CODEN: JASMAN

The Journal of the Acoustical Society of America

ISSN: 0001-4966

Vol. 120, No. 6 December 2006

(Continued)

CONTENTS—*Continued from preceding page*

(Continued)

CONTENTS—*Continued from preceding page*

(Continued)

CONTENTS—*Continued from preceding page*

Acoustic response from adherent targeted contrast agents

Shukui Zhao, Dustin E. Kruse, Katherine W. Ferrara, and Paul A. Dayton
Department of Biomedical Engineering, University of California, Davis, California 95616
kwferrara@ucdavis.edu

Abstract: In ultrasonic molecular imaging, encapsulated micron-sized gas bubbles are tethered to a blood vessel wall by targeting ligands. A challenging problem is to detect the echoes from adherent microbubbles and distinguish them from echoes from nonadherent agents and tissue. Echoes from adherent contrast agents are observed to include a high amplitude at the fundamental frequency, and significantly different spectral shape compared with free agents ($p < 0.0003$). Mechanisms for the observed acoustical difference and potential techniques to utilize these differences for molecular imaging are proposed.

© 2006 Acoustical Society of America
PACS numbers: 43.35.Ei, 43.35.Wa [TJM]
Date Received: August 14, 2006 **Date Accepted:** October 11, 2006

1. Introduction

Although the oscillation of cavitation bubbles near a boundary[1–3] and the dynamics of an encapsulated gas bubble far from a boundary[4] have been studied extensively, a unique problem arises when encapsulated micron-sized gas bubbles attach to a vessel wall and are insonified in medical ultrasound applications. In ultrasonic molecular imaging, micron-sized gas bubbles are coated with a shell that supports peptide- or antibody-based targeting ligands, where these ligands bind to receptors on a blood vessel wall. Thus, tethers on the order of nanometers in length connect these small bubbles to endothelial cells and bring them in close contact with a boundary. The oscillation of these adherent microbubbles was observed to be asymmetrical by high-speed photography[5] but their acoustic response has not been reported previously. Optimal detection of bound agents would require differentiating their echoes from those produced by freely circulating agents and the surrounding tissue.[6] Detection of the echoes from small bubbles tethered to the endothelium is a challenging problem since the quantity of microbubbles retained at a target site is small, and their signal can be easily masked by the background from freely circulating non-adherent agents.[7,8]

Ultrasound radiation force can facilitate binding between the agents and target site, increase the number of adherent agents available for imaging, and reduce the waiting period for accumulation of targeted agents.[9,10] Augmenting radiation force for bubble localization with signal processing schemes based on acoustic characteristics to differentiate free and bound agents could then produce a rapid and efficient molecular imaging scheme.

In this article, we report *in vitro* observations for the echo spectra of adherent and freely flowing contrast agents. By combining optical and acoustical experimental systems, a protocol was developed to force microbubbles to bind to a phantom vessel wall using radiation force, with the binding verified optically, and the echo spectra recorded acoustically. Differences in the acoustical response between free and bound contrast agents are observed, and possible mechanisms for these differences are examined with evidence from optical experiments and simulations. We conclude with proposed methods to specifically detect bound targeted contrast agents based on differences in their scattered echo spectrum.

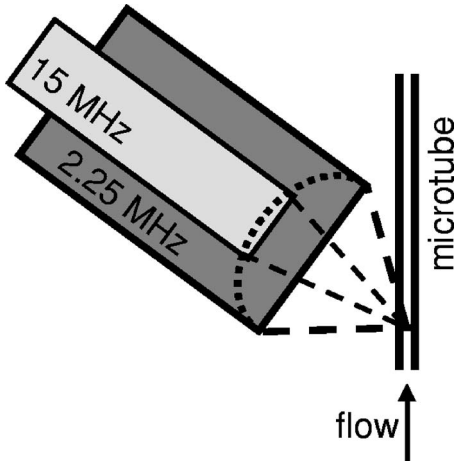

Fig. 1. Experimental diagram.

2. Methods

2.1 Optical experiments

Optical experiments were performed to observe the effect of an ultrasound radiation force pulse and localization of targeted microbubbles on a vessel wall. The experimental setup has been described in detail previously.[9] In short, a 200-μm cellulose tube was placed at the mutual focus of a 60× objective and a single element transducer [V3966, outer diameter (o.d.) 0.75 in. and inner diameter (i.d.) 0.47 in., Panametrics-NDT, Waltham, MA]. The radiation force pulse was at 4 MHz and ~50 kPa, and the microbubble concentration was ~4000 microbubbles per microliter. After application of ten radiation force pulses, the tube was scanned up and down by adjusting the focal plane and images of adherent microbubbles were saved.

2.2 Acoustical experiments

A custom two-element coaxial and confocal transducer facilitated the recording of the fundamental frequency and higher harmonics. Specifically, a 2.25 MHz outer annular element (V3966, o.d. 0.75 in. and i.d. 0.47 in., Panametrics-NDT, Waltham, MA) was used for transmission and a 15 MHz inner element (IM1502HR, 0.25 in., Valpey Fisher Corp., Hopkinton, MA) was used for reception, each with a one inch focal length (Fig. 1). The one-way −6 dB bandwidth was ~120% (0.9–3.6 MHz) and 90% (~10–23 MHz) for the outer and inner elements, respectively. The excitation pulse was either a Blackman-windowed ten-cycle pulse with a center frequency of 4 MHz or a five-cycle pulse with a center frequency of 2 MHz with matched pressure and intensity generated on an arbitrary wave generator (AWG 2021, Tektronix, Inc., Beaverton, OR). The received echoes were amplified 40 dB with a Panametrics receiver (5900PR, Panametrics-NDT, Waltham, MA), digitized by a 12-bit analog/digital board (PDA12A, Signatec Inc, Corona, CA) configured to sample at 125 MHz, and analyzed offline via MATLAB(v7.1, The Mathworks Inc, Natick, MA).

A 200-μm inner diameter cellulose microtube was placed at the focus of both transducer elements, and a solution of targeted microbubbles (~4000 microbubbles per microliter) was pumped through the tube with a mean velocity of 10 mm/s. The microtube was held vertically to reduce bubble accumulation along the wall due to floatation and the transducer was placed at an angle of about 45 deg to eliminate reflected echoes from the tube wall. The preparation of the targeted microbubbles and avidin-coated microtube have been described previously.[9] Echoes were recorded from the contrast agents for a peak negative pressure (PNP) of 40, 130, 210, and 290 kPa. Acoustic calibration was performed with a needle hydrophone (PZT-0400, Onda Corp, Sunnyvale, CA) placed at the transducer focus. Freely flowing

 © 2006 Acoustical Society of America

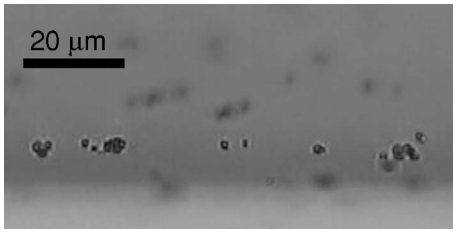

Fig. 2. Optical observation of adherent microbubbles on a vessel wall and formation of aggregates.

microbubbles were imaged first, followed by the application of 20 radiation force pulses. Each radiation force pulse consisted of five million cycles at 4 MHz and a PNP of ~50 kPa, promoting the adhesion of targeted agents to the tube wall. Optical observation confirmed bubble adhesion. Free contrast agents were then rinsed from the tube and echoes from the remaining adherent bubbles were acquired. Data were averaged over ten sets for adherent microbubbles and 33 sets for freely flowing agents.

2.3 Simulation

Simulations were carried out to investigate the effect of coherent echo summation due to the localization of contrast agents on a vessel wall. In these simplified simulations, microbubbles are assumed to be of the same size (1.2 μm in diameter), and either randomly distributed inside a vessel (free) or localized on one portion of a vessel wall within a 90-deg angle (adherent). The echo from the 1.2-μm microbubble driven by a ten-cycle Blackman-windowed pulse at 4 MHz and 210 kPa was calculated from a modified Rayleigh-Plesset equation[11] and summed for every microbubble according to their spatial positions. The diameter of the vessel was varied from 200 to 20 μm. The same number of microbubbles was involved for the free and adherent cases. Simulations were repeated 20 times for each case and statistical mean and standard deviations of the received echo power were reported in log scale.

3. Results

3.1 Experiments

No adherent microbubbles were observed on the tube wall before the radiation force pulse and approximately 100 adherent microbubbles were observed within a tube length of 100 μm after deflection. Some of the adherent microbubbles formed aggregates separated by ~20 μm or less (Fig. 2). Adherent microbubbles were spatially distributed on the side of the vessel wall away from the transducer.

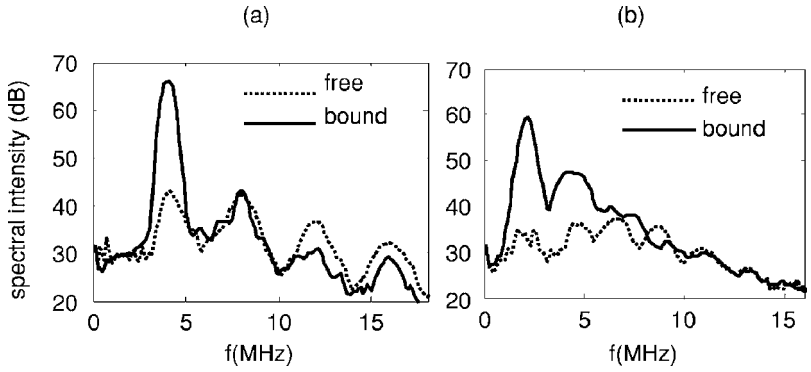

Fig. 3. Spectral intensity for echoes from free and bound microbubbles following transmission with a PNP of 210 kPa and a center frequency of 4 MHz (a) and 2 MHz (b).

 © 2006 Acoustical Society of America

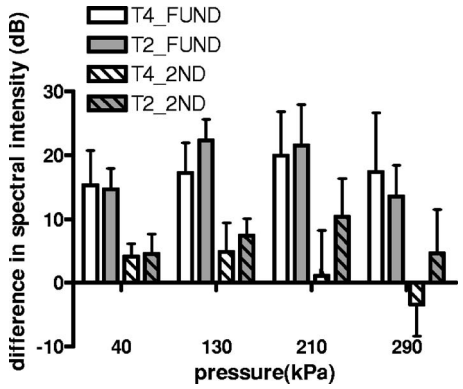

Fig. 4. Difference in spectral intensity at the fundamental (plain) and second harmonic (striped) frequency between bound and free agents, following transmission with a center frequency of 2 (gray) or 4 MHz (white).

With the wideband 15 MHz element used for echo reception, higher order harmonics were observed up to 20 MHz. Spectra shown in Fig. 3 were obtained using a PNP of 210 kPa, averaged over ten sets for bound contrast agents and over 33 sets for freely circulating agents, and then converted into decibels using a reference voltage of 1 mV. The spectral intensity at fundamental and harmonic frequencies was quantified by calculating the average intensity within a 1-MHz frequency band centered at different frequencies.

The fundamental spectral intensity increased 14–22 dB for bound agents compared with free agents with transmission at 2 and 4 MHz ($p < 0.0001$ and 0.0003, respectively) (Fig. 4). The second harmonic component also increased for bound relative to free agent echoes following transmission with a center frequency of 2 MHz at all four pressure levels ($p < 0.0001$ for PNP=40, 130, 210 kPa and $p < 0.001$ for PNP=290 kPa) and was significantly changed for transmission of 4 MHz at two pressure levels ($p < 0.0001$ and 0.0006 for PNP =40 and 130 kPa, respectively). Higher harmonic components increased as a result of the radiation force pulse only for 2 MHz transmission at 130 kPa ($p < 0.003$ and 0.005 for third and fourth harmonic, respectively, data not shown).

The echo spectrum from freely circulating agents demonstrates small differences between the fundamental echo intensity and the intensity of the second and third harmonic components; less than 6 and 10 dB for transmission center frequencies of 2 and 4 MHz, respectively [Figs. 5(a) and 5(b)]. In contrast, the difference between the fundamental intensity and the intensity of the second and third harmonic components for adherent agents can approach 18 and 30 dB, for 2 and 4 MHz transmission, respectively. For all cases studied here, the difference between the fundamental intensity and second and third harmonics of free agents was significantly smaller than this difference when computed for adherent agents ($p < 0.0001$).

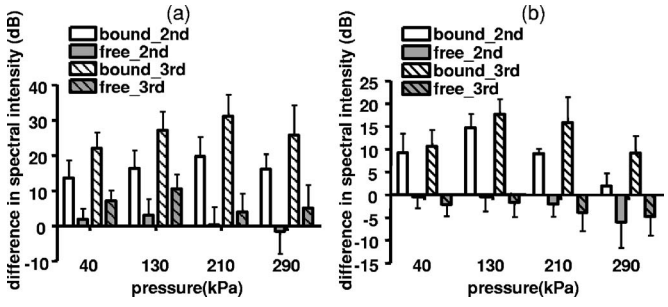

Fig. 5. Difference in echo spectral intensity of the second (plain) and third harmonic (striped) relative to the fundamental component for bound and free agents following transmission at 4 (a) and at 2 MHz (b).

 © 2006 Acoustical Society of America

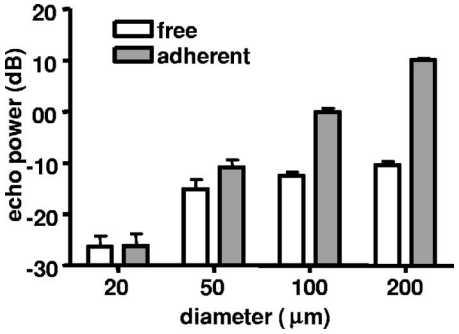

Fig. 6. Echo power from simulated free and adherent agents in different size vessels.

3.2 Simulation

A significant difference in received echo power was observed between uniformly distributed free microbubbles in a vessel and adherent microbubbles localized on a vessel wall for vessels with a diameter larger than 20 μm (Fig. 6). For a vessel with a diameter of 200 μm as in the experiments, echo power from microbubbles localized along the vessel wall was $\sim$20 dB higher than that for randomly distributed microbubbles ($p < 0.0001$). This difference becomes smaller (12 and 4 dB) but is significant for vessels with diameters of 100 and 50 μm, respectively ($p < 0.0001$), but not significant for a 20-μm vessel ($p = 0.86$).

4. Discussion and conclusions

The physical problem under investigation bears similarities to and differences from previous studies of cavitation bubble dynamics. In optical studies, the adherent microbubbles were observed to oscillate asymmetrically and form liquid jets,[5] similar to bubbles in cavitation studies. However, these targeted microbubbles are coated with a lipid shell, are tethered to a wall by ligands instead of simply in the proximity of the boundary, and are excited by an ultrasound pulse in the megahertz frequency range. Additionally, the goal is to detect the echoes from adherent microbubbles and distinguish them from echoes from non-adherent microbubbles and tissue. The boundary integral method and image method[2,12] used to simulate the dynamics of a cavitation bubble near a boundary may be adopted for these adherent microbubbles, although special care must be given to the adhesion between a microbubble and vessel wall and the effect of the bubble shell.

Two significant differences were observed between the echo spectrum of adherent microbubbles and that of free microbubbles, i.e., a significantly increased echo intensity at the fundamental frequency and a significantly larger difference between the echo intensity at the fundamental frequency and harmonics for adherent agents. We hypothesize three possible mechanisms for these experimentally observed differences.

First, when microbubbles are freely flowing in solution, their small diameter (less than 1/100th of an acoustic wavelength) and nearly uniform spatial distribution result in incoherent echo summation and a small backscattered intensity from each sample volume. Alternatively, a layer of contrast agents adherent to the inside of a vessel wall reflects ultrasound coherently, resulting in a large reflection of the fundamental component (Fig. 6). The formation of layers of perfluorocarbon nanoparticle contrast agents has also been reported to substantially increase their echogenicity over that observed when in solution.[13]

Second, optical observations indicated that adherent microbubbles formed aggregates (Fig. 2), which increases the coupling between adjacent agents and the effective scattering cross section. Secondary radiation force is responsible for the nonuniform microbubble distribution.[14] It has been demonstrated previously that aggregates of microbubbles produce a

 © 2006 Acoustical Society of America

more narrowband response with higher amplitude at the fundamental frequency,[15] and that microbubbles in close proximity couple acoustically and produce a harmonic response that is different from that produced by individual bubbles.[16]

Third, Zhao *et al.* observed previously that microbubbles adherent to a vessel wall oscillate asymmetrically in the plane normal to the boundary, in contrast to free microbubbles which oscillate symmetrically.[5] Further, for a low transmission pressure, the volume oscillation was observed to decrease in comparison with free agents. Asymmetrical oscillation of a cavitation bubble and formation of a jet near a boundary or within a vessel have been studied both theoretically and experimentally by number of research groups.[1–3,17] The effect of the decreased volume oscillation on the echo spectrum is the subject of future studies.

Finally, we note that our study involved the averaged echo spectrum over a pulse train. The largest spectral difference between adherent and free microbubbles is observed at 210 kPa for 4 MHz and ~130 kPa for 2 MHz, while the difference is smaller at the highest pressure of 290 kPa (Figs. 4 and 5). A decrease in signal power was also observed during acoustic experiments at 290 kPa and more noticeable at 2 MHz than 4 MHz. This acoustic study was supported by optical data (not shown) that demonstrated microbubble fragmentation at 290 kPa.

Regardless of the mechanisms responsible, the difference in spectral characteristics between bound and free contrast agents may be exploited in an imaging technique. Specifically, the application of imaging before and after a long, low amplitude pulse (designed to rapidly enhance the adhesion of targeted contrast agents) can be used to detect bound contrast agents. Given that echoes from the surrounding tissue should not change after the low amplitude radiation force pulse, the substantial spectral change before and after the radiation force pulse will facilitate the differentiation of tissue and bound agent echoes. Following the radiation force pulse, an increase in the spectral intensity at the fundamental frequency likely indicates the presence of bound agents. Characterization of the ratio of fundamental intensity to harmonics before and after the radiation force pulse can also be used to indicate the presence of adherent agents. Further studies will examine the implementation of specific targeted bubble detection techniques.

Acknowledgments

This work is supported by the National Institutes of Health through the NIH Roadmap for Medical Research, Grant No. R21EB005325-01, as well as R21CA098692, T32EB003827, R01CA 112356, and R01CA103828.

References and links

[1]Y. Tomita, P. B. Robinson, R. P. Tong, and J. R. Blake, "Growth and collapse of cavitation bubbles near a curved rigid boundary," J. Fluid Mech. **466**, 259–283 (2002).
[2]K. Sato, Y. Tomita, and A. Shima, "Numerical-analysis of a gas bubble near a rigid boundary in an oscillatory pressure field," J. Acoust. Soc. Am. **95**(5), 2416–2424 (1994).
[3]E. A. Brujan, K. Nahen, P. Schmidt, and A. Vogel, "Dynamics of laser-induced cavitation bubbles near an elastic boundary," J. Fluid Mech. **433**, 251–281 (2001).
[4]C. C. Church, "The effects of an elastic solid surface layer on the radial pulsations of gas-bubbles," J. Acoust. Soc. Am. **97**(3), 1510–1521 (1995).
[5]S. K. Zhao, K. W. Ferrara, and P. A. Dayton, "Asymmetric oscillation of adherent targeted ultrasound contrast agents," Appl. Phys. Lett. **87**(13), 134103 (2005).
[6]J. P. Christiansen and J. R. Lindner, "Molecular and cellular imaging with targeted contrast ultrasound," Proc. IEEE **93**(4), 809–818 (2005).
[7]P. A. Schumann, J. P. Christiansen, R. M. Quigley, T. P. McCreery, R. H. Sweitzer, E. C. Unger, J. R. Lindner, and T. O. Matsunaga, "Targeted-microbubble binding selectively to GPIIb IIIa receptors of platelet thrombi," Invest. Radiol., **37**(11), 587–593 (2002).
[8]H. Leong-Poi, J. Christiansen, A. L. Klibanov, S. Kaul, and J. R. Lindner, "Noninvasive assessment of angiogenesis by ultrasound and microbubbles targeted toalpha(v)-integrins," Circulation **107**(3), 455–460 (2003).
[9]S. Zhao, M. Borden, S. H. Bloch, D. Kruse, K. W. Ferrara, and P. A. Dayton, "Radiation-force assisted targeting facilitates ultrasonic molecular imaging," Mol. Imaging **3**(3), 135–148 (2004).
[10]J. J. Rychak, A. L. Klibanov, and J. A. Hossack, "Acoustic radiation force enhances targeted delivery of ultrasound contrast microbubbles: in vitro verification," IEEE Trans. Ultrason. Ferroelectr. Freq. Control **52**(3), 421–433 (2005).

 © 2006 Acoustical Society of America

[11]K. E. Morgan, J. S. Allen, P. A. Dayton, J. E. Chomas, A. L. Klibanov, and K. W. Ferrara, "Experimental and theoretical evaluation of microbubble behavior: Effect of transmitted phase and bubble size," IEEE Trans. Ultrason. Ferroelectr. Freq. Control **47**(6), 1494–1509 (2000).
[12]B. Krasovitski and E. Kimmel, "Gas bubble pulsation in a semiconfined space subjected to ultrasound," J. Acoust. Soc. Am. **109**(3), 891–898 (2001).
[13]G. M. Lanza, R. L. Trousil, K. D. Wallace, J. H. Rose, C. S. Hall, M. J. Scott, J. G. Miller, P. R. Eisenberg, P. J. Gaffney, and S. A. Wickline, "In vitro characterization of a novel, tissue-targeted ultrasonic contrast system with acoustic microscopy," J. Acoust. Soc. Am. **104**(6), 3665–3672 (1998).
[14]P. A. Dayton, K. E. Morgan, A. L. S. Klibanov, G. Brandenburger, K. R. Nightingale, and K. W. Ferrara, "A preliminary evaluation of the effects of primary and secondary radiation forces on acoustic contrast agents," IEEE Trans. Ultrason. Ferroelectr. Freq. Control **44**(6), 1264–1277 (1997).
[15]P. A. Dayton, K. E. Morgan, A. L. Klibanov, G. H. Brandenburger, and K. W. Ferrara, "Optical and acoustical observations of the effects of ultrasound on contrast agents," IEEE Trans. Ultrason. Ferroelectr. Freq. Control **46**(1), 220–232 (1999).
[16]J. S. Allen, D. E. Kruse, P. A. Dayton, and K. W. Ferrara, "Effect of coupled oscillations on microbubble behavior," J. Acoust. Soc. Am. **114**(3), 1678–1690 (2003).
[17]Y. T. Hu, S. P. Qin, T. Hu, K. W. Ferrara, and Q. Jiang, "Asymmetric oscillation of cavitation bubbles in a microvessel and its implications upon mechanisms of clinical vessel injury in shock-wave lithotripsy," Int. J. Non-Linear Mech. **40**(2–3), 341–350 (2005).

 © 2006 Acoustical Society of America

Synthesis of audio spectra using a diffraction model

V. Vijayakumar
FOSEE, Multimedia University, Jalan Air Keroh Lama, 75450 Melaka, Malaysia
vijaya@mmu.edu.my

C. Eswaran
Faculty of Information Technology, Multimedia University, Jalan Multimedia, 63100 Cyberjaya, Malaysia
eswaran@mmu.edu.my

Abstract: It is shown that the intensity variations of an audio signal in the frequency domain can be obtained by using a mathematical function containing a series of weighted complex Bessel functions. With proper choice of values for two parameters, this function can transform an input spectrum of discrete frequencies of unit intensity into the known spectra of different musical instruments. Specific examples of musical instruments are considered for evaluating the performance of this method. It is found that this function yields musical spectra with a good degree of accuracy.

© 2006 Acoustical Society of America
PACS numbers: 43.20.El, 43.75.Wx, 43.66.Jh [TDR]
Date Received: July 27, 2006 **Date Accepted:** October 10, 2006

1. Introduction

The aim of this paper is to propose a model for synthesizing musical sound that matches as closely as possible the actual steady-state spectrum of sound emanating from musical instruments. Based on the proposed model, it is possible to explain a number of phenomena observed in natural instruments such as dynamic frequency spectrum and nonlinear effects including chaos.[1–4] The model suggests a possible physical origin for the dynamic harmonic structure of musical instruments and their nonlinear character.

The use of FM can be considered as an important step in the synthesis of musical sounds. The FM equations give rise to a Bessel envelope for a given harmonic spectrum.[1] The Bessel functions appear to provide the cues for the amplitude for each harmonic of a given instrument note. The physical origin of the Bessel envelope in the FM-based synthesis models[1,5,6] is not discussed in the literature. The proposed diffraction model for the synthesis of musical spectra provides an explanation for the origin of Bessel envelopes.

In a typical musical instrument, the harmonic spectrum is due to the formation of multiple modes of standing waves. Each of these modes gives rise to a vibration of a definite frequency. A sound wave with a specific frequency undergoes diffraction as it passes through a circular aperture. The basic theory for diffraction through a circular aperture is well known[7] and it results in the intensity of the input wave being modulated by an envelope which can be constructed using Bessel functions.

In this paper, we use musical instrument data from MUMS (McGill University Master Samples)[8] which form the basis for the SHARC database.[9] For synthesizing the sound of any musical instrument using the proposed diffraction model, it is necessary to determine suitable values of two model parameters that will yield the appropriate envelope for the harmonics. These parameters are obtained by using a simple least-square fitting algorithm which repeatedly minimizes the error between the synthesized and the actual values of the amplitudes of the harmonics. The resulting spectrum is then compared with the actual spectrum.

 © 2006 Acoustical Society of America

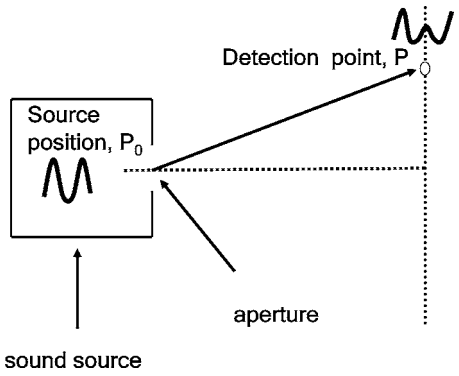

Fig. 1. Diffraction model.

2. Diffraction model

When sound wave of frequency, f, or angular frequency ω, and unit amplitude, originating from a point P_0, passes through a circular aperture, it is diffracted as shown in Fig. 1.[10] Let X and I denote, respectively, the amplitude and intensity of the sound wave at a point P which is at a specific distance from the center of the aperture as shown in Fig. 1. The values of X and I can be determined by using Lommel functions,[10] which are basically series expansions in Bessel functions.

The Lommel functions yield the intensity and phase of the diffracted sound wave at P, in terms of two Lommel variables u and v which are dependent on aperture size, distance of P, etc. for a fixed frequency of the originating sound wave.[10–12] In the proposed model, the intensity and phase of the diffracted sound wave at P are obtained for varying frequencies of the originating sound wave in terms of two new model parameters ξ and η, which can be expressed in terms of the Lommel variables, u and v as $\xi = v/u$ and $\eta = v/f$.

The originating and the diffracted waves denoted as $Y_{p0}(t)$ and $Y_p(t)$ can be written as

$$Y_{p0}(t) = \sin(2\pi ft) \quad \text{at} \quad P_0 \tag{1a}$$

$$Y_p(t) = X(f)\sin(2\pi ft) \quad \text{at} \quad P. \tag{1b}$$

$X(f)$ in Eq. (1a) denotes the complex value of the amplitude of the diffracted sound wave at point P when sound wave of frequency f with unit amplitude passes through the circular aperture. $X(f)$ can be expressed in terms of the model parameters, ξ and η, using the Lommel functions as shown in Eqs. (2),

$$X(f) = X^R - jX^I, \tag{2a}$$

where

$$\begin{aligned} X^R &= \cos\left(\frac{1}{2}\xi\eta f\right) + V_0(\xi,\eta)\cos\left(\frac{\eta f}{2\xi}\right) - V_1(\xi,\eta)\sin\left(\frac{\eta f}{2\xi}\right) \\ X^I &= \sin\left(\frac{1}{2}\xi\eta f\right) + V_0(\xi,\eta)\sin\left(\frac{\eta f}{2\xi}\right) - V_1(\xi,\eta)\cos\left(\frac{\eta f}{2\xi}\right) \end{aligned} \tag{2b}$$

for $\xi \leqslant 1$, and

 © 2006 Acoustical Society of America

$$X^R = U_1(\xi,\eta)\sin\left(\frac{\eta f}{2\xi}\right) - U_2(\xi,\eta)\cos\left(\frac{\eta f}{2\xi}\right)$$
$$X^I = U_1(\xi,\eta)\cos\left(\frac{\eta f}{2\xi}\right) + U_2(\xi,\eta)\sin\left(\frac{\eta f}{2\xi}\right) \quad (2c)$$

for $\xi > 1$.

The functions V_0, V_1, U_1, and U_2 in (2b) and (2c) are given by

$$V_0 = [J_0(\eta f) - \xi^2 J_2(\eta f) + \xi^4 J_4(\eta f) - \cdots],$$
$$V_1 = [\xi J_1(\eta f) - \xi^3 J_3(\eta f) + \xi^5 J_5(\eta f) - \cdots],$$
$$U_1 = \left[\left(\frac{1}{\xi}\right)J_1(\eta f) - \left(\frac{1}{\xi}\right)^3 J_3(\eta f) + \left(\frac{1}{\xi}\right)^5 J_5(\eta f) - \cdots\right], \quad (2d)$$
$$U_2 = \left[\left(\frac{1}{\xi}\right)^2 J_2(\eta f) - \left(\frac{1}{\xi}\right)^4 J_4(\eta f) + \left(\frac{1}{\xi}\right)^6 J_6(\eta f) - \cdots\right],$$

where J_i represents an ith order Bessel function of the first kind. Note that the correct equation, either, Eq. (2b) or Eq. (2c), must be used to ensure the convergence of the expansion depending on the value of ξ. The intensity and phase of the diffracted sound wave at point P are given by Eq. (2e) and Eq. (2f), respectively,

$$I_P = |X(f)|^2 = (X^R)^2 + (X^I)^2 \quad (2e)$$

$$\phi_P = \tan^{-1}\left(\frac{X^I}{X^R}\right). \quad (2f)$$

Special cases: At certain extremal values of the diffraction parameters, we can find closed-form solutions for $X(f)$. We will consider cases when ξ approaches zero, unity and large values.[10]

For large values of ξ, Eq. (2a), reduces to Eq. (3a), which is the Airy formula[10] for Frauhoffer diffraction.[10] When $\xi = 0$, we find that Eq. (2a) reduces to Eq. (3b), which is purely sinusoidal. When $\xi = 1$, Eq. (2a) reduces to Eq. (3c),

$$X(f) = -j\frac{J_1(\eta f)}{\xi}, \quad (3a)$$

$$X(f) = 1 - \cos\left(\frac{\eta f}{2\xi}\right) + j\sin\left(\frac{\eta f}{2\xi}\right), \quad (3b)$$

$$X(f) = \frac{1}{2}(1 - J_0(\eta f))\cos\left(\frac{\eta f}{2\xi}\right) - j\frac{1}{2}(1 + J_0(\eta f))\sin\left(\frac{\eta f}{2\xi}\right). \quad (3c)$$

For large values of ξ, and for an input sound signal composed of infinite harmonics, the instantaneous magnitude of the displacement of the sound wave at P can be obtained using Eqs. (1b) and (3a) as shown in Eq. (4),

$$Y(t) = \sum_{n=1}^{\infty} \frac{1}{\xi} J_1(n\beta)\sin(n\omega t), \quad (4)$$

where $\beta = \eta f$, $\omega = 2\pi f$, and n refers to the nth harmonic.

 © 2006 Acoustical Society of America

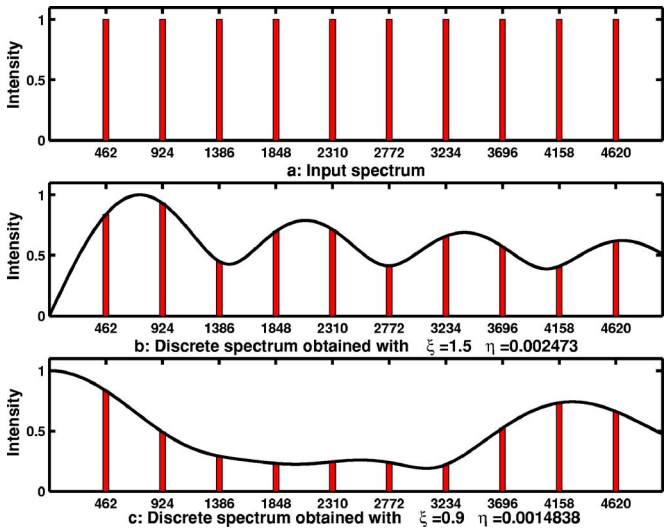

Fig. 2. (Color online) Continuous and discrete spectra: normalized intensity vs frequency (Hz).

It may be useful to compare the remarkable similarity of Eq. (4) with Tomisawa's FM synthesis equation, shown in Eq. (5)[13,14]

$$Y(t) = \sum_{n=1}^{\infty} \frac{2}{n\beta} J_n(n\beta)\sin(n\omega t). \tag{5}$$

3. Spectral characteristics of diffracted sound

When an input sound wave of unit amplitude with continuously varying frequencies is diffracted, the corresponding intensity values at point P will yield a continuous frequency spectrum.

If the sound wave undergoing diffraction is composed of discrete frequencies, the resulting spectrum after diffraction will also be composed of the same discrete frequencies but with their intensities modified.

Figure 2(a) shows a sound wave made up of a fundamental frequency of 462 Hz and 9 harmonics, each with a unit intensity value. Diffraction of this sound wave through a circular aperture will modify its spectrum depending on the values of the parameters η and ξ, as shown in Figs. 2(b) and 2(c).

The intensity modifying envelopes in Figs. 2(b) and 2(c), derived from Eq. (2), represent the continuous spectrum that are obtained when a sound wave comprising continuous frequencies in the range from 0 to 5000 Hz undergoes diffraction. The values of the diffraction parameters, η and ξ, will determine the exact shape of the modifying envelope.

It is shown in the following section that the diffraction model described above can be applied successfully for synthesizing the spectra of musical instruments.

4. Synthesis of spectra of musical instruments

It has been found by empirical methods that for synthesizing the steady-state spectra of the various musical instruments that were considered, the useful ranges of values of the two parameters are $0 \leqslant \eta \leqslant 1.0$ and $0 \leqslant \xi \leqslant 150$. To test the proposed model, we have selected the sound obtained from three musical instruments, namely the trumpet, the French horn, and the bass clarinet played at fundamental frequencies of 462, 220, and 110 Hz, respectively. The sound samples are taken from the MUMS database[8] and the details of the harmonics present as reported by Sandell are available in the SHARC database.[9]

 © 2006 Acoustical Society of America

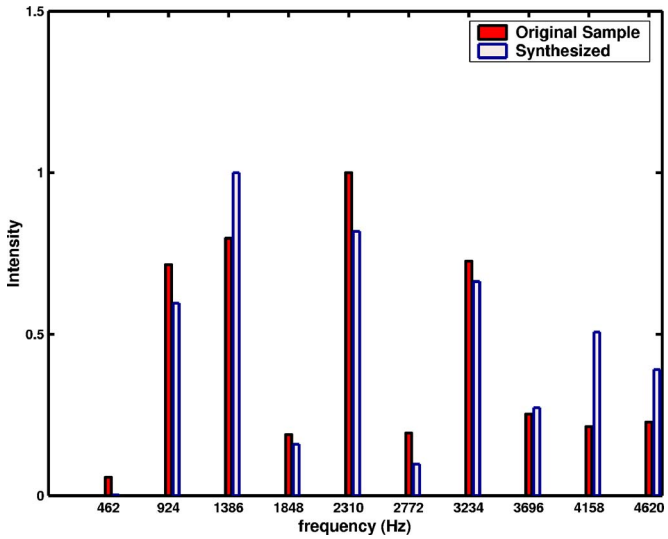

Fig. 3. (Color online) Trumpet: ξ=126; η=0.207 73; LSE=0.2204.

The steps involved in the synthesis of the spectrum of the trumpet are described below.

(1) The intensity values of the trumpet at the ten harmonic frequencies (with fundamental frequency=462 Hz) are normalized to lie in the range 0 to 1.
(2) Let the sum squared error E_s, between the synthesized and actual spectra be defined as in Eq. (6),

$$E_s = \sum_{n=1}^{n=10} [I_{Q_n} - I'_{Q_n}]^2, \tag{6}$$

where I_{Q_n} is the intensity value of the nth harmonic obtained using Eq. (2) and I'_{Q_n} is the actual (MUMS) intensity value of the nth harmonic.
(3) Using MATLAB, the optimum values of the parameters ξ and η which minimize E_s are determined. For trumpet, the optimum values obtained are ξ=126 and η=0.207 73 and the minimum value of E_s denoted as LSE is 0.2204.
(4) Using the optimum values of η and ξ in Eq. (2), the synthesized spectrum of the trumpet is obtained as shown in Fig. 3.

Using a similar procedure, the synthesized spectra of the French horn played at 220 Hz and bass clarinet played at 110 Hz are obtained as shown in Figs. 4 and 5, respectively, where the values of η, ξ and LSE are also shown. It can be seen from Figs. 3–5 that the synthesized spectra of the musical instruments match well with the actual spectra.

5. Dynamic spectra

If the model parameters in (2) evolve in time, we can then show that each harmonic of the spectrum will also independently evolve in time, giving rise to a dynamic spectrum.[1]

The parameter ξ depends on the model setup values such as aperture size, distance of point P, etc., which are assumed to remain constant. The parameter η, on the other hand, depends on the model setup values as well as the speed of sound.[10] Fuks has shown that the speed of sound changes significantly during the period of production of sound in wind instruments due to the changing ratio of oxygen and carbon dioxide in the air.[15,16] Hence, the parameter η can be assumed to evolve in time, which results in a dynamic spectrum.

 © 2006 Acoustical Society of America

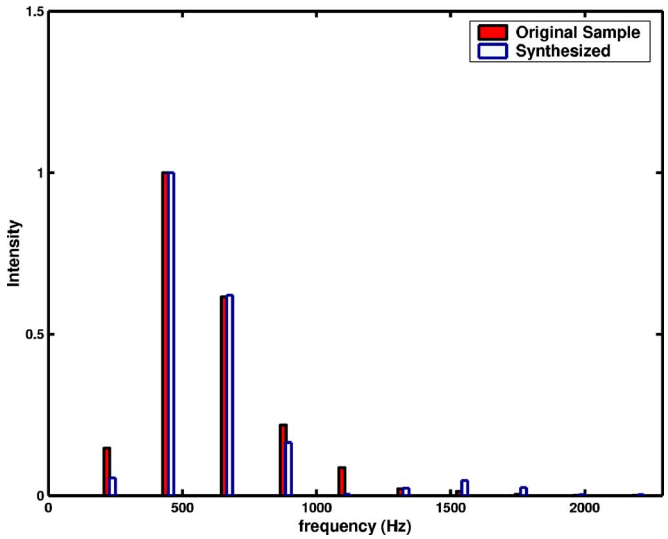

Fig. 4. (Color online) French horn: ξ=97; η=0.017 769; LSE=0.0200.

To illustrate the method, let us assume that the parameter η evolves in time, t, according to Eq. (7) keeping the value of ξ constant at 0.1,

$$\eta(t) = \eta_0(1 + 0.01e^{-500t})^{-1}. \tag{7}$$

In Eq. (7), the value of η is gradually increased from 0.2007 to 0.2020 in 2 ms with η_0 =0.2027. This corresponds to a gradual reduction in the speed of sound by about 0.35% of the original value.

To illustrate the spectral evolution, we begin by assuming an input sound signal of unit amplitude made up of a fundamental frequency of 500 Hz with ten harmonics. The intensity

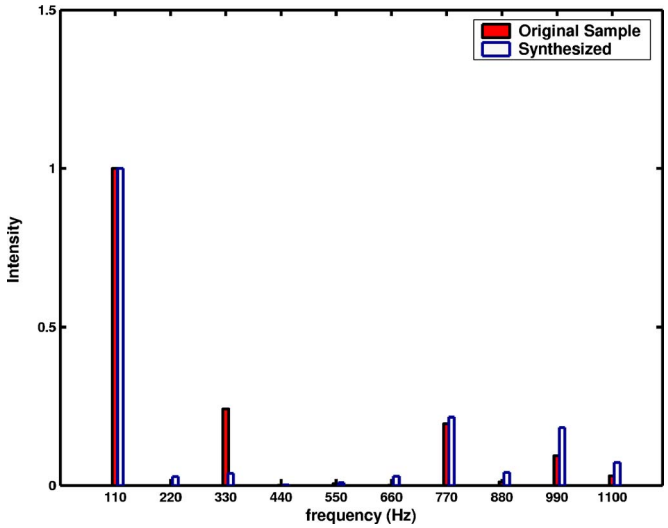

Fig. 5. (Color online) Bass clarinet: ξ=9.3; η=0.015 332; LSE=0.0312.

 © 2006 Acoustical Society of America

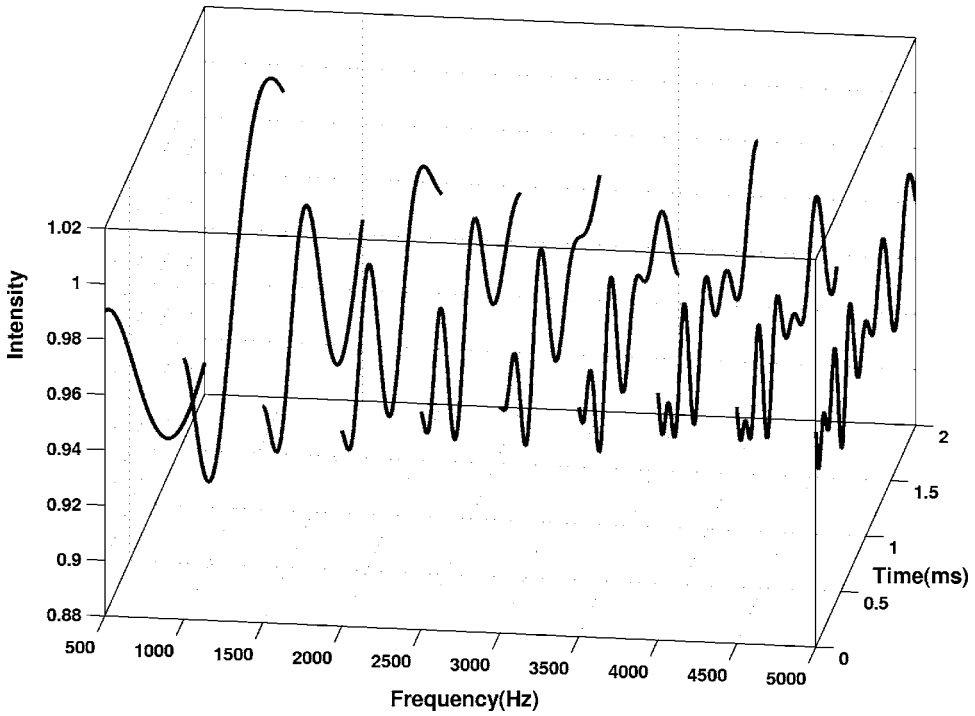

Fig. 6. Dynamic spectra showing the evolution of harmonics.

and phase values of the harmonics of the sound wave after diffraction are calculated using (2) for each value of $\eta(t)$, resulting in the dynamic spectrum as shown in Fig. 6 which forms the basis for the synthesis of musical sound.

Note that the choice of the evolution method for η will produce a unique dynamic spectrum and the resulting synthesized sound. The parameter η used in this model can thus be compared to the modulation index used in other FM synthesis models.[1,5,6]

6. Conclusion

We have proposed in this paper a diffraction model which can be used to synthesize the steady-state harmonic spectra of musical instruments with proper model parameter values.

Diffraction theory provides a possible physical meaning of the intensity-modifying envelope of the synthesized spectra of musical instruments. In real instruments, there could be additional causes for intensity modifications of the harmonics as described in Ref. 3.

It is also shown that the dynamic spectra of the musical instruments can be obtained by varying one of the model parameters η with respect to time.

References and links

[1]J. M. Chowning, "The synthesis of complex audio spectra by means of frequency modulation," J. Audio Eng. Soc. **21**, 526–534 (1973).
[2]N. H. Fletcher, "Nonlinear dynamics and chaos in musical instruments," Complexity International **1** (1994) http://www.complexity.org.au/ci/vol01/fletch01/. Last accessed 10/31/06.
[3]N. H. Fletcher, "The nonlinear physics of musical instruments," Rep. Prog. Phys. **62**(5), 723–764 (1999).
[4]A. Robel, "Synthesizing natural sounds using dynamic models of sound attractors," Comput. Music J. **25**(2), 46–61 (2001).
[5]J.-P. Palamin, P. Palamin, and A. Ronveaux, "A method of generating and controlling musical symmetrical spectra," J. Audio Eng. Soc. **36**, 671–685 (1988).
[6]B. T. G Tan, S. L. Gan, S. M. Lim, and S. H. Tang, "Real-time implementation of double frequency modulation (DFM) synthesis," J. Audio Eng. Soc. **42**(11), 918–925 (1994).
[7]E. Hecht, *Optics*, 4th ed. (Addison-Wesley, Reading, MA, 2002), pp. 467–476.

 © 2006 Acoustical Society of America

[8]MUMS, McGill University Master Samples; ⟨http://www.music.mcgill.ca/resources/mums/html/⟩. Last accessed 10/31/06.
[9]G. J. Sandell, Sandell Harmonic Archive (SHARC) (1994); ⟨http://people.cs.uchicago.edu/~odonnell/Scholar/Data/SHARC⟩. Last accessed 10/31/06
[10]K. D. Mielenz, "Algorithms for Fresnel diffraction at rectangular and circular apertures," Journal of the National Institute of Standards and Technology **103**(5), 505–509 (1998).
[11]C. Eswaran and V. Vijayakumar, "Synthesis and dynamic behavior of diffracted audio spectra," J. Acoust. Soc. Am. **119**(5), 3441 (2006).
[12]V. Vijayakumar and C. Eswaran, "Nonlinear behavior of interacting harmonics in audio spectra," J. Acoust. Soc. Am. **119**(5), 3274 (2006).
[13]N. Tomisawa, "Tone Production Method for an Electronic Musical Instrument," U.S. Patent 4,249,447 (1981).
[14]B. Schottstaedt, "The simulation of natural instrument tones using frequency modulation with a complex modulation wave," Comput. Music J. **1**(4), 51–52 (1977).
[15]L. Fuks, "Prediction of pitch effects from measured CO_2 content variations in wind instrument playing," KTH TMH-QPSR 4 1996 Stockholm, 37–43, 1996.
[16]L. Fuks, "Prediction and measurements of exhaled air-effects," in *Proceedings of the Institute of Physics, Vol. 19, Part 5, Book 2*, 373–378 (1997).

 © 2006 Acoustical Society of America

Geometrical effects on the tuning of Chinese and Korean stone chimes

Junehee Yoo
Department of Physics Education, Seoul National University, Seoul 151-742, Republic of Korea
yoo@snu.ac.kr

Thomas D. Rossing
Center for Computer Research in Music and Acoustics, Department of Music, Stanford University, Stanford, California 94305
rossing@ccrma.stanford.edu

Abstract: The vibrational mode frequencies and mode shapes of ancient stone chimes are analyzed and their dependence on stone shapes are discussed. Mode shapes and frequencies of several chime models are determined by using finite element methods, and these show good agreement with mode shapes and frequencies observed in Korean *pyeongyeong* chime stones using holographic interferometry and experimental modal testing. The dependence of mode shapes and frequencies on vertex angle and base curvature suggests that the geometries used in late Chinese *bianqing* and Korean *pyeongyeong* may have been selected to give the best sound.

© 2006 Acoustical Society of America
PACS numbers: 43.75.Kk, 43.40.Dx [DD]
Date Received: May 10, 2006 **Date Accepted:** July 5, 2006

1. Introduction

Stone chimes have been cherished musical instruments for centuries in several Asian countries. They have taken a number of different forms, but generally they have two legs which meet at a vertex. The longer leg is often called the drum, because it is where the chime is struck, and the shorter leg is called the femur or thigh.

Several sets of stone chimes have been found in ancient Chinese tombs dating from 400 BC and before. A *bianqing* of 32 stones was found in the tomb of the Marquis *Yi* of *Zheng* (the same tomb that contained the renowned set of 65 bells), dating from about 433 BC. Although many stones were found broken, Chinese scholars were able to determine their dimensions, and from these, Lehr determined scaling laws for their various dimensions.[1] Stones are scaled in lengths as well as thicknesses.

Another ancient *bianqing* from the Warring States period (450–221 BC) of the *Zhou* dynasty was found more or less intact, so that the fundamental frequencies of most of the stones, as well as the dimensions, could be determined.[2] Vertex angles of these stones ranged from 142 to 155 deg.

The Korean *pyeongyeong* consists of a set of 16 hard stones cut in the shape of an inverted letter L. The stones are hung from a wooden stand and struck, near the lower end of the longer side, by a mallet tipped with horn. The upper ridge of the longer side of a stone is about 1.5 times longer than the shorter side. Unlike most Chinese stone chimes, the *pyeongyeong* stones in a set have nearly the same shape except for the highest stone in which the long edge may be slightly shortened, but are scaled in thickness.[3]

Old *pyeongyeongs* are preserved in museums as national treasures, but replicas are built and played in concerts. Earlier we analyzed a *pyeongyeong* built by Hyungon Kim and played by the National Traditional Orchestra of Korea. The fundamental frequency was shown to be directly proportional to thickness over most of the range.[4] The second mode was found to be tuned to 1.5 times the nominal frequency, the third mode to about 2.3 times the nominal frequency, and the fourth mode about 3 times the nominal frequency up to the 12th stone.[4]

 © 2006 Acoustical Society of America

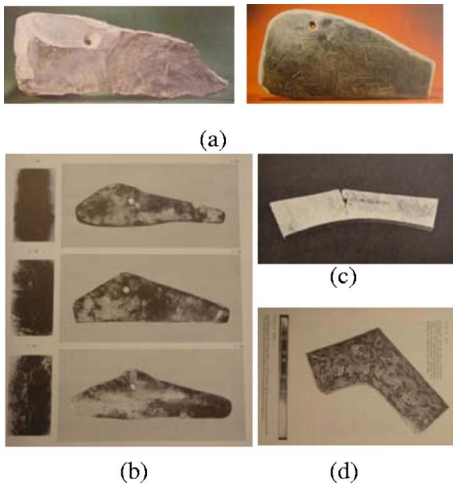

Fig. 1. (Color online) *Bianqing* stones from different ages: (a) ancient stones from *Shanxi* and *Henan* provinces; (b) ancient stones from *Henan*; (c) stone chime from Marquis *Yi* tomb (433 BC); (d) chime from 1717 AD.

In this paper, we report on studies designed to show how the vibrational frequencies of L-shaped chime stones, such as are found in the Korean *pyeongyeong* and the Chinese *bianqing*, depend upon the details of their geometry.

2. Shapes of *Pyeongyeong* and *Bianqing* chime stones

The shape of a *pyeongyeong* stone is said to be the "shape of the heaven that curves to cover the earth." The 115° angle between the drum part and the femur part and the concave curved base form a smooth L shape. In Korea, the *pyeongyeong* has been built in this smooth L shape for some five centuries, whereas Chinese *bianqing* stone chimes have varied in shape from time to time. Old stones from before the Christian era mostly have a straight base, or an arc-shaped base, for example, whereas stones from the *Qing* Dynasty (1644–1911) are L shaped.

According to Kuttner, stones with a straight base [Figs. 1(a) and 1(b)] are older than those with an arc-shaped base [Fig. 1(c)], and he concluded that the curved base resulted from experiments to improve the acoustical qualities of the stones. Also, the angle between the drum part and the femur part became narrower in stones from the *Qing* Dynasty and later.[5]

In this study, we examine the effects of geometry on the tuning and the sound quality of stone chimes, such as the Korean *pyeongyeong* and the Chinese *bianqing*. Modal shapes and modal frequencies are estimated by means of finite element methods (FEM) analysis, and these results are compared to modal shapes and frequencies of existing stones, determined by holographic interferometry and by experimental modal testing. Modal shapes and frequencies of stones of different shapes are calculated by finite element methods. Of particular interests are the effects of varying the vertex angle and the curvature of the base.

3. Modeling of stones and finite element analysis

Since the sound spectra and mode shapes of several *pyeongyeong* replica stones have previously been measured,[4] we used these stones as models for finite element analyses. The stone of lowest frequency is tuned to C5 (523 Hz), and we use that stone for (FEM) modeling and designate it as PGC 115, since the vertex angle α is 115°. The modal frequencies calculated for this stone are compared to the modal frequencies determined from the sound spectrum, from holographic interferometry, and from experimental modal testing using the (STAR) system. The agreement is very good, as shown in Table 1.

The upper seventh stone from the tomb of Marquis Yi is supposed to be tuned to C, but it was broken when it was excavated.[6] The size of each side, angle, and thickness are reported by the Museum of Hubei Province.[6] Since the vertex angle α is 163°, the model for this stone is

 © 2006 Acoustical Society of America

Table 1. Calculated (FEM) and measured mode frequencies in the first *gyeong*. Measured values are the average of the frequencies obtained by holographic interferometry, experimental modal testing, and analysis of the sound spectra.

	PGC116 Calculated data by ANSYS		PGC Average of experimental data		
Mode no.	Freq. (Hz)	Ratio to fund.	Freq. (Hz)	Ratio to fund.	Error (¢)
1	527	1.00	526	1.00	0.30
2	810	1.54	810	1.54	0
3	1233	2.34	1242	2.36	−1.14
4	1625	3.08	1634	3.10	−0.86
5	2203	4.18	2207	4.20	−0.28
6	2704	5.13	2704	5.14	0
7	3554	6.74	3553	6.75	0.04
8	3993	7.57	3957	7.52	1.42
9	4527	8.59	4489	8.53	1.32

designated as BQC 163. Keeping the principle lengths A, B, E, and F of stone the same, vertex angle α was then changed to 140° and 115°, and these models are designated BQC 140 and BQC 115, respectively. FEM was used to determine the mode frequencies and mode shapes of the three *bianqing* models and the *pyeongyeong* model. The four models are shown in the upper row in Fig. 2.

With the same angle α=115°, the base lines were changed from resembling the smooth arc of the *pyeongyeong* (BQ115 in Fig. 2) to a near right angle shape (BQ 115ra), three oblique lines (BQ 115to) and a straight line (BQ 115sb) as shown in the second row in Fig. 2. FEM was again used to determine the mode frequencies and mode shapes of the three new *bianqing* models.

The commercial program ANSYS Mechanical 8.1 was used for the FEM analysis. Since a *gyeong* is a flat plate of constant thickness, we adapted the three-dimensional eight-node Shell 93 element for modeling it. The shell element 93 was found to give the most accurate results. For the PGC 115 model, 13 key points were created to make the keypoints for modeling by ANSYS. We chose quadrilateral element shapes to construct the mesh.

Systematic ways of varying the vertex angle and base line were introduced. The first set of 19 alternative *gyeong* models was constructed by adding 5° increments to the vertex angle from 90°, the shape of an L, to 180°, the shape of a bar. In this series of shapes the baseline curvature was kept the same. Next we estimated the effect of baseline curvature on mode frequencies and shapes as the baseline was systematically varied.[3]

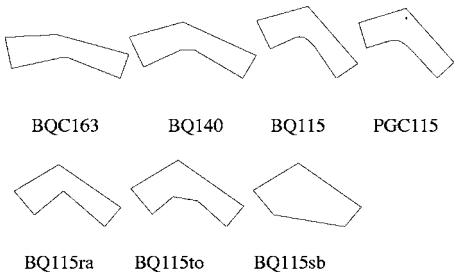

Fig. 2. *Bianqing* and *pyeongyeong* models used to test geometry dependence on tuning

 © 2006 Acoustical Society of America

Table 2. Model frequencies and frequency ratios for models with varying angle α.

	BQC163		BQC140		BQC115		PGC115	
No.	Freq. (Hz)	Ratio to fund.	Freq. (Hz)	Ratio to fund.	Freq. (Hz)	Ratio to fund.	Freq. (Hz)	Ratio to fund.
1	591	1.00	756	1.00	972	1.00	527	1.00
2	1357	2.29	1378	1.82	1471	1.51	809	1.54
3	1558	2.63	1781	2.35	2114	2.18	1232	2.34
4	1607	2.72	2963	3.92	3109	3.20	1624	3.08
5	3356	5.67	3657	4.84	4016	4.13	2202	4.18
6	5022	8.64	4893	6.47	5230	5.38	2701	5.13

4. Results and discussion

Table 2 shows the dependence of the modal frequencies on vertex angle as calculated by FEM. The models correspond to those in Fig. 2. Also shown are the frequencies relative to the lowest mode of vibration. Note that decreasing the vertex angle lowers the ratios of the higher modes and also brings them nearer to a harmonic relationship. This may have made them more sonorous. The ratios for BQC 115 are reasonably close to those of the Korean *pyeongyeong* model PGC 115.

Table 3 shows the dependence of the modal frequencies on baseline curvature. Also shown are the frequencies relative to the lowest mode of vibration. The differences between the smooth arc (BQC 115), the near right angle (BQC 115ra), and the three oblique lines (BQC 115to) are small, but in the stone with the straight base (BQC 115sb) the second, third, and fourth mode frequencies are raised substantially compared to the fundamental. The sound of this stone model would be expected to be quite different from the others and also different from the *pyeongyeong* stone PGC 115.

More details of the dependence of mode shapes and frequencies on vertex angle were provided by varying the vertex angle in five-degree increments from 90° to 180°. Figure 3 shows how the mode shape and frequency of the lowest mode changes as the vertex angle changes from 90° to 180°. Similar plots for the higher modes are shown online in file . Figure 4(a) shows how the mode frequencies depend on the vertex angle. A polynomial trend line calculated for best fit, also shown, is of the form $y=0.002x^3-0.0405x^2-3.0059x+1122.2$. Figure 4(a) shows the fundamental frequency, and Fig. 4(b) shows the frequency ratios of the higher modes to the fundamental.

Mm1 shows the dependence of mode shapes and frequencies on vertex angles (10.4MB). This is a file of the type avi.

Table 3. Modal frequencies and frequency ratios for models with varying baseline.

	BQC115ra		BQC115		BQC115to		BQC115sb	
No.	Freq. (Hz)	Ratio to fund.	Freq. (Hz)	Ratio to fund.	Freq. (Hz)	Ratio to fund.	Freq. (Hz)	Ratio to fund.
1	940	1.00	972	1.00	984	1.00	941	1.00
2	1403	1.49	1471	1.51	1532	1.56	1521	1.62
3	2036	2.17	2114	2.18	2312	2.35	2971	3.16
4	3122	3.32	3109	3.20	3075	3.12	3807	4.04
5	4031	4.29	4016	4.13	3987	4.05	4010	4.26
6	5179	5.51	5230	5.38	5641	5.73	5166	5.49

 © 2006 Acoustical Society of America

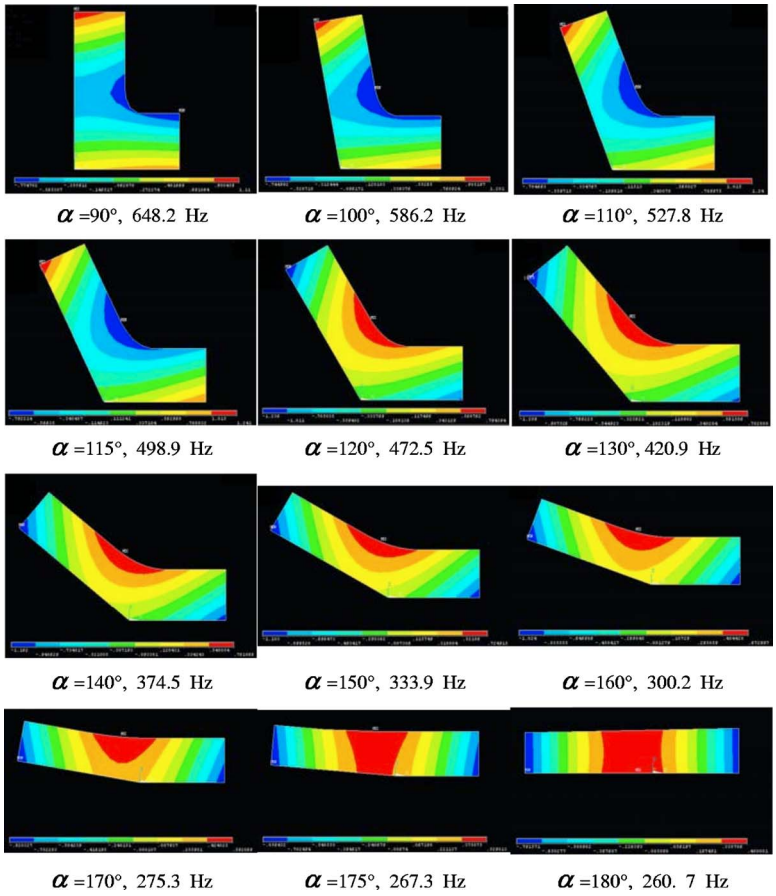

Fig. 3. (Color online) First mode shapes and frequencies of chimelike models with varying vertex angles. (This figure is intended for color viewing.)

The frequency ratios of the various partials might be expected to determine the timbre of the sound. A vertex angle of about 115° was adopted by both the makers of Korean *pyeongyoung* and the Chinese *bianqing* of the *Qing* dynasty and later.

From examining existing Chinese *bianqing*, it appears that the L shape with a gently curved base gradually evolved over several centuries. The 18th century stone in Fig. 1(d) has a vertex angle of approximately 113°, as measured from the photograph. This is very close to the angle of 115° measured in Korean *pyeongyeong* stones of about the same age, which is not surprising since the earliest *pyeongyeong* were imported from China. This vertex angle was probably arrived at by attempting to maximize sonority.

The dependence of modal frequency, and especially the ratios of the higher mode frequencies to the fundamental, on chime shape suggests that the ancient Chinese and Korean chime makers tuned their chimes by adjusting the shape of the chimes to obtain the most pleasing sound. This was probably done through centuries in China, and when the Koreans began making stone chimes, they were guided by the Chinese chimes having the best sound. The most important parameter is the vertex angle, with the curvature of the base having a much smaller influence.

5. Conclusion

By means of finite element methods (FEM) analysis, we have shown how changing the vertex angle α and the curvature of the base changes the relative frequencies of the modes of vibration

 © 2006 Acoustical Society of America

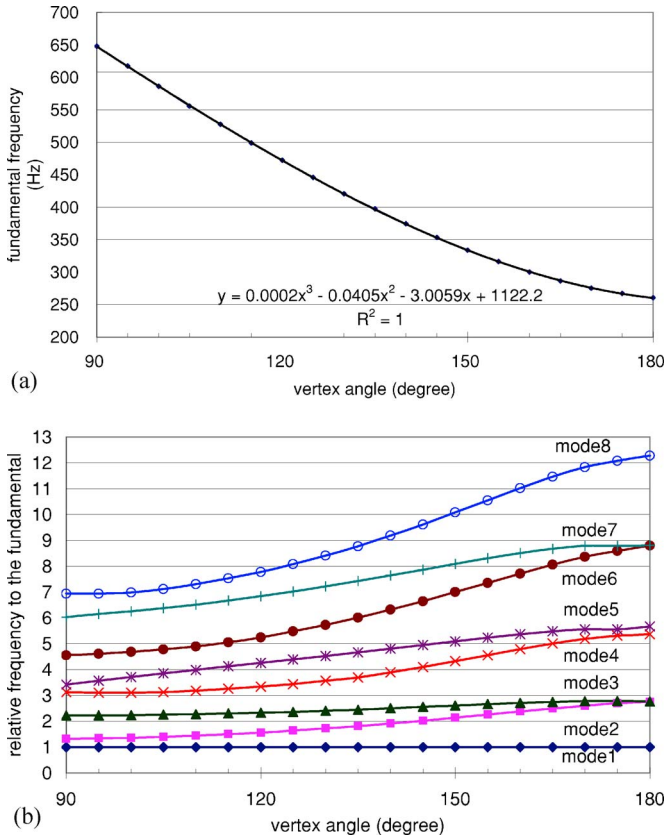

Fig. 4. (Color online) Frequency dependence on vertex angle α in chimelike models: (a) fundamental frequency; (b) ratio of higher mode frequencies to the fundamental. (This figure is intended for color viewing.)

of stone chimes (lithophones) and hence the character of the sound. *Pyeongyeong* stone chimes in Korea have maintained pretty much the same shape during the past five centuries, and the same appears to be true of Chinese *bianqing*. Our calculations show that relative modal frequencies are changed considerably by changing the vertex angle, but are less sensitive to changes in curvature of the base. The L shape with vertex angle around 115° appears to produce stones with maximum sonority.

The fabricators of ancient lithophones no doubt discovered the same thing, albeit by years and years of trial and error.

The agreement between mode frequencies and mode shapes calculated by FEM and measured by holographic interferometry and by experimental modal testing under playing conditions was found to be quite satisfactory, and this validated the use of FEM to study the effects of varying the model shapes.

References and links

[1]A. Lehr, "Designing chimes and carillons in history," Acust. Acta Acust. 83, 320–336 (1997).
[2]A. Lehr, "Chinese lithophone," Berichten uit het National Beiaardmuseum **6**, 3–6 (1993).
[3]J. Yoo, "Acoustics of Korean percussion instruments: Pyeongyeong and pyeonjong," (Ph.D. dissertation, Northern Illinois University, DeKalb, IL, 2005).
[4]J. Yoo and T. D. Rossing, "Vibrational modes of pyeon-gyoung, Korean chime stone," in *Proceedings of ISMA 2004: International symposium on musical acoustics*, edited by S. Adachi Nara, Japan (2004).
[5]F. A. Kuttner, *The Archaeology of Music in Ancient China: 2,000 Years of Acoustical Experimentation 1400 BC-AD 750* (Paragon House, New York, 1990).
[6]The Museum of Hubei Province, *The Tomb of Marquis Yi of State of Zeng* (Cultural Relics Publishing House, Beijing, 1989), in Chinese.

 © 2006 Acoustical Society of America

The acoustic signature of bubbles fragmenting in sheared flow

Grant B. Deane and M. Dale Stokes
Scripps Institution of Oceanography, University of California at San Diego, La Jolla, California 92093-0238
gdeane@ucsd.edu, dstokes@ucsd.edu

Abstract: Measurements of the sound of bubbles fragmenting in fluid shear are presented and analyzed. The frequency, amplitude, and decay rate of the acoustic emissions from 1.8-mm-radius bubbles fragmenting between opposed fluid jets have been determined. A broad band of frequencies (1.8 to 30 kHz) is observed with peak pressure amplitudes in the range of 0.03 to 2 Pa. While the peak pressure amplitudes show no significant scaling with frequency, the frequency dependence of the decay rates is consistent with the sum of thermal and acoustic radiation losses.

© 2006 Acoustical Society of America
PACS numbers: 43.30.Nb [DKW]
Date Received: July 26, 2006 **Date Accepted:** October 10, 2006

1. Introduction

Understanding the wind-driven component of ambient noise in the open ocean is a long-standing problem in ocean acoustics, dating back to the seminal works of Knudsen *et al.*[1] and Wenz.[2] Bubbles have been implicated in this process, but a complete physical description of air entrainment and sound radiation by open ocean waves remains to be presented.

There are several key processes that must be characterized in a model of wave noise emission.[3,4] These are (1) the creation rate of bubbles as a function of space, time, and bubble size; (2) the emission amplitude and decay rate of newly formed, ringing bubbles; and (3) the passive acoustic absorption of the population of quiescent bubbles within the breaking wave crest. Passive acoustic absorption may not be important for very gently spilling breakers, but is likely to significantly modify the emission spectrum of energetic breakers.

Recent studies of bubbles within open ocean and laboratory breakers have shown that bubble fragmentation is an important process shaping the bubble spectrum,[5–7] and, presumably, also the noise radiated by individual bubbles created within whitecaps. Figure 1 shows a series of images illustrating bubble fragmentation in a laboratory breaking wave. The images were taken through the glass side wall of the Scripps Institution of Oceanography Hydraulics Facility wave flume at the break point of a focused wave packet.[5] The first slide shows the region of air entrainment in the leading edge of the wave directly beneath the plunging crest. The arrows in the top right and bottom left images point to a bubble deforming under the action of fluid shear stress. The final image (bottom right) shows the separating fragmentation products. At the moment of their creation, these bubbles begin breathing mode oscillations and emit an exponentially decaying sinusoidal pulse of sound.[8] This paper presents the results of a study designed to characterize the amplitude and decay of the acoustic emissions from individual bubbles fragmenting in fluid shear under controlled conditions.

2. Experimental setup

The objective of the experiment was to study the acoustic signature of bubbles fragmenting in fluid shear. To achieve this, two opposing fluid jets were created approximately 20 cm above a bubble injection device, and a hydrophone was used to record the sound of fragmentation events (Fig. 2). The jets were fan-shaped (spread in the horizontal plane) and slightly offset in the vertical to create a relatively thin region of high fluid shear (see Fig. 3 for measurements of the velocity structure).

 © 2006 Acoustical Society of America

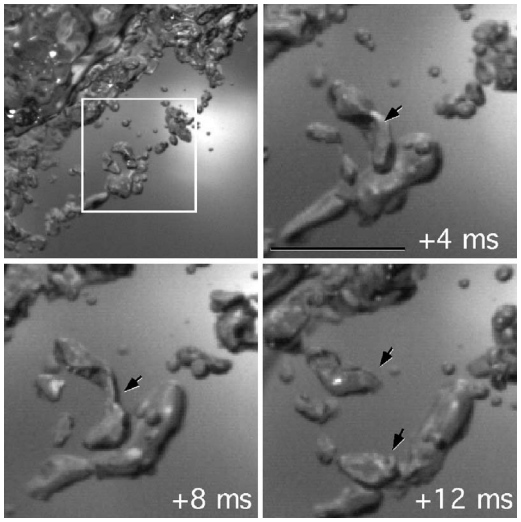

Fig. 1. These images show bubble fragmentation in a region of high fluid shear generated by an overturning wave jet impacting the wave face of a laboratory plunging breaker. The bubbles highlighted by the white box in the first image are the fragmented remnants of a filament of air trapped between the jet and the wave face. The following images detail the elongation and subsequent fragmentation of an individual bubble within the remnants. The scale bar is 1 cm.

The bubble injector consisted of a differential pressure regulator that provided a constant 60 kPa above ambient pressure and fed a bubble injection needle via a constant gas flow valve. This ensured a depth-independent gas injection rate and a constant bubble size of ap-

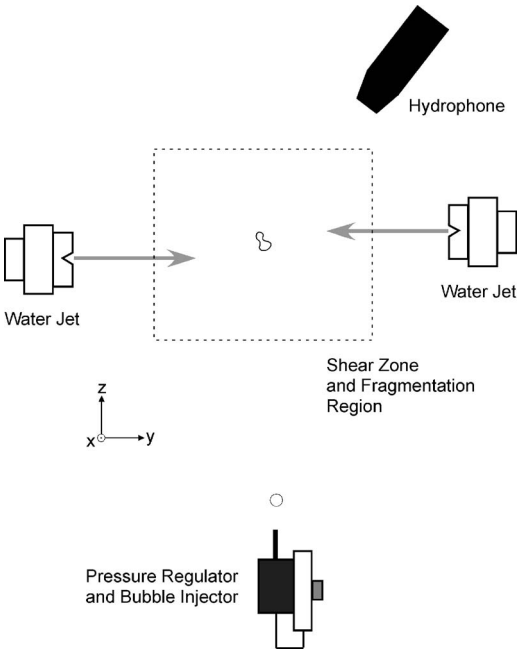

Fig. 2. A schematic of the bubble fragmentation system. Bubbles are created by a differential pressure regulator and gas flow valve below apposing water jets. The bubbles rise into the high fluid shear region and fragment. An ITC 6050C hydrophone positioned 25 cm from the jet was used to measure the acoustic emissions of the fragmentation products. A high-speed video camera (not shown) was used to image the fragmentation.

 © 2006 Acoustical Society of America

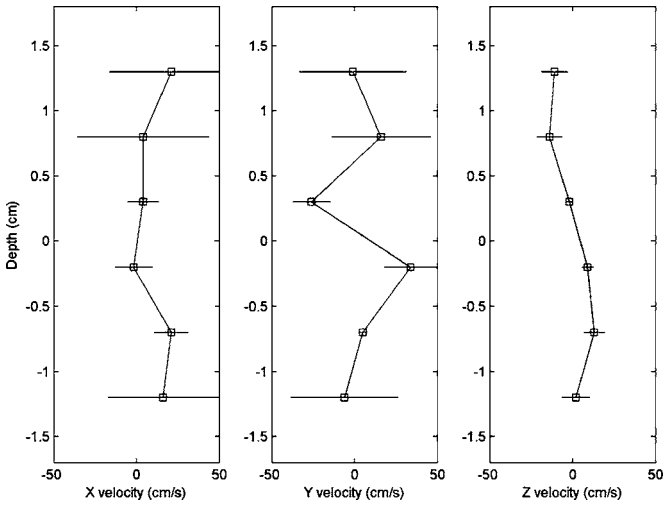

Fig. 3. The three plots show the three components of velocity measured with a 5-MHz acoustic Doppler velocimeter along the jet centerline. Zero depth corresponds to the center midpoint of the jets, the x and y axes lie in a horizontal plane, with the y axis running between the jet nozzles, and the z axis is vertical (see Fig. 2). The horizontal bars on the plots indicate the root-mean-square velocity deviation about the mean.

proximately 1.8 mm radius when deployed 2 m below the water surface. Bubbles were injected at a rate of about 1 every 2 s, permitting the study of individual fragmentation events. Injected bubbles rose through the jet region, with approximately one in three fragmenting. A high-speed camera was positioned in front of the jet to image the details of bubble deformation and the fragmentation products.

An International Transducer Corporation 6050C hydrophone was positioned 25 cm above and to the side of the fragmentation region. The hydrophone output was recorded with a 16-bit National Instruments data acquisition card at a sample rate of 75 k samples/s.

The equipment (hydrophone, jets, bubble injector, and high-speed camera) was mounted on a frame and deployed in a 15-m-deep equipment test pool. The nearest reflecting boundary was the surface, 2 m away. Geometrical spreading ensured that the surface return was at least 16 times smaller in amplitude than the direct path radiation from fragmentation events (boundary reverberation is discussed further in the next section). Fragmentation experiments were carried out in both fresh water and sea water.

3. Analysis

The fate of a bubble rising through the jet region varied according to its trajectory. Approximately two out of every three bubbles passed through the region intact. The mode of bubble fracture, when it occurred, varied depending on the intensity of the local fluid shear. Bubbles entrained near either of the jet nozzles underwent a rapid and energetic fragmentation cascade, resulting in the superposition of multiple acoustic signatures. Less energetic events tended to result in the simultaneous production of either two or three bubbles of varying sizes. The objective of the analysis was to estimate the amplitude and decay of acoustic emissions from bubble fragmentation products. As each bubble signature requires the estimation of five parameters (see below), we have limited the analysis to binary fragmentation events (events that result in only two products), or ten signature parameters.

The sound emission from individual fragmentation products was assumed to be of the form[9]

$$p(t) = A\cos(\omega_b(t-t_0)+\phi)\exp(-\omega_b\delta(t-t_0)/2); \quad t \geq t_0, \tag{1}$$

where A is the pressure amplitude in pascal referenced to 1 m, ω_b is the bubble resonant frequency in radians per second, δ is the damping factor, t_0 is the time at which fragmentation

 © 2006 Acoustical Society of America

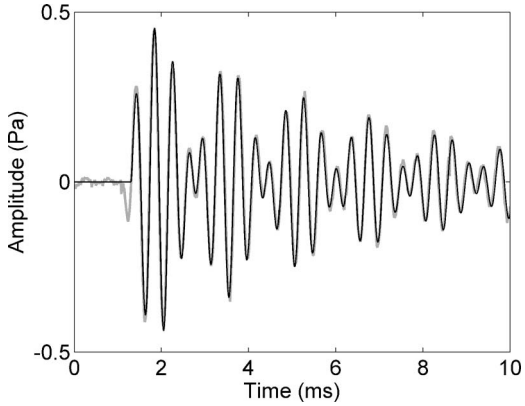

Fig. 4. The acoustic emission from a binary fragmentation event (solid, gray line) is plotted along with a ten-parameter model fit (solid line). The amplitude is in units of pascal at a reference distance of 1 m. The water surface was 2 m above the fragmentation event, corresponding to a propagation delay of approximately 2.7 ms.

occurs, and ϕ is a phase factor. The ten parameters for the two bubbles comprising a binary event are estimated by searching through parameter space and optimizing them in a least mean-square error sense. This was achieved through a combination of automated processing and human intervention. A graphical user interface was written in MATLAB to display individual events and their power spectrum. This permitted both the selection of binary events and the estimation of initial parameters for the multidimensional parameter search. An unconstrained, nonlinear optimization for the best fit between the sum of the two bubble pluses and the measured emission signature was then implemented with the simplex search method.[10]

An example of a binary fragmentation event and the optimal model fit [given by the superposition of two bubble pulses of the form specified by Eq. (1)] is shown in Fig. 4. The parameter estimates were $A_0=0.247$ Pa, $A_1=-0.264$ Pa, $\omega_0=12\,750$ radians/s, $\omega_1=16\,630$ radians/s, $t_0=t_1=1.32$ ms, $\phi_0=-0.109$ radians, $\phi_1=0.4708$ radians, $\delta_0=0.0340$, and $\delta_1=0.0183$. As the two bubbles produce sound at different frequencies, the interference of their signatures results in a series of maxima and minima in the waveform amplitude (a "beat" pattern). The close agreement between the measured emission and the optimal model fit shown in the figure is representative of the results obtained across the entire data set.

Because the experiment was conducted in a pool (albeit a large one), it is worth discussing reverberation. The nearest boundary to the fragmentation region was the surface, which was 2 m distant. The travel time for this path is approximately 2.7 ms and any evidence for a surface return contaminating the data would show up approximately 7 cycles into the acoustic signature in Fig. 4. Geometrical spreading would set the amplitude for surface returns at approximately 0.03 Pa, which is too small to be noticeable in the figure. It was possible to see evidence of surface reverberation in the residue of the model fit but it was not of sufficient magnitude to significantly impact the parameter estimation.

Figures 5 and 6 show amplitude and decay rate estimates for 505 binary fragmentation events.

4. Discussion

The first point worth noting is that this data set does not show any large differences in the spread of amplitude, decay rate, and frequency of bubbles fragmenting in fresh versus salt water. It is evident from the broad spread of frequencies radiated by the bubble products that shear-induced fragmentation results in a broad range of bubble sizes. The smallest bubble product analyzed in this study was 100 microns in radius, an upper limit that was set by the sampling frequency of the data acquisition system.

 © 2006 Acoustical Society of America

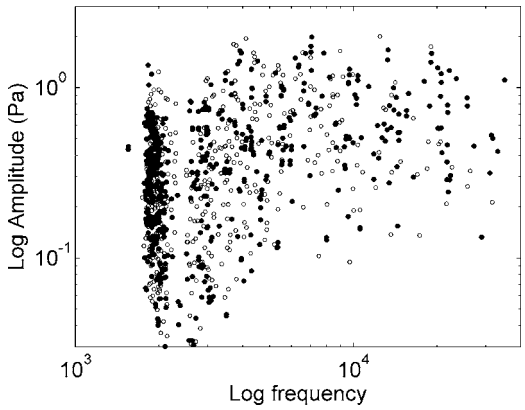

Fig. 5. A scatter plot of the estimated amplitude of acoustic emissions from 505 binary fragmentation events (exactly two products) versus frequency. The open and filled circles correspond to fresh water (at 14.0 °Celsius) and salt water (at 13.4 °Celsius) environments, respectively.

One of the most significant results of this study is the estimate of acoustic signature amplitude of bubbles fragmenting in sheared flow, summarized in Fig. 5. There is a broad spread in radiation amplitude ranging from 0.03 Pa or less to about 2 Pa (almost a factor of 100) across a broad band of frequencies. There does not appear to be a significant trend in the maximum amplitude observed. The minimum amplitude does exhibit frequency dependence below 5 kHz, with larger bubbles radiating at lower amplitudes. The peak oscillation pressures reported here are consistent with the frequency independent levels of between 0.2 and 1.2 Pa reported by Updegraff[11] below gently spilling waves in the ocean.

The estimates of acoustic decay rate (summarized in Fig. 6) show a considerable spread in value. The lower bound for the losses is largely consistent with thermal damping[12,13] (indicated by the broken line), and mean losses are reasonably well predicted by the sum of thermal and acoustic radiation losses (the solid line, given by Eq. 8.2.31b in Medwin and Clay[14]). The scatter in the measured damping for a specified frequency may be due to interactions between the bubble products and the sheared flow. It was noted during the experiment (data not shown) that bubbles rising through the jet region would sometime emit noticeable tone bursts without fragmenting, leading to the speculation that bubble-flow interactions could act to modify the observed decay rate of newly created bubble products.

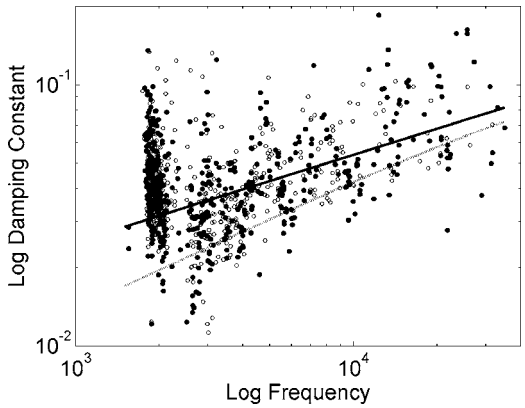

Fig. 6. A scatter plot of the estimated decay rate of acoustic emissions from the same fragmentation events in Fig. 5. The solid black line shows the theoretical decay rate from thermal damping and acoustic radiation losses, while the broken black line shows thermal losses only.

 © 2006 Acoustical Society of America

The data show that binary bubble fragmentation induced by fluid shear can spread an initially monochromatic bubble size spectrum into a wide range of bubble sizes. In addition, the acoustic emission from these products does not show a significant scaling with frequency between 2 to 30 kHz but does show a wide variation in peak pressure amplitude (from 0.03 to 2 Pa). The decay rate of the acoustic emissions shows a frequency scaling commensurate with the sum of thermal and acoustic radiation losses, although there is considerable scatter in the data.

These results have important implications for understanding the noise radiated by oceanic whitecaps. The data suggest that the fragmentation process within whitecaps may be modeled as an ensemble of acoustic pulses over a broad band of frequencies with frequency-independent amplitude scaling and damping determined by thermal and radiation losses. They also suggest that the process of bubble fragmentation may be responsible for the creation of a broader range of bubble sizes than previously thought.[5,6]

Acknowledgments

We are pleased to acknowledge Cary Humphries, James Uyloan, and Beswick Engineering for their help in the fabrication and deployment of the bubble smasher and assistance with the data analysis. This work has been supported by a grant from the Office of Naval Research Ocean Acoustics Division, Grant Number N00014-04-1-0728.

References and links

[1]V. O. Knudsen, R. S. Alford, and J. W. Emling, "Underwater ambient noise," J. Mar. Res. **7**, 410–429 (1948).
[2]G. M. Wenz, "Acoustic ambient noise in the ocean: Spectra and sources," J. Acoust. Soc. Am. **34**, 1936–1956 (1962).
[3]G. B. Deane, "Sound generation and air entrainment by breaking waves in the surf zone," J. Acoust. Soc. Am. **102**, 2671–2689 (1997).
[4]M. R. Loewen and W. K. Melville, "A model of the sound generated by breaking waves," J. Acoust. Soc. Am. **90**, 2075–2080 (1991).
[5]G. B. Deane and M. D. Stokes, "Scale dependence of bubble creation mechanisms in breaking waves," Nature (London) **418**, 839–844 (2002).
[6]C. Garrett, M. Li, and D. Farmer, "The connection between bubble size spectra and energy dissipation rates in the upper ocean," J. Phys. Oceanogr. **30**, 2163–2171 (2000).
[7]M. S. Longuet-Higgins, "The crushing of air cavities in a liquid," Proc. R. Soc. London, Ser. A **439**, 611–626 (1992).
[8]M. Minnaert, "On musical air bubbles and the sound of running water," Philos. Mag. **16**, 235–248 (1933).
[9]T. G. Leighton, *The Acoustic Bubble* (Academic, San Diego, 1994).
[10]J. C. Lagarias, J. A. Reeds, M. H. Wright, and P. E. Wright, "Convergence properties of the Nelder-Mead simplex method in low dimensions," SIAM J. Optim. **9**(1), 112–147 (1998).
[11]G. E. Updegraff, "*In situ* investigation of sea surface noise for a depth of one meter," Ph.D. thesis, University of California, San Diego (1989).
[12]P. A. Crowther, "Bubble noise creation mechanisms," in *Sea Surface Sound*, edited by B. R. Kerman (Kluwer Academic, Boston, 1988), pp. 131–150.
[13]C. Devin, "Survey of thermal, radiation, and viscous damping of pulsating air bubbles in water," J. Acoust. Soc. Am. **31**, 1654–1667 (1959).
[14]H. Medwin and C. S. Clay, *Fundamentals of Acoustical Oceanography* (Academic, San Diego, 1998).

 © 2006 Acoustical Society of America

ACOUSTICAL NEWS—USA

E. Moran
Acoustical Society of America, Suite 1NO1, 2 Huntington Quadrangle, Melville, NY 11747-4502

***Editor's Note**: Readers of the journal are encouraged to submit news items on awards, appointments, and other activities about themselves or their colleagues. Deadline dates for news items and notices are 2 months prior to publication.*

New Fellows of the Acoustical Society of America

Charles W. Holland
For contributions to seafloor acoustics.

Marehalli G. Prasad
For contributions to the acoustics of ducts and mufflers.

USA Meetings Calendar

Listed below is a summary of meetings related to acoustics to be held in the U.S. in the near future. The month/year notation refers to the issue in which a complete meeting announcement appeared.

2007

4–8 June	153rd Meeting of the Acoustical Society of America, Salt Lake City, UT. [Acoustical Society of America, Suite 1NO1, 2 Huntington Quadrangle, Melville, NY 11747-4502; Tel.: 516-576-2360; Fax: 516-576-2377; E-mail: asa@aip.org; www:http://asa.aip.org].
22–24 Oct.	NoiseCon 2007, Reno, NV [Website is: www.inceusa.org/nc07
27 Nov.–2 Dec.	154th Meeting of the Acoustical Society of America, New Orleans, LA (note Tuesday through Saturday) [Acoustical Society of America, Suite 1NO1, 2 Huntington Quadrangle, Melville, NY 11747-4502; Tel.: 516-576-2360; Fax: 516-576-2377; E-mail: asa@aip.org; www:http://asa.aip.org].

2008

28 July–1 Aug.	9th International Congress on Noise as a Public Health Problem (Quintennial meeting of ICBEN, the International Commission on Biological Effects of Noise). Foxwoods Resort, Mashantucket, CT [Jerry V. Tobias, ICBEN 9, Post Office Box 1609, Groton, CT 06340-1609, Tel. 860-572-0680; Web: www.icben.org. E-mail icben2008@att.net.

Cumulative Indexes to the Journal of the Acoustical Society of America

Ordering information: Orders must be paid by check or money order in U.S. funds drawn on a U.S. bank or by Mastercard, Visa, or American Express credit cards. Send orders to Circulation and Fulfillment Division, American Institute of Physics, Suite 1NO1, 2 Huntington Quadrangle, Melville, NY 11747-4502; Tel.: 516-576-2270. Non-U.S. orders add $11 per index.

Some indexes are out of print as noted below.

Volumes 1–10, 1929–1938: JASA, and Contemporary Literature, 1937–1939. Classified by subject and indexed by author. Pp. 131. Price: ASA members $5; Nonmembers $10.

Volumes 11–20, 1939–1948: JASA, Contemporary Literature and Patents. Classified by subject and indexed by author and inventor. Pp. 395. Out of Print.

Volumes 11–20, 1939–1948: JASA, Contemporary Literature and Patents. Classified by subject and indexed by author and inventor. Pp. 395. Out of Print.

Volumes 21–30, 1949–1958: JASA, Contemporary Literature and Patents. Classified by subject and indexed by author and inventor. Pp. 952. Price: ASA members $20; Nonmembers $75.

Volumes 31–35, 1959–1963: JASA, Contemporary Literature and Patents. Classified by subject and indexed by author and inventor. Pp. 1140. Price: ASA members $20; Nonmembers $90.

Volumes 36–44, 1964–1968: JASA and Patents. Classified by subject and indexed by author and inventor. Pp. 485. Out of Print.

Volumes 36–44, 1964–1968: Contemporary Literature. Classified by subject and indexed by author. Pp. 1060. Out of Print.

Volumes 45–54, 1969–1973: JASA and Patents. Classified by subject and-indexed by author and inventor. Pp. 540. Price: $20 (paperbound); ASA members $25 (clothbound); Nonmembers $60 (clothbound).

Volumes 55–64, 1974–1978: JASA and Patents. Classified by subject and indexed by author and inventor. Pp. 816. Price: $20 (paperbound); ASA members $25 (clothbound); Nonmembers $60 (clothbound).

Volumes 65–74, 1979–1983: JASA and Patents. Classified by subject and indexed by author and inventor. Pp. 624. Price: ASA members $25 (paperbound); Nonmembers $75 (clothbound).

Volumes 75–84, 1984–1988: JASA and Patents. Classified by subject and indexed by author and inventor. Pp. 625. Price: ASA members $30 (paper--bound); Nonmembers $80 (clothbound).

Volumes 85–94, 1989–1993: JASA and Patents. Classified by subject and indexed by author and inventor. Pp. 736. Price: ASA members $30 (paperbound); Nonmembers $80 (clothbound).

Volumes 95–104, 1994–1998: JASA and Patents. Classified by subject and indexed by author and inventor. Pp. 632, Price: ASA members $40 (paperbound); Nonmembers $90 (clothbound).

Volumes 105–114, 1999–2003: JASA and Patents. Classified by subject and indexed by author and inventor. Pp. 616, Price: ASA members $50; Nonmembers $90 (paperbound).

ACOUSTICAL NEWS—INTERNATIONAL

Walter G. Mayer
Physics Department, Georgetown University, Washington, DC 20057

International Meetings Calendar

Below are announcements of meetings and conferences to be held abroad. Entries preceded by an * are new or updated listings.

March 2007

13–15 **Spring Meeting of the Acoustical Society of Japan**, Tokyo, Japan (Acoustical Society of Japan, Nakaura 5th-Bldg., 2-18-20 Sotokanda, Chiyoda-ku, Tokyo 101-0021, Japan; Fax: +81 3 5256 1022; Web: www.asj.gr.jp/index-en.html).

15–17 **AES 30th International Conference on Intelligent Audio Environments**, Saariselkä, Finland (Web: www.aes.fi/aes30/).

19–22 **German Acoustical Society Meeting (DAGA2007)**, Stuttgart, Germany (Web: www.daga2007.de).

April 2007

9–12 **International Congress on Ultrasonics (2007 ICU)**, Vienna, Austria (Fax: +43 158801 13499; Web: www.icultrasonics.org).

10–12 **4th International Conference on Bio-Acoustics**, Loughboro, UK (Web: www.ioa.org.uk/viewupcoming.asp).

16–18 **29th International Symposium on Acoustical Imaging**, Shonan Village Center, Kanagawa Pref., Japan (Web: publicweb.shonan-it.ac.jp/ai29/AI29.html).

24–25 *__Institute of Acoustics (UK) Spring Conference__, Cambridge, UK (Web: www.ioa.org.uk/viewupcoming.asp).

June 2007

1–3 *__Second International Symposium on Advanced Technology of Vibration and Sound__, Lanzhou, China (Web: www.jsme.or.jp/dmc/Meeting/VSTech2007.pdf).

3–7 **11th International Conference on Hand-Arm Vibration**, Bologna, Italy (Web: associazioneitalianadiacustica.it/HAV2007/index.htm).

4–6 *__Japan-China Joint Conference on Acoustics__, Sendai, Japan (Fax: +81 3 5256 1022; Web: www.asj.gr.jp/eng/imdex.html).

18–21 **Oceans07 Conference**, Aberdeen, Scotland, UK (Web: www.oceans07ieeeaberdeen.org).

25–29 **2nd International Conference on Underwater Acoustic Measurements: Technologies and Results**, Heraklion, Crete, Greece (Web: www.uam2007.gr).

July 2007

2–6 **8th International Conference on Theoretical and Computational Acoustics**, Heraklion, Crete, Greece (Web: www.iacm.forth.gr/~ictca07).

3–5 *__First European Forum on Effective Solutions for Managing Occupational Noise Risks__, Lille, France (Web: www.noiseatwork.eu).

4–7 **International Clarinet Association Clarinetfest**, Vancouver, British Columbia, Canada (E-mail: john.cipolla@wku.edu; Phone: 1 270 745 7093).

9–12 **14th International Congress on Sound and Vibration (ICSV14)**, Cairns, Australia (Web: www.icsv14.com).

16–21 **12th International Conference on Phonon Scattering in Condensed Matter**, Paris, France (Web: www.isen.fr/phonons2007).

August 2007

6–10 **16th International Congress of Phonetic Sciences (ICPhS2007)**, Saarbrücken, Germany (Web: www.icphs2007.de).

28–31 **inter-noise 2007**, İstanbul, Turkey (Web: www.internoise2007.org.tr).

27–31 **Interspeech 2007**, Antwerp, Belgium (Web: www.interspeech2007.org).

September 2007

2–7 **19th International Congress on Acoustics (ICA2007)**, Madrid, Spain (SEA, Serrano 144, 28006 Madrid, Spain; Web: www.ica2007madrid.org).

9–12 **ICA Satellite Symposium on Musical Acoustics (ISMA2007)**, Barcelona, Spain (SEA, Serano 144, 28006 Madrid, Spain; Web: www.ica2007madrid.org).

9–12 **ICA Satellite Symposium on Room Acoustics (ISRA2007)**, Sevilla, Spain (Web: www.ica2007madrid.org).

17–19 **3rd International Symposium on Fan Noise**, Lyon, France (Web: www.fannoise.org).

19–21 *__Autumn Meeting of the Acoustical Society of Japan__, Kofu, Japan (Acoustical Society of Japan, Nakaura 5th-Bldg., 2-18-20 Sotokanda, Chiyoda-ku, Tokyo 101-0021, Japan; Fax: +81 3 5256 1022; Web: www.asj.gr.jp/index-en.html).

24–28 *__XIX Session of the Russian Acoustical Society__, Nizhny Novgorod, Russia (Web: www.akin.ru).

June 2008

30–4 **Acoustics'08 Paris: 155th ASA Meeting +5th Forum Acusticum (EAA) +9th Congrès Français d'Acoustique (SFA)**, Paris, France (Web: www.acoustics08-paris.org).

July 2008

7–10 **18th International Symposium on Nonlinear Acoustics (ISNA18)**, Stockholm, Sweden (Temporary e-mail: ⟨Bengt Enfla⟩benflo@mech.kth.se).

28–1 **9th International Congress on Noise as a Public Health Problem**, Mashantucket, Pequot Tribal Nation (ICBEN 9, P.O. Box 1609, Groton, CT 06340-1609, USA, Web: www.icben.org).

September 2008

22–26 **INTERSPEECH 2008–10th ICSLP**, Brisbane, Australia (Web: www.interspeech2008.org).

November 2008

1–5 **IEEE International Ultrasonics Symposium**, Beijing, China (Web: www.ieee-uffc.org/ulmain.asp?page=symposia).

August 2010

23–27 **20th International Congress on Acoustics (ICA2010)**, Sydney, Australia (Web: www.ica2010sydney.org/).

 0001-4966/2006/120(6)/3431/1/$22.50 © 2006 Acoustical Society of America

BOOK REVIEWS

P. L. Marston
Physics Department, Washington State University, Pullman, Washington 99164

These reviews of books and other forms of information express the opinions of the individual reviewers and are not necessarily endorsed by the Editorial Board of this Journal.

Editorial Policy: *If there is a negative review, the author of the book will be given a chance to respond to the review in this section of the Journal and the reviewer will be allowed to respond to the author's comments. [See "Book Reviews Editor's note," J. Acoust. Soc. Am.* **81***, 1651 (May 1987).]*

Urban Forest Acoustics

Voichita Bucur

Springer-Verlag, Berlin, 2006. 181 pp. Price: $129 (hardcover), ISBN: 3540307834

The author, Voichita Bucur, a member of the science faculty at the Henri Poincare University in Nancy, is prominent in the field of the acoustics of wood materials. Her previous work includes *Acoustics of Wood*, now in its second edition (Springer-Verlag, Berlin, 2006). This latest text on the acoustics of urban forests should be of interest to environmental managers and foresters as well as acousticians and advanced students.

The book consists of nine chapters. The first chapter contrasts the concept of urban trees, located on streets, in parks, and gardens with that of forest trees. Urban trees are subject to greater environments stresses but constitute essential components in populated areas aesthetically, culturally, and climatically. Chapter 2 deals with noise in the urban forest. An overview of sound parameters, such as SPL, speed of sound, sound intensity, weight sound pressure levels, L_{eq}, etc. is given, followed by a description of equipment for noise measurement and a discussion on how outdoor measurements are influenced by the distance effect, frequency content, and visibility. Chapter 3 covers the morphological and mechanical characteristics of trees and the measurement procedures requisite for management inventory of forests, timber volume, and for forestry planning and protection. Development of ultrasonic and laser sensors over the last decade or two has provided noncontact methods of measuring trunk diameters, cross-section estimates, and heights of trees. Collection and entry of data are facilitated without the need for tedious manual entry. Mechanical characteristics, such as moduli of elasticity, are used in the study of genotypic characteristics of different clones. Sylvicultural practices exemplified by the effect of spacing on the wood quality of standing trees, are described primarily in terms of modulus of elasticity.

Noise attenuation with plant material is described in Chap. 4. Factors influencing noise attenuation in a forest include the presence of trees, soil surface, ground vegetation, topography, and meteorological factors. Sound transmission by plant material is expressed as excess attenuation, i.e., the measured sound pressure level corrected for air absorption, minus the free field level (which would have existed if there was neither obstacle nor sound velocity gradient present). Acoustic characteristics of the constitutive elements of the tree, such as trunk, bark, canopy, and forest floor, affect the mechanisms of acoustic absorption. The trunk, branches, and foliage help to scatter incident acoustic energy, and the effectiveness of scattering is determined by the geometry of the scatterers. It is certainly interesting to learn that audible reverberation in a forest is due to interference between direct and ground-reflected sounds and the scattering effects caused by trees, branches, and meteorological conditions. Using these considerations, modeling and simulation may be rendered possible to gain a better understanding of the complex phenomena of sound propagation. Vegetation belts and barriers are also useful for traffic noise control by reflection and attenuation, and this topic is treated in more detail in Chap. 5. The principal sources of outdoor noise are those generated by traffic on streets and highways, by rail transportation, and by aircraft. An overview of outdoor community noise, legislative action (e.g., the 1996 Green Paper on future noise policy by the European Commission); sources and measurement parameters of traffic, rail, and aircraft noise, techniques for improvement of the soundscape through strategic placement of vegetation, topographic modifications, etc. are given, and there are brief mentions of modeling programs for predicting traffic noise.

At the beginning of Chap. 6 (Noise Abatement and Dwellings), an excellent definition is rendered of the term "soundscape," originally coined by the Canadian musician Murray Schafre in the late 1960s. Soundscape refers to the sounds produced by human beings, different kinds of traffic noise, background music, birds, animals, waterfalls, or streams, bells, broadcasting, and other natural, artificial, or social sounds—all of which unite into one sound environment, that evokes personal feelings in humans under various circumstances. The concept of soundscapes is fraught with social, historical, cultural, and environmental implications. It thus becomes evident that the design of a comfortable environment includes paying attention to the soundscape as well as landscape design. In urban residential areas, the deployment of trees around houses should be rendered to maximize noise reduction, thereby improving the aesthetics and air quality. In the case of residential suburban areas, noise is generated principally by vehicular traffic, and it can be reduced by creating tree belts and noise barriers.

Noise by birds and insects in urban forest environment, the subject of Chap. 7, add to the cacophony generated by the presence of humans and machinery (vehicular traffic, aircraft, etc.). Bird sounds are perceived in both time and frequency domains, and they are certainly subject to attenuation through scattering and medium absorption as well as meteorological effects. The overall environmental noise level due to nonhuman sources lies between 45 and 55 dB. The insects that are of the greatest concern are the tree-destroying termites. It is important to detect them so that they can be exterminated, and acoustic emission methods operating at more than 40 kH have been successful in detecting termites in trees.

A very brief Chap. 8 describes the remote sensing techniques used to detect fires in forests. While these methods include employing electromagnetic energy, aerial photography with thermal imagery, radar imagery, and satellite detection, there is one acoustic method that depends on backscattered sound, which also happens to be highly affected by atmospheric turbulence along the path of the original pulse. No infrastructure project planning is complete without a costs/benefits analysis, so the economic aspects of urban forestry are outlined in the final Chap. 9. Aesthetics obviously counts, but there is also the benefit of trees removing environmental pollutants, providing cooling shades, slowing storm water runoff, preventing soil erosion, reducing heating and cooling costs, and enhancing property values,

The first appendix (called "annex" in this text) lists the nomenclature of the mathematical symbols used in the text, and the second appendix covers the very basic equations of acoustics. Appendix 3 gives the standard frequency weight graph for A, B, C weighting network. Appendix 4 lists the ANSI and ISO standards applicable to acoustic definitions, measurement methods, measurements of specific types of sources, and measurement of structures used in noise control. Annex 5 lists the physical units used in the book. An excellent listing of references pertinent to the topic of urban forestry is given at the end.

This is a text that an environmentalist should have in his/her library; and it should be obvious to the reader that no landscape design or community planning is complete without considering the soundscape.

DANIEL R. RAICHEL
Eilar Associates and CUNY Graduate Center
2727 Moore Lane
Fort Collins, CO 80526-2192

 0001-4966/2006/120(6)/3433/1/$22.50 © 2006 Acoustical Society of America

REVIEWS OF ACOUSTICAL PATENTS

Lloyd Rice
11222 Flatiron Drive, Lafayette, Colorado 80026

The purpose of these acoustical patent reviews is to provide enough information for a Journal reader to decide whether to seek more information from the patent itself. Any opinions expressed here are those of reviewers as individuals and are not legal opinions. Printed copies of United States Patents may be ordered at $3.00 each from the Commissioner of Patents and Trademarks, Washington, DC 20231. Patents are available via the Internet at http://www.uspto.gov.

Reviewers for this issue:

GEORGE L. AUGSPURGER, *Perception, Incorporated, Box 39536, Los Angeles, California 90039*
ANGELO CAMPANELLA, *3201 Ridgewood Drive, Hilliard, Ohio 43026-2453*
ALIREZA DIBAZAR, *Department of BioMed Engineering, University of Southern California, Los Angeles, California 90089*
JOHN M. EARGLE, *JME Consulting Corporation, 7034 Macapa Drive, Los Angeles, California 90068*
SEAN A. FULOP, *California State University, Fresno, 5245 N. Backer Avenue M/S PB92, Fresno, California 93740-8001*
JEROME A. HELFFRICH, *Southwest Research Institute, San Antonio, Texas 78228*
DAVID PREVES, *Starkey Laboratories, 6600 Washington Ave. S., Eden Prairie, Minnesota 55344*
DANIEL R. RAICHEL, *2727 Moore Lane, Fort Collins, Colorado 80526*
CARL J. ROSENBERG, *Acentech Incorporated, 33 Moulton Street, Cambridge, Massachusetts 02138*
NEIL A. SHAW, *Menlo Scientific Acoustics, Inc., Post Office Box 1610, Topanga, California 90290*
WILLIAM THOMPSON, JR., *Pennsylvania State University, University Park, Pennsylvania 16802*
ERIC E. UNGAR, *Acentech, Incorporated, 33 Moulton Street, Cambridge, Massachusetts 02138*
ROBERT C. WAAG, *University of Rochester, Department of Electrical and Computer Engineering, Rochester, New York 14627*

7,056,366

43.25.Nm METHOD AND APPARATUS FOR INCREASING THE OPERATING LIFETIME OF GAS FILTERS BY AN ACOUSTIC FIELD

Matityahu Fichman *et al.*, assignors to Technion Research and Development Foundation, Limited
6 June 2006 (Class 95/29); filed 12 June 2003

Sound from an acoustic source is applied to the gas that is to be filtered as it flows into the filter so as to produce steady secondary acoustic streaming around dust particles already deposited on the filter. This reduces the pressure drop across the filter resulting from the initial clogging, and thus permits extended use of the filter before the pressure drop becomes excessively great.—EEU

7,066,894

43.28.Dm SENSOR AND METHOD FOR DETECTING VERY LOW FREQUENCY ACOUSTIC SIGNALS

Michael E. Halleck *et al.*, assignors to iLife Solutions, Incorporated
27 June 2006 (Class 600/586); filed 8 July 2002

A sensor and method for detecting very-low-frequency signals is disclosed. The sensor is capable of detecting acoustic signals in the frequency range of 0.1–30 Hz. The sensor consists of a chamber with a cavity and a low-frequency microphone placed within the cavity. Another embodiment consists of a chamber with a resonant cavity, a low-frequency microphone

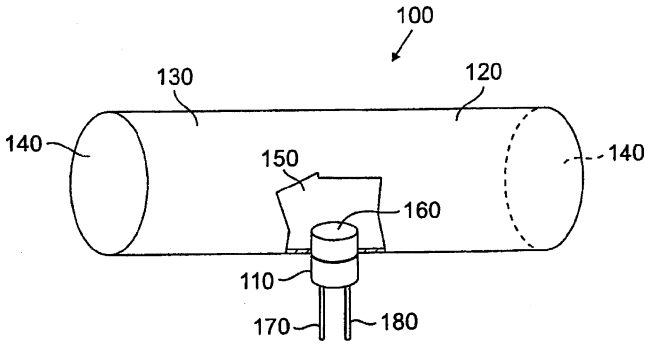

placed within the cavity, and a membrane covering the cavity. Low-frequency acoustic signals incident upon the membrane cause the membrane to move and amplify the acoustic signals within the resonant cavity.—DRR

7,062,919

43.28.Kt VORTEX FUEL NOZZLE TO REDUCE NOISE LEVELS AND IMPROVE MIXING

Hisham Alkabie, assignor to Pratt & Whitney Canada Corporation
20 June 2006 (Class 60/776); filed 11 February 2005

Low-frequency turbine engine noise brought on by combustion-pressure fluctuations reentering upstream past the post ignition chamber into the nozzle mixing chambers is reduced by the claimed nozzle **12**, where compressed air flows from the compressed air plenum **5** through air inlet openings **13**, then to mixing chamber **21**, then exits toward ignition through annulus **24**. Curved surfaces **20** and **28** create counter-rotating air vortices that move in a direction that traverses the fuel spray emitted from fuel orifices **16**. The counter-rotating, stream-wise vorticity eliminates or reduces the acoustic pressure coupling effect on the fuel-air mixture before combus-

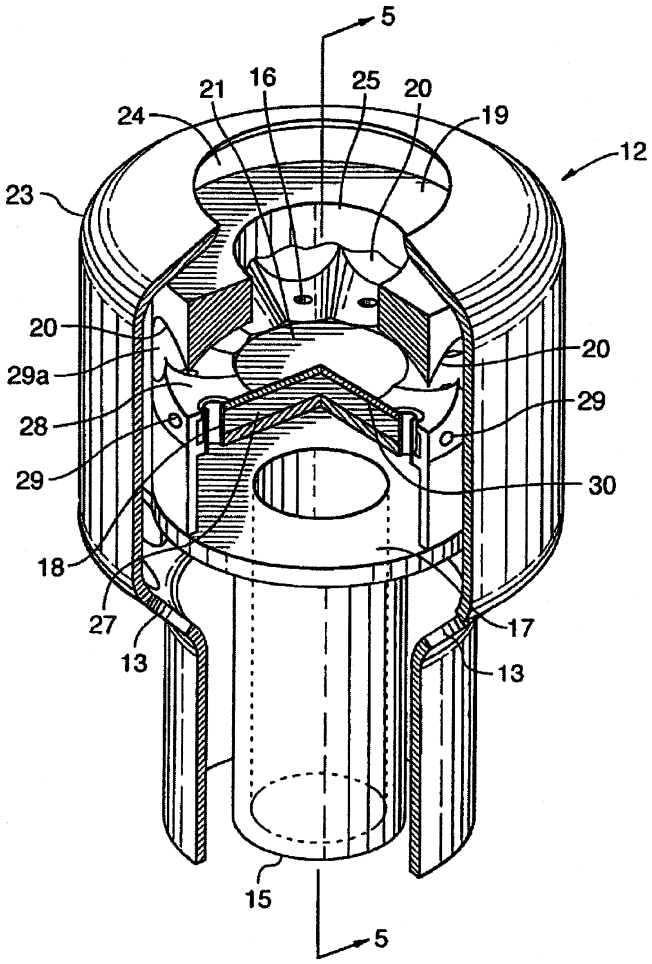

tion takes place, enhances combustion efficiency, and reduces emissions from the combustion process. The claims include the decoupling of acoustic and hydrodynamic fluctuations of a combustor and that the fuel-laden vortices swirl with diminished velocity as they move from deflecting surfaces toward the mixing chamber.—AJC

7,066,888

43.35.Yb METHOD AND APPARATUS FOR DETERMINING AN ULTRASOUND FLUID FLOW CENTERLINE

Kenneth Abend and Alan Stein, assignors to Allez Physionix Limited
27 June 2006 (Class 600/454); filed 29 October 2004

This is a method for determining the location of an effective center of fluid flow in a vessel through the use of an ultrasound transducer array that can propagate and receive ultrasound energy. Ultrasound energy is propagated along an axis of propagation and projects upon the vessel. A Doppler-shifted signal reflected from the fluid in the vessel is received and a set of quantities expressed as a density is derived from the Doppler-shifted signal for each set of coordinates. The mean, mode, or median is calculated for

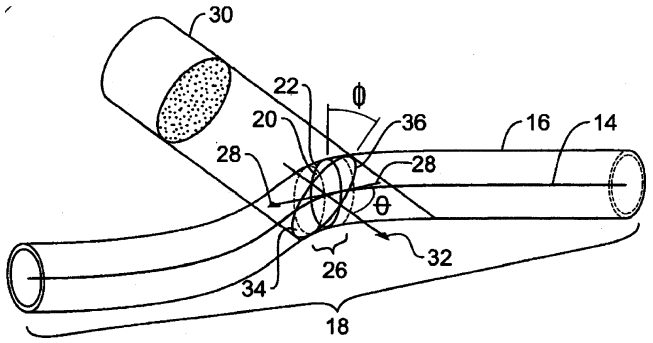

each of the dimensions of the set of coordinates in conjunction with the density associated therewith. The calculation is repeated throughout the field of view of the vessel to define a centerline.—DRR

7,068,867

43.35.Yb ULTRASONIC POSITION INDICATOR

Avner Adoram *et al.*, assignors to Glucon Medical Limited
27 June 2006 (Class 385/12); filed 2 January 2003

A system is provided for monitoring the position of an instrument (e.g., a catheter, an endoscope, a needle, a guidewire, etc.) in a patient during surgery. The system includes a light-transmission medium configured

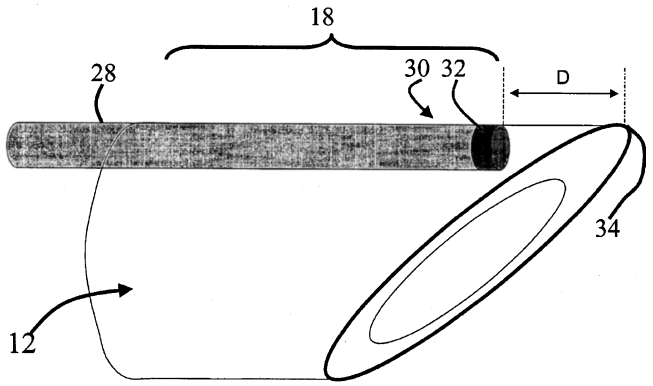

to transmit light pulses to a desired region to produce an acoustic signal, at least one ultrasound sensor configured to receive and transduce the acoustic signal, and a processing unit connected to the sensor(s) and configured to locate the source of the acoustic signal using the transduced signal.—DRR

7,055,389

43.35.Zc ACOUSTIC COUPLING WITH A FLUID RETAINER

Dennis William Mueller, assignor to MetScan Technologies, LLC
6 June 2006 (Class 73/620); filed 31 May 2002

The device described in this patent is intended for use in ultrasonic inspection of extended surfaces, such as wings of aircraft. A frame that is placed against the surface to be inspected carries a cross member that can move along the frame and this cross member carries a transducer support that can move along the cross member. The transducer thus can be positioned at any point in an *X-Y* coordinate system based on the frame. The transducer itself can be rotated so as to make contact with curved inspection surfaces. All motions are controlled by a computer system, which also records and displays the data. Two ways are described for introducing fluid between the transducer and the inspection surface in order to increase the coupling: in the form of a continuous stream introduced along a side of the transducer or from a jacket surrounding the transducer.—EEU

7,062,972

43.35.Zc ACOUSTIC TRANSDUCER

James A. Hill, assignor to Horiba Instruments, Incorporated
20 June 2006 (Class 73/632); filed 21 July 2003

An exhaust gas analyzer sensor to measure exhaust gas temperature and flow velocity is claimed where the piezo elements are protected from the exhaust heat. Transducers **30-30** send ultrasound waves through the exhaust gas (called a "fluid" in the descriptions). This transducer includes a

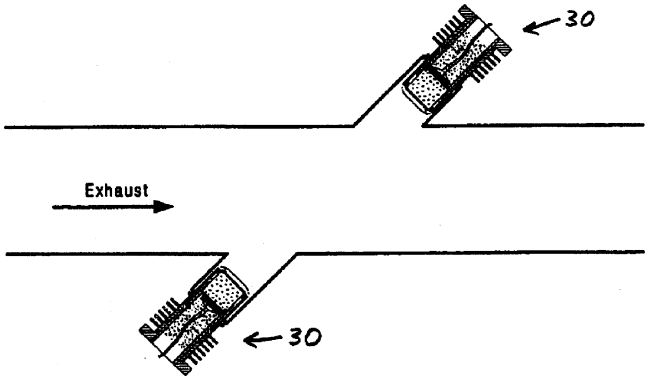

piezo-ceramic pulse generator, an impedance matching layer between the pulse generator and the fluid, a thermal management system that includes a plurality of fins, also a sampling system that brings a fluid sample to the transducer set **30-30**, means to dilute the fluid flow, and a transducer pair arranged in opposition.—AJC

7,062,977

43.35.Zc VIBRATORY TRANSDUCER

Alfred Wenger and Martin Anklin, assignors to Endress+Hauser **Flowtec AG**
20 June 2006 (Class 73/861.355); filed in the European Patent Office 21 September 2001

A coriolis-force mass-flow-densitometer transducer with reduced pressure cross-sensitivity is claimed. Subject to fluid flows in tubes **101** and **102**, vibration exciter **113** converts exciting power P_{exc} into pulsing or harmonic forces, driving tubes **101** and **102** in phase opposition. Sensor **114** detects the relative motion between tube segments **101a** and **102a** while sensor **115** detects relative motion between **101b** and **102b**. Both sensors send signals

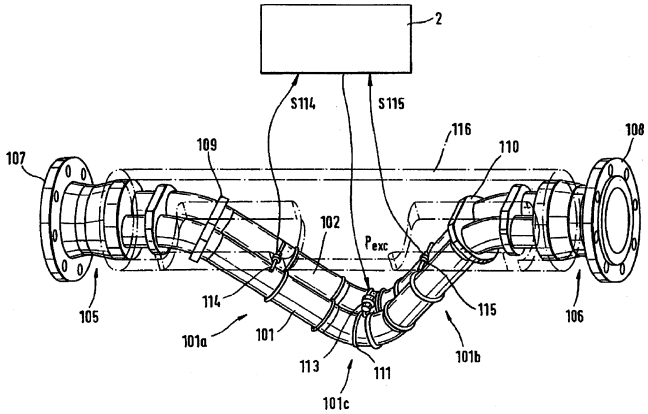

to processor **2**. The resonant frequency of the wagging mode having its axis as the line from the inlet **107** to the outlet **108** depends on fluid density. The frequency and amplitude of the curved-loop, bending-mode signal—being the difference between signals **S114** and **S115**—provides the coriolis signal proportional to the mass flow rate. The author argues that adding stiffening rings **111** and **112**, or a single ring at the elbow, provides the reduced cross-sensitivity to static pressure.—AJC

7,053,534

43.38.Ar PIEZOELECTRIC VIBRATION GYRO-SENSOR

Yoshiro Tomikawa and Yoshiaki Tanaka, assignors to Epson Toyocom Corporation
30 May 2006 (Class 310/370); filed in Japan 6 September 2002

This patent discloses a tuning-fork-style gyro having interdigitated drive transducers designed for use on quartz or another crystalline piezoelectric material. It is not clear what is new or different about this configuration, but the discussion is limited to the electronics, so it is of little interest to most acousticians.—JAH

7,062,053

43.38.Ar CONDENSER MICROPHONE STRUCTURE

Masayoshi Hohjyo, assignor to Matsushita Electric Industrial Company, Limited
13 June 2006 (Class 381/174); filed in Japan 31 May 2002

The patent describes structural methods of extending the upper frequency range of noise cancelling in typical gradient microphones that might be used in cellular phones and similar applications.—JME

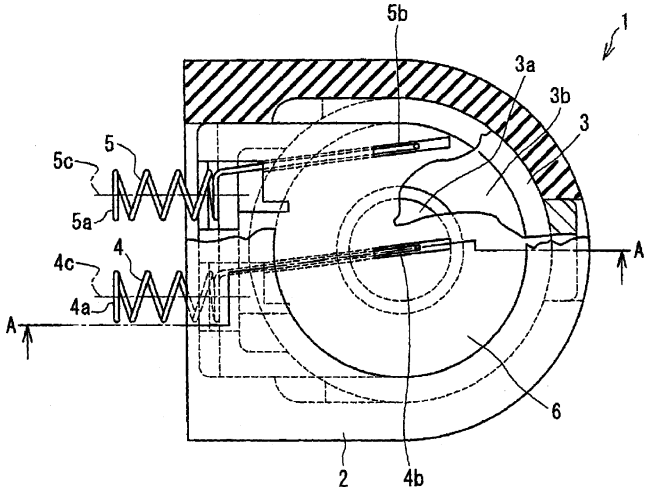

7,035,425

43.38.Dv FREQUENCY RESPONSE ENHANCEMENTS FOR ELECTRO-DYNAMIC LOUDSPEAKERS

Steven W. Hutt *et al.*, assignors to Harman International Industries, Incorporated
25 April 2006 (Class 381/431); filed 2 May 2003

A means of calculating the amount of metal in frame **102** is described, specifically the percentage of metal between openings, which is said to improve motor strength and frequency response. The claims include the use

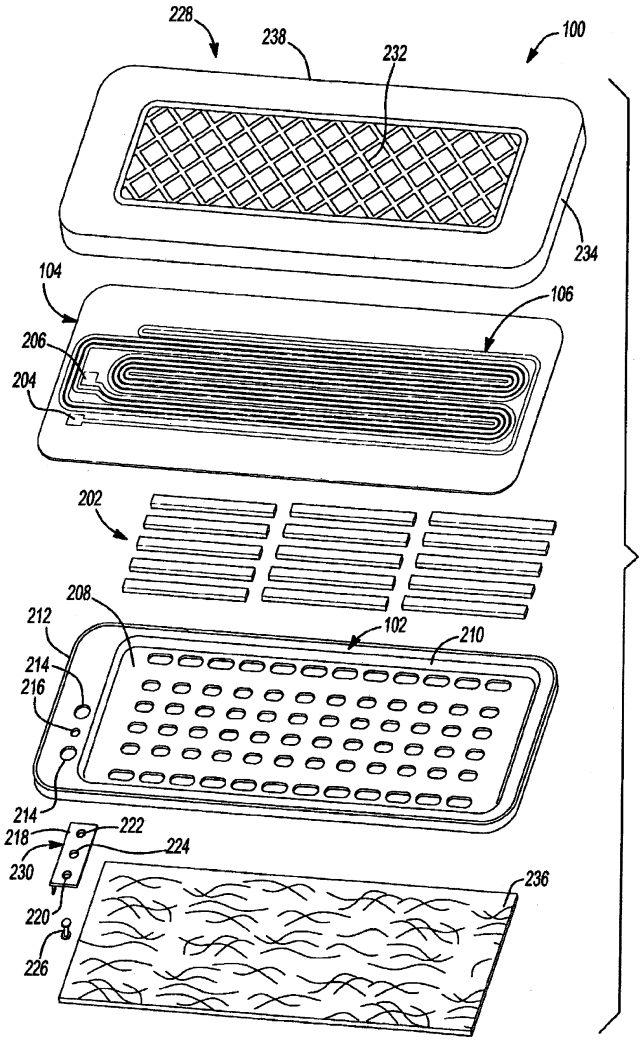

of adhesives to attach diaphragm **104** to the frame, the use of porous material **236**, a range (about 20% to 45%) for the amount of metal between openings, and, it seems, for percentages less than 20% and greater than 45%.—NAS

7,065,221

43.38.Ew SPEAKER APPARATUS

Hidekazu Tanaka, assignor to Matsushita Electric Industrial Company, Limited
20 June 2006 (Class 381/96); filed in Japan 1 December 1998

This is a companion to United States Patent 7,058,186, reviewed in this issue. In this case, the basic premise is much iffier, however. Consider the situation in which a loudspeaker **1** is located in the rear portion of a TV set, and its output is conducted through a narrow waveguide **2** to emerge from a vertical slit beside the viewing screen. It seems obvious that sound quality will be degraded by pipe resonances. These can be corrected to some degree with acoustical filters, entailing additional cost and complexity. The patent asserts that if microphone **4** is placed at just the right location, it can be used

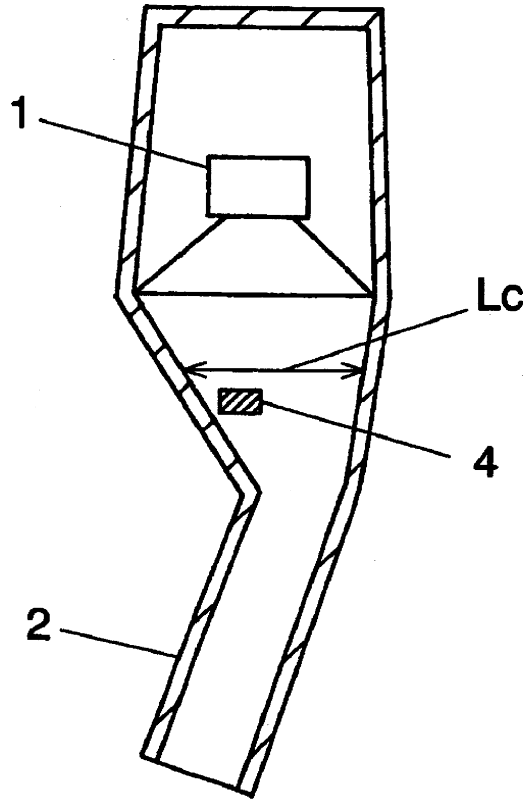

as a feedback sensor for automatic electronic correction instead. The patent includes diagrams of amplitude and phase responses, suggesting that stable operation is possible up to several kilohertz.—GLA

7,058,186

43.38.Ew LOUDSPEAKER DEVICE

Hidekazu Tanaka, assignor to Matsushita Electric Industrial Company, Limited
6 June 2006 (Class 381/95); filed in Japan 1 December 1999

This is a companion to United States Patent 7,065,221, also reviewed in this issue. During the past 50 years, loudspeaker designers have devoted considerable brain power to the concept of motional feedback, i.e., including

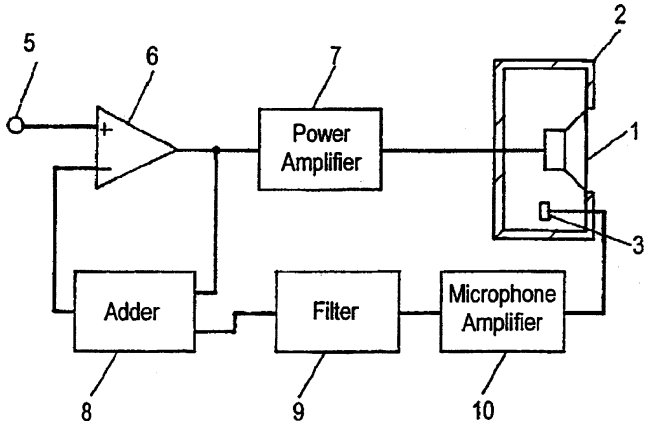

a loudspeaker's acoustic output in a negative feedback loop. Various methods of deriving a suitable electrical feedback signal include sensing electrical impedance, cone motion, near-field sound pressure, and sound pressure inside the cabinet. To the best of my knowledge, all but the last have been used in commercial loudspeaker systems at one time or another. Matsushita has decided to fill the remaining gap. Since the first acoustic mode of a rectangular closed box occurs when its largest internal dimension equals a

half-wavelength, it would seem necessary to limit motional feedback to the region well below this critical frequency. According to this patent, however, if the sensing microphone is placed near a location where sound pressure from the first two or three modes is at a minimum, stable operation can be extended to a higher frequency.—GLA

7,066,026

43.38.Fx UNDERWATER ACOUSTIC VECTOR SENSOR USING TRANSVERSE-RESPONSE FREE, SHEAR MODE, PMN-PT CRYSTAL

Ken Kan Deng, assignor to Wilcoxon Research, Incorporated
27 June 2006 (Class 73/514.34); filed 9 July 2004

An acoustic particle-velocity sensor, or vector sensor, is fashioned using a single shear-mode coupled relaxor crystal with an exceptionally large piezoelectric shear coefficient as the sensing element. The crystal is cut at a special orientation relative to its crystallographic axes to provide maximum response in the desired sensing direction and minimum response in the two orthogonal directions. The sensor includes a proof mass **202**, the mounting

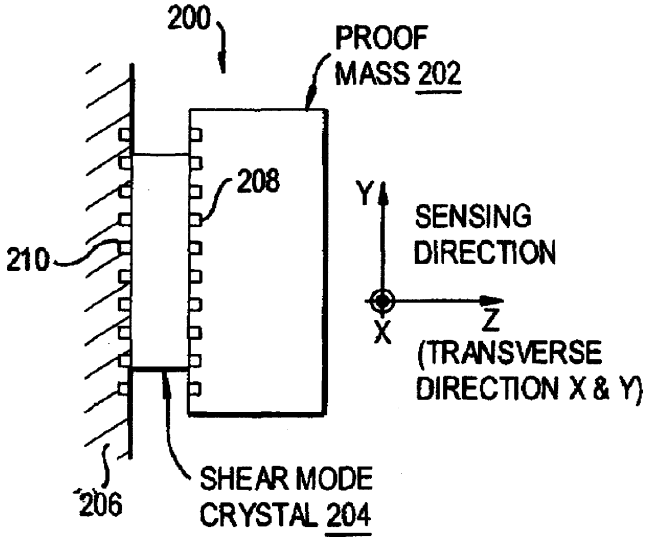

base **206**, and the crystal **204**. To mitigate the adverse lateral constraint problem, or clamping effect, associated with a relaxor crystal, reduced bonding area between either the proof mass or the base and the crystal is realized by castellated, or tongue and groove, surfaces **208** and **210**. Three such orthogonally oriented sensors are mounted in a rigid but neutrally buoyant housing to form a small-vector sensor with high signal-to-noise ratio and broad bandwidth.—WT

6,978,159

43.38.Hz BINAURAL SIGNAL PROCESSING USING MULTIPLE ACOUSTIC SENSORS AND DIGITAL FILTERING

Albert S. Feng *et al.*, assignors to Board of Trustees of the University of Illinois
20 December 2005 (Class 455/570); filed 13 March 2001

This system is similar to a two-microphone, subtractive noise reducer, but with additional processing, in which spectral transforms are extracted from each microphone signal. The subtractive noise reduction then takes place with respect to each spectral component, rather than the signal as a whole, with each spectral component also being subjected to a specific delay. An inverse FFT then reconstructs the clean signal. The result is said to allow the reconstruction of individual audio sources within the pickup space.

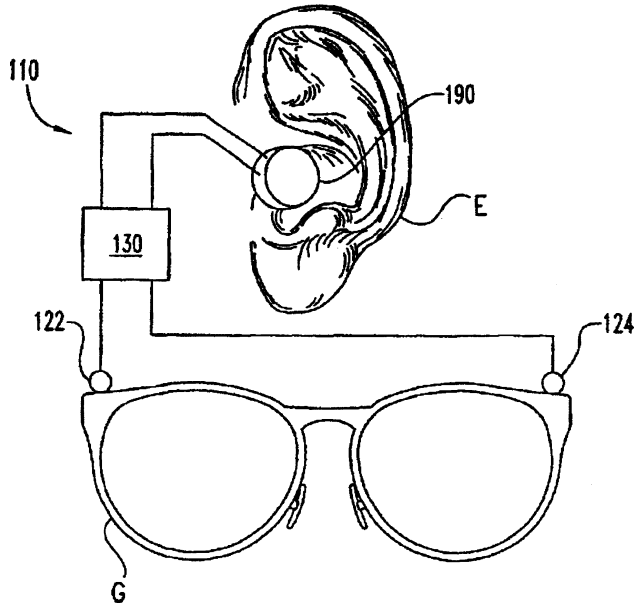

In a typical application, the spectral component delays would be adjusted so as to isolate a specific desired input signal, but other arrangements are possible.—DLR

7,065,220

43.38.Hz MICROPHONE ARRAY HAVING A SECOND ORDER DIRECTIONAL PATTERN

Daniel Max Warren and Stephen C. Thompson, assignors to Knowles Electronics, Incorporated
20 June 2006 (Class 381/92); filed 28 September 2001

This clear and cogent patent describes ways of using first-order elements at low frequencies with second-order elements at high frequencies to

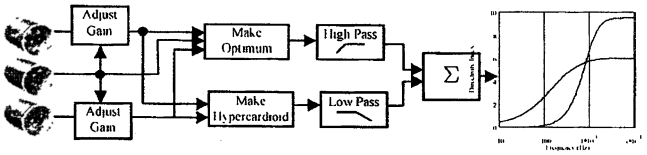

achieve uniform output, along with increased directivity index and improved noise floor. The patent should be read by all microphone designers—if for nothing more than as a part of one's on-going technical education.—JME

7,068,796

43.38.Hz ULTRA-DIRECTIONAL MICROPHONES

James A. Moorer, San Rafael, California
27 June 2006 (Class 381/92); filed 31 July 2001

According to the abstract, "The present invention provides a highly directional audio response that is flat over five octaves or more by the use of multiple collinear arrays followed by signal processing. Each of the collinear arrays has a common center, but a different spacing so that it can be used for a different frequency range. The responses of the microphones for each

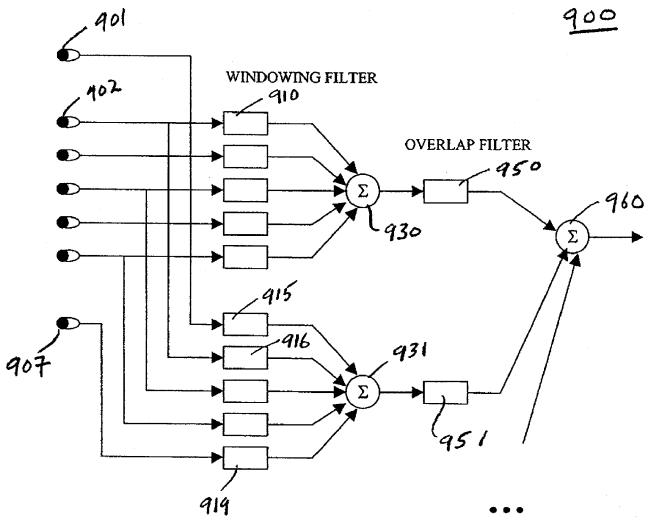

spacing are combined and filtered for a given array spacing so that it can be used for a different frequency range." The patent is a model of clarity and should be read by anyone involved in microphone arrays.—JME

7,068,800

43.38.Hz SPEAKER APPARATUS

Naoshi Matsuo, assignor to Fujitsu Limited
27 June 2006 (Class 381/152); filed in Japan 9 September 1998

At least one earlier patent has addressed the possibility of simulating a loudspeaker array by using multiple transducers **20** to drive a single flat diaphragm **10**. Such an approach offers practical advantages but it would seem difficult to localize the effects of individual drivers. A key feature of

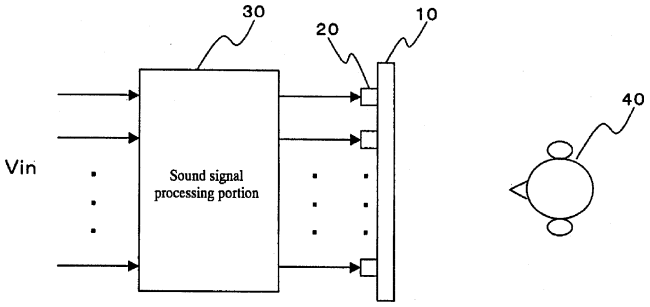

this patent is the introduction of interference signals. When isolation between two or more areas is required, an interfering signal is calculated and fed to transducers located between the target areas.—GLA

7,068,801

43.38.Hz MICROPHONE ARRAY DIFFRACTING STRUCTURE

Michael R. Stinson and James G. Ryan, assignors to National Research Council of Canada
27 June 2006 (Class 381/160); filed 17 December 1999

This may be described as a patent in principle, inasmuch as no specific embodiment is presented. A wide family of three-dimensional constructions is presented which can all represent a pattern or cluster of individual cells that lead from the outer surface to an internally placed microphone(s). The

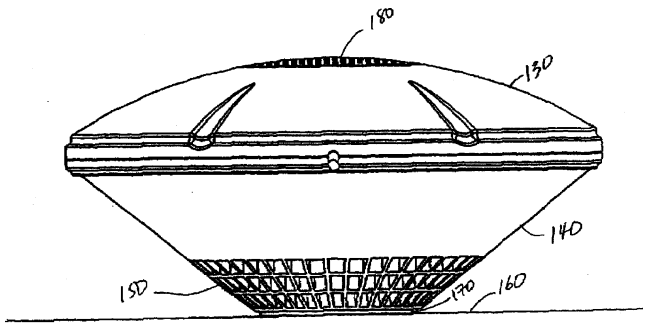

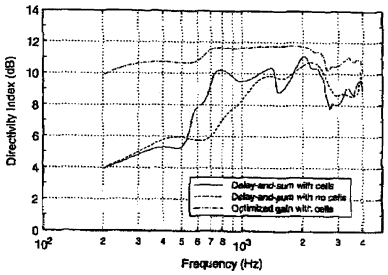

microphone's three-dimensional polar response is thus influenced by the imposed cell cluster. Like the once-popular multicellular horn of yore, the actual polar patterns are very wavelength dependent. I would not be surprised to see the National Research Council of Canada come up with a real-world problem that this patent can successfully address.—JME

7,027,605

43.38.Ja MID-RANGE LOUDSPEAKER

Bernard M. Werner, assignor to Harman International Industries, Incorporated
11 April 2006 (Class 381/99); filed 12 May 2003

For a long time, cinema loudspeaker systems were two-way affairs. The 1970s saw the development of three-way systems. The mouths of the horns for both were, of necessity, large in order to control the directivity down to the lower-frequency limit (or there about) of the horn passband.

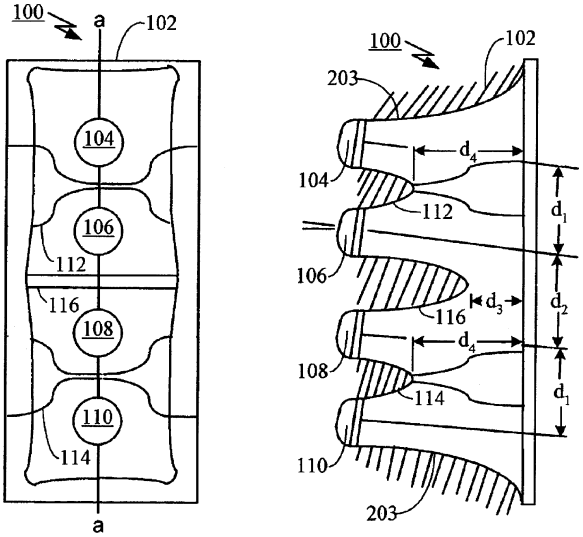

Large meant that they were deep. Deep meant there needed to be a large void behind the screen. Large voids meant that there was wasted space (which, for a first run multiplex, could be a fair amount). This patent describes a waveguide that is shallow, uses four mid-range cone-type trans-

ducers, and has a filtering network that has more than one output. Basically, all drivers are active at the low end of the passband and only one appears to be active at the high end of the passband. A midrange loudspeaker module based on the patent is used in the JBL Screen Array cinema systems.—NAS

7,031,488

43.38.Ja SUPER TWEETER

Tzu-Chung Chang, assignor to Sun Technique Electric Company, Limited
18 April 2006 (Class 381/398); filed 23 April 2004

A "super tweeter," with performance from below 1000 Hz to about 100 kHz (a range of almost 8 octaves) is described using a "magnetic base, a voice coil, a frame annularly mounted to the magnetic base, a central supporting member mounted on a central portion of the magnetic base, a diaphragm, an annular inner supporting member, and an annular outer

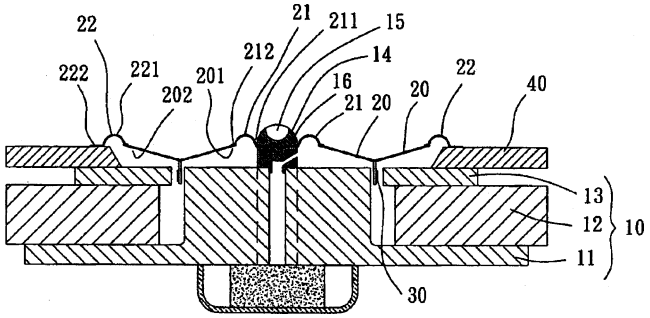

supporting member." Although two patents (one from 1972 and one from 2001) are listed as references, this reviewer had the strange sense of, as Yogi Berra once said, "deja vu all over again." One can see using this tweeter for acoustic modeling studies and the investigation of certain aspects of the bioacoustics of some animal species.—NAS

7,039,211

43.38.Ja HORN-LOADED COMPRESSION DRIVER SYSTEM

Bernard M. Werner, assignor to Harman International Industries, Incorporated
2 May 2006 (Class 381/343); filed 28 March 2003

A phase plug is described for use with an electrodynamic transducer

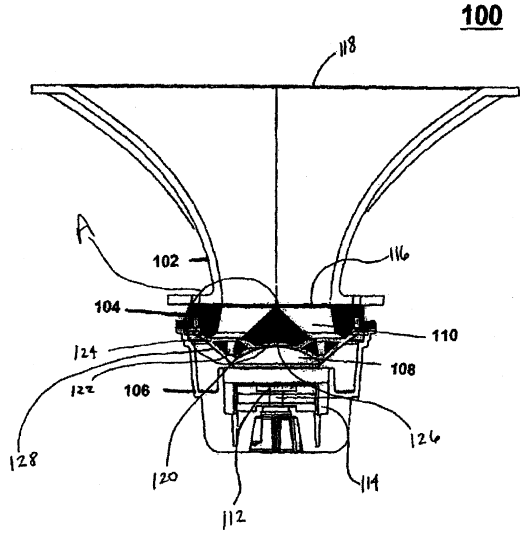

and a horn. Harvey Fletcher, Fancher Murray, and others would be interested to see the claims.—NAS

7,054,459

43.38.Ja SURROUNDING STRUCTURE OF A LOUDSPEAKER

Mitsukazu Kuze *et al.*, assignors to Matsushita Electric Industrial Company, Limited
30 May 2006 (Class 381/398); filed in Japan 17 May 2002

At least one earlier patent describes a half-roll loudspeaker surround **22** that is semi-elliptical in shape. In this case, however, the molded

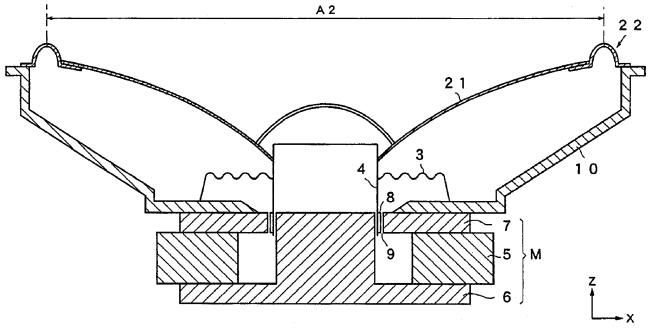

surround also includes radial or diagonal grooves to relieve hoop stresses.—GLA

7,062,051

43.38.Ja ACOUSTIC DEVICE

Neil Harris and Henry Azima, assignors to New Transducers Limited
13 June 2006 (Class 381/152); filed in the United Kingdom 17 August 2001

The inventors have obtained numerous earlier patents describing how the response of a distributed mode (flat panel) loudspeaker can be controlled by the design of the panel itself, the location of the driving transducer, additional damping, and mass loading at specific points. This patent goes into the theory of mass loading in considerable detail and shows how this technique can be used, for example, to compensate for less than optimum panel dimensions.—GLA

7,068,806

43.38.Ja CONDENSED SPEAKER SYSTEM

Casey P. Walsh, Arroyo Grande, California
27 June 2006 (Class 381/351); filed 14 January 2003

It is theoretically possible to build a closed-box loudspeaker system like an aneroid barometer; the pesky air spring is eliminated by eliminating the air. Not surprisingly, the idea has already been patented, but the variant shown here includes a separate high-pressure chamber **24** to provide the required restoring force. Skeptics may point out that whether the restoring

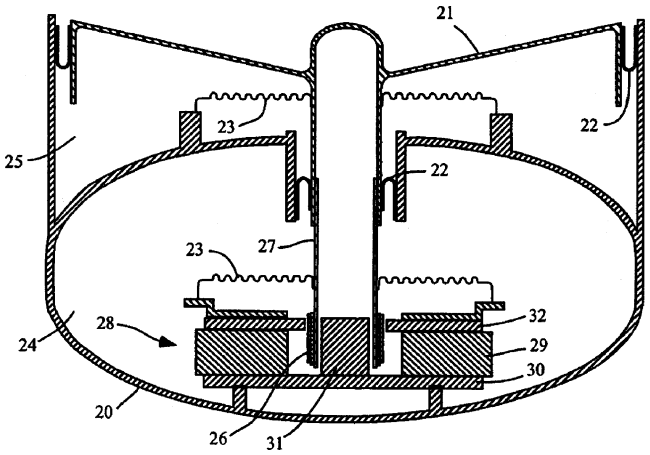

spring is mechanical or pneumatic, the cone itself must withstand a surface pressure of several hundred pounds without deformation, which may explain the apparent lack of a working model.—GLA

7,061,327

43.38.Lc SINGLE SUPPLY HEADPHONE DRIVER/ CHARGE PUMP COMBINATION

Tony Doy, assignor to Maxim Integrated Products, Incorporated
13 June 2006 (Class 330/297); filed 24 January 2002

Small, portable audio devices are usually powered by a single low-voltage battery. As a result, large output coupling capacitors are required to block direct current from headphones. To eliminate the capacitors, yet keep

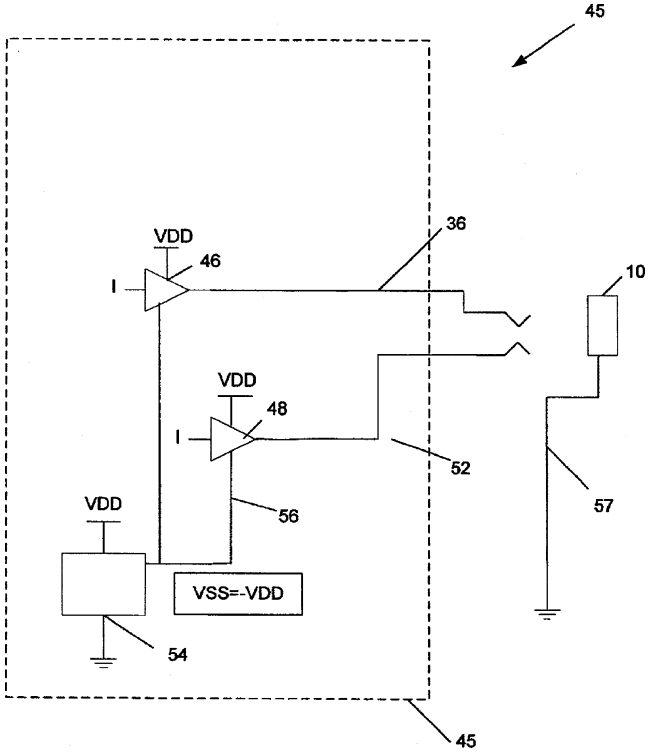

the common output terminal at ground potential, a negative supply is needed. This patent suggests that an onboard charge pump circuit will do the job. Reading the patent text is like swimming in molasses, but the illustrations and claims can be understood without too much difficulty.—GLA

7,061,328

43.38.Lc INTEGRATED DIRECT DRIVE INDUCTOR MEANS ENABLED HEADPHONE AMPLIFIER

Tony Doy, assignor to Maxim Integrated Products, Incorporated
13 June 2006 (Class 330/297); filed 17 November 2005

This is a companion patent to United States Patent 7,061,327, reviewed above. It contains additional details about suitable charge pump circuitry.—GLA

7,068,095

43.38.Lc AMPLIFIER CIRCUIT

Derek Bernardon, assignor to Infineon Technologies AG
27 June 2006 (Class 330/9); filed in Germany 10 July 2002

A class D audio power amplifier is described which includes a signal generator controlled by a phase-locked loop to provide a stable sawtooth waveform for pulse-width modulation. In this design, however, the ampli-

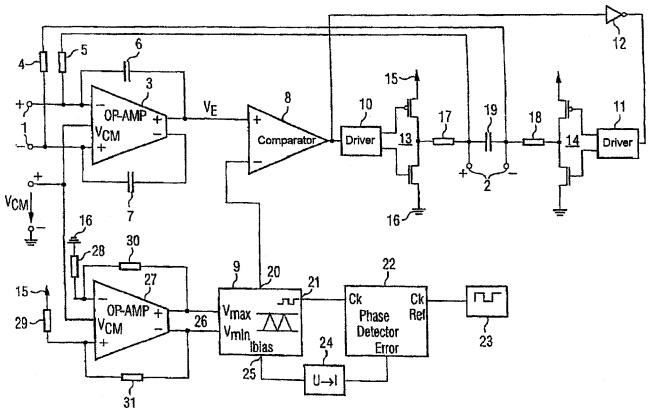

tude of the sawtooth signal tracks the power supply voltage, thus substantially improving power supply rejection without lowering overall efficiency.—GLA

7,067,956

43.38.Rh SURFACE ACOUSTIC WAVE DEVICE, FILTER DEVICE AND METHOD OF PRODUCING THE SURFACE ACOUSTIC WAVE DEVICE

Masahiko Imai *et al.*, assignors to Fujitsu Media Devices Limited
27 June 2006 (Class 310/313 D); filed in Japan 4 September 2002

A method is claimed for temperature stabilization of the frequency passband limits of a surface acoustic wave (SAW) device **10**, where low-expansion substrate **1** has cavities **1a** and **2a** etched away under the

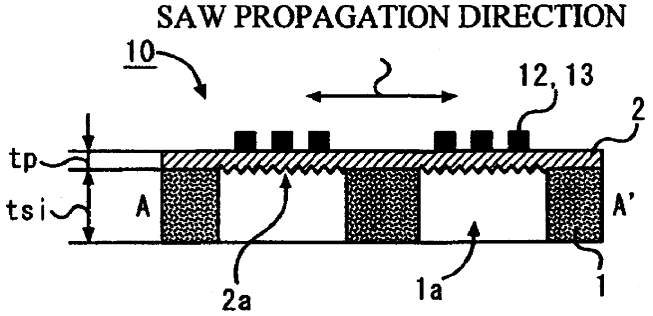

piezoelectric layer **2** carrying SAW electrodes **12**, **13**, etc. Top and bottom sealing covers (not shown) are bonded to the piezoelectric and substrate layers, and the SAW volume is filled with inert gas.—AJC

7,062,109

43.38.Rh ACOUSTO-OPTIC DEVICE

Yukito Tsunoda and Hiroshi Miyata, assignors to Fujitsu Limited
13 June 2006 (Class 385/7); filed in Japan 25 June 2004

To reduce the energy required to operate an acousto-optical tunable filter using a surface acoustic wave (SAW) device—used, for instance, as an optical add-drop multiplexer (OADM)—the SAW-piezoelectric substrate **11**

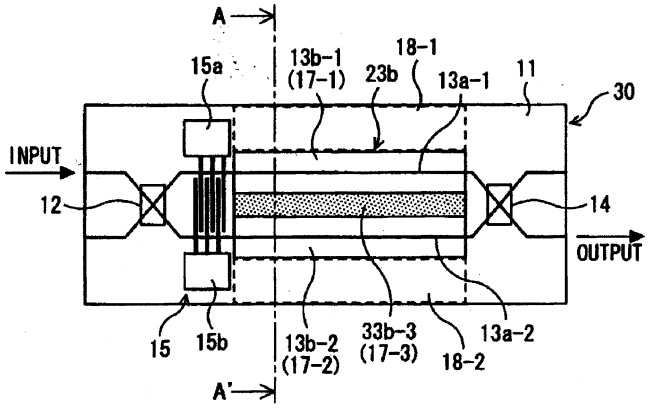

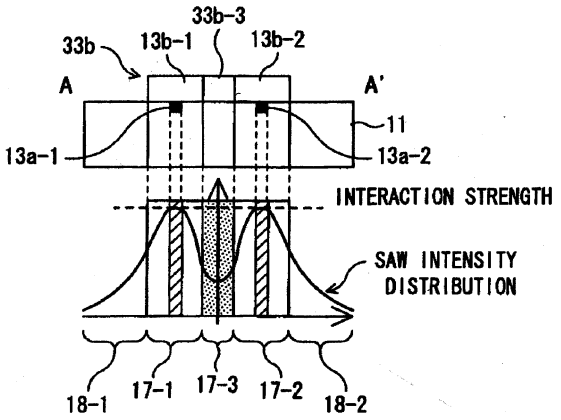

is divided into two propagation paths **13b-1** and **13b-2** with isolation **33b-3** so as to concentrate the SAW energy propagation to be mainly adjacent to, and in contact with, the optical wave guides **13a-1** and **13a-2**.—AJC

7,064,471

43.38.Rh SURFACE ACOUSTIC WAVE DEVICE, METHOD OF MANUFACTURING THE DEVICE, AND ELECTRONIC COMPONENT USING THE DEVICE AND METHOD

Kazuo Ikeda *et al.*, assignors to Matsushita Electric Industrial Company, Limited
20 June 2006 (Class 310/313 D); filed in Japan 21 June 2001

Upon being subjected to violent heat or strain during the manufacture of SAW device **1**, e.g., batch dicing (cutting), strong electrostatic charges and potentials are generated on piezoelectric substrate **1** that can damage the SAW fingers **2-3**. By adding metal strips **18** and **20** connected to electrodes **6a** and **6b**, such spurious charges are drawn off or stabilized so that the

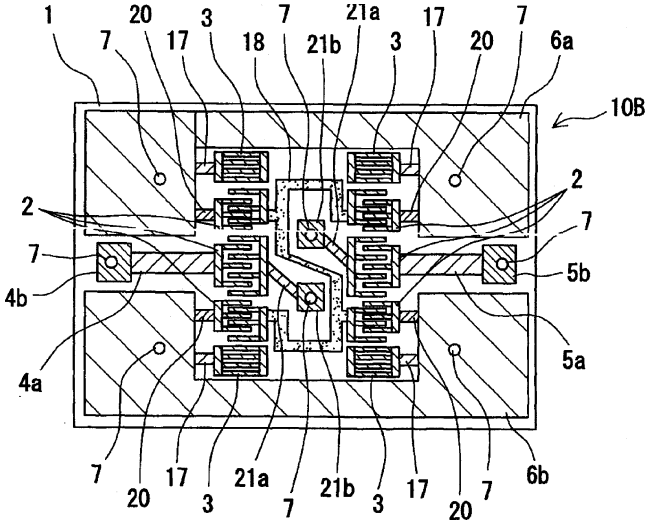

damaging high potentials will not occur. The claims include symmetry and area of the added conductors and a sealed volume including the SAW surfaces.—AJC

7,058,366

43.38.Si WIRELESS TERMINAL PROVIDING SOUND PRESSURE LEVEL DISSIPATION THROUGH CHANNELED PORTING OF SOUND

Gregory S. Patterson, assignor to Sony Ericsson Mobile Communications AB
6 June 2006 (Class 455/90.3); filed 9 December 2002

The tiny loudspeaker in a cell phone may be called upon to produce audible sound in free air (ring tones and hands-free communication) yet serve as a headphone receiver when the case is held tightly to the user's ear.

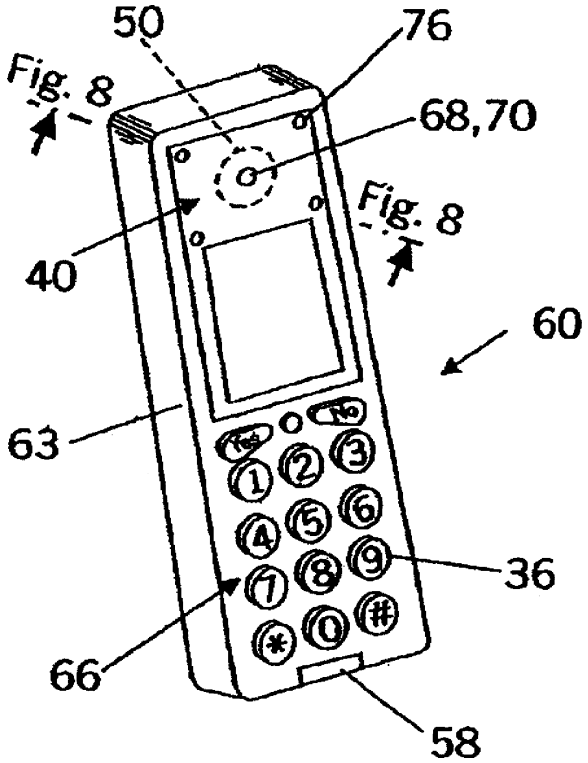

An output suitable for the former usage may produce hearing damage when used for the latter. Worse yet, the partially deaf user may then decide to sue the manufacturer. One known alternative is to conduct only a portion of the

speaker's output through the central earphone hole **68**, **70**, and divert the remainder to branch ports on the side or rear of the case. The novel feature of this patent is to place relief ports **76** on the front of the case, but outside the area needed for an ear seal.—GLA

7,062,023

43.38.Si TELEPHONE TERMINAL WITH ALARM

Takeshi Izaki, assignor to Brother Kogyo Kabushiki Kaisha
13 June 2006 (Class 379/110.01); filed in Japan 30 September 2003

Some wireless telephones can be programmed to generate an alarm signal at a predetermined time. If the alarm signal emanates from the handset, and if the handset happens to be near the user's ear at that time, hearing damage can result. This patent describes a set of preloaded programming instructions designed to forestall such an unhappy event.—GLA

7,064,655

43.38.Si VARIABLE-ECCENTRICITY TACTILE GENERATOR

Matthew J. Murray *et al.*, assignors to Sony Ericsson Mobile Communications AB
20 June 2006 (Class 340/407.1); filed 19 April 2004

An electric motor **12** driving an off-center mass **16** forms a common type of vibrator, one that can be used in a cellular telephone as a silent ring signal. If the distance between the mass and the axis of rotation is varied,

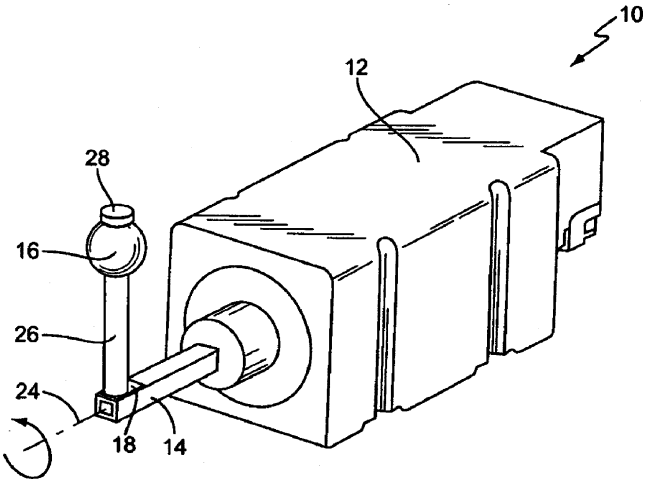

then the amount of vibration varies accordingly, allowing control over the intensity of the silent signal. As a bonus, such variable eccentricity can be used to minimize the electrical current drawn during startup.—GLA

7,065,219

43.38.Si ACOUSTIC APPARATUS AND HEADPHONE

Kensaku Abe *et al.*, assignors to Sony Corporation
20 June 2006 (Class 381/74); filed in Japan 13 August 1998

Most noise-cancelling headphones are self-contained and can be plugged into any portable audio device. This patent suggests that certain benefits can be obtained by moving the associated circuitry to a separate

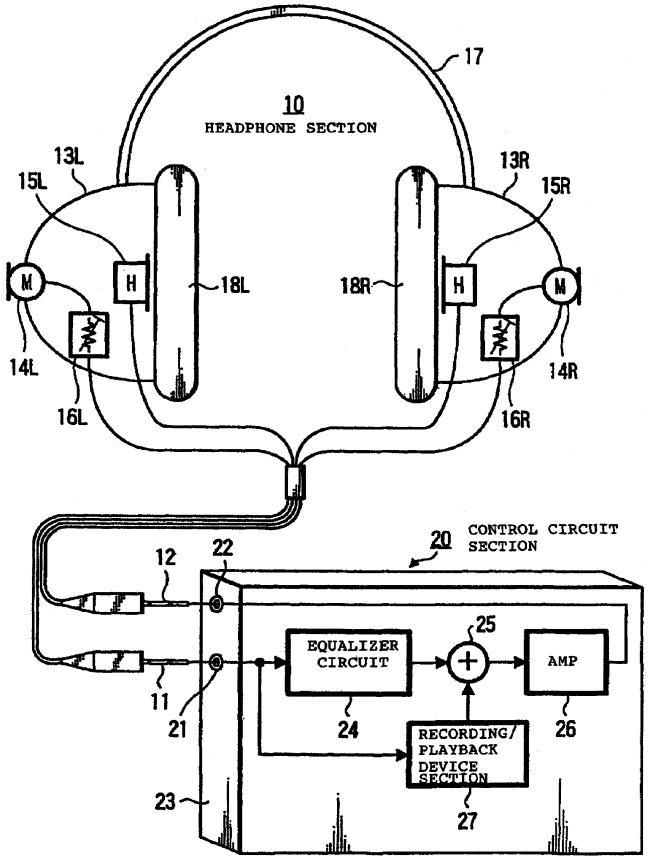

control box, or to the audio playback device. Among those benefits is the possibility of using the headset for binaural recording as well as playback.—GLA

7,068,782

43.38.Si COMMUNICATIONS DEVICES WITH RECEIVER EARPIECES AND METHODS THEREFOR

Karl F. Mueller and David M. Yeager, assignors to Motorola, Incorporated
27 June 2006 (Class 379/433.02); filed 27 June 2002

In a typical cellular phone, sound from a tiny loudspeaker **210** is conducted to the user's ear through a single hole or a small cluster of holes

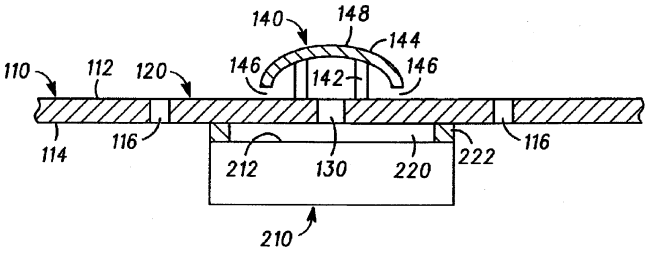

130. If the earpiece is not positioned correctly, it is easy for sound to be blocked by soft tissue. In this variant, the sound emerges around the circumference of rounded button **140** to avoid the problem.—GLA

7,031,476

43.38.Tj METHOD AND APPARATUS FOR INTELLIGENT SPEAKER

Roy Kenneth Chrisop *et al.*, assignors to Sharp Laboratories of America, Incorporated
18 April 2006 (Class 381/77); filed 13 June 2000

Communications module **28** is powered by a high-frequency carrier signal that is impressed on the audio signal feeding speaker system **12** via connections **20**. The communications module, powered via filter **24** and rectifier **26**, sends coded information back to an amplifier using amplitude modulation, phase shift keying, or two-tone modulation of the carrier signal.

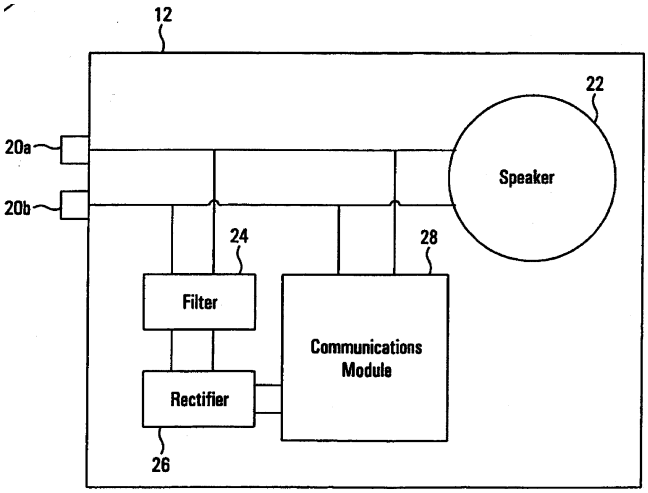

The amplifier would need a module capable of decoding the information signal. A signal may also be sent from the amplifier to the speaker system. What effect the carrier and coded information signals may have on the performance of the audio signal and the resulting acoustic signal emanating from the speaker is not discussed, but one hopes that all this extra information is well outside the audio passband.—NAS

7,054,816

43.38.Tj AUDIO SIGNAL PROCESSING DEVICE

Ronaldus Maria Aarts *et al.*, assignors to Koninklijke Philips Electronics N.V.
30 May 2006 (Class 704/270); filed in the European Patent Office 24 December 1999

How refreshing it is to come across a patent that has a single figure and less than two pages of text! The patent describes a device that has uses in the area of teleconferencing, where both speech and music signals may be combined in a single audio channel. The intent is to separate music and speech so that speech can be assigned as needed and the music can be ''widened'' in pseudostereo fashion. According to the patent, the speech content can be substantially isolated via principal component analysis (PCA) techniques. The resulting speech and music components can then be redirected as desired.—JME

7,035,422

43.38.Vk WEARABLE SPEAKER GARMENTS

David Wiener, assignor to Soundtube Entertainment, Incorporated
25 April 2006 (Class 381/388); filed 12 April 2000

Many people like to listen to music while engaging in a variety of other activities. While headphones and earphones are presently used for this, ''earphones and headphones are often uncomfortable to wear for long periods of time, are not an attractive fashion statement, can be dislodged as a result of physical activity, and can attenuate environmental sounds compromising the wearer's safety.'' The invention offers a solution to these problems.—NAS

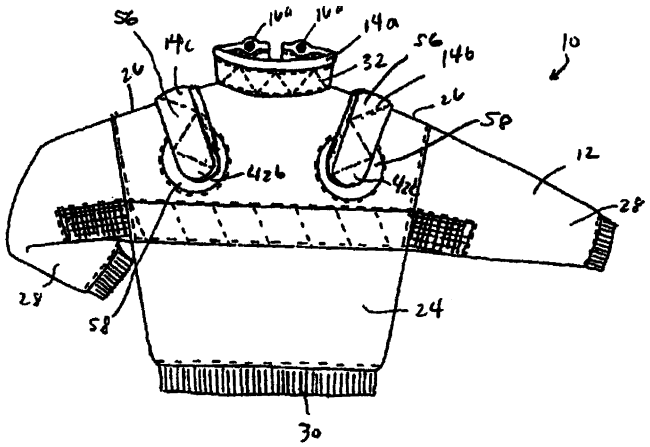

7,065,217

43.38.Vk APPARATUS AND METHOD FOR MULTICHANNEL SOUND REPRODUCTION SYSTEM

Stefan Gierl *et al.*, assignors to Harman/Becker Automotive Systems (Becker division) GmbH
20 June 2006 (Class 381/10); filed in Germany 5 March 2001

This patent describes, in principle only, a method of encoding FM radio signals so that, at the receiving end, they engage various methods of converting the basic stereo or mono program into a semblance of multichannel. ''For example, stereo, pseudostereo or mono reproduction are provided in the multichannel sound reproduction system in response to the stereo component within the output signal.''—JME

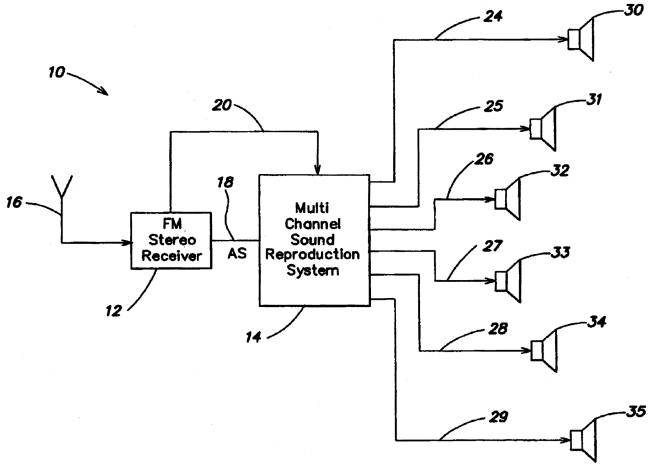

7,066,898

43.40.Ng VIBRATOR, VIBRATION UNIT, AND VIBRATOR CONTROL METHOD

Kentaro Mori *et al.*, assignors to OMRON Corporation
27 June 2006 (Class 601/99); filed in Japan 30 June 2000

We have here a fairly complex massaging device that is essentially a vibrator having massaging balls moving back and forth along guiding

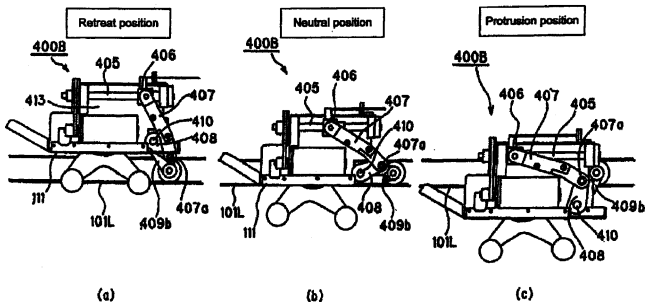

members over a treatment area. A means of adjustment is provided for altering the position and direction of the treatment unit.—DRR

7,032,708

43.40.Tm FLUSH MOUNTABLE VIBRATION REDUCING LOUDSPEAKER MOUNTING ASSEMBLY

Ian Popken *et al.*, assignors to Russound/FMP, Incorporated
25 April 2006 (Class 181/150); filed 27 August 2003

A damping gasket **14** is attached to baffle **12** by forcing forward lips **28a** through baffle openings **18b**. Baffle and gasket are attached to frame member **16** using quarter-turn fasteners, which do not require any tools to

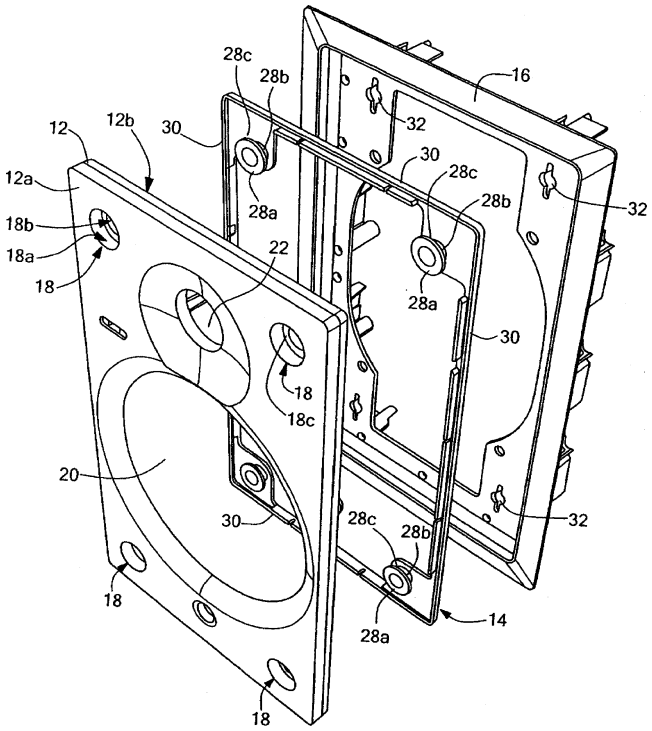

insert and turn. The baffle is thereby isolated from the frame member and supporting wall.—NAS

7,055,811

43.40.Tm VIBRATION ISOLATING DEVICE

Yoshio Ihara *et al.*, assignors to Toyo Tire and Rubber Company, Limited
6 June 2006 (Class 267/140.13); filed 3 May 2004

Isolator assembly **7** connects vehicle engine mount **4** (subject to engine vibration) with vehicle body **B** through bolt **41**, boss **2**, elastomer **3**, and shell **71-73**. This isolator includes a load bearing elastomer **3** to isolate the engine vibrations in **4** from vehicle body **B** during normal running, and a stiffer snubber elastomer **51-53**. During body acceleration forward via the carriage and drive wheels, engine inertia force rearward will deflect the soft

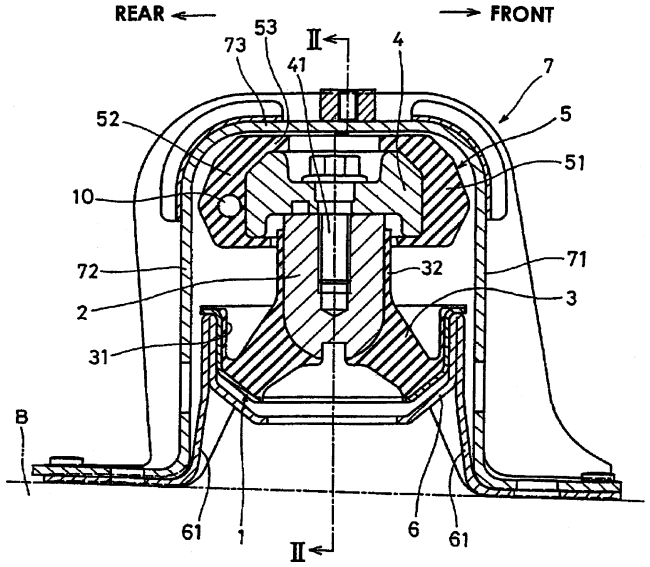

elastomer causing snubber **52** to contact assembly frame **71-73**. A more graduated such contact force is implemented by air cavity **10** (apparently the major claim) in the stiffer elastomer **52**, thus providing better vibration isolation at 40–170 Hz (2400–4200 RPM) during acceleration. Open and closed cavities **10** are claimed, with the rear cavity claimed especially.—AJC

7,059,353

43.40.Tm POWER STEERING NOISE AND VIBRATION ATTENUATOR

Brian Muscat and G. Michael Wooley, assignors to DaimlerChrysler Corporation
13 June 2006 (Class 138/26); filed 10 July 2003

Power steering pump noise and vibration traveling along hose **58** connected by fasteners **62** or **64** to a vehicle power steering actuator (not shown) is reduced by the inertia mass damping collar **10** fastened to the hose. Collar **10** is installed by compressing the hose to pass through slot **18**.

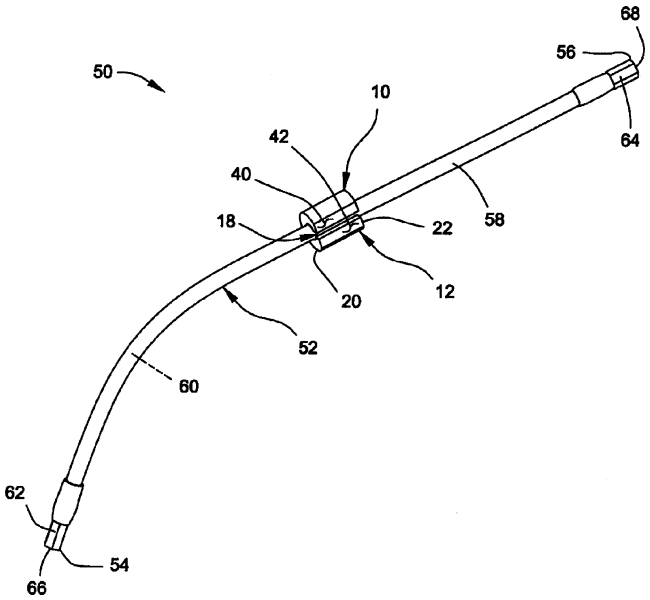

An alternative method for stiff hoses and pipes is to install collar **10** before fastener **62** or **64** is installed. The position of the collar along the hose is selected according to the type of hose, the length of hose, and the frequency

of the vibrations specific to each application. The claims include an inner bore of collar **10** that is slightly smaller than the outer diameter of hose **58** to effect friction to retain the position of the collar on the hose.—AJC

7,066,064

43.40.Tm METHOD AND APPARATUS FOR VIBRATION DAMPENING OF BARFEEDERS

Raymond O. Varady, Collinsville, Illinois
27 June 2006 (Class 82/127); filed 1 November 2002

The purpose of a barfeeder is to push a long bar into the workspace of a production lathe up to a specified length. A certain length of the bar then is supported within the headstock or spindle of the lathe, but the rest of the bar stock (which may be quite long) must be supported by the bar-feeding device. This length of the stock tends to whip and vibrate as the turning speed is increased, adversely affecting the machining quality. An array of hydrodynamic bearings, spaced along the length of the barfeeder, is provided to limit this vibration. In order to increase the range of bar stock diameters and turning speeds for which these bearings provide effective vibration control, these bearings are made to work with an electro-rheological or a magneto-rheological fluid whose effective viscosity can be controlled by appropriate application of electrical of magnetic fields.—EEU

7,063,192

43.40.Vn ACTIVE VIBRATION SUPPRESSION APPARATUS, CONTROL METHOD THEREFOR, AND EXPOSURE APPARATUS HAVING ACTIVE VIBRATION SUPPRESSION APPARATUS

Takehiko Mayama, assignor to Canon Kabushiki Kaisha
20 June 2006 (Class 188/378); filed in Japan 27 November 2000

An active vibration-suppression method for precision 3D semiconductor photo-optical etching apparatuses is claimed. Pedestal **1** carries a vibration sensor **3** that feeds controller **50** to stabilize the photo-etching target holder **45**. Stabilizing computer **4** provides approximate compensation according to the natural modes of base **1** and isolating support **2**. The control algorithm **4-5** seems to be the familiar ''three-function controller'' (proportional/integral/differential) method that includes feed forward, velocity damping and acceleration sensing, plus nonlinear compensation, including a gain reduction as a mechanical limit is approached. The claims include the three-function, phase lead/lag, and monotonic nonlinear compensation methods, and composites thereof.—AJC

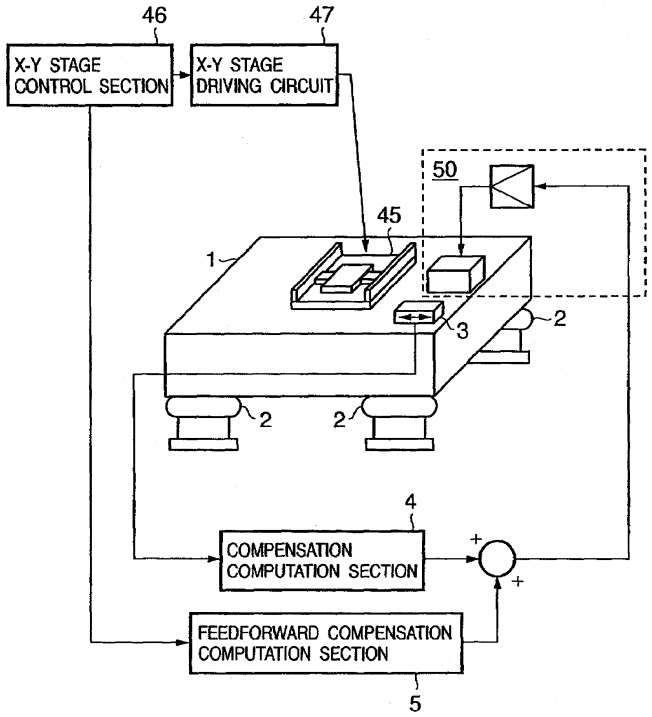

7,066,454

43.40.Vn ACTIVE TYPE VIBRATION ISOLATING SUPPORT SYSTEM

Hirozumi Kon *et al.*, assignors to Keihin Corporation
27 June 2006 (Class 267/140.14); filed in Japan 26 March 2003

A support for a vibration isolator is claimed where vibrations from engine **E** are isolated from body frame **F** by elastomer **14**, fluidized chambers **24** and **25** separated by plunger **19**, and elastomer diaphragm **18**. A spring under plunger **20** supports the engine weight. Actuator **31** is not engaged during idle shaking; passive damping is afforded by small orifices (not shown) between fluid volumes **24** and **25**. For higher engine speeds, where the orifice flow impedance is high, the coil magnetic actuator **31** is energized through connector **40** by the electronic control unit **U**, driving plunger **20** to prevent engine vibrations from entering the vehicle body. The claims include the electromagnetic actuator, the liquid chambers, and the support spring.—AJC

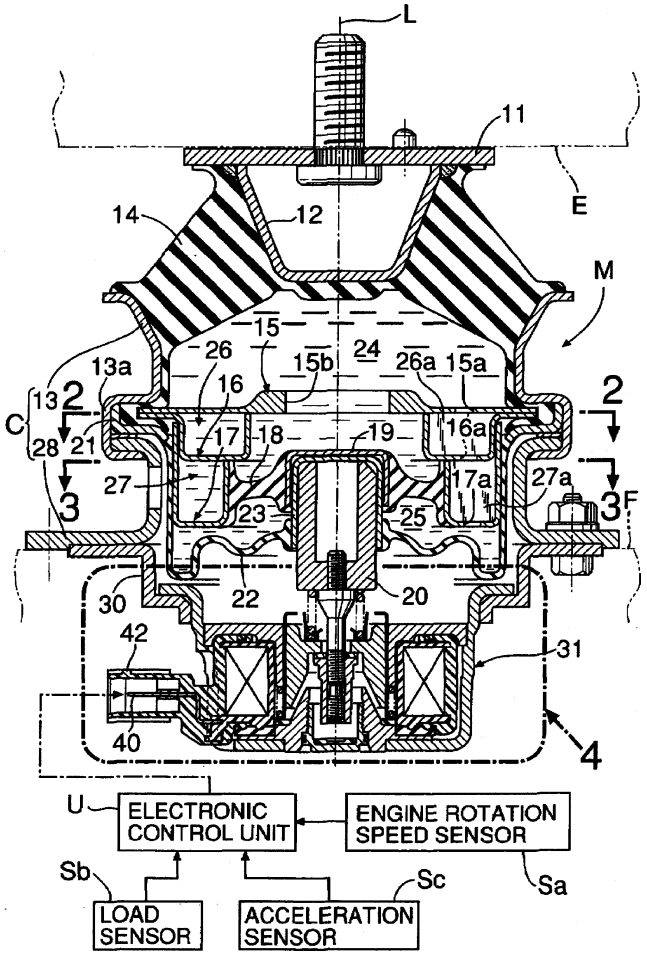

7,043,867

43.40.Yq FISH-BITE INDICATOR

Clifford Royston Fox, assignor to Fox Design International Limited
16 May 2006 (Class 43/17); filed in the United Kingdom 6 December 1994

A fish-bite indicator incorporates a vibration sensor (a piezoelectric bimorph) in contact with the fishing line that detects vibrations as a result of a fish bite, but which also allows playout or retrieval of the line. The signals generated by the vibrations are used to trigger a buzzer to alert the fisherman. The volume and tone of the buzzer, as well as the sensitivity of the device, are adjustable. The device, including associated circuitry and battery power supply, is contained within a plastic injection-molded housing.—WT

7,054,596

43.40.Yq WIRELESS VIBRATION DIAGNOSTIC INSTRUMENT

Robert T. Arntz, assignor to DaimlerChrysler Corporation
30 May 2006 (Class 455/66.1); filed 21 December 2001

This self-contained tool for helping to locate and diagnose automotive chassis sounds in essence consists of a clamp to which there is attached a vibration sensor and a compact electronics package. The electronic circuit processes the vibration signals and transmits them to a suitable receiver, such as a technician's earphones or a FM radio. The primary advantage of this device over earlier ones is that it does away with the inconvenient wire connections that earlier systems require.—EEU

7,062,049

43.50.Lj ACTIVE NOISE CONTROL SYSTEM

Toshio Inoue *et al.*, assignors to Honda Giken Kogyo Kabushiki Kaisha
13 June 2006 (Class 381/71.4); filed in Japan 9 March 1999

Low-frequency noise in the passenger compartment **24** of a wide range of vehicles is highly correlated with suspension and vehicle-body vibrations resulting in a longitudinal standing wave around 40 Hz and one around 80 Hz. Active noise control (ANC) is implemented using feed-forward signals from sensor microphones **40** under the driver seat, **40A**, **41**, **42A** under the roof, and **42** in the truck space. These sensor signals are combined in a

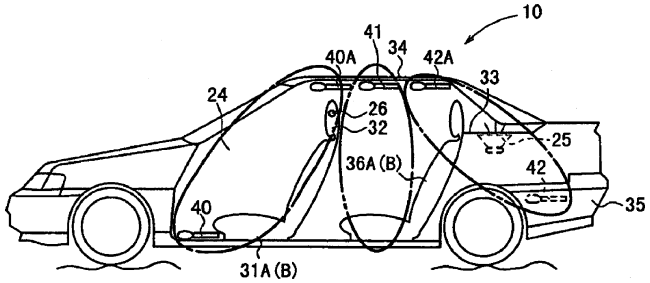

controller containing multiple adaptive filters. A single speaker **25** emits the canceling sound based on the error signal from head-position microphone **26**. The claims include such ANC for vehicles with a fixed roof in the frequency range of 20–120 Hz, a narrower range of 40–80 Hz, and a control box with a microphone placed where the antinode sound pressure is high.—AJC

7,063,184

43.55.Ev SOUND REDUCING PANEL

Lahnie Johnson, Tampa, Florida
20 June 2006 (Class 181/290); filed 11 June 2003

This patent describes a sound absorbing panel suitable for outdoor use. The panel comprises a water-resistant element with a porous covering sheet with a curable polymeric material forming an internal frame.—CJR

7,068,794

43.55.Ti SMART PANEL FOR DECREASING NOISE IN WIDE BAND FREQUENCY

Jae Hwan Kim, assignor to INHA Industry Partnership Institute
27 June 2006 (Class 381/71.7); filed in the Republic of Korea 15 March 2000

The patent asserts that the panel has improved transmission-loss performance due to resonating piezoelectric members that are attached to the

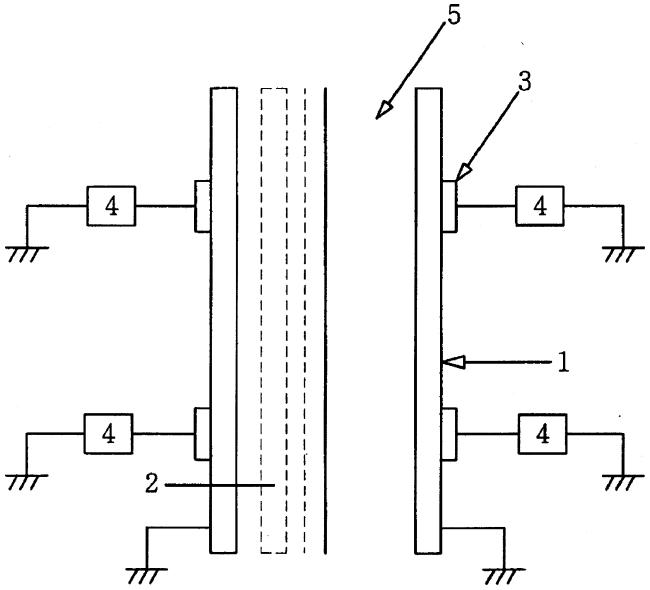

board structure of the panel. The piezoelectric units adjust the impedance value of the board at its resonant frequency.—CJR

7,062,056

43.58.Kr DIRECTIONAL HEARING AID TESTER

Jacobus Jonkman, assignor to Etymonic Design Incorporated
13 June 2006 (Class 381/312); filed 10 September 2003

For a more realistic estimate of the directionality provided by a directional microphone system in a hearing aid that performs level-dependent

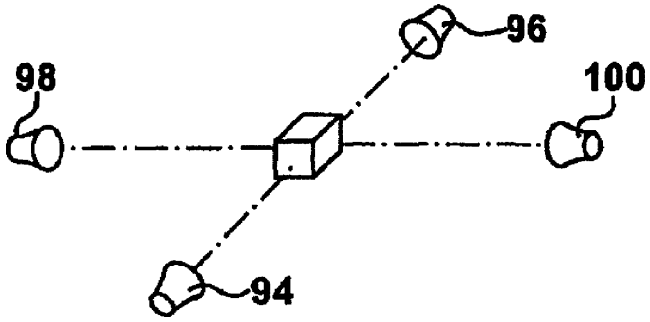

gain and frequency shaping, simultaneous broadband excitation signals are used from two or more loudspeakers placed in an acoustic enclosure at

certain positions relative to the hearing aid. If the excitation signals for the loudspeakers have components that are orthogonal to each other, the response of the hearing aid to each excitation signal can be extracted.—DAP

7,058,190

43.60.Bf ACOUSTIC SIGNAL ENHANCEMENT SYSTEM

Pierre Zakarauskas *et al.*, assignors to Harman Becker Automotive Systems-Wavemakers, Incorporated
6 June 2006 (Class 381/122); filed 22 May 2000

The patented system would monitor the signal spectrum from a microphone in an effort to measure the signal quality, including whether the microphone is switched on and what the signal/noise ratio is. If the signal is deemed to fall below a certain quality threshold, the user is warned in some way to take action (e.g., to talk into the microphone, to turn the microphone on, etc.). The title of this patent is somewhat misleading, since, in fact, the onus is on the user to enhance his/her own signal (e.g., speech), after receiving a warning from the system.—SAF

7,054,448

43.60.Dh AUTOMATIC SOUND FIELD CORRECTING DEVICE

Hajime Yoshino and Kazuya Tsukada, assignors to Pioneer Corporation
30 May 2006 (Class 381/59); filed in Japan 27 April 2001

In this age of very complex home entertainment systems, the user can certainly appreciate just about any degree of setup assistance—as long as that assistance is automatic, foolproof, and turns itself off when it has finished its job. Described here is an elaborate means for calibrating such a system. A microphone is placed at the intended listening position. One at a time, the system goes through each channel, setting levels, equalization, and relative delays. The unaided user could easily spend hours doing this job.—JME

7,054,451

43.60.Dh SOUND REINFORCEMENT SYSTEM HAVING AN ECHO SUPPRESSOR AND LOUDSPEAKER BEAMFORMER

Cornelis Pieter Janse and Harm Jan Willem Belt, assignors to Koninklijke Philips Electronics N.V.
30 May 2006 (Class 381/83); filed in the European Patent Office 20 July 2001

This short patent describes several improvements in the operation of just about any kind of speech reinforcement system. The advantage of echo

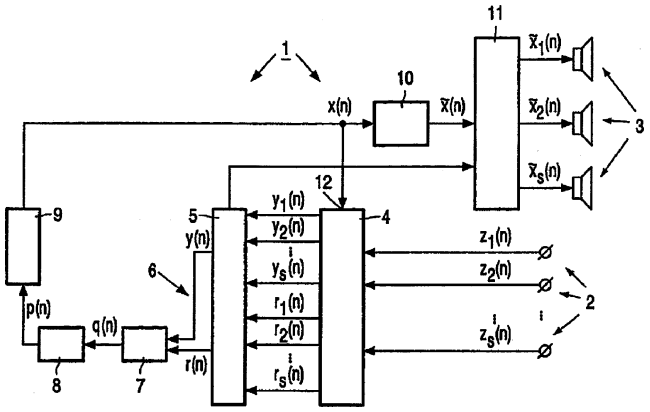

suppression is clear to everyone in that it improves signal intelligibility. Likewise, the creating of a loudspeaker null zone in the neighborhood of an active microphone diminishes the likelihood of system "howling" or feedback.—JME

7,058,187

43.60.Dh AUTOMATIC SOUND FIELD CORRECTING SYSTEM AND A SOUND FIELD CORRECTING METHOD

Yoshiki Ohta, assignor to Pioneer Corporation
6 June 2006 (Class 381/98); filed in Japan 14 February 2000

This patent describes the use of both pink noise and impulse signals for automated setup of surround-sound loudspeaker arrays, primarily in the

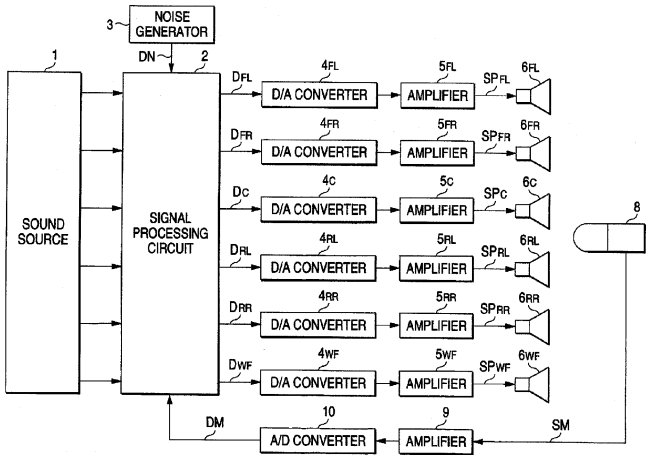

home environment. As with the other systems that have been described in these pages, channel level, polarity, equalization, and delay functions are all adjusted.—JME

7,068,799

43.60.Dh SOUND FIELD CORRECTING METHOD IN AUDIO SYSTEM

Yoshiki Ohta, assignor to Pioneer Corporation
27 June 2006 (Class 381/98); filed in Japan 14 February 2000

Here is yet another entry in the automated surround-sound adjustment sweepstakes. It appears, at least in this case, that the differentiae among patents of this special class are not so much what actually happens when one presses the START button—but rather how the controlling software is written!—JME

7,058,184

43.60.Fg ACOUSTIC MEASUREMENT METHOD AND APPARATUS

Robert Hickling, Huntington Woods, Michigan
6 June 2006 (Class 381/92); filed 25 March 2003

The patent describes an intensity probe consisting of an array of small omnidirectional microphones positioned at the vertices of a regular tetrahedron. The component signals can be linearly combined to produce the three

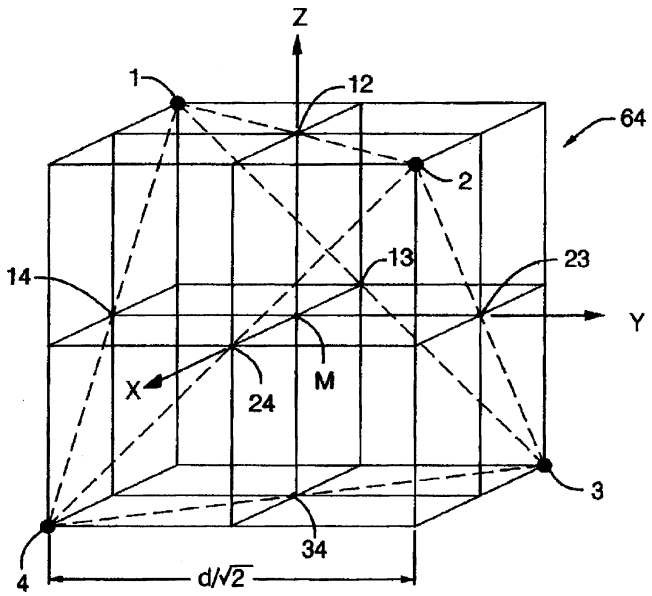

orthogonal acoustical velocity vectors, and directly summed to produce the pressure component. The outputs are converted to digital form for further processing.—JME

7,064,132

43.64.Gz COMPOSITION AND METHOD FOR TREATMENT OF OTITIS EXTERNAL

Alan J. Mautone, assignor to Scientific Development and Research, Incorporated
20 June 2006 (Class 514/310); filed 11 December 2001

The patent describes a compound, process, and method for increasing auditory canal patency while simultaneously preventing the occurrence of otitis externa. An aerosolized mixture of liquid crystals consisting of a mixture of one or more lipid surfactants, one or more spreading agents, and one or more fluorocarbon propellants is administrated directly to the external auditory canal. Spreading agents are selected from a group consisting of sterols, lipids, fatty acids, cholesteryl esters, phospholipids, carbohydrates, nucleic acids, and proteins, in powder form. Upon administration, the propellant(s) evaporate from the mixture and the lipid crystals are deposited upon an air/liquid interface resident upon the epithelial tissue lining the external auditory canal. When the lipid crystals make contact with the epithelial lining, an amorphous spread film is formed, thereby forming a barrier against exogenous water, while simultaneously decreasing the surface tension of the lining, so as to increase the patency thereof. In a second embodiment, a therapeutically active agent effective in the treatment of otitis externa is added to the mixture of lipid crystals.—DRR

7,054,457

43.66.Ts HEARING INSTRUMENT RECEIVER MOUNTING ARRANGEMENT FOR A HEARING INSTRUMENT HOUSING

Oleg Saltykov, assignor to Siemens Hearing Instruments, Incorporated
30 May 2006 (Class 381/328); filed 13 August 2002

Components for a hearing aid are inserted in a keyed tubing that slides into a channel in the hearing aid housing and conducts sound to the ear canal of the wearer. The tubing assembly has a peripheral ring that hits a wall

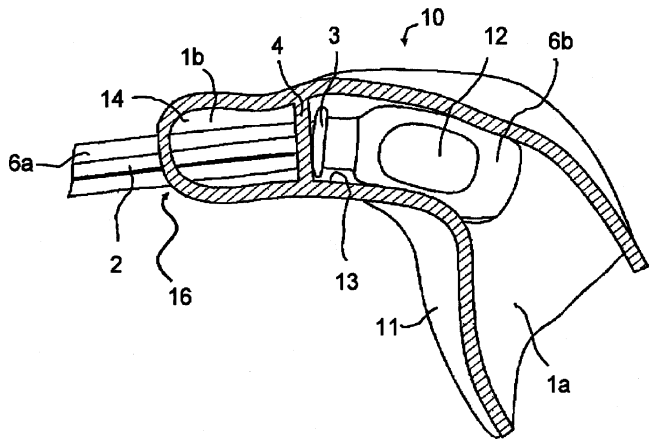

while going through the hearing aid housing, thus stopping it during insertion. The tubing assembly is said to help prevent the occurrence of acoustic feedback oscillation during hearing aid use.—DAP

7,054,957

43.66.Ts SYSTEM FOR PROGRAMMING HEARING AIDS

Scott T. Armitage, assignor to Micro Ear Technology, Incorporated
30 May 2006 (Class 710/8); filed 28 February 2001

Described is a system to program hearing aids from a host computer that incorporates a PCMCIA, USB, RS-232, SCSI, Firewire, or wireless interface. The program for programming hearing aids may be stored as a dynamic link library (DLL) file in a memory within the programming device. Electrical isolation is provided between an interface in the programming device and the computer.—DAP

7,058,182

43.66.Ts APPARATUS AND METHODS FOR HEARING AID PERFORMANCE MEASUREMENT, FITTING, AND INITIALIZATION

James Mitchell Kates, assignor to GN ReSound A/S
6 June 2006 (Class 381/60); filed 17 May 2002

A hearing aid performs self-tests by generating signals and recording responses of specific components, or of the entire hearing aid, particularly with respect to feedback canceller operation and maximum stable gain

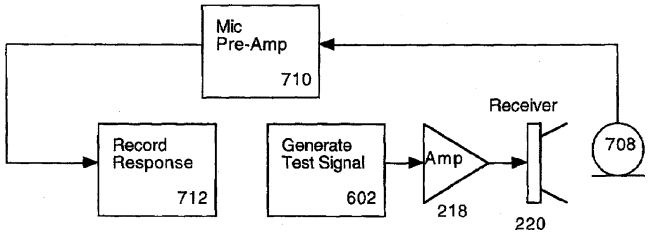

versus prescribed gain. Under control of a test program loaded into the hearing aid, the tests may be run during manufacturing or *in situ* during an evaluation of the hearing aid fitting.—DAP

7,058,191

43.66.Ts HEARING AID WITH A RADIO FREQUENCY RECEIVER

Lars Ballisager and Bjarne Klemmensen, assignors to Oticon A/S
6 June 2006 (Class 381/312); filed in Denmark 4 October 2000

Upon activation of a switch, a radio-frequency receiver for a hearing aid with a single-crystal oscillator scans for the presence of a carrier

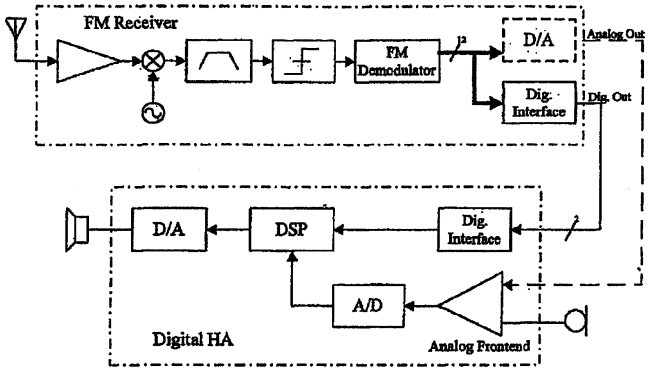

frequency. If the carrier level exceeds a predetermined threshold, the receiver automatically synthesizes the appropriate receiving frequency without having to physically interchange crystals.—DAP

7,068,802

43.66.Ts METHOD FOR THE OPERATION OF A DIGITAL, PROGRAMMABLE HEARING AID AS WELL AS A DIGITALLY PROGRAMMABLE HEARING AID

Hervé Schulz and Tom Weidner, assignors to Siemens Audiologische Technik GmbH
27 June 2006 (Class 381/318); filed in Germany 2 July 2001

To prevent acoustic feedback oscillation, maximum amplification values are programmed and stored for individual channels in a multichannel hearing aid. These values are determined either by the hearing aid wearer and/or are generated by the hearing aid signal processor. The maximum gain values may be derived from the initial amplification and the wearer's short-term volume-control changes and used in conjunction with other signal processing algorithms, including automatic gain control, situational analyses, and noise reduction.—DAP

7,065,224

43.66.Ts MICROPHONE FOR A HEARING AID OR LISTENING DEVICE WITH IMPROVED INTERNAL DAMPING AND FOREIGN MATERIAL PROTECTION

Elrick Lennaert Cornelius *et al.*, assignors to Sonionmicrotronic Nederland B.V.
20 June 2006 (Class 381/369); filed 28 September 2001

The peak in the frequency response of a hearing aid microphone is attenuated without the use of screens that can become clogged with debris. An edge of a damping frame is placed against the microphone diaphragm in

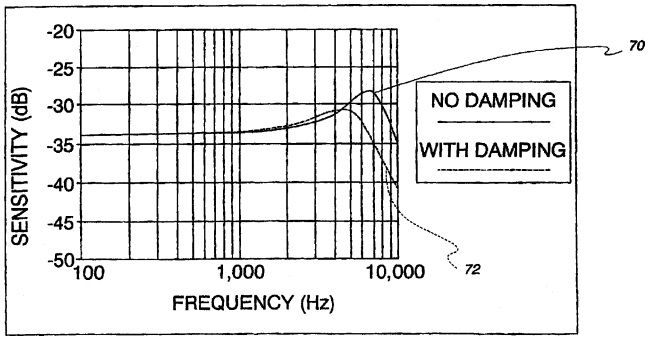

the rear volume of the microphone. The backplate is positioned at a known distance close to the damping frame, which has a slit that defines an aperture through which air escapes into the rear volume.—DAP

7,062,441

43.71.Gv AUTOMATED LANGUAGE ASSESSMENT USING SPEECH RECOGNITION MODELING

Brent Townshend, assignor to Ordinate Corporation
13 June 2006 (Class 704/270); filed 13 May 1999

This is a system for automated measurement of a person's ability to understand and speak a language. The system provides a set of tasks that requires the subject to provide one or more spoken responses. A speech-recognition evaluation of the spoken responses may be an estimate of the linguistic content or other characteristics of the response or of elements of

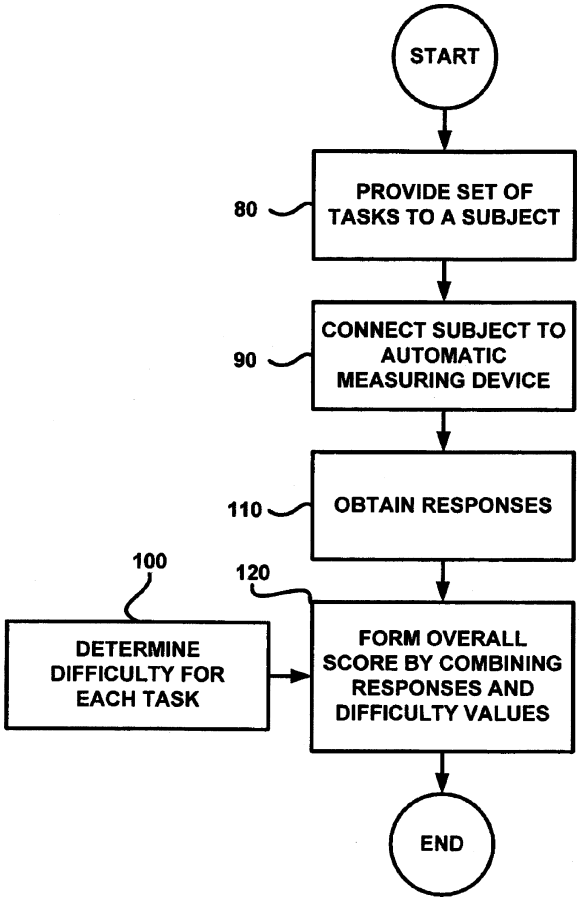

the response. A scoring device converts the response evaluation into one or more item scores. A computation device generates a subject score on the basis of a scoring computation model that depends upon the expected item-dependent operating characteristics of the speech recognition system.—DRR

7,054,808

43.72.Dv NOISE SUPPRESSING APPARATUS AND NOISE SUPPRESSING METHOD

Koji Yoshida, assignor to Matsushita Electric Industrial Company, Limited
30 May 2006 (Class 704/226); filed in Japan 31 August 2000

This patent introduces a system for noise suppression for speech recognition tools. The system estimates the signal-to-noise ratio (SNR) by using the speech-signal power from a speech interval and the noise power from a nonspeech interval. The noise-suppression-level coefficients are adjusted based on the value of SNR. Spectral subtraction is then performed based on the speech/nonspeech determination and the values of the noise-suppression-level coefficients.—AAD

7,065,486

43.72.Dv LINEAR PREDICTION BASED NOISE SUPPRESSION

Jes Thyssen, assignor to Mindspeed Technologies, Incorporated
20 June 2006 (Class 704/227); filed 11 April 2002

Linear filters derived from linear predictive coding analysis are used as models of a speech signal and the noise accompanying it. This requires detection of signal frames containing noise only, so that a noise model can be effectively constructed and kept updated. If the noise, excluding the speech, has been modeled correctly, simple methods for suppressing the noise in a LPC resynthesized signal present themselves.—SAF

7,068,798

43.72.Dv METHOD AND SYSTEM FOR SUPPRESSING ECHOES AND NOISES IN ENVIRONMENTS UNDER VARIABLE ACOUSTIC AND HIGHLY FEEDBACK CONDITIONS

Fernando Gallego Hugas *et al.*, assignors to Lear Corporation
27 June 2006 (Class 381/93); filed 11 December 2003

The general objective here is quite intriguing, as a unified in-vehicle system is envisioned, which would allow any automobile occupant to communicate peacefully with the others through a setup of microphones and speakers even during noisy road conditions, and which would also allow any occupant to make a mobile phone call under the same kinds of noisy conditions. The patented techniques focus on ways of deriving noise-canceling filters and echo-canceling filters adaptively during the noisy drive, although standard techniques are uniformly employed for the filters themselves (e.g., Wiener filters) and the adaptive schemes. Previous patents are also referred to for complete procedures.—SAF

7,065,485

43.72.Ew ENHANCING SPEECH INTELLIGIBILITY USING VARIABLE-RATE TIME-SCALE MODIFICATION

Nicola R. Chong-White and Richard Vandervoort Cox, assignors to AT&T Corporation
20 June 2006 (Class 704/208); filed 9 January 2002

A scheme is described that would modify a speech signal by endowing it with more of the typical characteristics of ''clear speech'' that have been documented in the literature. Such modifications would include strengthening of consonantal cues by lengthening formant transitions using a new variation of the overlap-add technique (called waveform similarity overlap-add), and adaptive spectral enhancement to make the spectral peaks (formants) more distinct. These suggestions are of great interest, but the patent goes vague in approaching the key hurdle of correctly identifying the consonants and vowels of each syllable in the performance of the desired syllable segmentation.—SAF

7,062,050

43.72.Gy PREPROCESSING METHOD FOR NONLINEAR ACOUSTIC SYSTEM

Prank Joseph Pompei, Wayland, Massachusetts
13 June 2006 (Class 381/77); filed 27 February 2001

Nonlinear distortion of an audio signal transmitted by an ultrasonic carrier is reduced by processing audio signals applying an inversion to the

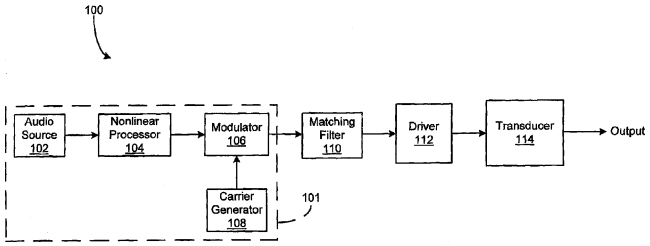

modeled representation of signal demodulation through a propagation medium. The method is said to be effective for ultrasonic output levels ranging from 20 Pa to about 1000 Pa.—DAP

7,069,210

43.72.Gy METHOD OF AND SYSTEM FOR CODING AND DECODING SOUND SIGNALS

Rakesh Taori, assignor to Koninklijke Philips Electronics N.V.
27 June 2006 (Class 704/220); filed in the European Patent Office 1 December 1999

Sound-signal segments are encoded independently into numbered frames that are subdivided into several streams. Each frame is decoded for a sound segment independently from other frames, so if a frame is omitted in a stream, the sound signal can still be reconstructed by interpolation from the available surrounding frames.—DAP

7,069,212

43.72.Gy AUDIO DECODING APPARATUS AND METHOD FOR BAND EXPANSION WITH ALIASING ADJUSTMENT

Naoya Tanaka *et al.*, assignors to Matsushita Elecric Industrial Company, Limited
27 June 2006 (Class 704/225); filed in Japan 19 September 2002

Spectral band replication (SBR) compensates for high-frequency band components that are lost in an audio coding process by adding pseudo-high-frequency components to the low-frequency components. The number of

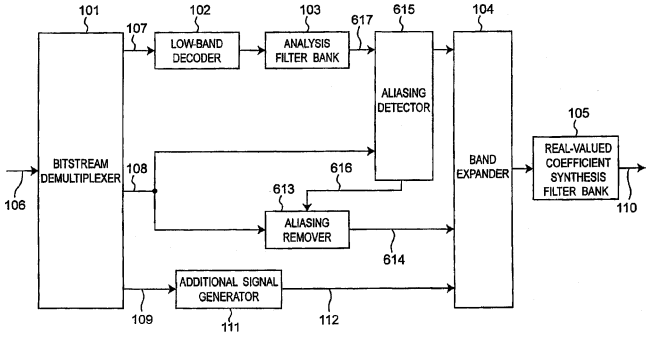

operations required in decoding for SBR band expansion is reduced by using real-valued rather than complex-valued coefficient filter banks, which may produce aliasing of image components that can reduce sound quality. Alias-

ing is detected and removed by adjusting the gains of adjacent subband signals.—DAP

6,975,989

43.72.Ja TEXT TO SPEECH SYNTHESIZER WITH FACIAL CHARACTER READING ASSIGNMENT UNIT

Hiroshi Sasaki, assignor to Oki Electric Industry Company, Limited
13 December 2005 (Class 704/260); filed in Japan 13 March 2001

This patent describes a method of including emotional or expressive elements into synthesized speech. The included elements are created from a specified inventory of character combinations, somewhat akin to the current practice in e-mails and text messaging, known as emoticons. The patent

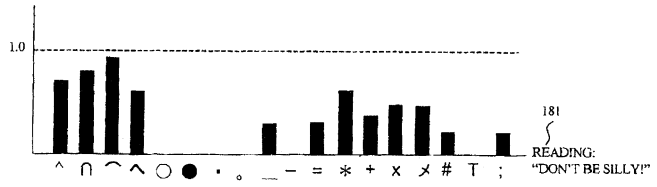

EXAMPLE OF SELECTED TYPICAL VECTORS

includes numerous tables of these allowed character sets, referred to here as ''facial characters,'' rules for their use, and their meanings. Apparently, numerical values from the character tables are used in some way to construct corresponding prosodic patterns for use by the speech synthesizer.—DLR

6,978,239

43.72.Ja METHOD AND APPARATUS FOR SPEECH SYNTHESIS WITHOUT PROSODY MODIFICATION

Min Chu and Hu Peng, assignors to Microsoft Corporation
20 December 2005 (Class 704/258); filed 7 May 2001

The intent of this concatenative speech synthesizer is to be able to produce realistic-sounding phonetic and prosodic structures without doing any modification of the speech segments from which the result is constructed. Needless to say, the system requires a vast assortment of stored speech segments to accomplish this goal. Content-based search methods are described by which suitable speech segments are located for use by the synthesizer.—DLR

7,069,216

43.72.Ja CORPUS-BASED PROSODY TRANSLATION SYSTEM

Jan DeMoortel *et al.*, assignors to Nuance Communications, Incorporated
27 June 2006 (Class 704/260); filed 1 October 2001

Transcribed spoken-language corpora exist that have been annotated for linguistic prosody. There has not been, however, a single standardized way of annotating a textual corpus, or a text-to-speech system output, for prosodic information. This patent describes a machine learning (instance-based supervised) technique that could learn the principles of translating between two different prosodic annotation schemes, and then put these into practice on annotated text to change its prosodic annotations to the format desired by the user. Such a method requires, for training, a large database of natural speech with prosodic descriptions at various degrees of coarseness from the syllable sequence on up to the sentence pitch track.—SAF

6,975,994

43.72.Ne DEVICE FOR PROVIDING SPEECH DRIVEN CONTROL OF A MEDIA PRESENTATION

Sarah Leslie Black and Michael L. Weiner, assignors to Technology Innovations, LLC
13 December 2005 (Class 704/275); filed 12 September 2001

A system is described for the editing and presentation of media events, such as a slide presentation, all of which would be under the control of a speech-recognition computer system. Many examples are given of the speech commands that would be used to control video and/or audio sequences, inclusion of Internet segments in the form of web pages, timing of these, video display details, audio volume, and so forth. There is some discussion of the types of computer controls available, slide advances, etc., but almost nothing about the speech recognition methods or mechanisms.—DLR

6,978,237

43.72.Ne SPEECH RECOGNITION SUPPORT METHOD AND APPARATUS

Mitsuyoshi Tachimori and Hiroshi Kanazawa, assignors to Kabushiki Kaisha Toshiba
20 December 2005 (Class 704/238); filed in Japan 30 June 1999

A speech recognition engine is here being applied to the task of generating a map of the area of interest, possibly for the purpose of vehicle navigation. If a specific location is indicated by the recognized speech input, then the distance from the user's present location to the named location is

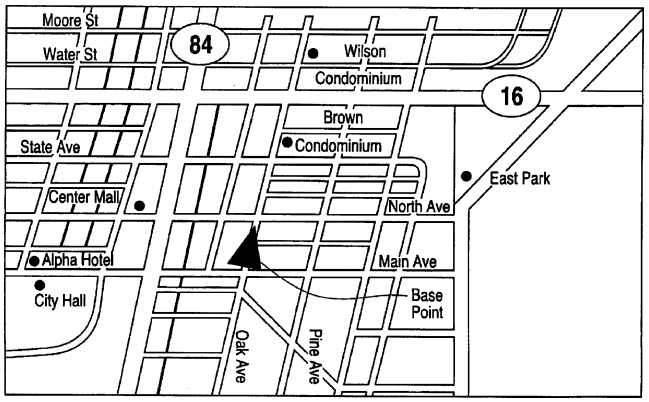

computed and announced. The application described here is a place locator to be used in a car or by a pedestrian trying to find his or her way around a city. In one embodiment, the recognizer would produce a list of *n*-best candidates, from which the user would select, perhaps by a second speech input utterance.—DLR

7,054,817

43.72.Ne USER INTERFACE FOR SPEECH MODEL GENERATION AND TESTING

Yuan Shao, assignor to Canon Europa N.V.
30 May 2006 (Class 704/270); filed 25 January 2002

As pointed out in the patent, speech models that lie within the core of a speech recognition engine must normally be created by highly skilled speech engineers in a specialized development environment. The ability to create or tweak speech models is not normally within the range of the clients of speech recognition software companies. The patent proposes to remedy this situation by presenting a user-friendly environment within which relatively novice users can create a speaker and word database and make use of it in a controlled fashion to develop speech models of the sort used in typical speech recognition engines.—SAF

7,058,580

43.72.Ne CLIENT-SERVER SPEECH PROCESSING SYSTEM, APPARATUS, METHOD, AND STORAGE MEDIUM

Teruhiko Ueyama *et al.*, assignors to Canon Kabushiki Kaisha
6 June 2006 (Class 704/270.1); filed in Japan 24 May 2000

To reduce the amount of data transfer between a client in a portable device and a server that performs speech recognition, compression-encoded

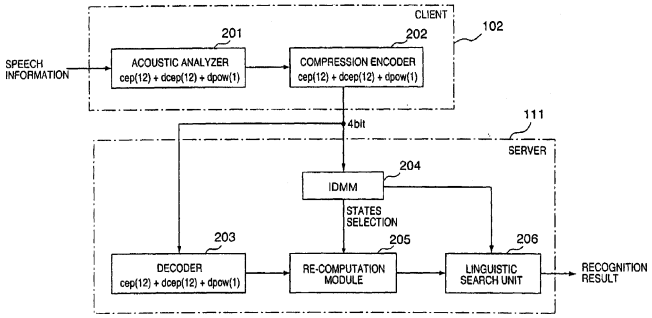

speech parameters rather than actual speech are transmitted to the server. Scalar quantization is used to reduce 25-dimensional speech parameters into four bits per dimension.—DAP

7,062,433

43.72.Ne METHOD OF SPEECH RECOGNITION WITH COMPENSATION FOR BOTH CHANNEL DISTORTION AND BACKGROUND NOISE

Yifan Gong, assignor to Texas Instruments Incorporated
13 June 2006 (Class 704/226); filed 18 January 2002

This very brief six-page patent is nonetheless crammed with details, presenting a specific method of compensation for convolutive (channel) and additive (background) distortions during the operation of an otherwise typical hidden Markov model speech recognition system trained on clean speech. The method involves modifying the mean vectors of the original model space in evidently novel ways.—SAF

7,062,436

43.72.Ne WORD-SPECIFIC ACOUSTIC MODELS IN A SPEECH RECOGNITION SYSTEM

Julian J. Odell and Shahid Durrani, assignors to Microsoft Corporation
13 June 2006 (Class 704/255); filed 11 February 2003

The number of acoustic models used by a recognizer is reduced by using word-specific models that model phones specific to candidate words. A subseries of the general phones representing each candidate word is modeled by at least one new phone dedicated to the candidate word or to a small group of similar words. Examples of the candidate words include letters, digits, dates, and commands.—DAP

7,065,487

43.72.Ne SPEECH RECOGNITION METHOD, PROGRAM AND APPARATUS USING MULTIPLE ACOUSTIC MODELS

Yasunaga Miyazawa, assignor to Seiko Epson Corporation
20 June 2006 (Class 704/233); filed in Japan 23 October 2000

This verbose patent doesn't present very much new material, but it is still hard to follow the logic. It presents a means of using one of a set of six acoustic models for each speech frame during a typical speech recognition process. Each of the six models has been created by first adding one of six predetermined noise patterns (which are not described), and then undergoing a noise elimination procedure, based upon the noise models. The best model of the lot is chosen to drive recognition at each frame. The idea seems to be that the real speech to be recognized is expected to have undergone a noise-suppression process.—SAF

7,062,297

43.72.Ne METHOD AND SYSTEM FOR ACCESSING A NETWORK USING VOICE RECOGNITION

Sten Minör *et al.*, assignors to Telefonaktiebolaget L M Ericsson (publ)
13 June 2006 (Class 455/563); filed in the United Kingdom 21 July 2000

Unique applications on a network are found via speech recognition using a location address consisting of several address components for each

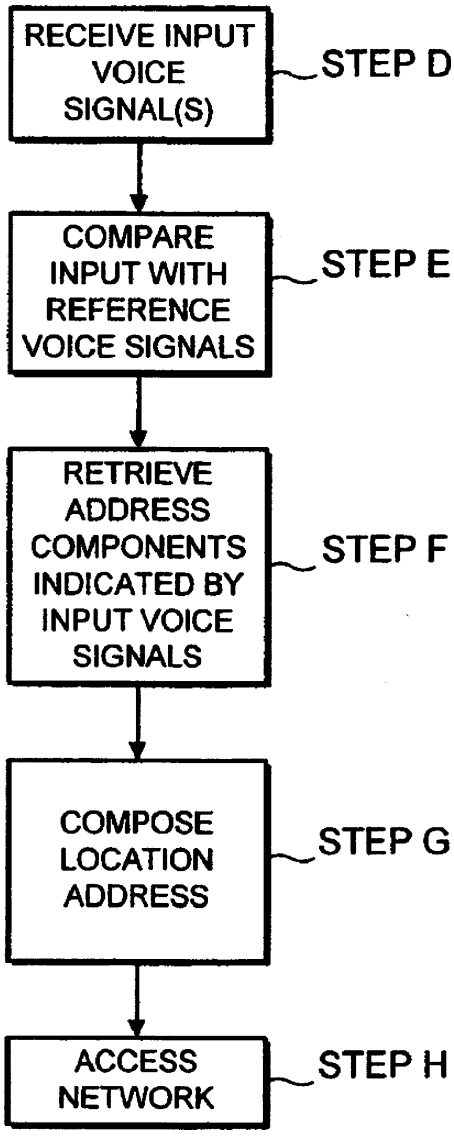

application on the network. Voice-reference signals that are associated with the address components are stored for later comparison to input voice signals.—DAP

7,065,488

43.72.Ne SPEECH RECOGNITION SYSTEM WITH AN ADAPTIVE ACOUSTIC MODEL

Kiyoshi Yajima and Soichi Toyama, assignors to Pioneer Corporation
20 June 2006 (Class 704/255); filed in Japan 29 September 2000

Another variation on the theme of speech recognition with speaker and noise adaptation, this patent suggests a particular scheme of comparison among several feature vectors, each created differently from the same utterance or utterance model. A ''standard'' vector, a noise-reduced vector, and a vector from the signal with the noise still intact are each generated for a received utterance, and are used in concert to derive a speaker-adapted acoustic model. Detailed procedures are provided, which all work with well-established acoustic vector forms such as cepstral coefficients, etc.—SAF

7,054,811

43.72.Pf METHOD AND SYSTEM FOR VERIFYING AND ENABLING USER ACCESS BASED ON VOICE PARAMETERS

Ziv Barzilay, assignor to Cellmax Systems Limited
30 May 2006 (Class 704/246); filed 6 October 2004

This patent makes grandiose promises of a method to provide ''absolute verification of an identity'' from among a known number of users, and to provide such verification by means of fancy and hitherto untapped features of speech, like the degree of chaos as measured by Lyapunov exponents. While we are sympathetic to the idea that tapping into such veins could one day provide individuating biometrics of speech, the assertion that ''the Lyapunov exponents characterize the voice registration sample uniquely'' is simply not credible without substantiation, especially given that the recent literature on chaotic time-series analysis is at odds with itself where the measurement and ultimate value of various chaos metrics are concerned.—SAF

7,059,168

43.80.Qf ULTRASOUND PHANTOM

Yasushi Hibi *et al.*, assignors to Olympus Corporation
13 June 2006 (Class 73/1.86); filed in Japan 1 October 2002

The patent pertains to an ultrasound phantom that emulates a human body with regard to ultrasonic waves. It is a training tool for medical students to learn the techniques of medical checkup of the body cavity with an ultrasonic probe and/or an ultrasonic endoscope. The device consists of a base member that is formed of a material that transmits ultrasound waves in order to simulate at least a part of the body, and includes a storage portion with a small width connected to another storage portion with a greater width, one or more organ models, which are stored in either or both of these storage portions, for imitating internal human organs. A jellylike member

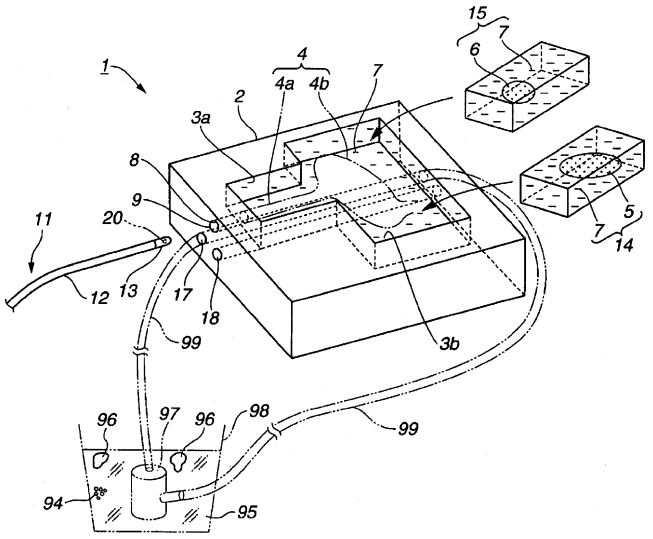

that transmits ultrasound waves fills in the spaces around these organ models.—DRR

7,063,668

43.80.Qf METHOD AND ARRANGEMENT FOR ACOUSTIC DETERMINATION OF MOISTURE CONTENT OF A GAS MIXTURE

Erik Cardelius *et al.*, assignors to Maquet Critical Care AB
20 June 2006 (Class 600/532); filed in Sweden 28 April 2003

The goal of the device is to provide a simpler method and arrangement for the acoustic determination of the moisture content of a gas mixture in a breathing aid that is used in medical critical care. The mechanical breathing aid has two inlets, an air source and an oxygen source. A mixing location controls the amounts of air and oxygen from these respective inlets. An

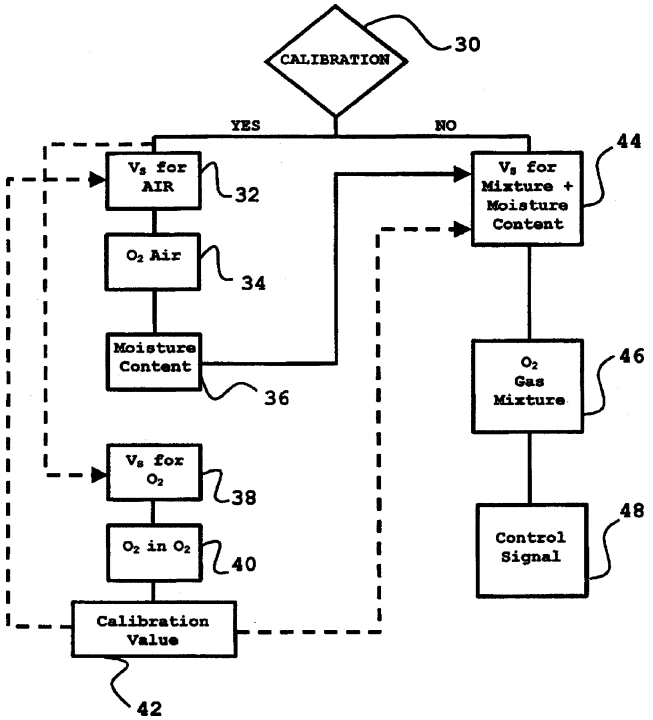

acoustic analyzer operates during the measurement procedure to yield a moisture content value for air from the air source to generate acoustic velocity-based information from acoustic energy interaction with the breathing gas, and to determine therefrom oxygen content. The analyzer also operates during a calibration procedure to generate acoustic velocity-based

information from the interaction of acoustic energy with the air from the air source and to determine therefrom oxygen content for the air, from which a moisture content value for the air is determined. The analyzer can be equipped to provide a warning signal if the calculated value for the moisture content indicates an abnormally low or abnormally high moisture content in the air being supplied to the mechanical breathing aid.—DRR

7,066,895

43.80.Sh ULTRASONIC RADIAL FOCUSED TRANSDUCER FOR PULMONARY VEIN ABLATION

Vaclav O. Podany, assignor to Ethicon, Incorporated
27 June 2006 (Class 601/3); filed 30 June 2003

This is an ultrasonic, radial, focused transducer designed to provide sufficiently high energy for pulmonary vein (PV) ablation. The method con

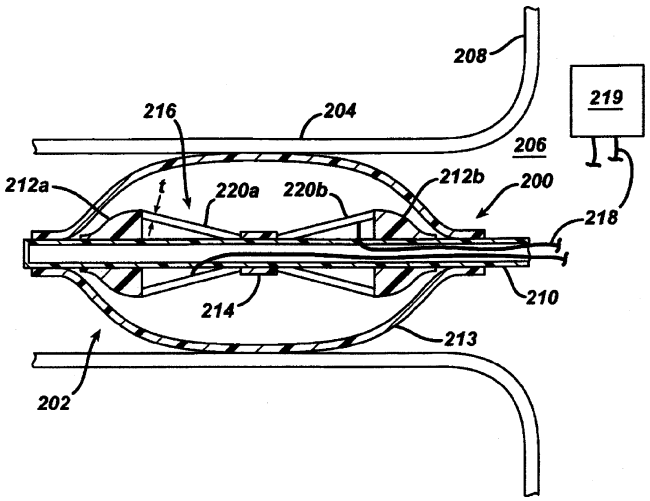

sists of generating ultrasonic energy from one or more ultrasonic transducers and focusing the ultrasonic energy in the radial direction either by shaping the transducers or by arranging one or more lenses proximate to the transducers.—DRR

7,063,666

43.80.Vj ULTRASOUND TRANSDUCERS FOR IMAGING AND THERAPY

Lee Weng *et al.*, assignors to Therus Corporation
20 June 2006 (Class 600/439); filed 17 February 2004

Element excitations in these transducers are electronically phased to position the focal point of an ultrasound beam. The beam can also be electronically steered. For imaging, the transducer bandwidth is increased by an electronic switch that places a resistance in parallel with the array elements. Additionally, the array can be flexed to vary its radius of curvature and, thus, control the position of the focus, or the elements may be individually pivoted to steer the ultrasonic beam produced by the array.—RCW

7,066,886

43.80.Vj ULTRASOUND IMAGING SYSTEM AND METHOD BASED ON SIMULTANEOUS MULTIPLE TRANSMIT-FOCUSING USING WEIGHTED ORTHOGONAL CHIRP SIGNALS

Tai Kyong Song and Young Kwan Jeong, assignors to Medison Company, Limited
27 June 2006 (Class 600/443); filed in the Republic of Korea 26 December 2001

Weighted orthogonal signals are transmitted by this system to produce a number of focuses. Echoes received from the focuses are processed using pulse compression to improve axial resolution without sacrificing frame rate.—RCW

7,068,827

43.80.Vj SYSTEM AND METHOD OF MEASURING FAT CONTENT IN TARGET ORGAN AND RECORDING MEDIUM OF RECORDING FAT CONTENT MEASURING PROGRAM

Ji Wook Jeong *et al.*, assignors to Electronics and Telecommunications Research Institute
27 June 2006 (Class 382/128); filed in the Republic of Korea 26 September 2002

Fat content is quantified by comparing amplitudes in selected regions of ultrasonic images.—RCW

7,066,889

43.80.Vj SCANNING PROBE

James D. Taylor, assignor to Envisioneering, LLC
27 June 2006 (Class 600/459); filed 22 March 2004

This ultrasound probe includes a pair of motors in one end of the probe housing. The shaft of one motor has a hollow interior and is used to produce a longitudinal movement of an ultrasound transducer. A shaft that extends

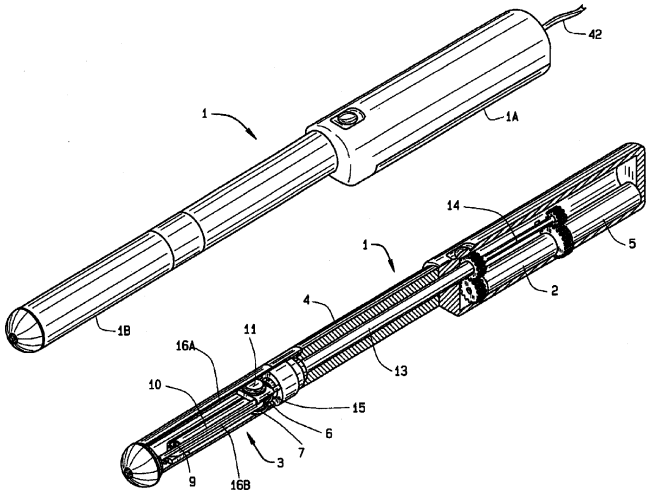

through the interior of the first shaft is used to pivot or rotate the ultrasound transducer to produce a cross-sectional view of the surrounding anatomy. Volumes of anatomy are scanned by motion of the first shaft.—RCW

7,056,290

43.80.Vj CONTINUOUS DEPTH HARMONIC IMAGING USING TRANSMITTED AND NONLINEARLY GENERATED SECOND HARMONICS

Matthew Rielly and James Jago, assignors to Koninklijke Philips Electronics, N.V.
6 June 2006 (Class 600/447); filed 30 September 2002

An ultrasound beam is transmitted at a fundamental frequency to produce harmonics nonlinearly and echos from the harmonics at far ranges. An ultrasound beam is also transmitted at a harmonic frequency to produce echos at near ranges to compensate for the lack of harmonically produced echos at near ranges.—RCW

7,060,033

43.80.Vj ULTRASOUND IMAGING GUIDEWIRE WITH STATIC CENTRAL CORE AND TIP

David A. White and W. Martin Belef, assignors to Boston Scientific Corporation
13 June 2006 (Class 600/463); filed 14 June 2004

This guidewire contains an ultrasonic scanning device that is rotated around the axis of the guidewire to obtain images at all azimuthal angles around the guidewire axis. The imaging device is also translated within the guidewire to obtain images at other positions along the guidewire axis without moving the guidewire.—RCW

LETTERS TO THE EDITOR

This Letters section is for publishing (a) brief acoustical research or applied acoustical reports, (b) comments on articles or letters previously published in this Journal, and (c) a reply by the article author to criticism by the Letter author in (b). Extensive reports should be submitted as articles, not in a letter series. Letters are peer-reviewed on the same basis as articles, but usually require less review time before acceptance. Letters cannot exceed four printed pages (approximately 3000–4000 words) including figures, tables, references, and a required abstract of about 100 words.

High-frequency hearing in phocid and otariid pinnipeds: An interpretation based on inertial and cochlear constraints (L)

Simo Hemilä
Department of Biological and Environmental Sciences, University of Helsinki, FI-00014 Helsinki, Finland

Sirpa Nummela[a)]
Department of Anatomy, Northeastern Ohio Universities College of Medicine, Rootstown, Ohio 44272-0095 and Department of Biological and Environmental Sciences, University of Helsinki, FI-00014 Helsinki, Finland

Annalisa Berta
Department of Biology, San Diego State University, San Diego, California 92182-4614

Tom Reuter
Department of Biological and Environmental Sciences, University of Helsinki, FI-00014 Helsinki, Finland

(Received 20 January 2006; revised 12 September 2006; accepted 2 October 2006)

Audiograms in air and underwater, determined by previous workers for four pinniped species, two eared seals (Otariidae) and two phocids (Phocidae), are supplemented here by measurements on their middle ear ossicular mass, enabling mechanistic interpretations of high-frequency hearing and audiogram differences. Otariid hearing is not largely affected by the medium (air/water). This indicates that cochlear constraints limit high-frequency hearing in otariids. Phocids, however, have massive middle ear ossicles, and underwater hearing has radically shifted towards higher frequencies. This suggests that the high-frequency hearing of phocids in air is constrained by ossicle inertia. © *2006 Acoustical Society of America.* [DOI: 10.1121/1.2372712]

PACS number(s): 43.64.Bt, 43.80.Lb [WWA] Pages: 3463–3466

Pinnipeds are adapted to hearing in both air and water,[1–4] two media with radically different acoustic properties. In air pinnipeds probably hear like terrestrial mammals; sound waves enter through the external auditory meatus and set the tympanic membrane and the middle ear ossicles into vibration, producing movements of the oval window and pressure fluctuations in the cochlear fluid. In this situation the middle ear acts as a filter limiting the hearing range, and the inertia of the middle ear ossicles is relevant as it may affect the high frequency hearing limit (HFHL).[5–8] Cochlear factors may also limit high frequency hearing.[9]

While the detailed mechanism for pinniped hearing underwater still remains unknown, it is well-known that these animals close their outer ear canal in water,[10,11] and that several options for hearing through bone conduction are possible. Sound may, for instance, set the whole head into vibration and then the inertia of massive ossicles has a very different role, leading to differential motion between the stapes and the vibrating cochlear capsule.[11–15] In such a situation massive ossicles are of great advantage. Skull vibrations may also cause movements and deformations of the cochlea, producing fluid movement and hair cell stimulation.[11,12,14] Direct recordings of skull and ossicle vibrations suggest, however, that ossicle rather than fluid inertia is the main mechanism behind bone conduction in humans.[16]

In order to appreciate the different roles of inertia in air and water it is useful to consider the differences in sound dissipation in these media. Let us compare two plane waves of equal intensity and frequency, one in air and the other in water. As the ratio of the characteristic acoustic impedances between water and air is ≈ 3700, the sound pressure ratio is $\sqrt{3700} = 61$, and the ratio of particle velocities and accelerations is $1/61$. In water, sound can bring heavy masses into vibration, as a result of the large sound pressure, but due to the small particle velocity and acceleration the inertial forces are much reduced. Thus it is understandable that in water sound can set an animal's head into vibration, even at fairly high frequencies, and lead to bone conduction hearing.

[a)]Author to whom correspondence should be addressed. Electronic mail: snummela@fastmail.fm

TABLE I. Data on hearing and middle ear ossicles for four pinnipeds. High-frequency hearing limit in air (f_{Ha}), and underwater (f_{Hw}), predicted high-frequency hearing limit in air (f_H), combined mass of malleus and incus (m, mean value for several ears, sex and side given when available). For institutional abbreviations, see the Acknowledgments.

Taxon	f_{Ha} kHz	f_{Hw} kHz	f_H kHz	m mg	Material studied
Phocidae					
Phoca vitulina	22	100	17	164	(see Ref. 18)
Mirounga angustirostris	24	80–100	8	1390	LACM 54767 (female, right and left)
Otariidae					
Callorhinus ursinus	35	40	39	13.0	AMNH 245298 (left), NMNH 286106 (female), 286149 (male), SDSNH 16326 (right)
Zalophus californianus	31	34	33	21.9	SDSNH 22862 (male, left), 22981 (left)

Phocid ears differ anatomically from otariid ears in several respects. In phocids, the auditory bulla is inflated, the tympanic membrane and oval window are relatively large, and the round window and the fossula into which it opens are immense. Further, the round window is partly shielded from direct access to the middle ear, and in extreme cases (*Mirounga*) it opens outside the middle ear cavity, external to the skull.[12] Phocid middle ear ossicles are bulbous and massive, ten times larger than in terrestrial mammals with a similar skull size, whereas the otariids ossicles do not deviate in size from those of their terrestrial carnivore relatives, indicating that the phocid hearing system is clearly more specialized for aquatic hearing.[11,12,17,18]

Consequently, it is possible that in air the interaction between the middle and inner ear in seals is very different from that in water. However, given the current knowledge of cochlear physiology, there is no reason to expect significant changes, when the animal's head is submerged just below the surface. Thus a comparison of phocid and otariid audiograms measured in air and underwater[1,17,19–25] may provide valuable information on the relative roles of the middle and the inner ear in shaping the high-frequency part of the audiograms. To study various functional interpretations previously published audiogram data are here supplemented by the middle ear ossicular mass (malleus+incus) for several phocids and otariids (Table I). The stapes mass is not included; it forms a constant fraction of 5% of the combined mass of malleus and incus.[18]

When a bone with mass m vibrates with angular frequency ω, acceleration a, and velocity v, the inertial force is $ma=m\omega v$. Thus the role of inertial forces increases with an increasing frequency. The ossicle inertia in air-conducted hearing and the inertia of the skull bones in bone-conducted hearing most likely limit the hearing sensitivity at high frequencies. The inertia may, however, lose its physiological relevance for high-frequency hearing in case the tonotopic organization of the basilar membrane, or the molecular mechanisms of the individual hair cells prevent the cochlea from following high frequencies.[9,26,27] This means that cochlear factors may set limits to hearing already at somewhat lower frequencies, well before the inertia becomes a critical factor that would limit the hearing sensitivity. While inertia causes the hearing threshold to rise rather steadily toward higher frequencies, cochlear effects apparently result in an abrupt high-frequency cutoff.[8,28,29]

Behavioral audiograms of four pinniped species are of interest here (Fig. 1). Instead of sound pressure levels the corresponding plane wave intensity levels are being used. This quantity enables direct comparison of results from the

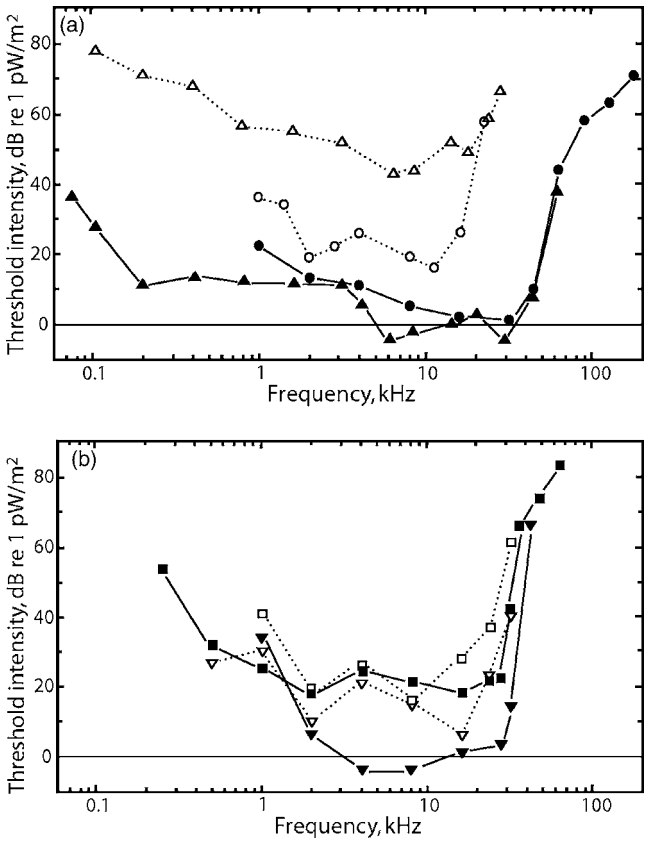

FIG. 1. Audiograms for phocids (a) and otariids (b). All threshold intensities are given in decibels relative to 1 pW/m^2, in order to compare thresholds in water and air. Open symbols in-air, filled symbols underwater. ○, ● *Phoca vitulina* (Ref. 1); △, ▲ *Mirounga angustirostris* (Ref. 23); □, ■ *Zalophus californianus* (Refs. 19 and 20); ▽, ▼ *Callorhinus ursinus* (Ref. 20, the values for Lori).

two media.[1,11,23,28] All threshold intensities are given in decibels relative to 1 pW/m^2. In-air and underwater audiograms are shown for two phocids, *Phoca vitulina* (harbor seal) and *Mirounga angustirostris* (northern elephant seal) [Fig. 1(a)], and for two otariids, *Callorhinus ursinus* (northern fur seal) and *Zalophus californianus* (California sea lion) [Fig. 1(b)]. The high frequency hearing limits (HFHLs) of each pinniped in air and underwater are given in Table I; the HFHL is taken to be the frequency where the curve crosses the threshold of 60 dB at the high-frequency part of the curve.

The phocid underwater audiograms, with high sensitivities up to 50 kHz [Fig. 1(a)], are amply supported by similar audiograms for three other phocid species, the harp seal (*Pagophilus groenlandicus*), the ringed seal (*Pusa hispida*), and the grey seal (*Halichoerus grypus*).[17,24,25] These species also have massive ossicles, the malleus+incus mass is ≈200, 150 and 300 mg, respectively,[18] similar to that of *Phoca vitulina* (164 mg, Table I). The harp seal shows a slight deviation from the other phocids; within the frequency range 16–32 kHz the hearing threshold in air remains constant, as opposed to the rising threshold in *Phoca and Mirounga*.[25] It is possible that in air the harp seal uses a somewhat different hearing mechanism than other phocids.

According to current understanding the middle ear remains air-filled when a seal is submerged just below the surface.[11,12] This implies that in typical behavioral experiments where the animal's head is usually about 1 m below the water surface and the static pressure increase is approximately 10%, no radical changes in the cochlear physiology are to be expected. Thus the large difference between the phocid HFHL values in air and underwater [Fig. 1(a)] hardly reflect any cochlear changes but more likely differences between sound transmission in air and in water, and the different mechanisms by which these sound stimuli reach the cochlea. The inertia of the middle ear ossicles limits high-frequency hearing in air,[5–8] but in water the bone conduction mechanism described above may stimulate the cochlea at higher frequencies. The effect of inertia thus explains the differences of HFHL values of phocids underwater and in air.

The otariid HFHL values in air and underwater are almost equal [Fig. 1(b)]. A parsimonious explanation for this is that in otariids the high-frequency hearing limit has a cochlear origin at sound frequencies around 35 kHz. This limit constrained by the cochlea is thus responsible for the final cutoff in air, and for a very sharp sensitivity cutoff underwater at about the same frequency. It is plausible that even in otariids the cochlea might be stimulated through bone conduction at higher frequencies, but according to the hypothesis presented above their cochlea is not evolutionarily adapted for high-frequency hearing in air or in water.

These pinniped results support the notion that both the middle ear and the inner ear contribute to the threshold rise toward high frequencies, the middle ear causing an inertial effect, mostly seen in phocids, and the inner ear producing an absolute cochlear cutoff, encountered in otariids. In terrestrial mammals, adapted to hearing in air, and whales, adapted to hearing underwater, the contributions of the middle and inner ear to the HFHL apparently overlap.[9,26,28] Middle ear and inner ear have coevolved, and we cannot expect high cochlear sensitivity to frequencies which cannot reach the inner ear.

If the middle ears of different mammals are isometric and certain other conditions are met, the HFHL values limited by inertia are inversely proportional to the cubic root of ossicle mass m.[8] The middle ears of terrestrial mammals are approximately isometric, and indeed the experimental HFHL values as a function of $1/\sqrt[3]{m}$, where m is given in milligrams, follow approximately the line $f_H = 91\ \text{kHz}/\sqrt[3]{m}$.[8,18] Table I shows the experimentally determined high-frequency hearing limits of seals in air (f_{Ha}) and the values calculated using the equation above (f_H). In *Phoca*, *Callorhinus*, and *Zalophus* f_{Ha} and f_H agree reasonably well, suggesting that the middle ears of these seals are functionally isometric with the middle ears of terrestrial mammals.[8,18] The effect of inertia is also apparent in the otariid audiograms in air. The ossicles of *Zalophus* are heavier than those of *Callorhinus*, and indeed the threshold of *Zalophus* starts to rise at a lower frequency than the threshold of *Callorhinus*.

The experimental HFHL value of *Mirounga* in air, 24 kHz, is much higher than the value 8 kHz predicted on the basis of its heavy ossicles. However, the absolute sensitivity of *Mirounga* in air is poor, 27 dB lower than in *Phoca*, suggesting a functional difference between the hearing mechanisms of these species. Thus deviations from isometry and possible contributions from bone conduction may explain the exceptional HFHL of *Mirounga*.

It remains to be studied whether anatomical or functional differences exist in the inner ear of otariids and phocids. Our future work on pinnipeds will focus on the evolutionary aspects of the middle ear and hearing (in preparation).

ACKNOWLEDGMENTS

We thank the following persons for access to their collections and for loan of material under their care: Tom Deméré at the San Diego Natural History Museum (SDSNH), Jim Mead and Charley Potter at the National Museum of Natural History (NMNH), John Heyning at the Los Angeles County Museum (LACM), and Nancy Simmons and Eileen Westwig at the American Museum of Natural History (AMNH). We thank the editor Whitlow Au, and John Rosowski and an anonymous referee for their criticism and comments. This work was partly supported by the Ella and Georg Ehrnrooth Foundation (S.N.) and NSF DEB 9419802 (A.B.).

[1] B. Møhl, "Auditory sensitivity of the common seal in air and water," J. Aud. Res. **8**, 27–38 (1968).
[2] D. Wartzok and D. R. Ketten, "Marine mammal sensory systems," in *Biology of Marine Mammals*, edited by J. E. Reynolds III and S. A. Rommel (Smithsonian Institution Press, Washington, D. C., 1999), pp. 117–175.
[3] A. Ya. Supin, V. V. Popov, and A. M. Mass, *The Sensory Physiology of Aquatic Mammals* (Kluwer Academic, Boston, 2001).
[4] A. Berta, J. L. Sumich, and K. M. Kovacs, *Marine Mammals: Evolutionary Biology*, 2nd ed. (Elsevier, San Diego, 2006).
[5] A. R. Møller, "Function of the middle ear," in *Handbook of Sensory Physiology, vol V/I, Auditory System*, edited by W. D. Keidel and W. D. Neff (Springer-Verlag, Berlin, 1974), pp. 491–517.
[6] J. J. Zwislocki, "The role of the external and middle ear in sound transmission," in *The Nervous System*, edited by D. B. Tower (Raven, New York, 1975), Vol. 3, pp. 45–55.

[7]J. J. Rosowski, "Hearing in transitional mammals: Predictions from the middle-ear anatomy and hearing capabilities of extant mammals," in *The Evolutionary Biology of Hearing*, edited by D. B. Webster, R. R. Fay, and A. N. Popper (Springer-Verlag, New York, 1992), pp. 615–631.
[8]S. Hemilä, S. Nummela, and T. Reuter, "What middle ear parameters tell about impedance matching and high frequency hearing," Hear. Res. **85**, 31–44 (1995).
[9]M. A. Ruggero and A. N. Temchin, "The roles of external, middle, and inner ears in determining the bandwidth of hearing," Proc. Natl. Acad. Sci. U.S.A. **99**, 13206–13210 (2002).
[10]F. Ramprashad, S. Corey, and K. Ronald, "Anatomy of the seal's ear (*Pagophilus groenlandicus*) (Erxleben, 1777)," in *Functional Anatomy of Marine Mammals*, edited by R. J. Harrison (Academic, London, 1972), pp. 263–306.
[11]B. Møhl, "Hearing in seals," in *The Behavior and Physiology of Pinnipeds*, edited by R. J. Harrison, R. C. Hubbard, R. S. Peterson, C. E. Rice, and R. J. Schusterman (Appleton-Century-Crofts, New York, 1968b), pp. 172–195.
[12]C. A. Repenning, "Underwater hearing in seals: Functional morphology," in *Functional Anatomy of Marine Mammals*, edited by R. J. Harrison (Academic, London, 1972), pp. 307–331.
[13]E. Bárány, "A contribution to the physiology of bone conduction," Acta Oto-Laryngol., Suppl. **26**, 1–223 (1938).
[14]J. Tonndorf, "A new concept of bone conduction," Arch. Otolaryngol. **87**, 49–54 (1968).
[15]T. Reuter, S. Nummela, and S. Hemilä, "Elephant hearing," J. Acoust. Soc. Am. **104**, 1122–1123 (1998).
[16]S. Stenfelt, N. Hato, and R. L. Goode, "Factors contributing to bone conduction: The middle ear," J. Acoust. Soc. Am. **111**, 947–959 (2002).
[17]J. M. Terhune and K. Ronald, "Underwater hearing sensitivity of two ringed seals (*Pusa hispida*)," Can. J. Zool. **53**, 227–231 (1975).
[18]S. Nummela, "Scaling of the mammalian middle ear," Hear. Res. **85**, 18–30 (1995).
[19]R. J. Schusterman, R. F. Balliet, and J. Nixon, "Underwater audiogram of the California sea lion by the conditioned vocalization technique," J. Exp. Anal. Behav. **17**, 339–350 (1972).
[20]P. W. B. Moore and R. J. Schusterman, "Audiometric assessment of northern fur seals, *Callorhinus ursinus*," Marine Mammal Sci. **3**, 31–53 (1987).
[21]Ye. S. Babushina, G. L. Zaslavskii, and L. I. Yurkevich, "Air and underwater hearing of the northern fur seal: Audiograms and auditory frequency discrimination," Biophysics (Engl. Transl.) **36**, 909–913 (1991).
[22]D. Kastak and R. J. Schusterman, "Low-frequency amphibious hearing in pinnipeds: Methods, measurements, noise, and ecology," J. Acoust. Soc. Am. **103**, 2216–2228 (1998).
[23]D. Kastak and R. J. Schusterman, "In-air and underwater hearing sensitivity of a northern elephant seal (*Mirounga angustirostris*)," Can. J. Zool. **77**, 1751–1758 (1999).
[24]J. M. Terhune and K. Ronald, "The harp seal, *Pagophilus groenlandicus* (Erxleben, 1777). III. The underwater audiogram," Can. J. Zool. **50**, 565–569 (1972).
[25]J. M. Terhune and K. Ronald, "The harp seal, *Pagophilus groenlandicus* (Erxleben, 1777). X. The air audiogram," Can. J. Zool. **49**, 385–390 (1971).
[26]J. E. Gale and J. F. Ashmore, "An intrinsic frequency limit to the cochlear amplifier," Nature (London) **389**, 63–66 (1997).
[27]R. H. Withnell, L. A. Shaffer, and D. J. Lilly, "What drives mechanical amplification in the mammalian cochlea?," Ear Hear. **23**, 49–57 (2002).
[28]S. Hemilä, S. Nummela, and T. Reuter, "A model of the odontocete middle ear," Hear. Res. **133**, 82–97 (1999).
[29]S. Nummela, "Scaling and modeling the mammalian middle ear," Comments on Modern Biology, Part C, Comments on Theoretical Biology **4**, 387–412 (1997).

A note on the low-frequency noise reduction of cylindrical capsules (L)

Eric E. Ungar[a)]
Acentech, Incorporated, 33 Moulton Street, Cambridge, Massachusetts 02138-1118

(Received 14 July 2006; revised 21 September 2006; accepted 22 September 2006)

The noise reductions provided by capsules consisting of uniform cylindrical shells whose two ends are closed off by like circular plates are analyzed for the low-frequency regime in which a capsule acts quasi-statically, much like a pressure vessel. The change in the confined volume is determined from the structural deflections produced by a net pressure difference, taking account of the interactions of the shell and end plates. Expressions for the noise reduction of a single capsule and of two nested capsules are derived. Some insights into the noise reduction effects of interaction between the shell and end plates are discussed, as are the contributions of these components.
© *2006 Acoustical Society of America.* [DOI: 10.1121/1.2363936]

PACS number(s): 43.40.Ey, 43.40.Dx, 43.40.Qi [DF] Pages: 3467–3470

I. INTRODUCTION

In many practical applications it is desired to employ an enclosure to shield a sensitive item from noise (for example, to reduce the noise exposure of an experimental animal in magnetic resonance imaging) or to protect the surroundings from noise produced by a source. In cases where all dimensions of the enclosure are much smaller than an acoustic wavelength, the effect of the sound field on the enclosure is essentially like that of a fluctuating uniform pressure. If the frequencies of the acoustic pressure fluctuations are significantly lower than the fundamental natural frequency of the enclosure structure, then that structure deflects quasi-statically and may be analyzed essentially like a pressure vessel. This analysis approach is applied here to a capsule consisting in essence of a thin-walled pipe with flat end caps.

II. COMPONENT DEFLECTIONS

A. Cylindrical shell

Figure 1 shows a section through a cylindrical shell along its axis and indicates the sign convention of Timoshenko,[1] which is used in the present analysis. If the origin of the axial coordinate x is taken at midlength of the shell in order to take advantage of symmetry about the midpoint, then the *inward* deflection w due to a net *internal* pressure p may be written as[1]

$$w(x)/p = A \sin \beta x \sinh \beta x + B \cos \beta x \cosh \beta x - a^2/E_S h_S, \tag{1}$$

where a and h_S denote the shell's radius and thickness, respectively, and E_S represents the modulus of elasticity of its material. The parameter β is defined as

$$\beta = [E_S h_S/4a^2 D_S]^{1/4} = [3(1-\nu_S^2)/a^2 h^2]^{1/4}, \tag{2}$$

where D_S denotes the shell wall's flexural rigidity and obeys

$$D_S = E_S h_S^3/12(1-\nu_S^2) \tag{3}$$

with ν_S representing Poisson's ratio of the shell's material. The constants A and B need to be evaluated from the end conditions.

If the end plates restrain the radial deflection of the shell fully, then the end conditions are

$$w(L/2) = 0 \quad \text{and} \quad M_S = -D_S \frac{d^2 w(L/2)}{dx^2}, \tag{4}$$

where M_S denotes the moment acting on the shell's edge per unit edge length. By applying these two boundary conditions to Eq. (1) one obtains two equations, which may be written compactly as

$$AsS + BcC = a^2/E_S h_S \equiv \Phi \tag{5a}$$

$$AcC - BsS = -M_S/2p\beta^2 D_S \equiv -\mu, \tag{5b}$$

where Φ and μ, as well as the notation

$$s = \sin \alpha, \quad c = \cos \alpha, \quad S = \sinh \alpha, \quad C = \cosh \alpha \tag{6}$$

have been introduced for the sake of convenience, with α defined as

$$\alpha = \beta L/2. \tag{7}$$

Solution of these equations yields

$$A = (\Phi sS - \mu cC)/\Delta \tag{8a}$$

$$B = (\mu sS + \Phi cC)/\Delta, \tag{8b}$$

with

$$\Delta = C^2 - s^2. \tag{8c}$$

One then finds from Eq. (1) that the slope $\theta_S = dw(L/2)/dx$ at the shell's edge obeys

a)Electronic mail: eungar@acentech.com

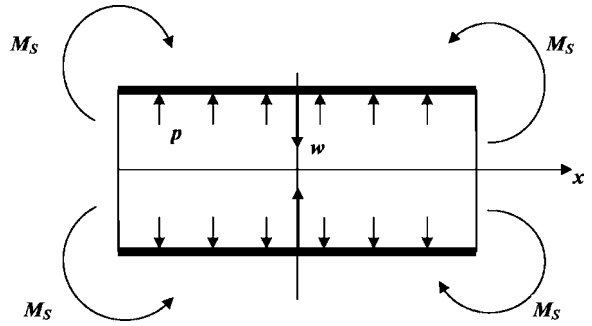

FIG. 1. Axial section through cylindrical shell, showing sign conventions for pressure p, radial deflection w, and edge moment per unit edge length M_S, after Timoshenko.

$$\theta_S \Delta/p\beta = \Phi(SC - sc) - \mu(SC + sc). \tag{9}$$

With $M_S=0$ the foregoing equations apply to a shell with hinged edges. For a shell with clamped edges, at which the slope is equal to zero, Eq. (9) implies that moment at a clamped end obeys

$$M_{S,\ \text{clamped}} = a\sqrt{\frac{D_S}{E_S h_S}}\left(\frac{SC - sc}{SC + sc}\right) = \frac{a h_S}{2\sqrt{3(1-\nu_S^2)}}\left(\frac{SC - sc}{SC + sc}\right). \tag{10}$$

B. Circular plate

With the sign convention shown in Fig. 2, the displacement y at radius r of a plate in the direction of the applied pressure p obeys[1]

$$y(r)/p = (r^4 - a^4)/64D_P + C(r^2 - a^2), \tag{11}$$

where D_P represents the flexural rigidity of the plate (given by the same expression as for the shell, but here involving the parameters relevant to the plate), C is a constant, and the deflection at the rim has been taken to be zero, $y(a)=0$.

Substitution of the foregoing expression into that for the moment M_P at the rim of the plate per unit length along the rim,

$$M_P(a) = -D_P\left[\frac{d^2y}{dr^2} + \frac{\nu_P}{r}\frac{dy}{dr}\right]_{r=a} \tag{12}$$

where ν_P represents the plate material's Poisson's ratio, permits one to find that

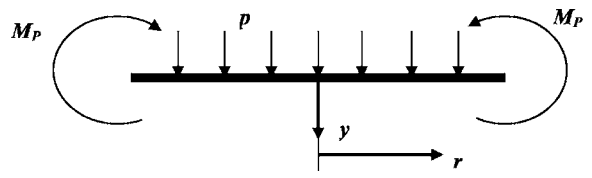

FIG. 2. Section through circular plate along a diameter, indicating sign conventions for pressure p, radial coordinate r, deflection y, and edge moment per unit edge length M_P, after Timoshenko.

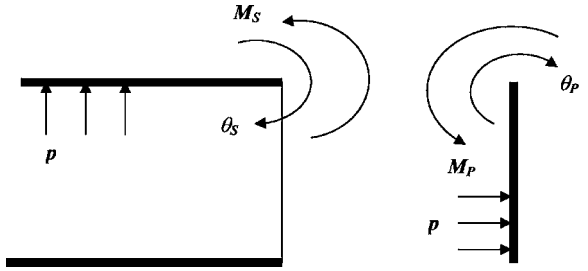

FIG. 3. Moments and rotations at interconnection of cylindrical shell and end plate.

$$C = -\frac{1}{2(1+\nu_P)D_P}\left[\frac{M_P}{p} + \frac{a^2(3+\nu_P)}{16}\right]. \tag{13}$$

From Eq. (11) one may then obtain the following expression for the slope θ_P at the rim:

$$\frac{\theta_P}{p} = \frac{dy(a)}{pdr} = -\frac{a}{D_P(1+\nu_P)}\left(\frac{M_P}{p} + \frac{a^2}{8}\right). \tag{14}$$

With $M_P=0$ the foregoing expressions apply for a plate with a hinged edge. At a clamped edge the slope vanishes, so that one may find from Eq. (14) that at such an edge the moment obeys

$$M_{P,\ \text{clamped}} = -pa^2/8. \tag{15}$$

C. Interconnection of shell and end plates

If the shell is rigidly connected to the end plates, then the slopes and moments at the shell and plate edges must match. Taking account of the sign conventions (see Fig. 3) this matching requires that

$$\theta_S = \theta_P \quad \text{and} \quad M_S = -M_P. \tag{16}$$

Application of Eqs. (9) and (14) to the foregoing relations then permits one to determine the moment at the rim:

$$\frac{M_S}{p} = a^2\frac{\frac{1}{8} + \frac{\beta D_P(1+\nu_P)(SC - sc)}{E_S h_S \Delta}}{1 + \frac{D_P(1+\nu_P)(SC + sc)}{2\beta a D_S \Delta}}. \tag{17}$$

This moment is always positive and thus always opposes the deflection induced by the pressure, as one would expect.

For the case where the plate rigidity is much greater than that of the shell [that is, for $D_P \gg D_S$] Eq. (17) reduces to the moment for a clamped-edge shell, corresponding to Eq. (10). This result agrees with intuition, since a comparatively rigid end plate essentially fixes the shell edge. Similarly, for the case where the shell is much more rigid than the plate (that is, for $D_P \ll D_S$) Eq. (17) reduces to the moment for a clamped-edge plate, as given by Eq. (15). This again agrees with intuition, since a comparatively rigid shell in essence serves to keep the plate edge fixed. Note that the latter moment does not depend on the plate's rigidity and that Eq. (17) does not apply to the case where end plates are absent (or $D_P=0$).

III. DISPLACED VOLUMES

The volume V_S displaced by the deflection of the cylindrical shell may be calculated from Eq. (1):

$$V_S/p = -2\int_0^{L/2} 2\pi a(w/p)dx$$

$$= -4\pi a[AI_A + BI_B - (1-\nu_S/2)a^2L/2E_Sh_S]. \quad (18)$$

Here the last term has been multiplied by $(1-\nu_S/2)$ to account for the Poisson effect, which restricts the radial expansion of the shell as the result of the axial force that acts on the shell due to the pressure on the end plates. The minus sign has been added to make the expression correspond to an increase in the contained volume for an internal pressure (or a decrease in the volume for an external pressure) in view of the sign convention applicable to Eq. (1). I_A and I_B are defined as

$$I_A = \int_0^{L/2} \sin\beta x \sinh\beta x dx = (sC - cS)/2\beta \quad (19a)$$

$$I_B = \int_0^{L/2} \cos\beta x \cosh\beta x dx = (sC + cS)/2\beta. \quad (19b)$$

Substitution for A and B from Eqs. (8a) and (8b) then yields[2]

$$\frac{V_S}{p} = \frac{2\pi a^3 L}{E_s h_s}\left(1 - \frac{\nu_S}{2} - \frac{SC+sc}{2\alpha\Delta}\right) - \frac{\pi a M_S/p}{D_S\beta^3}\cdot\frac{SC-sc}{\Delta}. \quad (20)$$

The volume V_{SA} due to the axial expansion of the shell may readily be found to obey

$$\frac{V_{SA}}{p} = \frac{\pi a^3 L}{2h_S E_S}. \quad (21)$$

The volume V_P displaced by the two end plates may be found to be given by[3]

$$\frac{V_P}{p} = 4\pi\int_0^a \frac{y}{p} r dr = \frac{\pi a^4}{2(1+\nu_P)D_P}\left[\frac{-M_S}{p} + \frac{a^2(7+\nu_P)}{48}\right] \quad (22)$$

on the basis of Eqs. (11) and substitution of C from Eq. (13).

The total volume decrease $V_D = V_S + V_{SA} + V_P$ due to an external pressure may then be found from the three foregoing equations.

IV. SOUND ATTENUATION OF CAPSULES

A decrease V_V of a confined volume results in an increase p_i in the pressure in that volume. For rapidly changing small (i.e., acoustic) pressures, the volume compliance of the confined volume—that is, the ratio B of the volume reduction to the pressure increase—obeys

$$B \equiv V_V/p_i = V_0/\gamma p_0, \quad (23)$$

where V_0 represents the initial volume and p_0 the initial pressure in that volume; the symbol γ represents the ratio of specific heats in the confined gas (equal to 1.4 for air).

In the foregoing analysis of the volume change resulting from a pressure p applied to a capsule structure, the pressure p tacitly was taken to represent the difference between the external pressure p_e and the internal pressure p_i. If one takes account of this fact and replaces p by $p_e - p_i$ one may write the volume compliance of the capsule structure as

$$\Gamma \equiv V_D/p = V_D/(p_e - p_i). \quad (24)$$

Since the reduction V_V of the confined volume is the same as the volume reduction V_D resulting from the capsule deformation, one may readily find from the two foregoing equations that

$$p_e/p_i = 1 + B/\Gamma. \quad (25)$$

Thus, the attenuation (or noise reduction) NR obeys

$$NR = 20\log_{10}(p_e/p_i)$$

$$= 20\log_{10}(1 + B/\Gamma) = 20\log_{10}\left(1 + \frac{V_0}{\Gamma\gamma p_0}\right). \quad (26)$$

It should be noted that the confined volume V_0 may be smaller than the entire volume of the cylindrical enclosure if that enclosure contains acoustically incompressible objects.

In order to consider two nested enclosures (capsules) with an air space between the inner and outer one, one may define the volume compliances Γ_E and Γ_I of the outer and inner enclosures, respectively, in analogy to Γ of Eq. (24), in terms of the volume decreases V_E and V_I resulting from deformations of these enclosures. Similarly, one may define the compliances B_I and B_M of the interior volume and of the volume between the exterior and interior capsule in analogy to Eq. (23). Then, taking account of the fact that the reduction V_M in the volume between the two capsules results from deformations of both capsules, one may write

$$V_M = B_M p_m = V_E - V_I = \Gamma_E(p_e - p_m) - \Gamma_I(p_m - p_i), \quad (27)$$

where p_m denotes the pressure increase in the space between the two capsules. Since the reduction V_I of the volume inside the interior capsule results from the deformation of the interior capsule, one also may write

$$V_I = B_I p_i = \Gamma_I(p_m - p_i). \quad (28)$$

By solving the foregoing relation for p_m and introducing the result into Eq. (24), one may find after some manipulation that

$$\frac{p_e}{p_i} = \left(1 + \frac{B_M}{\Gamma_E}\right)\left(1 + \frac{B_I}{\Gamma_I}\right) + \frac{B_I}{\Gamma_E}. \quad (29)$$

The corresponding NR is equal to $20\log_{10}$ of the foregoing pressure ratio.

V. SOME OBSERVATIONS, DESIGN IMPLICATIONS

From Eq. (17) it is evident that the edge moment M_S due to interconnection of the shell and the end plates is always positive. Equations (20) and (22) show that an increase in this moment results in reduced volume displacement, and therefore in greater noise reduction. One thus may conclude that rigid connection between the shell and its end plates

results in greater *NR* than hinged connection (for which $M_S = 0$), as one would expect intuitively.

From Eqs. (10) and (15) one finds that the ratio of the two limiting edge moments can be written as

$$\frac{M_S(D_P \gg D_S)}{M_S(D_P \ll D_S)} = \frac{\mathbf{4}}{\mathbf{3}\sqrt{\mathbf{1}-\nu_S^2}} \cdot \frac{SC - sc}{SC + sc} \cdot \frac{h_S}{a}. \tag{30}$$

Since $h_S/a \ll 1$ for the usually considered thin shells, it follows that the foregoing ratio is less than unity, implying that a comparatively rigid end plate exerts a smaller edge moment on the shell than does a comparatively compliant end plate. In fact, one may show from Eq. (17) that dM_S/dD_P is always negative (for $h_S/a \ll 1$). This implies that M_S always decreases as D_P increases and thus that a less rigid end plate results in a greater moment and therefore in a smaller volume displacement by the shell—contrary to what one would expect intuitively at first glance. However, one may explain this phenomenon by noting that a given pressure tends to cause a less rigid end plate to deflect more, resulting in greater rotation at the interconnected edges and thus in exertion of a greater moment on the shell edge.

For a capsule configuration for which the moment M_S given by Eq. (17) is greater than that corresponding to a shell with clamped edges, as given by Eq. (10), it follows from Eq. (20) that the volume displaced by the shell is smaller than the volume the shell would displace if its edges were clamped. Similarly, it follows from Eq. (22) that for a configuration for which the moment M_S given by Eq. (17) is greater than the moment corresponding to a plate with clamped edges, as given by Eq. (15), the volume displaced by the plate is smaller than that the plate would displace if its edge were clamped.

With more flexible end plates the volume displaced by the shell is reduced, but the volume displaced by the plates is increased. Since *NR* depends on the sum of the volumes displaced by the shell and the end plates, one would want to minimize this sum, subject to such constraints as the total weight of the assembly. Such optimizations probably are best investigated numerically for specific cases of interest.

One may determine from Eqs. (20) and (22) that the ratio V_S/V_P of the volume displaced by the shell to that displaced by the end plates is of the order of $(E_P/E_S) \times (h_P/a)^3 (L/h_S)$. Since $(h_P/a)^3$ typically is very small, the volume displaced by the shell in most cases is considerably smaller than that displaced by the end plates. This suggests that in order to obtain a large *NR* one should make the end plates as rigid as possible by making them thick and of a material with a high modulus of elasticity, and ideally also by affixing them to stiff flanges.

Throughout all of the foregoing discussion it was tacitly assumed that the sound field that excites the capsule structures is known and not changed by the motions of these structures. In most practical cases such changes in the sound field only have small effects on the relatively large noise reductions that well-conceived capsules can provide. It is important to note also that the capsule considered here consists of a uniform cylindrical shell and that ribs or other disruptions of the shell's circumferential uniformity may increase the volume compliance of the shell and thus decrease the capsule's noise reduction.

ACKNOWLEDGMENT

The work reported here was carried out under National Institute of Mental Health Grant No. 1 R43 MH075466-01.

[1] S.Timoshenko, *Theory of Plates and Shells* (McGraw–Hill, New York, 1940).

[2] In agreement with the sign convention of Fig. 1 this expression indicates that an interior pressure increases the outward volume displaced due to bulging, whereas an increased edge moment decreases this volume. With $M_S = 0$ this expression corresponds to simply supported edges. For a shell with clamped edges,

$$\frac{V_S}{p} = \frac{2\pi a^3 L}{E_s h_s}\left[1 - \frac{\nu_S}{2} - \frac{C^2 - c^2}{\alpha(SC + sc)}\right]$$

[3] In agreement with the sign convention of Fig. 2 this expression indicates that both the pressure and the edge moment $M_P = -M_S$ increase the displaced volume. With $M_S = 0$ this expression corresponds to simply supported edges. For two end plates with clamped edges,

$$\frac{V_P}{p} = \frac{\pi a^6}{96 D_P}$$

Lateralization of sine tones–interaural time vs phase (L)

Peter Xinya Zhang[a] and William M. Hartmann
Department of Physics and Astronomy, Michigan State University, East Lansing, Michigan 48824

(Received 25 May 2006; revised 8 September 2006; accepted 27 September 2006)

Listeners estimated the lateral positions of 50 sine tones with interaural phase differences ranging from −150° to +150° and with different frequencies, all in the range where signal fine structure supports lateralization. The estimates indicated that listeners lateralize sine tones on the basis of interaural time differences and not interaural phase differences. © *2006 Acoustical Society of America.* [DOI: 10.1121/1.2372456]

PACS number(s): 43.66.Pn, 43.66.Qp [AK] Pages: 3471–3474

I. INTRODUCTION

Since the time of Lord Rayleigh (Strutt, 1907) it has been known that human listeners can localize or lateralize tones on the basis of interaural phase differences (IPDs) or interaural time differences (ITDs). For a tone of given frequency there is a simple relationship between the two interaural parameters, IPD=360°f(ITD), where IPD is measured in degrees. Thus IPD and ITD are almost the same thing, but there is a proportionality factor which is the frequency of the tone, f.

The distinction between IPD and ITD causes one to wonder if one of these two measures of interaural difference correlates better with the human perception of sidedness. *A priori*, the IPD has a built-in advantage in that there is a fixed physical terminus for the measure. As the phase increases to 180°, the IPD of a sine tone loses its significance whatever the ITD or the frequency. Further, measurements of just noticeable deviations from the midline show that the JND in IPD is roughly independent of frequency, whereas the JND in ITD is not (Yost and Hafter, 1987).

On the other hand, the azimuth of free-field sources correlates better with ITD because, for a given azimuth, the ITD changes little as the frequency varies while the IPD changes a lot (Kuhn, 1979). If human listeners gain their internal measures of laterality from experience with the physical positions of audible objects, then the ITD would have a natural advantage.

Auditory models following the Jeffress model (Jeffress, 1948) tend to emphasize the ITD because fixed internal delay lines that compensate externally imposed ITDs lead to a topographic encoding based on ITD. However, this encoding is confined to frequency-specific channels. Within any tuned channel, the ITD is approximately equivalent to an IPD. Consequently, it is not possible to argue that the ITD enjoys a clear advantage based on neural architecture. On the contrary, the distribution of IPD-sensitive neurons across frequency, as observed in the inferior colliculus of guinea pig (McAlpine *et al.*, 2001) suggests that IPD may be more fundamental physiologically, because the neural population seems to be distributed according to IPD.

On the other hand, cross-frequency models used to study human lateralization of broad-band stimuli are based on a common ITD in different frequency channels (Stern *et al.*, 1988). The "straightness" criterion for ITD is a frequency-independent ITD and not a frequency-independent IPD. To the extent that straightness is perceptually important, the ITD has the edge.

In 1981, Yost performed a series of experiments on the lateral position of sine tones as a function of interaural phase difference. In separate IPD experiments, he measured the perceived location of tones with frequencies between 200 and 1500 Hz. In these experiments, the interaural phase varied from −150° to +180°. Listeners were required to indicate the position of the tone image on a scale from left to right.

Yost found that the overall aspect of the laterality-vs-IPD curves seemed to be independent of frequency. By contrast, the lateralization responses were different functions of ITD for different frequencies. Consequently, the experiments suggested that the human binaural system was acting more as an IPD meter than as an ITD meter.

A potential problem with Yost's experiments is that trials were blocked on frequency. Therefore, if listeners use the full range of available responses for each experimental block, then experiments in which the range of IPD is the same in each block would lead to the conclusion that laterality is the same function of IPD whatever the frequency of the tone. Yost was aware of this possibility and performed spot checks with pairs of tone frequencies to test his results. The checks supported the dominant position of the IPD, but those checks fell short of a full experiment.

Recent measurements of Huggins pitch laterality (Zhang and Hartmann, 2004) caused us to become aware of context sensitivity for lateralization judgements made by listeners. A similar informal observation had been made for tones by Sayers (1964). To pursue these observations, we performed an experiment on sine-tone laterality using IPD as the principal variable, as in the experiments done by Yost. The difference was that trials were not blocked on frequency.

II. EXPERIMENT

The experiment used two fixed sets of 25 sine tones with parameters selected to be in ranges where tones can be lateralized on the basis of ITDs or IPDs in the fine structure (Zwislocki and Feldman, 1956; Yost and Hafter, 1987). The

[a]Author to whom correspondence should be addressed. Electronic mail: zhangx11@msu.edu

TABLE I. Interaural Parameters—Stimulus Set 1.

Stim. No.	ITD (μs)	IPD (°)	Freq. (Hz)
1	−200	−30	417
2	+400	+30	208
3	−600	−30	139
4	+800	+30	104
5	−200	−60	833
6	+400	+60	417
7	−600	−60	278
8	+800	+60	208
9	−1000	−60	167
10	+200	+90	1250
11	−400	−90	625
12	+600	+90	417
13	−800	−90	313
14	+1000	+90	250
15	−400	−120	833
16	+600	+120	556
17	−800	−120	417
18	+1000	+120	333
19	−400	−150	1042
20	+600	+150	694
21	−800	−150	521
22	+1000	+150	417
23	0	0	167
24	0	0	333
25	0	0	694

intention was to cover the entire range of IPD, frequency, and ITD where discrimination is good while remaining mainly within that range. Such "reasonable" parameters were selected as follows: First, the IPDs were 0°, ±30°, ±60°, ±90°, ±120°, and ±150°, the same as those used by Yost, except for 180°. Here, a positive sign means that the fine structure leads on the right. Second, the ITDs were well distributed, never greater than 1000 μs, and normally less than the low-frequency head-diffraction physiological range of 763 μs. Third, the frequencies resulting from the IPDs and ITDs were in the range from 100 to 1250 Hz and were normally less than 1000 HZ.

A. Stimuli

The ITDs, IPDs, and frequencies of Stimulus Set 1 are shown in Table I. Stimulus Set 2 was identical except that plus and minus signs in the table were reversed. Consequently, the experiment was left-right symmetrical overall.

The tones were calculated by an array processor and were stored in buffers with a length of 32,768 words per channel. The buffer contents were converted to analog signals by two 16 bit digital-to-analog converters at a sample rate of 20 ksps. Hence, the total stimulus duration was 1.6 s. The onsets and offsets were smoothed by raised-cosine functions 100 ms in duration. The phase delay for the signal for one ear was applied to the waveform fine structure only, not to the raised-cosine envelope. Converted signals were low-pass filtered at 2.5 kHz with Brickwall filters with a slope of −115 dB/octave. Digital recordings made at the output of the filters verified the waveform phase shifts and envelopes. The listener heard the stimuli through Sennheiser HD 414 headphones while seated in a double-walled sound-treated room. The level of the tones was 60 dB sound pressure level.

B. Listeners

Five listeners participated in the experiment: A (age 19), C (65), W (66), X (31), and Z (33). Listeners were male except for C. Listeners all had normal hearing, defined as thresholds within 15 dB of nominal, throughout the frequency range of this experiment. They were all experienced in binaural listening tasks and were right handed. Listeners X and W were the authors.

C. Procedure

The listening tests were organized as runs of 25 trials. Each run employed the 25 stimuli of Set 1 or Set 2, presented in random order. Runs with Set 1 and runs with Set 2 alternated.

On each trial, a listener heard one of the tones from the stimulus set. The listener could repeat the tone as many times as desired. Then the listener responded with a number between −40 and +40 to indicate the lateral position of the image of the tone. Except for A, listeners had extensive experience in lateralizing tones on the −40 to +40 scale in connection with another experiment. There was no feedback. A typical run lasted 3–5 min, depending on the listener. Final data were based on the last ten runs for a given listener.

D. Results

The first step in analyzing the data was to determine an average response, for each listener, to each of the 44 different stimuli with nonzero IPD and to each of the six stimuli with zero IPD. Occasionally, a tone with a positive or negative IPD led to a response with the opposite sign (opposite side of the head). In order to avoid unwarranted cancellation of positive and negative responses in finding the mean, it was necessary to perform some filtering on the data. Responses to stimuli with IPD greater than or equal to 90° were excluded if the responses had a sign opposite to the IPD. All other data were included. Out of 440 data points for each listener, 20 were excluded for listener A, 27 for C, 55 for W, 23 for X, and 22 for Z.

Next, the included responses for stimuli having a particular IPD were collected and averaged. The standard deviation was also found. These values of mean and standard deviation are shown in Fig. 1. Similarly, means and standard deviations for stimuli having particular ITD values were found, and those are shown in Fig. 2.

1. Standard deviations

If the sensation of lateral position is a function of IPD, the standard deviations, shown as error bars in Fig. 1, should be small. To test this idea, standard deviations for individual listeners were computed in the following way: First, the mean response was calculated for each of the 50 stimuli. Next, a mean and variance were calculated for each IPD value based on the means for individual stimuli, using as a weighting factor the number of included responses for each

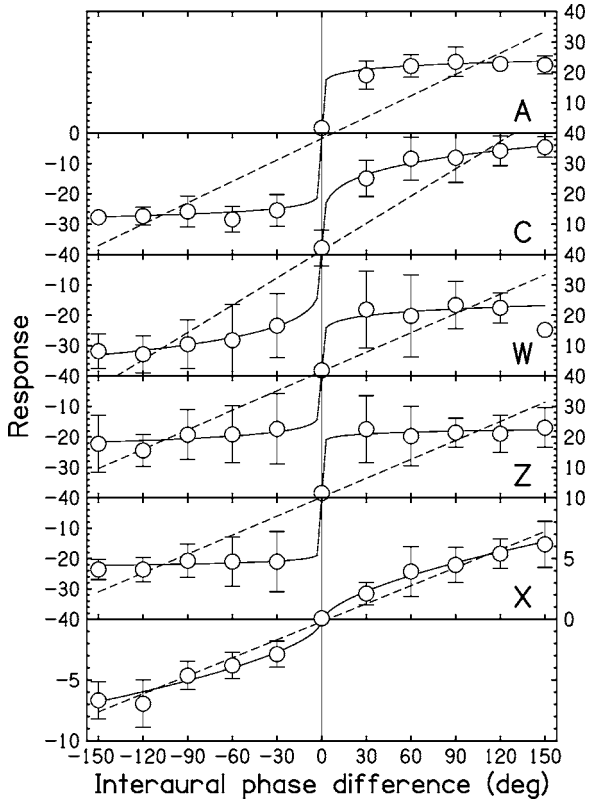

FIG. 1. Lateral position responses for five listeners plotted as a function of interaural phase difference (IPD). Each symbol shows the mean response to four or five tones with a given IPD. Error bars are two standard deviations in overall length. Dashed lines show the best linear fits. Solid lines show the best nonlinear fits.

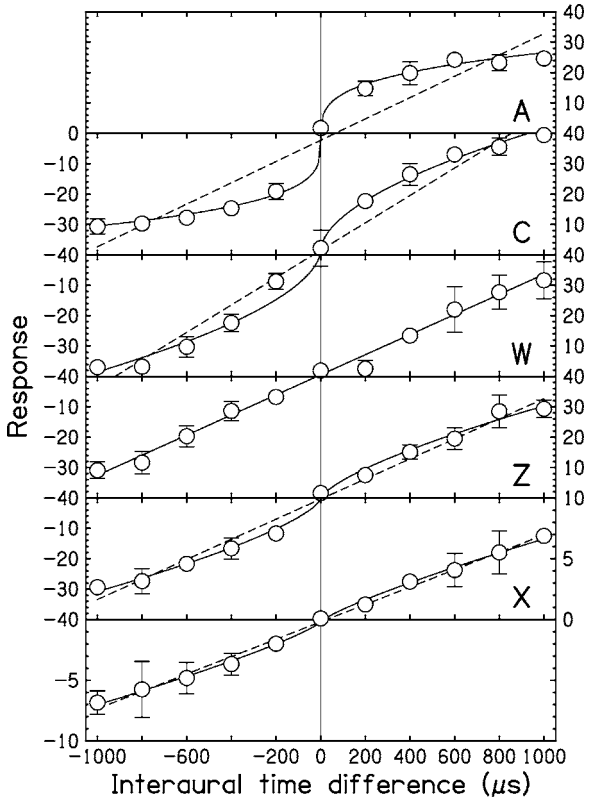

FIG. 2. Same as Fig. 1, but plotted against interaural time difference (ITD). Where no error bars are shown the standard deviation is smaller than the data points.

stimulus. The square roots of the variances are the standard deviations in Fig. 1. The standard deviations averaged over the ten finite IPD values are reported in Table II. Similarly, standard deviations were computed from the same raw data regarded as functions of ITD, and averaged over the ten finite ITD values.

Table II shows that the standard deviations are smaller when responses are regarded as a function of ITD, not of IPD. Such a result argues in favor of ITD as the effective interaural parameter. A two-sample t-test, based on ten means for finite IPD and ten means for finite ITD, showed that the standard deviations are significantly smaller for ITD than for IPD for all five listeners, with p-values shown in Table II.

An alternative calculation of the variances simply averaged the raw responses for each IPD (or ITD). The means were the same as in the figures, but the standard deviations were sufficiently larger that the distinction between IPD and ITD was significant at the 0.01 level only for listeners C, W, and Z. Although standard deviations were smaller for ITD than for IPD for the other two listeners as well, the difference was not significant. The disadvantage of this later computation is that it incorporates all the variation on individual trials.

2. Restricted range of IPD

When the absolute value of the IPD is 90° or less, one expects that lateralization judgments are only little affected by alias images outside the region of centrality. Therefore, we performed a new test excluding all the data with IPDs greater than 90°, but with no other filtering. The test was otherwise identical to that of Sec. II D 1 above. The test showed that the standard errors were significantly smaller for ITD than for IPD, with $p<0.001$ for all listeners except for listener A. For A, $p<0.02$.

3. Straight-line fits

If the perceived lateral position is an accurate IPD meter, then the responses in Fig. 1 above should be a linear function of IPD. Straight lines were fitted to the data by minimizing the rms error. Similarly straight lines were fitted to the ITD data in Fig. 2. The fitting procedure simply fitted all included responses for all values of IPD or ITD.

The rms error was smaller for the ITD straight line than for the IPD straight line for all five listeners. Averaged over

TABLE II. Standard deviation for each listener averaged over ten mean responses to tones with nonzero IPD or ITD. The p-values less than 0.05 support the hypothesis that the standard deviations for ITD are less than those for IPD.

Listener	IPD	ITD	p-value
A	3.7	2.2	0.01
C	7.3	2.2	$\ll$0.01
W	8.5	3.9	$<$0.01
Z	6.9	2.9	$\ll$0.01
X	1.4	1.1	0.05

TABLE III. Best-fit parameters for the nonlinear model and rms error, E.

	$L=a(\text{IPD})^q+b$				$L=a(\text{ITD})^q+b$			
Listener	a	b	q	E	a	b	q	E
A	18.1	−1.9	0.07	4.1	4.12	−2.0	0.28	2.8
C	12.6	1.4	0.20	7.6	0.84	1.5	0.56	3.7
W	13.6	0.8	0.10	9.3	0.03	0.5	1.00	4.5
Z	18.3	0.1	0.04	7.0	0.24	−0.3	0.70	3.5
X	0.3	−0.2	0.60	1.4	0.02	−0.2	0.82	1.2

listeners, the error for ITD was less than half the error for IPD, indicating that lateral position is better represented as a linear ITD meter than as a linear IPD meter. However, neither representation is good because lateral position is clearly a nonlinear function of the interaural parameters for most listeners. The linear fits are shown by dashed lines in Figs. 1 and 2.

4. Nonlinear fits

A reasonable fit to the lateral position data can be obtained with a function of three parameters: constant bias, scale factor, and exponent. Exponents less than 1.0 indicate compression. Such nonlinear functions were fitted to the data as functions of IPD and of ITD to minimize rms error. The final parameters and rms error are shown in Table III. The table shows that the rms errors are always smaller for the ITD functions, suggesting that lateral position is a better monotonic function of ITD than of IPD. The nonlinear fits are shown by solid lines in Figs. 1 and 2.

For listeners A, W, and Z, the exponents are close to zero ($q \leqslant 0.1$) for the IPD fits, corresponding to constant values of the model responses independent of IPD except for the sign. Therefore, for these three listeners it can be said that the lateralization responses are essentially not functions of IPD.

5. Individual differences

The plots in Figs. 1 and 2 show that the five listeners were rather different in several important respects. Whereas most of the listeners lateralized the stimuli over a large range of azimuths and gave responses over the allowed range from −40 to +40, listener X lateralized all the stimuli close to the midline. Listeners exhibited different amount of compression. But despite such individual differences, all listeners appeared to base their lateralization judgements on ITD and not on IPD.

III. CONCLUSION

Five listeners estimated the lateral positions of 50 sine tones with interaural phase differences of 0°, ±30°, ±60°, ±90°, ±120°, and ±150°. The interaural time differences ranged from −1000 to +1000 μs, and the frequencies were all in the range where lateralization can be based on signal fine structure.

The lateralization estimates were evaluated as functions of IPD and of ITD. The evaluations revealed that the estimates were well described as functions of ITD and not as functions of IPD. Evaluations included standard deviations of estimates for given interaural parameters as well as goodness of fits for simple linear and nonlinear functions. The conclusion that human listeners lateralize tones based on ITD and not on IPD agrees with results by Schiano *et al.* (1986)–limited to ITDs smaller than ours–but is at variance with other previous research (Sayers, 1964; Yost, 1981). It appears that these previous experiments were biased by blocking experimental trials with respect to frequency. It seems likely that listeners learn their sine-tone localization scales from objects in the real world, which leads to a scale based on ITD. However, the extreme limits of the scale are established by the IPD, as is logically necessary. The dominant role of the ITD no longer holds when the IPD exceeds an extreme value, somewhere in the vicinity of 180°. The results support a direct application of cross-correlation models, such as the Jeffress model, to human sound localization.

ACKNOWLEDGMENT

This work was supported by the NIH-NIDCD Grant No. DC00181.

Jeffress, L. A. (**1948**). "A place theory of sound localization," J. Comp. Physiol. Psychol. **41**, 35–39.

Kuhn, G. F. (**1979**). "The pressure transformation from a diffuse sound field to the external ear and to the body and head surface," J. Acoust. Soc. Am. **65**, 991–1000.

McAlpine, D., Jiang, D., and Palmer, A. R. (**2001**). "A neural code for low-frequency sound localization in mammals," Nat. Neurosci. **4**, 396–401.

Sayers, B., McA. (**1964**). "Acoustic-image lateralization judgements with binaural tones," J. Acoust. Soc. Am. **36**, 923–926.

Schiano, J. L., Trahiotis, C., and Bernstein, L. R. (**1986**). "Lateralization of low-frequency tones and narrow bands of noise," J. Acoust. Soc. Am. **79**, 1563–1570.

Stern, R. M., Zeiberg, A. S., and Trahiotis, C. (**1988**). "Lateralization of complex binaural stimuli A weighted-image model," J. Acoust. Soc. Am. **84**, 156–165.

Strutt, J. W. (**1907**). "On our perception of sound direction," Philos. Mag. **13**, 214–232.

Yost, W. A. (**1981**). "Lateral position of sinusoids presented with interaural intensive and temporal differences," J. Acoust. Soc. Am. **70**, 397–409.

Yost, W. A., and Hafter, E. R. (**1987**). "Lateralization," in *Directional Hearing*, edited by W. A. Yost and G. Gourevitch (Springer, New York), p. 62.

Zhang, P. X., and Hartmann, W. M. (**2004**). "Lateralization of the Huggins pitch," J. Acoust. Soc. Am. **115**, 2534.

Zwislocki, J., and Feldman, R. S. (**1956**). "Just noticeable differences in dichotic phase," J. Acoust. Soc. Am. **28**, 860–864.

Acoustic beams with angular momentum

John Lekner
School of Chemical and Physical Sciences, Victoria University of Wellington, P.O. Box 600, Wellington, New Zealand

(Received 19 January 2006; revised 11 September 2006; accepted 13 September 2006)

A family of exact solutions of the Helmholtz equation is used to represent transversely bounded helicoidal sound beams. Simple results are obtained for the energy content per unit length, the momentum content per unit length, and the angular momentum content per unit length. The analysis is restricted to lossless media; scattering and viscous damping are neglected. The energy, momentum, and angular momentum are calculated to second order in the velocity potential. The angular momentum content is always equal to m/ω times the energy content, where m (an integer) is the topological charge and ω is the angular frequency. © *2006 Acoustical Society of America.*
[DOI: 10.1121/1.2360420]

PACS number(s): 43.20.Bi [RMW] Pages: 3475–3478

I. INTRODUCTION

Hefner and Marston[1,2] have studied acoustical helicoidal beams, both theoretically and experimentally. The associated vortex structure has been explored.[3–5] The theoretical analysis has so far been restricted[1,2,5] to the Laguerre-Gaussian approximate set of solutions of the Helmholtz equation. These approximate solutions fail when the beams are strongly focused. Strong focusing is needed for *acoustical tweezers*[6,7] to work. Should *acoustical spanners* (the sound analog of optical spanners[8]) ever be developed, there will be a need for exact (nonparaxial) helicoidal solutions of the Helmholtz equation. Indeed, such solutions are needed for exact treatment of acoustical tweezers also. The purpose of this note is to present a set of such exact solutions, and discuss their properties.

The emphasis here is on the intrinsic angular momentum properties of transversely bounded acoustic beams. Note that a sound beam can supply torque on an insonified object without itself possessing intrinsic angular momentum; the Rayleigh disk[9,10] is the prime example of this. In such cases the torque applied depends on the positioning of the object in relation to the propagation direction of the (laterally infinite) sound beam.[11,12] Our interest is in the elucidation of the properties of laterally finite acoustic helicoidal beams. The calculation of the torques such beams exert on insonified objects (and the associated problem of the forces exerted by transversely finite sound beams) is left to a later publication.

II. GENERALIZED BESSEL BEAMS

It is well known[13] that linear sound is represented by solutions of the homogeneous wave equation

$$(\nabla^2 - \partial_{ct}^2)\Psi = 0. \tag{1}$$

Here Ψ is a complex velocity potential. The real first-order fluid velocity is given by the gradient of either the real or imaginary part of Ψ,

$$\mathbf{v}_1 = \nabla V, \quad V = \mathrm{Re}\,\Psi \text{ or } \mathrm{Im}\,\Psi. \tag{2}$$

The corresponding first order density ρ_1 and pressure p_1 are then given by

$$\rho_1 = -\left(\frac{\rho_0}{c}\right)\partial_{ct} V, \quad p_1 = c^2\rho_1 = -\rho_0 \partial_t V. \tag{3}$$

It has recently been shown[14] that the second-order quantities are also determined by Ψ, because they satisfy inhomogeneous linear second-order partial differential equations where the source terms are second-order in Ψ. For lossless, homentropic, irrotational flow of an ideal gas, an equation valid to all orders is known.[15]

In this note we shall consider single-frequency solutions of the wave equation (1). We write $\Psi(\mathbf{r},t) = e^{-i\omega t}\psi(\mathbf{r})$. Then $\psi(\mathbf{r})$ satisfies the Helmholtz equation

$$(\nabla^2 + K^2)\psi = 0, \quad K = \omega/c. \tag{4}$$

The wave equation and the Helmholtz equation are separable[16] in cylindrical polar coordinates (r, z, ϕ), where $r = \sqrt{x^2+y^2}$ is the distance from the z axis. A general solution which is nonsingular on the z axis (i.e., at $r=0$) can be written as

$$\psi_m(\mathbf{r}) = e^{im\phi}\int_0^K dk f(k) e^{iqz} J_m(kr), \quad k^2 + q^2 = K^2. \tag{5}$$

Note that the range of k ensures that both k and q are real, so there are no terms with exponentially increasing or decreasing amplitude contributing to ψ_m. Solutions of the form (5) are in use in electrodynamics.[17,18] The function $f(k)$ can be complex. It is arbitrary, but we shall restrict ourselves to those $f(k)$ for which the following integrals exist:

$$\int_0^K dk\sqrt{k} f(k), \quad \int_0^K dk k^{-1}|f(k)|^2, \quad \int_0^K dk k^{-1} q |f(k)|^2. \tag{6}$$

The existence of the first of these enables us to use Hankel's integral formula[18,19]

$$\int_0^\infty dr r J_m(kr) J_m(k' r) = k^{-1} \delta(k - k'). \tag{7}$$

The last two integrals give the energy, momentum, and angular momentum content of a generalized Bessel acoustic beam, as we shall see.

III. THE ENERGY, MOMENTUM, AND ANGULAR MOMENTUM DENSITIES OF A BEAM

The energy density in a fluid is[13,14]

$$e(\mathbf{r},t) = e_0 + e_1(\mathbf{r},t) + e_2(\mathbf{r},t) + \cdots. \tag{8}$$

[Note that $(\mathbf{r},t)$ is a point in space-time, not the position of a fluid particle; the Eulerian rather than the Lagrangian formulation is being used.] The zero-order term e_0 is not associated with the sound wave. The first-order term is $e_1 = -(e_0 + p_0) c^{-1} \partial_{ct} V$, and cycle-averages to zero when V is linear in $\cos \omega t$ and $\sin \omega t$. The second-order term is

$$e_2(\mathbf{r},t) = \frac{1}{2} \rho_0 [(\nabla V)^2 + (\partial_{ct} V)^2]. \tag{9}$$

When V is equal to the real or the imaginary part of $\Psi(\mathbf{r},t) = e^{-i\omega t} \psi(\mathbf{r})$, the cycle-average of e_2 is

$$\bar{e}(\mathbf{r}) = \frac{1}{4} \rho_0 [|\nabla \psi|^2 + K^2 |\psi|^2]. \tag{10}$$

The momentum density is $\mathbf{p} = \rho \mathbf{v}$, where $\rho = \rho_0 + \rho_1 + \rho_2 + \cdots$ and $\mathbf{v} = \mathbf{v}_1 + \mathbf{v}_2 + \cdots$. The first-order term $\rho_0 \mathbf{v}_1$ cycle-averages to zero. There are two second-order terms, $\rho_1 \mathbf{v}_1$ and $\rho_0 \mathbf{v}_2$. The latter term is omitted by Landau and Lifshitz,[13] but since $\mathbf{v}_2$ is irrotational[14] it can be expressed as the gradient of a potential, $\mathbf{v}_2 = \nabla W$. From Eqs. (A6) and (A7) of Ref. 14 we find that W satisfies the inhomogeneous wave equation

$$c^2 \nabla^2 W - \partial_t^2 W = 2(\partial_t \nabla V) \cdot \nabla V + 2\alpha (\partial_t V) \nabla^2 V, \tag{11}$$

where the constant α is given by Eq. (8) of Ref. 14. Cycle averaging of Eq. (11), i.e., operating with $T^{-1} \int_0^T dt$, where $T = 2\pi/\omega$ is the time period everywhere in the beam, gives zero on the right-hand side. To show this, we write the velocity potential as

$$V(\mathbf{r},t) = C(\mathbf{r}) \cos \omega t + S(\mathbf{r}) \sin \omega t. \tag{12}$$

Denoting the cycle average by a bar, we have

$$\overline{(\partial_t \nabla V) \cdot \nabla V} = -\omega \nabla C \cdot \nabla S \overline{(\cos^2 \omega t - \sin^2 \omega t)} = 0,$$

$$\overline{(\partial_t V) \nabla^2 V} = -\omega K^2 C S \overline{(\cos^2 \omega t - \sin^2 \omega t)} = 0. \tag{13}$$

(We have used the fact that C and S satisfy the Helmholtz equation.) Also $\overline{\partial_t^2 W} = 0$. Thus $\nabla^2 \bar{W} = 0 : \bar{W}(\mathbf{r})$ is a harmonic function, which cannot have a maximum or a minimum except at domain boundaries. For acoustic beams in unbounded media this implies that $\bar{W}$ is constant in space. Thus $\overline{\mathbf{v}_2}$ is zero.

The nonzero cycle-averaged part of the momentum density is thus

$$\overline{\mathbf{p}(\mathbf{r})} = \overline{\rho_1 \mathbf{v}_1} = -\frac{\rho_0}{c} \overline{(\partial_{ct} V) \nabla V} = \frac{K \rho_0}{2c} \operatorname{Im}(\psi^* \nabla \psi). \tag{14}$$

(This holds for both choices of the velocity potential, $V = \operatorname{Re} \Psi$ and $V = \operatorname{Im} \Psi$.) The result (14) is in close correspondence with the momentum density in quantum mechanics,[20]

$$\mathbf{p}(\mathbf{r},t) = \hbar \operatorname{Im}(\Psi^* \nabla \Psi), \tag{15}$$

where the wave function Ψ is a solution of the time-dependent Schrödinger equation.

In this paper we have chosen (as is customary) to have the acoustic beam propagate along the z axis. The momentum component along the beam axis has the cycle average $\overline{p_z}$. We have, from Eqs. (10) and (14),

$$\bar{e} - c\overline{p_z} = \frac{\rho_0}{4} |(\nabla - iK\hat{\mathbf{z}}) \psi|^2 \geq 0. \tag{16}$$

The cycle-average of the energy density is never smaller than c times the cycle-average of the momentum density component along the beam propagation direction. Equality in Eq. (16) is possible only for a transversely infinite plane wave beam, $\psi \sim e^{iKz}$. The quantities on the left-hand side of Eq. (16) are the Eulerian cycle-averaged energy density and momentum density. The local Eulerian cycle-averaged energy *flow* and momentum density are equal.[21]

Finally, we need the z component of the cycle-averaged angular momentum density. We have, omitting the $\rho_0 \mathbf{v}_2$ term which has zero cycle-average,

$$j_z = (\mathbf{r} \times \mathbf{p})_z = x p_y - y p_x = r p_\phi = -\left(\frac{\rho_0}{c}\right) (\partial_{ct} V)(\partial_\phi V). \tag{17}$$

(Note that j_z is zero unless the velocity potential has azimuthal dependence.) The cycle-average of Eq. (17) is, for $V = \operatorname{Re} \psi$ or $\operatorname{Im} \psi$,

$$\overline{j_z} = \frac{K \rho_0}{2c} \operatorname{Im}(\psi^* \partial_\phi \psi). \tag{18}$$

In the special case where the azimuthal dependence is entirely in the factor $e^{im\phi}$ [as it is for the generalized Bessel beams of Eq. (5)],

$$\overline{j_z} = \frac{K \rho_0}{2c} m |\psi|^2. \tag{19}$$

In this case the cycle-averaged angular momentum density is proportional to the topological charge,[3] m.

IV. APPLICATION TO GENERALIZED BESSEL BEAMS

We shall calculate the cycle-averaged contents per unit length of the beam, specifically

$$E' = \int d^2 r \bar{e}, \quad P_z' = \int d^2 r \overline{p_z}, \quad J_z' = \int d^2 r \overline{j_z}. \tag{20}$$

Here $\int d^2 r$ stands for $\int_{-\infty}^{\infty} dx \int_{-\infty}^{\infty} dy = \int_0^\infty dr r \int_0^{2\pi} d\phi$, i.e., we are taking a transverse slice through the beam. The reason for the prime notation is as follows: $dE = E' dz$ is the energy con-

tent in a slice of thickness dz of the beam, so E' may be viewed as dE/dz, etc.

Let us calculate J_z' first, because it is the simplest. We have, from Eqs. (5), (19), and (20),

$$J_z' = 2\pi\frac{K\rho_0}{2c}m\int_0^\infty drr\int_0^K dkf^*(k)e^{-iqz}J_m(kr) \times\int_0^K dk'f(k')e^{iq'z}J_m(k'r) = \pi\frac{K\rho_0}{c}m\int_0^K dkk^{-1}|f(k)|^2. \quad (21)$$

The last expression follows from the Hankel integral formula (7).

Next, consider the momentum content per unit length. This is

$$P_z' = 2\pi\frac{K\rho_0}{2c}\,\mathrm{Im}\int_0^\infty drr\int_0^K dkf^*(k)e^{-iqz}J_m(kr) \times\int_0^K dk'f(k')iq'e^{iq'z}J_m(k'r) = \pi\frac{K\rho_0}{c}\int_0^K dkk^{-1}q|f(k)|^2. \quad (22)$$

Finally, the energy content per unit length. We have

$$|\nabla\psi|^2 = (\nabla\psi^*)\cdot\nabla\psi = |\partial_r\psi|^2 + |\partial_z\psi|^2 + r^{-2}|\partial_\phi\psi|^2 = |\partial_r\psi|^2 + |\partial_z\psi|^2 + \frac{m^2}{r^2}|\psi|^2. \quad (23)$$

(The last line applies only to wave functions with $e^{im\phi}$ azimuthal dependence.) In integrating over $|\partial_r\psi|^2$ we have the r integration,

$$\int_0^\infty drr[\partial_r J_m(kr)][\partial_r J_m(k'r)] = -\int_0^\infty drr\frac{1}{r}\partial_r[r\partial_r J_m(kr)]J_m(k'r) = \int_0^\infty drr\left(k^2 - \frac{m^2}{r^2}\right)J_m(kr)J_m(k'r) \quad (24)$$

because $J_m(kr)$ satisfies the differential equation

$$\frac{1}{r}\partial_r[r\partial_r J_m(kr)] + \left(k^2 - \frac{m^2}{r^2}\right)J_m(kr) = 0. \quad (25)$$

Thus the m^2/r^2 terms cancel, and we are left with

$$E' = 2\pi\frac{\rho_0}{4}\int_0^\infty drr\int_0^K dkf^*(k)\int_0^K dk'f(k')e^{i(q'-q)z} \times\{k^2 + qq' + K^2\}J_m(kr)J_m(k'r) = \pi\rho_0 K^2\int_0^K dkk^{-1}|f(k)|^2. \quad (26)$$

From Eqs. (21), (22), and (26) we see that

$$cP_z' \le E', \quad cKJ_z' = mE'. \quad (27)$$

The inequality follows from the fact that $q = \sqrt{K^2 - k^2} \le K$ within the range of integration. The equality can be written as

$$\omega J_z' = mE', \quad (28)$$

and is consistent with the sound beam being made up of phonons, each of energy $\hbar\omega$ and each carrying angular momentum $\hbar m$. We may, if we wish, think of each phonon carrying momentum $\hbar\mathbf{K}$ (with $K=\omega/c$). This is consistent with the inequality in Eq. (27) because not all the phonons are travelling parallel to the z axis; a transversely finite acoustic beam is necessarily either converging or diverging to some extent. A similar interpretation can be made for sound pulses.[22]

V. DISCUSSION

The results we have just given are exact in the absence of scattering and viscous damping. They are rather remarkable in several ways:

(i) The energy and momentum per unit length, E' and P_z', are independent of the topological charge m;
(ii) The angular momentum content per unit length J_z' is proportional to m;
(iii) J_z' is always equal to $(m/\omega)E'$.

To be precise about point (i), if we take the same amplitude function $f(k)$ for the infinity of beams with $m=0, \pm1, \pm2, \ldots$, we shall find that they all have the same energy and momentum per unit length, despite the fact that the beams have a very different radial dependence, determined by $J_m(kr)$. Likewise for (ii), the proportionality of J_z' to m holds when $f(k)$ does not depend on m.

We should comment finally on the difference between Eq. (28) and an equation of similar form derived by Hefner and Marston.[1,2] They find, for beams with azimuthal dependence $e^{im\phi}$, that the ratio of the angular momentum flux to the beam power is ω/m. This is the same ratio as for J_z'/E', but the quantities are different; J_z' and E' are angular momentum and energy contents per unit length of the beam, not fluxes.

ACKNOWLEDGMENTS

The author is indebted to Professor Philip Marston and to an anonymous reviewer for helpful comments, suggestions, and references.

[1]B. T. Hefner and P. L. Marston, "Acoustical helicoidal waves and Laguerre-Gaussian beams: Applications to scattering and to angular momentum transport," J. Acoust. Soc. Am. **103**, 2971 (1998). *Proceedings of the Joint Meeting of the 16th International Congress on Acoustics and the 137th Meeting of the Acoustical Society of America* (Acoustical Society of America, 1998), pp. 1921–1922.
[2]B. T. Hefner and P. L. Marston, "An acoustical helicoidal wave transducer with applications for the alignment of ultrasonic and underwater systems," J. Acoust. Soc. Am. **106**, 3313–3316 (1999).
[3]J-L. Thomas and R. Marchiano, "Pseudo angular momentum and topological charge conservation for nonlinear acoustical vortices," Phys. Rev. Lett. **91**, 244302 (2003).
[4]S. Gspan, A. Meyer, S. Bernet, and M. Ritsch-Marte, "Optoacoustic gen-

eration of a helicoidal ultrasonic beam," J. Acoust. Soc. Am. **115**, 1142–1146 (2004).
[5]R. Marchiano and J-L. Thomas, "Synthesis and analysis of linear and nonlinear acoustic vortices," Phys. Rev. E **71**, 066616 (2005).
[6]J. Wu, "Acoustical tweezers," J. Acoust. Soc. Am. **89**, 2140–2143 (1991).
[7]J. Lee, K. Ha, and K. Shung, "A theoretical study of the feasibility of acoustical tweezers: Ray acoustics approach," J. Acoust. Soc. Am. **117**, 3273–3280 (2005).
[8]L. Allen, S. M. Padgett, and M. J. Padgett, *Optical Angular Momentum* (IOP, Bristol, 2003), Chap. 4.
[9]J. W. S. Rayleigh, "On an instrument capable of measuring the intensity of aerial vibrations," Philos. Mag. **14**, 186 (1882).
[10]J. W. S. Rayleigh, *Theory of Sound* (Dover, New York, 1896/1945), Vol. **2**, Sec. 253b.
[11]J. B. Keller, "Acoustic torques and forces on disks," J. Acoust. Soc. Am. **29**, 1085–1090 (1957).
[12]G. Maidanik, "Torques due to acoustical radiation pressure," J. Acoust. Soc. Am. **30**, 620–623 (1958).
[13]L. D. Landau and E. M. Lifshitz, *Fluid Mechanics* (Pergamon, Oxford, 1959), Chap. VIII.
[14]J. Lekner, "Energy and momentum of sound pulses," Physica A **363**, 217–225 (2006).
[15]M. F. Hamilton and C. L. Morfey, "Model equations," in *Nonlinear Acoustics*, edited by M. F. Hamilton and D. T. Blackstock (Academic, San Diego, 1998), Chap. 3, Eq. (26).
[16]J. A. Stratton, *Electromagnetic Theory* (McGraw-Hill, New York, 1941), p. 356.
[17]S. M. Barnett and L. Allen, "Orbital angular momentum and nonparaxial light beams," Opt. Commun. **110**, 670–678 (1994).
[18]J. Lekner, "Invariants of three types of generalized Bessel beams," J. Opt. A, Pure Appl. Opt. **6**, 837–843 (2004).
[19]G. N. Watson, *Theory of Bessel Functions*, 2nd ed. (Cambridge University Press, Cambridge, 1944), Sec. 14.4.
[20]J. Lekner, "Invariants of atom beams," J. Phys. B **37**, 1725–1736 (2004).
[21]J. Lighthill, "Acoustic streaming," J. Sound Vib. **61**, 391–418 (1978), Eq. (12).
[22]J. Lekner, "Angular momentum of sound pulses," J. Phys.: Condens. Matter **18**, 6149–6158 (2006).

Anomalous postcritical refraction behavior for certain transversely isotropic media

Lin Fa[a)]
The Department of Electronics and Information Engineering, Xi'an Institute of Post and Telecommunication, Weiguo Road, Xi'an, Shaanxi 710121, People's Republic of China

Ray L. Brown[b)]
Oklahoma Geological Survey, Sarkeys Energy Center, 100 East Boyd Street, Norman, Oklahoma 73019

John P. Castagna[c)]
Department of Earth and Atmospheric Sciences, University of Houston, 4800 Calhoun Road, Houston, Texas 77004

(Received 30 June 2005; revised 31 August 2006; accepted 13 September 2006)

Snell's law at the boundary between two transversely isotropic media with a vertical axis of symmetry (VTI media) can be solved by setting up a fourth order polynomial for the sine of the reflection/transmission angles. This approach reveals the possible presence of an anomalous postcritical angle for certain transversely isotropic media. There are thus possibly three incident angle regimes for the reflection/refraction of longitudinal or transverse waves incident upon a VTI medium: precritical, postcritical/preanomalous, and postanomalous. The anomalous angle occurs for certain strongly anisotropic media where the required root to the phase velocity equation must be switched in order to obey Snell's law. The reflection/transmission coefficients, polarization directions, and the phase velocity are all affected by both the anisotropy and the incident angle. The incident critical angles are also effected by the anisotropy. © *2006 Acoustical Society of America.*
[DOI: 10.1121/1.2360419]

PACS number(s): 43.20.Fn, 43.20.Dk, 43.20.El [LLT] Pages: 3479–3492

I. INTRODUCTION

Postcritical refraction/reflection of seismic/acoustic waves in transversely isotropic materials is potentially important in a variety of applications including earthquake seismology, environmental and geotechnical seismic investigation, seismic exploration, underwater acoustics, and nondestructive testing. In this paper postcritical reflection/transmission coefficients, polarization directions, and magnitude of phase velocities in strongly transversely isotropic media are determined using Snell's law at the interface between layers by solving a fourth order polynomial for the sine of the reflection/refraction angles. This approach can potentially be used to characterize anomalous interface behaviors and to calculate the reflection/transmission (R/T) coefficients for layered sedimentary rocks. The mathematical expressions for the polarization coefficient vector are given in terms of both the anisotropic elastic moduli of the VTI medium and the phase velocity direction, and allow calculation of the differences between the polarization direction and the phase velocity direction and between the energy velocity direction and the phase velocity direction. The treatment of the polarization coefficient vector for inhomogeneous waves is also discussed.

Sedimentary rocks such as shale are thought to be or are commonly treated as being transversely isotropic. A transversely isotropic medium with a vertical axis of symmetry is called a VTI medium. The phase velocity in anisotropic media was, in principle, known to Kelvin[1] and to Christoffel.[2] Thomsen,[3] Vernik and Nur,[4] and Wang[5] reported the measured anisotropic parameters of some sedimentary rocks. Daley and Hron,[6] and Carcione[7] described the phase velocities of longitudinal and transverse waves for an infinite elastic VTI medium. Henneke,[8] Rokhlin *et al.*,[9] and Mandal[10] discussed the reflection/refraction of an elastic wave at an interface between generally anisotropic media. Due to the complexity of the exact calculation of the R/T coefficients, Daley and Hron[11] performed the calculations of the R/T coefficients only for the case of elliptically anisotropic media. Rüger[12] approximated the R/T coefficients for layered VTI and HTI media as did Klimeš[13] in order to simplify the form of the R/T coefficients and to increase computation speed. Hosten[14] and Lanceleur *et al.*[15] described the polarization coefficient vector for the inhomogeneous wave. Aki and Richards[16] gave the sign convention of the converted waves related to the incident wave in the precritical angle regime.

In our analysis, we first set up a fourth order equation for the sine of the angle of propagation. The phase velocity is obtained from the Christoffel equation. We illustrate how solutions for the phase velocity apply to the solution of Snell's law. We use this approach to determine the real and imaginary values of the phase velocity and the sine of the angle of propagation. The selected roots that satisfy Snell's law depend on the anisotropy of the layered VTI media. This leads to unusual postcritical reflection/refraction behavior for certain types of interfaces. Next, we will set up the math-

a)Electronic mail: fa_yy@yahoo.com.cn
b)Electronic mail: raybrown@ou.edu
c)Electronic mail: jcastagna@uh.edu

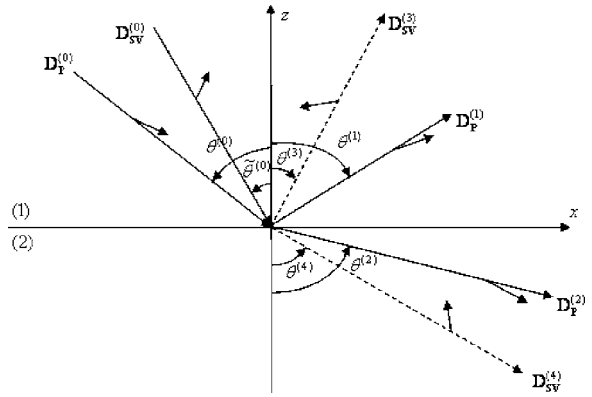

FIG. 1. Geometry of both wave front normal and displacement vectors for incident wave and converted waves at the interface between two kinds of VTI media. $\mathbf{D}_{\mathbf{P}}^{(0)}$ or $\mathbf{D}_{\mathbf{SV}}^{(0)}$ stand for the incident *P*-wave or *SV*-wave; $\mathbf{D}_{\mathbf{P}}^{(1)}$ and $\mathbf{D}_{\mathbf{SV}}^{(3)}$ are the reflection *P*- and *SV*-waves; and $\mathbf{D}_{\mathbf{P}}^{(2)}$ and $\mathbf{D}_{\mathbf{SV}}^{(4)}$ are the refracted *P*- and *SV*-waves. The arrowheads on the long lines indicate the direction of the phase velocity of each wave and those on the short lines indicate the direction of the each polarization coefficient vector.

ematical relationship of the polarization direction versus both the anisotropic parameters and phase the velocity directions of the waves, give expressions for the sign convention of polarization directions of converted waves relative to that of the incident wave and describe the treatment of the polarization coefficient vector including inhomogeneous waves. The expression for the polarization coefficient vector can be used to show the variation of the polarization direction with the incident angle and to explain anomalous polarization for the incident wave and converted waves. Finally, we will use these ideas to numerically investigate postcritical reflection/refraction for two types of VTI interfaces. We find that the postcritical refraction process can differ significantly from previous treatments and that the anomalous behavior observed can be particularly important for some strongly anisotropic materials.

II. VTI SNELL'S LAW USING FOURTH ORDER POLYNOMIALS

For two homogeneous elastic half-spaces in contact at the *xy* plane and for an incident *P*-wave or *SV* wave (*SV* denotes a vertical direction of particle displacement parallel to the *xz* plane), rays for incident and converted (reflected and refracted) waves are in the *xz* plane as shown in Fig. 1. In most anisotropic cases, none of the waves will be purely longitudinal or purely transverse, except for the case of anomalous polarization.[18] The subscripts $\{x,y,z\}=\{i\}$ denote Cartesian coordinates; the superscripts $\{0,1,2,3,\text{and } 4\}=\{m\}$ denote the cases of the incident *P*-wave or *SV*-wave ($m=0$), the reflected ($m=1$), and refracted ($m=2$) *P*-waves and the reflected ($m=3$) and refracted ($m=4$) *SV*-waves, respectively; the superscripts $\{\text{in},\text{re}\}=\{n\}$ denote the incidence medium and refraction medium, respectively. We denote by θ_0 and $\tilde{\theta}_0$, respectively, the incident angles of *P*- and *SV*-waves.

In this section, first we illustrate that the phase velocity of the converted waves may have different types of solutions in different incident angle regimes for certain layered VTI media with strong anisotropy. Then we determine the polarization coefficient vector of the incident and converted waves and give the sign convention of the polarization coefficient vector of the converted waves relative to the incident wave, as well as the relation of the polarization direction versus the elastic moduli and the phase velocities. Finally we present an approach to solving Snell's law at an interface and a fast algorithm of calculating R/T coefficients.

For a VTI medium, the transverse wave (*SH*-wave) propagates independently of both *P*-wavefronts and *SV*-wavefronts (*SH* denotes that the direction of particle displacement is orthogonal to the *xz* plane). Consequently, the equations for the investigation of the *P*- and *SV*-wave motions can be analyzed assuming an effective two-dimensional motion (i.e., in the $y=0$ plane) without any loss of generality.

A. Solutions of phase velocity for the incident wave and converted waves

In the absence of body forces and for the incident wave and all resulting waves (reflected, refracted, or converted waves) in layered VTI media, the Christoffel equation can be written as[18,6]

$$\begin{bmatrix} \Gamma_{11}^{(m)}-[v^{(m)}]^2 & 0 & \Gamma_{13}^{(m)} \\ 0 & \Gamma_{22}^{(m)}-[v^{(m)}]^2 & 0 \\ \Gamma_{31}^{(m)} & 0 & \Gamma_{33}^{(m)}-[v^{(m)}]^2 \end{bmatrix} \begin{bmatrix} u_x^{(m)} \\ u_y^{(m)} \\ u_z^{(m)} \end{bmatrix} = 0, \tag{1}$$

where $\rho^{(n)}$ and $c_{jl}^{(n)}$ (j, $l=1$, 2, 3, 4, 5, and 6) are the mass density and moduli relating stress and strain in the incidence and refraction media; $u_i^{(0)}$ is the component of the particle displacement (i.e., polarization coefficient vector) $\boldsymbol{u}^{(0)}$ ($m=0$) for the incident wave and $u_i^{(m)}$ is the component of the particle displacement $\boldsymbol{u}^{(m)}$ ($m=1$, 2, 3, and 4) for each resulting wave; $v^{(m)}$ is the phase velocity of the incident wave and resulting waves ($m=0$, 1, 2, 3, and 4); ω is angular frequency; $k^{(m)}=\omega/v^{(m)}$, $l_x^{(m)}=k_x^{(m)}/k^{(m)}=\sin\theta^{(m)}$, $l_z^{(m)}=k_z^{(m)}/k^{(m)}=\cos\theta^{(m)}$, $A_{ji}^{(n)}=c_{jl}^{(n)}/\rho^{(n)}$, $\Gamma_{13}^{(m)}=\Gamma_{31}^{(m)}=(A_{13}^{(n)}+A_{44}^{(n)})\sin 2\theta^{(m)}/2$, $\Gamma_{11}^{(m)}=A_{11}^{(n)}\sin^2\theta^{(m)}+A_{44}^{(n)}\cos^2\theta^{(m)}$, $\Gamma_{22}^{(m)}=A_{44}^{(n)}\cos^2\theta^{(m)}+A_{66}^{(n)}\sin^2\theta^{(m)}$, $\Gamma_{33}^{(m)}=A_{33}^{(n)}\cos^2\theta^{(m)}+A_{44}^{(n)}\sin^2\theta^{(m)}$ and the scattering (refraction or reflection) angle $\theta^{(m)}$ ($m=1$, 2, 3, and 4) is a function of the incident angle θ (θ_0 or $\tilde{\theta}_0$).

From Eq. (1), the solution of the phase velocity for the *SH*-wave can be written as

$$v_{\text{sh}}^{(m)}=\sqrt{\Gamma_{22}^{(m)}}=\sqrt{A_{66}^{(m)}\sin^2\theta^{(m)}+A_{44}^{(m)}\cos^2\theta^{(m)}}. \tag{2}$$

Because the *SH*-wave is independent of the *P*- and *SV*-waves, we do not consider it in the following calculation and analysis.

According to Eq. (1), the solutions of phase velocities of the incident wave (*P*-wave or *SV*-wave) and resulting waves at a given angle $\theta^{(m)}$ are given by

$$v_1^{(m)}=\sqrt{(A_4^{(n)}\sin^2\theta^{(m)}+A_5^{(n)}+Q^{(m)})/2}, \tag{3}$$

or

$$v_2^{(m)} = \sqrt{(A_4^{(n)} \sin^2 \theta^{(m)} + A_5^{(n)} - Q^{(m)})/2}, \tag{4}$$

where $A_1^{(n)} = A_{11}^{(n)} - A_{44}^{(n)}$, $A_2^{(n)} = A_{44}^{(n)} - A_{33}^{(n)}$, $A_3^{(n)} = A_{13}^{(n)} + A_{44}^{(n)}$, $A_4^{(n)} = A_{11}^{(n)} - A_{33}^{(n)}$, $A_5^{(n)} = A_{33}^{(n)} + A_{44}^{(n)}$, and $Q^{(m)} = \sqrt{[A_1^{(n)} \sin^2 \theta^{(m)} + A_2^{(n)} \cos^2 \theta^{(m)}]^2 + [A_3^{(n)}]^2 \sin^2 2\theta^{(m)}}$.

These phase velocity expressions are the same as those given by Daley and Hron[6] and Carcione.[7] These authors chose $v_1^{(m)}$ as the solution of the phase velocity of the incident *P*-wave and resulting *P*-waves and $v_2^{(m)}$ as the solution of the phase velocity of the incident *SV*-wave and resulting *SV*-waves. These solutions are valid for the *P*- and *SV*-waves in an infinite VTI medium but are only sometimes valid for the resulting reflected and refracted waves (we shall see that strongly anisotropic VTI media may require that the phase velocity roots be switched beyond a certain angle). Furthering the work of Daley and Hron[6] and Carcione,[7] we determine that (1) for some layered VTI media with strong anisotropy, the value of $\sin \theta^{(m)}$ for the inhomogeneous wave can become an imaginary number at a certain postcritical incident angle referred to as the "anomalous angle" notated as $\theta_a^{(m)}$, and (2) the solution of the phase velocity should be switched from $v_1^{(m)}$ to $v_2^{(m)}$ for the inhomogeneous *P*-wave at this anomalous incident angle or the solution of the phase velocity should be switched from $v_2^{(m)}$ to $v_1^{(m)}$ for the inhomogeneous *SV*-wave at the anomalous angle, i.e., the phase velocity becomes imaginary. The existence of the anomalous angle depends on the well-known[6] anisotropic parameters, $\varepsilon^{(\mathrm{re})}$ and $\delta^{(\mathrm{re})}$, of the refraction medium and, $\varepsilon^{(\mathrm{in})}$ and $\delta^{(\mathrm{in})}$, of the incidence medium. In the case where the anomalous angle exists, for the refracted *P*-wave or the reflected *P*-wave, $v_1^{(m)}$ is the solution of the phase velocity in the preanomalous angle regime, and $v_2^{(m)}$ is the solution of the phase velocity in the postanomalous angle regime; for the refracted *SV*-wave, $v_2^{(m)}$ is the solution of the phase velocity in the preanomalous angle regime, and $v_1^{(m)}$ is the solution of the phase velocity in the postanomalous angle regime. The anomalous polarization implies that the first arrival becomes a purely transverse wave. Helbig and Schoenbeg[18] gave a condition of anomalous polarization in a homogeneous anisotropic elastic medium; $c_{13}+c_{44}>0$ indicates that the polarization is normal and $c_{13}+c_{44}<0$ indicates that the polarization is anomalous. The mathematical expressions of the polarization coefficient vector given below will also give the relation of particle displacement direction versus both the elastic moduli of the VTI media and the phase velocity direction, and it can be used to explain the anomalous polarization. The condition of the anomalous refraction (or anomalous reflection) in the postcritical incidence angle regime is different from that of the anomalous polarization described by Helbig and Schoenbeg.[18] It not only strongly depends on the anisotropy of the incidence and refraction media, but also on the incident angle. Even though the values of both $c_{13}^{(\mathrm{in})}+c_{44}^{(\mathrm{in})}$ of the incidence medium and $c_{13}^{(\mathrm{re})}+c_{44}^{(\mathrm{re})}$ of the refraction medium are greater than zero, anomalous refraction (or anomalous reflection) may occur. Slawinski, Slawinski, Brown, and Parkin[19] illustrated the application of the general Snell's law by using an approximate expression for the phase velocity of weak anisotropic media[3] without considering anomalous reflection or refraction. We will show that the solution of Snell's law for phase velocity of the corresponding converted wave must be changed as noted above at the anomalous angle.

B. Determination of polarization coefficient vectors for the incident wave and converted waves

The orientation of the displacement vector of a plane wave in a homogeneous anisotropic elastic medium is the polarization of that plane wave.[18] As we only consider *P*- and *SV*-waves, Eq. (1) can be rewritten as

$$\begin{bmatrix} \Gamma_{11}^{(m)} - [v^{(m)}]^2 & \Gamma_{13}^{(m)} \\ \Gamma_{31}^{(m)} & \Gamma_{33}^{(m)} - [v^{(m)}]^2 \end{bmatrix} \begin{bmatrix} u_x^{(m)} \\ u_z^{(m)} \end{bmatrix} = 0. \tag{5}$$

The complex polarization coefficient vector can be written as[16,17]

$$\begin{bmatrix} u_x^{(m)} \\ u_z^{(m)} \end{bmatrix} = \begin{bmatrix} a_1^{(m)} & b_1^{(m)} \\ a_3^{(m)} & b_3^{(m)} \end{bmatrix} \begin{bmatrix} 1 \\ j \end{bmatrix}, \tag{6}$$

where $a_1^{(m)}$, $b_1^{(m)}$, $a_3^{(m)}$, and $b_3^{(m)}$ are real and j is a unit imaginary number.

The anisotropic elastic moduli of a VTI medium and the wave phase velocity direction can influence the polarization direction for the infinite VTI medium. The anisotropic parameters of the incidence and refraction media and the incidence angle determine the polarization direction of each converted wave for layered VTI media. From Eq. (5), we obtain

$$\frac{u_z^{(m)}}{u_x^{(m)}} = -\frac{\Gamma_{11}^{(m)} - [v^{(m)}]^2}{\Gamma_{13}^{(m)}} \tag{7}$$

and

$$\frac{u_x^{(m)}}{u_z^{(m)}} = -\frac{\Gamma_{33}^{(m)} - [v^{(m)}]^2}{\Gamma_{31}^{(m)}}. \tag{8}$$

Equations (7) and (8), and the normalized condition $u_x^{(m)}[u_x^{(m)}]^* + u_z^{(m)}[u_z^{(m)}]^* = 1$ yield

$$\frac{u_x^{(m)}}{u_z^{(m)}} + \frac{[u_z^{(m)}]^*}{[u_x^{(m)}]^*} = \frac{u_x^{(m)}[u_x^{(m)}]^* + u_z^{(m)}[u_z^{(m)}]^*}{[u_x^{(m)}]^* u_z^{(m)}}, \tag{9}$$

or

$$\frac{[u_x^{(m)}]^*}{[u_z^{(m)}]^*} + \frac{u_z^{(m)}}{u_x^{(m)}} = \frac{[u_x^{(m)}]^* u_x^{(m)} + [u_z^{(m)}]^* u_z^{(m)}}{u_x^{(m)}[u_z^{(m)}]^*}. \tag{10}$$

Thus, we can obtain the polarization direction of each resulting wave relative to a given incident wave. The sign of each component of polarization coefficient vector must obey the following relation:

$$u_x^{(m)}[u_z^{(m)}]^* = -\frac{|\Gamma_{13}^{(m)}|^2}{\Gamma_{13}^{(m)}\{\Gamma_{33}^{(m)} - [v^{(m)}]^2\}^* + [\Gamma_{13}^{(m)}]^*\{\Gamma_{11}^{(m)} - [v^{(m)}]^2\}}, \tag{11}$$

or

$$[u_x^{(m)}]^* u_z^{(m)} = -\frac{|\Gamma_{13}^{(m)}|^2}{[\Gamma_{13}^{(m)}]^*\{\Gamma_{33}^{(m)} - [v^{(m)}]^2\} + \Gamma_{13}^{(m)}\{\Gamma_{11}^{(m)} - [v_v^{(m)}]^2\}^*}, \tag{12}$$

where the superscript $*$ signifies the complex conjugate.

Now, we begin to derive the mathematical expressions of polarization coefficient vectors of the incident wave and all converted waves. From Eqs. (8) and (11), we can obtain the x component of the complex polarization coefficient vector as follows:

$$u_x^{(m)}[u_x^{(m)}]^* = |u_x^{(m)}|^2 = u_x^{(m)}[u_z^{(m)}]^* \left[\frac{u_x^{(m)}}{u_z^{(m)}}\right]^* = \frac{\Gamma_{13}^{(m)}[\Gamma_{13}^{(m)}]^*}{\Gamma_{13}^{(m)}[\Gamma_{13}^{(m)}]^* + \{\Gamma_{11}^{(m)} - [v^{(m)}]^2\}\{\Gamma_{11}^{(m)} - [v^{(m)}]^2\}^*}. \tag{13}$$

From Eqs. (7) and (12), we get the z component of the complex polarization coefficient vector,

$$u_z^{(m)}[u_z^{(m)}]^* = |u_z^{(m)}|^2 = [u_x^{(m)}]^* u_z^{(m)} \left[\frac{u_z^{(m)}}{u_x^{(m)}}\right]^* = \frac{\Gamma_{13}^{(m)}[\Gamma_{13}^{(m)}]^*}{\Gamma_{13}^{(m)}[\Gamma_{13}^{(m)}]^* + \{\Gamma_{33}^{(m)} - [v^{(m)}]^2\}\{\Gamma_{33}^{(m)} - [v^{(m)}]^2\}^*}. \tag{14}$$

Equations (11)–(14) give the polarization directions of the incident and converted waves as functions of the anisotropic elastic moduli and the incident angle. Using Eqs. (11)–(14), the polarization directions of all converted waves related to that of the incident wave can be determined analytically and the anomalous polarization[18] can be studied.

For the incident wave and homogeneous converted waves, the polarization coefficient vectors are real. Therefore, $b_1^{(m)}=0$ and $b_3^{(m)}=0$. By rewriting Eqs. (13) and (14), we get each component of the polarization coefficient vector as follows:

$$u_x^{(m)} = a_1^{(m)} = \sqrt{\frac{\Gamma_{33}^{(m)} - [v^{(m)}]^2}{\Gamma_{11}^{(m)} + \Gamma_{33}^{(m)} - 2[v^{(m)}]^2}} = \frac{\Gamma_{13}^{(m)}}{\sqrt{[\Gamma_{33}^{(m)}]^2 + \{\Gamma_{11}^{(m)} - [v^{(m)}]^2\}^2}}, \tag{15}$$

$$u_z^{(m)} = a_3^{(m)} = \sqrt{\frac{\Gamma_{11}^{(m)} - [v^{(m)}]^2}{\Gamma_{11}^{(m)} + \Gamma_{33}^{(m)} - 2[v^{(m)}]^2}} = \frac{\Gamma_{13}^{(m)}}{\sqrt{[\Gamma_{13}^{(m)}]^2 + \{\Gamma_{33}^{(m)} - [v^{(m)}]^2\}^2}}. \tag{16}$$

As the reflection and refraction angles $\theta^{(m)}$ ($m=1$, 2, 3, and 4) are a function of the incident angle θ, the polarization directions of the incident plane wave and the converted waves depend on the incident angle θ as well as the anisotropic parameters of the media.

We assume an incident plane wave moving in the negative z direction incident upon a VTI boundary with a horizontal component of motion along the x axis, as shown in Fig. 1. According to the sign convention of the polarization coefficient vectors [Eq. (11) or Eq. (12)] for a harmonic particle vibration with a given angular frequency ω, the relation between the particle displacement vector and the polarization coefficient vector for the incident wave can be written as

$$\mathbf{D}_{\mathbf{p}}^{(0)} = \begin{pmatrix} u_x^{(0)} \\ -u_z^{(0)} \end{pmatrix} \exp[j(\omega t - k^{(0)} x \sin\theta + k^{(0)} z \cos\theta)]$$

(P-wave incidence) (17)

or

$$\mathbf{D}_{\mathbf{sv}}^{(0)} = \begin{pmatrix} -u_z^{(0)} \\ u_x^{(0)} \end{pmatrix} \exp[j(\omega t - k^{(0)} x \sin\theta + k^{(0)} z \cos\theta)]$$

(SV-wave incidence), (18)

where $k^{(0)}$ is the wave number of the incident P-wave or that of the incident SV-wave. The relation between the particle displacement vectors, the polarization coefficient vectors, and the corresponding scattering coefficients for the converted waves can be written as

$$\mathbf{D}_{\mathbf{p}}^{(1)} = R^{(1)} \begin{pmatrix} u_x^{(1)} \\ u_z^{(1)} \end{pmatrix} \exp[j(\omega t - k^{(1)} x \sin\theta^{(1)} - k^{(1)} z \cos\theta^{(1)})], \tag{19}$$

$$\mathbf{D}_{\mathbf{p}}^{(2)} = R^{(2)} \begin{pmatrix} u_x^{(2)} \\ -u_z^{(2)} \end{pmatrix} \exp[j(\omega t - k^{(2)} x \sin\theta^{(2)} + k^{(2)} z \cos\theta^{(2)})], \tag{20}$$

$$\mathbf{D}_{\mathbf{sv}}^{(3)} = R^{(3)} \begin{pmatrix} -u_z^{(3)} \\ -u_x^{(3)} \end{pmatrix} \exp[j(\omega t - k^{(3)} x \sin\theta^{(3)} - k^{(3)} z \cos\theta^{(3)})], \tag{21}$$

and

$$\mathbf{D}_{\mathbf{sv}}^{(4)} = R^{(4)} \begin{pmatrix} -u_z^{(4)} \\ u_x^{(4)} \end{pmatrix} \exp[j(\omega t - k^{(4)} x \sin\theta^{(4)} + k^{(4)} z \cos\theta^{(4)})], \tag{22}$$

where $k^{(m)}$ is the wave number of the converted waves, $R^{(1)}$ is the reflection coefficient of quasi-P to quasi-P wave reflection, $R^{(2)}$ is the transmission coefficient of quasi-P to quasi-P wave refraction, $R^{(3)}$ is the reflection coefficient of quasi-P to quasi-SV wave reflection, and $R^{(4)}$ is the transmission coefficient of quasi-P to quasi-SV wave refraction.

When the phase velocity of the incident wave is smaller than that of the refracted or converted wave, there is a corresponding incident critical angle $\theta_c^{(m)}$ ($m=1$ or 2 or 4). When the incident angle θ is greater than the incident critical angle $\theta_c^{(m)}$, the corresponding converted wave becomes an inhomogeneous wave.

For the incident quasi-P wave or for the incident quasi-SV wave, the z component of the power density flux can be written as (see Appendices A and B)

$$P_z^{(0)} = -\frac{\omega k^{(0)}}{2}\{[u_x^{(0)}]^* c_{44}^{(\mathrm{in})}[u_x^{(0)}\cos\theta + u_z^{(0)}\sin\theta] + [u_z^{(0)}]^*[c_{13}^{(\mathrm{in})}u_x^{(0)}\sin\theta + c_{33}^{(\mathrm{in})}u_z^{(0)}\cos\theta]\} \quad (23)$$

or

$$P_z^{(0)} = -\frac{\omega k^{(0)}}{2}\{[u_z^{(0)}]^* c_{44}^{(\mathrm{in})}[u_z^{(0)}\cos\theta + u_x^{(0)}\sin\theta] + [u_x^{(0)}]^*[c_{13}^{(\mathrm{in})}u_z^{(0)}\sin\theta + (c_{13}^{(\mathrm{in})}u_x^{(0)}\cos\theta)]\}. \quad (24)$$

For the reflected and refracted waves, the z components of their power density fluxes can be written as

$$P_z^{(1)} = \frac{\omega k^{(1)}|R^{(1)}|^2}{2}\{[u_x^{(1)}]^* c_{44}^{(\mathrm{in})}[u_x^{(1)}\cos\theta^{(1)} + u_z^{(1)}\sin\theta^{(1)}] + [u_z^{(1)}]^*[c_{13}^{(\mathrm{in})}u_x^{(1)}\sin\theta^{(1)} + (c_{33}^{(\mathrm{in})}u_z^{(1)}\cos\theta^{(1)})]\}, \quad (25)$$

$$P_z^{(2)} = -\frac{\omega k^{(2)}|R^{(2)}|^2}{2}\{[u_x^{(2)}]^* c_{44}^{(\mathrm{re})}[u_x^{(2)}\cos\theta^{(2)} + u_z^{(2)}\sin\theta^{(2)}] + [u_z^{(2)}]^*[c_{13}^{(\mathrm{re})}u_x^{(2)}\sin\theta^{(2)} + c_{33}^{(\mathrm{re})}u_z^{(2)}\cos\theta^{(2)}]\}, \quad (26)$$

$$P_z^{(3)} = \frac{\omega k^{(3)}|R^{(3)}|^2}{2}\{[u_z^{(3)}]^* c_{44}^{(\mathrm{in})}[u_z^{(3)}\cos\theta^{(3)} + u_x^{(3)}\sin\theta^{(3)}] + [u_x^{(3)}]^*[c_{13}^{(\mathrm{in})}u_z^{(3)}\sin\theta^{(3)} + (c_{13}^{(\mathrm{in})}u_x^{(3)}\cos\theta^{(3)})]\}, \quad (27)$$

and

$$P_z^{(4)} = -\frac{\omega k^{(4)}|R^{(4)}|^2}{2}\{[u_z^{(4)}]^* c_{44}^{(\mathrm{re})}[u_z^{(4)}\cos\theta^{(4)} + u_x^{(4)}\sin\theta^{(4)}] + [u_x^{(4)}]^*[c_{13}^{(\mathrm{re})}u_z^{(4)}\sin\theta^{(4)} + (c_{13}^{(\mathrm{re})}u_x^{(4)}\cos\theta^{(4)})]\}. \quad (28)$$

For the inhomogeneous wave, the real part of the z component of the power density flux should be equal to zero or the component normal to the interface of the energy flux vector is always nonexistent.[11] Substitution of both $u_x^{(m)} = a_1^{(m)} + jb_1^{(m)}$ and $u_z^{(m)} = a_3^{(m)} + jb_3^{(m)}$ into Eqs. (25)–(28), leads to

$$(a_1^{(m)}a_3^{(m)} + b_1^{(m)}b_3^{(m)}) = 0, \quad (29)$$

where for a quasi-P wave incidence, $m=2$, or $m=2$ and 4, respectively; for a quasi-SV wave incidence, $m=1$, or $m=1$ and 2, or $m=1$, 2 and 4, respectively.

Using Eq. (29), we obtain the relation

$$u_x^{(m)}[u_z^{(m)}]^* = (a_1^{(m)} + jb_1^{(m)})(a_3^{(m)} - jb_3^{(m)}) = j(b_1^{(m)}a_3^{(m)} - a_1^{(m)}b_3^{(m)}), \quad (30)$$

or

$$u_z^{(m)}[u_x^{(m)}]^* = (a_1^{(m)} - jb_1^{(m)})(a_3^{(m)} + jb_3^{(m)}) = -j(b_1^{(m)}a_3^{(m)} - a_1^{(m)}b_3^{(m)}). \quad (31)$$

Equations (30) or (31) guarantee that if $u_x^{(m)}$ is real, then $u_z^{(m)}$ must be imaginary (or vice versa). For the refracted and reflected inhomogeneous P-waves, we take $u_x^{(m)}$ as a real number and $u_z^{(m)}$ as an imaginary number. For the refracted inhomogeneous SV-wave, we take $u_x^{(m)}$ as an imaginary number and $u_z^{(m)}$ as a real number. Therefore, the polarization coefficients for the inhomogeneous wave can be written as

$$u_x^{(m)} = a_1^{(m)} = \sqrt{\frac{\Gamma_{33}^{(m)} - [v^{(m)}]^2}{\Gamma_{11}^{(m)} + \Gamma_{33}^{(m)} - 2[v^{(m)}]^2}} = \frac{\Gamma_{13}^{(m)}}{\sqrt{[\Gamma_{33}^{(m)}]^2 + \{\Gamma_{11}^{(m)} - [v^{(m)}]^2\}^2}}, \quad (32)$$

$$u_z^{(m)} = jb_3^{(m)} = j|\Gamma_{13}^{(m)}|\sqrt{\frac{\{\Gamma_{11}^{(m)} - [v^{(m)}]^2\}^*}{\{[\Gamma_{13}^{(m)}]^*\}^2\{\Gamma_{33}^{(m)} - [v^{(m)}]^2\} + |\Gamma_{11}^{(m)}|^2\{\Gamma_{11}^{(m)} - [v^{(m)}]^2\}^*}}, \quad (33)$$

where $b_1^{(m)}=0$ and $a_3^{(m)}=0$.

C. An approach to Snell's law and a fast algorithm of calculating R/T coefficients

At the interface between VTI media, according to Snell's law, we have

$$\mathrm{const}(\theta) = \left[\frac{\sin\theta^{(1)}}{v^{(1)}}\right]^2 = \left[\frac{\sin\theta^{(2)}}{v^{(2)}}\right]^2 = \left[\frac{\sin\theta^{(3)}}{v^{(3)}}\right]^2 = \left[\frac{\sin\theta^{(4)}}{v^{(4)}}\right]^2, \quad (34)$$

where $\theta=\theta_0$ or $\theta=\tilde{\theta}_0$, which stands for the incident angle of P-wave or the incident angle of SV-wave; and $\mathrm{const}(\theta) = \{\sin\theta/[v^{(0)}]\}^2 = 2\sin^2\theta/[A_5^{(\mathrm{in})} + A_4^{(\mathrm{in})}\sin^2\theta \pm Q^{(1)}]$. $v^{(0)}$ is the phase velocity of the incident P-wave or that of the incident SV-wave. From Eq. (34), we obtain two fourth order equations for $\sin\theta^{(m)}$ as follows (see Appendix C):

$$B_1^{(\mathrm{in})}(\theta)\sin^4\theta^{(1,3)} + B_3^{(\mathrm{in})}(\theta)\sin^2\theta^{(1,3)} + B_5^{(\mathrm{in})} = 0, \quad (35)$$

and

$$B_1^{(\mathrm{re})}(\theta)\sin^4\theta^{(2,4)} + B_3^{(\mathrm{re})}(\theta)\sin^2\theta^{(2,4)} + B_5^{(\mathrm{re})} = 0, \quad (36)$$

where $B_1^{(\mathrm{in})}(\theta) = A_2^{(\mathrm{in})} - [K_1(\theta)]^2$, $B_3^{(\mathrm{in})}(\theta) = 2[A_1^{(\mathrm{in})} - A_4^{(\mathrm{in})}K_1(\theta)]$, $B_5^{(\mathrm{in})} = A_3^{(\mathrm{in})} - [A_4^{(\mathrm{in})}]^2$, $K_1(\theta) = 2/\mathrm{const}(\theta) - A_4^{(\mathrm{in})}$, $B_1^{(\mathrm{re})}(\theta) = A_2^{(\mathrm{re})} - [K_2(\theta)]^2$, $B_3^{(\mathrm{re})}(\theta) = 2[A_1^{(\mathrm{re})} - A_4^{(\mathrm{re})}K_2(\theta)]$, $B_5^{(\mathrm{re})} = A_3^{(\mathrm{re})} - [A_4^{(\mathrm{re})}]^2$, and $K_2(\theta) = 2/\mathrm{const}(\theta) - A_4^{(\mathrm{re})}$.

According to Eqs. (35) and (36), the reflection/refraction angles are given in terms of $\sin\theta^{(m)}$ and thus, the R/T coefficients can be calculated. We can use the energy balance principle to verify whether the calculated R/T coefficients are correct. When there is at least one incident critical angle and the incident angle is greater than this critical angle, the corresponding converted wave becomes an inhomogeneous wave.

The case of a P-wave impinging on the interface between VTI media provides an instructive example. The relations of both displacement and traction across interface in terms of the R/T coefficients can be written as

$$\begin{bmatrix} u_x^{(1)} & -u_x^{(2)} & -u_z^{(3)} & u_z^{(4)} \\ u_z^{(1)} & u_z^{(2)} & -u_x^{(3)} & -u_x^{(4)} \\ \dfrac{c_{13}^{(\mathrm{in})}u_x^{(1)}\sin\theta^{(1)}+c_{33}^{(1)}u_z^{(1)}\cos\theta^{(1)}}{v^{(1)}(\theta^{(1)})} & -\dfrac{c_{13}^{(\mathrm{re})}u_x^{(2)}\sin\theta^{(2)}+C_{33}^{(\mathrm{re})}u_z^{(2)}\cos\theta^{(2)}}{v^{(2)}(\theta^{(2)})} & -\dfrac{c_{13}^{(\mathrm{in})}u_z^{(3)}\sin\theta^{(3)}+C_{33}^{(\mathrm{in})}u_x^{(3)}\cos\theta^{(3)}}{v^{(3)}(\theta^{(3)})} & -\dfrac{c_{33}^{(\mathrm{re})}u_x^{(4)}\sin\theta^{(4)}+c_{13}^{(\mathrm{re})}u_z^{(4)}\cos\theta^{(4)}}{v^{(4)}(\theta^{(4)})} \\ \dfrac{c_{44}^{(\mathrm{in})}(u_x^{(1)}\cos\theta^{(1)}+u_z^{(1)}\sin\theta^{(1)})}{v^{(1)}(\theta^{(1)})} & \dfrac{C_{44}^{(\mathrm{re})}(u_x^{(2)}\cos\theta_2+u_z^{(2)}\sin\theta_2)}{v^{(2)}(\theta^{(2)})} & -\dfrac{c_{44}^{(\mathrm{in})}(u_x^{(3)}\sin\theta^{(3)}+u_z^{(3)}\cos\theta^{(3)})}{v^{(3)}(\theta^{(3)})} & -\dfrac{c_{44}^{(\mathrm{re})}(u_z^{(4)}\cos\theta^{(4)}+u_x^{(4)}\sin\theta^{(4)})}{v^{(4)}(\theta^{(4)})} \end{bmatrix}$$

$$\times \begin{bmatrix} R^{(1)} \\ R^{(2)} \\ R^{(3)} \\ R^{(4)} \end{bmatrix} = \begin{bmatrix} -u_x^{(1)} \\ u_z^{(1)} \\ -\dfrac{c_{13}^{(\mathrm{in})}u_x^{(1)}\sin\theta^{(1)}+c_{33}^{(\mathrm{in})}u_z^{(1)}\cos\theta^{(1)}}{v^{(1)}(\theta_1)} \\ \dfrac{c_{44}^{(\mathrm{in})}(u_x^{(1)}\cos\theta^{(1)}+u_z^{(1)}\sin\theta^{(1)})}{v^{(1)}(\theta^{(1)})} \end{bmatrix}. \tag{37}$$

This equation can be solved for the R/T coefficients.

III. CALCULATION AND DISCUSSION

For the interface between two VTI media with given anisotropic and physical parameters, the coefficients $B_1^{(\mathrm{in})}(\theta)$ and $B_1^{(\mathrm{re})}(\theta)$ in Eqs. (35) and (36) are functions of the incident angle θ. The coefficient $B_1^{(\mathrm{in})}(\theta)$ determines the solution of the phase velocity of the reflected *P*-wave for the case of the *SV*-wave incidence. The coefficient $B_1^{(\mathrm{re})}(\theta)$ determines the solution of the phase velocities of the refracted *P*- and *SV*-waves for the case of *P*-wave incidence or the case of *SV*-wave incidence.

Here we discuss the case when there is an incident critical-angle for the refracted *P*-wave. Analysis for the cases of incident critical angle involving the refracted-SV wave is analogous and therefore need not be repeated here.

For VTI media for which $B_1^{(\mathrm{re})}(\theta)$ is smaller than zero for all incident angles, the phase velocity of the refracted *P*-wave has only one solution: $v^{(2)}=v_1^{(2)}$. For some VTI media with strong anisotropy, $B_1^{(\mathrm{re})}(\theta)$ is smaller than zero in an incident angle regime from zero to a certain anomalous postcritical angle and $B_1^{(\mathrm{re})}(\theta)$ is greater than zero from this anomalous angle to 90°. At the anomalous angle, $\sin\theta^{(2)}$ obtained from Eq. (36) becomes imaginary, and the solution of the phase velocity of refracted *P*-wave should be switched from $v_1^{(2)}$ to $v_2^{(2)}$. This anomalous angle of the refracted *P*-wave is denoted as $\theta_a^{(2)}$. As the incident angle θ approaches the anomalous angle from the preanomalous angle regime, the coefficient, $B_1^{(\mathrm{re})}(\theta)$, of Eq. (36) approaches zero from the negative side and the solution for $\sin^2\theta^{(2)}(>1)$ approaches infinity. Therefore, the value of the calculated phase velocity for the refracted inhomogeneous *P*-wave approaches infinity according to Eqs. (36) and (3). When the incident angle approaches the anomalous angle, $\theta_a^{(2)}$ from the postanomalous angle regime, the coefficient, $B_1^{(\mathrm{re})}(\theta)$, of Eq. (36) is almost zero and slightly positive and the value of the solution of $\sin^2\theta^{(2)}(<-1)$ approaches negative infinity. Therefore, the value of the calculated phase velocity for the inhomogeneous refracted *P*-wave is imaginary and its absolute value approaches infinity according to Eqs. (36) and (4). For any inhomogeneous wave, the solved phase velocity is not an actual wave velocity since $\sin\theta^{(2)}$ is greater than one and $\cos\theta^{(2)}$ is imaginary or $\cos\theta^{(2)}$ is greater than one and $\sin\theta^{(2)}$ is imaginary. No matter how big the absolute value of the solved phase velocity of the inhomogeneous refracted *P*-wave is in the vicinity of the anomalous angle $\theta_a^{(2)}$, the calculated phase velocity and the refraction angle of the inhomogeneous refracted *P*-wave always obeys Snell's law, i.e., $\sin\theta^{(2)}/v^{(2)}=\sin\theta/v^{(0)}=\sqrt{\mathrm{const}(\theta)}$. Therefore, the behavior of the inhomogeneous refracted *P*-wave is the same as that of a general inhomogenous wave. The physical explanation of this phenomenon requires consideration of Eqs. (38) and (39) below.

Based on the anisotropic parameters of some sedimentary rocks given by Thomsen,[3] Vernik and Nur,[4] and Wang,[5] the physical and anisotropic parameters of two model cases are given in Tables I and II. These models are transversely isotropic. The elastic moduli are given by $c_{13}^{(n)}=\rho^{(n)}\sqrt{[\delta^{*(n)}(\alpha^{(n)})^4]+[(\alpha^{(n)})^2-(\beta^{(n)})_v^2][(\varepsilon^{(n)}+1)(\alpha^{(n)})^2-(\beta^{(n)})^2]}-\rho^{(n)}(\beta^{(n)})^2$, $c_{33}^{(n)}=\rho^{(n)}(\alpha^{(n)})^2$, $c_{11}^{(n)}=[2\varepsilon^{(n)}+1]\rho^{(n)}[\alpha^{(n)}]^2$, $c_{44}^{(n)}=\rho^{(n)}(\beta^{(n)})^2$, and $c_{66}^{(n)}=[2\gamma^{(n)}+1]\rho^{(n)}(\beta^{(n)})$; $\alpha^{(n)}$ and $\beta^{(n)}$ are the vertical phase velocities of both *P*- and *SV*-waves in these rocks, respectively; $\varepsilon^{(n)}$, $\delta^{*(n)}$, and $\gamma^{(n)}$ are the anisotropic parameters of the rocks. The superscript * of the anisotropic parameter $\delta^{*(n)}$ does not indicate the complex conjugate of the anisotropic parameter $\delta^{(n)}$ and is used for

TABLE I. Parameters for model 1. Both sand and shale are weakly anisotropic.

Medium	$\alpha^{(n)}$ (m/s)	$\beta^{(n)}$ (m/s)	$\rho^{(n)}$ (g/cm^3)	Thomsen parameters			Elastic constants (GPa)				
				$\varepsilon^{(n)}$	$\delta^{*(n)}$	$\gamma^{(n)}$	$c_{11}^{(n)}$	$c_{13}^{(n)}$	$c_{33}^{(n)}$	$c_{44}^{(n)}$	$c_{66}^{(n)}$
A-shale	2745	1508	2.340	0.103	−0.073	0.345	21.264	6.976	17.632	5.321	8.993
T-sandstone	3368	1829	2.500	0.110	−0.127	0.255	34.597	10.612	28.359	8.363	12.628

TABLE II. Parameters for model 2. The O-shale is a strongly anisotropic oil shale.

Medium	$\alpha^{(n)}$ (m/s)	$\beta^{(n)}$ (m/s)	$\rho^{(n)}$ (g/cm^3)	Thomsen parameters			Elastic constants (GPa)				
				$\varepsilon^{(n)}$	$\delta^{*(n)}$	$\gamma^{(n)}$	$c_{11}^{(n)}$	$c_{13}^{(n)}$	$c_{33}^{(n)}$	$c_{44}^{(n)}$	$c_{66}^{(n)}$
A-shale	2745	1508	2.340	0.103	−0.073	0.345	21.264	6.976	17.632	5.321	8.993
O-shale	4231	2539	2.370	0.200	0.000	0.145	59.397	15.824	42.426	15.278	19.709

consistency with prior work (see Ref. 3). Model 1 is a case where no anomalous angle exists for the interface between the two VTI media while model 2 is a case where the anomalous angle for the refracted *P*-wave does exist. The calculated slowness curves are shown in Figs. 2(a) and 2(b) for models 1 and 2. These curves show that there is one reflected *P*-wave, one refracted *P*-wave, one reflected *SV*-wave, and one refracted *SV*-wave created when a *P*-wave or an *SV*-wave impinges on the interface between VTI media. For *P*-wave incidence, there is only one incident critical angle, $\theta_c^{(2)}$, of the refracted *P*-wave for both models.

A. Model 1

In terms of the parameters in Table I and the relation $B_1^{(\mathrm{re})}(\theta)=A_2^{(\mathrm{re})}-[K_2(\theta)]^2$, the calculated coefficient, $B_1^{(\mathrm{re})}(\theta)$ of Eq. (36) is smaller than zero for all incident angles. In this case, the phase velocity of the refracted *P*-wave has only one solution. The reflected *P*- and *SV*-waves and the refracted *SV*-wave are general converted waves. In the precritical regime $[0°<\theta<\theta_c^{(2)}]$ of the refracted *P*-wave, because $0<\sin\theta^{(2)}<1$, the refracted *P*-wave is a general converted wave. For postcritical angles, $(\theta_c^{(2)}<\theta<90°)$, since $\sin\theta^{(2)}$ is greater than 1 and $\cos\theta^{(2)}$ is imaginary, the refracted *P*-wave is a general inhomogeneous wave. The incident wave and all converted waves abide by Snell's law in all incidence angle regimes, i.e.,

$$\frac{\sin\theta^{(0)}}{v^{(0)}}=\frac{\sin\theta^{(1)}}{v^{(1)}}=\frac{\sin\theta^{(2)}}{v^{(2)}}=\frac{\sin\theta^{(3)}}{v^{(3)}}=\frac{\sin\theta^{(4)}}{v^{(4)}}.$$

Consequently, as for the results given by the previous work, $v_1^{(2)}$ is the solution of the phase velocity, $v^{(2)}$, of the refracted *P*-wave. In other words, $v^{(2)}=v_1^{(2)}$ for all incident angles.

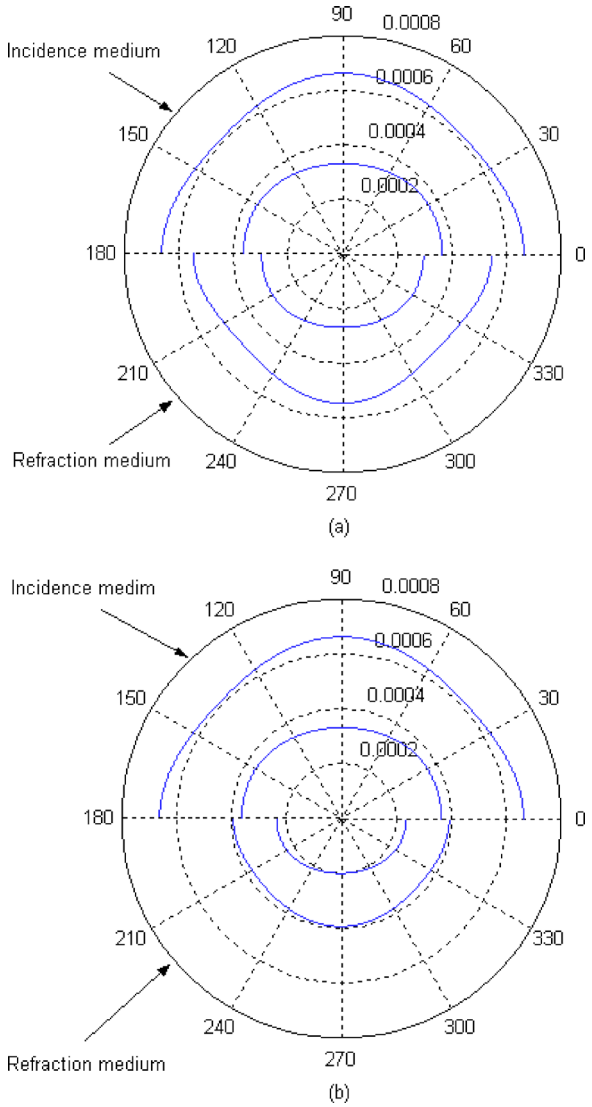

FIG. 2. Calculated slowness curves: (a) model 1; (b) model 2.

Figure 3 shows the relation of the R/T coefficients versus both θ and $\varepsilon^{(\mathrm{re})}$ given by Eq. (37) with all other physical and anisotropic parameters of the incidence and refraction media constant. Some observations include the following: (1) anisotropy can cause the R/T coefficients to vary; (2) the maximum of $R^{(2)}$ decreases with increasing $\varepsilon^{(\mathrm{re})}$; (3) the local maximum of $R^{(3)}$ decreases with increasing $\varepsilon^{(\mathrm{re})}$ and its maximum increases with $\theta^{(2)}$; (4) the maximum of $R^{(4)}$ increases with $\varepsilon^{(\mathrm{re})}$; and (5) $\theta_c^{(2)}$ decreases with increasing $\varepsilon^{(\mathrm{re})}$.

For the isotropic case, the calculated $\theta_c^{(2)}$ is equal to 54.5897°, and for the anisotropic case, the calculated $\theta_c^{(2)}$ is equal to 49.9154°. The relations of both the *z* component, $P_z^{(0)}$, of power density flux of the incident wave and the real part summation, $P_z^{(s)}=[\Sigma_{m=1}^{4}\mathrm{real}(P_z^{(m)})]$, of *z* components of power density flux of all converted waves versus the incident angle θ are shown in Fig. 4. As should be the case, the calculated R/T coefficients obey the principle of conservation of energy for all incident angles.

B. Model 2

Figure 5 is the calculated relation between the coefficient, $B_1^{(\mathrm{re})}(\theta)$, of Eq. (36) and the incidence angle θ with the parameters for model 2 given in Table II. Because no incidence critical-angle exists for each of the reflected *P*-wave, reflected *SV*-wave, and the refracted *SV*-wave, they are general converted waves. In other words, $v_1^{(1)}$ is the solution of the phase velocity of the reflected *P*-wave, and $v_2^{(3)}$ and $v_2^{(4)}$ are the solutions of the phase velocities of the reflected and refracted *SV*-waves, respectively. The calculated incident critical-angle, $\theta_c^{(2)}$, of the refracted *P*-wave is about equal to 33.6322°. From Fig. 5, it can be seen that there is a zero value for the coefficient $B_1^{(\mathrm{re})}(\theta)$ at $\theta=62.0600°$, which is

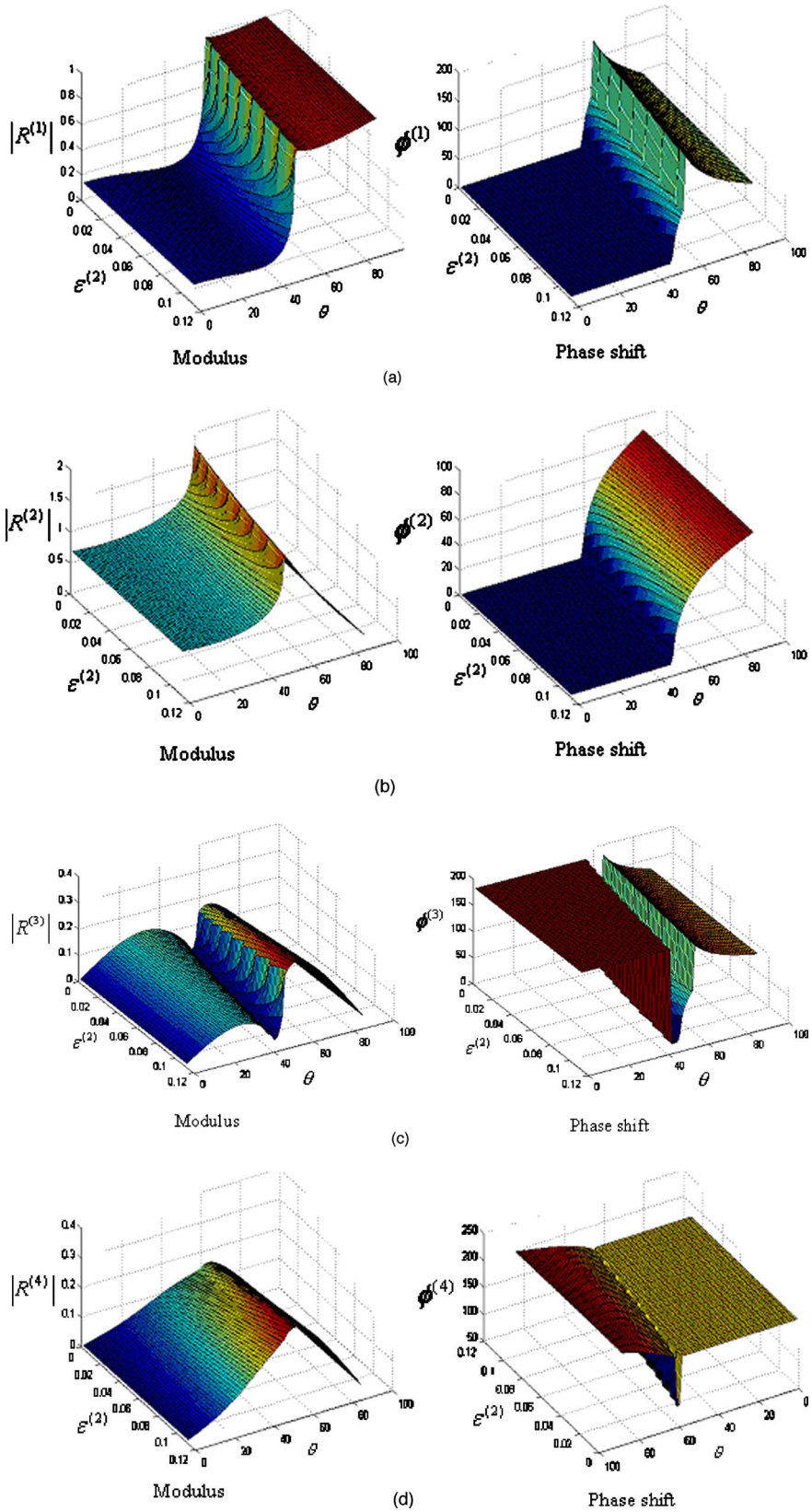

FIG. 3. R/T coefficients versus both θ and $\varepsilon^{(\mathrm{re})}$ when $\varepsilon^{(\mathrm{in})}$, $\delta^{*(\mathrm{in})}$ and $\delta^{*(\mathrm{re})}$ are constant for model 1. $\varepsilon^{(\mathrm{in})}$ and $\delta^{*(\mathrm{in})}$ are the anisotropic parameters of the incidence medium; $\varepsilon^{(\mathrm{re})}$ and $\delta^{*(\mathrm{re})}$ are the anisotropic parameters of the refraction medium. The left is modulus $|R^{(m)}|$, the right is phase $\phi^{(m)}$ (in degrees) and $m=1$, 2, 3, and 4, respectively. (a) $R^{(1)}$ versus θ and $\varepsilon^{(\mathrm{re})}$; (b) $R^{(2)}$ versus θ and $\varepsilon^{(\mathrm{re})}$; (c) $R^{(3)}$ versus θ and $\varepsilon^{(\mathrm{re})}$; (d) $R^{(4)}$ versus θ and $\varepsilon^{(\mathrm{re})}$.

greater than $\theta_c^{(2)}$. The calculations also show that when the incident angle $\theta<62.0600°$ [i.e., $B_1^{(\mathrm{re})}(\theta)<0$], the solution of the phase velocity of the refracted P-wave is $v_1^{(2)}$ and when $\theta>62.0600°$ [i.e., $B_1^{(\mathrm{re})}(\theta)>0$], the solution is $v_2^{(2)}$. In other words, only when the solution of the phase velocity of the refracted P-wave is switched at $\theta=62.0600°$ from $v_1^{(2)}$ to $v_2^{(2)}$, will the calculated phase velocity and the refraction angle of the refracted P-wave in terms of Eqs. (3), (4), and (36) obey

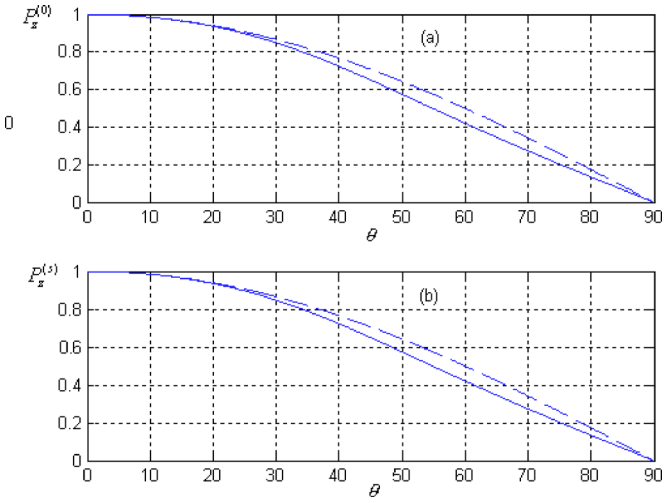

FIG. 4. $P_z^{(0)}$ and $P_z^{(s)}$ versus θ for model 1. The dashed line is the isotropic case and the solid line is the anisotropic case, where, $P_z^{(0)}$ and $P_z^{(s)}$ are normalized by the maximum of the power density flux of the incident wave.

Snell's law and the calculated R/T coefficients according to Eq. (37) abide by the energy balance principle.

Now, we analyze and discuss the refracted *P*-wave for various angle ranges:

1. For $0° < \theta < 62.0600°$: In this incident angle regime, Fig. 5 shows that $B_1^{(\mathrm{re})}(\theta)$ is smaller than zero, and $\sin^2\theta^{(2)}$ is greater than zero.

Due to $0 < \sin^2\theta^{(2)}$ [or $\sin\theta^{(2)}$] < 1 in the incident angle regime from 0° to the critical angle, $\theta_c^{(2)}(< 62.0600°)$, of the refracted *P*-wave, the refracted *P*-wave is a general converted wave and its particle displacement is expressed by Eq. (20).

Due to $\sin^2\theta^{(2)} > 1$ and $\cos^2\theta^{(2)} < 0$ in the incident angle regime from $\theta_c^{(2)}$ to 62.0600°, in terms of Eq. (20), the particle displacement of the refracted *P*-wave can be rewritten as

$$\begin{aligned}\mathbf{D}_{\mathbf{p}}^{(2)} &= R^{(2)}\begin{pmatrix} u_x^{(2)} \\ -u_z^{(2)} \end{pmatrix}\exp[-\alpha_c^{(2)}z]\exp[j(\omega t - k^{(2)}x\sin\theta^{(2)})] \\ &= R^{(2)}\begin{pmatrix} u_x^{(2)} \\ -u_z^{(2)} \end{pmatrix}\exp[-\alpha_c^{(2)}z]\exp\left[j\omega\left(t - \frac{\sin\theta^{(2)}}{v_1^{(2)}}x\right)\right] \\ &= R^{(2)}\begin{pmatrix} u_x^{(2)} \\ -u_z^{(2)} \end{pmatrix}\exp[-\alpha_c^{(2)}z]\exp\left[j\omega\left(t - \frac{\sin\theta^{(0)}}{v_1^{(0)}}x\right)\right] \\ &= R^{(2)}\begin{pmatrix} u_x^{(2)} \\ -u_z^{(2)} \end{pmatrix}\exp[-\alpha_c^{(2)}z]\exp[j(\omega t - k^{(0)}x\sin\theta],\end{aligned} \tag{38}$$

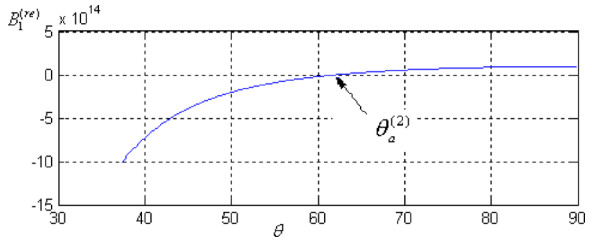

FIG. 5. $B_1^{(2)}$ versus the incident angle θ for model 2.

where $\alpha_c^{(2)} = -jk^{(2)}\cos\theta^{(2)} = \omega\sqrt{\sin^2\theta^{(2)} - 1}/v_1^{(2)}$, which is a real number. Equation (38) shows that in the incident angle regime from $\theta_c^{(2)}$ to 62.0600°, because $v_1^{(2)}$ and $\alpha_c^{(2)}$ are real, the refracted *P*-wave attenuates far from the interface and propagates in the *x* direction and its wave number $k_x^{(2)}(=k^{(2)}\sin\theta^{(2)})$ is equal to the projection, $k^{(0)}\sin\theta$, of the wave number vector of the incident *P*-wave on the *x* axis.

Now we analyze the case of the incidence angle θ being approximate to and slightly less than 62.0600°. When θ approaches 62.0600°, calculated $\sin\theta^{(2)}$ and $v_1^{(2)}$ approach infinity but are of the same order and still obey Snell's law such that $k^{(2)}\sin\theta^{(2)} = \omega\sin\theta^{(2)}/v_2^{(2)} = \omega\sin\theta/v_1^{(0)} = \omega\sqrt{\mathrm{const}(\theta)}$, which is a finite value and, $\alpha_c^{(2)} = \omega\sqrt{[\sin\theta^{(2)}/v_1^{(2)}]^2 - [1/v_1^{(2)}]^2} \approx \omega\sin\theta^{(2)}/v_1^{(2)} = \omega\sin\theta/v_1^{(0)}$. The refracted *P*-wave can be still expressed by Eq. (38) and its behavior is the same as that of the general inhomogeneous wave in the preanomalous angle regime near to the incident angle of 62.0600°.

2. At $\theta = 62.0600°$: $B_1^{(\mathrm{re})}(\theta)$ equals zero and $\sin^2\theta^{(2)} = \sin^2\theta^{(4)} = -[B_5^{(\mathrm{re})}/B_3^{(2)}(\theta)]$. When θ is greater than 62.0600°, $\sin^2\theta^{(2)}$ anomalously becomes negative. This incident angle is the anomalous angle, $\theta_a^{(2)}$, of the refracted *P*-wave.

3. In the incident angle regime from 62.0600° to 90°: Figure 5 shows that $B_1^{(\mathrm{re})}(\theta)$ is greater than zero in this incident angle regime. In terms of Eq. (36), the calculated $\sin^2\theta^{(2)}$ is smaller than zero and $\cos^2\theta^{(2)}$ is greater than one. In the incident angle regime from $\theta_a^{(2)}$ (62.0600°) to 90°, only choosing $v_2^{(2)}$ as the solution of the refracted *P*-wave can guarantee that the calculated $\sin\theta^{(2)}$ and the phase velocity of the refracted *P*-wave abide by the Snell's law. Because the calculated $\sin\theta^{(2)}$ is smaller than zero, $\cos^2\theta^{(2)}$ is greater than one. Both $\sin\theta^{(2)}$ and $v_2^{(2)}$ are imaginary, and the particle displacement of the refracted *P*-wave can be rewritten as

$$\begin{aligned}\mathrm{D}_{\mathrm{P}}^{(2)} &= R^{(2)}\begin{pmatrix} u_x^{(2)} \\ -u_z^{(2)} \end{pmatrix}\exp[-\alpha_a^{(2)}z]\exp[j(\omega t - k^{(2)}x\sin\theta^{(2)})] \\ &= R^{(2)}\begin{pmatrix} u_x^{(2)} \\ -u_z^{(2)} \end{pmatrix}\exp[-\alpha_a^{(2)}z]\exp\left[j\omega\left(t - \frac{\sin\theta^{(2)}}{v_2^{(2)}}x\right)\right] \\ &= R^{(2)}\begin{pmatrix} u_x^{(2)} \\ -u_z^{(2)} \end{pmatrix}\exp[-\alpha_a^{(2)}z]\exp\left[j\omega\left(t - \frac{\sin\theta}{v_1^{(0)}}\right)\right] \\ &= R^{(2)}\begin{pmatrix} u_x^{(2)} \\ -u_z^{(2)} \end{pmatrix}\exp[-\alpha_a^{(2)}z]\exp[j(\omega t - k^{(0)}x\sin\theta)],\end{aligned} \tag{39}$$

where as $v_2^{(2)}$ and $\sin\theta^{(2)}$ are imaginary, and both $\alpha_a^{(2)}$ $[= jk^{(2)}\cos\theta^{(2)} = j\omega\cos\theta^{(2)}/v_2^{(2)}]$ and $k^{(2)}\sin\theta^{(2)}$ $[= \omega\sin\theta^{(2)}/v_2^{(2)} = \omega\sin\theta/v_1^{(0)} = \omega\sqrt{\mathrm{const}(\theta)}]$ are real. The refracted *P*-wave still attenuates far from the interface and propagates in the *x* direction in the postanomalous angle regime. Its wave number $k_x^{(2)}[=k^{(2)}\sin\theta^{(2)}]$ is equal to the projection, $k^{(0)}\sin\theta$, of the wave number vector of the incident *P*-wave on the *x* axis.

When θ is approximate to and slightly larger than 62.0600°, the absolute values of the calculated $\sin\theta^{(2)}$ and $v_1^{(2)}$ which are imaginary are approximate to infinity. They

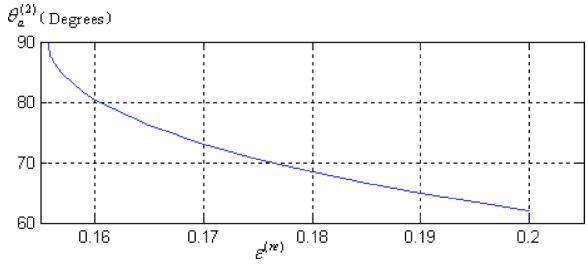

FIG. 6. $\theta_a^{(2)}$ versus $\varepsilon^{(\mathrm{re})}$.

are approximate to infinity with same order and still obey Snell's law, i.e., $\sin\theta^{(2)}/v_1^{(2)}=\sin\theta/v_1^{(0)}=\sqrt{\mathrm{const}(\theta)}$, and $\alpha_c^{(2)}=\omega\sqrt{[\sin\theta^{(2)}/v_1^{(2)}]^2-[1/v_1^{(2)}]^2}\approx\omega\sin\theta^{(2)}/v_1^{(2)}=\omega\sin\theta/v_1^{(0)}$. The refracted *P*-wave is still expressed by Eq. (39) and its behavior is the same as that of the general inhomogeneous wave in the postanomalous angle regime near to the anomalous angle.

Now we analyze the effect of anisotropy on the anomalous angle, $\theta_a^{(2)}$, of the refracted *P*-wave and discuss the relationship of the R/T coefficients versus both the incident angle and the anisotropic parameters. For the curves shown below, the incident angle, θ, and the anisotropic parameter, $\varepsilon^{(\mathrm{re})}$, are variables and the other physical and anisotropic parameters of the incidence and refraction media are held constant. The calculated relation of $\theta_a^{(2)}$ versus $\varepsilon^{(\mathrm{re})}$ is shown in Fig. 6 indicating that the anomalous angle, $\theta_a^{(2)}$, increases with decreasing anisotropic parameter, $\varepsilon^{(\mathrm{re})}$. When $\varepsilon^{(\mathrm{re})}$ decreases to 0.15578, the anomalous angle, $\theta_a^{(2)}$, and the zero point of the coefficient $B_1^{(\mathrm{re})}$ of Eq. (36) disappear at the same time. Figure 7 is the calculated relationship of the R/T coefficient versus both incident angle θ and anisotropic parameter, $\varepsilon^{(\mathrm{re})}$. Figure 6 shows that (1) $\theta_c^{(2)}$ decreases with increasing $\varepsilon^{(\mathrm{re})}$; (2) both the local maximum of $R^{(1)}$ and the maximum of $R^{(2)}$ decrease with increasing $\varepsilon^{(\mathrm{re})}$; and (3) the maximum of $R^{(3)}$ increases with $\varepsilon^{(\mathrm{re})}$ and its local maximum decreases with increasing $\varepsilon^{(\mathrm{re})}$.

In the isotropic case, the calculated incident critical angle, $\theta_c^{(2)}$, of the refracted *P*-wave is equal to 40.4499°. In the anisotropic case, the calculated $\theta_c^{(2)}$ and $\theta_a^{(2)}$ are about equal to 33.6322° and 62.0600°, respectively.

The relations of both the *z* component, $P_z^{(0)}$, of the power density flux of the incident wave and the real part summation, $P_z^{(s)}[=\Sigma_{m=1}^{4}\mathrm{real}(P_z^{(m)})]$, of *z* components of the power density flux of all converted waves versus the incident angle θ are shown in Fig. 8. The dashed line is the isotropic case and both the solid line and the dotted line are the anisotropic cases. In the anisotropic cases, because we take $v_1^{(2)}$ as the solution of the phase velocity of the refracted *P*-wave in the preanomalous angle regime, and $v_2^{(2)}$ as the solution of its phase velocity in the postanomalous angle regime, the calculated R/T coefficients abide by the energy balance throughout all incident angles, as shown by the solid lines in Figs. 8(a) and 8(b). The dashed lines and solid lines in Fig. 8 are the same as those in Fig. 4. The reason for this is that the real part summation of the *z* components of the power density flux of all converted waves only depends on the *z* component of power density flux of the incident wave, and is not related to the properties of the refraction medium.

The dotted line in Fig. 8(b) is the calculated result when we only take $v_1^{(2)}$ as the solution of the phase velocity of the refracted *P*-wave throughout all incident angles for the anisotropic case.

From the results for model 2, it can be seen that if we only choose $v_1^{(2)}$ as the solution of the phase velocity of the refracted *P*-wave throughout all incident angle regimes, for the postanomalous angle regime (1) the reflection/refraction angles and the phase velocity do not obey Snell's law and (2) the calculated R/T coefficients do not satisfy principle of conservation of energy, as evidenced by the dotted line in Fig. 8(b).

IV. RESULTS

From the above derivations, calculations, and analyses for models 1 and 2, we have found that:

(i) For the interface between some combinations of VTI media, such as those selected for model 1, the anomalous angle does not exist and the anisotropy only causes variation of R/T coefficients.

(ii) For the interface between other combinations of VTI media, as represented by model 2, there is an incident critical angle $\theta_c^{(2)}$ and an anomalous angle $\theta_a^{(2)}$. The anomalous angle $\theta_a^{(2)}$ is in the postcritical regime. Therefore, for a refracted *P*-wave, the incident angle can be divided into three regimes: (1) from 0° to the incident critical angle $\theta_c^{(2)}$, (2) from the angle $\theta_c^{(2)}$ to anomalous angle $\theta_a^{(2)}$, and (3) from the angle $\theta_a^{(2)}$ to 90°. In the preanomalous angle regime $(0°-\theta_a^{(2)})$ of the refracted *P*-wave, the solution of the phase velocity of the corresponding converted *P*-wave is real. In the postanomalous angle regime $(\theta_a^{(2)}-90°)$, the solution of the phase velocity is imaginary. In the post incident critical-angle regime, the solutions for the phase velocity of the refracted *P*-wave are not an actual wave velocity. If the incident angle is approximate to the anomalous angle $\theta_a^{(2)}$, although the absolute value (or value) of the phase velocity, $v_1^{(2)}$ [or $v_2^{(2)}$], of the inhomogeneous refracted *P*-wave approximates infinity, $v_1^{(2)}$ [or $|v_2^{(2)}|$] and $\sin\theta^{(2)}$ are of same order and obey Snell's law. Therefore, in this incident angle regime, the behavior of the inhomogeneous refracted *P*-wave is the same as that of the general inhomogenous wave. In our treatments of both R/T coefficients and Snell's law, the selected phase velocity is required. The related anisotropy across an interface not only causes variation of R/T coefficients, but also variable behavior of the calculated phase velocity and refraction angle in the vicinity of the anomalous angle.

(iii) We have found similar results for the case when *S-V* waves are incident.

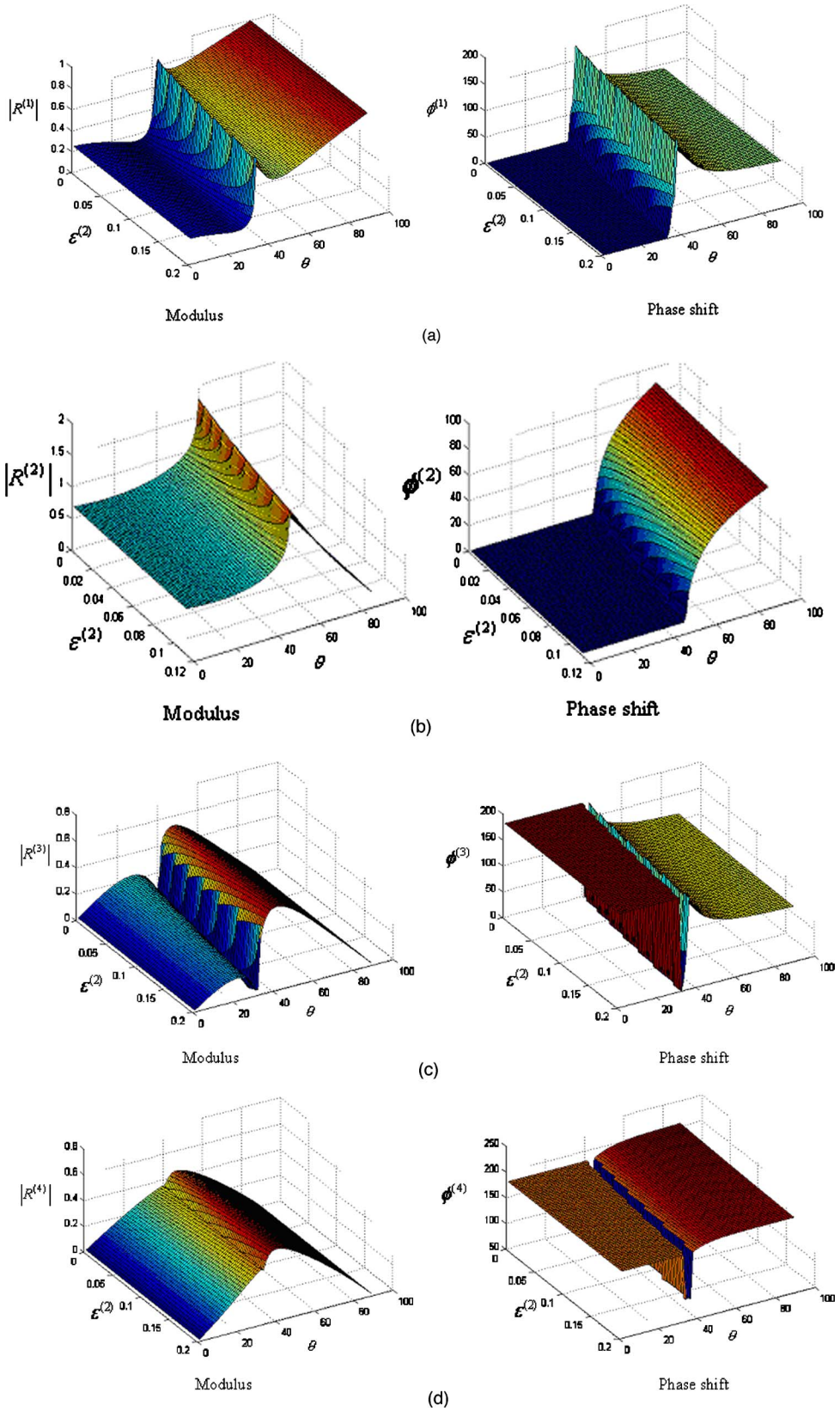

FIG. 7. R/T coefficients versus θ and $\varepsilon^{(\mathrm{re})}$ for constant $\varepsilon^{(\mathrm{in})}$, $\delta^{*(\mathrm{in})}$, and $\delta^{*(\mathrm{re})}$ for model 2. The left is modulus $|R^{(m)}|$, the right is phase $\phi^{(m)}$ (in degrees) and $m=1$, 2, 3, and 4, respectively. (a) $R^{(1)}$ versus both θ and $\varepsilon^{(\mathrm{re})}$. (b) $R^{(2)}$ versus θ and $\varepsilon^{(\mathrm{re})}$. (c) $R^{(3)}$ versus θ and $\varepsilon^{(\mathrm{re})}$. (d) $R^{(4)}$ versus θ and $\varepsilon^{(\mathrm{re})}$.

(iv) In the postanomalous angle regime, because both $\sin\theta^{(m)}$ and the phase velocity $v^{(m)}$ are imaginary, the corresponding inhomogeneous wave still attenuates far from the interface and propagates in the x direction. The corresponding wave number $k_x^{(m)}[=k^{(m)}\sin\theta^{(m)}]$ is equal to the projection, $k^{(0)}\sin\theta$, of the wave number vector of the incident P-wave on the x axis.

(v) For model 2, we also found that with the decreasing $\varepsilon^{(\mathrm{re})}$, the zero point of the coefficient, $B_1^{(\mathrm{re})}$, of Eq. (36)

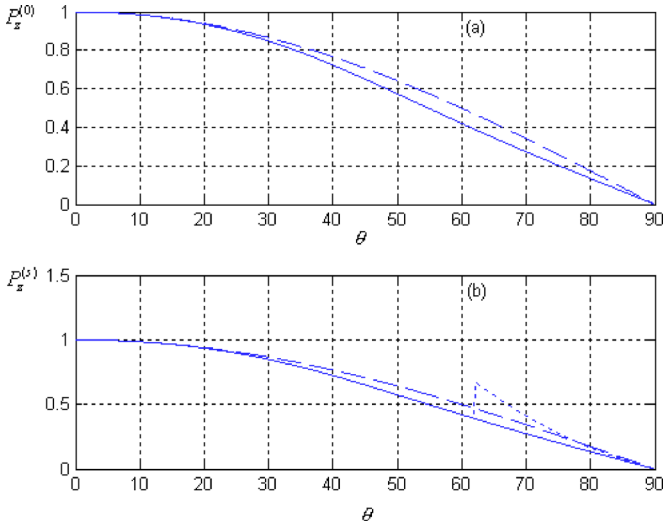

FIG. 8. $P_z^{(0)}$ and $P_z^{(s)}$ versus θ for model 2, where $P_z^{(0)}$ and $P_z^{(s)}$ are normalized by the maximum of the power density flux of the incident wave.

shifts towards higher incident angle and the anomalous angle increases. When $\varepsilon^{(\mathrm{re})}$ decreases to a certain value, the zero point of $B_1^{(\mathrm{re})}$ and the anomalous angle disappear at the same time.

(vi) We infer that the anomalous angle is more likely to occur when there are very strong contrasts in anisotropy across the interface.

V. CONCLUSIONS AND FUTURE WORK

(i) An alternative approach to Snell's law for the analysis of postcritical refraction/reflection of layered VTI media is presented. The method is based upon a fourth order equation for $\sin\theta^{(m)}$.

(ii) For the interface between certain layered VTI media with strong anisotropy, there can be an anomalous angle $\theta_a^{(m)}$, which is in the postcritical incident angle regime.

(iii) When the incident angle is greater than $\theta_a^{(m)}$, then $\sin^2\theta^{(m)}$ anomalously becomes a real negative number and the root of the phase velocity of the corresponding converted wave must be switched.

(iv) When the incident angle is approximately equal to the anomalous angle $\theta_a^{(m)}$, the absolute value of the calculated phase velocity of the corresponding inhomogeneous wave increases greatly although it is not an actual wave velocity of the inhomogeneous wave.

(v) Rapid calculation of R/T coefficients is accomplished by picking different solutions of the phase velocity of the converted wave in different incident angle regimes for the case when the anomalous angle exists. This manuscript describes a new algorithm, which can rapidly calculate the R/T coefficients in terms of their strict analytic expressions for both elliptical anisotropic media and nonelliptical anisotropic media. This algorithm is not only valid for the weak anisotropy, but also valid for general anisotropy.

(vi) We have shown how to determine the polarization coefficient vector for the different waves in the postcritical regime and a method of determining the polarization direction of the converted waves relative to the incident wave. The Snell's law approach used provides another means of comparing the reflection and transmission effects of relative anisotropy between two VTI media.

Future research should include detailed analysis of the relations between the polarization direction, the direction of phase velocity, the direction of the power density flux, the anisotropic parameters and the incidence angle, as well as the condition of creating anomalous polarization.

ACKNOWLEDGMENTS

We would like to thank the sponsors of the OU Reservoir Characterization Consortium for financial support.

APPENDIX A

In an infinite anisotropic medium, the matrix expressions of particle displacement (or polarization coefficient vector), strain, stress and gradient operator are given below:

(1)

$$\text{The particle displacement: } \mathbf{u} = \begin{pmatrix} u_s \\ u_y \\ u_z \end{pmatrix} \text{ (a three-element column matrix).}$$

(2)

$$\text{The strain: } \mathbf{S} = \begin{pmatrix} S_1 \\ S_2 \\ S_3 \\ S_4 \\ S_5 \\ S_4 \end{pmatrix} \text{ (in the form of a six-element column matrix) or}$$

$$\mathbf{S} = \begin{pmatrix} S_{xx} & S_{xy} & S_{xz} \\ S_{yx} & S_{yy} & S_{yz} \\ S_{zx} & S_{zy} & S_{zz} \end{pmatrix} = \begin{pmatrix} S_1 & \frac{S_6}{2} & \frac{S_5}{2} \\ \frac{S_6}{2} & S_2 & \frac{S_4}{2} \\ \frac{S_5}{2} & \frac{S_4}{2} & S_3 \end{pmatrix} \text{ (in the form of a nine-element square matrix)}$$

(3)

The stress: $\mathbf{T}=\begin{pmatrix} T_1 \\ T_2 \\ T_3 \\ T_4 \\ T_5 \\ T_4 \end{pmatrix}$ (in the form of a six-element column matrix) or

$$\mathbf{T}=\begin{pmatrix} T_{xx} & T_{xy} & T_{xz} \\ T_{yx} & T_{yy} & T_{yz} \\ T_{zx} & T_{zy} & T_{zz} \end{pmatrix} = \begin{pmatrix} T_1 & T_6 & T_5 \\ T_6 & T_2 & T_4 \\ T_5 & T_4 & T_3 \end{pmatrix}$$ (in the form of a nine-element square matrix).

(4)

The gradient operator $\nabla_s=\begin{pmatrix} \frac{\partial}{\partial x} & 0 & 0 \\ 0 & \frac{\partial}{\partial y} & 0 \\ 0 & 0 & \frac{\partial}{\partial z} \\ 0 & \frac{\partial}{\partial z} & \frac{\partial}{\partial y} \\ \frac{\partial}{\partial z} & 0 & \frac{\partial}{\partial x} \\ \frac{\partial}{\partial y} & \frac{\partial}{\partial x} & 0 \end{pmatrix}$.

For the above expressions, $S_1=S_{xx}$, $S_2=S_{yy}$, $S_3=S_{zz}$, $S_4=2S_{yz}=2S_{zy}$, $S_5=2S_{xz}=2S_{zx}$, $S_6=2S_{xy}=2S_{xy}$, $T_1=T_{xx}$, $T_2=T_{yy}$, $T_3=T_{zz}$, $S_4=T_{yz}=T_{zy}$, $T_5=Z_{xz}=T_{zx}$, and $T_6=T_{xy}=T_{xy}$.

APPENDIX B

For an infinite perfectly elastic medium, the basic relation between the stress **T**, the moduli matrix, C, of the medium and the strain **S** is

$$\mathbf{T}=\mathrm{C}:\mathbf{S}, \tag{B1}$$

where the symbol : is the double-dot product operator of matrix operation.

Bringing the relation between the strain **S** and the particle displacement **D**,

$$\mathbf{S}=\nabla_s\mathbf{D} \tag{B2}$$

into Eq. (B1), we obtain

$$\mathbf{T}=\mathrm{C}:\nabla_s\mathbf{D}. \tag{B3}$$

For the case of plane P- and SV-waves propagating on the xz plane of an infinite VTI medium, Eq. (B3) can be rewritten as

$$\begin{pmatrix} T_1 \\ T_2 \\ T_3 \\ T_4 \\ T_5 \\ T_4 \end{pmatrix} = \begin{pmatrix} c_{11} & c_{12} & c_{13} & 0 & 0 & 0 \\ c_{12} & c_{22} & c_{13} & 0 & 0 & 0 \\ c_{13} & c_{13} & c_{33} & 0 & 0 & 0 \\ 0 & 0 & 0 & c_{44} & 0 & 0 \\ 0 & 0 & 0 & 0 & c_{44} & 0 \\ 0 & 0 & 0 & 0 & 0 & c_{66} \end{pmatrix} \times \begin{pmatrix} \frac{\partial}{\partial x} & 0 & 0 \\ 0 & 0 & 0 \\ 0 & 0 & \frac{\partial}{\partial z} \\ 0 & \frac{\partial}{\partial z} & 0 \\ \frac{\partial}{\partial z} & 0 & \frac{\partial}{\partial x} \\ 0 & \frac{\partial}{\partial x} & 0 \end{pmatrix} \begin{pmatrix} D_x \\ 0 \\ D_z \end{pmatrix} = \begin{pmatrix} c_{11}\frac{\partial D_x}{\partial x}+c_{13}\frac{\partial D_z}{\partial z} \\ c_{11}\frac{\partial D_x}{\partial x}+c_{13}\frac{\partial D_z}{\partial z} \\ c_{13}\frac{\partial D_x}{\partial x}+c_{33}\frac{\partial D_z}{\partial z} \\ 0 \\ c_{44}\left(\frac{\partial D_x}{\partial z}+\frac{\partial D_z}{\partial x}\right) \\ 0 \end{pmatrix}, \tag{B4}$$

where the stress components T_4 and T_6 are equal to zero.

Suppose that the particle vibrates harmonically with a given angular frequency ω. The particle displacement velocity of the plane wave can be written as

$$\mathbf{V}=\frac{\partial \mathrm{D}}{\partial t}=j\omega\mathbf{D}, \tag{B5}$$

and its complex conjugate can be expressed by

$$\mathbf{V}^*=-j\omega\mathbf{D}^*. \tag{B6}$$

The power density flux vector of the plane P- and SV-waves can be written as

$$\mathbf{p} = -\frac{\mathbf{V}^* \cdot \mathbf{T}}{\mathbf{2}} = -\frac{1}{2}(V_x\ V_y\ V_z)^* \begin{pmatrix} T_1 & T_6 & T_5 \\ T_6 & T_2 & T_4 \\ T_5 & T_4 & T_3 \end{pmatrix}$$
$$= -\frac{1}{2}(V_x\ 0\ V_z)^* \begin{pmatrix} T_1 & 0 & T_5 \\ 0 & T_2 & 0 \\ T_5 & 0 & T_3 \end{pmatrix} = -\frac{1}{2}\begin{pmatrix} V_x^* T_1 + V_z^* T_5 \\ 0 \\ V_x^* T_5 + V_z^* T_3 \end{pmatrix}, \tag{B7}$$

where the symbol • is the dot product operator of matrix operation.

As shown in Fig. 1, the incident wave propagates on an *xz* plane and impinges on the interface between two kinds of VTI media and four converted waves create. Bringing Eqs. (17)–(22) into Eq. (B6) gives the complex conjugate of the particle displacement velocities of the incident and converted waves. Further bringing the complex conjugate and the stress components related to the power density flux expressed by Eq. (B4) into Eq. (B7) yields Eqs. (23)–(28).

APPENDIX C

From Eq. (30), we have

$$\text{const}(\theta)[v^{(m)}]^2 = [\sin\theta^{(m)}]^2, \tag{C1}$$

where $m=1$, 2, 3, and 4.

Inserting Eqs. (3) and (4) into Eq. (C1), we obtain the following relations:

$$Q^{(m)} = \pm\left\{\left[\frac{2}{\text{const}(\theta)} - A_4^{(n)}\right][\sin\theta^{(m)}]^2 - A_5^{(n)}\right\}$$
$$= \pm\{K_{1,2}[\sin\theta^{(m)}]^2 - A_5^{(n)}\}, \tag{C2}$$

and

$$[A_1^{(n)}\sin^2\theta^{(m)} + A_2^{(n)}\cos^2\theta^{(m)}]^2 + 4[A_3^{(n)}]^2\sin^2\theta^{(m)}\cos^2\theta^{(m)}$$
$$= \{K_{1,2}[\sin\theta^{(m)}]^2 - A_5^{(n)}\}^2, \tag{C3}$$

where $K_{1,2}(\theta) = 2/\text{const}(\theta) - A_4^{(\text{in,re})}$. Rearranging Eq. (C3) gives Eqs. (35) and (36).

[1] W. Thomson (Lord Kelvin), "Elements of a mathematical theory of elasticity, Part 1, On stresses and strains," Philos. Trans. R. Soc. London **146**, 481–498 (1856).

[2] E. B. Christoffel, "On the propagation of shocks through elastic solids" (in German), Annali di Matematica **8**, 193–243 (1877); English translation: Ann. Math. **8**, 193–243 (1877).

[3] L. Thomsen, "Weak elastic anisotropy," Geophys. J. **51**, 1954–1966 (1986).

[4] L. Vernik and A. Nur, "Ultrasonic velocity and anisotropy of hydrocarbon source rocks," Geophysics **57**, 727–735 (1992).

[5] Z. Wang, "Seismic anisotropy in sedimentary rocks, Part 2: Laboratory data," Geophysics **67**, 1423–1440 (2002).

[6] P. F. Daley and F. Hron, "Reflection and transmission coefficients for transversely isotropic media," Bull. Seismol. Soc. Am. **67**, 661–675 (1977).

[7] J. M. Carcione, *Wave Fields in Real Media: Wave Propagation in Anisotropic, Anelastic and Porous Media* (Pergamon, Amsterdam, 2001).

[8] E. G. Henneke, "Reflection-refraction of a stress wave at a plane boundary between anisotropic media," J. Acoust. Soc. Am. **51**, 210–217 (1972).

[9] S. L. Rokhlin, T. K. Boland, and L. Adler, "Reflection and refraction of elastic waves on plane interface between two generally anisotropic media," J. Acoust. Soc. Am. **79**, 906–918 (1986).

[10] B. Mandal, "Reflection and transmission properties of elastic waves on a plane interface for general anisotropic media," J. Acoust. Soc. Am. **90**, 1106–1118 (1991).

[11] P. F. Daley and F. Hron, "Reflection and transmission coefficients for seismic waves in ellipsoidally isotropic media," Geophysics **44**, 27–38 (1979).

[12] A. Rüger, "*P*-wave reflection coefficients for transversely isotropic models with vertical and horizontal axis of symmetry," Geophysics **62**, 713–722 (1997).

[13] L. Klimeš, "Weak-contrast reflection-transmission coefficients in a generally anisotropic background," Geophysics **68**, 2063–2071 (2003).

[14] B. Hosten, "Reflection and transmission of acoustic plane waves on an immersed orthotropic and viscoelastic solid layer," J. Acoust. Soc. Am. **89**, 2745–2753 (1991).

[15] P. Lanceleur, H. Ribeiro, and J. D. Belleval, "The use of inhomogenous waves in the reflection-transmission problem at a plane interface between two anisotropic media," J. Acoust. Soc. Am. **93**, 1882–1892 (1993).

[16] K. Aki and P. G. Richards, *Quantitative seismology: Theory and methods* (Freeman, New York, 1980), Vol. 1.

[17] K. Helbig and M. Schoenberg, "Anomalous polarization of elastic waves in transversely isotropic media," J. Acoust. Soc. Am. **91**, 1235–1245 (1987).

[18] B. A. Auld, *Acoustic Fields and Waves in Solids* (Wiley, New York, 1973).

[19] M. A. Slawinski, R. A. Slawinski, R. J. Brown, and J. M. Parkin, "A generalized form of Snell's Law in anisotropic media," Geophysics **65**, 632–637 (2000).

Finite element analysis of broadband acoustic pulses through inhomogenous media with power law attenuation

Margaret G. Wismer
Bucknell University, Lewisburg, Pennsylvania 17837

(Received 19 October 2005; revised 17 August 2006; accepted 18 August 2006)

Acoustic waves in tissues and weakly attenuative fluids often have an attenuation parameter, $\alpha(\omega)$, satisfying $\alpha(\omega)=\alpha_0\omega^y$ in which α_0 is a constant, ω is the frequency, and y is between 1 and 2. This power law attenuation is not predicted by the classical thermoviscous wave equation and researchers have proposed different modified viscous wave equations in which the loss term is a convolution operator or a fractional spatial or temporal derivative. In this paper, acoustic waves undergoing power law attenuation are modeled by a modification to the thermoviscous wave equation in which the time derivative of the viscous term is replaced by a fractional time derivative. An explicit time domain, finite element formulation leads to a stable algorithm capable of simulating axisymmetric, broadband acoustic pulses propagating through attenuative and dispersive media. The algorithm does not depend on the Born approximation, long wavelength limit, or plane wave assumptions. The algorithm is validated for planar and focused transducers and results include radiation patterns from a viscous scatterer in a lossless background and signals reflected from a viscous layer. The program can be used to determine scattering parameters for large, strong, possibly viscous scatterers, in either a lossless or viscous background, for which analytic results are scarce. © *2006 Acoustical Society of America.* [DOI: 10.1121/1.2354032]

PACS number(s): 43.20.Hq [TDM] Pages: 3493–3502

I. INTRODUCTION

Continued interest in the mechanisms and models of ultrasonic attenuation is motivated by the fact that loss parameters can dramatically influence sound wave propagation and affect the size, shape, and time delay of propagating pulses. Media with acoustic attenuation, whether caused by molecular relaxations or scattered by small random particles, will result in scattering coefficients that are frequency dependent. General quantitative ultrasound imaging algorithms are being developed based on this fact, as found in Oelze, *et al.* (2002), Zhang, *et al.* (2001), and Padilla, *et al.* (2003). Algorithms that compensate for attenuation in the background media are found in Oelze and O'Brien (2002) and Hughes and Duck (1997). Sophisticated techniques for determining the exact values of attenuation and dispersion are given in He (1999); and Girault, *et al.* (1998).

Acoustic attenuation in biological tissue generally satisfies a power law relationship such that attenuation increases with frequency according to some noninteger exponent. The modeling of power law attenuation and its associated dispersion can be particularly challenging. The classical Navier-Stokes viscous wave equation, with analytic solutions given in Blackstock (1967) and more recently in Cobbold, *et al.* (2004), predicts pressure with an attenuation coefficient that is quadratically dependent on frequency and with very little dispersion. This has led researchers to seek a modified wave equation, many of which contain a convolution integral term or a fractional derivative term (Szabo, 1994; Waters, *et al.* 2003), and that with these terms, more accurately models power law attenuation. Typically the convolution or fractional derivative is in the temporal domain although equations with spatial fractional derivatives are given in Chen and Holm (2004). Experimental verification of the equations in Szabo (1994) is given in He (1999). Fractional calculus is the study of modeling physical systems based on derivatives and integrals of fractional order and in depth explanations and examples are provided by Podlubny (1999)).

Recent efforts to provide analytic solutions of the modified viscous wave equations are provided in Cobbold *et al.* (2004) and Sushilov and Cobbold (2004) and in Shorter (2004) for solids. Even more examples of numerical solutions to wave equations with a convolution or summation operator are presented in Norton and Novarini (2003) to model dispersive waves in underwater environments, in Wochner, Atchley, and Sparrow (2005) to simulate the effects of absorption in air, in Wilson, *et al.* (2005) to model sound propagation in a porous media, in Stucky and Lord (2001) to predict lossy ultrasonic signals in solids, and in Padilla *et al.* (2003) and Lerch and Friedrich (1986) to predict sound signals in biological tissues. Numerical modeling of nonlinear sound propagation with power law attenuation can be found in Wallace, *et al.* (2001); Liebler, Ginter, Dreyer, and Riedlinger (2005). Further examples of the use of fractional derivatives to model diffusive and dissipative wave phenomena are found in Mainardi and Paradisi (2001); Hilfer (2003).

In this paper a modified form of the viscous wave equation for acoustic pressure waves is proposed in which the first order temporal derivative of the damping term is replaced with a fractional order temporal derivative. It is empirically shown through the wavenumber that this equation is an accurate model of power law attenuation and the assumed dispersion of Szabo (1994). The equation is solved numerically using a spatial finite element method and a temporal finite difference method. The boundary condition between

two media with different attenuation coefficients is enforced. The numerical solutions are based on an axisymmetric geometry and results are provided for a broadband pulsed signal launched from a planar piston or focused transducer and impinging upon scatterers of various sizes and material parameters.

The remainder of this paper is organized as follows: in Sec. II we review more of the theory of power law attenuation and how it can be modeled with a modified viscous wave equation based on fractional time derivatives. Section III presents the numerical solution of this equation. The axisymmetric form of the equation is solved and the resulting pressure waves are compared to analytic solutions for piston transducers, both planar and focused. In Sec. IV we present some simulation results and a discussion on the reflection coefficient for attenuative materials is included. In Sec. V we discuss the results and the implications for using the attenuation parameter in an imaging system.

II. THEORETICAL MODEL OF ATTENUATION

In 1967, Blackstock (Blackstock, 1967) analyzed transient pressure signals through a viscous medium based on the homogenous viscous wave equation, given as

$$\nabla^2 p - \frac{1}{c_0^2}\frac{\partial^2 p}{\partial t^2} + \tau\frac{\partial}{\partial t}\nabla^2 p = 0, \tag{1}$$

in which c_0 is sound velocity, τ is a first order time constant that models a molecular relaxation and/or bulk viscosity, and p is the small-signal or excess pressure. This model assumes that the attenuation is relatively light and causes negligible temperature effects in the surrounding media. The one-dimensional plane wave solution for this equation in dimension z is written in phasor form as

$$p(z) = p_0 e^{j(\omega t - \mathbf{k}z)},$$

in which the complex wavenumber, $\mathbf{k}$, is given as

$$\mathbf{k} = \frac{\omega}{c_0}\sqrt{\frac{1}{1+j\omega\tau}} = \beta - j\alpha, \tag{2}$$

and the boundary condition is $p(0)=p_0 e^{j\omega t}$. The plane wave solution is significant because any temporal-spatial pressure field, in a homogenous medium, can be expressed as a sum of plane waves. If one assumes that the fluid has a relatively short time constant, consistent with adiabatic processes such that $(\omega\tau)\ll 1$; then $\alpha\approx\alpha_0\omega^2$, $\alpha_0=\tau/2c_0$, $\beta=\omega/c_0$, and the plane wave becomes an exponentially, decaying sinusoid such that

$$p(z) = p_0 e^{-\alpha z} e^{j(\omega t - \beta z)}. \tag{3}$$

Experimental investigations have revealed that for many thick or gelatinous fluid substances, biological tissues, attenuation does increase with frequency, but not as much to the frequency squared. In Szabo (1994), one will find plots of attenuation versus frequency for representative thick fluids and viscous materials in which the power law exponent is between 1 and 2. It is well accepted that absorption in most fluids satisfies a power law such that

$$\alpha(\omega) = \alpha_0|\omega|^y, \tag{4}$$

in which y is a noninteger and is often close to 1. It is often assumed that this plot is part of a resonance curve in which the attenuation peaks at a certain frequency and then decreases, but these high frequencies are rarely seen in ultrasound transducers.

A slight modification of (1) in which the partial time derivative is changed to a fractional derivative yields a modified viscous wave equation of the form

$$\nabla^2 p - \frac{1}{c_0^2}\frac{\partial^2 p}{\partial t^2} + \tau^{y-1}\frac{\partial^{(y-1)}}{\partial t^{y-1}}\nabla^2 p = 0. \tag{5}$$

Fractional derivatives have long been used to model systems either with light damping or that otherwise could not be described with a single time constant. Several books have been published on fractional calculus including Podlubny (1999), in which the continuous time Riemann fractional derivative of $f(t)$ is defined as

$$\frac{\partial^\nu f}{\partial t^\nu} = \frac{1}{\Gamma(\upsilon)}\frac{\partial^n}{\partial t^n}\int_0^t (t-x)^{\upsilon-1} f(x)dx, \tag{6}$$

in which $\upsilon = n-\nu$ and n is the smallest integer greater than ν. The gamma function, $\Gamma(\upsilon)$, is defined by

$$\Gamma(\upsilon) = (\upsilon-1)\,! = \int_0^\infty u^{\upsilon-1}e^{-u}\,du. \tag{7}$$

Thus, whereas integer time derivatives of a function describe what is happening to a function at an instant in time, fractional derivatives depend on how the function has evolved over time. For this reason they are well suited to model systems with damping.

The complex wavenumber for eq. (5) is

$$\mathbf{k} = \frac{\omega}{c_0}\frac{1}{\sqrt{1+(j\omega\tau)^{(y-1)}}}. \tag{8}$$

The negative imaginary part of this complex number is the attenuation and can be empirically proven to satisfy

$$\alpha(\omega) = -\,\mathrm{Imag}[\mathbf{k}] \approx \frac{(y-1)}{y}\frac{\tau^{y-1}}{c_0}|\omega|^y, \tag{9}$$

if the modified *smallness approximation* of $(\omega\tau)^{y-1}\ll 1$ is true, consistent with the attenuation factor found in Blackstock (1967) for $y=2$. In order for broadband signals to be causal, the sound velocity must also be frequency dependent or, equivalently, the propagation factor, $\beta=\omega/c(\omega)$, is nonlinearly dependent on frequency. The Kramers-Kronig theory, based on signal causality, has been applied to the damped wave solutions to determine the exact nature of $\beta(\omega)$. An alternative theory based on generalized functions and causality has been proposed in Szabo (1994). In both cases, $c_0=c(\infty)$. A rigorous explanation and experimental validation of these theories is provided in Waters, *et al.*

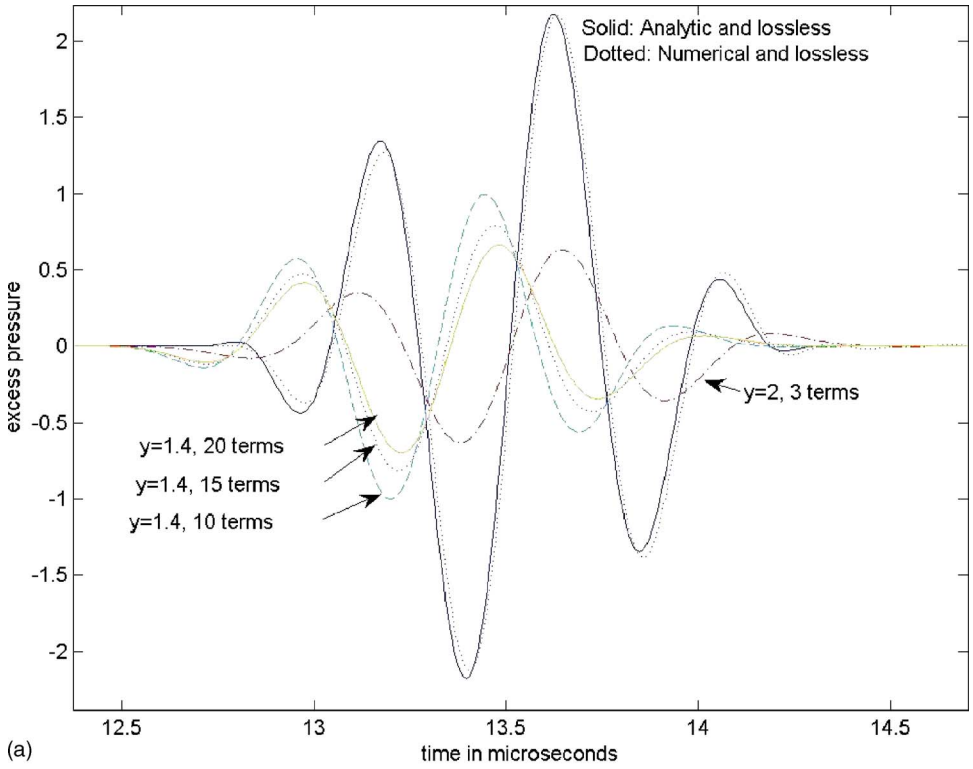

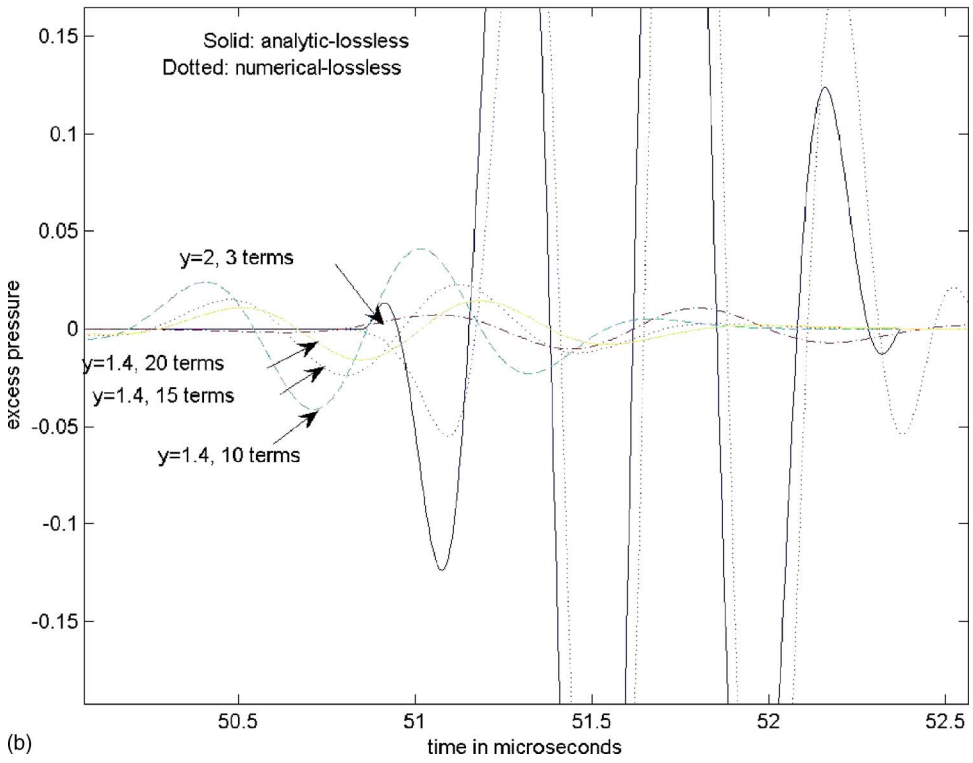

FIG. 1. (a) The calculated excess pressure 2 cm in front of a 2.5 mm (radius), 2 MHz planar transducer. A comparison of numerical and analytic lossless media with two different absorptive media and two different values for the number of power series terms. (b) The calculated excess pressure 8 cm in front of a 2.5 mm (radius), 2 MHz planar transducer. A comparison of numerical and analytic lossless media with two different absorptive media and two different values for the number of power series terms.

(2005). It can be shown, empirically, that consistent with Szabo (1994), the propagation constant for (5), defined as the real part of the complex wavenumber is

$$\beta(\omega) = \beta_0 - \beta'(\omega) = \mathrm{Real}[\mathbf{k}] \approx \frac{\omega}{c_0} - \frac{y-1}{y}\frac{\tau^{y-1}}{c_0}\cot\left((y+1)\frac{\pi}{2}\right)\omega|\omega|^{y-1}. \quad (10)$$

Note that as $(\omega\tau)^{y-1}$ approaches 1, the approximations in (9) and (10) become less accurate.

III. NUMERICAL IMPLEMENTATION

Finite element simulation of the pressure wave equation allows one to determine the scattered pressure field in complex geometries without resorting to simplifying approxima-

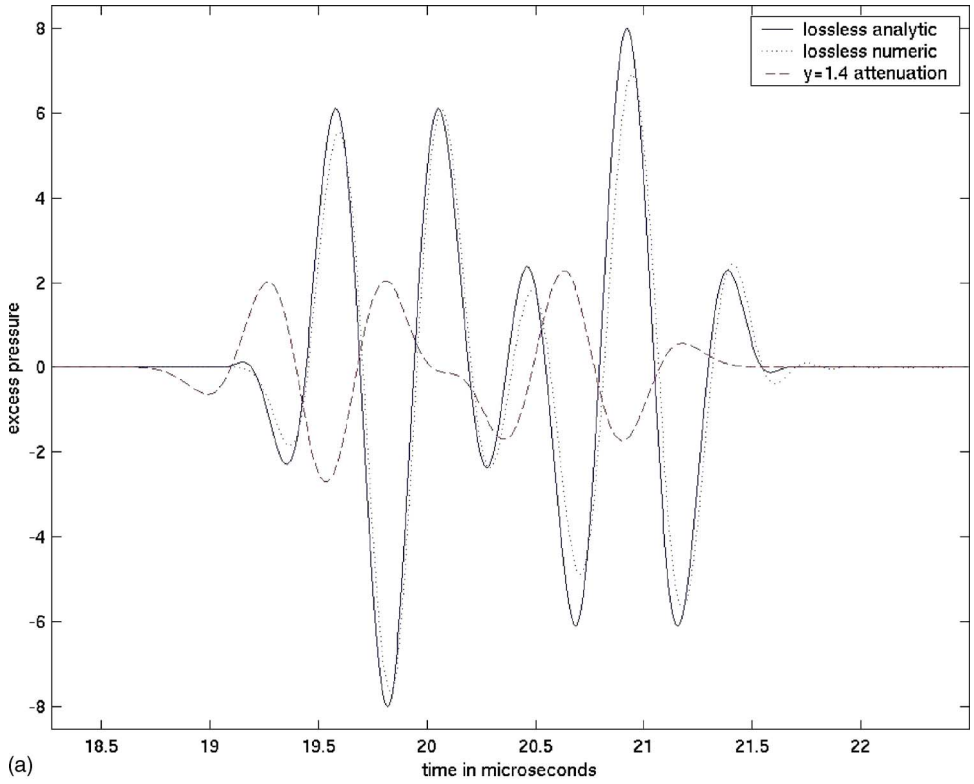

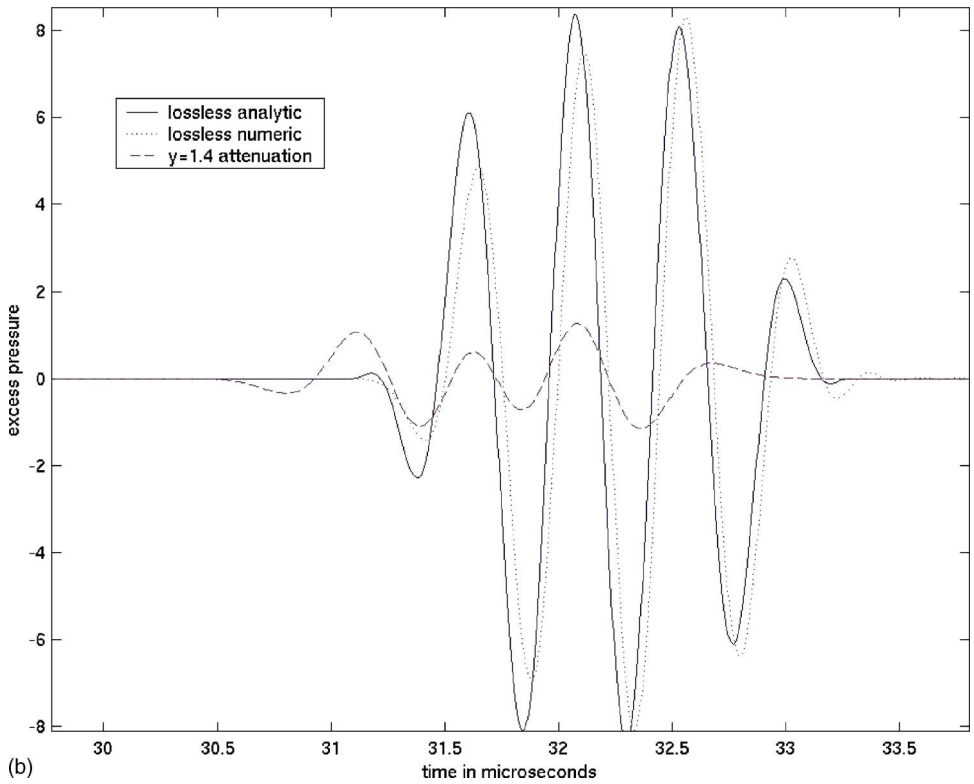

FIG. 2. (a) The calculated excess pressure 3 cm in front of a strongly focused 2 MHz transducer with focal point at 4 cm and radius 2 cm. A comparison of numerical and analytical lossless media with those for absorptive media. (b) The calculated excess pressure 5 cm in front of a strongly focused 2 MHz transducer with focal point at 4 cm and radius of 2 cm. A comparison of numerical and analytical lossless media with those for absorptive media.

tions such as the use of plane waves, the Born approximation of weak scattering, or the Rayleigh limit of very small scatterers. In order to simulate wave propagation through inhomogenous media, one must use the viscous wave equation whose solution will account for position-dependent material parameters in density, ρ, compressibility, κ, time constants, τ, and attenuation frequency exponent y, such that (5) appears as

$$\nabla \cdot \frac{1}{\rho(\mathbf{r})}\nabla p - \kappa(\mathbf{r})\frac{\partial^2 p}{\partial t^2} + \frac{\partial^{(y(\mathbf{r})-1)}}{\partial t^{y(\mathbf{r})-1}}\nabla \cdot \frac{\tau(\mathbf{r})^{y(\mathbf{r})-1}}{\rho(\mathbf{r})}\nabla p = 0, \tag{11}$$

in which $\mathbf{r}$ represents a position vector within the solution domain.

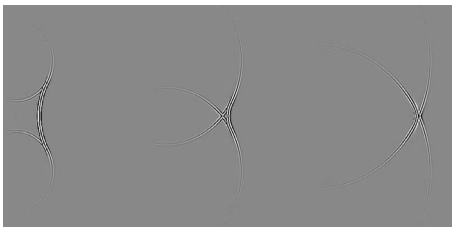

FIG. 3. Three intensity plots illustrating the propagation of the wave field in front of a strongly focused transducer. Areas of white indicate positive excess pressure while black is negative excess pressure. The signal at three different times are displayed from left to right, 10, 20, and 30 μs after the signal is launched from the face of the transducer. Each frame is 8 cm in the vertical direction and 6 cm horizontally.

An explicit time-domain finite element method is used to solve this equation in which the solution domain is broken up into a uniform rectangular grid of elements. The size of the elements is related to solution accuracy and the smallest element distance (width or length) should be no bigger than the smallest wavelength to be calculated. For an axisymmetric geometry in which signal propagation depends only on the radius, r, and depth, z, the pressure p is calculated at each node via

$$p(t;r,z) = \sum_i p_i(t) N_i(r,z), \tag{12}$$

in which p_i is the excess pressure at node i and $N_i(r,z)$ is an interpolation function or shape function that is equal to one at node i and either linearly or quadratically decays to zero at the other nodes of the element. The Galerkin finite element method of numerical analysis can be used to determine (12), by defining a so-called weak form of (11) in the solution domain to be

$$\int_V N(\mathbf{r}) \left(\nabla \cdot \frac{1}{\rho(\mathbf{r})} \nabla p - \kappa(\mathbf{r}) \frac{\partial^2 p}{\partial t^2} + \frac{\partial^{(y(\mathbf{r})-1)}}{\partial t^{y(\mathbf{r})-1}} \nabla \cdot \frac{\tau(\mathbf{r})^{y(\mathbf{r})-1}}{\rho(\mathbf{r})} \nabla p \right) dV = 0. \tag{13}$$

Invoking the divergence theorem, assuming an axisymmetric solution space, and substituting for $N(\mathbf{r})$ the same well behaved basis function used in (12), one obtains a linear system of differential equations given as

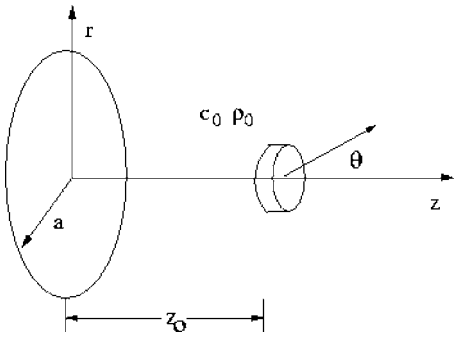

FIG. 4. Simulation geometry of small scatterer in front of a planar transducer.

$$[K_{\text{stiff}}]\{p_i\} - [M]\left\{ \frac{\partial^2 p_i}{\partial t^2} \right\} + [K_\tau]\left\{ \frac{\partial^{y_i-1} p_i}{\partial t^{y_i-1}} \right\} = \int_S N_j \left(\frac{1}{\rho_i} + \frac{\tau_i^{y_i-1}}{\rho_i} \frac{\partial^{y_i-1}}{\partial t^{y_i-1}} \right) p_i \nabla N_i \cdot \mathbf{n}\, dS, \tag{14}$$

in which

$$[K_{\text{stiff}}] = -\int_V \frac{1}{\rho_i} \nabla N_j \cdot \nabla N_i\, dV, \tag{15}$$

$$[M] = -\int_V \kappa_i N_j N_i\, dV, \tag{16}$$

and

$$[K_\tau] = -\int_V \frac{\tau_i^{y_i-1}}{\rho_i} \nabla N_j \cdot \nabla N_i\, dV. \tag{17}$$

in which i and j indicate node indicies.

For a more comprehensive derivation of (14), the reader is referred to Segerlind (1984), one of the many classical texts on the finite element method. The right hand side of (14) are integrals over the element surfaces and ensure the flux, $[1/\rho + (\tau^{y-1}/\rho)(\partial^{y-1}/\partial t^{y-1})]\nabla p \cdot \mathbf{n}$, the continuity condition between elements. It also ensures that the flux boundary condition, at the interface between materials a and b, given as

$$\left(\frac{1}{\rho_a} + \frac{\tau_a^{y_a-1}}{\rho_a} \frac{\partial^{y_a-1}}{\partial t^{y_a-1}} \right) \nabla p_a \cdot \mathbf{n} = \left(\frac{1}{\rho_b} + \frac{\tau_b^{y_b-1}}{\rho_b} \frac{\partial^{y_b-1}}{\partial t^{y_b-1}} \right) \nabla p_b \cdot \mathbf{n} \tag{18}$$

is satisfied.

The nodal potentials are determined from (14) by approximating the second order time derivative by a centered difference equation,

$$\frac{\partial^2 p_i}{\partial t^2} = \frac{p_i^{t+\Delta t} - 2p_i^t + p_i^{t-\Delta t}}{\Delta t^2} \tag{19}$$

and replacing the fractional time derivative with a backward difference power series, similar to Wismer and Ludwig (1995), such that

$$\frac{\partial^{y-1} p_i}{\partial t^{y-1}} = \frac{(1-z^{-1})^{y-1}}{\Delta t^{y-1}} = \frac{1}{\Delta t^{y-1}} \sum_{n=0}^{N} (-1)^n y_n p_i^{t-n\,\Delta t}, \tag{20}$$

in which p_i is the excess pressure at node i, t is time, Δt is the time step and must be smaller than $\sqrt{\Delta \mathbf{r}^2 + \Delta \mathbf{z}^2}/c$ in order to ensure solution stability and $y_1 = (y-1), y_2 = y_1(y_1 - 1)/2!, y_3 = y_1(y_1-1)(y_1-2)/3!$, etc. In this derivation z^{-1} is used to indicate a time delay. It is noted that (20) is numerically equivalent to the Grünwald-Letnikov (Podlubny, 1999) definition for the fractional derivative, given as

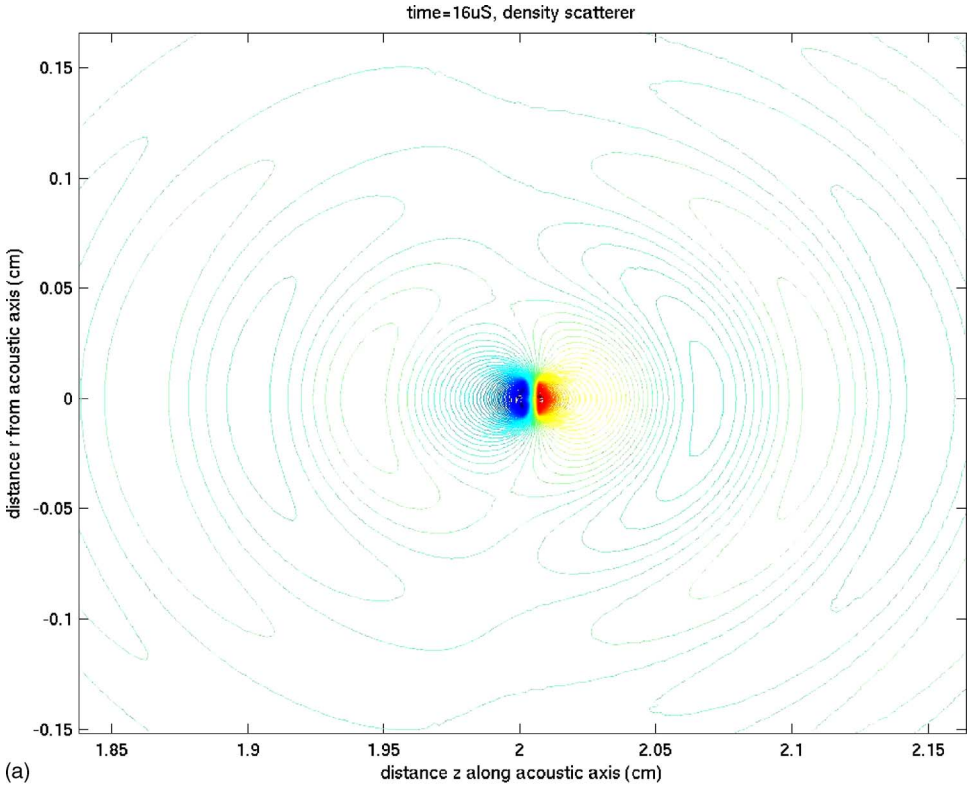

(a)

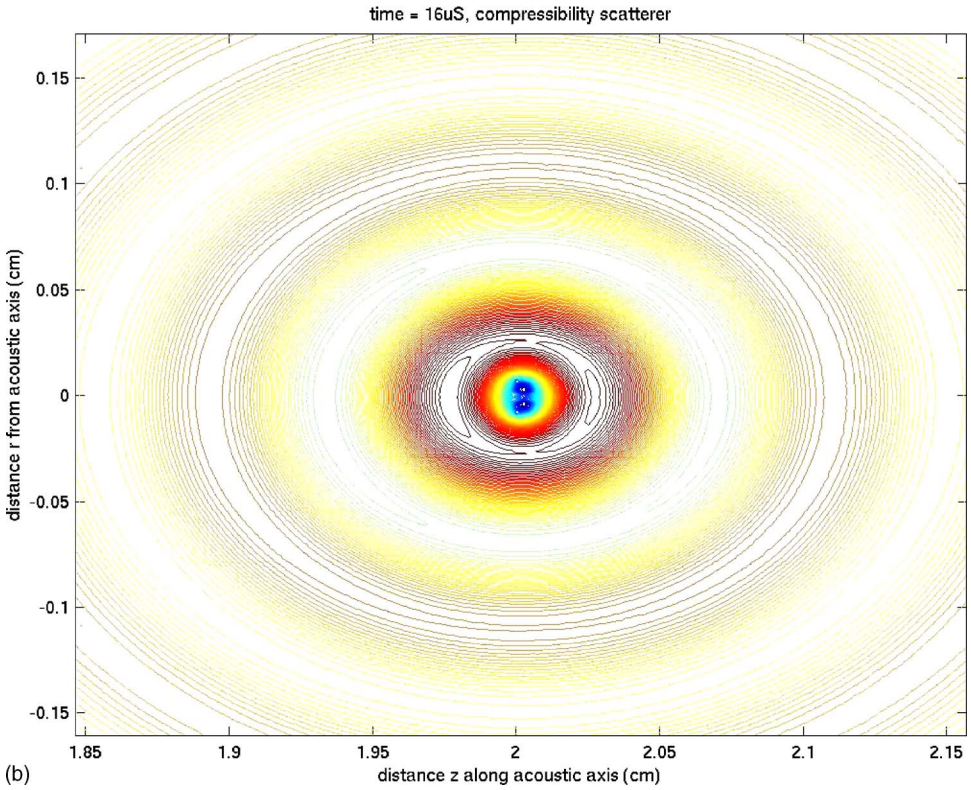

(b)

FIG. 5. (a) Contour plots showing lines of constant, excess, scattered pressure scattered from a small density inclusion located 2 cm in front of a finite planar transducer. Scattered signal recorded at time $t=16$ μs. The radiation pattern is indicative of the transient dipole pattern resulting from a relatively small, weak density scatterer. (b) Contour plots showing lines of constant, excess, scattered pressure scattered from a small compressibility inclusion located 2 cm in front of a finite planar transducer. Scattered signal recorded at time $t=16$ μs. The radiation pattern is indicative of the transient monopole pattern resulting from a relatively small, weak compressibility scatterer.

$$\frac{\partial^{y-1}p}{\partial t^{y-1}} = \frac{1}{\Gamma(y-1)}\sum_{k=0}^{N}\left(\frac{\Gamma(k-y-1)}{\Gamma(k+1)}p^{t-k\,\Delta t}\right), \tag{21}$$

in which $\Gamma(x)$ is defined in (7). Thus, if (19) and (20) or (21) are inserted into (14), the potential $p_i^{t+\Delta t}$ can be determined without inverting any matrices. This is possible because a mass lumping technique is used to approximate the matrix $[M]$ such that it is diagonal. Also, because the mesh can have over five million nodes, memory saving techniques are employed for the uniform grid whereby only unique rows and columns of the matrices $[K_{\text{stiff}}]$, $[M]$ and $[K_\tau]$ are stored.

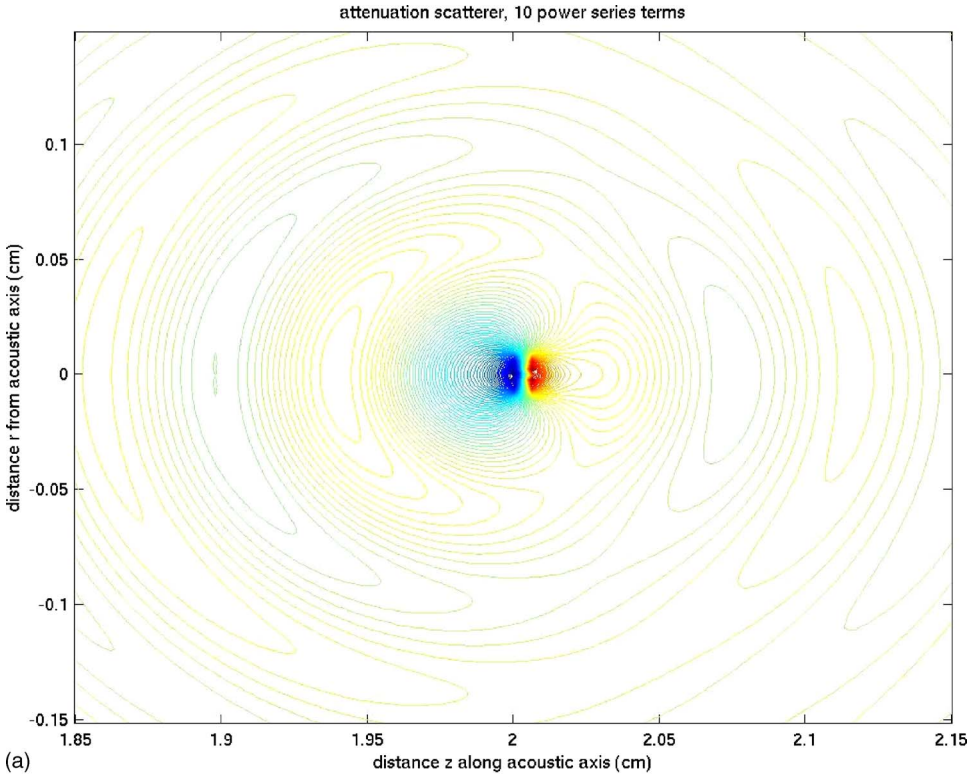

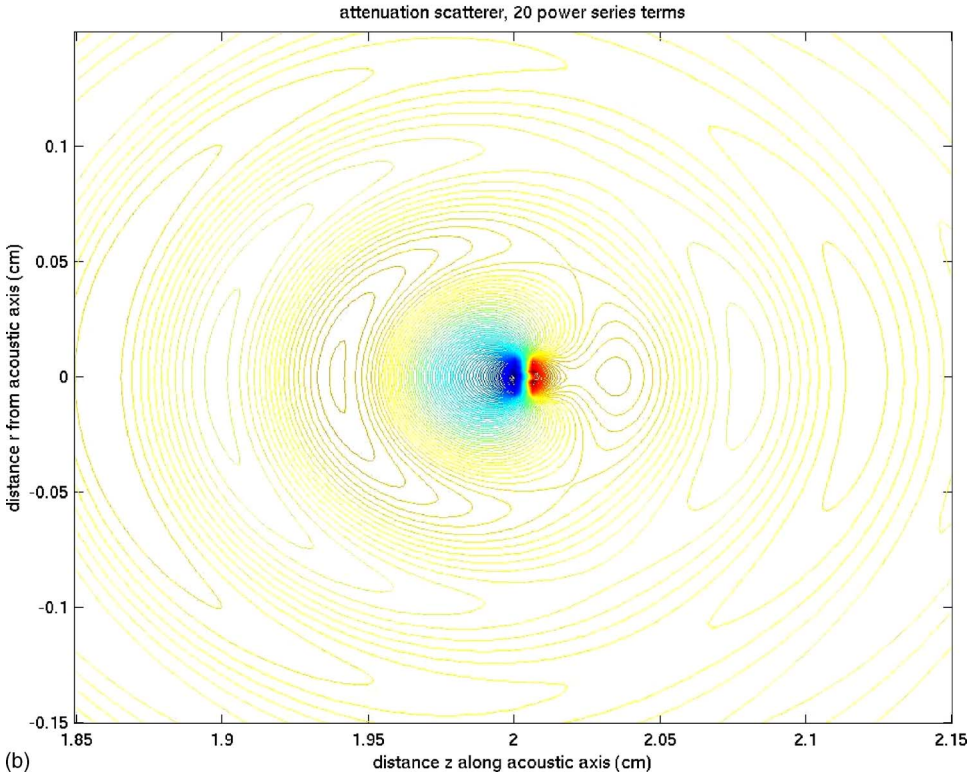

FIG. 6. (a) Contour plots showing lines of constant, excess, scattered pressure scattered from a small viscous inclusion, simulated with 10 power series terms, located 2 cm in front of a finite planar transducer. The scattered signal was recorded at time $t=16$ μs. The radiation pattern is indicative of a distorted transient dipole pattern resulting from a relatively small, viscous scatterer. (b) Similar specifications as for Fig. 6(a), except that 20 power series terms are used for the fractional derivative term.

The resulting algorithm is equivalent to a nine point finite difference stencil in space.

Validation of the code is achieved by comparing the results to analytic solutions for planar piston and focused transducers and for the transmission of signals through lossless and lossy media in both the nearfield and farfield. The input signal is assumed to be a uniform pressure across the face of the transducer with a time dependency given as

$$p_{\text{in}}(t) = \cos(2\pi f_0 t)\left[1 - \cos(2\pi f_1 t)\right], \tag{22}$$

in which f_0 is the center frequency and f_1 controls the bandwidth. The on-axis pressure solution, for a planar transducer, at point z and time t in a medium with sound speed c, is therefore

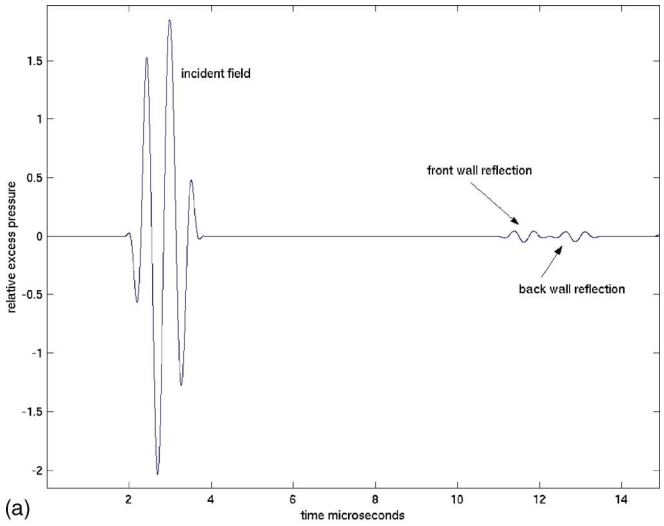

(a)

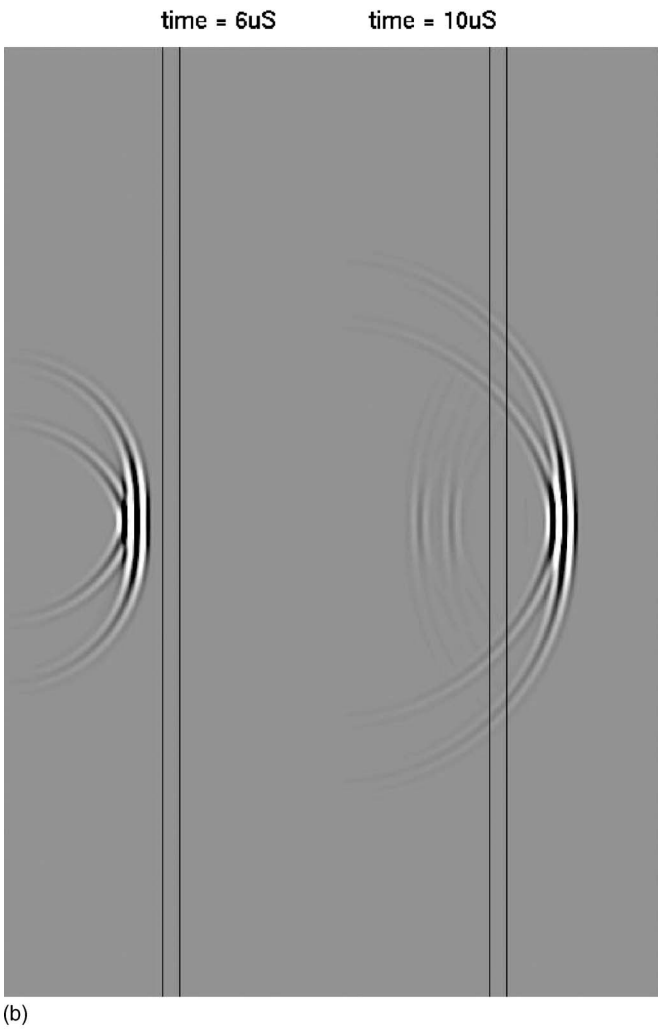

(b)

FIG. 7. (a) Time traces showing the incident and reflected signals from a three layer system in which the viscous middle layer is 1 mm thick and is 1 cm from the face of a 2 mm (radius), 2 MHz transducer. The front and back layer are the same lossless material. Signals are recorded at a point 6 mm in front of the transmit transducer. (b) Intensity plots of the wave field for the three layer system. Dark bands identify the front and back wall of the 1 mm viscous layer. Each frame is 6 cm vertically by 2.1 cm horizontally.

$$p(t,z) = p_{\text{in}} * \left[\delta\left(t - \frac{z}{c}\right) - \delta\left(t - \frac{\sqrt{z^2 + a^2}}{c}\right) \right], \tag{23}$$

in which * is the convolution operator and a is the transducer radius. For $a=2.5$ mm, 2 MHz transducer, insonifying a medium with a sound speed of 1573 m/s and density 1000 kg/m^3 results are given in Fig. 1. In this case the signal is broadband with a −6 dB bandwidth of 2 MHz with and a uniform amplitude of 1 across the surface. The pressure versus time is plotted for 2 cm (near field), and 8 cm (farfield), away from the transducer face. The lossless numerical [$\tau=0$ in (14)] and analytical [in (23)] results are plotted along with a numerical simulated signal in a lossy medium in which $y=1.4$ and $\tau^{y-1}=(5e-5)$ s$^{0.4}$. Note that τ^{y-1} is a fractional time delay for which the units are given in terms of seconds^{y-1}(s^{y-1}). At 2 MHz this yields an attenuation, defined by the imaginary part of (8), of $\alpha=77.85$ Np/m (6.7 dB/cm), a phase speed of $c_p = \omega/\beta(\omega) = 1595$ m/s and a group speed of $c_g = [\partial\beta(\omega)/\partial\omega]^{-1} = 1604$ m/s, in which $\beta(\omega)=\text{real}(k(\omega))$. In this case $(\omega\tau)^{y-1}=0.0346$, resulting in an approximate 1.4% difference between (9) and the imaginary part of (8). The pressure wave propagating through a system with fractional power law attenuation was simulated and plotted for three different number of power series terms [$N=10, N=15$, and $N=20$ in (20)]. A fifth signal is also included for a media with quadratic loss ($y=2$) and for which the attenuation at 2 MHz is 6.5 dB/cm. As predicted by (8), the signal in the $y=2$ medium undergoes broadening, but minimal dispersion or velocity shifts while the $y=1.4$ system causes the anticipated signal shift as frequencies propagate at different speeds. The results also show that the time trace determined with the higher number of power terms results in greater attenuation, close to that for the $y=2$ medium, and therefore more accurate. Note that the $y=1.4$ dispersive medium and the $y=2$ nondispersive medium have approximately the same attenuation at 2 MHz. The convergence of the power series depends on the exponent y and will converge with fewer terms the closer y is to 2. If $y=1$ in (20), the series essentially never converges, whereas if $y=2$ the series converges with just three terms. Since each term requires the storage of an additional time-step simulation of weakly attenuating and highly dispersive media will be more memory intensive. The farfield results in Fig. 1(b) are noticeably less accurate, as numerical errors accumulate over time, but the percent error is within 5%.

The program can accomodate focused transducers and results are shown in Fig. 2 for a source with $F=2a/\text{focal-length}=1.0$ ($a=2$ cm, $f=4$ cm). Shown in Fig. 2 is a comparison between the lossless numerical and analytic results, from Hamilton (1992), of the on-axis pressure. The effects of acoustic absorption are also displayed. Found in Fig. 3 are intensity plots of the entire pressure field at times of 10, 30, and 50 μs and demonstrate how the propagating waves add coherently at the focal point.

IV. RESULTS FOR THE SMALL SCATTERER-RAYLEIGH LIMIT

The advantage of finite element and/or finite difference simulation is that relatively complex inhomogenous systems can be modeled without the need for simplifying assumptions. The acoustic system under consideration consists of a planar piston transducer, with a user specified radius, center frequency, and bandwidth, insonifying a region of space with different material parameters. For the axisymmetric algorithm, the inhomogenous region can consist of layered media or disk inclusions of arbitrary thickness and radius, as shown in Fig. 4. The resultant pressure will therefore be rotationally symmetrical about the acoustic axis, and only half of the problem space needs to be simulated. The algorithm allows the user to specify material parameters, number of layers, number of inclusions, inclusion radius and thickness and transducer center frequency, bandwidth and radius.

An analytic solution, for the scattered wave, $p_s(\mathbf{r})$, is available for plane waves impinging upon a small, weak scatterer, and is given as

$$p_s(\mathbf{r}) \approx P_0 \frac{e^{-j\mathbf{k}\cdot\mathbf{r}}}{r}\Phi(\theta), \tag{24}$$

in which $\Phi(\theta)$ is the radiation pattern and is given by

$$\Phi(\theta) = \frac{k_0^2 V_s}{4\pi}\left(\frac{\kappa_s - \kappa_0}{\kappa_0} + \frac{\rho_s - \rho_0}{\rho_0}\cos(\theta)\right). \tag{25}$$

The 0 subscript refers to material parameters in the background medium and s the scatterer. The angle θ is between the direction of the incident wave and the acoustic axis, as shown in Fig. 4, and V_s is the scatterer volume. Weak scatterers are ones whose material properties do not differ significantly from the background material, thereby ensuring that the scattered signal is at least an order of magnitude smaller than the incident wave, and the Born approximation is thus justified.

The signal calculated via (14) is assumed to consist of two components p_s, the scattered signal and p_{inc}, the incident wave. Thus, in order to find the scattered signal, the numerical simulation needs to be implemented twice. First, the system with the scatterer is modeled in order to compute the total small-signal pressure field, p_{tot} and then a system without the scatterer is modeled to find the incident field, p_{inc}. The scattered field is then simply

$$p_s = p_{\text{tot}} - p_{\text{inc}}, \tag{26}$$

and the scattered radiated field can be compared to the result in (24).

Shown in Fig. 5 are results of the scattered waves for a small disk scatterer. Relevant simulation parameters include a planar transducer radius of 5 mm, a 2 MHz narrow band input signal with a half-power bandwidth of 0.4 MHz and a distance $z_0=2$ cm. The background medium has a compressibility of $\kappa_0=405\times10^{-12}$ $[\text{kg}/(\text{m s}^2)]^{-1}$ and a density of $\rho_0=1000$ kg/m^3 for a sound speed of $c_0=1573$ m/s. The scatterer has a thickness and radius of $a=0.0623$ mm to make $k_0 a \approx 0.5$, which, although not an order of magnitude less than 1, is still small enough to observe the scattering effects of (25). Simulating very small scatterers is difficult because it requires a very fine grid and since a uniform grid is used this makes the memory requirements and simulation times increase accordingly.

In Fig. 5(a) the scatterer has a density of 1050 kg/m^3 and the same compressibility as the background, whereas in Fig. 5(b) the scatterer has a compressibility of 730×10^{-12} $[\text{kg}/(\text{m s}^2)]^{-1}$ but the same density as the background material. In keeping with theory, the scattered wave due to the inclusion, more dense than the background, exhibits a dipole radiation pattern while the scattered wave due to the inclusion more compressible than the background has a monopole pattern.

In Fig. 6(a) a scatterer has the same density and compressibility as the background but now has a fractional time constant given as $\tau^{y-1}=2e-2s^{0.2}$, with $y=1.2$. In light of (9), this corresponds to an attenuation coefficient of $\alpha=3.5$ Np/cm (30 dB/cm) at 2 MHz. While this may be an untypically high absorption rate, it also is a limiting case for the program. Larger values of τ^{y-1} cause computational instabilities. In order for the algorithm in (14) to remain stable, the damping matrix $[K_\tau]$ must be at least an order of magnitude smaller than the stiffness matrix, $[K_{\text{stiff}}]$.

Scattered signal results are shown in Fig. 6(b), for the same absorptive scatterer as in Fig. 6(a), but for which the number of power series terms is increased from 10 to 20. Increasing the number of power series terms in the fractional time operator appears to improve the spatial accuracy of the radiation field for the absorptive scatterer. This field is essentially a distorted dipole pattern and results from the fact that the pressure is attenuated as it propagates through the scatterer, and therefore the radiation on the front side is stronger than the radiation on the backside.

Finally results are given for a three layer system in which the middle layer consists of a viscous material. All three layers have the same density of 1000 kg/m^3 and lossless sound speed of 1573 m/S. The middle layer is 1 cm in front of a 4 mm transducer, has a thickness of 1 mm and a fractional time-delay parameter of $\tau^{y-1}=2e-4s^{0.4}$ for which $y=1.4$, resulting in an attenuation of 24 dB/cm at 2 MHz. The time signal in Fig. 7(a) is recorded at a point 0.6 cm in front of the transducer; indicative of a point hydrophone receiver with infinite bandwidth. The reflection coefficient between two viscous media, 1 and 2 is given as

$$\mathbf{R}_{\text{LOSS}} = \frac{\mathbf{z}_2 - \mathbf{z}_1}{\mathbf{z}_1 + \mathbf{z}_2} = \frac{\dfrac{1}{\rho_2 c_2\sqrt{1+(j\omega\tau_2)^{y_2-1}}} - \dfrac{1}{\rho_1 c_1\sqrt{1+(j\omega\tau_1)^{y_1-1}}}}{\dfrac{1}{\rho_2 c_2\sqrt{1+(j\omega\tau_2)^{y_2-1}}} + \dfrac{1}{\rho_1 c_1\sqrt{1+(j\omega\tau_1)^{y_1-1}}}}. \tag{27}$$

If it is assumed that the media have the same sound velocity, $c_1=c_2$, and density, $\rho_1=\rho_2$, and fluid 1 is lossless, then, with (9) and (10), the reflection coefficient becomes

$$\mathbf{R}_{\mathrm{LOSS}} = \frac{j[\alpha_1(\omega) - \alpha_2(\omega)] + \beta_1'(\omega) - \beta_2'(\omega)}{\frac{2}{c_1} - j[\alpha_1(\omega) + \alpha_2(\omega)] - [\beta_1'(\omega) + \beta_2'(\omega)]}$$

$$\approx -\frac{(y_2 - 1)}{2y_2}(\omega\tau_2)^{y_2-1}(j + C_y), \tag{28}$$

in which $c_y = \cot[(y_2 + 1\pi/2)]$. Thus, signals reflected from a lossless/viscous interface are highpass filtered with the sharpness of the filter, depending on the power law exponent of the absorptive material. The reflection coefficient for the lossless/viscous interface has an absolute value of 0.0012 at 2 MHz and the frequency spectrum of the time signals indicate a shift of 0.4 MHz in the front wall reflection relative to the incident field. Intensity plots, showing the entire wave field as it propagates through the layer, are provided in Fig. 7(b).

V. DISCUSSION

A modified viscous wave equation is proposed to model ultrasonic signals as they propagate through biological tissues. The modified equation includes a fractional derivative and it is empirically shown that the resulting propagation factor has an imaginary part that yields power law attenuation and a real part that satisfies the requisite velocity dispersion. An explicit, axisymmetric, time-domain algorithm is coded to solve this equation. The results demonstrate that signal scattering and reflections can depend solely on differences in attenuation parameters. Stronger attenuation should yield bigger reflections, although if the damping factor is too big the algorithm suffers from stability problems as the viscous term $\tau^{y-1}[\partial^{(y-1)}/\partial t^{y-1}]\nabla^2$ of (5) may become larger than the mass or stiffness terms. The results can be used to test imaging algorithms that incorporate frequency dependent scattering and backscatter coefficients.

ACKNOWLEDGMENTS

The author gratefully acknowledges the many insightful and judicious comments provided by the anonymous reviewers.

Blackstock, D. (**1967**). "Transient solution for sound radiated into a viscous fluid," J. Acoust. Soc. Am. **41**, **1312–1319**.

Chen, W., and Holm, S. (**2004**). "Fractional Laplacian time-space models for linear and nonlinear lossy media exhibiting arbitrary frequency dependency," J. Acoust. Soc. Am. **115**, 1424–1430.

Cobbold, R., Sushilov, N., and Weatherman, A. (**2004**). "Transient propagation in media with classical or power law loss," J. Acoust. Soc. Am. **116**, 3294–3303.

Girault, J.-M., Ossant, F., Ouahabi, A., Kouamé, and Patat, F. (**1998**). "Time-varying autoregressive spectral estimation for ultrasound attenuation in tissue characterization," IEEE Trans. Ultrason. Ferroelectr. Freq. Control **45**, 650–659.

Hamilton, M. (**1992**). "Comparison of three transient solutions for the axial pressure in a focused sound beam," J. Acoust. Soc. Am. **92**, 527–532.

He, P. (**1999**). "Experimental verification of models for determining dispersion from attenuation," IEEE Trans. Ultrason. Ferroelectr. Freq. Control **46**, 706–714.

Hilfer, R. (**2003**). "On fractional relaxation," Fractals **11**, 251–257.

Hughes, D. I., and Duck, F. A. (**1997**). "Automatic attenuation compensation for ultrasonic imaging," Ultrasound Med. Biol. **23**, 651–664.

Lerch, R., and Friedrich, W. (**1986**). "Ultrasonic waves in attenuating media," J. Acoust. Soc. Am. **80**, 1140–1147.

Liebler, M., Ginter, S., Dreyer, T., and Riedlinger, R. (**2005**). "Full wave modeling of therapeutic ultrasound: efficient time domain implementation of the frequency power law attenuation," J. Acoust. Soc. Am. **116**, 2742–2750.

Mainardi, F., and Paradisi, P. (**2001**). "Fractional diffusive waves," J. Comput. Acoust. **9**, 1417–1436.

Norton, G., and Novarini, J. (**2003**). "Including dispersion and attenuation directly in the time domain for wave propagation in isotropic media," J. Acoust. Soc. Am. **113**, 3024–3031.

Oelze, M. L., and O'Brien, W. D. (**2002**). "Frequency dependent attenuation-compensation functions for ultrasonic signals backscattered from random media," J. Acoust. Soc. Am. **111**, 2308–2319.

Oelze, M., Zachary, J., and O'Brien, W. (**2002**). "Characterization of tissue microstructure using ultrasonic backscatter: Theory and technique for optimization using a Gaussian form factor," J. Acoust. Soc. Am. **112**, 1202–1211.

Padilla, F., Peyrin, F., and Laugier, P. (**2003**). "Measure of attenuation and backscatter coefficient in trabecular bones using a numerical model of three-dimensional microstructure," J. Acoust. Soc. Am. **113**, 1122–1129.

Podlubny, I. (**1999**). *Fractional Differential Equations* (Academic, San Diego).

Segerlind, L. (**1984**). *Applied Finite Element Analysis* (Wiley, New York).

Shorter, P. (**2004**). "Wave propagation and damping in linear viscoelastic laminates," J. Acoust. Soc. Am. **115**, 1917–1925.

Stucky, P., and Lord, W. (**2001**). "Finite element modeling of transient ultrasonic waves in linear viscoelastic media," IEEE Trans. Ultrason. Ferroelectr. Freq. Control **48**, 6–16.

Sushilov, N., and Cobbold, R. (**2004**). "Frequency-domain wave equation and its time-domain solutions in attenuating media," J. Acoust. Soc. Am. **115**, 1431–1436.

Szabo, T. (**1994**). "Time-domain wave equations for lossy media obeying a frequency power law," J. Acoust. Soc. Am. **96**, 491–500.

Wallace, K., Holland, M., and Miller, J. (**2001**). "Improved description of shock wave evolution in media with frequency power law attenuation," J. Acoust. Soc. Am. **109**, 2263–2265.

Waters, K., Hughes, M., Mobley, J., and Miller, J. (**2003**). "Differential forms of the Kramer-Kronig dispersion relations," IEEE Trans. Ultrason. Ferroelectr. Freq. Control **50**, 68–76.

Waters, K. R., Mobley, J., and Miller, J. (**2005**). "Causality-imposed (Kramers-Kronig) relationships between attenuation and dispersion," IEEE Trans. Ultrason. Ferroelectr. Freq. Control **52**, 822–833.

Wilson, K., Ostashev, V., and Collier, S. (**2005**). "Time domain equations for sound progation in rigid frame porous media," J. Acoust. Soc. Am. **116**, 1889–1892.

Wismer, M., and Ludwig, R. (**1995**). "An explicit numerical time domain formulation to simulate pulsed pressure waves in viscous fluid exhibiting orbitrary frequency power law dissipation," IEEE Trans. Ultrason. Ferroelectr. Freq. Control **42**, 1040–1049.

Wochner, M., Atchley, A., and Sparrow, V. (**2005**). "Numerical simulation of finite amplitude wave propagation in air using a realistic atmospheric absorption model," J. Acoust. Soc. Am. **ll8**, 2891–2898.

Zhang, X., Broschat, S., and Flynn, P. (**2001**). "A comparison of material classification techniques for ultrasound inverse imaging," J. Acoust. Soc. Am. **111**, 457–467.

Stability of self-similar plane shocks with Hertzian nonlinearity

B. Edward McDonald
Naval Research Laboratory, Washington, DC 20375

(Received 22 April 2005; revised 19 September 2006; accepted 25 September 2006)

The nonlinear progressive wave equation [McDonald and Kuperman, J. Acoust. Soc. Am. **81**, 1406–1417 (1987)] is expressed in a form to accommodate Hertzian nonlinearity of order $n=3/2$ typical of granular media. Stability of self-similar plane weak shocks against perturbations in three dimensions is demonstrated for arbitrary order nonlinearity with $1<n<3$. Investigation of stability in the presence of Hertzian nonlinearity is motivated by the nonlinearity coefficient being arbitrarily large in the unstressed state. Energy in the perturbation field is shown to fall off at least as fast as $1/t$, while energy in the self-similar wave falls off slower than $1/t$. For an initial wave profile increasing in the direction of propagation, it is shown that where the quadratic nonlinearity coefficient diverges, the slope of the wave goes to zero. [DOI: 10.1121/1.2363946]

PACS number(s): 43.25.−x, 43.30.Lz [MFH] Pages: 3503–3508

I. INTRODUCTION

Relevant scenarios in mine countermeasures (MCM) using explosives to clear buried mines emphasize the physically interesting problem of a nonlinear compressional wave propagating from a fluid medium (ocean or atmosphere) into an unstressed granular medium (seafloor or dry earth). When the overdensity in the fluid medium is small but finite, the wave is well described by nonlinear acoustics with quadratic nonlinearity.[1,2] In a granular medium, however, the lowest order nonlinearity in the equation of state is no longer quadratic, but the Hertzian nonlinearity of order 3/2.[3–5] The nonlinearity coefficient of a medium is linearly related to the second derivative of pressure with respect to overdensity, and thus diverges near the unstressed state for the Hertzian nonlinearity.

A recent experiment[4] shows an interesting transition from quadratic nonlinearity at low (but finite) wave amplitude to Hertzian nonlinearity at high amplitude. In this case the transition is caused by prestressed granules being separated and clapping together when the sinusoidal exciting wave exceeds a level determined by the prestress. The experiment used transverse forcing to bring about the clapping of granules. Unfortunately, there seems to be no equivalent data using compressional forcing. In the seafloor or earth, initially unstressed granules may be driven together by a strong compressive wave if the bulk modulus of the grain material (e.g., quartz) is sufficiently higher than that of the interstitial fluid. A transition from quadratic to Hertzian nonlinearity would begin as intergranular stresses become significant.

If one wishes to model a nonlinear wave propagating in an unstressed granular medium taking the usual assumption of quadratic nonlinearity, one has to decide what value of the nonlinearity coefficient to use. It begins at an arbitrarily high value when grains first come in contact, and decreases to a finite value at maximum stress. If the granular medium is prestressed, the quadratic theory may be assumed valid over a limited interval by Taylor's expansion of the bulk stress - strain relation about a nonzero baseline strain rate ϵ_0. One is left, however, with the problem of the nonlinearity coefficient diverging at least as fast as $\epsilon_0^{-1/2}$ in the limit of small strain.[3]

What are the physical consequences of an arbitrarily large nonlinearity coefficient on a propagating wave? Does the wave develop pathological behavior perhaps leading to its instability? Resolution of these questions arises from stating the nonlinearity explicitly without Taylor's expansion. One can do this by augmenting the equation of state with a term of fractional order and proceeding without Taylor expanding the additional term. (This paper argues that the diverging nonlinearity coefficient is an artifact of Taylor's expansion of a nonanalytic equation of state.) Using the ratio of perturbation energy to unperturbed energy as a stability measure, we will show that linear stability of a wave subject to Hertzian nonlinearity appears to be weakened slightly (but not destroyed) relative to a wave with quadratic nonlinearity.

Self-similar nonlinear acoustic plane waves are descriptive of explosive shock waves and sonic booms in homogeneous media at late times. The equations of nonlinear acoustics without dissipation admit similarity solutions with similarity variable x/t.[6,7] With the addition of viscous dissipation, similarity solutions exist in the form of a function of time multiplied by a function of $x/t^{1/2}$. In the limit of small viscosity, these solutions tend toward the inviscid solutions depending on x/t.

The analysis presented here investigates the idealized but physically incomplete inviscid limit. Four reasons exist for doing this: (1) granular materials exhibit frequency-linear attenuation for which similarity solutions are not available; (2) the inviscid limit yields compact closed-form solutions for shock evolution which are valuable to benchmark a numerical model in the limit of low attenuation; (3) inviscid solutions reveal clear tendencies between higher order nonlinearity and increased wave stability; (4) inviscid solutions reveal the physical consequences of a diverging nonlinearity coefficient.

While it is conventional wisdom that shock waves in uniform media evolve toward similarity profiles, analyses leading to asymptotic decay rates of perturbations to plane

shock waves of arbitrary strength have been lengthy and mathematically detailed.[8–12] Perturbations to particular shock systems have been shown to decay at least as fast as an inverse fractional power of time.[8,11,12] When the entropy increase behind the shock is neglected,[8] the asymptotic behavior of perturbation amplitude is $t^{-1/2}$; when entropy increase is included[12] the asymptotic behavior is $t^{-3/2}$. Weak shocks are defined as those having small fractional changes in density. For self-similar weak shocks depending on x/t, the analysis of small perturbations is greatly simplified, and perturbation energy will be shown to fall off at least as fast as t^{-1}. Since weak shocks are isentropic up to third order in amplitude,[7] this result is consistent with that of Ref. 8.

We will derive asymptotic recovery rates for perturbed self-similar weak shocks subject to arbitrary order nonlinearity $1<n<3$ using the nonlinear progressive wave equation[2] (NPE). Results are applicable to the recovery of weak shocks which are temporarily subjected to environmental inhomogeneities (including turbulence[13–15] in the fluid case $n=2$), and then emerge into a homogeneous environment.

The analysis to follow does not include configurations in which either planar waves or inviscid flow are not appropriate. Examples are Mach reflections[16] from an interface and propagation within a turbulent flow.

II. THEORY

The NPE describes evolution of finite-amplitude acoustic density fluctuations ρ' in a wave-following coordinate system moving in the x direction at a nominal sound speed c_0, where subscript zero refers to the undisturbed medium ahead of the wave,

$$\partial_t \rho' = -\frac{1}{2c_0}\partial_x[p(\rho') + c_0^2(\rho'^2/\rho_0 - \rho')] - \frac{c_0}{2}\int_\infty^x \nabla_\perp^2 \rho' dx, \tag{1}$$

where ∂_t is the time derivative in the moving frame, $x=x' - c_0 t$ is the reduced x coordinate (x' refers to a frame fixed in the medium), ρ_0 is the unperturbed density of the medium with $\rho=\rho_0+\rho'$, p is pressure, and $\nabla_\perp^2 \equiv (\partial_y^2+\partial_z^2)$. The x- integration path in (1) begins in the quiescent medium ahead of the wave where ρ' and its derivatives are zero. Error terms in (1) are $O(\rho'^3, \rho'^2\theta^2)$, where θ is the wave-normal angle with respect to x. For this reason it is sufficient to use an adiabatic equation of state $p(\rho')$ since weak shock heating is cubic in shock amplitude.[7] We must also confine attention to nonlinearity of order $1<n<3$ in order to remain within the error limits of Eq. (1).

For media which support acoustic waves (e.g., fluids, saturated granular media, or prestressed granular media), c_0 is the linear sound speed of the undisturbed medium. For dry granular media, the sound speed varies with the local strain rate as $\epsilon^{1/4}$, and is thus zero in the unstressed state. Such a medium does not support acoustic waves, and the use of Eq. (1) is not appropriate. (A Riemann solution applicable to unstressed dry granular media without transformation to a moving frame will be given below.)

Nonlinear plane waves are described by Eq. (1) in one dimension, resulting in the Riemann equation

$$\partial_t \rho' = -f(\rho')\partial_x \rho', \tag{2}$$

where

$$f(\rho') = \frac{1}{2c_0}\left(\frac{\partial p}{\partial \rho'} + c_0^2(2\rho'/\rho_0 - 1)\right), \tag{3}$$

and f is the sound speed relative to c_0: $c=c_0+f(\rho')$. It is helpful to leave (3) expressed as is rather than assume the usual Taylor's expansion with coefficient of quadratic nonlinearity in order to accommodate nonanalytic $p(\rho')$.

In Eq. (2) we introduce the similarity variable ξ and seek solutions of the form $\rho'(x,t)=\rho'(\xi)$,

$$\xi \equiv \frac{x}{t} \rightarrow \quad \partial_x = \frac{1}{t}\frac{d}{d\xi} \quad \partial_t = -\frac{\xi}{t}\frac{d}{d\xi}. \tag{4}$$

Equation (2) becomes

$$-\frac{\xi}{t}\frac{d\rho'}{d\xi} = -\frac{f(\rho')}{t}\frac{d\rho'}{d\xi}, \tag{5}$$

which yields the condition for plane-wave self-similarity,

$$f(\rho') = \xi = x/t. \tag{6}$$

The self-similar profile is thus

$$\rho'(x,t) = f^{-1}(x/t). \tag{7}$$

Assuming $f(\rho')$ is a monotonically increasing and continuous function (7) implies that ρ' is a monotonically increasing function of x. Then, in order for ρ' to remain bounded, it must vary smoothly in segments except for shock locations where its amplitude decreases discontinuously, with proper jump conditions at the discontinuities.

It should be noted that special analytic solutions[17] of the KZ equation[1] including shocks exist which are neither planar nor self-similar. The analysis below implies that at late times such nonplanar shocks propagating in a homogeneous medium evolve toward self-similar planar shocks. One should note that numerical methods used in the solution of the KZ equation apply only to quadratic nonlinearity.

A. Linear perturbation in one dimension

We now perturb Eq. (2) to determine the stability of the self-similar wave. First, consider perturbations in one dimension on a region where ρ' is continuous,

$$\rho'(x,t) \rightarrow \rho'(x,t) + \delta\rho(x,t). \tag{8}$$

Equation (2) yields

$$\partial_t \delta\rho = -f(\rho')\partial_x \delta\rho - \frac{df}{d\rho'}\partial_x \rho' \delta\rho. \tag{9}$$

From (4) and (6) we find

$$\partial_x \rho' = \frac{1}{t}\frac{d\rho'}{d\xi}, \tag{10}$$

and

$$\frac{df}{d\rho'} = \frac{d\xi}{d\rho'}. \tag{11}$$

With (6), (10), and (11), Eq. (9) yields

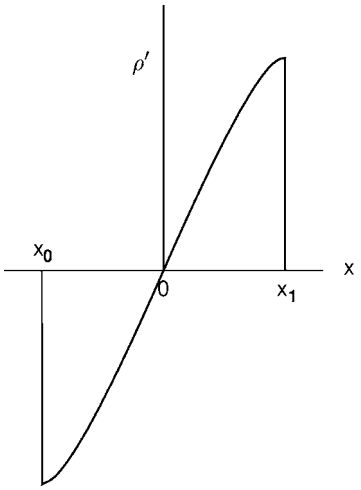

FIG. 1. Schematic diagram for a self-similar wave in one dimension with shock discontinuities at x_0 and x_1. The origin is taken where the wave reaches zero continuously.

$$\partial_t \delta\rho = -\frac{x}{t}\partial_x \delta\rho - \frac{1}{t}\delta\rho. \tag{12}$$

It is straightforward to show that, for $t \geqslant t_0 > 0$ (12) has the solution

$$\delta\rho(x,t) = \frac{t_0}{t}\delta\rho\left(x\frac{t_0}{t}, t_0\right), \tag{13}$$

where $\delta\rho(x,t_0)$ is the perturbation at $t=t_0$.

B. Shock discontinuities

We examine freely propagating waves as could be generated by an explosive source. Consider a profile $\rho'(x)$ which varies continuously with a single zero between shock discontinuities as in Fig. 1. We take the origin at the zero, which remains fixed in the reduced x coordinate frame, so that $\rho'(0)=0$ without loss of generality. The shock illustrated in Fig. 1 happens to be symmetric about the origin, but this is not a necessity. Expressing Eq. (2) as

$$\partial_t \rho' = -\partial_x \Phi(\rho'), \tag{14}$$

where

$$\Phi(\rho') = \int^{\rho'} f(\rho)d\rho = \frac{1}{2c_0}\left(p(\rho') + c_0^2\left(\frac{\rho'^2}{\rho_0} - \rho'\right)\right), \tag{15}$$

the Rankine-Hugoniot condition[18] for mass conservation across a shock at x_s may be stated

$$\frac{dx_s}{dt} = \frac{[\Phi]}{[\rho']} = \left.\frac{\Phi(\rho')}{\rho'}\right|_{x_s}, \tag{16}$$

where the brackets indicate the jump across the shock. Equations (14) and (16) imply mass conservation as follows:

$$\int_0^{x_s} \rho' dx = \text{const}. \tag{17}$$

As a result of Eqs. (2) and (6), one finds that on $(0,x_s)$ the self-similar wave is related to its initial state as follows:

$$\rho'(x,t) = \rho'(xt_0/t, t_0). \tag{18}$$

Thus, at late times the self-similar profile is determined by its behavior at an early time near $x=0$. If we take $\rho'(x,t_0) \propto x^m$ near $x=0$ where m is a positive constant, then Eqs. (6) and (7) imply $\rho'(x,t) \propto (x/t)^m$. Allowing that m is not necessarily an integer, the proportionality is stated

$$\rho'(x,t) = b \cdot \left(\frac{x}{t}\right)^m, \tag{19}$$

where b is constant. Then, from (7)

$$f(\rho') = \left(\frac{\rho'}{b}\right)^{1/m}. \tag{20}$$

Equations (3) and (20) imply that when the dominant nonlinearity in the equation of state is of order $1 < n < 3$, one has

$$p \propto \rho'^n \rightarrow m = 1/(n-1). \tag{21}$$

Thus, a quadratic nonlinearity $n=2$ gives $m=1$, descriptive of an N wave, while Hertzian nonlinearity $n=3/2$ gives $m=2$, or a parabolic profile. The divergent nonlinearity coefficient near $\rho'=0$ for the Hertzian nonlinearity is accompanied by $\partial_x \rho'$ going to zero.

C. Consequences of divergent nonlinearity parameter

A general result illustrating the effect of divergent nonlinearity coefficient upon the wave slope for a nonlinear plane wave may be derived by using the method of characteristics to solve Eqs. (2) and (3),

$$\rho'(x,t) = g(x - tf(\rho')), \tag{22}$$

where

$$g(x) = \rho'(x,0). \tag{23}$$

Forming the x derivative of Eq. (22) and bringing $\partial_x \rho'(x,t)$ to the left side gives

$$\partial_x \rho'(x,t) = \frac{\rho_x'(x_r,0)}{1 + t\rho_x'(x_r,0)\left(\frac{\partial^2 p}{\partial \rho'^2} + \frac{2c_0^2}{\rho_0}\right)/2c_0}$$

$$= \frac{\rho_x'(x_r,0)}{1 + c_0 t\beta\rho_x'(x_r,0)/\rho_0}, \tag{24}$$

where $\rho_x'(x_r,0)$ refers to $\partial_x \rho'$ evaluated at $t=0$, $x_r = x - tf(\rho'(x,t))$, and the coefficient of quadratic nonlinearity is given by

$$\beta \equiv 1 + \left.\frac{\partial \log c}{\partial \log \rho}\right|_0 = 1 + \left.\frac{1}{2}\frac{\rho_0}{c_0^2}\frac{\partial^2 p}{\partial \rho'^2}\right|_0. \tag{25}$$

When Hertzian nonlinearity is present, $p(\rho)$ contains a term proportional to $\rho'^{3/2}$, so that $\beta \propto \rho'^{-1/2}$ as $\rho' \rightarrow 0$. The second expression in (24) reveals the following for $\beta \rightarrow \infty$ and $t > 0$: (a) when the initial condition has a zero with positive slope in the direction of propagation, the wave slope $\partial_x \rho'$ at $x=0$ is forced to zero; (b) when the initial condition has a zero with negative slope in the direction of propagation, the wave slope at $x=0$ becomes infinite (a shock begins to form) immediately. The shock discontinuity in case (b) begins at

zero amplitude and increases with time until the wave ages sufficiently; then, it decreases as the wave becomes self-similar.

Returning to the self-similar shock resulting from the equation of state (21), the shock location and strength from (19), (15), and (16) are

$$x_s(t) = x_s(t_0)(t/t_0)^{m/(m+1)} \tag{26}$$

$$\rho_s'(t) = \rho_s'(t_0)(t/t_0)^{-m/(m+1)}. \tag{27}$$

The energy in the basic state may be obtained from (19) and (26) to give

$$\int_0^{x_s} \rho'^2 dx \propto t^{-m/(m+1)}, \tag{28}$$

which falls off slower than $1/t$. When the slope at $x=0$ is nonzero, one has $m=1$, which results in a classic N-wave shock with $\rho'(x,t) \propto x/t$, $x_s \propto \sqrt{t}$, and both ρ_s' and the energy integral (28) decrease as $1/\sqrt{t}$. For Hertzian nonlinearity, $m=2$, so that $x_s \propto t^{2/3}$, and both ρ_s' and the energy integral (28) decrease as $t^{-2/3}$.

The energy in the perturbation may be integrated from (13) to give

$$\int_0^{x_s} \delta\rho^2 dx = \frac{t_0}{t}\int_0^{x_s t_0/t} \delta\rho^2(x,t_0)dx. \tag{29}$$

It is permissible to use the unperturbed shock location in (29), since inclusion of the perturbed value δx_s would add a term of third order in $\delta\rho$. Since the upper limit of integration on the right side of (29) decreases with time, the energy in the perturbation decreases at least as fast as $1/t$. From (28) and (29), stability of the self-similar plane wave in one dimension is established including shock jump conditions. In particular, the ratio of perturbation energy (29) to the wave's unperturbed energy (28) decreases at least as fast as $t^{-1/(m+1)} = t^{-1+1/n}$.

D. Linear stability against three-dimensional perturbations

Consider now a three-dimensional perturbation of a nonlinear plane wave,

$$\rho'(x,t) \to \rho'(x,t) + \delta\rho(x,y,z,t). \tag{30}$$

From Eq. (1) and the steps leading to Eq. (12), the three-dimensional version of Eq. (12) becomes

$$\partial_t \delta\rho = -\frac{x}{t}\partial_x \delta\rho - \frac{1}{t}\delta\rho - \frac{c_0}{2}\int_\infty^x \nabla_\perp^2 \delta\rho dx. \tag{31}$$

While direct solution of this equation is not available as in the one-dimensional case, it is possible to demonstrate that the perturbation energy decays at least as fast as $1/t$. Multiplying Eq. (31) by $2\delta\rho$ yields

$$\partial_t \delta\rho^2 = -\frac{x}{t}\partial_x \delta\rho^2 - \frac{2}{t}\delta\rho^2 - c_0\delta\rho\int_\infty^x \nabla_\perp^2 \delta\rho dx \tag{32a}$$

$$= -\frac{x}{t}\partial_x \delta\rho^2 - \frac{2}{t}\delta\rho^2 - c_0\nabla_\perp \cdot \left(\delta\rho\int_\infty^x \nabla_\perp \delta\rho dx\right) + \frac{c_0}{2}\partial_x\left(\nabla_\perp\int_\infty^x \delta\rho dx\right)^2. \tag{32b}$$

Near shock discontinuities, we consider $\delta\rho$ as the limit of a continuous function which falls to zero rapidly for x outside the shock. Integrating (32b) over all space, with $\delta\rho=0$ at infinity, leads to the following:

$$\partial_t \int \delta\rho^2 dxdydz = -\frac{1}{t}\int \delta\rho^2 dxdydz - \frac{c_0}{2}\int dydz\left(\nabla_\perp\int_{-\infty}^\infty \delta\rho dx\right)^2. \tag{33}$$

To achieve this result, the first term on the right side of (32b) was integrated by parts, and the third term on the right yields a surface term which vanishes at infinity. Equation (33) shows that the energy in the three-dimensional perturbation field falls off at least as fast as $1/t$. We conclude from (28) and (33) that the basic state is stable against three-dimensional perturbations: as in the one dimensional case, the ratio of perturbation energy (33) to the wave's energy (28) decreases at least as fast as $t^{-1/(m+1)} = t^{-1+1/n}$.

It is worth noting that (33) yields stability of self-similar plane waves against arbitrary three-dimensional perturbations explicitly. In many physical systems stability analysis must resort to local dispersion relations, treating differential equation coefficients as locally constant.

E. Riemann solution for unstressed dry granular media

Returning to the issue of a medium with zero sound speed in the unstressed state, we invoke the equation for the right-propagating Riemann invariant[7] for an isentropic self-similar wave, which may be stated

$$(\partial_t + (v+c)\partial_{x'})\rho' = 0, \tag{34}$$

where $v = \int_0^{\rho'} c/(\rho_0+w)dw$ is the particle velocity and $c^2 = \partial p/\partial\rho'$. As before, x' refers to a coordinate system fixed in the medium. Equation (34), which may be regarded as exact, agrees with Eqs. (2) and (3) up through second order. The condition for self-similarity corresponding to (6) is

$$\xi \equiv x'/t = (v+c). \tag{35}$$

Taking $p \propto \rho'^{3/2}$ gives $f(\rho') = (v+c) \propto \rho'^{1/4} + O(\rho'^{5/4})$. The lowest order expression for the similarity solution corresponding to (19), (26), and (27) is

$$\rho'(x',t) \propto (x'/t)^4,$$

$$x_s'(t) = x_s'(t_0)(t/t_0)^{4/5},$$

$$\rho_s'(t) = \rho_s'(t_0)(t/t_0)^{-4/5}. \tag{36}$$

Equation (36) reveals that Hertzian nonlinearity in a dry unstressed granular medium results in different self-similar shock behavior from that found in a fluid or a saturated granular medium at onset of Hertzian nonlinearity as discussed after Eq. (28). In particular, the shock amplitude decreases faster and the zero stress point remains fixed in the medium.

Stability of the similarity solution (36) against one-dimensional perturbations follows from the analysis of Sec. II A, with x replaced by x'. The ratio of perturbation energy to the wave's total energy falls as $t^{-1/5}$. Since the NPE applies only to media which support acoustic waves in the unperturbed state, one must rely on the more general stability proofs of Refs. 8–12 for stability against three-dimensional perturbations.

III. A NUMERICAL EXAMPLE WITH MIXED NONLINEARITY

Given the lack of experimental data on nonlinear compressional waves in fluid-saturated granular media, we give a numerical result illustrating nonlinear wave behavior subject to Hertz forces of various amplitudes in a fluid medium. The numerical experiment applies to a Hertzian chain that might be realized by placing spheres in a long, fluid-filled cylinder whose diameter equals that of the spheres. This configuration traps fluid between spheres so that there is no differential flow.

When an elastic sphere is compressed by a force F in the x direction, the resulting decrement h in diameter along x is given by[5]

$$F = \frac{\sqrt{2}}{3}\frac{E}{1-\sigma^2}h^{3/2}R^{1/2}, \tag{37}$$

where E is the Young's modulus of the sphere material, σ is Poisson's ratio, and R is the sphere radius. Taking $h \ll R$, the density perturbation in the resulting effective medium (spheres plus fluid) is

$$\frac{\rho'}{\rho_0} \simeq \frac{h}{2R}, \tag{38}$$

where ρ_0 is the unperturbed density of the bulk medium. An equation of state for the Hertzian chain treated as a bulk medium is obtained by adding the fluid pressure to the intergranular Hertz force F divided by the area of the cylinder πR^2,

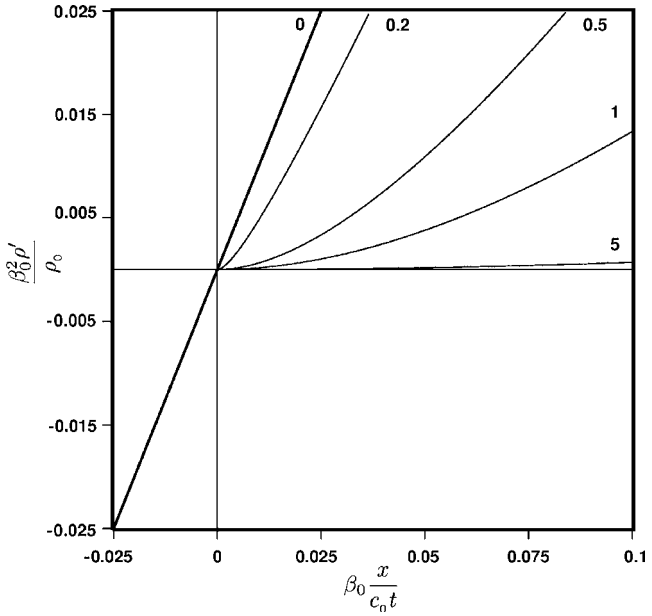

FIG. 2. Self-similar wave profiles for the equation of state (39). The curves are labeled with the value of the Hertz force parameter a.

$$p = \rho_0 c_0^2(u + (\beta_0 - 1)u^2 + a \cdot \max(0,u)^{3/2}), \tag{39}$$

where

$$u = \frac{\rho'}{\rho_0}, \tag{40}$$

c_0 and β_0 are the bulk medium's unperturbed sound speed and quadratic nonlinearity coefficient[19] in the absence of Hertz forces, respectively, and

$$a = \frac{4}{3\pi}\frac{E}{\rho_0 c_0^2}(1-\sigma^2)^{-1} \tag{41}$$

is a nondimensional quantity specifying the amplitude of the Hertz force. The max function in Eq. (39) reflects the fact that grains can only transmit positive stress. Applying Eqs. (3) and (6) to (39), we find for the similarity solution

$$u\beta_0 + \frac{3}{4}au^{1/2} = \frac{x}{c_0 t}, \quad x > 0. \tag{42}$$

For $x \leqslant 0$, the second term on the left side of (42) is absent. The physically relevant solution to (42) is

$$\frac{\rho'}{\rho_0} = \begin{cases} \left[2\left(\frac{3}{4}a\right)^2 - \frac{3}{2}a\sqrt{\left(\frac{3}{4}a\right)^2 + 4\beta_0\frac{x}{c_0 t}} + 4\beta_0\frac{x}{c_0 t}\right]/(4\beta_0^2), & x > 0, \\ x/\beta_0 c_0 t, & x \leqslant 0. \end{cases} \tag{43}$$

Figure 2 illustrates the self-similar waveforms from Eq. (43) for various values of the Hertz force parameter a. Shock discontinuities are not shown since their location depends on the initial condition from which the self-similar wave evolved, and the values of β_0 and t. Figure 2 supports the vanishing slope of the waveform near a zero crossing with initially positive slope in the presence of Hertz forces [Eq. (24)], as can be shown directly from Eq. (43) for $a > 0$. The

discontinuity in slope at the origin for $a>0$ in Fig. 2 reflects the fluidlike behavior of the medium for negative strain, and the sudden onset of Hertz forces for positive strain.

IV. SUMMARY

For media which support acoustic waves the NPE,[2] Eq. (1) predicts stability of self-similar plane waves including shocks subject to Hertzian and other low-order nonlinearities despite the divergence of the quadratic nonlinearity coefficient at zero stress. This stability implies that the fate of all nonlinear acoustic plane waves in lossless homogeneous media is self-similarity. Equation (33) shows that the energy in a three-dimensional perturbation falls off at least as fast as $1/t$, while Eq. (28) shows that energy in the self-similar plane wave falls off slower than $1/t$ for nonlinearity of order $1<n<3$. The ratio of the perturbation energy to the wave's unperturbed energy falls off at least as fast as $t^{-1+1/n}$, where $n=2$ for fluidlike media, and $n=3/2$ for the Hertzian nonlinearity of intergranular contacts. In this measure, stability is positively correlated with increasing order nonlinearity. For purely one-dimensional cases [Eq. (8)], the detailed evolution of the perturbation field is given in Eq. (13).

It has been shown in Eq. (24) that for general nonlinear plane waves with initial amplitude increasing in the direction of propagation, the slope of the wave goes to zero where the nonlinearity coefficient diverges as in Fig. 2. For waves with amplitude initially decreasing in the direction of propagation, divergent nonlinearity coefficient causes the wave to steepen toward shock formation immediately.

Since a nonanalytic component in the equation of state (i.e., Hertzian nonlinearity) has physical consequences not amenable to the use of a quadratic nonlinearity coefficient, it seems reasonable to treat the analytic portion of $p(\rho')$ in Eq. (1) with traditional methods, and add the nonanalytic component separately without Taylor's expansion [see Eq. (39) for an example]. The NPE is well suited for this approach, whereas the method used in numerical solution of the KZ equation[1] is limited to quadratic nonlinearity.

ACKNOWLEDGMENT

Work supported by the Office of Naval Research.

[1] E. A. Zabolotskaya and R. V. Khokhlov, "Quasi-plane waves in the nonlinear acoustics of confined beams," Sov. Phys. Acoust. **15**, 35–40 (1969).
[2] B. E. McDonald and W. A. Kuperman, "Time domain formulation for pulse propagation including nonlinear behavior at a caustic," J. Acoust. Soc. Am. **81**, 1406–1417 (1987).
[3] I. Y. Belyaeva, V. Y. Ziatsev, and L. A. Ostrovskii, "Nonlinear acoustoelastic properties of elastic media," J. Acoust. Soc. Am. **39**, 11–15 (1993).
[4] V. Tournat, V. Zaitsev, V. Gusev, V. Nazarov, P. Bequin, and B. Castagnede, "Probing weak forces in granular media through nonlinear dynamic dilatancy: clapping contacts and polarization anisotropy," Phys. Rev. Lett. **92**, 085502 (1-4) (2004).
[5] L. D. Landau and E. M. Lifschitz, *Theory of Elasticity* (Addison-Wesley, Reading, MA, 1959).
[6] B. E. McDonald and J. Ambrosiano, "Similarity solution for low mach number spherical shocks," J. Acoust. Soc. Am. **84**, 1497–1503 (1988).
[7] L. D. Landau and E. M. Lifschitz, *Fluid Mechanics* (Addison-Wesley, Reading, MA, 1959).
[8] A. E. Roberts, "Stability of a steady plane shock," Los Alamos Scientific Laboratory Report No. LA-299 (1945), 27 pp., Document PB2004-100597, National Technical Information Service, 5285 Port Royal Road, Springfield, VA 22161.
[9] W. C. Lien and T. P. Liu, "Nonlinear stability of a self-similar 3-dimensional gas flow," Chem. Phys. **204**, 525–549 (1999).
[10] X. B. Lin and S. Schecter, "Stability of self-similar solutions of the Dafermos regularization of a system of conservation laws," SIAM J. Math. Anal. **35**, 884–921 (2003).
[11] T. P. Liu and K. Zumbrun, "On nonlinear stability of general undercompressive viscous shock waves," Chem. Phys. **174**, 319–345 (1995).
[12] J. W. Bates, "Initial-value-problem solution for isolated rippled shock fronts in arbitrary fluid media," Phys. Rev. E **69**, 056313 (2004).
[13] A. A. Piacsek, "A numerical study of weak step shocks that focus in two dimensions," Ph.D. Thesis, Penn State University (1995).
[14] A. A. Piacsek, "Atmospheric turbulence conditions leading to focused and folded sonic boom wave fronts," J. Acoust. Soc. Am. **111**, 520–529 (2002).
[15] S. N. Gurbatov, A. Malakhov, and A. Saichev, *Nonlinear Random Waves and Turbulence in Nondispersive Media: Waves, Rays, Particles* (Manchester University Press, New York, 1991).
[16] B. E. McDonald, "Weak shock interaction with a free - slip interface at low grazing angles," J. Acoust. Soc. Am. **91**, 718–733 (1992).
[17] Y. N. Makov, "Universal automodeling solution to the Khokhlov-Zabolotskaya equation for waves with shock fronts," Acoust. Phys. **43**, 722–727 (1997).
[18] A. D. Pierce, *Acoustics* (Acoustic Society of America, New York, 1989), Sec. 11.3.
[19] R. E. Apfel, ""The effective nonlinearity parameter B/A for immiscible liquid mixtures," J. Acoust. Soc. Am. **74**, 1866–1868 (1983).

Application of a nonlinear boundary condition model to adhesion interphase damage and failure

Brian E. O'Neill and Roman Gr. Maev
Department of Physics, University of Windsor, Windsor, Ontario N9B 3P4, Canada

(Received 31 August 2005; revised 21 August 2006; accepted 2 September 2006)

In an earlier paper [J. Sadler, B. O'Neill, and R. Maev, J. Acoust. Soc. Am. **118**, 51–59 (2005)], a set of generalized boundary conditions were proposed, based on a thin layer (thickness $\ll$ wavelength) model of the acoustic interface. In this paper, the model is extended to cover the more pathological nonlinearity of the adhesion interphase—that is, the critically important thin layer where bonds are formed between adhesive and substrate. First, the boundary conditions are shown to be sufficiently general to cope with all manner of interphase nonlinearity, including unilateral cases such as clapping or slipping. To maintain this generality, an analytic time domain solution is proposed based on expansion in terms of the layer thickness rather than the conventional expansion in terms of harmonics. Finally, the boundary conditions are applied to an interphase failure model based upon basic continuum damage mechanics principles. It is proposed that such a model, which can predict the evolution of the interphase damage under stressful conditions, may allow a proper prediction of the ultimate adhesion strength based on nonlinear parameters measured nondestructively with ultrasound. © *2006 Acoustical Society of America.*
[DOI: 10.1121/1.2357996]

PACS number(s): 43.25.Ts, 43.35.Zc, 43.25.Jh, 43.35.Ty [MFH] Pages: 3509–3517

I. INTRODUCTION—GENERALIZATION OF BOUNDARY CONDITIONS

"Boundaries" in continuum mechanics are an abstraction that allows for the application of a simple piecewise continuous model to the inhomogeneous problem of two homogeneous media joined at some interface. Provided the variation occurs over a small enough region, much smaller than the wavelength of any probing beam, this is a reasonable approximation, and simple equations relate the fields on one side to those on the other.[1] Similar equations can be derived for any narrow layer using a linear expansion and the equations of motion; in other words, the motion can be related quasistatically from one side of any sufficiently thin layer to the other, treating it as a boundary.[2–4] In a previous paper,[5] we argued, with little justification, that the generalized boundary conditions developed from a thin layer expansion can be applied to model cases of imperfect interfaces, such as adhesion failure. This meshes well with the so-called interphase theory of adhesion failure,[6–8] which argues that adhesion failure most often occurs in the mating region where bonds are formed (or not) between particles of two different species, and that the immediate neighborhood of this region (the "interphase") often has properties that are significantly different from those of either bulk material. As this region fails, it becomes increasingly nonlinear, with, in particular, an increasing lack of tensile strength. A recent paper by Rokhlin *et al.*[9] demonstrated how this very idea could be exploited by using high amplitude, low frequency vibrations to increase the sensitivity of reflected high frequency ultrasound to adhesive bonding degradation. The basis of the approach is that the low frequency vibrations put the bond quasistatically into a state of compression or tension, which is then probed with the high frequency ultrasound. By way of explaining their results, the authors modeled the adhesive bonding region as a static distribution of springs of varying lengths. The effective elastic constant of the bondline is dependent on the number of springs in contact across the interface at any given moment. They then applied a previously published linear thin layer boundary condition model,[10] to calculate the effect of the stressed interphase on a high frequency ultrasonic probe wave.

In this paper, we set out to show what happens when we treat the correspondence between a nonlinear adhesion interphase region and the nonlinear thin layer in our the previously published boundary model.[5] That model is fully capable of dealing with the quasistatic case in Ref. 9, but can also handle the nonlinearity induced in hypothetical high power ultrasonic waves propagating across the damaged region. This latter situation is one that many experimentalists have attempted to exploit, with little success, and is precisely the case we consider in this paper. Incidently, one of the conclusions reached here is that multimodal techniques may well be the only practical way to test the interphase region of a bond. Also, in this paper, as in our previous one, we have suggested an unconventional approach to solving the ultrasonic nonlinear thin layer interaction problem in the time domain. This allows us to deal dynamically with any reasonable combination of layer nonlinearity and incident ultrasonic wave form while maintaining the general nature of the solution. Furthermore, instead of relying on the typical static spring models, we here demonstrate how a simple continuum damage mechanics may be applied to an adhesive interphase region in order to model the continuous development of failure behavior, from perfectly welded to completely broken. This approach is based on the notion that bond failure is an incremental process, and any complete theory of adhesion failure should be able to handle all aspects of this process.

II. GENERALIZED BOUNDARY CONDITIONS APPLIED TO THE NONLINEAR INTERFACE

As mentioned, the generalized boundary conditions, including some nonlinear expressions, were derived in a previous paper.[5] The key expressions connecting the fields on either side of a thin layer are

$$u_i^{\mathrm{II}}(\delta n_k,t) - u_i^{\mathrm{I}}(0,t) = n_p \frac{\partial u_i^L(0,t)}{\partial x_p}\delta, \tag{1}$$

$$n_j[T_{ij}^{\mathrm{II}}(\delta n_k,t) - T_{ij}^{\mathrm{I}}(0,t)] = n_j n_p \frac{\partial T_{ij}^L(0,t)}{\partial x_p}\delta, \tag{2}$$

where u and T are the displacement and stress, respectively, and the superscripts I, II, and L refer to fields in the material on the left side of the interface, the right side of the interface and the interface layer itself. δ is the interface layer thickness, and n_j is the jth component of the unit vector perpendicular to the interface. In general, these expressions are linked by the continuity of displacement and traction, thus it is possible to remove all reference to the fields in the layer with appeals to its constitutive and inertial laws. The linear case was dealt with in our previously mentioned paper. In the case of possibly nonlinear interface relations, one can appeal to a more general form of the constitutive Hooke's Law. This might be written

$$T_{ij} = C_{ij}\left[\frac{\partial u_k}{\partial x_l}\right], \tag{3}$$

where the C_{ij} are some general functions of the displacement gradients. Most commonly, the second and higher order terms are orders of magnitude smaller than the linear term, which is more explicitly suggested by an expansion

$$T_{ij} = c_{ijkl}\left(1 + F^L\left[\frac{\partial u_s}{\partial x_t}\right]\right)\frac{\partial u_k}{\partial x_l}, \tag{4}$$

where $F^L[\ ]$ is some small function.

Using the Kronecker delta, we can define a projection operator, $\xi_{ij} \equiv \delta_{ij} - n_i n_j$, to separate tensor components acting perpendicular and parallel to the interface. It is then possible to use the continuity of the traction and parallel gradients to rewrite the constitutive equation of the layer

$$n_j n_p T_{ip}^{\mathrm{ave}} + \xi_{jp} T_{ip}^L = c_{ijkl}^L\left(1 + F^L\left[n_t n_q \frac{\partial u_s^L}{\partial x_q} + \xi_{qt}\frac{\partial u_s^{\mathrm{ave}}}{\partial x_q}\right]\right) \times \left(n_l n_q \frac{\partial u_k^L}{\partial x_q} + \xi_{ql}\frac{\partial u_k^{\mathrm{ave}}}{\partial x_q}\right), \tag{5}$$

where ave refers to the continuous field components approximated as the average of those in the two substrates: $u_i^{\mathrm{ave}} = 1/2(u_i^{\mathrm{I}} + u_i^{\mathrm{II}})$. (Although this notation is preferable, it should be little different from simply evaluating in the more convenient of I or II.) It is clear that what we have is a set of six equations that may be solved to evaluate the six unknown directed derivatives of displacement and traction that appear on the right sides of Eqs. (1) and (2). Multiplying by n_j, it is possible to find the unknown directional derivatives of the displacement, taking advantage of the small size of F^L to get a first order inversion

$$n_q \frac{\partial u_i^L}{\partial x_q} = \left(\Lambda_{ij}^L T_{jp}^{\mathrm{ave}} n_p - \Lambda_{ilk}^L \xi_{ql}\frac{\partial u_k^{\mathrm{ave}}}{\partial x_q}\right)(1 - F^L[\cdots])\,\delta, \tag{6}$$

where $\Lambda_{ij}^L = (n_l n_k c_{ikjl}^L)^{-1}$ with $(n_r n_t c_{irst}^L)^{-1}(n_j n_l c_{ijkl}^L) = \delta_{ks}$, $\Lambda_{ilk}^L = \Lambda_{ij}^L n_s c_{jskl}^L$, and

$$[\cdots] = \left[n_t \Lambda_{sj}^L T_{jp}^{\mathrm{ave}} n_p + (\delta_{lt}\delta_{ks} - n_t \Lambda_{slk}^L)\xi_{ql}\frac{\partial u_k^{\mathrm{ave}}}{\partial x_q}\right], \tag{7}$$

is found by replacing the unknown term in the argument of F^L with its zeroth order approximation. The stresses in the layer may then be found (making use of $(1+F^L)(1-F^L) \approx 1$):

$$T_{ij}^L = \Gamma_{ijk}^L n_p T_{kp}^{\mathrm{ave}} + (\Gamma_{ijkl}^L + c_{ijkl}^L F^L[\cdots])\xi_{ql}\frac{\partial u_k^{\mathrm{ave}}}{\partial x_q}, \tag{8}$$

where $\Gamma_{ijk}^L = c_{ijrl}^L n_l \Lambda_{kr}^L$ and $\Gamma_{ijkl}^L = [c_{ijkl}^L - c_{ijvt}^L n_t \Lambda_{vlk}^L]$.

The results for the traction boundary condition are somewhat easier. Noting that particle velocities and accelerations are continuous across the layer, Newton's second law gives

$$\rho\frac{\partial^2 u_i^{\mathrm{ave}}}{\partial t^2} = \frac{\partial T_{pi}^L}{\partial x_p} = \frac{\partial T_{ip}^L}{\partial x_p} = \frac{\partial}{\partial x_p}(T_{ij}^L n_p n_j + \xi_{jp} T_{ij}^L) = n_p \frac{\partial T_{ij}^L n_j}{\partial x_p} + \xi_{jp}\frac{\partial T_{ij}^L}{\partial x_p}.$$

It is clear that

$$n_j n_p \frac{\partial T_{ij}^L}{\partial x_p} = \rho^L \frac{\partial^2 u_i^{\mathrm{ave}}}{\partial t^2} - \xi_{jp}\frac{\partial T_{ij}^L}{\partial x_p}, \tag{9}$$

and

$$n_j n_p \frac{\partial T_{ij}^L}{\partial x_p} = \rho^L \frac{\partial^2 u_i^{\mathrm{ave}}}{\partial t^2} - \Gamma_{ijk}^L n_q \xi_{jp}\frac{\partial T_{kq}^{\mathrm{ave}}}{\partial x_p} - (\Gamma_{ijkl}^L + c_{ijkl}^L F^L)\xi_{jp}\xi_{ql}\frac{\partial^2 u_k^{\mathrm{ave}}}{\partial x_p\,\partial x_q}. \tag{10}$$

It is worth noting, however, that in general, ρ^L is also field dependent, in fact, it is inversely proportional to the local material volume

$$\frac{\rho_0^L}{\rho^L} = \frac{\mathrm{Vol}}{\mathrm{Vol}_0} = 1 + \epsilon_{ii}^L, \tag{11}$$

where ϵ_{ij} is the strain tensor. This could also be expressed in terms of the substrate fields as

$$\rho^L = \rho_0^L\left[1 + n_i \Lambda_j^L (1 - F^L[\cdots])T_{jp}^I n_p + (\delta_{kl} - n_i \Lambda_{ilk}^L)\xi_{ql}\frac{\partial u_k^I}{\partial x_q}\right]^{-1}. \tag{12}$$

It is expected that, in most cases, the contribution of this term will be somewhat smaller than that of the nonlinearity in Eqs. (6) and (10).

With the complete boundary conditions given above, it is possible to build general models for multiple layer systems in the usual manner, however, algebraic expressions can only be found by using a perturbation expansion of some sort. For harmonic excitation and weak layer nonlinearity, it is conve-

nient to use an expansion in terms of higher harmonics. This has been the approach of most theorists. Such an approach should be suspect for cases of nonclassical interphase nonlinearity, for example, clapping or slipping cases, based as it is on the superposition principle. It is possible, however, to approach the problem in the time domain, using an expansion in terms of the layer thickness. This approach was outlined, although for normal incidence only, in our previous paper. In brief, it involves partial wave expansions on either side of the layer of the form

$$A(s_j x_j \pm t) + A'(s_j x_j \pm t)\phi(s_j x_j \pm t)\delta + O(\delta^2), \tag{13}$$

where s_i is the slowness, and the layer is presumed at $x_3=0$. These partial waves are phase matched at the interface, and may be related to the incident wave form to the zeroth order by setting $\delta=0$, to first order by setting $\delta^2=0$, and so on. It will also be necessary to relate the traction and displacement boundary conditions by integrating or differentiating the partial waves with respect to time. Since time derivatives are continuous across the interface layer, this approach is perfectly valid, resulting in a set of algebraic equations that may be expressed generally as

$$\sum_{\beta} p_i^{\bar{\beta}} R_\beta \phi_\beta^{\{n\}}(-t) + \sum_{\alpha} p_i^{\bar{\alpha}} R_\alpha \phi_\alpha^{\{n\}}(t) = \mathcal{F}_i^{\{n\}}$$

$$-\sum_{\beta} P_{i3}^{\bar{\beta}} R_\beta \phi_\beta^{\{n\}}(-t) + \sum_{\alpha} P_{i3}^{\bar{\alpha}} R_\alpha \phi_\alpha^{\{n\}}(t) = \mathcal{G}_i^{\{n\}}, \tag{14}$$

where α and β refer to reflected and transmitted partial modes with displacement and traction polarizations at the interface, p_i and $P_{i3}=c_{i3kl}p_k s_l$, respectively. $R_{\alpha,\beta}$ are the usual transmission and reflection coefficients for the partial wave modes. The $\phi^{\{n\}}$ are the nth order corrections while $\mathcal{F}_i^{\{n\}}$ and $\mathcal{G}_i^{\{n\}}$ are the nth order driving factors. For zeroth order, clearly $\phi^{\{0\}}=1$ and $\mathcal{F}_i^{\{0\}}$ and $\mathcal{G}_i^{\{0\}}$ are derived directly from the displacement and traction polarizations of the incident waves.

Most often the full solution may be significantly simplified to address a particular case. For the work below, which is intended mainly to demonstrate the concept of the damaged interface, or interphase, our consideration is restricted, for simplicity, to normal incidence and isotropic media. In that case, the equations simplify to set of nonlinear variants of the so-called "quasistatic" boundary conditions[11,12]

$$u_i^{\mathrm{II}} - u_i^{\mathrm{I}} = \Lambda_{ij}^L (1 - F^L[\cdots]) T_{jp}^{\mathrm{I}} n_p \delta \tag{15}$$

$$n_p T_{ip}^{\mathrm{II}} - n_p T_{ip}^{\mathrm{I}} = \rho^L \frac{\partial^2 u_i^{\mathrm{ave}}}{\partial t^2}\delta. \tag{16}$$

Typically, the expression is used in its linear form, with $F^L=0$, in which case the Λ_{ij}^L may be directly related to the "spring constants": $K_{ij}=n_l n_k c_{ikjl}^L=(\Lambda_{ij}^L)^{-1}$; as well, often the layer inertia is ignored by setting the layer density, ρ^L, to zero. Notice that these equations are valid for both longitudinal and shear polarizations. If the layer is linear and isotropic, it is possible to write $c_{ikjl}^L=\lambda^L\delta_{ik}\delta_{jl}+2\mu^L\delta_{ij}\delta_{kl}$, resulting in $K_{ij}=2\mu^L\xi_{ij}+(\lambda^L+2\mu^L)n_i n_j$, or, in the notation of the quasistatic approach, $K_{ij}=K_T\xi_{ij}+K_L n_i n_j$. It is clear, however, that the usual quasistatic boundary conditions will generally fail for oblique incidence for purely geometrical reasons. Even for the simplest case of an isotropic, linear layer, the boundary conditions will have additional terms (also noted by Rokhlin and Wang)[3]

$$u_i^{\mathrm{II}} - u_i^{\mathrm{I}} = \left(K_{ik}^{-1} n_p T_{kp}^{\mathrm{ave}} - \frac{K_T}{K_L} n_i \xi_{pk} \frac{\partial u_k^{\mathrm{ave}}}{\partial x_p} \right)\delta, \tag{17}$$

$$n_p T_{ip}^{\mathrm{II}} - n_p T_{ip}^{\mathrm{I}} = \left[\rho^L \frac{\partial^2 u_i^{\mathrm{ave}}}{\partial t^2} - \xi_{iq} \frac{\partial T_{rp}^{\mathrm{ave}}}{\partial x_q} n_r n_p - (K_L - K_T) \times \xi_{pq} \frac{\partial^2 u_i^{\mathrm{ave}}}{\partial x_q \partial x_p} - 2K_T \xi_{iq}\xi_{kp} \frac{\partial^2 u_k^{\mathrm{ave}}}{\partial x_q \partial x_p} \right]\delta. \tag{18}$$

While it is now clear that we can apply our generalized boundary conditions to a layer of nonlinear media, it is less clear that this makes this model suitable to the more pathological cases of failing and damaged interphases. In particular, the derivation of these expressions relied on a formal statement of material continuity. Certain types of interface failure, such as partial or complete disbonds, would appear to be outside the scope of this theory. It is not necessary, however, to cling to this view of the theory. Instead, it is possible to view the right hand sides of Eqs. (1) and (2) as simply providing a connection between the two media, which may be made as general as one might wish. In particular, this theory has been extended to deal with cases of unilateral boundary conditions, such as clapping or sliding interfaces. In this paper, we will not be explicitly using those results, so they have been relegated to Appendix A, for those who are interested. In general, the unilateral results may be most simply approximated using a bilinear layer model, where the layer density is zero, and the layer stiffness approaches infinity when the surfaces are in contact, but approaches zero when they are not.

III. THE "THIN LAYER" MODEL APPLIED TO THE DAMAGED INTERPHASE

A. Bonding failure as damage

Over the past decade or so, much attention has been given to the problems of the ultrasonic nondestructive evaluation of adhesively bonded structures.[9,13–15] While certain defects are easily detected by the most common techniques, and the presence of such defects are clear indications of weakness, their absence has not proven to be an indication of strength. This unhappy situation arises because other structural defects, such as zero-volume disbonds, may occur, to which contemporary ultrasonic techniques are not particularly sensitive. Much effort has therefore been expended in developing techniques which might be more sensitive to such defects, for example, the measurement of the nonlinear properties of the interface itself. Although much has been claimed over the years, and some success has been shown for specific examples, a lot of suspicion remains regarding the efficacy of these various proposals, hindering their acceptance in the broader community. In the authors' opinion, one

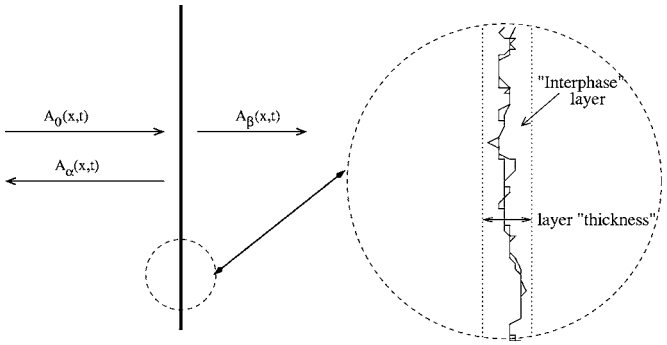

FIG. 1. Reflection from an interphase layer modeled as a thin, nonlinear layer. The region of adhesion bonds and defects is best thought of as a layer having physical properties significantly different from either substrate.

of the major reasons for this is a lack of any universal model that can effectively link the parameters of the wave, a dynamic, hopefully nondestructive, probe, to the bond strength, defined quasistatically and destructively. This section proposes a possible solution to this problem. The basis of the idea is the following. Each adhesion-substrate interphase may be considered as a weak layer (see Fig. 1), an invitation for localized damage to take place. The damage may be of two varieties, one being the damage which occurs as a result of the mechanical and environmental stresses on the working part; the other is built-in due to shortcomings in joining process. Fundamentally, one would expect similar behavior from these two situations, however, this does mean that the properties used for the "undamaged" state must be carefully calibrated based on the best case scenarios, rather than the "as-cured" initial state of the material. Using these parameters, it is possible to develop two sets of equations: the damage impacted elastic constitutive equations and the damage evolution equations for the interphase layer. This gives the possibility of designing a technique for using strong ultrasonic waves to evaluate the current damage state, while keeping new damage introduction to acceptable levels. The ultimate strength of the bond, as would be determined by a pull test, is then inferred from the damage model. The damage model itself must be validated through standard tensile tests.

B. A simple one-dimensional damage model of the interphase

In a simple model, the damaged interphase may be thought of as comprised of two parts, the delaminated fraction, ϕ, and the intact fraction, $1-\phi$.[16] For the one-dimensional (1D) case, the undamaged interphase will be treated as a thin linear material, with a constitutive relation like $T=\bar{C}\epsilon$, where ϵ is the nominal strain of the interface: $\epsilon\delta=u^{\mathrm{II}}-u^{\mathrm{I}}$. Any delaminated region is presumed to have full strength under compression and no strength under tension. In that case, the simplest possible model for the constitutive relation of the entire region would be $T=\bar{C}(1-\phi)\epsilon$ under tension, and $T=\bar{C}\epsilon$ under compression. Although this model is clearly only a first approximation, there is little consensus in the literature regarding how to improve upon it, and it well illustrates the general idea. Such a bilinear model is easily introduced into the results of the previous sections, even for multiple interphases.

The second task is to build a model controlling the damage evolution. Such a model could be quite complicated, taking into account plastic deformation, hardening, creep, etc. Here, for simplicity, it is assumed that the evolution of the interface is dominated by brittle damage, that is, that plastic flow and hardening are negligible. This would mean that such a model is most appropriate for the more brittle adhesives—cyanoacrylates, or diffusion bonds, for example, and not really suitable for rubbery or highly plastic adhesives. One expression that gives a reasonable damage behavior is

$$\phi-\phi_0=\left(\frac{\bar{C}}{X}\right)^{\eta}\epsilon^{2\eta}, \tag{19}$$

where ϕ_0 is the initial damage, $\bar{C}$ is the undamaged elastic modulus, and the evolution parameters X and η control, in combination, the failure rate and the peak strength of the virgin material. This expression may be rewritten as

$$X(\phi-\phi_0)^{\frac{1}{\eta}}=\bar{C}\epsilon^2, \tag{20}$$

from which it more apparent that it gives the relation between damage and elastic potential energy. Specifically, it determines how damage is driven by a relaxation in strain energy. This expression, with η typically set to unity, is common in the literature of continuum damage mechanics. Under monotonic loading, it results in stress-strain curves and damage evolution as shown in Fig. 2. The basic features of this curve may be fit to experiment. More details regarding the origins of this curve may be found in Appendix B and Refs. 16–18.

Once the interface damage characteristics, in the form of the damage impacted constitutive equation and the damage evolution equations, are written, it is possible to model the interface behavior under the influence of strong acoustic waves (or virtually any other disturbance). The major difficulty lies in the nonlinearities inherent in this situation. Fortunately, the situation involves two quite different timescales during most of the motion. Because the idea is to be as nondestructive as possible, these investigations should take place in the regime where the evolution in the damage happens over a great many cycles of the wave. Thus the period of the wave is the fast time scale and the damage evolution, for the most part, is the slow time scale. The model may be implemented in the following way. At time t, acoustic waves impinge on the damaged interface, possibly multiple modes on either side. The $\delta=0$ (perfect interface) boundary conditions are solved to approximate the modal amplitudes at this instant. Superpositions of the these zeroth order solutions are then used to approximate the stress and acceleration at the interface. These are used in the right hand side of the boundary conditions expressions, along with the current magnitude of the damage $[\phi(t-\Delta t)]$, to find first order corrections to the wave and stress amplitudes. $\epsilon(t)$, the strain across the interface, is then inferred from the first order fields, and used either directly or incrementally, as $\Delta\epsilon=\epsilon(t)-\epsilon(t-\Delta t)$, in or-

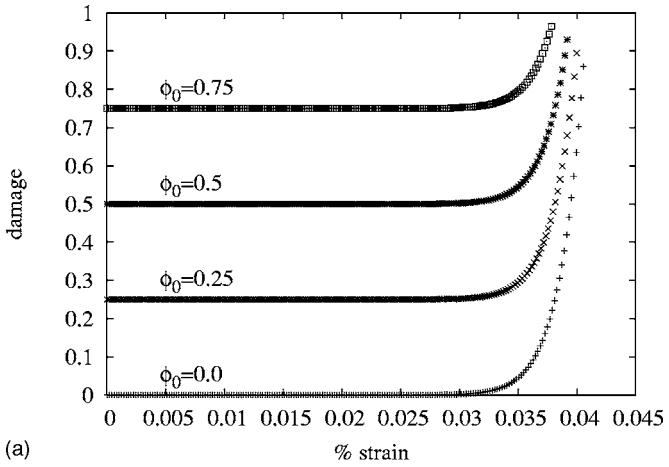

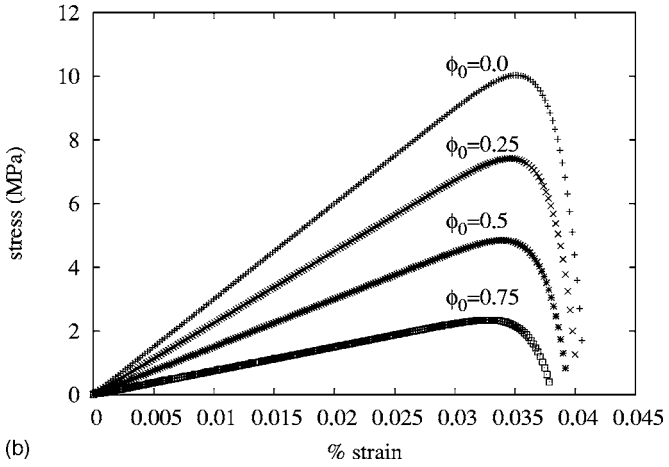

FIG. 2. Evolution of damage (upper) and stress (lower) during monotonic strain loading for various initial damage states. Here the virgin material was assumed to have an elastic modulus, $\bar{C}$ of 30 GPa, an ultimate strength of 10 MPa and failing slope of $20\bar{C}$.

der to determine the new damage, $\phi(t)$. The process is repeated for the next time step. The fact that ϕ changes relatively slowly compared to the period of the wave means that it is unnecessary to improve on this by imposing some sort of cyclic self consistency algorithm.

C. Interphase damage simulations

The 1D model of the damaged interphase is quite simple to implement as described. This was done for values of the material meant to roughly simulate the adhesion layer between a metal and an epoxy adhesive impinged upon by a high power ultrasonic wave. A single damaged interphase, of thickness 0.01 mm, elastic modulus 30 GPa, and virgin strength of 10 MPa (see Fig. 2) is located between a pair of dissimilar half spaces, with reflection coefficient 0.5. A 1 MHz longitudinal wave, normally incident at the interface, with stress amplitude of 1 MPa was chosen. This amplitude is large enough to show noticeable bilinear distortion, but not large enough to significantly increase the interphase damage in any given period. Figure 3 shows the interphase strain curves for damage levels of 0%, 25%, 50%, and 75%. The bilinear distortion is quite clear here. Unfortunately, however, this distortion is not detected independently, but only its

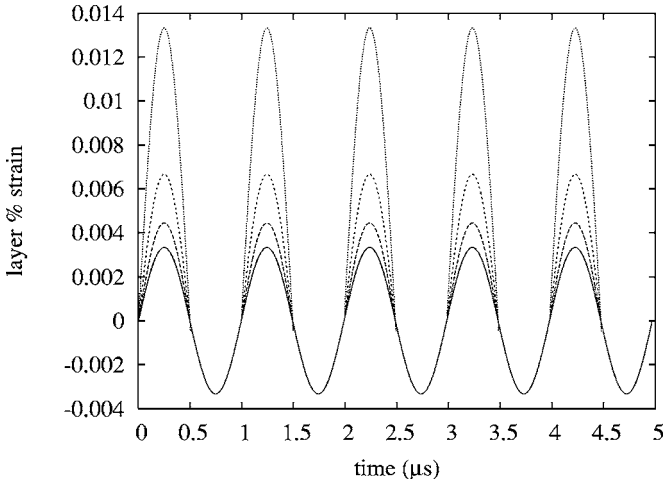

FIG. 3. Interface strain due to a 1 MPa pulse (10% T_{max}) reflecting from the damaged interphase between dissimilar media. From least to greatest distortion: 0%–75% initial damage. The damage increase calculated for all of these cases is negligible. This would change if the amplitude or length of the toneburst were increased.

impact on the reflected or transmitted wave, where its impact is reduced by a factor of the interphase layer thickness. The result is a slight phase shift correction in the tension side of the waves (Fig. 4) compared to the undamaged material. Clearly this is not easily discerned in the wave form itself. One way to detect the effect is to make use of spectral analysis. Table I shows the harmonic content for the interphase strain and the reflected and transmitted signals. Note that, because of the simple constitutive model chosen here, the even harmonics are seen to dominate over the odd ones. We do not wish to imply that this effect will be noticeable in the typical nonlinear experiment dealing with adhesive bonds. Such experiments typically measure the sum total of nonlinear effects, including the strong material nonlinearities of the adhesives themselves. The interphase defects that are so critical to understanding adhesion failure likely do not generate harmonic distortions strong enough to be detected without significant effort. However, when interphase effects dominate the nonlinearity, such as occurs near regions of local delamination, the nonuniform generation of harmonics is well documented.[19] The suppression of odd harmonics shown here is just the simplest instance of this phenomenon.

In the continuum damage model described, damage can accumulate even if the wave amplitude is small. It should be noted that most damage models make use of a threshold value of the strain below which it is assumed that no damage occurs. The discussion here would apply only to waves having amplitudes above this rather arbitrary limit. Even for the case analyzed above, where the maximum stress in the wave is significantly below the interphase layer strength, the layer could fail after a sufficiently long pulse. As the vibration continues, damage buildup continues, as a result, the effective tensile elastic modulus and the ultimate tensile strength both decrease, until it drops below the maximum stress of the wave, and delamination occurs.

One of the more interesting prospects, then, is the use of pulses to probe damaged interfaces. In conventional nonlinear ultrasound, long tonebursts are used—due to their narrow

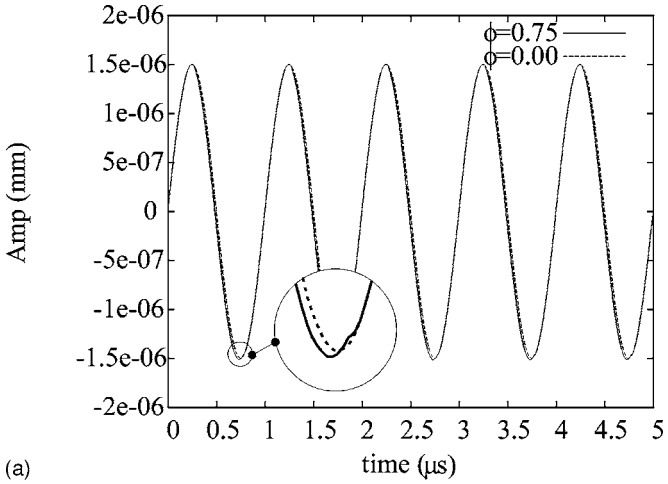

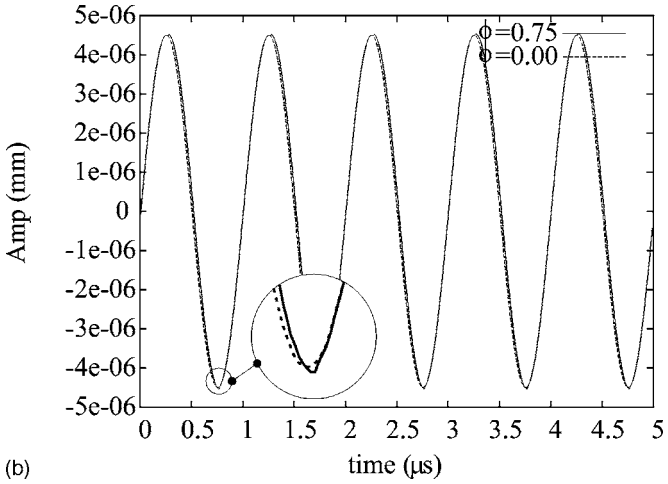

FIG. 4. Reflected (upper) and transmitted (lower) waves from a damaged interphase between dissimilar media. The nonlinear distortion here is much less obvious than that in Fig. 3 might have suggested; with increasing complexity and additional layers, the situation becomes more difficult to interpret.

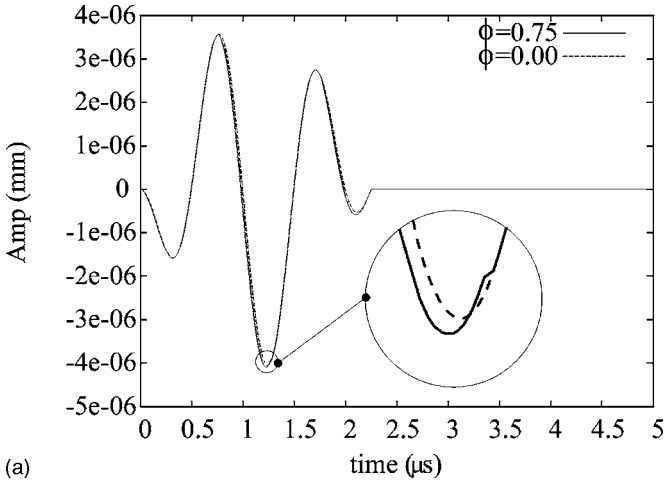

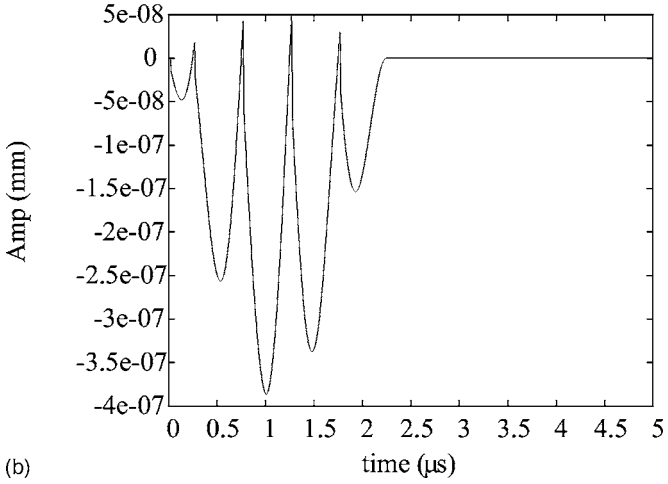

FIG. 5. Pulse reflected from a damaged interphase between dissimilar media (upper). Phase inversion processing can be used to remove the fundamental (lower), that is, the superposition of two signals reflected from the interface, the direct signal plus the signal with inverse phase.

bandwidth, it is much easier to investigate the harmonics. As is clear above, however, a long, strong, toneburst could damage the interface significantly. An alternative would be to use a short, sharp spike. Because of its short duration, a single such spike could have a significantly larger amplitude, probing more of the stress-strain curve, and still create less damage than a toneburst. Obviously, spectral analysis may not be an option in this case, however, given the asymmetrical aspect of this nonlinear distortion, it is possible to get good results using inverse phase processing. That is, following a pulse, $A(t)$, apply a second pulse of inverse phase, $-A(t)$. The reflected (or transmitted) pulses from each are then added, effectively eliminating the symmetric parts of the response. Figure 5 demonstrates how effective such an analysis can be in this particular case.

TABLE I. Normalized harmonic amplitudes for the interphase strain (Fig. 3), reflected and transmitted signals (Fig. 4) for a harmonic wave incident on a boundary with 75% damage.

	Harmonic				
Damage 75%	1st	2nd	3rd	4th	5th
At interphase	1.0	0.25	2.9*e*-6	0.052	1.0*e*-6
Reflected	1.0	0.020	9.2*e*-5	0.0045	9.2*e*-5
Transmitted	1.0	0.021	0.0001	0.0047	0.0001

While the damage analysis was demonstrated here in 1D only, there is nothing preventing its extension to two-dimensions or three-dimensions using the results of previous sections. The main thing missing is a damage evolution and damage response for shear stresses applied to the interface. This might be similar in form to those proposed for the longitudinal stress, except that the result would not have the same symmetry. In fact, from a previous analysis of friction coupled interfaces,[20] it is expected that we would find the dominance of odd rather than even harmonics.

IV. CONCLUSION

We have shown in this paper how generalized boundary conditions can be adapted to deal with a large variety of dynamic behavior. This provides a unique opportunity to develop a model which is capable of demonstrating the entire range of interphase behavior. Such a model may be derived

from continuum damage mechanics, as demonstrated in the final sections of the paper. In that model, the damage may be inferred, at least under ideal conditions, from the nonlinear distortion it introduces into passing ultrasonic waves, and at the same time may be used to estimate the remaining strength of the interface, as defined using monotonic loading. One drawback is that the acoustic power required to generate nonlinear effects is a significant fraction of the remaining strength of the material, and may result in the rapid failure of bonds with even a little damage. That is, there is only a narrow amplitude window where significant harmonics are produced without introducing significant new damage. This likely explains the difficulty the nonlinear ultrasonics community has had in making such a scheme operational—either the harmonic generation is small, or the part has already failed. However, with a clear, validated theory connecting the damage and the acoustic nonlinearity, it should be possible to monitor a threshold. For example, if the minimum strength required is $T_{\max}$, the damage evolution theory can be used to determine the allowed initial damage ϕ_0, which corresponds to this strength. Then the nonlinear layer theory can be used to establish the amplitude of an interrogating wave or pulse needed to have some measurable nonlinear distortion. This then becomes the determining factor in whether a part is good or bad. If it proves difficult to achieve a sufficient signal to noise ratio using ultrasonics alone, it is our opinion that this could be significantly enhanced using a multi-modal approach, for example, ultrasonics plus static loading, ultrasonics plus thermal pulse, or ultrasonics plus vibration. Some of these approaches are already being explored in the lab.[9,19,21] However, further work is needed to establish the link between the parameters measured via these techniques and the actual bond strength.

ACKNOWLEDGMENTS

The authors would like to acknowledge the funding and support of the Natural Sciences and Engineering Research Council of Canada. They would also like to thank Jeff Sadler and Sergei Titov for helpful discussions.

APPENDIX A: GENERALIZED BOUNDARY CONDITIONS EXTENDED TO THE UNILATERAL INTERFACE

Two cases of particular interest involving nonlinear behavior at interfaces are the so-called clapping nonlinearity and slipping nonlinearity. Both of these unilateral boundary cases involve unbonded surfaces in close contact, which give rise to time varying boundary conditions involving discontinuous, but well behaved, displacements.[22–24] Perhaps more of an issue, common to both these cases, is that the boundary conditions for at least half of the bilinear motion are formulated entirely in terms of the tractions, whereas standard boundary conditions always consist of one set of conditions relating the tractions and one set relating the displacements. As will be demonstrated, this does not pose a huge problem in either case, as one may simply reformulate traction boundary conditions in terms of displacements.

First, begin by considering the clapping case. For this to be interesting, a static compressive external pressure, P, is required, which forces the open gap to close. (It is simple to include a spring-like closing model if it is of interest. Doing so does away with the unilateral nature of the problem, however.) Thus the boundary conditions, for the closed interface, are (see Ref. 24)

$$u^{\mathrm{II}} - u^{\mathrm{I}} = 0, \tag{A1}$$

$$T^{\mathrm{II}} - T^{\mathrm{I}} = 0, \tag{A2}$$

which may be easily achieved by setting the interface "layer" density and stiffness to 0 and ∞, respectively.

After the gap opens, no absolute condition exists on the displacements beyond $u^{\mathrm{II}} > u^{\mathrm{I}}$, but independent conditions on the tractions do exist

$$T^{\mathrm{II}} = 0, \tag{A3}$$

$$T^{\mathrm{I}} = 0. \tag{A4}$$

First, it is clear that $T^{\mathrm{II}} - T^{\mathrm{I}} = 0$, as before. Second, this implies, in terms of partial waves, that, after integration

$$-\omega Z_{\mathrm{I}} A_0'(\omega t) + \omega Z_{\mathrm{I}} A_\alpha'(\omega t) - P = 0$$

$$\Rightarrow A_\alpha(\omega t) = A_0(\omega t) + \frac{P}{Z_{\mathrm{I}}} t + \mathrm{C}_\alpha, \tag{A5}$$

$$-\omega Z_{\mathrm{II}} A_\beta'(\omega t) - P = 0$$

$$\Rightarrow A_\beta(\omega t) = -\frac{P}{Z_{\mathrm{II}}} t + \mathrm{C}_\beta. \tag{A6}$$

It is therefore also true that

$$u^{\mathrm{II}} - u^{\mathrm{I}} = A_\beta(\omega t) - A_0(\omega t) - A_\alpha(\omega t)$$
$$= -2A_0(\omega t) + 2A_0(\omega t_0) - \left(\frac{1}{Z_{\mathrm{I}}} + \frac{1}{Z_{\mathrm{II}}}\right) P(t - t_0). \tag{A7}$$

Here, as in Eqs. (14), the subscript α refers to mode reflected back from the interface and β to the transmitted mode. The Z are the acoustic impedances: $\omega Z = \omega \rho v = kC$ where C is the pertinent elastic constant. The integration constants C_α and C_β were determined by the initial condition that $u^{\mathrm{II}} - u^{\mathrm{I}} = 0$ at t_0, the instant that the interface opens. This instant is that in which the traction $T^{\mathrm{I}}(t)$, initially positive, passes through zero going negative. The other transition time, back to the closed state, occurs when $u^{\mathrm{II}} - u^{\mathrm{I}}$ next goes to zero. These times, which are essential to the form of the resulting nonlinearity, can either be found *a priori* by an analytical analysis,[24] or, in an incremental time domain simulation, with a simple test. It is clear that, although perhaps somewhat different than initially construed, the generalized boundary conditions are sufficiently flexible to deal with this case.

The sliding case works in a similar manner. During the sliding motion, assuming a classical two-constant frictional force, only traction boundary conditions[20] exist

$$T^{\mathrm{II}} = -\operatorname{sgn}(v)\mu_k P, \tag{A8}$$

$$T^{\mathrm{I}} = -\operatorname{sgn}(v)\mu_k P, \tag{A9}$$

where $\operatorname{sgn}(v)$ is the sign of the relative velocity and μ_k is the coefficient of kinetic friction. Using the same technique as before, it is possible to recast these equations as

$$u^{\mathrm{II}} - u^{\mathrm{I}} = -2A_1(\omega t) + 2A_1(\omega t_0) - \left(\frac{1}{Z_{\mathrm{I}}} + \frac{1}{Z_{\mathrm{II}}}\right)\operatorname{sgn}(v)\mu_k P(t - t_0) + \Delta_0. \tag{A10}$$

The rest of the motion works as in the clapping case, with the transition from the stuck motion to the slipping motion occurring at the point where the acoustic stress exceeds the static friction, μ_s. The transition back to stuck motion occurs when the acoustic stress drops below the kinetic friction. It is possible, with some effort, to generalize the ideas above to oblique incidence.

APPENDIX B: DAMAGE MODEL PARAMETERS FROM THE MONOTONIC LOADING CURVE

The brittle damage mechanics model used here is a generalization of that found in the first chapters of Ref. 18. The main extension is to propose a two parameter "damage strengthening parameter" that results in a sufficiently flexible monotonic loading curve, that could conceivably be matched to experimental data. Such a curve will ideally increase from zero along a nearly straight line, reach a peak value (the strength of the material), then drop rapidly until failure (see Fig. 2). For the damage evolution described in Eq. (19), such a curve is the result of plotting T, the measured stress, versus ϵ, the total strain, as it increases from zero. Clearly, as ϵ increases, so does the damage, thus

$$T = \left[1 - \phi_0 - \left(\frac{\bar{C}}{X}\right)^{\eta}\epsilon^{2\eta}\right]\bar{C}\epsilon. \tag{B1}$$

It is then a simple thing to link the parameters of this theory, $\bar{C}$, ϕ_0, X, and η to the features of this curve. While a great many ways may be conceived of going about this, including a least squares approach, the form of the expression chosen makes it simple to perform this analytically. We will concentrate, then on the relationships between the following sets of prominent features:

- the location of the nonzero root,
- the slopes at the zero crossings, and
- the location and height of the peak stress.

Clearly, this gives more than enough information to determine our set of parameters. Practically, however, not all are so easily accessible, so it is possible to choose to use those that are most convenient.

The simplest feature to analyze is the second root or zero crossing location, found by setting $T=0$ above. The first root is clearly at $\epsilon=0$. The second occurs at

$$\epsilon_0^2 = \frac{X}{\bar{C}}(1 - \phi_0)^{\frac{1}{\eta}}. \tag{B2}$$

If we are looking at an initially virgin material, with $\phi_0=0$, this is just the ratio between the modulus and the X parameter.

The slope of the curve at any point is the first derivative of Eq. (B1):

$$\frac{dT}{d\epsilon} = (1 - \phi_0)\bar{C} - (2\eta - 1)\left(\frac{\bar{C}^{\eta+1}}{X^{\eta}}\right)\epsilon^{2\eta}. \tag{B3}$$

At $\epsilon=0$, this is, not surprisingly $(1-\phi_0)\bar{C}$. This slope gives, for the virgin material, the elastic modulus; for the fatigued material, it gives the initial damage, as explained above.

At the second root, one finds a slope of: $-2\eta(1-\phi)\bar{C}$. Given the initial damage and elastic modulus, this is the clearest way to find the η parameter.

Unfortunately, because a continuum damage theory is generally not considered to be valid as failure takes over, it may not be a great idea to rely too heavily on values taken near the second zero crossing of the curve. More important is to match the values near the peak stress. The peak stress will occur at the point where Eq. (B3) is set to zero, that is, when

$$\epsilon_m^2 = \frac{X}{\bar{C}}(1 - \phi_0)^{\frac{1}{\eta}}(2\eta + 1)^{-\frac{1}{\eta}}. \tag{B4}$$

It is notable that the ratio $\epsilon_m^2/\epsilon_0^2$ is independent of X:

$$\frac{\epsilon_m^2}{\epsilon_0^2} = (2\eta + 1)^{-\frac{1}{\eta}}. \tag{B5}$$

The peak stress, found by plugging Eq. (B4) into Eq. (B1), is

$$T_m = 2\eta\left(\frac{1 - \phi_0}{2\eta + 1}\right)^{\frac{2\eta+1}{2\eta}}\sqrt{\bar{C}X}. \tag{B6}$$

The damage at peak stress is found to be independent of X:

$$\phi_m = \frac{2\eta\phi_0 + 1}{2\eta + 1}. \tag{B7}$$

Although it is initially not obvious how to take advantage of this result, it is possible to use it to simply relate the peak stress to its location. The result is also independent of X, and gives an alternative method for finding η:

$$\frac{T_m}{\epsilon_m} = \frac{2\eta(1 - \phi_0)\bar{C}}{(2\eta + 1)}. \tag{B8}$$

[1] L. M. Brekhovskikh, *Waves in Layered Media*, 2nd ed. (Academic, New York, 1980).

[2] W. Huang and S. I. Rokhlin, "Interface waves along an anisotropic imperfect interface between anisotropic solids," J. Nondestruct. Eval. **11**, 185–198 (1992).

[3] S. I. Rokhlin and W. Huang, "Ultrasonic wave interaction with a thin anisotropic layer between two anisotropic solids: Second-order asymptotic boundary conditions," J. Acoust. Soc. Am. **94**, 3405–3420 (1993).

[4] A. Niklasson, S. Datta, and M. Dunn, "On ultrasonic guided waves in a thin anisotropic layer lying between two isotropic layers," J. Acoust. Soc. Am. **108**, 2005–2011 (2000).

[5] J. Sadler, B. O'Neill, and R. Gr. Maev, "Ultrasonic wave propagation across a thin nonlinear anisotropic layer between two half-spaces," J.

Acoust. Soc. Am. **118**, 51–59 (2005).
[6]B. Pukanszky, "Interfaces and interphases in multicomponent materials: Past, present, future," Eur. Polym. J. **41**, 645–662 (2005).
[7]J. Bouchet and A. A. Roche, "The formation of epoxy/metal interphases: Mechanisms and their role in practical adhesion," J. Adhes. **78**, 799–830 (2002).
[8]J. F. Maguire, P. L. Talley, and M. Lupkowski, "The interphase in adhesion: Bridging the gap," J. Adhes. **45**, 269–290 (1994).
[9]S. I. Rokhlin, L. Wang, B. Xie, V. A. Yakolev, and L. Adler, "Modulated angle beam ultrasonic spectroscopy for evaluation of imperfect interfaces and adhesive bonds," Ultrasonics **42**, 1037–1047 (2004).
[10]L. Wang and S. I. Rokhlin, "Stable reformulation of transfer matrix method for wave propagation in layered anisotropic media," Ultrasonics **39**, 413–424 (2001).
[11]D. Palmer, D. Rehbein, J. Smith, and O. Buck, "Nondestructive characterization of the mechanical strength of diffusion bonds: Application of a quasi-static spring model," J. Nondestruct. Eval. **7**, 167–174 (1988).
[12]A. Baltazar, S. Rokhlin, and C. Pecorari, "On the relationship between ultrasonic and microstructural properties of imperfect interfaces in layered solids," in *Rev. of Prog. QNDE, Vol. 18*, edited by D. E. Thompson and D. E. Chimenti (Kluwer/Plenum, New York, 1999), pp. 1463–1470.
[13]J. Achenbach and O. Parikh, "Ultrasonic analysis of nonlinear response and strength of adhesive bonds," J. Adhes. Sci. Technol. **5**, 601–618 (1991).
[14]S. Hirsekorn, "Nonlinear transfer of ultrasound by adhesive joints—A theoretical description," Ultrasonics **39**, 57–68 (2001).
[15]C. Bockenheimer, D. Fata, W. Possart, M. Rothenfusser, U. Netzelmann, and H. Schaefer, "The method of non-linear ultrasound as a tool for the non-destructive inspection of structural epoxy-metal bonds: A resume," Int. J. Adhes. Adhes. **22**, 227–233 (2002).
[16]J. Lemaitre, *A Course on Damage Mechanics* (Springer-Verlag, New York, 1992).
[17]D. Krajcinovic, "Damage mechanics: Accomplishments, trends and needs," Int. J. Solids Struct. **37**, 267–277 (2000).
[18]G. Z. Voyiadjis and P. I. Kattan, *Advances in Damage Mechanics: Metals and Metal Matrix Composites* (Elsevier, New York, 1999).
[19]I. Solodov, N. Krohn, and G. Busse, "CAN: An example of nonclassical acoustic nonlinearity in solids," Ultrasonics **40**, 621–625 (2002).
[20]B. O'Neill, R. Gr. Maev, and F. Severin, "Distortion of shear waves passing through a friction coupled interface" in *2000 IEEE Ultrasonics Symposium Proceedings, Vol. 1*, edited by S. C. Schneider, M. Levy, and B. R. McAvoy (IEEE, New York, 2001), pp. 819–823.
[21]Z. Yan and P. Nagy "Thermo-optical modulation of ultrasonic surface waves for NDE," Ultrasonics **40**, 689–696 (2002).
[22]M. Comninou and J. Dundurs, "Interaction of elastic waves with a unilateral interface," Proc. R. Soc. London, Ser. A **368**, 141–154 (1979).
[23]N. Yoshioka, "A review of the micromechanical approach to the physics of contacting surfaces," Tectonophysics **277**, 29–40 (1997).
[24]J. Richardson, "Harmonic generation at an unbonded interface—i. Planar interface between semi-infinite elastic media," Int. J. Eng. Sci. **17**, 73–85 (1979).

Axial radiation force of a Bessel beam on a sphere and direction reversal of the force

Philip L. Marston[a)]
Department of Physics and Astronomy, Washington State University, Pullman, Washington 99164-2814

(Received 1 September 2006; accepted 18 September 2006)

An expression is derived for the radiation force on a sphere placed on the axis of an ideal acoustic Bessel beam propagating in an inviscid fluid. The expression uses the partial-wave coefficients found in the analysis of the scattering when the sphere is placed in a plane wave traveling in the same external fluid. The Bessel beam is characterized by the cone angle β of its plane wave components where $\beta=0$ gives the limiting case of an ordinary plane wave. Examples are found for fluid spheres where the radiation force reverses in direction so the force is opposite the direction of the beam propagation. Negative axial forces are found to be correlated with conditions giving reduced backscattering by the beam. This condition may also be helpful in the design of acoustic tweezers for biophysical applications. Other potential applications include the manipulation of objects in microgravity. Islands in the (ka,β) parameter plane having a negative radiation force are calculated for the case of a hexane drop in water. Here k is the wave number and a is the drop radius. Low frequency approximations to the radiation force are noted for rigid, fluid, and elastic solid spheres in an inviscid fluid. © *2006 Acoustical Society of America.* [DOI: 10.1121/1.2361185]

PACS number(s): 43.25.Qp, 43.25.Uv, 43.20.Fn, 43.80.Jz [MFH] Pages: 3518–3524

I. INTRODUCTION

There have been numerous theoretical investigations of the acoustical radiation force of plane traveling waves (often referred to as progressive waves) incident on spherical objects in an inviscid fluid.[1–7] Some aspects of the radiation force of focused acoustic beams on spheres have also been calculated.[7–11] Some research suggests the possibility of trapping small objects (such as biological cells) near the focus of a single traveling wave.[10,11] The ability to either trap an object or pull it back toward the source of a single beam of sound may be a desirable alternative to the better known form of "acoustic tweezers" based on counterpropagating sound beams from a pair of transducers.[9] Such single-beam acoustic tweezers may provide an alternative to "optical tweezers" widely investigated for the purpose of trapping biological cells or other small objects.[12–15] In either the acoustic or electromagnetic case an important property of focused beams is that conditions have been predicted where the radiation force is in the opposite direction of the beam propagation even in the absence of significant dissipation. For *plane wave illumination* of spheres having isotropic properties in situations where dissipation can be neglected, the radiation force is directed along the direction of propagation for the reasons reviewed below in Sec. III.

The purpose of this paper is to calculate the radiation force caused by an acoustic Bessel beam[16–19] in an inviscid ideal fluid incident on a sphere having isotropic material properties in the case where the sphere is centered on the Bessel beam. As an example, the force is calculated for the case of a spherical drop of a hydrocarbon liquid in water. For an appropriate choice of frequency and Bessel beam parameters, the force is predicted to be opposite the direction of the beam propagation.

Scalar wave acoustic Bessel beams are an axisymmetric solution of the Helmholtz equation for the complex velocity potential of the form[20]

$$\psi_B(x,y,z) = \psi_0 \exp(i\kappa z) J_0(\mu \sqrt{(x^2+y^2)}), \tag{1}$$

where ψ_0 determines the beam amplitude, z and (x,y) denote the axial and transverse coordinates, κ and μ denote the axial and radial wave numbers, J_0 is a zero-order Bessel function, and $\kappa^2+\mu^2=k^2=(\omega/c_0)^2$, where c_0 denotes the phase velocity of the fluid. Here and in subsequent discussions of first order quantities the complex time factor of the form $\exp(-i\omega t)$ has been separated from the spatial dependence of complex functions. The complex first order acoustic velocity and pressure are $u_B=\nabla\psi_B$ and $p_B=i\omega\rho_0\psi_B$ where ρ_0 is the density of the surrounding fluid. The radiation force calculation uses Marston's solution[21] for the scattering of an ideal Bessel beam by a sphere centered on the beam. Relevant aspects of that solution are noted here in Appendix A.

An important parameter in the characterization of a Bessel beam is the cone angle β which describes the angle of the planar wave components of the beam relative to the z axis.[20–23] That angle is related to the parameters in Eq. (1) by

$$\beta = \arccos(\kappa/k) = \arcsin(\mu/k). \tag{2}$$

That angle is illustrated in Fig. 1 for the problem under consideration. The other important parameters in the evaluation of the radiation pressure are the wave-number-radius product ka of the sphere and the sphere's material properties relative to those of the surrounding fluid. As discussed in Sec. III, the usual plane wave limit[5,6] is recovered for the general radiation force expression Eq. (10) for the case $\beta=0$. As a con-

[a)]Electronic mail: marston@wsu.edu

 © 2006 Acoustical Society of America

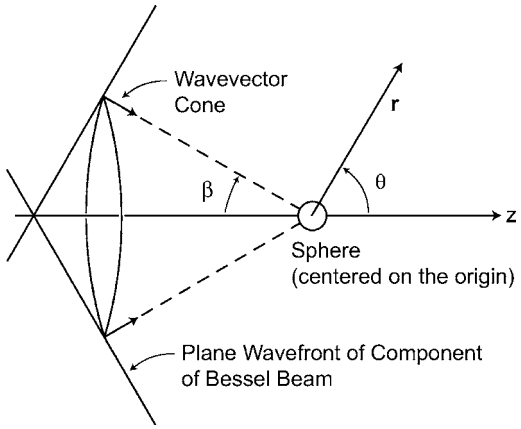

FIG. 1. Geometry of the radiation force calculation. The sphere is located on the axis z of an ideal Bessel beam. As explained in Refs. 20–22, the beam may represented by a superposition of plane waves having a cone angle β. The scattering angle relative to the beam axis is denoted by θ.

sequence of the finite width of all sources, Bessel-like beams only retain their form over a finite propagation distance.[16–23] The incident wave considered here is an ideal Bessel beam.

In addition to extending the understanding of situations where radiation forces are negative relative to the axis of a beam and related aspects of acoustic tweezers, some other potential applications of this analysis include the manipulation of fluid objects (such as liquid drops,[24,25] localized gas clouds,[26] or flames[27]) in reduced gravity (associated with space flight) where small forces acting over a long time duration can significantly affect the dynamics and positioning of objects. In addition since the analysis is sufficiently general to allow for the sphere to be metallic or ceramic there may be applications to the measurement of the acoustic intensity of approximate realizations of Bessel beams[16,18,22,23] as has long been the case for approximate realizations of plane waves.[3,4]

The present analysis completely ignores the complications resulting from thermal-viscous effects and from acoustic streaming. Analytical studies by Doinikov[28–30] indicate that there are numerous situations where such corrections to the radiation force may be especially significant for the case of traveling waves. For situations where the fluids used have sufficiently small viscosities, experiments have given satisfactory agreement with the inviscid radiation force of a traveling wave. Examples include low viscosity hydrocarbon liquid drops in water as well as the case of various solid spheres illuminated by quasiplane waves.[3,4] The thickness of the oscillating viscous external boundary layer (and in the liquid drop case, the thickness of oscillating internal boundary layer) must be much less than both the wavelength and the sphere radius a. It is assumed that this condition holds for the situation considered here. It is noteworthy that Doinikov[30] has predicted that as a consequence of *viscous corrections* a bubble may be attracted to a source of sound, however the mechanism in that case differs from the *inviscid radiation force* illustrated here for liquid drops.

II. RADIATION FORCE ON A SPHERE IN A BESSEL BEAM

It is convenient to evaluate the radiation force by using the farfield scattering summarized in Appendix A. The analysis of radiation forces based on farfield properties[27,31–33] is an alternative to the nearfield approach of King[1] and Yosioka and Kawasina.[2] The analysis is facilitated by the property of the radiation stress tensor[27,33] $\mathbf{S}_T$ for an ideal fluid that $\nabla \cdot \mathbf{S}_T = 0$. As a consequence, by application of the divergence theorem, the integral for the radiation force on the object can be transformed to a surface located at a large distance from the object.[27,33] In the present case this surface is taken to be a spherical surface of radius r with $kr \gg 1$. Let Re and Im designate real and imaginary parts of a complex quantity. The axial radiation force on the sphere is[33]

$$\mathsf{F}_z = -\pi\rho_0 k^2 (I_1 + I_2 - I_3), \tag{3}$$

$$I_1 = (\psi_0 a/2)^2 \int_{-1}^{1} |F(ka,w,b)|^2 w dw, \tag{4}$$

$$I_2 = (\psi_0 ra/2) \int_{-1}^{1} \mathrm{Re}[\psi_B^* F(ka,w,b) e^{ikr}] w dw, \tag{5}$$

$$I_3 = (\psi_0 ra/2k) \int_{-1}^{1} \mathrm{Im}[(\partial\psi_B/\partial z)^* F(ka,w,b) e^{ikr}] dw, \tag{6}$$

where $w = \cos\theta$, θ is the scattering angle shown in Fig. 1, $b = \cos\beta$, and * denotes complex conjugation. Equations (3)–(6) follow from Eq. (6) of Ref. 33 after expressing the scattering with the normalization used in Eq. (A1) in which the amplitude F is dimensionless. The expression has been simplified by taking the amplitude factor ψ_0 to be real and by omitting two terms proportional to ψ_0^2 (shown in Ref. 33) which do not contain F. The sum of the omitted terms vanishes. (The radiation force F_z vanishes when the scatterer is removed from the volume considered[27] so that then there is no scattering and $F = 0$.) The integrals in Eqs. (4)–(6) may be evaluated in the limit of large kr by using the partial-wave representations of F and ψ_B given in Eqs. (A2), (A4), and (A6) and by using properties of the Legendre polynomials listed in Appendix B. The partial wave coefficients α_n and β_n are related by Eqs. (A3) and (A4) to the partial wave expansion of the scattering for plane wave incidence. The integrals reduce to

$$I_1 = (2\psi_0/k)^2 \sum_{n=0}^{\infty} (n+1)(\alpha_n \alpha_{n+1} + \beta_n \beta_{n+1}) P_n(b) P_{n+1}(b), \tag{7}$$

$$I_2 = (\psi_0/k)^2 \sum_{n=0}^{\infty} (n+1)(\alpha_n + \alpha_{n+1}) P_n(b) P_{n+1}(b), \tag{8}$$

$$I_3 = -(\kappa/k)(\psi_0/k)^2 \sum_{n=0}^{\infty} (2n+1) \alpha_n P_n^2(b). \tag{9}$$

Notice that $\kappa/k = \cos\beta = P_1(b)$. Using Eq. (B3), gives $I_3 = -I_2$. The acoustic intensity (in W/m^2) along the axis of the Bessel beam is $I_0 = (\rho_0 c_0/2)(\kappa k \psi_0^2) = (\rho_0 c_0/2)(k\psi_0)^2 \cos\beta$. The axial radiation force on the sphere becomes

$$\mathsf{F}_z = (\pi a^2)(I_0/c_0)(1/\cos\beta) Y_P(ka, \cos\beta), \tag{10a}$$

$$Y_P = -(2/ka)^2 \sum_{n=0}^{\infty} (n+1) \times [\alpha_n + \alpha_{n+1} + 2(\alpha_n \alpha_{n+1} + \beta_n \beta_{n+1})] \times P_n(\cos\beta) P_{n+1}(\cos\beta), \quad (10b)$$

where the normalization of the dimensionless function Y_P was selected for ease of comparison with standard results for plane traveling waves.[3–7] When β is 90° the product $P_n(\cos\beta)P_{n+1}(\cos\beta)$ vanishes for all n because either n or $n+1$ is odd. Consequently Y_P vanishes in that limit as required by symmetry.

III. RADIATION FORCE IN THE PLANE-WAVE LIMIT

In the limit of a plane traveling wave, $\cos\beta = 1$ and $P_n(\cos\beta) = 1$ for all n. Consequently Y_P reduces to the standard expression given by Hasegawa *et al.*[5,6] Notice that while the present derivation uses the $\exp(-i\omega t)$ convention and Hasagawa *et al.* use the $\exp(i\omega t)$ convention, the form of Y_P is retained since the dependence on β_n always appears as the product $\beta_n \beta_{n+1}$. This limit also agrees with a result for Y_P based on the $\exp(-i\omega t)$ convention.[34] For plane waves, Eqs. (8), (9), and (A2) give

$$I_2 - I_3 = -2I_3 = 2(\psi_0/k)^2 \sum_{n=0}^{\infty} (2n+1)\alpha_n = -ka(\psi_0/k)^2 \, \mathrm{Im}[f(ka,1)], \quad (11)$$

where $f(ka, \cos\theta) = F(ka, \cos\theta, 1)$ is the dimensionless form function in the plane wave limit. In the case of a scatterer having no dissipation, $|s_n| = 1$ and the optical theorem[35] gives for the imaginary part of the *forward scattering* form function,

$$\mathrm{Im}[f(ka,1)] = (ka/2) \int_0^{\pi} |f|^2 \sin\theta d\theta. \quad (12)$$

Combining Eqs. (3), (4), (10a), (11), and (12) gives in that case,

$$Y_P = (1/2) \int_0^{\pi} |f(ka, \cos\theta)|^2 (1 - \cos\theta) \sin\theta d\theta, \quad (13)$$

which is *non-negative*. Equation (13) is equivalent to an early result of Westervelt[31] specialized to the case of no absorption and in the case of light scattering, an early result of Debye.[36,37] Inspection of Eq. (13) shows that the behavior of $|f|^2$ for θ near π is significantly weighted in the evaluation of Y_P. Reducing the scattering into the backward hemisphere reduces the radiation force. For a perfectly reflecting sphere having $ka \gg 1$, except near a narrow forward diffraction peak[21,35] $|f| \approx 1$ and Eq. (13) gives $Y_P \approx 1$. Including the absorption of a sphere introduces a positive term,[31] not in Eq. (13), which is proportional to the ratio of the absorption cross section to the geometric cross section πa^2.

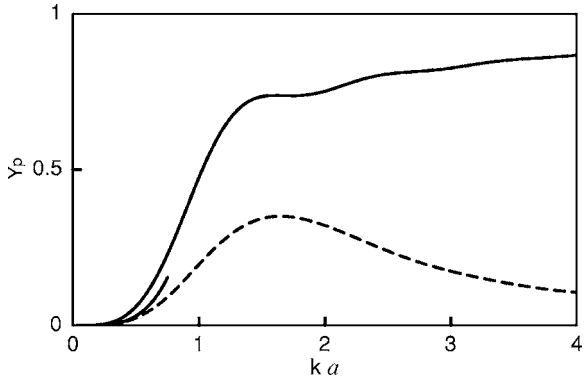

FIG. 2. Dimensionless radiation force function Y_P from Eq. (10b) for a fixed rigid sphere for an incident plane wave (upper solid curve) and an incident Bessel beam having $\beta = 60°$. The results are expressed in terms of the size parameter ka for the sphere. The short lower solid curve is the low frequency approximation from Eq. (14) for $\beta = 60°$.

IV. FORCE ON A RIGID SPHERE IN A BESSEL BEAM

Consider now the case of a fixed rigid sphere placed on the axis of a Bessel beam. In that case the s_n are given by[21] $s_n = -h_n^{(2)}(ka)'/h_n^{(1)}(ka)'$, where h_n is a spherical Hankel function of the indicated kind and primes denote differentiation. Figure 2 shows Y_P from Eq. (10b) for a plane wave (the upper solid curve) and a Bessel beam having $\beta = 60°$ (the dashed curve). It was numerically found that the series in Eq. (10) may be truncated for n somewhat in excess of ka. A large value of β was selected so as to clearly show the reduction in Y_P. When ka is very small, less than approximately 0.3, the scattering is dominated by the monopole ($n = 0$) and dipole ($n = 1$) terms of Eq. (A2). Using Mathematica® to obtain the leading order term in the small ka expansion of Y_P, gives the following low frequency approximation:

$$Y_{\mathrm{PLF}}(ka, \cos\beta) = (ka)^4 [1 + (2/9) P_2(\cos\beta)] P_1(\cos\beta). \quad (14)$$

Only s_0 and s_1 were found to influence Y_P to this order of ka. The lower solid curve in Fig. 2 shows Y_{PLF} when ka is small for $\beta = 60°$. Comparison with the dashed curve shows that at small ka the result from Eq. (10b) is recovered. Taking $\beta = 0$ in Eq. (14) gives $Y_P \approx (ka)^4 (11/9)$, which is King's result[1] for a massive rigid sphere.

V. FORCE ON AN IDEAL FLUID SPHERE IN A BESSEL BEAM

In this case the s_n are given in Appendix A. When expressing the relative fluid properties it is convenient to use the dimensionless parameters of Yosioka and Kawasima[2] and of Lee and Wang[38] which are $\sigma = c_i/c_0$ and $\lambda = \rho_i/\rho_0$ for the inner-to-outer fluid sound speed and density ratios. In the plane wave case, the Y_P for several ka for a liquid drop having $\sigma = 1/1.15$ and $\lambda = 1.005$ were tabulated by Yosioka *et al.*[3] The numerical algorithm used here was found to agree with the tabulated values of Y_P. Crum[39] lists typical values of these ratios for immiscible hydrocarbon liquid drops *in water* at near room temperature conditions. The example of a liquid

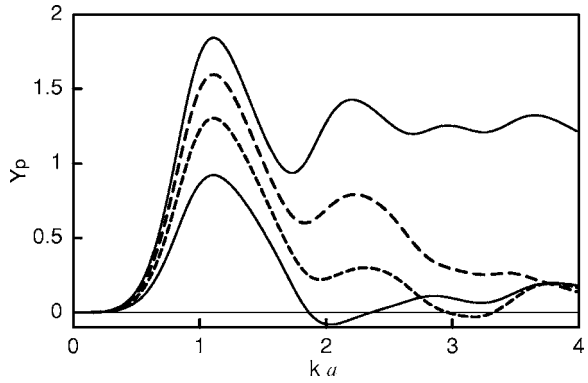

FIG. 3. Dimensionless radiation force function Y_P from Eq. (10b) for a sphere of ideal fluid having the relative properties of a liquid hexane drop in water for four values of β:0° (upper solid curve), 30° (upper dashed curve), 45° (lower dashed curve), and 60° (lower solid curve). For β=45° and 60° there are regions where Y_P is negative so that the radiation force is directed opposite to the propagation direction of the Bessel beam.

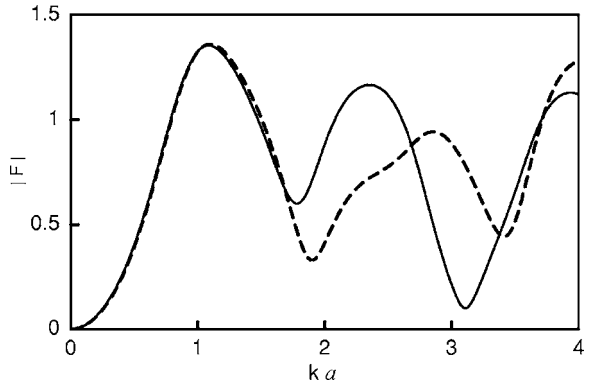

FIG. 4. Dimensionless form function magnitude from Eq. (A2) calculated for backscattering for the fluid sphere considered in Fig. 3 for β=45° (solid curve) and β=60° (dashed curve). The regions where Y_P is negative in Fig. 3 are associated with reduced backscattering.

drop in a Bessel beam considered in Fig. 3 is a hexane drop for which σ=0.719 and λ=0.656. Figure 3 shows Y_P for several values of β including the plane wave case. It was numerically found that the series in Eq. (10) may be truncated for n somewhat in excess of ka.

The anomalous regions where Y_P is negative are discussed in Sec. VI. Consider here the reduction in Y_P with increasing β when ka is less than 0.5. As reviewed in Sec. IV when ka is small the scattering is dominated by the monopole and dipole terms in Eq. (A2). Only those partial waves contribute to the leading order in the small ka expansion of Y_P. By using Mathematica® the leading order term in the low frequency approximation is found to be

$$Y_{\mathrm{PLF}} = [4(ka)^4/\Delta^2][G^2 + (2/9)(1-\lambda)^2 P_2(b)]\cos\beta, \tag{15a}$$

$$G(\lambda,\sigma) = \lambda - (\Delta/3\lambda\sigma^2), \tag{15b}$$

where $\Delta=1+2\lambda$ and $b=\cos\beta$. The result of Yosioka and Kawasima[2] (also found by Lee and Wang[38]) is recovered when β=0. Equation (15) shows that while the $\cos\beta$ factor causes a reduction in Y_{PLF} with increasing β, the dependence on β is complicated by the term involving $P_2(\cos\beta)$. The low-frequency approximation for an incompressible (but movable) sphere is found by taking the limit $\sigma^2\to\infty$ in Eq. (15b) so that G in Eq. (15a) is replaced by $G=\lambda$ where λ is the density ratio. In the plane wave limit Y_{PLF} reduces to $[4(ka)^4/\Delta^2][\lambda^2+(2/9)(1-\lambda)^2]$ in agreement with King's analysis for a movable incompressible sphere.[1] The fixed-rigid sphere limit for a Bessel beam, Eq. (14), is recovered by taking $\lambda\to\infty$ and $\sigma^2\to\infty$ in Eq. (15).

VI. NEGATIVE AXIAL RADIATION FORCES IN A BESSEL BEAM

Inspection of Fig. 3 reveals for β=45° and 60°, there are ka regions where Y_P becomes negative. When Y_P is negative the radiation force is directed opposite the direction of beam propagation. To understand the reversal in the direction of the force, recall from the plane-wave example discussed in Sec. III that the backscattering amplitude strongly influences Y_P. Figure 4 shows the backscattering form function magnitude $|F(ka,-1,\cos\beta)|$ for β=45° and 60° for the fluid sphere considered in Fig. 3. Inspection of Fig. 4 shows that there are prominent *minima* in $|F|$ for the regions where Y_P is negative. This property is also evident by comparing the θ dependence of $|F(ka,\cos\theta,\cos\beta)|$ for ka at or near the center of the regions where Y_P is negative with the case where β=0. Figure 5 shows this comparison for a hexane sphere with ka=3.17 in a beam with β=45°. The scattering in the entire backward hemisphere is suppressed in the Bessel beam case relative to the plane-wave case. Since ka is not large only a few partial waves contribute significantly to the scattering in Eq. (A2) and $|F|$ is found to be a slowly varying function of θ in comparison to large ka examples for rigid and soft spheres shown in Ref. 21. Inspection of Fig. 5 and Eq. (B2) suggests that scattering into the backward hemisphere is suppressed because the factor $P_n(\cos\beta)$ affects the significant partial waves. Figure 6 shows a similar comparison for β=60° and ka=2 which corresponds to a region where Y_P is negative. In that case, however, fewer partial waves are significant. The most negative value of Y_P for the example in Fig. 3 is Y_P=−0.081 at ka=2.03 for β=60°. For β=45° the most negative Y_P value is −0.0297 which is at

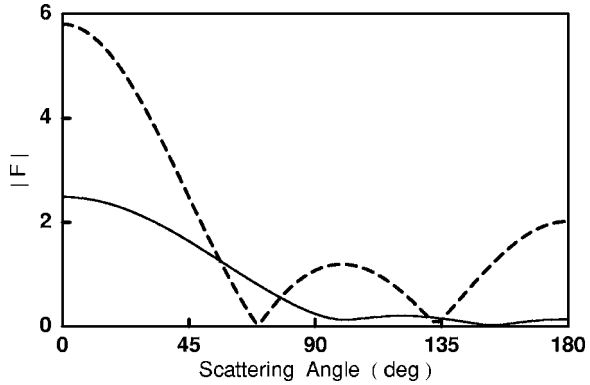

FIG. 5. The solid curve is the angular distribution of the scattering amplitude $|F|$ from Eq. (A2) for the liquid drop considered in Fig. 3 for a condition where Y_P is negative: ka=3.17 and β=45°. The dashed curve is for ka=3.17 with phase wave incidence (β=0°). The comparison shows that the scattering into the backward hemisphere is significantly depressed in the Bessel beam case.

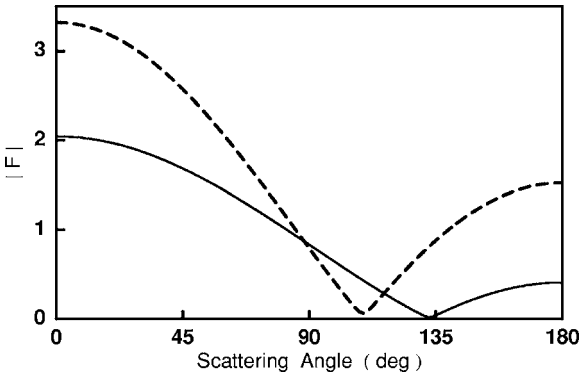

FIG. 6. Like Fig. 5 except that for the solid curve $ka=2$ and $\beta=60°$ and the dashed curve is $ka=2$ and $\beta=0°$.

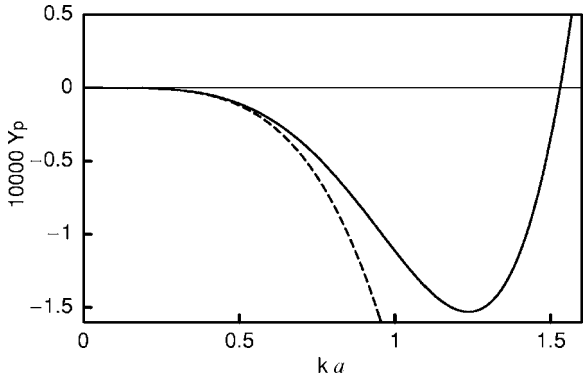

FIG. 8. The solid curve is Y_P from Eq. (10b) for a fluid sphere with relative fluid properties selected to give $G(\lambda,\sigma)=0$ in Eq. (15) by taking $\lambda=1.2$ and $\sigma=\sqrt{(3.4/4.32)}$. The dashed curve is the low frequency approximation in Eq. (15). The solid curve Y_P is negative for ka between 0 and 1.52.

$ka=3.17$. For $\beta=60°$ the small local *maximum* in Y_P in Fig. 3 at $ka=2.86$ corresponds to a local *maximum* in $|F|$ at $ka=2.85$ in Fig. 4.

To search for other regions having negative radiation force, Y_P from Eq. (10b) was evaluated for a sphere having the properties of an ideal hexane drop in water ($\sigma=0.719$, $\lambda=0.656$) for a dense grid of points on the region $0<ka<6$, $0°<\beta<90°$. Negative values were found only in the part with $1<ka<6$, $40°<\beta<90°$. Figure 7 shows that Y_P is negative on *islands* within that subregion. From symmetry and from the form of Eq. (10), Y_P vanishes when $\beta=90°$. For $\beta=30°$ with this σ and λ, Y_P was computed to be nonnegative for $ka<20$.

A systematic search for regions of negative Y_P in the four parameter domain (ka, β, λ, σ) was beyond the scope of this investigation. Restricting attention to β of 45° and 60°, examples giving negative Y_P are easy to find even for spheres having different properties than hexane spheres in water. For a carbon tetrachloride sphere in water[39] ($\lambda=1.587$, $\sigma=0.619$) there are negative Y_P peaks at (ka, β, Y_P) of (2.98, 45°, −0.0269) and (2.29, 60°, −0.0309). For a benzene sphere in water[39] ($\lambda=0.874$, $\sigma=0.861$) there are negative Y_P peaks at (ka, β, Y_P) of (3.75, 45°, −0.00455) and (2.55, 60°, −0.0111).

Inspection of Eq. (15) suggests that for small ka, Y_P becomes negative when the fluid parameters λ and σ are selected to give $G(\lambda,\sigma)=0$. It is also necessary for β to lie between 54.7346° and 90° so that $P_2(\cos\beta)<0$ and $\cos\beta>0$. The condition $G(\lambda,\sigma)=0$ gives $\sigma=\sqrt{[(1+2\lambda)/(3\lambda^2)]}$. Figure 8 shows $10^4 Y_P$ for $\lambda=1.2$ and $\sigma=\sqrt{(3.4/4.32)}\approx 0.887$. Also shown is $10^4 Y_{\mathrm{PLF}}$ from Eq. (15). Notice that Y_P is negative as predicted but that when ka exceeds 1.52, Y_P becomes positive. As noted in Sec. V, Y_{PLF} is influenced by only the monopole and dipole scattering terms in Eq. (A2). Positive Y_P may be due to partial waves in Eq. (B2) with $n>1$. The 10^4 prefactor was included in Fig. 8 because of the very small magnitude of Y_P which is typically less than 10^{-4} in this region.

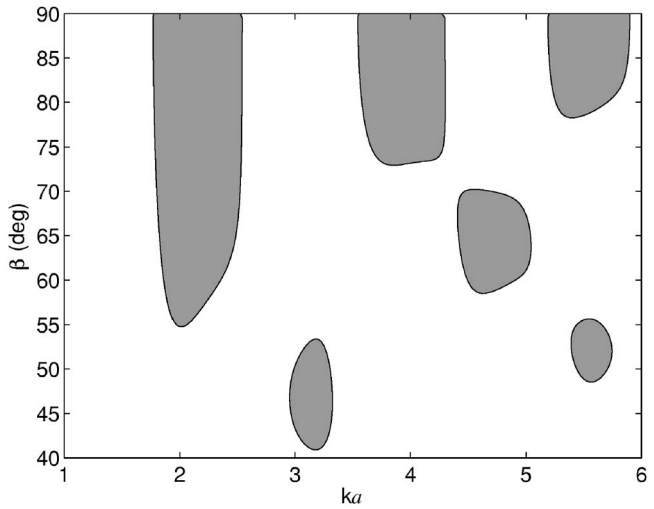

FIG. 7. Islands where Y_P is computed by Eq. (10b) to be negative are shown as dark patches that are bounded by a contour at $Y_P=0$. These are shown for a hexane sphere in water. The examples where Y_P is negative in Fig. 3 are in the leftmost islands.

VII. DISCUSSION AND CONCLUSIONS

The main result in Eq. (10) gives the radiation force for an isotropic sphere centered on an ideal Bessel beam. The partial wave coefficients α_n and β_n are related by Eqs. (A3) and (A4) to the partial wave expansion of the scattering for plane wave incidence. The derivation of Eq. (10) was sufficiently general to allow for the case where the absorption of acoustic energy by the sphere cannot be neglected. This is often the case for plastic or polymer spheres placed in water.[5,40] Including absorption causes $|s_n|<1$ while the connection with α_n and β_n in Eq. (A4) remains applicable. In the numerical examples for Y_P and the analytical approximations of the low frequency behavior, Eqs. (14) and (15), absorption is neglected.

When absorption is negligible, the approximation in Eq. (15) becomes applicable to a small solid elastic sphere by taking the inner sound speed to be $c_i=\sqrt{[c_L^2-(4/3)c_T^2]}$ where c_L and c_T are the longitudinal and transverse wave velocities of the elastic material. That replacement has been shown to yield the proper monopole and dipole scattering contributions for the equivalent fluid sphere when ka is small in the present case where the viscous properties of the outer fluid are neglected.[41] For that replacement to be applicable it is

necessary for ka to be much less than the ka of any low-frequency resonance, including that of the $n=2$ partial wave.[40]

The existence of conditions where Y_P becomes negative suggests that it may be feasible to point a Bessel beam at a sphere and use the acoustic radiation force to *pull the sphere back towards the source*. This application is plausible in reduced gravity (space-based platforms) where small radiation forces can significantly affect the motion of spheres over an extended period of time. For a more definitive analysis, however, it would be necessary to analyze the transverse force on the sphere for spheres displaced slightly from the axis of the Bessel beam. That analysis is outside the scope of the present discussion since Eqs. (10) and (A2) are only directly applicable for a sphere centered on a Bessel beam.

The comparison of Fig. 3 with plots of the scattering shown in Figs. 4–6 (and other results not shown here) indicate that the regions where Y_P is negative with a significant magnitude tend to occur where the backscattering amplitude is suppressed as a consequence of the illumination by a Bessel beam. It is plausible that this correlation with backscattering may be used to find regions of enhanced performance of acoustic tweezers or other devices for biophysical applications.[9–11,42] When ka is small so that Eq. (15) is applicable, from the example in Fig. 8, negative Y_P appear unfortunately to be small in magnitude.

Concerning the unresolved question of the transverse stability of spheres on the axis of a Bessel beam, the following observations are noteworthy. Liquid filled circular cylindrical acoustic levitators produce a standing wave pressure distribution where the radial dependence of the pressure is typically of the form $J_0(\mu\sqrt{(x^2+y^2)})$ as in the Bessel beam case. Numerous examples have been demonstrated where small drops and bubbles in water (or in other liquids) are attracted to the axis of such cylinders.[24,39,43,44] Much less is known about the radial stability when ka is not small. The mathematical existence of conditions for ideal spheres to have transverse stability in acoustic Gaussian beams[11] makes it plausible that conditions can also be found for acoustic Bessel beams. The existence of transverse stability of objects trapped in light beams is also supportive.[12–15] Ordinarily transverse stability of gas bubbles in liquids subjected to the *optical* radiation pressure of a laser beam requires that the beam has an axial irradiance minimum.[45] Stability of bubbles in light beams of a different type was recently demonstrated.[46] If necessary the transverse stability of spheres in *acoustic* Bessel beams could be altered by superposing a second acoustic beam (at a different frequency) having an axial pressure minimum.[47]

ACKNOWLEDGMENTS

This research was supported in part by NASA. Appendix A and Ref. 21 were supported by ONR. The author is grateful to Dr. David B. Thiessen for helpful comments.

APPENDIX A: FARFIELD SCATTERING BY A SPHERE

For a sphere having isotropic material properties centered on the Bessel beam and placed at $z=0$, using the coordinate system shown in Fig. 1, the farfield scattering is given by

$$\psi_s(r,\theta) = (a/2r)\psi_0 F e^{ikr}, \tag{A1}$$

where the partial wave series for the dimensionless form function is found to be[21]

$$F(ka,\cos\theta,\cos\beta) = (-i/ka)\sum_{n=0}^{\infty}(2n+1)(s_n-1) \times P_n(\cos\theta)P_n(\cos\beta). \tag{A2}$$

The scattering angle relative to the z axis is denoted by θ. Here the coefficient (s_n-1) is the same as the partial wave coefficient for the dimensionless form function associated with scattering caused by plane wave illumination[35]

$$f(ka,\cos\theta) = (-i/ka)\sum_{n=0}^{\infty}(2n+1)(s_n-1)P_n(\cos\theta). \tag{A3}$$

It is convenient for the purposes of the present paper to introduce a normalized partial wave coefficient $\alpha_n+i\beta_n=(s_n-1)/2$ where

$$\alpha_n = [\mathrm{Re}(s_n)-1]/2, \quad \beta_n = \mathrm{Im}(s_n)/2 \tag{A4}$$

and Re and Im designate real and imaginary parts. As reviewed in Ref. 21, the s_n and the factors (s_n-1) are known for many types of spheres. When none of the incident acoustic energy is absorbed, the complex s_n are unimodular.[35] For example in the case of an inviscid fluid sphere s_n is given by $s_n=-D_n^*/D_n$ where the denominator is[48]

$$D_n = \rho_i ka j_n(ka/\sigma)h_n^{(1)\prime}(ka) - \rho_0(ka/\sigma)j_n'(ka/\sigma)h_n^{(1)}(ka), \tag{A5}$$

ρ_i and ρ_0 are the densities of the sphere and the surrounding fluid and $\sigma=c_i/c_0$ is the corresponding ratio of sound velocities. In Eq. (A5), primes denote differentiation of spherical Bessel and Hankel functions and * denotes complex conjugation.

The partial wave series for the incident wave, the Bessel beam in Eq. (1), is[21]

$$\psi_B = \psi_0\sum_{n=0}^{\infty} i^n(2n+1)j_n(kr)P_n(\cos\theta)P_n(\cos\beta). \tag{A6}$$

APPENDIX B: PROPERTIES OF LEGENDRE POLYNOMIALS

Properties of the $P_n(w)$ used in the derivation of Eqs. (7)–(10) include[49]

$$\int_{-1}^{1} P_m(w)P_n(w)dw = [2/(2n+1)]\delta_{mn}, \tag{B1}$$

$$\int_{-1}^{1} wP_m(w)P_n(w)dw = I_{mn}, \tag{B2}$$

where $I_{mn}=0$ unless $m=n\pm1$, $I_{n+1n}=2(n+1)/[(2n+1)(2n+3)]$ and $I_{n-1n}=2n/[(2n-1)(2n+1)]$. The following[49] was also used:

$$(n+1)P_{n+1}(w) - (2n+1)wP_n(w) + nP_{n-1}(w) = 0. \tag{B3}$$

The following special cases are noteworthy: $P_0(w)=1$, $P_1(w)=w$, $P_2(w)=(3w^2-1)/2$, and $P_2(\cos\beta)=0$ for $\beta=54.7356°$.

[1]L. V. King, "On the acoustic radiation pressure on spheres," Proc. R. Soc. London **147**, 212–240 (1934).
[2]K. Yosioka and Y. Kawasima, "Acoustic radiation pressure on a compressible sphere," Acustica **5**, 167–173 (1955).
[3]K. Yosioka, T. Hasegawa, and A. Omura, "Comparison of ultrasonic intensity from radiation force on steel spheres with that on liquid spheres," Acustica **22**, 145–152 (1969).
[4]T. Hasegawa and K. Yosioka, "Acoustic radiation force on fused silica spheres, and intensity determination," J. Acoust. Soc. Am. **58**, 581–585 (1975).
[5]T. Hasegawa and Y. Watanabe, "Acoustic radiation pressure on an absorbing sphere," J. Acoust. Soc. Am. **63**, 1733–1737 (1978).
[6]T. Hasegawa, Y. Hino, A. Annou, H. Noda, M. Kato, and N. Inoue, "Acoustic radiation pressure acting on spherical and cylindrical shells," J. Acoust. Soc. Am. **93**, 154–161 (1993).
[7]X. C. Chen and R. E. Apfel, "Radiation force on a spherical object in an axisymmetric wave field and its application to the calibration of high-frequency transducers," J. Acoust. Soc. Am. **99**, 713–724 (1996).
[8]J. R. Wu and G. Du, "Acoustic radiation force on a small compressible sphere in a focused beam," J. Acoust. Soc. Am. **87**, 997–1003 (1990).
[9]J. R. Wu, "Acoustical tweezers," J. Acoust. Soc. Am. **89**, 2140–2143 (1991).
[10]J. W. Lee, K. L. Ha, and K. K. Shung, "A theoretical study of the feasibility of acoustical tweezers: Ray acoustics approach," J. Acoust. Soc. Am. **117**, 3273–3280 (2005).
[11]J. W. Lee and K. K. Shung, "Radiation forces exerted on arbitrarily located sphere by acoustic tweezer," J. Acoust. Soc. Am. **120**, 1084–1094 (2006).
[12]A. Ashkin, J. M. Dziedzic, J. E. Bjorkholm, and S. Chu, "Observation of a single-beam gradient force optical trap for dielectric particles," Opt. Lett. **11**, 288–290 (1986).
[13]A. Ashkin, "Forces of a single beam gradient laser trap on a dielectric sphere in the ray optics regime," Biophys. J. **61**, 569–582 (1992).
[14]K. Svoboda and S. M. Block, "Biological applications of optical forces," Annu. Rev. Biophys. Biomol. Struct. **23**, 247–285 (1994).
[15]J. A. Lock, S. Y. Wrbanek, and K. E. Weiland, "Scattering of a tightly focused beam by an optically trapped particle," Appl. Opt. **45**, 3634–3645 (2006).
[16]D. K. Hsu, F. J. Margetan, and D. O. Thompson, "Bessel beam ultrasonic transducer: Fabrication method and experimental results," Appl. Phys. Lett. **55**, 2066–2068 (1989).
[17]J. A. Campbell and S. Soloway, "Generation of a nondiffracting beam with frequency-independent beamwidth," J. Acoust. Soc. Am. **88**, 2467–2477 (1990).
[18]J.-y. Lu and J. F. Greenleaf, "Ultrasonic nondiffracting transducer for medical ultrasonics," IEEE Trans. Ultrason. Ferroelectr. Freq. Control **37**, 438–447 (1990).
[19]K. B. Cunningham and M. F. Hamilton, "Bessel beams of finite amplitude in absorbing fluids," J. Acoust. Soc. Am. **108**, 519–525 (2000).
[20]J. Durnin, "Exact solutions for nondiffracting beams. I. The scalar theory," J. Opt. Soc. Am. A **4**, 651–654 (1987).
[21]P. L. Marston, "Scattering of a Bessel beam by a sphere," (submitted).
[22]J. Durnin, J. J. Miceli, Jr., and J. H. Eberly, "Diffraction-free beams," Phys. Rev. Lett. **58**, 1499–1501 (1987).
[23]D. McGloin and K. Dholakia, "Bessel beams: Diffraction in a new light," Contemp. Phys. **46**, 15–28 (2005).
[24]P. L. Marston and D. B. Thiessen, "Manipulation of fluid objects with acoustic radiation pressure," Ann. N.Y. Acad. Sci. **1027**, 414–434 (2004).
[25]S. K. Chung and E. H. Trinh, "Containerless protein crystal growth in rotating levitated drops," J. Cryst. Growth **194**, 384–397 (1998).
[26]R. Tuckermann, B. Neidhart, E. G. Lierke, and S. Bauerecker, "Trapping of heavy gases in stationary ultrasonic fields," Chem. Phys. Lett. **363**, 349–354 (2002).
[27]W. Wei, D. B. Thiessen, and P. L. Marston, "Acoustic radiation force on a compressible cylinder in a standing wave," J. Acoust. Soc. Am. **116**, 201–208 (2004).
[28]A. A. Doinikov, "Acoustic radiation pressure on a rigid sphere in a viscous fluid," Proc. R. Soc. London, Ser. A **447**, 447–466 (1994).
[29]A. A. Doinikov, "Acoustic radiation force on a spherical particle in a viscous heat-conducting fluid. III. Force on a liquid drop," J. Acoust. Soc. Am. **101**, 731–740 (1997).
[30]A. A. Doinikov, "Acoustic radiation pressure exerted by a spherical wave on a bubble in a viscous liquid," Wave Motion **24**, 275–279 (1996).
[31]P. J. Westervelt, "The theory of steady forces caused by sound waves," J. Acoust. Soc. Am. **23**, 312–315 (1951).
[32]L. P. Gorkov, "On the forces acting on a small particle in an acoustical field in an ideal fluid," Sov. Phys. Dokl. **6**, 773–775 (1962).
[33]C. P. Lee and T. G. Wang, "Acoustic radiation force on a bubble," J. Acoust. Soc. Am. **93**, 1637–1640 (1993).
[34]F. G. Mitri, "Acoustic radiation force due to incident plane-progressive waves on coated spheres immersed in ideal fluids," Eur. Phys. J. B **43**, 379–386 (2005).
[35]P. L. Marston, "Generalized optical theorem for scatterers having inversion symmetry: Applications to acoustic backscattering," J. Acoust. Soc. Am. **109**, 1291–1295 (2001).
[36]P. Debye, "Der Lichtdruck auf Kugeln von beliebigem Material," Ann. Phys. **30**, 57–136 (1909).
[37]H. C. van de Hulst, *Light Scattering by Small Particles* (Wiley, New York, 1957), pp. 124–130.
[38]C. P. Lee and T. G. Wang, "Radiation pressure and acoustic levitation," *Nonlinear Acoustics*, edited by M. F. Hamilton and D. T. Blackstock (Academic, New York, 1998), pp. 177–205.
[39]L. A. Crum, "Acoustic force on a liquid droplet in an acoustic stationary wave," J. Acoust. Soc. Am. **50**, 157–163 (1971).
[40]B. T. Hefner and P. L. Marston, "Backscattering enhancements associated with subsonic Rayleigh waves on polymer spheres in water: Observation and modeling for acrylic spheres," J. Acoust. Soc. Am. **107**, 1930–1936 (2000).
[41]R. A. Roy and R. E. Apfel, "Mechanical characterization of microparticles by scattered ultrasound," J. Acoust. Soc. Am. **87**, 2332–2341 (1990).
[42]W. T. Coakley, "Ultrasonic separations in analytical biotechnology," Trends Biotechnol. **15**, 506–511 (1997).
[43]R. E. Apfel, "Technique for measuring the adiabatic compressibility, density, and sound speed of submicroliter liquid samples," J. Acoust. Soc. Am. **59**, 339–343 (1976).
[44]D. F. Gaitan, L. A. Crum, C. C. Church, and R. A. Roy, "Sonoluminescence and bubble dynamics for a single, stable, cavitation bubble," J. Acoust. Soc. Am. **91**, 3166–3183 (1992).
[45]B. T. Unger and P. L. Marston, "Optical levitation of bubbles in water by the radiation pressure of a laser beam: An acoustically quiet levitator," J. Acoust. Soc. Am. **83**, 970–975 (1988).
[46]J. Y. Ye, G. Chang, T. B. Norris, C. Tse, M. J. Zohdy, K. W. Hollman, M. O'Donnell, and J. R. Baker, Jr., "Trapping cavitation bubbles with a self-focused laser beam," Opt. Lett. **29**, 2136–2138 (2004).
[47]B. T. Hefner and P. L. Marston, "An acoustical helicoidal wave transducer with applications for the alignment of ultrasonic and underwater systems," J. Acoust. Soc. Am. **106**, 3313–3316 (1999).
[48]K. A. Sage, J. George, and H. Uberall, "Multipole resonances in sound scattering from gas bubbles in a liquid," J. Acoust. Soc. Am. **65**, 1413–1422 (1979).
[49]J. D. Jackson, *Classical Electrodynamics*, 3rd ed. (Wiley, New York, 1999), Sec. 3.2, pp. 96–101.

Precursor arrivals in the Yellow Sea, their distinction from first-order head waves, and their geoacoustic inversion

Peter H. Dahl and Jee Woong Choi
Applied Physics Laboratory, University of Washington, 1013 NE 40th Street, Seattle, Washington 98105-6698

(Received 11 May 2006; revised 21 September 2006; accepted 21 September 2006)

Measurements made as part of the 1996 Yellow Sea experiment at location 37° N, 124° E, undertaken by China and the U.S. are analyzed. Signals generated by explosive sources were received by a 60-m-length vertical line array deployed in waters 75 m deep. Evidence is presented that precursor arrivals measured at ranges less than 1 km are refracted waves that are zeroth order in their ray series classification, and this directly points to the existence of a gradient in sediment sound speed. In contrast, first-order head waves, which are much weaker in amplitude, would exist only if this gradient were absent. It is found that the energy spectrum of precursor arrivals agrees well with a zeroth-order model, i.e., it is proportional to the source amplitude spectrum, $S(f)$, where f is frequency, rather than a first-order model, which would have it proportional to $S(f)/f$. From travel time analysis the sediment sound speed just below the water-sediment interface is estimated to be 1573 m/s with a gradient of 1.1 s^{-1}, and from analysis of the energy spectrum of the precursor arrivals the sediment attenuation is estimated to be 0.08 dB/m/kHz over the frequency range 150–420 Hz. The results apply to a nominal sediment depth of 100 m. © *2006 Acoustical Society of America.*
[DOI: 10.1121/1.2363938]

PACS number(s): 43.30.Cq, 43.30.Ma, 43.30.Pc [AIT] Pages: 3525–3533

I. INTRODUCTION

In Choi and Dahl,[1] the influence of a sound speed gradient in surficial sediments on the set of precursor arrivals defined as signals arriving prior to the water wave is analyzed. The distinction between a first-order head wave (constant sound speed in the seabed) and a zeroth-order refracted wave (positive sound-speed gradient in the seabed) is highlighted, with the latter being much more energetic. Figure 1 shows the two types of precursors: one represented by a single ray path and identified as a first-order head wave and the other consisting of multiple ray paths for which the term zeroth order is used. The first-order and zeroth-order nomenclature is from Choi and Dahl[1] and originates from a ray series classification as discussed in Červený and Ravindra.[2]

For the zeroth-order case the earliest arrival is the C_0 wave (also called a refracted wave or diving wave) with subsequent arrivals (C_n waves, $n=1,2,\ldots$) being multiple refracting-seabed reflecting; these are also known as diving wave multiples.[3] The C_0 wave undergoes upward refraction with a single turning point (Fig. 1), with an initial grazing angle at the water-seabed interface, θ_0, which exceeds the critical angle θ_c, and subsequent arrivals (C_n waves, $n=1,2,\ldots$) have initial grazing angles $\theta_c<\theta_n<\theta_0$. Following the linear gradient assumption, the travel time difference between the C_0 wave and C_1 wave is given by $\Delta T_{0\_1}=a^2L_2^3/32c_{1s}^3$, where c_{1s} is the seabed sound speed at the water-sediment interface, a is the coefficient describing a linear gradient in sound speed in the sediment, and L_2 is the horizontal range (Fig. 1) that corresponds to the first-order head wave[2] generated within a (hypothetical) seabed of constant sound speed c_{1s}.

For the first-order head wave, the amplitude spectrum of the precursor arrival goes as $S(f)/f$, where $S(f)$ is the source amplitude spectrum as function of frequency f, while generally for the zeroth-order case, the amplitude spectrum of the precursor arrival goes as $S(f)$. The exception is the transition between the two cases as represented by the interference head wave[2] that arises from the superposition of the C_n waves ($n=0,1,\ldots$) that are not separated in time, i.e., $\Delta T_{0\_1}<\delta t$, where δt is the characteristic time duration of the incident wave. In this case, the parameter $\zeta=(32f\Delta T_{0\_1})^{1/3}$ also applies[1,2]. For $\zeta<1$, the interference head wave assumes spectral properties akin to first-order head waves; for $\zeta>1$ the spectral properties tend toward zeroth order and the amplitude is significantly greater.

In this paper, field observations of precursor arrivals made in the Yellow Sea are described, and evidence is presented that these arrivals are zeroth-order refracted waves. Synthetic time series generated using parabolic equation (PE) methods are used to support this evidence, and geoacoustic parameters describing a linear gradient in compressional sound speed and attenuation in the seabed are inverted from the data. Since these observations are zeroth order, they relate directly to a positive gradient in sediment sound speed, and an equivalent (or effective) half-space geoacoustic model consistent with these observations cannot be identified.

This paper is organized as follows. A short description of the field measurements and the marine geology at the experimental site is given in Sec. II. In Sec. III the arrival structure versus time and depth is analyzed, and an inversion based on travel time is carried out to estimate sound speed just below the water-sediment interface and its gradient. Sec-

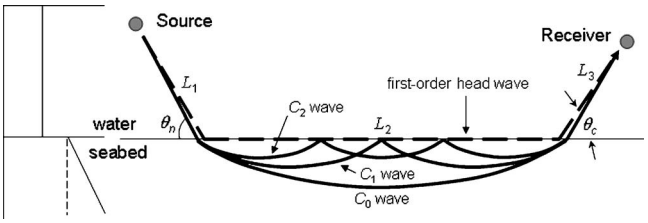

FIG. 1. Left side: sound-speed profile in seabed showing constant sound speed, zero gradient (dashed line), and nonzero positive gradient (solid line). Right side: Equivalent ray path for a first-order head wave corresponding to a constant sediment sound speed (dashed line), and multiple ray paths, C_n waves ($n=0,1,\ldots$), constituting a zeroth-order refracted wave, which corresponds to a positive gradient for sound speed (solid line). Note that grazing angle θ_n varies slightly with C_n wave, and is greater than the critical angle θ_c.

tion IV discusses the spectrum of the precursors and inversion for an estimate of the sediment compressional wave attenuation. The spectra represent clear evidence that the precursors are zeroth-order refracted waves. A summary and short discussion are given in Sec. V, along with additional evidence relating to the amplitude of the precursor arrivals that supports our conclusions.

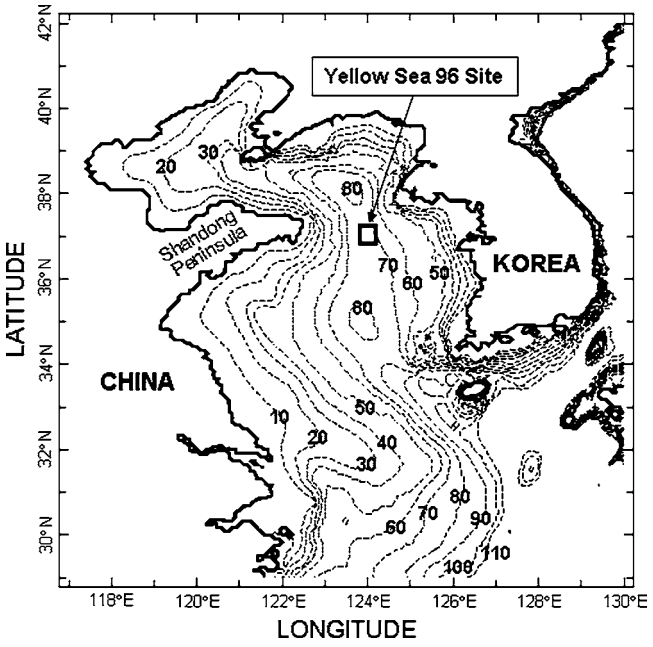

FIG. 2. Location of the 1996 Yellow Sea experiment conducted by China and the U.S. including bathymetry contours in meters.

II. THE EXPERIMENT AND SITE

The measurements were made as a part of the 1996 Yellow Sea experiment undertaken by China and the U.S. (YS96) and involving the Chinese research vessels SHI YAN 3 and SHI YAN 2. Although occurring less than 8 months later, several works published in the proceedings of the 1997 Beijing Shallow Water Acoustics Conference[4] provide additional experimental overview and some preliminary results from YS96.

The experimental site (37°N, 124°E) in the central Yellow Sea was centered roughly between the tip of the China's Shandong Peninsula and the landmass of Korea, in waters 75 m deep (Fig. 2). Here, the Yellow Sea is representative of an epicontinental sea with a flat and broad seafloor with terrigenous sediment.[5] Coring data reported in a marine atlas of the Yellow Sea[6] suggest that the surficial sediment within the first meter consists of silty sand composed of 50%–70% sand and 10%–20% clay, with some shell components and mean grain size (in phi scale) of $3-4\phi$. Based on this mean grain size the compressional sound speed and density ranges would be 1570–1610 m/s and 1.84–1.92 g/cm^3, respectively, according to the empirical relations given in Jackson and Richardson.[7] However, both grain size and porosity can affect sound speed[8,9] and we do not have information on the latter.

Seismic profile records (500–3000 Hz), for which one profile line nearly precisely overlaps the experimental site,[10] show an absence of layered sequences to a sediment depth of ~100 m. High-resolution chirp sonar records (3.5–12 kHz) that also overlap with the experimental site[5] are devoid of layered structure to their maximum penetration depth of ~10 m into the sediment. Thus, a conceptual geoacoustic model for the experimental site consistent with these marine geological observations is that of a nonlayered sediment extending to depth ~100 m below the seafloor. It is also reasonable to assume that a positive, linear gradient in compressional sound speed applies over this ~100-m depth scale for terrigenous sediment.[11,12]

The YS96 data set analyzed here originates from the broadband propagation measurements made at range less than 1 km, on 22 August 1996 within a few minutes of 12:15 UTC. The R/V SHI YAN 2 starting at range ~0.4 nm from the R/V SHI YAN 3, deployed 38-g explosive sources set to detonate at 7 m and, ~15 s later, 50 m, and continued to open in range from the SHI YAN 3, which held station at position 124°E, 37°N. Signals were recorded on Chinese and U.S. vertical line arrays deployed over the side of the SHI YAN 3. Measurements studied here were made with the 16-element vertical line array (VLA), element spacing 4 m, deployed by the Applied Physics Laboratory, University of Washington (APL-UW) at a position approximately 36 m from the bow of the 104-m-long SHI YAN 3 on its starboard side. These data were first bandpass filtered between 75 and 750 Hz, then digitized at a 2-kHz sampling rate.

As noted previously, the focus of this paper is on the precursor arrivals for which evidence is given that these arrivals represent noninterfering C_n waves. Such arrivals show in the data only at close range owing to sediment attenuation, and also require the deeper (50 m) source to be visible within the arrival structure. Accordingly, the primary data for this work are grouped into four sets corresponding to four source detonations from the SHI YAN 2, at ranges defined as distance from the stern of the SHI YAN 2 to the deployment location of the APL-UW VLA on the SHI YAN 3, estimated to be 699, 701, 723, and 869 m, for sets 1–4, respectively. An uncertainty of ±10 m in range separation applies to each case based on quadrature addition of GPS ship positioning errors. The source depth estimates are 54, 47, 50, and 49 m, for sets 1–4, respectively, based on measurements of the bubble pulse duration, with a ±3-m uncertainty based on bubble

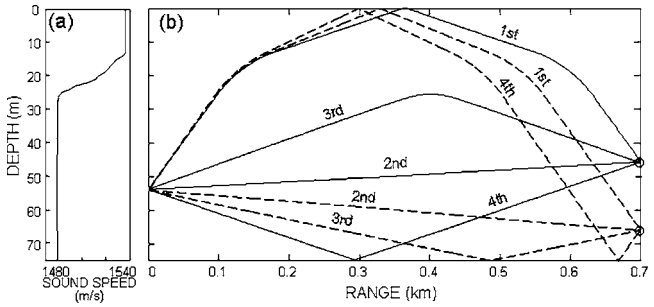

FIG. 3. (a) Sound speed versus depth determined by the conductivity-temperature-depth (CTD) casts from the R/V SHI YAN 3. (The CTD measurements were made by the South China Sea Institute of Oceanology.) (b) Ray diagram showing the first four water-borne ray arrivals for receiver depths of 46 m (solid line) and 66 m (dashed line). The ray corresponding to the first arrival (labeled 1st) undergoes reflection from the sea surface; other labels indicate order of subsequent arrivals.

pulse measurement precision.[13] Finally, results of a study of the measurements made from the VLA deployed by the Institute of Acoustics, Beijing, at a position closer to the stern of the SHI YAN 3, and involving sources deployed at longer ranges, is given by Rogers *et al.*;[17] these results are compared with ours in Section IV.

III. TRAVEL TIME ANALYSIS AND INVERSION

A. Identification of contributions to the arrival structure

The ray diagram [Fig. 3(b)] shows for set 1 the first four water-borne rays (eigenrays) received by the 46- and 66-m depth hydrophones from source at depth 54 m. These are predicted with a ray-tracing code that carries out horizontal range step integration for travel time, depth, and angle, using fourth-order Runge-Kutta methods.[18] (We define a water-borne ray as one with path in the water column, although it may have undergone reflection from the bottom and or sea surface.) The sound-speed profile [Fig. 3(a)] used in the ray computations originates from the conductivity-temperature-depth (CTD) cast made from the SHI YAN 3 within a few minutes of the acoustic measurements, which shows a strong thermocline that is common to the Yellow Sea in late summer. The first water-borne ray arrival (henceforth referred to as the "first arrival") corresponds to the path reflected from the sea surface once for all receivers between 66 and 10 m. For receivers between 66 and 34 m the second arrival corresponds to the direct path which has approximately 10 dB less spreading loss, whereas for shallower receivers the second arrival interacts with the seabed and then the sea surface. (The shallowest receiver at 6 m is inoperable.)

Figure 4(a) displays the arrival structure versus time and depth within the 75–750-Hz band for all 16 receivers. Using the aforementioned ray code, the solid red lines trace the computed arrival time fronts associated with the first ten water-borne rays, which are aligned on the figure by matching the location of the first arrival associated with receiver depth 46 m. The dashed red line traces the measured arrival time front of the precursor arrival relative to the first arrival that is associated with water-borne rays. In the geometry used in this experiment, the precursor arrival and the first arrival are the only arrivals that can be resolved given the bandwidth of the receiving VLA. Because absolute time measurements are not available, the difference in their travel times is a key observable that is used for travel time analysis and inversion. Call this difference τ_{ij}, where subscripts i and j represent the ith element of the receiving array and the experimental data set j, respectively. Figure 4(b) shows the selective narrow bandpass outputs for the arrival structure received at depth 66 m, with the shaded area highlighting the very distinct precursor arrival that exists only at lower frequencies. The two vertical dotted lines correspond to the time interval, T_1, between the shock wave and first bubble pulse for this set where $T_1=19$ ms as estimated using autocorrelation. At this receiver depth the interval T_1 is also manifested as a duplicate precursor arrival, although the interfering first arrival makes the duplicate precursor less distinct; for progressively shallower hydrophones the first arrival interferes with and eventually masks the duplicate precursor arrival. Note that although the interval T_1 is readily visible in the time series data, portions of the data with travel times beyond the first arrival exceed the dynamic range of the VLA's receiving network owing to the close range of the source; prior to this time the received levels are within the dynamic range and the response is linear. In the following section, ray theory estimates for the travel time difference between the precursor arrival and the first arrival, $\hat{\tau}_{ij}$, are defined and compared with measured τ_{ij} as defined above. These comparisons are limited to 46–66-m depths because precursor arrival travel times are more reliably estimated at these depths.

B. Travel time analysis for the C_0 wave

A reasonable physical model for the precursor travel time observations is one corresponding to the zeroth-order ray picture of Fig. 1, depicting upward refraction owing to a positive sound-speed gradient in the sediment. Although there are other options for canonical geoacoustic models involving gradients (e.g., see Ref. 19), a linear gradient model for the compressional sound speed in the seabed of the form $c_{1s}+az$ will be assumed here, where z is depth below the water-sediment interface. This assumption is made because of its simplicity and analytic form for travel time, and because other relational properties for refracted waves developed around the linear model can be exploited. Evidence given in Sec. II, involving seismic profile, and chirp sonar records also support using a nonlayered sediment structure.

A model for the travel time T_{C_0} of the first-arriving C_0 wave is given by

$$T_{C_0}=\frac{1}{a}\left|\ln\left(\frac{1-\sin\theta_t}{1+\sin\theta_t}\right)\right|+\frac{H_S+H_R}{c_w\sin\theta_0}, \tag{1}$$

where the first term covers the sediment-borne phase, parametrized by θ_t, the transmitted grazing angle in the sediment, and the gradient a. The second term covers the water-borne phase of the C_0 wave assuming this phase is governed by the (known) constant water sound speed, $c_w=1479.8$ m/s, a reasonable assumption given the ~50-m source depth and receiver depths greater than 46 m, where H_S and H_R are,

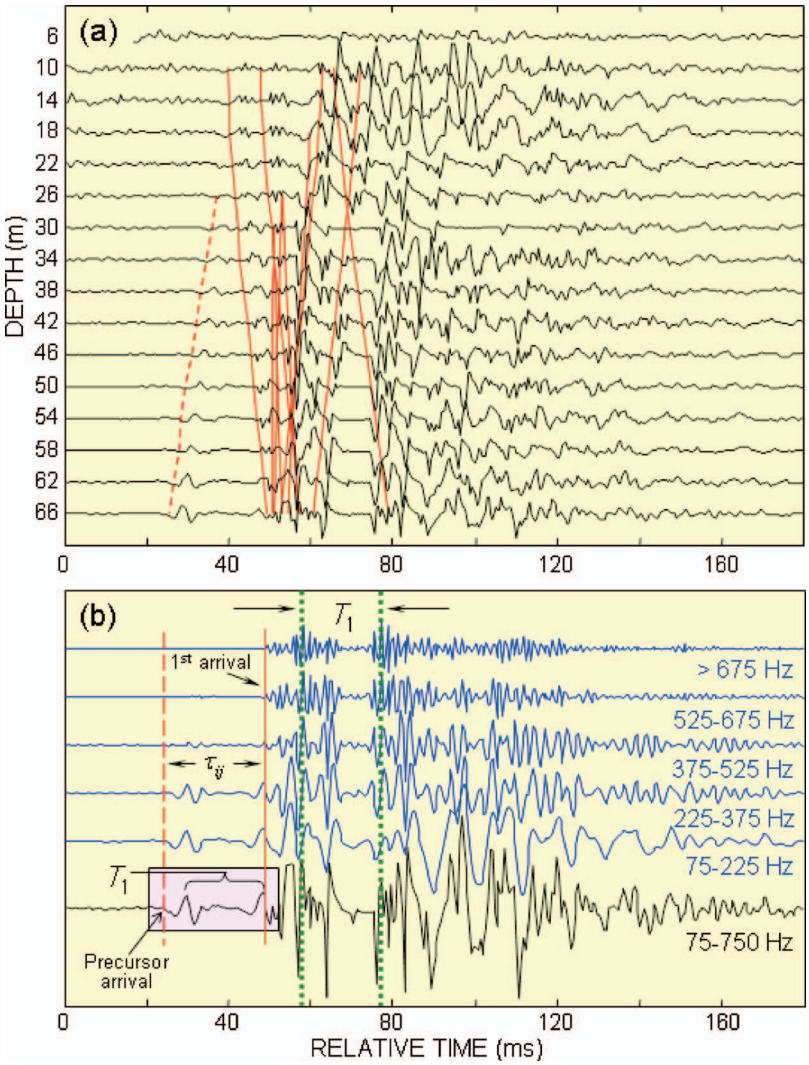

FIG. 4. (a) The set 1 arrival structure versus time and depth for 16 channels (top channel at depth 6 m is damaged) and computed arrival time fronts (red solid lines) corresponding to the first 10 eigenrays. The dashed red line traces the measured arrival time front of the precursor arrival relative to the first arrival associated with the water-borne rays. Time series data in the region to the left of time 40 ms is amplified by a factor of 2 for clarity. (b) Narrow bandpass outputs for the arrival structure for the 66-m depth hydrophone; shaded area highlights the precursor arrival phase. The two vertical dotted lines correspond to the time interval T_1 between the shock wave and first bubble pulse; τ_{ij} is the arrival difference between the precursor arrival and the first arrival.

respectively, the source and receiver heights above the water-sediment interface. Computed travel times for the C_0 wave from Eq. (1) minus ray-based estimates of travel time for the first arrival, using the sound-speed profile in Fig. 3(a), give the calculated values, $\hat{\tau}_{ij}$, to be compared with measured τ_{ij}.

Following an approach similar to that in Chapman *et al.*,[20] a Monte Carlo simulation is used to estimate c_{1s} and a with an objective function to be minimized for the inversion defined by

$$E = \sum_i \sum_j \sqrt{(\tau_{ij} - \hat{\tau}_{ij})^2}. \tag{2}$$

A subset of ~500 best models, selected on the basis of satisfying $E < 1$ ms, is obtained from 50 000 uniformly random configurations, for which the search space of c_{1s} and a is 1480–1650 m/s and 0.1–2.0 s^{-1}, respectively. Mean values and standard deviations of c_{1s} and a estimated from the model subset are 1573 m/s±5 m/s and 1.1 s^{-1}±0.1 s^{-1}, respectively. Figure 5 displays the arrival structure for the bottom six hydrophones for all sets in a more expanded scale to allow comparison between the measured data and the modeled relative travel times. The closed (C_0 wave arrival time) and open (first arrival time) symbols reflect the final inversion result, for which the modeled travel times of first arrival are plotted over their corresponding estimated times to provide the absolute time reference. We take the inversion to apply to a depth into the sediment corresponding to the turning depth of the C_0 wave, or ~50 m.

Note that it is important to keep in mind that travel time versus depth (or range) for an zeroth-order refracted wave can appear very similar to that of a first-order head wave (also called a pure head wave).[2] Carrying out the same inversion using instead a physical model based on the travel time for a first-order head wave, T_{1HW}, given by

$$T_{1HW} = \frac{r}{c_1} + \frac{(H_S + H_R)c_w}{\sqrt{1 - \left(\frac{c_w}{c_1}\right)^2}}\left(\frac{1}{c_w^2} - \frac{1}{c_1^2}\right), \tag{3}$$

where r is the source-receiver range, yields an estimate c_1, the constant sound speed in the sediment (1587 m/s), and corresponding critical angle ($\theta_c = 21°$). Assuming the linear gradient model for the sediment and using the estimated values for c_{1s} and a, then the theoretical arrival angles at the VLA for sets 1–3, i.e., θ_0 in Eq. (1), range between 23° and 24° for receiver depths between 66 and

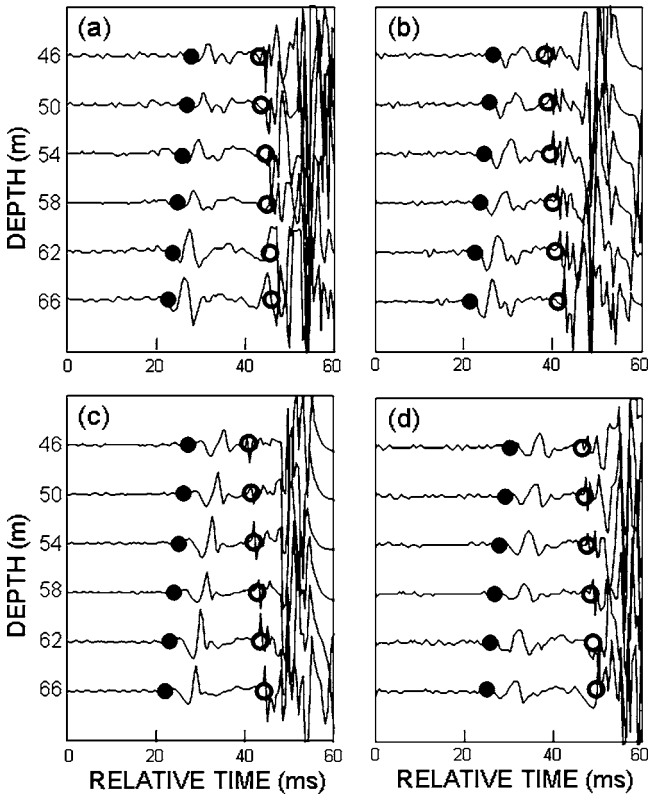

FIG. 5. (a) The arrival structure versus time and depth for the bottom six hydrophones for set 1. The closed (C_0 wave arrival time) and open (first arrival time) symbols reflect the final inversion result, for which the modeled travel times of first arrival are plotted over their corresponding estimated times to provide the absolute time reference. (b)–(d) Same displays for sets 2–4.

46 m, respectively, and between 24.5° and 25.5° for the same depth range for set 4. Estimates of arrival angle from the VLA data are consistent with these values, but unambiguous confirmation of the theoretical arrival angles with this field data is not possible. Specifically, the difference in travel times between two elements is used for an angle-of-arrival estimate, which puts the arrival angle between 22° and 25° depending on data set. Owing to strong currents there was some degree of array tilting; e.g., the array's tilt sensor at depth 17 m indicated a tilt of varying degree, with an rms tilt of nominally ~2°, although there is ambiguity as to the orientation of the tilt components with respect to the line-of-site between source and the VLA. Furthermore, the uncertainty in the estimate for travel time difference at a hydrophone separation of 20 m is ±0.25 ms, which translates to uncertainty of ±1°.

IV. ESTIMATES OF THE PRECURSOR ENERGY SPECTRAL DENSITY AND INVERSION FOR SEDIMENT ATTENUATION

Inversion for sediment compressional wave attenuation is based on an estimate of the transient precursor energy spectral density (ESD). Note that Godin *et al.*[21] used spectra from first-order head-wave arrivals to invert for the compressional sound-speed attenuation in the sediment, though the inversion approach used here, including assumptions concerning the nature of precursor arrivals, differs from their work. The ESD is expressed in the decibel equivalent of units proportional to energy flux density per hertz, along with a noise ESD that is comparable on this relative scale. A reference ESD (defined below) is also required which has an arbitrary offset from the precursor and noise ESD.

For sets 1, 2, and 4 signal time series segments of duration 22.5 ms are extracted from the bottom five channels because of their stronger signal-to-noise ratio (SNR). Although used in the travel time analysis, data from set 3 are not used for this purpose because it is significantly different from the other sets in its spectral character for reasons unknown. An example time series is that shown in the left-hand shaded box in Fig. 4(b). The extracted time series data are demeaned and tapered with an equal-length Tukey window (cosine-tapered window, parameter 0.4); this effectively smoothes the transition of the beginning and ending 10 sample points while leaving the middle 25 sample points untapered. A spectrum is then estimated with a 90-point rectangular window FFT and the five estimates of the ESD are averaged, giving 10 degrees of freedom to the final spectral estimate for a given set, which puts the 90% confidence interval at −2.6 and +4 dB about a spectral estimate.

The equivalent noise ESD is estimated from the 0.5 s of data recorded prior to the precursor arrival and on the bottom two array channels. The time series for each channel is divided into 44 subrecords of length 45 points, from which the noise ESD is estimated in the manner described above for the signal case but with much greater precision (90% confidence interval is approximately ±1 dB). The primary source of noise is the engine and machinery sound emanating from the SHI YAN 3, which is readily audible from the time series.

Sediment attenuation is estimated from the noise-corrected precursor ESD by comparing it with a reference ESD representing the spectral density of the explosive source signal plus linear effects associated with the channel and receiving system. It is important to emphasize that the short-duration precursor arrivals do not originate from the entire explosive source time function containing both shock and bubble pulse features, but instead originate from the shock wave only. In some instances, as in Fig. 4(b), a duplicate precursor arrival can be seen in the data with arrival time delay (~19 ms) with respect to the initial precursor corresponding to the primary bubble pulse. Thus, the source spectral density used here does not have the frequency modulation property associated with the interference between the shock wave and the bubble pulse.

To generate a reference ESD the explosive source time series measurements reported in Peng *et al.*[22] are used; they were recorded during the ASIAEX experiment in the East China Sea using the same weight and type of sources as those used in this experiment. The ASIAEX time series data show a shock pulse of duration ~1 ms with characteristic rise time, $t_0 \sim 0.2$ ms, based on a 10%-to-90% amplitude rise-time measure. Thus, for the shock wave alone, for frequencies $f \ll 1/(2\pi t_0)$, we expect the spectrum to be flat then go as $1/f^2$ for higher frequencies.[23] It is expected that some additional portion of the explosion time series is operative in generating the precursor arrivals, e.g., a portion up to but not including the first bubble pulse. A reasonable approximation

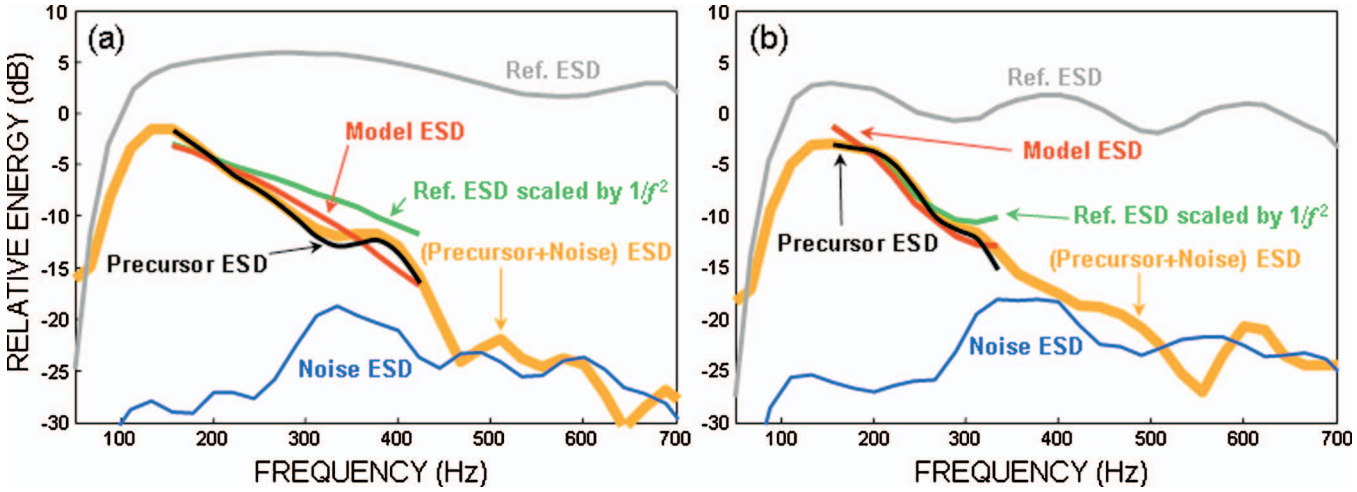

FIG. 6. (a) Estimate of the energy spectral density (ESD) of the precursor arrival based on the average of set 1 and set 2 data (black line) compared with model ESD (red line). The precursor ESD is corrected for noise (uncorrected is orange line) with values reliable to frequencies between 150 and 420 Hz. The model ESD is the reference ESD (gray line) corrected for sediment attenuation according to Eq. (5), for frequencies 150–420 Hz. Within the same frequency range the reference ESD is also shown scaled by $1/f^2$ (green line), which corresponds to a first-order head wave without sediment attenuation. The precursor and noise ESD are directly comparable in this relative decibel scale, whereas the reference ESD is displayed with an arbitrary decibel offset. (b) Same for set 4 data, but with frequency range inversion restricted to frequencies between 150 and 350 Hz.

is to take the spectrum of the shock pulse plus the first negative phase, of total duration ~11 ms. There remains some uncertainty as to which spectrum, shock wave alone or shock wave plus first negative phase, applies; given that these spectra are not substantially different we take the average of the two and identify the resulting energy spectral density as $|S_0(f)|^2$.

The result for $|S_0(f)|^2$ is modified slightly to account for the transfer function associated with the channel, $|H_1(f)|^2$, plus the analog receiving network of the VLA, $|H_2(f)|^2$. For this, a precursor arrival originating from a source spectrum much wider than $|H_2(f)|^2$ is simulated without seabed attenuation using the range-dependent acoustic model (RAM) PE code,[24] with result identified as $|H_1(f)|^2$. (For this simulation, the inverted $c_{1s}=1573$ m/s and gradient $a=1.1$ s^{-1} are used, which apply to a sediment depth of 500 m at which point a false bottom is imposed, and for sediment density we use 1.85 g/cm^3 as suggested in Ref. 17.) Next, a function $|H_2(f)|^2$ is defined that approximates the receiving network between ~75 and 750 Hz, and finally the transfer function is defined as $|H_1(f)|^2|H_2(f)|^2$. Note that $|H_1(f)|$ does not apply to the entire underwater sound channel *per se*, but instead represents the effects of the path identified as a plausible physical model for the YS96 observations and is associated with an identifiable arrival precursor phase. This is the zeroth-order refracted wave for which the constituent ray paths (C_n wave, $n=0,1,\ldots$) are shown in Fig. 1. There is a small degree modulation in $|H_1(f)|$ resulting from the separation of the C_0 wave and subsequent (weaker) C_n wave ($n=1,2,\ldots$). Specifically, L_2 is ~600 m for sets 1 and 2, and ~750 m for set 4; using the inverted values for a and c_{1s}, the travel time difference between the C_0 wave and the C_1 wave, ΔT_{0_1}, is ~2.5 ms for sets 1 and 2, and ~4.5 ms for set 4, and a slight modulation at frequency intervals, given by $\sim 1/\Delta T_{0\_1}$, can be seen in $|H_1(f)|$. This is discussed further in Sec. V.

The reference ESD, $|S_{\mathrm{ref}}(f)|^2$, in Fig. 6 is defined as

$$|S_{\mathrm{ref}}(f)|^2 = |S_0(f)|^2|H_1(f)|^2|H_2(f)|^2. \tag{4}$$

Sediment attenuation is estimated by finding the weighted least-squares fit between the measured precursor ESD expressed in decibels, and the following model:

$$10\log_{10}|S_{\mathrm{ref}}(f)|^2 - \alpha\hat{L}_2 f/1000 + K, \tag{5}$$

where α is sediment attenuation coefficient in dB/m/kHz, $\hat{L}_2$ is the path length of C_0 wave in the sediment (approximately equal to L_2 for ranges $<c_{1s}/a$), and K is an arbitrary decibel offset that emerges from the inversion algorithm. For sets 1 and 2 the estimate for the sediment attenuation is 0.08 ± 0.01 dB/m/kHz. When this value for attenuation is applied to Eq. (5) the result is the red line in Fig. 6(a). For set 4 the estimate is 0.07 ± 0.02 dB/m/kHz, and similar comparison is shown in Fig. 6(b). The final result obtained by a weighted average is 0.08 ± 0.01 dB/m/kHz. This estimate should be interpreted as a depth-average, i.e., averaged over approximately 50 m, corresponding to the turning depth of the C_0 wave.

Despite some degree of uncertainty in the reference spectrum, the results strongly suggest that the spectrum of the precursor arrival is not that of a first-order head wave, unless unrealistically negligible sediment compressional wave attenuation is assumed, which is not plausible. This is because, in the case of a first-order head wave, the ESD of the head wave is already related to the reference spectrum by $1/f^2$ scaling [green lines in Figs. 6(a) and 6(b)] in the absence of any additional sediment attenuation. In both data examples shown in Fig. 6 the attenuation estimates extend down to 150 Hz, which is the lowest frequency that lies sufficiently within the passband for which the −3-dB frequency is nominally 75 Hz. The upper frequency limit for estimating attenuation depends on SNR. For the average of set 1 and 2 data, this frequency is 420 Hz given that for higher frequencies the SNR is less than 3 dB; for the same reason the upper

frequency limit for set 4 data is 350 Hz. Thus, we take 150–420 Hz as the frequency range applicable to the sediment attenuation inversion, and the result is nominally consistent with the inversion result based on longer range propagation measurements from YS96.[17] Specifically, the two inversion results give the same estimate for attenuation at a frequency of ~250 Hz, whereas those from Ref. 17 give slightly lower and higher estimates for attenuation at lower and higher frequencies, respectively, owing to their nonlinear trend for sediment attenuation as a function of frequency, compared with the linear trend given here. A trend substantially different from a linear one was not observable over our relatively small frequency range.

V. SUMMARY AND DISCUSSION

Short-range (<1 km) propagation measurements taken in the Yellow Sea have been analyzed with emphasis on understanding the nature of the precursor arrivals that are distinguished by their arriving prior to any water-borne arrival. The signals were generated by broadband explosive sources and received on a 16-element vertical line array (VLA), receiver separation 4 m, roughly spanning the water column of depth 75 m. Evidence has been presented that the precursor arrivals are zeroth-order refracted waves that directly point to the existence of a gradient in sediment sound speed. Using travel time analysis involving the precursor arrival and the first-arriving water-borne ray, the sound speed just below the water-sediment interface was estimated to be 1573 m/s, with gradient estimated to be 1.1 s^{-1}.

The characteristic time duration of the incident wave, δt, is less than 2 ms. As discussed in Sec. I, the estimated travel time difference between the C_0 wave and the C_1 wave, ΔT_{0_1}, exceeds this bound, and thus the precursor arrival is assumed to consist of a C_0 wave that does not interfere with subsequent C_n waves ($n=1,2,\ldots$). In this case, however, a true observation of the time-separated C_0 and C_n waves is not possible owing to sediment attenuation. For example, ΔT_{0_1} for set 4 is estimated to be ~4.5 ms, and a PE simulation (Fig. 7) of the precursor arrival shows that well-separated C_0 and C_1 waves in the absence of attenuation are not distinguishable when attenuation is included in the simulation. Note that the term *noninterfering* as used here is based on the separation of the C_0 wave from the C_1 wave; later-arriving C_n waves ($n=2,3,\ldots$) can still interfere with the C_1 wave if their travel time difference is small compared to δt. For example, for the C_1 and C_2 waves, $\Delta T_{1\_2}=a^2L_2^3/172.8c_{1s}^3$, which is $\lesssim$1 ms.

The energy spectrum of the precursor arrival constitutes a direct observable of frequency-dependent attenuation originating from propagation in the sediment over a relatively precisely known range. Using this energy spectrum, sediment compressional wave attenuation was estimated to be 0.08 dB/m/kHz over the nominal frequency range 150–420 Hz. Observations outside this frequency are not possible with these data owing to high-pass filtering on the low-frequency end and insufficient SNR on the high-frequency end. Given that the frequency of experimental data was >150 Hz, it is assumed that this attenuation is compressional wave attenuation rather than that associated with an energy loss due to conversion to shear waves.

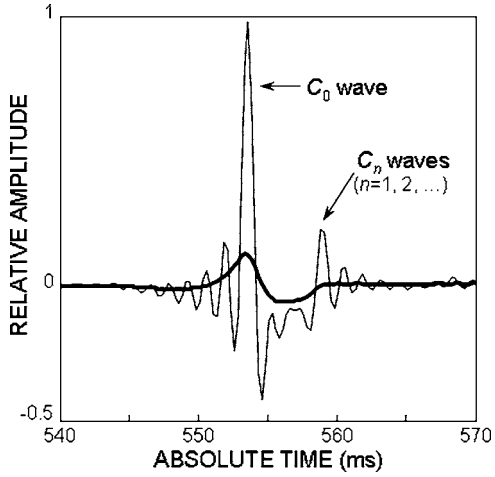

FIG. 7. Comparison between PE-simulated C_n waves ($n=0,1,\ldots$) without sediment attenuation (thin line) and with sediment attenuation of 0.08 dB/m/kHz (thick line) for source bandwidth of 75–750 Hz; geometry is the same as for set 4 with receiver depth equal to 66 m.

The amplitude of the precursor arrival provides additional evidence that points to the nature of the Yellow Sea observations insofar as a zeroth-order refracted wave propagating within sediment with a positive sound-speed gradient can be readily distinguished from a very weak first-order head-wave arrival. Figure 8 shows a comparison of the measured and synthetic (PE) time series data corresponding to the bottom seven receivers for set 2. Note that a duplicate synthetic time series with a time lag equal to the bubble pulse period T_1 was coherently added to the PE result to approximate the effect of the first bubble pulse. The two dashed lines in Fig. 8(a) highlight the arrival time front of the precursor arrival and the first arrival displayed in both the data and the synthetics. These lines trace out the symbols denoting relative travel time, originally plotted in Fig. 5(b) for set 2, and therefore reconfirm overall agreement in travel time analysis involving ray theory, inversion using Eq. (1), and the PE synthetics. Excluding results in Fig. 8(c), the PE simulation is based on the final inversion result (c_{1s} =1573 m/s, a=1.1 s^{-1}, α=0.08 dB/m/kHz), and the synthetic time series for all depths are calibrated by matching the amplitude of negative phase of the precursor arrival measured by the receiver at depth 54 m [see Fig. 8(b) and its inset]. As noted previously, the VLA receiver dynamic range is exceeded at these short source-to-receiver ranges for acoustic energy arriving after the first arrival, and data corresponding to these travel times are not interpreted. Nevertheless, the calibration as so defined maintains a satisfactory agreement between simulation and measurement for the amplitude of the first arrival and precursor arrival as recorded by the other receivers. The ratio of precursor arrival to first arrival amplitude is ~0 to 3 dB for the PE simulation, and ~0 to 4 dB for the data, depending on receiver depth.

To compare with the above, the PE simulation is repeated [Fig. 8(c)] using a geoacoustic model based on a constant sound speed (1587 m/s) in the sediment without sediment attenuation to produce a first-order head wave. This

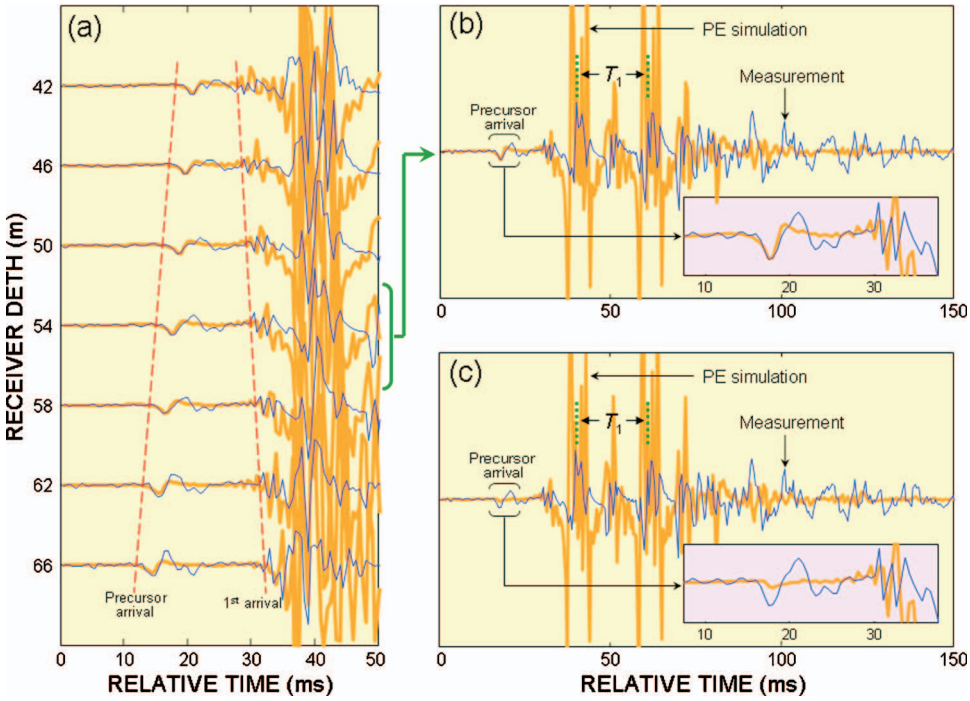

FIG. 8. (a) Comparison between measured (thin blue line) and PE simulated (thick orange line) time series for the bottom seven receivers (set 2). The PE simulation is based on a geoacoustic model for the inversion result c_{1s}=1573 m/s, a=1.1 s^{-1}, α=0.08 dB/m/kHz. The two dashed lines highlight the arrival time fronts corresponding to the precursor arrival and first arrival (see also the text). The PE results are calibrated to match the negative phase of the precursor arrival amplitude measured by the receiver at depth 54 m. (b) Expanded scale display for the receiver depth at 54 m, with the inset showing further expansion. (c) Similar expanded scale display of measured and PE simulated time series (using same-calibration factor) for the receiver at depth 54 m, with PE simulation now based on a half-space geoacoustic model using a constant sound equal to 1587 m/s without sediment attenuation. Speculation on the origin of low-frequency oscillation in the data between 100 and 150 ms is discussed in the text.

value for the sound speed in a half-space yields a similar relation between the arrival times for the precursor arrival and first arrival (Sec. III). Using the same factor to calibrate the synthetic data in Fig. 8(c), the synthetic amplitude is approximately the same as the synthetic data shown in Fig. 8(b) for arrival times beyond the precursor phase. However, in this case the ratio of precursor arrival amplitude to first arrival amplitude is now about −20 dB, even though sediment attenuation is set to zero, and it is thus difficult to imagine the first-order head wave actually being observable in field data.

Although the field measurements discussed here have provided much information on the nature of precursor arrivals in the Yellow Sea, their analysis is limited to the amplitudes of these precursor arrivals and of the first water-borne ray arrivals, plus their relative travel times, owing to system dynamic range. This is the reason the peak amplitude of the synthetic time series exceeds that of the measured time series as in Fig. 8(b). Yet, the measured time series amplitude also eventually exceeds that of the synthetic time series, e.g., as in Fig. 8(b) between 100 and 150 ms. Here, we cannot rule out the inclusion of bistatic reverberation from the hull of the SHI YAN 3. However, another possible explanation is the existence of a reflecting layer located deeper than the C_0 wave turning depth that we can readily speculate further on using PE synthetics. For example, adding a reflecting half-space layer to the above geoacoustic model at a sediment depth of 200 m, for which sound speed increases abruptly by ~100 m/s, produces similar low-frequency oscillations in the synthetic time series between 100 and 150 ms, with the time series prior to this point being unchanged. Thus, based on the approximately 50-m turning depth of the C_0 wave, our results should be viewed as applying only to this depth extent into the sediment. However, insofar as Ref. 10 provides evidence for the absence of reflecting layers to a nominal depth of 100 m in this region of the Yellow Sea, we adopt this depth as an upper bound.

ACKNOWLEDGMENT

This work was funded by the Office of Naval Research Code 321 Ocean Acoustics.

[1]J. W. Choi and P. H. Dahl, "First-order and zeroth-order head waves, their sequences, and implications for geoacoustic inversion," J. Acoust. Soc. Am. **119**, 3660–3668 (2006).
[2]V. Červený and R. Ravindra, *Theory of Seismic Head Waves* (University of Toronto Press, Toronto, 1971), Chaps. 2, 3, 6.
[3]M. E. Dougherty and R. A. Stephen, "Geoacoustic scattering from seafloor features in the ROSE area," J. Acoust. Soc. Am. **82**, 238–256 (1987).
[4]*Shallow-water Acoustics*, edited by R. Zhang and J. Zhou (China Ocean, Beijing, 1997).
[5]S. K. Chough, H. J. Lee, S. S. Chun, and Y. J. Shinn, "Depositional processes of late Quaternary sediments in the Yellow Sea: A review," Geosci. J. **8**, 211–264 (2004).
[6]*Marine Atlas of the Bohai Sea, Yellow Sea and East China Sea: Geology and Geophysics*, edited by L. Quanxing (China Ocean, Beijing, 1990).
[7]D. R. Jackson and M. D. Richardson, *High-Frequency Seafloor Acoustics* (Springer, NY, 2006).
[8]E. L. Hamilton and R. T. Bachman, "Sound velocity and related properties of marine sediments," J. Acoust. Soc. Am. **72**, 1891–1904 (1982).
[9]E. L. Hamilton, "Compressional-wave attenuation in marine sediments,"

Geophysics **37**, 620–646 (1972).
[10]J. P. Liu, J. D. Milliman, S. Gao, and P. Cheng, "Holocene development of the Yellow River's subaqueous delta, North Yellow Sea," Mar. Geol. **209**, 45–67 (2004).
[11]E. L. Hamilton, "Sound velocity gradients in marine sediments," J. Acoust. Soc. Am. **65**, 909–922 (1979).
[12]E. L. Hamilton, "Geoacoustic modeling of the sea floor," J. Acoust. Soc. Am. **68**, 1313–1340 (1980).
[13]Estimates of the bubble pulse period from this experiment (18.5 to 20 ms) are not consistent with that expected for the explosive charge weight (38 g) and detonation depth (50 m) based on the frequently used semi-empirical equation for bubble pulse period, e.g., as in Chapman (Ref. 14), which puts the period of the first bubble pulse at ~23 ms. The issue is the empirical coefficient, 2.11; according to Cole (Ref. 15) this coefficient is valid only for TNT charges exceeding 230 g (and up to 140 kg). The same (38-g) sources were also detonated at depth 50 m in the Asian Seas International Acoustics Experiment (ASIAEX), with similarly reduced bubble pulse periods, yet there is very compelling acoustic evidence that the sources in fact detonated at their preset depth of 50 m with an overall variation of ±5 m (Ref. 16). Thus, based on nominal depth of 50 m, we re-estimated the coefficient to be 1.82 for the 38-g sources used in YS96.
[14]N. R. Chapman, "Measurement of the waveform parameters of shallow explosive charges," J. Acoust. Soc. Am. **78**, 672–681 (1985).
[15]R. H. Cole, *Underwater Explosions* (Princeton University Press, Princeton, 1948), Chap. 8.
[16]R. Zhang, Z. Li, J. Yan, Z. Peng, and F. Li, "Broad-band matched-field source localization in the East China Sea," IEEE J. Ocean. Eng. **29**, 1049–1054 (2004).
[17]P. H. Rogers, J. X. Zhoi, X. Z. Zhang, and F. Li, "Seabottom acoustic parameters from inversion of Yellow Sea experimental data," in *Experimental Acoustic Inversion Methods for Exploration of the Shallow Water Environment*, edited by A. Carti, J.-P. Hermand, S. M. Jesus, and M. B. Porter (Kluwer Academic, Dordrecht, 2000), pp. 219–234.
[18]B. D. Dushaw and J. A. Colosi, "Ray tracing for Ocean Acoustic Tomography," Applied Physics Laboratory, Technical Memo APL-UW TM 3-98, December (1998).
[19]H. Kawahara and G. V. Frisk, "A canonical ocean-bottom sound velocity profile," J. Acoust. Soc. Am. **76**, 1254–1257 (1984).
[20]N. R. Chapman, L. Jaschke, and A. D. Kennedy, "The Haro strait geoacoustic tomography experiment," in *Experimental Acoustic Inversion Methods for Exploration of the Shallow Water Environment*, edited by A. Carti, J.-P. Hermand, S. M. Jesus, and M. B. Porter (Kluwer Academic, Dordrecht, 2000), pp. 51–72.
[21]O. A. Godin, N. R. Chapman, M. C. A. Laidlaw, and D. E. Hannay, "Head wave data inversion for geoacoustic parameters of the ocean bottom off Vancouver Island," J. Acoust. Soc. Am. **106**, 2540–2551 (1999).
[22]Z. Peng, J. X. Zhou, P. H. Dahl, and R. Zhang, "Sea-bed acoustic parameters from dispersion analysis and transmission loss in the East China Sea," IEEE J. Ocean. Eng. **29**, 1038–1045 (2004).
[23]D. E. Weston, "Underwater explosions as acoustic sources," Proc. Phys. Soc. London, Sect. B **76**, 233–249 (1960).
[24]M. D. Collins, "A split-step Padé solution for the parabolic equation method," J. Acoust. Soc. Am. **93**, 1736–1742 (1993).

Generalization of the rotated parabolic equation to variable slopes

Donald A. Outing[a] and William L. Siegmann
Rensselaer Polytechnic Institute, Troy, New York 12180

Michael D. Collins
Naval Research Laboratory, Washington, D.C. 20375

Evan K. Westwood
Applied Research Laboratories, Austin, Texas 78713

(Received 14 November 2005; revised 26 September 2006; accepted 30 September 2006)

The rotated parabolic equation [J. Acoust. Soc. Am. **87**, 1035–1037 (1990)] is generalized to problems involving ocean-sediment interfaces of variable slope. The approach is based on approximating a variable slope in terms of a series of constant slope regions. The original rotated parabolic equation algorithm is used to march the field through each region. An interpolation-extrapolation approach is used to generate a starting field at the beginning of each region beyond the one containing the source. For the elastic case, a series of operators is applied to rotate the dependent variable vector along with the coordinate system. The variable rotated parabolic equation should provide accurate solutions to a large class of range-dependent seismo-acoustics problems. For the fluid case, the accuracy of the approach is confirmed through comparisons with reference solutions. For the elastic case, variable rotated parabolic equation solutions are compared with energy-conserving and mapping solutions. © *2006 Acoustical Society of America.*
[DOI: 10.1121/1.2372590]

PACS number(s): 43.30.Dr, 43.30.Ma [ADP] Pages: 3534–3538

I. INTRODUCTION

The parabolic equation method is a powerful approach for solving range-dependent problems in ocean acoustics.[1] An important issue in this area is to improve accuracy for problems involving shear waves.[2–5] In this paper, we present a parabolic equation solution that should be accurate for a large class of ocean acoustics problems that involve elastic sediments and sloping bathymetry. Such problems can also be solved using normal modes,[6,7] the wave-number spectrum,[8,9] finite differences,[10] and finite elements,[11] but the parabolic equation method is very efficient for range-dependent problems.

A parabolic wave equation is obtained by factoring the operator in the wave equation into a product of incoming and outgoing operators. If range dependence in the medium is sufficiently gradual, outgoing energy dominates incoming energy, and the problem can be simplified by obtaining an approximate solution in terms of the outgoing operator. Parabolic wave equations are exact in a stratified medium. The factorization of the operator is an approximation for range-dependent problems. Even when the range dependence is gradual, significant errors may accumulate with range. Efforts to reduce these errors have been underway since the late 1980s.

A series of range-dependent benchmark problems was designed for testing the accuracy of parabolic equation solutions, and amplitude errors were observed for problems involving sloping ocean bottoms.[12] It was initially believed that these errors are due to two-way effects and that the parabolic equation method has serious accuracy limitations for range-dependent problems. A complex ray solution was used to demonstrate that back-scattered energy is negligible for one of the benchmark problems.[13] This provided hope that parabolic equation solutions could be modified to provide accurate solutions to range-dependent problems. The first progress in this direction was the rotated parabolic equation,[14] which accurately handles a sloping ocean bottom by working in a rotated coordinate system that is aligned with the interface. Although the ocean surface is not aligned with this coordinate system, it is easy to enforce the pressure release boundary condition on a sloping boundary.

Since the rotated parabolic equation was restricted to constant slopes, other techniques for handling range dependence were developed. More general types of range dependence can be handled by approximating the medium in terms of a series of range-independent regions, using the parabolic equation to propagate the field through each region, and then applying a correction at the vertical interfaces between regions. Energy-conservation corrections have proven to be effective when shear wave effects can be neglected.[15,16] Single-scattering corrections also provide accurate solutions.[17] Since the energy-conservation and single-scattering corrections have had limited success for problems involving shear waves,[18–20] there has recently been a renewed interest in the rotated parabolic equation and related approaches. When range dependence is sufficiently gradual, accurate solutions can be obtained using a mapping approach,[21] which is

[a]Present address: United States Military Academy, West Point, New York 10996.

 © 2006 Acoustical Society of America

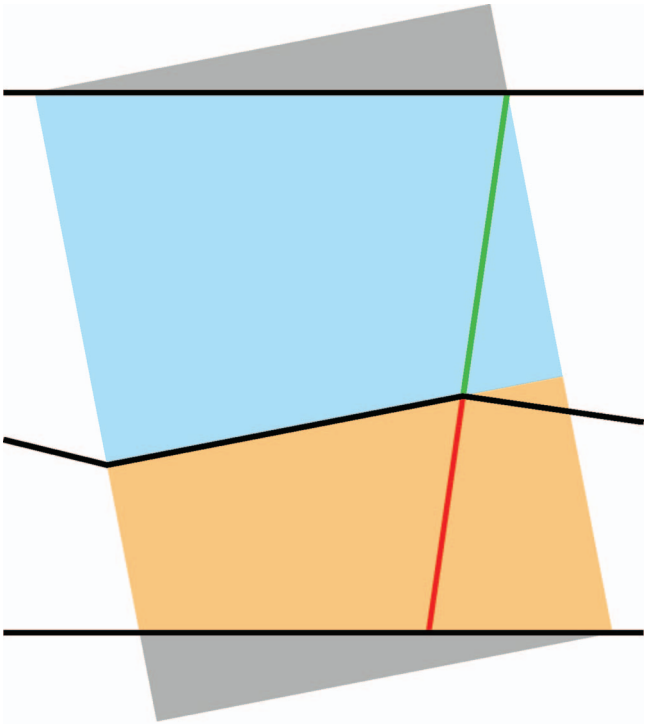

FIG. 1. Geometry of the variable rotated solution. The horizontal black lines are the ocean surface (above) and the bottom of the computational grid (below). The sloping black line segments indicate an ocean-sediment interface that has been approximated in terms of a series of constant slopes. On the colored line that is orthogonal to the interface, an initial condition is obtained by interpolation (red) and extrapolation (green). The field is extrapolated slightly beyond the change in slope by overshooting a short distance while keeping the slope constant, as indicated by the blue (ocean) and tan (sediment) regions. The gray areas above and below the horizontal lines represent zero padding, which can be used to simplify the bookkeeping.

based on mapping the ocean bottom to a horizontal interface. The mapping gives rise to additional terms in the wave equation that would be difficult to handle in a parabolic equation solution, but the effect of these terms are easy to handle approximately when slopes are small.

In this paper, we generalize the rotated parabolic equation to problems involving variable slopes. In Sec. II, the basic idea is described and tested for fluid problems. In Sec. III, the variable rotated parabolic equation is generalized to problem involving elastic sediments.

II. VARIABLE SLOPES

In this section, we describe the variable rotated parabolic equation and test it for problems involving fluid sediments. The ocean-sediment interface is approximated in terms of a series of constant slope regions. The field is propagated through a given region using a parabolic equation in a coordinate system that is aligned with the interface. This approach was applied in the original implementation of the rotated parabolic equation for constant slope problems.[14] Using the approach illustrated in Fig. 1, an initial condition for the next region is obtained on a line that is orthogonal to the interface. On the red part of the line, the initial condition is obtained by interpolating the solution in the current region. On the green part of the line, the initial condition is obtained by extrapolating the solution a short distance into the next region by overshooting the point where the slope changes. Linear interpolation and extrapolation provides sufficient solution accuracy. As indicated by the blue (ocean) and tan (sediment) regions in Fig. 1, the slope artificially remains constant in the overshoot region. If the change in slope is small, this approximation should be accurate away from the interface, including on the green part of the line. If changes in slope are sufficiently large or frequent, the red part of the line may not be confined to the current region. It is straightforward but tedious to obtain solution values on a (r,z) grid by using the successive coordinate rotations.

We test the variable rotated parabolic equation by comparing with energy-conserving parabolic equation solutions, which are known to be accurate for many problems. In order to illustrate the magnitude of the error when range dependence is not treated properly, we also present solutions that conserve pressure across vertical interfaces (the approach that was used before energy-conserving solutions were introduced). We work in cylindrical coordinates, where r is the range from the source and z is the depth below the ocean surface.

Example A consists of upslope and downslope cases. A 25 Hz source is located at $z=100$ m. The sound speed is 1500 m/s in the water column and 1700 m/s in the sediment, where the density is 1.5 g/cm^3 and the attenuation is 0.5 dB/λ. For the upslope case, the bathymetry is 400 m for $r<2$ km, 200 m for $r>8$ km, and linear for 2 km$<r<$8 km. For the downslope case, the bathymetry is 200 m for $r<2$ km, 400 m for $r>8$ km, and linear for 2 km$<r<$8 km. Solutions for example A appear in Fig. 2. The pressure conserving solution has significant errors for both cases. For the upslope case, the variable rotated and energy-conserving parabolic equation solutions are nearly identical. For the downslope case, the agreement is good but there are some small differences.

Example B illustrates that the difference between the rotated and energy-conserving parabolic equation solutions can be significant and that it is the energy-conserving solution that breaks down. For this downslope problem, the bathymetry increases linearly from 300 m at the source to 600 m at $r=10$ km. A 25 Hz source is located at $z=100$ m, and the sound speed is 1500 m/s in the water column. In the sediment, the sound speed is 1850 m/s, the density is 5 g/cm^3, and the attenuation is 0.5 dB/λ. An artificially large value is used for the density in order to magnify the difference between the solutions. Since the bottom slope is constant, this problem can be solved by the method of complex rays.[7] Solutions for example B appear in Fig. 3. The rotated parabolic equation solution agrees with the complex ray solution. The errors in the energy-conserving solution are apparently due to the large density contrast, the stair-step approximation of the interface, and the neglect of nonpropagating modes, which can contribute to the transmission of energy to long ranges for some range-dependent problems.

III. SEISMO-ACOUSTICS PROBLEMS

In this section, we generalize the variable rotated parabolic equation to problems involving elastic sediments. For

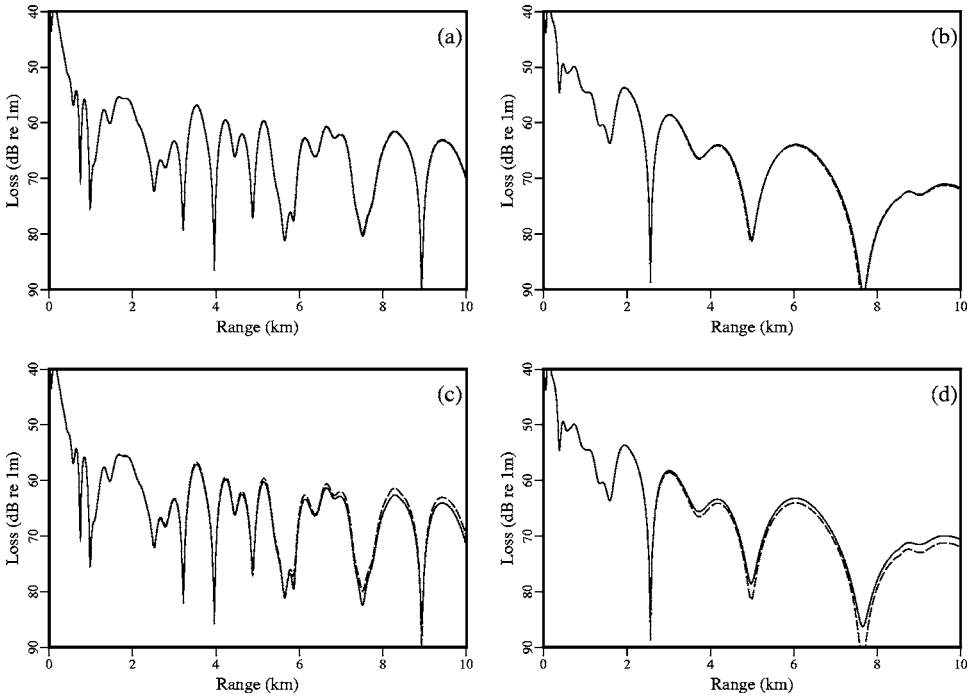

FIG. 2. Transmission loss at $z=30$ m for example A, which involves a 10 Hz source in shallow water. There are uplope (left column) and downslope (right column) cases, with changes in slope at $r=2$ km and $r=8$ km. The variable rotated solutions are shown as dashed curves. (a, b) The energy-conserving solutions are in agreement with the variable rotated solutions, but there is a slight difference for the downslope case. (c, d) There are significant errors in the pressure-conserving solutions.

this case, the dependent variable is a vector, which must be rotated along with the coordinate system. We use a rotated version of the (u_x,w) formulation of elasticity,[22,23] where u_x is the horizontal derivative of the horizontal displacement and w is the vertical displacement. In this formulation, it is easy to handle solid-solid interfaces in the sediment.[23] In each region of constant slope, x is the tangential variable, u_x is the tangential derivative of the tangential displacement, and w is the normal displacement. The elastic parabolic equation is of the form[22,23]

$$\frac{\partial}{\partial x}\begin{pmatrix} u_x \\ w \end{pmatrix} = L\begin{pmatrix} u_x \\ w \end{pmatrix}, \tag{1}$$

where L is a depth operator.

In a series of four steps, the field in the current region is interpolated, extrapolated, and rotated to obtain an initial condition in the next region. In the first step, we apply the inverse of L to the field in the current region to obtain

$$\begin{pmatrix} u \\ \int w \end{pmatrix} = L^{-1}\begin{pmatrix} u_x \\ w \end{pmatrix}. \tag{2}$$

We now have both components of the displacement vector (u,w) in the current region. In the second step, we rotate (u,w) to obtain w in the next region. In the third step, we obtain the dilatation Δ in the current region as follows:

$$\begin{pmatrix} \Delta \\ w \end{pmatrix} = D\begin{pmatrix} u_x \\ w \end{pmatrix}, \tag{3}$$

$$D \equiv \begin{pmatrix} 1 & \partial/\partial z \\ 0 & 1 \end{pmatrix}. \tag{4}$$

Since Δ is invariant under rotation, we now have Δ and w in the next region. In the fourth and final step, we obtain the initial condition in the next region by applying D^{-1}.

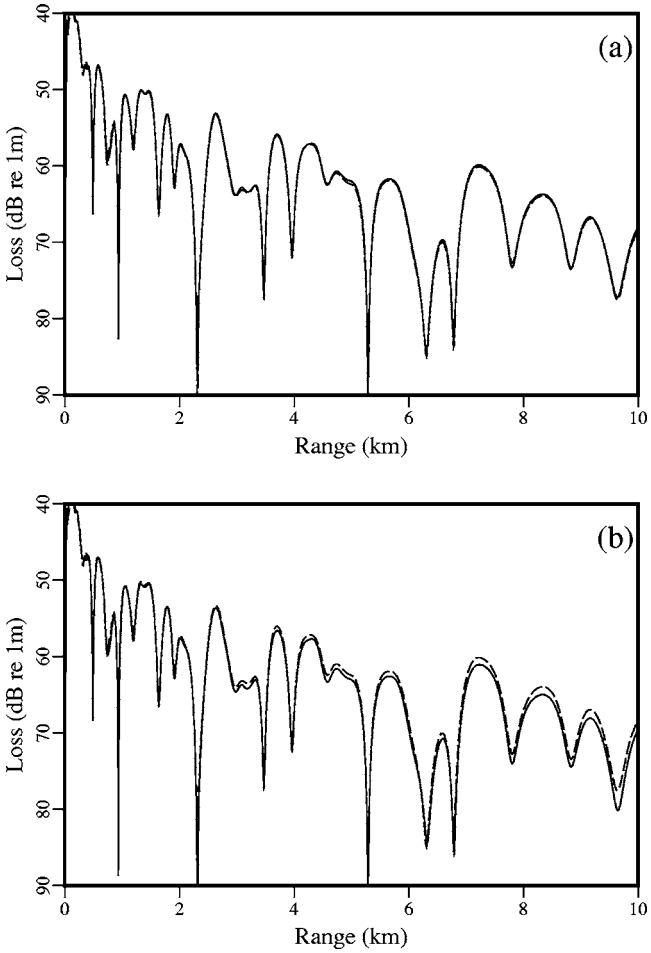

FIG. 3. Transmission loss at $z=30$ m for example B, which involves a 25 Hz source in an environment with a large density contrast across the ocean-sediment interface and bathymetry increasing linearly from 300 m to 600 m over $0<r<10$ km. The complex ray solution (dashed curves) is known to be accurate for this problem. (a) The variable rotated solution is in agreement with the reference solution. (b) The energy-conserving solution has significant errors.

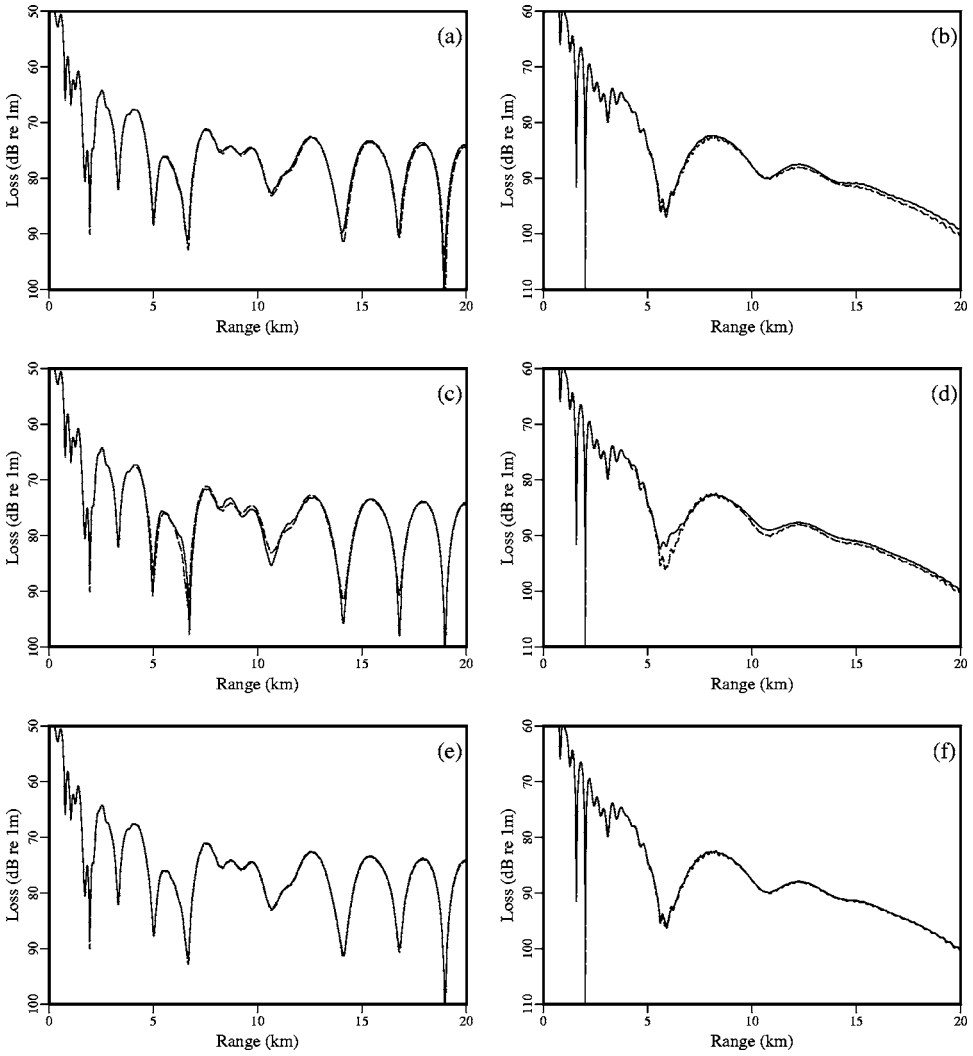

FIG. 4. Transmission loss at $z=30$ m for example C, which involves a 10 Hz source in an environment with 600 m bathymetry for $r<4$ km and a constant upslope to 300 m at $r=20$ km. There are high and low wave speed cases involving compressional and shear speeds of 3400 m/s and 1700 m/s (left column) and 2400 m/s and 1200 m/s (right column). The variable rotated solutions are shown as dashed curves. (a, b) The solution that approximately conserves energy has errors for both cases, but the errors are larger for the low wave speed case. (c, d) The uncorrected mapping solution has significant errors for both cases. (e, f) The corrected mapping solution agrees with the variable rotated solution for both cases.

For the examples, we compare variable rotated solutions with energy-conserving[18] and mapping[21] solutions. The energy-conserving correction for elastic media is approximate, but it provides fairly accurate solutions for many problems. The corrected mapping solution is accurate when range dependence is sufficiently gradual. It is also related to the variable rotated solution. The ocean-sediment interface is aligned with the coordinate system in both solutions, which differ in the way that changes in slope are handled. In the mapping solution, the field is extrapolated with a leading-order correction factor. In the variable rotated solution, the extrapolation is correct to higher order. In order to illustrate the magnitude of the error when range dependence is not treated properly, we also present the uncorrected mapping solution.[21]

Example C is an upslope problem consisting of two sediment types and different slopes. A 10 Hz source is placed at $z=390$ m in an ocean in which the sound speed is 1500 m/s. The bathymetry is 600 m for $r<4$ km and linearly decreases to 300 m over 4 km$<r<r_{\max}$. In the sediment, the density is 1.5 g/cm^3, the compressional attenuation is 0.2 dB/λ, and the shear attenuation is 0.4 dB/λ. The compressional and shear speeds are 3400 m/s and 1700 m/s for the high speed case and 2400 m/s and 1200 m/s for the low speed case. Solutions appear in Fig. 4 for the case $r_{\max}=20$ km. Based on the results for the acoustic examples, we would expect the variable rotated solution to be accurate for these problems. The energy-conserving solution has small errors for the high speed case and moderate errors for the low speed case. There are significant errors in the uncorrected mapping solutions. The corrected mapping solutions agree with the variable rotated solutions. Solutions appear in Fig. 5 for the cases $r_{\max}=8$ km and $r_{\max}=12$ km. There are errors in the corrected mapping solutions, which are larger for the larger slope.

IV. CONCLUSION

The rotated parabolic equation has been generalized to problems involving variable slopes. The medium is approximated in terms of a series of regions of constant slope. The original rotated parabolic equation algorithm is used to propagate the field through each region. In order to obtain an overlap between regions, the field is extrapolated a short distance beyond each change in slope. A starting field in the next region is then obtained by interpolating and extrapolating from the field in the current region. For the elastic case, the solution vector is rotated along with the coordinate system by applying a series of operators. We confirmed the accuracy of the approach for the fluid case and found that

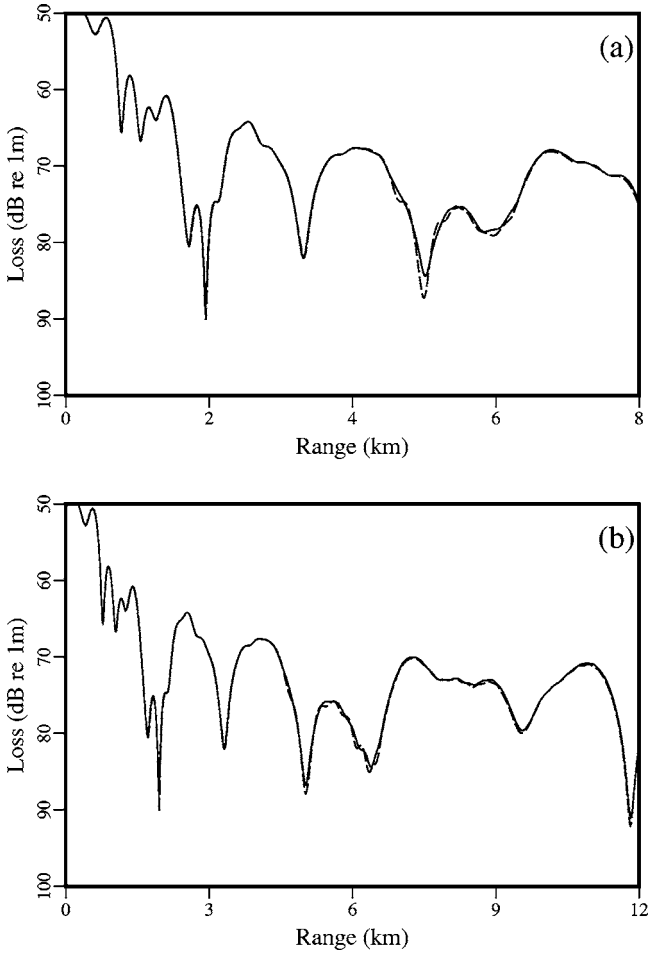

FIG. 5. Transmission loss for versions of example C that are modified to have steeper slopes. (a) The upslope region occurs over 4 km$<r<$8 km. (a) The upslope region occurs over 4 km$<r<$12 km. The variable rotated parabolic equation solutions are shown as dashed curves. There are significant errors in the corrected mapping solutions.

energy-conserving solutions break down for some downslope problems. The results presented for the elastic case suggest that the variable rotated parabolic equation is accurate for a large class of seismo-acoustic problems.

ACKNOWLEDGMENTS

This work was supported by the Office of Naval Research.

[1]F. B. Jensen, W. A. Kuperman, M. B. Porter, and H. Schmidt, *Computational Ocean Acoustics* (American Institute of Physics, New York, 1994), pp. 343–412.
[2]R. R. Greene, "A high-angle one-way wave equation for seismic wave propagation along rough and sloping interfaces," J. Acoust. Soc. Am. **77**, 1991–1998 (1985).
[3]M. D. Collins, "A higher-order parabolic equation for wave propagation in an ocean overlying an elastic bottom," J. Acoust. Soc. Am. **86**, 1459–1464 (1989).
[4]B. T. R. Wetton and G. H. Brooke, "One-way wave equations for seismoacoustic propagation in elastic waveguides," J. Acoust. Soc. Am. **87**, 624–632 (1990).
[5]M. D. Collins, "Higher-order parabolic approximations for accurate and stable elastic parabolic equations with application to interface wave propagation," J. Acoust. Soc. Am. **89**, 1050–1057 (1991).
[6]R. I. Odom, M. Park, J. A. Mercer, R. S. Crosson, and P. Paik, "Effects of transverse isotropy on modes and mode coupling in shallow water," J. Acoust. Soc. Am. **100**, 2079–2092 (1996).
[7]M. Park and R. I. Odom, "Effects of elastic heterogeneities and anisotropy on mode coupling and signals in shallow water," J. Acoust. Soc. Am. **104**, 747–757 (1998).
[8]H. Schmidt, W. Seong, and J. T. Goh, "Spectral super-element approach to range-dependent ocean acoustic modeling," J. Acoust. Soc. Am. **98**, 465–472 (1995).
[9]J. T. Goh and H. Schmidt, "A hybrid coupled wave-number integration approach to range-dependent seismoacoustic modeling," J. Acoust. Soc. Am. **100**, 1409–1420 (1996).
[10]R. A. Stephen, "A review of finite difference methods for seismo-acoustic problems at the sea floor," Rev. Geophys. **26**, 445–458 (1988).
[11]J. E. Murphy and S. A. Chin-Bing, "A finite-element model for ocean acoustics propagation and scattering," J. Acoust. Soc. Am. **86**, 1478–1483 (1989).
[12]F. B. Jensen and C. M. Ferla, "Numerical solutions of range-dependent benchmark problems," J. Acoust. Soc. Am. **87**, 1499–1510 (1990).
[13]E. K. Westwood, "Ray methods for flat and sloping shallow-water waveguides," J. Acoust. Soc. Am. **85**, 1885–1894 (1989).
[14]M. D. Collins, "The rotated parabolic equation and sloping ocean bottoms," J. Acoust. Soc. Am. **87**, 1035–1037 (1990).
[15]M. B. Porter, F. B. Jensen, and C. M. Ferla, "The problem of energy conservation in one-way models," J. Acoust. Soc. Am. **89**, 1058–1067 (1991).
[16]M. D. Collins and E. K. Westwood, "A higher-order energy-conserving parabolic equation for range-dependent ocean depth, sound speed, and density," J. Acoust. Soc. Am. **89**, 1068–1075 (1991).
[17]M. D. Collins and R. B. Evans, "A two-way parabolic equation for acoustic back scattering in the ocean," J. Acoust. Soc. Am. **91**, 1357–1368 (1992).
[18]M. D. Collins, "An energy-conserving parabolic equation for elastic media," J. Acoust. Soc. Am. **94**, 975–982 (1993).
[19]M. D. Collins and W. L. Siegmann, "A complete energy conservation correction for the elastic parabolic equation," J. Acoust. Soc. Am. **104**, 687–692 (1999).
[20]M. D. Collins, "A two-way parabolic equation for elastic media," J. Acoust. Soc. Am. **93**, 1815–1825 (1993).
[21]M. D. Collins and D. K. Dacol, "A mapping approach for handling sloping interfaces," J. Acoust. Soc. Am. **107**, 1937–1942 (2000).
[22]A. J. Fredricks, W. L. Siegmann, and M. D. Collins, "A parabolic equation for anisotropic elastic media," Wave Motion **31**, 139–146 (2000).
[23]W. Jerzak, W. L. Siegmann, and M. D. Collins, "Modeling Rayleigh and Stoneley waves and other interface and boundary effects with the parabolic equation," J. Acoust. Soc. Am. **117**, 3497–3503 (2005).

Simulations of large acoustic scintillations in the Straits of Florida

Xin Tang[a] and F. D. Tappert[b]
Division of Applied Marine Physics, University of Miami, RSMAS, Miami, FL 33149

Dennis B. Creamer[c]
Code 5580, US Naval Research Laboratory, Washington DC 20375

(Received 25 July 2005; revised 6 September 2006; accepted 11 September 2006)

Using a full-wave acoustic model, Monte Carlo numerical studies of intensity fluctuations in a realistic shallow water environment that simulates the Straits of Florida, including internal wave fluctuations and bottom roughness, have been performed. Results show that the sound intensity at distant receivers scintillates dramatically. The acoustic scintillation index *SI* increases rapidly with propagation range and is significantly greater than unity at ranges beyond about 10 km. This result supports a theoretical prediction by one of the authors. Statistical analyses show that the distribution of intensity of the random wave field saturates to the expected Rayleigh distribution with $SI=1$ at short range due to multipath interference effects, and then *SI* continues to increase to large values. This effect, which is denoted supersaturation, is universal at long ranges in waveguides having lossy boundaries (where there is differential mode attenuation). The intensity distribution approaches a log-normal distribution to an excellent approximation; it may not be a universal distribution and comparison is also made to a *K* distribution. The long tails of the log-normal distribution cause "acoustic intermittency" in which very high, but rare, intensities occur. © *2006 Acoustical Society of America.* [DOI: 10.1121/1.2372446]

PACS number(s): 43.30.Dr, 43.30.Pc, 43.30.Re [DRD] Pages: 3539–3552

I. INTRODUCTION

Since the sonar detection process is probabilistic in nature, more than 50 years of research has been directed toward understanding intensity fluctuations of acoustic signals propagating in the ocean.[1] Sound-speed variability due to oceanic heterogeneities leads to distortion and variability of the acoustic signals propagating in such an environment. This temporal and spatial variability is caused by oceanic processes with dynamics that are inherently nonlinear and imposes physical limits on sonar detection systems. Applications such as coherent signal processing must take into account this variability of the acoustic signal. The statistical behavior of the fluctuations of intensity in sonar applications is crucial in the theory of signal detection and a change in the probability distribution describing these fluctuations may lead to revision of such theories.

Most of the research activity on understanding the behavior of acoustic signals in the presence of such inhomogeneities has concentrated on deep-water environments where bottom interaction of the acoustic signals can be ignored, and acoustic propagation conserves energy, i.e., there is no appreciable attenuation. Applications of wave propagation through random media (WPRM) theory to deep-water waveguides focused, for example, on understanding the transmission of acoustic pulses and extracting intensity moments, e.g. the variance of intensity, called the scintillation index,

$$SI = \langle (I - \langle I \rangle)^2 \rangle / \langle I \rangle^2, \tag{1}$$

where I denotes the signal intensity. A perfectly coherent signal has $SI=0$. In this paper, the average intensity $\langle I \rangle$ is normalized to unity.

In weakly fluctuating media or propagation over short distances, the distortion of the acoustic wave fronts is sufficiently small that the variation of the signal amplitude in the cross-range direction is a small fraction of the average amplitude. This is the weak scattering or unsaturated regime and has been shown[2] to accurately describe wave transmission when the scintillation index is less than 0.3. The amplitude of the signal is then distributed according to a log-normal distribution.[3] Over long propagation paths or in strongly fluctuating media, wave front distortion is severe, causing spatial and temporal decorrelation of the signal. This is the fully saturated regime of scattering characterized by large intensity fluctuations with a variance comparable to the average intensity (i.e., the scintillation index is near one). The asymptotic distribution determining the intensity statistics is the Rayleigh (exponential) distribution so that the scintillation index is unity. This asymptotic distribution is universal in the sense that, within a broad class of sound-speed variability, the exact form of this variability is irrelevant.

In reality, this asymptotic regime is often never reached in the ocean. Many experiments at very long ranges show that the saturated region of acoustic propagation is never reached. There can be many reasons for this, an example

[a]Contact address: ExxonMobil Upstream Research Corporation, Houston, TX 77252.
[b]Deceased.
[c]Author to whom correspondence should be addressed; electronic mail: creamer@ait.nrl.navy.mil

being the existence of very large (spatially) fluctuations of the sound speed (mesoscale eddies). This "outer-scale" problem also exists in radio wave propagation through interstellar media,[4] which is a case where there is a power-law turbulent fluctuation spectrum with effectively no "largest" scale. The regime of saturated scattering only applies at ranges large enough where the propagation region (e.g., Fresnel zone) is much larger than the scales associated with the physics of the propagation medium. Many experimental situations are just never in this asymptotic regime and the analysis of the scintillations and intensity distributions in such experiments are not easily explained (and therefore more interesting).

The Rayleigh distribution of intensity,[1,5] derived from the central limit theorem applied to additive scattering processes, has long dominated the thinking of researchers concerned with the saturation regime of acoustic signal fluctuations using statistical theories of WPRM. The first theory of WPRM that led to the Rayleigh distribution is due to Shishov,[6] who considered a plane wave incident on a randomly fluctuating medium with uniform background and homogeneous, isotropic fluctuations. This theory was later extended by many researchers[7] with the goal of predicting the transient behavior of SI and the intensity distribution before the saturation regime is reached, where $SI=1$ and the Rayleigh distribution is obtained. More relevant to ocean acoustics, the intensity distribution at the center of a ray tube in an ocean with a general sound speed profile was shown by Dashen[8] to asymptotically approach the Rayleigh distribution, and be even calculated a small correction term. A basic assumption in that work is that a single ray tube can be analyzed without regard to the many other ray tubes that contribute to the signal at long ranges, i.e., multipath interference effects are ignored. Dashen's ray-based theory was later refined and developed into a quantitative method for estimating the range to saturation for a single ray tube in realistic ocean environments.[3,9] In a different vein, Dozier and Tappert[10] developed a stochastic coupled mode theory and showed that if there are N propagating modes then saturation at long ranges corresponds to an equipartition of modal power, and the intensity is uniformly distributed on the surface of an N-dimensional sphere. For large N this intensity distribution approaches the Rayleigh distribution. The range to saturation was numerically computed for realistic internal wave fluctuations[11] and since this theory explicitly includes multipath interference effects, the saturation range was found to be surprisingly small. The Rayleigh distribution of intensity, with the random phase approximation built in, is generally believed to represent the final state of statistical equilibrium beyond which no change is possible. It is considered to correspond to thermodynamic equilibrium, the maximum entropy state, and according to ergodic theory the state of equipartition on the energy surface.

In the shallow-water ocean, the physical boundaries radically change the nature of wave propagation—the boundaries themselves lead to severe multi pathing while subbottom absorption and conversion to nonacoustic forms of energy lead to loss mechanisms that invalidate conservation of energy. Since this energy conservation is such a fundamental concept in the long-range behavior of intensity statistics discussed above (e.g., it is necessary for equilibrium to exist), it is not too surprising that intensity statistics would be very different in shallow-water oceans. WPRM theory was extended to include the effects of lossy bottom interactions by several researchers,[12–14] but the effects of these losses on intensity fluctuations was not considered until the work of one of the author.[15] There, the intensity distribution describing the asymptotic (in range) state of the system was shown not to be the equilibrium, or Gaussian, distribution by determining that acoustic signals propagating in a lossy shallow water waveguide asymptotically have a scintillation index that increases exponentially with range. This is a universal situation as long as there is a nonzero difference in the attenuation between modes (in a modal picture) and random mode coupling. Of course, varying these parameters will change the length scale determining the exponential increase, but this will always occur unless the differential attenuation between modes vanishes.

By extending the statistical theory of mode coupling[10,11] to include lossy boundary interactions and by examining the fourth moment statistics, it was shown in Ref. 15 that the mean intensity asymptotically (i.e., as $r\to\infty$) decays with range according to $\langle I\rangle = I_0 \exp(-\lambda_1 r)$ and the mean square intensity asymptotically decays in range according to $\langle I^2\rangle = I_1^2 \exp(-\lambda_2 r)$. Letting $\lambda = 2\lambda_1 - \lambda_2 \geqslant 0$, then the asymptotic form of the scintillation index is

$$SI = A\exp(-\lambda r) - 1, \quad \lambda r \to \infty, \tag{2}$$

where A does not depend on range. As noted above, this result is universal in the presence of differential mode attenuation. This surprising result, which does not violate any known law of physics or mathematics, shows that the Rayleigh distribution cannot represent the range asymptotic state of intensity fluctuations in such a system. This behavior of the scintillation index was confirmed in numerical simulations through a realistic internal wave field by Tielburger, Finette, and Wolf.[16] This state of large scintillations is referred to as "supersaturation." The exponent λ is called the "generalized Lyapunov exponent" by analogy to the "Lyapunov exponent" familiar from studies of chaos theory in underwater acoustics.[17] Both exponents are difficult to estimate from theory, from numerical simulations, or from experimental observations. The term generalized Lyapunov exponent comes from work on the theory of random matrices[18] (especially as it applies to localization in wave propagation in disordered media).

This paper proposes that the long-range intensity distribution function is log-normal instead of Rayleigh, although comparison is also made to a modified Bessel or K distribution. It should be emphasized that the appearance of the log-normal distribution is an asymptotic phenomena in a very similar way that the appearance of the Rayleigh distribution is asymptotic; applications to long-range shallow-water propagation experiments should have the same caveats as discussed previously for the Rayleigh distribution. The log-normal distribution has appeared previously in WPRM; as mentioned earlier, it has been used to describe weak intensity fluctuations with a small scintillation index. Jakeman[19] has suggested it as a possible intensity distribution in the "strong

focusing" regime (where random caustics appear) and notes that it is natural when the scattering processes are multiplicative (as in random matrix theory) and numerous. In the supersaturation region, the log-normal distribution appears asymptotically; the variances are large because the tail in the appropriate log-normal distribution for the intensity is wide (becoming wider with range) and decays slowly with increasing intensity.

In this work, numerical simulations of sound propagation in the Straits of Florida, a well characterized oceanic environment with random fluctuations[20–22] are performed with the aim of improving the understanding of signal intensity fluctuations. A parabolic-equation numerical method[23] is used to study sound propagation in a realistic shallow water environment that simulates the Straits of Florida. As in many other shallow water areas, internal wave activity is found to be the dominant cause of sound speed fluctuations in the Straits of Florida affecting acoustic wave propagation.[20,22] In the frequency range of interest, mode coupling due to multiple scattering is strong, implying that both the amplitudes and phases of the sound pressure vary. Because of the existence of a strong thermocline layer, sound propagation in the Straits of Florida is characterized by downward refraction and frequent bottom interactions. Additionally, the bottom sediments in the Straits of Florida are mostly sandy carbonates that allow acoustic energy at grazing angles exceeding the critical angle to penetrate and be absorbed. This gives an ideal environment to study scintillation statistics. In this environment, the University of Miami Parabolic Equation[24] (UMPE) numerical model is exercised for a large number of realizations of the internal wave field, equivalent to sampling the ocean over a large geophysical time interval. The scintillation index of the sound intensities is then obtained by a Monte Carlo average of the simulated data, and the probability distribution of the sound intensities is determined.

It is found that a log-normal distribution provides an excellent description of the intensity distribution. By contrast, the K distribution is found not to provide as good a description. By fitting the log-normal model to simulated data using standard quantitative statistical tests, it is found that the parameter of the best log-normal fit, equivalent to λr in Eq. (2) grows linearly with the propagation range at long ranges.

In the sequel, Sec. II provides information about the intensity distributions that are used to describe "saturated" and supersaturated behavior. Section III describes the simulations performed using the UMPE numerical code, and the environmental inputs, internal waves in particular, are detailed. The sound attenuation and intensity scintillations are then displayed, and a large simulation data set is obtained. Section IV describes the statistical analysis whereby the scintillation index is calculated, and both the log-normal and K probability distributions are tested as candidate distributions. In addition, the parameters that give the best fit to the data are determined as a function of range. Discussion and conclusions are contained in Sec. V.

II. INTENSITY DISTRIBUTIONS

For later reference and to establish notation, properties of intensity distributions are defined and reviewed. The intensity distribution function ρ is defined such that the probability that the intensity I lies in the interval between I and $I+dI$ is $\rho(I)dI$. The nth moment of $\rho(I)$ is

$$\langle I^n \rangle = \int_0^\infty I^n \rho(I) dI \tag{3}$$

The mean intensity is normalized to $\langle I \rangle = 1$ for all the statistical analyses in this paper. The cumulative probability function is

$$P(I) = \int_0^I \rho(I') dI' \tag{4}$$

and $P(\infty) = 1$. The median intensity I_m is defined by

$$P(I_m) = 1/2. \tag{5}$$

Half of the intensities are expected to have values respectively less than and greater than I_m.

The Rayleigh distribution for the intensity follows from the assumption that the real and imaginary parts are drawn from a Gaussian distribution. If the mean intensity is set to unity, there are no free parameters in the distribution; thus, the scintillation index cannot increase exponentially with range. The log-normal has a free parameter that can be used to allow range dependence for the scintillation index. Another one-parameter distribution often used in scintillation theory is the modified Bessel or K distribution. This paper compares the simulation results to these three distributions and uses the behavior of the scintillation index to determine free parameters (i.e., the free parameter becomes the scintillation index). Another distribution often used is the generalized gamma distribution, which has more than one free parameter; additionally it includes the log-normal distribution as a limiting case. If the log-normal distribution provides a good fit of the results then so does the generalized gamma distribution.

A. Rayleigh distribution

The Rayleigh distribution of intensity is well known to be

$$\rho_R(I) = \exp(-I) \tag{6}$$

and the moments of the Rayleigh distribution are

$$\langle I^n \rangle = n\,!\,, \tag{7}$$

which gives $SI = \langle I^2 \rangle - 1 = 1$. The cumulative probability is

$$P_R(I) = 1 - \exp(-I), \tag{8}$$

giving $I_m = \ln 2$.

B. Log-normal distribution

Since the Rayleigh distribution cannot be used to describe the strong scintillations discussed earlier and because the numerical simulations discussed below support the picture of a supersaturation region, the log-normal intensity dis-

tribution is examined as a possible candidate. Recalling that the mean intensity is normalized to unity, the log-normal distribution (see, e.g., Ref. 25 pp. 220-221) becomes

$$\rho_L(I) = (I\sqrt{2\pi\nu})^{-1}\exp[-(\ln I + \nu/2)^2/2\nu], \tag{9}$$

where the single parameter ν in this distribution is the variance of $\ln I$:

$$\nu = \langle(\ln I - \langle \ln I\rangle)^2\rangle \geq 0. \tag{10}$$

The mean value of $\ln I$ is

$$\langle \ln I\rangle = -\nu/2. \tag{11}$$

The intensity moments according to the log-normal distribution are

$$\langle I^n\rangle = \exp[n(n-1)\nu/2], \tag{12}$$

and in particular, for $n=2$, it is seen that

$$SI = \exp(\nu) - 1. \tag{13}$$

The cumulative log-normal probability distribution is

$$P_L(I) = \frac{1}{2}\left[1 + \mathrm{erf}\left(\frac{\ln I + \nu/2}{\sqrt{2\nu}}\right)\right], \tag{14}$$

where erf(…) is the error function and giving the median intensity

$$I_m = \exp(-\nu/2). \tag{15}$$

The coincidence of Eq. (13) with $\nu = \lambda r + \ln A$ to the result in Eq. (2) is one of the clues that led to consideration of the log-normal distribution.

The log-normal distribution has previously been used to describe weak intensity fluctuations in the limit $\nu \to 0$. Then, with the constraint that the mean intensity is unity, the Gaussian distribution is obtained

$$\rho_L(I) \approx (2\pi\nu)^{-1/2}\exp[-(I-1)^2/2\nu]. \tag{16}$$

It follows that $SI = \nu \ll 1$. This paper is concerned with large intensity fluctuations, $\nu \gg 1$, and the log-normal distribution appears to be novel in this context. For large ν, the median intensity is exponentially small, the mean intensity is unity, and the rms intensity is exponentially large, $\langle I^2\rangle^{1/2} = \exp(\nu/2)$. Thus the log-normal distribution for large ν is relatively flat over an enormous range of intensities. In particular, the log-normal distribution for large ν has a long "tail" at the high intensity end that would be observed as very strong scintillations that occur as intermittent events. This phenomenon is called acoustic intermittency, and is due solely to acoustic propagation effects. The numerical simulations discussed below show exactly this expected behavior.

C. *K* distribution

Other distributions have been used to look at the non-Gaussian behavior of the statistics in wave propagation in random media. Jakeman[26] has been a strong proponent of the *K* distribution, based on using modified Bessel functions. Like the log-normal distribution this distribution has a single parameter (when the mean intensity is unity) that can be determined by the intensity variance. The probability function for the amplitude is

$$\rho_K(A) = \frac{4b}{\Gamma(\alpha)}(bA)^{\alpha}K_{\alpha-1}(2bA) \tag{17}$$

with $b = \sqrt{\alpha/\langle A^2\rangle}$ and where Γ is the gamma function and K_α is the modified Bessel function. With the mean intensity set to unity, the intensity distribution is then

$$\rho_K(I) = \frac{2\alpha}{\Gamma(\alpha)}(\alpha I)^{(\alpha-1)/2}K_{\alpha-1}(2\sqrt{\alpha I}). \tag{18}$$

For the *K* distribution the normalized intensity moments are

$$\langle I^n\rangle = n!\,\frac{\Gamma(n+\alpha)}{\alpha^n\Gamma(\alpha)}. \tag{19}$$

In the particular the scintillation index is

$$SI = 1 + \frac{2}{\alpha}. \tag{20}$$

As $\alpha \to \infty$, the *K* distribution reduces to the Rayleigh distribution. Large values of the scintillation index occur when α is small, in which case it plays a similar role as $\exp(-\nu)$ for the log-normal distribution. In the limit as $\alpha \to 0$, the moments have the leading behavior

$$\langle I^n\rangle \approx n!\,(n-1)!\,\alpha^{-n} = n!\,(n-1)!\,e^{n[-\ln(\alpha)]}. \tag{21}$$

The scaling of the argument of the exponent with the moment number is completely different than for the log-normal distribution, Eq. (12). Values of the higher moments are substantially smaller than for the log-normal distribution when the intensity variance is large.

The function in Eq. (18) does not have a simple analytical expression; however, a useful integral representation[27] for the modified Bessel function gives

$$\rho_K(I) = \frac{\alpha}{\Gamma(\alpha)}\int_0^\infty \frac{dt}{t^\alpha}e^{-\alpha It - 1/t}, \tag{22}$$

valid for $\alpha > 0$. Thus the cumulative *K* distribution is

$$P_K(I) = \frac{1}{\Gamma(\alpha)}\int_0^\infty \frac{dt}{t^{1+\alpha}}e^{-1/t}(1 - e^{-\alpha It}). \tag{23}$$

When α is small the median intensity, I_m, is also expected to be small (as it was for the log-normal distribution). The leading behavior for small α is

$$P_K(I) = (\alpha I)^\alpha, \tag{24}$$

giving $I_m = 2^{-1/\alpha}/\alpha$.

For a large scintillation index it is seen that the *K* distribution is also a very broad distribution and has a very long tail at high intensities.

III. NUMERICAL SIMULATIONS

Sound propagation in the shallow water Straits of Florida environment has been studied experimentally for many years.[20] Recently, numerical simulations in that environment have been performed with a high fidelity acoustic

model that includes internal wave fluctuations and bottom roughness, and good agreement with observed temporal coherence of broadband signals has been achieved.[22] In this paper, the same acoustic model and environmental model are used to study intensity fluctuations of continuous wave (cw) signals.

A. Environmental inputs

A two-layer environmental model is used, with a 200 m water layer overlying a semi-infinite sediment layer. The ocean sound speed is expressed as

$$c(z,r,t) = c_1(z) + c_2(z,r,t), \tag{25}$$

with (z,r) being two space coordinates and t being the time component, representing geophysical time. Here $c_1(z)$ is the range independent deterministic sound speed, and $c_2(z,r,t)$ is the random component due to the statistical nature of the small-scale oceanic variability. In this paper, only internal-wave induced temporal fluctuations are considered.

As is typical of most shallow water regions, there is a strong thermocline in the water of the Straits of Florida. Especially during the summer time, the thermocline layer stretches all the way from the surface to the bottom. The temperature, T, is assumed to decrease linearly throughout the whole water column, giving a characteristic downward refracting sound speed profile

$$c_1(z) = a_0 + a_1 T(z), \tag{26}$$

where $a_0 = 1450$ m/s and $a_1 = 4.0$ m/s °C. Based on the average of a number of sound speed profiles taken from various measurements,[20] a linear sound speed profile with sound speed 1545 m/s at the surface, 1490 m/s at the bottom of water layer, and a constant negative gradient of $dc_1/dz = -0.275\ \mathrm{s}^{-1}$ is used as the deterministic sound speed profile. The limiting grazing angle at the bottom is $\theta_1 = \cos^{-1}(1490/1545) = 15.3°$. From previous studies[21] the bottom is modeled as a range independent fluid layer with constant compressional sound speed of 1650 m/s, constant density of 1.5 g/cm^3, and constant compressional attenuation of 0.06 dB/km Hz. The sound speed gradient in the sediment is assumed zero, implying that the penetrating acoustic energy does not return to the water layer; instead, it is absorbed. The critical grazing angle at the bottom is $\theta_c = \cos^{-1}(1490/1650) = 25.4°$.

Volume attenuation in the water column is set to zero and the water density is set to a constant of 1.025 g/cm^3. Density fluctuations, which induce internal waves, are converted to sound speed fluctuations and are discussed later. In this two layer model, the deterministic water-sediment interface is assumed to be smooth and flat. A random component of bathymetric variation is simulated using a power-law spectrum and is superimposed on the deterministic boundary as has been described before.[28] An rms vertical displacement of 5 m and a horizontal correlation length 1000 m is used, so the rms slope is very small. The sea surface is modeled as a smooth and flat pressure release boundary.

Internal waves are known to exist in the ocean due to perturbations of the density stratification. In shallow water, density is controlled mainly by temperature, and the radian buoyancy frequency profile is determined by

$$N(z) = \sqrt{-g\alpha \cdot dT/dz}, \tag{27}$$

where g is the acceleration of gravity and α is the coefficient of thermal expansion, $\alpha = 10^{-4}(°\mathrm{C})^{-1}$. Since the sound speed is approximately a linear function of temperature, it follows from Eq. (27) that

$$N(z) = \sqrt{-\beta \cdot dc_1/dz}, \tag{28}$$

where $\beta = g\alpha/a_1 = 2.45 \times 10^{-4}\ \mathrm{s}^{-1}$. With the simplified model of sound speed introduced above for the Straits of Florida, the buoyancy frequency is constant and the corresponding period is 12.76 min. Thus, a consistent model of sound speed and internal waves has been achieved.

The goal here is to construct a realistic, stochastic, internal-wave field that induces small-scale sound speed inhomogeneities. Thus any possible long period deterministic solitary waves are disregarded, and the internal waves are described by a homogeneous and stationary spectrum that is similar to a Garret-Munk-type spectrum,[22] i.e., the vertical and horizontal scales of the internal waves are substantially different. If the internal wave fluctuations are horizontally isotropic, they may be modeled by a power-law spectrum in continuous wave number space according to

$$S(k_z,k) = (L_V L_H/2\pi)(1 + L_V^2 k_z^2 + L_H^2 k^2)^{-3/2}, \tag{29}$$

where k_z and k are vertical wave number and horizontal wave number, respectively, and L_V and L_H are the vertical and horizontal correlation length, respectively. The spectrum is normalized

$$\int_{-\infty}^{\infty}\int_{-\infty}^{\infty} S(k_z,k)\,dk_z\,dk = 1. \tag{30}$$

The dispersion relation of internal wave motion can be obtained as

$$\omega(k_z,k) = Nk/\sqrt{k_z^2 + k^2}. \tag{31}$$

Note that the periods of all internal-wave modes are greater than $N^{-1} = 12.76\ \mathrm{min}^{-1}$. The effect of the earth's rotation has been neglected in the above equations.

The fluctuating part of the sound speed is expressed as

$$c_2(z,r,t) = \xi(z)\mu(z,r,t), \tag{32}$$

where the function $\mu(z,r,t)$ is the random field with unit variance and $\xi(z)$ represents the fact that internal-wave sound-speed fluctuations can have a strength that is depth dependent. The random field $\mu(z,r,t)$ is efficiently obtained from the two-dimensional internal-wave spectrum by a two-dimensional Fourier transform

$$\mu(z,r,t) = \mathrm{Re}\sum_{k_z}\sum_{k} \hat{a}(k_z,k)e^{i[k_z z + kr - \omega(k_z,k)t]}, \tag{33}$$

where the Fourier coefficients $\hat{a}(k_z,k)$ have uniformly distributed random phases and Rayleigh distributed random amplitudes specified by the given power spectrum. This guar-

antees that $\mu(z,r,t)$ is a Gaussian random function having zero mean. The standard deviation $\xi(z)$ follows from $\xi(z) = \langle c_2^2(z,r,t)\rangle^{1/2}$ but generally a Wentzel-Kramer-Brillouin-Jeffreys approximation is used to determine it as a function of depth. In this paper, however, the buoyancy frequency is a depth independent constant. Together with the boundary conditions that internal waves vanish at both surface and bottom, the vertical mode functions of internal waves become pure sine functions. The vertical wave number k_z may be directly linked to the vertical mode number n according to $k_z = n\pi/H$, and the complex Fourier transform in k_z is replaced with a sine transform.

The above procedure is used to construct sound-speed profiles in the presence of internal waves. Using the values of the parameters $L_H = 5000$ m gives a realistic model of sound-speed fluctuations.[22] In order to generate totally independent internal wave fields, different realizations of $\hat{a}(k_z,k)$ are generated by a Monte Carlo procedure, this being equivalent to advancing t by large amounts. Note that the Monte Carlo procedure provides a good representation of the probability function of the fluctuations $\hat{a}(k_z,k)$; whether or not it provides a good sampling for the probability function of the intensity of the acoustic field is not apparent.

B. Sound transmission

With the described realistic environment, the UMPE numerical model[16] is used to simulate sound propagation in the Straits of Florida. A point source located at 170 m depth (30 m above the bottom) projects a single harmonic frequency of 500 Hz. In the absence of bathymetric variations, the water depth is $H = 200$ m. The acoustic field is displayed in Fig. 1 by computing the transmission loss in dB units, which is defined in the usual way as

$$TL(z,r) = -10\log_{10}|p(z,r)|^2, \tag{34}$$

where $p(z,r)$ is the sound pressure at the field point (z,r) relative to the value at reference range 1 m from the source. The gray scale is chosen such that black represents low transmission loss or high intensity, and white represents high transmission loss or low intensity. The displayed dynamic range is 100 dB. Water depth is shown as a solid black curve.

For comparison, the internal wave induced sound speed fluctuations and the bottom roughness are turned off in the numerical input described above. The sound propagation is then range independent. The acoustic field plot is shown in the upper panel of Fig. 1. It is seen that, although bottom penetration is quite noticeable, acoustic power is well contained in the water column. The confining ability of the sound channel (due to downward refraction and bottom reflection) is clear since the acoustic field is relatively strong in the bottom part of the water column and the general sound levels are reasonably high, even at receivers 100 km away from the source. It is easily understood that the high order modes penetrate into the bottom and are quickly attenuated, while attenuation of the low order modes is much weaker. This propagation pattern, however, is very different when range dependent sound speed fluctuations are introduced.

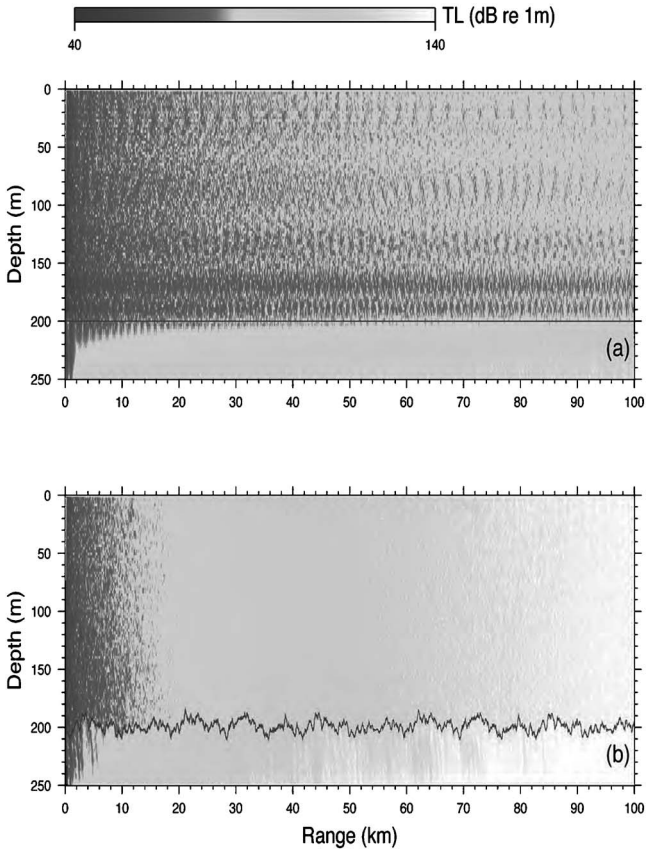

FIG. 1. Field plots of cw transmission loss. (a) No fluctuations, range independent; (b) with one realization of the internal wave field and bottom roughness.

In the lower panel of Fig. 1, both the internal wave induced sound-speed fluctuations and bottom roughness are included, with the parameters of internal wave fields and bottom roughness as specified in last subsection. The source signal strength and the numerical parameters of UMPE model are the same as used for the range independent case. There are two main differences between plot (a) and plot (b) in Fig. 1. First, the sound channel focusing ability has been destroyed, or at least diluted so that the acoustic wave field in plot (b) is not structured at all. This can be explained by multiple scattering due to sound-speed inhomogeneities introduced by either internal waves or bottom roughness, or both. Second, due to more acoustic energy penetrating the bottom, the acoustic wave field in (b) is much weaker, about 50 dB less at 100 km, compared to the range independent case in plot (a). Here the bottom interaction plays an important role in the damping of sound energy (mode stripping).

Multiple scattering from sound-speed inhomogeneities, in general, speeds up the mode stripping process by putting more energy into higher order modes, and therefore, indirectly attenuates the sound signal. One should note that either internal waves or a rough bottom may independently influence sound propagation as discussed. A physical picture of this process is as follows. Small grazing angle rays are preferentially scattered to steeper grazing angles by the environmental fluctuations, until the critical grazing angle is exceeded, whereupon the steep rays penetrate the bottom and are absorbed.[29] This creates a cascade of energy flowing

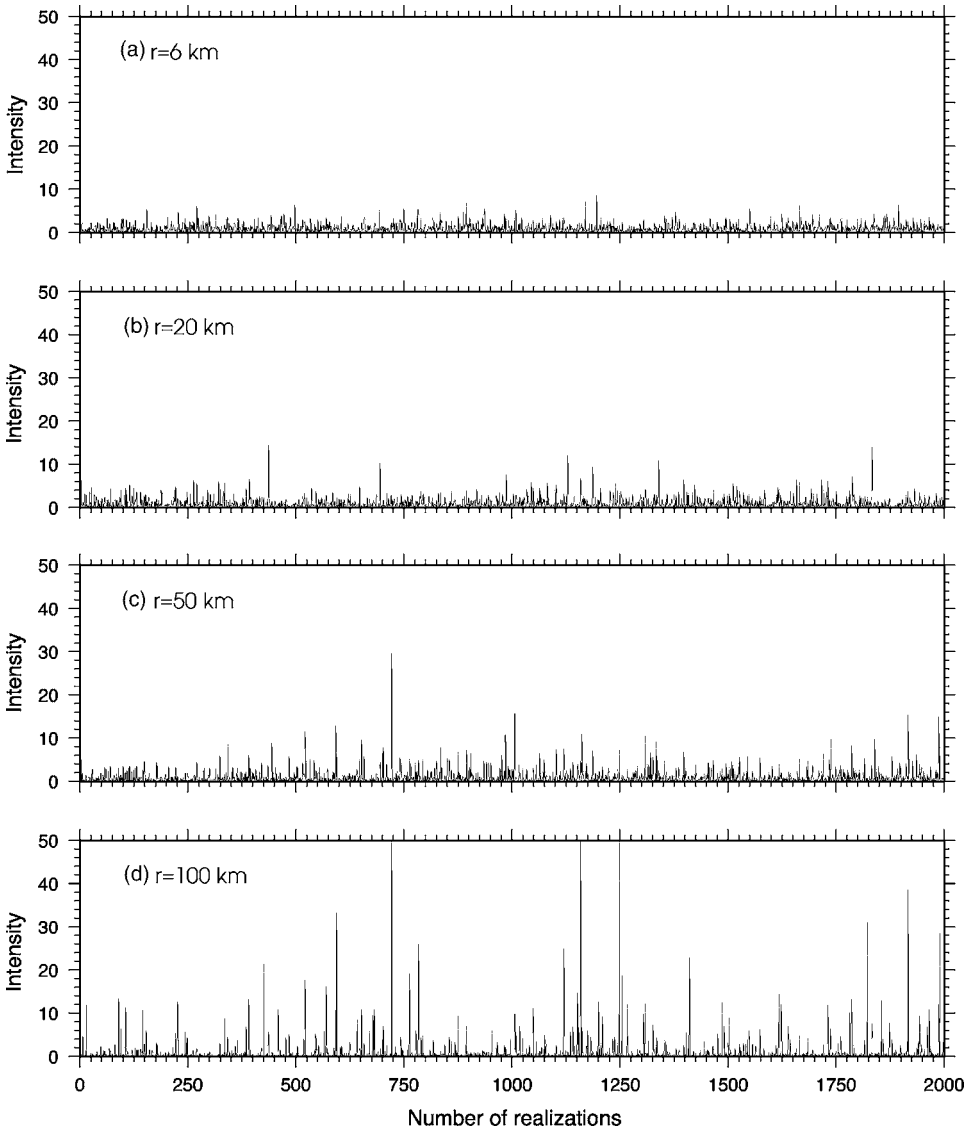

FIG. 2. Time series of normalized intensity fluctuations at four ranges. The realizations of the environmental fluctuations are independent.

from smaller to larger grazing angles where dissipation occurs due to bottom penetration. In acoustic normal mode space, the cascade of energy is from lower modes to higher modes where dissipation occurs due to mode stripping. This process is analogous to the Kolmogorov cascade of energy from larger eddies to smaller eddies where dissipation occurs due to viscosity that is familiar from turbulence theory. This process also explains why thermodynamic equilibrium statistics, i.e., the Rayleigh distribution, are not applicable to propagation in real oceanic waveguides.

The details of the scattered acoustic wave fields greatly depend on the randomly generated internal wave field and bottom roughness. One phenomenon that is not clearly apparent in Fig. 1(b) is that the sound energy may occasionally be focused at some small areas forming randomly distributed "hot spots" on the weak background wave field. This is what is referred to as large acoustic scintillations. To study this effect, 2000 single frequency PE simulations are made, each using a different randomly generated internal wave field, corresponding to sampling the fluctuating ocean at a large geophysical time interval so that each realization of the internal wave field is independent. The receivers are fixed at the source depth (30 m above the bottom), and at four different horizontal ranges: 6, 20, 50, and 100 km. The normalized sound intensities (mean intensity is unity) of 2000 realizations are plotted in Fig. 2 in the form of an undersampled time series. It is clear that, from plot (a) to plot (d) in Fig. 2, the acoustic intensity scintillations increase with the propagation range and none of them shows any regularity. At the longer ranges, the appearance of hot spots is intermittent and unpredictable. This is called acoustic intermittency. Since the environmental fluctuations are not intermittent (they follow from a Gaussian probability distribution function and thus there no spikes or hot spots in the sound speed profile) this intermittency is due to propagation effects in this environment. The growth rate of the scintillation can be estimated by calculating a higher moment, the scintillation index, which is discussed in the next section.

IV. STATISTICAL ANALYSIS

As with many other problems of wave propagation in random media, the description of an acoustic wave propagating through an inhomogeneous sound-speed field, e.g., due

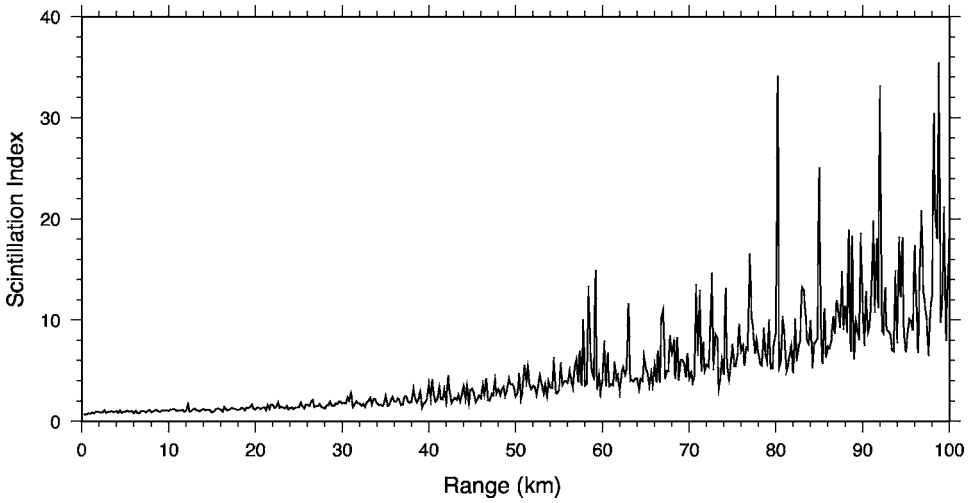

FIG. 3. Scintillation index as a function of range for 5000 realizations.

to internal waves, must depend on a statistical method rather than a deterministic one. The scintillation index and the intensity distribution are two important statistical measures. The numerical simulations are discussed based on these two key concepts.

The intensity at a field point (z,r) for the jth realization is denoted by I_j. The mean over N realizations is calculated as the sample average

$$\bar{I}_N = \frac{1}{N}\sum_{j=1}^{N} I_j. \tag{35}$$

Then each I_j is divided by $\bar{I}_N$, which makes the new sample average exactly equal to unity. The scintillation index is then calculated as

$$SI_N = \frac{I}{N}\sum_{j=1}^{N}\left(\frac{I_j}{\bar{I}_N} - 1\right)^2. \tag{36}$$

In principle, Eqs. (35) and (36) could be computed together in a single do loop. Numerically, this generally leads to severe cancellation errors and so a two-pass summation algorithm is used; Eq. (35) is first calculated and the result is used in Eq. (36).

A. Scintillation index

The acoustic data used in this calculation are obtained from the aforementioned repeated numerical sound transmissions where each transmission uses an independent simulation of the random internal wave field and bottom roughness. The total number of realizations is extended to 5000 to help with sampling the intensity distribution. Figure 3 shows the scintillation index at a receiver that is displaced horizontally from the source location to a range of 100 km.

The scintillation index increases with propagation range and is significantly greater than unity at ranges beyond about 10 km, in accordance with the prediction.[15] In an inhomogeneous shallow water environment, saturation is reached quickly at ranges as short as 5 km, due to multipath interference effects.[9] As shown in Fig. 1, the difference of transmission loss between the range independent propagation, plot (a), and range dependent propagation, plot (b), becomes significant at ranges around 5 km, and keeps growing afterward. At about this range, the scintillation index begins to deviate from the expected saturation value of unity. Figure 2 is another indication of such a phenomenon. At a range of 6 km, the normalized intensities fluctuate as expected at saturation. At longer ranges, the sound intensity scintillations increase dramatically, reaching values larger than 50 times the average intensity.

There are two necessary conditions for the scintillation index to be greater than unity: first, the average sound intensity should be low; and second, the sound intensity should fluctuate. Large values of the scintillation index are a consequence of sound intensity fluctuations on a low background intensity (the average intensity), similar to the way a remote star scintillates in the evening's dark sky. In the ocean acoustics case, these two conditions are met by the multiple scattering by internal waves and boundary roughness, and the frequent bottom interactions and penetrations. Although large scintillations are rare events, they are readily detectable when they do occur.

Figures 2 and 3 illustrate a serious difficulty in using Monte Carlo simulations when looking at higher order moments of the acoustic intensity. The probability function describing the environmental fluctuations is Gaussian and can be well simulated by the Monte Carlo procedure (whether done uniformly over an interval by some more refined technique). If the intensity followed a Rayleigh distribution then events with intensities much larger than the mean are extremely rare, implying that the contribution to the scintillation index (or any other moment of the intensity) of high intensity events is negligible, and therefore the part of the intensity distribution containing these "outliers" does not have to be well sampled. However, the probability function describing the acoustic intensity is not *a priori* determined; it is not clear which sound-speed fluctuations (i.e., which part of the Monte Carlo distribution describing the sound-speed fluctuations) would lead to intermittent, large intensities. Reiterating, Monte Carlo sampling is over the distribution describing the sound-speed fluctuations, not over the distribution describing the resulting acoustic intensity; how the two distributions are linked is not well determined at present. The stochastic trajectories of the intensities responsible for these

intermittent events are not determined by the probability distribution for the intensity even if it was known (this is known as "large deviation" theory in the stochastics literature[18]); however, these high intensity events provide the major contribution to the scintillation index when it is large compared to unity. The effect of this inadequate sampling can be seen in the scintillation plot shown in Fig. 3: as the range increases, the scintillation index (which is an averaged, statistical quantity) becomes highly variable, indicating that even 5000 realizations are not large enough to sample the important portion of the intensity distribution. The consequence of under sampling the intensity distribution is to underestimate *SI*; thus the actual values of *SI* at long ranges are even larger than indicated in Fig. 3. This issue is revisited later, after simulation results for the intensity distribution are presented.

As shown in Ref. 15, there exists a mismatch between the mode-coupling terms, which redistribute the modal energies, and the mode stripping, resulting in an irreversible loss of energy. As a result, the expected Rayleigh distribution can no longer describe the long-range wave propagation behavior in inhomogeneous waveguides having lossy boundaries. It is seen that the abnormal large scintillation index beyond about 5 km shown in Fig. 3 is associated with the fact that extremely small and random wave fields are not Rayleigh distributed. Other statistical distributions must be introduced in order to describe this supersaturation effect.

At this stage, it is not possible to calculate a critical propagation range for such a supersaturation effect to appear. It depends on the source signal strength, the sound channel, and many parameters of the random media. It is found that the growth rate of the scintillation index is more sensitive to the strength of the internal wave fluctuations than to the details of the internal wave structure. One more interesting question is whether the growth of the scintillation index ceases beyond some range. This possibility is tested by either increasing the propagation range (to 1000 km) or increasing the intensity of internal wave induced sound speed fluctuations to 15 m/s rms. No significant indication of a slowing down of the growth of the scintillation index has been seen. In both cases the transmission losses are as large as 300 dB *re* 1 m. This confirms the effect of exponentially increasing scintillation index predicted by Creamer, who also showed that this effect was universal in shallow-water environments. The universality of the probability distribution function is an open question.

B. Probability distributions

The evaluation of either the log-normal distribution or the *K* distribution defined in Sec. II requires that the parameters ν and α be estimated. For the *K* distribution, Eq. (20) can be used to relate α and the estimated scintillation index, SI_N. For the log-normal the simplest method is to insert the value of SI_N obtained from Eq. (36) into Eq. (13) to obtain the estimate

$$\nu_N = \ln(SI_N + 1). \tag{37}$$

If the intensity distribution is log normal, then $\nu_N \to \nu$ as $N \to \infty$. The convergence is quite slow when ν is large. Inadequate sampling of the high intensity tails leads to an underestimate of SI_N and therefore of ν_N. A better way to estimate ν_N is to use Eq. (11) in the form

$$\nu_N = -\frac{2}{N}\sum_{j=1}^{N} \ln I_j \tag{38}$$

or to estimate ν directly from its definition in Eq. (10)

$$\nu_N = \frac{1}{N}\sum_{j=1}^{N} (\ln I_j - \langle \ln I \rangle)^2, \tag{39}$$

where Eq. (38) is used to estimate $\langle \ln I \rangle = -\nu_N/2$. These two formulas are found to yield more accurate and stable estimates of the parameter ν than Eq. (37). The best estimate of ν is obtained by fitting the cumulative probability functions as explained in the next subsection.

Both the *K* distribution, Eq. (18), and the log-normal distribution, Eq. (9), have larger probabilities at the high intensity end as compared to the Rayleigh distribution. Additionally, the shape of these distributions varies with the propagation range, instead of being a fixed curve. In order to visualize the difference of the high intensity tails between these two distributions, the distributions are displayed on logarithm scales as shown in the left column of Fig. 4. Receiver ranges at 6, 20, 50, and 100 km are used. On this logarithmic plot, the Rayleigh distribution is the straight line independent of range, and the other distributions are curves that depend on range. For the *K* distributions, the parameter α is estimated from Eq. (20), while for the log-normal distributions, the parameter ν is estimated according to Eq. (39) above. The thick jagged curves are the probability distributions of the simulated data obtained by counting the "events," and producing histogram plots with bin size ΔI chosen so that each bin has enough events in it to be statistically meaningful (error in each bin is square root of the number of events in each bin). The number of events *N* is equal to the total number of acoustic realizations at one designated receiver range. In order to increase *N*, it is assumed that sound intensities in a small interval around the designated range have the same probability distribution. This procedure gives enough data points to calculate statistics without carrying out a huge number of PE realizations. For example, in the bottom panel of Fig. 4, the total PE realization number is 5000, and data at five ranges around 100 km (the maximum distance is 200 m) are used, so the total number is $N = 25{,}000$.

These probability distribution plots indicate that sound intensity fluctuations of the simulated data are close to a Rayleigh distribution at short ranges, $R = 6$ km for example, and change to a another distribution at longer ranges. At the shorter ranges, the *K* distribution might be an acceptable candidate, but inadequate at the longer ranges. This distribution adequately provides for the high-intensity tails but is completely wrong at small and moderate intensities. At long ranges, the log normal provides a good account of the intensity distribution. The switch over from Rayleigh to log-normal behavior is smooth and gradual, particularly at the low intensity end where the Rayleigh and log-normal distributions are nearly indistinguishable. The plots in Fig. 4 illus-

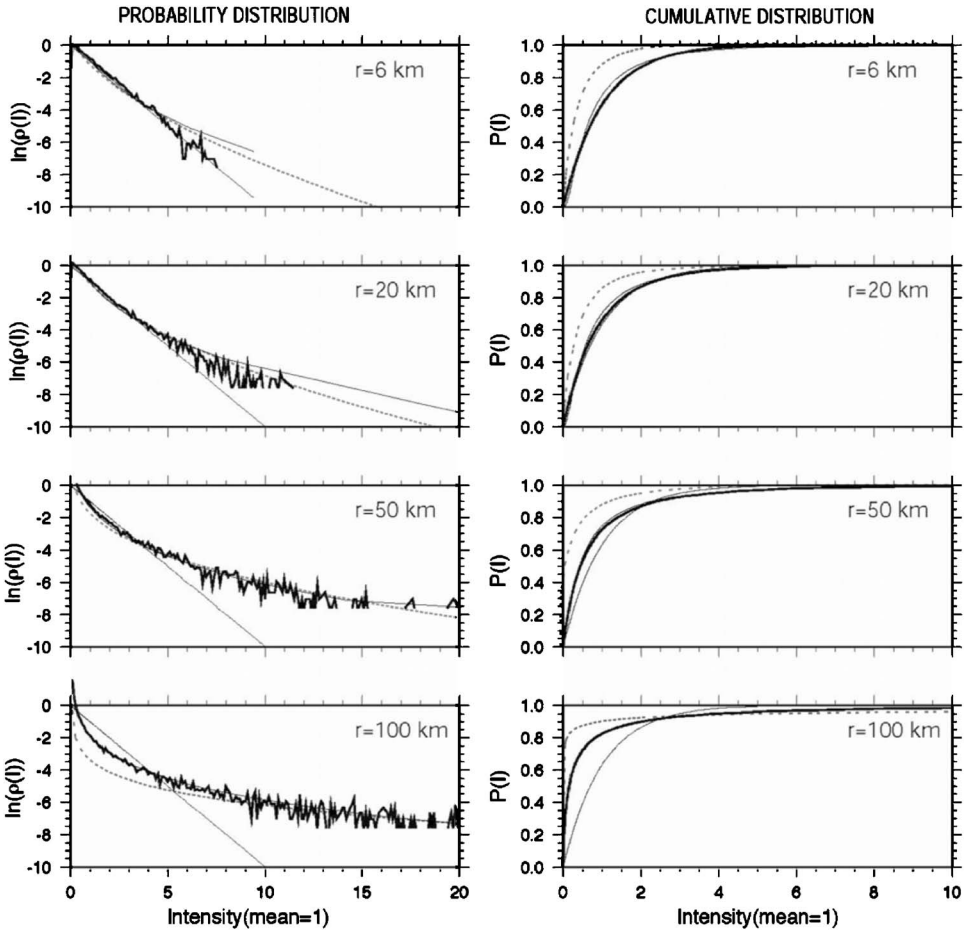

FIG. 4. Probability density functions (left) and cumulative probability distributions (right) for normalized sound intensities at four ranges. The simulated data are the thick curves; the Rayleigh distributions (range independent) and the log-normal distributions (range dependent) are the thin lines, while the K distributions are the dotted lines. The clipping in the simulated data is due to the finite number of digits retained in the data files for the intensity.

trate the sampling (of the intensity distribution) problem that was discussed earlier. It is seen that, while the probability of high intensity events is low (e.g., $\approx 10^{-3}$ for $I=20$ at the 100 km range), a quantity such as $I^2\rho(I)$ is much larger (near unity). From Fig. 4, it can be inferred that this quantity is roughly flat, or even slightly increasing, over the intensity range from 5 to 20. This incomplete sampling is the cause of the extreme variability in the scintillation index seen in Fig. 3 at the longer ranges.

The above comparison is not conclusive because an arbitrary bin size ΔI is used to make the histograms of the simulated data. A better statistic for this purpose is the cumulative probability distribution, which is computed for the simulated data according to the methods recommended in *Numerical Recipes*.[30] The cumulative distributions at four different ranges are plotted in the right column of Fig. 4 corresponding to their probability distributions in the left column. The solid thin curves that change with range are for log-normal distributions while the dotted thin curve is for the K distribution. The thin curves that do not change with range are for Rayleigh distributions and the thick curves are for the simulated data set. Once again, the comparisons of these cumulative distribution functions show that sound intensity fluctuations tend toward the log-normal distribution at long ranges while they are Rayleigh distributed at short ranges. The K distribution is completely inadequate at all ranges. At ranges greater than about 50 km it appears that the best fit is to a log-normal distribution. At 100 km, as shown in the bottom right corner of Fig. 4, the cumulative probability distribution is almost exactly a log-normal distribution, and it differs significantly from the Rayleigh distribution. In the following subsection, the parameter ν for the log-normal distribution is obtained by fitting the distribution functions instead of estimating ν from a moment calculation, which should provide a better description of the simulated data.

C. Fitted log-normal probability distribution

In general, there are two quantitative methods, the Kolmogorov-Smirnov test and the chi-square test, to examine the differences between two statistical distributions.[30] Since the mean intensity is normalized to unity at each range, the Rayleigh distribution contains no parameters and the log-normal distribution contains one parameter, ν. The goodness of fit for the log-normal distribution depends on the accuracy of the estimate of the parameter ν.

Suppose $G(I)$ is the cumulative distribution function of the simulated data. It is assumed that $G(I)$ can be represented by $P_L(I,\bar{\nu})$, a log-normal distribution with an estimated value of the parameter ν. The estimated parameter $\bar{\nu}$ is obtained by fitting $P_L(I,\bar{\nu})$ to $G(I)$. It is called the fitted log-normal distribution. The fitting process is done by minimizing the chi-square function

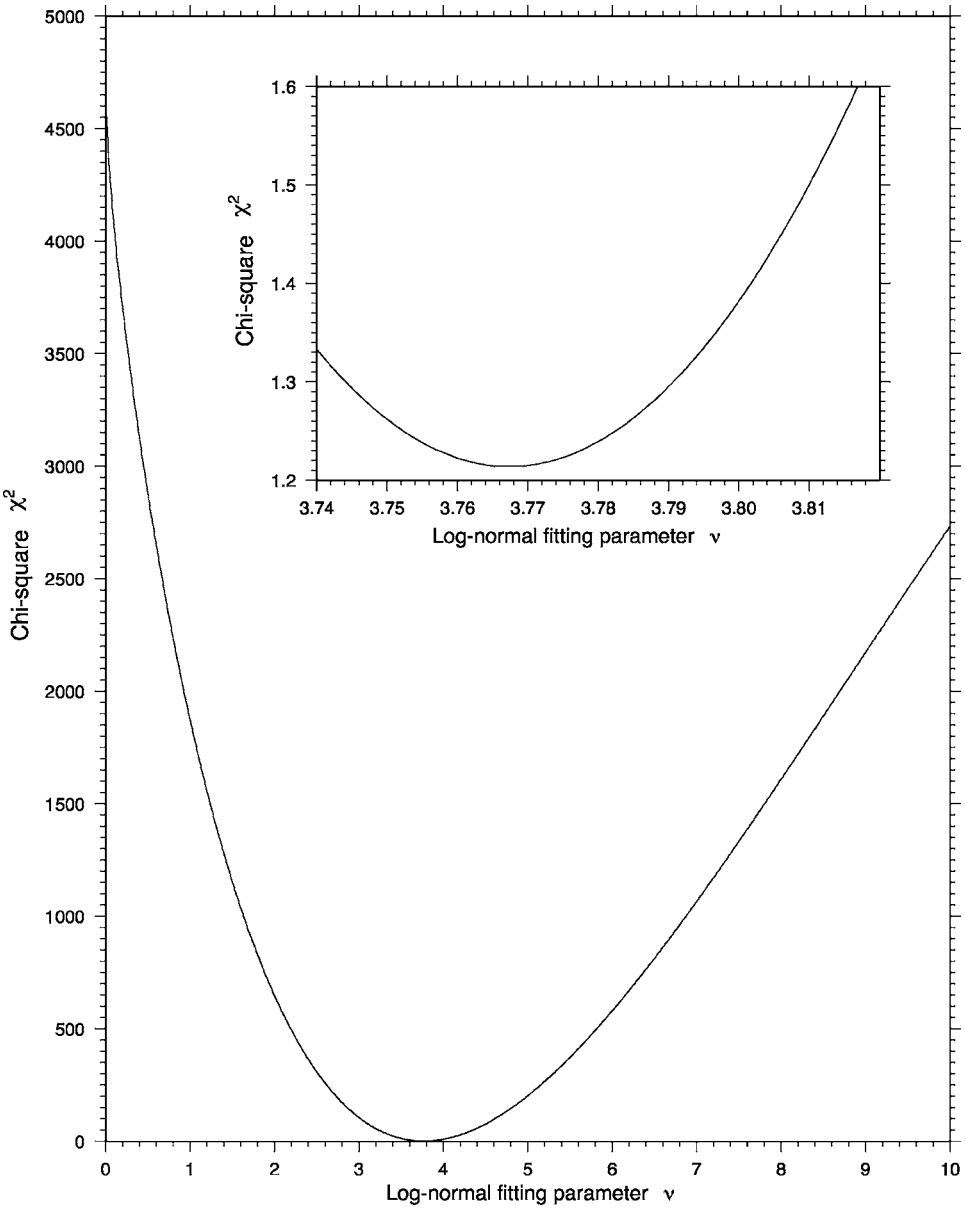

FIG. 5. Chi-squared, χ^2, of the fit [from Eq. (32)] vs the fitting parameter ν, at a range of 95 km. The upper-right corner is the magnified area around the minimum chi-squared value.

$$\chi^2(\bar{\nu}) = \sum_j [P_L(I_j, \bar{\nu}) - G(I_j)]^2, \tag{40}$$

$$D = \max_{0<I<\infty} |P(I) - G(I)|. \tag{41}$$

where the sum is carried over the normalized intensities I_j until χ^2 converges. Algorithms from *Numerical Recipes*[5] are employed. Figure 5 shows the $\chi^2(\bar{\nu})$ curve calculated at a range of 95 km. Also plotted is the magnified area around the minimum of χ^2. The fact that the $\chi^2(\bar{\nu})$ curve is smooth and has a single minimum enables a quick determination of $\bar{\nu}$. It is found that $\chi^2(\bar{\nu})$ decreases with range, and thus the intensity distribution of the simulated data set $G(I)$ approaches a log-normal distribution as the propagation range increases.

The Kolmogorov-Smirnov test calculates the maximum of the absolute difference, called the Kolmogorov-Smirnov D, between two cumulative distribution functions. Comparing to the given cumulative distribution function $P(I)$ the K-S statistic is

Shown in Fig. 6, curves (a) and (b) are the results obtained by applying this equation to Rayleigh distribution $P_R(I)$ and the fitted log-normal distribution $P_L(I)$, respectively. It is clear that the fit to the Rayleigh distribution is best around $R=5$ km and worsens beyond this range. Thus, full saturation occurs at about 5 km. The log-normal distributions provide much better fits at ranges greater than about 50 km, which is the supersaturation regime.

The results of fitting the log-normal parameter ν at 500 ranges with equal intervals (200 m) from 0 to 100 km are displayed in Fig. 7. Since the χ^2 test shows that the intensity distribution is reasonably close to the log-normal distribution only if the ranges are greater than about 50 km, the results shown in Fig. 7 for smaller ranges are not meaningful. Figure 7 indicates that the estimated ν may be approaching a linear relation with range, $\nu \sim \lambda r$ for r greater than about

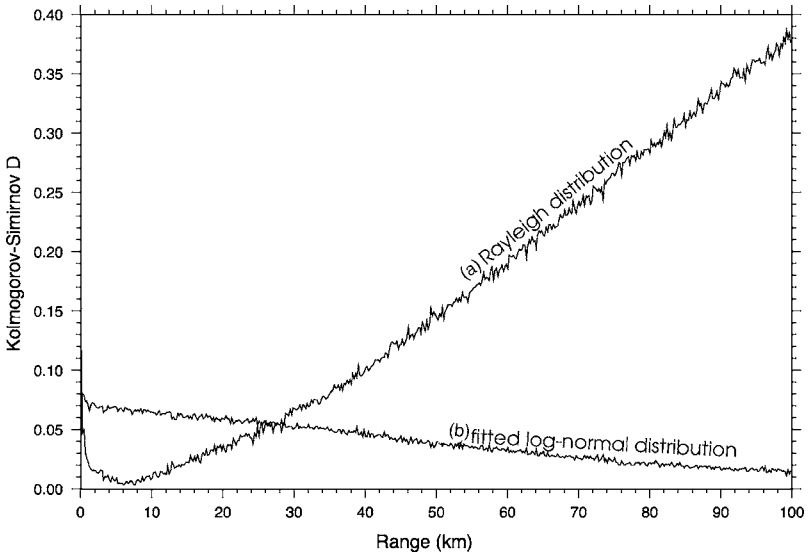

FIG. 6. Results of the Kolmogorov-Smirnov test as a function of range for (a) Rayleigh distribution and (b) fitted log-normal distribution.

80 km. Here the parameter λ is the "generalized Lyapunov exponent." It is difficult to estimate this exponent, because the estimated values of ν are increasingly uncertain as r increases, in accordance with the sampling difficulty discussed above.

Using the data shown in Fig. 7, a linear regression fit to $\nu = a + br$ is performed from range R to 100 km for various values of R, in an attempt to estimate coefficient $\lambda = b$ from the simulated data set. The resulting estimates of a and b, as well as their standard deviations, varied considerably and inconsistently depending on R. Spurning statistical techniques, which seem to be unreliable for this difficult estimation problem, a graphical technique is used to obtain the result $\lambda = (0.04 \pm 0.01)\text{km}^{-1}$. The best estimate of the e-folding distance for the growth of the scintillation index in the Straits of Florida at 500 Hz is about $\lambda^{-1} = (25 \pm 10)\text{km}^{-1}$.

To improve this estimate, the numerical simulations are extended to range 200 km with $N = 5000$ realizations. Values of SI are many hundred, the fit to a log-normal intensity distribution is better, but the estimated values of ν are not convincingly linear in range. The asymptotic regime predicted by Creamer[15] where a single eigenvalue of the mode coupling matrices dominates the decay of the mean and mean-square intensity, appears to be at ranges greater than about 200 km. A more reliable prediction is the supersaturation effect: the scintillation index increases monotonically with range to extremely large values and the intensity distribution function approaches a log-normal distribution.

The above relatively crude estimate of the e-folding distance shows that it nevertheless might be possible with good experimental techniques to observe large acoustic scintillations in the Straits of Florida, or in comparable shallow water environments such as the Yellow Sea.

V. DISCUSSION

In this paper the statistical properties of the acoustic intensity have been investigated by means of Monte Carlo simulation in a well-studied environment, the Straits of Florida. A conclusion based on this study is that the probability distribution function (pdf) of the intensity closely approximates that of a log-normal distribution at long ranges; it certainly does not follow a Rayleigh distribution. Additional comparison was made to the K distribution and as a candidate distribution was ruled out. By normalizing the distribution function to have unit mean intensity, the log-normal distribution then involves a single parameter, ν, which is the variance of log intensity. It is found that this variance, at large distances, increases approximately linearly with range.

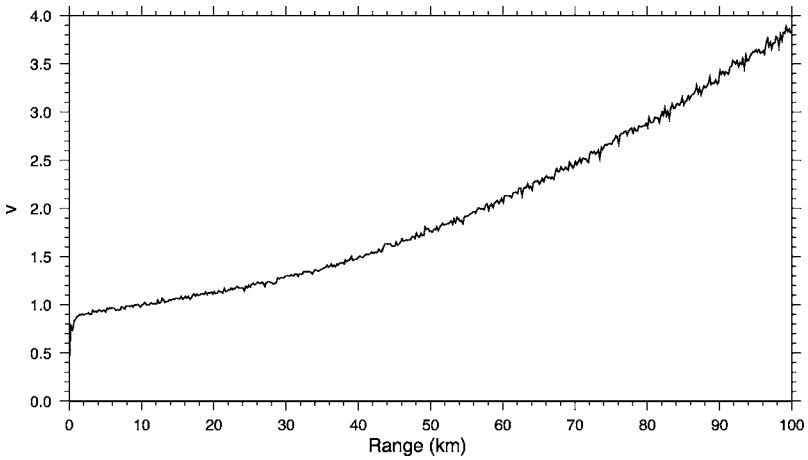

FIG. 7. Fitted values of the log-normal parameter ν as a function of range. At long ranges it is found that $\nu = \lambda r$, where λ is the generalized Lyapunov exponent.

This explains the surprising result[2] that the scintillation index increases exponentially in range for lossy waveguides.

The specific simulation environment chosen in this paper corresponds to underwater acoustic propagation in the Straits of Florida. The exponential increase in the scintillation index as shown to be universal[15] in lossy waveguides. Parameter variation in the present acoustic environment indicates that the PDF of intensity being log-normal persists with an attendant change in log-intensity variance. A theoretical modal analysis of the intensity moments[31] shows that the PDF is not log normal when only a small number of modes propagates; the variance of log intensity still increases linearly with range, but higher order moments do not increase as quickly as a log-normal distribution would indicate. However, with a large number of propagating modes, the pdf approximates a log-normal distribution. The situation is reminiscent of that for the derivation of a Rayleigh distribution—a large number of contributions leads to a universal behavior independent of the number of contributors.

These considerations lead to a possible physical model, which is adapted from the discussion in Ref. 25, pp. 219–220. Suppose that the acoustic intensity satisfies

$$dI/dr = -\alpha(r)I, \tag{42}$$

where the attenuation $\alpha(r)$ is a random function of range r. The solution is

$$\ln I(r) = \text{const} - \int_0^r \alpha(r')dr'. \tag{43}$$

In the above reference, it is shown that the central limit theorem implies that the random function defined by the integral in the above equation becomes normally distributed as $r \to \infty$ if the correlation distance of $\alpha(r)$ is small. It follows that $\ln I(r)$ is normally distributed for large r, and hence $I(r)$ approaches a log-normal distribution. This model is further extended by assuming that $\alpha(r) = \langle\alpha\rangle + \delta\alpha(r)$, where $\langle\alpha\rangle$ is a constant and $\delta\alpha(r)$ is a zero-mean stationary random function of r. Based on Eq. (43), an elementary statistical calculation yields the variance

$$\nu = \langle(\ln I - \langle\ln I\rangle)^2\rangle \to \lambda r, \tag{44}$$

where

$$\lambda = \int_{-\infty}^{\infty} \langle \delta\alpha(r)\delta\alpha(r+r')\rangle dr'. \tag{45}$$

This is an explicit formula for the generalized Lyapunov exponent in terms of the integral correlation length of the fluctuating part of the attenuation.

The above physical model begs the question why the intensity should satisfy an equation of the type Eq. (42). A physically intuitive picture is that the environmental fluctuations rapidly transfer acoustic intensity back and forth between a large number of ray paths or normal modes that have very different attenuation coefficients α. Thus the acoustic intensity in an "average" ray path or normal mode suffers an attenuation that may be described as a random function of the attenuations in different ray paths or modes. This picture leads directly to Eq. (42), which in turn implies log-normal statistics. Recall that the attenuation α is, in general, the sum of the absorption and scattering losses. Thus there exists the possibility that large acoustic scintillations may be observed even when there is negligible absorption. This might occur, for example, deep in the "shadow zones" where scattering is the sole cause of intensity fluctuations. Quantitative predictions of the exponent λ according to Eq. (45) are beyond the scope of this paper.

The main implication for experiments on propagation in lossy waveguides centers on the earlier discussion of sampling the outliers in the intensity distribution. In WPRM experiments, different realizations are achieved by invoking the ergodic hypothesis—time averages are equal to ensemble averages. Because of the outliers on the high intensity tail of the distribution that cause acoustic intermittency, it is difficult experimentally to take enough independent samples (in the ergodic sense) to fully characterize such infrequent but not rare events.

[1] P. G. Bergman, Editor of Part I, Chapter 7, "Intensity Fluctuations," in *Physics of Sound in the Sea*, reprinted by Naval Material Command, Washington D.C. (1969), originally (1946).
[2] R. L. Fante, "Electromagnetic beam propagation in turbulent media," Proc. IEEE **68**, 1424 (1975).
[3] S. M. Flatté, editor, *Sound Transmission Through a Fluctuating Ocean* (Cambridge University Press, Cambridge, England, 1979).
[4] B. J. Rickett, "Interstellar scattering and scintillation of radio waves," Annu. Rev. Astron. Astrophys. **15**, 2479–504 (1977).
[5] I. Dyer, "Statistics of sound propagation in the ocean," J. Acoust. Soc. Am. **48**, 337–345 (1970).
[6] V. I. Shishov, "Strong fluctuations of the intensity of a plane wave propagating in a random refractive medium," Sov. Phys. JETP **34**, 744–748 (1972).
[7] V. I. Tatarskii, A. Ishimaru, and V. U. Zavorotny, *Wave Propagation in Random Media (Scintillation)* (SPIE, Washington and IOP, Bristol, 1993).
[8] R. Dashen, "Path integrals for waves in random media," J. Math. Phys. **20**, 894–920 (1979).
[9] J. L. Codona, D. B. Creamer, S. M. Flatté, R. G. Frehlich, and F. S. Henyey, "Solution for the fourth moment of waves propagating in random media," Radio Sci. **21**, 929–948 (1986).
[10] L. B. Dozier and F. D. Tappert, "Statistics of normal mode amplitudes in a random ocean. I. Theory," J. Acoust. Soc. Am. **63**, 353–365 (1978).
[11] L. B. Dozier and F. D. Tappert, "Statistics of normal mode amplitudes in a random ocean. II. Computations," J. Acoust. Soc. Am. **64**, 533–547 (1978).
[12] L. B. Dozier, "A Coupled-Mode Model for Spatial Coherence of Bottom-Refracting Energy," in *Proceedings of Stochastic Modeling Workshop*, October 26–28, 1982, C. W. Spofford and J. M. Haynes, editors (Applied Research Laboratories, University of Texas at Austin, 1983).
[13] N. S. Gorskaya and M. A. Raevskii, "Influence of a random internal-wave field on sound propagation in the ocean," Sov. Phys. Acoust. **30**, 108–113 (1984).
[14] A. G. Sazontov and V. A. Farfel, "Calculation of low-frequency sound attenuation in the ocean in connection with scattering by internal waves," Sov. Phys. Acoust. **32**, 307–310 (1987).
[15] D. B. Creamer, "Scintillating shallow-water waveguides," J. Acoust. Soc. Am. **99**, 2825 (1996).
[16] D. Tielburger, S. Finette, and S. Wolf, "Acoustic propagation through an internal wave field in a shallow water waveguide," J. Acoust. Soc. Am. **101**, 789–808 (1997).
[17] K. B. Smith, M. G. Brown, and F. D. Tappert, "Ray chaos in underwater acoustics," J. Acoust. Soc. Am. **91**, 1939–1949 (1992).
[18] A. Crisanti, G. Paladin, and A. Vulpiani, *Products of Random Matrices in Statistical Physics* (Springer, New York, 1993).
[19] E. Jakeman and R. J. A. Tough, "Non-Gaussian models for the statistics of scattered waves," Adv. Phys. **37**, 471 (1988).
[20] H. A. DeFerrari and H. B. Nguyen, "Acoustic reciprocal transmission experiments, Florida Straits," J. Acoust. Soc. Am. **79**, 299–315 (1986).
[21] C. A. Monjo and H. A. DeFerrari, "Analysis of pulse propagation in the

bottom-limited sound channel with a surface duct," J. Acoust. Soc. Am. **95**, 3129–3148 (1994).
[22]X. Tang and F. D. Tappert, "Effects of internal waves on sound pulse propagation in the Straits of Florida," IEEE J. Ocean. Eng. **22**, 245 (1997).
[23]F. D. Tappert, "The parabolic approximation method," in *Wave Propagation and Underwater Acoustics*, Lecture Notes in Physics, Vol. **70**, edited by J. B. Keller and J. S. Papadakis (Springer-Verlag, New York, 1977), Chap. V, pp. 224–287.
[24]K. B. Smith and F. D. Tappert, *UMPE: The University of Miami Parabolic Equation Model*, Version 1.3, MPL Technical Memorandum 432, May 1993.
[25]H. Cramér, *Mathematical Methods of Statistics* (Princeton Univ. Press, Princeton, NJ., 1946).
[26]E. Jakeman, "On the statistics of *K*-distributed noise," J. Phys. A **13**, 31–48 (1980).
[27]I. S. Gradshteyn and I. M. Ryzhik, *Table of Integrals, Series, and Products* (Academic, New York, 1980).
[28]F. D. Tappert and L. Nghiem-Phu, "Modeling of pulse response function of bottom interacting sound using the parabolic equation method," in *Ocean Seismo-Acoustics*, edited by T. Akal and J. M. Berkson (Plenum, New York, 1986), pp. 129–137.
[29]H. L. Wilson and F. D. Tappert, "Acoustic propagation in random oceans using the radiation transport equation," J. Acoust. Soc. Am. **66**, 256–274 (1979).
[30]W. H. Press, S. A. Teukolsky, W. T. Vetterling, and B. P. Flannery, *Numerical Recipes in FORTRAN*, 2nd ed. (Cambridge University Press, Cambridge, England, 1992), Chap. 14.
[31]D. B. Creamer, "Theoretical analysis of scintillating lossy waveguides," in *Proceedings of the International Conference on Shallow-Water Acoustics*, April 2–25, 1997, edited by R. Zhang and J. Zhou (China Ocean Press, Beijing, 1997).

Acoustic scattering from mud volcanoes and carbonate mounds

Charles W. Holland[a)]
The Pennsylvania State University, Applied Research Laboratory, State College, Pennsylvania 16804-0030

Thomas C. Weber
University of New Hampshire, Center for Coastal and Ocean Mapping, Durham, New Hampshire 03824

Giuseppe Etiope
Istituto Nazionale di Geofisica e Vulcanologia, Rome, Italy 00143

(Received 5 April 2006; revised 8 August 2006; accepted 31 August 2006)

Submarine mud volcanoes occur in many parts of the world's oceans and form an aperture for gas and fluidized mud emission from within the earth's crust. Their characteristics are of considerable interest to the geology, geophysics, geochemistry, and underwater acoustics communities. For the latter, mud volcanoes are of interest in part because they pose a potential source of clutter for active sonar. Close-range (single-interaction) scattering measurements from a mud volcano in the Straits of Sicily show scattering 10–15 dB above the background. Three hypotheses were examined concerning the scattering mechanism: (1) gas entrained in sediment at/near mud volcano, (2) gas bubbles and/or particulates (emitted) in the water column, (3) the carbonate bio-construction covering the mud volcano edifice. The experimental evidence, including visual, acoustic, and nonacoustic sensors, rules out the second hypothesis (at least during the observation time) and suggests that, for this particular mud volcano the dominant mechanism is associated with carbonate chimneys on the mud volcano. In terms of scattering levels, target strengths of 4–14 dB were observed from 800 to 3600 Hz for a monostatic geometry with grazing angles of 3–5°. Similar target strengths were measured for vertically bistatic paths with incident and scattered grazing angles of 3–5° and 33–50°, respectively. © *2006 Acoustical Society of America.*
[DOI: 10.1121/1.2357707]

PACS number(s): 43.30.Gv, 43.30.Ma, 43.30.Vh [RAS] Pages: 3553–3565

I. INTRODUCTION

One of the important problems limiting active sonar performance in shallow water is the large number of false targets. Scattering that produces "target-like" echoes is defined here as clutter. Sonar clutter can arise from a variety of ocean features. High scattering has been observed from biologics (e.g., Ref. 1) and anthropogenic features such as wellheads and wrecks (e.g., Refs. 2 and 3). In shallow water, much of the observed clutter is believed to arise from features on and under the seabed. Seabed features (and the associated scattering mechanisms) that lead to clutter have not been well studied in the past; in particular the characteristic scattering and its dependencies upon incident and scattered vertical angle, azimuth and frequency are poorly understood.

One potential source of clutter from the seabed is mud volcanoes and carbonate mounds. Mud volcanoes form due to the rise of fluidized sediments and/or gas along a fault or on top of a seafloor-piercing shale diapir. They may occur in sedimentary areas with hydrocarbon generation at depth, originate from thick clay beds, usually erupt along fault lines, and often bubble gas (mostly methane), and sometimes oil. At least 300 mud volcanoes are known to exist on the ocean shelves,[4] mainly within the petroliferous basins. They are known to occur in a variety of geologic settings, including the abyssal parts of inland seas, active margins, continental slopes of passive margins, and continental shelves. A recent review article estimates the number of deep-water submarine mud volcanoes at 10^3–10^5.[5] Mud volcanoes studied along the Mediterranean Ridge at water depths ~2000 m are of order several 10^3 m in diameter and 10^2 m in height (e.g., Ref. 6). Deep-water mud volcanoes often are associated with gas hydrates.

Much less is known about shallow water mud volcanoes, and it is anticipated that continued advances in ocean exploration will bring new discoveries of mud volcanoes in areas presently not associated with mud volcanism. The recently discovered mud volcanoes in the Straits of Sicily[7] are much smaller (of order 10^1 to 10^2 in diameter and several meters in height) than their deep-water counterparts. They occur in water depths of 70–170 m (too shallow for gas hydrates) along the Scicli fault zone. Seismic reflection data (discussed in Ref. 7 and Sec. III B) show diapiric structures beneath cone-shaped structures, which are typical of mud volcanism. Though we do not have absolute proof that these features are mud volcanoes (a core sample would be required), we use the term mud volcanoes in the same sense as Ref. 8, given the apparent presence of carbonate mounds.

The objectives of this research were to identify the scattering mechanism associated with a single mud volcano

[a)]Author to whom correspondence should be addressed; electronic mail: holland-cw@psu.edu

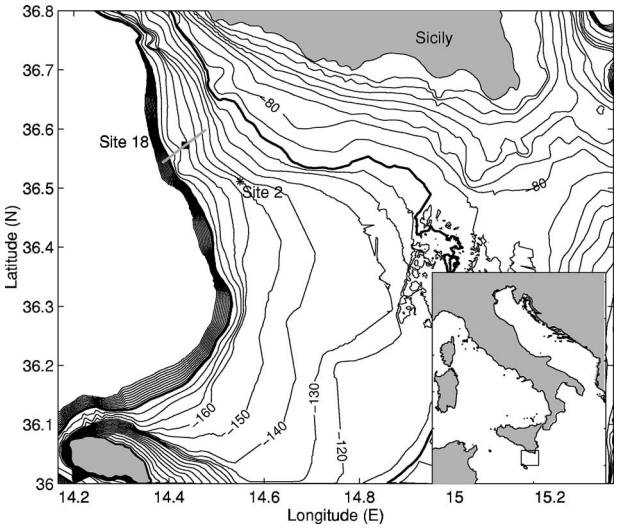

FIG. 1. Map of experiment area in the Straits of Sicily. The mud volcanoes of interest are located at Site 18. The black box at site 18 corresponds to the precise area of the multibeam measurements of Fig. 2. The gray line intersecting Site 18 is the sub-bottom profiling track (see Fig. 5). Seabed reflection measurements were conducted at Site 2.

(MV) and determine the frequency and angular dependence of the scattering. For the scattering mechanism, the three hypotheses that seem most probable are:

(1) gas bubbles (emitted) in the water column;
(2) gas entrained in sediment at/near mud volcano; and
(3) structure itself (carbonate pavements and/or chimneys)

The measurements were designed to determine which mechanism(s) play a significant role in the scattering and the commensurate clutter.

II. APPROACH

Through long-range reverberation, clutter features can be detected and localized. Long-range broadband (200–2000 Hz) reverberation measurements in the Malta Plateau (unpublished data) have shown significant clutter at the locations of some of the mud volcanoes (MVs). In the area of interest (see Site 18 box in Fig. 1) scattered returns from the MVs are 10–20 dB above the background reverberation and have been observed from distances up to 22 km. However, at long ranges, quantifying scattering characteristics of the feature, e.g., identifying the scattering mechanism, can be difficult or impossible. This is because uncertainties in the propagation paths, i.e., mechanisms dominating the propagation to and from the scatterer (both related to the oceanography and the seabed geoacoustics) are typically quite large.

An alternative approach is to probe the clutter features at close range using a direct path scattering technique. Direct path scattering observations offer two significant advantages: (a) the uncertainties associated with propagation (through a generally sparsely sampled ocean) are minimized, and (b) the measurement geometries are favorable to producing data from which hypotheses about the scattering mechanisms can be directly tested. Our experimental approach, adapted from a scattering technique designed for diffuse scattering, is discussed in more detail in Sec. IV A. Before discussing the scattering technique, we summarize (in Sec. III) what is known about the mud volcanoes from geophysical sensors and visual observations.

III. MUD VOLCANO CHARACTERISTICS

In order to identify potential scattering mechanisms, a variety of measurements were made on and around the MVs. These include bathymetry and seafloor backscatter data collected with a Reason 8101 240 kHz multibeam echo sounder, 300 kHz water column backscatter collected with an RDI acoustic Doppler current profiler (ADCP), and temperature, salinity, and dissolved oxygen above the suspected mud volcano using a Seabird CTD sensor. Additionally, an instrumented module (GAS-SCIPACK)[9] was deployed. These data were collected during the Boundary2004 Experiment within a few days of the low frequency acoustic scattering experiment (described later in Sec. IV). Seismic reflection data and sidescan data were collected during prior campaigns (2000 and 2002).

A. Multibeam bathymetry and backscatter

The experimental area, the Malta Plateau in the Straits of Sicily (Fig. 1), occupies the northern edge of the North African passive continental margin and is a submerged section of the Hyblean Plateau of mainland Sicily. While several

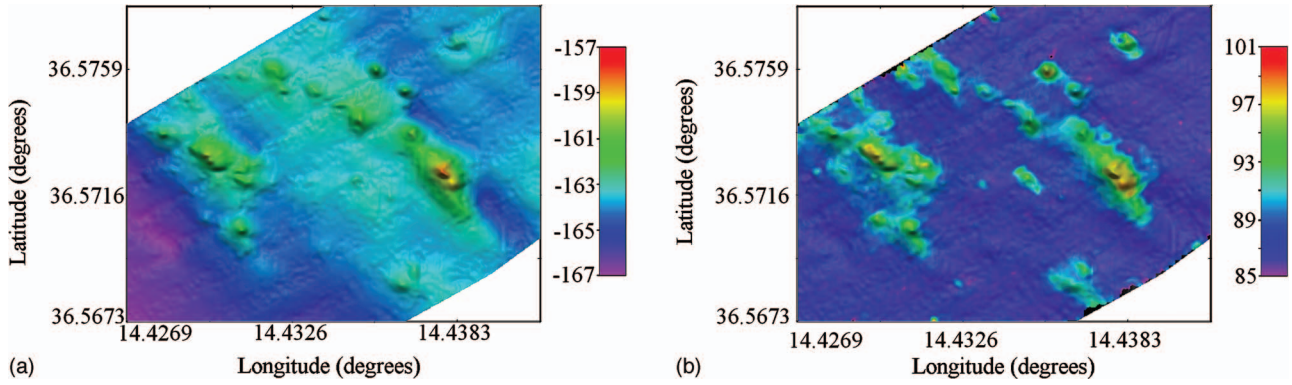

FIG. 2. (a) Multibeam bathymetry showing mud volcanoes at Site 18; the area is approximately 1350×1200 meters. Color corresponds to depth in meters. (b) A mosaic of values proportional to backscattering strength in dB (arbitrary units), corrected to 70°.

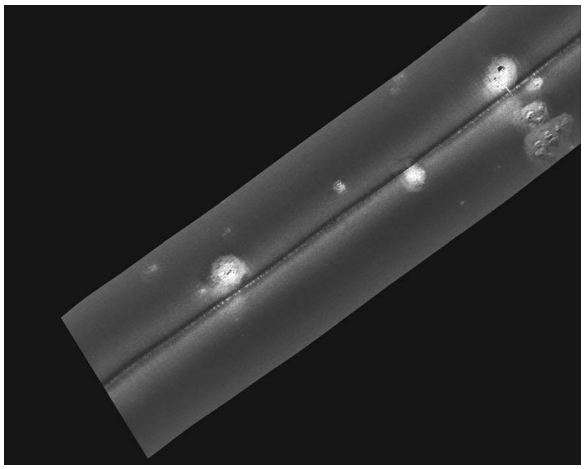

FIG. 3. Georeferenced 100 kHz sidescan image along the track (black line) in Fig. 7(b). The length of the track is approximately 1000 m and the cross-range dimension is 320 m.

clusters of mud volcanoes have been identified on the Malta Plateau, our interest here is focused on the MV cluster at Site 18 shown in Fig. 2.

The seafloor in Fig. 2 is gently sloped, from a depth of 164 m in the northeast corner of the survey to 167 m in the southwest corner. Several MVs are visible, rising to a maximum of approximately 5 m above the mean seafloor depth. The outer length scales observed in these features are quite variable, ranging from 40 to 400 m. Also visible in the data are nearly linear depressions adjacent to some of the larger MVs that may be associated with faults and/or regions of fluid escape. The multibeam sounding resolution varied across the swath from approximately 4 to 10 m in the across-track direction, and 2.5 m in the along-track direction. In postprocessing, the data have been low pass filtered, so that the resolution of in Fig. 2 is approximately 10 m.

An acoustic backscatter value associated with each multibeam bottom detection (one value for each beam on every ping) was also recorded in the raw multibeam data record. In order to compare different areas on the seafloor, these data were first corrected for any range and angle dependencies not associated with seafloor characteristics (similar to Ref. 10). Our main interest here is only in distinguishing between different types of seafloor, and so only relative backscatter values are required.

The strong angular dependence in the backscatter makes it difficult to identify different seafloor types in the data, and so the backscatter data are converted into a mosaic of values representing the backscatter that would be expected at a fixed grazing angle (70°). For each backscatter value, this is done by subtracting a predicted difference (in dB) for the backscatter at its true grazing angle from the predicted backscatter at 70°. Predicted backscatter values are derived from an empirical second degree polynomial fit that describes the angular dependence of all of the backscatter data within 40 m of the backscatter value in question. Although this method can introduce artifacts into the resulting mosaic, these artifacts should be on scales that are less than approximately 40 m, and the larger scale seafloor structure should remain largely unchanged.

The result of this process is shown in Fig. 2(b). Note that for each of the MVs (bathymetric highs) the corresponding scattering is relatively high. In general, for regions between

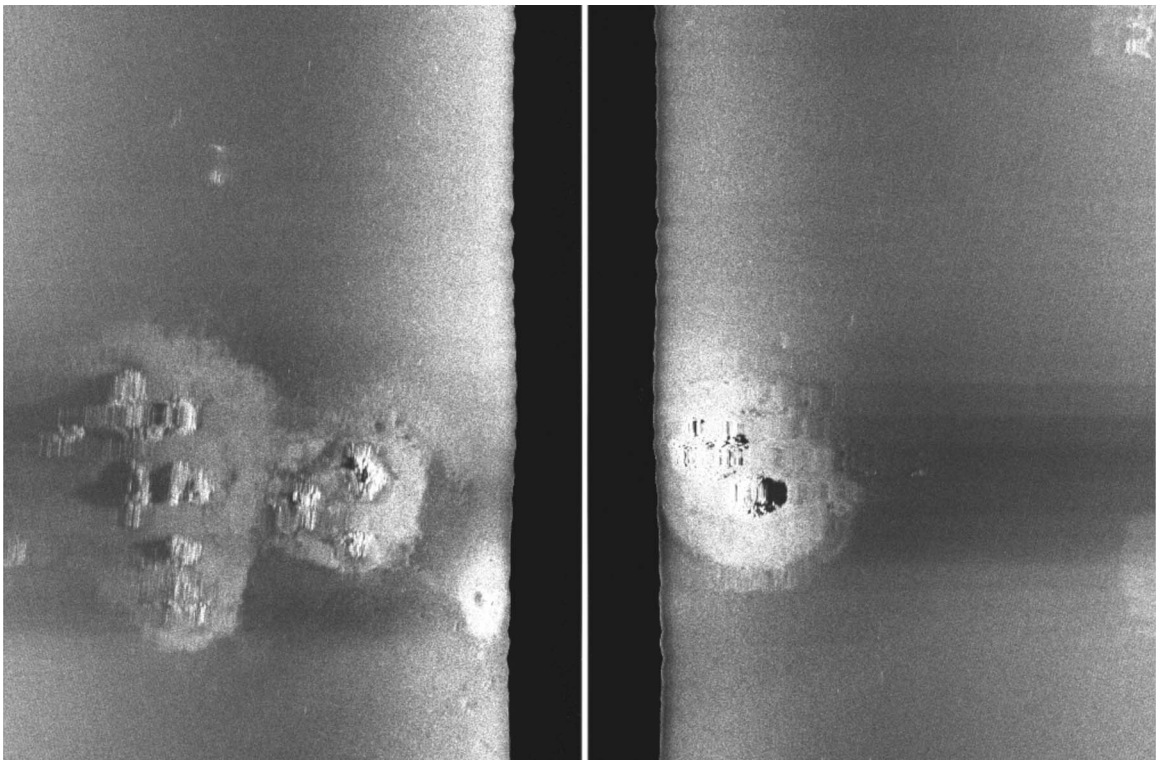

FIG. 4. A 100 kHz raw sidescan image (from Ref. 7) of the northernmost MV of Fig. 3 and the largest mound of Fig. 2. The scale is 320 m in cross range with approximately square pixel size; white indicates high scattering. The data indicate protrusions or carbonate chimneys on the MV roughly 10 m in lateral dimensions and 2–4 m in height. The altitude of the sonar was 19 m above the seabed.

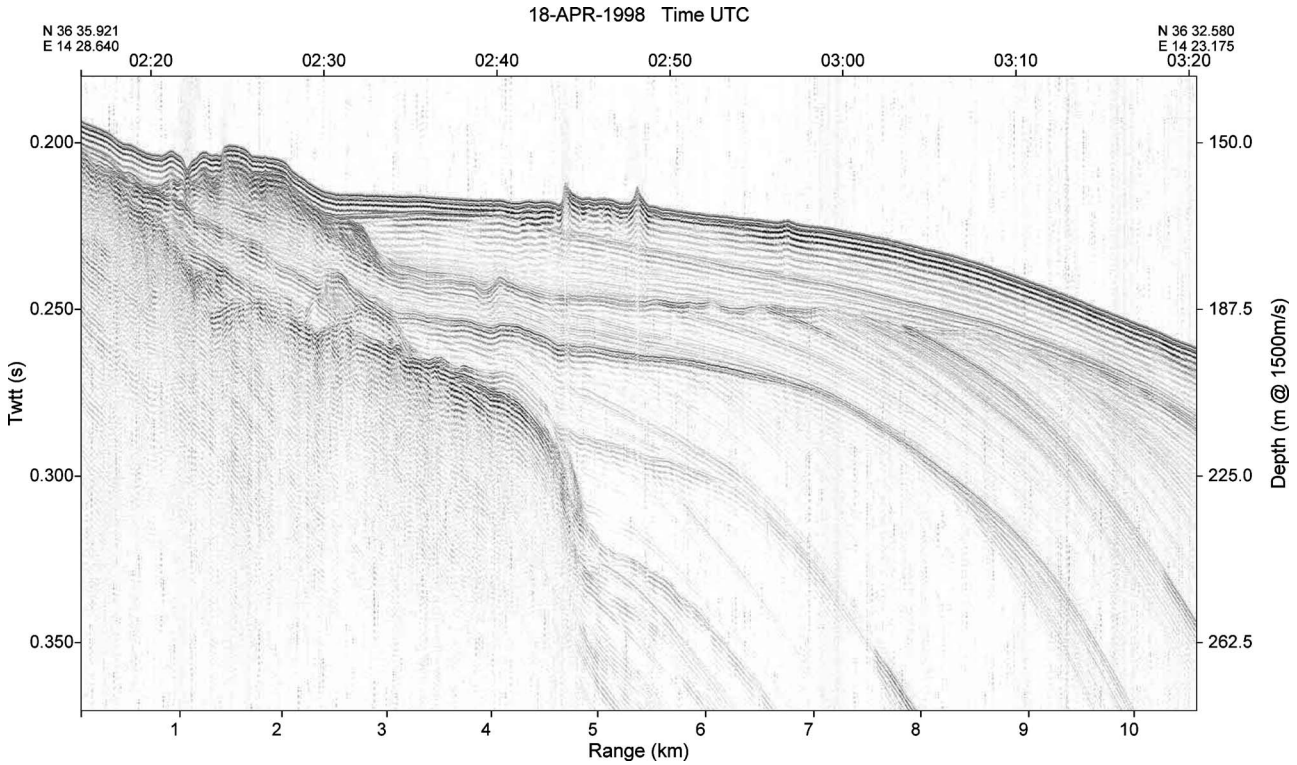

FIG. 5. Seismic reflection data showing the mud volcanoes (between 4 and 6 km). Vertical exaggeration is 350:1. The track location is shown as a gray line in Fig. 1.

the bathymetric highs, the scattering strength is lower. However, there are several discrete high scattering patches that do not correspond with an apparent bathymetric high (which might be because there are small mounds below the multibeam resolution). The backscattering data show three distinct regions: the background (~87 dB, arbitrary units that are proportional to acoustic backscatter), intermediate regions that are 2–4 dB above the background, and high backscatter regions which are 6–10 dB above the background. These three regions will be discussed again in the context of the visual observations (Sec. III C).

B. Seismic reflection and sidescan sonar

Sidescan data (Fig. 3) were collected using an Edgetech DF-100 along a 6 km line that cut through the central part of the multibeam survey box [see thick gray line in Fig. 7(b)]. The sidescan data clearly show three groups of features with high scattering; the easternmost and westernmost features can be clearly seen in the multibeam bathymetry and backscatter data (Fig. 2). The high scattering from near the center of the image does not have a clear counterpart in the bathymetry [Fig. 2(a)] but does in the multibeam backscatter data [Fig. 2(b)]. Raw sidescan data at the largest mound (Fig. 4) show protrusions on the mound roughly 10 m in lateral dimension and up to 4 m in height (calculated from the shadow length). From the shadow characteristics (also see Fig. 4 of Ref. 7) these protrusions appear to be constructed of cemented or consolidated sediment. These protrusions are believed to be carbonate chimneys. Note that the carbonate chimneys are not resolved in the multibeam data (Fig. 2).

Sub-bottom seismic reflection data were collected with an EG&G Uniboomer (Fig. 5). The western most and easternmost MVs are clearly seen at around 5 and 5.5 km, respectively. Note the indication of an acoustic shadow underneath the MVs which might be caused by the high impedance associated with the mounds, or possibly gas. Deeper layers show no clear indications of gas.

C. Geochemical and visual

Geochemical and visual oceanographic observations were performed using the GAS-SCIPACK module, an instrumented module for casts and towed surveys close to the seabed.[9] The module was equipped with two solid-state methane sensors (K-METS, Capsum, Germany), CTD and transmissometer (Idronaut 316), 12 Niskin 2.5 l bottles (General Oceanics 1015), echo sounder (Tritech PA500), color camera (Deep Sea Power & Light MULTI-SEACAM 2050 color), Light DL 1040 (120 V/250 W), attitude sensors (heading, pitch, roll) and internal status sensors (internal T, voltage, current, water detector). Sensor data and images were displayed in real time in an onboard console composed by a PC, TV, and video recorder. GAS-SCIPACK depth and direction were controlled following communications among console operators, winch driver, and navigating officer. Tow depths were typically a few meters above the seafloor. Though measurements were conducted at eight different sites on the Malta Plateau, we report here mainly on the Site 18 results.

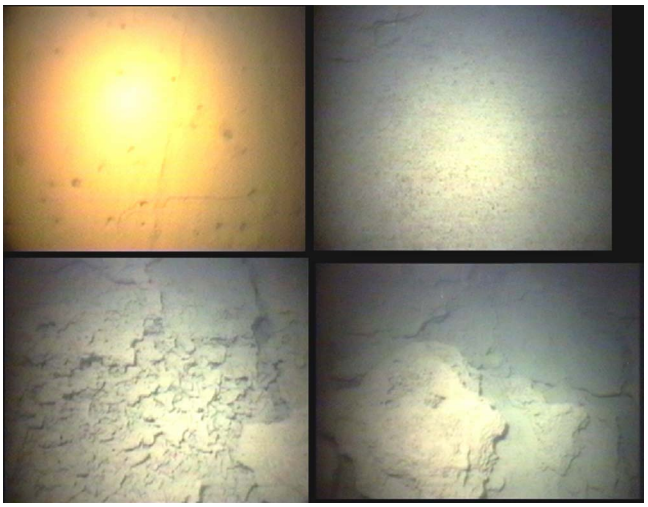

FIG. 6. Seafloor images (left to right) from the study area exhibiting (a) a soft fine-grained sediment; (b) coarse grained sediment surrounding the MVs; (c)-(d) carbonate heterogeneous crust and blocks on the MVs, ranging from centimeter to meter scale. The field of view is approximately 3 $\times$2.5 m.

1. Visual inspection

Bubbles were not visually detected at any of the eight sites. Two of the sites showed enriched benthic and pelagic biomass (Gorgonia, worms, fishes) and calcareous algae fixed on apparently cemented sediments. Only Site 18 (where the scattering measurements were conducted, see Fig. 1) was characterized by large and heterogeneous blocks without significant biomass. Such features are known to occur over mud volcanoes and in methane seepage areas. The images do not show classic mud volcanic edifices or mud flows, but these can be covered by the bio-constructions. The seismic profiles (see Fig. 5 and Ref. 7) suggest more clearly the occurrence of outcropping and buried mud volcanic (diapiric) structures.

The underwater video observations from Site 18 indicate seabed variability that is characterized by three distinct classes. The seafloor image in Fig. 6(a) shows a very soft, fine-grained sediment with evidence of bioturbation, which is characteristic of large areas of the seafloor a few tens of meters away from the MVs. This soft seafloor is in stark contrast to the seafloor image shown in Figs. 6(c) and 6(d) over the MVs. A third seafloor type—Fig. 6(b), found on the perimeter of the MVs, appears to be coarse-grained material (presumably weathered/eroded material from the carbonate mounds) and shows no evidence of bioturbation. These three bottom types—fine-grained, coarse-grained, and carbonate blocks and fragments—correspond reasonably well to the three different 240 kHz backscatter regions: background, intermediate, and high backscatter, respectively (see Sec. III A).

2. Methane analysis

A total of 18 seawater samples were collected at eight sites. Seawater samples were collected in 200 ml glass bottles, sealed with silicon septa and aluminium caps. Methane analyses were performed on board by head-space extraction (double syringe technique[11,12]), in thermostatic conditions, and GC-FID (gas chromatography-flame ionization detector); Autofim II, Telegan, UK; detection limit 0.1 ppm, accuracy 4%–5%. The reproducibility of replicate head-space samples was within ±15%, as determined from ten water samples in atmospheric equilibrium. Calibration was performed using atmospheric samples and Scotty II standards.

Concentrations of methane above 2–4 *n*Mol/l (equilibrium value with the atmosphere at the site-specific salinity temperature) are considered anomalous. Methane anomalies (tens of *n*Mol/l) were detected in all seawater samples collected close to the seafloor sediments. The highest concentrations (>200 *n*Mol/l) were found at two locations (36.4275° N 14.6434° E and 36.5708° N 14.4313° E) exhibiting similar bathymetric features as in Fig. 2. The latter location corresponds to Site 18—close to the location of the acoustic scattering measurements. At Site 18 a concentration of 300 *n*Mol/l was measured.

The solid-state methane sensors provided three pieces of useful information. First, they confirmed background levels of tens of *n*Mol/l across the area. At locations where the GC-FID showed high levels of methane, the solid-state sensors generally did not detect an increase. This is attributed to the relatively slow response time of the sensors (2–3 min). Second, given the response time and the drift speed of the vessel (less than about 1 knot), the indication is that the high levels of methane must exist over lateral dimension much smaller than ~50 m (at several meters above the seafloor). Finally, the sensors are quite sensitive to the presence of bubbles; however, no bubbles were detected during any of the tows.

D. ADCP and CTD drift results

Acoustic backscatter data from the hull-mounted ADCP on *R/V Alliance* were collected during one night where the *R/V Alliance* rotated between several MVs at Site 18, performing station keeping maneuvers for 20–45 min at each position. An example of the data collected corresponding to one of the four ADCP beams is shown in Fig. 7(a), with the ship's position during this time shown in Fig. 7(b). There are two distinct types of features in this data: (1) a group of scatterers spread over the entire bathymetric feature in a thin layer at a nearly constant depth of ~95 m, and (2) one or more plumes that are relatively large in their vertical extent (between 100 and 150 m). The acoustic backscatter in the horizontal layer is much lower than the backscatter from the vertical plumes, indicating that these are clouds of scatterers with either different number densities, different types, or both. Further, note that the plumes present over the mound located at 36.5725 N, 14.438 E between 01:10 and 01:55 local time appear to be gone $5\frac{1}{2}$ h later, although it is possible that the ADCP beam simply did not intersect the plume at that later time. The plumes found at 36.573 N, 14.430 E are present during both times that the ship was at that station. Measurements with a SeaBird CTD system (with an SBE 43 Oxygen sensor) taken between 22:08 and 22:51 local time several nights later show a very slight increase in dissolved

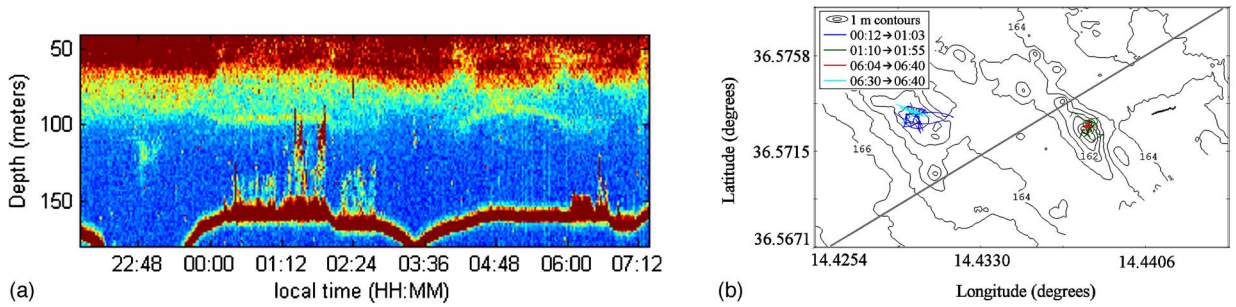

FIG. 7. (a) Acoustic backscatter from a single beam of the ship-mounted ADCP. (b) Tracklines including ADCP drift less than 0.5 m/s (colored lines); drift for low frequency scattering measurement (black short curved track ENE corner of plot); sidescan and seismic reflection track (diagonal gray line).

oxygen over the largest MV as compared to the surrounding regions (slightly less than a 1% difference).

These data indicate that a chemotrophic food chain may be present, where the base of the food chain uses methane rather than photosynthesis as its energy source (similar to that described for pockmarks found in the North Sea, (Ref. 13, see page 56]). Such a food chain may also support plankton and possibly nekton, which seems the most likely cause of the "plumes" in the ADCP backscatter data. Hovland and Judd[13] also suggest that fluid seepages can suspend nutrients that would otherwise be trapped in sediments, acting as an alternate mechanism at the base of the food chain. Although no evidence of seepage was found during the CTD drift, it is difficult to rule this out because of the possibility that the seepage is episodic. Another hypothesis that could explain the backscatter in the water column is that bubbles are being released from the sites where mounds are present. If this were happening, however, the O_2 anomaly would be expected to have the opposite sign, since dissolved oxygen would be diffusing into the methane bubbles as they rose through the water column, e.g., Ref. 4 (although the ADCP and the CTD measurements were not taken simultaneously).

E. Summary observations

Mud volcanoes of sizes $O(10^{1-2})$ m in lateral dimension and several meters in height were observed on the outer shelf of the western Malta Plateau. There was no biomass observed on these MVs (in contrast to significant biomass observed on MVs roughly 25 km to the southeast). This may be because this is an active or recently active site, so that there may be insufficient time for biomass to have developed. The presence of high aqueous concentrations of methane near the MVs is certain, although there was no clear indication of gas in bubbles either in the sediment or in the water column. Between the sidescan and multibeam data our picture is of protrusions or carbonate chimneys roughly 10 m in lateral dimension and several meters high that are sometimes isolated but typically clustered on larger mounds.

Given the observations, it appears that the most likely mechanism for low frequency scattering is scattering from the carbonate mound itself and/or the carbonate chimneys on top of the mounds. While no measurements have been made on the material, it is apparently consolidated and so would have a relatively large impedance contrast relative to the water column which means not only that the scattering could be potentially large, but that scattering from within the MV (e.g., from gas bubbles entrained in the sediment) might be relatively hard to detect. While the observations suggest the lack of free gas bubbles, perhaps none of the hypotheses can be completely ruled out due to the potentially episodic nature of gas release.

IV. LOW FREQUENCY SCATTERING MEASUREMENTS AND MODELING

The objective of the low-frequency (800–3600 Hz) scattering experiment was to measure the scattering associated with a single mud volcano at close range. The MV selected for the scattering measurements, the largest mound in the cluster (at 36.5716° N 14.4383° E in Fig. 2), is roughly elliptical with dimension 150 m × 50 m and oriented at 145° (re North).

During the measurement period (1559–1609 UTC 21 May, 2004) the winds were light, less than a few m/s, with a sea state 1 and the vessel drifted along the track shown in Fig. 7(b), about 75° relative to the axis of the MV.

A. Experiment design

The main challenge of the short-range scattering experiment is to avoid or control multipaths. One multipath problem is potential contamination by sub-bottom reflections. It is well known that scattering may arise from not only the interface but also from sub-bottom inhomogeneities or horizons. However, sub-bottom reflections at normal incidence contaminate the scattering measurement, since the normal incidence reflections (even from sub-bottom horizons) are often at higher amplitude than scattering at lower angles.

A second multipath problem is contamination from hybrid paths. Hybrid paths are paths that belong to a different family of scattering events that arrive at the same time as the scattering path that is being measured. Figures 8 and 9 show the various paths and their relationship in time and angle. For example, in this geometry, beyond about 0.4 s, the monostatic (path *a*) and vertically bistatic paths (*b*, *c*, and *d*) cannot be separated in time or angle. By vertically bistatic we mean that the incident and scattered angles are different in the vertical plane. A receive and/or source array with vertical aperture can be used to control both types of multipaths, i.e., by reducing the contribution of the normal incidence reflections and also providing some discrimination against the various scattering paths.

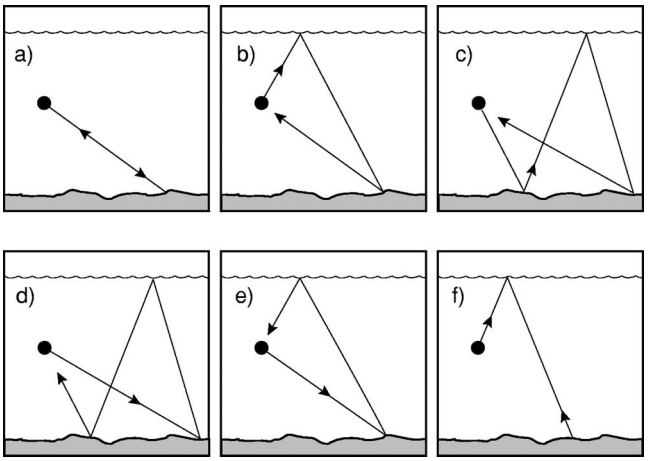

FIG. 8. Seabed scattering multipaths (from Ref. 15). Only those paths that have less than two surface interactions are depicted.

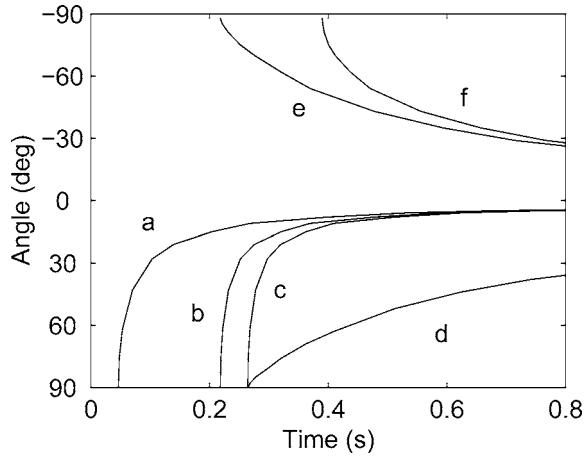

FIG. 9. Vertical arrival angles vs time for various bottom scattering paths. Time is referenced to source initiation. The geometry corresponds with the geometry of the experiment. Angles are measured with −90° towards the sea surface. Path (a) is the monostatic backscattering path. See Fig. 8 for other path descriptions.

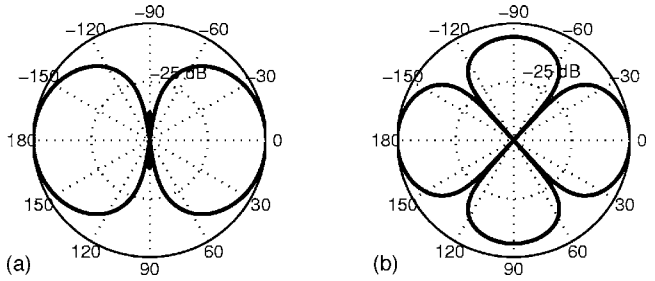

FIG. 11. Theoretical source beam patterns for: (a) 3600 and 1800 Hz and (b) 2400 Hz. The inter-element spacings for the three frequencies were 20.8, 41.7, and 41.7 cm, respectively. The beam pattern at 800 Hz is omnidirectional (a single Mod 40 transducer was employed). For analysis in this paper, only transmitted paths near 0° are employed, where the theoretical curves are quite accurate.

Figure 10 depicts the system employed in this study. The vertical aperture of the receive array helps minimize effects of multipath. Short pulses (typically 15 ms) from transducers near the bottom of the array provided a repeatable and stable source. The equipment is deployed from the forecastle and the ship was left to drift. The weight of the Mod-40s (90 kg in water) provides enough ballast to keep the array straight when the current shear is small. A small fin (not shown) on the Mod40 frame stabilizes the array against rotational forces.

The source array was constructed with pairs at $\lambda/2$ spacing in the vertical so that transmitting in phase would yield a null in the vertical plane. The mid-frequency source array was constructed of 3 ITC-4001 transducers spaced at 20.8 and 41.7 cm, to yield $\lambda/2$ spacing at 3600, 1800, and 1200 Hz. The top of this array was placed 1 m below the bottom phone of the receive array. The low frequency array consisted of 2 Mod 40 flextensional transducers spaced at 1.27 m (or $\lambda/2$ spacing at ~600 Hz). Theoretical beam patterns are shown in Fig. 11. Beam pattern measurements (see Ref. 15) showed some deviations from the theoretical re-

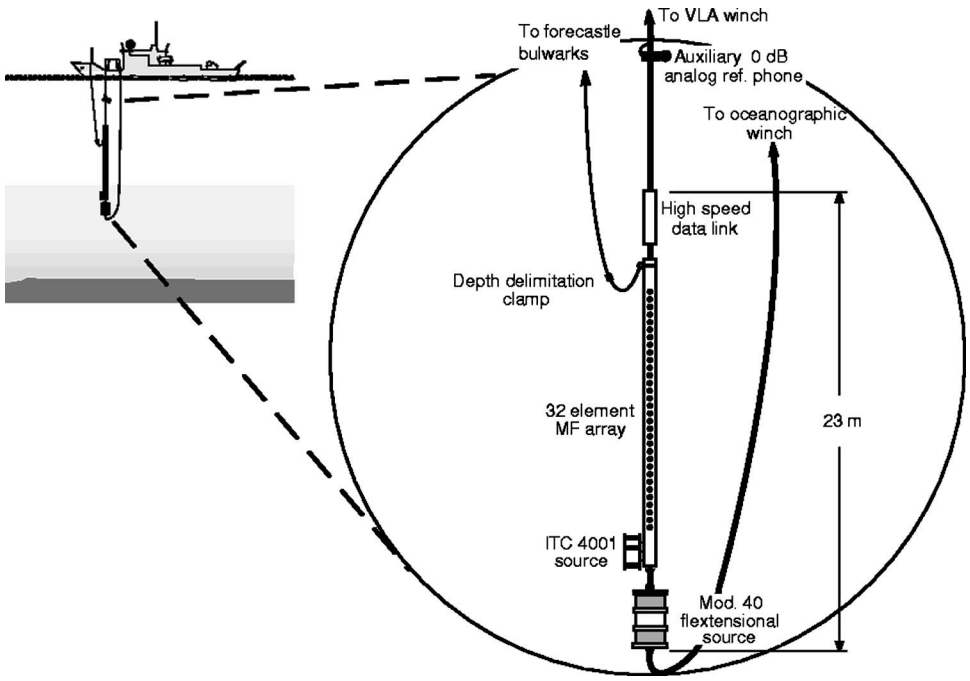

FIG. 10. Experiment geometry used for measuring bottom scattering (from Ref. 15). Details of the source and receive arrays are found in the text.

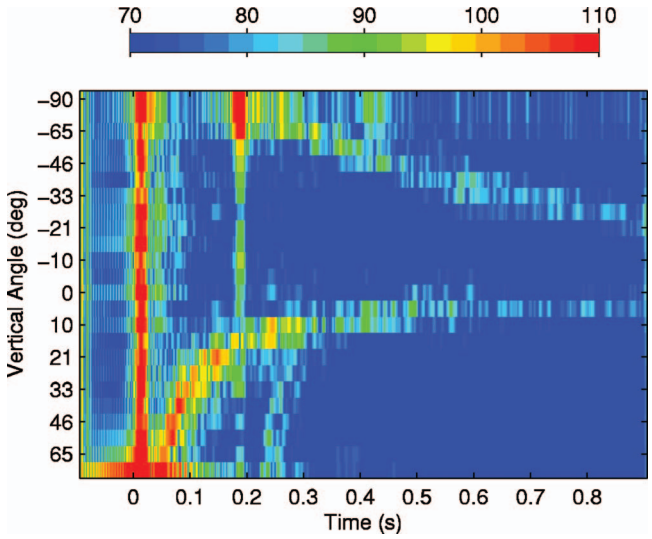

FIG. 12. Scattering (in dB) from a "uniform" seabed as seen by the vertical array from a single ping at 3600 Hz. The various paths evolution in time and angle correspond to those shown in Fig. 9. The arrival at 0.18 s, observed on nearly all beams, is the surface reflected path.

sponse, but the differences are not significant for this study, since the focus is on low grazing angle scattering that would be important for long-range clutter. Ping types included both CW and LFM pulses of 15 ms pulse length. Repetition rates of 6 pings/min were used, and the acquisition system was triggered 1 s before transmit to acquire ambient noise for each ping. Fifteen pings were collected for each frequency.

The receive array consisted of 32 Benthos AQ-4 hydrophones with a 0.18 m spacing hardwired directly to the NATO Research Vessel (NRV) *Alliance*. The data were sampled at 12 kHz and low pass filtered at 3.8 kHz with a seven-pole six-zero elliptic (70 dB per octave roll off) antialias filter. The RC high pass filter (6 dB per octave roll off) was set at 500 Hz. A high speed digital link within the array provided programmable signal conditioning, digitization, and serialization of the signals. Following signal conditioning, data were beamformed (Hanning shading) using a plane wave time domain beamformer.[16] Beams were spaced to yield 3 dB down crossing points at the design frequency of the array. The data are filtered in 200 Hz bands with a sixth order low pass digital elliptic filter with 0.5 dB of ripple in the passband and a stopband 50 dB down. Receive array depth and the total water depth are determined using the arrival times of the surface and bottom reflected paths.

Experimental results from a control area (i.e., flat seabed) are shown in Fig. 12. The water depth and source depth are 128 and 91 m, respectively. Zero time in the figure corresponds to the direct blast, which overloads the array and is seen on all beams. The surface reflection is visible at 0.18 s. Clear arrival paths can be understood in terms of the various monostatic and bistatic scattering paths of Figs. 8 and 9. This experimental method has been used in the past (e.g., Refs. 15 and 17) to obtain diffuse scattering strength, i.e., scattering strength versus angle for seabeds that are homogenous (in a gross sense) over scales of hundreds of meters. In the following, we adapt the method to be able to measure scattering from discrete scatterers.

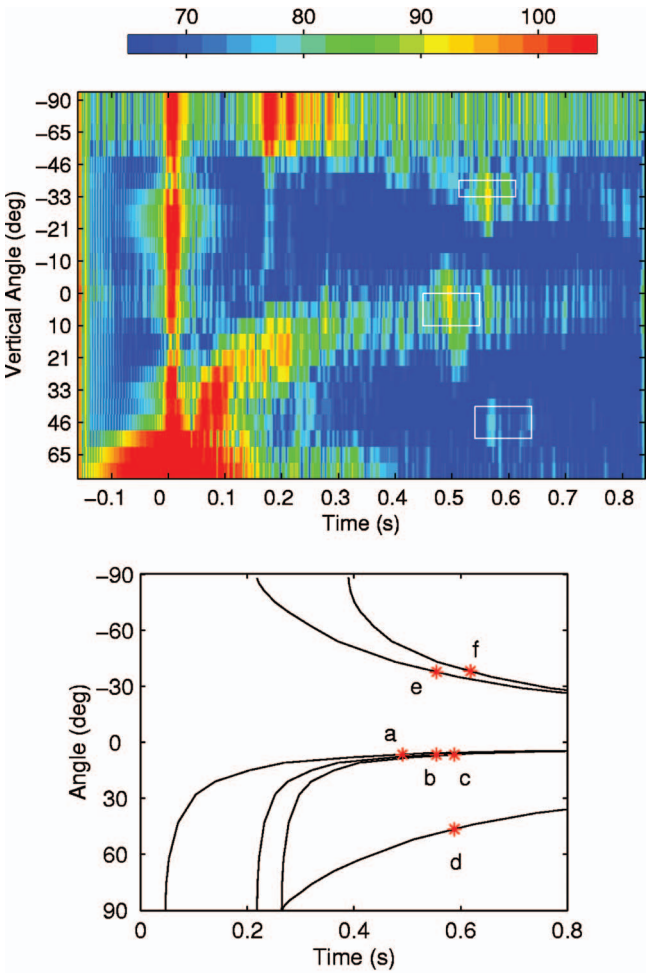

FIG. 13. Scattering at 1800 Hz (in dB) from a single ping along track 5. The scattered arrivals from the MV are clearly observed along several paths and are highlighted by the white boxes. Note returns from direct-direct (path a), direct-surface reflected (path e) and surface bottom (path d). The surface-direct (path b) can also be faintly seen at the same time as the direct-surface (path e) and on the same beam as the direct-direct (path a). The path geometries are shown in Fig. 8. The key points of the figure are that scattering from the MV is ~10–15 dB above the scattering from the surrounding seabed, that the scattering occurs at grazing angles slightly lower (closer to the horizontal) than from the background sediment, and finally that there is no significant scattering in the water column.

B. Scattering from the MVs

An example of the measured beam time series near the MV is provided in Fig. 13(a). A discrete scatterer would be expected to be visible in the beam time series along one or more of the various paths [see Fig. 13(b)]. The scattering from the MV can be seen on the monostatic path (path *a*) at about 0.48 s and is ~10–15 dB above the diffuse scattering from the surrounding seabed. The angle associated with this path and range is +5° (i.e., 5° down). The bistatic MV-surface reflected path (path *e*) is seen at −40° at 0.55 s. The reciprocal path (surface-MV or path *b*) occurs at the same time but at +5°. Note that its level is reduced relative to path *e* because of the source beampattern. The MV-surface-bottom path (path *d*) occurs at 0.57 s and a scattered angle of about 45°.

One of the important aspects of the analysis pertains to identification of the scattering mechanism. Each of the hy-

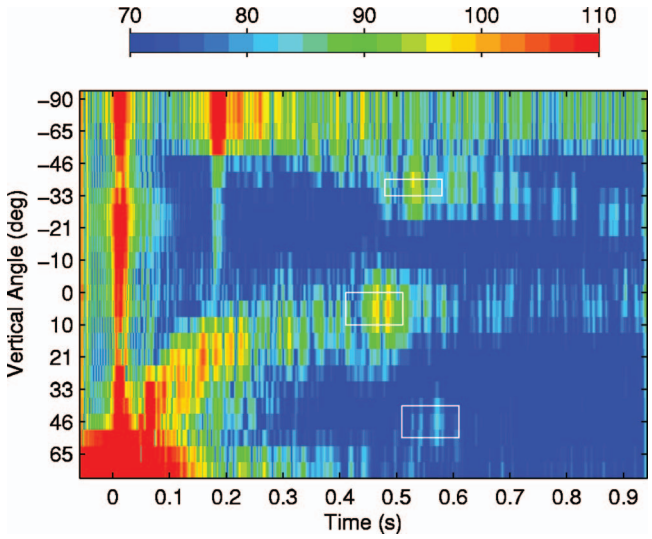

FIG. 14. Multiple scattered returns from the MV could be observed occasionally (see the two closely spaced returns on the direct-direct path).

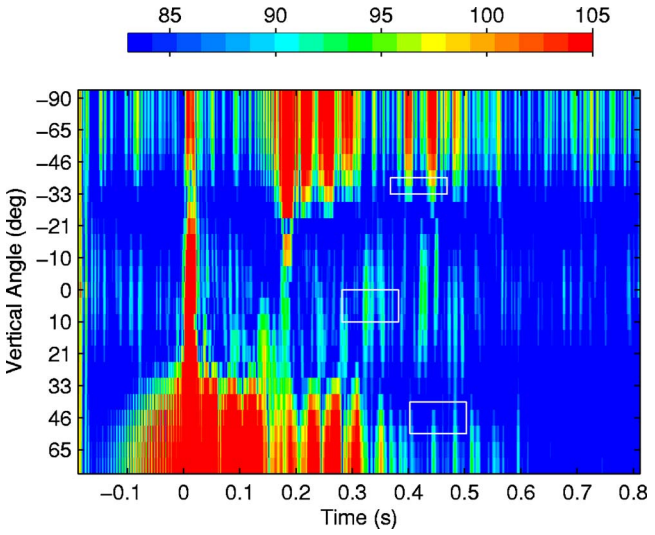

FIG. 15. (Color online) Beam time series at 800 Hz showing the direct-direct, surface-direct and direct-surface-bottom scattering paths. The direct-surface path is obscured because of the wide beams and the surface scattered paths. The direct path (white box at about 5°) is visible along with the surface-direct path on the same beam 0.1 s later.

potheses can be examined in light of the beam-time series data [Fig. 13(a)]. Hypothesis (1) was that the dominant scattering mechanism was from bubbles and particulates emitted from the MV. If this hypothesis was correct, then we would expect to see high scattering in the water column (i.e., in the beams corresponding to 0° to −48° (the angle associated with surface scattering at that range). However, there is no evidence in the data of scattering within the water column (scattering levels in the water column are ~40 dB lower than the scattering from the seabed). The data indicate that hypothesis 1 is not correct during the time period of the observations.

Hypothesis 2 stated that the dominant scattering mechanism was from gas trapped under, around or within the MV. Inspection of Fig. 13 shows that the strongest arrival is actually a few degrees higher than the scattering from the surrounding seabed at the same instant in time. It is easiest to see this on the monostatic path, path *a*. This means that the scattering is coming from above the seabed (though the vertical resolution is insufficient to quantify how high). In Fig. 14, beam time series are shown for a different ping. In this ping several scattering highlights on given path from the MV are apparent (seems to occur in less than 50% of the pings). These events occur 18 ms apart (27 m in round trip travel) and it seems most likely that they come from two distinct features on the MV. At 800 Hz (Fig. 15), the receive beams are so wide in the vertical, that it becomes nearly impossible to distinguish paths *d* and *e* from surface scattering and bottom scattering events. Since the source beam pattern is omni directional, generally both paths *a* and *b* are visible.

Hypothesis 3 was that the dominant scattering mechanism was from the structure itself. The evidence from the beam-times series data indicates that this is the most likely mechanism. Futhermore, it seems most likely that the scattering arises from the carbonate chimneys which rise from the top of the MV. However, bubbles in the MV itself (but higher than the water depths surrounding the MV) cannot be completely ruled out.

C. Target strength estimation

The scattered intensity I from the MV can be written:

$$I = I_o \delta_i \delta_s s_t, \tag{1}$$

where I_o is the source intensity, $10\log_{10}(s_t)$ is the target strength and δ is a transmission factor from the source to the scattering patch (subscript i) and the reverse path (subscript s); $-10\log_{10}(\delta)$ is the one-way transmission loss). The scattered intensity is measured by taking the peak level within a small time window around the expected arrival time. The source intensity was monitored by a hydrophone above the source, but since the hydrophone is in the null of the source beam pattern, a more robust estimate was made using the recorded power amplifier drive voltage and the calibrated transducer response curves.

The transmission factors are estimated by assuming spherical spreading. This is reasonable since the sound speed profile is nearly isovelocity near the seabed (see Fig. 16) and the surface reflected paths are at steep angles (>30°). For the angles probed, the difference between the two-way transmission loss using the isovelocity assumption and that using the measured profile is less than 1 dB and the difference in angles between source and receiver above 3° is less than 0.3°. Assuming incoherent summation of paths:

$$\delta_i \delta_s = \frac{N_i}{r_i^2} \frac{N_s}{r_s^2} \prod_{m=1}^{M} R_m, \tag{2}$$

where r is the distance along the path (incident i or scattered s), N is the number of arrivals that contribute within the pulse length, and R is the intensity reflection coefficient from M boundary interactions. Assuming that the scattering event takes place on the MV (i.e., elevated somewhat relative to the surrounding seabed) both the direct and the bottom reflected paths contribute to the observed scattering (see Fig. 16). The direct and bottom reflected paths arrive at the scat-

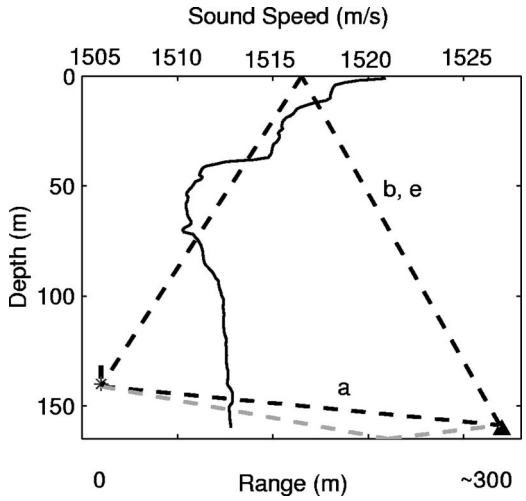

FIG. 16. Sound speed profile and geometry of the experiment showing the source (*), receiver (|) MV (▲) and ray paths (---). Vertical exaggeration is 2:1. The ray paths are identified by the labels of Fig. 8. For clarity, path d is not shown, but is similar to paths b,e with a bottom reflection following the surface reflection.

tering patch within less than a millisecond (i.e., much smaller than a pulse length) so $N_i=2$. For the monostatic[18] path (path a) since the paths are reciprocal $N_s=2$. However, for the bistatic paths (paths b, d, and e) the receiver is high enough above the seabed that only one path contributes, $N_s=1$.

The reflection coefficients of the seabed R_b and sea surface R_s are estimated in the following way. For the monostatic path, path a, R_b is required at 5–6° grazing (depending on the range between source and MV). These angles are below the critical angle (approximately 12°) so $R_b \sim 1$. The exact reflection coefficient below critical angle depends upon the attenuation which is not known to very high accuracy, nevertheless the error in target strength induced by the approximation $R_b=1$ is expected to be very small. For path d (direct-surface-bottom path), an estimate of R_b (39–51°) is required for 1800–3600 Hz and spherical wave reflection coefficient measurements at a similar water depth (Site 2, for see location in Fig. 1) are used as a proxy. At large kd (where k is the wave number and d is the distance from source to bottom to receiver) the spherical and plane wave coefficients are very similar. For the reflection coefficient measurements $d>180$ and $k>7$; for the scattering measurements $d>\sim 35$ and $k>7$. Therefore, we assume that the spherical reflection coefficient for both the reflection and the scattering measurements is comparable and very nearly equal to the plane wave coefficient. The measured reflection loss data ($-10\log(|R|)$) are shown in Fig. 17; and the values at the angles of interest are given in Table I.

TABLE I. Bottom loss (BL) estimates. the BL measured at site 2 includes the frequency band over which it was averaged (closest 1/3 band or bands) and the number of angles over which the data were averaged.

Frequency (Hz)	Angles (deg)	BL (dB) Derived from TS	BL (dB) Measured at Site 2
1800	39–47°	11.0±2.8	13.5±1.0; 1400–2200 Hz (11)
2400	44–48°	14.1±1.8	14.5±1.0; 2200–2800 Hz (5)
3600	47–51°	13.6±2.6	14.4±0.9; 3550–4470 Hz (3)

As a check on the assumption that using the measured reflection coefficient from Site 2 is reasonable near the MV, R_b can be computed in another way. Given the fact the angles between paths d and e are so similar, R_b can be estimated from the beam time series data at the MV as

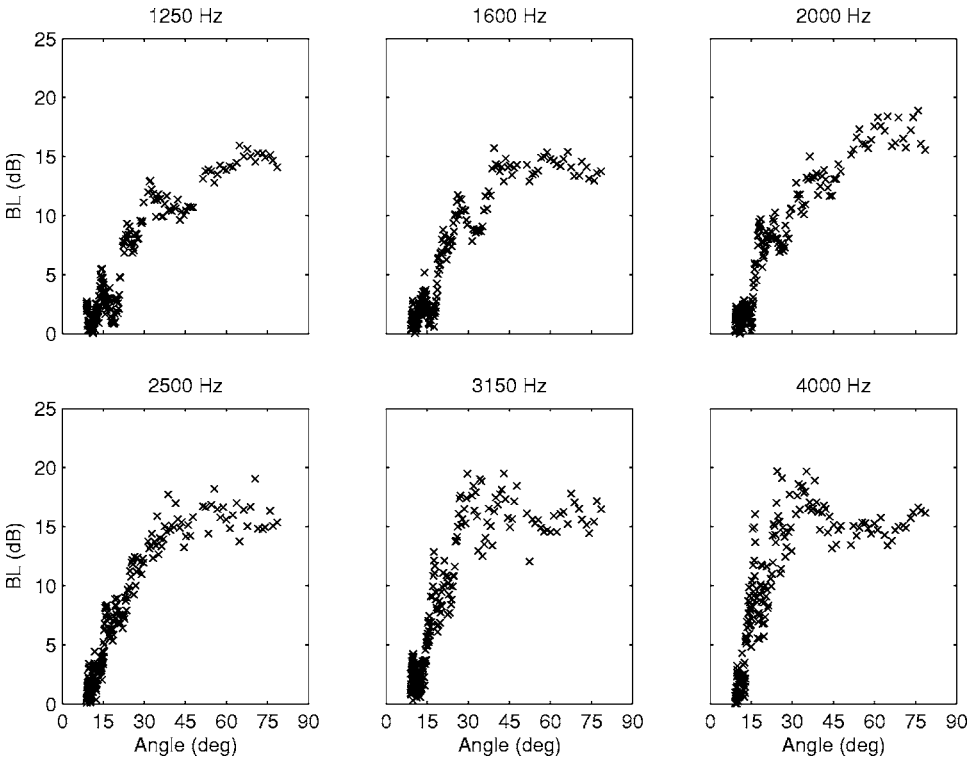

FIG. 17. Seabed reflection loss measured at Site 2 on the Malta Plateau. The data are averaged in 1/3 octave bins.

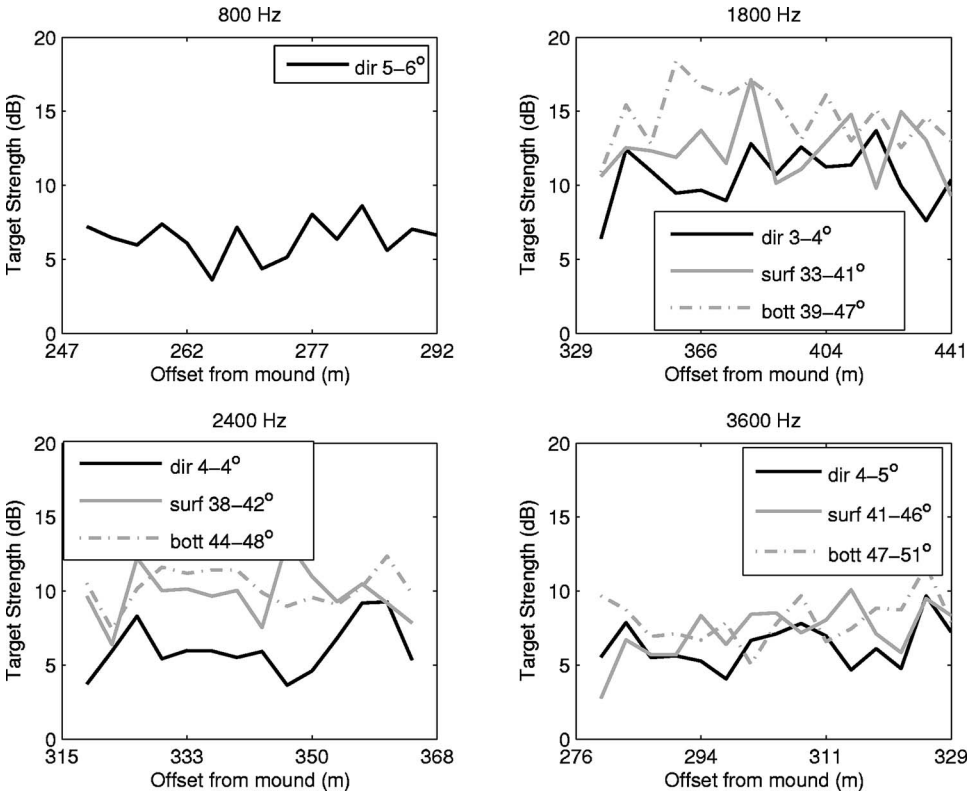

FIG. 18. Target strength of mound at Site 18 as a function of frequency, angle, and path. Monostatic (path a) is indicated by "*dir*," surface reflected path is indicated by "*surf*" and surface-bottom reflected is indicated by "*bott*."

$$R_b \simeq \frac{I_d}{I_e}\frac{\gamma_{\mathrm{se}}}{\gamma_{\mathrm{sd}}}, \tag{3}$$

where I_d and I_e are the received intensities from paths d and e, respectively, and γ_s is the transmission factor along the path from scatterer to receiver (although the transmission factors were computed, their ratio is very nearly unity since the paths are nearly identical at these ranges). The values of R_b derived in this fashion agree with those from Site 2 (see Table I) within the error bounds and thus give confidence that the reflection coefficient near the MV is similar that at Site 2.

For sea surface reflection we use (see Ref. 19)

$$|R_s(\theta,f)| = 1 - 0.21(k\sigma)^{3/2}\sin\theta, \tag{4}$$

where σ is the rms waveheight and the phase is assumed to be $-\pi$. The rms waveheight measured by a directional waverider buoy during the experimental period leads to $0.95 < |R_s(38-46^\circ, 1800-3600\ \mathrm{Hz})| < 1$.

The measured monostatic $(-)$ target strength computed with the model above is shown in Fig. 18. The grazing angles associated with the direct path (indicated by "*dir*") are provided in the legend. Also shown is the vertically bistatic target strengths (surface reflected path e) and (surface-bottom reflected path d) except at 800 Hz, where the beamwidths were too large for adequate spatial separation. In principle, we could have used the reciprocal paths b and c at 800 Hz, but in practice there was too much uncertainty in the path identification. The ordinate in Fig. 18 (offset from the MV) is estimated using the travel time. Note that each frequency has a distinct set of ranges/angles because the 15 pings for each frequency were transmitted serially (i.e., not interleaved). So Fig. 18 may depend upon geometry as well as frequency, although it should be noted that the angles at the various frequencies are quite similar.

There are several aspects of Fig. 18 that are important. First of all, note that the target strengths are fairly high, 4–14 dB, which means (in conjunction with its size) that the MV could be capable of producing clutter. Second, note that the scattering is fairly stable from ping to ping (one ping cycle is ~2.5 min) even though geometry is changing—grazing angles decreasing slightly with range. For each path type the standard deviation is typically less than 2 dB (see Table II). This stability suggests that the scattering mechanism is not hypersensitive to the precise geometry or geotime. This seems consistent with the evidence from the vertical array that the scattering mechanism is not due to bubble plumes in water column (which might lead to substantial temporal variability). This stability also indicates that there is a weak dependence of the scattering with vertical angle at least over a few degrees.

Third, note that in Fig. 18 (and Table II) that the target strength for paths a, e and d are similar. This suggests that the scattering may be nearly isotropic in the vertical, at least from 3° to 51° (although clearly the entire angular range is sparsely sampled). It is important to have some knowledge

TABLE II. Target strength (TS) estimates.

Frequency (Hz)	Monostatic TS (dB)	Surface-Direct TS (dB)	Surface-Direct-Bottom TS (dB)
800	6.1±1.6	⋯	⋯
1800	10.2±2.1	12.2±2.4	14.7±2.1
2400	6.0±1.7	9.9±1.7	10.3±1.3
3600	6.3±1.5	7.2±1.8	8.0±1.6

TABLE III. Properties of mud volcano used for modeling scattering from a visco-elastic sphere.

Set	Compressional speed (m/s)	Shear speed (m/s)	Compressional attenuation (dB/m/kHz)	Shear attenuation (dB/m/kHz)	Density (g/cm^3)
1	2200	1000	0.1	20	2.2
2	4000	1800	0.02	0.3	2.2

about the vertical angle dependence of the scattering for two reasons: (1) the dependence may help eliminate hypotheses about the scattering mechanism and (2) once the scattering mechanism is understood it may help suggest a reasonable physical model.

D. Simple modeling

The most likely scattering mechanism being the carbonate chimneys coupled with the nearly isotropic behavior of the scattering suggested that to first order, the MV might be considered as a visco-elastic sphere. The expressions developed by Faran[20] for an elastic sphere were extended to the visco-elastic case by allowing the wave number to become complex. The solution is written as an infinite sum of spherical basis functions; for the following cases 60 terms were sufficient to achieve convergence.

The fact that the carbonate chimneys cast a sharp shadow (see Fig. 4) is indicative of consolidated sediment, which we assume is carbonate. Since the carbonate properties are not known, we have used two plausible "end members" as listed in Table III. The theory is compared with the measured target strengths in Fig. 19 where it should be noted that the overall levels of the target strength are not very sensitive to the material properties. The theoretical target strength has the familiar shape with Rayleigh scattering rising as k^4 below $ka_o \sim 1$ (a_o is radius) and a roughly constant value above. The overall level is mostly controlled by the radius and scales approximately as a_o^2. The theoretical target strength for radius of $a_o=5$ m corresponding to the radii of the observed carbonate chimneys is in reasonable agreement with the measurements.

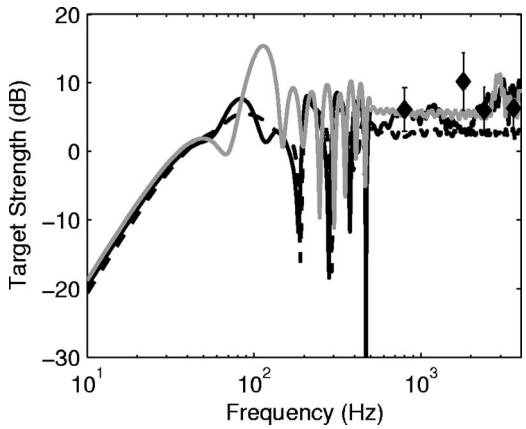

FIG. 19. Theoretical predictions of scattering from a visco-elastic sphere (solid and dashed lines) and measured monostatic data (♦) with ±2 standard deviations (I). The monostatic path is the solid black line and the vertically bistatic path (path *e* with 40° difference in incident and scattered angle) is the black dashed line. The gray line shows the monostatic path for geoparameter set 2 (see Table III). Above 500 Hz, the theoretical predictions are averaged over 200 Hz, commensurate with the data.

Both the monostatic target strength and the vertically bistatic target strength (relative angle difference of 40°) were computed and are shown in Fig. 19. Only the monostatic data are shown. While the data indicate that the vertically bistatic TS is a few dB lower than the monostatic case (Table II), the theoretical model for the sphere predicts the converse (Fig. 19)—though in a gross sense both the measurements and the model predict a weak dependence on vertical bistatic angle.

Though it may not be possible to draw absolute conclusions from the modeling, the results (i.e., agreement between model and data) are in accordance with and help substantiate the hypothesis that the scattering comes from the carbonate chimneys (Fig. 4). These features have dimensions close to that of the proxy sphere: lateral radial dimension of ~5 m and heights of around 2–4 m. Recall that the pulse in water has a radial dimension of 11 m, so one or several protrusions might be insonified at a given instant in time. The occurrence of multiple highlights in some pings (see Fig. 14) could arise from scattering from multiple protrusions spaced far enough apart to be temporally resolved. While the multiple highlights could also arise from near specular scattering from various facets or curved surfaces on the mound, facets and curved surfaces would not necessarily be expected to result in isotropic scattering in the vertical plane. In summary, the sphere model certainly adds weight to, but does not necessarily prove, the carbonate chimney scattering mechanism hypothesis. At the very least, the sphere model can be considered as a simple proxy, producing approximately the right levels as a function of frequency and angle.

V. SUMMARY AND CONCLUSIONS

Target strength measurements on an individual mud volcano indicate that it (and by extension other MVs) are a potential source of clutter for active sonar. Target strengths of 4–14 dB were observed from 800 to 3600 Hz for a monostatic geometry with grazing angles of 3–5°. Similar target strengths were measured for vertically bistatic paths with incident grazing angles of 3–5° and scattered angles of 33–50°. The target strengths were not very sensitive to precise geometry or geotime; typical standard deviations were ±2 dB over distances of tens of meters and order minutes.

The dominant scattering mechanism for this MV appears to be scattering from the protruding carbonate chimneys; free gas bubbles did not play a significant role. However, since ebullition of bubbles, particulates and fluids from MVs may be episodic, scattering from bubbles and particulates may be important for this particular MV at other times (perhaps associated with regional seismic events) and for other MVs in general. A simple visco-elastic model predicts reasonable first-order dependencies of the scattering as a function of frequency and vertical bistatic angle. With multibeam coverage over a larger area, we plan to develop a statistical clutter model based on the initial simple model developed here.

The short-range scattering measurement technique itself may be of importance to the community inasmuch as it is a fairly general way to probe small-scale features, dimensions of O(10–100) m. The key advantages of the technique (as compared to long-range techniques) are that: (a) the uncertainties associated with propagation through a generally sparsely sampled ocean are minimized, and (b) the proximity to the feature allows measurement geometries and concomitant analysis that can directly test hypotheses about the scattering mechanisms. One potential challenge with a vertical array (insonification is over 2π) is that the feature of interest must have a large scattering cross section compared to the background sediment. However, in practice, this is not expected to be a serious limitation since interest in clutter is focused on those features that have a high scattering cross section.

Future work will focus on the interpretation of long-range scattering from this same mud volcano. The observation that the scattering is nearly isotropic in the vertical plane should simplify that analysis inasmuch as the simple metric target strength can be employed.

ACKNOWLEDGMENTS

This research was supported by the Office of Naval Research in collaboration with the NATO Undersea Research Centre (NURC) under whose auspices the data were collected during experiment campaigns in 1998, 2002 and 2004. The authors express appreciation to Peter Nielsen, Chief Scientist of the Boundary 2002, Boundary 2004 Experiments under the aegis of the Boundary Characterization Joint Research Project, as well as the NURC ocean engineering personnel, the officers and crew of the *R/V Alliance* and the *ITS Tavolara* from which the GAS-SCIPACK measurements were performed.

[1]P. Ratilal, Y. Lai, D. Symonds, L. Ruhlman, J. Goff, C. Holland, J. R. Preston, E. Scheer, M. Sundvik, and N. Makris, "Long-range acoustic imaging of the continental shelf environment: the Acoustic Clutter Reconnaisance Experiment 2001," J. Acoust. Soc. Am. **117**, 1977–1998 (2005).
[2]M. K. Prior, "A scatterer map for the Malta Plateau," IEEE J. Ocean. Eng. **30**, 676–690 (2005).
[3]C. W. Holland, "Mapping seabed variability: Rapid surveying of coastal regions," J. Acoust. Soc. Am. **119**, 1373–1387 (2006).
[4]G. Etiope and A. V. Milkov, "A new estimate of global methane flux from onshore and shallow submarine mud volcanoes to the atmosphere," Envir. Geosciences **46**, 997–1002 (2004).
[5]A. V. Milkov, "Worldwide distribution of submarine mud volcanoes and associated gas hydrates," Mar. Geol. **167**, 29–42 (2000).
[6]G. Cifci, A. Limonov, L. Dimitrov, and V. Gainanov, "Mud volcanoes and dome-like structures an the Eastern Mediterranean Ridge," Mar. Geophys. Res. **19**, 421–438 (1997).
[7]C. W. Holland, G. Etiope, A. V. Milkov, E. Michelozzi, and P. Favali, "Mud volcanoes discovered offshore Sicily," Mar. Geol. **199**, 1–6 (2003).
[8]P. Yin, S. Berne, P. Vagner, B. Loubrieu, and Z. Liu, "Mud volcanoes at the shelf margin of the East China Sea," Mar. Geol. **194**, 135–149 (2003).
[9]G. Etiope, G. Marinaro, P. Favali, F. Furlan, S. Cenedese, and F. Gasparoni, "New technologies for methane leakage monitoring from seafloor-Description and first operational results," OMC-2005, Paper 177A, *Offshore Mediterranean Conference and Exhibition*, Ravenna, Italy, March 16–18, 2005.
[10]C. de Moustier and D. Alexandrou, "Angular dependence of 12 kHz seafloor acoustic backscatter," J. Acoust. Soc. Am. **90**, 522–531 (1991).
[11]G. Etiope, "Evaluation of a micro-gas chromatographic technique for environmental analyses of CO_2 and C_1–C_6 alkanes," J. Chromatogr. A 775, 243–249 (1997).
[12]G. Rehder, R. S. Keir, E. Suess, and T. Pohlmann, "The multiple sources and patterns of methane in North Sea waters," Aquat. Geochem. **4**, 403–427 (1998).
[13]M. Hovland and A. G. Judd, *Seabed Pockmarks and Seepage* (Graham and Trotman, London, 1988), p. 293.
[14]I. Leifer and R. Patro, "The bubble mechanism for methane transport from the shallow sea bed to the surface: A review and sensitivity study," Continental Shelf Res. **22**, 2409–2428 (2002).
[15]C. W. Holland, R. Hollett, and L. Troiano, "A measurement technique for bottom scattering in shallow water," J. Acoust. Soc. Am. **108**, 997–1011 (2000).
[16]P. Sylva, P. Menard, and D. Roy, "A reconfigurable real-time interpolation beamformer," IEEE J. Ocean. Eng. **11**, 123–126 (1986).
[17]C. W. Holland, "Shallow water coupled scattering and reflection measurements," IEEE J. Ocean. Eng. **27**, 454–470 (2002).
[18]For the monostatic case, two of the paths (direct-bottom and bottom-direct) arrive at the same instant in time, however, the incoherent assumption might still be reasonable since the incident and scattered angles are different for the two paths; thus the phases are not expected to be identical. If the two paths did sum completely coherently, the transmission loss would be 1.8 dB lower than modeled here.
[19]F. Li, J. Liu, and R. Zhang, "A model/data comparison for shallow-water reverberation," IEEE J. Ocean. Eng. **29**, 1060–1066 (2004).
[20]J. F. Faran, "Sound scattering by solid cylinders and spheres," J. Acoust. Soc. Am. **23**, 405–418 (1951).

Subcritical scattering from buried elastic shells

Irena Lucifredi and Henrik Schmidt
Department of Ocean Engineering, Massachusetts Institute of Technology, Cambridge, Massachusetts 02139

(Received 5 July 2005; revised 31 August 2006; accepted 31 August 2006)

Buried objects have been largely undetectable by traditional high-frequency sonars due to their insignificant bottom penetration. Further, even a high grazing angle sonar approach is vastly limited by the coverage rate dictated by the finite water depth, making the detection and classification of buried objects using low frequency, subcritical sonar an interesting alternative. On the other hand, such a concept would require classification clues different from the traditional high-resolution imaging and shadows to maintain low false alarm rates. A potential alternative, even for buried targets, is classification based on the acoustic signatures of man-made elastic targets. However, the elastic responses of buried and proud targets are significantly different. The objective of this work is to identify, analyze, and explain some of the effects of the sediment and the proximity of the seabed interface on the scattering of sound from completely and partially buried elastic shells. The analysis was performed using focused array processing of data from the GOATS98 experiment carried out jointly by MIT and SACLANTCEN, and a new hybrid modeling capability combining a virtual source—or wave-field superposition—approach with an exact spectral integral representation of the Green's functions for a stratified ocean waveguide, incorporating all multiple scattering between the object and the seabed. Among the principal results is the demonstration of the significant role of structural circumferential waves in converting incident, evanescent waves into backscattered body waves, emanating to the receivers at supercritical grazing angles, in effect making the target appear closer to the sonar than predicted by traditional ray theory.
© *2006 Acoustical Society of America.* [DOI: 10.1121/1.2357711]

PACS number(s): 43.30.Jx, 43.40.Ey, 43.40.Rj [RAS] Pages: 3566–3583

I. INTRODUCTION

Buried objects have been largely undetectable by conventional high-frequency sonars, due to the low levels of energy penetrating into the sediment, in particular at subcritical insonification angles. Use of supercritical insonification has been limited by the small area coverage rate in shallow water. Critical grazing angles are typically $20°-30°$, causing the range coverage of such a sonar to be limited to about twice the ocean depth. With subcritical penetration depth being inversely exponential with frequency,[1] a low-frequency sonar concept is therefore an attractive alternative. On the other hand, the reduced resolution at the lower frequencies makes traditional classification by imaging impossible, raising the need for alternative classification clues to keep the false alarm rates acceptable.

In this regard, the use of acoustic target signatures for classification may be a realistic alternative, in particular in the mid-frequency regime $1<ka<10$, where the structural signatures are rich in information about target shape and composition, as demonstrated by decades of analysis of scattering by elastic shells, such as spheres and cylinders.[2,3] For such acoustic signature classification, it is obviously critical that the relation between the target characteristics and the acoustic scattering is well understood. Resonance scattering theory[2] can be used to link both the position and the damping of the target resonances to the geometrical and physical properties of the elastic object, and some attempts have been made to set up a target recognition scheme based on the analysis of the resonance spectrum. In these, and the studies that followed, the characterization of the scattering problem was mainly performed in the frequency domain.

Among the past theoretical solutions, exact formulations have emerged for calculating the scattered field from general elastic bodies embedded in a fluid half-space,[4–7] in an elastic half-space,[8] and in fluid layered waveguides.[9,10] The work to follow was concentrated on the salient features of the scattering in the vicinity of medium boundaries[11–13] and formed the basis for understanding the physics of acoustic interaction with objects that are either suspended in shallow water or buried.

Throughout the late 1980s authors such as Kargl and Marston[14] have made observations and done modeling of the backscattering of short tone bursts from elastic spherical shells in terms of Lamb wave returns, axial reverberations, and glory effects often using a generalization of the geometric theory of diffraction to elastic objects in water described in Refs. 15 and 16. Thus far, theoretical analysis focusing on the scattering from elastic shells near boundaries has dealt with how the free-field resonance structure of the shell is influenced by the sediment loading and interface interactions. In particular, the discussion[9–11] was concentrated on the origin of modifications to the resonance structure giving rise to the classically observed symmetric and antisymmetric Lamb modes on shells and plates. Others[17] have used resonance scattering theory (RST) models in combination with experimental results to address the dynamics of elastic waves

 © 2006 Acoustical Society of America

reradiated from spherical shells buried at different depths and insonified with a bounded beam at supercritical incident angles.

In mine countermeasures (MCMs) applications, resonance of man-made elastic targets is a pivotal concept that distinguishes them from rocks or other clutter that may have a similar minelike shape. Nevertheless, burial of an elastic target in the seabed results in a variety of modifications to the scattered response caused by different physical mechanisms, geometric constraints, and intrinsic properties of the sediment. While considerable attention has been devoted to the problem of scattering from submerged shells, and some attention to scattering from partially buried shells, flush-buried shells have rarely been investigated, owing to the fact that flush-buried targets are difficult to detect and, even more so, the response they produce is challenging to analyze as the complete burial into sediment greatly affects the shell response observable in the water column.

While the initial response in the sonar detection community was to investigate the modes of energy coupling in the sediment through both the seabed roughness scattering and the frequency-selective phase matching from the ripple structure,[1] much of the attention is now being devoted to the analysis and the classification of the sediment altered elastic target scattering response. Being evident that lower frequencies possess better sediment penetration properties due to lower attenuation as well as a slower decaying evanescent field below the seabed interface, they become a preferred choice for detection of buried objects using subcritical incidence. In addition, it has been established that at lower frequencies, man-made targets, such as elastic shells, support the excitation and radiation of strong structural waves and resonances that create a specific acoustic signature that distinguishes them from other objects, and therefore can be used in detection and classification of targets.

In addition, knowledge of bistatic buried target responses may have potential in new multi-platform, autonomous surveillance systems. A leap from more traditional supercritical monostatic receiver-target configuration to a bistatic configuration is a logical step to obtain additional useful information for target classification.

On this background the motivation of the research presented here was to investigate the scattering from flush and partially buried targets in near-field bistatic configuration, insonified using subcritical incidence. To alleviate the shortcomings of the single-domain representation inherent in, e.g., the resonance scattering theory,[2] this work concentrates on a time-frequency representation rather than pure characterization of the scattering problem in the frequency domain. Furthermore, while ignored in the past, multiple scattering will be considered in the modeling and analysis, as it may play a significant role in complex shallow water environments where sound waves scatter from and between different objects and interfaces in close vicinity to each other.

This work aims to identify, analyze, and explain the fundamental effects of the sediment and the proximity of the seabed interface on the scattering of sound from elastic spherical shells insonified at low frequencies and subcritical incident angles. The global objective of this work is to develop an improved understanding of the fundamental physics of scattering from buried targets and subsequently to develop a robust methodology for their acoustic signature classification.

This paper describes the modeling and processing tools applied in the analysis, and then applies them to analyze and confirm a previously hypothesized dominance of elastic, circumferential waves in shaping the scattering from flush-buried spherical shells. Presenting the newly developed target scattering model and a beamforming approach are as much in the center of interest of this work as is using those tools to confirm a hypothesis about a flexural Lamb wave phenomenon observed in the experimental data as well as in the model. Thus, a preliminary investigation of bistatic scattering from buried targets[18] has postulated that at low frequencies (2–5 kHz range) and subcritical insonification, the target scattering is dominated by the specular scattering of the evanescent lateral wave, with the backscattering being excited by evanescent wave tunneling, similar to the behavior of a perfectly rigid target. In contrast, at high frequencies (10–15 kHz) the specular component becomes less significant due to the shallow penetration depth of the lateral wave, and instead a significant amount of energy is coupled into flexural, supersonic Lamb waves that radiate directly into the sediment and subsequently transmit energy into the water column at supercritical angles. This would suggest that the traditional plane-wave, ray-tracing approach to the propagation to and from the target is inadequate and should be replaced by a wave theory propagation model, adequately coupled to the target scattering model.

II. GOATS98 EXPERIMENT

A series of GOATS experiments was conducted with a long-term objective of developing new sonar concepts that exploit the information about target characteristics available in the 3-D multistatic field, and to attain improved detection and classification of buried targets.

The GOATS98 experiment was primarily aimed at developing an improved fundamental understanding of the physics of three-dimensional acoustic scattering from proud and buried objects. In addition, GOATS98 focused on exploring some of the fundamental aspects of the autonomous ocean sampling network technology for shallow and very shallow water MCMs. The GOATS98 experiment provided a first step towards the development of future MCM sonar concepts, by achieving a unique measurement of full three-dimensional scattering by man-made and natural objects, along with the associated seabed reverberation. At the same time it demonstrated the use of AUVs as acoustic receiver platforms for MCMs, and their potential for rapid environmental assessment in shallow littoral environments.

Detection and classification potential of multi-static configurations was explored by investigating the differences in 3-D characteristics of seabed reverberation and target returns. Since both aspect-dependent targets and seabed ripples produce strongly anisotropic scattered fields, the differences in their spatial and temporal structure are better exploited by multi-static sonar configurations, with a potential for both

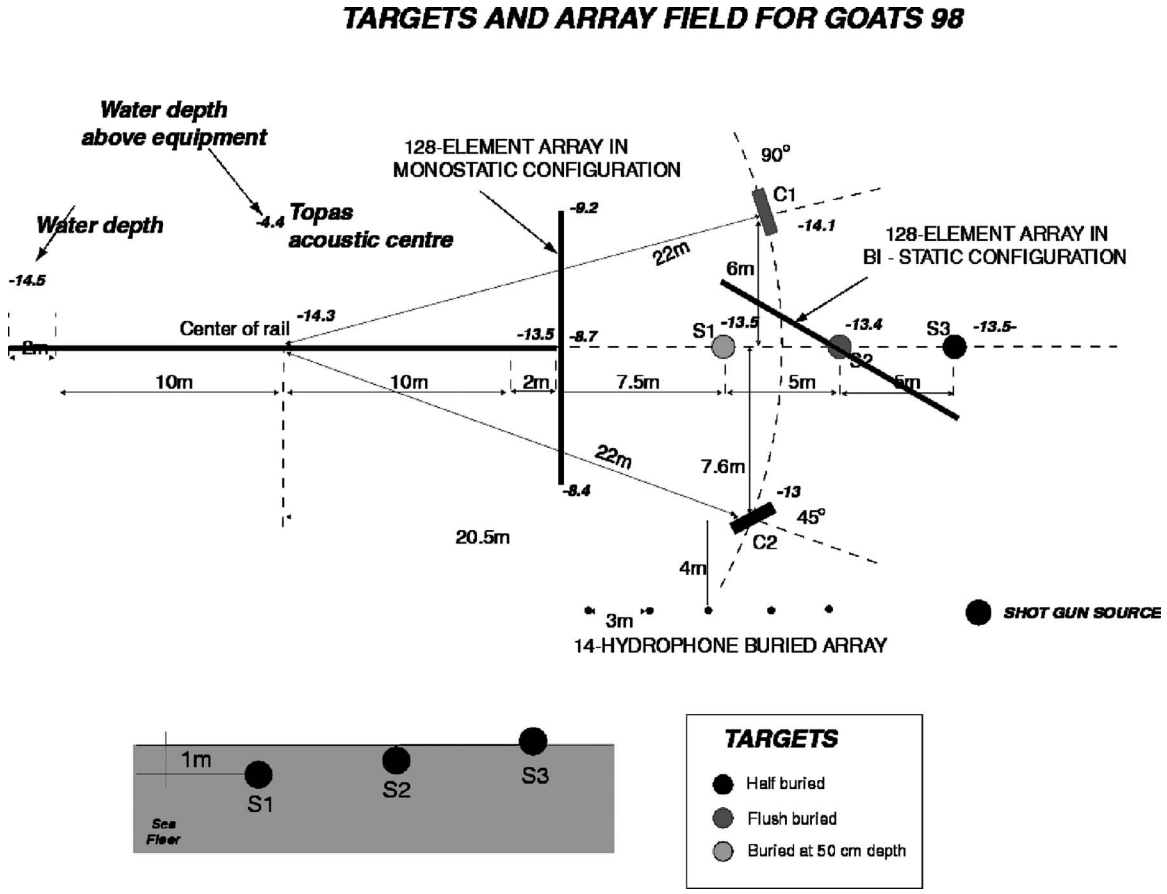

FIG. 1. Top view of GOATS98 experimental configuration. A stationary parametric source TOPAS parametric projector with a frequency range of 12–16 kHz was mounted on a 10-m-tall tower allowing target insonification at grazing angles below the critical grazing angle of 24°. The target field of interest consisted of three identical air-filled steel spherical shells S1 deeply buried, S2 flush buried, and S3 half buried. A 128-element HLA was placed 5 m vertically above the flush-buried target S2.

detection and classification performance enhancements compared to the more classical sonar systems.[19] With the limited spatial coherence of target signals, the new multi-static sonar concepts exploit the differences in scattering directionality between targets and reverberation. The anisotropic spatial structure of the target field is critical for detection and classification enhancement of bi- and multi-static MCM concepts. In addition, the frequency dependence of monostatic and bistatic target scattering may be exploited for detection and classification of buried objects. Some of the previous modeling studies[20] have suggested that significant gains can be achieved by operating in a lower frequency regime (i.e., 1–3 kHz), where the evanescent penetration coupling is strong.

A. Experimental configuration

The GOATS98 experiment was carried out in May 1998 in 12–15-m-deep water off the coast of the island of Elba, Italy. Prior to the experiment a number of spherical and cylindrical targets were buried at different depths, within a 10 $\times 10$ m^2 area of sandy bottom. The thickness of the sand was several meters and it has provided an environment for the penetration and the target scattering investigation. A bistatic phase of the GOATS98 experiment consisted of a stationary parametric source (TOPAS) insonifying a target field. As depicted in Fig. 1, the parametric projector was mounted on a 10-m-tall tower that could be repositioned along a 20-m-long rail on the seabed, allowing target insonification at grazing angles below as well as above the critical grazing angle of 24°. The TOPAS transducer was used to insonify the target field with a highly directional beam. It consists of 24 horizontal staves, electronically controlled to form a beam in a selected direction. The secondary frequency range of the source was 2–16 kHz.

The target field consisted of three identical air-filled steel spherical shells S1 deeply buried, S2 flush buried, and S3 half buried, each of 1.06-m-o.d. and 3-cm shell thickness. The spheres were deployed in line with the TOPAS rail. The rationale behind having three identical spheres was to make it possible to evaluate the variation of detection of performance as a function of burial depth and grazing angle in monostatic, but primarily in bistatic, configuration. In addition, two steel cylinders were flush buried at aspect angles of 90° for C1 and 45° for C2. The 2-m-long and 50-cm-diam. cylinders were both water filled, having a shell thickness of 6 mm. Both of the cylinders were flush buried in the sediment. The different cylinder orientations effectively emphasized the fundamental difference in the bistatic target returns as well as providing a base for multiple aspect response analysis. The source transmitting a Ricker pulse with a frequency band of 2–16 kHz and the center frequency of

8 kHz insonified sphere S2 at a subcritical incidence of 18° using a highly directive beam. A combination of fixed and mobile arrays was available for recording the 3-D scattered field. Among them, a 128-element horizontal line array (HLA) in bistatic configuration with 9-cm element spacing was suspended 5 m vertically above the flush-buried spherical shell S2. The data received on the HLA proved to be of high quality and represents an important contribution towards establishing the validity of numerical models and investigating the above-stated target scattering physical phenomena.

B. Observations and hypotheses

In an effort to explain anomalous high-frequency scattering observed experimentally from flush-buried targets, an earlier paper[18] presented a hypothesis regarding the role of elastic circumferential waves providing a strong mechanism for converting evanescent incident waves into propagating waves, which efficiently couple back into the water column. The findings of this preliminary study suggested that for subcritical insonification of buried targets, the traditional plane-wave, ray-tracing approach to the propagation to and from the targets is inadequate and must be replaced by full wave theory modeling. In the following, a more comprehensive analysis is performed, using experimental data and new modeling capabilities.

Thus, the GOATS98 experimental data set has been analyzed using a new focused beamforming approach, leading to identification of specular and elastic arrivals, and determining the different elevation angles at which they emerge from the seabed into the water column. As a result, this confirms the earlier hypothesis.

The target scattering scenario was modeled using the OASES-3D modeling framework, described later. As shown in Fig. 2, the TOPAS source was positioned on a 10-m-tall tower 29.5 m from the target S2, which was insonified at 18.7° grazing angle, well below the critical grazing angle of 24°. The AUV track was approximately perpendicular to the source-target axis, passing between the two at the distance 3.8 m from S2 at the point of closest approach. In this particular case a single scattering target modeling capability was employed. The resulting synthetic time series and spectrogram was obtained at 1-m spacing over a 10-m synthetic aperture. The time-frequency results of the above-described setup were quite unexpected and consisted of an initial strong low-pass-filtered specular response at 5 kHz, followed by a strong flexural response at a high frequency of 10 kHz, also followed by the flexural multiples at lower frequencies. While this result compares well to the actual AUV GOATS 98 experimental results, it is in contrast with the supercritical insonification results investigated by Tesei *et al.*[17] that seem to follow the plane-wave ray-tracing theory and show a maximum in the flexural response at 8 kHz. Based on these results, the following physical mechanisms of subcritical scattering from flush-buried spherical shells were postulated. As depicted in Fig. 3, at low frequencies backscattering is dominated by the specular scattering of the evanescent, lateral wave. Therefore, for a subcritical receiver in the backscattering direction the evanescent wave is being excited by wave tunneling, with exponential decay in frequency. In contrast, as shown in Fig. 4, it is postulated that at higher frequencies the specular component becomes insignificant because of the shallow penetration depth of the lateral wave. However, for shallow burial depth the target curvature near the seabed allows the evanescent tail to couple efficiently into the flexural Lamb waves of which the supersonic component radiates into the sediment and transmits into the water column at supercritical angles. It therefore follows that the associated energy will arrive at water-column receivers at angles ranging from vertical, for a receiver above the target, to the critical angle at distant receivers.

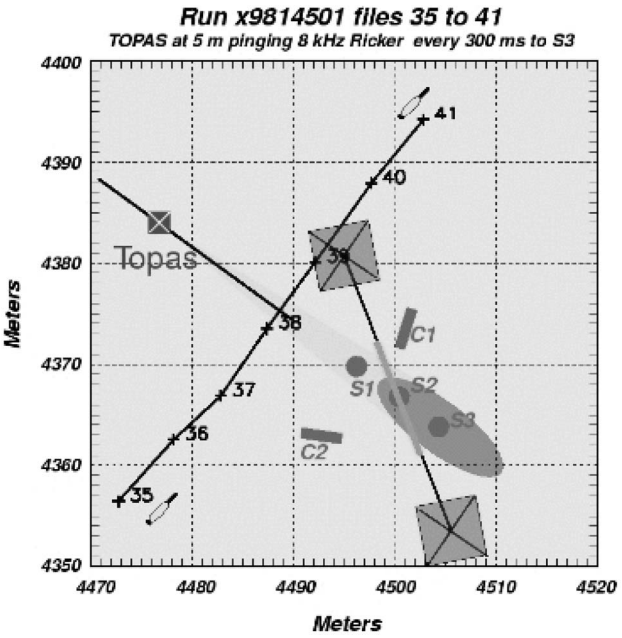

FIG. 2. Layout of the GOATS98 bistatic imaging experiment. A TOPAS parametric source is mounted on a tower, which may be relocated along a horizontal rail to change angles of incidence on the seabed targets. A fixed 128-element horizontal hydrophone array was suspended 5 m over the targets for fixed bistatic measurements, while an AUV equipped with a receiving array and acquisition system was used as a moving receiver platform, creating synthetic apertures at different offsets from the target field.

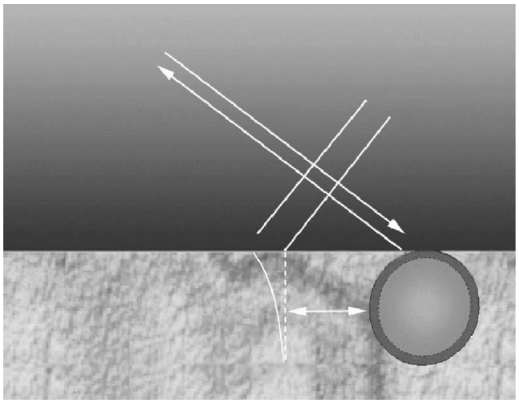

FIG. 3. Low-frequency representation of subcritical scattering from a flush-buried spherical shell. According to the hypothesis, the scattering at low frequency is dominated by the specular scattering of the evanescent lateral wave.

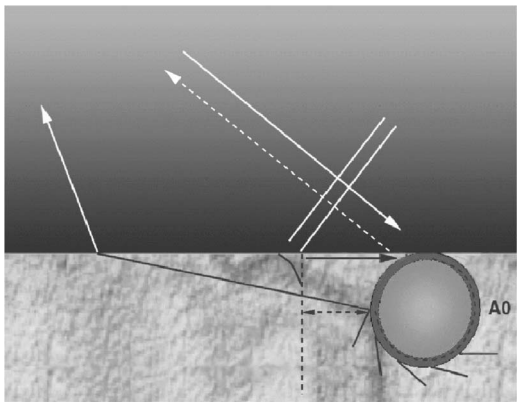

FIG. 4. High-frequency representation of subcritical scattering from a flush-buried spherical shell. In contrast to the low frequencies, at higher frequencies the scattering is dominated by the A0 Lamb wave, which radiates into the sediment and transmits into the water column at supercritical angles.

Consequently, for subcritical insonification the specular arrival will be low-pass filtered relative to the incident field, while the flexural Lamb wave becomes high-pass filtered because of the more effective reradiation of the supersonic component into the sediment and back into the water column. In Sec. IV B 3 beamforming of the synthetic and experimental data was applied in order to test this hypothesis regarding subcritical insonification.

III. TARGET SCATTERING MODEL

A. Overview

The analysis of the scattering from buried targets is performed using a combination of array processing and the modeling using a new hybrid, wave theory framework (OASES-3D) combining a virtual source approach to target scattering with an established wave number integration model for the ocean waveguide propagation to and from the target.[21] The virtual source approach, described in the following, is a generalization to arbitrary 3-D target geometry and composition of the classical wave-field superposition approach, e.g., the internal source density method, used by Stepanishen[22] to model 3-D scattering from objects of revolution with Dirichlet or Neumann boundary conditions in an infinite, homogeneous fluid. This virtual source approach to target scattering can be considered a full 3-D generalization of virtual source approaches such as the one proposed by Veljkovic[23,24] to model 2-D scattering from arbitrarily shaped objects near a seabed-water interface. All reported implementations of the method have had similar simplifications, which are avoided in OASES-3D. For example, Kessel[25] used a similar internal multipole expansion method in combination with a modal Green's function to model the scattering from objects in horizontally stratified waveguides, but again using ideal, homogeneous boundary conditions. Also, Kessel's, like Miller's,[26] approach does not allow the target to penetrate the waveguide interfaces and does not incorporate multiple scattering between the target and the adjacent boundaries. In addition, Sarkissian[27] did use a virtual source model to describe scattering by discrete objects in a waveguide, but the objects were not elastic and they were not buried in the sediment, therefore simplifying the theoretical approach, eliminating the structural and a number of environmental effects. Different from Lim's[7] approach, which employs the T-matrix formulation with multiple scattering, we develop and implement a different multiple scattering approach, which can handle realistic multiple scatterers of an arbitrary shape buried fully or partially in the sediment, as well as scattering from a nondiscrete entity such as a rough water-seabed interface. Additionally, in Lim's approach the bottom layer of the sediment is ignored, while we combine our scattering module with the OASES-3D wave-number integration approach, which fully incorporates the incident and scattered field interaction with all of the horizontally stratified layer interfaces.

B. Virtual source approach

The virtual source approach as implemented in OASES-3D involves three steps.[28] First, the incident field at the fully or partially buried target position in a stratified fluid-elastic waveguide is computed using standard wave-number integration.[29] The scattered field is then represented by removing the target and replacing it by a distribution of virtual sources inside the volume occupied by the target. After superimposing the incident field with the virtual source field, the virtual source strengths are determined by satisfying the boundary conditions on the surface of the target. The boundary conditions for any elastic target may be expressed in terms of the dynamic stiffness matrix, expressing the unique relationship between the surface pressure and the normal displacement. As opposed to other coupling approaches such as the "scattering chamber" approach, the replacement of the target by its unique stiffness matrix does not require the treatment of the outer medium in the target model. Therefore, once the dynamic stiffness matrix for the target is determined, it can be used for arbitrary orientation and burial of the target. This characteristic of the approach makes the investigation of the sensitivity of the scattered field to the parameters, such as seabed properties, burial depth, and insonificaton geometry, exceedingly convenient.

Different from Kessel's[25] and Stepanishen's[22] methods, this approach applies to general elastic objects with full 3-D geometry, requiring only a frequency-dependent stiffness matrix, associated with the target's internal structure and composition. In addition, the present approach allows the target to penetrate any interface in a horizontally stratified ocean environment, therefore providing a versatile numerical method for analysis of scattering from partially and fully buried targets. Furthermore, it takes into account multiple scattering effects within the target, as well as between the target and the environmental stratification as further investigated in Ref. 30.

The modeling of the target stiffness matrix is flexible and can be done using any target appropriate approach: a so-called "reverse" virtual source approach can be applied for a homogeneous fluid object, exact spherical harmonics representation can be used for spherical shells, or a more general numerical method such as finite elements can be used for other objects.

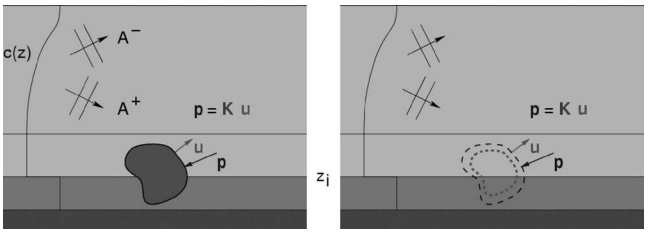

FIG. 5. Virtual source approach to scattering from partially buried targets in stratified ocean waveguides. The target is replaced by an internal, virtual source distribution generating a field in the background environment, which superimposed with the incident field, satisfies the boundary condition $\mathbf{p}=\mathbf{K}\mathbf{u}$, representing the target's dynamic stiffness properties.

The wave-field superposition principle is illustrated in Fig. 5. An arbitrarily shaped object in a stratified ocean is partially buried in the seabed. The stratification can include fluid as well as elastic layers, but it is assumed here for simplicity that the layers containing the target are isovelocity fluid media. The actual target is removed and replaced by a continuously stratified medium with a discrete distribution of N simple point sources, the unknown, complex strengths of which are represented by a dotted line. This source distribution is assumed to generate a field that is identical to the scattering produced by the target. Thus, if the surface of the target is discretized in N nodes, the total pressure $\mathbf{p}$ and normal displacement $\mathbf{u}$ are decomposed into the known incident field contribution $\mathbf{p_i}$, $\mathbf{u_i}$ and the scattered field $\mathbf{p_s}$, $\mathbf{u_s}$:

$$\mathbf{p}=\mathbf{p}_i+\mathbf{p}_s, \quad \mathbf{u}=\mathbf{u}_i+\mathbf{u}_s. \tag{1}$$

The scattered field is generated by the virtual source distribution $\mathbf{s}$:

$$\mathbf{p}_s=\mathbf{P}\mathbf{s}, \quad \mathbf{u}_s=\mathbf{U}\mathbf{s}, \tag{2}$$

with $\mathbf{P}$ and $\mathbf{U}$ representing $N\times N$ matrices containing the pressure and normal displacement Green's functions, respectively, between N virtual sources and N surface nodes.

The superimposed field on the virtual target surface must satisfy the boundary conditions associated with the real target. Thus, the field inside the true target must satisfy Green's theorem, providing a unique relation between the pressure and normal displacement on the surface. In a discrete representation with N surface nodes, this relation can be expressed in terms of a dynamic, frequency-dependent stiffness matrix $\mathbf{K}$:

$$\mathbf{p}=\mathbf{K}\mathbf{u}. \tag{3}$$

Combining Eqs. (1)–(3) leads to the following matrix representation for the virtual source strengths:

$$\mathbf{s}=[\mathbf{P}-\mathbf{K}\mathbf{U}]^{-1}[\mathbf{K}\mathbf{u_i}-\mathbf{p_i}]. \tag{4}$$

The components of the stiffness matrix obtained using spherical harmonics representation are given in Ref. 31. Once the virtual source strengths are found from Eq. (4), the scattered field is obtained anywhere in the external medium by superposition, using the continuous medium Green's function, in this case the stratified ocean waveguide.

1. Green's functions

The Green's function for a stratified ocean may be computed using any approach valid in the vicinity of the source and at all angles. Here we apply the exact Fourier-Bessel wave-number integration formulation[32] for stratified waveguides. Thus, the field produced by a horizontal distribution of sources can be expressed in an azimuthal Fourier series of the displacement potential $\phi(\mathbf{r})=\phi(r,\theta,z)$,

$$\begin{aligned}\phi(r,\theta,z)&=\phi_S+\phi_H\\&=\sum_{m=0}^{\infty}[\phi_S^m(r,z)+\phi_H^m(r,z)]\begin{Bmatrix}\cos m\theta\\ \sin m\theta\end{Bmatrix},\end{aligned} \tag{5}$$

where $\phi_S^m(r,z)$ and $\phi_H^m(r,z)$ are Fourier coefficients for the direct source contribution and the field produced by the boundary interactions, respectively. Both components are represented in terms of horizontal wave-number integrals,

$$\begin{aligned}\phi_S^m(r,\theta,z)=\frac{\epsilon_m}{4\pi}\int_0^{\infty}\left[\sum_{j=1}^{N}s_j\begin{Bmatrix}\cos m\theta_j\\ \sin m\theta_j\end{Bmatrix}\right.\\ \left.\times J_m(k_r r_j)\frac{e^{jk_r|z-z_j|}}{jk_z}\right]k_r J_m(k_r r)\,dk_r,\end{aligned} \tag{6}$$

$$\phi_H^m(r,\theta,z)=\int_0^{\infty}[A_m^+(k_r)e^{jk_z z}+A_m^-(k_r)e^{-jk_z z}]k_r J_m(k_r r)\,dk_r, \tag{7}$$

where k_r, k_z are the horizontal and vertical numbers, s_j is the complex source strength of source j at (r_j,θ_j,z_j), and $A_m^+(k_r)$ and $A_m^-(k_r)$ are the complex azimuthal Fourier coefficients of the up-and-downgoing wave-field amplitudes produced by the multiple boundary interactions. They are found by matching the boundary conditions at all horizontal interfaces. ϵ_m is a factor that is 1 for $m=0$ and 2 otherwise.

Considering only the multiple scattering between the target and the seabed, all that is needed for generating the Green's function matrices in Eq. (4) is the two-half-space Green's function, which for the virtual source and receiver both being in the water column above the seabed becomes

$$\begin{aligned}G_\omega(\mathbf{r}_i,\mathbf{r}_j)=s_j\frac{e^{ik_1|\mathbf{r}_i-\mathbf{r}_j|}}{4\pi|\mathbf{r}_i-\mathbf{r}_j|}+s_j\sum_{m=0}^{\infty}\begin{Bmatrix}\cos m\theta_i\cos m\theta_j\\ \sin m\theta_i\sin m\theta_j\end{Bmatrix}\\ \times\frac{\epsilon_m}{4\pi}\int_0^{\infty}\left[J_m(k_r r_j)R_{11}(k_r)\frac{e^{ik_{z;1}(z_I-z_j-z_i)}}{ik_{z;1}}\right]\\ \times k_r J_m(k_r r_i)\,dk_r,\end{aligned} \tag{8}$$

where R_{11} is the plane wave reflection coefficient for the seabed. Similarly, for the virtual receiver in the seabed, the Fourier-Bessel integral representation for the Green's function is

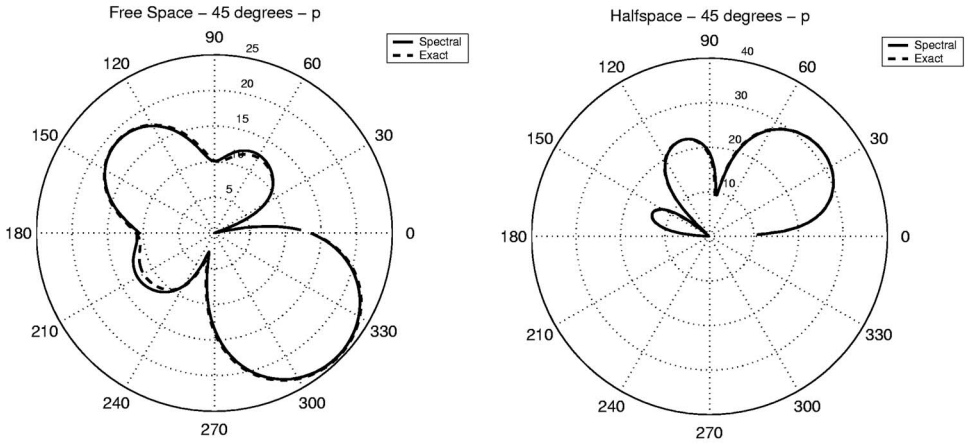

FIG. 6. Validation of spectral Green's functions. (a) Scattered acoustic pressure at 1 kHz 1 m from the center of the elastic sphere in an infinite fluid medium, with insonification at 45°. Solid curve shows the virtual source result using the spectral Green's function in. Eqs. (8) and (9). A dummy interface separating two identical water half-spaces passes through the center of the sphere. The result using the exact free-field Green's function is shown as a dashed curve. (b) Same, except lower half-space is air, and the dashed curve here shows the result obtained with the exact half-space Green's function using the method of images.

$$G_\omega(\mathbf{r}_i,\mathbf{r}_j) = s_j \sum_{m=0}^{\infty} \begin{Bmatrix} \cos m\theta_i \cos m\theta_j \\ \sin m\theta_i \sin m\theta_j \end{Bmatrix} \times \frac{\epsilon_m}{4\pi} \int_0^\infty \left[J_m(k_r r_j) T_{12}(k_r) \times \frac{e^{i(k_{z;1}(z_I - z_j) + k_{z;2}(z_i - z_I))}}{ik_{z;1}} \right] k_r J_m(k_r r_i)\, dk_r, \qquad (9)$$

with $T_{12}(k_r)$ being the transmission coefficient at horizontal wave number k_r.

C. Numerical implementation and validation

1. Virtual source distribution

Although the virtual source approach is, in principle, exact, the numerical stability of the solution is dependent on the virtual source distribution being such that it produces linearly-independent Green's function distributions over the surface nodes. In that regard it has been found empirically that a consistent convergence is achieved by distributing the surface nodes with a separation that is proportional to the local radii of curvature, and by placing a virtual source along the inward normal at each node, at a depth of approximately 0.6 times the node separation. This seems to provide the optimal compromise between diagonal dominance of the matrix to be inverted in Eq. (4) and efficient use of the dynamic range.

The numerical convergence of a virtual source scattering model has been validated by comparisons to exact spherical harmonic solutions for spherical shells[21] and by comparison to full finite element solutions for general shapes.[28]

2. Spectral Green's function

The computationally most intensive component of the present approach is the evaluation of the $N \times N$ pressure and displacement Green's function matrices **P** and **U** in Eq. (4) through the Fourier-Bessel representations in Eqs. (8) and (9). Here it is extremely important to take advantage of any target symmetries and variables of limited dimension. Thus, for example, for targets with vertical axisymmetry, the virtual sources and surface nodes are naturally placed in "rings" at constant depth, thus heavily reducing the number of required values of Bessel functions. Other computational gains can be achieved by careful use of numerical devices such as precomputed tabulations of the exponential and Bessel functions, precomputing the wave-number functions, etc. Further gains are achieved by embedding the virtual source geometry within the integration kernels. In other words, instead of evaluating the spectral integrals for each source-receiver combination, the integral is performed simultaneously for all identical source-receiver combinations, leading to a reduction in computation order from $O(N^2)$ to $O(N)$, with N being the number of the virtual sources and surface nodes.

Another key to the convergence and efficiency is the adherence to all the standard sampling guidelines for wave-number integration,[29] including the use of complex integration contours, leading to very robust and accurate solutions as illustrated in Fig. 6. Thus, Fig. 6 compares the results of the virtual source approach using the spectral Green's functions in Eqs. (8) and (9) with the result obtained with exact Green's functions for an infinite medium with a dummy interface dividing the spherical target in two, and a homogeneous half-space with a pressure-release surface. Although these cases have very simple constant reflection and transmission coefficients of either unity or zero, the fact that a closed-form Green's function exists makes them ideal "sanity checks" for the spectral integrals. Figure 6(a) shows the scattered acoustic pressure at 1 kHz 1 m from center of an elastic sphere in infinite fluid medium, with insonification at 45°. The solid curve shows the virtual source result using the spectral Green's functions, while the result using the exact free-field Green's function is shown as a dashed curve. Figure 6(b) shows the comparison of the spectral and exact Green's function results when the lower half-space is replaced by air. Here the dashed curve shows the result obtained with the exact half-space Green's function computed using the method of images.

IV. ANALYSIS OF EXPERIMENTAL AND SYNTHETIC DATA

The analysis is performed using parallel, identical processing of the experimental data and the associated synthetics generated using the OASES-3D modeling framework. The analysis included time-frequency processing of the real and synthetic time series, as described in Sec. IV B 2. The array processing of both data sets are compared in Sec. IV B 3. In addition to providing a physical explanation of the observed behavior, the analysis verifies and validates the models.

A. Tools and approaches

1. Arrival time analysis

The first step in the analysis is the characterization of the dispersion of compressional S0 and flexural A0 waves as they revolve around the shell. Tesei[17] has completed a comprehensive analysis of the dispersion of the structural response of the spherical shells applied in the GOATS98 experiment.

Using the results of this analysis, a travel-time tool was developed to facilitate quick calculation of expected arrival times of specular, A0, and S0 waves from a point on the shell to a particular point in the water column.

Using 3-D vector calculus, the travel-time modeling tool determines the points on the shell from which A0 and S0 waves emanate to any point in the water column. Given known locations of the HLA receivers, it calculates the time it takes for the specular and the elastic returns to reach a given receiver. Therefore, corresponding travel times in the shell, the sediment, and the water are obtained. Snell's law is used to calculate the refraction effects at the water-sediment interface.

The procedure is carriedout as follows. Knowing the point at which the specular reflection is located on the shell, the distance traveled along the shell in both clockwise and counter-clockwise directions is calculated. The angle of radiation from each waveform is known by utilizing the phase matching formula given by

$$\theta_c^* = \arcsin\left(\frac{c_{\text{ext}}}{c_{\text{shell}}^*}\right), \tag{10}$$

where c_{shell}^* the shell membrane wave speed and c_{ext} is the shell exterior medium speed. The point of the emanation on the shell can be obtained by a dot product between the vector path in the sediment and the shell radial vector. The point at which the ray hits the water-seabed interface is determined by the location of the receiver and the angle obtained by Snell's law.

Once the distances connecting the points of interest are determined, the corresponding wave speeds are necessary to determine the times of travel. In the study conducted by Tesei *et al.*,[17] an auto-regressive spectral method was used to determine the phase and group speeds of compressional S0 and flexural A0 waves for a sediment- and water-loaded elastic shell. Dispersion curves of S0 and A0 waves give frequency-dependent speeds in the 2–15 kHz regime, which coincides with the frequency regime of the GOATS98 experiment. For the purpose of the travel-time calculation for the expected times of specular and flexural wave arrivals, speeds of A0 and S0 waves at the center frequency of 8 kHz are calculated from the group speed dispersion curves provided by Tesei,[17] with a result of 2200 m/s for the A0 wave group speed and 5650 m/s for the S0 wave group speed, when the shell was flush loaded in sediment. Once the speeds of elastic waves are established, and the compressional wave speeds in the sediment and water were determined *in situ*[1] to be 1640 and 1520 m/s correspondingly, the travel time calculation of particular arrivals can be carried out. In addition, it was also established[1] that the sediment attenuation was 0.5 dB/λ. The times of travel in shell, sediment, and water for clockwise and counter-clockwise A0 and S0 waveforms and their multiples can be used to identify the arrivals in time-frequency plots as it was done in Sec. IV B 2.

In the sections to follow, these theoretical expected arrival times are superimposed on the target scattering model results as well as on target scattering experimental results. By carrying out this procedure, the waveforms that comprise the target elastic response are identified in time, and the peculiarities of the amplitude and the frequency contents of identified arrivals can then be attributed to a particular waveform and further analyzed.

2. Focused beamforming approach

In addition to the time of arrival analysis, the following analysis was also done on a 1–46 receiver subarray, positioned in the backscattering direction with respect to the flush-buried target S2, as shown in Fig. 14. By focusing the beamformer to different points on the seabed, the range and the elevation of different wave types were determined, therefore determining the effective radiation strength of the particular area of the seabed. In order to obtain the information of interest, focused beamforming was repeated for each discrete elevation ϕ and the ranging azimuth θ. Therefore, a matrix that contained arrivals at different elevation-azimuth point pairs was generated.

The next stage consisted of projecting the elevation-azimuth pairs to the seabed interface. Since the positions of the subarray sensors and the position of the flush-buried target was known, an intersection of the beamforming cone and the plane containing the seabed producing a hyperbola had to be calculated to obtain a set of XY points on the seabed surface. For this purpose, as shown in Fig. 7, a new coordinate system is introduced where the array is temporarily aligned with the y axis on the ground, and thus the following expression for the equation of the cone and the equation of the seabed are obtained:

$$\frac{x^2}{a^2} + \frac{(z-z_0)^2}{a^2} - \frac{y^2}{b^2} = 0, \quad z = 0. \tag{11}$$

At the intersection of the cone and the seabed the following equation is obtained

$$x^2 + z_0^2 - (\tan^2 \alpha) y^2 = 0, \tag{12}$$

where $\tan \alpha = a/b$ and $\alpha = \phi - \pi/2$, giving

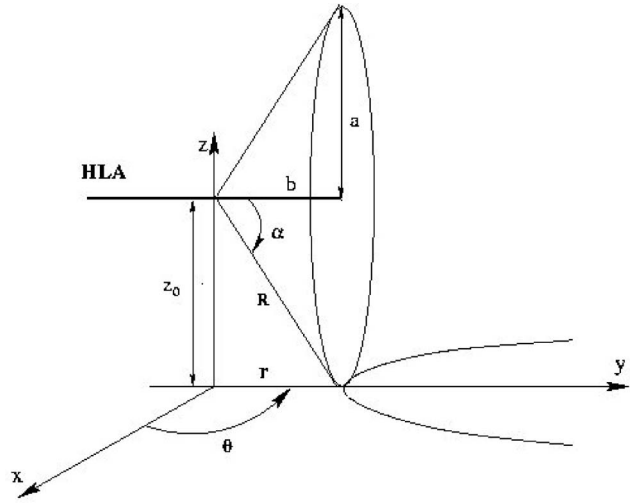

FIG. 7. Focused beamforming, projection of elevation, and azimuth angle on to an (X,Y) point on the seabed.

$$r = \frac{z_0}{\sqrt{\tan^2 \alpha \sin^2 \theta - \cos^2 \theta}} \tag{13}$$

from which the desired coordinate point pairs $(\bar{X},\bar{Y})$ for each α and θ are readily available. A rotation needs to be introduced to obtain the actual seabed coordinates (X,Y) that correspond to the GOATS98 experimental configuration:

$$X = \bar{X} \cos \theta_0 - \bar{Y} \sin \theta_0, \tag{14}$$

$$Y = \bar{X} \sin \theta_0 - \bar{Y} \cos \theta_0, \tag{15}$$

where θ_0 is the angle of azimuthal rotation of the HLA with respect to the y axis. This procedure was repeated for varying ϕ and θ angles, giving a family of hyperbole on the seabed comprised of different XY pairs. Figure 8 shows the XY pairs, on the seabed marked with dots, for ranging θ and ϕ. For each elevation and a range of azimuth angles, the intersection is a single hyperbola in the XY plane. As the elevation angle ϕ increases, different hyperbole describe a map of points on the seabed.

The final stage consisted of properly delaying the matrix of focus beamformed results, creating a real-time map of beamformed seabed radiation strength caused by the elastic shell response beneath it. The matrix, up to that point, contained beamformed results that represent repetition of a fixed set of events at different elevation angles used for beamforming. However, what was wanted for the projection on the seabed was a sequence of snapshots of the radiation strength of the seabed surface in real time, that is, an actual beamformed response of the effect of the radiating elastic target producing first the specular and then the set of elastic waves that hit the seabed surface at a certain elevation and azimuth in real time.

As shown in Fig. 9, to obtain this real-time map of seabed radiation strength, beamformed arrivals at each (X,Y) coordinate pair were shifted in time by Δt_i, which is the time necessary for the return to travel through water from the point of emanation on the seabed, (X_i,Y_i), to the center of the subarray:

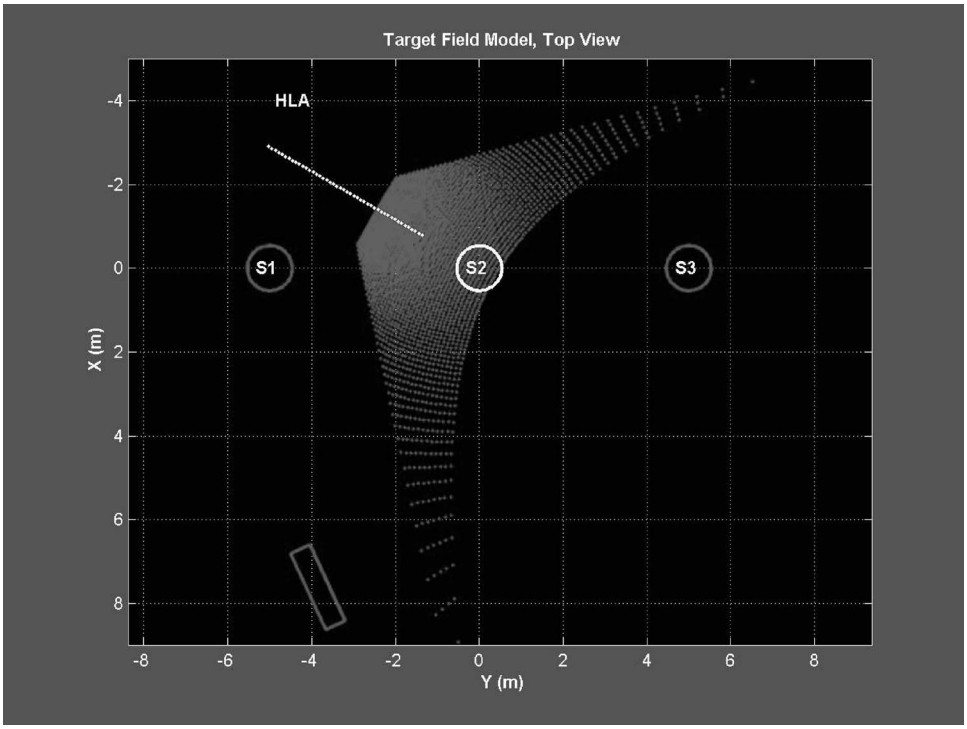

FIG. 8. Focused beamforming target field. The dots represent the calculated XY point pairs that comprise a family of hyperbole generated by the intersection of the beamforming cone and the seabed for varying elevation and azimuth.

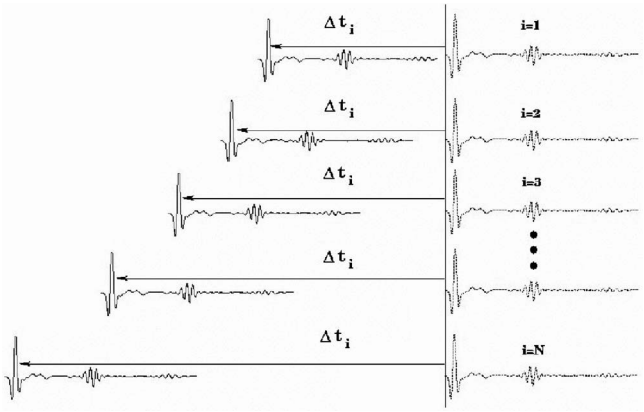

FIG. 9. In order to obtain the real-time map of seabed radiation strength, beam-formed arrivals at each (X,Y) coordinate pair were shifted in time by Δt_i, which is the time it takes for the return to travel through water from the point of emanation on the seabed (X_i,Y_i) to the center of the subarray.

$$\Delta t_i = \frac{R_{X_i,Y_i}}{c_\omega}. \tag{16}$$

As a result of this novel focus beamforming approach, various types of specular and elastic arrivals were identified, demonstrating the different elevation angles at which they emerge from the seabed into the water column.

B. Subcritical scattering by the flush-buried sphere—Results and discussion

1. Multiple scattering effects

One of the central objectives of this work is to analyze the mechanisms of scattering from buried targets under subcritical insonification, distinguish them from the ones generated using supercritical insonifications, and identify the target signature features that can be used to enhance detection and classification of buried mines. While multiple scattering has often not been taken into account in supercritical scattering from targets, it is likely to play a more significant role here, and it may become a possible classification clue for flush-buried target signatures for targets insonified using evanescent insonification. One of the goals in the study was to identify the features in the elastic shell scattering response brought about by multiple scattering, and use models that can incorporate it, in order to be able to compare the experimental and model data.

The snapshots of the results shown in Fig. 10 illustrate the effects of multiple scattering while also showing the peculiarities of the evanescent incidence on a flush-buried elastic spherical shell generated using the numerical target scattering module described in Sec. III that incorporates multiple scattering. The input parameters used for model runs were as follows: the incident field frequency was 3 kHz, the radius of the 3-cm-thick, 7700-kg/m^3 dense steel shell was 0.503 m, the shell compressional wave speed was 5950 m/s, and the shell shear wave speed was 3240 m/s. The compressional speeds of sand and water were 1640 and 1520 m/s, respectively, with the sand having 0.5 dB/λ attenuation. On the left-hand side, a plane wave is supercritically incident at 35°

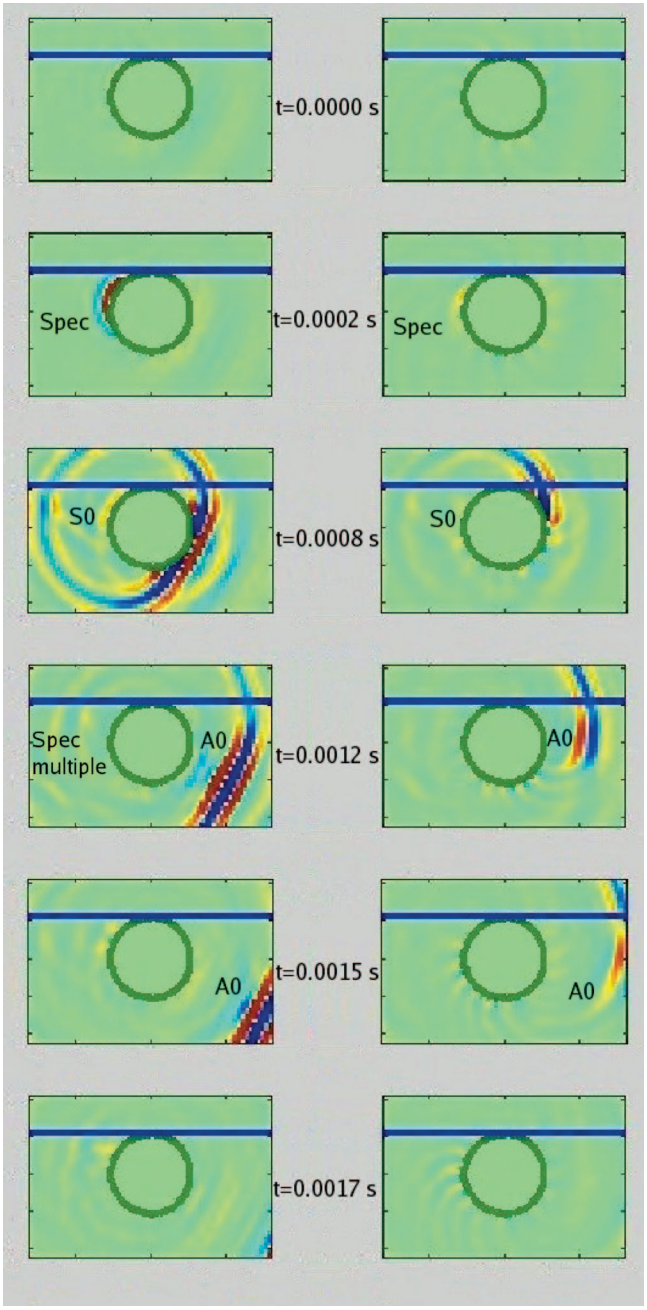

FIG. 10. Propagating (left) versus evanescent (right) incidence on a flush-buried spherical shell—multiple scattering included. The difference between the propagating and the evanescent incidence on a flush-buried elastic spherical shell was shown. The result was generated using the multiple scattering numerical model described in Sec. III. The figure also illustrates the contribution of multiple scattering to the flush-buried target response, and it is most obvious in the snapshots in the third and the fourth rows, where we can see the multiple reflections of the specular of the target hitting the water seabed interface, coming back to the target, and being reflected from it again towards the sediment-water interface.

on the flush-buried shell. The pronounced specular response of the target is visible, followed by the clockwise and counter-clockwise S0 compressional elastic waves, and the A0 flexural elastic wave. It is worth noting that clockwise and counter-clockwise components of the elastic waves are of similar amplitudes. The fourth row illustrates the effect of the clockwise and counter-clockwise components of the flexural A0 wave meeting and interacting after each one has traveled a full revolution around the shell.

On the right-hand side, a plane wave is incident subcritically on the seabed, producing an evanescent field that interacts with the flush-buried shell. In this case the response is quite different. The shell specular return is less pronounced, with the strongest response caused by the evanescent field coupling with the shell and the A0 wave circumnavigating the shell in the clockwise direction. The compressional S0 responses are apparent as yellow spots around the shell radiating as they travel faster than the A0 waves. The clockwise part of A0 response is shown here to be considerably stronger than its counter-clockwise counterpart, owing to the nature of the insonifying evanescent field that exponentially decays in depth.

This particular result is related to the Lamb wave hypothesis discussed in Sec. II B. It is the pronounced A0 Lamb wave, which according to the hypothesis, revolves around the target, radiates into the sediment, and transmits into the water column at supercritical angles.

Figure 10 also illustrates the contribution of multiple scattering to the flush-buried target response. This manifestation is the most obvious in the third and fourth row snapshots, where we can see the multiple reflections of the specular of the target hitting the water seabed interface, coming back to the target, and being reflected from it again towards the sediment-water interface. While the phenomenon is the most obvious in the propagating case on the left, due to the higher strength of the transmitted field, it is also visible in the evanescent incident case on the right. The multiple reflections of the flexural A0 and compressional S0 waves are also visible in the following rows.

2. Time-frequency analysis of the flush-buried shell

When a plane wave is incident on a shell in free space, the clockwise and the counter-clockwise returns travel the same path to the receiver in a monostatic configuration. As they revolve around the target, the flexural A0 returns radiate at a phase matching angle θ_c^* almost perpendicular to the target radius. The compressional S0 waves radiate, in turn, at a phase matching angle θ_c^* that is smaller than the A0 angle.

However, when the shell is flush buried in the sediment, and insonified at subcritical angles, an evanescent field is created in the sediment. For evanescent insonification, and the HLA receiver in bi-static configuration, such as the case in the GOATS98 experiment, Fig. 11 shows that when the time it takes to travel around the shell, through the sediment, and through the water column is added, A0I arrives at the receiver location before A0II. The same applies to S0I and S0II arrivals as well.

An out-of-plane source-receiver configuration (i.e., HLA receivers that are azimuthally away from the source-target axis in Fig. 1) is considered in Fig. 12. It represents the time series and the spectrogram of the GOATS98 experiment for a flush-buried target and receiver 26, located out of plane in the backscattering direction. The significance of the out-of-plane receivers in bistatic configuration is that they measure the 3-D target scattered field, supplying the classification and detection information, which a traditional monostatic in-plane receiver configuration[17] is not capable of providing.

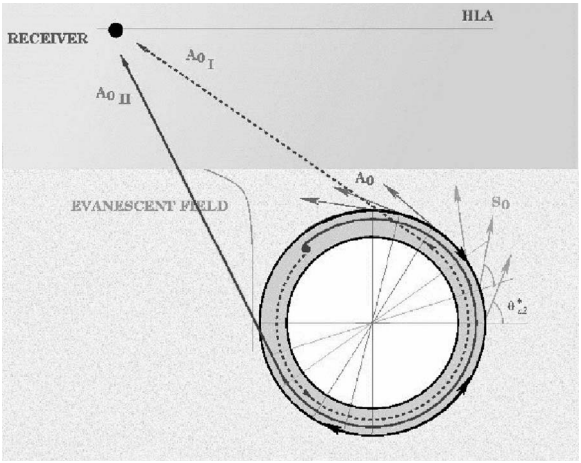

FIG. 11. Schematic of an evanescent field incident on a flush-buried elastic shell. For evanescent insonification and the HLA receiver in bi-static configuration, when the time it takes to travel around the shell, through the sediment, and through the water column is added, A0I arrives at the receiver location before A0II.

The locations of the arrivals on the spectrogram point towards the fact that the time of arrival calculations are accurate, as the specular and elastic arrivals coincide with the calculated expected times marked with black and green lines and calculated using the arrival time method from Sec. IV A 1. The spectrograms in Figs. 12 and 13 were both calculated using discrete Fourier transforms of Hanning windowed, well-overlapping segments of the corresponding time series. The number of FFT points used was 1024 giving the frequency resolution of 50 Hz, while the window length was 0.16 ms with the overlap of 0.12 ms, making the time resolution of the result about 0.1 ms. Due to the particular wave speeds and the configuration, S0I arrives before the specular, which is centered around 8 kHz. S0II is of considerably high-frequency content as it arrives at 12 kHz, and the following S0Ix2 at 10 kHz. Close to 23.5 ms, an A0I waveform arrives at a high frequency of 10 kHz, which is significantly higher than the expected center frequency of 8 kHz. At 24 ms A0II arrives at significantly high 12 kHz center frequency. The fact that S0I, A0I, and A0II have higher frequency content than the expected 8 kHz center frequency to begin with, provides evidence for the hypothesis from Sec. II B, where it is suggested that, under subcritical insonification, the flexural Lamb wave becomes high-pass filtered because of the more effective reradiation of the supersonic component into the sediment and the water column. By extension, the observed high frequency of the compressional part of the response can potentially also be affected by the more efficient coupling of the incident evanescent wave. It is believed that this is the first time in literature that the high-pass filter anomaly is demonstrated using experimental data under these conditions. It should be also noted that, unlike what is observed for propagating incidence,[17] the magnitude of the A0II flexural response is 8 dB higher than that of the specular response for the highly out-of-plane receivers in the backscattering direction.

Both the frequency content and the amplitude content differences described in the above paragraph present new

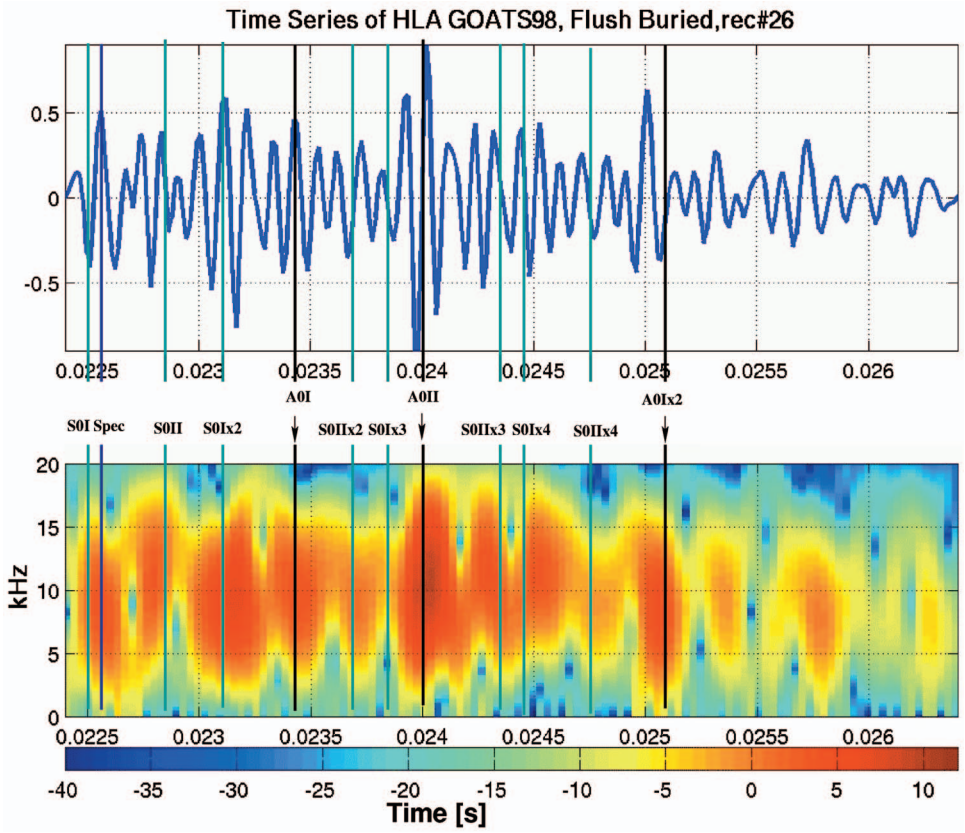

FIG. 12. Time series and spectrogram for a flush-buried target—experimental data, receiver 26. Calculated time of arrival expectations for S0 arrivals are marked with vertical green lines, while the expectations of A0 arrivals are marked with black lines. S0II is of considerably high-frequency content as it arrives at 12 kHz. Close to 24 ms, a strong A0II waveform arrives at a high frequency of 12 kHz, which is significantly higher that the expected center frequency of 8 kHz. Therefore, the high-pass filter anomaly of the flexural target response is identifiable in the experimental data. Also, the magnitude of the A0II flexural response is 8 dB higher than that of the specular response.

identification points for bistatic classification of buried targets insonified using evanescent incident fields.

Figure 13 shows the model result in the form of the time series and the spectrogram for the flush-buried target and the out-of-plane receiver 26. As before, S0I arrives before the shell specular return due to the target-receiver configuration. This agrees well with the corresponding experimental result in Fig. 12. The obvious high amplitude and 8 kHz center frequency specular is followed by S0II arrival at 7 kHz. This is lower than the corresponding experimental result in Fig. 12 that arrives at 12 KHz. Here, and for the rest of the time series record, experimental data consistently assign higher frequency contribution throughout the various wave types of the elastic response than the corresponding model results, even though the sediment attenuation used in the model corresponds to the measured value in an elaborate study by Maguer.[1] A few possible explanations of these discrepancies to be investigated in the future are shear and porosity effects not included in the fluid sediment model. Thus, energy is radiated into the shear waves, which are much slower than the flexural wave field.

Going down the time axis, the combined S0Ix2 and A0I effect is of significantly smaller amplitude and lower frequency content than that shown in the experimental results in Fig. 12. Also, the distinctive A0II flexural arrival dominates the elastic response, and it arrives at 9 kHz frequency, which is lower than in the in-plane receiver case but still higher than the 8 kHz center frequency traditionally observed with supercritical insonification and monostatic configuration. Yet again, this time for the modeled result, it is shown that the A0II flexural return arrives at higher frequencies than the corresponding specular return, validating the flexural Lamb wave high-pass filtering hypothesis. After the following several multiples of S0 returns, a repetition of weak A0Ix2 arrivals and a strong A0Ix2 flexural arrivals is observed.

Concerning the timing of the arrivals in the model data in Fig. 13, while the dominant A0II arrivals coincide with the black line predictions, S0Ix2 and A0I are offset from their prediction times by 0.1 and −.0.1 ms, respectively. On the other hand, those same expected times of arrival for S0Ix, A0I, and A0II agree well for the experimental data in Fig. 12. The fact that in Fig. 12 virtually all of the calculated expected times of arrival coincide with the experimental data, but are in some instances offset from model data in Fig. 13, might suggest some small inconsistencies in the timing of arrivals generated using the model. Additionally, the model result overall does have a more synthetic, clean quality to it, compared to the experimental response, which seems to be noisier.

In summary, the basic characteristic observed for a bistatic receiver for a flush-buried target under evanescent insonification confirms the high-pass filtering Lamb wave hypothesis. In addition, they present new identification points for bistatic classification of buried targets by pointing at the

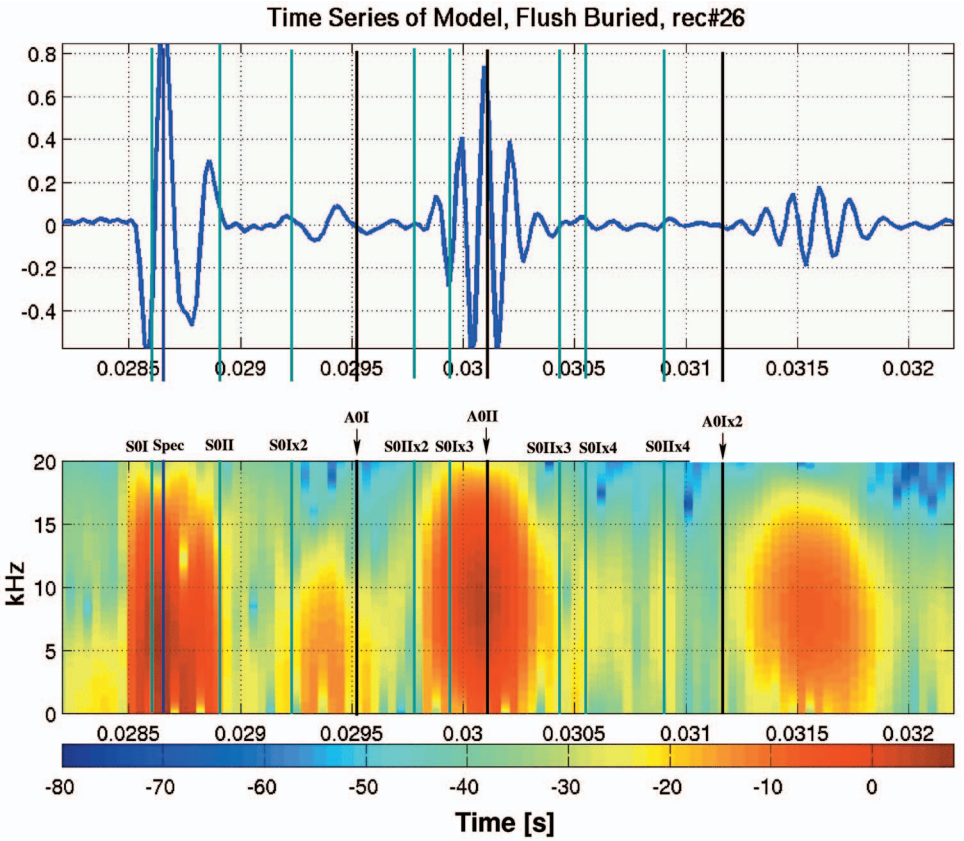

FIG. 13. Time series and spectrogram for a flush-buried target—model data, receiver 26. Calculated time of arrival expectations for S0 arrivals are marked with vertical green lines, while the expectations of A0 arrivals are marked with black lines. The combined S0Ix2 and A0I effect is of smaller amplitude and lower frequency content than that shown in the experimental results in Fig. 12. Also, the distinctive A0II flexural arrival dominates the elastic response, and it arrives at 9 kHz frequency.

amplitude and frequency differences between the specular, the clockwise, and the counter-clockwise components of the flexural waves as further discussed in Ref. 30.

3. Focused beamforming results

Array processing was applied to the HLA experimental and model data, to establish the elevation angle ϕ at which the specular and the elastic returns emerge from the seabed into the water column. This particular angle would provide information about the sediment propagation paths of the scattered wave types, and therefore gives insight in the physical phenomena that take place around the radiating sediment loaded shell.

Since the HLA was operated in a very near field with respect to the S2 target, focused wideband beamforming along sections of the HLA was initially done to determine the azimuthal angle of arrival of returns. The near field is defined as $r \leq L^2/\lambda$, where in our case the distance to the target is $r=5$ m, and at the center frequency of 8 kHz, the wavelength $\lambda=0.19$ m, with the length L of the whole array aperture of 11.43 m. Also, the HLA was segmented in three subarrays in order for the beamformer to be able to handle the wave-field inhomogeneities, but at the expense of the focusing ability. Figure 14 represents the configuration of a backscattering segment of the array, receivers 1–46, in its coordinate system where the center of the coordinate system is lying on the seabed, ϕ is the elevation angle with respect to the vertical z axis, and θ is the azimuth angle with respect to the x axis. At a range R, the beamforming cone intersects the seabed, creating a set of intersection points that describe a hyperbola.

As we are about to see, a fairly conventional practice of implementing a fixed-elevation focused beamformer, which has been implemented by other authors to experimental data in monostatic configuration,[33] ends up being marginally useful for our purposes, and therefore a new type of a beamforming approach was here developed in Sec. IV A 2 to extract more meaningful information about the physical mechanisms occurring during the elastic shell radiation process.

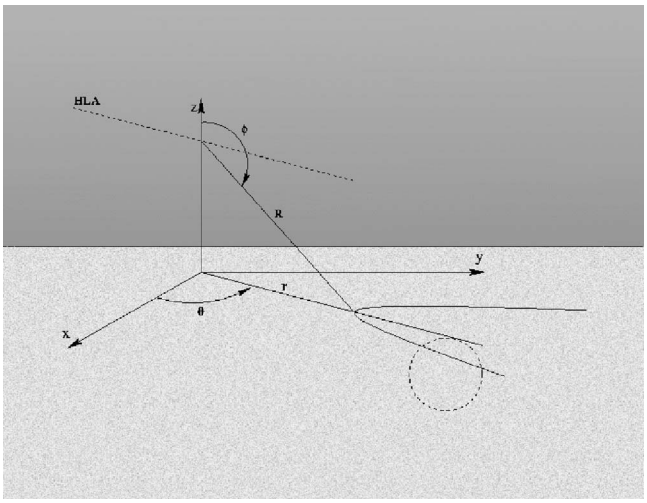

FIG. 14. Focused beamforming configuration of a back-scattering segment of the array, receivers 1–46, in the focused beamforming coordinate system where the center of the coordinate system is lying on the seabed, ϕ is the elevation angle with respect to the vertical z axis, and θ is the azimuth angle with respect to the x axis. At a range R, the beamforming cone intersects the seabed, creating a set of intersection points that describe a hyperbola. Note: The spherical target is flush buried in the sediment.

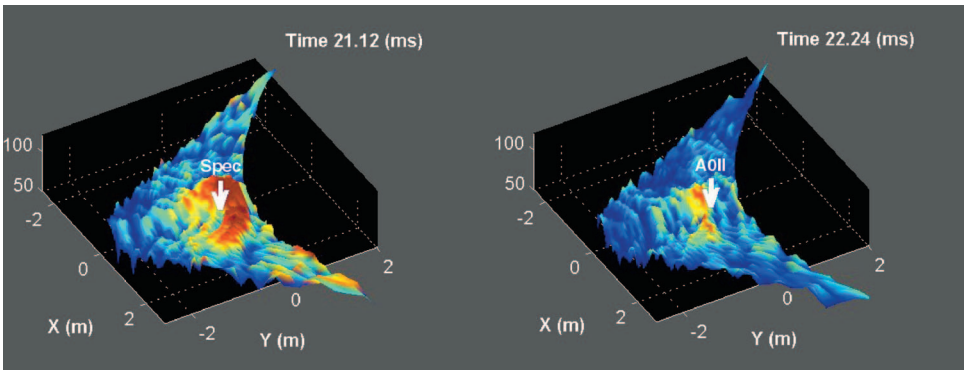

FIG. 15. Focused beamforming, flush-buried target—experimental data. This figure represents a part of a filmstrip of a 3-D representation of the location XY at which different beamformed target responses and their multiples emerge, and the strength of the response at that particular point is represented along the Z axis. The XY location of the flush-buried target is marked with a white vertical arrow, and the real time of the radiating shell response is marked in the upper right corner of each snapshot. Note that the arrow designates the target location, not the emerging wave location. The left snapshot shows that at 21.12 ms the specular arrival emerges at a seabed spot that corresponds to the coordinate (X,Y) pair of $(-0.5,0)$ m. The physical significance of this result is related to the fact that this particular point on the seabed corresponds to a particular elevation and azimuth angle pair $(\phi_{\text{spec}},\theta_{\text{spec}})$ at which the specular response is scattered from the buried elastic shell S2. In the right snapshot the A0II return is shown to arrive at a seabed point $(X,Y)=(-0.8,0)$ m, which is different from the specular, pointing at a different elevation angle of the elastic waves propagation through the sediment and coupling into the water column than the specular target return.

4. Experiment beamforming results

Figure 15 represents filmstrips of a 3-D representation of the beamformed scattering process from the flush-buried sphere S2 that was captured in time as snapshots of specular and elastic waveforms radiating from different points on the seabed. X and Y coordinates on the seabed are obtained from ϕ and θ as described in the previous section, and the strength of the response at that particular point is represented along the Z axis. The XY location of the flush buried target is marked with a white vertical arrow, and the real time of the radiating shell response is marked in the upper-right-hand corner of each snapshot.

In Fig. 15 the left snapshot shows that at 21.12 ms the specular arrival emerges at a seabed spot that corresponds to the coordinate (X,Y) pair of $(-0.5,0)$ m. The physical significance of this result is related to the fact that this particular point on the seabed corresponds to a particular elevation and azimuth angle pair $(\phi_{\text{spec}},\theta_{\text{spec}})$ at which the specular response is scattered from the buried elastic shell S2. In the right snapshot we can see the radiation strength of the sand for the stronger A0II, which emanates from the seabed into the water column at a different point that corresponds to a new (X,Y) pair of $(-0.8,0)$ m.

To more precisely determine the angles of arrival of specular and elastic returns, Fig. 16 was created using filmstrip snapshots of beamforming results with the elevation angle ϕ on the X axes and the azimuth angle θ on the Y axes. It shows at what particular elevation and azimuth angles the arrivals emerge from the seabed into the water column. The purple circle on the snapshots marks the (ϕ,θ) location of the target with respect to the subarray center. Specular, compressional S0, and flexural A0 waves and their multiples are identified on different time snapshots of the figure, where time is shown in the upper right hand corner. The first snapshot shows that the shell specular arrives at the sediment at an elevation ϕ of 143° and the azimuthal angle of 80°. The reader could refer to Fig. 14 for the graphical definition of the HLA-target elevation angle ϕ and the azimuthal angle θ.

The next snapshot on the right shows that the shell compressional return S0II arrives at roughly the same azimuth but very different elevation, namely $\phi=150°$. It should be noted that the higher elevation angle from the HLA to a point on the sediment surface means a shallower elevation angle from the target to that point of waveform emanation on the sediment surface. Therefore, this snapshot shows that the elastic shell compressional wave travels through the sediment at a 7° shallower angle than the target specular return.

The next snapshot shows the elevation of the S0Ix2 wave, which arrives at $\phi=151°$ and is also shallower than the specular arrival. The next snapshot on the right shows that the elevation angle of the first flexural A0I arrival is 147°, which also makes it shallower than the specular arrival. In the following snapshot the elevation angle of the flexural A0II arrival is 146°. The last snapshot shows the second revolution of the A0II return, A0IIx2, coming in at a distinctly shallow 161°. A possible explanation for A0Ix2 emerging at a different point than A0I follows from a sequence of physical mechanisms taking place during the target scattering process: longer distance circumnavigated, in form of revolutions, causes more attenuation to the waveforms, higher frequencies attenuate faster than the low ones, a change in frequency translates to a change in velocity governed by dispersion curves, a change in velocity means that the waveforms emerge at a different angle θ_c^* to the shell as demonstrated by the phase matching equation (10), which in turn causes the arrivals to hit the seabed at a different point and therefore at a different elevation angle. In addition, the overall resolution of the beamformed results is about 3° depending on the wave type, while the differences in the elevation angle between the specular and the first set of elastic arrivals are 7° and 4°, respectively, confirming that the beamforming resolution is high enough to support the conclusions.

Using this novel type of focused beamforming, the actual at-sea experimental results give quantitative base for the hypothesis about the physics of the propagation of elastic

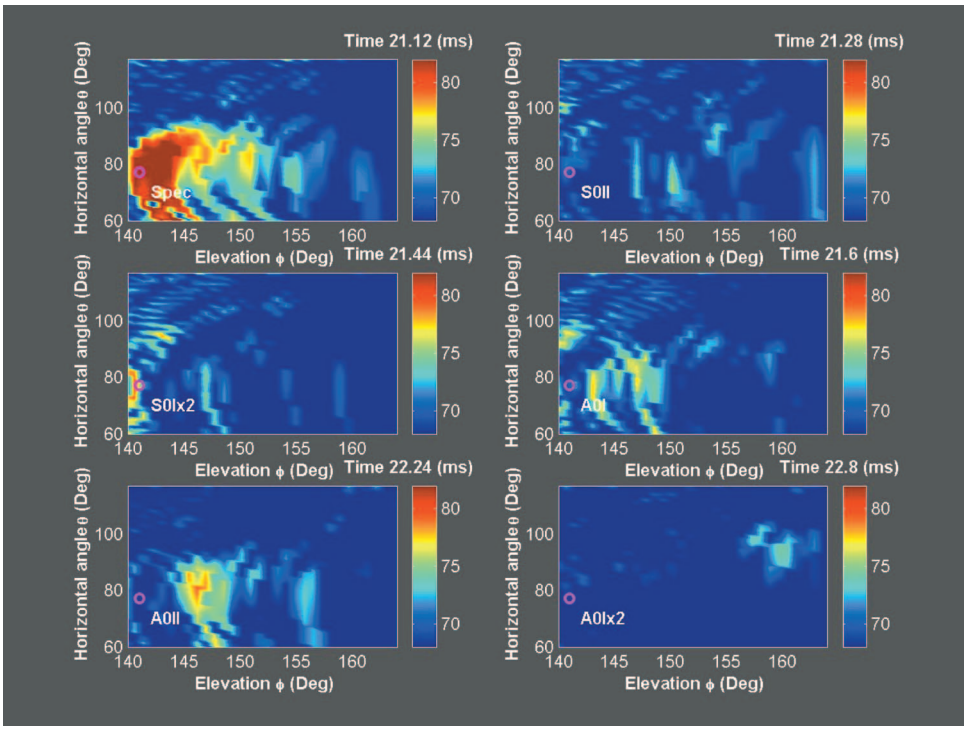

FIG. 16. Elevation-azimuth focused beamformed results—experimental data. This figure shows at what particular elevation and azimuth angles the target-radiated arrivals emerge from the seabed into the water column. The purple circle on the snapshots marks the (ϕ,θ) location of the target with respect to the subarray center. Specular, compressional S0, and flexural A0 waves and their multiples are identified on different time snapshots of the figure. The first snapshot on the left shows that the shell specular arrives at the sediment at an elevation ϕ of 143° and the azimuthal angle of 80°. The next snapshot on the right shows that the shell compressional return S0II arrives at roughly the same azimuth but different elevation, namely ϕ=150°, a 7° shallower angle than the target specular return. The figure also shows that the elevation angle of the first flexural A0I arrival is 147° and A0II is 146°, which makes the flexural waves also shallower than the specular target return. In the last snapshot the second revolution of the A0II return, A0IIx2, comes in considerably shallow at 161°.

waves under evanescent insonification described in Sec. II B, and make currently used wave-tracing arguments that assume all of the wave paths as to and from the target, unsound. The results and the analysis presented here differ from those presented by Lim[7] in the fact that he shows the angular dependence of the entire compound backscattered response, but does not assign the angular dependence of the individual emerging wavetypes such as specular, compressional, and flexural waves. He seems to be mostly concentrated on the differences in the compound backscattered field between the attenuating and nonattenuating sediment cases.

In addition, the result presented here confirms experimentally the proposed potential of yet another way of using structural waves to aid in the buried target classification, rather than the currently commonly used specular response alone, which often carries only a limited amount of useful information.

5. Model beamforming results

The whole multiple elevation beamforming procedure described in Sec. IV A 2 was repeated on the model data. In Fig. 17 the left snapshot shows that at 24.9414 ms the specular arrival emerges at a seabed spot whose center corresponds to the coordinate (X,Y) pair of $(-2,-0.2)$ m. On the right, the seabed radiation strength due to the stronger A0II return is seen to arrive at $(X,Y)=(-1.6,0)$ m at its own azimuth-elevation pair $(\phi_{A0II},\theta_{A0II})$ characterized by the specific physics of radiation around the shell and propagation through the sediment. This process is continued in time for the elastic responses that follow. The full sequence of film strips showing the emanation of the specular and all of the compressional and flexural responses can be found in Lucifredi's dissertation.[30]

The physical significance of the results shown above lies in the fact that they unambiguously show that the elevation angles of specular and elastic arrivals at which they emerge from the seabed into the water column are different, and therefore travel to the seabed-water interface at different elevation angles, a realization that is contrary to the traditional wave-tracing argument and in agreement with the hypothesis described in Sec. II B. In predicting this phenomenon, the virtual source model results are in agreement with the experimental results described in the previous paragraphs. Nonetheless, the differences between the experimental and model results do exist and are further addressed below.

In order to further investigate the phenomenon and, more precisely, determine the angles of arrival of specular and elastic returns, Fig. 18 was created using filmstrip snapshots of beamforming results with the elevation angle ϕ on the X axes and the azimuth angle θ on the Y axes. It shows at what particular elevation and azimuth angles the arrivals emerge from the seabed into the water column. The first snapshot shows that the shell specular arrives at the sediment at an elevation ϕ of 147° and the azimuthal angle of 82°. This is in agreement with the expected elevation and the

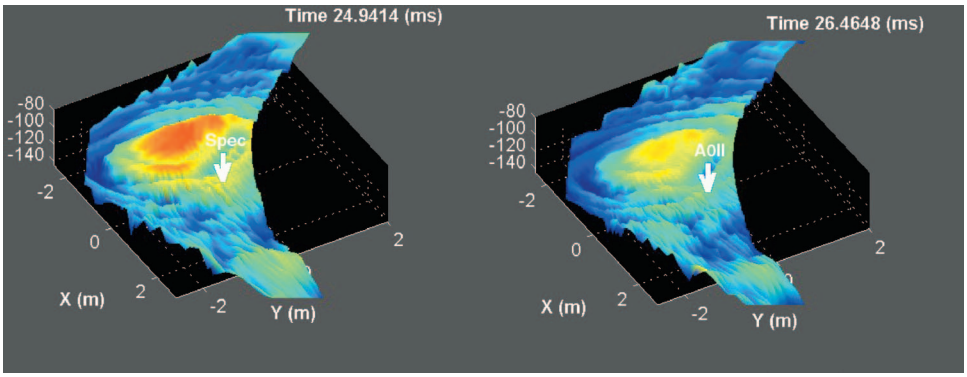

FIG. 17. Focused beamforming, flush-buried target—Model data. This figure is a filmstrip of a 3-D representation of the location XY at which different beamformed target responses emerge from the seabed, while the strength of the beamformed response at that particular point is represented along the Z axis. The XY location of the flush-buried target is marked with a white vertical arrow, and the real time of the radiating shell response is marked in the upper right corner of each snapshot. Note that the arrow designates the target location, not the emerging wave location. The left snapshot shows that at 24.9414 ms the specular arrival emerges at a seabed spot whose center corresponds to the coordinate (X,Y) pair of $(-2,-0.2)$ m. The physical significance of this result is related to the fact that this particular point on the seabed corresponds to a particular elevation and azimuth angle pair $(\phi_{\text{spec}},\theta_{\text{spec}})$ at which the specular response is scattered from the buried elastic shell. The snapshot on the right shows the beamformed radiation strength due to the A0II return, which is seen to arrive at $(X,Y)=(-1.6,0)$ m and its own azimuth-elevation pair $(\phi_{A0II},\theta_{A0II})$.

azimuth of the specular arrival in the backscattering direction from the geometric configuration of the target field.

The next snapshot on the right shows that the shell compressional return S0II arrives at almost the same azimuth, but very different elevation, namely $\phi=155°$. It should be noted that the higher elevation angle from the HLA to a point on the sediment surface means a shallower elevation angle from the target to that point of waveform emanation on the sediment surface. Therefore, this snapshot shows that the elastic shell compressional wave emerges from the sediment at an 8° angle difference with respect to the target specular return. In the experimental result in Fig. 16 the difference between the specular and the compressional returns was 7°.

The next snapshot shows the elevation of the S0Ix2 wave, which arrives at $\phi=151°$, which is also shallower than the specular arrival. The next snapshot on the right shows that the elevation angle of the first flexural A0I arrival is 154°, which also makes it shallower than the specular arrival. In the following snapshot the elevation angle of the flexural A0II arrival is 153°, and the one next to it is its next revolution arrival.

Therefore, much like the experimental data, the model consistently predicts flexural waves emanating at shallower angles than the corresponding shell specular return. However, in the model predictions the differences between the specular and the flexural angles are higher than what is observed with the experimental data. In addition, the focused beamforming processing seems to have been more effective on the experimental data where the point of emanation of the various waves is more concentrated around a certain

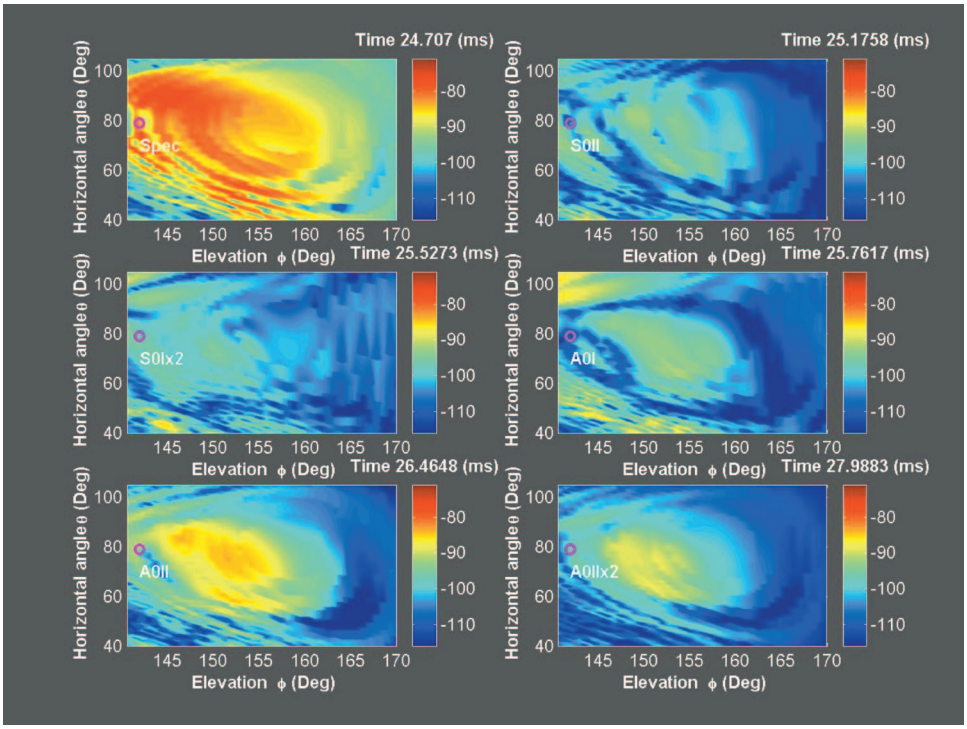

FIG. 18. Elevation-azimuth focused beamformed results, flush-buried target—Model data. This figure shows at what particular elevation and azimuth angles the target-radiated arrivals emerge from the seabed into the water-column. The purple circle on the snapshots marks the (ϕ,θ) location of the target with respect to the subarray center. Specular, compressional S0, and flexural A0 waves and their multiples are identified on different time snapshots of the figure. The first snapshot shows that the shell specular arrives at the sediment at an elevation ϕ of 147° and the azimuthal angle of 82°. The next snapshot on the right shows that the shell compressional return S0II arrives at roughly the same azimuth but very different elevation, namely $\phi=155°$, an 8° shallower angle than the target specular return. The figure also shows that the elevation angle of the first flexural A0I arrival is 154° and A0II is 153°, which makes the flexural waves also shallower than the specular target return.

elevation/azimuth pair, while the model-focused beamforming region is broader and more ambiguous, possibly related to the modeled time series shape, suggesting that the focusing was more successful on the experimental data set. Another point is somewhat of a difference in the horizontal angle of the array between the modeling and the experimental focused beamforming geometry. While the model-focused beamforming, which is an involved procedure, was done for the original array configuration, it was later established that the array orientation has somewhat changed during this particular phase of the experiment. Nevertheless, both of the array orientations were properly taken into account, and none of the focused beamforming conclusions drawn from the model were affected by this difference.

This result now quantitatively confirms the hypothesis about the physics of the propagation of elastic waves under evanescent insonification, showing that the nature of the physical processing taking place cannot be described using the traditional wave-tracing arguments that assume all of the wave paths as to and from the target, rendering them inadequate. Furthermore, related to the detection of fully buried targets, which was so far considered a challenging problem, here-shown specifics of the structural waves' radiation from the shell, propagation through the sediment, and coupling back into the water column as propagating waves provide a clear and an efficient way of so-called "smoke-shifting" these, otherwise hardly detectable, targets.

V. CONCLUSIONS

This paper has addressed the fundamental physics associated with scattering from targets buried in a shallow water seabed, specifically addressing and confirming earlier stated hypotheses regarding the dominant scattering mechanisms and the role of structural waves in shaping the acoustic signatures of such targets. A new hybrid modeling framework for complex targets in stratified waveguides was applied to generate controlled synthetics that were passed through the same processing chain as the experimental data, allowing for identification of physical mechanisms associated with the observed signal features. Time-frequency and array processing methods are developed and applied for extracting properties of buried target signatures that can be used to classify the targets based on their reradiated returns. A theoretical time-of-arrival tool was created and implemented to obtain the expected times of arrival of specular and elastic responses of buried elastic targets and therefore identify the target waveforms. In addition, a new focused beamforming approach that was formulated and implemented was used to determine the elevation angles at which specular and elastic returns emerge from the seabed into the water column.

Through the analysis of GOATS98 experimental data, validation of target scattering models, and hypothesis validation, the frequency and the amplitude content as well as the times of arrival of target elastic response have been examined. Among the most notable results is the finding of a difference in the frequency content of clockwise and counterclockwise Lamb wave components under subcritical insonification. New identification points for bistatic classification of buried targets were presented by pointing at the amplitude and frequency differences between the specular, the clockwise, and the counter-clockwise components of Lamb waves.

Even though the desired high-pass filtering effects and the elevation angles of different wave types are both shown in the model and the experimental data, discrepancies between the model and experimental results were observed. A few possible explanations of these discrepancies, to be investigated in the future, are shear and porosity effects not included in the fluid sediment model. As a result of sediment shear effects, energy is radiated into the shear waves, which are much slower than the flexural wave field, causing the discrepancy between the experimental and model result. In theory, the virtual source approach employed by the model can be generalized to elastic media, but the procedure is intricate.

Using focused beamforming, specular and elastic arrivals were identified and their associated radiation angles were estimated, providing evidence for an earlier stated hypothesis regarding the role of structural Lamb waves in converting the evanescent insonification to a radiating scattered field. Furthermore, regarding the detection of fully buried targets, which was so far considered a challenging problem, here-shown specifics concerning the structural waves provide a clear and an efficient way of so-called "smoke-shifting" these barely detectable targets.

ACKNOWLEDGMENTS

The authors would like to thank A. Tesei and R. Hollet at SACLANTCEN for their help and useful discussions. In addition, thanks to all of the scientists and engineers who made the GOATS98 experiment a success that resulted in a variety of rich and intricate datasets. Finally, the support of the Office of Naval Research is greatly appreciated.

[1]A. Maguer, W. Fox, H. Schmidt, E. Pouliquen, and E. Bovio, "Mechanisms for sub-critical penetration into sandy bottom: Experimental and modeling results," J. Acoust. Soc. Am. **107**, 1215–1225 (2000).
[2]H. L. P. Flax and W. G. Neubauer, "Reflection of elastic waves by a cylindrical cavity in an absorptive medium," J. Acoust. Soc. Am. **63**, 675–680 (1978).
[3]H. N. D. Veksler, J. L. Izbicki, and J. M. Conoir, "Bending a wave in the scattering by a circular cylindrical shell: Its relation with the bending free modes," J. Acoust. Soc. Am. **96**, 287–293 (1994).
[4]G. Kristensson and S. Ström, "Scattering from buried inhomogeneities-a general three dimensional formalism," J. Acoust. Soc. Am. **64**, 917–936 (1978).
[5]G. Kristensson and S. Ström, "The t matrix approach to scattering from buried inhomogeneities," in *Acoustic, Electromagnetic and Elastic Wave Scattering-Focus on T-Matrix Approach*, edited by V. K. Varadan and V. V. Varadan (Pergamon, New York, 1980).
[6]A. Karlsson, "Scattering from inhomogeneities in layered structures," J. Acoust. Soc. Am. **71**, 1083–1092 (1982).
[7]R. Lim, J. L. Lopes, R. H. Hackman, and D. G. Todoroff, "Scattering by objects buried in underwater sediments: Theory and experiment," J. Acoust. Soc. Am. **93**, 1762–1783 (1993).
[8]A. Boström and G. Kristensson, "Elastic wave scattering by a three dimensional inhomogeneity in an elastic half space," Wave Motion **2**, 335–353 (1980).
[9]R. H. Hackman and G. S. Sammelmann, "Acoustics scattering in an inhomogeneous waveguide," J. Acoust. Soc. Am. **80**, 1447–1458 (1986).
[10]R. H. Hackman and G. S. Sammelmann, "Multiple scattering analysis for a target in an oceanic waveguide," J. Acoust. Soc. Am. **84**, 1813–1825

(1988).
[11]G. S. Sammelmann and R. H. Hackman, "Acoustic scattering in a range independent shallow water waveguide with a penetrable bottom," *Proc. Oceans'89* (1989), pp. 1162–1167.
[12]G. S. Sammelmann and R. H. Hackman, "Acoustic scattering in a homogeneous waveguide," J. Acoust. Soc. Am. **82**, 324–336 (1987).
[13]R. H. Hackman, V. B. Johnson, R. Lim, L. Lopes, and G. S. Sammelmann, "Acoustic scattering from thin shells in bounded media and in sediments," *Proc. Oceans'89* (1989), pp. 1176–1180.
[14]S. G. Kargl and P. L. Marston, "Observations and modeling of the backscattering of short tone bursts from a spherical shell: Lamb wave echos, glory, and axial reverberations," J. Acoust. Soc. Am. **85**, 1014–1028 (1989).
[15]P. L. Marston, "Gtd for backscattering from elastic waves and cylinders in water, and the coupling of surface elastic waves with the acoustic field," J. Acoust. Soc. Am. **83**, 25–37 (1988).
[16]P. L. Marston, "Coupling coefficient g for Fabry-Perot representation of backscattering from spheres and cylinders: Quantitative gtd for elastic objects in water," J. Acoust. Soc. Am. (Suppl 1) **81**, 1014–1028 (1987).
[17]A. Tesei, R. Lim, A. Maguer, W. L. Fox, and H. Schmidt, "Measurements of acoustic scattering from partially and completely buried spherical shells," J. Acoust. Soc. Am. **112**, 1817–1830 (2002).
[18]H. Schmidt, "Bistatic scattering from buried targets in shallow water," *Proceedings, GOATS 2000 Conference*, SACLANTCEN Conference Proceedings CP-46, La Spezia, Italy, 21–22 August 2001.
[19]H. Schmidt, "Physics of 3-d scattering from rippled seabeds and buried targets in shallow water," SR 289, SACLANT Undersea Reserch Centre, La Specia, Italy (1998).
[20]W. Fox and A. Maguer, "Detection of buried objects at low grazing angles: Preliminary experimental results," SR 293, SACLANT Undersea Research Centre, La Specia, Italy (1998).
[21]H. Schmidt, "Virtual source approach to scattering from partially buried elastic targets," *Proceedings High Frequency Acoustics Conference*, San Diego, 1–5 March 2004.
[22]P. Stepanishen, "A generalized internal source density method for the forward and backward projection of harmonic pressure fields from complex bodies," J. Acoust. Soc. Am. **101**, 3270–3277 (1997).
[23]I. Veljkovic, G. Sandri, and R. J. Nagem, "Extended images in the theory of scattering," Aerotec., Missili Spazio **77**, 100–103 (1998).
[24]I. Veljkovic, "Acoustic scattering by the method of effective sources," M.S. thesis, Boston University, 1998.
[25]R. T. Kessel, "Scattering of elastic waves in layered media: a boundary integral-normal mode method," Ph.D. thesis, University of Victoria, 1996.
[26]R. D. Miller, E. T. Moyer, H. Huang, and H. Überall, "A comparison between the boundary element method and the wave superposition approach for the analysis of the scattered fields from rigid bodies and elastic shells," J. Acoust. Soc. Am. **89**, 2185–2196 (1991).
[27]A. Sarkissian, "Multiple scattering effects when scattering from a target in a bounded medium," J. Acoust. Soc. Am. **96**, 3137–3144 (1994).
[28]H. Schmidt, "Bistatic scattering from buried targets in shallow water - experiment and modeling," 7th European Conference on Underwater Acoustics, Delft, July 2004.
[29]F. Jensen, W. Kuperman, M. Porter, and H. Schmidt, *Computational Ocean Acoustics* (AIP, New York, 1994).
[30]I. Lucifredi, "Scattering from sub-critically insonified buried elastic shells," Ph.D. thesis, Massachusetts Institute of Technology, 2004.
[31]J. Lee, "Multi-static scattering of targets and rough interfaces in ocean waveguides," Ph.D. thesis, Massachusetts Institute of Technology, 1999.
[32]H. Schmidt and J. Glattetre, "A fast field model for three-dimensional wave propagation in stratified environments based on the global matrix method," J. Acoust. Soc. Am. **78**, 2105–2114 (1985).
[33]M. A. Pinto, A. Bellettini, R. Hollett, and A. Tesei, "Real- and synthetic-array signal processing of buried targets," J. Acoust. Soc. Am. **27**, 484–494 (2002).

A comparison of broadband models for sand sediments

James L. Buchanan
Mathematics Department, United States Naval Academy, Annapolis, Maryland 21402

(Received 4 September 2005; revised 11 August 2006; accepted 31 August 2006)

Chotiros and Isakson [J. Acoust. Soc. Am. **116**(4), 2011–2022 (2004)] recently proposed an extension of the Biot-Stoll model for poroelastic sediments that makes predictions for compressional wave speed and attenuation, which are in much better accord with the experimental measurements of these quantities extant in the literature than either those of the conventional Biot-Stoll model or the rival model of Buckingham [J. Acoust. Soc. Am. **108**(6), 2796–2815 (2000)]. Using a local minimizer, the Nelder-Mead simplex method, it is shown that there are generally at least two choices of the Chotiros-Isakson parameters which produce good agreement with experimental measurements. Since one postulate of the Chotiros-Isakson model is that, due to the presence of air bubbles in the pore space, the pore fluid compressibility is greater than that of water, an alternative model based on a conjecture by Biot [J. Acoust. Soc. Am. **34**(5), 1254–1264 (1962)], air bubble resonance, is considered. While this model does as well or better than the Chotiros-Isakson model in predicting measured values of wave speed and attenuation, the Rayleigh-Plesset theory of bubble oscillation casts doubt on its plausibility as a general explanation of large dispersion of velocity with respect to frequency. © *2006 Acoustical Society of America.*
[DOI: 10.1121/1.2357709]

PACS number(s): 43.30.Ma, 43.30.Pc [RAS] Pages: 3584–3598

I. INTRODUCTION

Neither the Biot-Stoll model (Biot,[1,2] Stoll[3]) for an unconsolidated sediment nor the more recently proposed model of Buckingham[4–7] made predictions for compressional wave speed and attenuation that were qualitatively in agreement with the measurements of the Sediment Acoustics Experiment 1999 (SAX99) (Thorsos *et al.*,[8] Richardson *et al.*[9]) The shortcomings of each model are illustrated in Fig. 1. As can be seen the Biot-Stoll model, using the parameters assigned by Williams *et al.*[10] overestimated the measured wave speeds below 1 kHz and underestimated the measured attenuation above 100 kHz. On the other hand the predictions of the Buckingham model were in accord with the measured wave speeds and attenuations in the region above 10 kHz, but the predicted wave speeds were higher and the attenuations lower than those measured below 10 kHz. As can also be seen in Fig. 1 the "Biot model with grain contact squirt flow and shear drag" (BICSQS) proposed by Chotiros and Isakson[11] improves upon both the low frequency predictions for wave speed and the high frequency predictions for wave attenuation of the Biot-Stoll model.

Other than the SAX99 measurements the case for strong dispersion of velocities at low frequencies is ambiguous. The wave speed and attenuation measurements from the cross-hole tomography experiments of Turgut and Yamamoto[12] shown in Fig. 2 also indicate strong dispersion. Shown in this figure are the predictions of the Biot-Stoll model based on the parameter values given by Turgut and Yamamoto, as well as the predictions of the BICSQS using the parameter values given by Chotiros and Isakson. The BICSQS again did noticeably better than the conventional Biot-Stoll model, though as Chotiros and Isakson note, the BICSQS is unable to track the oscillations in the Turgut and Yamamoto (TY90) data. On the other hand the recent measurements of Simpson *et al.*[13] in the 3–100 kHz (Fig. 6), which were not considered by Chotiros and Isakson, show only moderate velocity dispersion and seem consistent with the Buckingham model.

Buckingham[6] argues that an unconsolidated sediment is best treated as a generalized fluid in the sense that acoustic propagation is governed by the linearized Navier-Stokes equations. Buckingham disputes the applicability of Biot's model, which treats a poroelastic medium as an elastic frame with interstitial pore fluid, to the case of an unconsolidated sediment asserting that the elastic moduli of an uncemented sediment are effectively zero.[7] In the Buckingham model it is assumed that intergranular shearing suffices to give the sediment enough rigidity to support the propagation of shear waves. The model's prediction that, to the first order in the strain-hardening index, compressional wave attenuation increases linearly with frequency is in accord with the finding of Hamilton[14] and is supported by the SAX99 data in the higher frequency range. The Buckingham model predicts that compressional wave speed is only logarithmically dispersive with respect to frequency, as is required by the Kramers-Krönig causality relations, if attenuation is assumed to increase linearly with frequency. In this sense the Buckingham model may be regarded as a causal version of the widely used elastic model of a seabed. The Buckingham model has the virtue that its parameters can be calculated from fewer measurements: Compressional wave speed at a single frequency, and shear wave speed and attenuation at a single frequency as well as porosity and the densities and bulk moduli of the sand grains and pore fluid suffice. Because its prediction of only weak dispersion of velocity, the Buckingham model cannot explain the strong dispersion exhibited in the TY90 data, and in the SAX99 data, if the wave speed measurements at the two lowest frequencies are given credence.

 © 2006 Acoustical Society of America

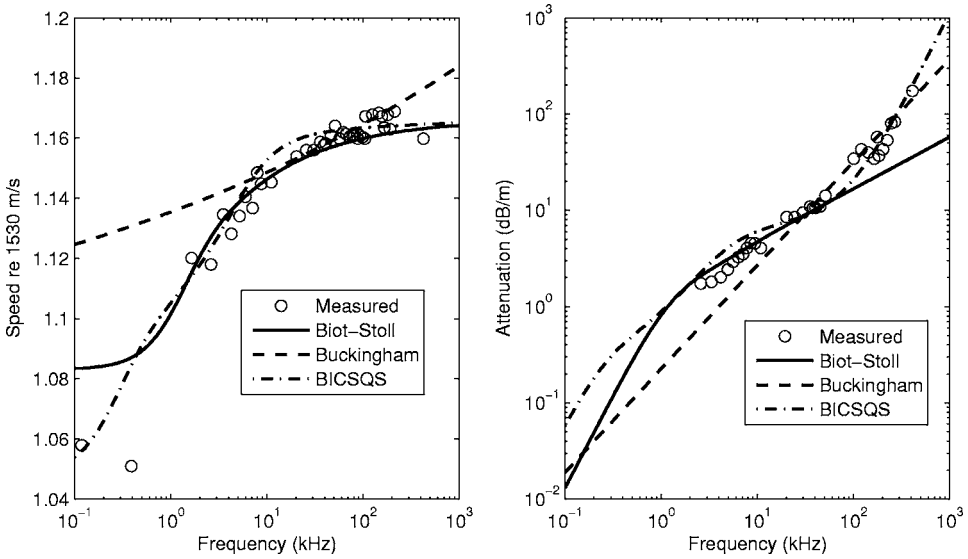

FIG. 1. Compressional wave speed and attenuation measurements and predictions for the SAX99 data. The measured values were normalized by the measured sound speed in water at the time and place of the experiment. The predictions of the models were normalized using a "typical" value of 1530 m/s. The Biot-Stoll parameters used for the predictions of the Biot-Stoll model are the "best fit" parameters found by Williams *et al.* (Ref. 10). The parameters used for the Buckingham model were a wave speed of 1771 m/s at 38 kHz, a shear wave speed of 129 m/s at 1 kHz and a shear wave attenuation of 30 dB/m.

II. THE CHOTIROS-ISAKSON BICSQS

Chotiros and Isakson were able to obtain much improved agreement with the SAX99 and TY90 data sets by augmenting the Biot-Stoll model with the assumptions (1) that the effective pore fluid modulus was less than that of water because of the presence of air bubbles in the pore space, and (2) that two Biot-Stoll parameters, the frame bulk modulus K_b^* and the frame shear modulus μ^*, depend upon frequency. As evidence for the first assumption, they cited the attempts to measure gas content of sediment cores described in Richardson *et al.*[9] which resulted in measurements ranging from 20 to 150 ppm. Because the amounts measured were less than that which the system was designed to resolve, the authors did not rule out the possibility that the gas content was zero. Thus the air bubble hypothesis is speculative. There are two other hypotheses, the composite material hypothesis and the independent coefficient of fluid increment hypothesis of Chotiros[15] which also could explain the low frequency SAX99 measurements. Further discussion of these hypotheses can be found in Buchanan.[16]

To obtain frequency-dependent moduli Chotiros and Isakson take the region between two sand grains to consist of an area of solid contact and a gap into and out of which fluid can flow when the frame is subjected to expansion and compression. Following Dvorkin and Nur,[17] they term this "squirt flow." The solid contact is modeled as a spring of modulus K_c and the effect of the flow in the gap, which will depend on the compressibility of the fluid and the resistance to radial expansion normal to the direction of the force is treated as a serial spring-dashpot (Maxwell) element with modulus K_y and damping constant η_y. The two mechanisms are assumed to act in parallel resulting in what is referred to in viscoelastic theory as the standard linear element [Fig. 3(a)]. Under a shearing force the absence of fluid loading for shear causes the viscoelastic element to simplify to a Kelvin-Voigt element with modulus G_c and damping constant η_s [Fig. 3(b)]. The effective moduli for the two types of elements undergoing time-harmonic oscillations $e^{-i\omega t}$ are (cf. Gittus,[18] for instance)

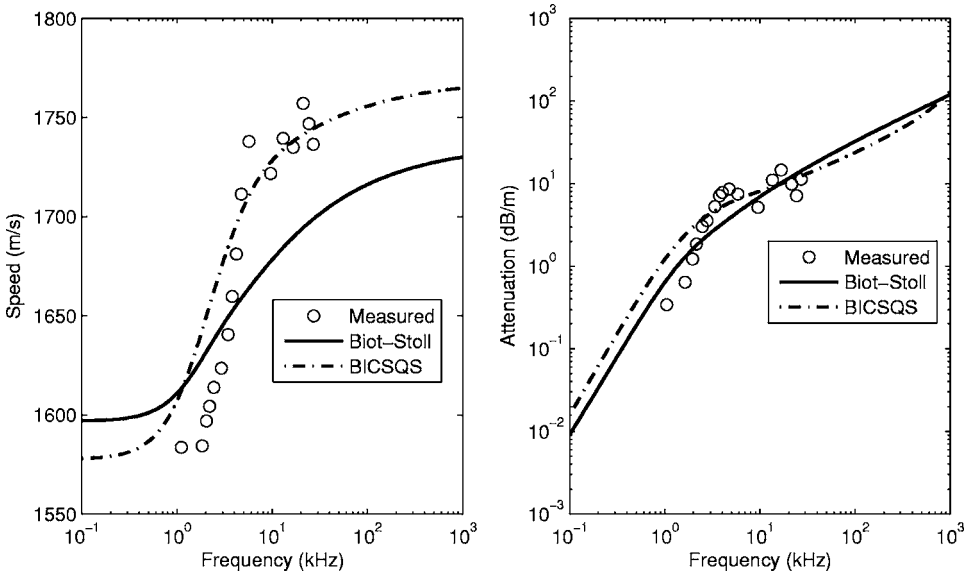

FIG. 2. Compressional wave speed and attenuation measurements and predictions for the TY90 data. The parameters used are those of Table I.

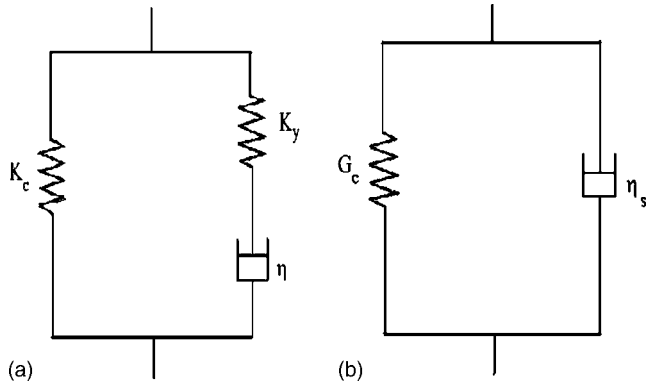

FIG. 3. (a) Standard linear viscoelastic element. (b) Kelvin-Voigt viscoelastic element.

$$K_b^* = K_c + \frac{K_y}{1 + i(\omega_k/\omega)}, \quad \mu^* = G_c\left(1 - i\frac{\omega}{\omega_\mu}\right),$$
$$\omega_k = \frac{K_y}{\eta_y}, \quad \omega_\mu = \frac{G_c}{\eta_s}. \tag{1}$$

Chotiros and Isakson identify these effective moduli with the Biot-Stoll parameters K_b^* and μ^*. Their argument for this is that the compressibility of the frame minerals is much less than that of the fluid and thus storage and loss mechanisms modelled by the two viscoelastic elements will predominate.

The zero-frequency values K_c and G_c of the two moduli are assumed to be related by an equation of elasticity

$$K_c = \frac{2}{3}G_c\frac{1+\nu}{1-2\nu}, \tag{2}$$

where ν is the Poisson ratio, and thus the four independent Biot-Stoll parameters $\mathrm{Re}\,K_b^*$, $\mathrm{Im}\,K_b^*$, $\mathrm{Re}\,\mu^*$, $\mathrm{Im}\,\mu^*$ are replaced by the five parameters G_c, K_y, ν, and the two relaxation frequencies

$$f_k = \frac{\omega_k}{2\pi}, \quad f_\mu = \frac{\omega_\mu}{2\pi}.$$

The shear modulus G_c can be determined from a measurement of shear wave speed at a low frequency and the contact modulus K_c computed from (2) with a Poisson ratio assigned a generic value consistent with the literature. Thus there are three "free" parameters K_y, f_k, and f_μ in (1) which are available to fit measured values of compressional wave speed and attenuation.

The values of the parameters that were used to generate the graphs labelled "BICSQS" in Figs. 1 and 2 are given in Table I. The process by which they were arrived at, as described by Chotiros and Isakson, was to choose an effective pore fluid bulk modulus K_f^{eff} which was consistent with the low-frequency data for wave speed and then to perform several iterations of sequentially manipulating K_y, f_k, f_μ, and permeability k to agree with the target wave speed and attenuation curves. Thus the BICSQS has five free parameters whose values are determined from wave speed and attenuation data. While this process arrived at a value of permeability very near that measured by Turgut and Yamamoto[12] using a constant head technique in the case of the TY90 data, it produced an estimate of permeability of $k=115\ \mu\mathrm{m}^2$ for the SAX99 sediment. For this sediment Williams *et al.*[10] gave a range for permeability of $[21,45]\ \mu\mathrm{m}^2$ as a 95% confidence interval for the method they regarded as most reliable, a constant head technique on divers cores. Another technique, image analysis of resin impregnated cores, produced a 95% confidence interval of $[7.5,48]\ \mu\mathrm{m}^2$ and an *in situ* constant head technique produced a 95% confidence interval of $[3.0,61]\ \mu\mathrm{m}^2$. Thus the entire range of measured values for permeability was $3-61\ \mu\mathrm{m}^2$, but Chotiros and Isakson's value is still outside of it. In defense of their high value for permeability the authors assert that permeability measurements may be accurate only to within an order of magnitude, but also speculate that the permeability in a sediment undergoing acoustic vibration is simply different from the permeability measured by constant head techniques. This assertion will be called the acoustic permeability hypothesis.

TABLE I. SAX-CI: Parameters for the SAX99 sediment used by Chotiros and Isakson. TY-CI: Parameters for the TY90 sediment used by Chotiros and Isakson.

Parameter	Units	SAX-CI	TY-CI
Porosity β		0.37	0.44
Grain density ρ_r	kg/m^3	2690	2650
Fluid density ρ_f	kg/m^3	1023	1000
Grain bulk modulus K_r	GPa	36	36
Fluid bulk modulus K_f	GPa	2.395	2.30
Effective fluid bulk modulus K_f^{eff}	GPa	2.15	2.25
Fluid viscosity η	kg/m-s	0.001	0.001
Permeability k	μm^2	115	17.5
Pore size a	μm	57	28
Structure factor α		1.35	1.24
Frame shear modulus μ	GPa	0.028	0.024
Gap modulus K_y	GPa	0.97	0.90
Bulk relaxation frequency f_k	kHz	4.8	3.2
Shear relaxation frequency f_μ	kHz	56	∞
Poisson Ratio ν		0.15	0.15

The approach that was taken in this work to determining parameter values was to use MATLAB's *fminsearch*, an implementation of the Nelder-Mead simplex multivariate minimization algorithm. Its use is not straightforward since problems of the sort being treated here typically have many local minima and thus the solution obtained may vary with the initial guess for the parameters. Also the solution may have parameter values that are implausible or even nonphysical. Empirically it is observed that the more parameters the algorithm is permitted to manipulate, the more likely this outcome is. Many of the simplex algorithm solutions presented in this work were not easy to find. Finding good solutions is a matter of persistence and even luck. The failure to find a solution having certain characteristics provides only circumstantial evidence that such a solution does not exist.

The use of the simplex algorithm requires an objective function to minimize. Given a set of measurements $c^* = \{c_n^*\}_{n=1}^N$ and a corresponding set of predictions $c = \{c_n\}_{n=1}^N$ by the model under consideration, the L_2 norm

TABLE II. CI: The Chotiros-Isakson parameters for the SAX99 sediment. S1, S1k, and S2 are simplex algorithm solutions of the BICSQS with norm weight 0.99. The parameters marked with * were those that were manipulated directly. B: The norms for the Buckingham model predictions.

Parameter	Units	CI	S1	S1k	S2	B
Effective fluid bulk modulus K_f^{eff}	GPa	2.15*	2.23*	2.21*	2.13*	
Permeability k	μm^2	115*	48*	43*	4.5*	
Pore size a	μm	57	37	36	11.4	
Gap modulus K_y	GPa	0.97*	0.50*	0.61*	1.2*	
Bulk relaxation frequency f_k	kHz	4.8*	9.2*	4.8	0.74*	
Shear relaxation frequency f_μ	kHz	56*	72*	68*	125*	
$\|c\|_{c^*}$	$\times 10^{-2}$	0.63	0.53	0.47	0.39	1.5
$\|a\|_{a^*}$		0.35	0.24	0.31	0.24	0.55

$$\|c\|_{c^*} = \frac{1}{\sqrt{N}} \sqrt{\sum_{n=1}^{N} \left(\frac{c_n - c_n^*}{c_n^*} \right)^2},$$

was be used to measure the discrepancy between measurement and prediction. Denoting the norms for compressional wave speed and attenuation by $\|c\|_{c^*}$ and $\|a\|_{a^*}$, respectively, the simplex algorithm was used to minimize the objective function

$$f(c,a) = w\|c\|_{c^*} + (1-w)\|a\|_{a^*}.$$

It turned out that for the data sets under consideration the c-norm was always much smaller than the a-norm and so a norm weight of $w=0.99$ was effective in mediating between the wave speed and attenuation data.

Tables II and III show the result of applying the simplex algorithm to the SAX99 and TY90 data sets using the BICSQS as the predictor model. Figure 4 shows the wave speeds and attenuations predicted by the three solutions of Table II. The parameters that the simplex method was allowed to manipulate were $K_f^{\text{eff}}, K_y, f_k, f_\mu$, and k with the pore size parameter being determined from the formula of Johnson, Koplik, and Dashen[19]

$$a = \sqrt{\frac{8\alpha k}{\beta}}. \tag{3}$$

The parameters not manipulated were given the values in the SAX-CI and TY-CI columns of Table I. For the SAX99 data two simplex algorithm solutions are given. S1 had lower c- and a-norms than the Chotiros-Isakson solution and a permeability almost within the range $[21,45]$ μm^2 favored by Williams *et al.*[10] Thus there is no need to assume as high a value for permeability as did Chotiros and Isakson. Solution S2, which had the lowest norms for any BICSQS solution found for the SAX99 data, had a much lower permeability, but one which was still within the range $[3,61]$ μm^2 of all measurements for SAX99. Both simplex solutions had higher shear relaxation frequencies than did Chotiros and Isakson's. Also Chotiros and Isakson found the bulk relaxation frequency f_k to be in the 3–5 kHz range for all five data sets they considered. They conjecture that this uniformity may be due to the average dimensions of the fluid film between grains. Solutions S1 and S2 have values well outside of this range, however, but in different directions. The solution S1k in Table II was obtained by setting the bulk relaxation frequency to $f_k = 4.8$ kHz assigned to it by Chotiros and Isakson and not permitting it to vary. The resulting solution has lower c- and a-norms than the Chotiros-Isakson solution and a permeability within the range favored by Williams *et al.* It could not have been arrived at without expectations concerning the value of f_k, however. As indicated in Table II the c-norms were about one-third and the a-norms about one-half the magnitude of those of the Buckingham model.

Which of the solutions S1,S1k, and S2 is most plausible depends upon what other information and expectations are brought to bear. If the permeability was unknown, S2 would be the best solution because of its lower c-norm, but if the

TABLE III. CI: The parameters Chotiros and Isakson used for the TY90 sediment. S1, S2 S2f: Simplex algorithm solutions. The parameters marked with * were those that were manipulated directly. The norm weight was 0.99.

Parameter	Units	CI	S1	S2	S2f
Effective fluid bulk modulus K_f^{eff}	GPa	2.25*	2.21*	2.26*	2.26*
Permeability k	μm^2	17.5*	17.5	8.0*	8.0*
Pore size a	μm	28	20	13	13
Gap modulus K_y	GPa	0.90*	1.00*	0.93*	0.93*
Bulk relaxation frequency f_k	kHz	3.2*	7.0*	5.3*	5.2*
Shear relaxation frequency f_μ	kHz	1000*	∞*	∞*	100
$\|c\|_{c^*}$	$\times 10^{-2}$	2.2	1.2	1.1	1.1
$\|a\|_{a^*}$		1.15	1.02	0.83	0.84

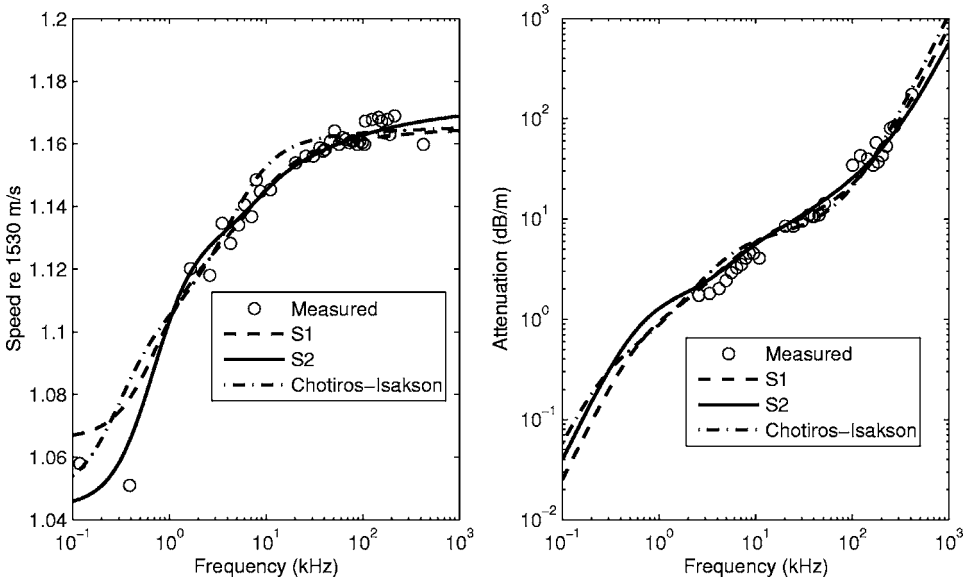

FIG. 4. Wave speed and attenuation predictions for the parameter sets given in Table II.

permeability was known to be well above S2's value, then S1 would become the most plausible solution. The estimates for the shear relaxation frequency and the gap modulus differ by a factor of about two for the two solutions. While solution S2 has a lower c-norm than solution S1, this is mostly due to its better agreement with the wave speed measurement at about 400 kHz. Williams *et al.*,[10] Fig. 3, assign a very high uncertainty to this measurement, however, placing the normalized wave speed between 1.02 and 1.08. Taking this into account S1 and S2 could be adjudged equally plausible, but if information on permeability is absent, or the acoustic permeability hypothesis accepted, there is no way to choose between them and their rather different determinations of the BICSQS parameters.

Table III gives two simplex solutions for the TY90 data set. Solution S1 was obtained by setting the permeability to its measured value and not allowing the simplex algorithm to manipulate it. For solution S2 permeability was a free parameter and the value determined by the simplex algorithm is about one-half the measured value. The improvement over S1, as measured by the c- and a-norms, is not large. Chotiros and Isakson found the shear relaxation frequency f_μ to be "infinity," thus making shear drag nonexistent. In Table III and subsequent tables f_μ was assigned the value ∞ if the value found by the simplex algorithm exceeded 1 MHz. Solution S2f of Table III indicates, however, that setting $f_\mu = 100$ kHZ changed the parameter values of S2 very little. Figure 5 shows that the predictions of S2 and S2f for attenuation diverged only above 30 kHz, the highest frequency at which there were measurements. Thus, rather than asserting that shear drag was for some reason absent, or inconsequential in the TY90, but not the SAX99 sediment, it seems more reasonable to conclude that it was unascertainable from measurements in the frequency range 1–30 kHz.

Chotiros and Isakson applied their model to five data sets, but only the SAX99 and TY90 data had both compressional wave speed and attenuation measurements over similar frequency ranges. A data set not considered is the *in situ* measurements of Simpson *et al.*[13] using a buried vertical synthetic array. The information given about the seabed pa-

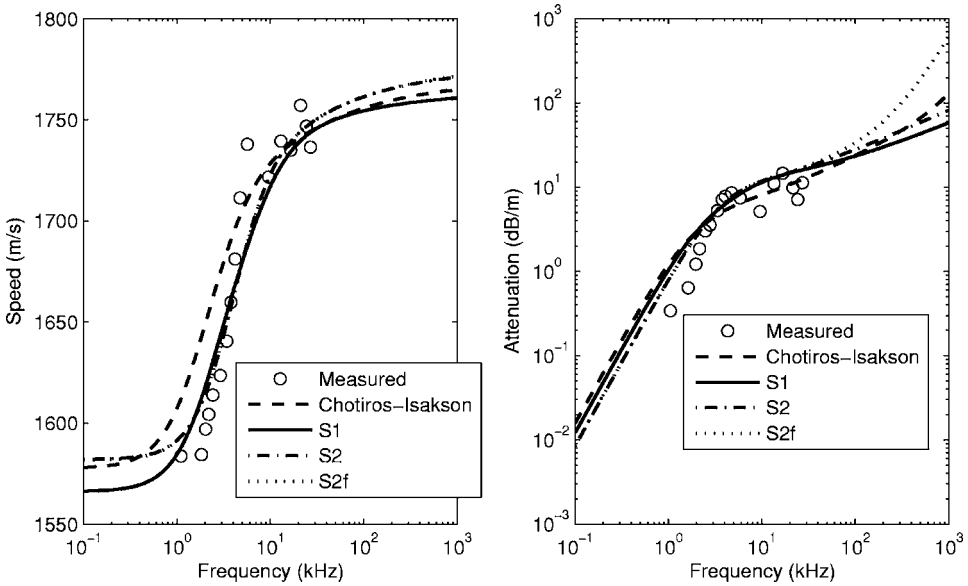

FIG. 5. Comparison of the wave speed and attenuation predictions of the parameter sets given in Table III.

TABLE IV. Solutions for the S03 data. S1 and S2 are simplex algorithm solutions of the BICSQS with norm weight 0.99. The parameters marked with * were those that were manipulated directly. For the Buckingham model (B) the parameters used were: Compressional wave speed, 1730 m/s at 73 kHz; shear wave speed, 130 m/s at 1 kHz (assumed); shear wave attenuation 30 dB/m (assumed).

Parameter	Units	S1	S2	B
Effective fluid bulk modulus K_f^{eff}	GPa	2.11*	1.98*	
Permeability k	μm^2	637*	2.2*	
Pore size a	μm	135	7.9	
Gap modulus K_y	GPa	0.48*	1.40*	
Bulk relaxation frequency f_k	kHz	21*	0.18*	
Shear relaxation frequency f_μ	kHz	31*	73*	
$\|c\|_{c^*}$	$\times 10^{-2}$	0.27	0.29	0.31
$\|a\|_{a^*}$		0.18	0.18	0.20

rameters is sparse. The averaged measured porosity was 0.379 and the averaged wet bulk density was 2035 kg/m^3. No measurement of shear wave speed was made, but the authors suggest that a value between 50 and 150 m/s would be expected for this type of sediment. Since the porosity was close to that of the SAX99 sediment, the parameters given in Table I were used with the porosity changed to the value given by Simpson *et al.* and the grain density changed to ρ_r=2670 kg/m^3 to accommodate the measured wet bulk density and porosity.

Table IV gives two BICSQS parameter sets fitting the data of Simpson *et al.*, which will be designated S03. The predictions for compressional wave speed and attenuation are shown in Fig. 6. As with the SAX99 sediment two solutions were found with quite different parameter values, but with similar, in this case almost identical, c- and a-norms. There was no measurement or estimate of permeability for the S03 sediment, but relative to the measured values for the SAX99 and TY90 sediments, solution S1 has a very high permeability and solution S2 a very low one. No solution was found with a permeability intermediate to these two solutions. Attempts to fix the permeability at values k =20 μm^2, which is similar to the measured permeabilities of the SAX99 and TY90 sediments, caused some other free parameter to drift to an implausible value. Also shown in Fig. 6 are the predictions of the Buckingham model. The norms given in Table IV add support to Buckingham's assertion that the S03 data is consistent with his model.[7]

III. BIOT'S VISCODYNAMIC COMPRESSIBILITY MODELS

Prior to Chotiros and Isakson,[11] investigators, following the suggestion of Stoll[3] (see also Stoll and Bryan[20]), attempted to incorporate inter- and intragranular viscoelastic losses by giving the moduli μ^* and K_b^* small imaginary parts which were independent of frequency. However, as noted by Turgut,[21] this model is not consistent with the Kramers-Krönig causality relations. Moreover, as indicated above, Chotiros and Isakson's BICSQS model, which assumes that the moduli K_b^* and μ^* are frequency-dependent, is the only version of the Biot-Stoll model that can accurately predict the measured wave attenuation in the higher frequency range for the SAX99 data. In this section it is noted that Biot[22] considered the problem of fluid-filled gaps and cracks and arrived at a general model of which the BICSQS is a specific instance.

The partial differential equations of the Biot-Stoll model contain as coefficients three moduli which are calculated from the values of the frame bulk modulus K_b^*, the shear modulus μ^*, the grain bulk modulus K_r, and the fluid bulk modulus K_f using the relations

$$H = K_b^* + \frac{4}{3}\mu + \frac{(K_r - K_b^*)^2}{D - K_b^*}, \tag{4}$$

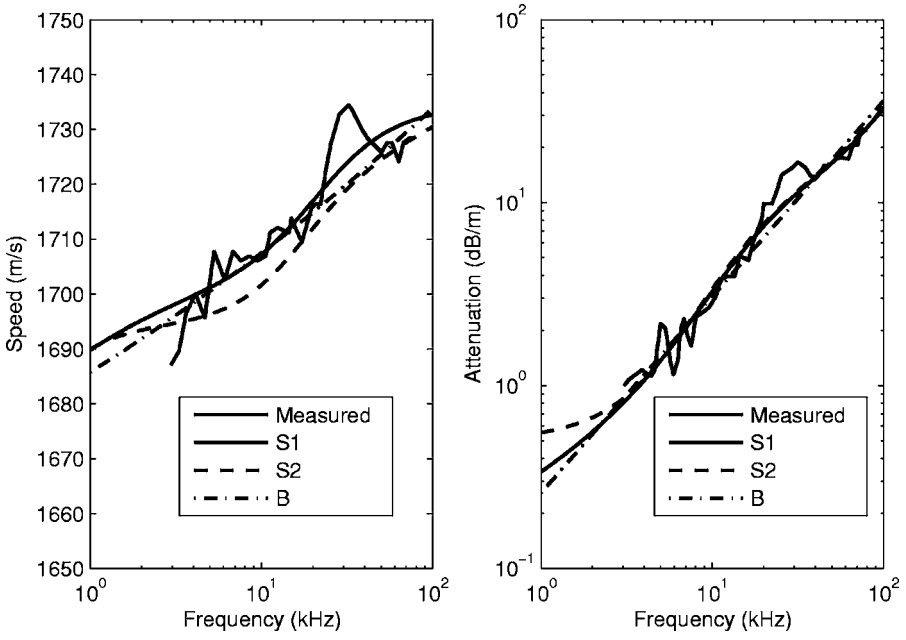

FIG. 6. The predictions for compressional wave speed and attenuation for the solutions of Table IV. The measured data was extracted from Simpson *et al.* (Ref. 13), Fig. 6.

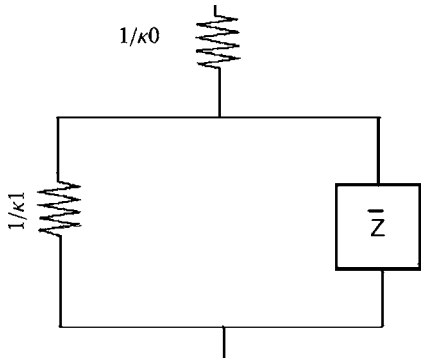

FIG. 7. The viscoelastic element assumed by Biot for fluid-filled cracks and gaps; after Biot (Ref. 22), Fig. 7.

$$C = \frac{K_r(K_r - K_b^*)}{D - K_b^*}, \quad M = \frac{K_r^2}{D - K_b^*},$$

where

$$D = K_r(1 + \beta(K_r/K_f - 1)).$$

Introducing the compressibilities

$$\kappa^* = K_b^{*-1}, \quad \delta = K_r^{-1}, \quad c^* = K_f^{-1}, \quad \gamma = \beta(c^* - \delta),$$

into (4) gives

$$H^* = \frac{4}{3}\mu^* + \frac{\kappa^* + \gamma - \delta}{\kappa^*(\gamma + \delta) - \delta^2},$$

$$M^* = \frac{1}{\gamma + \delta - \delta^2/\kappa^*}, \quad C^* = \frac{1 - \delta/\kappa^*}{\gamma + \delta - \delta^2/\kappa^*}, \tag{5}$$

however, under what he terms the *correspondence principle*: "Known results for elastic media may be immediately extended to the case of viscoelasticity by substituting operators for the elastic coefficients."[22] Biot considers the compressibilities with * to be differential operators, rather than constants.

For fluid-filled cracks and gaps Biot assumed a viscoelastic element of the form shown in Fig. 7. Thus he assumed

$$\kappa^* = \kappa_0 + \frac{1}{1/\kappa_1 + \bar{Z}}. \tag{6}$$

He evidently meant this model to apply to both fluid-filled cracks and gaps, but did not state what the compressibilities κ_0 and κ_1 represent physically in each case. For a fluid-filled gap Biot found that pore fluid pressure satisfies the diffusion equation

$$\frac{\partial^2 p_f}{\partial x^2} = \frac{12\eta c_f}{h^2}\frac{\partial p_f}{\partial t},$$

where η and c_f are the fluid viscosity and compressibility, respectively, and h is the width of the gap (Biot,[22] Fig. 5). Thus, assuming $p_f(0,t) = p_f(D,t) = 0, p_f(x,0) = \rho_{f0}$, a constant, where D is the length of the gap

$$p_f = \sum_{n=1}^{\infty} B_n \exp\left(-\frac{12\eta c_f}{h^2}\left(\frac{2n-1}{D}\pi\right)^2 t\right)\sin\left(\frac{2n-1}{D}\pi x\right),$$

$$B_n = \frac{4\rho_{f0}}{(2n-1)\pi}. \tag{7}$$

Assuming that the normal pressure P on the gap and the change in gap width Δh are related by $P = \bar{Z}\Delta h$, Biot concluded that a fluid-filled gap should be modeled as a series of Maxwell elements in parallel (Biot,[22] Fig. 6), giving

$$\bar{Z} = \sum_{n=1}^{\infty} \frac{a_n p}{p + r_n}, \tag{8}$$

where p is in general the time-derivative operator d/dt, and for the particular case of time-harmonic oscillations is given by $p = -i\omega$, and the relaxation frequencies are

$$r_n = \frac{h^2}{12\eta c_f}\left(\frac{2n-1}{D}\pi\right)^2. \tag{9}$$

Thus Biot's compressibility operator for a fluid filled crack or gap is

$$\kappa^* = \kappa_0 + \frac{1}{1/\kappa_1 - \sum_{n=1}^{\infty} \frac{i\omega a_n}{r_n - i\omega}}, \tag{10}$$

in the time-harmonic case. Comparing Chotiros and Isakson's equation (1), with Biot's equation (10), they are mathematically identical upon setting the compressibility $\kappa_0 \approx 0$, perhaps because the small quantity K_r^{-1} can be identified, setting the higher mode moduli $a_n, n > 1$ to zero and making the identifications $\kappa_1 = K_c^{-1}, a_1 = K_y, r_1 = \omega_k$. Thus by considering a similar problem Biot arrived at a general form for the compressibility operator κ^* which subsumes that used by Chotiros and Isakson.

As indicated, Biot assumed that dissipation was due to fluid viscosity, rather than the radial resistance to flow assumed by Chotiros and Isakson. Fluid viscosity cannot serve as an alternative physical mechanism for dissipation, however: If the gap length D is taken to be on one-half of the the mean grain size for the SAX99 sediment, 1.27 phi units (Richardson *et al.*[9]), and the gap width h is taken to be an order of magnitude smaller than the pore size parameter, say 1 μm, then (9) gives $f_k \approx 7$ MHz. Thus with the assumed values for D and h, fluid viscosity cannot explain the finding above (Table II) that f_k is on the order of 1–10 kHz unless the gap width h is taken to be much smaller. A value of $h = 0.03$ μm gives $f_k \approx 7$ kHz, but as Biot notes after doing this analysis with slightly different values for D and h "the behavior of water in gaps this size or smaller may depart from that of a Newtonian fluid, due to strong surface effects." Thus, rather than regarding the BICSQS compressibility κ^* as an instance of (10), it is more accurate to say that it is a specific instance of (6) with $\kappa_0 \approx 0, \kappa_1 = K_c^{-1}$ and, due to squirt flow, $\bar{Z} = -i\omega K_y(\omega_k - i\omega)^{-1}$. This analysis indicates a shortcoming of the BICSQS: There is presently no relation

such as (9) which relates f_k to measurable quantities and thus permits the plausibility of the squirt flow mechanism to be tested.

Biot gave the following general form for the shear modulus:

$$\mu^* = \int_0^\infty \frac{p}{p+r}\mu(r)dr + \mu_0 + \mu_1 p. \tag{11}$$

This form is sufficiently general to subsume the BICSQS equation $(1)_3$ $(p=-i\omega, \mu_0=G_c, \mu_1=G_c/\omega_\mu, \mu(r)\equiv 0)$, however, Biot did not suggest any physical meaning for the $\mu_1 p$ term and did not propose a form for μ^* in the particular case of fluid-filled cracks and gaps. For solid dissipation due to shear he did suggest the representation

$$\mu^* = \mu_0 + a(-i\omega)^s, 0 < s < 1, \tag{12}$$

which follows from assuming the relaxation spectrum

$$\mu(r) = \frac{a}{\pi} r^{s-1} \sin s\pi.$$

With the parameter s set to a value slightly less than one, this would give essentially the same form as assumed by Chotiros and Isakson, but with a different physical rationale.

To explore whether Biot's more general model might improve agreement with the extant data the following model was tested:

$$\kappa^* = \kappa_0 + \frac{1}{\frac{1}{\kappa_1} - \frac{i\omega K_y}{\omega_k - i\omega}},$$
$$c^* = (1-\phi)K_f^{-1} + \phi K_a^{-1}, \quad \mu^* = G_c\left(1 - i\frac{\omega}{\omega_\mu}\right). \tag{13}$$

where ϕ is the gas volume fraction and $K_a \approx 0.142$ MPa was used as the bulk modulus of the air in the bubbles assumed present in the pore fluid. Thus the compressibility operator is assumed to obey the Reuss law for the modulus of a composite material. The investigations supported the assumption $\kappa_0 \approx 0$ made, by Chotiros and Isakson and so in the results reported κ_0 was set equal to the small quantity K_r^{-1} and not permitted to vary. The parameter κ_1 could be calculated from the elastic relation (2), however, since the applicability of such relations to unconsolidated sediments was challenged earlier by Chotiros,[23] it was left as a free parameter in order to test (2). For all three sediments under consideration Table V shows that a solution was found that had a substantially lower value for κ_1 than that given by (2), but c- and a-norms similar to those of Tables II–IV. For the SAX99 sediment the solution was similar to Table II, S2. For the solution for the TY90 sediment the shear relaxation frequency was set to $f_\mu = 100$ kHz, since as noted above, its influence is slight in the 1–30 kHz range covered by the TY90 data. The permeability was set to the measured value of 17.5 μm^2 since the simplex algorithm tended to reduce it to nearly zero. The results for the S03 sediment were the most interesting. Whereas the solutions found when (2) was assumed had very high or low permeabilities (Table IV), a solution with permeability $k = 15.4$ μm^2 was found when κ_1 was left as a free parameter. This is much closer to the measured permeabilities of the SAX99 and TY90 sediments. For the S03 sediment the low frequency shear modulus G_c was given the same value as the SAX99 sediment, since no measurement of shear speed was available. Thus the investigation of the effect of abrogating (2) was inconclusive. It produced a more plausible estimate for the unknown permeability of the S03 sediment, but was unable to arrive at values for permeability that were near those measured for the SAX99 and TY90 sediments.

TABLE V. Solutions for the extended BICSQS in which frame compressibility was permitted to vary. The parameters marked with * were those that were manipulated directly. The values of the frame compressibility in parentheses were calculated from Eq. (2).

Parameter	Units	SAX99	TY90	S03
Permeability k	μm^2	3.2*	17.5	15.4*
Frame compressibility κ_1	GPa^{-1}	3.5*(33)	0.34*(38)	0.50*(31)
Gap modulus K_y	GPa	1.28*	1.32*	0.30*
Bulk relaxation frequency f_k	kHz	0.94*	4.5*	23*
Low freq. shear mod. G_c	GPa	0.028	0.024	0.028
Shear relaxation frequency f_μ	kHz	125*	100	41*
Gas bulk modulus K_a	MPa	0.453	0.195	0.355
Gas volume fraction ϕ	$\times 10^{-6}$	29*	93*	54*
$\|c\|_{c^*}$	$\times 10^{-2}$	0.40	1.1	0.26
$\|a\|_{a^*}$		0.21	0.75	0.18

The values for frame compressibility κ_1 in Table V are in all cases an order of magnitude more or less than those calculated from Eq. (2) when the Poisson ratio is 0.15. Hickey and Sabatier[24] give the constraint $\beta < 1 - K_b/K_r$ on K_b. This gives the bound $\kappa_1 = K_b^{-1} > 0.04 - 0.05$ GPa^{-1} for the three sediments under consideration. Thus the values for κ_1 in Table V comply with the given bound.

IV. BIOT'S AIR BUBBLE RESONANCE MODEL

As noted in Sec. II, Chotiros and Isakson suggest that the presence of air bubbles in the pore space might reduce the effective fluid bulk modulus and thereby explain wave speeds that were lower than predicted by the conventional Biot-Stoll model for frequencies below 1 kHz for the SAX99 data. Biot[22] modeled the presence of air bubbles in the pore fluid by assuming the fluid compressibility is given by the operator

$$c^* = c_\infty + \frac{1}{k_r - m_r\omega^2 - ib_r\omega} = c_\infty + \frac{c_1}{1 - (\omega/\omega_r)^2 - i\lambda_r(\omega/\omega_r)}, \tag{14}$$

where

TABLE VI. Simplex algorithm solutions for the SAX99, TY90, and S03 data sets for the free-parameter bubble resonance model. The norm weight was 0.99. The parameters marked with * were those that were manipulated directly.

Parameter	Units	SAX99	TY90a	TY90b	S03
Permeability k	μm^2	18.8^*	4.6^*	17.5	11.0^*
Shear relaxation frequency f_μ	kHz	87^*	100	100	24^*
Frame compressibility κ_1	GPa^{-1}	33	1.02^*	1.22^*	0.61^*
Fluid compression coeff. c_∞	GPa^{-1}	0.43^*	0.45^*	0.45^*	0.53^*
Bubble resonant frequency f_{r1}	kHz	0.76^*	4.4^*	4.5^*	25^*
Bubble compression coeff. c_1	GPa^{-1}	0.031^*	0.075^*	0.055^*	0.0076^*
Bubble damping coeff. λ_1		1	1.04^*	0.85^*	0.58^*
Gas bulk modulus K_a	MPa	0.453	0.195	0.195	0.355
Gas volume fraction ϕ	$\times 10^{-6}$	20	17	14	40
$\|c\|_{c^*}$	$\times 10^{-2}$	0.33	0.50	0.59	0.18
$\|a\|_{a^*}$		0.23	0.54	0.59	0.16

$$c_1 = \frac{1}{k_r}, \quad \omega_r = \sqrt{\frac{k_r}{m_r}}, \quad \lambda_r = b_r \omega_r.$$

Other models for the acoustics of gassy sediments, subsequent to Biot's, can be found in Anderson and Hampton,[25,26] and Bedford and Stern.[27]

To investigate the air bubble resonance hypothesis the model

$$\kappa^* = \kappa_1,$$

$$c^* = c_\infty + \frac{c_1}{1 - (\omega/\omega_{r1})^2 - i\lambda_1(\omega/\omega_{r1})},$$

$$\mu^* = G_c\left(1 - i\frac{\omega}{\omega_\mu}\right), \tag{15}$$

was considered. Thus it is posited that a compressibility operator incorporating air bubble resonance suffices to predict wave speed and attenuation and that the viscoelastic relaxation process of squirt flow modeled by the BICSQS κ^* in (1) is inconsequential. The constant $\kappa_1 = K_b^{-1}$, since it is real-valued, does not violate Kramers-Krönig causality (Turgut[21]). The free parameters which the simplex algorithm was allowed to manipulate were then the frame bulk compressibility κ_1, the bubble-resonant frequency $f_{r1} = \omega_{r1}/2\pi$, the fluid compressibility coefficients c_∞, c_1 the fluid compressibility damping coefficient λ_1, the shear relaxation frequency f_μ, and the permeability k. The BICSQS shear modulus equation was retained, since it adequately predicts the high frequency SAX99 wave attenuation data. The frame compressibility κ_1 could be eliminated as a free parameter by use of the elastic relation (2), however, as in the investigations of Sec. III, it is left as a free parameter. Gas volume fractions were computed from the zero-frequency fluid compressibility $c_\infty + c_1$ using the Reuss composite medium model (13). Use of the Reuss-Voigt-Hill model instead would roughly double the value of ϕ. The values for the bulk modulus of air, K_a, used in the computation of ϕ are shown in Table VI. They were adjusted for overburden pressure as follows: For the TY90 measurements, which were made in beach sand, water depth was taken to be zero. For the SAX99 measurements a water depth of 18.5 m[8] was used. For the S03 data no water depth information was available and a depth of 10 m was simply assumed. For all three measurements a representative depth into the sediment of 2 m was assumed.

Simplex algorithm solutions for the three sediments under consideration are given in Table VI. For the SAX99 data the lowest-norm solution placed an implausibly sharp resonance at the data point with a frequency of about 400 Hz. Assigning the damping parameter a value of $\lambda_1 = 1$, which was similar to that found for the other two sediments, produced a solution with norms similar to those of Tables II and V. Frame compressibility was also assigned since it tended to drift to implausibly large values. For the TY90 sediment the shear relaxation frequency was assumed to be $f_\mu = 100$ kHz. The permeability found for the TY90 data set (solution TY90a) was less than one-third of the measured value. Use of the measured value (solution TY90b) still produced better agreement, as measured by the c- and a-norms, than the models of Tables II and V. As Fig. 8 indicates, the bubble resonance model does well in matching the rapid increase in wave speed at about 4 kHz observed in the TY90 data. The free-permeability solution TY90a had slightly better agreement than the fixed-permeability solution TY90b with the data at around 30 kHz. For the SAX99 data the permeability found was almost in the interval $[21,45]$ μm^2 favored by Williams *et al.*[10] The value of permeability found for the S03 data was similar to the measured permeabilities of the SAX99 and TY90 sediments. The predictions for wave speed and attenuation for the SAX99 and S03 sediments are shown in Fig. 9.

If the bubble resonance model is accorded the same status as the BICSQS, that is, its parameters are simply manipulated to obtain agreement with measured data, then it is arguably the best model of those considered. It does as well as any of the other models for the SAX99 and S03 data sets, though the improvement in predicting wave speed and attenuation, as measured by the c- and a-norms, is modest at best. The improvement for the TY90 data is greater, both quantitatively in terms of the norms and qualitatively in its ability to predict the rapid rise in wave speed at about 4 kHz. While there is not currently any theory relating the BICSQS parameters to other quantities of known magnitude which

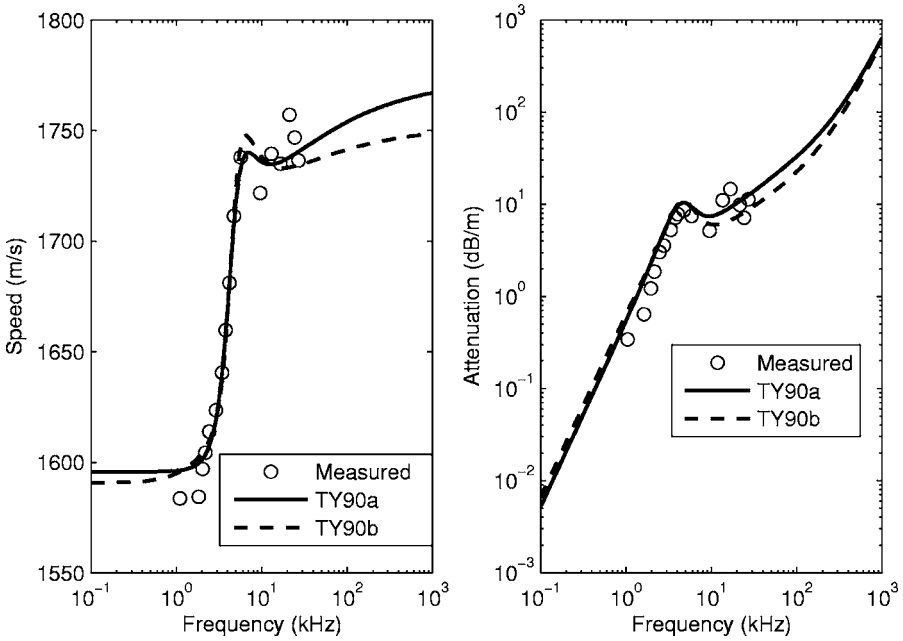

FIG. 8. The predictions for compressional wave speed and attenuation of the free-parameter bubble resonance model for the TY90 data. The parameter values are given in Table VI.

would permit its credibility to be examined, there is an extensive literature on the acoustical properties of a pulsating bubble (cf. Leighton,[28] Brennan[29]). Since the Rayleigh-Plesset equation (A7), which governs the oscillations of a bubble in a liquid, is derived for a single spherical bubble in an unbounded medium, its applicability to bubbles in the pore fluid of a sediment is not clear, at least if the size of the bubble is on the order of the dimension of the pore space. It is nonetheless of interest to see what the Rayleigh-Plesset theory, says about the plausibility of the bubble resonance model (15).

As shown in the Appendix, assuming bubbles of equilibrium radius R_{En} with gas volume fractions ϕ_n, the linearized Rayleigh-Plesset theory does lead to the form (14) assumed by Biot

$$c^* = c_\infty + \sum_{n=1}^{N} \frac{c_n}{1-(\omega/\omega_{rn})^2 - i\lambda_n(\omega/\omega_{rn})}, \tag{16}$$

with

$$c_\infty = K_f^{-1}\left(1-\sum_{n=1}^{N}\phi_n\right), \quad \omega_{rn}^2 = \frac{6kS+3kp_E R_{En}}{\rho_f R_{En}^3},$$
$$\lambda_n = \frac{4\eta_E \omega_{rn} R_{En}}{6kS+3kp_E R_{En}}, \quad c_n = \frac{3\phi_n R_{En}}{6kS+3kp_E R_{En}}. \tag{17}$$

The effective polytropic exponent is given by the formula (Brennen[29])

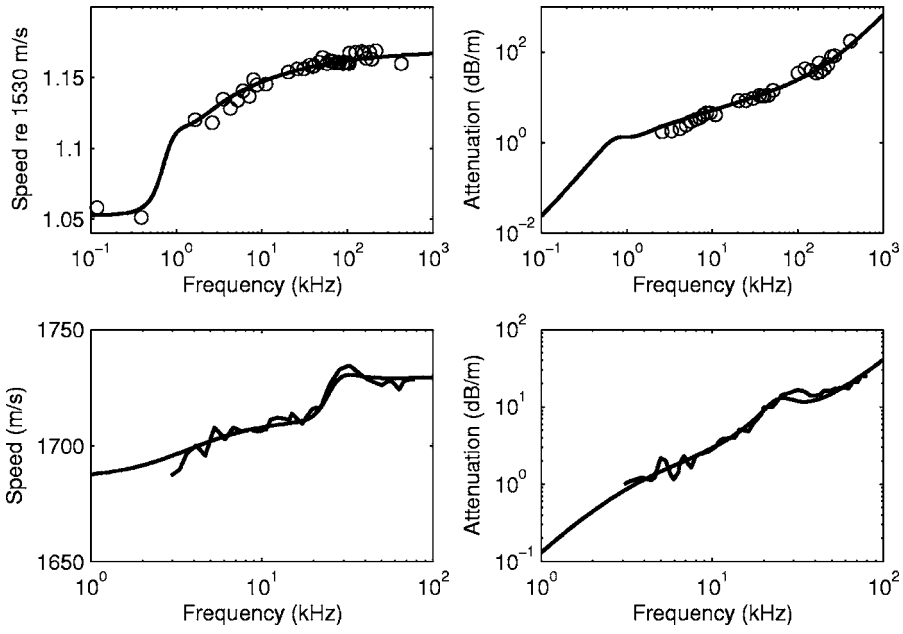

FIG. 9. The predictions for compressional wave speed and attenuation of the free-parameter bubble resonance model for the SAX99 (top) and S03 (bottom) data. The parameter values are given in Table VI.

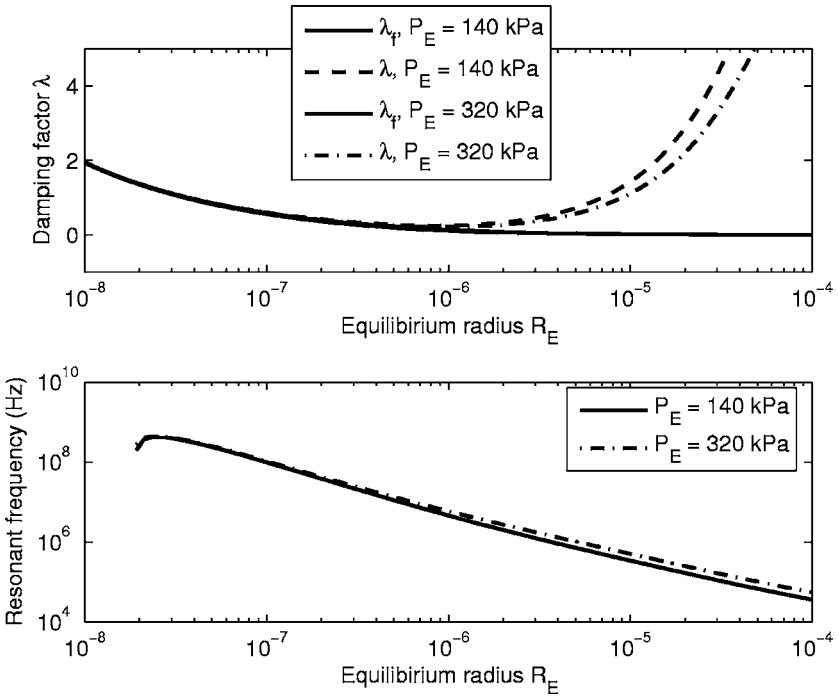

FIG. 10. Top: The values of the damping coefficient when only the fluid viscosity is used (λ_f) and when all three viscosities are used and the frequency of excitation was 10 kHz (λ). Bottom: The resonant frequency as calculated from (20) with $\lambda=\lambda_f$.

$$k=\tfrac{1}{3}\,\mathrm{Re}\,\Upsilon,$$

$$\Upsilon=\frac{3\gamma}{1-3(\gamma-1)i\upsilon\left(\sqrt{i/\upsilon}\coth\sqrt{i/\upsilon}-1\right)},\quad \upsilon=\frac{\alpha_G}{\omega R_E},$$

where α_G is the thermal diffusivity of the gas and γ is the ratio of specific heats. The effective viscosity is

$$\eta_E=\eta_F+\eta_T+\eta_A, \tag{18}$$

where η_F is the viscosity of the surrounding liquid and the thermal and acoustic components of the effective viscosity are given by

$$\eta_A=\frac{\rho_L\omega^2R_E^2}{4c_F},\quad \eta_T=\frac{P_E+2S/R_E}{4\omega}\,\mathrm{Im}\,\Upsilon. \tag{19}$$

While the linearized Rayleigh-Plesset theory does lead to the form (14) proposed by Biot, the damping parameter λ_n is dependent upon the frequency of excitation $\omega=2\pi f_e$ when the thermal and acoustic components of effective viscosity are not negligible. Also all three of the parameters ω_{rn},λ_n, and c_n depend upon the effective polytropic exponent k, which also depends upon ω. To explore this further parameter values are required. Several gases are observed in sediments.[25] For illustrative purposes the parameters for an air bubble in water, $S=0.07$ N/m (Brennen[29]), $\rho_f=1000$ kg/m^3, $c_f=1500$ m/s, $\alpha_G=2.3\times10^{-5}$ m^2/s, $\gamma=1.4$ (diatomic gas) were assumed. The far-field pressure was computed as atmospheric pressure plus the overburden pressure of water and sediment. For the TY90 measurements, which were made in beach sand, water depth was taken to be zero. For the SAX99 measurements a water depth of 18.5 m[8]was used. For both measurements a depth into the sediment of 2 m was assumed. This gave values of $P_E=140$ kPa and $P_E=320$ kPa for the TY90 and SAX99 sediments, respectively. Figure 10 (top) plots the damping factor against the equilibrium bubble radius for the two choices of P_E. The curves labeled λ_f were computed from (17) using $\eta_E=\eta_F$ as the effective viscosity. The curves labeled λ were computed using (18) with a frequency of excitation of $f_e=10$ kHz. As can be seen λ and λ_f agree for bubble radii $R_E<1$ μm. Using $f_e<10$ kHz extends the range of agreement to larger radii. Since the other parameter with frequency dependence, the polytropic exponent k, is near one in this range, the coefficients are for practical purposesindependent of f_e and the formula

$$f_r=\frac{\omega_r}{2\pi}\sqrt{1-\frac{1}{2}\lambda^2}, \tag{20}$$

can be used to compute the bubble-resonant frequency in the range $f_e<10$ kHz, $R_E<1$ μm. As Fig. 10 (bottom) shows the bubble-resonant frequency is then above 1 MHz for all $R_E<1$ μm. Thus the bubble resonant frequencies of less than 10 kHz shown in Table VI for the TY90 and SAX99 data are inconsistent with the linearized Rayleigh-Plesset compressibility operator when the bubble radii are much smaller than the dimension of the pore space, which based on the pore size parameters of Tables II and III is in the 10–60 μm range. That the presence of small volume fractions of bubbles in the pore fluid is commonplace is one of the assumptions of the Chotiros-Isakson model and, while it has not been verified experimentally, it seems plausible. The analysis above argues against using a bubble resonance model as a universal explanation of rapid changes in wave speed with respect to frequency.

V. AN ALTERNATIVE: DIFFERENT PHYSICAL EXPLANATIONS

A premise of Chotiros and Isakson's article[11] is that a single model is needed to explain all of the extant data. The model must then be able to predict the rapid changes in wave

TABLE VII. Simplex algorithm solutions for the SAX99, TY90, and S03 data sets when the linearized Rayleigh-Plesset compressibility opeartor was used and the sediment was treated as the surrounding fluid. The parameters marked with * were those that were manipulated directly.

Parameter	Units	SAX99	TY90a	TY90b	S03
Permeability k	μm^2	13^*	1.3^*	17.5	3.7^*
Shear relaxation frequency f_μ	kHz	123	100	100	39^*
Frame compressibility κ_1	GPa^{-1}	33	0.82^*	1.4^*	0.69^*
Equilibrium bubble radius R_E	mm	4.5^*	0.18^*	0.17^*	$1.6\times10^{-5}*$
Equilibrium pressure P_E	kPa	320	140	140	240
Viscosity of "fluid" η_F	kg/m-s	$\approx0^*$	0.0003^*	$\approx0^*$	$\approx0^*$
Sound speed in "fluid" c_F	m/s	1750	1700	1700	1725
Gas volume fraction ϕ	$\times10^{-6}$	15^*	19^*	11^*	774^*
$\|c\|_{c^*}$	$\times10^{-2}$	0.48	0.47	0.54	0.27
$\|a\|_{a^*}$		0.34	0.30	0.49	0.23

speed with respect to frequency observed in the TY90 data and also in the SAX99 data, if the two lowest frequency wave speed measurements are given credence. These two SAX99 measurements were obtained by different techniques from each other and from the higher frequency measurements[10] and there seems to be some skepticism concerning them. Figure 1 indicates that if these two measurements are disregarded, then the conventional Biot-Stoll model, augmented by Chotiros and Isakson's assumption that the shear modulus depends linearly on frequency, would do well at explaining the remaining SAX99 data. The TY90 data would still require explanation, however. Table VII shows the result of using the simplex method to determine some of the parameters in the Rayleigh-Plesset version of the compressibility operator [Eqs. (16) and (17)] for the SAX99, TY90, and S03 data sets. Since the analysis presented above indicates that bubble radii on the order of the dimension of the pore space or larger will be required, the surrounding medium was assumed to be the sediment, rather than the pore fluid, and the values used in (17) for the density and wave speed were those representative of the sediment. Since there was no obvious value for the viscosity of the sediment, it was made a free parameter. The values arrived at were smaller than the viscosity of water, but this presumably is due to the fact that the thermal and acoustic velocity terms in (18) dominate, making η_F difficult to determine.

As expected from the analysis above, explaining the rapid ascent of wave speed with respect to frequency in the SAX99 and TY90 data requires equilibrium bubble radii much greater than $R_E=1$ μm. For the TY90 data both the free and fixed permeability solutions arrived at about the same bubble radius, 0.2 mm. The c- and a-norms were slightly better than those of the free-parameter bubble resonance model (15) (Table VI) and about one-half the magnitude of the norms of the BICSQS for the corresponding case (Table III). The predictions for wave speed and attenuation are shown in Fig. 11. Thus it is a question of whether the linearized Rayleigh-Plesset compressibility operator is accurate for bubble radii exceeding the estimated dimension of the pore space and, if so, whether a bubble diameter on the order of a half a millimeter is plausible. Anderson and Hampton[25] give 0.5–5 mm as the most common range of bubble diameters in sediments and the value found for the TY90 sediment is close to the lower end of this range. For

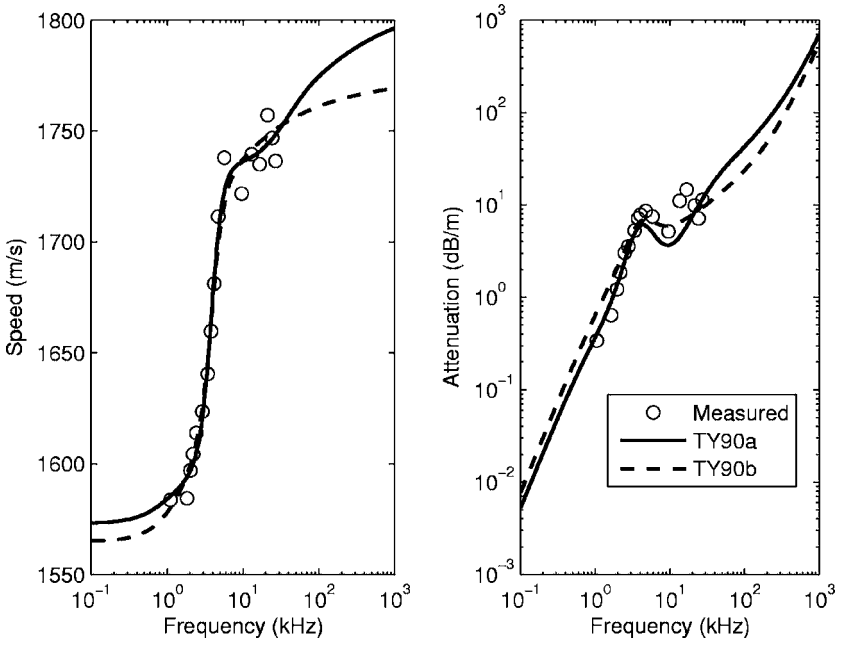

FIG. 11. The predictions for compressional wave speed and attenuation of the linearized Rayleigh-Plesset model for the TY90 data. The parameter values are given in Table VII.

TABLE VIII. Simplex algorithm solutions for the SAX99 and S03 sediment for the simplified model (21). For the SAX99 data the two lowest frequency wave speed measurements were disregarded. The parameters marked with * were those that were manipulated directly. The norms for the Buckingham model for the restricted SAX99 data were 0.60 and 0.55 for the c- and a-norms, respectively. For the S03 data they were 0.31 and 0.20.

Parameter	Units	SAX99a	SAX99b	S03a	S03b
Permeability k	μm^2	8.5*	33	3.7*	20
Shear relaxation frequency f_μ	kHz	100*	68*	39*	20*
Frame compressibility κ_1	GPa^{-1}	1.18*	33	0.67*	0.82*
Gas volume fraction ϕ	$\times 10^{-6}$	16*	6.8*	33*	32*
$\|c\\|_{c^*}$	$\times 10^{-2}$	0.27	0.44	0.27	0.37
$\|a\\|_{a^*}$		0.16	0.17	0.23	0.28

the SAX99 data set the bubble radius found was about 5 mm, which is outside of the given range, but not impossible.[25] For the S03 data the simplex method returned a very small bubble radius, one less than the minimum stable bubble size of about 1 μm given by Anderson and Hampton. As can be seen in Table VII the c- and a-norms for the SAX99 and S03 data sets were no better than the corresponding BICSQS solutions. Thus a bubble "resonance" explanation for the TY90, but not for the SAX99 and S03 data seems plausible and, if the improvement in agreement with the data is deemed significant, useful.

If it is accepted that the TY90 data is amenable to a different explanation, bubble "resonance" perhaps, and the two lowest frequency measurements of wave speed for the SAX99 data deemed unreliable, then the following simplified model merits consideration:

$$\kappa^* = \kappa_0 + \kappa_1 \approx \kappa_1,$$
$$c^* = (1-\phi)K_f^{-1} + \phi K_a^{-1}, \quad \mu^* = G_c\left(1 - i\frac{\omega}{\omega_\mu}\right). \tag{21}$$

This of course is just the Biot model augmented by Chotiros and Isakson's assumptions that the shear modulus has a linear dependence upon frequency and that, due to the presence of air bubbles, $c^* < K_f^{-1}$. Thus, as with the free-parameter bubble resonance model (15), it is posited that the squirt flow mechanism is inconsequential. Table VIII shows some simplex algorithm solutions for the S03 data and the SAX99 data when the two lowest frequency wave speed measurements were disregarded. The predictions for wave speed and attenuation are shown in Fig. 12. When permeability was a free parameter the result for the SAX99 data was a solution with c- and a-norms that were less than one-half the magnitude of those for the Buckingham model when the two lowest frequency wave speed measurements were disregarded. For both the SAX99 and S03 sediments the lower permeability solution had higher shear relaxation frequencies. This correlation is also present in the solutions of Tables II and IV. This is not to suggest that the correlation is necessarily physical, however. The frequency domains in which the permeability and the shear relaxation are influential overlap and because of this wave speed and attenuation data alone may be insufficient to determine them unambiguously.

VI. SUMMARY AND DISCUSSION

If a single model is sought to predict all of the measurements in all three data sets considered above, then Chotiros and Isakson's BICSQS is perhaps the most suitable. It is capable of explaining the large changes in wave speed over

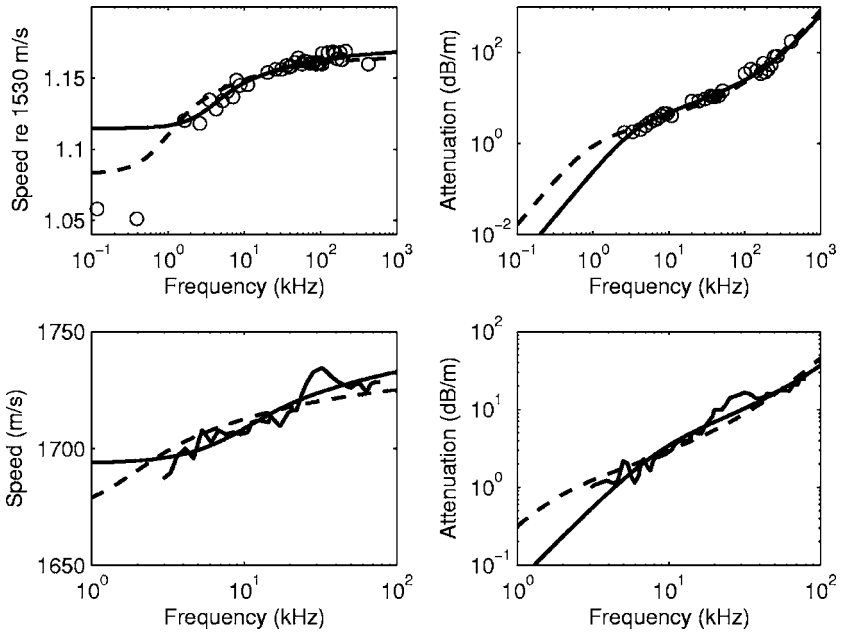

FIG. 12. The predictions for compressional wave speed and attenuation of the simplified model for the SAX99 (top) and S03 (bottom) data. The parameter values are given in Table VIII. The solid and dashed lines are the free- and fixed-permeability solutions, respectively.

relatively narrow intervals of frequency clearly observed in the TY90 data and also in the SAX99 data, if the two lowest frequency wave speed measurements are deemed reliable. The rival Buckingham model cannot predict such rapid increases in velocity with respect to frequency.

This conclusion requires qualification:

First, Biot's free-parameter bubble resonance model (14) does as well, and arguably better, at explaining the data. The reason that it is rejected as a general explanation of rapid changes in wave speed with respect to frequency is that acceptance of this model would require the denial of the applicability of the linearized Rayleigh-Plesset theory of bubble oscillations. While the derivation of mathematical models of complicated physical processes typically entail assumptions and approximations that might cast doubt on their applicability to practically any situation, there seems to be no particular reason to deny the applicability of the Rayleigh-Plesset theory when the bubble radii are much smaller than the dimension of the pore space. As indicated above the linearized Rayleigh-Plesset compressibility operator does not predict resonances in the frequency range in which the apparent resonances in the data occur unless the bubble radii are larger than the dimension of the pore space.

Second, the plausibility of the proposed physical mechanisms of the BICSQS, squirt flow and shear drag, has not been established. All that is really being tested is the mathematical form (1) of the frame compressibility and shear modulus operators. Two instances discussed above, Biot's model of fluid-filled cracks and gaps and the Rayleigh-Plesset version of the bubble resonance model illustrate the hazards of uncritically accepting equations with several free parameters. In both cases it was found that the model could not predict the observed relaxation or resonant frequency unless some parameter was given a value that contradicted a premise of the model. Absent any means to relate the free parameters in the BICSQS to measurable quantities, it is optimistic to assume that the same sort of difficulties will not arise if such connections are found.

Third, the number of free parameters in the BICSQS poses practical difficulties. Because of the intersections in the intervals of frequency in which the various parameters are influential, it is likely that two or more combinations of parameter values will produce approximately the same agreement with the data. This is illustrated by the BICSQS solutions S1 and S2 of Tables II and IV for the SAX99 and S03 data sets, respectively. It is noteworthy that if both the acoustic permeability hypothesis and the applicability of the elastic relation (2) are denied, then this difficulty diminishes. The parameter sets Table II: S1, Table V: TY90, and Table V: S03 then become the best BICSQS solutions for the SAX99, TY90, and S03 data, respectively, if it is assumed that the permeability of the S03 sediment is similar to that of the other two.

An alternative to seeking a model capable of explaining all of the data in all three of the data sets considered is to conjecture that the TY90 data may require different explanation and to disregard the two lowest frequency wave speed measurements in the SAX99 data set. Bubble "resonance" is a candidate explanation for the TY90 data, but a speculative one. Be that as it may, this partition of the data sets admits a simpler model consisting of the Biot model augmented by Chotiros and Isakson's hypotheses that air bubbles may be present in the pore fluid, and the shear modulus depends linearly on frequency.

If the suggested partition of the data is accepted, then the much simpler Buckingham model becomes more competitive. Its predictions fit the S03 data about as well as any other model considered above. It is then a question of whether the SAX99 data in the 1–10 kHz range, all of which was obtained with chirp sonar measurements,[10] is reliable and favors the Biot model sufficiently to justify its added complexity and the difficulty in determining its parameters. The SAX04 exercise may shed light here.

ACKNOWLEDGMENT

This work is the outgrowth of a summer spent at NRL-DC under the Naval Research Laboratory/United States Naval Academy Cooperative Program for Scientific Interchange.

APPENDIX: DERIVATION OF THE COMPRESSIBILITY OPERATOR FROM THE RAYLEIGH-PLESSET EQUATION

To derive a compressibility operator from the Rayleigh-Plesset equation take as a starting point the Reuss model for a composite medium

$$c^* = K_f^{-1}(1-\phi) + \sum_{n=1}^{N} K_{Rn}^{-1}\phi_n, \tag{A1}$$

where the ϕ_n is the gas volume fraction corresponding to bubbles of radius R_n and $\phi = \Sigma_{n=1}^{N}\phi_n$. The bulk modulus for a bubble is

$$K_R = -\frac{\Delta p_b}{\Delta V_b/V_b}, \tag{A2}$$

where p_b is the pressure in the bubble and V_b is its volume. According to the generalized Rayleigh-Plesset equation[29]

$$p_b = p_\infty + \rho_f\left(R\frac{d^2R}{dt^2} + \frac{3}{2}\left(\frac{dR}{dt}\right)^2 + 4\frac{\eta}{\rho_f R}\frac{dR}{dt} + 2\frac{S}{\rho_f R}\right), \tag{A3}$$

where R is the radius of the bubble, S is its surface tension, p_∞ is pressure in the fluid far away from the bubble, ρ_f is the density of the fluid and η is its viscosity. The changes over one-quarter of a cycle of the oscillation are

$$\Delta p_b = p_b\left(\frac{\pi}{2\omega}\right) - p_b(0), \quad \Delta V_b = V_b\left(\frac{\pi}{2\omega}\right) - V_b(0). \tag{A4}$$

To linearize the bulk modulus K_R assume

$$p_\infty = p_E - p_A e^{-i\omega t}, \quad R = R_E\left(1 + \chi e^{-i\omega t}\right), \tag{A5}$$

where $\chi \ll 1$. Substituting (A5) into (A3), then into (A4) and finally into (A2), gives upon expansion in powers of χ

$$K_R = \frac{1}{3\chi}p_A + \left(\frac{2}{3} + \frac{1}{3}i\right)p_A + \left(\frac{1}{6} - \frac{1}{6}i\right) \times \rho_f\left(4i\eta\frac{\omega}{\rho_f} + \omega^2 R_E^2 + 2\frac{S}{R_E\rho_f}\right) + \left(\frac{1}{6} - \frac{1}{6}i\right) \times \rho_f\left(-4\eta\frac{\omega}{\rho_f} + i\omega^2 R_E^2 + 2i\frac{S}{R_E\rho_f}\right) + O(\chi).$$

Since $\chi \ll 1$, only the R_E^{-1} terms, which might be large for small radii bubbles, in the $O(\chi^0)$ term need be retained. Thus the linearized bulk modulus for a bubble is

$$K_R = \frac{1}{3\chi}p_A + \frac{2}{3}\frac{S}{R_E}. \tag{A6}$$

By virtue of the R_E^{-1} term, this expression is slightly different from that arrived at by Leighton (A7) by similar considerations.

The radius of an air bubble is governed by the Rayleigh-Plesset equation

$$R\frac{d^2R}{dt^2} + \frac{3}{2}\left(\frac{dR}{dt}\right)^2 + 4\frac{\eta}{\rho_f R}\frac{dR}{dt} + 2\frac{S}{\rho_f R} - \frac{P_{GE}}{\rho_f}\left(\frac{R_E}{R}\right)^{3k} = -\frac{p_\infty}{\rho_f}, \tag{A7}$$

where R_E is the equilibrium radius, P_{GE} is the equilibrium partial gas pressure, and k_p is polytropic exponent. Vapor pressure in the bubble has been neglected.

Again assuming (A5) where $\chi \ll 1$, gives, upon neglecting powers of χ^2 and higher, and utilizing the equilibrium condition

$$P_{GE} = 2\frac{S}{R_E} + p_E,$$

leads to the equation

$$\chi(\omega) = \frac{p_A R_E}{2(3k-1)S + 3kp_E R_E - 4i\mu R_E\omega - \omega^2\rho_f R_E^3}.$$

Substitution of this expression into (A6) and the result into (A1) gives (16) with the coefficients determined by (17).

[1] M. A. Biot, "Theory of propagation of elastic waves in a fluid-saturated porous solid. I. Lower frequency range," J. Acoust. Soc. Am. **28**(2), 168–178 (1956).

[2] M. A. Biot, "Theory of propagation of elastic waves in a fluid-saturated porous solid. II. Higher frequency range," J. Acoust. Soc. Am. **28**(2), 179–191 (1956).

[3] R. D. Stoll, "Acoustic waves in saturated sediments," *Physics of Sound in Marine Sediments*, edited by L. Hampton (Plenum, New York, 1974), pp. 19–39.

[4] M. J. Buckingham, "Theory of acoustic attenuation, dispersion, and pulse propagation in unconsolidated granular materials including marine sediments," J. Acoust. Soc. Am. **102**(5), 2579–2596 (1997).

[5] M. J. Buckingham, "Theory of compressional and shear waves in fluid like marine sediments," J. Acoust. Soc. Am. **103**(1), 288–299 (1998).

[6] M. J. Buckingham, "Wave propagation, stress relaxation, and grain-to-grain shearing in saturated unconsolidated sediments," J. Acoust. Soc. Am. **108**(6), 2796–2815 (2000).

[7] M. J. Buckingham, "Compressional and shear wave properties of marine sediments: Comparisons between theory and data," J. Acoust. Soc. Am. **117**(1), 137–152 (2005).

[8] E. I. Thorsos, K. L. Williams, N. P. Chotiros, J. T. Christoff, K. W. Commander, C. F. Greenlaw, D. V. Holliday, D. R Jackson, J. L. Lopes, D. E. Magehee, J. E. Piper, M. D. Richardson, and D. Tang, "An overview of SAX99: Acoustic measurements," IEEE J. Ocean. Eng. **26**(1), 4–25 (2001).

[9] M. D. Richardson, K. B. Briggs, L. D. Bibee, P. A. Jumars, W. B. Sawyer, D. B. Albert, R. H. Bennet, T. K. Berger, M. J. Buckingham, N. P. Chotiros, P. H. Dahl, N. T. Dewitt, P. Fleischer, R. Flood, C. F. Greenlaw, D. V. Holliday, M. H. Hulbert, M. P. Hutnak, P. D. Jackson, J. S. Jaffe, H. P. Johnson, D. L. Lavoie, A. P. Lyons, C. S. Martens, D. E. McGehee, K. D. Moore, T. H. Orsi, J. N. Piper, R. I. Ray, A. H. Reed, R. F. Liko Self, J. L. Schmidt, S. G. Schock, F. Simonet, R. D. Stoll, D. Tang, D. E. Thistle, E. I. Thorsos, D. J. Walter, and R. A. Wheatcroft, "An overview of SAX99: Environmental considerations," IEEE J. Ocean. Eng. **26**(1), 26–53 (2001).

[10] K. L. Williams, D. R. Jackson, E. I. Thorsos, D. Tang, and S. G. Schock, "Comparison of sound speed and attenuation measured in a sandy sediment to predictions based on the Biot theory of porous media," IEEE J. Ocean. Eng. **27**(3), 413–428 (2002).

[11] N. P. Chotiros and M. J. Isakson, "A broadband model of sandy ocean sediments: Biot-Stoll with contact squirt flow and shear drag," J. Acoust. Soc. Am. **116**(4), 2011–2022 (2004).

[12] A. Turgut and T. Yamamoto, "Measurements of acoustic wave velocities and attenuation in marine sediments," J. Acoust. Soc. Am. **87**(6), 2376–2383 (1990).

[13] H. J. Simpson, B. H. Houston, S. W. Liskey, P. A. Frank, A. R. Berdoz, L. A. Kraus, C. K. Frederickson, and S. Stanic, "At-sea measurements of sound penetration into sediments using a buried vertical synthetic array," J. Acoust. Soc. Am. **114**(3), 1281–1290 (2003).

[14] E. L. Hamilton, "Geoacoustic modeling of the seafloor," J. Acoust. Soc. Am. **68**(5), 1313–1340 (1980).

[15] N. P. Chotiros, "An inversion for Biot parameters in water-saturated sands," J. Acoust. Soc. Am. **112**(5), 1853–1868 (2002).

[16] J. L. Buchanan, "An assessment of the Biot-Stoll model of a poroelastic seabed," Naval Research Laboratory Memorandum Report 7140-05-8885, Washington, D.C., August 5, 2005.

[17] J. Dvorkin and A. Nur, "Dynamic poroelasticity: A unified model with the squirt and the Biot mechanisms," Geophysics **58**(4), 524–533 (1993).

[18] J. Gittus, *Creep, Viscoelasticity and Creep Fracture in Solids* (Wiley, New York, 1975).

[19] D. L. Johnson, J. Koplik, and R. Dashen, "Theory of dynamic permeability and tortuosity in fluid-saturated porous media," J. Fluid Mech. **176**, 379–402 (1987).

[20] R. D. Stoll and G. M. Bryan, "Wave attenuation in saturated sediments," J. Acoust. Soc. Am. **47**(5 (Part 2)), 1440–1447 (1970).

[21] A. Turgut, An investigation of causality for Biot models by using Kramers-Kronig relations," in *Shear Waves in Marine Sediments*, edited by J. M. Hovem, M. D. Richardson, and R. D. Stoll (Kluwer, Dordrecht, 1991), pp. 403–410.

[22] M. A. Biot, "Generalized theory of acoustic propagation in porous dissipative media," J. Acoust. Soc. Am. **34**(5), 1254–1264 (1962).

[23] N. P. Chotiros, "Biot model of sound propagation in water-saturated sand," J. Acoust. Soc. Am. **97**(1), 199–214 (1995).

[24] C. J. Hickey and J. M. Sabatier, "Choosing Biot parameters for modeling water-saturated sands," J. Acoust. Soc. Am. **102**(3), 1480–1484 (1997).

[25] A. L. Anderson and L. D. Hampton, "Acoustics of gas-bearing sediments I. Background," J. Acoust. Soc. Am. **67**(6), 1865–1889 (1980).

[26] A. L. Anderson and L. D. Hampton, "Acoustics of gas-bearing sediments II. Measurements and models," J. Acoust. Soc. Am. **67**(6), 1890–1903 (1980).

[27] A. Bedford and M. Stern, "A model for wave propagation in gassy sediments," J. Acoust. Soc. Am. **73**(2), 409–417 (1983).

[28] T. G. Leighton, *The Acoustic Bubble* (Academic, New York, 1994).

[29] C. E. Brennen, *Cavitation and Bubble Dynamics* (Oxford University Press, New York, 1995).

Observations of polarized seismoacoustic *T* waves at and beneath the seafloor in the abyssal Pacific ocean

Rhett Butler
University of Hawaii at Manoa, 1680 East West Road, Honolulu, Hawaii 96822 and
The IRIS Consortium, 1200 New York Avenue NW, Washington, DC 20005

(Received 8 April 2004; revised 16 August 2006; accepted 19 August 2006)

Combined seismic and hydrophone observations show that the traditional *T* wave propagates as a seismoacoustic polarized interface wave (*Ti*) coupled to the seafloor. Seismoacoustic *Ti* waves propagating at the sound speed of water are routinely observed over megameter distances at the deep (4979 m) seafloor Hawaii-2 Observatory (H2O) between Hawaii and California, even though the seafloor site is within a shadow zone for acoustic wave propagation. *Ti* has also been observed on seismometers 225 km SSW of Oahu at the OSN1 site at the seafloor and within an ODP borehole into the basalt basement. Analyses of timing, apparent velocity, energy, and polarization of these interface waves are presented. At low frequency ($<\sim 5$ Hz) *Ti* propagates dominantly in the sediments and is consistent with higher-mode Rayleigh waves. At higher frequencies the observed *Ti* waves dominantly propagate acoustically with characteristics suggesting local scattering. The observation of *Ti* from an earthquake in Guatemala at OSN1, whose path is blocked by the Island of Hawaii, is consistent with scattering from the vicinity of the Cross Seamount. © *2006 Acoustical Society of America.* [DOI: 10.1121/1.2354066]

PACS number(s): 43.30.Ma, 43.30.Qd, 43.35.Pt [ADP] Pages: 3599–3606

I. INTRODUCTION

T waves generated by earthquakes propagate acoustically for great distances in the ocean. They are routinely used for monitoring oceanic earthquake locations (e.g., Fox *et al.*, 2001) and for nuclear treaty monitoring using a combination of hydrophone arrays and seismic stations on islands (e.g., Okal, 2001). Although the Hawaii-2 Observatory (H2O) (Butler *et al.*, 2000, 2004) between Hawaii and California at 4979-m depth lies nearly a kilometer below the conjugate depth of the SOFAR channel, interface *T* waves (*Ti*) are observed (Fig. 1) from circum-Pacific earthquakes at thousands of kilometers, propagating as coupled higher mode Rayleigh waves at the seismoacoustic boundary at the seafloor (Butler and Lomnitz, 2002). Although *Ti* waves at H2O typically have frequencies up to about 35 Hz, energy up to 80 Hz has been observed. Acoustic arrivals at hydrophones near the H2O site on the seafloor in the shadow zone below the conjugate depth, which have been observed by the Acoustic Thermometry of Ocean Climate experiment (ATOC) from acoustic sources (75 Hz) at megameter distances, remain unexplained (Dushaw *et al.*, 1999). Seismoacoustic *Ti* has also been observed below the conjugate depth at the OSN1 site 225 km SSW of Oahu, on a seismometer buried in the sediments at the seafloor at 4400-m depth, and by a borehole seismometer emplaced below the sediment-basalt interface 242.5 m below the seafloor from earthquakes 300 km distant in Hawaii and 7270 km distant near Guatemala (Butler, 2001).

The observational study presented in this paper uses apparent velocity, seismoacoustic energy partitioning, and polarization analyses of H2O and OSN1 data to characterize *Ti* wave observations at the seafloor.

II. OBSERVATIONS

A. H2O

The sound speed at the axis of the SOFAR channel is about 1.48 km/s, whereas at the seafloor at H2O the speed is about 1.54 km/s (Levitus *et al.*, 1994; Levitus and Boyer, 1994; Dushaw, 1999). Oceanic earthquakes often lack local epicentral control and the trade-offs between origin time, depth, and location create large uncertainty in estimating apparent velocity of the *T* waves to this precision. However, since this velocity uncertainty decreases with distance, the most distant earthquakes can be used to discriminate the apparent velocity (Fig. 2). The *Ti* waves from events over 5000 km northwest of H2O and over 9000 km south of H2O arrive with apparent velocities of about 1.48 to 1.49 km/s. Acoustic wave propagation modeling of the most distant event using a standard Pacific ocean acoustic and bathymetric model predicts arrivals in the SOFAR channel at these corresponding arrival times, but not at the depth of H2O (Dushaw, personal communication, 2002). This circumstantial evidence indicates that the *Ti* arrivals at H2O travel in or coupled with the SOFAR channel.

The seismoacoustic *Ti* wave arrivals are recorded on both a seismometer, buried about 0.5 m in the seafloor, and on a hydrophone located about 0.5 m above the seafloor. The partitioning of energy above and below the seafloor interface is diagnostic of the propagation mode of the *Ti* waves (Fig. 3). The horizontal components of seismic motion are rotated into radial and transverse direction with respect to the great circle from the source. The seismoacoustic modal structure observed by Butler and Lomnitz (2002) is clearly evident. Both for these two distant events and for closer events analyzed, the energy on the hydrophone channel is greater than the sum of the three-component seismic channels at frequen-

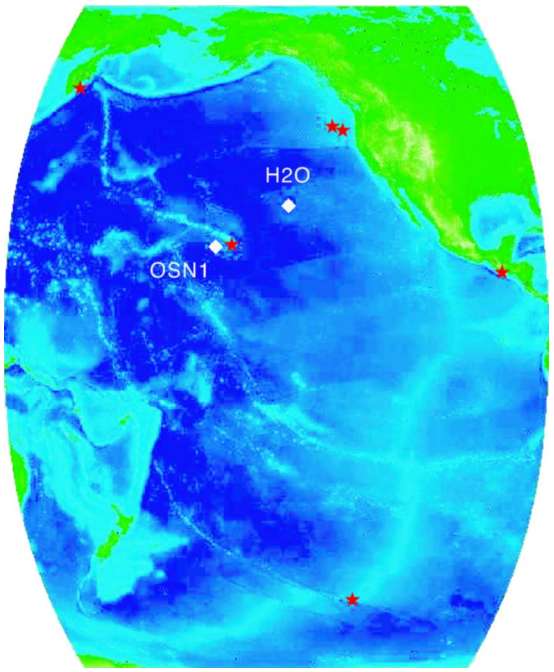

FIG. 1. *T* waves are the most energetic arrivals at frequencies greater than 1 Hz on the hydrophone and the buried seafloor seismometer at the H2O site, and have been observed from events at distances of nearly 10 000 km. *T* waves have also been observed at the OSN1 site, both on the buried seafloor seismometer and on the borehole seismometer 245 m below the seafloor beneath the sediment-basalt interface. Locations of earthquakes discussed herein and by Butler and Lomnitz (2002) are plotted, which are a subset of dozens of events analyzed.

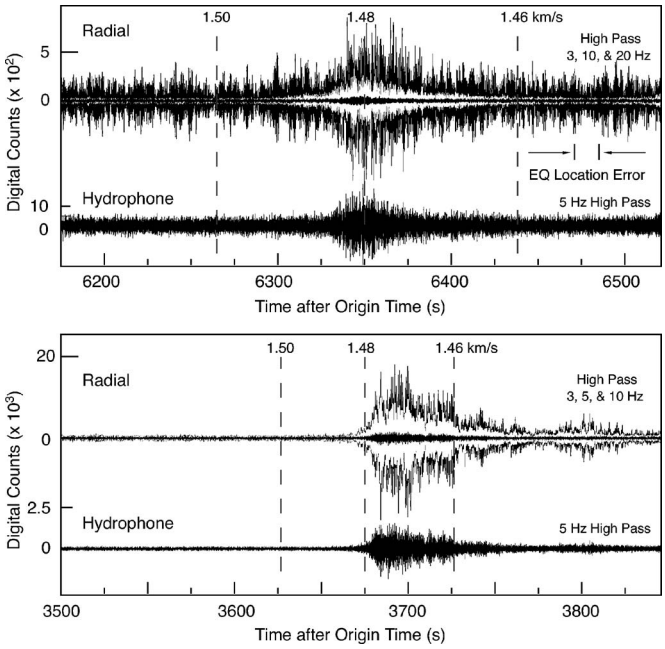

FIG. 2. *T* waves recorded on the seismometer and hydrophone at H2O have an apparent velocity of about 1.48 km/s, corresponding with the velocity near the axis of the SOFAR channel 4 km above the seafloor site. (above) An earthquake (magnitude Mw=6.7) on the South Pacific Ridge at 9400 km on 8 August 2001. Uncertainty of apparent velocity is estimated from epicentral uncertainty. (below) An earthquake (Mw=6.5) near the coast of Kamchatka at a distance of 5440 km on 8 October 2001. Radial components are shown in successively high-pass filtered in three stages plotted overlapping (black, white, then black, respectively, for low, intermediate, and highest frequency filter bands) for direct comparison of amplitude and time. The hydrophone is high-pass filtered at 5 Hz. The seismic wave field is polarized, and only the largest component, radial, is shown.

cies above about 5 Hz. Below 5 Hz, the energy on the radial component of the seismometer dominates for all earthquakes observed. Strong polarization is characteristic of *Ti* waves at frequencies ~5 Hz observed at H2O (Fig. 4) with dominant motion in the radial direction dipping ~2° downward and away from the earthquake source. Thus, whereas below about 5 Hz, the energy of the *Ti* wave is dominantly in the seafloor, above 5 Hz there is more energy propagating acoustically in the water. Since the sound speed of water near the seafloor of the H2O site is much greater (1.54 km/s), the dominance of acoustic energy above 5 Hz traveling with an apparent velocity at 1.48–1.49 km/s suggests that this energy is being scattered from the SOFAR channel to the seafloor, where it locally couples to seismoacoustic modes.

Without benefit from a spatial array of sensors, a single hydrophone provides no information on the directionality of a propagating wave. However, the seismometer provides indirect indication of the directionality of acoustic particle velocity through the polarization of the coupled seismic wave field. By examining the seismic polarization of specific seismoacoustic modes (Fig. 5), we can infer properties of the acoustic propagation. The propagation of low-frequency (<5 Hz) *Ti* waves as higher-order Rayleigh waves is clearly indicated by the prograde and retrograde elliptical particle motion in the sagittal plane (radial-vertical). The mode propagates at an angle of about 2° from horizontal (down and away from the source), and within 4° of azimuth of the great circle axis. At higher frequencies the seismoacoustic modes display a wider range of polarization characteristics. At times some of the modes (Fig. 5) show a nearly rectilinear pattern characteristic of a body wave being scattered from above at large angles (>30° from the horizontal). Other modes sometimes display elliptical motion, indicating modal coupling, along an axis at greater angle to the horizontal (5° to 45°) than exhibited by the low-frequency modes that propagate dominantly in the seafloor. These characteristics vary temporally within a given mode. Both the dominant polarization angle and range of angles increase with frequency for observed *Ti* modes from earthquakes at widely varying distances and azimuths to H2O (Fig. 6). The azimuth of propagation varies as well (not shown), with both near radial and wide angles (>30°) to radial.

Scatter may be expected from the sediment-basalt interface at ~30 m below the H2O sensors, as well as from rough bathymetry. Observations of three nanoearthquakes ($M<0$) located 3.7 km from the H2O site show simple waveforms not congruent with a strongly heterogeneous local structure (Butler, 2003); e.g., there are unambiguous observations of polarized birefringence of 15-Hz shear waves and radial polarization of compressional waves. Although the local receiver structure plays a significant role in the polarization angle, the observed variability of polarization characteristics for events at nearly the same time, range, and azimuth (e.g., the *Ti* mode at ~10.7 Hz in Fig. 6) suggests this cannot be the sole factor. The seafloor at the H2O site is very flat and varies by tens of meters over kilometer ranges. Although there are abyssal hills less than 500 m above the

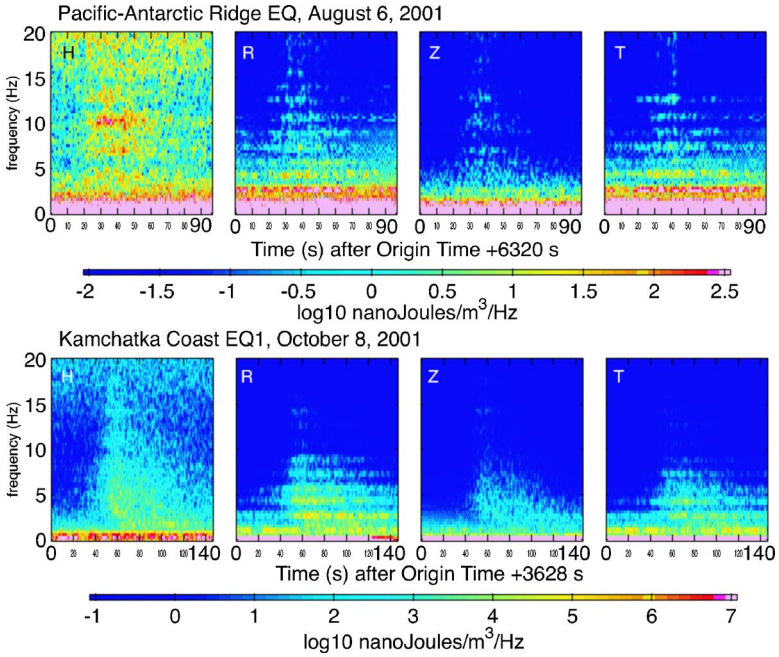

FIG. 3. (Color) Spectragrams plot energy versus frequency and time corresponding to the two events in Fig. 2. The four plots (left to right) show the hydrophone (H), and seismic radial (R), vertical (Z), and tangential (T) components of motion, respectively, all at the same scale for a given event. For the Kamchatka event and for all other earthquakes less distant from H2O, at frequencies below about 5 Hz the total energy on the seismic components buried 0.5 m within the seafloor sediment is greater than observed on the hydrophone located in the water 0.5 m above the seafloor. For the most distant event on the Pacific-Antarctic Ridge, no substantial hydrophone arrival is observed at low frequency (<5 Hz) above the background noise. All earthquakes observed have greater power at higher frequencies (>5 Hz) in the hydrophone signal than on the seismic components. The banded structure in the traces is indicative of modal coupling to the seafloor sediments.

seafloor at 30 km southwest of the H2O site, most of the seafloor in an area >5000 km^2 around the site varies by less than 100 m from the H2O depth [see sonar scan in Butler (2003)]. It is difficult to reconcile the observed dominance of acoustic energy in higher frequency (>5 Hz) *Ti* wave arrivals from the scattering of seismic energy at and within the seafloor.

B. OSN1

The OSN1 pilot experiment (Collins *et al.*, 2001; Stephen *et al.*, 2003) simultaneously recorded seismometers deployed on the seafloor, shallow buried in the sediments, and below the sediment-basalt interface during a 6-month period in early 1998 (Fig. 1). No hydrophone was deployed. Observations of *Ti* at both the OSN1B and OSN1 vertical sensors from a Guatemala earthquake are shown in Fig. 7. These arrivals are clearly discernible only when the data are high-pass (5 Hz) filtered. Given the 20 sps sampling and antialiasing filters on the data streams, the effective bandwidth of the OSN1 signal is only from 5 to 7 Hz. The signal-to-noise ratio (SNR) of the data on the OSN1B buried seismometer is substantial and comparable to H2O observations.

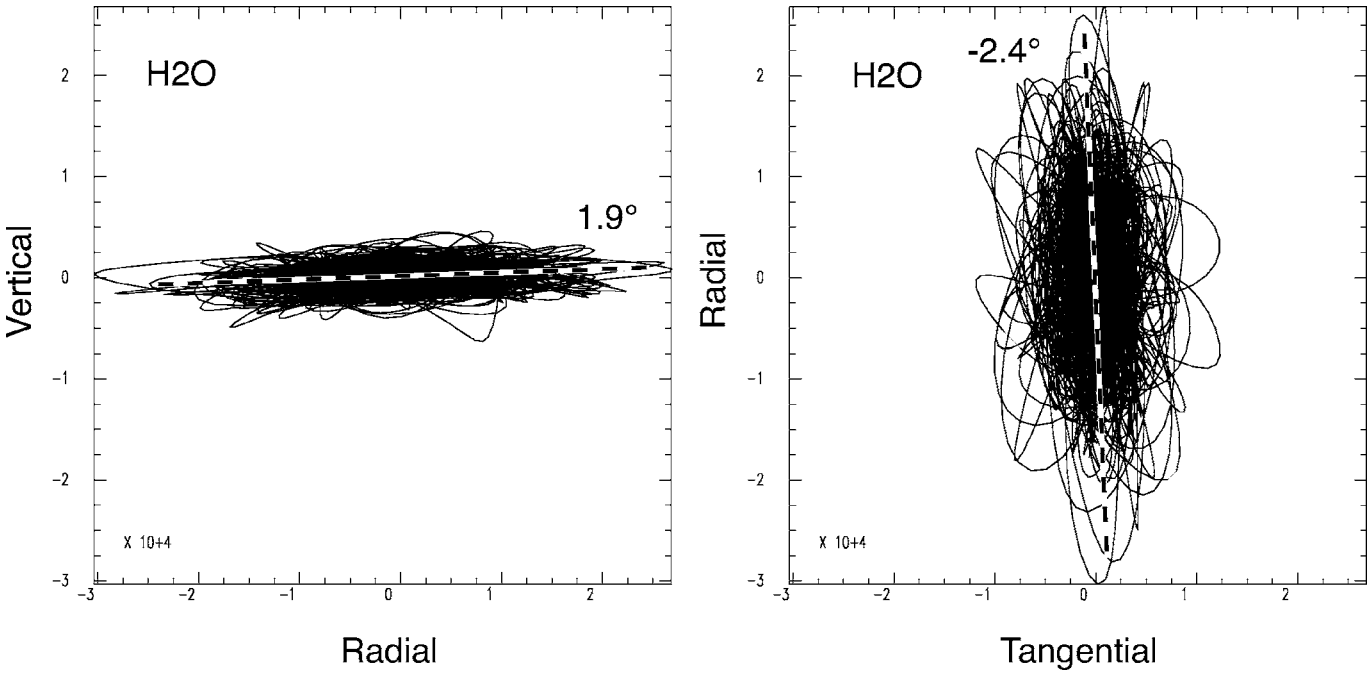

FIG. 4. *Ti* observed from the 8 October 2001 earthquake (Fig. 1) near Kamchatka shows strong radial polarization on the Guralp seismometer buried in sediments. Acceleration records are normalized for instrument response, high pass filtered at 5 Hz. The left figure is vertical and radial motion, and the right figure is radial and tangential. Both are at the same scale for direct comparison. Positive radial is toward the source, positive tangential is +90° clockwise from the radial. Dotted lines show the least-squares fitting line, computed iteratively without assuming either axis as the dependent or independent variable.

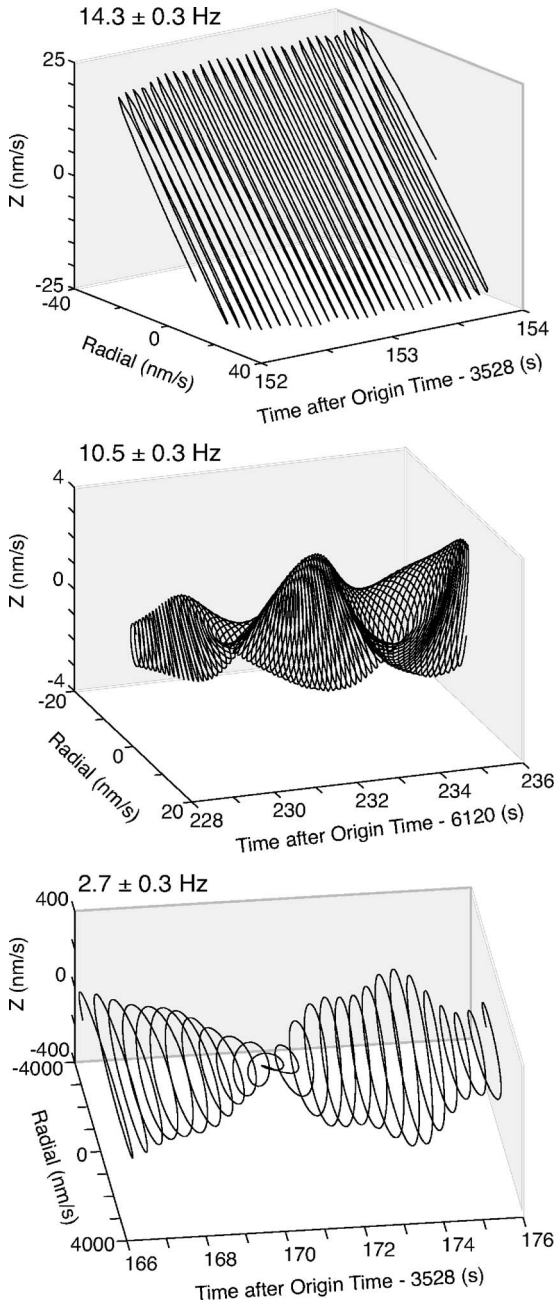

FIG. 5. Examples of *Ti* polarization observations in the sagittal plane are shown for three frequency bands from events shown in Figs. 1 and 2. Gaussian band-pass filters were used with filter parameters, $fc \pm \sigma$ Hz, noted above each subplot, where fc is the center frequency and σ is the characteristic width of the Gaussian. The upper and lower examples are from the earthquake near Kamchatka, whereas the middle example is from the Pacific-Antarctic Ridge earthquake. The lowest frequency is polarized within 1° of horizontal and displays elliptical particle motion characteristic of seismoacoustic coupled Rayleigh waves. Higher frequency bands display a wide range of steeper polarization angles, and both rectilinear and elliptical particle motions characteristic of acoustic energy from the upper ocean being scattered incident upon and coupling to the seafloor. The middle and upper observations show average polarizations at 9.5° and 40.9°, respectively, from horizontal. Note that the scales for the three subplots differ.

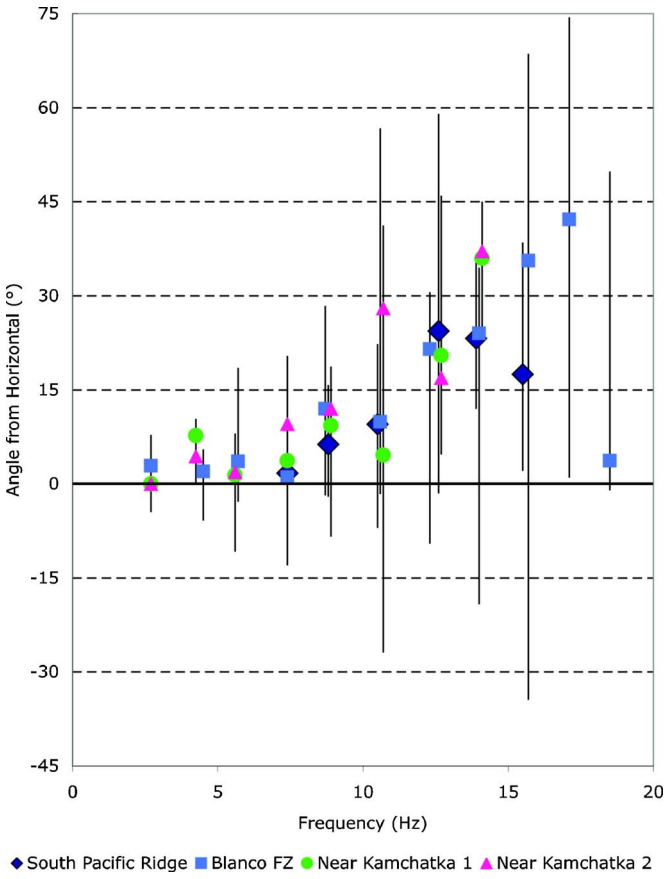

FIG. 6. The sagittal polarization (radial-vertical) angles of individual *Ti* modes are shown as a function of frequency for four earthquakes. Positive angle is down and radially away from the source. The Pacific-Antarctic Ridge and first near-Kamchatka events are shown in earlier figures. The second event near Kamchatka (Mw=6.4) occurred 6 min after the first and at the same location (distance and azimuth within 0.02% of first event from H2O). The Blanco Fracture Zone earthquake (Mw=6.2) on 2 June 2000 occurred at a distance of 2130 km northeast of H2O. Low-frequency modes (<5 Hz) have near radial orientation whereas higher frequencies (>5 Hz) show increasingly steeper angles and greater scatter. A symbol is plotted at the polarization of the maximum energy, whereas the vertical line spans the range of polarizations observed for the mode. Small variations in frequencies of individual modes are observed between events. Note the polarization variation of *Ti* mode at 10.7 Hz between the first and second earthquakes near Kamchatka, which have almost identical paths.

Although the SNR for *Ti* on the OSN1 borehole seismometer is only about 2:1, the *Ti* wave arrives with no appreciable difference in time from its counterpart at the seafloor 242 m above.

Polarization of *Ti* is observed both on the shallow-buried OSN1B and the OSN1 borehole sensor from nearby, small (M=4) Hawaii Island earthquakes (Butler, 2001). The *Ti* observed on the OSN1B shallow-buried sensor shares characteristics with its H2O counterpart. The energy is horizontally polarized, dominantly radial, and inclined <5° from the horizontal dipping downward and away from the source. However, the OSN1 borehole sensor indicates a different *Ti* polarization character—the energy is dominantly in the sagittal plane and vertically polarized. The *Ti* wave from the Guatemala earthquake shares this characteristic (Fig. 8).

The propagation path of *Ti* from the Guatemala earthquake to OSN1 presents an interesting puzzle, as shown in Fig. 9. The Island of Hawaii lies directly in the middle of the great circle propagation path. It is well known that islands may effectively block the propagation of SOFAR *T* waves. However, it is evident that *Ti* may still be observed at and beneath the seafloor of OSN1. The travel times of the *T* waves offer one clue, as shown in Fig. 10. The OSN1 obser-

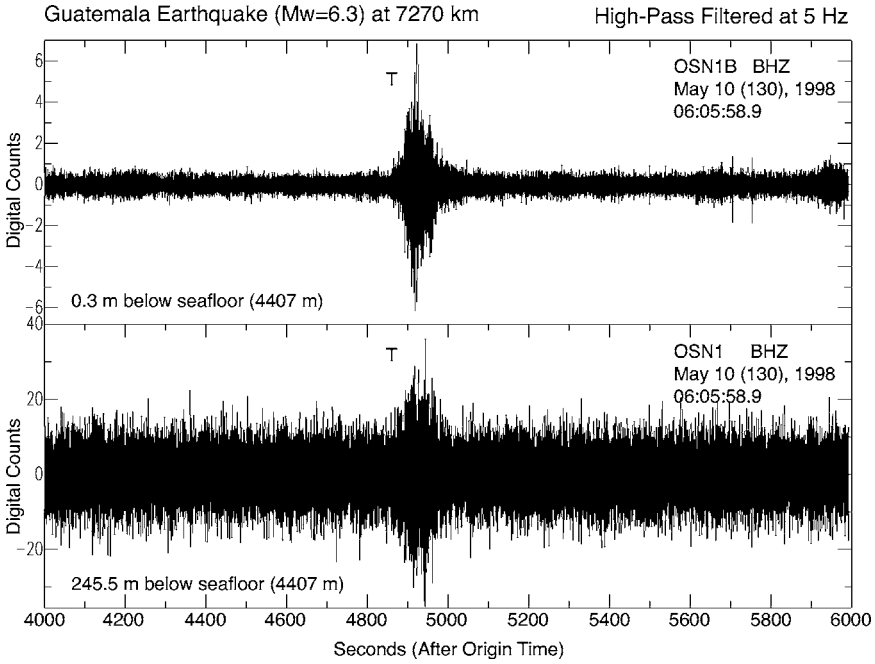

FIG. 7. *Ti* is observed from an earthquake near Guatemala on the OSN1 borehole seismometer 245 m below the OSN1B seafloor-buried sensor. Data from a seismometer sitting on the seafloor (OSN1S), which also clearly observed *Ti*, are not shown. Data have limited bandwidth due to 20 sps sampling. The vertical-component records shown are not corrected for instrument response—digital amplitude counts are nominal. The *Ti* amplitude (velocity response) on OSN1 is about 30% of OSN1B. Although many *Ti* are observed from local Hawaii events during the 6-month Ocean Seismic Network (OSN) Pilot Experiment, this is the only circum-Pacific event seen.

vation arrives about 30 s late relative to island stations. Hence, it may be deduced that it did not travel through the island of Hawaii (since conversion and transmission partly as a compressional *P* wave within the island would result as a faster, early arrival). About 10 s of the observed apparent delay for OSN1 may be accounted from *T*-to-*P* conversion for the island stations.

The key to unraveling the observation of *Ti* from the Guatemala earthquake at OSN1 lies in polarization analysis of the OSN1B buried sensor (Fig. 11), which displays a dominant polarization direction along in the azimuth $135.5° \pm 180°$. Rotating the coordinate frame along this azimuth and viewing the polarization with respect to the vertical component of motion, the horizontal polarization again dominates over the vertical motion with the direction of polarization inclined at about 3° from the horizontal, consistent with H2O observations in general and OSN1B observations from Hawaii earthquakes. If an apparent propagation direction from southeast to northwest is selected, then the orientation of the motion in this apparent sagittal plane is consistent with the other polarization observations, i.e., down and away from the apparent source.

South of Hawaii there are a number of seamounts that intersect the SOFAR channel which lie near the apparent azimuth of the OSN1 *Ti* observation from the Guatemala earthquake (Fig. 9). The Cross Seamount (18°43'N, 158°17'W), which rises into the SOFAR channel within 500 m of the sea surface, fits the approximate timing

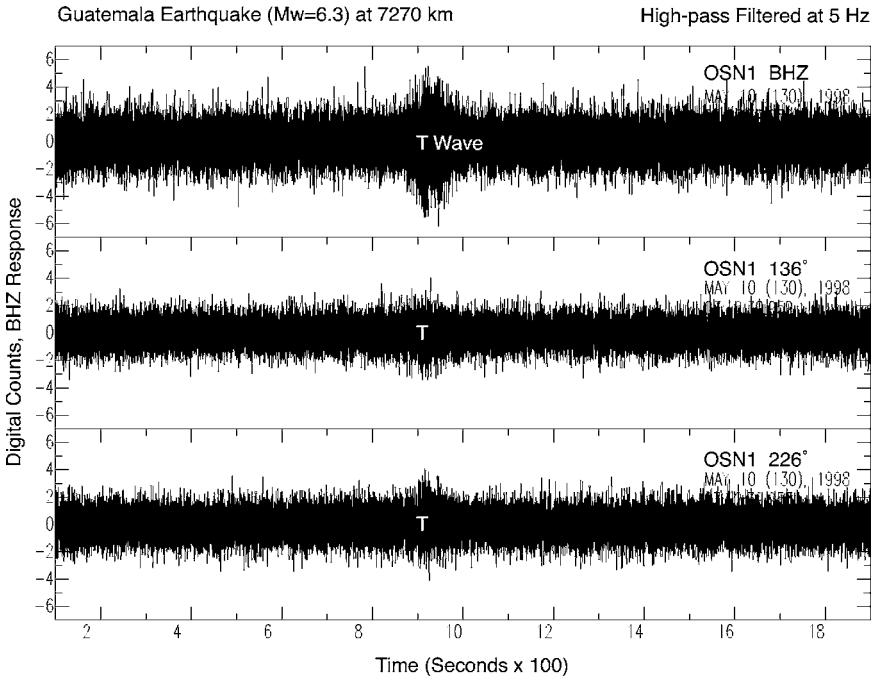

FIG. 8. Observation of vertically polarized *Ti* from the Guatemala earthquake on the vertical and horizontal components of OSN1 borehole sensor, high-pass filtered at 5 Hz. Horizontal components have been rotated into orthogonal azimuths determined from OSN1B sensor polarization (Fig. 11) and normalized to the vertical (BHZ) instrument response.

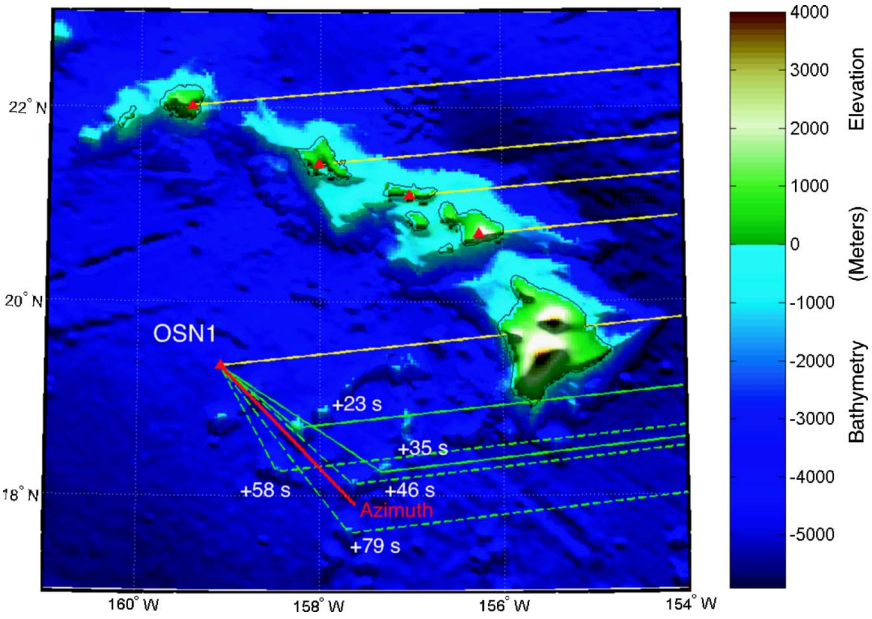

FIG. 9. The great circle paths (yellow) from the Guatemala Earthquake to OSN1 and Hawaiian Islands seismic stations are shown. The apparent great circle to OSN1 is blocked by the Island of Hawaii. The apparent propagation direction of *Ti* derived from polarization analysis (Fig. 12) is shown as the red line. The green lines indicate propagation delays for paths scattered from seamounts to the southeast.

(+23 s), but it is also possible that the observed *Ti* signal at OSN1 is due to scattering contributions from several seamounts. Reviewing the seismic recording observed on Kauai from this Guatemala earthquake, there is a clear, distinct secondary arrival observed 77 s following the main *T* wave. The relative timing of this secondary arrival is consistent with scattering from the vicinity of the Cross Seamount, and corroborates this interpretation of the OSN1 data.

III. DISCUSSION

A. Interface modes

The energy distribution and polarization characteristics of the low-frequency ($<\sim 5$ Hz) component of the *Ti* observed at H2O are consistent with Butler and Lomnitz (2002), who interpreted the seismoacoustic modes as energy trapped near the sediment-water interface by the low shear wave velocity of sediments. Analogous Rayleigh modes have been observed at the air-soil interface (e.g., Langston, 2004). Butler (2003) observed at the H2O site average shear wave velocities of 97 m/s in the sediment cover and about 1.5 km/s in the basalt basement. Hence, another possible interpretation for the observed seismoacoustic modes is that they are Scholte waves (fluid-solid interface Rayleigh waves) traveling at velocities just below the shear wave speed of the basalt basement, comparable to the sound speed of water.

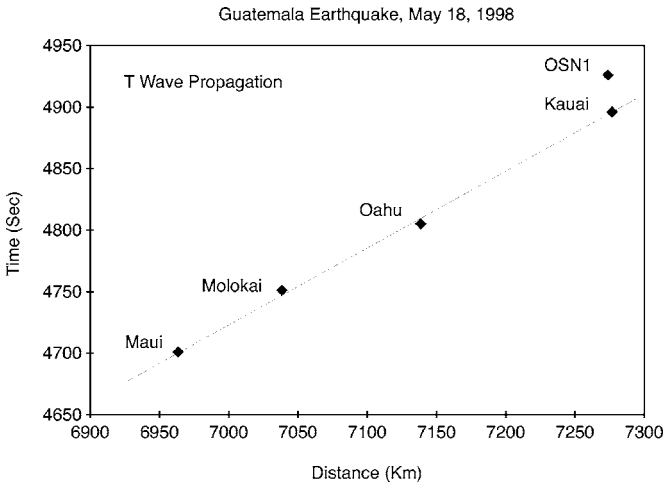

FIG. 10. The travel times of *T* waves are plotted for the sites in Fig. 9. The travel time corresponds to the maximum of the low-pass filtered envelope of the respective *T* wave. Note that the OSN1 arrival is delayed by about 30 s relative to the Hawaiian Island observations: Pelenet sites (Wolfe *et al.*, 2002) and the GSN station KIP on Oahu (Butler *et al.*, 2004).

The vertical polarization of *Ti* is a characteristic observed on the OSN1 borehole seismometer located in the basalt both from nearby Hawaii earthquakes and the distant Guatemala earthquake. For the seafloor-buried sensors at H2O and OSN1, the radial component dominates in the sediments. Crossing the sediment-basalt interface, the sagittal polarization of *Ti* rotates from radial to vertical. This is consistent with *Ti* propagation in the basalt layer as an evanescent mode balancing the vertical momentum of shallow-angle, postcritically reflecting waves propagating above the sediment-basalt interface (e.g., Sykes and Oliver, 1964).

B. Scattering

The OSN1 *Ti* observation from the Guatemala earthquake appears to be due the scattering from nearby seamounts (e.g., Johnson *et al.*, 1968). However, the limited data and the lack of a hydrophone do not permit a more detailed analysis about the nature of the scattering. For example, is the scattered energy dominantly in the water column, or has it propagated from the seamount as an interface wave (Butler and Lomnitz, 2002)? Seamount scattering cannot explain the H2O *Ti* observations. The marked consistency of the observed horizontal polarization within a few degrees of the back-azimuth to the earthquake source for all events observed cannot be mimicked by a plausible distribution of seamount scatters.

Shadow zone arrivals (Spiesberger and Tappert, 1996) have been observed at a hydrophone array near the H2O site and at several other deep arrays in both the Atlantic and

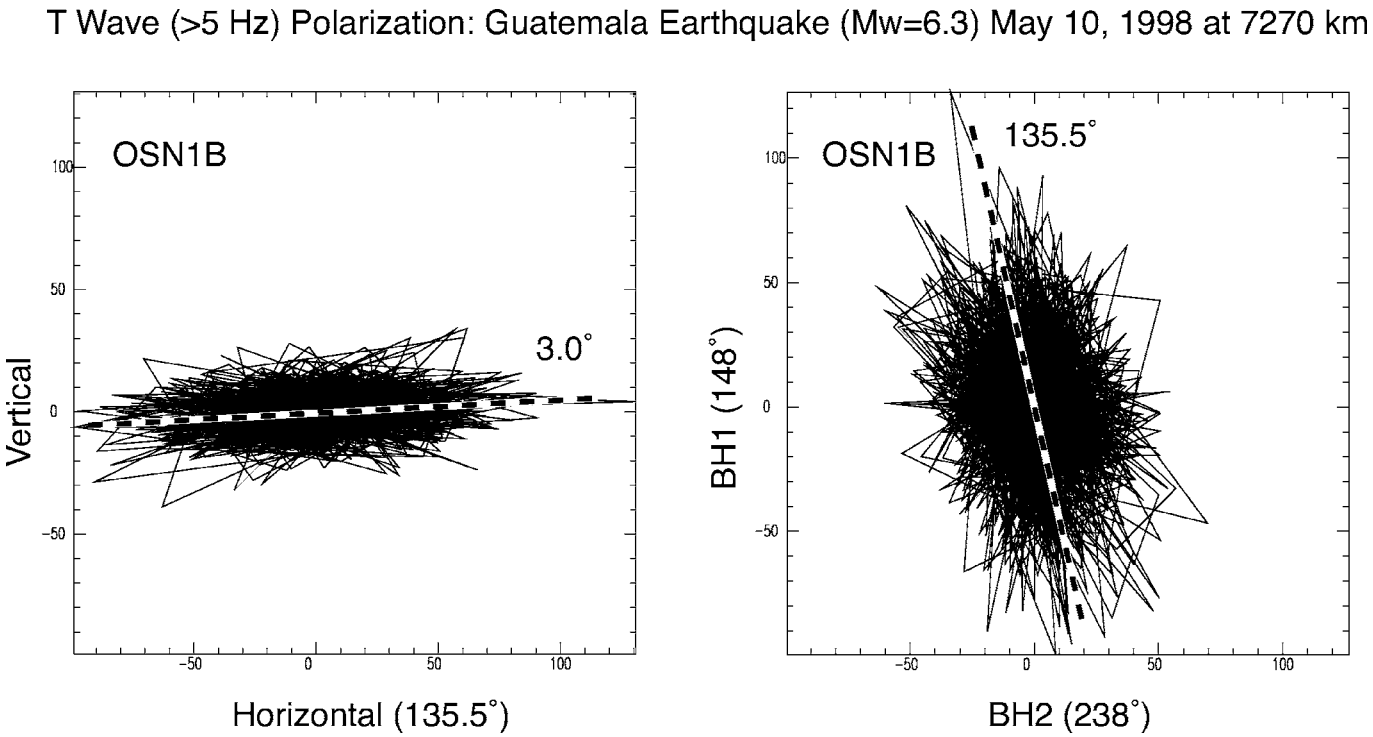

FIG. 11. *Ti* polarization for the Guatemala earthquake observed at the OSN1B shallow buried sensor, high-pass filtered at 5 Hz. The right figure shows horizontal components as oriented *in situ*; the dotted line show the least-squares fitting line oriented at 135.5°. The left figure is vertical and horizontal rotated into the orientation at 135.5°. Both are at the same scale for direct comparison. Consistent with OSN1B polarizations from Hawaii earthquakes and H2O observations, the *Ti* arrival at OSN1B for the Guatemala earthquake appears to be propagating from an azimuth 135.5° towards the northwest.

Pacific by Dushaw *et al.* (1999), who state "To date, no known mechanism, e.g., diffraction leakage from caustics or diffusion of acoustic energy by internal wave scattering, can explain the extreme diffusion of acoustic energy that must be occurring." Thermohaline fine structure (i.e., spice; Munk, 1981) has been observed near the H2O site from a physical oceanographic survey in early 1997 (Rudnick and Ferrari, 1999; Ferrari and Rudnick, 2000). Dzieciuch *et al.* (2004) present a thorough analysis of the 1997 Spice Experiment data set, separating internal wave and spice contributions. Numerical simulations of acoustic propagation through the structure do not indicate substantial penetration of acoustic energy into the shadow zone (M. Dzieciuch, personal communication, 2003).

The preponderance of acoustic energy observed at higher frequencies (>5 Hz) at H2O and the variability and character of the observed polarization of seismoacoustically coupled waves, together with apparent velocities appropriate for the SOFAR channel, suggest that local acoustic scatter near the H2O site may have a role in the observations. However, no specific mechanism is indicated from the data.

IV. CONCLUSIONS

The combination of a hydrophone above the sea floor with broadband seismic instrumentation within the sediments and in the basalt beneath the seafloor provide new observational constraints on the polarization, energy distribution, and apparent velocity for *T* wave propagation near the seafloor. Seismoacoustic, interface *Ti* waves are routinely observed at the H2O and OSN sites, below the conjugate depth of the SOFAR channel. *Ti* waves have been routinely observed on a borehole seismometer in the basement 242 m below the seafloor. The seismoacoustic energy propagates dominantly within the seafloor at low (<5 Hz) frequencies, and the energy distribution and polarization characteristics indicate higher-mode Rayleigh/Scholte wave propagation. Scattering from a nearby seamount has been observed at OSN1. At frequencies above 5 Hz the energy distribution, apparent velocity, and polarization characteristics of *Ti* suggest a contribution from acoustic scattering processes. Detailed phase and group velocity measurements from a horizontal seismoacoustic array, collocated with a borehole seismometer in the seafloor basement and a vertical hydrophone array throughout the water column, would aid substantially in understanding the nature and propagation of these seismoacoustic modes.

ACKNOWLEDGMENTS

This work was supported by NSF Cooperative Agreement No. EAR-0004370. I have enjoyed discussions with John Colosi, Fred Duennebier, Brian Dushaw, Matt Dzieciuch, Neil Frazer, Bruce Howe, Cinna Lomnitz, Walter Munk, Marco Olivieri, Dan Rudnick, and Henrik Schmidt. I thank Cecily Wolfe for Pelenet data. HIGP Contribution No. 1465 and SOEST Contribution No. 6838.

Butler, R. (**2001**). "Observation of seismo-acoustic T phases at and below the seafloor in the Northeastern Pacific at the Hawaii-2 Observatory and OSN1 site," EOS Trans AGU, **82**(47), Fall Meet. Suppl. Abstract S21A-0557.

Butler, R. (**2003**). "The Hawaii-2 Observatory: Observation of Na-

noearthquakes," Seismol. Res. Lett. **74**(10), 290–297.
Butler, R., and Lomnitz, C. (**2002**). "Coupled seismoacoustic modes on the seafloor, Geophys. Res. Lett. **29**(10), 1418.
Butler, R., Lay, T., Creager, K., Earl, P., Fischer, K., Gaherty, J., Laske, G., Leith, W., Park, J., Ritzwoller, M., Tromp, J., and Wen, L. (**2004**). "The Global Seismographic Network surpasses its design goal," EOS Trans. Am. Geophys. Union **85**(23), 225–232.
Butler, R., Chave, A. D., Duennebier, F. K., Yoerger, D. R., Petitt, R., Harris, D., Wooding, F. B., Bowen, A. D., Bailey, J., Jolly, J., Hobart, E., Hildebrand, J. A., and Dodeman, A. H. (**2000**). "Hawaii-2 Observatory pioneers opportunities for remote instrumentation in ocean studies," EOS (Wash. D.C.) **81**, 157–163.
Collins, J. A., Vernon, F. L., Orcutt, J. A., Stephen, R. A., Peal, K. R., Wooding, F. B., Spiess, F. N., and Hildebrand, J. A. (**2001**). "Broadband seismology in the oceans: lessons from the Ocean Seismic Network Pilot Experiment," Geophys. Res. Lett. **28**, 49–52.
Dushaw, B. D. (**1999**). "Inversion of multimegameter-range acoustics data," IEEE J. Ocean. Eng. **24**, 215–223.
Dushaw, B. D., Howe, B. M., Mercer, J. A., and Spindel, R. C. (**1999**). "Multimegameter-range acoustic data obtained by bottom-mounted hydrophone arrays for measurement of ocean temperature," IEEE J. Ocean. Eng. **24**, 202–214.
Dzieciuch, M., Munk, W., and Rudnick, D. L. (**2004**). "The propagation of sound through a spicy ocean, the SOFAR overture," J. Acoust. Soc. Am. **116**(3), 1447–1462.
Ferrari, R., and Rudnick, D. L. (**2000**). "Thermohaline variability in the upper ocean," J. Geophys. Res. **105**(C7), 16857–16883.
Fox, C. G., Matsumoto, H., and Lau, T.-K. A. (**2001**). "Monitoring Pacific Ocean seismicity from an autonomous hydrophone array," J. Geophys. Res. **106**, 4183–4206.
Johnson, R. H., Norris, R. A., and Duennebier, F. K. (**1968**). "Abyssally generated *T* phases," in *The Crust and Upper Mantle of the Pacific Area*, edited by L. Knopoff, C. L. Drake, and P. J. Hart, AGU Monograph, pp. 70–78.
Langston, C. A. (**2004**). "Seismic ground motions from a bolide shock wave," J. Geophys. Res. **109**, B12309.
Levitus, S., and Boyer, T. P. (**1994**). *World Ocean Atlas 1994, Vol. 4. Temperature*, NOAA Atlas NESDIS 4 (U.S. Government Printing Office, Washington, DC).
Levitus, S., Burgett, R., and Boyer, T. P. (**1994**). *World Ocean Atlas 1994, Vol. 3: Salinity*, NOAA Atlas NESDIS 3 (U.S. Government Printing Office, Washington, DC).
Munk, W. (**1981**). "Internal waves and small scale processes," in *Evolution of Physical Oceanography: Scientific Surveys in Honor of Henry Stommel*, edited by B. A. Warren and C. Wunsch (MIT, Cambridge, MA), pp 264–291.
Okal, E. A. (**2001**). "T-phase stations for the International Monitoring System of the Comprehensive Nuclear Test-Ban Treaty: A global perspective," Seismol. Res. Lett. **72**, 186–196.
Rudnick, D. L., and Ferrari, R. (**1999**). "Compensation of horizontal temperature and salinity gradients in the ocean mixed layer," Science **283**, 526–529.
Spiesberger, J. L., and Tappert, F. (**1996**). "Kaneohe acoustic thermometer further validated with rays over 3700 km and the demise of the idea of axially trapped energy," J. Acoust. Soc. Am. **99**, 173–184.
Stephen, R. A., Spiess, F. N., Collins, J. A., Hildebrand, J. A., Orcutt, J. A., Peal, K. R., Vernon, F. L., and Wooding, F. B. (**2003**). "Ocean Seismic Network Pilot Experiment," Geochem., Geophys., Geosyst. **4**(10), 1092.
Sykes, L. R., and Oliver, J. (**1964**). "The propagation of short period seismic surface waves across oceanic areas, Part I—Theoretical Study," Bull. Seismol. Soc. Am. **54**(5), 1349-1372.
Wolfe, C. J., Solomon, S. C., Silver, P. G., Russo, R. M., and VanDecar, J. C. (**2002**). "Inversion of body wave delay times for mantle structure beneath the Hawaiian islands: Results from the PELENET experiment," Earth Planet. Sci. Lett. **198**, 129–145.

Geoacoustic inversion of short range source data using a plane wave reflection coefficient approach

S. A. Stotts, D. P. Knobles, J. A. Keller, J. N. Piper, and L. A. Thompson
Applied Research Laboratories, The University of Texas at Austin, P.O. Box 8029, Austin, Texas 78713-8029

(Received 2 December 2005; revised 12 July 2006; accepted 15 September 2006)

Acoustic time series data were collected in a shallow, hard bottom lake environment located in central Texas using both short range (2 m) implosive data, obtained with the source and a single hydrophone located near mid-depth in the waveguide, along with longer range implosive and explosive data from a near surface source to a bottom mounted hydrophone. Matched field inversions using simulated annealing were performed with a ray trace plus complex plane wave reflection coefficient forward propagation model that was validated in previous work. Isolating bottom interacting paths to perform the inversions is shown to be essential to reduce parameter uncertainties in the hard bottom environment and enables a systematic approach to the inversions which establishes the number of layers needed to represent the lake environment. Measured transmission loss data from a towed source were compared through a RMS error analysis to modeled transmission loss, constructed with the parameters from inversions of data from several source types, to further establish the validity of the inversion approach for this environment. Geoacoustic parameters obtained by inversions of short range, low frequency impulsive data are used to predict transmission loss at longer ranges and higher frequencies. The range dependence of the global minimum is discussed. © *2006 Acoustical Society of America.*
[DOI: 10.1121/1.2361181]

PACS number(s): 43.30.Pc, 43.30.Cq [AIT] Pages: 3607–3626

I. INTRODUCTION

The purpose of this study was to determine what geoacoustic information can be obtained in an extremely limited, highly controlled experiment in a very shallow hard bottom environment. A systematic approach is presented to obtain unique geoacoustic parameters by adjusting the number of layers in the sediment representation. Separating the bottom interacting energy from the total received energy, prior to performing the inversions, facilitates a substantial reduction in parameter uncertainties. This paper presents details of the approach to achieve this objective.

Geoacoustic inversion experiments performed in real ocean environments often require expensive resources and can involve computationally intensive calculations. For instance, horizontal moored or towed line arrays and vertical line arrays have all been used in shallow water experiments and involve complicated setups.[1–6] The types of sources and data used in previous experiments include implosive sources,[7,8] explosive sources,[9,10] source tows,[11] transmission loss (TL) measurements from towed sources,[12–14] and ship noise.[15–17] To decrease the computation required to perform inversions some recent works in shallow water environments have attempted to utilize limited data and more rapid analysis by using single hydrophone measurement techniques.[18,19] For the inversions in Ref. 19, for example, the forward model contained only single bounce ray path information for comparison to measured data, thus decreasing the required computational effort.

There are several other significant findings emphasized in this work. First, the analysis presented here demonstrates that the parameters obtained from the inversion of short range (2 m) implosive data in a hard bottom environment can model the long range TL as accurately as model predictions based on parameter values obtained from inversions with longer range data. Second, it is demonstrated that for shallow environments such as the one described in this experiment and for longer range sources, separation of the surface and direct paths was not necessary to obtain valid parameter values from the inversions of the longer range source data. Third, the parameters obtained from the inversions at short ranges and low frequencies can be used to model TL which accurately predicts measured TL data at much longer ranges and higher frequencies. One additional underlying theme in this work is that at relatively low frequencies a fluid model description can be used to represent a hard bottom environment.

The development of this approach was a result of several important factors including the type of environment, the source data, the received data selection, and the model. Detailed discussions of each of these elements are given in Sec. II to support the systematic inversion approach presented in Sec. III. A synopsis here will introduce some of these points.

The type of environment used to perform the inversions was important for several reasons. First, acoustic propagation data were collected at the Lake Travis Test Station (LTTS) located on Lake Travis, approximately 12 miles west of Austin, TX. The LTTS is maintained and operated by The Applied Research Laboratories: The University of Texas at Austin (ARL:UT). Second, the lake facility provides an opportunity to perform approximately range-independent experiments out to ranges of approximately 40 water depths

and provides an excellent environment to test experimental setups and inversion analysis techniques prior to deployment in a real ocean environment (particularly shallow water). Third, the temporal stability of this lake environment offers an advantage over performing experiments in typical ocean environments where additional variables such as ocean internal waves, noise sources, and atmospheric conditions can limit the ability to reproduce measurements at different times. More specifically, this advantage permits experimental data collected in different years, but at the same time of year to be used collectively in order to infer the bottom characteristics of this environment.

Ocean environments considered thus far have varied from soft to moderately hard sediment types; however, there exists few inversion datasets from environments with hard bottom types, such as areas where the top sediment has been swept away by strong currents, leaving only a gravel or gravel-sand mixture where sound speed ratios at the water sediment interface can be as high as 1.2 or greater.[20] Examples of these hard shallow environments can be found throughout the world. For instance, the coast of Nova Scotia contains gravel-sand mixtures out to several kilometers from the coast.[21] Also, a thin hard layer overlying sand was found to exist approximately 70 m east of Jacksonville, Florida.[8]

Single hydrophone data were obtained for a variety of source-receiver geometries. The analysis presents for the first time a complete study involving three source types in the same experimental analysis. Useful data were collected from implosive, explosive, and continuous tonal sources during the summers of 2000 and 2001 in a shallow water lake environment where ground truth geoacoustic data exist.

Previous work has assumed independent knowledge of the source spectrum.[7,8,14] In this analysis the source spectrum is extracted from the received time series used in the inversion.

Measured TL is reported for a wide band of continuous wave (CW) tonals obtained from a J-9 source.[22] The parameters obtained from the inversions of the impulsive data were used to model TL at several frequencies ranging from 257 to 1000 Hz to independently validate the solutions obtained from the inversions. TL predictions generated with models using accurate parameter values obtained from geoacoustic inversions can provide valuable propagation information.

Inversions thus far have employed relatively long source-receiver separations. That approach was applied in this analysis as well with both implosive and explosive sources; however, important geoacoustic information was also extracted from inversions of data collected at the extremely short (2 m) source-receiver separations with implosive sources and the values of these parameters will be compared to values obtained from longer range source data inversions. Placing the source and receiver at positions in the middle of the water-column for the shorter range implosive data enables the separation of the paths of the receiver arrivals into direct, surface reflected, and bottom reflected components allowing a ray description of the propagation to provide a direct correspondence to the measured data.

Recent inversion studies have dealt with sources operating at depths where the direct path contribution to the source spectrum is easily separated from other paths, such as the surface reflected path.[7,8] In this paper a unique aspect is that the source depths were very near the surface except for the short range implosive sources. As a result the direct path and surface reflected arrivals were not separable for the longer range sources. Instead, the source waveforms were extracted by separating the initial arrival from the subsequent bottom interacting arrivals. From the time segment with just the initial arrival it is possible to construct an effective source spectrum called the direct plus surface reflected (DSR) spectrum, since it consists of both a direct path and a surface reflected path. This is another unique aspect of this work in that the source spectra are extracted from the received time series used in the inversion rather than requiring separate measurements of the source spectrum.

For this environment, the direct and surface reflected paths dominate the propagation, especially for the short range data. In addition, limited penetration in the sediment was found for this test site. The combination of these factors produced broad minima in the geoacoustic parameter distributions. This result led to the systematic inversion approach whereby the direct and surface reflected paths were excluded prior to the inversions to reduce the parameter uncertainties and to determine the layers needed for the bottom representation. Note that the direct and surface reflected paths are needed in order to obtain the source range and source depth.

Many propagation models, applied to both real and synthetic geacoustic inversion data, have been presented.[23–30] Other models have been successfully applied to benchmark problems.[31] Choosing an appropriate forward model to search for inverted parameters requires consideration, and a thorough evaluation of the model must be obtained under a variety of conditions to understand the accuracy and limitation of the given model. The inversions presented here were performed by matching the measured data with the calculated field from a hybrid ray trace plus plane wave reflection coefficient (PWRC) model which was previously applied to three test cases for the Inversion Technology (IT) workshop held in May 2001.[30] The PWRC method was recently applied to a range-dependent shallow-water ocean environment.[8] The PWRC method is highly versatile and can accommodate reflection coefficients from any bottom model. A ray-based approach can provide insight into the data arrival structure as well, and permits the separation of the different arrivals, which is essential to the determination of the geoacoustic parameter values with minimal uncertainty from the inversions.

The inversion method is presented in Sec. II. Sections II A and II B contains a description of the experimental setup. A discussion of estimating the source spectrum from the DSR spectrum is presented in Sec. II C, and more details of the accuracy of this technique are presented in Appendix A. Analyses of the inversion results for the short range implosive source, the longer range explosive sources, and the longer range implosive sources are presented in Secs. II D–II F, respectively. Section II G gives a summary of the solutions obtained by the inversions presented in Secs. II D–II F. A brief discussion of the source data SNR is also given in Sec. II G, with a quantitative discussion presented in

Appendix B. The sound speed at the top of the first layer is discussed in detail in Sec. II G, and other important first and second layer parameters are discussed in Appendix C.

Section III gives the systematic approach to characterize the uncertainty of the geoacoustic inversions.[32–36] The approach is to start the inversions with a half-space model and then *bootstrapping* each successive inversion by adding an underlying layer to determine the validity of using a particular number of layers. Here, the number of sediment layers that overlie a half-space is specified in a model. This technique was also used for inversions of data with only bottom interacting arrivals. Section III A presents the extraction method whereby the direct and surface reflected paths are excluded from the inversions. Section III B gives the procedure to minimize the parameter uncertainty. Eliminating the direct and surface reflected paths provides better sensitivity to the bottom structure.

Section IV presents the measured and modeled TL. Section IV A contains a discussion of the measured and modeled TL (calculated with the parameter values from the inversions of the short range implosive data). Section IV B compares, via the RMS error, TL data, and the modeled TL calculated with the parameters obtained by the inversion of the data from the various source types. The RMS error is used to independently validate the parameters obtained from the inversions. A summary is presented in Sec. V.

II. INVERSION METHOD

In this section an initial discussion of the data collection is followed by details of the cost function used in the inversions. The parameter values obtained from the inversions using all arrival paths are presented for three source types: short range implosive sources, longer range explosive sources, and longer range implosive sources. Comparisons of some of the important parameter values between the various source types obtained from the individual inversions, as well as, cost distributions that have broad minima are discussed here. The effect of excluding the direct and surface reflected paths prior to the inversions is presented in Sec. III to reduce the uncertainties of the important bottom parameters discussed in this section.

A. Experimental setup

The data were collected in the shallow waveguide of Lake Travis. Figure 1 shows a topographical map of the experimental site. The water depth at this environment corresponded to approximately 7λ for an example frequency of 250 Hz (the approximate peak of the energy source level for the implosive source). Every important aspect of the problem geometry was known. GPS recordings marked source and receiver locations to approximately 1–2 m accuracy throughout the experiment. The data recorder was located at the LTTS facility. Some of the data being analyzed were recorded from a hydrophone receiver located on the bottom in a channel approximately 1.5 km in length, or approximately 39 water depths (longer range data). Additional data were recorded from a hydrophone suspended mid-depth at the LTTS facility (shorter range data). Bathymetry along the channel was recorded from a depth sounder with a digital readout. In both geometries the bathymetry was range-independent, and the water depth was approximately 38 m.

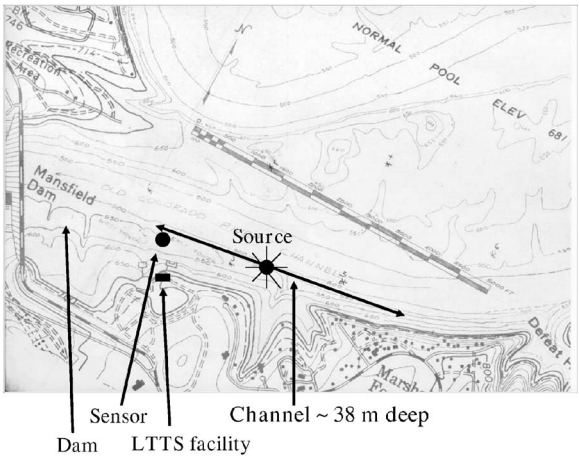

FIG. 1. Topological map of the experiment area near the dam of Lake Travis, located approximately 12 miles west of Austin, TX.

Noise contributions were minimized by simply waiting for boat traffic to clear the experiment area and by performing experiments early in the day. Other noise sources, such as nearby construction, vehicle traffic on area roadways, and the motor from the boat used for the source tows were shown to be negligible by spectral analysis of the data.

B. Measured temperature profiles

An underwater probe located at the LTTS records daily the temperature down to depths of approximately 18 m. For the experiment discussed in this paper a diver recorded the temperature on the bottom, enabling the extrapolation of the sound speed profile (SSP) down to the bottom.[37] In addition a single temperature reading was made at the bottom near the sensor at the edge of the channel in July, 2000, two days prior to the experiment dates. Sound speed profiles (SSPs) were calculated from these temperature readings using Medwin's formula with zero salinity.[38] The sound speeds were linearly interpolated between the deepest probe depth and the depth at the bottom sensor. An average sound speed profile was obtained from a set of four temperature readings recorded hourly beginning at 7:50 AM on each day.

Two such averaged SSPs from recordings separated by three days in mid-July, 2000 are shown in Fig. 2. The shorter range and longer range implosive data were analyzed with the SSP measured on July 10, 2000. SSPs were not measured in 2001 because only the short range data were recorded and differences in the SSPs at these ranges are assumed negligible. It will be shown that valid parameter values were obtained with inversions of the shorter range implosive data recorded in 2001 using the previous year SSPs. This is in part because the source to receiver range was 2 m, and in part because the data were recorded at approximately the same day as the previous year recordings with similarly dry stable weather conditions as a testament to the temporal sta-

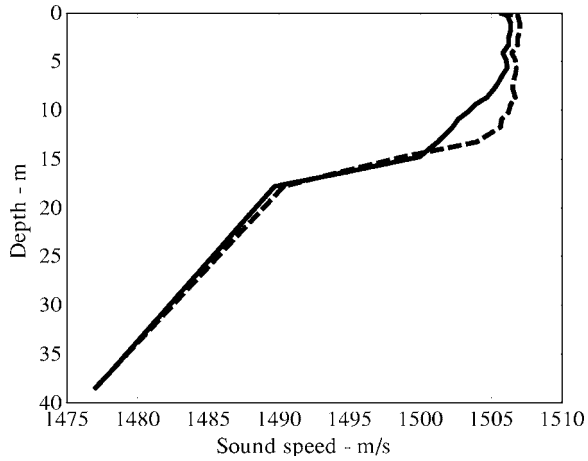

FIG. 2. Two average sound speed profiles obtained from hourly recorded temperature readings on July 10 (solid) and July 13 (dashed), 2000.

bility of the environment. The explosive data were analyzed with the SSP measured on the day that the explosive sources were recorded, specifically July 13, 2000.

C. Cost function calculation

The measured time series is correlated with the model field using a Bartlett cost function for a single receiver.[7,8] The cost function is

$$\Phi = 1 - \frac{1}{N}\sum_{i=1}^{N} \phi_i, \tag{1}$$

where N is the number of sources used in the inversion. The contribution for each source is

$$\phi_i \equiv \phi_{i,k_{\max}}, \tag{2}$$

with

$$\phi_{i,k} = \frac{|\Sigma_j M_{i,j} D_{i,j}^* e^{i\omega_j \delta\tau_{i,k}}|}{\sqrt{M_i \times D_i}}, \tag{3}$$

with $M_{i,j}$ the model value and $D_{i,j}$ the data value, for the ith source and the jth frequency $f_j = \omega_j/2\pi$. The model norm is

$$M_i = \sum_j |M_{i,j} M_{i,j}^*|, \tag{4}$$

with a similar expression for the data norm, D_i. The time delay $\delta\tau_{i,k}$ is relative to the start of a time delay window that contains the peak correlation, with the index k identifying the sampling number of the time delay window and $k = k_{\max}$ maximizes the correlation. Although the absolute value of the time delay between the data and model time series at the peak correlation is not physically significant, it must be identified for effective inversion processing. Initially, the time delay window is very wide to locate the time of the peak correlation because the source and received time series were not synchronized; however, for efficiency in subsequent calls to the forward model the window width is reduced. This cost function is a coherent sum over frequency for each source. The sum over sources is an incoherent average of the peak correlation of data and model time series for each source, although much of the analyses presented here are for single sources.

The model field is calculated from the time series of a point source impulse response convolved with the time series obtained from the measured source spectrum. The model field is $M_{i,j} = S_j R_{i,j}$ where the source spectrum S_j is obtained either from the single source used in a given inversion or from the closest source used in a multisource inversion because of the increased signal to noise ratio (SNR). The model point source impulse response is $R_{i,j}$ for the ith source at the jth frequency bin. Absolute determinations of received amplitudes were not necessary since both the model and data amplitudes were normalized in the cost functions.

1. Inversion data

The inversion of data from three types of sources are presented in this section, i.e., a short range implosive source, a longer range explosive source, and two longer range implosive sources. (Data from the two implosive sources were also used in a simultaneous inversion in an attempt to ascertain parameter values that are often poorly defined by an inversion analysis, such as attenuations, but no additional information was obtained from these inversions and will not be emphasized here.) Inversions of the longer range explosive source data did not produce more information than the data from an implosive source at longer ranges due to SNR limitations. Differences in the parameter values obtained from inversions of the source data presented in Secs. II D–II F for some of the top layer parameters will be noted; however, the geoacoustic parameters from the inversions of the data from all three source types are used to construct model TL that are shown in Sec. IV to have comparable range dependence, and in this context the geoacoustic solutions are described as being consistent.

The most important parameters to be determined for the Lake Travis environment for the purpose of accurately predicting TL were sound speed and attenuation at the top of the first layer, and the ratio of the sound speed at the top of the second layer to the speed at the bottom of the first layer. (For a bottom with no overlying sediment layer the relevant sound speed ratio is the ratio of the substrate speed to the bottom water sound speed.) Source level variations among the various source types suggests that some parameters are better determined with specific sources due to the differences in the SNR between the various source types and also due to different geometries. For example, for the shorter range data the layer thickness and sound speeds are determined, whereas the attenuations are determined with the longer range data.

2. Propagation model

The inversions were performed with a simulated annealing[39] algorithm in combination with the PWRC propagation model. Basically, the PWRC method separates the water-column propagation from the bottom physics and allows detailed analysis of the effects of the underlying sediment layers. The waterborne eigenray path information is calculated once and stored. Subsequent calls to the forward model include the bottom interactions via a complex valued

reflection coefficient. In both the synthetic and real data the inversion results compared well with other forward models such as the Parabolic Equation (PE) and normal modes. For comparison, some of the inversions were performed using ORCA,[40] a normal mode propagation model.

3. Sediment model

For the inversions in this section the assumed sediment representation is a two-layer range-invariant fluid bottom overlying a half-space. The bottom structure consists of a very hard layered limestone underneath a few meters of a chalk/limestone combination which is in turn underneath only a few inches of unconsolidated mud. This chalk/limestone geology referred to as the Austin Chalk Group persists throughout the central Texas region to the west of and along Interstate Highway 35 and consists of a number of chalky stratigraphic zones. This description is consistent with the inversion results obtained within the limits of a two-layer model. The overlying gaseous mud layer was ignored for all the analyses presented in this paper.

4. Source spectrum model

The measured source spectrum, obtained at short ranges from the 2 m implosive sources, was constructed from a direct path arrival. (Indeed, one of the purposes of part of the experiment was to obtain the direct path source spectrum and to apply it to inversion data obtained for a different experiment in an ocean environment.[8])

For the longer range implosive sources, it is demonstrated that inversion results obtained by extracting the source spectrum from the same received data processed in the given inversion produced similar model TL predictions as those generated from the parameters obtained with inversions of the short range implosive data with the source spectrum obtained from the direct path time segment only. Since the sources were located near the surface, separating the direct path from the surface reflected paths in the data was not possible, i.e., the travel time difference between the two paths is less than the duration of the source due to the presence of bubble pulses produced by the fluid restoring forces.

For the short range (2 m) implosive sources the travel time difference between each path is observed to be greater than the duration of the source due to the presence of bubble pulses because the various path arrivals are identifiable in the time series. Additional bubble pulses are not identified and are negligible.

No short range (2 m) explosive source spectra were measured since the detonation time was too short to allow a separation in the direct and surface reflected arrivals; therefore, extracting the source spectrum from the time series processed for the long range explosive source data was essential for the inversions of the explosive source data. This means that using the source spectrum extracted from the same received time series of the longer range data used in the inversion circumvented the need for repeatability of the explosive sources, although a comparison of two example spectra is discussed in Sec. II E. Appendix A contains a quantitative analysis of the result of applying the DSR spectrum to inversions with the longer range source data.

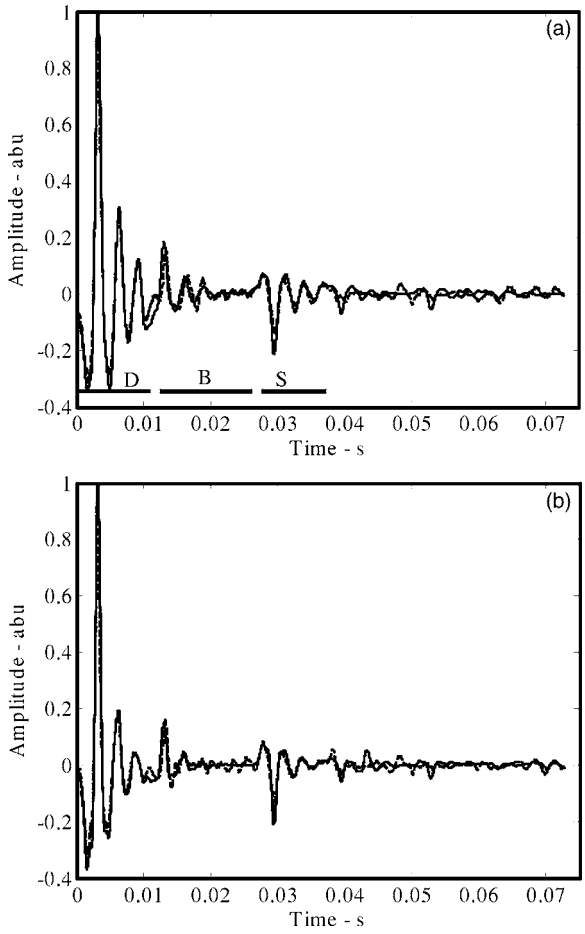

FIG. 3. (a) Data time series (solid) from a 100 W 3-way light bulb implosion below the LTTS barge (solid). **D**irect, **B**ottom reflected, and **S**urface reflected path arrivals are indicated. Model time series (dash) calculated with GAMARAY. (b) Data time series (solid) from a 60 W standard Sylvania®, and a model time series (dash) generated from the bottom description obtained from the inversion of the data in (a).

D. Implosive short range sources

Inversions were performed with data from short range implosive light bulb sources deployed at the LTTS test facility during 2001. The source and receiver at depths of 30 m and 20 m, respectively, were separated in range by 2 m. The data time series were recorded with a sampling rate of 48 kHz. The time series shown in Figs. 3(a) and 3(b) were obtained by resampling the original time series at 2400 Hz and reproduce all of the original data structure observed for a 48 kHz sampling rate. The small scale arrivals before (not shown) and after the total combination of the direct path, the first bottom bounce, and the surface reflected arrivals designated in Figs. 3(a) and 3(b) and after a few additional boundary reflected arrivals, are attributed to the noise in the environment and not to some effect such as applying a boxcar filter window to the data. The oscillations shown after the initial arrival and after the subsequent boundary reflected arrivals are components of the source waveform bubble pulse that result from the fluid restoring force after the initial

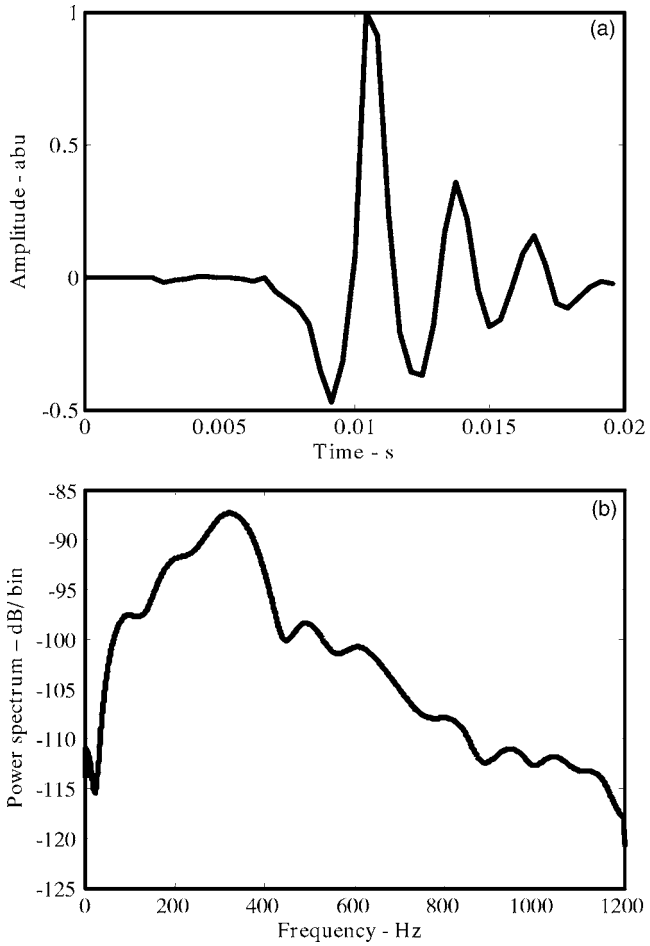

FIG. 4. (a) Time series and (b) corresponding energy spectrum for the source (direct path data) extracted from Fig. 3(a).

vacuum of the implosion. Noise levels between the additional boundary reflected arrivals are negligible compared to the signal levels from bubble pulses.

Time series from several light bulb source types were measured. The proximity of the source and receiver produced well-separated multipath arrivals, as seen in the example time series in Fig. 3(a) from a 100 W three-way bulb source. The data-model comparison in Fig. 3(a) shows that the direct path, first bottom bounce, and surface reflected pulses are accurately modeled with GAMARAY, a range-independent ray model, since only a few paths are needed to reproduce the time series for the shorter range source data.[41] The model field included ray paths with up to six bottom interactions.

The direct path data were extracted from the time series of Fig. 3(a). The direct path components [shown in Fig. 4(a)], after zero padding, provide the source spectrum [Fig. 4(b)] in 0.586 Hz increments, obtained from a 4096 point Fourier transform, for the cost function evaluation. For the inversion data, a band of frequencies from 200 to 400 Hz, encompassing the peak of the spectrum in Fig. 4(b) was selected. For this source, the spectrum is peaked near 300 Hz and has decreasing energy with decreasing frequency; therefore, the information obtained from the inversions at low frequencies is limited for this source type and hinders the determination of the deep sediment properties. The data for the inversion were extracted from the entire time series shown in Fig. 3(a) and includes the direct path arrival.

TABLE I. Two-layer plus half-space geoacoustic parameter value solution from the PWRC method range-independent inversion processing of the 2 m range implosive source data.

Parameter	Solution value	Lower bound	Upper bound
Min. cost	0.0556		
C_{t1} (m/s)	1717.2499	1550	2900
H_1 (m)	1.4296	0.300	2.5
C_{g1} (1/s)	3.3531	0.0	4.0
ρ_1 (g/cm^3)	1.5604	1.55	2.2
C_{t2}/C_{b1}	1.1255	0.90	1.6
α_{t1} [dB/(m kHz)]	1.5735	0.1	2.5
α_{g1} [dB/(m^2 kHz)]	0.0090	-1.0×10^{-2}	1.0×10^{-2}
H_2 (m)	26.8712	5.0	40.00
C_{g2} (1/s)	0.9620	0.4	4.0
ρ_2 (g/cm^3)	1.9453	1.6	2.1
C_{sub}/C_{b2}	1.4768	0.95	2.0
α_{t2} [dB/(m kHz)]	2.1865	0.10	2.5
α_{g2} [dB/(m^2 kHz)]	0.0190	-2.0×10^{-2}	2.0×10^{-2}
α_{sub} [dB/(m kHz)]	2.3977	0.1	2.5
ρ_{sub} [g/cm^3]	2.0470	1.6	2.2

The results for the geoacoustic parameter values from this inversion for the parameters of a bottom model with two sediment layers and a substrate are listed in the second column of Table I. The first layer surficial sound speed is C_{t1}. The first layer thickness is H_1 and the attenuation at the top of the first layer is α_{t1}. The other parameters are layer density ρ_i, layer attenuation α_i, sound speed gradient C_{gi}, attenuation gradient α_{gi}, and sound speed ratio C_{ti+1}/C_{bi} at each internal layer interface i with $t(b)$ designating the top (bottom) of each layer.

From the parameter values in the second column of Table I the impulse response in the 200–400 Hz band was calculated with GAMARAY, multiplied by the extracted source spectrum, and inverse Fourier transformed to obtain a model time series. Figure 3(a) shows the agreement of this model time series with the measured time series data with a reproduction of the surface and bottom reflected paths. In addition, the measured and modeled time series for a 60 W Sylvania® bulb for the same source/receiver geometry as Fig. 3(a) are shown in Fig. 3(b), where the measured source spectrum extracted from the time series in Fig. 3(b) and the geoacoustic parameter values from inverting the time series data in Fig. 3(a) were used to generate the model time series in Fig. 3(b). The comparison of data and model time series in Fig. 3(a) demonstrates that the bottom description was sufficiently accurate to reproduce the first bottom bounce from the short range implosive light bulb sources; however, one important point illustrated in Figs. 3(a) and 3(b) is that the initial direct path pulse amplitude and first bubble pulse have the highest amplitudes in the time series and the bottom and surface reflected arrivals each have less magnitude as compared to the direct path arrival. The levels of the first bottom interaction, as well as, any additional bottom interactions are much lower than the direct path, which necessarily dominates the correlation. Therefore, further analysis excluding

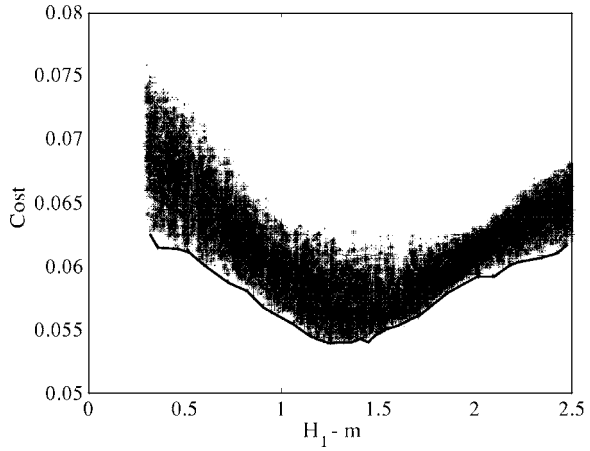

FIG. 5. The distribution of cost function values and the envelope of their minima as a function of the first layer thickness. Distribution obtained from an inversion of data from the short range implosive source.

these paths to isolate the bottom interactions is needed and will be discussed in Sec. III. In Secs. II D–II G, a comparison of similar parameter values obtained from the individual inversions of the various source types using all the arrival paths is presented along with a discussion of the parameter distributions for the important parameters.

The data-model agreement for the surface reflected pulse in Fig. 3 suggests that the source to receiver geometry was the same for both implosive sources. No noise was included in the model time series; therefore, many of the small scale arrivals after the surface reflected path are not reproduced and are attributed to noise in the data, although some additional arrivals due to multipaths are present in the time series but were not specifically identified. The band for the model time series was the same 200–400 Hz band of the inversion data. Even though no filter window tapering was employed with this wide band, no Gibb's phenomena were seen in the resulting time series. The data time series for both low (100–300 Hz) and high (200–600 Hz) bands showed good agreement with the model time series in Figs. 3(a) and 3(b). This is because most of the source energy is contained in the 200–400 Hz band, as shown in Fig. 4(b). Hence, the source spectra for the data inversions and for the model time series generation exhibit a tapering of the intensity on either side of the peak, producing an effective tapering of the box-car window filter applied in the inverse transform for the model time series. Most of the useful information from inversions of the data with the short range implosive sources pertains to the first layer parameters because no appreciable data is available at the low frequencies needed to penetrate and return from the deeper portion of the bottom.

An example cost distribution is shown in Fig. 5 as a function of the first layer thickness. An envelope of the minima of the cost distribution is also depicted in Fig. 5. (In subsequent figures of cost distributions these envelopes of the distribution minima will be employed to represent the cost distributions as a function of the inversion parameters. The envelopes are obtained by inspection of the lowest cost function values in selected intervals of the parameter value.) The differences in the parameter values from the different

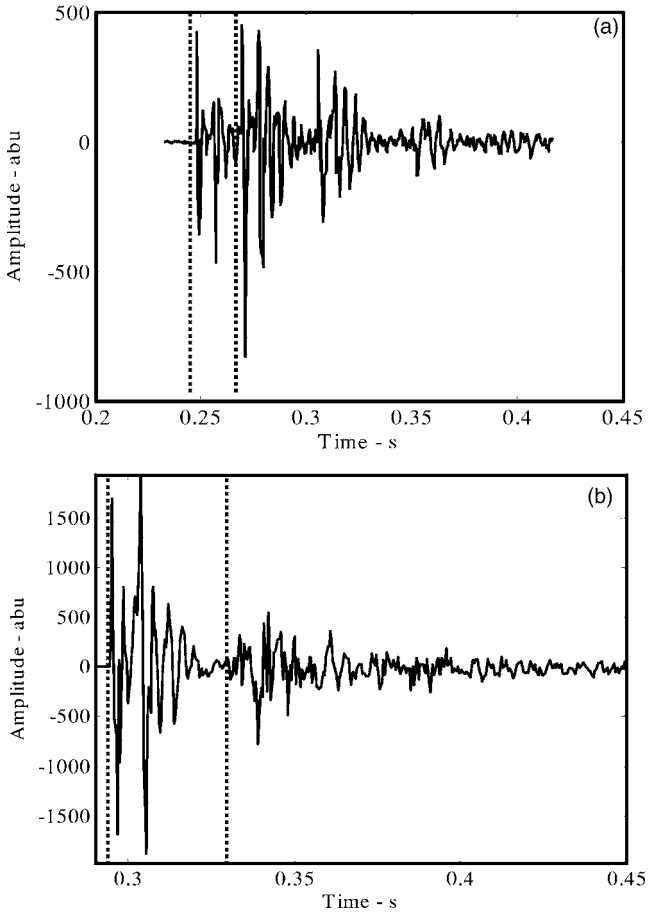

FIG. 6. Received time series from an explosive charge at ranges of (a) 200.3 m and (b) 57.9 m. Vertical dashed lines bracket the direct path arrivals.

source types discussed in Secs. II E and II F are due in part to the near flatness of the distributions. Nevertheless, some of the distribution minima are discernible as in Fig. 5. The sensitivity of the layer thickness to the inversion is attributed to the smaller amplitude of the bottom interactions relative to the direct path arrivals as seen in Fig. 3(a).

E. Explosive sources

Inversions of data from several explosive sources were also performed. The explosive charges were easily obtainable firecrackers and were practical for underwater applications because they contained waterproof fuses and produced broadband data. The firecrackers were taped to a plastic pipe and then lowered into the water to a fixed depth after the fuses were lit. The fuses burned sufficiently slowly underwater such that a source depth of 2.74 m (9 ft.) was achieved. The results of inversions from the explosive source data are presented in this section. The inversions are performed with the data from a single source at 200.3 m range, approximately 5 water depths away from the receiver.

The time series data from the 200.3 m range source are shown in Fig. 6(a), and the data from another explosive source obtained at a range of 57.9 m are shown in Fig. 6(b). The time series in Figs. 6(a) and 6(b) for the two ranges differ. The GAMARAY model of the arrival structure was used to identify the direct plus surface reflected arrivals and

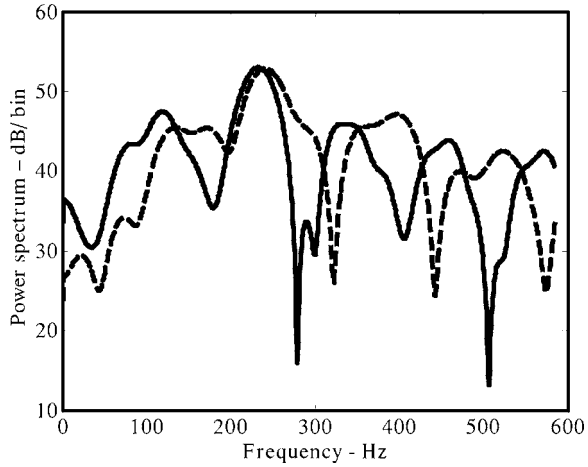

FIG. 7. Spectrum levels for the source time series from Fig. 6(a) (dashed) and from Fig. 6(b) (solid).

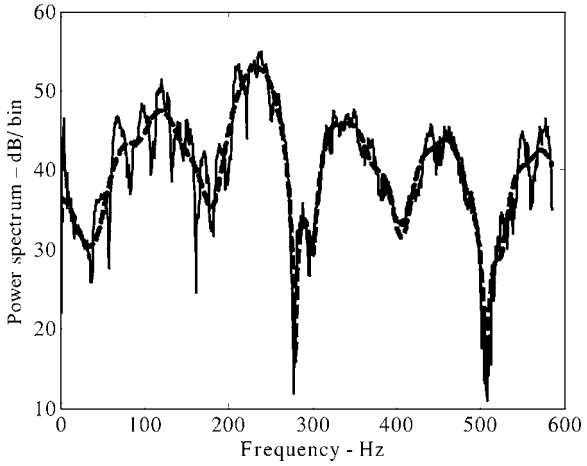

FIG. 8. Spectra for the source time series from the DSR arrivals in Fig. 6(b) (dashed) and for the total time series (solid) in Fig. 6(b).

subsequent bottom path arrivals in the time series obtained from the explosive sources. Several bottom interacting arrivals are apparent. Arrivals with up to four bottom interactions are seen in each time series; however, the time series from the shorter range explosive source show more attenuation of each successive pulse due to the higher grazing angle with the bottom.

Since the firecracker explosions were closer to the surface than the short range implosions, the separation of the direct and surface reflected arrivals in the mixture of the arrivals from the firecracker source bubble pulses was not possible. Therefore, the inversions of these data were performed using the DSR spectrum as discussed in Sec. II B. The DSR spectra are shown in Fig. 7 and were obtained from the time series segments bracketed by the vertical lines in Fig. 6. The vertical scale in Fig. 7 is arbitrary, and the peak levels of the spectra from the two sources have been assigned the same values for ease of comparison. The spectra from both of the explosive sources are relatively flat and extend across a broader band of frequencies as compared to the light bulb source spectrum in Fig. 4.

The spectrum from the time series containing bottom interactions is similar to the spectrum of just the DSR arrivals, as demonstrated in Fig. 8, except the former contains more interference structure than the spectrum of the DSR arrivals due to the multiple bottom interactions. The point is that the spectrum analysis reveals the dominance of the direct and surface reflected paths even for the longer range data.

Due to manufacturing variability and arrival path length differences, the two extracted source spectra shown in Fig. 7 are not identical. Most of the difference appears to be in the form of a shift in the pattern of peaks and nulls; therefore, using the DSR spectrum from the same explosive source used in the inversion avoided considering these differences.

The second column in Table II contains the results for the parameter values from the inversions of data from an explosive source at 200.3 m range and shows that some of the parameter values are different than the values from the results of the inversions of the short range implosive source data discussed in Sec. II D; namely, the sound speed at the top of the first layer differs from the value obtained from the inversion of the short range implosive source data by approximately 58 m/s. Also, in column two of Table II the attenuation at the top of the first layer differs by 0.26 dB/(m kHz) from the value obtained from inversion of the short range implosive data. The first layer density, however, is close to the value listed in Table I obtained from the inversion of the short range data.

Sound speed and thickness values obtained from inversions of the data from other explosive sources produced similar results to those in Table II. As with the results from the inversions of the data from short range sources, there is less information about the second layer from the inversions of the explosive source data. Also, the parameter distributions were broad even for the first layer parameter values; therefore, for the longer range explosive data, as well as, the

TABLE II. Two layer plus half-space geoacoustic parameter value solution from the PWRC method range-independent inversion processing of data from an explosive source at a range of 200.3 m and from two light bulb sources at ranges of 187.7 m and 552.7 m. The fourth column contains parameters from the inversion of data with only two bottom interacting arrivals from a light bulb at a range of 187.7 m.

Parameter	Explosive source	Implosive sources	Two bottom interactions
Min. cost	0.2801	0.537	0.267
C_{t1} (m/s)	1775.3264	1756.7785	1708.24
H_1 (m)	2.3185	1.1304	1.089
C_{g1} (1/s)	2.2420	2.9854	0.960
ρ_1 (g/cm^3)	1.5667	1.8611	1.701
C_{t2}/C_{b1}	1.1674	1.0841	0.938
α_{t1} [dB/(m kHz)]	1.3057	1.8326	1.175
α_{g1} [dB/(m^2 kHz)]	–0.0044	–0.0095	–0.0026
H_2 (m)	28.5245	15.5724	20.26
C_{g2} (1/s)	3.7657	0.879	2.522
ρ_2 (g/cm^3)	1.9858	2.0616	1.668
C_{sub}/C_{b2}	1.2305	1.7020	1.225
α_{t2} [dB/(m kHz)]	0.2486	0.1941	0.341
α_{g2} [dB/(m^2 kHz)]	0.0096	0.0095	–0.0098
α_{sub} [dB/(m kHz)]	0.2328	2.4270	1.492
ρ_{sub} [g/cm^3]	2.0273	1.727	1.835

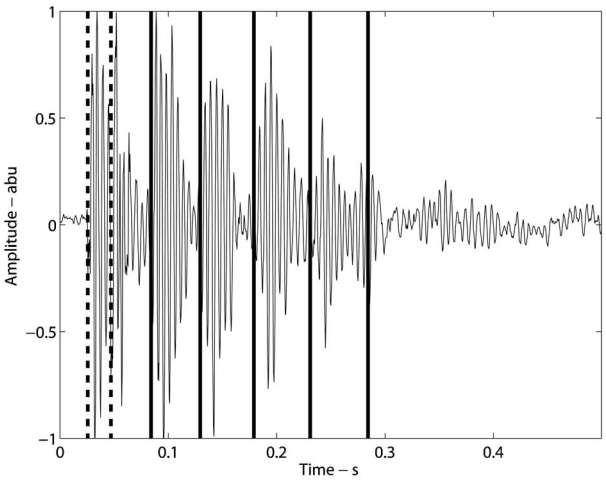

FIG. 9. Time series from the implosion of a 60 W standard Sylvania® light bulb at a range of 187.7 m. The vertical lines identify travel time interval separations for modeled eigenrays that reflect off the bottom. Dashed lines bracket the time series used to construct the DSR spectrum. Solid lines identify the leading edge of subsequent bottom interacions beginning with the second bounce.

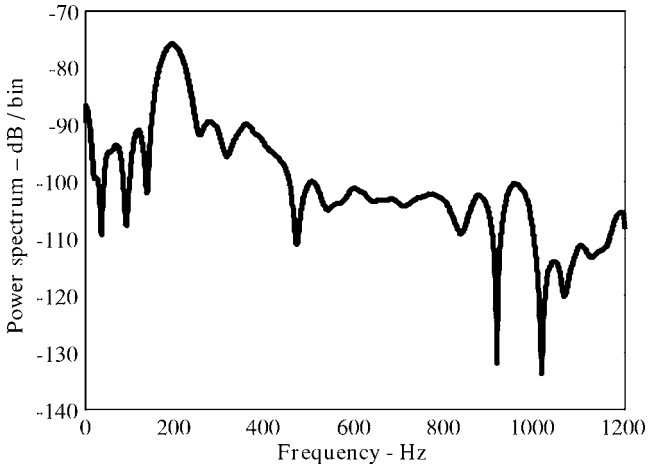

FIG. 10. Source spectrum extracted from the portions of time series in Fig. 9 containing only the direct path and surface reflected path arrivals.

shorter range implosive data in Sec. II D, the exclusion of the direct and surface arrivals will be shown in Sec. III to be crucial in reducing the parameter uncertainties to obtain a unique representation of the lake environment.

F. Longer range implosive sources

An example time series from an implosive light bulb source at a range of 187.7 m is shown in Fig. 9. The strongest peak has been arbitrarily normalized to one. (Data calibration is not necessary since the cost function for the inversion is independent of signal level, as discussed in Sec. II B.) Multiple arrivals, including the direct path, and several paths with bottom interactions are observed in Fig. 9, along with several weaker arrivals afterwards. The eigenray relative arrival times in Fig. 9, designated by the vertical lines, were calculated with GAMARAY. The source depth is 7.01 m. The agreement of the model and data relative arrival times suggests that the source depth, bottom depth, and SSP were accurately measured. The time series segment containing the direct and surface reflected paths is shown between the first two brackets in Fig. 9.

The spectrum of the implosive source at a range of 187.7 m is obtained by separating the DSR path arrivals from the bottom interacting arrivals and is shown in Fig. 10. The peak energy of this source, a 60 W Sylvania® light bulb, is shown in Fig. 10 to be at approximately 200 Hz. The inversions from the longer range implosive source data employed the signal in the band from 50.4 Hz to 257 Hz.

An inversion was performed from a combination of the time series data in Fig. 9 and the time series data from an implosive source at a range of 552.7 m. The third column of Table II gives this geoacoustic parameter values from the inversion. This geoacoustic solution was obtained by initializing the inversion with the values in the solution from the inversion with the short range implosive source data discussed in Sec. II D. The initial annealing temperature was set high and equal to the initial temperature in the inversion of the short range implosive source data. The parameter values in column three of Table II were obtained after approximately 2000 iterations.

The data from implosions of light bulbs at the longer ranges gave useful information about several of the parameters in the upper two sediment layers, although the cost distributions were shown to have broad minima similar to the inversions presented in Secs. II D and II E. The value obtained from these inversions for the sound speed at the top of the first layer differs from that for the inversion of the data from the other source types discussed in Secs. II D and II E by $\lesssim 40$ m/s, and the first layer sediment thickness is on the order of 1 m, similar to the value for that parameter obtained from the inversion of the short range implosive source data. A high value of the attenuation for the top of the first layer is also obtained from the inversion of the data from two long range implosive sources.

In Sec. II G a discussion of the parameter values obtained from the inversions that included all the propagation paths is given. The broad nature of the distributions for the important first and second layer parameter values will be evident, although it will be shown in Sec. IV, that the inversion results presented in this section were consistent in that all of these parameters can be used to model consistent TL.

G. Inversion summary for data with all arrivals

All of the inversion results presented in Secs. II D–II F were obtained using the same parameter bounds. Additional comparisons of some of the parameters values obtained from the two layer inversions are made in this section. Envelopes of the cost distribution minima as a function of the first layer sound speed from the inversions of data from each of the three source types are shown in Fig. 11. The sound speed at the top of the first layer for the short range implosive source data inversion is lower than the value of the same parameter for the inversions from the explosive source data, and from the longer range implosive source data, by $\lesssim 68$ m/s. The cost distribution envelopes produced from the inversions of data from all three source types exhibit broad minima for the

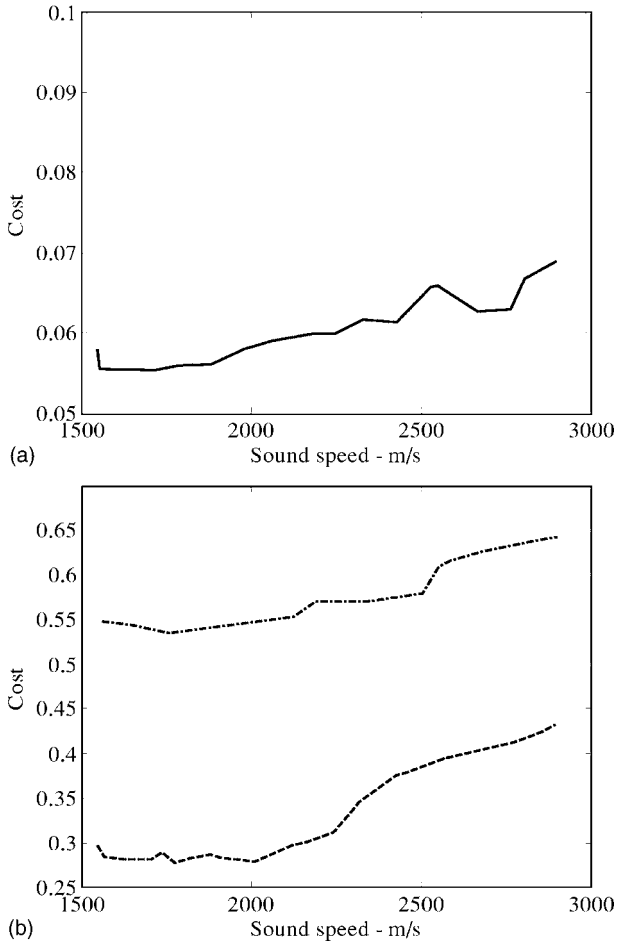

FIG. 11. Cost distribution envelopes as a function of the sound speed at the top of the first layer from inversions of data (a) from an implosive source at a range of 2 m, and (b) from two implosive sources at ranges of 187.7 m and 552.7 m (dashed-dotted), and from an explosive source at a range of 200.3 m (dashed).

first layer sound speed and have similar shapes. The cost values at the global minimum in Fig. 11 are different for each source type. Appendix B discusses the relationship of the range dependence of the cost values and the data SNR. Figure 11 reveals that the values of the sound speed varies from approximately 1600 m/s to 1900 m/s. These values have approximately the same cost value as the global minimum and show a high uncertainty. This is one of the sensitive parameters of the sediment and in Sec. III a parameter value is produced with much smaller uncertainty than shown in Fig. 11.

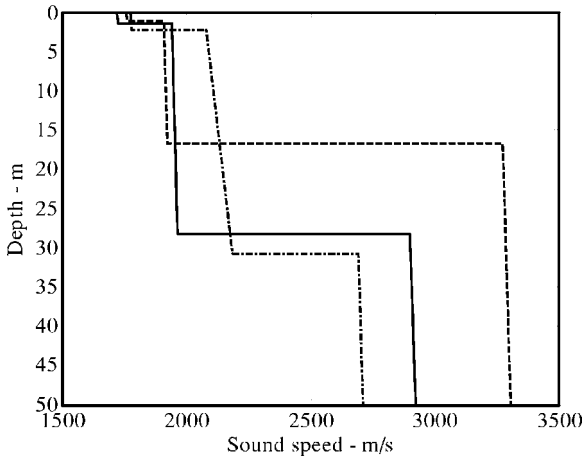

FIG. 12. Bottom sound speed as a function of depth from PWRC inversions (Tables I and II) of data from an implosive source at a range of 2 m (solid), of data from two implosive sources at ranges of 187.7 m and 552.7 m (dashed), and of data from an explosive source at a range of 200.3 m (dashed-dotted).

Values for several of the first layer geoacoustic parameters from the inversions of various source data using the PWRC method are collected in Table III. Inversions of the implosive source data were also performed with modeled fields from ORCA to show that the large uncertainties in the distributions are due to the environment, independent of the model used in the inversions. The first layer geoacoustic parameter values are included in Table III for inversions from several source data. The sound speed at the top of the first layer obtained from the inversions with PWRC and ORCA are within the range of those from the sources presented in Secs. II D–II F (also listed in Table III for comparison).

Figure 12 shows the bottom sound speed profiles from the geoacoustic parameter values in Tables I and II for the PWRC method. The sound speeds for the second layer in the inversion solutions from the short range implosive source lie approximately at the midpoint between the solutions for the other two source types. The second layer sound speed has a range of values from approximately 1900 m/s to 2200 m/s and is within the range of values expected for a limestone sediment. The inversion sound speeds are in the range of the values from seismic measurements made approximately 10 miles from the LTTS facility, using a geophone array with an elastic wave generator.[42] Below approximately 0.6 m of soil, an approximately 30 m thick layer of chalk/limestone with a compressional speed ranging from 2100 to 2400 m/s was

TABLE III. First layer parameter values from inversions of the data from several source types with PWRC and normal mode (NM) forward models.

Sources	Model	Range (m)	C_{t1} (m/s)	H_1 (m)	α_{t1} [dB/(m kHz)]
Two bulbs	PWRC	188, 553	1756.78	1.13	1.83
Two bulbs	NM	188, 553	1777.87	1.24	2.27
Three bulbs	NM	188, 553, 752	1738.52	2.23	2.29
Three bulbs	PWRC	188, 553, 752	1721.97	1.99	1.04
Firecracker	PWRC	200	1775.33	2.31	1.31
Single bulb	PWRC	2	1717.25	1.43	1.57
Single bulb	NM	2	1738.62	1.24	1.94

found, overlying a dense limestone substrate with a compressional speed of approximately 3400 m/s. Also, sound speed and density values from the inversion are within the bounds measured by Hamilton for chalk/limestone.[20]

The parameters distributions were shown to be broad for other important first and second layer parameters obtained from the inversions that included all the propagation paths. Several of the first and second layer parameters distributions are discussed in Appendix C. Data path selection may not be possible for some environments; however, for this environment it was possible and was essential to quantify the uniqueness of the parameters obtained by the inversions presented in Sec. II.

III. SYSTEMATIC INVERSIONS WITH DATA FROM SEPARATED ARRIVALS

The purpose of this section is to eliminate the direct and surface reflected arrivals and thus increase the sensitivity of the bottom parameter values obtained by the inversion of the impulsive source data. This data selection resolves the ambiguities in the values of a few important parameters produced from inversions of the data from the three source types discussed in Sec. II and also determines the minimum number of layers needed to describe the environment. The accuracy of the results is assessed by varying the number of layers used in the inversion model systematically and comparing the variation in the layer parameter values and the effect on the parameter uncertainties.

A. Separating arrivals

The solutions to the inversions presented in this section demonstrates the ability to separate arrivals in the model and also in the data, thereby demonstrating the versatility of the PWRC method in isolating the bottom effects. This technique of path separation may also prove useful for a soft bottom sediment, as opposed to the hard limestone present in this environment, although separating the bottom arrival paths may be more difficult (if possible) for other types of environments. A complete analysis of the details of the inversion using each separated bottom time series segment is not presented here. Rather, an overview of several points is used to demonstrate the technique.

To begin, the first two paths were excluded from the model corresponding to the direct path and surface reflected arrival contributions to the time series, as shown for example, by the time series segment between the vertical bars in Figs. 6(a) and 6(b). The data spectra, excluding the direct path plus surface reflected arrival, were extracted and inversions were performed. The data from a single implosive source at 187.7 m was used for the analysis. The starting parameter values for the inversions presented in this section were those in Table I, column two. Table II, column four shows the results for the geoacoustic parameter values from an inversion of only the data from the first two bottom interactions. The sound speed at the top of the first layer differs by approximately 9 m/s from the value obtained for that parameter from inversions of the short range implosive source data. For this source range the sound speed ratio at the top of the second layer to the bottom of the first layer is not resolved and is lower than the value from the inversions of the source data discussed in Secs. II D–II F due to the lack of energy penetration and limited bottom interaction at this range.

Another analysis was performed by isolating the first bottom interacting arrival from the data from the explosive source at a range of 200.3 m and using this time segment to construct an alternative source spectrum for subsequent inversion processing, again excluding the DSR paths in the inversions. Since this was a hard bottom environment, the structure of the initial explosion and subsequent bubble pulses was well preserved after the first bottom interaction. The inversion results using the source spectrum obtained from the first bottom interaction were similar to those reported in Table II, column two for inversions with the DSR spectrum as the representative spectrum from an explosive source. If there were no DSR paths due to a refracting SSP or if no measurements of the source spectrum were obtained, the inversion techniques presented here may still be applicable.

A more detailed analysis of the parameter distributions obtained by the inversions that excluded the direct and surface reflected paths is presented in Sec. III B and substantiates the inversion results of Sec. II. A method is also presented to determine the number of layers needed to describe the environment. The approach is to uniquely determine which environmental description is appropriate using only the cost values and distributions from the inversions. Then the inversion solutions are evaluated independently with the TL data cost function, i.e., the RMS error in Sec. IV. The importance of this method is that it verifies that geoaoustic parameters obtained from inversions using one type of data can then accurately estimate another type of data (TL) at frequencies and ranges beyond those used in the inversions.

B. Dependence on the number of layers

A general approach to understanding the importance of the individual parameters is to build up an environmental model by successively adding layers to each previous model, perform the inversions, and then compare both the cost function minimum and the cost distribution envelopes for important parameters as a function of the number of layers. Convergence of the minimum cost values at the inversion solutions will be used to determine the minimum number of sediment layers needed to obtain accurate parameter values from a geoacoustic inversion. Inversions of the short range implosive source data with a varying number of sediment layers were performed by applying a bootstrap technique. For the half-space model (referred to as the zero or no sediment layer model) three inversions parameters were used, the half-space sound speed, density, and attenuation. Once the zero sediment layer inversion was performed, a layer over the half-space was added, and the parameter values at the top of this layer were initialized to the values obtained from the previous inversion, i.e., the zero sediment layer model parameter values, and layer thickness, layer sound speed gradient, and layer attenuation gradient parameters were added.

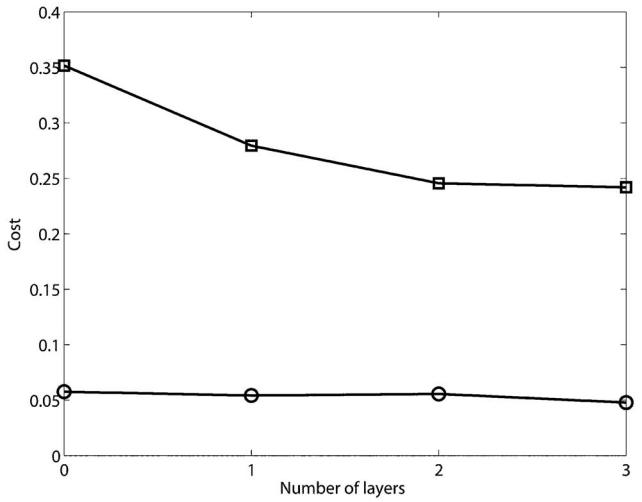

FIG. 13. Cost values for inversions as a function of the number of layers for the short range implosive source (circle) and for the bottom interactions of the implosive source at a range of 187.7 m (square).

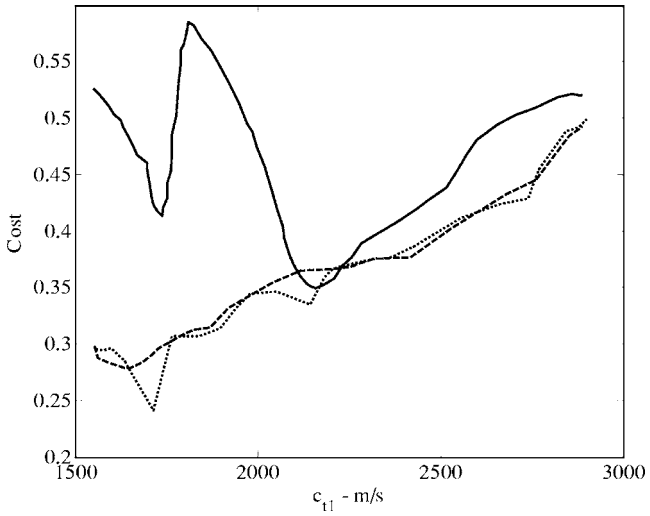

FIG. 14. Cost distribution envelopes for sound speed obtained from the inversions of implosive source data at a range of 187.7 m by excluding the direct and surface reflected paths. At the top of the half-space for the zero sediment layer model (solid), at the top of the first sediment layer for the one layer model (dashed), and at the top of the first layer for the two layer model (dotted).

This procedure was repeated to build a two sediment layer model in which the parameters specifying the top of the second layer were initialized to those of the half-space parameters obtained from the one sediment layer inversions. Similarly, the three sediment layer model representation is initialized from the solution for the two sediment layer model.

The minimum cost values for each inversion as a function of the number of layers are shown in Fig. 13. The cost value as the number of layers increases is expected to decrease until the minimum number of layers needed to represent the environment is encountered. The minimum correlation cost values as a function of the number of layers varies little for the short range implosive data when all the path contributions are used in the inversion.

To remove the effect of the direct path on the correlation cost values, data from a longer range (187.7 m) implosive source was processed and the direct and surface reflected paths were excluded from the inversion data to isolate the bottom contributions to the cost function. Then, Fig. 13 shows that the minimum cost value definitely decreases as the number of sediment layers increases from zero to one. Performing the inversions with a second sediment layer below a first layer initialized with the one sediment layer solution produced a lower cost value minimum than was achieved for the one sediment layer model. Thus, it is expected that a two layer model is a better representation of the environment than either a zero or one sediment layer model. Finally, adding a third layer below the second layer produced a negligible change in the cost value minimum obtained from the inversion.

The values of some important first layer parameters $(C_{t1}, C_{t2}/C_{b1}, \alpha_{t1})$ were more well-defined by the inversions that excluded data from the direct and surface reflected path arrivals than if data from these arrival paths was included. Namely, discernable minima in the cost distributions of $C_{t1}, C_{t2}/C_{b1}$, and α_{t1} were obtained from the inversions once data from the direct and surface reflected path arrivals were excluded. The cost distribution envelopes of these parameters were broader when the inversion was performed on data from all arrivals, as discussed in Sec. II. Cost distribution envelopes for the sound speed at the water sediment interface as a function of the number of sediment layers is shown in Fig. 14 for inversions of the long range implosive data referenced in Fig. 13. For the model that contains no sediment layers, the minimum cost value is much greater than the cost value at the minimum for either the one or two layer solutions. In addition a double minimum exists in the distribution for the zero layer as shown in Fig. 13. The value of C_{t1} at the cost distribution minimum for the zero layer model solution is greater than 2100 m/s. The value of C_{t1} at the cost distribution minimum for the one layer model solution is lower by approximately 70 m/s than the value in the inversion solution for a two layer model, whereas C_{t1} in the solution for the two layer model is approximately 5 m/s less than the value listed in Table I obtained from the inversion of the short range implosive source data.

A convergence of the distribution envelopes as a function of the number of layers was found for the minimum in the cost distribution for the attenuation α_{t1} obtained from the inversion of the longer range implosive source data excluding the direct and surface reflected paths as shown in Fig. 15. For the zero layer model α_1 is probably unphysically low for the ground truth sediment description and the minimum cost value is well above the minimum cost distribution values obtained from the inversion of either the one or two layer models. The cost distribution envelopes obtained for α_1 from the inversion of the one layer model exhibits a broad but discernible minimum, whereas the cost distribution envelopes for α_1 from the inversion for a two layer model shows a more distinct minimum with a lower cost value. The minima in the cost distribution envelopes in Fig. 15 are better resolved than the minima in the envelopes from the inversions of the two layer models presented in Sec. II.

The inversions with the longer range implosive source

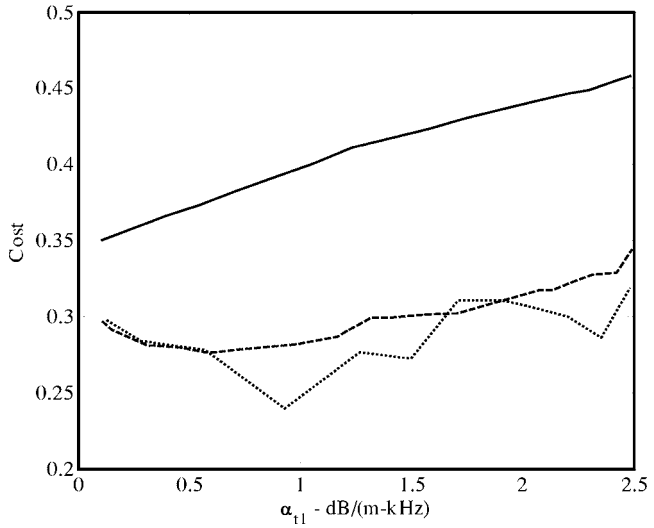

FIG. 15. Cost distribution envelopes for attenuation obtained by the inversions of implosive source data at a range of 187.7 m by excluding the direct and surface reflected paths. At the top of the half-space for the zero sediment layer model (solid), at the top of the first sediment layer for the one layer model (dashed), and at the top of the first layer for the two layer model (dotted).

data at a range of 187.7 m that produced Figs. 14 and 15 contained only three bottom interactions out of more than six and could not resolve the sound speed ratio C_{t2}/C_{b1}. Therefore, inversions were performed with the longer range explosive source data at 200.3 m that contained at least four bottom interactions and excluded the direct and surface reflected paths. The cost distribution envelopes for the sound speed ratio C_{t2}/C_{b1} from the inversions for the one and two layer sediment models are shown in Fig. 16 (C_{t2} for the one layer model is the sound speed in the half-space). The cost distribution minimum for this parameter is also well determined in both the one and two layer model solutions, and the cost at the minimum value is only slightly smaller than the cost at the minimum for the one layer model.

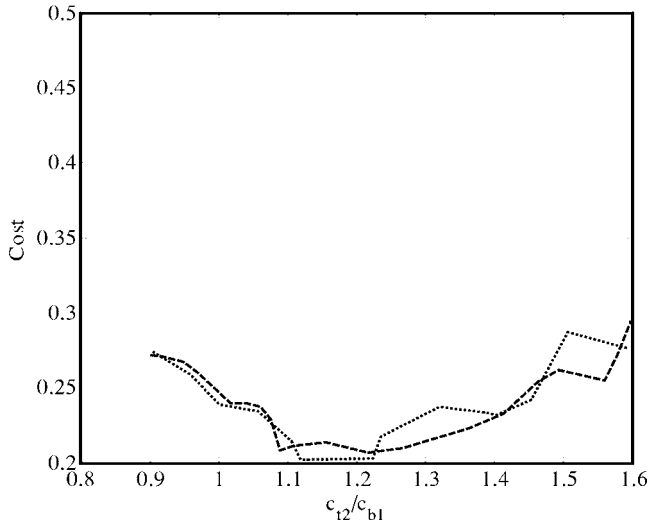

FIG. 16. Cost distribution envelopes for sound speed ratio C_{t2}/C_{b1} obtained by the inversions of the explosive source at a range of 200.3 m by excluding the direct and surface reflected paths. For the one layer model (dashed) and for the two layer model (dotted).

The three layer solution had no parameter values that differed appreciably from the corresponding values in the two layer solution. Therefore, the distribution envelopes essentially converged with two sediment layers. This result will be corroborated next by comparing the data TL with the model TL predicted from the parameter values obtained from the inversions as a function of the number of layers in the sediment models.

IV. TRANSMISSION LOSS

A discussion of the measured TL is presented in Sec. IV A. The accuracy of model TL predictions calculated from the geoacoustic parameter solutions obtained with inversions is examined in Sec. III B by evaluating another cost function, i.e., the RMS error between the data TL presented in Sec. IV A and the model TL constructed with the geoacoustic parameter values obtained from the inversion.

A. Model predictions

TL at several frequencies was measured from the received levels from a towed J-9 source mounted on the side of a small boat equipped with a gas powered generator. The J-9 source can operate in either a single CW mode at fixed output line level or in a multiple CW mode at a reduced output line level, as compared to the single mode operation. To maximize the source level in this high bottom attenuation environment, the source was operated in single CW mode. The data at each frequency were collected on separate passes, and multiple passes were performed for some of the frequencies. The boat maintained a slow constant speed of approximately 1.5 m/s down the length of the channel to a maximum distance of approximately 1.5 km from the receiver located on the bottom (Fig. 1), although the total range for each frequency varied from this maximum range. The source depth was approximately constant at 7 m on each of the five passes reported here. Readings from a handheld global positioning system (GPS) were converted to the source track range as a function of time.

The recorded time series from the received signals with the continuous wave lines were fast Fourier transformed (FFTd) to produce spectragrams. The frequency bins with the maximum line levels were determined, and a sum of the intensity in the three bins centered on the bin with the peak line level produced the received signal plus noise levels. An estimate of the noise was calculated from the average of the intensity over approximately ten bins each to the left and to the right of the three bins centered about the bin with peak intensity. The noise levels were negligible compared to the signal levels. Measured TL was obtained by subtracting the received dB level from the source dB level. The source levels were set and measured prior to deployment at the LTTS barge and are referred to as the calibrated source levels. Table IV, column two, lists the calibrated source levels of the tonals at frequencies of 257 Hz, 511 Hz, 788 Hz, and 998 Hz.

Model TL was calculated using ORCA with the inversion parameters listed in the second column of Table I for comparison to the measured TL. The measured TL data vali-

TABLE IV. Source levels for cw tones. Derived levels [Eq. (6)] obtained with the solution from inversion of the short range implosive source data. The fourth column is the difference of the calibrated and derived source levels.

Frequency (Hz)	Calibrated (dB)	Derivative (dB)	Difference (dB)
257	148.24	146.02	2.22
511	148.78	147.89	0.89
788	149.97	150.96	−0.99
998	150.16	149.86	0.30

date the solutions obtained by the inversions. A normal mode model was used to generate the model TL and shows that the parameter values obtained by the inversions are independent of the forward model used in the inversions. A ray model could have been used to produce similar TL model predictions; however, for a shallow water waveguide at these frequencies many multipaths must be included to reproduce the field at longer ranges.

The resulting measured and modeled TL comparisons are shown in Figs. 17 and 18 for frequencies of 257, 511, 788, and 998 Hz. Another set of source tow passes was performed later during the experiment, and the measured TL from those passes produced similar comparisons with the modeled TL, although the exact path on the various passes varied, and the second set of source tow passes did not extend as far from the sensor as those from the first set. The other solutions listed in Table II, columns two and three, were also used to model the TL with ORCA and produced similar comparisons to the data TL.

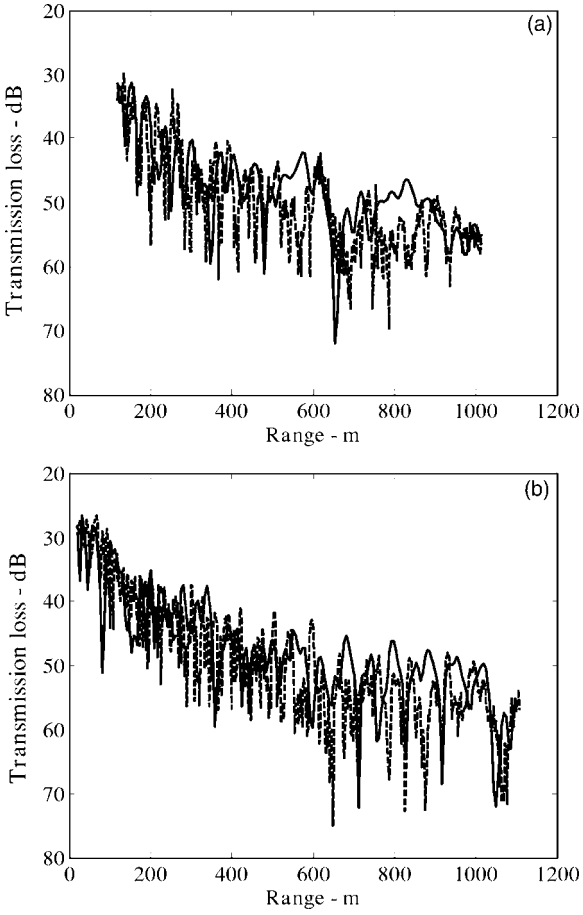

FIG. 17. Transmission loss from the tonal data (dashed) and the normal mode model TL (solid) for (a) 257 Hz and (b) 511 Hz.

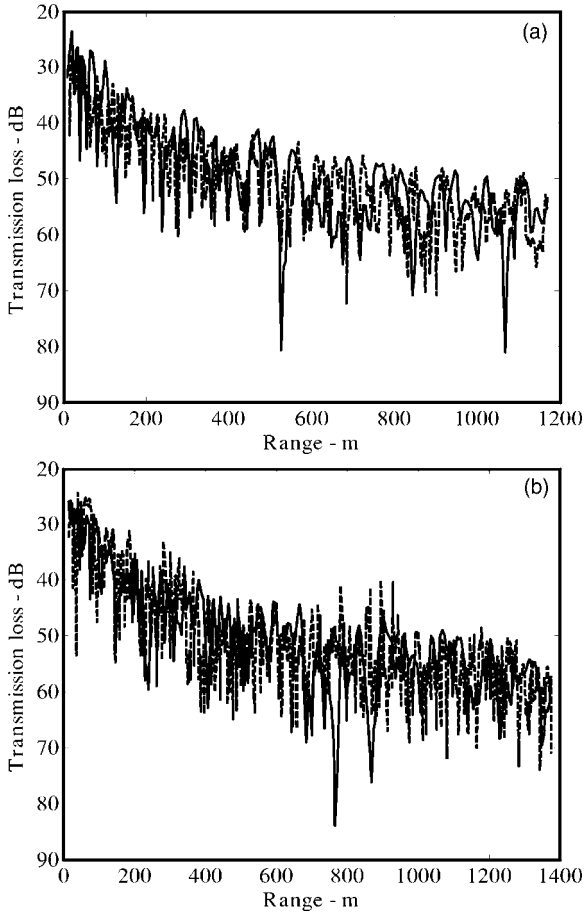

FIG. 18. Transmission loss from data (dashed) and model TL (solid) at (a) 788 Hz and (b) 998 Hz.

The qualitative agreement between modeled and measured TL validates the geoacoustic parameter values obtained from the various inversions with broadband data by showing that they can be used to predict independently measured TL over a broad range of frequencies well above those used in the inversion. This also shows that a bottom model with fluid layers can accurately predict the propagation in a hard bottom environment. A quantitative comparison of the measured and model TL based on RMS error is presented in Sec. IV B.

B. RMS error

The RMS error between the data and model TL for a fixed frequency, f, is

$$\mathrm{RMS}_{\mathrm{TL}}(f) \equiv \sqrt{\frac{1}{N}\sum_{i=1}^{N}[\mathrm{TL}_{i,D}(f) - \mathrm{TL}_{i,M}(f)]^2}, \tag{5}$$

where i is the range index, N is the total number of ranges, and $\mathrm{TL}_{i,D(M)}$ is the data (model) TL for the ith range.

For these data, the RMS error was calculated from the model TL predicted with the solutions for the geoacoustic parameter values listed in Table I and in Table II, columns

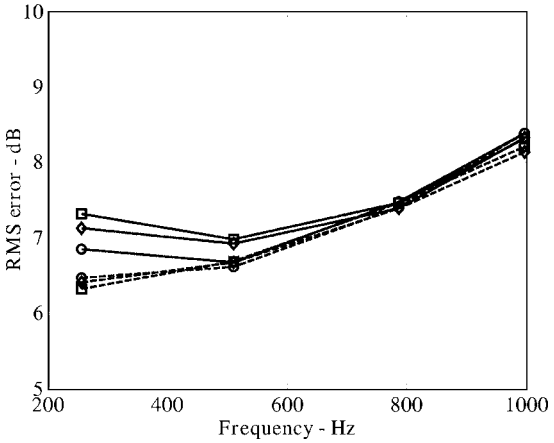

FIG. 19. Frequency dependence of the RMS error between the data TL and the model TL calculated with geoacoustic parameter values from the inversions of the short range implosive source data (circle), of the data from the two longer range implosive sources (square), and of the longer range explosive source data (diamond). Data TL computed from calibrated source levels (solid lines) and data TL computed from the source levels obtained Eq. (6) (dashed lines).

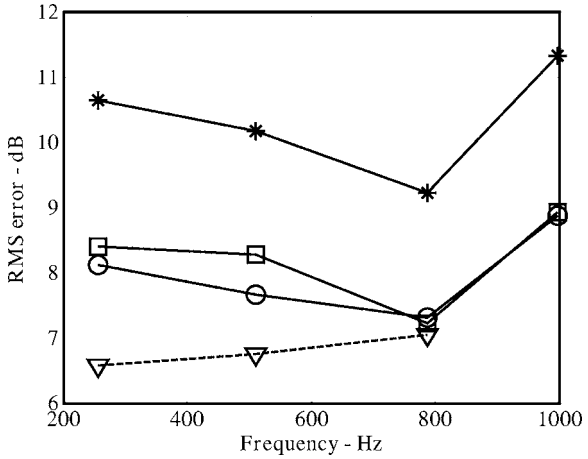

FIG. 20. Layer dependence of the RMS error for the model parameters obtained by the inversion of data from an implosive source at a range of 187.7 m, excluding the direct and surface reflected path arrivals. Zero sediment layer model (star), one layer model (square), and two layer model (circle). RMS errors calculated from two data passes are shown for comparison (triangle).

two and three, i.e., with the two layer sediment representations from the individual inversions of the data from three source types. Two sets of results are depicted in Fig. 19. The first was obtained from TL measurements based on the calibrated source levels recorded prior to the source tow passes (column two of Table IV). The second set of results in Fig. 19, with the slightly lower RMS error, were obtained by replacing $\mathrm{TL}_{i,D}(f)$ with $\mathrm{SL}(f)-\mathrm{RL}_{i,D}(f)$ in Eq. (5) and adjusting $\mathrm{SL}(f)$ to minimize the error:

$$\mathrm{SL}(f) = \frac{1}{N}\sum_{i=1}^{N} [\mathrm{RL}_{i,D}(f) - \mathrm{TL}_{i,M}(f)], \tag{6}$$

where SL is the source level, and $\mathrm{RL}_{i,D}$ is the received level at frequency f. The source levels determined from Eq. (6) are listed in the third column of Table IV. Table IV, column four, displays the difference between the calibrated source levels and those obtained from Eq. (6) for the geoacoustic solution from the inversion of the short range implosive source data as shown in Fig. 19. Except for the 257 Hz tonal, for which the SL difference between the calibrated and derived values is 2.2 dB, the SL differences are less than approximately 1 dB.

The main result shown in Fig. 19 is that the RMS error is nearly independent of which source type produced the data for the inversions from which the model geoacoustic parameter values were obtained. This study demonstrates that inversions from the short range source data, and from longer range source data in various geometries, produced equivalent geoacoustic parameter values for TL model predictions that are valid at longer ranges and at higher frequencies than those in the data for the inversions.

Next, the RMS errors for TL models generated from the inversions of the implosive source data with zero, one, two, and three sediment layer representations were examined as a function of frequency. By examining the cost distribution envelopes for the surficial sound speeds and attenuations obtained from the inversion of the longer range implosive source data the zero sediment layer model was shown in Sec. III B to be an inadequate description of the environment. Also, cost distribution envelopes from the inversions for the three layer sediment model were not discernibly different from the distribution envelopes with inversions obtained using the two layer model. To determine the relevance of the RMS error values, the RMS error between the measured TL data from the two data passes at each frequency (excluding the 998 Hz data which had a much shorter second pass) was computed, i.e., $\mathrm{TL}_{i,D}(f)$ was substituted for $\mathrm{TL}_{i,M}(f)$ in Eq. (5). The data-data RMS errors give an estimate of the lower limit of the RMS error expected for the data-model correlations.

Figure 20 shows the frequency dependence of the RMS errors from the inversion solutions discussed in Figs. 14 and 15 as a function of the number of sediment layers in the sediment model. The zero sediment layer model solution from the inversion of the longer range implosive source, excluding the direct and surface reflected path arrivals, produced the largest difference in the RMS error as compared to the data-data RMS error. The one layer model solution gives a better fit to the RMS error than the zero layer solution; however, at 257 and 511 Hz the difference between the one layer RMS error and the data-data RMS error is still approximately 2 dB. The two layer model solution obtained using the same data as the one layer solution produced a data-model RMS error closest to the data-data RMS error. In summary, the one and two layer solutions converge to the same prediction for the surficial sediment layer parameter values and produced at 788 Hz a data-model RMS error close to the value of the data-data RMS error. This is expected since, as the frequency increases, the penetration depth decreases thus decreasing the influence of the second layer parameters on the model TL.

The best prediction of the model TL was obtained using the two layer model parameters in Table I. Comparisons of the RMS errors as a function of the number of sediment layers in the solutions obtained from inversions of the short

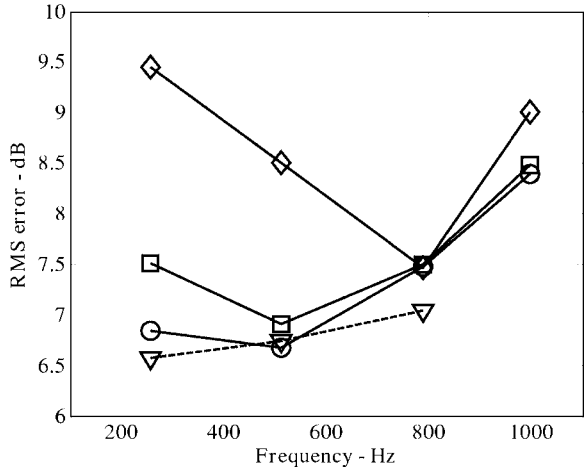

FIG. 21. Layer dependence of the RMS error for the model parameters obtained by the inversion of the short range implosive source at a range of 2 m for the three sediment layer model (diamond), the one layer model (square), and the two layer model (circle). RMS errors calculated from two data passes (Sec. IV B) are shown for comparison (triangle).

range implosive source data are shown in Fig. 21. The RMS error for the two layer model solution has the best agreement with the data-data RMS error at 257 Hz. For the higher frequencies, both the one and two layer solutions have nearly the same RMS error at values close to those of the data-data RMS errors. Overall, there is a slight decrease in the RMS model-data error at the lower frequencies.

In Fig. 21 the RMS model-data error from the three layer model is significantly higher than from the one or two layer model solutions. This is because α_1 is too small in the three layer solutions. The peak energy of the short range implosive source data used in the inversions may have been at frequencies that are too high [see Fig. 4(b)] to use a three layer model representation of the environment, because the source level of the data was insufficient at the lower frequencies that provide significant arrivals with deeper penetration into the sediment.

One final point is that inversions with the short range implosive source which excluded the direct and surface reflected paths showed that the three layer solution was indistinguishable from the two layer solution obtained with the same data. The resulting data-model RMS errors from the one and two layer solutions obtained from these inversions as a function of the number of layers had similar behavior as those shown in Fig. 20 for the longer range source data.

V. CONCLUSION

Developing and testing ocean environment inversion techniques prior to performing the actual ocean experiments in a stable environment such as the LTTS facility is extremely useful. Data collected during the same summer months, but separated by a year, were successfully used to infer bottom properties and to test new inversion techniques without the inconsistencies introduced by the inherent temporal variability of an ocean environment.

Geoacousic inversions of data from a single receiver and sources in two different geometries were performed. Water sound speed profiles obtained from measured temperature profiles were used in a ray trace plus plane wave reflection coefficient propagation model to perform a simulated annealing optimization. Inversion results for geoacoustic parameter values from short range implosive source data were consistent with those obtained from inversions of additional implosive and explosive source data at longer ranges. An examination of the cost distributions obtained from inversions of the longer range data showed that excluding the direct and surface reflected paths gave more precise estimates for several of the surficial sediment parameters and also determined the number of layers needed to represent the environment. The ability to process arrivals separately makes the PWRC method useful for geoacoustic inversions even with data from a single sensor located on the bottom.

TL predictions calculated from the geoacoustic parameter values determined from inversions were compared to measured TL from a towed source. Measured and modeled TL agree for frequencies and ranges well above those used to perform the inversions. A sensitivity study was performed using the RMS error between model and data TL confirming that the number of layers needed to represent the environment had been determined from the parameter distributions obtained by inversions.

It was demonstrated here for the first time that separation of the direct and surface reflected paths to estimate the source spectrum was not necessary to obtain valid inversion results, especially for the upper layer parameter solutions from inversions of the longer range impulsive source data. The source range dependence of the cost values was associated with the SNR and was attributed to spreading loss.

Finally, all of the analyses presented here show that even in hard environments at these frequencies a fluid model description can be used to accurately predict propagation.

ACKNOWLEDGMENTS

This work was supported by the Independent Research and Development Program of Applied Research Laboratories, The University of Texas at Austin. The authors express their appreciation to Dr. R. A. Koch for many insightful discussions and the editing of this manuscript.

APPENDIX A: DSR SPECTRUM

The DSR spectrum contains both direct path plus surface reflected arrivals; therefore, it is necessary to demonstrate that no appreciable error is introduced by using the DSR spectrum in place of the actual source spectrum, S_j. For inversions involving multiple sources, the closest source to the receiver is used to determine the DSR spectrum, $S_{j,\mathrm{DSR}}$, although this is not a necessary procedure but does account for the increased SNR of the closer source. In the application of the DSR spectrum only the source spectrum is modified and therefore every individual path from the model calculation is included in the inversions (unless the direct and surface reflected paths are explicitly excluded as in Sec. III). The path separations increase as the number of bottom interactions increases and all of these contributions must be included in evaluating the cost function.

Details of the DSR spectrum that was used in the inversions of the longer range data presented in Secs. II and III are given here. The derivation of the DSR spectrum is followed by an example which quantifies this effect. The direct and surface reflected paths were modeled and then used to deconvolve the two paths of the DSR spectrum in order to isolate the actual source spectrum. The DSR spectrum is defined by

$$S_{j,\mathrm{DSR}} = S_j \sum_{i=1}^{2} R_{i,j} = S_j [G_D e^{i\omega_j \tau_D} - G_{\mathrm{SR}} e^{i\omega_j \tau_{\mathrm{SR}}}], \tag{A1}$$

where G_D (G_{SR}), and τ_D (τ_{SR}) are the geometric spreading loss and ray path travel time, respectively, for the direct (surface reflected) paths. Equation (A1) is conveniently written

$$S_{j,\mathrm{DSR}} = e^{i\omega_j \tau_D} G_D [1 - G_{\mathrm{DSR}} e^{i\omega_j \tau_{\mathrm{DSR}}}] S_j, \tag{A2}$$

where $G_{\mathrm{SR}}/G_D \equiv G_{\mathrm{DSR}}$ and $\tau_{\mathrm{SR}} - \tau_D \equiv \tau_{\mathrm{DSR}}$. For convenience, $[1 - G_{\mathrm{DSR}} e^{i\omega_j \tau_{\mathrm{DSR}}}]$ is referred to as the "bracketed expression."

The amplitude factor, G_D, and the phase factor τ_D need not be determined since the cost function is normalized and includes the time delay $\delta\tau_{i,k}$ in Eq. (3) which accounts for arbitrary phase shifts. However, the bracketed expression on the right-hand side of Eq. (A2) must be considered since it is frequency dependent, periodic, and can produce nulls in the $S_{j,\mathrm{DSR}}$ spectrum. It is interesting to note that for a single frequency, substituting Eq. (A2) into Eq. (3) produces an arbitrary phase factor; however, the frequency integrations in Eq. (3) destroys this result for multiple frequencies.

To quantify the location of the nulls Eq. (A2) is approximated by

$$S_{j,\mathrm{DSR}} \approx e^{-i\omega_j \tau_{\mathrm{DSR}}/2} \sin(\omega_j \tau_{\mathrm{DSR}}/2) S_j, \tag{A3}$$

where the overall phase and magnitude terms in Eq. (A2) have been neglected and G_{DSR} is assumed to be approximately 1 for illustration. This shows that the first null is expected to be at zero frequency. For actual data, however, there is significant noise offset at zero frequency as shown in Figs. 7 and 8, preventing this null from occurring. The important point is the location of the second null, which is shown to be at frequencies greater than those used in the inversions of impulsive data due to the lack of energy at these frequencies.

For sources near the surface and for relatively short source-to-receiver ranges the difference in the path length between the direct and surface reflected path is negligible. For example, the longer range explosive source at the 200.3 m range with a source depth of 2.74 m gives $\tau_{\mathrm{DSR}} \approx 6.17 \times 10^{-4}$ s. Similarly, for this example, $G_{\mathrm{DSR}} \approx 0.984$ [justifying the assumption made in the derivation of Eq. (A3)]. The frequency value of the second null in Eq. (A3) is approximately 1620 Hz, well above the frequencies considered in the inversion for the longer range sources.

The bracketed expression in Eq. (A1) was evaluated for the 200.3 m explosive source since it could produce a degradation in the correlation function given in Eq. (3). The power spectrum from the direct plus surface reflected path extracted from the longer range explosive source at 200.3 m range is shown in Fig. 22 along with a relative plot of the bracketed expression to illustrate the behavior of the effect. The curves have been normalized to the peak at approximately 250 Hz. Some degradation could have been realized for the lowest frequencies; however, the specral content falls off at a much faster rate than the bracketed expression and the lower frequencies do not contribute significantly to the cost function evaluation. For the higher frequencies, the bracketed expression is relatively constant. Therefore, no appreciable affect on the cost values is expected.

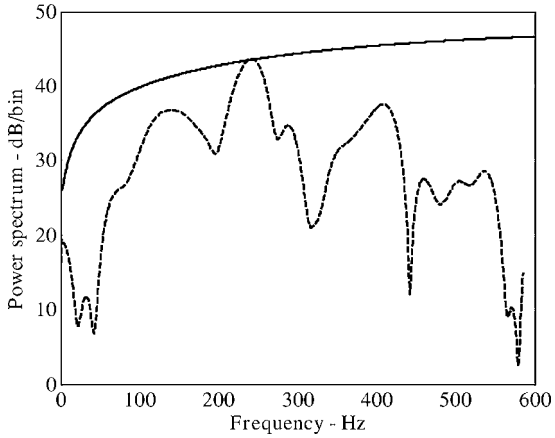

FIG. 22. Power spectrum for the direct plus surface reflected path from the explosive source data at a range of 200.3 m (dashed) and a relative plot of the expression $[1 - G_{\mathrm{DSR}} e^{i\omega_j \tau_{\mathrm{DSR}}}]$ (solid) normalized to the peak energy of the power spectrum.

To verify these results, the inversion solutions discussed in Secs. II D and II F were obtained by using the DSR spectrum, yielding the final cost function values of 0.536 from using two implosive sources and 0.280 for a single explosive source. The parameter values producing these cost values were then used to evaluate the cost with the source spectrum S_j calculated from Eq. (A1). The resulting cost values were 0.540 and 0.280, respectively, i.e., nearly the same as those obtained using $S_{j,\mathrm{DSR}}$. Therefore, the assumptions made in using the DSR spectrum should not affect the cost values for the inversions presented in Secs. II D–II F.

APPENDIX B: DATA SNR

The values of the global cost minimum for the inversions of data from each type of source depend on the SNR data. The SNR values for the longer range data were shown to be relatively low by their limited penetration into the bottom. For a high SNR environment, high cost values would be attributed to environmental mismatch, i.e., incorrect inversion results. However, the agreement of the parameter values from the solutions of the inversions with the different source types rules this out as the cause. Concerning the inversions of the data from the short range implosive sources, from the long range implosive sources, and from the explosive sources, the cost values, for comparable samples of data, decrease as the range decreases. Also, for the explosive sources, multiple bottom interactions were less visible in the data due to the lower received SNR from the sources at longer range. Based on consistent minimum cost values ob-

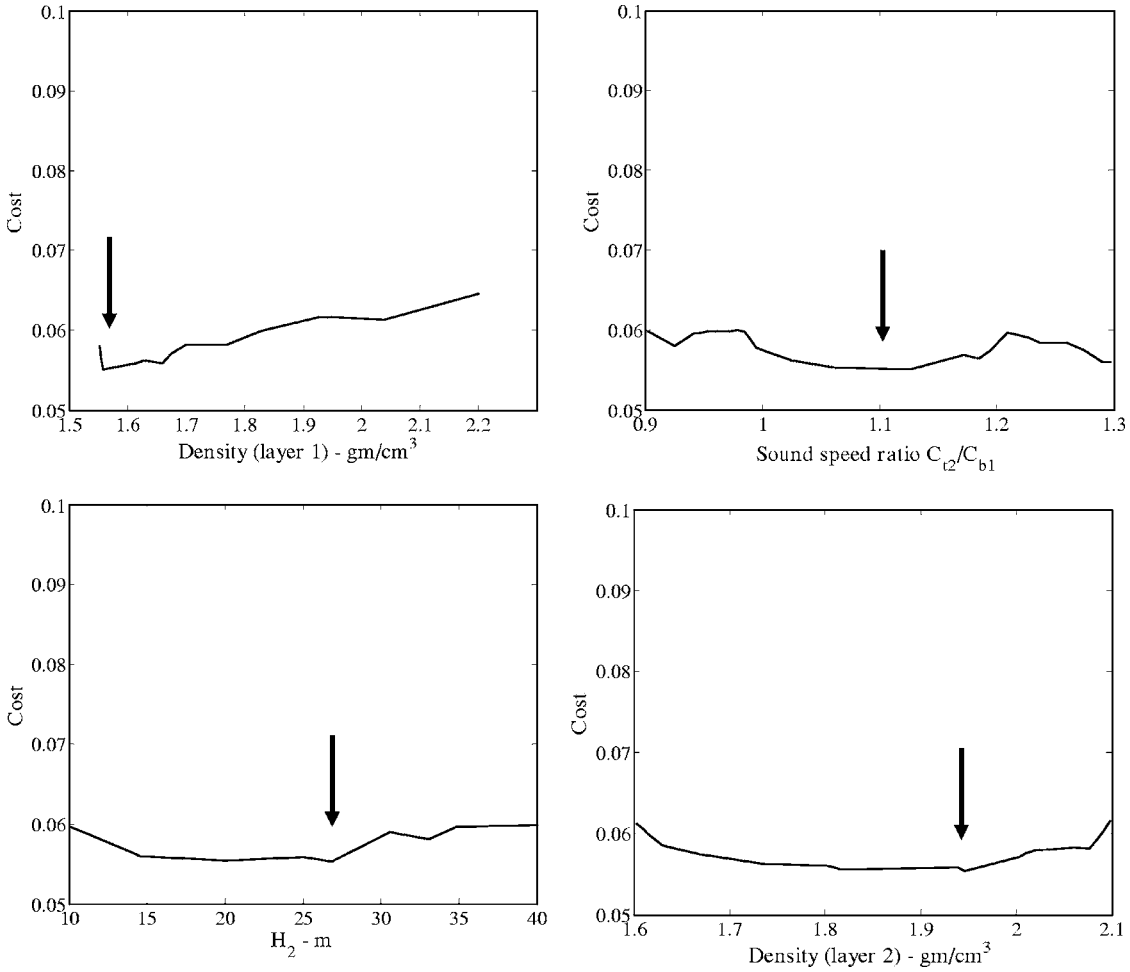

FIG. 23. Cost distributions envelopes as a function of (a) first layer density, (b) sound speed ratio, C_{t2}/C_{b1}, (c) second layer thickness, and (d) second layer density, from inversions of the data from the short range implosive source. Arrows identify the location of minima.

tained from the inversions of similar source type data as those presented in Secs. II D–II F and the inability to penetrate deep into the bottom structure for the longer range sources a low SNR for the data is plausible.

The minimum cost function values at the inversion solutions differ substantially in Figs. 11(a) and 11(b). This range dependence of the SNR is due mostly to increased spreading loss with increasing range. To demonstrate this the broadband energy is calculated for the received time series from a given source. The SNR is defined by the ratio of this received signal energy to the total broadband energy of the noise estimated from a time sample taken just before the source signal arrives. The range dependence of the SNR is then compared to a simple spherical spreading loss model [$20\log(r)$, where r is the slant range] by comparing the difference between the SNR from sources at two ranges to the TL differences for the same ranges. The SNR difference is

$$\mathrm{SNR_{diff}} = \mathrm{SNR_{fire}} - \mathrm{SNR_{bulb}} = 65.8 - 57.5 = 8.3\ \mathrm{dB}, \tag{B1}$$

where the subscripts diff, fire, and bulb refer to the difference of the SNR values for the longer range explosive source at 200.3 m (fire) and for the longer range implosive source at 552.7 m (bulb). For TL the difference is

$$\mathrm{TL_{diff}} = |\mathrm{TL_{fire}} - \mathrm{TL_{bulb}}| = |46.21 - 54.86| = 8.65\ \mathrm{dB}. \tag{B2}$$

The TL and SNR differences agree to within 0.35 dB, which verifies that in this hard bottom environment spreading loss accounts for the range dependence of the SNR.

As a consistency check another estimate of the SNR can be obtained from[43]

$$1 - \Phi = \frac{\mathrm{SNR}}{1 + \mathrm{SNR}}. \tag{B3}$$

Solving for the SNR value from Eq. (B3), converting to decibels, and then taking the difference between the two sources yields the relative SNR in terms of the relative cost function values. Substituting $\Phi_{\mathrm{fire}}=0.28$ and $\Phi_{\mathrm{bulb}}=0.537$ from Table I gives $\mathrm{SNR_{cost}}=6.92$ dB, which differs from the result in Eq. (B1) by 1.38 dB.

Many other inversions were performed using data from other similar source types and gave similar results.

APPENDIX C: INVERSIONS USING ALL PROPAGATION PATHS

Figure 23 shows the cost distribution envelopes for several parameters other than the first layer sound speed (dis-

cussed in Sec. II G) from the inversion of the short range implosive source data. The distribution envelope for the density of the first layer has a minimum near the lower bound placed on the inversions for this parameter. The cost distribution envelopes from the inversions of data from the other source types exhibited a broad minimum for all the layer densities as compared to the minima in the distribution envelopes for the thickness of the first layer, which suggests that the cost function is less sensitive to the values of the layer densities. The distribution envelope for the ratio of the sound speed at the top of the second layer to the speed at the bottom of the first layer also produced a minimum, suggesting that some information from the second layer is obtainable with the short range implosive source. This latter parameter distribution was also shown to be more resolved in Sec. III by excluding the direct and surface reflected paths in the inversions of the longer range explosive source data.

Broad minima were also present in the cost distribution envelopes obtained for most of the inversion parameters associated with the second layer and made a unique determination of the parameter values inconclusive. The distribution envelopes for the second layer parameters from the inversion of the short range implosive data were examined and also showed barely resolvable minima. For example, the minima for the second layer thickness and density are marginally discernible in the distribution envelopes in Figs. 23(c) and 23(d), respectively. The second layer thickness varies from approximately 16 m from inversions of the longer range implosive source data to approximately 30 m from inversion of short range implosive source data. The reason is that the longer range source bottom bounce arrivals have less penetration into the sediment due to the lower grazing angles and do not sample the thickness of the second layer. The cost envelopes, produced by the inversions of the source data discussed in Secs. II D–II F, for the first and second layer gradients in the sound speeds and attenuations were almost flat.

The number of arrivals seen in Fig. 9 from the longer range implosive source, as discussed in Sec. II F, is more than the number recorded from the explosive sources at similar ranges. This supports the hypothesis that the explosive sources had lower levels than the implosive sources and would not have yielded much better results at comparably longer ranges than did the implosive sources.

[1]S. D. Rajan, J. F. Lynch, and G. V. Frisk, "Perturbative inversion methods for obtaining bottom geo-acoustic parameters in shallow water," J. Acoust. Soc. Am. **82**, 998–1017 (1987).

[2]M. D. Collins, W. A. Kuperman, and H. Schmidt, "Nonlinear inversion for ocean bottom properties," J. Acoust. Soc. Am. **92**, 2770–2783 (1992).

[3]C. E. Lindsay and N. R. Chapmann, "Matched field inversion for geophysical parameters using adaptive simulated annealing," IEEE J. Ocean. Eng. **18**, 224–231 (1993).

[4]M. R. Fallat, P. L. Nielsen, and S. E. Dosso, "Hybrid geoacoustic inversion of broadband Mediterranean Sea data," J. Acoust. Soc. Am. **107**, 1967–1977 (2000).

[5]A. Caiti, S. M. Jesus, and A. Kristensen, "Geo-acoustic seafloor exploration with a towed array in a shallow water area of the Strait of Sicily," IEEE J. Ocean. Eng. **21**, 347–354 (1996).

[6]A. Tolstoy, *Matched Field Processing for Underwater Acoustics* (World Scientific, Englewood Cliffs, 1993).

[7]D. P. Knobles, R. A. Koch, L. A. Thompson, and P. E. Eisman, "Broadband sound propagation in shallow water and geoacoustic inversion," J. Acoust. Soc. Am. **113**, 205–222 (2003).

[8]S.A. Stotts, D. P. Knobles, R. A. Koch, D. E. Grant, K. C. Focke, and A. J. Cook, "Geoacoustic inversion in range-dependent ocean environments using a plane wave reflection coefficient approach," J. Acoust. Soc. Am. **115**, 1078–1102 (2004).

[9]G. R. Potty, J. H. Miller, P. H. Dahl, and C. J. Lazauski, "Geoacoustic inversion results from the ASIAEX East China Sea experiment," IEEE J. Ocean. Eng. **29**, 1000–1010 (2004).

[10]K. Yang, Y. Ma, C. Sun, J. H. Miller, and G. R. Potty, "Multistep matched-field inversion for broad-band data from ASIAEX2001," IEEE J. Ocean. Eng. **29**, 964–972 (2004).

[11]C. Park, W. Seong, P. Gerstoft, and M. Siderius, "Time-domain geoacoustic inversion of high-frequency chirp signal from a simple towed system," IEEE J. Ocean. Eng. **28**, 468–478 (2003).

[12]J. Zhou, X. Zhang, P. H. Rogers, and J. Jarzunski, "Geo-acoustic parameters in a stratified seabottom from shallow water acoustic propagation," J. Acoust. Soc. Am. **82**, 2068–2074 (1987).

[13]I. Rozenfeld, W. M. Carey, P. G. Cable, and W. L. Siegmann, "Modeling and analysis of sound transmission in the Strait of Korea," IEEE J. Ocean. Eng. **26**, 809–820 (2001).

[14]D. P. Knobles, T. Yudichak, R. A. Koch, P. Cable, J. Miller, and G. Potty, "Inferences on seabed attenuation in the East China Sea from distributed acoustic measurements," IEEE J. Oceanic Eng. **31**, 129–144 (2006).

[15]M. Nicholas, J. S. Perkins, G. J. Orris, L. T. Fialkowski, and G. J. Heard, "Environmental inversion and matched-field tracking with a surface ship and an L-shaped receiver array," J. Acoust. Soc. Am. **116**, 2891–2901 (2004).

[16]R. A. Koch and D. P. Knobles, "Geoacoustic inversion with ships as sources," J. Acoust. Soc. Am. **117**, 626–637 (2005).

[17]C. Park, W. Seong, and P. Gerstoft, "Geoacoustic inversion in time domain using ship of opportunity noise recorded on a horizontal towed array," J. Acoust. Soc. Am. **117**, 1933–1941 (2005).

[18]J. P. Hermand, "Broadband geo-acoustic inversion in shallow water from waveguide impulse response measurements on a single hydrophone: Theory and experimental results," IEEE J. Ocean. Eng. **24**, 41–66 (1999).

[19]J.-C. Le Gac, M. Asch, Y. Stephan, and X. Demoulin, "Geoacoustic inversion of broad-band acoustic data in shallow water on a single hydrophone," IEEE J. Ocean. Eng. **28**, 479–493 (2003).

[20]E. L. Hamilton, "Sound velocity-density relations in sea-floor sediments and rocks," J. Acoust. Soc. Am. **63**, 366–377 (1978).

[21]J. H. Beebe, S. T. McDaniel, and L. A. Rubano, "Shallow-water transmission loss prediction using the Biot sediment model," J. Acoust. Soc. Am. **71**, 1417–1426 (1982).

[22]"Underwater Electracoustic Standard Transducers Catalogue," Naval Research Laboratory, Underwater Sound Reference Detachment, Transducer Branch, Standards Section, May 1982.

[23]P. Gerstoft, "Inversion of seismoacoustic data using genetic algorithms and *a posteriori* probability distributions," J. Acoust. Soc. Am. **95**, 770–782 (1994).

[24]D. P. Knobles, R. A. Koch, E. K. Westwood, and T. Udagawa, "The inversion of ocean waveguide parameters using a nonlinear least squares approach," J. Comput. Acoust. **6**(1 and 2), 83–97 (1998).

[25]M. D. Collins and L. Fishman, "Efficient navigation of parameter landscapes," J. Acoust. Soc. Am. **98**, 1637–1644 (1995).

[26]T. B. Neilsen, "An iterative implementation of rotated coordinates for inverse problems," J. Acoust. Soc. Am. **113**, 2574–2586 (2003).

[27]P. Gerstoft, "Inversion of acoustic data using a combination of genetic algorithms and the Gauss-Newton approach," J. Acoust. Soc. Am. **97**, 2181–2190 (1995).

[28]M. R. Fallat and S. E. Dosso, "Geoacoustic inversion via local, global, and hybrid algorithms," J. Acoust. Soc. Am. **105**, 3219–3230 (1999).

[29]M. Haire, "Geoacoustic Inversion Using a Hybrid Optimization Algorithm," M.Sc. thesis, The University of Texas at Austin (2001).

[30]D. P. Knobles, R. A. Koch, S. A. Stotts, and T. B. Neilsen, "Numerical study of geoacoustic inversion in range-dependent ocean environments," IEEE J. Ocean. Eng. **28**, 355–369 (2003).

[31]R. Chapman, S. Chin-Bing, D. King, and R. Evans, editors, "Special issue on geoacoustic inversion in range-dependent shallow-water environments," IEEE J. Ocean. Eng. **28**, 317–563 (2003).

[32]S. E. Dosso, "Quantifying uncertainty in geoacoustic inversion. I. A fast Gibbs sampler approach," J. Acoust. Soc. Am. **111**, 129–142 (2002).

[33]S. E. Dosso and P. L. Nielsen, "Quantifying uncertainty in geoacoustic inversion. II. Application to broadband, shallow-water data," J. Acoust. Soc. Am. **111**, 143–159 (2002).

[34]A.-L. S. Lapinski and D. M. Chapman, "The effects of ignored seabed variability in geoacoustic inversion," J. Acoust. Soc. Am. **117**, 3524–3538 (2005).
[35]S. E. Dosso, P. L. Nielsen, and M. J. Wilmut, "Data error covariance in matched-field geoacoustic inversion," J. Acoust. Soc. Am. **119**, 208–219 (2006).
[36]C.-F. Huang, P. Gerstoft, and W. S. Hodgkiss, "Uncertainty analysis in matched-field geoacoustic inversions," J. Acoust. Soc. Am. **119**, 197–207 (2006).
[37]J. N. Piper, Diving Safety Officer, ARL:UT Research Dive Team (2000).
[38]H. Medwin, "Speed of sound in water for realistic parameters," J. Acoust. Soc. Am. **58**, 1318 (1975).
[39]W. K. Goffe, G. D. Ferrier, and J. Rogers, "Global optimization of statistical functions with simulated annealing," J. Econometr. **60**, 65–100 (1994).
[40]E. K. Westwood, C. T. Tindle, and N. R. Chapman, "A normal mode model for multilayered acoustoelastic ocean environments based on an analytic reflection coefficient method," J. Acoust. Soc. Am. **95**(5), Pt. 2, 2908 (1994).
[41]E. K. Westwood and P. J. Vidmar, "Eigenray finding and time series simulation in a layered-bottom ocean," J. Acoust. Soc. Am. **81**, 912–924 (1987).
[42]S. A. Stotts, R. A. Gramann, and M. B. Bennett, "Seismic wave excitation from impulsive sources," ARL:UT Technical Letter ARL-TL-EV-99-17, Applied Research Laboratories, The University of Texas at Austin (1999).
[43]R. A. Koch (private communication).

Noise suppression using the coherent onion peeler

James H. Wilson[a)]
Planning Systems, Inc., 3834 Vista Azul, San Clemente, California 92672

Albert H. Nuttall
P. O. Box 401, Old Lyme, Connecticut 06371

Robert A. Prater
Planning Systems, Inc., San Diego, California 92110

(Received 3 March 2006; revised 11 August 2006; accepted 19 August 2006)

An innovative noise suppression algorithm, called the coherent onion peeler (COP) (patent detained) is derived by minimizing the error in the coherent subtraction of the data from a single plane wave model. The COP solution "collapses" for all beamforming algorithms to the same solution at the complex hydrophone FFT level. Thus, any beamformer can be applied to the residual FFTs after the COP has been applied. The COP is applied to the strongest interferer first and the residual FFTs represent the acoustic field with this interferer coherently "peeled back" like the outer skin of an onion. This procedure can be repeated any number of times to coherently suppress the noise from all interferers present. A new nonadaptive beamformer is developed that "blends" together the best beam pattern properties of conventional beamforming (CBF) near array design frequency and the generalized fourier integral method (GFIM) at very low frequencies (VLF). In between these frequency extremes, the GFIM-CBF Blend (patent pending) (G-C Blend) is a frequency-dependent weighted average of both individual beamformers. COP and G-C Blend are applied to the broadband noise emitted by the tow ship, which severely degrades the performance of the towed array; COP reduced this broadband noise by over 19 dB in a single pass. © *2006 Acoustical Society of America.*
[DOI: 10.1121/1.2354045]

PACS number(s): 43.30.Wi, 43.30.Nb, 43.30.Zk, 43.60.Ac, 43.60.Mn [EJS] Pages: 3627–3634

I. INTRODUCTION

A recent article (Nuttall and Wilson, 2000) showed that the performance of the Fourier integral method (FIM) (patent detained) (Nuttall and Wilson, 1991) and generalized FIM (GFIM)[1] outperformed conventional beamforming (CBF), the minimum variance distortionless response (MVDR), and enhanced MVDR (EMVDR) at very low frequencies (VLF) using simulated data. This result caused controversy when some readers incorrectly assumed that the authors claimed the result held near the design frequency, $f_o = c/2d$, of an equally spaced line array with spacing d.

The authors never made this claim, and the CBF, FIM, and GFIM beam patterns shown in Fig. 2 of Nuttall and Wilson (2000) were for $f/f_o = 0.04$, or 4% of design frequency. The authors have now developed a GFIM/CBF "blended" beamformer (called G-C Blend) that is, CBF at the design frequency $f = f_o$, and gradually transitions to FIM or GFIM at VLF as the frequency decreases. There is no reason to use FIM or GFIM at the design frequency because of their higher peak side lode levels compared to CBF. On the other hand, there is no reason to use CBF at VLF (defined to be $f/f_o \leq 0.1$), because FIM/GFIM has a narrower beamwidth than CBF by a factor of 2/3, and FIM/GFIM have no sidelobes at the VLF frequencies. In Sec. II, the blended GFIM/FIM and CBF nonadaptive beamformer is derived.

MVDR and EMVDR depend on the inverse of the complex estimated covariance matrix, and are, thus, highly nonlinear methods. The highly nonlinear impact of MVDR and EMVDR was discussed thoroughly in Nuttall and Wilson (2000), and its performance degradation at VLF was demonstrated quantitatively for time-varying environments, such as those in most shallow water areas. Wilson and Veenhuis (1997) addressed the limitations of MVDR, and the complete theoretical background of FIM is discussed in detail in Wilson (1995), Nuttall and Wilson (1991), and Wilson (1983). Tests on simulated data (Fabre and Wilson, 1995) and on measured towed array data (Solomon *et al.*, 1999) also showed the performance degradation of MVDR and CBF relative to FIM and GFIM.

One objective of this paper is to produce an adaptive beamforming alternative to MVDR and EMVDR that is linear in the covariance matrix of the received data. By linear we mean that the noise suppression method depends on the estimated covariance matrix (not its inverse) to the first power. We have developed the coherent onion peeler (COP)[2] and tested it on measured data. The results have been exceptionally good on two sets of measured data, and some results from one data set are presented in this paper. The word "coherent" in COP means that both amplitude and phase are used in the noise suppression part of the algorithm, and the term "onion peeler" refers to the process of subtracting the strongest planewave interferer coherently first, and then beamforming the residual acoustic field with "the onion peeled," or loudest noise source suppressed. Our mathemati-

a)Electronic mail: jhwilson@cox.net

cal derivation of COP presented in Sec. III for a single plane wave was surprising to us, in that the noise suppression in the COP solution takes place at the hydrophone FFT level, not the beamformer output level. We attempted to perform the noise suppression at the CBF, FIM/GFIM, and MVDR/EMVDR level, but the answer converged to the same result for all three beamforming methods and, thus, any beamformer can be applied to the residual FFTs after COP noise suppression. Therefore, COP is a beamformer-independent noise suppression procedure.

Section IV shows some COP results on broadband propeller data on a towed array, and conclusions and recommendations are given in Sec. V.

II. THE NONADAPTIVE GFIM/FIM AND CBF BLENDED BEAMFORMER

A quantitative set of metrics must be specified for one to claim that a nonadaptive beamformer is optimum. By nonadaptive, we mean that the beamforming weights applied to the covariance matrix are constant in time, and do not depend on the measured data in any way. Burdic (1991) and many others (e.g., Shultheis, 1968) have shown that CBF is the "optimum" detector in an ideal signal (perfect single plane wave arrival) and noise environment (spatially incoherent noise); however, this ideal acoustic field is hardly ever a close approximation to the measured acoustic fields encountered in the real world. Therefore, the claim of optimality in this case is not physically very meaningful. CBF is widely used in sonar systems throughout the world because it is robust and easily implemented, and performs well in deep water in nonmultipath environments. However, in almost all shallow water environments, and in deep water multipath environments (e.g., strong bottom bounce areas), CBF by itself is highly nonoptimal. To find a more nearly optimal beamformer in these nonideal acoustic environments, there have been numerous adaptive beamforming efforts, mainly based on the minimum variance distortionless response (MVDR), where the beam power output is minimized relative to a unity gain constraint in the signal direction (see Kneipfer, 1997). One of the authors (Nuttall) invented MVDR (Nuttall and Hyde, 1969) with Capon (1969), and there are numerous articles (see Booth *et al.*, 1997 for a core list of references) on element-based MVDR or beam-based algorithms with hard or soft constraints.

The GFIM/FIM and CBF Blended (G-C Blend) beamforming algorithm is a nonadaptive algorithm and will not be compared to MVDR or any other adaptive algorithm directly. The G-C Blend algorithm produces a nearly optimum, nonadaptive beam pattern, and is discussed in this section. The derivation of our adaptive beamforming algorithm, COP, is presented in the next section with the G-C Blend algorithm as COP's beamformer of choice.

The G-C Blend algorithm is a frequency-weighted linear combination of FIM and CBF, as specified in Eqs. (14) and (15) of Nuttall and Wilson, 2000,

$$N(u,f) = r(f/f_o)\frac{fd}{c} \times \sum_{1-M}^{M-1} \left[\exp(-i2\pi fmdu/c)\hat{G}_f(md)w'_m + p(f/f_o)\frac{fd}{c}\exp(-i2\pi fmdu/c)\hat{G}_f(md) \right], \quad (1)$$

where

$$w_m = (M - |m|)/M \text{ for CBF},$$

$$w'_m = \begin{cases} 1 \text{ for FIM} \\ \text{or} \\ 1 - \cos(2\pi m/M) \text{ for GFIM} \end{cases} \quad (2)$$

for $1-M \le m \le M-1$.

In Eqs. (1) and (2), an M-element equally-spaced line array of spacing d is assumed, with $u = \cos\theta$, with $\hat{G}_f(md)$ being the covariance value at separation md in frequency bin f, with c equal to the speed of sound at the array location, and the array design frequency $f_o = c/(2d)$. The frequency weighting factors are given by

$$r(f/f_o) = f/f_o \text{ and } p(f/f_o) = (1 - f/f_o). \quad (3)$$

A simple linear weighting, transitioning from CBF to GFIM/FIM, was selected until a measured data analysis shows that another weighting will improve performance. The advantages of weighting covariance matrix element pairs as in Eqs. (1) and (2) have been discussed in detail in Nuttall and Wilson (2000) and will not be repeated here. This is very different than amplitude weighting of single elements (e.g., Taylor weighting); thus FIM and GFIM cannot be derived from amplitude weighting of single elements.

Equations (1)–(3) show that the authors are not advocating using FIM or GFIM instead of CBF at all frequencies $0.0 \le f/f_o \le 1.0$. At design frequency ($f = f_o$), Eq. (1) defaults to CBF. At very low frequencies (VLF) ($f/f_o \le 0.1$) Eq. (1) becomes heavily weighted toward FIM/GFIM (as desired) so that FIM's or GFIM's narrower beamwidth (a factor of 2/3 of the CBF beamwidth) improves performance significantly. The number of peak sidelobes and their levels are minimal at VLF (see Fig. 2 in Nuttall and Wilson, 2000). At this point we can say qualitatively that the G-C Blend algorithm gives us the "best of both worlds" in a nonadaptive beamformer. Near design frequency, the algorithm defaults to CBF and the higher peak sidelobes of FIM and GFIM do not degrade performance.

We will only suggest a preliminary, qualitative cost function (cf) to be tested on measured data:

$$\text{cf} = 1/(\text{area under the beam pattern curve}) \times (\text{maximum peak sidelobe level}) \times (\text{number of sidelobes in the beam pattern}). \quad (4)$$

The only justification for maximizing this cf will be *performance on measured data*, but for now we state qualitatively that it is "good" to minimize the area under the beam pattern curve (or maximize AG), while minimizing both the number

and values of the peak sidelobe levels. The actual, rather than theoretical, beam pattern must be used in this cf, as determined from measured data. In the next section, we will show how COP and G-C Blend work well together to provide excellent performance on measured data. COP and G-C Blend working together defines our approach to adaptive beamforming.

III. THE COHERENT ONION PEELER: AN ADAPTIVE NOISE SUPPRESSION ALGORITHM FOR ALL BEAMFORMERS

The initial objective of the authors was to derive an adaptive beamformer for FIM, GFIM, and CBF to suppress noise from interferers, with the constraint that the algorithm be linear in the covariance matrix. The authors feel that MVDR's performance is degraded in time nonstationary acoustic environments as exist in the littoral (Nuttall and Wilson, 2000) because MVDR is highly nonlinear in the covariance matrix. However, the mathematical modeling of the linear noise suppression algorithm for each beamformer led to the same mathematical solution, which we call COP. COP depends only on the hydrophone FFTs and not on the beamformer selected. COP can be applied to FIM, GFIM, CBF, MVDR, or any other beamforming method which uses FFTs as inputs.

Derivation of the single plane wave COP algorithm for an unequally spaced line array: Assume a pressure field $\bar{p}(t,x)$ at time t and location x, with time samples collected at $t=n\Delta$ for $n=0:N-1$, and spatial samples at locations $x=x(m)$ for $m=0:M-1$. We use the colon symbol $J:K$ to denote $\{J,J+1,\ldots,K\}$ with $J<K$. The total data available is $p(n,m)\equiv\bar{p}(n\Delta,x(m))$ for $n=0:N-1$, $m=0:M-1$.

If a single plane wave arrives from an angle $u_1=\sin\theta_1$ comprised of frequencies $\{f_1(k)\}_{k_a}^{k_b}$, the observed complex pressure field at (t,x) is modeled as a superposition of plane waves in the frequency band $f_1(k_a):f_1(k_b)$ as

$$\bar{p}_1(t,x)=\sum_{k=k_a}^{k_b} a_1(k)\exp\left[i2\pi f_1(k)\left(t-\frac{x}{c}u_1\right)\right], \tag{5}$$

where the amplitudes $\{a_1(k)\}_{k_a}^{k_b}$ are complex. For given frequencies $\{f_1(k)\}_{k_a}^{k_b}$ and arrival angle u_1, we want to choose amplitudes $\{a_1(k)\}_{k_a}^{k_b}$ so that the total weighted model/data error e is minimized. Here, the error e is given by

$$\begin{aligned} e &\equiv \sum_{n=0}^{N-1}\sum_{m=0}^{M-1} w_t(n)w_x(m)\left|\overset{\text{data}}{p(n,m)}-\overset{\text{model}}{\bar{p}_1(n\Delta,x(m))}\right|^2 \\ &=\sum_{n,m} w_t(n)w_x(m)\left|p(n,m)\right. \\ &\quad\left.-\sum_k a_1(k)\exp\{i\alpha_1(k)[n-\beta(m)u_1]\}\right|^2, \end{aligned} \tag{6}$$

where the temporal and spatial weights, $\{w_t(n)\}$ and $\{w_x(m)\}$, are real and positive, and the known dimensionless parameters

$$\alpha_1(k)\equiv 2\pi f_1(k)\Delta, \quad \beta(m)\equiv\frac{x(m)}{c\Delta}. \tag{7}$$

To minimize e, consider the partial derivatives

$$\begin{aligned} \frac{\partial e}{\partial a_1^*(\underline{k})} &= -\sum_{n,m} w_t(n)w_x(m)\Big(p(n,m) \\ &\quad -\sum_k a_1(k)\exp\{i\alpha_1(k)[n-\beta(m)u_1]\}\Big) \\ &\quad\times\exp\{-i\alpha_1(\underline{k})[n-\beta(m)u_1]\} \quad \text{for } \underline{k}=k_a:k_b. \end{aligned} \tag{8}$$

Define the temporal and spatial windows:

$$W_t(\alpha)=\sum_{n=0}^{N-1} w_t(n)\exp(-i\alpha n) \text{ for all } \alpha, \quad W_t(0)=1, \tag{9}$$

$$W_x(\gamma)=\sum_{m=0}^{M-1} w_x(m)\exp(i\beta(m)\gamma) \text{ for all } \gamma, \quad W_x(0)=1, \tag{10}$$

and the two-dimensional data spectrum

$$P(\alpha,\gamma)=\sum_{n,m} w_t(n)w_x(m)p(n,m)\exp[-i\alpha n+i\beta(m)\gamma] \tag{11}$$

for all α,γ.

Then from Eq. (8), the optimal complex amplitudes $\{\underline{a}_1(k)\}_{k_a}^{k_b}$ satisfy the simultaneous linear equations

$$\begin{aligned} &\sum_{k=k_a}^{k_b}\underline{a}_1(k)W_t(\alpha_1(\underline{k})-\alpha_1(k))W_x\{[\alpha_1(\underline{k})-\alpha_1(k)]u_1\} \\ &\quad=P[\alpha_1(\underline{k}),\alpha_1(\underline{k})u_1], \text{ for } \underline{k}=k_a:k_b. \end{aligned} \tag{12}$$

Henceforth, we consider only the case of flat temporal weighting:

$$w_t(n)=\frac{1}{N} \quad \text{for } n=0{:}N-1. \tag{13}$$

Then

$$W_t(\alpha)=\exp\left(-i\alpha\frac{N-I}{2}\right)\frac{\sin(N\alpha/2)}{N\sin(\alpha/2)}, \tag{14}$$

with

$$W_t(2\pi k/N)=\left\{\begin{matrix}1 \text{ for } k=0\\ 0 \text{ for } k\neq 0\end{matrix}\right\}, \quad |k|<N. \tag{15}$$

Also, we take fitting frequencies

$$f_1(k)=\frac{k}{N\Delta} \quad \text{for } k=k_a:k_b, \quad \alpha_1(k)=2\pi k/N \tag{16}$$

and there follows

$$W_t[\alpha_1(\underline{k})-\alpha_1(k)]=W_t\left[\frac{2\pi}{N}(\underline{k}-k)\right]=\delta(\underline{k}-k). \tag{17}$$

Hence, we can write an explicit solution to Eq. (12) for the optimal amplitudes, namely,

$$\underline{a}_1(k)=P[\alpha_1(k),\alpha_1(k)u_1] \quad \text{for } k=k_a:k_b. \tag{18}$$

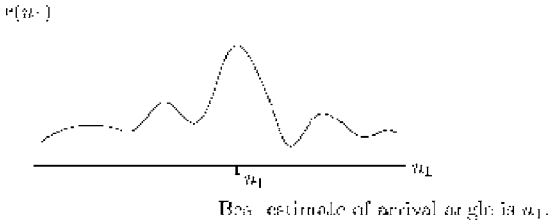

FIG. 1. Minimizing angular model/data errors in COP.

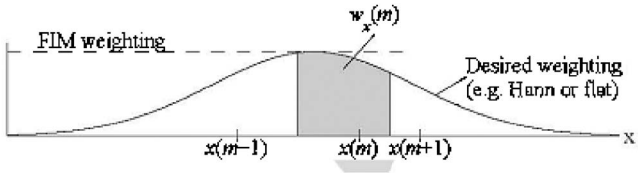

FIG. 2. Optimum spatial weights in COP.

To find the value of the minimum error, express Eq. (6) as

$$\begin{aligned}\underline{e} &= \sum_{n,m} w_t(n)w_x(m)\Bigg[p(n,m) \\ &\quad - \sum_k \underline{a}_1(k)\exp\{i\alpha_1(k)[n-\beta(m)u_1]\}\Bigg]p^*(n,m) \\ &= \sum_{n,m} w_t(n)w_x(m)|p(n,m)|^2 - \sum_k \underline{a}_1(k) \\ &\quad \times \underbrace{\sum_{n,m} w_t(n)w_x(m)p^*(n,m)\exp\{i\alpha_1(k)[n-\beta(m)u_1]\}}_{P^*(\alpha_1(k),\alpha_1(k)u_1) \text{ from equation(11)}}.\end{aligned} \tag{19}$$

Now substitute the optimal amplitudes [Eq. (18)] to get the minimum error

$$\underline{e} = \sum_{n,m} w_t(n)w_x(m)|p(n,m)|^2 - \underbrace{\sum_k |P(\alpha_1(k),\alpha_1(k)u_1)|^2}_{\equiv r(u_1)/N^2}. \tag{20}$$

We now further minimize the error $\underline{e}$ by choosing the fitting angle u_1 that maximizes $r(u_1)$. Using the definition of the data spectrum P [Eq. (11)] and the flat temporal weighting [Eq. (18)], we get

$$\begin{aligned}r(u_1) &= \sum_k \left| \sum_{n,m} w_x(m)p(n,m) \right. \\ &\quad \left. \times \exp\left[-i\frac{2\pi}{N}kn + i\beta(m)\frac{2\pi}{N}ku_1\right]\right|^2 \\ &= \sum_{k=k_a}^{k_b} \left| \sum_{m=0}^{M-1} w_x(m)q(k,m)\exp\left[-i\frac{2\pi k}{N}\beta(m)u_1\right]\right|^2,\end{aligned} \tag{21}$$

where

$$q(k,m) = \sum_{n=0}^{N-1} p(n,m)\exp(-i2\pi kn/N) \tag{22}$$

for $k = 0{:}N-1, m = 0{:}M-1$

is the temporal discrete Fourier transform of the mth element data. The maximization of $r(u_1)$ by choice of u_1 is depicted in Fig. 1.

The processing given by Eq. (21) has a very plausible form. First, the time-space data $\{p(n,m)\}$ is transformed into the frequency-space domain $\{q(k,m)\}$. Then, for hypothesized arrival angle u_1, scale and phase shift the mth element component in frequency bin k by $(2\pi k/N)\beta(m)u_1$. But this phase shift exactly compensates for that of a single frequency plane wave arriving at angle u_1,

$$\text{phase shift } (k,m) = 2\pi\frac{kx(m)}{N\Delta c}u_1 = \frac{2\pi k}{N}\beta(m)u_1. \tag{23}$$

Thus, the inner complex sum over m in Eq. (21) is a coherent one for any plane wave arriving at angle u_1. Finally, the outer sum over k in Eq. (21) is an incoherent sum over frequencies in the band of interest. This incoherent sum is necessary because no interrelations have been assumed for individual frequency components in the plane wave arrivals. After the sum over k is complete, then one can plot $r(u_1)$ for all u_1 in the angular sector of interest.

The complex sum on element number m in Eq. (21) cannot be accomplished by a FFT because, in general, $\beta(m)=x(m)/(c\Delta)$ is not linear in m for an unequally-spaced line array (but a FFT calculation can be utilized for an equally-spaced or a sparse equispaced line array). This complex sum must be carried out by brute force. However one short-cut available is to use the recursion

$$\begin{aligned}\exp\left[i\frac{2\pi k}{N}\beta(m)u_1\right] &= \exp\left[i\frac{2\pi(k-1)}{N}\beta(m)u_1\right] \\ &\quad \times \exp\left[i\frac{2\pi}{N}\beta(m)u_1\right]\end{aligned} \tag{24}$$

for each m and u_1 in order to generate the k values needed for the exponentials.

Finding the best spatial weights $\{w_x(m)\}$ is not trivial; they should not simply be taken as flat but should reflect known element locations $\{x(m)\}$. For example, $w_x(m)$ might be taken to be proportional to the shaded area between adjacent element midpoints in Fig. 2.

After finding the best coefficients $\{\underline{a}_1(k)\}$ for a specified u_1, the minimal residual is, from Eqs. (5) and (6),

$$\begin{aligned}\underline{p}(n,m) &\equiv p(n,m) - \bar{p}_1[n\Delta, x(m)] \\ &= p(n,m) - \sum_k \underline{a}_1(k) \\ &\quad \times \exp\left\{i\frac{2\pi k}{N}[n-\beta(m)u_1]\right\}.\end{aligned} \tag{25}$$

The corresponding FFT of this residual is

$$\underline{q}(\underline{k},m)=\sum_{n=0}^{N-1}\underline{p}(n,m)\exp(-i2\pi\underline{k}n/N)$$

$$=q(\underline{k},m)-\sum_{k=k_a}^{k_b}\underline{a}_1(k)\exp\left[-i\frac{2\pi k}{N}\beta(m)u_1\right]\times\underbrace{\sum_{n=0}^{N-1}\exp[-i2\pi(\underline{k}-k)n/N]}_{N\delta(\underline{k}-\underline{k})}$$

$$=q(\underline{k},m)-N\underline{a}_1(\underline{k})\exp\left[-i\frac{2\pi\underline{k}}{N}\beta(m)u_1\right],\quad\text{for }\underline{k}=k_a{:}k_b. \tag{26}$$

The optimal amplitudes are, from Eqs. (16), (10), and (19),

$$\hat{a}_1(k)=P[\alpha_1(k),\alpha_1(k)u_1]=\frac{1}{N}\sum_{m=0}^{M-1}w_x(m)q(k,m)\exp\left[i\frac{2\pi k}{N}\beta(m)u_1\right] \tag{27}$$

for $k=k_a{:}k_b$.

These complex amplitudes should be evaluated only after the best arrival angle u_1, namely $\hat{u}_1$, has been determined. Then, Eq. (26) should be evaluated, using $\hat{u}_1$ in place of u_1. That is,

$$\hat{a}_1(k)=P[\alpha_1(k),\alpha_1(k)\hat{u}_1] \tag{28}$$

$$=\frac{1}{N}\sum_{m=0}^{M-1}w_x(m)q(k,m)\exp\left[i\frac{2\pi k}{N}\beta(m)\hat{u}_1\right]\quad\text{for }k=k_a{:}k_b, \tag{29}$$

$$\hat{q}(k,m)=q(k,m)-N\hat{a}_1(k)\exp\left[-i\frac{2\pi k}{N}\beta(m)\hat{u}_1\right] \tag{30}$$

for $k=k_a{:}k_b$.

The latter quantity is the minimal residual in the frequency-space domain. Also,

$$\hat{q}(k,m)=q(k,m)\quad\text{for }k\notin k_a{:}k_b. \tag{31}$$

Let the spatially weighted FFT at frequency bin k be defined as

$$q_w(k,m)=q(k,m)w_x(m) \tag{32}$$

and its spatial autocorrelation for frequency bin k be

$$\phi(k,j)=\sum_m q_w(k,m)q_w^*(k,m-j). \tag{33}$$

Then, from Eq. (21), if $x(m)=dm$ (equally spaced line array)

$$r(u_1)=\sum_{k=k_a}^{k_b}\left|\sum_{m=0}^{M-1}q_w(k,m)\exp\left[i\frac{2\pi k}{N}\frac{dm}{c\Delta}u_1\right]\right|^2$$

$$=\sum_{k_a}^{k_b}\sum_{j=1-M}^{M-1}\phi(k,j)\exp\left(i\frac{2\pi k}{N}\frac{d}{c\Delta}ju_1\right). \tag{34}$$

A FIM (patent detained)-like generalization would be to weight the sum over j, to get

$$r_s(u_1)=\sum_{k=k_a}^{k_b}\sum_{j=1-M}^{M-1}w_s(j)\phi(k,j)\exp\left(i\frac{2\pi k}{N}\frac{d}{c\Delta}ju_1\right), \tag{35}$$

where the $\{w_s(j)\}_{1-M}^{M-1}$ are separation weights (real and even about $j=0$).

Equally spaced or sparse equispaced line array: From Eq. (21) with $z(m)=w_x(m)q(k,m)$ (holding k fixed), let

$$f(v)\equiv\sum_{m=0}^{M-1}z(m)\exp[iv\beta(m)],\quad\beta(m)=\frac{x(m)}{c\Delta},\qquad v=\frac{2\pi k}{N}u_1. \tag{36}$$

As an example of a sparse equispaced line array, consider

$$\{x(m)\}=[x(0)x(1)\ldots x(M-1)]=\left[0\quad\underbrace{d}_{1\text{ missing}}\quad 3d\quad 4d\quad\underbrace{\quad}_{2\text{ missing}}\quad 7d\quad 8d\quad 9d\quad\cdots\right], \tag{37}$$

then

$$\{\beta(m)\}=\beta[0\ 1\ 3\ 4\ 7\ 8\ 9\cdots],\quad\beta\equiv\frac{d}{c\Delta} \tag{38}$$

and

$$f(v)=z(0)+z(1)\exp(iv\beta)+z(2)\exp(iv\beta3)+z(3)\exp(iv\beta4)+z(4)\exp(iv\beta7)+z(5)\exp(iv\beta8)+z(6)\exp(iv\beta9)+\cdots. \tag{39}$$

Let

$$y=[z(0)\ z(1)\ 0\ z(2)\ z(3)\ 0\ 0\ z(4)\ z(5)\ z(6)\cdots]. \tag{40}$$

Then

$$f(v)=y(0)+y(1)\exp(iv\beta)+y(3)\exp(iv3\beta)+y(4)\exp(iv4\beta)+y(7)\exp(iv7\beta)+y(8)\exp(iv8\beta)+y(9)\exp(iv9\beta)+\cdots.$$

$$=\sum_{j=0}y(j)\exp(iv\beta j)=\sum_{j=0}y(j)\exp\left[i2\pi\frac{k}{N}\frac{d}{c\Delta}u_1j\right]. \tag{41}$$

By taking

$$\frac{k}{N}\frac{d}{c\Delta}u_1=\frac{n'}{N'}$$

this operation can be done by an N'-point FFT. Sequence $\{y(j)\}$ has zeros in it, dictated by the missing element locations. As a result, the $\{z(m)\}$ are merely "spaced out" by the missing element locations.

COP has now been extended to a two, three, or any multiple coherently interfering planewave model, simply by adding additional plane wave components into the model in Eq. (6). Also, a moving source model has been developed where the source is allowed to change bearing during each FFT period. These more complex versions of COP will be analyzed in future research.

IV. COP CONCEPT OF OPERATIONS (CONOPS)

It is now clear that the word "coherent" in COP means that both amplitude and phase are adaptively estimated every FFT period, and a "residual FFT" is calculated. Since it is relatively easy to track a strong interferer in relative bearing versus time, one can implement COP in a sonar system in real time as a noise suppression algorithm. When the beamforming is performed on the residual FFT, we say that the "onion has been peeled" and we can display the residual acoustic beamformed field with the strong interferer suppressed. One can continue to track and suppress the next strongest interferer until all interferers have been suppressed, and, hopefully, the weak signals of interest will be detected.

Very efficient C^{++} software has been developed to implement COP in a real time processor with a choice of FIM, GFIM, CBF or G-C Blend as beamformers. The M-of-N Tracker (Wilson, 1995) is used to "track" the interferer, and COP is applied every FFT interval in a user-specified relative bearing sector and frequency band centered on the M-of-N Tracker relative bearing position and multiple frequency intervals to be suppressed. The residual FFT is then rebeamformed and the strong interferer is suppressed. This process can continue for all interferers that are tracked by the Quiet Interlude Processing System (QuIPS), a real time, automated, multi-Intelligence (multi-INT) processing system in which the M-of-N Tracker is embedded. The acoustic sensor is just one sensor input to be data fused with tracks from numerous other nonacoustic sensors. It is strongly emphasized that the coherent track data from the interferers suppressed by COP are not lost, and can be tracked and plotted separately. The QuIPS tracker and COP are not yet integrated into a real time system.

V. COP PERFORMANCE ON MEASURED DATA

COP has been run for two very different applications using different data sets. The first involved the suppression of a surface ship interferer's narrowband (NB) harmonic lines so that a weaker target was detected after COP was applied. The results were exceptionally good, and will be addressed in a future report.

A second data set was from a towed array sonar system, where broadband (BB) acoustic energy from the propeller of the tow ship continually degraded performance, even when the tow ship slowed to four knots. COP was applied to this BB noise suppression application, and the results are described in this section.

Two sets of towed array hydrophone time series data were supplied with the array geometry, data format, sample rates, FFT lengths, and processing band (1200–1600 Hz). The towed array is a 48 element equally spaced line array

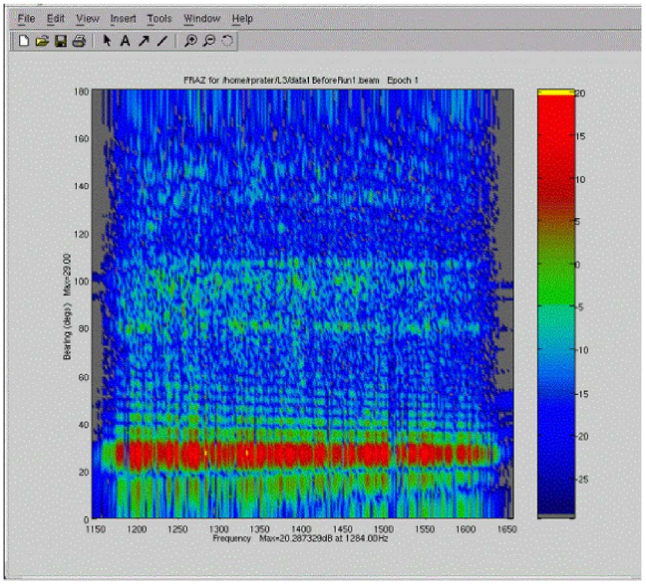

FIG. 3. (Color online) Beamformed FRAZ surface before COP with 2 Hz FFT resolution.

with a design frequency of 1725 Hz. Tow ship noise level was more than 30 dB above the noise in other directions, and the main lobe relative bearing of the noise peak depends on array depth and tow cable scope. For the two towed array data sets, the own ship propeller noise:

- peaked at approximately 25° 51 s relative for data set I with an array depth of 135 m and cable scope of 100 m.
- peaked at approximately 50° 47 s relative for data set II with an array depth of 81 m and cable scope of 300 m.

The data were filtered, decimated and heterodyned to ±200 Hz of dc and this necessitated the adaptation of the COP algorithm described in the previous section to heterodyned data.

Data results: Figures 3–6 illustrate the COP noise sup-

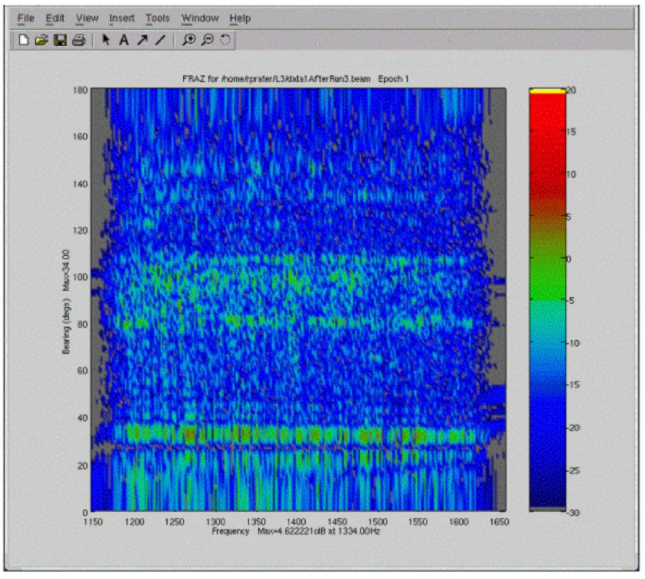

FIG. 4. (Color online) Beamformed FRAZ surface after COP is applied to the entire band with a 2 Hz FFT resolution.

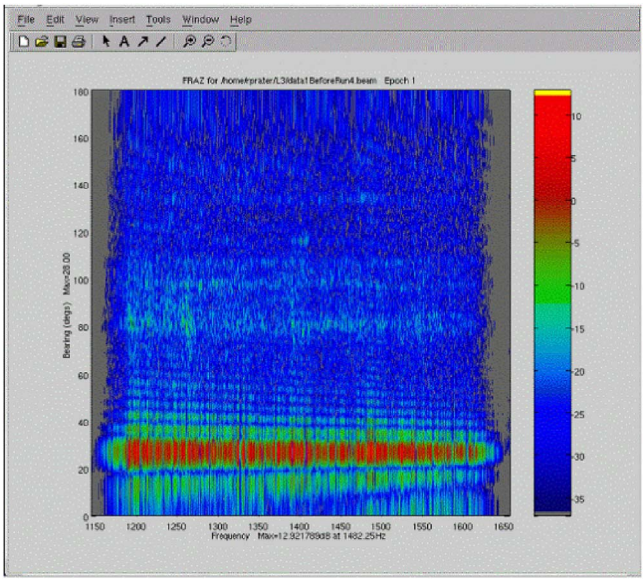

FIG. 5. (Color online) Beamformed FRAZ surface before COP with 0.125 Hz FFT resolution.

pression results. These figures represent a one pass noise suppression COP application; the results would improve even more with multiple COP passes, and that will be addressed in a future paper.

Figure 3 shows a typical COP 2 Hz resolution frequency azimuth (FRAZ) surface to illustrate the BB interferer's beamformed output with broadband (BB) resolution before COP noise suppression; the propeller self-noise is 20–30 dB above the background noise levels. Figure 4 shows COP applied over the entire band, and now one can clearly detect two or three other contacts near broadside. There is almost a 30 dB reduction in noise level after COP! The residual acoustic energy near the propeller noise main lobe after COP can be "cleaned up" with multiple COP passes; current results suffer from limitations of using a single planewave model.

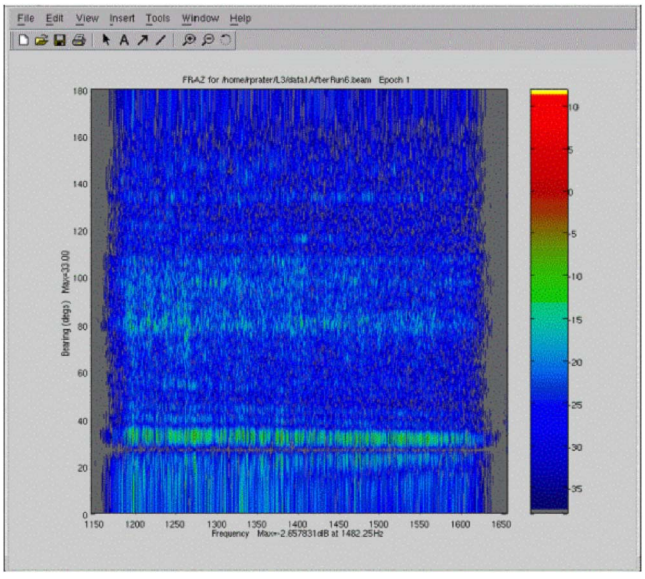

FIG. 6. (Color online) Beamformed FRAZ surface after COP is applied to the entire band with a 0.125 Hz FFT resolution.

Figure 5 shows a typical COP 0.125 Hz resolution FRAZ surface to illustrate the beamformed output with narrowband (NB) resolution before COP noise suppression. Figure 6 shows the FRAZ surface after COP suppression over the entire band, respectively. Again, 2 or 3 surface ship contacts are now clearly seen near broadside, and the residual energy near the relative bearing of the propeller noise can be further suppressed with multiple COP passes. COP suppressed the main noise lobe by 20–30 dB on one pass!

By autoscaling the FRAZ surfaces after COP noise suppression in Fig. 4 (2 Hz bandwidth (BW)) and Fig. 6 (0.125 Hz BW), one finds that the maximum beam noise level on the FRAZ surfaces in Figs. 3 and 5 are 20.3 dB and 12.9 dB, respectively, before COP noise suppression. After COP noise suppression, maximum beam noise levels of 4.6 dB and 2.6 dB are found. When the maximum beamformed noise levels are corrected to spectrum levels, the COP noise suppression was far greater at the 0.125 Hz resolution (19.3 dB) compared to the COP noise suppression at the 2.0 Hz resolution (12.7 dB).

COP could be run for a second pass on the FRAZ surface after noise suppression to further suppress the first sidelobe region from 30° to 38° relative and from 24° to 0° relative. The authors are not sure why the first sidelobe regions did not get suppressed by COP after a single pass as well as desired and offer the following two possible reasons for the nonplanewave beam patterns:

(1) The propeller noise is a spherical wave, not a plane wave, and this may impact the positions of the first sidelobe (on either side) peak bearing location.
(2) There may be a weak bottom bounce arrival interfering with the direct spherical arrival.

The multiple pass results of COP over this data will be addressed in a future paper.

VI. CONCLUSIONS

COP reduced the broadband noise interference by over 19 dB for the towed array data analyzed and displayed in this paper. COP shows great promise for incorporation in all sonar systems worldwide. The results on measured towed array data with a strong interferer present were also excellent, and will be addressed in a future paper. COP is protected by its patent, and potential users should contact the authors for applications to each of their sonar systems.

[1]FIM and GFIM are patented beamforming algorithms.
[2]COP is a patented noise suppression and adaptive beamforming technique.

Booth, N. O., Baxley, P. A., Rice, J. A., Schey, P. W., Hodgkiss, W. S., D'Spain, G. L., and Murray, J. J. (**1997**). "Source localization with broadband matched field processing in shallow water," Spawar Systems Center – San Diego Technical Report.

Burdic, W. S. (**1991**). *Underwater Acoustic System Analysis*, 2nd ed. (Prentice-Hall, Englewood Cliffs), pp. 192–203.

Capon, J. (**1969**). "High-resolution frequency-wavenumber spectrum analysis," Proc. IEEE **57**, 1408–1418.

Fabre, J. P., and Wilson, J. H. (**1995**). "Minimum detectable level evaluation of inverse beamforming using outpost sunrise data," J. Acoust. Soc. Am. **98**, 3262–3278.

Kneipfer, R. (**1997**). "Algorithm description for a beam space, minimum

variance soft constraint (MVSC) adaptive beamformer," NUWC-NPT Technical Report No. 10, p. 682.
Nuttall, A. H., and Hyde, D. W. (**1969**). "Unified approach to optimum and suboptimum processing for arrays," USL Report No. 992, Naval Underwater Systems Center, New London, CT, 22 April 1969.
Nuttall, A. H., and Wilson, J. H. (**1991**). "Estimation of the acoustic field directionality by use of planar and volumetric arrays via the Fourier integral method," J. Acoust. Soc. Am. **90**, 2004–2019.
Nuttall, A. H., and Wilson, J. H. (**2000**). "Adaptive inverse beamforming," J. Acoust. Soc. Am. **108**, 2259–2265.
Solomon, J. S. D., Knight, A. J., and Greening, M. V. (**1999**). "Sonar array signal processing for sparse linear arrays," Defense Science and Technology Organization (DSTO) Technical Report, June 1999.
Shultheis, (**1968**). private communication.
Wilson, J. H. (**1983**). "Signal detection and localization using the Fourier series method (FSM) and cross-sensor data," J. Acoust. Soc. Am. **73**, 1648–1656.
Wilson, J. H. (**1995**). "Applications of inverse beamforming (IBF)," J. Acoust. Soc. Am. **98**, 3250–3261.
Wilson, J., and Veenhuis, R. (**1997**). "Shallow water beamforming with small aperture, horizontal towed arrays," J. Acoust. Soc. Am. **101**, 384–394.

Active control of passive acoustic fields: Passive synthetic aperture/Doppler beamforming with data from an autonomous vehicle

Gerald L. D'Spain,[a] Eric Terrill, C. David Chadwell,
Jerome A. Smith, and Stephen D. Lynch
Marine Physical Laboratory, Scripps Institution of Oceanography, University of California, San Diego, La Jolla, California 93940-0701

(Received 26 July 2005; revised 31 July 2006; accepted 8 August 2006)

The maneuverability of autonomous underwater vehicles (AUVs) equipped with hull-mounted arrays provides the opportunity to actively modify received acoustic fields to optimize extraction of information. This paper uses ocean acoustic data collected by an AUV-mounted two-dimensional hydrophone array, with overall dimension one-tenth wavelength at 200–500 Hz, to demonstrate aspects of this control through vehicle motion. Source localization is performed using Doppler shifts measured at a set of receiver velocities by both single elements and a physical array. Results show that a source in the presence of a 10-dB higher-level interferer having exactly the same frequency content (as measured by a stationary receiver) is properly localized and that white-noise-constrained adaptive beamforming applied to the physical aperture data in combination with Doppler beamforming provides greater spatial resolution than physical-aperture-alone beamforming and significantly lower sidelobes than single element Doppler beamforming. A new broadband beamformer that adjusts for variations in vehicle velocity on a sample by sample basis is demonstrated with data collected during a high-acceleration maneuver. The importance of including the cost of energy expenditure in determining optimal vehicle motion is demonstrated through simulation, further illustrating how the vehicle characteristics are an integral part of the signal/array processing structure. © *2006 Acoustical Society of America.* [DOI: 10.1121/1.2346177]

PACS number(s): 43.30.Wi, 43.60.Fg, 43.60.Gk, 43.30.Es [EJS] Pages: 3635–3654

I. INTRODUCTION

Synthetic aperture processing converts temporal processing gain into spatial gain through the use of a moving receiver and/or source. This approach has been used extensively in the radar community where synthetic aperture radar techniques provide high resolution images of the earth's surface. These techniques have been extended to the problem of acoustically imaging the underwater environment. In both applications, the source of the wave field energy used to probe the environment is located on, and is under the control of, the platform creating the synthetic aperture. In ocean acoustics, active synthetic aperture imaging methods have undergone significant development and now are widely applied, particularly in high frequency surveys of the ocean bottom.

Aperture also can be synthesized without the use of an active source under control by the receiver. In this passive case, the properties of the source are part of the set of unknowns to be determined and typically are the quantities of greatest interest. Passive synthetic aperture sonar has no analog in the radar community. In contrast to the active case, it has not received a significant amount of attention. Early research efforts in ocean acoustics were made by Williams (1976) and Fitzgerald, Guthrie, and Shaffer (1976). In 1988, Autrey showed that under certain assumptions, a passive synthetic aperture system is equivalent in both implementation and performance to a narrowband spectrum analyzer (Autrey, 1988). Subsequent work in the published literature include algorithms to perform synthetic aperture processing with horizontal towed array data such as Yen and Carey's coherent sum of subaperture beams (Yen and Carey, 1989), the maximum likelihood estimation method (Nuttall, 1992), combined synthetic aperture and Doppler processing (Williams and Harris, 1992), and the Extended Towed Array Measurements algorithm (Stergiopoulos and Sullivan, 1989). This latter algorithm uses the correlation between overlapping synthetic and physical array elements to obtain phase corrections that account for deformation in array shape and fluctuations in the environment to some extent. It also decreases the coherence time requirements of the acoustic field from that needed to synthesize the whole aperture to that needed to perform the phase corrections from one overlap period to the next. Recently, synthetic aperture beamforming has been placed into the framework of model-based processing (Sullivan and Candy, 1997). This formulation uses a signal model that explicitly accounts for receiver motion (the same signal model as used in Sec. II), a vital step in improving processing performance. A few results of creating synthetic aperture passively using actual ocean acoustic data also have been published. Examples, in addition to the aforementioned works published in 1976, include those of Yen and Carey (1989), Roderick, Maiocco, and Kanabis (1989), Stergiopoulos (1990), Stergiopoulos and Urban (1992a, b),

[a]Electronic mail: gld@mpl.ucsd.edu

and Sullivan (2003). Quantitative assessment of the performance of specific algorithms has been conducted (e.g., Edelson and Sullivan, 1991; 1992; Yen and Carey, 1989; Stergiopoulos and Urban, 1992b; Sullivan and Candy, 1997). A special issue of IEEE Journal of Oceanic Engineering (Vol. 1) devoted to passive synthetic aperture in ocean acoustics appeared in 1992.

Almost all the work with moving receivers has dealt with towing a single hydrophone or hydrophone line array, thereby creating synthetic aperture in a single spatial dimension and in the same dimension as the physical aperture. In most cases, only situations where a single source transmitting a single narrowband signal have been considered. Noteable exceptions are the theoretical demonstration that large array gains may be achievable with modest increases in effective aperture in anisotropic noise fields (e.g., acoustically cluttered environments) (Sullivan, Carey, and Stergiopoulos, 1992) and the use of a general model-based processing approach that allows for multiple sources transmitting at multiple frequencies (Sullivan and Candy, 1997). The analyses for the most part are limited to a single frequency and do not consider broadband sources and/or the presence of broadband noise. Also not discussed to any great extent in the existing literature are the limitations imposed by the ocean environment on synthetic aperture creation. Characteristics of the ocean environment place limits on the information that can be extracted using synthetic aperture techniques, but the supporting data required to understand these environmental limitations rarely is collected.

The at-sea data collected in previous passive synthetic aperture studies made use of manned platforms. However, over the past few decades, autonomous underwater vehicles (AUVs) have undergone significant development and now are highly capable data collection platforms (e.g., National Research Council, 1996; 2004). In the field of underwater acoustics, most of the research to date with AUVs has involved active acoustic transmissions, for imaging the ocean bottom and subbottom and near-surface properties. Recently, AUVs have begun to be used in passive acoustics studies (e.g., Glegg *et al.*, 2001).

In the work presented in this paper, the receiving platform is an older-design, mid-size AUV. The distortions of the received acoustic field caused by the AUV's motion provide most of the information used in this paper to estimate the directional properties of the ocean acoustic field. The maneuverability and adaptability of AUVs provide opportunities for ocean acoustic data collection not afforded by other types of underwater acoustic sensor systems. As an example, an AUV has the capability to adapt its motion to purposefully impart a specific structure to the received field to optimize extraction of quantities of interest. This concept of active control of received acoustic fields through receiver motion is pursued further in this paper. An important consideration is the cost of motion due to the expenditure of finite propulsion energy available on the AUV.

An autonomous vehicle's maneuverability and hydrodynamic efficiency can be retained through the use of hull-mounted acoustic arrays, as opposed to the use of towed arrays. Deployment and retrieval also are much simpler. Added benefits are that the relative positions of hull-mounted array elements can be determined with little effort and they are independent of time. One important consequence of this fact is that hull-mounted array data are not degraded during a maneuver. Vehicle maneuvers are used in this paper to create synthetic aperture in more than one dimension in order to resolve some of the ambiguities and/or reduce the beamformer sidelobes arising in passive synthetic aperture processing. In addition, vehicle accelerations during the maneuver itself actually can help in estimating the directionality of the sound field, as demonstrated by the resampling beamformer presented in Sec. III. Although the radiated acoustic and vibration noise of the vehicle is a more serious consideration with hull-mounted systems, this self noise can be effectively eliminated (Zimmerman, D'Spain, and Chadwell, 2005) since the propellers on most autonomous vehicles do not rotate sufficiently fast to cause cavitation. The one serious drawback of hull-mounted systems is that the physical aperture is limited by the size of the vehicle. Therefore, the aperture must be either created using a Taylor series expansion approach (D'Spain, Hodgkiss, and Edmonds, 1991) or synthesized through motion.

The purpose of this paper is to develop and demonstrate the beamforming performance at low frequencies (200–500 Hz) of a set of techniques that take advantage of vehicle motion using ocean acoustic data collected by a hydrophone array mounted within the outer shroud of an AUV. The array has physical aperture in two horizontal dimensions, but its overall size is about a tenth of a wavelength at the low frequencies of interest. Beamforming performance is demonstrated in multisource conditions as well as for broadband signals. Section II summarizes the beamforming approach, based on the Doppler shifts in frequency imparted by the vehicle motion, and the underlying assumptions. A new type of beamformer that takes advantage of vehicle accelerations is introduced in Sec. III. In Sec. IV, brief descriptions of the ocean acoustics experiment and the AUV receiving system are presented, followed by the results from the synthetic aperture/Doppler and "resampling" beamforming algorithms using the AUV data in Sec. V. The concept of active control of passive acoustic fields through the motion of a receiving AUV is pursued further through simulation in Sec. VI. Finally, Sec. VII summarizes the conclusions of this work.

II. BEAMFORMING APPROACH AND ASSUMPTIONS

A. Analogy between passive synthetic aperture and Doppler beamforming

The basis of synthetic aperture processing is the exchange of temporal gain for spatial gain (Autrey, 1988). However, the transformation from time to space does not need to be performed explicitly to extract the available information on the directional characteristics of the sound field. Under plane wave propagation, synthetic aperture beamforming and Doppler processing are equivalent processes (the equivalence does not necessarily hold for other types of wave fields as pointed out by Carey, 1989). To illustrate this point and to introduce notation, consider a single tone plane

wave from a fixed source propagating across a fixed physical aperture in a medium whose properties do not change with time. The complex pressure at position $\underline{x}$ is then

$$p_r(\omega_s,\underline{x}) = A_p(\omega_s)\exp[i(\omega_s t + \underline{k}_s \cdot \underline{x})]. \quad (1)$$

The subscript "s" for the circular frequency ω_s and spatial frequency $\underline{k}_s$ signifies that these quantities are measured by a stationary receiver. In synthetic aperture beamforming, the array elements are synthesized by receiver motion with constant velocity $\underline{v}_r$, i.e., $\underline{x}=\underline{v}_r t$. The received field becomes

$$\begin{aligned} p_r(\omega_r,\underline{v}_r t) &= A_p(\omega_s)\exp[i(\omega_s t + \underline{k}_s \cdot \underline{v}_r t)] \\ &= A_p(\omega_s)\exp[i(\omega_s + \underline{k}_s \cdot \underline{v}_r)t] \\ &\equiv A_p(\omega_s)\exp[i\omega_r t]. \end{aligned} \quad (2)$$

The quantity ω_r is the frequency as measured by a moving receiver. The amplitude at ω_r measured by a moving receiver is the same amplitude at ω_s measured by a fixed receiver. The expression for the received frequency

$$\begin{aligned} \omega_r &= \omega_s + \underline{k}_s \cdot \underline{v}_r = \omega_s\left(1 + \frac{\underline{v}_r \cdot \hat{r}}{c_p}\right) \\ &= \omega_s\left(1 + \frac{v_r}{c_p}\cos[\theta_s - \Psi_r]\right) \end{aligned} \quad (3)$$

is the dispersion relation for sound propagating at phase velocity c_p to a moving receiver in a stationary medium (e.g., Pierce, 1989). The unit vector, $\hat{r}$, is defined to point in the direction opposite to the direction of propagation ($\underline{k}_s/|\underline{k}_s| = -\hat{r}$). The source azimuth is θ_s, the direction of receiver motion is Ψ_r, and v_r without the underscore is the magnitude (speed) of $\underline{v}_r$.

Equation (2) illustrates the point made by Autrey (1998) that all the gain from synthetic aperture processing of a single plane wave in a homogeneous, isotropic noise field can be obtained through temporal processing. For single tone signals, this gain can be obtained by a Fourier transform over time. In addition, Eq. (2) shows that all the available information on the directionality of the sound field also can be obtained by temporal processing. This information is contained in the frequency shifts due to motion of the receiver and the resulting redistribution of energy in the received pressure spectrum. Therefore, all the techniques developed for spectral estimation, including high resolution methods, can be used in passive synthetic aperture beamforming. Equation (2) also illustrates how synthetic aperture processing blurs the distinction between temporal and spatial frequency; the distribution of energy in the temporal frequency domain becomes intertwined with the directional distribution of the acoustic sources (given by the spatial frequency). This observation implies that to achieve significant array gains through creation of synthetic aperture in anisotropic ("acoustically cluttered") noise conditions, spectrally nonwhite noise conditions must also exist. The latter requirement is implicitly assumed in previous derivations of passive synthetic aperture array gain given that only single-tone signals were considered.

B. Stationary source approximation

The time-dependent Doppler shifted frequency of a tone generated by a source moving at velocity, $\underline{v}_s(t)$, and measured by a receiver moving at velocity $\underline{v}_r(t)$ is (Pierce, 1989)

$$\omega_r(t) = \omega_s(t)\left[1 + \frac{\underline{v}_r(t) - \underline{v}_s(t)}{c_p} \cdot \hat{r}(t)\right]. \quad (4)$$

The unknown source properties are the true source frequency, $\omega_s(t)$ (i.e., the frequency measured by a fixed receiver when the source is stationary), the source velocity (where $\underline{v}_s \equiv (v_s\cos[\phi_s], v_s\sin[\phi_s])$), and the direction from the receiver to the source, $\hat{r}(t)$. The quantity of primary interest in this paper is the source bearing, determined by $\hat{r}(t)$. Therefore, an "effective" source frequency for an equivalent stationary source can be defined that provides a good approximation to Eq. (4) and reduces the number of unknowns by half. Rewriting Eq. (4) gives

$$\begin{aligned} \omega_r(t) = &\left\{\omega_s(t)\left[1 - \frac{\underline{v}_s(t)}{c_p} \cdot \hat{r}(t)\right]\right\}\left[1 + \frac{\underline{v}_r(t)}{c_p} \cdot \hat{r}(t)\right] \\ &+ \omega_s(t)\left[\frac{(\underline{v}_s \cdot \hat{r})(\underline{v}_r \cdot \hat{r})}{c_p^2}\right]. \end{aligned} \quad (5)$$

Given that $v_s/c_p \leqslant 10^{-2} \ll 1$ and $v_r/c_p \leqslant 10^{-3} \ll 1$, then the second term on the right-hand side of Eq. (5) is negligible compared to the first term. Therefore, an "effective" source frequency for an equivalent stationary source can be defined as

$$\omega_s^{\text{eff}}(t) \equiv \omega_s(t)\left[1 - \frac{\underline{v}_s(t)}{c_p} \cdot \hat{r}(t)\right] \quad (6)$$

so that

$$\omega_r(t) \approx \omega_s^{\text{eff}}(t)\left[1 + \frac{\underline{v}_r(t)}{c_p} \cdot \hat{r}(t)\right]. \quad (7)$$

This approximation reduces the number of unknown source parameters to two, ω_s^{eff} and $\hat{r}$ (or equivalently, θ_s, the source azimuth) since no effort is made to derive information on the track of the source. The following developments make use of this approximation and ω_s will be used to specify ω_s^{eff}.

The stationary source approximation models any frequency spreading arising from the differential Doppler shifts of multipath components excited by a moving source as part of the radiated spectrum of an equivalent "fixed" source. (A way of combining multifrequency energy from a single source is outlined in Sec. II G). In addition, it assumes the source remains at approximately constant azimuth during the processing period.

C. Energy integration along hypothesized curves

The Doppler beamforming process presented in this section involves the integration of spectral energy collected over a set of straight-line tracks. The first step for a given assumed source frequency and assumed source azimuth (i.e., look direction) is to select a set of frequency bins, one from each straight-line track ("leg"). These frequency bins are deter-

mined by a cosine-dependent curve over leg number that is a function of source frequency and azimuth [Eq. (3)]. The average AUV speed and direction of motion for each leg, and the effective phase velocity of the received acoustic field, are taken as known inputs to the beamformer. In the case of moving physical aperture, the spectral levels are those measured by the physical beam pointed in the look direction of interest. The beamformer output then is the incoherent sum of the weighted spectral levels in these frequency bins; $\Sigma_n^{\mathrm{NT}} w_n A_n^2(\omega_r^n)$ where n is the leg number, NT is the total number of legs, and w_n is the weighting of the nth leg's selected bin level $A_n^2(\omega_r^n)$ at received frequency ω_r^n. Various weightings can be used when summing the bin spectral levels. A data-independent equal weighting ($w_n \sim 1/\mathrm{NT}$), a data-adaptive weighting in which the bin level is normalized by the average bin level in the processing band ($w_n \sim 1/\Sigma_i^{\mathrm{NF}}(A_n^i)^2$, where NF is the number of frequency bins in the processing band), and a weighting inversely proportional to the peak level in the processing band, ($w_n \sim 1/(A_n^{\max})^2$) were used with the AUV-collected data. Results are summarized in Sec. V.

D. Simultaneous search over source frequency and azimuth

Once the stationary source approximation (Sec. II B) is made, the two unknowns to be determined are the effective source frequency as measured by a stationary receiver, ω_s, and the source azimuth, θ_s. Two or more moving receivers allow for a unique solution (e.g., Sullivan, 2003) since two independent equations are obtained from the Doppler-shifted received frequency and the relative phase shift between the two receivers [for two hydrophones with spatial separation in the same direction as $\underline{v}_r$, then $\omega_s = \omega_r - v_r \Delta\hat{e}$ and $\cos(\theta_s - \Psi_r) = (c_p)(\omega_r - v_r \Delta\hat{e})^{-1}\Delta\hat{e}$, where $\Delta\hat{e}$ equals the phase difference between the hydrophones normalized by their spatial separation]. For a single omnidirectional receiver, these two source unknowns also can be determined uniquely along a single straight-line track using the differential Doppler shifts of two or more multipath components in a waveguide. An alternative approach is to make a change in receiver speed at fixed heading, which can be equated to an effective change in phase velocity as shown by Eq. (3). Another method is to make a change in receiver heading. With these latter two approaches, the two unknowns can be determined simultaneously through cooperative behavior of two or more vehicles. A special case of a receiver speed change is for one of the receiver speeds to be zero, which can be implemented by a constant-velocity receiver sharing information with a fixed receiving system.

The magnitude of the changes in received frequency due to changes in phase velocity, in receiver speed, and in receiver heading is a measure of the Doppler beamforming sensitivity of these approaches. Differentiating Eq. (3):

$$\delta\omega_r(\delta c_p) = -\omega_s \frac{v_r}{c_p^2} \cos[\theta_s - \Psi_r]\delta c_p, \tag{8}$$

$$\delta\omega_r(\delta v_r) = \omega_s \frac{1}{c_p} \cos[\theta_s - \Psi_r]\delta v_r, \tag{9}$$

$$\delta\omega_r(\delta\Psi_r) = \omega_s \frac{v_r}{c_p} \sin[\theta_s - \Psi_r]\delta\Psi_r. \tag{10}$$

The magnitude of δv_r is order 1 m/s for commercially available AUVs and that of $\delta\Psi_r$ can be as large as π corresponding to a 180° reversal in the direction of motion. The quantity δc_p is determined by propagation conditions. For a shallow water waveguide with approximately constant sound speed of c and a critical angle of the bottom of χ_c, then $\delta c_p = c(1/\cos[\chi_c] - 1)$, approximately equal to 100 m/s for a bottom critical angle of 20°. Therefore,

$$\delta\omega_r(\delta v_r)/\delta\omega_r(\delta c_p) = -\frac{\delta v_r/v_r}{\delta c_p/c_p} \approx -15. \tag{11}$$

This result indicates that Doppler/synthetic aperture beamforming is an order of magnitude more sensitive to changes in receiver speed than to phase differences between multipath arrivals in typical shallow water environments. In fact, the speeds attainable by the AUV used to collect the data in this paper are not sufficiently high to allow multipath differential Doppler approaches to be effective.

As an aside, Eq. (8) and the value of δc_p of 100 m/s for a typical shallow water site off the Southern California coast provide the information necessary to estimate the fractional spectral spreading, $\delta\omega_r/\omega_s$, recorded by a moving AUV due to the spatial bandwidth of the channel. It is about 0.004% for motion toward or away from the source, half that associated with uncontrolled variations in vehicle velocity along straight-line tracks (see Sec. IV) and on the same order as that due to medium fluctuations (Sec. V D).

In a similar way,

$$\delta\omega_r(\delta v_r)/\delta\omega_r(\delta\Psi_r) = \frac{1}{\tan[\theta_s - \Psi_r]} \frac{\delta v_r/v_r}{\delta\Psi_r}. \tag{12}$$

Here, the relative sensitivity is dependent upon the receiver's direction of motion with respect to the source azimuth, being more sensitive to speed changes when moving toward or away from the source (endfire) and more sensitive to heading changes when moving at right angles to the source direction (broadside). For directions of motion and source azimuths such that the tangent term is approximately unity, then the relative sensitivity also is of order unity. The results presented in the first part of Sec. V use a combination of different receiver directions of motion each at about the same receiver speed. The resampling beamformer discussed in Sec. III combines both changes in speed and in direction of motion into one method.

As shown in Sec. V, the ambiguity surface (beamforming output) with Doppler/synthetic aperture processing for the simultaneous search of effective source frequency and source azimuth using data from a single receiver displays a pattern of smoothly evolving sidelobes. The behavior of these sidelobes in the source frequency/azimuth plane can be determined by variations in source frequency and source azimuth such that the received frequency remains unchanged:

$$\delta\omega_r = 0 = \left(1 + \frac{v_r}{c_p}\cos[\theta_s - \Psi_r]\right)\delta\omega_s - \omega_s \frac{v_r}{c_p}\sin[\theta_s - \Psi_r]\delta\theta_s, \quad (13)$$

which simplifies to

$$\frac{\delta\omega_s}{\omega_s} \approx \frac{v_r}{c_p}\sin[\theta_s - \Psi_r]\delta\theta_s. \quad (14)$$

For a single straight-line track traversed at constant speed, Eq. (14) describes the sinusoidally varying slopes of the trajectory of the beamformer sidelobe in the source frequency/azimuth plane. For a set of straight-line tracks, the true source frequency and azimuth are determined by the intersection of these trajectories.

The appropriate search grid in the source frequency/azimuth plane is determined by the spatial (distribution in azimuth) and spectral bandwidths of the source, and by the frequency resolution of the fast Fourier transform (FFT) used in the processing. Equation (3) shows that the change is nearly one-to-one for changes in assumed source frequency bin and resulting calculated received frequency bin. Therefore, two to three grid points per binwidth is appropriate for received signals with bandwidth on the order of, or less than, the FFT resolution. The change in calculated received frequency bin for a change in assumed source azimuth is dependent upon direction of motion with respect to the source azimuth. For the FFT resolution used in Sec. V, a 10° change in assumed source azimuth results in a maximum received frequency change of about one binwidth.

Section V presents results from the simultaneous search over source frequency and azimuth.

E. Length of time on each leg

Several parameters determine the appropriate length of time traveled on each leg. First, the spatial resolution is determined by the resolution in frequency

$$\frac{2\pi}{T} = \delta\omega_r = -\omega_s \frac{v_r}{c_p}\sin[\theta(\hat{l}) - \Psi_r]\delta\theta(\hat{l}), \quad (15)$$

where T is the time required on each leg to obtain data for a single FFT. [Note that Eq. (15) is a restatement of the expression for the angular resolution of a line array of length L; given that $2\pi c_p/\omega_s = \lambda_s$ and $v_r T = L$, then $\delta\theta = \lambda_s/(L\sin[\theta])$ where λ_s is the acoustic wavelength at the frequency of the source, L is the spatial length of the track, and θ is the angle with respect to endfire.] Therefore, for a given vehicle speed and frequency of interest, increasing FFTL, the FFT length for Doppler/synthetic aperture beamforming, increases the frequency resolution and therefore provides finer spatial resolution. Longer periods of time are required as the AUV speed and the frequency band of interest decrease. The sine dependence is associated with the spatial resolution properties of linear arrays; poor spatial resolution at endfire and best resolution at broadside.

However, greater frequency resolution implies a greater period of time required to obtain an estimate of the sound field's directionality and a greater period over which the field conditions must remain stationary. In addition, a greater amount of energy is consumed by the AUV in transiting along longer tracks. (Given that the cost of motion increases with increasing vehicle speed, the best strategy is to travel as slowly as possible to traverse the necessary track length, L, as long as the acoustic field properties remain approximately stationary. However, this latter requirement rarely is known *a priori*). Even if conditions otherwise permit it, a maximum achievable frequency resolution is determined by uncontrolled variations in vehicle velocity (speed and direction of motion) along the tracks (re Fig. 4) unless they are taken into account (as in Sec. III) and by frequency spreading from Doppler shifting imparted by the environment, as discussed in Sec. V D.

The variance of the spectral estimate is reduced by incoherently averaging statistically independent realizations of the spectrum (e.g., Bendat and Piersol, 1986). These independent realizations can be obtained by taking sequential FFTs in time using the ergodic assumption. Therefore, one approach is to maintain constant velocity on a given track for a longer period of time to collect the data required for the additional realizations. In this case, the same frequency bins from one realization to the next are incoherently averaged, and no new information on the directionality of the sound field is obtained. Alternatively, a maneuver to a different track can be made as soon as sufficient data for a single long FFT have been recorded. With this approach, the frequency bins to average together are determined by the Doppler beamformer look direction. This incoherent accumulation technique reduces the variance of the beamformer output estimate and so increases the deflection ratio for detection (e.g., Urick, 1983).

With broadband sources, incoherent averaging across frequency bands can be used to reduce the estimate's variance. This method requires that some *a priori* knowledge of the frequency content of the source signal be known (e.g., harmonically related spectral lines of surface ships; Ross, 1987), and is discussed further in Sec. II G and in Sec. V. As for incoherently averaging across hydrophone elements, the physical size of the AUV with respect to the acoustic wavelengths at low frequencies (frequencies less than 1 kHz) usually does not permit the individual hydrophones to have sufficient spatial separation to provide statistically independent estimates of ocean acoustic noise. The separation, however, is usually adequate for cases where the background noise is dominated by flow noise and sometimes vehicle vibration noise.

F. Doppler/synthetic aperture beamforming with a moving array

The method used in this paper to form synthetic aperture with a moving sensor array allows for both adaptive as well as conventional beamforming techniques to be applied to the physical array data. It assumes that all moving array elements experience the same Doppler shift.

Frequency domain adaptive beamforming relies upon statistically stable estimates of the data cross spectral density matrix. This stability typically is achieved by dividing a time

series record into segments and averaging FFT realizations for each segment. However, this division then prevents the long FFTs for fine frequency resolution required to perform Doppler/synthetic aperture beamforming at low frequencies and low receiver speeds. The approach used here is to estimate adaptive array weights for a given frequency band within which Doppler beamforming is performed, and to assume that these weights pertain to all the finely resolved frequency bins within the band. The first step is to determine the number of time series samples, FFTL, required for Doppler beamforming along a given leg (re the previous part of this section). Then, this record is divided into a number of shorter segments of sample length FFT_*short* to provide statistically independent realizations required for estimating the data cross spectral density matrix (CSDM). The number of independent realizations in adaptive beamforming usually is set equal to or greater than the number of array elements M (the dimension of the data CSDM) in order to stabilize the matrix inversion (e.g., Noble, 1969), so that FFT_*short* $\leqslant$ FFTL/M. In addition, the frequency resolution provided by the segment length FFT_*short* defines the frequency band within which Doppler beamforming will be performed and so is taken to be equal to, or greater than, the Doppler beamforming bandwidth, $2\omega_c(v_r/c_p)$ for center frequency, ω_c. In summary,

$$\text{FFT}\_short \leqslant \min\left\{\text{FFT}L/M, \left(2\frac{v_r}{c_p}\frac{\omega_c}{\Omega_0}\right)^{-1}\right\}, \tag{16}$$

where $\Omega_0/2\pi$ is the data sampling rate. The resulting (complex) adaptive array weights then are used to form physical aperture beams in each of the narrow frequency bins defined by the long FFT length, FFTL. After transforming the beam directions from an AUV-based coordinate system to one in absolute space using the AUV heading, θ_r (which often differs from the AUV direction of motion, Ψ_r; see Fig. 3), the Doppler processing proceeds in a way identical to that with single element data described in Sec. II C. Although this approach provides only relatively coarse frequency resolution at the adaptive beamforming step, it does allow for finer spatial resolution and lower sidelobes compared to conventional beamforming. In Sec. V, results of Doppler beamforming with array weights determined by white-noise-constrained adaptive beamforming (Cox, Zeskind, and Owen, 1987; Gamann, 1992) are compared to those from conventional beamforming, to those using physical aperture alone, and to those where only data from a single omnidirectional receiver are used.

G. Broadband sources

The "relative" received frequency $\hat{\omega}_r$ using an assumed center frequency of ω_c is

$$\hat{\omega}_r \equiv \frac{\omega_r - \omega_c}{\omega_c} = \frac{\omega_s - \omega_c}{\omega_c} + \frac{\omega_s}{\omega_c}\frac{v_r}{c_p}\cos[\theta_s - \Psi_r]. \tag{17}$$

Given that the center frequencies are not too different from the true effective source frequencies, then the relative frequencies are approximately frequency independent and can be combined as in Fig. 5. Note that for a multitone signal from a single source, only one ω_s must be known (or estimated) since all others can be derived from the relative frequency or the ratio of received frequencies, leaving θ_s as the only unknown.

H. Deviations from underlying assumptions

The Doppler/passive synthetic aperture processing presented in this section is based on several assumptions regarding the source, the propagation characteristics, and the receiver. First, the source is modeled as fixed in space. For a constant velocity source in the far field, use of an effective source frequency provides a good approximation to this assumption, as discussed in Sec. II B. A second assumption is that the radiated frequency content of the source is assumed to not vary with time. Therefore, the properties of sources that accelerate (by a change in heading and/or change in speed), undergo a significant change in azimuth, and/or generate nonstationary source spectra over the Doppler processing period may not be well estimated. The acoustic signals in the data set used in this paper are transmitted by a controlled source deployed from a moored platform (Sec. IV) and so do not provide a rigorous test of the stationary source approximation.

As for propagation effects, the processing approach assumes that the incoming acoustic field from a source of interest approximates a plane wave traveling in a stationary, homogeneous whole space with known phase velocity. Multipath propagation conditions give rise to azimuthally dependent spreading in frequency, which can be used to obtain information on the source and the environment (by providing a measure of the spatial bandwidth of the channel given the source and receiver depths). However, the typical maximum speeds of midsize AUVs is not sufficiently great to permit this information to be extracted. Temporal fluctuations in the medium, as discussed at the end of Sec. V, cause Doppler spreading that is independent of the source characteristics and therefore introduces a type of noise ("multiplicative" noise; Tuzlukov, 2002) in the estimation of source properties.

With the standard processing approach, the receiver is assumed to travel at constant and known velocity over the time period required to obtain the FFT. However, a resampling beamforming approach (Sec. III) can correct for any known variations in receiver velocity. In addition to knowing its velocity, a directional receiver (directional sensor and/or physical aperture array) also must determine its orientation in absolute space (heading, pitch, and roll) as a function of time to properly align its beams.

III. ACCOUNTING FOR VARIATIONS IN RECEIVER VELOCITY: THE "RESAMPLING BEAMFORMER"

The variations in AUV velocity along one of its tracks, as measured by the Doppler velocity log (DVL), are shown in Fig. 4. These uncontrolled variations cause spreading of the received energy in the frequency domain. In fact, as the calculations at the end of Sec. IV demonstrate, the spreading caused by unaccounted-for AUV velocity variations is a major limiting factor in creating synthetic aperture and Doppler beamforming at the source/receiver ranges of this experi-

ment. One approach is to account for these velocity variations explicitly in the signal model, i.e., to replace v_r by $v_r(t)$ in Eqs. (2) and (3). The purpose of this section is to present an alternative method of accounting for these velocity variations that operates on all frequencies simultaneously. The approach allows a new type of beamformer to be defined whose properties are outlined in this section.

The quantity actually measured by the AUV-based digital data acquisition system is not the received frequency itself, but rather the fractional sampling frequency, given by the received frequency normalized by the data sampling rate, $\omega_r(t)/\Omega_0$. The variations in AUV velocity cause the received frequency to be dependent upon time so that the received energy from a single transmitted tone appears to be spread across a finite band of frequencies over the time period of the long FFTs required for low frequency Doppler/synthetic aperture beamforming. A time-dependent data sampling rate, $\Omega(t)/2\pi$, has a similar effect. (In fact, underwater acoustic measurements were made with the AUV in a calibration tank to verify that the frequency spreading caused by temporal variations in the AUV hydrophone data acquisition sampling rate is negligible). The approach taken here is to redigitize the hydrophone data with a sampling rate that varies with time to exactly cancel the temporal variations in received frequency caused by the known AUV velocity variations.

The sampling theorem (e.g., Bendat and Piersol, 1986) states that a continuous signal can be reconstructed exactly from equally spaced digital samples of the signal as long as the continuous signal is band-limited and that the digital sampling rate is more than twice the highest frequency component in the continuous signal. Therefore, the underlying continuous signals recorded by the AUV-mounted hydrophones can be reconstructed and redigitized to compensate for the AUV motion variations. The requirement for canceling the AUV-motion-induced frequency variations is

$$\frac{d}{dt}\left[\frac{\omega_r(t)}{\Omega(t)}\right]=0\rightarrow\frac{1}{\omega_r(t)}\frac{d\omega_r(t)}{dt}=\frac{1}{\Omega(t)}\frac{d\Omega(t)}{dt}. \tag{18}$$

This result can be integrated between times t_0 and t_1 to give

$$\frac{\omega_r(t_1)}{\omega_r(t_0)}=\frac{\Omega(t_1)}{\Omega(t_0)}=\frac{\Delta t(t_0)}{\Delta t(t_1)}, \tag{19}$$

where Δt is the time interval between data samples. The expression for $\omega_r(t)$ is given by Eq. (3) where the AUV speed, $v_r(t)$ and direction of motion, $\Psi_r(t)$, are assumed to vary with time. An assumed source bearing, $\theta(\hat{l})$, determined by a given look direction, is used in the equation. Substituting the resulting expression into Eq. (19) results in

$$\begin{aligned}\Delta t(t_i)&=\frac{\omega_r(t_{i-l})}{\omega_r(t_i)}\Delta t(t_{i-l})\\&=\frac{c_p+v_r(t_{i-l})\cos[\theta(\hat{l})-\Psi_r(t_{i-l})]}{c_p+v_r(t_i)\cos[\theta(\hat{l})-\Psi_r(t_i)]}\Delta t(t_{i-1})\\&=\frac{\omega_r(t_0)}{\omega_r(t_i)}\Delta t(t_0)\\&=\frac{c_p+v_r(t_0)\cos[\theta(\hat{l})-\Psi_r(t_0)]}{c_p+v_r(t_i)\cos[\theta(\hat{l})-\Psi_r(t_i)]}\Delta t(t_0).\end{aligned} \tag{20}$$

Equation (20) shows that the change in data sampling rate to compensate for variations in AUV velocity is different for each look direction. This observation provides the basis for a new beamforming approach. The output squared amplitude of this "resampling beamformer" is given by the spectrum of the time series received by a moving receiver, $r(t)$, after resampling based on a given look direction. That is, if the nth sample of the time series originally digitized at a time-independent sampling rate of $1/\Delta t(t_0)\equiv 1/\Delta t_0$ is $r(n\Delta t_0)$ then the corresponding sample of the resampled time series is $r[\Sigma_{i=1}^{n}\Delta t(t_i)]$ where $\Delta t(t_i)$ is given by Eq. (20). Therefore, the resampling beamformer output squared is

$$B_{\hat{l}}(f)=\left|\mathrm{FFT}\left\{r\left[\sum_{i=1}^{n}\Delta t(t_i)\right]\right\}\right|^2,\quad n=1,\ldots,\mathrm{FFT}L. \tag{21}$$

The expression for the received fractional sampling frequency, η_r after resampling based on an assumed source bearing of $\theta(\hat{l})$ given that the true source bearing is θ_s is

$$\begin{aligned}\eta_r(t)=\frac{\omega_r(t)}{\Omega(t)}&=\eta_r^0\left[\frac{c_p+v_r(t)\cos[\theta_s-\Psi_r(t)]}{c_p+v_r(t)\cos[\theta(\hat{l})-\Psi_r(t)]}\right]\\&=\left[\frac{\omega_s}{\Omega_0}\left(1+\frac{v_r^0}{c_p}\cos[\theta(\hat{l})-\Psi_r^0]\right)\right]\\&\quad\times\left[\frac{c_p+v_r(t)\cos[\theta_s-\Psi_r(t)]}{c_p+v_r(t)\cos[\theta(\hat{l})-\Psi_r(t)]}\right],\end{aligned} \tag{22}$$

where $v_r^0\equiv v_r(t_0)$ and similarly for Ψ_r^0. The first term in square brackets in the last expression in Eq. (22) is independent of time and equals the assumed received fractional sampling frequency at t_0 for the given look direction, $\hat{l}$. The second term in brackets contains the time dependence due to the variations in AUV velocity. When the assumed source bearing (look direction) equals the true source direction, then this second term becomes unity and η_r is time-independent. Simultaneously, the first term in square brackets becomes equal to the true received fractional sampling frequency at t_0. Therefore, the basis of the beamforming operation is the degradation in the output of the FFT due to temporal variability in the fractional sampling frequency that arises from "mismatch" between the true and assumed source bearings. The number of frequency bins over which a single tone's source energy is spread when the look direction does not correspond to the true source direction is determined by the FFT length (i.e., the synthetic aperture array length).

Equation (22) shows that the beamformer sensitivity (i.e., the temporal variability of the fractional sampling frequency) also increases with increasing source frequency and increasing temporal variations in AUV speed and heading (increasing acceleration). The relative importance of changes in speed and in heading can be determined by differentiating Eq. (22) with respect to time. To first order, it is

$$\frac{d\eta_r(t)}{dt} \approx \frac{\eta_r^0}{c_p}\left[\frac{dv_r(t)}{dt}(\cos[\theta_s - \Psi_r(t)] - \cos[\theta(\hat{l}) - \Psi_r(t)]) + v_r(t)\frac{d\Psi_r(t)}{dt}(\sin[\theta_s - \Psi_r(t)] - \sin[\theta(\hat{l}) - \Psi_r(t)])\right]. \quad (23)$$

Changes in receiver speed amplify the cosine differences in the mismatch whereas the difference in sines is amplified by receiver heading changes. For the special case of constant acceleration along a linear track (dv_r/dt=constant, $d\Psi_r/dt=0$), then η_r is independent of time both when $\theta(\hat{l})=\theta_s$ and when $\theta(\hat{l})=2\Psi_r-\theta_s$. This ambiguity disappears when either $\Psi_r=\theta_s$ or $\Psi_r=\theta_s\pm\pi$. It is equivalent to the typical left-right ambiguity that exists in beamforming with data from line arrays of omnidirectional elements. In this case, the ambiguity occurs about the line formed by the direction of motion because the change in received frequency of a tone is the same whether the source is at a given angle clockwise from the direction of motion or at that same angle in the counterclockwise direction. In contrast, the case of circular motion at constant speed ($dv_r/dt=0$, $d\Psi_r/dt$=constant) displays an ambiguity at $\theta(\hat{l})=\pi+2\Psi_r(t)-\theta_s$. That is, the left-right ambiguity occurs about a line perpendicular to the direction of motion and disappears at broadside ($\Psi_r=\theta_s\pm\pi/2$). The reason for this ambiguity is that the increase in the Doppler-upshifted received frequency from a single tone source as the receiver's heading becomes more oriented toward the direction of source is exactly the same as that due to a decrease in Doppler-downshifted frequency as the receiver's heading becomes less oriented in a direction heading away from a source. Since the vehicle heading is constantly changing along a circular arc, this ambiguity (sidelobe) decreases with increasing distance traveled along the arc. Examples of the behavior of the resampling beamformer and its sidelobe character for circular track motion are presented in Sec. V.

The time-domain resampling implementation presented here is inherently broadband; it works for all frequencies simultaneously. Therefore, it is well suited for use with time-delay-and-sum beamforming, and can be used in conjunction with the Doppler beamforming methods in the previous section.

To extend mission durations, an autonomous vehicle must conserve energy by intermittently coming to rest with respect to the surrounding medium, either by becoming neutrally buoyant and freely drifting in the water column or by sitting upon the ocean bottom. The foregoing discussion demonstrates that the receiver accelerations associated with transitions from resting to relative medium motion provide a unique opportunity for obtaining information on the directional properties of the sound field. More generally, the character of the receiver motion becomes an integral part of the beamforming operation.

IV. THE EXPERIMENT AND AUV HYDROPHONE SYSTEM

Ocean acoustic data collected during an experiment in April, 2004 by an AUV-mounted hydrophone system are presented in this paper. A brief description of the experiment is presented in Sec. IV A, the features of the AUV and its hydrophone data acquisition system are summarized in Sec. IV B, and Sec. IV C contains information on the AUV navigation systems.

A. Description of the experiment

The location of the 6-day experiment was 67 km west of San Diego at 32 deg, 38.5 min N, 117 deg, 57.5 min W (see Fig. 1). R/P FLIP, a 100-m-long manned spar buoy, was deployed in 180-m water in a three-point mooring that restricted its motion to a 50-m watch circle. The AUV, whose tracks during one of its events are plotted in Fig. 1, was deployed and retrieved from R/V Sproul, a 38-m-long ship operated by the Scripps Institution of Oceanography. Also shown in Fig. 1 are the locations of the three acoustic transponders with 500-m interelement separation that allowed the AUV location in two dimensions to be determined to submeter accuracy as a function of time using a high precision, long baseline navigation technique (Kussat, Chadwell, and Zimmerman, 2005).

During the 24 AUV events conducted during the 2004 test, a variety of signal waveforms, including sets of continuous-wave tones, frequency-modulated chirps, and pseudorandom noise sequences, were transmitted from three controlled acoustic sources deployed from FLIP at fixed depths from 10 to 50 m. One source generated signals in the low frequency band (200–800 Hz) and the other two operated at midfrequencies (1–7 and 5–10 kHz, respectively). Attached to the source cable were tilt meters to monitor depth and motion of the sources. The transmitted signals were received by the AUV running tracks in a variety of geometries and at various depths from 20 to 100 m. Also deployed from FLIP were a collection of environmental sensors including three 16-element strings of temperature sensors and a conductivity/temperature/depth (CTD) profiling sensor. A sound speed profile derived from one of the CTD casts is shown in Fig. 2 along with the nominal deployment depths of 50 m for the acoustic sources and 60 m for the AUV during the event plotted in Fig. 1. The profile shows a mixed surface layer of about 20 m thickness overlying the thermocline in the 20–30 m depth interval. At greater depths, the sound speed was approximately independent of depth with a value of 1490 m/s.

B. The AUV and its hydrophone data collection system

The AUV used during the experiment is an Odyssey IIb formerly manufactured by Bluefin Robotics, Inc. The vehicle's propulsion system was replaced by the ducted-fan, vectored-thrust system installed on all modern Bluefin vehicles, and then modified to minimize radiated acoustic and vibration noise (Zimmerman, D'Spain, and Chadwell, 2005).

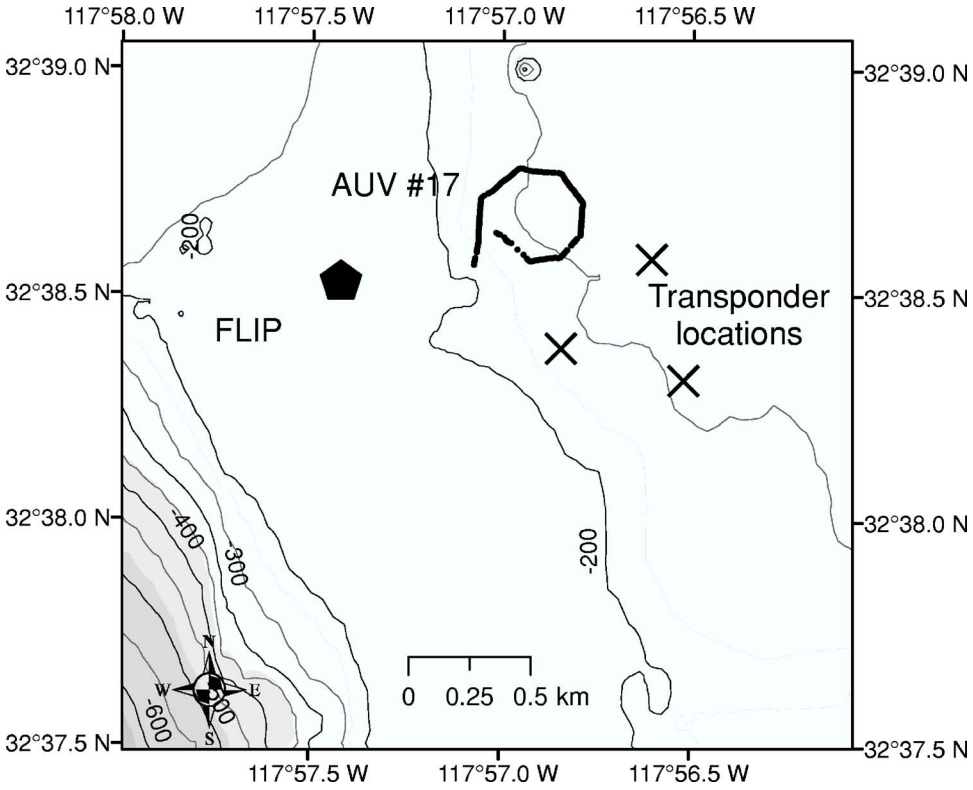

FIG. 1. Map of the location of the April, 2004 experiment on the 40-Mile Bank west of San Diego. The three-point mooring location of R/P FLIP is indicated by a solid pentagon, the three high-precision acoustic transponder positions are marked with × symbols, and the octagon-shaped track of the AUV during one of the events (No. 17) as measured by the acoustic navigation system is plotted as a series of small circles. The event started with the AUV heading almost due north, and then making a series of seven 45° turns to starboard as it traveled in a clockwise direction. Bathymetry contours are plotted at 50-m intervals.

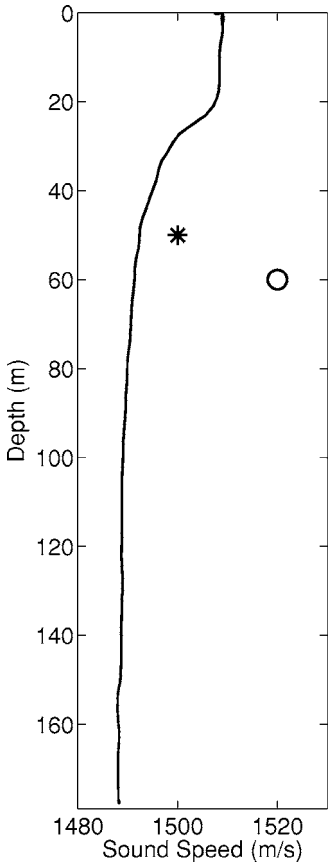

FIG. 2. Sound speed profile derived from a CTD cast taken from FLIP during the April, 2004 experiment along with the acoustic source depth (asterisk) and the deployment depth of the AUV (open circle) during event 17 whose track is plotted in Fig. 1.

The self noise levels recorded by the elements of the hydrophone array mounted inside the AUV (described in the next paragraph) now are at, or below, typical shallow water ocean background noise levels at sea state 2 at almost all frequencies above 300 Hz. (However, the interrogation pings transmitted every 10 s by the AUV acoustic navigation system, described in the next part of this section, did contaminate the passive acoustic data as did pulses generated every 2–3 s by the AUV's steering mechanism). The vehicle is 2.2 m long, 0.58 m in diameter, and has a maximum speed and mission duration of 1.2 m/s and 4 h, respectively.

An 8-element hydrophone array was mounted inside the outer shroud of the AUV to retain the hydrodynamic efficiency and maneuverability of the vehicle. The hydrophone locations along with the main components of the AUV are shown in Fig. 3. The time series from each of the 8 elements was digitized at a 20 ksample/s rate by a low-power data acquisition system inside the AUV and then recorded con-

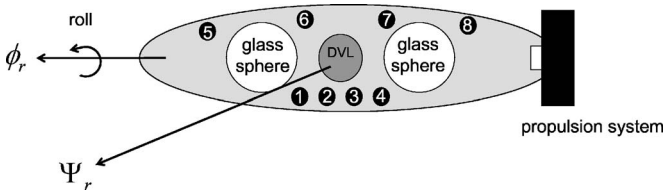

FIG. 3. Schematic of the top view of the AUV with the eight shroud-mounted hydrophone locations specified as numbered black circles. The vehicle's two instrumentation glass spheres and DVL are drawn as large circles. The nomenclature for the vehicle heading, ϕ_r, and direction of motion, Ψ_r, used in the paper are indicated as well as the direction of roll. Pitch (not shown) is the angle of rotation in and out of the plane of the page about an axis in the vertical direction in the schematic.

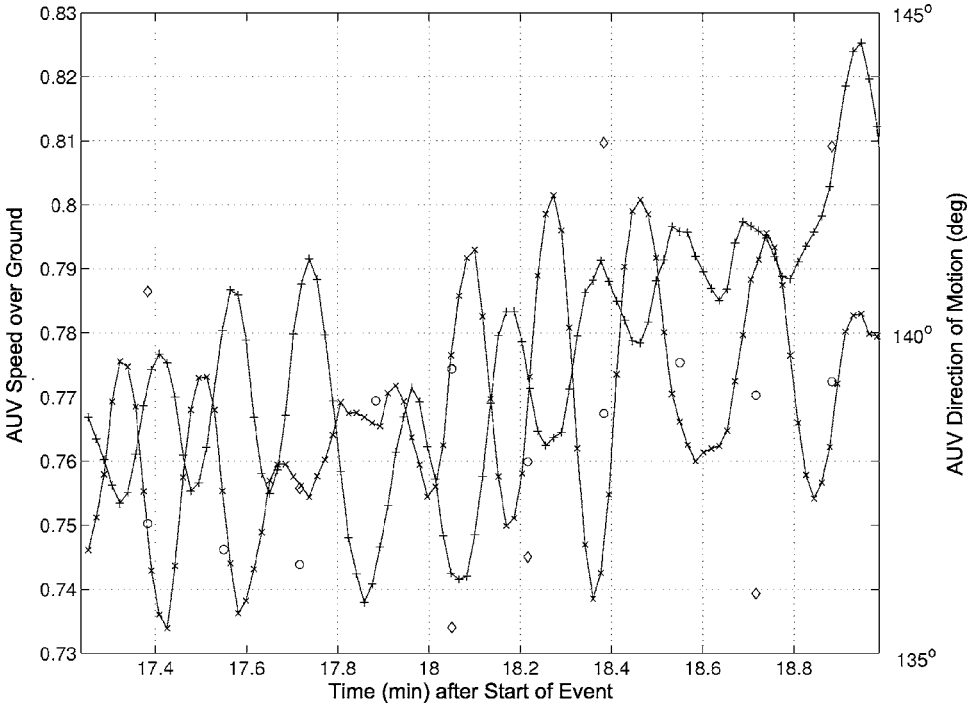

FIG. 4. Plot of the AUV speed over ground in m/sec (connected ×'s) and direction of motion (connected plus signs) measured by the DVL during the fourth straight section of the octagon-shaped event in Fig. 1 (traveling to the southeast). For comparison, the plot also shows the AUV direction of motion (diamonds) and speed over ground (circles) estimates derived from the high-precision acoustic navigation data during this period.

tinuously onto hard disk. Additional details on the data acquisition system and the other components of the modified Odyssey IIb are provided in Zimmerman, D'Spain, and Chadwell (2005).

C. AUV navigation

During the experiment, four independent systems were installed on the vehicle to determine its position in three dimensions as a function of time. These systems were required to measure the vehicle's depth, its 2D position in absolute space, its velocity (speed and direction of motion) over ground, its heading, and its pitch and roll. A pressure gauge capable of measuring depth with 0.7 m accuracy provided readings of the AUV depth every 0.1 s. A high precision acoustic navigation system with demonstrated decimeter-level navigation accuracy (Kussat, Chadwell, and Zimmerman, 2005) measured the vehicle position in 2D absolute space. (The locations of this system's three transponders are shown in Fig. 1.) Interrogation pings were issued from the AUV once every 10 s during an event. The resulting position fixes can be differenced to provide estimates of speed and direction of motion over ground with time. Estimates obtained this way agreed quite well with those obtained by the Doppler velocity log (DVL), as shown in Fig. 4 for one of the straight-line tracks. The DVL provided estimates of speed and direction of motion over ground approximately once every second using measured Doppler shifts from bottom reflections on each of four 300-kHz acoustic beams oriented in a Janus configuration. The DVL also contained a fluxgate compass to provide vehicle heading. Because of its location and electromagnetic shielding provided by its housing, the DVL compass provided more accurate heading measurements than the vehicle's attitude and heading reference system (AHRS). However, the AHRS did provide useful measurements of AUV pitch and roll (see Fig. 3 and its caption for definitions of pitch and roll).

Figure 4 shows a plot of the AUV speed and direction of motion along a track as derived from the DVL data. The vehicle had been programmed to travel in a straight line at constant speed over this track. However, the vehicle's actual speed and direction of motion were not constant, but varied with a periodicity of 12–18 s. The magnitude of the variation in speed approaches $\Delta v_r \approx 0.1$ m/s about a mean speed of slightly less than 0.8 m/s. In heading, the variation is $\Delta\Psi_r \approx 10°$. These variations, associated with the properties of the AUV's control system, result in spreading of the signal energy in the received frequency spectrum. The resulting spread in the relative received frequency due to these two components of vehicle velocity variation is $\Delta\hat{\omega}_r = \Delta v_r / c \approx 0.007\%$ and $\Delta\hat{\omega}_r = (v_r/c)\Delta\Psi_r \approx 0.009\%$, respectively.

These variations in vehicle velocity over the processing period required for Doppler processing at low frequencies, if unaccounted for, are the limiting factor in synthetic aperture beamforming at the medium ranges in this experiment. The resampling beamformer approach, introduced in Sec. III, corrects for these variations so that the limiting factor approaches that imposed by the environment, as discussed in Sec. V D.

V. BEAMFORMING PERFORMANCE WITH AT-SEA DATA

A. Creation of acoustically cluttered conditions

During the sea test, an effort was made to reduce the amount of acoustic contamination and interfering noise from sources such as transiting ships during the AUV events. (The interrogation pulses created once every 10 s by the acoustic navigation system and the pulses every 2–3 s from the AUV's steering system did contaminate the hydrophone ar-

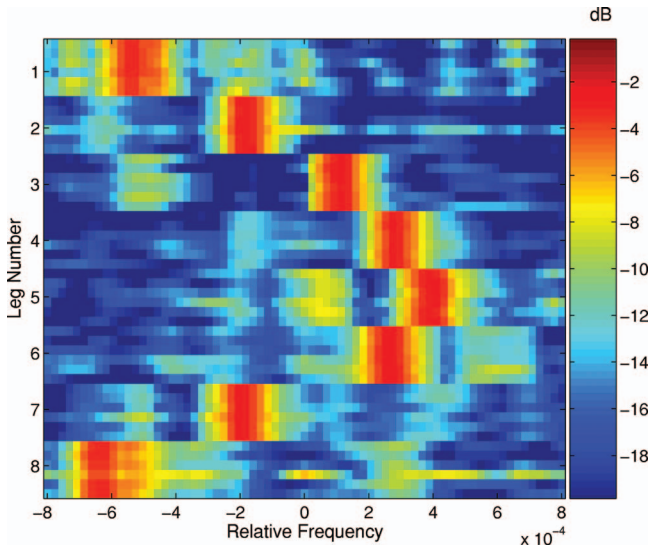

FIG. 5. Single element spectra from the data collected by the AUV-mounted hydrophones along each of the eight legs of the octagon event in Fig. 1 as a function of relative frequency. The time series used in calculating the spectra were combined so that two sources with exactly the same frequency content, the true one at an azimuth to the west-southwest (average azimuth of 254°) and a second, artificial one with 10 dB higher spectral levels to the south-southeast (at 164°), are present in the data. The spectra as a function of relative frequency were averaged over four frequencies centered at 220, 280, 370, and 460 Hz and normalized to a maximum value of 0 dB on each leg.

ray data, but no effort was made to extract them from the time series.) Therefore, acoustically cluttered conditions were created artificially with the AUV data. The approach was to add the time series recorded during one or more straight-line tracks ("legs") to those from the track of interest after multiplying by a factor less than one. Using this method, interfering sources of specified relative levels and at chosen locations with exactly the same frequency content as the source of interest could be generated. An important aspect of this approach is that the average AUV speed, changes in average direction of motion, and changes in average heading from one leg to the next are not quite equal, resulting in some smearing of the interfering source energy in the received spectra. These leg-to-leg variations in AUV velocity and heading changes can be corrected for with some preprocessing effort; however, that step has not been taken in the results presented in the following.

B. Passive synthetic aperture/Doppler beamforming results

The received spectra estimated from the data from six of the eight AUV-mounted hydrophones are plotted in Fig. 5. These data were recorded along each of the eight legs of the octagon event in Fig. 1; leg 1 is the westernmost leg where the AUV direction of motion was nearly due north and the final leg 8 was traversed in a direction to the northwest. For each leg number, listed along the vertical axis in Fig. 5, the six horizontal lines in the plot represent the six single element spectra collected by elements 1–4, 6, and 7. (Relative positions of these hydrophones are indicated in Fig. 3.) The time series processed for leg 1 were generated by first multiplying those originally recorded along leg 1 by a factor of 0.3 (equivalent to about 10-dB attenuation) and then adding those recorded during leg 3. Similarly, each subsequent leg's time series were attenuated by a factor of 0.3 and then added to those recorded two legs later in the sequence, e.g., the attenuated version of those from leg 2 were added to leg 4's time series, the attenuated leg 3 time series were added to those from leg 5, etc. Given that the source on FLIP was located to the west-southwest from the AUV tracks (average bearing of 254°), this process created an artificial source with exactly the same frequency content but with 10 dB greater levels at about 90° counterclockwise from the FLIP location, or at 164°.

The spectra from each leg's time series, generated by the above-noted method, was calculated from 52 s of data to provide a frequency resolution of 0.02 Hz. The normalized spectra are plotted in Fig. 5 as a function of relative frequency, $\hat{\omega}_r$, since statistical stability of the estimates was achieved by averaging over four tones with center frequencies of 220, 280, 370, and 460 Hz.

The results in Fig. 5 show that the lowest relative frequencies for the artificial high-level source at 164° were measured along legs 1 and 8 since the AUV was traveling in directions away from the source whereas leg 5's spectra contain the highest relative frequencies since the direction of motion was toward the source. The weaker (true) source at 254° also can be detected in the figure, particularly along leg 3 at about −5 relative frequency and along leg 5 just above 0. Since this weaker source, by construction, generates exactly the same set of signals as the higher-level interferer, it would not be detectable by a fixed omnidirectional receiver. By pushing and pulling energy around in the received spectrum, the motion of the AUV has improved detection under these anisotropic/spectrally nonwhite conditions.

The variations in received frequency as a function of AUV direction of motion, such as displayed in Fig. 5, can be combined in various ways to obtain directional estimates of the sound field. The results of conducting a simultaneous search for source frequency and source azimuth using the Doppler beamforming method described in Sec. II C are plotted in Fig. 6. Only the data collected by a single hydrophone were used in the processing. Also, only the 71 frequency bins about 220 Hz over the eight legs of the octagon event in Fig. 1 were included. Various intersecting arcs are present in the figure; their behavior is described by Eq. (14). The intersection of the reddest-colored arcs (highest sidelobes) indicates the beamformer's best estimate of the azimuth and frequency of the high-level source at about 164° azimuth.

In Fig. 7, the dotted curve is a 2D plot of the beamformer output extracted from Fig. 6 along the horizontal line at the source frequency with the maximum beamformer output. Also plotted with a solid curve are the results obtained by Doppler beamforming separately about center frequencies of 220, 280, 370, and 460 Hz, and then incoherently averaging the outputs (before conversion to decibels) after normalizing each to a maximum value of unity. Both curves show significant structure with a peak value close to, or at, the azimuthal location of the high-level source at 164°. (The peak value of the frequency-averaged curve is not 0 dB be-

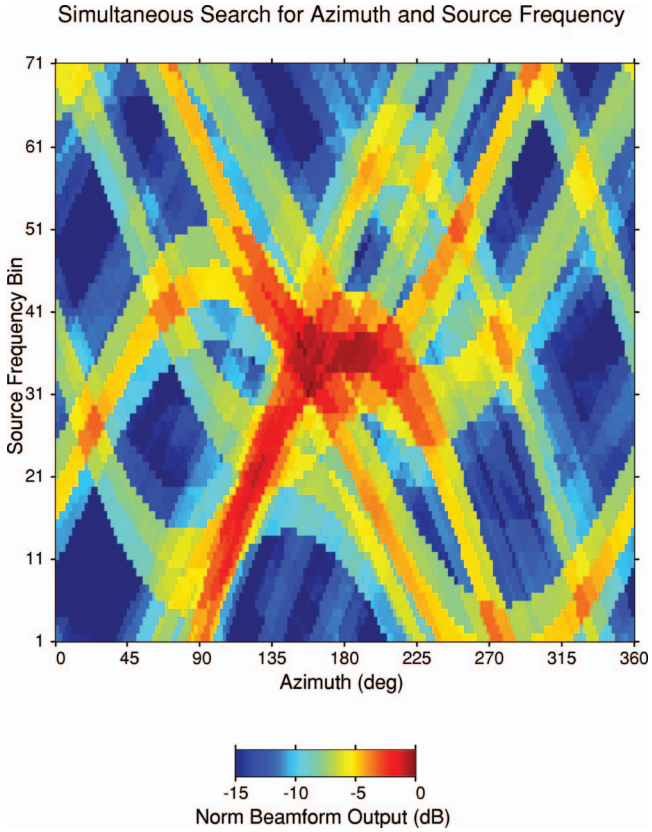

FIG. 6. Doppler beamformer output as a function of assumed source frequency and assumed source azimuth using the data collected by hydrophone 1 in Fig. 3 over the eight legs of the octagon-shaped event in Fig. 1. The 71 source frequency bins, each with 0.02-Hz resolution, are centered about 220 Hz. The time series were constructed as in Fig. 5 in order to contain two sources with identical frequency content.

cause the azimuths where the peak output occurs at each frequency are not quite the same.) In addition, both curves clearly show the weak source at 254° although the location of the peak is shifted 20° or so to greater azimuthal angles. The beamformer output peak for the weaker source is nearly equal in level and significantly narrower in azimuth in comparison to the artificial source with 10 dB greater received levels. One reason is that the variations in average AUV velocity from one leg to the next were not taken into account when creating the multisource time series, as explained earlier. This reason also helps explain the 20° bias in the weak

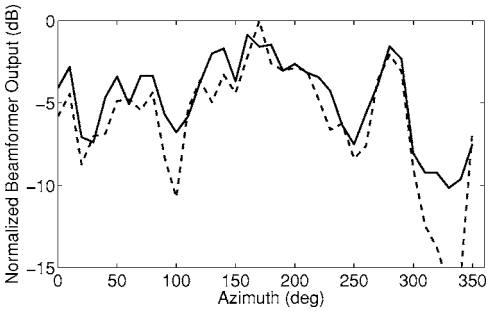

FIG. 7. Doppler beamformer output for hydrophone 1 at the source frequency with the maximum beamformer output in Fig. 6. The dotted curve is the normalized output at 220 Hz and the solid curve is the average of the normalized output for the four tones at 220, 280, 370, and 460 Hz.

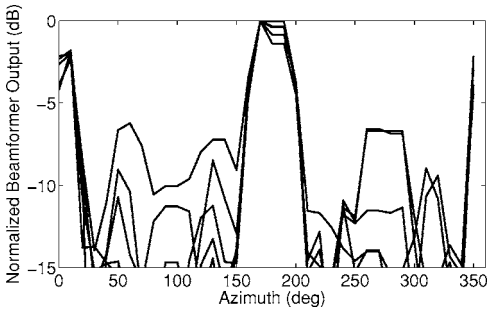

FIG. 8. Doppler beamformer output at 220 Hz for all 6 AUV hydrophones using only the time series collected along legs 1 and 3 (direction of motion to the north and to the east, respectively) of the octagon event shown in Fig. 1. All other aspects of the plot are the same as in Fig. 7.

source location; smearing of the high-level source results in a small error in estimated source frequency resulting in a shift along a sidelobe in the estimated weak source location. Another reason why the beamformer output levels for the weaker source are nearly equal to those of the stronger source is due to leakage of the stronger source energy on those legs where the Doppler-shifted energy from the two sources occurs near the same frequency. One way to reduce this leakage is to exclude from the integration those legs where significant leakage occurs, in effect creating a notch in the direction of the strong source. In any case, if the center frequency of the weak single-tone source is not assumed to be the same as that of the higher-level source, the color-scale plot in Fig. 6 illustrates the difficulty of finding this source with these single element data. Note that the width of the main lobe in Fig. 7 is increased by 25° or so, partly because of the actual difference in average source azimuth along one leg to the next. Since only 25% of the data collected on each leg is used in the processing, the octagon could have been one-fourth its size in Fig. 1.

The Doppler beamformer output as a function of assumed source frequency and look direction is the incoherent sum of the weighted spectral levels collected over a set of straight-line tracks. The frequency bins for each leg number are determined by cosine-dependent curves that are functions of assumed source frequency and look direction (Sec. II). Various weightings were used in summing the bin levels. Results from several events in the April, 2004 experiment indicate that a data-independent equal weighting ($w_n \sim 1/\mathrm{NT}$) provided slightly poorer results (i.e., sidelobes that were up to 2 dB higher) than normalizing the bin level by the average bin level in the processing band ($w_n \sim 1\Sigma_i^{\mathrm{NF}}(A_n^i)^2$). The output from this latter weighting was not statistically different than scaling each leg's spectrum in the processing band by the peak level in that band ($w_n \sim 1/(A_n^{\max})^2$). The results presented in Fig. 7 used this second data-adaptive peak level scaling, followed by the aforementioned normalization to a maximum 0-dB value across azimuth at each frequency.

One aspect of the beamforming process that has a significant effect on the results is the selection of the legs to include in the processing. For example, Fig. 8 shows the results of including only the first and third legs of the octagon event, i.e., those where the direction of motion was to

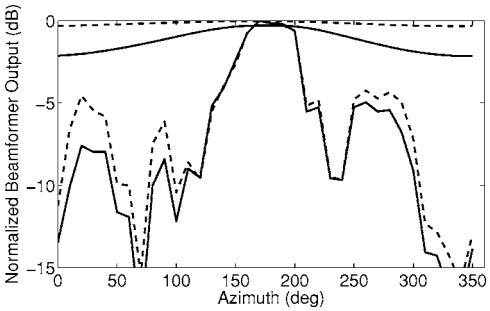

FIG. 9. Conventional (two dotted curves) and adaptive white-noise-constrained (two solid curves) beamformer output using only the physical aperture of the AUV array (upper two curves) and Doppler beamforming with the moving physical aperture (lower two curves). The processing was done for a single tone at 220 Hz.

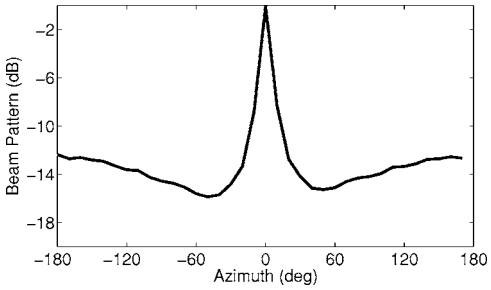

FIG. 10. The resampling beamformer beam pattern at 500 Hz for a complete circular track of radius 8.4 m traversed at a constant 1 m/s speed. The frequency resolution of the FFT used in the processing is 0.02 Hz.

the north and to the east, respectively. The peak for the high-level source is significantly narrower than in the previous figure for two reasons; no mismatch exists in the assumed and actual direction of motion changes between the two legs, and the actual bearings of the source for these two legs do not differ by a significant amount. Although the overall sidelobe level appears lower than in the previous figure, high sidelobes exist near 20° and 200° due to the left-right ambiguity in Doppler beamforming about 0° and 90° directions of motion. In addition, because only two legs have been summed, the statistical variability of the output is sufficiently large that it is difficult to detect the presence of the weaker source at 254°. As discussed in Sec. II C, the incoherent accumulation of the spectral energy in Doppler processing reduces the variance of the beamformer output estimate as the number of legs increase. Assuming energy from one leg to the next represents realizations of the same underlying χ^2 random process (the real and imaginary parts of the FFT in a given frequency bin are assumed to be independent and Gaussian distributed; Bendat and Piersol, 1986), and with equal weighting of the realizations, then confidence intervals can be placed on the beamformer output estimates. The 80% confidence limits for the beamformer output estimate with equal weighting that corresponds to the dotted curve in Fig. 7 are +2.4 to −1.7 dB, and +1.1 to −0.9 dB for the estimate corresponding to the solid curve.

The benefits of using Doppler/synthetic aperture beamforming techniques with moving physical aperture are illustrated in the lower two curves in Fig. 9. For comparison, the upper two curves in the figure show the beamforming results using physical aperture only. The physical array was created by hydrophone elements 1 through 4, 6, and 7 (see Fig. 3), forming a 2D square-shaped array with approximate 0.5-m length per side. The physical aperture-only results were obtained both by conventional and white-noise-constrained adaptive beamforming with frequency resolution of 0.61 Hz, 32 times poorer than the approximate 0.02-Hz resolution used for Doppler/synthetic aperture beamforming. The lower frequency resolution allowed for 32 nonoverlapping realizations of the data cross spectral density matrix along each leg, which were averaged together to obtain statistically stable estimates. The resulting directional estimates for each leg then were normalized to unity and incoherently averaged over all eight legs. Figure 9 shows that the overall dimension of the physical array, on the order of one-tenth of an acoustic wavelength at the frequencies of interest here, is too small by itself to resolve the presence of two sources even with white-noise-constrained adaptive beamforming. However, the combination of Doppler and physical aperture beamforming provides significantly improved results compared to either physical aperture alone (very broad main lobe) or Doppler beamforming with a single omnidirectional element (see Fig. 7; high sidelobes). The combined adaptive/Doppler beamforming approach gives lower sidelobes than that using conventional/Doppler beamforming.

As with the single-hydrophone results, the size of the octagon event with respect to the source/receiver range results in broadening of the peaks in Fig. 9, and the main peak is further broadened due to the method of creating multisource conditions. In the case of moving physical aperture, additional broadening of the high-level source peak occurs because the average heading of the AUV does not change by exactly the same amount from one leg to the next.

C. Results of applying the resampling beamformer

As discussed in Sec. III, the properties of the resampling beamformer are dictated by the character of the vehicle acceleration. A special case with interesting properties is that of circular motion at constant speed. Figure 10 shows the synthesized resampling beamformer beam pattern for AUV motion in the clockwise direction starting at 0°, at a constant speed of 1.0 m/s, and with a constant radius of curvature of 8.4 m. This value for the curvature allows the AUV to complete one circular track over the time period required for a FFT with 0.02-Hz resolution. In the figure, the true source location is at 0° azimuth and its transmitted signal is modeled as a single tone at 500 Hz. The resulting beam pattern shows a narrow main lobe with sidelobes at least 12 dB down from the main lobe peak level. This performance is achieved because of the spectral smearing effects of the centripetal acceleration associated with the small radius of curvature.

During the 2004 experiment, most of the tracks traversed by the AUV were designed to maintain constant speed and heading. However, significant vehicle accelerations occurred during turns from one straight track to the next. For example, the AUV event shown in Fig. 1 involved a sequence of 45° turns in which the vehicle traversed approxi-

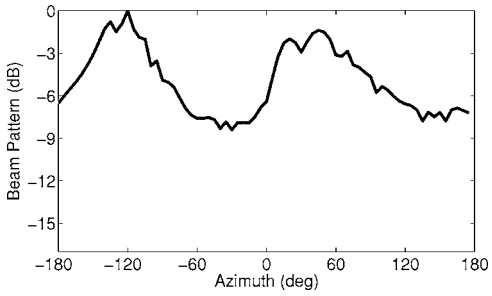

FIG. 11. The synthesized beam pattern for the resampling beamformer as a function of azimuth at 370 Hz using the actual DVL data recorded as the AUV was in the process of turning from the first to the second straight-track segment of the octagon event in Fig. 1.

mate circular arcs at a fairly constant speed. AUV data collected during the first turn, from a heading of due north to 45° east of north, were extracted to evaluate the beamforming performance of the resampling beamformer with at-sea AUV data. During this turn, the acoustic source deployed from FLIP was located at approximately endfire to the arc of the turn. The DVL data recorded during the turn indicate that the vehicle's direction of motion actually rotated through an angle of 60° and its speed increased from 0.9 to 1.0 m/s before settling on the second leg. The synthesized beam pattern for the resampling beamformer at 370 Hz using the actual DVL data from this time period is plotted in Fig. 11. The hydrophone time series were synthesized using a source transmitting the 370-Hz tone signal at an azimuth of −130° in the plot, corresponding to the actual bearing of FLIP of 230° true. In addition to the main lobe, a high sidelobe exists in the 10° to 50° azimuth interval. It is due to the ambiguity about the broadside direction for circular-type motion as discussed in Sec. III. That is, the average AUV direction of motion during the turn was about 35° so that broadside was at 125°. Given the true source azimuth of 230° (equal to −130°), then a high sidelobe can be expected to occur around 20°, corresponding to the sidelobe location in Fig. 11. The results of resampling the actual individual AUV hydrophone time series recorded during the turn for the 370-Hz tone transmitted from FLIP are displayed in Fig. 12. The original hydrophone time series recorded at sea were used in the processing rather than an artificial multisource data set as in the

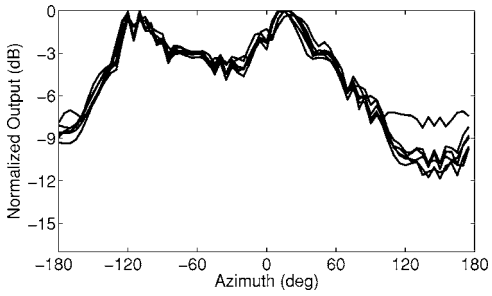

FIG. 12. The results for 370 Hz of applying the resampling beamformer to the time series of six of the eight AUV-mounted hydrophones during the turn from the first to the second straight-track segment of the octagon event in Fig. 1.

previous part of this section. The behavior of these curves agrees quite well with that expected from the beam pattern plot in Fig. 11.

D. Effects of environmental fluctuations

Frequency spreading imparted by the environment is a result both of multipath (e.g., different modes are Doppler shifted by different amounts) and also of the time-varying motion of the medium. The former is determined by the spatial bandwidth of the underwater channel and is discussed in Sec. II D. Once variations in vehicle velocity are taken into account (e.g., by the resampling beamformer), the combination of these two environmental effects determines the degree of frequency spreading measured during the experiment. This part of the section is devoted to the effects of temporal fluctuations in the medium. These medium fluctuations must involve accelerations of the fluid in order to induce a Doppler shift; a steady current flow does not Doppler shift an acoustic field propagating between a fixed source and a fixed receiver (Salmon, 1998).

For a pure tone signal of finite duration, its spectrum is the sinc squared function. In the examination of the frequency spreading of single tone transmissions caused by propagation effects, sufficiently long time series were used so that the width of the sinc squared function's main lobe was significantly narrower than the measured frequency spreading.

Very long FFTs of time series recorded with high received signal-to-noise ratio from moored source transmissions to ocean bottom hydrophones over ranges from 1 to 4 km were used to characterize the frequency spreading in the reception of single tone signals. It was found that the quantity $\Delta\omega/\omega_c$, where $\Delta\omega$ is the spread about the center frequency ω_c, was approximately frequency independent over two decades from 70 Hz to 7 kHz. Calibration data collected in a large, fresh water tank verify that the energy spreading observed at sea is significantly greater than that caused by the combined acoustic source transmission system and AUV hydrophone data acquisition system. The frequency spreading measured at sea was most often approximately Gaussian distributed with a standard deviation of roughly order $\Delta\omega/\omega_c \approx 0.001\%$, somewhat smaller than the estimated spreading due to multipath (see Sec. II D) and to variations in vehicle velocity along straight-line tracks (see Sec. IV). (The spreading during a few time periods showed a surprisingly different behavior which was correlated with the character of the ocean surface wave activity; Lynch, D'Spain, and Terrill, 2004). The skewness of the spectral energy distributions is approximately zero, suggesting that the spreading is caused by processes with equal average amounts of forward and backward motion along the trajectory between source and receiver. This property is a basic aspect of the orbital motion of oceanographic waves such as ocean surface and internal waves. The effective range-integrated speeds of water motion projected along the propagation path that give rise to this Doppler spreading are up to 0.03 m/s [equal to $2c\ (\Delta\omega/\omega_c)$]. The kurtosis of the energy distributions also is nearly zero. Gaussian spreading in the

spectrum recorded by a fixed receiver of a single tone transmitted from a stationary source is equivalent to Gaussian modulation of the autocorrelation of the sinusoid in the time domain. This Gaussian modulation of the autocorrelation is a direct measure of the temporal decorrelation caused by the environment and $1/\Delta\omega$ is a quantitative measure of temporal decorrelation. The effects of this type of noise, appropriately modeled as multiplicative noise (rather than the typical additive noise), cannot be reduced by increasing the level of the transmitted signal. It is rarely taken into account in sonar and radar system design (Tuzlukov, 2002).

VI. ACTIVE CONTROL OF PASSIVE ACOUSTIC FIELDS

A. Basic formulation

An autonomous vehicle is capable of pushing and pulling acoustic energy around in the received pressure spectrum through its motion. Therefore, it has the potential to adjust its motion to optimize extraction of information of interest. For example, the previous section demonstrated the results of Doppler shifting a low-level signal with respect to a high level interferer with exactly the same inherent frequency content. Receiver motion can increase detection capability under anisotropic, spectrally nonwhite noise conditions. Moving toward a source both shifts the received spectrum to higher frequencies and increases its spectral bandwidth slightly. In contrast, motion away from a source shifts the received spectrum to lower frequencies and compresses the spectral bandwidth. Without additional knowledge about the spectral characteristics of a signal of interest, the best strategy is to initially move away from an interferer (assuming the fixed receiver is able to estimate the direction toward the interferer). However, autonomous vehicles have a limited amount of on-board propulsion energy to effect this motion. Therefore, an important issue is the proper strategy for a vehicle to use to most effectively accomplish a given objective given this energy constraint. The issue of receiver strategies is pursued further in this section for the case of a single omnidirectional receiver moving at constant velocity.

One problem of this type can be formulated in the following way. Assume that the AUV's goal is to optimize detection at a specific frequency, ω_0, and in a specific direction, $\hat{k}_0$, in the presence of a known interference distribution, $S_N(\omega,\hat{k})$. The vehicle's speed and direction of motion are v_r and Ψ_r, respectively. Therefore, the frequency of interest in the received spectrum is

$$\omega_0^r(t) = \omega_0\left[1 + \frac{v_r}{c_p}\cos[\theta(\hat{k}_0) - \Psi_r]\right]. \tag{24}$$

The question is what motion should the vehicle undergo in order to minimize the contribution from the interferers to the received energy at ω_0^r. The processing approach employed will be the Doppler/synthetic aperture beamforming discussed in Sec. II. Also, the duration of time spent on any track is assumed fixed; only the vehicle speed and vehicle heading are allowed to vary from one straight-line track to the next in order to minimize the interferers' effects. The contribution of an interferer in direction $\hat{k}$ to the received acoustic energy at the desired received frequency is that from the frequency ω_s such that

$$\omega_0^r = \omega_0\left[1 + \frac{v_r}{c_p}\cos[\theta(\hat{k}_0) - \Psi_r]\right] = \omega_s\left[1 + \frac{v_r}{c_p}\cos[\theta(\hat{k}) - \Psi_r]\right]. \tag{25}$$

Therefore, the optimization problem is to determine $\underline{v}_r$ (with components v_r and Ψ_r) in order to minimize

$$\min_{\underline{v}_r}\{S_I^r(\omega_0^r)\} = \min_{\underline{v}_r}\left\{\sum_{n=1}^{Nsrc} S_N^n(\omega_s^n)\right\}. \tag{26}$$

The quantity $S_I^r(\omega)$ is the received spectrum from the interfering sources, $S_N(\omega,\hat{k})$ (measured by a fixed receiver) is modeled as the sum of *Nsrc* interfering sources with the *n*th source having spectrum $S_N^n(\omega)$, and where

$$\omega_s^n = \omega_0\left[\frac{1 + (v_r/c_p)\cos[\theta(\hat{k}_0) - \Psi_r]}{1 + (v_r/c_p)\cos[\theta(\hat{k}_n) - \Psi_r]}\right]. \tag{27}$$

A somewhat different approach to this problem is to maximize the spacing between the center frequency of the interfering spectral peaks and the frequency of interest. That is, the AUV motion, v_r and Ψ_r, is sought to maximize the following sum of weighted squared differences:

$$\max_{\underline{v}_r}\{\mathrm{SS}\} \equiv \max_{\underline{v}_r}\left\{\sum_{n=1}^{Nsrc} a_n(\omega_I^n - \omega_0^r)^2\right\}, \tag{28}$$

where a_n is a weighting that depends upon the *n*th interfering peak's spectral level and bandwidth around its received center frequency, ω_I^n. Setting to zero the partial derivatives of the weighted sum of squared differences in Eq. (28) with respect to direction of motion and speed gives

$$\frac{\partial \mathrm{SS}}{\partial \Psi_r} = 0 = \sum a_n(\omega_I^n - \omega_0^r)\left[\frac{\partial \omega_I^n}{\partial \Psi_r} - \frac{\partial \omega_0^r}{\partial \Psi_r}\right], \tag{29a}$$

$$\frac{\partial \mathrm{SS}}{\partial v_r} = 0 = \sum a_n(\omega_I^n - \omega_0^r)\left[\frac{\partial \omega_I^n}{\partial v_r} - \frac{\partial \omega_0^r}{\partial v_r}\right], \tag{29b}$$

These two equations result in

$$\sum a_n(\omega_s^n - \omega_0)\{\omega_s^n \sin[\theta_s^n - \Psi_r] - \omega_0 \sin[\theta_0 - \Psi_r]\} = -\frac{v_r}{c_p}\sum a_n\{\omega_s^n \cos[\theta_s^n - \Psi_r] - \omega_0 \cos[\theta_0 - \Psi_r]\} \times\{\omega_s^n \sin[\theta_s^n - \Psi_r] - \omega_0 \sin[\theta_0 - \Psi_r]\}, \tag{30a}$$

$$\sum a_n(\omega_s^n - \omega_0)\{\omega_s^n \cos[\theta_s^n - \Psi_r] - \omega_0 \cos[\theta_0 - \Psi_r]\} = -\frac{v_r}{c_p}\sum a_n\{\omega_s^n \cos[\theta_s^n - \Psi_r] - \omega_0 \cos[\theta_0 - \Psi_r]\}^2. \tag{30b}$$

[Note that Eqs. (29a) and (29b) are functions of the frequencies, ω_I^n and ω_0^r, as measured by a moving receiver, whereas

Eqs. (30a) and (30b) pertain to frequencies, ω_s^n and ω_0, measured by a fixed receiver.]

B. One interfering source

It is revealing to examine the results of these equations in the limiting case of a single interfering source at circular frequency ω_s. Then

$$\mathrm{SS} = \left[(\omega_s - \omega_0) + \frac{v_r}{c_p}[\omega_s \cos[\theta_s - \Psi_r] - \omega_0 \cos[\theta_0 - \Psi_r]] \right]^2. \tag{31}$$

This equation shows that in most cases, Ψ_r can be chosen so that the squared difference can increase without bound by increasing the AUV speed, v_r. In effect, minimizing contamination by interfering noise sources is achieved by the receiver traveling as fast as possible in order to maximize its ability to push and pull acoustic energy around in the received spectrum. However, since an underwater vehicle cannot go arbitrarily fast, an upper bound, $v_r^{\max}$, must be set. (An alternative approach is to incorporate a vehicle-specific energy efficiency curve in the formulation, as discussed in Sec. VI C). Therefore, only the vehicle direction of motion, Ψ_r, and its corresponding Eq. (30a) need to be considered in the present optimization problem. For a single interfering source, it becomes

$$\begin{aligned}(\omega_s - \omega_0)\{\omega_s \sin[\theta_s - \Psi_r] - \omega_0 \sin[\theta_0 - \Psi_r]\} \\ = -\frac{v_r^{\max}}{c_p}\{\omega_s \cos[\theta_s - \Psi_r] - \omega_0 \cos[\theta_0 - \Psi_r]\} \\ \times \{\omega_s \sin[\theta_s - \Psi_r] - \omega_0 \sin[\theta_0 - \Psi_r]\}.\end{aligned} \tag{32}$$

If the term involving the difference of sines that appears on both sides of the equation is canceled, then the resulting expression can only be satisfied when $\omega_s \approx \omega_0$, yielding $\cos[\theta_s - \Psi_r] \approx \cos[\theta_0 - \Psi_r]$. Equation (31) shows that this result gives $\mathrm{SS} \approx 0$, providing a minimum of SS rather than a maximum, and so can be discarded. Therefore, the useful result from Eq. (32) is to choose Ψ_r such that

$$\omega_s \sin[\theta_s - \Psi_r] = \omega_0 \sin[\theta_0 - \Psi_r]. \tag{33}$$

This expression can be solved graphically. In the special case of $\omega_s = \omega_0$, the solution for the vehicle direction of motion that maximizes SS can be obtained analytically and is

$$\Psi_r = \frac{\theta_s + \theta_0}{2} \pm \frac{\pi}{2}. \tag{34}$$

That is, the optimal direction of motion for the AUV is at a right angle to the average of the interfering source direction and the direction of interest. This direction of motion maximizes the difference in Doppler shift from these two directions.

C. Constraints on vehicle motion

In the preceding discussion, a simple constraint on vehicle motion was incorporated by placing an upper limit on speed. A more realistic approach is to determine a cost function associated with the amount of energy expended by the vehicle during motion. If $f(v_r)$ represents this cost of motion, then Eq. (28) becomes

$$\max_{v_r}\{\mathrm{SS}\} \equiv \max_{v_r}\left\{ \frac{1}{f(v_r)} \sum_{n=1}^{Nsrc} a_n(\omega_I^n - \omega_0^r)^2 \right\}. \tag{35}$$

With this formulation, Eqs. (29a) and (30a) remain unchanged. However, in Eq. (29b), rather than the right-hand side being equal to zero, it is

$$\begin{aligned}\sum a_n(\omega_I^n - \omega_0^r)\left[\frac{\partial \omega_I^n}{\partial v_r} - \frac{\partial \omega_0^r}{\partial v_r} \right] \\ = \frac{1}{2}\left[\sum a_n(\omega_I^n - \omega_0^r)^2\right] \frac{1}{f^2(v_r)} \frac{\partial f(v_r)}{\partial v_r}.\end{aligned} \tag{36}$$

Rewriting gives

$$\begin{aligned}\sum a_n(\omega_I^n - \omega_0^r)\left[\frac{\partial \omega_I^n}{\partial v_r} - \frac{\partial \omega_0^r}{\partial v_r} - \frac{1}{2}\frac{1}{f^2(v_r)} \frac{\partial f(v_r)}{\partial v_r}(\omega_I^n - \omega_0^r) \right] \\ = 0.\end{aligned} \tag{37}$$

As before, insight into the character of Eq. (37) can be obtained by considering a single interferer. The solution of setting $(\omega_I - \omega_0^r)$ equal to zero yields a minimum value for SS, as Eq. (35) shows, and so can be discarded. Therefore, the useful solution is determined by setting the term in brackets in Eq. (37) to zero, which again can be found graphically. When $\omega_s = \omega_0$, the analytical solution is

$$\begin{aligned}\left[\frac{1}{2}\frac{1}{f^2(v_r)} \frac{\partial f(v_r)}{\partial v_r} v_r - 1 \right][\cos[\theta_s - \Psi_r] - \cos[\theta_0 - \Psi_r]] \\ = 0.\end{aligned} \tag{38}$$

The left-hand term in square brackets provides the optimal solution for v_r, which is independent of vehicle heading. As an example, assume the vehicle speed cost function has the form

$$f(v_r) = a_0 + a_3 v_r^3. \tag{39}$$

This expression is based on the fact that vehicle drag forces typically scale as the square of the speed so that the mechanical power expended to overcome these forces scale with speed cubed. The a_0 term represents speed-independent "overhead" (e.g., vehicle hotel and payloads). Plugging this expression into the left-hand term in square brackets in Eq. (38) gives

$$2a_3^2 v_r^6 + (4a_0 a_3 - 3a_3)v_r^3 + 2a_0^2 = 0. \tag{40}$$

Application of the quadratic formula gives

$$v_r^3(\mathrm{opt}) = \frac{(3 - 4a_0) \pm \sqrt{9 - 24a_0}}{4a_3}. \tag{41}$$

Equation (41) shows that the optimal vehicle speed is inversely proportional to the cube root of the coefficient for the speed cubed term in Eq. (39), with smaller coefficients leading to higher optimal speeds, and vice versa.

TABLE I. The azimuth, center frequency, spectral level, and frequency spread of the three Gaussian-shaped spectral peaks that comprise the anisotropic (interference) component of the noise field.

Azimuth (deg)	Center freq (Hz)	Spectral peak level (linear units)	Spread s.d. (linear units)
0	500	1.0	0.1
90	501	1.0	1.0
180	500	0.5	0.1

D. Multiple interfering sources

In the general case of multiple interfering spectral peaks, the equations for the optimal AUV velocity involve the weighted sum of transcendental functions which can only be solved using numerical techniques. A synthetic example is presented in this part of the section to illustrate some of the concepts.

Consider an interference field composed of three spectral peaks arriving from 0°, 90°, and 180°. These peaks are modeled as Gaussian functions with center frequencies, peak levels, and spectral bandwidths (as measured by a stationary receiver) listed in Table I. Isotropic background noise with a level one-tenth that of the two highest spectral peaks is added to the interference field. The received levels as a function of frequency bin number (corresponding to 497.3–504.7 Hz) and as a function of AUV direction of motion for a fixed speed of 2.0 m/s are shown in Fig. 13. Optimal directions of motion for a given frequency band and look direction of interest are those along the appropriate cosine-varying curve where the received levels are lowest. As an example, if the desired look direction is 315° at a source frequency of 500 Hz (bin No. 140), then the optimal direction of motion is 110°.

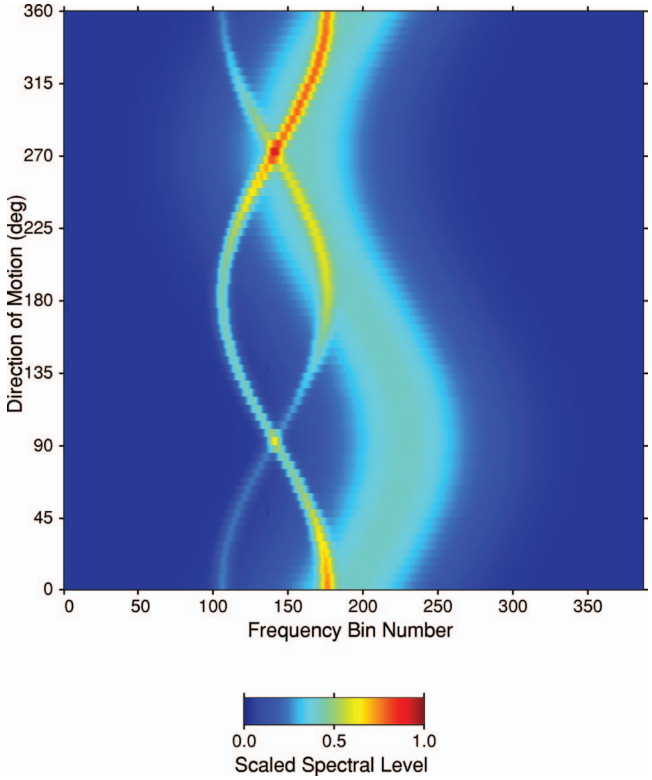

FIG. 13. Simulation of the scaled received spectrum as a function of the direction of motion for an AUV traveling in a straight line at a constant speed of 2 m/s. The horizontal axis spans the band from 497.3 to 504.7 Hz. The noise field is composed of three sources; at 0° with 500-Hz center frequency, 90° with a center frequency of 501 Hz, and at 180° with 500-Hz center frequency. The source spectra are modeled as Gaussian functions with parameters given in the text.

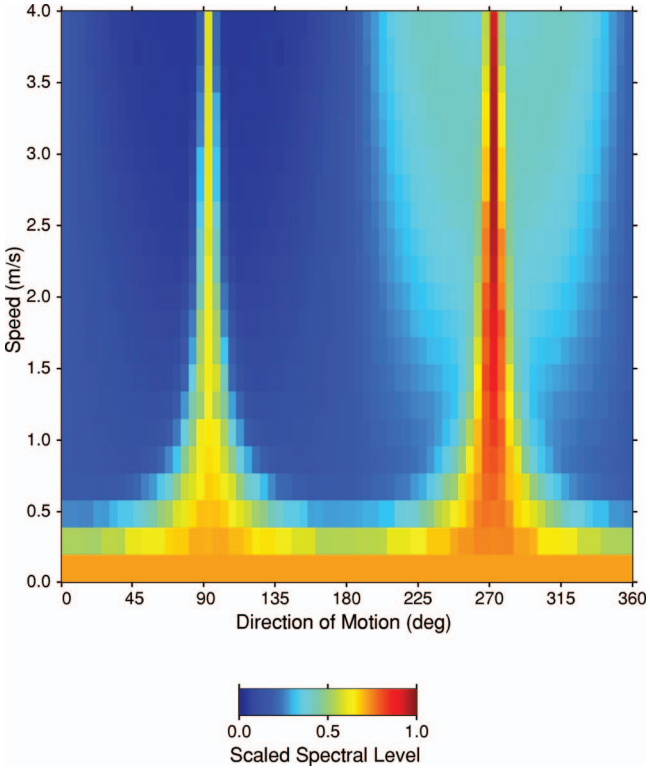

FIG. 14. Simulation of the scaled received spectrum at 500.0 Hz as a function of receiver speed and direction of motion for the case of a speed-independent energy cost function. The characteristics of the noise sources are the same as in Fig. 13.

The corresponding plot of received level as a function of AUV direction of motion and vehicle speed at a frequency of 500.0 Hz is shown in Fig. 14. The cost-of-motion function, $f(v_r)$, is set to a speed-independent value of 3/8. The plot shows that the lowest received levels in the 500.0 Hz bin are achieved by traveling at high speeds to the east-northeast (40°–70°) or to the east-southeast (110°–140°). Motion due east or due west leaves the energy from the interferers at 0° and 180° in the received frequency band of interest (vertical red and yellow lines in Fig. 14) and motion in westerly directions pulls some of the broader-band contamination centered at 501 Hz to lower frequencies.

The effects of incorporating a more realistic cost-of-motion function in the search for the optimal receiver speed is shown in Fig. 15. The function has the form given by Eq. (39) with $a_0=3/8$ and $a_3=1/5$. High AUV speeds are penalized so that the optimal speed in Fig. 15 is 0.8 m/s at a 35° direction of motion whereas it is as large as possible at either 45° or 135° in Fig. 14.

This synthetic example illustrates that significant improvements in array performance can be obtained by Doppler/passive synthetic aperture processing in anisotropic/spectrally nonwhite noise conditions. Because an autono-

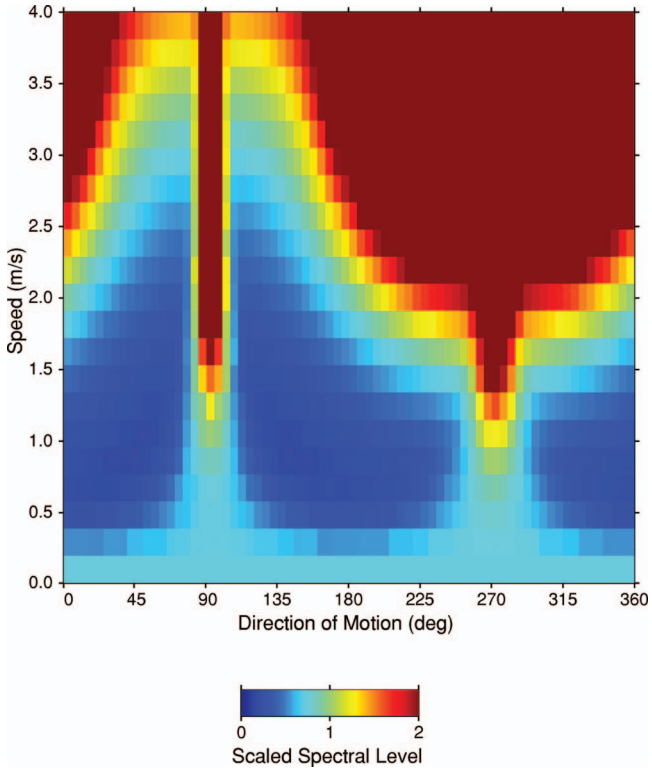

FIG. 15. The same simulation as in Fig. 14 but now with an energy cost function that varies with the cube of the receiver speed (see the text for details).

mous vehicle has control over its motion, it can manipulate the changes in the received field resulting from its motion to optimize extraction of information of interest. With this approach, the vehicle capabilities and characteristics become an integral part of the array processing structure.

VII. CONCLUSIONS

Underwater autonomous vehicles provide unique opportunities and considerations in the passive measurement of ocean acoustic fields. They have the ability to adapt and maneuver in response to received sounds in their environment. Even more so, they can alter the structure of received signals to optimize extraction of information of interest. One way of actively modifying the character of received sounds is through motion, as discussed in this paper. However, motion requires expenditure of energy, in limited supply on autonomous vehicles. Therefore, these energy costs must be accounted for in developing vehicle measurement strategies. In fact, the characteristics of the autonomous vehicle, e.g., its maneuverability and energy efficiency, become an integral part of the signal and array processing.

One processing approach used in this paper to form the basis of active control of received acoustic fields through motion is Doppler beamforming. Passive synthetic aperture processing is equivalent to Doppler beamforming under certain conditions (Autrey, 1988; Carey, 1989). Therefore, rather than formulate the passive synthetic aperture beamforming problem in space and spatial frequency (bearing), an alternative approach is to remain in the time and temporal frequency domains. As a result, all the techniques developed for spectral estimation, including high-resolution methods, can be applied to the passive synthetic aperture problem. The trade-off between time and space in passive synthetic aperture processing equates to a trade-off between temporal frequency and spatial frequency. Therefore, in order to achieve large array gains from synthetic aperture processing in anisotropic noise conditions (Sullivan, Carey, and Stergiopoulos, 1992), spectrally nonwhite conditions must also exist. A ubiquitous example of an interfering noise source in ocean acoustics that creates anisotropic, spectrally nonwhite conditions at low frequencies are transiting surface ships (e.g., Ross, 1987).

The results presented in this paper demonstrate the use of passive synthetic aperture/Doppler beamforming with low frequency ocean acoustic data collected by a hydrophone array mounted on the hull of an older-model AUV. Whereas active synthetic aperture methods place stringent requirements on vehicle navigation and stability because the same region of the surface or object of interest at close range must be repeatedly imaged, the requirements in the passive case are more lax. Vehicle velocity, both speed and direction of motion, is the critical quantity and can be measured by a Doppler velocity logging (DVL) instrument. In addition, an attitude/heading reference system (AHRS) is important for measuring vehicle orientation, particularly heading, in cases of moving physical aperture.

Various algorithms are introduced and demonstrated with the AUV hull-mounted hydrophone array data, under both single and multiple source conditions. A stationary source approximation is employed to reduce the number of source unknowns from four (source frequency, speed, direction of motion, and azimuth) to two (effective source frequency and azimuth). These unknowns are resolved by forming synthetic aperture in two or more horizontal directions. The Doppler/synthetic aperture processing approach involves incoherent accumulation of spectral energy obtained along each of a set of straight-line tracks. The accumulation is performed along cosine-shaped trajectories in the frequency domain that are specified by the assumed effective source frequency and look direction, providing estimates of these source properties as well as statistically independent realizations to reduce the variance of the beamformer output estimate. In the simultaneous search for source frequency and azimuth, the beamformer sidelobes for a single moving receiver in the source frequency/azimuth plane follow smooth, sinusoidally varying trajectories whose behavior can be quantified by a perturbation approach.

The approach with moving physical aperture is to perform Doppler/passive synthetic aperture beamforming in each of the physical array beams. The complex element weights to form these beams are derived by either a conventional or adaptive beamforming method. They are determined at a courser frequency resolution than that used with the Doppler beamforming in order to obtain a statistically stable estimate of the physical array data cross spectral density matrix on a given leg. Results using the AUV data show that white-noise-constrained adaptive beamforming applied to the physical aperture data and combined with high-frequency-resolution Doppler beamforming gives much

greater spatial resolution than beamforming with physical aperture alone (the characteristic overall dimension of the physical array is order one-tenth that of the acoustic wavelengths of interest). It also provides somewhat lower sidelobes than when conventional beamforming is used instead with the physical aperture data, and significantly lower sidelobes compared to Doppler beamforming with single hydrophone elements. This combined approach allows a 10-dB lower-level source with exactly the same frequency content as that of an interfering source to be clearly identified in the beamforming output.

A new type of beamformer is defined and demonstrated with the AUV data. The "resampling beamformer" accounts for variations in receiver velocity on a data sample by sample basis by resampling the time series with a time-dependent sampling rate that exactly compensates for the time-dependent Doppler shifts resulting from the known receiver velocity variations. This resampling is broadband since it operates in the time domain and so works for all frequencies simultaneously. It results in high-resolution estimates of the directionality of the sound field during high vehicle accelerations such as those during tight maneuvers and start-up/slow-down in transitions between resting and actively mobile states. Once correction for variations in receiver velocity is made by the resampling process, the limitation in Doppler/synthetic aperture beamforming with this experimental data set approaches that caused by the frequency spreading imparted by the environment.

Finally, the concept of active control of passive acoustic fields through receiver motion is further investigated through simulation. The problem is to determine at what speed and in what direction an AUV should move to optimize detection of a weak signal in a specified frequency band and in a given direction, given the spatial and temporal frequency distribution of a set of noise interferers. In the case of a single interferer with a center frequency in the middle of the frequency band of interest (as measured by a stationary receiver), analytical results show that the optimal direction of motion is at right angles to the average of the azimuth of the interferer and the azimuth of interest. In determining optimal vehicle speed, a function expressing the cost of motion must be incorporated into the formulation to prevent the optimal speed from increasing without bound. For a cost function that varies with the cube of the vehicle speed (vehicle drag typically depends on the speed squared so that the mechanical power required to overcome the drag varies as the speed cubed), the optimal vehicle speed in the case of a single interferer with identical frequency is inversely proportional to the cube root of the coefficient for the speed cubed term in the cost function, with smaller coefficients leading to higher optimal speeds, and vice versa. In the general case of several spatially distributed interferers with different spectral levels and frequency content, the solution must be determined numerically, as illustrated by a simulation with three interfering sources at different azimuths and slightly different frequencies. The simulation further emphasizes that for these types of problems, the autonomous vehicle characteristics are an integral part of the signal/array processing structure.

ACKNOWLEDGMENTS

Richard Zimmerman, Dennis Rimington, and David Price at the Marine Physical Laboratory provided all the engineering support for the AUV operations in the 2004 experiment. Galina Rovner did most of the data processing and Scott Jenkins provided information on the speed dependence of the cost of vehicle motion. Dave Ensberg, Heidi Batchelor, and Neil Kussat at MPL helped with at-sea data collection. The assistance of the crews of the R/P FLIP and R/V Sproul is greatly appreciated. This work was supported by the Office of Naval Research, Code 321(US) as part of the Applied Research Laboratory program at the Marine Physical Laboratory.

Autrey, S. W. (**1988**). "Passive synthetic arrays," J. Acoust. Soc. Am. **84**, 592–598.

Bendat, J. S., and Piersol, A. G. (**1986**). *Random Data: Analysis and Measurement Procedures* (Wiley, New York), 2nd ed.

Carey, W. M. (**1989**). "Commits on "Passive synthetic arrays" [J. Acoust. Soc. Am. 84, 592–598 (1988)]," J. Acoust. Soc. Am. **85**, 1372.

Cox, H., Zeskind, R. M., and Owen, M. M. (**1987**). "Robust adaptive beamforming," IEEE Trans. Acoust., Speech, Signal Process. **35**(10), 1365–1376.

D'Spain, G. L., Hodgkiss, W. S., and Edmonds, G. L. (**1991**). "Energetics of the deep ocean's infrasonic sound field," J. Acoust. Soc. Am. **89**(3), 1134–1158.

Edelson, G. S., and Sullivan, E. J. (**1991**). "On the performance of the overlap-correlator synthetic-aperture technique," J. Acoust. Soc. Am. **90**(4), 2000–2003.

Edelson, G. S., and Sullivan, E. J. (**1992**). "Limitations on the overlap-correlator method imposed by noise and signal characteristics," IEEE J. Ocean. Eng. **OE-1**, 30–39.

Fitzgerald, R. M., Guthrie, A. N., and Shaffer, J. D. (**1976**). "Low-frequency coherence transverse to the direction of propagation," J. Acoust. Soc. Am. **60**, 752–753.

Glegg, S. A. L., Olivieri, M., Coulson, R. K., and Smith, S. M. (**2001**). "A passive sonar system based on an autonomous underwater vehicle," IEEE J. Ocean. Eng. **26**(4), 700–710.

Gramann, R. A. (**1992**). "ABF algorithms implemented at ARL-UT," ARL Tech. Letter ARL-TL-EV-92-31, Applied Research Laboratories, The University of Texas at Austin, Austin, TX.

Kussat, N. H., Chadwell, C. D., and Zimmerman, R. (**2005**). "Absolute positioning of an autonomous underwater vehicle using GPS and acoustic measurements," IEEE J. Ocean. Eng. **30**(1), 153–164.

Lynch, S. D., D'Spain, G. L., and Terrill, E. (**2004**). "Internal- and surface-wave-induced fluctuations and frequency spreading in shallow water acoustic propagation over short ranges," J. Acoust. Soc. Am. **116**(4), 2534–2535.

National Research Council (**1996**). *Undersea Vehicles and National Needs* (National Academy Press, Washington, DC).

National Research Council (**2004**). *Future Needs in Deep Submergence Science; Occupied and Unoccupied Vehicles in Basic Ocean Research* (National Academy Press, Washington, DC).

Noble, B. (**1969**). *Applied Linear Algebra* (Prentice-Hall, New York).

Nuttall, A. H. (**1992**). "The maximum likelihood estimator for acoustic synthetic aperture processing," IEEE J. Ocean. Eng. **OE-1**, 26–30.

Pierce, A. D. (**1989**). *Acoustics; An Introduction to Its Physical Principles and Applications* (Acoustical Society of America, New York).

Roderick, W. I., Maiocco, L. M., and Kanabis, W. G. (**1989**). "Project DIVA-deep integrating virtual aperture," J. Underwater Acoustics **2**, 157–167.

Ross, D. (**1987**). *Mechanics of Underwater Noise* (Peninsula, Los Altos, CA).

Salmon, R. (**1998**). *Lectures on Geophysical Fluid Dynamics* (Oxford University Press, New York).

Stergiopoulos, S. (**1990**). "Optimum bearing resolution for a moving towed array and extension of its physical aperture," J. Acoust. Soc. Am. **87**, 2128–2140.

Stergiopoulos, S., and Sullivan, E. J. (**1989**). "Extended towed array processing by an overlap correlator," J. Acoust. Soc. Am. **86**, 158–171.

Stergiopoulos, S., and Urban, H. (**1992a**). "A new passive synthetic aperture technique for towed arrays," IEEE J. Ocean. Eng. **OE-1**, 16–25.
Stergiopoulos, S., and Urban, H. (**1992b**). "An experimental study in forming a long synthetic aperture at sea," IEEE J. Ocean. Eng. **OE-1**, 62–72.
Sullivan, E. J. (**2003**). "Passive acoustic synthetic aperture processing," IEEE J. of Oceanic Engineering Soc. Newsletter **38**(1), 21–24.
Sullivan, E. J., and Candy, J. V. (**1997**). "Space-time array processing: The model-based approach," J. Acoust. Soc. Am. **102**(5), 2809–2820.
Sullivan, E. J., Carey, W. M., and Stergiopoulos, S. (**1992**). "Guest Editorial," IEEE J. Ocean. Eng. **OE-1**, 1.
Tuzlukov, V. P. (**2002**). *Signal Processing Noise* (CRC Press, New York), 663 pp.
Urick, R. (**1983**). *Principles of Underwater Sound*, 3rd ed. (McGraw-Hill, New York).
Williams, R. E. (**1976**). "Creating an acoustic synthetic aperture in the ocean," J. Acoust. Soc. Am. **60**, 60–73.
Williams, R., and Harris, B. (**1992**). "Passive acoustic synthetic aperture processing techniques," IEEE J. Ocean. Eng. **OE-1**, 8–15.
Yen, N. C., and Carey, W. (**1989**). "Application of synthetic-aperture processing to towed array data," J. Acoust. Soc. Am. **86**, 754–765.
Zimmerman, R., D'Spain, G. L., and David Chadwell, C. (**2005**). "Decreasing the radiated acoustic and vibration noise of a mid-size AUV," IEEE J. Ocean. Eng. **30**(1), 179–187.

Studying the mechanical behavior of a plastic, shock-resisting, antitank landmine

W. C. Kirkpatrick Alberts II,[a] Roger Waxler, and James M. Sabatier
National Center for Physical Acoustics, University of Mississippi, University, Mississippi, 38677

(Received 21 April 2006; revised 29 August 2006; accepted 3 September 2006)

Modal behavior in landmines has recently become a topic of interest for acoustic landmine detection. It is well known that landmines exhibit mechanical resonance behavior that enhances the soil velocity over a buried landmine. Recent experimental work by Zagrai *et al.* [A. Zagrai, D. Donskoy, and A. Ekimov, J. Acoust. Soc. Am. **118** (6), 3619–3628 (2005)] demonstrates the existence of structural modes in several landmines. The work reported herein parallels the work of Zagrai *et al.* in studying the structural modes of the pressure plate of a plastic, cylindrically symmetric, antitank landmine. The pressure plate is considered to act as an elastically supported thin elastic plate. An observed perturbation of the first symmetric mode of the pressure plate is caused by the landmine's shock-resisting mechanism. This is validated by a lumped element model for the first symmetric mode coupled to the shock-resisting mechanism. © *2006 Acoustical Society of America.* [DOI: 10.1121/1.2357999]

PACS number(s): 43.40.At, 43.40.Dx, 43.20.Tb [KA] Pages: 3655–3663

I. INTRODUCTION

Although structural vibrations of landmines have become a topic of recent interest in the acoustic landmine detection community,[1] resonance behavior in landmines has been reported in much of the literature.[2–4] Early works by Scott *et al.*[2] and Donskoy *et al.*[3] show clear resonances in experimental work performed on both un-buried and buried landmines. Most recently, Zagrai *et al.*[1] show two-dimensional structural modes present in the pressure plates and casings of several landmines.

The initial modeling efforts by Donskoy *et al.*[3] consisted of modeling the resonance of the landmine by considering the pressure plate to act as a damped simple harmonic oscillator. This type of model is reasonable because the wavelengths of sound in the air and in the ground that correspond to the typically measured resonance frequencies of landmines are larger than the dimensions of most landmines. With this one-dimensional model, the authors achieve good results when comparing the model to their suite of single point impedance measurements taken for many different landmine types.

Building upon the work of Donskoy *et al.*,[3] Zagrai *et al.*[1] observed two-dimensional structural modes during their experimental work. Since these modes still occur at low frequencies, the authors, using the solution to the equation of motion for an elastically supported thin elastic plate as a basis, describe each mode of a plate by a spatially dependant mass, spring, and dashpot. This allows each mode to be separately inserted into the previously mentioned lumped element model. Effectively, this extends the one-dimensional lumped element model to a two-dimensional model because of the spatial dependence of the effective mode parameters. Again, good results are achieved when matching this model to observations.

For a landmine to operate, it must respond to an applied force by deforming enough to activate its detonator. The ability of the casing to deform allows a landmine to exhibit mechanical resonance behavior. Each type of landmine has its own set of resonance frequencies and modes determined by its elastic and dimensional properties. Because there are many different types of landmines constructed out of various materials, it is not reasonable to expect a single theoretical model to be able to explain the behavior of all landmines. This work focuses on a single plastic landmine that has a large acoustic response, an Italian VS 1.6.

The following section of the paper describes, in detail, the landmine used throughout this study. After the description of the landmine are descriptions of experimental procedures used to characterize the mechanical vibrations of the VS 1.6 when free and when subjected to a load on the chassis of the landmine. The experimental observations are then described theoretically with particular attention paid to two interesting experimentally observed effects: a large shift of the first symmetric mode of the landmine and a reordering of modes upon flush burial of the landmine in sand.

II. THE ITALIAN VS 1.6 LANDMINE

A cross-sectioned example of a VS 1.6 landmine is shown in Fig. 1. The large cavity at the bottom of the landmine is the chamber that houses the explosive. The central portion contains the fuse and the detonating assembly. The pressure plate makes up the top of the landmine and can be removed by unscrewing the threaded locking ring. All parts are assembled using o-rings making the VS 1.6 air tight and waterproof. Visible near the center of Fig. 1 is the detonating assembly, which is activated by a steady pressure on the pressure plate. A steady pressure is required to allow enough

[a]Author to whom correspondence should be addressed. Present address: U.S. Army Research Laboratory, ATTN: AMSRD-ARL-CI-ES, 2800 Powder Mill Road, Adelphi, MD 20783.
Electronic mail: kirk.alberts@arl.army.mil

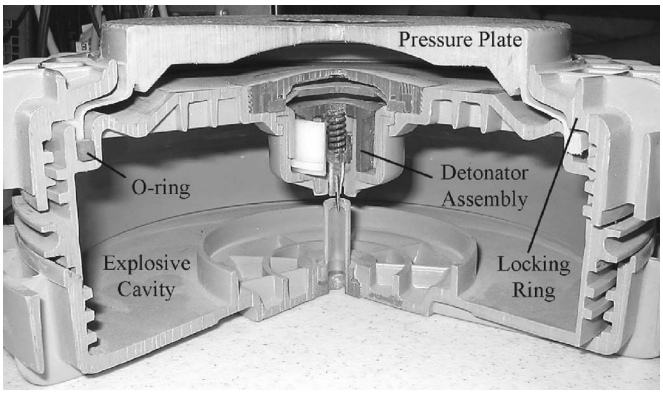

FIG. 1. Cross-sectioned example of a VS 1.6 antitank landmine.

time for air to pass through a small nozzle to a much smaller volume. The air causes a diaphragm to distort, which, in turn, causes a plunger to transfer pressure through the spring to the striker. The striker then initiates the fuse, which explodes the landmine. Highly impulsive forces do not occur on a long enough time scale to allow air to pass through the nozzle to initiate the fuse, thereby making the landmine shock resistant.[5] By scaling measurements taken from Fig. 1 to the size of the landmine, the size of the large volume beneath the pressure plate was found to be approximately 180 cm^3.

It is believed that the acoustic behavior of the VS 1.6 is associated with the modal response of the pressure plate. Examination of Fig. 1 reveals the varying thickness of the pressure plate of the VS 1.6 landmine. From the center of the plate to roughly 56% of the radius of 7.2 cm, there is an increase in plate thickness along a slight arc. The thickness then becomes uniform until approximately 78% of the radius where the thickness increases linearly. There is then a small decrease in thickness until the edge support is reached. The plate's minimum thickness occurs at the center and is 5 mm. It is seen in Fig. 1 that the pressure plate is symmetric about the center. The mass of a complete pressure plate from a disassembled VS 1.6 was measured to be 256.1 g with a volume of 223 cm^3 found by measuring the height of water displaced by submerging the plate in a container of known size. This yields a density of 1150 kg/m^3, which is approximately that of a family of polyamide, polyamide 6/6.[6,7] Also visible in Fig. 1 is the edge support of the pressure plate. Notice that the support is very thin compared to the thickness of the plate. If a force is applied to the plate, the edge support will deform before the plate itself. Beneath the support there is a small square space labeled o-ring. The locking ring that holds the pressure plate in place presses the edge support against the o-ring, which compresses to form a watertight and airtight seal.

The detonating assembly visible at the center of the landmine, Fig. 1, contains a small nozzle and a set of channels in the shape of a wheel. The channels have been measured to determine the volume of air in the small cavity. The channels that form the spokes have a width of 1.6 mm. The outer ring has a width of 4 mm. All channels have a depth of 1.5 mm. These measurements yield a cavity volume of 0.8 cm^3. The nozzle has also been measured by scaling from Fig. 1. It has a length of 5.1 mm and a constant diameter of 0.8 mm.

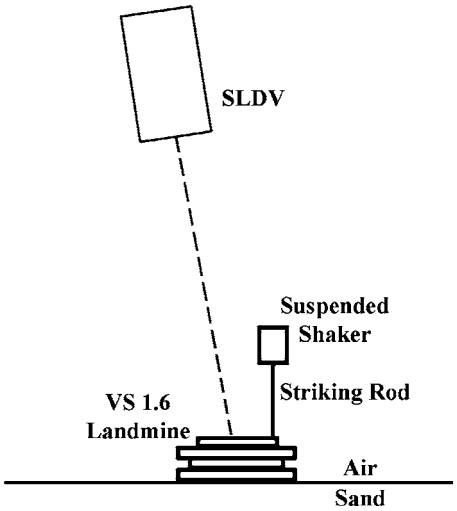

FIG. 2. Experimental configuration used during the modal analysis of the VS 1.6.

When examining the cross sectioned VS 1.6, several features of the pressure plate and chassis are to be noted. These are the varying thickness, the thin edge support that controls the deflection of the pressure plate, the air cavities, and the nozzle. The cavity-nozzle system is airtight and undergoes a change in pressure when the pressure plate of the landmine vibrates in any modes that produce a significant net volume change of the large cavity.

III. EXPERIMENTAL PROCEDURES AND RESULTS

A. Modal analysis of the unburied VS 1.6

Before beginning experiments on a buried landmine, it is necessary to know the unburied (free) response of the landmine. Initially, typical modal analysis techniques using impulse hammer excitation were used. However, in an attempt to automate the modal analysis of the VS 1.6, a measurement method using a shaker as the excitation source was developed. Modal analysis via a shaker is not new,[8,9] but the typical method requires the use of a force sensor at the point of contact between the shaker and the object under study. Such a sensor was not available and was deemed detrimental to the experiment because of the added load on the pressure plate of the landmine.

The structural modes of the VS 1.6 were measured with the landmine resting on top of sand housed in a large container. Excitation of the pressure plate was accomplished via a suspended electromechanical shaker striking the plate through a 3 mm diameter aluminum rod. The shaker was driven every two seconds with a 1 V single cycle pulse of 1 kHz sent to the shaker from a function generator after passing through a power amplifier. Simultaneous to the excitation pulse, a trigger pulse was sent to a scanning laser Doppler velocimeter (SLDV), which measured the velocity of the pressure plate at a given point.

The shaker was suspended such that it struck the pressure plate at a point near the edge. This configuration, Fig. 2,

allows the shaker's pulse to excite both the symmetric and asymmetric modes in the pressure plate, should they exist. The shaker was clamped to a framework in such a manner that very little vibration was produced at the back of the shaker. The thin rod was placed to be in slight contact with the pressure plate. This allowed only a small amount of point loading on the pressure plate in the rod's rest position.

The SLDV, triggered from the function generator, was set to scan a 200-point grid drawn over the pressure plate of the VS 1.6 yielding a spatial resolution of 1.53 points per square centimeter. The SLDV, thus triggered, measured the velocity at each point as described above. The internal analyzer in the SLDV was set to measure over a frequency range of 0–1.6 kHz with a frequency resolution of 1 Hz. The analyzer window was set to force/expo with the velocity signal of the SLDV given the expo window. Enhancement of the SLDV signal was set to standard for this measurement, meaning that the SLDV software would take up to nine fast Fourier transforms (FFTs) before computing the average consisting of three of the nine FFTs. Remeasure was activated so that the SLDV would return to measurement points deemed by the software to be necessary for rescan. No software filters or other external filters were used on the SLDV signal. The height of the SLDV from the landmine was 1.24 m. This height corresponds to a coherence maximum of the SLDV laser. Many heights are available, the reported height was chosen only for convenience.

Results of this measurement are seen in Fig. 3. Seven modes are apparent in the measurement range. The modes are tabulated by the integers "*m*" and "*n*," where *m* refers to the number of nodal diameters and *n* refers to the number of nodal circles. Also seen in Fig. 3 are the resonance frequencies of each mode and their relative mechanical admittance in m/s/N. The admittance was calculated manually after measuring the velocity of the thin rod during its contact with the plate (the positive portion of the excitation pulse) and calculating the force imparted to the plate by the rod. Figure 3 also shows a most interesting result, the frequency of the first symmetric mode is higher than that of the first asymmetric mode. Generally, it is expected that the simplest geometric modes occur lowest in frequency. It will be shown that this shift of the first symmetric mode can be attributed to the large volume beneath the pressure plate. It should also be noted that some of the higher modes are distorted. This distortion is believed to be caused mostly by the point loading of the rod used for the excitation, although some distortions are inherent to this nonideal device. Similar measurements using different excitation (impulse hammer or loudspeaker) reveal the same seven modes without the point load distortion. The only information not obtained from the SLDV software in this measurement is the damping ratio of each mode. These may be obtained by looking at the quality factor of each resonance peak. This was not done, as the data were not critical to this work.

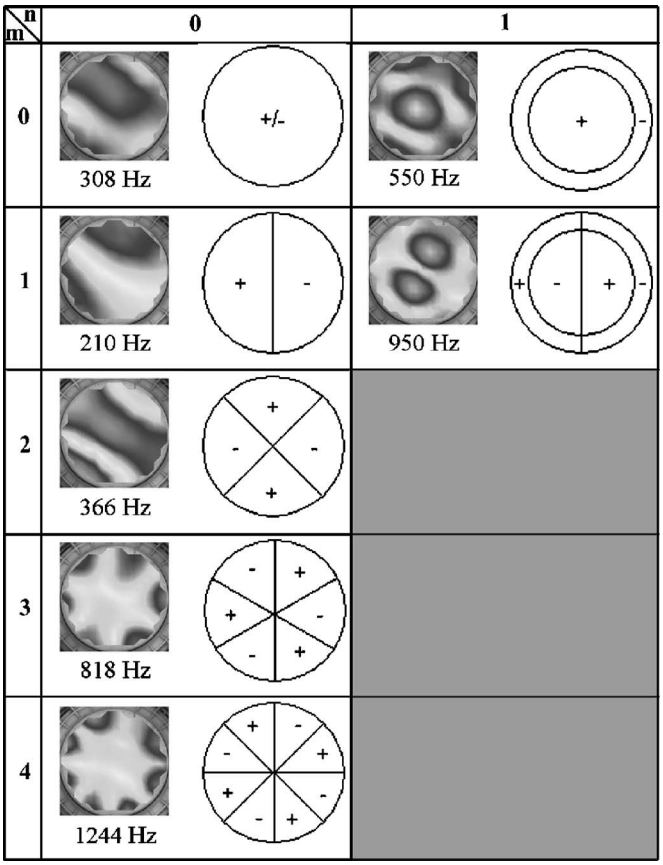

FIG. 3. Results of the modal analysis of the VS 1.6. Dark gray areas correspond to maximum mechanical admittances of 0.44, 0.53, 0.19, 0.40, 0.16, 0.08, and 0.05 m/s/N with increasing frequency.

B. Chassis loading of the VS 1.6

In order to test the effects a chassis load might have on the structural modes of the pressure plate, chassis loading experiments were performed in both water and sand so that shear effects could be studied as well. All software and hardware settings remain as described in previous sections. Prior to initiating the water experiments, the studied landmine was soaked in water for 4 days to attempt to allow the polyamide 6/6 to saturate.[6,7]

The height of the water was brought up the side of the landmine's chassis in increments determined by the chassis' geometry. These increments can be seen in Fig. 4. At each point indicated in the figure, a scan of the pressure plate was performed. The modal frequencies were then recorded and plotted as a function of percent landmine height as seen in Fig. 5. As water was brought up the sides of the chassis, there was very little change in the modal frequencies of the pressure plate until the water reached 100% landmine height, at which point the modes all exhibit a downward shift in frequency. This downward shift in frequency is possibly due to mass loading of the plate by water in the small crevice between the pressure plate and the chassis. The reader will note that the (1,1) and the (4,0) modes are absent at 100% landmine height. When 100% landmine height was reached in this experiment, the (1,1) and the (4,0) modes were not high enough in amplitude for good resonance frequency recognition. The height increment at 95% was left out of this experiment since mass loading by the water was believed to be the dominant effect on the mode frequencies.

In order to study possible shear effects, the previous

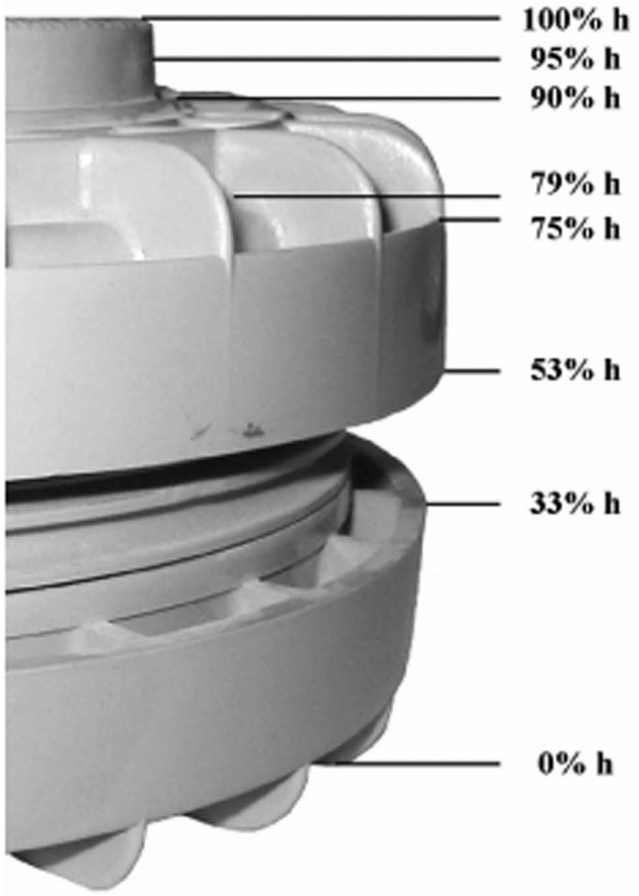

FIG. 4. Height steps used when chassis loading the VS 1.6 in both water and sand. Heights are listed in percent "*h*," where *h* is the height of the landmine, 9.1 cm.

experiment was repeated in a controlled sand environment. A large, 96 by 146 by 29 cm, box filled with dry, unconsolidated sand was used for this sand loading experiment. 10 cm of sand was excavated from the box and the landmine was placed into the excavated box in the same height steps as in the water experiment. Each time the landmine was buried deeper into the sand, the SLDV was used to scan, with the same settings as above, the pressure plate of the landmine. The resonance frequencies were recorded and plotted in Fig. 6. Each mode again stays at essentially the same frequency

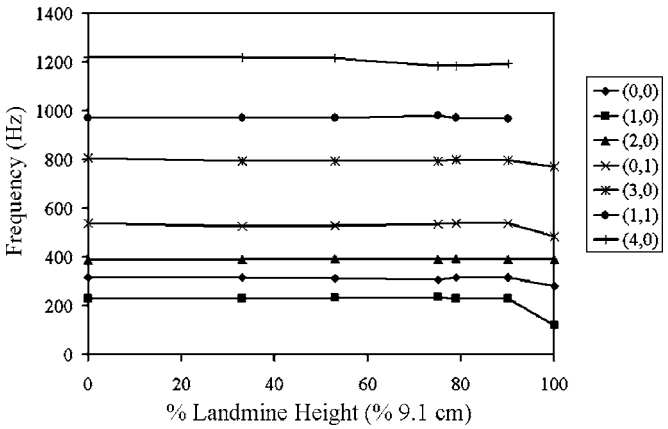

FIG. 5. Results of the chassis loading experiment in water.

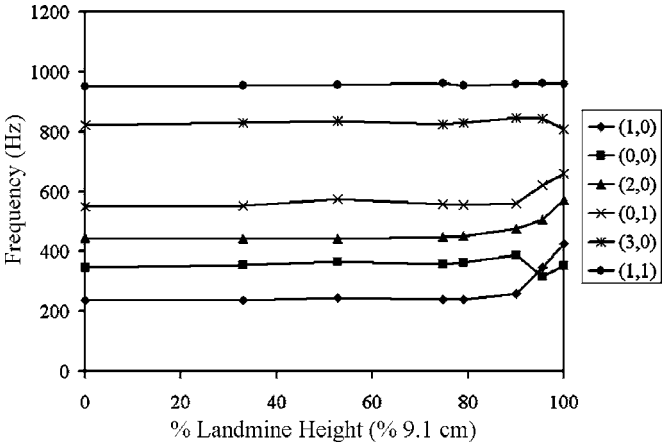

FIG. 6. Results of the chassis loading experiment in sand.

until 75% of the landmine's height is reached. Between 75% and 90% of the height, all of the modes exhibit a slow upward frequency shift. At 95% of the height, an interesting phenomenon occurs. All modes, excepting the first symmetric mode, continue their upward shift in frequency. The first symmetric mode, however, shifts downward in frequency by 70 Hz and then shifts up by another 35 Hz once the sand is level with the pressure plate of the landmine. This causes a reordering of the first symmetric and first asymmetric modes such that they return to their expected order.

IV. THEORETICAL MODELS

A. Elastically supported thin plate

In a fashion similar to that reported by Zagrai *et al.*,[1] the thin plate equation subject to circumferential elastic boundary conditions is used here to model the modes of the VS 1.6. The equation of motion describing the transverse displacement, $w(r,\theta)$, of the surface of a thin elastic plate driven by an arbitrary force $f(r,\theta)$ is well known and is given as[10–13]

$$\left(\nabla^4 - \frac{\rho h \omega^2}{D}\right) w(r,\theta) = \frac{f(r,\theta)}{D}, \tag{1}$$

where ω is the circular frequency of the plate obtained by assuming harmonic time dependence, ρ is the mass density of the plate, and D is known as the flexural rigidity of the plate and is given by Eq. (2) below

$$D = \frac{Yh^3}{12(1-\sigma^2)}. \tag{2}$$

In Eq. (2), Y is Young's modulus, h is the plate thickness, and σ is Poisson's ratio. Figure 7 shows the geometry of the

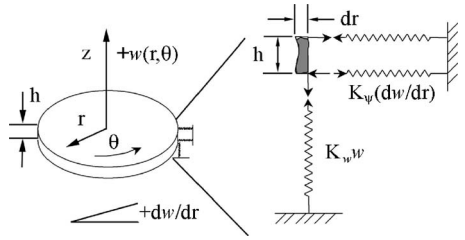

FIG. 7. Geometry of the plate model for the pressure plate of the VS 1.6.

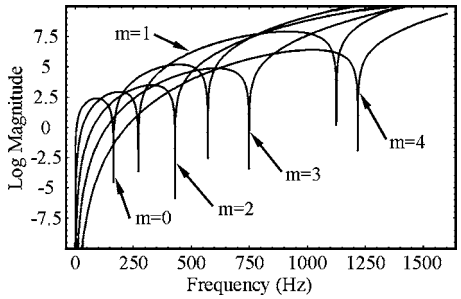

FIG. 8. Numerically generated plot showing the mode frequencies (zeros in each curve) for several values of m.

plate along with the elastic boundary conditions acting on the plate edge. K_w resists vertical motion of the plate edge and K_ψ resists rotation of the plate edge about the radial axis. Both K_w and K_ψ are circumferentially distributed about the edge of the plate.[11]

The solution for the free vibration, $f(r,\theta)$ equal zero in Eq. (1), of the plate is given below[11]

$$w(r,\theta) = \sum_{m=-\infty}^{\infty} \sum_{n=0}^{\infty} [A_m J_m(k_{mn} r) + C_m I_m(k_{mn} r)] e^{im\theta}. \tag{3}$$

The term multiplying r in the arguments of the Bessel functions, k_{mn}, is defined by the following:

$$k_{mn}^4 = \frac{\rho h \omega_{mn}^2}{D}, \tag{4}$$

where ω_{mn} are the resonance frequencies. The boundary conditions at the edge of the elastically supported thin plate are

$$-K_w w(r,\theta) = -D\left[\frac{\partial}{\partial r}(\nabla^2) + \frac{1}{r}(1 - \sigma)\frac{\partial}{\partial r}\left(\frac{1}{r}\frac{\partial^2}{\partial \theta^2}\right)\right] w(r,\theta),$$

$$K_\psi \frac{\partial}{\partial r} w(r,\theta) = -D\left[\frac{\partial^2}{\partial r^2} + \sigma\left(\frac{1}{r}\frac{\partial}{\partial r} + \frac{1}{r^2}\frac{\partial^2}{\partial \theta^2}\right)\right] w(r,\theta). \tag{5}$$

On substituting Eq. (3) into Eqs. (5) for each m two linear equations for A_m and C_m are obtained. For nontrivial solutions to exist, the determinant of the coefficient matrix of A_m and C_m must equal zero for nonzero frequencies. Figure 8 shows a plot of the determinant of the coefficient matrix for the first five values of m, recall that m determines the number of nodal diameters. Zeros in the value of the determinant correspond to resonance frequencies, ω_{mn}. Parameters used in the creation of Fig. 8 were Young's modulus, plate density, plate thickness, Poisson's ratio, K_w, and K_ψ. Of these parameters, only K_w and the plate density were measured. However, the previously mentioned density of 1150 kg/m^3 was replaced by 1245 kg/m^3. This larger density was used for all subsequent calculations. The circumferentially distributed vertical spring constant, K_w, was measured by a simple point-mass loading experiment to be approximately 0.22 MPa. Poisson's ratio was taken as 0.3. The remaining parameters (Young's modulus, plate thickness, and K_ψ) were determined by performing a nonlinear least squares type fit to the measured frequencies. This resulted in effective values of Young's modulus and plate thickness of approximately 2.4 GPa and 4.7 mm, respectively. The resonance frequencies showed little sensitivity to K_ψ, so it was set to zero for all elastic plate calculations. It should be noted that the material parameters, although effective because this model neglects the cross section of the plate, align reasonably well with those of polyamide 6/6.[6,7] It is apparent that, with the exception of the (0,0), the (1,1), and the (4,0) modes, the calculated modal frequencies align reasonably well with the measured frequencies shown in Fig. 3 considering that the complicated cross section of the VS 1.6 pressure plate has been ignored.

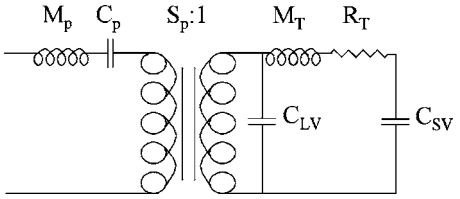

FIG. 9. Electrical equivalent circuit for the (0,0) mode of the VS 1.6.

B. Electrical equivalent circuit for the (0,0) mode

As is apparent from the results of the modal analysis of the free landmine, there is a large perturbation of the (0,0) mode of the pressure plate from the value obtained from the elastically supported thin plate model; the (0,0) mode has been shifted to a frequency higher than that of the (1,0) mode. If the construction of the VS 1.6 is considered, the large cavity, possibly the small tube, and small cavity as well, could have an influence on the first symmetric mode of the landmine since it involves the largest net change in volume relative to other modes. To investigate this possibility, an electrical equivalent circuit[14] for the first symmetric mode coupled to the landmine's shock-resisting mechanism was written and its impedance calculated. This type of model is reasonable since, at the mode frequency in question, the wavelength in air is larger than all dimensions of the system in question.

Figure 9 shows a pictorial representation of the lumped acoustic circuit that will be used to represent the landmine, volumes, and nozzle. In Fig. 9, M_P and C_P are the mass and compliance of the plate, respectively. These are combined into the plate impedance calculated below. S_P is the area of the plate and acts to couple the acoustic portion of the circuit to the mechanical portion. C_{LV} is the compliance of the large volume beneath the plate. M_T and R_T are the mass and resistance of the nozzle and C_{SV} is the compliance of the small volume.

The first calculation is that of the impedance of the plate vibrating in its first symmetric mode. The treatment presented here follows the method described by Mason[14] for determining the impedance of a thin elastic plate clamped at the edges. First, the equation of motion, Eq. (1), is modified by replacing $f(r,\theta)$ with a spatially constant driving pressure, P. In the subsequent solution, m is set to zero since only the symmetric modes are of interest here. In addition,

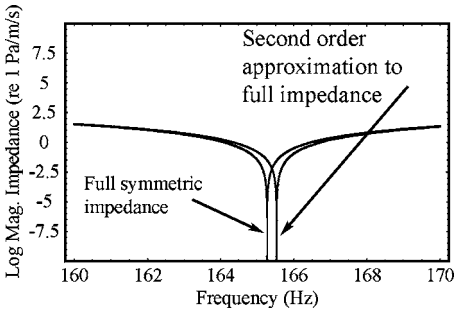

FIG. 10. Plots of the full impedance and its second order approximation showing a small shift in resonance frequency due to the approximation.

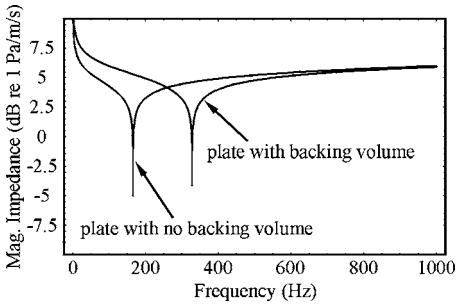

FIG. 11. Plot of the impedance of the (0,0) mode of an elastically supported plate with and without a backing volume.

λ/a is substituted for k_{mn} in the argument of the Bessel functions in the solution. The elastic boundary conditions are then applied noting that they have been significantly reduced because the only concern is with the symmetric modes; i.e., the terms dependent on polar angle are ignored.

Just as in the discussion of the free plate, a matrix equation similar to that described above results from the application of the boundary conditions to the solution. This is used to solve for the coefficients of the Bessel functions, which are then reinserted into the solution giving the displacement of the plate when it vibrates in its symmetric, m equal zero, modes.

With the solution for the symmetric modes of the plate, the volume velocity of the plate can now be calculated. This is done by integrating over the surface of the plate in the following manner:

$$V = i2\pi\omega \int_0^a w(r) r dr. \tag{6}$$

The input pressure, P, is simply divided by the volume velocity calculated above to arrive at the full impedance of the symmetric modes plate.

The full impedance of the symmetric modes of the plate is now realized (see the Appendix). However, for the lumped element approximation only the low frequency impedance of the plate is necessary. Therefore, by assuming that λ is small the Maclaurin series of the plate impedance is formed keeping only terms to second order in λ, following the treatment in Mason,[14] which further restricts the impedance of the elastically supported plate to its first symmetric mode, (0,0). Plots of the full impedance and the series approximation appear in Fig. 10, created using the same parameters as those used in the creation of Fig. 8. It should be noted that the second order approximation introduces roughly a 0.2 Hz change in the resonance frequency of the first symmetric mode. This change equates to only a 0.1% change in frequency, which gives validity to the approximation. To further validate the impedance as calculated above, the limit of the expansion as both K_w and K_ψ tend to infinity is taken. This effectively clamps the plate and reduces the impedance to that found in Mason[14] for the symmetric modes of a clamped plate, verifying the accuracy of what has been done here.

With the low frequency approximation to the plate's impedance, the rest of the lumped acoustic element circuit can be calculated to obtain the effect of the cavity on the response of the plate. The compliances of the two cavities, C_{LV} and C_{SV}, each considered as a cylinder, are calculated from the following equation:[14]

$$\text{Compliance} = \frac{V_C}{\rho_0 c^2}, \tag{7}$$

where V_C is the volume of the cavity, ρ_0 is the density of the air in the cavity, and c is the speed of sound in air.

Because this approximation lies in the low-frequency regime, the air inside the nozzle acts as a mass moving in and out of the tube. Because the size of the nozzle is so narrow, thermoviscous attenuation at the walls of the tube must be taken into account. The impedance of the tube, including the mass of the air in the tube and the resistance to the motion of the air, is[14]

$$Z_{\mathrm{tube}} = \frac{\omega\rho_0 kL}{S(k^2+\alpha^2)}\alpha + i\frac{\omega\rho_0 k^2 L}{S(k^2+\alpha^2)}, \tag{8}$$

where α is the thermoviscous attenuation at the walls of the nozzle, k is ω divided by the speed of sound in air, and L is the length of the tube.

The impedance of every element shown in Fig. 9 has been derived. Calculating the impedance of the entire circuit yields

$$Z_{\mathrm{Total}} = S_P^2\left[Z_{\mathrm{Plate}} + \frac{\left(Z_{\mathrm{Tube}} - \frac{i}{\omega C_{\mathrm{SV}}}\right)\left(\frac{-i}{\omega C_{\mathrm{LV}}}\right)}{\left(Z_{\mathrm{Tube}} - \frac{i}{\omega C_{\mathrm{SV}}}\right) + \left(\frac{-i}{\omega C_{\mathrm{LV}}}\right)}\right], \tag{9}$$

where S_P is the area of the plate and the quantities containing the compliances are the impedances of the large and small volumes beneath the plate. All that is left is to insert a value for the attenuation, α. This was found in Mason[14] to be

$$\alpha = \frac{2.8\times 10^{-3}}{\sqrt{2\pi}}\frac{\sqrt{\omega}}{r}\ \mathrm{Np/m}, \tag{10}$$

where r is the radius of the tube in meters.

The impedance given by Eq. (9), including attenuation, was evaluated numerically and is plotted in Fig. 11 using the previously listed parameters as well as the measured parameters presented in the description of the cavities landmine. The impedance shows a result similar to experimental observations in that the impedance predicts a large shift in the first

symmetric mode of the plate, a shift so large that the first symmetric mode would occur higher in frequency than the first asymmetric mode. The impedance of the circuit, Fig. 11, demonstrates a shift of roughly 200 Hz of the first symmetric mode of an elastically supported thin plate. The frequency of the circuit resonance is approximately 350 Hz, which agrees well with the experimental observations of the free VS 1.6. Similar effects have been observed in timpani when the volume below the drumhead was made smaller.[15,16] Fletcher and Rossing[15] demonstrate experimentally that a kettle volume one-half its original size shifts the frequency of the drum's first symmetric mode to frequency higher than that of the first asymmetric mode. Further, Christian *et al.*[16] show that a kettle one half its original size will produce a similar shift in frequency. If a center vibration speed of 1 m/s is assumed for the 182 Hz timpani mode listed in Christian *et al.* (Table VI, column 8),[16] then a percentage kettle volume change of 0.24% can be calculated. This volume change is calculated on the assumption of a uniform membrane displacement, which overestimates the actual volume change. Similarly, if the volume change is calculated for the (0,0) mode of the VS 1.6, with a measured maximum vibration speed of 70 μm/s, the percent change in volume is 0.47%. These comparable estimated changes in volume lend validity to the model.

An experiment to change the size of the volume beneath the pressure plate would be a prudent attempt at further verification of the theoretical results presented above. Such an experiment was designed, but attempts to remove the locking ring securing the pressure plate of the landmine used in this study showed a great potential for destruction of the landmine's casing. Thus, the experiment was abandoned because of the availability of the landmine type under test.

C. Shear contact at flush condition

The measurement to determine the effect of sand loading on the chassis exhibits a most interesting phenomenon. The contact of the sand against the side of the pressure plate, 95% h and 100% h, forces a reordering of the modes from their measured free positions. As mentioned previously, at 95% h the first symmetric mode shifts to a position lower in frequency than the first asymmetric mode and all of the higher frequency modes show an upward shift in frequency. Qualitatively, these observations can be described by considering the boundary conditions between two elastic half-spaces separated by a vertical boundary. The boundary conditions for contact without slip are continuity of normal and tangential stress and strain.[17] For this qualitative explanation, the interest lies only with the tangential components of the boundary conditions, namely the vertical component of the stress and the strain. Applying Hooke's Law to write the stress in terms of the strain gives

$$\sigma_{zr} = 2\mu u_{zr}, \tag{11}$$

where μ is a Lamé constant. Written in terms of the compressional wave speed in the soil matrix and the density of the soil, the Lamé constant becomes

$$\mu = \frac{1-2\sigma}{2(1-\sigma)}\rho V_p^2, \tag{12}$$

where σ, ρ, and V_p are Poisson's ratio, density, and compressional wave speed in the soil matrix, respectively. Equation (12) is derived from the following equations where V_s is the shear wave speed in the soil matrix[18]

$$V_s = \sqrt{\frac{\mu}{\rho}},$$

$$V_p = \sqrt{\frac{\lambda + 2\mu}{\rho}},$$

$$\frac{V_p^2}{V_s^2} = \frac{2(1-\sigma)}{(1-2\sigma)}. \tag{13}$$

Using Eq. (12), the values of the Lamé constant for the sand box using the compressional wave speed and density of the sand were calculated.

Because the reordering of modes in the VS 1.6 occurs at the flush-buried condition, the compressional wave speed at the surface is of greatest interest. Taking 100 m/s to be the compressional wave speed at the surface of the sand and measuring the density of the dry sand to be 1600 kg/m^3, finding Poisson's ratio for sand to be 0.1,[19,20] and inserting these values into Eq. (12), it is found that μ is on the order of 10^6 Pa. Bachrach[19] considers Poisson's ratio of sand at some buried depth. Near the surface of the sand, however, sand becomes more fluid-like. Therefore, a Poisson's ratio on the order of 0.4 might be expected. Substitution of a Poisson's ratio of 0.4 into Eq. (12) gives a μ of about the same order as when using a Poisson's ratio of 0.1. For this qualitative argument, the order of the Lamé constant is of greatest importance. Since both Poisson's ratios yield similar results, the Lamé constant of order 10^6 Pa can be applied. In order to make use of this result, how Eq. (12) is incorporated into the boundary conditions of the plate must be considered.

Equation (12), vertical stress in terms of vertical strain, yields a force per unit length. The left-hand side of the first of Eqs. (5) is a distributed spring constant, K_w, multiplied by the displacement of the plate, $w(r,\theta)$. This gives units of force per unit length. Therefore, in this first approximation, the vertical stress can simply be added to the left-hand side of the first of Eqs. (5). Addition of the vertical stress to K_w results in a 1000% increase in the edge stiffness of the plate which forces the plate into a more clamped condition. Fitting using K_w as a parameter, with all others fixed, confirms that large K_w will move the modal frequencies as observed in the experiments. In addition, the shift in the first symmetric mode created by the volumes beneath the plate is much smaller for a clamped plate and does not cause a reordering of modes. The circuit impedance depicted in Fig. 12 is that of a clamped plate. Figure 12 was created using the same parameters as in previous numerical calculations, except Young's modulus and the circumferential spring constants. Young's modulus became 130 MPa and the spring constants were allowed to go to infinity. The change in Young's modulus was necessary to allow the frequency of the first symmet-

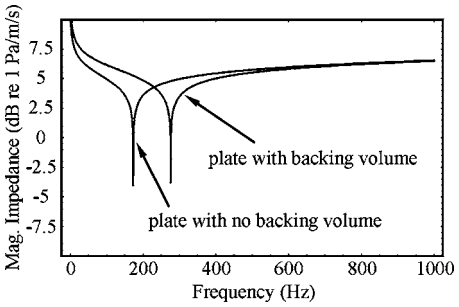

FIG. 12. Plot of the impedance of the (0,1) mode of a clamped plate with and without a backing volume.

ric mode of the clamped plate to be very close to that of the first symmetric mode of the elastic plate. It is of note that the shifted impedance in Fig. 12 does not match well with the observations in Fig. 6 at 100% landmine height. However, Fig. 12 serves to demonstrate that stiffening the edge supports of an elastic plate will lessen its susceptibility to a small backing volume. Therefore, it can be stated that flush burial of the VS 1.6 lessens the effect of the volumes and nozzle beneath the plate by not allowing the flexure of the pressure plate to change the large volume as much as when the pressure plate is free. The implication of this result is that measurements of a landmine's modes must be performed *in situ* in order to truly know the order of the modes when the landmine is buried.

V. CONCLUDING REMARKS

Seven structural modes, similar to those expected in a drumhead, have been observed in the cylindrically symmetric pressure plate of the VS 1.6 antitank landmine. An elastically supported, thin, elastic plate acceptably models many of the observed modes even though the complicated cross section of the plate has been neglected. Discrepancies between observations and the predictions of the basic thin plate model arise because of the mechanisms below the pressure plate of the landmine, specifically the large volume beneath the plate that forces a stiffening of the first symmetric mode of the landmine. This stiffening results in a shift of the first symmetric mode that places it higher in frequency than the first asymmetric mode of the landmine. This has been confirmed by a lumped element model of the plate-volume system.

Chassis loading experiments in both water and sand reveal little, if any, effect on the modes of the landmine. Flush burial in sand, however, reorders the first symmetric and asymmetric modes. This reordering of modes can be qualitatively explained by shear stiffening of the vertical elastic edge support of the landmine, which forces the pressure plate to approach a clamped condition. A clamped plate, vibrating in its first symmetric mode over a sealed volume, undergoes more flexure than a similarly vibrating elastically supported plate, which does not create as large a volume change. This smaller volume change diminishes the amount of volume induced stiffening of the plate, thus lessening any resonance frequency shift.

The study reported herein has shown several interesting effects caused by the complex structure of the landmine under study. Further, the landmine's interaction with the sand upon flush burial has shown a complex relationship between the sand's shear and the order of the vibration modes of the plate. The observations and subsequent explanations suggest that studies of vibrating landmines should consider the effects of the mechanism(s) beneath the pressure plates on the vibrations of those plates as well as the vibrational characteristics of the landmines *in situ*.

ACKNOWLEDGMENTS

This material is based upon work supported by the U. S. Army Research, Development, and Engineering Command, Communications-Electronics Research, Development, and Engineering Center, Night Vision and Electronic Sensors Directorate under Contract No. DAAB15-02-C-0024 and the Department of the Navy, Office of Naval Research under Grant No. N00014-02-1-0878. Any opinions, findings, and conclusions or recommendations expressed in this material are those of the authors and do not necessarily reflect the views of the sponsors. The authors would like to thank Craig Hickey for discussions regarding the contact of the pressure plate with the sand.

APPENDIX: THE IMPEDANCE OF THE SYMMETRIC MODES OF AN ELASTICALLY SUPPORTED THIN PLATE AND ITS LOW-FREQUENCY APPROXIMATION

In Ref. 14, Mason shows the impedance of the symmetric modes of a clamped thin plate. Here, in Sec. IV B, the derivation of the impedance of the symmetric modes of an elastically supported thin plate has been described. The results of the first part of the derivation are shown below, in the expression for the impedance of the symmetric modes of an elastically supported thin plate

$$Z_{\text{symm}}(\omega) = \frac{i\dfrac{\lambda^2\sqrt{Dh\rho}}{a^2}(\gamma\varphi - \beta\zeta)}{\pi a^2\left[-\dfrac{2K_w}{\lambda}(\zeta \mathrm{J}_1 - \varphi \mathrm{I}_1) + (\gamma\varphi - \beta\zeta)\right]}, \quad \text{(A1)}$$

where

$$\zeta = (\mathrm{I}_0 + \mathrm{I}_2)\frac{\lambda^2}{2a^2} + \left(\frac{K_\psi\lambda}{aD} + \frac{\sigma\lambda}{a^2}\right)\mathrm{I}_1,$$

$$\varphi = -(\mathrm{J}_0 - \mathrm{J}_2)\frac{\lambda^2}{2a^2} - \left(\frac{K_\psi\lambda}{aD} + \frac{\sigma\lambda}{a^2}\right)\mathrm{J}_1,$$

$$\gamma = -\left(\frac{K_w}{D} - \frac{\lambda^2}{2a^3}\right)\mathrm{I}_0 - \left(\frac{\lambda}{a^3} - \frac{3\lambda^3}{4a^3}\right)\mathrm{I}_1 + \frac{\lambda^2}{2a^3}\mathrm{I}_2 + \frac{\lambda^3}{4a^3}\mathrm{I}_3,$$

$$\beta = -\left(\frac{K_w}{D} + \frac{\lambda^2}{2a^3}\right)\mathrm{J}_0 + \left(\frac{\lambda}{a^3} + \frac{3\lambda^3}{4a^3}\right)\mathrm{J}_1 + \frac{\lambda^2}{2a^3}\mathrm{J}_2 - \frac{\lambda^3}{4a^3}\mathrm{J}_3. \tag{A2}$$

In (A1) and (A2), the arguments of the Bessel functions (J and I), λ, have been left off for compactness and the subscript on each Bessel function refers to its order. Following the second portion of the description in Sec. IV B, the results of the low-frequency approximation of the impedance of the symmetric modes of the plate, $Z_{\mathrm{plate}}(\omega)$, appear below

$$\begin{aligned} Z_{\mathrm{plate}}(\omega) = i\frac{192K_wD(D + aK_\psi + D\sigma)}{a^3\pi\omega\Xi} \\ + i\frac{3h\rho\omega}{\pi a^2\Xi^2}\Bigg[\left(\frac{3}{5}a^8K_w^2K_\psi^2 + 3(2^{10})D^4(1+\sigma)^2 \\ + 2a^5DK_wK_\psi\left[2^5K_\psi + \frac{3}{5}a^2K_w(6+\sigma)\right] \\ + 2^6aD^3(1+\sigma)[96K_\psi + a^2K_w(7+\sigma)] \\ + D^2\Bigg\{3(2^{10})a^2K_\psi^2 + 2^7a^4K_wK_\psi(4+\sigma) \\ + \frac{a^6K_w^2}{5}[113 + 3\sigma(12+\sigma)]\Bigg\}\Bigg)\Bigg]. \end{aligned} \tag{A3}$$

In (A3), a is the radius of the plate and the quantity Ξ is given by

$$\Xi = a^4K_wK_\psi + 96D^2(1+\sigma) + D[96aK_\psi + a^3K_w(7+\sigma)]. \tag{A4}$$

[1] A. Zagrai, D. Donskoy, and A. Ekimov, "Structural vibrations of buried land mines," J. Acoust. Soc. Am. **118**(6), 3619–3628 (2005).

[2] W. R. Scott, Jr. and J. S. Martin, "Experimental investigation of the acousto-electromagnetic sensor for locating land mines," Proc. SPIE **3710**, 204–214 (1999).

[3] D. Donskoy, A. Ekimov, N. Sedunov, and M. Tsionskiy, "Nonlinear seismo-acoustic land mine detection and discrimination," J. Acoust. Soc. Am. **111**(6), 2705–2714 (2002).

[4] M. S. Korman, W. C. K. Alberts II, and J. M. Sabatier, "Nonlinear acoustic experiments for landmine detection: The significance of the top plate normal modes," Proc. SPIE **5415**, 42–50 (2004).

[5] *Jane's Mines and Mine Clearance 2001–2002*, edited by C. King (Jane's Information Group, Inc., Alexandria, VA, 2001).

[6] A. Freeman, S. C. Mantell, and J. H. Davidson, "Mechanical performance of polysulfone, polybutylene, and polyamide 6/6 in hot chlorinated water," Sol. Energy **79**(6), 624–637 (2005).

[7] C.-C. Pai, R.-J. Jeng, S. J. Grossman, and J.-C. Huang, "Effects of moisture on thermal and mechanical properties of Nylon-6,6," Adv. Polym. Technol. **9**(2), 157–163 (1989).

[8] D. J. Inman, *Engineering Vibrations*, 2nd ed. (Prentice-Hall, Englewood Cliffs NJ, 2001).

[9] P. Avitabile, "Experimental modal analysis: A simple non-mathematical presentation," Sound Vib. **35**(1), 20–31 (2001).

[10] L. D. Landau and E. M. Lifshitz, *Theory of Elasticity*, 2nd ed., translated by J. B. Sykes and W. H. Reid (Pergamon Books, New York, 1970).

[11] A. W. Leissa, *Vibration of Plates* (Acoustical Society of America, Melville, NY, 1993).

[12] S. Timoshenko and J. N. Goodier, *Theory of Elasticity*, 2nd ed. (McGraw-Hill, New York, 1951).

[13] S. Timoshenko and S. Woinowsky-Krieger, *Theory of Plates and Shells*, 2nd ed. (McGraw-Hill, New York, 1959).

[14] W. P. Mason, *Electromechanical Transducers and Wave Filters*, 2nd ed. (Van Nostrand, Princeton, NJ, 1948).

[15] N. H. Fletcher and T. D. Rossing, *The Physics of Musical Instruments*, 2nd ed. (Springer-Verlag, New York, 1998).

[16] R. S. Christian, R. E. Davis, A. Tubis, C. A. Anderson, R. I. Mills, and T. D. Rossing, "Effects of air loading on timpani membrane vibrations," J. Acoust. Soc. Am. **76**(5), 1336–1345 (1984).

[17] L. M. Brekhovskikh and V. Goncharov, *Mechanics of Continua and Wave Dynamics*, 2nd ed. (Springer-Verlag, Berlin, 1994).

[18] J. D. AchenBach, *Wave Propagation in Elastic Solids* (North-Holland, Amsterdam, 1973).

[19] R. Bachrach, J. Dvorkin, and A. M. Nur, "Seismic velocities and Poisson's ratio of shallow unconsolidated sands," Geophys. J. **65**(2), 559–564 (2000).

[20] G. Mavko, T. Mukerji, and J. Dvorkin, *The Rock Physics Handbook: Tools for Seismic Analysis in Porous Media* (Cambridge University Press, Cambridge, 1998).

Computation of the homogeneous and forced solutions of a finite length, line-driven, submerged plate

Daniel T. DiPerna,[a] William K. Blake,[b] and Xingguang Z. DiPerna[c]
Naval Surface Warfare Center, 9500 MacArthur Boulevard, West Bethesda, Maryland 20817

(Received 7 February 2006; revised 10 August 2006; accepted 31 August 2006)

A formulation is developed to predict the vibration response of a finite length, submerged plate due to a line drive. The formulation starts by describing the fluid in terms of elliptic cylinder coordinates, which allows the fluid loading term to be expressed in terms of Mathieu functions. By moving the fluid loading term to the right-hand side of the equation, it is considered to be a force. The operator that remains on the left-hand side is the same as that of the *in vacuo* plate: a fourth-order, constant coefficient, ordinary differential equation. Therefore, the problem appears to be an inhomogeneous ordinary differential equation. The solution that results has the same form as that of the *in vacuo* plate: the sum of a forced solution, and four homogeneous solutions, each of which is multiplied by an arbitrary constant. These constants are then chosen to satisfy the structural boundary conditions on the two ends of the plate. Results for the finite plate are compared to the infinite plate in both the wave number and spatial domains. The theoretical predictions of the plate velocity response are also compared to results from finite element analysis and show reasonable agreement over a large frequency range. [DOI: 10.1121/1.2357716]

PACS number(s): 43.40.Dx, 43.40.Rj [DF] Pages: 3664–3671

I. INTRODUCTION

In structural acoustics, there are a limited number of geometries in which a closed form solution has been obtained.[1] These include the spherical shell,[2] infinite cylindrical shell, and infinite plate. The details of these solutions are given by Skelton and James.[3] For the infinite cylindrical shell and the infinite plate, the equations of motion are Fourier transformed and the resulting equations are then solved to yield a closed form solution for the transform. The inverse transform is then a sum of two parts: the propagating and decaying waves associated with the structure, which can be obtained using contour integration, and a branch cut contribution, which is due to fluid that extends to infinity. For the spherical shell, both the structural equations and the surrounding fluid are described in spherical coordinates, and the solution is obtained using separation of variables. One of the qualitative differences between the solutions for the spherical shell, which is finite, and the infinite cylindrical shell and plate is that the solution for the spherical shell has no branch cut contribution, whereas both infinite geometries contain branch cut contributions. Methods of approximating the contributions of the branch cut were described by DiPerna and Feit.[4,5] The above solutions have been frequently studied for several reasons: they are relatively simple to solve and they give insight as to the physics of the coupled structural/acoustic motion. Fourier transform solutions have also been used as starting points for the semi-infinite plate using the Wiener-Hopf technique[6] and the baffled plate. For problems other than the above-mentioned geometries, recourse must be made to numerical solutions. For example, Photiadis[7] treated the problem of the scattering of an acoustic wave by a finite length plate by numerically solving an integral equation.

For the finite length, submerged plate, the Fourier transform solution becomes problematic. This is because the equation of motion for the plate/fluid system is only defined on a finite interval, whereas the Fourier transform requires an integration over an infinite interval. Typically what has been done to circumvent this problem is to assume that the plate is baffled, which means that the velocity is assumed to vanish beyond the edge of the plate. The underlying reason that the Fourier transform solution of a fluid-loaded finite plate does not easily lead to an exact solution is because the range of integration required for the transform does not coincide with the interface of the plate and the fluid.

In the formulation described in this paper an approach will be used that is more appropriate for a finite geometry than the Fourier transform solution. Instead of using Cartesian coordinates for both the plate and the fluid, Cartesian coordinates will be used to describe the plate, and elliptic cylinder coordinates to describe the fluid. While these coordinate systems may seem incompatible, they happen to coincide precisely at the interface between the fluid and the plate since the limiting case of elliptic cylinder coordinates (as the radial coordinate goes to 0) is a finite length strip.[8] The solution for the acoustic field in the fluid is then expanded in terms of the separable solutions of the Helmholtz equation in elliptic cylinder coordinates, namely Mathieu functions.[8–10] The use of elliptic cylinder coordinates to model radiation and scattering from impenetrable strips is not new. Their use for electromagnetic and acoustic scattering problems is described in Ref. 11 and references therein. The case of the diffraction of electromagnetic waves from a dielectric elliptic cylinder of finite thickness was treated by Yeh.[12] Blake[13]

[a]Electronic mail: daniel.diperna@navy.mil
[b]Electronic mail: hydroacoustics@aol.com
[c]Electronic mail: xingguang.diperna@navy.mil

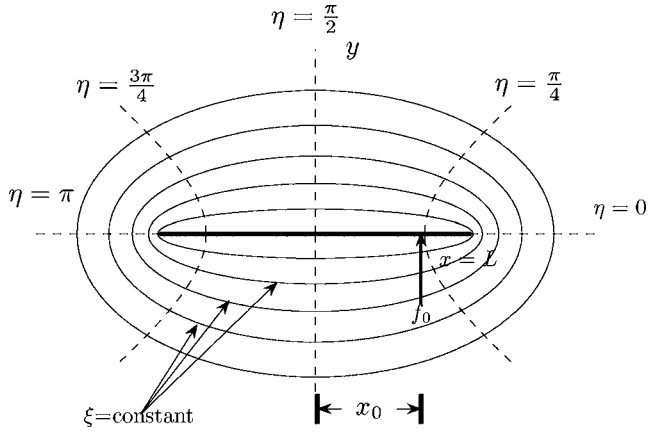

FIG. 1. Geometry of a line driven plate.

used elliptic cylinder coordinates to describe the acoustic field outside of a beam, with an assumed velocity distribution that approximated the *in vacuo* mode shapes to describe the beam vibration. Thus he did not solve the fully coupled problem.

Presumably, the reason elliptic cylinder coordinates have not been used extensively in structural acoustics is that Mathieu functions are not commonly available and are nontrivial to calculate. However, with the increase in computing power and availability of linear algebra packages, it has become simpler to calculate the coefficients required for Mathieu functions as the solution of an eigenvalue problem, rather than using standard recursion formula.

An additional benefit of expanding the acoustic field in terms of Mathieu functions is that the singularity of the velocity field associated with the assumption that the plate is infinitely thin is automatically accounted for via the scale factor of the transformation. This effect has been noted previously in the solution of diffraction problems using coordinate transformations.[14]

By expanding the acoustic field in terms of Mathieu functions and utilizing their orthogonality properties, an expression for the plate velocity is obtained in terms of the eigenfunctions and Green's function of the *in vacuo* plate. The form of the fluid-loaded solution is the same as that of the *in vacuo* plate: the sum of a forced solution (Green's function) and four homogeneous solutions multiplied by arbitrary constants that are then chosen to match the boundary conditions.

II. THEORY

The cross-sectional geometry of the problem being considered here is shown in Fig. 1, with the z coordinate running from $-\infty$ to ∞ into the paper. The fluid is described in elliptical cylinder coordinates, with radial coordinate $\xi=0$ coinciding with the plate, and the curves $\xi=$const being ellipses. The angular coordinate η is defined on $0 \leq \eta < 2\pi$. The plate is described in Cartesian coordinates, with midplane of the plate being located on $-L \leq x \leq L$, $y=0$. The plate is driven by an applied force per unit length of magnitude f_0 at $x=x_0$. The upper surface of the plate corresponds to $\xi=0$, $0 \leq \eta < \pi$ in the fluid, and the lower surface of the plate corresponds to $\xi=0$, and $\pi \leq \eta < 2\pi$ in the fluid. The transformation from elliptic coordinates to Cartesian coordinates is given by

$$x = L \cosh \xi \cos \eta,$$
$$y = L \sinh \xi \sin \eta. \tag{1}$$

The equation of motion for a plate with fluid loading on both sides is given by

$$\mathcal{L}[u(x)] + 2P[u(x)] = f_0 \delta(x - x_0), \tag{2}$$

where $u(x)$ is the plate velocity, $P[u(x)]$ is acoustic pressure, and $\mathcal{L}$ is the structural operator of the *in vacuo* plate. The structural operator is

$$\mathcal{L} = \frac{iD}{\omega} \frac{\partial^4}{\partial x^4} - i\omega m, \tag{3}$$

where ω is the angular frequency, $D=Eh^3/(12(1-\nu^2))$ is the flexural rigidity, E is Young's modulus, ν is Poisson's ratio, h is the thickness of the plate, and m is the mass per unit length of the plate. The factor of 2 in Eq. (2) accounts for the fact that fluid is acting on both the upper and lower surfaces of the plate.

By rearranging Eq. (2) the equation of motion becomes

$$\mathcal{L}[u(x)] = f_0 \delta(x - x_0) - 2P[u(x)], \tag{4}$$

and the fluid loading term now appears to be a forcing function. The left side of the equation is simply the *in vacuo* structural operator, which is an inhomogeneous, constant coefficient, differential equation. From the theory of ordinary differential equations,[15] the solution is the sum of a homogeneous solution and a particular solution, or

$$u(x) = \sum_{n=1}^{4} q_n E_n(x) + f_0 G(x|x_0) - 2\int_{-L}^{L} G(x|\tau) P[u(\tau)]\, d\tau, \tag{5}$$

where q_n are arbitrary constants, $E_n(x)$ are the homogeneous solutions, and $G(x|x_0)$ is the Green's function of the *in vacuo* plate, which satisfy

$$\mathcal{L}[E_n(x)] = 0,$$
$$\mathcal{L}[G(x|x_0)] = \delta(x - x_0), \tag{6}$$

respectively. The homogeneous solutions and Green's functions are given by

$$E_1(x) = e^{ik_f(x+L)},$$
$$E_2(x) = e^{-ik_f(x-L)},$$
$$E_3(x) = e^{k_f(x-L)},$$
$$E_4(x) = e^{-k_f(x+L)},$$

$$G(x|x_0) = \frac{\omega}{4Dk_f^3}[e^{ik_f|x-x_0|} + ie^{-k_f|x-x_0|}], \tag{7}$$

where the flexural wave number $k_f=(m\omega^2/D)^{1/4}$. Note that solutions are normalized as described in Ref. 16 to avoid numerical problems, which can arise if the real part of the argument of the exponential is large and positive. The above normalization assures that the real part of the argument is always less than or equal to zero, and thus the maximum value of $E_n(x)$ is one. It is straightforward to verify that Eq. (5) satisfies Eq. (2) by simply substituting and performing the required operations.

A. Solution of the plate/fluid system

As shown in the Appendix, the acoustic pressure $P(\xi_0, \eta)$ and normal velocity of the fluid $V(\xi_0, \eta)$ on the plate surface $\xi_0=0$ can be expanded in terms of the separable solutions of the Helmholtz equation in elliptic coordinates as follows:

$$P(\xi_0, \eta) = \sum_{n=1}^{\infty} c_n Ms_n^{(3)}(\xi_0, q) se_n(\eta, q) \tag{8a}$$

$$V(\xi_0, \eta) = \frac{1}{i\omega\rho h_\xi(\xi_0, \eta)} \sum_{n=1}^{\infty} c_n Ms_n'^{(3)}(\xi_0, q) se_n(\eta, q), \tag{8b}$$

where $se_n(\eta,q)$ and $Ms_n^{(3)}(\xi_0,q)$ are the odd angular and corresponding radial Mathieu functions, $h_\xi(\xi_0, \eta)$ is the scale factor of the transformation, and c_n are the expansion coefficients of the acoustic field and will be chosen to match the boundary conditions between the fluid and plate. The boundary condition between the fluid and the plate is that the normal acoustic velocity match the plate velocity. Since the normal is defined in opposite directions on the upper and lower surface, and because the angular Mathieu functions have been chosen to be odd, enforcing the following boundary condition on the upper surface of the plate $0 \leq \eta < \pi$ will automatically ensure that the velocity is also matched on the lower surface $\pi \leq \eta < 2\pi$:

$$u[x(\eta)] = \frac{1}{i\omega\rho h_\xi(\xi_0, \eta)} \sum_{n=1}^{\infty} c_n Ms_n'^{(3)}(\xi_0, q) se_n(\eta, q). \tag{9}$$

Utilizing the orthogonality properties of the angular Mathieu functions, the expansion coefficients c_n of the acoustic field can be solved for as follows:

$$c_n = \frac{2i\omega\rho}{\pi Ms_n'^{(3)}(\xi_0, q)} \int_0^{\pi} h_\xi(\xi_0, \eta) se_n(\eta, q) u[x(\eta)]\, d\eta. \tag{10}$$

Inserting this expression for c_n into Eq. (8a) yields the following for the acoustic pressure on the surface of the plate:

$$P(\xi_0, \eta) = \frac{2i\omega\rho}{\pi} \sum_{n=1}^{\infty} F_n se_n(\eta, q), \tag{11}$$

where the modal reaction forces F_n are given by

$$F_n = \frac{Ms_n^{(3)}(\xi_0, q)}{Ms_n'^{(3)}(\xi_0, q)} \int_0^{\pi} h_\xi(\xi_0, \eta) se_n(\eta, q) u[x(\eta)]\, d\eta. \tag{12}$$

Inserting Eq. (11) into Eq. (5) and performing the integration yields the following expression for the plate velocity:

$$u(x) = \sum_{n=1}^{4} q_n E_n(x) + f_0 G(x|x_0) - \frac{4i\omega\rho}{\pi} \sum_{n=1}^{\infty} F_n H_n(x), \tag{13}$$

where the modal coupling function $H_n(x)$ is given by

$$H_n(x) = \int_{-L}^{L} se_n(\eta(\tau), q) G(x|\tau)\, d\tau. \tag{14}$$

The velocity of the plate is now known in terms of four unknown constants, q_n, which will be chosen to match the boundary conditions on the edges of the plate, and the modal reaction forces F_n. These forces can be solved for by inserting Eq. (13) into Eq. (12), and integrating, to yield the following system of equations:

$$F_n + \frac{4i\omega\rho}{\pi} \sum_{m=1}^{\infty} M_{nm} F_m = \sum_{m=1}^{4} E_{nm} q_m + f_0 G_n \tag{15}$$

where the following definitions have been made:

$$M_{nm} = \frac{Ms_n^{(3)}(\xi_0, q)}{Ms_n'^{(3)}(\xi_0, q)} \int_0^{\pi} se_n(\eta, q) h_\xi(\xi_0, \eta) H_m[x(\eta)]\, d\eta,$$

$$E_{nm} = \frac{Ms_n^{(3)}(\xi_0, q)}{Ms_n'^{(3)}(\xi_0, q)} \int_0^{\pi} se_n(\eta, q) h_\xi(\xi_0, \eta) E_m[x(\eta)]\, d\eta,$$

$$G_n = \frac{Ms_n^{(3)}(\xi_0, q)}{Ms_n'^{(3)}(\xi_0, q)} \int_0^{\pi} se_n(\eta, q) h_\xi(\xi_0, \eta) G[x(\eta)|x_0]\, d\eta. \tag{16}$$

By truncating the system of equations in Eq. (15) at a value of $M=O(k_{\max}2L)$, where $k_{\max}=\max(k,k_f)$, the solution for the modal reaction forces $\underline{F}$, in matrix notation is as follows:

$$\underline{F} = \underbrace{\left[I + \frac{4i\omega\rho}{\pi}\mathbf{M}\right]^{-1}\mathbf{E}}_{\mathbf{F}^q}\,\underline{q} + \underbrace{\left[I + \frac{4i\omega\rho}{\pi}\mathbf{M}\right]^{-1}\underline{G}}_{\underline{F}^{dr}} f_0. \tag{17}$$

Note that the modal reactions forces are a sum of two terms: the first term $\mathbf{F}^q$ is the reaction of the fluid due to the homogeneous solutions of the *in vacuo* plate, and the second term $\underline{F}^{dr}$ is the reaction of the fluid to the Green's function of the *in vacuo* plate. Inserting this expression into Eq. (13) yields

$$u(x) = \sum_{n=1}^{4} E_n^{fl}(x) q_n + G^{fl}(x|x_0) f_0, \tag{18}$$

where the homogeneous solutions $E_m^{fl}(x)$ and Green's function $G^{fl}(x|x_0)$ of the **fluid-loaded** plate are given by

$$E_n^{fl}(x) = E_n(x) - \frac{4i\omega\rho}{\pi} \sum_{m=1}^{M} \mathbf{F}_{mn}^q H_m(x), \tag{19a}$$

$$G^{fl}(x|x_0) = G(x|x_0) - \frac{4i\omega\rho}{\pi}\sum_{m=1}^{M} F_m^{dr} H_m(x). \tag{19b}$$

Note that the fundamental form of the solution for the fluid-loaded plate is the same as that of the *in vacuo* plate, the sum of the particular solution and four homogeneous solutions, which will be chosen to match the structural boundary conditions.

B. Boundary conditions

Equation (18) gives the complete solution for the velocity on a fluid-loaded plate. There are four arbitrary constants, q_n, that may be used to satisfy the boundary conditions on the structure. The typical boundary conditions on a plate are that the edges are clamped or free. Each of these boundary conditions imposes two constraints on the field at each end of the plate, yielding a total of four constraints. For a clamped boundary, the displacement and its derivative with respect to x must vanish, and for a free edge the second and third derivatives with respect to x must vanish.[6] For example, for a plate with both edges free, the boundary conditions lead to the following system of equations:

$$\sum_{m=1}^{4} E_m''^{fl}(-L)q_m = -G''^{fl}(-L|x_0)f_0,$$

$$\sum_{m=1}^{4} E_m'''^{fl}(-L)q_m = -G'''^{fl}(-L|x_0)f_0,$$

$$\sum_{m=1}^{4} E_m''^{fl}(L)q_m = -G''^{fl}(L|x_0)f_0,$$

$$\sum_{m=1}^{4} E_m'''^{fl}(L)q_m = -G'''^{fl}(L|x_0)f_0, \tag{20}$$

from which it is trivial to solve for the constants q_m. In general, in order to calculate the derivatives of the fluid-loaded Green's functions and homogeneous solutions, which are required for the boundary conditions, the following will need to be calculated:

$$H_n(x) = \int_{-L}^{L} se_n(\eta(\tau),q)G(x|\tau)\,d\tau,$$

$$H_n'(x) = \int_{-L}^{L} se_n(\eta(\tau),q)\frac{\partial G(x|\tau)}{\partial x}\,d\tau,$$

$$H_n''(x) = \int_{-L}^{L} se_n(\eta(\tau),q)\frac{\partial^2 G(x|\tau)}{\partial x^2}\,d\tau,$$

$$H_n'''(x) = \int_{-L}^{L} se_n(\eta(\tau),q)\frac{\partial^3 G(x|\tau)}{\partial x^3}\,d\tau. \tag{21}$$

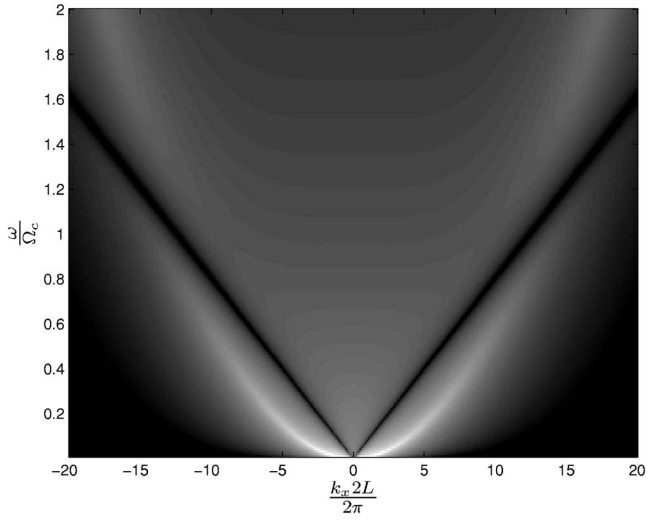

FIG. 2. Gray-scale map of the logarithm of the Fourier transform of the velocity on an infinite plate due to a line drive located at $x=x_0$.

III. RESULTS

In this section, results for the line-driven, finite, fluid-loaded plate will be compared to analogous results for the line-driven infinite plate, and additionally to results from finite element analysis.

A. Comparison to an infinite plate

The case being considered in this section is that of a 1-in.-thick steel plate with a total length of 2 m ($L=1$ m), immersed in water, with no structural damping. Figure 2 shows a gray-scale image of the logarithm of the magnitude of the Fourier transform of the velocity of an infinite plate due to a line drive as a function of frequency, or $\tilde{G}^{\infty}(k_x,f)$. White represents a large velocity, and black a small velocity. The notable features are the flexural wave dispersion curve, which appears as a white parabola and has a large response, and the acoustic lines, which form the dark "V." Along these lines, the fluid has a large impedance and thus the velocity of the plate is small along these lines. For frequencies above the critical frequency $\Omega_c=\sqrt{12}c^2/(hc_p)$, where the flexural wave number crosses the acoustic line, the flexural waves are strongly radiating, and the flexural waves have lower magnitude and are somewhat broader than below the coincidence frequency. Note that the assumptions leading to the thin plate equations are typically violated above the coincidence frequency. Figure 3 shows the Fourier transform of the velocity on the fluid-loaded finite plate in the absence of boundary conditions on the edge of the plate, $\tilde{G}^{fl}(k_x,f)$, where the fluid-loaded Green's function is given by Eq. (19b), driven at its center. This is a notable point since the Green's function for the finite plate is not a function of $|x-x_0|$, as is the case for an infinite plate. Because the plate is only defined over $-L<x<L$, the limits of the Fourier transform are also limited to this range. As can be seen, the results are strikingly different than that of the infinite plate. While the flexural wave dispersion curve can still be seen, superimposed on it are aliased versions of the infinite plate dispersion curve,

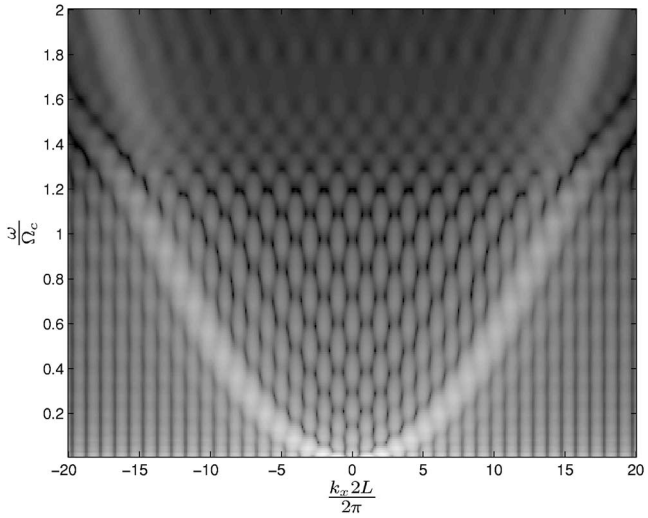

FIG. 3. Gray-scale map of the logarithm of the Fourier transform of the velocity on a finite plate due to a line drive located at $x=x_0$. Note that no boundary conditions have been imposed on the ends of the plate.

which are spaced at intervals of $2\pi/2L$. This phenomenon is very similar to the behavior observed on periodically stiffened plates and shells.[17]

Figure 4 shows the Fourier transform of the velocity of the finite plate now subject to free boundary conditions at each end, or $\tilde{u}(k_{x,f})$, with $u(x)$ as defined in Eq. (18), and the constants q_n chosen to satisfy free boundary conditions at both ends of the plate. Below the coincidence frequency $\omega/\Omega_c=1$, there are a series of horizontal stripes at discrete frequencies. These large velocities correspond to resonances that are not seen in the infinite plate. There are no resonances above the coincidence frequency due to the fact that the flexural waves are radiating strongly, and therefore the two edges are only interacting weakly. Note that in both Fig. 3 and Fig. 4, there was no structural loss, which means the only loss

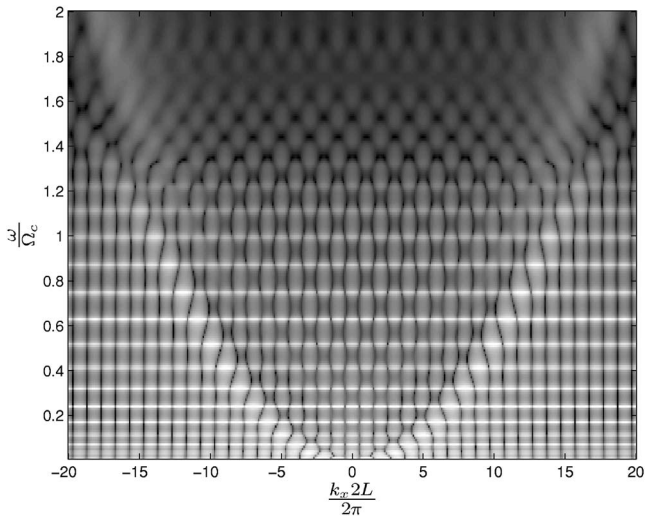

FIG. 4. Gray-scale map of the logarithm of the Fourier transform of the velocity on a finite plate due to a line drive located at $x=x_0$, where free boundary conditions have been imposed at each end of the plate. Note the length resonances that show up as horizontal stripes at discrete frequencies.

was due to radiation into the fluid. This is why the effects of the plate having a finite length are much more prominent below the coincidence frequency, where the loss due to radiation is small. If there were a large structural loss factor, the effects of the plate having a finite length would be diminished even below coincidence since the waves on the structure would be highly damped and most of the energy would never reach the edges.

Figure 5 shows the fluid-loaded Green's function as given in Eq. (19b), for a finite plate driven at its center, normalized by the drive point admittance of the *in vacuo* plate, compared to that of the infinite plate, for several frequencies. Notably, the velocity for the finite plate only goes out the length of the plate. For the two frequencies below coincidence, there is a substantial difference between the finite length plate and the infinite plate, with the difference being larger near the end of the plate. For the frequency above coincidence, the finite plate velocity is closer to that of the infinite plate because the flexural waves are strongly radiating, and most of the vibrational energy has shed before interacting with the edges of the plate.

B. Comparison to numerical solution

In order to confirm the validity of the solution developed in this paper, a two-dimensional finite element analysis (FEA) of the submerged, line-driven plate, with $x_0=0$ and free/free boundary conditions, was performed using the finite element code ABAQUS. The case being considered is a 0.2-in.-thick brass plate immersed in water, with L=8in., and a structural loss factor of 0.001. The plate is modeled by four-node bilinear plane strain elements with 8 elements across the thickness of the plate and 600 elements across the length of the plate. Acoustic elements are used to model the region between the plate and a surface on which a radiating (nonreflecting) boundary condition is applied. These two aspects of the finite element model are somewhat different than the theory developed here, which satisfied the Sommerfeld radiation condition in the fluid and used thin plate theory to represent the plate. The only approximation in the theory presented here is the truncation of the matrix in Eq. (15). Figure 6 shows the comparison between the drive point admittance predicted by FEA and the theory presented in this paper. Over the entire frequency range the agreement is quite reasonable. The resonance frequencies predicted by FEA are slightly higher than the theory, which is typical of FEA predictions. Additionally, the peaks of the resonances are not precisely the same level, which is also to be expected since the internal loss of the plate was small. Figure 7 shows a comparison of the velocity at the end of the plate due to a drive at $x_0=0$. Again, the agreement is very close.

Although the primary goal of this paper was to develop a procedure to calculate the vibrational response of the plate, it is a trivial exercise to calculate the radiated pressure. Once

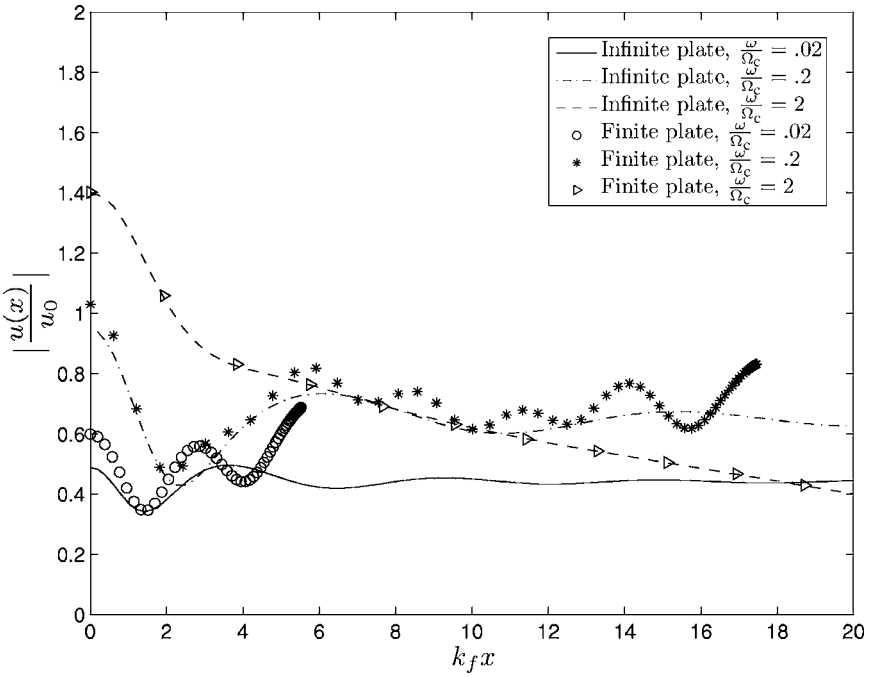

FIG. 5. Finite plate velocity normalized by $u_0=k_f/(4\omega m)$ as a function of nondimensional distance $k_f x$ for three frequencies compared to infinite plate.

the velocity on the surface has been calculated, the expansion coefficients c_n can be calculated via Eq. (10). The pressure anywhere in the fluid is then given by

$$P(\xi,\eta)=\sum_{n=1}^{\infty} c_n Ms_n^{(3)}(\xi,q)se_n(\eta,q). \tag{22}$$

The pressure per unit force was calculated at the point $x=0$, $y=2.25L$ and compared to finite element results. The comparison is shown in Fig. 8. Again, there is close agreement.

C. Convergence

In Sec. II it was stated the number of terms should be truncated at $M=O(k_{\max}2L)$. This follows directly from the Nyquist criterion that a function must be sampled at least two points per wave. For what follows, the number of modes M will correspond to be the number of points. Consider below the coincidence frequency, where the largest wave number is the flexural wave number k_f. Then $k_f 2L=2\pi\Lambda$, where $\Lambda=2L/\lambda_f$ is the total number of waves on the length of the plate. Therefore, the criteria is $M/\Lambda=O(2\pi)$, which says that the number of unknowns per wave must be on the order of 6, which is consistent with the Nyquist criterion. To check this

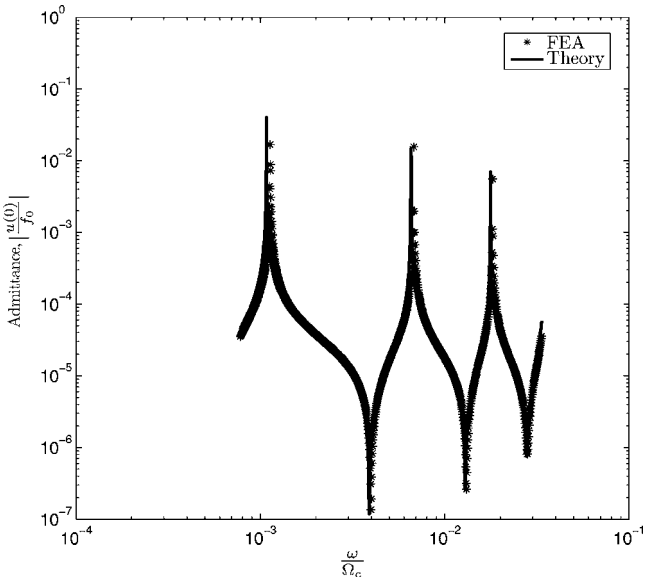

FIG. 6. Velocity at drive point due to a drive at $x_0=0$ with free/free boundary conditions computed from theory compared to results from finite element analysis.

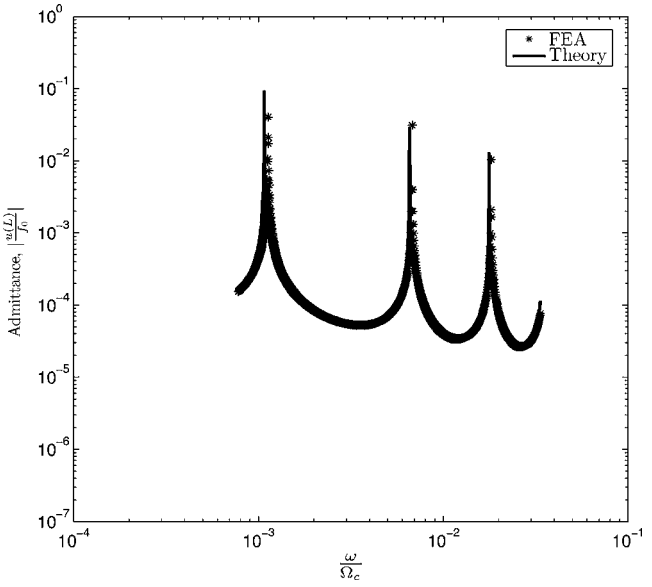

FIG. 7. Velocity at $x=L$ due to a drive at $x_0=0$ with free/free boundary conditions computed from theory compared to results from finite element analysis.

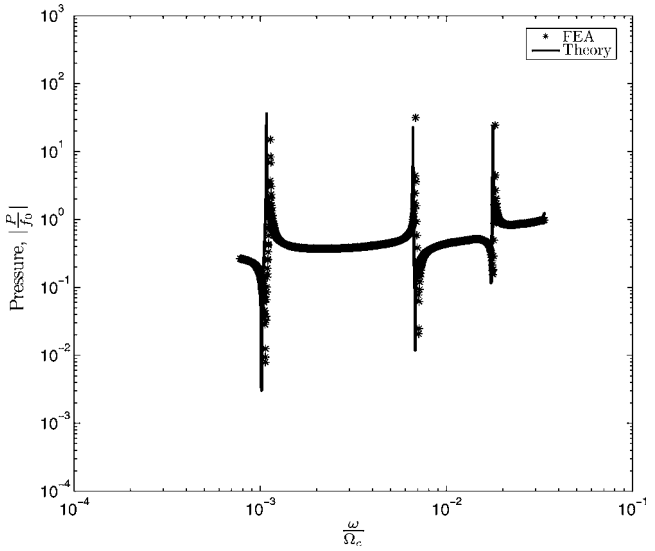

FIG. 8. Radiated pressure at $x=0$, $y=2.25L$ due to a drive at $x_0=0$ with free/free boundary conditions computed from theory compared to results from finite element analysis.

numerically, the velocity on the free/free plate was computed as a function of the number of terms per wave M/Λ for several frequencies below the coincidence frequency. The metric being used is

$$\epsilon(M) = \left\{ \left[\frac{\int_{-L}^{L} [u^M(x) - u^{M-1}(x)]^2 \, dx}{\int_{-L}^{L} [u^{M_{\max}}(x)]^2 \, dx} \right] \right\}^{1/2}, \tag{23}$$

where $u^M(x)$ is the estimate of the plate velocity using M terms and $M^{\max}$ is number of terms used in the converged solution. Therefore the metric is a measure of how much the solution is changing as one more term is used. The denominator is simply for normalization. The results are shown in Fig. 9. When M/Λ is less than 1, every time an extra term is added, the solution changes about the same amount $\epsilon(M) \approx 0.01$. Above $M/\Lambda=2$, the Nyquist rate, the amount of change in the solution is decreasing about two orders of magnitude as the number of terms is doubled.

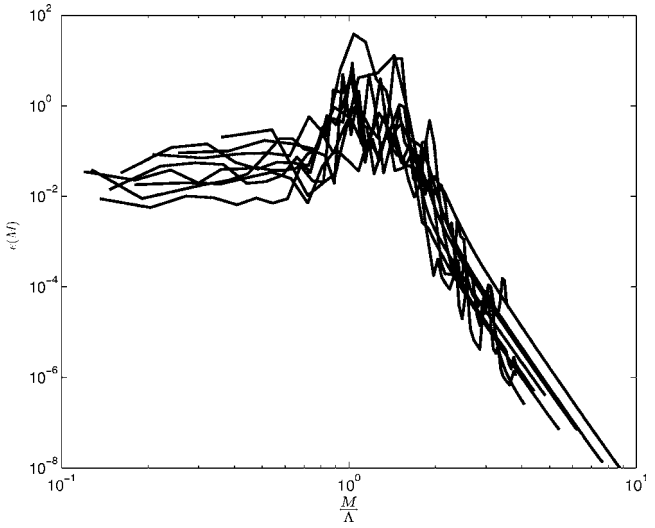

FIG. 9. Convergence of the series as a function of the number of terms per wave.

IV. SUMMARY

A formulation has been developed to predict the velocity of a submerged finite plate due to a line drive. By expanding the acoustic pressure and velocity in terms of the eigenfunctions of the Helmholtz equation in elliptic cylinder coordinates, a description of the plate velocity is obtained in the same form as that of the *in vacuo* plate. The velocity of the submerged plate is found to be the sum of four homogeneous solutions, each of which can exist in the absence of an applied force and therefore can be multiplied by an arbitrary constant, and a Green's function, which is the response of the submerged plate due to a concentrated line force. The four arbitrary constants are then chosen to satisfy the four structural boundary conditions on the edges of the plate.

The velocity of the finite plate as predicted by this formulation is compared to the corresponding result for the infinite plate to get an idea of the physical phenomena due solely to the finite length of the plate, such as resonances at discrete frequencies. Predictions from the theory were also compared to results from FEA and show reasonable agreement.

ACKNOWLEDGMENTS

This work was sponsored by the Office of Naval Research, under the direction of Lynn Petersen, William Martin, and Stephen Schreppler.

APPENDIX: MATHIEU FUNCTIONS

In elliptic cylinder coordinates, the governing equation for the acoustic field can be written as

$$P_{\xi\xi}(\xi,\eta) + P_{\eta\eta}(\xi,\eta) + \frac{k^2L^2}{2}(\cosh 2\xi - \cos 2\eta)P(\xi,\eta) = 0. \tag{A1}$$

$k=\omega/c$ is the acoustic wave number, c is the speed of sound in the fluid, ω is the angular frequency, and η is the angular coordinate defined on $[0,2\pi]$, the upper surface of the plate being $[0,\pi]$, and the lower surface being $[\pi,2\pi]$. The radial coordinate is ξ, with $\xi_0=0$ being a strip corresponding to the plate surface. This equation can be solved through separation of variables, and its solutions are, in the notation used by Abramowitz and Stegun,[9]

$$P(\xi,\eta) = \sum_{n=1}^{\infty} [a_n Se_n(\xi,q) + c_n Ms_n^{(3)}(\xi,q)] se_n(\eta,q) + \sum_{n=0}^{\infty} [b_n Ce_n(\xi,q) + d_n Mc_n^{(3)}(\xi,q)] ce_n(\eta,q), \tag{A2}$$

where are $se_n(\eta,q)$ and $ce_n(\eta,q)$ are the odd and even angular Mathieu functions, respectively, which correspond to sine and cosine functions in a circular coordinate system,

$Se_n(\xi,q)$ and $Ce_n(\xi,q)$ are radial Mathieu functions, which are the incoming radial solutions corresponding to Bessel functions of the first kind in circular coordinates, $Ms_n^{(3)}(\xi,q)$ and $Mc_n^{(3)}(\xi,q)$ are the outgoing radial solutions corresponding to Hankel functions in a circular coordinate system, and $q=(kL/2)^2$. Since the subject of the paper is the response of the plate due to a line drive on the structure, only the outgoing solutions are required, and therefore the coefficients a_n and b_n, which multiply the incoming solutions, must be zero. If the scattering problem were being considered that is, where the source is in the fluid instead of on the structure, the field due to the source could be represented in terms of the incoming solutions.

The normal acoustic velocity can be found from

$$V(\xi_0,\eta) = \frac{1}{i\omega\rho h_\xi(\xi_0,\eta)} \frac{\partial P(\xi,\eta)}{\partial \xi}\bigg|_{\xi=\xi_0}, \tag{A3}$$

where the scale factor[18] is given by

$$h_\xi(\xi_0,\eta) = \frac{L}{\sqrt{2}}\sqrt{\cosh 2\xi_0 - \cos 2\eta}. \tag{A4}$$

The pressure and velocity are now given by

$$P(\xi_0,\eta) = \sum_{n=1}^{\infty} [c_n Ms_n^{(3)}(\xi_0,q)se_n(\eta,q) + d_n Mc_n^{(3)}(\xi_0,q)ce_n(\eta,q)],$$

$$V(\xi_0,\eta) = \frac{1}{i\omega\rho h_\xi(\xi_0,\eta)} \sum_{n=1}^{\infty} [c_n Ms_n'^{(3)}(\xi_0,q)se_n(\eta,q) + d_n Mc_n'^{(3)}(\xi_0,q)ce_n(\eta,q)]. \tag{A5}$$

The expression for the normal acoustic velocity is comprised of two sets of terms, one that is odd and one that is even. Because the normal on the upper surface of the plate ($0 \le \eta < \pi$) is pointing up, and the normal on the lower surface ($\pi \le \eta < 2\pi$) is pointing down, in order for the velocity on both surfaces to match the plate velocity, the coefficients of the even terms must be zero, or $d_n=0$, which leaves the following:

$$P(\xi_0,\eta) = \sum_{n=1}^{\infty} c_n Ms_n^{(3)}(\xi_0,q)se_n(\eta,q),$$

$$V(\xi_0,\eta) = \frac{1}{i\omega\rho h_\xi(\xi_0,\eta)} \sum_{n=1}^{\infty} c_n Ms_n'^{(3)}(\xi_0,q)se_n(\eta,q). \tag{A6}$$

The following orthogonality relationship will also be useful,

$$\int_0^\pi se_n(\eta,q)se_m(\eta,q)d\eta = \frac{\pi}{2}\delta_{nm}, \tag{A7}$$

where δ_{nm} is the Kronecker delta function.

[1] M. Junger and D. Feit, *Sound, Structures, and Their Interaction*, 2nd ed. (Acoustical Society of America, New York, 1993).
[2] M. C. Junger, "Sound scattering by thin elastic shells," J. Acoust. Soc. Am. **24**(4), 366–373 (1951).
[3] E. A. Skelton and J. H. James, *Theoretical Acoustics of Underwater Structures* (Imperial College, London, 1997).
[4] D. T. DiPerna and D. Feit, "An approximate Green's function for a locally excited fluid-loaded plate," J. Acoust. Soc. Am. **114**(1), 194–199 (2003).
[5] D. T. DiPerna and D. Feit, "An approximate analytic solution for the radiation from a line-driven fluid-loaded plate," J. Acoust. Soc. Am. **110**, 3018–3024 (2001).
[6] A. N. Norris and G. R. Wickham, "Acoustic diffraction from the junction of two flat plates," Proc. R. Soc. London, Ser. A **451**, 631–655 (1995).
[7] D. M. Photiadis, "The scattering of sound from fluid-loaded plates," J. Acoust. Soc. Am. **85**(6), 2440–2451 (1989).
[8] P. M. Morse and H. Feshbach, *Methods of Theoretical Physics*, Volume II (McGraw-Hill, New York, 1953).
[9] M. Abramowitz and I. A. Stegun, *Handbook of Mathematical Functions* (National Bureau of Standards, Washington, DC, 1970).
[10] N. W. McLachlan, *Theory and Application of Mathieu Functions* (Oxford U. P., Oxford, 1951).
[11] T. B. A. Senior, J. J. Bowman, and P. L. E. Uslenghi, *Electromagnetic and Acoustic Scattering by Simple Shapes* (Hemisphere, New York, 1987).
[12] C. Yeh, "The diffraction of waves by a penetrable ribbon," J. Math. Phys. **4**, 65–71 (1963).
[13] W. K. Blake, "The radiation from free-free beams in air and in water," J. Sound Vib. **33**(4), 427–250 (1974).
[14] L. Shafai, "An improved integral equation for the numerical solution of two-dimensional diffraction problems," Can. J. Phys. **48**, 954–963 (1970).
[15] P. M. Morse and H. Feshbach, *Methods of Theoretical Physics*, Volume I (McGraw-Hill, New York, 1953).
[16] F. B. Jensen, W. A. Kuperman, M. B. Porter, and H. Schmidt, *Computational Ocean Acoustics* (AIP, Woodbury, NY, 1994).
[17] D. M. Photiadis, E. G. Williams, and B. H. Houston, "Wave-number space response of a near periodically ribbed shell," J. Acoust. Soc. Am. **101**(2), 877–886 (1997).
[18] F. B. Hildebrand, *Advanced Calculus for Applications*, 2nd ed. (Prentice-Hall, Englewood Cliff, NJ, 1976).

On formulation of a transition matrix for electroporoelastic medium and application to analysis of scattered electroseismic wave

Chau-Shioung Yeh[a)]
Department of Civil Engineering, and Institute of Applied Mechanics, National Taiwan University, Taipei, Taiwan

Szu-Miau Chen
Department of Civil Engineering, National Taiwan University, Taipei, Taiwan

Tsung-Jen Teng
National Center for Research on Earthquake Engineering, Taipei, Taiwan

Yang-Jye Lee
Department of Civil Engineering, National Ilan University, Ilan, Taiwan

(Received 4 January 2006; revised 20 August 2006; accepted 31 August 2006)

On the basis of Pride's theory (1994) which couples Biot's theory for poroelastic medium (1956) and Maxwell equations via flux/force transport equations, we extend Yeh *et al.* (2004) approach for poroelastic medium to develop a transition matrix for electroporoelastic medium. The transition matrix, which relates the coefficients of scattered waves to those of incident waves, is then derived through the application of Betti's third identity and the associated orthogonality conditions for the electroporoelastic medium. To illustrate the application, a simple case of the scattering problem of a spherical electroporoelastic inclusion, embedded within the surrounding electroporoelastic medium subjected to an incident plane compressional wave is considered.
© *2006 Acoustical Society of America.* [DOI: 10.1121/1.2357713]

PACS number(s): 43.40.Ph, 43.20.Bi, 43.20.Gp, 43.30.Ma [PEB] Pages: 3672–3693

I. INTRODUCTION

The phenomenon of electroseismic effect has been studied for about 60 years. This has led to applications in the monitoring of electrical properties for the control of pollution (Roberts and Lin, 1997), the monitoring for the movement of volcanic fluids and detecting the precursory electromagnetic signals associated with an eruption (Revil *et al.*, 2003), hydrothermal energy and the studies of earthquake prediction (Mogi, 1985), oil and gas reservoir monitoring (Block and Harris, 2006) and so on. On the theoretical side, Frenkel (1944) has postulated equations that can be used to estimate the amount of relative fluid motion induced by a seismic wave. Neev and Yeatts (1989) have also postulated a set of equations to model the interaction between mechanical waves and electric fields due to electrokinetics. Pride (1994) has proposed a volume-averaged method for deriving the continuum equations that have the form of Maxwell's equations coupled with Biot's (1956) equations. On the numerical side, Pride and Haartsen (1996) and Mikhailov *et al.* (1997) have applied an analytical Green's function to obtain eignevector solutions for porous media, which can be used to simulate layered media. Garambois and Dietrich (2001) have extended Haartsen and Pride's (1997) work, adopted the approach of the generalized reflection and transmission matrix method (GRTM) (Kennett and Kerry, 1979) and employed the discrete wave number integration method of Bouchon (1981) to handle the calculations of the coupled seismic and electromagnetic waves in a fluid-saturated stratified porous medium. Han and Wang (2001) have presented a fast finite-element method to simulate the electroseismic conversion in the time domain. Pain *et al.* (2005) have described a finite-element formulation that can be utilized to solve the Biot poroelastic equations coupled to a single electrokinetic conversion equation (a simplification of Maxwell's equations). White (2005) has derived an asymptotic theory that enables forward modeling of the electroseismic response for full three-dimensional geometries on a scale that is relevant to exploration.

Previous studies about electroseismic problems most often focus on two-dimensional cases. Only simplified or asymptotic form of solutions with regular geometry boundaries has been considered. To go beyond these limitations, we will develop a formulation based on transition matrix to solve electroseismic wave scattering problems.

In this paper, on the basis of Pride's theory, the transition matrix for electroporoelstic media is developed by applying the approach used for elastic media (Pao, 1978) and poroelastic media (Berryman, 1985; Yeh *et al.*, 2004). The coupled equations of motion are decomposed into two parts: One describing the dilatational (longitudinal) waves and the other the rotational (transverse) waves. The former ones include Biot's fast and slow waves, and the latter ones contain the mechanical shear and electromagnetic waves. In our formulation, we present the basis functions in an analytical

[a)]Author to whom correspondence should be addressed. Fax: +886-2-2363-9290. Electronic mail: csyeh@iam.ntu.edu.tw

 © 2006 Acoustical Society of America

form such that orthogonality relationships are preserved. Instead of asymptotic methods, we apply the Wronskian formula which has been applied by Yeh *et al.* (2004) for the derivation of poroelastic medium to prove the orthogonality conditions. To illustrate the application of the transition matrix formulation, we present a solution for the scattering of the incident plane waves by an embedded spherical electroporoelastic inclusion in a electroporoelastic medium.

The composition of the paper is designated as follows. In Sec. II, the governing equations for an isotropic and homogeneous porous continuum are presented and decoupled. The basis functions in spherical coordinates and their orthogonality conditions are then given. In Sec. III, we show a series expansions of an incident wave with given coefficients, and determine the coefficients of the refracted and scattered waves. Then, the transition matrix for a spherical electroporoelastic inclusion is obtained. In Sec. IV, a solution for a spherical electroporoelastic inclusion subjected to a plane compressional wave is illustrated.

II. THE BASIS FUNCTIONS AND THE ORTHOGONALITY CONDITIONS

A. Governing equations

Pride (1994) has adopted volume-averaging arguments to derive a complete set of equations that describe the coupled seismic and electromagnetic waves in a porous continuum. With an $\exp(i\omega t)$ time dependence for motion with circular frequency ω in a homogeneous and isotropic space, the Pride's governing equations for electroporoelastic medium can be written as follows:

$$\nabla \times \mathbf{E} = -i\omega \mathbf{B}, \tag{1}$$

$$\nabla \times \mathbf{H} = i\omega \mathbf{D} + \mathbf{J}, \tag{2}$$

$$\nabla \cdot \boldsymbol{\tau} = -\omega^2(\rho \mathbf{u} + \rho_f \mathbf{w}), \tag{3}$$

$$\mathbf{J} = \sigma \mathbf{E} + L(-\nabla p + \omega^2 \rho_f \mathbf{u}), \tag{4}$$

$$i\omega \mathbf{w} = L\mathbf{E} + \frac{k(\omega)}{\eta}(-\nabla p + \omega^2 \rho_f \mathbf{u}), \tag{5}$$

$$\boldsymbol{\tau} = (H - 2G)(\nabla \cdot \mathbf{u})\mathbf{I} + G(\nabla \mathbf{u} + \mathbf{u}\nabla) + C(\nabla \cdot \mathbf{w})\mathbf{I}, \tag{6}$$

$$-p = C\nabla \cdot \mathbf{u} + M\nabla \cdot \mathbf{w}, \tag{7}$$

$$\mathbf{B} = \mu \mathbf{H}, \tag{8}$$

$$\mathbf{D} = \epsilon \mathbf{E}, \tag{9}$$

where $\mathbf{u}$ is the average displacement of the solid grains, $\mathbf{w} = \phi(\mathbf{u}_f - \mathbf{u})$ is the "filtration displacement," ϕ is the porosity, $\mathbf{u}_f$ is the average displacement of pore fluid, p is the pore-fluid pressure, ρ is the bulk density, ρ_f is the pore fluid density, η is the fluid viscosity, $\mathbf{E}$ is the electric field, $\mathbf{H}$ is the magnetic field, $\mathbf{B}$ is the magnetic flux, $\mathbf{D}$ is the dielectric displacement, $\boldsymbol{\tau}$ is the bulk-stress tensor, ϵ is the electrical permittivity, μ is the magnetic permeability, and $\mathbf{I}$ is the identity matrix. The electrical conductivity of the material $\sigma(\omega)$, the electrokinetic coupling coefficient $L(\omega)$ and the dynamic permeability $k(\omega)$ are complex and frequency-dependent. The parameters H, G, C, and M are the material constants for the poroelastic material defined by Biot (1962).

B. Decomposition of equations of motion

Substitutions of Eqs. (6) and (7) into Eqs. (3) and (5), respectively, yield the equations of motion for a homogeneous poroelastic material coupled with electromagnetic field

$$(H - G)\nabla\nabla \cdot \mathbf{u} + G\nabla^2 \mathbf{u} + \omega^2 \rho \mathbf{u} + C\nabla\nabla \cdot \mathbf{w} + \omega^2 \rho_f \mathbf{w} = \mathbf{0}, \tag{10}$$

$$C\nabla\nabla \cdot \mathbf{u} + \omega^2 \rho_f \mathbf{u} + M\nabla\nabla \cdot \mathbf{w} + \omega^2 \tilde{\rho} \mathbf{w} + i\omega \tilde{\rho} L\mathbf{E} = \mathbf{0}, \tag{11}$$

where

$$\tilde{\rho}(\omega) = \frac{\eta}{i\omega k(\omega)} \tag{12}$$

is the effective density of the fluid in relative motion.

General solutions expressed in terms of the displacement vectors $\mathbf{u}$ and $\mathbf{w}$ directly are usually difficult because these vectors are coupled in the original equations of motions Eqs. (10) and (11). Therefore, a formulation for general solutions in terms of some potentials is proposed, and on the basis of Helmholtz's theorem (Gregory 1996), any general solutions for displacement vectors $\mathbf{u}$ and $\mathbf{w}$, which are assumed to exist continuous derivatives up to at least the second order, can be decomposed into two scalar potentials ϕ_1 and ϕ_2, and two divergence-free vector potentials $\boldsymbol{\psi}_1$ and $\boldsymbol{\psi}_2$

$$\mathbf{u} = \nabla \phi_1 + \nabla \times \boldsymbol{\psi}_1, \tag{13}$$

$$\mathbf{w} = \nabla \phi_2 + \nabla \times \boldsymbol{\psi}_2. \tag{14}$$

It should be noted that each of the two Helmholtz's decompositions in Eqs. (13) and (14) is unique up to the additive gradient of a scalar harmonic function or the additive curl of a vector harmonic function. And then, completeness of the above representations is questionable. Therefore, a solution scheme adapted from the "Lamé's potentials" which are developed by Lamé for the solutions of elastodynamic problems (Sternberg, 1960; Olsson, 1984) is utilized in order to make some adaptation which can fix the questions of completeness. Detailed derivations of this solution scheme can be found in Appendix C.

According to Eqs. (2), (4), (7), and (9), we have

$$\mathbf{E} = -\frac{L}{i\omega \bar{\epsilon}} \nabla [C\nabla \cdot \mathbf{u} + M\nabla \cdot \mathbf{w}] - \frac{\omega^2 \rho_f L}{i\omega \bar{\epsilon}} \mathbf{u} + \frac{1}{i\omega \bar{\epsilon}} \nabla \times \mathbf{H}, \tag{15}$$

where

$$\bar{\epsilon}(\omega) = \epsilon(\omega) + \frac{\sigma(\omega)}{i\omega}, \tag{16}$$

is the effective electrical permittivity of the porous continuum.

Substitution of Eqs. (13)–(15) into the coupled equations (10) and (11) yields two parts: The dilatational part and the rotational one. The dilatational part can be written in a matrix form (detailed derivations can be found in Appendix C)

$$\begin{bmatrix} H & C \\ C & M \end{bmatrix} \begin{Bmatrix} \nabla^2\phi_1 \\ \nabla^2\phi_2 \end{Bmatrix} + \omega^2 \begin{bmatrix} \rho & \rho_f \\ \rho_f & \rho_n \end{bmatrix} \begin{Bmatrix} \phi_1 \\ \phi_2 \end{Bmatrix} = \begin{Bmatrix} 0 \\ 0 \end{Bmatrix}, \tag{17}$$

where

$$\rho_n = \left(\frac{\bar{\epsilon}}{\bar{\epsilon} - \tilde{\rho} L^2} \right) \tilde{\rho}. \tag{18}$$

Two eigenvalues of Eq. (17) can be obtained as shown below

$$(k_{p1,p2}/\omega)^2 = (B \mp \sqrt{B^2 - 4AD})/2A, \tag{19}$$

where

$$\begin{aligned} A &= HM - C^2, \\ B &= \rho_n H + \rho M - 2\rho_f C, \\ D &= \rho\rho_n - \rho_f^2, \end{aligned} \tag{20}$$

and their associated eigenvectors are

$$\mathbf{\Phi} = \begin{bmatrix} \mu_1 & 1 \\ 1 & \mu_2 \end{bmatrix}, \tag{21}$$

with

$$\langle \mu_1, 1 \rangle^T = \langle -f/2d, 1 \rangle^T \quad \text{and} \quad \langle 1, \mu_2 \rangle^T = \langle 1, f/2a \rangle^T, \tag{22}$$

where

$$\begin{aligned} a &= C\rho_n - M\rho_f, \\ b &= M\rho - H\rho_n, \\ d &= C\rho - H\rho_f, \\ f &= b - \sqrt{b^2 + 4ad}. \end{aligned} \tag{23}$$

Equation (17) can be decoupled into the following form:

$$\begin{bmatrix} H^* & 0 \\ 0 & M^* \end{bmatrix} \begin{Bmatrix} \nabla^2\Phi_1 \\ \nabla^2\Phi_2 \end{Bmatrix} + \omega^2 \begin{bmatrix} \rho^* & 0 \\ 0 & \rho_n^* \end{bmatrix} \begin{Bmatrix} \Phi_1 \\ \Phi_2 \end{Bmatrix} = \begin{Bmatrix} 0 \\ 0 \end{Bmatrix}, \tag{24}$$

where

$$\begin{aligned} \Phi_1 &= \frac{1}{(\mu_1\mu_2 - 1)}(\mu_2\phi_1 - \phi_2), \\ \Phi_2 &= \frac{1}{(\mu_1\mu_2 - 1)}(\mu_1\phi_2 - \phi_1), \end{aligned} \tag{25}$$

and

$$\begin{aligned} H^* &= H\mu_1^2 + 2C\mu_1 + M, \\ M^* &= M\mu_2^2 + 2C\mu_2 + H, \\ \rho^* &= \rho\mu_1^2 + 2\rho_f\mu_1 + \rho_n, \\ \rho_n^* &= \rho_n\mu_2^2 + 2\rho_f\mu_2 + \rho. \end{aligned} \tag{26}$$

The details in the derivation of Eq. (24) are shown in Appendix A. From Eq. (24), we readily obtain two uncoupled scalar Helmholtz equations

$$\begin{aligned} \nabla^2\Phi_1 + k_{p1}^2\Phi_1 &= 0, \\ \nabla^2\Phi_2 + k_{p2}^2\Phi_2 &= 0, \end{aligned} \tag{27}$$

where $k_{p1} = \omega/\sqrt{H^*/\rho^*}$ and $k_{p2} = \omega/\sqrt{M^*/\rho_n^*}$ denote the fast and slow dilatational wave numbers, respectively. Indeed, Eq. (27) is the same as Eq. (19).

According to Eqs. (10), (11), and (13)–(15), we have the rotational part (detailed derivations can be found in Appendix C)

$$G\nabla^2\boldsymbol{\psi}_1 + \omega^2\rho\boldsymbol{\psi}_1 + \omega^2\rho_f\boldsymbol{\psi}_2 = \mathbf{0}, \tag{28}$$

$$\frac{\rho_f L^2}{\bar{\epsilon}} \left(\frac{\mathbf{H}}{\omega^2\rho_f L} \right) + \frac{\rho_f}{\rho_n}\boldsymbol{\psi}_1 + \boldsymbol{\psi}_2 = \mathbf{0}. \tag{29}$$

Equation (29) can substituted into Eq. (28) to eliminate $\boldsymbol{\psi}_2$. With Eqs. (8) and (13)–(15) substituted into Eq. (1) and using Eq. (17) to simplify the resulting equation, the rotational part can be rewritten in a matrix form

$$\begin{bmatrix} 1 & 0 \\ -1 & 1 \end{bmatrix} \begin{Bmatrix} \nabla^2\boldsymbol{\psi}_1 \\ \nabla^2\left(\dfrac{\mathbf{H}}{\omega^2\rho_f L} \right) \end{Bmatrix} + \omega^2 \begin{bmatrix} \dfrac{\left(\rho - \dfrac{\rho_f^2}{\rho_n} \right)}{G} & -\dfrac{\rho_f^2 L^2}{\bar{\epsilon} G} \\ 0 & \mu\bar{\epsilon} \end{bmatrix} \times \begin{Bmatrix} \boldsymbol{\psi}_1 \\ \left(\dfrac{\mathbf{H}}{\omega^2\rho_f L} \right) \end{Bmatrix} = \begin{Bmatrix} \mathbf{0} \\ \mathbf{0} \end{Bmatrix}. \tag{30}$$

Eigenvalues of this equation are

$$\begin{aligned} k_{s1} &= \sqrt{1 - \xi} S_A \omega, \\ k_{s2} &= S_B \omega / \sqrt{1 - \xi}, \end{aligned} \tag{31}$$

where

$$\begin{aligned} S_A^2 &= \left(\rho - \frac{\rho_f^2}{\rho_n} \right) \Big/ G, \\ S_B^2 &= \mu\bar{\epsilon}, \\ S_C^2 &= \frac{\rho_f^2 L^2}{\bar{\epsilon} G}, \\ \xi &= \frac{(S_A^2 - S_B^2 + S_C^2) - \sqrt{(S_A^2 - S_B^2 + S_C^2)^2 - 4S_A^2 S_C^2}}{2S_A^2}. \end{aligned} \tag{32}$$

After similar manipulations as we have done for Eq. (21), a set of eigenvectors can be obtained

$$\boldsymbol{\Psi} = \begin{bmatrix} 1 & \xi \\ \xi\dfrac{S_A^2}{S_C^2} & 1 \end{bmatrix}. \tag{34}$$

And then Eq. (30) can be decoupled into the form

$$\begin{bmatrix} G^* & 0 \\ 0 & \mu^* \end{bmatrix} \begin{Bmatrix} \nabla^2\boldsymbol{\Psi}_1 \\ \nabla^2\boldsymbol{\Psi}_2 \end{Bmatrix} + \omega^2 \begin{bmatrix} \rho^{**} & 0 \\ 0 & \rho_n^{**} \end{bmatrix} \begin{Bmatrix} \boldsymbol{\Psi}_1 \\ \boldsymbol{\Psi}_2 \end{Bmatrix} = \begin{Bmatrix} \mathbf{0} \\ \mathbf{0} \end{Bmatrix}, \tag{35}$$

where

$$\boldsymbol{\Psi}_1 = \frac{1}{\left(\xi^2\dfrac{S_A^2}{S_C^2} - 1\right)} \left[\xi\left(\frac{\mathbf{H}}{\omega^2\rho_f L}\right) - \boldsymbol{\psi}_1 \right],$$

$$\boldsymbol{\Psi}_2 = \frac{1}{\left(\xi^2\dfrac{S_A^2}{S_C^2} - 1\right)} \left[\xi\frac{S_A^2}{S_C^2}\boldsymbol{\psi}_1 - \left(\frac{\mathbf{H}}{\omega^2\rho_f L}\right) \right], \tag{36}$$

and

$$G^* = 1 + \left(1 - \xi\frac{S_A^2}{S_C^2}\right)\frac{\xi}{(1-\xi)},$$

$$\mu^* = 1 - \xi^2\frac{S_A^2}{S_C^2},$$

$$\rho^{**} = \left(1 - \xi^2\frac{S_A^2}{S_C^2}\right)S_A^2,$$

$$\rho_n^{**} = \left[\left(1 - \xi\frac{S_A^2}{S_C^2}\right)\frac{\xi}{(1-\xi)} + 1\right]S_B^2. \tag{37}$$

The details in the derivation of Eq. (35) are also shown in Appendix A. From Eq. (35), we readily obtain two uncoupled vector Helmholtz equations

$$\nabla^2\boldsymbol{\Psi}_1 + k_{s1}^2\boldsymbol{\Psi}_1 = \mathbf{0},$$

$$\nabla^2\boldsymbol{\Psi}_2 + k_{s2}^2\boldsymbol{\Psi}_2 = \mathbf{0}, \tag{38}$$

where $k_{s1} = \omega/\sqrt{G^*/\rho^{**}}$ and $k_{s2} = \omega/\sqrt{\mu^*/\rho_n^{**}}$ denote the mechanical shear and electromagnetic wave numbers, respectively. Indeed, Eq. (38) is the same as Eq. (35).

According to Eqs. (29) and (36), we have

$$\boldsymbol{\psi}_2 = \mu_3\boldsymbol{\Psi}_1 + \mu_4\boldsymbol{\Psi}_2, \tag{39}$$

where

$$\mu_3 = -\left[\frac{\rho_f}{\rho_n} + \xi\frac{S_A^2}{S_D^2}\right],$$

$$\mu_4 = -\left[\frac{\rho_f}{\rho_n}\xi + \frac{S_C^2}{S_D^2}\right], \tag{40}$$

$$S_D^2 = \frac{\rho_f}{G}. \tag{41}$$

C. Basis functions in spherical coordinates

For waves in a three-dimensional electroporoelastic medium, the motion may be decomposed into six groups: $\mathbf{L}_1$, $\mathbf{L}_2$, $\mathbf{M}_1$, $\mathbf{M}_2$, $\mathbf{N}_1$, and $\mathbf{N}_2$. Group $\mathbf{L}_1$ and $\mathbf{L}_2$ represent the dilatational motions propagating with speeds c_{p1} and c_{p2}, and associated wave numbers $k_{p1} = \omega/c_{p1}$ and $k_{p2} = \omega/c_{p2}$; Group $\mathbf{M}_1$, $\mathbf{N}_1$, and $\mathbf{M}_2$, $\mathbf{N}_2$ are the rotational motions propagating with speed c_{s1} and c_{s2}, and associated wave numbers $k_{s1} = \omega/c_{s1}$ and $k_{s2} = \omega/c_{s2}$. The four wave speeds are given by $c_{p1} = \sqrt{H^*/\rho^*}$, $c_{p2} = \sqrt{M^*/\rho_n^*}$, $c_{s1} = \sqrt{G^*/\rho^{**}}$, and $c_{s2} = \sqrt{\mu^*/\rho_n^{**}}$, respectively.

In spherical coordinates (R, θ, ϕ), similar to the expression for elastic media (Morse and Feshbach, 1953), we propose six vector wave functions with the superscripts $1, 2, \ldots, 6$ for the electroporoelastic medium as follows:

$$\mathbf{u}_{\sigma mn}^{(1)} = \mathbf{L}_{1\sigma mn} = \frac{\mu_1}{k_p}\nabla\left[h_n^{(2)}(k_{p1}R)Y_{\sigma mn}(\theta,\phi)\right] = \frac{\mu_1 k_{p1}}{k_p}\left\{h_n^{(2)\prime}(k_{p1}R)\mathbf{A}_{\sigma mn} + (n^2+n)^{1/2}\frac{h_n^{(2)}(k_{p1}R)}{k_{p1}R}\mathbf{B}_{\sigma mn}\right\}, \tag{42}$$

$$\mathbf{u}_{\sigma mn}^{(2)} = \mathbf{L}_{2\sigma mn} = \frac{1}{k_p}\nabla\left[h_n^{(2)}(k_{p2}R)Y_{\sigma mn}(\theta,\phi)\right] = \frac{k_{p2}}{k_p}\left\{h_n^{(2)\prime}(k_{p2}R)\mathbf{A}_{\sigma mn} + (n^2+n)^{1/2}\frac{h_n^{(2)}(k_{p2}R)}{k_{p2}R}\mathbf{B}_{\sigma mn}\right\}, \tag{43}$$

$$\mathbf{u}_{\sigma mn}^{(3)} = \mathbf{M}_{1\sigma mn} = \nabla\times\left[h_n^{(2)}(k_{s1}R)Y_{\sigma mn}(\theta,\phi)R\mathbf{e}_R\right] = (n^2+n)^{1/2}h_n^{(2)}(k_{s1}R)\mathbf{C}_{\sigma mn}, \tag{44}$$

$$\mathbf{u}_{\sigma mn}^{(4)} = \mathbf{N}_{1\sigma mn} = \frac{1}{k_{s1}}\nabla\times\mathbf{M}_{1\sigma mn} = \left\{(n^2+n)\left(\frac{h_n^{(2)}(k_{s1}R)}{k_{s1}R}\right)\mathbf{A}_{\sigma mn} + (n^2+n)^{1/2}\frac{[k_{s1}Rh_n^{(2)}(k_{s1}R)]'}{k_{s1}R}\mathbf{B}_{\sigma mn}\right\}, \tag{45}$$

$$\mathbf{u}_{\sigma mn}^{(5)} = \xi\mathbf{M}_{2\sigma mn} = \xi\nabla\times\left[h_n^{(2)}(k_{s2}R)Y_{\sigma mn}(\theta,\phi)R\mathbf{e}_R\right] = \xi(n^2+n)^{1/2}h_n^{(2)}(k_{s2}R)\mathbf{C}_{\sigma mn}, \tag{46}$$

$$\mathbf{u}_{\sigma mn}^{(6)} = \xi\mathbf{N}_{2\sigma mn} = \frac{\xi}{k_{s2}}\nabla\times\mathbf{M}_{2\sigma mn} = \xi\left\{(n^2+n)\left(\frac{h_n^{(2)}(k_{s2}R)}{k_{s2}R}\right)\mathbf{A}_{\sigma mn} + (n^2+n)^{1/2}\frac{[k_{s2}Rh_n^{(2)}(k_{s2}R)]'}{k_{s2}R}\mathbf{B}_{\sigma mn}\right\}, \tag{47}$$

where the superscripts, $1, 2, \ldots, 6$ are designated for the quantities contributed by $\mathbf{L}_1$, $\mathbf{L}_2$, $\mathbf{M}_1$, $\mathbf{N}_1$, $\mathbf{M}_2$, and $\mathbf{N}_2$, respectively. $k_p \equiv \sqrt{\omega^2\rho/H}$ is the common wave number used to make the basis function dimensionless, $h_n^{(2)}(x)$ is the

spherical Hankel function of the second kind, $[xh_n^{(2)}(x)]' = xh_n^{(2)\prime}(x) + h_n^{(2)}(x)$ and $h_n^{(2)\prime}(x) = dh_n^{(2)}(x)/dx$. The spherical surface harmonics $Y_{\sigma mn}(\theta,\phi)$ consists of an even part ($\sigma = 1$) and an odd one ($\sigma = 2$)

$$Y_{1mn}(\theta,\phi) = P_n^m(\cos\theta)\cos m\phi,$$

$$Y_{2mn}(\theta,\phi) = P_n^m(\cos\theta)\sin m\phi, \tag{48}$$

where $P_n^m(\cos\theta)$ are the associated Legendre polynomials, $m = 0, 1, \ldots, n$ and $n = 0, 1, \ldots, \infty$. The three mutually perpendicular vectors $\mathbf{A}_{\sigma mn}$, $\mathbf{B}_{\sigma mn}$, and $\mathbf{C}_{\sigma mn}$ are related to the three unit vector $\mathbf{e}_R$, $\mathbf{e}_\theta$, and $\mathbf{e}_\phi$ in the spherical coordinates

$$\mathbf{A}_{\sigma mn} = \mathbf{e}_R Y_{\sigma mn},$$

$$\mathbf{B}_{\sigma mn} = (n^2+n)^{-1/2}\left[\mathbf{e}_\theta \frac{\partial}{\partial\theta} + \mathbf{e}_\phi \frac{\partial}{\sin\theta\,\partial\phi}\right] Y_{\sigma mn} = \mathbf{e}_R \times \mathbf{C}_{\sigma mn},$$

$$\mathbf{C}_{\sigma mn} = (n^2+n)^{-1/2}\left[\mathbf{e}_\theta \frac{\partial}{\sin\theta\,\partial\phi} - \mathbf{e}_\phi \frac{\partial}{\partial\theta}\right] Y_{\sigma mn} = -\mathbf{e}_R \times \mathbf{B}_{\sigma mn}. \tag{49}$$

According to Eqs. (14), (25), and (39), the vector operators of the filtration displacement are obtained as follows:

$$\mathbf{w}_{\sigma mn}^{(1)} = \frac{k_{p1}}{k_p}\left\{h_n^{(2)\prime}(k_{p1}R)\mathbf{A}_{\sigma mn} + (n^2+n)^{1/2}\frac{h_n^{(2)}(k_{p1}R)}{k_{p1}R}\mathbf{B}_{\sigma mn}\right\}, \tag{50}$$

$$\mathbf{w}_{\sigma mn}^{(2)} = \frac{\mu_2 k_{p2}}{k_p}\left\{h_n^{(2)\prime}(k_{p2}R)\mathbf{A}_{\sigma mn} + (n^2+n)^{1/2}\frac{h_n^{(2)}(k_{p2}R)}{k_{p2}R}\mathbf{B}_{\sigma mn}\right\}, \tag{51}$$

$$\mathbf{w}_{\sigma mn}^{(3)} = \mu_3(n^2+n)^{1/2}h_n^{(2)}(k_{s1}R)\mathbf{C}_{\sigma mn}, \tag{52}$$

$$\mathbf{w}_{\sigma mn}^{(4)} = \mu_3\left\{(n^2+n)\left(\frac{h_n^{(2)}(k_{s1}R)}{k_{s1}R}\right)\mathbf{A}_{\sigma mn} + (n^2+n)^{1/2}\frac{[k_{s1}Rh_n^{(2)}(k_{s1}R)]'}{k_{s1}R}\mathbf{B}_{\sigma mn}\right\}, \tag{53}$$

$$\mathbf{w}_{\sigma mn}^{(5)} = \mu_4(n^2+n)^{1/2}h_n^{(2)}(k_{s2}R)\mathbf{C}_{\sigma mn}, \tag{54}$$

$$\mathbf{w}_{\sigma mn}^{(6)} = \mu_4\left\{(n^2+n)\left(\frac{h_n^{(2)}(k_{s2}R)}{k_{s2}R}\right)\mathbf{A}_{\sigma mn} + (n^2+n)^{1/2}\frac{[k_{s2}Rh_n^{(2)}(k_{s2}R)]'}{k_{s2}R}\mathbf{B}_{\sigma mn}\right\}. \tag{55}$$

According to Eqs. (13)–(15), (17), (25), and (36), the vector operators of the electric field are obtained as follows:

$$\mathbf{E}_{\sigma mn}^{(1)} = -i\omega\frac{\rho_n L k_{p1}}{\bar{\epsilon}k_p}\left\{h_n^{(2)\prime}(k_{p1}R)\mathbf{A}_{\sigma mn} + (n^2+n)^{1/2}\left(\frac{h_n^{(2)}(k_{p1}R)}{k_{p1}R}\right)\mathbf{B}_{\sigma mn}\right\}, \tag{56}$$

$$\mathbf{E}_{\sigma mn}^{(2)} = -i\omega\frac{\mu_2\rho_n L k_{p2}}{\bar{\epsilon}k_p}\left\{h_n^{(2)\prime}(k_{p2}R)\mathbf{A}_{\sigma mn} + (n^2+n)^{1/2}\left(\frac{h_n^{(2)}(k_{p2}R)}{k_{p2}R}\right)\mathbf{B}_{\sigma mn}\right\}, \tag{57}$$

$$\mathbf{E}_{\sigma mn}^{(3)} = -i\omega\frac{\mu_5\rho_f L}{\bar{\epsilon}}(n^2+n)^{1/2}h_n^{(2)}(k_{s1}R)\mathbf{C}_{\sigma mn}, \tag{58}$$

$$\mathbf{E}_{\sigma mn}^{(4)} = -i\omega\frac{\mu_5\rho_f L}{\bar{\epsilon}}\left\{(n^2+n)\left(\frac{h_n^{(2)}(k_{s1}R)}{k_{s1}R}\right)\mathbf{A}_{\sigma mn} + (n^2+n)^{1/2}\frac{[k_{s1}Rh_n^{(2)}(k_{s1}R)]'}{k_{s1}R}\mathbf{B}_{\sigma mn}\right\}, \tag{59}$$

$$\mathbf{E}_{\sigma mn}^{(5)} = -i\omega\frac{\mu_6\rho_f L}{\bar{\epsilon}}(n^2+n)^{1/2}h_n^{(2)}(k_{s2}R)\mathbf{C}_{\sigma mn}, \tag{60}$$

$$\mathbf{E}_{\sigma mn}^{(6)} = -i\omega\frac{\mu_6\rho_f L}{\bar{\epsilon}}\left\{(n^2+n)\left(\frac{h_n^{(2)}(k_{s2}R)}{k_{s2}R}\right)\mathbf{A}_{\sigma mn} + (n^2+n)^{1/2}\frac{[k_{s2}Rh_n^{(2)}(k_{s2}R)]'}{k_{s2}R}\mathbf{B}_{\sigma mn}\right\}, \tag{61}$$

where

$$\mu_5 = \xi\frac{S_A^2}{S_C^2} - 1,$$

$$\mu_6 = 1 - \xi, \tag{62}$$

According to Eq. (36), the vector operators of the magnetic field are obtained as follows:

$$\mathbf{H}_{\sigma mn}^{(1)} = \mathbf{0}, \tag{63}$$

$$\mathbf{H}_{\sigma mn}^{(2)} = \mathbf{0}, \tag{64}$$

$$\mathbf{H}_{\sigma mn}^{(3)} = \frac{\mu_5\rho_f L k_{s1}}{\mu\bar{\epsilon}}\left\{(n^2+n)\left(\frac{h_n^{(2)}(k_{s1}R)}{k_{s1}R}\right)\mathbf{A}_{\sigma mn} + (n^2+n)^{1/2}\frac{[k_{s1}Rh_n^{(2)}(k_{s1}R)]'}{k_{s1}R}\mathbf{B}_{\sigma mn}\right\}, \tag{65}$$

$$\mathbf{H}_{\sigma mn}^{(4)} = \frac{\mu_5\rho_f L k_{s1}}{\mu\bar{\epsilon}}(n^2+n)^{1/2}h_n^{(2)}(k_{s1}R)\mathbf{C}_{\sigma mn}, \tag{66}$$

$$\mathbf{H}_{\sigma mn}^{(5)} = \frac{\mu_6\rho_f L k_{s2}}{\mu\bar{\epsilon}}\left\{(n^2+n)\left(\frac{h_n^{(2)}(k_{s2}R)}{k_{s2}R}\right)\mathbf{A}_{\sigma mn} + (n^2+n)^{1/2}\frac{[k_{s2}Rh_n^{(2)}(k_{s2}R)]'}{k_{s2}R}\mathbf{B}_{\sigma mn}\right\}, \tag{67}$$

$$\mathbf{H}_{\sigma mn}^{(6)} = \frac{\mu_6\rho_f L k_{s2}}{\mu\bar{\epsilon}}(n^2+n)^{1/2}h_n^{(2)}(k_{s2}R)\mathbf{C}_{\sigma mn}. \tag{68}$$

Whereas according to the constitutive relation Eq. (7), the scalar operators of fluid pressures are shown below

$$p_{\sigma mn}^{(1)} = (C\mu_1 + M)\frac{k_{p1}^2}{k_p} h_n^{(2)}(k_{p1}R) Y_{\sigma mn}, \tag{69}$$

$$p_{\sigma mn}^{(2)} = (C + M\mu_2)\frac{k_{p2}^2}{k_p} h_n^{(2)}(k_{p2}R) Y_{\sigma mn}, \tag{70}$$

$$p_{\sigma mn}^{(3)} = 0, \tag{71}$$

$$p_{\sigma mn}^{(4)} = 0, \tag{72}$$

$$p_{\sigma mn}^{(5)} = 0, \tag{73}$$

$$p_{\sigma mn}^{(6)} = 0. \tag{74}$$

The vector operators for the tractions at a surface with an unit outward normal $\mathbf{n}$ can be calculated from $\mathbf{t}(\mathbf{u}) = \mathbf{n} \cdot \boldsymbol{\tau}(\mathbf{u})$ and Eq. (6) are shown as follows:

$$\mathbf{t}_{\sigma mn}^{(1)} = [(H - 2G) + C/\mu_1](\nabla \cdot \mathbf{L}_{1\sigma mn})\mathbf{n} + G\mathbf{n} \cdot (\nabla \mathbf{L}_{1\sigma mn} + (\nabla \mathbf{L}_{1\sigma mn})^T), \tag{75}$$

$$\mathbf{t}_{\sigma mn}^{(2)} = [(H - 2G) + C\mu_2](\nabla \cdot \mathbf{L}_{2\sigma mn})\mathbf{n} + G\mathbf{n} \cdot (\nabla \mathbf{L}_{2\sigma mn} + (\nabla \mathbf{L}_{2\sigma mn})^T), \tag{76}$$

$$\mathbf{t}_{\sigma mn}^{(3)} = G\mathbf{n} \cdot (\nabla \mathbf{M}_{1\sigma mn} + (\nabla \mathbf{M}_{1\sigma mn})^T), \tag{77}$$

$$\mathbf{t}_{\sigma mn}^{(4)} = G\mathbf{n} \cdot (\nabla \mathbf{N}_{1\sigma mn} + (\nabla \mathbf{N}_{1\sigma mn})^T), \tag{78}$$

$$\mathbf{t}_{\sigma mn}^{(5)} = \xi G\mathbf{n} \cdot (\nabla \mathbf{M}_{2\sigma mn} + (\nabla \mathbf{M}_{2\sigma mn})^T), \tag{79}$$

$$\mathbf{t}_{\sigma mn}^{(6)} = \xi G\mathbf{n} \cdot (\nabla \mathbf{N}_{2\sigma mn} + (\nabla \mathbf{N}_{2\sigma mn})^T). \tag{80}$$

If we consider a special case of a spherical surface $\mathbf{n} = \mathbf{e}_R$, the six traction operators are reduced to the following simpler forms:

$$\mathbf{t}_{\sigma mn}^{r(1)} = \left\{ -\frac{k_{p1}^2}{k_p}[(H - 2G)\mu_1 + C] h_n^{(2)}(k_{p1}R) + G\left[-2\mu_1 \frac{k_{p1}^2}{k_p} h_n^{(2)}(k_{p1}R) + \frac{2\mu_1(n^2+n)}{k_p R^2} h_n^{(2)}(k_{p1}R) - \frac{4\mu_1 k_{p1}}{k_p R} h_n^{(2)'}(k_{p1}R) \right] \right\} \mathbf{A}_{\sigma mn} + 2G\frac{\mu_1 k_{p1}}{k_p} \times (n^2+n)^{1/2} \left[\frac{h_n^{(2)'}(k_{p1}R)}{R} - \frac{h_n^{(2)}(k_{p1}R)}{k_{p1}R^2} \right] \mathbf{B}_{\sigma mn}, \tag{81}$$

$$\mathbf{t}_{\sigma mn}^{r(2)} = \left\{ -\frac{k_{p2}^2}{k_p}[(H - 2G) + C\mu_2] h_n^{(2)}(k_{p2}R) + G\left[-2\frac{k_{p2}^2}{k_p} h_n^{(2)}(k_{p2}R) + \frac{2(n^2+n)}{k_p R^2} h_n^{(2)}(k_{p2}R) - \frac{4k_{p2}}{k_p R} h_n^{(2)'}(k_{p2}R) \right] \right\} \mathbf{A}_{\sigma mn} + 2G\frac{k_{p2}}{k_p}(n^2+n)^{1/2} \times \left[\frac{h_n^{(2)'}(k_{p2}R)}{R} - \frac{h_n^{(2)}(k_{p2}R)}{k_{p2}R^2} \right] \mathbf{B}_{\sigma mn}, \tag{82}$$

$$\mathbf{t}_{\sigma mn}^{r(3)} = G\left[k_{s1} h_n^{(2)'}(k_{s1}R) - \frac{h_n^{(2)}(k_{s1}R)}{R} \right] (n^2+n)^{1/2} \mathbf{C}_{\sigma mn}, \tag{83}$$

$$\mathbf{t}_{\sigma mn}^{r(4)} = 2Gk_{s1} \left\{ (n^2+n) \left[\frac{h_n^{(2)}(k_{s1}R)}{k_{s1}R} \right]' \mathbf{A}_{\sigma mn} + \left[\left(n^2 + n - 1 - \frac{(k_{s1}R)^2}{2} \right) \frac{h_n^{(2)}(k_{s1}R)}{(k_{s1}R)^2} - \frac{h_n^{(2)'}(k_{s1}R)}{k_{s1}R} \right] \times (n^2+n)^{1/2} \mathbf{B}_{\sigma mn} \right\}, \tag{84}$$

$$\mathbf{t}_{\sigma mn}^{r(5)} = \xi G\left[k_{s2} h_n^{(2)'}(k_{s2}R) - \frac{h_n^{(2)}(k_{s2}R)}{R} \right] (n^2+n)^{1/2} \mathbf{C}_{\sigma mn}, \tag{85}$$

$$\mathbf{t}_{\sigma mn}^{r(6)} = 2\xi Gk_{s2} \left\{ (n^2+n) \left[\frac{h_n^{(2)}(k_{s2}R)}{k_{s2}R} \right]' \mathbf{A}_{\sigma mn} + \left[\left(n^2 + n - 1 - \frac{(k_{s2}R)^2}{2} \right) \frac{h_n^{(2)}(k_{s2}R)}{(k_{s2}R)^2} - \frac{h_n^{(2)'}(k_{s2}R)}{k_{s2}R} \right] \times (n^2+n)^{1/2} \mathbf{B}_{\sigma mn} \right\}. \tag{86}$$

D. Orthogonality conditions for the spherical basis functions

The three vector functions $\mathbf{A}_{\sigma mn}$, $\mathbf{B}_{\sigma mn}$, and $\mathbf{C}_{\sigma mn}$ satisfy the following orthogonal relations (Morse and Feshbach, 1953):

$$\mathbf{A}_{\sigma mn} \cdot \mathbf{B}_{\sigma mn} = 0, \quad \mathbf{A}_{\sigma mn} \cdot \mathbf{C}_{\sigma mn} = 0, \quad \mathbf{B}_{\sigma mn} \cdot \mathbf{C}_{\sigma mn} = 0, \tag{87}$$

and the integrations over a spherical surface yield the following equations:

$$\int_0^{2\pi} \int_0^{\pi} \mathbf{A}_{\sigma mn} \cdot \mathbf{A}_{\sigma' m' n'} \sin\theta d\theta d\phi = (1/\gamma_m)\delta_{mm'}\delta_{nn'}\delta_{\sigma\sigma'},$$

$$\int_0^{2\pi} \int_0^{\pi} \mathbf{B}_{\sigma mn} \cdot \mathbf{B}_{\sigma' m' n'} \sin\theta d\theta d\phi = (1/\gamma_m)\delta_{mm'}\delta_{nn'}\delta_{\sigma\sigma'},$$

$$\int_0^{2\pi} \int_0^{\pi} \mathbf{C}_{\sigma mn} \cdot \mathbf{C}_{\sigma' m' n'} \sin\theta d\theta d\phi = (1/\gamma_m)\delta_{mm'}\delta_{nn'}\delta_{\sigma\sigma'}. \tag{88}$$

The normalization constant is

$$\gamma_m = \epsilon_m (2n+1)(n-m)!/4\pi(n+m)!, \tag{89}$$

where $\epsilon_m = 1$ when $m = 0$, and $\epsilon_m = 2$ when $m > 0$.

For the wave fields which are regular in the region enclosing the origin of the coordinate system, we use six regular basis functions $\hat{\mathbf{u}}_{\sigma mn}^{(\alpha)}$ ($\alpha = 1, 2, 3, 4, 5,$ or 6) which are obtained from $\mathbf{u}_{\sigma mn}^{(\alpha)}$ by replacing the spherical Hankel function $h_n^{(2)}$, in $\mathbf{L}_{1\sigma mn}$, $\mathbf{L}_{2\sigma mn}$, $\mathbf{M}_{1\sigma mn}$, $\mathbf{N}_{1\sigma mn}$, $\mathbf{M}_{2\sigma mn}$, and $\mathbf{N}_{2\sigma mn}$, with the spherical Bessel function j_n.

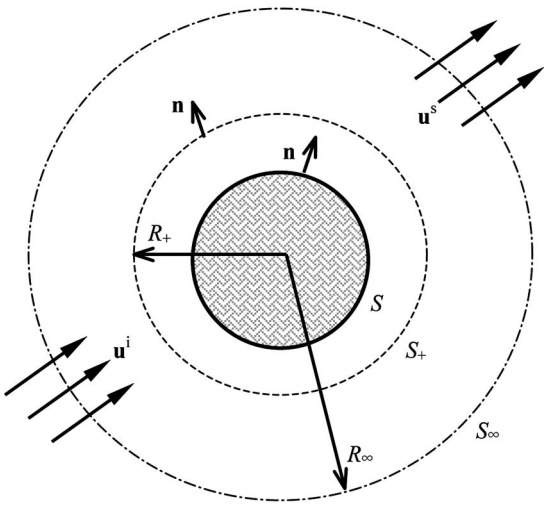

FIG. 1. Waves scattered by an inclusion bounded by the surfaces S.

Consider an infinite region divided by a surface S of a spherical shape as shown in Fig. 1, where we add an artificial spherical surface S_+ exterior to S with radius R_+.

Similar to Pride and Haartsen's approach (1996), we can derive the statement of reciprocity as

$$\oiint_{S_V} \{[\mathbf{E}^{(B)} \times \mathbf{H}^{(A)} - \mathbf{E}^{(A)} \times \mathbf{H}^{(B)}] \cdot \mathbf{n} + i\omega[\mathbf{u}^{(B)} \cdot \mathbf{t}^{(A)} - \mathbf{u}^{(A)} \cdot \mathbf{t}^{(B)} - p^{(A)}\mathbf{n} \cdot \mathbf{w}^{(B)} + p^{(B)}\mathbf{n} \cdot \mathbf{w}^{(A)}]\} dS_V = 0. \quad (90)$$

Let V be the region inside S_+ first, and then let set (A) be one of the regular sets and (B) be another regular set inside region S_+. Equation (90) reduces to the following equation

$$\oiint_{S_+} \{[\hat{\mathbf{E}}^{(\beta)}_{\sigma' m' n'} \times \hat{\mathbf{H}}^{(\alpha)}_{\sigma m n} - \hat{\mathbf{E}}^{(\alpha)}_{\sigma m n} \times \hat{\mathbf{H}}^{(\beta)}_{\sigma' m' n'}] \cdot \mathbf{n} + i\omega[\hat{\mathbf{t}}^{(\alpha)}_{\sigma m n} \cdot \hat{\mathbf{u}}^{(\beta)}_{\sigma' m' n'} - \hat{t}^{(\beta)}_{\sigma' m' n'} \cdot \hat{u}^{(\alpha)}_{\sigma m n} - \hat{p}^{(\alpha)}_{\sigma m n}\mathbf{n} \cdot \hat{\mathbf{w}}^{(\beta)}_{\sigma' m' n'} + \hat{p}^{(\beta)}_{\sigma' m' n'}\mathbf{n} \cdot \hat{\mathbf{w}}^{(\alpha)}_{\sigma m n}]\} dS = 0, \quad (91)$$

where $\alpha, \beta = 1, 2, 3, 4, 5,$ or 6. Next, let set (A) be one of the singular sets and (B) be another singular one. Choose control volume to be the region bounded internally by S_+ and externally by S_∞, then all $\mathbf{u}^{(\alpha)}_{\sigma m n}$ are regular in this region. Thus the second orthogonality condition can be obtained as

$$\left(\iint_{S_\infty} - \iint_{S_+}\right)\{[\mathbf{E}^{(\beta)}_{\sigma' m' n'} \times \mathbf{H}^{(\alpha)}_{\sigma m n} - \mathbf{E}^{(\alpha)}_{\sigma m n} \times \mathbf{H}^{(\beta)}_{\sigma' m' n'}] \cdot \mathbf{n} + i\omega[\mathbf{t}^{(\alpha)}_{\sigma m n} \cdot \mathbf{u}^{(\beta)}_{\sigma' m' n'} - \mathbf{t}^{(\beta)}_{\sigma' m' n'} \cdot \mathbf{u}^{(\alpha)}_{\sigma m n} - p^{(\alpha)}_{\sigma m n}\mathbf{n} \cdot \mathbf{w}^{(\beta)}_{\sigma' m' n'} + p^{(\beta)}_{\sigma' m' n'}\mathbf{n} \cdot \mathbf{w}^{(\alpha)}_{\sigma m n}]\} dS = 0. \quad (92)$$

The minus sign of the second integral is used because the outer normal at S_+ in this case is $-\mathbf{e}_R$. Through the zero value of Wronskian formula (Abramowitz and Stegun, 1964) (i.e., both are Bessel functions) and the relationship of material properties, we can prove that the integrals on both surfaces S_∞ and S_+ vanish. Finally, let the set (A) be one of the regular sets and the set (B) be a singular one outside the surface S_+ and inside the surface S_∞. Through Eqs. (49) and (88) and the application of the Wronskian formula (Abramowitz and Stegun, 1964), the third orthogonality condition can be obtained as

$$\iint_{S_+} \{[\hat{\mathbf{E}}^{(\beta)}_{\sigma' m' n'} \times \mathbf{H}^{(\alpha)}_{\sigma m n} - \mathbf{E}^{(\alpha)}_{\sigma m n} \times \hat{\mathbf{H}}^{(\beta)}_{\sigma' m' n'}] \cdot \mathbf{n} + i\omega[\mathbf{t}^{(\alpha)}_{\sigma m n} \cdot \hat{\mathbf{u}}^{(\beta)}_{\sigma' m' n'} - \hat{t}^{(\beta)}_{\sigma' m' n'} \cdot \mathbf{u}^{(\alpha)}_{\sigma m n} - p^{(\alpha)}_{\sigma m n}\mathbf{n} \cdot \hat{\mathbf{w}}^{(\beta)}_{\sigma' m' n'} + \hat{p}^{(\beta)}_{\sigma' m' n'}\mathbf{n} \cdot \mathbf{w}^{(\alpha)}_{\sigma m n}]\} dS = (\omega G/k_s) D^{(\alpha)}_{\sigma m n} \delta_{\sigma\sigma'} \delta_{mm'} \delta_{nn'} \delta_{\alpha\beta}, \quad (93)$$

where

$$D^{(\alpha)}_{\sigma m n} = \begin{cases} \gamma_{(\alpha)} \cdot 4\pi(n+m)!/[\epsilon_m \cdot (2n+1)(n-m)!], \\ 0, \quad \text{if } \sigma = \text{odd, and } m = 0, \end{cases} \quad (94)$$

and

$$\gamma_{(\alpha)} = \begin{cases} H^* \dfrac{k_s k_{p1}}{G k_p^2} & \text{if } \alpha = 1, \\ M^* \dfrac{k_s k_{p2}}{G k_p^2} & \text{if } \alpha = 2, \\ (n^2+n)\left(1 - \dfrac{\mu_5^2 \rho_f^2 L^2}{G\mu\bar{\epsilon}^2}\right)\dfrac{k_s}{k_{s1}} & \text{if } \alpha = 3, \quad or\ 4, \\ (n^2+n)\left(\xi^2 - \dfrac{\mu_6^2 \rho_f^2 L^2}{G\mu\bar{\epsilon}^2}\right)\dfrac{k_s}{k_{s2}} & \text{if } \alpha = 5, \quad or\ 6, \end{cases} \quad (95)$$

where $k_s \equiv \sqrt{\omega^2\rho/G}$. Equations (91)–(93) are the desired orthogonality conditions among the basis functions that are critical in the derivation of the transition matrix. Notice that the surface integrals in Eqs. (91)–(93) are independent of radius R_+. These invariant properties imply a conservation law and mean that the shape of S_+ may be deformed to any spherical surface S, and the surface integral over S_+ can be replaced with the one over S. The details of the derivation of Eqs. (91)–(93) are presented in Appendix B.

III. DEVELOPMENT OF TRANSITION MATRIX

A. Series expansions of the incident, refracted, and scattered waves

Let a region inside S as shown in Fig. 1 be filled with a material different from that of the surrounding medium, and all material constants inside S are designated by a subscript (0). An incident wave $\mathbf{u}^i(R)$ impinging on the inclusion is refracted into the inclusion with the displacement $\mathbf{u}_-(R)$ and scattered into the surrounding medium as $\mathbf{u}^s(R)$. Each of these three kinds of waves can be represented by a series representation of the basis functions within a specific region

$$\mathbf{u}^i(R) = \sum_{\sigma' m' n'} \sum_{\beta=1}^{6} a^{(\beta)}_{\sigma' m' n'} \hat{\mathbf{u}}^{(\beta)}_{\sigma' m' n'}, \quad (96)$$

$$\mathbf{u}^s(R) = \sum_{\sigma' m' n'} \sum_{\beta=1}^{6} c^{(\beta)}_{\sigma' m' n'} \mathbf{u}^{(\beta)}_{\sigma' m' n'}, \tag{97}$$

$$\mathbf{u}_-(R) = \sum_{\sigma' m' n'} \sum_{\beta=1}^{6} f^{(\beta)}_{\sigma' m' n} \hat{\mathbf{u}}^{(\beta)}_{\sigma' m' n'(0)}. \tag{98}$$

The symbol $\sum_{\sigma' m' n'}$ is an abbreviation for three summations over the indexes. The quantities $a^{(\beta)}_{\sigma' m' n'}$, $c^{(\beta)}_{\sigma' m' n'}$, and $f^{(\beta)}_{\sigma' m' n'}$ denote the incident, scattered, and refracted coefficients, respectively. The incident wave in Eq. (96) is uniformly convergent for $R < R_\infty$. The basis functions for $\mathbf{u}^s(R)$ are regular outside and at the interface of the inclusion. Similarly, the series for $\mathbf{u}_-(R)$ are uniformly convergent inside and at the interface of the inclusion. The total displacement field in the exterior region can be represented by the series in Eqs. (96) and (97)

$$\mathbf{u} = \mathbf{u}^i(R) + \mathbf{u}^s(R) = \sum_{\sigma' m' n'} \sum_{\beta=1}^{6} a^{(\beta)}_{\sigma' m' n'} \hat{u}^{(\beta)}_{\sigma' m' n'} + \sum_{\sigma' m' n'} \sum_{\beta=1}^{6} c^{(\beta)}_{\sigma' m' n'} \mathbf{u}^{(\beta)}_{\sigma' m' n'}. \tag{99}$$

Since both series are uniformly convergent, we can apply the associated operators $\mathbf{w}$, $\mathbf{E}$, $\mathbf{H}$, $\mathbf{t}$, and p to Eq. (99), such that

$$\mathbf{w}(\mathbf{u}) = \sum_{\sigma' m' n'} \sum_{\beta=1}^{6} a^{(\beta)}_{\sigma' m' n'} \hat{\mathbf{w}}^{(\beta)}_{\sigma' m' n'} + \sum_{\sigma' m' n'} \sum_{\beta=1}^{6} c^{(\beta)}_{\sigma' m' n'} \mathbf{w}^{(\beta)}_{\sigma' m' n'},$$

$$\mathbf{E}(\mathbf{u}) = \sum_{\sigma' m' n'} \sum_{\beta=1}^{6} a^{(\beta)}_{\sigma' m' n'} \hat{\mathbf{E}}^{(\beta)}_{\sigma' m' n'} + \sum_{\sigma' m' n'} \sum_{\beta=1}^{6} c^{(\beta)}_{\sigma' m' n'} \mathbf{E}^{(\beta)}_{\sigma' m' n'},$$

$$\mathbf{H}(\mathbf{u}) = \sum_{\sigma' m' n'} \sum_{\beta=1}^{6} a^{(\beta)}_{\sigma' m' n'} \hat{\mathbf{H}}^{(\beta)}_{\sigma' m' n'} + \sum_{\sigma' m' n'} \sum_{\beta=1}^{6} c^{(\beta)}_{\sigma' m' n'} \mathbf{H}^{(\beta)}_{\sigma' m' n'},$$

$$p(\mathbf{u}) = \sum_{\sigma' m' n'} \sum_{\beta=1}^{6} a^{(\beta)}_{\sigma' m' n'} \hat{p}^{(\beta)}_{\sigma' m' n'} + \sum_{\sigma' m' n'} \sum_{\beta=1}^{6} c^{(\beta)}_{\sigma' m' n'} p^{(\beta)}_{\sigma' m' n'},$$

$$\mathbf{t}(\mathbf{u}) = \sum_{\sigma' m' n'} \sum_{\beta=1}^{6} a^{(\beta)}_{\sigma' m' n'} \hat{\mathbf{t}}^{(\beta)}_{\sigma' m' n'} + \sum_{\sigma' m' n'} \sum_{\beta=1}^{6} c^{(\beta)}_{\sigma' m' n'} \mathbf{t}^{(\beta)}_{\sigma' m' n'}. \tag{100}$$

Analogous to the exterior region, the same operators can also be applied to the refracted fields as follows:

$$\mathbf{w}(\mathbf{u}_-) = \sum_{\sigma' m' n'} \sum_{\beta=1}^{6} f^{(\beta)}_{\sigma' m' n} \hat{\mathbf{w}}^{(\beta)}_{\sigma' m' n'(0)},$$

$$\mathbf{E}(\mathbf{u}_-) = \sum_{\sigma' m' n'} \sum_{\beta=1}^{6} f^{(\beta)}_{\sigma' m' n} \hat{\mathbf{E}}^{(\beta)}_{\sigma' m' n'(0)},$$

$$\mathbf{H}(\mathbf{u}_-) = \sum_{\sigma' m' n'} \sum_{\beta=1}^{6} f^{(\beta)}_{\sigma' m' n} \hat{\mathbf{H}}^{(\beta)}_{\sigma' m' n'(0)},$$

$$p(\mathbf{u}_-) = \sum_{\sigma' m' n'} \sum_{\beta=1}^{6} f^{(\beta)}_{\sigma' m' n} \hat{p}^{(\beta)}_{\sigma' m' n'(0)},$$

$$\mathbf{t}(\mathbf{u}_-) = \sum_{\sigma' m' n'} \sum_{\beta=1}^{6} f^{(\beta)}_{\sigma' m' n} \hat{\mathbf{t}}^{(\beta)}_{\sigma' m' n'(0)}. \tag{101}$$

B. The transition matrix for a spherical electroporoelastic inclusion

Consider the region V in Eq. (90) to be bounded by S_+ and S, and let $\mathbf{u}^{(A)} = \mathbf{u}^{(\alpha)}_{\sigma mn}$ and $\mathbf{u}^{(B)} = \mathbf{u}$ at the surface S_+, and, $\mathbf{u}^{(B)} = \mathbf{u}_+$, $\mathbf{w}^{(B)} = \mathbf{w}_+$, $\mathbf{E}^{(B)} = \mathbf{E}_+$, $\mathbf{H}^{(B)} = \mathbf{H}_+$, $p^{(B)} = p_+$, and $\mathbf{t}^{(B)} = \mathbf{t}_+$ at the surface S. Then Eq. (90) yields

$$\begin{aligned} &\iint_S \{[\mathbf{E}_+ \times \mathbf{H}^{(\alpha)}_{\sigma mn} - \mathbf{E}^{(\alpha)}_{\sigma mn} \times \mathbf{H}_+] \cdot \mathbf{n} + i\omega[\mathbf{t}^{(\alpha)}_{\sigma mn} \cdot \mathbf{u}_+ \\ &\quad - \mathbf{t}_+ \cdot \mathbf{u}^{(\alpha)}_{\sigma mn} - p^{(\alpha)}_{\sigma mn} \mathbf{n} \cdot \mathbf{w}_+ + p_+ \mathbf{n} \cdot \mathbf{w}^{(\alpha)}_{\sigma mn}]\} dS \\ &= \iint_{S+} \{[\mathbf{E} \times \mathbf{H}^{(\alpha)}_{\sigma mn} - \mathbf{E}^{(\alpha)}_{\sigma mn} \times \mathbf{H}] \cdot \mathbf{n} + i\omega[\mathbf{t}^{(\alpha)}_{\sigma mn} \cdot \mathbf{u} \\ &\quad - \mathbf{t} \cdot \mathbf{u}^{(\alpha)}_{\sigma mn} - p^{(\alpha)}_{\sigma mn} \mathbf{n} \cdot \mathbf{w} + p \mathbf{n} \cdot \mathbf{w}^{(\alpha)}_{\sigma mn}]\} dS, \\ &\quad \alpha = 1,2,3,4,5 \text{ or } 6. \end{aligned} \tag{102}$$

where the normal vector $\mathbf{n}$ for $\mathbf{t}$ at S_+ is in the direction $\mathbf{e}_R$. Substitution of Eqs. (99) and (100) into Eq. (102) yields the following relationship:

$$\begin{aligned} &\iint_S \{[\mathbf{E}_+ \times \mathbf{H}^{(\alpha)}_{\sigma mn} - \mathbf{E}^{(\alpha)}_{\sigma mn} \times \mathbf{H}_+] \cdot \mathbf{n} + i\omega[\mathbf{t}^{(\alpha)}_{\sigma mn} \cdot \mathbf{u}_+ \\ &\quad - \mathbf{t}_+ \cdot \mathbf{u}^{(\alpha)}_{\sigma mn} - p^{(\alpha)}_{\sigma mn} \mathbf{n} \cdot \mathbf{w}_+ + p_+ \mathbf{n} \cdot \mathbf{w}^{(\alpha)}_{\sigma mn}]\} dS \\ &= \sum_{\sigma' m' n'} \sum_{\beta=1}^{6} a^{(\beta)}_{\sigma' m' n} \iint_{S+} \{[\hat{\mathbf{E}}^{(\beta)}_{\sigma' m' n'} \times \mathbf{H}^{(\alpha)}_{\sigma mn} - \mathbf{E}^{(\alpha)}_{\sigma mn} \\ &\quad \times \hat{\mathbf{H}}^{(\beta)}_{\sigma' m' n'}] \cdot \mathbf{n} + i\omega[\mathbf{t}^{(\alpha)}_{\sigma mn} \cdot \hat{\mathbf{u}}^{(\beta)}_{\sigma' m' n'} - \hat{\mathbf{t}}^{(\beta)}_{\sigma' m' n'} \cdot \mathbf{u}^{(\alpha)}_{\sigma mn} \\ &\quad - p^{(\alpha)}_{\sigma mn} \mathbf{n} \cdot \hat{\mathbf{w}}^{(\beta)}_{\sigma' m' n'} + \hat{p}^{(\beta)}_{\sigma' m' n'} \mathbf{n} \cdot \mathbf{w}^{(\alpha)}_{\sigma mn}]\} dS \end{aligned}$$

$$+\sum_{\sigma'm'n'}\sum_{\beta=1}^{6} c_{\sigma'm'n}^{(\beta)} \iint_{S+} \{[\mathbf{E}_{\sigma'm'n'}^{(\beta)} \times \mathbf{H}_{\sigma mn}^{(\alpha)} - \mathbf{E}_{\sigma mn}^{(\alpha)} \times \mathbf{H}_{\sigma'm'n'}^{(\beta)}] \cdot \mathbf{n} + i\omega[\mathbf{t}_{\sigma mn}^{(\alpha)} \cdot \mathbf{u}_{\sigma'm'n'}^{(\beta)} - \mathbf{t}_{\sigma'm'n'}^{(\beta)} \cdot \mathbf{u}_{\sigma mn}^{(\alpha)} - p_{\sigma mn}^{(\alpha)} \mathbf{n} \cdot \mathbf{w}_{\sigma'm'n'}^{(\beta)} + p_{\sigma'm'n'}^{(\beta)} \mathbf{n} \cdot \mathbf{w}_{\sigma mn}^{(\alpha)}]\} ds,$$

$$\alpha = 1,2,3,4,5 \text{ or } 6. \tag{103}$$

The surface integral associated with $c_{\sigma'm'n}^{(\beta)}$ vanishes because of Eq. (92), and the remaining surface integral on the right hand side of Eq. (103) is equal to $(\omega G/k_s)D_{\sigma mn}^{(\alpha)}\delta_{\sigma\sigma'}\delta_{mm'}\delta_{nn'}\delta_{\alpha\beta}$ because of Eq. (93). Hence, the incident coefficient can be obtained as follows:

$$a_{\sigma mn}^{(\alpha)} = \frac{k_s}{\omega G D_{\sigma mn}^{(\alpha)}} \iint_S \{[\mathbf{E}_+ \times \mathbf{H}_{\sigma mn}^{(\alpha)} - \mathbf{E}_{\sigma mn}^{(\alpha)} \times \mathbf{H}_+] \cdot \mathbf{n} + i\omega[\mathbf{t}_{\sigma mn}^{(\alpha)} \cdot \mathbf{u}_+ - \mathbf{t}_+ \cdot \mathbf{u}_{\sigma mn}^{(\alpha)} - p_{\sigma mn}^{(\alpha)} \mathbf{n} \cdot \mathbf{w}_+ + p_+ \mathbf{n} \cdot \mathbf{w}_{\sigma mn}^{(\alpha)}]\} dS. \tag{104}$$

The subscript "+" denotes the field on S approaching from the+$\mathbf{n}$ side. Similarly, assigning $\mathbf{u}^{(A)} = \hat{\mathbf{u}}_{\sigma mn}^{(\alpha)}$ in Eq. (90) and making use of the procedure for determining $a_{\sigma mn}^{(\alpha)}$, we obtain the scattered coefficient

$$c_{\sigma mn}^{(\alpha)} = \frac{-k_s}{\omega G D_{\sigma mn}^{(\alpha)}} \iint_S \{[\mathbf{E}_+ \times \hat{\mathbf{H}}_{\sigma mn}^{(\alpha)} - \hat{\mathbf{E}}_{\sigma mn}^{(\alpha)} \times \mathbf{H}_+] \cdot \mathbf{n} + i\omega[\hat{\mathbf{t}}_{\sigma mn}^{(\alpha)} \cdot \mathbf{u}_+ - \mathbf{t}_+ \cdot \hat{\mathbf{u}}_{\sigma mn}^{(\alpha)} - \hat{p}_{\sigma mn}^{(\alpha)} \mathbf{n} \cdot \mathbf{w}_+ + p_+ \mathbf{n} \cdot \hat{\mathbf{w}}_{\sigma mn}^{(\alpha)}]\} ds. \tag{105}$$

This equation shows clearly that the coefficient of the scattered waves is determined by the dynamic sources $\mathbf{u}_+$, $\mathbf{w}_+$, $\mathbf{E}_+$, $\mathbf{H}_+$, $\mathbf{t}_+$, and p_+ at the surface S. Equations (104) and (105) reveal the Huygens' principle for electroseismic waves. If a poroelastic inclusion is perfectly welded to the surrounding medium, the following fields must be continuous at the interface S (Pride and Haartsen, 1996):

$$\mathbf{u}_+ = \mathbf{u}_-, \quad \mathbf{w}_+ \cdot \mathbf{n} = \mathbf{w}_- \cdot \mathbf{n}, \quad \mathbf{n} \times \mathbf{E}_+ = \mathbf{n} \times \mathbf{E}_-, \quad \mathbf{n} \times \mathbf{H}_+ = \mathbf{n} \times \mathbf{H}_-, \; p_+ = p_-, \quad \mathbf{t}_+ = \mathbf{t}_-, \quad on \; S. \tag{106}$$

Thus $\mathbf{u}_+$, $\mathbf{w}_+ \cdot \mathbf{n}$, $\mathbf{n} \times \mathbf{E}_+$, $\mathbf{n} \times \mathbf{H}_+$, $\mathbf{t}_+$, and p_+, defined in Eqs. (104) and (105), can be replaced by $\mathbf{u}_-$, $\mathbf{w}_- \cdot \mathbf{n}$, $\mathbf{n} \times \mathbf{E}_-$, $\mathbf{n} \times \mathbf{H}_-$, $\mathbf{t}_-$, and p_-, respectively. Therefore, we can extend the series representation for $\mathbf{u}_-$ of Eq. (98) to interface S. Substitution of this series of $\mathbf{u}_-$, $\mathbf{w}_- \cdot \mathbf{n}$, $\mathbf{n} \times \mathbf{E}_-$, $\mathbf{n} \times \mathbf{H}_-$, $\mathbf{t}_-$, and p_- into Eq. (104) for $\mathbf{u}_+$, $\mathbf{w}_+ \cdot \mathbf{n}$, $\mathbf{n} \times \mathbf{E}_+$, $\mathbf{n} \times \mathbf{H}_+$, $\mathbf{t}_+$, and p_+ yields the relationship between the incident and refracted coefficients

$$a_{\sigma mn}^{(\alpha)} = \sum_{\sigma'm'n'}\sum_{\beta=1}^{6} \mathbf{Q}_{\sigma mn,\sigma'm'n'}^{(\alpha,\beta)} f_{\sigma'm'n'}^{(\beta)}, \tag{107}$$

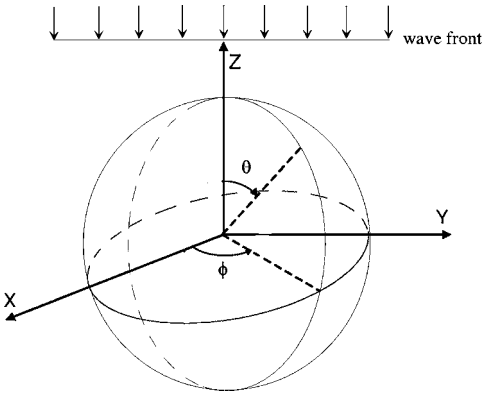

FIG. 2. A plane harmonic wave impinges on an inclusion embedded in an infinite medium.

where

$$\mathbf{Q}_{\sigma mn,\sigma'm'n'}^{(\alpha,\beta)} = \frac{k_s}{\omega G D_{\sigma mn}^{(\alpha)}} \iint_S \{[\hat{\mathbf{E}}_{\sigma'm'n'(0)}^{(\beta)} \times \mathbf{H}_{\sigma mn}^{(\alpha)} - \mathbf{E}_{\sigma mn}^{(\alpha)} \times \hat{\mathbf{H}}_{\sigma'm'n'(0)}^{(\beta)}] \cdot \mathbf{n} + i\omega[\mathbf{t}_{\sigma mn}^{(\alpha)} \cdot \hat{\mathbf{u}}_{\sigma'm'n'(0)}^{(\beta)} - \hat{\mathbf{t}}_{\sigma'm'n'(0)}^{(\beta)} \cdot \mathbf{u}_{\sigma mn}^{(\alpha)} - p_{\sigma mn}^{(\alpha)} \mathbf{n} \cdot \hat{\mathbf{w}}_{\sigma'm'n'(0)}^{(\beta)}]$$

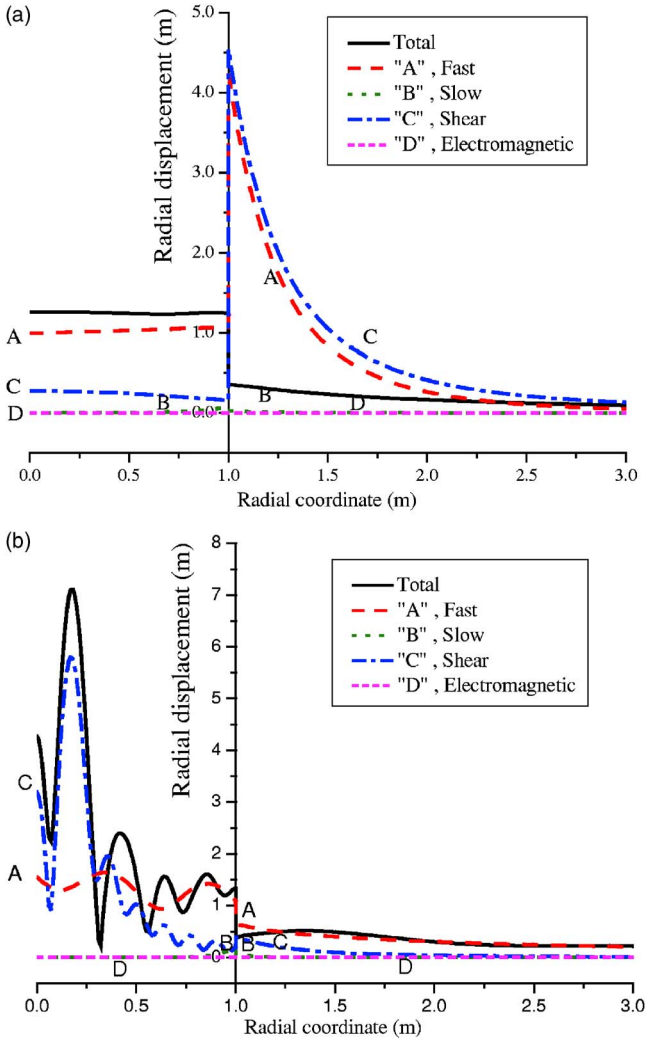

FIG. 3. (Color online) The total reflected wave amplitude of radial displacement along z-axis at (a) 200 Hz and (b) 2000 Hz and whose components contributed by the fast, slow, shear, and electromagnetic wave.

TABLE I. Material properties for the cases studied.

		Exterior surrounding	Interior inclusion
		electroporoelasticity	electroporoelasticity
porosity	$\phi(\%)$	30	30
permeability	$k_0(\mathrm{m}^2)$	10^{-11}	10^{-11}
bulk modulus solid	k_s(Pa)	3.6×10^{10}	3.5×10^{10}
bulk modulus fluid	k_f(Pa)	2.2×10^{9}	2.2×10^{9}
bulk modulus frame	k_{fr}(Pa)	7.0×10^{9}	4.0×10^{8}
shear modulus frame	g_{fr}(Pa)	5.0×10^{9}	5.0×10^{8}
viscosity	η(Pa·s)	10^{-3}	10^{-3}
solid density	$\rho_s(\mathrm{kg/m}^3)$	2.7×10^{3}	2.6×10^{3}
fluid density	$\rho_f(\mathrm{kg/m}^3)$	10^{3}	10^{3}
salinity	C(mol/L)	10^{-3}	10^{-3}
temperature	$T(K)$	298	298
fluid dielectric constant	κ_f	80	80
solid dielectric constant	κ_s	4	4
tortuosity	α_∞	3	3

$$+\hat{p}^{(\beta)}_{\sigma' m' n'(0)}\mathbf{n}\cdot\mathbf{w}^{(\alpha)}_{\sigma mn}]\}dS. \tag{108}$$

Similarly, substitution of the series representation of $\mathbf{u}_-$ into Eq. (105) yields the relationship between the scattered and refracted coefficients

$$c^{(\alpha)}_{\sigma mn} = -\sum_{\sigma' m' n'}\sum_{\beta=1}^{6}\hat{\mathbf{Q}}^{(\alpha,\beta)}_{\sigma mn,\sigma' m' n'} f^{(\beta)}_{\sigma' m' n'}, \tag{109}$$

in which

$$\hat{\mathbf{Q}}^{(\alpha,\beta)}_{\sigma mn,\sigma' m' n'} = \frac{k_s}{\omega G D^{(\alpha)}_{\sigma mn}}\iint_S \{[\hat{\mathbf{E}}^{(\beta)}_{\sigma' m' n'(0)}\times\hat{\mathbf{H}}^{(\alpha)}_{\sigma mn} - \hat{\mathbf{E}}^{(\alpha)}_{\sigma mn}\times\hat{\mathbf{H}}^{(\beta)}_{\sigma' m' n'(0)}]\cdot\mathbf{n} + i\omega[\hat{\mathbf{t}}^{(\alpha)}_{\sigma mn}\cdot\hat{\mathbf{u}}^{(\beta)}_{\sigma' m' n'(0)} - \hat{\mathbf{t}}^{(\beta)}_{\sigma' m' n'(0)}\cdot\hat{\mathbf{u}}^{(\alpha)}_{\sigma mn} - \hat{p}^{(\alpha)}_{\sigma mn}\mathbf{n}\cdot\hat{\mathbf{w}}^{(\beta)}_{\sigma' m' n'(0)} + \hat{p}^{(\beta)}_{\sigma' m' n'(0)}\mathbf{n}\cdot\hat{\mathbf{w}}^{(\alpha)}_{\sigma mn}]\}dS. \tag{110}$$

In matrix notation, we can write Eqs. (107) and (109) as

$$\mathbf{a} = \mathbf{Q}\mathbf{f}, \tag{111}$$

$$\mathbf{c} = -\hat{\mathbf{Q}}\mathbf{f}, \tag{112}$$

where $\mathbf{a}$, $\mathbf{c}$, and $\mathbf{f}$ are column matrices for fixed σ, m, and n; moreover, $\mathbf{Q}$ and $\hat{\mathbf{Q}}$ are square matrices with the indexes (α,β) and infinite matrices with indexes $m=0,\ldots,n$ and $n=0,\ldots,\infty$. Denoting the inverse of the matrix $\mathbf{Q}$ by $\mathbf{Q}^{-1}$, we have the results

$$\mathbf{f} = \mathbf{Q}^{-1}\mathbf{a}, \tag{113}$$

$$\mathbf{c} = -(\hat{\mathbf{Q}}\mathbf{Q}^{-1})\mathbf{a} = \mathbf{T}\mathbf{a}. \tag{114}$$

The product $-\hat{\mathbf{Q}}\mathbf{Q}^{-1}$ is called the transition matrix

$$\mathbf{T} \equiv -\hat{\mathbf{Q}}\mathbf{Q}^{-1}, \tag{115}$$

for the electroporoelastic medium. The transition matrix relates directly the unknown scattered coefficient $\mathbf{c}$ to the given incident coefficient $\mathbf{a}$. The refracted coefficient $\mathbf{f}$ is related to $\mathbf{a}$ through $\mathbf{Q}^{-1}$ matrix.

Let S be a spherical surface with radius a, the traction $\mathbf{t}(\mathbf{u}^{(\beta)}_{\sigma mn})$ in the surface integrals for $\mathbf{Q}^{(\alpha,\beta)}_{\sigma mn,\sigma' m' n'}$ and

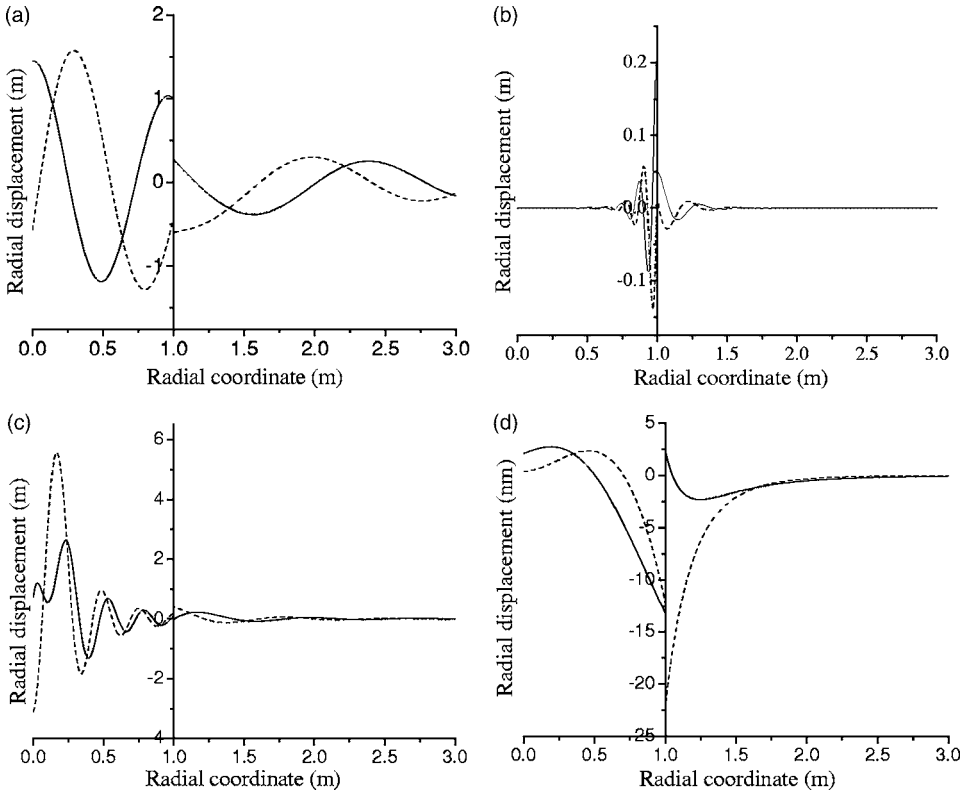

FIG. 4. Radial displacement for each coupling part (the real (solid line) and imaginary part (dashed line) of (a) $\mathbf{u}^{(1)}$ (fast), (b) $\mathbf{u}^{(2)}$ (slow), (c) $\mathbf{u}^{(4)}$ (shear), and (d) $\mathbf{u}^{(6)}$ (electromagnetic) components of the reflected wave) along z-axis at 2000 Hz.

$\hat{\mathbf{Q}}^{(\alpha,\beta)}_{\sigma mn,\sigma' m' n'}$ is replaced by $\mathbf{t}^r(\mathbf{u}^{(\beta)}_{\sigma mn})$ defined in Eqs. (81)–(86). The resulted integrals can be evaluated in a closed form by using Eqs. (49), (87), and (88). The corresponding elements of $\mathbf{Q}^{(\alpha,\beta)}_{\sigma mn,\sigma' m' n'}$ obtained from Eq. (108) are listed in Appendix B, and those of $\hat{\mathbf{Q}}^{(\alpha,\beta)}_{\sigma mn,\sigma' m' n'}$ can be obtained from $\mathbf{Q}^{(\alpha,\beta)}_{\sigma mn,\sigma' m' n'}$ by replacing the spherical Hankel function $h_n^{(2)}$ with the spherical Bessel function j_n. Note that $\mathbf{Q}$-matrix for the spherical electroporoelastic inclusion are diagonal matrices with the indexes $(\sigma mn, \sigma' m' n')$,

$$\mathbf{Q}^{(\alpha,\beta)}_{\sigma mn,\sigma' m' n'} \begin{cases} \neq 0, & \text{when } \sigma = \sigma', m = m', n = n', \\ = 0, & \text{otherwise.} \end{cases} \tag{116}$$

Furthermore, the associated transition matrix is also diagonal with the same indexes,

$$[\mathbf{T}^{(\alpha,\beta)}]_{\sigma mn,\sigma' m' n'} \begin{cases} \neq 0, & \text{when } \sigma = \sigma', m = m', n = n', \\ = 0, & \text{otherwise.} \end{cases} \tag{117}$$

On the other hand, concerning the indexes (α, β), the transition matrix is not in a diagonal form. Substituting the above results into Eqs. (113) and (114), we can determine the solutions for the waves scattered by a spherical electroporoelastic inclusion. The relationships between the incident coefficients and scattered coefficients for the case of the spherical electroporoelastic inclusion are obtained as follows:

$$\begin{aligned} c^1 &= T^{11}a^1 + T^{12}a^2 + T^{14}a^4 + T^{16}a^6, \\ c^2 &= T^{21}a^1 + T^{22}a^2 + T^{24}a^4 + T^{26}a^6, \\ c^3 &= T^{33}a^3 + T^{35}a^5, \\ c^4 &= T^{41}a^1 + T^{42}a^2 + T^{44}a^4 + T^{46}a^6, \\ c^5 &= T^{53}a^3 + T^{55}a^5, \\ c^6 &= T^{61}a^1 + T^{62}a^2 + T^{64}a^4 + T^{66}a^6. \end{aligned} \tag{118}$$

IV. APPLICATION TO ANALYSIS OF ELECTROSEISMIC WAVE SCATTERING BY A SPHERICAL INCLUSION

For an incident plane compressional wave impinging on the inclusion, the incident coefficients for the transition matrix can be obtained by appling Eq. (104). Let the incident wave be a fast dilatational plane wave with a wave number k_{p1} and unit amplitude traveling in the negative z-direction as shown in the Fig. 2. The potential of this plane wave can be represented as

$$\phi_1^i = \frac{\phi_0}{\mu_1} e^{ik_{p1}(z-a)}. \tag{119}$$

With the series expansion, the exponential term can be expanded into the series of the spherical Bessel function and the Legendre polynomials (Ying and Truell, 1956) as

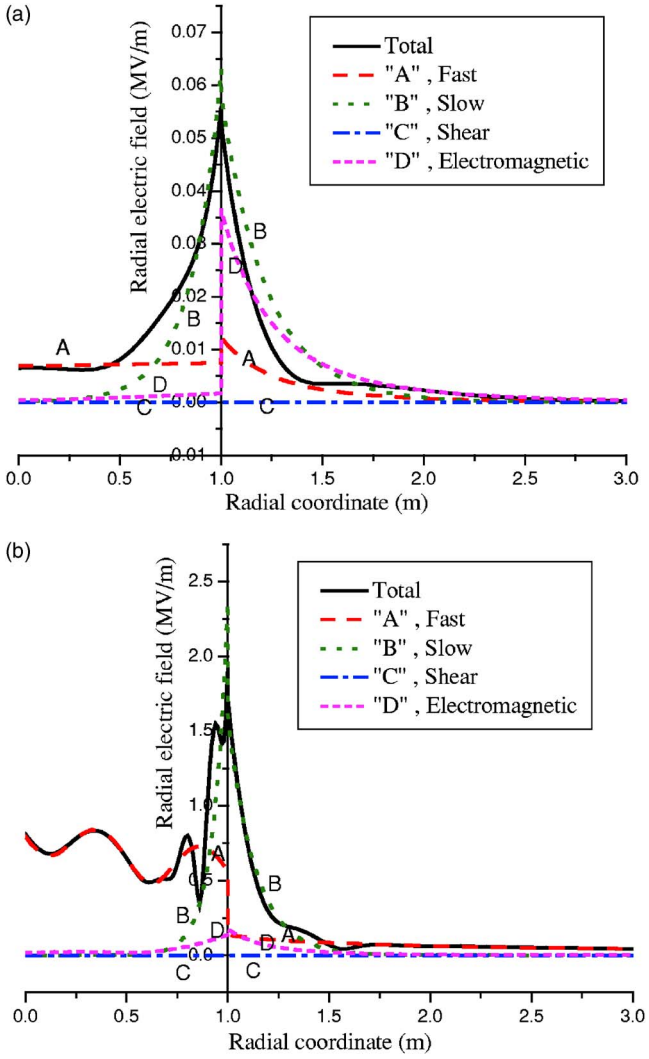

FIG. 5. The total reflected wave amplitude of radial electric field along z-axis at (a) 200 Hz and (b) 2000 Hz and whose components contributed by the fast, slow, shear and electromagnetic wave.

$$\begin{aligned} \phi_1^i &= \frac{\phi_0}{\mu_1} e^{ik_{p1}z} e^{-ik_{p1}a} \\ &= \frac{\phi_0}{\mu_1} e^{-ik_{p1}a} \sum_{n=0}^{\infty} (2n+1) i^n j_n(k_{p1}R) P_n(\cos\theta), \end{aligned} \tag{120}$$

where $P_n(\cos\theta)$ is the Legendre polynomial. At the same time, we set $\sigma = 1$ (even) through comparing Eq. (120) with the spherical surface harmonics in Eq. (48). Thus the associated displacement field is determined from Eqs. (13) and (25)

$$\mathbf{u}^i = \nabla(\phi_0 e^{ik_{p1}z}) e^{-ik_{p1}a} = \frac{k_p}{\mu_1} \phi_0 e^{-ik_{p1}a} \sum_{n=0}^{\infty} (2n+1) i^n \hat{\mathbf{u}}^{(1)}_{10n}. \tag{121}$$

Substituting Eq. (121) into Eq. (104), we obtain the incident coefficients

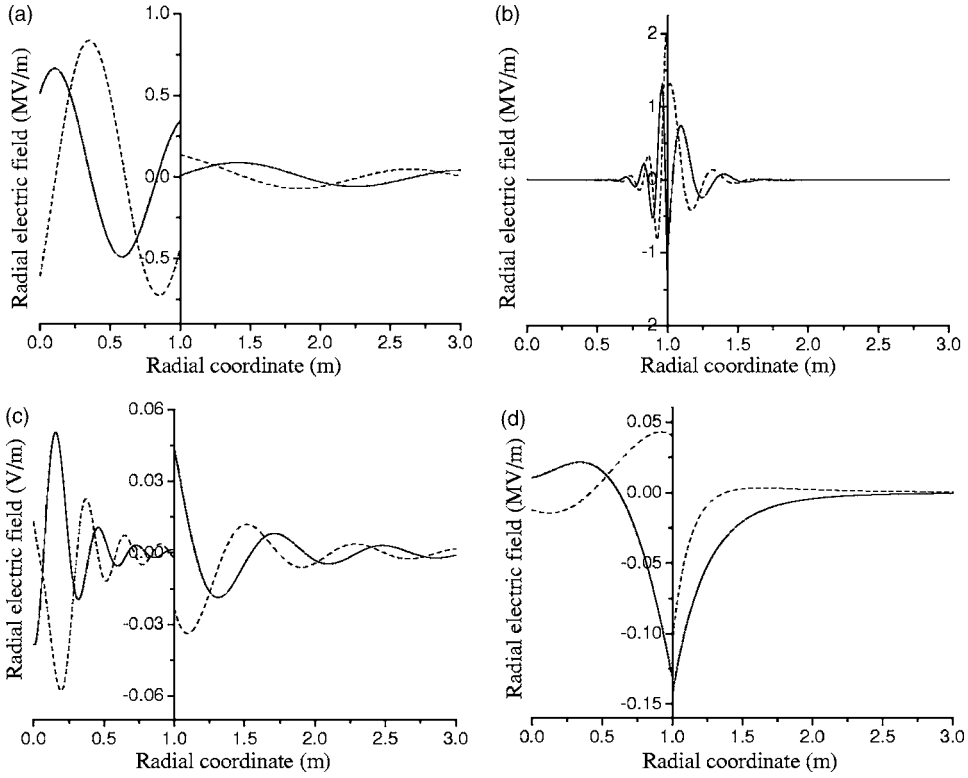

FIG. 6. Radial electric field for each coupling part [the real (solid line) and imaginary part (dashed line) of (a) $\mathbf{E}^{(1)}$ (fast), (b) $\mathbf{E}^{(2)}$ (slow), (c) $\mathbf{E}^{(4)}$ (shear), and (d) $\mathbf{E}^{(6)}$ (electromagnetic) components of the reflected wave] along z-axis at 2000 Hz.

$$a_{\sigma mn}^{(\alpha)} = \begin{cases} \phi_0 e^{-ik_{p1}a}(2n+1)i^n k_p/\mu_1, & \alpha=1,\sigma=1,m=0, \quad \text{and} \quad n \in N, \\ 0, & \text{otherwise}. \end{cases} \tag{122}$$

All results pertain to a spherical inclusion with $a=1.0m$. The material properties in the exterior and interior media are converted from those chosen by Garambois and Dietrich (2002). The corresponding material constants are listed in Table I. The results shown in Fig. 3 display the amplitudes of the radial displacements for the scattered (radial coordinate $\geqslant$1.0 m) and the refracted (radial coordinate $\leqslant$1.0 m) waves along the z-axis at the two different frequencies. In fact, the amplitude obtained from Eqs. (97) and (98) consist of six parts: $\mathbf{u}^{(1)}$, $\mathbf{u}^{(2)}$, $\mathbf{u}^{(3)}$, $\mathbf{u}^{(4)}$, $\mathbf{u}^{(5)}$, and $\mathbf{u}^{(6)}$. Under the incidence of the fast dilatational plane wave, the contribution of the mode conversion for the third and fifth parts $\mathbf{u}^{(3)}$ and $\mathbf{u}^{(5)}$ are zero. From Fig. 3, it reveals that at both 200 and 2000 Hz, the slow wave attenuates out quickly; the electromagnetic contribution is very small. For the scattered part, the shear wave contribution is larger than the fast part at 200 Hz, but at 2000 Hz, the fast wave becomes more significant. For the refracted part, the shear wave contribution at 200 Hz is very small, but at 2000 Hz the shear wave becomes more significant. This is analogous to the selective transmission for elastic wave (Pao and Mow, 1976). In order to further illustrate the above-mentioned statements at 2000 Hz, we plot the second, fourth, and sixth parts in the region near the interface in Fig. 4. Figure 5 displays the amplitudes of the radial electric field for the scattered (radial coordinate $\geqslant$1.0 m) waves and the refracted (radial coordinate $\leqslant$1.0 m) waves along the z-axis at the two different frequencies. Figure 6 shows the amplitude of $f=2000$ Hz obtained from Eqs. (100) (only the scattered part) and (101) consisting of six parts: $\mathbf{E}^{(1)}$, $\mathbf{E}^{(2)}$, $\mathbf{E}^{(3)}$, $\mathbf{E}^{(4)}$, $\mathbf{E}^{(5)}$, and $\mathbf{E}^{(6)}$. Under the incidence of the fast dilatational plane wave, the contribution of the mode conversion for the third and fifth parts $\mathbf{E}^{(3)}$ and $\mathbf{E}^{(5)}$ are also zero. From Figs. 5 and 6, we see that at both 200 and 2000 Hz, the slow wave attenuates out quickly and the shear wave contribution is very small. It is also observed that near the surface of the sphere, slow wave contributions are quite significant. Figure 7 presents the results for the radial surface electric field ($\phi=0$, $\theta=0\sim2\pi$) for the electroporoelastic inclusion at 200 and 2000 Hz. At 2000 Hz, we find that the selective transmission is present with the scattered part being smaller and the refracted part being larger.

V. CONCLUDING REMARKS

In this paper we adopt the approach introduced by Yeh *et al.* (2004) for poroelastic scattering problem to develop the transition matrix for the analysis of electroseismic wave scattered in an electroporoelastic medium. A set of basis functions for an electroporoelastic medium is presented. The related orthogonality conditions are obtained by applying Betti's third identity generalized for the electroporoelasticity and the transition matrix is derived accordingly.

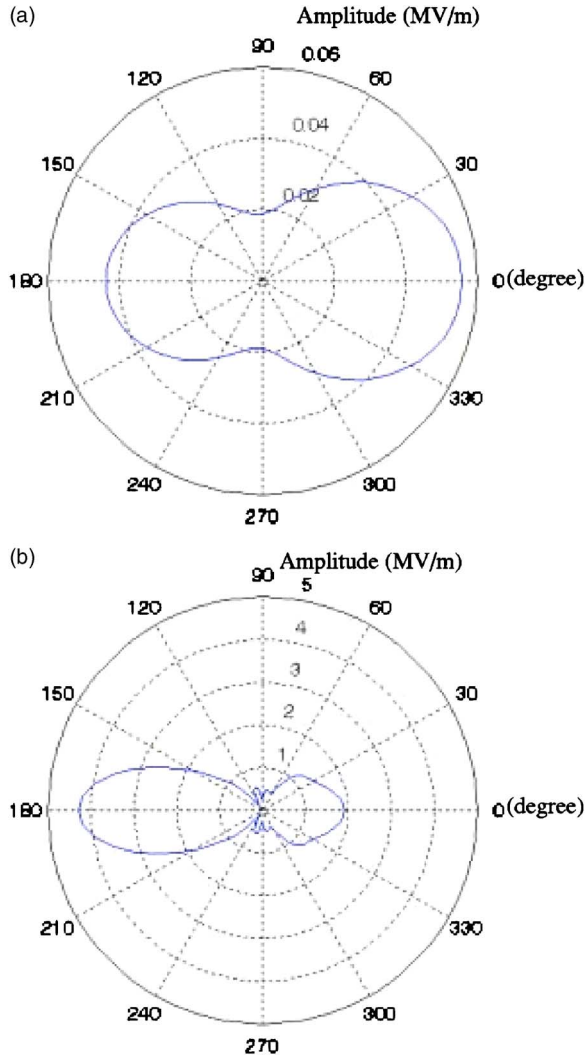

FIG. 7. (Color online) Amplitude of radial electric field at surface at (a) 200 Hz and (b) 2000 Hz.

In order to show its applicability, the transition matrix is employed to study the wave scattered by an electroporoelastic spherical inclusion embedded in electroporoelastic media. The results are obtained for Biot's fast and slow, shear and electromagnetic waves. Moreover, it is shown that the phenomenon of the selective transmission is present. For electric field, near the surface of the spherical inclusion, contributions of the slow wave are more pronounced. This phenomenon reflects the coupling electroseismic effects. The example demonstrates that the method proposed in this paper is an useful approach for analysis of scattered electroseismic waves.

ACKNOWLEDGMENTS

The authors gratefully acknowledge the financial support granted by the National Science Council, R.O.C. (NSC-093-2811-E-002-057). The facility of calculation provided by National Taiwan University is also highly appreciated.

APPENDIX A: DECOUPLING THE DILATATIONAL AND ROTATIONAL WAVES

This Appendix presents the decoupling procedure for the dilatational and rotational waves.

1. Dilatational waves

The determinant of the coefficients from the characteristic equation in Eq. (17) is set to be zero as

$$\begin{vmatrix} \rho - H\frac{k^2}{\omega^2} & \rho_f - C\frac{k^2}{\omega^2} \\ \rho_f - C\frac{k^2}{\omega^2} & \rho_n - M\frac{k^2}{\omega^2} \end{vmatrix} = 0. \tag{A1}$$

Equation (A1) provides the eigenvalues as

$$k_{p1}^2/\omega^2 = (B - \sqrt{B^2 - 4AC})/2A,$$

$$k_{p2}^2/\omega^2 = (B + \sqrt{B^2 - 4AC})/2A, \tag{A2}$$

where A, B, and C are defined in Eq. (20). Substitution of Eq. (A2) into (A1) gives two associated eigenvectors

$$\langle \mu_1, 1 \rangle^T = \left\langle -\left(\rho_n - M\frac{k_{p1}^2}{\omega^2}\right) \Big/ \left(\rho_f - C\frac{k_{p1}^2}{\omega^2}\right), 1 \right\rangle^T,$$

$$\langle 1, \mu_2 \rangle^T = \left\langle 1, -\left[\rho - H\frac{k_{p2}^2}{\omega^2}\right] \Big/ \left(\rho_f - C\frac{k_{p2}^2}{\omega^2}\right) \right\rangle^T. \tag{A3}$$

In order to decouple Eq. (17), we rewrite the parameters μ_1 and μ_2 shown in the preceding equations in a common denominator form

$$\mu_1 = -\left(\rho_n - M\frac{k_{p1}^2}{\omega^2}\right)\left(\rho_f - C\frac{k_{p2}^2}{\omega^2}\right) \Big/ \left[\left(\rho_f - C\frac{k_{p1}^2}{\omega^2}\right) \times \left(\rho_f - C\frac{k_{p2}^2}{\omega^2}\right)\right],$$

$$\mu_2 = -\left[\rho - H\frac{k_{p2}^2}{\omega^2}\right]\left(\rho_f - C\frac{k_{p1}^2}{\omega^2}\right) \Big/ \left[\left(\rho_f - C\frac{k_{p1}^2}{\omega^2}\right) \times \left(\rho_f - C\frac{k_{p2}^2}{\omega^2}\right)\right], \tag{A4}$$

where Eq. (A4) can be further simplified into the equations presented in Eq. (22). The diagonal matrices with regard to Eq. (17) are expressed as

$$\begin{bmatrix} H^* & 0 \\ 0 & M^* \end{bmatrix} = \begin{bmatrix} \mu_1 & 1 \\ 1 & \mu_2 \end{bmatrix}^T \begin{bmatrix} H & C \\ C & M \end{bmatrix} \begin{bmatrix} \mu_1 & 1 \\ 1 & \mu_2 \end{bmatrix} = \begin{bmatrix} H\mu_1^2 + 2C\mu_1 + M & H\mu_1 + C\mu_1\mu_2 + C + M\mu_2 \\ H\mu_1 + C\mu_1\mu_2 + C + M\mu_2 & H + 2C\mu_2 + M\mu_2^2 \end{bmatrix} \tag{A5}$$

and

$$\begin{bmatrix} \rho^* & 0 \\ 0 & \rho_n^* \end{bmatrix} = \begin{bmatrix} \mu_1 & 1 \\ 1 & \mu_2 \end{bmatrix}^T \begin{bmatrix} \rho & \rho_f \\ \rho_f & \rho_n \end{bmatrix} \begin{bmatrix} \mu_1 & 1 \\ 1 & \mu_2 \end{bmatrix} = \begin{bmatrix} \rho\mu_1^2 + 2\rho_f\mu_1 + \rho_n & \rho\mu_1 + \rho_f\mu_1\mu_2 + \rho_f + \rho_n\mu_2 \\ \rho\mu_1 + \rho_f\mu_1\mu_2 + \rho_f + \rho_n\mu_2 & \rho + 2\rho_f\mu_2 + \rho_n\mu_2^2 \end{bmatrix}. \tag{A6}$$

With the aid of the following equation:

$$4ad - f^2 = -2b^2 + 2b\sqrt{b^2 + 4ad}, \tag{A7}$$

the symmetric off-diagonal elements of Eq. (A5) vanish

$$H\mu_1 + C\mu_1\mu_2 + C + M\mu_2 = 0. \tag{A8}$$

2. Rotational waves

The determinant of the coefficients from the characteristic equation in Eq. (30) is set to be zero as

$$\begin{vmatrix} S_A^2 - \dfrac{k^2}{\omega^2} & -S_C^2 \\ \dfrac{k^2}{\omega^2} & S_B^2 - \dfrac{k^2}{\omega^2} \end{vmatrix} = 0, \tag{A9}$$

where S_A^2, S_B^2, and S_C^2 are defined in Eq. (32).

Equation (A9) provides the eigenvalues as

$$(k_{s1}/\omega)^2 = (1-\xi)S_A^2,$$

$$(k_{s2}/\omega)^2 = \left(\frac{1}{1-\xi}\right)S_B^2, \tag{A10}$$

where ξ is defined in Eq. (33). Substitution of Eq. (A10) into (A9) gives a set of eigenvectors

$$\mathbf{\Psi} = \begin{bmatrix} 1 & \xi \\ \xi\dfrac{S_A^2}{S_C^2} & 1 \end{bmatrix}. \tag{A11}$$

According to Eq. (30), in order to diagonalize the matrix $\begin{bmatrix} 1 & 0 \\ -1 & 1 \end{bmatrix}$, we assume a matrix $\begin{bmatrix} 1 & \gamma \\ \varsigma & 1 \end{bmatrix}$, and then

$$\begin{bmatrix} G^* & 0 \\ 0 & \mu^* \end{bmatrix} = \begin{bmatrix} 1 & \gamma \\ \varsigma & 1 \end{bmatrix} \begin{bmatrix} 1 & 0 \\ -1 & 1 \end{bmatrix} \begin{bmatrix} 1 & \xi \\ \xi\dfrac{S_A^2}{S_C^2} & 1 \end{bmatrix} = \begin{bmatrix} 1 + \gamma\left(\xi\dfrac{S_A^2}{S_C^2} - 1\right) & \xi + \gamma(1-\xi) \\ \varsigma + \left(\xi\dfrac{S_A^2}{S_C^2} - 1\right) & \xi\varsigma + (1-\xi) \end{bmatrix}. \tag{A12}$$

Let off-diagonal terms be zero, we can find

$$\gamma = \frac{\xi}{\xi - 1},$$

$$\varsigma = 1 - \xi\frac{S_A^2}{S_C^2}, \tag{A13}$$

and the diagonal terms are

$$G^* = 1 + \left(1 - \xi\frac{S_A^2}{S_C^2}\right)\frac{\xi}{(1-\xi)},$$

$$\mu^* = 1 - \xi^2\frac{S_A^2}{S_C^2}. \tag{A14}$$

The other part of Eq. (30), can be diagonalized to

$$\begin{bmatrix} \rho^{**} & 0 \\ 0 & \rho_n^{**} \end{bmatrix} = \begin{bmatrix} 1 & \dfrac{\xi}{(\xi-1)} \\ 1 - \xi\dfrac{S_A^2}{S_C^2} & 1 \end{bmatrix} \begin{bmatrix} S_A^2 & -S_C^2 \\ 0 & S_B^2 \end{bmatrix} \begin{bmatrix} 1 & \xi \\ \xi\dfrac{S_A^2}{S_C^2} & 1 \end{bmatrix}$$

$$= \begin{bmatrix} \left(1 - \xi^2\dfrac{S_A^2}{S_C^2}\right)S_A^2 & \dfrac{1}{(\xi-1)}[(\xi-1)(\xi S_A^2 - S_C^2) + \xi S_B^2] \\ \dfrac{S_A^2}{S_C^2}[(1-\xi)(S_C^2 - \xi S_A^2) + \xi S_B^2] & \left[\left(1 - \xi\dfrac{S_A^2}{S_C^2}\right)\dfrac{\xi}{(1-\xi)} + 1\right]S_B^2 \end{bmatrix}. \tag{A15}$$

With the aid of the following equation [i.e., Eq. (33)]:

$$(\xi-1)(\xi S_A^2 - S_C^2) + \xi S_B^2 = 0, \tag{A16}$$

the symmetric off-diagonal elements of Eq. (A15) vanish.

From Eqs. (A16), (32), and (62), we can write the other form

$$\frac{\mu_5\mu_6\rho_f^2 L^2}{\mu\bar{\epsilon}^2} - \xi G = 0. \tag{A17}$$

Furthermore, we also use some algebraic techniques to obtain the following identities among the factors: μ_1, μ_2, μ_3, μ_4, μ_5, and μ_6

$$H\mu_1 + C - \left(G\mu_1 - \frac{\mu_5\rho_n\rho_f L^2}{\bar{\epsilon}^2\mu}\right)\frac{k_{s1}^2}{k_{p1}^2} + \mu_3(C\mu_1 + M) = 0, \tag{A18}$$

$$(H\mu_1 + C)\xi - \left(\mu_1 G\xi - \frac{\mu_6\rho_n\rho_f L^2}{\bar{\epsilon}^2\mu}\right)\frac{k_{s2}^2}{k_{p1}^2} + \mu_4(C\mu_1 + M) = 0, \tag{A19}$$

$$H + C\mu_2 - \left(G - \frac{\mu_2\mu_5\rho_n\rho_f L^2}{\bar{\epsilon}^2\mu}\right)\frac{k_{s1}^2}{k_{p2}^2} + \mu_3(C + M\mu_2) = 0, \tag{A20}$$

$$(H + C\mu_2)\xi - \left(G\xi - \frac{\mu_2\mu_6\rho_n\rho_f L^2}{\bar{\epsilon}^2\mu}\right)\frac{k_{s2}^2}{k_{p2}^2} + \mu_4(C + M\mu_2) = 0. \tag{A21}$$

These results will be useful in the evaluation of Eq. (B28).

APPENDIX B: ELEMENTS IN Q-MATRIX FOR A ELECTRO-POROELASTIC SPHERICAL INCLUSION AND THE DERIVATION OF ORTHOGONALITY CONDITIONS

This appendix enumerates the elements of $\mathbf{Q}$ for a electroporoelastic spherical inclusion with radius a. In addition, we apply the $\mathbf{Q}^*$ matrix to derive the orthogonality conditions defined in Eqs. (91)–(93). An opening interface condition is assumed between the sphere inclusion and the surrounding medium. To utilize the spherical symmetry and choose the origin of the coordinate system to be located at the center of the sphere and designate the outward unit surface-normal vector $\mathbf{n}=\mathbf{e}_R$ in the evaluation of $\mathbf{Q}^{(\alpha,\beta)}_{\sigma mn,\sigma' m' n'}$. We can calculate the surface integral in Eq. (108). The $\mathbf{Q}$ matrix is written as

$$\mathbf{Q}^{(\alpha,\beta)}_{\sigma mn,\sigma mn} = \frac{k_s}{\omega G D^{(\alpha)}_{\sigma mn}} \times \begin{bmatrix} \mathbf{Q}^{*(1,1)} & \mathbf{Q}^{*(1,2)} & \mathbf{Q}^{*(1,3)} & \mathbf{Q}^{*(1,4)} & \mathbf{Q}^{*(1,5)} & \mathbf{Q}^{*(1,6)} \\ \mathbf{Q}^{*(2,1)} & \mathbf{Q}^{*(2,2)} & \mathbf{Q}^{*(2,3)} & \mathbf{Q}^{*(2,4)} & \mathbf{Q}^{*(2,5)} & \mathbf{Q}^{*(2,6)} \\ \mathbf{Q}^{*(3,1)} & \mathbf{Q}^{*(3,2)} & \mathbf{Q}^{*(3,3)} & \mathbf{Q}^{*(3,4)} & \mathbf{Q}^{*(3,5)} & \mathbf{Q}^{*(3,6)} \\ \mathbf{Q}^{*(4,1)} & \mathbf{Q}^{*(4,2)} & \mathbf{Q}^{*(4,3)} & \mathbf{Q}^{*(4,4)} & \mathbf{Q}^{*(4,5)} & \mathbf{Q}^{*(4,6)} \\ \mathbf{Q}^{*(5,1)} & \mathbf{Q}^{*(5,2)} & \mathbf{Q}^{*(5,3)} & \mathbf{Q}^{*(5,4)} & \mathbf{Q}^{*(5,5)} & \mathbf{Q}^{*(5,6)} \\ \mathbf{Q}^{*(6,1)} & \mathbf{Q}^{*(6,2)} & \mathbf{Q}^{*(6,3)} & \mathbf{Q}^{*(6,4)} & \mathbf{Q}^{*(6,5)} & \mathbf{Q}^{*(6,6)} \end{bmatrix}_{\sigma mn,\sigma mn}, \tag{B1}$$

where $\mathbf{Q}$ matrix is diagonal with the indexes $(\sigma mn, \sigma' m' n')$. The elements of $\mathbf{Q}^*$ are shown as follows:

$$\begin{aligned}\mathbf{Q}^{*(1,1)}_{\sigma mn,\sigma mn} = i\frac{4\pi(n+m)!\,a^2\omega}{\epsilon_m(2n+1)(n-m)!}\Bigg\{ & h_n^{(2)}(k_{p1}a)j_n(k_{p1(0)}a)\left(\frac{-2\mu_1\mu_{1(0)}n(n+1)}{k_p k_{p(0)}a^3}\right)(G-G_{(0)}) + h_n^{(2)}(k_{p1}a)j_n'(k_{p1(0)}a)\left(\frac{k_{p1}^2 k_{p1(0)}}{k_p k_{p(0)}}\right) \\ & \times\left[-H\mu_1\mu_{1(0)} - C\mu_{1(0)} - C\mu_1 - M + \left(\frac{2\mu_1\mu_{1(0)}n(n+1)}{k_{p1}^2 a^2}\right)(G-G_{(0)})\right] + h_n^{(2)\prime}(k_{p1}a)j_n(k_{p1(0)}a)\left(\frac{k_{p1}k_{p1(0)}^2}{k_p k_{p(0)}}\right) \\ & \times\left[H_{(0)}\mu_1\mu_{1(0)} + \mu_1 C_{(0)} + \mu_{1(0)}C_{(0)} + M_{(0)} + \left(\frac{2\mu_1\mu_{1(0)}n(n+1)}{k_{p1(0)}^2 a^2}\right)(G-G_{(0)})\right] + h_n^{(2)\prime}(k_{p1}a)j_n'(k_{p1(0)}a) \\ & \times\left(\frac{-4\mu_1\mu_{1(0)}k_{p1}k_{p1(0)}}{k_p k_{p(0)}a}\right)(G-G_{(0)})\Bigg\},\end{aligned} \tag{B2}$$

$$\mathbf{Q}^{*(1,2)}_{\sigma mn,\sigma mn} = i\frac{4\pi(n+m)!\,a^2\omega}{\epsilon_m(2n+1)(n-m)!}\Bigg\{h_n^{(2)}(k_{p1}a)j_n(k_{p2(0)}a)\left(\frac{-2\mu_1 n(n+1)}{k_p k_{p(0)}a^3}\right)(G-G_{(0)}) + h_n^{(2)}(k_{p1}a)j_n'(k_{p2(0)}a)\left(\frac{k_{p1}^2 k_{p2(0)}}{k_p k_{p(0)}}\right)$$
$$\times\left[-\mu_1 H - \mu_1\mu_{2(0)}C - C - \mu_{2(0)}M + \left(\frac{2\mu_1 n(n+1)}{k_{p1}^2 a^2}\right)(G-G_{(0)})\right] + h_n^{(2)\prime}(k_{p1}a)j_n(k_{p2(0)}a)\left(\frac{k_{p1}k_{p2(0)}^2}{k_p k_{p(0)}}\right)$$
$$\times\left[\mu_1 H_{(0)} + \mu_1\mu_{2(0)}C_{(0)} + C_{(0)} + \mu_{2(0)}M_{(0)} + \left(\frac{2\mu_1 n(n+1)}{k_{p2(0)}^2 a^2}\right)(G-G_{(0)})\right] + h_n^{(2)\prime}(k_{p1}a)j_n'(k_{p2(0)}a)$$
$$\times\left(\frac{-4\mu_1 k_{p1}k_{p2(0)}}{k_p k_{p(0)}a}\right)(G-G_{(0)})\Bigg\}, \tag{B3}$$

$$\mathbf{Q}^{*(1,4)}_{\sigma mn,\sigma mn} = in(n+1)\frac{4\pi(n+m)!\,a^2\omega}{\epsilon_m(2n+1)(n-m)!}\Bigg\{h_n^{(2)}(k_{p1}a)j_n(k_{s1(0)}a)\left(\frac{k_{p1}^2}{k_p k_{s1(0)}a}\right)\Bigg[-H\mu_1 - C + 2\mu_1\left(\frac{n^2+n-1}{k_{p1}^2a^2}\right)(G-G_{(0)})$$
$$+\left(\mu_1 G_{(0)} - \frac{\mu_{5(0)}\rho_n L\rho_{f(0)}L_{(0)}}{\bar{\epsilon}_{(0)}\bar{\epsilon}\mu_{(0)}}\right)\frac{k_{s1(0)}^2}{k_{p1}^2} - \mu_{3(0)}(C\mu_1 + M)\Bigg] + h_n^{(2)}(k_{p1}a)j_n'(k_{s1(0)}a)\left(\frac{-2\mu_1}{k_p a^2}\right)(G-G_{(0)})$$
$$+ h_n^{(2)\prime}(k_{p1}a)j_n(k_{s1(0)}a)\left(\frac{-2\mu_1 k_{p1}}{k_p k_{s1(0)}a^2}\right)(G-G_{(0)}) + h_n^{(2)\prime}(k_{p1}a)j_n'(k_{s1(0)}a)\left(\frac{2\mu_1 k_{p1}}{k_p a}\right)(G-G_{(0)})\Bigg\}, \tag{B4}$$

$$\mathbf{Q}^{*(1,6)}_{\sigma mn,\sigma mn} = in(n+1)\frac{4\pi(n+m)!\,a^2\omega}{\epsilon_m(2n+1)(n-m)!}\Bigg\{h_n^{(2)}(k_{p1}a)j_n(k_{s2(0)}a)\left(\frac{k_{p1}^2}{k_p k_{s2(0)}a}\right)\Bigg[-H\mu_1\xi_{(0)} - C\xi_{(0)} + 2\mu_1\xi_{(0)}\left(\frac{n^2+n-1}{k_{p1}^2a^2}\right)$$
$$\times(G-G_{(0)}) + \left(\mu_1 G_{(0)}\xi_{(0)} - \frac{\mu_{6(0)}\rho_n L\rho_{f(0)}L_{(0)}}{\bar{\epsilon}_{(0)}\bar{\epsilon}\mu_{(0)}}\right)\frac{k_{s2(0)}^2}{k_{p1}^2} - \mu_{4(0)}(C\mu_1 + M)\Bigg] + h_n^{(2)}(k_{p1}a)j_n'(k_{s2(0)}a)\left(\frac{-2\mu_1\xi_{(0)}}{k_p a^2}\right)$$
$$\times(G-G_{(0)}) + h_n^{(2)\prime}(k_{p1}a)j_n(k_{s2(0)}a)\left(\frac{-2\mu_1 k_{p1}\xi_{(0)}}{k_p k_{s2(0)}a^2}\right)(G-G_{(0)}) + h_n^{(2)\prime}(k_{p1}a)j_n'(k_{s2(0)}a)\left(\frac{2\mu_1 k_{p1}\xi_{(0)}}{k_p a}\right)(G-G_{(0)})\Bigg\}, \tag{B5}$$

$$\mathbf{Q}^{*(2,1)}_{\sigma mn,\sigma mn} = i\frac{4\pi(n+m)!\,a^2\omega}{\epsilon_m(2n+1)(n-m)!}\Bigg\{h_n^{(2)}(k_{p2}a)j_n(k_{p1(0)}a)\left(\frac{-2\mu_{1(0)}n(n+1)}{k_p k_{p(0)}a^3}\right)(G-G_{(0)}) + h_n^{(2)}(k_{p2}a)j_n'(k_{p1(0)}a)\left(\frac{k_{p2}^2 k_{p1(0)}}{k_p k_{p(0)}}\right)$$
$$\times\left[-H\mu_{1(0)} - C\mu_2\mu_{1(0)} - C - M\mu_2 + \left(\frac{2\mu_{1(0)}n(n+1)}{k_{p2}^2a^2}\right)(G-G_{(0)})\right] + h_n^{(2)\prime}(k_{p2}a)j_n(k_{p1(0)}a)\left(\frac{k_{p2}k_{p1(0)}^2}{k_p k_{p(0)}}\right)$$
$$\times\left[H_{(0)}\mu_{1(0)} + \mu_2\mu_{1(0)}C_{(0)} + C_{(0)} + \mu_2 M_{(0)} + \left(\frac{2\mu_{1(0)}n(n+1)}{k_{p1(0)}^2a^2}\right)(G-G_{(0)})\right] + h_n^{(2)\prime}(k_{p2}a)j_n'(k_{p1(0)}a)$$
$$\times\left(\frac{-4\mu_{1(0)}k_{p1(0)}k_{p2}}{k_p k_{p(0)}a}\right)(G-G_{(0)})\Bigg\}, \tag{B6}$$

$$\mathbf{Q}^{*(2,2)}_{\sigma mn,\sigma mn} = i\frac{4\pi(n+m)!\,a^2\omega}{\epsilon_m(2n+1)(n-m)!}\Bigg\{h_n^{(2)}(k_{p2}a)j_n(k_{p2(0)}a)\left(\frac{-2n(n+1)}{k_p k_{p(0)}a^3}\right)(G-G_{(0)}) + h_n^{(2)}(k_{p2}a)j_n'(k_{p2(0)}a)\left(\frac{k_{p2}^2 k_{p2(0)}}{k_p k_{p(0)}}\right)$$
$$\times\left[-H - C\mu_2 - C\mu_{2(0)} - M\mu_2\mu_{2(0)} + \left(\frac{2n(n+1)}{k_{p2}^2a^2}\right)(G-G_{(0)})\right] + h_n^{(2)\prime}(k_{p2}a)j_n(k_{p2(0)}a)\left(\frac{k_{p2}k_{p2(0)}^2}{k_p k_{p(0)}}\right)$$
$$\times\left[H_{(0)} + C_{(0)}\mu_{2(0)} + \mu_2 C_{(0)} + \mu_2\mu_{2(0)}M_{(0)} + \left(\frac{2n(n+1)}{k_{p2(0)}^2a^2}\right)(G-G_{(0)})\right]$$
$$+ h_n^{(2)\prime}(k_{p2}a)j_n'(k_{p2(0)}a)\left(\frac{-4k_{p2}k_{p2(0)}}{k_p k_{p(0)}a}\right)(G-G_{(0)})\Bigg\}, \tag{B7}$$

$$\mathbf{Q}^{*(2,4)}_{\sigma mn,\sigma mn} = in(n+1)\frac{4\pi(n+m)!\,a^2\omega}{\epsilon_m(2n+1)(n-m)!}\left\{h_n^{(2)}(k_{p2}a)j_n(k_{s1(0)}a)\left(\frac{k_{p2}^2}{k_p k_{s1(0)}a}\right)\left[-H-C\mu_2+2\left(\frac{n^2+n-1}{k_{p2}^2a^2}\right)(G-G_{(0)})\right.\right.$$
$$+\left.\left(G_{(0)}-\frac{\mu_2\mu_{5(0)}\rho_n L\rho_{f(0)}L_{(0)}}{\bar{\epsilon}_{(0)}\bar{\epsilon}\mu_{(0)}}\right)\frac{k_{s1(0)}^2}{k_{p2}^2}-\mu_{3(0)}(C+M\mu_2)\right]+h_n^{(2)}(k_{p2}a)j_n'(k_{s1(0)}a)\left(\frac{-2}{k_p a^2}\right)(G-G_{(0)})$$
$$\left.+h_n^{(2)\prime}(k_{p2}a)j_n(k_{s1(0)}a)\left(\frac{-2k_{p2}}{k_p k_{s1(0)}a^2}\right)(G-G_{(0)})+h_n^{(2)\prime}(k_{p2}a)j_n'(k_{s1(0)}a)\left(\frac{2k_{p2}}{k_p a}\right)(G-G_{(0)})\right\}, \tag{B8}$$

$$\mathbf{Q}^{*(2,6)}_{\sigma mn,\sigma mn} = in(n+1)\frac{4\pi(n+m)!\,a^2\omega}{\epsilon_m(2n+1)(n-m)!}\left\{h_n^{(2)}(k_{p2}a)j_n(k_{s2(0)}a)\left(\frac{k_{p2}^2}{k_p k_{s2(0)}a}\right)\left[-H\xi_{(0)}-C\mu_2\xi_{(0)}+2\xi_{(0)}\left(\frac{n^2+n-1}{k_{p2}^2a^2}\right)(G-G_{(0)})\right.\right.$$
$$+\left.\left(G_{(0)}\xi_{(0)}-\frac{\mu_2\mu_{6(0)}\rho_n L\rho_{f(0)}L_{(0)}}{\bar{\epsilon}_{(0)}\bar{\epsilon}\mu_{(0)}}\right)\frac{k_{s2(0)}^2}{k_{p2}^2}-\mu_{4(0)}(C+M\mu_2)\right]+h_n^{(2)}(k_{p2}a)j_n'(k_{s2(0)}a)\left(\frac{-2\xi_{(0)}}{k_p a^2}\right)(G-G_{(0)})$$
$$\left.+h_n^{(2)\prime}(k_{p2}a)j_n(k_{s2(0)}a)\left(\frac{-2k_{p2}\xi_{(0)}}{k_p k_{s2(0)}a^2}\right)(G-G_{(0)})+h_n^{(2)\prime}(k_{p2}a)j_n'(k_{s2(0)}a)\left(\frac{2k_{p2}\xi_{(0)}}{k_p a}\right)(G-G_{(0)})\right\}, \tag{B9}$$

$$\mathbf{Q}^{*(3,3)}_{\sigma mn,\sigma mn} = in(n+1)\frac{4\pi(n+m)!\,a^2\omega}{\epsilon_m(2n+1)(n-m)!}\left\{h_n^{(2)}(k_{s1}a)j_n(k_{s1(0)}a)\left[\left(\frac{-\mu_5\mu_{5(0)}\rho_f L\rho_{f(0)}L_{(0)}}{\bar{\epsilon}_{(0)}\bar{\epsilon}a}\right)\left(\frac{1}{\mu}-\frac{1}{\mu_{(0)}}\right)+\left(\frac{-1}{a}\right)(G-G_{(0)})\right]\right.$$
$$+h_n^{(2)}(k_{s1}a)j_n'(k_{s1(0)}a)k_{s1(0)}\left[\frac{\mu_5\mu_{5(0)}\rho_f L\rho_{f(0)}L_{(0)}}{\mu_{(0)}\bar{\epsilon}_{(0)}\bar{\epsilon}}-G_{(0)}\right]+h_n^{(2)\prime}(k_{s1}a)j_n(k_{s1(0)}a)k_{s1}$$
$$\left.\times\left[\frac{-\mu_5\mu_{5(0)}\rho_f L\rho_{f(0)}L_{(0)}}{\mu\bar{\epsilon}_{(0)}\bar{\epsilon}}+G\right]\right\}, \tag{B10}$$

$$\mathbf{Q}^{*(3,5)}_{\sigma mn,\sigma mn} = in(n+1)\frac{4\pi(n+m)!\,a^2\omega}{\epsilon_m(2n+1)(n-m)!}\left\{h_n^{(2)}(k_{s1}a)j_n(k_{s2(0)}a)\left[\left(\frac{-\mu_5\mu_{6(0)}\rho_f L\rho_{f(0)}L_{(0)}}{\bar{\epsilon}_{(0)}\bar{\epsilon}a}\right)\left(\frac{1}{\mu}-\frac{1}{\mu_{(0)}}\right)+\left(\frac{-\xi_{(0)}}{a}\right)(G-G_{(0)})\right]\right.$$
$$+h_n^{(2)}(k_{s1}a)j_n'(k_{s2(0)}a)k_{s2(0)}\left[\frac{\mu_5\mu_{6(0)}\rho_f L\rho_{f(0)}L_{(0)}}{\bar{\epsilon}_{(0)}\bar{\epsilon}\mu_{(0)}}-\xi_{(0)}G_{(0)}\right]+h_n^{(2)\prime}(k_{s1}a)j_n(k_{s2(0)}a)k_{s1}$$
$$\left.\times\left[\frac{-\mu_5\mu_{6(0)}\rho_f L\rho_{f(0)}L_{(0)}}{\bar{\epsilon}_{(0)}\bar{\epsilon}\mu}+\xi_{(0)}G\right]\right\}, \tag{B11}$$

$$\mathbf{Q}^{*(4,1)}_{\sigma mn,\sigma mn} = in(n+1)\frac{4\pi(n+m)!\,a^2\omega}{\epsilon_m(2n+1)(n-m)!}\left\{h_n^{(2)}(k_{s1}a)j_n(k_{p1(0)}a)\left(\frac{k_{p1(0)}^2}{k_{p(0)}k_{s1}a}\right)\left[H_{(0)}\mu_{1(0)}+C_{(0)}+2\mu_{1(0)}\left(\frac{n^2+n-1}{k_{p1(0)}^2a^2}\right)(G-G_{(0)})\right.\right.$$
$$-\left.\left(G\mu_{1(0)}-\frac{\mu_5\rho_{n(0)}L_{(0)}\rho_f L}{\bar{\epsilon}_{(0)}\bar{\epsilon}\mu}\right)\frac{k_{s1}^2}{k_{p1(0)}^2}+\mu_3(C_{(0)}\mu_{1(0)}+M_{(0)})\right]+h_n^{(2)}(k_{s1}a)j_n'(k_{p1(0)}a)\left(\frac{-2\mu_{1(0)}k_{p1(0)}}{k_{p(0)}k_{s1}a^2}\right)(G-G_{(0)})$$
$$\left.+h_n^{(2)\prime}(k_{s1}a)j_n(k_{p1(0)}a)\left(\frac{-2\mu_{1(0)}}{k_{p(0)}a^2}\right)(G-G_{(0)})+h_n^{(2)\prime}(k_{s1}a)j_n'(k_{p1(0)}a)\left(\frac{2\mu_{1(0)}k_{p1(0)}}{k_{p(0)}a}\right)(G-G_{(0)})\right\}, \tag{B12}$$

$$\mathbf{Q}^{*(4,2)}_{\sigma mn,\sigma mn} = in(n+1)\frac{4\pi(n+m)!\,a^2\omega}{\epsilon_m(2n+1)(n-m)!}\left\{h_n^{(2)}(k_{s1}a)j_n(k_{p2(0)}a)\left(\frac{k_{p2(0)}^2}{k_{p(0)}k_{s1}a}\right)\left[H_{(0)}+\mu_{2(0)}C_{(0)}+2\left(\frac{n^2+n-1}{k_{p2(0)}^2a^2}\right)(G-G_{(0)})\right.\right.$$
$$-\left.\left(G-\frac{\mu_{2(0)}\mu_5\rho_{n(0)}L_{(0)}\rho_f L}{\bar{\epsilon}_{(0)}\bar{\epsilon}\mu}\right)\frac{k_{s1}^2}{k_{p2(0)}^2}+\mu_3(C_{(0)}+M_{(0)}\mu_{2(0)})\right]+h_n^{(2)}(k_{s1}a)j_n'(k_{p2(0)}a)\left(\frac{-2k_{p2(0)}}{k_{p(0)}k_{s1}a^2}\right)(G-G_{(0)})$$
$$\left.+h_n^{(2)\prime}(k_{s1}a)j_n(k_{p2(0)}a)\left(\frac{-2}{k_{p(0)}a^2}\right)(G-G_{(0)})+h_n^{(2)\prime}(k_{s1}a)j_n'(k_{p2(0)}a)\left(\frac{2k_{p2(0)}}{k_{p(0)}a}\right)(G-G_{(0)})\right\}, \tag{B13}$$

$$\mathbf{Q}^{*(4,4)}_{\sigma mn,\sigma mn} = in(n+1)\frac{4\pi(n+m)!\,a^2\omega}{\epsilon_m(2n+1)(n-m)!}\left\{h_n^{(2)}(k_{s1}a)j_n(k_{s1(0)}a)\left(\frac{-1}{k_{s1}k_{s1(0)}a^3}\right)\left[-a^2\frac{\mu_5\mu_{5(0)}\rho_f L\rho_{f(0)}L_{(0)}}{\bar{\epsilon}_{(0)}\bar{\epsilon}}\left(\frac{k_{s1}^2}{\mu}-\frac{k_{s1(0)}^2}{\mu_{(0)}}\right)\right.\right.$$
$$\left.+2(G-G_{(0)})+a^2(Gk_{s1}^2-G_{(0)}k_{s1(0)}^2)\right]+h_n^{(2)}(k_{s1}a)j_n'(k_{s1(0)}a)\left(\frac{1}{k_{s1}a^2}\right)\left[\frac{k_{s1}^2a^2}{\mu}\frac{\mu_5\mu_{5(0)}\rho_f L\rho_{f(0)}L_{(0)}}{\bar{\epsilon}_{(0)}\bar{\epsilon}}\right.$$
$$\left.+2(n^2+n-1)(G-G_{(0)})-a^2Gk_{s1}^2\right]+h_n^{(2)\prime}(k_{s1}a)j_n(k_{s1(0)}a)\left(\frac{1}{k_{s1(0)}a^2}\right)\left[\frac{-k_{s1(0)}^2a^2}{\mu_{(0)}}\frac{\mu_5\mu_{5(0)}\rho_f L\rho_{f(0)}L_{(0)}}{\bar{\epsilon}_{(0)}\bar{\epsilon}}\right.$$
$$\left.\left.+2(n^2+n-1)(G-G_{(0)})+a^2G_{(0)}k_{s1(0)}^2\right]+h_n^{(2)\prime}(k_{s1}a)j_n'(k_{s1(0)}a)\left(\frac{-2}{a}\right)(G-G_{(0)})\right\}, \tag{B14}$$

$$\mathbf{Q}^{*(4,6)}_{\sigma mn,\sigma mn} = in(n+1)\frac{4\pi(n+m)!\,a^2\omega}{\epsilon_m(2n+1)(n-m)!}\left\{h_n^{(2)}(k_{s1}a)j_n(k_{s2(0)}a)\left(\frac{-1}{k_{s1}k_{s2(0)}a^3}\right)\left[-a^2\frac{\mu_5\mu_{6(0)}\rho_f L\rho_{f(0)}L_{(0)}}{\bar{\epsilon}_{(0)}\bar{\epsilon}}\left(\frac{k_{s1}^2}{\mu}-\frac{k_{s2(0)}^2}{\mu_{(0)}}\right)\right.\right.$$
$$\left.+2\xi_{(0)}(G-G_{(0)})+\xi_{(0)}a^2(Gk_{s1}^2-G_{(0)}k_{s2(0)}^2)\right]+h_n^{(2)}(k_{s1}a)j_n'(k_{s2(0)}a)\left(\frac{1}{k_{s1}a^2}\right)\left[\frac{k_{s1}^2a^2}{\mu}\frac{\mu_5\mu_{6(0)}\rho_f L\rho_{f(0)}L_{(0)}}{\bar{\epsilon}_{(0)}\bar{\epsilon}}\right.$$
$$\left.+2\xi_{(0)}(n^2+n-1)(G-G_{(0)})-a^2\xi_{(0)}Gk_{s1}^2\right]+h_n^{(2)\prime}(k_{s1}a)j_n(k_{s2(0)}a)\left(\frac{1}{k_{s2(0)}a^2}\right)\left[\frac{-k_{s2(0)}^2a^2}{\mu_{(0)}}\frac{\mu_5\mu_{6(0)}\rho_f L\rho_{f(0)}L_{(0)}}{\bar{\epsilon}_{(0)}\bar{\epsilon}}\right.$$
$$\left.\left.+2\xi_{(0)}(n^2+n-1)(G-G_{(0)})+a^2\xi_{(0)}G_{(0)}k_{s2(0)}^2\right]+h_n^{(2)\prime}(k_{s1}a)j_n'(k_{s2(0)}a)\left(\frac{-2\xi_{(0)}}{a}\right)(G-G_{(0)})\right\}, \tag{B15}$$

$$\mathbf{Q}^{*(5,3)}_{\sigma mn,\sigma mn} = in(n+1)\frac{4\pi(n+m)!\,a^2\omega}{\epsilon_m(2n+1)(n-m)!}\left\{h_n^{(2)}(k_{s2}a)j_n(k_{s1(0)}a)\left[\left(\frac{-\mu_{5(0)}\mu_6\rho_f L\rho_{f(0)}L_{(0)}}{\bar{\epsilon}_{(0)}\bar{\epsilon}a}\right)\left(\frac{1}{\mu}-\frac{1}{\mu_{(0)}}\right)+\left(\frac{-\xi}{a}\right)(G-G_{(0)})\right]\right.$$
$$+h_n^{(2)}(k_{s2}a)j_n'(k_{s1(0)}a)k_{s1(0)}\left[\frac{\mu_{5(0)}\mu_6\rho_f L\rho_{f(0)}L_{(0)}}{\bar{\epsilon}_{(0)}\bar{\epsilon}\mu_{(0)}}-\xi G_{(0)}\right]+h_n^{(2)\prime}(k_{s2}a)j_n(k_{s1(0)}a)k_{s2}$$
$$\left.\times\left[\frac{-\mu_{5(0)}\mu_6\rho_f L\rho_{f(0)}L_{(0)}}{\bar{\epsilon}_{(0)}\bar{\epsilon}\mu}+\xi G\right]\right\}, \tag{B16}$$

$$\mathbf{Q}^{*(5,5)}_{\sigma mn,\sigma mn} = in(n+1)\frac{4\pi(n+m)!\,a^2\omega}{\epsilon_m(2n+1)(n-m)!}\left\{h_n^{(2)}(k_{s2}a)j_n(k_{s2(0)}a)\left[\left(\frac{-\mu_6\mu_{6(0)}\rho_f L\rho_{f(0)}L_{(0)}}{\bar{\epsilon}_{(0)}\bar{\epsilon}a}\right)\left(\frac{1}{\mu}-\frac{1}{\mu_{(0)}}\right)+\left(\frac{-\xi\xi_{(0)}}{a}\right)(G-G_{(0)})\right]\right.$$
$$+h_n^{(2)}(k_{s2}a)j_n'(k_{s2(0)}a)k_{s2(0)}\left[\frac{\mu_6\mu_{6(0)}\rho_f L\rho_{f(0)}L_{(0)}}{\bar{\epsilon}_{(0)}\bar{\epsilon}\mu_{(0)}}-\xi\xi_{(0)}G_{(0)}\right]+h_n^{(2)\prime}(k_{s2}a)j_n(k_{s2(0)}a)k_{s2}$$
$$\left.\times\left[\frac{-\mu_6\mu_{6(0)}\rho_f L\rho_{f(0)}L_{(0)}}{\bar{\epsilon}_{(0)}\bar{\epsilon}\mu}+\xi\xi_{(0)}G\right]\right\}, \tag{B17}$$

$$\mathbf{Q}^{*(6,1)}_{\sigma mn,\sigma mn} = in(n+1)\frac{4\pi(n+m)!\,a^2\omega}{\epsilon_m(2n+1)(n-m)!}\left\{h_n^{(2)}(k_{s2}a)j_n(k_{p1(0)}a)\left(\frac{k_{p1(0)}^2}{k_{p(0)}k_{s2}a}\right)\left[H_{(0)}\mu_{1(0)}\xi+C_{(0)}\xi+2\mu_{1(0)}\xi\left(\frac{n^2+n-1}{k_{p1(0)}^2a^2}\right)\right.\right.$$
$$\times(G-G_{(0)})-\left(G\mu_{1(0)}\xi-\frac{\mu_6\rho_{n(0)}L_{(0)}\rho_f L}{\bar{\epsilon}_{(0)}\bar{\epsilon}\mu}\right)\frac{k_{s2}^2}{k_{p1(0)}^2}+\mu_4(C_{(0)}\mu_{1(0)}+M_{(0)})\left.\right]+h_n^{(2)}(k_{s2}a)j_n'(k_{p1(0)}a)$$
$$\times\left(\frac{-2\mu_{1(0)}k_{p1(0)}\xi}{k_{p(0)}k_{s2}a^2}\right)(G-G_{(0)})+h_n^{(2)\prime}(k_{s2}a)j_n(k_{p1(0)}a)\left(\frac{-2\mu_{1(0)}\xi}{k_{p(0)}a^2}\right)(G-G_{(0)})$$
$$\left.+h_n^{(2)\prime}(k_{s2}a)j_n'(k_{p1(0)}a)\left(\frac{2\mu_{1(0)}k_{p1(0)}\xi}{k_{p(0)}a}\right)(G-G_{(0)})\right\}, \tag{B18}$$

$$\mathbf{Q}^{*(6,2)}_{\sigma mn,\sigma mn} = in(n+1)\frac{4\pi(n+m)!\,a^2\omega}{\epsilon_m(2n+1)(n-m)!}\left\{h_n^{(2)}(k_{s2}a)j_n(k_{p2(0)}a)\left(\frac{k_{p2(0)}^2}{k_{p(0)}k_{s2}a}\right)\left[H_{(0)}\xi+\mu_{2(0)}C_{(0)}\xi+2\xi\left(\frac{n^2+n-1}{k_{p2(0)}^2a^2}\right)(G-G_{(0)})\right.\right.$$
$$\left.-\left(G\xi-\frac{\mu_{2(0)}\mu_6\rho_{n(0)}L_{(0)}\rho_f L}{\bar{\epsilon}_{(0)}\bar{\epsilon}\mu}\right)\frac{k_{s2}^2}{k_{p2(0)}^2}+\mu_4(C_{(0)}+M_{(0)}\mu_{2(0)})\right]+h_n^{(2)}(k_{s2}a)j_n'(k_{p2(0)}a)\left(\frac{-2k_{p2(0)}\xi}{k_{p(0)}k_{s2}a^2}\right)(G-G_{(0)})$$
$$\left.+h_n^{(2)\prime}(k_{s2}a)j_n(k_{p2(0)}a)\left(\frac{-2\xi}{k_{p(0)}a^2}\right)(G-G_{(0)})+h_n^{(2)\prime}(k_{s2}a)j_n'(k_{p2(0)}a)\left(\frac{2k_{p2(0)}\xi}{k_{p(0)}a}\right)(G-G_{(0)})\right\}, \tag{B19}$$

$$\mathbf{Q}^{*(6,4)}_{\sigma mn,\sigma mn} = in(n+1)\frac{4\pi(n+m)!\,a^2\omega}{\epsilon_m(2n+1)(n-m)!}\left\{h_n^{(2)}(k_{s2}a)j_n(k_{s1(0)}a)\left(\frac{-1}{k_{s2}k_{s1(0)}a^3}\right)\left[-a^2\frac{\mu_{5(0)}\mu_6\rho_{f(0)}L_{(0)}\rho_f L}{\bar{\epsilon}_{(0)}\bar{\epsilon}}\left(\frac{k_{s2}^2}{\mu}-\frac{k_{s1(0)}^2}{\mu_{(0)}}\right)\right.\right.$$
$$\left.+2\xi(G-G_{(0)})+\xi a^2(Gk_{s2}^2-G_{(0)}k_{s1(0)}^2)\right]+h_n^{(2)}(k_{s2}a)j_n'(k_{s1(0)}a)\left(\frac{1}{k_{s2}a^2}\right)\left[\frac{k_{s2}^2a^2}{\mu}\frac{\mu_{5(0)}\mu_6\rho_{f(0)}L_{(0)}\rho_f L}{\bar{\epsilon}_{(0)}\bar{\epsilon}}\right.$$
$$\left.+2\xi(n^2+n-1)(G-G_{(0)})-a^2\xi Gk_{s2}^2\right]+h_n^{(2)\prime}(k_{s2}a)j_n(k_{s1(0)}a)\left(\frac{1}{k_{s1(0)}a^2}\right)\left[\frac{-k_{s1(0)}^2a^2}{\mu_{(0)}}\frac{\mu_{5(0)}\mu_6\rho_{f(0)}L_{(0)}\rho_f L}{\bar{\epsilon}_{(0)}\bar{\epsilon}}\right.$$
$$\left.\left.+2\xi(n^2+n-1)(G-G_{(0)})+a^2\xi G_{(0)}k_{s1(0)}^2\right]+h_n^{(2)\prime}(k_{s2}a)j_n'(k_{s1(0)}a)\left(\frac{-2\xi}{a}\right)(G-G_{(0)})\right\}, \tag{B20}$$

$$\mathbf{Q}^{*(6,6)}_{\sigma mn,\sigma mn} = in(n+1)\frac{4\pi(n+m)!\,a^2\omega}{\epsilon_m(2n+1)(n-m)!}\left\{h_n^{(2)}(k_{s2}a)j_n(k_{s2(0)}a)\left(\frac{-1}{k_{s2}k_{s2(0)}a^3}\right)\left[-a^2\frac{\mu_6\mu_{6(0)}\rho_f L\rho_{f(0)}L_{(0)}}{\bar{\epsilon}_{(0)}\bar{\epsilon}}\left(\frac{k_{s2}^2}{\mu}-\frac{k_{s2(0)}^2}{\mu_{(0)}}\right)\right.\right.$$
$$\left.+2\xi\xi_{(0)}(G-G_{(0)})+a^2\xi\xi_{(0)}(Gk_{s2}^2-G_{(0)}k_{s2(0)}^2)\right]+h_n^{(2)}(k_{s2}a)j_n'(k_{s2(0)}a)\left(\frac{1}{k_{s2}a^2}\right)\left[\frac{k_{s2}^2a^2}{\mu}\frac{\mu_6\mu_{6(0)}\rho_f L\rho_{f(0)}L_{(0)}}{\bar{\epsilon}_{(0)}\bar{\epsilon}}\right.$$
$$\left.+2\xi\xi_{(0)}(n^2+n-1)(G-G_{(0)})-a^2\xi\xi_{(0)}Gk_{s2}^2\right]+h_n^{(2)\prime}(k_{s2}a)j_n(k_{s2(0)}a)\left(\frac{1}{k_{s2(0)}a^2}\right)\left[\frac{-k_{s2(0)}^2a^2}{\mu_{(0)}}\frac{\mu_6\mu_{6(0)}\rho_f L\rho_{f(0)}L_{(0)}}{\bar{\epsilon}_{(0)}\bar{\epsilon}}\right.$$
$$\left.\left.+2\xi\xi_{(0)}(n^2+n-1)(G-G_{(0)})+a^2\xi\xi_{(0)}G_{(0)}k_{s2(0)}^2\right]+h_n^{(2)\prime}(k_{s2}a)j_n'(k_{s2(0)}a)\left(\frac{-2\xi\xi_{(0)}}{a}\right)(G-G_{(0)})\right\}, \tag{B21}$$

and

$$\begin{aligned}
&\mathbf{Q}^{*(1,3)}_{\sigma mn,\sigma mn}=0, \quad \mathbf{Q}^{*(1,5)}_{\sigma mn,\sigma mn}=0, \quad \mathbf{Q}^{*(2,3)}_{\sigma mn,\sigma mn}=0,\\
&\mathbf{Q}^{*(2,5)}_{\sigma mn,\sigma mn}=0, \quad \mathbf{Q}^{*(3,1)}_{\sigma mn,\sigma mn}=0, \quad \mathbf{Q}^{*(3,2)}_{\sigma mn,\sigma mn}=0,\\
&\mathbf{Q}^{*(3,4)}_{\sigma mn,\sigma mn}=0, \quad \mathbf{Q}^{*(3,6)}_{\sigma mn,\sigma mn}=0, \quad \mathbf{Q}^{*(4,3)}_{\sigma mn,\sigma mn}=0,\\
&\mathbf{Q}^{*(4,5)}_{\sigma mn,\sigma mn}=0, \quad \mathbf{Q}^{*(5,1)}_{\sigma mn,\sigma mn}=0, \quad \mathbf{Q}^{*(5,2)}_{\sigma mn,\sigma mn}=0,\\
&\mathbf{Q}^{*(5,4)}_{\sigma mn,\sigma mn}=0, \quad \mathbf{Q}^{*(5,6)}_{\sigma mn,\sigma mn}=0, \quad \mathbf{Q}^{*(6,3)}_{\sigma mn,\sigma mn}=0,\\
&\mathbf{Q}^{*(6,5)}_{\sigma mn,\sigma mn}=0.
\end{aligned} \tag{B22}$$

Recall that a subscript (0) is used to indicate the parameters of the interior material. The elements of $\hat{\mathbf{Q}}$ are obtained from those of $\mathbf{Q}$ by replacing the spherical Hankel function $h_n^{(2)}$ with the spherical Bessel function j_n.

If the interior medium is identical with the exterior one, the subscript (0) is directly removed. Consider on a specific surface S_+ with radius a, the elements of $\mathbf{Q}^*$ matrix reduce to the third orthogonality condition presented in Eq. (93). They are

$$\begin{aligned}
\mathbf{Q}^{*(1,1)}_{\sigma mn,\sigma mn} &= i\frac{4\pi(n+m)!\,a^2\omega}{\epsilon_m(2n+1)(n-m)!}\left(\frac{-k_{p1}^3}{k_p^2}\right)W\{h_n^{(2)}\\
&\quad\times(k_{p1}a),j_n(k_{p1}a)\}[H\mu_1^2+2C\mu_1+M]\\
&= \left(\frac{\omega G}{k_s}\right)\frac{4\pi(n+m)!}{\epsilon_m(2n+1)(n-m)!}\left[H^*\frac{k_sk_{p1}}{Gk_p^2}\right],
\end{aligned} \tag{B23}$$

where the Wronskian formula (Abramowitz and Stegun, 1964) is defined as

$$\begin{aligned}
W\{h_n^{(2)}(ka),j_n(ka)\} &= h_n^{(2)}(ka)j_n'(ka)-h_n^{(2)\prime}(ka)j_n(ka)\\
&= i/(ka)^2,
\end{aligned} \tag{B24}$$

and H^* has been defined in Eq. (26)

$$\mathbf{Q}^{*(2,2)}_{\sigma mn,\sigma mn} = i\frac{4\pi(n+m)!\,a^2\omega}{\epsilon_m(2n+1)(n-m)!}\left(\frac{-k_{p2}^3}{k_p^2}\right)W\{h_n^{(2)} \times (k_{p2}a), j_n(k_{p2}a)\} \times [H + 2C\mu_2 + M\mu_2^2] = \left(\frac{\omega G}{k_s}\right)\frac{4\pi(n+m)!}{\epsilon_m(2n+1)(n-m)!}\left[M^*\frac{k_s k_{p2}}{Gk_p^2}\right], \tag{B25}$$

where M^* has also been defined in Eq. (26)

$$\mathbf{Q}^{*(1,2)}_{\sigma mn,\sigma mn} = i\frac{4\pi(n+m)!\,a^2\omega}{\epsilon_m(2n+1)(n-m)!}\left(\frac{-k_{p1}k_{p2}}{k_p^2}\right)[k_{p1}h_n^{(2)} \times (k_{p1}a)j_n'(k_{p2}a) - k_{p2}h_n^{(2)\prime}(k_{p1}a)j_n(k_{p2}a)] \times [H\mu_1 + C\mu_1\mu_2 + C + M\mu_2] = 0 \tag{B26}$$

and

$$\mathbf{Q}^{*(2,1)}_{\sigma mn,\sigma mn} = i\frac{4\pi(n+m)!\,a^2\omega}{\epsilon_m(2n+1)(n-m)!}\left(\frac{-k_{p1}k_{p2}}{k_p^2}\right)[k_{p2}h_n^{(2)} \times (k_{p2}a)j_n'(k_{p1}a) - k_{p1}h_n^{(2)\prime}(k_{p2}a)j_n(k_{p1}a)] \times [H\mu_1 + C\mu_1\mu_2 + C + M\mu_2] = 0, \tag{B27}$$

where the zero value is given from Eq. (A8). In addition

$$\mathbf{Q}^{*(1,4)}_{\sigma mn,\sigma mn} = 0, \quad \mathbf{Q}^{*(4,1)}_{\sigma mn,\sigma mn} = 0, \quad \mathbf{Q}^{*(2,4)}_{\sigma mn,\sigma mn} = 0,$$

$$\mathbf{Q}^{*(4,2)}_{\sigma mn,\sigma mn} = 0, \quad \mathbf{Q}^{*(1,6)}_{\sigma mn,\sigma mn} = 0, \quad \mathbf{Q}^{*(6,1)}_{\sigma mn,\sigma mn} = 0, \tag{B28}$$

$$\mathbf{Q}^{*(2,6)}_{\sigma mn,\sigma mn} = 0, \quad \mathbf{Q}^{*(6,2)}_{\sigma mn,\sigma mn} = 0,$$

where we have made use of the relations in Eqs. (A18)–(A21). If Eq. (A17) is used, we have

$$\mathbf{Q}^{*(4,6)}_{\sigma mn,\sigma mn} = 0, \quad \mathbf{Q}^{*(6,4)}_{\sigma mn,\sigma mn} = 0. \tag{B29}$$

Finally, we evaluate the last two elements:

$$\mathbf{Q}^{*(3,3)}_{\sigma mn,\sigma mn} = \mathbf{Q}^{*(4,4)}_{\sigma mn,\sigma mn} = \left(\frac{\omega G}{k_s}\right)\frac{4\pi(n+m)!}{\epsilon_m(2n+1)(n-m)!} \times \left[n(n+1)\left(1 - \frac{\mu_5^2\rho_f^2L^2}{G\mu\bar{\epsilon}^2}\right)\frac{k_s}{k_{s1}}\right], \tag{B30}$$

$$\mathbf{Q}^{*(5,5)}_{\sigma mn,\sigma mn} = \mathbf{Q}^{*(6,6)}_{\sigma mn,\sigma mn} = \left(\frac{\omega G}{k_s}\right)\frac{4\pi(n+m)!}{\epsilon_m(2n+1)(n-m)!} \times \left[n(n+1)\left(\xi^2 - \frac{\mu_6^2\rho_f^2L^2}{G\mu\bar{\epsilon}^2}\right)\frac{k_s}{k_{s2}}\right]. \tag{B31}$$

When the spherical Bessel function is replaced by the spherical Hankel function from the Wronskian formulation of Eqs. (B2)–(B21), we obtain the zero value identically on any spherical surface S (outside S_+ and inside S_∞), and this result leads the second orthogonality condition. When the spherical Hankel function is replaced by the spherical Bessel function in Eqs. (B2)–(B21) on a specific surface inside S_+, we derive the first orthogonality condition.

APPENDIX C: SOLUTION SCHEME ADAPTED FROM LAMÉ'S POTENTIALS

After eliminating **B**, **D**, **J**, and p from Eqs. (1), (2), (4), (5), and (7)–(9), the coupled terms related to electric field **E** can be expressed as

$$(i\omega\tilde{\rho}L)\mathbf{E} = \left(\frac{\tilde{\rho}L}{\bar{\epsilon} - \tilde{\rho}L^2}\right)(\nabla\times\mathbf{H} + \omega^2\tilde{\rho}L\mathbf{w}). \tag{C1}$$

Combining Eqs. (11) and (C1) yields

$$C\nabla\nabla\cdot\mathbf{u} + M\nabla\nabla\cdot\mathbf{w} + \omega^2\rho_f\mathbf{u} + \omega^2\rho_n\mathbf{w} + \left(\frac{\tilde{\rho}L}{\bar{\epsilon} - \tilde{\rho}L^2}\right)(\nabla\times\mathbf{H}) = \mathbf{0}, \tag{C2}$$

General solutions expressed in terms of the displacement vectors **u** and **w** directly are usually difficult because these vectors are coupled in the original equations of motions Eqs. (10) and (C2). Therefore, a formulation for general solutions in terms of some potentials is proposed, and on the basis of Helmholtz's theorem (Gregory 1996), any general solutions for displacement vectors **u** and **w**, which are assumed to exist continuous derivatives up to at least the second order, can be decomposed into two scalar potentials $\tilde{\phi}_1$ and $\tilde{\phi}_2$, and two divergence-free vector potentials $\tilde{\boldsymbol{\psi}}_1$ and $\tilde{\boldsymbol{\psi}}_2$

$$\mathbf{u} = \nabla\tilde{\phi}_1 + \nabla\times\tilde{\boldsymbol{\psi}}_1, \quad \mathbf{w} = \nabla\tilde{\phi}_2 + \nabla\times\tilde{\boldsymbol{\psi}}_2. \tag{C3}$$

Substituting **u** and **w** from Eq. (C3) into the coupled equations (10) and (C2) yields

$$\nabla\tilde{\chi}_1 + \nabla\times\tilde{\boldsymbol{\xi}}_1 = \mathbf{0}, \quad \nabla\tilde{\chi}_2 + \nabla\times\tilde{\boldsymbol{\xi}}_2 = \mathbf{0}, \tag{C4}$$

where the two dilatational parts, written in matrix form, are

$$\begin{Bmatrix}\tilde{\chi}_1\\ \tilde{\chi}_2\end{Bmatrix} = \begin{bmatrix}H & C\\ C & M\end{bmatrix}\begin{Bmatrix}\nabla^2\tilde{\phi}_1\\ \nabla^2\tilde{\phi}_2\end{Bmatrix} + \omega^2\begin{bmatrix}\rho & \rho_f\\ \rho_f & \rho_n\end{bmatrix}\begin{Bmatrix}\tilde{\phi}_1\\ \tilde{\phi}_2\end{Bmatrix}, \tag{C5}$$

and the two rotational parts, written in matrix form, are

$$\begin{Bmatrix}\tilde{\boldsymbol{\xi}}_1\\ \tilde{\boldsymbol{\xi}}_2\end{Bmatrix} = \begin{bmatrix}G & 0\\ 0 & \rho_nL/\bar{\epsilon}\end{bmatrix}\begin{Bmatrix}\nabla^2\tilde{\boldsymbol{\psi}}_1\\ \mathbf{H}\end{Bmatrix} + \omega^2\begin{bmatrix}\rho & \rho_f\\ \rho_f & \rho_n\end{bmatrix}\begin{Bmatrix}\tilde{\boldsymbol{\psi}}_1\\ \tilde{\boldsymbol{\psi}}_2\end{Bmatrix}. \tag{C6}$$

It should be noted that:

(1) The two dilatational parts generated in Eq. (C4) by the above four potentials are not necessary zeros. This statement is a contradiction of Eq. (17);
(2) the two rotational parts generated in Eq. (C4) by the above four potentials are not necessary zeros. This statement is a contradiction of Eqs. (28) and (29).

It is the purpose of this Appendix C to construct a new set of scalar potentials (ϕ_1, ϕ_2) from the old set of scalar potentials $(\tilde{\phi}_1, \tilde{\phi}_2)$ and a new set of vector potentials $(\boldsymbol{\psi}_1, \boldsymbol{\psi}_2)$ from $\tilde{\boldsymbol{\psi}}_1$ and **H**

$$\begin{Bmatrix}\phi_1\\ \phi_2\end{Bmatrix} = -\omega^{-2}\begin{bmatrix}\rho & \rho_f\\ \rho_f & \rho_n\end{bmatrix}^{-1}\begin{bmatrix}H & C\\ C & M\end{bmatrix}\begin{Bmatrix}\nabla^2\tilde{\phi}_1\\ \nabla^2\tilde{\phi}_2\end{Bmatrix}, \tag{C7}$$

$$\begin{Bmatrix} \boldsymbol{\psi}_1 \\ \boldsymbol{\psi}_2 \end{Bmatrix} = -\omega^{-2}\begin{bmatrix} \rho & \rho_f \\ \rho_f & \rho_n \end{bmatrix}^{-1}\begin{bmatrix} G & 0 \\ 0 & \rho_n L/\bar{\epsilon} \end{bmatrix}\begin{Bmatrix} \nabla^2\tilde{\boldsymbol{\psi}}_1 \\ \mathbf{H} \end{Bmatrix}. \quad \text{(C8)}$$

In the remaining text of this Appendix, detailed derivations will be presented to show that these four potential functions $(\phi_1, \phi_2, \boldsymbol{\psi}_1, \boldsymbol{\psi}_2)$, which are constructed with Eqs. (C7) and (C8), satisfy the following four properties, which are required in Sec. II B in the main text:

$$\mathbf{u} = \nabla\phi_1 + \nabla \times \boldsymbol{\psi}_1,$$

$$\mathbf{w} = \nabla\phi_2 + \nabla \times \boldsymbol{\psi}_2, \quad \text{(C9)}$$

$$\nabla \cdot \boldsymbol{\psi}_1 = 0, \quad \nabla \cdot \boldsymbol{\psi}_2 = 0, \quad \text{(C10)}$$

$$\begin{bmatrix} H & C \\ C & M \end{bmatrix}\begin{Bmatrix} \nabla^2\phi_1 \\ \nabla^2\phi_2 \end{Bmatrix} + \omega^2\begin{bmatrix} \rho & \rho_f \\ \rho_f & \rho_n \end{bmatrix}\begin{Bmatrix} \phi_1 \\ \phi_2 \end{Bmatrix} = \begin{Bmatrix} 0 \\ 0 \end{Bmatrix}, \quad \text{(C11)}$$

$$\begin{bmatrix} G & 0 \\ 0 & \rho_n L/\bar{\epsilon} \end{bmatrix}\begin{Bmatrix} \nabla^2\boldsymbol{\psi}_1 \\ \mathbf{H} \end{Bmatrix} + \omega^2\begin{bmatrix} \rho & \rho_f \\ \rho_f & \rho_n \end{bmatrix}\begin{Bmatrix} \boldsymbol{\psi}_1 \\ \boldsymbol{\psi}_2 \end{Bmatrix} = \begin{Bmatrix} \mathbf{0} \\ \mathbf{0} \end{Bmatrix}. \quad \text{(C12)}$$

Upon this, it can be asserted that every solution of displacement vectors **u** and **w** for governing Eqs. (1)–(9) admits the representations defined by Eqs. (C9)–(C12).

1. Proof of Eqs. (C9) and (C10)

Combining Eqs. (C7) and (C8), we have the following assertions:

$$\begin{Bmatrix} \nabla\phi_1 \\ \nabla\phi_2 \end{Bmatrix} = -\omega^{-2}\begin{bmatrix} \rho & \rho_f \\ \rho_f & \rho_n \end{bmatrix}^{-1}\begin{bmatrix} H & C \\ C & M \end{bmatrix}\begin{Bmatrix} \nabla\nabla^2\tilde{\phi}_1 \\ \nabla\nabla^2\tilde{\phi}_2 \end{Bmatrix}, \quad \text{(C13)}$$

$$\begin{Bmatrix} \nabla \times \boldsymbol{\psi}_1 \\ \nabla \times \boldsymbol{\psi}_2 \end{Bmatrix} = -\omega^{-2}\begin{bmatrix} \rho & \rho_f \\ \rho_f & \rho_n \end{bmatrix}^{-1}\begin{bmatrix} G & 0 \\ 0 & \rho_n L/\bar{\epsilon} \end{bmatrix}\begin{Bmatrix} \nabla \times \nabla^2\tilde{\boldsymbol{\psi}}_1 \\ \nabla \times \mathbf{H} \end{Bmatrix}. \quad \text{(C14)}$$

$$\begin{Bmatrix} \nabla\phi_1 + \nabla \times \boldsymbol{\psi}_1 \\ \nabla\phi_2 + \nabla \times \boldsymbol{\psi}_2 \end{Bmatrix} = -\omega^{-2}\begin{bmatrix} \rho & \rho_f \\ \rho_f & \rho_n \end{bmatrix}^{-1}\begin{bmatrix} H & C \\ C & M \end{bmatrix}\begin{Bmatrix} \nabla\nabla^2\tilde{\phi}_1 \\ \nabla\nabla^2\tilde{\phi}_2 \end{Bmatrix} - \omega^{-2}\begin{bmatrix} \rho & \rho_f \\ \rho_f & \rho_n \end{bmatrix}^{-1}\begin{bmatrix} G & 0 \\ 0 & \rho_n L/\bar{\epsilon} \end{bmatrix}\begin{Bmatrix} \nabla \times \nabla^2\tilde{\boldsymbol{\psi}}_1 \\ \nabla \times \mathbf{H} \end{Bmatrix}. \quad \text{(C15)}$$

The combination of Eqs. (C3)–(C6) yields to the following assertions:

$$\begin{Bmatrix} \nabla\tilde{\chi}_1 \\ \nabla\tilde{\chi}_2 \end{Bmatrix} = \begin{bmatrix} H & C \\ C & M \end{bmatrix}\begin{Bmatrix} \nabla\nabla^2\tilde{\phi}_1 \\ \nabla\nabla^2\tilde{\phi}_2 \end{Bmatrix} + \omega^2\begin{bmatrix} \rho & \rho_f \\ \rho_f & \rho_n \end{bmatrix}\begin{Bmatrix} \nabla\tilde{\phi}_1 \\ \nabla\tilde{\phi}_2 \end{Bmatrix}, \quad \text{(C16)}$$

$$\begin{Bmatrix} \nabla \times \tilde{\boldsymbol{\xi}}_1 \\ \nabla \times \tilde{\boldsymbol{\xi}}_2 \end{Bmatrix} = \begin{bmatrix} G & 0 \\ 0 & \rho_n L/\bar{\epsilon} \end{bmatrix}\begin{Bmatrix} \nabla \times \nabla^2\tilde{\boldsymbol{\psi}}_1 \\ \nabla \times \mathbf{H} \end{Bmatrix} + \omega^2\begin{bmatrix} \rho & \rho_f \\ \rho_f & \rho_n \end{bmatrix} \times \begin{Bmatrix} \nabla \times \tilde{\boldsymbol{\psi}}_1 \\ \nabla \times \tilde{\boldsymbol{\psi}}_2 \end{Bmatrix}, \quad \text{(C17)}$$

$$\begin{Bmatrix} \nabla\tilde{\chi}_1 + \nabla \times \tilde{\boldsymbol{\xi}}_1 \\ \nabla\tilde{\chi}_2 + \nabla \times \tilde{\boldsymbol{\xi}}_2 \end{Bmatrix} = \omega^2\begin{bmatrix} \rho & \rho_f \\ \rho_f & \rho_n \end{bmatrix}\begin{Bmatrix} \nabla\tilde{\phi}_1 + \nabla \times \tilde{\boldsymbol{\psi}}_1 \\ \nabla\tilde{\phi}_2 + \nabla \times \tilde{\boldsymbol{\psi}}_2 \end{Bmatrix} + \begin{bmatrix} H & C \\ C & M \end{bmatrix}\begin{Bmatrix} \nabla\nabla^2\tilde{\phi}_1 \\ \nabla\nabla^2\tilde{\phi}_2 \end{Bmatrix} + \begin{bmatrix} G & 0 \\ 0 & \rho_n L/\bar{\epsilon} \end{bmatrix} \times \begin{Bmatrix} \nabla \times \nabla^2\tilde{\boldsymbol{\psi}}_1 \\ \nabla \times \mathbf{H} \end{Bmatrix}, \quad \text{(C18)}$$

$$\begin{Bmatrix} \mathbf{0} \\ \mathbf{0} \end{Bmatrix} = \omega^2\begin{bmatrix} \rho & \rho_f \\ \rho_f & \rho_n \end{bmatrix}\begin{Bmatrix} \nabla\tilde{\phi}_1 + \nabla \times \tilde{\boldsymbol{\psi}}_1 \\ \nabla\tilde{\phi}_2 + \nabla \times \tilde{\boldsymbol{\psi}}_2 \end{Bmatrix} + \begin{bmatrix} H & C \\ C & M \end{bmatrix} \times \begin{Bmatrix} \nabla\nabla^2\tilde{\phi}_1 \\ \nabla\nabla^2\tilde{\phi}_2 \end{Bmatrix} + \begin{bmatrix} G & 0 \\ 0 & \rho_n L/\bar{\epsilon} \end{bmatrix}\begin{Bmatrix} \nabla \times \nabla^2\tilde{\boldsymbol{\psi}}_1 \\ \nabla \times \mathbf{H} \end{Bmatrix}, \quad \text{(C19)}$$

$$\begin{Bmatrix} \mathbf{u} \\ \mathbf{w} \end{Bmatrix} = \begin{Bmatrix} \nabla\tilde{\phi}_1 + \nabla \times \tilde{\boldsymbol{\psi}}_1 \\ \nabla\tilde{\phi}_2 + \nabla \times \tilde{\boldsymbol{\psi}}_2 \end{Bmatrix} = -\omega^{-2}\begin{bmatrix} \rho & \rho_f \\ \rho_f & \rho_n \end{bmatrix}^{-1}\begin{bmatrix} H & C \\ C & M \end{bmatrix} \times \begin{Bmatrix} \nabla\nabla^2\tilde{\phi}_1 \\ \nabla\nabla^2\tilde{\phi}_2 \end{Bmatrix} - \omega^{-2}\begin{bmatrix} \rho & \rho_f \\ \rho_f & \rho_n \end{bmatrix}^{-1}\begin{bmatrix} G & 0 \\ 0 & \rho_n L/\bar{\epsilon} \end{bmatrix} \times \begin{Bmatrix} \nabla \times \nabla^2\tilde{\boldsymbol{\psi}}_1 \\ \nabla \times \mathbf{H} \end{Bmatrix}, \quad \text{(C20)}$$

If the right hand side of Eq. (C15) is compared with the right hand side of Eq. (C20), then the coincidence of them yields

$$\begin{Bmatrix} \mathbf{u} \\ \mathbf{w} \end{Bmatrix} = \begin{Bmatrix} \nabla\tilde{\phi}_1 + \nabla \times \tilde{\boldsymbol{\psi}}_1 \\ \nabla\tilde{\phi}_2 + \nabla \times \tilde{\boldsymbol{\psi}}_2 \end{Bmatrix} = \begin{Bmatrix} \nabla\phi_1 + \nabla \times \boldsymbol{\psi}_1 \\ \nabla\phi_2 + \nabla \times \boldsymbol{\psi}_2 \end{Bmatrix}. \quad \text{(C21)}$$

Because that $\tilde{\boldsymbol{\psi}}_1$ and **H** are all divergence-free, therefore

$$\begin{Bmatrix} \nabla \cdot \boldsymbol{\psi}_1 \\ \nabla \cdot \boldsymbol{\psi}_2 \end{Bmatrix} = -\omega^{-2}\begin{bmatrix} \rho & \rho_f \\ \rho_f & \rho_n \end{bmatrix}^{-1}\begin{bmatrix} G & 0 \\ 0 & \rho_n L/\bar{\epsilon} \end{bmatrix}\begin{Bmatrix} \nabla^2\nabla \cdot \tilde{\boldsymbol{\psi}}_1 \\ \nabla \cdot \mathbf{H} \end{Bmatrix} = \begin{Bmatrix} 0 \\ 0 \end{Bmatrix}. \quad \text{(C22)}$$

2. Proof of Eqs. (C11) and (C12)

Equaions (C7) and (C8) yield

$$\omega^2\begin{bmatrix} \rho & \rho_f \\ \rho_f & \rho_n \end{bmatrix}\begin{Bmatrix} \phi_1 \\ \phi_2 \end{Bmatrix} + \begin{bmatrix} H & C \\ C & M \end{bmatrix}\begin{Bmatrix} \nabla^2\tilde{\phi}_1 \\ \nabla^2\tilde{\phi}_2 \end{Bmatrix} = \begin{Bmatrix} 0 \\ 0 \end{Bmatrix}, \quad \text{(C23)}$$

$$\omega^2\begin{bmatrix} \rho & \rho_f \\ \rho_f & \rho_n \end{bmatrix}\begin{Bmatrix} \boldsymbol{\psi}_1 \\ \boldsymbol{\psi}_2 \end{Bmatrix} + \begin{bmatrix} G & 0 \\ 0 & \rho_n L/\bar{\epsilon} \end{bmatrix}\begin{Bmatrix} \nabla^2\tilde{\boldsymbol{\psi}}_1 \\ \mathbf{H} \end{Bmatrix} = \begin{Bmatrix} \mathbf{0} \\ \mathbf{0} \end{Bmatrix}. \quad \text{(C24)}$$

Applying div and curl operators on Eqs. (C21), we have

$$\begin{Bmatrix} \nabla \cdot \mathbf{u} \\ \nabla \cdot \mathbf{w} \end{Bmatrix} = \begin{Bmatrix} \nabla^2\tilde{\phi}_1 \\ \nabla^2\tilde{\phi}_2 \end{Bmatrix} = \begin{Bmatrix} \nabla^2\phi_1 \\ \nabla^2\phi_2 \end{Bmatrix}, \quad \text{(C25)}$$

$$\begin{Bmatrix} -\nabla \times \mathbf{u} \\ -\nabla \times \mathbf{w} \end{Bmatrix} = \begin{Bmatrix} \nabla^2 \tilde{\boldsymbol{\psi}}_1 \\ \nabla^2 \tilde{\boldsymbol{\psi}}_2 \end{Bmatrix} = \begin{Bmatrix} \nabla^2 \boldsymbol{\psi}_1 \\ \nabla^2 \boldsymbol{\psi}_2 \end{Bmatrix}. \tag{C26}$$

From Eqs. (C23)–(C26), we have

$$\begin{bmatrix} H & C \\ C & M \end{bmatrix} \begin{Bmatrix} \nabla^2 \phi_1 \\ \nabla^2 \phi_2 \end{Bmatrix} + \omega^2 \begin{bmatrix} \rho & \rho_f \\ \rho_f & \rho_n \end{bmatrix} \begin{Bmatrix} \phi_1 \\ \phi_2 \end{Bmatrix} = \begin{bmatrix} H & C \\ C & M \end{bmatrix} \times \begin{Bmatrix} \nabla^2 \tilde{\phi}_1 \\ \nabla^2 \tilde{\phi}_2 \end{Bmatrix} + \omega^2 \begin{bmatrix} \rho & \rho_f \\ \rho_f & \rho_n \end{bmatrix} \begin{Bmatrix} \phi_1 \\ \phi_2 \end{Bmatrix} = \begin{Bmatrix} 0 \\ 0 \end{Bmatrix}, \tag{C27}$$

$$\begin{bmatrix} G & 0 \\ 0 & \rho_n L/\bar{\epsilon} \end{bmatrix} \begin{Bmatrix} \nabla^2 \boldsymbol{\psi}_1 \\ \mathbf{H} \end{Bmatrix} + \omega^2 \begin{bmatrix} \rho & \rho_f \\ \rho_f & \rho_n \end{bmatrix} \begin{Bmatrix} \boldsymbol{\psi}_1 \\ \boldsymbol{\psi}_2 \end{Bmatrix} = \begin{bmatrix} G & 0 \\ 0 & \rho_n L/\bar{\epsilon} \end{bmatrix} \times \begin{Bmatrix} \nabla^2 \tilde{\boldsymbol{\psi}}_1 \\ \mathbf{H} \end{Bmatrix} + \omega^2 \begin{bmatrix} \rho & \rho_f \\ \rho_f & \rho_n \end{bmatrix} \begin{Bmatrix} \boldsymbol{\psi}_1 \\ \boldsymbol{\psi}_2 \end{Bmatrix} = \begin{Bmatrix} \mathbf{0} \\ \mathbf{0} \end{Bmatrix}. \tag{C28}$$

Abramowitz, M., and Stegun, I. A. (**1964**). *Handbook of Mathematical Functions With Formulas, Graphs, and Mathematical Tables*, National Bureau of Standards Applied Mathematics Series Vol. 55 (National Bureau of Standards, Washington, DC), Eq. (10.17), p. 437.

Berryman, J. G. (**1985**). "Scattering by a spherical inhomogeneity in a fluid-saturated porous medium," J. Math. Phys. **26**, 1408–1419.

Biot, M. A. (**1956**). "Theory of propagation of elastic waves in a fluid-saturated porous solid. I. Low-frequency range," J. Acoust. Soc. Am. **28**, 168–178.

Biot, M. A. (**1962**). "Mechanics of deformation and acoustic propagation in porous media," J. Appl. Phys. **33**, 1482–1498.

Block, G. I., and Harris, J. G. (**2006**). "Conductivity dependence of seismoelectric wave phenomena in fluid-saturated sediments," J. Geophys. Res. **111**, B01304.

Bouchon, M. (**1981**). "A simple method to calculate Green's functions for elastic layered media," Bull. Seismol. Soc. Am. **71**, 959–971.

Frenkel, J. (**1944**). "On the theory of seismic and seismoelectric phenomena in a moist soil," J. Phys. (USSR) **8**, 230–241.

Garambois, S., and Dietrich, M. (**2001**). "Seismo-electric wave conversions in porous media: Field measurements and transfer function analysis," Geophysics **66**, 1417–1430.

Garambois, S., and Dietrich, M. (**2002**). "Full waveform numerical simulations of seismoelectromagnetic wave conversions in fluid-saturated stratified porous media," J. Geophys. Res. **107**, ESE 5-1–5-18.

Gregory, R. D. (**1996**). "Helmholtz's theorem when the domain is infinite and when the field has singular points," Q. J. Mech. Appl. Math. **49**, 439–450.

Haartsen, M. W., and Pride, S. R. (**1997**). "Electroseismic waves from point sources in layered media," J. Geophys. Res. **102**(B11), 24745–24769.

Han, Q. Y., and Wang, Z. J. (**2001**). "Time-domain simulation of SH-wave-induced electromagnetic field in heterogeneous porous media: A fast finite-element algorithm," Geophysics **66**(2), 448–461.

Kennett, B. L. N., and Kerry, N. J. (**1979**). "Seismic waves in a stratified half space," Geophys. J. R. Astron. Soc. **57**, 557–583.

Mikhailov, O. V., Haartsen, M. W., and Toksöz, M. N. (**1997**). "Electroseismic investigation of the shallow surface: Field measurements and numerical modeling," Geophysics **62**, 97–105.

Mogi, K. (**1985**). *Earthquake Prediction* (Academic, New York).

Morse, P. M., and Feshbach, H. (**1953**). *Methods of Theoretical Physics* (McGraw-Hill, New York), Eq. (9), p. 1865.

Neev, J., and Yeatts, F. R. (**1989**). "Electrokinetic effects in fluid-saturated poroelastic media," Phys. Rev. B **40**, 9135–9141.

Olsson, P. (**1984**). "Elastostatics as a limit of elastodynamics – a matrix formulation," Appl. Sci. Res. **41**, 125–151.

Pain, C. C., Saunders, J. H., Worthington, M. H., Singer, J. M., Stuart-Bruges, W., Mason, G., and Goddard, A. (**2005**). "A mixed finite-element method for solving the poroelastic Biot equations with electrokinetic coupling," Geophys. J. Int. **160**(2), 592–608.

Pao, Y. H., and Mow, C. C. (**1976**). "Theory of normal modes and ultrasonic spectral analysis of the scattering of waves in solids," J. Acoust. Soc. Am. **59**, 1046–1056.

Pao, Y. H. (**1978**). "Betti's identity and transition matrix for elastic waves," J. Acoust. Soc. Am. **64**, 302–310.

Pride, S. R. (**1994**). "Governing equations for the coupled electromagnetics and acoustics of porous media," Phys. Rev. B **50**, 15678–15696.

Pride, S. R., and Haartsen, M. W. (**1996**). "Electroseismic wave properties," J. Acoust. Soc. Am. **100**, 1301–1315.

Revil, A., Saracco, G., and Labazuy, P. (**2003**). "The volcano-electric effect," J. Geophys. Res. **108**(B5), art. no. 2251.

Roberts, J. J., and Lin, W. N. (**1997**). "Electrical properties of partially saturated Topopah Spring tuff: Water distribution as a function of saturation," Water Resour. Res. **33**(4), 577–587.

Sternberg, E. (**1960**). "On the integration of the equations of motion in the classical theory of elasticity," Arch. Ration. Mech. Anal. **6**, 34–50.

White, B. S. (**2005**). "Asymptotic theory of electroseismic prospecting," SIAM J. Appl. Math. **65**(4), 1443–1462.

Yeh, C. S., Teng, T. J., and Shih, P. J. (**2004**). "On formulation of a transition matrix for poroelastic medium and application to analysis of scattering problem," J. Acoust. Soc. Am. **116**(2), 655–676.

Ying, C. F., and Truell, R. (**1956**). "Scattering of a plane longitudinal wave by a spherical obstacle in an isotropically elastic solid," J. Appl. Phys. **27**, 1086–1097.

Study of the comparison of the methods of equivalent sources and boundary element methods for near-field acoustic holography

Nicolas P. Valdivia[a] and Earl G. Williams[b]
Code 7130, Naval Research Laboratory, Washington, DC 20375

(Received 12 May 2006; revised 6 September 2006; accepted 12 September 2006)

Boundary element methods (BEM) based near-field acoustic holography (NAH) has been used successfully in order to reconstruct the normal velocity on an arbitrarily shaped structure surface from measurements of the pressure field on a nearby conformal surface. An alternative approach for this reconstruction on a general structure utilizes the equivalent sources method (ESM). In ESM the acoustic field is represented by a set of point sources located over a surface that is close to the structure surface. This approach is attractive mainly for its simplicity of implementation and speed. In this work ESM as an approximation of BEM based NAH is studied and the necessary conditions for the successful application of this approach in NAH is discussed. A cylindrical fuselage surface excited by a point force as an example to validate the results is used. © *2006 Acoustical Society of America.* [DOI: 10.1121/1.2359284]

PACS number(s): 43.40.Sk, 43.20.Rz, 43.40.Yq [SFW] Pages: 3694–3705

I. INTRODUCTION

Near-field acoustical holography (NAH)[1] provides a reconstruction of the acoustic field (pressure, normal velocity, and intensity) on a surface from measurements of the radiated field on a near concentric surface. The problem is ill posed because of the presence of evanescent waves that decay rapidly from the structure surface to the measurement surface. The measurements are typically made very close to the structure in order to obtain a high resolution reconstruction. To treat the ill-posed nature of the problem, for planar surfaces[2] Fourier decomposition is used with the series truncated to remove the very short wavelength components of the field that decay very rapidly. For an arbitrarily shaped structure, boundary elements methods (BEM)[3,4] may be applied to discretize the integral equation representations of the acoustical pressure in order to obtain a relation between the pressure measurements and the acoustic field over the structure surface in matrix form. The resultant matrix system is ill posed and requires the use of regularization methods[5] for its solution. The common implementation procedure of regularization is based on the calculation of the singular value decomposition (SVD). The calculation of the SVD considerably increases the computation time and storage requirements of the regularization method. As an alternative, regularization methods can be implemented via iterative procedures like conjugate gradients.[5,6]

The discretization of integral equations utilizing BEM requires the numerical computation of integrals that can considerably reduce speed and efficiency of any numerical method that uses this technique. An alternative method known as the equivalent sources method (ESM) produces a matrix relation similar to the one in BEM without numerical computation of integrals, considerably increasing the speed of the computations. In ESM the acoustic field is represented by a set of sources distributed over a surface closed to the structure surface. The theoretical justification of ESM was given first by Vekua[7] and Kupradze,[8] and later improved by Müller and Kersten.[9] The paper of Koopman[10] introduced the method of superposition (other name for ESM) applied to scattering problems to the acoustical community. Since then, several authors[11–13] utilized this method for scattering problems. ESM applied to NAH was first suggested by Sarkissian.[14,15] Recently Semenova and Wu[16] compared ESM with the Helmholtz least squares method for NAH.

The goal of this work is to study ESM as an approximation to the integral equations used by BEM. Other issues addressed will include the correct location and distribution of the sources. Finally, we will compare the error produced by BEM based NAH and ESM based NAH using a vibrating cylinder.

II. ACOUSTIC REPRESENTATIONS

Let G be a domain in $\mathbb{R}^3$, interior to the closed boundary surface Γ where we assume that Γ is allowed to have edges and corners. Similarly we will denote as G^+ the region outside of G that shares the same boundary Γ (see Fig. 1). For a time-harmonic ($e^{-i\omega t}$) disturbance of frequency ω the sound pressure p satisfies the homogeneous Helmholtz equation in G (or G^+)

$$\Delta p + k^2 p = 0, \tag{1}$$

where $k=\omega/c$ is the wave number and c the constant for the speed of sound. A solution p that satisfies Eq. (1) in G^+ also needs to satisfy the Sommerfeld radiation condition.[17]

[a]Author to whom correspondence should be addressed; electronic mail: valdivia@pa.nrl.navy.mil
[b]Electronic mail: williams@pa.nrl.navy.mil

 © 2006 Acoustical Society of America

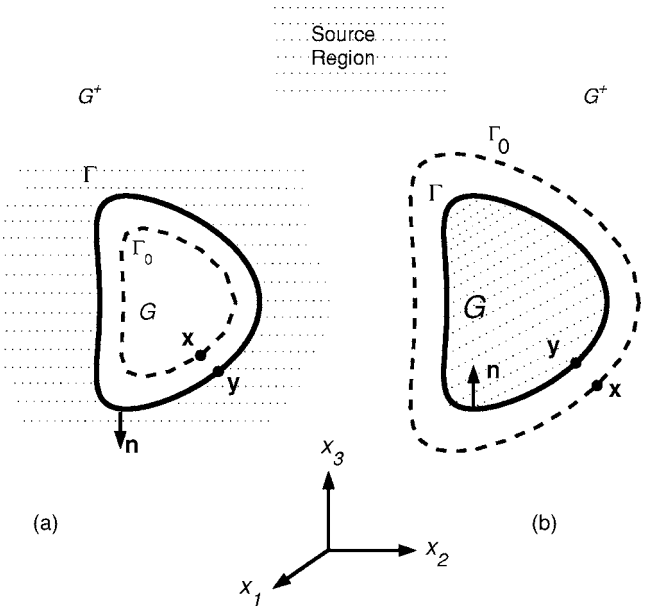

FIG. 1. Formulation for (a) interior NAH, (b) exterior NAH.

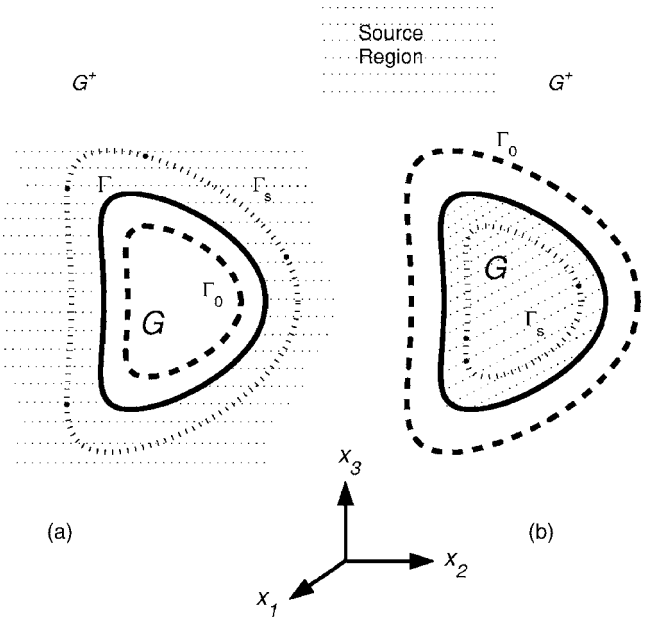

FIG. 2. The source surface Γ_s position for (a) interior NAH and (b) exterior NAH.

A. Integral equation representation

A solution p of Eq. (1) can be represented by the indirect formulation[18–20] for $\mathbf{x}=(x_1,x_2,x_3)$ as

$$p(\mathbf{x}) = \int_{\Gamma} \Phi(\mathbf{x},\mathbf{y})\varphi(\mathbf{y})dS(\mathbf{y}), \tag{2}$$

where

$$\Phi(\mathbf{x},\mathbf{y}) = \frac{\exp(ik|\mathbf{x}-\mathbf{y}|)}{4\pi|\mathbf{x}-\mathbf{y}|}. \tag{3}$$

In interior (exterior) NAH the acoustical sensors are placed on a surface Γ_0 inside (outside) the domain G (see Fig. 1). These are used to measure the pressure p and the fundamental problem is to recover the normal velocity on Γ. The solution to NAH is reduced to the solution of

$$p(\mathbf{x}) = \int_{\Gamma} \Phi(\mathbf{x},\mathbf{y})\varphi(\mathbf{y})dS(\mathbf{y}), \quad \mathbf{x} \in \Gamma_0, \tag{4}$$

for the density function φ on Γ. The normal derivative of the single source at Γ is given by the jump relation[18] of the normal derivative of Eq. (2) and Euler's equation

$$i\rho\omega v(\mathbf{x})^{\pm} = \int_{\Gamma} \frac{\partial\Phi(\mathbf{x},\mathbf{y})}{\partial\mathbf{n}(\mathbf{x})}\varphi(\mathbf{y})dS(\mathbf{y}) \mp \Omega(\mathbf{x})\varphi(\mathbf{x}), \quad \mathbf{x} \in \Gamma. \tag{5}$$

In Eq. (5), ρ is the mean fluid density, $\mathbf{n}$ is the unit normal with direction shown in Fig. 1, and $\Omega(\mathbf{x})$ is the solid angle coefficient. The superscript sign "+" in Eq. (5) is used for exterior NAH and "–" for interior NAH. This notation will be kept through the rest of this work.

B. Equivalent sources

A solution p of Eq. (1) can be represented by the method of equivalent sources.[14,15] In this method we are required to define the source surface Γ_s and distribute N_s source points over this surface. As shown by Fig. 2, for interior (exterior) NAH the source surface Γ_s is placed outside (inside) the domain G. Then we have the representation

$$p(\mathbf{x}) = \sum_{j=1}^{N_s} q_j\Phi(\mathbf{x},\mathbf{z_j}), \quad \mathbf{z}_j \in \Gamma_s, \tag{6}$$

where $\mathbf{z}_j$, $q_j, j=1,\ldots,N_s$ are, respectively, the source points and the source coefficients. The solution to NAH is reduced to solve Eq. (6) for the source coefficients q_j, then the normal derivative is calculated using

$$i\rho\omega v(\mathbf{y}) = \sum_{j=1}^{N_s} q_j \frac{\partial\Phi(\mathbf{y},\mathbf{z}_j)}{\partial\mathbf{n}(\mathbf{y})}, \quad \mathbf{y} \in \Gamma. \tag{7}$$

C. Modified integral equation representation

We modify the integral in Eq. (2), Eq. (4), and Eq. (5) by moving the integration surface Γ to a conformal position on the exterior (interior) Γ_s as shown in Fig. 2. The corresponding boundary integral representation

$$p(\mathbf{x}) = \int_{\Gamma_s} \Phi(\mathbf{x},\mathbf{y})\phi(\mathbf{y})dS(\mathbf{y}), \quad \mathbf{x} \in \mathbb{R}^3. \tag{8}$$

Note that the surface Γ_s is the same as that used for ESM.

The solution to NAH is reduced to the solution of

$$p(\mathbf{x}) = \int_{\Gamma_s} \Phi(\mathbf{x},\mathbf{y})\phi(\mathbf{y})dS(\mathbf{y}), \quad \mathbf{x} \in \Gamma_0, \tag{9}$$

for the density function ϕ on Γ. The normal derivative of the single source layer at Γ is given by the normal derivative of Eq. (8) and Euler's equation

$$i\rho\omega v(\mathbf{x}) = \int_{\Gamma_s} \frac{\partial \Phi(\mathbf{x},\mathbf{y})}{\partial \mathbf{n}(\mathbf{x})} \phi(\mathbf{y}) dS(\mathbf{y}), \quad \mathbf{x} \in \Gamma. \tag{10}$$

We will present results comparing this approach with ESM and regular inverse boundary element method (IBEM).

III. NUMERICAL SOLUTION

A. Boundary element methods

The boundary surfaces Γ, Γ_s are discretized into triangular elements with three nodes or quadrilateral elements with four nodes. As applied in previous works,[6,19,20] isoparametric linear functions are selected for interpolating the geometric and acoustical quantities. Given M pressure measurements on Γ_0, contained in the column vector $\mathbf{p}$, recover N pressure and normal velocity points on Γ, given by the column vectors $\mathbf{p}^s$ and $\mathbf{v}^s$, respectively. When $\mathbf{x} \in \Gamma_0$, Eq. (4) is discretized as

$$[\mathbf{S}]\boldsymbol{\varphi} = \mathbf{p}, \tag{11}$$

where $[\mathbf{S}]$ is an $M \times N$ complex matrix and $\boldsymbol{\varphi}$ is the vector that represents the density φ over N points in Γ. Similarly, when $\mathbf{x} \in \Gamma$, Eq. (5) is discretized as

$$\mathbf{v}^s = \frac{1}{i\rho\omega}[\mathbf{K}^{\pm}]\boldsymbol{\varphi}, \tag{12}$$

where $[\mathbf{K}^{\pm}]$ is an $N \times N$ complex matrix.

When $\mathbf{x} \in \Gamma_0$, Eq. (9) is discretized as

$$[\mathbf{S_m}]\boldsymbol{\varphi} = \mathbf{p}, \tag{13}$$

where $[\mathbf{S_m}]$ is an $M \times N_s$ complex matrix and $\boldsymbol{\phi}$ is the vector that represent the density ϕ over N_s points in Γ_s. Similarly, when $\mathbf{x} \in \Gamma$, Eq. (10) is discretized as

$$\mathbf{v}^s = \frac{1}{i\rho\omega}[\mathbf{K_m}]\boldsymbol{\varphi}, \tag{14}$$

where $[\mathbf{K_m}]$ is an $N \times N_s$ complex matrix.

B. Equivalent sources

We obtain the following matrix system from Eq. (6)

$$[\mathbf{G}]\mathbf{q} = \mathbf{p}, \tag{15}$$

where the coefficients of the $M \times N_s$ complex matrix $[\mathbf{G}]$ are given by $G_{ij} = \Phi(\mathbf{x}_i, \mathbf{z}_j)$. Here $\mathbf{x}_i$ are the points in Γ_0 and $\mathbf{z}_j$ are the points in Γ_s. Similarly, we obtain the relationship

$$\mathbf{v}^s = \frac{1}{i\rho\omega}[\mathbf{G}^{sv}]\mathbf{q}, \tag{16}$$

where the coefficients of the $N \times N_s$ complex matrix $[\mathbf{G}^{sv}]$ are given by $G^{sv}_{ij} = \frac{\partial \Phi(\mathbf{y}_i, \mathbf{z}_j)}{\partial \mathbf{n}(\mathbf{y}_i)}$ and $\mathbf{y}_i$ are the points in Γ.

C. Regularization

For the experimental problem, the exact pressure $\mathbf{p}$ is perturbed by measurement errors. We denote the measured pressure as $\mathbf{p}_m$. If the elements of the perturbation $\mathbf{e} = \mathbf{p}_m - \mathbf{p}$ are Gaussian (unbiased and uncorrelated) with covariance matrix $\sigma_0^2[\mathbf{I}]$, then $E(\|\mathbf{e}\|_2^2) = M\sigma_0^2$, where $\|\cdot\|_2$ is the 2 norm. It is well known that the linear systems Eq. (11), Eq. (13), and Eq. (15) are ill posed, i.e., the errors in $\mathbf{p}_m$ will be amplified on the solutions $\boldsymbol{\varphi}$, $\boldsymbol{\phi}$ or $\mathbf{q}$, and in most of the cases the recovery will be useless. For that reason special *regularization methods* are used to find the solution of these linear systems.

Consider the solution of the generic ill-posed linear matrix system

$$[\mathbf{A}]\mathbf{x} = \mathbf{p}_m, \tag{17}$$

where $[\mathbf{A}]$ represents the $M \times N$ (or $M \times N_s$) complex matrix in the ill-posed linear systems Eq. (11), Eq. (13), or Eq. (15). Similarly $\mathbf{x}$ represents the solution vector $\boldsymbol{\varphi}$ or $\mathbf{q}$. As explained in Hansen,[5] there are two types of regularization methods: direct and iterative. The direct regularization methods require the calculation of the singular value decomposition (SVD) of $[\mathbf{A}]$, which can be a prohibitive practice when the dimensions of $[\mathbf{A}]$ are big. Iterative regularization methods like conjugate gradients for the normal equations (CGNE) should be used instead, since it accesses the matrix $[\mathbf{A}]$ only via matrix-vector multiplication with $[\mathbf{A}]$ and $[\mathbf{A}]^H$ (see Table below).

Starting vector $\mathbf{x}_{(0)} = 0$
$\mathbf{r}_{(0)} = \mathbf{p}_m$
$\mathbf{d}_{(0)} = [\mathbf{A}]^H \mathbf{r}_{(0)}$
for $l = 1, 2, \ldots (\leqslant \min(M, N))$
$\alpha_{(l)} = \|[\mathbf{A}]^H \mathbf{r}_{(l-1)}\|_2^2 / \|[\mathbf{A}]\mathbf{d}_{(l-1)}\|_2^2$,
$\mathbf{x}_{(l)} = \mathbf{x}_{(l-1)} + \alpha_{(l)} \mathbf{d}_{(l-1)}$,
$\mathbf{r}_{(l)} = \mathbf{r}_{(l-1)} - \alpha_{(l)} [\mathbf{A}]\mathbf{d}_{(l-1)}$
$\beta_{(l)} = \|[\mathbf{A}]^H \mathbf{r}_{(l)}\|_2^2 / \|[\mathbf{A}]^H \mathbf{r}_{(l-1)}\|_2^2$,
$\mathbf{d}_{(l)} = [\mathbf{A}]^H \mathbf{r}_{(l)} + \beta_{(l)} \mathbf{d}_{(l-1)}$,

CGNE produces a sequence of iteration vectors $\mathbf{x}_{(l)}$, $l = 1, 2, 3, \ldots$. that approaches the optimal regularization after a few iterations. If the iteration is not stopped, the solution $\mathbf{x}_{(l)}$ amplifies the noisy data $\mathbf{p}_m$. This phenomena is known as "semiconvergence." For that reason it is crucial to obtain a reliable stopping rule for the CGNE iterations and we refer the reader to our previous work[6] for more details.

The regularized solution (using CGNE or another method) $\boldsymbol{\varphi}$ of the matrix system in Eq. (11) combined with Eq. (12) gives the normal velocity $\mathbf{v}^s$, and this method of solution is known as the indirect-implicit (IM) method.[20] Similarly the regularized solution $\boldsymbol{\phi}$ to Eq. (13) combined with Eq. (14) gives $\mathbf{v}^s$, and this method of solution will be named the nonsingular indirect-implicit (NIM) method. The name is given by the fact that the integral in Eq. (10) avoids the singularity produced by the integral in Eq. (5). In general these two methods belong to the more general methods of solution known as inverse boundary element methods (IBEMs). Finally, the equivalent sources method (ESM) uses the regularized solution $\mathbf{q}$ of the matrix system in Eq. (15) combined with Eq. (16) to obtain $\mathbf{v}^s$.

IV. INTEGRAL APPROXIMATION FOR ESM

In this section we will summarize some of the important implications found in the Appendix and apply them for the purpose of understanding ESM as an approximation of BEM.

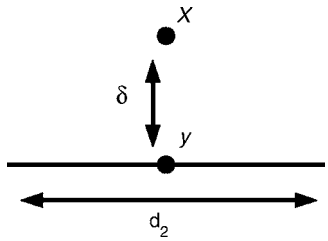

FIG. 3. Setup of integral approximation over element.

Let Ψ be a quadrilateral element of the surface Γ_s. Then, as proved in lemma 5.1.2 of Atkinson,[3] the function φ can be replaced by an interpolating polynomial function φ_p, and we get a resultant error estimate

$$\int_{\Psi} \varphi(\mathbf{z})\Phi(\mathbf{x},\mathbf{z})dS(\mathbf{z}) = \int_{\Psi} \varphi_p(\mathbf{z})\Phi(\mathbf{x},\mathbf{z})dS(\mathbf{z}) + C_1 d_2^{r+3}, \tag{18}$$

where d_2 is the maximum arc length of the sides in Ψ, r is the degree of the polynomial approximation, and C_1 a constant that depends on r. In BEM for NAH we use a polynomial approximation with $r=1$, since we have proved that NAH approximations with $r \geqslant 2$ yield an increase in the reconstruction error.[20]

ESM can be understood as an approximation to φ by a polynomial with $r=0$, i.e., approximation by a constant polynomial. Then ESM is based on the approximation of the integral

$$\int_{\Psi} \Phi(\mathbf{x},\mathbf{z})dS(\mathbf{z}) = \Phi(\mathbf{x},\mathbf{y})S_{\Psi} + C_2 D(k,\delta,d_2), \tag{19}$$

where $\mathbf{y}$ is a point in Ψ, C_2 is a constant that depends on the curvature of Ψ, S_{Ψ} is the area of the surface of Ψ, and $D(k,\delta,d_2)$ is a function given in the Appendix. As shown in Fig. 3, δ is the distance from $\mathbf{x}$ to $\mathbf{y}$. When Ψ is planar then $D(k,\delta,d_2)$ is given by Eq. (A6), and by Eq. (A4) otherwise.

For the planar case $C_2 \approx 1/12$. In Fig. 4 we show some plots of the comparison between the real errors produced by approximating Eq. (19) and the errors approximated by the estimate given in Eq. (A6). In this comparison $d_2=0.1$ m. Notice that, although the estimates are not accurate for $\delta < d_2$, they still follow the behavior of the error.

Finally, also for a planar quadrilateral element Ψ we use the estimate in Eq. (A6) to create the error surface shown in Fig. 5. In this figure we observe that the error reduces as we increase the distance δ, and, on the other hand, this error slightly increases when the frequency increases. We can conclude in this case that the integral approximation error will be small as long as $\delta \geqslant d_2$. This result can be generalized for an arbitrarily shaped surface using the integral estimates in Eq. (A4).

V. EVANESCENT WAVES' EFFECT IN ESM

From the previous section the reader can be misled to think that the bigger δ will lead to better accuracy in the reconstruction. But we need to clarify that the previous section just described the numerical error for the calculation of the integral equations. In NAH we have to consider the physical part of the reconstruction that has to deal with the presence of evanescent waves.

We will illustrate this effect of the evanescent waves using data from a vibrating plate (see our previous work[6] for more details). A steel rectangular plate (of 55.9×26.7 cm and thickness of 1.6 mm) was driven by a Wilcoxon F3/F9 inertial shaker (0–3000 Hz) fixed in the underneath corner of the plate in order to generate a broad spectrum of spatial wave numbers. The data are given over a rectangular $x-y$ plane Γ_0 located at $z=0.004$ m and possess 35×23 points with a uniform spacing over both coordinates of 0.025 m. The reconstruction plane Γ will also be a rectangular $x-y$ plane located at $z=0$ with the same dimensions and distribution of points in the $x-y$ plane as Γ_0, and the plate surface is located at the center of this area. The source surface Γ_s will

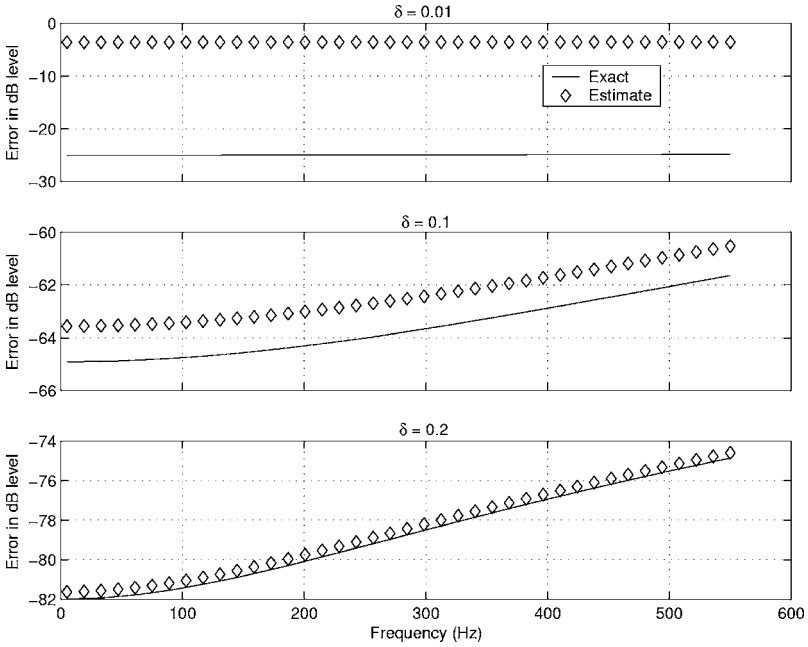

FIG. 4. Comparison between real approximation error and error given by estimates. Ψ is planar, $d_2=0.1$ m, (a) $\delta=0.01$ m, (b) $\delta=0.1$ m, and (c) $\delta=0.2$ m. The vertical coordinate is the error in dB level.

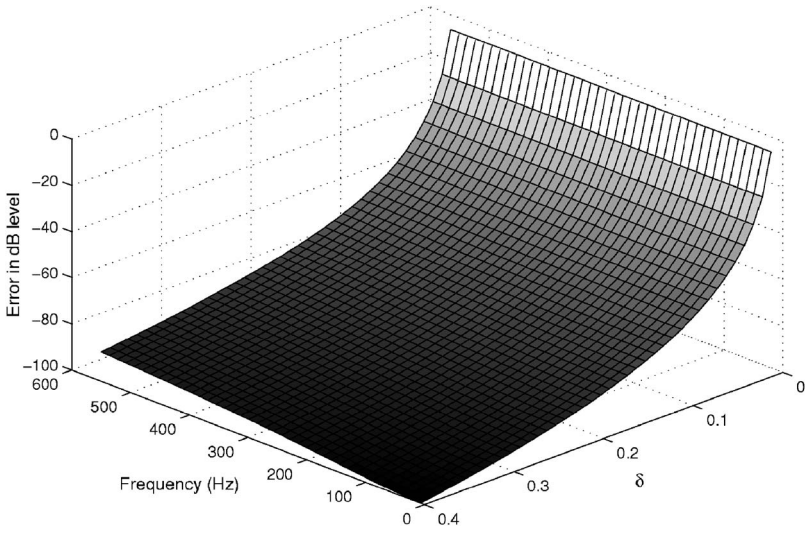

FIG. 5. Surface approximation error given by integral estimates when Ψ is planar, $d_2=0.1$.

be a rectangular $x-y$ plane located at $z=-\delta$ with the same dimensions and distribution of points in the $x-y$ plane as Γ_0.

Notice that the measurement aperture of Γ_0 almost doubles the size of the source (the plate), so this guarantees that the measured pressure field drops significantly towards the edges of the aperture. This condition allows us to use ESM for the reconstruction of the normal velocity over open surface Γ without the use of special continuation techniques.[21]

In the error results which follow, the "exact" normal velocity $\mathbf{v}^s$ on the plate was determined using the standard planar NAH. It has been demonstrated that the reconstructions with the over-scanned hologram are extremely accurate.[2] The reconstructed normal velocity $\mathbf{v}_r^s$ is obtained by using ESM with different values of δ. Equation (15) is solved using CGNE with the optimal iteration value, i.e., the CGNE iteration that has the smallest relative error $\|\mathbf{v}^s - |\mathbf{v}_r^s\|_2 / \|\mathbf{v}^s\|_2 \times 100\%$. In Fig. 6 we show the relative error of the reconstructed normal velocity for ESM with different values of δ. Notice that the error is similar for values of δ between 0.025 and 0.05 m. When $\delta=0.1$ m, the error increases slightly, but when $\delta=0.2$ m there is a considerable increase in the reconstruction error. This phenomena is related to the fact that the larger δ improves the accuracy of the integration, but is far away from the measurement surface. When the measurements are far away from the source surface, then very little evanescent wave information is obtained and it results in a very low resolution reconstruction. That is, the equivalent sources exhibit a natural $1/R$ decay so it is difficult for them to match on exponential decay in space, especially as δ increases.

In conclusion, we recommend using a value of δ between d_2 and $2d_2$ (here d_2 as in the previous section is the maximum length of a side in the mesh quadrilateral).

VI. INTERPOLATION PROPERTIES IN ESM

In this section we will discuss some of the problems that are found in ESM when the distribution of the points in the Γ surface and Γ_s surface is different. For that purpose we use the same example as the previous section, with variations in the distribution of the points in the Γ_s rectangular $x-y$ plane.

We define three different distributions of the points in the source surface. The point distributions in the $x-y$ plane denoted by $\Gamma_{s,i}, i=1,\ldots,4$, respectively, are shown in Figs. 7(a)–7(d). The distribution of points in $\Gamma_{s,1}$ is the same as in Γ. In $\Gamma_{s,2}$ there is a uniform distribution of points that coincide with the center midpoints of $\Gamma_{s,1}$. $\Gamma_{s,3}$ shows a distribution created from removing every other point in the $x-y$ coordinates. Finally in $\Gamma_{s,4}$ the distribution of points is uniform as in $\Gamma_{s,1}$, but just corresponds to a part of $\Gamma_{s,1}$.

Figure 8 shows the reconstruction errors using ESM with $\delta=0.025$ m over the different point distributions $\Gamma_{s,j}$. As in the previous section Eq. (15) is solved using CGNE for the optimal iteration. The first important result in this figure is that the reconstruction using $\Gamma_{s,1}$ possesses the smallest

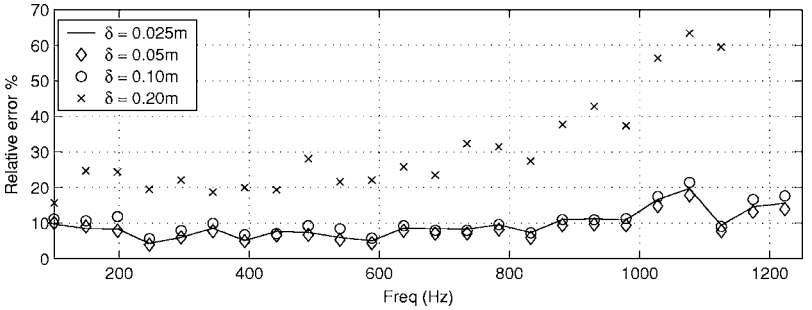

FIG. 6. Relative error for the reconstruction of the normal velocity of the vibrating plate using ESM for different values of δ.

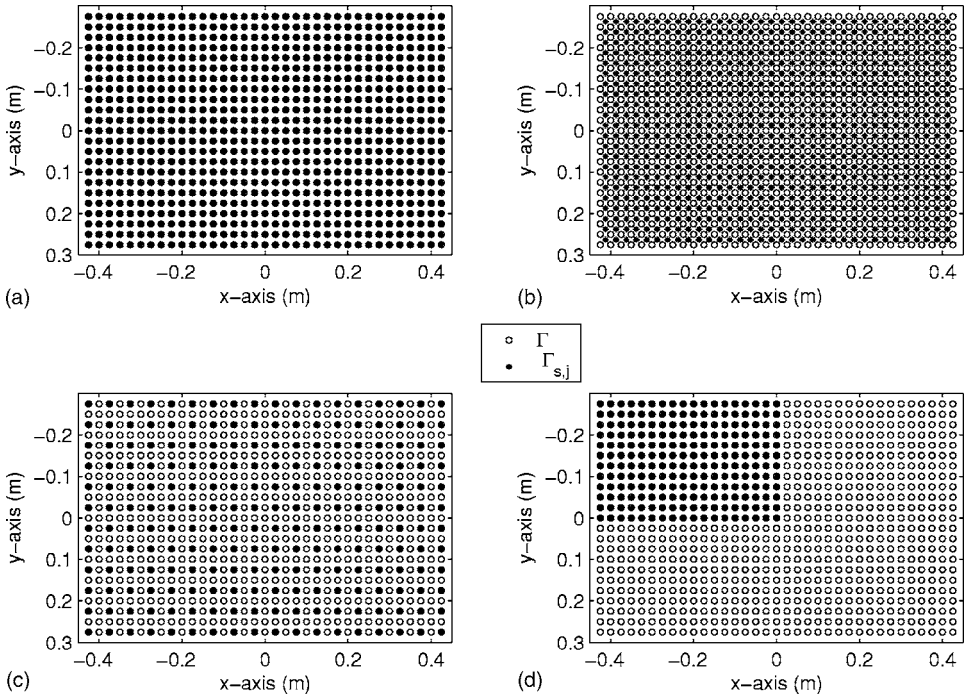

FIG. 7. Distribution of points over $x-y$ plane. Distribution for (a) $\Gamma_{s,1}$, (b) $\Gamma_{s,2}$, (c) $\Gamma_{s,3}$, and (d) $\Gamma_{s,4}$. Here $\delta=0.025$ m.

error. The reconstruction using $\Gamma_{s,2}$ is slightly worse. Finally, the reconstructions using $\Gamma_{s,3}$ or $\Gamma_{s,4}$ show a considerable increase in the relative error.

In Fig. 9, Fig. 10, and Fig. 11 we show a gray scale rendition of the magnitude of the normal velocity on the plane Γ recovered by ESM with $\delta=0.025$ m, respectively, using $\Gamma_{s,2}$, $\Gamma_{s,3}$, and $\Gamma_{s,4}$. Figure 9 shows that the reconstruction using $\Gamma_{s,2}$, although having a higher relative error than the reconstruction using $\Gamma_{s,1}$, still produces a smooth reconstruction. On the other hand, Fig. 10 shows a different result. The distribution of the points in $\Gamma_{s,3}$ is coarser than in Γ, and we can clearly see that the use of ESM translates this situation into magnitude irregularities that will negatively influence the reconstruction error. Figure 11 shows the reconstruction using the source surface $\Gamma_{s,4}$, where the source points are uniformly distributed as in Γ but just over a portion of the surface. The result as expected is only accurate over that particular portion of the surface Γ that is closer to the source points in $\Gamma_{s,4}$.

We can conclude from these examples that the optimal error will be obtained when the distribution of the points in Γ_s is equal to the distribution of points in Γ, and that the use of other points distributions in the best case will slightly increase the reconstruction error.

VII. COMPARISON OF IBEM AND ESM USING PHYSICAL EXPERIMENTS

The experimental configuration for the holographic measurement is similar to the previous work of Herdic.[22] The surface Γ is an aluminium stiffened cylindrical shell [0.81 m radius, 2.55 m length and the shell thickness varies between 0.8 and 1.2 mm, see Fig. 12(a)] excited by an exterior point force applied to a rib/stringer intersection near one end of the cylinder. The measurements were conducted using a chirp wave form over a band from 10 to 1000 Hz with 0.61 Hz resolution. The measurement surface Γ_0 is a cylinder of 0.7045 m radius and 2.32 m length as shown in Fig. 12(b).

The pressure on Γ_0 was measured on a grid of 32 points over the circumference, 29 points over the length, and at the cylinder ends the pressure is taken over five rings with 32 points at each ring [see Figs. 12(c) and 12(d)]. The normal velocity on Γ was measured with a vibrometer on a grid of 64 points over the circumference and 32 points over the length. At the ends of the cylinder in Γ there are no normal velocity measurements.

The vector $\mathbf{v}^s$ contains the measured normal velocity considered "truth" at the surface of the cylinder. Finally the vector $\mathbf{v}_r^s$, contains the reconstructed normal velocity ob-

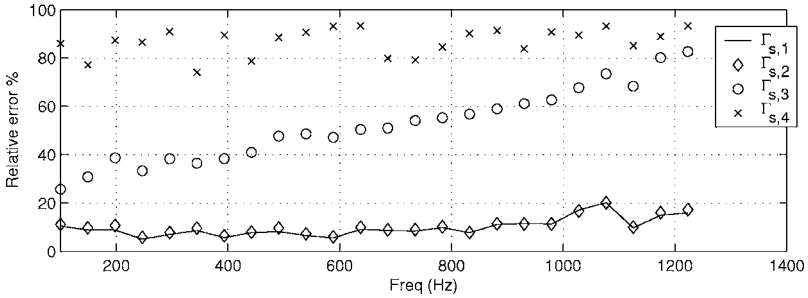

FIG. 8. Relative error for the reconstruction of the normal velocity of the vibrating plate for different point distributions of the source surface Γ_s for ESM with $\delta=0.025$ m.

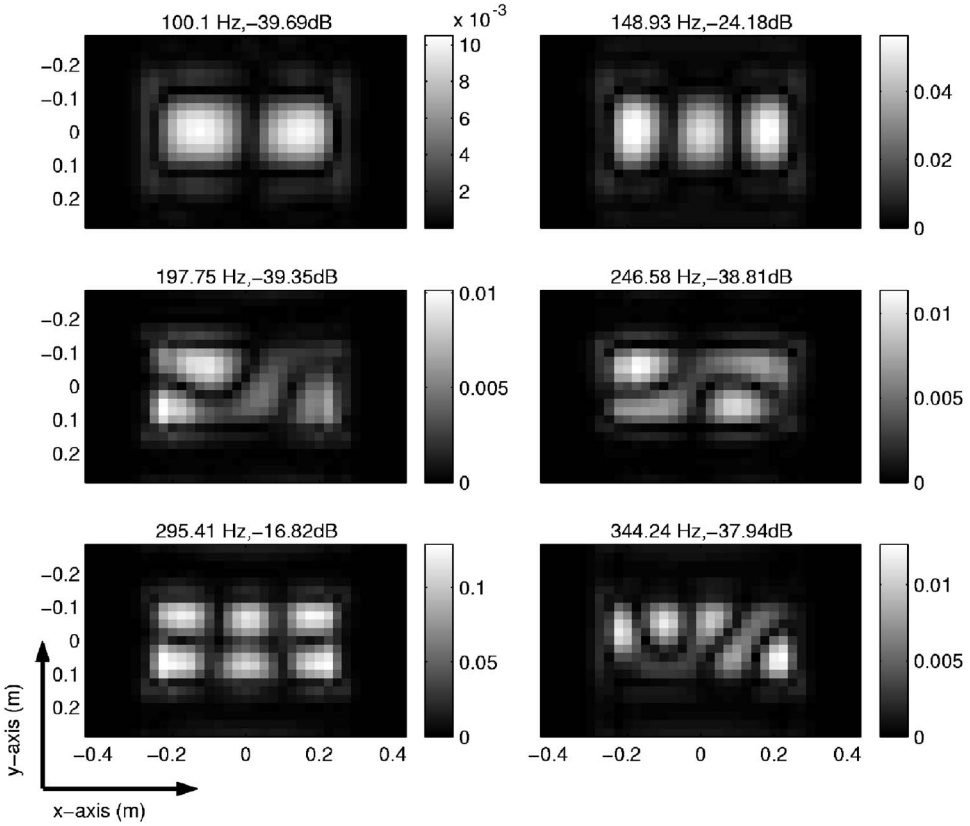

FIG. 9. Gray scale rendition of the magnitude of the normal velocity recovered on Γ using ESM with $\delta = 0.025$ m and source surface $\Gamma_{s,2}$. At each frequency we show the maximum dB level over the plane.

tained by any of the methods discussed in Secs. II and III combined with CGNE. For CGNE we use the optimal regularization parameter, i.e., the iteration is chosen in such a way that the relative error $\|\mathbf{v}^s - \mathbf{v}_r^s\|_2 / \|\mathbf{v}^2\|_2 \times 100$ is the smallest.

Figure 13 shows the relative error of reconstructed normal velocity for 16 frequencies equally spaced from 88.5 to 180 Hz. We remind the reader that IBEM-IM is applied by solving Eq. (11) with CGNE, and then apply Eq. (12) to obtain the reconstructed normal velocity. Similarly, IBEM-

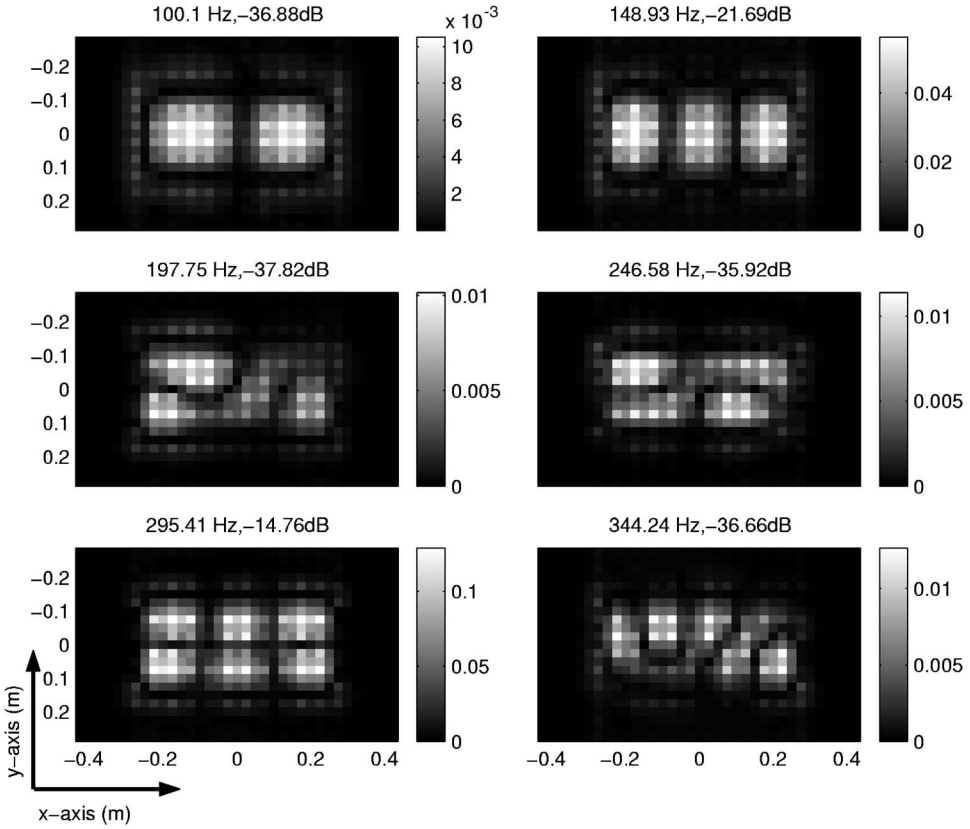

FIG. 10. Gray scale rendition of the magnitude of the normal velocity recovered on Γ using ESM with $\delta = 0.025$ m and source surface $\Gamma_{s,3}$. At each frequency we show the maximum dB level over the plane.

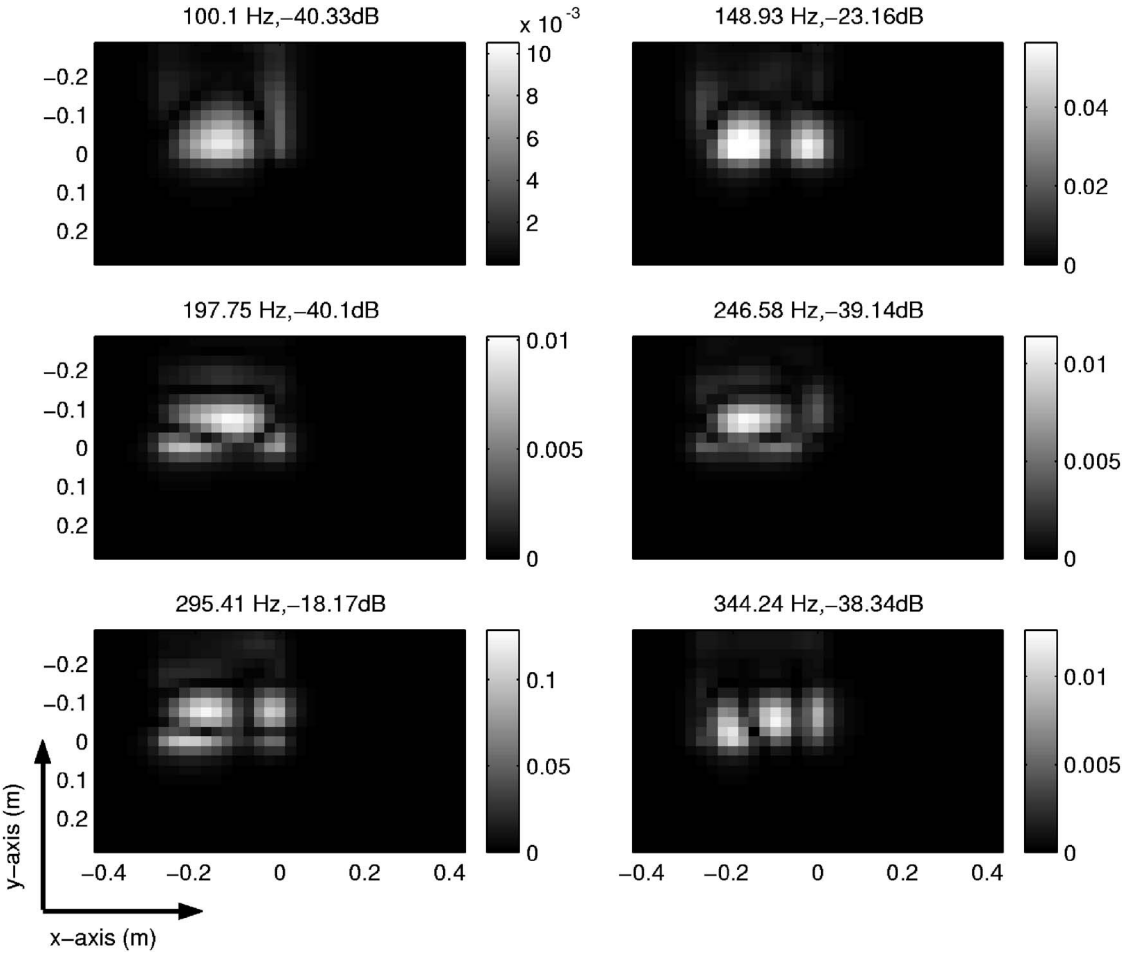

FIG. 11. Gray scale rendition of the magnitude of the normal velocity recovered on Γ using ESM with $\delta=0.025$ m and source surface $\Gamma_{s,4}$. At each frequency we show the maximum dB level over the plane.

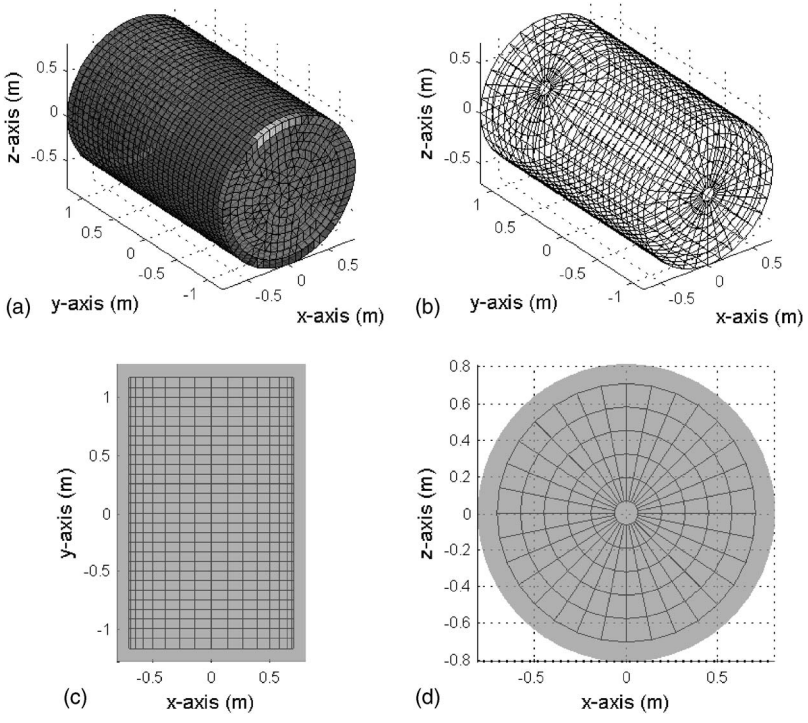

FIG. 12. Setup for physical interior problem experiment. (a) Surface Γ is an aluminum cylindrical shell, (b) measurement surface Γ_0, (c) measurements along the length (top view down on the cylinder) and (d) side-end measurements (side view on the cylinder).

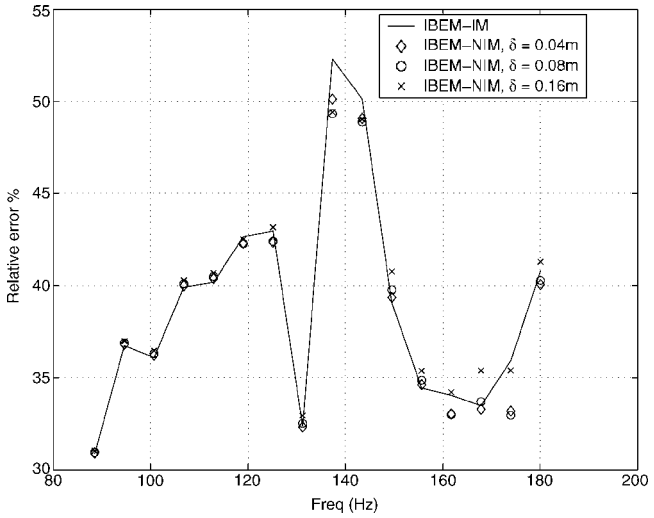

FIG. 13. Comparison between relative error of normal velocity reconstruction for different frequencies by IBEM-IM and IBEM-NIM with different values of δ.

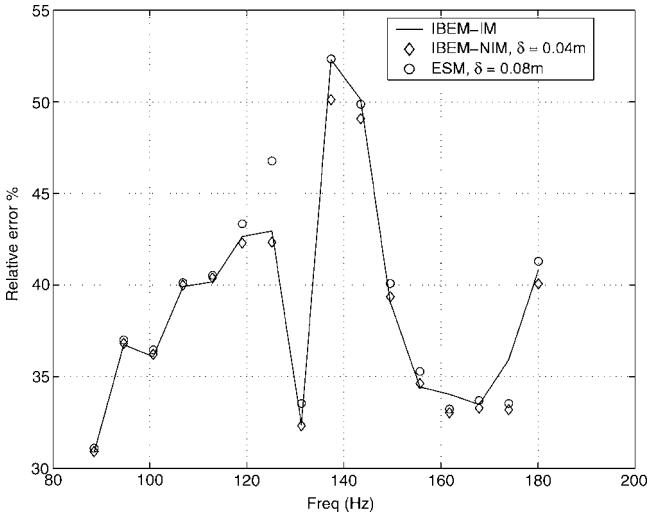

FIG. 15. Comparison between relative error of normal velocity reconstruction for different frequencies by IBEM-IM, IBEM-NIM with δ=0.04 m and ESM with δ=0.08 m.

NIM is applied by solving Eq. (13) with CGNE, and then apply Eq. (14) to obtain the reconstructed normal velocity. Figure 13 shows that the errors in the reconstructed normal velocity using IBEM-IM are similar to the errors using IBEM-NIM with different values of δ. Note that as δ becomes bigger, the error starts to increase, most likely due to the evanescent wave effect discussed in Sec. V.

Figure 14 shows the relative error of reconstructed normal velocity for the same frequencies as in Fig. 13, but using ESM for different values of δ. These results agree with the integral estimates of Sec. IV, in the sense that we require $\delta \geqslant d_2$ to make the integration error acceptable, or for our purpose, to obtain an accurate result in the reconstruction. Here the maximum diameter d_2=0.08 m, and in agreement with Sec. IV we see that the errors for $\delta \geqslant 8$ cm are similar.

Figure 15 shows a comparison of the relative error of the reconstructed normal velocity (same frequencies as in Figs. 13 and 14) using IBEM-IM, IBEM-NIM with δ=0.04 m and ESM with δ=0.08 m. We can clearly see that the three methods give similar error results, but IBEM-NIM gives slightly better reconstruction errors.

Finally, in Fig. 16 we show a gray scale rendition of the real part of the normal velocity measurements $\mathbf{v}^s$ in Γ and in Fig. 17 the reconstructed normal velocity $\mathbf{v}_r^s$ using IBEM-NIM with δ=0.04 m.

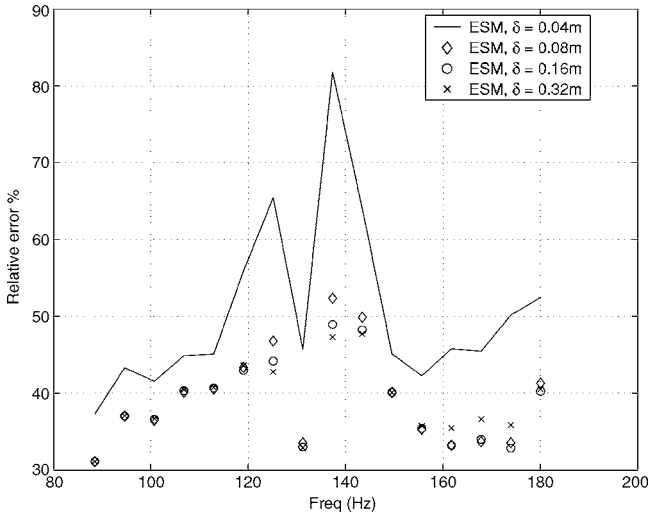

FIG. 14. Comparison between relative error of normal velocity reconstruction for different frequencies by ESM with different values of δ.

VIII. CONCLUSIONS

In this work we have studied three methods for the reconstruction of the acoustic field: IBEM-IM, IBEM-NIM, and ESM. The first two methods require the numerical discretization of integral equations, which can be an expensive technique when the number of reconstruction and measurement points is large. The matrix system required for ESM is obtained by the evaluation of the fundamental solution in Eq. (3) at the source points, and no boundary elements are used.

In Sec. IV we explained how ESM can be understood as an approximation to IBEM-NIM. The integral estimates showed that distance from the source surface Γ_s to the reconstruction surface should be greater or equal than d_2, the maximum diameter of a quadrilateral element in Γ_s, in order to obtain small integration error approximation.

In Sec. V we showed that in ESM when the size of the parameter δ is big, then the reconstruction error of the normal velocity will increase. This is the result of placing the source surface too far away from the measurements, obtaining very little information on the evanescent waves. We recommend δ to be between d_2 and $2d_2$.

In Sec. VI showed that for ESM the optimal distribution of points in Γ_s should be the same as the distribution of points in Γ. Using a different distribution of points than the optimal in the best case will result in a slight increase of the reconstruction error.

In Sec. VII, the physical experiment was used to compare the three methods using the reconstruction error. We found that IBEM-IM, IBEM-NIM, and ESM yield similar reconstruction errors. We can conclude from this result that

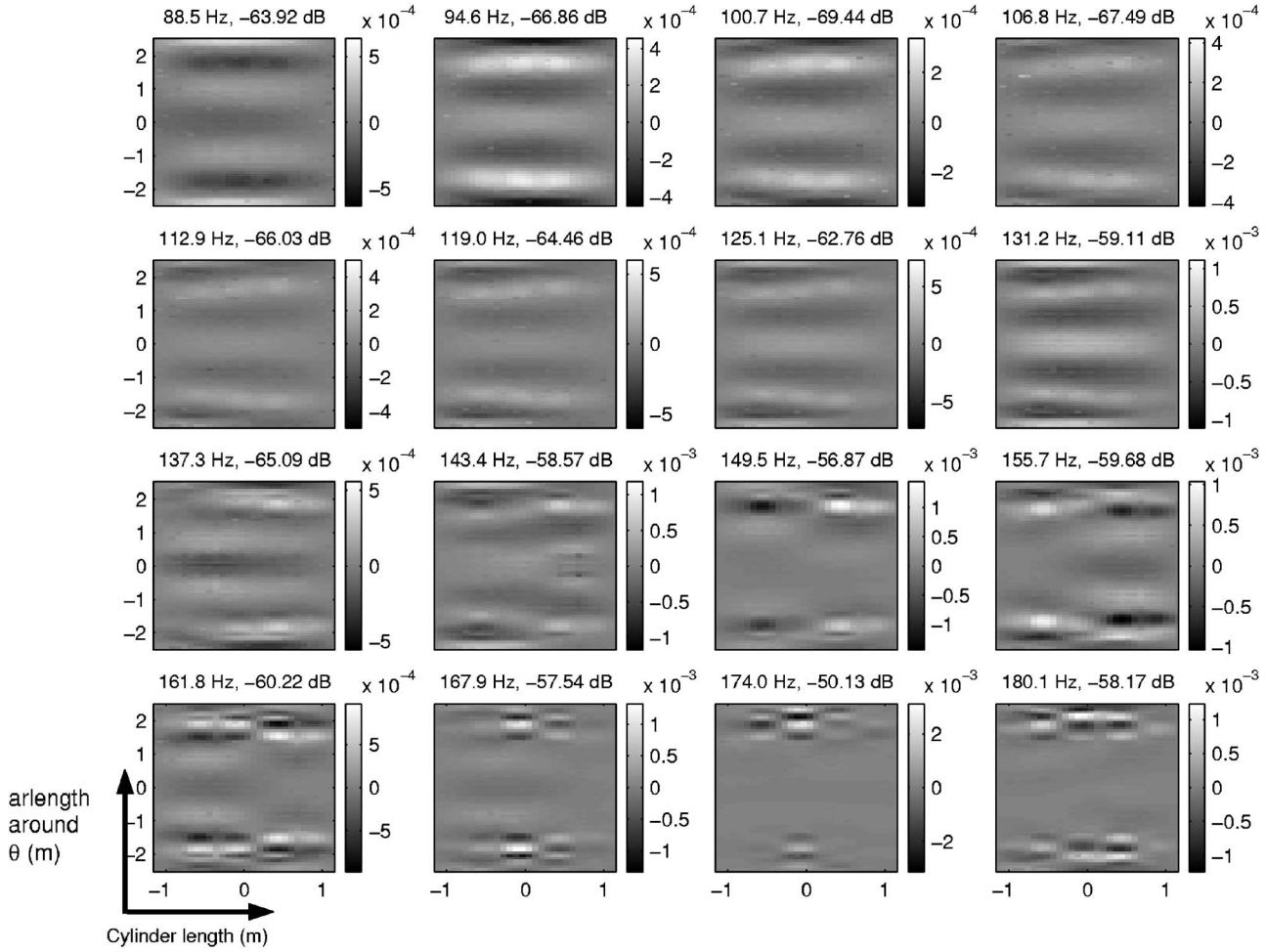

FIG. 16. Gray scale rendition of the real part of the measured normal velocity over the cylinder Γ for 16 frequencies corresponding to Fig. 15. At each frequency we show the maximum dB level over the plane.

as long that we satisfy the requirements for ESM discussed in Secs. IV–VI, this method can be used efficiently for NAH problems.

ACKNOWLEDGMENT

This work was supported by the Office of Naval Research.

APPENDIX: INTEGRATION ESTIMATES

Assume that Ψ is a quadrilateral element (see Fig. 18) and that $d_2>0$ is the maximum arc length of the sides in Ψ. The quantity $\delta>0$ is the distance from a point $\mathbf{x}$ to the quadrilateral element Ψ, i.e., there is $\mathbf{x}'\in\Psi$ such that $|\mathbf{x}-\mathbf{x}'|=\delta$.

We will be interested in the approximation of the integral

$$\int_{\Psi}\Phi(\mathbf{x},\mathbf{z})dS(\mathbf{z}). \tag{A1}$$

The mean value theorem applied to Eq. (A1) gives that

$$\int_{\Psi}\Phi(\mathbf{x},\mathbf{z})dS(\mathbf{z})=\Phi(\mathbf{x},\boldsymbol{\xi})S_{\Psi}, \tag{A2}$$

for certain $\boldsymbol{\xi}\in\Psi$. Here $S_{\Psi}=\text{area}(\Psi)$.

The multi-dimensional Taylor series are used to expand

$$\Phi(\mathbf{x},\boldsymbol{\xi})=\Phi(\mathbf{x},\mathbf{y})+D_1+D_2+\ldots$$

where

$$D_1=\sum_{i=1}^{3}\Phi_i(\mathbf{x},\mathbf{y})(\boldsymbol{\xi}_i-\mathbf{y}_i),$$

$$D_2=\sum_{i=1}^{3}\Phi_{ii}(\mathbf{x},\mathbf{y})\frac{(\boldsymbol{\xi}_i-\mathbf{y}_i)^2}{2}+\sum_{i,j=1,i\neq j}^{3}\Phi_{ij}(\mathbf{x},\mathbf{y})(\boldsymbol{\xi}_i-\mathbf{y}_i)(\boldsymbol{\xi}_j-\mathbf{y}_j).$$

Here $\Phi_i(\mathbf{x},\mathbf{y})$, $\Phi_{ij}(\mathbf{x},\mathbf{y})$ are, respectively, the first order and second order derivatives of $\Phi(\mathbf{x},\mathbf{y})$ with respect to $\mathbf{y}_i$ (or $\mathbf{y}_j$). The general error estimate is given by

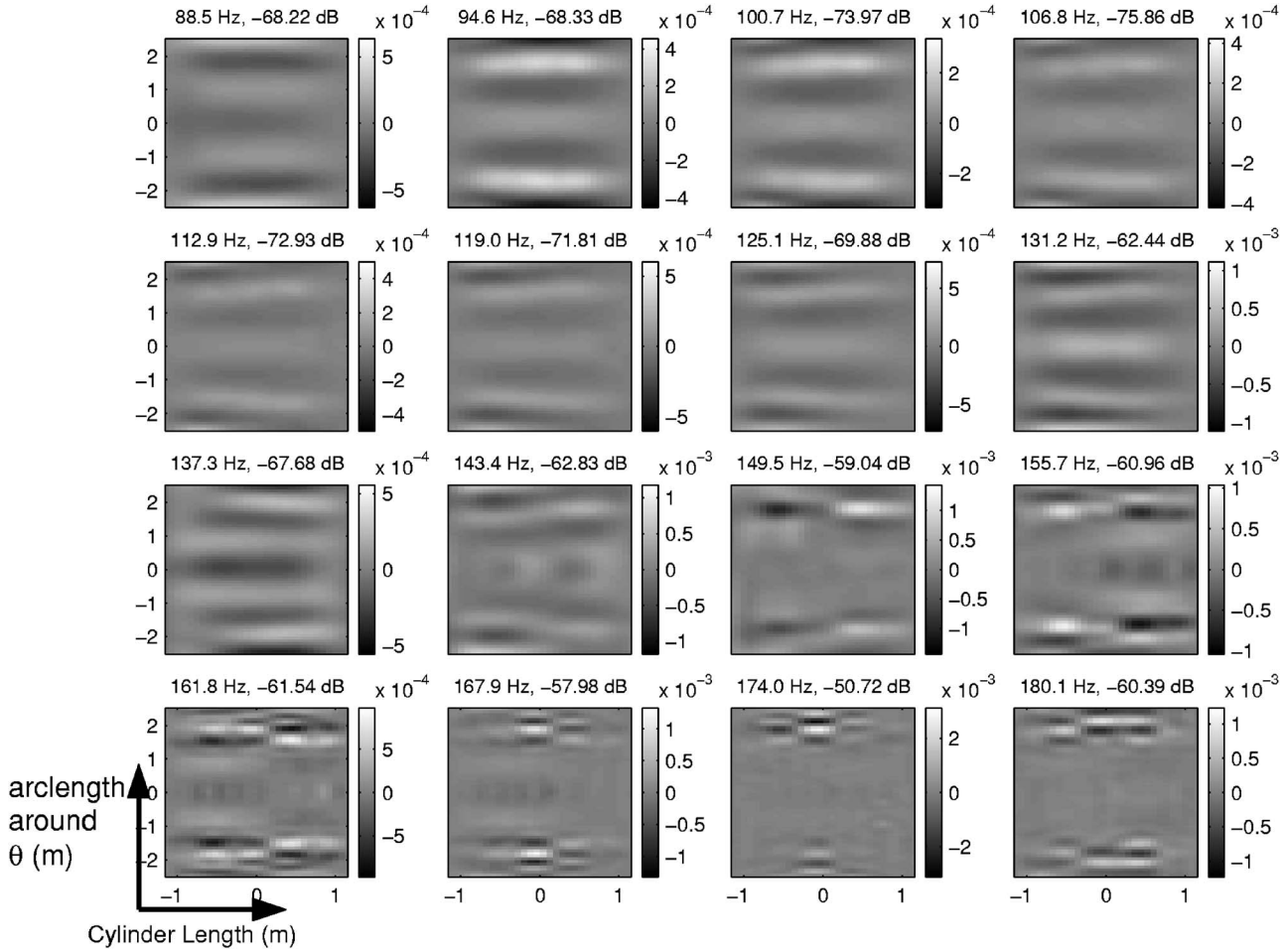

FIG. 17. Gray scale rendition of the real part of the recovered normal velocity using IBEM-NIM with $\delta=0.04$ cm over the cylinder Γ for 16 frequencies corresponding to Fig. 15. At each frequency we show the maximum dB level over the plane.

$$\int_{\Psi} \Phi(\mathbf{x},\mathbf{z})dS(\mathbf{y}) = \Phi(\mathbf{x},\mathbf{y})S_{\Psi} + CD_1S_{\Psi}, \tag{A3}$$

where C is a constant that will depend on the curvature of the surface quadrilateral Ψ.

Using the estimates $\delta<|\mathbf{x}-\mathbf{y}|\leqslant\delta+d_1$ and $|\mathbf{y}-\boldsymbol{\xi}|<\sqrt{2}d_2$ we get that

$$|D_1| \leqslant |(\mathbf{x}-\mathbf{y})\cdot(\boldsymbol{\xi}-\mathbf{y})|\frac{|ik|\mathbf{x}-\mathbf{y}|-1|}{4\pi|\mathbf{x}-\mathbf{y}|^3}$$

$$\leqslant \frac{\sqrt{2}d_2(\delta+d_1)}{4\pi\delta^3}\sqrt{1+k^2(\delta+d_1)^2}. \tag{A4}$$

Here, as shown in Fig. 18, d_1 is the arc length between $\mathbf{x}'$ and $\mathbf{y}$.

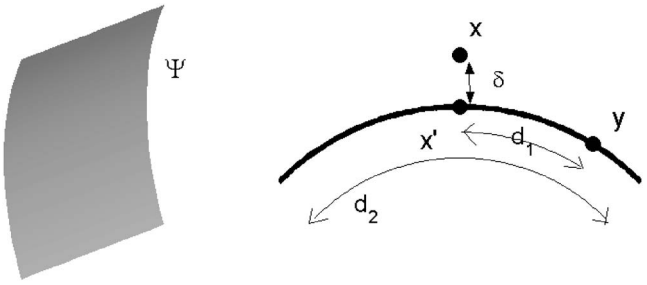

FIG. 18. Setup of integral approximation over element.

We will mention the special case when Ψ is a planar quadrilateral element (see Fig. 3) and $\mathbf{y}=\mathbf{x}'$. Since $(\mathbf{x}-\mathbf{y})\cdot(\boldsymbol{\xi}-\mathbf{y})=0$, then the estimate for D_1 is useless. In this particular case we use

$$\int_{\Psi} \Phi(\mathbf{x},\mathbf{z})dS(\mathbf{y}) = \Phi(\mathbf{x},\mathbf{y})S_{\Psi} + CD_2S_{\Psi}. \tag{A5}$$

We have that $d_1=0$, $(x_1-y_1)=(x_2-y_2)=(\xi_3-y_3)=0$ and $\Phi_{ij}(\mathbf{x},\mathbf{y})=0$ when $i\neq j$. So we obtain the estimate

$$|D_2| \leqslant \frac{|\boldsymbol{\xi}-\mathbf{y}|^2}{2}\frac{|ik|\mathbf{x}-\mathbf{y}|-1|}{4\pi|\mathbf{x}-\mathbf{y}|^3} = \frac{d_2^2}{4\pi\delta^3}\sqrt{1+k^2\delta^2}. \tag{A6}$$

[1]E. G. Williams and J. D. Maynard, "Holographic imaging without the wavelength resolution limit," Phys. Rev. Lett. **45**, 554–557 (1980).
[2]E. G. Williams, *Fourier Acoustics: Sound Radiation and Nearfield Acoustical Holography* (Academic, London, 1999).
[3]K. E. Atkinson, *The Numerical Solution of Integral Equations of the Second Kind* (Cambridge University Press, New York, 1997).
[4]M. R. Bai, "Application of bem (boundary element method)-based acoustic holography to radiation analysis of sound sources with arbitrarily shaped geometries," J. Acoust. Soc. Am. **92**, 533–549 (1992).
[5]P. C. Hansen, *Rank-Deficient and Discrete Ill-Posed Problems* (Siam, Philadelphia, 1998).
[6]N. Valdivia and E. G. Williams, "Krylov subspace iterative methods for boundary element method based near-field acoustic holography," J. Acoust. Soc. Am. **117**, 711–724 (2005).
[7]I. N. Vekua, "About the completeness of the system of metaharmonic

functions," Dokl. Akad. Nauk SSSR **90**, 715–718 (1953).
[8]V. D. Kupradze, *Potential Methods in the Theory of Elasticity* (Fitzmatizdat, Moscow, 1965).
[9]C. Müller and H. Kersten, "Two classes of complete systems of functions for the treatment of boundary value problems for the reduced wave equation $\Delta u+k^2u=0$," Math. Methods Appl. Sci. **2**, 48–67 (1980).
[10]G. H. Koopmann, L. Song, and J. Fahnline, "A method for computing acoustic fields based on the principle of wave superposition," J. Acoust. Soc. Am. **86**, 2433–2438 (1989).
[11]R. D. Miller, J. E. T. Moyer, H. Huang, and H. Uberall, "A comparison between the boundary element method and the wave superposition approach for the analysis of the scattered fields from rigid bodies and elastic shells," J. Acoust. Soc. Am. **89**, 2185–2196 (1991).
[12]A. Sarkissian, "Method of superposition applied to scattering from a target in shallow water," J. Acoust. Soc. Am. **95**, 2340–2345 (1994).
[13]Y. I. Bobrovnitskii and T. M. Tomilina, "General properties and fundamental errors of the method of equivalent sources," Acoust. Phys. **41**, 649–660 (1995).
[14]A. Sarkissian, "Extension of measurement surface in near-field acoustic holography," J. Acoust. Soc. Am. **115**, 1593–1596 (2004).
[15]A. Sarkissian, "Method of superposition applied to patch near-field acoustic holography," J. Acoust. Soc. Am. **118**, 671–678 (2005).
[16]T. Semenova and S. F. Wu, "On the choice of expansion functions in the Helmholtz equation least-squares method," J. Acoust. Soc. Am. **117**, 701–710 (2005).
[17]D. Colton and R. Kress, *Inverse Acoustics and Electromagnetic Scattering Theory* (Springer-Verlag, New York, 1992).
[18]D. Colton and R. Kress, *Integral Equation Methods in Scattering Theory* (Wiley-Interscience, New York, 1983).
[19]T. K. DeLillo, V. Isakov, N. Valdivia, and L. Wang, "The detection of surface vibrations from interior acoustical pressure," Inverse Probl. **19**, 507–524 (2003).
[20]N. Valdivia and E. G. Williams, "Implicit methods of solution to integral formulations in boundary element methods based near-field acoustic holography," J. Acoust. Soc. Am. **116**, 1559–1572 (2004).
[21]E. G. Williams, "Continuation of acoustic near-fields," J. Acoust. Soc. Am. **113**, 1273–1281 (2002).
[22]P. Herdic, B. Houston, M. Marcus, E. Williams, and A. Baz, "The vibro-acoustic response and analysis of a full-scale aircraft fuselage section for interior noise reduction," J. Acoust. Soc. Am. **117**, 3667–3678 (2005).

Impact of perforation impedance on the transmission loss of reactive and dissipative silencers

Iljae Lee and Ahmet Selamet[a)]
Department of Mechanical Engineering and The Center for Automotive Research, The Ohio State University, 930 Kinnear Rd., Columbus, Ohio 43212

Norman T. Huff
Owens Corning, 4600 Humboldt Drive, Novi, Michigan 48377

(Received 12 May 2006; revised 11 September 2006; accepted 13 September 2006)

The effect of perforation impedance on the acoustic behavior of reactive and dissipative silencers is investigated using experimental and computational approaches. The boundary element method (BEM) is applied for the prediction of transmission loss of silencers with different perforation geometries. The variations are considered in the porosity (8.4 and 25.7%) and hole diameter (0.249 and 0.498 cm) of perforations for both reactive and dissipative silencers, as well as the fiber filling density (100 and 200 kg/m^3) for the latter. The acoustic impedance for a number of perforations in contact with air alone and fibrous material has been incorporated into the predictions, which are then compared with the measured transmission loss using an impedance tube setup. The results demonstrate the significance of the accuracy of the perforation impedance in the predictions for both reactive and dissipative silencers. © *2006 Acoustical Society of America.*
[DOI: 10.1121/1.2359703]

PACS number(s): 43.50.Gf [KA] Pages: 3706–3713

I. INTRODUCTION

Perforated ducts are used extensively in both reactive and dissipative silencers to control the acoustic behavior of the element, guide the flow, and retain the absorbing material when incorporated. To predict the acoustic behavior of these silencers, analytical and numerical [finite element method (FEM) and boundary element method (BEM)] techniques have been developed, for example, by Sullivan (1979), Eriksson *et al.* (1983), Munjal (1987), Cummings and Chang (1988), Peat and Rathi (1995), and Kirby (2003). However, only a small number of publications have incorporated the acoustic characteristics of perforations into such predictions, particularly for the dissipative silencers. This may be attributed to the limitations in availability and applicability of representative expressions for the perforation impedance.

The perforation impedance without fibrous material in the absence of mean flow is relatively well understood by, for example, Sullivan and Crocker (1978). They also present the effect of perforation impedance on the transmission loss (TL) of reactive silencers. Their empirical formulation has been widely used to predict TL, for example, by Thawani and Jayaraman (1983), Luo *et al.* (1995), and Wang and Liao (1998). Its applicability, however, may be confined to relatively low values of porosity ϕ, since the development is based on $\phi=4.2\%$. Studies on the acoustic characteristics of perforated ducts in the presence of fibrous material (dissipative silencers) are further limited compared to those without such material. Cummings (1976) suggests an expression for the impedance of perforation in contact with fibrous material by using characteristic impedance and wave number of the absorbent. Kirby and Cummings (1998) provide a similar semiempirical impedance formulation for such a configuration subject to grazing mean flow, which has been later utilized by Kirby (2001, 2003) in predicting the transmission loss of dissipative silencers. Selamet *et al.* (2001) have adapted their approach by modifying the formulation of Sullivan and Crocker (1978) for the perforations facing air-fibrous material (air on one side and the absorbent on the other), and demonstrated the impact of perforation impedance on the TL of dissipative silencers. However, in both Kirby and Cummings (1998) and Selamet *et al.* (2001), the perforation impedance with fibrous material is intuitively modified from the one without the absorbent.

Recently, Lee (2005) and Lee *et al.* (2006) have developed empirical expressions for the acoustic impedance of perforations with and without the fibrous material, which are suitable to determine the silencer characteristics with various porosities and different hole diameters. In light of such expressions, the objective of the present study is then to illustrate the effect of perforation impedance on the acoustic behavior of reactive and dissipative silencers. TL is used to assess the acoustic performance since it is independent of the input and termination impedances, therefore, representative of the silencer itself. Different duct porosities ($\phi=8.4$ and 25.7%), hole diameters ($d_h=0.249$ and 0.498 cm), and fiber filling densities ($\rho_f=100$ and 200 kg/m^3) are employed to demonstrate the effect of such parameters on the TL of silencers. The expressions for perforation impedance and the acoustic properties (complex characteristic impedance and wave number) of fibrous material provided by Lee *et al.* (2006) are applied in BEM predictions. The experimental TL

[a)]Electronic mail: Selamet.1@osu.edu

 © 2006 Acoustical Society of America

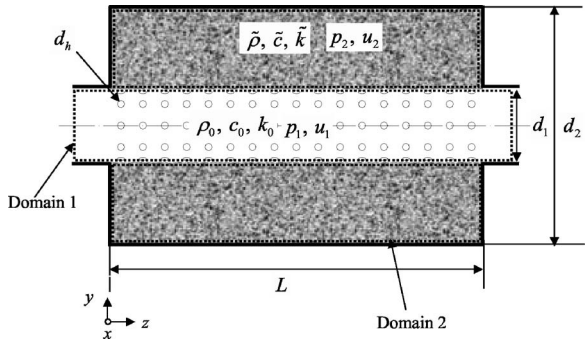

FIG. 1. Wave propagation in a perforated dissipative silencer in three-dimensions.

results from the impedance tube setup are then compared with predictions from the BEM, supporting the expressions developed for the perforation impedance.

Following this Introduction, Sec. II briefly describes the BEM and Sec. III presents the acoustic properties of the fibrous material and perforation impedance. Section IV compares the experimental results with predictions, followed by the concluding remarks in Sec. V.

II. BOUNDARY ELEMENT METHOD

This section describes the BEM used in this study for the predictions of silencers. A dissipative silencer in Fig. 1, for example, can be first divided into unfilled and filled acoustic domains. Impedance matrix for each domain is then obtained using boundary integration method. These impedance matrices are then combined by applying the boundary conditions between the two domains. The matrix for filled acoustic domain can be evaluated by using the complex acoustic characteristics of the absorbing material, such as density and speed of sound.

For the perforated main duct (domain 1), the three-dimensional wave equation in the absence of mean flow is expressed as

$$\nabla^2 p + k_0^2 p = 0, \tag{1}$$

where p is the acoustic pressure and k_0 is the wave number in air. The adjoint of Eq. (1) is given by

$$\frac{\partial^2 p^*}{\partial x^2} + \frac{\partial^2 p^*}{\partial y^2} + \frac{\partial^2 p^*}{\partial z^2} + k_0^2 p^* + \delta(x - x_i)(y - y_i)(z - z_i) = 0, \tag{2}$$

with its fundamental solution (Green's function) expressed as

$$p^* = \frac{1}{4\pi r} e^{-ik_0 r}, \tag{3}$$

where

$$r = \sqrt{(x - x_i)^2 + (y - y_i)^2 + (z - z_i)^2}, \tag{4}$$

and δ is the Dirac delta function. The weighted residual integral of Eq. (1) is written as

$$\int_V p^* (\nabla^2 p + k_0^2 p) dV = 0, \tag{5}$$

where V is the acoustic domain volume. Integrating the first term by parts twice and the second term once

$$\int_V p(\nabla^2 p^* + k_0^2 p^*) dV + \int_\Gamma \left[p^* \frac{\partial p}{\partial \boldsymbol{n}} - p \frac{\partial p^*}{\partial \boldsymbol{n}} \right] d\Gamma = 0, \tag{6}$$

where Γ is the boundary surface of the acoustic domain, and $\boldsymbol{n}$ is the unit outward normal vector to the surface. Rearranging Eq. (6)

$$C_i p_i + \int_\Gamma \frac{\partial p^*}{\partial \boldsymbol{n}} p d\Gamma = \int_\Gamma p^* \frac{\partial p}{\partial \boldsymbol{n}} d\Gamma, \tag{7}$$

where C_i are the edge or corner point coefficients. Discretizing the boundary surfaces into a number of elements Γ_j, Eq. (7) yields

$$C_i p_i + \sum_{j=1}^{N} \int_{\Gamma_j} \frac{\partial p^*}{\partial \boldsymbol{n}} p d\Gamma = \sum_{j=1}^{N} \int_{\Gamma_j} p^* \frac{\partial p}{\partial \boldsymbol{n}} d\Gamma, \tag{8}$$

which can be expressed in the matrix format as

$$[H]\{p\} = [G']\left\{ \frac{\partial p}{\partial \boldsymbol{n}} \right\}. \tag{9}$$

Equation (9) can be rewritten in terms of pressure and particle velocity which is outward normal to the boundary surface of domain 1 as

$$[H]\{p_1\} = [G]\{u_1\}. \tag{10}$$

The acoustic pressure and velocity on the boundary can be generally categorized as inlet, outlet, rigid wall, and perforations. Applying rigid boundary condition on the solid wall, the impedance matrix of the main duct ($[TC]$) may be expressed, in terms of inlet, outlet, and perforations, as

$$\begin{Bmatrix} \{p_1^i\} \\ \{p_1^o\} \\ \{p_1^p\} \end{Bmatrix} = \begin{bmatrix} [TC_{11}] & [TC_{12}] & [TC_{13}] \\ [TC_{21}] & [TC_{22}] & [TC_{23}] \\ [TC_{31}] & [TC_{32}] & [TC_{33}] \end{bmatrix} \begin{Bmatrix} \{u_1^i\} \\ \{u_1^o\} \\ \{u_1^p\} \end{Bmatrix}, \tag{11}$$

where superscripts i, o, and p denote inlet, outlet, and perforations.

Impedance matrix of the dissipative chamber (domain 2) ($[TD]$) can also be derived by a similar method as explained earlier [through Eqs. (1)–(10)] with complex density $\tilde{\rho}$ and speed of sound $\tilde{c}$. Applying the rigid boundary condition at the wall, impedance matrix for the dissipative chamber becomes

$$\{p_2^p\} = [TD]\{u_2^p\}. \tag{12}$$

The impedance matrices of perforated main duct and outer chamber may be coupled by the boundary conditions at the perforation interface. The acoustic velocity continuity at the interface yields

$$\{u_1^p\} = -\{u_2^p\}, \tag{13}$$

where the negative sign is assigned since u_1 and u_2 are normal outward acoustic velocities for each domain. For a per-

foration thickness much smaller than the wavelength, the pressure difference across the perforation may be expressed as

$$\{p_1^p\} - \{p_2^p\} = \rho_0 c_0 \tilde{\zeta}_p \{u_1^p\}, \tag{14}$$

where $\tilde{\zeta}_p$ is the nondimensional acoustic impedance of perforations. Combining Eqs. (11)–(14) yields the impedance matrix $[TI]$ of the silencer, defined by

$$\begin{Bmatrix} \{p_1^i\} \\ \{p_1^O\} \end{Bmatrix} = \begin{bmatrix} [TI_{11}] & [TI_{12}] \\ [TI_{21}] & [TI_{22}] \end{bmatrix} \begin{Bmatrix} \{u_1^i\} \\ \{u_1^O\} \end{Bmatrix}, \tag{15}$$

where

$$[TI_{11}] = [TC_{11}] + [TC_{13}](\tilde{\zeta}_p[I] - ([TC_{33}] + [TD]))^{-1}[TC_{31}], \tag{16}$$

$$[TI_{12}] = [TC_{12}] + [TC_{13}](\tilde{\zeta}_p[I] - ([TC_{33}] + [TD]))^{-1}[TC_{32}], \tag{17}$$

$$[TI_{21}] = [TC_{21}] + [TC_{23}](\tilde{\zeta}_p[I] - ([TC_{33}] + [TD]))^{-1}[TC_{31}], \tag{18}$$

$$[TI_{22}] = [TC_{22}] + [TC_{23}](\tilde{\zeta}_p[I] - ([TC_{33}] + [TD]))^{-1}[TC_{32}], \tag{19}$$

and $[I]$ is the identity matrix.

The averages of acoustic pressure and velocity from Eq. (15) at nodes on the inlet and outlet planes determine first the transfer matrix

$$\begin{bmatrix} p_1(0) \\ \rho_0 c_0 u_1(0) \end{bmatrix} = \begin{bmatrix} T_{11} & T_{12} \\ T_{21} & T_{22} \end{bmatrix} \begin{bmatrix} p_1(L) \\ \rho_0 c_0 u_1(L) \end{bmatrix}. \tag{20}$$

Assuming a main duct with a constant cross-sectional area, the TL of the silencer can then be calculated from the transfer matrix as follows:

$$TL = 20 \log_{10}\left(\tfrac{1}{2}|T_{11} + T_{12} + T_{21} + T_{22}|\right). \tag{21}$$

III. ACOUSTIC PROPERTIES OF FIBROUS MATERIAL AND PERFORATION IMPEDANCE

While the acoustic impedance of perforations is crucial in predicting the performance of both reactive and dissipative silencers, the acoustic properties of the fibrous material are also important for accurate predictions in dissipative silencers. This section provides the complex characteristic impedance and wave number of fibrous material for $\rho_f = 100$ and 200 kg/m^3, and the acoustic impedance of perforations in contact with air alone and fibrous material. The details of the experimental setups and the procedures to measure such properties are presented elsewhere [Lee *et al.* (2006)].

A. Acoustic properties of fibrous material

The empirical complex characteristic impedance $\tilde{Z}$ $(=\tilde{\rho}\tilde{c})$ and the wave number $\tilde{k}$ of Delany and Bazley (1970) for fibrous materials have been widely used due to its simplicity. Although the Delany and Bazley formulation is well representative of the acoustic behavior of fibrous material in general, Lee *et al.* (2006) have experimentally determined the complex characteristic impedance and wave number of specific fibrous material since the process of data reduction for perforation impedance requires accurate (rather than somewhat representative) acoustic properties of the material in contact with the perforation. The form of Delany and Bazley, which is convenient for the fits, has been retained. The complex characteristic impedance and wave number based on the values averaged over five experiments are then expressed by

$$\frac{\tilde{Z}}{Z_0} = (1 - a_1 f^{-b_1}) - i a_2 f^{-b_2}, \tag{22}$$

$$\frac{\tilde{k}}{k_0} = (1 + a_3 f^{-b_3}) - i a_4 f^{-b_4}, \tag{23}$$

with the fit coefficients $a_1 - a_4$ and $b_1 - b_4$ given earlier (Lee *et al.*, 2006, Table I) for both filling densities of $\rho_f = 100$ and 200 kg/m^3. These empirical expressions are used next for the predictions of the TL of dissipative silencers.

B. Acoustic impedance of perforations

The specific acoustic impedance of perforations may be defined as

$$\zeta_p = \frac{R + i k_0 (t_w + \alpha d_h)}{\phi}, \tag{24}$$

where R is the nondimensional resistance, t_w the perforated duct wall thickness, and α the end correction coefficient. The empirical relationship of Sullivan and Crocker (1978) given in the same form of Eq. (24) as

$$\zeta_p = \frac{0.006 + i k_0 (t_w + 0.75 d_h)}{\phi} \tag{25}$$

has been widely used for the perforation impedance with air-air contact (air on both sides). This expression was obtained using perforations with $\phi = 4.2\%$. In Eq. (25), the coefficient 0.75 is associated with the end correction of the perforations and may vary as a function of distance among holes.

Eleven samples of circular plates studied by Lee *et al.* (2006) include variations in porosity ϕ (2.1, 8.4, 13.6, and 25.2%), wall thickness t_w (0.08 and 0.16 cm), and hole diameter d_h (0.249 and 0.498 cm). The same work has also provided the experimental results for R and α of the perforations facing an absorbent with $\rho_f = 100$ and 200 kg/m^3 as well as air alone, which are used next for the TL predictions of reactive and dissipative silencers.

IV. TRANSMISSION LOSS

The measured and predicted transmission losses of reactive and dissipative silencers are presented in this section. The details of the experimental setup are described elsewhere [Lee (2005)]. The acoustic properties of fibrous material and perforation impedance provided in Sec. III are incorporated

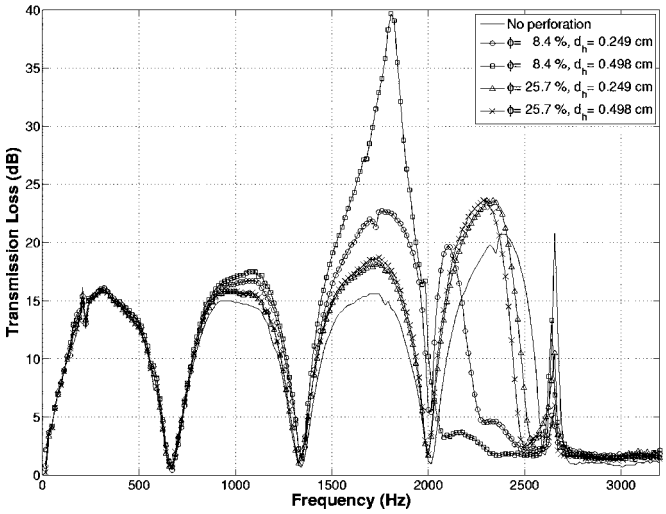

FIG. 2. The transmission loss of the perforated reactive silencer; experimental results.

into the BEM to obtain the TL of silencers. The experimental results for both reactive and dissipative silencers are presented next demonstrating the effect of porosity, hole diameter, and fiber filling density on the TL, followed by the comparison of these experiments with the BEM predictions for both silencers.

A. Experimental results

A cylindrical concentric perforated chamber with fixed outer dimensions (d_2=16.44 cm and L=25.72 cm in Fig. 1) is used for the TL measurements. The porosity and hole diameter of perforations along with the absorbent density are varied. Four perforated brass tubes with different porosities (ϕ=8.4 and 25.7%) and hole diameters (d_h=0.249 and 0.498 cm) are fabricated and mounted inside an expansion chamber. The inner diameter of the tubes is d_1=4.9 cm and the wall thickness is t_w=0.09 cm. The tubes are designed to have comparable distance between holes in both the axial and circumferential directions. The experimental results demonstrate next the effect of perforation impedance on the TL of both reactive and dissipative silencers, along with the impact of fibrous material.

Figure 2 shows the measured TL of the perforated reactive silencers with different duct porosities and hole diameters along with that of a simple expansion chamber. While the perforations do not affect the TL in the first dome, lower porosity, in general, increases the TL at the second and third domes. The impact from different hole diameters (d_h =0.249 and 0.498 cm) for the same ϕ is more significant for lower porosity (ϕ=8.4%) than for ϕ=25.7%. These reactive silencers are then used as baselines for the dissipative silencers, with the filling densities of ρ_f=100 and 200 kg/m^3 in the outer chamber.

Figure 3 shows the experimental results for dissipative silencers with different duct porosities (ϕ=8.4 and 25.7%), hole diameters (d_h=0.249 and 0.498 cm), and filling densities (ρ_f=100 and 200 kg/m^3) along with those of perforated reactive silencers. Filling the chamber with fibrous material dramatically changes the TL from a multi-dome behavior to

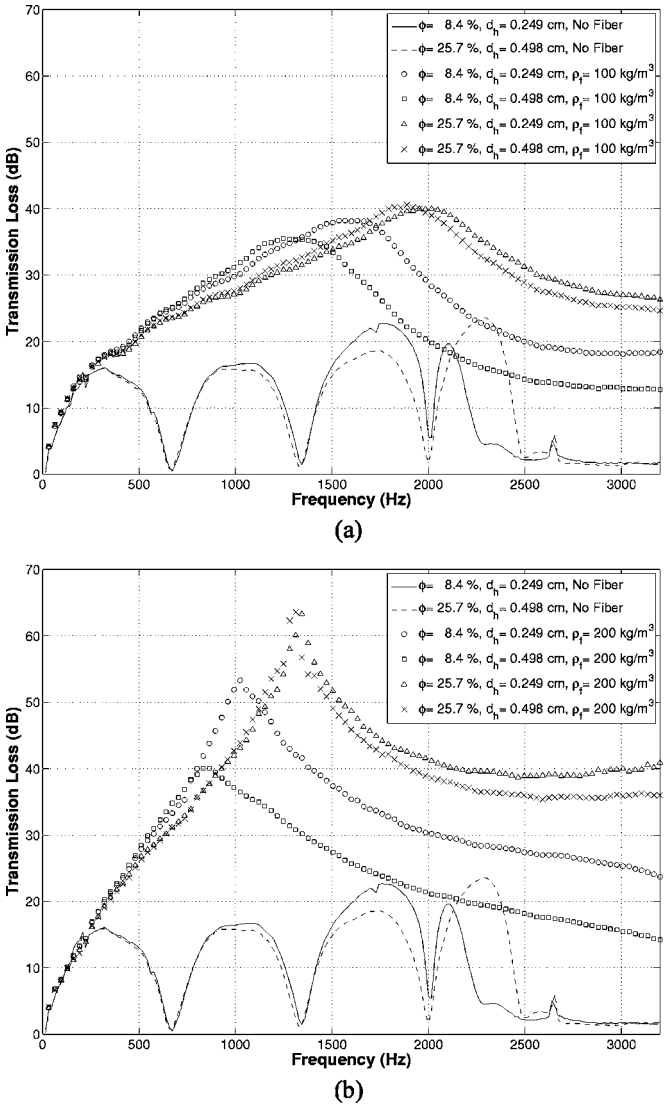

FIG. 3. The transmission loss of the perforated dissipative silencer; experimental results; (a) ρ_f=100 kg/m^3 and (b) ρ_f=200 kg/m^3.

a single peak with substantially higher attenuation except at low frequencies, illustrating the effectiveness of absorbent. Figure 3 also demonstrates the dependence of the TL of dissipative silencers on ϕ, ρ_f, and d_h. Thus, the understanding of the effects of such parameters on the TL is important for the predictions and design of dissipative silencers. Higher filling density (ρ_f=200 kg/m^3) generally increases the magnitude of peak TL and shifts the peak locations to lower frequencies compared to ρ_f=100 kg/m^3. For both filling densities, the impact of hole diameter is more significant for low porosity (ϕ=8.4%) than for high porosity (ϕ=25.7%). For low porosity (ϕ=8.4%), the filled silencers with large hole diameter (d_h=0.498 cm) exhibit, in general, lower TL than those with small hole diameter (d_h=0.249 cm). However, the hole diameter impact for silencers at high porosity (ϕ=25.7%) appears to diminish.

B. Comparison of experiments and BEM predictions—reactive silencers

By comparing the TL from experiments and predictions, this section provides an assessment of the acoustic imped-

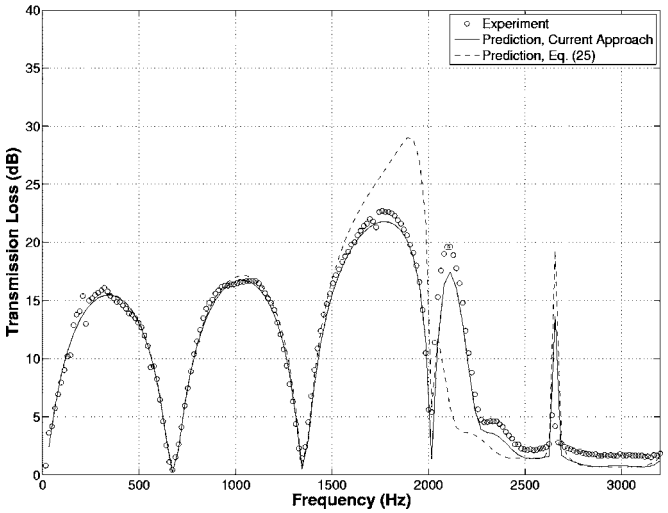

FIG. 4. The transmission loss of the perforated reactive silencer (ϕ=8.4%, d_h=0.249 cm); predictions vs measurements.

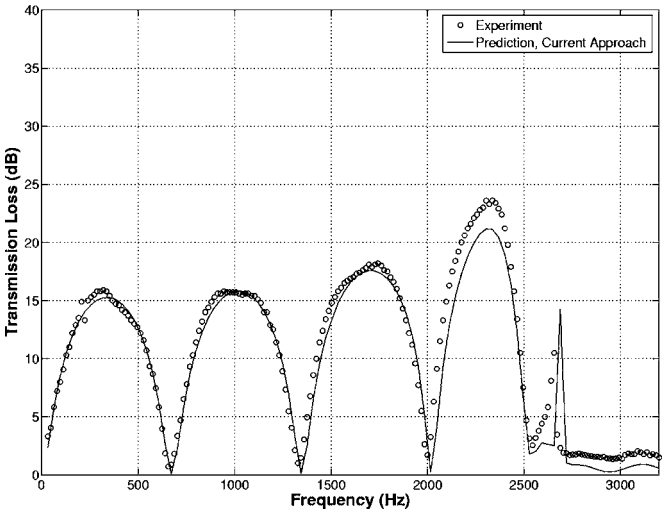

FIG. 6. The transmission loss of the perforated reactive silencer (ϕ =25.7%, d_h=0.249 cm); predictions vs measurements.

ance of perforations measured by Lee *et al.* (2006) in contact with air only. The porosities and hole diameters of the main ducts are close to those of the flat circular perforation samples used for the measurement of perforation impedance. The TL measured using the impedance tube setup is compared next with the predictions using the perforation impedance of Sullivan and Crocker (1978) and Lee *et al.* (2006).

The measured and predicted TL of perforated reactive silencers with ϕ=8.4% and hole diameters d_h=0.249 and 0.498 cm are presented in Figs. 4 and 5, respectively. The perforation impedance of Eq. (24) along with Table III of Lee *et al.* (2006) (hereafter referred to as the current approach) and Eq. (25) (Sullivan and Crocker, 1978) are used for the predictions. The BEM predictions using the current approach show an improved agreement with experiments compared to those using Eq. (25). Figure 6 presents the comparison of the measurements with the predictions for ϕ =25.7% and d_h=0.249 cm using only the current approach since Eq. (25) based on ϕ=4.2% may be less suitable for such high porosities. The BEM predictions show a reasonably good agreement with the experiments.

Figure 7 shows the experimental and predicted results of TL with different hole spacings, depicted in Fig. 8, while retaining the same porosity (ϕ=8.4%) and the hole diameter (d_h=0.249 cm). The unequal spacing between holes tends to increase the peak attenuation compared to the one with nearly equal spacing. The noticeable effect of the spacing illustrates the difficulty in obtaining a generalized perforation impedance for various porosity, and the hole size and shape.

C. Comparison of experiments and BEM predictions—dissipative silencers

BEM is used next for the TL predictions of dissipative silencers, along with the complex characteristic impedance and wave number and perforation impedance given in Sec. III. For ϕ=8.4 and 25.7%, Figs. 9 and 10, respectively, compares the TL from predictions and experiments for silencers

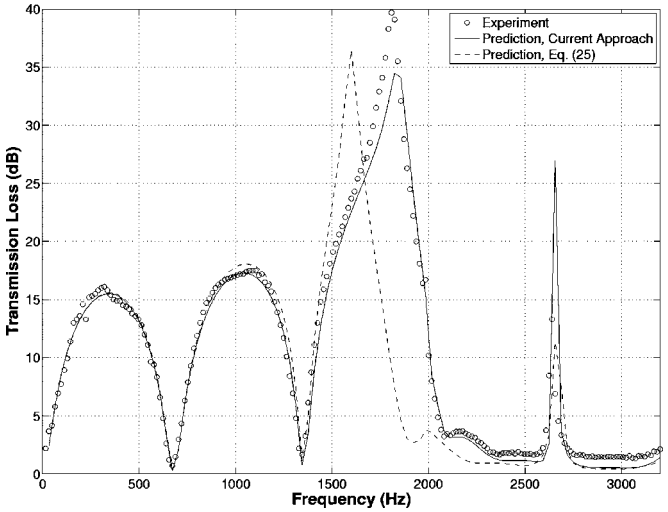

FIG. 5. The transmission loss of the perforated reactive silencer (ϕ=8.4%, d_h=0.498 cm); predictions vs measurements.

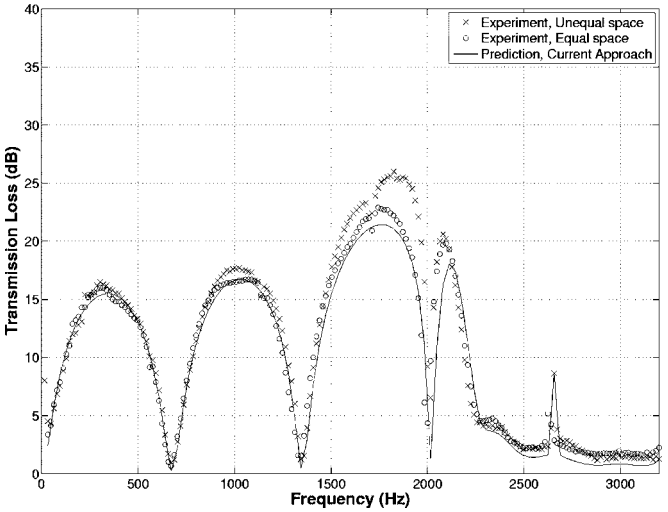

FIG. 7. The effect of hole spacing on the transmission loss of a perforated reactive silencer (ϕ=8.4%, d_h=0.249 cm); predictions vs measurements.

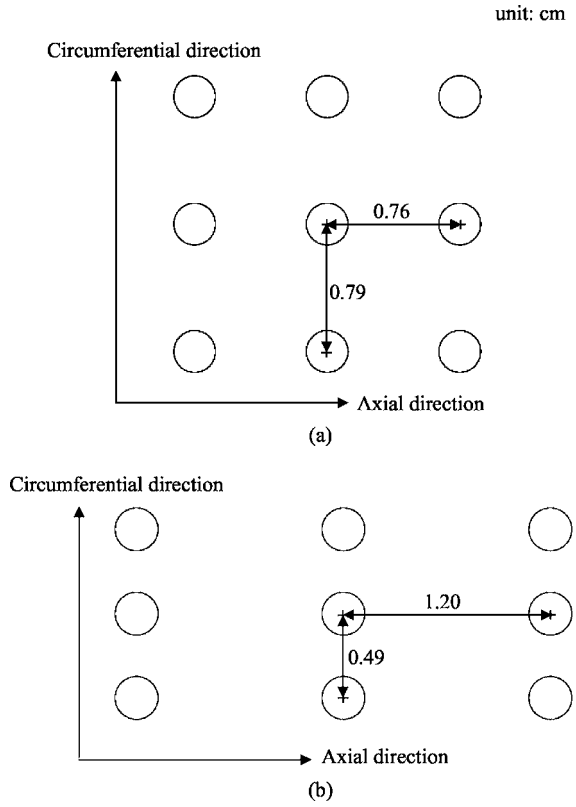

FIG. 8. The distances between holes for two different perforated ducts (ϕ =8.4%, d_h=0.249 cm); (a) equal spacing and (b) unequal spacing.

with d_h=0.249 cm and filling densities of ρ_f=100 and 200 kg/m^3. The predictions in Fig. 9 (ϕ=8.4%) show a good agreement with the experiments except near the peak TL for ρ_f=200 kg/m^3. Figure 10 (ϕ=25.7%) exhibits a reasonable overall agreement along with some deviations from the experiments at high frequencies. The deviations at higher filling densities and/or porosity may be attributed to the effect of variation in fiber filling conditions on the perforation impedance.

The acoustic impedance of perforations in contact with air-air has often been used in the predictions for dissipative

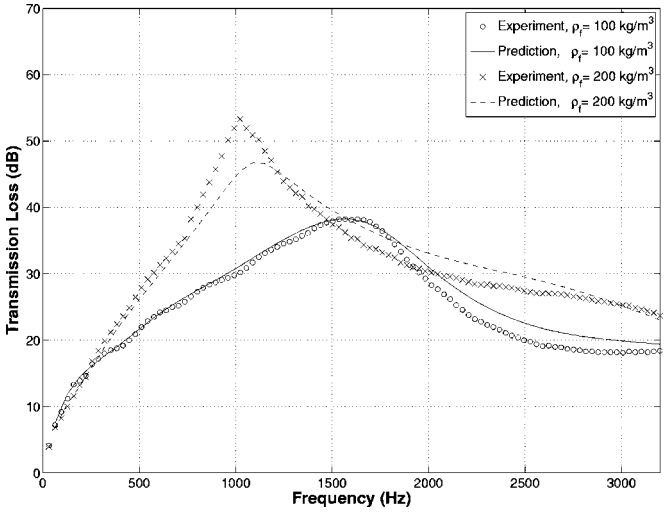

FIG. 9. The transmission loss of the perforated dissipative silencer (ϕ =8.4%, d_h=0.249 cm); predictions vs measurements.

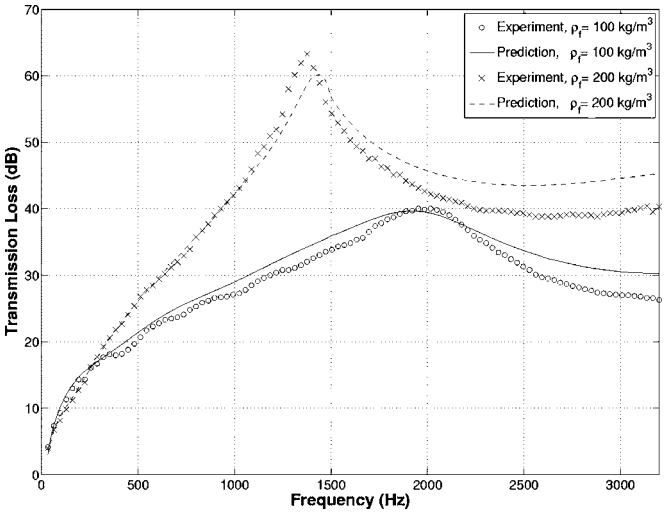

FIG. 10. Transmission loss of the perforated dissipative silencer (ϕ =25.7%, d_h=0.249 cm); predictions vs measurements.

silencers due to lack of information on perforations in contact with the fibrous material. Figure 11 shows the comparisons of experiments with the predictions using the perforation impedance with air-air and air-absorbent of the current approach. While the predictions using the impedance of perforations facing air-fibrous material show a good agreement with the experiments, those employing the perforation impedance with air alone exhibit a substantial deviation from the measurements particularly at high filling densities and frequencies. Thus, Fig. 11 illustrates the importance of appropriate perforation impedance in accurate predictions for dissipative silencers. That is, the substantial increases of both the resistance R and end correction coefficient α due to the contact with the fibrous material need to be incorporated into the predictions of dissipative silencers. The predictions from the heuristic method of Kirby and Cummings (1998) by employing the acoustic properties measured by Lee *et al.* (2006) are also provided in Fig. 11, showing a reasonable agreement with the experiments. This comparison, therefore, suggests that their method, with known acoustic impedance of perforations in contact with air-air and absorbent properties, is capable of capturing the effect of absorbing material on the perforation impedance in dissipative silencers.

V. CONCLUSIONS

The acoustic properties of fibrous material and perforation impedance measured in the experiments have been integrated, in the present study, into the BEM predictions of TL for silencers. First, the measured TL of reactive perforated silencers with different porosities (ϕ=8.4 and 25.7%) and hole diameters (d_h=0.249 and 0.498 cm) are presented illustrating the effect of such parameters on the TL. The reactive silencers are then filled with fibrous material with different densities (ρ_f=100 and 200 kg/m^3). The experimental results show that the use of fibrous material significantly increases the TL, except at low frequencies, changing its shape from multi-dome to a single resonance type. The peak frequency and magnitude of the TL are significantly affected by different filling densities of the material.

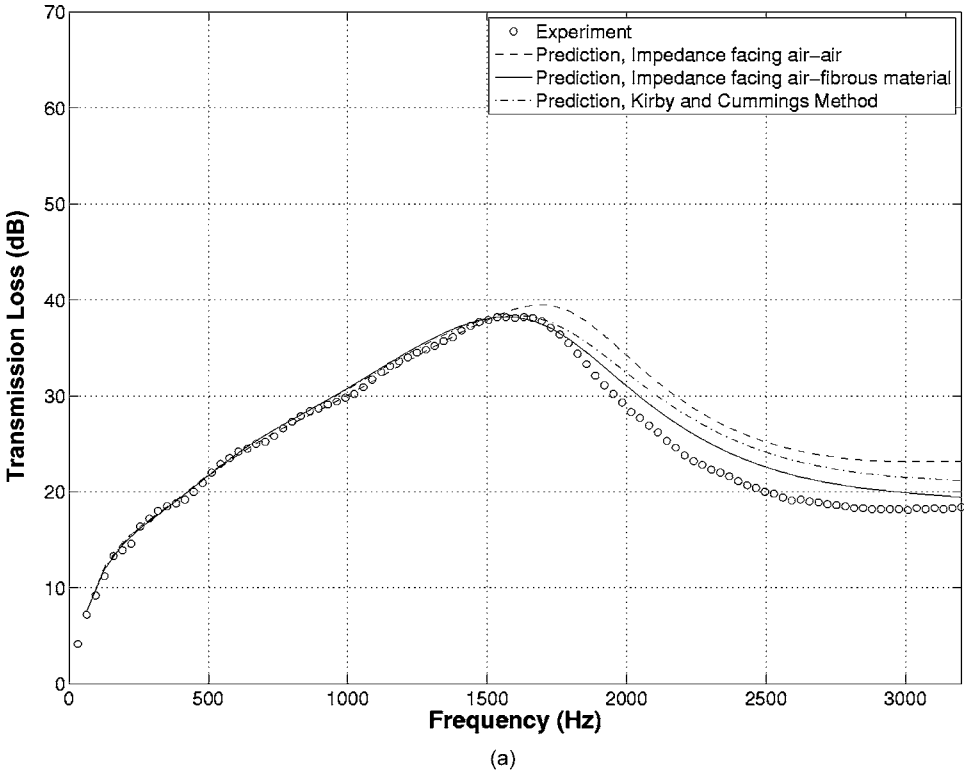

(a)

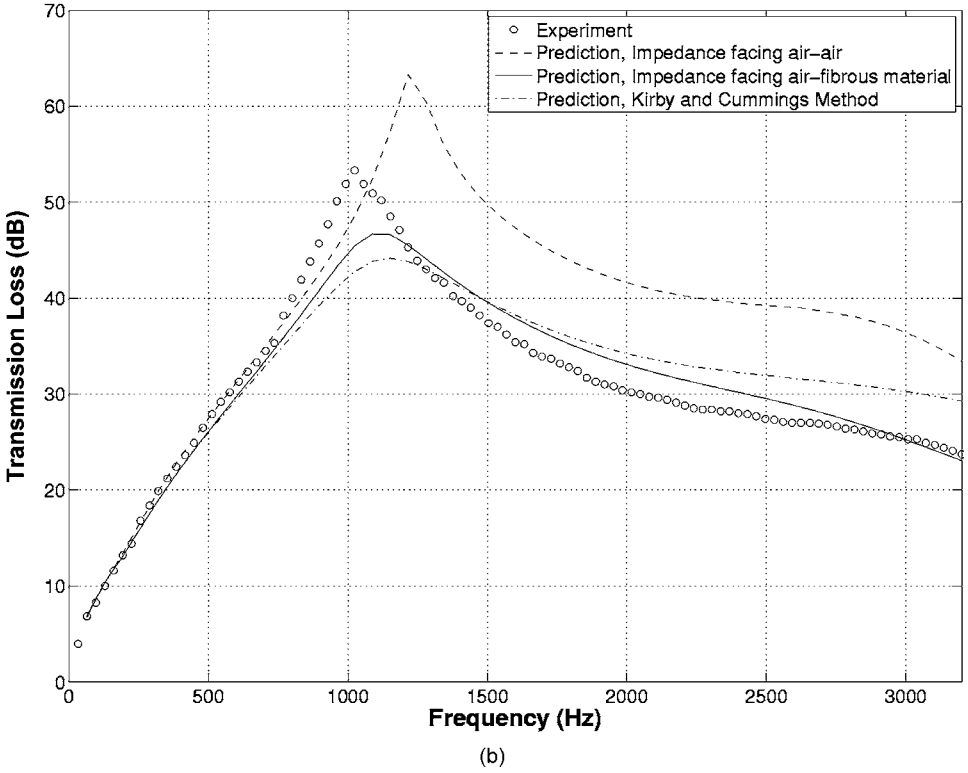

(b)

FIG. 11. The effect of perforation impedance on the transmission loss of the perforated dissipative silencer (ϕ =8.4%, d_h=0.249 cm): predictions vs measurements; (a) ρ_f=100 kg/m^3 and (b) ρ_f=200 kg/m^3.

The measured TL of reactive silencers is then compared with the predictions using different perforation impedances. The perforation impedance given by Lee *et al.* (2006) for reactive silencers leads to a good agreement with the measurements. The experimental and numerical results illustrate that the effect of different hole diameters (with the same porosity) on the TL is more significant at lower duct porosities. Varying relative distances between the holes are also observed to affect the TL of the reactive silencer with the same porosity and hole diameter.

The measured TL of dissipative silencers is also compared with the predictions which incorporate the acoustic properties of fibrous material and perforation impedance measured by Lee *et al.* (2006), exhibiting a satisfactory

agreement with the experiments. It should be noted that the acoustic impedance of perforations has been developed thus far with specific fibrous material used in the present study, and additional measurements may be necessary for a perforation facing an absorbent with substantially different acoustic properties and/or filling density.

Nomenclature

$a_{1,2,3,4}, b_{1,2,3,4}$ = coefficients of wave number and characteristic impedance of fibrous material
c_0 = speed of sound in air
$\tilde{c}$ = complex speed of sound in the absorbing material
C_i = edge point coefficient
d_1 = main duct diameter
d_2 = outer chamber diameter
d_h = perforate hole diameter
f = frequency
$[G], [G'], [H]$ = boundary element coefficient matrices
$[I]$ = the identity matrix
i = imaginary unit $(=\sqrt{-1})$
$\tilde{k}$ = complex wave number in the absorbing material
k_0 = wave number in air
L = silencer length
$\boldsymbol{n}$ = unit outward normal vector to the acoustic domain surface
p = acoustic pressure
p_1 = acoustic pressure in domain 1
p_2 = acoustic pressure in domain 2
R = resistance of perforation impedance
t_w = wall thickness of perforated duct
T_{ij} = transfer matrix elements
$[TC]$ = impedance matrix of domain I (main duct)
$[TD]$ = impedance matrix of domain II (chamber)
$[TI]$ = impedance matrix of silencer
TL = transmission loss
u_1 = particle velocity which is outward normal to the boundary surface of domain 1
u_2 = particle velocity which is outward normal to the boundary surface of domain 2
V = acoustic domain volume
x, y, z = coordinate axes
x_i, y_i, z_i = coordinate of ith node point
Z_0 = $\rho_0 c_0$, characteristic impedance of air
$\tilde{Z}$ = $\tilde{\rho}\tilde{c}$, complex characteristic impedance of the absorbing material
α = end correction coefficient of perforation impedance
δ = Dirac delta function
ϕ = duct porosity
Γ = boundary surface
Γ_j = boundary surface of jth discrete acoustic domain
ρ_0 = density of air
ρ_f = filling or bulk density of fibrous material
$\tilde{\rho}$ = effective density of the absorbing material
ζ_p = nondimensionalized acoustic impedance of a perforated duct in contact with air alone
$\tilde{\zeta}_p$ = nondimensionalized acoustic impedance of a perforated duct in contact with fibrous material
∇ = del operator

Superscript

i = inlet
o = outlet
p = perforations

Cummings, A. (**1976**). "Sound attenuation in ducts lined on two opposite walls with porous material, with some applications to splitters," J. Sound Vib. **49**, 9–35.

Cummings, A., and Chang, I.-J. (**1988**). "Sound attenuation of a finite length dissipative flow duct silencer with internal mean flow in the absorbent," J. Sound Vib. **127**, 1–17.

Delany, M. E., and Bazley, E. N. (**1970**). "Acoustical properties of fibrous absorbent materials," Appl. Acoust. **3**, 105–116.

Eriksson, J. J., Thawani, P. T., and Hoops, R. H. (**1983**). "Acoustics design and evaluation of silencers," Sound Vib. **17**, 20–27.

Kirby, R. (**2001**). "Simplified techniques for predicting the transmission loss of a circular dissipative silencer," J. Sound Vib. **243**, 403–426.

Kirby, R. (**2003**). "Transmission loss predictions for dissipative silencers of arbitrary cross section in the presence of mean flow," J. Acoust. Soc. Am. **114**, 200–209.

Kirby, R., and Cummings, A. (**1998**). "The impedance of perforated plates subjected to grazing gas flow and backed by porous media," J. Sound Vib. **217**, 619–636.

Lee, I.-J. (**2005**). "Acoustic characteristics of perforated dissipative and hybrid silencers," Ph.D. Dissertation (The Ohio State University, Columbus, OH).

Lee, I.-J., Selamet, A., and Huff, N. T. (**2006**). "Acoustic impedance of perforations in contact with fibrous material," J. Acoust. Soc. Am. **119**, 2785–2797.

Luo, H., Tse, C. C., and Chen, Y. N. (**1995**). "Modeling and applications of partially perforated intruding tube mufflers," Appl. Acoust. **44**, 99–116.

Munjal, M. L. (**1987**). *Acoustics of Ducts and Mufflers* (Wiley, New York).

Peat, K. S., and Rathi, K. L. (**1995**). "A finite element analysis of the convected acoustic wave motion in dissipative silencers," J. Sound Vib. **184**, 529–545.

Selamet, A., Lee, I.-J., Ji, Z. L., and Huff, N. T. (**2001**). "Acoustic attenuation performance of perforated concentric absorbing silencers," SAE Noise and Vibration Conference and Exposition, April 30–May 3, Traverse City, MI, SAE Paper 2001-01-1435.

Sullivan, J. W. (**1979**). "A method for modeling perforated tube muffler components. I. Theory," J. Acoust. Soc. Am. **66**, 772–778.

Sullivan, J. W., and Crocker, M. J. (**1978**). "Analysis of concentric-tube resonators having unpartitioned cavities," J. Acoust. Soc. Am. **64**, 207–215.

Thawani, P. T., and Jayaraman, K. (**1983**). "Modeling and applications of straight-through resonators," J. Acoust. Soc. Am. **73**, 1387–1389.

Wang, C.-N., and Liao, C.-Y. (**1998**). "Boundary integral equation method for evaluating the performance of straight-through resonator with mean flow," J. Sound Vib. **216**, 281–294.

A laboratory investigation of noise reduction by riblike structures on the ground

Hocine Bougdah,[a] Inan Ekici,[b] and Jian Kang[c]
Canterbury School of Architecture, University for the Creative Arts at Canterbury, New Dover Road, Canterbury, Kent CT1 3AN, United Kingdom

(Received 13 March 2006; revised 28 September 2006; accepted 2 October 2006)

This paper investigates the use of periodically spaced edges or wells for the control of road traffic noise. The wells have uniform height and width and are placed on the ground. Physical scale modeling is used to assess the acoustic performance of these structures under laboratory conditions. It is shown that, in certain situations where the use of conventional barriers would not be appropriate, strategically designed riblike structures can provide insertion losses of typically 10–15 dB. The findings are explained in terms of acoustic scattering with the approaches used in the study of resonators and diffraction/interference gratings. © *2006 Acoustical Society of America.*
[DOI: 10.1121/1.2372594]

PACS number(s): 43.50.Gf, 43.50.Lj, 43.50.Rq [KA] Pages: 3714–3722

I. INTRODUCTION

Environmental noise barriers are commonly used as a means of controlling road traffic noise. There are many barrier profiles which have been designed to utilize various physical phenomena for achieving noise reductions. A comprehensive review of various types of barriers has been undertaken by Ekici and Bougdah.[1]

Tilted reflective barriers reflect the noise towards relatively less harmful directions and avoid reverberant build-up of noise in the case of multiple barrier situations. This can also be achieved by the use of vertical barriers with absorptive faces which absorb the sound energy incident on the barrier surface rather than reflecting it. The use of absorbing materials has also been considered around the tops of barriers to reduce the sound diffracted into the shadow zone. Noise barriers with multiple diffracting edges have been shown to provide beneficial noise reductions too. The barrier types described above have been commonly used in practice. Further account of different barrier profiles is given elsewhere.[2–4]

An alternative noise barrier type, which has been shown to provide substantial noise reduction, consists of so-called acoustically soft pressure release surfaces mounted on top of conventional barriers. Van der Heijden and Martens[5] investigated the use of a series of wells on the ground for reducing traffic noise. The noise reductions were explained to be due to surface wave exclusion. Various similar applications consisted of a series of tubes mounted on top of conventional barriers with horizontal[6] and cylindrical caps.[7] The depth of these tubes corresponded to the quarter wavelength of the frequency which was targeted.

Experimental studies on near-grazing propagation of sound over theatre seating have shown large attenuations at low frequencies.[8,9] This paper explores further the parameters studied previously. However the geometrical setup relates to situations that could arise in environmental noise where the receivers are set back from the noise reducing surfaces. The attenuations at mid to high frequencies are important and any noise reducing device has to operate within a finite space.

Conventional "wall type" barriers are subject to various nonacoustical constraints, two of which are structural limitations and visual impact on environment. A series of low height edges used to control road traffic noise, minimize structural loading, and reduce visual impact are investigated in this paper. This paper starts with a short review and discussion of the theoretical concepts that are likely to influence the acoustic behavior of riblike structures. This is followed by a description of the experimental method used to investigate the performance of these structures. The paper then presents the results of the investigation and puts them in the context of the theories behind the acoustic performance of such structures.

II. ACOUSTIC BEHAVIOR OF RIBLIKE STRUCTURES

The noise attenuation and amplification achieved by riblike structures can be explained by a number of mechanisms. In addition to the long wave scattering effects and diffraction effects, surface wave generation mechanisms and interference effects all appear to play a certain part.

The discussion below reviews how various mechanisms could influence the performance of riblike structures and identifies the relevant physical parameters. The findings of this discussion, in turn, would inform the experimental model described in the forthcoming sections.

A. Quarter-wave resonators

The theory of quarter wavelength resonance may be a contributing phenomenon to scattering. A quarter-wave resonator can be thought of as a cavity closed at one end and open at the other. Under certain conditions the body of air

[a]Electronic mail: hbougdah@ucreative.ac.uk; Tel: 00441227817393; Fax: 00441227817500.
[b]Electronic mail: Inan.Ekici@atkinsglobal.com
[c]Electronic mail: j.kang@sheffield.ac.uk

 © 2006 Acoustical Society of America

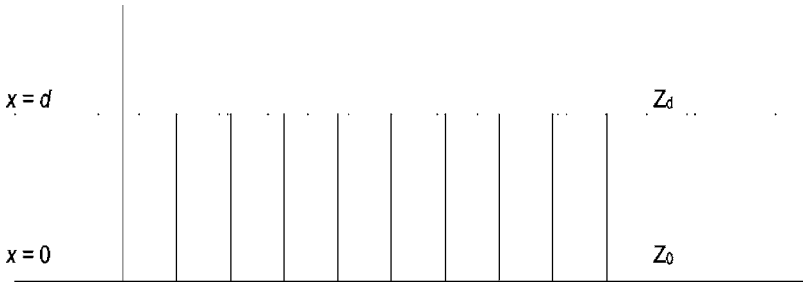

FIG. 1. A series of quarter-wave resonators.

confined within the cavity can be brought to a state of resonance.[10] It is assumed that the walls and the closed end of the channels shown in Fig. 1 are rigid and they are sufficiently wide for viscous and thermal conduction effects to be negligible.[6]

At resonance the reactive component of the impedance Z_d becomes zero and the input impedance of the resonator has been shown to be[11]

$$Z_d = \frac{\frac{\rho_o c}{S}\left(Z_o - j\frac{\rho_o c}{S}\tan kd\right)}{\frac{\rho_o c}{S} - jZ_o \tan kd}, \tag{1}$$

where Z_o is the impedance of the rigid end (Pa s/m^3), Z_d is the impedance of the open end (Pa s/m^3), k is the wave number, $k=2\pi/\lambda$ (1/m), S is the cross-section area of the resonator (m^2), ρ_o is the density of air (kg/m^3), c is the sound velocity in air (m/s). Assuming rigid end termination ($Z_0=\infty$), the specific input impedance of the open side of a rigid rectangular channel can be represented approximately as

$$Z_{in} = i\cot(kd). \tag{2}$$

According to Eq. (2), ($Z_{in}=0$), would correspond to a pressure release surface if

$$d = (2n+1)\frac{\lambda}{4}, \tag{3}$$

where $n=0,1,2$, and so on. Therefore, at well depths corresponding to odd multiples of the quarter wavelength of a sound, a surface could be considered to be a pressure release or reactive surface.

However, in all practical cases some resistive components will exist.[6] The specific input impedance of a surface would therefore depend on the nature of the components, as well as the depth of the wells and the wavelength of sound. This approach does not take into account the width of the wells, or the nature of edges. The theory of diffraction gratings is used below to explain the effects of some of other parameters.

B. Diffraction gratings

For the purpose of this paper, a diffraction grating is defined as a collection of reflecting elements, separated by a distance comparable to the wavelength of sound wave under consideration. A sound wave incident on a regularly spaced grating will, upon diffraction, have its amplitude, or phase, or both, modified in a predictable manner.[12] When a sound wave, with a wavelength λ, is incident on a grating surface, it is diffracted into discrete directions as shown in Fig. 2, where α is the angle of incidence, β is the angle of diffraction, m is the order of diffraction ($=0,\pm1,\pm2$, etc.), w is the horizontal spacing between diffracting elements.

The angles are measured from the grating normal which is perpendicular to the grating surface at its center. The sign convention for these angles is that those to the left of the grating normal (anticlockwise) are positive and the ones to the right (clockwise) are negative. The zero diffraction order ($m=0$) represents specular reflection. The positive diffraction

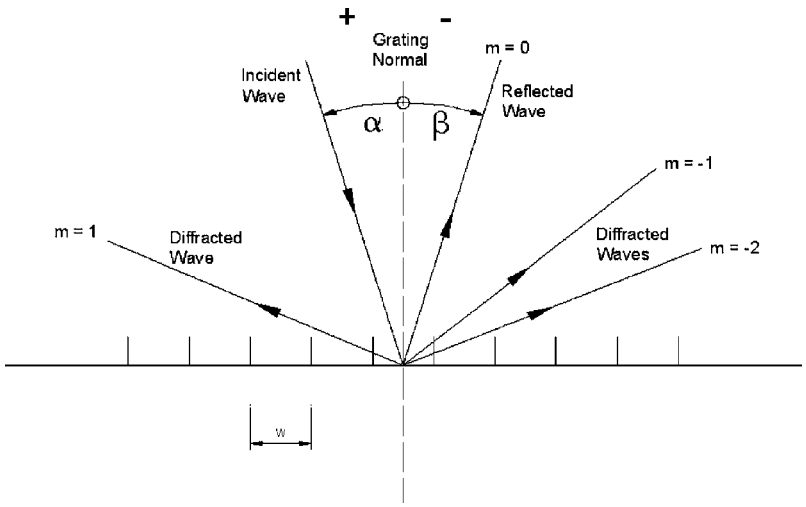

FIG. 2. A typical diffraction grating.

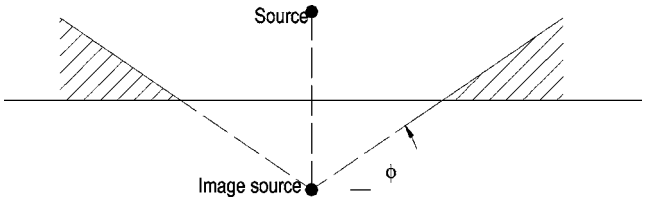

FIG. 3. Existence criteria for surface waves.

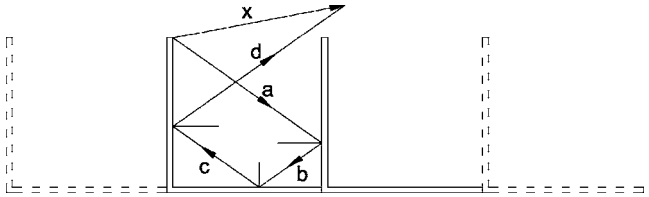

FIG. 4. Reflections within a well.

orders appear at the same side of the normal as the incident wave and the negative orders lie on the opposite side.

The diffracted wave front is formed by contributions from individual diffracting elements, each of which acts as a point source. These contributions can yield constructive and destructive interference patterns at varying diffraction angles.

The geometrical path difference δ between an incident and reflected plane wave from adjacent elements can be expressed as $\sin\alpha+\sin\beta$. For constructive interference the diffracted rays from the adjacent elements should be in phase and therefore the path length difference should equal the wavelength or its integral multiples. At all other angles, there will be some measure of destructive interference between the wavelets originating from the groove facets. These relationships are expressed by the grating equation.

Constructive interference can be defined by

$$m\lambda = w(\sin\alpha + \sin\beta). \tag{4}$$

Since the maximum possible value of $\sin\alpha+\sin\beta$ is 2, for a particular wavelength λ, all values of m for which $|m\lambda/w|<2$ would correspond to physically realizable diffraction orders.

The maximum value of destructive interference can similarly be expressed as appearing when

$$\frac{m\lambda}{2} = w(\sin\alpha + \sin\beta) \tag{5}$$

In the above grating equations the diffraction pattern is independent of the shape of the diffracting elements. In reality, however, the intensity of a general grating is proportional to a diffraction factor and an interference factor.[13] These take into account properties of the individual diffracting elements of the grating as well as the total number of diffracting elements. Different shapes of diffracting elements have been investigated by Boulanger *et al.*[14] They observed a shift in the measured spectra to lower frequencies than that expected for a smooth acoustically hard surface. A surface wave generation mechanism could be responsible for this.

C. Surface waves

Surface wave propagation has been investigated by model[15] and outdoor[16] experiments. These waves exist between the flat ground and a conical surface as shown in Fig. 3.[17] The apex of the cone coincides with the image source position. The hatched zone indicates the area where surface waves are possible. The value of the incidence angle ϕ which defines the extent of this zone can be expressed as follows:

$$\sin(\phi) < \frac{[\mathrm{Im}(Z_s) - \mathrm{Re}(Z_s)]}{|Z_s|^2}. \tag{6}$$

For grazing incidence wave with $\phi=0$, this general condition requires only that the imaginary part $\mathrm{Im}(Z_s)$ of the surface impedance exceed the real part Re (Z_s). This criterion also applies to the existence of surface waves for propagation of near-grazing incidence of plane waves traveling over an impedance ground.

The surface impedance Z_s of a thin homogeneous layer of thickness d, situated over a rigid semi-infinite backing, can be written in terms of characteristic impedance Z_c as follows:

$$Z_s = Z_c \coth(-ik_b \cdot d), \tag{7}$$

where k_b is the acoustic propagation constant for layer media. According to the "thin layer model" approach, increasing the height of the edges would effectively increase the thickness of the layer.

The significant effect of surface waves, therefore, would be expected at low frequencies for the lowest flow resistivities due to greater reactive components (i.e., imaginary component) of surface impedance for a hard-backed layer model for the ground. As the source height becomes lower or as the number of edges becomes higher, the likelihood of generating surface waves would also increase. These would make the potential improvements due to a series of edges less apparent, or even negative, over certain frequencies.[6]

D. Interference effects within the grooves

The interference between diffracted and reflected waves within the grooves (wells) is another likely mechanism which defines attenuation maxima and minima. Typical reflection paths within a single well are shown in Fig. 4. The direct path is represented by path x and the multiple reflections are indicated by the path $\boldsymbol{a}$, $\boldsymbol{b}$, $\boldsymbol{c}$, and $\boldsymbol{d}$. This particular diagram shows only 3 reflection paths however a number of alternative path diagrams would be possible for this geometry.

Over a hard ground, attenuation maxima (destructive interference) would occur at frequencies corresponding to path length differences δ_x which are odd multiples of half-wavelength. These frequencies can be represented as follows:

$$\delta_x = (2n+1)\frac{\lambda}{2}, \tag{8}$$

where $n=0,1,2$, etc. Similarly, an attenuation minimum (constructive interference) would be expected to occur at fre-

quencies corresponding to path length differences δ_x which are even multiples of half-wavelength. This can be represented as shown below,

$$\delta_x = (2n)\frac{\lambda}{2}, \tag{9}$$

where $n=0,1,2$, etc. The interference effects could manifest themselves in the forms of peaks (maxima and minima) in the insertion loss spectra. The relative positions of these peaks could indicate if these are due to interference effects between direct and multiple-reflected (within the well) ray paths.

E. Overall effects

The discussion above highlighted four mechanisms which could be used in explaining attenuations and amplifications achieved by riblike structures. In certain situations, the wavelength at which the maximum noise attenuations occur would be expected to correspond to four times the well depth. At grazing incidence, this could define the lowest limit of noise attenuations. Long wave scattering effects would be the main noise attenuation mechanism at these frequencies. At higher frequencies, diffraction effects could become the dominant mechanism. Interference effects between direct and multiple-reflected (within the grooves) paths can cause constructive and destructive interference peaks at certain frequencies. On the other hand, at frequencies lower than the limiting frequency, noise amplifications could occur due to surface wave generation mechanisms.

A number of physical parameters have been found to influence noise propagation over rib structures, as listed below:

- wavelength of the incident wave, λ
- well depth, d
- total number of diffracting elements
- well width, w
- source and receiver locations
- nature of the individual diffracting elements
- overall distance covered by diffracting elements

The likely effects of the four mechanisms and parameters identified above will be investigated using a number of physical scale models.

III. EXPERIMENTAL METHOD

The experimental investigation into the performance of riblike structures was carried out in a semi-anechoic chamber 3 m long $\times$3 m wide $\times$2.75 m high. Aluminum sheets used to simulate reflective ground surfaces were 2 mm thick, and the edges used to simulate riblike structures with reactive surfaces consisted of 1 mm thick aluminum angles.

The modeling scale was 1:10. The frequency range at which the testing was carried out was 1 600 Hz–12 500 Hz at 1/3 octave band intervals, corresponding to full scale frequencies in the range between 160 Hz and 1250 Hz. This frequency range represents the lower and peak frequencies of a typical A-weighted road traffic noise spectrum where noise attenuation in practice is more difficult to achieve compared with the higher frequency end. The air absorption correction was not applied in this study, given that the frequency range was relatively low, the distances were small, and the analysis focused mainly on relative comparisons. In this paper full scale dimensions and frequencies are reported throughout, except where indicated.

TABLE I. Directivity characteristics of the source.

Frequency (kHz)	1.6	2	2.5	3.15	4	5	6.3	8	10	12.5
Directivity index (dB)	2	2	2.8	3.5	3.7	3.9	4.1	6.7	4.5	9.2

The noise source was a small sized tweeter speaker connected to a white noise generator through an amplifier. The source approximated to a "point source." Although not investigated as part of this paper, a more accurate 2D system can be obtained by the use of a "line source." The noise output was kept constant throughout the test. The directivity characteristics of the source in the frequency of interest are shown in Table I. The physical center of the source was 0.4 m above the ground. The receiver was a $\frac{1}{2}$ in. microphone connected to a B&K 2260 sound level meter.

The background sound pressure levels (SPL) were less than 10 dB at the frequency range of interest. The signal levels varied between 50 dB and 85 dB depending on the setup, receiver position, and the frequency. The signal levels were monitored at the receiver positions under consideration and at a reference point which was 0.3 m (1:10 scale) from the source and remained the same in all tests to enable comparisons between different configurations. The SPL with the configurations under consideration were monitored and compared with those for a single or no edge cases, as appropriate.

The investigation consisted of three sets of experiments. In the first set of tests described in Sec. IV A, the effects of multiple edges situated on the ground were studied. A single edge consisting of a 90° aluminum angle with dimensions of 0.25 m $\times$ 0.25 m was first placed between the source and the receiver at a distance of 5 m from both. The progressive increase in the number of edges from 1 to 17 was then investigated at a single receiver location. The maximum width of the barrier was 4 m. This receiver position was chosen such that the line-of-sight from the physical center of the source to the receiver was grazing the top of the edge. This ensured the subsequent addition of edges in the direction of the receiver did not affect the path length of the sound. The geometrical configuration and results for this setup are presented in Sec. IV A.

The second set of experiments investigated the effects of a riblike structure at a number of receivers with different vertical heights without varying the horizontal separation between source and receiver or modifying the edge configuration. This geometry was intended to look at the effect of attenuations or amplifications at different diffraction angles. In these experiments, a riblike structure consisting of 21 edges spaced at 0.08 m and a height of 0.17 m was used. The width of the barrier was 1.6 m. Seven receivers were horizontally situated 12 m from the source (or 7 m from the edge nearest to source), at heights between 0 m and 3 m above the ground and spaced at 0.5 m increments above each other.

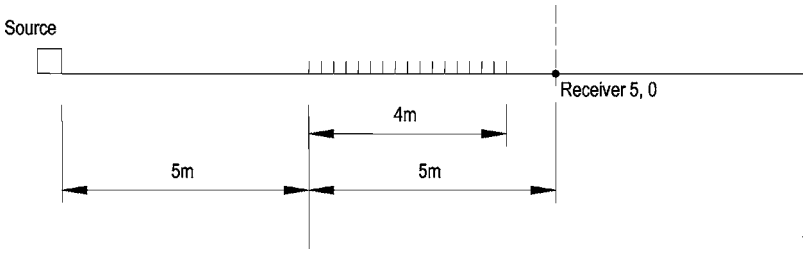

FIG. 5. Experimental setup for investigating the effect of progressive increase in the number of edges.

SPL measurements were made at each receiver location for no edge, single edge, and 21 edge configurations, respectively. The results are described in Sec. IV B.

The third set of experiments, described in Sec. IV C, used three different well depths to identify the effect of these on the lowest frequency at which attenuation occurs. In these experiments 14 edges and three different combinations of edge height and spacing were used at six different receiver locations, two distances, and three heights as before. The width of barriers varied between 1 m and 3.25 m depending on the setup.

IV. RESULTS

This section will present the results of the experimental investigation for all three sets of experiments.

A. Progressive increase in the number of edges

As previously stated, the objective of this experiment is to investigate the effects of progressive addition of edges, at a typical receiver. The basic geometry is shown in Fig. 5. The depth of wells in this experiment is 0.25 m. Maximum attenuations would be expected at the wavelength which corresponds to four times the well depth as discussed before, namely $\lambda = 1$ m and $f = 340$ Hz. Figure 6 shows the SPL for the various geometric configurations ranging from 1 to 17 edges.

Above about 315 Hz, the SPL is gradually reduced with increased number of edges. Between 400 Hz and 1250 Hz, the reductions in SPL due to the 17-edge case are between 17 dB and 26 dB which is rather significant. At lower frequencies, the addition of further edges increases the SPL by up to 4 dB. This could be due to surface wave generation discussed earlier. At 250 Hz the 8-edge configuration achieves the maximum sound reduction and the addition of subsequent edges led to an increase in the SPL. At 315 Hz, the addition of 4 edges achieved most of the reductions and the remaining edges up to 17 did not contribute substantially to the overall noise reduction at this frequency band.

This receiver is situated on the ground and the addition of the first edge obstructs the line of sight from source to receiver. However the subsequent addition of edges does not affect the path length difference significantly and therefore SPL reductions are caused by other factors. From the trend in the SPL reductions, further substantial reductions by the addition of even more edges appear achievable. However this is beyond the scope of this paper.

B. Effect of receiver height

In order to investigate the effect of the receiver height on the performance of the riblike structure, a series of tests were carried out on a geometry consisting of 21 edges combined with seven receiver heights. The setup is shown in Fig.

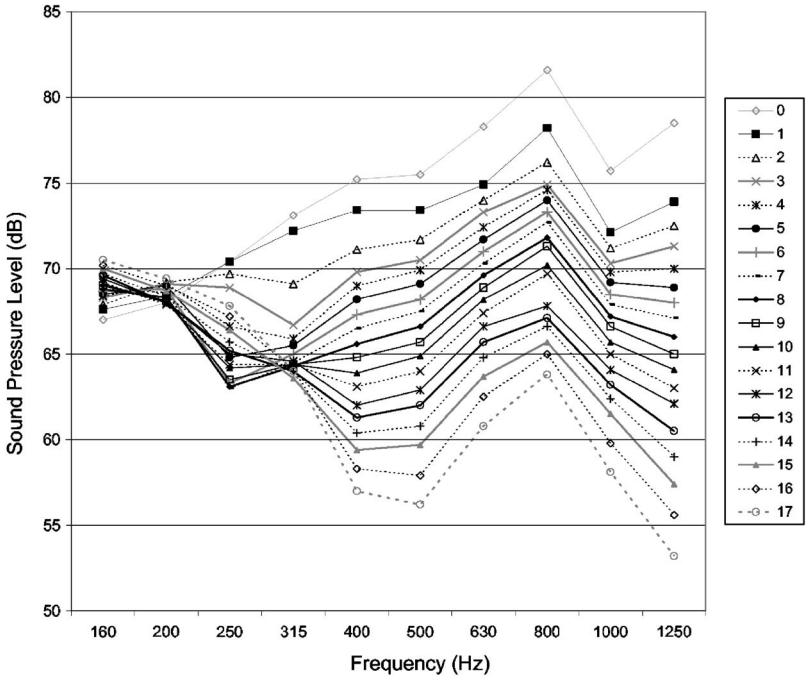

FIG. 6. Variation in SPL with increased number of edges, receiver 5, 0.

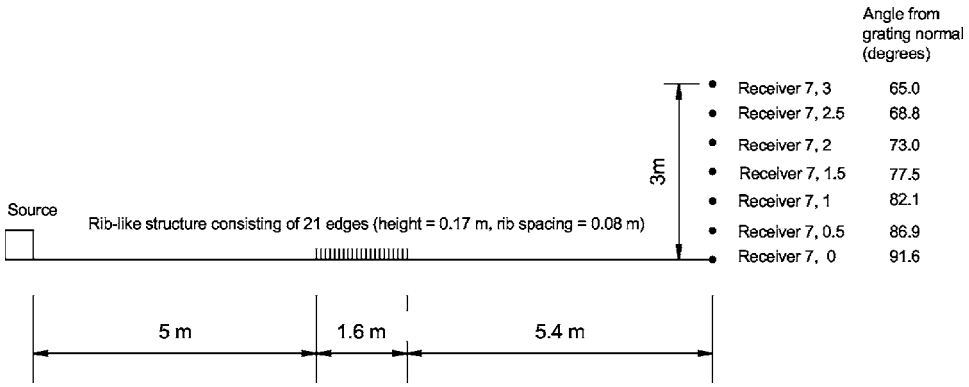

FIG. 7. Experimental setup for 21 edges and 7 receiver heights.

7 together with the diffraction angles of various receivers. The resulting insertion loss values for each of the receiver heights are shown in Fig. 8.

At receiver heights of 0 m and 0.5 m the largest insertion loss occurred at 500 Hz. As the height of the receiver is increased, this maximum benefit shifts to lower frequencies. This coincides with 315 Hz at a 1 m high receiver, with 250 Hz at 1.5 m high receiver and with 200 Hz at higher receivers.

At 160 Hz, decreasing the height of the receivers reduces the performance. The receiver at 3 m above the ground has a +3 dB insertion loss whereas the receiver at ground level, which is also the only receiver partially in the shadow zone, has a −3 dB insertion loss. The influence of the single edge is negligible at this frequency and therefore these effects can be attributed to the riblike structure.

At around 630 Hz, the situation appears to be reversed. As the height of the receiver increases, the noise levels at the receiver increase hence the insertion loss decreases. The exception is the 0.5 m high receiver at grazing incidence which possesses a higher insertion loss than the receiver on the ground, which is partially in the shadow zone. At 1250 Hz, the situation is similar to that described above.

The frequency which corresponds to the quarter-wavelength of the well depths in this case is 500 Hz according to Eq. (3). Based on the testing frequency range of 160–1250 Hz and the grating separation distance of approximately $w=0.1$ m, the only mode permitted by the grating equation at incidence and diffracted angles of 90° is $m=0$, occurring at around receivers 1 and 2 positioned at heights of 0 m and 0.5 m above ground, respectively. Therefore with the present setup it may prove difficult to identify the diffraction angles at which these effects may be taking place.

C. Effect of well depths

Figure 9 shows the setup for the third experiment, where the edge number is fixed as 14, whereas three well depths, 0.08 m, 0.17 m, and 0.25 m are compared. Corresponding to the second experiment, there are 6 receiver positions. The insertion loss of different reactive surfaces over that of a single edge are given as single figure insertion loss values in Table II. These are a simple linear average of the insertion loss values measured at individual frequency bands in an attempt to eliminate the influence of actual spectrum shape. The spectra of insertion loss values obtained for the three well depths at each of the six receiver locations are shown in Fig. 10.

For receivers (5, 0), (5, 0.4), (10, 0), and (10, 0.4) the general pattern of the differences between the three well

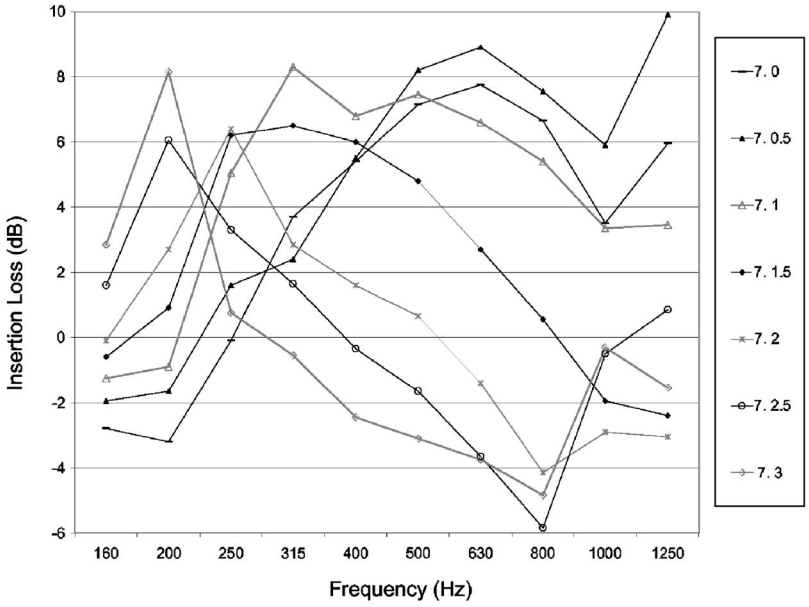

FIG. 8. Insertion loss of 21-edge configuration (well depth=0.17 m) at various receivers.

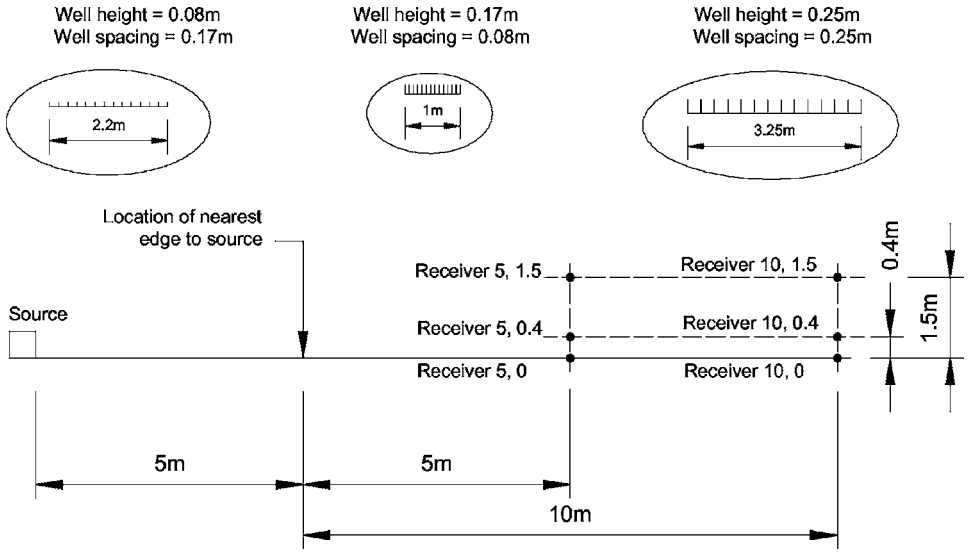

FIG. 9. Experimental setup for investigating different well heights.

depths is similar. This is characterized by two distinct regions in the insertion loss spectrum. Between 250 and 500 Hz the insertion loss values seem to correspond to the depth of the well. As the well depth increases, so does the insertion loss. At 630 Hz and above, the trend is slightly different as the 0.17 m well yields the worst performance. At these frequencies, it seems that the insertion loss follows the spacing of edges rather than their height. This is due to the width of the reactive surface.

The remaining two receivers (5, 1.5) and (10, 1.5), seem to have a similar pattern of insertion loss values, which is different than that observed previously. At lower frequencies, the insertion loss values seem to increase with well depth, the change in pattern (drop in insertion loss) occurs at lower frequencies than those above, and at a higher rate to the point where the values are negative. The peak insertion loss for the 0.08 m deep well occurs at a frequency of two 1/3 octave bands higher than that for the 0.07 m and the 0.25 m deep wells.

The maximum attenuations at the 0.25 m wells correspond to the quarter-wavelength of the well depth. This was not observed for other two well depths. It should be stressed that the proportion of area covered by the 0.17 m and 0.08 m edges is much smaller than that covered by the 0.25 m edges, even though the total number of wells is identical for all three cases.

In the case of 0.17 m wells, the magnitudes of peaks are less pronounced. For the maximum attenuations at resonant frequencies to be realized, the wavelength of the sound wave has to be smaller than half of the overall width of the reactive surface. The 0.17 m wells do not meet this requirement as shown in Table III.

The effects of surface waves can be seen in Fig. 10, for the two receivers at 1.5 m above ground. As the well depth is increased lower receivers are further in the shadow zone and some of the attenuations would be due to line-of-sight being intercepted.

This experiment showed that the overall width of the reactive surface is important for ensuring high frequency performance.

TABLE II. Linear average of insertion loss values (in dB) for 14-edge configurations at three different well heights

	Average insertion loss (dB) with three well heights		
Receiver	0.08 m	0.17 m	0.25 m
(5, 0)	3.1	3.9	10.2
(5, 0.4)	3.6	4.2	10.3
(5, 1.5)	0.1	0.8	2.1
(10, 0)	2.1	3.4	7.6
(10, 0.4)	2.7	3.4	8.4
(10, 1.5)	1.6	3.6	5.4

V. DISCUSSIONS AND CONCLUSIONS

This paper presents the findings of a series of tests undertaken in a semianechoic chamber to investigate the performance of riblike structures consisting of multiple edges. With strategic designs riblike structures can be very effective in providing insertion loss, typically 10–15 dB.

Quarter-wavelength resonance and surface wave generation play a significant role in determining their performance at lower frequencies. It was found that mainly the depth of the wells determined the lower frequency limit of attenuations. At frequencies lower than the limiting frequency, and at certain receiver locations, the attenuation could be negative due to surface wave generation. The attenuations were found to be greatest for receivers which were situated at propagation angles and horizontal distances close to the reactive surface.

The significant effect of surface waves can be seen at low frequencies for the lowest flow resistivities due to greater reactive component (i.e., imaginary component) of surface impedance for a hard-backed layer model for the ground. As the source height becomes lower or as the number of edges becomes higher, the likelihood of generating surface waves would also increase. These would make the potential improvements due to a series of edges less apparent, or even negative, over certain frequencies. This can be

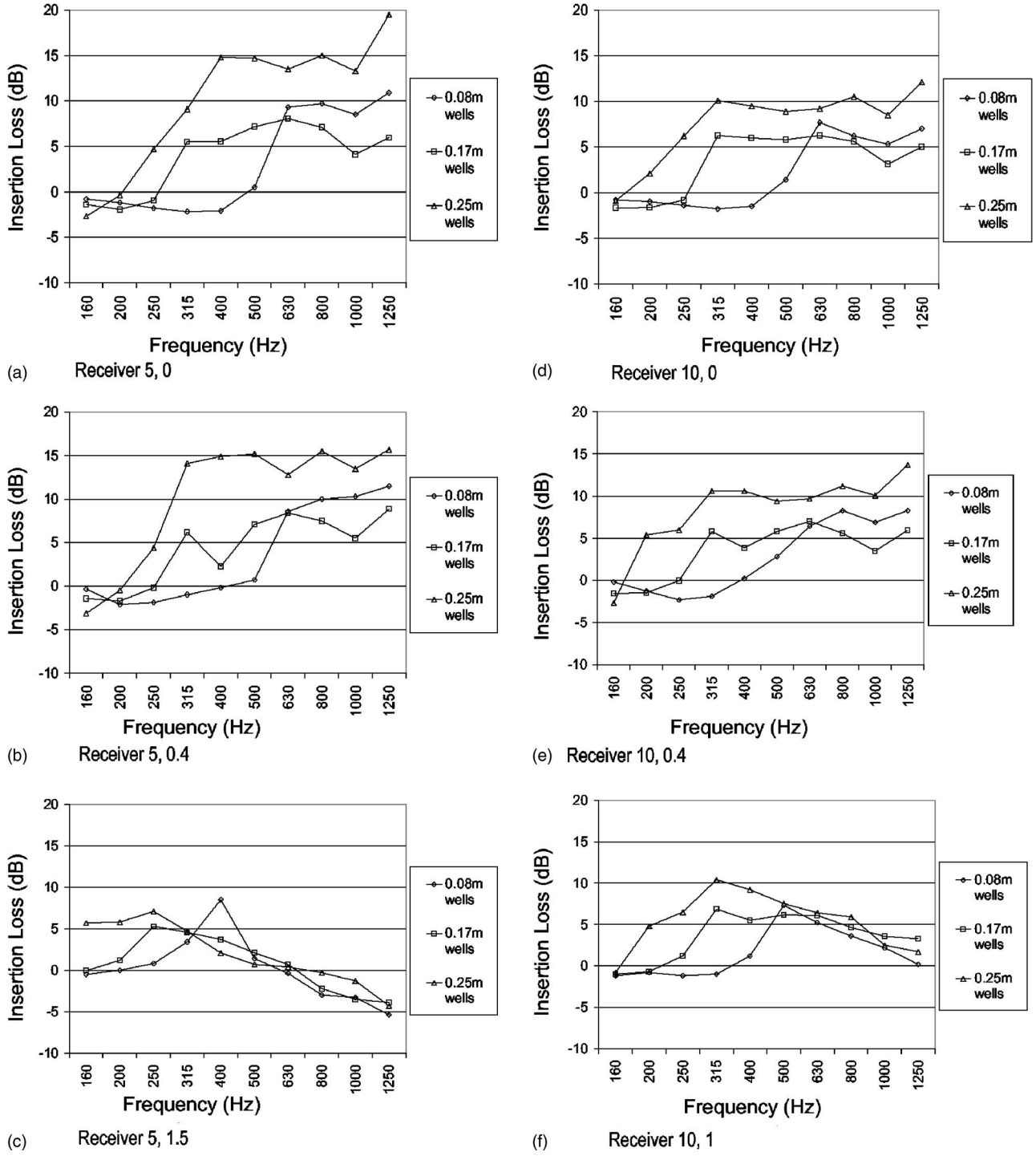

FIG. 10. Insertion loss of 14-edge configuration at different well heights.

TABLE III. Acoustic characteristics of the 14-edge configuration at different well heights.

Well depth (m)	Approximate resonant frequency (Hz)	Corresponding wavelength (m)	Half-width of reactive surface (m)
0.25	340	1.0	1.6
0.17	500	0.68	0.5
0.08	1075	0.32	1.1

seen in Fig. 10, for the two receivers at 1.5 m above ground.

In addition, interference between direct and reflected (within the grooves) paths was shown to be a possible explanation for the measured peaks (maxima and minima) in attenuation spectra, although these observations did not hold for some of the configurations with smaller edge heights. At higher frequencies diffraction effects were shown to be the likely mechanism responsible for the attenuations, although the geometries investigated did not allow these attenuations to be related to diffraction grating effects at various diffraction angles.

Some of the configurations described in this paper have been studied elsewhere[18] using 1/24 octave band frequency resolution. Although the presence of maxima and minima was clearly noted, the work did not identify any correlation between the location of these and various geometric setups. Such a correlation may strongly depend on small variations in the experimental setup including the position of receiver. This would need to be investigated as part of better controlled experiments.

The high frequency performance appeared to be dependent on diffraction effects characterized by the overall surface area the wells and the total number of edges. This was not necessarily the case for receivers which were in direct line of sight of the source. It was found that the there was an optimum number of edges for the most favourable attenuations, depending on the diffraction angles and the frequencies.

As the diffraction angles as measured from the grating normal were reduced, the attenuations were observed to shift to lower frequencies. The high frequency gains at these receivers were negative. For the maximum attenuations at resonant frequencies to be realized, the wavelength of the sound wave would need to be smaller than the half-wavelength of the overall width of the reactive surface.

Possible applications for these structures would include central reservations on motorways and on top of other structures (such as earth bunds or rows of garages). These applications however need to be considered from a maintenance point of view. The effect of dust built-up and rubbish clogging up the wells need to be considered.

The separation distance between the edges and the nature of the scattering objects have not been investigated as part of this work. Further study would also be required on the use of absorbing treatment in and around the wells and the use of the riblike structure in conjunction with absorbing ground and vegetation.

[1] I. Ekici and H. Bougdah, "A review of research on environmental noise barriers," Build. Acoust. **10**, 289–323 (2003).

[2] G. Watts, "Acoustic performance of traffic noise barriers. A state-of-the art review," Euro Symposium 1992, The Mitigation of Traffic Noise in Urban Areas, pp. 219–246 (1992).

[3] D. C. Hothersall, "Modelling the performance of noise barriers," Euro Symposium 1992, The Mitigation Traffic Noise in Urban Areas, pp. 247–258 (1992).

[4] G. A. Daigle, Report by the Institute of Noise Control Engineering Working Party on the Effectiveness of Noise Walls, Noise/News International **7**, 13–35 (1998).

[5] L. A. M. Van Der Haijden and M. J. M. Martens, "Traffic noise reduction by means of surface wave exclusion above parallel grooves in the roadside," Appl. Acoust. **15**, 329–339 (1982).

[6] K. Fujiwara, D. C. Hothersall, and C. Kim, "Noise barriers with reactive surfaces," Appl. Acoust. **53**, pp. 255–272 (1998).

[7] T. Okubo and K. Fujiwara, "Efficiency of noise barrier on the ground with an acoustically soft cylindrical edge," J. Sound Vib. **216**, 771–790 (1998).

[8] T. J. Shultz and B. G. Watters, "Propagation of sound across audience seating," J. Acoust. Soc. Am. **36**, 885–896 (1964).

[9] J. E. West and G. M. Sessler, "Sound transmission over theatre seats," J. Acoust. Soc. Am. **36**, 1725–1732 (1964).

[10] C. D. Field and F. R. Fricke, "Theory and applications of quarter-wave resonators: A prelude to their use for attenuating noise entering buildings through ventilation openings," Appl. Acoust. **53**, 117–132 (1998).

[11] L. E. Kinsler, A. R. Frey, A. B. Coppens, and J. V. Sanders, *Fundamentals of Acoustics*, 4th ed. (Wiley, New York, 2000).

[12] *Diffraction Grating Handbook*, 5th ed., edited by Christopher Palmer (Thermo RGL, Richardson Gratings Laboratory, 2002).

[13] W. C. Elmore and M. A. Heald, *Physics of Waves* (Dover, New York, 1985) ISBN 0-486-64926-1.

[14] P. Boulanger, K. Attenborough, S. Taherzadeh, T. Waters-Fuller, and K. Ming Li, "Ground effect over hard rough surfaces," J. Acoust. Soc. Am. **104**, 1474–1482 (1998).

[15] R. J. Donato, "Model experiments on surface waves," J. Acoust. Soc. Am. **63**, 700–703 (1978).

[16] D. G. Albert, "Observations of acoustic surface wave propagation above a snow cover," in Proceedings of the Fifth International Symposium on Long Range Sound Propagation, pp. 10–16 (1992).

[17] L. C. Sutherland and G. A. Daigle, "Atmospheric sound propagation," in *Handbook of Acoustics*, edited by M. J. Crocker, Chap. 28, pp. 305–329 (1998).

[18] I. Ekici, "Road traffic noise barrier design: measurements and models concerning multiple-walls and augmented earth mounds," Ph.D. thesis, Sheffield Hallam University (2004).

Orthogonal adaptation for multichannel feedforward control

Jing Yuan[a)]
Department of Mechanical Engineering, The Hong Kong Polytechnic University, Hunghom, Kowloon, Hong Kong

(Received 29 May 2006; revised 1 September 2006; accepted 6 September 2006)

In active noise control, it is desired to generate destructive interference by model-independent control. This is possible for single-channel systems to which a recently proposed method, called orthogonal adaptation, is applicable. In this study, the new method is extended to multichannel systems. An important issue is how to optimize a feedforward controller in the minimum H_2 norm sense. In practice, secondary paths of some multichannel systems may be nonminimum phase. It is a difficult problem to design H_2 feedforward controllers for multichannel systems with nonminimum phase secondary paths. The problem is solved analytically here with the best achievable, a practical and an economical solution. A recursive least squares algorithm is presented for online identification of multiple paths without persistent excitations. These solutions make it possible to implement noninvasive mode-independent controllers for multichannel systems. Experiment results are presented to verify the analytical results. © *2006 Acoustical Society of America.* [DOI: 10.1121/1.2358012]

PACS number(s): 43.50.Ki, 43.50.Gf [KA] Pages: 3723–3729

I. INTRODUCTION

Feedforward control is a popular method for active noise control[1,2] (ANC) when the primary signal is either available or recoverable as the reference signal. Secondary sources are excited to generate destructive interference in noise fields. Analytically, eigenfunctions of noise fields are the best tools for ANC design. Practically, eigenfunctions are not available accurately. Take a one-dimensional (1D) duct for example, its eigenfunctions depend on the impedance of duct ends, which is approximated by zero/infinity for an open/closed end. If the impedance of duct ends changes from ∞-∞ to ∞-0, the kth eigenfunction of the duct changes from $\cos[(k\pi/L)x]$ to $\cos\{[(2k-1)\pi/2L]x\}$ where L is the duct length.[3] Since impedance of an open/closed duct end is not really zero/infinity, it is not possible to obtain accurate eigenfunctions for 1D ducts, let alone three-dimensional noise fields whose eigenfunctions depend on more unknown parameters.

In a practical approach, error sensors are placed in a noise field to anchor a designated quiet zone. Transfer functions from secondary sources to error sensors become the minimum information for an ANC system. The filtered-x least mean squares (FxLMS) is a popular tool for controller adaptation, whose stability depends on the accuracy of path models. A system may be unstable if phase errors in a model exceed 90°.[4–6] Since transfer functions in noise fields may drift due to variation of environmental or boundary conditions, many ANC systems apply online modeling to keep path models close to true transfer functions. These are called model independent ANC (MIANC) systems for ease of reference. Proposed here is a new MIANC system.

In most ANC systems, path models are finite impulse response (FIR) filters with many parameters. Accurate estimation of model parameters requires "persistent excitations"[7]—the invasive injection of probing signals into actuation signals.[8] Some researchers try to regulate the magnitudes of invasive signals,[9,10] others investigate noninvasive modeling of secondary. paths.[11–13]

Recently, a method called orthogonal adaptation has been proposed for single-channel systems to implement noninvasive MIANC systems.[14] It is extended here to multichannel systems. A major difficulty is how to force the regression vector as orthogonal as possible to the online models. For multichannel systems, it is more difficult to meet the orthogonal requirement if the secondary path is nonminimum phase (NMP). The problem is solved here with the best achievable, a practical and an economical solution. A recursive least squares (RLS) algorithm is proposed for online modeling of multichannel systems. Experimental results are presented to verify the extended algorithm when applied to multichannel systems.

II. BACKGROUND INFORMATION

In an ANC system, transfer functions from primary and secondary sources to error sensors are represented by $P(z)$ and $\boldsymbol{S}(z)$ as the *p*rimary *t*ransfer vector and *s*econdary transfer matrix. The actuation signal is generated by $a(z) = C(z)r(z)$ where $C(z)$ is the controller transfer vector and $r(z)$ is the reference signal. The error signals are given by

$$e(z) = P(z)r(z) + \boldsymbol{S}(z)a(z) = [P(z) + \boldsymbol{S}(z)C(z)]r(z). \quad (1)$$

when $r(z)$ is broadband noise, $e(z)=0$ requires an ideal controller

$$C(z) = -\boldsymbol{S}^{-1}(z)P(z). \quad (2)$$

Equation (2) is stable if $\boldsymbol{S}(z)$ is minimum phase (MP), which requires a nonsingular $\boldsymbol{S}(z)$ for all $|z| \geqslant 1$. Otherwise, the secondary path is NMP, Eq. (2) is unstable and an achievable objective is to minimize

a)Electronic mail: mmjyuan@polyu.edu.hk

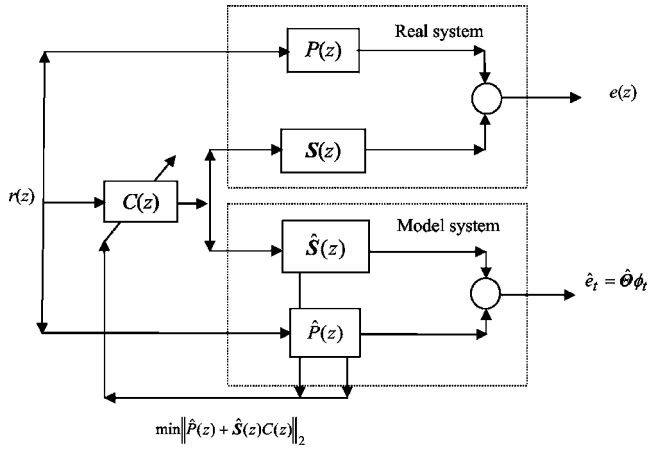

FIG. 1. Block diagram of the proposed ANC system.

$$\|e(z)\|_2 = \|P(z) + \boldsymbol{S}(z)C(z)\|_2. \tag{3}$$

The proposed system achieves this objective with a block diagram shown in Fig. 1.

It is assumed by many researchers that $P(z)$ and $\boldsymbol{S}(z)$ are approximated by FIR filters with negligible errors, which is adopted in this study. Let $P=[P_0P_1,\ldots,P_m]$ and $\boldsymbol{S}=[\boldsymbol{S}_0\boldsymbol{S}_1,\ldots,\boldsymbol{S}_m]$ denote coefficients of $P(z)$ and $\boldsymbol{S}(z)$ respectively, the time-domain version of Eq. (1) is a discrete-time convolution

$$e_t = \sum_{k=0}^{m} P_k r_{t-k} - \sum_{k=0}^{m} \boldsymbol{S}_k a_{t-k}, \tag{4}$$

where e_t, r_t, and a_t, denote respective samples of $e(z), r(z)$, and $a(z)$. Introducing coefficient matrix $\boldsymbol{\Theta}=[P\ \boldsymbol{S}]$ and regression vector $\boldsymbol{\phi}_t=[r_t r_{t-1},\ldots,r_{t-m}a_t a_{t-1},\ldots,a_{t-m}]^T$, one may rewrite Eq. (4) to

$$e_t = \boldsymbol{\Theta}\boldsymbol{\phi}_t. \tag{5}$$

Since the regression vector $\boldsymbol{\phi}_t$ contains actuation signal a_t, controllers are designed to regulate $\boldsymbol{\phi}_t$ and minimize objective function

$$J_t = \sum e_t^T e_t = \sum \boldsymbol{\phi}_t^T \boldsymbol{\Theta}^T \boldsymbol{\Theta} \boldsymbol{\phi}_t, \tag{6}$$

where the summation is over a sliding time window.

Like other MIANC systems, the proposed one minimizes J_t, when $\boldsymbol{\Theta}=[P\ \boldsymbol{S}]$ is not available. Online estimates of $P(z)$ and $\boldsymbol{S}(z)$ are denoted as $\hat{P}(z)$ and $\hat{\boldsymbol{S}}(z)$, which are obtained by minimizing estimation error

$$\begin{aligned}\boldsymbol{\varepsilon}(z) &= e(z) - \hat{P}(z)r(z) - \hat{\boldsymbol{S}}(z)a(z) \\ &= \Delta P(z)r(z) + \Delta \boldsymbol{S}(z)a(z).\end{aligned} \tag{7}$$

Here $\Delta P(z)=P(z)-\hat{P}(z)$ and $\Delta \boldsymbol{S}(z)=\boldsymbol{S}(z)-\hat{\boldsymbol{S}}(z)$ are model errors. If $\hat{\boldsymbol{\Theta}}=[\hat{P}\ \hat{\boldsymbol{S}}]$ denotes online estimate of $\boldsymbol{\Theta}=[P\ \boldsymbol{S}]$, then $\hat{P}=[\hat{P}_0\hat{P}_1\cdots\hat{P}_m]$ and $\hat{\boldsymbol{S}}=[\hat{\boldsymbol{S}}_0\hat{\boldsymbol{S}}_1\cdots\hat{\boldsymbol{S}}_m]$ contain coefficient matrices of $\hat{P}(z)$ and $\hat{\boldsymbol{S}}(z)$, respectively. The time-domain version of Eq. (7) is

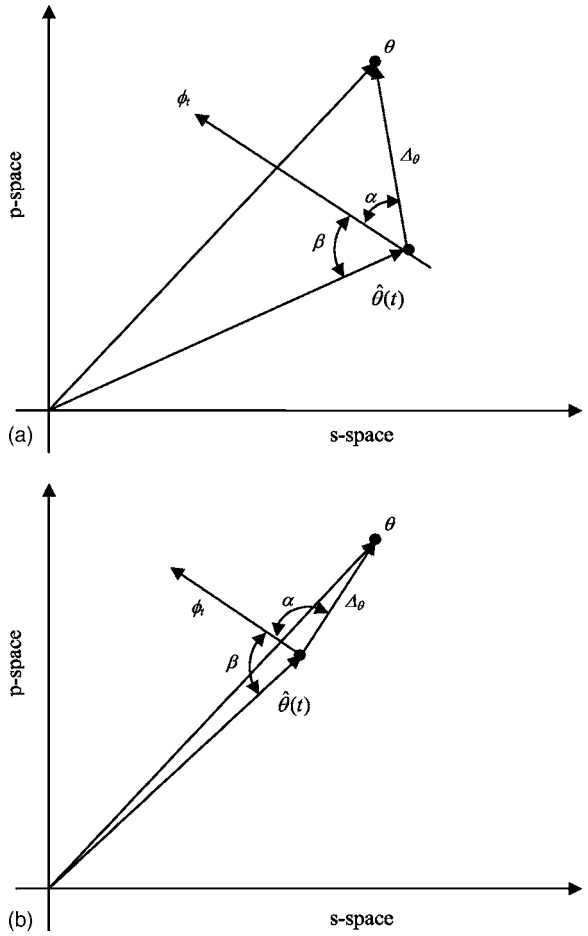

FIG. 2. Illustration of orthogonal adaptation: (a) adapting and (b) converging.

$$\boldsymbol{\varepsilon}_t = e_t - \hat{\boldsymbol{\Theta}}\boldsymbol{\phi}_t = \Delta\boldsymbol{\Theta}\boldsymbol{\phi}_t, \tag{8}$$

where $\Delta\boldsymbol{\Theta}=\boldsymbol{\Theta}-\hat{\boldsymbol{\Theta}}$. The system performs two online tasks. One is a modeling task to drive $\boldsymbol{\varepsilon}_t \to 0$ and the other is an optimizing task to force $\hat{e}_t=\hat{\boldsymbol{\Theta}}\boldsymbol{\phi}_t \approx 0$. Here $\hat{e}_t$ is the error signal of the model system in Fig. 1. Similar to the derivation from Eq. (1) to Eq. (5), one can see that $\hat{e}_t=\hat{\boldsymbol{\Theta}}\boldsymbol{\phi}_t$ is equivalent to

$$\hat{e}(z) = \hat{P}(z)r(z) + \hat{\boldsymbol{S}}(z)a(z) = [\hat{P}(z) + \hat{\boldsymbol{S}}(z)C(z)]r(z). \tag{9}$$

The optimization task solves $C(z)$ by minimizing $\|\hat{P}(z) + \hat{\boldsymbol{S}}(z)C(z)\|_2$.

Let $\theta^T=[p^T\ S^T]$ denote one row of $\boldsymbol{\Theta}$, then $\hat{\theta}^T=\lfloor\hat{p}^T\ \hat{s}^T]$ and $\Delta_\theta^T=[\Delta p^T, \Delta s^T]$ are the corresponding rows of $\hat{\boldsymbol{\Theta}}$ and $\Delta\boldsymbol{\Theta}$, respectively. Objectives $\boldsymbol{\varepsilon}_t=\Delta\boldsymbol{\Theta}\boldsymbol{\phi}_t \to 0$ and $\hat{e}_t=\hat{\boldsymbol{\Theta}}\boldsymbol{\phi}_t \approx 0$ are equivalent to $\Delta_\theta^T\boldsymbol{\phi}_t \to 0$ and $|\hat{\theta}^T\boldsymbol{\phi}_t| \approx 0$ for all rows. Effects of the two tasks are illustrated in Fig. 2 where the two axes represent the p- and s spaces of $\theta^T=[p^T\ s^T]$. Driving $\Delta_\theta^T\boldsymbol{\phi}_t \to 0$ is equivalent to driving $\alpha \to 90°$ while forcing $|\hat{\theta}^T\boldsymbol{\phi}_t| \approx 0$ is equivalent to forcing $\beta \approx 90°$. When the controller starts, $\alpha \neq 90°$ and $\beta \neq 90°$ in Fig. 2(a). One may find respective algorithms, such that $\Delta_\theta^T\boldsymbol{\phi}_t \to 0$ and $|\hat{\theta}^T\boldsymbol{\phi}_t| \approx 0$ are

achieved, respectively. If the system converges to $\alpha=90^{\circ}$ and $\beta=90^{\circ}$, ϕ_t is orthogonal to Δ_θ, $\hat{\theta}$ and θ simultaneously and J_t is minimized in view of Eq. (6).

Analytically, one may understand the joined effects of the two online tasks via

$$\|e_t\| = \|\varepsilon_t + \hat{\boldsymbol{\Theta}}\boldsymbol{\phi}_t\| = \|\varepsilon_t + \hat{e_t}\| \leqslant \|\varepsilon_t\| + \|\hat{e_t}\|, \tag{10}$$

which is obtained by adding $\hat{e}_t=\hat{\boldsymbol{\Theta}}\boldsymbol{\phi}_t$ to both sides of Eq. (8). On the left hand side of Eq. (10), e_t, represents the ANC error. On the right hand side, $\varepsilon_t=\Delta\boldsymbol{\Theta}\boldsymbol{\phi}_t$ is the estimation error, and $\hat{e}_t$ is the error of the model system in Fig. 1. If $\Delta_\theta^T\boldsymbol{\phi}_t \to 0$ and $|\hat{\theta}^T\boldsymbol{\phi}_t| \approx 0$ for all components of $\varepsilon_t=\Delta\boldsymbol{\Theta}\boldsymbol{\phi}_t$ and $\hat{\boldsymbol{\Theta}}\boldsymbol{\phi}_t$, then $\|\varepsilon_t\| \to 0$ and $\|\hat{e_t}\| \approx 0$ imply $\|e_t\| \approx 0$ even $\Delta_\theta \neq 0$.

III. CONTROLLER OPTIMIZATION

It may not be difficult to minimize $\|\hat{e}_t\|$ if $\hat{\boldsymbol{S}}(z)$ is MP in every step of estimation. One can substitute $C(z)=-\hat{\boldsymbol{S}}^{-1}(z)\hat{P}(z)$ into Eq. (9) such that $[\hat{P}(z)-\hat{\boldsymbol{S}}(z)\hat{\boldsymbol{S}}^{-1}(z)\hat{P}(z)]r(z)=0$ and equivalently $\hat{e_t}=0$. Unfortunately, $\hat{\boldsymbol{S}}^{-1}(z)$ is unstable if $\hat{\boldsymbol{S}}(z)$ is NMP, in which case a stable $C(z)$ is sought to minimize $\|\hat{P}(z)+\hat{\boldsymbol{S}}(z)C(z)\|_2$. This is a difficult problem for multichannel systems.

A. Best achievable solution

For systems with equal inputs and outputs, the inverse of $\hat{\boldsymbol{S}}(z)$ has the form of

$$\hat{\boldsymbol{S}}^{-1}(z) = \hat{D}^{-1}(z)\hat{\boldsymbol{S}}_a(z), \tag{11}$$

where $\hat{D}(z)$ and $\hat{\boldsymbol{S}}_a(z)$ are the determinant and adjoint of $\hat{\boldsymbol{S}}(z)$, respectively. Singularities of $\hat{\boldsymbol{S}}(z)$ depend on roots of $\hat{D}(z)$. Let r_i denote the ith root of $\hat{D}(z)$, then $\hat{\boldsymbol{S}}(z)$ is NMP if there exist some $\{r_i\}$ such that $|r_i|>1$.

The optimal controller is related to $\hat{D}(z)=D_m(z)D_n(z)$, where $D_m(z)$ and $D_n(z)$ are the MP and NMP parts of $\hat{D}(z)$, respectively. One may obtain a mirror polynomial $R_n(z)$ by using coefficients of $D_n(z)$ in the reversed order. It can be shown[15] that $W_a(z)=D_n(z)/R_n(z)$ is a stable all-pass filter. It then follows that

$$\hat{D}(z) = D_n(z)D_m(z) = \frac{D_n(z)}{R_n(n)}R_n(z)D_m(z) = W_a(z)W_m(z), \tag{12}$$

where $W_m(z)=R_n(z)D_m(z)$ is a MP filter. The optimal controller has the form of

$$C_o(z) = \hat{\boldsymbol{S}}_a(z)G(z). \tag{13}$$

Using Eqs. (11) and (12), one can see that $\hat{\boldsymbol{S}}_a(z)$ and $\hat{\boldsymbol{S}}(z)$ are related to each other by

$$\hat{\boldsymbol{S}}(z)\hat{\boldsymbol{S}}_a(z) = \hat{D}(z)\boldsymbol{I} = W_a(z)W_m(z)\boldsymbol{I}, \tag{14}$$

where $\boldsymbol{I}$ is an identity matrix. Substituting Eqs. (13) and (14) into $\|[\hat{P}(z)+\hat{\boldsymbol{S}}(z)C_o(z)]\|_2$, one obtains

$$\|\hat{P}(z)+\hat{\boldsymbol{S}}(z)C_o(z)\|_2 = \|\hat{P}(z)+W_a(z)W_m(z)G(z)\|_2. \tag{15}$$

The above equation may be rewritten to

$$\begin{aligned}\|\hat{P}(z)+\hat{\boldsymbol{S}}(z)C_o(z)\|_2 &= \|W_a\|_2\|W_a^{-1}\hat{P}+W_mG\|_2 \\ &= \|W_a^{-1}(z)\hat{P}(z)+W_m(z)G(z)\|_2,\end{aligned} \tag{16}$$

where $\|W_a(z)\|_2=1$ since it is an all-pass filter. The next step is to apply the long-division and obtain

$$W_a^{-1}(z)\hat{P}(z) = \frac{R_n(z)\hat{P}(z)}{D_n(z)} = \frac{P_r(z)}{D_n(z)} + P_q(z), \tag{17}$$

where $P_q(z)$ and $P_r(z)$ are the quotient and remainder polynomial vectors. The two parts on the right hand side of Eq. (17) are orthogonal to each other in the H_2 norm sense, such that Eq. (16) may be expressed as

$$\begin{aligned}\|\hat{P}(z)+\hat{\boldsymbol{S}}(z)C_0(z)\|_2 &= \|W_a^{-1}(z)\hat{P}(z)+W_m(z)G(z)\|_2 \\ &= \left\|\frac{P_r(z)}{D_n(z)}\right\|_2 + \|P_q(z)+W_m(z)G(z)\|_2.\end{aligned} \tag{18}$$

When $D_n(z)$ is the NMP part of $\hat{D}(z)$, $P_r(z)/D_n(z)$ is unstable and cannot be cancelled by any stable feedforward controller. The best achievable result is $\|P_q(z)+W_m(z)G(z)\|_2=0$ by controller

$$G(z) = -W_m^{-1}(z)P_q(z) = -\frac{P_q(z)}{R_n(z)D_m(z)} \quad \text{or}$$

$$C_o(z) = -\frac{\hat{\boldsymbol{S}}_a(z)P_q(z)}{R_n(z)D_m(z)}. \tag{19}$$

Any other feedforward controller only increases Eq. (18) if it is not given by Eq. (19).

A key step in the above.derivations is the use of Eqs. (13) and (14). To the best of author's knowledge, this is the first reported method to find a H_2 feedforward controller for multichannel systems with square and NMP secondary paths. It is not perfect since Eqs. (13) and (14) are applicable only if $\hat{\boldsymbol{S}}(z)$ is square. When there are different inputs and outputs, a suboptimal controller is solvable by methods presented in the next two subsections.

B. Practical solution

One may also design a practical and suboptimal controller $C(z)$ to minimize

$$\|\hat{P}(z)+\hat{\boldsymbol{S}}(z)C(z)\|_2 = \|F(z)\|_2, \tag{20}$$

where $C(z)$ and $F(z)$ are FIR filters. The impulse response of Eq. (20) is given by

$$F=\begin{bmatrix} F_1 \\ F_2 \\ \vdots \\ \vdots \\ F_{2m-1} \end{bmatrix}=\begin{bmatrix} \hat{P}_1 \\ \hat{P}_2 \\ \vdots \\ \hat{P}_m \end{bmatrix}+\begin{bmatrix} \hat{S}_1 & & & \\ \hat{S}_2 & \hat{S}_1 & & \\ \vdots & \hat{S}_2 & \ddots & \\ \hat{S}_m & \vdots & \ddots & \hat{S}_1 \\ & \hat{S}_m & \vdots & \hat{S}_2 \\ & & \ddots & \vdots \\ & & & \hat{S}_m \end{bmatrix}\begin{bmatrix} C_1 \\ C_2 \\ \vdots \\ C_m \end{bmatrix}=\hat{P}+\mathbf{\Gamma}_s C, \tag{21}$$

where $F^T=[F_1,\ldots,F_{2m-1}]$ and $C^T=[C_1,\ldots,C_m]$ are coefficient vectors of $F(z)$ and $C(z)$ respectively, coefficient matrices of $\hat{S}(z)$ are used to construct matrix

$$\mathbf{\Gamma}_s=\begin{bmatrix} \hat{S}_1 & & & \\ \hat{S}_2 & \hat{S}_1 & & \\ \vdots & \hat{S}_2 & \ddots & \\ \hat{S}_m & \vdots & \ddots & \hat{S}_1 \\ & \hat{S}_m & \vdots & \hat{S}_2 \\ & & \ddots & \vdots \\ & & & \hat{S}_m \end{bmatrix}. \tag{22}$$

According to Parserval's theorem, minimizing $\|\hat{P}(z)+\hat{S}(z)C(z)\|_2=\|F(z)\|_2$ is equivalent to minimizing $\|F\|^2$. The objective function is

$$\begin{aligned} F^TF&=(\hat{P}+\mathbf{\Gamma}_s C)^T(\hat{P}+\mathbf{\Gamma}_s C)\\ &=\hat{P}^T\hat{P}+\hat{P}^T\mathbf{\Gamma}_s C+C^T\mathbf{\Gamma}_s^T\hat{P}+C^T\mathbf{\Psi}_s C, \end{aligned} \tag{23}$$

where $\mathbf{\Psi}_s=\mathbf{\Gamma}_s^T\mathbf{\Gamma}_s$ is the autocorrelation matrix of the impulse response of $\hat{\boldsymbol{S}}(z)$. One may introduce $\mathbf{\Xi}=\mathbf{\Gamma}_s^T\hat{P}$ and substitute $C^T\mathbf{\Gamma}_s^T\hat{P}=C^T\mathbf{\Psi}_s\mathbf{\Psi}_s^{-1}\mathbf{\Xi}$ into Eq. (23). This leads to

$$F^TF=\hat{P}^T\hat{P}-\mathbf{\Xi}^T\mathbf{\Psi}_s^{-1}\mathbf{\Xi}+(\mathbf{\Psi}_s C+\mathbf{\Xi})^T\mathbf{\Psi}_s^{-1}(\mathbf{\Psi}_s C+\mathbf{\Xi}), \tag{24}$$

where parameter vector C only affects $(\mathbf{\Psi}_s C+\mathbf{\Xi})^T\mathbf{\Psi}_s^{-1}(\mathbf{\Psi}_s C+\mathbf{\Xi})$.

In this solution, $C(z)$ minimizes F^TF if $\mathbf{\Psi}_s C=-\mathbf{\Xi}$ is solvable or the rank of $\mathbf{\Gamma}_s$ equals its row size. This is not a problem for single-channel systems. For multichannel systems, however, special care has to be taken to satisfy the rank requirement. The resultant controller is suboptimal if compared with $C_o(z)$ in Eq. (19), but it is more practical and less computationally expensive.

Since $\mathbf{\Gamma}_s$ depends on coefficient matrices of $\hat{S}(z)$, its rank could change as the system identifies $\hat{S}(z)$. There may be instants when $\mathbf{\Gamma}_s$ is rank defective and $\mathbf{\Psi}_s=\mathbf{\Gamma}_s^T\mathbf{\Gamma}_s$ is singular. A pseudoinverse of $\mathbf{\Psi}_s$ may be used to minimize $\mathbf{\Psi}_s C+\mathbf{\Xi}\approx 0$ in such cases. Substituting into Eq. (24), one can see that F^TF is not minimized to the full extent when $\mathbf{\Psi}_s C+\mathbf{\Xi}\approx 0$. While a rank defective $\mathbf{\Gamma}_s$ degrades ANC performance, it does not affect system stability as long as $C(z)$ is bounded.

C. Economic solution

In many ANC applications, $P(z)$ and $\boldsymbol{S}(z)$ are approximated by FIR filters with large numbers of coefficients. The dimension of $\mathbf{\Psi}_s$ is $(l\times m)^2$ if a multichannel system has l actuators and the degree of $C(z)$ is m. Calculation of $\mathbf{\Psi}_s$ and $\mathbf{\Xi}$ requires additional work. Online solution of $\mathbf{\Psi}_s C=-\mathbf{\Xi}$ is very expensive.

Alternatively, one may consider a positive definite function $O=0.5F^TF$ and a recursive algorithm that updates C and minimizes O. The time derivative of O is given by

$$\dot{O}=F^T\mathbf{\Gamma}_s\dot{C}, \tag{25}$$

where Eq. (21) is used to link $\dot{F}$ to $\dot{C}$. The above equation suggests a very simple way to modify C. It is given by

$$\dot{C}=-\mu\mathbf{\Gamma}_s^TF \quad \text{or} \quad C_{t+1}=C_t-\mu\mathbf{\Gamma}_s^TF\delta t, \tag{26}$$

where μ is a small positive constant and δt is the sampling interval. Combining Eqs. (25) and (26), one obtains $\dot{O}=-\mu F^T\mathbf{\Gamma}_s\mathbf{\Gamma}_s^TF\leqslant 0$. Therefore $O=0.5F^TF$ will be minimized by the recursive use of Eq. (26).

The advantage of this solution is to avoid online inverse of $\mathbf{\Psi}_s$. The method is not able to minimize $O=0.5F^TF$ in every step of identification, though it reduces the computational cost. Mathematically, this solution is equivalent to the practical one upon the convergence of Eq. (26). Therefore the same rank condition is preferred. In case $\mathbf{\Gamma}_s$ is rank defective, $\mathbf{\Psi}_s$ is singular and there does not exist a suboptimal C for $\mathbf{\Psi}_s C=-\mathbf{\Xi}$ no matter what method is used to solve $C(z)$. In view of Eq. (24), F^TF cannot be minimized to the full extent as C_t converges to a finite vector C but $\mathbf{\Psi}_s C+\mathbf{\Xi}\neq 0$. System stability, however, will not be affected by the rank of $\mathbf{\Gamma}_s$ as long as $C(z)$ is bounded.

IV. CONVERGENCE OF PATH MODELING

In the previous section, a rank condition on $\mathbf{\Gamma}_s$ is preferred by the optimization task. According to Eq. (22), $\mathbf{\Gamma}_s$ consists of coefficient matrices of $\hat{S}(z)$ and $\hat{S}(z)$ is an estimate of $\boldsymbol{S}(z)$. If $P(z)$ and $\boldsymbol{S}(z)$ were available accurately, the optimization should be applied to $P(z)$ and $\boldsymbol{S}(z)$. The rank condition basically depends on $\boldsymbol{S}(z)$ and system configuration such as locations of actuators and error sensors. This is actually a preferred condition for all multichannel ANC systems. It has not been discussed in the literature since most ANC systems update controllers by FxLMS. A controller obtained by FxLMS is not necessarily optimal. In view of Eq. (24), a multichannel feedforward controller is not optimal in the minimum H_2 norm sense if the rank condition is not satisfied, in which case satisfying the rank condition is a new hint for system improvement.

Here $\boldsymbol{S}(z)$ and $\hat{S}(z)$ are said to satisfy the rank condition respectively, if $\mathbf{\Gamma}_s$ satisfies the rank condition when coefficient matrices of $\boldsymbol{S}(z)$ and $\hat{S}(z)$ are substituted in Eq. (22), respectively. There are two possible cases when $\mathbf{\Gamma}_s$ does not satisfy the rank condition: (1) $\boldsymbol{S}(z)$ does not satisfy the rank condition and $\hat{S}(z)$ converges to $\boldsymbol{S}(z)$; and (2) $\boldsymbol{S}(z)$ satisfies the rank condition but $\hat{S}(z)$ does not converge to $\boldsymbol{S}(z)$. One

must adjust system configuration such that $\boldsymbol{S}(z)$ satisfies the rank condition in the first place. It is then possible to identify $\hat{S}(z)$ that satisfies the rank condition at each step of estimation. This requires a very complicated algorithm[16] and is an additional restriction to online modeling.

In this section, a simple RLS algorithm is proposed to drive $\varepsilon_t = \Delta\boldsymbol{\Theta}\phi_t \to 0$ and satisfy the rank requirement on $\boldsymbol{\Gamma}_s$. The algorithm has a matrix form

$$\hat{\boldsymbol{\Theta}}(t+1) = \hat{\boldsymbol{\Theta}}(t) + \frac{\varepsilon_t \phi^T}{\phi^T \phi}. \tag{27}$$

One may use positive definite function $V(t) = \mathrm{Tr}\{\Delta\boldsymbol{\Theta}^T(t)\Delta\boldsymbol{\Theta}(t)\}$ to analyze the convergence of Eq. (27). Similar to identity $a^2 - b^2 = (a-b)(a+b)$, it can be verified that

$$V(t+1) - V(t) = \mathrm{Tr}\{ \times[\Delta\boldsymbol{\Theta}(t+1) - \Delta\boldsymbol{\Theta}(t)]^T[\Delta\boldsymbol{\Theta}(t+1) + \Delta\boldsymbol{\Theta}(t)]\}. \tag{28}$$

with the help of Eq. (27) and $\Delta\boldsymbol{\Theta} = \boldsymbol{\Theta} - \hat{\boldsymbol{\Theta}}$, one can obtain

$$\Delta\boldsymbol{\Theta}(t+1) - \Delta\boldsymbol{\Theta}(t) = \hat{\boldsymbol{\Theta}}(t) - \hat{\boldsymbol{\Theta}}(t+1) = \varepsilon_t \phi^T(t)/\phi^T\phi \tag{29}$$

and

$$\Delta\boldsymbol{\Theta}(t+1) + \Delta\boldsymbol{\Theta}(t) = 2\boldsymbol{\Theta} - \hat{\boldsymbol{\Theta}}(t) - \hat{\boldsymbol{\Theta}}(t+1) = 2\Delta\boldsymbol{\Theta}(t) - \varepsilon_t \phi^T(t)/\phi^T\phi. \tag{30}$$

The next step is to substitute Eqs. (29) and (30) into Eq. (28), which leads to

$$V(t+1) - V(t) = \mathrm{Tr}\left\{ \frac{-\phi\varepsilon_t^T}{\phi^T\phi}\left[2\Delta\boldsymbol{\Theta}(t) - \frac{\varepsilon_t \phi^T}{\phi^T\phi} \right] \right\}. \tag{31}$$

Substituting $\mathrm{Tr}\{\phi\varepsilon_t^T\Delta\boldsymbol{\Theta}\} = \varepsilon_t^T\Delta\boldsymbol{\Theta}\phi = \varepsilon_t^T\varepsilon_t$ and $\mathrm{Tr}\{\phi\varepsilon_t^T\varepsilon_t\phi^T\} = \varepsilon_t^T\varepsilon_t \mathrm{Tr}\{\phi\phi^T\}\varepsilon_t^T\varepsilon_t\phi^T\phi$ into Eq. (31), one can finish the derivation with

$$V(t+1) - V(t) = -\frac{\varepsilon_t^T\varepsilon_t}{\phi^T\phi} \leqslant 0. \tag{32}$$

It indicates monotonous decrease of $V(t) = \mathrm{Tr}\{\Delta\boldsymbol{\Theta}^T(t)\Delta\boldsymbol{\Theta}(t)\}$ until $\varepsilon_t \to 0$.

A simple attempt to meet the rank condition on $\boldsymbol{\Gamma}_s$ is a proper choice of initial guess for $\hat{S}(z)$. When the secondary path is square, a possible initial guess of $\hat{S}(z)$ would be an identity matrix. When there are different inputs and outputs, one may initialize $\hat{S}(z)$ with pseudorandom values such that the initial rank of $\boldsymbol{\Gamma}_s$ equals its row size. This is an effective way to avoid heavy computations and maintain good ANC performance. In simulations, the ANC performance degrades drastically if the initial guess of $\hat{S}(z)$ does not meet the rank condition while other conditions remain unchanged.

V. COMPARISON WITH OTHER MIANC SYSTEMS

Model independent by online modeling is the common feature of all MIANC systems including the proposed one. While there are slight differences in identification algorithms, the computational cost of online modeling is almost the same. The main difference is how to design the controller and how to evaluate performance, which are the subjects of comparison.

Most MIANC systems need another task for controller adaptation by FxLMS, which requires manageable computations in one sample but takes many samples for $C(z)$ to converge after the convergence of $\hat{S}(z)$ in online modeling. Since FxLMS is an estimation algorithm, there are inevitable estimation errors in $C(z)$. System stability is a problem if the phase error of $\hat{S}(z)$ exceeds 90°. After FxLMS drives the convergence of $C(z)$, it is difficult to see if $C(z)$ is optimal or not. In case $C(z)$ is not optimal, it is not clear how to improve system performance.

The proposed system optimizes $C(z)$ without adaptation. If $\hat{S}(z)$ is square, the best achievable solution is proposed. If $\hat{S}(z)$ is not square, two suboptimal solutions are proposed. Advantages of the proposed method are weak points of FxLMS: (a) The methods are stable and optimal even $\hat{S}(z)$ does not converge to $\boldsymbol{S}(z)$; (b) it is possible to achieve the best achievable performance; (c) if hardware is fast enough, $C(z)$ can be solved by minimizing $\|\hat{P}(z) + \hat{\boldsymbol{S}}(z)C(z)\|_2$ immediately after the convergence of $\hat{P}(z)$ and $\hat{S}(z)$; (d) there are no estimation errors in $C(z)$; and (e) the controller is optimal in the minimum H_2 norm sense if a rank condition on $\hat{S}(z)$ is satisfied.

With available hardware, the first two solutions are too computationally expensive to be done in every sample interval. The economic solution requires roughly m times the storage and computations required by FxLMS, where m is the degree of $C(z)$. These methods are no match to FxLMS in terms of computational cost in each sample interval. Advantages of the proposed system will eventually become attractive when faster optimization algorithms are available or computers are faster and less expensive to offset drawbacks of heavy online computations.

VI. IMPLEMENTATION AND VERIFICATION

An experiment was conducted to test orthogonal adaptation for multichannel systems. The controller was implemented in a dSPACE 1103 board. The degrees of $C(z)$, $\hat{P}(z)$, and $\hat{\boldsymbol{S}}(z)$ were $m = 300$. The primary source and secondary sources were 6 in. speakers. The online tasks were implemented using Eqs. (26) and (27) with initial guesses $\hat{P}(z) = 0$, $\hat{\boldsymbol{S}}(z) = \boldsymbol{I}$ and $C(z) = [1,1,1]^T$. The system sampling rate was 1538 samples/s and all signals were low-pass filtered with cutoff frequency 500 Hz. In the experiment, $r(z)$ was broadband noise. While it is possible to recover $r(z)$ from a measured signal, it would take additional computer time for online modeling of feedback paths and cancellation of acoustical feedbacks. To save computer time for the main focus, $r(z)$ was directly available to the controller. Figure 3 shows the experiment configuration.

The experiment was conducted in an anechoic chamber. The controller was turned off first to collect signals from the

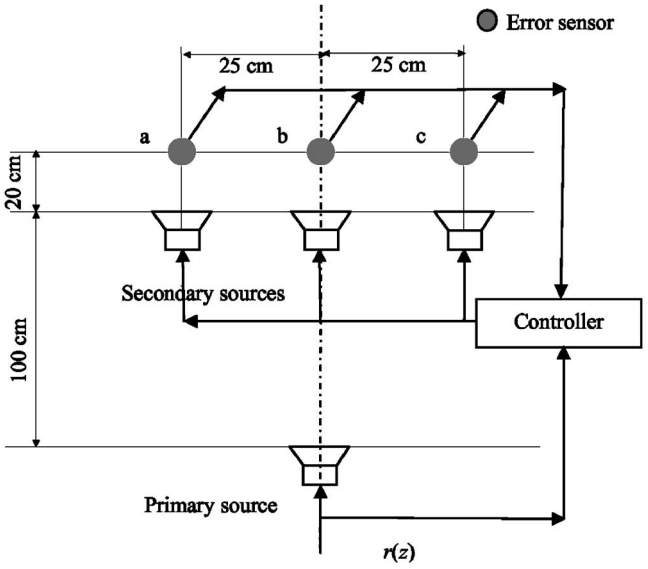

FIG. 3. Sensor/actuator configuration in the experiment.

error sensors. Power spectral densities (PSDs) of the signals were normalize by the PSD of $r(z)$ as the comparison references, which are shown as the gray curves in Figs. 4(a)–4(c). The ANC was then turned on for a while before taking signals from the error sensors. The black curves in Figs. 4(a)–4(c) represent normalized PSDs of the error signals collected after the ANC was active. Significant noise reduction is observed in the entire frequency range of interest. It is verified by the experiment that orthogonal adaptation is an effective approach for model-independent feedforward control of multichannel systems.

Like other MIANC systems, the proposed one only minimizes error signals. Due to hardware limit, the experimental system only had three error sensors. Its bandwidth was half the sampling frequency with the shortest wavelength of 48.23 cm. The range of the quiet zone was limited by two main facts: (1) an error sensor anchors a quiet region whose range is a small fraction of shortest wavelength; and (2) any combination of three anchors is in a two-dimensional plane. A larger quiet zone could be possible if it is sheltered by many closely spaced anchors to prevent noise from penetrating between anchors. It is not yet possible to test the proposed methods in such a large scale with our available hardware and programming skills.

A further study is in the way to find faster algorithms for minimizing $\|\hat{e}_i\|$, or program available ones in a more efficient way. A possible attempt is to combine online economic solution with offline best solution to improve performance

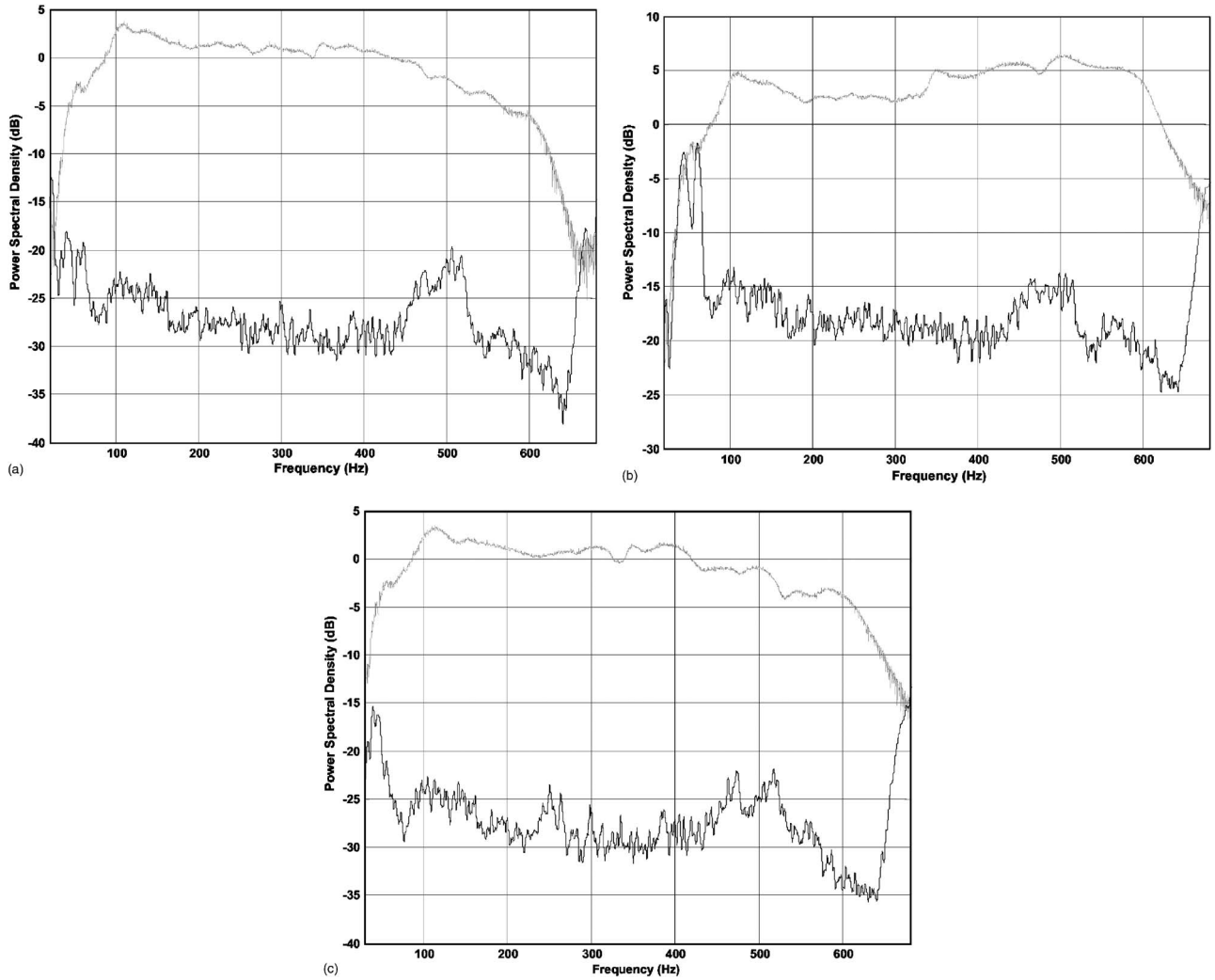

FIG. 4. Normalized PSDs of uncontrolled (gray) and controlled (black) noise, measured by error sensors (a), (b), and (c).

without heavy online computations. It is reasonable to expect more inputs/outputs in the near future when faster hardware or algorithms are available.

VII. CONCLUSION

Orthogonal adaptation is extended to multichannel MIANC systems in this study. An important issue is online optimization of a feedforward controller. This problem is solved here with the best achievable, a practical and an economical solution. A simple RLS algorithm is presented for online modeling of multichannel systems. Experimental results are presented to verify the performance of the extended algorithm. In the present stage, only the economical solution is implemented in experiments with limited inputs/outputs. As a result of rapid advance of technologies, it will eventually become possible to implement the best solution with more inputs/outputs when faster hardware is available.

ACKNOWLEDGMENT

The author acknowledges the help of Wu Wei who selected sensor/actuator locations and collected experiment data in this project.

[1]C. H. Hansen and S. D. Snyder, *Active Control of Noise and Vibration* (E and FN Spon, London, 1997).
[2]P. A. Nelson and S. J. Elliott, *Active Control of Sound* (Academic, London, 1992).
[3]D. E. Hall, *Basic Acoustics* (Wiley, New York, 1987).
[4]M. A. Vaudrey, W. T. Baumann, and W. R. Saunders, "Stability and operation constraints of adaptive LMS-based feedback control," Automatica **39**, 595–605 (2003).
[5]E. Bjarnason, "Analysis of the filtered-x LMS algorithm," IEEE Trans. Speech Audio Process. **3**(3), 504–514 (1995).
[6]S. D. Snyder and C. H. Hansen, "The influence of transducer transfer functions and acoustic time delay on the LMS algorithm in active noise control systems," J. Sound Vib. **140**(3), 409–424 (1990).
[7]G. C. Goodwin and K. S. Sin, *Adaptive Filtering, Prediction and Control* (Prentice-Hall, Englewood Cliffs, NJ, l984).
[8]L. J. Eriksson and M. C. Allie, "Use of random noise for on-line transducer modeling in an adaptive active attenuation system," J. Acoust. Soc. Am. **85**, 797–802 (1989).
[9]M. Zhang, H. Lan, and W. Ser, "Cross-updated active noise control system with online secondary path modeling," IEEE Trans. Speech Audio Process. **9**, 598–602 (2000).
[10]M. Zhang, H. Lan, and W. Ser, "A robust online secondary path modeling method with auxiliary noise power scheduling strategy and norm constraint manipulation," IEEE Trans. Speech Audio Process. **11**(1), 45–53 (2003).
[11]W. C. Nowlin, G. S. Guthart, and G. K. Toth, "Noninvasive system identification for multichannel broadband active noise control," J. Acoust. Soc. Am. **107**, 2049–2060 (2000).
[12]X. Qiu and C. H. Hansen, "An algorithm for active control of transformer noise with online cancellation path modelling based on the perturbation method," J. Sound Vib. **240**(4), 647–665 (2001).
[13]B. J. Kim and D. C. Swanson, "Linear independence method for system identification/secondary path modeling for active control," J. Acoust. Soc. Am. **118**(3), 1452–1468 (2005).
[14]J. Yuan, "Orthogonal adaptation for active noise control," J. Acoust. Soc. Am. **120**(1), 204–210 (2006).
[15]P. A. Regalia, *Adaptive IIR Filtering in Signal Processing and Control* (Dekker, New York, 1995).
[16]J. Yuan, "Improving an adaptive controller for non-minimum phase plants," Automatica **38**, 869–8735 (2002).

Geometrical perturbation of an inclined wall on decay times of acoustic modes in a trapezoidal cavity with an impedance surface

K. S. Sum[a] and J. Pan[b]
School of Mechanical Engineering, The University of Western Australia, 35 Stirling Highway, Crawley, Western Australia 6009

(Received 5 April 2006; revised 27 August 2006; accepted 1 September 2006)

Decay times of acoustic modes of a trapezoidal cavity (TC modes) with an inclined wall are studied. Each cavity wall is successively assigned an impedance surface and the other five walls are rigid. The decay times are obtained from the coupling between rigid-walled modes of the rectangular cavity (RC modes) that bounds the trapezoidal cavity. Two coupling mechanisms are identified, namely, the damping coupling and the geometrical coupling. The former is related to the coupling of RC modes at the impedance surface, while the latter is related to the coupling of RC modes at the inclined wall. Both mechanisms include the same volume coupling where RC modes couple throughout the trapezoidal cavity. When the impedance surface is at either of the two trapezoidal walls, the grouping of TC modes with same decay times and the decay time variation with the wall inclination are determined only by the damping coupling. When the surface is at any of the other rectangular walls, both the damping and geometrical couplings are at work. This paper provides an understanding of how the inclined wall and the impedance surface location affect the TC-mode grouping, and what determines the decay time variation with the inclination. © *2006 Acoustical Society of America.* [DOI: 10.1121/1.2357718]

PACS number(s): 43.55.Br, 43.55.Ka, 43.20.Ks [NX] Pages: 3730–3743

I. INTRODUCTION

In room acoustics, reverberation time is one of the important parameters that provides a physical measure of acoustical quality in rooms. It is determined by the decay times of acoustic modes in the rooms. In the past, a lot of research works have been conducted to relate the decay times to the sound absorption of room boundaries, where two different theoretical frameworks were established through the concepts of modally and locally reactive walls. The surface of a modally reactive wall is elastic and possesses structural modes that vibrate flexurally, where the decay times are related to the wall absorption by the coupling between the structural and acoustic modes. The concept is often applicable to bare flexible walls.[1] The effects of modally reactive walls on the decay times have been studied but the works only focused on rectangular enclosures.[2,3] The surface of a locally reactive wall is inelastic, where the decay times are related to the wall absorption by the normal acoustical impedance of the surface.[4] This concept is used for thick porous or fibrous materials, and usually still applicable even when such material is backed by a flexible wall because the locally reactive surface is in front of the sound field.[5] In this case, the average surface absorption can be described by the combined acoustical impedance of the material and the flexible wall.[6] The effects of locally reactive walls on the decay times have also been investigated,[7–10] and the analysis was extended to include walls with nonuniform surface impedance.[11,12] However, these studies were also concerned with rectangular rooms only.

In practice, rooms of irregular shapes can often be found. In an early mathematical work, an analytical technique has been developed for the prediction of sound fields in irregular rooms.[13] In this technique, each acoustic mode of an irregular room is expressed as the normal expansion of rigid-walled modes of the rectangular room that bounds the irregular room. The technique has been successfully used in various studies of sound fields in irregular enclosures.[14–17] But, all these works only focused on the prediction of resonance frequencies and sound pressure distributions or mode shapes in the enclosures. The same acoustical properties were also of concern even in those investigations using finite element and boundary element methods or direct numerical calculations.[18,19] Despite the importance of the decay times of acoustic modes in room acoustics, none of these previous works reported the effects of geometrical irregularity of enclosures on the decay times. In some recent studies using irregular cavities with fractal lateral walls that were locally reactive, the damping of acoustic modes was found to increase with the irregularity of the cavities.[20,21] However, the irregularity was produced by fragmenting the walls into unevenly corrugated shapes, where one deals with highly complicated surface profiles of the walls due to their high surface irregularities. Although such fractal cavity shapes could not be found in ordinary rooms, the works have demonstrated that the cavity irregularity significantly affected the damping of acoustic modes.

[a]Electronic mail: ksum@mech.uwa.edu.au
[b]Electronic mail: pan@mech.uwa.edu.au

 © 2006 Acoustical Society of America

In the architectural design of modern buildings, irregular spaces with tilted walls of regular geometry are very common. In this case, one would concern with how the inclination of the walls affects the reverberation times of such spaces in the presence of absorptive surfaces on either the tilted or other nontilted walls. One would also be interested to know whether the reverberation times can be tuned to desired values by tilting certain walls. Since there is little reported work on the effects of geometrical irregularity of rooms on the decay times of acoustic modes, and no relevant studies have been carried out for modally or locally reactive walls of regular shapes, it is clear that such effects are still not well understood. It is then necessary to establish an explicit means that can highlight the relationship between the decay times and the wall inclination, and investigate how this relationship is affected by modally or locally reactive surface locations on tilted or nontilted walls. There is also a need to understand the way that the decay times vary with the inclination and what determines the variation.

In this paper, a detailed study is conducted on the decay times of acoustic modes in a trapezoidal cavity (TC modes) with an inclined wall. The sound absorption by a locally reactive wall (also called impedance wall) is considered, where a locally reactive/impedance surface is successively assigned to each cavity wall including the inclined wall, and the other five walls are rigid. By employing the same analytical technique which has been validated[15,16] and widely used in previous works on irregular enclosures,[13–17] the trapezoidal cavity response is composed by rigid-walled modes of its bounding rectangular cavity (RC modes). The edges of the bounding cavity enclose exactly the trapezoidal shape, and TC modes are defined to evolve from individual RC modes. The decay time of each TC mode is obtained from the coupling of the RC mode that evolves it with other RC modes, where an analytical relationship between the decay time and the wall inclination is developed. Effects of the wall inclination on the decay times of TC modes are then studied when the inclination is altered by retaining a same volume of the trapezoidal cavity. The constant volume is used so that the modal density of the trapezoidal cavity is about the same for any inclination, and decay times for different inclinations can be compared under the condition of a same number of TC modes. It is found that the decay times are controlled by two different mechanisms of coupling between RC modes, namely, the damping coupling and the geometrical coupling. The characteristic of each mechanism is explained in terms of the wall inclination and the impedance surface location. Since locally reactive surfaces have a specific feature of producing RC-mode groups with same decay times as previously observed for rectangular cavities,[7–10] mathematical descriptions are used to show how both couplings generate TC-mode groups with same decay times, and the types of RC modes that evolve these TC modes. The similarity and difference between the RC-mode grouping for rectangular cavities and the TC-mode grouping for the trapezoidal cavity are then shown. A maximum or minimum or both can also exist in the decay time of each TC mode. Examples are used to illustrate how the damping and geometrical couplings act upon each other to produce extrema in the decay times of TC modes that evolve from various types of RC modes. This study provides a basic understanding of the decay time behavior in a trapezoidal space in terms of the effects of the inclined wall and the impedance surface location, and the physical mechanisms involved.

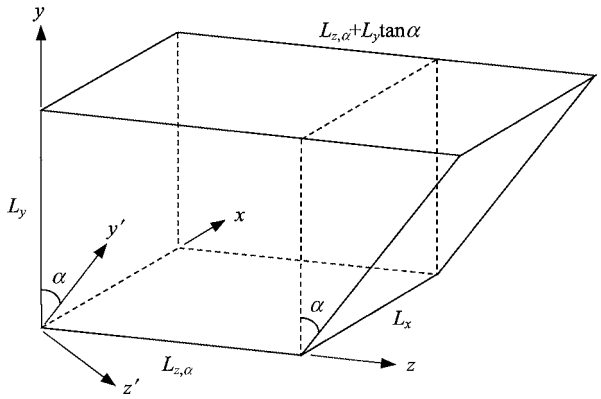

FIG. 1. Schematic illustration of the trapezoidal cavity with an inclined wall.

II. DECAY TIMES OF TC MODES

A. Solutions to the decay times

Consider the trapezoidal cavity shown in Fig. 1, which has a wall that is inclined at an angle, α. In a free vibration of the sound field in the cavity, the sound pressure at any position in the cavity, p, is described by the homogeneous acoustic wave equation as

$$\nabla^2 p + (\omega/c_0)^2 p = 0. \tag{1}$$

ω is the angular frequency (rad/s) and c_0 is the speed of sound in air. At the inclined wall, α is related to the height of a given location, y, and cavity length at this height, z, as $z = L_{z,\alpha} + y \tan\alpha$ where $L_{z,\alpha}$ is the cavity length at $y=0$. Since y and z are dependent on each other, p cannot be analytically resolved into independent components in the x, y, and z directions. As a result, Eq. (1) is not analytically solvable for the trapezoidal geometry.

However, rigid-walled modes of the bounding rectangular cavity (RC modes) can be used to compose the sound field in the trapezoidal cavity.[13,15–17] The rectangular cavity has dimensions of $L_x \times L_y \times (L_{z,\alpha} + L_y \tan\alpha)$ and it exactly encloses the trapezoidal cavity. If ω_{ai} and Φ_{ai} are the resonance frequency and shape function of the ith RC mode, they are solutions of the wave equation for the rectangular cavity such that

$$\nabla^2 \Phi_{ai} + (\omega_{ai}/c_0)^2 \Phi_{ai} = 0, \tag{2}$$

$$\omega_{ai} = c_0 \sqrt{(l_i\pi/L_x)^2 + (m_i\pi/L_y)^2 + [n_i\pi/(L_{z,\alpha} + L_y \tan\alpha)]^2}, \tag{3}$$

$$\Phi_{ai} = \cos(l_i\pi x/L_x)\cos(m_i\pi y/L_y) \times \cos[n_i\pi z/(L_{z,\alpha} + L_y \tan\alpha)]. \tag{4}$$

In the above, l_i, m_i, and n_i are indices which represent the number of nodes of the RC mode in the x, y, and z directions,

respectively. The pressure in the trapezoidal cavity can then be expressed as

$$p = \sum_{i=1}^{N} P_i \Phi_{ai}, \tag{5}$$

where P_i is the complex pressure amplitude of the ith RC mode that is determined by the boundary conditions of the trapezoidal cavity. Since Φ_{ai} is used as a basis function in the normal expansion of p, Eq. (1) can be converted into an eigenvalue equation, where ω that gives an eigenvalue of the trapezoidal cavity and P_i's that correspond to this eigenvalue, are solved.

In the derivation of the eigenvalue equation for the trapezoidal cavity, Eq. (2) is multiplied with p and Eq. (1) is multiplied with Φ_{ai}, and the former is then subtracted from the latter. When the result is integrated over the trapezoidal volume, V_T,

$$c_0^2 \int_{V_T} (\Phi_{ai} \nabla^2 p - p \nabla^2 \Phi_{ai}) dV = (\omega_{ai}^2 - \omega^2) \int_{V_T} p \Phi_{ai} dV. \tag{6}$$

The volume integral on the left hand side of Eq. (6) can be converted into a surface integral by using the second Green's formula,[22] and the equation becomes

$$c_0^2 \int_A \left(\Phi_{ai} \frac{\partial p}{\partial n} - p \frac{\partial \Phi_{ai}}{\partial n} \right) dA = (\omega_{ai}^2 - \omega^2) \int_{V_T} p \Phi_{ai} dV. \tag{7}$$

The two differentials in Eq. (7) describe the boundary conditions of the trapezoidal cavity, where A denotes the surface area of the cavity wall under consideration and n denotes the unit vector for the direction normal to the surface (positive outward). At the five noninclined walls, $\partial \Phi_{ai}/\partial n = 0$ but at the inclined wall, $\partial \Phi_{ai}/\partial n$ does not necessarily equal to zero. If a wall of interest is rigid, then $\partial p/\partial n = 0$ at the wall. If it is locally reactive (i.e., the entire wall has an impedance surface that faces the enclosed sound field), then $\partial p/\partial n = -j\omega p/c_0 \zeta_L$ at the wall, where ζ_L is the specific normal acoustical impedance of the wall surface. $|\zeta_L| \gg 1$ is considered so that the use of Φ_{ai} as a basis function is valid (i.e., the impedance surface absorption is small and it negligibly distorts the RC-mode shapes).

Consider that the trapezoidal cavity has a wall with an impedance surface and five rigid walls. By substituting Eq. (5) into Eq. (7) and then using the above boundary conditions as described by $\partial \Phi_{ai}/\partial n$ and $\partial p/\partial n$, the eigenvalue equation for the trapezoidal cavity can be obtained from Eq. (7) as

$$(\omega_{ai}^2 - \omega^2) \sum_{k=1}^{N} M_{i,k} P_k + \frac{j \rho_0 c_0 A_L \omega}{\zeta_L} \sum_{k=1}^{N} J_{i,k} P_k + \rho_0 c_0^2 A_w \sum_{k=1}^{N} I_{i,k} P_k = 0, \tag{8}$$

$$M_{i,k} = \rho_0 \int_{V_T} \Phi_{ai} \Phi_{ak} dV, \tag{9}$$

$$I_{i,k} = \frac{1}{A_w} \int_{A_w} \Phi_{ak} \frac{\partial \Phi_{ai}}{\partial n} dA, \tag{10}$$

$$J_{i,k} = \frac{1}{A_L} \int_{A_L} \Phi_{ai} \Phi_{ak} dA. \tag{11}$$

ρ_0 is the air density, A_w is the surface area of the inclined wall, and A_L is the surface area of the wall that has the impedance surface. Analytical expressions for $I_{i,k}$ can be derived from Eq. (10) after a coordinate transformation from y and z to y' and z' (see Fig. 1). If the impedance surface is at the inclined wall, then $A_L = A_w$ and the same transformation is also required before $J_{i,k}$ can be analytically obtained from Eq. (11).

From Eq. (8), a matrix equation can be formed after a substitution of $\lambda = -j\omega$ is used:

$$(\lambda^2 \mathbf{M} + \lambda \mathbf{D} + \mathbf{S}) \mathbf{P} = 0. \tag{12}$$

$\mathbf{M}$, $\mathbf{D}$, and $\mathbf{S}$ are the mass, damping, and stiffness matrices:

$$\mathbf{M} = \begin{bmatrix} M_{1,1} & \cdots & M_{1,N} \\ \vdots & \ddots & \vdots \\ M_{N,1} & \cdots & M_{N,N} \end{bmatrix}, \tag{13}$$

$$\mathbf{D} = -\frac{\rho_0 c_0 A_L}{\zeta_L} \begin{bmatrix} J_{1,1} & \cdots & J_{1,N} \\ \vdots & \ddots & \vdots \\ J_{N,1} & \cdots & J_{N,N} \end{bmatrix}, \tag{14}$$

$$\mathbf{S} = \begin{bmatrix} \omega_{a1}^2 M_{1,1} + \rho_0 c_0^2 A_w I_{1,1} & \cdots & \omega_{a1}^2 M_{1,N} + \rho_0 c_0^2 A_w I_{1,N} \\ \vdots & \ddots & \vdots \\ \omega_{aN}^2 M_{N,1} + \rho_0 c_0^2 A_w I_{N,1} & \cdots & \omega_{aN}^2 M_{N,N} + \rho_0 c_0^2 A_w I_{N,N} \end{bmatrix}. \tag{15}$$

Equation (12) is not a standard eigenvalue matrix equation. However, by using a substitution of $\mathbf{Q} = \lambda \mathbf{P}$, it can be converted to a standard equation[2,23] that is derived as

$$\begin{bmatrix} -\mathbf{M}^{-1}\mathbf{D} & -\mathbf{M}^{-1}\mathbf{S} \\ \mathbf{I} & \mathbf{0} \end{bmatrix} \begin{bmatrix} \mathbf{Q} \\ \mathbf{P} \end{bmatrix} = \lambda \begin{bmatrix} \mathbf{Q} \\ \mathbf{P} \end{bmatrix}. \tag{16}$$

$[\ ]^{-1}$ denotes the matrix inverse, $\mathbf{I}$ is an $N \times N$ identity matrix, and $\mathbf{0}$ is an $N \times N$ zero matrix. Equation (16) can now be numerically solved as an eigenvalue problem and $2N$ solutions to λ are produced, which contain N pairs of values of λ that are approximately complex conjugates. As a result, N eigenvalues that correspond to N trapezoidal cavity modes (TC modes) can be deduced. For the jth eigenvalue, λ_j, there is a corresponding set of modal pressure amplitudes, $\mathbf{P_j} = [P_1^{(j)} P_2^{(j)} \cdots P_N^{(j)}]^{\mathrm{T}}$, where $[\ ]^{\mathrm{T}}$ denotes the matrix transpose. Associated with $\lambda_j (= \lambda_{j,re} + j\lambda_{j,im})$, the resonance frequency and decay time of the jth TC mode can then be obtained as $f_{aj}^T = \omega_{aj}^T / 2\pi = \lambda_{j,im} / 2\pi$ and $T_{aj}^T = 2.2\pi / \lambda_{j,re}$. Superscript T on f_{aj}^T, ω_{aj}^T, and T_{aj}^T indicates that the characteristics are for a TC mode. As a finite value of N is used, T_{aj}^T contains a truncation error. Consequently, it is anticipated that for this error to be negligibly small, N would need to increase with α. This will be discussed in the

results and discussion section where the convergence of T_{aj}^T is illustrated.

B. Damping coupling and geometrical coupling

In order to describe the effects of α on T_{aj}^T and understand what determines the behavior of T_{aj}^T, an explicit analytical expression for T_{aj}^T is established in this subsection. Since Eq. (16) originates from Eq. (8), each eigenvalue of the trapezoidal cavity obtained by Eq. (16) actually satisfies Eq. (8) when the values of P_k's for the eigenvalue are used. For the jth eigenvalue (i.e., the jth TC mode), $\omega=\omega_a^{T(j)}$ and $P_k=P_k^{(j)}$, and Eq. (8) can be written as a quadratic equation of $\omega_a^{T(j)}$ as

$$\left(\sum_{k=1}^{N} M_{i,k}P_k^{(j)}\right)(\omega_a^{T(j)})^2 - \left(\frac{j\rho_0 c_0 A_L}{\zeta_L}\sum_{k=1}^{N} J_{i,k}P_k^{(j)}\right)\omega_a^{T(j)} - \left(\omega_{ai}^2\sum_{k=1}^{N} M_{i,k}P_k^{(j)} + \rho_0 c_0^2 A_w\sum_{k=1}^{N} I_{i,k}P_k^{(j)}\right) = 0. \quad (17)$$

Equation (17) yields a complex $\omega_a^{T(j)}$ whose real and imaginary parts, respectively, give ω_{aj}^T and T_{aj}^T.

As Eq. (17) can be satisfied by N RC modes and there are N different $\omega_a^{T(j)}$'s from which N equations in the form of Eq. (17) can result, a method is required to distinguish all the $\omega_a^{T(j)}$'s. Due to the orthogonality of RC modes in the x direction, the inclined wall only allows the coupling between those RC modes with the same modal index in the x direction, l, for a given $\omega_a^{T(j)}$. Thus, only these modes have nonzero $P_k^{(j)}$'s, and l can be obtained from a modal decomposition of the jth TC mode into $P_k^{(j)}$'s (i.e., by noting the common l of those RC modes with nonzero $P_k^{(j)}$'s). For other $\omega_a^{T(j)}$'s (i.e., other TC modes), the same way is used to determine the corresponding l's. Based on an ascending order of ω_{aj}^T's, all the l's are then sorted. On the other hand, based on an ascending order of ω_{ai}'s, the l_i's of RC modes for $\alpha=0°$ are also sorted (only the bounding rectangular cavity volume for $\alpha=0°$ is the same as V_T). The sorted l's and l_i's are then compared, where individual $\omega_a^{T(j)}$'s are successively assigned to individual RC modes when their l's and l_i's match each other. So, each TC mode [with a given $\omega_a^{T(j)}$ (i.e., ω_{aj}^T and T_{aj}^T)] can be defined to evolve from each RC mode. By using this method of defining TC modes, it was shown that a TC mode is dominated by the RC mode that evolves it when α is small, and by many RC modes of comparable pressure amplitudes when α is large.[24] If the jth TC mode is defined to evolve from the ith RC mode, then ω_{aj}^T and T_{aj}^T can be replaced by $\omega_{a(i)}^T$ and $T_{a(i)}^T$. A bracket is used for the subscript i to show that the ith RC mode does not necessarily evolve the ith TC mode as previously illustrated.[24] Hence, by analytically solving Eq. (17) for $\omega_a^{T(j)}$, the real and imaginary parts of the solutions give

$$f_{a(i)}^T = \omega_{a(i)}^T/2\pi = [-D_{ai,im}^{(j)} + \sqrt{B_{ai}^{(j)} + \sqrt{(B_{ai}^{(j)})^2 + (C_{ai}^{(j)})^2}}]/4\pi, \quad (18)$$

$$T_{a(i)}^T = 4.4\pi/(D_{ai,re}^{(j)} + G_{ai}^{(j)}), \quad (19)$$

where

$$B_{ai}^{(j)} = 2\omega_{ai}^2 + 2R_{ai,re}^{(j)} + [(D_{ai,im}^{(j)})^2 - (D_{ai,re}^{(j)})^2]/2, \quad (20)$$

$$C_{ai}^{(j)} = 2R_{ai,im}^{(j)} - D_{ai,re}^{(j)}D_{ai,im}^{(j)}, \quad (21)$$

$$R_{ai,re}^{(j)} + jR_{ai,im}^{(j)} = \rho_0 c_0^2 A_w\sum_{k=1}^{N} I_{i,k}P_k^{(j)}/\sum_{k=1}^{N} M_{i,k}P_k^{(j)}, \quad (22)$$

$$D_{ai,re}^{(j)} + jD_{ai,im}^{(j)} = \frac{\rho_0 c_0 A_L}{\zeta_L}\sum_{k=1}^{N} J_{i,k}P_k^{(j)}/\sum_{k=1}^{N} M_{i,k}P_k^{(j)}, \quad (23)$$

$$G_{ai}^{(j)} = C_{ai}^{(j)}/\sqrt{B_{ai}^{(j)} + \sqrt{(B_{ai}^{(j)})^2 + (C_{ai}^{(j)})^2}} \approx R_{ai,im}^{(j)}/\sqrt{\omega_{ai}^2 + R_{ai,re}^{(j)}}. \quad (24)$$

From Eq. (19), it can be seen that $T_{a(i)}^T$ depends on $D_{ai,re}^{(j)}$ and $G_{ai}^{(j)}$ which correspond to two different physical mechanisms. $D_{ai,re}^{(j)}$ is the real part of the damping coupling of the ith RC mode for the jth eigenvalue. It is related to the coupling of the ith RC mode with itself and other RC modes at the impedance wall [see the impedance surface coupling, $\Sigma_{k=1}^N J_{i,k}P_k^{(j)}$, in Eq. (23)], where $T_{a(i)}^T$ is altered through changes in $P_k^{(j)}$'s due to the damping of the RC modes induced by the coupling. In other words, this mechanism mainly describes the coupling between RC modes by the impedance surface. $G_{ai}^{(j)}$ is called the geometrical coupling of the ith RC mode for the jth eigenvalue. It is related to the coupling of the ith RC mode with itself and other RC modes at the inclined wall [see Eq. (24) and the inclined surface coupling, $\Sigma_{k=1}^N I_{i,k}P_k^{(j)}$, in Eq. (22)], where $T_{a(i)}^T$ is altered through changes in $P_k^{(j)}$'s induced by the coupling. In other words, this mechanism mainly describes the coupling between RC modes by the inclined wall even though it exists only with the impedance surface as explained below.

When the trapezoidal cavity does not have the impedance surface, $\zeta_L\to\infty$, and $D_{ai,re}^{(j)}$ and $D_{ai,im}^{(j)}$ given by Eq. (23) and thus, $\mathbf{D}$ given by Eq. (14), vanish. Consequently, all $P_k^{(j)}$'s in $\mathbf{P_j}$ obtained from Eq. (12) only have real values such that $R_{ai,im}^{(j)}=0$ from Eq. (22) and thus, $G_{ai}^{(j)}=0$ from Eq. (24). It follows from Eq. (19) that $T_{a(i)}^T$ is infinite (i.e., although one of the cavity walls is inclined, none of them absorb sound). On the other hand, when the cavity is rectangular but has the impedance surface, $I_{i,k}=0$ from Eq. (12) (because $\partial\Phi_{ai}/\partial n=0$) and hence, $R_{ai,re}^{(j)}=0$ and $R_{ai,im}^{(j)}=0$ from Eq. (22). So, $G_{ai}^{(j)}\approx 0$ from Eq. (24). It follows from Eq. (19) that $T_{a(i)}^T$ is finite since $D_{ai,re}^{(j)}\neq 0$ (i.e., the impedance surface absorbs sound even though all the cavity walls are noninclined).

However, $D_{ai,re}^{(j)}$ and $G_{ai}^{(j)}$ include the same coupling of the ith RC mode with itself and other RC modes throughout the trapezoidal cavity [i.e., Eqs. (22) and (23) have the same volume coupling, $\Sigma_{k=1}^N M_{i,k}P_k^{(j)}$]. Here, the coupling of the ith RC mode with other RC modes is caused by the nonorthogonality of the RC-mode shapes in the trapezoidal volume, which can be verified by substituting Eq. (4) into Eq. (9) and solving the integral. The volume coupling always exists even

TABLE I. (a) The expressions of various coupling terms and decay time, and (b) the RC-mode grouping, for $\alpha=0°$.

(a)	Impedance surface location		
	$x=0$ or L_x	$y=0$ or L_y	$z=0$ or $L_{z,0}$
$\Sigma_{k=1}^{N} M_{i,k} P_k^{(j)} (\times \rho_0)$		$\varphi_{i,i}^{(x)} \varphi_{i,i}^{(y)} \varphi_{i,i}^{(z)} P_i^{(j)}$	
$\Sigma_{k=1}^{N} J_{i,k} P_k^{(j)} (\times 1/A_L)$	$\varphi_{i,i}^{(y)} \varphi_{i,i}^{(z)} P_i^{(j)}$	$\varphi_{i,i}^{(x)} \varphi_{i,i}^{(z)} P_i^{(j)}$	$\varphi_{i,i}^{(x)} \varphi_{i,i}^{(y)} P_i^{(j)}$
$D_{ai,re}^{(j)} (\times c_0/\zeta_{L,re})$ [Eq. (23)]	$1/\varphi_{i,i}^{(x)}$	$1/\varphi_{i,i}^{(y)}$	$1/\varphi_{i,i}^{(z)}$
$G_{ai}^{(j)}$ [Eq. (24)]		0	
$T_{ai} (\times 4.4\pi\zeta_{L,re}/c_0)$ [Eq. (19)]	$\varphi_{i,i}^{(x)}$	$\varphi_{i,i}^{(y)}$	$\varphi_{i,i}^{(z)}$

(b)		Impedance surface location		
RC-mode group	RC-mode subgroup	$x=0$ or L_x	$y=0$ or L_y	$z=0$ or $L_{z,0}$
Grazing	$T_{ai} (\times 4.4\pi\zeta_{L,re}/c_0)$	L_x	L_y	$L_{z,0}$
	Fundamental	(0,0,0)	(0,0,0)	(0,0,0)
	Axial	(0,0,#), (0,#,0)	(0,0,#), (#,0,0)	(0,#,0), (#,0,0)
	Tangential	(0,#,#)	(#,0,#)	(#,#,0)
Nongrazing	$T_{ai} (\times 4.4\pi\zeta_{L,re}/c_0)$	$0.5L_x$	$0.5L_y$	$0.5L_{z,0}$
	Axial	(#,0,0)	(0,#,0)	(0,0,#)
	Tangential	(#,0,#), (#,#,0)	(#,#,0), (0,#,#)	(0,#,#), (#,0,#)
	Oblique	(#,#,#)	(#,#,#)	(#,#,#)

when the cavity is rectangular. In this case, the ith RC mode is coupled to itself only because the RC-mode shapes are orthogonal to each other in the rectangular volume, and $\Sigma_{k=1}^{N} M_{i,k} P_k^{(j)}$ then becomes $M_{i,i} P_i^{(j)}$.

C. Grouping of acoustic modes

One way to understand how the inclined wall affects $T_{a(i)}^T$ due to the impedance surface is to examine whether groups of TC modes with same decay times would be generated. It is also necessary to know whether the TC-mode grouping is similar to the RC-mode grouping for rectangular cavities in previous studies,[7–10] and whether the TC-mode grouping would change with the impedance surface location at different walls of the trapezoidal cavity. In this respect, a fixed ζ_L is used in the present work so that changes in $T_{a(i)}^T$ are due to the wall inclination only. The true geometrical influence of the inclined wall on $T_{a(i)}^T$ can then be uniquely quantified when it is not masked by the effect of a frequency-varying ζ_L, which only relates to the material properties of the impedance surface. (Note: $T_{a(i)}^T$'s are subject to different values of ζ_L because they are definable at different $f_{a(i)}^T$'s, but ζ_L varies with frequency and the variation is different for different materials). However, as $T_{a(i)}^T$ is nearly proportional to ζ_L [this can be examined from Eqs. (19) and (23), and will be shown in Sec. III A], the effect of a varying ζ_L can be approximately included as a multiplication factor to $T_{a(i)}^T$ if the frequency variation of ζ_L of the material under consideration is known. Also, since decay times and resonance frequencies are mainly affected by the real and imaginary parts of ζ_L (i.e., $\zeta_{L,re}$ and $\zeta_{L,im}$), respectively,[6,8] and $\zeta_{L,im}$ is generally small for most materials, $\zeta_{L,re} \gg \zeta_{L,im}$ is considered so that $|\zeta_L| \gg 1$ is satisfied. In this subsection, $D_{ai,re}^{(j)}$ and $G_{ai}^{(j)}$ explained in Sec. II B are used to analytically describe the effects of α on $T_{a(i)}^T$ for the impedance surface location at a given wall. Mathematical descriptions are employed to show how the TC-mode grouping is determined by the behaviors of $D_{ai,re}^{(j)}$'s and $G_{ai}^{(j)}$'s of the RC modes that evolve the TC modes.

1. Grouping of RC modes

Consider $\alpha=0°$ (i.e., the cavity is rectangular). When Eqs. (9) and (11) are expanded after the substitution of Eq. (4), the elements in the analytical expressions of $M_{i,k}$ and $J_{i,k}$ are

$$\varphi_{i,k}^{(x)} = \int_0^{L_x} \cos(l_i \pi x/L_x) \cos(l_k \pi x/L_x) dx, \tag{25a}$$

$$\varphi_{i,k}^{(y)} = \int_0^{L_y} \cos(m_i \pi y/L_y) \cos(m_k \pi y/L_y) dy, \tag{25b}$$

$$\varphi_{i,k}^{(z)} = \int_0^{L_{z,0}} \cos(n_i \pi z/L_{z,0}) \cos(n_k \pi z/L_{z,0}) dz, \tag{25c}$$

where $L_{z,0}$ is the cavity length. The orthogonality of RC modes in the rectangular volume implies the expression of $\Sigma_{k=1}^{N} M_{i,k} P_k^{(j)}$ given in Table I(a). Since the cavity response at $\omega_{a(i)}^T (=\omega_{ai})$ is dominated by the ith RC mode only (i.e., $P_i^{(j)}$ is very large compared to all the other $P_k^{(j)}$'s), $\Sigma_{k=1}^{N} J_{i,k} P_k^{(j)} \approx J_{i,i} P_i^{(j)}$. This leads to the expressions of $\Sigma_{k=1}^{N} J_{i,k} P_k^{(j)}$ given in the table for the impedance surface at $x=0$ or L_x, $y=0$ or L_y, and $z=0$ or $L_{z,0}$. Also shown, are the expressions of $D_{ai,re}^{(j)}$ after $\Sigma_{k=1}^{N} J_{i,k} P_k^{(j)}$ is divided by $\Sigma_{k=1}^{N} M_{i,k} P_k^{(j)}$ as in Eq. (23). As $G_{ai}^{(j)} \approx 0$ for the rectangular cavity, Eq. (19) gives $T_{a(i)}^T = T_{ai} \approx 4.4\pi/D_{ai,re}^{(j)}$ where T_{ai} is the decay time of the ith RC mode. Therefore, for the three cases of impedance surface location, $T_{ai} \propto \varphi_{i,i}^{(x)}$, $T_{ai} \propto \varphi_{i,i}^{(y)}$, and $T_{ai} \propto \varphi_{i,i}^{(z)}$, respectively [see Table I(a)].

If $*$ denotes a non-negative integer and # denotes a non-zero positive integer, it can be mathematically shown from Eqs. (25a)–(25c) that $\varphi_{i,i}^{(x)}$ is equaled to L_x for $(0,*,*)$ and $0.5L_x$ for $(\#,*,*)$, $\varphi_{i,i}^{(y)}$ is equaled to L_y for $(*,0,*)$ and $0.5L_y$ for $(*,\#,*)$, and $\varphi_{i,i}^{(z)}$ is equaled to $L_{z,0}$ for $(*,*,0)$ and $0.5L_{z,0}$ for $(*,*,\#)$. Thus, in terms of T_{ai}, $(0,*,*)$ has twice of that for $(\#,*,*)$, $(*,0,*)$ has twice of that for $(*,\#,*)$, and $(*,*,0)$ has twice of that for $(*,*,\#)$ [see Table I(b)]. This means that for each of the three cases of impedance surface location, the T_{ai}'s of the RC modes that graze the surface have a same value, and those of the RC modes that do not graze the surface have another same value. The former is two times higher than the latter. In an orthogonal direction parallel to the surface, a grazing RC mode has a zero index [either $(0,*,*)$, $(*,0,*)$, or $(*,*,0)$], and a nongrazing RC mode has a nonzero index [either $(\#,*,*)$, $(*,\#,*)$, or $(*,*,\#)$]. Hence, for the impedance surface location at a given wall of the rectangular cavity, there are altogether two RC-mode groups, namely, the grazing group and the nongrazing group. As summarized in Table I(b), the grazing group has four subgroups that consist of one fundamental [i.e., (0,0,0)], one tangential, and two axial subgroups, while the non-grazing group also has four subgroups that consist of one axial, one oblique, and two tangential subgroups. (Note: An axial RC mode has two zero indices, a tangential RC mode has one zero index, and an oblique RC mode has nonzero indices).[8,10]

2. Grouping of TC modes

Consider $\alpha>0°$ (i.e., the cavity is trapezoidal). The impedance surface is trapezoidal when it is at $x=0$ or L_x, and rectangular when it is at $y=0$ or L_y, $z=0$, or the inclined wall. When Eqs. (9)–(11) are expanded, the elements in the analytical expressions of $M_{i,k}$, $I_{i,k}$, and $J_{i,k}$ are

$$\varphi_{i,k}^{(yz)} = \int_0^{L_y} \cos\left(\frac{m_i\pi y}{L_y}\right)\cos\left(\frac{m_k\pi y}{L_y}\right) \times \int_0^{L_{z,\alpha}+y\tan\alpha} \cos\left(\frac{n_i\pi z}{L_{z,\alpha}+L_y\tan\alpha}\right) \times\cos\left(\frac{n_k\pi z}{L_{z,\alpha}+L_y\tan\alpha}\right)dzdy, \tag{26a}$$

$$\varphi_{i,k}^{(z0)} = \int_0^{L_{z,\alpha}} \cos\left(\frac{n_i\pi z}{L_{z,\alpha}+L_y\tan\alpha}\right)\cos\left(\frac{n_k\pi z}{L_{z,\alpha}+L_y\tan\alpha}\right)dz, \tag{26b}$$

$$\varphi_{i,k}^{(zL)} = \int_0^{L_{z,\alpha}+L_y\tan\alpha} \cos\left(\frac{n_i\pi z}{L_{z,\alpha}+L_y\tan\alpha}\right) \times\cos\left(\frac{n_k\pi z}{L_{z,\alpha}+L_y\tan\alpha}\right)dz, \tag{26c}$$

$$\varphi_{i,k}^{(y1)} = \int_0^{L_y/\cos\alpha} \cos\left(\frac{m_i\pi y}{L_y}\right)\cos\left(\frac{m_k\pi y}{L_y}\right) \times\cos\left(\frac{n_i\pi z}{L_{z,\alpha}+L_y\tan\alpha}\right)\cos\left(\frac{n_k\pi z}{L_{z,\alpha}+L_y\tan\alpha}\right)dy', \tag{26d}$$

$$\varphi_{i,k}^{(y2)} = \int_0^{L_y/\cos\alpha} \cos\left(\frac{m_k\pi y}{L_y}\right)\cos\left(\frac{n_k\pi z}{L_{z,\alpha}+L_y\tan\alpha}\right) \times\frac{\partial}{\partial n}\left[\cos\left(\frac{m_i\pi y}{L_y}\right)\cos\left(\frac{n_i\pi z}{L_{z,\alpha}+L_y\tan\alpha}\right)\right]dy'. \tag{26e}$$

As $\cos(l_i\pi x/L_x)$ is orthogonal to $\cos(l_k\pi x/L_x)$ for $0\leqslant x\leqslant L_x$, $\varphi_{i,k}^{(x)}\neq 0$ only if $l_k=l_i=l$ where Eq. (25a) becomes

$$\varphi_l^{(x)} = \int_0^{L_x} \cos^2(l\pi x/L_x)dx. \tag{27}$$

The expressions of $\Sigma_{k=1}^N M_{i,k}P_k^{(j)}$ and $\Sigma_{k=1}^N J_{i,k}P_k^{(j)}$ are then obtained as shown in Table II(a), where N_l in the table is the number of RC modes with the l index. Also shown, are the expressions of $D_{ai,re}^{(j)}$ for the impedance surface location at $x=0$ or L_x, $y=0$ or L_y, $z=0$, and the inclined wall after $\Sigma_{k=1}^N J_{i,k}P_k^{(j)}$ is divided by $\Sigma_{k=1}^N M_{i,k}P_k^{(j)}$ as in Eq. (23). It can be seen from the table that in terms of the indices of the ith RC mode that evolves a TC mode, $D_{ai,re}^{(j)}$ depends only on $l_i(=l)$ in the first case via $\varphi_l^{(x)}$, but only on m_i and n_i in the last four cases via $\varphi_{i,k}^{(yz)}$, $\varphi_{i,k}^{(z0)}$, $\varphi_{i,k}^{(zL)}$, $\varphi_{i,k}^{(y)}$, and $\varphi_{i,k}^{(y1)}$. So, in the first case, the $D_{ai,re}^{(j)}$'s of RC modes have a same value when $l=0$ and another same value when $l>0$, and the former is half of the latter [because from Eq. (27), $\varphi_l^{(x)}=L_x$ for $l=0$, and $0.5L_x$ for $l>0$]. Also, in each of the last four cases, the $D_{ai,re}^{(j)}$'s of those RC modes with same m_i's and n_i's are the same (i.e., the RC modes have a common dependence of these indices when they have the same m_i's and n_i's).

Next, the behavior of $G_{ai}^{(j)}$ is analytically described. From Eq. (23),

$$D_{ai,im}^{(j)} \approx \frac{\rho_0 c_0 A_L}{\zeta_{L,re}}\left(\sum_{k=1}^N J_{i,k}P_{k,im}^{(j)}\sum_{k=1}^N M_{i,k}P_{k,re}^{(j)} - \sum_{k=1}^N J_{i,k}P_{k,re}^{(j)}\sum_{k=1}^N M_{i,k}P_{k,im}^{(j)}\right) \Bigg/ \left[\left(\sum_{k=1}^N M_{i,k}P_{k,re}^{(j)}\right)^2 + \left(\sum_{k=1}^N M_{i,k}P_{k,im}^{(j)}\right)^2\right], \tag{28}$$

where $P_{k,re}^{(j)}$ and $P_{k,im}^{(j)}$ are the real and imaginary parts of $P_k^{(j)}$. When the impedance surface is at $x=0$ or L_x, $\Sigma_{k=1}^N J_{i,k}P_{k,re}^{(j)}$, $\Sigma_{k=1}^N J_{i,k}P_{k,im}^{(j)}$, $\Sigma_{k=1}^N M_{i,k}P_{k,re}^{(j)}$, and $\Sigma_{k=1}^N M_{i,k}P_{k,im}^{(j)}$ in Eq. (28) are, respectively, given by $\Sigma_{k=1}^{N_l}\varphi_{i,k}^{(yz)}P_{k,re}^{(j)}/A_L$, $\Sigma_{k=1}^{N_l}\varphi_{i,k}^{(yz)}P_{k,im}^{(j)}/A_L$, $\rho_0\varphi_l^{(x)}\Sigma_{k=1}^{N_l}\varphi_{i,k}^{(yz)}P_{k,re}^{(j)}$, and $\rho_0\varphi_l^{(x)}\Sigma_{k=1}^{N_l}\varphi_{i,k}^{(yz)}P_{k,im}^{(j)}$. Thus, $D_{ai,im}^{(j)}\approx 0$ which implies that $P_{k,im}^{(j)}\approx 0$. It follows that $R_{ai,im}^{(j)}\approx 0$ from Eq. (22) and $G_{ai}^{(j)}$

TABLE II. (a) The expressions of various coupling terms and decay time, and (b) the TC-mode grouping, for $\alpha > 0°$. Re[ ] and Im[ ] denote the real and imaginary parts of the complex quantity. T_{y0}, T_{yL}, T_{z0}, and T_{Inc}, respectively, denote the decay times of those TC modes that evolve from the $(*,m,n)$ modes for the impedance surface location at $y=0$, $y=L_y$, $z=0$, and the inclined wall. $H^{(j)}_{i(yz)}=\Sigma^{N_l}_{k=1}\varphi^{(yz)}_{i,k}P^{(j)}_k$, $H^{(j)}_{i(z0)}=\Sigma^{N_l}_{k=1}\varphi^{(z0)}_{i,k}P^{(j)}_k$, $H^{(j)}_{i(zL)}=\Sigma^{N_l}_{k=1}\varphi^{(zL)}_{i,k}P^{(j)}_k$, $H^{(j)}_{i(y)}=\Sigma^{N_l}_{k=1}\varphi^{(y)}_{i,k}P^{(j)}_k$, $H^{(j)}_{i(y1)}=\Sigma^{N_l}_{k=1}\varphi^{(y1)}_{i,k}P^{(j)}_k$, and $H^{(j)}_{i(y2)}=\Sigma^{N_l}_{k=1}\varphi^{(y2)}_{i,k}P^{(j)}_k$.

(a)

	Impedance surface location				
	$x=0$ or L_x	$y=0$	$y=L_y$	$z=0$	Inclined wall
$\Sigma^N_{k=1}M_{i,k}P^{(j)}_k(\times\rho_0)$			$\varphi^{(x)}_l H^{(j)}_{i(yz)}$		
$\Sigma^N_{k=1}J_{i,k}P^{(j)}_k(\times 1/A_L)$	$H^{(j)}_{i(yz)}$	$\varphi^{(x)}_l H^{(j)}_{i(z0)}$	$\varphi^{(x)}_l H^{(j)}_{i(zL)}$	$\varphi^{(x)}_l H^{(j)}_{i(y)}$	$\varphi^{(x)}_l H^{(j)}_{i(y1)}$
$D^{(j)}_{ai,re}(\times c_0/\zeta_{L,re})$ [Eq. (23)]	$1/\varphi^{(x)}_l$	$\mathrm{Re}[H^{(j)}_{i(z0)}/H^{(j)}_{i(yz)}]$	$\mathrm{Re}[H^{(j)}_{i(zL)}/H^{(j)}_{i(yz)}]$	$\mathrm{Re}[H^{(j)}_{i(y)}/H^{(j)}_{i(yz)}]$	$\mathrm{Re}[H^{(j)}_{i(y1)}/H^{(j)}_{i(yz)}]$
$\Sigma^N_{k=1}I_{i,k}P^{(j)}_k(\times 1/A_w)$			$\varphi^{(x)}_l H^{(j)}_{i(y2)}$		
$R^{(j)}_{ai,re}+jR^{(j)}_{ai,im}(\times c_0^2)$ [Eq. (22)]	$\mathrm{Re}[H^{(j)}_{i(y2)}/H^{(j)}_{i(yz)}]+j0$		$H^{(j)}_{i(y2)}/H^{(j)}_{i(yz)}$		
$G^{(j)}_{ai}(\times c_0^2)$ [Eq. (24)]	0		$\mathrm{Im}[H^{(j)}_{i(y2)}/H^{(j)}_{i(yz)}]/\sqrt{\omega^2_{ai}+c_0^2\mathrm{Re}[H^{(j)}_{i(y2)}/H^{(j)}_{i(yz)}]}$		
$T^T_{a(i)}(\times 4.4\pi\zeta_{L,re})$ [Eq. (19)]	$\varphi^{(x)}_l/c_0$	$\dfrac{1}{c_0\mathrm{Re}\left[\dfrac{H^{(j)}_{i(z0)}}{H^{(j)}_{i(yz)}}\right]+\zeta_{L,re}G^{(j)}_{ai}}$	$\dfrac{1}{c_0\mathrm{Re}\left[\dfrac{H^{(j)}_{i(zL)}}{H^{(j)}_{i(yz)}}\right]+\zeta_{L,re}G^{(j)}_{ai}}$	$\dfrac{1}{c_0\mathrm{Re}\left[\dfrac{H^{(j)}_{i(y)}}{H^{(j)}_{i(yz)}}\right]+\zeta_{L,re}G^{(j)}_{ai}}$	$\dfrac{1}{c_0\mathrm{Re}\left[\dfrac{H^{(j)}_{i(y1)}}{H^{(j)}_{i(yz)}}\right]+\zeta_{L,re}G^{(j)}_{ai}}$

(b)

	Impedance surface location at $x=0$ or L_x					
RC-mode group that evolves TC modes	Grazing group			Nongrazing group		
RC-mode subgroup	Fundamental: (0,0,0); Axial: (0,0,#), (0,#,0); Tangential: (0,#,#)			Axial: (#,0,0); Tangential: (#,0,#), (#,#,0); Oblique: (#,#,#)		
$T^T_{a(i)}(\times 4.4\pi\zeta_{L,re}/c_0)$	L_x			$0.5L_x$		
	Impedance surface location					
	$y=0$	$y=L_y$		$z=0$		Inclined wall
$T^T_{a(i)}$ [evolved from $(*,m,n)$]	T_{y0}	T_{yL}		T_{z0}		T_{Inc}
Forms of $(*,m,n)$ modes (i.e., many groups of RC modes)	$(*,\#,0)$, $(\#,*,0)$, $(*,0,\#)$, $(\#,0,*)$, $(0,*,\#)$, or $(0,\#,*)$	$(*,*,0)$, $(*,0,*)$, or $(0,*,*)$	$(*,*,\#)$, $(*,\#,*)$, or $(\#,*,*)$	$(*,\#,\#)$, $(\#,*,\#)$, or $(\#,\#,*)$	$(\#,\#,0)$, $(\#,0,\#)$, or $(0,\#,\#)$	$(\#,0,0)$, $(0,\#,0)$, or $(0,0,\#)$
RC-mode subgroups for each form (F: Fundamental, A: Axial, T: Tangential, O: Oblique)	One A, one T	One F, two A's, one T	One A, two T's, one O	One T, one O	One T	One A

≈ 0 from Eq. (24). Hence, from Eq. (19), $T^T_{a(i)} \approx 4.4\pi/D^{(j)}_{ai,re} \propto \varphi^{(x)}_l$ [see Table II(a)] where the wall inclination negligibly affects $T^T_{a(i)}$ because $\varphi^{(x)}_l$ is independent of α. In other words, as the impedance surface shape is trapezoidal at $x=0$ or L_x, $\Sigma^N_{k=1} J_{i,k} P^{(j)}_k$ has a common dependence of α as $\Sigma^N_{k=1} M_{i,k} P^{(j)}_k$ [i.e., $\varphi^{(yz)}_{i,k}$ given by Eq. (26a)]. Both couplings act in an exactly opposite way such that the geometrical effect of the inclined wall (i.e., geometrical coupling, $G^{(j)}_{ai}$) on $T^T_{a(i)}$ is negligible. Therefore, the result is similar to that for $\alpha=0°$, where the $T^T_{a(i)}$'s of the TC modes that evolve from RC modes which graze the impedance surface have a same value, and those of the TC modes that evolve from RC modes which do not graze the surface have another same value [see Table II(b) for the surface location at $x=0$ or L_x]. The former is two times higher than the latter because $\varphi^{(x)}_l$ is equaled to L_x for grazing RC modes and $0.5L_x$ for nongrazing RC modes. It can be seen that the TC-mode grouping is also similar, where there are altogether two groups of TC modes that evolve from the grazing and nongrazing RC modes, respectively. The grazing group has four subgroups (one fundamental, one tangential, two axial) and the nongrazing group also has four subgroups (one axial, one oblique, two tangential).

When the impedance surface is at $y=0$ or L_y, $z=0$, or the inclined wall, both the impedance surface and volume couplings depend differently on α such that $G^{(j)}_{ai}$ can be significant to $T^T_{a(i)}$ (i.e., $\varphi^{(yz)}_{i,k}$ has a different dependence of α to $\varphi^{(z0)}_{i,k}$, $\varphi^{(zL)}_{i,k}$, $\varphi^{(y)}_{i,k}$, and $\varphi^{(y1)}_{i,k}$). The expressions of $\Sigma^N_{k=1} I_{i,k} P^{(j)}_k$, $R^{(j)}_{ai,re} + jR^{(j)}_{ai,im}$, and $G^{(j)}_{ai}$ for any of these impedance surface locations are given in Table II(a). Since $G^{(j)}_{ai}$ depends on $\sqrt{\omega^2_{ai} + R^{(j)}_{ai,re}}$ and $R^{(j)}_{ai,im}$ [see Eq. (24)], which are in common that both depend on m_i and n_i via $\varphi^{(y2)}_{i,k}$ and $\varphi^{(yz)}_{i,k}$ [see Table II(a)], the $G^{(j)}_{ai}$'s of those RC modes with same m_i's and n_i's are the same. As $T^T_{a(i)} \propto 1/(D^{(j)}_{ai,re} + G^{(j)}_{ai})$ from Eq. (19), only the $T^T_{a(i)}$'s of the TC modes that evolve from those RC modes with same m_i's and n_i's would have a same value (i.e., one combination of values of m_i's and n_i's yields one decay time value and thus, one group of TC modes). So, there are many groups of TC modes from many different combinations of values of m_i's and n_i's. Table II(b) summarizes all possible forms of RC modes that evolve the TC modes, and the associated RC-mode subgroups for each form.

III. RESULTS AND DISCUSSION

Examples are presented to illustrate how the impedance surface location and the inclined wall affect the grouping of TC modes based on their decay times, and what determines the decay time variation with the wall inclination. The width and height of the trapezoidal cavity used in the examples are $L_x=0.5$ m and $L_y=0.575$ m, and values of α from 0° to 45° inclusive are considered in 5° steps. Since V_T is maintained the same when α is changed, $L_{z,\alpha} + L_y \tan\alpha$ (the cavity length at $y=L_y$) has to increase with α, and $L_{z,\alpha}$ (the cavity length at $y=0$) has to decrease with α (see Fig. 1). For $\alpha = (0°, 5°, 10°, 15°, 20°, 25°, 30°, 35°, 40°, 45°)$, the corresponding values used for both lengths are $L_{z,\alpha} + L_y \tan\alpha = (0.434, 0.459, 0.485, 0.511, 0.539, 0.568, 0.6, 0.635, 0.675, 0.722)$ m and $L_{z,\alpha} = (0.434, 0.409, 0.383, 0.357, 0.329, 0.3, 0.268, 0.233, 0.193, 0.147)$ m.

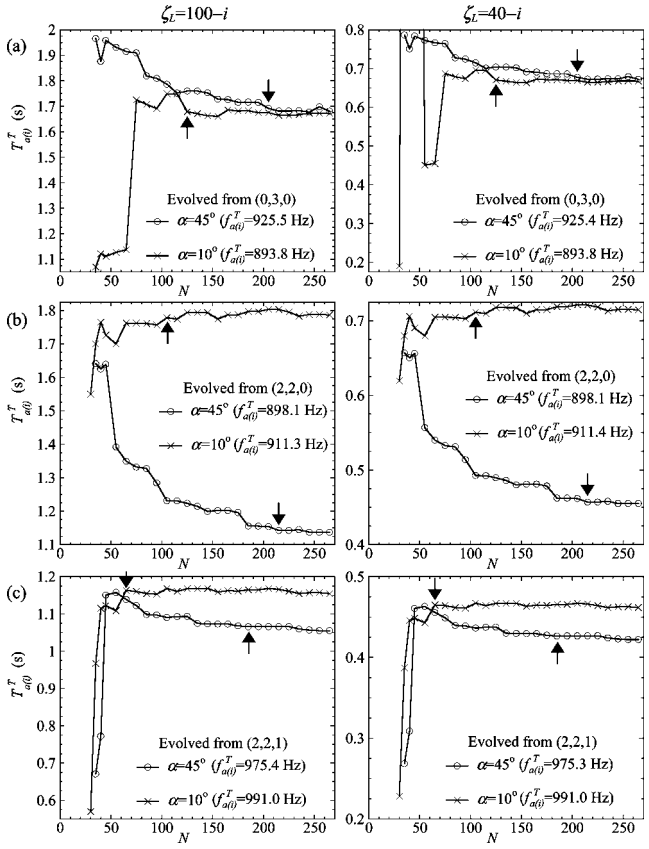

FIG. 2. Decay times of the TC modes that evolve from (a) (0,3,0), (b) (2,2,0), and (c) (2,2,1), as a function of the number of RC modes used in the decay time calculation, N, for the impedance surface at the inclined wall of the trapezoidal cavity. The arrows indicate the points beyond which adjacent values of the individual decay times are within about 1% from each other.

A. Convergence of decay times of TC modes

For the values of the trapezoidal cavity dimensions given above, $T^T_{a(i)}$'s are evaluated by solving Eq. (16). Figure 2 depicts the values of $T^T_{a(i)}$'s of the TC modes that evolve from (0,3,0), (2,2,0), and (2,2,1), as a function of the number of RC modes used in the decay time calculation, N. The case of the impedance surface location at the inclined wall is shown, where a lightly ($\zeta_L = 100 - i$) and a moderately ($\zeta_L = 40 - i$) absorptive impedance surface as well as $\alpha = 10°$ and 45° are considered. For each value of α, the arrows in the figure indicate the points beyond which adjacent values of the individual $T^T_{a(i)}$'s are within about 1% from each other. It can be seen that the $T^T_{a(i)}$'s converge when N increases, but the three TC modes have some discrepancies in the values of N associated with the arrow positions. Therefore, the convergence rates of their $T^T_{a(i)}$'s are different, and these are due to the different volume, impedance surface, and inclined surface couplings of (0,3,0), (2,2,0), and (2,2,1). In addition, the

values of N associated with the arrow positions for $\alpha=45°$ are much higher than those for $\alpha=10°$ (see Fig. 2) even though V_T does not change, because the size of the bounding rectangular cavity increases with α. The bounding cavity for $\alpha=45°$ is thus larger and has more RC modes than that for $\alpha=10°$. So, in order to achieve the same truncation error limit (i.e., 1% or less) in the $T^T_{a(i)}$'s, the values of N for $\alpha=45°$ need to be higher than those for $\alpha=10°$. Figure 2 also indicates that for each TC mode, the arrow positions are the same for $\zeta_L=100-i$ and $40-i$, which suggest that the value of ζ_L does not affect the convergence rates of the individual $T^T_{a(i)}$'s. The reason is because ζ_L is only a multiplication factor for the impedance surface and volume couplings [see Eq. (23)], where these couplings of the respective (0,3,0), (2,2,0), and (2,2,1) with themselves and other RC modes are altered by the same amount when ζ_L changes. As a result, if ζ_L changes from $100-i$ to $40-i$, only the values of the $T^T_{a(i)}$'s are reduced by about 2.5 times as can be examined from Fig. 2, but their variations with N are negligibly changed. Similar observations can also be obtained for the impedance surface location at other walls. In the following, values of N of several hundreds have been used and they are larger for higher values of α. These values of N are sufficient for the truncation errors in the first 26 TC modes to be ignored, since the $T^T_{a(i)}$'s of only these modes are of interest and the highest resonance frequency of the modes is around 1000 Hz.

B. Decay time behavior of RC modes

$\alpha=0°$ is first considered. Figure 3 shows the T_{ai}'s of six RC modes for the impedance surface location at $x=0$ or L_x, $y=0$ or L_y, and $z=0$ or $L_{z,0}$. For these three cases, respectively, (0,0,1), (0,2,0), and (0,2,1) [i.e., $(0,*,*)$], (0,0,1), (1,0,1), and (2,0,1) [i.e., $(*,0,*)$], and (0,2,0), (1,2,0), and (2,2,0) [i.e., $(*,*,0)$] are the grazing modes, but (1,0,1), (1,2,0), and (2,2,0) [i.e., $(\#,*,*)$], (0,2,0), (1,2,0), and (2,2,0) [i.e., $(*,\#,*)$], and (0,2,1), (1,2,1), and (2,2,1) [i.e., $(*,*,\#)$] are the nongrazing modes. In all cases, it is obvious from Fig. 3 that the T_{ai}'s for the grazing modes are twice of those for the nongrazing modes. The decay time behavior and the associated RC-mode grouping (i.e., grazing and nongrazing) are determined by the $D^{(j)}_{ai,re}$'s of the individual RC modes. The $D^{(j)}_{ai,re}$'s further depend on the $J_{i,i}P^{(j)}_i$-to-$M_{i,i}P^{(j)}_i$ ratios of the modes. Figure 4 presents the $J_{i,i}P^{(j)}_i$'s, $M_{i,i}P^{(j)}_i$'s, $D^{(j)}_{ai,re}$'s, and $G^{(j)}_{ai}$'s of the RC modes. Only the real parts of $J_{i,i}P^{(j)}_i$'s and $M_{i,i}P^{(j)}_i$'s are illustrated because the imaginary parts are negligibly small due to $\zeta_{L,re} \gg \zeta_{L,im}$. As described in Sec. II C, when the impedance surface is at $x=0$ or L_x, $y=0$ or L_y, or $z=0$ or $L_{z,0}$, the $\varphi^{(x)}_{i,i}, \varphi^{(y)}_{i,i}$, or $\varphi^{(z)}_{i,i}$ of each RC mode, respectively, controls the $J_{i,i}P^{(j)}_i$-to-$M_{i,i}P^{(j)}_i$ ratio (thus, $D^{(j)}_{ai,re}$ and T_{ai}) of the mode. So, as can be examined from Fig. 4, for each case of impedance surface location, the grazing modes have a same $J_{i,i}P^{(j)}_i$-to-$M_{i,i}P^{(j)}_i$ ratio (or same $D^{(j)}_{ai,re}$'s), the nongrazing modes have another same ratio, and the $D^{(j)}_{ai,re}$'s for the grazing modes are half of those for the nongrazing modes. Also, the $G^{(j)}_{ai}$'s of the modes are zero (see Fig. 4) because all the cavity walls are non inclined. Hence, the T_{ai}'s of the grazing modes have same values and those of the nongrazing modes have other same values as seen in Fig. 3. The former are twice of the latter [i.e., opposite to the $D^{(j)}_{ai,re}$'s in Fig. 4. Also, see Eq. (19)].

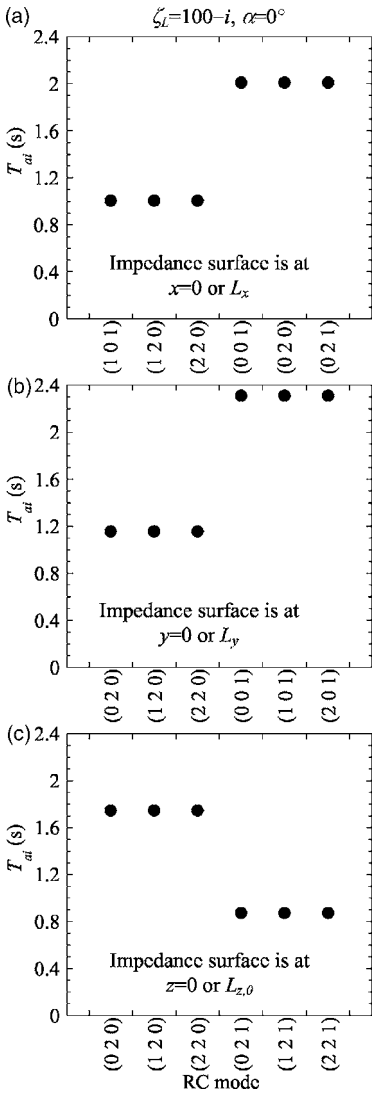

FIG. 3. Decay times of six RC modes for the impedance surface location at (a) $x=0$ or L_x, (b) $y=0$ or L_y, and (c) $z=0$ or $L_{z,0}$ of the rectangular cavity.

C. Decay time behavior of TC modes

$\alpha>0°$ is now considered. Figure 5 shows the $T^T_{a(i)}$'s of six TC modes that evolve from (0,2,0), (1,2,0), (2,2,0), (0,2,1), (1,2,1), and (2,2,1), as a function of α for the impedance surface location at $z=0$, $y=L_y$, $x=0$, and the inclined wall. The $T^T_{a(i)}$'s are evaluated by solving Eq. (16). From Fig. 5, two features of the $T^T_{a(i)}$'s can be observed. First, when the impedance surface is at $z=0$, $y=L_y$, or the inclined wall, the $T^T_{a(i)}$'s of (0,2,0), (1,2,0), and (2,2,0) [i.e., $(*,2,0)$] are the same, and those of (0,2,1), (1,2,1), and (2,2,1) [i.e., $(*,2,1)$] are the same [see Figs. 5(a), 5(b), and 5(d)]. In other words, the $T^T_{a(i)}$'s of the TC modes with same m_i's and n_i's are the same. However, when the surface is at $x=0$, the $T^T_{a(i)}$'s of (0,2,0) and (0,2,1) [i.e., $(0,*,*)$] have a same value of 2.0 s, and those of (1,2,0), (1,2,1), (2,2,0), and (2,2,1) [i.e., $(\#,*,*)$] have another same value of 1.0 s (i.e., the former

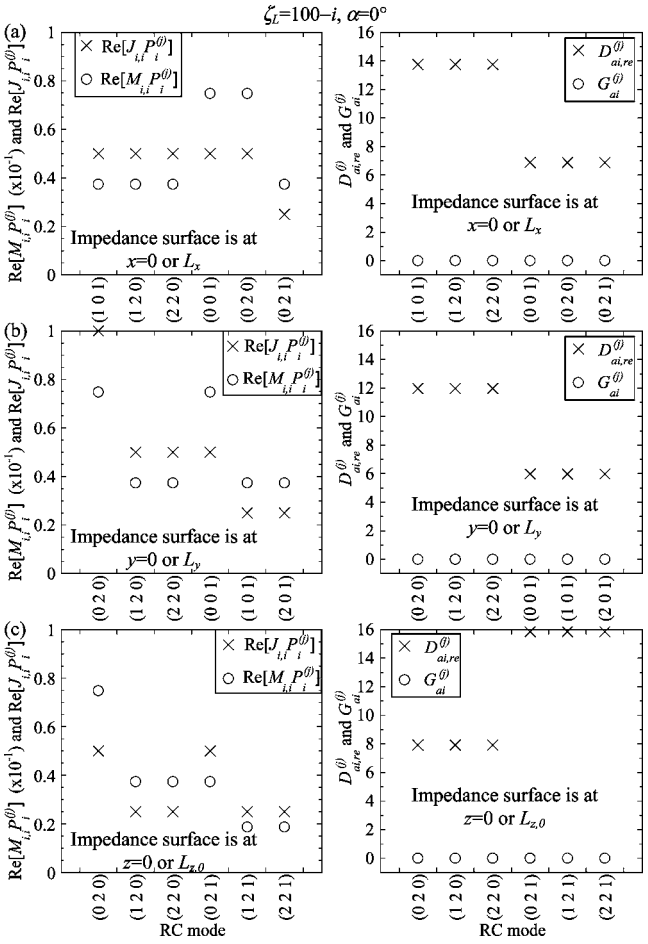

FIG. 4. Real parts of the impedance surface and volume couplings, and the geometrical coupling and the real part of the damping coupling of six RC modes, for the impedance surface location at (a) $x=0$ or L_x, (b) $y=0$ or L_y, and (c) $z=0$ or $L_{z,0}$ of the rectangular cavity.

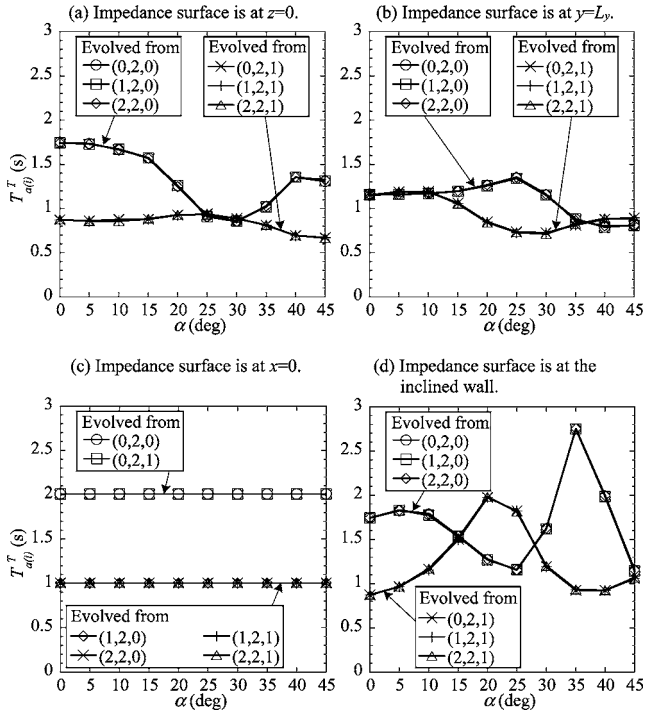

FIG. 5. Decay times of the TC modes that evolve from six RC modes, as a function of α for the impedance surface location at (a) $z=0$, (b) $y=L_y$, (c) $x=0$, and (d) the inclined wall of the trapezoidal cavity.

is two times higher than the latter) [see Fig. 5(c)]. Second, for the surface at $z=0$, $y=L_y$, or the inclined wall, the $T^T_{a(i)}$'s vary with α where a maximum or minimum or both can exist. This means that the impedance surface absorption can be adjusted by changing α, and it is unnecessary for the surface to change area (only when the surface is at $z=0$), change location to another wall, or be at the inclined wall [see Figs. 5(a), 5(b), and 5(d)]. For the surface at $x=0$, the $T^T_{a(i)}$'s are independent of α so there are no extrema [see Fig. 5(c)]. In other words, if the impedance surface is at this location, its absorption is not affected by the wall inclination. The first feature is explained below, and the second feature is further illustrated later in the discussion.

The decay time behavior and the associated TC-mode grouping in Fig. 5 are determined by both the $D^{(j)}_{ai,re}$'s and $G^{(i)}_{ai}$'s of the RC modes that evolve the TC modes. The $D^{(j)}_{ai,re}$'s and $G^{(j)}_{ai}$'s further depend on the impedance surface, inclined surface, and volume couplings of the RC modes. Since a TC mode is composed by more than one RC mode, the RC mode that evolves the TC mode does not only couple with itself but also, with other RC modes. So, $\Sigma^N_{k=1}J_{i,k}P^{(j)}_k$ and $\Sigma^N_{k=1}M_{i,k}P^{(j)}_k$ control $D^{(j)}_{ai,re}$ rather than $J_{i,i}P^{(j)}_i$ and $M_{i,i}P^{(j)}_i$, and $\Sigma^N_{k=1}I_{i,k}P^{(j)}_k$ and $\Sigma^N_{k=1}M_{i,k}P^{(j)}_k$ control $G^{(j)}_{ai}$ rather than $I_{i,i}P^{(j)}_i$ and $M_{i,i}P^{(j)}_i$ Figure 6 presents the impedance surface and volume couplings, as well as the $|R^{(j)}_{ai,im}|$'s and $\sqrt{\omega^2_{ai}+R^{(j)}_{ai,re}}$'s of the RC modes for $\alpha=45°$. As can be examined from Fig. 6(a), although both couplings vary among the RC modes, the $\Sigma^N_{k=1}J_{i,k}P^{(j)}_k$-to-$\Sigma^N_{k=1}M_{i,k}P^{(j)}_k$ ratios of (0,2,0), (1,2,0), and (2,2,0) [i.e., (∗,2,0)] are the same, and those of (0,2,1), (1,2,1), and (2,2,1) [i.e., (∗,2,1)] are the same when the impedance surface is at $z=0$, $y=L_y$, or the inclined wall (can be judged as equal spacings between the markers for both couplings), In addition, although $|R^{(j)}_{ai,im}|$ and $\sqrt{\omega^2_{ai}+R^{(j)}_{ai,re}}$ also vary among the RC modes, (0,2,0), (1,2,0), and (2,2,0) have a same $|R^{(j)}_{ai,im}|$-to-$\sqrt{\omega^2_{ai}+R^{(j)}_{ai,re}}$ ratio, and (0,2,1), (1,2,1), and (2,2,1) have another same ratio [see Fig. 6(b)]. However, when the surface is at $x=0$, (0,2,0) and (0,2,1) [i.e., $(0,*,*)$] have a same $\Sigma^N_{k=1}J_{i,k}P^{(j)}_k$-to-$\Sigma^N_{k=1}M_{i,k}P^{(j)}_k$ ratio, (1,2,0), (2,2,0), (1,2,1), and (2,2,1) [i.e., $(\#,*,*)$] have another same ratio, and the former is half of the latter. Also, the $|R^{(j)}_{ai,im}|$-to-$\sqrt{\omega^2_{ai}+R^{(j)}_{ai,re}}$ ratios of the RC modes are close to zero [i.e., $|R^{(j)}_{ai,im}|\approx 0$ in the third graph in Fig. 6(b)] because $P^{(j)}_{k,im}$'s are zero, which can be shown to cause by the exactly opposite effects of $\Sigma^N_{k=1}J_{i,k}P^{(j)}_k$ and $\Sigma^N_{k=1}M_{i,k}P^{(j)}_k$ as explained in Sec. II C. As an example, Fig. 7 shows the magnitudes and phases of the inclined surface and volume couplings (i.e., $|I_{i,k}P^{(j)}_k|$, $|M_{i,k}P^{(j)}_k|$, $\theta^{(j)}_{(IP)i,k}$, and $\theta^{(j)}_{(MP)i,k}$) of (0,2,1) for $\alpha=45°$, and the impedance surface location at $x=0$ and $z=0$. It is obvious from Fig. 7(a) that when the surface is at $x=0$, the $\theta^{(j)}_{(IP)i,k}$'s and $\theta^{(j)}_{(MP)i,k}$'s of the individual couplings of (0,2,1) with itself and other RC modes are either close to 0° or ±180°, which result in the net phases in $\Sigma^N_{k=1}I_{i,k}P^{(j)}_k$ and $\Sigma^N_{k=1}M_{i,k}P^{(j)}_k$ and thus, $|R^{(j)}_{ai,im}|$ to be near zero. When the surface is at $z=0$, the $\theta^{(j)}_{(IP)i,k}$'s and $\theta^{(j)}_{(MP)i,k}$'s are more scattered [see Fig. 7(b)],

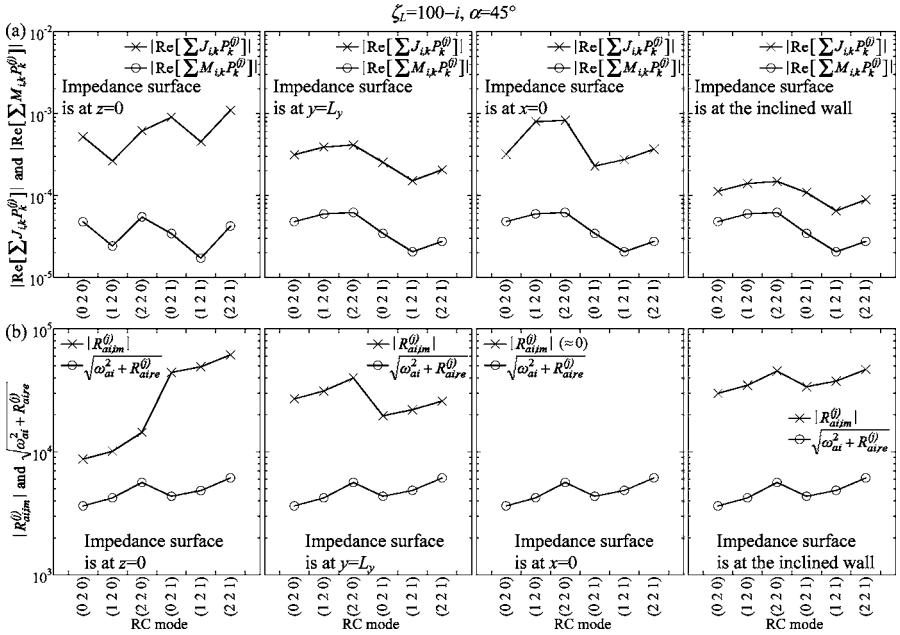

FIG. 6. Magnitudes of the real parts of the (a) impedance surface and volume couplings, and (b) denominator and magnitude of the numerator of the geometrical coupling [see Eq. (24)] of six RC modes at the resonance frequencies of their evolved TC modes.

which suggest that the net phases in $\Sigma_{k=1}^{N} I_{i,k} P_k^{(j)}$ and $\Sigma_{k=1}^{N} M_{i,k} P_k^{(j)}$ can be significant, and $|R_{ai,im}^{(j)}|$ is then considerable.

Due to the characteristics of the $\Sigma_{k=1}^{N} J_{i,k} P_k^{(j)}$-to-$\Sigma_{k=1}^{N} M_{i,k} P_k^{(j)}$ and $|R_{ai,im}^{(j)}|$-to-$\sqrt{\omega_{ai}^2 + R_{ai,re}^{(j)}}$ ratios in Fig. 6, when the surface is at $x=0$, the $D_{ai,re}^{(j)}$'s of (0,2,0) and (0,2,1) have a same value, those of (1,2,0), (2,2,0), (1,2,1), and (2,2,1) have another same value, the former is half of the latter, and the $G_{ai}^{(j)}$'s of the modes are close to zero [see Fig. 8(c)]. Also, when the surface is at the other locations, the $D_{ai,re}^{(j)}$'s and $G_{ai}^{(j)}$'s [thus, $(D_{ai,re}^{(j)} + G_{ai}^{(j)})$'s] of (0,2,0), (1,2,0), and (2,2,0) are the same, and those of (0,2,1), (1,2,1), and (2,2,1) are the same [see Figs. 8(a), 8(b), and 8(d)]. These behaviors of $D_{ai,re}^{(j)}$'s and $G_{ai}^{(j)}$'s explain the reason for the same $T_{a(i)}^{T}$'s of

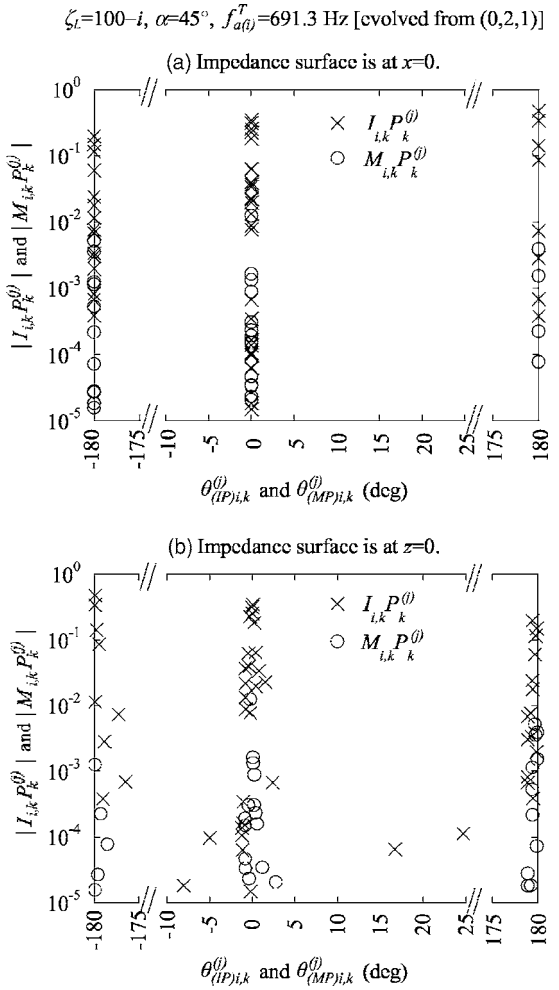

FIG. 7. Magnitudes and phases of the inclined surface and volume couplings of (0,2,1) with itself and other RC modes at the resonance frequency of its evolved TC mode, for the impedance surface location at (a) $x=0$ and (b) $z=0$ of the trapezoidal cavity.

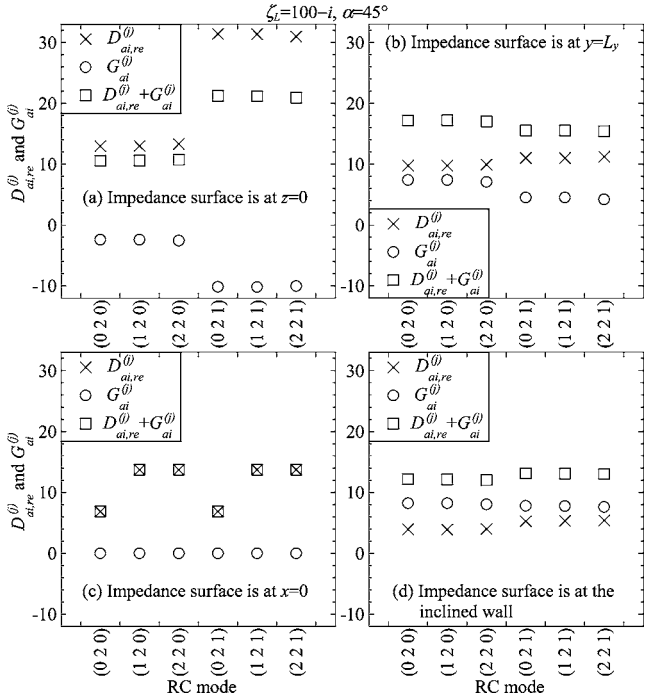

FIG. 8. Geometrical coupling and the real part of the damping coupling of six RC modes at the resonance frequencies of their evolved TC modes, for the impedance surface location at (a) $z=0$, (b) $y=L_y$, (c) $x=0$, and (d) the inclined wall of the trapezoidal cavity.

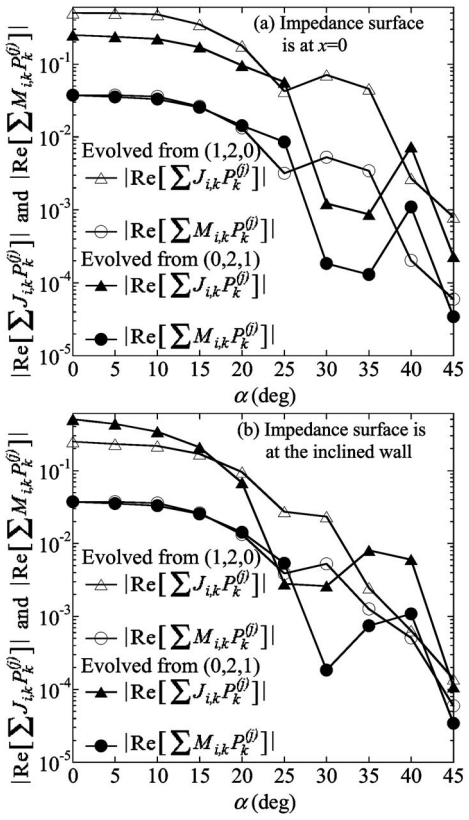

FIG. 9. Magnitudes of the real parts of the impedance surface and volume couplings of (1,2,0) and (0,2,1), as a function of α for the impedance surface location at (a) $x=0$ and (b) the inclined wall of the trapezoidal cavity.

the TC modes that evolve from RC modes with zero or nonzero l_i's when the surface is at $x=0$, and the same $T^T_{a(i)}$'s of the TC modes that evolve from RC modes with same m_i's and n_i's when the surface is at the other locations, as in Fig. 5. The observation in Fig. 8 is also consistent with the description in Sec. II C that the TC-mode grouping is controlled by the l_i's (either zero or nonzero) of the RC modes that evolve the TC modes when the impedance surface is at $x=0$ or L_x, but the m_i's and n_i's of the RC modes when the surface is at any of the other locations.

The variation of $T^T_{a(i)}$ with α in Fig. 5 is determined by the variations of $D^{(j)}_{ai,re}$ and $G^{(j)}_{ai}$ with α. The latter further depend on the variations of the $\Sigma^N_{k=1}J_{i,k}P^{(j)}_k$-to-$\Sigma^N_{k=1}M_{i,k}P^{(j)}_k$ and $R^{(j)}_{ai,im}$-to-$\sqrt{\omega^2_{ai}+R^{(j)}_{ai,re}}$ ratios with α. As examples, Fig. 9 depicts the impedance surface and volume couplings, as well as the $R^{(j)}_{ai,im}$'s and $\sqrt{\omega^2_{ai}+R^{(j)}_{ai,re}}$'s of (1,2,0) and (0,2,1), as a function of α for the impedance surface location at $x=0$ and the inclined wall. It can be examined from Fig. 9(a) that the $\Sigma^N_{k=1}J_{i,k}P^{(j)}_k$-to-$\Sigma^N_{k=1}M_{i,k}P^{(j)}_k$ ratio of each mode is the same for different values of α when the surface is at $x=0$ [i.e., $D^{(j)}_{ai,re}$'s in Fig. 11(a) do not vary with α]. Figure 10(a) also indicates that for the values of α shown, the values of $R^{(j)}_{ai,im}$'s are near zero, which cause the $R^{(j)}_{ai,im}$-to-$\sqrt{\omega^2_{ai}+R^{(j)}_{ai,re}}$ ratios to be close to zero although the $\sqrt{\omega^2_{ai}+R^{(j)}_{ai,re}}$'s vary with α. Hence, as illustrated in Fig. 11(a), the $G^{(j)}_{ai}$'s can be neglected when compared to the $D^{(j)}_{ai,re}$'s, where the variation of the $T^T_{a(i)}$'s with α is then fully controlled by the $D^{(j)}_{ai,re}$'s. So, the $T^T_{a(i)}$'s

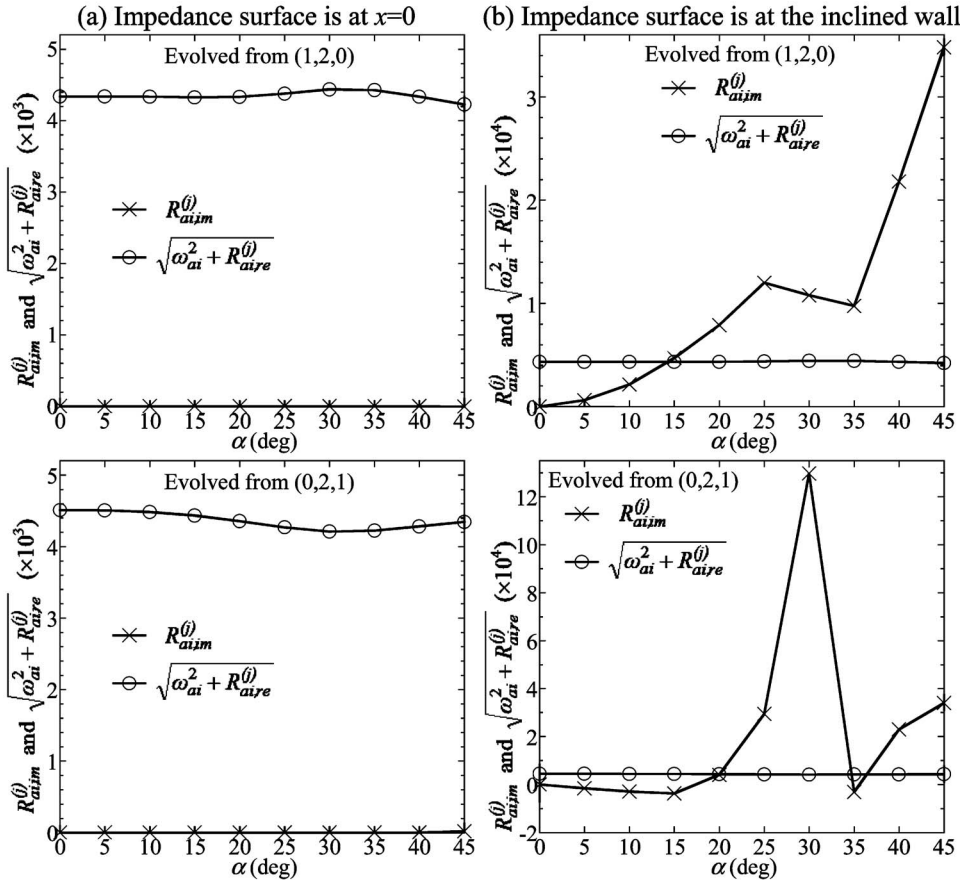

FIG. 10. The denominator and numerator of the geometrical coupling [see Eq. (24)] of (1,2,0) and (0,2,1), as a function of α for the impedance surface location at (a) $x=0$ and (b) the inclined wall of the trapezoidal cavity.

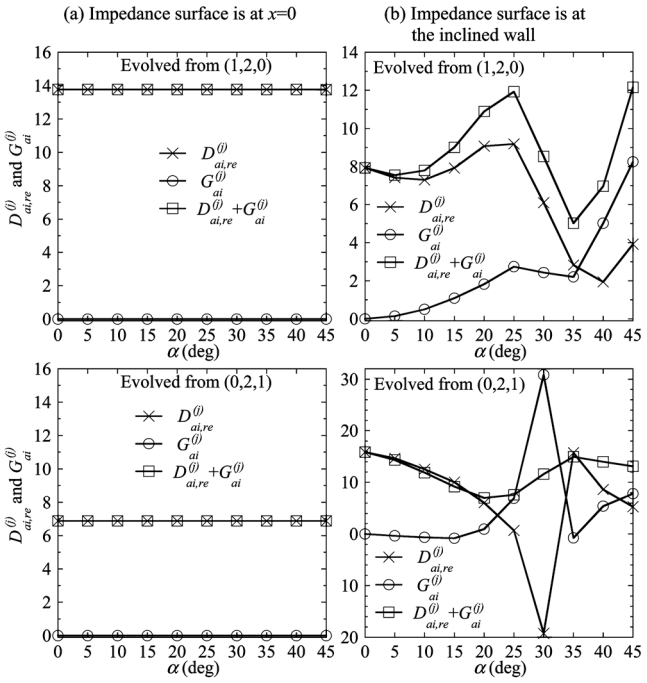

FIG. 11. Geometrical coupling and the real part of the damping coupling of (1,2,0) and (0,2,1), as a function of α for the impedance surface location at (a) $x=0$ and (b) the inclined wall of the trapezoidal cavity.

of the TC modes that evolve from the two RC modes do not have any extrema when α is altered, and this behavior is also applicable to the $T^T_{a(i)}$'s of the TC modes that evolve from other RC modes in Fig. 5(c).

When the surface is at the inclined wall, the $\Sigma^N_{k=1}J_{i,k}P^{(j)}_k$-to-$\Sigma^N_{k=1}M_{i,k}P^{(j)}_k$ and $R^{(j)}_{ai,im}$-to-$\sqrt{\omega^2_{ai}+R^{(j)}_{ai,re}}$ ratios and thus, the $D^{(j)}_{ai,re}$'s and $G^{(j)}_{ai}$'s of (1,2,0) and (0,2,1) change with α [see Figs. 9(b), 10(b), and 11(b)]. It is obvious from Fig. 10(b) that the values of $R^{(j)}_{ai,im}$'s and $\sqrt{\omega^2_{ai}+R^{(j)}_{ai,re}}$'s are of about the same order of magnitude, although the variation of the latter with α is negligible compared to the former. Hence, the $R^{(j)}_{ai,im}$-to-$\sqrt{\omega^2_{ai}+R^{(j)}_{ai,re}}$ ratios are significant in which the values of the $G^{(j)}_{ai}$'s are comparable to the $D^{(j)}_{ai,re}$'s [see Fig. 11(b)]. As a result, the variation of the $T^T_{a(i)}$'s with α is controlled by the $(D^{(j)}_{ai,re}+G^{(j)}_{ai})$'s of the RC modes [also, see Eq. (19)] rather than the $D^{(j)}_{ai,re}$'s alone. Due to the variations of the $\Sigma^N_{k=1}J_{i,k}P^{(j)}_k$-to-$\Sigma^N_{k=1}M_{i,k}P^{(j)}_k$ and $R^{(j)}_{ai,im}$-to-$\sqrt{\omega^2_{ai}+R^{(j)}_{ai,re}}$ ratios and thus, the $D^{(j)}_{ai,re}$'s and $G^{(j)}_{ai}$'s with α, extrema are generated in the $(D^{(j)}_{ai,re}+G^{(j)}_{ai})$'s. A maximum occurs when the damping and geometrical couplings act maximally constructive (i.e., both $D^{(j)}_{ai,re}$ and $G^{(j)}_{ai}$ have positive values) or minimally destructive (i.e., the values of $D^{(j)}_{ai,re}$ and $G^{(j)}_{ai}$ have opposite signs) upon each other [e.g., at $\alpha=25°$ for (1,2,0) and $\alpha=35°$ for (0,2,1) in Fig. 11(b)]. In this case, the impedance surface absorption is maximum, where a minimum is produced in the $T^T_{a(i)}$ [e.g., $T^T_{a(i)}$'s of the TC modes that evolve from (1,2,0) and (0,2,1), respectively, at $\alpha=25°$ and 35° in Fig. 5(d)]. On the other hand, a minimum in the $(D^{(j)}_{ai,re}+G^{(j)}_{ai})$ exists when the damping and geometrical couplings act minimally constructive or maximally destructive upon each other [e.g., at $\alpha=35°$ for (1,2,0) and $\alpha=20°$ for (0,2,1) in Fig. 11(b)]. Due to a large destructive or small constructive effect of both couplings, the impedance surface does not absorb much sound and thus, the $T^T_{a(i)}$ has a maximum [e.g., $T^T_{a(i)}$'s of the TC modes that evolve from (1,2,0) and (0,2,1), respectively, at $\alpha=35°$ and 20° in Fig. 5(d)]. The same explanation of the variations of $D^{(j)}_{ai,re}$ and $G^{(j)}_{ai}$ with α is also applicable for the variation of the $T^T_{a(i)}$'s of the TC modes that evolve from other RC modes for the impedance surface location at $z=0$ or $y=L_y$ in Figs. 5(a) and 5(b).

IV. CONCLUSIONS

The coupling between rigid-walled modes of a rectangular cavity (RC modes) is used to study the decay times of acoustic modes of a trapezoidal cavity (TC modes), $T^T_{a(i)}$'s. The trapezoidal cavity has an inclined wall described by an inclination angle, α, as well as an impedance surface. The grouping of TC modes based on their $T^T_{a(i)}$'s and the variation of the $T^T_{a(i)}$'s with α, are determined by two different coupling mechanisms of the individual RC modes that evolve the TC modes, namely, the damping coupling, $D^{(j)}_{ai,re}$, and the geometrical coupling, $G^{(j)}_{ai}$. The damping coupling is related to the coupling of RC modes at the impedance surface (i.e., impedance surface coupling). The geometrical coupling is related to the coupling of RC modes at the inclined wall (i.e., inclined surface coupling). For $\alpha=0°$, $G^{(j)}_{ai}\approx 0$, and the behavior of the decay times of RC modes, T_{ai}'s, and the RC-mode grouping are fully determined by the $D^{(j)}_{ai,re}$'s of the modes. For the impedance surface location at a given wall, there are two RC-mode groups, namely, the grazing group and the nongrazing group. The T_{ai}'s for the grazing modes are twice of those for the nongrazing modes. For $\alpha>0°$, the impedance surface and volume couplings have a common dependence of α when the impedance surface is at either of the two trapezoidal walls of the cavity. Therefore, both couplings act in an exactly opposite way such that the geometrical effect of the inclined wall (i.e., $G^{(j)}_{ai}$) on $T^T_{a(i)}$ is negligible, and $D^{(j)}_{ai,re}$ is independent of α. Thus, similar to $\alpha=0°$, the behavior of $T^T_{a(i)}$'s and the TC-mode grouping are fully determined by the $D^{(j)}_{ai,re}$'s of the RC modes that evolve the TC modes (i.e., there are two groups of TC modes that evolve from the grazing and nongrazing RC modes, and the $T^T_{a(i)}$'s for the former are twice of those for the latter). Also, the $T^T_{a(i)}$'s are independent of α and do not have any extrema. When the impedance surface is at any of the other walls, the behavior of $T^T_{a(i)}$'s and the TC-mode grouping are determined by both $D^{(j)}_{ai,re}$'s and $G^{(j)}_{ai}$'s which are, respectively, the same for those RC modes with same number of nodes in the directions across and towards the inclination (the y and z directions in this paper). Thus, TC modes that evolve from these RC modes have same decay times. So, many groups of TC modes exist because there are many different combinations of the number of nodes of RC modes in the two directions. As $D^{(j)}_{ai,re}$ and $G^{(j)}_{ai}$ vary with α, extrema are generated in $(D^{(j)}_{ai,re}+G^{(j)}_{ai})$. A maximum occurs when the damping and geometrical couplings act maximally constructive or minimally destructive upon each other, where the impedance surface absorption is maximum and a minimum is produced in

$T^T_{a(i)}$. A minimum in $(D^{(j)}_{ai,re}+G^{(j)}_{ai})$ exists when the damping and geometrical couplings act maximally destructive or minimally constructive upon each other, where the impedance surface does not absorb much sound and a maximum is produced in $T^T_{a(i)}$. Hence, with the exception of the impedance surface location at either of the two trapezoidal walls, the absorption of the surface can be adjusted by changing α. It is unnecessary for the surface to change area (only when the surface is at the opposite wall to the inclined wall), change location to another wall, or be at the inclined wall. Both experimental works on the decay times of TC modes subject to a locally and an extensively reactive surface are underway.

ACKNOWLEDGMENT

Financial support for this work by the Australia Research Council through the ARC Discovery Project Grant is gratefully acknowledged.

[1]J. Pan and D. A. Bies, "An experimental investigation into the interaction between a sound field and its boundaries," J. Acoust. Soc. Am. **83**, 1436–1444 (1988).
[2]J. Pan and D. A. Bies, "The effect of fluid-structural coupling on sound waves in an enclosure—Theoretical part," J. Acoust. Soc. Am. **87**, 691–707 (1990).
[3]J. Pan and D. A. Bies, "The effect of fluid-structural coupling on sound waves in an enclosure—Experimental part," J. Acoust. Soc. Am. **87**, 708–717 (1990).
[4]P. M. Morse, "Some aspects of the theory of room acoustics," J. Acoust. Soc. Am. **11**, 56–66 (1939).
[5]N. B. Bhatt, "Effect of an absorbing wall on the decay of normal frequencies," J. Acoust. Soc. Am. **11**, 67–73 (1939).
[6]J. Pan, S. J. Elliott, and K. H. Baek, "Analysis of low frequency acoustic response in a damped rectangular enclosure," J. Sound Vib. **223**, 543–566 (1999).
[7]F. V. Hunt, L. L. Beranek, and D. Y. Maa, "Analysis of sound decay in rectangular rooms," J. Acoust. Soc. Am. **11**, 80–94 (1939).
[8]P. M. Morse and R. H. Bolt, "Sound waves in rooms," Rev. Mod. Phys. **16**, 69–150 (1944).
[9]E. H. Dowell, "Reverberation time, absorption, and impedance," J. Acoust. Soc. Am. **64**, 181–191 (1978).
[10]L. E. Kinsler, A. R. Frey, A. B. Coppens, and V. J. Sanders, "Architectural acoustics," in *Fundamentals of Acoustics*, 3rd ed. (Wiley, New York, 1982), Chap. 13, pp. 313–341.
[11]D. Y. Maa, "Nonuniform acoustical boundaries in rectangular rooms," J. Acoust. Soc. Am. **12**, 20–33 (1940).
[12]P. M. Morse and K. U. Ingard, "Sound waves in ducts and rooms," in *Theoretical Acoustics* (McGraw-Hill, New York, 1968), Chap. 9, pp. 554–576.
[13]P. M. Morse and H. Feshbach, "Approximate methods," in *Methods of Theoretical Physics–Part II* (McGraw-Hill, New York, 1953), Chap. 9, pp. 999–1064.
[14]J. Missaoui and L. Cheng, "A combined integro-modal approach for predicting acoustic properties of irregular-shaped cavities," J. Acoust. Soc. Am. **101**, 3313–3321 (1997).
[15]I. J. Cooper and H. F. Pollard, "Low frequency resonances in unsymmetrical enclosures," Acustica **41**, 86–93 (1978).
[16]P. Hamery, P. Dupire, and M. Bruneau, "Acoustic fields in trapezoidal cavities," Acust. Acta Acust. **83**, 13–18 (1997).
[17]Y. Y. Li and L. Cheng, "Modifications of acoustic modes and coupling due to a leaning wall in a rectangular cavity," J. Acoust. Soc. Am. **116**, 3312–3318 (2004).
[18]M. Petyt, J. Lea, and G. H. Koopman, "A finite element method for determining the acoustic modes of irregular shaped cavities," J. Sound Vib. **45**, 497–502 (1976).
[19]P. Herzog and M. Bruneau, "Shape perturbation and inertial mode coupling in cavities," J. Acoust. Soc. Am. **86**, 2377–2384 (1989).
[20]B. Sapoval, O. Haeberle, and S. Russ, "Acoustical properties of irregular and fractal cavities," J. Acoust. Soc. Am. **102**, 2014–2019 (1997).
[21]B. Hebert, B. Sapoval, and S. Russ, "Experimental study of a fractal acoustical cavity," J. Acoust. Soc. Am. **105**, 1567–1574 (1999).
[22]E. Kreyszig, "Vector integral calculus. Integral theorems," in *Advanced Engineering Mathematics*, 8th ed. (Wiley, New York, 1999), Chap. 9, 505–513.
[23]G. L. Anderson, "Application of a variational method to dissipative, nonconservative problems of elastic stability," J. Sound Vib. **27**, 279–296 (1973).
[24]K. S. Sum and J. Pan, "Effects of the inclination of a rigid wall on the free vibration characteristics of acoustic modes in a trapezoidal cavity," J. Acoust. Soc. Am. **119**, 2201–2210 (2006).

Evaluation of decay times in coupled spaces: An efficient search algorithm within the Bayesian framework[a)]

Ning Xiang[b)] and Tomislav Jasa
School of Architecture and Department of Electrical, Computer, and Systems Engineering, Rensselaer Polytechnic Institute, Troy, New York 12180

(Received 9 June 2006; revised 16 September 2006; accepted 20 September 2006)

This paper discusses an efficient method for evaluating multiple decay times within the Bayesian framework. Previous works [N. Xiang and P. M. Goggans, J. Acoust. Soc. Am. **110**, 1415–1424 (2001); **113**, 2685–2697 (2003); N. Xiang, P. M. Goggans, T. Jasa, and M. Kleiner, **117**, 3707–3715 (2005)] have applied the Bayesian inference to cope with demanding tasks in estimating multiple decay times from Schroeder decay functions measured or calculated in acoustically coupled spaces. Since then a number of recent works call for efficient estimation methods within the Bayesian framework. An efficient analysis is of practical significance for better understanding and modeling the sound energy decay process in acoustically coupled spaces or even in single spaces for reverberation time estimation. This paper will first formulate the Bayesian posterior probability distribution function (PPDF) in a matrix form to reduce the dimensionality as applied to the decay time evaluation. Based on existence of only global extremes of PPDFs as observed from extensive experimental data, this paper describes a dedicated search algorithm for an efficient estimation of decay times. © *2006 Acoustical Society of America.* [DOI: 10.1121/1.2363932]

PACS number(s): 43.55.Br, 43.55.Mc [EJS] Pages: 3744–3749

I. INTRODUCTION

Recent research in acoustically coupled spaces[1–5] requires a set of practical tools to evaluate the sound energy decay from experimentally measured data or from computer-based simulations. One of the demanding tasks for better understanding and design of acoustics in coupled spaces lies in sound energy decay analysis. Applications of Bayesian probability theory in decay time evaluation in acoustically coupled spaces[6–8] have demonstrated a useful framework for analyzing Schroeder decay functions[9] from room impulse response measurements. The Bayesian framework proves to be able to estimate not only the decay parameters from Schroeder decay model,[6] but also to determine the decay order,[7] to quantify uncertainties of decay time estimates and the interrelationship between multiple decay times.[8]

Bayesian probability theory provides useful tools to formulate posterior probability density function (PPDF) of decay parameters. One approach to estimation of respective decay parameters is to localize global extremes of the PPDF over the parameter space, leading to an effective estimation of relevant decay parameters,[6] so-called maximum *a posterior* (MAP) estimation. Recent research in the acoustically coupled spaces demands an efficient way in performing Bayesian decay analysis. The subject of this paper is to show how one can accomplish the multiple decay time estimation with a low computation burden based on the MAP estimation. This effort is to speed up evaluations of relevant decay parameters from Schroeder decay functions using Bayesian probability theory. A practical significance of efficient methods is that architectural acousticians need to evaluate the multiple decay times over a number of octave/one-third octave bands, normally 5–20 evaluations to cover the frequency range of interest. For systematic investigations, a large number of room impulse responses need to be analyzed.

This paper is organized as follows, Sec. II briefly describes Bayesian formulation of posterior distributions over the decay time space. In Sec. II, one difference from previous work (Ref. 6), is the introduction of the Bayesian formalism in a matrix form, partially based on previous works.[10,11] This formulation along with that documented in Ref. 6 may piece together a coherent understanding of the model-based Bayesian inference, and help architectural acousticians to apply the Bayesian inference to the practical problems. On the application level the matrix formulation will particularly help those readers who want to implement the method using MATLAB. Section III discusses the proposed search method, its implementation and computation load evaluation. Finally, Sec. IV concludes the paper.

II. BAYESIAN FORMULATION

A. Schroeder decay models

This section begins with Schroeder decay function data $\mathbf{D}=[d_1,d_2,\ldots,d_K]^{Tr}$, a column vector of K elements, $()^{\mathrm{Tr}}$ stands for matrix transpose. A parametric model has been established based on the nature of Schroeder's integration[6,12]

$$\mathbf{D} = \mathbf{GA} + \mathbf{e}, \tag{1}$$

which approximates the data $\mathbf{D}$ with an error vector $\mathbf{e}$. $\mathbf{A}$ is a column vector of m coefficients, termed *linear parameter*

[a)]Aspects of this work have been presented at the 151st ASA Meeting, JASA **119** (2006), pp. 3208 (A).

[b)]Author to whom correspondence should be addressed; electronic mail: xiangn@rpi.edu

 © 2006 Acoustical Society of America

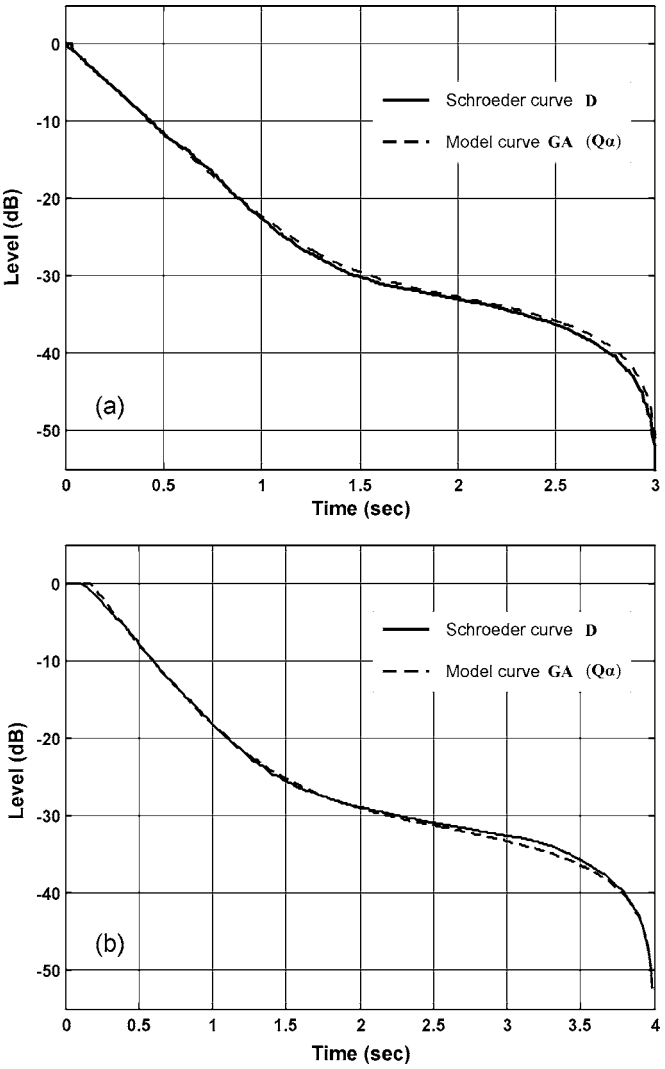

FIG. 1. Comparison between Schroeder decay function (**D**) measured in real halls and their model function (**GA**, or equivalently $\mathbf{Q}\boldsymbol{\alpha}$). (a) Room impulse response measured in Troy Savings Bank Music Hall, filtered at 500 Hz octave band. (b) Room impulse response measured in San. Patrick Church, filtered at 4 kHz ocatve band.

vector. **G** is a matrix of $K \times m$; jth column of **G** is given by

$$G_{kj}(T_j,t_k) = \begin{cases} t_K - t_k & \text{for } j = 0 \\ \exp(-13.8 \cdot t_k/T_j) & \text{for } 1,2,\ldots,m-1, \end{cases} \tag{2}$$

where T_j is jth decay time to be determined for $0 \le j \le m-1$, $T_0 = \infty$. $0 \le k \le K-1$; t_K represents the upper limit of Schroeder's integration. Recent works[8,12] have experimentally proven the validity of this model, especially when t_K is large enough. Figure 1 illustrates two examples of the Schroeder decay function **D** calculated from real hall measurements and its model function **GA** with properly estimated model parameters.

The decay model in Eq. (1) is in the form of generalized linear models.[10,11] This special form has gained general interest since one can analytically formulate the PPDF within the Bayesian framework in a tractable form. To proceed, an eigen decomposition of $m \times m$ square matrix $\mathbf{G}^{\mathbf{Tr}}\mathbf{G}$ comes into use:

$$\mathbf{G}^{\mathbf{Tr}}\mathbf{G} = \mathbf{E}\boldsymbol{\Lambda}\mathbf{E}^{\mathbf{Tr}}, \tag{3}$$

where $()^{\mathrm{Tr}}$ represents matrix transpose, **E** is a square matrix containing m eigenvectors, while $\boldsymbol{\Lambda}$ is a diagonal matrix containing m eigenvalues of the eigenvectors. The eigen decomposition facilitates converting **G** into an orthonormalized one **Q** or vice versa (see Appendix A):

$$\mathbf{Q} = \mathbf{G}\mathbf{E}\boldsymbol{\Delta}^{-1}; \quad \mathbf{G} = \mathbf{Q}\boldsymbol{\Delta}\mathbf{E} \tag{4}$$

with

$$\boldsymbol{\Delta}^{\mathbf{Tr}}\boldsymbol{\Delta} = \boldsymbol{\Lambda}. \tag{5}$$

In similar fashion, the linear parameter vector **A** can be converted into the orthonormalized one $\boldsymbol{\alpha}$, or vice versa:

$$\boldsymbol{\alpha} = \boldsymbol{\Delta}\mathbf{E}\mathbf{A}; \quad \mathbf{A} = \mathbf{E}\boldsymbol{\Delta}^{-1}\boldsymbol{\alpha}, \tag{6}$$

such that the error function **e** can be equivalently expressed in terms of Schroeder decay function **D** and the orthonormalized model $\mathbf{Q}\boldsymbol{\alpha}$:

$$\mathbf{e} = \mathbf{D} - \mathbf{Q}\boldsymbol{\alpha}. \tag{7}$$

B. Bayesian decay parameter estimation

Bayesian theory formulates the PPDF through the prior probability density and likelihood function via Bayes' theorem:

$$p(\mathbf{A},\mathbf{T}|\mathbf{D},I) = \frac{p(\mathbf{A},\mathbf{T}|I)p(\mathbf{D}|\mathbf{A},\mathbf{T},I)}{p(\mathbf{D}|I)}, \tag{8}$$

where $p(\mathbf{D}|I)$ acts in the context of decay time estimation as a normalization constant. **T** is a vector matrix of m coefficients, termed *nonlinear parameter vector*. $p(\mathbf{A},\mathbf{T}|I)$ is the prior distribution function of **A** and **T**. Bayes' theorem in Eq. (8), therefore, represents how our prior knowledge $p(\mathbf{A},\mathbf{T}|I)$ is modified in presence of data through the likelihood function $p(\mathbf{D}|\mathbf{A},\mathbf{T},I)$. Background information I includes that the Schroeder decay model in Eq. (2) through Eq. (1) describes the data **D** reasonably well so that all errors in **e** are bounded by a finite value. Given finite errors and a reasonable model as the only available information, application of the principle of the maximum entropy[6] assigns a Gaussian distribution to the likelihood function $p(\mathbf{D}|\mathbf{A},\mathbf{T},I)$ and an independence to errors e_i from each other, so that

$$p(\mathbf{D}|\mathbf{A},\mathbf{T},\sigma,I) = (\sqrt{2\pi}\sigma)^{-K}\exp\left(\frac{\mathbf{e}^{\mathbf{Tr}}\mathbf{e}}{2\sigma^2}\right), \tag{9}$$

with a finite, but unspecified error variance σ^2. The likelihood function $p(\mathbf{D}|\mathbf{A},\mathbf{T},\sigma,I)$ implies that the error variance σ^2 at this stage is still unknown.

A substitute of Eq. (7) into Eq. (9) yields the posterior probability density function $p(\boldsymbol{\alpha},\mathbf{T}|\mathbf{D},\sigma,I)$ in terms of the likelihood $p(\mathbf{D}|\boldsymbol{\alpha},\mathbf{T},\sigma,I)$ and prior probability function $p(\boldsymbol{\alpha},\mathbf{T}|I)$:

$$p(\boldsymbol{\alpha},\mathbf{T}|\mathbf{D},\sigma,I) \propto p(\boldsymbol{\alpha},\mathbf{T}|I)(\sqrt{2\pi}\sigma)^{-K} \times \exp\left[-\frac{(\mathbf{D}-\mathbf{Q}\boldsymbol{\alpha})^{\mathbf{Tr}}(\mathbf{D}-\mathbf{Q}\boldsymbol{\alpha})}{2\sigma^2}\right], \tag{10}$$

where $p(\boldsymbol{\alpha},\mathbf{T}|\mathbf{D},\sigma,I)$ and $p(\boldsymbol{\alpha},\mathbf{T}|I)$ reflect the fact that the

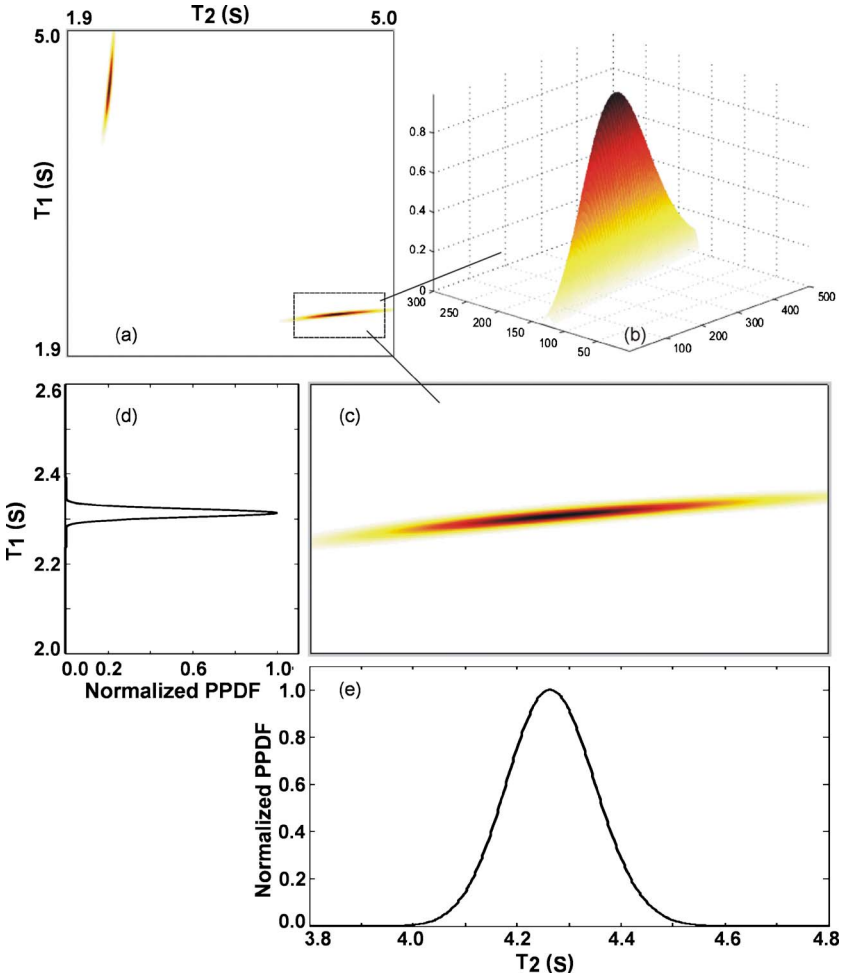

FIG. 2. (Color online) Posterior probability density function (PPDF) over decay time space $\{T_1, T_2\}$ evaluated for the room impulse response measured in San. Patrick Church as shown in Fig. 1(b). The PPDF in 2D presentation between 1.9 and 5.0 s. (b) One of the PPDF mode in three-dimensional (3D) presentation over $\{2.0s, 2.6s\}$ and $\{3.8s, 4.8s\}$ with a grid of 300×500. (c) One of the PPDF mode in 2D presentation over $\{2.0s, 2.6s\}$ and $\{3.8s, 4.8s\}$. (d), (e) Projections onto two decay time axes from slices across the peak of the mode.

equivalent orthonormalized model $\mathbf{Q}\boldsymbol{\alpha}$ has substituted the Schroeder decay model **GA** through Eqs. (4), (6), and (7), so the linear vector **A** has been substituted by $\boldsymbol{\alpha}$.

The marginalization over $\boldsymbol{\alpha}$ with a uniform prior, and over σ by assigning Jeffreys' prior along with the orthonormalization stated in Sec. II A lead to an analytically tractable PPDF in the form of the student-T distribution (see Appendix B):

$$p(\mathbf{T}|\mathbf{D},I) \propto [\mathbf{D}^{\mathbf{Tr}}\mathbf{D} - \mathbf{q}^{\mathbf{Tr}}\mathbf{q}]^{(m-K)/2}, \tag{11}$$

with

$$\mathbf{q} = \mathbf{Q}^{\mathbf{Tr}}\mathbf{D} \tag{12}$$

Similar to the formulation in Ref. 7, the marginalization removes $\boldsymbol{\alpha}$ and σ from the current problem, and results in the student-T PPDF over only the decay time space. The decay time estimation can, therefore, be carried out in a dramatically reduced dimensionality. Once the decay times are estimated, an expected linear parameter vector $\langle \mathbf{A} \rangle$ can be determined through Eq. (6) and $\langle \boldsymbol{\alpha} \rangle = \hat{\mathbf{q}}$ with $\hat{\mathbf{q}}$ being a MAP estimate of $\mathbf{q}$ in Eq. (12).

C. Numerical examples

Figure 1(a) shows the Schroeder decay function **D** of 3000 elements within 500 Hz (oct) measured in the Troy Savings Bank Music Hall, Troy, NY, and the decay model **GA**

$$\mathbf{GA} = \begin{pmatrix} t_K - t_0 & e^{-13.8 \cdot t_0/T} \\ t_K - t_1 & e^{-13.8 \cdot t_1/T} \\ \vdots & \vdots \\ t_K - t_{K-1} & e^{-13.8 \cdot t_{K-1}/T} \end{pmatrix} \begin{pmatrix} 4.339E-7 \\ 1.002 \end{pmatrix} \tag{13}$$

with $K=3000$, reverberation time $T=2.60$ s. Figure 1(b) shows the Schroeder decay function **D** of 4000 elements measured in San. Patrick Church, Watervliet, NY, and the decay model **GA**

$$\mathbf{GA} = \begin{pmatrix} t_K - t_0 & e^{-13.8 \cdot t_0/T_1} & e^{-13.8 \cdot t_0/T_2} \\ t_K - t_1 & e^{-13.8 \cdot t_1/T_1} & e^{-13.8 \cdot t_1/T_2} \\ \vdots & \vdots & \vdots \\ t_K - t_{K-1} & e^{-13.8 \cdot t_{K-1}/T_1} & e^{-13.8 \cdot t_{K-1}/T_2} \end{pmatrix} \times \begin{pmatrix} 2.168E-7 \\ 2.596 \\ 0.205 \end{pmatrix}, \tag{14}$$

with $K=4000$, decay times $T_1=2.29$ s, $T_2=4.21$ s.

Figure 2 illustrates normalized PPDFs over decay time space $\{T_1, T_2\}$ given the model in Eq. (14) and the measured Schroeder decay function **D** as shown in Fig. 1(b). The PPDF over a two-dimensional (2D) decay time space between 1.9 and 5 s includes two distinct, well-separated distribution modes of equal height. Figures 2(d) and 2(e) illustrate the projections onto two decay time axes from slices

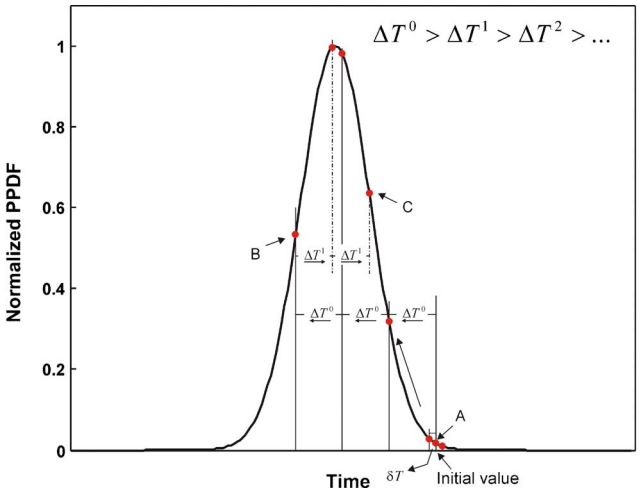

FIG. 3. (Color online) Search method within one-dimensional parameter space. Point "A" represents the starting sample determined by a random set of decay times (initial value). Two more samples with the smallest step size δT determine the up-hill moving direction along which a large step size ΔT^0 is kept until point "B". Then a reduced step size ΔT^1 and an opposite moving direction are kept until point "C". From point C the moving direction will be reversed with an even smaller step size ΔT^2, and so on.

across the peak of the mode. Extensive evaluations of a large number of measured results confirm that the student-T distribution in Eq. (11) over n-dimensional decay time space demonstrates $n!$ distinctly separated distribution modes of equal height.[6,7] For this reason, only one mode serves the estimation purpose. Besides these modes, no local extremes so far have been found. This fact gives a rise to a simplified search algorithm elaborated in the following: localization of the peak position of one of these modes will serve estimation of decay times.[13]

III. A FAST SEARCH ALGORITHM

The PPDF associated with any particular set of values for the decay parameters is a measure of how much one believes that they really lie in the neighborhood of that range. Therefore, localization of one of the PPDF global extremes in the parameter space will lead to an effective estimation of relevant decay parameters,[6] the MAP estimation. Previous works have applied Gibbs sampling technique[6,14] within the Bayesian framework. Gibbs sampler breaks the problem of drawing samples from a multivariante density down to densities of smaller dimensionality in a rotational pattern. Gibbs sampler may still require a large number of random samples within each single rotation process. In Bayesian decay analysis, however, one can exploit the fact that the student-T distribution within the subspace of a single mode will not exhibit local extremes, which means that there is only one "hill" along one decay-time axis within the subspace around the single mode.

A. Search algorithm

Inspired by the rotational pattern of the Gibbs sampler, one begins a search along one decay-time axis while fixing the others. At the initial point, randomly chosen value of T_i with its PPDF sample indicated by point "A" in Fig. 3, a proper moving direction can be estimated by comparing PPDF values in Eq. (11) at two other adjacent T_i's on each side with a tiny step size, *the smallest step size* δT (defined according to required precision prior to the search). After determination of the moving "up-hill" direction, a relative large step size (termed *initial step size* ΔT^0 within each iteration in this paper) is recommended to search the one dimensional space coarsely. The same step size is kept until the PPDF value becomes smaller than the previous one as indicated by point "B" in Fig. 3. This causes reversing of the moving direction and decreasing of the step size $\Delta T^1 < \Delta T^0$; with this moving direction and step size the search goes until the point "C" in Fig. 3. Conceivably both the moving-direction reversion and the step-size reduction could happen many times until the step size becomes the smallest one (δT) as initially defined. With this smallest step size one more search along the corresponding moving direction keeps going up hill until the PPDF value turns "down hill," and the search within this dimension can be stopped. By fixing the value of the last T_i^1, the search goes on to the next one-dimensional space of T_{i+1}, if any, until all the dimensions are searched; this finishes up one iteration (rotation) with $T_1^1, T_2^1, \ldots$.All T_i^1s and their corresponding PPDF values are kept in the memory of the search algorithm.[15–20]

The next iteration begins with $T_1^1, T_2^1, \ldots$ as initial values. A breaking mechanism to stop overall search can be determined by the fact that the (large) step size is reduced to the smallest step size $\Delta T^n = \delta T$ and differences between the current PPDF value and the previous one fall below a threshold Δp as defined according to the required precision. The decay time values associated with the maximum value of the PPDF determined by Eq. (11) among the search iterations will be kept as the MAP estimates.

B. Implementation and discussion

Previous work[8] shows very different, varied shapes of PPDF modes from data to data. In double-slope cases, in particular, often the PPDF mode along one dimension can be so different from the one along the other dimension over the decay time space, so that there will not be general rules of how the initial step size, the step size reduction can be selected. Experimental results as shown in this paper use the following values

- The smallest step size: $\delta T = 1.0 \times 10^{-4}$ s
- The initial (large) step size: $\Delta T^0 = X \cdot \delta T$ with an initial step size factor $X = 81$
- The step size factor X reduces for ΔX when reserving the search direction: At the first direction reversion $\Delta X = 10$, the step size factor becomes $X - \Delta X$, ΔX reduces 2 at every direction reversion until $\Delta X = 1$ or $X = 1$
- The threshold of the PPDF difference: $20lg(\Delta p) = 2.0 \times 10^{-3}$

This work calculates the Schroeder decay functions from room impulse responses at an integration interval of 1 ms, which results in Schroeder decay functions of several hundreds till several thousand points [with K in Eq. (11) being on order of 10^3]. For this reason the calculation of the PPDF

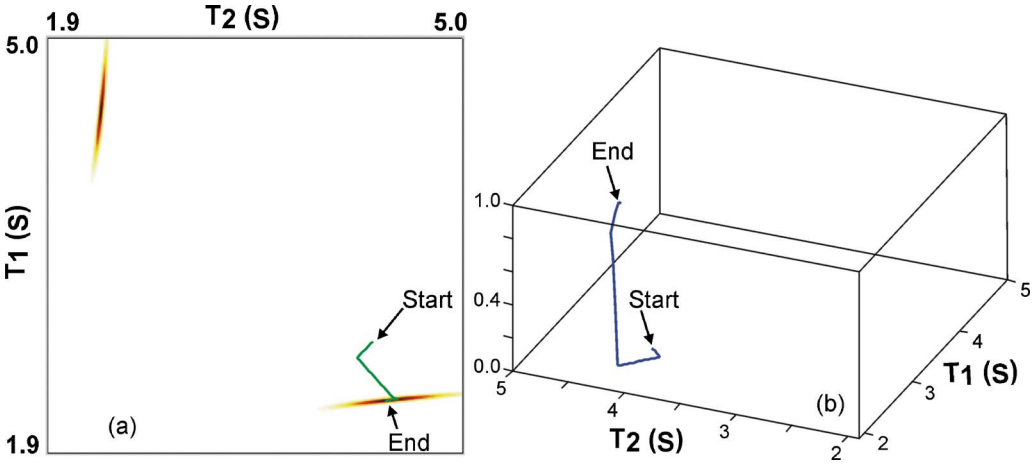

FIG. 4. (Color online) Search trace over decay time space $\{T_1, T_2\}$ evaluated for the experimental data measured in San. Patrick Church as shown in Fig. 2. The MAP values T_1=2.29 s, T_2=4.21 s as from iteration 28. (a) Search trace overlapped with the 2D PPDF over the decay time space $\{T_1, T_2\}$ between 1.9 and 5.0 s. (b) Search trace in a 3D presentation.

using Eq. (11) is conveniently pursued on a logarithmic basis $20lg[p(\mathbf{T}|\mathbf{D},\mathbf{I})]$, where quantity $\mathbf{D}^{\mathbf{Tr}}\mathbf{D}$ needs to be calculated only once throughout the overall search. Figure 4 illustrates the search iterations for a double-slope case of the experimental data shown in Fig. 2. Figure 4(a) shows its search trace overlayed on top of the 2D presentation of the PPDF over the decay time space of $\{1.9s, 5.0s\}$, while Fig. 4(b) illustrates how the search iteratively climbs one of the PPDF modes upwards.

The dynamic step-size reduction has been proven to be a reasonable way to reduce the computational load while achieving high search resolution. As demonstrated by this numerical example, 28 iterations for the double-slope case converge the search; each iteration requires only a few of search steps, while the search with a fixed step size as small as δT will require hundreds, even thousands of the small steps, especially when the random sampling begins in ranges where the PPDF is of low values. The single-slope cases using the dynamic step-size reduction often require significantly less search effort, since only a few of the step-size reductions associated with search direction reversions within one single iteration are needed. Using traditional Gibbs sampling,[6,10] however, a relatively large number of samples have to be evaluated within each iteration, in order of thousand samples, since the PPDF shape within each iteration is in general not known.

The search algorithm with the dynamic step-size reduction as implemented in this work runs efficiently, usually takes a few seconds for double-slope cases on a currently available personal computer when the Schroeder decay data are in order of thousands points, while for single-slope cases it usually takes less than 1 s or less. The search process also has a "burn-in" phase like other classical Markov Chain Monte Carlo methods.[10] The burn-in process can be significantly shortened by a simple estimate of T_1^0 using a small portion of the Schroeder decay function, say between −5 and −10 dB, particularly for the single-slope case. In this work an initial value of $T_2^0 = 1.5 \times T_1^0$ is always set for the double-slope case. The search algorithm itself is then not a random process at all. When starting at the same initial point in the decay time space, the search algorithm will converge at the same ending point given the step sizes, the reduction size and the breaking threshold as mentioned above.

Note that there might be even more efficient algorithms for this specific application, if substantial optimization would be undertaken. In addition, only in this specific application, the search algorithm can be effected. If the PPDF over the parameter space of other applications shows not only the global extreme, but is accompanied by possible local extremes, one should resort to the traditional Gibbs sampling method or other Markov Chain Monte Carlo methods.

IV. CONCLUSIONS

This work exploits the Schroeder decay function model which is in the form of the generalized linear models. This specific model form makes it possible to reduce the dimensionality of the posterior probability distribution functions (PPDFs) within the Bayesian framework by probabilistic marginalization to a compact form termed student-T distribution. This paper derives the student-T distribution in a matrix form. At the end, the student-T distribution is a function of only decay times and there are only global extremes over the decay time space, so as to implement a dramatically simplified search algorithm. Inspired by rotational patterns of Gibbs sampling, a dynamic reduction of search step sizes with similar rotational iterations results in an efficient search algorithm for the Bayesian decay time estimation. When the PPDF contains not only global extremes, but is accompanied by possible local extremes, more general approaches such as Markov Chain Monte Carlo methods should be applied.

ACKNOWLEDGMENTS

The authors would like to thank Dr. Paul Goggans and Dr. Kevin Knuth for their valuable discussion and advice. The authors would also like to express their gratitude to Dr. Chris Jaffe, Dr. Mendel Kleiner, and Dr. Rendell R. Torres, who supported this work with enthusiasm, to Donghua Li and Zühre Sü, who participated in extensive room-acoustic data collection in the scope of their M.S. Degree theses.

APPENDIX A

$\mathbf{E}$ of Eq. (3) has following properties:

$$\mathbf{E}^{\mathbf{Tr}} = \mathbf{E}; \quad \mathbf{E}^{\mathbf{Tr}}\mathbf{E} = \delta, \tag{A1}$$

where δ is an identity matrix. Using Eqs. (3)–(5) one can derive that

$$\mathbf{Q}^{\mathbf{Tr}}\mathbf{Q} = \delta. \tag{A2}$$

APPENDIX B

From Eqs. (10), (12), and (A2)

$$\begin{aligned}(\mathbf{D} - \mathbf{Q}\boldsymbol{\alpha})^{\mathbf{Tr}}(\mathbf{D} - \mathbf{Q}\boldsymbol{\alpha}) &= \mathbf{D}^{\mathbf{Tr}}\mathbf{D} - \boldsymbol{\alpha}^{\mathbf{Tr}}\mathbf{Q}^{\mathbf{Tr}}\mathbf{D} - \mathbf{D}^{\mathbf{Tr}}\mathbf{Q}\boldsymbol{\alpha} + \boldsymbol{\alpha}^{\mathbf{Tr}}\mathbf{Q}^{\mathbf{Tr}}\mathbf{Q}\boldsymbol{\alpha} \\ &= (\mathbf{D}^{\mathbf{Tr}}\mathbf{D} - \mathbf{q}^{\mathbf{Tr}}\mathbf{q}) + (\boldsymbol{\alpha} - \mathbf{q})^{\mathbf{Tr}}(\boldsymbol{\alpha} - \mathbf{q}) \end{aligned} \tag{B1}$$

$$p(\boldsymbol{\alpha}, \mathbf{T}|\mathbf{D}, \sigma, I) \propto (\sqrt{2\pi}\sigma)^{-K} \exp\left[\frac{-(\mathbf{D}^{\mathbf{Tr}}\mathbf{D} - \mathbf{q}^{\mathbf{Tr}}\mathbf{q})}{2\sigma^2}\right] \times \exp\left[-\frac{(\boldsymbol{\alpha} - \mathbf{q})^{\mathbf{Tr}}(\boldsymbol{\alpha} - \mathbf{q})}{2\sigma^2}\right]. \tag{B2}$$

The marginalization over the nuisance parameters $\boldsymbol{\alpha}$ by assigning a uniform prior $p(\boldsymbol{\alpha}|\mathbf{I})$=const, $p(\mathbf{T}|\boldsymbol{\alpha}, \mathbf{I})$=const:

$$p(\mathbf{T}|\mathbf{D}, \sigma, \mathbf{I}) \propto \int_{-\infty}^{\infty} p(\boldsymbol{\alpha}, \mathbf{T}|\mathbf{D}, \sigma, \mathbf{I}) d\boldsymbol{\alpha}. \tag{B3}$$

$$p(\mathbf{T}|\mathbf{D}, \sigma, I) \propto (\sqrt{2\pi}\sigma)^{-K+m} \times \int_{-\infty}^{\infty} \exp\left[\frac{-(\mathbf{D}^{\mathbf{Tr}}\mathbf{D} - \mathbf{q}^{\mathbf{Tr}}\mathbf{q})}{2\sigma^2}\right] d\boldsymbol{\alpha}, \tag{B4}$$

according to Eq. (A5) in Ref. 6:

$$\int_{-\infty}^{\infty} \exp\left[\frac{-(\boldsymbol{\alpha} - \mathbf{q})^{\mathbf{Tr}}(\boldsymbol{\alpha} - \mathbf{q})}{2\sigma^2}\right] d\boldsymbol{\alpha} = (\sqrt{2\pi}\sigma)^m \tag{B5}$$

and an integration of Eq. (B4) over σ by assigning Jeffrey's prior $1/\sigma^6$ yields Eq. (11).

[1] J. S. Anderson, M. Bratos-Anderson, and P. Doany, "The acoustics of a large space with a repetitive pattern of coupled rooms," J. Sound Vib. **208**, 313–329 (1997).

[2] J. E. Summers, R. R. Torres, and Y. Shimizu, "Statitical-acoustics models of energy decay in systems of coupled rooms and their relation to geometrical acoustics," J. Acoust. Soc. Am. **116**, 958–969 (2004).

[3] J. E. Summers, R. R. Torres, Y. Shimizu, and Bengt-Inge L. Dalenbäck, "Adapting a randomized beam-axis-tracing algorithm to modeling of coupled rooms via late-part ray tracing," J. Acoust. Soc. Am. **118**, 1491–1502 (2005).

[4] D. T. Bradley and L. M. Wang, "The effects of simple coupled volume geometry on the objective and subjective results from nonexponential decay," J. Acoust. Soc. Am. **118**, 1480–1490 (2005).

[5] V. Valeau, J. Picaut, and M. Hodgson, "On the use of a diffusion equation for room-acoustic predictions," J. Acoust. Soc. Am. **119**, 1504–1513 (2006).

[6] N. Xiang and P. M. Goggans, "Evaluation of decay times in coupled spaces: Bayesian parameter estimation," J. Acoust. Soc. Am. **110**, 1415–1424 (2001).

[7] N. Xiang and P. M. Goggans, "Evaluation of decay times in coupled spaces: Bayesian decay model selection," J. Acoust. Soc. Am. **113**, 2685–2697 (2003).

[8] N. Xiang, P. M. Goggans, T. Jasa, and M. Kleiner, "Evaluation of decay times in coupled spaces: Reliability analysis of Bayesian decay time estimation," J. Acoust. Soc. Am., **117**, 3705–3715 (2005).

[9] M. R. Schroeder, "New method of measuring reverberation time," J. Acoust. Soc. Am. **37**, 409–412 (1965).

[10] J. J. K. O'Ruanaidh and W. J. Fitzgerald, *Numerical Bayesian Methods Applied to Signal Processing* (Springer, New York, 1996).

[11] G. L. Bretthorst, "Bayesian analysis. I. Parameter estimation using quadrature NMR models," J. Magn. Reson. (1969-1992) **88**, 533–551 (1990).

[12] N. Xiang, "Evaluation of reverberation times using a non-linear regression approach," J. Acoust. Soc. Am. **98**, 2112–2121 (1995).

[13] S. Dosso, "Quantifying uncertainty in geoacoustic inversion. I. A fast Gibbs sampler approach," J. Acoust. Soc. Am. **111**, 129–142 (2002).

[14] Z. H. Michalopoulou and M. Picarelli, "Gibbs sampling for time-delay and amplitude estimation in underwater acoustics," J. Acoust. Soc. Am. **117**, 799–808 (2005).

[15] E. T. Jaynes, *Probability Theory: The Logic of Science* (Cambridge University Press, Cambridge, 2003).

[16] F. Jacobsen, "A note on acoustic decay measurements," J. Sound Vib. **115**, 165–170 (1987).

[17] M. Vorländer and H. Bietz, "Comparison of methods for measuring reverberation time," Acustica **80**, 205-215 (1994).

[18] A. Lundeby, T. E. Vigran, H. Bietz, and M. Vorländer, Uncertainties of measurements in room acoustics," Acustica **81**, 344–355 (1995).

[19] D. S. Sivia, *Data Analysis: A Bayesian Tutorial* (Clarendon Press, Oxford, 1996).

[20] H. Jeffreys, *Theory of Probability*, 3rd ed. (Oxford University Press, London, 1961).

Modal decomposition method for acoustic impedance testing in square ducts[a)]

Todd Schultz, Louis N. Cattafesta III, and Mark Sheplak[b)]
Interdisciplinary Microsystems Group, Department of Mechanical and Aerospace Engineering, University of Florida, Gainesville, Florida 32611-6250

(Received 17 February 2006; revised 13 September 2006; accepted 15 September 2006)

Accurate duct acoustic propagation models are required to predict and reduce aircraft engine noise. These models ultimately rely on measurements of the acoustic impedance to characterize candidate engine nacelle liners. This research effort increases the frequency range of normal-incidence acoustic impedance testing in square ducts by extending the standard two-microphone method (TMM), which is limited to plane wave propagation, to include higher-order modes. The modal decomposition method (MDM) presented includes four normal modes in the model of the sound field, thus increasing the bandwidth from 6.7 to 13.5 kHz for a 25.4 mm square waveguide. The MDM characterizes the test specimen for normal- and oblique-incident acoustic impedance and mode scattering coefficients. The MDM is first formulated and then applied to the measurement of the reflection coefficient matrix for a ceramic tubular specimen. The experimental results are consistent with results from the TMM for the same specimen to within the 95% confidence intervals for the TMM. The MDM results show a series of resonances for the ceramic tubular material exhibiting a monotonic decrease in the resonant peaks of the acoustic resistance with increasing frequency, resembling a rigidly-terminated viscous tube, and also evidence of mode scattering is visible at the higher frequencies. © *2006 Acoustical Society of America.* [DOI: 10.1121/1.2360423]

PACS number(s): 43.58.Bh, 43.20.Ye, 43.20.Mv [AJZ] Pages: 3750–3758

I. INTRODUCTION

Acoustic liners are used in turbofan engines to suppress radiated engine noise. These liners provide an acoustic impedance boundary condition for modes inside the engine duct.[1] Liner design requires experimental verification of the acoustic properties of candidate configurations. The two-microphone method (TMM) is a popular standardized technique for determining the normal-incidence acoustic impedance of materials.[2–6] In this method, a compression driver is mounted at one end of an acoustic waveguide, and the test specimen is mounted at the other. Two microphones are flush-mounted in the duct wall at two locations near the specimen to determine the incident and reflected plane waves. The microphone data are used to estimate the complex-valued reflection coefficient and the corresponding acoustic impedance of the test specimen.

Current 1/5th-scale aeroacoustic impedance testing requires a frequency range of at least 20 kHz.[7,8] However, the frequency range of the TMM is restricted by the plane wave assumption. For example, the upper frequency limit of the TMM is limited to 6.7 kHz in a 25.4 mm square waveguide. To extend the range further, the duct and specimen size must be reduced. For example, the side length of the square duct would have to be 8.5 mm to reach the desired 20 kHz bandwidth. Unfortunately, small specimen sizes result in installation and fabrication issues and in local material variations that can cause changes in the measured acoustic impedance. The installation and fabrication issues arise from having to cut a finite specimen, often resulting in damage to its edges. Furthermore, the smaller the specimen size, the larger the percentage of the total area composed of the damaged edges. For the local material variations, testing a large number of specimens can quantify these statistical variations. However, this approach is time consuming and costly.

Another method to increase the frequency range is to permit the propagation of higher-order modes. This allows large specimens but increases the complexity of the measurement setup and data reduction routine. For a 25.4 mm square duct, the bandwidth is increased to 13.5 kHz if the first four modes propagate or to 20 kHz if the first nine modes propagate. The advantage to this modal decomposition method (MDM) is that the higher-order modes can also be modeled as plane waves at oblique angles of incidence; thus this method can yield information regarding the effects of angle of incidence. The oblique-incidence information can be used to verify the local reactivity assumption, which states that the acoustic impedance is independent of the angle of incidence.[9]

Modal decomposition methods presented in the literature can be separated into two different schemes: correlation and direct methods.[10] Correlation approaches determine the modal amplitudes by measuring the temporal and spatial correlation of acoustic properties inside the waveguide. Direct methods, however, use point measurements to compute the modal amplitudes from a system of equations derived from

[a)]Portions of this work were presented in "Modal decomposition method for acoustic impedance testing in rectangular ducts" at the 44th AIAA Aerospace Sciences Meeting and Exhibit, Reno, NV, 9–12 January 2006, paper number AIAA 2006-2695, and in "Modal Decomposition Method for High Frequency Acoustic Impedance Testing," ASA Fall Meeting, Minneapolis, MN, 17–21 October 2005.

[b)]Electronic mail: sheplak@ufl.edu

 © 2006 Acoustical Society of America

an analytical propagation model. Accurate propagation models exist for rectangular, square, or cylindrical ducts with rigid walls. However, multiple independent sources are required to resolve the acoustic properties of the test specimen, such as the reflection coefficients, mode scattering coefficients, and acoustic impedances. This paper uses the latter approach and computes the modal amplitudes by solving a system of linear equations. This method is also amenable to a least-squares solution for added robustness.

Focusing now on prior research on direct methods, early work by Eversman investigated the energy flow of acoustic waves in rectangular ducts but did not consider the decomposition of modal components.[11] Moore was one of the first to investigate direct methods to determine the source distribution for ducted fans but limited his results to estimates of the sound pressure levels for each circumferential mode and neglected radial modes.[12] Following this, Zinn *et al.* investigated measuring acoustic impedance for higher-order modes by adapting the standing-wave method.[13] Yardley then added the effects of mean flow and reflected waves to determine the source distribution of a fan but did not expand the method to compute the reflection coefficient matrix.[14] Yardley also suggested that the microphones should all be mounted flush to the waveguide or duct. Pickett *et al.* continued to improve the direct method by adding a discussion of optimum microphone locations but limited their algorithms to a deterministic system of equations.[15] Only results at the fan blade passage frequency were reported. Moore continued the analysis evolution by comparing integral algorithms for the solution of the deterministic set of equations to the least-squares approach.[16] He concluded that the deterministic system was susceptible to measurement noise, and the least-squares solution provided robustness and approached the integral method solution in the limit of infinite measurement points. Again, his results were limited to estimates of the modal amplitudes.

Subsequently, Kerschen and Johnston developed a direct technique for random signals, but restricted the method to only incident waves.[17] Pasqualini *et al.* concentrated their efforts on a transform scheme for a direct method for circular or annular ducts only using a spinning-mode synthesizer with nine elements as the acoustic source.[18] A spinning-mode synthesizer is an array of compression drivers mounted on a waveguide, usually circular, in such a way that by changing the relative amplitude and phase of the sources, different modal distributions in the waveguide can be obtained. A method for use with transient signals was then developed by Salikuddin and Ramakrishnan.[19,20] Continuing this line of work, Åbom extended the direct method to any type of signal by measuring the frequency response function between microphone pairs.[10] Åbom noted difficulties associated with generating the necessary independent sources to calculate the reflection coefficient matrix. Akoum and Ville then developed and applied a direct method based on a Fourier-Lommel transform to the measurement of the reflection coefficient matrix at the baffled end of a pipe.[21] They developed a spinning-mode synthesizer using two compression drivers by mounting the compression drivers to the side of a circular waveguide on a rotating ring to generate the necessary independent sources. Their results were in good agreement with theoretical predictions for the normal mode, but they state that discrepancies existed for the higher-order modes since all of the data were near the cut-on frequency. Most recently, Kraft *et al.* discussed the development of a modal decomposition experiment using four microphones but did not provide any results.[7]

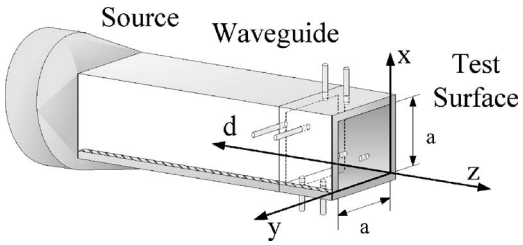

FIG. 1. Waveguide coordinate system. Note that the side wall has been removed to show the internal duct.

The contribution of this paper is to adapt a direct MDM based on a least-squares scheme to a square duct and to use simple sources to acquire the data necessary to estimate the entire reflection coefficient matrix and the acoustic impedance at frequencies beyond the cut-on frequency of higher-order modes. The outline of the paper is as follows: Sec. II derives the data reduction procedure for estimating the complex modal amplitudes, the reflection coefficient matrix, and the acoustic impedance values from the measured data. Section III outlines the experimental procedure and analysis parameters. This section concludes with a brief discussion concerning the sources of error. Section IV presents the experimental results for a single impedance specimen and compares the MDM results to TMM results for the same specimen. This paper then offers conclusions from the experimental results and offers suggestions for future work.

II. DATA REDUCTION ALGORITHM

The MDM developed here is restricted to time-harmonic, linear, lossless acoustics without mean flow governed by the Helmholtz equation for pressure

$$\nabla^2 \underline{P} + k^2 \underline{P} = 0, \tag{1}$$

where $\underline{P}$ is the complex acoustic pressure amplitude, $k = \omega/c_0$ is the wave number, ω is the angular frequency, c_0 is the isentropic speed of sound, and the $+j\omega t$ time convention is assumed.[22,23] The coordinate system is shown in Fig. 1, and the x, y, d coordinates will be used for this paper. The origin of the x, y, d coordinates is located in the lower right-hand corner of the internal duct at the plane where the test specimen is mounted. The general solution to Helmholtz equation, assuming propagation in the d direction, is a summation of normal modes

$$\underline{P} = \sum_m \sum_n \psi_{mn}(x,y)(A_{mn}e^{jk_z d} + B_{mn}e^{-jk_z d}), \tag{2}$$

where $j = \sqrt{-1}$, A_{mn} and B_{mn} are the complex modal amplitudes of the incident and reflected wave, respectively, m and n are the mode numbers, k_z is the axial wave number, $\psi(x,y)$ is the transverse factor determined by the boundary

conditions. The transverse factor is the product of the two eigenfunctions for a rigid-walled square duct,

$$\psi_{mn}(x,y) = \cos\left(\frac{m\pi}{a}x\right)\cos\left(\frac{n\pi}{a}y\right), \tag{3}$$

where a is the side length of the waveguide. The corresponding dispersion relation is

$$k_z = \sqrt{\left(\frac{\omega}{c_0}\right)^2 - \left(\frac{m\pi}{a}\right)^2 - \left(\frac{n\pi}{a}\right)^2}. \tag{4}$$

For a normal mode to propagate, k_z must be real-valued. The cut-on frequencies are determined by setting $k_z=0$ in Eq. (4),

$$f_{mn}^{\mathrm{co}} = \frac{c_0}{2}\sqrt{\left(\frac{m}{a}\right)^2 + \left(\frac{n}{a}\right)^2}. \tag{5}$$

Below f_{mn}^{co}, a higher-order mode (m,n) will not propagate and is evanescent. The angle of incidence for a propagating higher-order mode is[22]

$$\phi_{mn} = \cos^{-1}\left(\sqrt{1 - \left(\frac{f_{mn}^{\mathrm{co}}}{f}\right)^2}\right). \tag{6}$$

A. Complex modal amplitudes

The experimental procedure flush mounts a number of microphones in the sides of the waveguide, as in the TMM. The number and locations of the microphones are selected to observe the desired modes. A test frequency is selected and the total number of propagating modes, σ, are found from Eq. (5) for that frequency. The minimum number of microphone measurements required to uniquely determine the acoustic pressure is for this test frequency is 2σ.[10] Next, Eq. (2) is written for each microphone measurement, summing only over the propagating modes for that frequency, to form a system of equations

$$\begin{aligned}
\underline{P}_1 &= \sum_m \sum_n \psi_{mn}(x_1,y_1)(A_{mn}e^{jk_z d_1} + B_{mn}e^{-jk_z d_1}),\\
\underline{P}_2 &= \sum_m \sum_n \psi_{mn}(x_2,y_2)(A_{mn}e^{jk_z d_2} + B_{mn}e^{-jk_z d_2}),\\
&\vdots\\
\underline{P}_\eta &= \sum_m \sum_n \psi_{mn}(x_\eta,y_\eta)(A_{mn}e^{jk_z d_\eta} + B_{mn}e^{-jk_z d_\eta}),
\end{aligned} \tag{7}$$

where the subscript on $\underline{P}$ represents the microphone location and η is the number of microphone measurements, which must be equal to or larger than 2σ. To decompose the sound field, the microphones should be located with some transverse separation and some axial separation. A simple way to configure the microphone locations is to group the microphones into two groups and locate each group at a separate axial location. The system of equations can be compactly expressed in matrix form as

$$\{\underline{P}\} = \mathbf{L}\{G\}, \tag{8}$$

where $\{\underline{P}\}$ is the $\eta\times 1$ vector of measured complex acoustic pressure amplitudes, $\{G\}$ is the $2\sigma\times 1$ vector of the complex modal amplitudes given by

$$\{G\} = \begin{Bmatrix}\{A\}\\ \{B\}\end{Bmatrix}, \tag{9}$$

and $\mathbf{L}$ is the $\eta\times 2\sigma$ matrix of the coefficients from Eq. (7), composed of the transverse function and the propagation complex exponential.

The coefficient matrix has a special form; it is composed of two sub-matrices that are complex conjugates. As a result of this structure, the determinant of the $\mathbf{L}$ matrix has an imaginary part that is identically equal to zero. To avoid this problem, the matrix equation is transformed into a system of two real-valued matrix equations, each with a coefficient matrix that has a nonzero determinant

$$\{\underline{P}_R\} + j\{\underline{P}_I\} = (\mathbf{L}_R + j\mathbf{L}_I)(\{G_R\} + j\{G_I\}), \tag{10}$$

where the subscripts "R" and "I" denote the real and imaginary parts, respectively.[24] The expression is rearranged by carrying out the multiplication and collecting the real and imaginary parts

$$\begin{Bmatrix}\{\underline{P}_R\}\\ \{\underline{P}_I\}\end{Bmatrix} = \begin{bmatrix}\mathbf{L}_R & -\mathbf{L}_I\\ \mathbf{L}_I & \mathbf{L}_R\end{bmatrix}\begin{Bmatrix}\{G_R\}\\ \{G_I\}\end{Bmatrix}. \tag{11}$$

The solution to Eq. (11) is found, for example, via Gaussian elimination for the deterministic case in which $\eta=2\sigma$. For the overdetermined case, in which $\eta>2\sigma$, a least-squares solution to Eq. (11) is desired for a robust solution and can be found by solving the normal equations

$$\begin{aligned}
\begin{bmatrix}\mathbf{L}_R & -\mathbf{L}_I\\ \mathbf{L}_I & \mathbf{L}_R\end{bmatrix}^{\mathbf{T}}\begin{Bmatrix}\{\underline{P}_R\}\\ \{\underline{P}_I\}\end{Bmatrix} &= \begin{bmatrix}\mathbf{L}_R & -\mathbf{L}_I\\ \mathbf{L}_I & \mathbf{L}_R\end{bmatrix}^{\mathbf{T}}\begin{bmatrix}\mathbf{L}_R & -\mathbf{L}_I\\ \mathbf{L}_I & \mathbf{L}_R\end{bmatrix}\\
&\times\begin{Bmatrix}\{G_R\}\\ \{G_I\}\end{Bmatrix},
\end{aligned} \tag{12}$$

where the superscript $\mathbf{T}$ represents the transpose of the matrix.[25]

B. Reflection coefficient matrix

With the existence of higher-order propagating modes, an incident acoustic mode now may reflect as the same mode or scatter into different modes. This increases the complexity of characterizing the specimen, as a single reflection coefficient can no longer describe the acoustic interaction. Instead, the reflection coefficient matrix is defined as

$$\{B\} = \mathbf{R}\{A\}, \tag{13}$$

where the size of $\mathbf{R}$ is $\sigma\times\sigma$ and the vectors $\{A\}$ and $\{B\}$ are $\sigma\times 1$.[10,11] The elements of $\mathbf{R}$ are represented by $R_{mn,qr}$, where the first index, mn, is the mode number for the reflected mode and the second index, qr, is the mode number for the incident mode. The diagonal elements, $R_{mn,mn}$, represent same-mode reflection coefficients, while the off-diagonal elements, $R_{mn,qr}$, represent the mode scattering coefficients. To determine the unknown reflection coefficient

matrix, a minimum of σ linearly independent source conditions must be measured.[10,21] The additional vectors of the incident and reflected complex modal amplitudes can be used to form linearly independent expressions for Eq. (13) and then are combined together to form matrices such that

$$[\{B\}_1\ \{B\}_2\ \cdots\ \{B\}_\sigma] = \mathbf{R}[\{A\}_1\ \{A\}_2\ \cdots\ \{A\}_\sigma], \tag{14}$$

which can then be solved for the reflection coefficient matrix.[10,21] For the deterministic case where there are equal number of independent sources and modes, the solution to Eq. (14) is

$$\mathbf{R} = [B][A]^{-1}. \tag{15}$$

The solution of the overdetermined case is found in a least-squares sense by solving the normal equations. In this work various restrictor plates are placed between the waveguide and the compression driver to generate multiple independent sources. As will be seen below, each plate emphasizes the generation of one higher-order mode. The use of the restrictor plates with a single compression driver is in contrast to the spinning-mode synthesizers with multiple drivers used by previous researchers.[10,18,21]

C. Acoustic impedance

The acoustic impedance ratio is defined only for same-mode reflections as[22]

$$\xi_{mn} = \frac{\dfrac{Z_{\text{specimen}}}{\cos(\phi_{mn}^{\text{tr}})}}{\dfrac{Z_0}{\cos(\phi_{mn})}} = \frac{1 + R_{mn,mn}}{1 - R_{mn,mn}}, \tag{16}$$

where Z_{specimen} and Z_0 are the characteristic impedances of the specimen and medium, respectively, and ϕ_{mn}^{tr} is the angle of transmission for the m,n mode. The normalized specific acoustic impedance or normalized characteristic impedance is obtained from Eq. (16),

$$\frac{Z_{\text{specimen}}}{Z_0} = \frac{\cos(\phi_{mn}^{\text{tr}})}{\cos(\phi_{mn})}\frac{1 + R_{mn,mn}}{1 - R_{mn,mn}}. \tag{17}$$

Without further information concerning ϕ_{mn}^{tr}, only the normalized acoustic impedance can be computed from the results of the MDM. However, locally reactive materials are commonly tested.[26,27] A locally reactive material is a material whose impedance is independent of the angle of incidence and therefore is assumed to have a transmission angle of approximately zero.[28] In this case, Eq. (17) simplifies to

$$\frac{Z_{\text{specimen}}}{Z_0} = \frac{1}{\cos(\phi_{mn})}\frac{1 + R_{mn,mn}}{1 - R_{mn,mn}}, \tag{18}$$

which represents the normalized surface response impedance[9] and can be estimated from the MDM. The locally-reactive assumption is valid if the normalized specific acoustic impedances for all modes at a given frequency are equal.

For the TMM, only plane waves are present and, hence, only the normal incident acoustic impedance is determined. The higher-order modes can be thought of as plane waves at an oblique angle of incidence, as stated earlier. The effect of angle of incidence causes the acoustic impedance value to differ from the specific acoustic impedance value, and that both estimates of impedance must be considered to fully characterize the specimen.

D. Acoustic power

In addition to the normalized acoustic impedance, the absorption coefficient is an important parameter to characterize acoustic materials. The absorption coefficient, α, is defined as the amount of acoustic power absorbed by the specimen normalized by the incident power and is given as

$$\alpha = \frac{W_i - W_r}{W_i} = 1 - \frac{W_r}{W_i}, \tag{19}$$

where W_i and W_r represent the power in the incident and reflected acoustic fields, respectively. In the case of the TMM, the absorption coefficient only considers the power contained in the plane wave mode, but in the MDM, the absorption coefficient will encompass the total power absorbed in all of the propagating modes. Equation (19) assumes that no acoustic power is transmitted through the waveguide into the surrounding environment, hence demonstrating the need for terminating the specimen with a rigid back plate and for ensuring proper sealing of the waveguide. Expressions for the incident and reflected powers are derived from integrating the acoustic intensity in the d direction over the cross section of the waveguide to obtain the total power, W, given by

$$W(f) = \int\int_S I_d dS = \int_{y=0}^{a}\int_{x=0}^{a} \frac{1}{2}\,\text{Re}[\underline{P}\underline{U}_d^*]dxdy, \tag{20}$$

where $\underline{U}_d$ is the acoustic velocity perturbation in the frequency domain and is found from Euler's equation[22]

$$\underline{U}_d = \frac{j}{\rho c_0 k}\frac{\partial \underline{P}}{\partial d}. \tag{21}$$

The orthogonal properties of the normal modes in the acoustic pressure solution given in Eq. (2), and in the acoustic velocity perturbation solution, given in Eq. (21), allow for the expression of the total power to be simplified and ultimately separated into two parts. Each part only contains the modal amplitudes for either the incident waves or the reflected waves. The resulting expressions for the incident and reflected powers are

$$W_i = \frac{a^2}{8\rho c_0 k}\sum_{m=0}^{M}\sum_{n=0}^{N} k_{z,mn}|A_{mn}|^2, \tag{22}$$

and

$$W_r = \frac{a^2}{8\rho c_0 k}\sum_{m=0}^{M}\sum_{n=0}^{N} k_{z,mn}|B_{mn}|^2. \tag{23}$$

The absorption coefficient not only provides an estimate of the sound absorption capabilities of a material, but also provides a check on the measurement. The absorption coeffi-

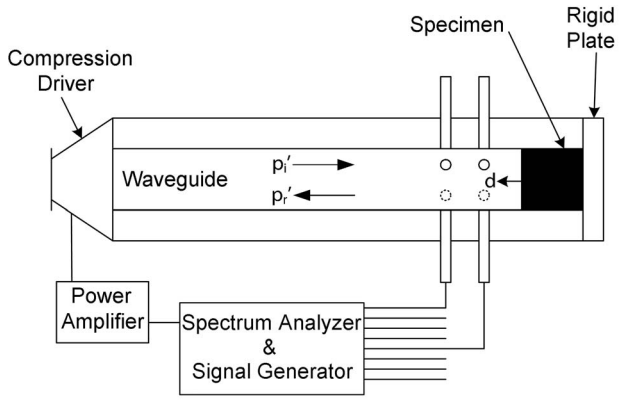

FIG. 2. Schematic of the experimental set up for the MDM (some microphone connections are left out for clarity).

cient is bounded between zero and unity, and values outside this range indicate a problem with the experimental setup and procedure.

III. EXPERIMENTAL METHODOLOGY

To verify the data reduction routine outlined above and obtain acoustic impedance data beyond the cut-on frequency, an experimental apparatus is developed. The experimental procedure to acquire and reduce the data is similar to the TMM. A compression driver is mounted at one end of a waveguide, and the test specimen is mounted at the other end. The specimen chosen for the analysis is a ceramic tubular specimen with 65% porosity (CT65) and a depth of 56 mm. The results for the same material are given by Jones *et al.*, but for a different depth of 77.5 mm.[27] For the MDM, eight microphones are flush-mounted in the duct wall at two axial locations near the specimen to resolve the incident and reflected waves, but far enough away for the evanescent modes to be negligible. Fourier transforms of the phase-locked, digitized pressure signals at each location are used to estimate the complex acoustic pressure and thus the modal coefficients and reflection coefficient matrix. A schematic of the experimental setup is shown in Fig. 2, with eight microphones flush-mounted into the waveguide. Each component of the experimental setup and the data acquisition and analysis routine are discussed in the following sections.

A. Waveguide

The waveguide used in the measurements presented is approximately 96 cm long and has a square cross section measuring 25.4 mm on a side. The walls of the waveguide are constructed of 22.9-mm thick aluminum (type 6061-T6). The cut-on frequencies for the higher-order modes, given in Table I, show that the limiting bandwidth for the TMM is 6.7 kHz for this waveguide, as opposed to 13.6 kHz when the MDM is used with the first four modes. To resolve these four modes, eight microphones are placed in two groups of four microphones at two axial locations. The placement is chosen such that each microphone is not located at the node line of any of the modes of interest and to achieve a sufficient signal to noise ratio. The locations of the eight microphones are provided in Table II.

TABLE I. Cut-on frequencies (kHz) for the higher-order modes.

m/n	0	1	2	3
0	0	6.83	13.6	20.5
1	6.83	9.66	15.3	21.6
2	13.6	15.3	19.3	24.6
3	20.5	21.6	24.6	29.0

B. Equipment description

The compression driver is a BMS 4590P, with an operating frequency range of 0.2–22 kHz, powered by a Techron 7540 power amplifier. The drive signal is generated by a Brüel and Kjær (B&K) Pulse Analyzer System, which also acquired and digitized the eight microphone signals with a 16-bit digitizer. The measurement microphones are B&K Type 4138 microphones (3.18 mm diameter) and are installed into the waveguide with their protective grids attached to the microphone. The microphones are calibrated only for magnitude before mounting in the waveguide. The phase mismatch between the eight microphones was measured up to 6.7 kHz and was found to be less than ±5°. This error is found to be acceptable as it resulted in less than 10% uncertainty in the magnitude and in the phase for the modal amplitudes and reflection coefficients. Atmospheric temperature is measured using a 100 Ω platinum resistive thermal device with an accuracy of ±2 K.

C. Signal processing

All eight microphone signals are measured and subsequently processed with a fast Fourier transform algorithm. The frequency resolution is 16 Hz with a frequency span from 0.3 to 13.5 kHz. The 1000 linear averages are processed using a uniform window with no overlap. Leakage is eliminated by the use of a pseudorandom periodic signal to excite the compression driver. To ensure synchronous data acquisition, the sampling is triggered by the start of the generator signal in a phase locked acquisition mode. The data are then processed using the MDM described above.

D. Numerical study of uncertainties

The main sources of error for the MDM are the signal to noise ratio, microphone phase mismatch, uncertainties in the measurements of the microphone locations, and the temperature. The frequency scaling of the uncertainty in the computed values from the MDM is also important, as the goal of the MDM is to extend the frequency range of acoustic impedance testing. Numerical studies have been conducted concerning the effects of the individual error sources and the

TABLE II. Measurement locations (a=25.4 mm).

Microphone	x,y,d Location (mm)	Microphone	x,y,d Location (mm)
1	$0.25a$, 0, $1.6a$	5	$0.25a$, 0, $1.1a$
2	a, $0.25a$, $1.6a$	6	a, $0.25a$, $1.1a$
3	$0.75a$, a, $1.6a$	7	$0.75a$, a, $1.1a$
4	0, $0.75a$, $1.6a$	8	0, $0.75a$, $1.1a$

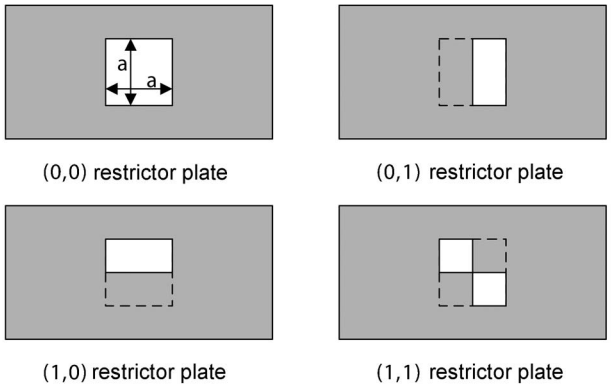

FIG. 3. Schematic of the four restrictor plates. (The dotted line represents the waveguide duct cross-section.)

frequency scaling of the total error, and are only summarized here for brevity.[29] These studies are performed for an approximate sound hard termination, with four different vectors of incident complex modal amplitudes. The reflected modal amplitudes are computed from Eq. (13) and the data are then used to calculate time-series data. The time-series data are then processed using the MDM described above. The root-mean-square (rms) normalized error between the elements of the calculated reflection coefficient matrix and the modeled reflection coefficient matrix is used to gage the uncertainty of the MDM. The numerical studies are performed at a frequency of 12 kHz to avoid pressure nodes for the microphone locations listed in Table II. The simulations varied the error introduced into the simulated input signals to the MDM and computed the perturbed output reflection coefficient matrix for each of the error sources individually. These results showed that the MDM gives reliable and accurate estimates ($\sim$10% uncertainty) for the complex modal coefficients and the reflection coefficient matrix.

IV. EXPERIMENTAL RESULTS

The MDM and TMM experimental results for the CT65 specimen are presented and compared using the same waveguide. The TMM results range from 0.3 to 6.7 kHz, while the MDM results range from 0.3 to 13.5 kHz. The cut-on frequencies for the higher-order modes are 6.83 kHz for the (1,0) and (0,1) modes and 9.66 kHz for the (1,1) mode based on the measured temperature. The independent sources for the MDM are generated via the four different restrictor plates shown in Fig. 3, each one is designed to emphasize one or more of the first four modes. Figure 4 shows the incident pressure field measured for each of the restrictor plates and reveals that one of the sources generates a pressure level approximately 5–10 dB higher than the other three sources for the higher-order modes. The exception is the plane wave mode, where the restrictor plate produces pressure levels only marginally higher than the others. The data for the reflected pressure field for each of the restrictor plates are presented in Fig. 5, and this figure shows evidence of mode scattering since there is no longer the same difference between the pressure amplitude of each of the sources as shown in the incident pressure field.

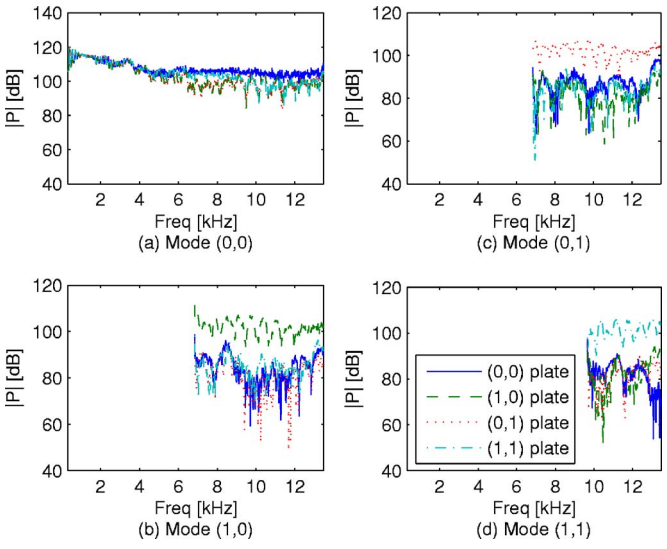

FIG. 4. (Color online) Incident pressure field. All dB units are referenced to 20 μPa.

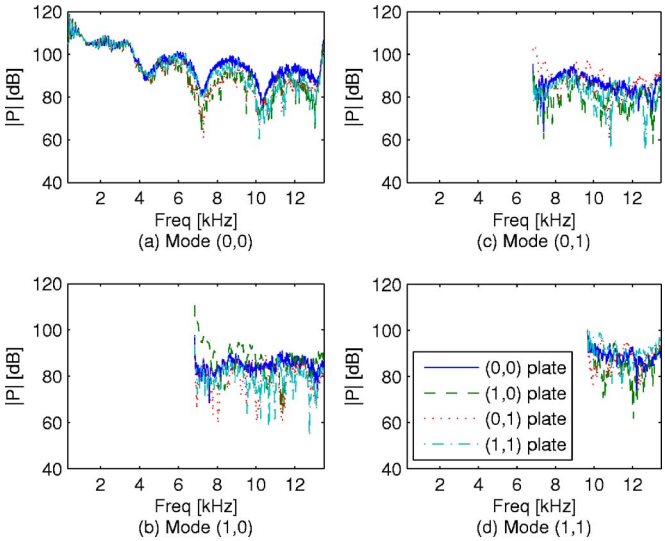

FIG. 5. (Color online) Reflected pressure field. All dB units are referenced to 20 μPa.

The absorption coefficient is shown in Fig. 6 for all four restrictor plates. The data show that the total power absorbed is dependent on the modal content of the acoustic field, since the absorption coefficient varies between the sources after the cut-on frequency for the first higher-order mode.

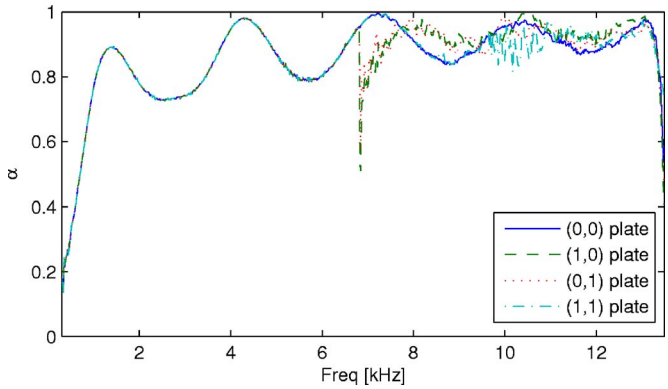

FIG. 6. (Color online) Absorption coefficient.

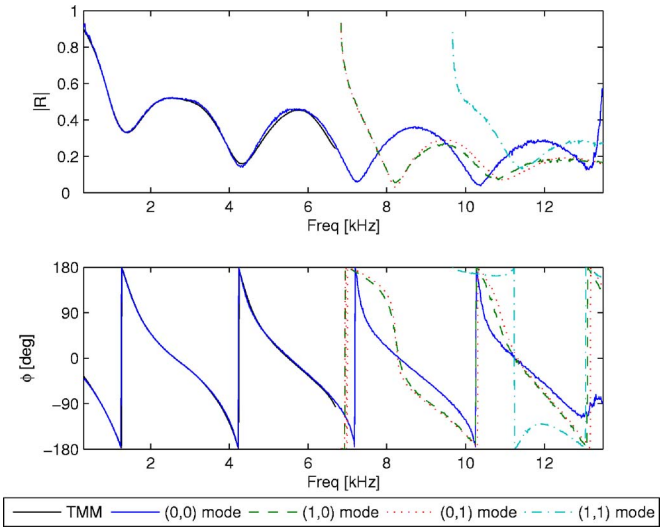

FIG. 7. (Color online) Reflection coefficients for the CT65 specimen. (TMM uncertainty estimates are not shown for clarity.)

The magnitude and argument of the reflection coefficients are shown in Fig. 7 along with results from the TMM. The estimate of the plane wave reflection coefficient provided by the MDM agrees with the TMM to within its 95% confidence interval estimates. The uncertainty estimates for the TMM are estimated using the procedure outlined in Schultz,[29] however, they are not shown in the figures for clarity. Figure 8 shows the mode scattering coefficients for the plane wave mode scattering into the higher-order modes. The other mode scattering coefficients are calculated but are not shown for brevity. The magnitude of the mode scattering coefficients is less than 0.2 for all frequencies except for the frequencies near the (1,1) mode cut-on. The maximum value for the magnitude of the other scattering coefficients is 0.2–0.3 for the (0,1) mode scattering into the (1,1) modes.

Figure 9 shows the normalized specific acoustic impedance. The test specimen is assumed to be a locally reactive material and thus the transmission angle is assumed to be normal to the surface. The data show a number of resonant

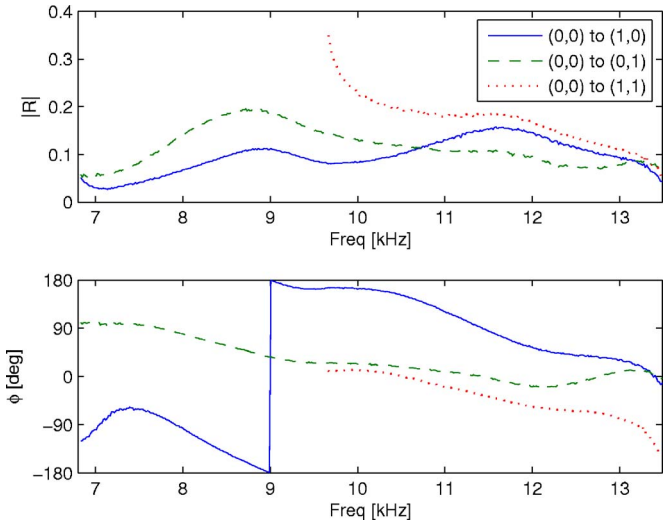

FIG. 8. (Color online) Mode scattering coefficients from the plane wave mode to the other higher-order modes.

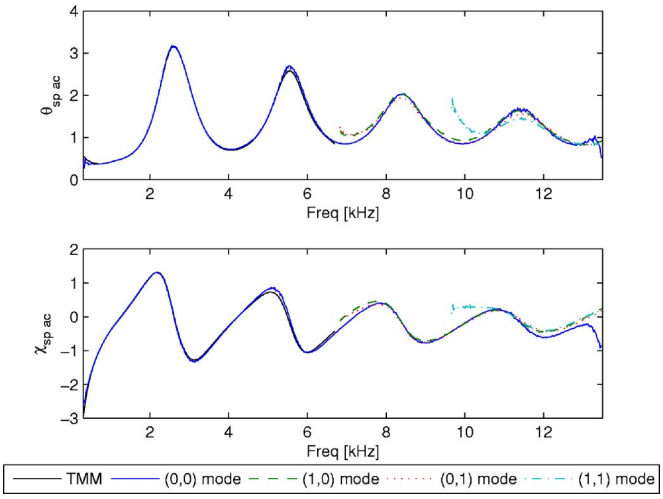

FIG. 9. (Color online) Normalized specific acoustic impedance estimates. (TMM uncertainty estimate are not shown for clarity.)

frequencies, which are 1.26, 4.24, 7.20, and 10.3 kHz as identified from the TMM and MDM results. If the ceramic cells are modeled as an ideal quarter-wave resonator, the first four resonant frequencies are 1.54, 4.61, 7.68, and 10.7 kHz. The comparisons between the experimental resonant frequencies and the calculated resonant frequencies are reasonable and provide physical insight into the mechanics of the ceramic tubular material as an acoustic liner. For the locally reactive assumption to be valid, the estimates for the normalized specific acoustic impedance should be identical, regardless of the mode. Uncertainty estimates of the normalized specific acoustic impedance are needed to fully evaluate this assumption, but the results show reasonable agreement, except at the cut-on for the (0,1), (1,0), and (1,1) modes and for frequencies above 13 kHz. These frequency ranges should be investigated further, but these results suggest that the locally reactive assumption is reasonable. The unreliable results at the cut-on frequencies are affected by theoretical phase and angle of incidence for the mode cutting on. At the cut-on frequency, the phase speed of the newly propagating mode approaches infinity and the incident angle approaches grazing incidence. Physically, this situation is unrealizable and results in the irregular behavior at the cut-on frequencies. Furthermore, even beyond the cut-on frequency the incidence angle is quite large and is 67° for the (1,1) mode at 10.5 kHz, where in Fig. 9, the data for the different modes appear to match. The MDM estimate of the normal incidence specific acoustic impedance is approximately independent of the transmission angle and agrees with the TMM estimate within the 95% confidence interval for the TMM. Again, the TMM uncertainty estimates are not shown for clarity.

V. DISCUSSION OF RESULTS

The MDM offers the ability to extend the bandwidth of acoustic impedance testing by accommodating the propagation of higher-order modes and maintaining a larger specimen size to avoid sample size effects. This also gives the ability to obtain acoustic impedance data at oblique angles of incidence, with the primary drawback being increased com-

plexity as compared to the TMM. A direct MDM procedure was developed for a square duct using the first four modes. This paper restricted the maximum number of propagating modes to four for a proof-of-concept demonstration. The routines presented can easily be expanded to handle more propagating modes through the addition of measurement microphones. As the bandwidth of the MDM is increased, spatial averaging of the microphone measurements may present an error source that can be reduced with probe tips attached to the microphones[30] or by using microphones with a smaller diameter such as MEMS-based microphones.[31] Also, diffraction effects of the sound scattering of the protective grids of the microphones can introduce error.[32] To achieve the 20 kHz bandwidth goal for the 25.4 mm square waveguide, up to and including the (2,2) must be accounted for. This requires 18 microphone measurements in order to resolve the nine propagating modes and will require nine independent source conditions. The additional microphones could be placed at new axial locations along with different locations along the perimeter of the waveguide. The additional source conditions could be created with additional restrictor plates. The routines can also be applied to rectangular and cylindrical ducts through substitution of the correct transverse factor, but a square duct was chosen because the geometry allows for the largest cross section for a given cut-on frequency for the first higher-order mode and allows for the microphones to be easily flush mounted to the duct walls.

VI. CONCLUSIONS

The present results demonstrate that the MDM can accurately resolve the sound field inside the waveguide and decompose the modal coefficients, except near the cut-on frequencies, and provide estimates for the complete reflection coefficient matrix. The MDM results are consistent with the TMM results to within the 95% confidence interval estimates for the TMM results. The MDM results show, for the example provided that the experimental method is successful at isolating the complex amplitudes of the incident and reflected waves. Evidence of mode scattering is present as seen from the higher incident amplitudes of one of the modes compared to the reflected mode. These amplitudes, repeatedly measured with various sources, provide the necessary information to determine the reflection coefficient matrix and the acoustic impedance of the test specimen. Again, for the example provided, the data tend to validate the independence of the specific acoustic impedance on the incident mode and indicate that the CT65 material is locally reactive.

The methodology and experimental apparatus presented can measure and decompose the entire sound field into incident and reflected modal components up to 13.5 kHz. The results for one material specimen are confirmed with a simple comparison to results from the standard two-microphone method. To fully characterize the MDM and validate the apparatus and methodology, uncertainty estimates are needed along with results for different material specimens. The inclusion of uncertainty estimates will allow for quantitative statements concerning the equality of the specific acoustic impedance for the different modes and thus will determine the validity of the locally reactive assumption. Another goal of future work should be to focus on extending the frequency range of the MDM up to approximately 20 kHz as desired for aeroacoustic testing.

ACKNOWLEDGMENTS

Financial support for the research project was provided by a NASA-Langley Research Center Grant (Grant No. NAG-1-2261) monitored by Mr. Michael Jones, who also provided material samples. The first author would like to thank the NASA Graduate Student Research Program Fellowship and the National Defense Science and Engineering Graduate Fellowship administered by the American Society for Engineering Education for their financial support.

[1] R. E. Motsinger and R. E. Kraft, in *Aeroacoustics of Flight Vehicles: Theory and Practice*, edited by H. H. Hubbard (Acoustical Society of America, New York, 1995), Vol. **2**, pp. 165–206.
[2] ASTM-E1050–98 (ASTM International, 1998).
[3] J. Y. Chung and D. A. Blaser, "Transfer function method of measuring in-duct acoustic properties, I-Theory, II-Experiment," J. Acoust. Soc. Am. **68**(3), 907–921 (1980).
[4] ISO-10534–2:1998 (International Organization for Standardization, 1998).
[5] M. G. Jones and T. L. Parrott, "Evaluation of a multipoint method for determining acoustic impedance," Mech. Syst. Signal Process. **3**(1), 15–35 (1989).
[6] M. G. Jones and P. E. Stiede, "Comparison of methods for determining specific acoustic impedance," J. Acoust. Soc. Am. **101**(5), 2694–2704 (1997).
[7] R. E. Kraft, J. Yu, H. W. Kwan, B. Beer, A. F. Seybert, and P. Tathavadekar, Acoustic Treatment Design Scaling Methods: Phase II Final Report No. NASA/CR-2003–212428 (2003).
[8] R. E. Kraft, J. Yu, H. W. Kwan, D. K. Echternach, A. A. Syed, and W. E. Chien, Acoustic Treatment Design Scaling Methods, NASA/CR-1999–209120, 1999.
[9] A. P. Dowling and J. E. Ffowcs-Williams, *Sound and Sound Sources* (Wiley, New York, 1983).
[10] M. Åbom, "Modal decomposition in ducts based on transfer function measurements between microphone pairs," J. Sound Vib. **135**(1), 95–114 (1989).
[11] W. Eversman, "Energy flow criteria for acoustic propagation in ducts with flow," J. Acoust. Soc. Am. **49**(6), 1717–1721 (1970).
[12] C. J. Moore, "In-duct investigation of subsonic fan rotor alone noise," J. Acoust. Soc. Am. **51**(5), 1471–1482 (1972).
[13] B. T. Zinn, W. A. Bell, B. R. Daniel, and A. J. Smith Jr., "Experimental determination of three-dimensional liquid rocket nozzle admittances," AIAA J. **11**(3), 267–272 (1973).
[14] P. D. Yardley, "Measurement of noise and turbulence generated by rotating machinery," Ph.D. dissertation, University of Southampton, 1974.
[15] G. F. Pickett, T. G. Sofrin, and R. A. Wells, Method of fan sound mode structure determination, NASA-CR-135293, 1977.
[16] C. J. Moore, "Measurement of radial and circumferential modes in annular and circular fan ducts," J. Sound Vib. **62**(2), 235–256 (1979).
[17] E. J. Kerschen and J. P. Johnston, "A modal separation measurement technique for broadband noise propagating inside circular ducts," J. Sound Vib. **76**(4), 499–515 (1981).
[18] J. P. Pasqualini, J. M. Ville, and J. F. de Belleval, "Development of a method of determining the transverse wave structure in a rigid wall axisymmetric duct," J. Acoust. Soc. Am. **77**(5), 1921–1926 (1985).
[19] M. Salikuddin, "Sound radiation from single and annular stream nozzles, with modal decomposition of in-duct acoustic power," J. Sound Vib. **113**(3), 473–501 (1987).
[20] M. Salikuddin and R. Ramakrishnan, "Acoustic power measurement for single and annular stream duct-nozzle systems utilizing a modal decomposition scheme," J. Sound Vib. **113**(3), 441–472 (1987).
[21] M. Akoum and J. M. Ville, "Measurement of the reflection matrix of a discontinuity in a duct," J. Acoust. Soc. Am. **103**(5), 2463–2468 (1998).
[22] D. T. Blackstock, *Fundamentals of Physical Acoustics* (Wiley, New York, 2000).
[23] P. M. Morse and K. U. Ingard, *Theoretical Acoustics* (Princeton University

Press, Princeton, 1986).
[24]S. S. Rao, *Applied Numerical Methods for Engineers and Scientists* (Prentice-Hall, New York, 2002), pp. 188–190.
[25]S. C. Chapra and R. P. Canale, in *Numerical Methods for Engineers* (McGraw-Hill, New York, 2002), pp. 231–261, 440–471.
[26]M. G. Jones, T. L. Parrott, and W. R. Watson, "Comparison of acoustic impedance eduction techniques for locally-reacting liners," AIAA-2003–3306, 9th AIAA/CEAS Aeroacoustics Conference and Exhibit, Hilton Head, South Carolina, 2003.
[27]M. G. Jones, W. R. Watson, and T. L. Parrott, "Design and evaluation of modifications to the NASA Langley flow impedance tube," AIAA-2004–2837, 10th AIAA/CEAS Aeroacoustics Conference, Manchester, United Kingdom, 2004.
[28]P. Morse, *Vibration and Sound* (Acoustical Society of America, Sewickley, 1981).
[29]T. Schultz, *Acoustic Impedance Testing for Aeroacoustic Applications*, Ph.D. dissertation, University of Florida, 2006.
[30]L. P. Franzoni and C. M. Elliott, "An innovative design of a probe-tube attachment for a (1/2)-in. microphone," J. Acoust. Soc. Am. **104**(5), 2903–2910 (1998).
[31]D. P. Arnold, T. Nishida, L. N. Cattafesta, and M. Sheplak, "A directional acoustic array using silicon micromachined piezoresistive microphones," J. Acoust. Soc. Am. **113**(1), 289–298 (2003).
[32]J. R. Underbrink, in *Aeroacoustic Measurements*, edited by Thomas J. Mueller (Springer, New York, 2002), pp. 165–179.

Objectively measured and subjectively perceived distortion in nonlinear systems[a)]

Åke Olofsson[b)]
Technical and Experimental Audiology, Karolinska Institutet, Blå vägen, Hus 15, SE-18230 Danderyd, Sweden

Martin Hansen[c)]
Widex Audiology Research Lab, Ny Vestergårdsvej 25, DK-3500 Værløse, Denmark

(Received 23 December 2005; revised 25 September 2006; accepted 1 October 2006)

A method for measuring nonlinear distortion, which is applicable to almost any transmission system and which can use any input signal as a test signal, is proposed. The method exploits the fact that a pair of signals, generated to form the real and imaginary parts of the analytical signal corresponding to the input signal to a system, lose their property of being a Hilbert pair after being passed through a nonlinear system. The method was tested by measuring 12 different hearing aid compression systems. These objective measurements were compared with the subjectively perceived amount of distortion, assessed by a group of 10 otologically normal subjects. A reasonably monotonic relation between the subjective and objective measures of distortion was observed. The objective Hilbert pair based measure can be related to both traditional total harmonic distortion and traditional signal to noise ratio. © *2006 Acoustical Society of America.* [DOI: 10.1121/1.2372591]

PACS number(s): 43.58.Ry, 43.66.Lj [AJZ] Pages: 3759–3769

I. INTRODUCTION

The introduction of digital signal processing techniques in hearing aids has made it common to use nonlinear signal processing schemes, which change the properties of the hearing aid depending upon the input signal. For example, amplitude compression in a hearing aid is designed to apply a time-varying and frequency dependent gain so that the level of the resulting output signal matches a desired target level. Other examples are noise reduction and/or speech enhancement and active feedback cancellation. If the properties of the hearing aid are varied too rapidly, the sound delivered by the hearing aid may be perceived as distorted. Until now there has not been a standardized objective measure which is directly related to this perceived distortion experienced in nonlinear hearing aids when listening to realistic, broadband input signals.

A definition of "distortion" is not always straightforward. Several definitions have focused on technical aspects of certain classes of transmission systems. Another view of distortion comes into play when one is interested in quantifying "distortion" as a perceptual entity, evoked during subjective listening tests. Naturally, one is interested in finding a close relation between the objectively measured distortion and the perceived distortion. For example, for a large class of linear transmission systems, which are disturbed by additive external or internal noise, the concept of the signal to noise ratio has proven to be an excellent predictor of the perceived amount of distortion resulting from these systems. For nonlinear systems, such a prediction tends to be more difficult and might, e.g., depend on the nature of the input signal. In measurements of nonlinear distortion in hearing aids according to standards (harmonic distortion and intermodulation distortion, ANSI, 1996 and IEC, 1983), steady-state or two-component sinusoidal signals are used. A more advanced method by Tan *et al.* (2003) used a 10-component multitone test signal. The frequencies were logarithmically spaced and the duration was 1 s. They investigated the distortions on this signal from a number of memoryless nonlinearities and showed a good correlation between measured distortions and subjective ratings.

These methods can, however, give highly unreliable results if the hearing aid changes its characteristics during the measurement. Sometimes this problem can be solved by measuring after the system has come to a steady state. However, a measurement with sinusoidal input signals will still be problematic, as it cannot be expected to reflect the behavior of the nonlinear signal-adaptive hearing aid during real use by the hearing aid wearer, e.g. with modulated time-varying signals like speech in background noise as input signal. An automatic gain control (AGC) hearing aid, for instance, changes its gain depending upon the level of the input signal and some aids may adaptively change their frequency response. Some aids may even try to enhance the signal to noise ratio by suppressing weak signals, or by differentiating between speech and noise and reducing the gain for noise signals. Moreover, even for a hearing aid comprising only of simple amplitude compression circuits, the amount of nonlinear distortion will depend on the compression thresholds, the attack and release times, the compression ratios, and the number of compression channels.

[a)]A poster with the same title was presented at IHCON, Lake Tahoe, 2002.
[b)]Electronic mail: Ake.Olofsson@ki.se
[c)]Current address: Fachhochschule Oldenburg/Ostfriesland/Wilhelmshaven, Inst. für Hörtechnik und Audiologie, Ofener Str. 16, D-26121 Oldenburg, Germany.

Several attempts to define alternative measures of nonlinear distortion using running speech and coherence between input and output signals have been reported (Kates, 1992; Dyrlund, 1989; Dyrlund *et al.*, 1994). This works well for a linear hearing aid but not so well for a signal-adaptive hearing aid, since the method does not distinguish between desired nonlinearity resulting from signal adaptive processing and nonlinear distortion produced, e.g., by undesired nonlinear side effects, or just by a poor transducer (Dyrlund *et al.*, 1994).

It can be shown (Olofsson 1992, also cited in Kates, 2000) that all systems which change their behavior during a measurement, will have coherence functions with magnitude less than 1. These coherence measurements reveal that the measured object is mathematically nonlinear. It is, however, not necessarily perceptually nonlinear, i.e., perceptually distorted.

Kates (2000) has used phase coherence to estimate nonlinear distortion. This works well for gain variations in a system but not for adaptive filtering where the phase of the system may change. Within the telecommunication area there has been a great interest in establishing standardized measurements methods, using speech test signals, which give a good prediction of the perceived overall speech transmission quality. These methods, Perceptual Speech Quality Measure (PSQM) (Beerends and Stemerdink, 1994), Perceptual Evaluation of Audio Quality (PEAQ) (Thiede *et al.*, 2000), Perceptual Evaluation of Speech Quality (PESQ), (Beerends *et al.*, 2002) use more or less sophisticated perceptual models, by which the input test signal and the output response signal are processed and transformed to a perceptual "internal representation." After normalizations the difference between the signals is calculated in the perceptual domain. The purpose of the normalizations is to equalize the average levels and frequency contents of the signals. In the case of an AGC hearing aid the difference between the transformed input and output signals can be large due to the temporal fluctuating gain of the aid. The PESQ has a procedure to compensate for slow broadband gain variations, but this could not compensate for the gain variations in a multichannel AGC aid or in a hearing aid with fast syllabic compression. In order to develop an objective distortion measure that is capable of predicting the perceived distortion in nonlinear hearing aids, it seems necessary to be able to tell apart the several aspects of the nonlinearity of the hearing aid. The hearing aid is designed deliberately to introduce a nonlinearity, such as occurs with amplitude compression. Amplitude compression has the intention of reducing gain at higher relative to lower input levels. However, parameters used in the design of the compressor can give rise to undesirable side effects, such as "spectral splatter," the spreading of the signal energy across a wider frequency range. This arises when the compressor gain changes rapidly, as occurs with fast-attack time constants. Conversely, nonlinearities can be unintentionally introduced by the use of poor design, circuitry or transducers.

With the exception of measurements of harmonic distortion and intermodulation, all methods described above, compare on a frame-by-frame basis the output signal with the input signal. A large error in the results can occur if the frames are not properly aligned along the time axis before the comparison (Kates, 1992).

As opposed to the methods described above, the measure we propose does not rely upon the relation between input and output signals, but on the linear relation between two output signals, which are the results from measurements with two input test signals, linearly related by the Hilbert transform. These output signals are time synchronized and do not possess the problem mentioned above. The distortion measure, which we describe below, is sensitive to fast acting nonlinearities, but not to nonlinearities due to slow acting AGC and similar signal-adaptive systems.

The purpose of the present project was to investigate whether it is possible to establish a monotonic relation between perceptually perceived distortion and the estimated distortion based on measurements with Hilbert-transform related input signals.

II. PROPOSED MEASURE OF NONLINEAR DISTORTION

The nonlinear distortion measure we propose is based on the analysis of pairs of signals which are related to each other by the Hilbert transform (Oppenheim and Schafer, 1975a). In this paper, we call two real-valued signals $x_1(t)$ and $x_2(t)$ a Hilbert pair, if $x_2(t)$ is the Hilbert transform of $x_1(t)$. If $x_1(t)$ and $x_2(t)$ are a Hilbert pair, then $x_2(t)$ and $-x_1(t)$ are also a Hilbert pair, and the complex-valued signal $x(t) = x_1(t) + jx_2(t)$ is the analytical signal of $x_1(t)$. As the Hilbert transform and the analytical signal play an important role in this paper, a short review about them is given in the next subsection.

A. The Hilbert transform

The Hilbert transform of a time signal can be defined in the time domain or in the frequency domain. In the frequency domain the Hilbert transform can be described by a linear filter $H(f)$,

$$H(f) = \begin{cases} j & f < 0 \\ 0 & f = 0 \\ -j & f > 0 \end{cases} \tag{1}$$

where $j = \sqrt{-1}$ and f is frequency. Given a time record $x(t)$ with Fourier transform $X(f)$, the Hilbert transform, $\tilde{x}(t)$, of $x(t)$ is calculated as

$$\tilde{X}(f) = H(f)X(f), \tag{2}$$

$$\tilde{x}(t) = F^{-1}\{\tilde{X}(f)\}, \tag{3}$$

where $\tilde{X}(f)$ is the Fourier transform of $\tilde{x}(t)$ and $F^{-1}\{\cdot\}$ is the inverse Fourier transform. The signal $\tilde{x}(t)$ will thus have a different phase spectrum but it has exactly the same amplitude spectrum as $x(t)$.

If we form the complex signal $u(t) = x(t) + j\tilde{x}(t)$, then $u(t)$ is the analytical signal corresponding to $x(t)$ and we can calculate its Fourier transform as

$$U(f) = X(f) + j\tilde{X}(f) = X(f) + jH(f)X(f) = \begin{cases} 0 & f < 0 \\ X(0) & f = 0 \\ 2X(f) & f > 0 \end{cases} \tag{4}$$

The analytical signal $u(t)$ will thus have zero energy for negative frequencies while it has the same spectrum as $x(t)$ at the positive frequencies, apart from the overall factor of 2. The absolute value $|u(t)|$ of the analytical signal is the Hilbert envelope of $x(t)$. If $\tilde{x}(t)$ is the Hilbert transform of $x(t)$, then $x(t)$ is the Hilbert transform of $-\tilde{x}(t)$, and $x(t)$ and $\tilde{x}(t)$ do therefore have exactly the same Hilbert envelope.

B. The product theorem for Hilbert transforms

The *product theorem for Hilbert transforms* states that, under certain circumstances, it is true that

$$\text{if} \quad y(t) = a(t)x(t), \tag{5}$$

$$\text{then} \quad \tilde{y}(t) = a(t)\tilde{x}(t). \tag{6}$$

with a real-valued function $a(t)$, where $\tilde{y}(t)$ is the Hilbert transform of $y(t)$. A sufficient requirement for the theorem to hold is that $A(f)=0$ when $|f| > f_0 > 0$ and $X(f)=0$ when $|f| < f_0$ where $A(f)$ is the Fourier transform of $a(t)$ and f_0 an arbitrary frequency (Brown, 1986). In other words, the Hilbert product theorem is fulfilled when $a(t)$ is a low-pass filtered signal and when the spectra of $x(t)$ and $a(t)$ do not overlap.

Let us consider a time varying system that at any given time t can have as its impulse response any linear combination of N possible linear impulse responses $h_i(\tau)$ $(0 \le i \le N-1)$ where τ is time lag. We can write the total impulse response at time t as

$$h(\tau,t) = \sum_{i=0}^{N-1} a_i(t)h_i(\tau) \tag{7}$$

where $a_i(t)$ is a time dependent weight factor for the ith impulse response. Note that time t specifies the long term global shape of the impulse response function while τ is the time lag within each of the constituent responses $h_i(\tau)$. For an input signal $u(t)$ we get an output signal

$$y(t) = \int_0^\infty h(\tau,t)u(t-\tau)d\tau = \int_0^\infty \sum_{i=0}^{N-1} a_i(t)h_i(\tau)u(t-\tau)d\tau. \tag{8}$$

Changing the order of integration and summation gives

$$y(t) = \sum_{i=0}^{N-1} a_i(t) \int_0^\infty h_i(\tau)u(t-\tau)d\tau = \sum_{i=0}^{N-1} a_i(t)x_i(t), \tag{9}$$

where $x_i(t)$ is the response of the filter with impulse response $h_i(\tau)$ to the input signal $u(t)$. If each pair of $a_i(t)$ and $x_i(t)$ fulfills the demands of the product theorem then obviously

$$\tilde{y}(t) = \sum_{i=0}^{N-1} a_i(t)\tilde{x}_i(t) \tag{10}$$

and the whole system fulfills the demands of the product theorem.

As an example we can think of the h_i to be impulse responses of band pass filters and the $a_i(t)$ to be the time-variant gain-scaling of an AGC-circuit in each channel i. In this case the $a_i(t)$ will depend on $u(t)$, traditionally on the short term envelope estimate of $u(t)$ from which a short term level estimate is derived to control the gain in the compressor. If the input signals $u(t)$ and $\tilde{u}(t)$ will generate gain regulating signals which are identical then the output signals will be a Hilbert transform pair, i.e., linearly related.

The above indicates that a slowly varying AGC system will be regarded as a more linear system in our proposed method, as opposed to systems containing memoryless nonlinearities (see Appendix). This is the motivation for measuring nonlinear distortion with Hilbert transform-related test signals.

C. Use of Hilbert pair signals for measuring linear and nonlinear systems

The method we propose exploits the fact that the real and imaginary part of the analytical signal corresponding to some test signal lose their property of being a Hilbert pair after being passed through a nonlinear system. The complex-valued analytical signal is made up of the real-valued real part and the real-valued imaginary part. These two real signals can be passed separately through the system under test, i.e., one after the other, thus yielding the two output signals separately, which in turn can be used to form the real and imaginary part of a complex-valued output signal. The amount of mismatch between the real and imaginary part of those two output signals, i.e. how much the real and the imaginary part deviate from being an exact Hilbert transformation pair, quantifies the degree of nonlinearity of the system and can be expressed as a signal to noise ratio. The degree to which the Hilbert pair properties are affected by a nonlinear transformation depends on the properties of the input signal and on the type of nonlinear processing. For a purely linear system, the output signals do in fact again form a perfect Hilbert pair. Note that the proposed method to measure nonlinear distortion is not based on relations between input and output signals but on relations between two different output signals from the hearing aid, resulting from two different input signals which are Hilbert-transform pairs. For a practical application, the following steps should be performed (see Fig. 1).

When a desired measurement signal $x_1(t)$ has been chosen and recorded to the computer, the corresponding analytical signal $u(t)=x_1(t)+jx_2(t)$ is calculated. We used the Matlab® function "hilbert" to perform the calculation of $x_2(t)$. The real part (RP signal) $x_1(t)$ and the imaginary part (IP signal) $x_2(t)$ of the signal $u(t)$ are used as two separate real-valued input test signals. For each of these test signals, the response signal from the measured object is sampled and stored separately. Note that this measurement method is not

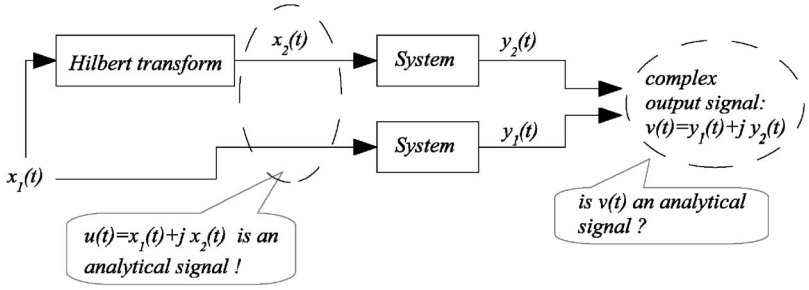

FIG. 1. Schematic illustration of the method for measuring nonlinearity with Hilbert pair signals.

at all restricted to digital systems that can only be simulated inside a computer. Any physical system can be analyzed if a precise timing of the beginning and the end of the input and output signals are controlled for. Of course, one has to keep in mind that the performance of everything in the electrical and acoustical signal pathway, including any D/A and A/D converters that present and record the acoustical signal to and from the system under test, affects the overall nonlinearity of the overall pathway. When measuring systems with memory, for instance AGC-systems, it is of course important that there is a sufficient pause between the two input signals, so the system is in the same state at the beginning of each recording.

After the recording of the two output signals $y_1(t)$ respectively $y_2(t)$, a new complex signal $v(t)=y_1(t)+jy_2(t)$ is formed with the output signal from the measurement with the RP test signal as the real part and the output signal from the measurement with the IP test signal as the imaginary part. The two-sided power spectral density (PSD) $S_{vv}(f)$ of this complex signal $v(t)$ is calculated. If the measured system is linear, this complex signal will have a PSD equal to zero for all negative frequencies, as can be seen from Eq. (4), and from the fact that a linear filter will not change the amplitude and phase relations between the RP and IP signals. At the positive frequencies, the output PSD $S_{vv}(f)$ divided by the respective input PSD $S_{uu}(f)$ defines the traditional transfer function of that linear system. However, any occurrence of a nonzero output PSD at negative frequencies indicates a nonlinearity in the system. The PSD at the negative frequencies, $S^-(f)=S_{vv}(-f)$, can then be related to the PSD at the corresponding positive frequencies, $S^+(f)=S_{vv}(f)$. If a nonlinearity is present in the system then of course the PSD at positive frequencies will also be influenced. There is, however, no way to tell how, as this will depend upon the actual nonlinearity. In the Appendix, Sec. 1, is shown that a sinusoidal test signal will give spectral contribution at both positive and negative frequencies if the nonlinearity is quadratic, but only contributions at negative frequencies if the nonlinearity is cubic. Uncorrelated noise, external or internal in the hearing aid, will also affect the measure giving spectral contributions to both positive and negative frequencies, as can be seen in the Appendix, Sec. 2. Therefore we *define* nonlinearity and linearity in a system according to the following: in case of a nonzero $S^-(f)$ we choose to identify $S^-(f)$ as stemming from the nonlinear part of the system response while we identify $S^+(f)$ as describing the linear part of the system response. Note that we only need to compute one PSD to get both the nonlinear and the linear part.

Figure 2 shows an example of measurements on a commercial behind-the-ear hearing aid with simulated speech as input signals (ICRA noise, one speaker simulation, Dreschler *et al.*, 2001). The solid curves show the PSD at positive frequencies [$S^+(f)$ spectra] and the dashed curves show the PSD at negative frequencies [$S^-(f)$ spectra], but drawn as a function of the positive frequencies. [The PSD was calculated using the MatLab® function for Welch estimates with frame size 4096 samples (82 ms) and overlap 2048 samples. Each frame was Hamming-windowed.]

The upper solid and dashed curves result from measurements with 90 dB SPL as the input level, the lower solid and dashed curves from the 70 dB SPL input signal, and the curves with an input level of 80 dB SPL are in between. The ratio between each $S^+(f)$ spectra and the corresponding $S^-(f)$ spectra gives the signal to distortion ratio SDR(f) as a function of frequency. The SDR(f) is the physical measure we propose.

To get a single number to describe the signal to distortion ratio, one possibility is to weigh the signal PSD and the distortion PSD with A-weighting filters, calculate the powers at the filter outputs, and express the difference in dB. This measure SDR_A was used in this investigation as an objective measure of distortion to be compared with results from the listening test (see below).

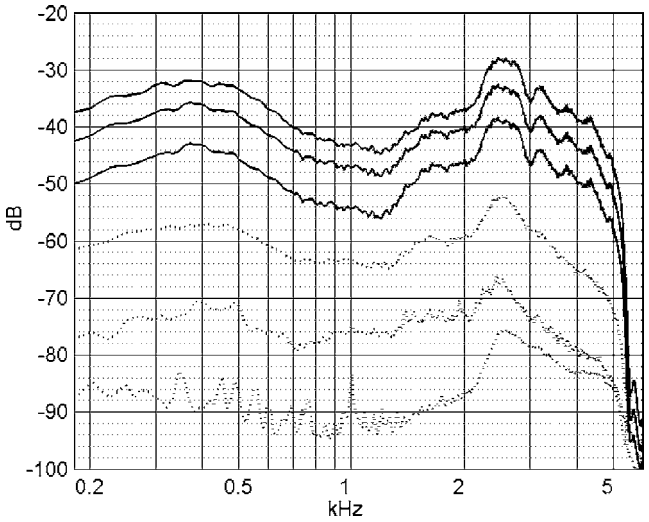

FIG. 2. Example of signal spectra (solid lines) and distortion spectra (dashed lines) from measurements of a behind-the-ear hearing aid. Input signals were simulated speech (ICRA-noise, one speaker). Input levels were 70 dB SPL (lowest solid and dashed curves), 80 db SPL and 90 dB SPL (upper solid and dashed curves), respectively.

TABLE I. Settings of the compression parameters of the 12 systems used in the subjective listening test experiment.

System id	Number of compression channels	Compression time constants	Compression kneepoint	Remarks
S01	3	fast	low	
S02	3	fast	high	
S03	3	fast	low	Hilbert violation
S04	3	fast	high	Hilbert violation
S05	3	instantaneous	low	
S06	3	instantaneous	low	postfiltering
S07	1	fast	low	
S08	1	fast	low	gain-filtering
S09	15	fast	low	
S10	15	fast	low	gain-filtering
S11	3	slow	low	
S12	15	slow	low	

In sum, the linear behavior of the measured object is defined from the PSD at positive frequencies and the distortion and noise behavior is defined from the PSD at negative frequencies. The calculation takes place by analysis of two real-valued output signals which are taken to form the real and imaginary part of a complex signal, rather than by comparing one input signal and its corresponding output signal.

III. LISTENING TEST

A. Systems

The systems used in the listening test were chosen from 26 simulated AGC systems. All program signals (see Sec. III B) were converted into Hilbert pair signals (real and imaginary parts) and all signals were then run through all systems. The measure SDR(f) was calculated for all systems, as a function of frequency. In order to compare the SDR with the subjective responses, the SDRs were collapsed into corresponding A-weighted signal to distortion measures, $\mathrm{SDR_A}$. Based on these measurements, twelve of the systems were selected for the listening test. They were chosen to be rather evenly spaced in signal to distortion values from very low to very high. All systems had a compressive characteristic with a static compression ratio of 2:1 in various numbers of separate channels (1, 3 or 15 channels). The compression time constants were either instantaneous (2 systems, see end of this subsection), fast (attack time 1 ms, release time 10 ms) or slow (attack time 10 ms, release time $>$4s). The kneepoints were either low (0 dB HL) or high (25 dB HL), and the compressor gain-signal could have a filter applied to it which limited the bandwidth of the gain-signal by use of a steep lowpass filter (fourth order at 100 Hz) prior to the multiplication with the bandpass signal. Two systems, S03 and S04, differed from, respectively, S01 and S02 only in that the Hilbert product theorem was not fulfilled for S03 and S04 (the lowpass filter had a higher corner frequency), i.e., the gain signals could have a spectral overlap with the input signals of the compressors. This also gave S03 and S04 a somewhat shorter attack and release times, as compared to S01 and S02, respectively. Table I shows the different parameter settings of the 12 test systems. Gain-filtering refers to the fact that the gain-signals in these systems (S08 and S10) were filtered with a low-pass filter.

The two systems S05 and S06 employed an instantaneous compression by means of a sample-by-sample square root compression of the bandpass signal $x(t)$ in each channel to reach the output signal $y(t)$. This idea relates back to a suggestion of Smoorenburg (1999). If the absolute value of $x(t)$ was below a compression threshold, c, the input signal was amplified linearly, with a certain gain $g_0 = 1/\sqrt{c}$ chosen so that $y(x)$ was continuous at $x = c$,

$$y(t) = \begin{cases} \mathrm{sign}(x(t)) \cdot \sqrt{\mathrm{sign}(x(t)) \cdot x(t)} & |x(t)| > c \\ g_0 \cdot x(t) & |x(t)| < c. \end{cases} \quad (11)$$

This processing compresses the waveform instantaneously and cannot be characterized by attack and release times. It introduced a higher amount of distortion than all other systems under test. The resulting sound quality was poor although the intelligibility for speech in quiet was very high (i.e., close to 100%, as was the case for all systems) as ascertained by informal testing with normal hearing subjects. System S06 differed from S05 by an additional postfiltering of the square-root-compressed output signals of each channel in the multichannel system. These postfilters filtered the compressed output with another bandpass filter with equal characteristics as the bandpass filters, which split the input signal into narrow bands.

B. Program material

The program material consisted of four stimuli, a male voice, a female voice, guitar music, and piano music. The voice signals were chosen, because human speech is the most important sound for a hearing aid user. To many hearing aid users, however, music is also important. We therefore included two pieces of music as stimuli in the test. The chosen test signals are meaningful to human test subjects, who in turn are optimally accustomed to the sound of these signals in their natural, undistorted state. At the same time, speech and music are complex signals that cover a broad frequency and level range and exhibit a temporal modulation spectrum which is independent in different frequency bands. It was decided to use only signals without any additive noise, to the extent possible by the use of excellent recording equipment. If additive background noise had been present in the recordings, the compressor in a hearing aid would lead to an amplified and possibly fluctuating level of that noise, which could be easily detectable and possibly objectionable for the subjects and thus influence their distortion rating (see below). Each stimulus had a length of 6–8 s. They were recorded with 16 bit A/D resolution and with a sampling frequency of 44.1 kHz. The voices were recorded with a low-noise microphone. After recording the signals were downsampled to 32 kHz and band pass filtered from 100 Hz to 10 kHz. After processing by the different systems the output spectra were equalized (over one-third octave bands) to have the same long time average spectra as the corresponding input signals regardless of system. All output signals were scaled to have the same rms value. These last two operations

are linear and therefore did not affect our objective measure, but they increased the probability that the test subjects were not biased in their ratings by the spectral shape or the overall loudness of the test stimuli.

A noise signal with a spectrum equal to the average of the spectra of the four original stimuli and with the same rms value as the processed sounds was generated. This signal was used to set the listening level of the headphone system. The headphone levels were measured on a Brüel&Kjaer type 4153 Artificial Ear (IEC 60318).

C. Equipment and method

The sound stimuli were stored in a computer. The controlling program randomized the order of stimulus presentation. First a test trial was run before the main test started. The listening level for the test trial was 70 dB SPL. Two different presentation levels were used in the main test, 65 dB SPL and 75 dB SPL. Half of the subjects listened to the lower level first and the other half to the higher. For each level, all combinations of systems and programs were presented. Additionally there were repetitions of four combinations, which were used to estimate the test-retest variability. These were also randomized into the total sequence.

The subject was seated in an audiometric booth (3 m $\times$3.5 m, height 2.1 m) and listened to the sounds diotically with AKG type K240 headphones. On a monitor placed in front of the subject, a screen with a vertical slider was presented. The slider could be moved with a mouse. All integer numbers from 0 (at the bottom) to 10 (at the top) were written beside the slider. To the left of number 1 the text "Mycket orent, oklart, otydligt" ("Very unclear"), beside 9 "Mycket rent, klart, tydligt" ("Very clear") and beside 5 "mittemellan" (midway) were written. To the right of number 0 "Mycket kraftig förvrängning" ("Very strong distortion") and to the right of number 10 "Helt fritt från förvrängning" ("Totally free from distortion") were written. A similar scale was used and discussed by Gabrielsson and Lindström (1985) and described in the IEC recommendation for listening tests on loudspeakers (IEC, 1985). The task for the subject was to move the slider to a position that corresponded with his listening impression. The subject had the opportunity to repeat the sound as often as he/she felt necessary. When he had decided upon a position for the slider he had to press a ready button ("Klar"). Then the next sound was presented after a delay of 3 s.

D. Subjects

Ten subjects with normal or close-to-normal hearing participated in the listening test. All except one were paid. They were between 25 and 69 years of age with a mean of 52.7. As their individual audiograms only were used to decide whether they could participate in the test or not, only the mean audiogram and range are shown in Fig. 3. Before the session the subject had to read a written instruction on paper, which described the task. The subject was instructed to listen to each sound and decide how free from distortion it was, and disregard all other aspects like music taste and the balance between bass and treble.

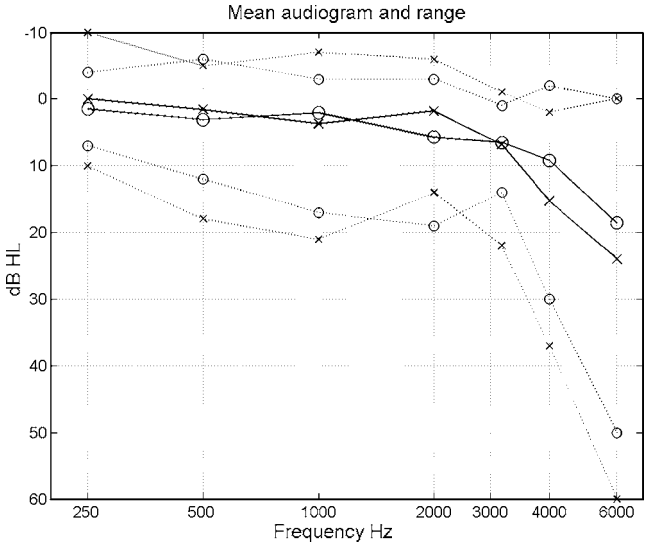

FIG. 3. Mean audiogram and range for 10 subjects. Circles represent right ears and crosses represent left ears.

IV. RESULTS

A. Subjective test

The subjective data, averaged across subjects, programs and levels, are plotted in Fig. 4, sorted in ascending order of subjective distortion to reveal the relation between subjective measurements and the compression parameters of the different systems.

There were three general trends that could be observed from the data in this figure: (1) The amount of perceived distortion decreased as the compression time constants increased. This is according to expectation because longer time constants mean slower gain variation and therefore a more linear behavior within a short period of time. (2) The amount of perceived distortion decreased as the compression thresholds increased (compare S01 with S02 and S03 with S04). This is also consistent with expectation as a high compression threshold means that the system is nonlinear for a smaller proportion of the time while it is linear at times where the signal level is below the compression threshold. (3) For fast compression, the amount of perceived distortion increased with increasing number of independent compression channels (compare S07 with S01 and S09, and compare S08 with S10). This last observation is also in line with expectation, as distortion from fast compression will be created in each individual channel. This distortion will spread into neighboring frequency bands. Also, the spectral contrast will be decreased by many fast acting compression channels, compared to only one wide band compression channel where the gain signal is controlled by the overall wide band level of the signal.

The subjective data show that filtering of the gain signal only improved the subjective scores slightly (compare system S07 with S08, and S09 with S10). Only for the strongest distortion introduced by the 3-band instantaneous square-root compression (S05 and S06), did postfiltering (of the compressed narrow band signals) give a clear improvement in the subjective scores. The introduction of a violation of

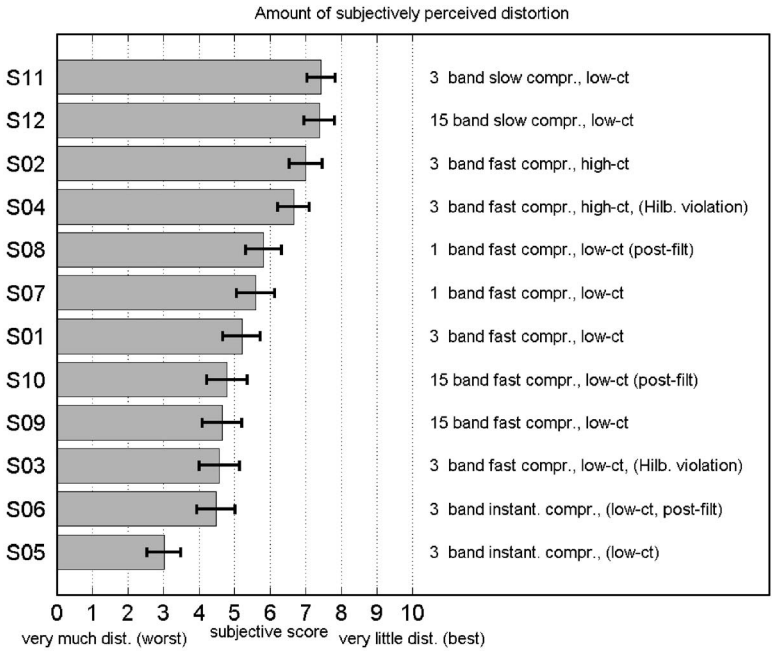

FIG. 4. Subjective amount of distortion for the twelve compression systems, averaged across subjects, levels, and programs, arranged in ascending order. The bars indicate the 95% confidence interval.

the Hilbert product theorem, produced only a minor decrease in the subjective score for a system (compare S02 with S04, and S01 with S03). Results from the listening test were analyzed by means of an analysis of variance of the subjective scores, the results of which are shown in Table II.

As can be seen from Table II the level did not influence the results systematically, although the interactions AD and CD were significant. Therefore all results were averaged over the level variable.

A Tukey HSD test of the difference in scores revealed, however, that out of the trends described above, only the differences between S01 and S02, between S03 and S04, between S05 and S06, between S07 and S09, and between S08 and S10 were significant ($p<0.05$).

There were some differences between subjects regarding average score, which can be seen in Fig. 5. Figure 6 shows that the guitar program (program 3) gave significantly higher average score, i.e., less perceived distortion, than the other programs.

TABLE II. Analysis of variance of the results of the subjective listening test.

Source	*Df*	Mean square	*F*-ratio	*P*-value
Main effects				
A: System	11	147.65	78.43	<0.0001
B: Program	3	138.638	73.64	<0.0001
C: Subject	9	178.921	95.04	<0.0001
D: Level	1	0.194655	0.10	0.7479
Interactions				
AB	33	14.8243	7.87	<0.0001
AC	99	5.04641	2.68	<0.0001
AD	11	3.50219	1.86	0.0413
BC	27	11.8939	6.32	<0.0001
BD	3	0.792749	0.42	0.7379
CD	9	4.2834	2.28	0.0162
Residual	753	1.88254		

There are clear interactions between some of the systems and the programs. Two of the systems (S09 and S10), for instance, got considerably lower average scores, meaning more perceived distortion, with the voices than with the music programs.

B. Objective measurements

Figure 7 shows output signal spectra and distortion/noise spectra for the four test programs using system S01 (3-band fast compression with low kneepoints) as an example system. From the measured signal and distortion/noise spectra the total signal power and the total distortion power for each combination of system and program were calculated.

As can be observed from Fig. 7, different program material resulted in different output spectra for the same system under test. This can be explained by the different temporal

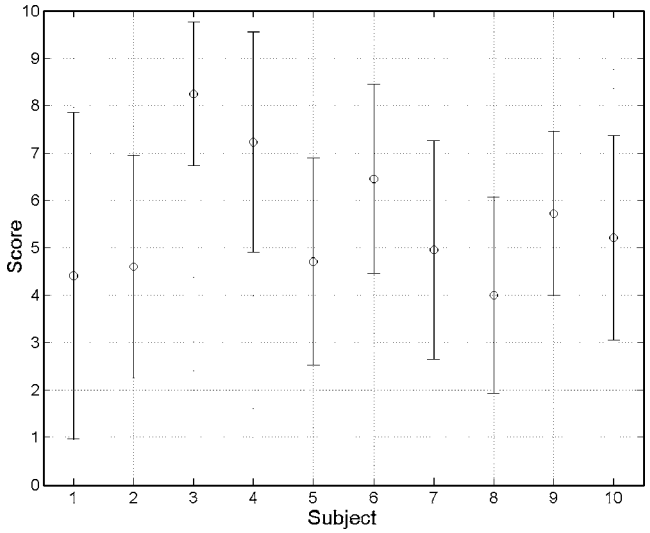

FIG. 5. Mean values and standard deviations of perceived distortion for the ten subjects, averaged across systems, levels, and programs.

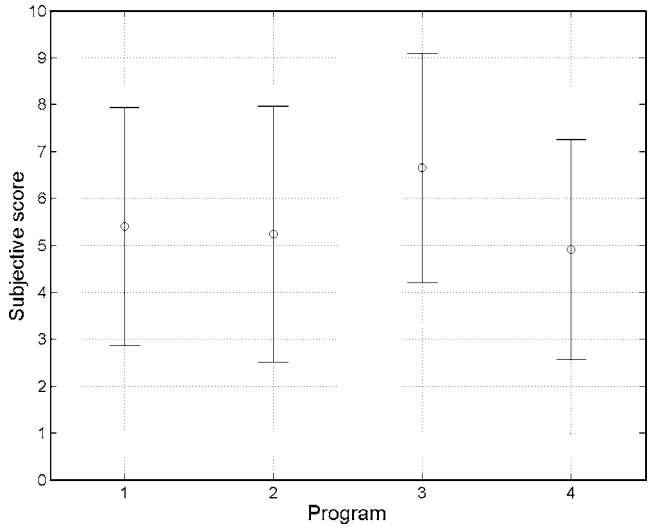

FIG. 6. Mean values and standard deviations of perceived distortion for the four programs, averaged across subjects, levels, and compression systems.

and spectral characteristics of the original sounds in combination with the nonlinearity of the system which can lead to spectral components at negative frequencies at "unpredictable" locations. Therefore, it is highly advisable to use a broad band signal as the input for each system, as was done in our case, to assure some average spreading of all newly introduced nonlinear components across the whole frequency range. The difference between the spectral power estimates at positive and negative frequencies, that is, the SDR as function of frequency, will depend on the precise choice of program material. Some of this dependency will be smoothed by averaging the different spectra across frequency, yielding SDR_A. However, a remaining dependence of the objective and subjective ratings on the program material could still be expected, and it was observed to a degree as summarized in Table II and shown in Fig. 7.

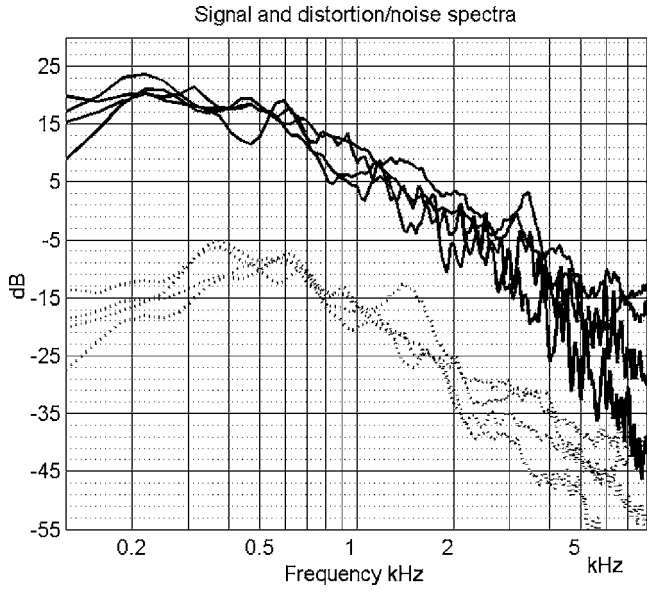

FIG. 7. Signal spectra at the positive frequencies (solid lines) and the noise/distortion spectra at the negative frequencies (dotted lines) for system S01 for the four test signals.

Different frequency components probably contribute differently to the perceived distortion. In an attempt to compensate for the importance of different frequency components, the spectra were weighted by the A-filter curve prior to the calculation of total power by integration across the whole frequency range. This calculation yielded the final objective scores, which are shown in Fig. 8. Postfiltering clearly raised (improved) the calculated SDR_A (compare system S07 with S08, and S09 with S10). A slight violation of the Hilbert product theorem gave rise to a minor decrease of the SDR_A (compare S01 with S03, and S02 with S04).

C. Relation between subjective and objective measurements

The subjective data are compared with the objective data in Fig. 9. A value of $r_s=0.797$ was calculated for Spearman's rank correlation coefficient, indicating a high correlation between objective and subjective data. Due to some deviation of the data from a straight line fit, a slightly smaller correlation coefficient of $r=0.677$ was found, but all in all, a rather monotonic relationship between calculated signal to distortion values and subjectively perceived absence of distortion could be observed, except for three systems, S08, S09, and S10. These systems gave lower subjective scores (more perceived distortion) than expected from the calculated signal to distortion values. The rest of the systems tended to line up on a monotonic function with a saturation at a score of 7.5 score units.

V. DISCUSSION

The subjects who participated in the listening test were all, except one, naive listeners. Three systems, S08, S09 and S10 gave lower scores than expected from the calculated signal to distortion values. Systems S09 and S10 had 15 filter bands with fast compressors. System S08 and S10 had gain filters. Filtering of the gain signal band limits the envelope (Oppenheim and Schafer, 1975b), and thus helps the systems to fulfill the product theorem for Hilbert transforms and thereby give low SDR values. They will, however, still generate perceptible nonlinear distortion. For example, the sounds generated by system S10 were subjectively perceived as harsh, rough, and metallic (judged by informal listening). As stated earlier, there is no unique measure of nonlinear distortion except when the input signal is sinusoidal. Nevertheless, when people listen to a piece of music or speech, which has passed a memoryless nonlinearity, they have a clear impression that the sound is distorted. Probably, different people use different cues to judge if a sound is distorted. What we call distortion may then be different things. Some people may differentiate between roughness and distortion, others not. It is also obvious that different program material gives different impression of distortion, as is shown in Fig. 6, where the guitar music gives higher scores (less perceived distortion) than the other programs, although the difference in SDR_A was minor. In sum, some of the subjective percepts associated with the interpretation of "distortion" may not be modeled completely by our proposed SDR measure. The levels of sound signals vary with time. It is quite possible that

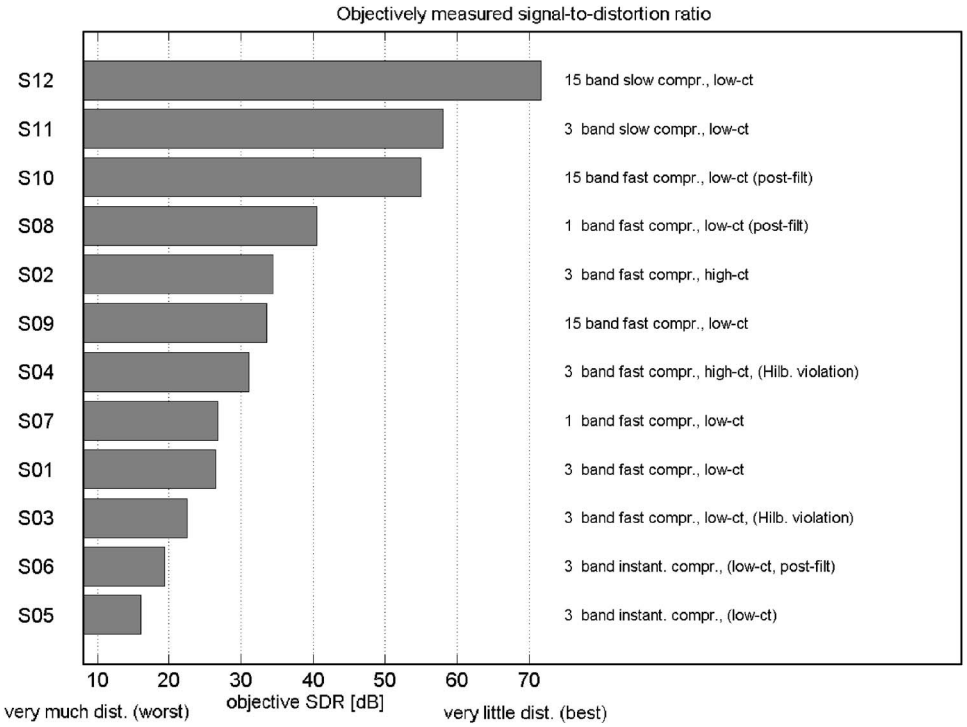

FIG. 8. Objective A-weighted signal-to-distortion ratio measurement for the twelve compression systems, arranged in ascending order.

strong audible distortions are created relatively seldom just for short time intervals. While this would not decrease the objective measure substantially, it might still be enough to result in a lowered subjective score (Gros and Chateau, 2001). However, the SDR predicted the subjective results nicely, except for the effects of the postfiltering technique. This technique was deemed interesting from a mathematical point of view, but it is, to our knowledge, hardly used in currently available hearing aids.

The methods, which until now have been proposed for measurement of nonlinear distortion, are not suited for measurements on signal-adaptive hearing aids, because they cannot separate nonlinearities introduced by purpose, like AGC, from memoryless nonlinearities. The method we propose is, on the contrary, sensible to memoryless nonlinearities, but not to well-designed AGC systems. It is therefore well suited for measurements of nonlinear distortion of signal-adaptive hearing aids.

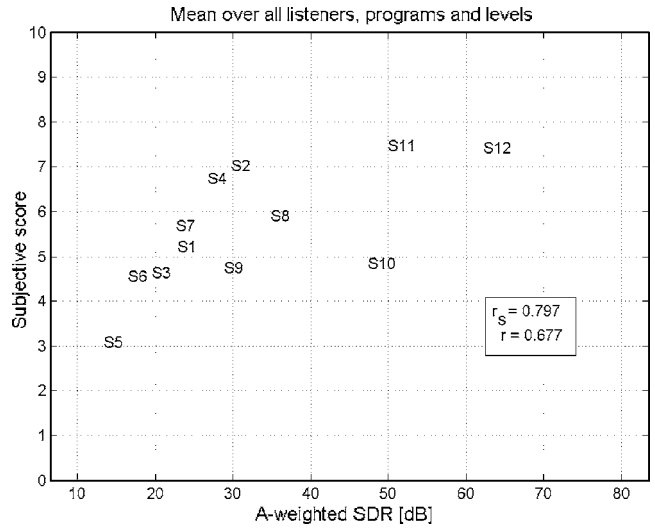

FIG. 9. Average subjective scores as a function of A-weighted signal to distortion ratio. The rank correlation coefficient r_s and the correlation coefficient r between subjective and objective data are given in the legend.

VI. CONCLUSIONS

The basic technical measure we have described is the frequency dependent SDR(f). To investigate whether this technical measure had any relation to a psychoacoustically perceived distortion, we compared subjective listening scores with a collapsed measure of the SDR(f), the A-weighted SDR_A. Nevertheless, this simple one-number measure showed a good correspondence with perceived distortion. The majority of the systems showed a monotonic relation between calculated signal to distortion values and subjectively perceived distortion, implying that our proposed objective measure gives a fair prediction of perceived distortion. The mathematically interesting postfiltering technique could lead to a clear improvement of the measured SDR, but only improved the perceived distortion slightly. Therefore, the requirement that the two output signals of a system form a Hilbert transform pair, when the respective input signals form a Hilbert transform pair, is a necessary but probably not sufficient condition for the system to be free from perceptible distortion. In sum, our proposed objective SDR measure seems suitable as a descriptive tool for nonlinear distortion but it should not be applied as the only design tool for optimizing a nonlinear hearing aid so as to be free from perceptible distortion.

ACKNOWLEDGMENTS

The authors wish to express their gratitude to Helena Norell, who did the subjective measurements, and to Björn Hagerman, Søren Westerman, and Carl Ludvigsen for valuable discussions and comments.

APPENDIX: RELATIONS TO OTHER MEASURES

1. Relation to harmonic distortion

Given a nonlinearity of a power series form

$$g(x) = x + a_2x^2 + a_3x^3 \tag{A1}$$

and an input signal $v(t)=\cos \omega t$ with radian frequency ω we get an output signal, $u_1(t)$, of the nonlinearity as

$$u_1(t) = \cos \omega t + a_2(1 + \cos 2\omega t) \cdot \frac{1}{2} + a_3(3 \cos \omega t + \cos 3\omega t) \cdot \frac{1}{4} = \frac{a_2}{2} + \left(1 + \frac{3a_3}{4}\right)\cos \omega t + \frac{a_2}{2} \cos 2\omega t + \frac{a_3}{4} \cos 3\omega t. \tag{A2}$$

If we, according to the method, instead use the Hilbert transform of $\cos \omega t$ as an input signal, i.e., $\sin \omega t$, we get

$$u_2(t) = \sin \omega t + a_2\big(1 - \cos 2\omega t\big) \cdot \frac{1}{2} + a_3(3 \sin \omega t - \sin 3\omega t) \cdot \frac{1}{4} = \frac{a_2}{2} + \left(1 + \frac{3a_3}{4}\right)\sin \omega t - \frac{a_2}{2} \cos 2\omega t - \frac{a_3}{4} \sin 3\omega t. \tag{A3}$$

If we calculate $v(t)=u_1(t)+ju_2(t)$ we get

$$v(t) = \frac{a_2}{2}(1 + j) + \left(1 + \frac{3a_3}{4}\right)e^{j\omega t} + \frac{a_2}{2}(1 - j)\frac{e^{j2\omega t} + e^{-j2\omega t}}{2} + \frac{a_3}{4}e^{-j3\omega t}. \tag{A4}$$

We can see that the quadratic term will introduce a frequency component at the positive radian frequency 2ω which in our new method will be regarded as signal while the distortion will be identified as those components at radian frequencies -2ω and -3ω. For small values of a_2 and a_3 our proposed new method will thus estimate the quadratic distortion as

$$d_2 = \left| \frac{a_2(1 - j)}{4 + 3a_3} \right| = \frac{a_2\sqrt{2}}{4 + 3a_3} \tag{A5}$$

and the cubic distortion as

$$d_3 = \frac{a_3}{4 + 3a_3} \tag{A6}$$

Conventionally, the quadratic and cubic distortions would be defined as

$$d_2' = \frac{a_2 \cdot 2}{4 + 3a_3} = \sqrt{2}d_2 \tag{A7}$$

and

$$d_3' = \frac{a_3}{4 + 3a_3} = d_3. \tag{A8}$$

Our new SDR method will obviously yield a smaller estimate of the quadratic distortion for this sinusoidal signal by a factor of $\sqrt{2}$ relative to the standard definition of harmonic distortion while the estimates of the cubic distortion are the same for both definitions.

2. Relation to signal to noise ratio

If we measure a linear system disturbed by additive noise with power spectral density $S_{nn}(f)$ we get the pair of output signals

$$y_1(t) = x(t) + n_1(t),$$

$$y_2(t) = \tilde{x}(t) + n_2(t), \tag{A9}$$

where $n_1(t)$ and $n_2(t)$ are independent realizations of the noise. We calculate the power spectrum, $S_{vv}(f)$, of

$$v(t) = y_1(t) + jy_2(t) = x(t) + j\tilde{x}(t) + n_1(t) + jn_2(t). \tag{A10}$$

The power spectrum of $\xi(t)=x(t)+j\tilde{x}(t)$ is

$$S_{\xi\xi}(f) = \begin{cases} 0 & f < 0 \\ 4S_{xx}(f) & f > 0 \end{cases} \tag{A11}$$

where $S_{xx}(f)$ is the power spectrum of $x(t)$. The power spectrum of $\eta(t)=n_1(t)+jn_2(t)$ is

$$S_{\eta\eta}(f) = 2S_{nn}(f) \tag{A12}$$

which gives

$$S_{vv}(f) = \begin{cases} 2S_{nn}(f) & f < 0 \\ 4S_{xx}(f) + 2S_{nn}(f) & f > 0 \end{cases} \tag{A13}$$

According to our definition the signal to distortion ratio (SDR) is defined by the relation of the Fourier magnitude at positive frequencies relative to the Fourier magnitude at negative frequencies. As $S_{nn}(-f)=S_{nn}(f)$ our estimate of SDR would then be

$$\mathrm{SDR}(f) = \frac{4S_{xx}(f) + 2S_{nn}(f)}{2S_{nn}(f)} = 2\frac{S_{xx}(f)}{S_{nn}(f)} + 1$$

which means that the SDR will overestimate the distortion relative to the classical measure for linear systems, the $\mathrm{SNR}(f)$, which of course is

$$\mathrm{SNR}(f) = \frac{S_{xx}(f)}{S_{nn}(f)}. \tag{A14}$$

ANSI S3.22-1996 (**1996**). "Specification of hearing aid characteristics," American National Standards Institute, New York.

Beerends, J. G., and Stemerdink, J. A. (**1994**). "A perceptual speech quality measure based on a psychoacoustic sound representation," J. Audio Eng. Soc. **42**, 115–123.

Beerends, J. G., Hekstra, A. P., Rix, A. W., and Hollier, M. P. (**2002**). "Perceptual evaluation of speech quality, (PESQ) the new ITU standard for end-to-end speech quality assessment, part II, Psychoacoustical model," J. Audio Eng. Soc. **50**, 765–778.

Brown, J. L. (**1986**). "A Hilbert transform product theorem," Proc. IEEE **74**, 520–521.

Dreschler, W. A., Verschuure, H., Ludvigsen, C., and Westermann, S.

(**2001**). "ICRA noises: Artificial noise signals with speech-like spectral and temporal properties for hearing instrument assessment," Audiology **40**, 148–157.
Dyrlund, O., Ludvigsen, C., Olofsson, Å., and Poulsen, T. (**1994**). "Hearing aid measurements with speech and noise signals," Scand. Audiol. **23**, 153–157.
Dyrlund, O. (**1989**). "Characterization of non-linear distortion in hearing aids using coherence analysis," Scand. Audiol. **18**, 143–148.
Gabrielsson, A., and Lindström, B. (**1985**). "Perceived sound quality of high-fidelity loudspeakers," J. Audio Eng. Soc. **33**, 33–53.
Gros, L., and Chateau, N. (**2001**). "Instantaneous and overall judgments for time-varying speech quality: Assessments and relationships," Acta. Acust. Acust. **87**, 367–377.
IEC 60118-0 (**1983**). Hearing aids. Part 0. "Measurement of electroacoustical characteristics," International Electrotechnical Commission, Geneva, Switzerland.
IEC 60268-13 (**1985**). Sound system equipment. Part 13. "Listening tests on loudspeakers," International Electrotechnical Commission, Geneva, Switzerland.
Kates, J. M. (**1992**). "On using coherence to measure distortion in hearing aids," J. Acoust. Soc. Am. **91**, 2236–2244.
Kates, J. M. (**2000**). "Cross-correlation procedures for measuring noise and distortion in AGC hearing aids," J. Acoust. Soc. Am. **107**, 3407–3414.
Olofsson, Å. (**1992**). "Measurements on AGC hearing instruments by use of broad-band test signals and a psychoacoustical model," Karolinska Institutet, Teknisk Audiologi, Report No. TA126, ISSN 0280-6819.
Oppenheim, A. V., and Schafer, R. W. (**1975a**). "*Digital signal processing*" (Prentice-Hall, Englewood Cliffs), ISBN 0-13-214635-5. pp. 337–366.
Oppenheim, A. V., and Schafer, R. W. (**1975b**). "*Digital signal processing*" (Prentice-Hall, Englewood Cliffs), ISBN 0-13-214635-5, pp. 363–366.
Smoorenburg, G. (**1999**). "What hearing aids can do and cannot do in view of the characteristics of cochlear disorders," in Proceedings of the 18th Danavox Symposium, "Auditory Models and Nonlinear Hearing Aid," edited by A. Rasmussen, P. Osterhammel, T. Andersen, and T. Poulsen (Kolding, Denmark), ISBN 87-982422-8-8.
Tan, C., Moore, B. C. J., and Zacharov, N. (**2003**). "The effect of nonlinear distortion on the perceived quality of music and speech signals,"J. Audio Eg. Soc., **51**, 1012–1031.
Thiede, T., Treurniet, W. C., Bitto, R., Schmidmer, C., Sporer, T., Beerends, J. G., Colomes, C., Keyhl, M., Stoll, G., Brandenburg, K., and Feiten, B. (**2000**). "PESQ — The ITU-standard for objective measurement of perceived audio quality," J. Audio Eng. Soc. **48**, 3–29.

Optimum beamformer in correlated source environments

Seungil Kim[a)]
Mobile Multimedia Laboratory, LG Electronics Institute of Technology, GS Gangnam Tower, Yeoksam-dong, Gangnam-gu, Seoul, 135-985, Korea

Chungyong Lee[b)] and Hong-Goo Kang[c)]
Department of Electrical and Electronic Engineering, Yonsei University, Seoul, 120-749, Korea

(Received 7 February 2006; revised 13 July 2006; accepted 13 July 2006)

A new method for overcoming signal cancellation problems due to correlated interferences which occur in a minimum variance distortionless response beamformer is proposed. Instead of decorrelating the correlated interferences, the coherently combining signal-to-interference plus noise ratio (CC-SINR) beamformer regards them as replicas of the desired signal and coherently combines them with the desired signal. This method uses an eigenvector constraint that suppresses only noise and uncorrelated interferences but retains the desired signal and correlated interferences. The CC-SINR beamformer does not require any preliminary information on correlated interferences. The signal-to-interference plus noise ratio (SINR) of the proposed beamformer output was compared to that of a conventional SINR beamformer when correlated interference, uncorrelated interference, and white noise exist. In addition, various key parameters that affect the performance of the beamformer, such as signal-to-noise ratio, uncorrelated interference-to-noise ratio, angular separation between signals, attenuation factor, phase delay of correlated interference, and the number of sensors were analyzed. All of the experimental results were in good agreement with the analytical results. © *2006 Acoustical Society of America.* [DOI: 10.1121/1.2329870]

PACS number(s): 43.60.Fg [EJS] Pages: 3770–3781

I. INTRODUCTION

An optimum beamformer uses several criteria represented by the second-order statistics of an array output.[1] A minimum variance distortionless response (MVDR) beamformer, which uses the correlation matrix of the received signal, imposes a constraint on the gain of unit look direction gain,[2] and it also assumes that the interference signals are not correlated with the desired signal. In correlated cases, therefore, the MVDR beamformer not only fails to form a null in the direction of the multipath interference, but also completely cancels the desired signal because the signal subspace is rank deficient.[3,4]

In order to overcome the problem caused by coherence, two representative methods have been considered. One simple method is the signal-to-interference plus noise (SINR) beamformer which utilizes the correlation matrix of noise.[5–7] Note that we refer to a method that uses the correlation matrix of the received signal as a MVDR beamformer. Clearly, the SINR beamformer requires information on a time period of interference plus noise.[2] The other is a method which destroys the correlation between the desired signal and interference. For this purpose, Reddy *et al.* proposed a spatial smoothing technique.[8] In order to overcome the rank deficiency problem caused by the correlated interference, Yang and Caveh proposed a frequency domain averaging technique, referred to as coherent signal-subspace transformation (CST).[4] Because the CST beamformer requires additional prior information on interference, Zeira and Friedlander developed the frequency domain averaging by array manifold interpolation.[9] In particular, Ward applied a constant directivity beamformer to reject the correlated interference.[10]

These approaches regard correlated interference as useless information. However, correlated interference can be considered to be additional information if it is appropriately combined, similar to a RAKE receiver in code division multiple access communications.[5] The RAKE receiver assumes that the time delays of the multipath components are perfectly known. This is a reasonable assumption, since time delay can be estimated by orthogonal codes in telecommunication environments. In many other applications, however, it is impossible to obtain preliminary information relative to correlated interferences such as time delays and incident angles. Therefore, Bresler *et al.* proposed an optimum combiner which is based on minimum mean square error beamformer.[11]

In this paper, a new beamformer which takes into account the correlated interferences as replicas of the desired signal and coherently combines them with the desired signal, instead of decorrelating them, is proposed. The CC-SINR beamformer estimates a correlation matrix of the signal and calculates an eigenvector corresponding to a principle eigenvalue. It then uses an eigenvector constraint that suppresses noise and uncorrelated interferences but retains the desired signal and correlated interferences. It is noteworthy that the CC-SINR beamformer does not require any preliminary information regarding correlated interferences because it uses the eigenvector corresponding to the principal eigenvalue which can be obtained from the statistics of the received

[a)]Electronic mail: goodksi@lge.com
[b)]Electronic mail: clee@mcsp.yonsei.ac.kr
[c)]Electronic mail: hgkang@mcsp.yonsei.ac.kr

 © 2006 Acoustical Society of America

signal. Since the CC-SINR beamformer can form beams toward both the direction of the desired signal and the correlated interference using the eigenvector, it further enhances the desired signal.

To verify the performance, we present a complete analysis of the SINR at the output of a conventional SINR beamformer and the CC-SINR beamformer as a function of various parameters. The analysis is based on a signal model, in which four signals—the desired signal, the correlated interference, the uncorrelated interference, and white Gaussian noise—are considered. The results of the analysis show that the CC-SINR beamformer has higher SINR outputs compared to the conventional SINR beamformer in the presence of correlated interference, and good agreement between the analytical and simulation results are obtained.

This paper is organized as follows. In Sec. II, the expression for the output SINR of the SINR beamformer in the presence of correlated interference is derived. In Sec. III, a steering vector in the presence of correlated interference is examined and the CC-SINR beamformer is derived. An analysis of the CC-SINR beamformer is also given, to compare its performance with the conventional SINR beamformer. Simulation results are presented to verify the analytical results in Sec. IV. In Sec. V, experimental results are described. Finally, conclusions follow in Sec. VI.

II. ANALYSIS OF A SINR BEAMFORMER IN THE PRESENCE OF CORRELATED INTERFERENCE

We consider a linear array with N sensors, equally spaced by distance d. The desired signal, correlated interferences, and uncorrelated interferences are assumed to be narrow-band. The noise is modeled as a zero-mean Gaussian random process, spatially white, and uncorrelated with the signal and the interferences. We also assume that the signal, interference, and noise are wide-sense stationary.

For simplicity, we restrict our analysis to the case of three sources. One is the desired signal $s(t)$ with incident angle θ_1, another is a fully correlated interference $s_c(t)$ with angle θ_2, and the other is an uncorrelated interference $s_u(t)$ with angle θ_u. The data vectors received at the array are represented by $\mathbf{s}(t)$, $\mathbf{s}_c(t)$, and $\mathbf{s}_u(t)$. The power of desired signal, uncorrelated interference, and noise are assumed to be σ_s^2, σ_u^2, and σ_n^2, respectively. From narrowband assumption for $s(t)$, the received signal vector can be written as

$$\begin{aligned}\mathbf{x}(t) &= \mathbf{s}(t) + \mathbf{s}_c(t) + \mathbf{s}_u(t) + \mathbf{n}(t)\\ &= s(t)\mathbf{a}(\theta_1) + \alpha s(t-\tau)\mathbf{a}(\theta_2) + s_u(t)\mathbf{a}(\theta_u) + \mathbf{n}(t)\\ &\cong [\mathbf{a}(\theta_1) + \alpha e^{-j\omega\tau}\mathbf{a}(\theta_2)]s(t) + s_u(t)\mathbf{a}(\theta_u) + \mathbf{n}(t)\\ &\triangleq \mathbf{b}(\theta_1,\theta_2)\cdot s(t) + \mathbf{u}(t),\end{aligned} \tag{1}$$

where α is a real-valued attenuation factor, τ indicates a time delay between the desired signal and the correlated signal. $\mathbf{a}(\theta)$ denotes a steering vector of the array, the undesired signal vector $\mathbf{u}(t)$ is defined by the sum of the uncorrelated interference and the noise vector, and $\mathbf{b}(\theta_1,\theta_2)$ is defined by $\mathbf{a}(\theta_1)+\alpha e^{-j\omega\tau}\mathbf{a}(\theta_2)$.

An optimal solution of the beamformer is given by well-known expression[7–9]

$$\mathbf{w} = c\cdot\mathbf{R}_{uu}^{-1}\mathbf{a}(\theta_1), \tag{2}$$

where $\mathbf{R}_{uu}^{-1}$ denotes the inverse of the correlation matrix of $\mathbf{u}(t)$ and c is a nonzero constant. When $c=\mathbf{a}^H(\theta_1)\mathbf{R}_{uu}^{-1}\mathbf{a}(\theta_1)$, it results in the optimal weight of the maximum likelihood beamformer. The superscript H denotes a Hermitian transpose operator.

From Eq. (2), the maximum achievable SINR of the SINR beamformer is given by

$$\mathrm{SINR}_{\mathrm{SINR}} = \left.\frac{\mathbf{w}^H\mathbf{R}_{ss}\mathbf{w}}{\mathbf{w}^H\mathbf{R}_{uu}\mathbf{w}}\right|_{\mathbf{w}=c\cdot\mathbf{R}_{uu}^{-1}\mathbf{a}(\theta_1)}, \tag{3}$$

where $\mathbf{R}_{ss}$ is the covariance matrix of the desired signal, which is expressed as

$$\begin{aligned}\mathbf{R}_{ss} &= E\{\mathbf{b}(\theta_1,\theta_2)s(t)s^*(t)\mathbf{b}^H(\theta_1,\theta_2)\}\\ &= \sigma_s^2\mathbf{b}(\theta_1,\theta_2)\mathbf{b}^H(\theta_1,\theta_2),\end{aligned} \tag{4}$$

where the superscript * denotes a complex conjugate. Substitution of Eqs. (2) and (4) into Eq. (3) yields

$$\mathrm{SINR}_{\mathrm{SINR}} = \frac{\sigma_s^2\mathbf{a}^H(\theta_1)\mathbf{R}_{uu}^{-1}\mathbf{b}(\theta_1,\theta_2)\mathbf{b}^H(\theta_1,\theta_2)\mathbf{R}_{uu}^{-1}\mathbf{a}(\theta_1)}{\mathbf{a}^H(\theta_1)\mathbf{R}_{uu}^{-1}\mathbf{a}(\theta_1)}. \tag{5}$$

The correlation matrix of summing all the undesired signals, $\mathbf{R}_{uu}$, can be written as

$$\mathbf{R}_{uu} = \sigma_u^2\mathbf{a}(\theta_u)\mathbf{a}^H(\theta_u) + \sigma_n^2\mathbf{I}, \tag{6}$$

where $\mathbf{I}$ is the $N\times N$ identity matrix. Applying the matrix inversion lemma[12] to Eq. (6), we obtain

$$\mathbf{R}_{uu}^{-1} = \sigma_n^{-2}\mathbf{I} - \frac{\sigma_u^2}{\sigma_n^2(\sigma_n^2+N\sigma_u^2)}\mathbf{a}(\theta_u)\mathbf{a}^H(\theta_u). \tag{7}$$

Let us define

$$\beta = \mathbf{a}^H(\theta_1)\mathbf{a}(\theta_2), \tag{8}$$

$$\gamma = \mathbf{a}^H(\theta_1)\mathbf{a}(\theta_u), \tag{9}$$

$$\delta = \mathbf{a}^H(\theta_u)\mathbf{a}(\theta_2). \tag{10}$$

β represents an output gain for the case in which the array is steered in direction θ_1 and an input signal arrives from the direction of θ_2. γ and δ are identical to β except for the steering and incident angles. Note that β, γ, and δ are proportional to the cosine of the angle between the steering vector of each signal and the interference.

Substituting Eq. (7) into Eq. (5) and using Eqs. (8)–(10), we obtain

$$\mathrm{SINR}_{\mathrm{SINR}} = \frac{\sigma_s^2}{\sigma_n^2\left[N - \left(\frac{\sigma_u^2}{\sigma_n^2 + N\sigma_u^2}\right)|\gamma|^2\right]} \cdot \left\{ N^2 + \alpha(\beta e^{-j\omega\tau} + \beta^* e^{j\omega\tau})N + \alpha^2|\beta|^2 \right.$$
$$+ \left(\frac{\sigma_u^2}{\sigma_n^2 + N\sigma_u^2}\right)^2 |\gamma|^2\left[|\gamma|^2 + \alpha(\gamma\delta e^{-j\omega\tau} + \gamma^*\delta^* e^{j\omega\tau}) + \alpha^2|\delta|^2\right]$$
$$- \left(\frac{\sigma_u^2}{\sigma_n^2 + N\sigma_u^2}\right)\left[|\gamma|^2 N + \alpha(\gamma\delta N e^{-j\omega\tau} + \beta^*|\gamma|^2 e^{j\omega\tau}) + \alpha^2\beta^*\gamma\delta\right]$$
$$\left. - \left(\frac{\sigma_u^2}{\sigma_n^2 + N\sigma_u^2}\right)\left[|\gamma|^2 N + \alpha(\gamma^*\delta^* N e^{j\omega\tau} + \beta|\gamma|^2 e^{-j\omega\tau}) + \alpha^2\beta\gamma^*\delta^*\right]\right\}. \quad (11)$$

The derivation of Eq. (11) is presented in the Appendix . This is the maximum achievable output SINR of a general SINR beamformer when correlated and uncorrelated interference exist. In order to obtain the meaning of Eq. (11) in detail, we investigated the variation in SINR by classifying the equation with three different cases.

Case 1. Only white noise exists ($\alpha=\beta=\gamma=\delta=\sigma_u=0$): In this case, we can easily obtain

$$\mathrm{SINR}_{\mathrm{SINR}}^{(1)} = \frac{\sigma_s^2}{\sigma_n^2}N. \quad (12)$$

Thus the SINR beamformer results in a SINR improvement of factor N compared to nonprocessing. This is reasonable, because the SINR beamformer also operates as a delay-and-sum beamformer, the performance of which is the same as Eq. (12) when only the desired signal and white noise exist.[13]

Case 2. Uncorrelated interference and white noise exist ($\alpha=\beta=\delta=0$): In this situation, there is no correlated interference and we only need to examine γ, which is proportional to the cosine of the angle between the steering vector of the desired signal and the uncorrelated interference. If we put $\alpha=\beta=\delta=0$ in Eq. (11), the maximum SINR becomes

$$\mathrm{SINR}_{\mathrm{SINR}}^{(2)} = \frac{\sigma_s^2}{\sigma_n^2}\left[N - \left(\frac{\sigma_u^2}{\sigma_n^2 + N\sigma_u^2}\right)|\gamma|^2\right] = \frac{\sigma_s^2}{\sigma_n^2}\left[N - \left(\frac{1}{N + \xi^{-1}}\right)|\gamma|^2\right], \quad (13)$$

where ξ is an uncorrelated interference-to-noise ratio (UINR) which is defined by $\xi=\sigma_u^2/\sigma_n^2$. Note that $|\gamma|^2$ denotes a gain in interference along the direction of θ_u, while the array is steered to the look direction θ_1 (see Eq. (9)). At a high UINR ($\xi \gg 1$), the maximum output SINR is decreased as much as the directivity gain of the array steered along θ_1, i.e., $|\gamma|^2/N$. If the uncorrelated interference is very close to the look direction, $|\gamma|^2$ approaches to N^2, and we find

$$\mathrm{SINR}_{\mathrm{SINR}}^{(2)} = \frac{N\sigma_s^2}{\sigma_n^2 + N\sigma_u^2} = \frac{\sigma_s^2}{\sigma_n^2} \cdot \left(\frac{N}{1 + N\xi}\right). \quad (14)$$

This implies that the desired signal and the uncorrelated interference are combined, but the white noise is summed incoherently. That is, the SINR beamformer cannot reject uncorrelated interference within the limits of the beamwidth. The maximum output SINR at low UINR($\xi \ll 1$), of course, approaches the same result shown in Eq. (12).

Figure 1 shows the relation between the output SINR and UINR. In this simulation, the array was assumed to be a 32-element uniform linear array with $d=6$ cm. The impinging sources consisted of a 500 Hz desired signal and a 200 Hz uncorrelated interference at directions of 10° and 20°, respectively. The SNR was fixed to 0 dB. The output SINR at low UINR is about 15 dB for the 32-element array, and it is the same result as the conventional beamformer represented in Eq. (12). When the UINR approaches infinity, the output SINR approaches the minimum value, $(\sigma_s^2/\sigma_n^2) \times (N - |\gamma|^2/N)$. This is shown by the dotted line in Fig. 1.

Case 3. Correlated interference and white noise exist ($\gamma=\delta=0$): Substituting $\gamma=\delta=0$ into Eq. (11), we obtain

$$\mathrm{SINR}_{\mathrm{SINR}}^{(3)} = \frac{\sigma_s^2[N^2 + \alpha(\beta e^{-j\omega\tau} + \beta^* e^{j\omega\tau})N + \alpha^2|\beta|^2]}{\sigma_n^2 N}. \quad (15)$$

To investigate the meaning of the SINR for this case, we partition it into three additive terms as follows:

$$\mathrm{SINR}_{\mathrm{SINR}}^{(3)} = \frac{\sigma_s^2}{\sigma_n^2}N + \frac{\alpha^2\sigma_s^2}{\sigma_n^2} \cdot \frac{|\beta|^2}{N} + \frac{\sigma_s^2}{\sigma_n^2} \cdot \alpha(\beta e^{-j\omega\tau} + \beta^* e^{j\omega\tau}). \quad (16)$$

The first term is the maximum SNR of *case 1*. The second term indicates that the correlated signal-to-noise ratio (CSNR) is increased by the normalized array gain $|\beta|^2/N$ multiplied by the square of the attenuation factor α, and it always has a positive value. However, the array gain obtained is represented by a sidelobe level of the beampattern which is steered in the direction of the desired signal. This means that the SINR beamformer accidentally increases the SINR output. We modify the third term slightly to describe its meaning. As shown in Eq. (8), β represents an array factor for interference along the direction of θ_2, while the array is steered in the look direction θ_1. For simplicity, we assume that the symmetric geometry of the linear array can be used and its sensor space d is set to the half-wavelength. As a result, β can be described by a real-value:[2]

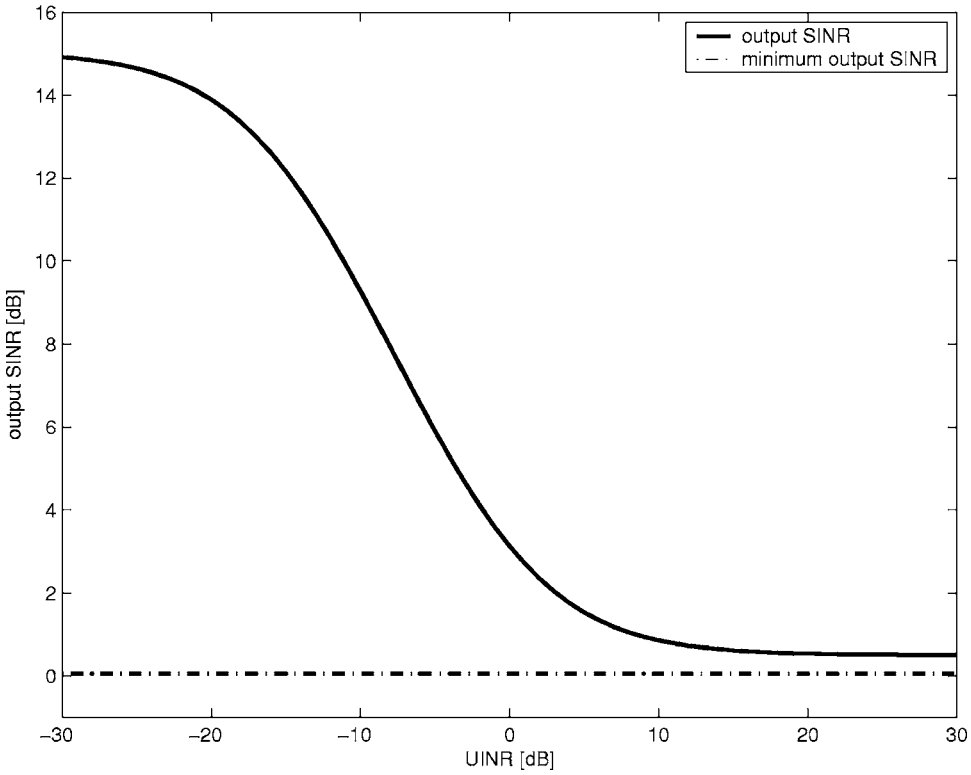

FIG. 1. Output SINR vs UINR for case 2. A 500 Hz desired signal and a 200 Hz uncorrelated interference impinge at a direction of 10° and 20°. The array is a 32-element uniform linear array with d=6 cm. The output SINR vs UINR (ξ) is shown. The dotted line represents the minimum value for the output SINR.

$$\beta = \frac{\sin[N\pi(\sin\theta_1 - \sin\theta_2)/2]}{\sin[\pi(\sin\theta_1 - \sin\theta_2)/2]}. \tag{17}$$

Therefore, the maximum SINR in Eq. (16) is expressed as

$$\mathrm{SINR}^{(3)}_{\mathrm{SINR}} = \frac{\sigma_s^2}{\sigma_n^2}N + \frac{\alpha^2\sigma_s^2}{\sigma_n^2}\cdot\frac{|\beta|^2}{N} + \frac{\sigma_s^2}{\sigma_n^2}\cdot\alpha\beta\cos(\omega\tau). \tag{18}$$

If $\omega\tau$ lies in $[-\pi/2, \pi/2]$, the third term has a positive value. Otherwise, it would decrease the output SINR by incoherent summing.

III. OPTIMUM BEAMFORMER FOR CORRELATED SOURCES

A. Proposed optimum beamformer in the presence of correlated sources

In order to analyze the characteristics of an optimum beamformer for correlated sources, we consider a more general signal model: the desired source, I correlated signals, J uncorrelated interferences, and white noise. We wish to show that the weight vector can be optimized by maximizing the SINR at the output of the beamformer in the presence of correlated signals. Various techniques for obtaining the optimum weight vector for correlated interferences have been discussed.[5–7] We now consider the simplest method, which employs Schwarz's inequality. First, Eq. (1) can be rewritten as

$$\begin{aligned}\mathbf{x}(t) &= \mathbf{s}(t) + \mathbf{s}_c(t) + \mathbf{s}_\mathbf{u}(t) + \mathbf{n}(t)\\ &= s(t)\mathbf{a}(\theta_{c,0}) + \sum_{i=1}^{I}\alpha_i s(t-\tau_i)\mathbf{a}(\theta_{c,i}) + \sum_{j=1}^{J} s_j(t)\mathbf{a}(\theta_{u,j}) + \mathbf{n}(t)\\ &= s(t)\sum_{i=0}^{I}\alpha_i e^{-jw\tau_i}\mathbf{a}(\theta_{c,i}) + \sum_{j=1}^{J} s_j(t)\mathbf{a}(\theta_{u,j}) + \mathbf{n}(t)\\ &= \mathbf{b}(\theta_{c,0},\theta_{c,1},\ldots,\theta_{c,I})\cdot s(t) + \mathbf{u}(t),\end{aligned} \tag{19}$$

where $\theta_{c,0}$, $\theta_{c,i}$, and $\theta_{u,j}$ represent the incident angles of the desired, correlated signal, and uncorrelated interferences, respectively. α_0 is 1, and τ_0 is 0. Vector $\mathbf{b}$ is a linear combination of steering vectors of signals correlated with the desired source.

From Eq. (19), the array output SINR is given by

$$\begin{aligned}\mathrm{SINR}_{\mathrm{out}} &= \frac{E\{|\mathbf{w}^H\mathbf{b}(\theta_{c,0},\theta_{c,1},\ldots,\theta_{c,I})\cdot s(t)|^2\}}{E\{|\mathbf{w}^H\mathbf{u}(t)|^2\}}\\ &= \frac{\sigma_s^2|\mathbf{w}^H\mathbf{b}(\theta_{c,0},\theta_{c,1},\ldots,\theta_{c,I})|^2}{\mathbf{w}^H\mathbf{R}_{uu}\mathbf{w}}.\end{aligned} \tag{20}$$

Using Schwarz' inequality in Eq. (20), we can derive the optimum weight $\mathbf{w}_{\text{CC-SINR}}$ for correlated sources as follows:

$$\begin{aligned}\mathrm{SINR}_{\mathrm{out}} &= \frac{\sigma_s^2|(\mathbf{R}_{uu}^{1/2}\mathbf{w})^H\cdot(\mathbf{R}_{uu}^{-1/2}\mathbf{b}(\theta_{c,0},\theta_{c,1},\ldots,\theta_{c,I}))|^2}{\mathbf{w}^H\mathbf{R}_{uu}\mathbf{w}}\\ &\le \sigma_s^2\mathbf{b}^H(\theta_{c,0},\theta_{c,1},\ldots,\theta_{c,I})\mathbf{R}_{uu}^{-1}\mathbf{b}(\theta_{c,0},\theta_{c,1},\ldots,\theta_{c,I})\\ &\overset{\text{def}}{=} \mathrm{SINR}_{\max},\end{aligned} \tag{21}$$

where equality is achieved with

$$\mathbf{w}_{\text{CC-SINR}} = c \cdot \mathbf{R}_{uu}^{-1}\mathbf{b}(\theta_{c,0}, \theta_{c,1}, \ldots, \theta_{c,I}). \quad (22)$$

Note, however, that it is too difficult to find time delays and the directions of the correlated interferences such as those in multipath environments. Therefore, a more appropriate approach is not to estimate the time delays and directions but $\mathbf{b}(\theta_{c,0}, \theta_{c,1}, \ldots, \theta_{c,I})$. The correlation matrix of an array output $\mathbf{R}_{xx}$ becomes

$$\mathbf{R}_{xx} = \sigma_s^2\mathbf{b}(\theta_{c,0}, \theta_{c,1}, \ldots, \theta_{c,I})\mathbf{b}^H(\theta_{c,0}, \theta_{c,1}, \ldots, \theta_{c,I}) + \mathbf{R}_{uu}, \quad (23)$$

where $\mathbf{R}_{uu}$ is the noise plus uncorrelated interference correlation matrix. Then,

$$\begin{aligned}\mathbf{R}_{ss} &= \mathbf{R}_{xx} - \mathbf{R}_{uu} \\ &= \sigma_s^2\mathbf{b}(\theta_{c,0}, \theta_{c,1}, \ldots, \theta_{c,I})\mathbf{b}^H(\theta_{c,0}, \theta_{c,1}, \ldots, \theta_{c,I}). \quad (24)\end{aligned}$$

Since $\mathbf{R}_{ss}$ is of unit rank, only one nonzero eigenvalue, λ_1, of $\mathbf{R}_{ss}$ exists. The eigenvector $\mathbf{e}_1$ corresponding to λ_1 is obtained by

$$\begin{aligned}&\mathbf{R}_{ss}\mathbf{b}(\theta_{c,0}, \theta_{c,1}, \ldots, \theta_{c,I}) \\ &\quad = \sigma_s^2\mathbf{b}(\theta_{c,0}, \theta_{c,1}, \ldots, \theta_{c,I})[\\ &\qquad \times\mathbf{b}^H(\theta_{c,0}, \theta_{c,1}, \ldots, \theta_{c,I})\mathbf{b}(\theta_{c,0}, \theta_{c,1}, \ldots, \theta_{c,I})] \\ &\quad = \sigma_s^2\mathbf{b}(\theta_{c,0}, \theta_{c,1}, \ldots, \theta_{c,I})\|\mathbf{b}(\theta_{c,0}, \theta_{c,1}, \ldots, \theta_{c,I})\|^2. \quad (25)\end{aligned}$$

From Eq. (25), the principal eigenvector $\mathbf{e}_1$ should be proportional to $\mathbf{b}(\theta_{c,0}, \theta_{c,1}, \ldots, \theta_{c,I})$.[13] That is, $\mathbf{e}_1$ is represented by a linear combination of steering vectors $\mathbf{a}(\theta_{c,i})$, $i = 0, 1, \ldots, I$, and contains complete information concerning the desired source and its correlated multipath sources. Hence, it follows that

$$\mathbf{w}_{\text{CC-SINR}} = c \cdot \mathbf{R}_{uu}^{-1}\mathbf{e}_1. \quad (26)$$

B. Analysis of the CC-SINR beamformer in the presence of correlated source

We recall the assumptions and the signal model described in Sec. II to compare the results presented in this section. Under these assumptions, the maximum achievable output SINR of the proposed CC-SINR beamformer, $\text{SINR}_{\text{prop}}$, is obtained by Eq. (21) as follows:

$$\text{SINR}_{\text{prop}} = \sigma_s^2\mathbf{b}^H(\theta_1, \theta_2)\mathbf{R}_{uu}^{-1}\mathbf{b}(\theta_1, \theta_2). \quad (27)$$

Substituting Eq. (7) into Eq. (27) and using Eqs. (7)–(10), we obtain

$$\text{SINR}_{\text{prop}} = \frac{\sigma_s^2}{\sigma_n^2}\left[\mathbf{b}^H(\theta_1, \theta_2)\mathbf{b}(\theta_1, \theta_2) - \frac{\sigma_u^2}{\sigma_n^2 + N\sigma_u^2}\mathbf{b}^H(\theta_1, \theta_2)\mathbf{a}(\theta_u)\mathbf{a}^H(\theta_u)\mathbf{b}(\theta_1, \theta_2)\right], \quad (28)$$

where

$$\begin{aligned}&\mathbf{b}^H(\theta_1, \theta_2)\mathbf{b}(\theta_1, \theta_2) \\ &\quad = [\mathbf{a}(\theta_1) + \alpha e^{-j\omega\tau}\mathbf{a}(\theta_2)]^H[\mathbf{a}(\theta_1) + \alpha e^{-j\omega\tau}\mathbf{a}(\theta_2)] \\ &\quad = N + \alpha(\beta^* e^{j\omega\tau} + \beta e^{-j\omega\tau}) + \alpha^2 N \quad (29)\end{aligned}$$

and

$$\begin{aligned}&\mathbf{b}^H(\theta_1, \theta_2)\mathbf{a}(\theta_u)\mathbf{a}^H(\theta_u)\mathbf{b}(\theta_1, \theta_2) \\ &\quad = \mathbf{a}^H(\theta_u)\mathbf{b}(\theta_1, \theta_2)\mathbf{b}^H(\theta_1, \theta_2)\mathbf{a}(\theta_u) \\ &\quad = \mathbf{a}^H(\theta_u)[\mathbf{a}(\theta_1) + \alpha e^{-j\omega\tau}\mathbf{a}(\theta_2)] \\ &\qquad \times[\mathbf{a}(\theta_1) + \alpha e^{-j\omega\tau}\mathbf{a}(\theta_2)]^H\mathbf{a}(\theta_u) \\ &\quad = |\gamma|^2 + \alpha(\gamma\delta e^{-j\omega\tau} + \gamma^*\delta^* e^{j\omega\tau}) + \alpha^2|\delta|^2. \quad (30)\end{aligned}$$

From Eqs. (28) to (30), we readily get

$$\begin{aligned}\text{SINR}_{\text{prop}} = \frac{\sigma_s^2}{\sigma_n^2}\Bigg\{&N + \alpha(\beta^* e^{j\omega\tau} + \beta e^{-j\omega\tau}) + \alpha^2 N \\ &- \frac{\sigma_u^2}{\sigma_n^2 + N\sigma_u^2}[|\gamma|^2 + \alpha(\gamma\delta e^{-j\omega\tau} + \gamma^*\delta^* e^{-j\omega\tau}) \\ &+ \alpha^2|\delta|^2]\Bigg\}. \quad (31)\end{aligned}$$

This is the maximum output SINR of the proposed beamformer when correlated interference and uncorrelated interference exist.

Case 1. Only white noise exist ($\alpha = \beta = \gamma = \delta = \sigma_u = 0$): Since there is no correlated interference, the same result as Eq. (12) is obtained.

Case 2. Uncorrelated interference and white noise exist ($\alpha = \beta = \delta = 0$): The same result as Eq. (13) is obtained.

Case 3. Correlated interference and white noise exist ($\gamma = \delta = 0$):

Substituting $\gamma = \delta = 0$ into Eq. (31), the following equation can be obtained:

$$\begin{aligned}\text{SINR}_{\text{prop}} &= \frac{\sigma_s^2}{\sigma_n^2}\{N + \alpha(\beta^* e^{j\omega\tau} + \beta e^{-j\omega\tau}) + \alpha^2 N\} \\ &= \frac{\sigma_s^2}{\sigma_n^2}N + \frac{\alpha^2\sigma_s^2}{\sigma_n^2} \cdot N + \frac{\sigma_s^2}{\sigma_n^2} \cdot \alpha\beta\cos(\omega\tau). \quad (32)\end{aligned}$$

Compared to the results for the SINR beamformer in the same environment (Eq. (18)), the result shown in Eq. (32) is different. In the second term of Eq. (18), the conventional SINR beamformer accidentally increases the SINR output with a gain pattern for the direction of the desired signal. However, the CC-SINR beamformer, as shown in Eq. (32), can increase the output SINR by beamforming in both the direction of the desired signal and the correlated interference. Since N is always greater than $|\beta|^2/N$ (because that $N^2 > |\beta|^2$), the CC-SINR beamformer can improve output SINR performance in the presence of a correlated source.

Figures 2–4 show an array output SINR computed using both the conventional SINR beamformer expressed in Eq. (18) and the CC-SINR beamformer proposed in Eq. (32). Figure 2 shows the output SINR as a function of the direction of interference for the case where the interference is

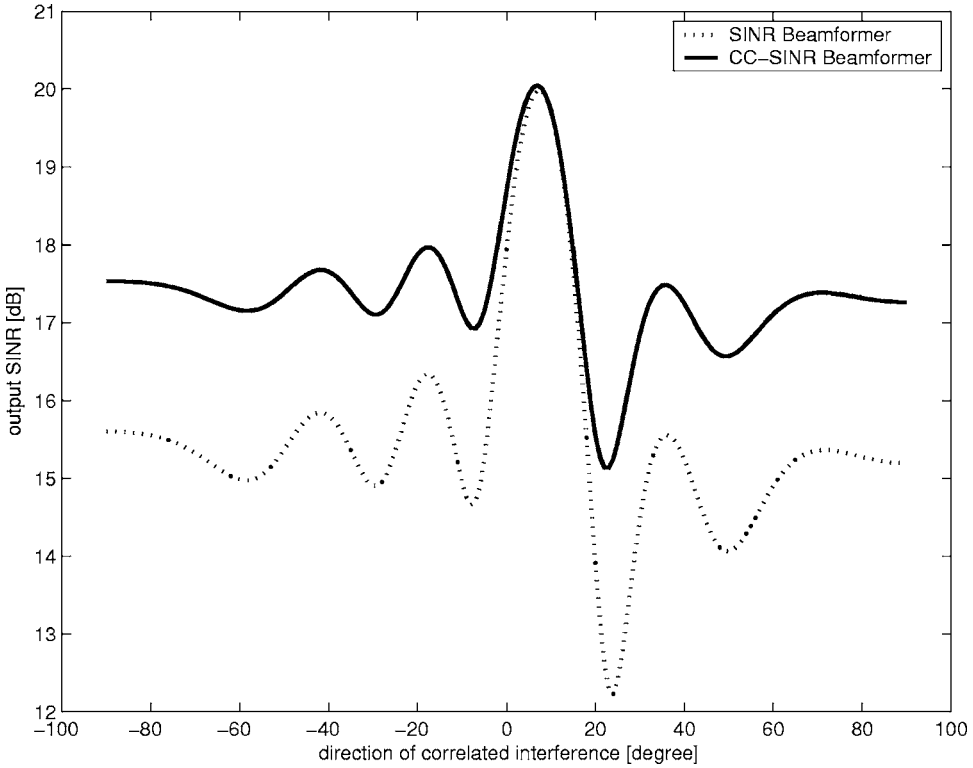

FIG. 2. Output SINR vs the direction of the correlated interference for case 3. The array configuration is the same as that used in Fig. 1. The impinging source is a 500 Hz desired signal and a single correlated interference. The SNR is set to 0 dB. An attenuation factor $\alpha=0.8$ and time delay $\tau=0.2$ ms. The dotted line represents the output SINR of the SINR beamformer and the solid line is that of the CC-SINR beamformer. The solid line is always greater than the dotted line.

correlated with the desired signal. In this simulation, the array configuration is the same as that used in Fig. 1. The impinging sources consist of a 500 Hz desired signal and a single correlated interference. The SNR was 0 dB. An attenuation factor $\alpha=0.8$ and time delay $\tau=0.2$ ms. Figure 2 implies that the CC-SINR beamformer guarantees higher SINR outputs in the presence of correlated interference at all incident angles.

Figure 3 shows essentially the same basic results as Fig. 2 but directions are replaced with an attenuation factor. It can easily be seen that, as the attenuation factor grows, so does the averaged output SINR difference between the CC-SINR beamformer and the SINR beamformer. In this example, note that the output SINR was averaged in all directions of correlated interference, i.e., $[-90°, 90°]$.

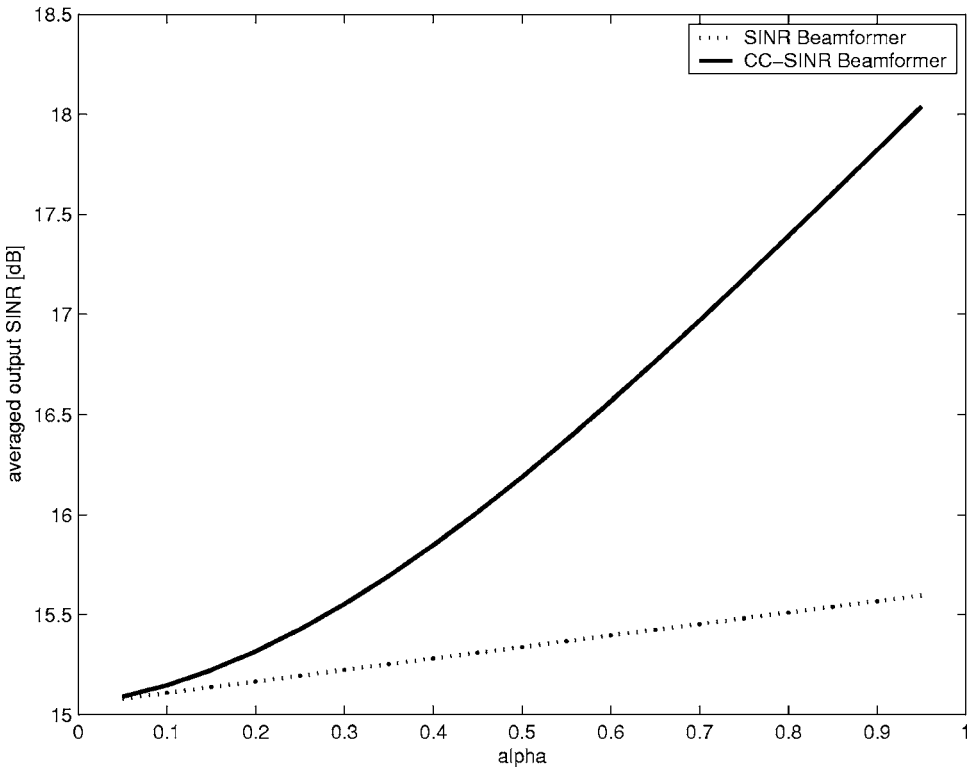

FIG. 3. Averaged output SINR vs attenuation factor. The array configuration and signal model is the same as that used in Fig. 1 except for the variable attenuation factor. The output SINR was averaged in all directions of the correlated interference, i.e. $[-90°, 90°]$. Accordingly, as the attenuation factor approaches 1, the CC-SINR beamformer shows good performance.

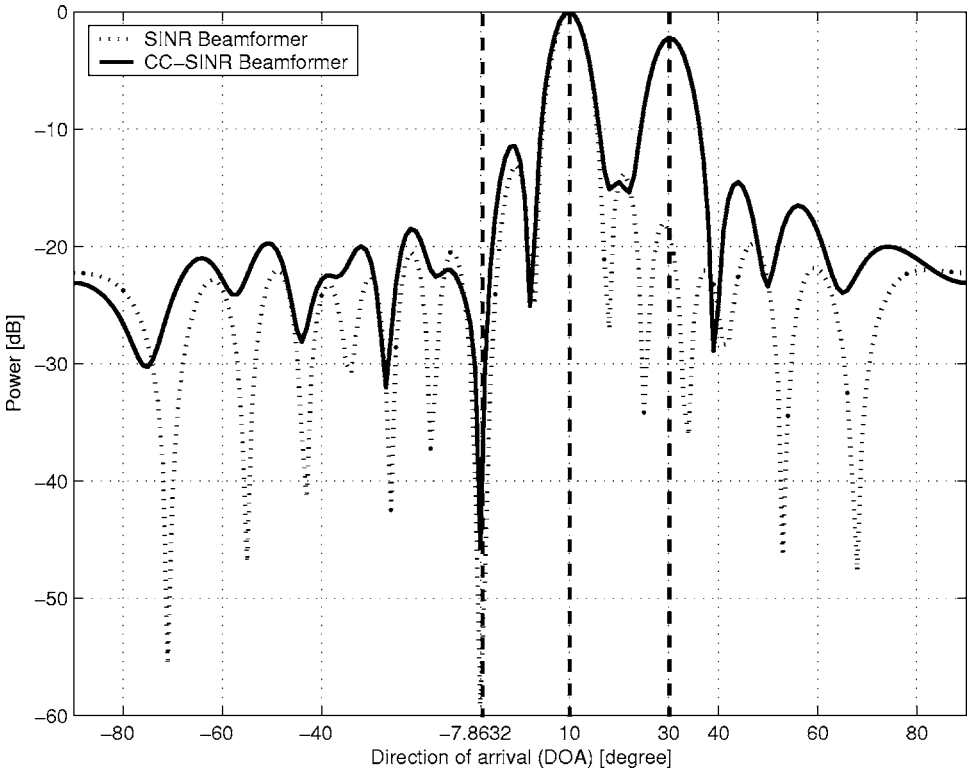

FIG. 4. Beam patterns of the optimum SINR beamformer and CC-SINR beamformer. A 500 Hz desired signal, one correlated interference and 200 Hz uncorrelated interference impinge at a direction of 10°, 30°, and −20°, respectively. The array is a 16-element uniform linear array with half-wavelength d. SNR and UINR are set to 0 dB.

IV. SIMULATION RESULTS

A. Beam pattern

Consider a 16-element uniform linear array in all experiments. Three far-field signals are impinging on the array: One is the desired signal, another is correlated interference, and the third is uncorrelated interference. The desired signal and the correlated interference are 500 Hz sinusoidal waves in directions of 10° and 30°, respectively. The attenuation factor, α, is fixed to 0.8 and the time delay τ is set to 0.2 ms. The uncorrelated interference is a 200 Hz sinusoidal wave in the direction of −20° and white Gaussian noise is also added. The sampling frequency is 8 kHz. The distance d between two sensors is set to the half wavelength of the desired signal.

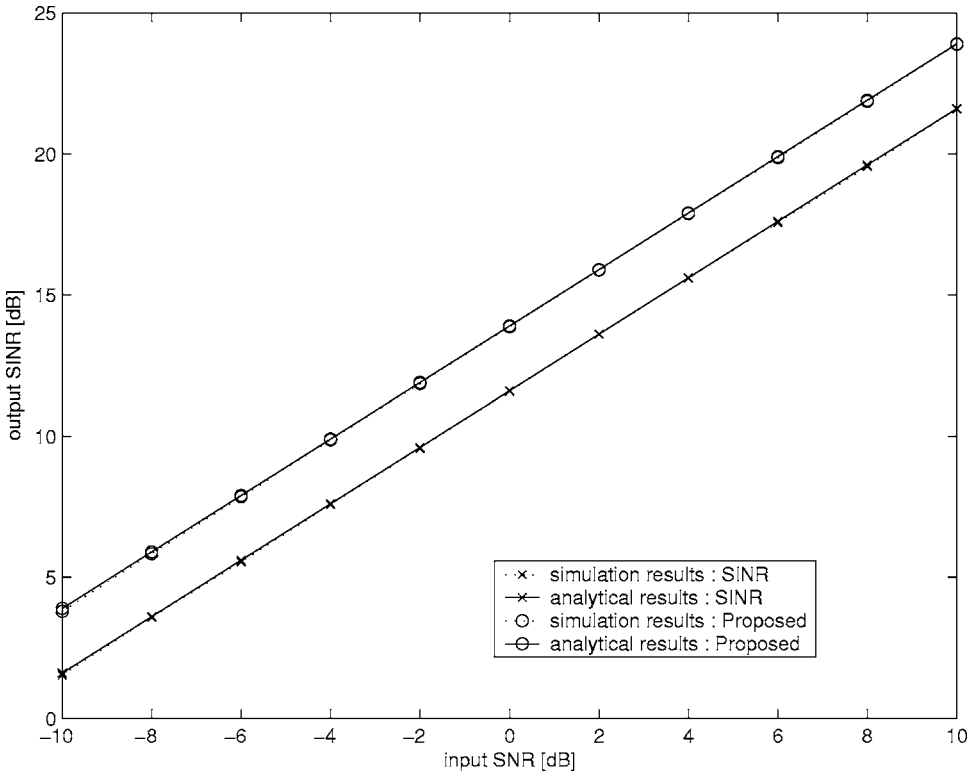

FIG. 5. Simulation and analytical results for output SINR vs input SNR. The scenario is the same as that used in Fig. 4 except for the variable input SNR.

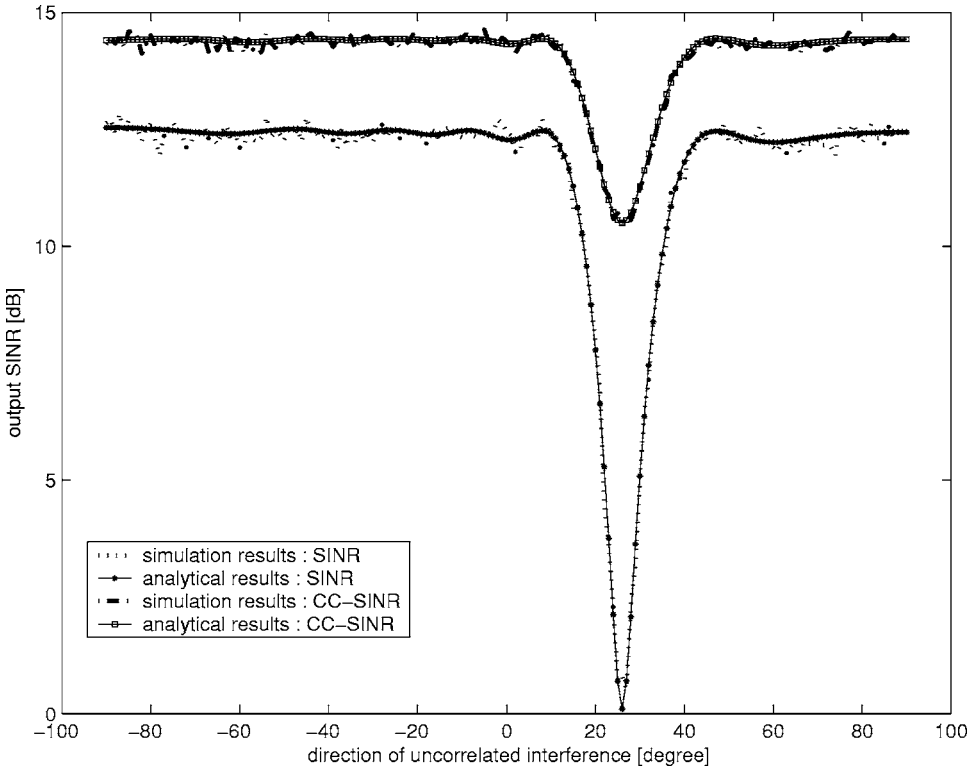

FIG. 6. Simulation and analytical results for output SINR vs the direction of the uncorrelated interference. The scenario is the same as that used in Fig. 4 except for the variable direction of the uncorrelated interference.

Figure 4 shows normalized beam patterns of the SINR beamformer and the CC-SINR beamformer in the case of SNR=0 dB and UINR=0 dB. The SINR beamformer has a deep null in the direction of uncorrelated interference, that is $\arcsin\left(\frac{2}{5}\sin(-20°)\right)=-7.8632°$. However, it steers in the desired direction only, since it cannot use any information for correlated interference. The CC-SINR beamformer uses the eigenvector corresponding to the principal eigenvalue of $\mathbf{R}_{ss}$, and it then forms a spatial beam to the correlated interference as well as the desired direction.

B. Signal-to-interference plus noise ratio

In order to verify the case-by-case analysis in Sec. III and to evaluate the achievable performance, simulations were performed for the conventional SINR beamformer and the CC-SINR beamformer in the presence of correlated interference. Figure 5 shows an example of the $\mathrm{SINR}_{\mathrm{SINR}}$ and $\mathrm{SINR}_{\mathrm{prop}}$ behavior computed using Eqs. (11) and (31) as a function of the input SNR. The results are depicted by a sample-average of 50 independent runs. It can easily be seen in Fig. 5 that the analytical results and the simulation results are in good agreement.

Figure 6 depicts the $\mathrm{SINR}_{\mathrm{SINR}}$ and the $\mathrm{SINR}_{\mathrm{prop}}$ as a function of the directions of uncorrelated interference. To plot the simulation results, 50 independent trials were used in this figure as well. No significant difference between the simulation results and the analytical results was found. The output SINR is decreased when the direction of the uncorrelated interference is near the incident angle of the desired signal, that is $\arcsin\left(\frac{5}{2}\sin(10°)\right)=25.7293°$.

V. EXPERIMENTAL RESULTS

In order to verify the performance of the CC-SINR beamformer in a real environment, two tests were performed. The conditions are as follows:

(1) The desired signal was generated to be a 1000 Hz sine wave which impinged on the microphone array (at the direction of 0°), and the uncorrelated interference signal was a 1500 Hz sine wave in the direction of 60° (The normal to the interference wave front makes a 30° angle with line joining the sensors in the linear array.)
(2) The desired signal and an uncorrelated interference signal with the same frequencies impinged in the direction of 60° and 0°, respectively.

The measurements were made in the Multimedia Room of the MCSP Lab. at Yonsei University. The uniform linear microphone array was mounted on a stand which enables accurate positioning for any distance between adjacent microphones, as shown in Fig. 7. It consists of seven omni-directional condenser microphones with distance $d=8$ cm. There were two loudspeakers, referred to as SPK1 and SPK2, which generate the desired signal and the uncorrelated interference. Two reference microphones (MIC A and MIC

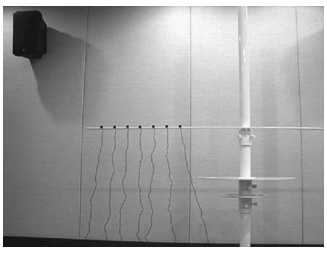

FIG. 7. The uniform linear microphone array. Seven omni-directional microphones are mounted on a stand which enables accurate positioning to distance of 8 cm between adjacent microphones.

TABLE I. Experimental environment I—0° desired signal and 60° interference signal.

	Input SINR (dB)	Input SNR (dB)	SINR beamformer (dB)	CC-SINR beamformer (dB)
Trial 1	7.2618	19.7799	21.0097	21.5907
Trial 2	11.3310	18.6182	20.2301	20.0506
Trial 3	6.3496	19.9001	21.2419	21.5214
Trial 4	8.3093	19.7891	21.1156	21.4677
Avg	8.3128	19.5218	20.8993	21.1576

TABLE II. Experimental environment II—60° desired signal and 0° interference signal.

	Input SINR (dB)	Input SNR (dB)	SINR beamformer (dB)	CC-SINR beamformer (dB)
Trial 1	0.2885	19.8115	21.3427	21.4142
Trial 2	0.9718	19.7749	21.3093	21.3911
Trial 3	0.0716	19.8475	21.5004	21.5536
Trial 4	1.0740	19.8086	21.6268	21.6304
Avg	0.6015	19.8106	21.4448	21.4973

B) were located in front of SPK1 and SPK2. The reference microphones and the microphone array were 0.2 and 2 m away from the speaker, respectively. The signal from the two speakers was measured by reference microphones and microphone arrays. The outputs of the microphones were sent to an A/D converter which was connected to a multichannel recording device interfaced with a personal computer. The sampling rate was 16 kHz in these experiments.

A. Environment I: 0° desired signal and 60° interference signal

Four independent experiments were performed in an identical environment to compare the output SINR of the conventional SINR beamformer with that of the CC-SINR beamformer. The desired SINR, the desired SNR, the output SINRs of the SINR beamformer and the CC-SINR beamformer are presented in Table I. As shown in Table II, the output SINR of the proposed beamformer is higher than that of the SINR beamformer by about 0.26 dB.

Figure 8(a) presents an impulse response of the transmission path between MIC A and MIC 4. The impulse response is determined by the cross-correlation of signals at two points in the room. To measure the impulse response, a pseudorandom noise (PN) test signal was used, which has properties similar to random noise.[14] The PN sequence is generated using a linear feedback shift-register and exclusive OR-gate circuits.[15,16]

To investigate shortly delayed reflections in a room environment, a further analysis is necessary. A reflectogram can display how the shortly delayed reflections are distributed in time. Since the CC-SINR beamformer combines the reflections, a reflectogram is very useful in predicting the performance of a beamformer. The reflectogram can be obtained by the squared envelope of the impulse response.[14] The squared envelope is defined as follows. Let $s(t)$ denote any signal, and its envelope is then represented by

$$e^2(t) = s^2(t) + \check{s}^2(t), \tag{33}$$

where $\check{s}(t)$, denotes the *Hilbert transform* of $s(t)$:

$$\check{s}(t) = \frac{1}{\pi}\int_{-\infty}^{\infty} \frac{s(t-t')}{t'}dt' \equiv H[s(t)]. \tag{34}$$

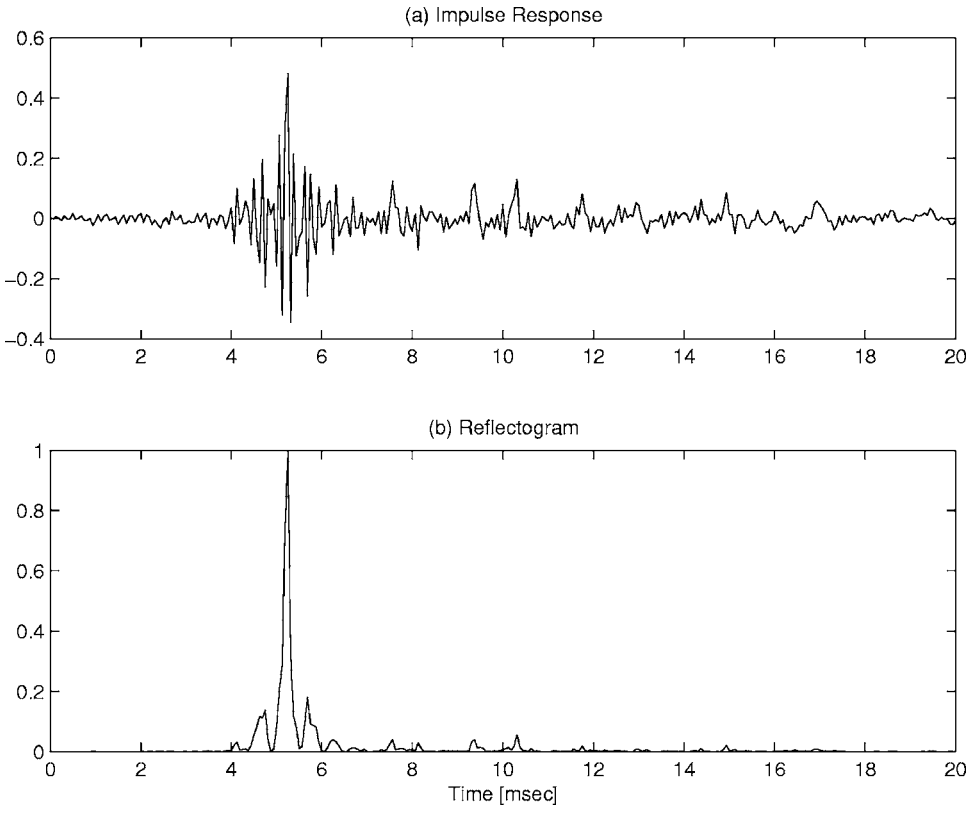

FIG. 8. The impulse response and reflectogram in experimental environment I. (a) Impulse response. (b) Reflectogram.

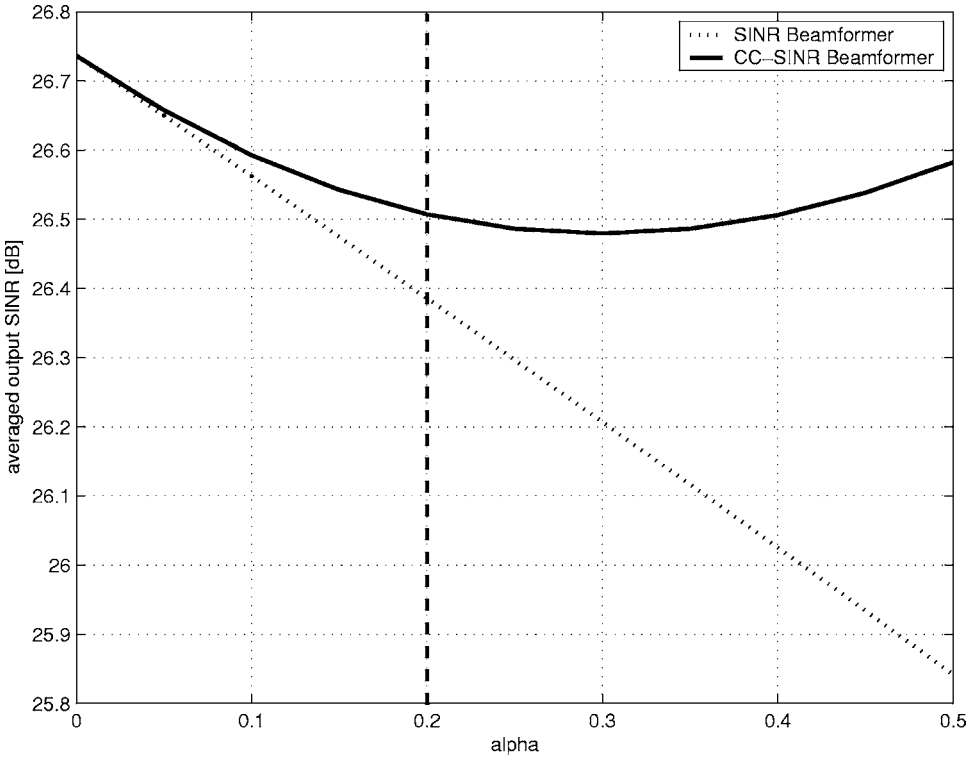

FIG. 9. Averaged output SINR vs an attenuation factor in experimental environment I. The output SINR of the proposed beamformer is 0.13 dB higher than that of the SINR beamformer, for an attenuation factor of 0.2.

Figure 8(b) shows a reflectogram of the impulse response used in the experiment. From the figure, we know that the attenuation factor α of the first reflection is approximately 0.2. From Table I, it can be seen that a significant reflection exists and that the output SINR of the proposed beamformer is 0.26 dB higher than that of the conventional SINR beamformer. The theoretically calculated SINR, which uses Eqs. (11) and (12) as a function of the attenuation factor in environment I, is depicted in Fig. 9. The analytical result shows that the output SINR of the proposed beamformer is also 0.13 dB greater than that of the SINR beamformer at an estimated value of α, which is in agreement with the experimental results.

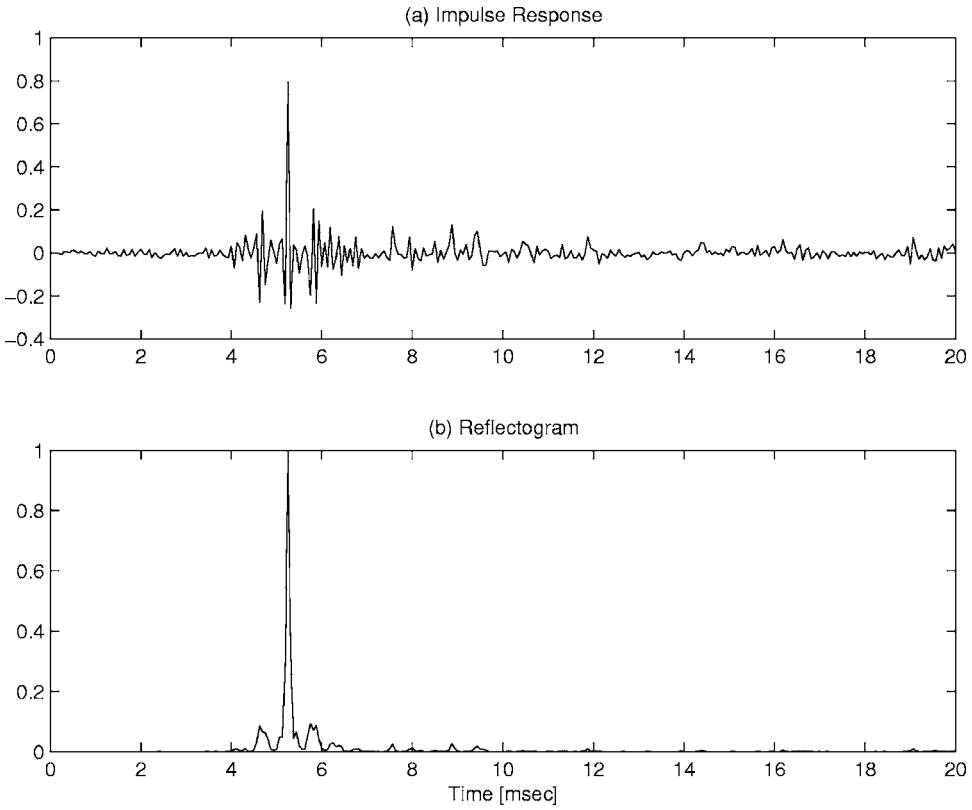

FIG. 10. The impulse response and reflectogram in experimental environment II.

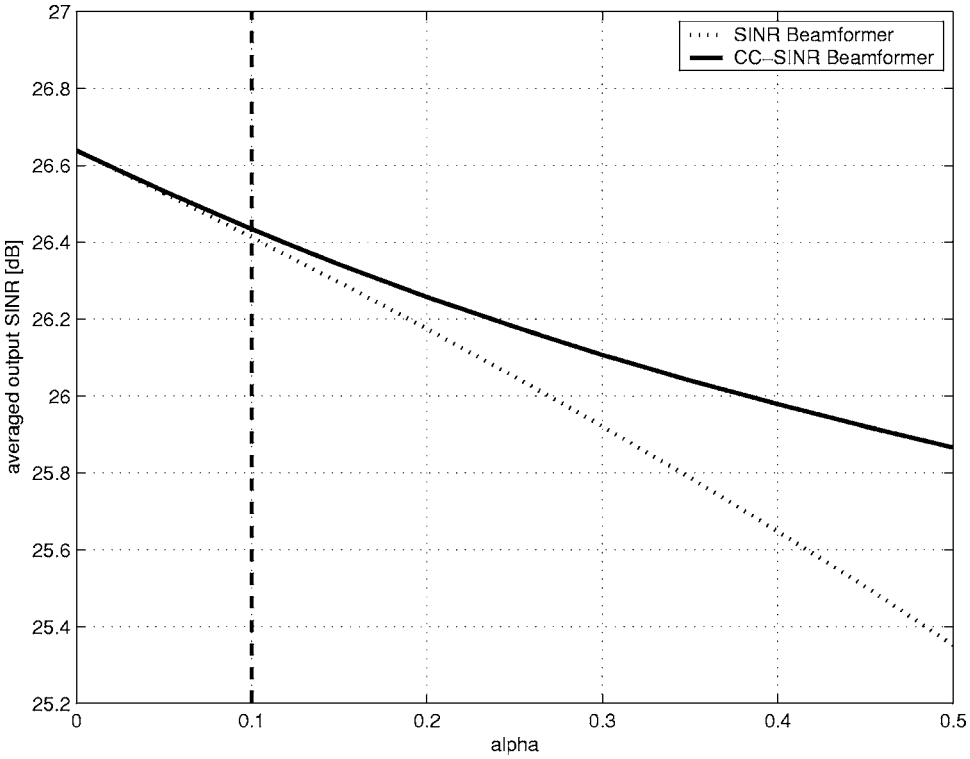

FIG. 11. Averaged output SINR vs an attenuation factor in experimental environment II.

B. Environment II: 60° desired signal and 0° interference signal

Four independent experiments were performed in the same environment to compare the output SINR of the conventional SINR beamformer with the CC-SINR beamformer. The desired SINR, the desired SNR, the output SINR of the SINR beamformer and the proposed beamformer are presented in Table II. As shown in Table II, the output SINR of the proposed beamformer is slightly higher than that of a SINR beamformer. Figure 10(a) presents an impulse response of the transmission path between MIC B and MIC 4. From Fig. 10(b), it can be seen that the attenuation factor α of the first reflection is approximately 0.1. It is known that strong reflections do not exist, contrary to environment I, as shown in Fig. 8(b). Figure 11 displays the theoretically calculated SINR at the output of the proposed beamformer and the SINR beamformer as a function of the attenuation factor in environment II. The output SINR of the proposed beamformer is almost the same as that of the SINR beamformer when $\alpha=0.1$.

VI. CONCLUSIONS

A method for improving the performance of a SINR beamformer in the presence of correlated interference is proposed. The CC-SINR beamformer regards correlated interferences as replicas of the desired signal and coherently combines them with the desired signal. We derived a theoretical expression for SINR at the outputs of the SINR beamformer and the CC-SINR beamformer, and also showed, based on analytical data, that the output SINR of the proposed beamformer was consistently always greater than that of a SINR beamformer. As the attenuation factor grew, so did the maximum achievable array gain of the CC-SINR beamformer.

ACKNOWLEDGMENTS

This work was supported by LG Yonam Foundation.

APPENDIX: MAXIMUM OUTPUT SINR OF THE SINR BEAMFORMER

In this appendix, the maximum achievable SINR of the SINR beamformer in the presence of the correlated interferences is derived. We begin by substituting Eq. (7) into Eq. (3) from Sec. II,

$$\mathrm{SINR}_{\mathrm{SINR}} = \frac{\sigma_s^2}{\sigma_n^2} \cdot \frac{\mathbf{a}^H(\theta_1)\left[\mathbf{I} - \left(\frac{\sigma_u^2}{\sigma_n^2 + N\sigma_u^2}\right)\mathbf{a}(\theta_u)\mathbf{a}^H(\theta_u)\right]\mathbf{b}\mathbf{b}^H\left[\mathbf{I} - \left(\frac{\sigma_u^2}{\sigma_n^2 + N\sigma_u^2}\right)\mathbf{a}(\theta_u)\mathbf{a}^H(\theta_u)\right]\mathbf{a}(\theta_1)}{\mathbf{a}^H(\theta_1)\left[\mathbf{I} - \left(\frac{\sigma_u^2}{\sigma_n^2 + N\sigma_u^2}\right)\mathbf{a}(\theta_u)\mathbf{a}^H(\theta_u)\right]\mathbf{a}(\theta_1)} = \frac{\sigma_s^2}{\sigma_n^2} \cdot \frac{Q}{P}, \tag{A1}$$

where P and Q is the denominator and nominator of Eq. (A1) except the input SNR, respectively. First, we consider the nominator part Q,

$$
\begin{aligned}
Q = {} & \mathbf{a}^H(\theta_1)\mathbf{b}\mathbf{b}^H\mathbf{a}(\theta_1) \\
& + \left(\frac{\sigma_u^2}{\sigma_n^2 + N\sigma_u^2}\right)^2 \mathbf{a}^H(\theta_1)\mathbf{a}(\theta_u)\mathbf{a}^H(\theta_u)\mathbf{b}\mathbf{b}^H\mathbf{a}(\theta_u)\mathbf{a}^H(\theta_u)\mathbf{a}(\theta_1) \\
& - \left(\frac{\sigma_u^2}{\sigma_n^2 + N\sigma_u^2}\right)\mathbf{a}^H(\theta_1)\mathbf{a}(\theta_u)\mathbf{a}^H(\theta_u)\mathbf{b}\mathbf{b}^H\mathbf{a}(\theta_1) \\
& - \left(\frac{\sigma_u^2}{\sigma_n^2 + N\sigma_u^2}\right)\mathbf{a}^H(\theta_1)\mathbf{b}\mathbf{b}^H\mathbf{a}(\theta_u)\mathbf{a}^H(\theta_u)\mathbf{a}(\theta_1). \qquad \text{(A2)}
\end{aligned}
$$

Equation (A2) can be separated into four sets of summations so that

$$
Q = Q_1 + Q_2 + Q_3 + Q_4, \qquad \text{(A3)}
$$

where, after some calculations and using Eqs. (8)–(10),

$$
Q_1 = N^2 + \alpha(\beta e^{-j\omega\tau} + \beta^* e^{j\omega\tau})N + \alpha^2|\beta|^2, \qquad \text{(A4)}
$$

$$
Q_2 = \left(\frac{\sigma_u^2}{\sigma_n^2 + N\sigma_u^2}\right)^2 |\gamma|^2[|\gamma|^2 + \alpha(\gamma\delta e^{-j\omega\tau} + \gamma^*\delta^* e^{j\omega\tau}) + \alpha^2|\delta|^2], \qquad \text{(A5)}
$$

$$
\begin{aligned}
Q_3 = {} & -\left(\frac{\sigma_u^2}{\sigma_n^2 + N\sigma_u^2}\right)[|\gamma|^2 N + \alpha(\gamma\delta N e^{-j\omega\tau} + \beta^*|\gamma|^2 e^{j\omega\tau}) \\
& + \alpha^2\beta^*\gamma\delta], \qquad \text{(A6)}
\end{aligned}
$$

$$
\begin{aligned}
Q_4 = {} & -\left(\frac{\sigma_u^2}{\sigma_n^2 + N\sigma_u^2}\right)[|\gamma|^2 N + \alpha(\gamma^*\delta^* N e^{j\omega\tau} + \beta|\gamma|^2 e^{-j\omega\tau}) \\
& + \alpha^2\beta\gamma^*\delta^*]. \qquad \text{(A7)}
\end{aligned}
$$

The denominator of Eq. (A1), P, is also given by

$$
\begin{aligned}
P &= \mathbf{a}^H(\theta_1)\mathbf{a}(\theta_1) - \left(\frac{\sigma_u^2}{\sigma_n^2 + N\sigma_u^2}\right)\mathbf{a}^H(\theta_1)\mathbf{a}(\theta_u)\mathbf{a}^H(\theta_u)\mathbf{a}(\theta_1) \\
&= N - \left(\frac{\sigma_u^2}{\sigma_n^2 + N\sigma_u^2}\right)|\gamma|^2. \qquad \text{(A8)}
\end{aligned}
$$

Combining Eqs. (A3)–(A8), we then have

$$
\begin{aligned}
\mathrm{SINR}_{\mathrm{SINR}} = {} & \frac{\sigma_s^2}{\sigma_n^2\left[N - \left(\frac{\sigma_u^2}{\sigma_n^2 + N\sigma_u^2}\right)|\gamma|^2\right]} \cdot \Bigg\{ N^2 + \alpha(\beta e^{-j\omega\tau} \\
& + \beta^* e^{j\omega\tau})N + \alpha^2|\beta|^2 + \left(\frac{\sigma_u^2}{\sigma_n^2 + N\sigma_u^2}\right)^2 |\gamma|^2[|\gamma|^2 \\
& + \alpha(\gamma\delta e^{-j\omega\tau} + \gamma^*\delta^* e^{j\omega\tau}) + \alpha^2|\delta|^2] \\
& - \left(\frac{\sigma_u^2}{\sigma_n^2 + N\sigma_u^2}\right)[|\gamma|^2 N + \alpha(\gamma\delta N e^{-j\omega\tau} \\
& + \beta^*|\gamma|^2 e^{j\omega\tau}) + \alpha^2\beta^*\gamma\delta] - \left(\frac{\sigma_u^2}{\sigma_n^2 + N\sigma_u^2}\right) \\
& \times [|\gamma|^2 N + \alpha(\gamma^*\delta^* N e^{j\omega\tau} + \beta|\gamma|^2 e^{-j\omega\tau}) \\
& + \alpha^2\beta\gamma^*\delta^*] \Bigg\}. \qquad \text{(A9)}
\end{aligned}
$$

[1] B. D. Van Veen and K. M. Buckley, "Beamforming: A versatile Approach to Spatial Filtering," IEEE ASSP Mag. **5**, 4–22 (1988).
[2] H. L. Van Trees, *Optimum Array Processing*, Detection, Estimation and Modulation Theory, Part IV (Wiley Interscience, New York, 2002).
[3] B. Widrow, K. M. Duvall, R. P. Gooch, and W. C. Newman, "Signal cancellation phenomena in adaptive antennas: Causes and cures," IEEE Trans. Antennas Propag. **AP-30**, 469–478 (1982).
[4] J. F. Yang and M. Kaveh, "Coherent signal-subspace transformation beamformer," IEE Proc., 137, 267–275 (**1990**).
[5] A. F. Naguib, "Adaptive antennas for CDMA wireless networks," Ph.D thesis, Standford University, 1996.
[6] J. E. Hudson, *Adaptive Array Principles* (Institution of Electrical Engineers, London, 1981).
[7] R. A. Monzingo and T. W. Miller, *Introduction to Adaptive Arrays* (Wiley & Sons, New York, 1980).
[8] V. U. Reddy, A. Paulraj, and T. Kailath, "Performance analysis of the optimum beamformer in the presence of correlated sources and its behavior under spatial smoothing," IEEE Trans. Acoust., Speech, Signal Process. **ASSP-35**, 927–936 (1987).
[9] A. Zeira and B. Friedlander, "Interpolated array minimum variance beamforming for correlated interference rejection," *Proceedings of the International Conference on Acoustics, Speech and Signal Processing (ICASSP-96)*, May 1996, pp. 3165–3168.
[10] D. B. Ward, "Technique for broadband correlated interference rejection in microphone arrays," IEEE Trans. Speech Audio Process. **6**, 414–417 (1998).
[11] Y. Bresler, V. U. Reddy, and T. Kailath, "Optimum beamforming for coherent signal and interferences," IEEE Trans. Acoust., Speech, Signal Process., **36**, 833–843 (1988).
[12] L. L. Scharf, *Statistical Signal Processing: Detection, Estimation, and Time Series Analysis* (Addison-Wesley, Reading, MA, 1991).
[13] S. U. Pillai, *Array Signal Processing* (Springer, New York, 1989).
[14] H. Kuttruff, *Room Acoustics*, 4th ed. (Spon, London, 2000).
[15] A. W. Lam and S. Tantaratnan, *Theory and Applications of Spread-Spectrum Systems–A Self-study Course* (IEEE, NJ, 1994).
[16] J. S. Lee and L. E. Miller, *CDMA Systems Engineering Handbook* (Artech House, Boston, 1998).

Noniterative analytical formula for inverse scattering of multiply scattering point targets

Edwin A. Marengo and Fred K. Gruber
Department of Electrical and Computer Engineering, Northeastern University, 409 Dana Research Center, Boston, Massachusetts 02115

(Received 18 January 2006; revised 8 August 2006; accepted 14 August 2006)

This paper derives, in the exact framework of multiple scattering theory for point targets, a noniterative analytical formula for the nonlinear inversion of the target scattering strengths from the scattering or response matrix that can be applied after the target positions have been estimated in a previous step via, e.g., time-reversal multiple signal classification or another approach. The new formula provides a noniterative analytical alternative to the iterative numerical solution approach for the same problem presented in a recent paper [A. J. Devaney, E. A. Marengo, and F. K. Gruber, "Time-reversal-based imaging and inverse scattering of multiply scattering point targets," J. Acoust. Soc. Am. **118**, 3129–3138 (2005)]. The two methods (noniterative versus iterative) are comparatively investigated with two numerical examples. © *2006 Acoustical Society of America.*
[DOI: 10.1121/1.2354018]

PACS number(s): 43.60.Pt, 43.60.Tj [DRD] Pages: 3782–3788

I. INTRODUCTION

A two-step approach for addressing the nonlinear inverse scattering problem for multiply scattering point targets has been recently derived and numerically validated in Devaney *et al.*[1] in which time-reversal multiple signal classification (MUSIC)[2–4] is employed for the super-resolution localization of the targets while an iterative numerical algorithm is used for the nonlinear inversion of the target reflectivities or scattering strengths. The present letter investigates further the second portion of the inversion process considered in Devaney *et al.*,[1] consisting of the determination of the target scattering strengths from knowledge of the multistatic response (MSR) matrix K of the system of targets as measured using an array of transmitters and receivers once the target positions have been estimated via, e.g., time-reversal MUSIC or another approach. Specifically, a direct analytical formula is derived for the determination of the target scattering strengths from knowledge of the MSR matrix K and the target positions which are assumed to have been estimated in the previous target localization step. The formula holds for general multiple scattering conditions despite the resulting nonlinearity of the map from the target scattering strengths to the data. The proposed method is based on a form of active nulling, a topic that has received recent interest within the time-reversal community.[5,6]

The developments are given in the framework of the scalar Helmholtz operator $(\nabla^2+k_0^2)$, where ∇^2 is the Laplacian operator in three-dimensional space, k_0 represents the known wave number of the field in the background medium and $G_0(\mathbf{r}, \mathbf{r}')$ is the known background Green's function pertinent to this partial differential operator for the boundary conditions relevant to the physical situation at hand, e.g., Sommerfeld's radiation condition. Within this framework, small scatterers are treated as "mathematical" point targets described as Dirac delta functions. As was explained by Chambers and Gautesen,[7] this idealized mathematical framework contrasts with the corresponding physical, acoustic scattering theory for small scatterers (corresponding to "physical" point targets) for which the scatterer size is much smaller than the wavelength. In particular, while idealized point targets act only as monopoles (scattering spherically symmetric waves only), physical point targets radiate both monopolar and dipolar fields, which gives a total of four radiation modes (nontrivial singular values of the respective scattering matrix) per point target (a monopole and three dipoles). Yet for certain special cases (see Chambers and Gautesen[7] as well as Refs. 5–7 in that paper), the monopole mode dominates, and it is in this spirit, which has been adopted before,[1–4] that the present formulation is derived.

The developments assume $M \leq \min(N_t, N_r)$ where M is the number of targets and N_t and N_r are the number of transmit and receive elements of the array, respectively, so that if the conditions for applicability of the time-reversal approach [in particular,[1,3] $M \leq \min(N_t, N_r)$ and $M < \max(N_t, N_r)$] hold, then the full program of inverse scattering can be carried out via the two-step approach of first localizing via time-reversal MUSIC and later inverting the scattering strengths via the formula of the present work.

That the singular system of the MSR matrix K contains information about the target scattering strengths is obvious and has been the subject of well-known investigations.[8,9] Extraction of useful general features (not of the actual scattering strength) is addressed in Colton and Kress.[9] In contrast, the present research is aimed at extracting the individual scattering strengths. For Born-approximable targets this problem can be solved trivially once the target positions have been found.[1,2] On the contrary, for the general multiple scattering regime the associated inversion is less straightforward due to the resulting nonlinearity of the reflectivities-to-MSR matrix mapping which traditionally would be handled via nonlinear optimization.[10] Despite this nonlinearity, the latter problem is solved in this paper analytically, noniteratively (unlike in Devaney *et al.*[1] which adopts the more conven-

 © 2006 Acoustical Society of America

tional numerical iterations route). Here it is worthwhile pointing out that the noniterative solution of nonlinear inverse problems is a topic of much importance[11] which remains open in inverse scattering of general scatterers if one seeks to reconstruct not only target support (which can be done via, e.g., the factorization and MUSIC methods,[12–14] the linear sampling method,[15] and so on) *but also* constitutive properties or scattering potential. It is the latter, less understood problem, which is of interest in this work. The derived results provide a novel noniterative framework which despite being emphasized here for the canonical case of point targets can also open new strategies for noniterative computational inverse scattering of certain large scatterers whose response can be modeled using a computational grid representing dominant scattering centers within the scatterer.

II. DIRECT AND INVERSE MULTIPLE SCATTERING THEORY

A. Basic relations

Consider, within the scalar Helmholtz operator framework outlined in the introduction, the inverse scattering problem of deducing the unknown positions $\mathbf{X}_m, m=1,2,\ldots,M$ and scattering strengths $\tau_m, m=1,2,\ldots,M$ of a collection of point scatterers from knowledge of the associated scattering matrix which when measured using an array of N_t point transmitters at positions $\mathbf{R}_t(j), j=1,2,\ldots,N_t$ and of N_r point receivers at positions $\mathbf{R}_r(l), l=1,2,\ldots,N_r$, can be shown to reduce to the $N_r \times N_t$ MSR matrix defined by[1,2,16]

$$K=\sum_{m=1}^{M} \tau_m g_{0,r}(\mathbf{X}_m)\psi_t^T(\mathbf{X}_m)=\sum_{m=1}^{M} \tau_m \psi_r(\mathbf{X}_m) g_{0,t}^T(\mathbf{X}_m), \quad (1)$$

where T denotes the transpose, where $g_{0,t}(\mathbf{X})$ is the $N_t \times 1$ transmit background Green's function vector defined by

$$g_{0,t}(\mathbf{X}) = \{G_0[\mathbf{X},\mathbf{R}_t(1)], G_0[\mathbf{X},\mathbf{R}_t(2)], \ldots, G_0[\mathbf{X},\mathbf{R}_t(N_t)]\}^T,$$

while $g_{0,r}(\mathbf{X})$ is the $N_r \times 1$ receive background Green's function vector defined by

$$g_{0,r}(\mathbf{X}) = \{G_0[\mathbf{R}_r(1),\mathbf{X}], G_0[\mathbf{R}_r(2),\mathbf{X}], \ldots, G_0[\mathbf{R}_r(N_r),\mathbf{X}]\}^T,$$

and where

$$\psi_t(\mathbf{X}_m)=g_{0,t}(\mathbf{X}_m)+\sum_{m' \neq m} \tau_{m'} G_0(\mathbf{X}_m,\mathbf{X}_{m'})\psi_t(\mathbf{X}_{m'})$$

$$\psi_r(\mathbf{X}_m)=g_{0,r}(\mathbf{X}_m)+\sum_{m' \neq m} \tau_{m'} \psi_r(\mathbf{X}_{m'}) G_0(\mathbf{X}_{m'},\mathbf{X}_m). \quad (2)$$

It is worthwhile to briefly discuss the meaning of relations (1) and (2) to place them in the particular deterministic context germane to the present discussion which contrasts with the original random media-oriented use of the same relations in the well-known works of Foldy[17] and Lax[18] on multiple scattering of waves, in particular, Eqs. (7) and (8) in Foldy,[17] and Eqs. (3.7) and (3.8) in Lax,[18] which are applicable deterministically, i.e., per realization of a statistical ensemble of targets, and which are used as a starting point for subsequent statistical treatment of multiple scattering in those papers. The same equations correspond to Eqs. 3 and 4 in Snieder and Scales,[16] Eqs. (14-7a) and (14-7b) in Ishimaru,[19] and Eqs. (7.2.5)–(7.2.17) in Tsang *et al.*[20] In the present study, as in the above mentioned references,[16–20] the vector ψ_t above corresponds to the "effective" or "exciting" field, in particular, the "final" exciting or incident field at the different scatterers after the multiple scattering interactions among scatterers have taken place. A similar interpretation applies to the receive counterpart ψ_r. The vectors ψ_r and ψ_t are auxiliary and, in particular, it is only after substitution of these vectors in Eq. (1) that the scattering or MSR matrix K which is the quantity of interest is fully determined. The forward scattering characterization given in Eqs. (1) and (2) is exact and can be generalized to the vector case readily.[20] For further details the reader is referred to Ishimaru,[19] pp. 246–248, and Tsang *et al.*,[20] pp. 376–382.

The map from the target scattering strengths $\tau_m, m=1,2,\ldots,M$ to the MSR matrix K is readily seen from Eqs. (1) and (2) to be nonlinear. This is so even if the target positions $\mathbf{X}_m, m=1,2,\ldots,M$ have been previously determined. The central goal of the next section is to show that despite this nonlinearity there exists an explicit reconstruction formula that yields in a single step the sought-after target scattering strengths $\tau_m, m=1,2,\ldots,M$ from knowledge of the MSR matrix K and the target positions $\mathbf{X}_m, m=1,2,\ldots,M$. The formula is derived in two complementary forms (the roles of the transmit and receive signals in one being the reverse of those in the other).

B. Noniterative inversion formula for the scattering strengths

The following discussion assumes that $M \leq \min(N_t, N_r)$. As shown in Devaney,[21] under these conditions, and with the exception of rare configurations, the receive background Green's function vectors $g_{0,r}(\mathbf{X}_m), m=1,2,\ldots,M$ form a linearly independent set so that

$$\sum_{m=1}^{M} \alpha_m g_{0,r}(\mathbf{X}_m)=0 \quad \text{if and only if } \alpha_m=0 \quad (3)$$

and, similarly, the transmit background Green's function vectors $g_{0,t}(\mathbf{X}_m), m=1,2,\ldots,M$ also form a linearly independent set so that

$$\sum_{m=1}^{M} \alpha_m g_{0,t}(\mathbf{X}_m)=0 \quad \text{if and only if } \alpha_m=0. \quad (4)$$

The MSR matrix K maps $\mathrm{C}^{N_t} \rightarrow \mathrm{C}^{N_r}$ where C^{N_t} and C^{N_r} represent N_t- and N_r-dimensional spaces of complex N_t and N_r tuples, respectively. To arrive at the desired formula, consider an "active target isolation," consisting of generating a transmit array vector $v=K^+ g_{0,r}(\mathbf{X}_1)+u \in \mathrm{C}^{N_t}$, where $K^+: \mathrm{C}^{N_r} \rightarrow \mathrm{C}^{N_t}$ is the Moore-Penrose generalized inverse of K (see, e.g., pp. 88 and 247–250 in Bertero and Boccacci[22]), in particular, $K^+=\Sigma_{m=1}^{M} \sigma_m^{-1} \rho_m \Psi_m^{\dagger}$ where $\dagger$ denotes complex adjoint (thus $\psi_m^{\dagger}=\psi_m^{T*}$ where $*$ denotes complex conjugate), and where $\sigma_m, m=1,2,\ldots,M$ are the nonzero singular values

[the rank of K being M (Refs. 1 and 21)], ρ_m are the right singular vectors and Ψ_m are the left singular vectors associated to the singular value decomposition of K, in particular, $K=\Sigma_{m=1}^{M}\sigma_m\Psi_m\rho_m^\dagger$, and u is any transmit signal in the null space of the MSR matrix K which is nonempty if $M<N_t$ and, in particular,[1,2] is the orthogonal complement of $\mathrm{Span}[g_{0,t}(\mathbf{X}_m), m=1,2,\ldots,M]$ in C^{N_t}. In particular, $v'=K^+g_{0,r}(\mathbf{X}_1)$ is the unique vector of minimum L^2 norm obeying *exactly* $Kv'=g_{0,r}(\mathbf{X}_1)$ (known as the normal solution[22]) while $v=K^+g_{0,r}(\mathbf{X}_1)+u$ where u is in the null space of K is the most general vector obeying the same equation. Then vector v, when used as excitation at the transmit array, yields an output Kv at the receive array equal to the background Green's function vector $g_{0,r}(\mathbf{X}_1)$ corresponding to target 1. Thus the entire received signal associated to this vector arises from target 1 only, a desirable property in isolating the effect of that target alone. Using expression (1) for the MSR matrix K one can express this in the convenient form

$$Kv=\sum_{m=1}^{M}\tau_m g_{0,r}(\mathbf{X}_m)\psi_t^T(\mathbf{X}_m)[K^+g_{0,r}(\mathbf{X}_1)+u]$$
$$=\sum_{m=1}^{M}\tau_m g_{0,r}(\mathbf{X}_m)\psi_t^T(\mathbf{X}_m)K^+g_{0,r}(\mathbf{X}_1)=g_{0,r}(\mathbf{X}_1). \quad (5)$$

In view of Eq. (3), expression (5) further translates for nontrivial $\tau_m, m=1,2,\ldots,M$ into

$$\tau_1\psi_t^T(\mathbf{X}_1)K^+g_{0,r}(\mathbf{X}_1)=1$$

$$\psi_t^T(\mathbf{X}_m)K^+g_{0,r}(\mathbf{X}_1)=0 \quad m=2,3,\ldots,M. \quad (6)$$

By applying Eq. (2) to the vector $\psi_t(\mathbf{X}_1)$, and substituting the thus obtained result in the top equation in Eq. (6) while using the bottom equation in Eq. (6) one arrives at the more convenient statement

$$\tau_1 g_{0,t}^T(\mathbf{X}_1)K^+g_{0,r}(\mathbf{X}_1)=1 \quad (7)$$

involving only the known MSR matrix K and the known background Green's function vectors $g_{0,r}(\mathbf{X}_1)$ and $g_{0,t}(\mathbf{X}_1)$ evaluated at the known target position $\mathbf{X}_1$, from which the unknown coefficient τ_1 can be readily (and uniquely) computed. Equation (7), with the substitution $1\to m$, is the sought-after reconstruction formula, in particular

$$\tau_m=[g_{0,t}^T(\mathbf{X}_m)K^+g_{0,r}(\mathbf{X}_m)]^{-1}. \quad (8)$$

A complementary approach can be established that is based on the adjoint $K^\dagger=K^{T*}$ of K or, equivalently, on the transpose K^T of K, instead. Thus if $V\in\mathrm{C}^{N_r}$ is a receive array vector of the form $V=(K^T)^+g_{0,t}(\mathbf{X}_1)+U$ where U is in the null space of the transpose K^T of K (which is nonempty if $M<N_r$), then $K^TV=g_{0,t}(\mathbf{X}_1)$, which according to Eq. (1) implies

$$\sum_{m=1}^{M}\tau_m g_{0,t}(\mathbf{X}_m)\psi_r^T(\mathbf{X}_m)(K^T)^+g_{0,t}(\mathbf{X}_1)=g_{0,t}(\mathbf{X}_1), \quad (9)$$

which in view of Eq. (4) implies for nontrivial τ_m, $m=1,2,\ldots,M$

$$\tau_1\psi_r^T(\mathbf{X}_1)(K^T)^+g_{0,t}(\mathbf{X}_1)=1,$$

$$\psi_r^T(\mathbf{X}_m)(K^T)^+g_{0,t}(\mathbf{X}_1)=0 \quad m=2,3,\ldots,M. \quad (10)$$

Finally, it follows from Eq. (10) and the bottom of the Foldy-Lax model expression Eq. (2) that

$$\tau_1=[g_{0,r}^T(\mathbf{X}_1)(K^T)^+g_{0,t}(\mathbf{X}_1)]^{-1}, \quad (11)$$

which implies the sought-after complementary formula

$$\tau_m=[g_{0,r}^T(\mathbf{X}_m)(K^T)^+g_{0,t}(\mathbf{X}_m)]^{-1}. \quad (12)$$

Inversion formulas (7) and (12) are exact in the sense that they yield no error under no noise. In particular, under no noise and the holding of the time-reversal MUSIC conditions the target positions $\mathbf{X}_m, m=1,2,\ldots,M$ can be determined (in the implicit previous target localization step) without error[1,2] and when these values are used in Eqs. (7) and (12) then the scattering strengths are found also perfectly, as desired. The effect of noise in the data is considered numerically next.

It is important to briefly discuss connections to the work of Shi and Nehorai[10] who investigated, under spatially white Gaussian noise, maximum likelihood estimation of scattering parameters of multiply scattering point targets. For the noisy data matrix $Y=K+W$ where the entries of the $N_r\times N_t$ noise matrix W are zero-mean jointly circularly symmetric complex Gaussian distributed random variables, the maximum likelihood estimates $\hat{\mathbf{X}}\equiv[\hat{\mathbf{X}}_1,\hat{\mathbf{X}}_2,\ldots,\hat{\mathbf{X}}_M]^T$ and $\hat{\tau}\equiv[\hat{\tau}_1,\hat{\tau}_2,\ldots,\hat{\tau}_M]^T$ of vectors describing, respectively, the positions and scattering strengths of all targets are found via the simultaneous minimization[10]

$$\hat{\mathbf{X}},\hat{\tau}=\mathrm{argmin}_{\tilde{\mathbf{X}},\tilde{\tau}}\|Y-\tilde{K}(\tilde{\mathbf{X}},\tilde{\tau})\|_F^2, \quad (13)$$

where F denotes the Frobenius norm and where the matrix $\tilde{K}(\tilde{\mathbf{X}},\tilde{\tau})$ is given by Eqs. (1) and (2) after the substitutions $K\to\tilde{K}$ and $\mathbf{X}_m\to\tilde{\mathbf{X}}_m, m=1,2,\ldots,M$ and $\tau_m\to\tilde{\tau}_m, m=1,2,\ldots,M$. Since the maximum likelihood estimator is known to be asymptotically optimal[23] (asymptotically attaining the Cramer-Rao lower bound for the variance) it will in general outperform the current approach which is not guaranteed to achieve that bound. On the other hand, the estimate of the scattering strengths in Eq. (13) requires exhaustive search in the high-dimensional parameter space of all target positions and all target strengths which for three spatial dimensions and complex-valued strengths corresponds to an exhaustive search involving $5M$ real parameters. This is more computationally intensive than the respective time-reversal MUSIC search in only three real parameters for the target localization part of the inversion. Note that the approach described in Eq. (13) is essentially one of nonlinear optimization and that its demanding computational intensity remains even in the absence of noise. This contrasts with the approach of the present paper which is a direct (noniterative, nonexhaustive search) formula for the target strengths after the target locations have been suitably estimated, e.g., by time-reversal MUSIC, or another method. Furthermore, the estimates of the reflectivities obtained from the noniterative approach can be used as a particularly good starting point for a nonlinear optimization technique solving Eq. (13).

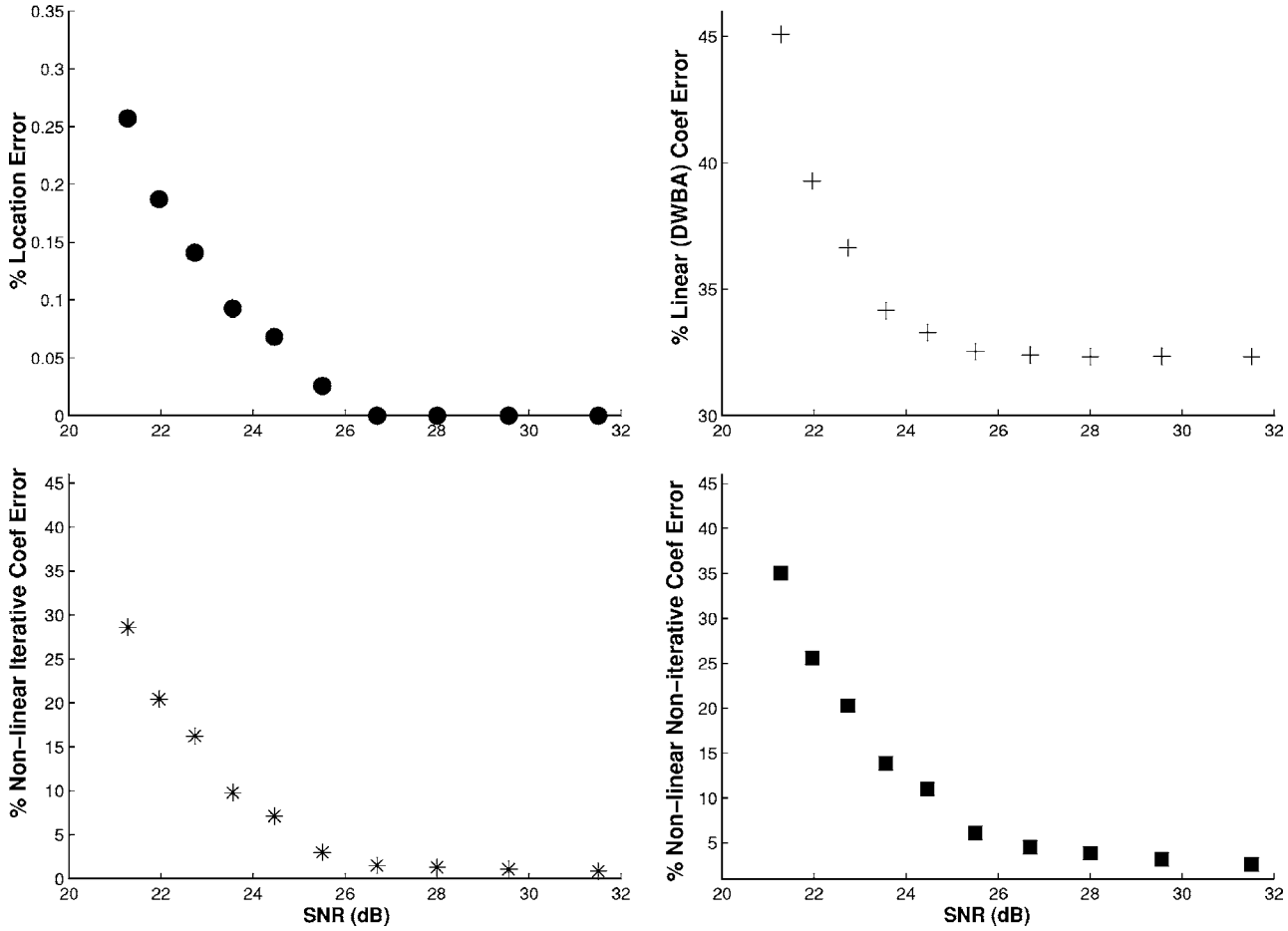

FIG. 1. Plots of the target location and scattering strength estimation errors for the noniterative inverse scattering method developed in this letter as well as the iterative method presented in Devaney *et al.*[1] For reference, the estimation errors on target scattering strength for the generally inapplicable Born approximation formula (indicated "DWBA") are also given. The errors are averages over 1000 repetitions.

III. NUMERICAL ILLUSTRATION

In this section the proposed noniterative nonlinear inversion algorithm for the reconstruction of the scattering strengths described in the previous section, in particular, the version of the formula given in Eq. (8), is tested and compared with the iterative one described in Devaney *et al.*[1] as well as with the respective reconstruction formula assuming the Born approximation.[1] The experiments are based on the same simulation geometry in two-dimensional free space presented in Devaney *et al.*[1] which considers four ($M=4$) point scatterers under interrogation by a set of seven ($N_t=N_r=7$) coincident ("same transmit, same receive") point transceivers. The transceiver array is a uniform linear array centered along the x axis at $z=0$ and having six wavelength interelement separation, where the wavelength$=1$. The four targets are located in a Cartesian grid at positions $(-2.25, -14.75)$, $(-0.25,-14.75)$, $(0.75,-15.75)$, and $(2.75,-15.75)$, all in units of a wavelength. All targets have unit-amplitude target scattering strengths, i.e., $\tau_m=1, m=1,2,3,4$ (but these values will be modified later in a complementary, second example). Because of the chosen target positions and scattering strengths there is strong multiple scattering between the targets, as shown in the results. As in Devaney *et al.*[1] the accuracy of the estimates was measured by means of a normalized percent error defined by

$$E = 100 \cdot \frac{\|\hat{\tau} - \tau\|}{\|\tau\|},$$

where $\|\cdot\|$ denotes L^2 (or 2) vector norm, $\hat{\tau}$ is a vector with the estimated reflectivities, and τ is a vector with the actual values. In the second example of this section, on the other hand, the errors of each target are addressed individually.

Under perfect data conditions (results not shown) both nonlinear methods yield errors which appear to be negligible, particularly relative to those of the linear approximation method which presents significant error, i.e., due to strong multiple scattering the Born approximation model is inapplicable. Figure 1 shows plots of the target location (estimated by means of the time-reversal MUSIC approach) and scattering strength estimation errors in the presence of additive white Gaussian noise. The errors are averages over 1000 repetitions. Note that the iterative approach yields slightly better results than the noniterative solution, which may be due to error canceling effects across iterations. Also note that below the 26 dB signal-to-noise ratio (SNR) level there are two sources of error affecting the algorithms: the error in the estimated positions and the noise in the MSR matrix. To isolate the effect of the noise in the data from the effect of the errors in the estimated target positions the experiments were repeated assuming the positions are known. The corre-

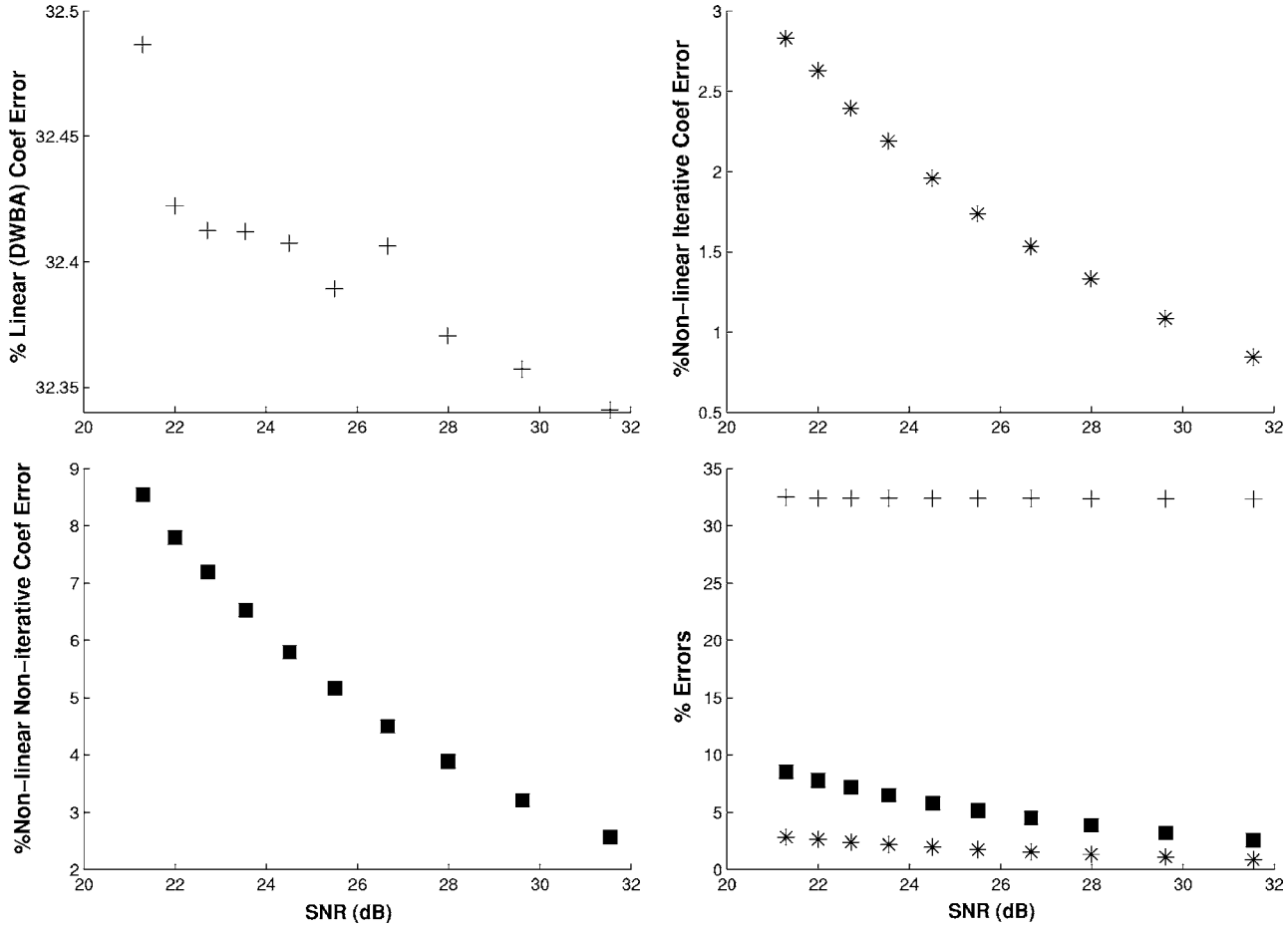

FIG. 2. Plots for the scattering strength estimation errors assuming the correct positions of the targets are known. Three algorithms are illustrated: the noniterative nonlinear inversion formula of this work, the iterative nonlinear inversion method of Devaney *et al.*,[1] and the generally inapplicable Born approximation formula. The errors are averages over 1000 repetitions. For comparison, all the results are put together in the plot at the bottom right.

sponding plots are presented in Fig. 2. The lower right plot shows a comparison of the three algorithms. As expected, in this case the level of errors is lower, and this is more noticeable for low SNR. Again the iterative algorithm exhibits slightly better performance than the noniterative one. But the iterative algorithm requires many iterations (more than 80) for convergence in these numerical experiments.

Among other numerical validation examples, the computer simulation study also considered, for the same general configuration of the previous example, targets with reflectivities given by $\tau_m = m, m = 1,2,3,4$ [target 1 corresponding to position $(-2.25, -14.75)$, target 2 corresponding to $(-0.25, -14.75)$, and so on]. It was found that in this case the iterative technique as proposed in Devaney *et al.*[1] diverged even in the absence of noise. This probably occurs because in that approach the initial estimate is based on the Born approximation which deteriorates as the values of the reflectivities increase. For this reason in this second example the values of the noniterative approach were used as initial estimates, yielding the results in Fig. 3. They show that for high SNR the iterative approach estimates have a lower percentage of error than those of the non-iterative approach. However, and surprisingly, for lower SNR the iterative approach breaks down and the noniterative approach performs better.

IV. CONCLUSION

The nonlinear inverse problem of estimating the target scattering amplitudes or reflectivities $\tau_m, m = 1,2,\ldots,M$ after the target locations $\mathbf{X}_m, m = 1,2,\ldots,M$ have been found consists of the inversion of the nonlinear map of the scattering strengths τ_m to the MSR matrix K as specified in Eqs. (1) and (2). This nonlinear inversion has been tackled in a recent paper[1] by means of an iterative numerical algorithm. Given the nonlinear nature of the problem, it is not obvious that under certain conditions it might be actually possible to carry out the inversion via an explicit formula, in particular, a noniterative analytical algorithm, in place of iterative numerical approaches such as the one discussed in Devaney *et al.*[1] On the other hand, a noniterative analytical approach is desirable, e.g., to clarify conditions for existence and uniqueness of the solution, and to establish a reference benchmark as well as novel conceptual tools to handle similar nonlinear inverse problems in wave propagation.

This letter showed that, surprisingly, despite the nonlinearity of the associated forward mapping, such a reconstruction formula does exist, and can be implemented rather trivially once the target positions have been properly estimated by other methods. Two forms of the formula [Eqs. (8) and (12)] were derived. The performance of the approach under

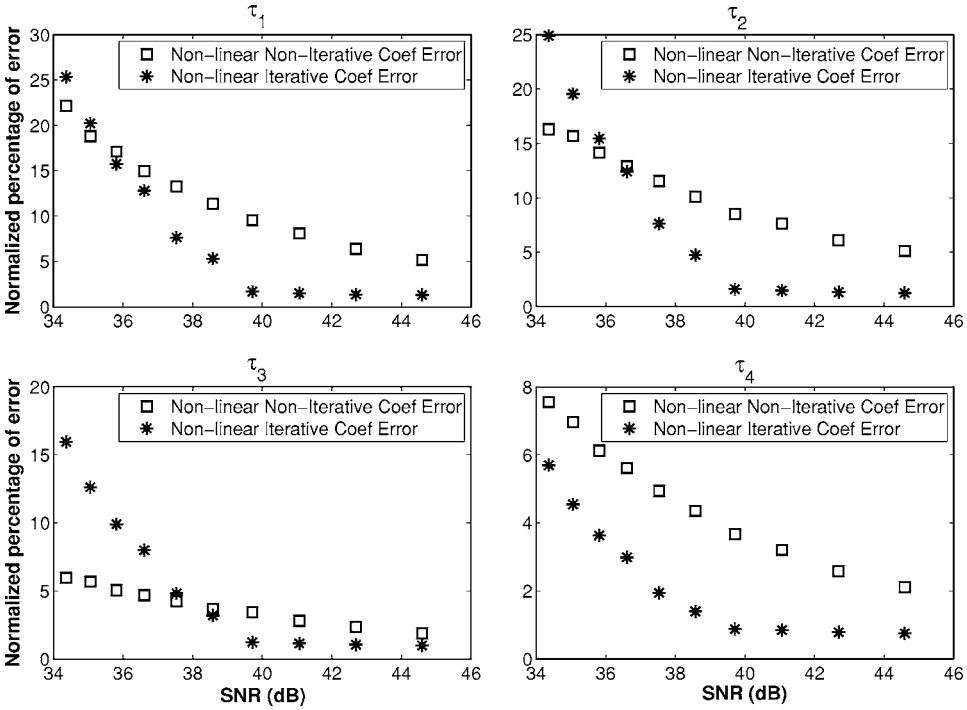

FIG. 3. Plots for the scattering strength estimation errors of four targets with scattering strengths given by $\tau=(\tau_1=1,\tau_2=2,\tau_3=3,\tau_4=4)$ assuming the correct positions of the targets are known. Two algorithms are illustrated: the noniterative nonlinear inversion formula of this work and the iterative nonlinear inversion method of Devaney *et al.*[1] using as initial value the noniterative estimate. The errors are averages over 1000 repetitions.

realistic noise was studied numerically. If the conditions for applicability of the time-reversal MUSIC method of the previous, target localization step hold, then the full inverse problem can be solved by that method combined with the formula of this work. The formula yields perfect results under no noise. It was found numerically that, expectationally, i.e., over many realizations, for noisy data the iterative numerical method of Devaney *et al.*[1] and the noniterative formula of this work perform comparably; yet in certain situations one of the two methods appears to perform better, with the main promise of the noniterative formula residing in strongly scattering and very noisy conditions as was illustrated with the last numerical example. The overall conclusion is that the noniterative approach, which is important both by itself and as a good first guess for the iterative approach, yields comparable performance relative to the iterative method while facilitating a clearer analytical characterization and being apparently more robust.

ACKNOWLEDGMENTS

This work was supported by the Air Force Office of Scientific Research under Grant No. FA9550-06-01-0013, and is affiliated with CenSSIS, the Center for Subsurface Sensing and Imaging Systems, under the Engineering Research Centers Program of the National Science Foundation (Award No. EEC-9986821).

[1]A. J. Devaney, E. A. Marengo, and F. K. Gruber, "Time-reversal-based imaging and inverse scattering of multiply scattering point targets," J. Acoust. Soc. Am. **118**, 3129–3138 (2005).
[2]F. K. Gruber, E. A. Marengo, and A. J. Devaney, "Time-reversal imaging with multiple signal classification considering multiple scattering between the targets," J. Acoust. Soc. Am. **115**, 3042–3047 (2004).
[3]S. K. Lehman and A. J. Devaney, "Transmission mode time-reversal super-resolution imaging," J. Acoust. Soc. Am. **113**, 2742–2753 (2003).
[4]C. Prada and J. L. Thomas, "Experimental subwavelength localization of scatterers by decomposition of the time reversal operator interpreted as a covariance matrix," J. Acoust. Soc. Am. **114**, 235–243 (2003).
[5]A. G. Cepni and D. D. Stancil, "Single antenna microwave nulling using time-reversal techniques," Microwave Symposium Digest, 2005 IEEE International Microwave Theory and Techniques Symposium, (June 12-17, 2005), pp. 1723–1726; A. G. Cepni, D. D. Stancil, J.-G. Zhu, and Y. Jiang, "Microwave signal nulling using multiple antennas and time-reversal methods," *Proceedings of the Vehicular Technology Conference*, Dallas, Texas, (Sept. 25-28, 2005), pp. 1274–1278.
[6]J. M. F. Moura, Y. Jin, D. Stancil, J.-G. Zhu, A. Cepni, Y. Jiang, and B. Henty, "Single antenna time reversal adaptive interference cancellation," *ICASSP 2005* (IEEE Cat. No. 05CH37625), Vol. 4, Part 4 (March 18-23, 2005), p. iv/1121–4.
[7]D. H. Chambers and A. K. Gautesen, "Time reversal for a single spherical scatterer," J. Acoust. Soc. Am. **109**, 2616–2624 (2001).
[8]M. Cheney, "The linear sampling method and the MUSIC algorithm," Inverse Probl. **17**, 591–595 (2001).
[9]D. Colton and R. Kress, "Eigenvalues of the far field operator for the Helmholtz equation in an absorbing medium," SIAM J. Appl. Math. **55**, 1724–1735 (1995).
[10]G. Shi and A. Nehorai, "Maximum likelihood estimation of point scatterers for computational time-reversal imaging," Commun. Inf. Syst. **5**, 227–256 (2005).
[11]J. L. Mueller, S. Siltanen, and D. Isaacson, "A direct reconstruction algorithm for electrical impedance tomography," IEEE Trans. Med. Imaging **21**, 555–559 (2002).
[12]A. Kirsch, "The MUSIC algorithm and the factorization method in inverse scattering theory for inhomogeneous media," Inverse Probl. **18**, 1025–1040 (2002).
[13]A. Kirsch, "Characterization of the shape of a scattering obstacle using the spectral data of the far field operator," Inverse Probl. **14**, 1489–1512 (1998).
[14]S. Hou, K. Solna, and H. Zhao, "Imaging of location and geometry for extended targets using the response matrix," J. Comput. Phys. **199**, 317–338 (2004).
[15]D. Colton and A. Kirsch, "A simple method for solving inverse scattering problems in the resonance region," Inverse Probl. **12**, 383–393 (1996).
[16]R. K. Snieder and J. A. Scales, "Time-reversed imaging as a diagnostic of wave and particle chaos," Phys. Rev. E **58**, 5668–5675 (1998).
[17]L. L. Foldy, "The multiple scattering of waves: I. General theory of isotropic scattering by randomly distributed scatterers," Phys. Rev. **67**, 107–119 (1945).
[18]M. Lax, "Multiple scattering of waves," Rev. Mod. Phys. **23**, 287–310

(1951).
[19]A. Ishimaru, *Wave Propagation and Scattering in Random Media* (IEEE Press, New York, 1997).
[20]L. Tsang, J. A. Kong, K.-H. Ding, and C. O. Ao, *Scattering of Electromagnetic Waves: Numerical Simulations* (Wiley, New York, 2001).
[21]A. J. Devaney, "Super-resolution processing of multi-static data using time-reversal and MUSIC," unpublished manuscript available in the website www.ece.neu.edu/faculty/devaney.
[22]M. Bertero and P. Boccacci, *Introduction to Inverse Problems in Imaging* (Institute of Physics Publishing, Bristol, 1998).
[23]S. M. Kay, *Fundamentals of Statistical Signal Processing: Estimation Theory* (Prentice Hall PTR, New Jersey, 1993).

A nonlinear finite-element model of the newborn ear canal

Li Qi and Hengjin Liu
Department of BioMedical Engineering, McGill University, Montréal H3A 2B4, Canada

Justyn Lutfy
Department of Anatomy and Cell Biology, McGill University, Montréal H3A 2B4, Canada

W. Robert J. Funnell[a)]
Departments of BioMedical Engineering and Otolaryngology, McGill University, Montréal H3A 2B4, Canada

Sam J. Daniel
Department of Otolaryngology, McGill University, Montréal H3H 1P3, Canada

(Received 1 March 2006; revised 20 September 2006; accepted 22 September 2006)

A three-dimensional nonlinear finite-element model of a 22-day-old newborn ear canal is presented. The geometry is based on a clinical x-ray CT scan. A nonlinear hyperelastic constitutive law is applied to model large deformations. The Young's modulus of the soft tissue is found to have a significant effect on the ear-canal volume change, which ranges from approximately 27% to 75% over the static-pressure range of ±3kPa. The effects of Poisson's ratio and of the ratio $C_{10}:C_{01}$ in the hyperelastic model are found to be small. The volume changes do not reach a plateau at high pressures, which implies that the newborn ear-canal wall would not be rigid in tympanometric measurements. The displacements and volume changes calculated from the model are compared with available experimental data. © *2006 Acoustical Society of America.*
[DOI: 10.1121/1.2363944]

PACS number(s): 43.64.Bt, 43.64.Ha [WPS] Pages: 3789–3798

I. INTRODUCTION

Children whose hearing loss is identified and corrected within six months of birth are likely to develop better language skills than children whose hearing loss is detected later (Yoshinaga-Itano *et al.*, 1998). It is recommended that all infants be screened for hearing loss before the age of 3 months (NIDCD, 1993; Joint Committee on Infant Hearing, 2000).

Although hearing loss is one of the most frequently occurring disorders in newborns, early diagnosis is difficult. Auditory brain-stem response screening tests and otoacoustic emissions tests can provide objective hearing-loss assessments. Neither test, however, can distinguish conductive hearing loss, which in newborns is often transient, from sensorineural hearing loss. The two types of hearing loss require different medical approaches.

Tympanometry is a fast and simple hearing test routinely used in clinics for the evaluation of conductive hearing loss. Tympanometry involves the measurement of the acoustic admittance of the middle ear in the presence of a range of static pressures. In order to obtain an accurate result for the middle-ear admittance as seen from the tympanic membrane, the complex admittance measured at the probe tip must be adjusted to compensate for the complex admittance due to the ear-canal volume between the probe tip and the tympanic membrane. The accuracy of the middle-ear admittance estimate therefore relies on obtaining an accurate estimate of the admittance of the enclosed air volume.

Studies have shown that middle-ear admittance measurements differ significantly between newborns and adults, in both low-frequency (226 Hz) and higher-frequency (e.g., 1 kHz) tympanometry (Paradise *et al.*, 1976); Holte *et al.*, 1990, 1991; Keefe *et al.*, 1993; Keefe and Levi, 1996; Shahnaz, 2002; Polka *et al.*, 2002; Margolis *et al.*, 2003; Margolis and Hunter, 1999). Holte *et al.* (1990) measured ear-canal wall movement in newborns of different ages and found that the diameter of the ear canal can change by up to 70% in response to high static pressures. Keefe *et al.* (1993) measured ear-canal reflectance over a wide frequency range. They concluded that significant differences between newborn and adult tympanograms are presumably due in part to the incomplete development of the newborn ear-canal wall and tympanic ring.

The outer ear and the middle ear in human newborns are not completely mature at birth, and various anatomical and physiological changes occur between birth and adulthood (Saunders *et al.*, 1983; Eby and Nadol, 1986). The tympanic membrane and the ossicles have reached adult size at birth but the external auditory canal is much smaller than its adult size. In adults the tympanic membrane lies at about a 45° angle from the horizontal, while in newborns it is nearly horizontal. The tympanic ring is not completely developed until the age of two years (Saunders *et al.*, 1983). Furthermore, in adults, the inner two thirds of the ear-canal wall are bony and the outer one third is composed of soft tissue; in

[a)]Author to whom correspondence should be addressed; electronic mail: robert.funnell@mcgill.ca

newborns, the ear canal is surrounded almost entirely by soft tissue (McLellan and Webb, 1957). This lack of ossification presumably allows the external ear canal to change volume significantly in response to large static pressures.

Although the importance of obtaining accurate ear-canal volume-change measurements has been acknowledged, few studies have been conducted to date. Owing to ethical issues and procedural problems it is difficult to measure newborn ear-canal volume change experimentally. The finite-element method is an invaluable research and design tool as it can be used to simulate the behavior of structures in conditions that cannot be achieved experimentally. Since the first finite-element model of the tympanic membrane was developed (Funnell and Laszlo, 1978), this method has been widely used to investigate the behavior of both human and animal ears (e.g., Wada *et al.*, 1992; Funnell, 1996; Funnell and Decraemer, 1996; Koike, 2002; Gan *et al.*, 2002, 2004; Elkhouri *et al.*, 2006). To the best of our knowledge, no finite-element model of the newborn ear canal has been produced until now.

The purpose of this study is to use modeling to investigate newborn ear-canal volume changes under high static pressures. We present here a nonlinear three-dimensional model of a healthy newborn ear canal. The geometry of the model is based on a clinical x-ray computed tomography (CT) scan of the ear of a 22-day-old newborn.

We chose a 22-day-old newborn ear canal for two reasons. First, during the first few days of a newborn's life, the outer ear may contain debris and the middle-ear cavity may be filled with amniotic fluid (Eavey, 1993). Newborns are therefore likely to present with conductive hearing loss during the immediate postnatal period, followed by an improvement in hearing as the debris and fluid are cleared. Consequently, hearing-screening tests conducted shortly after birth may lead to high false-positive rates. Second, as part of its Early Hearing Detection and Intervention program (EHDI, 2003), the American Academy of Pediatrics recommends that all infants be screened for hearing loss before the age of one month. For these reasons, a 22-day-old newborn is an appropriate study subject.

A hyperelastic constitutive law is applied to model soft tissue undergoing large deformations. Plausible ranges for material-property values are based on data from the literature. Model results are then compared with available experimental measurements.

II. MATERIALS AND METHODS

A. Three-dimensional reconstruction

The geometry of the model is based on a clinical x-ray CT scan (GE LightSpeed16, Montréal Children's Hospital) of the right ear of a 22-day-old newborn (study number A07-M69-02A, McGill University Institutional Review Board). The infant had a unilateral congenital atresia (absent external ear canal) on the left side. The external and middle ear on the right side was found to be entirely normal anatomically and exhibited normal hearing. The CT scan contained 47 horizontal slices, numbered from superior to inferior. The scan had 0.187 mm pixels and a slice spacing of 0.625 mm. The ear canal is present in slices 34–42. Figure 1 shows slices 11, 34, 37, 40, 42, and 47. The region surrounding the right ear canal in Fig. 1 (slice 37) has been enlarged, segmented, and labeled in Fig. 2. Figure 2 includes the ear canal itself, the soft tissue surrounding the ear canal, the tympanic membrane, the ossicles, the temporal bones, and the simulated probe tip. Rather than including the entire head in the model, the anterior, posterior, and medial surfaces were positioned so as to include the temporal bone and a generous amount of soft tissue. More details are given in Sec. III A.

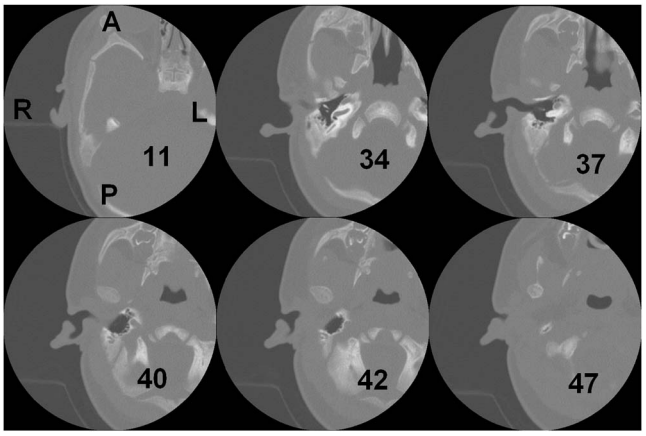

FIG. 1. X-ray CT data for 22-day newborn. Slices 11, 34, 37, 40, 42, and 47 are shown. Slices 34–42 include the ear canal. A is anterior; P is posterior; R is right; L is left.

In this study we used 37 slices, from slice 11 to slice 47. From slice 11 to slice 33, every second slice was used; from 34 to 47, every slice was used. A locally developed program, *Fie*, was used to segment the cross sections of the temporal bone and soft tissue, as shown in Fig. 2. The contours were imported into a three-dimensional surface-triangulation program, *Tr*3, and the surface was generated by optimally connecting contours in adjacent slices. The surface model is shown in Fig. 3. Both *Fie* and *Tr*3 are available at http://audilab.bmed.mcgill.ca/~funnell/AudiLab/sw/. Figure 3(a) is

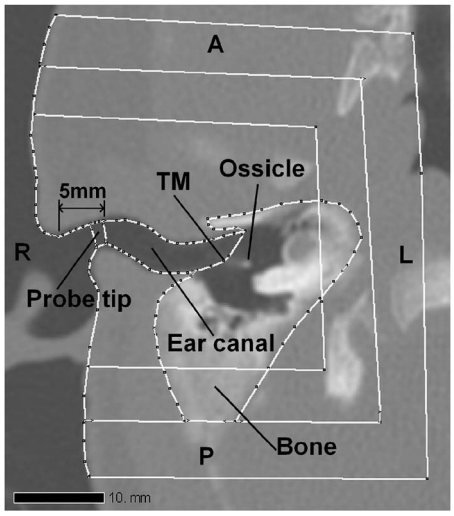

FIG. 2. Slice 37, showing segmented structures. TM is tympanic membrane. The probe tip is positioned at 5 mm from the entrance of the ear canal. A is anterior; P is posterior; R is right; L is left. Three different sizes of models are shown; more details are given in Sec. III A.

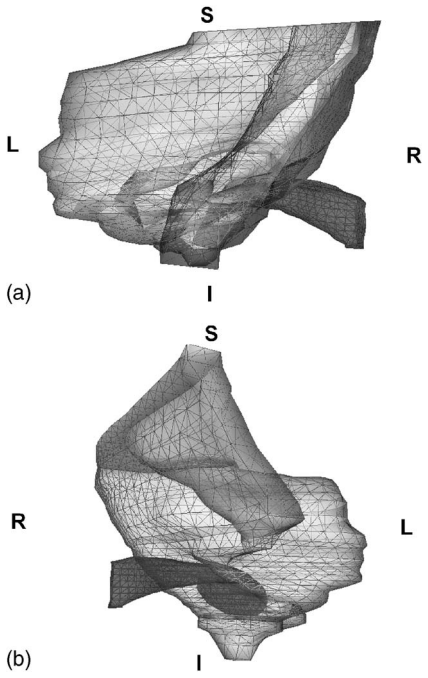

FIG. 3. Surface mesh of finite-element model. The ear canal and temporal bone surface are displayed; the soft tissue is not shown. (a) Posterior view. (b) Antero-lateral view. S is superior; I is inferior; R is right; L is left.

a posterior view of the ear canal and the temporal bone surface. Figure 3(b) is an antero-lateral view. In order to better display the relationships between the ear canal and the temporal bone, the soft tissue is not shown in Fig. 3. It can be seen that there is more temporal bone superior to the ear canal. Figure 4 shows the enclosed ear-canal surface. The ear-canal superior wall is much shorter than the inferior wall, as seen in Fig. 4(a). The tympanic membrane terminates the canal wall in a very horizontal position. It may be considered to form part of the ear canal wall for the innermost 8 mm or so of canal length. As shown in Fig. 4(b), the superior-inferior diameter (D1) is larger than the anterior-posterior diameter (D3), which agrees with the observations of McLellan and Webb (1957). Table I provides a summary of ear-canal and tympanic-membrane data from the literature for the adult ear and the newborn ear, and the corresponding data for the finite-element model.

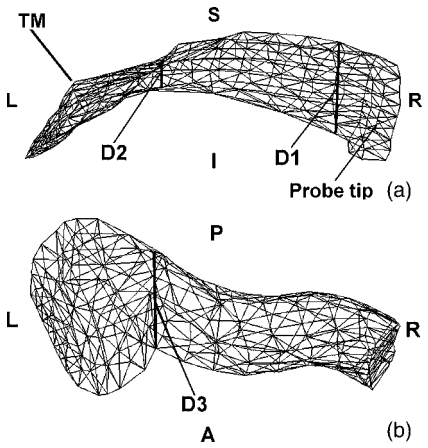

FIG. 4. Ear canal model. (a) Posterior view. (b) Inferior view. D1 (4.8 mm) is the maximum diameter, in the superior-inferior direction; D2 (1.6 mm) is the minimum diameter, in the superior-inferior direction; D3 (4.4 mm) is the maximum diameter in the anterior-posterior direction. S is superior; I is inferior; P is posterior; A is anterior; R is right; L is left.

TABLE I. Summary of adult and newborn ear canal and TM data.

	Adult	New born (Published Data)	Data in the model
Ear Canal			
Shape	S shape	Straight	Straight
Roof length (mm)	25–30[a,b]	13–22.5[c]	16
Floor length (mm)	25–30[a,b]	17–22.5[c]	22.5
Diameter (mm)	10[a]	4.44[d]	1.6–4.8
Bone	Inner 2/3[a]	None	None
Soft tissue	Outer 1/3[a]	Entire EAC	Entire EAC
TM			
Diameter along the manubrium (mm)	8–10[a]	Adult size[a]	8.7
Diameter perpendicular to the manubrium (mm)	7–9[a]	Adult size[a]	8.3
Surface area (mm^2)	55–85[a]	Adult size[a]	67

[a]Saunders *et al.*, 1983.
[b]Stinson and Lawton, 1989.
[c]2-month old newborn measurement (McLellan and Webb, 1957).
[d]Average ear-canal diameter for 1-month-old newborn (Keefe *et al.*, 1993).

A solid-element model with tetrahedral elements was generated from the triangulated surface using Gmsh (http://www.geuz.org/gmsh/) and imported into COMSOL™ version 3.2 (http://www.comsol.com) for finite-element analysis.

B. Material properties

There are three types of cartilage in the human body: articular cartilage, elastic cartilage, and fibrocartilage (Fung, 1993). Elastic cartilage is found in the wall of the external auditory canal (McLellan and Webb, 1957). Articular and elastic cartilage have a similar structure, both containing type II collagen, but elastic cartilage contains more elastic fibers and is therefore more flexible than articular cartilage (Fung, 1993). The Young's modulus of elastic cartilage in adults is between 100 kPa and 1 MPa (Zhang *et al.*, 1997; Liu *et al.*, 2004). The mechanical properties of cartilage are age dependent. Williamson *et al.* (2001) found that the tensile Young's modulus of bovine articular cartilage increased by an average of 275% from newborn to adult.

To the best of our knowledge, the stiffness of human newborn elastic cartilage has never been measured. In this study, we used three Young's moduli: 30, 60, and 90 kPa. The lowest value is close to the lowest stiffness of soft tissue such as fat (4.8 kPa, Wellman *et al.*, 1999) and gland (17.5 kPa, Wellman *et al.*, 1999) and 90 kPa is close to the lowest stiffness of cartilage in adult humans.

The ear-canal soft tissue is assumed to be homogeneous, isotropic, and nearly incompressible. The Poisson's ratio of elastic cartilage in newborns is taken to be 0.475. This value has been widely used in soft-tissue modeling (Torres-Moreno *et al.*, 1999; Cheung *et al.*, 2004; Chui *et al.*, 2004). The soft tissue is also assumed to be hyperelastic, as discussed in Sec. II D.

C. Boundary conditions and load

In newborn tympanometric measurement, the volume change caused by high static pressures has two sources. The first is tympanic-membrane movement; the second is ear-canal wall movement. The ear canal and the middle ear are configured as a parallel acoustic system. The same uniform static pressure is applied to the ear-canal wall and to the tympanic membrane. The total volume change is equal to the sum of the contributions of these two components. In this study, we focus only on the contribution of ear-canal-wall movement to volume change. We thus assume that the tympanic membrane is rigid and the ossicles, ligaments, etc., are not taken into account. Given that the bones are also assumed to be rigid in this model, only their surface representation is needed. The probe tip is also assumed to be rigid and its position is taken to be 5 mm inside the ear canal (Keefe *et al.*, 1993), as shown in Fig. 2. All other parts of the model are free to move. Static pressure is applied to the ear-canal wall from the inside of the canal.

D. Hyperelastic finite-element method

While undergoing tympanometry procedures, the newborn ear-canal wall deforms significantly under the high static pressures. Accordingly, linear elasticity with the infinitesimal-deformation formulation is not appropriate to formulate the finite-element model. As a result, we used a hyperelastic finite-deformation formulation.

In finite-deformation theory, the deformation gradient $\mathbf{F}=\partial\mathbf{x}/\partial\mathbf{X}$ is defined where $\mathbf{X}$ denotes a point in the reference configuration. The current position of the point is denoted by $\mathbf{x}=\mathbf{X}+\mathbf{u}$ where $\mathbf{u}$ is the displacement from the reference position to the current position. Using $\mathbf{C}=\mathbf{F}^T\mathbf{F}$, the "strain invariants" are defined as

$$I_1 = \mathrm{tr}(\mathbf{C}) \tag{1}$$

and

$$I_2 = \tfrac{1}{2}[I_1^2 - \mathrm{tr}(\mathbf{C}\cdot\mathbf{C})], \tag{2}$$

where tr is the trace operator.

Various strain-energy functions can be applied to soft tissue, such as neo-Hooke, Mooney-Rivlin, Arruda-Boyce, etc. In this study we focus on the polynomial method, which is a generalization of the neo-Hooke and Mooney-Rivlin methods and which has been widely used to simulate large deformations in almost incompressible soft tissues such as skin, brain tissue, breast tissue, and liver (e.g., Samani and Plewes, 2004; Cheung *et al.*, 2004). A second-order polynomial strain-energy function can be written as

$$W = C_{10}(I_1-3) + C_{01}(I_2-3) + \frac{\kappa}{2}(J-1)^2, \tag{3}$$

where W is the strain energy; C_{10} and C_{01} are material constants; κ is the bulk modulus; and J is the volume-change ratio. J is defined as

$$J = \det \mathbf{F}, \tag{4}$$

where det is the determinant operator.

Under small strains the Young's modulus of the material, E, may be written as

$$E = 6(C_{10} + C_{01}). \tag{5}$$

Further details about the hyperelastic model can be found elsewhere (e.g., Holzapfel, 2000).

The ratio $C_{10}:C_{01}$ is here taken to be 1:1, which has been widely used for biological soft tissue (e.g., Mendis *et al.*, 1995; Samani and Plewes, 2004).

E. Volume calculation

The air volume between the probe tip and the tympanic membrane can be calculated using the three-dimensional divergence theorem:

$$\iiint_M \mathrm{div}\,\mathbf{F}\,dV = \iint_S \mathbf{F}\cdot\mathbf{n}\,dS, \tag{6}$$

where M is a solid volume with a closed boundary surface, $\mathbf{S}$, whose unit normal vector is denoted by $\mathbf{n}$. The divergence of $\mathbf{F}$ defined as

$$\mathrm{div}\,\mathbf{F} = \frac{\partial F_x}{\partial x} + \frac{\partial F_y}{\partial y} + \frac{\partial F_z}{\partial z}. \tag{7}$$

By choosing $\mathbf{F}$ such that $\mathrm{div}\,\mathbf{F}=1$, we can easily obtain the ear-canal volume as

$$V = \iiint_M \mathrm{div}\,\mathbf{F}\,dV = \iint_S \mathbf{F}\cdot\mathbf{n}\,dA. \tag{8}$$

There is an infinite number of choices for $\mathbf{F}$ that have $\mathrm{div}\,\mathbf{F}=1$. In our study, we simply choose $\mathbf{F}=(x,0,0)$. The air volume can therefore be computed by integration over the deformed surface of the corresponding closed volume. Further details can be found elsewhere (e.g., Matthews, 2000, p. 97).

III. RESULTS

A. Convergence tests

Convergence tests are used to investigate how many elements should be used in the model. The results of a finite-element simulation depend in part on the resolution of the finite-element mesh, that is, on the numbers and sizes of the elements used. In general, the greater the number of elements the more accurate the results, but also the longer the time required for the computations. Nonlinear simulations in particular can be very time consuming.

In our convergence tests, the first step was to decide how much of the scan to incorporate in the x direction (from lateral to medial) and y direction (from posterior to anterior). The second step was to decide how many slices should be used in the model. For both step 1 and step 2, the surface models have a nominal mesh resolution of 18 elements per diameter. The last step was to decide what mesh resolution to use for the model. In the convergence tests the Young's modulus is 60 kPa and the Poisson's ratio is 0.475.

As shown in Fig. 2, three different models are compared. The first one (small model) has a lateral-medial size of about 32 mm and an anterior-posterior size of about 28 mm.

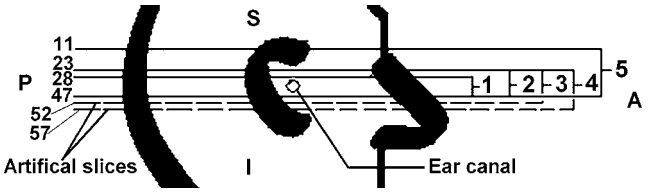

FIG. 5. Slices used in test models 1–5. Slices 48–57 are artificial slices, as discussed in the text. A is anterior; P is posterior; S is superior; I is inferior.

The second model (middle model) is about 36 mm by 39 mm. The third one (large model) is about 41 mm by 50 mm. All three models were generated based on slices 11–47.

The three models were compared based on the absolute values of the maximum displacements for both negative and positive pressures of 3 kPa, and on the ear-canal volume change for the same pressure. All three models have almost the same maximum displacements. The volume changes for model 1 were 6.7% larger than those of model 2 because model 1 contains less bone to constrain the wall motion, but models 2 and 3 differed by only about 1%. This implies that the middle model provides enough accuracy and it is the one used for the remaining simulations.

As mentioned earlier, the ear canal is present in slices 34–42. In order to investigate how many slices above and below the canal should be incorporated into the model, five different models were studied. Figure 5 illustrates the different configurations. Model 1 was composed of 20 slices, from slice 28 to slice 47. Model 2 included five more slices superiorly; it contains 25 slices, from 23 to 47. Model 3 included five more slices inferiorly. Since our CT scan did not include any slices inferior to slice 47, we created five artificial slices (numbered 48–52) by extrapolation and comparison with CT scans for newborns of about 3 months of age. The artificial slices included only soft tissue, the boundary conditions of which were made the same as those of the other soft tissue in the model. Model 3 was thus composed of 30 slices, from 23 to 52, slices 48–52 being artificial. Model 4 was based on model 3, the only difference being the incorporation of another five artificial slices inferiorly; the model thus contained 35 slices, from 23 to 57. Finally, model 5 was composed of 37 slices, from 11 to 47; no artificial slices were included in model 5.

As before, the different models were compared based on the absolute values of the maximum displacements and on the ear-canal volume changes for both negative and positive pressures of 3 kPa. The maximum displacements were almost the same; the differences were less than 2%. The volume changes for model 1 are up to 8.9% larger than those for the other models, presumably because it has fewer constraints due to the temporal bone superior to the canal, but the volume changes for models 2–5 are all within 1.3%. These results imply that our 37-slice dataset is sufficient even though there are not very many slices inferior to the ear canal. For the remainder of this paper we use model 5.

In order to decide what mesh resolution should be used, four different resolutions were compared. The initial surface models have nominal numbers of elements per diameter of

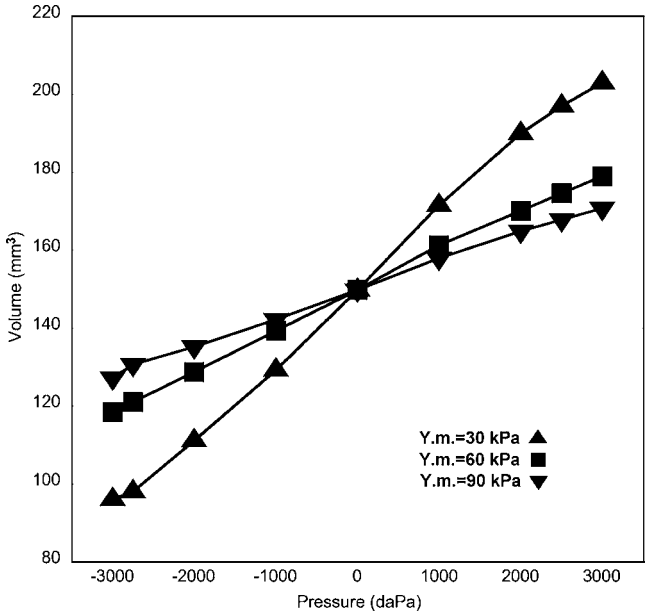

FIG. 6. Calculated ear-canal volume for three different Young's moduli (Y.m.). When pressure is 0, ear-canal volume is 150 mm^3.

12, 15, 18, and 22, respectively. The resulting solid models have 9076, 12786, 19233, and 23674 tetrahedral elements, respectively. As the mesh resolution increases, the maximum displacement of the entire model increases monotonically. The difference in maximum displacement between the 9076-element model and the 12,786-element model was about 4%, and the difference between the 12,786-element model and the 19,233-element one was about 5%. The difference between the 19,233-element model and the 23,674-element one, however, was less than 1%, and the location of the maximum displacement changed by less than 1 mm. The model with 19,233 elements was selected for further simulations.

B. Sensitivity analysis

Sensitivity analysis is used to investigate the relative importance of model parameters. In this study we focus on the ear-canal volume change under high static pressures, and therefore the effects of parameters on ear-canal volume changes were investigated. Sensitivity was analyzed for Young's modulus, Poisson's ratio, and the $C_{10}:C_{01}$ ratio. The Young's modulus was found to have the greatest impact on the volume change. Figure 6 shows ear-canal volumes corresponding to different Young's moduli for static pressures from −3 to +3 kPa. As Young's modulus increases, the model canal-wall volume changes decrease significantly.

Values from 0.45 to 0.499 have been used in the literature for Poisson's ratio for soft tissue (Li *et al.*, 2001; Samani and Plewes, 2004). A value of 0.5 corresponds to incompressibility. Increasing Poisson's ratio from 0.45 to 0.499, with a Young's modulus of 60 kPa, resulted in a 1.5% reduction in volume change at +3 kPa, and a change of only 1.1% at −3 kPa. The model is thus insensitive to Poisson's ratio, which is consistent with previous modeling (Funnell and Laszlo, 1978; Qi *et al.*, 2004).

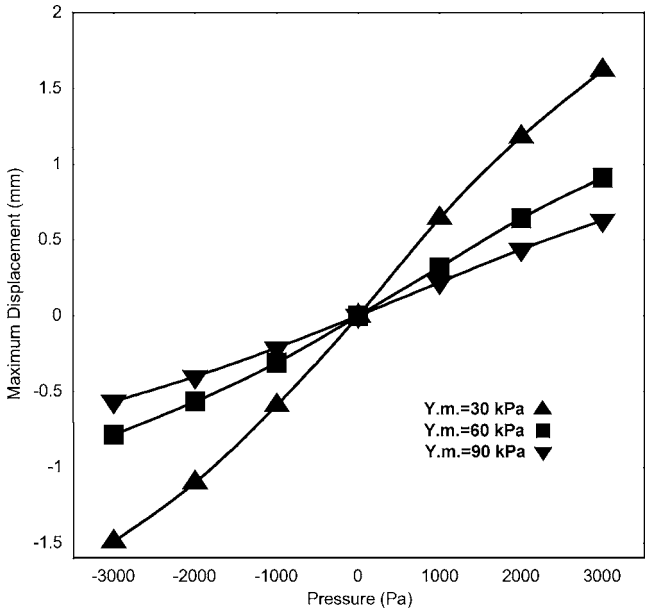

FIG. 7. Maximum displacement of the entire model for three different Young's moduli.

Three different ratios of C_{10} to C_{01} were studied, namely, 1:0, 1:1, and 0:1. The sum of C_{10} and C_{01} is kept constant at 10 kPa, corresponding to a small-strain Young's modulus of 60 kPa as given by Eq. (5). The volume changes occurring with the three combinations of C_{10} and C_{01} differ by less than 3% at +3 kPa and by even less at −3 kPa. The model is thus insensitive to the $C_{10}:C_{01}$ ratio when the sum of C_{10} and C_{01} remains constant. This is consistent with the results of Mendis (1995), who used a three-dimensional Mooney-Rivlin model for brain tissue and found that, when the deformation is under 30%, the different combinations of C_{10} and C_{01} had little effect on model displacements.

C. Model displacements and displacement patterns

The ear-canal wall of the model displays nonlinear elastic behavior leading to an *S*-shaped pressure-displacement relation under high static pressures, as shown in Fig. 7. The displacement curves are very similar in shape to the volume curves shown in Fig. 6. As the Young's modulus increases, the maximum displacement decreases in approximately inverse proportion.

The smaller the Young's modulus is and the larger the displacements are, the stronger the nonlinearity is. When Young's modulus is 90 kPa, the pressure-displacement relation becomes almost linear. When Young's modulus is 30 kPa, the slopes of the curves decrease significantly as the pressure becomes either more negative or more positive, but the displacement curve does not reach a plateau by either −3 kPa or +3 kPa.

The maximum displacement of the entire model occurs on the medial inferior surface of the ear canal. The maximum is quite localized. Figure 8 shows the displacement patterns on the superior and inferior surfaces of the canal for a pressure of +3 kPa, when Young's modulus is 60 kPa. The displacements of the inferior surface are bigger than those of the superior surface. This is because there is temporal bone around the top of the newborn ear canal but the bone around the bottom has not completely developed, as shown in Fig. 3.

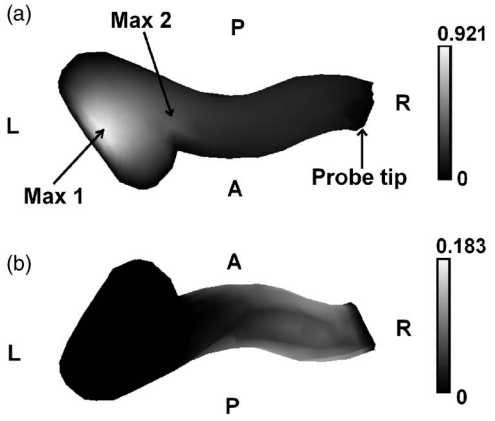

FIG. 8. Displacement pattern of ear-canal wall for static pressure of +3 kPa. (a) Ear-canal floor. Gray scale is from 0 to 0.921 mm. (b) Ear-canal roof. Gray scale is from 0 to 0.183 mm. Max 1, the maximum displacement of the entire model, is 0.921 mm. Max 2, the maximum displacement observable from the probe tip, is 0.452 mm. Since the tympanic membrane (TM) and the probe tip are assumed to be fixed, the corresponding displacements are zero. A is anterior; P is posterior; R is right; L is left.

D. Comparisons with experimental data

In this section we shall compare our simulation results with two sets of experimental data, maximum canal-wall displacement measurements (Holte *et al.*, 1990) and tympanometry (Shahnaz, 2002; Polka *et al.*, 2002).

1. Displacement measurements

Holte *et al.* (1990) measured the maximum displacements of ear-canal walls in newborns of different ages. Positive and negative pressures of 2.5–3 kPa were introduced by a syringe system. Displacements of the ear-canal wall and tympanic membrane were recorded by an otoscope with a videocassette recorder. The videotapes were reviewed, and ear-canal wall diameters at ambient pressure and at maximum static pressures were measured with a transparent ruler. The relative change in ear-canal wall diameter under maximum static pressure was expressed as a percentage of the resting diameter. For newborns aged from 11 to 22 days, the diameter change was $7.9\% \pm 11.1\%$ for the positive pressure, and $-15.0\% \pm 22.1\%$ for the negative pressure.

The maximum displacement in our model takes place on the medial inferior surface of the ear canal, which probably corresponds to a location beyond that which Holte *et al.* were able to observe. McLellan and Webb (1957) used an otoscope to examine 20 cleansed ear canals from ten healthy full-term newborns. They concluded that the inferior wall ascends from the tympanic membrane, and from the external orifice of the canal, to a transverse ridge which divides the inferior wall into inner and outer portions. Unlike the outer portion, the inner portion of the inferior wall can hardly be seen with an otoscope. Since Holte *et al.* also used an otoscope in their experiments, it would have been difficult for them to observe the inner part of the inferior wall. We conclude, therefore, that their diameter-change measurements were taken lateral to the ridge. As shown in Fig. 8, in our

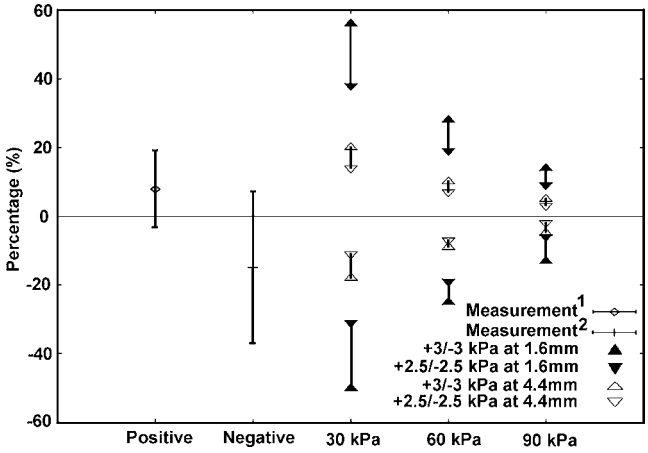

FIG. 9. Comparison of experimental data (Holte *et al.*, 1990) with simulation results. Positive = experimental data for pressures of +2.5 to +3 kPa; Negative = experimental data for pressures of −2.5 to −3 kPa. Triangles represent simulation results for Young's moduli of 30, 60, and 90 kPa, respectively. Filled and open triangles indicate the use of 1.6 and 4.4 mm, respectively, as the denominator when computing percentage changes. Upward-pointing and downward-pointing triangles indicate the use of ±3 kPa and ±2.5 kPa, respectively, as the pressure for the simulation results.

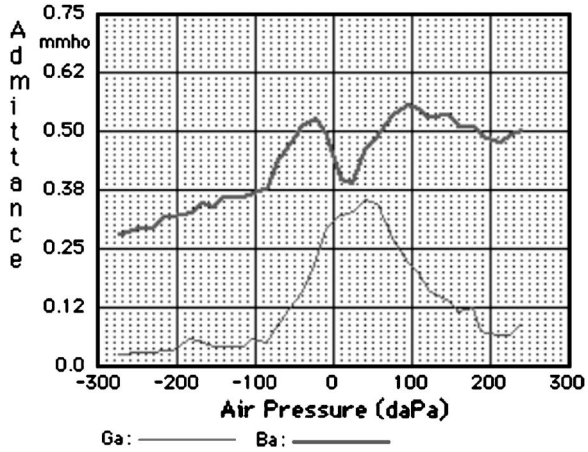

FIG. 10. Susceptance and conductance tympanogram at 226 Hz for 3-week-old newborn (based on Polka *et al.*, 2002).

model the displacements of the canal wall are larger at the ridge than they are lateral to the ridge; we therefore assume that Holte *et al.* measured the diameter changes at the ridge. In our model the ridge is located 11 mm from the probe tip. We use the model displacements at this point for comparison with the measurements of Holte *et al.*

McLellan and Webb (1957) observed a sagittal cross section at the ridge which appeared oval in shape in 16 ears, with the longer diameter being anterior-posterior. In our model, the resting diameters at the transverse ridge are shown in Fig. 4. The narrowest diameter (D2) at 11 mm is about 1.6 mm, and the widest diameter (D3) is about 4.4 mm. Since the resting diameters were not mentioned by Holte *et al.*, we do not know if the narrowest or the widest diameter was applied when the ratio of ear-canal wall displacements to resting diameters were calculated. Thus, for our model, the ratio of displacement (at the 11 mm position) to diameter was calculated for both resting diameters (1.6 and 4.4 mm), and for both ±2.5 kPa and ±3 kPa. The results are shown in Fig. 9 together with the experimental results of Holte *et al.* For positive pressures, when the narrowest resting diameter (1.6 mm) is applied, the results for the model with a Young's modulus of 30 kPa are beyond the experimental range; when Young's modulus is 60 kPa, the simulation results are partly within the experimental range; when Young's modulus is 90 kPa, they are totally within the experimental range. For negative pressures, the simulation results with a Young's modulus of 30 kPa are partly within the experimental range; for 60 and 90 kPa they are all within the experimental range. When the widest resting diameter (4.4 mm) is applied, all of the simulation results are within the experimental range for both positive and negative pressures.

2. Tympanometry

Polka *et al.* (2002) showed complete susceptance and conductance tympanograms for two 3-week-old infants measured at 226, 600, 800, and 1000 Hz. Both infants had normal hearing as measured by automated auditory brainstem response screening. Figure 10 shows one of the 226 Hz measurements.

For frequencies up to about 1 kHz, the adult ear canal can be modeled as a lumped acoustical element (e.g., Shanks and Lilly, 1981). This assumption is valid up to higher frequencies in the newborn canal because it is smaller than the adult canal. The susceptance measured at the probe tip includes the susceptance of the enclosed air volume (B_V), and the susceptances due to the vibration of the ear-canal wall (B_W) and tympanic membrane (B_{TM}) in response to the probe tone. Thus, the susceptances at the extreme positive pressure and negative pressure are given by

$$B^+ = B_V^+ + B_W^+ + B_{TM}^+ \tag{9}$$

and

$$B^- = B_V^- + B_W^- + B_{TM}^-. \tag{10}$$

The difference between the two is given by

$$\Delta B = B^+ - B^- = [B_V^+ - B_V^-] + [B_W^+ - B_W^-] + [B_{TM}^+ - B_{TM}^-]. \tag{11}$$

Given the near symmetry of the nonlinear response predicted by the model, as shown in Fig. 7, it may be reasonable to assume that the vibrations at the extreme positive and negative pressures are similar. In that case their effects cancel and the susceptance change is mainly determined by the actual volume change due to the static displacement of the canal wall and tympanic membrane.

Table II shows the susceptance and conductance values at the extreme static pressures (−275 and +250 daPa, i.e., −2.75 and +2.5 kPa), and their differences, from the measurements of Polka *et al.* (2002). The fact that the conductance changes are very small for seven out of the eight measurements supports the assumption that the vibrations are similar at the extreme positive and negative pressures.

The table also includes the equivalent-volume changes corresponding to the susceptance changes, computed using

TABLE II. Tympanometry results for two 3-week-old infants.

Newborn 1				
Frequency (Hz)	**226**	**630**	**800**	**1000**
B^+ (mmho)	0.5	1	0.875	1
B^- (mmho)	0.26	0.5	0.45	0.47
ΔB (mmho)	0.24	0.5	0.425	0.53
ΔV (mm^3)	240	180	120	120
G^+ (mmho)	0.05	0.5	0.8	1.1
G^- (mmho)	0	0.6	0.7	0.6
ΔG (mmho)	0.05	−0.1	0.1	0.5
Newborn 2				
Frequency (Hz)	**226**	**630**	**800**	**1000**
B^+ (mmho)	0.3	1.01	1.45	1.8
B^- (mmho)	0.25	0.5	0.8	1.1
ΔB (mmho)	0.05	0.51	0.65	0.7
ΔV (mm^3)	50	183	183	158
G^+ (mmho)	0.05	0.5	0.8	0.9
G^-(mmho)	0.05	0.65	0.8	0.9
ΔG (mmho)	0	−0.15	0	0

Tympanometry data are from Polka *et al.* (2002). B^+, B^-, G^+, and G^- are susceptance and conductance measurements at extreme positive and negative pressures. ΔB is the susceptance difference between extreme positive and negative pressures. ΔV is the equivalent-volume difference corresponding to ΔB. ΔG is the conductance difference between extreme positive and negative pressures.

$$\Delta V_{\text{eq}} = \Delta B \rho c^2 / 2\pi f, \tag{12}$$

where ρ is the air density (1.2 kg/m^3), c is the sound speed (343 m/s), and f is the frequency (cf. Shanks and Lilly, 1981).

Figure 11 shows model volume changes obtained for different Young's moduli, compared with the experimentally measured equivalent-volume changes from Table II. The volume changes obtained for the model are lower than those observed experimentally, which is consistent with the fact that the experimental equivalent-volume changes include contributions not only from ear-canal wall movement but also from tympanic-membrane movement.

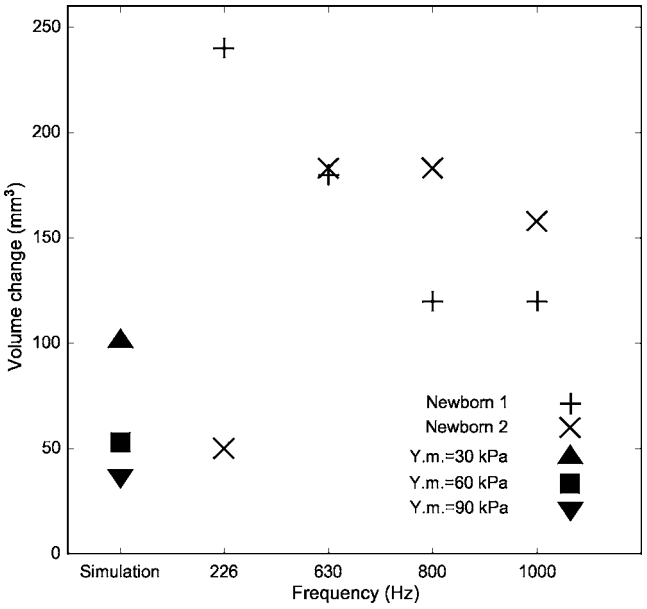

FIG. 11. Comparison of simulation results with equivalent-volume changes taken from tympanograms for two newborns. ▲, ■, and ▼ represent the volume changes from the simulation results for three different Young's moduli. + and × represent the tympanogram-based equivalent-volume changes for 226, 630, 800, and 1000 Hz.

IV. DISCUSSION AND CONCLUSIONS

A nonlinear hyperelastic model of the newborn ear canal is presented and compared with available experimental data.

For static pressures from −3 kPa to +3 kPa, the canal-wall displacements and volume changes are nonlinear, with the degree of nonlinearity increasing as the Young's modulus decreases and the displacements increase. Our sensitivity analysis indicates that the Young's modulus of the tissue in the ear-canal wall plays the most important role in determining volume changes. The effects of varying the Poisson's ratio and the C_{10}:C_{01} ratio are found to be small.

In our simulations, the displacements of the ear-canal wall are slightly larger under positive pressures than under negative pressures. In the measurements of Holte *et al.*, however, the mean diameter changes were much bigger for negative pressures than for positive pressures. In the measurements, a large overlap exists between the percentage displacement changes for the positive pressures and those for the negative pressures, as shown in Fig. 9. Possible reasons for the variability include individual differences between ears, age-related changes from 11 to 22 days, and uncertainty in the applied pressures. It is not clear whether the displacements under the positive pressures and the negative pressures are significantly different or not.

The cross section of the newborn ear canal is quite flattened; in our model, for example, the horizontal and vertical diameters are 1.6 and 4.4 mm, respectively, just lateral to the tympanic membrane. We do not know which diameter was used by Holte *et al.* in computing percentage changes. When the narrowest diameter was applied to our model results, the model with a Young's modulus of 30 kPa produces diameter changes far above the experimental range under positive pressures. In Holte's measurements, in a younger age group (1–11 days) the diameter changes may be up to 70%. This may indicate that Young's modulus of the newborn ear canal is 30 kPa for younger newborns, and between 60 and 90 kPa for older newborns. However, for a better comparison with the model, it would be desirable to be able to know where their measurements were made in the canal, and to know which diameter was used in the calculations.

In tympanometry a change of equivalent volume consists of two components. One component is the actual air-volume change caused by static pressures, which should be independent of frequency. The actual volume change is caused by the static displacement of both the ear-canal wall and the tympanic membrane. The other component is due to the vibration of the ear-canal wall and tympanic membrane in response to the probe tone. Assuming that the vibrations caused by the probe tone at the positive and negative extreme pressures cancel each other out, as discussed above, the difference between the experimental value and the simulation value may be taken to be the volume change caused by

the static displacement of the newborn tympanic membrane. The average equivalent-volume change across all four frequencies in Table II and Fig. 11 is 154 mm^3. The equivalent-volume changes at 630, 800, and 1000 Hz seem to fit the pattern of frequency independence quite well, but the values at 226 Hz do not—one is too high and the other is too low. It is not clear why this is so. Dropping these two values and taking the average over the three higher frequencies yields an equivalent-volume change of 157 mm^3, very close to the value obtained using all four frequencies. According to the simulation results, when the Young's modulus of the ear-canal wall is 30, 60, and 90 kPa, the ear-canal volume change is 101, 53, and 37 mm^3, respectively, from −2.75 kPa to 2.5 kPa. Subtracting these values from the average equivalent-volume change of 157 mm^3 yields predicted volume changes caused by tympanic-membrane displacement of about 56, 104, and 120 mm^3, respectively. No independent measurements of newborn tympanic-membrane volume displacements are available for comparison, and measurements in adult ears (e.g., Shanks and Lilly, 1981; Dirckx and Decraemer, 1992; Gaihede, 1999) may be quite different.

Shanks and Lilly (1981) measured adult ear-canal volume change over a static pressure range of ±4 kPa. They found a mean ear-canal volume change of 113 mm^3 caused by the movement of the cartilaginous part of the wall of the ear canal and the movement of the probe tip. Our simulated volume changes for the newborn are mostly less than those measured by Shanks and Lilly for adult ears. This is reasonable because the diameter and length of the newborn ear canal are much less than those of the adult ear canal. We also do not take probe-tip and tympanic-membrane movements into account and our pressure range is ±3 kPa rather than ±4 kPa. If we compare the ratio of volume change to the original volume, the results of Shanks and Lilly (1981) correspond to an average ratio of about 16% in the range ±4 kPa in adult, while the ratio in newborn is from 27% (for a Young's modulus of 90 kPa) to 75% (for a Young's modulus of 30 kPa) in the range of ±3 kPa based on our model results.

The simulated ear-canal volume changes do not reach a plateau when the pressure is varied between −3 kPa and +3 kPa, which is consistent with the report by Shanks and Lilly (1981) that even at ±4 kPa the adult ear canal is not rigid if the probe tip is placed on the cartilaginous part of the ear canal. The failure of the model to reach a plateau is also consistent with the nonflat tails often found in susceptance tympanograms in newborns (Paradise *et al.*, 1976; Holte *et al.*, 1990).

As a first step in modeling the newborn ear-canal wall, we have taken into account only the hyperelastic properties of the ear canal. Further work is required to incorporate in the model the tympanic membrane and the middle ear, and the probe tone itself. Modeling of the response to the probe tone will require inclusion of inertial and damping effects which are not in the current model. The addition of viscoelastic effects would permit simulation of the effects of the timing and direction of the large quasi-static pressure changes used in tympanometry (Osguthorpe and Lam, 1981). It will also be important to obtain a better idea of the types of tissue present: X-ray data will need to be supplemented by data obtained from sources such as MRI and histology.

ACKNOWLEDGMENTS

This work was supported by the Canadian Institutes of Health Research and the Natural Sciences and Engineering Research Council (Canada). We thank N. Shahnaz and L. Polka for providing the tympanometry data used here, as it appeared in their 2002 poster presented to the Acoustical Society of America.

Cheung, J. T. M., Zhang, M., Leung, A. K. L., and Fan, Y. B. (**2004**). "Three-dimensional finite element analysis of the foot during standing—A material sensitivity study," J. Biomech. **38**, 1045–1054.

Chui, C., Kobayashi, E., Chen, X., Hisada, T., and Sakuma, I. (**2004**). "Combined compression and elongation experiments and non-linear modelling of liver tissue for surgical simulation," Med. Biol. Eng. Comput. **42**, 787–798.

Dirckx, J. J. J., and Decraemer, W. F. (**1992**). "Area change and volume displacement of the human tympanic membrane under static pressure," Hear. Res. **62**, 99–104.

Early Hearing Detection and Intervention Program Guidance Manual (**2003**). http://www.cdc.gov/ncbddd/ehdi/nationalgoals.htm. Last accessed 10/30/2006.

Eavey, R. D. (**1993**). "Abnormalities of the neonatal ear: Otoscopic observations, histologic observations, and a model for contamination of the middle ear by cellular contents of amniotic fluid," Laryngoscope **103**, 1–31.

Eby, T. L., and Nadol, J. B., Jr. (**1986**). "Postnatal growth of the human temporal bone: implications for cochlear implants in children," Ann. Otol. Rhinol. Laryngol. **95**, 356–364.

Elkhouri, N., Liu, H., and Funnell, W. R. J., (**2006**). "Low-frequency finite-element modelling of the gerbil middle ear," J. Assoc. Res. Otolaryngol. (in press), DOI: 10.1007/s10162-006-0055-6

Fung, Y. C. (**1993**). *Biomechanics: Mechanical Properties of Living Tissues*, 2nd ed. (Springer-Verlag, Berlin).

Funnell, W. R.J., and Laszlo, C. A. (**1978**). "Modeling of the cat eardrum as a thin shell using the finite-element method," J. Acoust. Soc. Am. **63**, 1461–1467.

Funnell, W. R. J. (**1996**). "On the low-frequency coupling between eardrum and manubrium in a finite-element model," J. Acoust. Soc. Am. **99**, 3036–3043.

Funnell, W. R. J., and Decraemer, W. F. (**1996**). "On the incorporation of moiré shape measurements in finite-element models of the cat eardrum," J. Acoust. Soc. Am. **100**, 925–932.

Gaihede, M. (**1999**). "Mechanics of the middle ear system: Computerized measurements of its pressure-volume relationship," Auris Nasus Larynx **26**, 383–399.

Gan, R. Z., Sun, Q., Dyer, R. K., Jr., Chang, K. H., and Dormer, K. J. (**2002**). "Three-dimensional modeling of middle ear biomechanics and its applications," Otol. Neurotol. **23**, 271–280.

Gan, R. Z., Feng, B., and Sun, Q. (**2004**). "3-Dimensional finite element modeling of human ear for sound transmission," Ann. Biomed. Eng. **32**, 847–856.

Holte, L., Cavanaugh, R. M., Jr., and Margolis, R. H. (**1990**). "Ear canal wall mobility and tympanometric shape in young infants," J. Pediatr. (St. Louis) **117**, 77–80.

Holte, L., Margolis, R. H., and Cavanaugh, R. M., Jr. (**1991**). "Developmental changes in multifrequency tympanograms," Audiology **30**, l–24.

Holzapfel, G. A. (**2000**). *Nonlinear Solid Mechanics: A Continuum Approach for Engineering* (Wiley, Chichester).

Joint Committee on Infant Hearing, (**2000**). "Year 2000 position statement: Principles and guidelines for early hearing detection and intervention programs," Pediatrics **106**, 798–817.

Keefe, D. H., Bulen, J. C., Arehart, K. H., and Burns, E. M. (**1993**). "Ear-canal impedance and reflectance coefficient in human infants and adults," J. Acoust. Soc. Am. **94**, 2617–2637.

Keefe, D. H., and Levi, E. (**1996**). "Maturation of the middle and external ears: Acoustic power-based responses and reflectance tympanometry," Ear Hear. **17**, 361–372.

Koike, T., Wada, H., and Kobayashi, T. (**2002**). "Modeling of the human

middle ear using the finite-element method," J. Acoust. Soc. Am. **111**, 1306–1317.
Li, G., Lopez, O., and Rubash, H. (**2001**). "Variability of a three-dimensional finite element model constructed using magnetic resonance images of a knee for joint contact stress analysis," J. Biomech. Eng. **123**, 341–346.
Liu, Y., Kerdok, A. E., and Howe, R. D. (**2004**). "A nonlinear finite element model of soft tissue indentation," *Proceedings of Medical Simulation: International Symposium* (Cambridge, MA), 67–76.
Margolis, R. H., Bass-Ringdahl, S., Hanks, W. D., Holte, L., and Zapala, D. A. (**2003**). "Tympanometry in newborn infants—1 kHz norms," J. Am. Acad. Audiol **14**, 383–392.
Margolis, R. H., and Hunter, L. L. (**1999**). "Tympanometry-basic principles and clinical applications," *in Contemporary Perspective on Hearing Assessment*, edited by W. F. Rintelmann and F. Musiek (Allyn and Bacon, Boston).
Matthews, P. C. (**2000**). *Vector Calculus* (Springer, New York).
McLellan, M. S., and Webb, C. H. (**1957**). "Ear studies in the newborn infant," J. Pediatr. (St. Louis) **51**, 672–677.
Mendis, K. K., Stalnaker, R. L., and Advani, S. H. (**1995**). "A constitutive relationship for large deformation finite element modeling of brain tissue," J. Biomech. Eng. **117**, 279–285.
National Institute on Deafness and Other Communication Disorders, National Institutes of Health Consensus Statement: (**1993**). Early identification of hearing-impairment in infants and young children. Bethesda, MD.
Osguthorpe, J. D., and Lam, C. (**1981**). "Methodologic aspects of tympanometry in cats," Otolaryngol.-Head Neck Surg. **89**, 1037–1040.
Paradise, J. L., Smith, C. G., and Bluestone, C. D. (**1976**). "Tympanometric detection of middle ear effusion in infants and young children," Pediatrics **58**, 198–210.
Polka, L., Shahnaz, N., and Zeitouni, A. (**2002**). "A comparison of middle ear acoustic admittance in adults and 3-week-old infants based on multifrequency tympanometry," J. Acoust. Soc. Am. **112**, 2272 (abstract).
Qi, L., Mikhael, C. S., and Funnell, W. R. J. (**2004**). "Application of the Taguchi method to sensitivity analysis of a middle-ear finite-element model," *Proc. 28th Ann. Conf. Can. Med. Biol. Eng. Soc.* 153–156.
Samani, A., and Plewes, D. (**2004**). "A method to measure the hyperelastic parameters of ex vivo breast tissue sample," Phys. Med. Biol. **49**, 4395–4405.
Saunders, J. C., Kaltenbach, J. A., and Relkin, E. M. (**1983**). "The structural and functional development of the outer and middle ear," *Development of Auditory and Vestibular Systems* (Academic, New York).
Shahnaz, N. (**2002**). "Multifrequency, multicomponent tympanometry in 3-weeks old infants," *Second International Conference on Newborn Hearing Screening, Diagnosis & Intervention*, Como, Italy (abstract).
Shanks, J. E., and Lilly, D. J. (**1981**). "An evaluation of tympanometric estimates of ear canal volume," J. Speech Hear. Res. **24**, 557–566.
Stinson, M. R., and Lawton, B. W. (**1989**). "Specification of the geometry of the human ear canal for the prediction of sound-pressure level distribution," J. Acoust. Soc. Am. **85**, 2492–2503.
Torres-Moreno, R., Jones, D., Solomonidis, S. E., and Mackie, H. (**1999**). "Magnetic resonance imaging of residual soft tissues for computer-aided technology applications in prosthetics—A case study," J. Pros. Orth. **11**, 6–11.
Wada, H., Metoki, T., and Kobayashi, T. (**1992**). "Analysis of dynamic behavior of human middle ear using a finite-element method," J. Acoust. Soc. Am. **92**, 3157–3168.
Wellman, P., Howe, R. H., Dalton, E., and Kern, K. A. (**1999**). "Breast tissue stiffness in compression is correlated to histological diagnosis," Technical report, Harvard Biorobotics Laboratory, http://biorobotics.harvard.edu/pubs/mechprops.pdf. Last accessed 10/30/2006.
Williamson, A. K., Chen, A. C., and Sah, R. L. (**2001**). "Compressive properties and function-composition relationships of developing bovine articular cartilage," J. Orthop. Res. **19**, 1113–1121.
Yoshinaga-Itano, C., Sedey, A., Coulter, D. K., and Mehl, A. L. (**1998**). "Language of early and later identified children with hearing loss," Pediatrics **102**, 1161–1171.
Zhang, M., Zheng, Y. P., and Mak, A. F. (**1997**). "Estimating the effective Young's modulus of soft tissues from indentation tests—Nonlinear finite element analysis of effects of friction and large deformation," Med. Eng. Phys. **19**, 512–517.

Laser interferometry measurements of middle ear fluid and pressure effects on sound transmission

Rong Z. Gan[a] and Chenkai Dai
School of Aerospace and Mechanical Engineering and Bioengineering Center, University of Oklahoma, Norman, Oklahoma, 73019

Mark W. Wood
Hough Ear Institute, Oklahoma City, Oklahoma 73112

(Received 26 April 2006; revised 21 September 2006; accepted 26 September 2006)

An otitis media with effusion model in human temporal bones with two laser vibrometers was created in this study. By measuring the displacement of the stapes from the medial side of the footplate, the transfer function of the middle ear, which is defined as the displacement transmission ratio (DTR) of the tympanic membrane to footplate, was derived under different middle ear pressure and fluid in the cavity with a correction factor for cochlear load. The results suggest that the DTR increases with increasing frequency up to 4k Hz when the middle ear pressure was changing from 0 to 20 or −20 cm H_2O (e.g., ±196 daPa) and fluid level was increasing from 0 to a full middle ear cavity. The positive and negative pressures show different effects on the DTR. The effect of fluid on DTR varies between three frequency ranges: $f<1$k, between 1k and 4k, and $f>4$k Hz. These findings show how the efficiency of the middle ear system for sound transmission changes during the presence of fluid in the cavity and variations of middle ear pressure. © *2006 Acoustical Society of America.* [DOI: 10.1121/1.2372454]

PACS number(s): 43.64.Ha, 43.64.Bt [BLM] Pages: 3799–3810

I. INTRODUCTION

Otitis media with effusion as a middle ear disease is diagnosed with fluid in the middle ear cavity and commonly has the middle ear pressure differing from atmospheric pressure. These mechanical changes in the ear result in conductive hearing loss which can be characterized by a reduction of the middle ear admittance at the tympanic membrane or reduced movement of the tympanic membrane and ossicles.

Several clinical diagnostic and research tools have been developed for use with patients, animals, and human temporal bones for measuring middle ear mechanical changes caused by otitis media with effusion (Beery *et al.*, 1975; Lilly, 1984; Huttenbrink, 1988; Murakami *et al.*, 1997; Dirckx and Decraemer, 1992 and 2001; Rosowski *et al.*, 2003; Babb *et al.*, 2004; Ravicz *et al.*, 2004). The impedance changes of the middle ear induced by fluid in the cavity and changes of middle ear pressure are routinely tested in patients using tympanometry, a measurement of combined acoustic admittance of the ear canal and middle ear (Shakes and Shelton, 1991; Dirks and Morgan, 2000; Gaihede *et al.*, 2005). The tympanic membrane (TM) stiffness and shape changes caused by otitis media with effusion (OME) were observed in animal models using a moiré interferometer by von Unge *et al.*, (1993; 1997) and Larsson *et al.* (2003). The effect of positive and negative static pressure in the middle ear on mobility of the TM was measured in gerbil ears by Teoh *et al.* (1997), Lee and Rosowski (2001), and Rosowski and Lee (2002). The influence of static pressure variation from −5 to 25 cm H_2O on auditory threshold (the threshold of auditory nerve-brainstem evoked response) was recently reported on guinea pigs by Petrova *et al.* (2006). The mechanics of the middle ear at static air pressure difference across the TM was investigated in human cadaver temporal bones by measuring the vibration of the umbo and stapes head with a video measuring system by Murakami *et al.* (1997).

To detect the effect of fluid in the middle ear on TM movement, Ravicz *et al.* (2004) reported their measurement of umbo velocity in response to ear canal sound using a laser Doppler vibrometer while saline or silicone fluid was introduced into the middle ear in human temporal bones. Their results indicated that the reduction in umbo velocity at low frequencies was due to the decrease of air space with fluid in the middle ear. The primary mechanism for reduction of umbo velocity at high frequencies was an increasing mass of the TM by entrained fluid. However, the effects of middle ear fluid and pressure on ossicular movement, especially the stapes footplate, have not been reported.

Questions are raised such as: Do the middle ear fluid and air pressure have the same effect on stapes movement as that on the TM? How does the middle ear transfer function (e.g., velocity or displacement ratio between the TM and stapes footplate) change with middle ear pressure and fluid in the cavity? The lack of information in the literature regarding the effects of middle ear pressure and fluid on stapes footplate motion is primarily due to experimental challenge. When the middle ear cavity is filled with fluid, it is almost impossible to measure the motion of the stapes footplate with a sealed and intact middle ear and cochlea.

In this study, we report an alternative approach by measuring the velocity or displacement of the stapes footplate

[a]Author to whom correspondence should be addressed; electronic mail: rgan@ou.edu

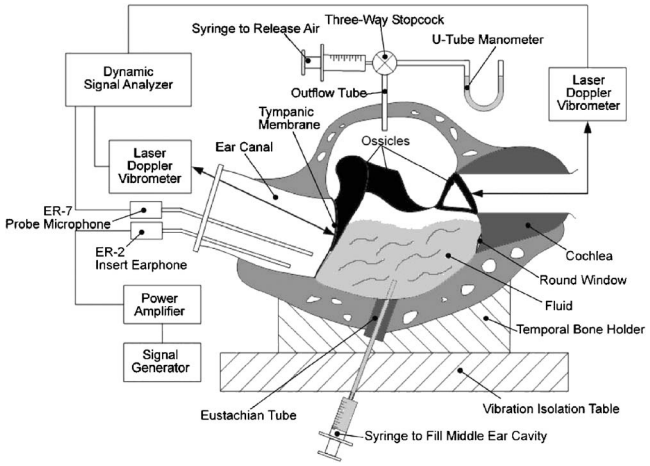

FIG. 1. Schematic diagram of the experimental setup in human temporal bones with two laser vibrometers for measurement of vibrations at the tympanic membrane (TM) and stapes footplate.

from the medial side of the footplate with an opened cochlea. Two laser interferometers (or vibrometers) were used on human temporal bones to simultaneously measure the TM and stapes footplate vibrations under various fluid levels in the cavity and different middle ear pressures. The transfer function of the middle ear with a correction factor for cochlear load was derived. The results reported in this paper provide new data on acoustic-mechanical transmission through the middle ear and the effect of cochlear load on middle ear function when fluid was present in the cavity and middle ear pressure was varied from zero to positive or negative.

II. METHODS

A. Human temporal bone preparation

Eleven fresh or fresh-frozen cadaver temporal bones, obtained through the University of Oklahoma Health Sciences Center or Organ-Share Organization, Oklahoma City were used in this study. The ages of individual donors ranged from 50 to 93 with a mean of 71 years (seven females and four males). All bones were used within one week of acquisition (Gan *et al.*, 2001; 2004).

Before acceptance into the study, each temporal bone was visually inspected under an operating microscope to confirm a normal ear canal and TM, and the absence of overt pathology. There was also a postexperimental check on each bone through a simple mastoidectomy to expose the middle ear cavity. The results of 11 bones reported in this paper are all without evidence of pathology in the middle ear after the postexperimental check.

The Eustachian tube (ET) meatus was identified and a silicone tube, outer diameter of 1 mm, was then advanced through the ET into the middle ear and glued in place at the skull base using cyanoacrylate gel glue. The silicone tube was connected to a syringe for injecting fluid into the middle ear cavity. The second silicone tube (2 mm outer diameter, named the outflow tube) was placed through the hole drilled on the top of the epitympanic tegmen. The tube was connected to a syringe and a U-tube manometer through a three-way stopcock as shown in Fig. 1. The manometer was used to measure middle ear pressure.

All surgically opened areas were sealed air tight using cyanoacrylate glue and silicone polymer. A leaking test was then conducted in every bone with the following procedures: the outflow tube was connected to the manometer and the middle ear pressure was varied from zero to ±20 cm H_2O (1 cm H_2O=98 Pa=9.8 daPa). The pressure at 20 or −20 cm H_2O was maintained for 20 s to confirm the middle ear system was sealed.

After the leaking test, a piece of laser reflective tape, 0.5 mm^2, weighing 0.04 mg (3M Co., St. Paul, MN), was placed as a laser target on the lateral surface of the umbo. The bone was wrapped in wet gauze (normal saline) to prevent desiccation of the specimen during the experiment. Note that before conducting any laser measurement on temporal bones, we used a tympanometer (Zodiac 901, Madsen, GN Otometrics, Denmark) to verify normal compliance of the TM. Most bones used in this study showed normal tympanograms and only two bones displayed a flat pattern indicating the possibility of fluid. For these bones, the middle ear was suctioned through the ET catheter while the outflow tube remained open to the atmosphere.

B. Temporal bone experimental setup with laser vibrometers

Figure 1 is the schematic diagram of the temporal bone experimental setup with two laser Doppler vibrometers to measure the TM and stapes footplate movements. The cochlea was opened from the medial side of the bone. The laser on the right side of the figure was aimed on the stapes footplate and another laser on the left side was aimed on the TM at the umbo. The experiment began with one laser only to measure the TM displacement in bones with intact cochlea.

The full description of similiar setup is available elsewhere (Gan *et al.*, 2004). Briefly, the temporal bone was placed in a temporal bone holder and the temporal bone assembly was set on a vibration isolation table. Pure tone sound signals of 90 dB sound pressure level (SPL) from a function generator (Model 193, Wavetek, San Diego, CA) were delivered to the ear canal near the TM by an inserted earphone (Model ER-2, Etymotic Research, Grove Village, IL). A probe microphone (Model ER-7, Etymotic Research) used for monitoring the input SPL was positioned approximately 2 mm from the umbo.

A hearing laser vibrometer (HLV; Model HLV-1000; Polytec PI, Tustin, CA) was used to measure the vibration of the TM (umbo). The helium–neon laser with an associated positioner-aiming prism was coupled to an operating microscope (Model OPMI-1FC, Zeiss) and the laser beam was directed through the ear canal at the reflective tape on the umbo (Fig. 1). The spectral magnitude and phase information from the laser vibrometer was obtained by a digitizing signal analyzer (Model DSA 601, Tektronix, Beaverton, OR) and recorded on a personal computer. Only data with a total harmonic distortion of less than 10% of pure tone signals according to the distortion index were accepted.

Currently, it is impossible to measure the movement of stapes footplate from lateral approach in an OME model of temporal bones with a sealed and intact middle ear and cochlea. Therefore, an alternative method from the medial ap-

proach to the footplate was proposed as follows. After the completion of measurement on the umbo with one laser, the medial surgical approach to the footplate was performed through the internal auditory canal (IAC) to open the vestibule. A reflective tape was then placed on the medial side in the middle of the footplate as a laser target.

The second laser Doppler vibrometer (LDV; Model OFV-501; Polytec PI, Tustin, CA) with a fiber optic cable with Nikon 50 mm focusing lens was used to measure movement of the footplate. The helium–neon laser was focused onto the reflective tape on the medial side of the footplate and perpendicular to the footplate. Velocity measures of the LDV on the footplate were simultaneously acquired with that measured by the HLV on the TM. The velocity data measured by both lasers were input into the digital signal analyzer (DSA 601, Tektronix) and finally converted as displacement data.

C. Experimental protocols

The control study in which the middle ear pressure remained at zero with no fluid in the cavity was performed first, with either one or two lasers. The following two types of experiments were performed in temporal bones after the control data were acquired.

1. Experiment I—Change of middle ear pressure

The middle ear air pressure was increased stepwise from 0 to +20, then down to −20 cm H_2O (1 cm H_2O=98 Pa, 20 cm H_2O=196 daPa), and finally, back to zero using the syringe attached to the ET catheter in 5 cm H_2O increment. At each step, the pressure was maintained for 30 s until the measurement was completed. Displacement of the umbo and footplate was measured at each middle ear pressure step across frequencies of 200–8k Hz. Note that pressure unit cm H_2O was used in this study and the conversion factor is 1 cm H_2O equal to 98 Pa or 9.8 daPa.

2. Experiment II—Change of middle ear fluid

Normal saline solution was injected into the middle ear cavity through the ET from zero to fully filling the middle ear cavity with the outflow tube open to the atmosphere. The fluid level was under control stepwise using a calibrated syringe filled with saline. The fully filled fluid level was identified by fluid appearance in the transparent outflow tube. Displacements of the umbo and footplate were measured at each fluid step (0.1 ml per step) across frequencies of 200–8k Hz.

Velocity or displacement of the umbo was measured in seven temporal bones (fresh-frozen bones) with an intact cochlea with one laser first. Next, the cochlea was opened and both TM and footplate displacements were measured by two lasers in every bone. For the remaining four bones (one fresh bone), the cochlea was opened at the beginning and two lasers were employed to measure the TM and footplate vibrations simultaneously through the Control, Experiment I (Exp. I), and Experiment II (Exp. II). No obvious difference in experimental measurements was found between fresh and fresh-frozen bones.

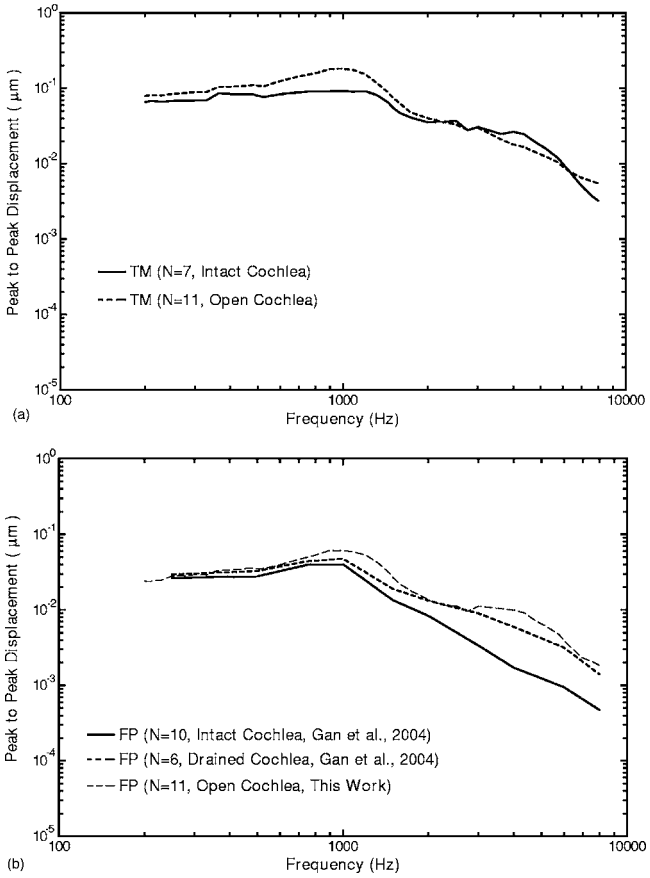

FIG. 2. Comparison of displacements measured at the TM and stapes footplate in temporal bones with intact cochlea and open cochlea. (a) Mean TM displacement curve measured in bones with intact cochlea (solid line) vs that measured with open cochlea (dashed line). (b) Mean footplate displacement (FP) measured from bones with intact cochlea (solid line), drained cochlea (thick broken line), and open cochlea (thin broken line).

III. RESULTS

A. Effect of cochlear load on TM and stapes footplate displacements (control study)

Figure 2(a) shows the mean spectral displacement of the TM (umbo) measured from seven temporal bones with intact cochlea at zero middle ear pressure and no fluid in the cavity (solid line) in comparison with the TM data obtained from 11 bones with opened cochlea (dashed line). The results show that cochlear load mainly affects the TM movement around frequency of 1k Hz. The increase of umbo displacement due to the release of cochlear load changed from 2 dB at 200 Hz to 6 dB at 1k Hz, and then reduced to 1 dB at 2k Hz. There was a small decrease of umbo displacement after the cochlea was opened around 4k and 5k Hz.

The mean control stapes footplate displacement obtained from 11 bones with open cochlea is displayed in Fig. 2(b) (broken line). The mean footplate displacement measured from 10 bones with intact cochlea (solid line) and from 6 bones with drained cochlea (dashed line) published by Gan *et al.* (2004) are also presented in Fig. 2(b). The results show that cochlear load mainly affects the footplate movement at high frequencies ($f \geqslant 1$k Hz), especially, around 4k Hz, consistent with the published data obtained with drained cochlea by Gan *et al.* (2004). The difference between the opened

cochlea and drained cochlea suggests that in the previous study with drained cochlea, the cochlear bony wall was not open and some fluid might still remain inside the cochlear cavity. Therefore, the displacement curve obtained in this study is higher than the curve obtained in previous study with drained cochlea. The TM and footplate data presented in Fig. 2 were used to estimate the effect of cochlear load on transfer function of the middle ear in Sec. IV of this paper.

B. Effect of middle ear pressure on TM and stapes footplate movements—Exp. I

Figure 3(a) shows the mean spectral displacement (magnitude) of the TM (umbo) with standard error (S.E.) bars measured from seven temporal bones with intact cochlea in response to positive middle ear pressure from 0 to 20 cm H_2O. The 90 dB sound pressure was applied in the ear canal near the umbo over the frequency range of 200–8k Hz. Figure 3(b) shows the mean phase angles of the umbo displacement measured from five bones. The curves in Fig. 3(a) clearly display that positive middle ear air pressure reduced the umbo displacement at frequencies less than 1500 Hz. Statistical analysis (P values) obtained from Student t test for the data shown in Fig. 3(a) reveals that there were significant differences between the control (zero pressure) and experimental data at pressure steps of 10, 15, and 20 cm H_2O at frequencies less or equal to 1000 Hz (P value <0.05). At 5 cm H_2O, the significant difference was only observed at 750 Hz.

The effect of negative middle ear pressure from 0 to −20 cm H_2O on TM (umbo) displacement measured from seven bones with intact cochlea are displayed in Fig. 4. The mean magnitude data are shown in Fig. 4(a). Figure 4(b) displays the mean phase angle data measured from five bones. Statistical analysis of the data in Fig. 4(a) shows that there were significant differences between the control (zero pressure) and experimental data of all pressure steps at less or equal to 1000 Hz (P value <0.05). Negative middle ear pressure of −5 cm H_2O resulted in a significant decrease of the umbo displacement at frequencies $\leqslant$1000 Hz and the positive 5 cm H_2O pressure only resulted in significant difference of the umbo displacement at 750 Hz.

The mean displacements simultaneously measured at the TM and stapes footplate using two laser vibrometers on 11 bones with opened cochlea are shown in Figs. 5 and 6 when the middle ear positive pressure was varied from 0 to 20 cm H_2O. Figures 5(a) and 6(a) present the mean displacement curves (magnitude) and Figs. 5(a) and 6(b) present the phase angle data obtained from one bone. There was a lack of statistical phase data measured from the bones with two lasers and we did not use mean ± S.E. data in Figs. 5(b) and 6(b). The statistical results from the umbo and footplate displacement magnitude data in Figs. 5(a) and 6(a) show that there were significant differences between the control (zero pressure) and experimental data for pressure steps of 10, 15, and 20 cm H_2O at frequencies $\leqslant$1000 Hz for both TM and footplate displacements (P value <0.05). At 5 cm H_2O, the significant difference was observed at frequencies $\leqslant$750 Hz.

The mean displacement curves simultaneously measured at the TM (umbo) and footplate are shown in Figs. 7 and 8

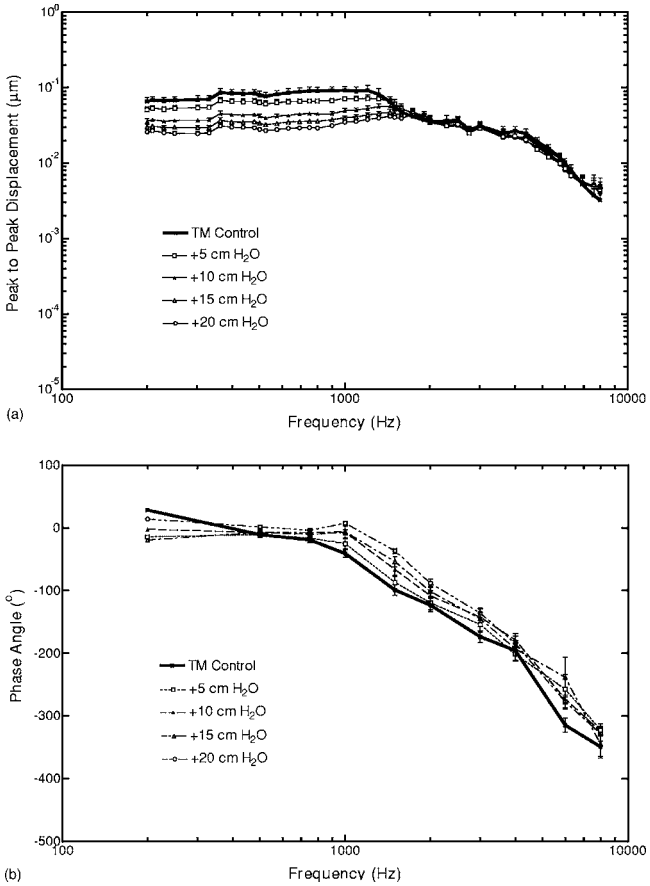

FIG. 3. Peak-to-peak displacement of the TM at the umbo (mean ± S.E.) measured from 7 bones with intact cochlea. The middle ear pressure was varied from 0 to +20 cm H_2O (1 cm H_2O=98 Pa). (a) Magnitude; (b) phase angle.

when the middle ear pressure was changed from 0 to −20 cm H_2O. Figures 7(a) and 8(a) display the mean displacement magnitude curves and Figs. 7(b) and 8(b) are the phase angle data measured from one bone. The statistical results for displacement magnitude show that displacement at the TM changed significantly when middle ear air pressure was varied from 0 to −5, −10, −15, and −20 cm H_2O at frequencies $\leqslant$1000 Hz (P value <0.05). At 1500 Hz, the umbo displacement had significant change only when pressure varied to −20 cm H_2O.

The displacement at the footplate had significant changes when middle ear pressure was varied from 0 to −10, −15, and −20 cm H_2O for frequencies $\leqslant$1000 Hz. At 1500 Hz, there was no significant change of the footplate movement for overall negative pressure changes. At −5 cm H_2O, the footplate displacement was affected significantly at frequencies $\leqslant$750 Hz.

In summary, the statistical analysis (the details not shown here) indicate that the positive and negative static pressures in the middle ear generally affect the movement of the TM and footplate at frequencies less than 1500 Hz.

C. Effect of fluid in middle ear cavity on TM and stapes footplate movements—Exp. II

Figure 9 shows the effect of normal saline solution in the middle ear cavity on displacement of the TM (umbo)

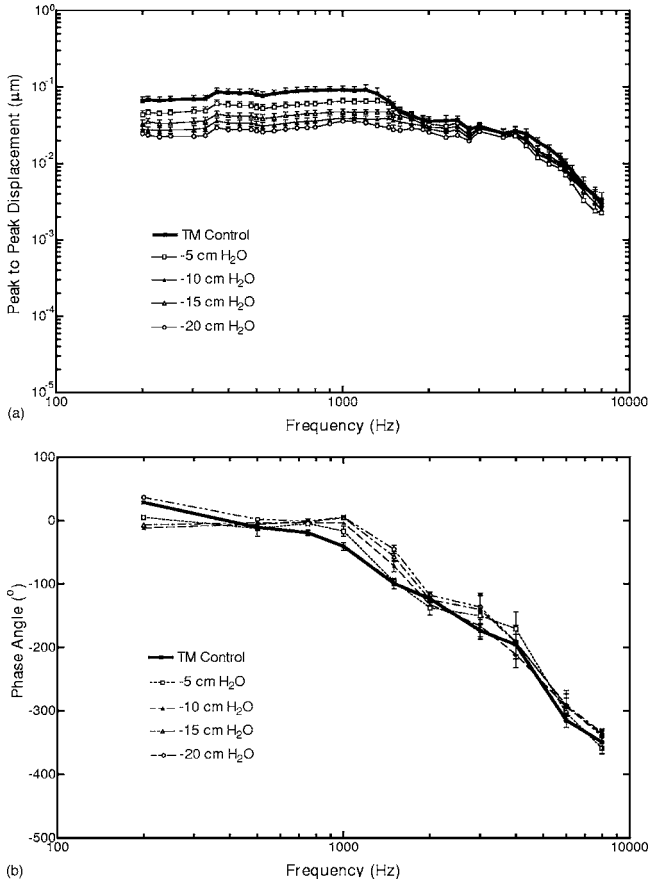

FIG. 4. Peak-to-peak displacement of the TM at umbo (mean ± S.E.) measured from seven bones with intact cochlea. The middle ear pressure was varied from 0 to −20 cm H_2O. (a) Magnitude; (b) phase angle.

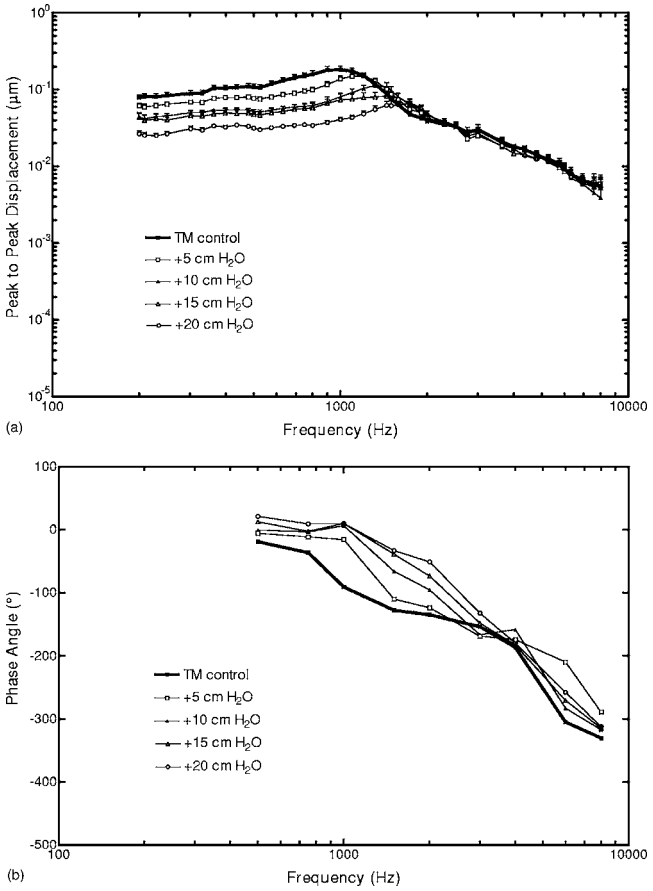

FIG. 5. Peak-to-peak displacement of the TM at the umbo (mean ± S.E.) measured from 11 bones with open cochlea. The middle ear pressure was varied from 0 to +20 cm H_2O. (a) Magnitude; (b) phase angle (one bone).

obtained from seven bones with intact cochlea. Saline solution was injected into the middle ear cavity through the syringe attached to the ET catheter from 0 to 0.6 ml, fully filling the cavity. Note that the maximum fill of 0.6 ml was not measured in all bones due to individual bone variations. Figure 9(a) displays the mean frequency response curves of the TM displacement magnitude and Fig. 9(b) presents the mean phase angles with S.E. obtained from five bones.

The curves in Fig. 9(a) demonstrate that fluid in the middle ear cavity caused reduction of the TM displacement, which was strongly dependent on frequency as well as the amount of fluid in the cavity. Statistical analysis of the TM displacement data in Fig. 9(a) reveals that the significant differences between the control (no fluid in the middle ear) and experimental data (with fluid in the middle ear) were observed when as little as 0.3 ml of fluid was injected into cavity at frequencies $\geqslant$1000 Hz. When the amount of fluid in the middle ear was increased to 0.4 and 0.5 ml, the TM displacement had significant reduction at frequencies $\geqslant$500 Hz. As fluid volume was increased to 0.6 ml, the reduction of TM movement became significant at 300 Hz. Therefore, as the amount of fluid in the middle ear was increased, the beginning frequency for significant reduction of the TM displacement moved to lower frequencies. There was a critical volume of fluid in the cavity at which the umbo velocity or displacement started decreasing significantly in comparison with the normal, no fluid condition. This critical value of 0.3 ml was identified from the experimental data in Fig. 9(a). The 0.3 ml is approximately equal to the fluid level filled up to the umbo or about 50% of the middle ear cavity volume.

The effects of fluid in the middle ear on displacement of the TM and footplate are displayed in Figs. 10 and 11, respectively. Figures 10(a) and 11(a) show the mean displacements of the TM and footplate obtained from 11 bones with opened cochlea. The reduction of the TM or footplate displacement measured from these mean curves was 20 dB across frequencies of 1k–6k Hz when the cavity was filled by saline solution (0.6 ml). Figures 10(b) and 11(b) present the phase angle data obtained from one bone. The statistical results from the umbo and footplate data in Figs. 10(a) and 11(a) show that there were significant reductions of both TM and footplate displacements at frequencies $\geqslant$1000 Hz when 0.2 ml fluid was injected in the middle ear. As the amount of fluid in the cavity reached 0.3 ml, the TM and footplate displacements dropped significantly at frequencies $\geqslant$750 Hz. With fluid volume reaching 0.4, 0.5, or 0.6 ml, the displacement curves of the umbo and footplate became close to each other. At frequencies $\leqslant$300 Hz, there were no significant differences between the control (no fluid) and Exp. (with fluid) on both TM and footplate displacements (detailed statistical data not shown here).

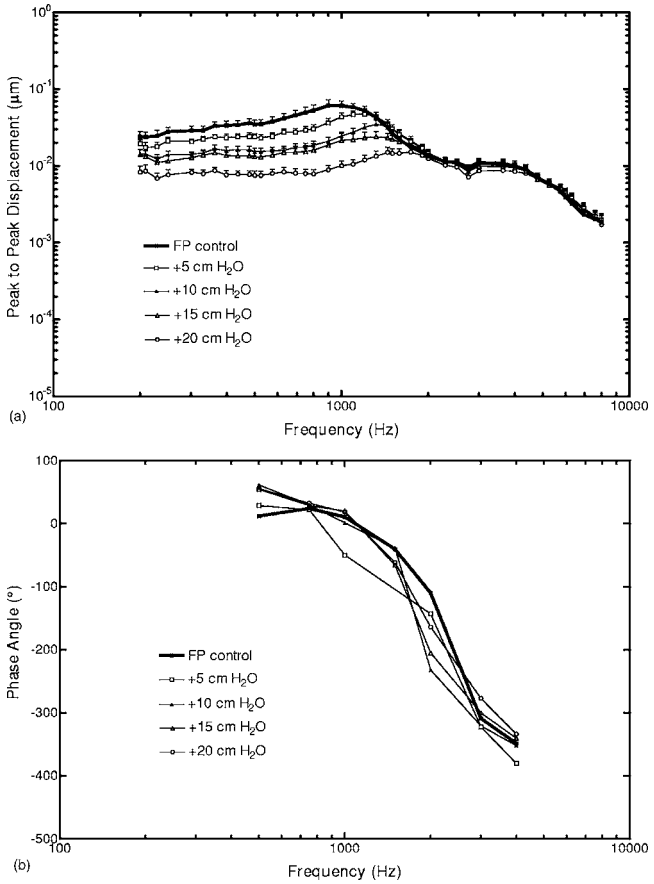

FIG. 6. Peak-to-peak displacement of the stapes footplate (FP, mean ± S.E.) measured from the medial side of the footplate in 11 bones with open cochlea. The middle ear pressure was varied from 0 to +20 cm H_2O. (a) Magnitude; (b) phase angle (one bone).

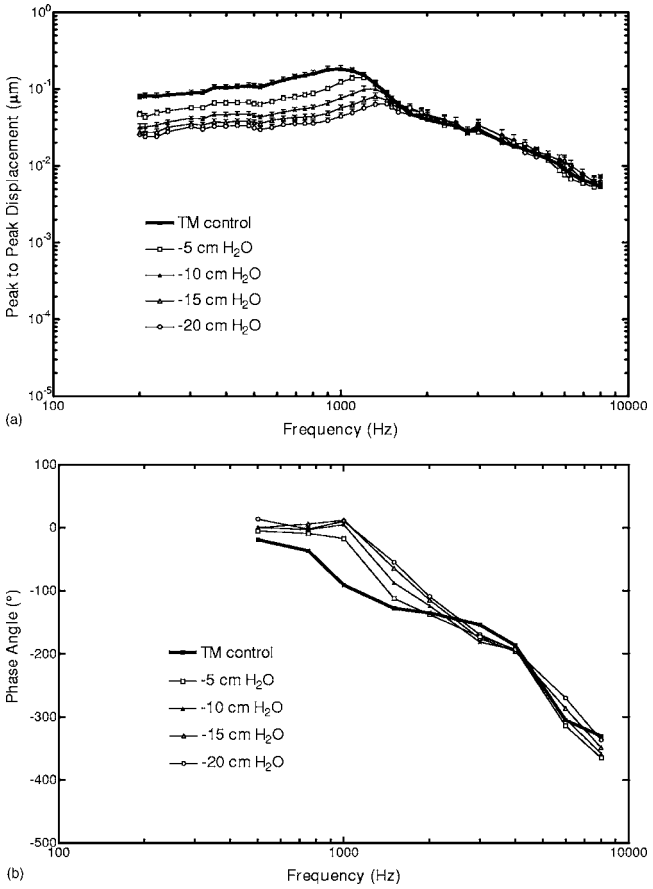

FIG. 7. Peak-to-peak displacement of the TM at the umbo (mean ± S.E.) measured from 11 bones with open cochlea. The middle ear pressure was varied from 0 to −20 cm H_2O. (a) Magnitude; (b) phase angle (one bone).

IV. DISCUSSION

A. Comparison with published data

1. Effect of middle ear pressure on TM movement

As can be seen in Figs. 3 and 4, there were significant reductions of the TM (umbo) displacement at low frequencies ($f \leqslant 1500$ Hz) when the middle ear pressure was varied from 0 to 20 cm H_2O or from 0 to −20 cm H_2O. There was no effect on TM movement at high frequencies ($f \geqslant 1500$ Hz). The reduction of TM displacement at 20 and −20 cm H_2O was about 8 dB and the rate of decrease in displacement was about 2 dB per 5 cm H_2O. This decreasing rate remained almost unchanged for either positive or negative pressure cycles.

The effect of graded variations in middle ear pressure on umbo movement in human temporal bones was reported by Murakami *et al.* (1997). They used a video measuring system to detect the umbo displacement when a constant sound pressure of 134 dB was delivered at the TM. The frequency range for their data was between 200 and 3.5k Hz. Figures 12(a) and 12(b) show the comparison of our data obtained at 0 (control), ±5, and ±20 cm H_2O with Murakami *et al.*'s data which were modified to 90 dB SPL. The umbo displacements reported by Murakami *et al.* at control and 5 or −5 cm H_2O were higher than our data at frequencies below 1.5k Hz. The displacements measured at 20 and −20 cm H_2O were close to our data. The umbo displacement had a significant reduction at frequencies below 1.5k Hz when positive or negative pressure was applied, which is similar to Murakami *et al.*'s results except that they found the umbo displacement decreased at frequencies less than 1.2k Hz.

Moreover, the different effect of positive and negative pressure on umbo movement reported by Murakami *et al.* is consistent with our results presented here. At positive middle ear pressure [Figs. 3 and 12(a)], there was almost no differentiation between the umbo displacements measured at different pressure steps at high frequencies ($f \geqslant 2$k Hz). When negative pressure steps were applied, there were obvious variations of the displacement at frequencies ⩾2k Hz [see Figs. 4 and 12(b)]. Murakami *et al.* reported the umbo displacement value was higher than the control data at frequencies of 1.4k to 3k Hz [see Fig. 12(b)].

The difference between our data and that reported by Murakami *et al.* was mainly due to different techniques for measuring vibration and a different experimental setup with temporal bones and input sound pressure levels. In our study, the middle ear pressure was monitored precisely and directly by a manometer instead of the tympanometer used by Murakami *et al.* The input sound pressure in our study was maintained at 90 dB which is considered to be in the linear response range of the middle ear. The sound pressure of 134 dB used by Murakami *et al.* may reach the nonlinear response range of the middle ear system (Bourgeade and

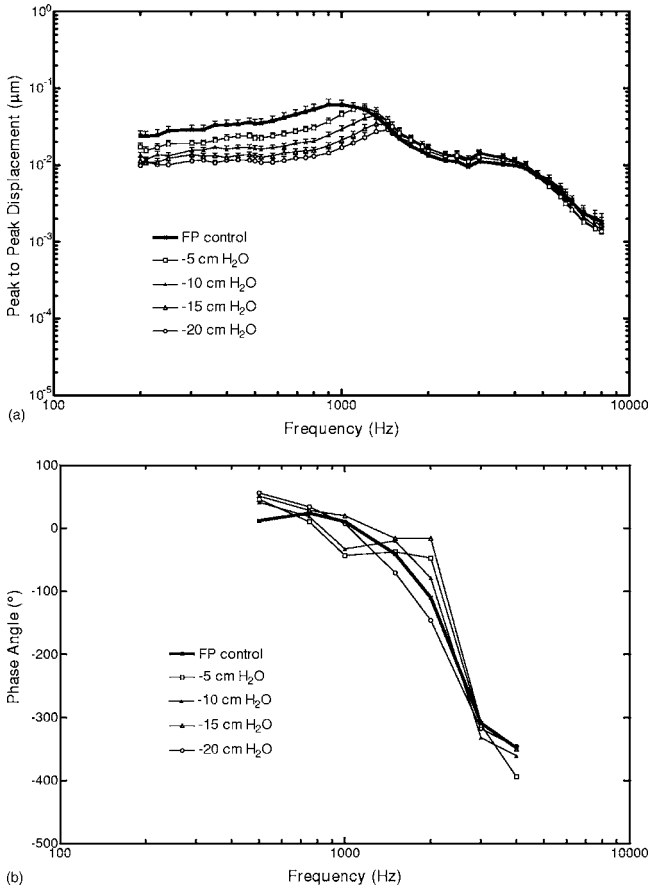

FIG. 8. Peak-to-peak displacement of the stapes footplate (FP, mean ± S.E.) measured from the medial side of the footplate in 11 bones with open cochlea. The middle ear pressure was varied from 0 to −20 cm H_2O. (a) Magnitude; (b) phase angle (one bone).

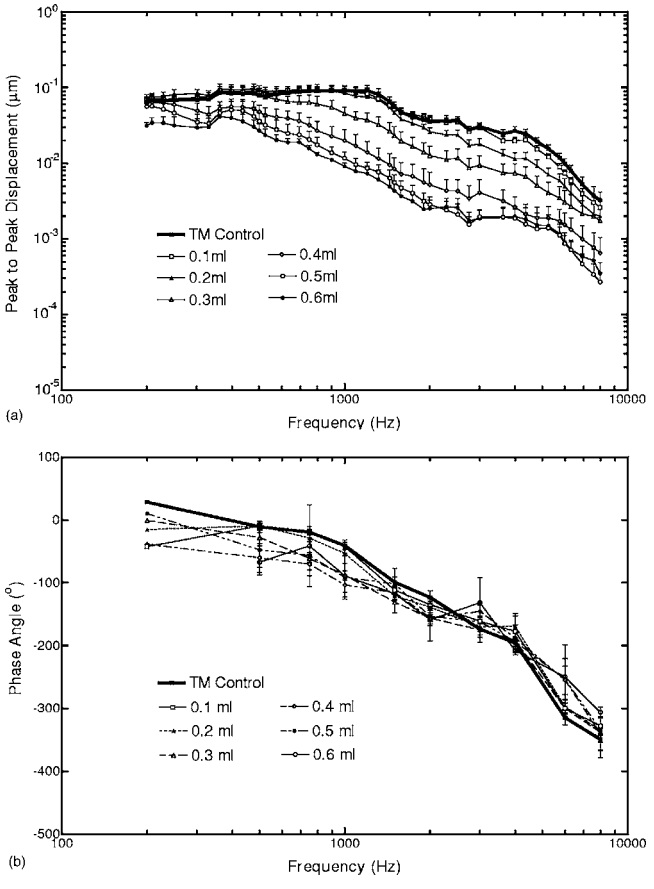

FIG. 9. Peak-to-peak displacement of the TM at the umbo (mean ± S.E.) measured from seven temporal bones with intact cochlea when saline solution was introduced into the middle ear cavity from 0 to 0.6 ml (filled the cavity). The middle ear pressure was maintained at zero. (a) Magnitude; (b) phase angle.

Pascal, 1998). However, the results published by Murakami *et al.* are generally consistent with the work we reported here.

A comparison between our data and other published data on TM displacement or velocity normalized with maximum value as middle ear pressure sweeps at 1k Hz is shown in Fig. 12(c). Lee and Rosowski's (2001) data were measured from gerbil ears at two locations on the TM, umbo (H_U) and pars flaccida (H_{PF}). Murakami *et al.*'s (1997) data were measured from cadaver temporal bones at the umbo. The measurements of H_U and H_{PF} from gerbil ears show an asymmetric response for middle ear pressure sweeps from negative to positive. Negative pressure caused a larger, reduction in umbo and pars flaccida velocity than positive pressure did. In human cadaver ears, both our and Murakami *et al.*'s data show that the umbo displacement data were almost symmetric and the absolute reduction value of the TM movement caused by positive and negative pressure is similar at 1k Hz.

2. Effect of fluid in middle ear on TM movement

The results in Fig. 9 show that significant reductions of TM (umbo) displacement were measured over almost all frequencies, particularly, the frequencies greater than 300 Hz and that TM displacement was strongly related to fluid volume in the cavity. TM displacement was decreased by 6 and 10.5 dB at frequencies of 1k and 6k Hz, respectively, when 0.3 ml saline solution was injected into the cavity. When the fluid level reached 0.6 ml (full), a 20 dB reduction of displacement was measured at the TM between 1k and 6k Hz.

The umbo displacement values with different fluid levels (Fig. 9) were compared with the data reported by Ravicz *et al.* (2004) in Fig. 13. The curves measured by Ravicz *et al.* on one bone (Fig. 4 of their paper) with no saline (control), saline on 50% of TM, and the middle ear cavity filled with saline (100% middle ear cavity) were compared to the curves measured at control (no fluid), 0.3 ml (fluid to umbo), and 0.6 ml (cavity full) in the present study. The frequency range covered by Ravicz *et al.* was up to 3k Hz and that conducted in this study was up to 8k Hz. As can be seen in Fig. 13, there were some variations between our data and Ravicz *et al.*'s results, but the measurements reported here generally agree with the data obtained by Ravicz *et al.*

The difference between our and Ravicz *et al.*'s data may be related to different bone experimental setup. In the present study, the temporal bone and entire middle ear system were maintained intact. Thus, the injected fluid may not completely fill the middle ear cavity or mastoid additus. However, in temporal bone experimental setup by Ravicz *et al.*, the mastoid air cells were removed, a facial recess approach was conducted, and the mastoid segment of the facial nerve was removed. Therefore, air trapped in the sinus tympani may respond differently and may affect TM movement.

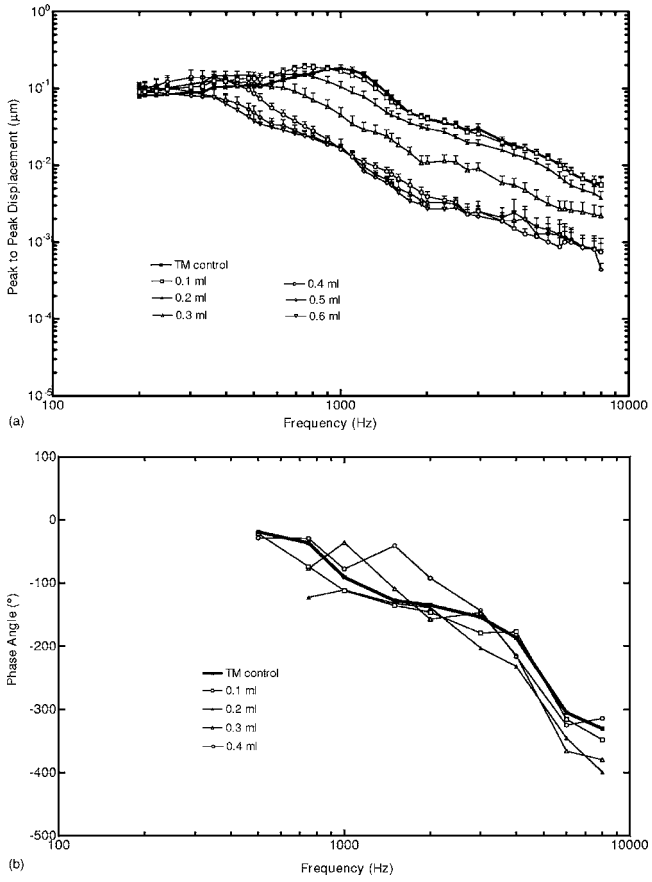

FIG. 10. Peak-to-peak displacement of the TM (mean ± S.E.) from 11 bones with open cochlea when saline was introduced into the middle ear cavity from 0 to 0.6 ml (filled middle ear cavity). The middle ear pressure was maintained at zero. (a) Magnitude; (b) phase angle (one bone).

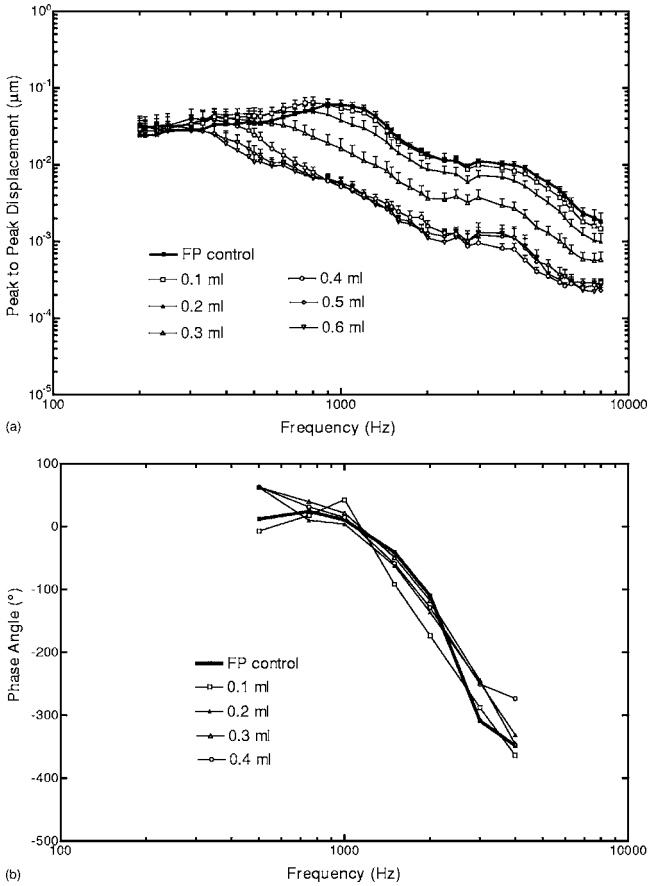

FIG. 11. Peak-to-peak displacement of the stapes footplate (FP, mean ± S.E.) from the medial side of the footplate in 11 bones with open cochlea when saline was introduced into the middle ear cavity from 0 to 0.6 ml (filled the cavity). The middle ear pressure was maintained at zero. (a) Magnitude; (b) phase angle (one bone).

B. Estimation of cochlear load effect

An alternative approach by measuring displacement of the stapes footplate from the medial side with an opened cochlea was performed in 11 bones with two lasers, one laser aiming on the umbo and another aiming on the medial site of the footplate. With the displacement data measured at the umbo and footplate, the transfer function of the middle ear for sound transmission can be described as the displacement transmission ratio of the TM to footplate (DTR). However, cochlear impedance, which is characterized by the mass and viscosity of cochlear fluid and stiffness of cochlear partitions, was removed when the cochlea was opened in those bone experiments. To estimate the effect of cochlear load on experimental data obtained in this study, we first compared the TM displacements measured from the bones with intact cochlea and that with open cochlea [Fig. 2(a)]. A maximum of 6 dB enhancement of the TM displacement due to the release of cochlear load was observed at 1k Hz. For stapes footplate displacement, we used published data measured in bones with intact cochlea (Gan *et al.*, 2004) and compared these data with the footplate displacement data obtained in bones with open cochlea in the present study [Fig. 2(b)]. The comparison of the TM and footplate movements under control condition, that is, zero middle ear pressure and no fluid in the cavity (Fig. 2), provides the base line for estimating the cochlear load effect on experimental data obtained in Exp. I and Exp. II or under middle ear pressure and fluid in the middle ear cavity.

Figure 14(a) shows the ratio of the TM displacement magnitude measured from 11 bones with open cochlea (mean value) to the mean displacement data measured from seven bones with intact cochlea when positive pressure was applied. Figure 14(b) displays the TM displacement ratio in response to negative pressure steps and Fig. 14(c) shows the TM displacement ratio when fluid in the middle ear was increased. As shown in Fig. 14(a), the peak value, or the maximum enhancement of the TM displacement by removing cochlear load, had a slight decrease (less than 1.6 dB) when the pressure was increased from 0 to 20 cm H_2O. When negative pressure was applied and varied from 0 to −20 cm H_2O [Fig. 14(b)], the peak value remained almost the same after an initial 0.8 dB increase in response to −5 cm H_2O pressure change. It is also observed that there is a peak frequency shift from 1k Hz to a higher frequency between 1 and 1.5k Hz in both positive and negative pressure situations. Note that the peak frequency change can be detected from the results in Figs. 3 and 5 for positive pressure and Figs. 4 and 6 for negative pressure as well.

These observations from experimental results on the effect of middle ear pressure on TM movement reveal that removing of cochlear load results in a maximum enhance-

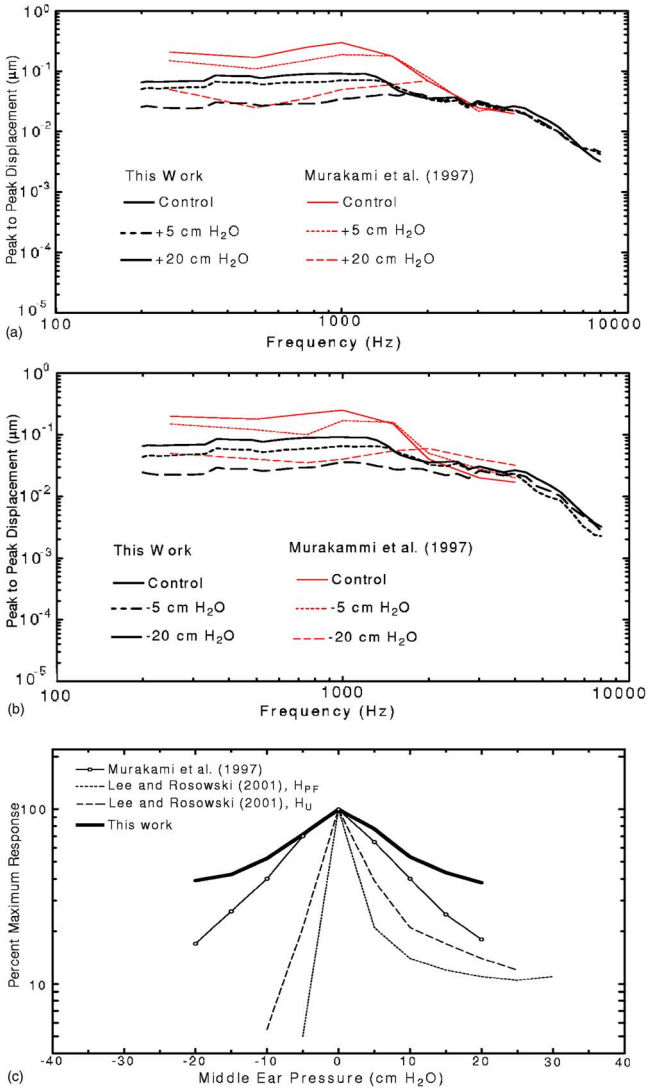

FIG. 12. (Color online) Comparison of our TM displacement data measured from seven bones with intact cochlea with previously published data. (a) Mean displacement of the TM obtained at positive middle ear pressure in this study compared with Murakami *et al.*'s (1997) results; (b) mean displacement of the TM obtained at negative middle ear pressure in this study compared with Murakami *et al.*'s (1997) results; (c) comparison of our TM displacement data obtained as middle ear pressure sweeps at 1000 Hz with Lee and Rosowski's (2001) and Murakami *et al.*'s (1997) results.

ment of the TM displacement of 6 dB at frequencies between 1 and 1.5k Hz in either control (zero pressure) or positive or negative middle ear pressure conditions. This finding suggests that the mechanical behavior of the middle ear system, which includes the stiffness and damping of the TM, ossicles, ossicular joints, and suspensory ligaments may not be affected by the cochlear load (or fluid inside cochlea) when the middle ear air pressure was changed.

When fluid in the middle ear cavity was increased from 0 to 0.3 ml, the peak enhancement of the TM displacement due to removal of cochlear load was decreased from 6 to 2.4 dB as shown in Fig. 14(c). The peak frequency was shifted to a low frequency between 600 and 1k Hz. When fluid volume reached 0.4 ml, the peak value did not change much from the control, but the peak frequency moved to a lower frequency about 300 Hz. A fluid volume of 0.4 ml was considered to reach the stapes in this study. The high jumps

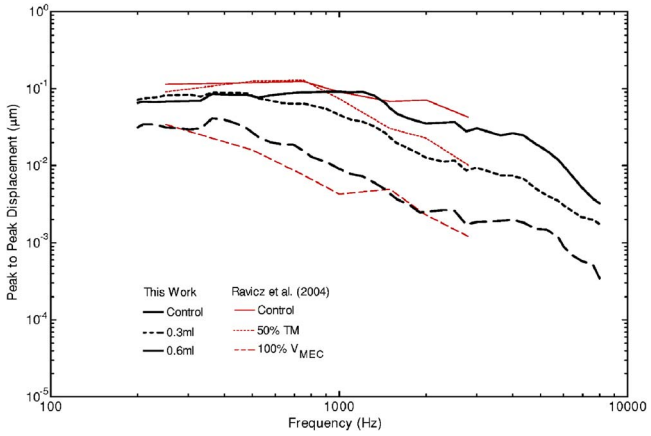

FIG. 13. (Color online) Comparison of our TM displacement measurements (mean) in seven bones with intact cochlea with Ravicz *et al.*'s (2004) data when saline was introduced to the middle ear cavity. There are three fluid levels for comparison: Control (no fluid), fluid level to umbo, and fluid filled cavity.

of the curves at 0.5 and 0.6 ml shown in Fig. 14(c) are considered not realistic, which may be caused by experimental errors when filling the cavity. The middle ear cavity might not be completely filled by the same maximum volume of fluid in the experiments with open cochlea as that with intact cochlea. There were also some effects from the anatomy variation of individual middle ear cavity and possible air bubbles trapped in with fluid.

In summary, the absolute value of the maximum increase of TM displacement reflects the effect of removing cochlear load. The peak frequency shift under middle ear pressure and fluid volume variations is mainly induced by middle ear pressure and fluid in the cavity.

C. Transfer function of middle ear

1. Transfer function of middle ear directly measured from bones with opened cochlea

There are three definitions of middle ear transfer function for the study of middle ear mechanics (Gan *et al.* 2004). In this paper, the DTR, displacement transmission ratio of the TM to footplate, was used to describe the middle ear transfer function. Figures 15(a)–15(c) show the DTR values calculated from the TM and footplate displacements (mean magnitude) in Figs. 5 and 6 (positive pressure), Figs. 7 and 8 (negative pressure), and Figs. 10 and 11 (middle ear fluid), respectively. These three figures present the transfer function of middle ear directly measured from 11 bones with open cochlea. As can be seen in Fig. 15(a), the DTR was increasing as positive middle ear pressure varied from 0 to 20 cm H_2O at frequencies from 200 to 2k Hz. At 4–8k Hz, the DTR decreased slightly as middle ear pressure increased, which is opposite to that observed at frequencies below 2k Hz. There was a transition frequency range of 2–4k Hz in which the DTR was across the control line as the pressure varied. The results in Fig. 15(a) indicate that the efficiency of sound transmission from the TM to footplate was decreased as middle ear positive pressure increased over the frequency range of 200 to 2k Hz.

The transfer function of middle ear shows different behavior in Fig. 15(b). The DTR decreased from the control

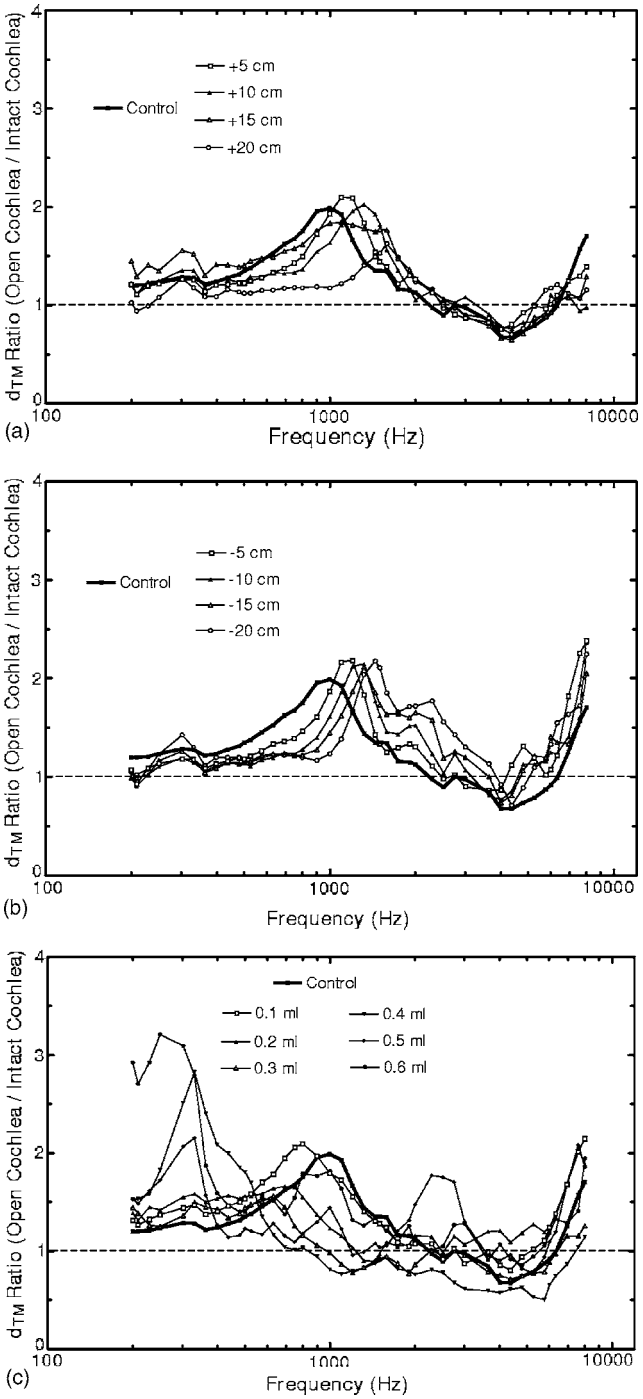

FIG. 14. Ratio of the TM displacement at the umbo (d_{TM}) between the d_{TM} measured in bones with open cochlea and that measured in bones with intact cochlea in three experimental situations: (a) Positive middle ear pressure increased from 0 (control) to 5, 10, 15, and 20 cm H_2O; (b) negative middle ear pressure decreased from 0 to −5, −10, −15, and −20 cm H_2O; (c) fluid volume in the cavity varied from 0 to 0.6 ml (a full middle ear cavity).

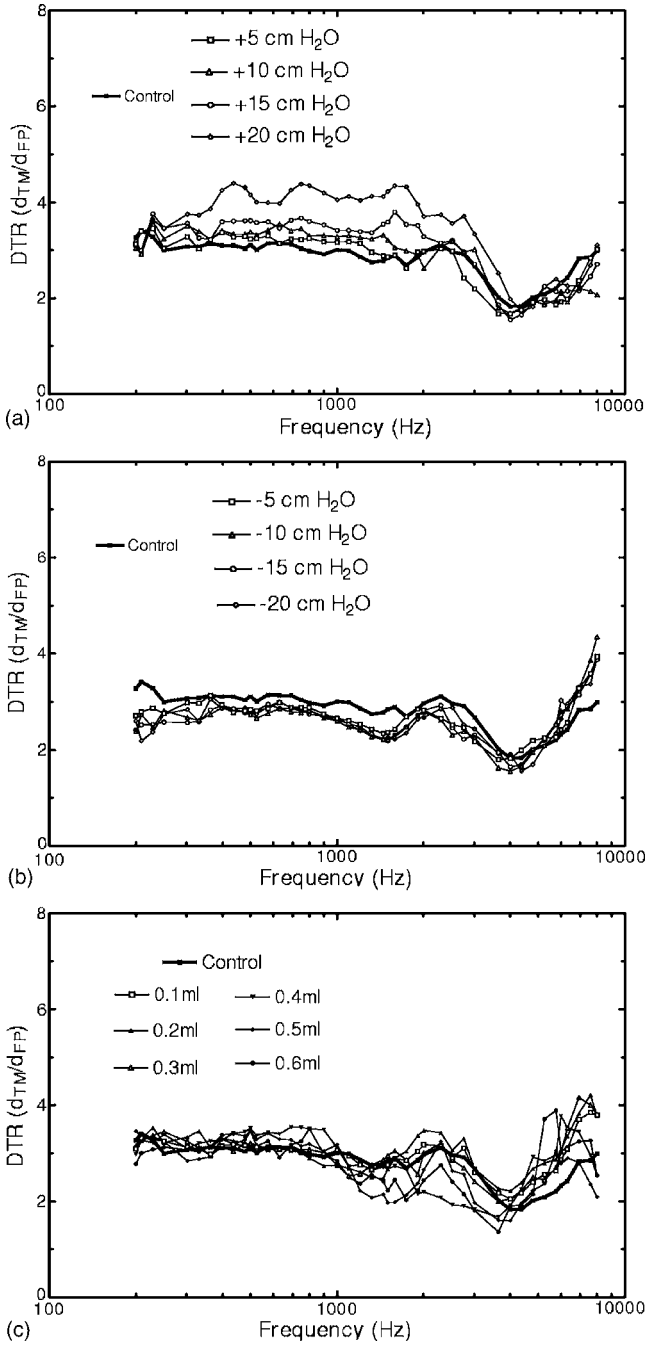

FIG. 15. Transfer function of the middle ear, or DTR, directly measured from 11 bones with open cochlea: (a) Positive middle ear pressure increased from 0 (control) to 5, 10, 15, and 20 cm H_2O; (b) negative middle ear pressure decreased from 0 to −5, −10, −15, and −20 cm H_2O; (c) fluid volume in the cavity varied from 0 to 0.6 ml.

line when middle ear pressure became negative at 200 to 4k Hz and there was no differentiation of the DTR when pressure was varying from −5 to −10, −15, and −20 cm H_2O. At higher frequencies (4–8k Hz), the DTR increased as the pressure became more negative (from −5 to −20 cm H_2O). The results in Fig. 15(b) suggest that the efficiency of vibration transmission from the umbo to footplate had a slight drop when −5 cm H_2O appeared in the middle ear, but this change was not sensitive to further decreases in pressure from −5 to −20 cm H_2O.

When fluid was introduced into the middle ear with a volume less than 0.3 ml, the effect on transfer function was very limited at frequencies below 1k Hz as shown in Fig. 15(c). The change of impedance and damping of middle ear system was not affected very much by a small amount of fluid at low frequencies. As the fluid increased to 0.4, 0.5, and 0.6 ml, the effect of fluid on DTR became obvious at three frequency ranges. The DTR was increased at $f < 800$ Hz and $f > 4$k Hz and decreased at 1–4k Hz.

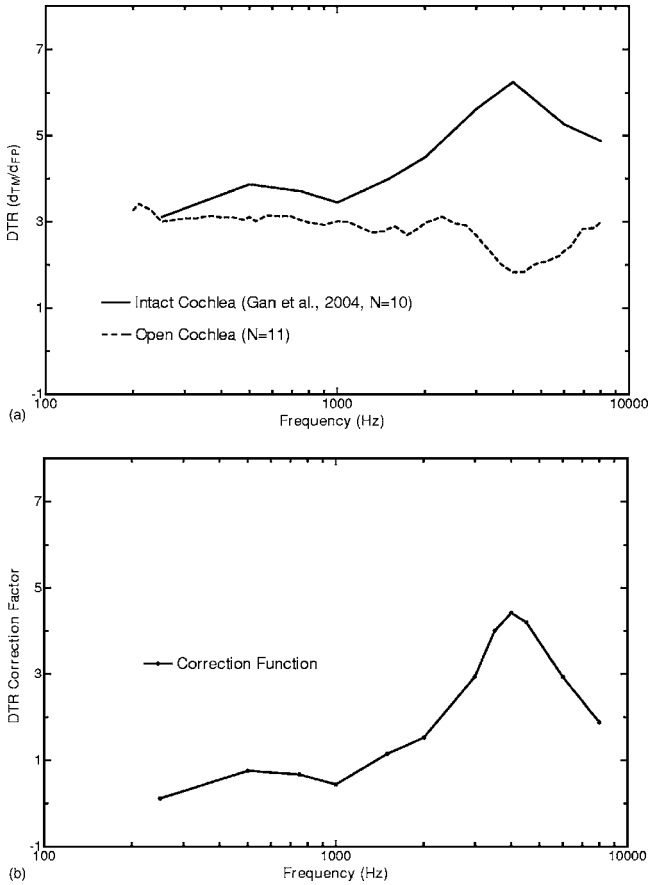

FIG. 16. DTR correction factor for cochlear load derived from this study and previously published data. (A) The DTR spectral curves obtained in bones with open cochlea in this study vs the curves obtained in bones with intact cochlea by Gan *et al.* (2004); (B) the DTR correction function for cochlear load calculated from part (A).

2. Transfer function of middle ear derived with cochlear load correction function

The transfer function of the middle ear, DTR, shown in Fig. 15 represents the "isolated" middle ear system in response to physical state changes in the middle ear for acoustic-mechanical transmission. There was no cochlear impedance applied on the medial side of the stapes footplate. To derive the transfer function of middle ear in normal cadaver bones, we generated a spectral correction factor to include the cochlear load effect on DTR as shown in Fig. 16. Of the two curves in Fig. 16(a), one was from published data with intact cochlea (Gan *et al.*, 2004) and another curve was obtained from the present study with open cochlea. Both curves were measured in temporal bones at zero middle ear pressure and no fluid in the cavity. The DTR difference between these two curves across the entire frequency range provides the correction factor for cochlear load shown in Fig. 16(b). The peak of the correction function at 4k Hz represents that cochlea has maximum effect on displacement transmission from the TM to footplate around 4k Hz.

Using the correction function we modified the data in Fig. 15 and derived the transfer function of middle ear under various middle ear pressure and fluid conditions. The calculation was based on the assumption that the middle ear is a

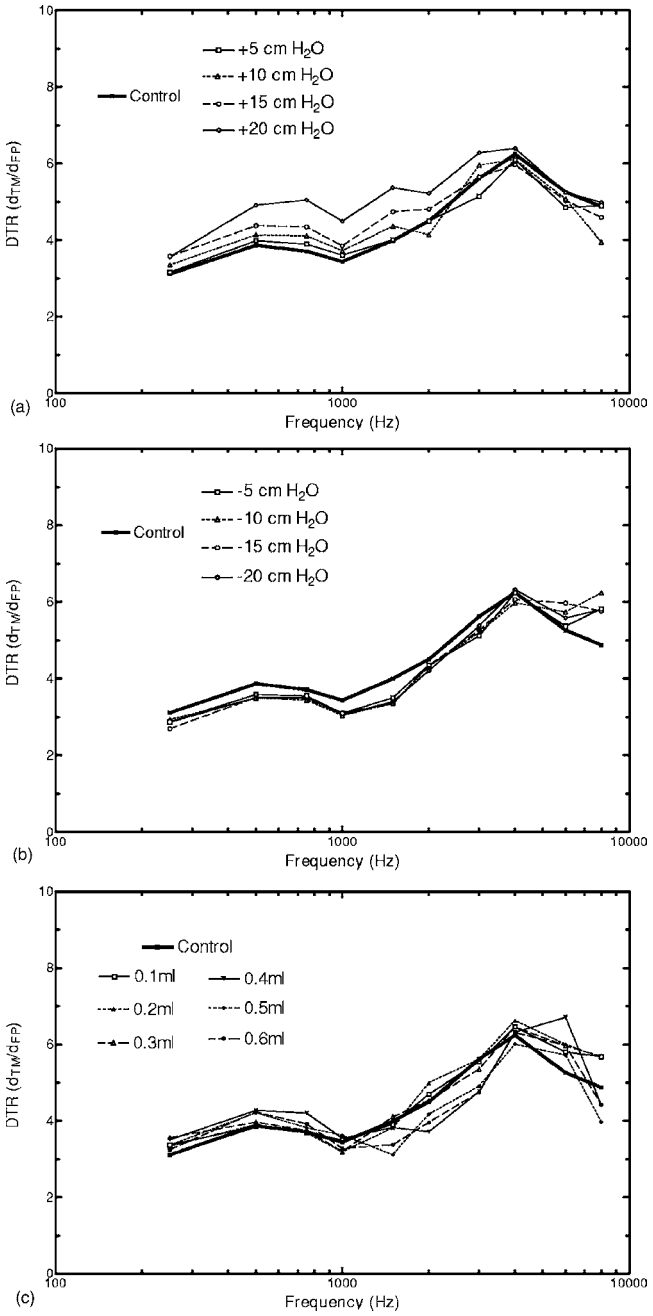

FIG. 17. DTR obtained in an otitis media with effusion model in human temporal bones with three mechanical changes in the ear: (a) Positive middle ear pressure increased from 0 (control) to 5, 10, 15, and 20 cm H_2O; (b) negative middle ear pressure decreased from 0 to −5, −10, −15, and −20 cm H_2O; (c) fluid in the cavity varied from 0 to 0.6 ml (a full middle ear cavity).

linear system. The mechanical properties of the middle ear system are not affected by cochlear load when the middle ear pressure and fluid variations were applied.

Figures 17(a) and 17(b) display the transfer function (DTR) when positive or negative middle ear pressure was applied stepwise, and Fig. 17(c) shows the DTR when fluid volume was varied in the middle ear cavity. These three figures reveal that: (1) The DTR increases with frequency increasing up to 4k Hz in all three experimental conditions, which indicates that the efficiency of the middle ear for sound transmission from the TM to footplate decreases as frequency increases to 4k Hz. At frequencies over 4k Hz, the

efficiency increases. (2) Middle ear pressure has different effects on middle ear transfer function. With positive pressure, the DTR increases with the pressure value increases. With negative pressure, there is no much change of the DTR in response to pressure variation (e.g., from −5 to −20 cm H_2O). (3) There are three frequency ranges in which the DTRs show different responses to fluid level variations in the middle ear. At frequencies below 1k Hz, a small increase of the DTR is observed as the fluid level increases. At frequencies between 1 and 4k Hz, the DTR is less than the control value as the fluid increases. At higher frequencies ($f > 4$k Hz), the opposite effect is observed.

It is important to clarify that the middle ear transfer function reported here represents the combined effect of the TM and stapes footplate movements in response to middle ear pressure and fluid variations. The DTR is more complicated than the umbo or footplate displacement. Therefore, the TM or footplate displacement curves may not reveal middle ear function completely.

The middle ear system consists of the tympanic membrane, middle ear ligaments, ossicles, and cavity. The stiffness or mechanical properties of the system change with the stress state which is dependent on the structure, and the air or fluid in the cavity. Mechanical analysis of the middle ear system under different air pressure and fluid volumes needs to be investigated further based on the biomechanics of middle ear tissues and the whole organ (Gan *et al.*, 2006). To fully understand the structure-function relationship with fluid and air in the middle ear, we are currently conducting multifield coupled finite element analysis on the established 3D model of the human ear.

V. CONCLUSION

A well-designed otitis media with effusion model in human temporal bones was created. By measuring the velocity or displacement of the stapes footplate from the medial side of the footplate, an alternative measurement approach was described. Two laser vibrometers were used to simultaneously measure the TM and footplate vibrations under various fluid levels in the cavity and different middle ear pressures. The transfer function of the middle ear, or the displacement transmission ratio of the TM to footplate (DTR), was derived under positive and negative middle ear pressure and fluid volume variation in the cavity with a correction factor for cochlear load. The results suggest that (1) the DTR increases with frequency increasing up to 4k Hz when the middle ear pressure was changed from 0 to 20 cm H_2O or from 0 to −20 cm H_2O and fluid level from 0 to a full middle ear cavity; (2) positive and negative middle ear pressures have shown different effects on the transfer function; and (3) the effect of fluid in the cavity on middle ear transfer function is different between three frequency ranges: $f < 1$k, between 1 and 4k, and $f > 4$k Hz. The data reported in this paper provide new knowledge on acoustic-mechanical transmission through the middle ear and the effect of cochlear load on middle ear function with fluid in the cavity and variations of middle ear pressure.

ACKNOWLEDGMENTS

The authors thank Don Nakmali, BSEE, for assisting temporal bone experiments and Kenneth J. Dormer, Ph.D., for acquiring temporal bones. This work was supported by the NIH/NIDCD Grant No. R01DC006632.

Beery, Q. C., Andrus, W. S., Bluestone, C. D., and Cantekin, E. I. (**1975**). "Tympanometric pattern classification in relation to middle ear effusions," Ann. Otol. Rhinol. Laryngol. **84**, 56–64.

Bourgeade, A., and Pascal, T. (**1998**). "Linear and nonlinear model of the human middle ear," J. Acoust. Soc. Am. **104**, 1509–1516.

Dirckx, J. J. J., and Decraemer, W. F. (**2001**). "Effect of middle ear components on eardrum quasi-static deformation," Hear. Res. **157**, 124–137.

Dirks, D. D., and Morgan, D. E. (**2000**). "Tympanometry and acoustic reflex testing," in *The Ear Comprehensive Otology*, edited by R. F. Canalis and P. R. Lambert (Lippincott Williams & Wilkins, Philadelphia, PA), 223–229.

Dirckx, J. J. J., and Decraemer, W. F. (**1992**). "Area change and volume displacement of the human tympanic membrane under static pressure," Hear. Res. **62**, 99–104.

Gaihede, M., Bramstoft, M., Thomsen, L. T., and Fogh, A. (**2005**). "Accuracy of tympanometric middle ear pressure determination in secretory otitis media: Dose-dependent overestimation related to the viscosity and amount of middle ear fluid," Otol. Neurotol. **26**, 5–11.

Gan, R. Z., Dyer, R. K., Wood, M. W., and Dormer, K. J. (**2001**). "Mass loading on ossicles and middle ear function," Ann. Otol. Rhinol. Laryngol. **110**, 478–585.

Gan, R. Z., Sun, Q., Dyer, R. K., Chang, K-H., and Dormer, K. J. (**2002**). "Three dimensional modeling of middle ear biomechanics and its application," Otol. Neurotol. **23**, 271–280.

Gan, R. Z., Wood, M. W., and Dormer, K. J. (**2004**). "Human middle ear transfer function measured by double laser interferometry system," Otol. Neurotol. **25**, 423–435.

Gan, R. Z., Dai, C. , and Wang, X. (2006). "Biomechanics of Otitis media with effusion in human ear," in The Fifth World Congress of Biomechanics, edited by Dieter Liepsch, Medimond Publishing, 527–533.

Huttenbrink, K. B. (**1988**). "The mechanics of the middle-ear at static air pressure," Acta Oto-Laryngol., Suppl. Suppl. **451**, 1–35.

Larsson, C., Dirckx, J. J. J., Decraemer, W. F., Bagger-Sjöbäck, D., and von Unge, M. (**2003**). "Pars flaccida displacement pattern in purulent otitis media in the gerbil," Otol. Neurotol. **24**, 358–364.

Lee, C.-Y., and Rosowski, J. J. (**2001**). "Effects of middle-ear static pressure on pars tensa and pars flaccida of gerbil ears," Hear. Res. **153**, 146–163.

Lilly, D. J. (**1984**). "Multiple frequency, multiple component tympanometry: New approaches to an old diagnostic problem," Ear Hear. **5**, 300–308.

Murakami, S., Guo, K., and Goode, R. L. (**1997**). "Effect of middle ear pressure change on middle ear mechanics," Acta Oto-Laryngol. **117**, 390–395.

Petrova, P., Freeman, S., and Sohmer, H. (**2006**). "The effects of positive and negative middle ear pressure on auditory threshold," Otol. Neurotol. **27**, 734–738.

Ravicz, M. E., Rosowski, J. J., and Merchant, S. N. (**2004**). "Mechanisms of hearing loss resulting from middle-ear fluid," Hear. Res. **95**, 103–130.

Rosowski, J. J., and Lee, C.-Y. (**2002**). "The effect of immobilizing the gerbil's pars flaccida on the middle-ear's response to static pressure," Hear. Res. **174**, 183–195.

Rosowski, J. J., Mehta, R. P., and Merchant, S. N. (**2003**). "Diagnostic utility of laser-Doppler vibrometry in conductive hearing loss with normal tympanic membrane," Otol. Neurotol. **24**, 165–175.

Shakes, J., and Shelton, C. (**1991**). "Basic principles and clinical applications of tympanometry," Otolaryngol. Clin. North Am. **24**, 288–328.

Teoh, S. W., Flandermeyer, D. T., and Rosowski, J. J. (**1997**). "Effects of pars flaccida on sound conduction in ears of Mongolian gerbil: Acoustic and anatomical measurements," Hear. Res. **106**, 39–65.

von Unge, M., Decraemer, W. F., Bagger-Sjöbäck, D., and Dirckx, J. J. J. (**1993**). "Displacement of the gerbil tympanic membrane under static pressure variations measured with real-time differential moire interferometer," Hear. Res. **70**, 229–242.

von Unge, M., Decraemer, W. F., Bagger-Sjöbäck, D., and Van den Berghe, D. (**1997**). "Tympanic membrane changes in experimental purulent otitis media," Hear. Res. **106**, 123–136.

Columella footplate motion and the cochlear microphonic potential in the embryo and hatchling chicken

Young S. Kim
Department of Electrical Engineering, College of Engineering, University of Missouri-Columbia, Columbia, MO 65212

Timothy A. Jones[a)]
Department of Otolaryngology, School of Medicine, University of Missouri-Columbia, Columbia, MO 65212

Mark E. Chertoff
Department of Hearing and Speech, School of Allied Health, University of Kansas Medical Center, Kanas City, KS 66160–7609

William C. Nunnally
Department of Electrical Engineering, College of Engineering, University of Missouri-Columbia, Columbia, MO 65212

(Received 14 June 2006; revised 25 August 2006; accepted 7 September 2006)

A piezoelectric (PZE) vibrator was used to mechanically drive the columella footplate and stimulate the cochlea of chicken embryos and hatchlings. Our objectives were to characterize the motion of the PZE driver and determine the relationship between columella footplate motion (displacement/velocity) and the cochlear microphonic recorded from the recessus scala tympani (CM_{rst}). At each frequency, displacement of the PZE driver probe tip was linearly related to the applied voltage over a wide range of attenuation levels (−60 to −20 dBre:50 $V_{p\text{-}p}$). The mean displacement across frequencies (100–4000 Hz) was 0.221 ± 0.042 $\mu m_{p\text{-}p}$ for a constant applied voltage level of −20 dBre:50 $V_{p\text{-}p}$. Displacement was within 1.5 dB of the mean for this stimulus level at all frequencies except for 4000 Hz, where it was ~3 dB higher ($p < 0.01$). CM_{rst} amplitudes in hatchlings were larger than amplitudes in embryos ($p = 0.003$). For a given frequency, *CM* was linearly related to footplate displacement and velocity at both ages. The transform ratio of CM_{rst}/A (*CM* amplitude/displacement) increased at ~6 dB/octave at frequencies between 100 and 1000 Hz in hatchlings suggesting that cochlear impedance (*Zc*) was resistive at these frequencies. In a large fraction of the embryos, *Zc* exhibited reactive behavior. © *2006 Acoustical Society of America.*
[DOI: 10.1121/1.2359236]

PACS number(s): 43.64.Ha, 43.64.Nf, 43.64.Yp, 43.80.Lb [BLM] Pages: 3811–3821

I. INTRODUCTION

During normal hearing, sound is conducted from air to the inner ear primarily by the middle ear (ME). The principal conducting elements of the middle ear are the tympanic membrane (TM) and ossicular chain. The ossicular chain is terminated by the stapes footplate in mammals and the columella footplate in birds. The footplate is inserted into the oval window and attached to the wall of the cochlea by the flexible annular ligament. Vibrations of the footplate and the corresponding pressures drive the displacement of the basilar membrane and lead to the transduction process in mechanoreceptive hair cells.

Understanding the transfer of sound vibration to the cochlea through the middle ear is essential for determining the relationship between sound pressures at the TM and the response of the cochlear sensor. This is especially true in developing animals where we cannot assume an effective transfer of sound in an immature middle ear and cochlea. Investigation of sound transfer requires the study of sound pressures or very small vibrations within the conduction system. Several approaches have been used to measure directly the displacement, velocity, and phase of motion at the tympanic membrane, columella footplate, as well as the resulting motion of the basilar membrane in the cochlea. For example, direct measurements have included the use of capacitive probes (Moller, 1963; Wilson and Johnstone, 1975; Relkin and Saunders, 1980), the Mössbauer technique (Gilad, Shtrikman *et al.*, 1967; Saunders and Johnstone, 1972; Manley, 1972a; Manley, 1972b; Manley and Johnstone, 1974; Sellick, Patuzzi *et al.*, 1982; Lynch, III, Nedzelnitsky *et al.*, 1982; Gummer, Smolders *et al.*, 1986; Gummer, Smolders *et al.*, 1987; Gummer, Smolders *et al.*, 1988), stroboscopic microscope (Guinan and Peake, 1967), time-averaged holography with laser interferometry (Khanna and Tonndorf, 1972) and laser vibrometers (interferometry) (Saunders, 1985; Cohen, Rubin *et al.*, 1992; Voss, Rosowski *et al.*, 2000; Overstreet, Temchin *et al.*, 2002)).

[a)]School of Allied Health Sciences, CSDI, East Carolina University, Library, Allied Health and Nursing Building, Room 3310A, Greenville, NC 27858-4353. Telephone 252-744-6088. Electronic mail: jonesti@ecu.edu

Most direct measurements of footplate velocity have been made in relatively mature animals and at relatively high sound levels. Use of direct methods to study the transfer characteristics of the embryonic middle ear has not been reported. This may be the case in part because direct measurements are not easily achieved in embryonic or early neonatal animals. An alternative approach for estimating the conductive status of the middle ear during development involves measuring the cochlear response (C_r) to airborne sound presented at the tympanic membrane (C_r/P_{tm}) and then determining the footplate velocity required to achieve the same cochlear response (C_r/v_{fp}). With these quantities, the transfer ratio v_{fp}/P_{tm} can be calculated. This provides an estimate of the velocity-pressure transform ratio for the middle ear; a value that reflects the effectiveness of the middle ear transfer function. The purpose of the research in this paper is to (1) develop a means to mechanically drive the footplate directly at known amplitudes and (2) to identify a cochlear response metric that is proportional to the amplitude of footplate motion. The cochlear microphonic has been used as a reliable indirect measure of footplate or basilar membrane motion by several investigators in mammals (Dallos, 1970; e.g., Ruggero, Robles *et al.*, 1986) and the *CM* response to direct stimulation of the stapes in neonates has been reported (Woolf and Ryan, 1988). Here we examine the cochlear microphonic as a cochlear response and an accurate measure of footplate motion in the chicken. The chicken was chosen since it is one of the most important and widely used developmental models available for the comparative study of the ontogeny of hearing.

II. METHODS

A. A piezoelectric motor as the columella footplate driver

A piezoelectric (PZE) driver (Burleigh PZL-007-20) was used to produce displacements of the columella footplate in the chicken (homolog for stapes footplate in mammals). Similar devices have been used by a number of investigators to produce relatively large displacements (up to 50 $\mu m_{p\text{-}p}$) (Dickman, Reder *et al.*, 1988; Rabbitt, Boyle *et al.*, 1995), and such drivers have been employed principally for stimulation at low frequencies. A PZE device has been used to drive the footplate directly in the mammal (Woolf and Ryan, 1988).

The PZL-007-20 PZE driver was a high output impedance pusher with a specified output mechanical stiffness of 16×10^9 dyne/cm and a maximum mechanical force output of 5.88×10^7 dynes (Burleigh Instruments). The driver was operated in a strictly compressional mode. The transfer function for the PZL-007-20 has not been described, and here we report the relationship between displacement, frequency, and applied voltage for small displacements on the order of 0.6–300 $nm_{p\text{-}p}$. The PZE driver was powered by a voltage amplifier (Burleigh PZ-150). A commercial signal generator provided a sine wave input to the amplifier. The level of voltage applied to the amplifier was controlled using an attenuator (TDT PA4). At 0 dB, the output of the voltage amplifier was adjusted to produce 50 $V_{p\text{-}p}$. In turn, the amplifier output was applied to the PZE crystal. Frequencies from 100 to 5000 Hz were evaluated. Voltages applied to the crystal ranged from −60 to 0 dBre:50 Vpp.

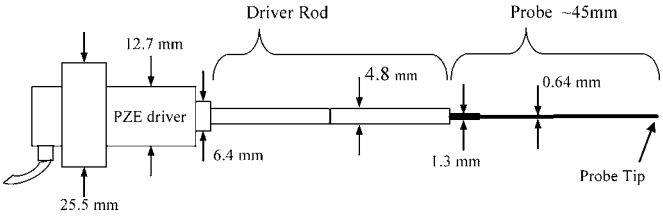

FIG. 1. Standard PZE driver and probe configuration. Key components of the assembly include the piezo driver, the driver rod (aluminum), and probe (stainless steel). The probe was a hollow tube having a length of ~45 mm. Not to scale.

B. Calibration of driver probe tip motion

For moderate to high levels of stimulation (−48–0 dBre:50 Vpp), interferometry was used to measure PZE driver probe tip displacement and velocity as a function of the voltage applied to the crystal. Linearity of the PZE driver was also evaluated at lower stimulus levels (−60 to −20 dBre:50 Vpp) by measuring the pressures developed in a calibration volume using a microphone.

1. Laser interferometers

Measurements of PZE probe tip velocity were made using laser interferometry. Two interferometers were used. One was fabricated in the laboratory and the second was a Polytech, HLV1000 hearing laser vibrometer. Several PZE driver configurations were tested using both interferometers. Calibration values for the different PZE driver configurations and different interferometers were not significantly different. Therefore, these data were combined for the purpose of this report. The PZE driver shown in Fig. 1 represents a configuration used here and elsewhere (Kim, 2002; Jones, Jones, and Paggett, 2006). Interferometer measurements were performed at 12 frequencies from 100 to 5000 Hz. For each frequency the velocity was measured at voltages ranging from −48 to 0 $dB_{re:50\ Vp\text{-}p}$ and executed in increments of 6 dB. In addition, PZE probe tip velocity was measured at a constant applied voltage of 5.0 $V_{p\text{-}p}$(−20 dBre:50 $V_{p\text{-}p}$) for frequencies from 100 to 4000 Hz These studies, along with those made using the microphone, provided a basis to evaluate the linearity of the PZE driver as a function of frequency and applied voltage.

Spectral analysis [fast Fourier transform, (FFT)] was used to determine the velocity levels that produced sine wave distortion. Time domain velocity waveforms were digitized (2048 points, 65 536 samples/s) and expressed in the frequency domain using the FFT (spectra: 1024 points, 32 Hz/point,). The amplitude of harmonic components was determined in relation to that of the fundamental frequency. Distortion harmonics were negligible for all stimulus levels below approximately −20 $dB_{re:50\ Vp\text{-}p}$ for all frequencies. Appreciable distortion (i.e., harmonics having amplitudes approaching within −25 dB of the amplitude of the fundamental) occurred at various levels above −20 $dB_{re:50\ Vp\text{-}p}$. These

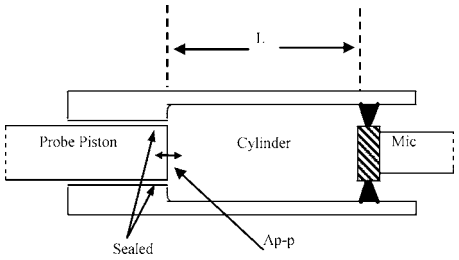

FIG. 2. Schematic of the sealed calibration cylinder, L: Length of the chamber ($L=10$ mm), $A_{p\text{-}p}$: Peak to peak piston displacement. The microphone (Mic) was inserted to form the major portion of one wall of the calibration chamber. The probe of the PZE diver was replaced by a cylindrical piston and the piston end was inserted into the calibration chamber to a position of length L from the microphone. Peak-to-peak displacements ($A_{p\text{-}p}$) were produced by the PZE driver. Displacement amplitude was calculated based upon pressure changes measured by the microphone in the cylinder chamber (cylinder diameter=8.03 mm, piston diameter=4.77 mm, cylinder volume $=5.0\times10^{-7}$ m^3, piston area$=17.85\times10^{-6}$ m^2).

levels were documented across frequencies and the values were used to define an upper voltage boundary for distortion-free operation of the PZE driver. Data presented here and elsewhere (Kim, 2002; Jones, Jones, and Paggett, 2006) were obtained at stimulus levels below this distortion boundary.

2. Microphone measurements

The microphone coupler is shown schematically in Fig. 2. The PZE driver rod assembly was configured as a piston forming the major portion of one wall of a cylindrical calibration chamber (Fig. 2). Pressure changes induced by the PZE piston motion in the calibration cylinder were monitored using a calibrated microphone (Brüel and Kjær's model 4231).

Pressure (in Pa) in the test volume (5.0×10^{-7} m^3, "Cylinder" of Fig. 2) was calculated based on the microphone output sensitivity (1.460 or 1.417 mV/Pa). Peak displacement (particle displacement, A_p in μm) and peak velocity (particle velocity, v_p in mm/s) were calculated from pressure values using Eqs. (1) and (2), assuming the acoustic input impedance of the microphone was considerably larger than air and conditions of standard temperature (20 °C) and atmospheric pressure (760 mmHg) as follows:

$$A_p = \frac{P_p \sin\left(\frac{\omega}{c_0}L\right)}{c_0\rho_0\omega}, \tag{1a}$$

$$= \frac{2\sqrt{2}\times10^{-5}\times10^{\mathrm{SPL}/20}\sin\left(\frac{\omega}{c_0}L\right)}{c_0\rho_0\omega}, \tag{1b}$$

$$v_p = \omega A_p, \tag{2}$$

where L=length of the cylinder (0.01 m), P_p=peak pressure (in Pascals, Pa), ω=angular velocity ($2\pi f$), f =frequency in Hz, c_0=sound speed in the air (343 m/s), ρ_0=density of air (1.21 kg/m^3) and SPL=sound pressure level, where SPL$=20\log(P_{\mathrm{rms}}/0.000\,02$ Pa) (dB)(Malecki, 1969; Seto, 1971; Temkin, 1981; Merhaut, 1981; Kreyzig, 1983; Ziomeck, 1995).

Microphone output was amplified (31.6 mV/Pa or 3.16 V/Pa, B&K NEXUS 2691 amplifier) and digitized using a 12 or 16 bit A/D converter and averaged to reduce random noise. Displacement ($\mu m_{p\text{-}p}$) and velocity ($mm/s_{p\text{-}p}$) of the piston were determined as a function of frequency and voltage applied to the PZE crystal. Frequencies tested in the calibration volume ranged from 100 to 4000 Hz whereas the voltage applied to the crystal ranged from −60 to −20 dBre:50 $V_{p\text{-}p}$.

C. Driving the columella footplate and electrophysiological recordings

1. General surgical preparation

Embryos incubated for 19 days and 14 to 15 day old chickens (Gallus domesticus) were used for this study. Each hatchling was anesthetized with EquiThesin (0.003 cc/g, intramuscular injection), a mixture of Na-pentobarbital (0.972 g), chloral hydrate (4.251 g), magnesium sulfate (2.125 g), ethanol (12.5 ml), and propylene glycol (42.6 ml), in distilled water to a total volume of 100 ml (Burkard, Jones *et al.*, 1994; Jones, Jones *et al.*, 1997). The columella of the right ear was removed and the trachea was cannulated to provide an open airway during experiments. The head was immobilized in plaster on a surgical platform and the tissue over the left ear canal was removed to visualize the TM and the movement of the PZE driver tip. The head was tilted so that the driver probe and the TM were approximately perpendicular. Core temperature of the chicken was maintained at a mean of 37.8±0.7 °C [mean±standard deviation (SD) unless otherwise stated] during recordings. A thermocouple was used to monitor temperature.

Mean beak (5.02±0.21 mm) and toe (18.1±0.42 mm) lengths of embryos corresponded to developmental stages of 44 to 45 (Hamburger and Hamilton, 1951). Each embryo's head was removed from the eggshell through a small opening and was secured in a customized plastic head holder. Embryos were given an intramuscular injection of EquiThesin: Saline [0.10 ml; 1:4 ratio]. Surface electrodes were used to monitor electrocardiographic (ECG) activity. The egg was placed on a heated platform in a sound attenuating booth and egg temperature was monitored with a calibrated thermistor inserted into amniotic fluids. A brain thermistor inserted into the neostriatum was utilized to monitor and maintain brain temperature at 37.1±2.1 °C.

2. Placement of PZE driver probe

Most of the surgical procedures outlined below were performed with the aid of a surgical microscope. The external auditory meatus (EAM) was dilated and widely exposed. A stainless steel hollow tube served as the PZE driver probe. It was secured to the end of the PZE driver rod as shown in the configuration of Fig. 1. The driver probe tube was rigidly coupled to the end of the central rod. The probe tube was ~45 mm long and the outside diameters 0.64 mm. An incision was made in the TM to visualize the base of the columella. In embryos, all middle ear fluid was carefully removed from the area of the footplate to ensure clear direct view of the footplate and columella. The columella was sev-

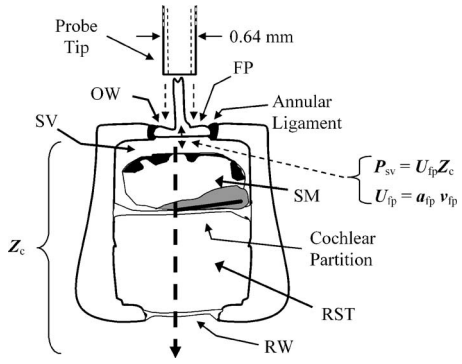

FIG. 3. Schematic diagram of coupling along the sound conduction path between the driver probe tip, columella footplate (FP), scala vestibuli (SV), scala media (SM), cochlear partition, recessus scala tympani (RST), and the round window (RW). OW=oval window. The probe tip was slipped over the columella stump and advanced until seated against the outer face of the footplate. Schematic represents the bony cochlear wall and membranous partitions showing the entrance of sound via the stapes footplate into the scala vestibuli. Pressure (P_{sv}) is developed in the scala vestibuli by the vibration of the footplate (footplate velocity, v_{fp}, footplate area, a_{fp}, volume velocity, U_{fp}) causing sound to be conducted across the cochlear partition along the cochlear impedance (Z_c) path to the round window (RW). Not to scale.

ered near the footplate, leaving a short columellar stub attached to the footplate. Care was taken to avoid damaging the round window (RW) membrane during the process since the RW is very near the columella at the point of separation. Placement of the PZE driver probe tube was made using a 10 μm precision micromanipulator. The remnant stump of the columella attached to the footplate was inserted into the lumen of the driver probe as the PZE probe tip was advanced (Fig. 3). Once the probe tip contacted the outer surface of the footplate, the driver tip and footplate were advanced slightly to induce a restoring force in the elastic elements of the annular ligament. The restoring force served to clamp the surface of the footplate to the driver tip. This ensured a snug and reliable mechanical coupling between the probe tip and the footplate such that the two moved in unison. The largest displacements possible with the PZE driver under voltage control were on the order of 2 microns$_{\text{p-p}}$.

3. Expressing driver vibrations in units of kinetic equivalent dB SPL (dB keSPL)

We have found it useful in our physiological studies to express the levels of stimulation associated with direct footplate driving in a way that relates to hearing in the normal animal. This may be done by expressing the vibration amplitudes in terms of a kinetic equivalent dB SPL (dB keSPL). We define dB keSPL simply as the dB SPL that would result in a plane wave in air at standard temperature and pressure (20 °C and 760 mmHg atmospheric pressure) in association with a particle velocity equivalent to that of the PZE driver probe tip. It is defined quantitatively in Eq. (3)

$$\text{X dB keSPL} = 20 \times \text{Log}\left(\frac{v_{\text{rms}} \times Z_{\text{air}}}{0.000\,02\ \text{Pa}}\right), \tag{3}$$

where v_{rms} is the root mean squared (rms) velocity of the driver probe tip (in mm/s) and Z_{air} is the specific acoustic impedance of air (0.4145 Pa·s/mm at 20 °C and 760 mmHg). Stimulus levels expressed in dB keSPL provide a means to appreciate the sound pressure levels in air that would produce air particle velocities identical to those of the corresponding footplate vibration.

4. Recording CM_{rst} responses

A tacit assumption in the present study is that displacement and velocity of the footplate itself are equal to the displacement and velocity of the calibrated driver probe tip. Based on this premise, footplate motion was determined and used to resolve the relationship between footplate motion and the amplitude of the cochlear microphonic recorded from the recessus scala tympani (CM_{rst}). The cochlea was accessed for recording the CM_{rst} and for administering drugs to the scala tympani via a posterolateral approach through the skull as reported elsewhere (Schermuly and Klinke, 1985; Manley, Gleich *et al.*, 1985; Klinke, Muller *et al.*, 1994; Jones and Jones, 1995a; Jones and Jones, 1995b; Jones, Jones, and Paggett, 2006). A small fenestration was made in the wall of the cochlea overlying the recessus scala tympani. A single silver electrode (0.762 mm in diameter) was placed in the scala tympani and used to record the CM_{rst}. The reference and ground electrodes were placed subcutaneously over the neck. Sine wave stimuli were used to elicit CM_{rst} responses and the function generator synchronization pulse was used to trigger the analog to digital (A/D) converter. CM_{rst} responses from the scala tympani were amplified (TDT DB4, gain: 20 000) filtered (10–10 kHz, band pass) and led to the input of an A/D converter (16 bit, 20 μs/point, 1024 points). Primary CM_{rst} responses were averaged (1024 sweeps) and the amplitudes of the averaged responses were determined. Experiments were conducted in a sound-attenuating booth. The neural action potential was eliminated from the cochlear response to stimuli by adding tetrodotoxin (TTX, Sigma 0.05 mg in 1.0 ml of 16% polyvinyl alcohol) (Narahashi, Moore *et al.*, 1964; Jones, 1992; Jones and Jones, 1996) or 50 mM kainic acid to the cochlear perilymph (scala tympani) (Zheng, Wang *et al.*, 1996; Shero, Salvi *et al.*, 1998; Sun, Salvi *et al.*, 2000; Sun, Hashino *et al.*, 2001; Irons-Brown and Jones, 2004). Recordings were made before and after drug application to confirm the effectiveness of neural blockade.

Statistical evaluation of CM_{rst} amplitudes as a function of age and frequency was completed using repeated measures, two factor ANOVA. Missing values were replaced with means.

III. RESULTS

A. Probe frequency response and linearity

Probe tip displacement ($\mu m_{\text{p-p}}$) is plotted as a function of frequency in Fig. 4. Results for both interferometry (filled circles) and microphone measurements (unfilled triangles) are shown. The mean displacement across frequencies (100–4000 Hz) based on interferometry was 0.221± 0.042 $\mu m_{\text{p-p}}$ for a constant applied voltage level of −20 dBre:50 $V_{\text{p-p}}$. Displacement was within 1.5 dB of the mean for this stimulus level at all frequencies except for 4000 Hz, where it was significantly higher (on average about 3 dB

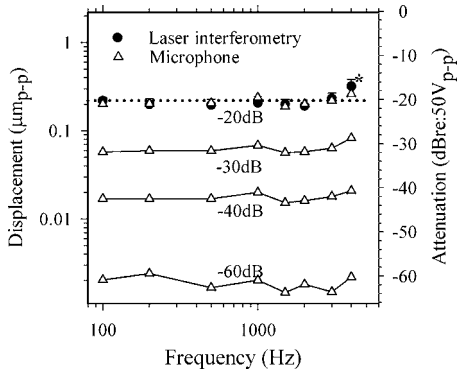

FIG. 4. PZE displacement ($\mu m_{p\text{-}p}$) of the PZE driver probe tip as a function of attenuation level and frequency (Hz). Displacement was measured using laser interferometry (filled circles) and pressure measurements (open triangles) in a calibration volume at −20 dB re: 50 $V_{p\text{-}p}$. Pressure measurements were also made at −30, −40 and −60 dB re:50 $V_{p\text{-}p}$. The dotted line represents the overall mean of interferometry measurements across frequencies of 0.221±0.042 $\mu m_{p\text{-}p}$ at −20 dB attenuation. * Indicates that the mean for 4 KHz was significantly higher ($p<0.01$) than the mean value across frequencies. Interferometry values for −20 dB re:50 $V_{p\text{-}p}$ are summarized in Table I.

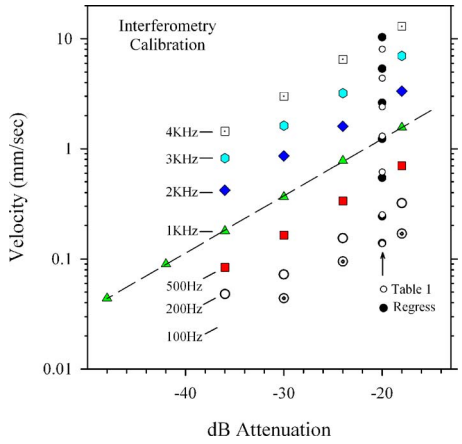

FIG. 5. Tip velocity [log scale (mm/s)] vs dB attenuation (dB re:50 $V_{p\text{-}p}$) as measured using a laser vibrometer. These are seven representative examples of 12 interferometry calibration sequences for stimulus levels between −18 and −48 dB attenuation. Measurements were made in 6 dB steps. Regression lines were calculated for each of 12 frequencies. In the interest of clarity we show only the regression line for 1000 Hz. All slopes were ~0.05 [log(velocity)/dB] and hence linear (equivalent to 1 decade/20 dB). Here we present seven of the twelve frequencies studied. The data for −20 dB attenuation are values from Table I, and values calculated using calibration regression lines for the respective individual frequencies "Regress." Here the Table I values may be contrasted with values at −20 dB re:50 $V_{p\text{-}p}$ predicted by the regression line for each frequency ("Regress," filled circles).

higher, one-way ANOVA, $p<0.001$, *post hoc* tests: Bonferroni, $p<0.01$). Similar estimates of displacement were obtained from microphone measurements at the same voltage level (−20 dBre:50 $V_{p\text{-}p}$) and for calibrations of probe tip displacement over a range of attenuation levels (−20 to −60 dBre:50 $V_{p\text{-}p}$). It is clear that displacement was linearly related to the attenuation level over the 40 dB range shown, thus representing displacements from ~0.221 microns at −20 $dB_{re:50\ Vp\text{-}p}$ to ~2 $nm_{p\text{-}p}$ at −60 $dB_{re:Vp\text{-}p}$. Table I summarizes interferometry findings at −20 $dB_{re:50\ Vp\text{-}p}$ across frequencies including numerical values for displacement, velocity and dB keSPL level.

Figure 5 illustrates seven representative velocity input-output curves of the twelve frequencies tested. The data reflect the linear relationship between the velocity of the probe tip as a function of the applied voltage. Similar curves were obtained at all 12 frequencies tested. Regressions for each frequency relating log(velocity) to dBre: 50 $V_{p\text{-}p}$ were significant ($p<0.002$) with R^2 values exceeding 0.995. Moreover, no significant difference in slopes was found across frequency. The mean slope across 12 frequencies was 0.05±0.002 log(mm/s)/dB. A slope of 0.05 (1 decade/20 dB) in these plots indicates that a direct linear relationship exists between applied voltage and the probe tip velocity at each frequency.

The mean particle velocities of the probe tip at −20 $dB_{re:50\ Vp\text{-}p}$ for each frequency from Table I are also plotted in Fig. 5. The velocity regression curves from the interferometry data predict values at −20 dB attenuation that are comparable to those of the means from Table I. Indeed, the values for the single calibration series shown in Fig. 5 are within approximately 2 dB of the mean values at −20 dB attenuation for each frequency given in Table I. The mean values thus may be used as calibration bench marks for velocity at the respective frequencies. Velocities at any given level of attenuation may be specified relative to the mean values at −20 $dB_{re:50\ Vp\text{-}p}$.

B. Columella motion and CM_{rst}

Representative examples of CM_{rst} waveforms generated in response to vibrations imposed on the columella footplate by the PZE driver are shown in Fig. 6. Waveforms produced in response to a 2000 Hz stimulus using displacements from ~20 to 2 $nm_{p\text{-}p}$ (−40 to −60 dBre:50 $V_{p\text{-}p}$) are illustrated for a hatchling and embryo. *CM* waveforms for both age groups were well formed at moderate stimulus levels and amplitudes

TABLE I. Displacement ($\mu m_{p\text{-}p}$), velocity (mm/sec) and dB keSPL values at −20 dB re: 50 $V_{p\text{-}p}$. Mean and standard deviation (SD) values are based on results from all laser interferometry measurements.

Frequency (Hz)	100	200	500	1000	1500	2000	3000	4000
Displacement ($\mu m_{p\text{-}p}$)	0.2193	0.1991	0.1958	0.2072	0.2008	0.1911	0.2325	0.3202
SD	0.0180	0.0317	0.0325	0.0376	0.0252	0.0125	0.0357	0.0636
$Velocity_{p\text{-}p}$ (mm/s)	0.1378	0.2502	0.6152	1.3017	1.8929	2.4014	4.3824	8.0464
dB keSPL	60.1	65.3	73.1	79.6	82.8	84.9	90.1	95.4

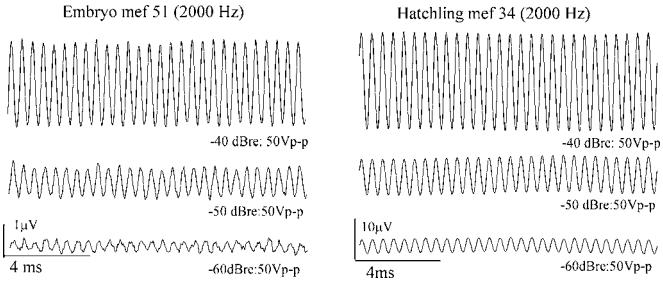

FIG. 6. Representative CM_{rst} recordings at three attenuation levels from one embryo (left) and hatchling (right). Calibration bars reflect scales for amplitude μV vertically, and time (ms) horizontally.

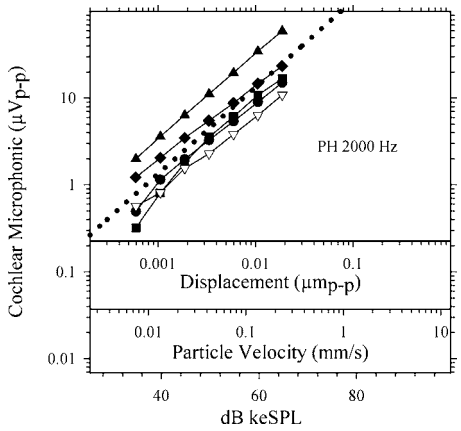

FIG. 7. Hatchling (PH) cochlear microphonic amplitude (CM_{rst}, $\mu V_{p\text{-}p}$) plotted against displacement for a 2000 Hz stimulus applied directly to the columella footplate. Curves for five hatchlings are shown. Horizontal axes show displacement ($\mu m_{p\text{-}p}$), particle velocity (mm/s) and dB keSPL.

varied systematically with footplate displacement. The preparation at both ages was quite stable permitting continuous recording over many hours. Table II summarizes mean values for embryos and hatchlings for footplate displacement of ~20 $nm_{p\text{-}p}$. As can be discerned from Table II and from Fig. 6, CM_{rst} amplitudes were considerably smaller in embryos at any given level of displacement ($p=0.003$, repeated measures, two factor ANOVA).

The CM_{rst} response to footplate motion at 2000 Hz as a function of footplate displacement, velocity and dB keSPL is illustrated in Fig. 7. As was the case generally, CM_{rst} amplitudes at 2000 Hz increased in direct relation to increases in displacement amplitudes over attenuation levels from less than −70 to −40 $dB_{re:50\ Vp\text{-}p}$, which correspond to displacements from ~0.5 to 200 nm.

Figure 8 provides summary illustrations of representative response curves for a selection of the various frequencies studied. As noted, when frequency was held constant, the CM_{rst} was systematically related to footplate motion (Figs. 6–8). The figure also provides a basis to contrast the response character across individuals for both embryos and hatchlings. Deviations from linearity at low stimulus levels appeared to be related to low signal-to-noise ratios in the primary CM_{rst} responses. Owing to smaller amplitudes generally, CM_{rst} responses in embryos had reduced signal-to-noise ratios compared to hatchlings. This contributed to an overall greater random variability in response curves of embryos when compared to hatchlings (e.g., compare Figs. 6 and 8). Robust linear response segments could be found in all curves at moderate stimulus levels in both embryos and hatchlings across frequencies. Generally across all animals the range of footplate displacement from ~0.5 to 200 nm was effective in producing well-resolved response magnitudes.

For each frequency, CM_{rst} amplitude was adequately described as a power function of displacement and was given by $CM_{rst}=b_0 \cdot A_{p\text{-}p}^{b_1}$. The CM_{rst} amplitude curves were best fit by regression using the following equation $\mathrm{Log}(CM_{rst})=\beta_0+\beta_1 \cdot \mathrm{Log}(A_{p\text{-}p})$, where $A_{p\text{-}p}$ is the footplate displacement in $\mu m_{p\text{-}p}$ and CM_{rst} is the CM amplitude in $\mu V_{p\text{-}p}$. A regression slope of $\beta_1=1$ indicated a linear relationship. The mean slope values across animals for each frequency ranged from 0.6 to 1.1 although most were close to 1.0 as summarized in Table III.

In Fig. 9, CM_{rst} is plotted as a function of frequency at two different displacement amplitudes. The results from two representative individuals (1 hatchling and 1 embryo) are presented. One can see from the figure that when footplate displacement was held constant and footplate velocity varied by changing stimulus frequency, the change in amplitude of CM_{rst} differed markedly from that obtained when velocity was increased and frequency held constant (e.g., compare CM_{rst} versus velocity in Fig. 7). The overall CM_{rst} amplitude response pattern with increasing frequency was similar for the two different stimulus displacement levels illustrated but the amplitude function itself was often nonlinear and non monotonic. That is, with increasing footplate velocity (frequency), CM_{rst} amplitudes remained constant, increased or

TABLE II. Mean *CM* amplitude ($\mu V_{p\text{-}p}$) at −40 dB re: 50 $V_{p\text{-}p}$ (displacement ~20 $nm_{p\text{-}p}$). *CM* amplitudes for embryos were significantly less than those for hatchlings ($p=0.003$).

A. Hatchlings	100 Hz	200 Hz	500 Hz	1000 Hz	1500 Hz	2000 Hz	3000 Hz	4000 Hz
mean	2.8	4.5	11.6	21.1	22.3	22.6	55.2	49.4
sd	1.0	1.2	7.9	14.8	10.1	20.8	45.5	49.7
n	5	5	5	5	5	5	5	5
B. Embryos	100 Hz	200 Hz	500 Hz	1000 Hz	1500 Hz	2000 Hz	3000 Hz	4000 Hz
mean	0.68	0.95	1.43	2.45	4.19	2.53	3.22	1.67
sd	0.35	0.81	1.21	2.07	3.49	2.52	3.62	2.14
n	5	7	8	7	8	8	8	8

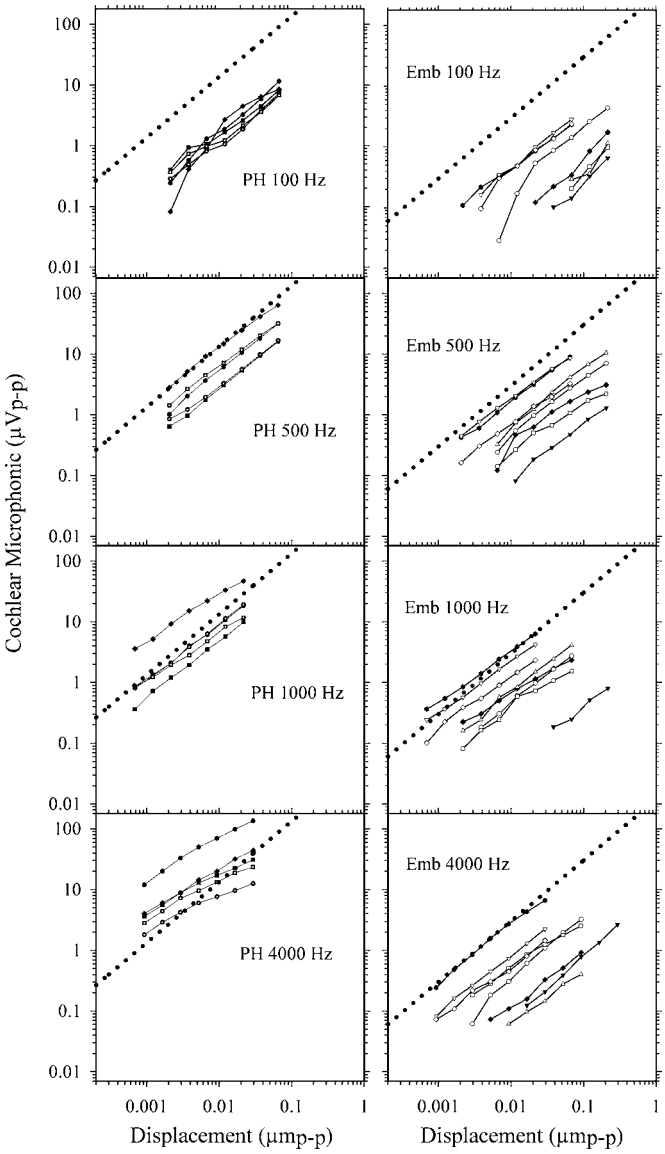

FIG. 8. Representative cochlear microphonic amplitudes ($CM_{\mathrm{rst}}, \mu V_{\mathrm{p\text{-}p}}$) are plotted as a function of footplate displacement ($\mu m_{\mathrm{p\text{-}p}}$). Each curve represents results for one animal. CM_{rst} amplitudes were recorded in response to direct footplate stimulation at four different frequencies. Left panel illustrates data for hatchings (PH). Right panel illustrates data for embryos (Emb). Dotted line represents a linear relation of slope=1.

even decreased. The response pattern was systematic and was repeated for each displacement level although shifted to the right or left thus reflecting the corresponding alternative set of velocities for each frequency. Similar findings were obtained in all animals. These response patterns were in striking contrast to those found with increasing footplate particle velocity when frequency was held constant.

C. Estimating cochlear input impedance

As argued and demonstrated persuasively by others (Dallos, 1970; Dallos, 1973; Ruggero, Robles, and Rich, 1986), the amplitude of the cochlear microphonic (CM_{rst}) is thought to be proportional to the displacement of the basilar membrane (x_{bm}), which in turn depends on the acoustic pressure gradient across the cochlear partition (e.g., see schematic of anatomical compartments in Fig. 3). Under normal circumstances, this pressure gradient is determined primarily by the pressure in the scala vestibuli near the insertion point of the stapes footplate (Nedzelnitsky, 1980). In the steady state, acoustic pressures at this insertion point may be described by the equation $P_{sv}=U_{fp}Zc$, where P_{sv} is the pressure in the scala vestibuli, U_{fp} is the volume velocity associated with the footplate particle velocity (v_{fp}), and Zc is the acoustic impedance presented by the cochlear sound conduction path. If the cochlear impedance (Zc) to sound conduction remains relatively constant at low frequencies, then the equation predicts that P_{sv}, and hence basilar membrane displacement and CM amplitude, will be proportional to footplate particle velocity at low frequencies. Under conditions where displacement is held constant ($x_{fp}=A$) and Zc remains unchanged, the equation predicts that the CM_{rst} will be directly proportional to frequency as follows:

$$CM_{rst} \propto x_{bm} \propto P_{sv} = U_{fp}Zc = v_{fp}a_{fp}Zc,$$

and substituting from Eq. (2)

$$CM_{rst} = j\omega A a_{fp} Zc,$$

where j introduces a 90 deg phase advance re: displacement, A is displacement (constant), and a_{fp} is the area of the footplate.

Rewriting and simplifying

$$CM_{rst} \propto k f_{fp} A Zc, \tag{4}$$

where $k=2\pi a_{fp}$ (k is constant for each animal) and f_{fp} is the frequency of stimulation. Dividing by displacement, we obtain the transform ratio CM_{rst}/A which varies in proportion only to frequency and Zc.

Figure 10 illustrates the transform ratio for hatchling data as a function of frequency. Generally for all hatchlings, the CM_{rst}/A ratio increases in parallel with the 6 dB/octave line (dashed) at least up to frequencies of about 1000 Hz. Above 1000 Hz the transform ratio plateaus for most animals. This suggests that Zc is essentially constant at frequencies of 1000 Hz and below in hatchlings.

In embryos, the resulting curves were complex and more variable than those of hatchlings. In one case the ratio appeared to be independent of frequency and generally considerably lower in magnitude than ratios in other animals (Fig. 10, bottom, mef 43). In four animals (Fig. 10, middle, mef: 46, 47, 49, and 50), the curves closely paralleled those of the hatchlings by increasing at 6 dB/octave up to ~1000 Hz. The remaining three embryos (Fig. 10, bottom, mef: 45, 51, and 48) exhibited intermediate behaviors. These results suggest that Zc may not be constant in all embryos at low frequencies.

IV. DISCUSSION

Our principle objectives in the current work were (1) to characterize displacement and velocity of the PZE driver probe tip as a function of the applied voltage and frequency and (2) to examine the relationship between footplate motion and the corresponding CM_{rst} response and test the hypothesis that the CM_{rst} is a faithful indicator of footplate velocity and

TABLE III. Log-Log regression line of *CM* vs PZE displacement plot for hatchling chicken. Units: $\beta_1 = > \log \mu V_{p\text{-}p} / \log \mu m_{p\text{-}p}$ and $\beta_0 = > \log \mu V_{p\text{-}p}$ across hatchlings (A) and embryos (B).

A. Hatchlings:	Hz	100	200	500	1000	1500	2000	3000	4000
Log scale slope	(β_1)	0.976	0.964	0.919	0.861	0.929	0.957	0.744	0.635
	SD	0.213	0.067	0.043	0.084	0.042	0.114	0.102	0.066
Scale factor	(β_0)	2.069	2.307	2.544	2.694	2.881	2.992	2.895	2.557
	SD	0.416	0.130	0.268	0.232	0.238	0.385	0.259	0.471
B. Embryos:	Hz	100	200	500	1000	1500	2000	3000	4000
Log scale slope	(β_1)	1.121	0.974	0.895	0.861	0.749	0.864	0.861	0.931
	SD	0.178	0.110	0.065	0.078	0.105	0.105	0.106	0.117
Scale factor	(β_0)	1.247	1.374	1.476	1.537	1.681	1.612	1.600	1.358
	SD	0.451	0.487	0.460	0.545	0.659	0.597	0.629	0.592

displacement in the chicken embryo and hatchling. In addition, the measurements so obtained provided an opportunity to examine the nature of cochlear input impedance (*Zc*) at low frequencies in the developing and mature chicken as we discuss below.

1. PZE driver response

The results of the present study demonstrated that the applied voltage controls displacement of the PZE driver probe tip and that this is true over the entire frequency range studied here. Probe tip velocity is therefore a function of both the applied voltage and of the driving frequency. This accounts for the range of dB keSPL levels across frequencies in Table I, since dB SPL is directly proportional to velocity. This is different than many acoustic drivers, wherein the applied voltage controls transducer particle velocity across a wide range of frequencies. In this latter case, the output pressure is proportional to the applied voltage and in practice more or less independent of the frequency. Obviously, this feature of the PZE driver must be taken into consideration when generating stimuli.

The present study provided bench mark displacement values for the PZE driver probe tip at eight frequencies as given in Table I. Moreover, the results indicated that the PZE driver operates linearly over a wide range of voltage levels (−60 to −20 dBre; 50 Vp-p) thus allowing linear control of displacements at least down to nanometer levels as has been shown for other piezoelectric drivers (Corey and Hudspeth, 1980; Woolf and Ryan, 1988). At a stimulus level of −20 dB re; 50 Vp-p, displacement amplitude remained within ±1.5 dB of the mean value 0.221 $\mu m_{p\text{-}p}$ across all frequencies except at 4000 Hz where displacement was on average 3 dB higher. The importance of the small deviation at 4000 Hz to studies employing the PZE driver depends on the nature of the study. Comparable error magnitudes for low frequencies of 100–4000 Hz were evident in the calibration data reported by Woolf and Ryan, 1988.

2. General features of the CM_{rst}

CM_{rst} amplitudes in E19 embryos were robust, suggesting that the cochlea is sufficiently mature to produce a substantial CM_{rst} that, at a given frequency, is linearly related to stapes displacement or velocity. At a given stimulus level, CM_{rst} amplitudes were significantly less in embryos compared to hatchlings, a finding that cannot be due to immaturities in the middle ear apparatus because the columella footplate was driven directly by the PZE driver. The reduced amplitudes therefore must reflect immaturities in the cochlea itself at these ages.

The *CM* response to direct footplate stimulation has

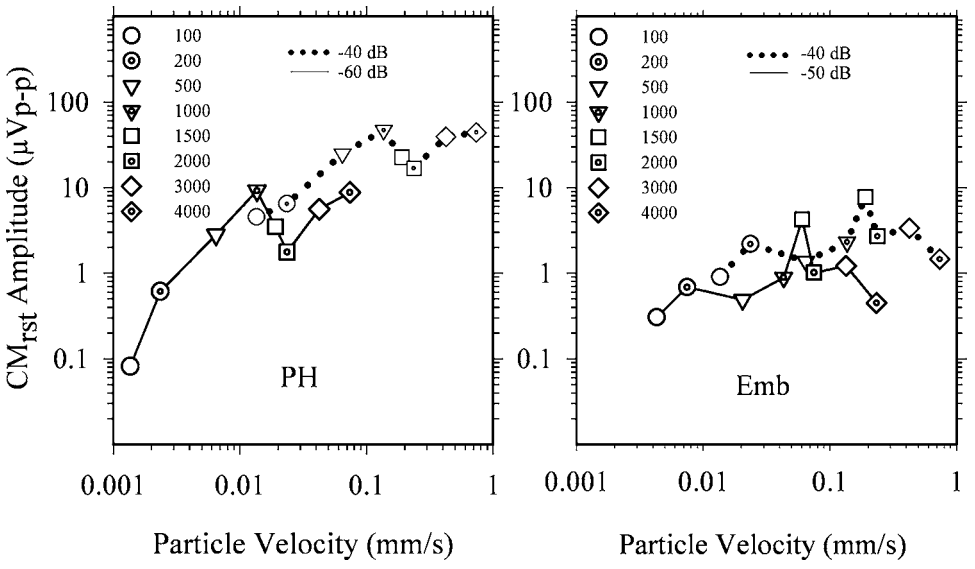

FIG. 9. Hatchling (PH) and embryo (Emb) cochlear microphonic response ($CM\rho\sigma\tau, \mu V_{p\text{-}p}$) to direct footplate stimulation. CM_{rst} amplitude is shown as a function of footplate particle velocity (mm/s) with displacement held constant. Two displacement levels are shown (Dotted lines −40 dB; solid lines −50 or −60 dB as shown). Frequency was increased in eight steps from 100 to 4000 Hz in order to introduce the corresponding stepped increases in footplate velocity. The legend identifies each symbol and frequency given in Hz.

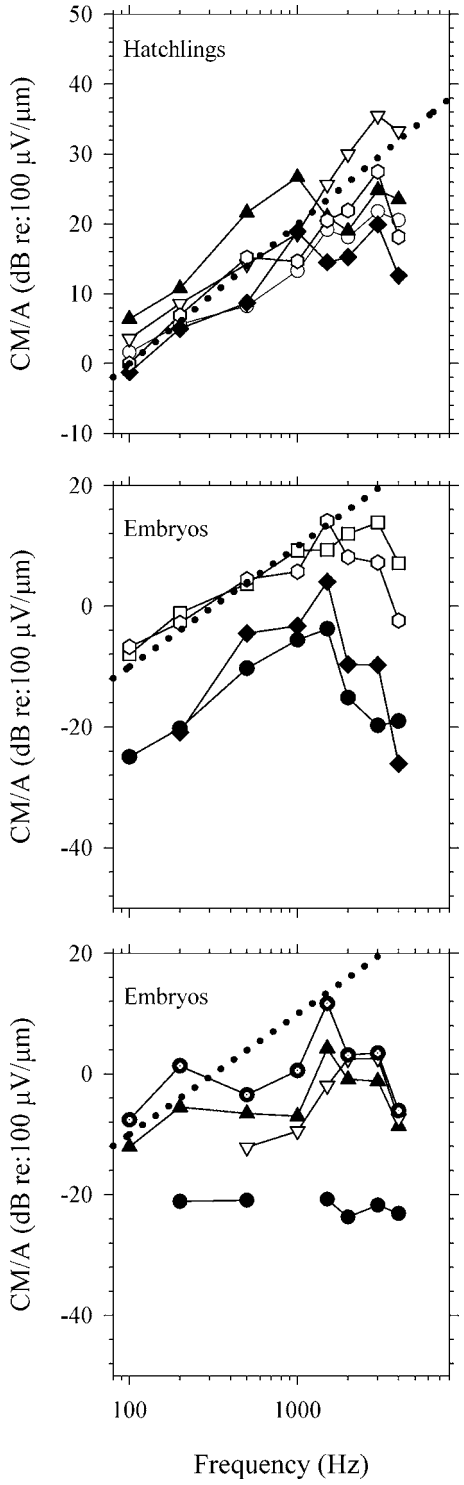

FIG. 10. Transform ratio of CM_{rst}/A plotted in dB re: 100 $\mu V/\mu m$ as a function of frequency for hatchlings (top) and embryos (middle and bottom). Dotted line shows 6 dB/octave slope.

been described in the mammal by others (Woolf and Ryan, 1988). Inspection of Fig. 2 suggests similar input-output functions (i.e., stimulus-response functions) to those presented here. We have employed a narrower range of stimulus levels to suit our objectives. Under the best conditions, *CM* amplitudes are linearly dependent on the applied pressure levels at the TM over a wide range of pressure levels (Dallos, 1973). When pressure levels are sufficiently high, the *CM* becomes distorted and input-output functions deviate significantly from linearity and the slope of the curve decreases. For the most part in the present study, the levels of stimulation achieved using direct footplate driving stayed within the linear range of *CM* functions. At the highest frequencies, we may have encroached slightly on the nonlinear segment of the *CM* input-output function since the slopes were slightly less than 1.0 for hatchlings (but not embryos). The slight compression of slopes may also be a consequence of the nondifferential method of recording the CM_{rst}. It is not likely, however, that a remotely recorded neural action potential contaminated the CM_{rst} in the present study since the nerve was blocked during all recordings. The shallow slopes are probably not due to factors related to the PZE driver, since we would expect to see such effects in both hatchlings and embryos and we did not. Due to the high output impedance of the PZE pusher, it is not probable that changes in stapes and cochlear impedance formed the basis for shallow slopes. A key attribute of CM_{rst} recordings in any case was that, when frequency was held constant, all curves were systematic, monotonic and approached linearity.

3. The CM_{rst} as a metric for footplate motion

One of our objectives was to evaluate the CM_{rst} as an effective indicator of footplate motion. Our ultimate aim was to use the CM_{rst} for estimating middle ear transfer characteristics. Although we did not endeavor to relate TM pressures to footplate motion in the present study, we have completed such studies recently (Kim, 2002). We noted in the Introduction that one may express middle ear transfer characteristics in the form of the transform ratio v_{fp}/P_{tm}. If we choose the CM_{rst} as our cochlear response metric, then we may determine the TM sound pressure (P_{tm}) required to produce a specific cochlear response, $C_r = CM_{rst}$ and in turn calculate the transform C_r/P_{tm}. Similarly, using the PZE driver and probe, we can adjust the footplate velocity (v_{fp}) to that required to produce an identical cochlear response (i.e., $CM_{rst} = C_r$) and in turn calculate the transform ratio C_r/v_{fp}. The middle ear transform ratio then is simply $v_{fp}/P_{tm} = (C_r/P_{tm})/(C_r/v_{fp})$. This relationship holds only if the CM_{rst} is a reliable metric, which accurately follows the cochlear response to footplate motion. The results of the present study support this hypothesis. It has long been appreciated that the CM_{rst} is proportional to the pressure applied to the TM during airborne sound stimulation (Dallos, 1970). Woolf and Ryan, 1988 have shown in the mammal and we have shown here in the bird, that for any given frequency, a range of stimulus levels may be chosen such that the CM_{rst} is proportional to footplate displacement. Based on these facts, it is reasonable to conclude that the CM_{rst} can meet the principal requirements for use in such sound transfer studies.

Our results clearly also demonstrate that there are some circumstances wherein the CM_{rst} does not faithfully and systematically follow footplate motion. There are sources of measurement error that can be identified and minimized if not eliminated. The variation of CM_{rst} response curves across individuals can be seen in Figs. 7 and 8. The variation reminds us that, although slopes may be similar across individuals, the curves nonetheless are not identical. This source

of variation can be eliminated if the use of the CM_{rst} versus displacement curve is restricted to the animal from which it was obtained. In other words, the CM_{rst} must be calibrated in each animal to minimize error. It is also clear for a given animal, that a CM_{rst} versus displacement curve for a particular frequency does not necessarily describe the magnitude of footplate motion at frequencies other than that used to establish the curve. This is clear from Figs. 8 and 9. The basis for this stems primarily from the fact that the CM_{rst} is a compound response that is produced at each frequency by a unique combination of generator sites in the cochlea. As illustrated in Fig. 9, CM_{rst} amplitude therefore may also be unique at each frequency despite identical displacement and velocity. Therefore, the CM_{rst} must be calibrated for each frequency used, a strategy that effectively eliminates this source of variability.

4. The relationship between footplate motion, CM and cochlear impedance(Zc)

Estimates of cochlear input impedance were also made using direct footplate driving in the present study. The CM_{rst}/A transform ratio for hatchlings increased in direct proportion to frequency from 100 to 1000 Hz in all hatchlings. A slope of 6 dB/octave is predicted for the ratio by Eq. (4) only if Zc is constant over these frequencies. Assuming that the contribution of *Zc* is not negligible, these results thus suggest that *Zc* is virtually constant at low frequencies between 100 and 1000 Hz and hence that cochlear input impedance is in essence resistive in the mature chicken at these frequencies. A resistive *Zc* has been reported for several mature mammals at frequencies ranging below 1000 Hz and extending variously as low as 500–100 Hz depending on species (Dallos, 1970; Lynch, III, Nedzelnitsky, and Peake, 1982; Kringlebotn, 2000) and for the human (Aibara, Welsh *et al.*, 2001). A resistive *Zc* at low frequencies is also suggested by the results of Gummer and colleagues (Gummer, Smolders, and Klinke, 1988) who showed in the pigeon that although the entire region of the curve from 100 to 1000 Hz shifted downward, the *general shape* of ME transfer characteristic (v_{fp}/P_{tm}) at these frequencies was minimally altered by removing the basilar papilla and cochlear fluids. In contrast, cochlear manipulation clearly altered distinct features of the transfer profile at frequencies above 1000 Hz, thus revealing major reactive transfer characteristics imposed by the cochlea on the ME at higher frequencies.

The embryos studied here presented much more complex transfer characteristics than hatchlings, as reflected in the CM_{rst}/A curves of Fig. 10. Clearly for 4 of the 8 embryos, the CM_{rst}/A ratio could not be explained simply on the basis of increasing frequency. If Eq. (4) holds in the embryo, then *Zc* must not be constant at low frequencies in these cases. We therefore hypothesize that there is a significant reactive component to *Zc* in a proportion of late embryos at low frequencies and this contrasts markedly with the mature animal. It is also clear that among this small sample of embryos the basic nature of the cochlear impedance was highly variable. The variability is not likely based in the CM_{rst} itself since the CM_{rst} was clearly shown in each animal to reliably reflect footplate motion at each frequency over a wide range of stimulus levels. It may be the case that in our random sample of late embryos, we caught individual animals at different stages in transition to a mature cochlear status. Although the embryos were all of similar chronological age, the actual status of the developing ear can vary considerably. In the present study, it was not possible to reliably document phase characteristics of the stimulus/response waveforms. In future studies we intend to use phase information to evaluate the nature of the reactive components of *Zc* that may be present in the embryo.

V. SUMMARY

PZE driver tip displacement was linearly related to the applied voltage. Displacement at a given voltage was relatively constant across frequencies from 100 to 4000 Hz with notable exceptions and had a mean value of 0.221 $\mu m_{p\text{-}p}$ with an applied voltage of 5 $V_{p\text{-}p}$. CM_{rst} recorded in response to direct footplate driving was linearly related to footplate displacement and velocity over a wide range of stimulus levels when frequency was held constant. In the hatchling chicken, the magnitude of the transfer ratio of CM_{rst}/A increased at ~6 dB/octave with increasing frequency suggesting that cochlear impedance (*Zc*) was resistive and constant at frequencies between 100 and 1000 Hz. This also holds for a portion of the embryos studied. However, a large fraction of embryos evidenced changes in impedance at low frequencies suggesting that *Zc* may exhibit important reactive components in the late embryo. In general, the present results indicated that the relationship between CM_{rst} amplitude and footplate displacement must be determined for each frequency and for each individual under study if the CM_{rst} is to provide an accurate quantitative indication of the amplitude of footplate motion. These findings may be used to facilitate measurements of middle ear sound transfer.

ACKNOWLEDGMENTS

This research was supported by NIH NIDCD 1R01DC02753 (T.A.J.), NASA NAG 5-4607 (T.A.J.), and NIH RO1 DC02117 (M. C.). The authors thank K. Paggett for competent assistance in working with embryos. Thanks are extended to Dr. R. McLaren who brought Y.S.K. and T.A.J. together and to Dr. S. Jones for solving many problems in the lab. Portions of the work reported here served in partial fulfillment of the requirements for the Ph.D degree, University of Missouri, Columbia (Y.S.K.).

Aibara, R., Welsh, J. T., Puria, S., and Goode, R. L. (**2001**). "Human middle-ear sound transfer function and cochlear input impedance," Hear. Res. **152**, 100–109.

Burkard, R., Jones, S. M., and Jones, T. A. (**1994**). "Conventional and cross-correlation brain-stem auditory evoked responses in the white leghorn chick: Rate manipulations," J. Acoust. Soc. Am. **95**, 2136–2144.

Cohen, Y. E., Rubin, D. M., and Saunders, J. C. (**1992**). "Middle ear development. I. Extra-stapedius response in the neonatal chick," Hear. Res. **58**, 1–8.

Corey, D. P., and Hudspeth, A. J. (**1980**). "Mechanical stimulation and micromanipulation with piezoelectric bimorph elements," J. Neurosci. Methods **3**, 183–202.

Dallos, P. (**1970**). "Low-frequency auditory characteristics: Species dependence," J. Acoust. Soc. Am. **48**, 489–499.

Dallos, P. (**1973**). *The Auditory Periphery* (Academic, New York).
Dickman, J. D., Reder, P. A., and Correia, M. J. (**1988**). "A method for controlled mechanical stimulation of single semicircular canals," J. Neurosci. Methods **25**, 111–119.
Gilad, P., Shtrikman, S., Hillman, P., Rubinstein, M., and Eviator, A. (**1967**). "Application of the Mossbauer method to ear vibrations," J. Acoust. Soc. Am. **41**(5), 1232–1236.
Guinan, J. J., and Peake, W. T. (**1967**). "Middle-ear characteristics of anesthetized cats," J. Acoust. Soc. Am. **41**, 1237–1261.
Gummer, A. W., Smolders, J. W. T., and Klinke, R. (**1987**). "Basilar membrane motion in the pigeon measured with the Mossbauer technique," Hear. Res. **29**, 63–92.
Gummer, A. W., Smolders, J. W. T. H., and Klinke, R. (**1986**). "The mechanics of the basilar membrane and middle ear in the pigeon," in *Peripheral Auditory Mechanisms*, edited by J. B. Allen, J. L. Hall, A. Hubbard, S. T. Neely, and A. Tubis, (Springer, Berlin), pp. 81–88.
Gummer, A. W., Smolders, J. W. T. H., and Klinke, R. (**1988**). "Determinants of high-frequency sensitivity in the bird," in *Cochlear Mechanisms: Structure, Function, and Models*, edited by J. P. Wilson and D. T. Kemp (Plenum, New York, pp. 377–385).
Hamburger, V., and Hamilton, H. L. (**1951**). "A series of normal stages in the development of the chick embryo," J. Morphol. **88**, 49–92.
Irons-Brown, S. R., and Jones, T. A. (**2004**). "Effects of selected pharmacological agents on avian auditory and vestibular compound action potentials," Hear. Res. **195**, 54–66.
Jones, S. M., and Jones, T. A. (**1995a**). "Neural tuning characteristics of auditory primary afferents in the chicken embryo," Hear. Res. **82**, 139–148.
Jones, S. M., and Jones, T. A. (**1995b**). "The tonotopic map in the embryonic chick cochlea," Hear. Res. **82**, 149–157.
Jones, S. M., and Jones, T. A. (**1996**). "Short latency vestibular evoked potentials in the chicken embryo," J. Vestib. Res. **6**, 71–83.
Jones, S. M., Jones, T. A., and Shukla, R. (**1997**). "Short latency vestibular evoked potentials in the Japanese quail (*Coturnix coturnix japonica*)," J. Comp. Physiol. [A] **180**, 631–638.
Jones, T. A. (**1992**). "Vestibular short latency responses to pulsed linear acceleration in unanesthetized animals," Electroencephalogr. Clin. Neurophysiol. **82**, 377–386.
Jones, T. A., Jones, S. M., and Paggett, K. C. (**2006**). "Emergence of hearing in the chicken embryo," J. Neurophysiol. **96**, 128–141.
Khanna, S. M., and Tonndorf, J. (**1972**). "Tympanic membrane vibrations in cats studied by time-averaged holography," J. Acoust. Soc. Am. **51**, 1904–1920.
Kim, Y. S. (**2002**). "Transfer function of the embryonic avian middle ear," Ph.D. Dissertation, University of Missouri, Columbia. pp. 1–229.
Klinke, R., Muller, M., Richter, C. P., and Smolders, J. (**1994**). "Preferred intervals in birds and mammals: A filter response to noise," Hear. Res. **74**, 238–246.
Kreyzig, E. (**1983**). *Advanced engineering mathematics* (Wiley, New York).
Kringlebotn, M. (**2000**). "Acoustic impedances at the oval window, and sound pressure transformation of the middle ear in Norwegian cattle," J. Acoust. Soc. Am. **108**, 1094–1104.
Lynch, T. J., III, Nedzelnitsky, V., and Peake, W. T. (**1982**). "Input impedance of the cochlea in cat," J. Acoust. Soc. Am. **72**, 108–130.
Malecki, I. (**1969**). "Acoustic wave propagation in extended fluid media with negligible dissipation," in *Physical foundations of technical acoustics* (Pergamon, New York), pp. 14–58.
Manley, G. A. (**1972a**). "Frequency response of the middle ear of geckos," J. Comp. Physiol. **81**, 251–258.
Manley, G. A. (**1972b**). "The middle ear of the Tokay gecko," J. Comp. Physiol. **81**, 239–250.
Manley, G. A., Gleich, O., Leppelsack, H. J., and Oeckinghaus, H. (**1985**). "Activity patterns of cochlear ganglion neurons in the starling," J. Comp. Physiol. [A] **157**, 161–181.
Manley, G. A., and Johnstone, B. M. (**1974**). "Middle-ear function in the guinea pig," J. Acoust. Soc. Am. **56**, 571–576.
Merhaut, J. (**1981**). "Sound waves in a gaseous medium," in *Theory of electroacoustics* (McGraw-Hill, New York), pp. 109–173.
Moller, A. (**1963**). "Transfer function of the middle ear," J. Acoust. Soc. Am. **35**, 1526–1534.
Narahashi, T., Moore, J. W., and Scott, W. R. (**1964**). "Tetrodotoxin blockage of sodium conductance increase in lobster giant axons," J. Gen. Physiol. **47**, 965–974.
Nedzelnitsky, V. (**1980**). "Sound pressures in the basal turn of the cat cochlea," J. Acoust. Soc. Am. **68**, 1676–1689.
Overstreet, E. H., Temchin, A. N., and Ruggero, M. A. (**2002**). "Passive basilar membrane vibrations in gerbil neonates: Mechanical bases of cochlear maturation," J. Physiol. (London) **545**, 279–288.
Rabbitt, R. D., Boyle, R., and Highstein, S. M. (**1995**). "Mechanical indentation of the vestibular labyrinth and its relationship to head rotation in the toadfish, opsanus tau," J. Neurosci. **73**, 2237–2260.
Relkin, E. M., and Saunders, J. C. (**1980**). "Displacement of the malleus in neonatal golden hamsters," Acta Oto-Laryngol. **90**, 6–15.
Ruggero, M. A., Robles, L., and Rich, N. C. (**1986**). "Basilar membrane mechanics at the base of the chinchilla cochlea. II. Responses to low-frequency tones and relationship to microphonics and spike initiation in the VIII nerve," J. Acoust. Soc. Am. **80**, 1375–1383.
Saunders, J. C. (**1985**). "Auditory structure and function in the bird middle ear: An evaluation by SEM and capacitive probe," Hear. Res. **18**, 253–268.
Saunders, J. C., and Johnstone, B. M. (**1972**). "A comparative analysis of middle-ear function in nonmammaliam vertebrates," Acta Oto-Laryngol. **73**, 353–361.
Schermuly, L., and Klinke, R. (**1985**). "Change of characteristic frequency of pigeon primary auditory afferents with temperature," J. Comp. Physiol. [A] **156**, 209–211.
Sellick, P. M., Patuzzi, R., and Johnstone, B. M. (**1982**). "Measurement of basilar membrane motion in the guinea pig using the Mossbauer technique," J. Acoust. Soc. Am. **72**(1), 131–141.
Seto, W. (**1971**). "Plane acoustic waves," in *Theory and Problems of Acoustics* (McGraw-Hill, New York), pp. 37–63.
Shero, M., Salvi, R. J., Chen, L., and Hashino, E. (**1998**). "Excitotoxic effect of kainic acid on chicken cochlear afferent neurons," Neurosci. Lett. **257**, 81–84.
Sun, H., Hashino, E., Ding, D. L., and Salvi, R. J. (**2001**). "Reversible and irreversible damage to cochlear afferent neurons by kainic acid excitotoxicity," J. Comp. Neurol. **430**, 172–181.
Sun, H., Salvi, R. J., Ding, D. L., Hashino, E., Shero, M., and Zheng, X.-Y. (**2000**). "Excitotoxic effect of kainic acid on chicken otoacoustic emissions and cochlear potentials," J. Acoust. Soc. Am. **107**, 2136–2142.
Temkin, S. (**1981**). "Reflection and transmission phenomena," in *Elements of acoustics* (Wiley, New York), pp. 77–198.
Voss, S. E., Rosowski, J. J., Merchant, S. N., and Peake, W. T. (**2000**). "Acoustic responses of the human middle ear," Hear. Res. **150**, 43–69.
Wilson, J. P., and Johnstone, J. R. (**1975**). "Basilar membrane and middle-ear vibration in guinea pig measured by capacitive probe," J. Acoust. Soc. Am. **57**, 705–722.
Woolf, N. K., and Ryan, A. F. (**1988**). "Contributions of the middle ear to the development of function in the cochlea," Hear. Res. **35**, 131–142.
Zheng, X.-Y., Wang, J., Salvi, R. J., and Henderson, D. (**1996**). "Effects of kainic acid on the cochlear potentials and distortion product otoacoustic emissions in chinchilla," Hear. Res. **95**, 161–167.
Ziomeck, L. J. (**1995**). "The linear wave equation and fundamental acoustical quantities," in *Fundamentals of Acoustic Field Theory and Space-Time Signal Processing* (CRC, Boca Raton), pp. 3–46.

L1,L2 maps of distortion-product otoacoustic emissions from a moth ear with only two auditory receptor neurons

Manfred Kössl[a)]
Institut für Zellbiologie und Neurowissenschaft, J. W. Goethe-Universität, Siesmayerstrasse 70, D-60323 Frankfurt am Main, Germany

Frank Coro
Departamento de Biologia Animal y Humana, Facultad de Biologia, Universidad de La Habana, Calle 25 num. 455, Vedado, La Habana, CP 10400

(Received 12 June 2006; revised 18 September 2006; accepted 21 September 2006)

The tympanal organ of the moth *Empyreuma affinis* emits physiologically vulnerable distortion-product otoacoustic emissions. To assess the nature of underlying mechanical nonlinearities, we measured L1,L2 maps by varying both stimulus levels. Two types of maps were found: (1) Maps containing dominant islands centered at the L1=L2 diagonal as it is typical for saturating nonlinearities that can be described by Boltzmann functions. In contrast to maps published for mammals and frogs, the shape of such islands includes sharp ridges at L1 or L2 levels close to 70 dB sound pressure level. This could be produced by a strongly asymmetric operating point of the respective transfer functions, consistent with the fact that the auditory sensory cells are not hair cells but primary mechanoreceptors with a single cilium. The saturating map components could be selectively reduced by acoustic suppression. (2) Maps where separated islands were less conspicuous but in which the dominant feature consisted of contour lines which were orthogonal to the $L1=2L2$ diagonal and could be generated by an expansive nonlinearity. Maps showing strong islands were found for $f2$ frequencies between 26.7 and 45 kHz, maps without strong islands for $f2$ between 42 and 57.5 kHz. This suggests a frequency-dependent change regarding the involved mechanical nonlinearities. © *2006 Acoustical Society of America.* [DOI: 10.1121/1.2363934]

PACS number(s): 43.64.Jb, 43.64.Kc [BLM] Pages: 3822–3831

I. INTRODUCTION

Auditory organs of insects exploit either a sound-velocity driven deflection of antennae as in the Johnston's organ of mosquitoes and flies or sound-level dependent displacement of a tympanum as it is found in grasshoppers and moths (Michelsen, 2003). The auditory sensory cells in both types of organs are quite similar and arranged in so-called scolopidia, in which auxiliary cells enclose each sensory neuron (Field, 2005). The receptor neuron is a primary mechanoreceptor with an axon and a dendrite that contains a single cilium (Gray, 1960). The main functional difference between the two types of organs is their working frequency range. Johnston's organs are sensitive to frequencies below 1 kHz, tympanal organs respond to higher frequencies of up to 100 kHz in some moth species.

The hearing range of our present animal model, the noctuoid moth *Empyreuma affinis*, is between 10 and 60 kHz, with the lowest auditory threshold of about 25 dB sound pressure level (SPL) at 35 kHz (Coro and Pérez, 1993). Each tympanal organ of *E. affinis* contains only two auditory receptor neurons (Coro and Pérez, 1987) whose dendrites are embedded in one cap cell that is attached to the tympanum (Coro and Trujillo, unpublished results). One of the neurons, the A1 cell, is about 25–30 dB more sensitive than the other one (Coro and Pérez, 1984). This simple design makes the ear of *E. affinis* a suitable model to study general principles of high frequency sound processing in insects. Similar to vertebrate ears, the tympanal organs of insects emit distortion product otoacoustic emissions (DPOAEs) that are most sensitive in the best hearing range of the species (Kössl and Boyan, 1998). In *E. affinis*, large DPOAEs that are vulnerable to anaesthesia can be measured between 15 and 60 kHz (Coro and Kössl, 1998, 2001). This may indicate the involvement of active mechanical feedback in producing high auditory sensitivity, similar to mechanisms in the vertebrate cochlea. In the case of Johnston's organs of mosquitoes and flies, it has been shown that they can spontaneously vibrate (Göpfert and Robert, 2001) and thus produce mechanical energy (Göpfert *et al.*, 2005). In the tympanal organs of insects, however, there are only a few functional data available to assess the micromechanics of auditory sensory transduction due to difficulties in measuring receptor currents in the dendrites of the sensory neurons.

DPOAE measurements can be used as a noninvasive method to derive mechanical characteristics of sensory transduction in hearing organs. In particular, the level dependence of DPOAEs, plotted in the form of L1,L2 maps provides clues about the type of nonlinearity involved. The characteristic map features in mammals (Mills *et al.*, 1994; Whitehead *et al.*, 1995a,b; Kummer *et al.*, 2000; Pibal *et al.*, 2002) are consistent with transfer characteristics as they are described by Boltzmann functions. In addition, frequency-selective

a)Author to whom correspondence should be addressed; electronic mail: koessl@zoology.uni-frankfurt.de

 © 2006 Acoustical Society of America

compression on the basilar membrane of mammals may further shape L1,L2 maps (Whitehead *et al.*, 1995b; Kummer *et al.*, 2000). In a detailed study on a frog species, Meenderink and van Dijk (2005) showed that L1,L2 maps have two components that can be modeled by a saturating, Boltzmann-type of nonlinearity at low levels and an expansive nonlinearity at high levels. In the frog, the two types of mechanical transduction characteristics seem to be represented in different auditory papillae (Meenderink and van Dijk, 2005). In the present study, we aim to derive mechanical transfer characteristics from the tympanal organ of the moth *E. affinis* by applying L1,L2 mapping techniques. In addition, for our L1,L2 map measurements we test if the nonlinear mechanism responsible for sensitive DPOAEs is suppressible by a third tone ($f3$) as it is the case with vertebrate DPOAEs (e.g., Brown and Kemp, 1984; Martin *et al.*, 1987).

II. MATERIALS

Recordings were made from 13 moths (seven females and six males) of *Empyreuma. affinis* (=*pugiòne*) (Lepidoptera, Arctiidae, Ctenuchinae) in Frankfurt am Main in April-May. Of these moths, six were brought from Havana as adults (four females, two males); the other seven (three females, four males) arrived in Germany as last-instars larvae, where they pupated and hatched. DPOAEs were measured more than three days after hatching, because we have shown previously that newly emerged moths do not produce DPOAEs (Coro and Kössl, 1998). The moths were fed with a saturated-sucrose solution.

For recordings, the wings and legs were cut off and the bulla amplificatrix, a structure that externally covers the tympanal organ of ctenuchinae moths (Kiriakoff, 1948), was also removed. In this way there was direct access to the tympanal membrane with an acoustic coupler for DPOAE recordings without displacement of body segments. The body was pinned dorsal side up to a cork platform atop a metal post. To avoid potential noxious effects of anaesthetics none were used in our experiments. The physiological state of the moths was assessed by the spontaneous movements of the antennae or by those evoked in response to light touch of one of the antennae.

To record DPOAEs, an acoustic coupler was positioned 0.5–1 mm from the tympanal membrane. The coupler has an overall tip diameter similar to that of the tympanal membrane and consists of two adjacent conical tubes for stimulation and recording. The tympanal organ was stimulated with two pure tones of different frequency, $f1<f2$, to obtain DPOAEs. One coupler channel was connected to a 1/4 in. Brüel & Kjaer 4135 microphone, and two 1 in. Microtech Gefell MK 103.1 microphone capsules served as speakers connected to the other coupler channel. The suppression tone $f3$ had a frequency in between $f1$ and $f2$, and was emitted by a 1/2 in. Brüel & Kjaer 4133 microphone capsule used as a speaker and connected to the stimulation tube of the coupler.

A Pentium PC with a Microstar DAP 840 Microstar board (sampling rates at 250 kHz) was used for generating the $f1$ and $f2$ frequencies and for controlling a Stanford Research Systems DS 335 synthesizer to produce the $f3$ frequency and three programmable attenuators (Tucker Davis Technologies System 3) to adjust stimulus levels. The Microstar board was also used for the fast Fourier transform (FFT) analysis of the microphone signal. A total of 100 recordings (recording time of 3.28 s) were averaged before FFT analysis. The $f1$ and $f2$ stimuli had a constant phase relation. The recording system was calibrated *in situ* for constant sound pressure level (SPL) at the microphone membrane using white noise, which was generated by addition of sinusoids of constant phase relation. We only used stimulus levels of up to 80 dB SPL since at levels above this value there were small setup-generated $2f1$-$f2$ distortions just above the noise level of the system of −13 to −19 dB SPL at certain stimulus frequencies. For a detailed description of the measuring procedures see Kössl *et al.* (1999).

The initial experimental procedures consisted in first obtaining a so-called DPOAE audiogram (see Coro and Kössl, 1998) at a fixed $f2/f1$ frequency ratio of 1.09 and levels of the two stimuli at 55/45 or 60/50 dB SPL. This DPOAE audiogram allowed the selection of $f2$ frequencies at which the specimen produced large levels of $2f1$-$f2$ distortion. At these selected $f2$ frequencies and using stimulus level combinations of L1=L2+10 dB, the optimum frequency ratio $f2/f1$ was determined that produces maximum emission level at low to medium L1 levels of 50–60 dB SPL within the range of tested frequency ratios f2/f1 between 1.01 and 1.45. The values of $f2$ ranged from 27.5 to 57.5 kHz, and the optimum frequency ratio values varied between 1.03 and 1.35, with most of the optimum ratios (11 of 18) between 1.07 and 1.11. The optimum ratios of 1.03 and 1.35 that are outside the mammalian-typical range of values are for insects still well within the range to evoke large DPOAEs, in particular since a reduction of DPOAE amplitude for small ratios as it is found in mammals does not occur in insects (Kössl and Boyan, 1998; Coro and Kössl, 1998). Using this procedure, the DPOAE levels that were measured at the optimum ratio were between 0 and 10 dB SPL. To obtain L1,L2 maps the $f2$ frequency was chosen as one that produced a maximum in the DPOAE audiogram and the $f1$frequency was adjusted according the optimum frequency ratio. We optimized the frequency ratio for the map measurements to obtain comparable DPOAE amplitudes for different $f2$ frequencies. For such an $f1,f2$ combination, the L1 level was increased stepwise by 2.5 dB while maintaining a constant L2 level. The L2 level was then increased by 2.5 dB and the procedure was repeated. Both stimulus levels were varied within the same range of intensities, which produced a square L1,L2 matrix containing from 400 to 729 data points for each stimulus frequency combination. The stimulus levels used varied between 10 and 82.5 dB SPL. For most maps (14 out of 18) the maximum stimulus level was at 75 or 77.5 dB SPL. Statistical analysis included the calculation of the mean, standard deviation (SD), and standard error of the mean. All data samples passed the normality test (Kolmogoroff-Smirnoff test) and comparison between two samples was done using an unpaired t test.

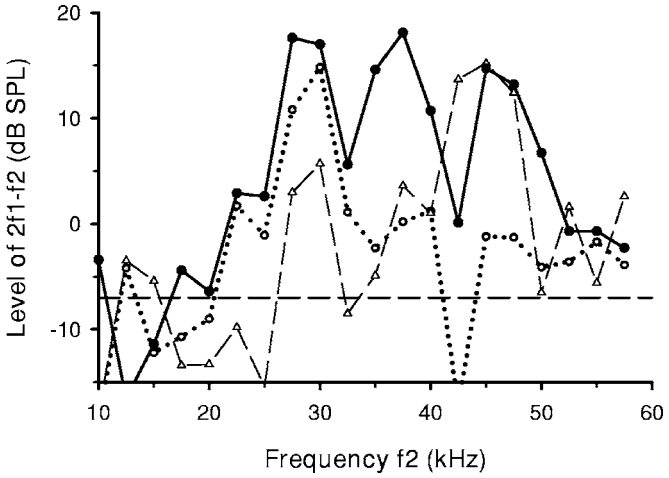

FIG. 1. DPOAE audiograms at a fixed $f2/f1$ frequency ratio of 1.09 and levels of the two stimuli at 60/50 dB SPL from three different *E. affinis* specimens, two females and one male. The horizontal dashed line represents the highest value of the mean plus 1 SD of noise level from these three experiments. In all three specimens there is a peak of $2f1$-$f2$ level close to 30 kHz, in two specimens there are peaks at 45 kHz.

III. RESULTS

In all ears tested we recorded DPOAEs, and those with the highest values at the lowest stimulus intensities were always at the $2f1$-$f2$ frequency. DPOAE audiograms obtained with the two stimuli set at intermediate levels (L1, L2 at 60,50 dB SPL) and at a constant frequency ratio $f2/f1$ of 1.09 reveal that maximum $2f1$-$f2$ amplitudes can be measured in an $f2$ frequency range from 20 to 60 kHz (Fig. 1). Depending on the specimen, either an $f2$-stimulus range of 20–40 kHz or of 40–57 kHz yields large DPOAEs. In some specimens both frequency ranges are efficient in evoking DPOAEs (Fig. 1).

We obtained 18 L1,L2 maps of the $2f1$-$f2$ DPOAE from 13 different specimens of *Empyreuma affinis*. An example of a map obtained with stimulus frequencies of 27 and 30 kHz is given in Fig. 2(a) where DPOAE levels above −10 dB SPL (>noise level+1 SD) are coded with gray shadings and consecutive contour lines. In this specimen, $2f1$-$f2$ levels were largest along the diagonal L1=L2, and a triangular-shaped island encloses maximum DPOAE levels for L1 levels between 50 and 70 dB SPL and L2 levels between 25 and 70 dB SPL. At the local DPOAE maximum within this island, the $2f1$-$f2$ level was 32.2 dB SPL at the combination of L1=67.5 and L2=65 dB SPL. For higher stimulus levels, a conspicuous dip is evident at the combination of L1=70 and L2=67.5 dB SPL with values below 0 dB SPL. The DPOAEs shift in phase by approximately 180° for stimulus levels just above the horizontal and vertical limits of the triangular-shaped island, at L1 or L2 between 72.5 and 75 dB SPL. A stimulus level increase by 2–7 dB is sufficient to induce this phase shift. At the highest stimulus levels used, close to 80 dB SPL, DPOAE levels reach a second maximum. L1,L2 maps obtained for the $2f2$-$f1$ DPOAE (not shown) displayed islands and wedges that are perpendicular to those in the corresponding $2f1$-$f2$ map from the same preparation and the contour shapes are mirrored at the L1=L2 diagonal.

The recordings shown in Fig. 2(a) were made immediately after the insect was prepared for the measurement (see methods). Afterwards, the animal was kept in place in the

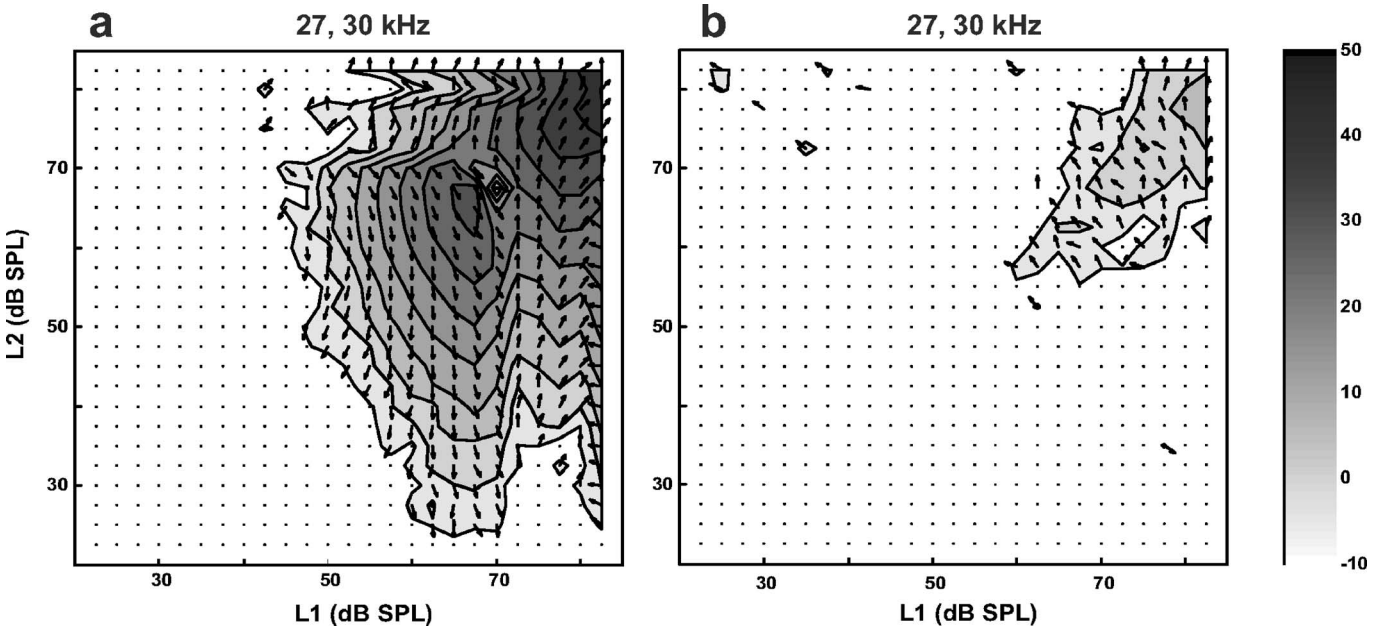

FIG. 2. Amplitude and phase of the $2f1$-$f2$ DPOAE as function of stimulus levels L1 and L2 from a living *Empyreuma affinis* (a) and from the same animal after 18 h had elapsed from the first recordings (b) with $f2=30.0$ kHz and $f2/f1=1.11$. The DPOAE amplitude is represented by shades of gray coding the range between −10 and 50 dB SPL (see scale bar at the right side) and by contour lines that are separated by 5 dB, starting at −5 dB SPL. Each L1/L2 combination tested is indicated by a dot. The arrows centered at the dots give the phase of the DPOAE. Phase data are only displayed if the DPOAE level is above −10 dB SPL. The phase is relative to that at L1=L2=82.5 dB SPL in this specimen (uppermost right data point). During the recordings shown in (a), the insect was moving its antennae spontaneously. The L1, L2 map shows a prominent triangular island at L1 levels between 50 and 70 dB SPL. During the recordings shown in (b) the insect did not move its antennae, and did not show any sign of being alive. The level of $2f1$-$f2$ is only above 0 dB SPL when the levels of both stimuli are larger than 55 dB SPL, and even at the highest L1 and L2 levels used there are no $2f1$-$f2$ responses above 10 dB SPL.

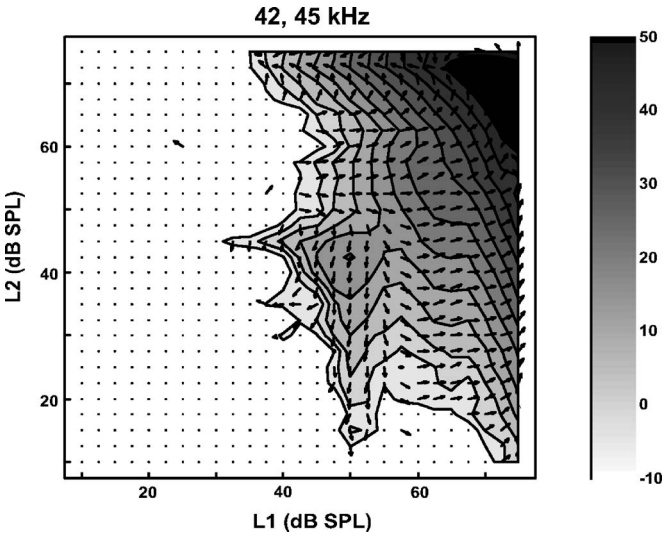

FIG. 3. Amplitude and phase of the $2f1$-$f2$ DPOAE as function of stimulus levels L1 and L2. These data were recorded from a specimen of *E. affinis* different than that shown in Fig. 2 and the stimuli used were $f2=45.0$ kHz and $f2/f1=1.07$. This map is dominated by parallel contour lines that are perpendicular to the L1=L2 diagonal.

recording chamber without changing the position of the coupler and the measurements were repeated 18 h later as shown in Fig. 2(b). At this time the animal did not show any signs of being alive and there was no antennae movement. The level of $2f1$-$f2$ was significantly reduced and even at the highest L1 and L2 levels there were no $2f1$-$f2$ responses above 10 dB SPL. In addition, the island-like shape has disappeared.

A. Frequency dependence of the shapes of L1, L2 maps

In living animals with spontaneous antennae movement two types of L1,L2 maps could be recorded. The characteristic feature of the first type of map is the triangular-shaped island of maximum DPOAE level at intermediate stimulus levels [Fig. 2(a)]. Within the range of stimulus levels used, the absolute maximum of DPOAE level is either within the limits of the island or at higher levels [Fig. 2(a)]. The second type of map is dominated by a larger region of parallel contour lines approximately orthogonal to the L1=2L2 diagonal at the highest stimulus levels used (Fig. 3). Such maps can also contain less conspicuous islands or ridges along the L1=L2 diagonal, e.g., close to L1=50 and L2=42.5 dB SPL (Fig. 3). In maps not showing strong islands, the DPOAE phase can shift by up to 180° when increasing the stimulus levels from the most sensitive region of the map towards higher levels. In contrast to maps with a strong island, a larger level increase of 20 dB or more is required to induce such a phase shift. Is has to be pointed out that the classification in two types of maps depending on the dominance of islands of course is limited for the range of used stimulus levels of up to 80 dB SPL and by the noise level of the recordings of −13 to −19 dB SPL.

When L1,L2 maps were recorded at different stimulus frequency combinations in the same specimen, maps with strong islands were always recorded for the lower stimulus frequencies and maps not showing strong islands for the higher frequencies (Fig. 4). In the two examples shown, the lower $f2$ frequencies of 27.5 and 45 kHz produced either a single triangular island [Fig. 4(c)] or a similarly shaped island flanked by two smaller additional DPOAE maxima along the L1-L2 diagonal [Fig. 4(a)]. In both cases [Figs. 4(b) and 4(d)], the higher $f2$ frequencies of 45.5 and 57.5 kHz, respectively, resulted in maps without strong islands and with dominant parallel contour lines at the highest stimulus levels used. Of course, outside our stimulus range such contours could form convex island-like shapes as it may occur in Fig. 4(b).

From 18 recorded maps, 16 were obtained from sensitive animals and were classified as maps with or as maps without dominant islands (Table I). The six maps that had islands as their dominating feature were measured using $f2$ frequencies between 27.5 and 45 kHz, while the ten maps without pronounced islands were obtained with $f2$ between 42.5 and 57.5 kHz. The other two maps were of an intermediate type and were obtained with $f2$ at 37.5 kHz. The average $f1$,$f2$ frequencies for the maps with strong islands were at 30.7, 34.1 kHz and at 44.9, 48.5 kHz for the maps without strong islands. This indicates that the two map types are associated with the low and the high frequency amplitude maxima of $2f1$-$f2$ DPOAE audiograms (see Fig. 1). To obtain the most sensitive DPOAE measurements that are comparable in DPOAE level we measured the maps at the optimum frequency ratio that was determined for each specimen and $f2$ frequency individually. This procedure introduces the frequency ratio as additional parameter (Table I), however there was no significant correlation between the map type or the used $f2$ frequency and the optimum frequency ratio (see legend of Table I). From the maps, the slope of DPOAE-amplitude growth along the L1=L2 diagonal was measured close to threshold, for a 7.5 dB increase of stimulus levels, starting at the first DPOAE-amplitude data point above −6.5 dB SPL. In the case of the maps with dominating islands, the slope was $3.14+0.57$ dB/dB($n=6$), for maps without strong islands the slope was at $2.82+0.65$ dB/dB($n=6$). The similarity of the slopes in both types of map may be due to the fact in most maps where islands were not the dominant feature [e.g., in Fig. 3 or Fig. 4(d)], nonetheless, small island-like shapes could appear at threshold just above the noise level.

B. DPOAE growth functions

To verify that the classification in two map types based on the shape of contour areas reflects quantitative differences in the change of DPOAE level with stimulus levels, we analyzed the individual relations between the $2f1$-$f2$ DPOAE value and the level of the $f1$ tone for a given value of L2, which will be called from now on, DPOAE growth functions. Of the 344 growth functions analyzed, 61.6% (212) show a local maximum of the $2f1$-$f2$ level at intermediate L1 levels [Fig. 5(a)]. The $2f1$-$f2$ decrease for L1 levels beyond the maximum is associated with an abrupt change of the $2f1$-$f2$ phase [Fig. 5(a)]. In 16% (55) of the growth func-

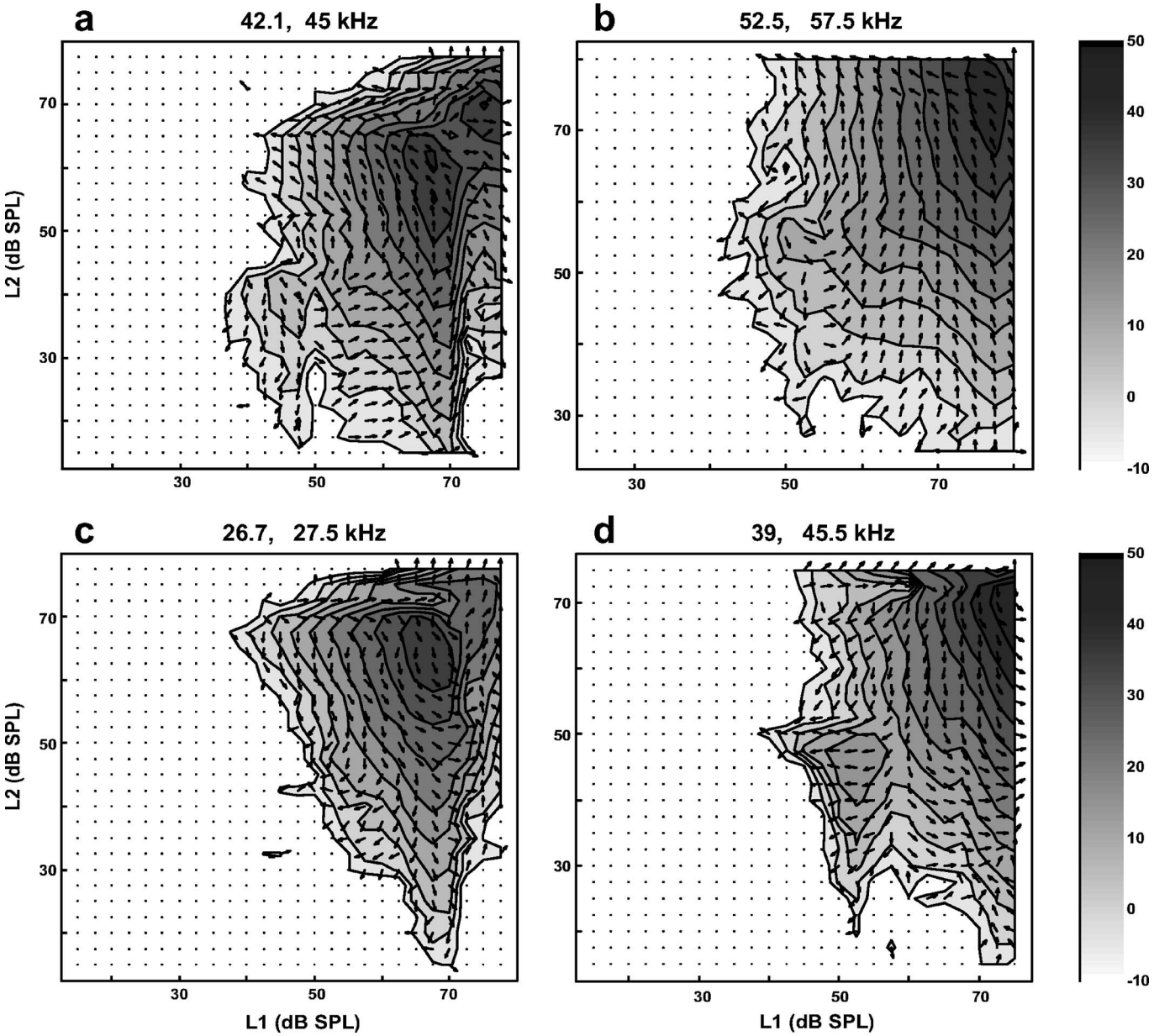

FIG. 4. Amplitude and phase of the $2f1$-$f2$ DPOAE as function of stimulus levels L1 and L2 in two moths (specimen 1: a,b specimen 2: c,d) for different stimulus frequencies. In both cases the lower frequency stimulus pairs evoked prominent triangular-shaped islands at intermediate stimulus levels in the map, whereas the higher frequency stimulus pairs produced parallel contours at the highest stimulus levels tested. In the latter cases, ridges or islands at intermediate stimulus levels are less prominent or absent.

tions, their shape is characterized by a "kneepoint," following the definition given by Meenderink *et al.* (2005), which indicates that at a certain L1,L2 stimulus combination below maximal intensity applied, there is a small decrease or flexion, but no dip as in the growth functions with a local maximum, and a further increase of the $2f1$-$f2$ DP value at higher intensities (result not shown). The rest of the growth functions, 22.4% (77) consists of a monotonous increase of DPOAE level over the whole stimulus intensity range used [Fig. 5(b)].

The percentage of the types of growth functions present in each map type differs significantly (unpaired t test, $p < 0.05$). For this analysis we considered 16 maps, six that had a strong island and ten without strong island. We excluded the two maps that could be classified as intermediate type. Maps with a strong island have a greater percentage of growth functions with a local maximum (86.3%), than the maps without strong island (46.1%) and show fewer monotonic growth functions (7.7%) and functions with a kneepoint (6.0%), than the maps without strong island (31.6% and 22.4%, respectively). The two types of maps also differ in the features of the growth functions with local maxima. In maps with strong islands, the value of the local maximum is significantly higher, (36.6±2.8 dB SPL, mean and standard error of the mean), than in the other type of map (16.3±1.7 dB SPL). In none of the maps without a strong island was the local maximum above 30 dB SPL, while five of the six maps that showed a dominant island had local maxima above this value.

TABLE I. The $f2$ frequencies and frequency ratios $f2/f1$ of the two types of L1,L2 maps. The maps with dominant island shapes were obtained from five specimens, the maps without dominant islands from nine specimens. The respective optimum frequency ratios that were used for the map measurement follow normality but differ significantly in their SD (Barlett test $p>0.05$). Therefore, a Welch t test was used which shows that the optimum ratios of both types of maps do not differ significantly (t Welch$=0.74, p=0.49$). This indicates that the type of the map does not depend on the used frequency ratio. In addition, there is no significant correlation between $f2$ and the corresponding $f2/f1$ ratio for maps with dominant islands, for maps without dominant islands, and for all maps grouped together ($P=0.68, p=0.73$, and $p=0.65$, respectively)

	Maps with dominant island ($n=6$)		Maps without dominant island ($n=10$)	
	f2	***f2/f1***	***f2***	***f2/f1***
	30	1.11	57.5	1.09
	45	1.07	45	1.07
	35	1.03	42.5	1.09
	27.5	1.03	57.5	1.05
	30	1.11	42.5	1.09
	37.5	1.35	42.5	1.09
			47.5	1.09
			45	1.05
			47.5	1.09
			57.5	1.09
Mean	34.1	1.12	48.5	1.08
SD	6.45	0.12	6.47	0.02

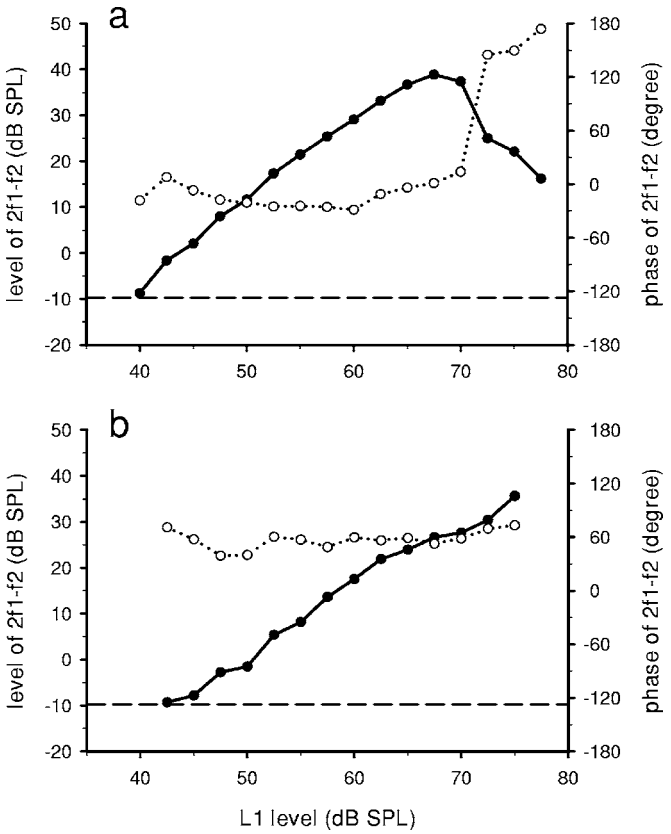

FIG. 5. Level of the $2f1$-$f2$ distortion product (solid circles) and $2f1$-$f2$ phase (open circles) as a function of L1 at a fixed L2 level of 62.5 dB SPL for (a) $f1=34$ kHz and $f2=35$ kHz and (b) $f1=54.7$ kHz and $f2=57.5$ kHz. The horizontal dashed lines represent the mean value of the noise plus one SD. The graph in (a) shows a local maximum of 39 dB SPL for the $2f1$-$f2$ DPOAE at an L1 level of 67.5 dB SPL, and a pronounced decrease of DPOAE level for higher L1 levels associated with a change of the $2f1$-$f2$ phase. The graph in (b) shows a monotonous growth of the $2f1$-$f2$ level with increasing values of L1 starting at around 45 dB SPL.

C. Effects of an *f3* suppression tone

In seven specimens we obtained L1,L2 maps while applying an $f3$ suppression tone, which was chosen to be between 0.6 and 1.6 kHz below $f2$ with the level of the suppressor between 52.5 and 70 dB SPL. The suppressor affects the shape of the $2f1$-$f2$ L1,L2 maps, since it reduces the DPOAE level at lower stimulus intensities, in particular close to the L1=L2 diagonal. There is a clear change in the convex contours and the identifiable wedges (Fig. 6). At higher stimulus levels, at and above 70 dB SPL, changes are absent or less conspicuous. Individual growth functions also reflect these changes. In Fig. 7 an example of a nonmonotonic DPOAE growth function is given, measured at an L2 level of 57.5 dB SPL. A suppression tone of 52.5 dB SPL preferentially affects the first component of the growth function (Fig. 7: open triangles). An increase in suppressor level to 62.5 dB SPL (Fig. 7: filled circles) leads to complete abolishment of the first component of the nonmonotonic growth function. Comparable changes during the presence of suppression tones were seen in the other five specimens tested.

IV. DISCUSSION

A. General properties of DPOAEs in *E. affinis*

The noctuoid moth *E. affinis* uses ultrasound for intraspecific communication during mating behavior (Sanderford *et al.*, 1998), and auditory nerve recordings show its ear is maximally sensitive at 30–35 kHz, a range where its own sound emissions have the highest intensity (Coro and Pérez, 1993). DPOAE audiograms recorded at low stimulus levels reach maximum amplitude in this frequency range (Coro and Kössl, 1998). At medium sound pressure levels of 60/50 dB SPL (Fig. 1) the frequency range that induces large DPOAE can extend up to about 50 kHz (Fig. 1; and Coro and Kössl, 1998). In the most sensitive preparations, the maximum amplitude of the $2f1$-$f2$ DPOAE is only about 15–20 dB below that of the $f1$ stimulus (Fig. 5). This indicates strongly nonlinear mechanical properties of the hearing organ. In addition, it also may reflect the fact that, by directly recording at the tympanal organ where the receptor cells are situated, any sound attenuation by auxiliary auditory structures is absent. Accordingly, when sound transmission to the tympanal organ involves an auxiliary conduction apparatus, like the acoustic trachea in another insect species such as the bushcricket *Mecopoda elongata*, the DPOAE amplitudes are reduced (Baumgarten, 2005).

Sensitive DPOAEs are only recorded when the moths are in good physiological condition. However, it is quite difficult to assess the physiological state of insects. Therefore, in the present study, we took spontaneous antennae movement of the nonanaesthetized animal as an indicator that the animal is alive (see also Coro and Kössl, 2001). Kept for more than 12 h in the recording chamber without sustaining it artificially, the moth did not show antennae movements or any other sign of being alive. The fact that at this time the DPOAEs had strongly deteriorated, of course, does not nec-

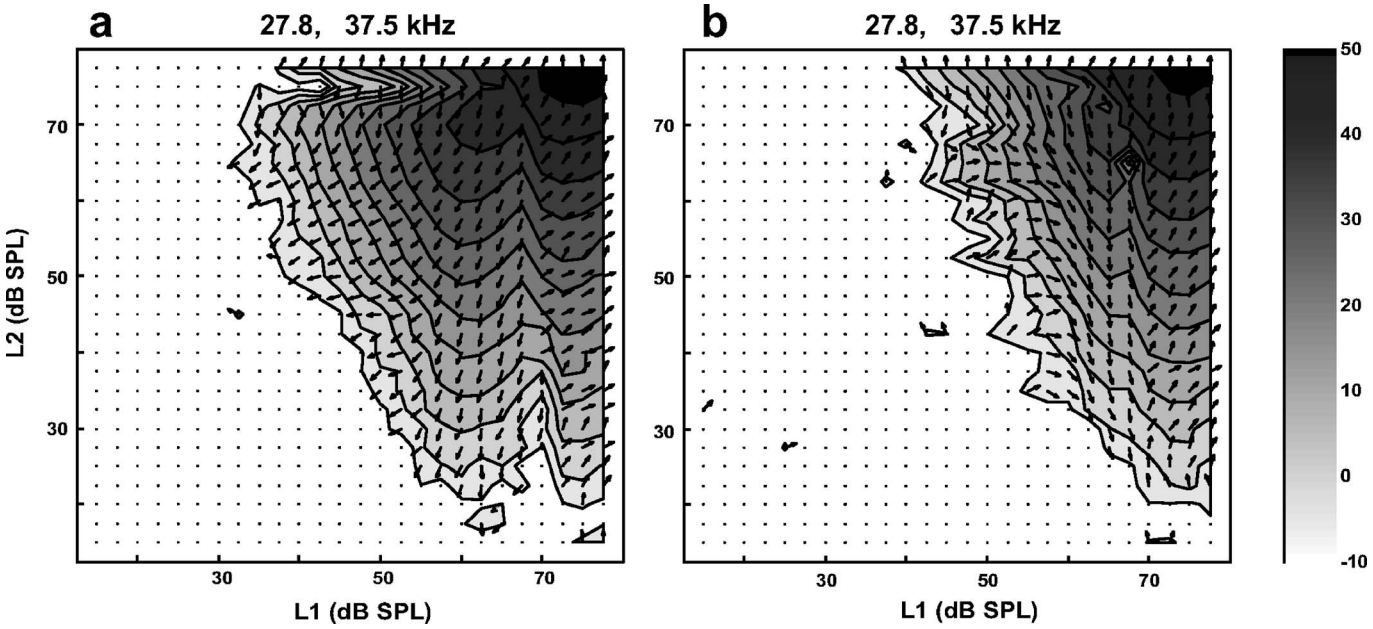

FIG. 6. Amplitude and phase of the $2f1$-$f2$ DPOAE as function of stimulus levels L1 and L2 in the absence (a) and the presence (b) of an $f3$ suppression tone. The stimuli used were $f1=27.8$ kHz and $f2=37.5$ kHz in (a), together with $f3=36.5$ kHz at 70 dB SPL in (b). The stimuli were applied alternatively with and without the suppression tone for each L1, L2 combination.

essarily prove that, e.g., metabolically active receptor cells or supporting cells are involved, since additional factors like dehydration could have changed general mechanical properties of the tympanum. But at this stage, the triangular-shaped map contours, which we take as an indicator of a compressive nonlinearity associated with transduction (see below), had disappeared. In addition, DPOAEs within these contours are strongly affected by acoustic suppression. This indicates that the most sensitive DPOAEs indeed reflect properties of the transduction apparatus in this species. Further evidence that sensitive DPOAEs in insects depend on active metabolism comes from studies where those DPOAEs were reduced during hypoxia or by using anaesthetics (Kössl and Boyan, 1998; Coro and Kössl, 2001).

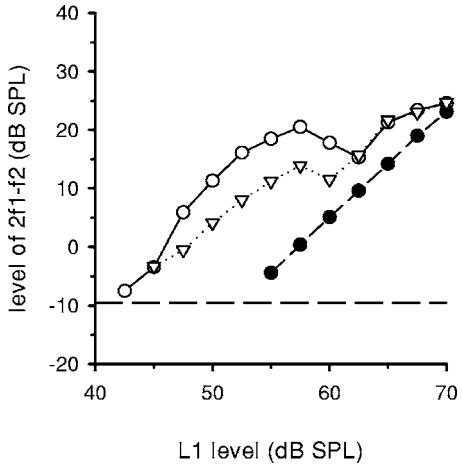

FIG. 7. Influence of an $f3$ suppression tone on a DPOAE growth function measured at an L2 level of 57.5 dB SPL. DPOAE levels without suppressor (open circles) are compared to values obtained during suppression with 52.5 dB SPL (open triangles) or 62.5 dB SPL (filled circles). The stimulus frequencies were $f1=34.4$ kHz, $f2=37.5$ kHz, and $f3=36.0$ kHz.

B. Level maps and types of nonlinearities in the ear of *E. affinis*

To be able to discuss the implications from the shape of L1,L2 maps for mechanical nonlinearities involved in auditory transduction in the hearing organ of *E. affinis*, a graphical illustration of the consequences of different nonlinearities on map contours is given in Fig. 8 (see also Meenderink and van Dijk, 2005). This simulation does not take into account mechanical frequency filtering prior to sensory transduction and is independent of the input frequencies. The intention of this simulation is to show that specific properties seen in the data could be produced by certain transfer functions.

Expansive nonlinearities like a cubic function [Fig. 8(a)] result in parallel contour lines with a slope of $L2=-2L1$ for the $2f1$-$f2$ distortion. In the maps from *E. affinis* such features are prominent in the maps without strong island with high frequency stimulation [Figs. 3, 4(b), and 4(d)]. In contrast, convex contours that run parallel to the $L1=L2$ diagonal are a characteristic of compressive or clipping nonlinearities as they are given by Boltzmann functions [Fig. 8(b)]. In *E. affinis* the island-dominated maps had maximum amplitudes close to the $L1=L2$ diagonal. The shape of the contour lines, however, was clearly different from that of a Boltzmann function with its operating point at a symmetric position [Fig. 8(b)]. The most characteristic features of island-dominated maps in *E. affinis* are triangular-shaped convex contours with quite an abrupt change of DPOAE level at a constant L1 or L2 level close to 70 dB SPL. Such abrupt level changes at a constant L1 or L2 level can be produced if the operating point of a Boltzmann function is asymmetric (Figs. 8(c) and 8(d); Lukashkin and Russell, 1999) and either minima or maxima at a constant L1 or L2 are the prominent features of such maps. Operating point shifts in both directions produce triangular-shaped contours at low to interme-

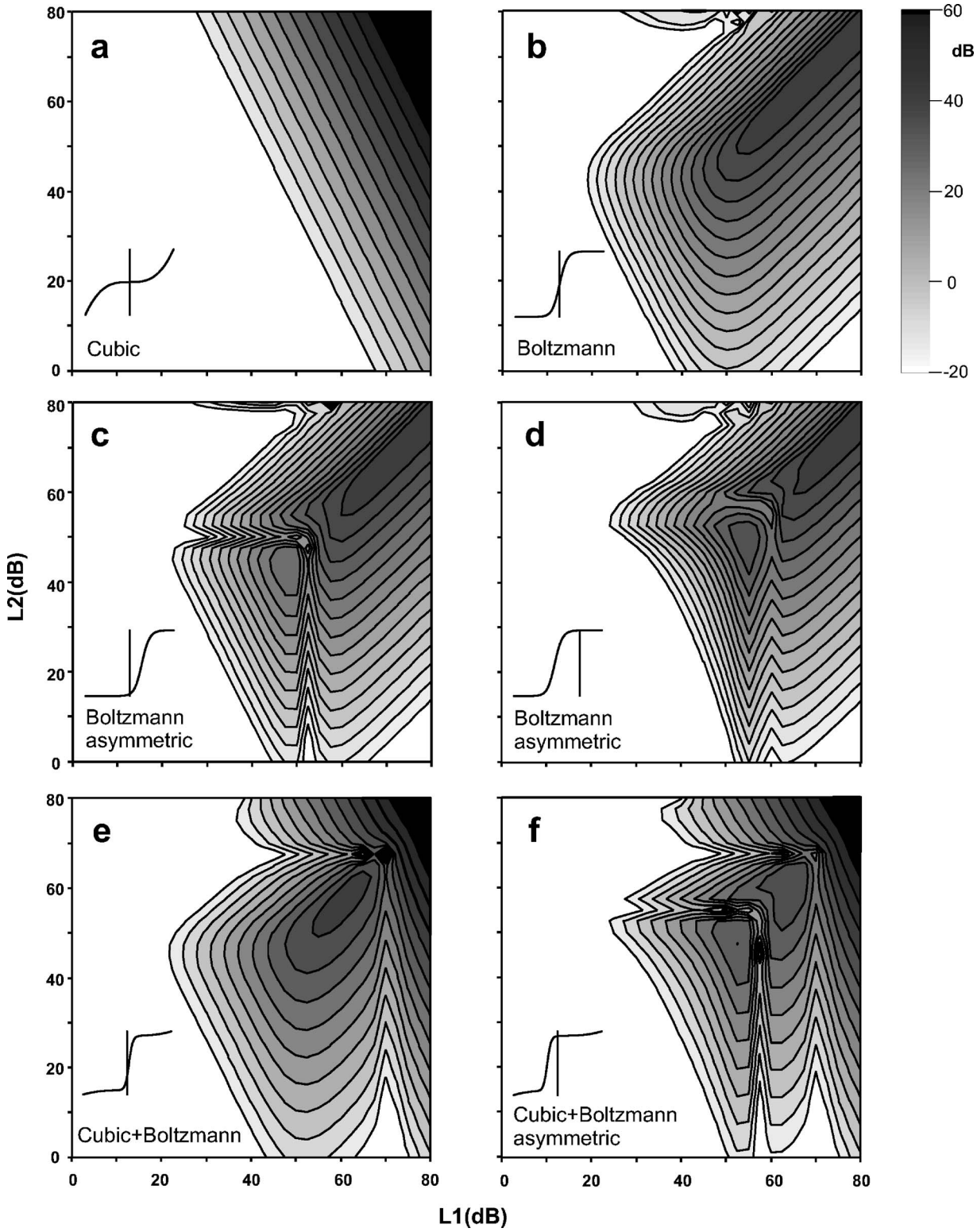

FIG. 8. Graphic illustration of L1,L2 maps for the $2f1$-$f2$ distortion derived from different types of nonlinear functions. The contour lines were calculated at 5 dB intervals. Insets show the respective nonlinear functions with a vertical line indicating the position of the operating point. (a) Cubic nonlinearity $y=x^3$ (b) Boltzmann function $y=[1+\exp[a*(x_a-x)]*[1+\exp(b*(x_b-x))]^{-1}$ similar to those that describe three state models of mechanoelectrical transduction in vertebrate hair cells (Corey and Hudspeth, 1983; Crawford *et al.*, 1989; Kros *et al.*, 1992) with $a=4$, $b=10$, $x_a=x_b=-0.054$. The function was optimized to obtain maximum overall symmetry, (c) Boltzmann function with operating point shifted to $x_a=x_b=0.225$, (d) Boltzmann function with operating point shifted $x_a=x_b=-0.785$, (e) symmetric Boltzmann function (operating point at $x_a=x_b=0.0015$) and cubic nonlinearity added (weighting factor 0.01), (f) Boltzmann function with shifted operating point ($x_a=x_b=-0.542$) and cubic nonlinearity added (weighting factor 0.01).

diate L1 and L2 levels that are reminiscent of the islands in the respective maps from the moth (Figs. 2(a), 4(a), and 4(c)). Distinct convex contours and separation of an island shape also can be produced if a symmetric Boltzmann function is combined with a cubic nonlinearity [Fig. 8(e)]; the form of the corresponding island, however, is different to the

typical triangle island shape in the moth data. Multiple separated areas of maximum distortion levels arise if cubic and asymmetric Boltzmann functions are combined [Fig. 8(f)]. In *E. affinis*, comparable phenomena are observed in some of the island-dominated maps [Fig. 4(a)].

The magnitude range of $2f1$-$f2$ levels produced by the Boltzmann functions in Figs. 8(b)–8(d) is about 60 dB for an L1=L2 input increase of 20 dB. This is comparable to an increase of DPOAE level in the maps with most pronounced islands (e.g., Fig. 4) from about −16 dB SPL (noise level) to maximum values of close to 40 dB SPL for a L1=L2 increase from 50 to about 70 dB SPL. It is important to note that the Boltzmann functions that are not combined with an expansive nonlinearity clip the input already at intermediate levels of about 60 dB and cause a saturation over most of the cycle of the output wave form. This would severely restrict the dynamic range of the system. From auditory nerve recordings in *E. affinis* it is known that spike responses of the sensory cells saturate about 20–30 dB above threshold (Coro and Perez 1984). A comparable restriction of dynamic range is found in other tympanal organs (Roeder, 1974; Imiazumi and Pollack, 2001) and could be due to a mechanical saturation, as seen in the Boltzmann functions, or/and to electrophysiological adaptation mechanisms in the cell membrane.

The comparison of L1,L2 maps of *E. affinis* with the properties of different nonlinear functions suggests, that at the moth's most sensitive frequency, close to 30 kHz, a compressive Boltzmann-like mechanical nonlinearity is involved, similar to those that are used to describe mechanical transduction in vertebrates. The initial slope of the respective L1,L2 maps along their diagonal of 3.14 dB/dB is close to the value of 3 dB/dB of a typical Boltzmann function. At higher frequencies, different nonlinear properties emerge, possibly described by an expansive nonlinearity. At present it is open if these are two mechanical processing modes of the same morphological substrate, most possibly the mechanical transduction apparatus, or if different components of the tympanal organ are involved. The observation that acoustic suppression with a third tone preferentially affects the triangular islands and the low level components of respective growth functions could indicate the presence of two sources of DPOAE generation.

The Boltzmann-like nonlinearity seems to be characterized by a strongly asymmetric operating point and thus the shape of the maps differs significantly from that seen in vertebrates (Mills *et al.*, 1994; Whitehead *et al.*, 1995a, b; Kummer *et al.*, 2000; Pibal *et al.*, 2002; Meenderink and van Dijk, 2005). A single compressive nonlinearity may be sufficient to explain the properties of maps with strong islands in accordance with models for DPOAE generation in mammals where a single localized Boltzmann nonlinearity, together with dynamic adjustment of the operating point, can account for level dependence of DPOAE (Lukashkin and Russell, 1998, 1999, 2005; Lukashkin *et al.*, 2002). Of course, in the moth, with its two sensory cells that are attached at the same point at the tympanum and the lack of tonotopicity, models that employ spatial separation of distributed nonlinear elements, as they could be provided by outer hair cells along the basilar membrane (Mills, 1997), would not work to explain the amplitude and phase behavior of nonmonotonic DPOAE growth functions.

C. Auditory transduction in tympanal organs

Auditory tympanal organs in insects contain primary sensory neurons with a single cilium. A dendritic sheet around the tip of the cilium is enclosed by an extracellular structure, the so-called cap that is embedded in attachment cells connected to the tympanum (Gray, 1960; Field, 2005). The sensory dendrites of insect auditory receptor neurons are not structurally polarized like vertebrate hair cells and may respond to mechanical pressure from any direction perpendicular to their length axis. Intracellular measurement of receptor potentials from the auditory receptors of locusts (Hill, 1983a, b) reveals that the cells only show depolarizing responses to sound and no hyperpolarization. Therefore it can be assumed that the operating point of mechanoelectrical transduction is shifted strongly towards a saturating region of the transduction transfer function, in contrast to the situation in vertebrates, where the structural polarity of the hair bundle and of the tip links produces either hyper- or depolarizing receptor currents. If, as in vertebrates, auditory receptor potentials trigger reverse electromechanical force generation in insects, the transfer characteristics of force generation would also be dominated by an asymmetric operating point as the triangular-shaped convex contours of sensitive L1,L2 maps at around 30 kHz indicate (Fig. 8).

Recently is has been shown that auditory transduction in the Johnston's organ of *Drosophila* most likely involves mechanosensitive channels of the TRP (Transient Receptor Potential) channel family (Kim *et al.*, 2003; Eberl *et al.*, 2000), similar to the situation in vertebrate hair cells (Sidi *et al.*, 2003; Corey *et al.*, 2004). In *Drosophila* mutants with defective putative channel proteins, or defective proteins that are responsible either for attachment of the cilia tip to the caps or important for the structural integrity of the cilium, spontaneous vibrations of the antennae of the Johnston's organ are absent or reduced (Göpfert and Robert, 2003; Göpfert *et al.*, 2005). The altered mechanical vibration characteristic in mutants gives strong evidence for an active mechanical amplification mechanism working at frequencies of a few hundred Hz (Göpfert *et al.*, 2005). In tympanal organs of moths, the sensory cells and their supporting cells are structurally similar to those of *Drosophila*; their working frequency range, however, is much higher and it remains to be tested if a possible mechanical amplifier based on proteins associated with forward transduction can be functional at such high frequencies.

ACKNOWLEDGMENTS

This study was supported by the DFG and Humboldt Foundation.

Baumgarten, D. (**2005**). "Otoakustische Emissionen bei der Laubheuschrecke *Mecopoda elongata*," ("Otoacoustic emissions from the bush cricket *Mecopoda elongata*"), Diploma thesis, Faculty of Biosciences, University of Frankfurt.

Brown, A. M., and Kemp, D. T. (**1984**). "Suppressibility of the 2f1-f2 stimu-

lated acoustic emissions in gerbil and man," Hear. Res. **13**, 29–37.
Corey, D. P., and Hudspeth, A. J. (**1983**). "Kinetics of the receptor current in bullfrog saccular hair cells," J. Neurosci. **3**, 962–976.
Corey, D. P., Garcia-Anoveros, J., Holt, J. R., Kwan, K. Y., Lin, S. Y., Vollrath, M. A., Amalfitano, A., Cheung, E. L., Derfler, B. H., and Duggan, A. (**2004**). "TRPAl is a candidate for the mechanosensitive transduction channel of vertebrate hair cells," Nature (London) **432**, 723–730.
Coro, F., and Kössl, M. (**1998**). "Distortion-product otoacoustic emissions from the tympanic organ in two noctuoid moths," J. Comp. Physiol., A **183**, 525–531.
Coro, F., and Kössl, M. (**2001**). "Components of the $2f_1$-f_2 distortion-product otoacoustic emission in a moth," Hear. Res. **162**, 126–133.
Coro, F., and Pérez, M. (**1984**). "Intensity coding by auditory receptors in *Empyreuma pugione* (Lepidotpera. Ctenuchidae)," J. Comp. Physiol., A **154**, 287–295.
Coro, F., and Pérez, J. (**1987**). "Estructura delórgano timpánico de *Empyreuma pugione* (Lepidoptera: Arctiidae)," ["Structure of the tympanal organ of *Empyreuma pugione* (Lepidoptera: Arctiidae)]." Cien. Biol. **17**, 31–41.
Coro, F., and Pérez, M. (**1993**). "Threshold and suprathreshold responses of the auditory receptors in an arctiid moth," Experientia **49**, 285–290.
Crawford, A. C., Evans, M. G., and Fettiplace, R. (**1989**). "Activation and adaptation of transducer currents in turtle hair cells," J. Physiol. **419**, 405–434.
Eberl, D. F., Hardy, R. W., and Kernan, M. J. (**2000**). "Genetically similar transduction mechanisms for touch and hearing in *Drosophila*," J. Neurosci. **20**, 5981–5988.
Field, L. H. (**2005**). "The chordotonal organ: A uniquely invertebrate mechanoreceptor," in *Methods in Insect Sensory Neuroscience*, edited by T. A. Christensen (CRC, New York), pp. 61–105.
Göpfert, M. C., and Robert, D. (**2001**). "Active auditory mechanics in mosquitoes," Proc. R. Soc. London, Ser. B **268**, 333–339.
Göpfert, M. C., and Robert, D. (**2003**). "Motion generation by Drosophila mechanosensory neurons," Proc. Natl. Acad. Sci. U.S.A. **100**, 5514–5519.
Göpfert, M. C., Humphris, A. D. L., Albert, J. T., Robert, D., and Hendrich, O. (**2005**). "Power gain exhibited by motile mechanosensory neurons in *Drosophila* ears," Proc. Natl. Acad. Sci. U.S.A. **102**, 325–330.
Gray, E. G. (**1960**). "The fine structure of the insect ear," Philos. Trans. R. Soc. London, Ser. B **243**, 75–94.
Hill, K. G. (**1983a**). "The physiology of locust auditory receptors I. Discrete depolarization of receptor cells," J. Comp. Physiol. **152**, 475–482.
Hill, K. G. (**1983b**). "The physiology of locust auditory receptors II. Membrane potentials associated with the response of the receptor cell," J. Comp. Physiol. **152**, 83–493.
Imiazumi, K., and Pollack, G. S. (**2001**). "Neural representation of sound amplitude by functionally different auditory receptors in crickets," J. Acoust. Soc. Am. **109**, 1247–1260.
Kim, J., Chung, Y. D., Park, D. Y., Choi, S., Shin, D. W., Sohk, H., Lee, W., Son, W., Yim, J., Parkk, C. S., and Kernan, M. J. (**2003**). "A TRPV family ion channel required for hearing in *Drosophila*," Nature (London) **424**, 81–84.
Kiriakoff, S. G. (**1948**). "Recherches sur les organes tympaniques des lepidopteres en rapport avec la classification. I. Ctenuchidae," ("Study on tympanal organs of lepidoptera in relation with their classification. I. Ctenuchidae"). Bull. & Ann. Soc. Entomol. Belgique **84**, 231–276.
Kössl, M., and Boyan, G. S. (**1998**). "Acoustic distortion products from the ear of a grasshopper," J. Acoust. Soc. Am. **104**, 326–335.
Kössl, M., Mayer, F., Frank, G., Faulstich, H., and Russell, I. J. (**1999**). "Evolutionary adaptations of inner ear function in Jamaican mormoopid bats," J. Comp. Physiol., A **185**, 217–228.
Kros, C. J., Rüsch, A., and Richardson, G. P. (**1992**). "Mechano-electrical transducer currents in hair cells of the cultured neonatal mouse cochlea," Proc. R. Soc. London, Ser. B **249**, 185–193.
Kummer, P., Janssen, Th., Hulin, P., and Arnold, W. (**2000**). "Optimal L1-L2 primary tone level separation remains independent of test frequency in humans," Hear. Res. **146**, 47–56.
Lukashkin, A. N., and Russell, I. J. (**1998**). "A descriptive model of the receptor potential nonlinearities generated by the hair cell mechanoelectrical transducer," J. Acoust. Soc. Am. **103**, 973–980.
Lukashkin, A. N., and Russell, I. J. (**1999**). "Analysis of the $f2-f1$ and $2f1-f2$ distortion components generated by the hair cell mechanoelectrical transducer: Dependence on the amplitudes of the primaries and feedback gain," J. Acoust. Soc. Am. **106**, 2661–2668.
Lukashkin, A. N., and Russell, I. J. (**2005**). "Dependence of the DPOAE amplitude pattern on acoustical biasing of the cochlear partition," Hear. Res. **203**, 45–53.
Lukashkin, A. N., Lukashkina, V. A., and Russell, I. J. (**2002**). "One source for distortion product otoacoustic emissions generated by low- and highlevel primaries," J. Acoust. Soc. Am. **111**, 2740–2748.
Martin, G. K., Probst, R., Scheinin, S. A., Coats, A. C., and Lonsbury-Martin, B. L. (**1987**). "Acoustic distortion products in rabbits, II. Sites of origin revealed by suppression and pure-tone exposures," Hear. Res. **28**, 191–208.
Meenderink, S. W. F., and van Dijk, P. (**2005**). "Characteristics of distortion product otoacoustic emissions in the frog from L_1, L_2 maps," J. Acoust. Soc. Am. **118**, 279–286.
Meenderink, S. W. F., Narins, P. M., and Van Dijk, P. (**2005**). "Detailed $f1$,$f2$ area study of distortion product otoacoustic emissions in the frog," J. Assoc. Res. Otolaryngol. **6**, 37–47.
Michelsen, A. (**2003**). "How Nature designs ears," in *Sensors and Sensing Biology and Engineering*, edited by F. G. Barth, J. A. C. Humphrey, and T. W. Secomb (Springer-Verlag, Wien), pp. 37–47.
Mills, D. M., Norton, S. J., and Rubel, E. W. (**1994**). "Development of active and passive mechanics in the mammalian cochlea," Aud. Neurosci. **1**, 77–99.
Mills, D. M. (**1997**). "Interpretation of distortion product otoacoustic emission measurements I. Two stimulus tones," J. Acoust. Soc. Am. **102**, 413–429.
Pibal, I., Drexl, M., and Kössl, M. (**2002**). "Level dependence of optimal level difference for evoking DPOAE in the gerbil," Hear. Res. **174**, 260–263.
Roeder, K. D. (**1974**). "Responses of the less sensitive acoustic sense cells in the tympanic organs of some noctuid and geometrid moths," J. Insect Physiol. **20**, 55–66.
Sanderford, M. V., Coro, F., and Conner, W. E. (**1998**). "Courtship behavior in *Empyreuma affinis* Roths. (Lepidoptera, Arctiidae, Ctenuchinae): Acoustic signals and tympanic organ response," Naturwiss. **85**, 82–87.
Sidi, S., Friedrich, R. W., and Nicolson, T. (**2003**). "NompC TRP channel required for vertebrate sensory hair cell mechanotransduction," Science **301**, 96–99.
Whitehead, M. L., McCoy, M. J., Lonsbury-Martin, B. L., and Martin, G. K. (**1995a**). "Dependence of distortion-product otoacoustic emissions on primary levels in normal and impaired ears: I. Effects of decreasing L2 below L1," J. Acoust. Soc. Am. **97**, 2346–2358.
Whitehead, M. L., Stagner, B. B., McCoy, M. J., Lonsbury-Martin, B. L., and Martin, G. K. L. (**1995b**). "Dependence of distortion-product otoacoustic emissions on primary levels in normal and impaired ears: II Asymmetry in the L1,L2 space," J. Acoust. Soc. Am. **97**, 2359–2377.

Effects of middle-ear immaturity on distortion product otoacoustic emission suppression tuning in infant ears[a)]

Carolina Abdala[b)]
House Ear Institute, 2100 West Third Street, Children's Auditory Research and Evaluation Center, Los Angeles, California 90057

Douglas H. Keefe
Boys Town National Research Hospital, Omaha, Nebraska 68131

(Received 16 June 2006; revised 28 August 2006; accepted 7 September 2006)

Distortion product otoacoustic emission (DPOAE) measures of cochlear function, including DPOAE suppression tuning curves and input/output (I/O) functions, are not adultlike in human infants. These findings suggest the cochlear amplifier might be functionally immature in newborns. However, many noncochlear factors influence DPOAEs and must be considered. This study examines whether age differences in DPOAE I/O functions recorded from infant and adult ears reflect maturation of ear-canal/middle-ear function or cochlear mechanics. A model based on linear middle-ear transmission and nonlinear cochlear generation was developed to fit the adult DPOAE I/O data. By varying only those model parameters related to middle-ear transmission (and holding cochlear parameters at adult values), the model successfully fitted I/O data from infants at birth through age 6 months. This suggests that cochlear mechanics are mature at birth. The model predicted an attenuation of stimulus energy through the immature ear canal and middle ear, and evaluated whether immaturities in forward transmission could explain the differences consistently observed between infant and adult DPOAE suppression. Results show that once the immaturity was compensated for by providing infants with a relative increase in primary tone level, DPOAE suppression tuning at f2=6000 Hz was similar in adults and infants. © *2006 Acoustical Society of America.* [DOI: 10.1121/1.2359237]

PACS number(s): 43.64.Jb, 43.64.Kc, 43.64.Ha [BLM] Pages: 3832–3842

I. INTRODUCTION

Distortion product otoacoustic emissions (DPOAEs) offer a noninvasive probe of cochlear function in humans. DPOAEs are generated when two stimulus tones (f_1,f_2) are presented simultaneously to the ear at sound pressure levels L_1 and L_2, respectively. The cochlea produces intermodulation distortion at frequencies mathematically related to the stimulus frequencies. The most robust of these distortion products is at $2f_1-f_2$. DPOAEs provide a window into human cochlear function and maturation, although they can be strongly affected by noncochlear factors.

A decade of work has shown that various features of the $2f_1-f_2$ DPOAE are not completely adultlike in human infants (Abdala, 1998, 2001, 2004; Brown *et al.*, 1995; Lasky, 1998). At $f_2=6000$ Hz, and to a lesser extent at 1500 Hz, DPOAE suppression tuning curves (STCs) are excessively narrow and sharp, and the low-frequency flank is steep in human infants relative to adults. These age differences have been observed in very premature infants, at term birth, and during the first 6 months of postnatal life (Abdala *et al.*, 2006). Additionally, the growth of suppression, which is measured by estimating a slope value from the DPOAE amplitude × suppressor level function, is more shallow for suppressor tones lower than f_2. The immaturities in suppression growth are restricted to the lowest frequency suppressor tones presented (3047–4559 Hz) nearly an octave below the f_2 frequency of 6000 Hz. In this range, suppression threshold (suppressor level required to just initiate DPOAE amplitude reduction) is elevated in infants. All of these nonadultlike characteristics are restricted to the STC at frequencies significantly lower than the f_2 frequency.

DPOAE input/output (I/O) functions at $f_2=6000$ Hz ($f_2/f_1=1.2$) are not adultlike in infants either. Adult I/O functions show growing DPOAE amplitude as stimulus level is increased from low to moderate levels, followed by saturation at moderate-high levels (Abdala, 2000). Although the specific configuration of the I/O function varies with frequency and subject to some extent, DPOAE amplitude growth generally follows this pattern in normal-hearing adults. The majority of infant DPOAE I/Os at $f_2=6000$ Hz also show amplitude growth with increasing level and saturation; however, up to 43% can show monotonic, nonsaturating functions (Abdala, 2000). When present, amplitude saturation is observed at elevated stimulus levels (mean =77–79 dB SPL) relative to adults. Abdala (2000) hypothesized that this age difference in the saturation characteristics of the I/O function arose from immaturities in operational range of cochlear amplifier function.

Lasky (1998) also studied the DPOAE I/O function in adults and neonates and found, in both groups, that the I/O

[a)]A preliminary report of this research was presented at the March 2006 meeting of the American Auditory Society in Scottsdale, AZ.
[b)]Electronic mail: cabdala@hei.org

 © 2006 Acoustical Society of America

function was generally similar in slope with the initial portion showing unity gain. In contrast to Abdala (2000), Lasky found adult I/O functions to be more linear with less evidence of saturation. One explanation for these seemingly discrepant results is that Lasky recorded DPOAEs using primary tone levels up to 65 dB SPL only, whereas Abdala and colleagues recorded I/O function with levels up to 85 dB SPL. Both investigators hypothesized a possible immaturity in cochlear amplifier function as the basis for the age differences observed, but cautioned that immature outer and middle ear function may have influenced the results.

Reports of cochlear immaturity in human infants, as measured with OAE methodology, have been mixed. Brown and colleagues reported immature cochlear filtering in newborns at 4000 Hz as measured by DPOAE f_2/f_1 ratio functions (Brown *et al.*, 1995). In contrast, Bargones and Burns (1988) recorded suppression tuning curves from spontaneous OAEs in 2–3-week-old newborns and found the tuning characteristics to be adultlike. Similarly, Eggermont *et al.* (1996) reported adultlike cochlear travel times calculated from DPOAE latency for term and preterm neonates. Clearly, reports about functional development of the human cochlea are equivocal. However, several studies (Abdala, 1998, 2001, 2004; Brown *et al.*, 1995; Lasky, 1998) have reported age differences between adults and infants using OAE methodology, known to be an assay of cochlear function.

The *source* of the DPOAE immaturity in infants has been scrutinized to a limited extent. A simple model producing reversible outer hair cell (OHC) dysfunction in human adults taking therapeutic doses of aspirin did not support the OHC as a source of DPOAE immaturity (Abdala, 2005). When the OHC motility was disabled in normal-hearing adult subjects taking aspirin, the resulting DPOAE STCs did not resemble infant tuning curves. Additionally, anatomical data indicate that OHCs are morphologically mature very early in gestation (Lavigne-Rebillard *et al.*, 1987). It is not known if the physical properties of the basilar membrane are immature in human newborns. It is possible that passive stiffness and mass characteristics of the basilar membrane are not adultlike, thus affecting the vibratory motion; however, this factor is difficult if not impossible to explore in human infants.

It is also possible that the nonadultlike DPOAE results observed in infants are due to a noncochlear immaturity. DPOAEs are evoked by pure tones that must travel though the outer and middle ear before reaching the cochlea to produce a response, thus they will be greatly affected by the forward transmission characteristics of the middle ear. Conversely, the OAE must travel from its points of origin on the basilar membrane, back out through the middle and outer ear, before being recorded by a probe microphone in the ear canal. The impact that an immature but healthy middle/outer ear system might have on OAEs recorded from human infants has not been well studied, although it has been shown that wideband acoustic transfer functions of the ear canal and middle ear are immature in infants (Keefe *et al.*, 1993, 2002) and remain nonadultlike until 11 years of age (Okabe *et al.*, 1988).

The anatomy of the human ear canal changes significantly during early childhood. The ear canal is relatively straight and short in infants and has a curved axis in adults (Northern and Downs, 1984). The ear-canal wall in infants has no bony portion and consists of a thin layer of cartilage that is highly compliant (Anson and Donaldson, 1981). The ear canal continues to mature up through age 9 years. The diameter and length of the ear-canal increase significantly from birth through 6 months of age (Keefe *et al.*, 1993).

Findings obtained in human temporal bones show how the anatomy of the human middle ear changes during childhood. The plane of the tympanic membrane relative to the ear canal axis is more horizontal in the term infant and is adultlike by age 3 years (Ikui *et al.*, 1997). The middle-ear ossicles are completely formed and ossified, and the middle-ear muscles are fully developed prior to birth (Saunders *et al.*, 1983). However, the middle-ear cavity volume increases postnatally until the late teenage years (Eby and Nadol, 1986) and may influence the ossicular orientation. The middle-ear cavity volume is 640 mm^3 in adults and 452 mm^3 in infants of age less than 1 year (Ikui *et al.*, 2000). The distance between the stapes footplate and the TM is larger in adults than in infants of postnatal age up through 6 months (Eby and Nadol, 1986). These postnatal changes in the human ear-canal and middle-ear structure are the likely source of changes in ear-canal and middle-ear functioning.

The DPOAE contains information on both cochlear and middle-ear functioning. Because middle-ear transmission is linear and cochlear generation is nonlinear, it is possible under some conditions to separate the effects of middle-ear and cochlear mechanics. DPOAE I/O functions have been used to indirectly estimate the effect of middle-ear transmission on the shapes of forward and reverse middle-ear transfer functions (Keefe, 2002). This model was based on an assumption that the distortion characteristics of the basilar membrane are uniform across a broad portion of its length, including the tonotopic region extending from 0.5 to 8 kHz. If this model is correct, the DPOAE I/O function should have an approximately invariant shape across frequency within this scaling region, with frequency-dependent changes due only to forward and reverse transmission through the middle ear. With respect to a reference DPOAE I/O function at 1 kHz, Keefe proposed that a translation of the I/O function along its stimulus-level dimension (L_2) represented differences in forward middle-ear transmission across frequency, while translations in DPOAE level represented differences across frequency in reverse middle-ear transmission. These translations were visually represented as a horizontal shift of the DPOAE I/O function on its stimulus axis and a vertical shift along its response axis.

Shera and Miller (2002) proposed an improved model that assumed distortion invariance on the composite L_1-L_2 stimulus dimensions of DPOAE responses rather than on the L_2 dimension assumed by Keefe (2002). Shera and Miller predicted relatively small bias errors in the Keefe (2002) method to estimate forward transmission, but larger bias errors in reverse transmission, especially at the highest f_2. The predicted bias errors were less than the variability found in

human temporal-bone measurements (Puria *et al.*, 2003) for f_2 up to 4000 Hz and were slightly larger at f_2=6000 Hz (Keefe, 2006).

In the present study, we examine whether age differences between DPOAE I/O functions, from infants at birth and through 6 months of age and from adults, reflect maturation of cochlear or middle-ear mechanics. A model was generated to fit DPOAE I/O function data. It is based on the linearity of middle-ear transmission (below the threshold of the middle-ear muscle reflex) and the nonlinearity of the cochlear-generation process. Only data at a single f_2 frequency are used to test the model. Thus, no assumption concerning distortion invariance across frequency is required. If the cochlear mechanics in the model is assumed to be mature at all ages, then the only remaining difference should be how middle-ear transmission varies with age.

If the model is unsuccessful at fitting DPOAE I/O functions measured in infants from birth to 6 months, by holding the cochlear-related parameters constant and varying only the middle-ear transmission parameters, then this would support the hypothesis that immaturities in DPOAE responses are at least partly due to immaturities in their cochlear mechanics. If the model is successful at fitting the data in this manner, then this would support the hypothesis that immaturities in DPOAE responses are due to immaturities in ear-canal and middle-ear functioning. In the latter case, it would also be possible to estimate the maturational shifts in forward and reverse transmission through the ear canal and middle ear in infants relative to adults. The main goal of this study is to address whether such immaturities in middle-ear transmission can explain the nonadultlike DPOAE suppression tuning results consistently observed at f_2=6000 Hz.

II. METHODS

A. Subjects

Twenty-seven normal-hearing adults and 35 healthy infants participated as subjects in this study. The 27 adults had a mean age of 27.8 years (range=18–35 years) and audiometric thresholds <15 dB HL for frequencies from 250 to 8000 Hz. Eleven right and 16 left ears were tested. Eighteen subjects were female and nine were male. All adult subjects had negative histories of hearing loss and otologic pathology.

Of the 35 infant subjects, 21 were term born and 14 were infants born prematurely (mean age at birth=35 postconceptional weeks) but tested after they reached termlike status, i.e., 37–41 weeks postconceptional age (PCA). Infants had a mean birth weight of 2920 g (range =1470–3955 grams) and mean one and five minute Apgar scores of 7.7 and 8.7 (range=5–10). There were 16 females and 19 male infants, 17 right and 18 left ears. Other than premature birth, none of the infants had high-risk factors for hearing loss and all infant subjects passed a hearing screening at 35 dB HL with a click-evoked auditory brainstem response (ABR) and a DP-gram (f_2 frequencies ranging from 1500 to 8000 Hz).

B. Instrumentation and signal processing

A custom-designed DPOAE acquisition system (SuprDP) was used to generate stimuli and acquire data under the control of custom software using a 48 000-Hz sampling rate. The data acquisition hardware was based on an Audio Processor developed by House Ear Institute Engineering Department. The hardware includes two-channel D/A, two-channel A/D, and a DSP processor (all 24-bit) as well as an analog high-pass filter (12 dB/oct; 700 Hz high-pass cutoff). The data acquisition system was connected to an Etymotic Research ER-10C probe microphone. The ER-10C probe contains two output transducers and a low-noise microphone. The two primary tones and suppressor tone were generated by the DSP processor. The primary tone at f_1 was generated by one D/A converter and delivered via one transducer. The primary tone at f_2 and the suppressor tone were produced by the second D/A converter and output through the second transducer. The microphone signal was high-pass filtered before being sampled by the A/D converter.

C. Data acceptance criteria

Twenty sweeps of the microphone signal were averaged by the DSP processor and comprised one block of data. Sweeps were accepted into a block only when the estimated root mean-squared level in that sweep did not exceed a user-controlled artifact rejection threshold. To ensure adequate subject state, a block of data was rejected whenever the acceptance criteria described below were not met. A minimum of 6 and a maximum of 12 acceptable blocks of data were averaged to compute the final DPOAE amplitude or the DPOAE grand average.

A DPOAE response was accepted if (1) the noise measurements for three frequency bins (11.7 Hz wide) on either side of the $2f_1-f_2$ frequency were <0 dB SPL and (2) the measured DPOAE level was at least 5 dB above the average noise measured in the six bins around $2f_1-f_2$. If the maximum number of blocks were collected (12 blocks or 240 sweeps) without meeting these criteria, no DPOAE response was accepted and the program moved on to the next test condition.

D. Calibration

Intermodulation distortion produced by the recording system at $2f_1-f_2$ was measured with the probe in a Zwislocki coupler for all test conditions. The mean level of distortion was −25 dB SPL. The recording system noise floor was determined using a similar method with no tones present. The level of system noise floor ranged between −23 and −30 dB SPL.

An *in situ* calibration procedure was conducted on both output transducers before each subject was tested. A chirp tone (swept-frequency signal from 10 to 10 000 Hz) with fixed voltage was presented to the transducer and the resulting SPL of the tone recorded in the ear canal. Based on this information, an equalization of output levels was performed for each subject to achieve target stimulus levels across test frequencies.

E. Procedure

All DPOAE testing was conducted at f_2=6000 Hz only. The most marked age effects for DPOAE suppression have been previously observed at f_2=6000 Hz. For this reason, 6000 Hz was chosen as the test frequency to enhance the probability of detecting age effects. Attempts were also made to collect low-frequency data. Thirty-eight newborns were tested at f_2=1500 Hz. However, noise in this frequency range was excessive at the older ages (3–6 months) and precluded successful completion of the protocol.

Adult subjects were tested within an IAC sound-attenuated booth at the House Ear Institute while sitting comfortably in a padded easy chair, reading or resting. One 1.5–2 h session was required for each adult. DPOAE I/O functions were generated with primary tones ranging from 30 to 85 dB SPL (L_1) in 5-dB steps and a 10-dB level separation ($L_1 > L_2$). Such a L_1-L_2 difference may not result in maximizing the DPOAE SPL at each L_2 (Kummer *et al.*, 1998), but the relevant issue in the current developmental study is that L_1-L_2 be the same for infants and adults. Two I/O functions were collected per subject. The mean of these two functions was used in subsequent analyses.

DPOAE suppression tuning was recorded at three stimulus levels in adults: ten adults were tested at 65–55 dB SPL, ten at 55–45 dB SPL, and seven at 50–40 dB SPL. To generate a suppression tuning curve (STC), 15 different suppressor tones were presented at frequencies around f_2 ranging from 3047 to 7239 Hz. The suppressor tone was presented ipsilaterally with the primary tones and increased in 5-dB intervals from 30 to 85 dB SPL. Unsuppressed DPOAE amplitude was measured at the start of data collection and prior to the presentation of each new suppressor frequency. Suppression tuning curves were generated with two suppression criteria: 2 and 6 dB. To generate STCs, the suppressor levels producing criterion suppression were calculated for each suppressor tone and plotted as a function of suppressor frequency.

Infant subjects were tested initially at 37–40 weeks postconceptional age. DPOAE I/O functions and DPOAE suppression tuning curves at f_2=6000 Hz were recorded at this initial test as described for adult subjects above. DPOAE STCs were only recorded at one primary tone level in infants: 65–55 dB SPL. Sixteen of the 35 infants were then followed for 6 months after birth and a DPOAE I/O function was recorded at ages 3 months (mean=85.4 days), 4 months (mean=117.4 days), 5 months (mean=148.7 days) and 6 months (mean=182.9 days). Infant testing took place at the Infant Auditory Research Laboratory, University of Southern California, Los Angeles County (USC+LAC), Women and Children's Hospital, in a quiet room away from the normal nursery and neonatal intensive care unit. Infants were tested in their hospital isolettes whenever possible, or occasionally tested while held in the parent's arms or, at older ages, while seated in a car seat. All infants were tested during natural sleep and a test session was typically 2 to 2.5 h in duration.

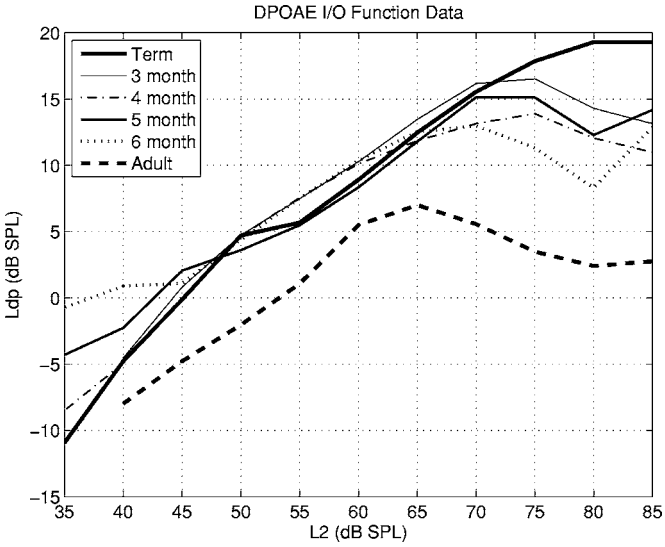

FIG. 1. Mean DPOAE levels are plotted vs L_2 at each age. Term infants and adults are plotted with thickest lines to facilitate comparison; otherwise, line thickness increases with increasing age. At birth, the number of observations comprising the mean ranged from n=12 to n=41. At 3 months through 6 months, observations ranged from n=6 to n=16. Reduced n always occurred at the lowest stimulus levels.

F. Analysis: DPOAE STCs

DPOAE STCs generated with 2- and 6-dB suppression criteria were recorded in adults and infants and analyzed in the following manner: (1) the STC width was measured 10 dB above the tip, and the tip frequency was divided by this width to obtain a Q_{10} measure; (2) the slope of the low- and high-frequency flank of the STC was quantified by fitting regression lines from the tip of the STC to end points on the low- and high-frequency flanks; (3) the tip-to-tail level was measured by subtracting the suppressor level at the tip of the STC from the level at the lowest suppressor frequency (3047 Hz); and (4) the STC tip frequency and the suppressor level at the tip frequency were measured.

G. Model to fit DPOAE I/O functions across age

The DPOAE I/O function data were fitted using a model based on the hypothesis that the cochlear mechanics is mature at birth, as described in the Introduction. If this hypothesis is correct, then all observed differences in the postnatal maturation of DPOAE I/O functions should be due to maturational differences in ear canal and middle-ear functioning. This hypothesis was tested by assessing the ability of the model to fit the measured I/O functions across age, based on the form of the cochlear nonlinearity observed in the I/O functions in adults. The model is further described in the Appendix.

III. RESULTS

A. Forward and reverse transmission effects from DPOAE I/O functions

The mean DPOAE I/O functions at f_2=6000 Hz for adults and infants at five ages are shown in Fig. 1. Clearly, the shape and configuration of the I/O functions vary with

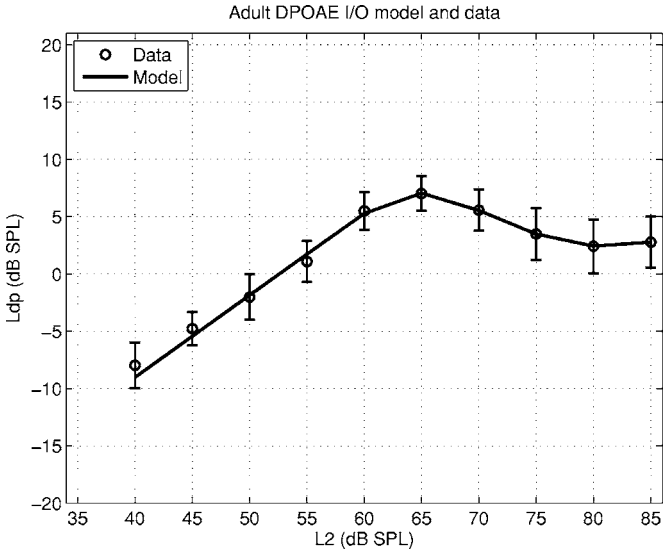

FIG. 2. The measured mean (circle symbol) DPOAE I/O function ±1 SE of the mean (error bar) are plotted along with the predicted DPOAE I/O function (line) from the model.

age. The mean adult function shows increasing DPOAE amplitude to moderate stimulus levels and an amplitude plateau typically beginning around 60–65 dB SPL. In contrast, term infants show amplitude increasing for stimulus levels through 80 dB SPL and saturation beyond this level. The intermediate ages (3, 4, 5, and 6 months of age) show amplitude saturation at varying stimulus levels, but always at elevated levels relative to the adult function. Another adult-infant difference in I/O function is present on the vertical dimension, where it is evident that DPOAE amplitude is always larger in the infants than adults. At some stimulus levels, the mean DPOAE amplitude was 17 dB larger in term infants than adults.

A nonlinear cochlear-generator model G was constructed to fit the adult DPOAE I/O function in Fig. 1. In terms of the root-mean squared pressure amplitude of $P_0 = 0.000\,02$ Pa, which defines 0 dB SPL, the mean DPOAE SPL (L_{DP}) in the adult group is fitted as a function of stimulus level L_2 by

$$L_{DP}(L_2) = 20 \log_{10} \frac{G(P_0 10^{L_2/20})}{P_0}. \quad (1)$$

This model implicitly includes ear-canal, middle-ear, and cochlear effects in the transformation from stimulus level to DPOAE level, but the important considerations are that (1) the function G is nonlinear and (2) the goal is to evaluate the changes in ear-canal and middle-ear transmission in infants relative to the corresponding transmission in adults. The mathematical form of the function G is described in the Appendix [see Eq. (A5)].

Figure 2 compares the model fit (solid line) to the mean DPOAE I/O function in adults (circle symbols and replotted from Fig. 1), in which the error bars denote ±1 standard error (SE) of the mean adult I/O function. The I/O function was approximately linear at low L_2, had a peak at moderate L_2 (65 dB SPL), and had a slight rolloff at higher L_2. The model and data agree to within ±1 SE of the data.

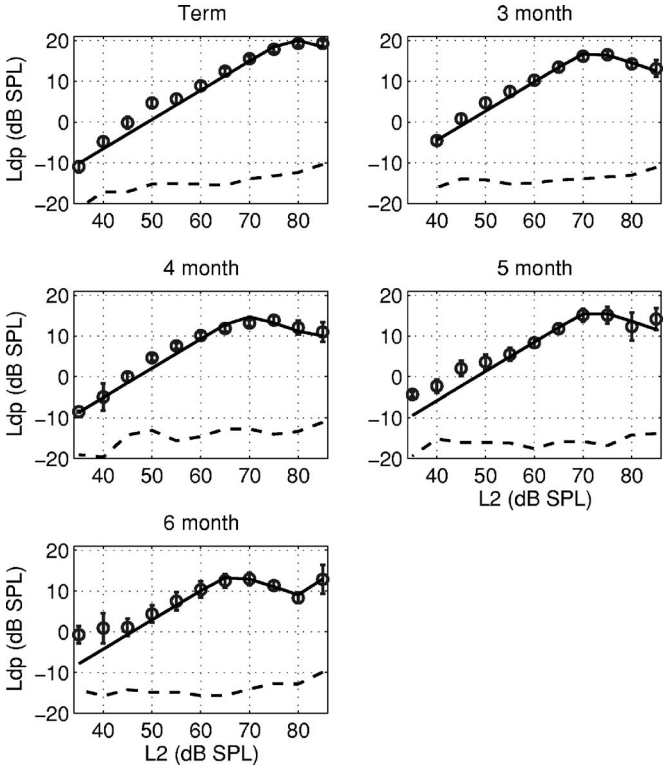

FIG. 3. Each panel shows results for one infant age group as labeled. Results include the measured mean (circle symbol) DPOAE I/O function and ±1 SE of the mean (error bar) along with the predicted DPOAE I/O function (line) from the model. The dashed lines show the mean noise SPL for each group.

Once the cochlear-model parameters were fixed by the particular form of G shown in Fig. 2, the infant I/O functions were modeled by calculating the relative change in forward transmission level ΔL_F and the relative change in reverse transmission level ΔL_R that provided the best fit between the model and the mean DPOAE I/O function for each infant group. This infant-group model is

$$L_{DP}(L_2) = \Delta L_R + 20 \log_{10} \frac{G(P_0 10^{(L_2+\Delta L_F)/20})}{P_0}, \quad (2)$$

in which the unknown parameters are ΔL_F and ΔL_R. This model agrees with the adult model of Eq. (1) when $\Delta L_F = \Delta L_R = 0$, and is further described in the Appendix. A conceptual interpretation of this model is as follows. Different values of ΔL_F and ΔL_R simply translate the model over the two-dimensional surface of each mean I/O function in infants relative to the mean I/O function for adults. A horizontal translation of the curve corresponds to changes in the forward ear-canal and middle-ear transmission, with larger forward attenuation shifting the curve to the right. A vertical translation of the curve corresponds to changes in reverse ear-canal and middle-ear transmission, with smaller reverse attenuation shifting the curve downward.

As shown in Fig. 3, the overall agreement between the model and data is adequate at every age. The model results support the hypothesis that maturational differences in the DPOAE I/O functions of adults and infants are controlled by maturational differences in ear-canal and middle-ear trans-

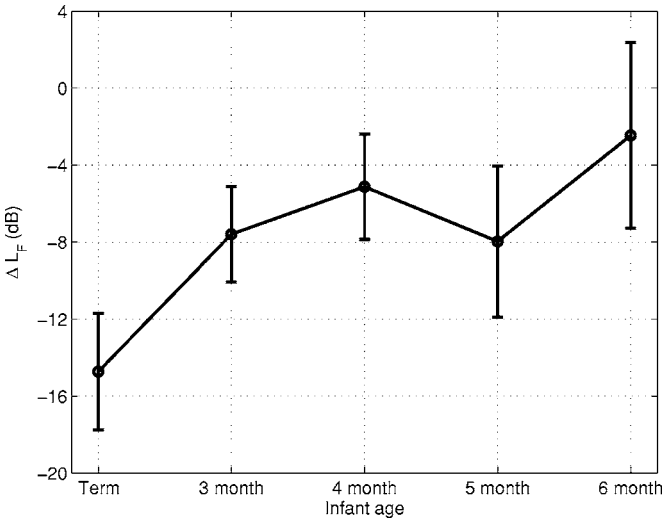

FIG. 4. The forward middle-ear level difference (ΔL_F) relative to adults is plotted as a function of age. The error bars show ±1 SE in the estimate of ΔL_F.

mission, not cochlear mechanics. The largest discrepancies in Fig. 3 occurred at low L_2 in the 5- and 6-month age groups.

Concerning forward transmission, the resulting ΔL_F at f_2 is plotted in Fig. 4 as a function of age, in which 0 dB is the adult baseline value. These predictions suggest that middle-ear forward transmission was 15 dB less in term infants than adults for the same L_2 in the ear canal. The magnitude of ΔL_F decreased with age towards adult values. Concerning reverse transmission, the resulting ΔL_R at f_{DP} is plotted in Fig. 5 as a function of age. The reverse middle-ear forward transmission was 13 dB larger in term infants than adults for the same L_2 in the ear canal, and ΔL_R decreased with age towards adult values. In the oldest infant group (6 months), the loss in forward transmission was approximately 3 dB while the gain in reverse transmission was 7 dB.

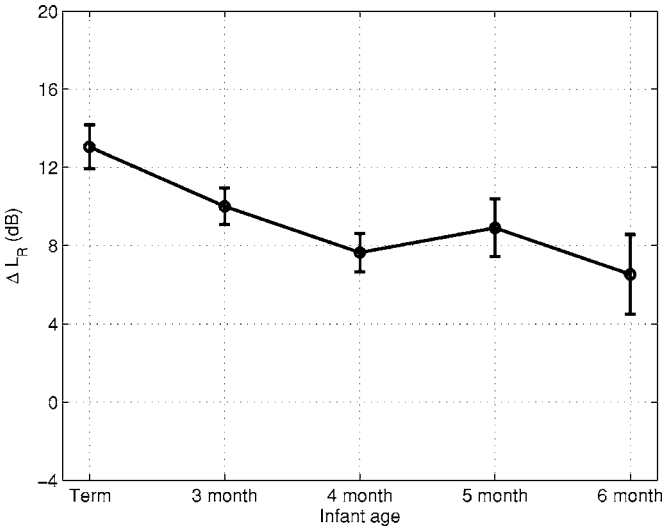

FIG. 5. The reverse middle-ear level difference (ΔL_R) relative to adults is plotted as a function of age. The error bars show ±1 SE in the estimate of ΔL_R.

These forward and reverse levels were calculated based on the mean DPOAE I/O function in each age group. The actual set of DPOAE I/O functions in each age group varied within the group, as is apparent from the standard errors (SEs) of the mean plotted in Figs. 2 and 3. This variability contributed variability to ΔL_F and ΔL_R. An added difficulty was that the inclusion criterion for the DPOAE assumed a 9 dB SNR, and this criterion level might be achieved in a given test ear at some L_2 values, but not at others, so that the number of observations varied with both age group and L_2. The effects of these sources of variability on the accuracy of ΔL_F and ΔL_R were assessed by use of the bootstrap method (Efron and Tibshirani, 1986), which enabled calculation of a (bootstrap) SE for ΔL_F and ΔL_R.

The bootstrap method analyzed 1000 synthetic data sets (using the Matlab Statistics Toolbox), in which each synthetic data set was created by randomly sampling N observations at a time with replacement from the actual N observations in each data set. A data set comprised the set of DPOAE SPLs in each ear for each age group at each L_2. For each synthetic data set, the mean DPOAE I/O function was calculated across the age groups, the adult I/O function was fitted using the cochlear model of Eq. (1), and the infant I/O function was fitted using the middle-ear model of Eq. (2) to provide an estimate of ΔL_F and ΔL_R. The SE of ΔL_F was calculated as the standard deviation of the 1000 estimates of ΔL_F across the synthetic data sets, and similarly for the SE of ΔL_R.

The SEs for ΔL_F (plotted as error bars in Fig. 4) were 2–3 dB for the full-term, 3-, and 4-month groups, 4 dB for the 5-month group, and 5 dB for the 6-month group. As a control, ΔL_F for adults had a mean of 0 dB, as expected for a transfer function level defined relative to adults, but its SE was 2 dB. Thus, 2 dB of the variability was due to variability in the adult group and, otherwise, the variability in infants increased with age. This may be due to the fact that the number of infants in each age group decreased with increasing age.

The SEs for ΔL_R (plotted as error bars in Fig. 5) varied from 1 dB for the full-term, 3-, 4-, and 5-month groups, and 2 dB for the 6-month group. As a control, ΔL_R for adults had a SE of 0.25 dB. Thus, the inaccuracies were greater in assessing relative forward-transmission effects than for reverse-transmission effects.

B. Forward transmission and DPOAE STCs

A further test of the hypothesis of cochlear maturity in newborn infants is whether the forward middle-ear transmission predictions in Fig. 4 can account for differences in DPOAE STCs recorded from infants and adults. The prediction of greater attenuation in forward middle-ear transmission for infants was applied to an analysis of DPOAE STC data collected in newborns (at term birth or equivalent for prematurely born infants) and adult subjects. In order to compensate for reduced stimulus levels reaching the infant cochlea (due to loss during forward transmission through the middle ear), STCs were recorded at the following stimulus levels (L_1,L_2): (1) infant and adult: 65–55 dB SPL; (2) in-

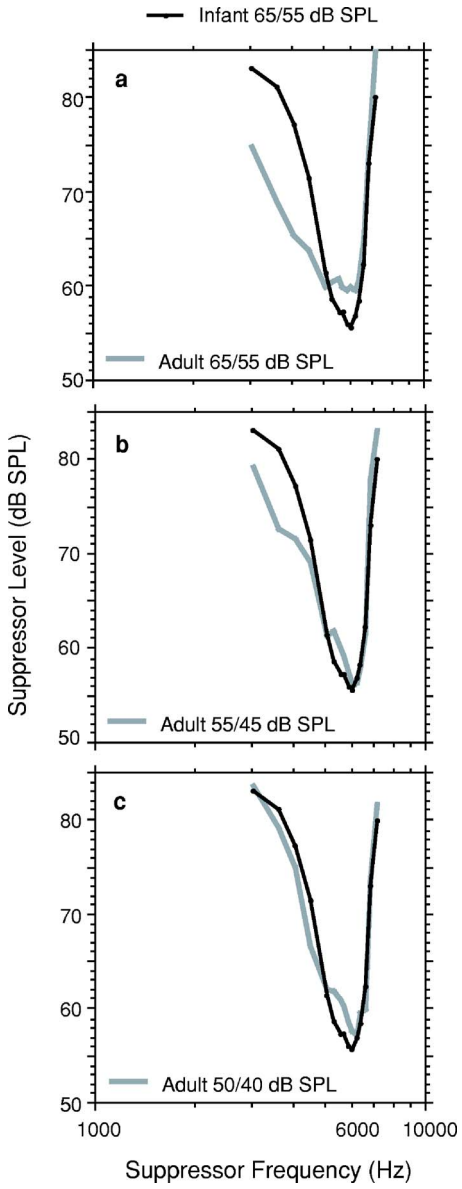

FIG. 6. Mean DPOAE STCs recorded at f2=6000 Hz with a suppression criteria of 6 dB in a group of adults and newborns: (a) STCs recorded in both adults and infants with primary tone levels of 65–55 dB SPL; (b) STCs recorded with primary tone levels +10 dB for infants; and (c) STCs recorded with primary tone levels +15 dB in infants

fant 65–55 dB SPL vs adult 55–45 dB SPL, and (3) infant 65–55 dB SPL vs adult 50–40 dB SPL. These comparisons would account for ΔL_F differences of 0, −10, and −15 dB, respectively (see Fig. 4). In addition to recording the adult STC with lower-level stimuli as detailed above, the mean adult tuning curves were scaled upward by adding 10 or 15 dB to each data point comprising the tuning curve.

Figure 6(a) shows the conventional comparison, in which infants and adults received the same ear-canal stimulus levels of 65–55 dB SPL. The age differences that have been reported consistently in the literature were present as expected in STCs recorded with both 2- and 6-dB suppression criteria. Only 6 dB STCs are shown in Fig. 6 although adult-infant comparisons were similar with both suppression criteria: narrower width for newborns (mean Q_{10}=3.20 for infants and 1.94 for adults), steeper low-frequency flank (mean tip-to-tail levels of 27.2 dB in infants and 15.3 dB in adults), and a lower tip level (mean tip levels of 55.6 dB for infants and 59.3 dB for adults).

Figure 6(b) shows the first adjusted STC comparison in which infants have stimulus levels presented +10 dB relative to adults. Such a comparison would compensate for a forward middle-ear attenuation of 10 dB in infants. The STCs were more similar: mean Q_{10}=3.20 for infants and 3.19 for adults. The mean tip-to-tail level was 27.2 dB for infants and 22.8 dB for adults; tip frequency and level showed increased similarity between adults and infants as well. However, there were still some marked age differences on the low-frequency flank, near the low-frequency outer boundaries of the tuning curve. The infant slope was still steeper, as evidenced by larger tip-to-tail levels, and tuning curve width was narrower away from the tip region.

Figure 6(c) shows mean STCs from infants that have received stimulus levels presented +15 dB relative to the adult levels. Such a comparison would compensate for a forward middle-ear attenuation of 15 dB in infants relative to adults, as predicted in Fig. 4. The curves are tightly superimposed and are difficult to distinguish for either suppression criteria. The adult-infant Q_{10} values (Q_{10} of 3.20 for infants and 2.76 for adults), tip-to-tail levels (27.2 dB for infants and 26.3 dB for adults), and tip levels (55.7 dB SPL for infants and 57.1 dB SPL for adults) were similar and adult and infant STCs were essentially superimposed throughout the range of suppressor frequencies presented, even at the outermost boundaries of the curve. These data suggest that, once the forward transmission is compensated for by providing infants with a relative increase of 15 dB in stimulus level, DPOAE suppression tuning at f_2=6000 Hz was similar between adults and infants.

IV. DISCUSSION

A. Ear-canal and middle-ear transmission effects on DPOAEs

Significant differences were observed between DPOAE I/O functions in infants and adults (see Fig. 1) measured using f_2=6000 Hz and f_{DP}=4000 Hz. The assumption that cochlear functioning is adultlike in term infants implies that such differences are due only to differences in ear-canal and middle-ear functioning. The adult mean DPOAE I/O functions were fitted using a nonlinear model of cochlear functioning (see Fig. 2). The infant mean I/O functions were fitted with a model that was altered only from the adult model by varying the forward and reverse transfer-function levels relative to that of the adults. The adequate fit between the model and measured data in the infant DPOAE I/O functions (see Fig. 3) supports the hypothesis that cochlear functioning is adultlike in newborns.

The resulting predictions of *forward* transmission show increased attenuation produced by the infant ear canal and middle ear relative to the adult ear canal and middle ear (Fig. 4). Although the present measurements were performed only at a single frequency, it is likely that forward transmission is attenuated at lower frequencies as well in infants. If so, such differences could degrade the transmission of speech and

other acoustic communication signals. Results over a range of frequencies would be helpful in better understanding forward and reverse ear-canal and middle-ear transmission differences between infants and adults across the audible frequency range.

The resulting predictions for *reverse* transmission show an increased level gain by as much as 13 dB in the ear canal and middle ear of infants relative to adults (Fig. 5). This added gain is evident from I/O functions presented in Fig. 1 where infant DPOAEs are always larger than adult responses. This observation is also consistent with multiple reports, summarized in Gorga *et al.* (2000), that DPOAE amplitude in the pediatric population is significantly larger than amplitude in adults. The results of experiments investigating maturation of the ABR in human infants show an influence of ear-canal length and volume on SPL measured in the ear canal. Sininger *et al.* (1997) measured ear-canal SPL in infants and adults by threading an ER-7 probe microphone tube into the ear canal while recording ABR thresholds to clicks and tonebursts. These investigators found, with a fixed voltage stimulus to the insert earphone receivers, that the stimulus level was between 0.8 and 27 dB higher in the ear canal of infants compared to adults. The higher-frequency tone bursts produced the largest gain in level. The average level difference for a broadband click was 20 dB in infant relative to adult ears. Likewise, when ABR thresholds were compared between adults and infants with the SPL held constant in each ear, the threshold differences were greatest at 4000 Hz (24 dB) and negligible at 500 Hz (3 dB). Sininger and colleagues attributed the differences in ear-canal SPL and the corresponding age differences in ABR threshold to the smaller enclosed ear-canal volume in infants relative to adults.

The tendency of the SEs of ΔL_F and ΔL_R to increase with increasing age is consistent with the fact that the full term infant group had as many as 41 observations whereas maximum number of observations (over all L_2) was 17 at age 3 months, 11 at age 4 months, 8 at age 5 months, and 10 at age 6 months. The fact that the maximum number of observations in any of the 4–6-month age groups never exceeded 11 ears reduced the accuracy (i.e., increased the SE) of the measurements of ΔL_F and ΔL_R. The trend in ΔL_F showing a nonmonotonic shape at 5 months relative to 4 and 6 months may not be significant inasmuch as the associated SEs overlap. Infants at ages 3–6 months have greater forward transmission than full-term infants but less than adults. The finding that the bootstrap SE of ΔL_F was larger than that of ΔL_R may reflect the fact that the cochlear nonlinearity compresses the forward-direct input from the ear canal to the cochlear vestibule, whereas the reverse-directed output is uncompressed.

B. Maturational differences in DPOAE suppression

It has been clearly established in previous investigations, and in this study, that DPOAE ipsilateral suppression is not adultlike at birth and remains immature through at least 6 months of age. Various possible sources of this immaturity have been discussed and considered in previous work, including potential cochlear sources. The reader can refer to these reports for more detailed discussion (Abdala, 1998; Abdala *et al.*, 1999; Abdala, 2000, 2005). The results of the present experiment indicate that one significant source of this immaturity in infant ears is an immaturity in both forward and reverse transmission through the ear canal and middle ear. The loss of energy in forward transmission from the ear canal to the cochlea is predicted to be approximately 15 dB for term-aged infants relative to adults at 6000 Hz. This attenuation of forward transmission produces lower stimulus levels in the cochlea relative to adults, which in turn results in sharper DPOAE suppression tuning in infants (Abdala, 2001). This sharper tuning is presumably because the cochlear amplifier has increased gain for lower-level stimuli on the basilar membrane.

It is possible to compensate for this attenuation in forward transmission with a corresponding increase in stimulus level (and suppressor level) for infant subjects. With this simple level compensation, the age differences in DPOAE suppression that have been described over the past decade are nearly eliminated [see Figs. 6(b) and 6(c)]. Thus, a relative attenuation of energy in forward transmission through the ear canal and middle ear of infants as old as 6 months should be expected and considered in OAE testing of babies in the hospital or audiology clinic. It should be considered also when implementing a research protocol that is dependent on a specific level presentation. When holding stimulus constant in the ear canal, it is important to consider that the resulting lower levels transmitted into the infant cochlea may activate cochlear amplification more effectively (i.e., provide enhanced gain and frequency resolution) than the higher levels transmitted into the adult cochlea.

To the extent that forward transmission was reduced in infants relative to adults at other frequencies than the f_1 and f_2 used in this study, the suppressor levels used in measuring the DPOAE STC would also be reduced in infants relative to adults. If this forward attenuation were constant across frequency, then the suppressor levels would be reduced by the same amount as the reductions in L_1 and L_2. The finding that the infant and adult STCs are similar in Fig. 6 after scaling the adult STC by 15 dB suggests that the relative forward attenuation across frequency is relatively small. It may be that ΔL_F varies with suppressor frequency, and a more detailed examination of this effect would require additional data collection over a range of probe frequencies, each with its corresponding suppressor frequencies.

C. Other contributing factors?

Early interpretations of DPOAE suppression tuning data in newborns suggested an immaturity in cochlear function (Abdala, 1998, 2001). The present findings allow for a more complete explanation of these age differences by including the effect of ear-canal and middle-ear immaturities. However, the findings reported here do not explain age differences in DPOAE suppression fully. Some features of DPOAE STC development seem to correspond well to our maturational predictions of outer and middle ear forward transmission, but, clearly, others do not. Maturation of sup-

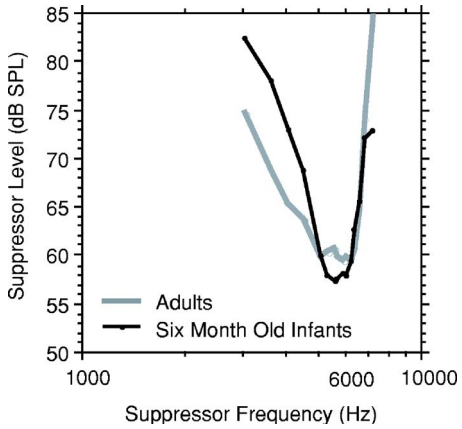

FIG. 7. Mean DPOAE STCs (f2=6000 Hz) with primary tone levels of 65–55 dB SPL and suppression critieria of 6 dB in a group of adults and 6-month-old infants.

pression growth at the lowest suppressor frequency (3047 Hz), for example, mirrors the predicted time course for development of middle ear function nicely. At birth, the slope of suppression growth is excessively shallow and nonadultlike as reported in numerous studies. However, this value becomes steeper and almost adultlike by 6 months of age. It is likely that suppressor levels presented to the newborn cochlea were attenuated at birth (due to inefficient forward transmission through the conductive pathways), and only a reduced range of suppressor levels could be presented. Consequently, the resulting growth slope was shallower because it was an incomplete function, lacking the highest suppressor levels. Once forward transmission through the middle ear approached, a more nearly adultlike status (Fig. 4 shows that forward transmission is within 3 dB of adult levels by 6 months of age), the suppressor tone at 3047 Hz showed an appropriately steep, adultlike, pattern of suppression.

Several other features of DPOAE suppression do not parallel the maturational time course predicted here for ear canal and middle ear forward transmission. DPOAE STC width (Q10) and steepness on the low-frequency flank remain nonadultlike at 6 months of age as shown in Fig. 7 (Abdala *et al.*, 2006) even though forward transmission predicted by our model should be nearly mature by this age. Since we have only described maturation of middle ear function around the primary tone frequencies of 5000 and 6000 Hz, it may be that the rate of maturation for frequencies lower than those tested here is slower and continues to develop beyond 6 months. Additionally, as reviewed in the Introduction, wideband energy reflectance and acoustic admittance measured in the ear canal are not adultlike until sometime after 11 years of age, suggesting that immaturity in ear-canal and middle-ear functioning has a much longer time course than 6 months. It should also be noted that reverse transmission through the ear canal and middle ear remains immature at age 6 months (see Fig. 5). Finally, although this work has implicated the middle ear as a significant factor in explaining age differences in DPOAE suppression, it is not possible to rule out that some aspect of cochlear function, probably related to micromechanics or even the physical properties of the basilar membrane, may remain immature into the first year of life. More research is needed to explain the remaining immaturities in DPOAE suppression at 6 months of age, which are apparent in Fig. 7.

V. CONCLUSIONS

In conclusion, our results, based on a model fitted to DPOAE I/O functions from infant and adult ears, support the hypothesis that cochlear function is adultlike in human infants at birth. These findings are consistent with morphological data suggesting that cochlear anatomy and structure are mature early in gestation. The data confirm that the underlying configuration of the I/O function is similar in adults and infants, once the functions are translated vertically and horizontally to compensate for immaturities in middle/outer-ear transmission. Additionally, the predicted attenuation in forward middle-ear transmission adequately explains the nonadultlike DPOAE STCs at $f_2=6000$ Hz, consistently recorded from infants over the past decade. Although these results suggest a normally functioning cochlea at birth (in the range of 4000–6000 Hz), it remains the case that normal sound transmission proceeds through the conductive pathways of the outer and middle ear. Therefore, these immaturities, though probably not cochlear in nature as originally hypothesized, have the potential to influence cochlear function by affecting the sound levels available to stimulate the cochlea and initiate basilar-membrane motion. The influence of immature conductive pathways must be considered in generating theories of auditory maturation and in interpreting clinical data. Clearly, only theories of auditory development that include the influence of the conductive pathway will be comprehensive enough to adequately describe the maturational process.

ACKNOWLEDGMENTS

This research was supported by the NIH (NIDCD Grant Nos. DC003552 and DC003784) and the House Ear Institute. Authors would like to thank Sandy Oba and Dr. Ellen Ma for their extensive and invaluable contributions to data collection and data management.

APPENDIX: MODEL TO ANALYZE MATURATIONAL DIFFERENCES IN DPOAE I/O RESPONSES

This appendix specifies the modeling of DPOAE I/O functions discussed in the main body of this report. A reference location in the cochlea is defined in a region sufficiently basal to the tonotopic place of f_2 that the basilar-membrane mechanics are approximately linear. Such a location might be at a tonotopic place a half-octave below f_2. The cochlear level describes the pressure difference acting across the basilar membrane. The cochlear level of the forward traveling wave at f_2 is L_2+L_F, in which $L_F=L_F(f_2)$ is the forward transfer function level at f_2 between the microphone and the reference cochlea location, including the forward pressure transfer function of the middle ear. The stimulus frequencies used in the measured data were sufficiently close ($f_2/f_1=1.2$) that L_F is approximately constant at f_1 and f_2. The corresponding cochlear level of the forward traveling wave

at f_1 is L_1+L_F. These stimuli produce a DPOAE signal at the reference cochlear location at $f_{DP}=2f_1-f_2$, which is reverse transmitted to the ear canal.

Because f_1, f_2, and L_1-L_2 are each fixed in the experiments and because $L_F(f_1)\approx L_F(f_2)=L_F$, the DPOAE level at the cochlear reference location is only a function $g(L_2+L_F)$ of the input level at that location. The DPOAE level L_{DP} at the probe microphone is related to the cochlear level g by the reverse transfer function $L_R=L_R(f_{DP})$ at frequency f_{DP} between the reference cochlear location and the probe microphone, so that

$$L_{DP}(L_2) = L_R + g(L_2 + L_F). \tag{A1}$$

An increase in L_F increases forward transmission from the ear canal to the cochlea, and an increase in L_R increases reverse transmission. The hypothesis that the cochlear mechanical source of DPOAE generation is mature at birth is represented by the fact that the nonlinear generator function g is independent of age. It follows that DPOAE level can vary with age only if at least one of the forward and reverse transfer-function levels varies with age. The cochlear generator function g may be specified by a single-source DPOAE model at the f_2 place or a two-source model at the f_2 place and f_{DP} place.

If present, multiple internal reflections of the DPOAE within the cochlea depend on both cochlear source characteristics (at the apical DP place in the cochlea) and middle-ear characteristics (at the oval window where the DPOAE is internally reflected from the middle ear). The model in Eq. (A1) is interpreted using a group of responses rather than a single-subject response so that effects of multiple internal cochlear reflections are assumed to average out.

The mean DPOAE level is written as $L_{DP,i}$ in infants and $L_{DP,a}$ in adults. The mean forward and reverse transmission levels are written as $L_{F,i}$ and $L_{R,i}$, respectively, in infants, and as $L_{F,a}$ and $L_{R,a}$, respectively, in adults. Without loss of generality, the mean forward and reverse transmission levels in adults are defined as zero, i.e., $L_{F,a}=L_{R,a}=0$ dB. The resulting mean forward and reverse transmission levels in infants are measured as level differences ΔL_F and ΔL_R, respectively, relative to the adult levels. The adult model simplifies to

$$L_{DP,a}(L_2) = g(L_2) \tag{A2}$$

so that the function g is a model that adequately fits the DPOAE I/O function in adults.

The stimulus level L_2 is converted to stimulus pressure magnitude q in terms of the reference pressure P_0 by

$$q = P_0 10^{L_2/20}. \tag{A3}$$

The predicted DPOAE magnitude p at the probe microphone is calculated at frequency f_{DP} using a nonlinear source function $G(q)$ with model parameters A_0, α, q_c, d_1, d_2, d_3, and d_4:

$$p = G(q) = \frac{P_0 A_0 q^{\alpha}}{(1 + [d_1(q/q_c) + d_2(q/q_c)^2 + d_3(q/q_c)^3 + d_4(q/q_c)^4]^8)^{1/8}}, \tag{A4}$$

The function $G(q)$ acts as a power-law fit for low-level stimuli ($q \ll q_c$) with $p \sim P_0 A_0 q^{\alpha}$. The parameter q_c is the critical stimulus amplitude defining the low-level regime, α is the power-law exponent, and A_0 scales the output amplitude. The parameters d_1, d_2, d_3, and d_4 specify a fourth-order polynomial in q/q_c describing the mid-level shape of the function. The exponent of $\frac{1}{8}$ (along with its inverse exponent 8) in the denominator was selected to best fit the data. This model performed better than models using exponents of $\frac{1}{6}$, $\frac{1}{4}$, or $\frac{1}{2}$.

Using Eq. (A2), the predicted ear-canal DPOAE level in the adult group is defined with the function g as follows:

$$L_{DP,a}(L_2) = g(L_2) = 20\log_{10}\frac{p}{P_0} = 20\log_{10}\frac{G(q)}{P_0} = 20\log_{10}\frac{G(P_0 10^{L_2/20})}{P_0}. \tag{A5}$$

The parameters in Eq. (A4) were calculated using a nonlinear least squares fit (the function lsqcurvefit in the Matlab Optimization Toolbox), with resulting values $A_0=0.0130$, $\alpha=0.717$, $q_c=0.632$ Pa, $d_1=2.122$, $d_2=-0.071$, $d_3=0.237$, and $d_4=-0.062$. The model fit remained within ±1 SE of the mean data (see Fig. 2). This model is only intended to fit DPOAE I/O data measured with $L_1=L_2+10$ dB, $f_2=6000$ Hz, and $f_2/f_1=1.2$.

With g determined from the adult data, the mean DPOAE I/O data measured in infants were fitted using the model in Eq. (A1), which is rewritten using Eq. (A5) as

$$L_{DP,i}(L_2) = \Delta L_R + g(L_2 + \Delta L_F), = \Delta L_R + 20\log_{10}\frac{G(P_0 10^{(L_2+\Delta L_F)/20})}{P_0}. \tag{A6}$$

The unknowns ΔL_F and ΔL_F were calculated in each age group using a nonlinear least squares fit.

Abdala, C. (**1998**). "A developmental study of DPOAE (2f1−f2) suppression in humans," Hear. Res. **121**, 125–138.

Abdala, C., Ma, E., and Sininger, Y. (**1999**). "Maturation of medial efferent system function in humans," J. Acoust. Soc. Am. **105**, 2392–2402.

Abdala, C. (**2000**). "Distortion product otoacoustic emission (2f1−f2) amplitude growth in human adults and neonates," J. Acoust. Soc. Am. **107**, 446–456.

Abdala, C. (**2001**). "Maturation of human cochlear amplifier function: DPOAE (2f1−f2) ipsilateral suppression at low- and high-levels in human adults and neonates," J. Acoust. Soc. Am. **110**, 1465–1476.

Abdala, C. (**2004**). "DPOAE (2f1−f2) suppression in three-month-old infants: Evidence for postnatal maturation of human cochlear function?" J. Acoust. Soc. Am. **116**, 3572–3580.

Abdala, C. (**2005**). "Effects of aspirin on distortion product otoacoustic emissions suppression in adults: A comparison with neonatal data," J. Acoust. Soc. Am. **118**(3), 1566–1575.

Abdala, C., Oba, S., and Keefe, D. H. (**2006**). "DPOAE ipsilateral suppression in infants through 6 months of age," Podium talk presented at the American Auditory Society, Scottsdale, AZ, 5–8 March 2006.

Anson, B. J., and Donaldson, J. A. (**1981**). "Surgical Anatomy of the Temporal Bone and Ear." (Saunders, Philadelphia).

Bargones, J., and Burns, E. (**1998**). "Suppression tuning curves for spontaneous otoacoustic emissions in infants and adults," J. Acoust. Soc. Am. **83**, 1809–1816.

Brown, A., Sheppard, S., and Russell, P. (**1995**). "Differences between neonate and adult cochlear mechanical responses," Aud. Neurosci. **1**, 169–181.

Eby, T. L., and Nadol, Jr., J. B. (**1986**). "Postnatal growth of the human temporal bone: Implications for cochlear implants in children," Ann. Otol.

Rhinol. Laryngol. **95**, 356–364.
Efron, B., and Tibshirani, R. (**1986**). "Bootstrap methods for standard errors, confidence intervals, and other measurements of statistical accuracy," Stat. Sci. **1**, 54–77.
Eggermont, J., Brown, D., Ponton, C., and Kimberley, B. (**1996**). "Comparisons of DPE and ABR traveling wave delay measurements suggests frequency specific synapse maturation," Ear Hear. **17**, 386–394.
Gorga, M. P., Norton, S. J., Sininger, Y. S., Cone-Wesson, B., Folsom, R. C., Vohr, B. R., Widen, J. E., and Neely, S. T. (**2000**). "Identification of neonatal hearing impairment: Distortion product otoacoustic emissions during the perinatal period," Ear Hear. **21**, 400–424.
Ikui, A., Sando, I., Haginomori, S.-I., and Sudo, M. (**2000**). "Postnatal development of the tympanic cavity: A computer-aided reconstruction and measurement study," Acta Oto-Laryngol. **120**, 375–379.
Ikui, A., Sando, I., Sudo, M., and Fujita, S. (**1997**). "Postnatal change in angle between the tympanic annulus and surrounding structures," Ann. Otol. Rhinol. Laryngol. **106**, 33–36.
Keefe, D. H. (**2002**). "Spectral shapes of forward and reverse transfer functions between ear canal and cochlea estimated using DPOAE input/output functions," J. Acoust. Soc. Am. **111**, 249–260.
Keefe, D. H. (**2006**). "Influence of middle-ear function and pathology on otoacoustic emissions," in *Otoacoustic Emissions: Clinical Applications*, 3rd ed. edited by M. S. Robinette and T. J. Glattke (Thieme Medical, New York), to be published.
Keefe, D. H., Bulen, J. C., Hoberg Arehart, K., and Burns, E. M. (**1993**). "Ear-canal impedance and reflection coefficient of human infants and adults," J. Acoust. Soc. Am. **94**, 2617–2638.
Keefe, D. H., Zhao, F., Neely, S. T., Gorga, M. P., and Vohr, B. R. (**2002**). "Ear-canal acoustic admittance and reflectance effects in human neonates. I. Predictions of otoacoustic emission and auditory brainstem responses," J. Acoust. Soc. Am. **113**, 389–406.
Kummer, P., Janssen, T., and Arnold, W. (**1998**). "The level and growth behavior of the $2f_1-f_2$ distortion product otoacoustic emission and its relationship to auditory sensitivity in normal hearing and cochlear hearing loss," J. Acoust. Soc. Am. **103**, 3431–3444.
Lasky, R. (**1998**). "Distortion product otoacoustic emissions in human newborns and adults. II. Level effects," J. Acoust. Soc. Am. **103**, 992–1000.
Lavigne-Rebillard, M., and Pujol, R. (**1987**). "Surface aspects of the developing human organ of Corti," Acta Oto-Laryngol., Suppl. **436**, 43–50.
Northern, J. L., and Downs, M. P. (**1984**). *Hearing in Children*, 3rd ed. (Williams & Wilkins, Baltimore).
Okabe, K., Tanaka, S., Hamada, H., Miura, T., and Funai, H. (**1988**). "Acoustic impedance measurement on normal ears of children," J. Acoust. Soc. Jpn. **9**, 287–294.
Puria, S. (**2003**). "Measurements of human middle ear forward and reverse acoustics: Implications for otoacoustic emissions," J. Acoust. Soc. Am. **113**, 2773–2789.
Saunders, J. C., Kaltenbach, J. A., and Relkin, E. M. (**1983**). "The structural and functional development of the outer and middle ear," In *Development of Auditory and Vestibular Systems*, edited by R. Romand and M.-R. Romand (Academic, New York), pp. 3–25.
Shera, C. A., and Miller, A. J. (**2002**). "Using DPOAEs to measure forward and reverse middle-ear transmission noninvasively," 25th annual meeting of the Association for Research in Otolaryngology, Abstract 760.
Sininger, Y. S., Abdala, C., and Cone-Wesson, B. (**1997**). "Auditory threshold sensitivity of the human neonate as measured by auditory brainstem response," Hear. Res. **104**, 27–38.

Role of suppression and retro-cochlear processes in comodulation masking release

Stephan M. A. Ernst and Jesko L. Verhey[a)]
AG Neurosensorik, Institut für Physik, Carl von Ossietzky Universität Oldenburg, D-26111 Oldenburg, Germany

(Received 25 January 2006; revised 7 September 2006; accepted 15 September 2006)

Recent physiological studies suggest that comodulation masking release (CMR) could be a consequence of wideband inhibition at the level of the cochlear nucleus. The present study investigates whether the existence region of psychophysical CMR is comparable to the inhibitory areas of units showing a physiological correlate of CMR. Since the inhibitory areas are similar to suppressive regions at the level of the basilar membrane, the amount of CMR that can be accounted for by suppression was determined by predicting the data with a model incorporating a peripheral nonlinearity. A CMR of up to 6 dB could still be experimentally observed for a flanking band (FB) four octaves below the on-frequency masker (OFM). For FB frequencies below the OFM, the suggested model predicts CMR equal to the measured CMR for high levels of the FB. The model underestimates the magnitude of CMR for midlevels of the FB, indicating that suppression alone cannot account for CMR. The data are consistent with the hypothesis that wideband inhibition plays a role in CMR. © *2006 Acoustical Society of America.* [DOI: 10.1121/1.2361183]

PACS number(s): 43.66.Ba, 43.66.Dc, 43.66.Mk, 43.66.Nm [JHG] Pages: 3843–3852

I. INTRODUCTION

The ability to detect a sinusoid in the presence of a narrow-band masker at the signal frequency may be enhanced by the addition of off-frequency masker components (referred to as flanking bands, FB), but only if the FBs are comodulated with the on-frequency masker (OFM). This effect is commonly referred to as comodulation masking release (CMR) and the type of experiment as a flanking band experiment (Hall *et al.*, 1984; Verhey *et al.*, 2003). Comodulation masking release has been studied primarily in humans but can also be observed in other mammals (Wagner *et al.*, 2002; Budelis *et al.*, 2002) and birds (Langemann and Klump, 2001). For FBs close to the signal frequency it has been assumed that a CMR is caused by information processing within the auditory filter at the signal frequency. The cue would be a change in the modulation depth of the beating masker components due to the presence of the signal (e.g., McFadden, 1986; Schooneveldt and Moore, 1987). Verhey *et al.* (1999) showed for another type of CMR experiment—the band-widening experiment—that most of the masking release could be predicted with a model that is sensitive to amplitude modulation within the auditory filter at the signal frequency. It is unlikely, however, that within-channel cues based on modulation perception could account for the observation that CMR occurs over a three-octave range when using an FB paradigm (Cohen, 1991). It was hypothesized that CMR in conditions with widely spaced masker components resulted from a process that combines the information across frequency bands, i.e., an across-channel process (Verhey *et al.*, 2003). The neurophysiological mechanisms, however, remain obscure.

Some recent physiological studies shed some light on possible neural mechanisms underlying CMR (Nelken *et al.*, 1999; Pressnitzer *et al.*, 2001; Nieder and Klump, 2001; Hofer and Klump, 2003; Neuert *et al.*, 2004; Las *et al.*, 2005; see Verhey *et al.*, 2003 for a review). For the primary auditory cortex (*A*1) of the cat, Nelken *et al.* (1999) suggested that disruption of the locking to the envelope of the slowly fluctuating noise was a possible cue for the detection of tonal signals in a modulated background noise. Las *et al.* (2005) showed that locking suppression similar to the one in *A*1 could also be found in some units at the level of the medial geniculate body (MGB) and was absent in the inferior colliculus (IC) of the cat. Nieder and Klump (2001) and Hofer and Klump (2003) studied CMR in a homologue of the primary cortex in birds, field *L*2. The *L*2 units did not show a similar envelope locking suppression to the units in *A*1 of the cat, which might indicate that locking suppression is specific to mammals (Las *et al.*, 2005).

Physiological data in Pressnitzer *et al.* (2001) and Neuert *et al.* (2004) indicated that the detection of the tone could already occur at a very early stage of the auditory pathway. In the cochlear nucleus (CN) of the guinea pig, they measured the response to stimuli of the FB type of CMR experiments. They found that the response of some units in the ventral cochlear nucleus (VCN) to the tonal signal was higher in the comodulated (CM) condition, i.e., in the presence of an OFM and a comodulated FB, than in a reference (RF) condition with only the OFM present. Pressnitzer *et al.* (2001) hypothesized that this physiological correlate of CMR might result from fast-acting wideband inhibition to a narrow-band cell (see also Verhey *et al.*, 2003). To test this hypothesis, Neuert *et al.* (2004) measured the response of units in the dorsal cochlear nucleus (DCN) using the same paradigm and positioning the FB in the inhibitory sidebands of the units. They observed that DCN units showed an even

[a)]Electronic mail: jesko.verhey@uni-oldenburg.de

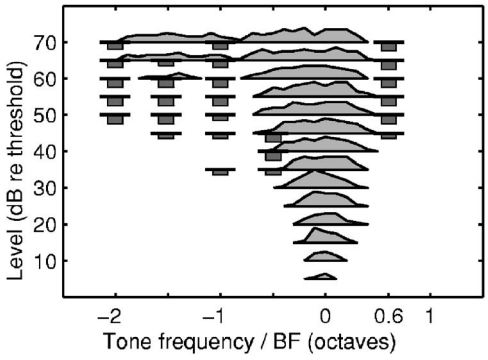

FIG. 1. Response map for a typical type III unit (1088001) in the dorsal cochlear nucleus of the guinea pig. The response of the unit to a tone at different frequencies relative to the best frequency (BF) of the unit is plotted as a function of the level of the tone relative to the threshold for a BF tone. The BF of the unit was 4580 Hz. Light-gray areas indicate the excitatory response. Inhibition is indicated by dark-gray bars pointing towards the bottom of the figure.

stronger enhancement of the signal representation in the CM condition compared to the response in the RF condition than VCN units. The difference was presumably partly due to the optimized positioning of the FB. In addition, dorsal CN units typically show stronger inhibitory sidebands than their VCN counterparts (Verhey *et al.*, 2003). Figure 1 shows the response map of a typical unit showing a strong correlate of CMR in the study of Neuert *et al.* (2004). This unit was classified as type III since it had a V-shaped excitatory response area with inhibitory sidebands and gave an excitatory response to noise, the maximum of which exceeded one-third of the maximum response to a tone at its best frequency (BF) (Stabler *et al.*, 1996). The majority of type III units showed the strongest enhancement of the signal in the CM condition. The light-gray areas in Fig. 1 indicate the excitatory response. Inhibition is indicated by dark gray bars pointing towards the bottom of the figure. Because this unit did not have spontaneous activity, the location of inhibitory sidebands was estimated from a two-tone response map. The two-tone response map was measured with an additional low-level excitatory tone at the BF of the unit, simultaneously gated with the probe tones. Inhibitory areas extend over several octaves below and, to a lesser extent, above the BF. The inhibition tends to increase as the level increases.

If the psychophysical CMR in humans originates from inhibition, then a large magnitude of CMR would be expected in conditions with high FB levels and low OFM levels. In addition, CMR should be observed up to large spectral distances between OFM and FB. Psychophysical studies on CMR do not agree on the effect of the FB level relative to the level of the OFM. Some studies show an increased CMR when the OFM level was lower than the level of the FB (Schooneveldt and Moore, 1987; Cohen, 1991). However, others found the largest release from masking for FBs with the same level as the OFM (Hall, 1986; McFadden, 1986; Moore and Shailer, 1991). Moore and Shailer (1991) and McFadden (1986) argued that the FB at levels above the OFM level might have caused an increase in the output of the auditory filter at the signal frequency. Thus, spectral masking might have been obliterating the measurement of CMR in their studies.

Large CMR for levels of the FB higher than the level of the OFM and for FB frequencies well below the signal frequency would, however, also be expected if CMR was caused by suppression at the level of the cochlea. Two-tone suppression was observed in physiological studies for frequencies above and below the characteristic frequency. Neural two-tone suppression at the level of the auditory nerve (e.g., Sachs and Kiang, 1968; Javel *et al.*, 1978) was similar to the mechanical two-tone suppression (e.g., Ruggero *et al.*, 1992; Cooper, 2004). Houtgast (1972) and Shannon (1976) presented psychophysical forward-masking data which were consistent with neural two-tone suppression. Recently, Plack *et al.* (2002) showed that a model including a dual-resonance nonlinear filter (DRNL) as the first stage can predict the psychophysical data on two-tone suppression.

In general, the frequency-level characteristics of suppressive regions and the inhibitory areas of the VCN and DCN units (see Fig. 1) showing a physiological correlate of CMR are very similar, but, in a study directly comparing two-tone suppression in single auditory-nerve fibers with wideband inhibition in single units in the CN, Rhode and Greenberg (1994) found that the frequency extent and the magnitude of wideband inhibition were stronger than two-tone suppression for the CMR showing unit types (choppers and pausers).

This study investigates whether CMR is observed psychophysically for a frequency-level range of the FB similar to the inhibitory areas in physiology. CMR is measured with a fixed signal frequency, a low-level OFM, and variable level and frequency of the FB. The choice of the levels and center frequencies of the masker components is motivated by the two-tone paradigm used in physiology to assess the inhibitory areas for a unit without spontaneous activity.

Psychoacoustical experiments always measure the response of the whole auditory system. Thus, in contrast to physiology, psychoacoustics has no direct access to the response of different stages of the auditory system. One way to determine the influence of the cochlea is to compare the CMR in a condition where the same stimulus is presented to both ears (diotic experiment) with CMR in a dichotic experiment, where the signal and OFM are presented to one ear and the FB to the other (dichotic experiment). The dichotic experiment can help determine how much the auditory system can benefit from comodulation across ears. The dichotic CMR can only originate from retro-cochlear processes. It is possible, however, that the retro-cochlear across-frequency process within one ear is different from the across-frequency process between the two ears, i.e., the difference between the CMR of the two experiments may not be a direct measure of the amount of CMR due to the nonlinear cochlear processes. Thus, apart from performing diotic and dichotic CMR experiments, the present study investigates the amount of CMR due to suppression by comparing predictions of a model simulating suppression to the results of the diotic CMR experiment.

II. EXPERIMENTS

A. Diotic presentation

1. Stimuli

All stimuli were generated digitally at a sampling rate of 44.1 kHz, converted to analog signals (RME ADI-8 DS), and amplified (Tucker-Davis HB7). The stimuli were presented to both ears through Sennheiser HD 580 headphones. The headphones had been coupler calibrated for each noise band separately using an artificial ear (Brüel & Kjaer type 4153).

The frequency of the sinusoidal signal was 2 kHz. The signal duration was 250 ms including 50-ms raised-cosine ramps. The signal was temporally centered in the 500-ms masker. The masker duration included 50-ms raised-cosine ramps at stimulus on- and offset. Depending on the masking condition, the masker was composed of one or two 20-Hz-wide noise bands. Each noise band was created by multiplying a sinusoidal carrier with a 10-Hz low-pass-filtered noise. The low-pass noise was generated in the frequency domain by filling portions of one 22 050-point buffer with constant magnitudes and portions of a second buffer with randomly selected phases (uniform distribution). All Fourier components outside the desired passband were set to zero. A subsequent inverse fast Fourier transform (iFFT) on the complex buffer pair yielded the desired 500-ms noise waveform. The multiplication with a sinusoidal carrier resulted in a 20-Hz-wide multiplied noise, extending from 10 Hz below the frequency of the sinusoidal carrier to 10 Hz above that frequency. The sinusoidal carrier of the masker was always in phase with the signal. For each stimulus presentation new noise bands were computed.

Signal threshold was determined for two conditions. In the refernce (RF) condition, the masker consisted of a bandpass noise centered at the signal frequency. The level of the OFM was 20 dB SPL. In the comodulated (CM) condition, a comodulated narrow-band off-frequency noise masker (flanking band, FB) was added to the OFM. Comodulated OFM and FB were generated by using the same low-pass-filtered noise for the two noise bands. The FB was centered at 125, 250, 500, 1000, 3000, or 4000 Hz. For each center frequency, five different levels were chosen in a 40-dB range using 10-dB steps. The highest level of the FB was chosen under the constraint that the excitation within the auditory filter at the signal frequency elicited by the FB was at least 10 dB less than the excitation elicited by the OFM. The excitation was calculated using a fourth-order gamma-tone filter centered at the signal frequency with an equivalent rectangular bandwidth (ERB, Glasberg and Moore, 1990) of 240 Hz. For FBs centered at either 1000, 3000, or 4000 Hz the highest level was 60 dB SPL. For a center frequency of 500 Hz, the highest level of the FB was 70 dB SPL; for the center frequencies of 250 and 125 Hz, the highest level of the FB was 80 dB SPL.

2. Procedure

A three-alternative, forced-choice (3-AFC) procedure with adaptive signal-level adjustment was used to determine the masked threshold of the sinusoidal signal. The three intervals in a trial were separated by gaps of 500 ms. Subjects had to indicate which of the intervals contained the signal. Visual feedback was provided after each response. The signal level was adjusted according to a two-down, one-up rule to estimate the 70.7% point of the psychometric function (Levitt, 1971). The initial step size was 8 dB. After every second reversal the step size was halved until a step size of 2 dB was reached. The run was then continued for another six reversals. From the level at these last six reversals, the mean was calculated and used as an estimate of the threshold.

The experiment was divided into sessions of six threshold estimates each. A session consisted of five CM conditions (five FB levels for one FB center frequency) and one RF condition. The final threshold estimate was taken as the mean over the threshold estimates from four sessions. For each FB center frequency, a separate final threshold estimate was determined for the RF condition.

3. Data analysis

To examine the statistical significance of the effects of stimulus variables and differences among subjects, a three-way ANOVA (FB center frequency $\times$ FB level $\times$ subject) for repeated measures was performed (MATLAB 7.2). The stimulus variables center frequency (5 levels: 250, 500, 1000, 3000, 4000 Hz) and level of the FB (6 levels: the 5 FB levels for the CM conditions and the RF condition) are fixed factors. Subject is a random factor. The dependent variable was the threshold in dB relative to the OFM level. Scheffé *posthoc* tests for contrast (MATLAB 7.2) were performed as appropriate to explore the sources of significant effects and interactions. Unless otherwise stated, differences were considered significant when these tests indicated a probability less than 0.05.

4. Subjects

Ten listeners with normal hearing participated in the experiment, varying in age from 24 to 35 years. None of the listeners had any history of hearing difficulties and their audiometric thresholds were 15 dB HL or better at 8 kHz and below. The audiometric threshold at the signal frequency (2 kHz) varied across subjects in a range between −5 and 5 dB HL. The average threshold at 2 kHz was about 0 dB HL. The subjects had at least 1 h experience in CMR experiments before collecting the data.

5. Results

Figure 2 shows average thresholds for the ten listeners (left panel) and the CMR (right panel) as a function of the center frequency of the FB (CF_{FB}). The thresholds in the left panel are expressed in decibels relative to the OFM level. In order to show the data for the CM condition for all FB levels within a single figure, the corresponding FB level was added to each threshold for the CM condition (gray bars). The FB level for each threshold is indicated by a short horizontal line. In addition the threshold for the RF condition—which is the same for all FB levels for each FB center frequency—is shown with a white bar, for comparison. Error bars indicate plus and minus one standard deviation.

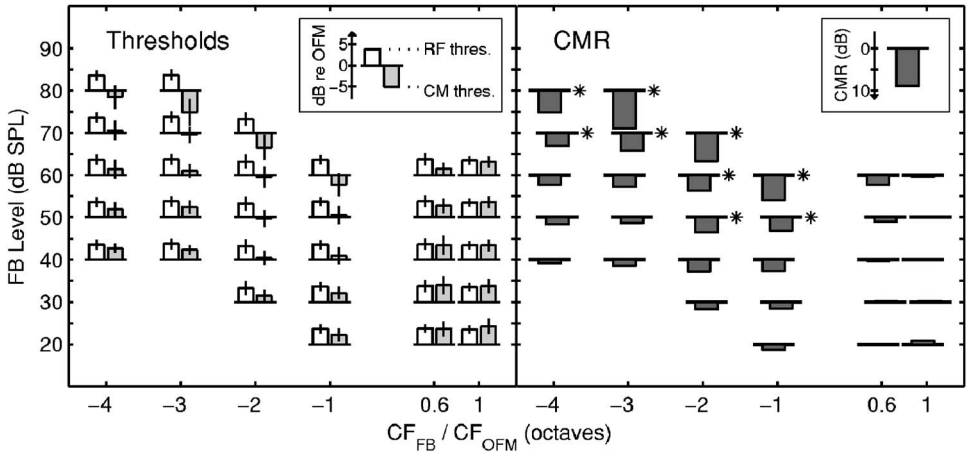

FIG. 2. Thresholds (left panel) and CMR (right panel) for the diotic presentation of signal and masker. Data are arranged in such a way that the ordinate indicates the FB level and the abscissa indicates the center frequency of the FB (CF_{FB}) relative to the center frequency of the OFM (CF_{OFM}). The thresholds (left panel) are expressed in dB relative to the OFM level. White bars represent the threshold measured for the RF condition and gray bars the threshold for the CM condition. Error bars indicate plus and minus one standard deviation. The right panel shows the amount of CMR, calculated as the difference between the thresholds for the RF and the CM condition. A bar pointing downwards indicates a positive CMR.

The thresholds for the RF condition are almost the same for all FB center frequencies. This is expected, since the RF condition is the same for all FB center frequencies. The mean of the RF threshold estimates averaged across the six FB center frequencies was 3.6 dB above the OFM level. Similar thresholds for a pure tone masked by a narrow-band noise were found in the literature (e.g., Bos and DeBoer, 1966; Moore and Shailer, 1991). In general, thresholds for the CM condition were similar to or slightly, lower than the threshold for the RF condition. Only for the highest FB levels and center frequencies of the FB below the OFM were CM thresholds markedly lower than the RF threshold. The lowest threshold for the CM condition of −5 dB relative to the OFM level was obtained for an FB with a center frequency of 250 Hz (i.e., three octaves below the signal frequency) and a level of 80 dB SPL. For FB positions above the signal frequency, thresholds were always close to the threshold for the RF condition.

The right panel of Fig. 2 shows the CMR for the different levels and center frequencies of the FB. CMR is calculated as the difference between the thresholds for the RF and CM conditions. A positive CMR is indicated by a bar pointing towards the bottom of the figure. The CMR for all FB positions spectrally below the signal frequency showed a positive CMR. The largest CMR of 9 dB was measured for a FB three octaves below the signal frequency at the highest tested FB level of 80 dB SPL. A CMR of up to 5 dB was obtained for a FB four octaves below the signal frequency. Two general trends were observed in the data for FBs spectrally below the CF_{OFM}: (i) CMR increased as the FB level increased and (ii) CMR decreased as the CF_{FB} decreased. CMR was generally absent for CF_{FB} higher than the signal frequency (less than 1 dB).

These effects are supported by the ANOVA. Both stimulus variables, the subjects, and all interactions had highly significant effects ($p \leq 0.0001$) on the threshold. The significant effect of subject and the interaction between the subject and the stimulus variables show individual differences in the thresholds.

The significant effect of center frequency of the FB shows that thresholds vary with spectral distance between FB and OFM. The Scheffé tests for contrast showed that, overall, thresholds for the center frequencies of the FB below the signal frequency are significantly lower than those for center frequencies above the signal frequency. The thresholds for the two center frequencies higher than the signal frequency are not significantly different from one another. The thresholds for the FB centered four octaves below the signal frequency are significantly higher than the thresholds for center frequencies of the FB of two and three octaves below the signal frequency.

The effect of level shows that the threshold depends on the FB level. The Scheffé tests for contrast showed that, overall, the thresholds for all CM conditions are significantly lower than the threshold for the RF condition. However, this effect depends both on center frequency and level of the FB as indicated by the significant interactions between the stimulus variables. For all center frequencies below the signal frequency, the Scheffé tests showed significant differences between the thresholds for the RF and CM conditions with the highest two FB levels. For a spectral distance between OFM and FB of two octaves, also the threshold for the CM condition with the third highest FB level was significantly lower than the threshold for the RF condition. All other differences between the thresholds for the RF and CM conditions were not significant.

B. Dichotic presentation

1. Methods

In contrast to the previous experiment, here the FB was presented to the left ear and the OFM and signal to the right ear. The procedure and measurement setup were identical to those of the previous experiment. Ten subjects participated in the experiment. Nine of the ten subjects had already participated in the first experiment. Since the CMR for FBs centered above the signal frequency was negligible, only FBs centered at frequencies below were considered.

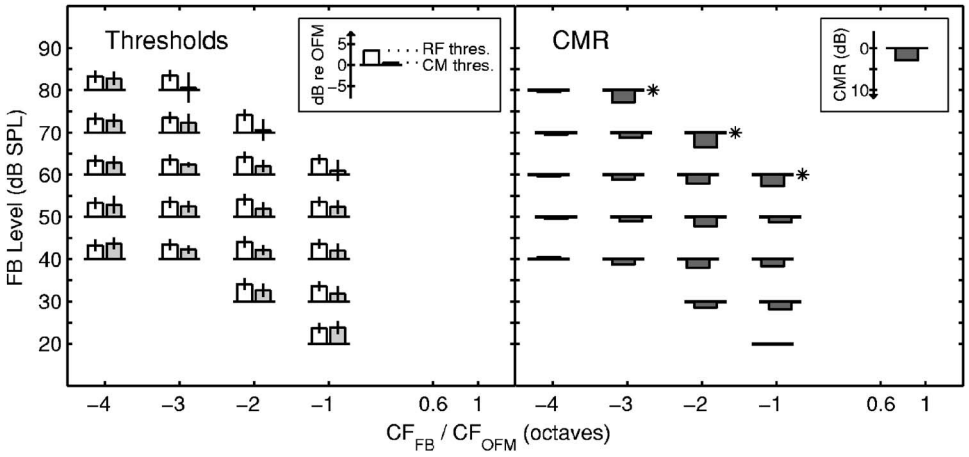

FIG. 3. Same as Fig. 2, but for a dichotic presentation of the masker where the OFM and signal were presented to only one ear and the FB was presented to the opposite ear.

2. Results

Figure 3 shows thresholds (left panel) and CMR (right panel). The data presentation is the same as in Fig. 2. The threshold for the RF condition was 3.5 dB, i.e., the same thresholds were obtained for the diotic and dichotic condition, as expected. The thresholds for the dichotic CM condition differ somewhat from those obtained for the diotic presentation.

In general, thresholds for the CM conditions were higher than the corresponding thresholds in the diotic presentation. This resulted in a reduced CMR (right panel). A CMR of 3 dB was observed for the highest FB level and the FB centered at one, two, or three octaves below the center frequency of the OFM. All other CMR magnitudes were less than 2 dB, i.e., of the same size as the average standard deviation for the CM condition (2 dB).

These effects are supported by the ANOVA. The effects of level and subject were highly significant ($p \leq 0.0001$). The effects of distance and all the interactions were significant. The significant effects of subject and the interaction between the subject and the stimulus variables show individual differences in the thresholds.

The significant effect of center frequency of the FB shows that thresholds vary with the spectral distance between FB and OFM. The Scheffé tests for contrast showed that, overall, thresholds for the lowest FB center frequency were significantly higher than for the other FB center frequencies. Thresholds for the FB centered at three octaves below signal frequency did not differ significantly form those for the FB closer to the signal frequency.

The significant effect of level shows that the threshold depends on the FB level. The Scheffé tests for contrast showed that, overall, the thresholds for the CM condition for the four highest FB levels are significantly lower than the threshold for the RF condition. However, this effect depends both on center frequency and level of the FB as indicated by the significant interactions between the stimulus variables. The Scheffé tests showed significant differences between the thresholds for the CM and RF conditions only for the highest FB levels and a center frequencies of one, two, and three octaves below the signal frequency.

III. MODEL

Plack *et al.* (2002) proposed a model that was able to describe two-tone suppression. The model combines the dual-resonance nonlinear (DRNL) filter (Meddis *et al.*, 2001) with a sliding temporal integrator (temporal window). A modified version of this model was used in the present study to predict the amount of CMR due to suppression.

A. Structure

The first stage of the model is a combined outer- and middle-ear filter. This stage was not part of the model proposed by Plack *et al.* (2002) but proved to be necessary for the stimuli used in the present study (see Sec. IV). The combined outer and middle ear transfer function is modeled by a first-order Butterworth bandpass filter with a lower cutoff frequency of 1 kHz and an upper cutoff frequency of 4 kHz [Breebaart *et al.* (2001); see Table I]. A low-level noise is added to the output of the filter to approximate the threshold in quiet.

The following two stages of the model (DRNL and temporal window) are essentially the same as proposed in Plack *et al.* (2002). The DRNL filter represents the compressive response of the basilar membrane (BM) to a tone at the characteristic frequency (CF) but linear response to a tone lower than the CF. The filter is divided into a linear pathway and a nonlinear pathway. The linear pathway consists of a gammatone filter followed by a low-pass filter. The nonlinear pathway consists of a gammatone filter, a compressive nonlinearity, and a second gammatone filter. The input is processed in parallel through each pathway and then added. The nonlinear pathway has a gain relative to the linear pathway. All DRNL parameters were taken from Plack *et al.* (2002) (see Table I). As in Plack *et al.* (2002), the model only uses the information out of the filter centered at the signal frequency. The output is squared and then smoothed with a sliding temporal window. The window comprises three exponential functions, one to describe backward masking, and two to describe forward masking. All parameters for the temporal window were taken from Oxenham (2001) (see Table I).

The last stage of the model is the decision device. Since stochastic stimuli were used in the present study, the decision

TABLE I. The model parameters for the combined outer and middle ear filter (Breebaart *et al.*, 2001), the DRNL filter (Plack *et al.*, 2002), and the temporal window (Oxenham, 2001).

Middle-ear filter parameter	Value
Bandpass filter lower cutoff (kHz)	1
Bandpass filter upper cutoff (kHz)	4
Bandpass filter order	1
DRNL parameter	**Value**
Lower slope of nonlinearity (dB/dB)	0.78
Upper slope of nonlinearity (dB/dB)	0.16
Transition level (dB SPL)	40
Gain of nonlinear pathway (dB)	39
1st nonlinear GT filter center frequency (re.CF)	1.10
1st nonlinear GT filter bandwidth (ERB re.CF)	0.14
2nd nonlinear GT filter center frequency (re.CF)	0.94
2nd nonlinear GT filter bandwidth (ERB re.CF)	0.08
Linear GT filter center frequency (re.CF)	0.93
Linear GT filter bandwidth (ERB re.CF)	0.12
Linear lowpass filter cutoff (re.CF)	0.91
Linear lowpass filter order	64
Temporal window parameter	**Value**
1st Forward masking time constant (ms)	3.1
2nd Forward masking time constant (ms)	21.0
Weighting factor	0.206
Backward masking time constant (ms)	3.5

device is slightly different from the one used in Plack *et al.* (2002). Plack *et al.* (2002) assumed that the detection is based on the ratio of the signal plus masker to the masker alone at the output of the model. They only considered the time where this ratio reaches its maximum value: Plack *et al.* (2002) used a very short signal in a nonsimultaneous masking condition with a deterministic masker. Thus, the position in time of the temporal window producing the maximum ratio was well defined.

In contrast to Plack *et al.* (2002), the present study used a stochastic masker. Since the masker was random noise, the output of the model was different for the different masker intervals. The present study used long signals in a simultaneous masking condition, i.e., the maximum for the signal plus masker at the output of the model varies from trial to trial. The same is true for the maximum of the masker alone. Figure 4 shows the output of the model for the masker alone (left panels) and for a signal added to the masker at a level of 26 dB SPL (right panels). Note that in each panel there is a different temporal position of the maximum (indicated by the open circle) since for each panel a different noise sample was used.

The decision variable is the quotient of the maximum intensity of the output of the model from the masker-plus-signal interval and the maximum intensity of the two masker-only intervals. The model considers only the temporal position between 125 and 375 ms, i.e., the temporal position of the signal, as indicated by the dotted lines and the horizontal bar in Fig. 4.

The model parameter k is the decision variable at threshold. When the value of the decision variable for a trial exceeds k, the signal is detected. The parameter k was set to 1.2, in order to match measured and simulated threshold for the RF condition. To determine the threshold with the model, the same adaptive 3-AFC procedure was used as in the experiment. The final threshold estimate was taken as the mean across 20 simulated sessions.

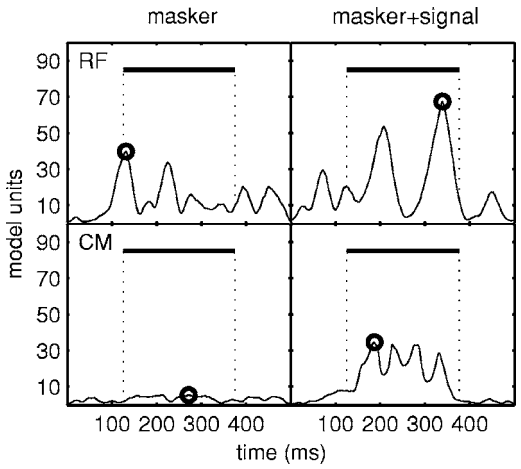

FIG. 4. Output of the DRNL temporal-window stage of the model to the masker alone (left panels) and the masker plus signal (right panels) for the RF condition (top) and the CM condition (bottom). The signal position in the waveform is indicated by the horizontal bar between the dotted lines and the maximum is indicated by an open circle. The ratio of the maximum in the masker-plus-signal interval and highest maximum of the two masker-alone intervals is the decision variable of the model.

B. Predictions

Figure 5 shows the predicted CMR (dark-gray bars) as a function of the center frequency of the FB relative to the signal frequency (i.e., the center frequency of the OFM). The representation of the data is the same as in the right panel of Fig. 2. In addition, the measured CMR (light-gray bars) is redrawn from Fig. 2.

The data indicate that the DRNL temporal window model is able to predict a release of masking due to the

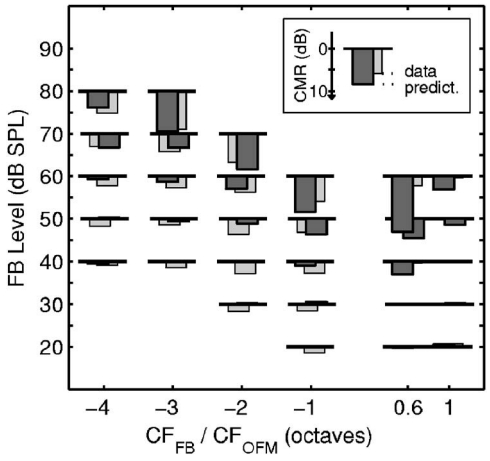

FIG. 5. Prediction of CMR with a modified version of the DRNL temporal window model. Data representation is the same as in the right panel of Fig. 2. Model predictions are shown with dark-gray bars. In addition, the measured diotic CMR is shown with light-gray bars. The bars were slightly shifted horizontally against each other.

presence of a comodulated FB. In comparison to the measured CMR a good match of CMR at high level differences for FB frequencies below the center frequency of the OFM was found. The mean difference between data and model prediction for the two highest level differences was less than 1 dB. However, the CMR is decreasing rapidly towards lower level differences. The predicted CMR for the three lowest levels of the FB was less than 1 dB; thus, the predicted CMR was up to 3 dB smaller than the measured CMR. For a FB spectrally higher than the OFM the model overestimated the CMR. The predicted CMR at the highest level differences was up to 10 dB larger than the measured CMR.

IV. DISCUSSION

A. Effects of level and center frequency of the FB on the amount of CMR

Several studies in the literature have already shown that the magnitude of CMR depends on the spectral position and the level of the FB [see Verhey *et al.* (2003) for a review]. In general, it was found that (i) the CMR decreases as the spectral separation of FB and OFM increases (Schooneveldt and Moore, 1987, 1989; Hall *et al.*, 1990), and (ii) CMR is smaller for FBs positioned above rather than below the signal frequency (Hall *et al.*, 1988; Schooneveldt and Moore, 1987, 1989). In addition, Cohen (1991) and Schooneveldt and Moore (1987) showed that CMR is larger with FB levels higher than the OFM. The data in the present study confirm the effect of frequency and level on the magnitude of CMR using a broader level and frequency range than the previous studies.

The CMR for an FB above the OFM at the same spectral separation of FB and OFM on an octave scale (1 octave) as well as on a linear frequency scale (1000 Hz) is smaller than the CMR with an FB below the OFM. A similar result was reported in Hall *et al.* (1988) and Schooneveldt and Moore (1987, 1989). The size of this effect depended on the signal frequency and the spectral distance between FB and OFM. For the FB level equal to or 10 dB higher than the OFM level, Schooneveldt and Moore (1987) measured a 2-dB-smaller CMR for the 2-kHz signal when the FB was centered at 3000 Hz instead of 1000 Hz, i.e., almost the same effect as in the present study.

Cohen (1991) measured CMR for an FB one octave below and for an FB one octave above the OFM. In contrast to the present study, she defined CMR as the difference between the CM condition and a condition where an uncorrelated FB is present, referred to as the deviant (DV) condition (Verhey *et al.*, 2003). In order to avoid confusion with the definition of CMR used in the present study, the CMR as calculated in Cohen (1991) will be referred to as CMR(DV-CM). At the same level of the FB and OFM, she found a 4-dB-higher CMR(DV-CM) for the FB one octave below the OFM than for the FB one octave above the OFM. This agrees qualitatively with the present data, although both magnitudes of CMR and the difference in CMR were larger than in the present data. This is presumably partly due to the different definitions of CMR. Several studies have shown that CMR(DV-CM) is slightly larger than the difference between the RF threshold and the CM threshold (Hall *et al.*, 1984; McFadden, 1986; Schooneveldt and Moore, 1987, 1989; Moore and Shailer, 1991; Verhey *et al.*, 2003). In addition, the level of OFM and FB was higher in Cohen's study (78 dB SPL) than in the present study (20 dB SPL). Moore and Shailer (1991) showed that CMR increased by about 5 dB as the spectrum level was increased from 10 to 30 dB. Another difference between the present study and the Cohen study are the center frequencies of the OFM and the FB. Whereas the present study varied the FB, Cohen varied the OFM frequency. Schooneveldt and Moore (1987) showed that the CMR for an FB one octave below the OFM and the same level for FB and OFM was greatly reduced when the center frequency of the OFM was changed from 24 to 8 kHz.

For a FB two or three octaves below the signal frequency, Cohen (1991) still obtained a significant CMR(DV-CM), especially at FB levels higher than the OFM level. Ernst and Verhey (2005) showed that a CMR can be obtained over a three-octave range when CMR is defined as the difference between thresholds in the RF and CM conditions, i.e., the same definition of CMR as used in the present study. Ernst and Verhey (2005) showed that CMR for a FB three octaves below the OFM increased as the level difference between FB and OFM increased in qualitative agreement with the present data. The present study also showed that a similar effect of FB level on the magnitude of CMR is observed for a FB four octaves below the OFM.

The magnitude of CMR was smaller in the dichotic experiment than in the diotic experiment. This effect is consistent with data in the literature (Schooneveldt and Moore, 1987; Cohen, 1991; Moore and Shailer, 1991). However, the dichotic CMR obtained by Cohen (1991) is markedly larger than the dichotic CMR found in this study. For an FB one octave below the OFM and with the same level of OFM and FB, she still found a dichotic CMR(DV-CM) of 5.6 dB. In contrast, no CMR was observed in the present study. The discrepancy may be due to the different definition of CMR in the two studies and the higher level used in the Cohen study.

B. Role of outer- and middle-ear filtering

In order to investigate the role of outer- and middle-ear filtering, CMR was simulated with a modified version of the model without the first stage of the model. Figure 6 shows the predicted CMR produced by this modified model compared to the prediction of the original model. The modified and the original versions of the model predicted the same CMR for a FB centered at frequencies above the signal frequency. In contrast, large discrepancies were observed for an FB centered at frequencies below the signal frequency. The modified version of the model predicted the largest CMR for a level of the FB of 60 dB SPL, irrespective of the center frequency of the FB. A negative CMR was predicted for higher levels of the FB. This was due to an excitation of the DRNL filter elicited by the FB. In the original version of the model, the excitation was negligible since the FB was attenuated by outer- and middle-ear filter stage. Since the outer- and middle-ear filter roughly corresponds to the threshold in

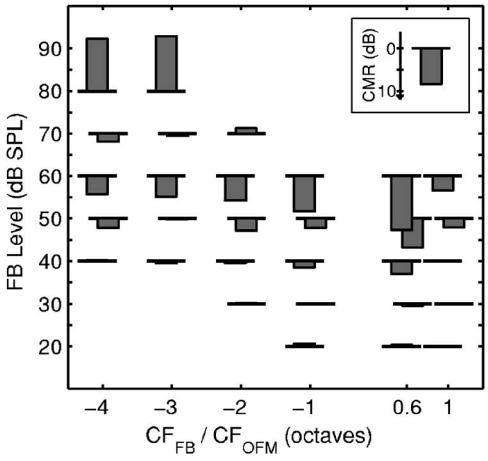

FIG. 6. CMR predicted with modified version of the model without the outer- and middle-ear filter (dark gray bars).

quiet, the simulations indicate that the level of the FB in SL and not in SPL might determine the magnitude of CMR.

C. Role of suppression

Hall *et al.* (1984) already discussed the role of suppression as a possible physiological mechanism underlying CMR. They pointed out that their results are inconsistent with the existence region of suppression. Adding a noise band just below the OFM was as effective as, or more effective than, adding a band just above the OFM. In contrast, data from physiological (Sachs and Kiang, 1968) and psychoacoustic (Shannon, 1976) studies indicate that at a level comparable to the OFM level used by Hall *et al.* (1984) suppression is substantially larger on the high-frequency side.

However, for the lower OFM level and broader frequency range considered in the present study, the level and frequency range for a positive CMR was similar to the psychoacoustical suppression data (Houtgast, 1974; Shannon, 1976). Oxenham and Plack (1998) suggested that suppression might be a possible mechanism underlying CMR for an FB centered at frequencies below the signal frequency. In line with this hypothesis, the model in the present study predicted a CMR which was similar in magnitude to the measured CMR for an FB centered at frequencies below the signal frequency.

The present study investigated the role of suppression in CMR using a modified version of the DRNL temporal window model proposed by Plack *et al.* (2002). The model predicts two-tone suppression because of the combined effects of compression and filtering in the nonlinear pathway of the model. The suppressor tone and the target tone are compressed together by the nonlinearity. The following bandpass filter largely attenuates the suppressor tone, whereas the target tone is essentially unaffected by the filter. Because the target is compressed with the suppressor tone, its level at the output of the second filter is less than it would be if it were presented alone. The bandpass filter prior to the nonlinearity determines the frequency-dependent strength of the suppression.

The suppressor in the CMR experiment of the present study is the FB. The strength of the suppression fluctuates over time due to the inherent envelope fluctuations of the narrow-band noise. The FB suppresses both the OFM and the target signal. However, since the FB and the OFM are comodulated in the CM condition, the FB largely removes the OFM, whereas the reduction in the average amplitude of the signal is comparatively small (see Fig. 4). Thus, the signal-to-masker ratio is larger for the CM condition than for the OFM alone (RF condition). An uncorrelated FB suppresses both the target tone and the OFM similarly, i.e., the threshold is the same as for the RF condition (Ernst and Verhey, 2006).

The model overestimated the CMR for FBs centered at frequencies above the signal frequency. This is presumably due to the inability of the model to predict suppression in this frequency region. Plack *et al.* (2002) showed that the DRNL temporal window model overestimated the suppression for suppressor frequencies above the signal frequency. The overestimation resulted from the first gammatone filter in the nonlinear pathway of the DRNL. An asymmetric first filter with a steeper slope on the high-frequency side such as the gammachirp (Irino and Patterson, 1997) would presumably yield to a better agreement between predictions and experimental data on suppression.

The simulations indicate that part of CMR for large spectral distances between OFM and FB can be accounted for by a within-channel cue. So far, it has only been shown that a large proportion of the CMR for low-level OFMs and high-level FBs can be predicted with a suppression model. Further studies are needed to investigate if CMR at the higher OFM levels can also be partly attributed to suppression.

Within-channel cues were usually discussed in terms of excitation produced by the off-frequency masker components at the signal frequency. Several authors have suggested that the beating between the FB and the OFM is reduced by the addition of the signal and may thus serve as a within-channel cue. An envelope cue was also proposed in Verhey *et al.* (1999) as an important cue for CMR in the band-widening type of CMR experiments. They showed that a within-channel model sensitive to envelope fluctuations predicted most of the CMR in this type of CMR experiments. A within-channel envelope cue is only likely to be used for small spectral distances between OFM and FB, since the sensitivity to high envelope frequencies is rather poor (e.g., Viemeister, 1979). The present study extends the definition of within-channel cues. A within-channel cue is defined as a cue based on the nonlinear processing within the filter at the signal frequency (see also Ernst and Verhey, 2005). In order to determine the amount of CMR due to within-channel cues for spectral distances between FB and OFM smaller than those considered in the present study, a combination of the present model and a model sensitive to envelope fluctuations as proposed in Verhey *et al.* (1999) is required.

D. Role of retro-cochlear processes

The model predicted most of the diotic CMR, indicating that CMR in this experiment was mainly a consequence of

suppression, i.e., resulted from a within-channel process. However, the model underestimated the CMR by up to 4 dB for midlevels of the FB and the FB centered below the signal frequency. The CMR for those levels and frequencies of the FB might result from retro-cochlear processes such as wideband inhibition at the level of the CN (Pressnitzer *et al.*, 2001; Meddis *et al.*, 2002; Verhey *et al.*, 2003; Neuert *et al.*, 2004). The receptive fields of the wideband cells were usually broad and extended over several octaves (Winter and Palmer, 1995; Jiang *et al.*, 1996; Verhey *et al.*, 2003). The inhibitory areas of the narrow-band cells cover a similar spectral range as the wideband cells. The range of frequencies and levels of the FB below the signal frequency producing considerable CMR in the present study corresponds to the physiological inhibitory area of the neurons showing CMR [e.g., Fig. 3A in Neuert *et al.* (2004); see also Fig. 1]. In addition to the large inhibitory area below the center frequency of the unit, Neuert *et al.* (2004) showed inhibitory areas above the center frequency. In general, the inhibitory area above the center frequency extends over a smaller frequency range than that below the signal frequency (see Fig. 1). Thus, in contrast to the present data, a physiological correlate of CMR may also be observed for an FB spectrally above the OFM if the FB center frequency is not too high. However, up to now it was not investigated systematically how the response of the units to CMR stimuli with FB center frequencies smaller than signal frequency differs from their response to CMR stimuli with FBs spectrally above the OFM.

Rhode and Greenberg (1994) directly compared two-tone suppression in single auditory-nerve fibers with wideband inhibition in single units in the CN. They concluded that wideband inhibition was stronger than two-tone suppression, both in frequency extent and magnitude, for some units in the CN. The slight discrepancy between the simulations and the data is in line with the hypothesis that an additional retro-cochlear process such as inhibition at the level of the CN is at least partly responsible for CMR, since suppression alone seemed to be unable to account for the CMR at midlevels of the FB.

Further evidence of the role of retro-cochlear processes in CMR is provided by the dichotic data. Dichotic CMR cannot be accounted for by suppression but could be a consequence of wideband inhibition at a level of the auditory pathway as early as the CN. Several studies have shown that wideband cells project to the contralateral CN (Joris and Smith, 1998; Doucet *et al.*, 1999; Davis, 2005).

There is a mismatch between the diotic CMR that was not accounted for by the suppression model and the dichotic CMR. However, such a discrepancy does not contradict the hypothesis of inhibition at the level of the CN as the underlying process, since recent physiological data indicate that the strength of the inhibition and the frequency extent of inhibitory areas within one ear and across ears are often dissimilar (Ingham *et al.*, 2005).

It is likely that stages of the auditory pathway higher than the CN will alter and probably further enhance the representation of the signal. One possible mechanism is the hypersensitive locking suppression as found in the MGB and the *A*1 (Las *et al.*, 2005): However it was only shown for a different CMR paradigm [band-widening type of experiment; see Verhey *et al.* (2003)]. It remains to be shown if such an effect is also observed in a flanking band type of CMR experiments as used in the present study.

V. CONCLUSIONS

(i) A diotic CMR was observed over a four-octave range. A dichotic CMR was only observed up to three octaves. The magnitude of CMR increased at a constant spectral separation between FB and OFM towards higher levels differences between the FB and OFM. CMR decreased towards broader spectral separations at a constant level of the FB.

(ii) The level and frequency region where CMR occurred corresponded to the inhibitory areas of CN neurons (Neuert *et al.*, 2004) as well as to the psychophysical suppression data (Houtgast, 1974).

(iii) A model incorporating a nonlinear peripheral filter stage predicted the diotic CMR for high FB levels, i.e., suppression might play an important role in CMR for large levels differences between OFM and FB.

(iv) The discrepancies between the predictions and diotic data at midlevels of the FB and the FB centered below the signal frequency indicated that higher level processes were involved in those conditions. The data with an FB presented to the opposite ear indicated that also at high levels of the FB, retro-cochlear processes might play a role in diehotic CMR.

ACKNOWLEDGMENTS

We thank Ian Winter for fruitful discussions related to the physiological aspects of CMR and providing the physiological data. We would also like to thank Chris Plack for support related to the dual-resonance nonlinear-filter model. This project was supported by the Deutsche Forschungsgemeinschaft.

Bos, C. E., and deBoer, E. (**1966**). "Masking and discrimination," J. Acoust. Soc. Am. **39**, 708–715.

Breebaart, J., van de Par, S., and Kohlrausch, A. (**2001**). "Binaural processing model based on contralateral inhibition. I. model structure," J. Acoust. Soc. Am. **110**, 1074–1088.

Budelis, J., Fishbach, A., and May, J. B. (**2002**). "Behavioral assessments of comodulation masking release in cats," J. Assoc. Res. Otolaryngol. Abs.:803.

Cohen, M. F. (**1991**). "Comodulation masking release over a three octave range," J. Acoust. Soc. Am. **90**, 1381–1384.

Cooper, N. P. (**2004**). "Compression in the peripheral auditory system," in *Compression from Cochlea to Cochlea Implants*, Springer Handbook of Auditory Research, edited by S. P. Bacon, R. R. Fay, and A. N. Popper (Springer, New York), pp. 18–61.

Davis, K. A. (**2005**). "Contralateral effects and binaural interactions in dorsal cochlear nucleus," J. Assoc. Res. Otolaryngol. **6**, 280–296.

Doucet, J. R., Ross, A. T., Gillespie, M. B., and Ryugo, D. K. (**1999**). "Glycine immunoreactivity of multipolar neurons in the ventral cochlear nucleus which project to the dorsal cochlear nucleus," J. Comp. Neurol. **408**, 515–531.

Ernst, S. M. A., and Verhey, J. L. (**2005**). "Comodulation masking release over a three octave range," Acta. Acust. Acust. **91**, 998–1006.

Ernst, S. M. A., and Verhey, J. L. (**2006**). Innenohrnichtlinearitten und frequenzbergreifende Prozesse (Cochlear nonlinearities and across-frequency

processes). *Fortschritte der Akustik - DAGA 2006, Oldenburg, Deutsche Gesellschaft für Akustik e.V*.
Glasberg, B. R., and Moore, B. C. J. (**1990**). "Derivation of auditory filter shapes from notched-noise," Hear. Res. **47**, 103–138.
Hall, J. W. (**1986**). "The effect of across-frequency differers in masking level on spectro-temporal patten analysis," J. Acoust. Soc. Am. **79**, 781–787.
Hall, J. W., Grose, J. H., and Haggard, M. P. (**1988**). "Comodulation masking release for multi component signals," J. Acoust. Soc. Am. **83**, 677–686.
Hall, J. W., Grose, J. H., and Haggard, M. P. (**1990**). "Effects of flanking band proximity, number and modulation pattern on comodulation masking release," J. Acoust. Soc. Am. **87**, 269–283.
Hall, J. W., Haggard, M. P., and Fernandes, M. A. (**1984**). "Detection in noise by spectrotemporal pattern analysis," J. Acoust. Soc. Am. **76**, 50–56.
Hofer, S. B., and Klump, G. M. (**2003**). "Within- and across-channel processing in auditory masking: A physiological study in the songbird forebrain," J. Neurosci. **23**, 5732–5739.
Houtgast, T. (**1972**). "Psychophysical evidence for lateral inhibition in hearing," J. Acoust. Soc. Am. **51**, 1885–1894.
Houtgast, T. (**1974**). "Lateral suppression in hearing: A psychophysical study on the ear's capability to preserve and enhance spectral contrast," Ph.D. dissertation (Academische Pers. B. V., Amsterdam).
Ingham, N., Bleeck, S., and Winter, I. M. (**2005**). "Contralateral single neuron receptive fields in the mammalian cochlear nucleus," Assoc. Res. Otolaryngoi. Abs.:28.
Irino, T., and Patterson, R. (**1997**). "A time-domain, level-dependent auditory filter: The gammachirp," J. Acoust. Soc. Am. **101**, 412–419.
Javel, E., Geisler, C., and Ravindran, A. (**1978**). "Two-tone suppression in auditory nerve of the cat: Rate-intensity and temporal analyses," J. Acoust. Soc. Am. **63**, 1093–1104.
Jiang, D., Palmer, A. R., and Winter, I. M. (**1996**). "The frequency extent of two tone facilitation in onset units in the ventral cochlear nucleus," J. Neurophysiol. **75**, 380–396.
Joris, P. X., and Smith, P. H. (**1998**). "Temporal and binaural properties in dorsal cochlear nucleus and its output tract," J. Neurosci. **18**, 10157–10170.
Langemann, U., and Klump, G. M. (**2001**). "Signal detection in amplitude-modulated maskers. I. Behavioural auditory thresholds in a songbird," Eur. J. Neurosci. **13**, 1025–1032.
Las, L., Stern, E. A., and Nelken, I. (**2005**). "Representation of tone in fluctuating maskers in the ascending auditory system," J. Neurosci. **25**, 1503–1513.
Levitt, H. (**1971**). "Transformed up-down methods in psychoacoustics," J. Acoust. Soc. Am. **49**, 467–477.
McFadden, D. (**1986**). "Comodulation masking release: Effects of varying the level, duration and time delay of a cue band," J. Acoust. Soc. Am. **80**, 1658–1667.
Meddis, R., O'Mard, L. P., and Lopez-Paveda, E. A. (**2001**). "A computational algorithm for computing nonlinear auditory frequency selectivity," J. Acoust. Soc. Am. **109**, 2852–2861.
Meddis, R., Delahaye, R., O'Mard, L., Sumner, C., Fantini, A., Winter, I., and Pressnitzer, D. (**2002**). "A model of signal processing in the cochlear nucleus: Comodulation masking release," Acta. Acust. Acust. **88**, 387–398.
Moore, B. C. J., and Shailer, M. J. (**1991**). "Comodulation masking release as a function of level," J. Acoust. Soc. Am. **90**, 829–835.
Nelken, I., Rotman, Y., and Yosef, O. B. (**1999**). "Responses of auditory-cortex neurons to structural features of natural sounds," Nature (London) **397**, 154–157.
Neuert, V., Verhey, J. L., and Winter, I. M. (**2004**). "Responses of dorsal cochlear nucleus neurons to signals in the presence of modulated maskers," J. Neurosci. **24**, 5789–5797.
Nieder, A., and Klump, G. M. (**2001**). "Signal detection in amplitudemodulated maskers. II. Processing in the songbird's auditory forebrain," Eur. J. Neurosci. **13**, 1033–1044.
Oxenham, A. J. (**2001**). "Forward masking: Adaptation or integration?" J. Acoust. Soc. Am. **109**, 732–741.
Oxenham, A. J., and Plack, C. J. (**1998**). "Suppression and the upward spread of masking," J. Acoust. Soc. Am. **104**, 3500–3510.
Plack, C. J., Oxenham, A. J., and Drga, V. (**2002**). "Linear and nonlinear processes in temporal masking," Acta. Acust. Acust. **88**, 348–358.
Pressnitzer, D., Meddis, R., Delahaye, R., and Winter, I. M. (**2001**). "Physiological correlates of comodulation masking release in the mammalian ventral cochlear nucleus," J. Neurosci. **21**, 6377–6386.
Rhode, W., and Greenberg, S. (**1994**). "Lateral suppression and inhibition in the cochlear nucleus of the cat," J. Neurophysiol. **71**, 493–514.
Ruggero, M., Robles, L., and Rich, N. C. (**1992**). "Two-tone suppression in the basilar membrane of the cochlea: Mechanical basis of auditory-nerve rate suppression," J. Neurophysiol. **68**, 1087–1099.
Sachs, M. B., and Kiang, N. Y. (**1968**). "Two-tone inhibition in auditory-nerve fibers," J. Acoust. Soc. Am. **43**, 1120–1128.
Schooneveldt, G. P., and Moore, B. C. J. (**1987**). "Comodulation masking release (CMR): Effects of signal frequency, flanking-band frequency, masker bandwidth, flanking-band level, and monotic versus dichotic presentation of the flanking band," J. Acoust. Soc. Am. **82**, 1944–1956.
Schooneveldt, G. P., and Moore, B. C. J. (**1989**). "Comodulation masking release for various monaural and binaural combinations of the signal, on-frequency, and flanking-band," J. Acoust. Soc. Am. **85**, 262–271.
Shannon, R. V. (**1976**). "Two-tone unmasking and suppression in a forward-masking situation," J. Acoust. Soc. Am. **59**, 1460–1470.
Stabler, S. E., Palmer, A. R., and Winter, I. M. (**1996**). "Temporal and mean rate discharge patters of single units in the dorsal cochlear nucleus of the anesthetized guinea pig," J. Neurophysiol. **3**, 1667–1688.
Verhey, J. L., Dau, T., and Kollmeier, B. (**1999**). "Within-channel cues in comodulation masking release (CMR): Experiments and model predictions using a modulation-filterbank model," J. Acoust. Soc. Am. **106**, 2733–2745.
Verhey, J. L., Pressnitzer, D., and Winter, I. M. (**2003**). "The psychophysics and physiology of comodulation masking release," Exp. Brain Res. **153**, 405–417.
Viemeister, N. F. (**1979**). "Temporal modulation transfer functions based upon modulation thresholds," J. Acoust. Soc. Am. **66**, 1364–1380.
Wagner, E., Kittel, M., and Klump, G. M. (**2002**). "Effects of signal duration on comodulation masking release (CMR) in the mongolian gerbil (*meriones unguiculatus*)," Assoc. Res. Otolaryngol. Abs.:804.
Winter, I. M., and Palmer, A. R. (**1995**). "Level dependence of cochlear nucleus onset unit responses and facilitation by second tones or broadband noise," J. Neurophysiol. **73**, 141–159.

Molecular analysis of the effect of relative tone level on multitone pattern discrimination

Robert A. Lutfi
Department of Communicative Disorders and Waisman Center, University of Wisconsin, Madison, Wisconsin 53706

Walt Jesteadt
Boys Town National Research Hospital, Omaha, Nebraska 68131

(Received 18 July 2005; revised 15 September 2006; accepted 15 September 2006)

Molecular psychophysics attempts to model the observer's response to stimuli as they vary from trial to trial. The approach has gained popularity in multitone pattern discrimination studies as a means of estimating the relative reliance or decision weight listeners give to different tones in the pattern. Various factors affecting decision weights have been examined, but one largely ignored is the relative level of tones in the pattern. In the present study listeners detected a level-increment in a sequence of 5, 100-ms, 2.0-kHz tone bursts alternating in level between 40 and 80 dB SPL. The level increment was made largest on the 40-dB tones, yet despite this all four highly-practiced listeners gave near exclusive weight to the 80-dB tones. The effect was the same when the tones were replaced by bursts of broadband Gaussian noise alternating in level. It was reduced only when the level differences were made <10 dB, and it was entirely reversed only when the low-level tones alternated with louder bursts of Gaussian noise. The results are discussed in terms of the effects of both sensory and perceptual factors on estimates of decision weights. © *2006 Acoustical Society of America.* [DOI: 10.1121/1.2361184]

PACS number(s): 43.66.Ba, 43.66.Fe [JHG] Pages: 3853–3860

I. INTRODUCTION

A fundamental goal of psychophysics is to determine how detection and discrimination are influenced by the different physical dimensions along which complex stimuli vary. Molecular psychophysics is an approach to this problem that focuses on the observer's decision process as it is reflected in the trial-by-trial data (Ahumada and Lovell, 1970; Gilkey and Robinson, 1986; Green, 1964; Watson, 1962). The approach has gained increasing application in recent years, particularly in studies of multitone pattern discrimination where the relative reliance or decision weight listeners give to the different tones in the stimulus is judged to be an important factor underlying performance (Alexander and Lutfi, 2004; Berg, 1989, 1990, 2004; Berg and Green, 1990; Buus, 1999; Dai and Berg, 1992; Doherty and Lutfi, 1996, 1999; Green and Berg, 1991; Lutfi, 1989, 1992; Lentz and Leek, 2002; Sadralodabai and Sorkin, 1999; Stellmack and Viemeister, 2000; Stellmack, Willihnganz, Wightman, and Lutfi, 1997; Willihnganz, Stellmack, Lutfi, and Wightman, 1997).

The techniques for estimating the weights differ in detail in these studies but are derived from the same general model taken to represent different stages of auditory processing leading to a decision (cf. Ahumada and Lovell, 1970; Berg, 1989, 1990; Lutfi, 1989, 1995; Richards and Zhu, 1994). Let x_i represent the value of the ith tone of the pattern (e.g., frequency or level). The listener is assumed to judge each pattern as a target or nontarget based on a linear combination of the x_i corrupted by additive internal noise,

$$\text{Respond Target iff } \sum_{i=1}^{N} a_i(x_i + e_{pi}) + e_c > C, \tag{1}$$

where, N is the total number of tones in the stimulus, e_{pi} and e_c are error terms representing fixed independent sources of internal noise, C is a response criterion, and the a_i are the relative decision weights ($\Sigma a_i = 1$). An important contribution of Berg (1989) was to show analytically that it is possible to estimate the a_i independently of e_{pi}, e_c, and C under this model. This provided a theoretical framework wherein the effect of listener weighing strategy on performance, typically interpreted as an attentional component of performance, could be evaluated separately from the influence of other limiting factors, such as sensory noise, response bias, and criterion variability.[1] The estimates of weights are given to within a constant of proportionality by the slopes b_i of the functions relating the probability of a target response to trial-by-trial variation in each x_i. Berg calls these functions COSS (conditioned-on-a-single-stimulus) functions and the analysis underlying the various molecular techniques for estimating the decision weights is now referred to as COSS analysis.

Since Berg's seminal paper, much of the focus of studies has been on the efficacy of the decision weights obtained; that is, how closely they approximate maximum-likelihood (ML) weights. ML weights maximize the likelihood of a correct response on each trial based on the known statistical properties of the tonal patterns. Deviations of the obtained weights from the ML weights are taken to reflect the effect of nonoptimal listening strategies on performance. This approach underlies the interpretation of the results of a variety of multitone detection and discrimination studies. In the most

notable cases it has been used to identify nonoptimal decision strategies responsible for informational masking (Lutfi, 1992, 1993, 1994; Oh and Lutfi, 1998), to account for differences among normal-hearing adults, young children, and the hard-of-hearing in multitone detection and discrimination experiments (Alexander and Lutfi, 2004; Doherty and Lutfi, 1996, 1999; Oh, Wightman, and Lutfi, 2001; Lentz and Leek, 2002; Stellmack *et al.*, 1997; Willihnganz *et al.*, 1997), to evaluate decision rules in profile analysis (Berg and Green, 1990; Dai and Berg, 1992; Dai, Nguyen, and Green, 1996; Green and Berg, 1991), and to test different models of temporal integration (Buus, 1999; Stellmack and Viemeister, 2000) and temporal pattern discrimination (Sadralodabai and Sorkin, 1999). The approach has even been used to evaluate the role of nonoptimal decision strategies in the identification of simple sound sources (Lutfi, 2001; Lutfi and Oh, 1997; Lutfi and Wang, 1999).

While studies have made great progress in identifying factors that influence decision weights of listeners in different conditions, one basic factor largely ignored is the relative level of tones in the pattern. This omission is surprising given that changes in the relative level of spectral components are known to be important for the identification of speech and everyday sounds. Detecting a change in relative level has also been the focus of numerous studies of auditory profile analysis (Green, 1988). Two studies so far have obtained consistent results regarding the effects of relative tone level on multitone pattern discrimination. Neff and Jesteadt (1996) report experiments in which listeners discriminated a change in the level of a single, fixed-frequency target tone occurring simultaneously with multiple distracter tones of random frequency. Discrimination thresholds improved as the target level was increased relative to the distracters, consistent with the interpretation that higher level tones were given greater decision weight. Berg (1990) conducted the only study, to our knowledge, in which a COSS analysis was undertaken specifically to evaluate the effects of relative tone level on estimates of decision weights. The task was discrimination of multitone sequences that differed in frequency. Only two listeners participated in the experiment, but both showed COSS slopes (weights) for the high-level tones to be greater than those for the low-level tones. Surprisingly, this was true even when low-level tones conveyed more reliable information regarding the to-be-discriminated change in frequency.

The goal of the present study was twofold. First, we wished to test the generality of the level result reported by Berg (1990) by obtaining COSS weights for a larger number of listeners in a different but equally basic psychophysical task, multitone level discrimination. Second, we wished to evaluate factors, both sensory and perceptual, that might reasonably be expected to yield greater decision weights on higher-level tones even when these tones provide less reliable information regarding the to-be-discriminated change.

II. EXPERIMENT 1: EFFECT OF THE NEAR MISS TO WEBER'S LAW

Decision weights in past studies have typically been interpreted to reflect the role of nonsensory factors pertaining to how the listener attends to different components of the pattern rather than to how well they can discriminate changes in those components. In this experiment, we examine a factor that can potentially affect the estimates of decision weights, but that is more commonly associated with sensory processes affecting discrimination. That factor is the near-miss to Weber's Law, the well-documented observation that threshold for a change in the intensity of a pure tone grows somewhat less than proportionally with the intensity of the tone (McGill and Goldberg, 1968). Expressed as a level difference in dB (ΔL), threshold decreases slightly as level is increased, whereas Weber's Law holds that threshold should remain constant. In contemporary models the near-miss is attributed to an effective increase in gain at high levels associated with spreading neural excitation. The spread of excitation is, moreover, presumed to occur at an early stage of processing, most likely as a result of basilar membrane mechanics, and so occurs prior to any attentional influence on decision weights (Florentine and Buus, 1981; Moore *et al.*, 1997; Viemeister, 1972; Zwicker, 1970).

The near miss has not been widely considered as a factor in multitone pattern discrimination studies; yet it can easily be expected to affect the estimates of decision weights that are obtained in these studies, particularly when the tones are of unequal level. To see why, consider that the psychometric function (PF) for pure-tone intensity discrimination is, in fact, a COSS function. It is a special type of COSS function, however, because it is not influenced by how other tones might compete for attention, as in the case of a multitone pattern. This is important because one well-known manifestation of the near miss is that the slope of the PF is greater for high-level tones than for low (Buus and Florentine, 1999). Given that this is true for single tones, then there is good reason to expect that the same would be true when the single tones are combined to form a pattern. We should expect in this case that the COSS slopes, and so the estimates of decision weights, would be greater for high-level tones than for low.

A. Method

The experiment was conducted in two phases. In the first, COSS functions (PFs) for level discrimination of a 100-ms, 2000-Hz pure tone were obtained as a function of tone level ranging from 20 to 80 dB SPL in 10 dB steps. A cued, yes-no procedure with feedback was used. The cue tone was identical to the comparison tone except it was fixed at one level (20–80 dB) within a block of trials. The level of the comparison was perturbed at random on each trial symmetrically about the level of the cue. The perturbation was normally distributed with standard deviation equal to 3 dB. Listeners indicated by button press whether the comparison level was greater than or less than the cue level and were given feedback regarding correctness of their response after each trial (note that there was never a trial in which the cue and comparison were the same level). All tones were computer generated and were played at a 16-bit resolution over a Dell SoundMAX Integrated Audio sound card at a 44.1 kHz sampling rate. The offset of the cue tone preceded the onset

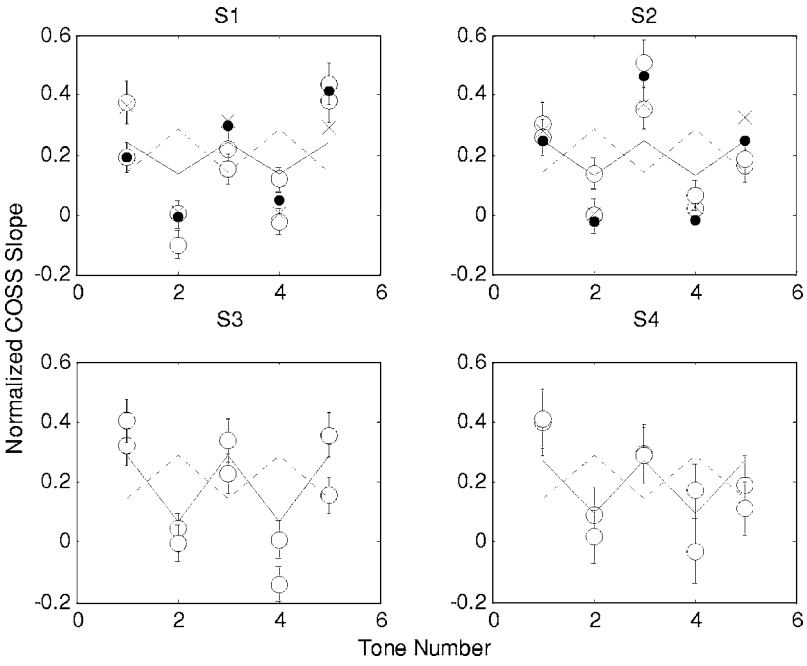

FIG. 1. Results for alternating 40/80 dB tone sequences. First tone is 80 dB. Unfilled circles give the estimates of the normalized COSS slopes ($b_i/\Sigma b_i$) with error bars as a function of position of each tone in the sequence. Two independent estimates are given for each position corresponding to increment-present and increment-absent trials. The dashed curve gives the predictions for an ideal listener that gives attentional weight a_i to each tone proportional to its stimulus index of sensitivity, $d'=\Delta/\sigma$. The continuous curve gives the prediction based on the estimated effect of the near miss assuming equal attentional weight given to all tones (see text for further details). Solid symbols give the mean estimates for a replication with tones separated by 100 ms. Crosses give the means estimates for a replication with the level increment on the 40 dB tones increased from 6 to 12 dB, and the magnitude of the level perturbations increased from 3 to 6 dB.

of the comparison tone by 200 ms. Both cue and comparison were gated on and off with 5-ms cosine-squared ramps. The tones were presented monaurally (right ear) through a Beyerdynamic DT 990 headphone. A TDH-50 earphone with known transfer function was used to calibrate the Beyerdynamic headphone using a binaural loudness balancing procedure at the pure-tone frequency of 2000 Hz (ANSI, 1996).

In the second phase of the experiment the stimulus was a multitone pattern consisting of a sequence of 5 tone bursts, each having the same duration, onset/offset ramps and frequency as the tone used in the first phase of the experiment. The offset of each tone coincided with the onset of the next at the 0 voltage points. The level of the tones alternated between 80 and 40 dB. The task of the listener was to detect an increment in the level of all 5 tones. The increment in levels were $\Delta_{HI}=3$ dB for the higher-level tones and $\Delta_{LO}=6$ dB for the lower-level tones in the pattern. Note that putting the largest increments on the lowest-level tones should encourage listeners to give greater attentional weight, a_i, to the lowest-level tones, which should result in greater COSS slopes for these tones. This is opposite to the predicted effect of the near-miss in which the COSS slopes are expected to be greatest for the highest-level tones, even given the smaller level increment on these tones. By generating counter expectations for the outcome in this experiment our intent was to provide a strong test of the hypothesized effect of the near miss. Listeners were instructed that the higher-level tones in the sequence would provide less reliable information for the task than the lower-level tones and that they should use the feedback to help them perform the task as accurately as possible. As in the first phase of the experiment a random perturbation in level with a standard deviation $\sigma=3$ dB was added independently to each tone on each presentation so as to permit derivation of COSS functions. All other conditions were identical to those described for the first phase with the exception that the yes-no procedure did not include a stimulus preview before each trial.

Four normal-hearing female adults, ages 21–30 years, were paid at an hourly rate for their participation. The listeners were graduate students in the Department of Communicative Disorders at the University of Wisconsin. All had extensive previous experience with the yes-no discrimination task and received at least 400 trials of practice in the present task prior to data collection. The data were collected in 1 sessions, including breaks, conducted on different days.

B. Results and discussion

Estimates of the slopes of the COSS functions were obtained by fitting the binary response data for each listener in each condition with logistic functions using the glmfit routine of the software application MATLAB version 7.0. A total of 400 or more trials per listener, per condition went into the estimate of each COSS function for the multitone patterns, 200 or more trials for the single tones. Analysis of the hit and false alarm rates revealed little or no response bias in any of these conditions. Figures 1 and 2 give the results. The unfilled symbols in each case show the normalized COSS slopes $b_i/\Sigma b_i$ (estimated decision weights) for each listener (panel) as a function of the temporal position of each tone of the multitone pattern. Separate estimates are given for trials in which the level increment was added and in which it was not. Error bars give the standard error of estimate of the slope resulting from the logistic fit to the binary response data conditioned on the level of each tone. The dashed curve in each panel is the prediction for an ideal observer. The ideal observer gives an attentional weight a_i to each tone proportional to its stimulus index of discriminability; $d'_{HI}=\Delta_{HI}/\sigma=1$ and $d'_{LO}=\Delta_{LO}/\sigma=2$ for the high and low level tones, respectively. The continuous curve in each panel gives the predicted effect of the near miss as estimated directly from the slopes of the COSS functions for the individually presented tones. The estimates were obtained by interpolation of a polynomial fit to the data relating COSS

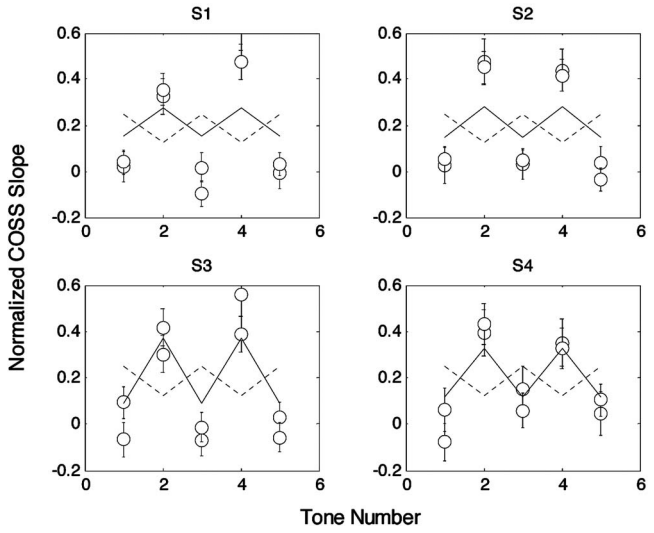

FIG. 2. Same as Fig. 1 except the temporal positions of the 40 and 80 dB tones in the sequence have been swapped.

slope to standard tone level and were in good agreement with the slopes of the psychometric functions for pure-tone intensity discrimination reported by Buus and Florentine (1999).

For all four listeners in both figures, the results agree more nearly with the predictions of the near-miss than they do with those of the ideal observer; the slopes of the COSS functions are greater for the higher-level tones even though these tones provide less reliable information for discrimination. A follow-up experiment ruled out the possibility that the results could be due to partial masking of the low- by the high-level tones. An identical pattern of results (filled symbols of Fig. 1) was obtained when the alternating 40 and 80 dB tones were separated by a 100 ms silent gap. We also tested the assumption that the near-miss can be modeled as a level-dependent gain. While often modeled in this way, the near miss has also been attributed to a level-dependent reduction of additive internal noise (Jesteadt *et al.*, 2003). This poses a problem for interpretation in the present experiment because, as previously noted, additive sources of internal noise are shown analytically not to influence the relative magnitude of the COSS slopes for different tones (Berg, 1989). If the internal noise model is correct, then the only effect of the near miss may be to cause listeners to give greater attentional weight to the 80 dB tones. To test the idea we replicated the conditions of Fig. 1 with the magnitude of the level increment on the 40 dB tones increased from $\Delta_{LO}=6$ to 12 dB, and the magnitude of the level perturbations increased from $\sigma_{LO}=3$ to 6 dB ($d'_{LO}=2$ unchanged). We reasoned that by increasing the external variation in level well beyond that of the internal noise changes in the level of the 40 dB tones would be equally as detectable, or more detectable, than those of the 80 dB tones. The results shown by the crosses in Fig. 1 are nearly identical to those previously obtained, consistent with the effect of the near miss modeled as a level-dependent gain.

The results of these conditions are generally consistent with the predicted effect of the near miss; however, two observations suggest that the near-miss is not the factor or, at least, not the only factor contributing to the disproportionate weight associated with the higher-level tones. First, the predictions tend to underestimate the weights given to the higher-level tones and overestimate the weights given to the lower-level tones. This is most evident, for example, for listeners S1 and S2 in Figs. 1 and 2. Second, the weights estimated for the lower-level tones are often at or near zero suggesting that the lower-level tones are simply ignored. Both of these outcomes appear to reflect an attentional effect on the weights that goes beyond the anticipated influence of the near miss. To evaluate the possible role of attentional factors in these conditions a second experiment was undertaken.

III. EXPERIMENT 2: EFFECT OF LOUDNESS AND PERCEPTUAL SIMILARITY

There are at least two ways in which attentional factors might have influenced the results of expt. 1. The first is that the higher-level tones might have dominated judgments simply because they were the loudest, most salient tones in the pattern. This idea, in fact, is consistent with the predictions of the component-relative-entropy (CoRE) model; a model that has been successfully applied to many results of multitone-pattern discrimination studies (Lutfi, 1993; Oh and Lutfi, 1998). The simplest version of the model presumes that listeners distribute their attention evenly across frequency and time. The result of the distributed attention is that each tone contributes to the listener's decision in proportion to its total power. We will simply refer to this as the *loudness* hypothesis. A second possibility is that listeners failed to selectively attend to the lower-level tones; perhaps because they were perceptually similar to the higher-level tones. Such similarity effects are described by Kidd *et al.* (1994, 2002) and would likely be exacerbated in expt. 1 where all tones were of the same frequency. We will call this the *similarity* hypothesis. Both hypotheses are readily distinguished from one another and the near-miss in terms of their predictions for conditions in which some or all tones in the pattern are replaced by bursts of broadband Gaussian noise. The near miss does not operate for broadband noise; hence, we should expect to see a pattern of weights closer to that of the ideal observer if all the tones are replaced by broadband noise. By comparison, both the loudness and similarity hypotheses predict results for broadband noise similar to those of expt. 1. This is because the higher-level noise bursts remain both louder than and perceptually similar to the lower-level noise bursts. Finally, the loudness and similarity hypotheses are distinguished in a second condition wherein the noise bursts replace only the higher-level tones in the pattern. Because the noise bursts are still the loudest elements of the pattern the loudness hypothesis continues to predict results like those of expt. 1. However, because the noise bursts are perceptually dissimilar from the tones they should promote selective attention; the similarity hypothesis therefore predicts weights closer to those of the ideal observer for this condition.

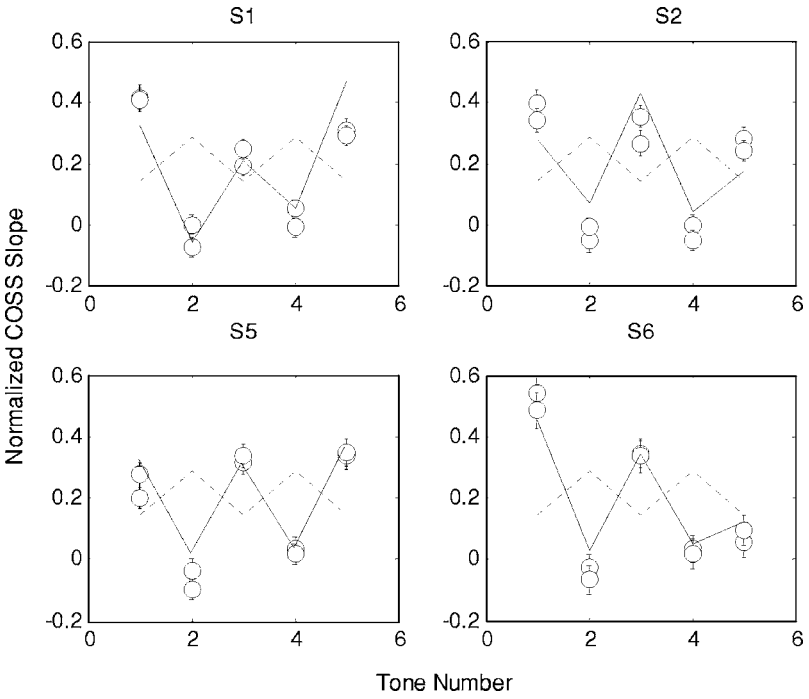

FIG. 3. Same as Fig. 1 except the tones in the sequence have been replaced by broadband Gaussian noise. Continuous lines give the normalized COSS slopes obtained from the 80/40 dB tone sequences of expt. 1.

A. Method

All conditions were identical to those of expt. 1 except that select tones in the pattern were replaced by equal-duration bursts of broadband Gaussian noise. The noise was generated using the randn routine of MATLAB version 7.0 and was filtered only by the Beyerdynamic DT 990 headphone. Two conditions were examined. In the first, all 5 tones were replaced by noise. The overall power of the bursts alternated between 80 and 40 dB SPL, beginning at 80 dB. As was the case for the tones in expt. 1, the level increment on the 80 and 40 dB bursts was 3 and 6 dB, respectively, and the perturbation in the level on all bursts was 3 dB. For the second condition the stimulus was identical to the first except the 40 dB noise bursts were replaced by 2.0 kHz tones. The spectrum level of the tones was equal to that of the 80 dB noise bursts (approximately 40 dB SPL) so that the noise bursts would be clearly louder than the tones. Two of the listeners who participated in the earlier experiment (S1 and S2) participated in this experiment. The remaining two listeners were new to the task but received at least 400 trials of practice in each condition before data collection began.

B. Results and discussion

Figures 3 and 4 show the results for the noise and noise +tone patterns, respectively. The data are plotted as before so as to allow direct comparison to the results of expt. 1.

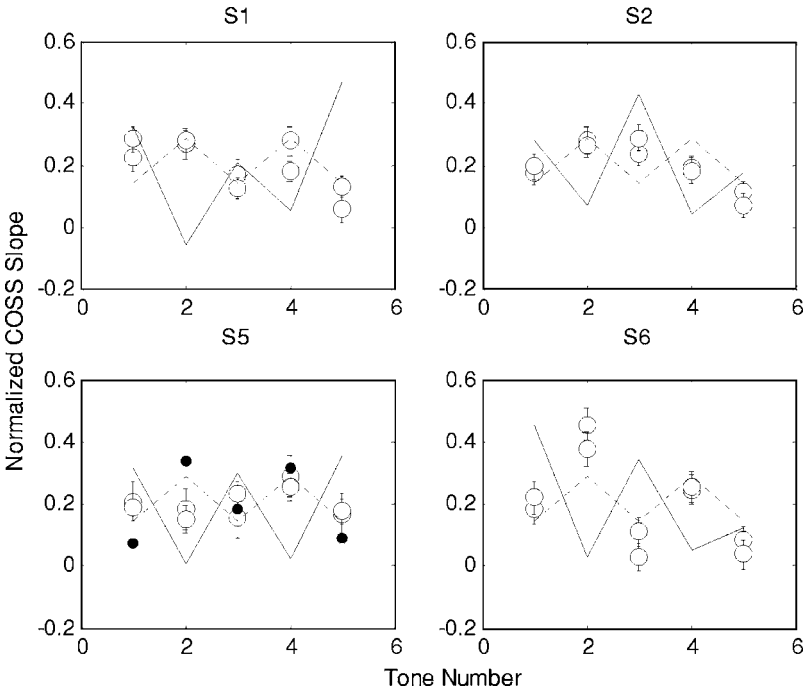

FIG. 4. Same as Fig. 3 except the lower-level noise bursts have been replaced with 2.0 kHz tones having the same spectrum level as the higher-level noise bursts. Small filled symbols for S3 show a replication with a 100 ms silent interval introduced between noise and tones.

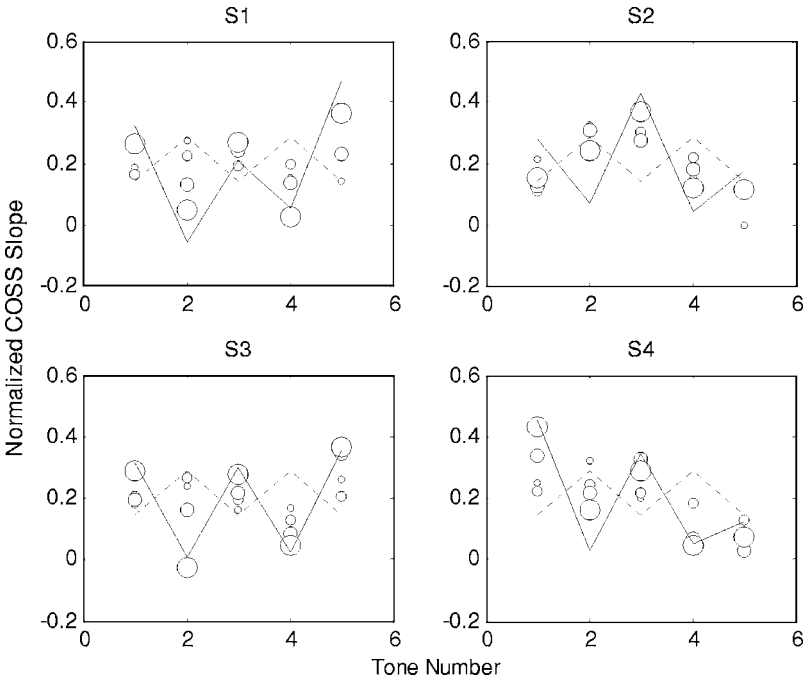

FIG. 5. Same as Fig. 1 except symbols represent the mean of the two estimates of decision weights for each listener as the level difference between tones is varied. Increasing symbol size denotes increasing level difference from 0, 1, 5, to 10 dB. Continuous curves give mean decision weights obtained from expt. 1 (level difference equals 40 dB).

Note that the solid lines for the two new listeners S5 and S6 were obtained from a replication of expt. 1. Of the three competing hypotheses the outcome clearly favors the similarity hypothesis. For the noise pattern the results are essentially unchanged from expt. 1. This would seem to pre-empt the previous interpretation in terms of the effect of the near miss as the near miss is not obtained for broadband noise. The results for the noise pattern are consistent with the loudness hypothesis, but the loudness hypothesis also predicts that the noise bursts would receive greater weight for the noise+tone pattern; clearly contrary to the data shown in Fig. 4. The similarity hypothesis is capable of predicting the results of all conditions of both experiments. Hence, it would appear that the loudness hypothesis is either incorrect or the effect of relative loudness on the decision weights can be overridden by reducing the similarity of patterns components.

IV. EXPERIMENT 3: HOW MUCH OF LEVEL DIFFERENCE?

The results of expts. 1 and 2 show that the tendency of the higher-level components in a pattern to dominate listener decisions is quite robust. However, the level-difference between components in these experiments was also quite large, 40 dB. Would similar results be obtained for much smaller level differences between components? One possibility is that the level effect is all or none; that there exists a level difference, somewhere between 0 and 40 dB, for which the decision weights abruptly shift from the higher-level, less-reliable tones to the lower-level, more-reliable tones. Such a result would reinforce the role of attention in establishing the effect. Expt. 3 was undertaken to test this possibility and to determine the smallest level difference for which the level effect is obtained.

A. Method

All conditions were identical to those of expt. 1 except the level difference between tones was selected to be 0, 1, 5, and 10 dB in different conditions. As before levels were symmetric around a value of 60 dB SPL. Listeners participating in the experiment were the same as those participating in expt. 2 and were given the same instructions regarding the reliability of the level increment on the higher- and lower-level tones.

B. Results and discussion

For simplicity in Fig. 5 we show only the mean of the two estimates of decision weights for each listener. The increasing symbol size denotes increasing level difference between tones. Dashed lines give the ideal decision weights as before. Continuous lines give the obtained decision weights from expt. 1 (level-difference equals 40 dB). Three points are to be noted from Fig. 5. First, decreasing the level difference by as much as 30 dB has little or no effect on the estimates of decision weights. The COSS slopes obtained for the tones differing by 10 dB are essentially equal to those obtained in expt. 1 where the difference was 40 dB. This is clearly inconsistent with the predictions of the near miss as there was little or no difference found for these listeners between the COSS slopes for single tones differing by 10 dB. Second, as the level difference is reduced further the estimates of decision weights converge gradually to the ideal. There is no evidence of a discrete change in decision weights that would be consistent with an abrupt shift in attention to the lower-level tones. Finally, it should be noted that the weights for the 0 dB difference condition are not as close to the ideal weights as they were for the condition in which the tones were alternated with broadband noise (cf. Fig. 4). The reason for this may again be related to the dif-

ficulty of selectively attending to tones having the same frequency (similarity hypothesis), which would tend to cause all tones to be given equal weight.

V. GENERAL DISCUSSION

The results of this study show that when detecting a change in the level of a multitone sequence, the highest-level components in the sequence typically have the greatest influence on the listener's judgments, even when the lower-level tones contain more information regarding the presence of a change. The effect is robust; it is obtained for highly practiced listeners, it occurs regardless of the position of the high-level tones in the sequence, it is undiminished when tones are separated by long (100 ms) silent intervals, and it is not reduced by imposing large level perturbations on the tones. The results are consistent with the predicted effect of the near miss to Weber's Law inasmuch as the relative slopes of the COSS functions obtained for the tones presented individually (where attentional weights are not a factor) are close to the relative slopes obtained for the tones presented within the pattern. However, two further results suggest that the near miss, at best, plays only a contributing role: The same effect is found for broadband Gaussian noise bursts where the near miss is absent, and it is undiminished for level differences as small as 10 dB where the near miss would predict a much smaller effect. The effect also appears to be not merely determined by the relative loudness of tones (louder tones being more salient in the pattern and so receiving greater weight). We find that the effect is entirely reversed (low-level tones given greater weight) when the higher-level tones are replaced by high-level noise bursts of equal or greater loudness. Only one interpretation is consistent with all of these results; it is that selective attention to individual pattern components is made difficult by perceptual similarity among components with the result that lower-level components are largely ignored.

The results have implications for assumptions underlying the most common interpretation of COSS weights. Given the widespread use of COSS analysis to evaluate the decision strategies of listeners, it is noteworthy that few papers have seriously evaluated the assumptions of the decision model underlying the analysis. There is cause for concern as early work shows these assumptions to be critical to the interpretation of the obtained decision weights (Lutfi, 1992; Richards, 2002). The Richards (2002) paper is particularly relevant in this regard. Simulations reported in this paper show that a level-dependent gain, as would be associated with the spread of excitation and the near miss, can produce a systematic bias in the estimates of weights, particularly when tones are of unequal level. The potential for a bias of this type has also been noted in the context of popular spectral shape discrimination tasks where the listener must detect a change in relative level within a stimulus (Lentz and Richards, 1997). The results of the present study suggest, however, that any bias resulting from the near miss is likely to be overridden by the influence of attentional factors on the estimates of decision weights. The results do little, therefore, to change the popular interpretation of decision weights as reflecting attentional factors in multitone pattern discrimination.

Though the present results only weakly establish a possible cause of the level effects, the results underscore the importance of the relative level as a factor influencing multitone pattern discrimination. Indeed, the only condition so far examined for which the relative level has not significantly influenced the outcome is the tone+noise condition of the present study. This condition takes on special significance because it suggests that listeners can overcome the detrimental tendency to give the greatest weight to higher-level components of a pattern if those components are made perceptually dissimilar from the lower-level components of the pattern, thereby permitting selective attention to the individual components. Such effects of perceptual dissimilarity on multitone pattern discrimination have been investigated at length by other authors (e.g., Kidd *et al.*, 1994, 2002), and it is beyond the scope of the present study to revisit these effects. However, they may ultimately prove key in understanding the consistently nonoptimal strategy of listeners to emphasize the component level over reliability in this study and that of Berg (1990) have so far reported similar results.

ACKNOWLEDGMENTS

The authors wish to thank Dr. Bruce Berg, Dr. John Grose, and an anonymous reviewer for comments on a previous version of this manuscript. This research was supported by grants from the NIDCD Nos. R01 DC006875-01 and R01 DC01262-14.

[1]Note that not attending to the tone in this case results effectively in an increase in e in this model not a reduction in a_i (cf. Lutfi, 1992; Lutfi *et al.*, 2003).

Ahumada, A. Jr., and Lovell, J. (**1970**). "Stimulus features in signal detection," J. Acoust. Soc. Am. **49**, 1751–1756.

Alexander, J. M., and Lutfi, R. A. (**2004**). "Informational masking in hearing-impaired and normal-hearing listeners: Sensation level and decision weights," J. Acoust. Soc. Am. **116**, 2234–2247.

ANSI (**1996**). ANSI S3.6-1996, "American National Standards specification for audiometers" (American National Standards Institute, New York).

Berg, B. G. (**1989**). "Analysis of weights in multiple observation tasks," J. Acoust. Soc. Am. **86**, 1743–1746.

Berg, B. G. (**1990**). "Observer efficiency and weights in a multiple observation task," J. Acoust. Soc. Am. **88**, 149–158.

Berg, B. G. (**2004**). "A molecular description of profile analysis: Decision weights and internal noise," J. Acoust. Soc. Am. **115**, 822.

Berg, B. G., and Green, D. M. (**1990**). "Spectral weights in profile listening," J. Acoust. Soc. Am. **88**, 758–766.

Buus, S. (**1999**). "Temporal integration and multiple looks, revisited: Weights as a function of time," J. Acoust. Soc. Am. **105**, 2466–2475.

Buus, S., and Florentine, M. (**1999**). "Psychometric functions for level discrimination," J. Acoust. Soc. Am. **90**, 1371–1380.

Dai, H., and Berg, B. G. (**1992**). "Spectral and temporal weights in spectral shape discrimination," J. Acoust. Soc. Am. **92**, 1346–1355.

Dai, H., Nguyen, Q., and Green, D. M. (**1996**). "Decision rules of listeners in spectral-shape discrimination with or without signal-frequency uncertainty," J. Acoust. Soc. Am. **99**, 2298–2306.

Doherty, K. A., and Lutfi, R. A. (**1996**). "Spectral weights for overall level discrimination in listeners with sensorineural hearing loss," J. Acoust. Soc. Am. **99**, 1053–1057.

Doherty, K. A., and Lutfi, R. A. (**1999**). "Level discrimination of single tones in a multitone complex by normal-hearing and hearing-impaired listeners," J. Acoust. Soc. Am. **105**, 1831–1840.

Florentine, M., and Buus, S. (**1981**). "An excitation-pattern model for intensity discrimination," J. Acoust. Soc. Am. **70**, 1646–1654.
Gilkey, R. H., and Robinson, D. E. (**1986**). "Models of masking: A molecular psychophysical approach," J. Acoust. Soc. Am. **79**, 1499–1510.
Green, D. M. (**1964**). "Consistency of auditory detection judgments," Psychol. Rev. **71**, 392–407.
Green, D. M. (**1988**). *Profile Analysis, Auditory Intensity Discrimination* (Oxford Science, New York).
Green, D. M., and Berg, B. G. (**1991**). "Spectral weights and the profile bowl," Q. J. Exp. Psychol. A **43**, 449–458.
Jesteadt, W., Wier, C. C., and Green, D. M. (**1977**). "Intensity discrimination as a function of frequency and sensation level," J. Acoust. Soc. Am. **61**, 169–177.
Kidd, G., Jr., Mason, C. R., and Arbogast, T. L. (**2002**). "Similarity, uncertainty, and masking in the identification of nonspeech auditory patterns," J. Acoust. Soc. Am. **111**, 1367–1376.
Kidd, G., Jr., Mason, C. R., Deliwala, P. S., Woods, W. S., and Colburn, H. S. (**1994**). "Reducing informational masking by sound segregation," J. Acoust. Soc. Am. **95**, 3475–3480.
Lentz, J. J., and Leek, M. R. (**2002**). "Decision strategies of hearing-impaired listener in spectral shape discrimination," J. Acoust. Soc. Am. **111**, 1389–1398.
Lentz, J. J., and Richards, V. M. (**1997**). "Sensitivity to changes in overall level and spectral shape: an evaluation of a channel model," J. Acoust. Soc. Am. **101**(6), 3625–3635.
Lutfi, R. A. (**1989**). "Informational processing of complex sound. I. Intensity discrimination," J. Acoust. Soc. Am. **86**, 934–944.
Lutfi, R. A. (**1992**). "Informational processing of complex sound. III. Interference," J. Acoust. Soc. Am. **91**, 3391–3401.
Lutfi, R. A. (**1993**). "A model of auditory pattern analysis based on component-relative-entropy," J. Acoust. Soc. Am. **94**, 748–758.
Lutfi, R. A. (**1994**). "Discrimination of random, time-varying spectra with statistical constraints," J. Acoust. Soc. Am. **95**, 1490–1500.
Lutfi, R. A. (**1995**). "Correlation coefficients and correlation ratios as estimates of observer weights in multiple-observation tasks," J. Acoust. Soc. Am. **97**, 1333–1334.
Lutfi, R. A. (**2001**). "Auditory detection of hollowness," J. Acoust. Soc. Am. **110**, 1010–1019.
Lutfi, R. A., Kistler, D. J., Callahan, M. R., and Wightman, F. L. (**2003**). "Psychometric functions for informational masking," J. Acoust. Soc. Am. **114**, 3273–3282.
Lutfi, R. A., and Oh, Eunmi (**1997**). "Auditory discrimination of material changes in a struck, clamped bar," J. Acoust. Soc. Am. **102**, 3647–3656.
Lutfi, R. A., and Wang, W. (**1999**). "Correlational analysis of acoustics cues for auditory motion," J. Acoust. Soc. Am. **106**, 919–928.
McGill, W. J., and Goldberg, J. P. (**1968**). "Pure-tone intensity discrimination and energy detection," J. Acoust. Soc. Am. **44**, 576–581.
Moore, B. C. J., Glasberg, B. R., and Baer, T. (**1997**). "A model for the prediction of thresholds, loudness and partial loudness," J. Audio Eng. Soc. **45**, 224–240.
Neff, D. L., and Jesteadt, W. (**1996**). "Intensity discrimination in the presence of random-frequency, multicomponent maskers and broadband noise," J. Acoust. Soc. Am. **100**, 2289–2298.
Oh, E. L., and Lutfi, R. A. (**1998**). "Nonmonotonicity of informational masking," J. Acoust. Soc. Am. **104**, 3489–3499.
Oh, E. L., Wightman, F. L., and Lutfi, R. A. (**2001**). "Children's detection of pure-tone signals with random multitone maskers," J. Acoust. Soc. Am. **109**, 2888–2895.
Richards, V. M. (**2002**). "Effects of a limited class of nonlinearities on estimates of relative weights," J. Acoust. Soc. Am. **111**, 1012–1017.
Richards, V. M., and Zhu, S. (**1994**). "Relative estimates of combination weights, decision criteria, and internal noise based on correlation coefficients," J. Acoust. Soc. Am. **95**, 423–434.
Sadralodabai, T., and Sorkin, R. D. (**1999**). "Effect of temporal position, proportional variance, and proportional duration on decision weights in temporal pattern discrimination," J. Acoust. Soc. Am. **105**, 358–365.
Stellmack, M. A., and Viemeister, N. F. (**2000**). "Observer weighting of monaural level information in a pair of tone pulses," J. Acoust. Soc. Am. **107**, 3382–3393.
Stellmack, M. A., Willihnganz, M. S., Wightman, F. L., and Lutfi, R. A. (**1997**). "Spectral weights in level discrimination by preschool children: Analytic listening conditions," J. Acoust. Soc. Am. **101**, 2811–2821.
Viemeister, N. (**1972**). "Intensity discrimination of pulsed sinusoids: The effects of filtered noise," J. Acoust. Soc. Am. **51**, 1265–1269.
Watson, C. S. (1962). "Signal detection and certain physical characteristics of the stimulus during the observation interval," Ph.D. thesis, Indiana University, Bloomington, IN.
Willihnganz, M. S., Stellmack, M. A., Lutfi, R. A., and Wightman, F. L. (**1997**). "Spectral weights in level discrimination by preschool children: Synthetic listening conditions," J. Acoust. Soc. Am. **101**, 2803–2810.
Zwicker (**1970**). "Masking and psychological excitation as consequences of the ear's frequency analysis," in *Frequency Analysis and Periodicity Detection in Hearing*, edited by R. Plomp and G. F. Smoorenburg (Sijthoff, Leiden), pp. 376–396.

Virtual pitch in a computational physiological model

Ray Meddis[a] and Lowel P. O'Mard
Department of Psychology, Essex University, Colchester, CO4 3SQ, United Kingdom

(Received 31 May 2006; revised 28 September 2006; accepted 2 October 2006)

A computational model of nervous activity in the auditory nerve, cochlear nucleus, and inferior colliculus is presented and evaluated in terms of its ability to simulate psychophysically-measured pitch perception. The model has a similar architecture to previous autocorrelation models except that the mathematical operations of autocorrelation are replaced by the combined action of thousands of physiologically plausible neuronal components. The evaluation employs pitch stimuli including complex tones with a missing fundamental frequency, tones with alternating phase, inharmonic tones with equally spaced frequencies and iterated rippled noise. Particular attention is paid to differences in response to resolved and unresolved component harmonics. The results indicate that the model is able to simulate qualitatively the related pitch-perceptions. This physiological model is similar in many respects to autocorrelation models of pitch and the success of the evaluations suggests that autocorrelation models may, after all, be physiologically plausible. © *2006 Acoustical Society of America.* [DOI: 10.1121/1.2372595]

PACS number(s): 43.66.Ba, 43.66.Hg, 43.66.Nm [BLM] Pages: 3861–3869

I. INTRODUCTION

Virtual pitch is a sensation of tone height created by broadband sounds. This pitch can be compared to the tone height of a pure tone even though the broadband stimulus may not contain any spectral energy in the frequency region of that tone. There are many different explanations of the origin of virtual pitches and these are often categorized as either "spectral" or "temporal." The model described below addresses a group of hypotheses in the "temporal" category (for example, Licklider, 1951; Yost *et al.*, 1978; Lyon, 1984; Assmann and Summerfield, 1990; Meddis and Hewitt, 1991; Meddis and O'Mard, 1997). These theories assume that virtual pitch arises from temporal regularity or periodicities in sounds and that these regularities can be characterized using mathematical methods such as autocorrelation. This approach makes many qualitatively detailed and often successful predictions concerning the outcome of a wide range of virtual pitch experiments, particularly for stimuli where the periodicity is invariant.

The status of the autocorrelation models remain controversial, however, because to many it appears to be physiologically implausible and positive evidence in its favor is elusive. There are no structures in the auditory brainstem that look capable of carrying out the "delay-and-multiply" operations required by autocorrelation. This is a major impediment to a general acceptance of an autocorrelation-type model of virtual pitch perception.

This paper seeks to address the issue by proposing a signal-processing scheme based on anatomical structures and physiological processes known to exist in the auditory periphery and brainstem. The aim is to show that a system based on these components can behave in some important respects like autocorrelation and can simulate a number of the most important virtual pitch phenomena.

The model is an extended version of an older computational model that was originally developed to simulate the response of single units in the auditory brainstem to sinusoidally amplitude modulated (SAM) tones (Hewitt and Meddis, 1992, 1994). In those studies it was shown that the model is able to simulate appropriate modulation transfer functions (MTFs) in ventral cochlear nucleus (VCN) neurons when stimulated using sinusoidal amplitude modulated (SAM) tones. It can also simulate appropriate *rate* MTFs in single inferior colliculus (IC) neurons. In this report the model will be expanded and evaluated using broadband stimuli with a pitch quality rather than SAM tones. An earlier study has shown that model VCN units can successfully simulate response of their physiological equivalents to broadband pitch stimuli (Wiegrebe and Meddis, 2004).

SAM tones do not themselves produce a strong pitch percept. It may seem strange that a model designed to process such stimuli should be regarded as a candidate explanation for pitch perception: However, the model's sensitivity to particular rates of amplitude modulation is based on its ability to respond to particular periodicities in the stimulus. Therefore, it is possible that it could also prove useful in responding to the periodicities present in pitch-evoking stimuli. This was the motivation for extending and re-evaluating the model.

The original model simulated nervous activity in a single best-frequency (BF) channel, i.e., a single site along the basilar membrane (BM). The new model is an expanded version that includes multiple parallel BF channels and many IC units in each channel. An additional cross-channel processing stage has been added to allow information to be aggregated across channels. Nevertheless, the basic component model of IC unit functioning is unchanged from its previously published form in all material respects.

It was necessary to include the aggregation of information across BF-channels (across BM sites) because the strongest sensation of pitch is created by stimuli whose frequency

[a]Electronic mail:rmeddis@essex.ac.uk

components are resolved by the auditory periphery, i.e., each component is processed in a different channel. For example, most IC units have only narrow receptive fields, sometimes responding to only one harmonic of a multiharmonic stimulus. It follows that a complete account of the extraction of the pitch of a multitone complex must involve a stage where the activity of units with different BFs is somehow combined. As a consequence, it is essential to add another layer of units above the narrowly-tuned units of the IC. This does not mean that the location of this layer is known, only that its inclusion was unavoidable.

The overall architecture of the model is the same as that of an autocorrelation model (Meddis and O'Mard, 1997a). It consists of a cascade of the following stages: (1) peripheral segregation of sound into frequency bands, (2) extraction of periodicities on a within-channel basis, and (3) aggregation of periodicity information across BF-channels. The novelty in the model lies in the way in which periodicity is extracted; using physiologically plausible circuits rather than an artificial mathematical device.

The model will be evaluated below by assessing its response to a range of stimuli commonly used in psychophysical experiments. These pitch-evoking stimuli include (1) complex tones with a missing fundamental frequency, (2) tones with alternating phase, (3) inharmonic tones with equally spaced frequencies, and (4) iterated rippled noise. The range of possible tests is virtually infinite and these stimuli have been carefully chosen to represent stimuli that raise difficulties for many pitch theories. Particular attention will be paid, for example, to differences in response to resolved and unresolved component harmonics. These stimuli have also been used previously to evaluate the autocorrelation model of pitch perception. The aim here is to demonstrate that a physiologically realizable circuit can substitute for autocorrelation and, qualitatively at least, it can perform just as well.

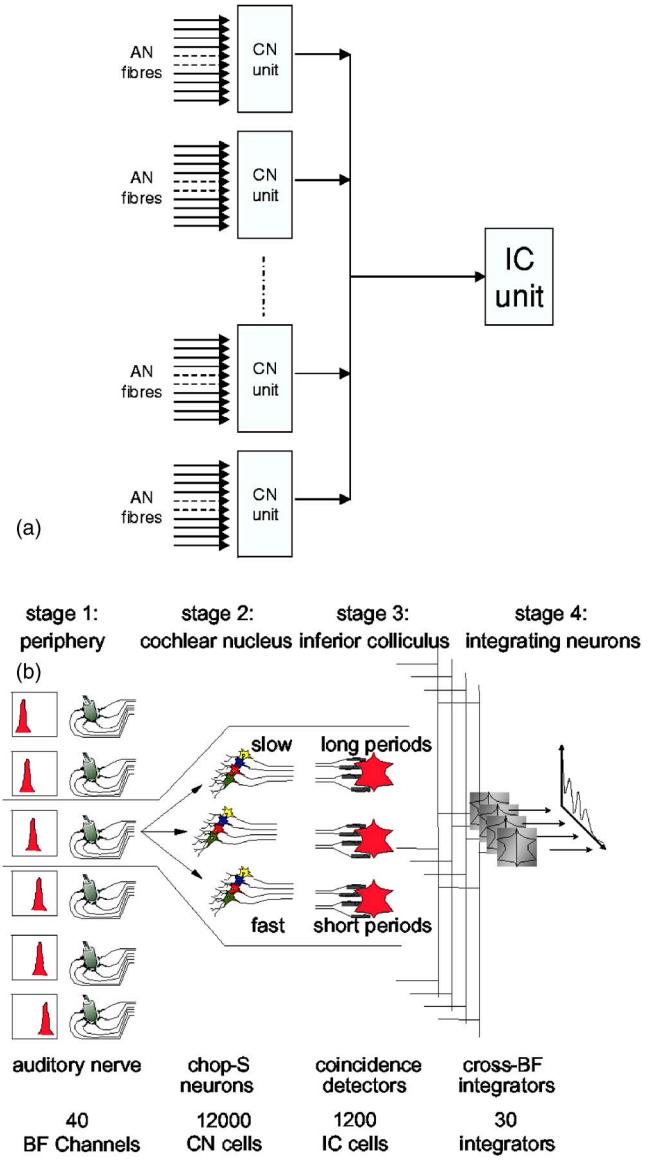

FIG. 1. (A) A single constituent module. A module consists of 10 VCN units feeding one IC unit. Each VCN unit receives input from 30 AN same-BF fibers. Within a module, all VCN units have the same saturated firing rate. (B) Arrangement of modules. There are 30 modules within each BF channel, each with a different characteristic firing rate. There are 40 channels with BFs ranging from 100 to 10000 Hz. A stage-4 unit receives one input from each channel from modules with the same saturated rate.

II. THE MODEL

The model contains thousands of individual components but is modular in structure [Fig. 1(A)]. The basic building block of the system is a module consisting of a cascade of three stages: auditory nerve (AN) fibers, VCN units, and an IC unit. Each module has a single IC cell receiving input from 10 VCN units *all with the same BF and saturated firing rate*. Each VCN unit receives input from 30 AN fibers *all with the same BF*. All modules are identical except for the BF and the saturated firing rate of the VCN units. Within a module, it is the saturated firing rate of the VCN units that determines the selectivity of the IC *rate* response to periodicity. The VCN units are modeled on VCN chopper units that fire at a fixed rate in response to moderately intense acoustic stimulation.

The VCN units are designed to imitate the behavior of sustained chopper units. These have low thresholds, a narrow dynamic range and a receptive field similar in width to that of an AN fiber (Blackburn and Sachs, 1989). The firing rate of VCN units is maximal about 20 dB above threshold and is largely independent of stimulus characteristics. As a consequence, the saturated chopping rate is referred to below as its *intrinsic* chopping rate. Different units have different intrinsic rates and these differences are fundamental to the ability of the model to detect and discriminate among different periodicities. The assumption that all units receive the same number of AN inputs is a simplifying assumption that may need to be revised at a future date. The assumption that all inputs to a VCN unit are from AN fibers with the same BF may also be a simplification. However, the narrowness of the receptive field of sustained chopper units is typically reported to be similar to that of a single auditory nerve fiber.

These modules are the same as those described in Hewitt and Meddis (1994) where it was shown that the VCN units

have appropriate modulation transfer functions (MTFs) and it was also shown that the module IC units have physiologically appropriate *rate*-MTFs. In other words the IC units show high firing rates for a restricted range of low-frequency modulations. These two MTFs are related in that the tuning of the IC unit depends on the chopping rate of VCN units supplying its input. If the intrinsic chopping rate of the VCN units is 100 spikes/s, the peak of the VCN MTF will be around 100 Hz and the peak of the IC *rate*-MTF is also at 100 Hz. A single IC unit can, therefore, be tuned to respond maximally to a particular modulation frequency by adjusting the chopping rate of its feeder VCN units.

The extended model replicates this core module many times within a single BF channel using different chopping rates in different modules. There are 10 VCN units in each block and, within a single channel, there are 30 blocks, each characterised by its chopping rate. This arrangement is replicated across 40 BF channels making a total of 12000 VCN units and 1200 IC units. The choice of 30 blocks and 40 BF channels is arbitrary and represents a trade-off against the considerable computational time involved.

This multirate, multi-BF architecture provides the basis for a further extension of the model; a fourth stage where periodicity information is aggregated *across* BF channels. This pitch-extraction stage is added to the model in the form of an array of hypothetical "stage 4" units called the "stage 4 profile." Each stage 4 unit receives input from one IC unit from each BF channel where all the contributing IC units have the same best modulation frequency and, hence, the same VCN chopping rate. Figure 1(B) illustrates the overall architecture. Each stage 4 unit has a unique pattern of sensitivities to periodicity.

The within-module details are unchanged from the original modeling studies. One minor change from earlier work is a reduction from 60 to 30 in the number of AN fibers providing input to a single VCN unit. This was to improve the fit of the model VCN MTFs to published animal data (Meddis and O'Mard, 1997b). Improvements to the detail of the AN model have also been included in order to be consistent with recent modeling work from this laboratory. The AN section of the model has, for example, been recently updated and is fully described in Meddis (2006). This updated version includes a nonlinear cochlear response and improved forward masking behavior (Meddis and O'Mard, 2005) and first-spike latencies (Meddis, 2006). The parameters of the dual resonance nonlinear (DRNL) filterbank are based on human psychophysical data (Lopez-Poveda and Meddis, 2001).

Stage 1: Auditory periphery. This stage of the model is exactly as described in Meddis (2006) where all equations and parameters are given in full. The effect of the outer-middle ear was simulated using a Butterworth first-order band pass filter with lower and upper cutoffs of 450 and 5000 Hz, respectively. The basilar membrane was modeled as 40 channels whose best frequencies (BFs) were equally spaced on a log scale across the range 100–10000 Hz. This was implemented as an array of dual resonance nonlinear (DRNL; Meddis *et al.*, 2001) filters using the parameters for human listeners given in Lopez-Poveda and Meddis (2001). All fibers were modeled identically, except for stochasticity, as high spontaneous rate (HSR) fibers with thresholds at 0 dB SPL at 1 kHz. The output of the auditory periphery was a stochastic stream of independent spike events in each auditory nerve fiber.

Stage 2: VCN units. These are implemented as modified McGregor cells (MacGregor, 1987) and are fully described in Hewitt and Meddis (1992) and Meddis (2006). Brief computational details and parameters are given in the Appendix. Each unit receives 30 AN fibers all with the same BF.

The saturated chopping rate of the VCN units is determined in the model by the potassium recovery time constant (τGk). This time constant is varied systematically across the array of units in such a way as to produce 30 different chopping rates equally spaced between 60 and 350 spikes/s. These values were chosen to be realistic with respect to physiological observations. The appropriate values of τGk were determined with an empirically derived formula; tau $=\text{rate}^{-1.441}$ based on the pure tone response at 65 dB SPL. Time constants varied between 2.8 ms (50 Hz) and 0.22 ms (350 Hz).

Stage 3: IC units. These are described in full in Hewitt and Meddis (1994) and are implemented here using the same MacGregor algorithm as used for the VCN units and using the parameters given in the Appendix. A single IC unit receives input from 10 VCN units. It is a critical (and speculative) feature of the model that each IC unit receives input only from VCN units with the *same intrinsic chopping rate*. The thresholds of the IC units are set to require coincidental input from many VCN units.

Stage 4 units. These units receive input from 40 IC units (one per BF-channel). All inputs to a single unit have the same rate-MTF as determined by the intrinsic saturated rate of the VCN units feeding the IC unit. It is assumed that each spike input to the stage 4 unit provokes an action potential. Therefore, stage 4 units are not coincidence detectors but simply counters of all the spikes occurring in their feeder units. They are intended purely as an indicator of the across-channel activity in the IC units tuned to a particular periodicity irrespective of BF channel. There are 30 stage 4 units, one for each VCN rate. The output of the model is, therefore, an array of 30 spike counts called the "stage-4 profile." The stage-4 profile rates are based on spike counts across the whole stimulus.

This profile is illustrated in Fig. 2 where it shows the response of the model to a simple harmonic stimulus. As the fundamental frequency of the stimulus rises, the profile shifts to the right. The change in pitch is coded in the change in the overall location of the profile. All profiles are the result of a single presentation of the stimulus. It must be stressed that this profile cannot be read as a pitch-meter that indicates a specific pitch frequency (e.g., 200 Hz). This is not a requirement of models of human pitch perception. The profile reflects the response of the whole system to a pitch-evoking stimulus. All of the values in the profile change when the pitch changes. In this sense, the pitch information is distributed throughout the profile which is used to detect *changes* in pitch as measured in most psychophysical experiments.

The model was evaluated at a refresh rate of 44 100 kHz on a dedicated Appro-4144H 4U Quad Opteron Server, a

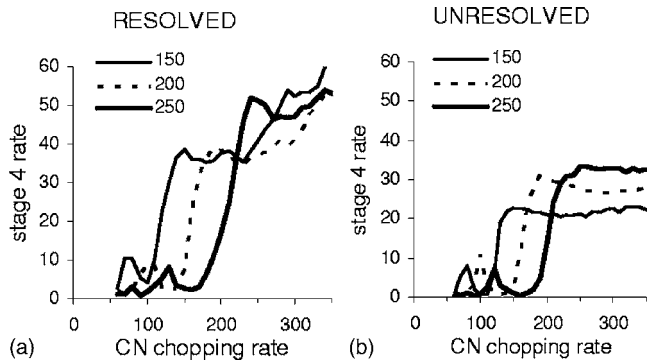

FIG. 2. Stage 4 rate profile for three 500-ms harmonic tones with F0=150, 200, and 250 Hz presented at 70 dB SPL. The *x* axis is the saturated rate of firing (spikes/s) of the VCN units at the base of the processing chain. The *y* axis is the rate of firing (spikes/s) of the stage 4 units. (A) Harmonics 3–8. (B) Harmonics 13–18.

quadruple parallel-processor computer. It was implemented using the Development System for Auditory Modeling (DSAM). The DSAM code is available from the authors at 'http://dsam.org.uk'

III. EVALUATION

The evaluation of the model follows a similar pattern and uses similar stimuli to an earlier evaluation of an autocorrelation model of pitch perception (Meddis and O'Mard, 1997a). The input consists of stimuli that are known from psychophysical studies to have a virtual pitch and whose pitch qualities vary with respect to the stimulus characteristics. The model's response is then compared qualitatively to published psychophysical observations.

A. Pitch of a harmonic tone

Figure 2(A) shows the stage 4 profile to three "missing fundamental" harmonic tones composed of harmonics 3–8 presented at 70 dB SPL for 500 ms. There is no spectral energy in the signals at their fundamental frequencies (F0 =150, 200, and 250 Hz). Figure 2(B) shows the profile for the same F0s where the tone is composed of harmonics 13–18 only. The effect of changing F0 is similar in that the profile shifts to the right as F0 increases. Despite differences in the overall shape, it is clear that the profiles in both figures discriminate easily among the three different pitches. The low harmonics in Fig. 2(A) are resolved by the human auditory periphery while the high harmonics in Fig. 2(B) are not (Plomp, 1964). Both are heard to have a clear pitch and listeners have little difficulty in detecting the changes in pitch despite the difference in peripheral resolvability.

The left to right upward trend in Fig. 2(A) is explained in terms of the intrinsic chopping rates of the different modules. High chopping rates in the VCN units give rise to more activity in those IC units that receive their input. As a consequence, the profile shows a higher stage 4 rate count for shorter intervals. It is significant, however, that the stimuli with unresolved harmonics [Fig. 2(B)] do not show this continued upward slope. The horizontal plateaux to the right of the functions suggests that the stage 4 rate is not reflecting the intrinsic chopping rate of the VCN units. On the contrary, for higher F0 the plateau is also higher. The stage 4 rate is reflecting the frequency of the envelope of the stimulus. In other words, some high-rate choppers are synchronizing to the envelope of the stimulus even though this has a longer period than the intrinsic chopping interval. The plateau is not seen for resolved harmonics because the signals in the individual channels do not have strongly modulated envelopes.

B. Alternating phase

Another difference between resolved and unresolved harmonics can be seen in the way phase affects the perceived pitch. An important characteristic of pitch perception is its insensitivity to the relative phase of the stimulus components among low, resolved harmonics. There is no change in perceived pitch when the phase relationship among the harmonics is altered. However, if the stimulus is composed of a group of high numbered (or "unresolved") harmonics, the pitch can be affected by the relative phases of the components. This is clearly demonstrated if the phases of successive harmonics are alternated (sin, cos, sin, cos, etc.) When this happens, the pitch of the stimulus is normally heard to rise by a whole octave. The pitch of unresolved harmonics in alternating phase reflects the period of the stimulus envelope which doubles when the phase is alternated.

Figure 3 shows the profiles for a harmonic complex when filtered to include either (a) low (resolved) harmonics (125–625 Hz) or (b) high (unresolved) harmonics (3900–5400 Hz). These stimuli are a subset of those used by Carlyon and Shackleton (1994) who found that the perceived pitch of HIGH harmonics reliably increased by an octave when the components were in alternating phase.

Figures 3(A) and 3(C) show the stage 4 profiles for SINE phase tones with F0=125 and 250 Hz. This should be compared with the profiles in Fig. 3(B) where F0 is 125 Hz and the components are in ALTERNATING (sine-cos) phase. The effect of changing the relative phase of the components is different for high and low numbered harmonics. The shape of the 125 Hz profile does not change much for low (resolved) harmonics when the phase is altered. However for high (resolved) harmonics, the shape changes substantially; the profile develops an extra upward slope at a chopping rate of 250 Hz and becomes similar to the stimulus with 250-Hz sine-phase tone. This result is qualitatively consistent with experimental observations of Shackleton and Carlyon.

It is unclear at this stage of the development of the model as to how this effect might be quantitatively assessed. However, a simple comparison of the profiles can be attempted using the mean Euclidean distance ($\sqrt{\Sigma d^2/n}$, where d is the difference between the values at corresponding points and n is the number of pairs of points). This statistic has the values 25 and 27 for *resolved* harmonics when the 125 Hz alternating phase stimulus is compared with 125 Hz and 250 Hz sine phase stimuli, respectively. This is a small difference indicating a preferred pitch of 125 Hz. However, corresponding mean Euclidean distances of 12 and 5 are obtained for *unresolved* harmonics indicating a clear preferred pitch match of 250 Hz for the unresolved 125 Hz alternating phase stimulus.

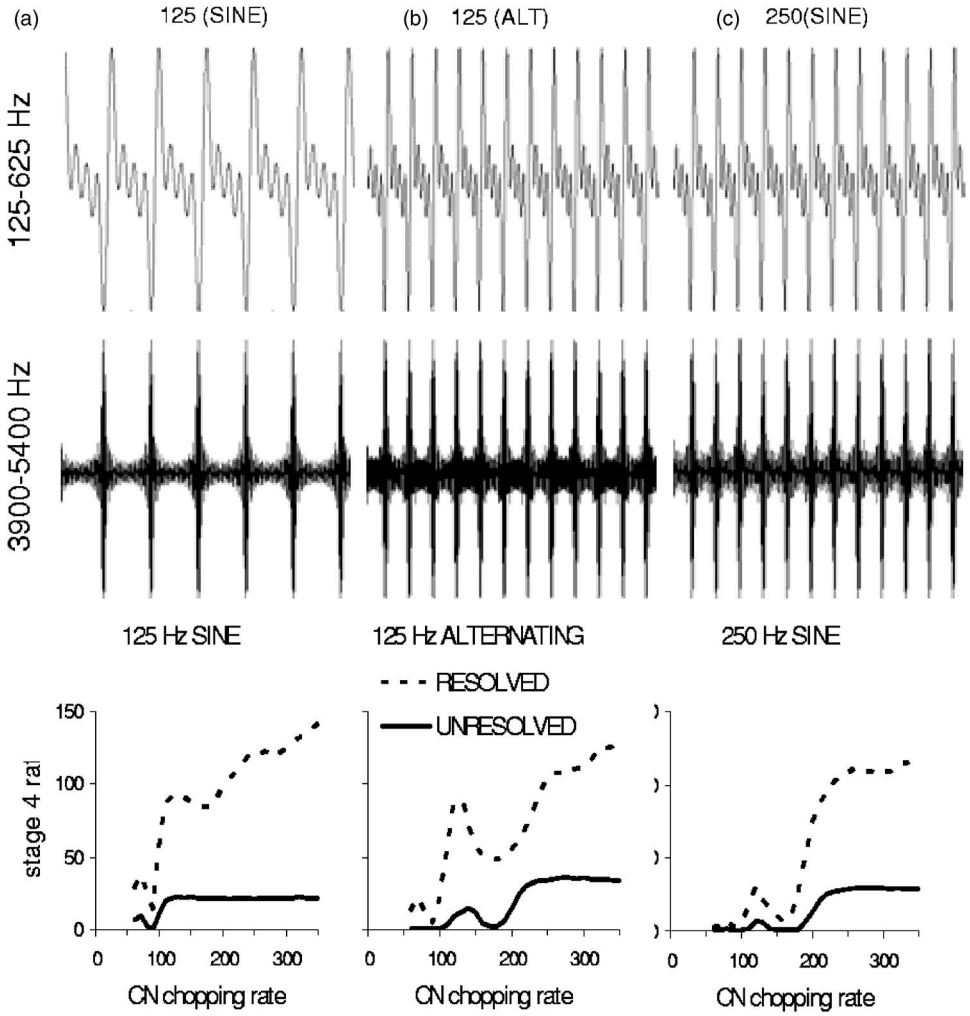

FIG. 3. Stage 4 rate profiles in response to stimuli consisting of low/resolved (125–625 Hz) and high/unresolved harmonics (3900–5400 Hz). (A) F0=125, sine phase. (B) F0=125 Hz alternating phase. (C) F0=250 Hz sine phase. Stimuli were 500 ms duration and presented at 70 dB SPL.

C. Inharmonic tones

De Boer (1956) showed that the pitch of a harmonic complex remained strong when the complex was made inharmonic by shifting the frequency of all components by an equal amount. The heard pitch of the complex shifts by a fraction of the shift of the individual components. This pitch shift is relatively large when the stimulus is composed of low harmonics but small for complexes composed of only high harmonics. For example, Moore and Moore (2003) showed that a complex composed of 3 resolved harmonics would show a pitch shift of 8% when the individual harmonics were all shifted by 24%. On the other hand, complexes of 3 unresolved harmonics showed much less pitch shift. The stimulus consisting of the least resolved (i.e., highest frequency) components showed little or no pitch shift. This was true for F0s of 50, 100, 200, and 400 Hz.

Two extreme examples of their stimuli were employed in the following demonstration which used 70-dB SPL, 500-ms tones consisting of either three resolved harmonics (3, 4, 5) or three unresolved harmonics (13, 14, 15) with F0=200 Hz. Pitch shifts were produced by shifting all component tones by either 0, 24%, or 48% and generating a stage 4 profile for each.

The resulting stage 4 profiles are shown in Fig. 4. The profiles for the *resolved* harmonics change with the shift. Shifting the frequencies of the *unresolved* harmonics [Fig. 4(B)] had little effect. Qualitatively at least, this replicates the results of Moore and Moore at least for their two extreme stimuli. When all harmonics are shifted by the same amount, the envelope of the signal is unchanged because it depends on the spacing between the harmonics which remains constant. The model reflects the unchanged periodicity of the envelope of the stimulus with unresolved harmonics in Fig. 4(B). On the other hand, the model reflects the changing

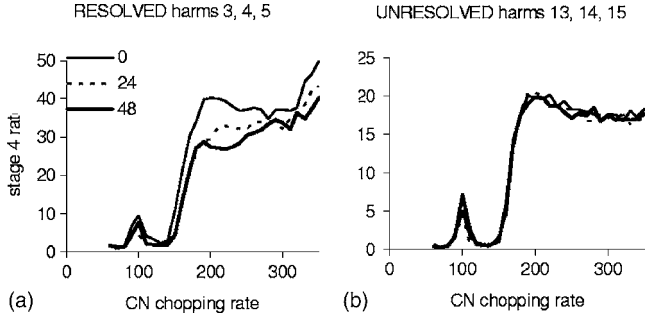

FIG. 4. Stage 4 rate profiles for shifted harmonic stimuli (F0=200 Hz). Shifts applied equally to all harmonics are 0, 24, or 48 Hz. (A) Harmonics 4, 5, and 6 (resolved). (B) Harmonics 13, 14, and 15 (unresolved). Shifting the harmonics has a smaller effect when the harmonics are unresolved.

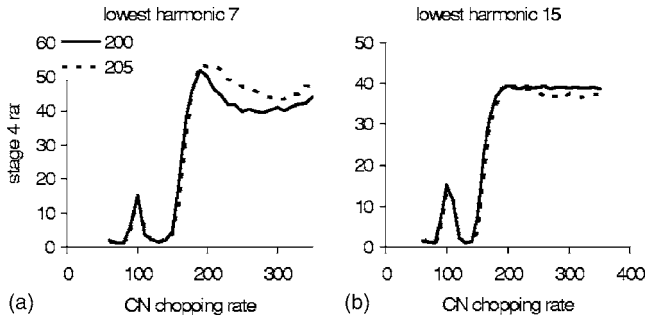

FIG. 5. Effects of pitch differences on the stage 4 rate profile for stimuli consisting of 11 successive harmonics. A shift of 5 Hz (F0=200, 205 Hz) is applied. Stimuli differ in terms of the number of the lowest harmonic in the series. (A) Lowest harmonic=7. (B) Lowest harmonics=15.

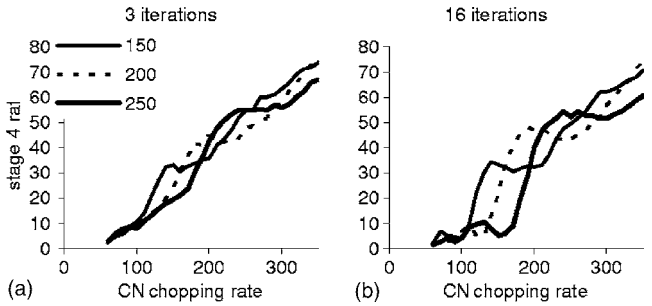

FIG. 6. Stage 4 rate profiles produced by the model in response to iterated rippled noise stimuli with iteration delays corresponding to pitches of 150, 200, and 250 Hz. (A) 3 iterations. (B) 16 iterations.

values of the resolved components when resolved stimuli are used [Fig. 4(A)].

This demonstration contrasts with the alternating phase demonstration in the previous section. The alternating phase effect occurs only when high harmonics are involved. On the other hand, when the pitch change is caused by inharmonic component frequency shifts, the effect is strongest when the shifts are applied to the low (resolved) harmonics.

D. Threshold for pitch difference

Harmonic number is also involved in determining the sensitivity to pitch differences. Houtsma and Smurzynski (1990) showed that the frequency difference threshold for the pitch of an 11 component harmonic complex was greater for high than for low harmonics. The model was therefore tested using tones consisting of either 11 successive low harmonics (lowest=7) or high harmonics (lowest=15), all in sine phase. F0 was 200 Hz and stimuli were presented for 500 ms. In both cases a second stimulus was presented with F0 increased to 205 Hz. A 5-Hz F0 difference was found by Houtsma and Smyrzinski to be close to the pitch difference threshold for stimuli when the lowest harmonic was 13 (see their Fig. 3).

The stage 4 rate profiles for each of these stimuli are given in Fig. 5. The 5-Hz shift in F0 has a greater effect for the stimulus composed of low harmonics [Fig. 5(A)] than for the stimulus consisting of high harmonics [Fig. 5(B)]. This is qualitatively consistent with Houtsma and Smyrzinski's result.

E. Iterated rippled noise

Iterated rippled noise (IRN) is of particular interest in the study of pitch because it produces a clear pitch percept but does not have the pronounced periodic envelope that is typical of harmonic and inharmonic tone complexes. When IRN is created by adding white noise to itself after a delay (d), the perceived pitch is typically matched to a pure tone or harmonic complex whose fundamental frequency is $1/d$. The strength of the pitch percept is also typically proportional to the number of times the delay-and-add process is repeated. The model was evaluated using stimuli constructed using a delays of 6.67, 5, and 4 ms reciprocals and a gain of 1. These stimuli have pitches around 150, 200, and 250 Hz. Figure 6 shows the rate profiles for these three values of IRN delay at two levels of iteration. Figure 6(A) shows only small differences in the profiles for the different delays when only three iterations are used. When 16 iterations are used [Fig. 6(B)] the differences between the profiles are more marked and this is consistent with what is heard.

F. Operation of the model

It is difficult to give a rapid intuitive insight into the operation of the model because of its complexity but the following may be helpful. While sustained chopping units fire regularly, their firing times are not necessarily in phase with one another even when the units have exactly the same chopping rate. However, the units will synchronize their firing to the phase of a pulsating stimulus if the pulse rate is the same as the intrinsic firing rate of the VCN unit. As a result all units with the same intrinsic firing rate will become synchronized with each other because they are synchronized to the same driving source.

An important consequence of this synchrony is that groups of VCN units will send synchronous volleys of spikes towards their target IC unit. The IC unit functions in the model as a coincidence detector. It produces the greatest response when the input from the VCN units is synchronized. This is most likely to occur when the period of the stimulus has some simple numerical relationship to the firing period of the VCN units. This gives the model its sensitivity to periodicity within BF-channels. Figure 7 illustrates the model response to a harmonic tone consisting of harmonics 3–8 of a 200-Hz F0. The IC response is shown for two different τGk values. The IC response across all channels is more vigorous and more consistent for $\tau Gk=0.52$ when the chopping rate ($\approx$200 Hz) is similar to the fundamental (Fig. 7, middle row). When $\tau Gk=0.85$ (chop rate $\approx$150 Hz) the pattern is less coherent across time (Fig. 7 bottom row). The best stimulus to recruit a chopper unit is a stimulus whose period is the same as that of the intrinsic firing of the chopper.

The model is sensitive to the period of a pure tone as well as the period of the envelope of a complex tone. This is important when the harmonics are resolved and the BM response in a single channel is a sinusoidal oscillation. It is also the case that the VCN units will synchronize to resolved low-frequency tones when the frequency of the tone is a whole multiple of the chopping rate of the VCN unit. For

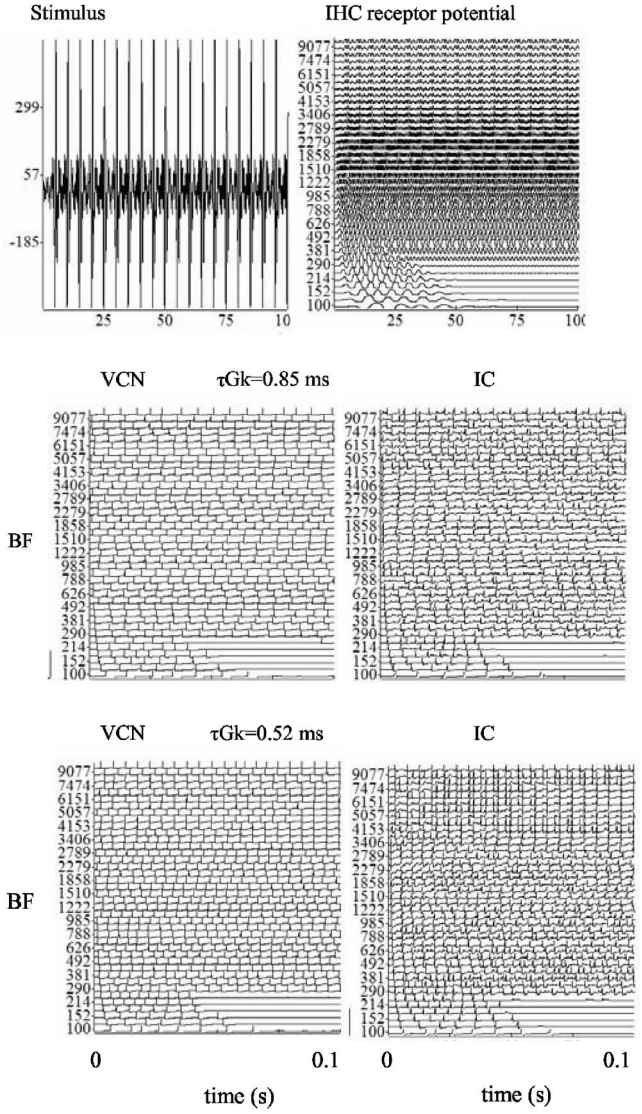

FIG. 7. Illustration of the model response to harmonic tone (F0=200 Hz, harmonics 3–8). The IC response is shown for two different τGk values. The IC response across all channels is more vigorous and more consistent when $\tau Gk=0.52$ (middle row, chop rate ≈200 Hz approx) compared to $\tau Gk=0.85$ (bottom row, chop rate ≈150 Hz).

example, a chopper with a spike rate of 150 spikes/s will synchronize with a 300-Hz pure tone or any multiple of 150 Hz although this effect becomes weaker as the tone frequency rises towards higher multiples of the unit's intrinsic rate. As a consequence, a complex tone consisting of the resolved harmonics of 150 Hz will stimulate choppers firing at a rate of 150 Hz in all of the different BM sites stimulated by the individual harmonic components.

IV. DISCUSSION

The aim of this study was to demonstrate that a model using physiological components could share some of the properties previously shown to characterize cross-channel autocorrelation models. The mathematical model and the new physiological model have a great deal in common. Both use an auditory first stage to represent auditory nerve spike activity. Both extract periodicity information on a within-channel basis. Both models accumulate information across channels to produce a periodicity profile. They differ only in the mechanism used to determine periodicities. In the physiological model, periodicity detection uses VCN units working together with their target IC units. This replaces the delay-and-multiply operations of the autocorrelation method.

The physiological mechanism depends on the synchronization properties of the model VCN chopper units. When the choppers are driven by a stimulus periodicity that coincides with their intrinsic driven firing rate, all the VCN units with the same firing rate will begin to fire in synchrony with the stimulus and with each other. This periodicity may originate either from low frequency pure tones or from modulations of a carrier frequency. It is this synchrony that drives the receiving IC units. This is not, of course, exactly the same process as autocorrelation. But it is similar in the sense that they both systematically extract periodicity information on a temporal basis.

At first sight, the rate profile does not look like an autocorrelation function. It progresses from long to short intervals and has a steep slope across VCN chopping rate. On the other hand, the summary autocorrelation function progresses from short to long lags and is normally presented as an approximately horizontal function across lags. However, Pressnitzer *et al.* (2001) have recommended that autocorrelation functions can give a better representation of some psychophysical results (e.g., lower limit of pitch) when they are weighted so that the contribution of longer time intervals is progressively reduced by a linear weighting function (see their Fig. 7). If their suggestion were applied to summary autocorrelation functions and the function reversed to go from long to short intervals, the parallel would become more visually apparent.

A simplifying assumption in the present model is that all IC units receive input from VCN units with the same intrinsic firing rate. This has recently been questioned by another modeling study showing that more realistic IC MTFs can be obtained using a spread of inputs across different chopping rates and a second converging layer within the IC (Guerin *et al.*, 2006). This surprising result was published too late to influence the study reported here. However, it does suggest that it might be possible to proceed successfully with fewer restrictive assumptions than those implemented above.

It would be premature to claim that the model described above is a complete pitch model. There are more pitch phenomena than those considered here and the new model needs to be tested on a much wider wide range of stimuli. Indeed some stimuli produce a pitch that is claimed not to be predicted by existing autocorrelation models (e.g. Carlyon *et al.*, 2002; Plack and White, 2000). These are matters for further investigation. Nevertheless, this study has demonstrated that a cross-channel autocorrelation model can be simulated, to a first approximation, by a physiological model and is worthy of further consideration.

This report has restricted itself to a qualitative assessment of the model to show that the stage 4 rate profiles demonstrate changes that parallel psychophysical changes. A quantitative study will clearly be necessary. However, this will require the solution of problems that lie beyond the scope of this study. One important problem is that the stage 4

TABLE I. MacGregor point neuron parameters for VCN units.

Dendritic low-pass filer cutoff (Hz)	400
tau$M$, membrane time constant (s)	5×10^{-4}
tauGk, potassium time constant (s)	3.7×10^{-3} to 0.25×10^{-3}
b, increment in Gk (Siemens/s)	0.1
Ek potassium reversal potential (V)	−10
Th0 threshold (mV)	2

TABLE II. MacGregor point neuron parameters for IC units.

Dendritic low-pass filer cutoff (Hz)	4000
tau$M$, membrane time constant (s)	1×10^{-3}
tauGk, potassium time constant (s)	1×10^{-4}
b, increment in Gk (Siemens/s)	0.1
Ek potassium reversal potential (V)	−10
Th0 threshold (mV)	25

profile reflects stimulus level as well as stimulus pitch. As the signal level is increased, the spread of activity across the channels is also increased. More IC units are recruited and the profile shows a higher overall activity count. Pitch perception is largely (but not completely) independent of level and two pitches can be matched even when levels are slightly different. These two variables must be disentangled before a fully quantitative comparison can be attempted.

It is likely that other models of IC functioning might do equally as well (Nelson and Carney, 2004; Langner, 1981) although this has not been tested. In particular, the Nelson and Carney model has been shown to simulate the response of IC units to SAM tones. This property is an important pre-requisite. The Hewitt and Meddis (1992, 1994) models were used only because they were more familiar to the authors. It is possible that any model of IC functioning would work so long as it reproduces rate MTFs as measured physiologically (e.g., Rees and Palmer, 1988; Krishna and Semple, 2000). However, these alternative IC models would need to be adapted to integrate periodicity information across BF channels in an additional layer of neuronal processing.

de Cheveigne (1998) has also developed a physiological model of periodicity extraction at the level of the cochlear nucleus using delay-and-inhibit circuits. This mechanism has been shown to be formally similar to autocorrelation. It is possible that delay-and-inhibit "building blocks" would serve the present purpose equally well although this again has not been tested. However, it remains to be seen whether the delay-and-inhibit idea is physiologically plausible given that it relies on an extensive range of graded inhibitory delays.

There is abundant evidence for VCN units that chop at the rates featured in this study (60–350 spikes/s). However, the physiological plausibility of the new model might itself be questioned in the light of the observations of Krishna and Semple (2000). Their results indicated that the rate MTF functions observed in the IC are more complex than was remarked on in earlier studies. They found not only rate-enhancement but also rate-suppression. Some IC units showed suppression of firing at some modulation frequencies and enhancement at others. Also rate MTFs [Krishna and Semple, 2000, Figs. 3(A), 3(C), and 3(D)] show enhancement peaks at 500, 400, and 100 Hz, respectively, but substantial suppression at lower modulation frequencies. Our IC units show none of these complexities and a more sophisticated model than that presented here should take this into account.

ACKNOWLEDGMENTS

This work was supported by a research grant from the Biotechnology and Biological Sciences Research Council. We thank Susan Shore, Ian Winter, Brian Moore, and an anonymous reviewer who provided helpful comments on the manuscript.

APPENDIX: SUSTAINED CHOPPER MODEL

The VCN unit model is based on MacGregor (1987) point neuron model. The present implementation consists of two stages: input at the dendrites and spike generation at the soma, respectively. The original MacGregor neuron provides for the possibility that the spiking threshold can vary over time but this has been omitted here. This is achieved by setting his parameter c to 0.

Each auditory nerve spike was represented as a 6 mV postsynaptic pulse lasting 50 μs. The dendritic input stage applies a first-order low pass filter (3 dB cutoff at 400 Hz, 0 dB gain) to the AN peri stimulus time histogram (PSTH) to produce a voltage change $I(t)$ at the soma.

The *trans*-membrane potential at the soma, E, is represented as a deviation from resting potential, Er, and tracked using the equation,

$$dE/dt = -E/\tau_m + I(t) + Gk(t)(Ek - E), \tag{A1}$$

where τ_m is the membrane time constant, Ek is the potassium reversal potential (relative to Er) and $Gk(t)$ is the cell potassium conductance. Conductance changes are tracked using

$$dGk = -Gk^* dt/\tau_{Gk} + b^* s, \tag{A2}$$

where τ_{Gk} is the potassium time constant, b is the increase in Gk following an action potential (AP) indicated when $s=1$. An AP is initiated when the membrane potential exceeds a threshold $E(t) > \mathrm{Th0}$. This threshold was fixed throughout. See Table I for parameter values.

The IC neuron used the same equations but some parameters were changed to produce tighter coincidence criteria (see Table II).

Assmann, P. F., and Summerfield, Q. (**1990**). "Modeling the perception of concurrent vowels: Vowels with different fundamental frequencies," J. Acoust. Soc. Am. **88**, 680–796.

Blackburn, C. C., and Sachs, M. B. (**1989**). "Classification of unit types in the anteroventral cochlear nucleus: PST histograms and regularity analysis," J. Neurophysiol. **62**, 1303–1329.

Carlyon, R. P., Wieringen, A., Long, C. J., Deeks, J. M., and Wouters, J. (**2002**). "Temporal pitch mechanisms in acoustic and electric hearing," J. Acoust. Soc. Am. **112**, 621–633.

Carlyon, R. P., and Shackleton, T. M. (**1994**). "Comparing the fundamental frequencies of resolved and unresolved harmonics: Evidence for two pitch mechanisms?" J. Acoust. Soc. Am. **95**, 3541–3554.

De Boer, E. (**1956**). "On the residue in hearing," Ph.D. thesis, University of Amsterdam.

Guérin, A., Le Bouquin Jeannès, R., Bès, J., Faucon, G., and Lorenzi, C. (**2006**). "Evaluation of two computational models of amplitude modulation coding in the inferior colliculus," Hear. Res. **211**, 54–62.

de Cheveigné, A. (**1998**). "Cancellation model of pitch perception," J. Acoust. Soc. Am. **103**, 1261–1271.
Hewitt, M. J., and Meddis, R. (**1992**). "A computer model of a cochlear-nucleus stellate cell: Responses to amplitude-modulated and pure-tone stimuli," J. Acoust. Soc. Am. **91**, 2096–2109.
Hewitt, M. J., and Meddis, R. (**1994**). "A Computer Model of Amplitude-Modulation Sensitivity of Single Units in the Inferior Colliculus," J. Acoust. Soc. Am. **95**, 2145–2159.
Houtsma, A. J. M., and Smurzynski, J. (**1990**). "Pitch identification and discrimination for complex tones with many harmonics," J. Acoust. Soc. Am. **87**, 304–310.
Krishna, B. S., and Semple, M. N. (**2000**). "Auditory temporal processing: Responses to sinusoidally amplitude-modulated tones in the inferior colliculus," J. Neurophysiol. **84**, 255–273.
Langner, G. (**1981**). "Neuronal mechanisms for pitch analysis in the time domain," Exp. Brain Res. **44**, 450–454.
Licklider, J. C. R. (**1951**). "A duplex theory of pitch perception," Experientia **7**, 128–133.
Lopez-Poveda, E. A., and Meddis, R. (**2001**). "A human nonlinear cochlear filterbank," J. Acoust. Soc. Am. **110**, 3107–3118.
Lyon, R. F. (**1984**). "Computational models of neural auditory processing," IEEE ICASSP **84**, 3.
MacGregor, R. J. (**1987**). *Neural and Brain Modeling* (Academic, San Diego).
Meddis, R., and O'Mard, L. P. (**2005**). "A computer model of the auditory nerve response to forward masking stimuli," J. Acoust. Soc. Am. **117**, 3787–3798.
Meddis, R., and O'Mard, L. P. (**1997a**). "A unitary model of pitch perception," J. Acoust. Soc. Am. **102**, 1811–1820.
Meddis, R., and O'Mard, L. P. (**1997b**). "Modeled chop-S and pauser/build-up responses in the cochlear nucleus: Further studies," ARO midwinter meeting, abstract 454.
Meddis, R. (**2006**). "Auditory-nerve first-spike latency and auditory absolute threshold: A computer model," J. Acoust. Soc. Am. **119**, 406–417.
Meddis, R., and Hewitt, M. J. (**1991**). "Virtual pitch and phase-sensitivity studied using a computer model of the auditory periphery: I pitch identification," J. Acoust. Soc. Am. **89**, 2866–2882.
Meddis, R., O'Mard, L. P., and Lopez-Poveda, E. A. (**2001**). "A computational algorithm for computing nonlinear auditory frequency selectivity," J. Acoust. Soc. Am. **109**, 2852–2861.
Meddis, R., and O'Mard, (**1997**). "A unitary theory of pitch perception," J. Acoust. Soc. Am. **102**, 1811–1820.
Moore, G. A., and Moore, B. C. J. (**2003**). "Perception of the low pitch of frequency-shifted complexes," J. Acoust. Soc. Am. **113**, 977–985.
Nelson, P. C., and Carney, L. H. (**2004**). "A phenomenological model of peripheral and central neural responses to amplitude-modulated tones," J. Acoust. Soc. Am. **116**, 2173–2186.
Plack, C. J., and White, L. (**2000**). "Pitch matches between unresolved complex tones differing by a single interpulse interval," J. Acoust. Soc. Am. **108**, 696–705.
Plomp, R. (**1964**). "The ear as a frequency analyzer," J. Acoust. Soc. Am. **36**, 1628–1636.
Pressnitzer, D., Patterson, R. D., and Krumbholz, K. (**2001**). "The lower limit of melodic pitch," J. Acoust. Soc. Am. **109**, 2074–2084.
Rees, A., and Palmer, A. R. (**1988**). "Neuronal responses to amplitude-modulated and pure tone stimuli in the guinea-pig inferior colliculus, and their modification by broadband noise," J. Acoust. Soc. Am. **85**, 1978–1994.
Wiegrebe, L., and Meddis, R. (**2004**). "The representation of periodic sounds in simulated sustained chopper units of the ventral cochlear nucleus," J. Acoust. Soc. Am. **115**, 1207–1218.
Yost, W. A., Hill, R., and Perez-Falcon, T. (**1978**). "Pitch and pitch discrimination of broadband signals with rippled power spectra," J. Acoust. Soc. Am. **63**, 1166–1173.

A test of the Binaural Equal-Loudness-Ratio hypothesis for tones[a)]

Jeremy Marozeau[b)]
Communication Research Laboratory, Department of Speech-Language Pathology and Audiology (106A FR), Institute for Hearing, Speech and Language, Northeastern University, 360 Huntington Avenue, Boston, Massachusetts 02115

Michael Epstein
Auditory Modeling and Processing Laboratory, Department of Speech-Language Pathology and Audiology (106A FR), Communications and Digital Signal Processing Center, ECE Department (440 DA), Institute for Hearing, Speech, and Language, Northeastern University, 360 Huntington Avenue, Boston, Massachusetts 02115

Mary Florentine and Becky Daley
Communication Research Laboratory, Department of Speech-Language Pathology and Audiology (106A FR), Institute for Hearing, Speech and Language, Northeastern University, 360 Huntington Avenue, Boston, Massachusetts 02115

(Received 4 April 2006; revised 19 September 2006; accepted 21 September 2006)

It is well known that a tone presented binaurally is louder than the same tone presented monaurally. It is less clear how this loudness ratio changes as a function of level. The present experiment was designed to directly test the Binaural Equal-Loudness-Ratio hypothesis (BELRH), which states that the loudness ratio between equal-SPL monaural and binaural tones is independent of SPL. If true, the BELRH implies that monaural and binaural loudness functions are parallel when plotted on a log scale. Cross-modality matches between string length and loudness were used to directly measure binaural and monaural loudness functions for nine normal listeners. Stimuli were 1-kHz 200-ms tones ranging in level from 5 dB SL to 100 dB SPL. A two-way ANOVA showed significant effects of level and mode (binaural or monaural) on loudness, but no interaction between the level and mode. Consequently, no significant variations were found in the binaural-to-monaural loudness ratio across the range of levels tested. This finding supports the BELRH. In addition, the present data were found to closely match loudness functions derived from binaural level differences for equal loudness using the model proposed by Whilby *et al.* [J. Acoust. Soc. Am. **119**, 3931–3939 (2006)]. © *2006 Acoustical Society of America.* [DOI: 10.1121/1.2363935]

PACS number(s): 43.66.Cb, 43.66.Pn, 43.66.Ba [AJO] Pages: 3870–3877

I. INTRODUCTION

A tone presented to both ears is perceived as louder than the same tone presented to only one ear (Fletcher and Munson, 1933; Scharf and Fishken, 1970; Marks, 1978). Generally, it is assumed that this ratio is equal to 2 for dichotic tones at the same loudness [for a review, see Marks (1978) and Hellman (1991)], but some studies have suggested a lower ratio (Scharf and Fishken, 1970; Zwicker and Zwicker, 1991; Whilby *et al.*, 2006). The ratio has been assumed to be independent of level, even though it is unclear if this is true (Fletcher and Munson, 1933; see also Fletcher, 1953). This assumption of a constant ratio between the binaural and monaural loudness growth functions is known as the Binaural Equal-Loudness-Ratio hypothesis (BELRH). Whereas Algom *et al.*'s (1989) magnitude estimation of monaural and binaural data lend support to the BELRH for tones, other studies report that the binaural loudness function is steeper than the monaural loudness function for tones (Hellman and Zwislocki, 1963) and for noises (Reynolds and Stevens, 1960), implying a monotonic increase of the ratio as function of level.

Binaural loudness summation can be studied with two different measures: the Binaural Level Difference for Equal Loudness (BLDEL) (Whilby *et al.*, 2006) and the binaural-to-monaural loudness ratio. When the binaural and the monaural loudness functions are presented in the same logarithmic plot, the first measure corresponds to the horizontal distance between the two functions, and the second to the vertical distance. If the BELRH is assumed, then the two functions should be parallel (i.e., the vertical distance is constant). In this case the slope of the loudness function will be proportional to the inverse of the BLDEL. Therefore, it is possible to derive a loudness function directly from the BLDEL data (Fletcher and Munson, 1933; Whilby *et al.*, 2006) using this assumption. On the other hand, without this

[a)]A portion of this work was presented at the Midwinter Meeting of the Association for Research in Otolaryngology [Marozeau *et al.*, "New method for deriving loudness functions from Binaural Level Differences for Equal Loudness" (2006)] and the American Auditory Society Meeting [Marozeau *et al.*, "Testing the Binaural Equal-Loudness-Ratio hypothesis using Cross-modality Matching" (2006)].

[b)]Electronic mail: j.marozeau@neu.edu

 © 2006 Acoustical Society of America

assumption, the BLDEL data alone do not provide any information on the shape of the loudness function. Therefore, in order to test the BELRH, binaural and monaural loudness functions must be measured directly over a large range of levels.

Such direct measurements of loudness functions have been previously performed for tones using magnitude estimation (Hellman and Zwislocki, 1963; Scharf and Fishken, 1970; Marks, 1978; Algom *et al.*, 1989). Unfortunately, this procedure may be susceptible to biases, especially at the extremes of the range (Poulton, 1989), and may not be suitable for the measurement of individual loudness functions (Epstein and Florentine, 2006). Therefore, insufficient data are available for accurately assessing the BELRH over a wide range of levels for pure tones in individual listeners. One of the two purposes of the present experiment is to obtain a reliable set of data that is comprehensive enough to permit testing the BELRH for individual listeners.

Obtaining reliable loudness functions for individual listeners requires proper psychophysical procedures. Given the high variability of magnitude-estimation data for loudness in individuals (Epstein and Florentine, 2006), Epstein and Florentine (2005) employed a cross-modality-matching procedure to measure loudness functions of 5- and 200-ms tones. Such cross-modality-matching procedures have been shown to yield reliable data for both groups and individuals (Teghtsoonian and Teghtsoonian, 1983; Hellman and Meiselman, 1988; 1990; 1993; Hellman, 1999). Epstein and Florentine (2005) used cross-modality matching to test the Equal-Loudness-Ratio hypothesis for duration, which states that the loudness ratio between short and long tones is independent of the level. Their data support this hypothesis, except at low levels. The present experiment uses the same protocol to test the BELRH, except for the type of stimuli (i.e., monaural and binaural tones were used instead of short and long tones) and the inclusion of a sequence of mid-to-high-level tones every five trials. This sequence was introduced to better replicate the conditions present in Whilby *et al.* (2006).

Similar conditions between Whilby *et al.* (2006) and the present study are important because the second purpose of the present experiment is to obtain data that can be used to test the loudness model proposed by Whilby *et al.* (2006). The model was derived from loudness matches between monaural and binaural tones using a wide range of stimulus levels that varied randomly within a session. According to Silva and Florentine (2006), such data may be affected by Induced Loudness Reduction (ILR). This effect occurs when a moderate-level tone is preceded by a louder *inducer* tone presented at the same or a nearby frequency [(Marks, 1994; Mapes-Riordan and Yost, 1999; Arieh and Marks, 2003), for a review see Wagner and Scharf (2006)]. The presence of an inducer tone can result in a decrease of the loudness level of the quieter tone by 10 to 15 phons. The amount of ILR can vary quite widely depending on the level, presentation mode, sequence, and duration of the preceding sounds (Mapes-Riordan and Yost, 1999; Nieder *et al.*, 2003). Because ILR most profoundly affects the perception of sounds at moderate levels, it can change the shape of the loudness function by making the slope shallower in the mid-range. The effects of loud inducer tones are time dependent and can last at least 10 min (Arieh and Marks, 2003; Epstein and Gifford, 2006). In order to reduce potential variability due to the context dependence of ILR, the present experiment was designed to maintain similar ILR-producing conditions for each trial throughout the entire experiment by exposing the listener to mid-to-high level tones at regular intervals. Although this design should reduce variability caused by different sequential contexts, it may also result in shallower slopes in the mid range of the measured loudness functions and smaller binaural-to-monaural loudness ratios than seen by other experimenters who utilize procedures that do not consider the sequentially evoked variability of the effects of ILR.

II. METHOD

A. Stimuli

The stimuli were 1-kHz tones with equivalent rectangular durations of 200 ms. The tones had 6.67-ms raised-cosine rises and falls and 195-ms steady-state portions to ensure that almost all the energy of the tone bursts was contained within the 160-Hz-wide critical band centered at 1 kHz (Scharf and Fishken, 1970; Zwicker and Fastl, 1990). Tones were presented both monaurally and binaurally. In the monaural condition, tones were presented to the ear with the higher threshold. In the binaural condition, tones were presented at approximately the same loudness to each ear. Because the threshold microstructure of the two ears differs, sounds presented at the same SL to each ear are closer in loudness than those presented at the same SPL, at least at low-to-moderate levels (Mauermann *et al.*, 2004). Therefore, an attenuation corresponding to the threshold difference between the two ears was applied to tones sent to the ear with the lower threshold to achieve binaural presentations at the same SL in each ear. The tone levels in the ear with the higher threshold ranged from the first multiple of 5 dB above threshold to 100 dB SPL in 5-dB steps.

Because the level presented to the ear with the lower threshold was always less than or equal to the level presented to the opposite ear, the total energy presented in the binaural condition was always less than or equal to two times the energy presented in the monaural condition. If, instead, tones presented to the higher threshold ear were amplified to match the opposite ear in SL, the total energy in the binaural condition could have exceeded two times the monaural energy. In that case, the loudness summation observed could have been attributed to a simple increase in energy.

B. Apparatus

A PC-compatible computer with a signal processor (TDT AP2) generated the stimuli via a 16-bit D/A converter (TDT DD1) with a 50-kHz sample rate. It also recorded the listeners' responses and executed the adaptive procedure. The output of the D/A converter was attenuated (TDT PA4), low-pass filtered (TDT FT5, $fc=20$ kHz, 135 dB/oct), attenuated again (TDT PA4), and led to a headphone amplifier (TDT HB6), which fed the earphone of the Sony MDR-V6 headset over the ear with the higher threshold. A third attenuator (TDT PA4) was used before the other headphone ampli-

fier and earphone. This setup ensured that the attenuators could control the stimulus level linearly over at least a 120-dB range and the signal was set to the same SL at both ears. For routine calibration, the output of the headphone amplifier was led to an A/D converter (TDT DD1), such that the computer could sample the waveform, calculate its spectrum and rms voltage, and display the results before each block of trials.

C. Procedure

The experiment was divided into two parts: measurements of absolute threshold and cross-modality matches.

1. Absolute thresholds

Absolute thresholds were measured separately for each ear at 1 kHz using a two-interval, two-alternative forced-choice paradigm with feedback. Each trial contained two observation intervals, which were marked by lights and separated by 500 ms. The stimulus was presented in the first or second observation interval with equal *a priori* probability for each interval. The listener's task was to indicate which interval contained the signal by pressing a key on a small computer terminal. One hundred milliseconds after the listener's response, the correct answer was indicated by a 200-ms light. Following the feedback, the next trial began after a 500-ms delay.

Each threshold measurement consisted of three interleaved tracks, each of which ended after five reversals. Reversals occurred when the signal level changed from increasing to decreasing or *vice versa.* On each trial, a track was selected at random from among the tracks that had not yet ended. For each track, the level of the signal was initially set approximately 15 dB above the listener's threshold. It decreased following three consecutive correct responses and increased following one incorrect response, such that the signal converged on the level yielding 79.4% correct responses (Levitt, 1971). The step size was 5 dB until the second reversal, after which it decreased to 2 dB.

The threshold for each track was calculated as the average signal level of the last two reversals and the average of the three tracks was considered the absolute threshold.

2. Cross-modality matching

Listeners were given a virtually unbounded ball of very thin but strong string (embroidery floss), scissors, adhesive tape, and a notebook. Each trial was presented in the middle of a 250-ms visually marked interval. They were asked to cut a piece of string that was as long as the sound was loud. After each presentation, the listeners taped the string segment into a notebook, turned the page, and pressed a button to indicate completion of the response. The next trial began 700 ms after the listener completed the response. In order to reduce any task-related biases, embroidery floss was selected because it is very thin and inelastic and can be cut very short. Listeners were encouraged to cut the string as short or as long as they wanted.

All levels and modes (monaural and binaural) were presented in random order. One block of trials contained three trials in each mode at each level. Two blocks of trials were completed such that six cross-modality matches were made for each level and mode. Each block lasted approximately 40 min and blocks were separated by a 15-min break. On each trial, a new tone level and mode were randomly selected from all other stimuli that had not yet been presented three times and had a level within 30 dB of the level of the previous trial. If no stimuli fulfilled these criteria, but some other stimuli still had been presented fewer than three times, a dummy trial was inserted. The dummy trial had the same mode and a level 30 dB above or below the preceding level, depending on the levels of the stimuli that remained to be presented. Large level differences between trials were avoided in order to prevent startling the listener from a sudden level increase or a missed stimulus from a sudden level decrease. The dummy trials were included in the final analysis.

As described earlier, this experiment was also designed to normalize the influence of ILR on listener responses. In order to achieve this, a random sequence of stimuli without repetition was presented to the listeners every five trials. The sequence was composed of all of the stimuli ranging from 50 to 100 dB SPL in 5-dB steps in both modes. Before each session, six such sequences were presented in a row to ensure that the same amount of ILR would affect all trials. The final cross-modality matches were the geometric means of the string lengths that were cut to match a given level.

D. Listeners

As shown in Table I, nine listeners (six females and three males) participated in this experiment. They ranged in age from 22 to 74 years old with a mean of 32 years. All listeners had audiometric thresholds less than 20 dB HL (ANSI, 2004) at octave frequencies from 250 to 8000 Hz in both ears when measured clinically and medical histories were consistent with normal hearing. The mean absolute threshold difference between the two ears was 3.7 dB at 1 kHz; no listener had a difference greater than 8 dB. Only L3 (the first author) and L5 had previous experience making loudness judgments.

E. Data analysis

Each data point shows the geometric mean of at least six string lengths. The standard deviation was determined from the logarithms of the string lengths. The group mean and standard error were calculated across the individual listeners' geometric means for each mode and level. The resulting data were transformed back into the string-length domain to show the probable range of each individual listener's responses. To compute average matches across listeners, string lengths for each individual were normalized by dividing by the geometric mean of that individual's string lengths for a binaural tone set to 40 dB SPL.

To examine the effects of stimulus variables, a two-way analysis of variance (ANOVA) for repeated measures was performed on the logarithms of the string lengths (level in dB SPL $\times$ presentation mode). The outcome was considered significant when $p \leq 0.05$.

TABLE I. Summary of the individual data (gender, age, thresholds at 1 kHz, and results). ΔL represents the absolute value of the threshold difference between the two ears of each listener. The Bi/Mono ratio is the averaged difference between the binaural and monaural polynomial fits to the data; Monaural exponent and Binaural exponent show the values of the exponents of the fitted power functions for levels above 40 dB SPL.

		Threshold measures in dB HL			Results			
Listener	Gender	Age	Left ear	Right ear	ΔL	Bi/Mono ratio	Monaural exponent	Binaural exponent
L1	F	44	13	7	6	1.24	0.17	0.18
L2	F	24	−4	−1	3	1.3	0.07	0.1
L3	M	30	−4	−4	0	1.4	0.14	0.16
L4	M	25	6	8	2	1.15	0.12	0.14
L5	F	22	3	−2	5	1.38	0.21	0.21
L6	F	74	−4	−9	5	-	-	-
L7	F	28	0	−8	8	1.33	0.15	0.14
L8	M	23	10	8	2	1.28	0.13	0.15
L9	F	22	4	6	2	1.25	0.14	0.15
Average		32	2.6	0.5	3.7	1.29	0.14	0.15

III. RESULTS

The geometric mean of string length is plotted on a log scale as a function of level in Fig. 1 for each individual listener. The full range of string lengths cut was from 0.1 to 36.6 cm with an average of 3.05 cm for the monaural and 4.24 cm for the binaural. The data for individual listeners were generally consistent, as indicated by the small standard deviations and the general monotonicity.

Third-order polynomials were used to estimate the monaural and binaural loudness functions for each listener using a least-squares fit. As is typical of loudness growth functions, there were clear differences among listeners. However, except for two listeners (L6 and L9 at low levels), the binaural fit was always higher than the monaural fit for any given level. This result implies that at an equal level, binaural tones were perceived as louder than monaural tones. Data from L6 in one session were corrupted because she taped the pieces of string on the wrong pages and skipped a page. Therefore, L6's data were not included in the average plot or statistical analysis. The binaural fit for L9 was lower than the monaural fit at low levels. This discrepancy can be attributed to the poor reliability of this listener's responses (i.e., large standard deviations) at those levels. However, except for low levels, the overall shapes of L9's loudness functions seem in agreement with those of the rest of the listeners, so L9's data were included in all subsequent analysis.

For most of the listeners, the cross-modality matching functions for tones were shallower at moderate levels than at low and high levels. They were also nearly parallel, as indicated by the roughly constant vertical distance between the two functions. The thick, solid lines in Fig. 1 show the ratio between the string lengths matched to equal-SPL monaural and binaural tones. Visually, it is approximately independent of SPL for most of the listeners, though some exceptions are apparent.

The mean ratios between the binaural and monaural loudness functions are summarized in Table I. These values ranged from 1.15 to 1.38. The range of ratios measured under very different conditions and found in other studies is about 1.5 to 2.0 (Zwicker and Zwicker, 1991; Marks, 1978).

The relationship between loudness and intensity is classically modeled as a power function of the intensity with an exponent of 0.3 (Stevens, 1955). However, this relationship is more complex than just a straight line on a log scale (Florentine and Epstein, 2006). Near threshold, the relationship between loudness and intensity can be approximated by a power function with an exponent of unity (Zwislocki, 1965; Buus *et al.*, 1998). At moderate levels, the slope of the loudness function is shallower than usually assumed (Florentine *et al.*, 1996), and the function can be locally approximated as a power function with an exponent of 0.2 (Buus and Florentine, 2001). However, in order to compare the present data with classical data in the literature, data from this experiment were fitted with a simple power function for all levels above 40 dB SPL. Table I shows the values of the exponents for individual listeners. These values are lower than the classical power function exponent of 0.3, but consistent with some other studies, as discussed later in Sec. IV A.

The group mean data and standard errors are plotted in Fig. 2. They are plotted in the same manner as Fig. 1, but the Y axis is the normalized string length. The average data show the same general trends as the majority of the individual data. Both loudness functions were shallower at moderate levels than at low and high levels. The thick line showing the binaural-to-monaural loudness ratio is nearly horizontal, indicating that it is approximately independent of SPL. This observation is supported by an ANOVA. The effects of the level and mode are both highly significant ($p<0.0001$), but the interaction between them is not ($p=0.12$), as is expected if the effect of mode is independent of the level. Accordingly, the results of the ANOVA support the BELRH.

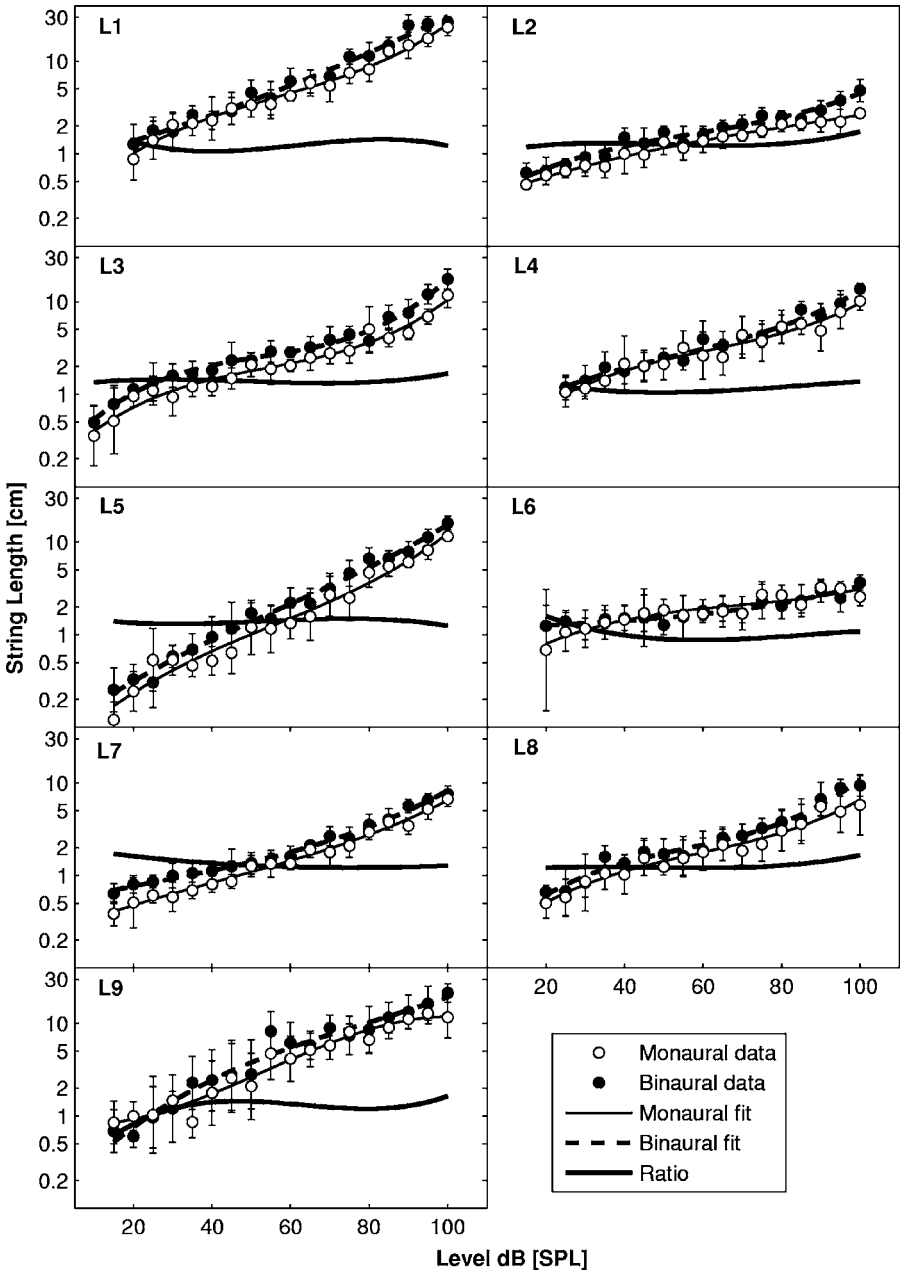

FIG. 1. Individual loudness functions obtained from all nine listeners. The geometric mean of the string length is plotted on a log scale as a function of level. The filled circles show data for the binaural tones and the open circles show the data for the monaural tones. The vertical bars show ± one standard deviation of the log of the string lengths. The solid thin lines show third-order polynomials fitted to the monaural average data and the dashed lines show third-order polynomials fitted to the binaural average data. The thick lines show the ratio of string lengths obtained for equal-SPL monaural and binaural tones as estimated from the polynomials.

IV. DISCUSSION

A. Comparison with data in the literature

1. Comparison with Epstein and Florentine (2005)

The present experimental protocol differed from that of Epstein and Florentine (2005) by only the type of stimuli used (i.e., monaural and binaural tones rather than 5- and 200-ms tones). Both experiments used monaural 200-ms tones at 1 kHz over a wide range of levels. Therefore, it is possible to directly compare the average loudness functions extracted from the two experiments. In order to be consistent with Epstein and Florentine (2005), the group means of the string lengths for monaural tones above 40 dB SPL were approximated with a power function. The value of the exponent fit to the data was 0.14 for both studies, indicating that the average loudness functions in the present experiment grew at nearly the same rate as the loudness functions measured by Epstein and Florentine (2005). Figure 3 shows the average data from the two experiments on the same graph. To facilitate comparison, the two loudness functions were normalized so that the match to the 40 dB SPL tone had a value of one. The two functions are quite similar, showing that the difference in methodology between the two experiments (i.e., the inclusion of a sequence of mid-to-high level tones) did not affect the slope of the loudness function for monaural tones.

2. Comparison with classical loudness experiments

Although the exponent of 0.14 found in the present study is quite similar to that found by Epstein and Florentine (2005), this value and the binaural-to-monaural loudness ratio of 1.29 are smaller than the values found in most prior studies using different experimental paradigms. It may be possible that judgments were influenced by the reluctance of listeners to cut long pieces of string, and the difficulty of

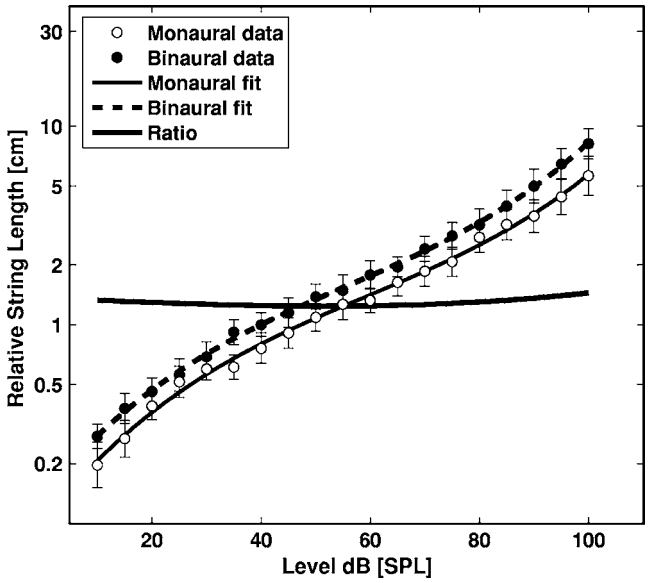

FIG. 2. Average data from the individual listeners (L6 omitted). The third-order polynomials fitted to the data were normalized by dividing each length by the average string length for the 40 dB SPL tone in the binaural condition. The vertical bars show ± one standard error of the log of the string length.

cutting very short pieces of string. Although this possibility cannot be completely ruled out, the data do not seem to show these effects (i.e., no unexpected compression appears at the very low and high levels). Most of these studies used magnitude estimation tasks to obtain loudness slopes and binaural-to-monaural ratios. Work by Treisman and Irwin (1967) indicates that different tasks may involve different perceptual processes and yield different results (i.e., the transformation of the psychological loudness scale to numbers can differ from the transformation to string lengths). Prior experimenters have made corrections to compensate for differences in methodology. For example, Marks (1987) raised each numerical estimate to the power of 0.3/0.2 to adjust the slope of his loudness function to the expected 0.3. If the current data were adjusted to match the slope of a fitted power function to 0.3, then the binaural-to-monaural loudness ratio would become 1.7. This ratio is well within the range of ratios found by other experimenters (Scharf and Fishken, 1970; Zwicker and Zwicker, 1991). This transformation suggests that the slope of the loudness function and the binaural-to-monaural loudness ratio are dependent on each other, and that both are dependent on the methodology.

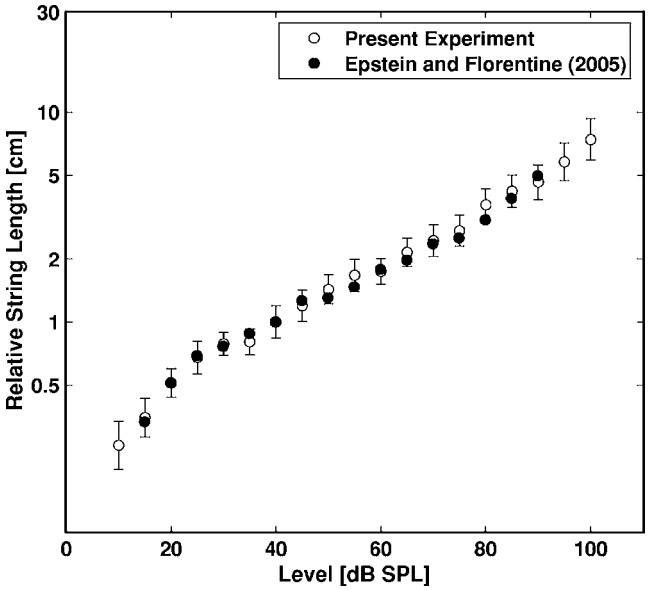

FIG. 3. Comparison between the average loudnesses of the monaural 200-ms tones obtained in the present paper (open circles) and the average loudnesses of the 200-ms tones (filled circles) obtained in Epstein and Florentine (2005).

B. Testing the Binaural Equal-Loudness-Ratio hypothesis

The present data clearly support the BELRH and are consistent with other studies that used magnitude estimation to measure the ratio (Scharf and Fishken, 1970; Marks, 1987; Algom *et al.*, 1989; Zwicker and Zwicker, 1991). Because the binaural and monaural loudness functions maintain a constant vertical distance on a log scale (as shown in Figs. 1 and 2) and the slopes of both functions change at moderate levels, the level difference between binaural and monaural tones required for equal loudness changes as a function of level. According to the present data, the Binaural Level Difference for Equal Loudness (BLDEL) is 5 dB at 20 dB SPL, 8 dB at 66 dB SPL, and 7 dB at 100 dB SPL.

C. The effect of induced loudness reduction in loudness judgments

The sequences of mid-to-high-level tones were introduced to better match the experimental conditions of Whilby *et al.* (2006) because it was hypothesized that Induced Loudness Reduction (ILR) affected those data. ILR is known to affect sounds differently as a function of level (Mapes-Riordan and Yost, 1999; Nieder *et al.*, 2003). Sounds below 40 dB SPL are not susceptible to ILR. Above 40 dB SPL the amount of ILR increases with level, at least up to 70 dB SPL (Scharf *et al.*, 2005). Consequently, loudness functions derived from data that are influenced by ILR are likely to have a shallower slope at moderate levels. The results, shown in Fig. 3, do not indicate that the amount of ILR produced by the sequence of tones used in the present experiment is greater than the amount of ILR seen due to the simple randomization of stimulus levels in Epstein and Florentine (2005). This is consistent with measures showing the rapidity of onset and the duration of the effects of ILR (Epstein and Gifford, 2006).

D. Modeling growth of loudness for individual listeners

Whilby *et al.* (2006) proposed a method for deriving loudness functions from BLDEL data. Briefly, the monaural loudness function, F_m, was defined as

$$F_m(L) = 10^{aL^3+bL^2+cL+d_m}, \quad (1)$$

where L was the level in dB SPL of the monaural stimulus and a, b, c, and d_m were the free parameters of the model. Because of the assumption of BELRH, the binaural loudness

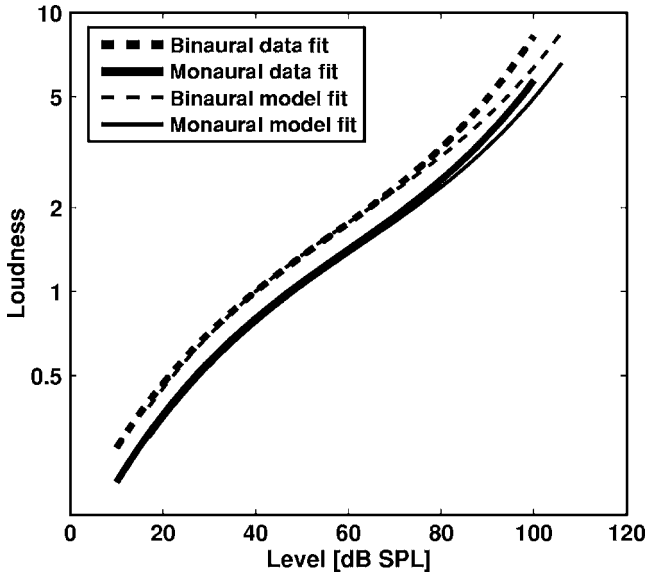

FIG. 4. Comparison between binaural (dashed lines) and monaural (solid lines) loudness functions extracted in the present paper (thick lines) and the loudness functions derived from the model (thin lines) Whilby *et al.* (2006).

function, F_b, *was* assumed to be proportional to F_m:

$$F_b(L) = \gamma F_m(L) = 10^{aL^3+bL^2+cL+d_b}, \tag{2}$$

where γ was the binaural-to-monaural loudness ratio and was equivalent to $10^{d_b-d_m}$. Because d_b can be set to normalize the scale and γ can be set at the value found in the present experiment, only three free parameters need to be determined to derive the two loudness functions. For a fixed selected level of the monaural stimulus, L_m, the BLDEL data from Whilby *et al.* (2006) were used to estimate the level of the binaural stimulus, L_b, at which the loudnesses of the monaural and binaural stimuli were equal. This can be expressed by the following equations:

$$\begin{aligned} &F_b(L_b) = F_m(L_m), \\ &\log\left(F_b(L_b)\right) = \log\left(F_m(L_m)\right), \\ &a(L_m^3 - L_b^3) + b(L_m^2 - L_b^2) + c(L_m - L_b) = d_b - d_m = \log(\gamma). \end{aligned} \tag{3}$$

First, the BLDEL data for each listener were fitted with a third-order polynomial. Then, by using a least-squares fit, the three free parameters (a, b, and c) were selected to minimize the error of the fit between the model and the BLDEL data.

Figure 4 shows the monaural and binaural loudness functions derived using the model compared with the functions extracted from the present experiment. The model-derived functions and the measured functions are quite similar up to 80 dB SPL. Above 80 dB SPL, the functions derived using the model are shallower than the experimentally obtained functions. These results show support for the model, at least up to 80 dB SPL.

This model may be valuable for predicting the shape of a loudness function for a given binaural-to-monaural loudness ratio. Although it does require experimental data, it has some advantages over the direct measurement of a loudness function using a task like magnitude estimation or cross-modality matching. First, the experimental data needed to derive loudness functions using the model are collected using a simple, reliable task; listeners adjust the level of the monaural tone to match the loudness of the binaural tone, and *vice versa*. Unfortunately, the variability of the two types of tasks cannot be easily compared because they involve different scales (i.e., string lengths versus dB SPL). However, it is worth noting that there is less difference between each individual loudness function when derived using the model than when extracted directly in the present experiment. Second, the present cross-modality matching results show great similarity to the data of Epstein and Florentine (2005). This suggests that a task like magnitude estimation or cross-modality matching, which involves the presentation of a wide range of levels in random order, causes the same amount of ILR as a sequence of tones chosen specifically to produce ILR. It is possible to present levels in ascending order to ensure that a listener never hears a high-level tone that precedes a moderate-level tone. Unfortunately, this may introduce another type of bias in which the listener will be able to anticipate the loudness of the upcoming tone presentation. It then seems difficult to design an experiment that can directly extract a loudness function that is unaffected by ILR. However, Silva and Florentine's (2006) data suggest that using an adaptive psychophysical loudness-matching procedure that presents levels in an ascending order can reduce the effects of ILR. Therefore, it may be possible to derive loudness functions that may not be affected by ILR from BLDEL data collected using this type of experimental design.

V. CONCLUSIONS

For most of the individual listeners, binaural and monaural loudness functions are parallel when plotted on a log scale. This result is even more clear in the average data. An ANOVA did not find a significant effect of level on the binaural-to-monaural loudness ratio and, thus, the ratio can be considered to be independent of level. This finding supports the Binaural Equal-Loudness-Ratio hypothesis (BELRH). A comparison of the present experiment with that of Epstein and Florentine (2005) suggests that a simple, random presentation of tones over a wide range of levels, as used in a typical magnitude estimation or cross-modality matching experiment, is sufficient to cause as much Induced Loudness Reduction (ILR) as a sequence of frequently presented mid-to-high level tones. The ratio between the average binaural and monaural loudness functions was found to be lower than the value often reported. This suggests that the binaural loudness summation for tones is less than perfect (i.e., the ratio is less than 2). Finally, the finding of no significant effect of level on the binaural-to-monaural loudness ratio lends support to the model proposed by Whilby *et al.* (2006) for deriving loudness functions from Binaural Level Difference for Equal Loudness (BLDEL) data.

ACKNOWLEDGMENTS

The authors wish to thank Andrew Oxenham, Brian Moore, and an anonymous reviewer for their helpful comments. This research was supported by NIH/NIDCD Grant No. R01DC02241.

Algom, D., Rubin, A., and Cohen-Raz, L. (**1989**). "Binaural and temporal integration of the loudness of tones and noises," Percept. Psychophys. **46**, 155–166.

American National Standards Institute (**2004**). "Specification for Audiometers (ANSI S3.6-2004)," (ANSI, New York).

Arieh, Y., and Marks, L. E. (**2003**). "Time course of loudness recalibration: Implications for loudness enhancement," J. Acoust. Soc. Am. **114**, 1550–1556.

Buus, S., and Florentine, M. (**2001**). "Modifications to the power function for loudness," in *Fechner Day 2001*, edited by E. Sommerfeld, R. Kompass, and T. Lachmann (Pabst, Berlin), 236–241.

Buus, S., Müsch, H., and Florentine, M. (**1998**). "On loudness at threshold," J. Acoust. Soc. Am. **104**, 399–410.

Epstein, M., and Florentine, M. (**2005**). "A test of the Equal-Loudness-Ratio hypothesis using cross-modality matching functions," J. Acoust. Soc. Am. **118**, 907–913.

Epstein, M., and Florentine, M. (**2006**). "Loudness of brief tones measured by magnitude estimation and loudness matching," J. Acoust. Soc. Am. **119**, 1943–1945.

Epstein, M., and Gifford, E. (**2006**). "A potential carry-over effect in the measurement of induced loudness reduction," J. Acoust. Soc. Am. **120**, 305–309.

Fletcher, H. (**1953**). *Speech and Hearing in Communication* (Van Nostrand, New York).

Fletcher, H., and Munson, W. A. (**1933**). "Loudness, its definition, measurement and calculation," J. Acoust. Soc. Am. **5**, 82–108.

Florentine, M., Buus, S., and Poulsen, T. (**1996**). "Temporal integration of loudness as a function of level," J. Acoust. Soc. Am. **99**, 1633–1644.

Florentine, M., and Epstein, M. (**2006**). "To honor Sevens and repeal his law (for the auditory system)," in *Fechner Day 2006*, edited by D. E. Kornbrot, R. M. Msetfi, and A. W. MacRae (St. Albans, England), 37–42.

Hellman, R. (**1991**). "Loudness measurements by magnitude scaling: Implications for intensity coding," in *Ratio Scaling of Psychological Magnitude* edited by S. J. Bolanowski and G. A. Gescheider (Erlbaum, Hillsdale, NJ), pp. 215–227.

Hellman, R. P. (**1999**). "Cross-modality matching: A tool for measuring loudness in sensorineural impairment," Ear Hear. **20**, 193–213.

Hellman, R. P., and Meiselman, C. H. (**1988**). "Prediction of individual loudness exponents from cross-modality matching," J. Speech Hear. Res. **31**, 605–615.

Hellman, R. P., and Meiselman, C. H. (**1990**). "Loudness relations for individuals and groups in normal and impaired hearing," J. Acoust. Soc. Am. **88**, 2596–2606.

Hellman, R. P., and Meiselman, C. H. (**1993**). "Rate of loudness growth for pure tones in normal and impaired hearing," J. Acoust. Soc. Am. **93**, 966–975.

Hellman, R. P., and Zwislocki, J. J. (**1963**). "Monaural loudness function at 1000 cps and interaural summation," J. Acoust. Soc. Am. **35**, 856–865.

Levitt, H. (**1971**). "Transformed up-down methods in psychoacoustics," J. Acoust. Soc. Am. **49**, 467–477.

Mapes-Riordan, D., and Yost, W. A. (**1999**). "Loudness recalibration as a function of level," J. Acoust. Soc. Am. **106**, 3506–3511.

Marks, L. E. (**1978**). "Binaural summation of the loudness of pure tones," J. Acoust. Soc. Am. **64**, 107–113.

Marks, L. E. (**1987**). "Binaural versus monaural loudness: Supersummation of tone partially masked by noise," J. Acoust. Soc. Am. **81**, 122–128.

Marks, L. E. (**1994**). "'Recalibrating' the auditory system: the perception of loudness," J. Exp. Psychol. Hum. Percept. Perform. **20**, 382–396.

Mauermann, M., Long, G. R., and Kollmeier, B., (**2004**). "Fine structure of hearing threshold and loudness perception," **116**, 1066–1080.

Nieder, B., Buus, S., Florentine, M., and Scharf, B. (**2003**). "Interactions between test- and inducer-tone durations in induced loudness reduction," J. Acoust. Soc. Am. **114**, 2846–2855.

Poulton, E. C. (**1989**). *Bias in Quantifying Judgments* (Erlbaum, Hillsdale, NJ).

Reynolds, G. S., and Stevens, S. S. (**1960**). "Binaural summation of loudness," J. Acoust. Soc. Am. **32**, 1337–1344.

Scharf, B., and Fishken, D. (**1970**). "Binaural summation of loudness: reconsidered," J. Exp. Psychol. **86**, 374–379.

Scharf, B., Wagner, E., and Nieder, B. (**2005**). "Induced loudness reduction: A review," J. Acoust. Soc. Am. **117**, 2454.

Silva, I., and Florentine, M. (**2006**). "Effect of adaptive psychophysical procedure on loudness matches," J. Acoust. Soc. Am. **120**, 2124–2131.

Stevens, S. S. (**1955**). "The measurement of loudness," J. Acoust. Soc. Am. **27**, 815–829.

Teghtsoonian, M., and Teghtsoonian, R. (**1983**). "Consistency of individual exponents in cross-modal matching," Percept. Psychophys. **33**, 203–214.

Treisman, M., and Irwin, R. J. (**1967**). "Auditory intensity discriminal scale I. Evidence derived from binaural intensity summation," J. Acoust. Soc. Am. **42**, 586–592.

Wagner, E., and Scharf, B. (**2006**). "Induced loudness reduction as a function of exposure time and signal frequency," J. Acoust. Soc. Am. **119**, 1012–1020.

Whilby, S., Florentine, M., Wagner, E., and Marozeau, J. (**2006**). "Monaural and binaural loudness of 5- and 200-ms tones in normal and impaired hearing," J. Acoust. Soc. Am. **119**, 3931–3939.

Zwicker, E., and Fastl, H. (**1990**). *Psychoacoustics: Facts and Models* (Springer, Berlin).

Zwicker, E., and Zwicker, U. T. (**1991**). "Dependence of binaural loudness summation on interaural level differences, spectral distribution, and temporal distribution," J. Acoust. Soc. Am. **89**, 756–764.

Zwislocki, J. J. (**1965**). "Analysis of some auditory characteristics," in *Handbook of Mathematical Psychology*, edited by R. D. Luce, R. R. Bush, and E. Galanter (Wiley, New York).

Binaural comodulation masking release: Effects of masker interaural correlation

Joseph W. Hall III,[a] Emily Buss, and John H. Grose
Department of Otolaryngology/Head and Neck Surgery, University of North Carolina School of Medicine, Chapel Hill, North Carolina 27599

(Received 18 May 2006; revised 31 August 2006; accepted 1 September 2006)

Binaural detection was examined for a signal presented in a narrow band of noise centered on the on-signal masking band (OSB) or in the presence of flanking noise bands that were random or comodulated with respect to the OSB. The noise had an interaural correlation of 1.0 (No), 0.99 or 0.95. In No noise, random flanking bands worsened $S\pi$ detection and comodulated bands improved $S\pi$ detection for some listeners but had no effect for other listeners. For the 0.99 or 0.95 interaural correlation conditions, random flanking bands were less detrimental to $S\pi$ detection and comodulated flanking bands improved $S\pi$ detection for all listeners. Analyses based on signal detection theory indicated that the improvement in $S\pi$ thresholds obtained with comodulated bands was not compatible with an optimal combination of monaural and binaural cues or to across-frequency analyses of dynamic interaural phase differences. Two accounts consistent with the improvement in $S\pi$ thresholds in comodulated noise were (1) envelope information carried by the flanking bands improves the weighting of binaural cues associated with the signal; (2) the auditory system is sensitive to across-frequency differences in ongoing interaural correlation. © *2006 Acoustical Society of America.* [DOI: 10.1121/1.2357989]

PACS number(s): 43.66.Dc, 43.66.Ba, 43.66.Pn [AK] Pages: 3878–3888

I. INTRODUCTION

The present study concerns binaural hearing and the ability of listeners to use energy at spectral locations removed from the signal frequency to aid signal detection. Before introducing the paradigm used here to investigate this ability, monaural and binaural findings pertinent to the question of across-frequency contributions to hearing performance will be briefly reviewed. Although monaural auditory performance appears to be based upon information in a limited frequency region around the signal in many paradigms (e.g., Fletcher, 1940; Patterson, 1976), other paradigms show that stimulus components well removed from the signal frequency can have important effects on monaural performance. For example, in modulation detection interference (MDI) (Yost and Sheft, 1989; Yost *et al.*, 1989) the presence of amplitude modulation on carriers removed from a target frequency impairs the ability to detect the presence of amplitude modulation at the target frequency. In the phenomenon of comodulation detection differences (CDD), the detection threshold of a narrowband of noise is impeded by the presence of comodulated noise bands at nontarget frequencies (Cohen and Schubert, 1987; McFadden, 1987). Both MDI and CDD results have been attributed, at least in part, to a failure of the auditory system to segregate the information at the target frequency from information present at surrounding frequencies (Cohen and Schubert, 1987; McFadden, 1987; Hall and Grose, 1991; Yost and Sheft, 1994; Oxenham and Dau, 2001; Hall *et al.*, 2006). Energy that is spectrally removed from a target frequency can also *improve* monaural performance in some paradigms. For example, in profile analysis (Green and Kidd, 1983; Green, 1988) the ability to detect intensity differences in a target tone that is roved in level is improved by the addition of further tones having the same rove as the target. In comodulation masking release (CMR) (Hall *et al.*, 1984) the ability to detect a tone in a narrow band of noise is improved by the addition of further noise bands that have the same temporal envelope as the noise band that is centered on the signal. Performance in these paradigms appears to depend, at least in part, on the ability of the auditory system to compare information across frequency channels. In a similar vein, the phenomenon of monaural envelope correlation perception (Richards, 1987) demonstrates the sensitivity of the ear to across-frequency correlation of temporal envelope. In summary, depending upon the nature of the monaural paradigm, energy removed from the target frequency can have little or no effect, a disadvantageous effect, or an advantageous effect on performance (for a review, see Grose *et al.*, 2005).

As with monaural hearing, there is abundant evidence that energy removed from the signal frequency can have a disadvantageous effect on binaural hearing. "Binaural interference" refers to phenomena wherein the ability to process binaural cues at a target frequency is hindered by the presence of binaural energy at other frequencies and has been demonstrated for interaural time discrimination, interaural level discrimination, binaural lateralization, and the masking-level difference (MLD) (e.g., McFadden and Pasanen, 1976; Dye, 1990; Trahiotis and Bernstein, 1990; Bernstein, 1991; Buell and Hafter, 1991; Woods and Colburn, 1992; Stellmack and Dye, 1993; Bernstein and Trahiotis, 1995). In contrast to monaural hearing, there is sparse evidence that energy in frequency regions removed from a

[a]Author to whom correspondence should be addressed; electronic mail: jwh@med.unc.edu

 © 2006 Acoustical Society of America

target frequency can have an advantageous effect on the ability to process interaural difference cues that are present at a target frequency. The term "binaural profile analysis" (Woods *et al.*, 1995) has been used to refer to the ability to base binaural performance on the pattern of binaural difference cues across frequency. Woods *et al.* (1995) examined the ability of listeners to discriminate an interaural time difference (ITD) at a target frequency on the basis of ITD information present across a range of frequencies. In this paradigm, a common ITD for both target and flanking energy was roved from interval to interval, but the target was given an additional ITD in the signal interval. Because of the ITD rove, performance could theoretically be improved by an ability to *compare* ITDs across frequency. Using a target of 500 Hz and flanking frequencies at harmonics of 100 Hz, Woods *et al.* (1995) found that the binaural profile information generally degraded performance. In a version of the paradigm that measured sensitivity to changes in interaural correlation, a spectrally continuous noise band was used and the listener was probed for the ability to discriminate a change in the interaural correlation in a 115-Hz-wide portion of the noise. Here, the presence of flanking profile information either had no effect or it degraded performance.

Hall *et al.* (1988) and Grose *et al.* (1995) used an MLD paradigm to investigate the possible utility of energy removed from the signal frequency in binaural signal detection. In their paradigm, $\mathrm{NoS}\pi$ thresholds were measured for an on-signal masking band (OSB), and for the OSB accompanied by comodulated No noise bands. The results from this paradigm have been mixed, with some listeners showing an improvement in $\mathrm{S}\pi$ threshold when the comodulated flanking bands were added, and other listeners showing similar OSB and comodulated noise thresholds. In this paper, the term "binaural CMR" will be used to refer to facilitation of binaural signal detection resulting from the addition of comodulated flanking bands. In similar MLD paradigms employing comodulated flanking bands, Cohen and Schubert (1991) did not find an improvement in binaural thresholds when comodulated flanking bands were added, whereas Schooneveldt and Moore (1989) did find such an improvement. Schooneveldt and Moore showed data averaged over listeners, so individual differences cannot be examined for those data. The data from the listeners who showed an improvement in $\mathrm{S}\pi$ thresholds when comodulated bands were added provide at least some indication that energy removed from the signal frequency can aid binaural detection. Hall *et al.* (1988) proposed a possible account of this masking release in terms of a version of the equalization/cancellation (EC) model (Durlach, 1963). In this account, the EC residuals resulting from cancellation of the time wave forms of comodulated noise bands are likewise comodulated. The residuals are comodulated because the timing errors are assumed to be small with respect to the pseudo periodicity of the envelope of the narrow bands of noise. Given a comodulation of masking noise residuals, a binaural CMR might arise via an across-frequency analysis of the envelopes at the output of an EC mechanism. For example, the envelopes of the residuals of the flanking bands might be used to give high weight to the envelope minima of the residuals of the OSB, as suggested by Buus (1985) for monaural CMR.

In summary, several findings indicate that energy spectrally removed from the signal frequency can be deleterious to binaural performance but evidence that such energy can be advantageous for binaural performance is limited and is not consistent across listeners or studies. The present study explored binaural CMR further, but with an important difference in the characteristics of the masking noise. In the present paradigm, the interaural correlation of the masking noise was either 1.0 (as in previous binaural CMR studies) or was reduced to either 0.99 or to 0.95. Although such slight reductions in masker interaural correlation result in an increase in the $\mathrm{S}\pi$ threshold, the MLD for such maskers is still substantial (e.g., Robinson and Jeffress, 1963; McFadden, 1968; van der Heijden and Trahiotis, 1998). It was hypothesized that the masking release for an $\mathrm{S}\pi$ signal obtained when comodulated flanking bands are added would be more reliable for maskers having interaural correlation slightly less than 1.0 than for the No maskers investigated in previous experiments. The basis of this hypothesis was related to the relative change in the $\mathrm{NoS}\pi$ OSB threshold that is obtained when *random* narrow bands of No flanking noise are added. Cokely and Hall (1991) previously showed that the OSB $\mathrm{NoS}\pi$ threshold for a narrowband noise is slightly higher (by approximately 3 dB) when random No flanking bands are added. Breebaart *et al.* (2001b) recently proposed an account of this effect in terms of an *across-frequency* integration of binaural information that arises from the spread of excitation associated with the narrowband OSB masker plus signal (van de Par and Kohlrausch, 1999; Breebaart *et al.*, 2001a). In this spectral integration account, it is assumed that (1) $\mathrm{S}\pi$ detection in No noise is limited by internal noise associated with the binaural detection process; (2) the binaural cues associated with the OSB masker plus signal are highly correlated across the different frequency channels to which excitation spreads; and (3) internal noise is uncorrelated across the different frequency channels. Under these assumptions, the detection of an $\mathrm{S}\pi$ signal presented in narrowband noise can benefit from an integration of information across the excitation pattern. By this account, $\mathrm{S}\pi$ thresholds increase when random No flanking bands are present because the flanking bands mask the spread of excitation associated with the OSB masker plus signal, thereby reducing or eliminating the advantage related to across-frequency integration of binaural information (Breebaart *et al.*, 2001a). This account has important implications for the interpretation of the previous results (Hall *et al.*, 1988; Grose *et al.*, 1995) where some listeners showed similar thresholds between the OSB $\mathrm{S}\pi$ condition and the conditions where comodulated flanking bands were added (a result that could easily be interpreted as indicating no binaural CMR). If the hypothesis is correct that flanking bands act to reduce the availability of across-frequency binaural cues arising from the OSB masker plus signal, then the possibility needs to be considered that any *positive* binaural CMR effects associated with the addition of comodulated flanking bands may be offset by *negative* effects that the flanking bands have on the availability of spread of excitation cues. In such a case, it would be incor-

rect to interpret a failure of comodulated flanking bands to improve the $S\pi$ threshold as necessarily indicating a failure to benefit from across-frequency comodulation of masker envelope.

If the above account is correct, then improvements in $S\pi$ thresholds when comodulated flanking bands are added should be more likely to occur in listeners when the masking noise interaural correlation is reduced from 1.0. The hypothesis that across-frequency excitation arising from an OSB masker plus signal can aid binaural detection hinges upon the assumption that the external noise has negligible variability in terms of binaural cues, and that the limits on $S\pi$ signal detection are imposed by internal noise that is independent across the different frequency channels to which the OSB masker-plus-signal excitation spreads (van de Par and Kohlrausch, 1999). Breebaart *et al.* (2001b) proposed that this assumption holds only when the interaural correlation of the masking noise is very close to 1.0. For reduced interaural correlations, the variability in the interaural cues of the masker take on a dominant role in limiting $S\pi$ detection (see also Breebaart and Kohlrausch (2001), where it was shown that $S\pi$ detection in narrowband noise appears to be limited by internal noise for an No masker and the variability of the binaural cues of the masker when the interaural correlation of the masker is reduced). Because the representation of the external noise variability is expected to be correlated across the excitation pattern of the narrowband masker, a detection benefit based upon across-frequency integration is not expected when the OSB has reduced interaural correlation. Thus, for noise having a reduced interaural correlation, comodulated noise bands should result in more reliable improvements in $S\pi$ detection because binaural CMR effects will not be offset by the loss of cues associated with the spectral integration. Experiment 1 examined this possibility. Experiment 2 investigated the possibility that a binaural CMR might arise from a combination of monaural and binaural information, and experiment 3 investigated possible binaural mechanisms that might underlie a binaural CMR.

II. EXPERIMENT 1. So AND $S\pi$ DETECTION IN NARROWBAND NOISE MASKERS AS A FUNCTION OF MASKER INTERAURAL CORRELATION

A. Methods

1. Conditions and rationale

Signal thresholds were estimated for two conditions of signal phase (So, $S\pi$) and three conditions of masker correlation (No, $N_{0.99}$, $N_{0.95}$). The masking conditions involved either a single, 25-Hz-wide noise centered on the signal frequency (500 Hz), or the OSB accompanied by comodulated, 25-Hz-wide flanking bands centered at 300, 400, 600, and 700 Hz. Multi-band conditions where the bands within a single ear were comodulated are referred to as COMOD. It was also the case that the interaural correlation was the same across all of the comodulated noise bands (see Stimuli section, below).

Control conditions were run in which the noise band envelopes were *random* across frequency, but the average interaural correlation for all bands was either 1.0, 0.99, or 0.95. These control conditions were used to help interpret any masking release that occurred for the $S\pi$ conditions for the comodulated noise bands. Specifically, they tested whether a masking release occurred for the $N_{0.99}$ and $N_{0.95}$ maskers when the flanking bands simply had the same *average* interaural correlation as the OSB. Random masker conditions (RAN), where the average interaural correlation was the same across all bands, allowed a test of this possibility. The RAN conditions also allowed examination of the previous finding that random No flanking bands are deleterious to $S\pi$ detection (Cokely and Hall, 1991), and a test of whether this effect also occurs for bands having reduced interaural correlation.

2. Listeners

There were six listeners, four female and two male. Listeners had audiometric thresholds that were better than 20 dB Hearing Level (HL) at octave frequencies from 250 to 8000 Hz. Listener age ranged between 24 and 51 years. All listeners had previous experience in binaural detection tasks.

3. Stimuli

The signal was a 500 Hz pure tone, 200 ms in duration including cosine-squared onset/offset ramps that had a total duration of 51 ms. The tonal signal was generated continuously in RPvds software (TDT) and was gated on and off during the signal interval. Because the tonal signal was free running and because the major factor controlling the timing of signal gating was the response time of the listener, the starting phase of the tonal signal was essentially random. Both level and interaural phase were controlled via multiplication with a scalar adjusted in the inter-stimulus interval.

When only one masker band was present (the OSB condition), it was centered on 500 Hz. When multiple bands were present, they were centered on 300, 400, 500, 600, and 700 Hz. Bands were played continuously at a pressure spectrum level of 50 dB. Maskers were generated in MATLAB prior to each threshold estimation track and were loaded into RPvds for presentation. Bands were generated in the frequency domain by assigning random draws from a normal distribution for the associated real and imaginary components. In the COMOD conditions, a single set of random draws was used to define all five noise bands. In the RAN conditions, different sets of random draws were used to define each band. In conditions where the masker interaural correlation was less than 1.0, two sets of masker bands were generated, set A and set B. Set A was presented to the left ear, and a weighted sum of A and B was presented to the right ear. The relative weights were computed so as to preserve the overall stimulus level and to produce an average interaural correlation of either 0.99 or 0.95. In the COMOD conditions, both A and B were composed of bands that fluctuated coherently across frequency, such that the combination of A and B presented to the right ear likewise fluctuated coherently across frequency. Because the bands centered on each frequency were based upon identical phase and amplitude draws for each ear, the interaural correlations were also identical among bands. In the RAN conditions, both A and B

were composed of independent noise samples. Masker arrays were transformed to the time domain using an inverse fast Fourier transform procedure. Each masker array was 2^{16} points, which, when played at 6.103 kHz, resulted in a 10.7 s sample. This masking stimulus was played continuously and repeated seamlessly.

Although the bands within each ear were comodulated in each of the COMOD conditions, the envelopes of the bands were not perfectly correlated across ears for COMOD conditions with interaural correlation of 0.99 or 0.95. The normalized envelope correlation (van de Par and Kohlrausch, 1995; Bernstein and Trahiotis, 1996) has been shown to be approximately the square root of the waveform correlation when the waveform correlation is close to 1.0 (van de Par and Kohlrausch, 1995). Therefore, the normalized interaural correlation of the envelopes of the noise bands was approximately 0.995 for the $N_{0.99}$ condition and approximately 0.975 for the $N_{0.95}$ condition.

4. Procedures

All testing was performed using a three-interval, three-alternative forced-choice paradigm. The inter-stimulus interval was 300 ms. Listeners indicated responses via a handheld response box. Listening intervals were indicated with light emitting diodes (LEDs), and feedback regarding the interval containing the signal was provided with a flashing LED following each response.

Using an adaptive threshold estimation procedure, the signal level was adjusted in a three-down, one-up track estimating approximately 79.4% correct (Levitt, 1971). Each track started with a signal level estimated to be approximately 5–10 dB above threshold. Initially the signal level was adjusted in steps of 4 dB. This step was reduced to 2 dB after the second track reversal. Each track continued until eight reversals were obtained, and the threshold estimate for a track was taken as the mean signal level at the last six track reversals. Three such estimates were obtained sequentially in each condition, with a fourth estimate taken in cases where results spanned 3 dB or more (a fourth estimate was obtained in approximately 25% of the conditions). For each listener, the order in which conditions were completed was random.

B. Results and discussion

Table I provides numerical values for the individual and the mean masked thresholds, and also shows the derived MLD and CMR values. In order to help portray the overall findings, the mean masked thresholds are also plotted in Fig. 1.

1. So effects

The So data will first be briefly considered. One clear finding was that the So thresholds for the OSB and the RAN conditions were very similar to each other, both within and across all three noise interaural correlation conditions (see Fig. 1 and details in Table I). The fact that the OSB and RAN So thresholds were similar is consistent with the random flanking bands being outside the monaural critical band centered on the signal (e.g., Fletcher, 1940). The fact that the So thresholds did not change with the interaural correlations examined here is consistent with previous results that have shown a very shallow change in So threshold with small reductions in interaural correlation (e.g., Robinson and Jeffress, 1963). In the present data, it was also the case that the So thresholds in the COMOD conditions were highly similar across all three noise correlation conditions, resulting in So CMRs that were also, on average, highly similar in all three noise correlation conditions (see Table I).

2. Binaural CMR

For each of the three conditions, OSB, RAN, and COMOD, MLDs were derived by subtracting the $S\pi$ threshold from the So threshold. The CMRs were derived by subtracting the COMOD threshold from the OSB threshold (separate CMRs were derived for So and $S\pi$ stimulation). As noted in the introduction, the results of previous studies, where the masking noise was perfectly correlated between ears, showed that improvement in the $S\pi$ threshold due to the presence of comodulated No flanking bands is inconsistent. The present No results are in good agreement with this, with L1–L3 showing nearly the same $S\pi$ threshold for the OSB and the COMOD No condition, and L4–L6 showing a threshold improvement of between 2.3 and 4.8 dB in the COMOD No condition. The main goal of the present experiment was to determine whether such a masking release is more consistent under conditions where the noise masker has an interaural correlation that is less than 1.0. The results are in agreement with this idea. For the $N_{0.99}$ and $N_{0.95}$ conditions, all six of the listeners showed better thresholds in the $S\pi$ COMOD condition than the $S\pi$ OSB condition (see trend in Fig. 1 and details in Table I). Across the No, $N_{0.99}$ and $N_{0.95}$ conditions, the average improvement in the $S\pi$ threshold when the comodulated flanking bands were added was 1.7, 3.5, and 6.2 dB, respectively. In the No$S\pi$ conditions, it is possible that masking release effects associated with binaural CMR are offset by a loss of spread of excitation cues. For example, although L1–L3 showed about the same $S\pi$ threshold in the No OSB and the No COMOD conditions, this apparent null effect may be a result of offsetting cues: the loss of a spread of excitation cue offsetting the gain of a binaural CMR cue. Note that an unresolved issue is the extent to which the $S\pi$ COMOD threshold may represent a combination of binaural masking release cues associated with the OSB and monaural masking release cues associated with an across frequency analysis (CMR). This will be considered further in the section below and in the following experiment.

Two results related to the addition of random flanking bands are important from the standpoint of binaural CMR. The first pertains to the relative change in the $S\pi$ OSB threshold when the random flanking noise bands were added. In the No condition, the addition of random flanking bands worsened the $S\pi$ threshold by an average of 3.7 dB. This is similar to the effect reported by Cokely and Hall (1991). As noted in the introduction, this kind of effect has recently been accounted for by Breebaart *et al.* (2001b) in terms of reduced availability of spread of excitation cues related to the OSB masker plus signal. Because this account hinges

TABLE I. Individual and mean thresholds (dB SPL) and derived MLDs and CMRs (dB) for experiment 1. Values in parentheses for mean data are inter-listener standard deviations.

	No			$N_{0.99}$			$N_{0.95}$		
	OSB	RAN	COMOD	OSB	RAN	COMOD	OSB	RAN	COMOD
L1 So	65.0	65.5	51.7	66.1	65.1	52.2	64.5	66.5	50.9
Sπ	43.3	48.2	43.6	47.4	48.2	44.7	54.5	55.5	48.9
MLD	21.7	17.3	8.1	18.7	16.9	7.5	10.0	11.0	2.0
So CMR			13.3			13.9			13.6
Sπ CMR			–0.3			2.7			5.6
L2 So	66.9	67.1	54.2	65.4	67.8	51.4	65.4	67.7	55.2
Sπ	45.8	50.4	46.3	50.6	53.7	46.4	54.1	54.1	49.6
MLD	21.1	16.7	7.9	14.8	14.1	5.0	11.3	13.6	5.6
So CMR			12.7			14.0			10.2
Sπ CMR			–0.5			4.2			4.5
L3 So	66.8	66.8	55.7	66.1	67.2	57.0	66.2	67.6	56.4
Sπ	46.4	53.4	46.1	51.2	53.1	49.1	57.2	56.8	50.8
MLD	20.4	13.4	9.6	14.9	14.1	7.9	9.0	10.8	5.6
So CMR			11.1			9.1			9.8
Sπ CMR			0.3			2.1			6.4
L4 So	68.1	67.2	54.8	67.9	65.8	56.0	67.7	66.1	53.2
Sπ	51.2	50.2	46.4	54.8	51.3	49.1	55.9	56.4	50.8
MLD	16.9	17.0	8.4	13.1	14.5	6.9	11.8	9.7	2.4
So CMR			13.3			11.9			14.5
Sπ CMR			4.8			5.7			5.1
L5 So	68.2	66.9	59.0	67.1	69.7	56.9	68.2	66.7	57.3
Sπ	50.0	52.6	47.7	54.7	55.7	49.4	60.3	59.3	51.4
MLD	18.2	14.3	11.3	12.4	14.0	7.5	7.9	7.4	5.9
So CMR			9.2			10.2			10.9
So CMR			2.3			5.3			8.9
L6 So	66.6	68.0	56.3	67.9	68.5	56.0	67.8	68.8	55.0
Sπ	48.7	53.1	45.5	51.7	55.7	50.2	58.8	57.7	52.3
MLD	17.9	14.9	10.8	16.2	12.8	5.8	9.0	11.1	2.7
So CMR			10.3			11.9			12.8
Sπ CMR			3.2			1.5			6.5
$\bar{X}$ So	66.9	66.9	55.3	66.7	67.3	54.9	66.6	67.2	54.7
	(1.2)	(0.8)	(2.4)	(1.0)	(1.7)	(2.5)	(1.5)	(1.0)	(2.3)
Sπ	47.6	51.3	45.9	51.7	53.0	48.2	56.8	56.6	50.6
	(2.9)	(2.0)	(1.4)	(2.8)	(2.8)	(2.1)	(2.4)	(1.8)	(1.2)
MLD	19.3	15.6	9.4	15.0	14.3	6.7	9.8	10.6	4.1
	(1.9)	(1.6)	(1.4)	(2.3)	(1.3)	(1.1)	(1.4)	(2.0)	(1.8)
So CMR			11.6			11.8			11.9
			(1.7)			(2.0)			(1.9)
Sπ CMR			1.7			3.5			6.2
			(2.1)			(1.7)			(1.5)

upon Sπ signal detection being limited by internal noise that is independent across the excitation pattern, such an effect is not expected when the variability in the binaural cues of the external noise limits Sπ detection performance (for example, with reduced masker interaural correlation). In agreement with this idea, the deleterious effect of the random flanking bands on Sπ detection was smaller or even absent in the conditions where the interaural correlation of the masking noise was reduced from 1.0. For example, in the $N_{0.95}$ condition, the average Sπ threshold in the OSB condition was 56.8 dB sound pressure level (SPL) and the average Sπ threshold in the random condition was 56.6 dB SPL.

The second random flanking band result that is of interest from the standpoint of binaural CMR pertains to the conditions where the noise correlation was less than 1.0. It is of interest whether the addition of noise bands that have the same average correlation as the OSB is sufficient to result in a masking release with respect to the OSB Sπ condition. The results indicate that the addition of the random flanking bands did not lower the Sπ threshold obtained in the OSB condition for either the $N_{0.99}$ or $N_{0.95}$ conditions. Therefore, the presence of flanking bands having the same *average* interaural correlation as the OSB was not a sufficient condition

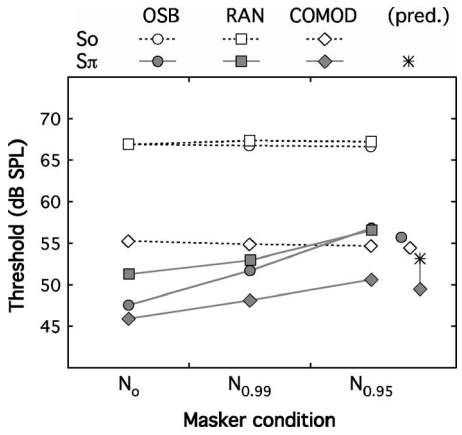

FIG. 1. Mean thresholds for experiments 1 (connected symbols on left for No, $N_{0.99}$ and $N_{0.95}$) and experiment 2 (symbols on far right). The unfilled symbols show So data and the filled symbols show $S\pi$ data. The circles, squares, and diamonds depict OSB, RAN, and COMOD thresholds, respectively. The asterisk represents the threshold predicted from optimal combination of d' from the $N_{0.95}S\pi$ OSB condition and the $N_{0.95}$So COMOD condition (experiment 2).

to obtain an improvement in relation to the $S\pi$ OSB condition.

3. Possible explanation of binaural CMR based upon the combination of an OSB binaural cue and an across-frequency monaural cue

One interpretation of the binaural CMR is that the comodulated flanking bands somehow result in an improvement in the processes underlying binaural signal detection. However, an alternative interpretation is that the masking release due to the comodulated flanking bands arises from the combination of a *binaural* MLD that is associated exclusively with the OSB portion of the stimulus with a *monaural* CMR that is associated with an across-frequency analysis. For the No condition, such a combination would appear to be unlikely. Here, the average $S\pi$ threshold for the OSB condition was 47.6 dB SPL, but the average So threshold associated with the COMOD condition was a considerably higher 55.3 dB SPL. It is therefore unlikely that the cues associated with monaural CMR would still be useful at the low signal-to-noise ratio associated with the OSB $S\pi$ threshold. However, in the $N_{0.99}$ and $N_{0.95}$ conditions, the $S\pi$ OSB thresholds and So COMOD thresholds were of more comparable magnitude, making a potential combination of on-signal binaural information with across-frequency monaural information more feasible. For example, in the $N_{0.95}$ condition, the average $S\pi$ OSB threshold was 56.8 dB and the average So COMOD threshold was 54.7 dB. As can be seen in Fig. 1, the convergence of the $S\pi$ OSB threshold with the So COMOD threshold for the conditions where the interaural correlation of the noise was slightly less than 1.0 was due entirely to the increase in $S\pi$ threshold that occurs with the decrease in the interaural correlation of the masking noise (Robinson and Jeffress, 1963; van der Heijden and Trahiotis, 1998). Experiment 2, below, was performed to test the idea that the binaural CMR for the maskers having interaural correlation slightly less than 1.0 was simply due to a combination of an OSB binaural masking release with across-frequency monaural masking release.

III. EXPERIMENT 2. A TEST OF WHETHER BINAURAL CMR RESULTS FROM THE COMBINATION OF OSB BINAURAL CUES WITH ACROSS-FREQUENCY MONAURAL CUES

As discussed above, although the improved $S\pi$ detection in the presence of comodulated flanking noise bands is compatible with an interpretation that comodulated flanking bands can enhance the binaural detection process, an alternative possibility is that the improvement simply reflects the combination of cues related to an OSB binaural masking release (MLD) and an across-frequency monaural masking release (CMR). The approach used here to differentiate between these alternatives incorporated fixed-block testing conditions from which psychometric functions were estimated for the $S\pi$ OSB and So COMOD conditions. These psychometric functions allowed the level of performance expected from a combination of OSB binaural and across-frequency monaural cues to be modeled (see details in results section, below). This modeled threshold was then compared to a fixed block threshold obtained for the $S\pi$ COMOD condition. Similar modeled and obtained $S\pi$ COMOD thresholds would be consistent with an interpretation that the obtained $S\pi$ COMOD threshold results from a combination of OSB binaural masking release information with across-frequency monaural masking release information. An obtained $S\pi$ COMOD threshold that is better than the modeled threshold would be consistent with an interpretation that the obtained $S\pi$ COMOD threshold reflects an enhancement of the binaural detection mechanism. The fixed-block conditions used the $N_{0.95}$ masking noise. The rationale for using the $N_{0.95}$ masking noise was that experiment 1 indicated that the $S\pi$ OSB threshold and the So COMOD threshold were most similar for this masker. Thus, this masker condition might reasonably be expected to be the one most likely to be associated with a combination of OSB binaural and across-frequency monaural detection cues.

A. Methods

1. Listeners and stimuli

The listeners were the same six individuals who participated in experiment 1. The signal and masker frequencies and the method of stimulus generation were the same as in experiment 1.

2. Procedures

Testing was performed using a fixed-block procedure. The signal level was held constant for each block of 50 trials. The levels chosen for each listener were based on the thresholds for the comparable condition in the adaptive tracks performed in experiment 1. Percent correct was assessed at a minimum of five signal levels, spanning 40%–90%, separated by 2 dB. At least two blocks were run at each signal level, with additional blocks obtained in conditions of high

variability (as assessed informally). Percent correct was assessed for three conditions for all listeners: $N_{0.95}S\pi$/OSB, $N_{0.95}$So/COMOD and $N_{0.95}S\pi$/COMOD.

B. Results and discussion

The construction of psychometric functions and subsequent modeling using signal detection theory (Green and Swets, 1966) enabled us to examine the underlying basis of the COMOD $S\pi$ thresholds. Psychometric functions were fitted to percent correct data for each listener separately. A logistic function was used, defined as:

$$f(x) = [(1/3) + (1 - (1/3))]\left(\frac{1}{1 + e^{-(x-\mu)/\theta}}\right),$$

where μ is the threshold parameter and θ is the slope parameter. These two variables were fitted to data in each of the three stimulus conditions using the FMINS function in MATLAB. Resulting fits were used to test the hypothesis that the $N_{0.95}S\pi$/COMOD condition was based on the combination of OSB binaural cues and across-frequency monaural cues, as independently estimated in the $N_{0.95}S\pi$/OSB and $N_{0.95}$So/COMOD conditions, respectively. The functions fitted to the data in these two conditions were used to predict percent correct for a range of signal levels, 35–60 dB in steps of 0.1 dB. These functions were then transformed into d' and combined optimally using the formula

$$d'_{a\&b} = \sqrt{d'^2_a + d'^2_b},$$

where d'_a and d'_b are the d' values associated with the NoSπ/OSB and NoSo/COMOD conditions, and $d'_{a\&b}$ is the function associated with the optimal combination of independent cues. The assumption of independent cues follows from the assumptions that the NoSo/COMOD threshold reflects the output of a monaural process, whereas the NoSπ/OSB threshold reflects the output of a binaural process. Values of $d'_{a\&b}$ were then converted back into units of percent correct. The signal level most closely approximating 79.4% was identified as the threshold predicted by optimal combination of the binaural and across-frequency cues. If performance in the $N_{0.95}S\pi$/COMOD condition is based on a combination of these cues, then the threshold estimated in this condition should closely match this prediction.

The data fits to the psychometric functions were quite good, accounting for between 90.6% and 99.9% of the variance in each function. Table II shows the threshold associated with the 79.4% point on the psychometric function for all six listeners. For every listener, the actual performance in the COMOD $S\pi$ condition was better than that predicted on the basis of the combination of binaural and monaural cues. On average, the obtained COMOD $S\pi$ threshold was 3.7 dB better than the threshold predicted on the basis of combined binaural and monaural cues. The four symbols on the far right of Fig. 1 summarize the mean results, with the circles, squares, and diamonds depicting the OSB, RAN, and COMOD thresholds, respectively, and the asterisk showing the threshold predicted from optimal combination of d' from the $N_{0.95}S\pi$ OSB condition and the $N_{0.95}$So COMOD condition. A pre-planned paired-samples t test indicated that the difference between the obtained threshold from the $N_{0.95}S\pi$ COMOD condition and the threshold predicted from optimal combination of d' from the $N_{0.95}S\pi$ OSB condition and the $N_{0.95}$So COMOD condition was significant ($t_5 = 6.8$; $p < 0.001$). Whereas this outcome is not consistent with a combination of OSB binaural and across-frequency monaural cues, it is consistent with the idea that the obtained binaural CMR reflects an enhancement in binaural detection.

TABLE II. Individual and mean thresholds (dB SPL) for experiment 2, predicted values of COMOD $S\pi$ thresholds (dB SPL) based upon optimal combination of OSB binaural and across-frequency monaural masking cues, and the Difference (dB) between the predicted and obtained COMOD $S\pi$ thresholds. Values in parentheses show the percent variance accounted for in the fits to the psychometric functions that were used to estimate the obtained thresholds. Values in parentheses for mean data are inter-listener standard deviations.

		Obtained		Predicted	
	OSB $S\pi$	COMOD So	COMOD $S\pi$	COMOD $S\pi$	Difference
L1	52.4	52.4	46.9	50.4	3.5
L2	55.6	53.2	49.9	52.5	2.6
L3	57.4	56.9	51.2	55.5	4.3
L4	55.7	54.8	48.1	53.5	5.4
L5	57.4	54.4	49.3	53.3	4.0
L6	55.9	55.2	51.7	53.9	2.2
$\bar{X}$	55.7	54.5	49.5	53.2	3.7
	(1.8)	(1.6)	(1.8)	(1.7)	(1.2)

IV. EXPERIMENT 3. SPECTRAL PROXIMITY AND THE NATURE OF THE BINAURAL CMR

The final experiment had two aims. The first was to determine the effect of spectrally shifting the flanking bands farther away from the OSB. It is known that monaural CMR effects are larger for relatively close spacing between the OSB and comodulated flanking bands. Whereas this effect may be due to a more potent across-channel effect for relatively proximal bands, it could also reflect a within-channel contribution related to beating between the OSB and flanking bands (Schooneveldt and Moore, 1987). It was of interest to determine whether increasing the spectral separation between the OSB and flanking bands would result in a different pattern of binaural CMR results.

The second aim of the experiment was to explore further the nature of mechanisms underlying the binaural CMR. One goal was to investigate the possible importance of the dynamic binaural difference cues associated with maskers having interaural correlations less than 1.0. One way to conceptualize the deleterious effect of reducing the interaural correlation of the masker on $S\pi$ detection is in terms of the change that the $S\pi$ signal introduces in the ongoing interaural differences of the masking noise. For an No masking noise (interaural correlation of 1.0), there are no interaural differences for the masker alone stimulus, but interaural differences are introduced when the $S\pi$ signal is presented. For a masker with an interaural correlation of less than 1.0, however, ongoing interaural differences exist in the stimulus even for the masker alone. In this case, the listener must be

able to differentiate the interaural differences inherent in the noise masker from the interaural differences resulting from the addition of the $S\pi$ signal. The comodulated flanking noise bands used in the present experiments could potentially aid in this differentiation. For example, when flanking noise bands introduce dynamic interaural differences that are identical to those of the noise band centered on the signal, the flanking bands can potentially be used as templates or covariates that could help distinguish the ongoing interaural differences of the noise from the interaural differences introduced by the signal. Provided that the listener is sensitive to the coherence of the dynamic binaural difference cues across frequency, then one possible cue for detection would be a discrepancy in the pattern of interaural cues across frequency. This issue was investigated in the present experiment by comparing performance in two comodulated noise conditions where the interaural correlation of the noise was 0.95, specifically examining the possible role of dynamic interaural phase cues. One condition was like that used in experiments 1 and 2, where the amplitudes and phases of the spectral components constituting each narrowband of noise were exactly the same within each ear. This meant that the dynamic interaural phase differences arising from the reduced interaural correlation were also the same across all bands. The second condition was similar, in that all bands within each ear were comodulated with one another. However, the individual Fourier components composing the OSB (for both ears) were modified: component phase and magnitude were assigned to sequential frequency bins in reverse order and component phase was multiplied by −1. As such, the magnitude spectrum was rotated around the spectral center of the stimulus, forming a "mirror image" of the nonrotated stimulus. Richards (1988) used this technique to examine the possible role of spectral cues in monaural envelope correlation perception. In a CMR experiment, Buss *et al.* (1998) found that the CMR was approximately the same whether the OSB was generated with the same magnitude spectrum as the comodulated bands or the magnitude spectrum of the OSB was rotated. When considering the effect of this mirror image manipulation on the $N_{0.95}$ stimulus in terms of its envelope and fine structure, the envelope is not changed but the fine structure is altered. The change in fine structure results in an ongoing pattern of interaural phase differences that is out of phase between the OSB and flanking bands (see Fig. 2). If the binaural CMR depends upon the dynamic interaural phase differences of the masker being the same across frequency, elimination of the binaural CMR would be expected for the "spectral mirror" manipulation. The previous negative "binaural profile analysis" findings of Woods *et al.* (1995) suggest that the ability to follow dynamic interaural phase differences is likely to be poor, and therefore that the spectral mirror manipulation might have little or no effect on the binaural CMR. However, the stimuli used by Woods *et al.* were different in several ways from those used here: in their experiment probing sensitivity to across-frequency differences in interaural phase, pure tones having nondynamic interaural phase differences were employed; in their experiment probing sensitivity to across-frequency differences in interaural correlation of noise, spectrally continuous stimuli were used. It is possible that the present approach, involving multiple narrowband noises having coherent, dynamically changing interaural phases changes would result in across-frequency interaural phase cues that were more salient. A finding of little effect on the binaural CMR in the spectral mirror condition would be consistent with an interpretation that the crucial stimulus characteristic underlying binaural CMR is envelope comodulation.

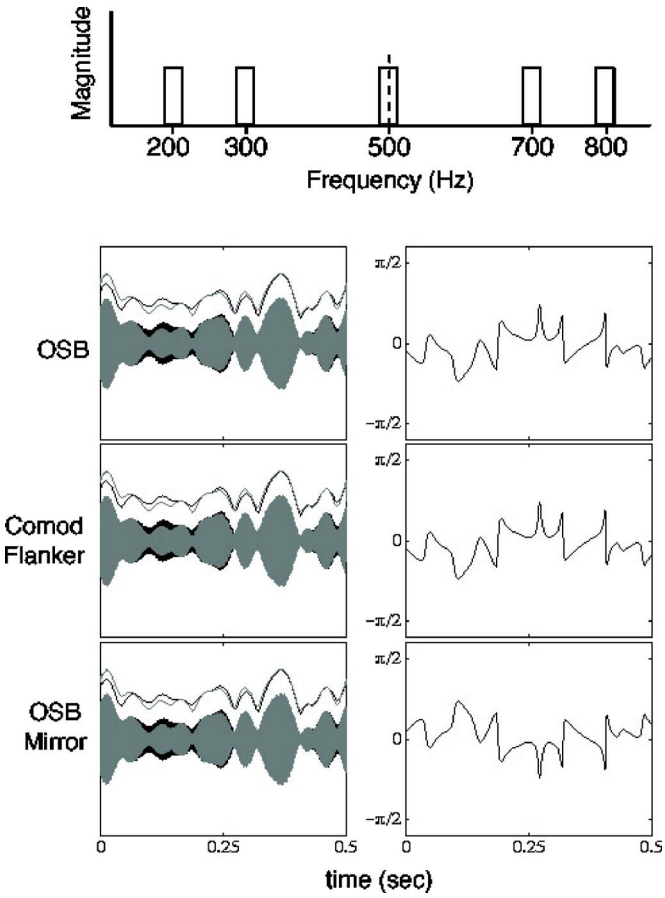

FIG. 2. The top panel shows a schematic of the noise bands used in conditions of experiment 3. The left-hand lower panels show time domain samples of representative noise stimuli having interaural correlation of 0.95. The left and right ear stimuli are overlaid, with the left ear shown in gray, and the right ear shown in black. The envelopes of the left and right ear stimuli are depicted above the time domain samples. The "OSB" and "Comod Flanker" panels can be compared to depict the relation between the OSB and a flanking band for the COMOD condition. The "OSB Mirror" and "Comod Flanker" panels can be compared to depict the relation between the OSB and a flanking band for the COMOD MIRROR condition. The right-hand lower panels show interaural phase as a function of time. The figure shows that although the interaural phase functions are in-phase for the COMOD conditions (compare "OSB" and "Comod Flanker"), they are out of phase for the COMOD MIRROR conditions (compare "OSB Mirror" and "Comod Flanker").

A. Methods

Five of the listeners from experiments 1 and 2 participated (listener L4 from the previous experiments did not participate). The stimuli were generated in the same way as in experiment 1 and 2, using the same stimulus parameters, with two exceptions. One exception was that psychometric function data for the OSB condition were not retaken, as the

TABLE III. Individual and mean thresholds (dB SPL) for experiment 3, predicted values of COMOD and COMOD MIRROR $S\pi$ thresholds (dB SPL) based upon optimal combination of OSB binaural and across-frequency monaural masking cues, and the Difference (dB) between the predicted and obtained COMOD $S\pi$ thresholds. Values in parentheses for mean data are inter-listener standard deviations.

		Obtained	Predicted		
		So	$S\pi$	$S\pi$	Difference
L1	COMOD	53.5	49.1	51.2	2.1
	MIRROR	54.0	50.4	51.3	0.9
L2	COMOD	55.1	49.8	53.6	3.8
	MIRROR	57.1	51.9	53.9	2.0
L3	COMOD	58.8	52.5	56.4	3.9
	MIRROR	59.0	53.6	56.3	2.7
L5	COMOD	54.8	50.4	54.0	3.6
	MIRROR	56.8	52.4	55.0	2.6
L6	COMOD	56.0	51.5	54.4	2.9
	MIRROR	58.6	53.3	55.1	1.8
$\bar{X}$	COMOD	55.6	50.7	53.9	3.2
		(2.0)	(1.3)	(1.9)	(0.8)
	MIRROR	57.1	52.3	54.3	2.0
		(2.0)	(1.2)	(1.9)	(0.7)

OSB data were available from experiment 2. The second exception was that the flanking bands were moved away from the OSB: whereas the center frequency of the OSB remained at 500 Hz, the two lower bands were now centered on 200 and 300 Hz and the two higher bands were now centered on 700 and 800 Hz. Percent correct was measured for a range of levels in the $N_{0.95}$So/COMOD and $N_{0.95}S\pi$/COMOD conditions using the same fixed-block testing procedures that were used in experiment 2. In the comodulated noise conditions, thresholds were obtained both for conditions where the noise was comodulated as in experiments 1 and 2 (COMOD) and for conditions where the spectral mirror manipulation was performed on the OSB (COMOD MIRROR).

B. Results and discussion

The data obtained from the psychometric functions were used in the same way as in experiment 2 to model the thresholds expected from optimal combination of binaural OSB and monaural across-frequency signal detection cues. The $S\pi$ thresholds for the COMOD condition were modeled from the psychometric functions that were fitted to the $N_{0.95}S\pi$ OSB data and the $N_{0.95}$So COMOD data. The $S\pi$ thresholds for the COMOD MIRROR condition were modeled from the psychometric functions that were fitted to the $N_{0.95}S\pi$ OSB data and the $N_{0.95}$So COMOD MIRROR data. Table III shows results from the data fits for the five listeners. The pattern of results was similar to that obtained in experiment 2. The function fits were again quite good, with the percent of variance accounted for ranging between 90.1% and 99.9%. For every listener, the actual performance in the COMOD and COMOD MIRROR $S\pi$ condition was again better than that predicted on the basis of the optimal combination of binaural and monaural cues. Pre-planned t tests indicated that the differences between predicted and obtained thresholds were significant both for the COMOD ($t_4=9.4$; $p=0.001$) and the COMOD MIRROR ($t_4=5.9$; $p=0.004$) conditions. These outcomes were again inconsistent with an interpretation that performance in these conditions results from an optimal combination of OSB binaural and across-frequency monaural cues. A finding of note was that the $S\pi$ threshold in the COMOD conditions was significantly better, by an average of 1.6 dB (see Table III), than that in the COMOD MIRROR conditions ($t_4=7.4$; $p=0.002$). One possible interpretation of this finding is that dynamic binaural phase differences contribute to binaural CMR and that the change in the across-frequency differences in these cues in the COMOD MIRROR condition reduces the binaural CMR. Even if this interpretation is correct, the finding that a significant binaural CMR occurs in the COMOD MIRROR condition indicates that across-frequency equivalence of dynamic binaural phase differences is not a necessary condition for a binaural CMR. Furthermore, it is not clear that the reduction of the binaural CMR in the COMOD MIRROR condition is binaural in origin, as there was a similar reduction in CMR in the So data. That is, the So threshold in comodulated noise was about 1.5 dB smaller on average in the COMOD MIRROR condition than the COMOD condition (see Table III). The source of this small effect is not clear.

Comparison of the present results to those of experiment 2 reveals that moving the flanking bands farther away from the OSB did not have a large effect on the obtained So and $S\pi$ thresholds. For example, in the closer spectral spacing used in experiment 2, the average $N_{0.95}$So COMOD threshold was 54.5 dB SPL, compared to an average $N_{0.95}$So COMOD threshold of 55.6 dB SPL in the present experiment. In experiment 2, the average $N_{0.95}S\pi$ COMOD threshold was 49.5 dB SPL, compared to an average $N_{0.95}S\pi$ COMOD threshold of 50.7 dB SPL in the present experiment. These results suggest that within-channel cues probably did not play a large role in the results of the COMOD conditions of experiment 2.

V. GENERAL DISCUSSION

One of the main findings of the present study was that although the masking release for an $S\pi$ signal was increased in only three of six listeners when comodulated No flanking bands were added to an No OSB, an increase in masking release occurred for all six listeners when comodulated flanking bands were added in the $N_{0.99}$ and $N_{0.95}$ conditions. One parsimonious interpretation of this consistent increase in masking release would involve the combination of a binaural OSB masking release cue with an across-frequency, monaural masking release cue. However, the analyses of the psychometric functions derived from the fixed block conditions did not support this interpretation.

The spectral mirror conditions were helpful in probing the nature of the processes that are likely to give rise to the binaural CMR. The results of these conditions indicated that a mechanism based upon the across-frequency analysis of dynamic binaural phase differences was not likely to form the basis of binaural CMR. This interpretation is consistent with previous "binaural profile analysis" results which indi-

cated poor sensitivity to across-frequency cues based upon binaural interaural time differences (Woods *et al.*, 1995).

A qualitative account of binaural CMR that is consistent with the present results is suggested by recent studies that have indicated that the $S\pi$ thresholds for tones presented in narrowband noise are determined largely by information coincident with masker envelope minima (Grose and Hall, 1998; Hall *et al.*, 1998; Buss *et al.*, 2003), where the binaural difference cues are the largest (Buss *et al.*, 2003). Because narrow bands of noise have prominent envelope fluctuations, the magnitude of the binaural difference cues associated with a signal will vary considerably as a function of time. Acute binaural signal detection for such stimuli may therefore depend upon a selective weighting of temporal epochs characterized by relatively high signal-to-noise ratios. This is similar to the idea proposed by Buus to account for monaural CMR (Buus, 1985). A factor that will limit the ability of the auditory system to identify such epochs is the presumed internal noise associated with the relevant binaural difference cues. A qualitative account of binaural CMR is that comodulated flanking bands provide information that can reduce the effect of such noise. Specifically, the envelopes of the comodulated flanking bands may be used to weight the binaural cues at the signal frequency such that relatively high weight is given to the temporal epochs associated with the masker envelope minima, and therefore the largest binaural difference cues. The envelope cues might arise either from the monaural representations of the flanking band temporal envelopes or, as noted in the introduction, from the envelopes available at the outputs of an EC process (Durlach, 1963).

Another qualitative account that is consistent with the binaural CMRs found for noise interaural correlations of 0.99 and 0.95 is that listeners can benefit from across-frequency comparisons of the ongoing interaural correlation. For example, consider a mechanism that monitors the interaural correlation at the outputs of sliding binaural temporal windows associated with different frequency channels. For both the COMOD and COMOD MIRROR cases, the interaural correlations at the outputs of the temporal windows would be the same across the frequency channels, except when the $S\pi$ signal was present. Note that this strategy would not be effective in the 0.99 and 0.95 interaural correlation RAN conditions of experiment 1 due to the fact that the interaural correlations of the noise would not be exactly the same when measured over finite temporal epochs (only the long-term average interaural correlation would be the same). Although this account is consistent with the results from the RAN, COMOD, and COMOD MIRROR 0.99 and 0.95 interaural correlation conditions, it does not appear to be consistent with the data from the No RAN condition. In the No RAN condition, the outputs of binaural temporal windows would be expected to indicate near perfect interaural correlation across frequency, except when the $S\pi$ signal was present. Whereas the across-frequency difference in interaural correlation resulting from signal presentation might be expected to aid detection in this case, the presence of the random No flanking bands actually led to a reduction in sensitivity to the $S\pi$ signal in relation to the OSB base line threshold (see Table I). One possibility is that any positive effect in terms of an across-frequency comparison of interaural correlation is more than offset by a loss of spread of excitation cues related to the OSB (Breebaart *et al.*, 2001b). It is therefore difficult to rule out the possibility that such a mechanism contributed to binaural masking release in conditions where the interaural noise correlation was less than 1.0.

VI. CONCLUSIONS

(1) Previous and present data indicated that the improvement in the threshold of an $S\pi$ signal when comodulated flanking bands are added to an OSB does not occur consistently across listeners when the masking noise has an interaural correlation of 1.0. The results of the present study showed that this masking release effect was consistent, occurring in all six of the listeners tested, when the interaural correlation was slightly less than 1.0. The present findings are consistent with an interpretation that binaural CMR may sometimes appear to be absent in No masking noise because of a separate factor related to the integration of binaural information resulting from spread of excitation associated with the OSB+signal. Whereas the addition of comodulated flanking bands provides information that can contribute to a binaural CMR, the bands may also mask binaural information that arises from spread of excitation associated with the OSB+signal.

(2) When flanking bands with random envelopes were added to an OSB, the $S\pi$ threshold increased when the noise was No, but this effect of random flanking bands was reduced or absent when the interaural correlation of the masking noise was reduced to 0.99 or 0.95.

(3) The results of fixed-block testing and associated psychometric functions were not consistent with an interpretation that the binaural CMR is a result of the combination of OSB binaural and across-frequency monaural masking release cues.

(4) The results of spectral mirror conditions indicated that across-frequency coherence of dynamic interaural phase differences is not a necessary condition for a binaural CMR.

(5) A qualitative account of binaural CMR that is consistent with the results obtained here is that the envelope minima associated with the comodulated flanking bands may be used by the auditory system to give relatively high weight to the temporal epochs associated with the largest binaural difference cues. The binaural masking release obtained in the $N_{0.99}$ and $N_{0.95}$ conditions is also consistent with an account based upon an across-frequency analysis of dynamic interaural correlation.

ACKNOWLEDGMENTS

This work was supported by NIH, RO1 DC00397. We thank Madhu B. Dev and Heidi Reklis for assistance in running subjects and technical support. We thank Armin Kohlrausch and three anonymous reviewers for many insightful comments that aided clarity and interpretation.

Bernstein, L. R. (**1991**). "Spectral interference in a binaural detection task," J. Acoust. Soc. Am. **89**, 1306–1313.
Bernstein, L. R., and Trahiotis, C. (**1995**). "Binaural interference effects measured with masking-level difference and with ITD- and IID-discrimination paradigms," J. Acoust. Soc. Am. **98**, 155–163.
Bernstein, L. R., and Trahiotis, C. (**1996**). "On the use of the normalized correlation as an index of interaural envelope correlation," J. Acoust. Soc. Am. **100**, 1754–1763.
Breebaart, J., and Kohlrausch, A. (**2001**). "The influence of interaural stimulus uncertainty on binaural signal detection," J. Acoust. Soc. Am. **109**, 331–345.
Breebaart, J., van de Par, S., and Kohlrausch, A. (**2001a**). "Binaural processing model based on contralateral inhibition. I. Model structure," J. Acoust. Soc. Am. **110**, 1074–1088.
Breebaart, J., van de Par, S., and Kohlrausch, A. (**2001b**). "Binaural processing model based on contralateral inhibition. II. Dependence on spectral parameters," J. Acoust. Soc. Am. **110**, 1089–1104.
Buell, T., and Hafter, E. (**1991**). "Combination of binaural information across frequency bands," J. Acoust. Soc. Am. **90**, 1894–1901.
Buss, E., Hall, J. W., and Grose, J. H. (**1998**). "Change in envelope beats as a possible cue in comodulation masking release (CMR)," J. Acoust. Soc. Am. **104**, 1592–1597.
Buss, E., Hall, J. W., and Grose, J. H. (**2003**). "The masking level difference for signals placed in masker envelope minima and maxima," J. Acoust. Soc. Am. **114**, 1557–1564.
Buus, S. (**1985**). "Release from masking caused by envelope fluctuations," J. Acoust. Soc. Am. **78**, 1958–1965.
Cohen, M. F., and Schubert, E. D. (**1987**). "The effect of cross-spectrum correlation on the detectability of a noise band," J. Acoust. Soc. Am. **81**, 721–723.
Cohen, M. F., and Schubert, E. D. (**1991**). "Comodulation masking release and the masking-level difference," J. Acoust. Soc. Am. **89**, 3007–3008.
Cokely, J. A., and Hall, J. W. (**1991**). "Frequency resolution for diotic and dichotic listening conditions compared using the bandlimiting measure and a modified bandlimiting measure," J. Acoust. Soc. Am. **89**, 1331–1340.
Durlach, N. I. (**1963**). "Equalization and cancellation theory of binaural masking-level differences," J. Acoust. Soc. Am. **35**, 1206–1218.
Dye, R. (**1990**). "The combination of interaural information across frequencies: Laterlization on the basis of interaural delay," J. Acoust. Soc. Am. **88**, 2159–2170.
Fletcher, H. (**1940**). "Auditory patterns," Rev. Mod. Phys. **12**, 47–65.
Green, D. M. (**1988**). *Profile Analysis* (Oxford University Press, Oxford).
Green, D. M., and Kidd, G., Jr. (**1983**). "Further studies of auditory profile analysis," J. Acoust. Soc. Am. **73**, 1260–1265.
Green, D. M., and Swets, J. A. (**1966**). *Signal Detection Theory and Psychophysics* (Wiley, New York).
Grose, J. H., Hall, J. W., and Buss, E. (**2005**). "Across-channel spectral processing," in *Auditory Spectral Processing*, edited by M. S. Malmierca and D. R. F. Irvine (Elsevier, Amsterdam), pp. 88–119.
Grose, J. H., and Hall, J. W., III (**1998**). "Masker fluctuation and the masking-level difference," J. Acoust. Soc. Am. **103**, 2590–2594.
Grose, J. H., Hall, J. W., and Mendoza, L. (**1995**). "Developmental effects in complex sound processing," in *10th International Symposium on Hearing*, edited by G. A. Manley, G. M. Klump, C. Koppl, H. Fastl, and H. Oekinghaus (World Scientific, Singapore), pp. 97–104.
Hall, J. W., Buss, E., and Grose, J. H. (**2006**). "Comodulation detection differences for fixed-frequency and roved-frequency maskers," J. Acoust. Soc. Am. **119**, 1021–1028.
Hall, J. W., Cokely, J., and Grose, J. H. (**1988**). "Signal detection for combined monaural and binaural masking release," J. Acoust. Soc. Am. **83**, 1839–1845.
Hall, J. W., and Grose, J. H. (**1991**). "Some effects of auditory grouping factors on modulation detection interference (MDI)," J. Acoust. Soc. Am. **90**, 3028–3036.
Hall, J. W., Grose, J. H., and Hartmann, W. M. (**1998**). "The masking-level difference in low-noise noise," J. Acoust. Soc. Am. **103**, 2573–2577.
Hall, J. W., Haggard, M. P., and Fernandes, M. A. (**1984**). "Detection in noise by spectro-temporal pattern analysis," J. Acoust. Soc. Am. **76**, 50–56.
Levitt, H. (**1971**). "Transformed up-down methods in psychoacoustics," J. Acoust. Soc. Am. **49**, 467–477.
McFadden, D. (**1968**). "Masking level differences determined with and without interaural disparities in masker intensity," J. Acoust. Soc. Am. **44**, 212–223.
McFadden, D. (**1987**). "Comodulation detection differences using noise-band signals," J. Acoust. Soc. Am. **81**, 1519–1527.
McFadden, D., and Pasanen, E. G. (**1976**). "Lateralization at high frequencies based on interaural time differences," J. Acoust. Soc. Am. **59**, 634–639.
Oxenham, A. J., and Dau, T. (**2001**). "Modulation detection interference: Effects of concurrent and sequential streaming," J. Acoust. Soc. Am. **110**, 402–408.
Patterson, R. D. (**1976**). "Auditory filter shapes derived with noise stimuli," J. Acoust. Soc. Am. **59**, 640–654.
Richards, V. M. (**1987**). "Monaural envelope correlation perception," J. Acoust. Soc. Am. **82**, 1621–1630.
Richards, V. M. (**1988**). "Components of monaural envelope correlation perception," Hear. Res. **35**, 47–58.
Robinson, D. E., and Jeffress, L. A. (**1963**). "Effect of varying the interaural noise correlation on the detectability of tonal signals," J. Acoust. Soc. Am. **35**, 1947–1952.
Schooneveldt, G. P., and Moore, B. C. J. (**1987**). "Comodulation masking release (CMR): Effects of signal frequency, flanking band frequency, masker bandwidth, flanking band level, and monotic vs dichotic presentation flanking bands," J. Acoust. Soc. Am. **82**, 1944–1956.
Schooneveldt, G. P., and Moore, B. C. J. (**1989**). "Comodulation masking release (CMR) for various monaural and binaural combinations of the signal, on-frequency, and flanking bands," J. Acoust. Soc. Am. **85**, 262–272.
Stellmack, M. A., and Dye, R. H. (**1993**). "The combination of interaural information across frequencies: The effects of number and spacing of components, onset asynchrony, and harmonicity," J. Acoust. Soc. Am. **93**, 2933–2947.
Trahiotis, C., and Bernstein, L. R. (**1990**). "Detectability of interaural delays over select spectral regions: Effects of flanking noise," J. Acoust. Soc. Am. **87**, 810–813.
van de Par, S., and Kohlrausch, A. (**1995**). "Analytical expressions for the envelope correlation of certain narrow-band stimuli," J. Acoust. Soc. Am. **98**, 3157–3169.
van de Par, S., and Kohlrausch, A. (**1999**). "Dependence of binaural masking level differences on center frequency, masker bandwidth, and interaural parameters," J. Acoust. Soc. Am. **106**, 1940–1947.
van der Heijden, M., and Trahiotis, C. (**1998**). "Binaural detection as a function of interaural correlation and bandwidth of masking noise: Implications for estimates of spectral resolution," J. Acoust. Soc. Am. **103**, 1609–1614.
Woods, W., Brughera, A., and Colburn, H. (**1995**). "Binaural profile analysis: On the comparison of interaural time difference and interaural correlation across frequency," J. Acoust. Soc. Am. **97**, 3280.
Woods, W. S., and Colburn, H. S. (**1992**). "Test of a model of auditory object formation using intensity and interaural time difference discrimination," J. Acoust. Soc. Am. **91**, 2894–2902.
Yost, W. A., and Sheft, S. (**1989**). "Across-critical-band processing of amplitude-modulated tones," J. Acoust. Soc. Am. **85**, 848–857.
Yost, W. A., and Sheft, S. (**1994**). "Modulation detection interference: Across-frequency processing and auditory grouping," Hear. Res. **79**, 48–58.
Yost, W. A., Sheft, S., and Opie, J. (**1989**). "Modulation interference in detection and discrimination of amplitude modulation," J. Acoust. Soc. Am. **86**, 2138–2147.

Electromotile hearing: Acoustic tones mask psychophysical response to high-frequency electrical stimulation of intact guinea pig cochleae[a)]

Colleen G. Le Prell,[b)] Kohei Kawamoto,[c)] Yehoash Raphael, and David F. Dolan
Kresge Hearing Research Institute, 1301 East Ann Street, Ann Arbor, Michigan 48109-0506

(Received 5 January 2006; revised 7 September 2006; accepted 11 September 2006)

When sinusoidal electric stimulation is applied to the intact cochlea, a frequency-specific acoustic emission can be recorded in the ear canal. Acoustic emissions are produced by basilar membrane motion, and have been used to suggest a corresponding acoustic sensation termed "electromotile hearing." Electromotile hearing has been specifically attributed to electric stimulation of outer hair cells in the intact organ of Corti. To determine the nature of the auditory perception produced by electric stimulation of a cochlea with intact outer hair cells, guinea pigs were tested in a psychophysical task. First, subjects were trained to report detection of sinusoidal acoustic stimuli and dynamic range was assessed using response latency. Subjects were then implanted with a ball electrode placed into scala tympani. Following the surgical implant procedure, subjects were transferred to a task in which acoustic signals were replaced by sinusoidal electric stimulation, and dynamic range was assessed again. Finally, the ability of acoustic pure-tone stimuli to mask the detection of the electric signals was assessed. Based on the masking effects, it is concluded that sinusoidal electric stimulation of the intact cochlea results in perception of a tonal (rather than a broadband or noisy) sound at a frequency of 8 kHz or above. © *2006 Acoustical Society of America.* [DOI: 10.1121/1.2359238]

PACS number(s): 43.66.Dc, 43.66.Gf, 43.64.Tk, 43.66.Ts [WPS] Pages: 3889–3900

I. INTRODUCTION

That electrical stimulation produces mechanical changes in the organ of Corti was first described in the pioneering studies of Moxon (1971), who reported frequency-specific and place-specific excitation, as well as acoustic masking of electrically evoked responses. We have more recently learned that sinusoidal electric stimulation of the intact cochlea produces a frequency-specific otoacoustic emission (OAE) in the ear canal (see Hubbard and Mountain, 1983; Xue *et al.*, 1993; Nuttall and Ren, 1995; Ren and Nuttall, 1995; Nakajima *et al.*, 1998; Nuttall *et al.*, 2001; Reyes *et al.*, 2001). These electrically evoked OAEs (EEOAEs) originate near the site of the stimulating electrode (Xue *et al.*, 1993; Ren and Nuttall, 1995; Nuttall *et al.*, 2001), where local electrical stimulation induces motile response (contractile motion, or elongation) of outer hair cells (OHCs). That OHCs change their shape in response to electric stimulation has been shown in cells dissociated from the organ of Corti (Brownell *et al.*, 1985; Kachar *et al.*, 1986; Ashmore, 1987) and cells maintained in a half-turn cochlear explant (Reuter and Zenner, 1990). In vivo electric stimulation of the cochlea results in OHC motile response leading to basilar membrane motion (Nuttall and Dolan, 1993; Nuttall and Ren, 1995; Xue *et al.*, 1995).

The basilar membrane motion observed by Nuttall and colleagues (Nuttall and Dolan, 1993; Nuttall and Ren, 1995) as well as Xue *et al.* (1995) presumably travels in the reverse direction as OAEs are produced by reverse traveling motion of the basilar membrane (i.e., projecting toward the stapes, through the middle ear, and into the ear canal, see Kemp, 1978; Shera and Guinan, 1999). However, electrically evoked motile response of OHCs also produces forward traveling motion of the basilar membrane (i.e., towards the helicotrema, see Nuttall and Dolan, 1993). Forward traveling waves generated in response to acoustic stimulation result in inner hair cell (IHC) neurotransmitter release, neural activity, and a corresponding auditory sensation (hearing). When a forward traveling wave is generated by electrical stimulation of OHCs, we presume that there is a corresponding auditory percept, which has been proposed as "electromotile hearing" (Nuttall and Ren, 1995). This work uses psychophysical measures of function to directly test the hypothesis that there is an auditory percept associated with electomotile hearing, and further, that the percept is a tonal acoustic sensation. We evaluated EEOAE generation in our subjects to confirm that electrical stimulation produced an EEOAE (which is a less invasive measure of traveling wave generation in the cochlea than direct measurement of basilar membrane motion) in addition to the acoustic sensation assessed with psychophysical procedures. The EEOAE data presented here provide key evidence that the electrical stimulation paradigm we used generated EEOAE responses that were equivalent to those in other studies.

[a)]Portions of this research were presented at the Midwinter Meetings of the Association for Research in Otolaryngology (for abstracts, see Le Prell *et al.*, 2000; 2002).

[b)]Author to whom correspondence should be addressed; electronic mail: colleeng@umich.edu
[c)]Current mailing address: Department of Otolaryngology, Kansai Medical University, 10-15 Fumizonocho, Moriguchi, Osaka, 570-8506, Japan.

II. MATERIALS AND METHODS

A. Subjects

Adult male guinea pigs (Elm Hill Breeding Labs, Chelmsford, MA) were individually housed with free access to water. All subjects weighed between 300-350 g at the onset of the experimental procedures. Weight gain was continual until subjects achieved a weight of at least 900 g. Food intake (Purina Guinea Pig Chow) was then moderately restricted. Animal treatment met or exceeded all guidelines in the Guide for the Care and Use of Laboratory Animals (National Research Council, 1996). The University Committee on the Use and Care of Animals of the University of Michigan approved all animal care and testing protocols.

B. Electrophysiology

Anesthetized guinea pigs (40 mg/kg ketamine, 10 mg/kg xylazine) were initially screened for normal acoustic sensitivity using the auditory brainstem response (ABR) to acoustic stimulation as in Le Prell *et al.* (2004). Threshold sensitivity was determined for 2, 4, 8 and 16 kHz tone bursts (10 m duration, 0.5 m rise/fall time) using Tucker Davis Technology (TDT) SigGen software (version 3.2) and TDT System II hardware. Sound-evoked brainstem responses were amplified (10 000x) and filtered (300–3000 Hz), digitized, then averaged (1020 presentations) and viewed using TDT BIOSIG (version 3.2) software. Thresholds were determined based on visual inspection of the ABR wave forms.

ABR thresholds were typically reevaluated within two weeks of surgically implanting an electrode inside the cochlea (see below). In addition, the electrical impedance (sinusoid wave form at 1000 Hz) of the electrode was measured and electrically evoked auditory brainstem responses (eABR) were assessed using the method described by Hall (1990; see also Mitchell *et al.*, 1997). Intra-cochlear stimulation used to evoke an eABR consisted of alternating-polarity monophasic current pulses (50 μs duration) presented at a rate of 50 pulses/s. Up to 2048 responses were collected for analysis at stimulus currents ranging from 30 to 1000 μA. Responses were amplified (gain=10 000), filtered (0.1 Hz–3 kHz) and digitized using in-house software. The eABR response was used to verify implant function, and to measure direct electrical stimulation of spiral ganglion cells based on visual inspection of wave P3 (see Black *et al.*, 1983; Tykocinski *et al.*, 1995; Shepherd and Javel, 1997). P3 was defined as the third peak of the eABR wave form occurring approximately 1.5 ms poststimulus onset (see Hall, 1990).

C. Psychophysical training and testing procedures

Subjects were tested five days per week for approximately 45 minutes using procedures described in Le Prell *et al.* (2004). In brief, subjects were trained using positive reinforcement procedures to depress a floor-mounted plastic response button at the start of each test trial; trial onset was signaled by illumination of a cue light mounted in front of the response button. The subjects' task was to depress the response button during a quiet listening interval (1–9 s), and release the button upon detecting an acoustic stimulus. Subjects received 45 mg Dustless Precision Pellets (Bio-Serv) for correct release responses. Acoustic stimuli were presented during 75% of the total trials ("test trials"). During the remaining trials, release rates in the absence of the test signal ("catch trials") were monitored. Subjects were punished with a brief (7 s) time out for any incorrect releases. During a time out, the cue light was extinguished and a new trial could not be initiated.

Acoustic tones were presented free field via an overhead piezoelectric speaker (Motorola model KSN 1001A) mounted approximately 8 in. above head level. Tone levels were calibrated using a microphone (Bruel & Kjaer type 4136 microphone, type 2619 preamp, type 2804 power supply) placed in the test cage in a position that approximated that of the guinea pig head when the animal was located in the front of the test cage and pressing the response button. Tone frequency (5.6, 8, 11.2, and 16 kHz) and level were varied based on the method of constant stimuli (see Niemiec and Moody, 1995). At each frequency, subjects were presented with one subthreshold stimulus and 4–5 suprathreshold stimuli. All tones were spaced in 10 dB increments, and each combination of frequency and stimulus level was presented up to 20 times. Threshold was defined as the stimulation level that produced a median response latency of 1500 ms; all thresholds were determined based on linear interpolation between adjacent data points. Response latency provides a sensitive measure of sensory effects, and equal latencies presumably indicate equal sensory effects (for review, see Moody, 1970). Thresholds assigned based on response latency closely corresponded to those assigned using the criteria of 50% correct detection responses.

A reinforcement contingency required subjects to respond rapidly after tone onset to receive a food pellet. This contingency was set such that reinforcement was delivered for approximately 90% of the correct releases, which ensured consistent responses throughout the test session. If the guinea pig did not respond within the trial duration (2550 ms, beginning at tone onset), a response latency of 2550 ms was recorded, the tone was turned off, and a new trial was initiated. If subjects did not complete at least ten test trials at each stimulus level (with no more than 20% catch trial releases), the daily latency data were discarded.

Initial operant response training required approximately 3 months; base line latency functions were established within another 2–3 months. Included in the latter 2–3 months was the introduction of the reinforcement contingency, and adjustment of this contingency as animals developed more rapid and more reliable response functions. Once reliable latency functions were established for acoustic stimulation, a ball electrode was implanted into the cochlea (see below). After establishing postimplant acoustic base lines, subjects were transferred to an electric stimulus detection task. We used a battery-powered optically isolated ac-coupled linear transconductance amplifier to deliver a constant current stimulus to the intra-cochlear electrode. Sinusoidal electric stimulation frequencies were the same as the acoustic test frequencies. Current level ranged from 1 to 374 μA rms (i.e.,

0–52 dB re 1 μA). Because the dynamic range between threshold and the maximum comfortable stimulation level is narrow for electric stimulation, electric stimulation levels were varied in 5 dB increments.

Electric response functions were first established in a quiet sound booth. Background acoustic stimuli were then added to assess masking efficiency. Order of testing for background tones was randomly selected. Only one background tone was presented during any given test session; multiple electrical sinusoids were tested with each of the acoustic maskers. Each background tone was tested for at least five days to verify that all response functions were stable. Based on the frequency-specific pattern of masking we observed, not all background tones were assessed with all test frequencies (i.e., having identified acoustic background tones with no masking effect for a given electrical target, acoustic tones with frequencies further from the electrical target were not probed for masking effects). Background tone level was approximately 10 dB above threshold; thresholds for background tone frequencies were estimated based on linear interpolation of thresholds determined using ABR (2, 4, 8, and 16 kHz) and psychophysical (5.6, 8, 11.2, and 16 kHz) procedures.

Initial subjects were tested with 5.6, 8 and 11.2 kHz electrical target signals and acoustic background tones spaced in approximately 500 Hz increments (5.6, 7, 7.5, 8, 8.5, 9, 10, 10.5, 11.2, 12, 12.3 kHz); completion of testing all desired combinations of acoustic backgrounds and electrical targets and periodic reevaluation of detection thresholds in quiet required upwards of 2 years per subject. Results from initial subjects indicated that masking effects were limited to acoustic frequencies within one critical band of the electrical target. Later subjects were therefore tested with 5.6, 8, 11.2, and 16 kHz electrical target signals and acoustic background tones that were at the same frequency as the electrical target, at frequencies that separated by approximately 1/2 critical band relative to the electrical target, and at frequencies that were separated by approximately 1 critical band relative to the electrical target (5.6, 7, 8, 9, 10, 11.2, 12, 14.5, 16, 17.5, and 19 kHz). Thus, the electrical target and the background acoustic tone were either at the same frequency, closely spaced frequencies, or at frequencies that were perceptually quite distinct. For detailed discussion of cochlear place and critical bandwidth, readers are referred to Greenwood (1961). This modification to the protocol resulted in masking functions with tuning equivalent to those produced by subjects with more densely spaced acoustic background tones and provided the added benefit of reducing the total duration of testing with electrical targets to approximately 1 year.

Because subjects showed continual improvement in electric thresholds throughout the 1–2 year duration of testing, testing in quiet was repeated at approximately bimonthly intervals. Given that threshold sensitivity changed over time in our subjects, all masking effects were assessed relative to the most temporally proximal set of base lines. Masking effects are reported as shift in electric stimulus detection threshold; masking functions were determined for four subjects.

D. Surgical procedures

For the current investigation, chronic electrodes were inserted into scala tympani as done by Nuttall *et al.* (2001). The surgical procedures were closely modeled after those used by Le Prell *et al.* (2005). In brief, a ball electrode (0.2–0.25 mm diameter, constructed of Teflon-coated platinum–iridium wire) was carefully inserted through the wall of the cochlea via a small fenestra slightly lateral to the round window. The site of the electrode was located at approximately 22.4 kHz (based on surgically induced threshold deficits described in Le Prell *et al.*, 2004). A silastic ball located 0.55 mm away from the end of the electrode prevented over insertion of the electrode and prevented leaking of the perilymph from the cochlea. Once appropriate placement of the electrode was confirmed, carboxylate cement (Durelon, ESPE, Germany) was used to seal the bulla defect and permanently fix the electrode in place. The opposing end of the electrode was soldered to a two-pin connector (HSS-132-G2, Samtec Inc., IN) prior to the onset of the surgical procedure. A ground wire, connected to the second pin of the connector, was then inserted into neck muscle. Methyl methacrylate cement (Jet Repair Acrylic, Lang Dental Manufacturing, IL) was used to fix the connector to the skull and to seal the tissue edges surrounding the head-mounted connector. The postauricular incision was then sutured and the incision cleaned. Subjects were treated with a multi-day postoperative regimen of chloramphenical (30 mg/kg) to prevent infection.

Prior to assessing the efficiency of acoustic background stimuli in masking the detection of electrical sinusoids, the subjects used in the masking experiments were unilaterally deafened in the ear contralateral to the implanted electrode (as in Le Prell *et al.*, 2004). The unilateral deafening procedure ensured that subjects listened for electric and acoustic stimulation with the same ear. To deafen the ear, we unilaterally injected neomycin sulfate (10% solution, 60 μl injection volume) through the round window membrane. Deafening was confirmed using ABR threshold assessment; morphological lesion was confirmed after euthanasia.

E. Electrically evoked otoacoustic emission assessment

Anesthetized guinea pigs (40 mg/kg ketamine, 10 mg/kg xylazine) were placed on a warmed heating pad. The ear canal and the tympanic membrane were visually inspected (with magnification) prior to insertion and after removal of a microphone (Etymotic Research, ER-10B+ Low Noise Microphone) from the ear canal. A short segment of flexible vinyl tubing selected to be minimally smaller than the guinea pig ear canal was placed around the microphone assembly to seal the ear canal to provide a closed field test condition. Tubing also served to prevent ear wax and other biological debris from directly entering and occluding the microphone itself; the tip of the tubing was close to, but did not contact, the tympanic membrane. Sinusoidal electric stimulation was delivered to the intra-cochlear electrode via the constant current stimulator used during behavioral testing.

Electrically evoked OAEs were assessed in nine animals; procedures were typically conducted within the first month postimplant, and repeated prior to euthanizing the animals at the conclusion of the experiments. For eight of these animals, sinusoidal wave forms were produced by an audio generator (LAG-120B; Leader) and amplified (1000x; amplifier constructed in house). Current ranged from 0 to 30 μA peak to peak (i.e., 0–10.6 μA rms). Current delivery was based on signal voltage, determined using an oscilloscope (40 MHz; Kenwood). Stimulation frequency was fine tuned such that the emission frequency was 5.6, 8, 11.2, or 16 kHz, and emission frequency and amplitude were determined using a lock-in-amplifier (SR530; Stanford Research Systems). For the ninth animal, current remained fixed between 0 (noise floor) and 30 μA; however, stimulation frequency (controlled by an SRS 830 lock-in amplifier) was stepped from 1 to 35 kHz in 22 Hz increments (1 s dwell time per frequency increment), with a time constant of 3 s (as described by Halsey *et al.*, 2006). Development of the latter procedure significantly improved frequency resolution for measuring the EEOAE response.

F. Morphological procedures

To confirm that daily electrical stimulation did not damage cochlear hair cells, organ of Corti tissue was evaluated at the conclusion of the psychophysical testing. Subjects were deeply anesthetized and decapitated, and the ears were harvested and gently perfused with fixative (4% paraformaldehyde in phosphate buffer). Placement of the electrode inside the cochlea was visually confirmed, and the middle ear and inner ear were carefully examined for any evidence of infection or other pathology. The following day, the otic capsule, lateral wall, and tectorial membrane were removed, and the bony modiolus was carefully detached at the base of the cochlea. Organ of Corti tissue, attached to the modiolus, was permeabilized with 0.3% Triton-X (Sigma, St. Louis, MO) in phosphate buffered saline (PBS) for 10 min and then incubated for 30 min with rhodamine phalloidin (Molecular Probes, Eugene, OR) diluted 1:100 in PBS (room temperature). After washing the tissues with PBS, individual turns from the organ of Corti were carefully dissected from the modiolus, mounted on microscope slides with GEL/Mount (Biomedia, Foster City, CA), and examined and photographed using a Leica (Eaton, PA) DMRB epifluorescence microscope.

III. RESULTS

A. Electrophysiology

Complete data sets were collected from four guinea pigs. Surgery-induced changes in ABR thresholds were generally 20 dB or less, although hearing loss was greater in one animal (P163, see Fig. 1). Surgically induced threshold deficits were greater than the changes of less than 10 dB in ABR (Prieskorn and Miller, 2000; Le Prell *et al.*, 2004) and psychophysical detection (Le Prell *et al.*, 2004) thresholds reported previously as a consequence of intra-cochlear insertion of polyimide tubing (outer diameter=0.16 mm). One possibility is that the larger fenestra required for inserting the ball electrode (outer diameter=0.2–0.25 mm) led to greater surgical trauma. Consistent with this hypothesis, Carvalho and Lalwani (1999) described greater ABR threshold shifts (>30 dB at 16 kHz and above) after implanting a larger intra-cochlear cannula (0.61 mm diameter).

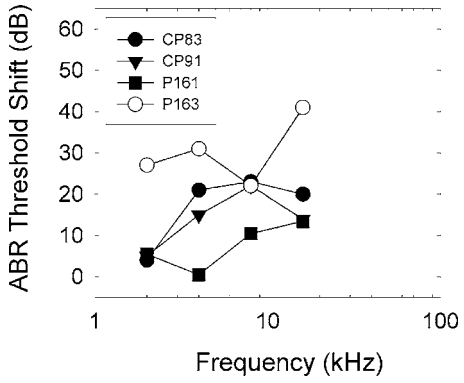

FIG. 1. Surgery-induced threshold shift was assessed as change in auditory brainstem response (ABR) threshold at 2, 4, 8 and 16 kHz. Data are shown for individual animals (CP83, CP91, P161, P163) to facilitate comparisons with psychophysical and morphological data. Threshold deficits were typically 20 dB or less, although one animal (P163) had surgically induced threshold deficits of 20–40 dB, suggesting significant trauma during surgery. Consistent with this, we observed significant intra-cochlear bone growth in P163 at the time of euthanasia.

Electrically evoked ABR neural response thresholds were less than 100 μA peak, with normal growth of input-output functions observed from 100 to 1000 μA. In the one animal (P163) in which threshold was carefully measured using 10 μA steps, threshold was 47 μA.

B. Electrically evoked otoacoustic emissions (EEOAEs)

EEOAEs were produced when current was applied to the cochlea for all animals except P163, which had significantly greater hearing loss postsurgery. For CP83 and CP91, emissions were produced at current levels as low as 2 μA rms at all stimulation frequencies (5.6, 8, 11.2, and 16 kHz), and EEOAE amplitude increased with current level. An EEOAE measured using a frequency sweep is illustrated in Fig. 2 (P161). Emissions were comparable, in both shape and amplitude, to those recorded from normal animals that have not undergone daily electric stimulation (Halsey *et al.*, 2006). To verify that the emissions we recorded depended on OHC integrity, EEOAEs were assessed in an animal deafened with subcutaneous kanamycin (400 mg/kg) followed 2 h later by intra-venous ethacrynic acid (40 mg/kg). This treatment elevated ABR thresholds to acoustic stimulation to >100 dB SPL, eliminated virtually all OHCs (evaluated histologically), and depressed EEOAE amplitude as previously described by Nuttall and Ren (1995).

C. Psychophysical testing: Base line functions

Examples of the dynamic ranges of acoustically and electrically evoked reactions are shown in Fig. 3; data are illustrated for animals CP83, CP91, and P163. All subjects readily responded to electrical stimulation when transferred from the acoustic signal detection task to the electrical signal

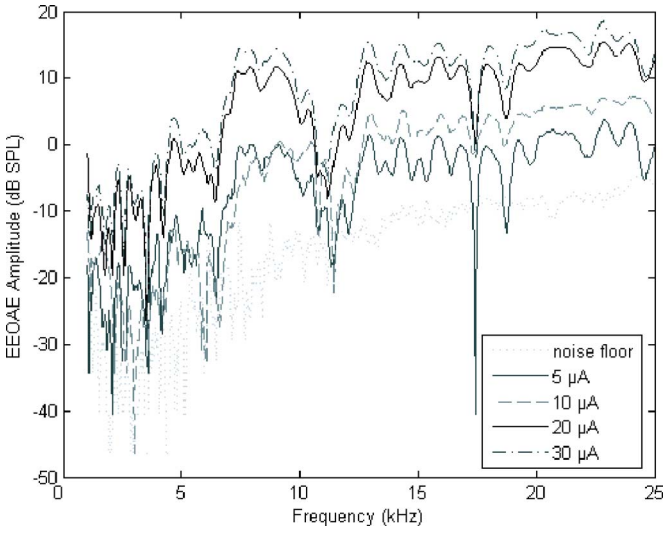

FIG. 2. Electrically evoked otoacoustic emissions (EEOAEs) were assessed in response to intra-cochlear electrical stimulation using a frequency sweep paradigm. Emissions were assessed using this paradigm for a single animal (P161); testing was conducted on day 45 postimplant. For all other subjects, testing was limited to 5.6, 8, 11.2, and 16 kHz, with each frequency presented at 0 (noise floor), 5, 10, 20, and 30 μA as shown above using the frequency sweep paradigm. The results were equivalent in that EEOAE amplitude grew with increasing current level.

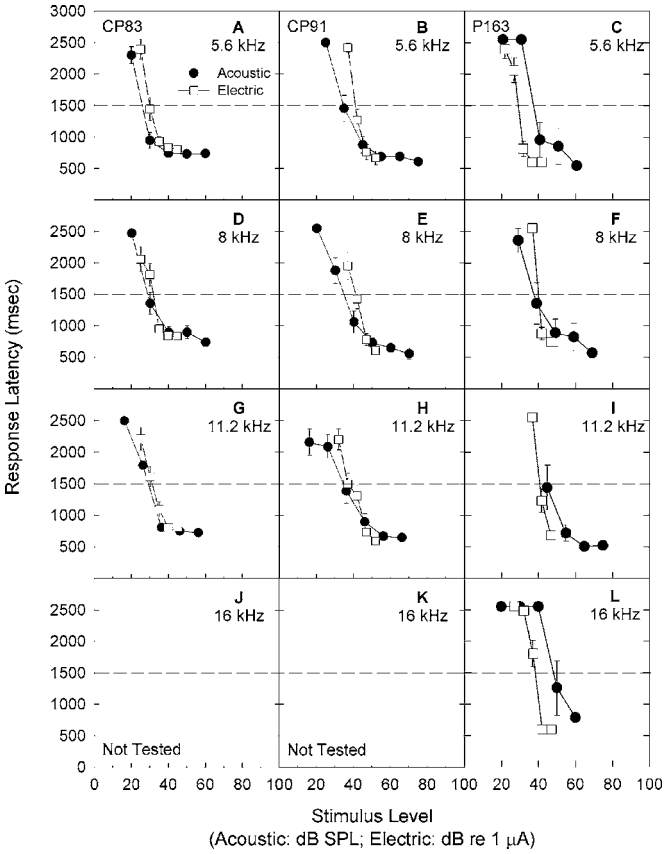

FIG. 3. Subjects were trained to report detection of 5.6 (A, B, C), 8 (D, E, F), 11.2 (G, H, I), and 16 (J, K, L) kHz acoustic signals. Once subjects were trained and producing reliable response latency functions, a process which typically required a total of 4–6 months, a ball electrode was implanted through the wall of the cochlea, into scala tympani, for delivery of sinusoidal electrical signals. Here, we illustrate detection response latency for 5.6, 8, 11.2, and 16 kHz acoustic test signals in quiet, with tests conducted over the first month postsurgery. Data are shown for subjects CP83 (A, D, G, J), CP91 (B, E, H, K) and P163 (C, F, I, J). Subjects were then switched to an electrical stimulus detection task. Subjects readily responded to electrical stimulation. Data shown here were collected during the first 1–2 months of testing; all data were collected in a quiet background. Responses were generally quite consistent, showing little improvement over any given 1–2 month test window, including the initial test period as illustrated here (response data are mean ±S.E.). Threshold was defined as the sound level corresponding to a response latency of 1500 ms, see dashed lines.

detection task. Acoustic data shown here were collected during the first month postimplant; electrical data shown here were collected during the next 1–2 months of testing. Dynamic range, i.e., the range of signal levels between maximum safe stimulation level (or, alternatively, the maximum level presented without discomfort) and minimum detectable level, was clearly narrower for electrical signals than for acoustic signals, a result that is consistent with numerous reports of narrower dynamic range for electrical signals. We monitored maximum comfort level by increasing maximum stimulus levels in small increments while carefully monitoring subject responses via a video camera located inside the test chamber with a monitor located remotely, outside the test chamber. Any signal levels that appeared to result in discomfort, evidenced, for example, by an animal "leaping" off the response key and hesitating to initiate a new trial, were not repeated.

Although responses indicating detection of electrical signals showed little change within any 1–2 month test window, detection thresholds tended to improve over longer periods of time. This result is shown in Fig. 4, where response data for 8 kHz electrical signals is illustrated for each animal at multiple times across the 1–2 year experimental duration. In between the base line reevaluation periods shown in each graph, animals were required to detect other electrical targets in quiet, or to detect electrical targets in the presence of a background tone. Because the subjects showed significant improvement over time, in some cases up to 20 dB re 1 μA, the effects of the background acoustic tones were evaluated relative to the most recent tests in quiet.

D. Psychophysical testing: Masking functions

Preliminary manipulations conducted with two subjects (CP83, CP91) revealed that masking of the electric signal by an acoustic background was level dependent. That is, when the acoustic stimulus and the electric target were the same frequency, increasing the level of the background tone increased masking (not depicted, see Le Prell *et al.*, 2000). During the remainder of testing, masker level was fixed at 10 dB sensation level (SL) and masker frequency was varied. Figure 5 depicts the frequency specificity and magnitude of the masking effect, assessed as shift in electric threshold. Background tones produced frequency-specific masking of electric sinusoids in animals with normal acoustic thresholds when the electric sinusoid was at least 8 kHz (see Fig. 5, panels D–L). Background tones had the greatest effect when the background tone and the electric stimulation fell within the same critical band (following Greenwood, 1961). These frequency-specific masking functions are consistent with characterizations of auditory nerve tuning that show very narrowly tuned (frequency specific) sound-driven responses at low signal levels, and broadly tuned responses across a

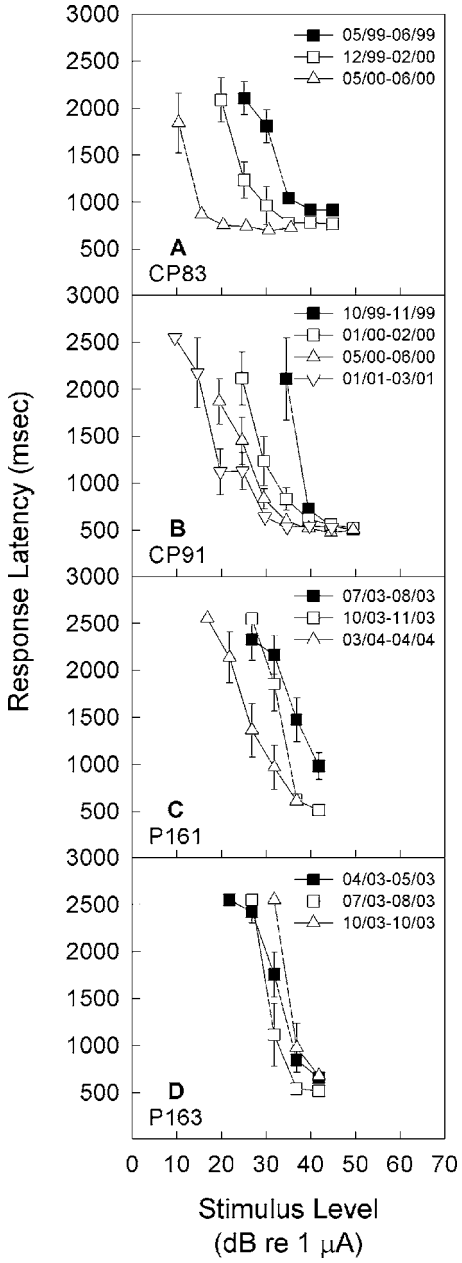

FIG. 4. Subjects were retested in quiet in the detection task requiring response to 5.6, 8, 11.2, and 16 kHz sinusoidal signals delivered via intracochlear electrical stimulation of a ball electrode. Here, we illustrate detection response latency for 8 kHz test signals in quiet, with tests conducted at various times over 1–2 year periods. Pronounced improvement with long-term testing was observed for three subjects (CP83, CP91, P161), with thresholds improving up to 20 dB re 1 μA. All masking effects were therefore assessed relative to the most recent data in quiet.

wider range of frequencies at higher signal levels (Liberman, 1978; Winter *et al.*, 1990; Wang *et al.*, 1997). When tested with 10 dB SL background tones, the animal with high-frequency hearing loss (P163, see Fig. 1) did not show frequency-specific masking effects with any electrical targets (Fig. 5, panels N–P). The 5.6 kHz electric target was not masked by acoustic pure tones for any of the animals (Fig. 5, panels A–C and M).

E. Morphology

The organ of Corti from the implanted ears of two subjects (CP83, P161) exhibited only mild and scattered OHC loss (see Fig. 6), consistent with age-related cell death (as described by Coleman, 1976). Little IHC loss was observed throughout the cochlear duct. Thus, the process of introducing the electrode into ears with intact hair cell populations and the daily electrical stimulation over extended temporal periods had no apparent negative consequences in these animals.

OHC loss for a third subject that underwent long-term daily electrical stimulation (CP91) was more widespread. While OHC loss was fairly limited in the basal turn (approximately 10%), scars indicating missing OHCs ranged from approximately 50% in the upper second turn to 85%–90% in the third turn and apex. This animal developed a hearing loss characterized by an abrupt and pronounced shift in electrical and acoustical detection thresholds approximately 21 months after the start of the daily electrical stimulation experiments. There was no evidence that this pathology progressed over time with the daily delivery of electric stimulation, as detection thresholds improved slowly over time throughout the first 21 months of testing (i.e., prior to the onset of the sudden and severe deficits). Two months later, after using behavioral techniques to characterize the hearing loss for both electrical and acoustic stimulation in this animal, it was euthanized. At that time, the OHC scars appeared thick and mature as previously described by Raphael and Altschuler (1991). IHC loss was limited to about 5% in the base and second turn, and 10% in the third turn and apex.

In the final animal to undergo long-term daily electrical stimulation tests (P163), the ball electrode was completely encased in bone inside the cochlea at the conclusion of the experiments. This bone appeared to project from the modiolus, such that a portion of the organ of Corti was also encased in bone. Evaluation of the organ of Corti revealed the first and second turns to have normal hair cell populations. In the third turn, there was approximately 15% OHC loss, predominantly within the third row of OHCs. IHC loss was limited to 8% in the third turn. Given the significant bone growth in this animal, in which the electrode was found to be encased in bone, it appears that surgical trauma clearly can induce a biological response. However, implants that are minimally invasive generally do not induce significant tissue response (see, for example, Brown *et al.*, 1993; Le Prell *et al.*, 2004); the current report of minimal tissue response across animals is consistent with results from earlier investigations using similarly minimally invasive implants.

IV. DISCUSSION

A. Electrical stimulation of ears with intact hair cells produces electrically evoked otoacoustic emissions

EEOAEs, generated by forward and reverse traveling motion along the basilar membrane, have been interpreted by others as likely to be accompanied by an acoustic percept termed electromotile hearing (Nuttall and Ren, 1995). In the current study, we used EEOAE measures primarily to confirm that sinusoidal electrical stimulation of our implants in our animals produces EEOAEs as described by others. For all but one test subject, EEOAE amplitude grew with current

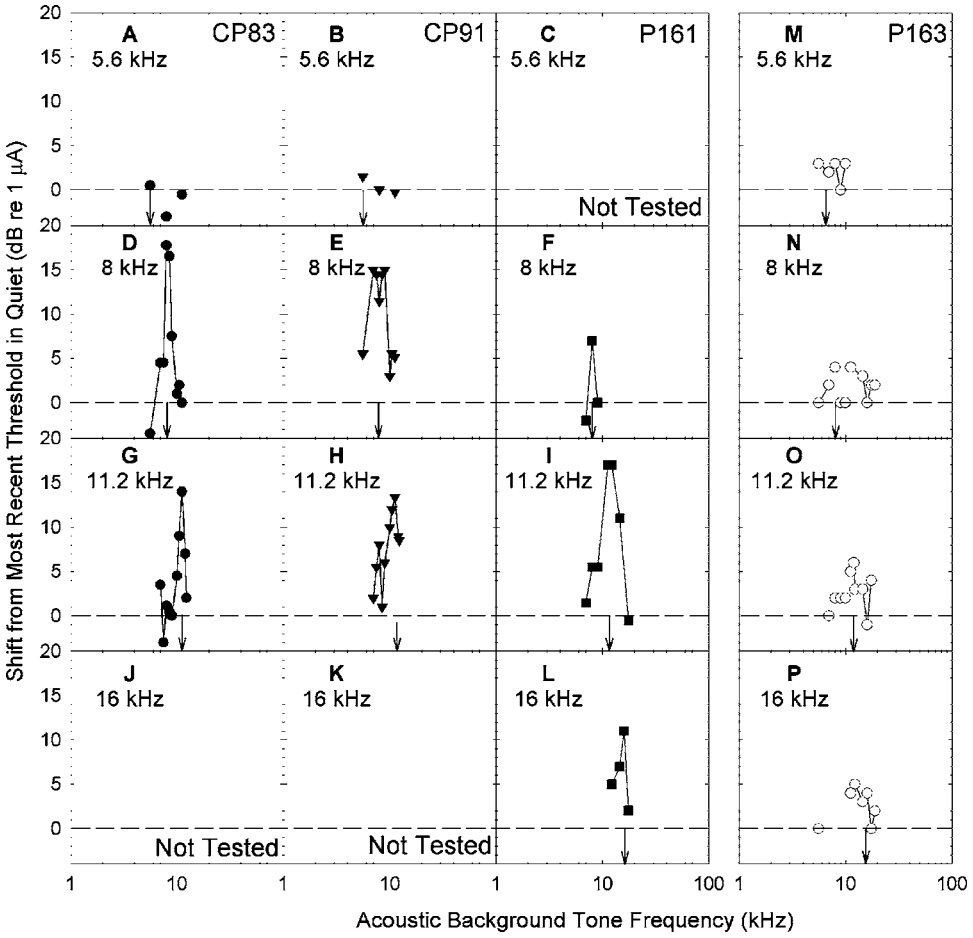

FIG. 5. Subjects were trained to report detection of 5.6 (A, B, C, M), 8 (D, E, F, N), 11.2 (G, H, I, O), and 16 (J, K, L, P) kHz sinusoidal signals. Sinusoidal signals were acoustic during initial training, and later delivered using intra-cochlear electrical stimulation. Here, we illustrate the shift in electrical sinusoid detection thresholds when 10–dB SL acoustic pure-tone background maskers were presented (see *x* axis). Target signal frequency is indicated in each panel using downwards arrows. Shift in detection threshold was calculated as the background-induced change from the most temporally proximate detection thresholds assessed in quiet; threshold shifts were greatest at frequencies closest to the electrical stimulation frequency except when the electrical target was a 5.6 kHz sinusoid. Anatomical evaluations were relatively normal in two animals (CP83, P161). The third animal (CP91) developed a sudden elevation in both acoustic and electrical signal detection thresholds and was found to have corresponding hair cell loss. In the fourth subject (P163, see right panels), the electrode was encased in bone.

level, and with frequency; results that are equivalent to those described in detail by others. Although EEOAEs were smaller in amplitude at the lowest test frequency (5.6 kHz) for those animals tested at a restricted set of frequencies (i.e., 5.6, 8, 11.2, and 16 kHz), responses were clearly above the noise floor even at the lowest frequency. Thus, there was not a clear relationship between EEOAE presence and efficacy of background masking signals; i.e., the lack of frequency specific masking at 5.6 kHz was not accompanied by lack of an EEOAE in response to 5.6 kHz stimulation. This is clearly illustrated in Fig. 2, which illustrates EEOAE responses at frequencies as low as 1 kHz. Because EEOAEs were evaluated in all subjects, we were also able to confirm that the single animal lacking an EEOAE in response to electrical stimulation (P163) had acoustic percepts that were distinctly different from those of other animals in which EEOAEs were generated by electrical stimulation of the implant.

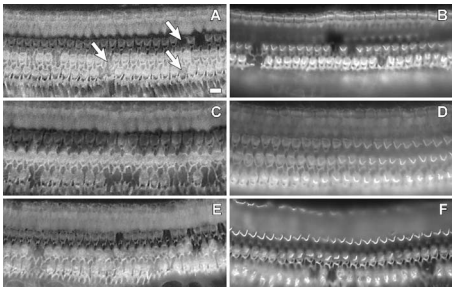

FIG. 6. Whole-mount surface preparations of cochlear tissues from CP83 (left) and P161 (right). Actin filaments in the organ of Corti were labeled using rhodamine-phalloidin and visualized under epifluorescence. Tissues are from the basal turn (A, B), second turn (C, D), and third turn (E, F). Images were focused at the level of the OHC apical surface. Only mild and scattered OHC loss, consistent with age-related cell death (see Coleman 1976), was observed in these tissues (for examples, see arrows in panel A, where each arrow points at a site of a single missing OHC). IHC loss was generally not observed.

B. Electrical stimulation of ears with intact hair cells produces frequency-specific masking, suggesting a tone-like sensation at higher frequencies

Anecdotal descriptions from human patients implanted with a cochlear prosthesis suggest the auditory percept associated with direct depolarization of auditory neurons is not tone-like (Jones *et al.*, 1940; House and Urban, 1973; Bilger, 1977b; 1977a; Bilger and Black, 1977; Eddington *et al.*, 1978; Tong *et al.*, 1982; Watson *et al.*, 1991; Dorman *et al.*, 1994; Blamey *et al.*, 1995; Collins *et al.*, 1997). In contrast, preliminary data from a study in which electrical current was applied to a cochlea with intact hair cells suggest that electric stimulation of intact hair cells results in a tonal percept. In a pitch-matching experiment using a single human subject, sinusoidal electric stimulation (8 kHz) of an electrode placed on the promontory was matched in pitch to approximately 8 kHz acoustic stimulation in the contralateral ear (A. Nuttall, personal communication).

Interactions of electric and acoustic stimuli have been

shown at the single-fiber level (Moxon, 1971; von Ilberg *et al.*, 1999) and with the whole-nerve compound action potential (CAP). Specific evidence includes masking of the acoustically evoked CAP by electric pulses (McAnally *et al.*, 1993; Kirk and Yates, 1994; McAnally and Clark, 1994; McAnally *et al.*, 1997c; 1997a; 1997b) and masking of the electrically evoked CAP by acoustic stimuli (Aran *et al.*, 1986; Kirk and Yates, 1994; James *et al.*, 2001). Our experiments revealed an interaction of electric and acoustic stimulation at the perceptual level. Background acoustic pure tones masked the detection of electrical stimulation provided that the stimulation frequencies were similar (i.e., within the same critical band) and that the electrical test frequency was 8 kHz or greater.

C. Does electrical stimulation of ears with intact hair cells produce an acoustic percept at lower frequencies?

There are several possible explanations for the observation that the 5.6 kHz electric sinusoid was not masked by acoustic stimulation. First, the 5.6 kHz electric stimulation may have resulted in an acoustic sensation that was not tone-like, such as would be expected if the auditory nerve were directly stimulated. A noise-like sensation would not be masked by pure-tone acoustic background tones. Alternatively, the 5.6 kHz electric stimulation may have produced a nonauditory sensation concurrent with, or, in the absence of, an auditory sensation. Thus, in the presence of the 5.6 kHz acoustic background, detection of an acoustic percept may have been masked but a nonauditory cue would provide a discriminative cue to perform the release response. Consistent with this suggestion, we observed a single guinea pig subject react to 4 kHz low-current electric stimulation as though the stimulation was painful. This stimulation was discontinued for this subject, and was not repeated with additional animals. Bipolar stimulation of the cochlea (i.e., stimulation of two intra-cochlear electrodes) was unpleasant when lower rates of pulsatile stimulation were applied near the round window (Fearn and Wolfe, 2000), and a single human subject described lower-frequency (2 kHz) electric stimulation delivered to the promontory as aversive (A. Nuttall, personal communication). Thus, some unknown tactile sensation may accompany lower frequency electric stimulation. That there may be an anomalous nonacoustic component to electric stimulation of the cochlea has been proposed previously, based on a single subject with consistent psychophysical detection responses in the absence of a reliable eABR (Miller *et al.*, 1995a).

D. Electromotile hearing?

Acoustic percepts may have been elicited through one or more of four distinct mechanisms. First, the tonotopically resonant basilar membrane motion that produced the EEOAE may have resulted in deflection of IHC stereocilia, release of excitatory neurotransmitter substance by the IHCs (for review, see Le Prell *et al.*, 2001), and auditory nerve activity (e.g., electromotile hearing). Alternatively, current injected into the cochlea may have directly stimulated spiral ganglion cells within the broad vicinity of the electrode (for discussion, see Spelman *et al.*, 1980; 1982; Clopton and Spelman, 1995; Spelman *et al.*, 1995; Kral *et al.*, 1998). Data from Cohen *et al.* (2003) suggest that spread of excitation falls off fairly sharply, with most probe/masker electrode interactions occurring within a region of about 10% of the length of the organ of Corti either basal to or apical to the site of stimulation. The placement of the electrode at approximately 22.4 kHz can be presumed to be located approximately 15% of the total cochlear length measured from the base, and the highest electrical stimulation frequency of 16 kHz can be presumed to be located approximately 20% of the total cochlear length measured from the base (from Tsuji and Liberman, 1997, percent distance from base $=66.4–38.2*\log(\text{kHz})$). Thus, it is possible that there was some direct stimulation of auditory neurons located in the vicinity of the organ of Corti that would best respond to 16 kHz stimulation. However, it is unlikely that there was any significant direct neural excitation of neurons responding best to the 11.2 kHz or lower test frequencies, which are located 26% (11.2 kHz), 32% (8 kHz), and 38% (5.6 kHz) of the total cochlear length measured from the base. Arguing against the notion that there was significant direct electrical neural excitation at the 16 kHz place in the cochlea, we note that direct electrical stimulation is typically not described as tonal by human listeners, whereas the 16 kHz stimulation was masked only by background tones that were similar in frequency relative to the 16 kHz electrical target. While it is conceivable that stimulation of the IHCs by the intracochlear electrical current triggered the release of excitatory neurotransmitter and the consequent auditory nerve activity and perception of sound, electrical stimulation of the IHCs would be subject to the same spatial constraints imposed by limited current spread as described for direct neural stimulation. Finally, while it is conceivable that stimulation of the facial nerve or vestibular system could occur, sensations generated via this mechanism would not be masked by pure-tone acoustic signals.

Based on the frequency map of the guinea pig cochlea provided by Tsuji and Liberman (1997), and the demonstration by Cohen *et al.* (2003) that spread of excitation falls off fairly sharply at distance extending beyond about 10% of the length of the organ of Corti, we consider it unlikely that direct electrical stimulation of auditory hair cells or auditory neurons generated the tone-like percepts associated with electrical stimulation at the higher stimulation frequencies. We can further attempt to discriminate among these mechanisms by estimating the thresholds for direct electrical stimulation of auditory neurons. Thresholds for detection of neural stimulation, in the absence of hair cell stimulation, are available from animals in which hair cell populations were eliminated with ototoxic drugs prior to implant with a cochlear prosthesis. eABR thresholds for our animals (with intact hair cell populations) were generally consistent with those reported by A. L. Miller and colleagues (1999), and somewhat lower than those reported by C. A. Miller and colleagues (1995b). From the limited existing data sets, we know that guinea pig eABR thresholds are approximately 16 μA for 3 kHz stimulation (Miller *et al.*, 1999), and that neural

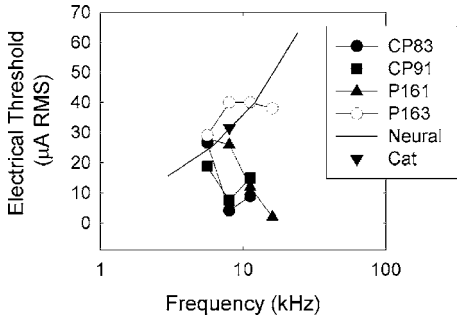

FIG. 7. Detection thresholds for electrical stimulation are plotted at all test frequencies (5.6, 8, 11.2, and 16 kHz) for each of our subjects (CP83, CP91, P161, P163). In addition, we plot the lowest current level predicted to result in detectable electrical stimulation of auditory neurons in animals without outer hair cells ("Neural"). Electric detection thresholds for 8 kHz (bipolar) sinusoidal stimulation in a single deafened cat (taken from Smith *et al.*, 1995) are consistent with the "predicted" neural thresholds. Empirically determined thresholds lower than the predicted neural stimulation thresholds are interpreted as the first direct perceptual evidence for the psychological phenomena termed "electromotile hearing".

stimulation thresholds increase by approximately 4 dB/octave (in monkeys, see Pfingst, 1984). Based on these data sets, we calculate that average detection thresholds for auditory nerve stimulation (in the absence of intact hair cell populations) might be expected to be approximately 25 μA rms at 6 kHz, 40 μA rms at 12 kHz, and 63 μA rms at 24 kHz. Electric detection thresholds for 8 kHz (bipolar) sinusoidal stimulation in a single cat (see Smith *et al.*, 1995) are consistent with the predicted thresholds (see Fig. 7). Although the data sets are disparate, including psychophysical and electrophysiological thresholds for sinusoidal, as well as monophasic/monopolar and biphasic/bipolar signals, psychophysical and electrophysiological thresholds are typically well correlated (Borg and Engstrom, 1983; Miller *et al.*, 1995b; Szymanski *et al.*, 1999; Wolski *et al.*, 2003; Le Prell *et al.*, 2004).

At our lowest test frequency (5.6 kHz), guinea pig thresholds were generally equivalent to predicted thresholds for detection of direct neural stimulation (see Fig. 7). Thus, direct neural stimulation probably provided a salient cue for detection of 5.6 kHz electric sinusoids. This effect is consistent with the failure of pure-tone acoustic signals to mask detection of the 5.6 kHz electric sinusoid (see Figs. 5(A)–5(C) and 5(M)). At higher test frequencies, most subjects (CP83, CP91, P161) detected sinusoidal electric stimulation at current levels well below those predicted to result in neural stimulation (see Fig. 7). These responses we interpret as electromotile hearing. Consistent with the purported nature of electromotile hearing, pure-tone acoustic stimuli had frequency-specific masking effects at 8, 11.2, and 16 kHz (see Figs. 5(D)–5(L)). In contrast, our subject P163, for whom the electrode was found to be encased in bone, had thresholds that were approximately equal to the predicted neural stimulation thresholds (Fig. 7). Consistent with the premise that direct neural stimulation does not result in a tone-like percept, we did not observe strong evidence of frequency-specific masking for this subject (see Figs. 5(M)–5(P)).

An alternative experimental approach that would have allowed more direct comparison of electrophonic responses and those driven by direct depolarization would include ototoxic drug treatment following the collection of base line electrical signal detection data. Ototoxic drugs would eliminate the electrophonic response, without disrupting the neural response driven by direct depolarization of auditory neurons. We considered this approach for our investigation; however, this approach does not permit us to identify any disruption of hair cell survival as a consequence of chronic electrical stimulation. Therefore, we did not choose to use this experimental approach. Such manipulations may represent an interesting approach for future investigations designed to clarify the mechanisms of perception across stimulation levels.

E. Electrical stimulation of ears with intact hair cells does not damage these cells

Although some patterns of electrical stimulation (i.e., continuous low frequency stimulation) can be detrimental to the survival of cochlear hair cells (Duckert, 1983; Duckert and Miller, 1984), other stimulation patterns do not produce functional or morphological deficits (Ni *et al.*, 1992). One animal in the present study demonstrated a sudden shift in thresholds following 21 months of testing (see Sec. III E, Morphology), but there was no evidence of any progressive deficits prior to this time. Data from our experiments with guinea pigs thus importantly suggest that intact hair cell populations are not damaged by daily electrical stimulation at levels that result in acoustic sensations. These data significantly extend the duration of testing from 85 days (von Ilberg *et al.*, 1999), during which time no changes in CAP were observed, to approximately 2 years (i.e., in the current experiments).

F. Clinical utility

The treatment of choice for those with profound hearing loss is the cochlear prosthesis; a device that directly stimulates the auditory nerve using electrical signals. Users of this device can comprehend open-set speech information without the aid of lip reading (Skinner *et al.*, 1994; 1997; Waltzman *et al.*, 1997; Firszt *et al.*, 2004). Historically, the benefits of the implant have been dependent on the density and excitability of surviving auditory nerve fibers (Clopton *et al.*, 1980; Nadol *et al.*, 1989; Incesulu and Nadol, 1998; see also Skinner *et al.*, 2002). However, as the criteria for implanting human patients with cochlear prostheses relax (NIH Consensus Statement, 1995), patients with greater residual hearing are being implanted with intra-cochlear electrode arrays.

Gantz and colleagues recently began to implant shorter (10 mm) intra-cochlear electrode arrays that preserve intact low-frequency hearing. They demonstrated that electrical stimulation of the base of the cochlea combined with acoustic stimulation of the intact apical cochlea (via hearing aid use) enhances perceptual experience for cochlear implant users (Gantz *et al.*, 2000; Tyler *et al.*, 2000; Gantz and Turner, 2003; 2004; Turner *et al.*, 2004). Similar results have been described in a case study by Skarzynski *et al.* (2003) and also by Kiefer and colleagues (von Ilberg *et al.*, 1999; Kiefer

et al., 2005), who report that patients can "merge" acoustic and electric stimuli into a unified sensation that is more pleasant than either the electric or acoustic component alone.

The suggestion that cochlear implant users with some residual hearing could benefit from cochlear stimulation strategies that take advantage of intact OHC populations is increasingly popular (Risberg *et al.*, 1990; McAnally and Clark, 1994; Nuttall and Ren, 1995; McAnally *et al.*, 1997b). By minimizing surgical trauma during cochlear implant procedures, residual populations of hair cells may be retained, resulting in superior implant performance. This concept of "soft surgery" for cochlear implants was first articulated by Lehnhardt (1993), and later described by Cohen (1997). In a population of 26 human patients implanted using the soft surgery technique, 62% retained their residual hearing 1 month postoperative, whereas 5% lost all residual hearing (Skarzynski *et al.*, 2002). The morphology of OHCs was normal following surgery designed to minimize trauma in guinea pigs euthanized 2–6 weeks postimplant (Rogowski *et al.*, 1995).

The current data set extends our understanding of interactions occurring as a consequence of combined use of acoustic and electric signals. Specifically, the current data illustrate the potential for generation of tone-like percepts with electromotile stimulation in the patient with a sufficient population of surviving hair cells. Improving the perception of tonal signals would have significant benefit for perception of music, which is typically quite poor in implant users (McDermott, 2004; Rubinstein, 2004; e.g., Gantz *et al.*, 2005; Gfeller *et al.*, 2005; Laneau *et al.*, 2006). Presumably, benefits of electromotile stimulation would also include improved speech discrimination by speakers of tonal languages (Huang *et al.*, 1995; 1996; Fu *et al.*, 1998; Lan *et al.*, 2004; Huang *et al.*, 2005; Lee and van Hasselt, 2005).

V. CONCLUSIONS

Psychophysical tuning curves are the gold standard for frequency-specific processing in the auditory periphery. Thus, these data provide clear and robust evidence of frequency-specific perception with electrical stimulation of the intact cochlea. Taken together, our results indicate intracochlear electric stimulation of OHCs in intact ears produces an acoustic sensation that is tone-like at least at higher frequencies (i.e., at or above 8 kHz). This behavioral result implies an electrically evoked traveling wave that is "acoustic-like." Our results suggest that if intact OHCs are present in cochleae with residual hearing, then stimulation of these hair cells may result in an acoustic sensation. These results may help to explain the recent observations that the perceptual experience of cochlear prosthesis users is improved by stimulation of remaining OHCs in patients that use both a hearing aid, and a cochlear prosthesis (von Ilberg *et al.*, 1999; Kiefer *et al.*, 2005).

ACKNOWLEDGMENTS

This research was supported by the National Organization for Hearing Research (CGL) and the Royal National Institute for the Deaf (YR) and by grants from the National Institutes of Health-National Institute of Deafness and Other Communication Disorders [NIH-NIDCD]: P01-DC00078 (DFD, DBM, YR), F32-DC00367 (CGL), and P30-DC05188]. We are grateful to David Moody for his expertise and assistance with the conduct of these experiments. We thank Masahiko Izumikawa and Ryosei Minoda for their expert assistance with histological procedures. We thank Kathryn Abele, Rebecca Diener, Elizabeth Hand, Edwin Labut, and Catherine Thompson for participating in the daily care and testing of these animals. We thank Amy Miller, John Middlebrooks, and Alfred Nuttall for valuable comments on earlier versions of this manuscript. Finally, we thank James Beals, Chris Ellinger, Kärin Halsey, Robert Masta, Alice Mitchell, Diane Prieskorn, and Donald Swiderski for technical contributions.

Aran, J. M., Erre, J. P., Hiel, H., Charlet de Sauvage, R., Goeury, P., and Rouanet, J. F. (**1986**). "Investigation of cochlear mechanisms using combined acoustical and electrical stimulations," Scand. Audiol. Suppl. **25**, 63–69.

Ashmore, J. F. (**1987**). "A fast motile response in guinea-pig outer hair cells: The cellular basis of the cochlear amplifier," J. Physiol. (London) **388**, 323–347.

Bilger, R. C. (**1977a**). "Psycoacoustic evaluation of current prostheses," Ann. Otol. Rhinol. Laryngol. Suppl. **86**, 92–140.

Bilger, R. C. (**1977b**). "Electrical stimulation of the auditory nerve and auditory prostheses: A review of the literature," Ann. Otol. Rhinol. Laryngol. Suppl. **86**, 11–20.

Bilger, R. C., and Black, F. O. (**1977**). "Auditory prostheses in perspective," Ann. Otol. Rhinol. Laryngol. Suppl. **86**, 3–10.

Black, R. C., Clark, G. M., O'Leary, S. J., and Walters, C. (**1983**). "Intracochlear electrical stimulation of normal and deaf cats investigated using brainstem response audiometry," Acta Oto-Laryngol., Suppl. **399**, 5–17.

Blamey, P. J., Parisi, E. S., and Clark, G. M. (**1995**). "Pitch matching of electric and acoustic stimuli," Ann. Otol. Rhinol. Laryngol. Suppl. **166**, 220-222.

Borg, E., and Engstrom, B. (**1983**). "Hearing thresholds in the rabbit. A behavioral and electrophysiological study," Acta Oto-Laryngol. **95**, 19–26.

Brown, J. N., Miller, J. M., Altschuler, R. A., and Nuttall, A. L. (**1993**). "Osmotic pump implant for chronic infusion of drugs into the inner ear," Hear. Res. **70**, 167–172.

Brownell, W. E., Bader, C. R., Bertrand, D., and de Ribaupierre, Y. (**1985**). "Evoked mechanical responses of isolated cochlear outer hair cells," Science **227**, 194–196.

Carvalho, G. J., and Lalwani, A. K. (**1999**). "The effect of cochleostomy and intracochlear infusion on auditory brain stem response threshold in the guinea pig," Am. J. Otol. **20**, 87–90.

Clopton, B. M., Spelman, F. A., and Miller, J. M. (**1980**). "Estimates of essential neural elements for stimulation through a cochlear prosthesis," Ann. Otol. Rhinol. Laryngol. Suppl. **89**, 5–7.

Clopton, B. M., and Spelman, F. A. (**1995**). "Electrode configuration and spread of neural excitation: Compartmental models of spiral ganglion cells," Ann. Otol. Rhinol. Laryngol. Suppl. **166**, 115–118.

Cohen, L. T., Richardson, L. M., Saunders, E., and Cowan, R. S. C. (**2003**). "Spatial spread of neural excitation in cochlear implant recipients: comparison of improved ECAP method and psychophysical forward masking," Hear. Res. **179**, 72–87.

Cohen, N. L. (**1997**). "Cochlear implant soft surgery: Fact or fantasy?," Otolaryngol.-Head Neck Surg. **117**, 214–216.

Coleman, J. W. (**1976**). "Hair cell loss as a function of age in the normal cochlea of the guinea pig," Acta Oto-Laryngol. **82**, 33–40.

Collins, L. M., Zwolan, T. A., and Wakefield, G. H. (**1997**). "Comparison of electrode discrimination, pitch ranking, and pitch scaling data in postlingually deafened adult cochlear implant subjects," J. Acoust. Soc. Am. **101**, 440–455.

Dorman, M. F., Smith, M., Smith, L., and Parkin, J. L. (**1994**). "The pitch of electrically presented sinusoids," J. Acoust. Soc. Am. **95**, 1677–1679.

Duckert, L. G. (**1983**). "Morphological changes in the normal and neomycin-perfused guinea pig cochlea following chronic prosthetic im-

plantation," Laryngoscope **93**, 841–855.
Duckert, L. G., and Miller, J. M. (**1984**). "Morphological changes following cochlear implantation in the animal model," Acta Oto-Laryngol., Suppl. **411**, 28–37.
Eddington, D. K., Dobelle, W. H., Brackmann, D. E., Mladejovsky, M. G., and Parkin, J. L. (**1978**). "Auditory prostheses research with multiple channel intracochlear stimulation in man," Ann. Otol. Rhinol. Laryngol. **87**, 1–39.
Fearn, R., and Wolfe, J. (**2000**). "Relative importance of rate and place: Experiments using pitch scaling techniques with cochlear implants recipients," Ann. Otol. Rhinol. Laryngol. Suppl. **185**, 51–53.
Firszt, J. B., Holden, L. K., Skinner, M. W., Tobey, E. A., Peterson, A., Gaggl, W., Runge-Samuelson, C. L., and Wackym, P. A. (**2004**). "Recognition of speech presented at soft to loud levels by adult cochlear implant recipients of three cochlear implant systems," Ear Hear. **25**, 375–387.
Fu, Q. J., Zeng, F. G., Shannon, R. V., and Soli, S. D. (**1998**). "Importance of tonal envelope cues in Chinese speech recognition," J. Acoust. Soc. Am. **104**, 505–510.
Gantz, B. J., Rubinstein, J. T., Tyler, R. S., Teagle, H. F., Cohen, N. L., Waltzman, S. B., Miyamoto, R. T., and Kirk, K. I. (**2000**). "Long-term results of cochlear implants in children with residual hearing," Ann. Otol. Rhinol. Laryngol. Suppl. **185**, 33–36.
Gantz, B. J., and Turner, C. W. (**2003**). "Combining acoustic and electrical hearing," Laryngoscope **113**, 1726–1730.
Gantz, B. J., and Turner, C. (**2004**). "Combining acoustic and electrical speech processing: Iowa/Nucleus hybrid implant," Acta Oto-Laryngol. **124**, 344–347.
Gantz, B. J., Turner, C., Gfeller, K. E., and Lowder, M. W. (**2005**). "Preservation of hearing in cochlear implant surgery: Advantages of combined electrical and acoustical speech processing," Laryngoscope **115**, 796–802.
Gfeller, K., Olszewski, C., Rychener, M., Sena, K., Knutson, J. F., Witt, S., and Macpherson, B. (**2005**). "Recognition of "real-world" musical excerpts by cochlear implant recipients and normal-hearing adults," Ear Hear. **26**, 237–250.
Greenwood, D. D. (**1961**). "Critical bandwidth and the frequency coordinates of the basilar membrane," J. Acoust. Soc. Am. **33**, 1344–1356.
Hall, R. D. (**1990**). "Estimation of surviving spiral ganglion cells in the deaf rat using the electrically evoked auditory brainstem response," Hear. Res. **49**, 155–168.
Halsey, K., Fegelman, K., Raphael, Y., Grosh, K., and Dolan, D. F. (**2006**). "Long-term effects of acoustic trauma on the electrically-evoked otoacoustic emission," J. Assoc. Res. Otolaryngol. **6**, 324–340.
House, W. F., and Urban, J. (**1973**). "Long term results of electrode implantation and electronic stimulation of the cochlea in man," Ann. Otol. Rhinol. Laryngol. Suppl. **82**, 504–517.
Huang, C. Y., Yang, H. M., Sher, Y. J., Lin, Y. H., and Wu, J. L. (**2005**). "Speech intelligibility of Mandarin-speaking deaf children with cochlear implants," Int. J. Ped Otorhinolaryngol. **69**, 505–511.
Huang, T. S., Wang, N. M., and Liu, S. Y. (**1995**). "Tone perception of Mandarin-speaking postlingually deaf implantees using the Nucleus 22-Channel Cochlear Mini System," Ann. Otol. Rhinol. Laryngol. Suppl. **166**, 294–298.
Huang, T. S., Wang, N. M., and Liu, S. Y. (**1996**). "Nucleus 22-channel cochlear mini-system implantations in Mandarin-speaking patients," Am. J. Otol. **17**, 46–52.
Hubbard, A. E., and Mountain, D. C. (**1983**). "Alternating current delivered into the scala media alters sound pressure at the eardrum," Science **222**, 510–512.
Incesulu, A., and Nadol, J. B., Jr. (**1998**). "Correlation of acoustic threshold measures and spiral ganglion cell survival in severe to profound sensorineural hearing loss: Implications for cochlear implantation," Ann. Otol. Rhinol. Laryngol. **107**, 906–911.
James, C., Blamey, P., Shallop, J. K., Incerti, P. V., and Nicholas, A. M. (**2001**). "Contralateral masking in cochlear implant users with residual hearing in the non-implanted ear," Audiol. Neuro-Otol. **6**, 87–97.
Jones, R. C., Stevens, S. S., and Lurie, M. H. (**1940**). "Three mechanisms of hearing by electrical stimulation," J. Acoust. Soc. Am. **12**, 281–290.
Kachar, B., Brownell, W. E., Altschuler, R., and Fex, J. (**1986**). "Electrokinetic shape changes of cochlear outer hair cells," Nature (London) **322**, 365–368.
Kemp, D. T. (**1978**). "Stimulated acoustic emissions from within the human auditory system," J. Acoust. Soc. Am. **64**, 1386–1391.
Kiefer, J., Pok, M., Adunka, O., Sturzebecher, E., Baumgartner, W., Schmidt, M., Tillein, J., Ye, Q., and Gstoettner, W. (**2005**). "Combined electric and acoustic stimulation of the auditory system: Results of a clinical study," Audiol. Neuro-Otol. **10**, 134–144.
Kirk, D. L., and Yates, G. K. (**1994**). "Evidence for electrically evoked traveling waves in the guinea pig cochlea," Hear. Res. **74**, 38–50.
Kral, A., Hartmann, R., Mortazavi, D., and Klinke, R. (**1998**). "Spatial resolution of cochlear implants: The electrical field and excitation of auditory afferents," Hear. Res. **121**, 11–28.
Lan, N., Nie, K. B., Gao, S. K., and Zeng, F. G. (**2004**). "A novel speech-processing strategy incorporating tonal information for cochlear implants," IEEE Trans. Biomed. Eng. **51**, 752–760.
Laneau, J., Wouters, J., and Moonen, M. (**2006**). "Improved music perception with explicit pitch coding in cochlear implants," Audiol. Neuro-Otol. **11**, 38–52.
Le Prell, C. G., Dolan, D., and Moody, D. B. (**2000**). "Electromotile hearing: Evidence that tone-like percepts are produced by electrical stimulation in the cochlea," Abs. Assoc. Res. Otolaryngol. **23**, 259.
Le Prell, C. G., Bledsoe, S. C., Jr., Bobbin, R. P., and Puel, J. L. (**2001**). "Neurotransmission in the inner ear: Functional and molecular analyses," in *Physiology of the Ear*, edited by A. F. Jahn and J. Santos-Sacchi (Singular, New York), pp. 575–611.
Le Prell, C. G., Kawamoto, K., Raphael, Y., Dolan, D., and Moody, D. B. (**2002**). "Electromotile hearing: Evidence that tone-like percepts are produced by electrical stimulation of cochlear outer hair cells," Abs. Assoc. Res. Otolaryngol. **25**, 165.
Le Prell, C. G., Yagi, M., Kawamoto, K., Beyer, L. A., Atkin, G., Raphael, Y., Dolan, D., Bledsoe, S. C., Jr., and Moody, D. B. (**2004**). "Chronic infusion of AMPA into the guinea pig cochlea induces temporary functional deficits and long-term morphological trauma," J. Acoust. Soc. Am. **116**, 1044–1056.
Le Prell, C. G., Halsey, K., Hughes, L. F., Dolan, D. F., and Bledsoe, S. C., Jr. (**2005**). "Disruption of lateral olivocochlear neurons via a dopaminergic neurotoxin depresses sound-evoked auditory nerve activity," J. Assoc. Res. Otolaryngol. **6**, 48–62.
Lee, K. Y., and van Hasselt, C. A. (**2005**). "Spoken word recognition in children with cochlear implants: A five-year study on speakers of a tonal language," Ear Hear. **26**(4), 30S-37S.
Lehnhardt, E. (**1993**). "Intracochleare plazierung der cochlear-implant-elektroden in soft surgery technique," HNO **41**, 356–359.
Liberman, M. C. (**1978**). "Auditory-nerve response from cats raised in a low-noise chamber," J. Acoust. Soc. Am. **63**, 442–455.
McAnally, K. I., Clark, G. M., and Syka, J. (**1993**). "Hair cell mediated responses of the auditory nerve to sinusoidal electrical stimulation of the cochlea in the cat," Hear. Res. **67**, 55–68.
McAnally, K. I., and Clark, G. M. (**1994**). "Stimulation of residual hearing in the cat by pulsatile electrical stimulation of the cochlea," Acta Oto-Laryngol. **114**, 366–372.
McAnally, K. I., Brown, M., and Clark, G. M. (**1997a**). "Estimating mechanical responses to pulsatile electrical stimulation of the cochlea," Hear. Res. **106**, 146–153.
McAnally, K. I., Brown, M., and Clark, G. M. (**1997b**). "Comparison of current waveforms for the electrical stimulation of residual low frequency hearing," Acta Oto-Laryngol. **117**, 831–835.
McAnally, K. I., Brown, M., and Clark, G. M. (**1997c**). "Acoustic and electric forward-masking of the auditory nerve compound action potential: Evidence for linearity of electro-mechanical transduction," Hear. Res. **106**, 137–145.
McDermott, H. J. (**2004**). "Music perception with cochlear implants: A review," Trends in Amplification **8**, 49–82.
Miller, A. L., Smith, D. W., and Pfingst, B. E. (**1999**). "Across-species comparisons of psychophysical detection thresholds for electrical stimulation of the cochlea: II. Strength-duration functions for single, biphasic pulses," Hear. Res. **135**, 47–55.
Miller, C. A., Faulkner, M. J., and Pfingst, B. E. (**1995a**). "Functional responses from guinea pigs with cochlear implants. II. Changes in electrophysiological and psychophysical measures over time," Hear. Res. **92**, 100–111.
Miller, C. A., Woodruff, K. E., and Pfingst, B. E. (**1995b**). "Functional responses from guinea pigs with cochlear implants. I. Electrophysiological and psychophysical measures," Hear. Res. **92**, 85–99.
Mitchell, A., Miller, J. M., Finger, P. A., Heller, J. W., Raphael, Y., and Altschuler, R. A. (**1997**). "Effects of chronic high-rate electrical stimulation on the cochlea and eighth nerve in the deafened guinea pig," Hear. Res. **105**, 30–43.
Moody, D. B. (**1970**). "Reaction time as an index of sensory function," in

Animal Psychophysics: The Design and Conduct of Psychophysical Experiments, edited by W. C. Stebbins, (Appleton-Century-Crofts, New York), pp. 277–302.
Moxon, E. C. (1971). "Neural and Mechanical Responses to Electrical Stimulation of the Cat's Inner Ear," Submitted to the Department of Electrical Engineering, at the Massachusetts Institute of Technology, Cambridge.
Nadol, J. B., Jr., Young, Y. S., and Glynn, R. J. (**1989**). "Survival of spiral ganglion cells in profound sensorineural hearing loss: Implications for cochlear implantation," Ann. Otol. Rhinol. Laryngol. **98**, 411–416.
Nakajima, H. H., Mountain, D. C., and Hubbard, A. E. (**1998**). "Nonlinear characteristics of electrically evoked otoacoustic emissions," Hear. Res. **122**, 109–118.
National Research Council (**1996**). *Guide for the Care and Use of Laboratory Animals* (National Academy Press, Washington D.C).
Ni, D., Shepherd, R. K., Seldon, H. L., Xu, S. A., Clark, G. M., and Millard, R. E. (**1992**). "Cochlear pathology following chronic electrical stimulation of the auditory nerve. I: Normal hearing kittens," Hear. Res. **62**, 63–81.
Niemiec, A. J., and Moody, D. B. (**1995**). "Constant stimulus and tracking procedures for measuring sensitivity," in *Methods in Comparative Psychoacoustics*, edited by G. M. Klump, R. J. Dooling, R. R. Fay, and W. C. Stebbins (Birkhauser Verlag, Basel), Vol. **6**, pp. 65–77.
NIH Consensus Statement (**1995**). "Cochlear implants in adults and children," Consens Statement **13**, 1–30.
Nuttall, A. L., and Dolan, D. F. (**1993**). "Basilar membrane velocity responses to acoustic and intracochlear electric stimuli," in *Biophysics of Hair Cell Sensory Systems*, edited by H. Duifuis, J. W. Horst, P. van Dijk, and S. M. van Netten (World Scientific, Singapore), pp. 288–295.
Nuttall, A. L., and Ren, T. (**1995**). "Electromotile hearing: Evidence from basilar membrane motion and otoacoustic emissions," Hear. Res. **92**, 170–177.
Nuttall, A. L., Zheng, J., Ren, T., and de Boer, E. (**2001**). "Electrically evoked otoacoustic emissions from apical and basal perilymphatic electrode positions in the guinea pig cochlea," Hear. Res. **152**, 77–89.
Pfingst, B. E. (**1984**). "Operating ranges and intensity psychophysics for cochlear implants. Implications for speech processing strategies," Arch. Otolaryngol. **110**, 140–144.
Prieskorn, D. M., and Miller, J. M. (**2000**). "Technical report: Chronic and acute intracochlear infusion in rodents," Hear. Res. **140**, 212–215.
Raphael, Y., and Altschuler, R. A. (**1991**). "Reorganization of cytoskeletal and junctional proteins during cochlear hair cell degeneration," Cell Motil. Cytoskeleton **18**, 215–227.
Ren, T., and Nuttall, A. L. (**1995**). "Extracochlear electrically evoked otoacoustic emissions: A model for in vivo assessment of outer hair cell electromotility," Hear. Res. **92**, 178–183.
Reuter, G., and Zenner, H. P. (**1990**). "Active radial and transverse motile responses of outer hair cells in the organ of Corti," Hear. Res. **43**, 219–230.
Reyes, S., Ding, D., Sun, W., and Salvi, R. (**2001**). "Effect of inner and outer hair cell lesions on electrically evoked otoacoustic emissions," Hear. Res. **158**, 139–150.
Risberg, A., Agelfors, E., Lindstrom, B., and Bredberg, G. (**1990**). "Electrophonic hearing and cochlear implants," Acta Oto-Laryngol., Suppl. **469**, 156–163.
Rogowski, M., Reiss, G., and Lehnhardt, E. (**1995**). "Morphologic study of the guinea pig cochlea after cochlear implantation using the "soft surgery" technique," Ann. Otol. Rhinol. Laryngol. Suppl. **166**, 434–436.
Rubinstein, J. T. (**2004**). "How cochlear implants encode speech," Curr. Opin. Otolaryngol. Head Neck Surg. **12**, 444–448.
Shepherd, R. K., and Javel, E. (**1997**). "Electrical stimulation of the auditory nerve. I. Correlation of physiological responses with cochlear status," Hear. Res. **108**, 112–144.
Shera, C. A., and Guinan, J. J., Jr. (**1999**). "Evoked otoacoustic emissions arise by two fundamentally different mechanisms: A taxonomy for mammalian OAEs," J. Acoust. Soc. Am. **105**, 782–798.
Skarzynski, H., Lorens, A., D'Haese, P., Walkowiak, A., Piotrowska, A., Sliwa, L., and Anderson, I. (**2002**). "Preservation of residual hearing in children and post-lingually deafened adults after cochlear implantation: An initial study," ORL **64**, 247–253.
Skarzynski, H., Lorens, A., and Piotrowska, A. (**2003**). "A new method of partial deafness treatment," Med. Sci. Monit. **9**, CS20–24.
Skinner, M. W., Clark, G. M., Whitford, L. A., Seligman, P. M., Staller, S. J., Shipp, D. B., Shallop, J. K., Everingham, C., Menapace, C. M., Arndt, P. L. *et al.* (**1994**). "Evaluation of a new spectral peak coding strategy for the Nucleus 22 Channel Cochlear Implant System," Am. J. Otol. **15**, Suppl. 2, 15–27.
Skinner, M. W., Holden, L. K., Holden, T. A., Demorest, M. E., and Fourakis, M. S. (**1997**). "Speech recognition at simulated soft, conversational, and raised-to-loud vocal efforts by adults with cochlear implants," J. Acoust. Soc. Am. **101**, 3766–3782.
Skinner, M. W., Ketten, D. R., Holden, L. K., Harding, G. W., Smith, P. G., Gates, G. A., Neely, J. G., Kletzker, G. R., Brunsden, B., and Blocker, B. (**2002**). "CT-derived estimation of cochlear morphology and electrode array position in relation to word recognition in Nucleus-22 recipients," J. Assoc. Res. Otolaryngol. **3**, 332–350.
Smith, D. W., Watt, S., Konrad, K. E., and Olszyk, V. B. (**1995**). "Behavioral auditory thresholds for sinusoidal electrical stimuli in the cat," J. Acoust. Soc. Am. **98**, 211–220.
Spelman, F. A., Pfingst, B. E., Miller, J. M., Hassul, M., Powers, W. E., and Clopton, B. M. (**1980**). "Biophysical measurements in the implanted cochlea," Otolaryngol.-Head Neck Surg. **88**, 183–187.
Spelman, F. A., Clopton, B. M., and Pfingst, B. E. (**1982**). "Tissue impedance and current flow in the implanted ear. Implications for the cochlear prosthesis," Ann. Otol. Rhinol. Laryngol. Suppl. **98**, 3–8.
Spelman, F. A., Pfingst, B. E., Clopton, B. M., Jolly, C. N., and Rodenhiser, K. L. (**1995**). "Effects of electrical current configuration on potential fields in the electrically stimulated cochlea: Field models and measurements," Ann. Otol. Rhinol. Laryngol. Suppl. **166**, 131–136.
Szymanski, M. D., Bain, D. E., Kiehl, K., Pennington, S., Wong, S., and Henry, K. R. (**1999**). "Killer whale (Orcinus orca) hearing: Auditory brainstem response and behavioral audiograms," J. Acoust. Soc. Am. **106**, 1134–1141.
Tong, Y. C., Clark, G. M., Blamey, P. J., Busby, P. A., and Dowell, R. C. (**1982**). "Psychophysical studies for two multiple-channel cochlear implant patients," J. Acoust. Soc. Am. **71**, 153–160.
Tsuji, J., and Liberman, M. C. (**1997**). "Intracellular labeling of auditory nerve fibers in guinea pig: Central and peripheral projections," J. Comp. Neurol. **381**, 188–202.
Turner, C. W., Gantz, B. J., Vidal, C., Behrens, A., and Henry, B. A. (**2004**). "Speech recognition in noise for cochlear implant listeners: Benefits of residual acoustic hearing," J. Acoust. Soc. Am. **115**, 1729–1735.
Tykocinski, M., Shepherd, R. K., and Clark, G. M. (**1995**). "Electrophysiologic effects following acute intracochlear direct current stimulation of the guinea pig cochlea," Ann. Otol. Rhinol. Laryngol. Suppl. **166**, 68–71.
Tyler, R. S., Kelsay, D. M., Teagle, H. F., Rubinstein, J. T., Gantz, B. J., and Christ, A. M. (**2000**). "7-year speech perception results and the effects of age, residual hearing and preimplant speech perception in prelingually deaf children using the Nucleus and Clarion cochlear implants," Adv. Oto-Rhino-Laryngol. **57**, 305–310.
von Ilberg, C., Kiefer, J., Tillein, J., Pfenningdorff, T., Hartmann, R., Sturzebecher, E., and Klinke, R. (**1999**). "Electric-acoustic stimulation of the auditory system. New technology for severe hearing loss," ORL **61**, 334–340.
Waltzman, S. B., Cohen, N. L., Gomolin, R. H., Green, J. E., Shapiro, W. H., Hoffman, R. A., and Roland, J. T., Jr. (**1997**). "Open-set speech perception in congenitally deaf children using cochlear implants," Am. J. Otol. **18**, 342–349.
Wang, J., Powers, N. L., Hofstetter, P., Trautwein, P., Ding, D., and Salvi, R. (**1997**). "Effects of selective inner hair cell loss on auditory nerve fiber threshold, tuning and spontaneous and driven discharge rate," Hear. Res. **107**, 67–82.
Watson, C. S., Dobie, R. A., Durlach, N., Humes, L. E., Levitt, H., Miller, J. D., Sherrick, C. E., Simmons, F. B., Studebaker, G. A., Tyler, R. S., and Widin, G. P. (**1991**). "Speech-perception aids for hearing-impaired people: Current status and needed research. Working Group on Communication Aids for the Hearing-Impaired," J. Acoust. Soc. Am. **90**, 637–683.
Winter, I. M., Robertson, D., and Yates, G. K. (**1990**). "Diversity of characteristic frequency rate-intensity functions in guinea pig auditory nerve fibres," Hear. Res. **45**, 191–202.
Wolski, L. F., Anderson, R. C., Bowles, A. E., and Yochem, P. K. (**2003**). "Measuring hearing in the harbor seal (Phoca vitulina): Comparison of behavioral and auditory brainstem response techniques," J. Acoust. Soc. Am. **113**, 629–637.
Xue, S., Mountain, D. C., and Hubbard, A. E. (**1993**). "Acoustic enhancement of electrically-evoked otoacoustic emissions reflects basilar membrane tuning: Experiment results," Hear. Res. **70**, 121–126.
Xue, S., Mountain, D. C., and Hubbard, A. E. (**1995**). "Electrically evoked basilar membrane motion," J. Acoust. Soc. Am. **97**, 3030–3041.

The kurtosis metric as an adjunct to energy in the prediction of trauma from continuous, nonGaussian noise exposures

Wei Qiu,[a] Roger P. Hamernik, and Bob Davis
Auditory Research Laboratory, State University of New York, 107 Beaumont Hall, Plattsburgh, New York 12901

(Received 16 June 2006; revised 21 September 2006; accepted 26 September 2006)

Data from an earlier study [Hamernik *et al.* (2003). J. Acoust. Soc. Am. **114**, 386–395] were consistent in showing that, for equivalent energy [L_{eq}=100 dB(A)] and spectra, exposure to a continuous, nonGaussian (nonG) noise could produce substantially greater hearing and sensory cell loss in the chinchilla model than a Gaussian (G) noise exposure and that the statistical metric, kurtosis, computed on the amplitude distribution of the noise could order the extent of the trauma. This paper extends these results to L_{eq}=90 and 110 dB(A), and to nonG noises that are generated using broadband noise bursts, and band limited impacts within a continuous G background noise. Data from nine new experimental groups with 11 or 12 chinchillas/group is presented. Evoked response audiometry established hearing thresholds and surface preparation histology quantified sensory cell loss. At the lowest level [L_{eq}=90 dB(A)] there were no differences in the trauma produced by G and nonG exposures. For $L_{eq}>90$ dB(A) nonG exposures produced increased trauma relative to equivalent G exposures. Removing energy from the impacts by limiting their bandwidth reduced trauma. The use of noise bursts to produce the nonG noise instead of impacts also reduced the amount of trauma. © *2006 Acoustical Society of America.*
[DOI: 10.1121/1.2372455]

PACS number(s): 43.66.Ed, 43.50.Pn [BLM] Pages: 3901–3906

I. INTRODUCTION

High-level nonGaussian (nonG) noise exposures are very common in industrial and military environments and clearly pose a hazard to hearing for large numbers of the exposed population. Over the past several decades a number of published papers have shown, in an animal model, that exposure to nonG noise produces more hearing and sensory cell loss than does an equivalent energy Gaussian (G) exposure (e.g., Dunn *et al.*, 1991; Lei *et al.*, 1994; Lataye and Campo, 1996; Hamernik and Qiu, 2001; Harding and Bohne, 2004). These results along with similar findings from human epidemiologic data (Sulkowski and Lipowczan, 1982; Taylor *et al.*, 1984; Thiery and Meyer-Bisch, 1988) challenge the use of the equal energy hypothesis (EEH) that forms the basis of current criteria for human exposure to noise (e.g., ISO 1999, 1990). One consequence of categorizing a temporally diverse and complex set of exposures with a single metric such as energy may be the appearance of large variability in the hearing threshold levels that is typically found in epidemiologic studies. This large variability (Mills *et al.*, 1996) precludes meaningful comparisons across exposure conditions as well as estimates of individual risk of hearing loss.

Since temporal variables do not affect an energy metric and since there are an infinite number of very different noise exposures characterized by the same Leq, it seems reasonable that a metric that would incorporate both temporal and level variables might be a useful adjunct to the Leq metric. One such metric is the kurtosis of a sample distribution that is defined as the ratio of the fourth-order central moment to the squared second-order moment of the amplitude distribution. This statistic, used to estimate the deviation of a distribution from the Gaussian, can be computed on the unfiltered and the filtered time-domain signal. All the variables that characterize a nonG noise such as transient peaks, intertransient intervals, transient durations, crest factor, etc., have an effect on the kurtosis. While the effect on kurtosis of any one of these variables can be predicted, the effect of them all acting in unison is less predictable.

Several years ago data were presented from a number of different exposures (Hamernik *et al.*, 2003) that were consistent with the above referenced work in showing that, for equivalent energy [L_{eq}=100 dB(A)] and spectra, exposure to a continuous, nonG noise could produce substantially greater hearing and sensory cell loss in the chinchilla model than a G noise exposure and that the statistical metric, kurtosis [$\beta(t)$], computed on the amplitude distribution of the noise, could order the extent of the trauma. This presentation extends these results to L_{eq}=90 and 110 dB(A) and to nonG noises that are generated using broadband noise bursts, and band-limited impacts. A metric based on some combination of kurtosis and energy may be useful in the assessment of industrial noise environments for hearing conservation purposes.

II. METHODS

The experimental design and methods were identical to those used in the Hamernik *et al.* (2003) paper. One hundred and six chinchillas, divided into nine experimental groups, were used as subjects. Briefly, each animal was made mon-

[a]author to whom correspondence should be addressed; electronic mail: wei.qiu@plattsburgh.edu

TABLE I. Summary of exposure conditions

L_{eq} dB(A)	$\beta(t)$	Noise type[a]	Group No.	N	Peak range dB SPL	Impulse probability	L_b-background dB(A)
90	3	(1)	47	12	⋯	⋯	⋯
90	32	(2)	48	11	[104, 118]	0.6	84
90	35	(3)	56	12	[105, 120]	0.6	83.5
100	21	(4)	50	11	[114, 128]	0.6	95.5
100	27	(5)	70(*)	12	[105, 115](**)	0.6	91
100	33	(3)	77	12	[115, 129]	0.22–0.35	91.5
100	45	(5)	82	12	[106, 117](**)	0.6	92
110	3	(1)	42	12	⋯	⋯	⋯
110	20	(2)	45	12	[129, 134]	0.6	104
110	27	(3)	78	12	[132, 137]	0.6	104

[a]Noise type: (1) Broadband Gaussian. (2) NonGaussian noise, with a Gaussian background component defined by L_b. The transients which provide the nonGaussian character of the noise were impacts created from three 400 Hz bands of energy centered at 1, 2, and 4 kHz. (3) Same as in (2) except the transients were broadband (710–5680 kHz). (4) Same as in (2) except the transients were narrow band (1800–2200 Hz). (5) For these exposures the transients were broadband (710–5680 Hz) noise bursts.
(*)Data of group 70 is taken from Hamernik *et al.* (2003).
(**)Levels represent the rms SPL of the noise burst.

aural by the surgical destruction, under anesthesia, of the left cochlea. During this procedure a bipolar electrode was implanted, under stereotaxic control, into the left inferior colliculus and the electrode plug cemented to the skull for the recording of auditory evoked potentials (AEP). The AEP was used to estimate pure tone thresholds and surface preparations of the organ of Corti were used to estimate the inner and outer hair cell (IHC, OHC) populations.

A. Experimental protocol

The animals were randomly assigned to one of nine experimental groups with 11 or 12 animals/group. Following a two-week postsurgical recovery, three AEP preexposure audiograms were obtained (on different days) on each animal at octave intervals between 0.5 and 16.0 kHz. If the mean of the three audiograms, at more than one test frequency, fell beyond one standard deviation of laboratory norms (Hamernik and Qiu, 2001) in the direction of poorer thresholds the animal was rejected.

The animals, confined to individual cages ($10\times11\times16$ in.) with free access to food and water, were exposed three or four at a time to one of the noise conditions summarized in Table I. Exposures lasted 24 h/day for five days and were interrupted once daily for approximately 20–30 min for AEP testing. The five-day exposures produced an asymptotic threshold shift. Thirty days following the last exposure day, three more audiograms were collected on different days and the mean used to define the postexposure threshold from which permanent threshold shift (PTS) was obtained.

B. Histology

Following the last AEP test protocol, each animal was euthanized under anesthesia and the right auditory bulla removed and opened to gain access to the cochlea for perfusion. Fixation solution consisting of 2.5% glutaraldehyde in veronal acetate buffer (final pH=7.3) was perfused through the cochlea. After 12–24 h of fixation the cochlea was postfixed in 1% OsO_4 in veronal acetate buffer. Surface preparation mounts of the entire organ of Corti were prepared and IHC and OHC populations were plotted as a function of frequency and location using the frequency-place map of Eldredge *et al.* (1981). Missing cells were identified by the presence of a characteristic phalangeal scar. For purposes of this presentation, sensory cell population data are presented as group averages (in percent missing) taken over octave band lengths of the cochlea centered on the primary AEP test frequencies or as the group mean total number of IHCs or OHCs missing.

C. Noise measurement and analyses

The design and digital generation of the acoustic signal is detailed in Hsueh and Hamernik (1990, 1991) and Hamernik *et al.* (2003). The noise was created using an Electro-Voice Xi-1152/94 speaker and amplifiers (Model P1200 and P2000). During exposure the sound level of noise field was monitored with a Larson Davis 814 sound level meter equipped with a 1/2 in. microphone. The sound field was recorded using a Bruel and Kjaer 1/2 in. microphone (Model 4134), amplified by a Bruel and Kjaer (Model 2610) measuring amplifier and digitalized by an analog-to-digital/digital-to-analog converter (Model PCI-6221, National Instrument Inc.). The signal was sampled at 48 kHz in 16 bits with a recording duration of 5.5 min. Several segments of the signal were recorded at each cage and saved on a hard disk for off line analysis. The sound preasure level (SPL) and spectral data on both impact and background noise were obtained from these recordings using programs developed using MATLAB. The SPLs, across cages, in the middle of each cage, varied within less than ±1 dB.

D. Noise exposures

Each exposure had in common approximately the same broadband (0.125–20 kHz) spectrum that was reasonably

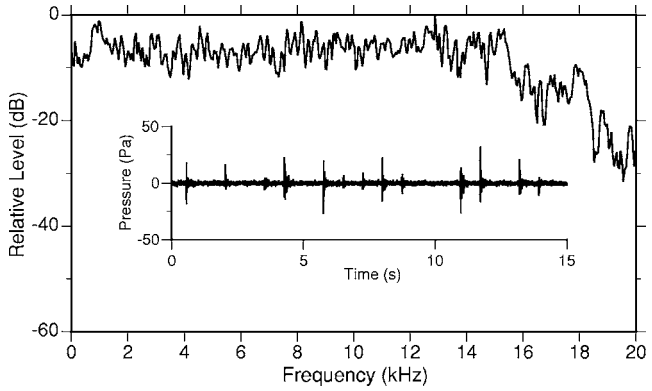

FIG. 1. The average spectrum of a 40 s sample of a nonG noise incorporating broadband impacts. This long-term spectrum was common to all the exposures. The inset shows a 15 s sample of one of the nonG wave forms.

flat between 0.125 and 10.0 kHz as shown in Fig. 1. It was this flat portion of the spectrum that was manipulated to produce the various types of nonG noises. The noise was presented at an L_{eq}=90, 100, or 110 dB(A) SPL. The nonG noises were created by inserting either impacts or noise bursts into the continuous G noise. The impact or noise burst transients were created from several different regions of the energy spectrum. The probability of a transient occurring in a 750 ms window was set at 0.6 for each exposure except for experimental group 77 where it was randomly varied between 0.225 and 0.35. For group 50, impact transients were created from the energy in a single 400 Hz wide band centered at 2 kHz; for groups 45 and 48 the energy in the impacts was derived from three, 400 Hz wide bands centered at 1, 2, and 4 kHz and for groups 56, 70, 78, and 82 the energy for either the impacts or the noise bursts was derived from the 710–5680 Hz region of the spectrum, i.e., broadband transients. The spectrum of the continuous G background noise (Fig. 2) consisted of the frequencies that were not used to produce the transients. The background noise level given as L_b in Table I was measured from digital recordings of the noise signal between impacts. The overall L_{eq} of the exposure was adjusted in an iterative fashion by adjusting the impact variables and the L_b to obtain the required L_{eq}.

III. RESULTS AND DISCUSSION

Summary data for the groups defined in Table I are shown as the symbols in Fig. 3 where they are identified by group numbers. Panel (a) shows the group mean total number of OHCs lost while panel (b) presents the group mean PTS averaged over the 2, 4, and 8 kHz ($PTS_{2,4,8}$) test frequencies as a function of the kurtosis, $\beta(t)$. Bars on the data points represent the standard error (s.e.). If a bar is not present the s.e. was less than the size of the symbol. For reference purposes, the total number of OHCs in the chinchilla cochlea is approximately 7300 (Bohne *et al.*, 1982 and Hamernik *et al.*, 1988). The two solid lines numbered (ii) and (iii) were taken from the Hamernik *et al.*, (2003) paper and represent the best fit of the function shown to the data that were obtained from a series of exposures extending from $\beta(t)$=3 to $\beta(t)>100$ at an L_{eq}=100 dB(A). Broadband impacts were used in the nonG exposures that produced curve

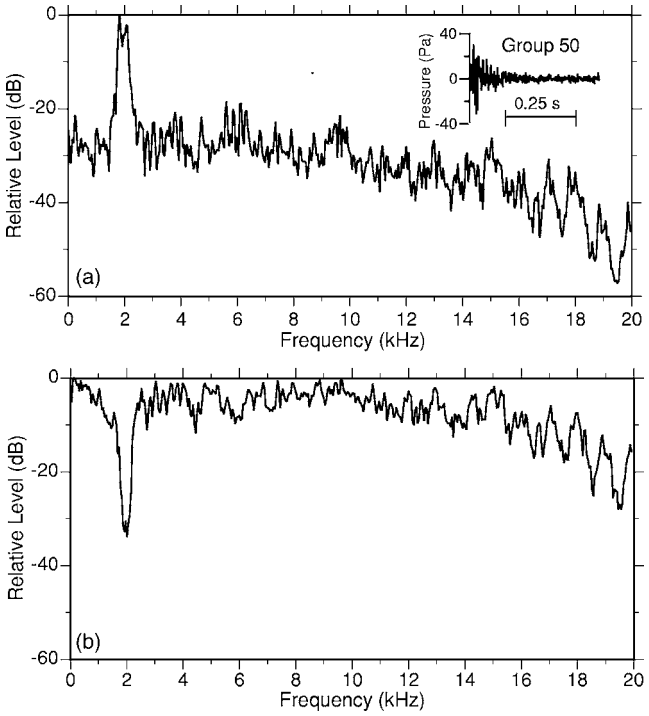

FIG. 2. The upper panel (a) shows the spectrum and wave form of the narrow band (1.8–2.2 kHz) impulse transient used in the exposure of group 50. The peak SPL was randomly varied between 114 and 128 dB and the probability of an impact occurring in a 750 ms window was set at 0.6. The lower panel (b) shows the complementary spectrum of the G background noise that was mixed with the impacts to create the nonG continuous noise.

(ii) while the impacts used in the nonG exposures that produced curve (iii) were created from the energy in three 400 Hz wide bands centered at 1, 2, and 4 kHz. These two pairs of curves show that the nonG exposures produced more OHC loss and PTS than did the energy and spectrally equivalent G noise, i.e., the exposures at a $\beta(t)$=3. For the nonG exposure containing broadband impacts [curve (ii)] the upper limit of OHC loss and PTS is 4515 missing OHCs and 49 dB PTS, respectively, while for the equivalent G exposure there are ~660 missing OHCs and a PTS of about 14 dB. IHC losses are not presented since they are much smaller than OHC losses and typically much less susceptible to noise damage than are the OHCs. IHC losses, however, did follow the trends presented for the OHCs.

Curve (iii) shows that as energy is removed from the impact and incorporated into the G background noise the degree of trauma is reduced considerably. The number of OHCs lost at the asymptotic value of this function drops to about 3000 and the PTS to about 33 dB, but this is still greater than for the $\beta(t)$=3, G exposure. This result could be anticipated since in the limit as the impact energy approaches zero the exposure approaches the Gaussian condition $\beta(t)$=3. These curves are used as a reference for the additional exposure conditions reported here. The same function will be used to relate the higher and lower level exposures [curves (i) and (iv) in Fig. 3] to this earlier data set.

The effect of increasing the L_{eq} to 110 dB(A) (groups 42 and 78) and fitting the same function as used for curve (ii) through the pair of data points (42 and 78) shifts the curves, as expected, upward. The G exposure (group 42) produced

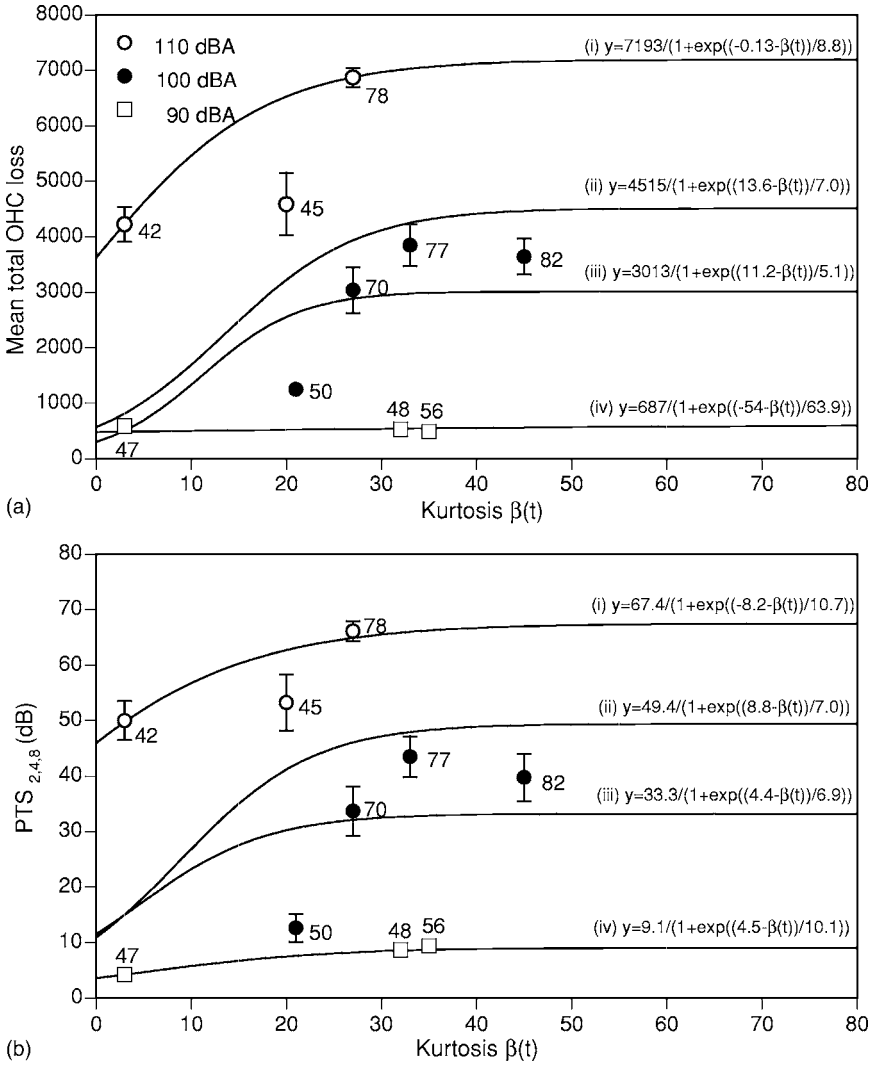

FIG. 3. (a) The group mean total outer hair cell (OHC) loss for the ten groups of animals exposed to the equal energy and spectrum Gaussian [$\beta(t)=3$] and nonGaussian [$\beta(t)>3$] noises. (b) The group mean permanent threshold shift averaged over the 2.0, 4.0 and 8.0 kHz AEP test frequencies ($PTS_{2,4,8}$). Numbers adjacent to data symbols identify the experimental groups outlined in Table I. Curves (ii) and (iii) represent the curve fit to data taken from Hamernik *et al.* (2003).

4230 missing OHCs and a $PTS_{2,4,8}=50$ dB while the nonG exposure (group 78) containing broadband impacts produced 6875 missing OHCs and a $PTS_{2,4,8}=66$ dB. Thus, at the higher L_{eq} the nonG exposure still produced considerably more trauma than did the equivalent G exposure. Removing energy from the impact by limiting its bandwidth and increasing the energy in the G component by a corresponding amount would be expected to cause a lessening of trauma. This is seen in the results from group 45. At an $L_{eq}=110$ dB(A) the total cell loss and mean PTS for group 45, an exposure that used the three, 400 Hz narrow bands of energy centered at 1, 2, and 4 kHz to produce the impacts, was statistically similar to the G exposure, condition 42. However, it is instructive to look at the frequency specific data when comparing the nonG and G groups 45 and 42, respectively.

Figure 4 compares the PTS and percent OHC loss for groups 42, 45, and 78 exposed to the 110 dB(A) noises. There are large differences in cell loss and PTS at the lower frequencies (0.5, 1.0, and 2.0 kHz) between groups 42 and 45 that are not reflected in the summary data shown in Fig. 3. Focusing on the high frequency mean $PTS_{2,4,8}$ and the group mean total OHC loss obscures the increased low frequency trauma produced by introducing nonG components into the exposure. The increased low frequency OHC loss in group 45 is reflected in the 12–15 dB increase in PTS at 0.5 and 1.0 kHz over the PTS produced by the G exposure (group 42). There is a group mean loss of 2031 OHCs in the 0.5 and 1.0 kHz octave band lengths of the basilar membrane following the nonG exposure of group 45 compared to 1164 missing as a result of the G exposure (group 42). Thus, the nonG exposure, incorporating the bandlimited impacts, also produced greater trauma than the equivalent G exposure but less than the group 78 that had more energy in the impacts. The series of curves in Fig. 4 clearly illustrate the increased trauma associated with high $\beta(t)$ exposures at 110 dB as well as the progression of the trauma toward the lower audiometric test frequencies as a greater fraction of the total energy is put into the impacts. At this level for the broadband impact condition a ceiling effect is beginning to appear. There is 100% OHC loss over a large part of the cochlea.

Group 50 was exposed to a nonG noise with $\beta(t)=21$ at 100 dB(A) in which the impacts were produced from a single 400 Hz wide band of the spectrum centered at 2 kHz. Using the points on curves (ii) and (iii) in Fig. 3 at the corresponding $\beta(t)=21$ as a reference it is clear that removing additional energy from the impacts, as in this one-band

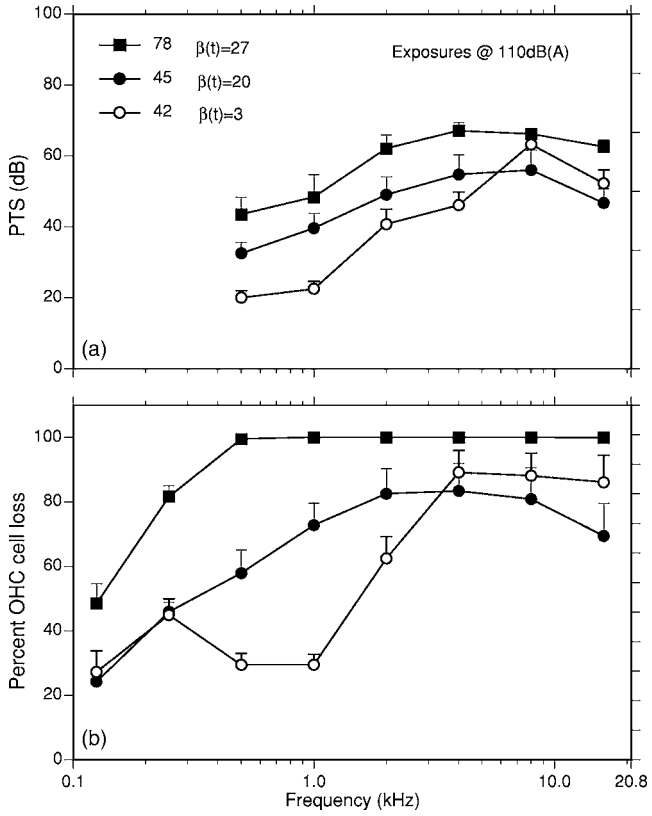

FIG. 4. (a) The frequency specific group mean permanent threshold shift (PTS) and (b) the group mean percent outer hair cell loss (OHC) for groups 42, 45, and 78 exposed to the 110 dB(A) Gaussian (42) and nonGaussian (45 and 78) noises. OHC data points represent average losses taken over octave band lengths of the basilar membrane at the indicated center frequencies.

exposure condition, causes a still further reduction in the trauma despite the presence of impact peaks that varied between 114 and 128 dB peak SPL. The impacts used in the exposures that produced curves (ii) and (iii) had approximately the same range of peak SPLs as those used in the exposure of group 50. The lessening of trauma from lower energy impacts having the same peaks suggests that the energy in the impact is more important in the production of hearing loss than is the impact peak SPL. Finally, it should be noted that despite the lower energy in the impacts the cell loss but not the $PTS_{2,4,8}$ for group 50 is statistically greater than the equivalent G exposure [i.e., the $\beta(t)=3$ point on curves (ii) and (iii) in Figs 3(a) and 3(b)]. The group mean total number of OHCs lost was 1250. This loss for group 50 was distributed across the entire basilar membrane and varied from 10% to 15% loss at the lower frequencies to 25% to 30% loss at 8 kHz and above. As with the OHC loss the PTS was evenly distributed across the test frequencies varying between 10 and 15 dB across the 0.5 through 16 kHz range.

The probability (P) of a transient occurring in a 750 ms window of the noise was set at 0.6 for all nonG exposures except group 77. For group 77, P was randomly varied such that $0.22<P<0.35$. The reduction of P resulted in less sensory cell loss and $PTS_{2,4,8}$ than for the $P=0.6$ conditions; curve (iii). This reduction in trauma agrees with a similar reduction reported in the Hamernik *et al.* (2003) paper when $P=0.1$ was used for several nonG exposures. Using broadband (710–5680 Hz) noise bursts instead of impacts to produce a nonG exposure condition as in groups 70 and 82 also had the effect of reducing the level of trauma at both values of $\beta(t)$ but the exposure still produced more trauma than the $\beta(t)=3$ exposure. The rms level of the noise bursts varied between 105 and 117 dB.

Groups 47, 48, and 56 received an $L_{eq}=90$ dB(A) exposure. At this Leq, both nonG groups (48 and 56), regardless of the bandwidth of the transients, produced the same degree of trauma as the G noise exposure group 47 (Fig. 3). While exposure conditions for the $L_{eq}=90$ dB are limited, the available data suggest that for exposures that produce relatively small amounts of PTS and sensory cell loss the EEH holds regardless of the value of the kurtosis. A similar conclusion was reached by Hamernik *et al.* (1981) using lower levels of nonG noise and a different experimental paradigm.

IV. CONCLUSIONS

The results presented above complement and extend our earlier results (Hamernik *et al.*, 2003) in showing that for noise exposures that have the potential for producing hearing loss a high kurtosis exposure will exacerbate the loss. Under such conditions the EEH does not apply. Temporally complex noise exposures having equivalent energy and spectrum if characterized by only an L_{eq} can result in hearing loss data showing extreme variability across exposed subjects. The kurtosis metric, which incorporates a number of variables that have in the past been examined individually such as impact peaks, inter-impact intervals, impact duration and crest factor can, however, separate exposed subjects into similarly exposed groups in a quantitative way and reduce variability. The kurtosis metric and the L_{eq} coupled with an examination of the transients in a complex exposure in terms of their range of peaks and spectrum may prove useful in the development of occupational noise exposure criteria for the protection of hearing.

ACKNOWLEDGMENTS

This work was supported by Grant No. 1-R01-OH02317 from the National Institute for Occupational Safety and Health. The technical assistance of George A. Turrentine, Ann Johnson, and Adam Bouchard is greatly appreciated. In conducting this research the investigators adhered to the "Guide for the Care and Use of Laboratory Animals," prepared by the Committee on Care and Use of Laboratory Animals of the Institute of Laboratory Animal Resources, National Research Council [DHHS Publication No. (NIH) 86-23, revised 1985].

Bohne, B., Kenworthy, A., and Carr, C. D. (**1982**). "Density of myelinated nerve fibers in the chinchilla cochlea," J. Acoust. Soc. Am. **72**, 102–107.

Dunn, D. E., Davis, R. R., Merry, C. J., and Franks, J. R. (**1991**). "Hearing loss in the chinchilla from impact and continuous noise exposure," J. Acoust. Soc. Am. **90**, 1979–1985.

Eldredge, D. H., Miller, J. D., and Bohne, B. A. (**1981**). "A frequency-position map for the chinchilla cochlea," J. Acoust. Soc. Am. **69**, 1091–1095.

Hamernik, R. P., Henderson, D., and Salvi, R. (**1981**). "Potential for interaction of low-level impulse and continuous noise," AFAMRL-TR-80-68,

Air Force Aerospace Medical Research Laboratory, Wright-Patterson Air Force Base, Ohio 45433.
Hamernik, R. P., Patterson, J. H., Turrentine, G. A., and Ahroon, W. A. (**1988**). "The quantitative relation between sensory cell loss and hearing thresholds," Hear. Res. **38**, 199–212.
Hamernik, R. P., and Qiu, W. (**2001**). "Energy-independent factors influencing noise-induced hearing loss in the chinchilla model," J. Acoust. Soc. Am. **110**, 3163–3168.
Hamernik, R. P., Qiu, W., and Davis, B. (**2003**). "The effects of the amplitude distribution of equal energy exposures on noise-induced hearing loss: The kurtosis metric," J. Acoust. Soc. Am. **114**, 386–395.
Harding, G. W., and Bohne, B. A. (**2004**). "Noise-induced hair-cell loss and total exposure energy: Analysis of a large data set," J. Acoust. Soc. Am. **115**, 2207–2220.
Hsueh, K. D., and Hamernik, R. P. (**1990**). "A generalized approach to random noise synthesis: Theory and computer simulation," J. Acoust. Soc. Am. **87**, 1207–1217.
Hsueh, K. D., and Hamernik, R. P. (**1991**). "Performance characteristics of a phase domain approach to random noise synthesis," Noise Control Eng. J. **36**, 18–32.
International Standard ISO 1999 (**1990**). "Acoustics-determination of occupational noise exposure and estimation of noise-induced hearing impairment," Technical Comm. ISO/TC43-Acoustics, International Organization for Standardization, Geneva, Switzerland.
Lei, S-F., Ahroon, W. A., and Hamernik, R. P. (**1994**). "The application of frequency and time domain kurtosis to the assessment of hazardous noise exposures," J. Acoust. Soc. Am. **96**, 1435–1444.
Lataye, R., and Campo, P. (**1996**). "Applicability of the L_{eq} as a damage-risk criterion: An animal experiment," J. Acoust. Soc. Am. **99**, 1621–1632.
Mills, J. H., Lee, F. S., Dubno, J. R., and Boettcher, F. A. (**1996**). "Interactions between age-related and noise-induced hearing loss," in *Scientific Basis of Noise-Induced Hearing Loss*, edited by A. Axelsson, H. Borchgrevink, R. P. Hamernik, P. A. Hellstrom, D. Henderson, and R. J. Salvi (Thieme, New York), pp. 193–121.
Sulkowski, W. J., and Lipowczan, A. (**1982**). "Impulse noise-induced hearing loss in drop forge operators and the energy concept," Noise Control Eng. **18**, 24–29.
Taylor, W., Lempert, B., Pelmear, P., Hemstock, I., and Kershaw, J. (**1984**). "Noise levels and hearing threshold in the drop forging industry," J. Acoust. Soc. Am. **76**, 807–819.
Thiery, L., and Meyer-Bisch, C. (**1988**). "Hearing loss due to partly impulsive industrial noise exposure at levels between 87 and 90 dB (A)," J. Acoust. Soc. Am. **84**, 651–659.

Individual differences in the sensitivity to pitch direction

Catherine Semal and Laurent Demany[a)]
Laboratoire de Neurophysiologie, UMR CNRS 5543, BP 63, Université Victor Segalen, 146 rue Leo Saignat, F-33076 Bordeaux, France

(Received 10 February 2006; revised 16 August 2006; accepted 31 August 2006)

It is commonly assumed that one can always assign a direction—upward or downward—to a percept of pitch change. The present study shows that this is true for some, but not all, listeners. Frequency difference limens (FDLs, in cents) for pure tones roved in frequency were measured in two conditions. In one condition, the task was to *detect* frequency changes; in the other condition, the task was to *identify* the direction of frequency changes. For three listeners, the identification FDL was about 1.5 times smaller than the detection FDL, as predicted (counterintuitively) by signal detection theory under the assumption that performance in the two conditions was limited by one and the same internal noise. For three other listeners, however, the identification FDL was much larger than the detection FDL. The latter listeners had relatively high detection FDLs. They had no difficulty in identifying the direction of just-detectable changes in intensity, or in the frequency of amplitude modulation. Their difficulty in perceiving the direction of small frequency/pitch changes showed up not only when the task required absolute judgments of direction, but also when the directions of two successive frequency changes had to be judged as identical or different. © *2006 Acoustical Society of America.* [DOI: 10.1121/1.2357708]

PACS number(s): 43.66.Hg, 43.66.Fe [AJO] Pages: 3907–3915

I. INTRODUCTION

The American National Standards Institute (ANSI, 1994) defines pitch as "that attribute of auditory sensation in terms of which sounds may be ordered on a scale extending from low to high." This definition tallies with the fact that, in numerous languages, the expression meaning "pitch" (e.g., *hauteur tonale* in French, *Tonhöhe* in German, *visina tona* in Croatian and Serbian) incorporates a notion of height. Several authors (e.g., Bachem, 1950) have argued that pitch is not reducible to "tone height" because two tones one octave apart, which are quite distinct with respect to tone height, share at the same time another pitch quality ("tone chroma"). Nevertheless, it is generally believed that one can always assign a *direction*—upward or downward—to a percept of pitch change. Is this actually true for every listener, regardless of the size of the pitch change?

Using pure-tone stimuli, Jesteadt and Bilger (1974) measured the frequency discrimination abilities of four listeners (ordinary students, apparently) in several psychophysical paradigms. One of these paradigms was a two-interval forced-choice (2IFC) task; on each trial, two successive tones differing in frequency (by ΔF) were presented and the listener had to indicate whether the second tone was higher or lower than the first; the frequency of the first tone varied randomly from trial to trial ("roving" procedure), between 795 and 1260 Hz. In a second paradigm, two successive tones were again presented on each trial, but this time they could be either identical or different in frequency and the listener had to make a same/different (SD) judgment; when the two tones differed from each other, the second tone was always higher; the frequency of the first tone was again roved from trial to trial. Whereas the 2IFC task required a sensitivity to the direction of frequency changes (and thus pitch changes, presumably), this was not the case for the SD task. For each task, Jesteadt and Bilger measured the slope of the individual psychometric functions ($d'/\Delta F$). Under the assumption that for both tasks the decision variable was a *signed* pitch difference, signal detection theory (Green and Swets, 1974) predicted that the slopes of the psychometric functions would be two times higher in the 2IFC task than in the SD task. The experimental results appeared to be consistent with this prediction. Therefore, Jesteadt and Bilger's study suggests that as soon as a pitch change between two tones is detected, its direction can be identified.

Contrary to Jesteadt and Bilger, however, Wickelgren (1969) suggested that SD judgments in the frequency/pitch domain are not based on the same internal variable as are higher/lower judgments. In Wickelgren's study, three listeners were presented with sequences of three tones (T1, T2, T3). On each trial, the frequency of T1 was selected randomly between 400 and 490 Hz, and T3 could be higher, lower, or identical to T1. The task was to identify the relation between T3 and T1 using three response categories (higher, lower, same) and a three-level confidence rating; T2 had a fixed frequency, always remote from those of T1 and T3. An analysis of the receiver operating characteristics (ROCs; cf. Green and Swets, 1974, chap. 2) led Wickelgren to argue that listeners' judgments were partly based on the relative "familiarity" of the pitch evoked by T3, a variable depending on the *unsigned* difference between T1 and T3. Wickelgren posited that this variable of familiarity is the main determinant of SD judgments on pitch when the differences to be detected are small.

[a)]Author to whom correspondence should be addressed. Telephone: +33 55757 1651; Fax: +33 55690 1421.
Electronic mail: laurent.demany@psyac.u-bordeaux2.fr

More recently, Neuhoff *et al.* (2002) performed on a large group of students (tested in an auditorium) a short experiment which was similar to that of Wickelgren, but in which there was no tonal interference between the two tones to be compared on each trial. Neuhoff *et al.* found that when the two tones differed in frequency, a large majority of errors consisted of incorrect judgments of direction ("higher" instead of "lower," or vice versa) rather than "same" responses. This finding was consistent with Wickelgren's main point. One possible interpretation of the results was that, for a significant fraction of human listeners, upward and downward pitch changes are *perceptually* confusable. However, Neuhoff *et al.* did not interpret their data in this way. They suggested instead that the incorrect judgments of direction were due partly to a failure to detect some shifts and partly, in the authors' words, to "conceptual errors," that is, the "lack of knowledge of the appropriate labels for rising and falling pitch."

In a fourth study, by Johnsrude *et al.* (2000), two groups of listeners were tested. One group was neurologically normal and the other consisted of patients with lesions in the left or right temporal lobe. In both groups, using adaptive procedures, the authors measured frequency difference limens (FDLs) for pure tones close to 1000 Hz. As in Jesteadt and Bilger's (1974) study, the listeners were required to perform, in separate blocks of trials, an SD task and a 2IFC task (higher/lower judgments). The mean FDLs measured in the SD task were similar for the two groups. In the 2IFC task, the mean FDLs of patients with lesions in the left temporal lobe were also similar to those of the normal group, but performance was significantly poorer for patients with lesions in the right temporal lobe when these lesions affected the gyrus of Heschl. This demonstrated a dissociation between the ability to detect frequency changes and the ability to identify the direction of such changes. Johnsrude *et al.* concluded that: (1) The ability to identify pitch direction crucially depends on neural processes taking place in the gyrus of Heschl of the right hemisphere; (2) lower-order neural processes are sufficient for pitch change detection. It should be noted, however, that the mean FDLs measured in normal listeners by Johnsrude *et al.* were very much higher than those previously obtained by other authors in very similar experimental conditions (see, e.g., Sek and Moore, 1995). The subjects of Johnsrude *et al.* were apparently not trained and it is likely that, after some training, their performances would have been quite different (see, e.g., Demany and Semal, 2002). In another neuropsychological investigation which was methodologically similar to that of Johnsrude *et al.*, Tramo *et al.* (2002) tested in particular a patient with bilateral lesions of the auditory cortex. This patient appeared to have abnormally high FDLs in the SD task as well as the 2IFC task. However, his deficit relative to normal controls was definitely larger in the 2IFC task, in accordance with the dissociation reported by Johnsrude *et al.*

The foregoing literature review shows that conflicting findings and conclusions have been reported regarding human listeners' sensitivity to pitch direction in small frequency/pitch changes. The starting point of the present research was the informal observation, by the authors, of a pronounced difference between them in this respect. Both authors are neurologically and audiologically normal. Moreover, both are able to detect small frequency changes in the absence of loudness cues and, therefore, neither of them is "tone deaf" (Peretz and Hyde, 2003; Foxton *et al.*, 2004). However, one of the authors is completely unable to identify the direction of small, but perfectly detectable, frequency/pitch changes, whereas this problem does not exist for the other author. The experiments reported here were intended to confirm the reality of such individual differences.

II. EXPERIMENT 1

In this experiment, performed on nine normal-hearing listeners, we measured FDLs in two conditions assessing, respectively, the ability to detect frequency changes and the ability to identify their direction. The frequencies and sound pressure level (SPL) of the pure tones used as stimuli were such that the perceptual correlate of a frequency change could always be assumed to be nothing but a pitch change. Trials had exactly the same form in the two conditions, and a two-alternative forced choice task was used in each case. The two conditions differed from each other only with respect to the question asked on each trial. The observed relations between the two types of FDLs were compared to the relation predicted by signal detection theory for an ideal listener.

A. Method

1. Subjects

The nine subjects (L1, L2, L3, ... L9) included the authors (L1 and L7) and seven college students who were paid for their services. Three of the students (L4, L8, and L9) were selected among 68 persons who were pre-tested collectively in an auditorium. The aim of this pre-test was to identify and recruit listeners having difficulties regarding the perception of pitch direction.[1] All subjects had normal audiograms from 125 to 4000 Hz, and considered themselves as neurologically healthy. None of the subjects had a thorough musical education, but two of them (L1 and L3) were amateur musicians. L1 and L7 had a considerable prior experience in psychoacoustical tasks (including frequency discrimination tasks), whereas the other subjects were novices.

2. Procedure

Subjects were tested individually in a sound-attenuating booth (Gisol, Bordeaux). On each trial, four successive pure tones were presented diotically, through headphones (Sennheiser HD265). They were generated via 24 bit digital-to-analog converters (RME), at a sampling rate of 44.1 kHz. They had equal amplitudes, a nominal SPL of 65 dB, a total duration of 250 ms, and were gated on and off with 20 ms cosinusoidal amplitude ramps. There was a silent interval (ISI) of 250 ms between the first two tones and between the last two tones. A longer ISI—700 ms—separated the second and third tones, thus segmenting the whole sequence into two pairs of tones. One of the pairs, selected at random, consisted of identical tones, whereas the two members of the other pair differed in frequency. The frequencies of the first members of the pairs were selected randomly, independently

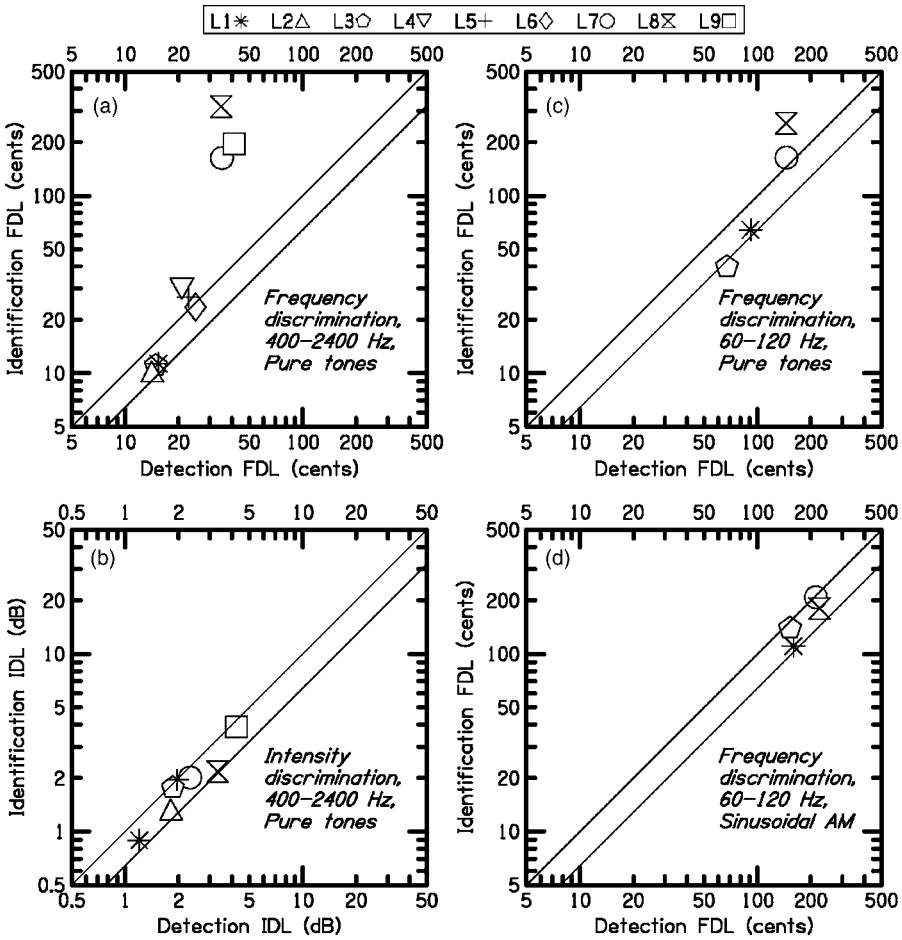

FIG. 1. (a) Detection and identification FDLs (frequency difference limens) of the nine listeners tested in experiment 1; FDLs were measured in musical cents and are here scaled logarithmically. (b) Detection and identification IDLs (intensity difference limens) of the seven listeners tested in experiment 4. (c) FDLs measured in experiment 5 for 60–120 Hz pure tones. (d) FDLs measured in experiment 5 for 60–120 Hz sinusoidal amplitude modulations. In each panel, the lower oblique line represents a prediction of signal detection theory (see the text).

of each other, between 400 and 2400 Hz (the probability distribution being rectangular on a log-frequency scale). In the pair including different tones, frequency changed either upwards or downwards, equiprobably.

FDLs were measured in a "detection" condition and an "identification" condition, corresponding to separate blocks of trials. In the detection condition, the task was to indicate on each trial if the pair including different tones was the first or the second pair. In the identification condition, the task was to identify the direction (upward or downward) of the frequency change that occurred within one pair, without specifying if this was the first or second pair. Responses were given by making a mouse-click on one of two labeled zones of a monitor screen, and were immediately followed by visual feedback. Response times were unlimited. Within a block of trials, there was a 600 ms pause between each response and the first tone of the next trial.

The critical frequency change occurring on each trial (ΔF) was defined in musical cents rather than in Hertz (1 cent=1/100 semitone=1/1200 octave). It was desirable to do so because, from 400 to 2400 Hz, FDLs vary markedly in terms of Hertz but are roughly constant in relative terms (see, e.g., Sek and Moore, 1995). In all blocks of trials, $|\Delta F|$ was initially large. It was decreased following each correct response, and increased following each incorrect response. A block ended after the 14th reversal in the variation of $|\Delta F|$. Up to the fourth reversal, $|\Delta F|$ was multiplied by 2.25 when it was increased, and divided by the cube root of the same factor when it was decreased. After the fourth reversal, $|\Delta F|$ was either multiplied by 1.5 or divided by the cube root of this factor. The FDL measured in a block of trials was defined as the geometric mean of all the $|\Delta F|$ values used from the fifth reversal on. This statistic estimated the 75% correct point of the psychometric function (Kaernbach, 1991).

In each test session, FDLs were measured alternately in the detection condition and the identification condition. The switch occurred after each FDL measurement. The number of FDL measurements varied from session to session but overall, for each listener, 50 FDL measurements were made in each condition; this corresponded to approximately 2000 trials per condition.

B. Results and discussion

For each condition and listener, we computed the geometric mean of the 50 measured FDLs. The results are displayed in Fig. 1(a). Here, each listener is represented by a specific symbol, as indicated on the top of the figure. The horizontal and vertical coordinates represent detection and identification performances, respectively, on identical logarithmic scales.

Two parallel oblique lines are drawn in each panel. The upper oblique line—i.e., the diagonal—indicates where the data points should be if identification performance [FDLs in the case of Fig. 1(a)] was equal to detection performance. Under the assumptions of "high-threshold theory" (Green

and Swets, 1974, chap. 5), if the detection of a frequency/pitch change was always sufficient for the identification of its direction, then the data points should be on this diagonal; moreover, it should be impossible to find a data point significantly below the diagonal because this would mean that the direction of *non*detectable frequency changes can be identified. The lower oblique line, on the other hand, represents the expected loci of the data points for an ideal listener defined in the framework of signal detection theory. For the ideal listener (Λ) in question: (1) A given pitch sensation is a point on an internal low-high continuum that is mathematically equivalent to a logarithmically scaled frequency axis; (2) performance in the two experimental conditions is limited only by a Gaussian random variability of the pitch sensations evoked by a tone of fixed frequency; (3) the variance of pitch for a given frequency corresponds to a given frequency ratio, independent of frequency. The strategy of Λ on each trial is optimal. In the detection condition, therefore, Λ measures the size of the pitch change elicited by each pair of tones, and then votes for the pair for which the change is larger. In the identification condition, Λ votes for the direction of the larger of the two pitch changes. We determined by means of computer simulations that in order to obtain, from Λ, 75% of correct responses in the two conditions, the signal (i.e., the frequency change presented in one pair of tones) had to be 1.56 times larger in the detection condition than in the identification condition.[2] This factor of 1.56 corresponds to the vertical or horizontal distance of the two oblique lines in each panel of Fig. 1.

Consider now the nine data points of Fig. 1(a). In the detection condition, the geometric standard errors of the nine mean FDLs had a mean value of 4.8% and ranged from 3.6% to 7.6%. In the identification condition, the corresponding standard errors had a mean value of 8.0% and ranged from 4.4% to 12.8%. So, the precision of the data is such that, vertically as well as horizontally, each of the nine symbols displayed in Fig. 1(a) has a size exceeding two standard errors. It can be seen that the nine data points form three clusters of three points. One cluster includes the data of three listeners (L1, L2, L3) for whom the detection FDLs were lowest (around 15 cents). For each of these three listeners, the identification FDL was lower than the detection FDL, and in each case the corresponding trend was statistically significant [$t(98) \geqslant 3.93$; $P < 0.001$]. The three data points are close to the lower oblique line, which means that L1, L2, and L3 behaved almost exactly like the ideal listener Λ defined above.[3] Let us point out that even for this subgroup of "best" listeners, the obtained detection and identification FDLs were higher than the FDLs reported by a number of authors (e.g., Wier *et al.*, 1977; Nelson *et al.*, 1983; Sek and Moore, 1995). This may be largely due to the fact that FDLs are generally measured for fixed standard tones, whereas we used here a roving procedure (see in this respect Demany and Semal, 2005).

L4, L5, and L6 produced a second cluster. Their detection FDLs (around 20 cents) are somewhat poorer that those of L1, L2, and L3. Their identification FDLs are approximately equal to their detection FDLs.

L7, L8, and L9 produced the third cluster. Their detection FDLs (around 35 cents) were the poorest. In the detection condition, however, these listeners' FDLs were only two or three times larger than those of L1, L2, or L3. By contrast, their identification FDLs were dramatically poor: They range from 163 to 317 cents. The ratio of the two types of FDL (identification/detection) is equal to 4.7 for L7, 4.8 for L9, and as much as 9.2 for L8. It is clear that these three listeners were completely unable to identify the direction of frequency changes that they nonetheless detected perfectly.

Globally, there was a correlation (Pearson r) of 0.90 between the logarithms of the detection FDLs and the logarithms of the ratios of the two types of FDL. This correlation is statistically significant ($\mathrm{d.f.} = 7$, $P < 0.01$).

In the experiment, as mentioned above, the response given on each trial was followed by visual feedback. In the identification condition, the feedback should have solved very rapidly the problem of a subject who would be able to perceive pitch direction without any difficulty but would not know the appropriate response for each direction. However, the feedback was also liable to have a more protracted benefit for listeners having difficulty in perceiving pitch direction: Thanks to the feedback, such listeners might have progressively learned to perceive pitch direction. This hypothesis led us to analyze the evolution of the FDLs measured in L7, L8, and L9 during the experiment. For each condition and listener, the geometric means of the FDLs measured in trial blocks $1-5, 6-10, \ldots 46-50$ are displayed in Fig. 2, where open and closed symbols represent detection and identification FDLs, respectively. The identification FDLs of L9 did improve during the experiment, and got closer and closer to her detection FDLs. For L7 and L8, in contrast, there was no sign of perceptual learning.

III. EXPERIMENT 2

In experiment 1, L7, L8, and L9 were unable to identify the direction of *frequency* changes that they nonetheless detected perfectly. This suggests that L7, L8, and L9 can perceive a *pitch* change without being able to identify its direction. However, an alternative interpretation of these listeners' results in experiment 1 was possible. It could be argued that they detected ΔF on the basis of some cue other than pitch, and that it was only for $|\Delta F|$ values close to the identification FDLs that they began to perceive ΔF as a genuine change in pitch. If so, all the listeners tested in experiment 1 would in fact be able to identify the direction of any pitch change detectable as such.

What could be the "cue other than pitch" used by L7, L8, and L9 in the detection condition of experiment 1? Since these listeners had normal audiograms, it is very unlikely that they detected ΔF on the basis of loudness changes. Another conceivable hypothesis is that, when they were presented with a given pair of tones, they monitored the excitation level of a single auditory filter activated by both tones. A change in frequency from the first tone to the second tone produced a change in the excitation level of the filter, thus allowing the listeners to perform not too badly in the detection condition. On the other hand, if the filter was chosen at random, on either side of the tones' excitation patterns, and if

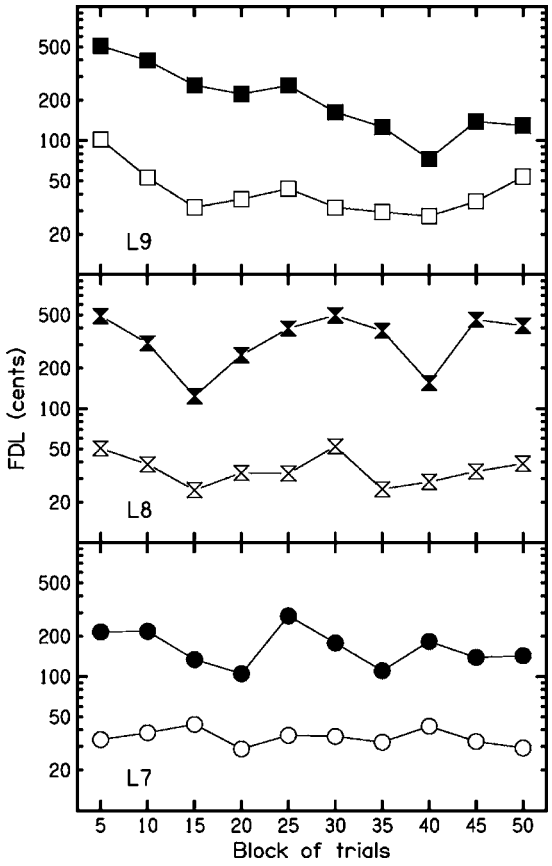

FIG. 2. Evolution of the FDLs measured in listeners L7, L8, and L9 during experiment 1. Open and closed symbols respectively represent detection and identification FDLs. Each data point is the geometric mean of five consecutive FDL measurements.

its center frequency was ignored, the direction of the change in excitation level did not provide information about the direction of the frequency change, which could explain the difficulty of the identification condition.

In experiment 2, this single-filter hypothesis was tested on L7 and L8 by replicating the detection condition of experiment 1 with the addition of random changes in intensity from tone to tone. In half of the FDL measurements, i.e., 20 blocks of trials for each subject, the SPL of every tone could take equiprobably any value between 60 and 70 dB. In the other half, the SPL was fixed at 65 dB, as in experiment 1. These two types of blocks were run alternately. If, on any given trial, L7 and L8 were monitoring the excitation level of a single auditory filter, then their FDLs should have been markedly larger with than without the intensity roving.

This was not the case. For L7, the geometric means of the FDLs obtained with and without the intensity roving were, respectively, 24.4 and 24.6 cents. For L8, the corresponding figures were 44.7 and 32.5 cents. So, on average, the roving of intensity increased the FDL by merely 17%. Moore and Glasberg (1989) and Emmerich *et al.* (1989) performed experiments comparable to the present one on listeners who had no difficulty in identifying pitch direction. The intensity roving range used by Moore and Glasberg (6 dB) was smaller than ours (10 dB). In their experiment, nonetheless, intensity roving had an average effect of the same size

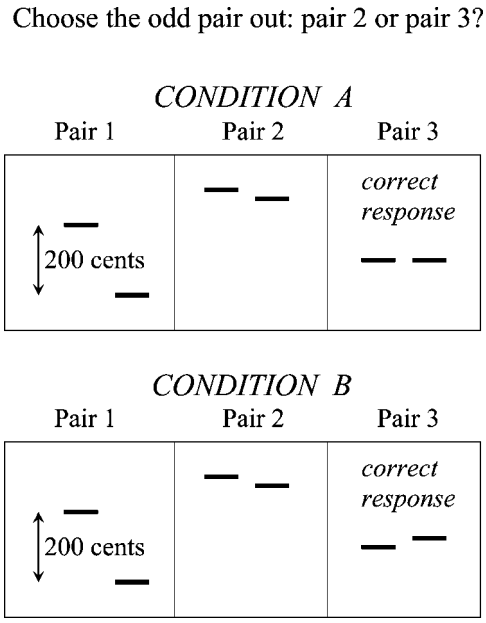

FIG. 3. The two conditions of experiment 3, illustrated by an example.

as the effect observed here. Emmerich *et al.* (1989), who used a 20 dB roving range, obtained a much larger effect.

In conclusion, experiment 2 did not support the idea that, in the detection condition of experiment 1, L7 and L8 used a perceptual cue other than pitch. It appears in any case that these listeners have no difficulty in dissociating pitch from loudness.

IV. EXPERIMENT 3

In the identification condition of experiment 1, subjects had to make *absolute* judgments on the direction of frequency changes. It is conceivable that a listener having difficulty in this task would nonetheless be able to perceive that a frequency change in a given direction is more similar to another frequency change in the same direction than to a frequency change in the opposite direction. The main goal of experiment 3 was to determine if this was true for L7, L8, and L9, the three listeners who had very poor identification FDLs in experiment 1.

A. Method

L1, L2, L3, L7, L8, and L9 were tested in two conditions, illustrated in Fig. 3. On each trial, three successive pairs of pure tones were presented. Within two of the three pairs, frequency changed in the same direction. In the remaining pair, there was either no frequency change (condition A) or a frequency change in the opposite direction (condition B). This "odd" pair was either Pair 2 or Pair 3, at random, and the subject's task was to identify its position in a 2AFC paradigm. The two elements of Pair 1 were always 200 cents apart, but the direction of the corresponding frequency change varied randomly from trial to trial. In condition B, therefore, the direction of the frequency change made in the odd pair also varied randomly from trial to trial. However, on every trial run in condition B, the changes made in Pairs 2 and 3 had identical sizes (in cents). As in experiment

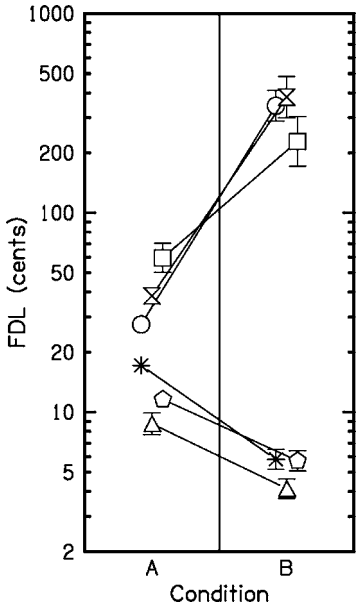

FIG. 4. Results of experiment 3. Each listener is represented by a specific symbol, the same as in Fig. 1. The error bars represent geometric standard errors. Error bars smaller than the symbol indicating the mean are not visible.

1, the tones had equal amplitudes, a nominal sound pressure level of 65 dB, and a duration of 250 ms. The ISI was again 250 ms within pairs and 700 ms between pairs. The frequency of the first member of each pair was again selected randomly between 400 and 2400 Hz. Visual feedback was once more provided following each response.

In each condition, the size of the frequency change ΔF made in Pair 2 and/or Pair 3 was varied from trial to trial, according to the same adaptive procedure as that used in experiment 1. We thus measured FDLs corresponding to the value of $|\Delta F|$ for which P(C) was 75%. For L1, L2, and L3, who can identify the direction of frequency in just-detectable frequency changes, our prediction was that FDLs would be lower in condition B than in condition A; this was to be expected because, for a given value of $|\Delta F|$, the difference between Pairs 2 and 3 was larger in condition B than in condition A. On the other hand, an opposite prediction was made for L7, L8, and L9, who were unable in experiment 1 to identify the direction of frequency changes well above their detection threshold; for these listeners, it could be expected that condition B would be the more difficult condition because it crucially required perceptual sensitivity to the direction of frequency changes, whereas this was not the case in condition A.

Within each test session, as in experiment 1, FDLs were measured alternately in the two conditions. The total number of FDL measurements per condition was equal to 6 for L1, 25 for L2, 10 for L3, 15 for L7 and L8, and 18 for L9.

B. Results and discussion

Figure 4 displays the geometric mean of the FDL measurements made for each condition and listener, as well as the associated standard errors. The results are extremely clear-cut and they agree with the predictions stated above: The FDLs of L1, L2, and L3 were lower in condition B than in condition A, whereas the opposite was true for L7, L8, and L9. In both conditions, L7, L8, and L9 were less efficient than L1, L2, and L3. However, the two groups do not differ dramatically from each other in condition A: Their average FDLs are in a ratio of about 3 for this condition. In condition B, by contrast, their average FDLs differ by a factor of about 60. Let us note that, in the blocks of trials estimating the FDL of L7, L8, and L9 in condition B, the initial value of $|\Delta F|$ was generally smaller than the FDL estimate eventually obtained. In consequence, the true FDLs of these listeners in condition B may be even higher than the estimates displayed in Fig. 4.

It is not surprising that L7, L8, and L9 were so inefficient in condition B given that the frequency change occurring in Pair 1 had a magnitude of 200 cents. This magnitude of change was well above all the detection FDLs measured in experiment 1, but not larger than the mean identification FDL of L7, L8, and L9 (216 cents). These three listeners might be somewhat more efficient in condition B if the frequency change produced in Pair 1 were larger. In any case, the present data make clear that their poor performance in the identification condition of experiment 1 is not due to the fact that the task required absolute judgments: L7, L8, and L9 show a perceptual insensitivity to the direction of frequency changes in relative as well as absolute judgments.

V. EXPERIMENT 4

We have shown above that there are pronounced individual differences regarding the perception of direction in frequency—and presumably pitch—changes. Is pitch special from that point of view? This question led us to perform a variant of experiment 1 in which the acoustic changes to be detected and identified as upward or downward changes were changes in intensity rather than frequency. Except for this novelty, the procedure and stimuli were identical to those of experiment 1. On each trial, therefore, four tones were presented in two pairs, and one tone (tone 2 or tone 4) differed in intensity from the other three (all at 65 dB). The intensity difference, ΔI, was at random positive or negative. Its absolute value $|\Delta I|$ was varied adaptively from trial to trial in order to find intensity difference limens (IDLs); the dB value of $|\Delta I|$ was manipulated exactly like $|\Delta F|$ (in cents) previously. On a given trial, the two elements of each pair of tones now had the same frequency. However, the frequencies of tones 1 and 3 were, as before, selected at random and independently of each other; in consequence, there was again a generally large frequency change from the first pair to the second pair. Since intensity comparisons between pure tones are markedly easier and more accurate for tones of the same frequency than for tones with different frequencies (Lim *et al.*, 1977), it was reasonable to assume that the IDLs measured here would be based exclusively on within-pair comparisons, as was the case for the FDLs measured in experiment 1.

The tested listeners included all those previously tested in experiment 1, except for L4 and L6. For each listener (with the exception of L9), 50 IDL measurements (15 for L9)

were made in the detection condition and in the identification condition. The results are displayed in Fig. 1(b). Each of the seven data points lies between the two oblique lines. Thus, the performance of all listeners was consistent with the idea that they could identify the direction of an intensity change as soon as they could detect it. In this respect, L7, L8, and L9 did not behave at all here as in experiment 1. Note, however, that they were in both experiments the three subjects for whom performance was poorest in the detection condition.

VI. EXPERIMENT 5

It could still be hypothesized, after experiment 4, that the perceptual problem of listeners such as L7, L8, and L9 is not exclusively a difficulty to perceive the direction of *pitch*, but more generally a difficulty to perceive the direction of *frequency*. The frequency of, for instance, a sinusoidal amplitude modulation imposed on a pure tone does not evoke a salient pitch percept when this modulation frequency is at least 15 times lower than the carrier frequency (Ritsma, 1962). On the other hand, a (sufficiently large) change in the modulation frequency can be heard (by many listeners, at least) as an increase or decrease in the number of modulation cycles per unit of time; by contrast, pure tones are perceived as smooth. In experiment 5, we replicated the procedure of experiment 1 on: (1) A continuum of *modulation* frequency, ranging from 60 to 120 Hz (for the first tone in each pair); (2) an *audio*-frequency continuum also ranging from 60 to 120 Hz. In the first of these two conditions, the modulations were sinusoidal and imposed on a sinusoidal carrier of 2000 Hz and 61 dB SPL. In the second condition, the stimuli were pure tones, approximately equalized in loudness at a level of 65 phons (by decreasing the SPL continuously from 85 to 75 dB between 60 and 120 Hz). The duration of all stimuli was set to 500 ms.

The experiment was performed on L1, L3, L7, and L8. For each continuum and listener, 15 FDL measurements were made in the detection condition and the identification condition. The results are displayed in Figs. 1(c) and 1(d). Not surprisingly, all the detection FDLs were much higher than those obtained in experiment 1. When the stimuli were pure tones [Fig. 1(c)], L1 and L3 behaved once more almost exactly like the ideal listener Λ, and for L8 the identification FDL was once more definitely larger than the detection FDL. However, contrary to what had been found in experiment 1, the identification FDL of L7 was very close to her detection FDL. When the manipulated frequency was a modulation frequency [Fig. 1(d)], the four listeners behaved similarly and none of them appeared to encounter a difficulty in the identification condition. It is remarkable that for L8, from Fig. 1(c) to Fig. 1(d), the detection FDL increases whereas the identification FDL decreases. Both of these trends are statistically significant $[t(28) \geqslant 2.53;\ P \leqslant 0.017]$. It is clear, therefore, that the perceptual problem of this listener is a difficulty to identify the direction of *pitch* rather than frequency per se.

For both L7 and L8, when the stimuli were pure tones, identification performance was not very much poorer than detection performance, in contrast to what had been found in experiment 1. Did this reflect an improvement, due to learning, in the ability of these listeners to perceive pitch direction? To answer that question, we retested L7 and L8 in the detection and identification conditions of experiment 1. A total of 20 new FDL measurements were made for each listener. The obtained geometric means of the detection and identification FDLs were, respectively, 24.8 and 317.8 cents for L7, and 37.3 and 238.8 cents for L8. Thus, the learning hypothesis had to be rejected. We believe instead that, for these listeners, a pitch change must exceed an approximately fixed magnitude in order to be identifiable as an upward change or a downward change. This conjecture makes sense of the fact that the identification FDLs of L7 and L8 for pure tones had similar values in experiments 1 and 5 (see Fig. 1).

VII. GENERAL DISCUSSION

As pointed out in the Introduction, Johnsrude *et al.* (2000) argued that the detection of frequency/pitch changes and the identification of their direction are distinct perceptual abilities, mediated by separate neural processes. The behavior of three of our subjects (L7, L8, and L9) was consistent with this thesis since these three subjects proved unable to identify the direction of frequency changes that, nonetheless, they detected perfectly and apparently heard as pitch changes. Although the subjects in question were neurologically normal, they showed the same dissociation as that observed by Johnsrude *et al.* (2000) or Tramo *et al.* (2002) in certain patients with brain lesions. On the other hand, the behavior of three other participants in our study (L1, L2, and L3) was quite different: In experiment 1, their identification FDLs were significantly *lower* than their detection FDLs. Their data were approximately consistent with the predictions of a model assuming that the detection of a frequency change and the identification of its direction are limited by one and the same internal noise: a random variability of the pitch sensations evoked by a tone of a given frequency.

In experiment 1, we also found that the ability to identify frequency direction in a just-detectable frequency change was strongly correlated with the detection FDL itself: The subjects who were efficient in the identification task were also efficient in the detection task. This result is remarkable because it suggests that, contrary to the thesis of Johnsrude *et al.*, the neural processes underlying the detection of frequency/pitch changes and the identification of their direction are not independent of each other. One possible speculation is that there are two separate detection mechanisms: an optimal mechanism which is sensitive to the direction of changes, and a non-optimal mechanism which is not direction-sensitive.

Although L7, L8, and L9 were unable to identify the direction of one-semitone changes in frequency, they could identify the direction of larger changes, and were indeed relatively successful for changes amounting to a few semitones. This effect of size is difficult to understand. The listeners themselves have little to say about the nature of their perceptual problem. Not surprisingly, the three of them are unable to sing in tune; but they are able to identify well-known melodies, and L8 enjoys listening to music. The per-

ceptual problem of some of the subjects who have difficulty in identifying the direction of small frequency/pitch changes may disappear following a long period of adequate training. However, this seems unlikely for L7 and L8 since, at the end of the present study, they had made no progress after more than 2000 identification trials run using an adaptive procedure including feedback. It would be interesting to get some idea of the prevalence of their apparently irremediable perceptual difficulty in the general population; let us emphasize in this regard that the group tested here may not be a representative sample.

Paavilainen *et al.* (1999) reported electro-encephalographic data concerning the sensitivity of human listeners to the direction of frequency changes. Their subjects were presented with a long sequence of pure tone pairs with randomly varying frequencies. Each tone had a duration of 50 ms and there was a 40 ms ISI within pairs. Frequency changed upward in most (87.5%) of the pairs, and downward in the remaining pairs. The authors' aim was to determine if the infrequent downward changes would elicit a significant mismatch negativity (MMN). This was indeed the case for the tested group as a whole. Because the MMN is a largely automatic (attention-independent) brain response, the authors suggested that the human brain contains neuronal populations which are selectively sensitive to the direction of discrete frequency changes. In the experiment of Paavilainen *et al.*, it was apparently not attempted to find differences between listeners. However, given that the frequency changes used had a minimum size of two semitones and were generally much larger, a significant MMN might have been found even in our subjects L7, L8, and L9. It would be interesting to perform a similar experiment using smaller frequency changes and separate subgroups of listeners, with different behavioral abilities to identify pitch direction.

Demany and Ramos (2005) also supported the hypothesis that the human brain contains direction-sensitive detectors of discrete frequency/pitch changes. They did so on the basis of purely psychophysical experiments. On each trial, their subjects were presented with a random "chord" of five simultaneous pure tones, followed after an ISI by a single tone (T). Because the component tones of the chords were gated on and off synchronously, they were very hard to hear out individually. This was confirmed in a condition where, on any trial, T could be either identical to a randomly selected component of the chord or halfway in (log) frequency between two components: Discriminating between the two corresponding types of chord-T sequences appeared to be very difficult. However, in another condition where T was instead one-semitone higher or lower than a randomly selected component of the chord and the task was to vote for "higher" or "lower," performance was much better (even when the ISI was several seconds long). In the latter condition, it appeared that listeners were able to perceive consciously the direction of a pitch movement produced by two tones without perceiving consciously the pitch of the first tone. This result, and those of related experiments, seemed to constitute strong evidence for the existence of automatic and direction-sensitive "frequency-shift detectors" in the human brain. Demany and Ramos conjectured that the detectors in question respond to frequency shifts of less than one semitone, and indeed respond to any frequency shift which is large enough to be audible. If this is true, then the results of the present research imply that such detectors do not exist in the brain of some listeners. We are inclined to think instead that they exist in the brain of every normal listener but that, for some listeners, they do not respond to very small shifts.

ACKNOWLEDGMENTS

We thank Hedwig Gockel, Maja Serman, and especially Christophe Micheyl for judicious comments on a previous version of this paper.

[1]More than 15% of the 68 pre-tested listeners were definitely less efficient in the identification task than in the detection task. Within this group, we selected three listeners for whom the difference was particularly large.

[2]A qualitative explanation of this outcome goes as follows. Suppose that, on a given trial, the larger of the two pitch changes measured by Λ has been evoked by the pair of identical tones. In the detection condition, the response of Λ on such a trial will be wrong with a probability of 1. In the identification condition, by contrast, the probability of a wrong response is only 1/2, because the pitch change evoked by the pair of identical tones was equiprobably ascending or descending. On a trial for which the larger of the two pitch changes measured by Λ takes place in the "right" pair (i.e., the pair of different tones), this larger change can nonetheless be in the wrong direction. However, the probability of such an event is smaller than 1/2. So, globally, for a given $|\Delta F|$, Λ is expected to perform better in the identification condition than in the detection condition. The psychophysical paradigm used in our detection condition has been analyzed mathematically in several publications (Macmillan *et al.*, 1977; Rousseau and Ennis, 2001; Micheyl and Messing, in press). For this paradigm, Rousseau and Ennis (2001) [see also Micheyl and Oxenham (2005)] provided an equation relating d' (that is, the subject's sensitivity to the signal to be detected, in our case ΔF) to the probability of a correct response, P. This equation is: $d'=2\mathbf{\Phi}^{-1}[1/2+(P/2-1/4)^{1/2}]$, where $\mathbf{\Phi}^{-1}$ denotes the inverse of the cumulative standard normal. For the same signal ΔF, in our identification condition, it can be shown that, more simply: $d'=2\mathbf{\Phi}^{-1}(P)$ (Micheyl, Kaernbach, and Demany, in preparation). Thus, when $P=0.75$, d' is 1.56 times larger in the identification condition than in the detection condition. Under the assumption that d' is proportional to $|\Delta F|$ in cents, this implies that, for Λ, the detection FDL is 1.56 times higher than the identification FDL.

[3]Nonetheless, for L1 and L3, the ratio of the two types of FDL (detection/identification) was significantly smaller than 1.56, the ratio expected for an ideal listener Λ [$t(98)\geqslant 1.99$; $P\leqslant 0.049$, two-tailed tests]. For L2, there was a marginally significant trend in the same direction [$t(98)=1.87$; $P=0.065$].

ANSI (**1994**). American National Standard Acoustical Terminology. ANSI S1.1-1994 (ASA 111-1994), 34.

Bachem, A. (**1950**). "Tone height and tone chroma as two different pitch qualities," Acta Psychol. **7**, 80–88.

Demany, L., and Ramos, C. (**2005**). "On the binding of successive sounds: Perceiving shifts in nonperceived pitches," J. Acoust. Soc. Am. **117**, 833–841.

Demany, L., and Semal, C. (**2002**). "Learning to perceive pitch differences," J. Acoust. Soc. Am. **111**, 1377–1388.

Demany, L., and Semal, C. (**2005**). "The slow formation of a pitch percept beyond the ending time of a short tone burst," Percept. Psychophys. **67**, 1376–1383.

Emmerich, D. S., Ellermeier, W., and Butensky, B. (**1989**). "A reexamination of the frequency discrimination of random-amplitude tones, and a test of Henning's modified energy-detector model," J. Acoust. Soc. Am. **85**, 1653–1659.

Foxton, J. M., Dean, J. L., Gee, R., Peretz, I., and Griffiths, T. D. (**2004**). "Characterization of deficits in pitch perception underlying 'tone deafness'," Brain **127**, 801–810.

Green, D. M., and Swets, J. A. (**1974**). *Signal Detection Theory and Psychophysics* (Krieger, New York).

Jesteadt, W., and Bilger, R. C. (**1974**). "Intensity and frequency discrimina-

tion in one- and two-interval paradigms," J. Acoust. Soc. Am. **55**, 1266–1276.
Johnsrude, I. S., Penhune, V. B., and Zatorre, R. J. (**2000**). "Functional specificity in the right human auditory cortex for perceiving pitch direction," Brain **123**, 155–163.
Kaernbach, C. (**1991**). "Simple adaptive testing with the weighted up-down method," Percept. Psychophys. **49**, 227–229.
Lim, J. S., Rabinowitz, L. D., Braida, L. D., and Durlach, N. I. (**1977**). "Intensity perception. VIII. Loudness comparisons between different types of stimuli," J. Acoust. Soc. Am. **62**, 1577–1587.
Macmillan, N. A., Kaplan, H. L., and Creelman, C. D. (**1977**). "The psychophysics of categorical perception," Psychol. Rev. **84**, 452–471.
Micheyl, C., and Messing, D. P. (in press). "Likelihood ratio, optimum decision rules, and correct-response probabilities in the 4IAX paradigm," Percept. Psychophys.
Micheyl, C., and Oxenham, A. J. (**2005**). "Comparing *F*0 discrimination in sequential and simultaneous conditions," J. Acoust. Soc. Am. **118**, 41–44.
Moore, B. C. J., and Glasberg, B. R. (**1989**). "Mechanisms underlying the frequency discrimination of pulsed tones and the detection of frequency modulation," J. Acoust. Soc. Am. **86**, 1722–1732.
Nelson, D. A., Stanton, M. E., and Freyman, R. L. (**1983**). "A general equation describing frequency discrimination as a function of frequency and sensation level," J. Acoust. Soc. Am. **73**, 2117–2123.
Neuhoff, J. G., Knight, R., and Wayand, J. (**2002**). "Pitch change, sonification, and musical expertise: Which way is up?," *Proceedings of the 2002 International Conference on Auditory Display*, Kyoto, Japan.
Paavilainen, P., Jaramillo, M., Näätänen, R., and Winkler, I. (**1999**). "Neuronal populations in the human brain extracting invariant relationships from acoustic variance," Neurosci. Lett. **265**, 179–182.
Peretz, I., and Hyde, K. L. (**2003**). "What is specific to musical processing? Insights from congenital amusia," Trends in Cognitive Science **7**, 362–367.
Ritsma, R. J. (**1962**). "Existence region of the tonal residue," J. Acoust. Soc. Am. **34**, 1224–1229.
Rousseau, B., and Ennis, D. M. (**2001**). "A Thurstonian model for the dual pair (4IAX) discrimination method," Percept. Psychophys. **63**, 1083–1090.
Sek, A., and Moore, B. C. J. (**1995**). "Frequency discrimination as a function of frequency, measured in several ways," J. Acoust. Soc. Am. **97**, 2479–2486.
Tramo, M. J., Shah, G. D., and Braida, L. D. (**2002**). "Functional role of auditory cortex in frequency processing and pitch perception," J. Neurophysiol. **87**, 122–139.
Wickelgren, W. A. (**1969**). "Associative strength theory of recognition memory for pitch," J. Math. Psychol. **6**, 13–61.
Wier, C. C., Jesteadt, W., and Green, D. M. (**1977**). "Frequency discrimination as a function of frequency and sensation level," J. Acoust. Soc. Am. **61**, 178–184.

The relationship between frequency selectivity and pitch discrimination: Effects of stimulus level

Joshua G. W. Bernstein[a] and Andrew J. Oxenham[b]
*Research Laboratory of Electronics, Massachusetts Institute of Technology, Cambridge, Massachusetts 02139 and Harvard-MIT Division of Health Sciences and Technology, Speech and Hearing Bioscience and Technology Program, Cambridge, Massachusetts 02139*I

(Received 7 June 2005; revised 12 September 2006; accepted 25 September 2006)

Three experiments tested the hypothesis that fundamental frequency (f_0) discrimination depends on the resolvability of harmonics within a tone complex. Fundamental frequency difference limens (f_0 DLs) were measured for random-phase harmonic complexes with eight f_0's between 75 and 400 Hz, bandpass filtered between 1.5 and 3.5 kHz, and presented at 12.5-dB/component average sensation level in threshold equalizing noise with levels of 10, 40, and 65 dB SPL per equivalent rectangular auditory filter bandwidth. With increasing level, the transition from large (poor) to small (good) f_0 DLs shifted to a higher f_0. This shift corresponded to a decrease in harmonic resolvability, as estimated in the same listeners with excitation patterns derived from measures of auditory filter shape and with a more direct measure that involved hearing out individual harmonics. The results are consistent with the idea that resolved harmonics are necessary for good f_0 discrimination. Additionally, f_0 DLs for high f_0's increased with stimulus level in the same way as pure-tone frequency DLs, suggesting that for this frequency range, the frequencies of harmonics are more poorly encoded at higher levels, even when harmonics are well resolved. © *2006 Acoustical Society of America.* [DOI: 10.1121/1.2372451]

PACS number(s): 43.66.Hg, 43.66.Fe, 43.66.Ba [JHG] Pages: 3916–3928

I. INTRODUCTION

Harmonic sounds, consisting of a sum of sinusoids, each with a frequency at a multiple of the fundamental frequency (f_0), are ubiquitous in our natural environment. Voiced human speech, the sounds of many musical instruments, animal vocalizations, and mechanical vibrations are all periodic signals whose frequency spectra are made up of sinusoids at discrete harmonically related frequencies. The auditory system tends to group the individual harmonic components together into a single percept with a pitch that usually corresponds to the f_0 of the complex, even if the component at the f_0 is absent from the stimulus or is masked (Schouten, 1940; Licklider, 1954).

Recent debates surrounding pitch perception have focused on the dependence of f_0 discrimination on harmonic number. The just-noticeable difference in the f_0 of a harmonic complex (the f_0 difference limen, or f_0 DL) has been shown to be smallest for complexes containing low-order harmonics, below about the tenth (Houtsma and Smurzynski, 1990; Shackleton and Carlyon, 1994; Krumbholz *et al.*, 2000; Kaernbach and Bering, 2001; Bernstein and Oxenham, 2003; 2005). This dependence of f_0 DLs on harmonic number has generally been ascribed to harmonic resolvability. On a linear frequency scale, individual components of a harmonic complex are equally spaced, whereas auditory filter bandwidths increase with increasing center frequency. As a result, low-order harmonics, spaced wider than filter bandwidths along the basilar membrane, are resolved by the auditory periphery, whereas multiple high-order harmonics fall within the bandwidth of a single auditory filter and are therefore unresolved.

Although many models of pitch perception are able to account for the dependence of f_0 discrimination on harmonic number, they do so in different ways. "Spectral" (Goldstein, 1973; Terhardt, 1974; 1979) and some "spectro-temporal" (Srulovicz and Goldstein, 1983; Shamma and Klein, 2000; Cedolin and Delgutte, 2005) models of pitch propose that the f_0 of a harmonic complex is identified by comparing the frequencies of individual harmonics to internally stored "harmonic templates." Because spectral models require spectrally resolved components to extract the f_0, they predict performance to worsen with increasing harmonic number due to a reduction in harmonic resolvability. "Temporal" models of pitch typically discard place information and extract f_0 information based on an autocorrelation or all-order interval analysis of auditory-nerve firing patterns, pooled across the population of fibers (Meddis and Hewitt, 1991; 1992; Cariani and Delgutte, 1996a,b; Meddis and O'Mard, 1997). These models predict a deterioration in f_0 discrimination with increasing absolute frequency (Cariani and Delgutte, 1996a; Carlyon, 1998), as a result of the roll-off of phase-locking in the auditory nerve (Weiss and Rose, 1988), but are unable to account for the dependence of f_0 discrimination on harmonic number *per se* (Carlyon, 1998). A recent modification of the

[a]Author to whom correspondence should be addressed. Present address: Army Audiology and Speech Center, Walter Reed Army Medical Center, 6900 Georgia Avenue NW, Washington, DC 20307. Electronic mail: joshua.bernstein@amedd.army.mil
[b]Present address: Department of Psychology, University of Minnesota, 75 East River Road, Minneapolis, MN 55455. Electronic mail: oxenham@umn.edu

 © 2006 Acoustical Society of America

autocorrelation model (Bernstein and Oxenham, 2005) was designed to account for the effects of harmonic number by limiting the range of periodicities over which the autocorrelation function is calculated relative to each filter's characteristic frequency (CF) (Schouten, 1970; Moore, 1982; Ghitza, 1986). However, the resulting dependence on harmonic number is not determined at the periphery and so is not based on harmonic resolvability. Although the inclusion of place information in this modified temporal model renders it "spectro-temporal" in nature, this type of model is referred to as "CF-dependent temporal" to differentiate it from the harmonic-template spectro-temporal models (e.g., Srulovicz and Goldstein, 1983; Shamma and Klein, 2000; Cedolin and Delgutte, 2005) mentioned above.

The question addressed in this study is whether the increase in f_0 DLs with increasing lowest harmonic number is directly related to a decrease in the resolvability of the harmonics (as predicted by spectral models), or whether the increase is related to harmonic number, independent of resolvability (as predicted by a CF-dependent temporal model). Our study exploits the fact that frequency selectivity, measured both physiologically (e.g., Rhode, 1971; Robles *et al.*, 1986) and psychophysically (e.g., Weber, 1977; Pick, 1980; Moore and Glasberg, 1987; Glasberg and Moore, 1990; Rosen and Stock, 1992; Hicks and Bacon, 1999), broadens at high levels, at least for frequencies of 1 kHz and above. The link between harmonic resolvability and pitch perception was examined by measuring the effects of stimulus level on complex-tone f_0 discrimination, pure-tone frequency discrimination, auditory filter bandwidths, and the ability to hear out the frequencies of individual harmonics in the same normal-hearing listeners. A companion paper (Bernstein and Oxenham, 2006) investigates the relationship between frequency selectivity and pitch discrimination in listeners with sensorineural hearing loss.

II. EXPERIMENT 1: FUNDAMENTAL FREQUENCY DISCRIMINATION

A. Rationale

Fundamental frequency DLs are known to increase with increasing lowest harmonic number present. Low-order harmonics yield small f_0 DLs ($<1\%$ of the f_0) and high-order harmonics yield large f_0 DLs (2 to 12% of the f_0, depending on the sensation level and phase relationships of the harmonics), with a steep transition between the two regions occurring around the tenth harmonic. This transition is seen whether harmonic complexes are bandpass filtered into a fixed spectral region and the f_0 adjusted (Hoekstra, 1979; Shackleton and Carlyon, 1994; Bernstein and Oxenham, 2005) or the f_0 is held constant and the harmonic number adjusted (Houtsma and Smurzynski, 1990; Bernstein and Oxenham, 2003). The aim of this experiment was to determine whether the f_0 DL transition point varies with stimulus level. Fundamental frequency DLs were measured as a function of f_0 for bandpass-filtered harmonic complexes. By using this paradigm instead of holding f_0 constant and adjusting harmonic number (Houtsma and Smurzynski, 1990; Bernstein and Oxenham, 2003), the spectral region remained constant for all stimuli, eliminating the potentially confounding effects of absolute frequency on the level dependence of frequency selectivity (Baker *et al.*, 1998). If small f_0 DLs are associated with resolved harmonics, then the transition between small and large f_0 DLs should occur at a higher f_0 (lower harmonic number) at high stimulus levels where frequency selectivity is poorer, because a wider frequency spacing would be required to resolve individual harmonics.

B. Methods

All stimuli were presented in threshold equalizing noise (TEN; Moore *et al.*, 2000), for four reasons. First, the use of a background noise enables the presentation of stimuli at a constant sensation level (SL) while varying the absolute sound-pressure level (SPL) over a wide range. This reduced the possibility that stimulus SL could have a confounding influence on f_0 DLs (Hoekstra, 1979). Second, TEN is intended to yield detection thresholds for pure tones in noise that are constant across frequency such that harmonics with equal SPL will also be equal in terms of SL. Third, the noise serves to mask any possible combination tones in the frequency region below the stimulus frequency range. Fourth, the presentation of harmonic complexes in a background noise is thought to aid the fusion of individual partials into a single perceptual object (Grose *et al.*, 2002), enabling the listeners to focus their attention more easily on the f_0 of the stimulus.

The stimulus levels presented in this experiment were referenced to the pure-tone detection thresholds for three TEN levels: 10, 40, and 65 dB SPL per equivalent rectangular auditory filter bandwidth (ERB_N; Glasberg and Moore, 1990). Because some of the stimuli presented in the high-level noise were uncomfortably loud for one of the listeners (S2), the highest-level noise was reduced by 3 dB to 62 dB SPL/ERB_N for this listener. To determine the SL reference, pure-tone detection thresholds were measured for each listener at each noise level for 1.5-, 2.5-, and 3.5-kHz tones, frequencies that, respectively, correspond to the lower-frequency cutoff, center frequency, and upper-frequency cutoff of the bandpass filter used in the f_0 discrimination experiment. Although TEN was intended to yield constant pure-tone detection thresholds, there was some small variation in the threshold SPL at the three frequencies tested. Therefore, we defined 0 dB SL for each noise level as the maximum of the thresholds measured across the three tested frequencies. Across listeners, the 0-dB SL reference ranged from 5.5 to 10.7, 36 to 38.5, and 60.5 to 64.5 dB SPL for the 10-, 40-, and 65-dB SPL/ERB_N TEN levels, respectively. Harmonic complex stimuli were presented at an average 12.5 dB SL per component. The absolute stimulus SPLs corresponding to this SL for the three levels of background TEN are referred to as the low, mid, and high levels, respectively. Although the across-frequency variation was greater at the low level (across-subject mean of the across-frequency standard deviation=2.2 dB) than the mid and high levels (standard deviation 1.0 dB in each case), this resulted in an average SL only 0.5 dB higher at the low level than at the mid and high levels.

The stimuli for this experiment consisted of 500-ms (including 30-ms raised-cosine rise and fall ramps) bandpass-filtered random-phase harmonic complexes. A new set of phases was selected independently from a uniform distribution for each stimulus. The large f_0 DLs produced by random-phase complexes for unresolved harmonics (Bernstein and Oxenham, 2005) should maximize the difference between f_0 DLs associated with low and high f_0's, thus providing the best opportunity to observe the transition between the two regions. The bandpass filter was held constant throughout the experiment, with 1.5- and 3.5-kHz corner frequencies and 50-dB/octave low- and high-frequency slopes. The filtering operation was implemented in the spectral domain by first adjusting the amplitude of each sinusoidal component, then summing all the components together. Stimuli were presented to the left ear in the TEN background at each of the three levels described above. Uncorrelated TEN with the same frequency content and level was also presented to the contralateral (right) ear to prevent detection of the stimulus in the contralateral ear via acoustic or electric crosstalk. Fundamental frequency discrimination was tested for eight average f_0's (75, 125, 150, 175, 200, 250, 325, and 400 Hz), at each of the three levels, with five repetitions per data point, for a total of 120 runs per listener. It is possible that with this bandpass-filter f_0 DL paradigm, listeners could have tracked individual frequencies rather than the f_0 in the case of resolved harmonics (Houtsma and Goldstein, 1972). However, Moore and Glasberg (1990) demonstrated that for harmonic complexes, listeners tend to base their pitch comparisons on the missing f_0 rather than on the frequencies of individual resolved components, even in cases where it would be advantageous to ignore the missing f_0. This suggests that listeners in the current study were also likely to base their responses on the f_0 and not on individual resolved frequencies.

The experimental method was similar to that described by Bernstein and Oxenham (2005). Fundamental frequency DLs were estimated in a three-interval, three-alternative forced-choice (3I-3AFC) adaptive procedure, using a two-down, one-up algorithm to track the 70.7% correct point on the psychometric function (Levitt, 1971). Two intervals contained a stimulus with a base f_0 ($f_{0,\mathrm{base}}$) and the other interval contained a complex with a higher f_0. The listener's task was to identify the interval containing the complex with the higher pitch. The f_0 difference (Δf_0), which was initially set to 20% of the f_0, changed by a factor of 1.59 until the second reversal and then changed by a factor of 1.26 for six more reversals. The f_0 DL was estimated as the geometric mean of the Δf_0's at the last six reversal points.

To reduce the effectiveness of loudness as an alternative discrimination cue, the root-mean-squared (rms) power was first equalized across the three intervals and then a random level perturbation was added to each interval, chosen from a uniform distribution of ±2.5 dB. In addition, $f_{0,\mathrm{base}}$ was roved from trial to trial within a run, chosen from a uniform distribution between ±5% of the average f_0. This was intended to encourage listeners to compare the pitches of the stimuli in each of the intervals of one trial, rather than comparing the pitch of each interval with some internally stored representation of the $f_{0,\mathrm{base}}$, although the f_0 roving may not have been effective for low f_0's where measured f_0 DLs were relatively large (8% or more).

After the f_0 DL measurements were completed, frequency DLs (FDLs) were measured for a pure tone with an average frequency of 1500 Hz, presented at an average SL of 12.5 dB in each of the three levels of background TEN. The 1500-Hz frequency was chosen for the FDL measurement because it represented the lower corner frequency of the bandpass-filtered harmonic tones, and was thus the most likely frequency region to yield resolved harmonics for the stimuli used in the f_0 DL measurements. FDL measurements were repeated four times at each level for each listener, using the same procedure as the f_0 DL measure, including level roving and frequency randomization.

Four normal-hearing listeners (one female) participated. Ages ranged from 22 to 30 years. All had audiometric thresholds of 15 dB HL or less *re* ANSI-1996 at octave frequencies between 250 and 8000 Hz. Two listeners (S2 and S3) were professional musicians with more than 10 years of formal musical training, and two (S1 and S4) were amateur musicians with at least 3 years of musical training. Each listener completed a training period of at least 4 h, which continued until FDLs and f_0 DLs no longer showed steady improvement.

The stimuli were generated digitally and played out via a soundcard (LynxStudio LynxOne) with 24-bit resolution and a sampling frequency of 32 kHz. The stimuli were then passed through a programmable attenuator (TDT PA4) and headphone buffer (TDT HB6) before being presented to the listener via Sennheiser HD 580 headphones. Listeners were seated in a double-walled sound-attenuating chamber. Intervals were marked by colored boxes on a computer screen, and feedback (correct/incorrect) was provided following each response.

C. Results

Figure 1 plots f_0 DLs and pure-tone FDLs for each of the individual listeners in the experiment (upper four panels) and the mean across the four listeners (lower panel). For all stimulus levels, f_0 DLs generally decreased with increasing f_0 (decreasing harmonic number), with a steep transition between large f_0 DLs for low f_0's and small f_0 DLs for high f_0's, consistent with previous findings (Hoekstra, 1979; Houtsma and Smurzynski, 1990; Shackleton and Carlyon, 1994; Bernstein and Oxenham, 2003; 2005). There were two effects of level on f_0 DLs, both of which occurred only as the level increased from mid to high. First, there was an increase in the f_0 at which the f_0 DL transition occurred. This effect was observed in the mean data as well as for three of the four individual listeners. In the mean data, f_0 DLs decreased to a low plateau level for a 200-Hz f_0 at the low and mid stimulus levels, but not until the f_0 reached approximately 250 Hz at the high level. Second, both the 1500-Hz pure-tone FDL and the minimum f_0 DL ($f_0\ \mathrm{DL}_{\mathrm{min}}$) achieved at the highest f_0's were elevated at the high level, an effect that was apparent in all four listeners and the mean data.

The f_0 DL data were parametrized to quantify and sta-

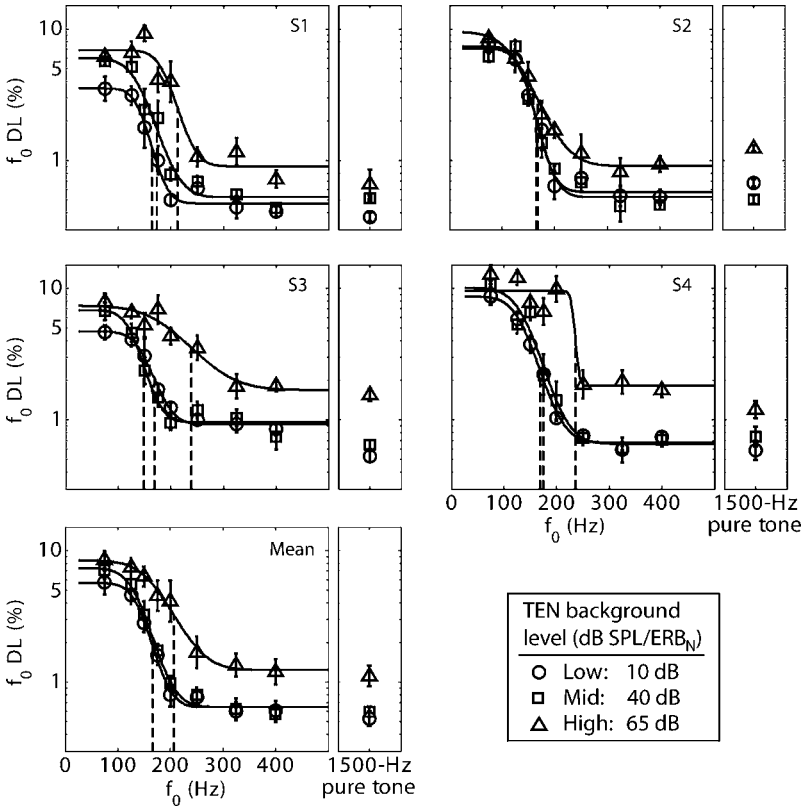

FIG. 1. Fundamental frequency DLs as a function of f_0 and FDLs for a 1500-Hz pure tone for the four individual listeners (upper four panels) and the mean data across the four listeners (lower panel). Stimuli were presented at an average 12.5 dB SL per component in the three TEN background levels specified in the legend. Error bars indicate ±1 standard error of the mean f_0 DL across the five runs for each condition, or across the four listeners in the case of the mean data. Solid lines represent the sigmoid functions [Eq. (1)] that best fit the data at each stimulus level. Vertical dashed lines indicate the f_0 DL transition derived from the sigmoid fit, where f_0 DLs are halfway (on a log scale) between minimum and maximum.

tistically test the two observed effects of level on f_0 DLs. A sigmoid function[1] with four free parameters was fitted to the log-transformed f_0 DLs. The sigmoid functions that best fit the f_0 DL data are depicted as solid curves in each panel of Fig. 1. The f_0 transition point ($f_{0,\mathrm{tr}}$, vertical dashed lines in Fig. 1) was defined as the estimate of the f_0 for which f_0 DLs were halfway (on a log scale) between the f_0 DL$_{\mathrm{min}}$ (achieved at high f_0's) and the maximum f_0 DL (f_0 DL$_{\mathrm{max}}$, achieved at low f_0's) for a given stimulus level.

The effects of level on $f_{0,\mathrm{tr}}$ and f_0DL$_{\mathrm{min}}$ were analyzed statistically using bootstrap resampling methods (Efron and Tibishirani, 1993). For each individual listener and level, 1000 estimates of each parameter were generated, with each estimate obtained by fitting the sigmoid function to a random resampling (with replacement) of five f_0 DL estimates at each f_0. For the group data, the bootstrap estimates were generated by randomly resampling (with replacement) four individual listener mean f_0 DLs at each f_0. Bootstrapped fits yielding $f_{0,\mathrm{tr}}$ estimates that fell outside of the 75 to 400-Hz range of f_0's tested were discarded. Two estimates were deemed to be significantly different if the 95% confidence interval (CI) of the difference between them, derived empirically by pairwise subtraction of the 1000 bootstrap estimates for each, did not overlap zero. The $f_{0,\mathrm{tr}}$ estimates are shown as circles in each panel of Fig. 2, with error bars representing the 95% CIs of each estimate (the other symbols represent frequency selectivity estimates from experiments 2 and 3, which will be described in Secs. III and IV, respectively). Significant differences between the high- and either the mid- (open symbols) or low-level (closed symbols) parameter estimates are identified by small symbols beneath the high-level estimates along the bottom of each panel of Fig. 2

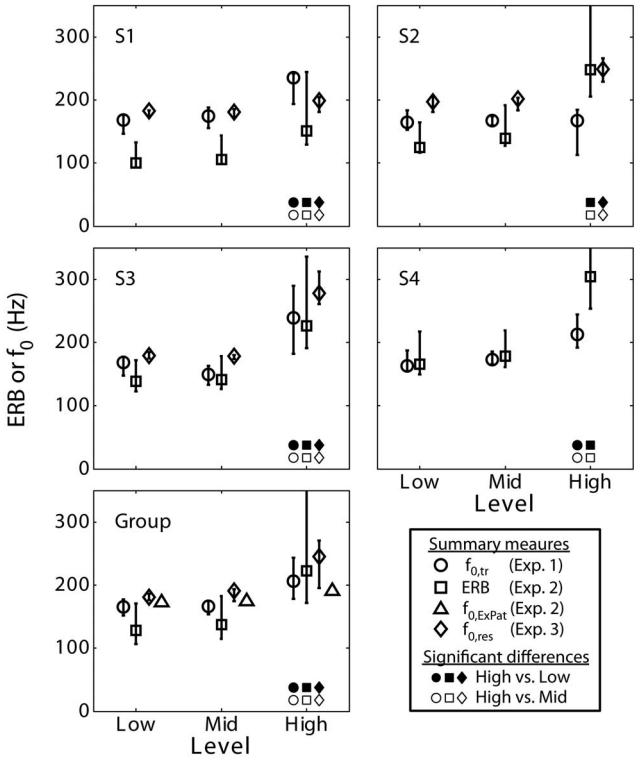

FIG. 2. Summary f_0 DL (experiment 1) and frequency selectivity measures (experiments 2 and 3) for each individual listener (upper four panels) and for the data pooled across listeners (lower panel). Small symbols at the bottom of the plot underneath the high-level data indicate that a given high-level parameter estimate was significantly different from the corresponding low- (closed symbols) or mid-level estimate (open symbols). Error bars represent the 95% confidence intervals obtained from bootstrap resampling of each measure (not available for the $f_{0,\mathrm{ExPat}}$ estimates based on the group data). Listener S4 did not participate in experiment 3.

(parameter estimates were never found to be significantly different between the mid and low levels). For example, for listener S1, the $f_{0,tr}$ was significantly different between the low and high conditions (small filled circle) and between the mid and high conditions (small open circle).

The high-level $f_{0,tr}$ was significantly larger ($p<0.05$) than both the low- and mid-level $f_{0,tr}$'s both for the group analysis and for three out of four listeners (S1, S3, and S4). Only listener S2 showed no significant differences in $f_{0,tr}$ across stimulus level. The log-transformed f_0 DL_{min} (Fig. 1) was also significantly larger at the high than at the low and mid levels in the group data and in three (S1, S2, and S4) out of four individual listeners (bootstrap CI estimates not shown). Although listener S3 showed no significant differences in f_0 DL_{min} across level, this may simply reflect the poor sigmoid fit for a large number of bootstrap resamplings of the high-level data for this subject, as an effect of level is visually apparent in the f_0 DL data for this subject. The observation that f_0 DL level effects only occurred between the mid and high conditions (where significant differences were observed) and not between the low and mid conditions (where no significant differences were observed) was confirmed by an additional bootstrap analysis comparing the high-mid versus mid-low differences in $f_{0,tr}$ and f_0 DL_{min}. The high-mid difference was significantly greater ($p<0.05$) than the mid-low difference for both group analyses ($f_{0,tr}$ and f_0 DL_{min}) and for two (S3 and S4) and three (S1, S2, and S4) out of four individual subjects for the $f_{0,tr}$ and f_0 DL_{min} estimates, respectively.

An effect of level similar to that observed in the f_0 DL_{min} was also observed in the 1500-Hz pure-tone FDLs (Fig. 1). Fisher LSD *t*-tests on the mean data showed that pure-tone FDLs were larger at the high level than at both the mid and low levels.

D. Discussion

The shift toward higher f_0's of the transition from large to small f_0 DLs at the high level is consistent with the hypothesis that good f_0 discrimination performance is associated with resolved harmonics. With reduced frequency selectivity at higher stimulus levels, higher f_0's would be needed to yield resolved harmonics in the considered spectral region. This hypothesis is tested further in experiments 2 and 3 by comparing the results with estimates of frequency selectivity. S2, the one listener who did not show this effect, was also the listener tested at a slightly lower level in the high-level condition than the other listeners (TEN level 62 dB instead of 65-dB SPL/ERB_N), and may have shown results more similar to the other listeners if tested at the slightly higher level.

The increase from the mid to the high level led not only to an increase in $f_{0,tr}$, but also to an increase in the f_0 DL_{min}. One possible interpretation for the increased f_0 DL_{min} is that frequency selectivity was reduced to such a degree that individual harmonics were not well resolved, even at the 400-Hz f_0, yielding poor f_0 DLs. However, two aspects of the data argue against this conclusion. First, it appears that a plateau was in fact reached, whereby f_0 DLs no longer decreased for f_0's above 250 Hz. Second, a similar effect was observed for the FDL of the 1500-Hz pure tone, which, being the only tone present and presented at an average level 12.5 dB above threshold, is resolved by definition. These two observations suggest another explanation, namely that the increase in f_0 DL_{min} and FDL at the high level reflects a deterioration in the frequency coding of the individual resolved components. A similar effect of level on FDLs for pure tones presented in background noise was observed by Dye and Hafter (1980), but at higher frequencies. Possible implications of this finding are addressed in Sec. V. Regardless of the mechanism by which individual pure-tone frequencies are encoded, it may be that a similar increase in pure-tone FDLs with level is not observed in the absence of background noise (e.g., Wier *et al.*, 1977) because information from off-frequency channels is available, which would not be affected by spectral or temporal distortions that may occur at high levels.

III. EXPERIMENT 2: AUDITORY FILTER SHAPES

A. Rationale

The central hypothesis of this study was that a reduction in frequency selectivity at higher signal levels would decrease the number of available resolved harmonics, thereby shifting the transition from large to small f_0 DLs to higher f_0's. This experiment was designed to verify the first part of this hypothesis, that frequency selectivity becomes worse with increasing level, which we expect given previous results (e.g., Weber, 1977; Pick, 1980; Moore and Glasberg, 1987; Rosen and Stock, 1992; Hicks and Bacon, 1999). Measurements of auditory filters in this experiment allowed a comparison between the variation in frequency selectivity with stimulus level and the f_0 DLs measured in the same listeners in experiment 1.

A version of the notched-noise method (Patterson, 1976), described by Rosen and Baker (1994), was used to measure the level of a noise that just masked a pure tone presented at a constant level, as a function of the width of the noise's spectral notch. A model auditory-filter shape was then fitted to the data. Stimulus levels and durations were similar to those of experiment 1 to ensure that the auditory filter shapes estimated in this experiment were as similar as possible to those presumably used by listeners for f_0 discrimination in the previous experiment. Auditory filter shapes were estimated using simultaneous rather than forward masking to mimic the simultaneous masking between components that occurs with the simultaneous presentation of the harmonics of a complex.

B. Methods

The notched-noise level that just masked a pure-tone signal was measured as a function of the masker notch width. Throughout the experiment, the pure-tone signal had a constant frequency (f_{sig}) of 1500 Hz, corresponding to the low-frequency edge of the passband in experiment 1, where harmonics were most likely to be resolved. Three level conditions were tested (low, mid, and high), whereby the signal was fixed at the SPL level corresponding to 10 dB SL

(adjusted for each listener) *re* one of the TEN levels that was used in experiment 1. This signal level was at the lower end of the 10–15-dB SL per component level range that was used in experiment 1. Although the signal SPL was adjusted relative to the detection threshold in TEN, the TEN background was not used in this experiment.

Each trial in the experiment consisted of three intervals, each with a 700-ms duration, separated by 500-ms silent gaps. Two of the intervals contained only a 700-ms noise burst (including 10-ms raised-cosine onset and offset ramps). The other interval also contained a 500-ms pure-tone signal (including 30-ms raised-cosine onset and offset ramps), temporally centered within the noise burst. The listeners' task was to identify which of the three intervals contained the pure-tone signal. A 3I-3AFC procedure with a two-up, one-down adaptive algorithm tracked the 70.7% correct point (Levitt, 1971). The spectrum level of the noise was initially set to −25, 5, and 30 dB SPL/Hz in the low, mid, and high conditions, respectively, and changed by 8 dB for the first two reversals, 4 dB for the next two reversals, and 2 dB for the last eight reversals. Threshold was estimated as the mean of the noise levels at the last eight reversal points.

To reduce the overall level of the masking noise at a given masker spectrum level, the two bandpass noises making up the noise masker had narrower bandwidths than in the Rosen and Baker (1994) study (200 Hz, or $0.13f_{\mathrm{sig}}$, compared to a range of 0.4 to $0.8f_{\mathrm{sig}}$ used by Rosen and Baker). The notch width was defined in terms of the deviations from the signal frequency, expressed as a proportion of f_{sig}, of the high-frequency edge of the lower-frequency noise band (Δf_l) and the low-frequency edge of the upper-frequency noise band (Δf_u). The maximum notch deviation relative to the signal frequency was also limited relative to the Rosen and Baker study ($\pm 0.2f_{\mathrm{sig}}$ as compared to $\pm 0.4f_{\mathrm{sig}}$). The limited range of notch widths reduced our ability to estimate the filter tail shapes, but was necessary to avoid the uncomfortably loud masker levels that would have been needed to mask the signal at wider notch widths. Three symmetrical notch conditions were tested, with equal Δf_l and Δf_u values of 0 (no notch), 0.1, and $0.2f_{\mathrm{sig}}$. To allow for the possibility of asymmetrical filters, there were also two asymmetric conditions, one with $\Delta f_l = 0.1f_{\mathrm{sig}}$ and $\Delta f_u = 0.2f_{\mathrm{sig}}$, and the other with $\Delta f_l = 0.2f_{\mathrm{sig}}$ and $\Delta f_u = 0.1f_{\mathrm{sig}}$. A further modification to the Rosen and Baker (1994) paradigm was the addition of a low-pass noise to mask any possible low-frequency combination bands (Greenwood, 1972) that could facilitate the detection of the signal. The low-pass noise had a cutoff frequency equal to the low-frequency edge of the lower-frequency noise band and a spectrum level 20 dB below that of the notched noise. To prevent the use of the contralateral ear for signal detection based on acoustic or electric crosstalk, an uncorrelated contralateral noise was presented, centered on f_{sig} with a bandwidth three times the ERB_N (Glasberg and Moore, 1990) and a spectrum level 40 dB below the signal level.

The same listeners took part in this experiment as had taken part in experiment 1. All listeners underwent a short training period where one masked threshold for each of the 15 (five notch widths at three levels) conditions was estimated. Listeners then completed four measurements for each data point, for a total of 60 runs.

C. Results and discussion

A standard fitting procedure was used to derive auditory filter shapes (Glasberg and Moore, 1990). Because of the small number of conditions tested (5 notch widths × 3 stimulus levels = 15 conditions), it was desirable to limit the number of free parameters in the filter shape model that were used to fit the data. This was accomplished by assuming the filter-tip shape (defined by the slope p) to be symmetrical and invariant across stimulus level, and assuming that both p and k (the signal-to-noise ratio in the filter output required for signal detection) were level invariant. Thus, the only parameter that was allowed to vary across level was the dynamic range limitation (r). The dynamic range limitation was applied only to the low-frequency side of the filter, representing the wide low-frequency tails observed in auditory-nerve fiber tuning curves (Kiang *et al.*, 1965). With these constraints, the 15 data points per listener were fitted with five free parameters: p, k, and three values of r. Limiting the number of free parameters to five only marginally sacrificed the overall goodness of fit. The root-mean-squared (rms) fitting error (resulting from fitting each the individual listener's data with a separate set of filters) was 1.95 dB in the five free parameter case and 1.45 dB in the case where r, p, and k were all allowed to vary with level (12 free parameters).

The assumed level invariance of the filter-tip shape is similar to the approach taken by Glasberg *et al.* (1999) and Glasberg and Moore (2000), whereby the filter tail and high-frequency slope of the filter tip were held constant across level, and only the gain of the filter tip and its low-frequency slope varied with stimulus level. In the present study, only the gain of the filter tip relative to the flat filter tail is allowed to vary with level, as modeled by the dynamic range limitation, r. The use of a level-invariant filter-tip shape models the physiologically observed two-component response of the basilar membrane (Ruggero, 1992; Ruggero *et al.*, 1997), with one broadly tuned linear filter corresponding to the passive mechanical properties of the basilar membrane, and one narrowly tuned variable-gain filter representing the level-dependent active mechanism thought to be governed by the outer hair cells (Ruggero and Rich, 1991).

The fitting procedure took into account the Sennheiser HD580 transfer function, the middle-ear transfer function, the possibility of off-frequency listening and variations in filter bandwidth in proportion with CF, as described by Glasberg and Moore (1990). Although the filter tip was assumed to be symmetric, the asymmetrical application of the dynamic-range limitation and the combination of off-frequency listening and proportional variation in filter bandwidth with CF accounted for unequal threshold measurements in the two asymmetric notch conditions.

The means and standard deviations (across the four listeners) of each of the best-fitting model parameters are listed in Table I.[2] Figure 3 shows the fitted filter shapes for each stimulus level based on the mean filter parameters from

TABLE I. Means and standard deviations across listeners of the filter-model parameters that best fit the notched-noise data of experiment 2.

Parameter	Level	Mean value	Standard deviation
p	All	47.18	9.99
r	Low	−35.30	2.85
	Mid	−22.23	2.63
	High	−11.82	1.97
k	All	−1.25	0.59

Table I. The main finding of this analysis is that the filter shape changed continuously with increasing level: the filter's dynamic range decreased as the stimulus level increased from the low to the mid to the high level. This trend is notably different from that observed in experiment 1, where f_0 DLs remained unchanged as the stimulus level increased from the low to the mid level, and then increased as the stimulus level increased from the mid to the high level.

D. Quantifying frequency selectivity

To directly test the hypothesis that small f_0 DLs are associated with resolved harmonics, two summary measures of frequency selectivity were derived and compared to the estimates of the $f_{0,\mathrm{tr}}$ (see Sec. II C). The first measure was the equivalent rectangular bandwidth (ERB) of the fitted filter shapes (Sec. III D 1). The second measure was an estimate of harmonic resolvability, based on peak-to-valley ratios (PVRs) in excitation patterns derived from the fitted filter shape functions and the spectra of the harmonic stimuli (Sec. III D 2).

1. Equivalent rectangular bandwidth (ERB)

Filter ERBs, calculated by integrating the fitted filter shape across frequency (Hartmann, 1998), are plotted as squares in Fig. 2 for individual listeners (upper four panels) and for filters derived from the data pooled across listeners (lower panel). Error bars indicate the 95% CIs derived from 1000 bootstrap estimates of each ERB. As for the $f_{0,\mathrm{tr}}$ and f_0 $\mathrm{DL}_{\mathrm{min}}$, there was little difference between the low- and mid-level ERBs, but an increase in the ERB from the mid to the high level. This was confirmed statistically, where ERBs were significantly greater at the high than both the mid (small filled squares) and the low levels (small open squares) for the group analysis and for all four listeners. Providing further support for this observation, the high-mid ERB difference was significantly larger than the mid-low difference in three out of four subjects (S2, S3, and S4), although this comparison failed to reach significance ($p=0.07$) in the group analysis. (The intersubject variability in ERBs did not match that observed in the $f_{0,\mathrm{tr}}$, where only listener S2 did not show a high-mid difference that was significantly greater than the mid-low difference.) Overall, the similar pattern of results for the effect of level on f_0 DLs and ERBs supports the idea that f_0 discrimination performance is related to frequency selectivity and that the poorer f_0 discrimination performance observed at the high level is related to the reduction in frequency selectivity associated with these stimuli.

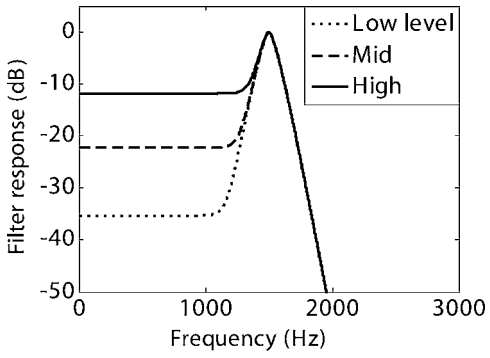

FIG. 3. Auditory filters at the three stimulus levels, based on the mean of each of four best-fitting filter parameters (p and three values of r) across the four listeners.

The ERBs (Fig. 2, squares) varied with level in a different manner than the auditory filter shapes (Fig. 3). Whereas auditory filter shapes changed continuously with level, the resulting ERBs remain unchanged until the stimulus level increased above the mid level. This result is related to the fact that only the dynamic range limitation (r) was allowed to vary with level. When r has a large negative value (in dB), the tail of the filter has little effect on the overall ERB. It is not until the dynamic range of the filter decreases substantially that the energy in the tail of the filter begins to affect the filter's ERB.

2. Excitation pattern model

The ERB measure provided a general statistic describing the frequency selectivity of the auditory system for comparison with the f_0 discrimination data. To more directly test the hypothesis that good f_0 discrimination is associated with resolved harmonics, harmonic resolvability was estimated based on the PVRs in peripheral excitation patterns, calculated using the fitted filters described above. The filterbank was produced using the mean filter parameters that best fit the notched-noise masking data for individual listeners (Table I). The filter parameter estimates for the 1.5-kHz CF were assumed to be scalable to other CFs along the cochlear partition, such that filters were identical on a logarithmic frequency scale across CF. The filterbank consisted of 501 model filters with CFs logarithmically spaced between 100 Hz and 10 kHz. Excitation patterns were calculated in the spectral domain, such that the excitation for each CF in the filterbank was the output power of the filter in response to the power spectrum of the harmonic stimulus plus background noise. The background noise was set at 10, 40, or 65-dB SPL/ERB_N and the signal level was set at 12.5 dB SL, where the 0-dB SL reference was averaged across the four listeners. A different excitation pattern was produced for each f_0 and stimulus level tested in experiment 1, with the appropriate filterbank used at each stimulus level, based on the filters derived in experiment 2.

Sample excitation patterns for the mid-level conditions are shown in Fig. 4 for 75-, 200-, and 400-Hz stimulus f_0's. For the lowest f_0 of 75 Hz, there are no discernible peaks present in the excitation pattern, because the frequency spacing between adjacent harmonic components is too narrow for the harmonics to be spectrally resolved by the filter bank. As

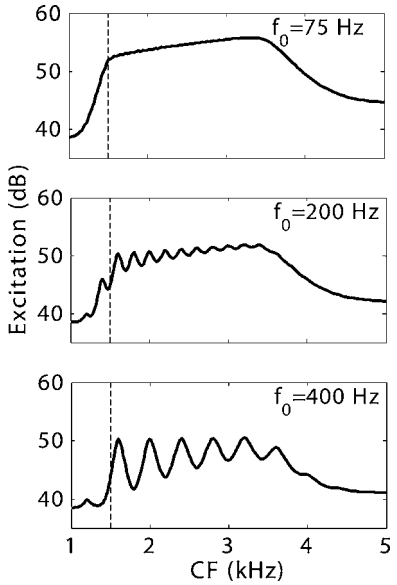

FIG. 4. Sample excitation patterns for three f_0's presented at the mid level.

the f_0 increases, peaks in the excitation pattern appear and become more prominent as individual components become increasingly spectrally resolved. The PVR quantified the degree to which harmonics were resolved by the filterbank. The PVR was measured between the first peak in the excitation pattern occurring at a CF $\geq$ 1.5 kHz (vertical dashed lines in Fig. 4), and the valley at a higher CF immediately adjacent to the peak.

Figure 5 shows PVRs as a function of f_0 for each stimulus level. PVRs are roughly equal for the low and mid stimulus levels, and are smaller at the high stimulus level, a trend similar to that observed for the ERB and $f_{0,tr}$ estimates. To directly compare the PVRs to the f_0 DL data, a threshold PVR (PVR_{th}), defined as the minimum PVR that yielded resolved harmonics, was varied as a single free parameter to fit the PVR estimates to the $f_{0,tr}$ estimates derived from the pooled f_0 DL data of experiment 1 (circles in Fig. 2, lower panel).[3] The PVR_{th} (horizontal dashed line in Fig. 5) was adjusted to minimize the least-squares difference between the f_0 needed to achieve the PVR_{th} (termed $f_{0,ExPat}$, vertical dashed lines in Fig. 5) and the $f_{0,tr}$ estimates derived from the

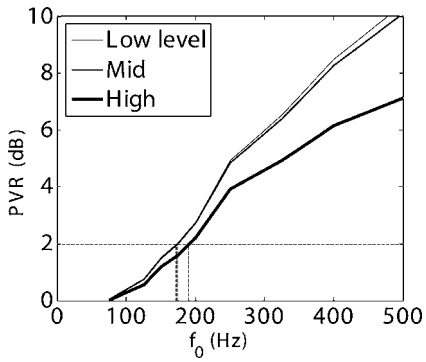

FIG. 5. Peak-to-valley ratios (PVRs) as a function of stimulus f_0 for the first excitation pattern peak occurring at a CF of 1500 Hz or higher. The horizontal dashed line indicates the PVR_{th} = 1.98 dB that minimized the mean-squared difference between the corresponding $f_{0,res}$ (vertical dashed lines) and the $f_{0,tr}$ estimates derived from the f_0 DL data (Fig. 1).

f_0 DL data. The PVRs for f_0's between those tested in experiment 1 were linearly interpolated as shown in Fig. 5. The fitted PVR_{th} represents the estimate of the PVR needed in the excitation pattern to yield f_0 DLs halfway (on a log scale) between f_0DL_{max} and f_0DL_{min}.

The estimated $f_{0,ExPat}$ at which the PVR was equal to the best-fitting PVR_{th} of 1.98 dB are plotted as triangles in the lower panel of Fig. 2. The pattern of results is qualitatively similar to the effect of stimulus level on the $f_{0,tr}$, with $f_{0,ExPat}$, remaining roughly constant between the low and mid levels (172.8 and 174.2 Hz, respectively), but increasing at the high level (190.8 Hz). The same trend was seen in the PVR versus f_0 plots of Fig. 5. As with the ERB, changes in the filter tail did not affect the PVR until the high level. Quantitatively, the excitation pattern model did not show as large of an effect of level on the $f_{0,ExPat}$ (approximately a 10% change) relative to that observed in the $f_{0,tr}$ (approximately a 25% change from the mid to the high level). It may be that f_0 discrimination is based on a complex analysis of several resolved harmonics, and not just the first resolved harmonic as modeled here. Supporting this idea, there was a smaller difference between the level effects on the $f_{0,ExPat}$ and $f_{0,tr}$ when the PVR for the $f_{0,ExPat}$ estimate was calculated for the second or third rather than the first peak in the excitation pattern (simulation results not shown).

3. Allowing the auditory filter tip shape to vary with level

Several filter-shape models that allowed the filter tip to vary with level were also investigated (results not shown). Three such models variations were tested: (1) symmetrical tip with low-frequency dynamic range limitation; (2) asymmetrical tip and low-frequency dynamic range limitation; and (3) asymmetrical tip without dynamic range limitation. For all three variations, the filter ERB increased regularly with increasing level, inconsistent with the trend observed in the $f_{0,tr}$. The trend in frequency selectivity was consistent with the trend in $f_{0,tr}$ as a function of level only when the filter tip was held constant across level as described in Sec. III C.

IV. EXPERIMENT 3: HEARING OUT HARMONICS

A. Rationale

This experiment measured the ability of listeners to hear out the frequencies of individual harmonics. A method similar to that of Bernstein and Oxenham (2003) measured performance in discriminating the frequency of a target harmonic embedded in a complex from that of a pure tone presented in isolation. The target harmonic was gated on and off repeatedly in order to draw listeners' attention to it without affecting peripheral resolvability. This approach was successful in the earlier study (Bernstein and Oxenham, 2003), estimating that approximately 9 to 11 harmonics are resolved for 100- and 200-Hz tone complexes, a number that closely corresponded to the transition from large to small f_0 DLs.

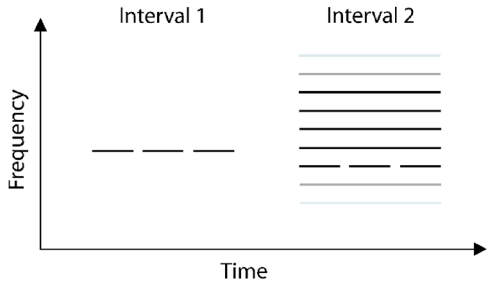

FIG. 6. Schematic of the stimulus paradigm used in experiment 3. Listeners compared the frequencies of the gated comparison tone presented in isolation (interval 1) with the frequency of a gated harmonic component of a bandpass filtered complex (interval 2). Shading represents the amplitude of each frequency component; components falling within the filter skirt are shown in lighter gray.

B. Methods

A schematic of the stimulus paradigm is shown in Fig. 6. Each trial consisted of two intervals, each with duration 500 ms, separated by 375 ms. The second interval contained a bandpass-filtered harmonic complex, identical to that of experiment 1, except that one harmonic (the target tone) was gated on and off in time, with three bursts of a 150-ms sinusoid (comparison tone), including 30-ms raised-cosine onset and offset ramps, separated by 25-ms silent gaps. The first interval contained a single stimulus frequency (the comparison tone) gated on and off in the same manner as the target tone. Harmonic complexes were presented in random phase. This reduced the possibility that the frequency of an unresolved harmonic could be detected based on the Duifhuis (1970) effect, whereby a sinusoid at the frequency of the missing harmonic may appear in the waveform during the temporal dips associated with sine-phase complexes (see Bernstein and Oxenham, 2003, footnote 2, for a discussion). Both intervals were presented to the left ear in the same wideband TEN background as experiment 1, which was turned on 250 ms before the start of the first interval, and turned off 250 ms following the end of the second interval. Again, uncorrelated TEN was presented to the contralateral ear to prevent the detection of the signal via acoustic or electric crosstalk. Each component (before filtering, where applicable) was presented at 12.5 dB SL (adjusted for each listener). Level randomization was not used in this experiment, because overall loudness variations would not have provided a usable cue. The frequency of the comparison tone (f_{comp}) was 3.5% higher or lower (each with probability 0.5) than the frequency of the target tone (f_{targ}). The listener was required to discriminate whether the target was higher or lower in frequency than the comparison tone. Feedback was provided following each response.

The target harmonic was chosen such that its nominal frequency fell between 1600 and 1750 Hz. For six of the nominal f_0's, only one harmonic fell in this range. For the 75- and 125-Hz f_0's, two harmonics fell within this range, and the total number of trials was evenly divided between the two possibilities. The limited range of f_{targ}'s created the possibility that listeners could obtain correct responses based on the absolute frequency of the comparison tone alone, without comparing it to the frequency of the target tone. In fact, an f_{comp} below 1600 Hz or above 1750 Hz could only be lower or higher, respectively, than an f_{targ}. Three steps were taken to reduce the likelihood that listeners would use such a strategy. First, the presentation order of the eight nominal f_0 values of the complex was randomized. Second, the actual value of the f_0 was roved, with the frequency of the target component chosen from a uniform distribution ranging from 50 Hz below to 50 Hz above the nominal target frequency, and the f_0 set accordingly. Third, dummy trials were added in such a way that the probability across dummy and nondummy trials that a given comparison tone frequency was higher than the target tone was roughly 50% for all possible comparison-tone frequencies. For example, in the $f_{comp} > 1750$ Hz range where in the nondummy trials f_{comp} would always be larger than f_{targ}, dummy trials were added where a similar f_{comp} was always lower than f_{targ}. The dummy trials were selected to have a mix of f_0's, comprising unresolved ($f_0 < 100$ Hz), partly unresolved ($f_0 = 150-200$ Hz), and mostly resolved ($f_0 > 300$ Hz) harmonics. The dummy comparison tones, which sometimes had frequencies below 1500 Hz, were not subjected to the slope of the bandpass filter. If listeners were responding based on the f_{comp} alone, then responses would have been biased toward "lower" and "higher" for low and high f_{comp}, respectively. However, an analysis of the data (not shown) indicated that this was not the case. Across all dummy and nondummy trials, listeners responded "lower" or "higher" with a probability of roughly 0.5 for the entire range of f_{comp}'s presented.

Each run consisted of 72 trials for one stimulus level condition. There were 48 nondummy trials (six trials for each of the eight f_0's tested in experiment 1), plus 24 dummy trials (two trials each for 12 combinations of f_0 and target frequency). There were 17 runs for each of the three stimulus levels, for a total of 102 nondummy trials for each f_0 and stimulus level. The stimulus level for each run was randomly selected, without replacement, until three runs were completed, and then the process was repeated.

Three of the four listeners from experiments 1 and 2 participated in this experiment (listener S4 did not participate). Each was given at least 1 h of additional training.

C. Results and discussion

The percentage correct as function of f_0 and level are plotted for each of the three individual listeners and for the mean data in Fig. 7. For each listener and stimulus level, there was a transition from chance performance (or below) at the lowest f_0's to near-perfect performance for the highest f_0's, consistent with the interpretation that harmonics are unresolved for low f_0's, and resolved for high f_0's. To compare with the f_0 DL data of experiment 1, the data were fitted to a psychometric function fixed to 50% and 100% correct at the extremes (solid curves in Fig. 7), and the f_0 required to reach 75% correct was defined as the limit of harmonic resolvability, termed the $f_{0,res}$ (vertical dashed lines in Fig. 7).

The effect of level on the $f_{0,res}$ (diamonds in each panel of Fig. 2) was similar to the level effects observed in the previous experiments. As for the $f_{0,tr}$ (circles) and ERB

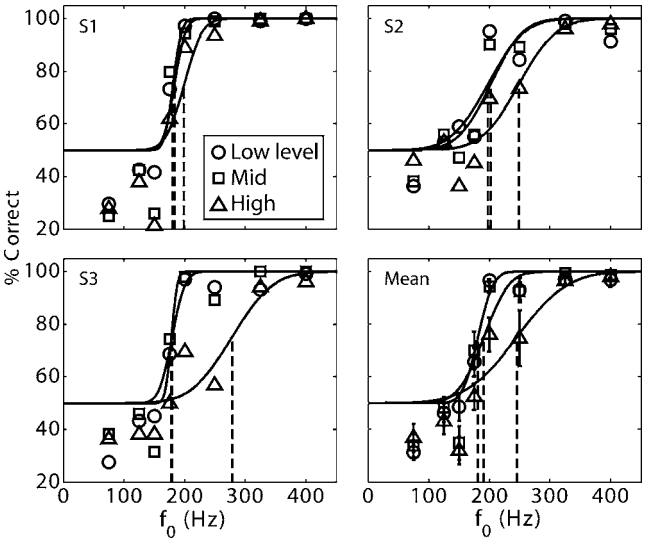

FIG. 7. Results of experiment 3 showing the percent correct in hearing out the frequency of an individual harmonic in the 1600–1750-Hz range as a function of stimulus f_0 for three stimulus levels for each individual listener (two upper panels and lower left panel) and for the mean data across the three listeners who participated in this experiment (lower right panel). Solid lines indicate the sigmoid function that best fit the data at each stimulus level, while vertical dashed lines represent the estimate of the limit of harmonic resolvability ($f_{0,\mathrm{res}}$) based on the 75% correct point. Error bars for the mean data represent ±1 standard error across the three listeners.

(squares), the $f_{0,\mathrm{res}}$ was similar at the low and mid levels, and then increased at the high level. This observation was supported by bootstrap resampling performed for each individual listener by randomly resampling (with replacement) 102 responses (correct/incorrect), and for the group data by resampling (with replacement) four individual-subject percent correct scores at each f_0 for a given level (95% CIs are shown as error bars in Fig. 2). The estimated $f_{0,\mathrm{res}}$ values were significantly larger at the high than both the mid and low levels for the group data and all three individual listeners (open diamonds at the bottom of each panel in Fig. 2). Furthermore, the high-mid $f_{0,\mathrm{res}}$ difference was significantly greater than the mid-low difference for all three subjects and the group analysis. The similarity in the overall pattern of results across the three experiments provides further evidence that the effects of stimulus level on f_0 DLs are related to frequency selectivity and the resolvability of individual harmonics.

Finally, below-chance performance was observed for the lowest f_0's, suggesting that listeners may have had access to information regarding the frequency of the gated target harmonic, but that they used this information incorrectly. Similar below-chance performance was sometimes observed for similar conditions in the Bernstein and Oxenham (2003) study. One possibility is that listeners were comparing the pure-tone frequency to that of a harmonic adjacent to the gated harmonic that sometimes became unmasked during the "off" intervals. However, the fact that listeners were not able to use this cue to produce better performance, despite feedback, suggests that the cue was unreliable and was fundamentally different from that used at the high f_0's, presumably reflecting a difference in harmonic resolvability.

V. GENERAL DISCUSSION

A. The relationship between f_0 discrimination and frequency selectivity

As pointed out by Shackleton and Carlyon (1994), a quantitative measure of the limit of harmonic resolvability may depend on the task and the detection criteria used in any given experiment. The current study to some extent avoids the problem of comparing results from different paradigms by comparing *patterns* of results, as a function of an independent variable (in this case level), rather than single values. Predictions based on the excitation pattern model (experiment 2) and the more direct hearing-out-harmonics paradigm (experiment 3) both led to the conclusion that harmonic resolvability depends on stimulus level in a similar way to the f_0 DL transition point in experiment 1. There was little or no change from the low to the mid stimulus level, but a similar increase in both the minimum f_0 for which harmonics could be heard out and the f_0 DL transition point from the mid to the high stimulus level. The fact that the two estimates of harmonic resolvability and the f_0 DL transition point depended on stimulus level in the same way provides support for the hypothesis that resolved harmonics are associated with good f_0 performance.

Some intersubject variability was observed in the experimental results, in that not all listeners showed an effect of level or a significantly greater high-mid versus mid-low difference for each f_0 discrimination and frequency selectivity measure. Moreover, on an individual listener basis the lack of a significant difference in one measure did not always correspond to the lack of significant difference in another. Nevertheless, each of these measures behaved similarly with respect to level when the data were averaged across listeners.

The results shown here may appear to be in conflict with the results of Krumbholz *et al.* (2000; see also Pressnitzer *et al.*, 2001). They concentrated on the lower limit of f_0 discrimination, and found that it corresponded more to a constant f_0 between 32 and 64 Hz, than to a constant harmonic number. Our conclusions can be reconciled with theirs if one assumes that pitch perception is constrained by two separate limits, one determined by the lower absolute limit of periodicity pitch (which appears to be between 30 and 60 Hz), and one determined by the spectral content, which is dependent on harmonic number, at least for f_0's between about 100 and 400 Hz.

B. Frequency selectivity and the coding of pure tones

In addition to the $f_{0,\mathrm{tr}}$ effect, this study also found that both the pure-tone FDL and the f_0 $\mathrm{DL}_{\mathrm{min}}$ (i.e. the f_0 DL associated with resolved harmonics) behaved in a similar manner to the various estimates of frequency selectivity, remaining constant from the low to the mid levels then increasing at the high stimulus level. It could be that level affected the two aspects of f_0 discrimination (i.e., increased f_0 $\mathrm{DL}_{\mathrm{min}}$ and increased $f_{0,\mathrm{tr}}$) in a similar manner simply because both rely on the frequency selectivity of the auditory system. This would be predicted by place-based models of pitch and frequency discrimination. On the other hand, the frequency coding of pure tones may rely on different mechanisms from

those that underlie harmonic resolvability, but which also deteriorate at high levels. In this case, the question arises as to whether the increase in the transition point, $f_{0,tr}$, really reflects harmonic resolvability, or whether it simply reflects poorer coding of individual harmonics (by a mechanism other than frequency selectivity, such as poorer temporal coding), making them more susceptible to interference by neighboring harmonics. We tested this possibility using a simple signal-detection model, with two independent additive noises representing the encoding accuracy of individual partials and the influence of neighboring partials, respectively. Using this simple model, we found that it was not possible to predict the observed shift in $f_{0,tr}$ by simply increasing the noise associated with the coding of individual harmonics. Instead, an increase in both types of noise was required to predict the changes in both $f_{0,tr}$ and f_0 DL_{min}. Thus, while we cannot completely rule out influences other than frequency selectivity and harmonic resolvability on $f_{0,tr}$, it appears reasonable to assume that a change in frequency selectivity is responsible for the increase in $f_{0,tr}$ at the high level.

C. Implications for theories of pitch perception

The results presented here, identifying a correspondence between f_0 discrimination performance and frequency selectivity, have implications for models of pitch perception, as discussed below.

1. Temporal models

"Temporal" models of pitch perception estimate f_0 using temporal information, often derived from auditory nerve firing patterns. Bernstein and Oxenham (2005) showed that a temporal autocorrelation model of pitch (Meddis and O'Mard, 1997) can account for the effect of harmonic number on f_0 discrimination performance if it is modified to include CF dependence, thus rendering it no longer a *purely* temporal model. In the modified model, "lag windows" limit the range of f_0's to which the model responds, relative to a given channel's CF, thereby forcing a dependence on harmonic number. However, because the dependence on harmonic number is not a consequence of harmonic resolvability or frequency selectivity, this model would be unlikely to predict a detrimental effect of reduced frequency selectivity on the f_0 DL transition point.

In a novel implementation of the autocorrelation model by de Cheveigné and Pressnitzer (2006), the range of lags achieved for a given CF is limited by the duration of the impulse response, and therefore the bandwidth, of the filter. For this model, the ability to efficiently code f_0 would be likely to depend on filter bandwidth, and hence on level, in a way similar to that found in our data. Furthermore, this model is also likely to resolve the apparent discrepancy between the current results that show a relationship between accurate f_0 and harmonic resolvability and those of Bernstein and Oxenham (2003) where increasing peripheral resolvability by presenting even and odd harmonics to opposite ears did not improve f_0 discrimination performance. The de Cheveigné and Pressnitzer (2006) model is in principle consistent with both sets of results because the model's dependence on harmonic number derives from the frequency selectivity of the auditory periphery, which would not be affected by dichotic presentation, but would be affected by changes in stimulus level.

It is not clear how temporal models, including that of de Cheveigné and Pressnitzer (2006), could account for the increase in f_0 DL_{min} and pure-tone FDLs observed at the high stimulus level, as phase locking in the auditory nerve does not generally deteriorate at high levels (Johnson, 1980). Furthermore, physiological evidence shows that when tones are presented in a background noise, the degree of phase locking is mainly dependent on the SNR (Rhode *et al.*, 1978; Abbas, 1981), rather than absolute level. In our experiment, stimuli were presented at equal SL across level, which is likely to have yielded a roughly constant SNR at the filter output. One possibility, suggested by a reviewer, is that the accuracy of phase locking to a pure-tone frequency could be disrupted at high stimulus levels by a relative increase in the ANF response to low-frequency background-noise energy resulting from the reduced filter tip-to-tail ratio.

2. Spectral models

Most spectral models of pitch are based on the concept that individual resolved frequencies are first identified and then compared to an internally stored template to derive the f_0 (e.g., Goldstein, 1973; Wightman, 1973; Terhardt, 1974; 1979). Models in this category are generally consistent with the observed shift in the f_0 DL transition point toward higher f_0's at a higher stimulus level. With increased filter bandwidths, higher f_0's will be needed to yield the increased separation between adjacent partials needed for resolved harmonics. Of course, all models that require resolved harmonics fail to predict the (albeit poor) pitch perception elicited by unresolved harmonics, and would therefore require a separate temporal envelope pitch extraction mechanism to account for these percepts.

The increase in the f_0 DL_{min} and the pure-tone FDL with level may also be consistent with spectral pure-tone frequency encoding. Dye and Hafter (1980) observed a similar effect of level on FDLs, but only for a relatively high-frequency (4 kHz) tone. For a 500-Hz or 1-kHz tone, FDLs decreased. This was interpreted in terms of reduced phase locking at 4 kHz, leading to frequency being encoded via spectral cues that are affected by the reduction in frequency selectivity with level. Although 1.5 kHz is lower than the frequency limits normally associated with a roll-off in phase locking in frequency discrimination (e.g., Moore and Sek, 1995), the similar effects of level observed in the Dye and Hafter and the current studies, together with the parallel dependence of frequency selectivity on level (experiment 2), suggest a possible role for spectral or spectro-temporal (as opposed to purely temporal) encoding in the 1.5- to 3.5 kHz frequency region tested in the current experiment. A spectral model might account for the effect of level on the f_0 DL_{min} and the pure-tone FDL in terms of a broadening of the excitation pattern (e.g., Zwicker, 1970) or in terms of rate saturation of the relatively large population of high spontaneous-rate auditory-nerve fibers (Liberman, 1978) at

high levels, leaving only a relatively small population of medium or low spontaneous-rate fibers for rate-based frequency encoding. However, a purely spectral model is unlikely to account for the observed deterioration in pure-tone frequency encoding (e.g., Moore and Sek, 1995) and resolved complex-tone f_0 discrimination performance (Moore *et al.*, 2006) at high absolute frequencies, thought to reflect the roll-off of phase locking in the auditory nerve (Weiss and Rose, 1988).

3. Harmonic-template spectro-temporal models

This class of pitch model uses a combination of place and temporal information to extract the individual frequencies of the harmonic components and calculate the f_0. Like purely spectral harmonic template models, these models also require the resolution of individual harmonic frequencies, and would therefore be likely to correctly predict an increase in $f_{0,\mathrm{tr}}$ with increasing level. In one type of model in this class, frequency information is extracted from the rapid transitions in the filter phase response near CF (Shamma, 1985; Cedolin and Delgutte, 2005). These models might also explain the observed effect of level on f_0 $\mathrm{DL}_{\mathrm{min}}$, in that phase transitions, as measured on the basilar membrane, tend to become more gradual with the increased filter bandwidths at high stimulus levels (Rhode and Cooper, 1996; Ruggero *et al.*, 1997).

Like the temporal models described above, spectro-temporal models that involve the extraction of individual resolved frequencies from phase-locking information in the auditory nerve (e.g., Srulovicz and Goldstein, 1983) do not depend on cochlear frequency selectivity to identify the frequencies of individual components. It is therefore not clear whether they could account for the observed increased in f_0 $\mathrm{DL}_{\mathrm{min}}$ with level. While these models might account for the increased $f_{0,\mathrm{tr}}$ in terms of a disruption of the temporal coding of individual frequency components due to the interaction of unresolved harmonics, Delgutte (1984) argued that the identification of individual frequency components based on a Fourier analysis of auditory-nerve responses would be robust to peripheral filtering.

VI. SUMMARY AND CONCLUSIONS

At high stimulus levels, f_0 DL performance for bandpass-filtered harmonic complexes deteriorates in two ways. First, the transition from high (poor) to low (good) f_0 DLs shifts to a higher f_0, implying that a larger spacing between adjacent harmonics is needed for good f_0 discrimination performance. The shift in the f_0 DL transition point as a function of level closely matches estimates of harmonic resolvability based on measures of auditory filter shapes and hearing out harmonics, consistent with the idea that resolved harmonics are necessary for accurate f_0 discrimination performance. Second, the minimum f_0 DL (at the highest f_0 tested) increases with increasing stimulus level, as does pure-tone FDLs at a comparable frequency, indicating that even resolved harmonic frequencies may be more poorly encoded at high stimulus levels. Overall, the results provide evidence in favor of spectral, spectro-temporal, or CF-dependent temporal models of pitch perception that depend on peripheral frequency selectivity to encode f_0 information, but not necessarily to the exclusion of temporal information.

ACKNOWLEDGMENTS

This work was supported by NIH Grants R01 DC 05216 and 5T32 DC 00038. An earlier version of this manuscript formed part of a Ph.D. thesis submitted by the first author to the Massachusetts Institute of Technology. We thank Christophe Micheyl, Louis Braida, Bertrand Delgutte, Gerald Kidd, John Grose, and two anonymous reviewers for their helpful comments on earlier versions of this manuscript.

[1]The sigmoid function was defined as

$$10\log_{10}[f_0\mathrm{DL}(\%)] = \mathrm{DL}_{\mathrm{min}} + [(\mathrm{DL}_{\mathrm{max}} - \mathrm{DL}_{\mathrm{min}})]/\sqrt{\pi} \times \int_{m(f_0 - f_{0,tr})}^{\infty} \exp[-(f_0')^2]df_0' \quad (1)$$

where $\mathrm{DL}_{\mathrm{max}}$ and $\mathrm{DL}_{\mathrm{min}}$ are the maximum and minimum values of $10\log_{10}(f_0\ \mathrm{DL}(\%))$ achieved at very low and very high f_0's, respectively, m is the slope of the function, and $f_{0,\mathrm{tr}}$ is the f_0 that yields an f_0 DL halfway (on a log scale) between $\mathrm{DL}_{\mathrm{min}}$ and $\mathrm{DL}_{\mathrm{max}}$.

[2]The set of filter parameters that best fit the masking data pooled across listeners (not shown) was similar to the mean of each filter parameters fit to the individual listeners shown in Table I.

[3]Excitation pattern model fits were not performed for each individual listener. Since the intersubject variability in the $f_{0,\mathrm{tr}}$ level effects did not match the intersubject variability in the ERB level effects, we would not expect the excitation pattern model based on the same data to closely fit the f_0 DL data on an individual subject basis.

Abbas, P. J. (**1981**). "Auditory-nerve fiber responses to tones in a noise masker," Hear. Res. **5**, 69–80.

Baker, R. J., Rosen, S., and Darling, A. M. (**1998**). "An efficient characterisation of human auditory filtering across level and frequency that is also physiologically reasonable," in *Psychophysical and Physiological Advances in Hearing*, edited by A. Rees, A. R. Palmer, A. Q. Summerfield, and R. Meddis (Whurr, London).

Bernstein, J. G., and Oxenham, A. J. (**2003**). "Pitch discrimination of diotic and dichotic tone complexes: Harmonic resolvability or harmonic number?," J. Acoust. Soc. Am. **113**, 3323–3334.

Bernstein, J. G. W., and Oxenham, A. J. (**2005**). "An autocorrelation model with place dependence to account for the effect of harmonic number on fundamental frequency discimnination," J. Acoust. Soc. Am. **117**, 3816–3831.

Bernstein, J. G. W., and Oxenham, A. J. (**2006**). "The relationship between frequency selectivity and pitch discrimination: Sensorineural hearing loss," J. Acoust. Soc. Am. **120**, 3929–3945.

Cariani, P. A., and Delgutte, B. (**1996a**). "Neural correlates of the pitch of complex tones. I. Pitch and pitch salience," J. Neurophysiol. **76**, 1698–1716.

Cariani, P. A., and Delgutte, B. (**1996b**). "Neural correlates of the pitch of complex tones. II. Pitch shift, pitch ambiguity, phase invariance, pitch circularity, rate pitch, and the dominance region for pitch," J. Neurophysiol. **76**, 1717–1734.

Carlyon, R. P. (**1998**). "Comments on 'A unitary model of pitch perception' [J. Acoust. Soc. Am. **102**, 1811–1820 (**1997**)]," J. Acoust. Soc. Am. **104**, 1118–1121.

Cedolin, L., and Delgutte, B. (**2005**). "Spatio-temporal representation of the pitch of complex tones in the auditory nerve," Assoc. Res. Otolaryngol. Abs., 1195.

de Cheveigné, A., and Pressnitzer, D. (**2006**). "The case of the missing delay lines: Synthetic delays obtained by cross-channel phase interaction," J. Acoust. Soc. Am. **119**, 3908–3918.

Delgutte, B. (**1984**). "Speech coding in the auditory nerve. II. Processing schemes for vowel-like sounds," J. Acoust. Soc. Am. **75**, 879–886.

Duifhuis, H. (**1970**). "Audibility of high harmonics in a periodic pulse," J. Acoust. Soc. Am. **48**, 888–893.

Dye, R. H., and Hafter, E. R. (**1980**). "Just-noticeable differences of fre-

quency for masked tones," J. Acoust. Soc. Am. **67**, 1746–1753.
Efron, B., and Tibishirani, R. J. (**1993**). *An Introduction to the Bootstrap* (Chapman & Hall, New York).
Ghitza, O. (**1986**). "Auditory nerve representation as a front-end for speech recognition in a noisy environment," Comput. Speech Lang. **1**, 109–130.
Glasberg, B. R., and Moore, B. C. J. (**1990**). "Derivation of auditory filter shapes from notched-noise data," Hear. Res. **47**, 103–138.
Glasberg, B. R., and Moore, B. C. J. (**2000**). "Frequency selectivity as a function of level and frequency measured with uniformly exciting notched noise," J. Acoust. Soc. Am. **108**, 2318–2328.
Glasberg, B. R., Moore, B. C. J., and Stone, M. A. (**1999**). "Modelling changes in frequency selectivity with level," in *Psychophysics, Physiology and Models of Hearing*, edited by V. Hohmann, T. Dau, and B. Kollmeier (World Scientific, Singapore).
Goldstein, J. L. (**1973**). "An optimum processor theory for the central formation of the pitch of complex tones," J. Acoust. Soc. Am. **54**, 1496–1516.
Greenwood, D. D. (**1972**). "Masking by combination bands: Estimation of the levels of the combination bands $(n+1)f_1-nf_h$," J. Acoust. Soc. Am. **52**, 1144–1154.
Grose, J. H., Hall, J. W., and Buss, E. (**2002**). "Virtual pitch integration for asynchronous harmonics," J. Acoust. Soc. Am. **112**, 2956–2961.
Hartmann, W. M. (**1998**). *Signals, Sound, and Sensation* (Springer, New York).
Hicks, M. L., and Bacon, S. P. (**1999**). "Psychophysical measures of auditory nonlinearities as a function of frequency in individuals with normal hearing," J. Acoust. Soc. Am. **105**, 326–338.
Hoekstra, A. (**1979**). "Frequency discrimination and frequency analysis in hearing," Ph.D. thesis, Institute of Audiology, University Hospital, Groningen, Netherlands.
Houtsma, A. J. M., and Goldstein, J. L. (**1972**). "The central origin of the pitch of pure tones: Evidence from musical interval recognition," J. Acoust. Soc. Am. **51**, 520–529.
Houtsma, A. J. M., and Smurzynski, J. (**1990**). "Pitch identification and discrimination for complex tones with many harmonics," J. Acoust. Soc. Am. **87**, 304–310.
Johnson, D. H. (**1980**). "The relationship between spike rate and synchrony in the responses of auditory-nerve fibers to single tones," J. Acoust. Soc. Am. **68**, 1115–1122.
Kaernbach, C., and Bering, C. (**2001**). "Exploring the temporal mechanisms involved in the pitch of unresolved complexes," J. Acoust. Soc. Am. **110**, 1039–1048.
Kiang, N. Y.-S., Watanabe, T., Thomas, E. C., and Clark, L. F. (**1965**). *Discharge Patterns of Single Fibers in the Cat's Auditory Nerve* (MIT Press, Cambridge, MA).
Krumbholz, K., Patterson, R. D., and Pressnitzer, D. (**2000**). "The lower limit of pitch as determined by rate discrimination," J. Acoust. Soc. Am. **108**, 1170–1180.
Levitt, H. (**1971**). "Transformed up-down methods in psychoacoustics," J. Acoust. Soc. Am. **49**, 467–477.
Liberman, M. C. (**1978**). "Auditory-nerve response from cats raised in a low-noise chamber," J. Acoust. Soc. Am. **63**, 442–455.
Licklider, J. C. R. (**1954**). "'Periodicity' pitch and 'place' pitch," J. Acoust. Soc. Am. **26**, 945.
Meddis, R., and Hewitt, M. (**1991**). "Virtual pitch and phase sensitivity studied of a computer model of the auditory periphery. II. Phase sensitivity," J. Acoust. Soc. Am. **89**, 2882–2894.
Meddis, R., and Hewitt, M. (**1992**). "Modeling the identification of concurrent vowels with different fundamental frequencies," J. Acoust. Soc. Am. **91**, 233–245.
Meddis, R., and O'Mard, L. (**1997**). "A unitary model of pitch perception," J. Acoust. Soc. Am. **102**, 1811–1820.
Moore, B. C. J. (**1982**). *An Introduction to the Psychology of Hearing*, 2nd ed. (Academic, London).
Moore, B. C. J., and Glasberg, B. R. (**1987**). "Formulae describing frequency selectivity as a function of frequency and level and their use in calculating excitation patterns," Hear. Res. **28**, 209–225.
Moore, B. C. J., and Glasberg, B. R. (**1990**). "Frequency discrimination of complex tones with overlapping and non-overlapping harmonics," J. Acoust. Soc. Am. **87**, 2163–2177.
Moore, B. C. J., and Sek, A. (**1995**). "Effects of carrier frequency, modulation rate, and modulation waveform on the detection of modulation and the discrimination of modulation type (amplitude modulation versus frequency modulation)," J. Acoust. Soc. Am. **97**, 2468–2478.
Moore, B. C. J., Glasberg, B. R., Flanagan, H., and Adams, J. (**2006**). "Frequency discrimination of complex tones; assessing the role of component resolvability and temporal fine structure," J. Acoust. Soc. Am. **119**, 480–490.
Moore, B. C. J., Huss, M., Vickers, D. A., Glasberg, B. R., and Alcantara, J. I. (**2000**). "A test for the diagnosis of dead regions in the cochlea," Br. J. Audiol. **34**, 205–224.
Patterson, R. D. (**1976**). "Auditory filter shapes derived with noise stimuli," J. Acoust. Soc. Am. **59**, 640–654.
Pick, G. (**1980**). "Level dependence of psychophysical frequency resolution and auditory filter shape," J. Acoust. Soc. Am. **68**, 1085–1095.
Pressnitzer, D., Patterson, R. D., and Krumbholz, K. (**2001**). "The lower limit of melodic pitch," J. Acoust. Soc. Am. **109**, 2074–2084.
Rhode, W. S. (**1971**). "Observations of the vibration of the basilar membrane in squirrel monkeys using the Mössbauer technique," J. Acoust. Soc. Am. **49**, 1218–1231.
Rhode, W. S., and Cooper, N. P. (**1996**). "Nonlinear mechanics in the apical turn of the chinchilla cochlea *in vivo*," Aud. Neurosci. **3**, 101–121.
Rhode, W. S., Geisler, C. D., and Kennedy, D. T. (**1978**). "Auditory nerve fiber responses to wide-band noise and tone combinations," J. Neurophysiol. **41**, 692–704.
Robles, L., Ruggero, M. A., and Rich, N. C. (**1986**). "Basilar membrane mechanics at the base of the chinchilla cochlea I. Input-output functions, tuning curves, and phase responses," J. Acoust. Soc. Am. **80**, 1364–1374.
Rosen, S., and Baker, R. J. (**1994**). "Characterising auditory filter nonlinearity," Hear. Res. **73**, 231–243.
Rosen, S., and Stock, D. (**1992**). "Auditory filter bandwidths as a function of level at low frequencies (125 Hz–1 kHz)," J. Acoust. Soc. Am. **92**, 773–781.
Ruggero, M. A. (**1992**). "Responses to sound of the basilar membrane of the mammalian cochlea," Curr. Opin. Neurobiol. **2**, 449–456.
Ruggero, M. A., and Rich, N. C. (**1991**). "Furosemide alters organ of Corti mechanics: Evidence for feedback of outer hair cells upon the basilar membrane," J. Neurosci. **11**, 1057–1067.
Ruggero, M. A., Rich, N. C., Recio, A., Narayan, S. S., and Robles, L. (**1997**). "Basilar-membrane responses to tones at the base of the chinchilla cochlea," J. Acoust. Soc. Am. **101**, 2151–2163.
Schouten, J. F. (**1940**). "The residue and the mechanism of hearing," Proc. K. Ned. Akad. Wet. **43**, 991–999.
Schouten, J. F. (**1970**). "The residue revisited," in *Frequency Analysis and Periodicity Detection in Hearing*, edited by R. Plomp and G. F. Smoorenburg (Sijthoff, Lieden, The Netherlands), pp. 41–54.
Shackleton, T. M., and Carlyon, R. P. (**1994**). "The role of resolved and unresolved harmonics in pitch perception and frequency modulation discrimination," J. Acoust. Soc. Am. **95**, 3529–3540.
Shamma, S. A. (**1985**). "Speech processing in the auditory system. II. Lateral inhibition and the central processing of speech evoked activity in the auditory nerve," J. Acoust. Soc. Am. **78**, 1622–1632.
Shamma, S., and Klein, D. (**2000**). "The case of the missing pitch templates: How harmonic templates emerge in the early auditory system," J. Acoust. Soc. Am. **107**, 2631–2644.
Srulovicz, P., and Goldstein, J. L. (**1983**). "A central spectrum model: A synthesis of auditory-nerve timing and place cues in monaural communication of frequency spectrum," J. Acoust. Soc. Am. **73**, 1266–1276.
Terhardt, E. (**1974**). "Pitch, consonance, and harmony," J. Acoust. Soc. Am. **55**, 1061–1069.
Terhardt, E. (**1979**). "Calculating virtual pitch," Hear. Res. **1**, 155–182.
Weber, D. L. (**1977**). "Growth of masking and the auditory filter," J. Acoust. Soc. Am. **62**, 424–429.
Weiss, T. F., and Rose, C. (**1988**). "A comparison of synchronization filters in different auditory receptor organs," Hear. Res. **33**, 175–180.
Wier, C. C., Jesteadt, W., and Green, D. M. (**1977**). "Frequency discrimination as a function of frequency and sensation level," J. Acoust. Soc. Am. **61**, 178–184.
Wightman, F. L. (**1973**). "The pattern-transformation model of pitch," J. Acoust. Soc. Am. **54**, 407–416.
Zwicker, E. (**1970**). "Masking and psychological excitation as consequences of the ear's frequency analysis," in *Frequency Analysis and Periodicity Detection in Hearing*, edited by R. Plomp and G. F. Smoorenburg (Sijthoff, Leiden, The Netherlands), pp. 376–394.

The relationship between frequency selectivity and pitch discrimination: Sensorineural hearing loss

Joshua G. W. Bernstein[a] and Andrew J. Oxenham[b]
*Research Laboratory of Electronics, Massachusetts Institute of Technology, Cambridge, Massachusetts 02139 and Harvard-MIT Division of Health Sciences and Technology, Speech and Hearing Bioscience and Technology Program, Cambridge, Massachusetts 02139*II

(Received 14 April 2006; revised 21 September 2006; accepted 25 September 2006)

This study tested the relationship between frequency selectivity and the minimum spacing between harmonics necessary for accurate f_0 discrimination. Fundamental frequency difference limens (f_0 DLs) were measured for ten listeners with moderate sensorineural hearing loss (SNHL) and three normal-hearing listeners for sine- and random-phase harmonic complexes, bandpass filtered between 1500 and 3500 Hz, with f_0's ranging from 75 to 500 Hz (or higher). All listeners showed a transition between small (good) f_0 DLs at high f_0's and large (poor) f_0 DLs at low f_0's, although the f_0 at which this transition occurred ($f_{0,\mathrm{tr}}$) varied across listeners. Three measures thought to reflect frequency selectivity were significantly correlated to both the $f_{0,\mathrm{tr}}$ and the minimum f_0 DL achieved at high f_0's: (1) the maximum f_0 for which f_0 DLs were phase dependent, (2) the maximum modulation frequency for which amplitude modulation and quasi-frequency modulation were discriminable, and (3) the equivalent rectangular bandwidth of the auditory filter, estimated using the notched-noise method. These results provide evidence of a relationship between f_0 discrimination performance and frequency selectivity in listeners with SNHL, supporting "spectral" and "spectro-temporal" theories of pitch perception that rely on sharp tuning in the auditory periphery to accurately extract f_0 information. © *2006 Acoustical Society of America.*
[DOI: 10.1121/1.2372452]

PACS number(s): 43.66.Hg, 43.66.Sr, 43.66.Fe, 43.66.Nm [JHG] Pages: 3929–3945

I. INTRODUCTION

Harmonic sounds are ubiquitous in the natural environment. The pitch of such sounds, usually corresponding to the fundamental frequency (f_0), is a useful attribute in an everyday listening environment. For example, pitch can convey musical melody, prosody in running speech, and linguistic information in Asiatic tonal languages. Pitch information can also provide a cue for the segregation of simultaneous talkers (e.g., Darwin and Hukin, 2000), thus aiding speech intelligibility in complex environments.

Listeners with sensorineural hearing loss (SNHL) are often faced with an impaired ability to discriminate the f_0 of complex sounds (Hoekstra and Ritsma, 1977; Hoekstra, 1979; Moore and Glasberg, 1988; 1990a; Moore and Peters, 1992; Arehart, 1994; Moore, 1995; Arehart and Burns, 1999; Moore and Moore, 2003; for a recent review, see Moore and Carlyon, 2005). The mechanisms underlying the pitch processing deficit that accompanies SNHL remain poorly understood. One possible cause is the reduction in peripheral frequency selectivity that often accompanies SNHL (Glasberg and Moore, 1986). "Spectral" (e.g., Goldstein, 1973; Wightman, 1973; Terhardt, 1974; 1979) and some "spectro-temporal" (e.g., Shamma and Klein, 2000; Cedolin and Delgutte, 2005) models of pitch are based on the assumption that individual harmonics of a complex tone must be resolved within the peripheral auditory system for the f_0 to be successfully extracted (for a recent review, see de Cheveigné, 2005). These models predict that reduced harmonic resolvability in listeners with SNHL due to the broadening of peripheral filters (e.g., Tyler *et al.*, 1983; Glasberg and Moore, 1986; Moore *et al.*, 1999) should impair pitch processing.

Certain results in normal-hearing (NH) listeners support the role of frequency selectivity and harmonic resolvability in f_0 discrimination. A number of studies have found that f_0 difference limens (DLs) increase substantially as the lowest harmonic number present in the stimulus increases beyond about 10 (Hoekstra, 1979; Houtsma and Smurzynski, 1990; Shackleton and Carlyon, 1994; Bernstein and Oxenham, 2003; 2005; 2006; Moore *et al.*, 2006). The transition from good to poor f_0 discrimination appears to correspond reasonably well with the point at which individual harmonics can no longer be heard out reliably (Bernstein and Oxenham, 2003), and the point at which the phase relation between components begins to affect f_0 DLs (Houtsma and Smurzynski, 1990; Bernstein and Oxenham, 2005), although the estimated limit of resolvability varies somewhat, depending on the method used (Plomp, 1964; Moore and Ohgushi, 1993; Shackleton and Carlyon, 1994; Moore *et al.*, 2006). Furthermore, our companion paper (Bernstein and Oxenham, 2006) found that the increase in auditory filter bandwidths at high

[a]Author to whom correspondence should be addressed. Current address: Army Audiology and Speech Center, Walter Reed Army Medical Center, 6900 Georgia Avenue N.W., Washington, DC 20307. Electronic mail: joshua.bernstein@amedd.army.mil
[b]Current address: Department of Psychology, University of Minnesota, 75 East River Road, Minneapolis, MN 55455. Electronic mail: oxenham@umn.edu

stimulus levels in NH listeners is accompanied by a shift in the transition point between good and poor f_0 discrimination towards higher f_0's (or lower harmonic numbers), as would be expected if low f_0 DLs required the presence of resolved harmonics.

Several studies have specifically investigated the relationship between frequency selectivity and f_0 discrimination in listeners with SNHL, but none has identified a strong correlation between the two (Hoekstra, 1979; Moore and Glasberg, 1990a; Moore and Peters, 1992). Moore and Glasberg (1990a) measured f_0 discrimination in listeners with unilateral SNHL for harmonic complexes containing both low- and high-order harmonics (1-12) and for complexes containing only high-order, less well resolved harmonics (6-12). They also estimated frequency selectivity by measuring auditory filter shapes (Glasberg and Moore, 1986). No significant correlation between frequency selectivity and f_0 discrimination was observed, although none of the listeners with poor frequency selectivity showed normal f_0 discrimination. In a related study, Moore and Peters (1992) investigated frequency selectivity and f_0 discrimination in both young and elderly NH and hearing-impaired (HI) listeners. While they found both reduced frequency selectivity and reduced f_0 discrimination performance for many of the HI listeners, there was only a weak correlation between the two measures.

Hoekstra (1979) and Hoekstra and Ritsma (1977) also measured f_0 discrimination in listeners with hearing impairment believed to be of cochlear origin. They used harmonic complexes with a range of f_0's, bandpass filtered into a fixed spectral region. They found that f_0 DLs decreased with increasing f_0, but that the transition between small and large f_0 DLs occurred at higher f_0's for HI listeners. This result is consistent with the idea that listeners with SNHL require a larger spacing between components to yield resolved harmonics and therefore good f_0 discrimination. Although Hoekstra (1979) and Hoekstra and Ritsma (1977) estimated frequency selectivity using psychophysical tuning curves (PTCs) in a subset of the HI listeners, the number of listeners in this subset was too small to permit a correlational analysis of the relationship between f_0 discrimination and frequency selectivity. Nevertheless, Hoekstra and Ritsma (1977) noted that those listeners with abnormally high f_0 DL transition f_0's also demonstrated abnormal PTCs, suggesting a relationship between the two measures. Arehart (1994), who varied the number of the lowest harmonic present, also found that the transition between small and large f_0 DLs occurred at a lower harmonic number for listeners with SNHL than for normal-hearing listeners, but did not relate this measure to estimates of peripheral frequency selectivity.

The goal of current study was to test the hypothesis that the harmonic spacing at which f_0 DLs change from large to small is dependent on peripheral frequency selectivity. This study differs from previous investigations of the relationship between f_0 discrimination and frequency selectivity in that it (1) focuses on the point of *transition* between large and small f_0 DLs (Experiment 1), and (2) relates this transition to measures of frequency selectivity (Experiments 2 and 3) in a sufficiently large and diverse population of HI listeners to enable a correlational analysis. The harmonic complexes were filtered into a passband extending from 1500 to 3500 Hz. Single-frequency measures of frequency selectivity and frequency discrimination used a signal frequency of 1500 Hz. This value, representing the lower cutoff of the passband for the complexes, was selected because it was the point at which the harmonics within the complex should have been best resolved, and is likely to represent the upper limit of performance (Houtsma and Smurzynski, 1990).

II. EXPERIMENT 1: FUNDAMENTAL FREQUENCY DIFFERENCE LIMENS

A. Rationale

Experiment 1 measured f_0 DLs as a function of f_0 for harmonic complexes, bandpass filtered into a fixed spectral region, in listeners with SNHL. By investigating the dependence of f_0 DLs on harmonic resolvability while keeping the frequency region constant, this paradigm avoided a possible confounding factor of SNHL that varies across frequency regions, which might arise in a paradigm that keeps f_0 constant while varying harmonic number (e.g. Houtsma and Smurzynski, 1990; Bernstein and Oxenham, 2003). With this paradigm, it is possible that listeners could have tracked individual frequencies rather than the f_0 in the case of resolved harmonics (Houtsma and Goldstein, 1972). However, Moore and Glasberg (1990b) demonstrated that listeners tend to base their pitch comparisons on the missing f_0 rather than on the frequencies of individual resolved components, even in cases where it would be advantageous to ignore the missing f_0.

Harmonic stimuli were presented in both sine and random phase to give an estimate of harmonic resolvability based on the phase dependence of f_0 DLs. In NH listeners, the phase relationships between harmonic components have been shown to affect f_0 DLs for complexes containing only high-order harmonics but not for those containing low-order harmonics (Moore, 1977; Houtsma and Smurzynski, 1990; Bernstein and Oxenham, 2005). This result is generally interpreted in terms of harmonic resolvability. For high-order unresolved harmonics that interact within individual peripheral filters, the phase relationship between components affects the temporal envelope and therefore the pitch percept associated with these complexes. In contrast, low-order resolved harmonics do not interact appreciably within individual peripheral filters, so the pitch percept associated with these harmonics is not affected by phase manipulations.

B. Listeners

Ten listeners (four female) with SNHL participated in the study. Pure-tone audiograms were measured using an AD229e diagnostic audiometer (Interacoustics) and TDH39 headphones. Bone-conduction threshold measurements (Radioear B-71) verified that the hearing loss for each listener was sensorineural in nature, based on the absence of any air-borne gaps larger than 10 dB. All listeners had moderate (30–65 dB HL *re* ANSI-1996) losses at audiometric frequencies between 1.5 and 4 kHz,[1] the relevant frequencies for the stimulus frequency range (1.5–3.5 kHz) used in the study, with two exceptions where the hearing loss still fell within

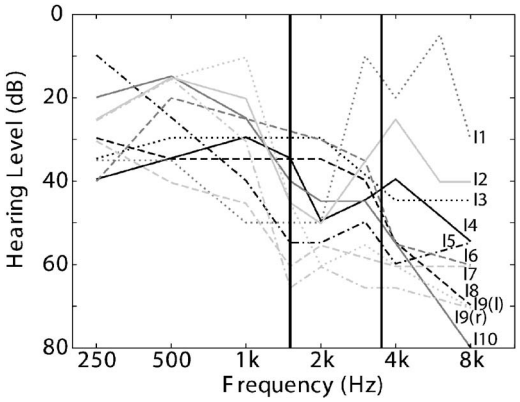

FIG. 1. Audiograms for the ten HI listeners (11 ears) who participated in the study. Vertical lines represent the 1.5–3.5 kHz stimulus region used in Experiments 1–3.

the specified range between 1.5 and 2 kHz, but was milder at higher frequencies.[2] A threshold equalizing noise (TEN) test for octave frequencies between 0.25 and 8 kHz verified the absence of "dead regions" in each listener (Moore *et al.*, 2000). Ages ranged from 27 to 78 years, with a mean of 49.7 and a median of 50.5 years. One HI listener (I6) was a trained musician with decades of musical experience, while the remaining HI listeners were nonmusicians. For each HI listener, measurements were made for the ear in which the hearing loss fell between 30 and 65 dB HL. If both ears met this criterion, the ear with the greater hearing loss was selected. Listeners with symmetrical losses were given their choice of test ear. One listener with an asymmetrical loss (I9) was tested in both ears. For simplicity, the two ears of this listener were treated as if they were from separate listeners [I9(l) and I9(r)], so that the total number of HI listeners was considered to be eleven. Audiograms for the 11 ears with SNHL are shown in Fig. 1, with vertical lines indicating the 1.5–3.5 kHz stimulus region tested in this study.

The study was designed to investigate correlations between f_0 discrimination and frequency selectivity within a group of listeners with SNHL, rather than to compare groups of NH and HI listeners. Nevertheless, three NH listeners (one female) were also included in the study to provide base line measurements. Normal-hearing listeners had audiometric thresholds of 15 dB HL or less *re* ANSI-1996 at octave frequencies between 0.25 and 8 kHz. The ages of the NH listeners were 19, 20, and 52 years. Each NH listener was tested with stimuli presented to the left ear. Two NH listeners (N1 and N2) were trained musicians with more than five years of formal training, while the third NH listener (N3) was a nonmusician. Table I provides audiological information for each NH and HI listener, as well as information regarding the stimulus level(s) tested in each of the three experiments (see Sec. II C 2). All listeners were paid for their time.

C. Method

The stimuli and methods for estimating f_0 DLs were similar to those used by Bernstein and Oxenham (2006), as described below.

1. Stimuli

Fundamental frequency DLs were measured as a function of f_0 for 500-ms (including 30-ms raised co-sine rise and fall ramps) random- and sine-phase harmonic complexes, bandpass filtered between 1.5 and 3.5 kHz, with 50 dB/oct. slopes. New phases were selected for each presentation of a random-phase complex. The filtering operation

TABLE I. Audiological and stimulus level information for the ten HI listeners (11 ears) and three NH listeners who participated in the study. (*) Measurements were made in both the left and right ears of listener I9. (**) Absolute thresholds were not measured in NH listeners using the adaptive technique and HD 580 headphones that were used in Experiments 1–3.

	Listener	Age	Sex	Test ear	Audiometric threshold at 1.5 kHz (dB HL) TDH 39	Max. adaptive threshold, 1.5–3.5 kHz (dB SPL) HD 580	TEN level (dB SPL/ ERB_N)
Hearing impaired	I1	29	F	R	50	49.3	50
	I2	58	M	L	45	46.3	50
	I3	67	M	R	30	36.5	50
	I4	58	F	L	35	44.8	50
	I5	52	M	R	55	48.2	50
	I6	78	F	R	27.5	47	50
	I7	27	M	L	60	57	60
	I8	33	M	L	35	50.2	50
	I9(l)*	46	F	L	45	58.7	60
	I9(r)*	46	F	R	65	61	62
	I10	49	M	L	40	46	50
Normal hearing	N1	19	M	L	−5	**	50,65
	N2	20	M	L	−2.5	**	50,65
	N3	52	F	L	5	**	50,65

was implemented in the spectral domain by first adjusting the amplitude of each sinusoidal component, and then summing all of the components together.

Random-phase harmonic complexes were chosen because they are known to yield very poor f_0 DLs (on the order of 5–10% of the f_0; Bernstein and Oxenham, 2003; 2005; 2006) when the harmonics are unresolved, thus producing a large f_0 DL difference between low and high f_0's and providing the best opportunity to observe the transition from large to small f_0 DLs. Sine-phase conditions were included to give an estimate of harmonic resolvability based on the phase dependence of f_0 DLs. At least nine f_0's were tested for each HI listener (75, 125, 150, 175, 200, 250, 325, 400, and 500 Hz). Higher f_0's (750 Hz and, in one case, 1500 Hz) were tested for some HI listeners for whom the 500-Hz f_0 DL appeared to be larger than the 1500-Hz pure-tone frequency difference limen (FDL) in a pilot run, suggesting that the f_0 DL had not reached its asymptotic value. For NH listeners, nine f_0's (75–500 Hz) were tested in the random-phase conditions. The 500-Hz f_0 was not tested for the sine-phase conditions, resulting in a total of eight f_0's tested in these listeners.

2. Stimulus level

It was desirable to keep both the sensation level (SL) and overall sound pressure level (SPL) similar for all listeners so as to control for the known influences of these two factors on f_0 discrimination performance (respectively, Hoekstra, 1979; Bernstein and Oxenham, 2006). Therefore, all stimuli were presented in a background of threshold equalizing noise (TEN; Moore *et al.*, 2000), which is intended to yield pure-tone detection thresholds in noise that are approximately constant across frequency. Presented in a TEN background, pure tones presented at equal SPL will also have roughly equal SL. For each HI listener, the TEN was set to a level that, in a NH listener, would yield tone-in-noise detection thresholds at least as high as the HI listener's detection thresholds in quiet. Initially, the TEN level was intended to be the same for all listeners. Tone-in-quiet thresholds, estimated using a three-interval three-alternative forced-choice, two-down, one-up adaptive procedure, were no higher than 50 dB SPL in the 1.5–3.5 kHz range for each of the first five HI listeners recruited for the study. For these listeners, the level of the background noise was set to 50 dB SPL per $\mathrm{ERB_N}$, where $\mathrm{ERB_N}$ is the equivalent rectangular bandwidth of auditory filters in NH listeners as described by Glasberg and Moore (1990). After measurements had been made for the initial five listeners, five additional listeners (six ears) were recruited for the study. Three of these six additional ears had at least one tone-in-quiet threshold in the 1.5–3.5 kHz range above 50 dB SPL. For these ears, the TEN level (Table I, column 7) was set to 60 dB SPL (two ears) or 62 dB SPL (one ear) depending on the maximum absolute threshold measured in the 1.5–3.5 kHz range (Table I, column 6).

To set stimulus levels, detection thresholds were measured for pure tones in the TEN background. The 0 dB SL reference was determined for each listener individually, and was taken as the mean of six threshold measurements, two estimates each for pure-tone frequencies of 1.5, 2, and 3 kHz. Across the HI listeners, the 0 dB SL reference ranged from −2.9 to +3.5 dB *re* the TEN level in dB $\mathrm{SPL/ERB_N}$.

Because of the different levels tested for the HI listeners, NH listeners were tested with both 50 dB $\mathrm{SPL/ERB_N}$ and 65 dB $\mathrm{SPL/ERB_N}$ TEN, to ensure that stimuli were presented at a level at least as high as the highest level presented to HI listeners. Due to a lack of testing time, sine-phase conditions were not tested at the higher level in NH listeners. Across the NH listeners, the 0 dB SL reference ranged from −3.8 to −1.8 dB and from −3.1 to −1.0 dB *re* the 50 and 65 dB $\mathrm{SPL/ERB_N}$ TEN levels, respectively.

Stimuli were presented at a nominal 12.5 dB SL per component in a TEN background at the levels specified in Table I. Exceptions to the procedure for setting the stimulus level were made for three listeners (two NH, one HI) where the stimuli presented in 62–65 dB $\mathrm{SPL/ERB_N}$ noise were uncomfortably loud at the 75- and/or 125-Hz f_0. For the listeners and conditions where this occurred, stimulus levels were reduced somewhat, or the conditions were eliminated.[3] To prevent contralateral detection of the stimuli, uncorrelated TEN was presented to the nontest ear at 20 dB below the level of that presented to the test ear.

3. Procedure

Five f_0 DL measurements were made for each combination of f_0, phase, and stimulus level. For each listener, all of the random-phase conditions were tested before the sine-phase conditions because the decision to include sine-phase measurements was not made until the random-phase data had already been collected for the first five HI listeners. FDLs for a 1500-Hz pure tone were measured as an additional condition interspersed with the f_0 DL estimates for harmonic complexes. Five FDL measurements each were interspersed with the measurements involving random- and sine-phase stimuli. The f_0 and stimulus level conditions were presented in random order.

Fundamental frequency DLs and FDLs were estimated in a three-interval three-alternative forced-choice (3I-3AFC) adaptive procedure, using a two-down, one-up algorithm to track the 70.7% correct point on the psychometric function (Levitt, 1971). Two intervals contained a stimulus with a reference f_0 ($f_{0,\mathrm{ref}}$) and the other interval contained a complex with a higher f_0. The listener's task was to identify the interval containing the complex with the higher pitch. The f_0 difference (Δf_0) was initially set to 20% of the f_0, changed by a factor of 1.59 until the second reversal, and then changed by a factor of 1.26 for six more reversals. The f_0 DL was estimated as the geometric mean of the Δf_0's at the last six reversal points.

To reduce the potential effectiveness of loudness as an alternative cue, the root-mean-squared (rms) power was first equalized across the three intervals by increasing the stimulus level per component for the interval containing the higher f_0, and then a random level perturbation was added to each interval, chosen from a uniform distribution of ±2.5 dB. In addition, $f_{0,\mathrm{ref}}$ was roved from trial to trial within a run, chosen from a uniform distribution between ±5% of the average f_0. This was intended to encourage listeners to com-

pare the pitches of the stimuli across each of the intervals of one trial, rather than comparing the pitch in each interval with some internally stored representation of the $f_{0,\mathrm{ref}}$, although the f_0 roving may not have been effective for low f_0's where the measured f_0 DLs were relatively large.

4. Apparatus

The stimuli were generated digitally and played out via a soundcard (LynxStudio LynxOne) with 24 bit resolution and a sampling frequency of 32 kHz. The stimuli were then passed through a programmable attenuator (TDT PA4) and headphone buffer (TDT HB6) before being presented to the listener via one earpiece of a Sennheiser HD 580 headset. Listeners were seated in a double-walled sound-attenuating chamber. Intervals were marked by colored boxes on a computer screen, and visual feedback (correct/incorrect) was provided following each response.

D. Results

Figure 2 plots f_0 DLs as a function of f_0 for six sample HI listeners [I5, I6, I7, I9(l), I9(r), and I10], representing the range of results observed across the 11 HI ears, and the mean f_0 DLs across the three NH listeners at each of the two stimulus levels. Each of the five HI listeners for whom data are not shown yielded very similar results to other subjects shown in Fig. 2. Results for listeners I2, I3, and I4 were, like I6 and I10, very similar to those for the NH listeners, while listeners I1 and I8 showed more abnormal results, comparable to those for I7 and I9(r). "Low" and "high" levels for NH listeners refer to stimuli presented in 50 and 65 dB SPL/$\mathrm{ERB_N}$ background TEN, respectively. Random-phase conditions are denoted by circles and sine-phase conditions by squares. The solid lines in Fig. 2 represent fitted functions to the random-phase data, and the dashed vertical lines represent midpoints of the transitions in the functions, as described in Sec. V A.

Four main findings are apparent in the results. First, for most listeners and phase conditions, f_0 DLs generally transitioned from large to small with increasing f_0. This is consistent with previous results in NH listeners (Hoekstra, 1979; Shackleton and Carlyon, 1994; Bernstein and Oxenham, 2005; 2006) and is thought to reflect the transition from all unresolved to some resolved harmonics, although Moore *et al.* (2006) have interpreted this result as reflecting a progressive decline in the ability to use temporal fine-structure information (see Sec. VI B). Second, the f_0 where the f_0 DL transition occurred (the f_0 transition point, $f_{0,tr}$), varied across listeners. NH listeners and listeners with relatively mild hearing loss (e.g., I6 and I10) showed the transition at a relatively low f_0 of around 200 Hz, whereas listeners with more severe hearing loss [e.g., I7 and I9(r)] tended to have transitions at higher f_0's of 500 Hz or more. The hypothesis that the across-listener variability in the f_0 DL transition point is related to frequency selectivity is examined quantitatively in Sec. V. Third, the results from some HI listeners show substantial nonmonotonicities in the pattern of results [e.g., I5, I7, and I9(r)]. For these listeners, f_0 DLs are elevated at moderate f_0's, which may result from unresolved

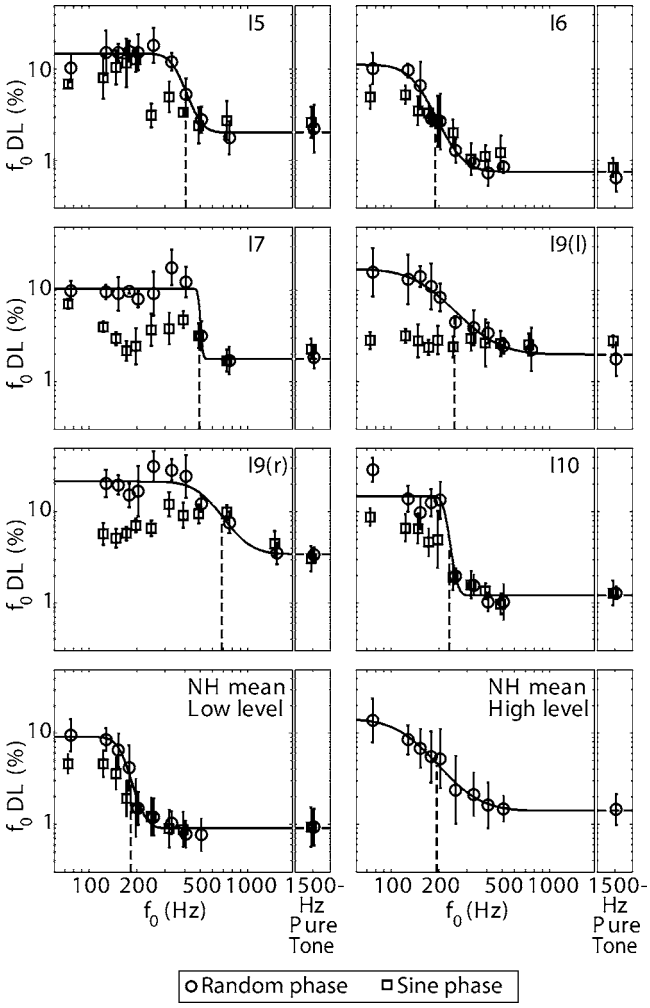

FIG. 2. (Top six panels) f_0 DLs plotted as a function of f_0, and FDLs for a 1500 Hz pure-tone FDL, for six example HI listeners. (Bottom two panels) mean f_0 DLs and FDLs across the three NH listeners at two stimulus levels. Error bars indicate the standard deviation of the five f_0 DL or FDL measurements for each HI listener, and the standard deviation across the three mean f_0 DLs or FDLs for NH listeners. Dashed curves indicate the sigmoid functions that best fit the random-phase data, for each individual HI listener or the mean NH data (see Sec. V A). Vertical dashed lines indicate the $f_{0,\mathrm{tr}}$, defined as the f_0 that yielded random-phase f_0 DLs halfway (on a log scale) between maximum and minimum.

harmonics that yield an envelope repetition rate too high to be processed efficiently (e.g., Kohlrausch *et al.*, 2000). Overall, flat or nonmonotonic f_0 DL functions were observed for three and five HI listeners (out of 11) in the random- and sine-phase conditions, respectively. Fourth, for most listeners, the phase relationships between harmonics affected f_0 DLs for low f_0's, but not high f_0's, consistent with previous results in NH hearing listeners (Houtsma and Smurzynski, 1990; Bernstein and Oxenham, 2003) and with the idea that complexes with high f_0's contain mostly resolved harmonics. This result provided an additional estimate of harmonic resolvability (see Sec. V A 3) based on the range of stimulus f_0's for which there was an f_0 DL phase effect.

III. EXPERIMENT 2: MODULATION DISCRIMINATION

A. Rationale

Frequency selectivity was estimated by measuring listeners' ability to discriminate between sinusoidal amplitude

modulation (SAM) and quasi-frequency modulation (QFM; Zwicker, 1952). The two sounds were three-tone complexes with identical amplitude spectra but different relative phases between components. Previous results have shown that HI listeners can perform this task out to higher modulation frequencies than can NH listeners (Nelson and Schroder, 1995), and that performance improves at high stimulus levels for NH listeners (Nelson, 1994). This is thought to be because the wider peripheral filters associated with SNHL (or high stimulus levels in NH listeners) increase the likelihood of peripheral interactions between components. The hypothesis that small f_0 DLs require resolved harmonics suggests that *better* SAM/QFM discrimination (i.e., a higher maximum modulation frequency) should correlate with *poorer* f_0 discrimination performance (i.e., a higher $f_{0,\mathrm{tr}}$). One advantage of testing this prediction is that HI listeners should perform better than NH listeners, such that the interpretation of the results should not be confounded by any nonspecific perceptual or cognitive deficits for the HI listeners (who were, on the average, older than the NH listeners). Also, this experiment estimates frequency selectivity by varying the spacing between adjacent frequency components, a situation analogous to that of the f_0 DL measures in Experiment 1.

B. Methods

As in the studies of Nelson (1994) and Nelson and Schroder (1995), the current experiment measured discrimination between SAM and QFM complexes as a function of the modulation frequency (f_m). The carrier frequency (f_c) was fixed at 1500 Hz (the lower cutoff frequency of the bandpass filter used in Experiment 1). In this three-interval three-alternative forced-choice task, two intervals contained SAM complexes and the third contained a QFM complex. Listeners were asked to identify the interval containing the stimulus that was different from the other two. Visual feedback (correct/incorrect) was provided. Each interval consisted of a three-component tone complex, with frequencies f_c-f_m, f_c, and f_c+f_m, and duration 500 ms (including 30 ms raised cosine onset and offset ramps). The intervals were separated by silent gaps of 375 ms.

The wideband background TEN was not used in this experiment because it was found to be too distracting and detrimental to performance in the modulation discrimination task. Instead, a low-pass TEN with a cutoff frequency of $(f_c-1.95f_m)$ was used to mask any distortion products occurring at frequencies of f_c-2f_m or below. The low-pass TEN had the same spectral characteristics as the wideband TEN of Experiment 1 for frequencies below its cutoff. The low-pass TEN was turned on 250 ms before the first interval and turned off 250 ms following the offset of the third interval, for a total duration of 2750 ms.

Although the wideband TEN was not used, the level of the center component was set at a SPL equal to the 12.5 dB SL level that was used in Experiment 1, adjusted for each listener. The level of each sideband was 6 dB below that of the center component, producing 100% amplitude modulation in the SAM case. The SAM complexes were generated by setting the three components to be in sine starting phase. The QFM complexes were identical to the SAM complexes except that the starting phase of the center component was advanced by 90°.

The f_m's were set to the f_0 values tested in the sine-phase conditions of Experiment 1 (eight f_m's for NH listeners, nine or ten f_m's for HI listeners). Each run included four trials for each f_m, presented in random order. Each HI listener completed 13 runs for a total of 52 stimulus presentations for each f_m, with two exceptions, detailed below. Each NH listener was tested with the stimulus level set relative to the detection threshold in both the 50 and 65 dB $\mathrm{SPL/ERB_N}$ TEN, with 13 runs presented at each level. The same 11 HI and 3 NH listeners from Experiment 1 participated in this experiment. Each listener completed at least 1 h of practice before the measurement period began.

Two HI listeners (I6 and I8) were unable to achieve much above chance performance even for the lowest f_m tested of 75 Hz, unless the randomization of f_m within a run was greatly diminished. For these two listeners, eight trials each of two f_m's were presented within a run. Seven runs were completed for each pair of f_m's for a total of 56 stimulus trials per f_m. With this modification, one of the listeners (I6) still failed to achieve 100% correct for the 75 Hz f_m. Two additional f_m's (25 and 50 Hz) were added for this listener, who achieved near-perfect performance at both f_m's.

C. Results

The upper six panels of Fig. 3 show the percent correct as a function of f_m for the same six sample HI listeners whose f_0 DLs were shown in Fig. 2. Again, the performance of the listeners not shown was generally within the range of those shown in the graphs. The lower two panels of Fig. 3 show the percent correct for each of the three NH listeners for each f_m at the low and high stimulus levels. Each listener showed qualitatively similar results, with performance decreasing from near 100% correct for the lowest f_m tested to near chance (33%) for the highest f_m tested. The solid lines represent sigmoidal fits, and the vertical dashed lines represent estimates of the 66.7% correct point based on the fitted functions, as described in Sec. V A 4. No consistent nonmonotonicities were observed in the results, suggesting that the nonmonotonicities observed by Nelson and Schroder (1995) may have derived from combination tones that were masked by the low-pass noise in the current experiment. The data shown in Fig. 3 generally support the hypothesis that listeners with poorer frequency selectivity can perform better than normal (i.e., out to a higher modulation frequency) in the modulation discrimination task. NH listeners and HI listeners with mild hearing loss (e.g., I6 and I10) who performed best at f_0 discrimination (Fig. 2) performed worst at discriminating QFM from SAM (Fig. 3). Conversely, listeners with more moderate-to-severe hearing loss who were poor discriminators of f_0 performed best at discriminating QFM from SAM at high modulation frequencies [e.g., I5, I7, I9(l), and I9(r)]. However, this was not always the case. For example, I8 had a relatively high $f_{0,\mathrm{tr}}$ but still showed difficulty in performing this task. The relationship between performance in this task and the f_0 DLs measured in Experiment 1 is evaluated in more detail for all listeners in Sec. V.

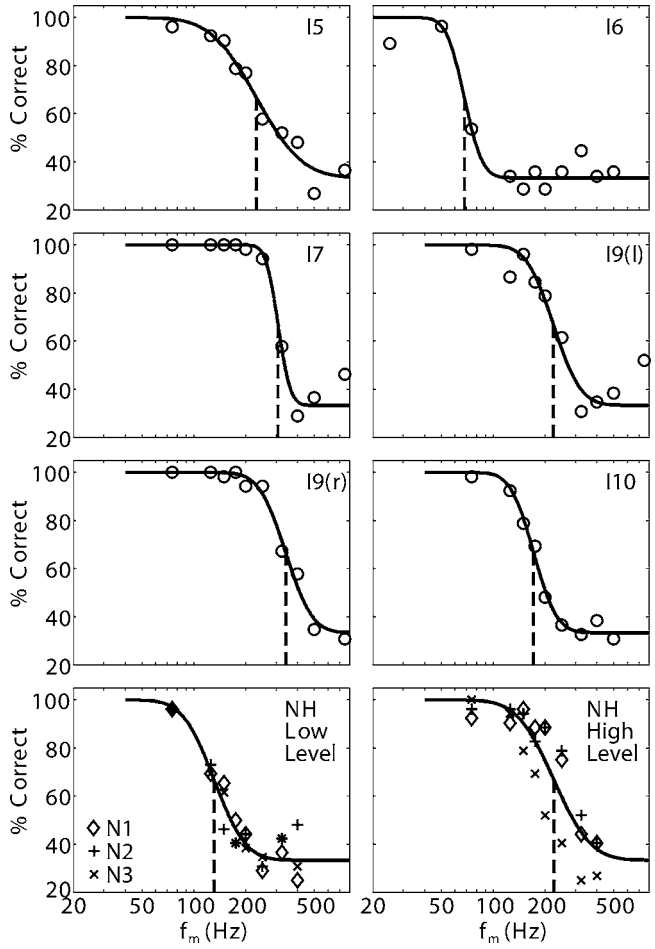

FIG. 3. Results of Experiment 2, showing the percentage correct in discriminating between SAM and QFM as a function of f_m, the frequency spacing between components, for the six sample HI listeners of Fig. 2 (top six panels), and for the three NH listeners at the two stimulus level (two lower panels). Dashed curves indicate the sigmoid function that best fit the data for each HI listener or for the pooled NH data at each level. Vertical dashed lines indicate the estimate of the threshold f_m ($f_{m,\mathrm{tr}}$) yielding 67% correct performance, halfway between perfect performance (100%) and guessing (33%).

IV. EXPERIMENT 3: AUDITORY FILTER SHAPES

A. Rationale

The current standard for evaluating peripheral frequency selectivity in the spectral domain is the notched-noise method of auditory filter-shape estimation (Patterson, 1976). This experiment used a "fixed signal level" version of the notched-noise method described by Rosen and Baker (1994) to estimate auditory filter bandwidths in the NH and HI listeners who participated in Experiments 1 and 2. The level of the notched-noise masker that just masked a pure tone was measured as a function of the masker's spectral notch width. At threshold, this paradigm is thought to deliver roughly constant overall (signal plus noise) power across notch widths at the output of auditory filter in question, thus reducing the possible confounding influence of variations in filter shape with input level.

B. Methods

Throughout the experiment, the pure-tone signal had a constant frequency (f_{sig}) of 1500 Hz, corresponding to the low-frequency edge of the passband in Experiment 1. The signal was fixed at the SPL level corresponding to 10 dB SL (adjusted for each listener individually) ***re*** the TEN level that was used in Experiment 1. Although the signal SPL was adjusted relative to the detection threshold in TEN, the TEN background was not used. The NH listeners were only tested with the signal at one level (10 dB *re* the detection threshold in 50 dB SPL/$\mathrm{ERB_N}$ TEN) because a signal at the higher level could not be comfortably masked for wide notch widths in these listeners.

Each trial in the experiment consisted of three intervals, each with a 700-ms duration, separated by 500-ms silent gaps. Two of the intervals contained only a 700 ms noise burst (including 10-ms raised-cosine onset and offset ramps). The other interval also contained a 500-ms pure-tone signal (including 30-ms raised-cosine onset and offset ramps), temporally centered within the noise burst. The listeners' task was to identify which of the three intervals contained the pure-tone signal. A 3I-3AFC procedure with a two-up, one-down adaptive algorithm tracked the 70.7% correct point (Levitt, 1971). The spectrum level of the noise (dB SPL/Hz) was initially set to −35 dB *re* the TEN noise level (dB SPL/$\mathrm{ERB_N}$) for each listener, and changed by 8 dB for the first two reversals, 4 dB for the next two reversals, and 2 dB for the last eight reversals. Threshold was estimated as the mean of the noise levels at the last eight reversal points. Reported thresholds are the means of three such threshold estimates.

The noise masker consisted of two bandpass noises, each with a bandwidth of 200 Hz. The notch width was defined in terms of the deviations from the signal fre quency, expressed as a proportion of f_{sig}, of both the high-frequency edge of the lower-frequency noise band (Δf_l) and the low-frequency edge of the upper-frequency noise band (Δf_u). Five symmetrical notch conditions were presented, with equal Δf_l and Δf_u values of 0, 0.1, 0.2, 0.3, and $0.4 f_{\mathrm{sig}}$. To allow for the possibility of asymmetrical filters, there were also four asymmetric conditions $[(\Delta f_l, \Delta f_u) = (0.1 f_{\mathrm{sig}}, 0.3 f_{\mathrm{sig}}), (0.2 f_{\mathrm{sig}}, 0.4 f_{\mathrm{sig}}), (0.3 f_{\mathrm{sig}}, 0.1_{\mathrm{sig}})$, and $(0.4 f_{\mathrm{sig}}, 0.2 f_{\mathrm{sig}})]$. A low-pass noise was included to mask any possible low-frequency combination bands (Greenwood, 1972) that could facilitate the detection of the signal, with a cutoff frequency equal to the low-frequency edge of the lower-frequency noise band and a spectrum level 20 dB below that of the notched noise.

C. Analysis

A standard fitting procedure was used to derive auditory filter shapes from the data (Glasberg and Moore, 1990). The fitting procedure took into account the Sennheiser H580 transfer function, the middle-ear transfer function, the possibility of off-frequency listening, and variations in filter bandwidth with center frequency (CF), as described by Glasberg and Moore (1990). Four different filter-shape models were tested, based on all permutations of symmetrical or asymmetrical filter tips (same or different upper- and lower-frequency slopes, p_l and p_u) and the presence or absence of a dynamic range limit (r) on the lower-frequency slope. The

TABLE II. The accuracy of four auditory filter models in fitting the notched-noise masking data across 14 NH and HI listeners.

Filter tip	Dynamic range limitation?	Free parameters	rms fitting error (dB)
Symmetric	Yes	3	1.24
Asymmetric	Yes	4	1.14
Symmetric	No	2	1.42
Asymmetric	No	3	1.31

dynamic range limit was never applied to the upper-frequency slope, thus simulating the uniformly steep upper slope often found in auditory-nerve and basilar-membrane tuning curves (e.g. Kiang *et al.*, 1965; Sellick *et al.*, 1982). The signal-to-noise ratio at the output of a model filter required for signal detection provided an additional free parameter in all four models. All four filter models yielded similar rms fitting errors (Table II), although there was a small advantage for filter models incorporating a larger number of free parameters. Bernstein and Oxenham (2006) found that variation in the $f_{0,\mathrm{tr}}$ across stimulus level in NH listeners was well accounted for by variation in the dynamic range limitation across level in the auditory filter model used to fit the notched-noise masking data. Therefore, in the current study, a filter model with a dynamic range limitation was chosen to characterize frequency selectivity for the regression analyses described in Sec. V. Because the rms error was only marginally improved by the addition of a fourth free parameter in the asymmetrical case, the filter model with a symmetrical tip was selected. The asymmetrical application of the dynamic-range limitation and the combination of off-frequency listening and proportional variation in filter bandwidth with CF accounted reasonably well for unequal threshold measurements in the four asymmetric notch conditions (overall rms fitting error 1.16 dB vs 1.31 dB for the symmetric conditions). The equivalent rectangular bandwidths (ERBs) of the filters were derived from the fitted parameters.

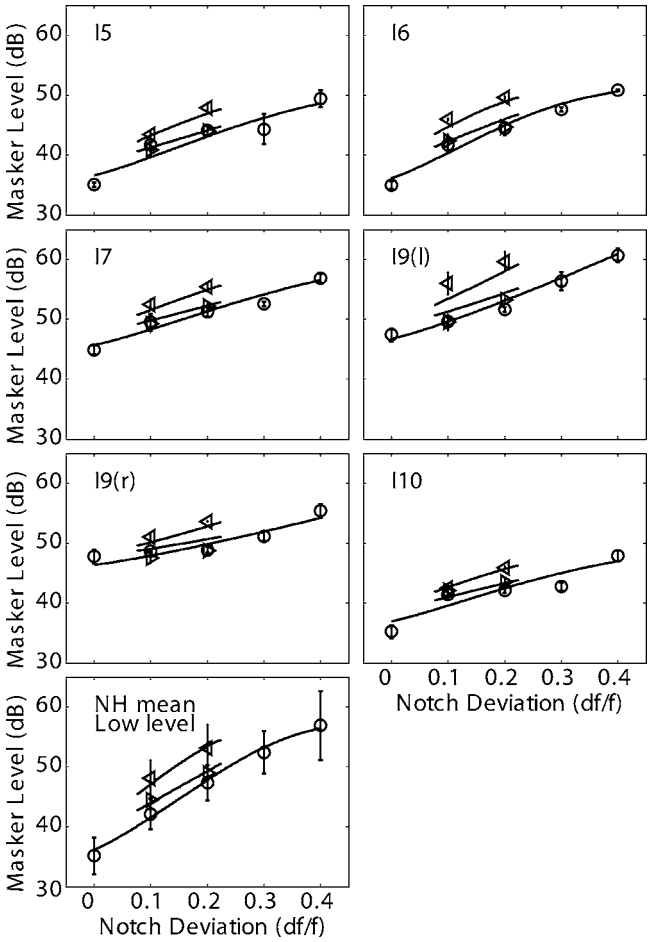

FIG. 4. The notched-noise masking level needed to just mask a 1500 Hz probe tone presented at 10 dB re the threshold in TEN at the level indicated in Table I. Circles indicate notches that are symmetrical around the probe-tone frequency. Left- and right-pointing triangles indicate asymmetrical notches, shifted toward lower and higher frequencies, respectively. For the asymmetrical conditions, data are plotted according to the notch edge closest to the probe frequency, and the second notch edge was $0.2/f_{\mathrm{sig}}$ farther away from the probe frequency. Solid lines indicate the predicted masker levels based on the best fitting auditory filter shape. Error bars indicate the standard deviation across the three masking measurements for the HI listeners, or across the three NH listeners.

D. Results

Figure 4 shows the notched-noise masking data along with the masking predictions based on the best-fitting filter functions (solid lines) for each of the six example HI listeners (upper six panels) from Figs. 2 and 3, and for the mean of the three NH listeners (lower panel). As in Figs. 2 and 3, the performance of the listeners not shown was generally within the range of those shown in the graphs. Circles represent conditions with symmetrical noise notches, while left- and right-pointing triangles represent asymmetrical conditions where Δf_l was greater than and less than Δf_u, respectively. The simple filter-shape model yielded a reasonable fit to the data for each listener. As expected, HI listeners generally showed broader frequency selectivity than did NH listeners. This can be seen in Fig. 4 by the generally shallower increase in masker level as a function of notch width in the HI than in the NH listeners. Although for illustrative purposes fits are shown for the mean NH data in the lower panel of Fig. 4, fits were performed for each individual NH listener for the across-listener analyses described in the following section.

V. ANALYSIS

A. Summary measures

Each of the experiments described above yielded summary values that were then used to derive correlations between the measures of f_0 discrimination (Experiment 1) and the measures of frequency selectivity (Experiments 1, 2, and 3). The different summary measures, and the way they are derived, are described below. The values for each of these measures for each listener are shown in Table III, with boldface entries indicating HI values that fell more than two standard deviations above the mean NH values (or above or below the mean NH values in the case of the f_0 DL slope, see Sec. V A 2) at a comparable stimulus level.[4] Although the experimental design was intended to investigate correlations

TABLE III. Best-fit estimates for individual listeners of four aspects of the f_0 DL data and three frequency selectivity estimates. Logarithmic transformations of the data shown here [except for m which is already in the logarithmic domain in Eq. (1)] were used in the correlation analyses of Figs. 6–8 and Table IV. Boldface entries indicate values for HI listeners that fell more than two standard deviations (of the NH values) above the mean NH values at a comparable level (or more than two standard deviations above *or* below the mean NH values in the case of m). Asterisks (*) indicate cases where the high-level HI values were compared to low-level NH mean values because no NH data were available at the high level.

		f_0 discrimination				Frequency selectivity		
	Listener	$f_{0,tr}$ (Hz)	f_0 DL_{min} (%)	f_0 DL_{max} (%)	Slope (m)	$f_{0,PE}$ (Hz)	$f_{m,tr}$ (Hz)	ERB (Hz)
Hearing impaired	I1	182.7	**1.84**	**32.86**	**1.70**	**275.7**	**287.7**	395.6
	I2	**214.9**	**1.44**	13.93	7.92	**246.2**	**143.3**	**406.2**
	I3	187.3	1.29	**21.61**	5.51	154.4	**166.0**	**482.0**
	I4	**203.5**	**1.38**	**25.31**	**3.46**	167.2	**153.2**	**517.2**
	I5	**403.2**	**2.02**	14.84	8.68	**489.0**	**230.7**	**543.1**
	I6	189.6	0.75	11.16	5.06	165.3	68.0	**409.4**
	I7	**493.6**	1.76	10.42	**54.53**	**446.9***	308.4	**618.7***
	I8	**345.1**	**3.60**	**23.86**	7.73	**330.9**	**152.0**	**454.0**
	I9(I)	250.5	**1.99**	17.17	3.11	**259.8***	223.9	**564.7***
	I9(r)	**687.4**	**3.45**	21.42	4.85	**462.7***	**341.0**	**941.5***
	I10	**231.9**	1.21	14.91	18.61	**241.1**	**171.6**	**623.0**
Normal hearing low level	N1	192.2	0.66	5.87	14.13	186.2	128.5	343.8
	N2	173.8	0.96	9.82	13.83	175.4	136.8	347.7
	N3	184.1	1.10	11.68	7.55	204.7	131.4	282.5
	Mean	183.4	0.91	9.12	11.84	188.8	132.2	324.7
	St. Dev.	9.2	0.22	2.97	3.72	14.8	4.2	36.6
Normal hearing high level	N1	196.4	1.06	5.79	14.52		269.4	
	N2	246.5	1.59	13.40	3.03		260.0	
	N3	160.8	1.48	31.40	2.62		174.5	
	Mean	201.2	1.38	16.86	6.72		234.6	
	St. Dev.	43.1	0.28	13.15	6.76		52.3	

between f_0 discrimination and frequency selectivity measures rather than to compare groups of impaired and normal listeners, this information is provided to demonstrate that many impaired listeners showed quantitatively abnormal results.

Four measures of f_0 discrimination performance were derived from the random-phase f_0 DL data. A sigmoid function[5] was fit to the log-transformed f_0 DL vs. log-transformed f_0 data (Fig. 2). A fit was made to the data for each HI listener and separately to the data at each of the two stimulus levels for each NH listener. The fitting procedure adjusted four free parameters, representing estimates of (1) the maximum (f_0 DL_{max}) and (2) the minimum f_0 DL (f_0 DL_{min}) attained at very low and very high f_0's, respectively, (3) the f_0 at which f_0 DLs transitioned from large to small ($f_{0,tr}$), and (4) the slope (m) of the transition. The FDL data measured for the 1500 Hz pure tone were included in the fitting procedure, with f_0 set to infinity, because a pure tone can be thought of as "infinitely" resolved.[6] With the f_0 set to infinity, the FDL data should only directly influence the estimate of the parameter f_0 DL_{min}, since changes in $f_{0,tr}$, f_0 DL_{max} and m do not affect the value of the sigmoid function at an f_0 of infinity. Because the nonmonotonicities observed in the sine-phase f_0 DL data prohibited a satisfactory fit for some listeners, only the random-phase data were analyzed in this way. The sigmoid functions that best fit the random-phase data are shown as solid curves in Fig. 2. While fitted curves are shown for the mean NH data in the lower two panels in Fig. 2, fits were made for each individual NH listener for the regression analyses described in Sec. V B, below.

1. The f_0 DL transition point ($f_{0,tr}$)

The $f_{0,tr}$, one of the parameters in the sigmoid fitting procedure, provides an estimate of the f_0 for which DLs were halfway (on a log scale) between maximum and minimum. Seven out of 11 HI ears had an $f_{0,tr}$ more than two standard deviations above the NH mean at a comparable level (boldfaced entries in Table III).

2. Maximum and minimum f_0 DL values (f_0 DL_{max} and f_0 DL_{min}) and the f_0 DL slope (m)

These values were also derived from the sigmoidal fits to data in Experiment 1. The values of f_0 DL_{max} and f_0 DL_{min} provide estimates of the f_0 discrimination performance associated with completely unresolved and resolved harmonics, respectively. The value of m provides an estimate of the rate at which the f_0 DL transitioned from its maximum to minimum value. These three summary measures did not form part of the original hypothesis regarding pitch discrimination and frequency selectivity, but certain relationships were found between f_0 DL_{min} and the other measures, which are described in the correlational analyses below. The f_0 DL_{min} was more than two standard deviations above the NH mean at a comparable level for seven out of the 11 impaired ears (boldfaced entries in Table III). The elevated f_0 DL_{min} in HI lis-

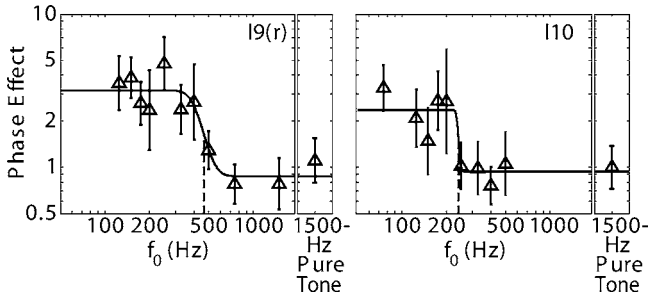

FIG. 5. The f_0 DL phase effect (PE), defined as the ratio between random- and sine-phase f_0 DLs, for two sample HI listeners. The ratio between pure-tone FDLs for trials that were interspersed with the sine- and random-phase f_0 DL conditions were also calculated to demonstrate any possible learning effects (right column of each panel). Error bars indicate the standard deviation across the 25 PE estimates for each HI listener. Solid curves indicate the sigmoid functions that best fit the PE data. Vertical dashed lines indicate the phase-effect transition f_0 ($f_{0,\mathrm{PE}}$) defined as the f_0 for which the phase effect was halfway (on a log scale) between maximal and minimal.

teners suggests that the frequencies of individual resolved harmonics are more poorly encoded, consistent with previous studies of pure-tone frequency discrimination in listeners with SNHL (e.g., Tyler *et al.*, 1983; Moore and Glasberg, 1986; Moore and Peters, 1992). The effects of hearing loss on f_0 $\mathrm{DL}_{\max}$ and m were less clear. Estimates of f_0 $\mathrm{DL}_{\max}$ were more than two standard deviations above the NH mean for only four HI ears (boldfaced entries in Table III). Estimates of m were more than two standard deviations above or below the NH mean for one and two HI ears, respectively.

3. The phase-effect transition point ($f_{0,PE}$)

The phase-effect transition point ($f_{0,\mathrm{PE}}$) is also derived from Experiment 1 (Fig. 2), but relates to the effect of phase on f_0 DLs, providing an estimate of harmonic resolvability based on the idea that the relative phase between successive components should only affect f_0 DLs if the components are unresolved and interact within individual auditory filters. In all listeners, f_0 DLs were larger in the random- than the sine-phase conditions for low but not for high f_0's, consistent with the idea that only complexes with high f_0's contain resolved harmonics. This observation was confirmed by two-factor (f_0 and phase) ANOVAS performed on the f_0 DL data for each individual listener, with all listeners showing a significant ($p<0.05$) interaction between f_0 and phase.

The f_0 DL phase effect (PE) was defined as the ratio between the f_0 DLs measured in random- and sine-phase conditions. Resampling was performed to obtain all possible estimates of the PE by recalculating the PE 25 times for each f_0, once for each combination of the five repeated f_0 DL measurements made for each phase relationship. The mean and standard deviations of the 25 PE estimates for each f_0 (and for the 1500 Hz pure tone) are plotted in Fig. 5 for two sample HI listeners that illustrate the range of observed responses. Because the random-phase conditions were always tested before the sine-phase conditions, general differences between the random- and sine-phase conditions might be attributable to learning effects. To control for this possibility, "phase-effect" ratios were also calculated for the 1500 Hz pure-tone FDL measurements that were interspersed in each f_0 DL phase condition.

For all listeners, the PE was generally greater than one for low f_0's (f_0 DLs affected by component phase), and approximately equal to one for high f_0's (no phase effect), although the maximum f_0 for which a PE was observed varied across listeners. To estimate the transition f_0 at which phase no longer affected f_0 DLs for each listener, a sigmoid function with four free parameters was fit to the log transforms of the 25 PE estimates at each f_0 (solid curves in Fig. 5).[7] As with the fits to the random-phase f_0 DL data, the PE estimates for the 1500 Hz pure tone were included in the fitting procedure, with f_0 set to infinity. This was done instead of setting the value of the sigmoid function to zero for infinite f_0's to allow some flexibility in the value of the PE function at high f_0's depending on the variance in the pure-tone FDLs. The PE transition f_0 ($f_{0,\mathrm{PE}}$) was defined as the f_0 for which the PE was halfway between its maximum and minimum log-transformed values (vertical dashed lines in Fig. 5). By characterizing the transition point of the PE function, any overall improvement due to learning effects in the sine-phase relative to the random-phase conditions would be factored out. Eight out of 11 HI ears had $f_{0,\mathrm{PE}}$'s more than two standard deviations above the NH low-level mean (boldfaced entries in Table III).

4. Modulation discrimination transition point

The modulation frequency at which QFM and SAM became indistinguishable (Experiment 2) provided another estimate of component resolvability, based on the idea that QFM and SAM should only be discriminable if the stimulus components are unresolved. A sigmoid function fixed at 100% and 33% correct at the extremes was fit (minimum least squares) to the percentage correct data as a function of the log-transformed f_m's (solid curves in Fig. 3). The 67% correct point of this function was taken as the estimate of the transition f_m ($f_{m,\mathrm{tr}}$) between resolved and unresolved components (vertical dashed lines in Fig. 3). The $f_{m,\mathrm{tr}}$ was more than two standard deviations above the NH mean at a comparable level for eight out of the 11 HI ears (boldfaced entries in Table III), supporting the hypothesis that HI listeners with wider peripheral filters should perform better than NH listeners in this task.

5. Equivalent rectangular bandwidth (ERB)

The ERB of the filter shape that best fit the notched-noise masking data (Experiment 3) provided a third estimate of frequency selectivity. ERBs were more than two standard deviations above the NH low-level mean for ten out of the 11 HI ears (boldfaced entries in Table III).

B. Regression analyses

Table IV lists the results of single regression analyses performed between each of the four measures of f_0 discrimination ($f_{0,\mathrm{tr}}$, f_0 $\mathrm{DL}_{\min}$, f_0 $\mathrm{DL}_{\max}$, and m), each of the three estimates of frequency selectivity ($f_{0,\mathrm{PE}}$, $f_{m,\mathrm{tr}}$, and ERB) and the degree of hearing loss at 1.5 kHz ($\mathrm{HL}_{1.5\mathrm{k}}$). Squared Pear-

TABLE IV. Squared Pearson correlation coefficients (R^2) for bivariate correlations between f_0 DL and frequency selectivity measures. Boldface entries indicate significant ($p<0.05$) correlations. Asterisks (*) indicate that partial correlations were significant when controlling for TEN level ($p<0.05$, partial R^2 values not shown). "N/A" indicates that 17 data points were not available because NH listeners were tested at only one level for at least one of the measures associated with a given cell.

Data included in analysis	Measure	$f_{0,tr}$	f_0 DL_{min}	f_0 DL_{max}	m	$f_{0,PE}$	$f_{m,tr}$	ERB
All listeners N=14	$HL_{1.5k}$	**0.50**	**0.52***	**0.38***	0.02	**0.51***	**0.52***	**0.68***
	$f_{0,tr}$		**0.54***	0.02	0.13	**0.80***	**0.44**	**0.62**
	f_0 DL_{min}			**0.45***	0.00	**0.57***	**0.48***	**0.38**
	f_0 DL_{max}				0.20	0.04	0.17	0.14
	m					0.13	0.08	0.04
	$f_{0,PE}$						**0.56***	**0.37**
	$f_{m,tr}$							**0.41**
HI listeners only N=11	$HL_{1.5k}$	**0.58**	0.34	0.01	0.13	**0.64***	**0.79***	**0.45**
	$f_{0,tr}$		**0.49**	0.04	0.18	**0.76***	**0.37**	**0.56**
	f_0 DL_{min}			0.18	0.00	**0.52***	**0.44**	0.19
	f_0 DL_{max}				0.35	0.02	0.08	0.00
	m					0.17	0.10	0.07
	$f_{0,PE}$						**0.51**	0.23
	$f_{m,tr}$							0.33
Two levels for each NH listener N=17	$HL_{1.5k}$	**0.46***	**0.39***	0.23	0.04	N/A	0.15	N/A
	$f_{0,tr}$		**0.51***	0.01	0.14	N/A	**0.31***	N/A
	f_0 DL_{min}			**0.38***	0.01	N/A	**0.37***	N/A
	f_0 DL_{max}				0.19	N/A	0.03	N/A
	m					N/A	0.06	N/A
	$f_{0,PE}$						N/A	N/A
	$f_{m,tr}$							N/A

son correlation coefficients (R^2) values are listed, along with an indication of the significance of each correlation (boldface indicates $p<0.05$), for analyses conducted with one data point per listener (N=14; only the low-level NH data included), only the HI listeners (N=11) and, where applicable, all data including two stimulus levels for each NH listener (N=17). Partial correlations, with the contribution of TEN level removed, were also computed to control for the possibility that observed correlations were due to differences in stimulus level rather than hearing impairment. Asterisks in Table IV indicate significant partial correlations ($p<0.05$, partial R^2 values not shown). The term N/A reflects the fact that NH listeners were only tested at the low level for one of the measures in a given correlation, so that 17 data points were not available. The R^2 and p values shown in each correlation plot (Figs. 6–8) are based on 14 data points, one for each NH listener tested at the low level and one for each HI listener. Correlations reported in the text are based on the same 14 data points, unless otherwise specified.

1. Relationships between the f_0 DL transition point and measures of frequency selectivity

Figure 6 shows the data and regression line for the log-transformed $f_{0,tr}$ plotted as a function of $HL_{1.5k}$ and each of the three log-transformed frequency selectivity estimates. The $f_{0,tr}$ was significantly correlated with $HL_{1.5k}$ [Fig. 6(a)], further supporting the conclusion that the deficit in f_0 discrimination performance is related to hearing impairment. The $f_{0,tr}$ was also significantly correlated with each of the three estimates of peripheral frequency selectivity. The correlation between $f_{0,tr}$ and $f_{0,PE}$ (as well as between $f_{0,tr}$ and both $HL_{1.5k}$ and $f_{m,tr}$ in the N=17 case) remained significant with TEN level removed from the analysis (asterisks in Table IV), suggesting that the correlation between the $f_{0,tr}$ and frequency selectivity was probably due to hearing impairment

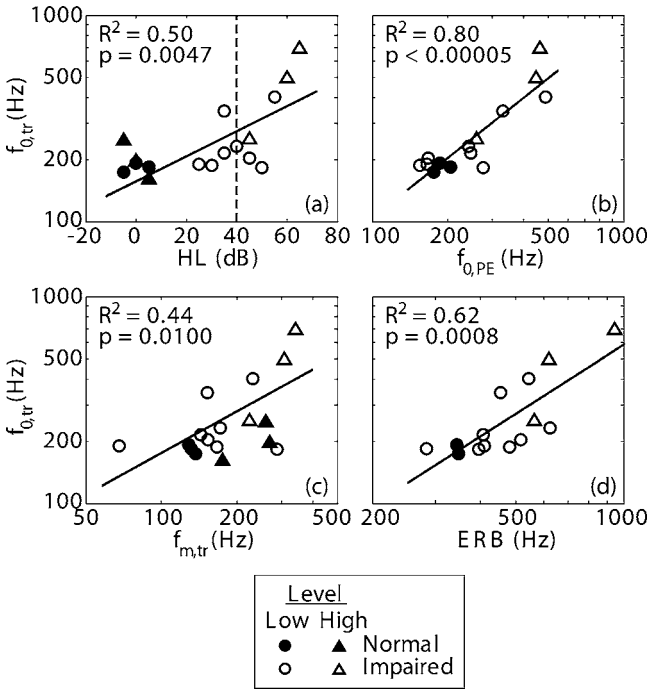

FIG. 6. The $f_{0,tr}$ was significantly correlated with (a) the audiometric threshold at 1.5 kHz ($HL_{1.5k}$), and each of the three estimates of frequency selectivity: (b) $f_{0,PE}$, (c) $f_{m,tr}$, and (d) ERB. The NH data for stimuli presented at the high level (filled triangles) were not included in the regression analyses. The vertical dashed line in (a) represents the cutoff between "normal-to-mild" and "moderate" hearing loss groups that yielded significantly different regression coefficients (see Sec. V B 1).

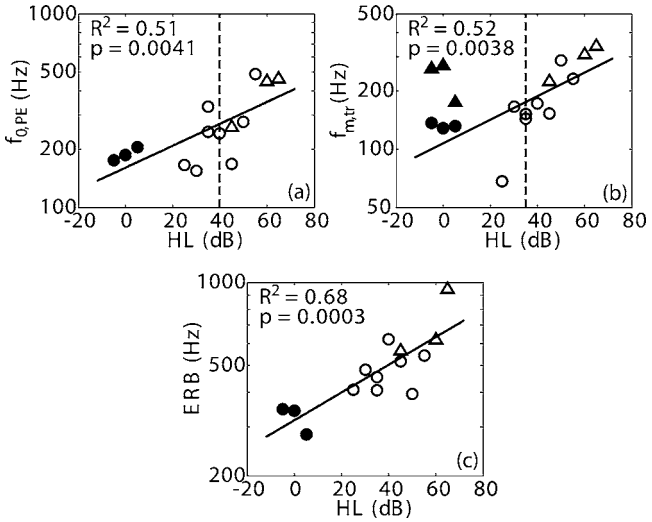

FIG. 7. The three estimates of frequency selectivity, (a) $f_{0,\mathrm{PE}}$, (b) $f_{m,\mathrm{tr}}$, and (c) ERB, were each significantly correlated to $\mathrm{HL}_{1.5\mathrm{k}}$. Vertical dashed lines in (a) and (b) represent the cutoffs between "normal-to-mild" and "moderate" hearing loss groups that yielded significantly different regression coefficients (see Sec. V B 1). See the legend of Fig. 6 for symbol definitions.

per se and not to variation in stimulus level.

Figure 7 shows that each of the measures of frequency selectivity were also significantly correlated with the degree of hearing loss. To investigate the possibility that the correlations between $f_{0,\mathrm{tr}}$ and each estimate of frequency selectivity could be an epiphenomena of their common dependencies on $\mathrm{HL}_{1.5\mathrm{k}}$, partial regression analyses were performed by removing from the analyses the contribution of $\mathrm{HL}_{1.5\mathrm{k}}$ to the variance in $f_{0,\mathrm{tr}}$ or f_0 $\mathrm{DL}_{\mathrm{min}}$. None of the resulting partial correlations involving $f_{m,\mathrm{tr}}$ or ERB as the frequency selectivity variable was significant ($p>0.05$). However, with $f_{0,\mathrm{PE}}$ as the frequency selectivity variable, the partial correlation with $f_{0,\mathrm{tr}}$ was statistically significant ($R^2=0.78, p<0.005$), suggesting that the correlation between $f_{0,\mathrm{tr}}$ and $f_{0,\mathrm{PE}}$ was not an epiphenomenon of their common dependence on $\mathrm{HL}_{1.5\mathrm{k}}$.

One additional aspect of the data that supports the idea that the $f_{0,\mathrm{tr}}$ depends on frequency selectivity *per se* is that the $f_{0,\mathrm{tr}}$ values show a similar dependence on HL as two of the three estimates of frequency selectivity. Consistent with earlier studies of frequency selectivity in HI listeners (Tyler *et al.*, 1983; Nelson, 1991; Moore, 1998; Moore *et al.*, 1999), hearing loss had little effect on the $f_{0,\mathrm{tr}}$, $f_{m,\mathrm{tr}}$ or $f_{0,\mathrm{PE}}$ until HL increased above approximately 30–40 dB HL [Figs. 6(a), 7(a), and 7(b)], suggesting that $f_{0,\mathrm{tr}}$ is better predicted by frequency selectivity than by audiometric threshold. To quantify this observation, the data were divided into two categories based on the degree of hearing loss at 1.5 kHz. Listeners with audiometric thresholds <40 dB HL [vertical dashed line in Figs. 6(a) and 7(a)] were assigned to the "normal-to-mild" group (N=7), while those with thresholds $\geqslant 40$ dB HL were assigned to the "moderate" group (N=7). A Potthoff (1966) analysis showed the regression coefficients to be statistically different ($p<0.05$) between the two groups for the $f_{0,\mathrm{tr}}$ and $f_{0,\mathrm{PE}}$, and for $f_{m,\mathrm{tr}}$, when the cutoff between the two groups was defined at 35 dB HL [vertical dashed line in Fig. 7(b)] instead of 40 dB HL. Regression coefficients were not significantly different between the two groups ($p=0.55$) for the ERB measure.

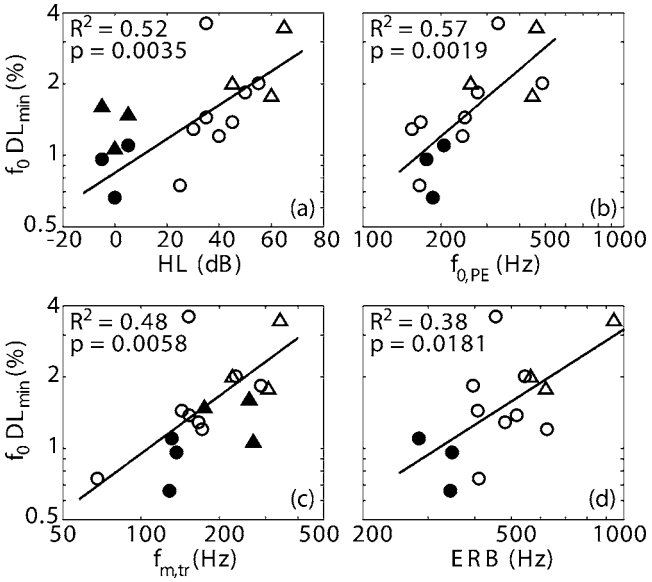

FIG. 8. The f_0 $\mathrm{DL}_{\mathrm{min}}$ was significantly correlated with (a) the audiometric threshold at 1.5 kHz ($\mathrm{HL}_{1.5\mathrm{k}}$), and each of the three estimates of frequency selectivity: (b) $f_{0,\mathrm{PE}}$, (c) $f_{m,\mathrm{tr}}$, and (d) ERB. See the legend of Fig. 6 for symbol definitions.

2. f_0 DL_{max}, f_0 DL_{min}, and m

The f_0 $\mathrm{DL}_{\mathrm{min}}$ was significantly correlated with $\mathrm{HL}_{1.5\mathrm{k}}$ and each of the three measures of frequency selectivity (Fig. 8), although the correlations with $\mathrm{HL}_{1.5\mathrm{k}}$ and with ERB were weak and became nonsignificant when the NH data were removed from the analysis. The correlations between f_0 $\mathrm{DL}_{\mathrm{min}}$ and $\mathrm{HL}_{1.5\mathrm{k}}$ and between f_0 $\mathrm{DL}_{\mathrm{min}}$ and both $f_{0,\mathrm{PE}}$ and $f_{m,\mathrm{tr}}$ remained significant with TEN level removed from the analysis (asterisks in Table IV), suggesting that the observed effects are related to the hearing loss and not to variation in stimulus level. However, none of the correlations between f_0 $\mathrm{DL}_{\mathrm{min}}$ and the three frequency selectivity estimates remained significant when $\mathrm{HL}_{1.5\mathrm{k}}$ was partialled out ($p>0.05$), leaving open the possibility that f_0 $\mathrm{DL}_{\mathrm{min}}$ may not be dependent on frequency selectivity *per se*.

Estimates of f_0 $\mathrm{DL}_{\mathrm{max}}$ were significantly correlated with $\mathrm{HL}_{1.5\mathrm{k}}$ (Table IV; plot not shown), suggesting that SNHL is associated with an impairment in f_0 discrimination for unresolved harmonics. However, the f_0 $\mathrm{DL}_{\mathrm{max}}$ was not significantly correlated with any of the three measures of peripheral frequency selectivity ($p>0.05$). This suggests that if there is a deficit in f_0 $\mathrm{DL}_{\mathrm{max}}$ related to HI, then some mechanism not directly related to peripheral frequency selectivity, such as the ability to process envelope modulations, may be responsible. Estimates of m were not significantly correlated with any other summary measure.

3. Relationships between the f_0 DL measures

The $f_{0,\mathrm{tr}}$ was found to be significantly correlated with the f_0 $\mathrm{DL}_{\mathrm{min}}$, mirroring a result observed by Bernstein and Oxenham (2006) whereby both the $f_{0,\mathrm{tr}}$ and the f_0 $\mathrm{DL}_{\mathrm{min}}$ increased at a high stimulus level (~80 dB SPL) in NH listen-

ers. This raises the possibility that more poorly encoded resolved component frequencies (as evidenced by the elevated f_0 DL_{min}) indirectly caused the $f_{0,tr}$ effect by reducing the auditory system's ability to process resolved harmonics. However, the correlations between $f_{0,tr}$ and both the $f_{0,PE}$ and the ERB remained significant ($p<0.05$) when the influence of f_0 DL_{min} was controlled in partial correlation analyses, suggesting that the $f_{0,tr}$ effect was not a direct result of poor frequency encoding of individual partials (the partial correlation between $f_{0,tr}$ and $f_{m,tr}$ was not significant). The f_0 DL_{min} and f_0 DL_{max} were also significantly correlated, suggesting that hearing-impaired listeners experience an overall deficit in f_0 discrimination performance.

4. Alternative transition-point definitions

In the correlation analyses described above, the various summary measures ($f_{0,tr}$,$f_{m,tr}$,$f_{0,PE}$) were calculated based on the midpoints of the transitions between best and worst performance levels. From a mathematical viewpoint, the midpoint is most accurately defined, because the slope of a sigmoid is steepest at that point. However, to assess harmonic resolvability, other points along the function might be more appropriate. For instance, an alternative measure might consider harmonics to be unresolved as soon as a phase effect first occurs (Moore *et al.*, 2006). The regression analyses described above were recalculated with the transition points defined as the f_0 for which performance was as follows: for the $f_{0,tr}$, 10% of the distance (on a log scale) between f_0 DL_{min} and f_0 DL_{max}; for the $f_{0,PE}$, 10% the distance (on a log scale) between the minimum and maximum f_0 DL phase effect; and for the $f_{m,tr}$, 10% of the distance (in percentage points) between the chance (33%) and perfect (100%) performance. The results of this analysis were largely the same (with regard to the significance of bivariate correlations) as those presented in Table IV, suggesting that the correlations observed between the various summary measures are robust with respect to the way in which the transition points are defined. There were, however, four exceptions. With the transitions defined based on the 10% points instead of the midpoints of the individual fitted curves, correlations became significant ($p<0.05$) between f_0 DL_{max} and $f_{0,tr}$ in the N=14 ($R^2=0.34$) and N=17 ($R^2=0.31$) analyses, and between f_0 DL_{max} and $f_{0,PE}$ ($R^2=0.30$) in the N=14 analysis. For this alternative definition, the correlation between $f_{0,tr}$ and the ERB in the N=11 analysis was no longer significant ($p=0.08$).

VI. DISCUSSION

A. Relationship between f_0 discrimination and frequency selectivity

1. The f_0 DL transition point

The strong correlations between the $f_{0,tr}$ and each of the three measures of frequency selectivity support the hypothesis that the spacing between harmonics required for good f_0 discrimination performance is related to peripheral frequency selectivity. The significant correlations between f_0 discrimination and frequency selectivity were not a result of generally poor performance in psychoacoustic tasks by HI listeners, because *good* performance in modulation discrimination (Experiment 2, large $f_{m,tr}$) was correlated with *poor* performance in f_0 discrimination (Experiment 1, large $f_{0,tr}$ and f_0 DL_{min}). The significant correlations between the $f_{0,tr}$ and frequency selectivity most likely represent a direct relationship between the two types of measure and not simply a common dependence on audiometric thresholds, as evidenced by the significant partial correlation between the $f_{0,tr}$ and the $f_{0,PE}$ when controlling for $HL_{1.5k}$, as well as the similar nonlinear dependence on $HL_{1.5k}$ exhibited by both types of measure [Fig. 6(a), 7(a) and 7(b)]. Furthermore, the data of Bernstein and Oxenham (2006) in NH listeners show that stimulus level affected both frequency selectivity and the $f_{0,tr}$ in the same way as hearing loss in the current study. Thus, frequency selectivity, the common denominator between these two studies, is likely to be responsible for the observed increases in $f_{0,tr}$ and f_0 DL_{min} in both cases.

2. Pure-tone FDLs and the f_0 DL_{min}

The current study also found significant correlations between each of the three estimates of frequency selectivity and the f_0 DL_{min}. As the f_0 DL_{min} estimate was tightly coupled to the 1500-Hz pure-tone FDLs, the log-transformed FDLs were also significantly correlated to each of the three log-transformed estimates of frequency selectivity ($f_{0,PE}$: $R^2=0.55$, $p<0.005$; $f_{m,tr}$: $R^2=0.51$, $p<0.005$; ERB: $R^2=0.32$, $p<0.05$). This result conflicts with several previous studies of the relationship between pure-tone frequency discrimination and peripheral frequency selectivity that have found only weak or nonsignificant correlations between the two types of measure (e.g., Tyler *et al.*, 1983; Moore and Glasberg, 1986; Moore and Peters, 1992).

One possible source of this discrepancy is the method of estimating frequency selectivity. In the Tyler *et al.* (1983) study, the small number of data points measured (three) on the PTC may have limited the accuracy of this frequency selectivity measure. Moore and Peters (1992) and Moore and Glasberg (1986) used an ERB measure derived from notched-noise data. This method yielded the weakest correlation with the FDL data in the current study, which may be due to differences in stimulus type or to the increased variability resulting from the additional step of fitting the masking data to a model auditory filter.

The use of background noise in the current study may also underlie the departure from previous investigations that found weak or absent correlations between FDLs and frequency selectivity when stimuli were presented in quiet. In NH listeners, reduced frequency selectivity at higher stimulus levels has been shown to negatively affect FDLs for pure tones presented in a background noise (e.g., Dye and Hafter, 1980; Bernstein and Oxenham, 2006) but not in isolation (e.g., Wier *et al.*, 1977). It may be that in the absence of a background noise, a higher-level stimulus excites a larger number of auditory nerve fibers, thereby distributing information for frequency discrimination over a broader tonotopic region and increasing the amount of information present (Green and Luce, 1974) in a way that offsets the effects of a reduction in frequency selectivity. Florentine and Buus (1981) invoked a similar idea involving the spread of exci-

tation to explain the deviation from Weber's law in pure-tone intensity discrimination. The use of TEN in the current study to reduce differences in SL and SPL across listeners may have also reduced the influence of absolute level (e.g. Bernstein and Oxenham, 2006) and sensation level (e.g. Hoekstra, 1979) on FDLs. In contrast, Moore and Glasberg (1986) and Tyler *et al.* (1983) presented pure tones to HI listeners at a constant SPL (80 and 94 dB, respectively), with the equivalent SL ranging from approximately 50 to 80 dB across listeners, respectively. Moore and Peters (1992) presented tones at a constant 25 dB SL, yielding an approximately 50 dB SPL range across the HI listeners.

Finally, the pure-tone frequency discrimination measurements reported here were only performed at a single frequency, 1500 Hz. It is not known whether similar effects would be obtained with hearing loss at lower frequencies. Dye and Hafter (1980) showed that for lower-frequency tones (500 and 1000 Hz), increasing the level of both the tone and the background noise tended to improve rather than impair frequency discrimination performance, suggesting that frequency selectivity may have less effect on lower-frequency tones. On the other hand, level is known to have less effect on frequency selectivity at low frequencies (1000 Hz and below) than at high frequencies (Baker *et al.*, 1998). Thus, the results of Dye and Hafter (1980) at low frequencies may reflect the reduction or absence of an effect of level on frequency selectivity rather than the absence of an effect of frequency selectivity on FDLs.

B. Possible role of temporal fine structure

The results clearly indicate a significant correlation between f_0 discrimination and frequency selectivity in the same listeners. Nevertheless, correlation is not causation, and the question remains whether the f_0 transition point depends on harmonic resolvability or some other aspect of auditory processing. One possibility is that impaired f_0 DLs may reflect a deficit in fine-structure processing. There are at least two ways in which such an impairment could arise. First, a reduction in fine-structure information could be the direct result of the impaired frequency selectivity in the HI listeners. Moore *et al.* (2006) argued that the transition from accurate to poor f_0 discrimination as a function of harmonic number in NH hearing listeners may reflect a reduction in the effectiveness of fine-structure coding as harmonics begin to interact, rather than a reduction in the resolvability of individual harmonics. With reduced frequency selectivity in HI listeners, harmonics would also be more likely to interact, possibly reducing the effectiveness of fine-structure coding. Second, HI listeners may have an inherent fine-structure impairment, perhaps due to a reduction of phase locking in the auditory nerve (e.g., Woolf *et al.*, 1981). Recent psychophysical evidence from interaural phase-difference (Lacher-Fougére and Demany, 2005) and low-rate FM discrimination (Buss *et al.*, 2004) measures in HI listeners support this idea. Because the current study did not perform psychophysical measures thought to directly depend on temporal fine-structure processing, the role of temporal fine-structure deficits in the observed f_0 discrimination impairment remains speculative.

C. Modulation discrimination

Some HI listeners showed better modulation discrimination performance than the NH listeners, consistent with the hypothesis that poorer frequency selectivity should yield better performance in this task. Nevertheless, the performance of the HI listeners was not as much better relative to the NH listeners as would be expected based on the f_0 DL results if both the $f_{0,\mathrm{tr}}$ and the $f_{m,\mathrm{tr}}$ reflected frequency selectivity. In Fig. 6(c), the $f_{m,\mathrm{tr}}$ for NH listeners tested at the higher level (filled triangles) generally fell to the right of the regression line, indicating that NH listeners performed better at modulation discrimination at this level than would be predicted from their f_0 DL data based on the relationship between $f_{0,\mathrm{tr}}$ and $f_{m,\mathrm{tr}}$ for the other 14 data points. This observation was supported by a significant one-tailed independent-sample t test, adjusted for unequal variances, comparing NH and HI listeners based on the log-transformed ratio $f_{0,\mathrm{tr}}/f_{m,\mathrm{tr}}$ $[t(13.7)=1.84, p<0.05]$. One interpretation of this result is that HI listeners may have some deficit in modulation processing that reduces their discrimination performance to below what they might achieve based on peripheral filter bandwidths alone. HI listeners do not generally show deficits in modulation processing when signals are presented to NH and HI listeners at an equal SL (Bacon and Gleitman, 1992). However, the wideband background noise was not used in Experiment 2, so that signals were presented at a higher SL for NH listeners. Alternatively, the relatively small $f_{m,\mathrm{tr}}$ (relative to $f_{0,\mathrm{tr}}$) in some HI listeners may reflect an absolute upper f_m limitation that would be experienced by any listener, not just HI listeners. For instance, it is known that modulation processing performance begins to deteriorate even in NH listeners for f_m's greater than about 150 Hz, independent of auditory filter bandwidth (Kohlrausch *et al.*, 2000). Because of the possible influence of limitations in post-filtering modulation detection efficiency, this task may not provide a fully accurate estimate of frequency selectivity (see, e.g., Moore and Sek, 1995).

Another aspect of the modulation discrimination data that may be related to a limitation in modulation processing, due either to SNHL or an absolute f_m limit, is that $f_{m,\mathrm{tr}}$ estimates were generally smaller than $f_{0,\mathrm{tr}}$ estimates. This result is reflected in the regression analysis (N=17), where the estimate of the linear regression coefficient (B_1) was significantly less than unity (0.56 with 95% confidence interval ±0.42). [While it could be argued (see Sec. V B 2) that the 10% point rather than the midpoint of the f_0 DL and f_m discrimination transitions may provide a more appropriate estimate of the limits of harmonic resolvability, the regression coefficient in this case was still less than unity, although not significantly so (0.64 ± 0.42)]. This would mean that the limit of harmonic resolvability, as estimated by the modulation discrimination task, occurs at a lower f_0 (*higher* harmonic number) than the $f_{0,\mathrm{tr}}$. One possible interpretation of this discrepancy is that the $f_{m,\mathrm{tr}}$, which relies on wide peripheral filters for good performance, provides an *upper* limit on the extent of harmonic resolvability, whereas estimates based on listeners' ability to hear out harmonics (Plomp, 1964; Moore and Ohgushi, 1993; Bernstein and Oxenham, 2003;

2006) or phase effects on f_0 DLs (Section V A 3; Moore *et al.*, 2006) which rely on narrow filters for better performance, provide a *lower* limit.

D. Did listeners extract the f_0?

With the f_0 discrimination paradigm employed in Experiment 1, it is possible that listeners could have performed the discrimination task by comparing the frequencies of individual resolved harmonics rather than by comparing the pitch of the missing f_0. However, Moore and Glasberg (1990b) demonstrated that NH listeners are unable to ignore the pitch of the missing f_0 in making sequential comparisons between the frequencies of individual partials, in that listeners performed much worse at discriminating the frequencies of the lowest harmonics for sequential harmonic complexes with different f_0's than for complexes with the same f_0. While this result strongly argues that NH listeners do not perform f_0 discrimination based on the frequencies of individual resolved components, we cannot rule out this possibility for the HI listeners. It is especially likely that the worst performing HI listeners may have based their judgments on individual partials. For example, listeners 17 and I9(r) did not achieve f_0 DL_{min} until f_0's reached 750 Hz or even 1500 Hz—respectively, f_0's that approach or exceed the limit of the existence region for the pitch of the missing f_0 (Plomp, 1964). Roving the spectral region of the harmonic complex can reduce the usefulness of a cue based on the lowest harmonic present (Houtsma and Smurzynski, 1990; Bernstein and Oxenham, 2003). However, in the case of the poorest performing hearing-impaired listeners, the large rove range necessary to eliminate the spectral cue could result in highly distracting changes in the timbre of the complexes, which are known to negatively affect pitch discrimination (Moore and Glasberg, 1990b; Moore and Moore, 2003).

E. Perceptual implications for HI listeners

The results shown here indicate that listeners with SNHL experience a deficit in f_0 processing, directly related to a loss of peripheral frequency selectivity, which manifests itself in at least three ways. First, a larger spacing between adjacent harmonics is needed to yield the smallest possible f_0 DLs for a given spectral region, implying that in everyday listening conditions a larger proportion of stimulus f_0's will yield a weak pitch percept in these listeners. Second, even when harmonics are widely separated, the f_0 DLs are larger (poorer) than in NH listeners. Finally, the results of Experiment 1 also show that listeners with SNHL had a higher $f_{0,PE}$ than normal, meaning that these listeners will experience potentially detrimental effects of component phase on f_0 discrimination over a larger range of f_0's. This effect may be of particular importance in a reverberant environment, where a heterogeneous mixture of reflection delays tends to "smear" the temporal envelopes (Houtgast *et al.*, 1980; Steeneken and Houtgast, 1980) at the output of auditory filters excited by unresolved harmonics (Qin and Oxenham, 2005). With wider filters, listeners with SNHL will be more susceptible to the negative impact of reverberation phase randomization on f_0 discrimination.

F. Implications for pitch models

The current findings corroborate the previous findings of Bernstein and Oxenham (2006) showing that in NH listeners, f_0 DL_{min} and $f_{0,tr}$ increased as a function of stimulus level in the same way as peripheral frequency selectivity. The current study extends this finding by establishing a relationship between f_0 discrimination and frequency selectivity in a large enough population of NH and HI listeners to yield significant correlations between the two measures. Because the findings of the two studies are similar with respect to the relationship between f_0 discrimination and frequency selectivity, the implications for models of pitch perception of the current HI results are the same as those discussed in the previous manuscript (for full discussion, see Bernstein and Oxenham, 2006). To summarize, these results are consistent with any pitch model that relies on peripheral frequency selectivity to explain why low-order harmonics yield better f_0 DLs than high-order harmonics. This includes spectral (e.g., Goldstein, 1973) and spectro-temporal (Shamma and Klein, 2000; Cedolin and Delgutte, 2005) models that use place or timing information to extract the frequencies of individual resolved harmonics, as well as a recent version of the autocorrelation model (de Cheveigné and Pressnitzer, 2006) that depends on temporal response characteristics of auditory filters that are related to the filter bandwidths.

VII. SUMMARY AND CONCLUSIONS

Listeners with SNHL experience a deficit in f_0 discrimination that manifests itself in terms of an increase in the minimum spacing between harmonics required for f_0 DLs to transition from large (poor) to small (good). The f_0 DL transition point was significantly correlated to three different estimates of frequency selectivity, supporting the hypothesis that good f_0 discrimination performance depends on sharp frequency selectivity, and that listeners with SNHL experience a deficit in f_0 processing due to a reduction in frequency selectivity. Additionally, the best f_0 discrimination performance achieved by HI listeners was worse than that attained by NH listeners even when harmonics were spaced widely enough in frequency to yield relatively good f_0 discrimination performance associated with resolved harmonics. This effect, also observed for pure tones, was also correlated with two estimates of frequency selectivity in HI listeners, suggesting a possible role for frequency selectivity in the frequency encoding of individual resolved harmonics. These results support spectral and spectro-temporal theories of pitch perception that rely on frequency selectivity to extract the frequencies of individual resolved harmonics, but may also be consistent with a place-dependent temporal model of pitch perception where the range of detectable periodicities is limited by the impulse response durations of cochlear filters.

ACKNOWLEDGMENTS

This work was supported by NIH Grant Nos. R01-DC-05216 and 5T32-DC-00038. A previous version of the manuscript formed part of a Ph.D. thesis submitted by the first author to the Massachusetts Institute of Technology. We thank Andrea Simonson for her help in the recruiting and

audiological evaluation of HI listeners and Louis Braida, Gerald Kidd, Bertrand Delgutte, Christophe Micheyl, Brian Moore, an anonymous reviewer and the associate editor, John Grose, for their helpful comments on earlier versions of this manuscript.

[1]Some listeners with audiometric thresholds at 1 and 2 kHz within 5 dB HL of each other were not tested at 1.5 kHz. For these listeners, the 1.5 kHz threshold is taken as the mean of the 1 and 2 kHz thresholds.

[2]Listener I1 had a low-frequency loss with near-normal thresholds at 3 and 4 kHz (10 and 20 dB HL, respectively), but impaired thresholds at lower frequencies (50 dB HL at 1 and 2kHz). Listener I2 had a notched loss, with impaired thresholds at 1.5 and 2 kHz (45 and 50 dB HL, respectively), but a mild loss of 25 dB HL at 4 kHz.

[3]For NH listener N1, the TEN and stimulus levels were each reduced by 5 dB for the 75- and 125-Hz f_0's. For NH listener N3, the stimulus level was reduced by 3 dB for the 75-Hz f_0, but the TEN was kept at 65 dB SPL/ERB_N. For HI listener I9(r), who completed more f_0 conditions than the other listeners, the 75-Hz f_0 conditions were not tested.

[4]HI $f_{0,PE}$ and ERB estimates measured at the high stimulus level were compared to the NH low-level estimates because no high-level NH data were available (asterisks in Table III).

[5]The sigmoid function was defined as:

$$\log[f_0DL(\%)] = \log(f_0DL_{\max}) + \frac{1}{\sqrt{\pi}}\log\left(\frac{f_0DL_{\min}}{f_0DL_{\max}}\right)\int_{m\,\log(f_0/f_{0,\mathrm{tr}})}^{\infty} e^{-[\log(f_0)]^2} d[\log(f_0')]. \quad (1)$$

[6]The assumption that the pure-tone case will yield the smallest possible DL may be questionable because the presence of multiple resolved harmonics could yield additional f_0 information. However, two-tailed t tests indicated that for each listener and level, with one exception, the f_0 DL at the largest f_0 tested (500, 750, or 1500 Hz) was not significantly different ($p > 0.05$) from the FDL for the 1500-Hz pure tone. [The exception was listener I1, where the f_0 DL at 750 Hz, the largest f_0 tested in this listener, was significantly smaller than the 1500 Hz pure-tone FDL ($P < 0.01$).]

[7]For the NH listeners, the data at 500 Hz were not included in the PE analysis because sine-phase measurements were not performed at that f_0.

Arehart, K. H. (**1994**). "Effects of harmonic content on complex-tone fundamental-frequency discrimination in hearing-impaired listeners," J. Acoust. Soc. Am. **95**, 3574–3585.

Arehart, K. H., and Burns, E. M. (**1999**). "A comparison of monotic and dichotic complex-tone pitch perception in listeners with hearing loss," J. Acoust. Soc. Am. **106**, 993–997.

Bacon, S. P., and Gleitman, R. M. (**1992**). "Modulation detection in subjects with relatively flat hearing losses," J. Speech Hear. Res. **35**, 642–653.

Baker, R. J., Rosen, S., and Darling, A. M. (**1998**). "An efficient characterization of human auditory filtering across level and frequency that is also physiologically reasonable," in *Psychophysical and Physiological Advances in Hearing*, edited by A. R. Palmer, A. Rees, A. Q. Summerfield, and R. Meddis (Whurr, London).

Bernstein, J. G., and Oxenham, A. J. (**2003**). "Pitch discrimination of diotic and dichotic tone complexes: Harmonic resolvability or harmonic number?" J. Acoust. Soc. Am. **113**, 3323–3334.

Bernstein, J. G. W., and Oxenham, A. J. (**2005**). "An autocorrelation model with place dependence to account for the effect of harmonic number on fundamental frequency discrimination," J. Acoust. Soc. Am. **117**, 3816–3831.

Bernstein, J. G. W., and Oxenham, A. J. (**2006**). "The relationship between frequency selectivity and pitch discrimination: Effects of stimulus level," J. Acoust. Soc. Am. **120**, 3916–3928.

Buss, E., Hall, J. W., and Grose, J. H. (**2004**). "Temporal fine-structure cues to speech and pure tone modulation in observers with sensorineural hearing loss," Ear Hear. **25**, 242–250.

Cedolin, L., and Delgutte, B. (**2005**). "Spatio-temporal representation of the pitch of complex tones in the auditory nerve," Assoc. Res. Otolaryngol. Abs. 1195.

Darwin, C. J., and Hukin, R. W. (**2000**). "Effectiveness of spatial cues, prosody, and talker characteristics in selective attention," J. Acoust. Soc. Am. **107**, 970–977.

de Cheveigné, A. (**2005**). "Pitch perception models," in *Springer Handbook of Auditory Research: Pitch Perception*, edited by C. J. Plack, A. J. Oxenham, A. N. Popper, and R. Fay (Springer, Berlin).

de Cheveigné, A., and Pressnitzer, D. (**2006**). "The case of the missing delay lines: Synthetic delays obtained by cross-channel phase interaction," J. Acoust. Soc. Am. **119**, 3908–3918.

Dye, R. H., and Hafter, E. R. (**1980**). "Just-noticeable differences of frequency for masked tones," J. Acoust. Soc. Am. **67**, 1746–1753.

Florentine, M., and Buus, S. (**1981**). "An excitation-pattern model for intensity discrimination," J. Acoust. Soc. Am. **70**, 1646–1654.

Glasberg, B. R., and Moore, B. C. J. (**1986**). "Auditory filter shapes in subjects with unilateral and bilateral cochlear impairments," J. Acoust. Soc. Am. **79**, 1020–1033.

Glasberg, B. R., and Moore, B. C. J. (**1990**). "Derivation of auditory filter shapes from notched-noise data," Hear. Res. **47**, 103–138.

Goldstein, J. L. (**1973**). "An optimum processor theory for the central formation of the pitch of complex tones," J. Acoust. Soc. Am. **54**, 1496–1516.

Green, D. M., and Luce, R. D. (**1974**). "Counting and timing mechanisms in auditory discrimination and reaction time," in *Contemporary Developments in Mathematical Psychology*, edited by D. H. Krantz, R. C. Atkinson, R. D. Luce, and P. Suppres (Freeman, San Francisco), Vol. II.

Greenwood, D. D. (**1972**). "Masking by combination bands: Estimation of the levels of the combination bands $(n+1)f_1 - nf_h$," J. Acoust. Soc. Am. **52**, 1144–1154.

Hoekstra, A. (**1979**). "Frequency discrimination and frequency analysis in hearing," Ph.D. thesis, Institute of Audiology, University Hospital, Groningen, Netherlands.

Hoekstra, A., and Ritsma, R. J. (**1977**). "Perceptive hearing loss and frequency selectivity," in *Psychophysics and Physiology of Hearing*, edited by E. F. Evans and J. P. Wilson (Academic, London).

Houtgast, T., Steeneken, H. J. M., and Plomp, R. (**1980**). "Predicting speech intelligibility in rooms from the modulation transfer function. I. General room acoustics," Acustica **46**, 60–72.

Houtsma, A. J. M., and Goldstein, J. L. (**1972**). "The central origin of the pitch of pure tones: Evidence from musical interval recognition," J. Acoust. Soc. Am. **51**, 520–529.

Houtsma, A. J. M., and Smurzynski, J. (**1990**). "Pitch identification and discrimination for complex tones with many harmonics," J. Acoust. Soc. Am. **87**, 304–310.

Kiang, N.Y.-S., Watanabe, T., Thomas, E. C., and Clark, L. F. (**1965**). *Discharge Patterns of Single Fibres in the Cat's Auditory Nerve* (MIT Press, Cambridge, MA).

Kohlrausch, A., Fassel, R., and Dau, T. (**2000**). "The influence of carrier level and frequency on modulation and beat-detection thresholds for sinusoidal carriers," J. Acoust. Soc. Am. **108**, 723–734.

Lacher-Fougére, S., and Demany, L. (**2005**). "Consequences of cochlear damage for the detection of interaural phase differences," J. Acoust. Soc. Am. **118**, 2519–2526.

Levitt, H. (**1971**). "Transformed up-down methods in psychoacoustics," J. Acoust. Soc. Am. **49**, 467–477.

Moore, B. C. J. (**1977**). "Effects of relative phase of the components on the pitch of three-component complex tones," *in Psychophysics and Physiology of Hearing*, edited by E. F. Evans and J. P. Wilson (Academic, London), pp. 349–358.

Moore, B. C. J. (**1995**). *Perceptual Consequences of Cochlear Damage* (OUP, Oxford).

Moore, B. C. J. (**1998**). *Cochlear Hearing Loss* (Whurr, London).

Moore, B. C. J., and Carlyon, R. P. (**2005**). "Perception of pitch by people with cochlear hearing loss and by cochlear implant users," in *Springer Handbook of Auditory Research: Pitch Perception*, edited by A. J. Oxenham, C. J. Plack, A. N. Popper, and R. Fay (Springer, Berlin).

Moore, B. C. J., and Glasberg, B. R. (**1986**). "The relationship between frequency selectivity and frequency discrimination for subjects with unilateral and bilateral cochlear impairments," in *Auditory Frequency Selectivity*, edited by B. C. J. Moore and R. D. Patterson (Plenum, New York).

Moore, B. C. J., and Glasberg, B. R. (**1988**). "Pitch perception and phase sensitivity for subjects with unilateral and bilateral cochlear hearing impairments," in *Clinical Audiology*, edited by A. Quaranta (Laterza, Bari, Italy).

Moore, B. C. J., and Glasberg, B. R. (**1990a**). "Frequency selectivity in subjects with cochlear loss and its effects on pitch discrimination and phase sensitivity," in *Advances in Audiology*, edited by F. Grandori, G.

Cianfrone, and D. T. Kemp (Karger, Basel), Vol. **7**, pp. 187–200.
Moore, B. C. J., and Glasberg, B. R. (**1990b**). "Frequency discrimination of complex tones with overlapping and non-overlapping harmonics," J. Acoust. Soc. Am. **87**, 2163–2177.
Moore, B. C. J., and Moore, G. A. (**2003**). "Discrimination of the fundamental frequency of complex tones with fixed and shifting spectral envelopes by normally hearing and hearing-impaired subjects," Hear. Res. **182**, 153–163.
Moore, B. C. J., and Ohgushi, K. (**1993**). "Audibility of partials in inharmonic complex tones," J. Acoust. Soc. Am. **93**, 452–461.
Moore, B. C. J., and Peters, R. W. (**1992**). "Pitch discrimination and phase sensitivity in young and elderly subjects and its relationship to frequency selectivity," J. Acoust. Soc. Am. **91**, 2881–2893.
Moore, B. C. J., and Sek, A. (**1995**). "Auditory filtering and the critical bandwidth at low frequencies," in *Advances in Hearing Research*, edited by G. A. Manley, G. M. Klump, C. Koppl, H. Fastl, and H. Oeckinghaus (World Scientific, Singapore).
Moore, B. C. J., Glasberg, B. R., Flanagan, H., and Adams, J. (**2006**). "Frequency discrimination of complex tones; assessing the role of component resolvability and temporal fine structure," J. Acoust. Soc. Am. **119**, 480–490.
Moore, B. C. J., Vickers, D. A., Plack, C. J., and Oxenham, A. J. (**1999**). "Inter-relationship between different psychoacoustic measures assumed to be related to the cochlear active mechanism," J. Acoust. Soc. Am. **106**, 2761–2778.
Moore, B. C. J., Huss, M., Vickers, D. A., Glasberg, B. R., and Alcantara, J. I. (**2000**). "A test for the diagnosis of dead regions in the cochlea," Br. J. Audiol. **34**, 205–224.
Nelson, D. A. (**1991**). "High-level psychophysical tuning curves: Forward masking in normal-hearing and hearing-impaired listeners," J. Speech Hear. Res. **34**, 1233–1249.
Nelson, D. A. (**1994**). "Level-dependent critical bandwidth for phase discrimination," J. Acoust. Soc. Am. **95**, 1514–1524.
Nelson, D. A., and Schroder, A. C. (**1995**). "Critical bandwidth for phase discrimination in hearing-impaired listeners," J. Acoust. Soc. Am. **98**, 1969–1976.
Patterson, R. D. (**1976**). "Auditory filter shapes derived with noise stimuli," J. Acoust. Soc. Am. **59**, 640–654.
Plomp, R. (**1964**). "The ear as a frequency analyzer," J. Acoust. Soc. Am. **36**, 1628–1636.
Potthoff, R. F. (**1966**). "Statistical aspects of the problem of biases in psychological tests. (Institute of Statistics Mimeo Series No. 479.)," Chapel Hill: University of North Carolina, Department of Statistics.
Qin, M. K., and Oxenham, A. J. (**2005**). "Effects of envelope-vocoder processing on F0 discrimination and concurrent-vowel identification," Ear Hear. **26**, 451–460.
Rosen, S., and Baker, R. J. (**1994**). "Characterizing auditory filter nonlinearity," Hear. Res. **73**, 231–243.
Sellick, P. M., Patuzzi, R., and Johnstone, B. M. (**1982**). "Measurement of basilar membrane motion in the guinea pig using the Mössbauer technique," J. Acoust. Soc. Am. **72**, 131–141.
Shackleton, T. M., and Carlyon, R. P. (**1994**). "The role of resolved and unresolved harmonics in pitch perception and frequency modulation discrimination," J. Acoust. Soc. Am. **95**, 3529–3540.
Shamma, S., and Klein, D. (**2000**). "The case of the missing pitch templates: How harmonic templates emerge in the early auditory system," J. Acoust. Soc. Am. **107**, 2631–2644.
Steeneken, H. J. M., and Houtgast, T. (**1980**). "A physical method for measuring speech-transmission quality," J. Acoust. Soc. Am. **69**, 318–326.
Terhardt, E. (**1974**). "Pitch, consonance, and harmony," J. Acoust. Soc. Am. **55**, 1061–1069.
Terhardt, E. (**1979**). "Calculating virtual pitch," Hear. Res. **1**, 155–182.
Tyler, R. S., Wood, E. J., and Fernandes, M. A. (**1983**). "Frequency resolution and discrimination of constant and dynamic tones in normal and hearing-impaired listeners," J. Acoust. Soc. Am. **74**, 1190–1199.
Wier, C. C., Jesteadt, W., and Green, D. M. (**1977**). "Frequency discrimination as a function of frequency and sensation level," J. Acoust. Soc. Am. **61**, 178–184.
Wightman, F. L. (**1973**). "The pattern-transformation model of pitch," J. Acoust. Soc. Am. **54**, 407–416.
Woolf, N. K., Ryan, A. F., and Bone, R. C. (**1981**). "Neural phase-locking properties in the absence of outer hair cells," Hear. Res. **4**, 335–346.
Zwicker, E. (**1952**). "Die Grenzen der Hörbarkeit der Amplitudenmodulation und der Frequenzmodulation eines Tones [The limits of audibility of amplitude and frequency modulation of tones]," Acustica, **2**, 125–133.

The influence of later-arriving sounds on the ability of listeners to judge the lateral position of a source[a)]

Raymond H. Dye, Jr., Christopher A. Brown,[b)] José A. Gallegos,[c)] and William A. Yost
Parmly Hearing Institute, Loyola University of Chicago, Chicago, Illinois 60626

Mark A. Stellmack
Department of Psychology, University of Minnesota, Minneapolis, Minnesota 55455

(Received 17 January 2006; revised 25 September 2006; accepted 26 September 2006)

This study examined the deleterious effects of a later-arriving sound on the processing of interaural differences of time (IDTs) from a preceding sound. A correlational analysis assessed the relative weight given to IDTs of source and echo clicks for echo delays of 1–64 ms when the echo click was attenuated relative to the source click (0–36 dB). Also measured were proportion correct and the proportion of responses predicted from the weights. The IDTs of source and echo clicks were selected independently from Gaussian distributions (μ=0 μs, σ=100 μs). Listeners were instructed to indicate the laterality of the source click. Equal weight was given to the source and echo clicks for echo delays of 64 ms with no echo attenuation. For echo delays of 16–64 ms, attenuating the echo had no substantial effect on source weight or proportion correct until the echo was attenuated by 18–30 dB. At echo delays $\leq$4 ms, source weights and proportions correct remained high regardless of echo attenuation. The proportions of responses predicted from the weights were lower at echo delays $\geq$16 ms. Results were discussed in terms of backward recognition masking and binaural sluggishness and compared to measurements of echo disturbance. © *2006 Acoustical Society of America.* [DOI: 10.1121/1.2372588]

PACS number(s): 43.66.Pn, 43.66.Mk [GDK] Pages: 3946–3956

I. INTRODUCTION

Since Wallach, Newman, and Rosenzweig (1949), the manner in which direct sounds (sources) and reflected sounds (echoes) combine to influence spatial perception has been framed as a question of the relative "weighting" given to the source and echo. Shinn-Cunningham *et al.* (1993) formalized this framework to account for both localization dominance and discrimination suppression based on interaural delay. In their study, listeners were presented via headphones two 1-ms noise bursts separated by either 1 ms or 10 ms to simulate a source and its echo. The interaural differences of time (IDTs) of the two bursts were selected independently from the set −500, −150, 0, +150, and +500 μs. Listeners were asked to adjust the IDT of a pointer until it matched the intracranial position of the fused burst pair for each of the 25 combinations of IDT_1 and IDT_2, representing the IDTs of the simulated source and echo, respectively. The relative contributions of the two clicks were assessed from the relative magnitudes of the regression coefficients obtained from multiple linear regression. Since a pointing task was employed, it was necessary that the interval between the leading and lagging 1-ms bursts be brief so that fused intracranial images would be formed (the maximum interval was 10 ms). Consistent with the precedence effect, the relative weight given to the leading burst increased as the interval between bursts was shortened to 1 ms. Others have also used this procedure to assess the precedence effect for bursts differing in spectral composition (Shinn-Cunningham *et al.*, 1995) and for stimuli presented in the free field (Stecker and Hafter, 2002). More recently, Litovsky and Shinn-Cunningham (2001) have applied this procedure to cases in which multiple images were heard, instructing listeners to match either the leftmost or rightmost intracranial image. Since the emphasis was on onset dominance, only echo delays as long as 15 ms were included in the study.

Another approach to assessing the relative contribution of the leading and lagging events has been to "jitter" the interaural delays of the clicks, selecting the IDTs from Gaussian distributions that were left leading versus right leading. By examining the slopes of the normalized response probability versus IDT functions separately for each event, the relative weight given to each event can be measured. Saberi (1996) performed such a COSS ("conditional on single stimulus," Berg, 1989) analysis for interclick intervals of 1.8, 3.0, and 12.0 ms for click trains of 2–16 clicks, finding the information carried in the first click weighted more heavily than that carried by subsequent clicks. This onset dominance tended to decrease as the interclick interval was increased. Because the IDTs carried by each click were all drawn from the same distribution, observers attempted to integrate information across samples. Since Buell and Hafter (1988) demonstrated suboptimal integration for interclick intervals shorter than approximately 10 ms (indicative of non-

[a)]Portions of these data were presented at the 138th meeting of the Acoustical Society of America [Dye, R. H., (1999). J. Acoust. Soc. Am.**106**, 2237].
[b)]Current address: Department of Speech and Hearing Science, Arizona State University, Tempe, Arizona 85287-1908.
[c)]Current address: Institute of Neuroscience, University of Oregon, Eugene, Oregon 97403.

 © 2006 Acoustical Society of America

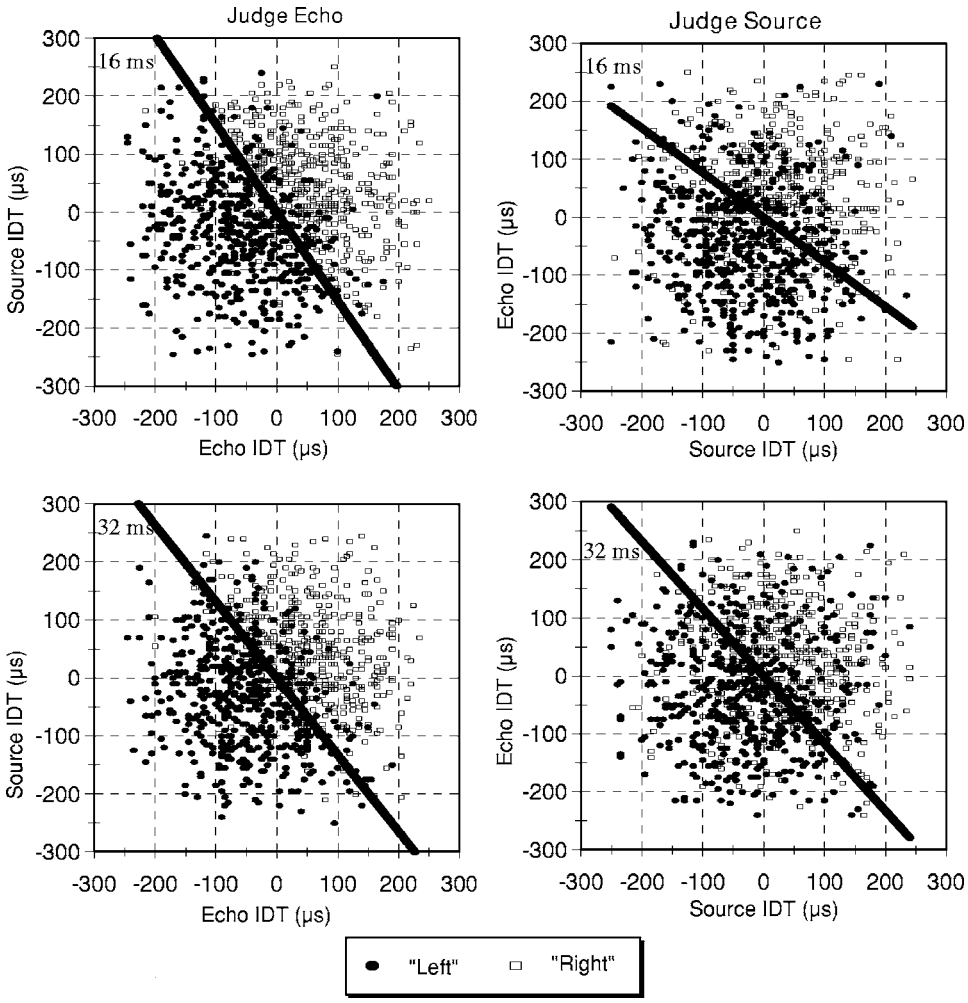

FIG. 1. Left panel: Left-right judgments are shown as a joint function of the interaural delays of the echo (abscissa) and source (ordinate) for one listener. Right panel: Left-right judgments are shown as a joint function of the interaural delays of the source (abscissa) and echo (ordinate). Results are shown separately for echo delays of 16 and 32 ms.

uniform weighting), the emphasis in studies using COSS analysis has been relatively short intervals between clicks.

Stellmack *et al.* (1999) used a different procedure to measure the relative weight given to the leading and lagging clicks, one based on an analysis of point-biserial correlations (Lutfi, 1995; Richards and Zhu, 1994). In this study, the listeners were instructed to respond according to the laterality of one click, ignoring the information carried by the other. As such, this procedure could be used for the study of interclick intervals (or echo delays) that led to either single or multiple auditory images. The stimuli that listeners judged were pairs of dichotic acoustic transients that were presented via headphones. A single, diotic pulse was presented during the first interval to mark the intracranial midline for the listener. In the second interval, two dichotic pulses were presented, separated by an "echo delay" of 1, 2, 4, 8, 16, 32, 64, 128 or 256 ms. The interaural delay of each of pulse was independently selected from a Gaussian distribution, with $(\mu, \sigma) = (0, 100\ \mu s)$. Data were obtained separately for conditions in which the source or echo was to be judged.

As the echo delay was increased from 1 to 8 ms, the normalized echo weight rose from nearly 0.0 to 0.5; both source and echo judgments were based entirely on the source at the shortest echo delays, but were based equally on the source and echo at delays of 8 ms. This marked the loss in onset dominance that others have found as the delay between the first event and latter events increases (see Zurek, 1987, and Litovsky *et al.*, 1999 for reviews). At these short echo delays, echo weights were essentially the same regardless of whether judgments were to be based on the echo or the source.

An important and unique aspect of this study was the fact that echo delay was extended beyond 8 out to 256 ms. Over this range, proportion correct increased with echo delay for conditions in which the echo served as the target. For conditions in which the source served as the target, proportion correct was high at short echo delays (less than 4 ms), since the precedence effect made the task easier to perform. Oddly, when the source was the target, proportion correct was lowest at intermediate echo delays (8–64 ms) and increased as echo delay was lengthened to 128 and 256 ms. Furthermore, source judgments were poorly predicted by weights at intermediate echo delays when the source served as the target—responses became more random, based neither on information in the source nor the echo. Figure 1 shows responses for one representative participant from that study to illustrate this point. Each row of panels shows results for a particular echo delay, either 16 or 32 ms. The left panels show data for conditions in which the responses were to the echo (2nd) click and the right panel shows responses to the source (1st) click. The lines in each panel depict the best-fitting linear boundaries between left and right responses,

which has a slope of $-(W_{echo}/W_{source})$ for the panels on the left and $-(W_{source}/W_{echo})$ for the panels on the right where W_{source} and W_{echo} are the normalized weights given to the first and second click, respectively. Although W_{source} and W_{echo} fell within a range of 0.4–0.6 for each of the four panels, note that there was much more variability in the responses when listeners were instructed to respond to the laterality of the first click. In other words, there were more right responses to the left of the boundary and more left responses to the right of the boundary. As such, the boundary did a poorer job of segregating left and right responses when the source was the target click, correctly classifying 0.71, and 0.68 of the responses for echo delays of 16 and 32 ms, as opposed to 0.86 and 0.84, when the echo was the target. The percentages of correct responses were also 14%–16% higher when the echo served as the target click. Clearly, for these intermediate echo delays (16–64 ms) listeners actually had more difficulty judging the source than the echo. This difficulty extracting interaural information from earlier events is the topic of this paper.

For listeners to perform well in these experiments, they must spatially resolve the two sounds, correctly identifying the locations of the intracranial images associated with the two clicks. Furthermore, they must correctly resolve temporal order (e.g., Hirsh, 1959; Hirsh and Sherrick, 1961). It is possible that listeners in Stellmack *et al.* (1999) correctly heard out separate images for the source and echo clicks, but were confused as to which arose first. To address this, they ran conditions in which the nontarget click was fixed at 0 interaural delay. When the source click served as the target and the echo was always diotic, proportion correct still showed a minimum at intermediate echo delays, although it was only 6%–7% lower (relative to what was obtained at the longest echo delays) instead of 18%–20% lower when the interaural delay of the echo was varied across trials. As such, it is most likely the case that other factors besides temporal-order confusion contributed to the impoverished ability to lateralize the preceding event when the interval between clicks was 16–64 ms. Supporting this conclusion is the fact that, for intermediate echo delays, responses were variable even on trials in which both clicks were to one side. There is a considerable degree of randomness for echo delays of 16 and 32 ms in the upper right and lower left quadrants of the right panels of Fig. 1, where the interaural delays of the source and echo clicks were consistent, i.e., there are many left responses (filled circles) when both source and echo were to the right (the upper right quadrant) and many right responses (open boxes) when both source and echo were to the left (the lower left quadrant). For these conditions, one could obtain correct responses by responding to the laterality of either click, so confusion over which came first could not lead to incorrect responses. It should also be pointed out that confusion about temporal order should not necessarily lead to better performance when the echo serves as the target than when the source serves as the target, since one should be just as likely to utilize the wrong click in the two conditions. Perhaps the last event overwrites or degrades the sensory trace arising from an earlier event, as was suggested by Massaro (1972). According to Massaro, when the last event serves as the target, performance would be superior to that obtained when a prior event serves as the target.

Although Massaro's work (Massaro (1970a; 1970b; 1971)), on backward recognition masking was mostly involved with pitch discrimination, the phenomenon is consistent with the data of Stellmack *et al.* (1999) at intermediate echo delays. In a study of backward recognition masking of binaural information, Massaro *et al.* (1976) asked listeners to lateralize a 20-ms 1000 Hz tone on the basis of an interaural difference of level (IDL) that was either −4 dB or +4 dB. This target tone was followed on most trials by a "backward interference" tone that was also 1000 Hz and 20 ms in duration. The interval between the target tone and the backward interferer was 0, 20, 40, 70, 120, 180, or 250 ms. The IDL of the interferer was −8, 0, or +8 dB, where negative IDLs were more intense at the left ear and positive IDLs were more intense at the right ear. They found evidence of backward interference for intervals shorter than 180 ms, particularly when the subsequent interferer was contralateral to the target tone. When the interferer and target carried IDLs that favored contralateral ears, responses were generally consistent with the side of the backward interferer at lags of 20 and 40 ms. Tolkmitt (1974) also demonstrated backward interference in a free-field localization task, with interference by broadband noise (400 ms in duration) of 20-ms target tones (1000 Hz in experiment 1, 560, 3560, and 6500 Hz in experiment 2) occurring for target-masker intervals as long as 200 ms. Von Békésy (1971) had previously reported what he termed "backward inhibition" for sequential sounds. His listeners were presented with two equally loud 35-ms tones, one 1000 Hz via a single loudspeaker and the other 1500 Hz via a ring of 12 loudspeakers having a radius of 60 cm. At a delay of 60 ms, whichever stimulus was presented second dominated the spatial percept.[1]

Although many studies have been carried out to examine the dominant role that early arriving sounds have on perceived spatial location, the focus of the current investigation is on the manner in which later arriving sounds (simulated reflections) affect the ability of human listeners to report the spatial location of earlier arriving sounds (simulated sources). The backward interference produced by the second transient at intermediate echo delays is an interesting phenomenon that warrants more study.

Because the waveforms associated with echoes in real acoustic environments are generally attenuated versions of the waveforms produced by sources, an important consideration in the study of backward interference concerns echo attenuation. The goal of the current study was to determine the range of relative levels over which an echo click continues to exert influence over judgments that are based upon the interaural delay of a source click. In the current experiment, the simulated echo was attenuated relative to the first click by 0, 6, 12, 18, 24, 30, or 36 dB. For each value of echo attenuation, the ability of listeners to judge the laterality of the source click was evaluated for echo delays of 1, 2, 4, 8, 16, 32, and 64 ms.

II. METHODS

The experimental methods were identical to those employed by Stellmack *et al.* (1999), except that the echo was attenuated by 0, 6, 12, 18, 24, 30, and 36 dB. Each trial consisted of two intervals. During the first, a diotic click was presented that marked the intracranial midline for the listeners. After 500 ms of silence, the observation interval, consisting of a dichotic sequence of two clicks, was presented. The interaural delays of the lead and lag clicks were independently selected from a Gaussian distribution with a mean of 0 μs and a standard deviation of 100 μs. We shall refer to the first and second clicks as the source and echo, respectively. As a consequence of the random selection of interaural delays from trial to trial, the source and echo could lead to the same or opposite ears. The echo delay refers to the interval of time between the onset of the leading source click and the onset of the leading echo click. Data were gathered at echo delays of 1, 2, 4, 8, 16, 32, and 64 ms.

The clicks were 50-μs rectangular pulses. Negative interaural delays correspond to left-leading clicks, while positive interaural delays correspond to right-leading clicks. The interaural delays were limited to ±2.5 standard deviations from the mean (±250 μs) in order to avoid excessively large interaural delays. The interaural delays were rounded to the nearest 5 μs so that the delays would correspond to integer multiples of the 200-kHz sampling rate that was used for generating the pulse trains.

The level of a continuous train (100/s) of equal-amplitude clicks was set to 52 dB SPL as measured by a digital rms voltmeter (Fluke PM 2525). The echo delay and echo level was fixed within a block of 50 trials. Twenty 50-trial blocks were run per condition, yielding 1000 trials per combination of echo delay and echo attenuation (7 echo delays by 7 echo attenuations). Feedback was provided immediately after each response on a trial-by-trial basis.

Stimuli were digitally generated via Gateway E4200 personal computer and converted to analog signals with 16-bit digital-to-analog converters (TDT DD1) using output rates of 200 kHz per channel. The levels of the clicks were set by TDT attenuators (PA4), and the clicks were low-pass filtered at 7.5 kHz (TDT PF1). The clicks were presented through Sennheiser HD 520 II headphones to listeners seated in IAC sound-attenuating chambers.

Listeners were instructed to use the information in the source click, ignoring the echo click, and to press one button on a keyboard if the source appeared to the left of midline and another key if the source appeared to the right, using the diotic cue presented in the first interval as a reference. For comparison, baseline conditions were run in which the source click was presented alone in the observation interval (without an echo click).

Prior to each block of trials, listeners were allowed to listen to as many practice trials as they desired. These trials had the same echo delay and echo attenuation as the test trials with interaural delays varying from trial to trial. Listeners were instructed to adjust the headphones during the practice trials so that the diotic click during the first interval sounded intracranially centered. When ready, listeners initiated a block of 50 test trials by pressing a particular key on the computer keyboard. Listeners were run in 1.5-h sessions during which 1000–1500 left-right judgments were made. All trials of a particular condition (echo delay/echo attenuation) were completed before moving on to a new condition. The order in which echo delays were run was random for each individual subject; however, data were collected at all echo attenuations at that particular echo delay before echo delay was changed. The order in which echo attenuations were run was random for each listener at each echo delay.

Three listeners participated in this study. Two had extensive experience in lateralization experiments, while the third had not previously participated in psychoacoustical experiments. All were naive to the hypotheses under investigation and all were given at least 10 000 trials of training before data collection began. Initially, listeners made lateralization judgments for a single click (interaural delays chosen randomly from Gaussian distribution with a mean of 0 μs and a standard deviation of 100 μs). It was required that proportion correct be at least 0.85 for single clicks (computed over 200 trials) before moving on to lateralization training sessions with two clicks. For all listeners in the study, this required fewer than 800 trials. Once this criterion was achieved for single clicks, 200 training trials were run for each of the 49 conditions (7 echo delays by 7 echo attenuations, run in a random order) without recording of the results. Each 200-trial training session consisted of four 50-trial blocks for fixed echo delays and echo attenuations. These blocks were run in the manner described above for experimental trials, including the ad lib practice trials during which listeners attempted to center the position of intracranial images associated with diotic (first interval) clicks through adjustment of headphone position.

Performance was assessed in three ways. First, simple proportion correct $[P(C)]$ was computed. This is the proportion of trials yielding responses consistent with the interaural delay of the first click. Second, the point-biserial correlation between the response made by the listener and the interaural delay of the "source" was computed, along with the point-biserial correlation between the response and the interaural delay of the "echo." Third, we predicted subjects' responses with a simple detection-theoretic model. From these two correlations, normalized source and echo weights, W_{source} and W_{echo}, were computed as a measure of relative influence of the source and echo on judgments,

$$W_{\text{Source}} = \frac{R_{\text{resp,IDT}_{\text{Source}}}}{|R_{\text{resp,IDT}_{\text{Source}}}| + |R_{\text{resp,IDT}_{\text{Echo}}}|}; \quad (1)$$

$$W_{\text{echo}} = 1 - W_{\text{Source}},$$

where $R_{\text{resp,IDT}_{\text{Source}}}$ and $R_{\text{resp,IDT}_{\text{Echo}}}$ are the point-biserial correlations between the left-right responses and the interaural delays of the source and echo clicks, respectively.

For conditions in which responses were to be based on the interaural delay of the source, optimal performance would be represented by $W_{\text{source}}=1.0$ and $W_{\text{echo}}=0.0$. From the two measured weights, a decision variable (D) was computed as a linear combination of source and echo IDTs,

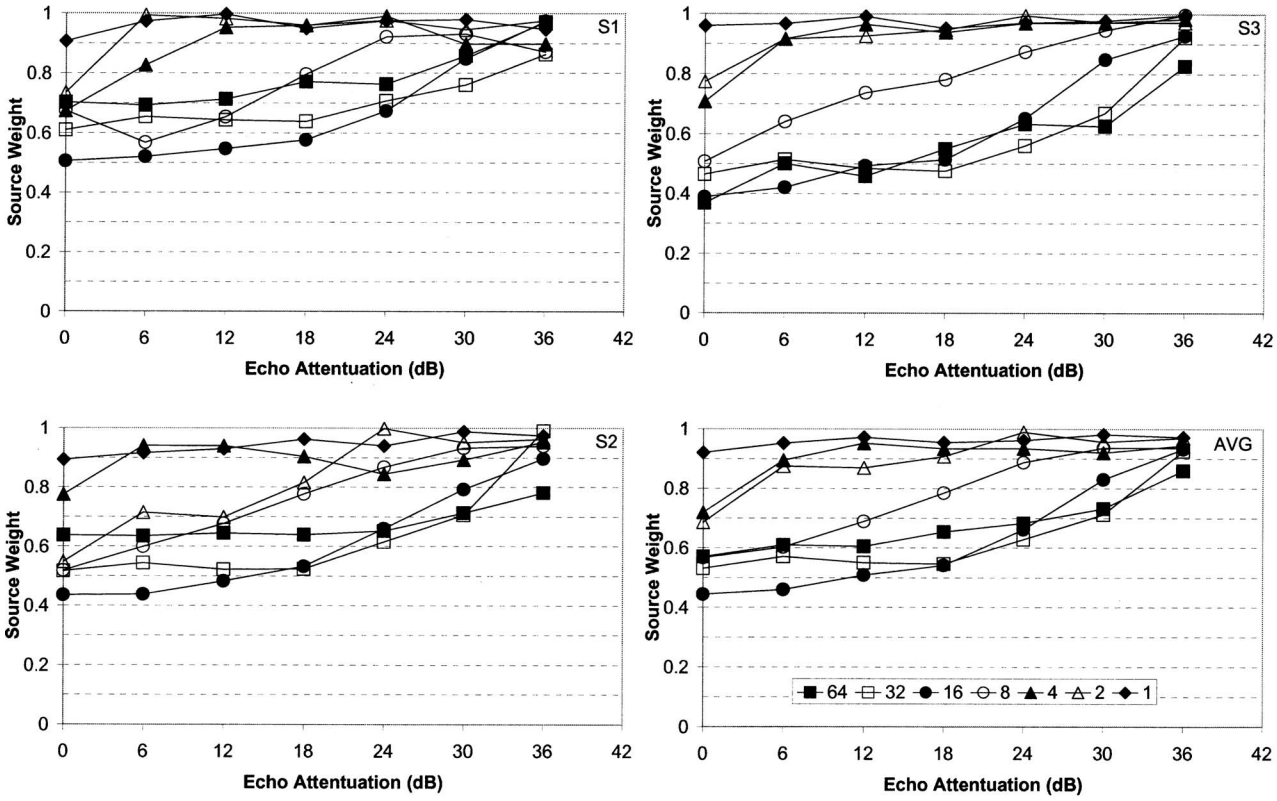

FIG. 2. Source weight is plotted as a function of echo attenuation and echo delay for three observers. Data are shown separately for three participants. The fourth panel shows the average values.

$$D = W_{\text{source}} IDT_{\text{source}} + W_{\text{echo}} IDT_{\text{echo}} + \varepsilon, \quad (2)$$

where ε represents prediction error. Responses were assumed to be based on the magnitude of D such that a listener would respond "left" if $D < 0.0$; "right" if $D > 0.0$; and randomly if $D = 0.0$, since there was no evidence for left-right response bias. The success of this simple model was assessed by computing the proportion of subjects' responses that were correctly predicted by the decision variable in Eq. (2). This was the third measure of performance, designated as $P(A)$.

III. RESULTS

Figures 2–4 plot W_{source}, $P(C)$, and $P(A)$, respectively, as functions of echo attenuation and echo delay. In each figure, the first three panels plot data for individual listeners, and the fourth (bottom right) plots data averaged across the three listeners.

The text will emphasize the average results (bottom right panels), since the three observers yielded data that were quite similar. As echo attenuation was increased from 0 to 18 dB there were only slight increases in source weight and proportion correct for echo delays of 16, 32, and 64 ms, with both source and echo weights remaining near 0.5. As the level of the echo click was reduced further at these delays, the source weights (Fig. 2) approached 1.0 and the percentages correct (Fig. 3) approached those obtained in the "no echo" condition (indicated by the single X at the far right). For an echo delay of 8 ms, source weights and proportions correct improved more quickly as the echo was attenuated. At echo delays of 4, 2, and 1 ms, the source weights and proportions correct were generally near their maximum values when the echo was unattenuated, so attenuating the echo had little effect, although the first 6 dB of attenuation did increase the source weight and proportion correct when the echo delays were 2 and 4 ms. These results are consistent with previous studies (see Litovsky *et al.*, 1999) that have demonstrated binaural precedence at these shorter echo delays. For these conditions, binaural precedence facilitates performance. The proportion of responses correctly predicted from the source and echo weights [Eq. (2)] shows an effect of echo delay, with proportion of responses correctly predicted being somewhat smaller for longer echo delays (Fig. 4).

To emphasize the minimal influence of echo level until the echo has been greatly attenuated, the left/right responses of one listener (S3) are shown in Fig. 5 for conditions in which the echo delay was set to 16 ms. Consistent with the fact that the source weights barely change with click attenuation up to 18 dB, the linear boundary (slope $= -(W_{\text{source}}/W_{\text{echo}})$) between left and right responses did not change appreciably until the echo was attenuated by 24 dB. Each panel also shows proportion correct, $P(C)$, and the proportion of responses correctly predicted from Eq. (2), $P(A)$.

Separate repeated measures analyses of variance (7 attenuations $\times 7$ echo delays) were carried out to examine the effects of echo delay and echo attenuation on the source weights, the proportions correct, and the proportions of responses accounted for by the weighted average model. Each analysis of variance was carried out on arcsine transformed

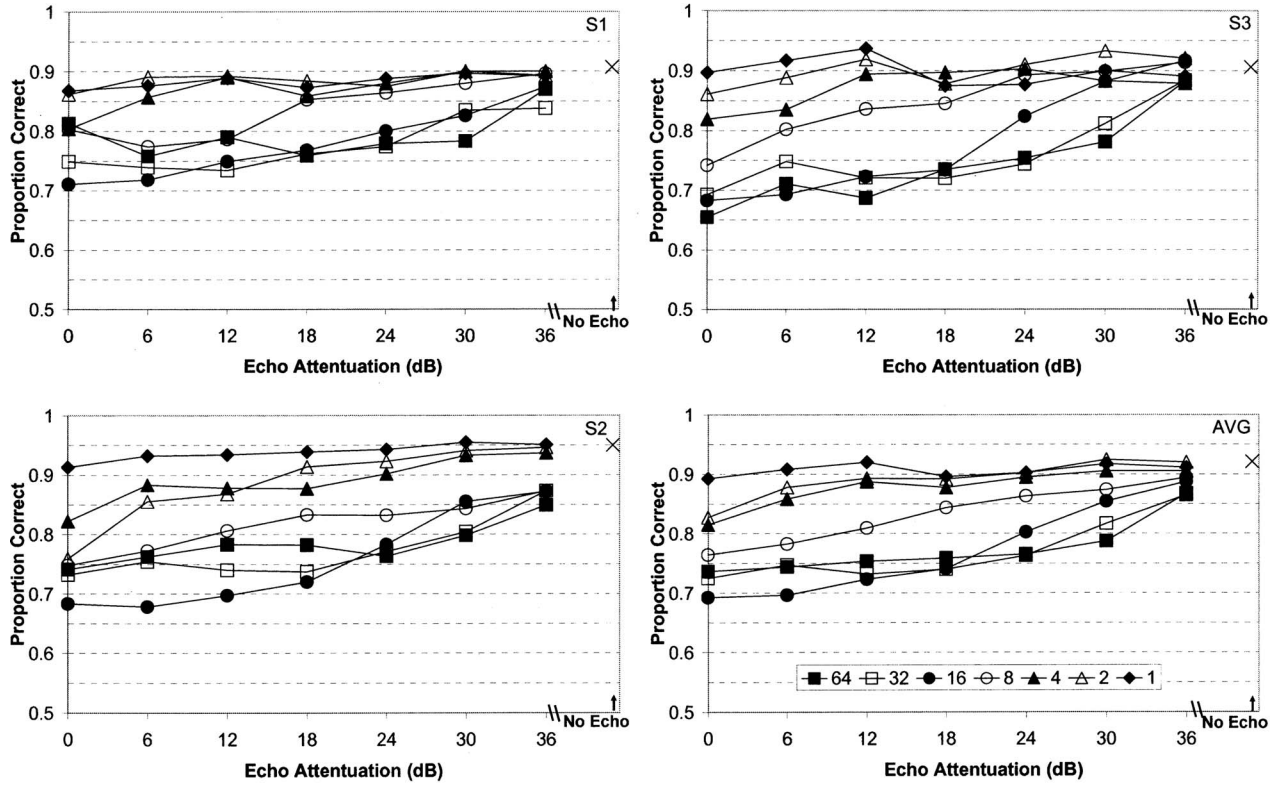

FIG. 3. Proportion correct is plotted as a joint function of echo attenuation and echo delay for three observers. The fourth panel shows the average values.

versions of the dependent variables in order to stabilize the variances (Collett, 1991), since all three variables are limited to a range of 0–1.0.

A. Source weight

There were significant main effects of echo delay [$F(6,12)=26.95$, $p<0.0001$, $\omega^2=0.511$ (ω^2 is the proportion of total variance accounted for by the independent variable)] and echo attenuation [$F(6,12)=62.31$, $p<0.0001$, $\omega^2=0.259$], as well as a significant interaction between echo attenuation and echo delay for source weight [$F(36,72)=4.59$, $p<0.0001$, $\omega^2=0.117$]. It was generally the case that larger source weights were observed at shorter echo delays and larger echo attenuations, with echo attenuation having a greater effect on source weights when the echo delays were longer. The significant interaction was further investigated with tests of simple main effects of echo attenuation. Significant effects of echo attenuation were found when the echo delay was 64 ms [$F(6,12)=10.84$, $p<0.01$], 32 ms [$F(6,12)=17.54$, $p<0.01$], 16 ms [$F(6,12)=152.14$, $p<0.01$], 8 ms [$F(6,12)=20.14$, $p<0.01$], 4 ms [$F(6,12)=5.22$, $p<0.01$], 2 ms [$F(6,12)=5.50$, $p<0.01$], but not 1 ms [$F(6,12)=2.11$, $p>0.05$]. To further elucidate the effects of echo attenuation, six contrasts were carried out at each echo delay showing a significant effect of echo attenuation to determine the attenuation at which source weight differed significantly from the weight obtained with no attenuation. The Bonferroni inequality was employed to cap the familywise error rate at 0.05 for the six comparisons (0 vs 6 dB, 0 vs 12 dB, 0 vs 18 dB, 0 vs 24 dB, 0 vs 30 dB, and 0 vs 36 dB).[2] For echo delays of 2, 4, 8, 16, 32, and 64 ms, the attenuations required to produce a source weight different from the one obtained with no attenuation were 6 dB, 6 dB, 18 dB, 18 dB, 30 dB, and 30 dB, respectively. Clearly, the elevation of source weight with attenuation of the echo occurs with less echo attenuation at shorter echo delays.

B. Proportion correct

Significant main effects were found for echo delay [$F(6,12)=26.75$, $p<0.01$, $\omega^2=0.578$] and echo attenuation [$F(6,12)=43.40$, $p<0.01$, $\omega^2=0.232$], as well a significant interaction between echo attenuation and echo delay for [$F(36,72)=3.46$, $p<0.01$, $\omega^2=0.085$]. Higher proportions correct were associated with shorter echo delays and greater amounts of echo attenuation, with the effect of echo attenuation on proportion correct being greater at longer echo delays. Again, the significant interaction was examined with tests of simple main effects of echo attenuation at each echo delay. As with source weights, significant effects were found at all echo delays except 1 ms [$F(6,12)=6.21$, $p<0.01$ at 64 ms; $F(6,12)=23.36$, $p<0.01$ at 32 ms; $F(6,12)=38.68$, $p<0.01$ at 16 ms; $F(6,12)=18.11$, $p<0.01$ at 8 ms; $F(6,12)=7.91$, $p<0.01$ at 4 ms; $F(6,12)=3.24$, $p<0.05$ at 2 ms; and $F(6,12)=1.31$, $p>0.05$ at 1 ms]. The effects of echo attenuation on proportions correct at each echo delay were further examined with six contrasts to determine the attenuation at which proportion correct differed significantly from that obtained with no attenuation. The Bonferroni inequality was employed to cap the familywise error rate at 0.05 for the 6 comparisons (0 vs 6 dB, 0 vs 12 dB, 0 vs

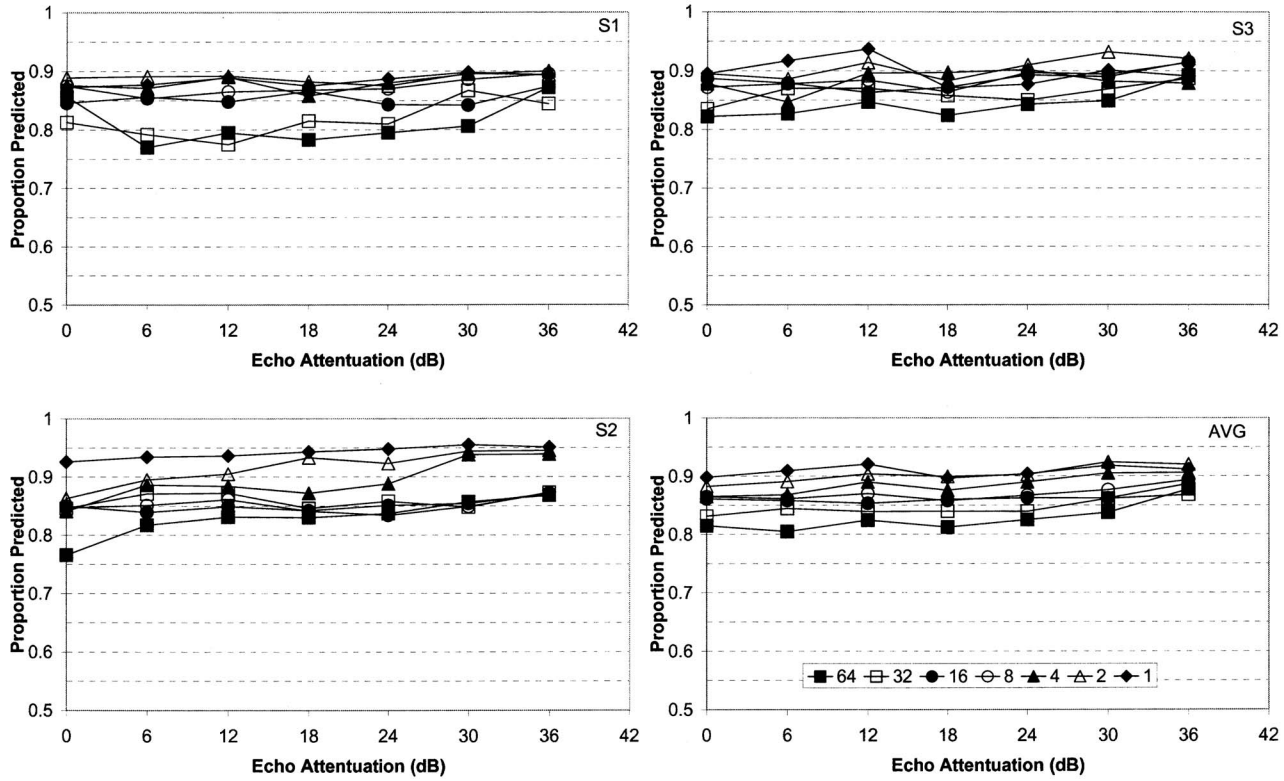

FIG. 4. The proportion of responses correctly predicted from the source and echo weights is plotted as a function of echo attenuation and echo delay. Data are shown separately for the three observers, with the average data shown in the fourth panel.

18 dB, 0 vs 24 dB, 0 vs 30 dB, and 0 vs 36 dB). For echo delays of 2, 4, 8, 16, 32, and 64 ms, the attenuations required to produce a proportion correct different from the one obtained with no attenuation were 12 dB, 12 dB, 18 dB, 24 dB, 30 dB, and 36 dB, respectively. As was the case for source weights, statistically significant elevation of proportion correct occurred with less attenuation of the echo at shorter echo delays.

C. Proportion of responses correctly predicted

Significant main effects were observed for echo delay [$F(6,12)=7.97$, $p<0.01$, $\omega^2=0.525$] and echo attenuation [$F(6,12)=8.21$, $p<0.01$, $\omega^2=0.103$], with higher proportions of responses correctly predicted associated with shorter echo delays and greater amounts of echo attenuation. The interaction between echo delay and echo attenuation was not significant for proportion of responses correctly predicted [$F(36,72)=0.69$, $p=0.865$].

IV. DISCUSSION

The most intriguing finding was that for echo delays of 64, 32, and 16 ms, attenuating the echo had little impact on the ability of listeners to properly weight the information arising from the source until the attenuation reached about 18–30 dB. For these echo delays, the two pulses were given nearly equal weight when they were the same level, so one might expect that reducing the level of one would increase the weight given to the other, since sensitivity to IDTs for acoustic transients is somewhat dependent on level (Hafter and DeMaio, 1975; Dye and Hafter, 1984). This demonstrates that presenting clicks at different levels does not enhance the ability to report the laterality of the source for these intermediate echo delays. Although the levels of reflections are influenced by the absorption characteristics of surfaces, it would be rare for a first reflection to be attenuated by 18–24 dB (Berkley, 1987; Ando, 2002). This finding indicates that backward interference in lateralization is quite robust and likely to influence localization in real world acoustic environments. For echo delays of 8, 4, and 2 ms, source weight and proportion correct increased rapidly as the echo was attenuated, particularly during the first 6 dB of attenuation for echo delays of 4 and 2 ms. At these shorter echo delays, the more intense preceding click actually masks the subsequent echo click (Ronken, 1970; Babkoff and Sutton, 1971). Presumably this forward masking of the echo click by the more intense source click decreases the salience of the binaural information carried by the echo click. It should be noted that the echo was always detectable at echo delays longer than 2 ms, even when it was attenuated by 36 dB (consistent with Raab, 1961).

For an echo delay of 16 ms, two of the three participants actually gave more weight the echo than the source when the source and echo clicks were presented at the same level. This resulted in the lowest average proportion correct in the study, 0.69. Stellmack *et al.* (1999) collected data from 15 individuals and found that 9 gave more weight to the echo than the source at an echo delay of 16 ms for conditions in which laterality judgments were based on IDT_{source}, leading to the lowest proportion correct (about 0.60). This finding confirms

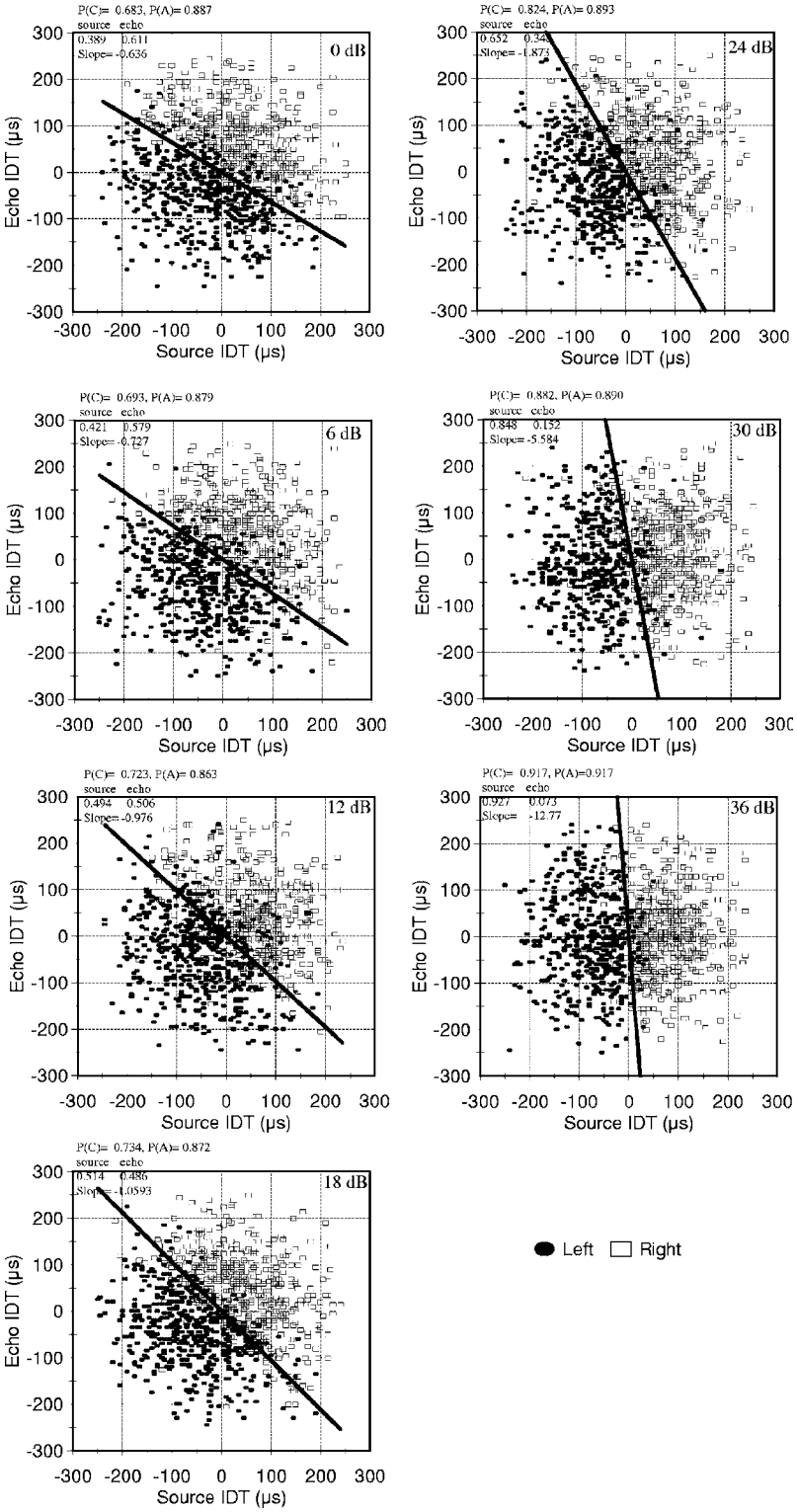

FIG. 5. An example of left-right judgments as a joint function of the interaural delays of the source (abscissa) and echo (ordinate) for S3 for data obtained with an echo delay of 16 ms. Results are shown separately for different echo attenuations. Each panel shows proportion correct, proportion of responses correctly predicted, source and echo weights, and the slope of the best fitting linear boundary between left and right responses.

the great difficulty that listeners have in lateralizing source events when the echo is no longer suppressed (echo delays longer than the 10-ms temporal window of the precedence effect for impulsive stimuli) but the temporal order of the source and echo cannot yet be determined (echo delays shorter than 20 ms; Hirsh and Sherrick, 1961).

As was mentioned in the Introduction, Massaro carried out a series of experiments that demonstrated the deleterious effects of later arriving sounds on the ability to identify the pitch (Massaro, 1970a; 1975), loudness (Massaro and Burke, 1991) or location (Massaro *et al.*, 1976) of previous sounds. Interference effects were evident for delays between the offset of brief signals and subsequent signals by as much as 180–240 ms. Findings like these led Massaro (1972) to propose a two-stage model of auditory short-term memory. An auditory stimulus produces a preperceptual, unanalyzed, auditory image containing information about the purely sensory features of the acoustic stimulus (frequency, level, location, etc.) that exceeds the duration of the stimulus. This preperceptual store provides the basic unit of sensory information,

with recognition of object features entailing readout to a "synthesized," postcategorical auditory perceptual memory. If a second sound follows before the first's features can be read out, the second sound overwrites the preperceptual store, effectively terminating processing of the first. Because one's ability to identify the properties of the initial stimulus is impoverished if the second occurs within 200–250 ms of the first, Massaro (1972) concluded that approximately 250 ms was required for read out of the preperceptual image to synthesized auditory memory. According to the simple two-stage model, there should be no effect of the similarity between the target and the backwards interferer, since it was presumed that the second event overwrites the features of the first. However, Kallman and Massaro (1979) found strong target-masker similarity effects for pitch judgments—participants tended to report the pitch of the backward interferer at delays less than 80 ms. This effect is reminiscent of Massaro *et al.*'s (1976) results for judgments of 20-ms 1000-Hz tones based on interaural level difference—at intertone intervals of 70 ms or less, left-right judgments were likely to be consistent with the laterality of the backward interferer. These similarity effects were explained by arguing that the masker terminates processing of the target tone, but also corrupts the memory representation at the stage of synthesized memory corrupted by the backward masker (Kallman and Massaro, 1979).[3] For echo delays of between 16 and 64 ms, the current study found that attenuating the echo click had no apparent effect on laterality judgments based on the source click until the echo click was attenuated more than 18 dB. It is as though the binaural information carried by this brief, less intense event some 32–64 ms after the to-be-lateralized target had been synthesized with the binaural information carried by the earlier event in forming the percept upon which responses were being made. The result is laterality judgments that are correlated with the interaural differences of time carried by both the source and echo clicks. Proportion correct and source weights were lowered by the second click at longer echo delays, as though the binaural information from the first and second event was combined. At shorter echo delays (8 ms or less), the precedence effect suppressed the binaural information carried in the echo click, leading to higher values of W_{source} and proportion correct.

The finding that interaural differences separated in time by up to 64 ms continue to interact is consistent with "binaural sluggishness" (Grantham and Wightman, 1978). When binaural parameters are varied sinusoidally at rates higher than 10 Hz, the stimulus is more difficult to discriminate from one with unmodulated binaural parameters (Grantham and Wightman, 1978; Grantham, 1982). These data have led to the conclusion that the binaural auditory system is "sluggish." This sluggishness has been modeled by a moving-average filter that integrates interaural values over the duration of its window. Several studies (Kollmeier and Gilkey, 1990; Culling and Summerfield, 1998; Akeroyd and Summerfield, 1999) have sought to measure the duration of the integration window, the equivalent rectangular duration (ERD). Estimates range from 40 to 200 ms, agreeing reasonably with our two-pulse lateralization data. Culling and Summerfield measured the shape of the integration window from measurements of the binaural masking level difference (BMLD), demonstrating a rearward lobe that was 1.3–2.3 times the duration of the forward lobe. Since a longer rearward lobe is consistent with greater forward integration, the direction of the asymmetry is not consistent with backward recognition masking of binaural information.

Comparison to free-field phenomena

When a sound is presented in any environment with reflective surfaces present, the first arriving sound comes directly from the source. It is followed by a group of early reflections off lateral walls, the floor, and the ceiling, reaching the listener within 50 ms of the direct sound (Kuttruff, 2000). This first group of reflections typically consists of discrete, identifiable events in time. Depending on the absorption characteristics of the reflective surfaces, these reflections will typically be reduced in magnitude when compared to the direct sound. Early reflections are often followed by a cluster of reflections that arrive quickly from many different directions. These events are lower in level and temporally contiguous, merging together to form reverberant sound. For stimuli that are nearly continuous, like speech or music, all reflections arriving during the first 35 or so ms are thought to reinforce the impression created by the direct sound. Humans do not perceive these events as separate from the source, and the perception of location is generally consistent with binaural information conveyed by the sound that arrives via the direct path (Haas, 1949) as long as the spectra and temporal envelopes of the reflections are reasonably similar to those arising from the source.

At longer echo delays, reflections may be heard as separate events, as echoes of the source, when they are sufficiently intense. For speech and music, these echoes may become annoying, distracting the listener from the speaker or music. Haas (1949) defined the threshold for echo disturbance as the echo delay at which 50% of the listeners judge the echo to be "disturbing." This "echo disturbance" (Haas, 1949) depends on the rate of speech, the reverberation time of the listening room, and the relative level of the reflection. For instance, speech presented at 7.4 syllables per second (fast speech), yielded an echo disturbance threshold of only 40 ms, while speech at 3.5 syllables per second (solemn speech) yielded echo disturbance thresholds of 92 ms. When the echo was reduced by 6 dB relative to the source, the echo disturbance threshold reached 175 ms (up from 68 ms for speech presented at 5.3 syllables/s with the source and echo of equal level). Muncey *et al.* (1953) measured echo disturbance thresholds with speech (5 syllables/s) and various types of music (e.g., fast and slow string music and fast and slow organ music), finding that echoes caused less annoyance for music than speech and least for slow music. Both Haas (1949) and Muncey *et al.* (1953) found that echoes became less disturbing as they were attenuated. For instance, Haas (1949) found that by an echo attenuation of 10 dB, there was no echo delay that participants found "disturbing." Although the range of delays over which echo disturbance exists coincides with the rather long delays over which back-

ward interference was observed here, the rather strong level dependence of echo disturbance is inconsistent with the effects observed in the current study. It should also be emphasized that Muncey *et al.* (1953) found the even relatively low level echoes (attenuated by30 dB relative to the source) continued to be "disturbing" as echo delays were extended to 1 s. This contrasts with Stellmack *et al.* (1999), who found that participants grew able to effectively ignore the echoes when judging the laterality of sources as the echo delay extended to 128 and 256 ms. It should be kept in mind, however, that both Haas and Muncey *et al.* presented continuous stimuli, with sources and echoes overlapping acoustically even at long echo delays. On the other hand, Stellmack *et al.* presented brief transients with simulated sources and echoes having no temporal overlap. As a consequence, the simulated echoes cease to impede processing of sources as the echo delay is extended to 128 ms. Another critical difference between "echo disturbance" studies (Haas, 1949; Muncey *et al.*, 1953) and studies in which lateralization of source or echo clicks is measured (the current study, Stellmack *et al.*, 1999) is the fact that participants in the lateralization studies are not specifically queried about how "disturbing" they find the echoes. Indeed, participants in lateralization studies may find the echoes annoying (their subjective impressions are generally not sought), but the echoes cease to affect judgments based on the preceding acoustic event.

Under what conditions would the first arriving echo follow the source by 16–64 ms? Under the assumption that the room were a perfect cube, reflections off the two lateral walls, the ceiling, and the floor would arrive at the listener simultaneously if the listener's head and the source were at an elevation that was equidistant between the floor, the ceiling, and the two lateral walls. Assuming a velocity of sound of 344 m/s, the direct-indirect sound path length differences would need to be 5.5, 11, and 22 m to produce echo delays of 16, 32, and 64 ms, respectively. If the listener's head and the speaker were on opposite ends of the room, these path length differences would be obtained for rooms having a height/width 13.28, 26.56, and 53.22 m for echo delays of 16, 32, and 64 ms. On the other hand, if the listener and the source were 1 m apart, but positioned in the middle of the room (equidistant from the floor, ceiling, and side walls), path length differences of 5.5, 11, and 22 m would only require the rooms to be 6.42, 11.96, and 22.98 m for echo delays of 16, 32, and 64 ms. Although a 6.42-m room is rather common, it is rare that rooms of this size are perfect cubes, and it would be extraordinary for the listener's head and the sound source to be positioned equidistant from walls, the ceiling and the floor. As a consequence, realistic rooms would undoubtedly be much larger if they were to produce the echo delays required for backward interference.

Given the low likelihood that acoustic events occurring 16 ms or longer after an event are reflections, it is our belief these events (reverberations or pulses that simulate them) are effectively treated as new sources, consistent with Buell and Hafter's (1988) finding of optimal integration of information once the interclick interval exceeds approximately10 ms. Perhaps the fact that these later-arriving acoustic events are treated as new sources, demanding processing resources, is what makes them "disturbing" (in the Haas and Muncey *et al.* sense). All listeners reported hearing multiple images at echo delays exceeding 8 ms; however, none were capable of lateralizing the first pulse (the simulated source) independently of the second (the simulated echo) until the second was attenuated by nearly 30 dB. It is our belief that the second, lower level events were simply treated as less intense subsequent sources, not reverberations of the initial pulse, when "echo" delays were greater than 16 ms. The mystery is that these two perceptual events continue to influence one another when they are separated by 64 ms, even for conditions that yield ideal integration, since one of the assumptions of ideal integration is statistical independence of the samples of IDT. Furthermore, it is evident that two seemingly segregated perceptual events can interfere with each other; interference can occur in the absence of perceptual fusion. The asymmetry of this influence, with events occurring 16–64 ms later having a greater impact on the ability to process earlier ones, was the main topic of this paper.

V. CONCLUSIONS

In summary, it was shown that simulated echo clicks had a deleterious effect on the ability to lateralize a source click when the interval between the source and echo fell in the range of 8–64 ms even when the latter click was attenuated by as much as 18 dB. This was ascertained by examining source weights, derived from point biserial correlations between responses and interaural differences of time of source and echo clicks, and the proportion of correct responses. There was also indication of a greater degree of randomness in laterality judgments at longer echo delays, since the proportion of responses predicted from the weights declined with increasing echo delay (out to 64 ms, the end of the range for the current experiment). A comparison between the data obtained here and so-called echo disturbance (Haas, 1949; Muncey *et al.*, 1953) showed a similar delay at which an echo becomes subjectively "disturbing" and when it interferes with the ability to lateralize a source click. However, there are important differences between the two phenomena. Most importantly, echoes continue to be disturbing as the delays are extended out to 1 s (Muncey *et al.*, 1953), yet the ability to lateralize leading clicks returns as delays are increased to 128 ms (Stellmack *et al.*, 1999). We believe that the deleterious effect of later acoustic events on the ability to lateralize previous ones is an example of backward recognition masking (e.g., Massaro, 1975), whereby subsequent events either terminate or overwrite sensory representations of events occurring earlier. Backward recognition masking of IDT information may be related to binaural sluggishness, although the direction of asymmetry of estimated temporal windows is opposite what would be required to account for the lateralization data (Culling and Summerfield, 1998). The range of echo delays over which backwards interference is evident leads to the conclusion that it would only exist for rather large rooms. It is also suggested that the auditory system treats acoustic events taking place more 10–16 ms later as new sources. Perhaps one of the reasons that they disrupt

processing of earlier events is that they garner auditory processing resources so that they may themselves be processed.

ACKNOWLEDGMENTS

We would like to thank our colleagues at the Parmly Hearing Institute for their support and advice while this experiment was conducted. We would also like to thank Dr. Wes Grantham, Dr. Gerald Kidd, and an anonymous reviewer for many helpful suggestions that improved the clarity of the manuscript. In particular, it was the anonymous reviewer who suggested that we consider room sizes for cases in which the source and the listener were in close proximity. José A. Gallegos was supported by the Mie Kim Najita Summer Fellowship. James Collier provided technical assistance and Noah Jurcin assisted with data collection. This work was supported by a grant from NIDCD (Program Project Grant No. DC000293).

[1]It should be noted that Blauert and Tüttemann (1978) failed to replicate Békésy's (1971) results, finding no evidence for backward inhibition.

[2]The decision to limit the post hoc comparisons to the six levels of attenuation versus no attenuation was based on our hesitancy to use a more conservative approach like Tukey's HSDs, which requires large mean differences for statistical significance, and our disinterest in most of the 21 possible pairwise comparisons.

[3]For a thorough discussion of why similarity effects are unlikely to reflect interactions between targets and backward maskers within preperceptual sensory memory, see Kallman and Massaro (1979).

Akeroyd, M. A. and Summerfield, A. Q.(**1999**). "A binaural analog of gap detection," J. Acoust. Soc. Am. **105**, 2807–2820.

Ando, Y. (**2002**). *Architectural Acoustics* (Springer-Verlag, Berlin).

Berkley, D. A. (**1987**). "Hearing in rooms," in *Directional Hearing*, edited by W. A. Yost and G. Gourevitch (Springer, New York), pp. 249–260.

Berg, B. G. (**1989**). "Analysis of weights in multiple observation tasks," J. Acoust. Soc. Am. **86**, 1743–1746.

Babkoff, and Sutton (**1971**). "Monaural temporal interactions," J. Acoust. Soc. Am. **50**, 459–465.

Blauert, J., and Tüttemann, G. (**1978**). "Auditory backward inhibition in concert halls," J. Audio Eng. Soc. **28**, 718–719.

Buell, T. N., and Hafter, E. R. (**1988**). "Discrimination of interaural differences of time in the envelopes of high-frequency signals: Integration times," J. Acoust. Soc. Am. **84**, 2063–2066.

Collett, D. (**1991**). *Modeling Binary Data* (Chapman & Hall, London).

Culling, J. F., and Summerfield, Q. (**1998**). "Measurements of the binaural temporal window using a detection task," J. Acoust. Soc. Am. **103**, 3540–3553.

Dye, R. H., Jr., and Hafter, E. R. (**1984**). "The effects of intensity on detection of interaural differences of time in high-frequency trains of clicks," J. Acoust. Soc. Am. **75**, 1593–1598.

Grantham, D. W. (**1982**). "Detection of time-varying interarual correlation in narrow band noise stimuli," J. Acoust. Soc. Am. **72**, 1178–1184.

Grantham, D. W., and Wightman, F. L. (**1978**). "Detectability of varying interaural temporal differences," J. Acoust. Soc. Am. **63**, 511–523.

Haas, H. (**1949**). "The influence of a single echo on the audibility of speech," J. Audio Eng. Soc. **20**, 145–159.

Hafter, E. R., and De Maio, J. (**1975**). "Difference thresholds for interaural delay," J. Acoust. Soc. Am. **57**, 181–187.

Hirsh, I. J. (**1959**). "Auditory perception of temporal order," J. Acoust. Soc. Am. **31**, 759–767.

Hirsh, I. J., and Sherrick, C. E., Jr.. (**1961**). "Perceived order in different sense modalities," J. Exp. Psychol. **62**, 423–432.

Kallman, H. J., and Massaro, D. W. (**1979**). "Similarity effects in backward recognition masking," J. Exp. Psychol. Hum. Percept. Perform. **5**, 110–128.

Kollmeier, B., and Gilkey, R. H. (**1990**). "Binaural forward and backward masking: Evidence for sluggishness in binaural detection," J. Acoust. Soc. Am. **87**, 1709–1719.

Kuttruff, H. (**2000**). *Room Acoustics*, 4th ed., (Taylor and Francis, London).

Litovsky, R. Y., and Shinn-Cunningham, B. G. (**2001**). "Investigation of the relationship among three common measures of precedence: Fusion, localization dominance, and discrimination suppression," J. Acoust. Soc. Am. **109**, 346–358.

Litovsky, R. Y., Colburn, H. W., Yost, W. A., and Guzman, S. J. (**1999**). "The precedence effect," J. Acoust. Soc. Am. **106**, 1633–1654.

Lutfi (**1995**). "Correlation coefficients and correlation ratios as estimates of observer weights in multiple-observation tasks," J. Acoust. Soc. Am. **97**, 1333–1334.

Massaro, D. W. (**1970a**). "Retroactive interference in short-term recognition memory for pitch," J. Exp. Psychol. **83**, 32–39.

Massaro, D. W. (**1970b**). "Preperceptual auditory images," J. Exp. Psychol. **85**, 411–417.

Massaro, D. W. (**1971**). "Effect of masking tone duration on preperceptual auditory images," J. Exp. Psychol. **87**, 146–148.

Massaro, D. W. (**1972**). "Preperceptual images, processing time, and perceptual units in auditory perception," Psychoanal. Rev. **79**, 124–145.

Massaro, D. W. (**1975**). "Backward recognition masking," J. Acoust. Soc. Am. **58**, 1059–1065.

Massaro, D. W., and Burke, D. (**1991**). "Perceptual development and auditory recognition masking," Dev. Psychol. **27**, 85–96.

Massaro, D. W., Cohen, M. M., and Idson, W. L. (**1976**). "Recognition masking of auditory lateralization and pitch judgments," J. Acoust. Soc. Am. **59**, 434–441.

Muncey, R. W., Nickson, A. F. B., and Dubout, P. (**1953**). "The acceptability of speech and music with a single artificial echo," Acustica **3**, 168–173.

Richards, V. M., and Zhu, S. (**1994**). "Relative estimates of combination weights, decision criteria, and internal noise based on correlation coefficients," J. Acoust. Soc. Am. **95**, 423–434.

Raab, D. H. (**1961**). "Forward and backward masking between acoustic clicks," J. Acoust. Soc. Am. **33**, 137–139.

Ronken, D. A. (**1970**). "Monaural detection of a phase difference between clicks," J. Acoust. Soc. Am. **47**, 1091–1099.

Saberi, K. (**1996**). "Observer weighting of interaural delays in filtered impulses," Percept. Psychophys. **58**, 1037–1046.

Shinn-Cunningham, B. G., Zurek, P. M., and Durlach, N. I. (**1993**). "Adjustment and discrimination measurements of the precedence effect," J. Acoust. Soc. Am. **93**, 2923–2932.

Shinn-Cunningham, B. G., Zurek, P. M., Durlach, N. I., and Clifton, R. K. (**1995**). "Cross-frequency interactions in the precedence effect," J. Acoust. Soc. Am. **98**, 164–171.

Stecker, G. C., and Hafter, E. R. (**2002**). "Temporal weighting in sound localization," J. Acoust. Soc. Am. **112**, 1046–1057.

Stellmack, M. A., Dye, R. H., and Guzman, S. J. (**1999**). "Observer weighting of interaural delays in source and echo clicks," J. Acoust. Soc. Am. **105**, 377–387.

Tolkmitt, F. J. (**1974**). "Latency of sound localization as a function of azimuth and frequency," Am. J. Psychol. **103**, 310–316.

von Békésy, G. (**1971**). "Auditory inhibition in concert halls," Science **171**, 529–536.

Wallach, H., Newman, E. B., and Rosenzweig, M. R. (**1949**). "The precedence effect in sound localization," Am. J. Psychol. **52**, 315–336.

Zurek, P. M. (**1987**). "The precedence effect," in *Directional Hearing*, edited by W. A. Yost and G. Gourevitch (Springer, New York), pp. 85–105.

Constructing and disrupting listeners' models of auditory space

Richard L. Freyman[a)]
Department of Communications Disorders, University of Massachusetts, 6 Arnold House, Amherst, Massachusetts 01003

Rachel Keen[b)]
Department of Psychology, University of Massachusetts, 407 Tobin Hall, Amherst, Massachusetts 01003

(Received 26 January 2006; revised 16 June 2006; accepted 16 August 2006)

A major problem for an auditory system exposed to sound in a reverberant environment is to distinguish reflections from true sound sources. Previous research indicates that the process of recognizing reflections is malleable from moment to moment. Three experiments report how ongoing input can prevent or disrupt the fusion of the delayed sound with the direct sound, a necessary component of the precedence effect. The buildup of fusion can be disrupted by presenting stimuli in alternation that simulate different reflecting surfaces. If buildup of fusion is accomplished first and then followed by an aberrant configuration, breakdown of the precedence effect occurs but it depends on the duration of the new sound configuration. The Djelani and Blauert (2001) finding that a brief disruption has no effect on fusion was confirmed; however, it was found that a more lengthy disruption produces breakdown. © *2006 Acoustical Society of America.*
[DOI: 10.1121/1.2354020]

PACS number(s): 43.66.Qp, 43.66.Pn [AK] Pages: 3957–3965

I. INTRODUCTION

When sound is produced in a room, complex interactions ensue as reflections of the original sound bounce off the surrounding surfaces. Under most circumstances, the source of sound and reflections are lumped into a single auditory image that is localized near the source of the original sound, a phenomenon known as the precedence effect. While the reflections do not have a strong effect on the perceived direction of the auditory image, they do affect other aspects of perception, such as the spatial width of the image and the loudness and quality of the perceived sound (Blauert, 1997). As shown by Bech (1995, 1996, 1998), we are exquisitely sensitive to the small timber and spatial differences that result from changing just one simulated reflection among many. This sensitivity makes it relatively easy to identify which of several rooms a sound was recorded in, i.e., a gym, a restroom, a classroom, or a small lab room (Robart and Rosenblum, 2005).

As the delay between a source and reflected sound increases, the listener begins to hear the delayed sounds as separate auditory images, "echoes" of the original source. The shortest time delay at which lead and lag sounds are heard as separate sources is defined as echo threshold (Blauert, 1997). Although echo threshold may logically be seen as a limit of basic auditory temporal resolution, the dependence of the threshold on the listener's auditory experience immediately preceding threshold measurement suggests that more complex processes are at work. For example, echo threshold can be raised by repeating brief stimuli such as a train of pulses or noise bursts. Echoes that are heard early in the train fade as the train continues, the "build-up" phenomenon first reported by Thurlow and Parks (1961). We have found that the built-up echo threshold is fragile, and can be lowered by several manipulations of a stimulus train, including changing the spectrum of the reflected sounds (McCall *et al.*, 1998), changing the lead-lag delay (Clifton *et al.*, 1994), and switching locations of lead and lag sound (Clifton, 1987). When lead and lag locations are switched, the listener's echo threshold drops so that lagging sounds previously unreported become audible echoes, localized at the site of the lag loudspeaker. If lead and lag sounds maintain their new positions, the precedence effect is reestablished and the echo fades as threshold rises (Clifton and Freyman, 1989).

The malleability of echo threshold holds great potential to aid our understanding of just how the brain responds to and recognizes certain sounds as true sources and other sounds as mere reflections. Under most normal circumstances it is the true sound source that is critical to localize whereas reflected sounds can be safely ignored. We have advanced a hypothesis about what auditory events can affect echo threshold and why. Underlying this hypothesis is the assumption that as listeners experience sound in a room, the acoustic properties of the room are coded as part of that auditory experience. We have proposed that when listeners are exposed to sound in a room they form expectations about how sound behaves in that room, and when acoustic properties of the room are changed in a sudden and improbable manner, echo threshold drops. We call this the "room acoustics hypothesis" (Clifton *et al.*, 1994; Clifton and Freyman 1997; Clifton *et al.*, 2002). In a series of studies we have found that fusion shown by higher echo thresholds is disrupted when loudspeakers are arranged to simulate movement of a wall toward or away from the listener (Clifton *et*

[a)]Author to whom all correspondence should be addressed. Electronic mail: rlf@comdis.umass.edu
[b)]Formerly, Rachel K. Clifton.

al., 1994), or a change in the reflective properties of the wall (McCall *et al.*, 1998). Listeners become suddenly aware of sound located at the wall's simulated position when delay or spectrum of the "echo" is changed.

Experiments on buildup have typically featured an unchanging train that ended with a test click identical to the preceding train, or a test click changed in a way calculated to break down the precedence effect (Clifton *et al.*, 1994; Grantham, 1996; McCall *et al.*, 1998). In these studies the questions concerned how to disrupt the strong precedence effect induced by the unchanging input preceding the test click. These studies have shown that following such sudden changes, echo threshold is much closer to what is measured when there is no preceding conditioning train. Presumably, this is because there has not yet been any buildup of echo threshold in the new "room." However, our own tests of our hypothesis have not dealt directly with the question of whether the built-up threshold for the original configuration is broken down after the sudden change. Recently, Djelani and Blauert (2001) asked the following: If the location of the lag sound was suddenly moved at the end of the train of lead-lag click pairs, but then immediately switched back to its original location, would the listener experience the breakdown of the precedence effect? The answer was "no;" the experience of a single switch in lag location had little effect on echo threshold in the original configuration. Djelani and Blauert (2001) concluded that there was no breakdown of precedence, only that the buildup had not yet occurred for the new configuration. The implication is that one can maintain or perhaps even acquire models of more than one room at the same time.

The purpose of the current experiments was to explore the process of both forming and disrupting a model for a particular auditory space. In particular, we investigated whether the acquisition or maintenance of such models is independent of concurrent or subsequent input that simulates alternative spaces. As did Djelani and Blauert (2001) we used click pairs as stimuli. Trains of standard click pairs featured a single sound source with a single reflection. We interleaved single clicks or click pairs within this standard click train to simulate different room characteristics from those present in the standard train. In experiment 1 we asked whether buildup for the standard lead-lag configuration could occur under conditions of fluctuating input about room acoustics. In experiments 2 and 3 we asked under what conditions buildup would be maintained in the face of various lead-lag conditions that differed from the original configuration. Experiment 2 contained a replication of the Djelani and Blauert conditions along with some extensions, while experiment 3 determined whether the buildup would be disrupted by a more dramatically different mixture of sounds that simulate variations in room acoustics.

II. EXPERIMENT 1: DOES BUILDUP OCCUR WHEN INPUT IS FLUCTUATING?

A. Method

1. Stimuli and apparatus

Stimuli were pairs of computer generated 50-μs pulses presented from two channels of a 16-bit digital-analog (D/A) converter (TTES QDA1). The outputs of the two signal channels were low-pass filtered at 8.5 kHz (TTE J1390), attenuated (TTES PAT1), amplified (CROWN D40), and delivered to a pair of loudspeakers (Realistic Minimus 7). The loudspeakers rested on a semicircular arc constructed of foam-covered wood which was housed in an anechoic chamber measuring $4.9 \times 4.1 \times 3.12$ m. The floor, ceiling, and walls of the chamber were lined with 0.72-m foam wedges. Subjects sat in a chair in the center of the room with the loudspeakers situated at 45 deg left (−45 deg) and 45 deg right (+45 deg) at a distance of 1.9 m. The center of the loudspeakers was 1.4 m above the wire mesh floor of the chamber at ear height for the typical listener seated in the chair. The stimulus level was measured by presenting the click stimuli through the loudspeakers at a rate of 4 clicks/s. A microphone was lowered to the position of the center of the subject's head with the subject absent. The microphone output was fed to a sound level meter (B&K 2204) set on the "fast" meter response on the A scale. Unattenuated outputs through the system were 61 dBA from either loudspeaker. The experiments were run at 43 dBA (with attenuators set to 18 dB).

2. Conditions

The primary conditions of the experiment used a train-test method used previously in a number of different studies (e.g., Freyman *et al.*, 1991; Clifton *et al.*, 1994; Grantham, 1996; Yost and Guzman, 1996; and Djelani and Blauert, 2001). On each trial, repeated pairs of clicks (one to each loudspeaker) were delivered at a rate of 4 clicks/s to form a click "train." Following the train, and a pause of 750 ms, a "test click" was presented. During both the train and test clicks, the clicks from the right loudspeaker were delayed relative to the left loudspeaker by 2 to 14 ms in 2 ms steps. The listeners' task was to report their judgment about whether they heard a sound in the vicinity of the right loudspeaker, which presented the lagging click. In this design, the test click pair had the same locations (lead left, lag right) in all conditions, so the effects of various conditioning trains on the same test click could be assessed.

In the baseline buildup condition, either 3, 5, 7, or 9 identical clicks with a fixed delay to right loudspeaker were presented during the train, with the test click having the same right-loudspeaker delay as the train. The rate for the baseline condition was 4 clicks/s. Figure 1, top trace, displays this baseline "buildup" condition for the example where there were nine clicks in the train and the test click is identical to the train. The remaining traces show the conditions in which single clicks or click pairs were interleaved halfway between the baseline click pairs. Interleaved stimuli are shown as open bars and baseline click pairs are shown as solid black bars. In the buildup+ condition, click pairs identical to the clicks in the train were interleaved, creating effectively a train consisting of almost double the number of clicks and a rate of 8 clicks/s. This condition served as a control for the more rapid rate that resulted from interleaving clicks in the experimental conditions. In the switch condition, the delay of the interleaved clicks was reversed, so that the composite train consisted of alternating left-leading and right-leading

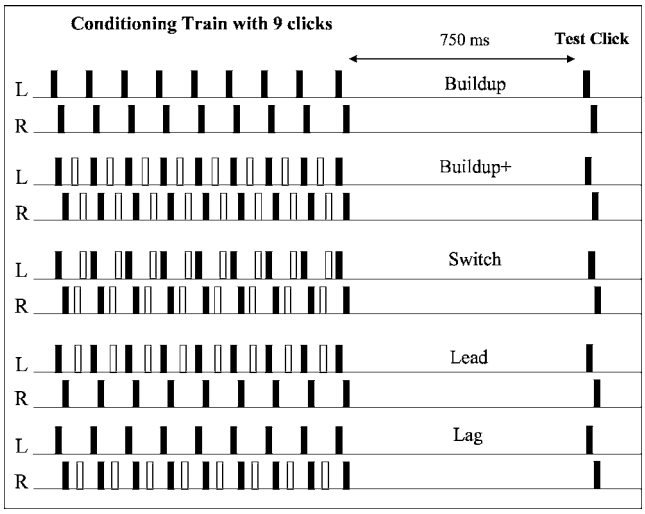

FIG. 1. Stimulus configurations for experiment 1 using the example of nine buildup click pairs in the conditioning train. After the trial, listeners reported whether or not they heard an echo from the vicinity of the right loudspeaker during the test click.

pairs. In the lead condition, only the lead (left) click was interleaved, and in the lag condition, only the right click was interleaved. In addition to these train-test stimuli, subjects listened to an "NC" condition, in which no conditioning train, only the test click, was presented. Hearing the echo for the NC condition represents the basic threshold for these click pairs with no interference and no buildup.

The switch, lead, and lag conditions were expected to disrupt buildup of the precedence effect because of the inconsistent room models being simulated. The switch condition presented the listener with two alternating models in which a reflecting surface is either on the right or left side. The lead condition keeps the sound source in one steady location but has a reflecting surface present or not present on alternating clicks pairs. This is most clearly a violation of the standard configuration. The lag condition features a source that moves back and forth. When the source is on the left side of the room there is a reflective surface simulated on the right side; when the source is on the right there are no simulated reflections. With all three conditions the simulated reflective surfaces are changed. However, with the switch and lag conditions the source locations are also moved, which complicates the situation. Violations of the original model of room acoustics could be less obvious than when the source is stable.

3. Procedure

The subjects were asked to face straight ahead, but were not physically restrained. They were told that they would hear a train of clicks followed by a test click separated from the train by a slight pause. Subjects were instructed to focus on the test click, not the train, and to listen for any sound coming from the vicinity of the right loudspeaker. They pressed one of two buttons to indicate whether or not they perceived a sound on the right during the test click. Note that a delayed sound was presented from the right loudspeaker on every trial, and this task is a subjective judgment of the subject's perception of the presence of an echo. Listeners were not given practice prior to data collection.

The stimuli were presented in blocks of 35 trials in which the interleave condition and the number of clicks in the train were fixed. Within each block, each of the seven delays (2, 4, 6, 8, 10, 12, and 14 ms) was presented five times in a random order. All five interleave conditions, including the baseline condition, were presented in a group of five blocks in which the number of clicks (N) in the train was fixed. The next group of five blocks again presented all five interleave conditions using a different number of clicks, and so forth, until all four N's were used and 20 blocks were completed. The ordering of the interleave conditions within a group of five blocks was random, as was the ordering of the number of clicks in the train across groups of five blocks. These random orders were different for each subject. After 20 blocks, five judgments had been obtained from each listener at each delay, interleave condition, and number of clicks in the train. The entire process was repeated with different random orders three additional times, so that across the total of 80 blocks, each subject made 20 judgments for each condition. Four 35-trial NC runs were interspersed within the train-test conditions, one in each set of 20 blocks. In total, a listener made 2800 judgments on train-test trials (20 judgments $\times$7 delays $\times$5 interleave conditions $\times$4 number of clicks in the train) in addition to 140 NC trials. These 2940 trials were typically spread through three-to-four listening sessions lasting one-and-one-half hours each.

4. Subjects

Ten listeners, nine female, one male, participated in this experiment. Their ages ranged from 21 to 31 years. Each subject passed a hearing screening at 20 dB HL at the octave frequencies from 500 to 4000 Hz.

B. Results

The initial analysis averaged across all ten subjects the percentage of trials on which an "echo" was reported as a function of delay for each condition. Examination of the data showed clearly that fewer echoes were reported for the buildup conditions relative to the NC condition, in agreement with the previous data reviewed in the Introduction. The buildup effect was well established with three clicks in the train, and did not appear to increase appreciably as N increased to five, seven, and nine clicks. Because the interleaved conditions also did not show an appreciable effect of increasing number, all plots and analyses collapsed the data across N. A more substantial number effect on buildup had been found in Freyman *et al.* (1991) with longer (150-μs) pulses compared with the 50-μs pulses used here. In future studies the potential effect of pulse duration on buildup should be explored.

As shown in Fig. 2, as delay increased the percentage of trials on which two clicks were reported increased smoothly for all the functions. The difference between the buildup conditions (open symbols) and NC (dashed line) reflects the

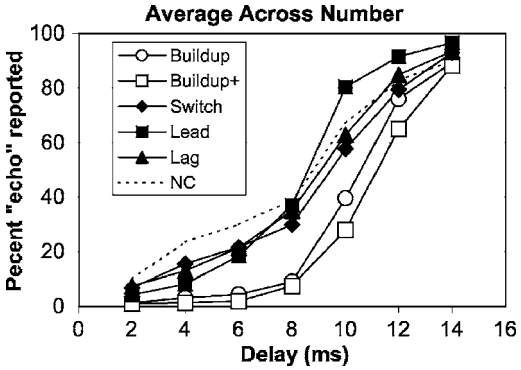

FIG. 2. Percentage of total trials on which listeners reported hearing an echo in experiment 1, plotted for each condition as a function of delay between leading and lagging clicks. The plotted data were collapsed across number of buildup clicks in the train for each condition.

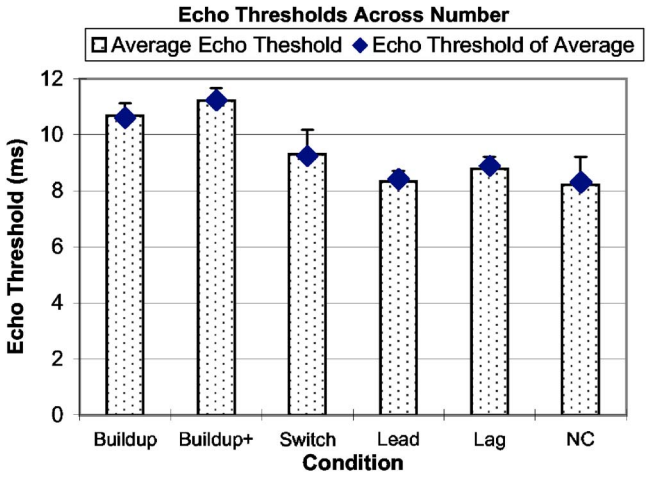

FIG. 3. Mean and +/− one standard error of echo thresholds derived from logistic fits to the individual functions obtained in experiment 1. For all of the train-test conditions, the standard errors are of the means across subjects after averages had been taken across number of clicks. Filled diamonds show the echo thresholds derived from the group psychometric functions displayed in Fig. 2.

buildup of echo threshold. That is, echoes are reported in fewer trials when the test click is preceded by a train of clicks identical to the test click.

Of primary interest for this paper is which, if any, of the trains with the interleaved click pairs would disrupt the buildup. As expected, the effect of the interleave condition that essentially inserted more repetitions of the same lead-lag pairs (buildup+), shown by the open squares, had only a small effect in the direction of increasing buildup. All three types of interleaved click pairs that represent a change in simulated room acoustics appear to increase the number of echoes reported relative to the buildup conditions.

To quantify the effects observed in Fig. 2, echo thresholds (the delay at which echoes were reported on 50% of the trials) were estimated from the functions obtained from each individual subject (see Appendix Table A1). Each function was fitted with a sigmoidal equation using nonlinear parameter estimation on MATLAB, which estimated the least-squares solution to logistic functions of the form $1/(1+\exp -[(\tau-m)/s)]$, where τ is the lag-click delay, m is the midpoint of the function, and s is the slope. The parameter m represents an estimate of the delay at which 50% echoes were reported, the echo threshold in this case. The fits were generally good, with 90% of the R^2 values above 0.95. In only one case (out of 210 total function fits) was the fit so poor that we felt it did not validly represent the echo threshold. In this case (subject 2's data at $N=3$, switch condition) only the data obtained at 2–10 ms were used in the fitting equation, with 12 and 14 ms excluded.

As in the analyses reported above, the echo thresholds for each subject were collapsed across N. These collapsed echo thresholds were then averaged across all ten subjects and are shown in Fig. 3 for each condition. The vertical lines extending from each bar represent one standard error of the mean across subjects after the collapse of the data across N. The diamonds shown on the columns represent the echo thresholds estimated from fitting the sigmoidal equations to the psychometric functions of the average data shown in Fig. 2. These estimates appear to agree quite well with the means of estimates of individual echo thresholds.

An analysis of variance performed on the echo thresholds across the six conditions yielded a main effect of condition $[F(5,45)=5.46,\ p<0.001]$. Planned comparisons were used to determine which conditions differed. The baseline buildup condition had a mean echo threshold of 10.7 ms. Mean echo threshold for the buildup+ condition, which interleaved the identical clicks, was slightly higher at 11.2 ms, although this difference was statistically significant $[F(1,9)=8.92,\ p<0.015]$. Echo threshold for the NC condition was 8.2 ms, so the buildup caused a shift of echo threshold of 2.5 to 3 ms for the buildup and buildup+ conditions, respectively, as expected, a significant difference $[F(1,9)=7.09,\ p<0.025]$. All three of the interleave conditions that were intended to simulate variations in room acoustics showed lower echo thresholds than either of the two standard buildup conditions. Planned comparisons contrasting the two buildup conditions against all others was highly significant $[F(1,9)=22.91,\ p<0.001]$. No comparisons among the three interleaved conditions were significantly different at alpha=0.05.

The results show that it is possible to severely disrupt the buildup by introducing variations during the train of clicks. Echo threshold did not increase unless the acoustic information in the preceding train designated a stable room model of source and reflections. As an example, consider the lead condition, which had a strong disruptive effect on the buildup. Here, an original stimulus and simulated reflection are paired, but between every pair the original source click is delivered with no "reflection" following it. Thus, the system should have difficulty building up a model of this auditory space, which is assumed by the room acoustics hypothesis to be responsible for the increased fusion of lead and lag. This confusing situation is analogous to the visual example of Escher's stairways that lead to impossible levels (Escher, 1984). Just as viewers of these visual incongruities may use various strategies in attempting to resolve the stairway problem, our listeners may experience these confusing auditory inputs in a number of different ways. At the moment these possibilities can only be speculated about, but future research

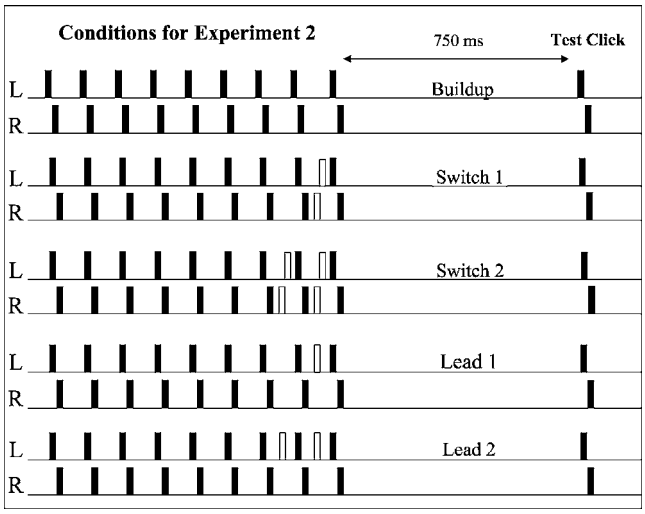

FIG. 4. Stimulus configurations for experiment 2.

may explicate what listeners do to attempt to resolve these inputs. Our data only allow us to conclude that alternation of impossible scenarios as we have conceived them disrupts buildup.

III. EXPERIMENT 2. DO VARIATIONS NEAR THE END OF THE TRAIN PRODUCE BREAKDOWN?

Experiment 1 showed the buildup of fusion could be disrupted by introducing variations in between the repeated lead-lag click pairs during a conditioning train. On the surface, this appears to be a different type of result than that obtained by Djelani and Blauert (2001) because they found that switching the lag position at the end of a preceding train had no effect on echo threshold. However, there were two key methodological differences. First, we introduced the variations much more aggressively; the variation clicks numbered only one less than the buildup clicks. Second, the variations were interleaved throughout the train, not allowing buildup to occur first. In contrast, Djelani and Blauert (2001) introduced only one variation after the precedence effect had already built up. In the current experiment, we replicate the Djelani and Blauert general procedures more directly, by introducing only one or two variations after buildup was allowed to occur.

Method and results

The same ten subjects who participated in experiment 1 served as listeners in this follow-up study. The stimuli used in this experiment are shown in Fig. 4. The baseline condition used trains of nine lead-lag pairs presented at 4 clicks/s ("buildup" train from experiment 1). Two of the experimental conditions from experiment 1, switch and lead, were modified for the current study. As shown in the figure, the variations were presented either once, between the eighth and ninth clicks in the buildup train, or twice, between the seventh and eighth click also. As in experiment 1, the stimuli were presented in 35-trial blocks with condition fixed and delay varied across trials in each block. Each of the seven delays was presented five times in each block, as before. The

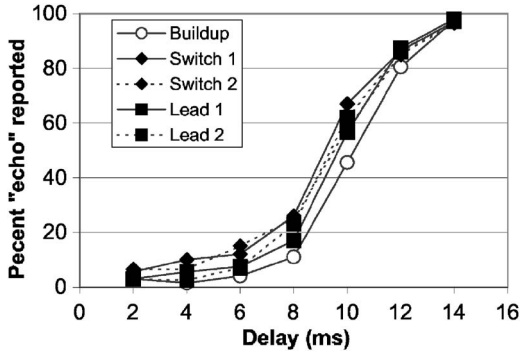

FIG. 5. Percentage of total trials on which listeners reported hearing an echo in experiment 2, plotted for each condition as a function of delay between leading and lagging clicks.

five conditions were presented in a random order in a set of five blocks. Four such sets of blocks were run for each subject, for a total of 20 blocks and 20 judgments for each delay in each condition.

Means of individual echo thresholds, computed as in experiment 1, varied by about 1 ms across conditions (see Appendix Table A2). Individual tests among all mean echo thresholds indicated that only switch 1 was statistically different from the basic buildup condition (Tukey HSD $p < 0.03$). The psychometric functions of the mean data, displayed in Fig. 5, show little effect of the interleaved clicks. Only slightly more echoes were reported in the experimental conditions than in the baseline buildup condition. These results are similar to those obtained by Djelani and Blauert (2001). Thus, it can be concluded that once the buildup of fusion has occurred during a click train, one or two aberrant clicks inserted at or near the end of the train does not appreciably reduce the built-up fusion.

IV. EXPERIMENT 3. CAN THE PRECEDENCE EFFECT BE BROKEN DOWN?

To this point we have determined that the buildup of fusion can be disrupted by interleaving variations that specify different acoustic spaces in between the repeated standard pairs in the conditioning train. On the other hand only one or two instances of such variations inserted at the end of the train had little effect on already built-up fusion, in agreement with Djelani and Blauert (2001). Thus, where the buildup was allowed to occur before any variations were introduced, disruption of the precedence effect was minimal. A remaining question is if buildup had been allowed to occur first, whether or not the more numerous variations that prevented buildup in experiment 1 would have produced a breakdown of the precedence effect. In experiment 3 buildup was induced by presenting a train of repeated identical click pairs followed by an equally long train of aberrant clicks that was intended to break down the built-up fusion.

A. Methods

Nine new normal-hearing subjects participated. The stimulus conditions for the experiment are shown in Fig. 6. There were two experimental conditions. In the first (shown at the top of the figure), a buildup train of five click pairs was

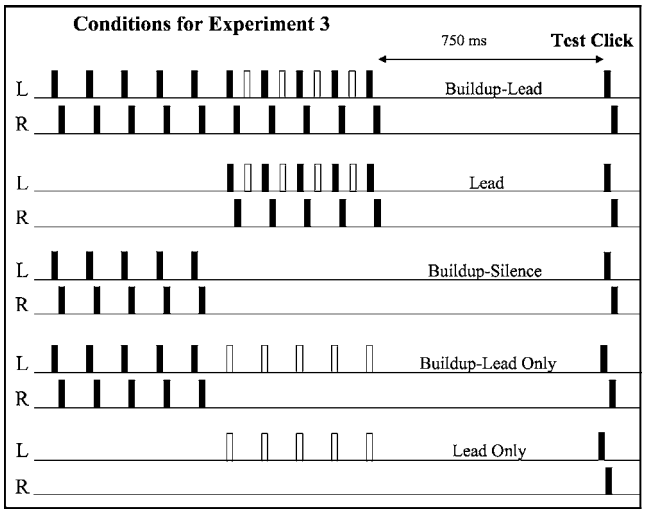

FIG. 6. Stimulus configurations for experiment 3. In addition to the conditions shown, the basic buildup condition from experiments 1 and 2 was repeated with this new set of subjects.

followed by five additional repeated pairs with lead interleaved (the "buildup-lead" condition). The primary control condition for this experiment was the lead condition itself, without the preceding buildup (second trace). A second control condition was buildup-silence condition (third trace), which was necessary in order to determine how much of the buildup would be expected to dissipate during the time period between the buildup train and the test click in the main experimental condition. Although not shown in Fig. 6, a final control condition was the basic buildup with five click pairs without the additional silent period, a repetition of the Buildup condition from experiment 1.

The second experimental condition was buildup-lead only, which was the strongest attempt to break down buildup fusion, as no maintenance of the original configuration was interleaved. A new control condition, lead only, in which no lag sound was presented until the test click, was used in addition to the buildup and buildup-silence conditions described above. As before, the test click on which subjects made their judgements was the same for all conditions, to allow comparisons for the effect of preceding input.

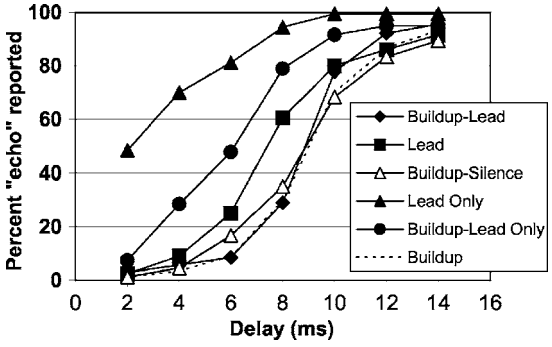

FIG. 7. Percentage of total trials on which listeners reported hearing an echo in experiment 3, plotted for each condition as a function of delay between leading and lagging clicks.

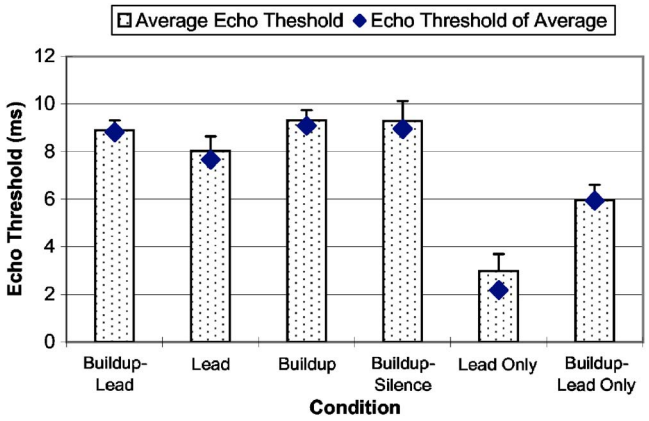

FIG. 8. Mean and +/− one standard error of echo thresholds derived from logistic fits to the individual functions obtained in experiment 3. Filled diamonds show the echo thresholds derived from the group psychometric functions displayed in Fig. 7.

B. Results

Echo thresholds were estimated from each subject's psychometric function, as in experiment 1 (see Appendix Table A3). An analysis of variance (ANOVA) computed on echo threshold yielded a main effect of conditions $[F(5,40)=25.04,\ P<0.0001]$. Follow-up comparisons were conducted as indicated below. The results of the buildup-lead and buildup-lead only conditions along with the relevant control conditions are shown in Fig. 7, which displays the percentage of trials on which an echo was reported averaged over subjects, and Fig. 8, which shows the computed echo thresholds. First, it should be noted that substituting silence for the second part of the train did not noticeably dissipate the buildup, so buildup-silence serves as a control for our two experimental conditions that had intervening stimuli after the buildup. Note the closely overlapping curves for the buildup-silence (open triangles) and buildup (dashed line) conditions in Fig. 7 and the similarity of the columns in Fig. 8. Data for the buildup-lead condition showed that interleaving aberrant clicks within the train did not cause a breakdown once fusion had already built up (buildup-lead versus buildup/buildup-silence $[F(1,8)=1.84 p>0.20]$.

When the lead only train was presented before the test click, the reporting of echoes increased substantially (solid triangles in Fig. 7). Echo threshold was between 2 and 3 ms compared with approximately 9 ms for the buildup-silence train (Fig. 8). A similar phenomenon was reported by Freyman *et al.* (1991) when the echo seemed to "pop out" if it was preceded by a train of single source clicks. When buildup was allowed to occur before the introduction of the lead only train (buildup-lead only), fewer echoes were reported when single lead clicks were presented (lead only), and the echo threshold was approximately 6 ms $[F(1,8)=40.85,\ p<0.001]$. However, a breakdown of echo threshold did occur, as shown by the substantial difference between buildup-silence and buildup-lead only $[F(1,8)=13.16,\ p<0.01]$. Echo threshold was substantially lower when aberrant clicks (compared to silence) were introduced between the buildup train and the test click. The most reasonable explanation for these data is that there was buildup during

the buildup portion of the train and then substantial, though not complete, breakdown during the lead-only train that cannot be explained by the additional time between the buildup train and the test click.

Finally, the results of the two experimental conditions differed from one another. After fusion had been allowed to buildup during repeated click pairs, introducing aberrant clicks from the lead side only created more disruption if they were presented unopposed (trace 4 in Fig. 6, displayed as solid circles in Fig. 7). If the same aberrant clicks were interleaved between the original fused click pairs, they had little effect on echo threshold (top trace in Fig. 6, displayed as solid diamonds in Fig. 7). A followup comparison of buildup-lead only versus buildup-lead was significant $[F(1,8)=18.45,\ p<0.002]$.

V. DISCUSSION

A major problem for any auditory system exposed to sound in a reverberant environment is to distinguish reflections from true sound sources. When reflections are below echo threshold, they are fused into a single auditory image, enabling accurate sound localization. Previous research on the precedence effect indicates that for human listeners the recognition process is swift and automatic, but subject to change by ongoing input (Clifton and Freyman, 1997). Under normal circumstances listeners experience consistent input when exposed to sound in enclosed spaces. Reflecting walls, ceilings, and floors do not jump around, disappear, and reappear. Although we experience changing acoustic environments as we move about through corridors and rooms, it is hard to imagine the circumstances under which one would experience the alternation of different acoustic spaces from one second to the next. By giving listeners this unnatural input, we have found that constructing a model of auditory space appears to require a certain amount of uninterrupted repetitions of the same acoustic information, but once acquired the model is fairly stable. Nevertheless, this too can be disrupted by the introduction of a radically different acoustic configuration.

In experiment 1 we asked whether having an inconsistent input comprised of very different auditory spaces in alternation would disrupt the buildup process. The standard buildup train featured a lead-lag click pair, with lead on the left side. Variations consisted of switching lead and lag locations between every pair of clicks in the train, and introducing single clicks from either the left (lead side) or the right (lag side). These variations simulated a change in the acoustic space by either removing a reflection or adding one in a new location. All variations we presented to listeners did indeed disrupt the buildup process, resulting in echo thresholds similar to that when a single click pair was presented in isolation.

Although alternating different acoustic environments succeeded in disrupting buildup, if one continued the train long enough the listener might be able to form a model for both acoustic configurations. In a preliminary report Blauert and Col (1992) presented a train lasting several seconds in which lead and lag locations switched on alternate click pairs. They reported that buildup occurred for both lead-lag configurations eventually, so that the listener localized only the lead click coming from alternate sides. Quantitative results were not presented in that report, so we do not know how many repetitions were required to produce this "double" buildup. We cannot rule out the possibility that had we continued all of the trains that disrupted buildup in experiment 1 for a long period, buildup would have occurred.

As part of this series of studies, we extended the Djelani and Blauert (2001) conditions in which they found no change in the built-up fusion of lead and lag pairs when tested after a brief switch in lag position. In experiment 2, a constant train of lead-lag clicks was presented, followed by interleaving a switch in lead-lag positions for either 1 or 2 clicks. In agreement with Djelani and Blauert we found that this brief introduction of aberrant click pairs was not enough to disrupt the built-up fusion. They interpreted their results as indicating that breakdown in fusion does not occur; in contrast, we conclude that fusion is relatively stable and is not easily broken down, but that conditions exist which do break down the precedence effect. When the system is presented with several (in our case five) consecutive instances of a new auditory space, the previous model of the lead-lag pair begins to break down. These findings lead us to propose that like the buildup, the breakdown does not occur instantaneously, but requires repeated alternative stimulation. In addition mere silence will not lead to breakdown of the precedence effect. The insertion of an additional 1.25 s of silence between the train and test clicks in experiment 3 produced no change in echo threshold, contributing to this picture of stability in built-up fusion. Longer periods of silence lead to deterioration of fusion (Djelani and Blauert, 2000).

Experiment 3 elaborated on what would and would not breakdown the acoustic model once it is established. We found that the same train that prevented formation of the model in experiment 1 did little to disturb it once the model was in place. The buildup-lead condition featured the buildup train followed by single clicks interspersed within the ongoing train; fusion was preserved. However, the introduction of a train of those same single clicks not interspersed within an ongoing train (buildup-lead only) did break down echo thresholds, but not completely. Echo thresholds were not reduced to the low levels of the lead only control condition (the 50% boundary was about 2–3 ms for lead only and 6 ms for buildup-lead only), indicating the lingering effect of buildup in the early part of the train. The fact that buildup-lead only is in between the buildup-lead and the lowest echo threshold (lead only) indicates the sensitivity of the auditory system to both repetition and interruption of the standard stimulus.

The significant difference between buildup-lead and buildup-lead only is intriguing. Why should single clicks from the left not disrupt a model when interleaved with the original configuration, but disrupt it when given as an independent train? The answer would seem to be that interleaving the original lead-lag pair between the disruptive single

clicks acted to reinforce or maintain the model, whereas giving the bare train of single clicks with no echo began the process of the system adjusting to a completely new acoustic configuration, to the detriment of maintaining the previous model of acoustic space. It is not clear how long that new configuration would have to continue before the original model would be completely gone.

To summarize our findings, it appears that constructing a model of auditory space involves a rapid mapping of reflected sounds in the space. This mapping is evidenced by increasing echo thresholds as information comes in. The function rises steeply and asymptotes quickly, a phenomenon we have termed buildup. Once established, this fusion is somewhat resistant to breakage, but will deteriorate if a new spatial configuration is introduced. The temporal parameters of its stability are unclear. Prolonged silence or lengthy continuation of the new configuration would be expected to displace a built-up model.

Our situation is a crude simulation of a person standing outside in an open area, but near a wall to the listener's right. A sound presented from the left reflects off the wall and reaches the listener as a single reflection. Using this pared down and precisely controlled situation enabled us to determine the effects of changing a single aspect of the stimulus. In order elaborate the room acoustics hypothesis so that it applies to real-room situations, more complex auditory environments with multiple reflections and realistic sounds should be created. Djelani and Blauert (2001) have begun this extension by using 12 reflections in a virtual room and spoken sentences lasting several seconds rather than brief clicks. They found buildup of echo suppression in a fashion similar to that for simpler stimuli. If the findings we report here with single reflections and click stimuli hold up under more complex stimulus conditions, we will have a much better understanding of how competing sounds are processed by the brain and localized in everyday settings.

APPENDIX

TABLE A1. Experiment 1. Individual echo thresholds averaged across number of clicks.

Condition	Subjects 1–10										Mean	Std error
Buildup	8.97	11.21	10.35	14.00	11.44	10.45	10.77	8.63	10.76	10.19	10.68	0.46
Buildup+	9.59	11.53	11.73	13.56	11.96	11.09	11.82	8.93	12.05	10.04	11.23	0.43
Switch	9.06	4.74	7.90	12.15	8.97	9.96	11.07	6.39	9.71	10.34	9.03	0.70
Lead	7.71	6.71	9.40	6.97	8.64	9.11	9.55	6.73	9.07	9.40	8.33	0.37
Lag	7.89	6.66	8.43	8.08	9.16	9.67	10.18	6.90	10.64	10.11	8.77	0.44
NC	5.80	12.79	10.05	4.80	10.85	10.66	8.62	3.56	5.16	9.88	8.22	0.99

TABLE A2. Experiment 2. Individual echo thresholds.

Condition	Subjects 1–10										Mean	Std error
Buildup	9.09	13.12	11.17	9.97	7.66	9.82	9.77	10.12	10.12	10.74	10.16	0.44
Switch 1	2.06	12.53	8.15	9.12	7.48	9.76	8.24	9.77	10.64	10.30	8.81	0.88
Switch 2	3.36	12.20	9.19	9.33	6.66	9.84	8.31	9.76	10.88	10.98	9.05	0.79
Lead 1	5.48	12.53	10.76	9.87	7.56	9.87	8.54	10.37	9.97	10.05	9.50	0.61
Lead 2	7.00	12.55	9.46	9.76	7.23	9.61	8.08	10.19	10.31	9.56	9.38	0.51

TABLE A3. Experiment 3. Individual echo thresholds.

Condition	Subjects 1–9									Mean	Std error
Buildup lead	8.50	8.49	8.36	8.84	8.78	9.47	9.18	11.56	6.80	8.89	0.42
Lead	9.11	7.33	7.22	9.89	8.40	6.65	5.60	11.37	6.55	8.01	0.61
Buildup silence	10.08	7.71	8.94	8.11	8.89	10.70	7.54	15.05	6.58	9.29	0.84
Buildup lead only	7.82	6.66	6.99	4.35	8.92	4.02	5.23	6.41	3.35	5.97	0.62
Lead only	6.32	2.16	2.54	2.03	7.01	1.68	2.67	1.00	1.40	2.98	0.72
Buildup	9.77	9.36	8.13	9.88	9.65	10.19	8.21	11.50	6.98	9.30	0.44

ACKNOWLEDGMENTS

This research was supported by a grant from the National Institute on Deafness and other Communicative Disorders (DC01625). The authors would like to thank Gail Brown, Lauren Sullo, and Laurel Slongwhite for their assistance in data collection.

Bech, S. (**1995**). "Timbral aspects of reproduced sound in small rooms. I," J. Acoust. Soc. Am. **97**, 1717–1726.

Bech, S. (**1996**). "Timbral aspects of reproduced sound in small rooms. II," J. Acoust. Soc. Am. **99**, 3539–3549.

Bech, S. (**1998**). "Spatial aspects of reproduced sound in small rooms," J. Acoust. Soc. Am. **103**, 434–445.

Blauert, J. (**1997**). *Spatial Hearing: The Psychophysics of Human Sound Localization* (MIT Press, Cambridge, MA).

Blauert, J., and Col, J. P. (**1992**). "A study of temporal effects in spatial hearing," in *Auditory Psychology and Perception*, edited by Y. Cazal, L. Demany, and K. Korner (Pergamon Press, Oxford, 1992), pp. 531–538.

Clifton, R. K. (**1987**). "Breakdown of echo suppression in the precedence effect," J. Acoust. Soc. Am. **82**, 1834–1835.

Clifton, R. K., and Freyman, R. L. (**1989**). "Effect of click rate and delay on breakdown of the precedence effect," Percept. Psychophys. **46**, 139–145.

Clifton, R. K., and Freyman, R. L. (**1997**). "The precedence effect: beyond echo suppression," in *Binaural and Spatial Hearing in Real and Virtual Environments*, edited by R. H. Gilkey and T. B. Anderson (Lawrence Erlbaum, Hillsdale, N.J.).

Clifton, R. K., Freyman, R. L., Litovsky, R. Y., and McCall, D. (**1994**). "Listener expectations about echoes can raise or lower echo threshold," J. Acoust. Soc. Am. **95**, 1525–1533.

Clifton, R. K., Freyman, R. L., and Meo, J. (**2002**). "What echoes tell us about the auditory environment," Percept. Psychophys. **64**, 180–188.

Djelani, T., and Blauert, J. (**2000**). "Some new aspects of the buildup and breakdown of the precedence effect," in *Physiological and Psychophysical Bases of Auditory Function*, edited by D. J. Breebart, A. J. Houtsma, A. Kohlrausch, V. F. Prijs, and R. Schoonhoven (Shaker, Maastricht, NL), pp. 200–207.

Djelani, T., and Blauert, J. (**2001**). "Investigations into the build-up and breakdown of the precedence effect," Acta. Acust. Acust. **87**, 253–261.

Escher, M. C. (**1984**). *The Graphic Work of M. C. Escher* (Gramercy, New York).

Freyman, R. L., Clifton, R. K., and Litovsky, R. Y. (**1991**). "Dynamic processes in the precedence effect," J. Acoust. Soc. Am. **90**, 874–884.

Grantham, D. W. (**1996**). "Left-right asymmetry in the buildup of echo suppression in normal-hearing adults," J. Acoust. Soc. Am. **99**, 1118–1122.

McCall, D. D., Freyman, R. L., and Clifton, R. K. (**1998**). "Sudden changes in room acoustics influence the precedence effect," Percept. Psychophys. **60**, 593–601.

Robart, R. L., and Rosenblum, L. D. (**2005**). "Hearing space: Identifying rooms by reflected sound," in *Studies in Perception and Action XIII*, edited by H. Heft and K. L. Marsh (Lawrence Erlbaum Associates, Inc.).

Thurlow, W. R., and Parks, T. E. (**1961**). "Precedence-suppression effects for two click sources," Perceptual and Motor Skills, **13**, pp. 7–12.

Yost, W. A., and Guzman, S. (**1996**). "Auditory processing of sound sources: Is there an echo in here?," Curr. Dir. Psychol. Sci. **5**, 125–131.

Amplitude modulation of turbulence noise by voicing in fricatives

Jonathan Pincas[a] and Philip J. B. Jackson
Centre for Vision, Speech & Signal Processing, University of Surrey, Guildford, GU2 7XH, United Kingdom

(Received 20 October 2005; revised 1 September 2006; accepted 5 September 2006)

The two principal sources of sound in speech, voicing and frication, occur simultaneously in voiced fricatives as well as at the vowel-fricative boundary in phonologically voiceless fricatives. Instead of simply overlapping, the two sources interact. This paper is an acoustic study of one such interaction effect: the amplitude modulation of the frication component when voicing is present. Corpora of sustained and fluent-speech English fricatives were recorded and analyzed using a signal-processing technique designed to extract estimates of modulation depth. Results reveal a pattern, consistent across speaking style, speaker, and place of articulation, for modulation at f_0 to rise at low voicing strengths and subsequently saturate. Voicing strength needed to produce saturation varied 60–66 dB across subjects and experimental conditions. Modulation depths at saturation varied little across speakers but significantly for place of articulation (with [z] showing particularly strong modulation) clustering at approximately 0.4–0.5 (a 40%–50% fluctuation above and below unmodulated amplitude); spectral analysis of modulating signals revealed weak but detectable modulation at the second and third harmonics (i.e., $2f_0$ and $3f_0$) © *2006 Acoustical Society of America.* [DOI: 10.1121/1.2358004]

PACS number(s): 43.70.Bk, 43.72.Ar [BHS] Pages: 3966–3977

I. INTRODUCTION

English has voiceless and voiced fricatives at four places of articulation: postalveolar /ʃ, ʒ/, alveolar /s, z/, dental /θ, ð/, and labiodental /f, v/. These speech sounds are produced by forcing air through a narrow constriction in the oral cavity (Shadle, 1985), generating noise within the jet and, more importantly, at or along a physical obstacle downstream, such as the teeth (sibilants /ʃ, ʒ, s, z/) and lips (nonsibilants /θ, ð, f, v/), as shown in Fig. 1.

Acoustic theory of noise generation from turbulence describes three types of source: monopole, dipole, and quadrupole (Lighthill, 1952). Monopoles arise from velocity fluctuations injected into the soundfield, dipole sources result from turbulent flow impinging on a solid obstacle, and quadrupoles occur in regions of turbulence through self-mixing. The intensity of these sources depends on the flow velocity as V^4, V^6, and V^8, respectively (Lighthill, 1954).

In fricatives, flow at the constriction exit produces a monopole, then quadrupoles just downstream in the jet core and dipoles at the teeth or lips (Stevens, 1998). It is widely accepted that dipole sources dominate noise generation in fricatives (Stevens, 1971; Shadle, 1985, 1990), although some studies have considered a monopole component (Pastel, 1987; Stevens, 1998; Narayanan and Alwan, 2000).

Voiced frication has both glottal and fricative sources, which produce the familiar "buzzy" quality. Yet it does not occur solely in voiced fricatives. Pincas (2004) recorded an average 16 ms of voicing overlapping frication at the vowel-fricative (/VF/) boundary of voiceless fricatives; Heid and Hawkins (1999) report 72% of voiceless fricatives having mixed excitation at the /VF/ boundary, according to an 8 ms minimum source overlap. Figure 2 shows a vowel transition into a *voiced* fricative. At transition, the formants move and fade; meanwhile, the high-frequency noise becomes prominent during the fricative segment.

The characteristics of voiced frication do not arise simply from the linear combination of independent sources. The articulatory, aerodynamic, and acoustic conditions required by and resulting from the simultaneous production of glottal vibration and frication noise produce "mutual interaction effects" (Pincas and Jackson, 2004): the presence of each source causes the other to be changed. The focus of this paper, amplitude modulation (AM) of the frication component, is one such effect and can be seen as vertical striations in the spectrogram of Fig. 2(a). Other effects include mutual amplitude reduction (Stevens, 1971), changes in fundamental frequency of voicing (Lofqvist *et al.*, 1989), and spectral changes both in the voicing component before, during, and after frication (Lofqvist *et al.*, 1995) and in the frication-noise component (Shadle, 1995).

A. Amplitude modulation formulation

Modulation depth m is the aspect of AM studied here. It can be conceptualized as the fraction of the carrier signal by which the modulated signal varies, e.g., if $m=0.5$, then the signal fluctuates by 50% above and below its original, unmodulated value. It is most often given in standard index form (in the range 0–1), but in the perceptual literature modulation depth is often quoted in dB: $20\log_{10}(m)$.

In AM, a carrier signal $w(n)$ is multiplied by a modulating signal $a(n)$ to produce the amplitude-modulated signal,

[a]Author to whom correspondence should be addressed; electronic mail: j.pincas@surrey.ac.uk

 © 2006 Acoustical Society of America

FIG. 1. Sound production mechanisms in schematic mid-sagittal view of the vocal tract in voiced fricative configuration: (G)lottis, (C)onstriction, (O)bstacle, (L)ip termination. Acoustic sources: △ periodic, ○ monopole, ◇ quadrupole, and ∞ dipole noise.

$x(n)=w(n)a(n)$. With a periodic modulating signal, $a(n)$ takes the form of a d.c. term and fundamental sinusoid of frequency f_0 plus harmonics:

$$x(n) = w(n)\left[1 + \sum_{h=1}^{H} m_h \cos\left(\frac{2\pi h f_0 n}{fs} + \phi_h\right)\right], \quad (1)$$

where $h \in 1..H$ are the harmonics, m_h is the modulation index at hf_0, $\int_S$ is discrete signal's sampling frequency, and ϕ_h is an arbitrary phase shift assumed to be constant. We assume $a(n)$ to be non-negative. With purely sinusoidal amplitude modulation $(H=1)$, $a(n)$ is completely specified by the f_0 component, i.e., by m_1 and ϕ_1. In natural voiced fricatives, the noise $w(n)$ is colored and the underlying modulation shape $a(n)$ is not a pure sinusoid.

B. Amplitude modulation in fricatives

During voiced frication, transglottal pressure and laryngeal tension maintain phonation. Glottal vibration causes AM indirectly though variations in flow through the constriction, assumed to be fixed (Shadle, 1985). Although the presence of AM noise in voiced fricatives is broadly acknowledged, fundamental questions remain. How does the result of glottal vibration reach the constriction? How does this perturbation affect the jet and the turbulence it forms? How does the perturbed turbulence go on to generate sound?

In his view of speech production, Stevens (1971) models noise sources under *static* aerodynamic conditions. From this perspective, the opening and closing of the vocal folds during one glottal cycle turns the flow on and off. Thus, the power of dipole sources is modulated proportional to V^6 while the flow velocity depends on the area and pressure across the constriction, ΔP_c (other sources accordingly). All these changes are considered to happen simultaneously.

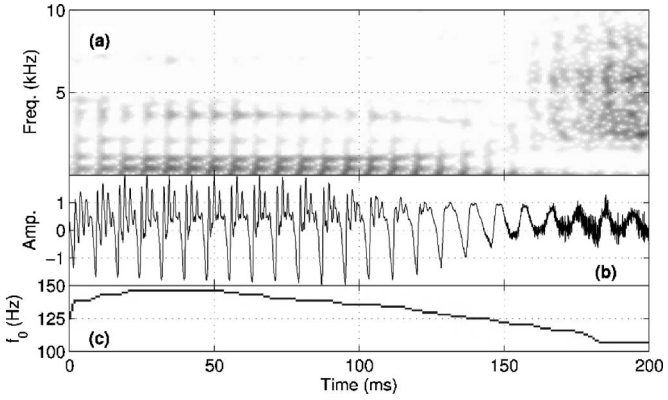

FIG. 2. (a) Spectrogram, (b) wave form, and (c) pitch track of /VF/ transition in [a:ʒ] token—16 kHz bandwidth.

Noise source fluctuations up to 15 dB (i.e., $m \sim 0.7$) have been attributed to this mechanism (Stevens, 1971).

However, this static view belies the true complexity of the aeroacoustics. Experiments on mechanical models of the VT reveal considerable irregularity near the glottis which changes drastically in character moving downstream (Barney *et al.*, 1999). Also, the phase of the noise modulation suggests that it takes time for the flow to generate noise (Jackson and Shadle, 2000).

An alternative view attributes AM to the interaction of the sound pressure wave created by phonation and the formation of turbulence in the jet exiting from the fricative constriction (Jackson and Shadle, 2000). Turbulent flows often exhibit large-scale regularity at certain ranges of flow rate and Reynolds number, $\mathrm{Re}=\rho VD/\mu$, (Sinder, 1999); furthermore, unstable vortex formation is sensitive to acoustic interference and a sound wave near the jet's natural Strouhal number $(\mathrm{St}=f_0 D/V)$ regularizes or *forces* the turbulence, causing rotational flow structures to grow periodically (Simcox and Hoglund, 1971; Crow and Champagne, 1971). Forced modulation depths of $m \sim 0.2$ at $\mathrm{St}=0.3$ were reported for their jet configuration. In voiced fricatives $(0.05 \leq \mathrm{St} \leq 0.2)$, voicing sets up the forcing wave, which then interacts with the jet to produce periodic vortices that convect downstream. These structures modulate the noise generation as, for example, the vortex train passes the obstacle. A further possible effect comes from the interaction of glottal vortices with the turbulence formed in the fricative jet, but data are incomplete (Barney *et al.*, 1999).

There is little quantitative data published describing the acoustic characteristics of AM noise in fricatives, and it remains unclear exactly how those of the pulsed noise relate to the voicing that induces the pulsing, which this paper seeks to address. In a study of modulation phase, Jackson and Shadle (2000) gave some measure of average modulation depth in sustained voiced fricatives: their results range from 0 dB in the case of the bilabial fricative [ß] to 2 dB in the case of [z] $(m \sim 0.25)$; modulation for the other fricatives tended to cluster around 1 dB $(m \sim 0.1)$.

In contrast to literature on modulation spectrograms [e.g., Tchorz and Kollmeier (2002)], signal processing techniques for cochlear implants [e.g., Rosen *et al.* (1999)] and temporal aspects of speech intelligibility [e.g., Shannon *et al.* (1995)], the modulation frequencies of interest in this paper are much higher (>100 Hz). The primary object is to characterize the relationship of the modulation index at f_0 to other properties of speech, such as voicing strength, place of articulation, and individual speaker differences. In particular, the modulation was examined at the voice fundamental frequency f_0, plus harmonics $2f_0$ and $3f_0$. To quantify the observed modulation, and to move toward an understanding of the forcing mechanism, an estimate of the modulation index $\hat{m}$ was computed from recorded speech signals.

C. Noise models in speech synthesis

In simple models of voiced fricatives, the individual contributions from voicing and frication sources are summed to form the output: voicing as a volume-velocity source at

the glottis; frication as a pressure source at the supraglottal constriction. Flanagan's electrical analogue model was one of the first to incorporate AM of the fricative source (Flanagan and Cherry, 1969). Band-passed Gaussian noise (0.5–4 kHz) was multiplied by the squared volume velocity at the constriction exit, including the d.c. component. Sondhi and Schroeter (1987) employed a similar model for aspiration at the glottis, gated by a threshold Reynolds number; for frication they placed a volume-velocity source 0.5 cm downstream of the constriction exit (or at the-lips for /f, v, θ, ð/). Klatt treated aspiration and frication identically, modulating the noise source by a square wave (50% burst duration) that was switched on during voicing, to achieve the effect he wanted (Klatt, 1980).

In Scully's work (Scully, 1990; Scully *et al.*, 1992), noise generation was based on Stevens' static experiments (Stevens, 1971): the strength of the pressure source was proportional to $\Delta P_C^{\frac{3}{2}}$, where ΔP_C is the pressure drop across the constriction. This source, depending on slowly varying articulatory and aerodynamic parameters, was applied equally to aspiration and frication sources. Since ΔP_C across the supraglottal constriction was lower for voiced than voiceless fricatives, this equation yields the weaker frication source, but does not encode any modulation. However, motivated by perceptual test results, aspiration noise was modulated, using the rapidly varying glottal area.

In his Ph.D. thesis, Sinder (1999) presented a model for fricative production based on aeroacoustic theory. Once the necessary flow-separation conditions had been met, vortices were shed which convected along the tract, generating sound as they went, particularly when encountering an obstacle. In the Portuguese articulatory synthesizer of Teixeira *et al.* (2003), the volume velocity at the fricative constriction is based on the flow at the glottis and transfer functions computed for noise sources at several instants during an f_0 pitch period, allowing them to activate and deactivate.

D. Organization

This research aims to extend current knowledge of AM noise generation by examining the relationship between the forcing glottal wave and modulation depth. Both-sustained fricatives and fluent fricatives embedded in phrases were analyzed to provide modulation values suitable for integration into model-based speech synthesizers. Section II describes the speech recordings, the algorithm, and parameters for estimating modulation depth in voiced frication. Section III discusses problems in applying the estimation algorithm to mixed-source speech and presents the preprocessing technique used to overcome them. The estimation procedure's overall accuracy is then discussed. Section IV presents results for the sustained and fluent-fricatives, considering effects of gender, place of articulation (PoA), vowel context, and voicing strength. Section V draws together the main findings, relating them to earlier AM work, explanations of the forcing mechanism, and current understanding of AM perception.

II. METHOD

A. Speech recordings

Two sets of fricative recordings were designed to capture the range of aeroacoustic conditions achievable by the human vocal apparatus in steady phonation and those typically realized in fluent speech. The *sustained fricative* set included laryngeal measurement of the vocal fold vibration and calibrated sound pressure from a microphone at a fixed distance from the subjects' lips for 16 subjects (12M, 4F). The *fluent-speech fricative* set provided a more natural environment with nonsense words framed in a standard phrase for eight subjects (4M, 4F). Four subjects took part in both experiments. Numbers of male and female subjects reflected availability, while providing at least four of each sex, so gender effects are treated cautiously. Subjects were unpaid staff and students of the University of Surrey, age range 20–35, all with British RP accents.

1. Sustained fricatives

Fricatives [ʒ, z, ð, v] were spoken in isolation. Both male and female subjects was asked to produce two types of utterance at three pitch settings, $f_0 \in \{125,150,175\ \text{Hz}\}$.[1] The first utterance type was an uninterrupted fricative where the subject smoothly adjusted loudness from their quietest possible fricative to loudest, and again to quiet, and loud (~3 s in total). The second type consisted of three separate sustained fricatives of increasing intensity (~1 s each). Each recording was preceded by a pitch-reference tone and short (2 s) pause to allow subjects to tune their pitch. Having three settings enabled an analysis for f_0. In total 24 recordings were made for each speaker (four fricatives × three f_0 values × two types).

Speech audio and electroglottograph (EGG) signals were captured simultaneously on PC by a Creative Labs Audigy soundcard via a Sony SRP-V110 desk (two channels at 44.1 kHz, 16 bit): mono audio from a Beyerdynamic M59 microphone, and EGG from a Laryngograph Lx Proc PCLX with adult-sized electrodes. A 1 kHz calibration tone was measured at the microphone and a B & K Type 2240 sound pressure level (SPL) meter, both 10 cm from the loudspeaker. During recording, subjects placed their head in a movement-restricting support and were instructed to keep still, to control the lip-microphone distance to within a few millimeters of 10 cm, at lip level and ~45° to the line of sight.[2]

2. Fluent fricatives

Speech-like tokens of F=/ʃ, ʒ, s, z, θ, ð, f, v/ were recorded from nonsense /VFə/ words with V=/a, *i*, u/, embedded in the phrase "What does /VFə/ mean?," using an acoustically sheltered cubicle and equipment as above. Subjects were given two kinds of prompt: a randomized list of sentences and an audio recording of the list read by one author in time to a metronome (with pauses for response), played through single-ear headphone.[3] To promote natural,

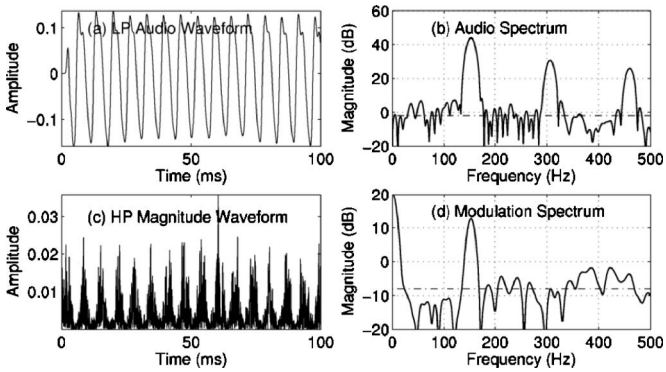

FIG. 3. Illustration of the harmonic structure of the voicing signal (top row) and the modulating signal (bottom row) for 100 ms of [z] ($f_0 \approx 150$ Hz). (a) Audio wave form low-pass filtered at 1 kHz. (b) Audio spectrum up to 500 Hz. (c) Magnitude of wave form high-pass filtered at 9 kHz. (d) Modulation spectrum. Dashed lines in spectra indicate noise floor.

fluent speech, subjects were left free to move their head. For each speaker, 216 sentences were recorded (nine reps. of every VF pair).

B. Measuring modulation depth

1. Estimating the modulation index m_h

With modulated broadband noise, the carrier signal $w(n)$ is an unknown random variable, which can be modeled as Gaussian white noise, and the signal $x(n)$ is as in Eq. (1). To estimate m_h, the instantaneous magnitude of the signal is taken $|x(n)| = |w(n)|a(n)$ which, unlike the modulated noise signal, contains a periodic component at f_0 and its strength is proportional to m_1. To extract this component, the Fourier transform is computed $\bar{X}(k) = \mathcal{F}\{|x(n)\}$, applying a Hamming window and zero padding:

$$\bar{X}(k) = \mathcal{F}\{|w(n)|\} \otimes \left[\Delta(k) + \sum_{h=1}^{H} \frac{m_h}{2} (\Delta(k - hk_0) e^{j\phi_h}) + \sum_{h=1}^{H} \frac{m_h}{2} (\Delta(k + hk_0) e^{-j\phi_h}) \right], \quad (2)$$

where $\otimes$ denotes convolution, $\Delta(\cdot)$ the Fourier transform of the window function, and $k_h = hNf_0/f_S$ is the frequency bin that contains harmonic hf_0. Figure 3(d) shows the *modulation spectrum*, $\bar{X}(k)$, for frication noise from a [z] token modulated at $f_0 \approx 150$ Hz, where the spike occurs. Hence, modulation index m_h can be estimated by comparing the coefficients at hf_0 and d.c.: $\hat{m}_h = 2|\bar{X}(k_h)|/|\bar{X}(0)|$.

2. Allowing for pitch variation

Although the processing window is short enough to exclude major changes in fundamental frequency, pitch variation within a window smears the modulation energy at each harmonic. To compensate for variable pitch and spectral smearing from windowing, our estimate $\hat{m}_h$ was based on the area under the spike at k_h and above the noise floor, including adjacent bins as appropriate.[4] This defined $\tilde{k}_h$ as the contiguous set of bins under the k_h spike [see Fig. 3(d)]. For the spike around zero frequency, a range of bins was also aggregated, $\tilde{0}$. Thus, with noise floor $\hat{\theta}^2 = \frac{1}{N}(1 - \frac{2}{\pi}) \sum_{k=0}^{N-1} |X(k)|^2$, an estimate similar to that above was formed:

$$\hat{m}_h = 2 \left(\frac{\sum_{\tilde{k}_h} |\bar{X}(k)|^2 - \hat{\theta}^2}{\sum_{\tilde{0}} |\bar{X}(k)|^2 - \hat{\theta}^2} \right)^{1/2}. \quad (3)$$

III. APPLICATION TO SPEECH

A. Periodic energy mixed with noise

Since voiced fricatives comprise periodic energy mixed with frication in the time wave form and much of the spectrum, it is not trivial to isolate the noise component for analysis. The f_0 component itself is confined to low frequencies (<400 Hz) and can easily be removed by high-pass (HP) filtering without losing any significant amount of fricative noise. However, bands of periodic energy, or voicing harmonics, persist into the higher spectral regions of the fricative noise, especially near formant frequencies.

For most speech sounds, interest is focused on the first two or three formants (up to perhaps 4 kHz) as higher formants tend to be weaker and are less important perceptually. In normal, fluent voiced fricative speech, voicing is often weak and its formants are rarely detectable much above 3 kHz; in strong fricatives with a loud voicing component (as in our sustained fricatives corpus), formants can be found up to 5 or 6 kHz. Consider the spectrum of a strongly voiced [v] in Fig. 4. Figure 4(b) shows the dominant periodic energy in the 0–4 kHz region (a harmonic spectrum with four defined formant peaks at 1.3, 2.2, 3.2, and 3.7 kHz); in Fig. 4(c), the spectrum is purely aperiodic, with no harmonics that can be ascertained in the 7–16 kHz range; in Fig. 4(a), 4–7 kHz contains mainly aperiodic energy though with a defined formant at 6.2 kHz, which can be seen in both the spectrum and the spectrogram in Fig. 4(d).

The effect on apparent modulation depth of mixing periodic energy with frication noise should be considered. Given that formants are damped resonances excited periodically by voicing at f_0, they will tend to have a fluctuating envelope similar to that of the aperiodic component. Unless the peaks are in phase with the bursts of frication, the presence of voicing will attenuate the apparent modulation depth of the noise. Consider the fricative [v] in Fig. 4. The spectrogram shows strongly modulated frication noise above 4 kHz, as well as fluctuating peaks in formant energy at lower frequencies. Careful inspection reveals that the pulses of frication are out of phase with the pulsed formant energy. Amplitude envelopes [or modulation signals, $a(n)$] for different frequency bands are shown underneath as Figs. 4(e) and 4(f), showing how they differ in phase. Figure 4(e) compares amplitude fluctuation in the overwhelmingly periodic, 1–4 kHz band [thick line, cf. Fig. 4(b)], to the mainly aperiodic, 7–16 kHz band [thin line, cf. Fig. 4(c)]. The phase difference between the two modulation signals is ~170°.

Envelopes in Fig. 4(f) demonstrate the attenuation of

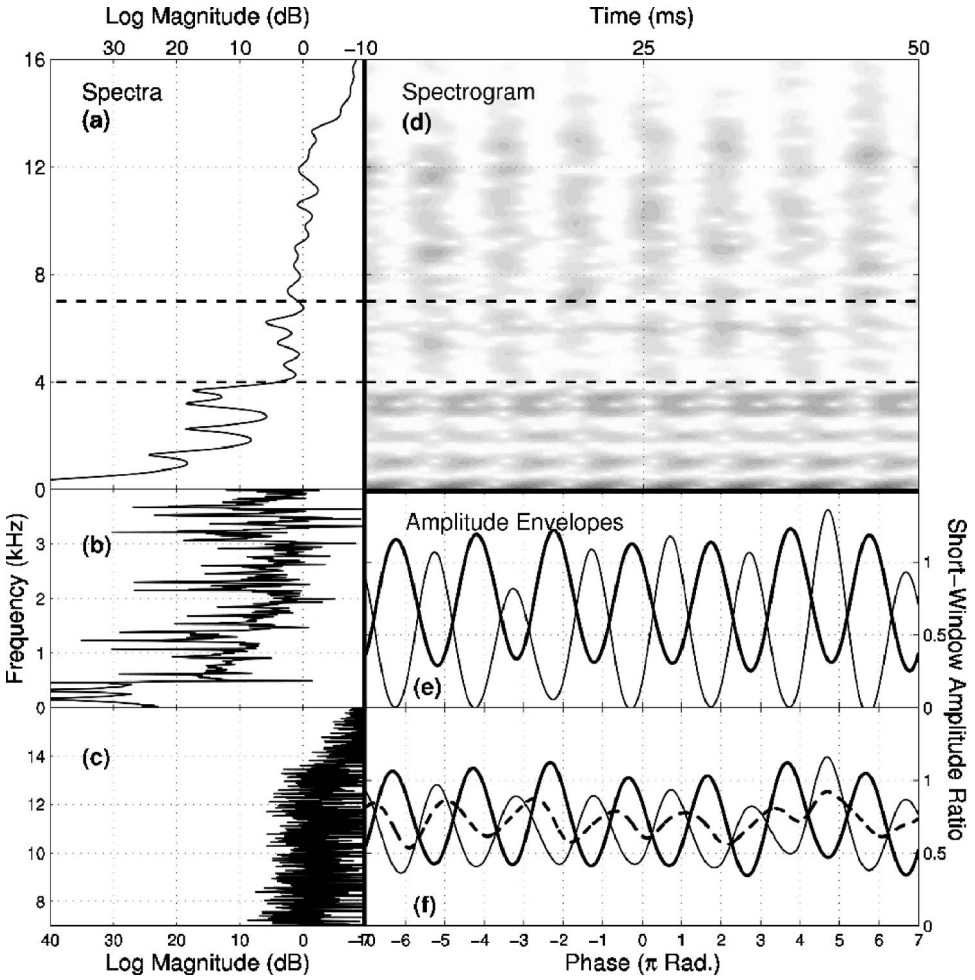

FIG. 4. (a) LPC spectrum (order 40), (b) close-up of spectrum in region 0–4 kHz, (c) close-up of spectrum in region 7–16 kHz, (d) spectrogram (5 ms, Hanning window, 4× zero-padded, fixed gray-scale, frequency-aligned with LPC spectrum and time-aligned with amplitude envelopes), and (e),(f) amplitude envelopes (magnitude signal, low-pass filtered at 200 Hz) for 50 ms section of sustained [v] ($f_0 \approx 153$ Hz, $f_s = 32$ KHz). Individual amplitude envelopes are for different frequency bands, f_{BP}. (e) $1 \leq f_{BP} \leq 4$ kHz (thick line, periodic energy) and $7 \leq f_{BP} \leq 16$ kHz (thin line, aperiodic energy); dashed horizontal lines on spectrogram identify these frequency regions, (f) $1 \leq f_{BP} \leq 16$ kHz (thick line, mainly periodic), $3.5 \leq f_{BP} \leq 16$ kHz (dashed line, balanced mix of periodic and aperiodic) and $4 \leq f_{BP} \leq 16$ kHz (thin line, mainly aperiodic).

apparent modulation from combining the out-of-phase periodic and aperiodic energy components. HP filtering with cutoff $f_{HP}=1$ kHz (thick solid line) removes the f_0 component *and first formant* but leaves the remaining periodic and aperiodic energy intact. Since the voicing source is stronger, the modulation signal is dominated by the periodic formant energy; the similarity in phase to the "periodic only" 1–4 kHz band [thick solid line in Fig. 4(e)] confirms this. However, in comparison to the 'periodic only' case, the depth of modulation has been reduced; this is due to the out-of-phase aperiodic energy in the region 4–16 kHz. Raising f_{HP} to 3.5 kHz (dashed line) excludes most (but not all) of the periodic energy (see formant at 3.7 kHz in the spectrum and spectrogram), which evens out the periodic and aperiodic components. Modulation shape and depth are disrupted, and the phase of the modulating signal resembles neither of the previous cases. A further increment to $f_{HP}=4$ kHz (thin line) excludes the last strong formant (a weaker one remains at ~6 kHz) and the resulting envelope is similar, if weaker, to the "aperiodic only" 7–16 kHz band [thin line in Fig. 4(e)].

Since we are interested only in modulation of the frication noise, it is paramount that the *aperiodic component* is successfully isolated before applying Eq. (3) to estimate the modulation depth. As Fig. 4 demonstrates, failure to remove periodic energy can seriously affect the accuracy of m_1 estimation for the frication noise. Periodic components could be removed by HP filtering with f_{HP} high enough to exclude all likely periodic energy.

Although fixing f_{HP} at a higher value has the advantage of effective removal of periodic energy, it substantially limits the bandwidth of noise from which modulation depth is measured. This causes two problems: first, modulation is unlikely to be uniform throughout the frication noise spectrum (see Sec. III B); second, filtering AM noise removes some modulated sidebands which gives underestimated modulation depth (see Sec. III E).

B. Nonuniformly modulated noise

Thus far, the noise signal has been treated as Gaussian white noise. In voiced fricatives, the carrier noise $w(n)$ is not white, but colored (filtered) depending on PoA. The spectral composition of the noise does not directly affect the modulation of different frequency regions. However, it cannot be assumed that the mechanism responsible for modulation in fricatives produces uniform modulation across all frequencies; in fact, spectrograms of voiced fricatives suggest that noise in very high frequency regions (>8 kHz) is more modulated than in the main region (3–7 kHz). More work is needed to understand how the modulation mechanism produces uneven modulation depths across the noise spectrum.

Figure 5 shows a short portion (100 ms) of a strongly modulated [ʒ] that happens to lack strong voicing formants,

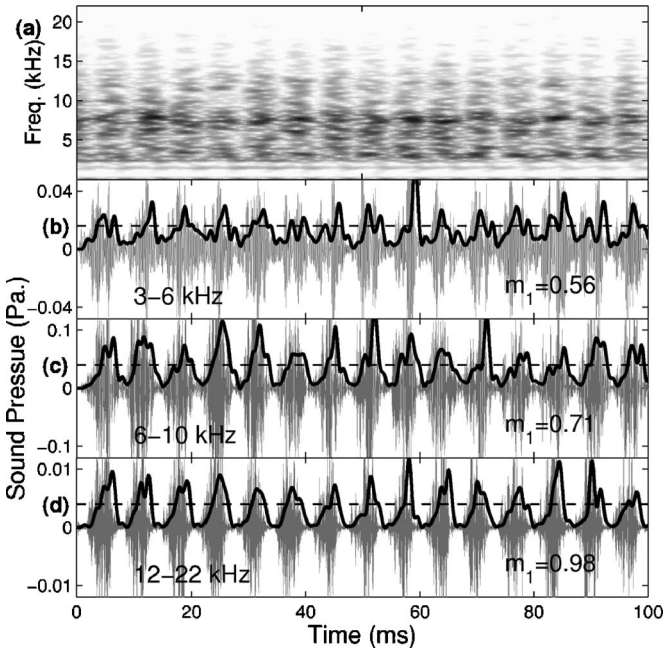

FIG. 5. (a) Spectrogram, and (b,c,d) time-aligned wave forms (light gray) with amplitude envelopes (black lines, magnitude signal low-pass filtered at 700 Hz) for 100 ms section of sustained [ʒ] ($f_0 \approx 152$ Hz, $f_s = 44.1$ kHz). Individual amplitude envelopes are for different frequency bands, f_{BP}, with axes scaled to $\pm 2\times$ rms amplitude (indicated by dashed lines; notice the different scale for each band). (a) $3 \leq f_{BP} \leq 6$ kHz; (b) $6 \leq f_{BP} \leq 10$ kHz; (c) $12 \leq f_{BP} \leq 22$ kHz; $\hat{m}_1$ values estimated for individual frequency bands as in Sec. II B.

allowing analysis of different frequency bands without interference from periodic energy. In the spectrogram, the frication noise looks modulated throughout the spectral range, but the weaker noise above 10 kHz comes in more distinct and separated bursts compared to the midrange noise. This observation is borne out by analysis: amplitude envelopes for three spectral bands (magnitude signals, low-pass filtered at 700 Hz to catch the first few modulation harmonics) illustrate variations in the modulation signal through the noise spectrum. In the 3–6 kHz range [Fig. 5(b)], the modulation signal is noisy and its fundamental is weak ($m_1 = 0.56$). For 6–10 kHz [Fig. 5(c)], m_1 grows to 0.71, the wave form becomes more regular, and the periodic structure of the modulation signal emerges, with steep-sided, rather than sinusoidal, pulses. At 12–22 kHz [Fig. 5(d)], modulation at the fundamental is almost complete ($m_1 = 0.98$) and the wave form has regularized into a train of sharp (steep-sided) pulses separated by a noticeable gap. This is akin to the "fundamental saturating under the action of its harmonic" described by Crow and Champagne (1971), where the fundamental can increase no further; instead, a significant harmonic structure develops where the modulation signal begins to adapt from sinusoid to pulse train. Thus, basing measurement of noise on the upper frequency bands could lead to an overestimation of m_1 with regard to the full spectrum of frication noise. To balance the need for effective removal of periodic components and accurate estimation of modulation depth, the voiced fricative signals were preprocessed using a technique designed to segregate periodic and aperiodic energy.

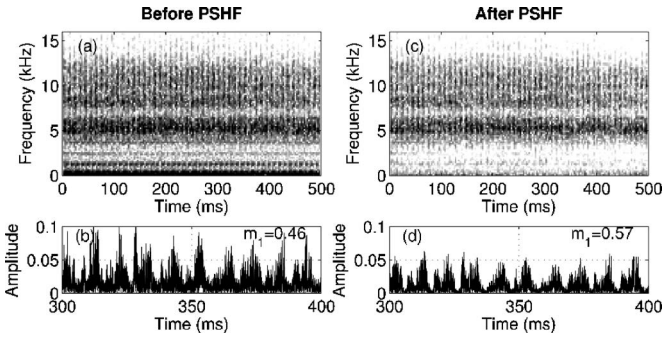

FIG. 6. 500 ms section of [z]; $f_0 \approx 125$ Hz. Left column: before PSHF. Right column: after PSHF. (a,c) Fixed gray-scale spectrograms. (b,d) $f_{HF} = 500$ Hz filtered magnitude wave forms, $|x(n)|$, for 300–400 ms portion of signal; $\hat{m}$ estimates obtained as in Sec. II B.

C. Pitch-scaled harmonic filtering

Separating periodic and aperiodic energy from a mixed-source signal is not a straightforward signal processing task. For speech signals, Yegnanarayana *et al.* (1998) and Jackson (2000) have proposed algorithms based on comb filtering of harmonics using adaptive pitch data. By testing the algorithms on synthetic signals, and through informal listening tests, they have shown that speech can be effectively decomposed into periodic and aperiodic streams. In this study, Jackson (2000)'s decomposition algorithm, the *pitch-scaled harmonic filter*. [PSHF, described in detail in Jackson and Shadle (2001)], was adopted as preprocessing to the modulation estimation procedure. Figure 6 shows the effect of applying the PSHF to 500 ms of [z] from the sustained fricative corpus. In spectrograms before and after, (a) and (c), the effects of pitch-scaled filtering are evident — formants below 4 kHz have been removed, although there remains some trace of the voicing fundamental. To ensure complete removal of the fundamental, high-pass filtering at a low frequency ($f_{HP} = 1$ kHz) was applied in addition to the PSHF. In Figs. 6(b) and 6(d), the effect on modulation depth of HP filtering employed alone is compared to the combination of PSHF and HP filtering. The HP filtered magnitude wave form, $|x(n)|$, from the PSHF's aperiodic signal [Fig. 6(d)] shows deeper and sharper modulation. This was confirmed by measurements of m_1 which gave an increase of 0.11 (from 0.46 to 0.57) after application of the PSHF. The increase is attributed to the attenuating effect of periodic energy on modulation, described in Sec. III A.

D. Processing conditions

Choice of window size is a trade-off between modulation depth resolution and time resolution, which affects variability such as from pitch glides. Simulations using synthesized signals evaluated different window sizes (see Table I). So, m_1 was estimated with a 100 ms window and a 5 ms step size for the sustained fricative corpus; for the fluent fricatives, a shorter 30 ms window was used. Processing windows were zero padded to $N = 2^{15}$ points. The required values of f_0 were obtained from analysis of the EGG signal, when available; otherwise, from the speech signal.

TABLE I. Estimation error (bias,deviation) over all frames in 100 files vs analysis window size, with 8× zero padding. Values are averaged across modulation index $m \in \{0.0, 0.1, \ldots, 1.0\}$.

		Window size	
f_0 (Hz)	Jitter (%)	1024 (23 ms)	4096 (93 ms)
150	0.0	−0.004, 0.037	0.003, 0.020
160–140	0.5	−0.005, 0.037	0.006, 0.019
180–120	1.5	−0.017, 0.039	0.003, 0.020

For later comparison, voicing strength v_1 was defined as the spectral amplitude at f_0 in the audio signal prior to high-pass filtering. For sustained fricatives, where subjects' lip-microphone distance was strictly controlled and the microphone calibrated, v_1 is expressed as SPL (in Pa). For fluent-speech fricatives, the calibration to SPL was estimated by comparing rms measurements averaged over all fluent-speech fricative wave forms to a calibrated test utterance recorded with the sustained fricatives. This estimated voicing strength $\hat{v}_1$ acts as a guide for comparing results from the two experiments.

E. Evaluation of modulation estimates

In estimating the underlying modulation depth for a section of voiced frication, errors come from three sources. Error A is due to the nature of the noise signal: random variation inevitably gives to the impression of some small modulation component. Error B is introduced by the modulation estimation procedure (Sec. III B), as a kind of bias. Finally, in the case of real voiced fricatives, imperfections in the preprocessing (Sec. III C) will introduce further artifacts, error C. Simulation tests were conducted to evaluate the magnitude of the combined estimation error $A+B$. These tests involved making estimates of the modulation index from Gaussian white noise samples with an imposed amplitude modulation.

Summary results for two window sizes are given in Table I under three voicing conditions, incorporating descending pitch glides and random pitch variation, or jitter. Errors between true and estimated values are given in terms of average bias and variance, quoted as standard deviation. In all cases, the bias was small compared to the deviation, which was twice as high for the short (23 ms) window as for the longer (93 ms) window. The longer window gave errors of $\pm 0.04(2\sigma)$ on the estimates under typical speech conditions.

Establishing the magnitude of error C is less simple. Filtering partially fills in "valleys" in the temporal wave form and thus reduces in modulation depth. Eddins (1993) ran simulations to evaluate the effect of band-pass filtering on m_1 of modulated white noise varying the bandwidth, $f_{BW} \in \{0.2, 0.4, 0.8, 1.6\}$ kHz. He concluded that modulation depth was "relatively unaffected" for these filter conditions. Our own simulations investigating the effects of limiting bandwidth of modulated noise by high-pass filtering showed the effect to be secondary, increasing the range to ±0.05 at the highest 11 kHz cut-on frequency (lowest bandwidth).

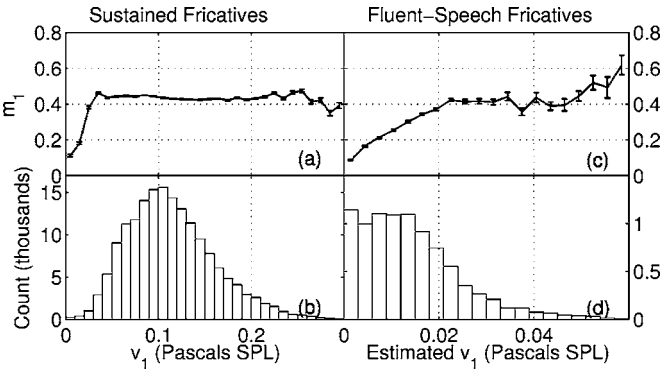

FIG. 7. Top: Modulation depth $\hat{m}_1$ as a function of voicing strength v_1 or $\hat{v}_1$. Bottom: v_1 or $\hat{v}_1$ distribution histograms for sustained fricatives (left column) and fluent-speech fricatives (right column). Data are means and counts of values falling within ±0.01 Pa bins (sustained fricatives) or ±0.003 Pa bins (fluent-speech fricatives). Error bars show standard error.

The 1 kHz HP filter applied here has negligible effect, as does the erroneous removal of some noise by the PSHF.

To validate use of the PSHF on voiced fricatives, its effect with known modulation was assessed. Phonetically trained subjects recorded voiced and noise components of voiced fricatives separately by producing sustained *voiceless* fricatives, introducing phonation, then gradually relaxing the constriction, leaving just voicing.

Recordings were edited to give voicing plus frication noise with an imposed m. Random, 100 ms sections of frication with known m (0.1–1) were mixed with sections of voicing (from same speaker/fricative) with amplitude varying 0–15 dB in comparison to the frication (periodic to aperiodic ratio, PAR) and preprocessed (Sec. III C) before measurement of m.

PAR significantly affected the accuracy of estimation for each preprocessing stage. For strongly voiced fricatives, the error with HP filtering was much improved by applying the PSHF. Where the voicing component was insignificant, HP filtering produced a better estimate alone, due to PSHF artifacts.

In 1000-trial simulation, where PAR varied freely (as in natural fricatives), overall bias was 0.03, suggesting a tendency to overestimate, and 2σ range rose to 0.10 (cf. 0.18 with HP filtering only). While justifying the use of the PSHF, this result is misleading in some respects. Most voiced fricatives are not very strongly voiced, so estimates produced using only HP filtering are fairly reliable; hence accuracy increases only slightly with the PSHF. Tokens with strong voicing, where using the PSHF gave large increases in accuracy, were less common but characteristic of particular speakers or PoAs. Without the PSHF, results for those speakers and fricatives would be inaccurate, though a fraction of all fricatives. Thus, the PSHF improves comparability of results.

IV. MODULATION RESULTS

A. The $\hat{m}_1$ vs v_1 relationship

Figure 7 summarizes $\hat{m}_1$ for all the data. To explore the relationship between voicing strength, v_1 or $\hat{v}_1$, and modula-

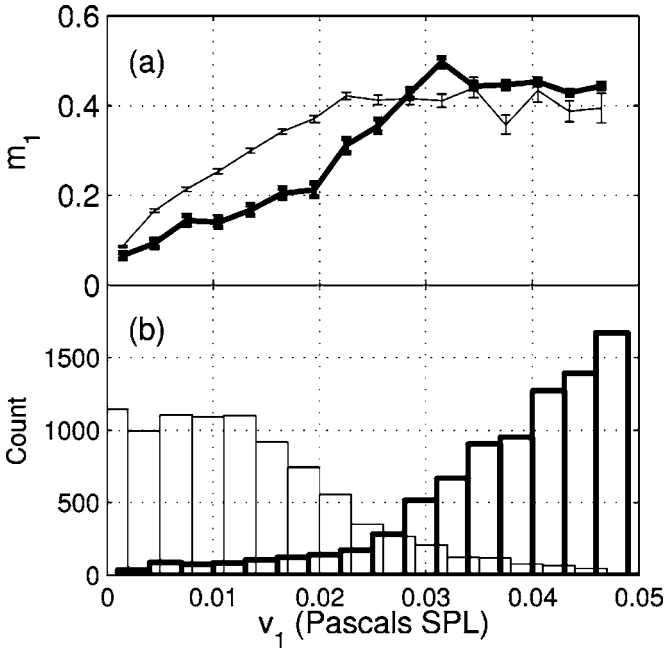

FIG. 8. (a) Modulation depth $\hat{m}_1$ as a function of voicing strength v_1 or $\hat{v}_1$, and (b) v_1 or $\hat{v}_1$ distribution histogram for sustained fricatives (thick line) and fluent-speech fricatives (thin line). Data are means and counts of values falling within ±0.003 Pa bins. Error bars show standard error.

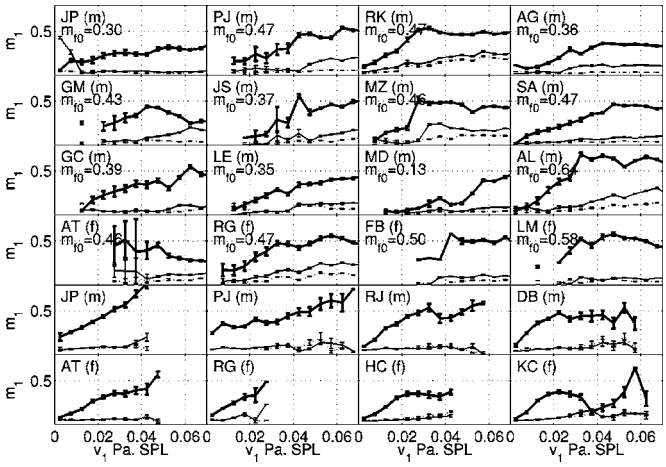

FIG. 9. Modulation depths at the fundamental frequency $\hat{m}_1$ (thick line), second harmonic $\hat{m}_2$ (thin line) and third harmonic $\hat{m}_3$ (dashed line), vs voicing strength v_1 or $\hat{v}_1$ for individual speakers for sustained fricatives (top four rows) and fluent-speech fricatives (bottom two rows). Data are means and counts of values falling within ±0.005 Pa bins. Error bars show standard error. Subjects' initials with male/female indication are given, m_1 values quoted for sustained fricatives are mean $\hat{m}_1$ over the voicing strength bin $0.05 \leq v_1 < 0.06$ Pa.

tion depth $\hat{m}_1, v_1$ ranges spanning all the data (0–0.3 Pa SPL for sustained fricatives; 0–0.07 Pa SPL for fluent-speech fricatives) were split into equal bins (0.01 and 0.003 Pa bin width for sustained and fluent-speech, respectively). The $\hat{m}_1$ vs v_1 relationship is represented as voicing strength bin centers plotted against average $\hat{m}_1$ reading for that bin. Histograms show number of frames in each bin.

In producing the sustained fricatives, very high or low levels of voicing were seldom used, resulting in an approximately normal distribution. Voicing levels in the fluent-speech case were significantly lower, as expected for short, intervocalic fricatives. The skew of the distribution toward lower values of $\hat{v}_1$ in Fig. 7(d) can be attributed to voice dynamics in intervocalic voiced fricatives: voicing rapidly decreases in amplitude as frication begins and either remains low until the vowel onset, or ceases (devoicing) (Pincas, 2004).

Figure 8 shows the low voicing strengths ($0 \leq v_1$ or $\hat{v}_1 \leq 0.05$). There are fewer data frames for the fluent-speech fricatives as each was so short; at higher values of $\hat{v}_1$ where $\hat{m}_1$ was stronger, the lack of data leads to wide error intervals, compared with the sustained fricatives. The $\hat{m}_1$ vs $\hat{v}_1$ curve for sustained fricatives levels off sharply at $v_1 = 0.03$ Pa, where modulation saturates, $\hat{m}_1 \approx 0.5$. Above $v_1 = 0.04$ Pa, $\hat{m}_1$ remains constant until $v_1 = 0.25$ Pa [Fig. 7(a)], where the data become too sparse to give meaningful results. For fluent-speech fricatives, $\hat{m}_1$ saturated earlier, by $\hat{v}_1 = 0.02$ Pa, and was slightly lower (~ 0.4) than for sustained fricatives. Above $\hat{v}_1 = 0.03$ Pa, data were sparse [Fig. 8(b), histogram counts fall below 250] and the bin averages beyond $\hat{v}_1 = 0.05$ Pa should be interpreted with caution.

Figure 9 (thick lines) illustrates the $\hat{m}_1$ vs v_1 relationship for individual speakers. In sustained fricatives, saturation occurred at a similar point (0.03–0.04 Pa) for all subjects except MD; saturation values of $\hat{m}_1$ were also similar for each speaker; quoted $\hat{m}_1$ readings were at 0.055 Pa, from the bin following saturation. Although mean $\hat{m}_1$ ranged 0.13–0.64, the distribution ($\mu = 0.43, \sigma = 0.12$) shows that, on average, speakers' modulation tends to lie around the 0.4–0.5 mark.

Given the imbalance of male to female subjects, only cautious comment can be made in comparison of their results. No difference is immediately discernible in $\hat{m}_1$ at saturation, although statistical comparison reveals a slight difference in mean and distribution (male $\mu = 0.40, \sigma = 0.12$; female $\mu = 0.50, \sigma = 0.05$).

Individual differences in degree of modulation could correspond to an aspect of voice quality. Significantly, the limiting values of $\hat{m}_1$ came well before modulation was complete ($m_1 = 1$), and imply saturation of a physical AM mechanism.

For the four speakers who took part in both experiments (JP, PJ, AT and RG; two male, two female), comparison of results suggests similar behavior across experiments (except JP, whose patterns for sustained and fluent-speech fricatives are obviously different). The fluent-speech curves for subjects PJ and RG appear to match the initial portions of their respective sustained fricative curves well. AT's fluent-speech and sustained fricative data complement one another, providing reliable readings at lower voicing strengths and a continuing pattern at higher strengths, respectively.

B. Effect of place of articulation

Differences among the four English voiced fricatives are seen in Fig. 10. Error intervals are wider than those in Figs. 7 and 8 but the basic $\hat{m}_1$ vs v_1 relationship remains the same for all four fricatives, with varying saturation parameters for each PoA. The curve for [z] (thick solid line) stands out: it is the quickest to saturate (at $v_1 \approx 0.035$) and does so at a highest modulation depth. Furthermore, the transition from the

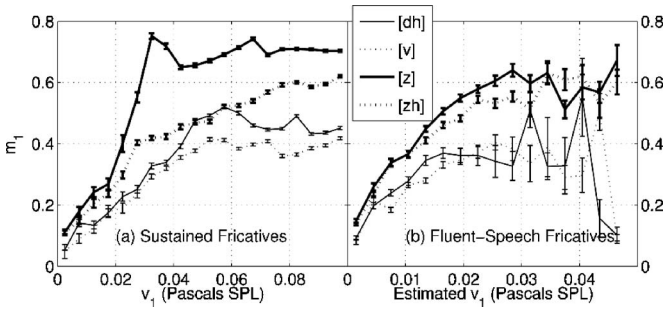

FIG. 10. Modulation depth $\hat{m}_1$ as a function of voicing strength v_1 or $\hat{v}_1$ for (a) sustained, and (b) fluent-speech fricatives: [ð] –solid thin; [v] –dotted thin; [z] –solid thick and [ʒ] –dotted thick. Data are means and counts of values falling within ±0.005 Pa bins (sustained fricatives) or ±0.003 Pa bins (fluent-speech fricatives). Error bars show standard error.

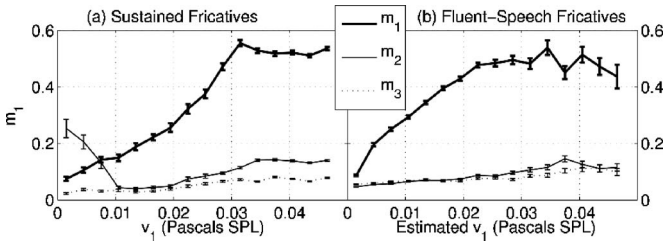

FIG. 11. Modulation depths at the fundamental frequency $\hat{m}_1$, second harmonic $\hat{m}_2$ and third harmonic $\hat{m}_3$ vs voicing strength v_1 or $\hat{v}_1$ for (a) sustained fricatives, and (b) fluent-speech fricatives. Means from all tokens. Data are means and counts of values falling within ±0.003 Pa bins. Error bars show standard error.

rising, linear part of the curve to the saturated part is more abrupt than for other fricatives. The high modulation depth at saturation for [z] in Fig. 10 is common to most speakers: 14 of 16 subjects have [z] as the most heavily modulated fricative at $v_1=0.05$ Pa.[5] These findings echo previous results for [z] in fluent speech (Pincas and Jackson, 2004). Considering the alternative views of modulated noise production discussed in the Introduction, there are several possible interpretations. According to the static view, the constriction area, A_C, determines the pressure drop across the constriction, ΔP_C, relative to that at the glottis (Stevens, 1971). So, for [z], which has a marginally smaller constriction (0.17 cm^2) compared to other places (0.19 cm^2) (Narayanan *et al.*, 1995), the modulation of ΔP_C, and hence of the flow velocity and noise intensity, would be lesser ($m \sim 0.6$). However, area differences may not be the most significant factor. The monopole, quadrupole, and dipole sources for each PoA have varied amplitudes and critical Reynolds numbers due to their particular geometry, which could account for the observed differences in m.

The view based on forced turbulence has the advantage that the greater acoustic pressure fluctuation in the smaller constriction would strengthen forcing, tending to raise noise modulation. Yet the precise geometry could have a more substantial influence, for the reasons above, but also since the constriction-obstacle distance and Strouhal number are critical for this mechanism. Modulation is maximal 2–6 diameters from the jet exit, i.e., 1–3 cm, and forcing closer to the natural Strouhal number can double the modulation (Crow and Champagne, 1971). Furthermore, the distribution of sources (e.g., dipoles along the upper lip in nonsibilants [v, dh]) affects modulation phase ϕ_h through turbulence convection [Coker *et al.* (1996)]. Thus distributed sources exhibit reduced modulation. Note that alveolar fricatives have the most concentrated dipole source at the lower incisors.

C. Harmonic structure of *a*(*n*)

The aeroacoustic processes that produce AM noise in voiced fricatives might be thought of as follows: a forcing glottal wave, $d(n)$, interacts with a noise generation process to produce AM noise near the fricative constriction. Following reflections within the VT, the noise radiates as the voiced fricative signal, $x(n)=a(n)w(n)$. The shape of $x(n)$'s envelope is described by the modulating signal $a(n)$ applied to an unmodulated frication noise signal $w(n)$ and its modulation spectrum has a component m_1 at the fundamental. In relating $d(n)$ to $a(n)$, the results discount the linear hypothesis that $d(n)$ is proportional to $a(n)$ (i.e., that the underlying modulation is identical in shape to the glottal wave that initiated it). This is demonstrated by the saturation of $\hat{m}_1$, the fundamental component of $a(n)$, as a function of v_1, the fundamental component of $d(n)$. Yet, the full $d(n)$ to $a(n)$ mapping requires further clarification.

Observations confirm that even the most strongly modulated frication noise shows negligible components above the second harmonic (i.e., only m_1 and m_2 are significant) and in many cases m_2 is so weak as to blend into the background fluctuations, leaving m_1 only. This is true even when the forcing wave shows significant harmonic structure. Figure 3 gives an example of such a situation for a token of [z] taken from the corpus: the forcing wave $d(n)$ is represented by the low-pass filtered audio wave form. This is compared to the high-pass filtered magnitude wave form $|x(n)|$, whose spectrum has peaks at harmonics of the modulating signal $a(n)$. Note how the harmonic structure of $d(n)$ in Fig. 3(b) was not preserved in the modulation spectrum of the noise, shown in Fig. 3(d).

Figure 11 shows $\hat{m}_h$ values at the first and second harmonics using the familiar binning procedure. As v_1 increased, a significant modulation harmonic $\hat{m}_2$ arose and $\hat{m}_3$ was detectable. Although the results cannot rule out the possibility that m_2 was caused by the same harmonic in the forcing wave (i.e., v_2), it seems more likely that they conform to the behavior observed by Crow and Champagne in a comparable study using turbulent jets forced by a *pure sinusoid* from a loudspeaker (Crow and Champagne, 1971).

Figure 9 shows the harmonic analysis for individual subjects. Some speakers (cf., JP-LM and MZ-RG) show relatively little modulation at the higher harmonics. To ascertain whether this difference depends on the forcing wave's harmonics (voice quality variation), or on natural variation in the modulating signal, requires further investigation.

D. Effect of f_0

Figure 12 analyzes the effect of voicing pitch on modulation depth for male and female subjects for both experiments. The relationship between voicing strength, v_1 or $\hat{v}_1$, and modulation depth $\hat{m}_1$ is plotted in Figs. 12(a), 12(b),

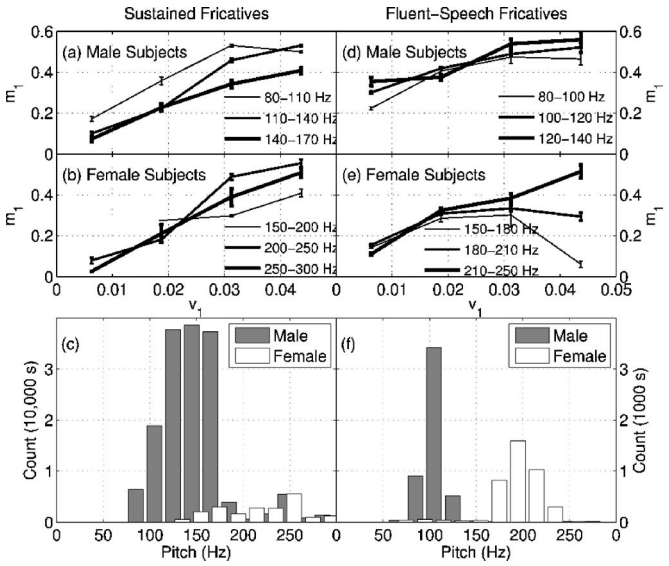

FIG. 12. Modulation depth $\hat{m}_1$ as a function of voicing strength v_1 or $\hat{v}_1$ for (a) sustained fricatives, male subjects; (b) sustained fricatives, female subjects; (d) fluent-speech fricatives, male subjects; (e) fluent-speech fricatives, female subjects. The f_0 data divided into three equally spaced pitch bins (different for each plot). In general: low range (thin line), middle range (medium line), and high range (thick line). For specific bin values see legends. Data for each f_0 bin are means of all frames whose measured f_o falls into that bin. Voicing strength, v_1 or $\hat{v}_1$, binning used ±0.005 Pa bins. Error bars show standard error. Bottom: measured f_0 distribution histograms for (c) sustained fricatives, and (f) fluent-speech fricatives. Data are means and counts of values falling within ±20 Hz bins from all tokens for male (gray bars) and female (clear bars) speakers.

12(d), and 12(e) grouped by fundamental frequency f_0 (bin edges determined by dividing the range of 95% of the data into three equal-width bins). The measured distributions of f_0 are shown in Figs. 12(c) and 12(f).

Figure 12(c) reveals that subjects were not very successful in attaining the required f_0 (125, 150, 175 Hz), in the sustained fricatives experiment. Female subjects, as might be expected, had particular difficulty with the lower pitches. The distribution of f_0 data is thus wider than anticipated, but nevertheless provides an appropriate base for analysis. In the fluent-speech fricative experiment, where subjects spoke at their natural pitch, f_0 distributions are significantly tighter. As a result, data are sparse in the lower pitch bins from female subjects [150–180 and 180–210 Hz; Fig. 12(e)], and dominated by one subject at higher voicing strengths, producing an anomalous curve (KC in Fig. 9, bottom right).

Fundamental frequency of voice has little consequence for the relationship between voicing strength and modulation depth, with similar shaped curves throughout. Furthermore, there is some suggestion in the sustained fricative experiment that male subjects [Fig. 12(a)] produce higher modulation at lower f_0 for all but one voicing level. However, this pattern is not replicated in any other results and we conclude that f_0 is not an important influence on modulation depth.

E. Perceptual considerations

The combination of harmonic and amplitude-modulated noise sources is special to voiced frication and presents an interesting and complex picture from a psychoacoustic perspective. On a basic level, it is known that modulation effects a change in the quality of the noise component, creating a sensation of "roughness" (Zwicker and Fastl, 1999). However, most previous work on the perception of AM noise is limited in relevance to voiced fricatives, due to their short duration and the presence of voicing.

1. Detection of amplitude modulation

The extent of the percept created by AM depends, of course, on the depth of noise modulation (m), but also on a number of other factors. Numerous authors have reported the relationship between the detection threshold θ of AM noise with a sinusoidal envelope, and its frequency f, referred to as the temporal modulation transfer function, or TMTF (Bacon and Viemeister, 1985; Patterson *et al.*, 1978; Viemeister, 1979). Detection thresholds at each f are measured using a forced choice paradigm: subjects must differentiate the modulated stimulus interval from one or two accompanying unmodulated noise intervals. The modulation depth of the target interval is adjusted gradually according to the subject's responses, to yield finally an estimate of the detection threshold. Thresholds are low in the region of frequencies applicable to speech (e.g., $\theta \approx 0.13$ at $f=125$ Hz), although they increase with f by $\sim 3-4$ dB/octave; hence a small difference in detection threshold is expected for typical male and female voices. The TMTF also has implications for the detectability of modulation at harmonics of f_0. With $f_0 = 125$ Hz, the second harmonic's modulation detection threshold is $\theta \approx 0.18$ ($f=250$ Hz). Given that m_2 tends to be below this level (Fig. 9), modulation at harmonics above f_0 is not likely to be detectable. In addition, deeper modulation at f_0 could mask shallower modulation at $2f_0$ in an effect in the modulation domain akin to regular psychoacoustic masking in the frequency domain [see literature on "modulation masking," e.g., Houtgast (1989)].

Stimulus duration also affects our ability to detect AM. In the literature, thresholds are almost always based on 500 ms stimuli, yet voiced fricatives are much shorter.[6] Lee and Bacon (1997) investigated the effect of stimulus duration on modulation detection threshold and showed that shorter stimuli did indeed yield higher thresholds.

The added effect of voicing is extremely hard to predict. A low frequency voicing component significantly louder than the noise component, as with nonsibilants [ð] and [v], would produce masking (in the regular, frequency-domain sense (Fletcher, 1940); i.e., an increase in absolute detection threshold of the noise). The consequences of this decrease in audibility for the detection of AM are not known, but it may be of note that Viemeister (1979) found minimal difference in AM detection for stimuli presented at different levels.

The combination of tone and noise further complicates the detection of AM. Wakefield and Viemeister (1985) performed what appears to be the only investigation into AM noise detection in the presence of a pure sinusoid with f equal to that of the modulating signal. Their results suggest a key role for the phase between tone and modulation, with the possibility of detection being *enhanced* where the two are in phase. The finding is hard to generalize, however, since they used only 3 kHz bandwidth noise.

2. Perceptual coherence

Correlated temporal patterns across disparate spectral components (such as those present in modulated noise) create or reinforce distinct auditory "objects" (Bregman, 1990). A commonly cited example of this effect is comodulation masking release [for a review see Verhey *et al.* (2003)], where modulation imposed on a masking noise band causes the detection threshold of a tone at the band's center to *decrease* (detection improves) as the bandwidth of the noise is widened, even past the critical bandwidth (CB) (Hall *et al.*, 1984); this contrasts with the classical psychophysical masking paradigm where increasing noise bandwidth beyond the CB has no effect on masking, (Fletcher, 1940), and suggests that listeners are able to use the "comodulated" temporal pattern of the noise to improve stream segregation and detection of the tone. The relevance of stream segregation and modulation to speech has previously been demonstrated by Hermes (1991), who found that the cohesive-ness of synthesized breathy vowels was enhanced by modulation of the aperiodic component. If this effect extends to voiced fricatives, modulation of frication could enhance the integrity or intelligibility of speech in noise.

V. CONCLUSION

In voiced fricatives, phonation induces amplitude modulation of frication noise. A technique was developed to estimate the depth of modulation and applied to turbulence noise from sustained and fluent-speech fricatives. Modulation depth rose approximately linearly with voicing strength for low voicing levels (below ~63 dB SPL); it saturated at a similar voicing level for different fricatives and speakers, although its value at this point varied. For example, modulation depth at a voicing strength of 0.04 Pa SPL (immediately after saturation) was largest for [z] (0.65; cf. 0.44 for [ʒ], 0.37 for [ð], 0.34 for [v]). Previous perceptual studies of modulated noise suggest that the levels of modulation observed are detectable. Further work could establish how amplitude-modulated noise in fricatives serves as a phonetic cue or voice-quality characteristic, and investigate the aeroacoustic mechanism responsible for producing modulation.

[1]Since the effect of f_0 on m was unknown, this control ensured comparability of results, especially between male and female speakers.

[2]A short lip-microphone distance helped to capture quiet frication over any background or electric noise.

[3]A pilot experiment revealed that some subjects had difficulty keeping their place on the printed list while speaking. The audio prompting was designed to aid them, but also as a natural control on speech rate and intonation.

[4]The present method diverges here from that used in Pincas and Jackson (2004).

[5]In contrast, saturation points and levels for the remaining fricatives, while relatively similar and consistently distinct from [z], vary for each speaker with no clear pattern. This could be explained by articulatory configurations varying less across speakers for [z], but more for the other fricatives which tend either to cause difficulty (e.g., [ʒ] is quite rare in English) or to be produced in a variety of ways (e.g., [ð] varies in degree of tongue protrusion). The slightly narrower confidence intervals for [z] at higher voicing strengths concur.

[6]Mean intervocalic fricative durations, averaged over 216 repetitions by eight subjects, according to Pincas (2004): [v]-70 ms, [ð]-69 ms, [z] -92 ms and [ʒ]-101 ms. ANOVA shows significant ($p<0.0005$) difference between sibilants [z, ʒ] and nonsibilants [ð, v] but no significant difference within these pairs.

Bacon, S., and Viemeister, N. (**1985**). "Temporal modulation transfer functions in normal-hearing and hearing-impaired subjects," J. Phys. D **24**, 117–134.

Barney, A., Shadle, C. H., and Davies, P. (**1999**). "Fluid flow in a dynamic mechanical model of the vocal folds and tract. 1. measurements and theory," J. Acoust. Soc. Am. **105**, 444–455.

Bregman, A. (**1990**). *Auditory Scene Analysis: The Perceptual Organisation of Sound*. MIT, Cambridge, MA.

Coker, C. H., Krane, M. H., Reis, B. Y., and Kubli, R. A. (**1996**). "Search for unexplored effects in speech production," In *Proc. Int. Conf. Spoken Language Processing 1996*, Philadelphia, **14**, pp. 415–422.

Crow, S. C., and Champagne, F. H. (**1971**). "Orderly structure in jet turbulence," J. Fluid Mech. **48**, 547–591.

Eddins, D. (**1993**). "Amplitude modulation detection of narrow-band noise: Effects of absolute bandwidth and frequency region," J. Acoust. Soc. Am. **93**, 470–479.

Flanagan, J. L., and Cherry, L. (**1969**). "Excitation of vocal-tract synthesizers," J. Acoust. Soc. Am. **45**, 764–769.

Fletcher, H. (**1940**). "Auditory patterns," Rev. Mod. Phys. **12**, 47–65.

Hall, J., Haggard, M., and Fernandes, M. (**1984**). "Detection in noise by spectro-temporal pattern analysis," J. Acoust. Soc. Am. **76**, 50–56.

Heid, S., and Hawkins, S. (**1999**). "Synthesizing systematic variation at the boundaries between vowels and obstruents," In *Proc. ICPhs*, San Fransisco, 511–514.

Hermes, D. J. (**1991**). "Synthesis of breathy vowels: Some research methods," Speech Commun. **10**, 497–502.

Houtgast, T. (**1989**). "Frequency selectivity in amplitude-modulation detection," J. Acoust. Soc. Am. **85**, 1676–1680.

Jackson, P. J. B. (**2000**). "Characterisation of plosive, fricative and aspiration components in speech production," Ph.D. thesis, Dept. Electronics and Computer Science, University of Southampton.

Jackson, P. J. B., and Shadle, C. H. (**2000**). "Frication noise modulated by voicing, as revealed by pitch-scaled decomposition," J. Acoust. Soc. Am. **108**, 1421–1434.

Jackson, P. J. B., and Shadle, C. H. (**2001**). "Pitch-scaled estimation of simultaneous voiced and turbulence-noise components in speech," IEEE Trans. Speech Audio Process. **9**(7), 713–726.

Klatt, D. H. (**1980**). "Software for a cascade/parallel formant synthesizer," J. Acoust. Soc. Am. **67**, 971–995.

Lee, J., and Bacon, S. P. (**1997**). "Amplitude modulation depth discrimination of a sinusoidal carrier: Effect of stimulus duration," J. Acoust. Soc. Am. **101**, 3688–3693.

Lighthill, M. (**1952**). "On sound generated aerodynamically. I. General theory," In *Proceedings of the Royal Society*, **211**, pp. 564–587.

Lighthill, M. (**1954**). "On sound generated aerodynamically. II. Turbulence as a source of sound," In *Proceedings of the Royal Socieiy*, **222**, pp. 1–34.

Lofqvist, A., Baer, T., McGarr, N. S., and Seider-Story, R. (**1989**). "The cricothyroid muscle in voicing control," J. Acoust. Soc. Am. **85**, 1314–1321.

Lofqvist, A., Koenig, L. L., and McGowan, R. S. (**1995**). "Vocal tract aerodynamics in /aCa/ utterances: Measurements," Speech Commun. **16**, 50–66.

Narayanan, S. S., and Alwan, A. A. (**2000**). "Noise source models for fricative consonants," IEEE Trans. Speech Audio Process. **8**, 328–344.

Narayanan, S. S., Alwan, A. A., and Haker, K. (**1995**). "An articulatory study of fricative consonants using magnetic resonance imaging," J. Acoust. Soc. Am. **98**, 1325–1347.

Pastel, L. (**1987**). "Turbulent noise sources in vocal tract models," Master's thesis, MIT, Cambridge, MA.

Patterson, R., Johnson-Davies, D., and Milroy, R. (**1978**). "Amplitude-modulated noise: The detection of modulation versus the detection of modulation rate," J. Acoust. Soc. Am. **63**, 1904–1911.

Pincas, J. (**2004**). "The interaction of voicing and frication sources in speech: An acoustic study," Master's thesis, School of Electronics and Physical Sciences, University of Surrey.

Pincas, J., and Jackson, P. J. B. (**2004**). "Acoustic correlates of voicing-frication interaction in fricatives," In *Proc. From Sound to Sense*, Cambridge, MA, O73-O78.

Rosen, S., Faulkner, A., and Wilson, L. (**1999**). "Adaptation by normal listeners to upward spectral shifts of speech: Implications for cochlear implants," J. Acoust. Soc. Am. **106**, 3629–3636.

Scully, C. (**1990**). "Articulatory synthesis," In *Speech Production and Speech Modelling*, edited by W. J. Hardcastle and A. Marchal (Kluwer, Dordrecht, Netherlands), pp. 151–186.
Scully, C., Castelli, E., Brearley, E., and Shirt, M. (**1992**). "Analysis and simulation of a speaker's aerodynamic and acoustic patterns for fricatives," J. Phonetics **20**, 39–51.
Shadle, C. (**1990**). "Articulatory-acoustic relationships in fricative consonants," In *Speech Production and Speech Modelling*, edited by W. J. Hardcastle and A. Marchal (Kluwer, Dordrecht, Netherlands) 187–209.
Shadle, C. H. (**1985**). "The acoustics of fricative consonants," Technical Report No. 506, RLE, Massachusetts Institute of Technology.
Shadle, C. H. (**1995**). "Modelling the noise source in voiced fricatives," In *Proc. 15th Int. Congress on Acoustics*, Trondheim, Norway, Vol. **3**.
Shannon, R. V., Zen, F.-G., Kamath, V., Wygonski, J., and Ekelid, M. (**1995**). "Speech recognition with temporal cues," Science **270**, 303–304.
Simcox, C. D., and Hoglund, R. F. (**1971**). "Acoustic interactions with turbulent jets," ASME J. Basic Eng. **93**, 42–46.
Sinder, D. J. (**1999**). "Speech synthesis using an aeroacoustic fricative model," Ph. D. thesis, Dept. Electrical Engineering, Rutgers University, New Brunswick, NJ.
Sondhi, M. M., and Schroeter, J. (**1987**). "A hybrid time-frequency domain articulatory speech synthesiser," IEEE Trans. Acoust., Speech, Signal Process. **35**, 955–967.
Stevens, K. N. (**1971**). "Airflow and turbulence noise for fricative and stop consonants: Static considerations," J. Acoust. Soc. Am. **50**, 1180–1192.
Stevens, K. N. (**1998**). *Acoustic Phonetics*, (MIT Press, Cambridge, MA).
Tchorz, J., and Kollmeier, B. (**2002**). "Estimation of the signal-to-noise ratio with amplitude modulation spectrograms," Speech Commun. **38**, 1–17.
Teixeira, A., Jesus, L. M. T., and Martinez, R. (**2003**). "Adding fricatives to the Portuguese articulatory synthesiser," In *Proc. Eurospeech 2003*, Geneva, Switzerland, 2949–2952.
Verhey, J. L., Pressnitzer, D., and Winter, I. M. (**2003**). "The psychophysics and physiology of comodulation masking release," Exp. Brain Res. **153**, 405–417.
Viemeister, N. (**1979**). "Temporal modulation transfer functions based upon modulation thresholds," J. Acoust. Soc. Am. **66**, 1364–1380.
Wakefield, G. H., and Viemeister, N. F. (**1985**). "Temporal interactions between pure tones and amplitude modulated noise," J. Acoust. Soc. Am. **77**, 1535–1542.
Yegnanarayana, B., d'Alessandro, C., and Darsinos, V. (**1998**). "An iterative algorithm for decomposition of speech signals into periodic and aperiodic components," IEEE Trans. Speech Audio Process. **6**, 1–11.
Zwicker, E., and Fastl, H. (**1999**). *Psychoacoustics: Facts and Models*, 2nd ed. (Springer-Verlag, Berlin).

Effect of intonation on Cantonese lexical tones[a)]

Joan K-Y Ma,[b)] Valter Ciocca, and Tara L. Whitehill
Division of Speech and Hearing Sciences, University of Hong Kong, 5/F, 34 Hospital Road, Hong Kong Special Administrative Region, People's Republic of China

(Received 8 October 2005; revised 5 September 2006; accepted 20 September 2006)

In tonal languages, there are potential conflicts between the F0-based changes due to the coexistence of intonation and lexical tones. In the present study, the interaction of tone and intonation in Cantonese was examined using acoustic and perceptual analyses. The acoustic patterns of tones at the initial, medial, and final positions of questions and statements were measured. Results showed that intonation affects both the F0 level and contour, while the duration of the six tones varied as a function of positions within intonation contexts. All six tones at the final position of questions showed rising F0 contour, regardless of their canonical form. Listeners were overall more accurate in the identification of tones presented within the original carrier than of the same tones in isolation. However, a large proportion of tones 33, 21, 23, and 22 at the final position of questions were misperceived as tone 25 both within the original carrier and as isolated words. These results suggest that although the intonation context provided cues for correct tone identification, the intonation-induced changes in F0 contour cannot always be perceptually compensated for, resulting in some erroneous perception of the identity of Cantonese tone. © *2006 Acoustical Society of America.* [DOI: 10.1121/1.2363927]

PACS number(s): 43.70.Kv, 43.71.Hw [AL] Pages: 3978–3987

I. INTRODUCTION

Cantonese is a tone language in which contrasts in tone mark a difference in lexical meaning. Cantonese tones are characterized by tone level (high, mid, and low) and tone contour (rising, falling, and level) (Fok-Chan, 1974). The six basic tones in Cantonese are high level (55), high rising (25), mid level (33), low falling (21), low rising (23), and low level (22). The numerical values in parenthesis describe the level of pitch at the beginning and the end point of the tone (Chao, 1947). Intonation is a universal feature shared by languages of different origins, and it plays an important role in conveying both linguistic and paralinguistic meanings in communication. The intonation of a sentence is mainly carried by fundamental frequency (F0) variations. The use of intonation in a tone language could be potentially confusing as F0 patterns are used to mark both tone at syllabic level and intonation at sentential level. This poses an interesting research question about the influence of intonation on the identity of lexical tones. The identification of lexical tones might be affected when the direction of F0 movement in a tone does not coincide with the F0 changes of intonation, such as when a low-falling tone is placed at the final position of question, which has a rising F0 contour.

The contrast between questions and statements is frequently used in studying the effect of intonation on F0 patterns of tone. The intonation patterns of Cantonese are similar to the reported intonation patterns of other world languages (Bauer and Benedict, 1997; Fok-Chan, 1974). It is commonly agreed that statements are characterized by a falling intonation, while questions have a rising intonation contour (Ohala, 1983). However, researchers disagree on how exactly the difference between questions and statements should be characterized. As summarized by Liu and Xu (2005), several features have been proposed to describe the rising intonation of questions: boundary tones (Pierrehumbert, 1980; Ladd, 1996; Lin, 2004), F0 increase of the entire sentence (Ho, 1977; Yuan, Shih, and Kochanski, 2002) and superposition of a baseline on the phrase curve (Thorsen, 1980; Liu and Xu, 2005). For Cantonese, Gu, Hirose, and Fujisaki (2005) and Ma, Ciocca, and Whitehill (2006b) analyzed the F0 patterns of questions and statements using the Fujisaki model (Fujisaki and Hirose, 1984). They observed that questions were marked by positive tone command values with amplitude larger than usual towards the end of the utterance for all six tones. Ma *et al.* (2006b) also found that there was an increase in the baseline frequency for questions. These two studies suggested that the question and statement contrasts in Cantonese are marked by both global and local F0 changes.

The effect of intonation on the acoustic properties of tone has been a subject of research in various Chinese tone languages such as Chengtu (Chang, 1958), Cantonese (Fok-Chan, 1974; Lee, 2004; Vance, 1976), and Mandarin (Ho, 1977; Rumjancev, cited in Lyovin, 1978; Shen, 1989; Lin, 2004). It is generally agreed that intonation is likely to modify the F0 patterns of tones, but the specific F0 patterns vary across tone languages. Two general patterns have been identified. At sentence final position, intonation-induced F0

[a)]Portions of this work were presented in "The effects of intonation patterns on lexical tone production in Cantonese," Proceedings of International Symposium on Tonal Aspects of Language: Emphasis on Tone Languages, Beijing, People's Republic of China, March 2004, and "The effect of intonation on perception of Cantonese lexical tones," Proceedings of International Conference on Spoken Language Processing, Jeju, Korea, October 2004.

[b)]Author to whom correspondence should be addressed; electronic mail: joanma@hkusua.hku.hk

 © 2006 Acoustical Society of America

perturbations of lexical tones mostly affect the F0 level, but not the F0 contour (Chang, 1958; Ho, 1977; Lin, 2004; Rumjancev, cited in Lyovin, 1978; Shen, 1989). Specifically, when the direction of F0 movement of tone and intonation are the same (e.g., a rising tone at the end of a rising intonation), the F0 level of the tone will increase further. However, when the direction of F0 movement of tone and intonation do not coincide, the F0 value of the tone would be neutralized such that, for example, the F0 of a falling tone would not fall as low at the end of a rising intonation. The second general pattern is that, in addition to the level of the tone being modified, the tone contour may also deviate from its canonical form due to the effect of sentence intonation (Fok-Chan, 1974; Lee, 2004). That is, while a rising tone at the end of a rising intonation gives rise to a higher F0 level, the contour of a falling/level tone would be changed to rising when it occurs at the end of a rising intonation.

Different results have also been reported on the perceptual effect of intonation on tone. Connell, Hogan, and Rozsypal (1983) claimed that the perturbation in F0 patterns of tones brought about by intonation has little effect on listeners' perception in Mandarin. In contrast, Fok-Chan (1974) reported that listeners' tone perception was poorer when presented with Cantonese stimuli produced in interrogative manner. She suggested that the modification in F0 patterns in tone as a result of intonation was likely to affect listeners' perception.

Although F0 is the primary acoustic correlate for tone, the significance of duration as a perceptual cue to tone identity has also been explored (Blicher, Diehl, and Cohen, 1990; Liu and Samuel, 2004; Tseng, Massaro, and Cohen, 1986). Tseng *et al.* (1986) demonstrated that duration might be used as a secondary cue for the perception of Mandarin tones when the F0 information is ambiguous. Ho (1977) observed that duration was likely to be a function of word position rather than intonation, except at word final position where tones produced in interrogative were found to have a longer duration than those in declarative in Mandarin. Vance (1976) pointed out that vowel duration was not significant for tone perception in Cantonese as similar vowel length was observed for all tones. However, Lee (2004) observed that the duration patterns among the six tones were not maintained at the final position of questions. She reported that tones 33, 21, and 22 produced at the final position of questions were longer than when produced in statements in Cantonese, while tones 55, 25, and 23 showed minimal contrast at the final position of questions and statements. However, she did not report a quantitative analysis of these differences. Therefore, it is not clear whether the duration contrast between the six tones at the final position of questions can provide an additional cue to listeners for tone identification.

The above discussion revealed different findings on the effects of intonation on both F0 patterns and duration of lexical tone in different tone languages. In order to explore the effects of intonation on the production and perception of lexical tones in Cantonese, acoustic and perceptual analyses were performed on the same set of Cantonese tones produced within statements and questions in the current study.

II. EXPERIMENT 1-ACOUSTIC ANALYSIS

The objective of experiment 1 was to investigate the F0 changes produced by different intonation patterns on Cantonese lexical tones. Comparison was made between tones at initial, medial and final positions within an utterance. Acoustic analysis was performed to measure the F0 and duration patterns of the target words.

A. Method

1. Speakers

Twenty native Cantonese speakers were recruited (ten males and ten females, aged 19 to 25 years). They were all undergraduates or graduates of Hong Kong universities. Nineteen speakers were born and raised in Hong Kong. The remaining speaker was born in the USA, but he was raised in Hong Kong since he was two months old. Cantonese was the native language, and English the second language, of all speakers. None of the speakers had a reported history of speech problems and all had passed a hearing screening ($\leqslant$20 dBHL at 250, 500,1000, 2000, and 4000 Hz).

2. Materials

Three sets of target words were derived from the roots /si/, /ji/, and /jɐu/. Each set consisted of six words that contrasted only in tone, giving a total of 18 target words. These words were embedded in three different positions within the following sentences: (a) initial position (/*X* tsi_{22} hou_{25} lan_{21} sɛ_{25}/ "*X* is difficult to write"), (b) medial position (/sɛ_{25} kɔ_{33} *X* tsi_{22} sin_{55}/ "Write the *X* word first"), and (c) final position (/lei_{55} kɔ_{33} tsi_{22} hɐi_{22} *X*/ "This word is *X*"). Two types of intonation were studied in the present experiment–question and statement. Each of the sentences could be produced as either a statement or a question by modifying only the intonation marking. Thus, each speaker produced a total of 108 different stimuli (18 target words by three different positions by two intonation patterns).

3. Procedures

Recording was carried out in a sound-attenuated room (IAC single-wall booth), with a Sony TCD-D3 DAT recorder and a Bruel and Kjær (4003) low-noise unidirectional microphone. A 10 cm mouth-to-microphone distance was maintained for the first 17 speakers. The mouth-to-microphone distance was increased to 15 cm for the last three speakers to prevent clipping of the recordings, as the sponge attached to the microphone was removed due to hygienic reasons during the outbreak of severe acute respiratory syndrome in Hong Kong.

In order to obtain naturally produced speech samples, speakers were engaged in a dialogue in which the first author initiated each exchange and speakers answered with one of the sentences. In each trial, the dialogues were presented visually on the screen of a G4 Apple Macintosh computer running a HyperCard (Apple^{TM}) custom program. The sequence of dialog presentation was randomized across sub-

jects. Each production was monitored by the first author, who is a qualified speech and language pathologist, to ensure that the correct tone was produced.

After the recording, each sentence was low-pass filtered at 22 kHz, digitized at sampling rate of 44.1 kHz and stored onto an Apple PowerMacintosh 7100 computer as a separate file, using a DigiDesign Audiomedia II DSP card.

4. Data analysis

Acoustic analysis was performed to measure the F0 values and the duration of each target word, using the Praat software (Version 4.0.46, Boersma and Weenink, 2003). The voiced segment of each word was identified visually from a wideband spectrogram and an amplitude waveform display. F0 was estimated at nine evenly spaced time points from the beginning to the end of the voiced segment of the word using an autocorrelation algorithm. Five time points were chosen for subsequent analysis (0%, 25%, 50%, 75%, and 100% of the total duration). Manual measurements from the amplitude waveform were used when the software produced F0 estimates that were largely different from those of adjacent time points. Out of a total of 2160 speech samples, 128 samples (5.93%) required manual measurement at one or more of the five time points used for analysis. Among these 128 samples, eight samples showed diplophonic features with F0 varying between high and low F0 values in consecutive cycles. For these samples, F0 estimates were obtained by averaging the manually estimated F0 of two consecutive cycles of the waveform. The duration of each target word was measured by calculating the difference in time between the 0% and 100% time points of the voiced segment. The average F0 of each tone at each time point and the average duration of each tone were then calculated for each position and intonation for each speaker. Group averages for male and female speakers were also calculated for later analysis.

Intra- and inter-rater reliabilities were calculated by repeating the analysis for two speakers (10% of the data) by the first author and a second rater, who is experienced in acoustic analysis. Pearson's correlation was used to calculate reliability. Intra-rater reliability was $0.97(p<0.001)$ and inter-rater reliability was $0.98(p<0.001)$.

B. Results

1. Fundamental frequency

The mean F0 values for questions and statements for male and female speakers in each tone at all nine time points are displayed in Figs. 1(a)–1(f). The F0 patterns of the six tones were similar for all targets in statements and at the initial and medial positions of questions. All the three level tones (tones 55, 33, and 22) had slightly falling contours, and the relative F0 distance between tones 55 and 33 was greater than between tones 33 and 22. Tones 25 and 23 had a rising tone contour; tone 25 had higher final F0 level than tone 23. Tone 21 started at about the same level as tone 22, and had a falling contour to the lowest F0 value of the six tones. At the final position of questions, both male and female speakers showed rising F0 contour for all six tones. Specifically, tones 55 and 33 showed an increase in F0 from 0% to 100% of the total duration; while tones 25, 21, 23, and 22 had a slight dip in F0 from the 0% to the 25% time points, followed by an increase in F0 from 25% to 100%. The F0 patterns for tones 25, 21, 23, and 22 were overlapping, with similar F0 levels; tones 55 (highest overall F0) and 33 (slightly lower F0 values) were distinct from the rest.

The mean F0 value for each tone at each intonation and position within each time point was calculated for each speaker. Four-way ANOVAs ($2\times2\times3\times5$) were used to analyze the data for each tone separately. Gender (male vs female) was the between subject factor; intonation (question vs statements), position (initial, medial, and final) and time point (0%, 25%, 50%, 75%, and 100%) were the within subject factors. Overall, females produced significantly higher F0 than male speakers for all six tones [main effect of gender: tone 55, $F(1,18)=189.00$, $p<0.001$; tone 25, $F(1,18)=262.23$, $p<0.001$; tone 33, $F(1,18)=298.16$, $p<0.001$; tone 21, $F(1,18)=250.36$, $p<0.001$; tone 23, $F(1,18)=294.06$, $p<0.001$; tone 22, $F(1,18)=394.22$, $p<0.001$].

Tones produced in questions had higher F0 levels than the same tones in statements [main effect of intonation: tone 55, $F(1,18)=132.77$, $p<0.001$; tone 25, $F(1,18)=262.23$, $p<0.001$; tone 33, $F(1,18)=148.12$, $p<0.001$; tone 21, $F(1,18)=123.48$, $p<0.001$; tone 23, $F(1,18)=153.54$, $p<0.001$; tone 22, $F(1,18)=197.55$, $p<0.001$]. Significant interaction effects between intonation and position were also found for all six tones [tone 55, $F(2,36)=36.46$, $p<0.001$; tone 25, $F(2,36)=36.51$, $p<0.001$; tone 33, $F(2,36)=120.22$, $p<0.001$; tone 21, $F(2,36)=89.78$, $p<0.001$; tone 23, $F(2,36)=88.73$, $p<0.001$; tone 22, $F(2,36)=125.73$, $p<0.001$]. Post hoc analysis showed that the F0 level of questions was significantly higher than that of statements for (i) all tones (Tukey HSD test, $p<0.01$) except tone 21 (Tukey HSD test, $p>0.05$) at the initial position, (ii) tones 55, 25, 33, and 23 at the medial position (Tukey HSD test, $p<0.01$ for all), and (iii) all six tones at the final position (Tukey HSD tests, $p<0.001$ for all).

The three positions (initial, medial, and final) were found to be significantly different from each other for each of the six tones [main effect of position: tone 55, $F(2,36)=80.99$, $p<0.001$; tone 25, $F(2,36)=125.76$, $p<0.001$; tone 33, $F(2,36)=127.19$, $p<0.001$; tone 21, $F(2,36)=19.00$, $p<0.001$; tone 23, $F(2,36)=80.75$, $p<0.001$; tone 22, $F(2,36)=50.85$, $p<0.001$]. In statements, tones at the initial position had higher F0 level than tones in medial position, which in turn had higher F0 than tones in final position. The difference in F0 level between the initial and the final positions was significant for both genders and all six tones (Tukey HSD test, $p<0.001$ for all). For questions, the differences in F0 between the initial and medial positions were significant for all six tones in both genders (Tukey HSD test, $p<0.001$ for all), except for tone 22 produced by male speakers (Tukey HSD test, $p>0.05$). At the final position, owing to the differences in tone contour compared with the other two positions, the differences in overall F0 level between the final and the initial positions and between the final and medial positions were not compared statistically. However, Figs. 1(a)–1(f) show that all tones at the final position of questions began at an F0 level below that of the initial and

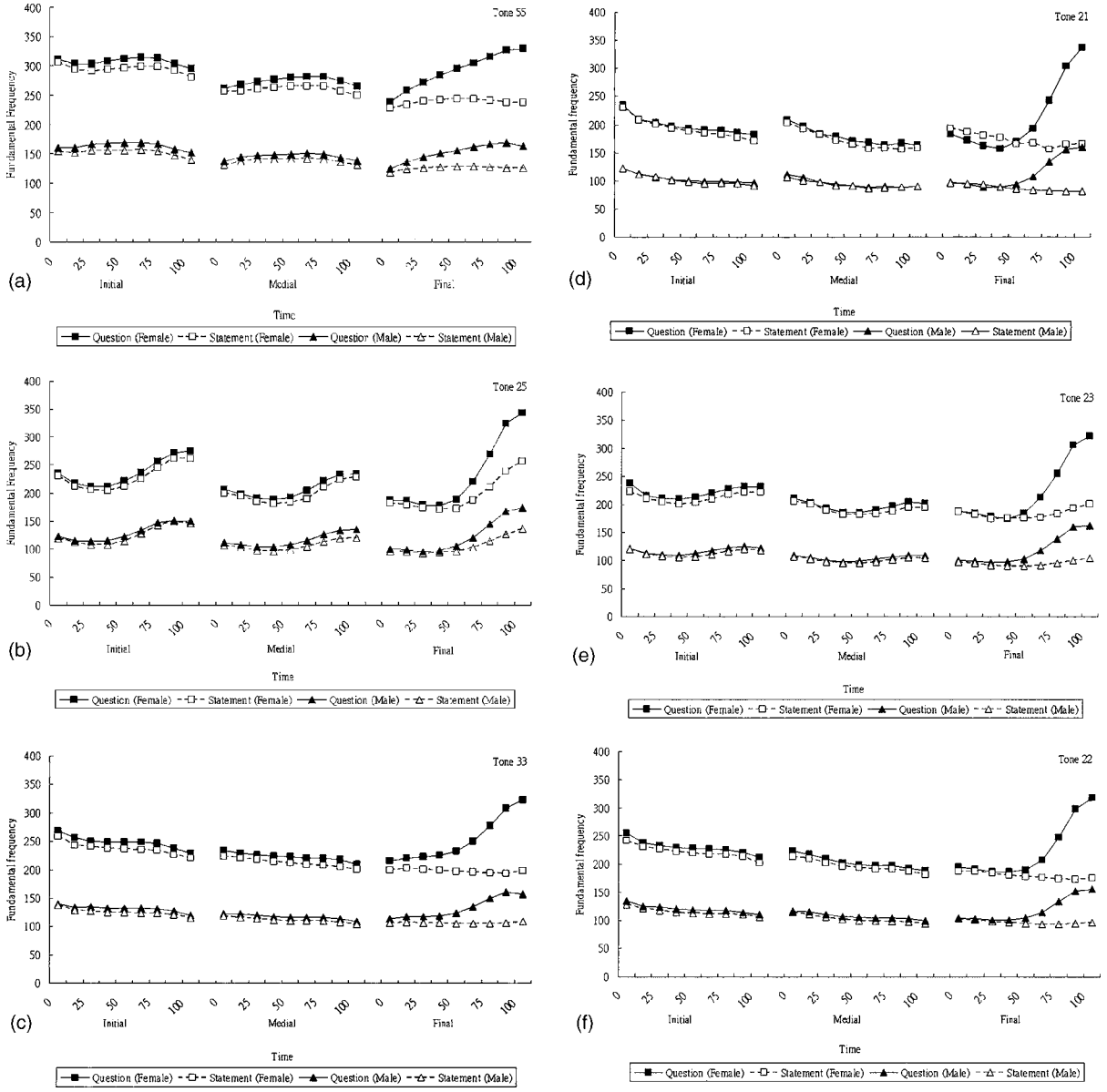

FIG. 1. (a)–(f). Mean F0 values for the six tones are displayed for (a) tone 55, (b) tone 25, (c) tone 33, (d) tone 21, (e) tone 23, and (f) tone 22. Within each figure, the F0 patterns at the initial, medial, and final positions are shown horizontally. For each tone, the mean F0 values at nine time points are displayed. Open symbols represent statements while filled symbols represent questions. Squares represent mean F0 values for female speakers and triangles represent male speakers.

medial positions, and increased to a level above that of the initial position from either 50% or 75% of the total duration onwards.

Analysis of the interaction of position, intonation, and time point showed the influence of intonation on F0 for different contexts at each time point. At the initial and medial positions, the F0 value of tones in questions was higher than in statements in all time points. Significant differences were noted at most of the time points for tones 55 (Tukey HSD test, $p<0.05$ at 25%, 50%, 75%, and 100% of the time) and 33 (Tukey HSD test, $p<0.05$ for all time points), but the differences between questions and statements were generally not significant across time points for tones 25, 21, 23, and 22 for both genders (Tukey HSD test, $p>0.05$). At the final position, tones produced in questions had higher F0 values than those of statements at most time points. The F0 values of tones produced in questions were significantly higher than in statements at 75% and 100% of the total duration for all six tones in both genders (Tukey HSD test, $p<0.001$ for all), suggesting that the difference in F0 between statements and questions grew bigger towards the end of the tones at the final position.

2. Duration

The mean duration of each tone at each position of the two intonations is shown in Fig. 2. A four-way repeated ANOVA ($2\times2\times3\times6$) was used to compare the differences in duration of the six tones between the two intonations across the three positions of both genders. Male and female speakers produced similar duration for the targets [$F(2,36)=195.18, p>0.05$]. The main effect of position was statisti-

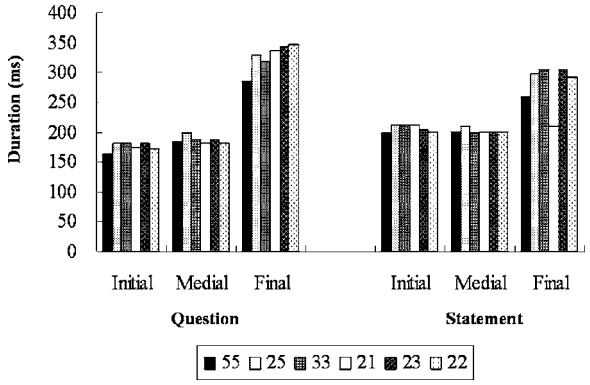

FIG. 2. Mean duration for the six tones across the three positions (initial, medial, and final) in questions and statements are displayed.

cally significant $[F(10,180)=13.52, p<0.05]$. Specifically, the duration of the targets at the final position was significantly longer than those in the initial and medial positions (Tukey HSD test, $p<0.05$ for both), while there was no significant difference in duration between the targets at initial and medial positions (Tukey HSD test, $p>0.05$). The position by tone interaction $[F(10,180)=13.52, p>0.05]$ showed that this pattern of differences among the three positions was the same for all six tones. Although the main effect for intonation was not significant $[F(1,18)=0.02, p>0.05]$, the intonation by position interaction $[F(2,36)=149.60, p<0.05]$ showed that targets at the initial and medial positions of statements had significantly longer duration than their counterparts produced in questions (Tukey HSD test, $p<0.05$ for both); while targets at the final position of questions had a longer duration than those in statements (Tukey HSD test, $p<0.05$). The main effect for tone was statistically significant $[F(5,90)=18.71, p<0.05]$. Tones 55 and 21 had significantly shorter durations when compared with the other four tones (Tukey HSD test, $p<0.05$ for all), while the differences between tones 25, 33, 23, and 22 were not significant (Tukey HSD test, $p>0.05$ for all). The tone by intonation interaction $[F(5,90)=9.79, p<0.05]$ showed that tone 55 had shorter duration than the other five tones when produced in questions and tones 25, 33, 23, and 22 when produced in statements (Tukey HSD test, $p<0.05$ for all); while tone 21 had shorter duration than the other five tones only when produced in statements (Tukey HSD test, $p<0.05$ for all). The interaction between tones, intonation, and position $[F(10,180)=15.68, p<0.05]$ showed that the abovementioned pattern between tones by intonation was only observed at the final position (Tukey HSD test, $p<0.05$ for all); while there was no significant contrast in duration between tones at initial and medial positions (Tukey HSD test, $p>0.05$ for all).

C. Discussion

The results of the above analysis showed that intonation affects the F0 patterns of tones across positions: tones produced within questions have a higher F0 level, the F0 level of tones varied across positions in both questions and statements, and a rising F0 contour was found for all tones at the final position of questions. The average F0 level of tones in questions was higher than their counterparts produced in statements (except for tone 21 at the initial and medial positions, and tone 23 at the medial position). The difference in F0 between intonation contexts was largest at the final position, which is consistent with the rising F0 contour associated with questions (Ohala, 1983). Liu and Xu (2005) proposed that the difference in F0 level between questions and statements is related to the meaning of surprise or incredulity carried in questions.

In statements, tones at the initial position had the highest F0 level, followed by tones at the medial and the final positions. The changes in F0 level for tones at various positions of statement support the findings of previous studies on the F0 pattern of declarative sentences (Ohala, 1978; Vance, 1976). Declarative sentences (or statements) are characterized by a lowering of F0 in successive words from the beginning to the end of the sentence ("downdrift;" Ohala, 1978), and by a final fall in the contour of the last syllable (Vance, 1976). This decrease in the F0 level of tones from the initial to the medial and final position supports the existence of a declination effect in statements in Cantonese.

F0 contours of the six tones remained consistent across positions and intonations, with the exception of contours of tones in the final positions of questions. The rising intonation contour of questions changed the F0 contour of all six tones from the canonical forms to rising contours at the final positions. This intonation-induced F0 change at the final position of questions was in agreement with the findings of Fok-Chan (1974) and Lee (2004) on the interaction between tone and intonation in Cantonese. In addition, tones 25, 21, 23, and 22 showed overlapping F0 contours at the final position of questions. The F0 patterns of these four tones resembled the original contour of tone 25.

The results of experiment 1 also showed that the duration of the targets varied as a function of positions within intonation contexts. The duration of the six tones remained similar within each condition (statement initial, statement medial, statement final, question initial, question medial, and question final), except for shorter duration for tone 55 at the final position of questions and statements, and tone 21 at the final position of statements. Besides the lengthening of tone 21 at the final position of questions, Lee (2004) also reported that tones 33 and 22 had lengthened durations at the final position of questions when compared with those in statements. Similar findings were not observed in this study. However, Lee (2004) did not perform statistical analyses for evaluating the difference in tone duration between intonations. Lee (2004) also reported variability among the four speakers in her study; some speakers showed no observable difference in duration. The findings of the present study also support the idea that duration effects vary among speakers.

III. EXPERIMENT 2—PERCEPTUAL ANALYSIS

The findings of experiment 1 showed that intonation affects both F0 level and contour. Intonation had no overall duration effect on tone, although interaction between position and intonation showed that the duration of six tones varied as a function of positions within intonation contexts.

The effect of intonation on F0 was especially strong at the final position of questions, where all six tones showed rising F0 contours regardless of their canonical forms, and overlapping of F0 patterns between tones 25, 21, 23, and 22 were found. Previous studies showed that F0 is the most important perceptual cue in tone perception (Fok-Chan, 1974; Vance, 1976; Gandour, 1981). Fok-Chan (1974) suggested that once the F0 structure of the tone is disrupted, then perception would be affected. The second experiment was designed to investigate whether intonation-induced changes in the F0 patterns of tones (i.e., F0 level and F0 contour) affect tone identity. Previous perceptual experiments in Mandarin showed that intonation-induced F0 changes do not necessarily change the lexical identity of tones for listeners (Connell, Hogan, and Rozsypal, 1983). Although the acoustic analysis showed different effect of intonation on the F0 contour of tones in Mandarin and Cantonese, the presence of extrinsic context (i.e., the intonation contour of the sentence) may provide listeners cues to perceptually "normalize" for the changes in the F0 pattern of the lexical tones. Therefore, three different experimental contexts (original carrier, isolation, and neutral carrier) were designed to test whether the extrinsic context can help listeners in the identification of tones whose F0 contour has undergone intonation-related changes.

A. Method

1. Listeners

Twelve females, aged 18–19 years old, served as listeners. They were all first-year undergraduates in the Division of Speech and Hearing Sciences, University of Hong Kong. None of them had participated in experiment 1. They were considered naïve listeners, as the experiment was carried out within their first two months at university, during which they received no phonetic training on tones. Cantonese was the first language for all the listeners. All listeners passed a hearing screening ($\leq$20 dBHL at 250, 500, 1000, 2000, and 4000 Hz). A tone perception screening, consisting of 24 trials (four trials for each tone), was carried out with all the listeners. Stimuli used were different from those in the experimental session. Listeners had to correctly identify each of the six tones in at least three out of four trials in order to pass the screening. They achieved an overall average accuracy of 99.3%.

2. Speech materials

Speech materials from two of the speakers in experiment 1, one male and one female, were used for the present experiment. The two speakers were selected because the F0 patterns of their target tones were closest to the average F0 patterns of their own gender. All 108 utterances of each speaker were used in this experiment (three sets of six tones of target words, three positions, and two intonations). Three presentation conditions (original carrier, isolation, and neutral carrier) were selected to investigate the use of extrinsic context by listeners in the perception of intonation-induced F0 changes in tones. In the original carrier condition, the targets were presented with the original carriers, as recorded in experiment 1. In the isolation condition, targets were presented as single words in order to determine the effect of a lack of extrinsic context on tone identification. Stimuli were manually extracted, using the Praat software (Boersma and Weenink, 2003), from the initial, medial, and final positions of the original utterances. The beginning and the end of the syllable were selected from the amplitude waveform display. The neutral carrier condition was designed to investigate whether the presence of a carrier sentence that provided cues about the average F0 and the F0 range of the speaker could be exploited to improve the accuracy of the identification of intonation-induced F0 changes. This condition was motivated by the finding that the presence of extrinsic context in the form of a carrier sentence results in sharper identification boundaries for level tones (Francis, Ciocca, and Ng, 2003). In the neutral carrier condition, all the target tones in isolation form were appended at the final position of the same carrier /lei_{55} kc_{33} tsi_{22} hɐi_{22}/ (This word is). The neutral carrier was synthesized from the production of the original carrier with targets in final position (/lei_{55} kɔ_{33} tsi_{22} hɐi_{22}/) by these two speakers. For each speaker, the average F0 of each syllable of all the 18 productions of /lei_{55} kɔ_{33} tsi_{22} hɐi_{22}/ was calculated. Among the 18 productions, the utterance with F0 values that were closest to the average F0 in each of the four syllables was chosen. The F0 of each syllable within the selected utterance was then resynthesized using the PSOLA algorithm of Praat software (Boersma and Weenink, 2003) to be within 2 Hz of the average F0 for each syllable at each of the nine time points. The two synthesized carriers (one for the male speaker and the other for the female speaker) were judged to sound natural by the first author and two other native Cantonese speakers (all qualified speech and language pathologists). All the target tones in isolation were then appended at the final position of the neutral carrier. In each presentation condition, the overall loudness of each of the stimuli was then equalized by the first author by modifying the overall amplitude of each token as necessary using the Praat software (Boersma and Weenink, 2003).

3. Procedures

The experiment was carried out in a single wall IAC sound-attenuated booth, with the speech materials presented to the listeners through a Sennheiser HD 545 headset, connected to a G4 Apple Macintosh computer, with an Aardvark USB 3 sound card. A HyperCard (Apple™) program was used to run the experiment. For each trial, six Chinese characters were presented on the screen, representing one set of contrastive tones. The carrier was also presented at the top of the screen with the target word represented by "_" for the original carrier and neutral carrier conditions.

The stimuli were divided into six blocks, according to presentation condition (original carrier, isolation form, and neutral carrier) and speaker. Within each block, there were a total of 216 trials, as each of the 108 stimuli was repeated once. Three experimental sessions were scheduled at least one week apart to minimize learning effects. In each session, two blocks (male and female) of one presentation condition were presented. The order of presentation for both presentation condition and speaker was randomized and counterbal-

anced across listeners. Each block took about 1/2 h to finish, and each session took about 1 h. Listeners were informed that the stimuli consisted of both questions and statements. Before each session, the 18 Chinese characters were read aloud by the first author to ensure that listeners were familiar with all the characters, as the same Chinese character may have more than one pronunciation in different contexts in Cantonese. Within each trial, listeners were asked to identify the Chinese character that matched the word they heard by clicking on the button representing the character. Each stimulus was presented once and the listener could opt to listen to it a second time by clicking on a "repeat sound" button.

B. Results

1. Overall perceptual accuracy

Confusion matrices were compiled separately according to presentation condition (original carrier, isolation, and neutral carrier), position (initial, medial, and final), and intonation context (question and statement) for each listener. Group confusion matrices were compiled by summing confusion matrices across 12 listeners. The overall percentages of correct identification for each of the three presentation conditions were compared using a series of Wilcoxon matched pair tests as ceiling effects were observed for some targets. The overall accuracy for tones presented within the original carrier (mean 90.57, SD=25.40) was significantly higher than for targets presented in isolation (mean 72.22, SD =33.43) ($T=0, p<0.005$) and for targets presented within the neutral carrier (mean 70.39, SD=35.72) ($T=0, p<0.005$); there was no difference between the isolation and the neutral carrier conditions ($T=29.5, p>0.05$). Statistically significant differences in perceptual accuracy were observed for original carrier and the other two conditions in all intonation contexts and positions ($p<0.05$ for all), except for the final targets of questions where the differences between original carrier, neutral carrier, and isolation were not significant ($p>0.05$ for all). Targets presented in isolation had significantly higher accuracy than when presented within the neutral carrier at initial and medial positions of questions, and initial position of statements ($p<0.05$ for all); while targets presented within neutral carrier had perceptual accuracy higher than those presented in isolation at the medial and final positions of statements ($p<0.05$ for all).

The percentages of correct identification of targets presented with the original carrier in each intonation context and position were compared individually for each tone. Performance was similar in all the conditions, except for the final targets of questions for tones 21, 23, and 22, for which accuracy was significantly lower than in other conditions ($T=0, p<0.005$ for all).

The confusion matrix for the perception of the six tones as final targets of questions in the original carrier condition is shown in Table I. The numbers in the cells represent the percentage of responses realized as that particular tone. For example, tone 25 at the final position of questions was correctly identified 81.9% of the time (118 out of 144 trials). Correct identifications are shown by the numbers appearing on the diagonal of the matrix (boldtype). The mean accuracy of the six tones in this context was compared using Wilcoxon matched-pair tests. The percentage of correct identification for tone 55 (mean=100%) was significantly higher than for the other five tones ($T=0, p<0.05$ for all). The accuracy for tones 25 (mean=82%) and 33 (mean=72%) was significantly higher than for tones 21, 23, and 22 ($p<0.05$ for all), but the difference between tones 25 and 33 was not statistically significant ($p>0.05$). The mean accuracy for tone 21 (mean=27%) was higher than for tones 23 (mean=10%) and 22 (mean=22%) ($T=0, p<0.05$ for both); no significant difference was found between tones 23 and 22 ($T=3, p>0.05$).

TABLE I. Confusion matrix for perceptual accuracy at the final position of questions within the original carrier condition.

	Perceived tone					
Target	55	25	33	21	23	22
55	**100.0**					
25		**81.9**		1.4	6.3	10.4
33		25.7	**71.5**		2.8	
21		71.5		**27.1**	1.4	
23		78.5	1.4		**9.7**	10.4
22		62.5	6.3		9.7	**21.5**

Note. Target tones are on the vertical axis, and perceived tones on the horizontal axis. Cell numbers represent the percentage of responses for each target tone.

2. Error patterns

Error patterns were analyzed by calculating the percentage of misidentifications of each tone out of the total number of identification errors observed for that tone within each presentation condition. As described in the previous section, in the original carrier condition, stimuli presented at the final position of questions were the least accurately perceived. Except for tones 55 and 25, most of the errors in this context involved misperceiving the target tone as tone 25. This error accounted for about 66% of the identification errors for tone 33, 93% of the identification errors for tone 21, 76% of the identification errors for tone 23, and 73% of the identification errors for tone 22. Two other common perceptual errors were noted in the original carrier condition. Tone 25 was misperceived as tone 23 (69% of all perceptual errors involving tone 25). The other common, but less frequent, error resulted from the mutual confusion between tones 33 and 22.

For targets presented with the neutral carrier and in isolation, the error pattern for the final targets of questions was similar to that for the original carrier condition. Tones 33, 21, 23, and 22 were misperceived as tone 25. Also, a large number of tone level errors were observed in these two presentation conditions in all six contexts, accounting for about 65%–96% of all the perception errors for each tone in each presentation condition. For the three level tones, tone 55 was perceived as tone 33, and tones 33 and 22 were perceived as tones 55, 33, or 22; the two rising tones (tones 25 and 23) were confused with each other.

TABLE II. Performance of individual listeners for the final position of questions within the original carrier condition.

	Tone					
Listeners	55	25	33	21	23	22
L1	100	33.3	100	91.7	33.3	83.3
L2	100	16.7	100	91.7	8.3	91.7
L3	100	100	0	0	0	0
L4	100	100	8.3	0	0	0
L5	100	100	0	0	0	0
L6	100	100	50	0	0	0
L7	100	83.3	100	8.3	0	0
L8	100	100	100	0	0	0
L9	100	100	100	8.3	8.3	8.3
L10	100	100	100	25	0	16.7
L11	100	75	100	50	50	25
L12	100	66.7	100	50	16.7	25

Note. Numbers in the cells represent the accuracy (percentage correct) for that particular tone by each listener.

3. Individual error patterns

The confusion matrices of all individual listeners were examined. The percentages of correct identification of each listener at the final position of questions are shown in Table II. Listeners could be classified into four groups according to their identification patterns:

a. Listeners 1 and 2 were able to correctly identify tones 55, 33, 21, and 22 for final targets of questions. Their perception of tones 25 and 23 was poor (tone 25 being misperceived as tone 23, 21, or 22, and tone 23 misperceived as tone 25 or 22).

b. Listeners 3, 4, 5, and 6 were able to correctly identify tones 55 and 25, but frequently misidentified the other tones as tone 25.

c. In addition to being able to perceive tones 55 and 25 correctly (as for listeners in the previous group), listeners 7, 8, 9, and 10 were able to perceive tone 33 with 100% accuracy, while tones 21, 23, and 22 were likely to be confused with tone 25.

d. Listeners 11 and 12 perceived tones 55 and 33 with a high level of accuracy. These listeners were also able to perceive tones 21, 23, and 22 more accurately than listeners in groups 2 and 3, but they were less accurate in identifying tone 25.

C. Discussion

For the targets presented with the original carriers, identification accuracy for all six tones was close to 100% (ranged from 91% to 100%) in all conditions except for the final targets in questions, whose F0 contours deviated from their canonical form. For these target tones, the identification accuracy ranged from 10% (tone 23) to 100% (tone 55). The results showed that a large proportion of tones 21, 23, and 22 were misperceived as tone 25 at the final position of questions, likely due to the overlapping rising F0 contours of these tones 21, 23, and 22 with tone 25, as shown in experiment 1. Therefore, listeners relied heavily on the intrinsic F0 patterns of these tones, as suggested in previous studies (Fok-Chan, 1974; Gandour, 1981; Vance, 1976). Although all three level tones (tones 55, 33, and 22) had a rising contour at the final position of questions, listeners showed better perceptual accuracy for tones 55 and 33. The distinctiveness in the F0 level of tones 55 and 33, especially at the initial portion of the tone, is likely to have cued an accurate identification of these tones, given that there are no other rising tones at the same F0 level during the first half of the segments. Tone 55 also showed a rise in F0 throughout the segment, while the other five tones had a level F0 pattern in the first half of the segment. The perceptual accuracy for targets at the final position of questions in the original carrier condition was lower than in the other five contexts with the original carrier, and similar to that of the isolation conditions. This finding suggests that F0 information provided by the extrinsic context, such as the intonation type and the position of a word within a sentence, may not be used effectively when intonation-induced changes result in F0 patterns that differ considerably from the canonical pattern.

The results of experiment 2 showed that while in the original carrier condition listeners were able to employ the F0 cues provided by the extrinsic context in order to compensate for the intonation-induced F0 changes, and when the extrinsic context was removed (isolation condition), identification accuracy decreased. It is possible that subjects may not have made the maximal use of the F0 information regarding intonation patterns with isolated tones, as listeners were not told explicitly the intonation of the original carrier from which each isolated tone was extracted. However, Ma, Ciocca, and Whitehill (2006a) found that listeners had no difficulty in identifying the intonation pattern when they heard isolated tones produced in sentence-final position.

The perceptual patterns of the targets presented with the neutral carriers showed how extrinsic context cued tone perception. Perceptual errors were most common for tones 33, 21, and 22 in initial position and tone 22 in medial position, and most of the errors involved confusions with tones of the same contour but of higher F0 level. As shown in experiment 1, the F0 level of tones varied across position, with F0 level being the highest at the initial position, followed by that of medial and final positions. When all targets were placed at the final position of the neutral carrier, targets of the initial and medial positions were of higher F0 level than typical targets at the final position. These results are consistent with the "recency strategy" (Wong and Diehl, 2003), according to which the immediate preceding context provides cues for listeners to infer the F0 range of the talker's voice when processing an utterance. The extracted F0 range (or average F0) is then used to identify tones by carrying out a tone normalization process (Francis *et al.*, 2006; Leather, 1983).

IV. GENERAL DISCUSSION

The results of the present study showed that the F0 patterns of tones in all positions of statements, and in the initial and medial positions of questions, were comparable with the canonical forms. By contrast, the F0 contours of all tones at the final position of questions were modified to rising by the final rise of the question. These results are in agreement with

the findings from other studies on the interaction between tone and intonation in Cantonese (Fok-Chan, 1974; Vance, 1976; Lee, 2004). These conclusions contrast with those from studies on Mandarin Chinese, which reported that the F0 contour of tones was not affected by sentence intonation (Ho, 1977; Rumjancev,; cited in Lyovin, 1978; Shen, 1989). This difference might be related to how question intonation is produced by speakers of the two languages. Studies on intonation in Cantonese suggested that the difference between questions and statements is modeled by both global F0 increase and local F0 changes at the end of the final syllable of questions (Gu, Hirose, and Fujisaki, 2005; Ma, Ciocca, and Whitehill, 2006b). Gu *et al.* (2005) also suggested that the increase in amplitude of the positive tone command is larger than usual at the end of questions. The local F0 changes observed at the final position of questions provided a possible explanation of the modification of F0 contour at the final position of questions in Cantonese. Lin (2004) also used the concept of "boundary tones," the F0 changes at the final one or two syllables of the utterance which convey information about sentence intonation (e.g., question vs statement), to explain the difference between questions and statements in Mandarin. He found that boundary tones reflect the F0 pattern of a question by changing the F0 level at the beginning of the boundary tone and/or the slope of the rising F0. By contrast, Yuan (2004) suggested that boundary tones are not necessary for modeling of questions in Mandarin. He proposed that the difference between the two intonations could be explained by an overall higher phrase curve and higher strength value towards the end of questions. Liu and Xu (2005) found that the F0 difference between the two intonations is mostly related to the superposition of an exponential or double-exponential F0 baseline on the phrase curve of the sentence, which attributed the final F0 rise in questions to part of the global intonation changes of questions. This suggests that questions are mainly marked by global F0 changes in Mandarin and, therefore, the tone structures are largely unaffected.

The current results also showed that the intonation-induced F0 changes observed at the final position of questions affect listeners' perception. A large proportion of tones 21, 23, and 22 were perceived as tone 25 at the final position of questions. These results agreed with previous reports that tones produced within questions were more difficult to recognize than those in declarative sentences (Fok-Chan, 1974). By contrast, a previous perceptual study of Mandarin found that the perturbation in F0 pattern caused by intonation had minimal effect on perception for native listeners (Connell, Hogan and Rozsypal, 1983). The higher tendency of misperception in Cantonese when compared with Mandarin is probably related to the difference in the effect of intonation on tone as mentioned above, as well as to the features of the tones in each language. In Cantonese, there are three level tones and two rising tones. Therefore, a slight modification in F0 level or contour may result in erroneous identification. For example, an increase in F0 range of tone 23 may lead to the perception of a tone 25; similarly, a slight increase in F0 level could cause a tone 22 to be perceived as tone 33. By contrast, Mandarin has four tones with distinctive F0 contours (level, rising, falling-rising and falling) and levels. Therefore, a small rise in the contour of the level tone (tone 1) caused by interrogative intonation, as shown in Ho's experiment (1977), might not affect the listeners' perception, as the resulting contour would still not resemble other tones in Mandarin. Furthermore, Tseng, Massaro, and Cohen (1986) found that duration and amplitude could become secondary cues in tone perception in Mandarin when F0-related cues are ambiguous. Several studies have explored the possibility that perceptual cues such as duration (Blicher, Diehl, and Cohen, 1990; Liu and Samuel, 2004; Tseng *et al.*, 1986) and amplitude envelope (Fu and Zeng, 2000; Whalen and Xu, 1992) are used for Mandarin tone identification. Unlike Mandarin tones, the present study showed that duration of tones varied as a function of position within intonations in Cantonese. Similar duration was observed for the six Cantonese tones of the same position and intonation, except for tones 55 and 21 at the final position of statements and tone 55 at the final position of questions. This suggests that the duration difference is unlikely to be a reliable cue in tone identification. Vance (1976) also found that the difference in vowel length among Cantonese tones was too small to be used for tone identification. It is possible that amplitude-related cues, not included in the present study, could be used as secondary cues to tone perception by Cantonese listeners.

The acoustic analysis in experiment 1 showed that the F0 contours of tones 21, 23, and 22 at the final position of questions were modified by the final-rise in questions to a surface F0 assimilating that of tone 25. Vance (1976) suggested that the tonal variations owing to intonation context could be classified as a form of tone sandhi. Wang and Li (1967) proposed that if a tone undergoes tone sandhi, it should be treated as a homophone of the resulting tone. In the current study, although most of the tones 21, 23, and 22 at the final position of questions were perceived as rising tones in experiment 2, the large amount of variability in the individual data (as shown in Table II) indicate that these tones were not homophonous to tone 25. This suggests that the tonal variations observed at the final position of question in Cantonese should be considered as the result of contextual modification by intonation rather than as a form of tone sandhi.

The large perceptual variability for tones at the final position of questions in the original carrier demonstrated that, although the canonical F0 patterns of tones were distorted by intonation context, some listeners were still able to recover the intended tones while some listeners took the distorted F0 pattern at "face value." One of the possible explanations is that different F0 cues were used by different listeners. Gandour (1981) proposed that Cantonese tones are perceived by features (like F0 level and F0 contour) rather than as whole tone units. The present results provided evidence that some listeners (listeners 1 and 2) placed more emphasis on tone level than contour; therefore, they were able to distinguish the closely spaced tones 21 and 22 accurately by the differences in F0 level, but failed to use the rising contour as a cue in perceiving both tones 25 and 23. By contrast, another group of listeners (listeners 3, 4, 5, and 6) weighed tone contour as the main perceptual cue, and

misperceived tones 33, 21, 23, and 22 as tone 25, while the contrast in F0 level between tone 33 and tone 25 was not perceived. For some listeners (listeners 7–12), both F0 contour and level were utilized as perceptual cues in tone perception. Therefore, they were able to perceive tones 55 and 33 accurately by exploiting the F0 level cue, while tones 21, 23, and 22 were confused with tone 25 due to their rising contour.

It is not clear how listeners weighed different F0 cues in tone identification. One possibility is that some listeners take into account the sentence intonation when they identify tones. When tones were presented with the original context, as in experiment 2, listeners tried to compensate for the final F0 rise in questions while trying to identify the tones of the target words. Therefore, they might have focused on the F0 level cues since all tones had rising F0 contours as a result of the final rise in questions. Alternatively, some listeners may have chosen to ignore the sentence intonation during the perception task, as they were asked to focus only on identifying the tones. In this case, listeners would perceive the tones on the basis of their surface F0 patterns and, therefore, fail to differentiate tones of similar F0 levels (tones 25, 21, 23, and 22). Further research on the perception of tones and intonation in Cantonese would be necessary to determine how different perceptual cues are utilized by individual listeners.

ACKNOWLEDGMENTS

The authors wish to thank Anders Löfqvist and two anonymous reviewers for their helpful comments on an earlier draft of the manuscript.

Bauer, R. S., and Benedict, P. K. (**1997**). *Modern Cantonese Phonology* (Mouton de Gruyter, Berlin).

Blicher, D. L., Diehl, R. L., and Cohen, L. B. (**1990**). "Effects of syllable duration on perception of Mandarin Tone 2/Tone 3 distinction: Evidence of auditory enhancement," J. Phonetics **18**, 37–49.

Boersma, P., and Weenink, D. (**2003**). Praat 4.0.46: A system for doing phonetics by computer (computer software) (University of Amsterdam, Amsterdam, The Netherlands). Available online: http://www.fon.hum.uva.nl/praat/ Last accessed 10/302006.

Chang, C. T. (**1958**). "Tones and intonation in Chengtu dialect," Phonetica **2**, 59–85.

Chao, Y. R. (**1947**). *Cantonese primer* (Greenwood Press, New York).

Connell, B. A., Hogan, J. T., and Rozsypal, A. J. (**1983**). "Experimental evidence of interaction between tone and intonation in Mandarin Chinese," J. Phonetics **11**, 337–351.

Fok-Chan, Y. Y. (**1974**). *A Perceptual Study of Tones in Cantonese* (University of Hong Kong Press, Hong Kong).

Francis, A., Ciocca, V., and Ng, B. K. C. (**2003**). "On the (non)categorical perception of Cantonese lexical tones," Percept. Psychophys. **65**, 1029–1044.

Francis, A., Ciocca, V., Wong, N. K. Y., Leung, W. H. Y., and Chu, P. C. Y. (**2006**). "Extrinsic context affects perceptual normalization of lexical tone," J. Acoust. Soc. Am. **119**, 1712–1726.

Fu, Q-J., and Zeng, F.-G. (**2000**). "Identification of temporal envelop cues in Chinese tone recognition," Asia Pac. J. Speech, Language Hearing **5**, 45–57.

Fujisaki, H., and Hirose, K. (**1984**). "Analysis of voice fundamental frequency contours for declarative sentences of Japanese," J. Acoust. Soc. Jpn. **5**, 233–242.

Gandour, J. (**1981**). "Perceptual dimensions of tone: Evidence from Cantonese," J. Chin. Linguist. **9**, 20–36.

Gu, W-T., Hirose, K., and Fujisaki, H. (**2005**). "Analysis of the effects of word emphasis and echo question on F0 contours of Cantonese utterances," *Proceedings of the Interspeech-2005*, Lisbon, Portugal, pp. 1825–2828.

Ho, A. T. (**1977**). "Intonation variation in a Mandarin sentence for three expressions: Interrogative, exclamatory and declarative," Phonetica **34**, 446–457.

Ladd, D. R. (**1996**). *Intonational Phonology* (Cambridge University Press, Cambridge).

Leather, J. (**1983**). "Speaker normalization in perception of lexical tone," J. Phonetics **11**, 373–382.

Lee, W-S. (**2004**). "The effect of intonation on the citation tones in Cantonese," *Proceedings of the First International Symposium on the Tonal Aspects of Languages*, Beijing, China, pp. 107–110.

Lin, M. (**2004**). "Boundary tone of Chinese intonation and its pitch (F0) pattern," in *From Traditional Phonology to Modern Speech Processing*, edited by G. Fant, H. Fujisaki, J. Cao, and Y. Xu (Foreign Language Teaching and Research Press, Beijing), pp. 309–327.

Liu, F., and Xu, Y. (**2005**). "Parallel encoding of focus and interrogative meaning in Mandarin intonation," Phonetica **62**, 70–87.

Liu, S-Y., and Samuel, A. G. (**2004**). "Perception of Mandarin Lexical tones when F0 information is neutralized," Lang Speech **47**, 109–128.

Lyovin, A. V. (**1978**). "Review of tone and intonation in Modern Chinese by M. K. Rumjancev," J. Chin. Linguist. **6**, 120–168.

Ma, J. K-Y, Ciocca, V, and Whitehill, T. L. (**2006a**). "Perception of intonation in Cantonese," *Proceedings of the Second International Symposium of Tonal Aspects of Languages*, La Rochelle, France, pp. 93–96.

Ma, J. K-Y, Ciocca, V., Whitehill, T. L. (**2006b**). "Quantitative analysis of intonation patterns in statements and questions in Cantonese," *Proceedings of the Third International Conference on Speech Prosody*, Dresden, Germany, pp. 277–280.

Ohala, J. J. (**1978**). "Tone Rules," in *Tone: A Linguistic Approach*, edited by V. A. Fromkin (Academic, New York), pp. 5–39.

Ohala, J. J. (**1983**). "Cross-language use of pitch: An ethological view." Phonetica **40**, 1–18.

Pierrehumbert, J. (**1980**). "The phonology and phonetics of English intonation," unpublished Ph.D. thesis, MIT.

Rumjancev, M. K. (**1972**). *Ton i intonacija v sovemennom kitajskom jazyke (Tone and intonation in Modern Chinese)*. (Izdatel'stvo Moskovskogo Universiteta, Moscow).

Shen, X. N. S. (**1989**). *The Prosody of Mandarin Chinese* (University of California Press, Berkeley, California).

Thorsen, N. G. (**1980**). "A study of the perception of sentence intonation—evidence from Danish," J. Acoust. Soc. Am. **67**, 1014–1030.

Tseng, C.-Y., Massaro, D. M. and Cohen, M. M. (**1986**). "Lexical tone perception in Mandarin Chinese: Evaluation and integration of acoustic features," in *Linguistics Psychology and the Chinese People*, edited by H. S. R. Kao and R. Hoosain (University of Hong Kong, Hong Kong), pp. 91–104.

Vance, T. J. (**1976**). "An experimental investigation of tone and intonation in Cantonese," Phonetica **33**, 368–392.

Wang, S-Y. W., and Li, K.-P. (**1967**). "Tone 3 in Pekinese," J. Speech Hear. Res. **10**, 629–636.

Whalen, D. H., and Xu, Y. (**1992**). "Information for Mandarin tones in the amplitude contour and in brief segments," Phonetica **49**, 25–47.

Wong, P. C. M., and Diehl, R. L. (**2003**). "Perceptual normalization for inter- and intratalker variation in Cantonese level tones," J. Speech Lang. Hear. Res. **46**, 413–421.

Yuan, J.-H. (**2004**). "Intonation in Mandarin Chinese: Acoustics, Perception, and Computational Modeling," unpublished Ph.D. thesis, Cornell University.

Yuan, J.-H., Shih, C.-L., and Kochanski, G. P. (**2002**). "Comparison of declarative and interrogative intonation in Chinese," *Proceedings of the Speech Prosody-2002*, Aix-en-Provence, France, pp. 711–714.

Extended speech intelligibility index for the prediction of the speech reception threshold in fluctuating noise

Koenraad S. Rhebergen,[a] Niek J. Versfeld,[b] and Wouter A. Dreschler[c]
Department of Clinical and Experimental Audiology, Academic Medical Center, Meibergdreef 9, 1105 AZ Amsterdam, The Netherlands

(Received 24 March 2006; revised 4 August 2006; accepted 5 September 2006)

The extension to the speech intelligibility index (SII; ANSI S3.5-1997 (1997)) proposed by Rhebergen and Versfeld [Rhebergen, K.S., and Versfeld, N.J. (2005). J. Acoust. Soc. Am. **117**(4), 2181–2192] is able to predict for normal-hearing listeners the speech intelligibility in both stationary and fluctuating noise maskers with reasonable accuracy. The extended SII model was validated with speech reception threshold (SRT) data from the literature. However, further validation is required and the present paper describes SRT experiments with nonstationary noise conditions that are critical to the extended model. From these data, it can be concluded that the extended SII model is able to predict the SRTs for the majority of conditions, but that predictions are better when the extended SII model includes a function to account for forward masking. © *2006 Acoustical Society of America.* [DOI: 10.1121/1.2358008]

PACS number(s): 43.71.An, 43.66.Ba, 43.71.Gv, 43.72.Kb [MSS] Pages: 3988–3997

I. INTRODUCTION

Speech intelligibility decreases due to the presence of a background noise. Parts of the speech signal then are masked by the noise such that not all speech information is available to the listener. French and Steinberg (1947), Fletcher and Galt (1950), and later Kryter (1962a, 1962b) developed a calculation method, known as the articulation index (AI), to predict the speech intelligibility under such masking conditions. The AI calculation scheme was re-examined in the 1980s and early 1990s, which led to a new method accepted as the ANSI S3.5-1997 (1997). Since its revision in 1997, the AI is named the speech intelligibility index (SII). A detailed description of the SII can be found in Pavlovic (1987), and the ANSI S3.5-1997 (1997) standard.

To date, the SII model has been designed and validated only for stationary masking noises. In fluctuating masking noises, speech intelligibility is usually much better for normal-hearing listeners, since the listener is able to take advantage of the relatively silent periods in the noise masker; for hearing impaired listeners this is often not the case (Festen and Plomp, 1990; Houtgast *et al.*, 1992; Versfeld and Dreschler, 2002). However, the SII model does not take into account any fluctuation in the masking noise since it uses only the long term speech and noise spectrum. Therefore, it predicts speech intelligibility inaccurately for these conditions. Since many daily-life background noises do fluctuate strongly over time (Koopman *et al.*, 2001), the SII model is unable to predict speech intelligibility in the majority of real-life situations adequately.

Recently, Rhebergen and Versfeld (2005) proposed an extension to the SII model, in order to improve the predictions for speech intelligibility in fluctuating noise. The basic principle of this approach is that both speech and noise signal are partitioned into small time frames. Within each time frame the instantaneous SII is determined, yielding the speech information available to the listener at that time frame. Next, the SII values of these time frames are averaged, resulting in the SII for that particular speech-in-noise condition. With the aid of various data available for a variety of noise types described in the literature, Rhebergen and Versfeld (2005) have shown that their extension allows a good account for most existing data, dealing with the speech reception threshold (SRT) for sentences. However, there still are conditions where the extended SII (ESII) model is unable to give accurate predictions. First, the ESII model is unable to predict SRTs for sentences in 100% sinusoidally intensity-modulated (SIM) speech noise, as measured by Festen (1987). Although the SRT values predicted by the ESII model yield an improvement over the original SII model, there are still some systematic deviations. Festen found lowest SRTs (i.e., best performance) for modulation frequencies of 16 and 32 Hz, whereas the ESII model predicts the best performance for a modulation frequency of 8 Hz.

Second, Rhebergen *et al.* (2005) measured SRTs with unintelligible interfering speech (foreign language) as a masker played normal and time reversed. By reversing the unintelligible speech masker in time, the SRT worsened about 2.3 dB. Rhebergen *et al.* (2005) argued that this difference could be attributed to differences in the amount of forward masking: The time-reversed speech masker (having a "ramped"-like envelope, i.e., a gradual increase with a sudden offset) provokes more forward masking than a normal speech masker (being more "damped"-like, i.e., a sharp onset followed by a gradual declination). A time-asymmetrical nonspeech-like noise masker may provide more insight into the effects of temporal forward masking on speech intelligibility. The ESII model is, in essence, a time-symmetrical model. It does not account for the differences in forward and

[a]Electronic mail: k.s.rhebergen@amc.uva.nl
[b]Electronic mail: n.j.versfeld@amc.uva.nl
[c]Electronic mail: w.a.dreschler@amc.uva.nl

 © 2006 Acoustical Society of America

backward masking. The model predicts the same speech intelligibility with a noise masker played normal and time reversed.

Third, the ESII is a model verified with SRT data described in the literature. To enable a fair comparison between the data obtained in different studies, Rhebergen and Versfeld (2005) restricted themselves to the use of SRT data obtained with one set of speech materials, viz., the Dutch speech corpus of Plomp and Mimpen (1979). Even though the corpus is similar, differences between studies sometimes are substantial: some conditions have been measured abundantly (SRT in stationary speech shaped noise), whereas other conditions have been measured sparsely (SRT in SIM noise) (Festen, 1987). Moreover, SRT data have been collected by different researchers in different experimental settings. This introduces additional variance in the data. For example, SRTs in quiet or interrupted noise differ largely between different papers (de Laat and Plomp, 1983; Festen, 1987; Noordhoek, 2000; Duquesnoy, 1983; Plomp and Mimpen 1979a; 1979b). For a good validation of the ESII model, only SRTs obtained from the same group of subjects and measured under the same experimental conditions should be used for ESII calculations. For instance, the ESII model predicts that SRTs in fluctuating noise, unlike stationary noise, may depend on the subject's absolute threshold, even in normal-hearing listeners.

This paper addresses the problems described above, with the aim to test and, where necessary, refine the ESII model. All experiments have been conducted with normal-hearing subjects.

In the first section, SRT tests are performed for nineteen different noise conditions (test and retest) using the speech material of Versfeld *et al.* (2000). The noise conditions comprise steady state noise, interrupted noise with different modulation frequencies and different duty cycles, SIM noise with different modulation frequencies, and two asymmetrically saw-tooth noises. The noise conditions have been selected such to test the ESII model critically.

In the next section, the observed SRTs are used to evaluate and refine the ESII model. Notably, the ESII calculations are extended by using a function to account for forward masking. Last, predictions and limitations of the finally obtained extended ESII model will be discussed.

II. EXPERIMENT

In this experiment, the SRTs for a number of noise conditions are measured. The results will be used to validate the SII model.

A. Subjects

Twelve normal-hearing subjects (one male, 11 females) participated. Their age ranged from 18 to 29 years and was on average 21.5 years. Subjects were native speakers of the Dutch language and had at least high school education. Each subject had pure-tone thresholds of 15 dB HL or better at octave frequencies from 125 to 8000 Hz (ANSI S3.6, 1996). Table I shows the average pure-tone thresholds.

TABLE I. Pure-tone thresholds averaged across the group of 12 normal-hearing subjects.

Frequency (Hz)	125	250	500	1000	2000	4000	8000
Threshold (dB HL)	8.2	5.9	4.1	0.0	1.8	3.6	5.0
Standard deviation (dB)	6.4	7.0	5.4	4.5	4.0	5.5	8.9

B. Stimuli

The target speech material consisted of short every-day sentences, uttered by a female speaker (Versfeld *et al.*, 2000). The speech material comprises 39 lists of 13 sentences and has been developed for a reliable measurement of the speech intelligibility in noise. The speech was stored at a sample rate of 44.1 kHz and a 16 bits resolution.

All 19 interfering noise conditions are given in Table II. The noise conditions comprise one condition with steady state noise, ten conditions with interrupted noise, two conditions with saw-tooth noise, and six conditions with SIM (sinusoidal intensity modulated) noise. Figure 1 illustrates the wave forms of the noise types. All noise conditions had a long-term average spectrum equal to the long-term average spectrum of the target female speech material (Versfeld *et al.*, 2000). The nonstationary noises were derived from the original stationary masking noise of Versfeld *et al.* (2000), where the envelope was modified with the aid of the MATLAB signal processing toolbox. The interrupted noise conditions were modulated with a duty cycle of 50% and a depth of 100%, and the modulation frequencies were 4, 8, 16, 32, 64, and 128 Hz. Four conditions had a modulation frequency of 8 Hz, but with a duty cycle of 40%, 45%, 55%, and 60%. The SIM noises were generated according to Festen (1987). The modulation frequencies were 4, 8, 16, 32, 64, and 128 Hz, and the modulation depth was 100%. The two saw-tooth noise conditions had a modulation frequency of 8 Hz and the envelope was exponentially increasing or decreasing in time (types 1 and 2, respectively), with a slope of about 40 dB/125 ms.

C. Procedure

Subjects were tested individually in a sound-insulated booth. Signals were played out via an Echo soundcard (Gina 24/96) on a personal computer at a sample frequency of 44.1 kHz, and were fed through a TDT Amplifier (MA2) and a TDT Headphone Buffer (PA4). Subjects received the signals monaurally at their best ear via TDH 39P headphones at a fixed noise level of 65 dB A. After the presentation of a sentence, the subject's task was to repeat the sentence he or she had just been presented. A sentence was scored correct if all words in that sentence were repeated without any error. A list of 13 sentences, unknown to the subject, was used to estimate the signal-to-noise ratio (SNR) at which 50% of the sentences was reproduced without any error, the so-called SRT. For a given condition, the first sentence of the list started far below the expected SRT. The sentence was repeated each time at a 4 dB higher level until the subject was able to reproduce it correctly. The twelve other sentences of that list were presented only once, following a simple up-

TABLE II. Schematic representation of the nineteen noise conditions.

Noise condition	Noise type	Modulation frequency	Modulation depth (%)	Duty cycle (%)	Envelope shape
Int 4 Hz	Interrupted	4	100	50	Square
Int 8 Hz	Interrupted	8	100	50	Square
Int 16 Hz	Interrupted	16	100	50	Square
Int 32 Hz	Interrupted	32	100	50	Square
Int 64 Hz	Interrupted	64	100	50	Square
Int 128 Hz	Interrupted	128	100	50	Square
Int 8 Hz dc40%	Interrupted	8	100	40	Square
Int 8 Hz dc45%	Interrupted	8	100	45	Square
Int 8 Hz dc55%	Interrupted	8	100	55	Square
Int 8 Hz dc60%	Interrupted	8	100	60	Square
Saw-tooth *T*1	Saw-tooth	8	-	-	Exponential increasing
Saw-tooth *T*2	Saw-tooth	8	-	-	Exponential decreasing
SIM 4 Hz	Sinusoidal intensity modulated	4	100	-	Sinusoidal
SIM 8 Hz	Sinusoidal intensity modulated	8	100	-	Sinusoidal
SIM 16 Hz	Sinusoidal intensity modulated	16	100	-	Sinusoidal
SIM 32 Hz	Sinusoidal intensity modulated	32	100	-	Sinusoidal
SIM 64 Hz	Sinusoidal intensity modulated	64	100	-	Sinusoidal
SIM 128 Hz	Sinusoidal intensity modulated	128	100	-	Sinusoidal
Steady state	Stationary	-	-	-	Flat

down procedure with a step size of 2 dB. The SRT was estimated according to the procedure described by Plomp and Mimpen (1979a), i.e., by taking the mean SNR of sentence 5–13 plus the SNR that would have been used for the fourteenth sentence. With each sentence presentation, a random sample of the interfering noise was taken. The noise onset was 1200 ms before the onset of the sentence; it stopped 800 ms after the offset of the sentence. Thus, the duration of the noise was in total 2000 ms longer than the sentence duration.

In total, 19 conditions were tested. The experiment was partitioned into two blocks, a test and a retest block. To avoid confounding of measurement condition order and sentence lists, the order of conditions and sentence lists was counterbalanced across subjects. In total, each subject received 38 lists of 13 sentences preceded by three practice lists.

III. RESULTS

A $19[\text{condition}]\times 2[\text{test/retest}]\times 12[\text{subject}]$ analysis of variance (ANOVA) was performed on the data. Of the main effects, "condition" ($F[18,198]=159.08$, $p<0.001$), and "test/retest" was significant ($F[1,11]=14.87$, $p<0.005$). The SRT of the retest was on average 0.8 dB better. Differences between subjects were not significant ($F[11,15.71]=2.14$, $p>0.05$). Of the interactions, conditions*test ($F[18,198]=1.88$, $p<0.05$) and conditions*subjects ($F[198,198]=1.36$, $p<0.05$) were weakly significant. Therefore, in the remainder of the paper, subjects have not been

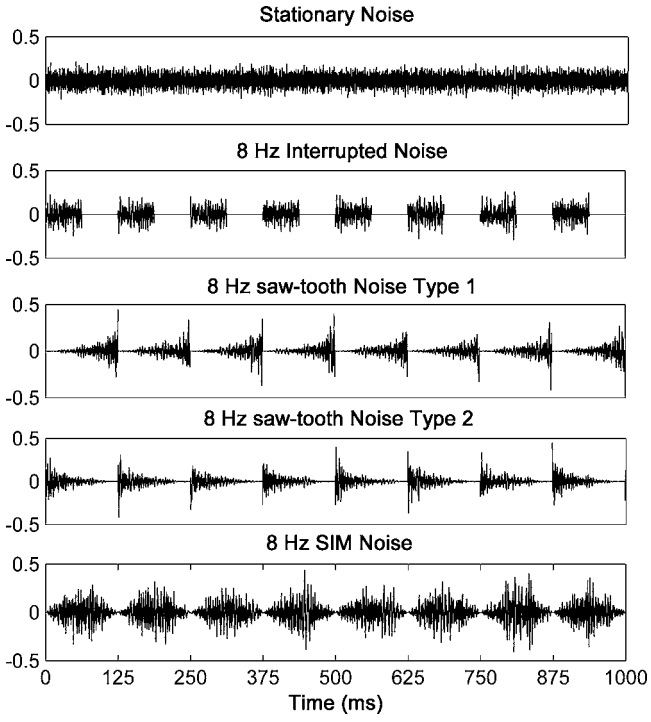

FIG. 1. Illustration of some masking noises used in the present experiment. In this selection all signals have a spectrum equal to the long-term average spectrum of the female target speech (Versfeld *et al.*, 2000) and, with exception of the upper panel, a modulation frequency of 8 Hz. The second panel shows interrupted noise with a duty cycle of 50%; the third panel saw-tooth noise (type 1), the fourth panel saw-tooth noise (type 2, time reversed version of type 1), and at the lower panel a SIM noise.

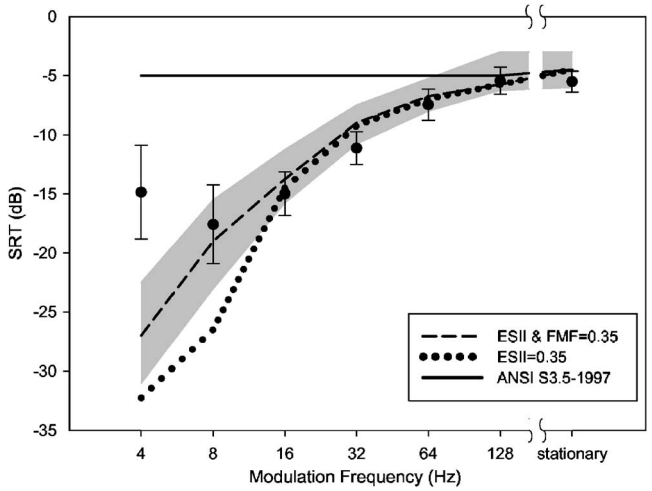

FIG. 2. Speech reception threshold (dB) as function of modulation frequency (Hz) for the steady state noise and the 4–128 Hz interrupted noise conditions. Error bars denote the standard deviations between subjects. The shaded area, the dashed, dotted, and solid lines are model predictions and are explained in Sec. V.

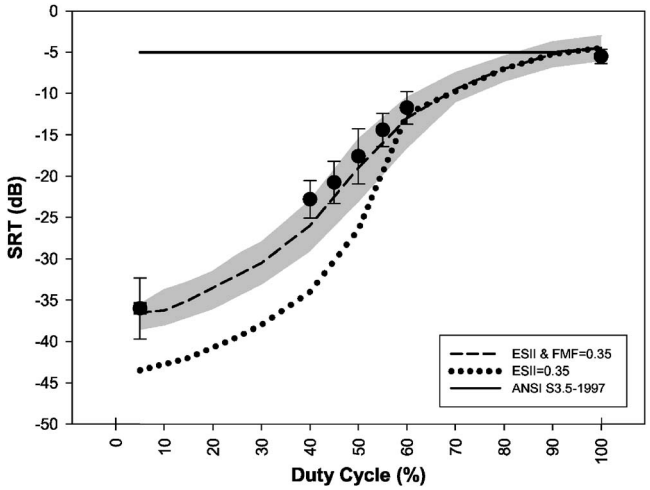

FIG. 3. Speech reception threshold (dB) as function of duty cycle (%) for interrupted noise with a modulation frequency of 8 Hz (circles). Error bars denote the standard deviations between subjects. An additional noise condition (duty cycle 5%, square) will be explained in Sec. IV. The shaded area, the dashed, dotted, and solid lines are model predictions and explained in Sec. V.

entered as a separate factor in the analyses. Because the present paper focuses on model predictions, and not on a possible learning effect, only the results of the retest data have been presented, although test/retest still has been entered as a factor in the data analysis. Below, additional analyses were performed on subsets of the data.

A. Interrupted noise

Figure 2 shows the SRT values (dB) for the retest data, averaged across subjects, as function of modulation frequency (Hz) for interrupted noise with a duty cycle of 50%. Error bars denote the standard deviation between subjects. The shaded area, the dashed, dotted, and solid lines in Fig. 2 are model predictions and are discussed below. A 7[condition]$\times$2[test/retest] ANOVA showed that the main effect of condition was significant ($F[6,1]=123.37$, $p<0.001$). Also, the main effect test/retest was significant ($F[1,1]=8.88$, $p<0.005$). The SRTs of the retest were on average 0.9 dB better. There was no significant interaction. The SRT is lowest with a modulation frequency of 8 Hz (−16.7 dB). This SRT is comparable, but somewhat higher than that obtained by de Laat and Plomp (1983), who found an SRT of −23 dB at a modulation frequency of 10 Hz. The SRT with a 4 Hz interrupted noise is somewhat higher compared to that with an 8 Hz interrupted noise. This may be accounted for by the fact that at these slow modulation rates noise bursts can mask complete words of a sentence. The trend in the present data is consistent with the results of Miller and Licklider (1950), Licklider and Guttman (1957), Gustfsson and Arlinger (1994), Trine (1995), Dubno *et al.* (2002, 2003), and Nelson *et al.* (2003). Bonferroni post hoc tests showed that the 8, 16, 32, and 64 Hz conditions differed significantly from each other. The 64, 128, and stationary noise conditions did not differ significantly.

Figure 3 shows the SRT values (dB) averaged across subjects, for the retest data only, as function of duty cycle (%) for interrupted noise with a modulation frequency of 8 Hz. Error bars denote the standard deviations between subjects. The shaded area, the dashed, dotted, and solid lines in Fig. 3 are model predictions and are discussed below. The duty cycles were 40%, 45%, 50%, 55%, 60%, and 100% (steady state noise). An additional data point, indicated with a filled square, obtained with a duty cycle of 5%, will be discussed below. A 6[condition]$\times$2[test/retest] ANOVA was performed on these data. Of the main effects, difference in condition was significant ($F[5,1]=121.83$, $p<0.001$). Also, the SRT of the retest was on average 1.3 dB better than the test, which was a significant effect ($F[1,1]=9.11$, $p<0.05$). There was no significant interaction between the main effects. Bonferroni post hoc tests showed no significant differences between the 40% and 45% condition, as well as between the 55% and 60% condition. Otherwise, the SRT of all conditions were significantly different. The data show a gradual and almost linear increase in SRT from −21.8 up to −11.6 dB as the duty cycle increases from 40% up to 60%.

B. Saw-tooth noise

For the retest, the mean SRT scores of saw-tooth type 1 and saw-tooth type 2 were −9.3 and −11.9 dB, respectively. A 3[condition]$\times$2[test/retest] ANOVA was performed on the data with the saw-tooth and steady state noise. Of the main effects, differences in condition were significant ($F[2,1]=249.69$, $p<0.001$). The SRT of the retest was on average 0.1 dB better than the test, which was not significant ($F[1,1]=0.368$ $p>0.05$). There was no significant interaction. Bonferroni post hoc tests showed that all three conditions differed significantly from each other.

C. SIM noise

Figure 4 shows the SRT values averaged across subjects, for the retest data, for each of the six conditions for the interfering SIM noises and for the steady state noise. Error bars denote the standard deviations between subjects. A

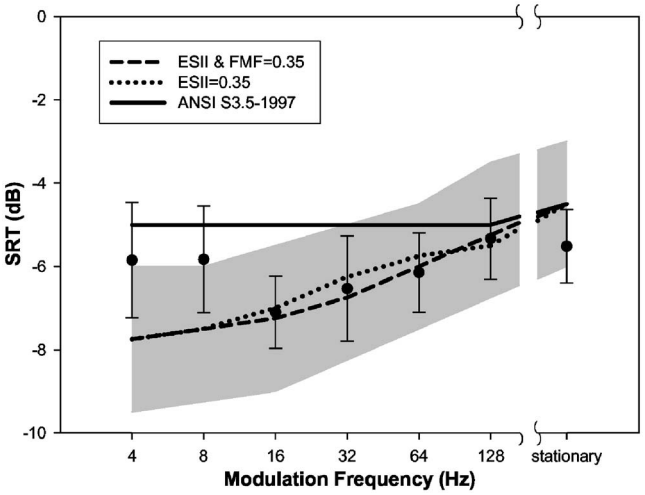

FIG. 4. Speech reception threshold (dB) as function of modulation frequency (Hz) for the conditions with SIM noise. Error bars denote the standard deviations between subjects. The shaded area, the dashed, dotted, and solid lines are model predictions and explained in Sec. V.

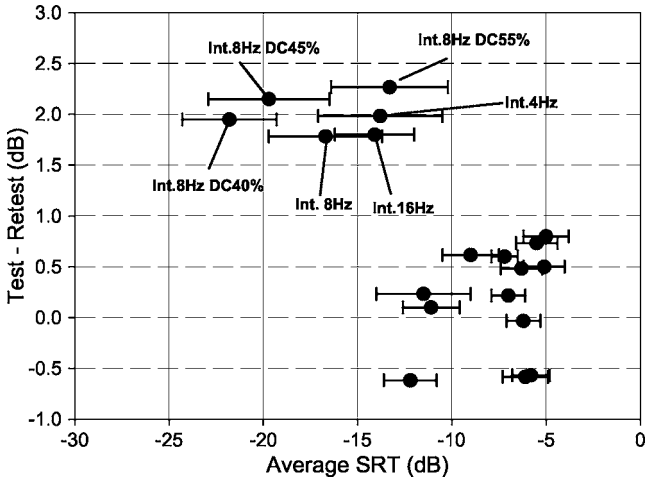

FIG. 5. Test-retest difference (dB) as function of the average SRT for all noise conditions.

7[condition]×2[test/retest] ANOVA showed that of the main effects, only differences in condition were significant ($F[6,1]=8.07$, $p<0.001$). The SRT of the retest was on average 0.1 dB better than the test, which was not significant ($F[1,1]=0.431$, $p>0.05$). There were no significant interactions. Bonferroni post hoc tests showed that the 8, 16, 32, and 64 Hz conditions were not significantly different from each other, and that the 16 Hz condition was significantly different from the 4, 128 Hz condition, and the stationary noise condition. The trends in the present data are not entirely consistent with the results of Festen (1987). He observed best SRTs for the 32 Hz condition, whereas in this study best SRTs were observed for the 16 Hz condition. Furthermore, the SRTs observed by Festen (1987) were 2–3 dB lower than the SRTs observed in this experiment.

IV. DISCUSSION

The results of the present experiment show some interesting aspects.

First of all, the SRTs of the retest were on average 0.8 dB lower than the SRTs of the first test. After separating the SRT data into subgroups, it was clear that this effect was only present in the interrupted noise conditions. A possible explanation may be that listening into the gaps of the interrupted noise requires practice. Hence, the learning effect is expected to be more prominent when the gaps are deeper. In other words: Lower (i.e., better) SRTs are accompanied by larger test-retest differences. Figure 5 displays the average test-retest difference as a function of the mean SRT for all conditions in the present study. The data in Fig. 5 form two subgroups: One subgroup is formed by those conditions where the test-retest difference does not exceed 1 dB, and the mean SRT is higher than about −12 dB. The other subgroup is formed by the conditions with relatively good SRTs of −13 dB or better. Here the test-retest differences are larger than 1.5 dB. The latter group consists of conditions with interrupted noise. It seems that the test-retest difference is related to the gap length and not particularly related to a specific modulation frequency. The lower boundary of the gap length where significant learning effects may occur then is in the order of 50 ms. To what degree the size of the learning effect is related to gap length, and how much practicing is required before thresholds stabilize, is left to future research. It is however important with respect to modeling the data (where one wants to avoid learning as much as possible), as well as with respect to clinical applications with the measurement of the SRT in fluctuating noise conditions (where one wants to reach stable thresholds as quickly as possible).

Second, the two conditions with saw-tooth noise gave a difference of 3.2 dB in SRT. The two conditions are identical, except for that saw-tooth type 2 is the time-reversed counterpart of type 1. It is likely that the difference in SRT is due to differences in forward masking. The temporal envelope of saw-tooth type 2 has a quick onset time (steep slope) and a slow decay (shallow slope), as can be seen in Fig. 1, and produces a plosive-like sound. Such an envelope has resemblance with the envelope of real speech (Rosen, 1992), since the envelope of speech is typically dominated by plosive sounds. The envelope of saw-tooth type 1 is the opposite of type 2: the envelope increases gradually and offsets abruptly. Forward masking is the phenomenon that weak sounds are masked by preceding strong sounds, and is a characteristic of the auditory system that it apparently cannot follow such abrupt offsets accurately. A signal (or speech) that is present directly after the abrupt offset is physically not masked by the saw-tooth noise, but it is masked due to the sluggishness of the auditory system. Hence, a more favorable signal-to-noise ratio is required to result in the same intelligibility as for speech in saw-tooth type 2 noise. Indeed, this is true in the present experiment. It is also true for the data of Rhebergen *et al.* (2005), who described an SRT test with intelligible and unintelligible interfering speech played normal and time-reversed. With Dutch listeners, (unintelligible) Swedish interfering speech gave a rise in SRT of 2.3 dB when played in reverse.

Third, between-subject differences appear to be larger with lower SRT values, as can be seen in Fig. 2. Rhebergen and Versfeld (2005) showed with their extended SII method

that the psychometric function (i.e., SII as a function of SNR) near SII=0.3 is relatively shallow for speech in interrupted noise compared to that for speech in stationary noise. Consequently, a given variation in SII corresponds to a large variation in the SNR with interrupted noise, but to a smaller variation with stationary noise. In the next section (Sec. V), SII calculations will show whether this explanation can fully account for the differences in variance between these conditions.

Fourth, the large difference in SRT (approximately 6 dB) obtained with interrupted noise between the present results and those of de Laat and Plomp (1983) possibly might be explained by differences in absolute threshold, since de Laat and Plomp (1983) found a high correlation between the SRT and the pure-tone average (PTA, averaged across 500, 1000, and 2000 Hz) in their group of subjects. However, the PTA of the present group of subjects is 7.6 dB better (viz., 2.0 dB HL with a standard deviation of 3.6 dB) compared to the average PTA of 9.6 dB HL (with a standard deviation of 3.6 dB) from the subjects of de Laat and Plomp (1983). Moreover, with the present data, a Pearson correlation coefficient was calculated between the individual PTAs and the noise conditions. Correlations were nonsignificant ($r=0.035$, $p>0.05$). The differences in observed SRTs must be due to other factors, such as perhaps the use of different speech corpuses (Plomp and Mimpen, 1979a, versus Versfeld *et al.*, 2000). Although Versfeld *et al.* (2000) found no significant differences between these sets when comparing them in stationary masking noise, van Wijngaarden and Houtgast (2004) did, be it in different listening conditions (such as reverberation). It is known that differences in intelligibility between different speech materials become more apparent under increasingly adverse listening situations (Mullennix *et al.*, 1989). But what properties of the speech signal cause these differences is yet unclear. A similar explanation holds for the differences in SRT with SIM noises obtained by Festen (1987) and the present data.

Next, the increase in SRT with increasing modulation frequency of the interrupted noise (from 8 to 128 Hz) is due to an increase in forward masking. In all conditions, the masker is absent in 50% of the time, but due to a decrease in "gap" duration (62.5 down to 3.9 ms), the forward masking induced by each masker pulse becomes more effective. The SRT with a 128 Hz interrupted noise is even worse than with a steady state noise. In this condition, the gaps are very short in duration, such that they are probably entirely masked. At the same time, the masker pulses must be 3 dB higher in level, in order to have the same long term root-mean-square level as stationary noise. Thus, 128 Hz interrupted noise is a more effective masker than is stationary noise.

The increase in SRT with interrupted noise when changing the modulation frequency from 8 to 4 Hz may be accounted for by the fact that with these slow modulation rates, masking of complete words in a sentence can occur. This phenomenon has also been observed by Miller and Licklider (1950) and Nelson *et al.* (2003), who found optimal performance around modulation rates of 10 and 8 Hz, respectively. Because in the SRT procedure every word of the sentence needs to be repeated correctly, it is unsuitable for these low modulation frequencies (less than 8 Hz).

Finally, a slight change in the duty cycle results in a large change in SRT, cf. Fig. 3. Considering the entire range, a decrease in duty cycle (more pulsed signals with longer gaps) will probably result in increasingly lower thresholds, with the SRT in quiet (absence of a noise masker) as a lower limit. The SRT in quiet is on average about 20 dB A (Duquesnoy, 1983; Duquesnoy and Plomp, 1983; Plomp and Mimpen, 1979b, Noordhoek, 2000), which is, compared to a 65 dB A noise level, equal to an SRT of −45 dB. Additional experiments show that the decrease holds at least to a duty cycle of 5%; resulting in an SRT of −36 dB (see Fig. 3, filled square).

V. SII MODEL PREDICTIONS

A detailed description of the conventional SII model is given in ANSI S3.5-1997 (1997) or Pavlovic (1987), and a detailed description of the ESII model is given in Rhebergen and Versfeld (2005). The basic principle of the conventional SII is that departing from the long term speech spectrum, the long term noise spectrum, and the absolute threshold of hearing, the amount of speech information that exceeds both noise and threshold is calculated. The extension proposed by Rhebergen and Versfeld (2005) is that the long term noise spectrum is replaced by the actual noise signal. Both speech (represented by stationary speech shaped noise) and noise signal are partitioned into small time frames, and within each time frame, the (now instantaneous) conventional SII is calculated, representing the speech information available to the listener at that time frame. The ESII for the condition under investigation is obtained by averaging the instantaneous SII across time. With the ESII, the length of the time frames is frequency dependent, and time constants are adapted from gap detection data (Moore, 1997). The length of a time frame ranges from approximately 35 ms in the lowest frequency band up to 9.4 ms in the highest frequency band. The present paper uses the SPIN 21 critical band weighting function (ANSI S3.5-1997, 1997, Table B.1).

Furthermore, all SII calculations are conducted with the long term speech spectrum of the female target speaker. In order to approach the sound level at the ear drum (as required by the SII model), all signals are filtered with a fifth order finite impulse response filter with the transfer characteristics of the TDH39P headphone that was used in the experiment. Also, if required, the background noise present in the sound proof booth was added to the noise signal. This seems unnecessary, but the SII model defines silence in each band as −50 dB SPL, whereas in a sound proof booth more realistic numbers are between 0 and 10 dB SPL in the mid and high frequencies and 35 to 50 dB SPL in the frequencies below 100 Hz. These levels have almost no effect with most noise types, except for conditions where noises contain relatively long silent periods, such as is the case with interrupted noise.

Since the purpose of the present paper is to evaluate the model, learning effects were eliminated as much as possible

TABLE III. For each condition of the present experiment, the SRTs of the retest and the results of the various SII calculation schemes are given. Lower rows yield the mean and standard deviation of the SII. FMF denotes the use of the forward masking function, asym.w. denotes the use of an asymmetrical integration window, and Lin.w. denotes the use of a fixed integration window of 4 ms.

Noise condition	SRT(dB)	stdv(dB)	Conventional SII	Extended SII (2005)	Extended SII & FMF (asym. w.)	Extended SII & FMF (Lin.w.)
Int 8 Hz	−17.6	3.3	0.000	0.388	0.357	0.359
Int 16 Hz	−15.0	1.8	0.031	0.333	0.291	0.299
Int 32 Hz	−11.1	1.4	0.012	0.271	0.260	0.276
Int 64 Hz	−7.5	1.3	0.239	0.309	0.299	0.292
Int 128 Hz	−5.4	1.1	0.297	0.339	0.299	0.305
Int 8 Hz dc40	−22.8	2.3	0.000	0.465	0.385	0.394
Int 8 Hz dc45	−20.8	2.6	0.000	0.432	0.367	0.376
Int 8 Hz dc55	−14.4	2.0	0.044	0.369	0.354	0.357
Int 8 Hz dc60	−11.7	2.0	0.117	0.365	0.361	0.364
Sawtooth *T*1	−9.3	1.5	0.178	0.389	0.369	0.376
Sawtooth *T*2	−11.9	1.6	0.102	0.310	0.330	0.335
SIM 8 Hz	−5.8	1.3	0.303	0.381	0.384	0.385
SIM 16 Hz	−7.1	0.9	0.260	0.322	0.331	0.335
SIM 32 Hz	−6.5	1.3	0.308	0.318	0.329	0.335
SIM 64 Hz	−6.2	0.9	0.289	0.314	0.315	0.323
SIM 128 Hz	−5.3	1.0	0.319	0.337	0.321	0.326
Steady state	−5.5	0.9	0.314	0.316	0.316	0.317
Mean SII			0.17	0.35	0.33	0.34
Std SII			0.13	0.05	0.04	0.04

by omitting the first test and considering only the average values of the retest. Furthermore, the noise conditions with modulation frequencies below 8 Hz were excluded from the SII calculations. As mentioned earlier, noise conditions with these low modulation frequencies give a rise in SRT due to the masking of complete words.

A. Conventional SII calculations

The fourth column of Table III shows the results of the calculations with the conventional SII model (ANSI S3.5-1997, 1997). By definition, at threshold one would expect the SII to be similar across conditions, since threshold is reached by the availability of a given fixed amount of speech information. Table III shows that for the conventional SII this certainly is not true, which makes the conventional SII model a poor predictor for the speech intelligibility in fluctuating noise. The SII has a mean of 0.17 and a large standard deviation between conditions of 0.13. The SRTs predicted by the conventional SII model are given in Figs. 2–4 by a solid line, where the SII has been kept fixed to 0.35. As can be seen, the predicted SRT is virtually independent on the type of fluctuation of the noise masker—as expected, because the model departs from the long term spectra of speech and noise.

B. Extended SII calculations

The fifth column of Table III shows the extended SII calculations (Rhebergen and Versfeld, 2005). Here, the mean SII value is 0.35 and its standard deviation is equal to 0.05. Predictions of the SRT for the present conditions are plotted in Figs. 2–4 as a dotted curve, where the SII has been kept fixed to 0.35. Predictions with the extended SII model are far better than with the ANSI S3.5-1997 method, described in the previous section. However, it can be seen from the figures that the model still fails to adequately describe the data for conditions with relatively large silent gaps. Apparently, the masking function used in the model underestimates the real amount of masking in these conditions. Also, since the ESII model is a time-symmetric model, it is unable to account for the difference in threshold between the two conditions with the saw-tooth masker. The ESII model always will predict identical thresholds for noises that are each others time reversal. Simple adaptation of the integration time cannot solve the problem, since this results in deviations for the ESII for the other conditions.

In order to overcome these two shortcomings of the model, in the next section a forward masking function is introduced.

C. Implementation of forward masking in the extended SII

A large number of studies have shown the possibility of masking a target signal by a preceding masker (so-called forward masking), and its relationship between masker level and the time interval between masker and target signal (Pollack, 1955; Plomp, 1964; Elliott, 1969; Duifhuis, 1973; Widin and Viemeister, 1979; Jesteadt *et al.*, 1982; Moore and Glasberg, 1983; Kidd and Feth, 1982). These studies show a decrease in masking threshold with increased masker-signal delay. The masking threshold returns in about 200 ms to the level of the unmasked target signal threshold (i.e., when no masker is present), regardless of masker level. When plotting the masking thresholds (dB) as a function of masker-target gap on a logarithmic time scale, a linear relationship exists (e.g., Plomp, 1964). Ludvigsen (1985) has modeled this

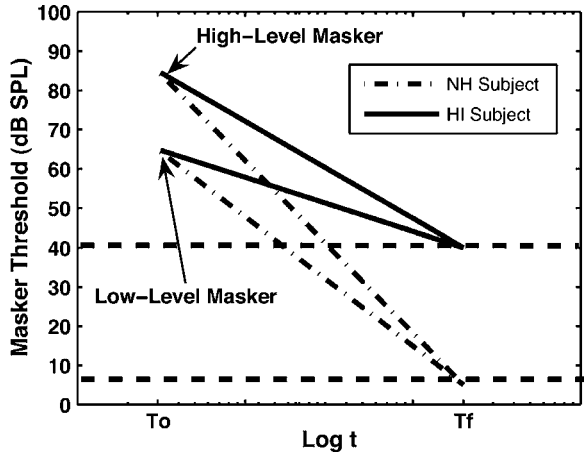

FIG. 6. Masked threshold (dB SPL) plotted as a function of time (on a logarithmic axis) for two masker levels (high-level masker and low-level masker) and for a normal-hearing and a hearing-impaired subject. Horizontal dashed lines indicate the absolute threshold of that subject. (Redrawn from Ludvigsen, 1985, Fig. 4, p. 1277.)

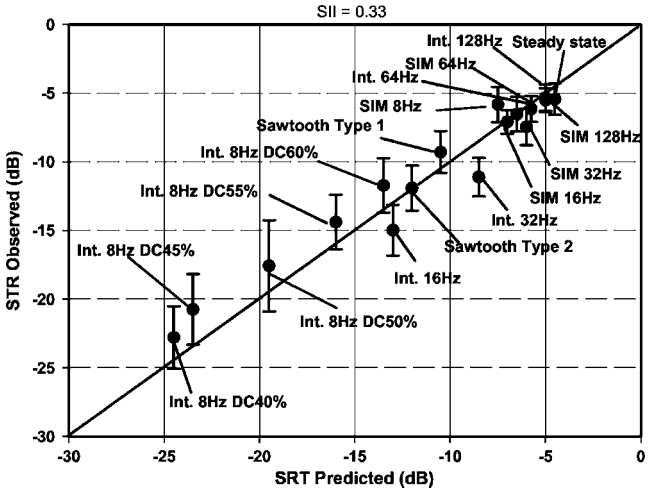

FIG. 7. For all conditions, the observed SRT (dB) is plotted as a function of the predicted SRT (dB), where the prediction has been made with the ESII model with the FMF included. Error bars denote the standard deviation between subjects.

function, which is called in this paper the forward-masking function (FMF). The model parameters were determined from the results of other studies reported in the literature, and the model predicts forward masking very well, not only for the normal hearing, but also for the hearing impaired. Figure 6 displays the FMF, i.e., the masked threshold as a function of time (reprinted from Ludvigsen, 1985) for two masker levels (high-level masker and low-level masker) and for a normal-hearing and a hearing-impaired subject. As can be seen in Fig. 6, the FMF is linear between T_0 and T_f when time is plotted on a logarithmic axis. Also, the duration of the FMF is always equal, regardless of hearing loss or masker level.

The middle portion of the FMF is a simple linear relationship, and is given by

$$E_{\mathrm{FMF}}(t) = E(T_0) - \frac{\log(t/T_0)}{\log(T_f/T_0)} * [E(T_0) - E(T_f)],$$

where at time T_0, the level of the linear portion $E(T_0)$ is equal to the level of the envelope of the masker, and where at time T_f, the linear function intersects with the absolute threshold of hearing $E(T_f)$. The values of the parameters T_0 and T_f are 2 and 200 ms, respectively. To take forward masking into account, the original envelope $E(t)$ is modified according to: $E(t) = \max[E(t), E_{\mathrm{FMF}}(t)]$. In this manner, sharp onsets in the envelope are followed instantaneously, but sharp offsets make that $E_{\mathrm{FMF}}(t)$ take over, resulting in a gradual decline of the envelope (due to forward masking). The FMF does not account for the phenomenon of backward masking, where a soft signal is masked by a louder signal that follows it. Backward masking is still poorly understood (Moore, 1997), and its effect on speech intelligibility is still unclear and probably not very large.

Note that the FMF is similar in the low and high frequency bands, whereas temporal integration is not. Both phenomena act separately on the signal, and probably are situated in different places in the auditory system. So far, forward masking was not modeled separately in the ESII, but rather was taken together with temporal integration. Effectively this gave longer integration times, which can explain that a best fit to the data of Rhebergen and Versfeld (2005) was obtained by multiplication of the time constants from Moore (1997) by a factor of 2.5. However, when forward masking is modeled separately from temporal integration, the original integration times (the original frequency dependent gap detection lengths) should be used.

The sixth column of Table III shows the ESII calculations with the FMF included. This addition of forward masking results in better predictions, i.e., SII values are closer together as can be deduced from the lower standard deviation (0.04). Indeed, the SII for those conditions with relatively long silent periods has decreased. In addition, the SII values for the two saw-tooth conditions are closer together.

When the calculation scheme is simplified by taking all integration times equal to 4 ms, the standard deviation in SII for all noise conditions remains the same (0.04), see the seventh column of Table III. This is because the time constants of the FMF are an order of magnitude larger than those of gap detection. Predictions of the ESII model with the FMF included are denoted in Figs. 2–4 with dashed lines, where the SII has been kept fixed to 0.35. Indeed, especially for conditions with larger silent gaps, this SII model predicts the data better. The shaded areas in Figs. 2–4 indicate the range of the predicted SRT when the SII value ranges between 0.30 and 0.40. With the exception of those noise conditions with a very low modulation frequency, all observed SRTs are close to the dashed line, and are situated in the shaded area. The benefit of the FMF is less clear in the SIM noise conditions (Fig. 4). Due to the fact that there are no complete silent periods in the SIM noise conditions (see Fig. 1 for comparison between SIM and interrupted noise), the differences between the ESII model with or without FMF is less clear.

Figure 7 displays for all conditions described in the previous section the relationship between the observed SRT and the SRT as predicted by the ESII model with the FMF. Predictions were made under similar assumptions as described

above, and the SII was taken equal to 0.33, the average value of the SII in Table III, column 6. If the data of Fig. 7 are considered in detail, some predicted SRTs lie above the diagonal. Since these conditions appear to be the conditions in which a learning effect was observed (see Fig. 5), it is expected that after all learning effects are overcome, SRTs will become better and, hence, lie closer to the diagonal.

Several conditions, especially those with low SRTs, show large between-subject differences. As argued above, these large differences are due to the shallowness of the psychometric function (SII as a function of SNR). When converting the observed individual SRTs to SII values, differences between subjects are comparable for all conditions. This indicates that no factors other than differences in the steepness of the psychometric function play a role. Alternatively, the width of the shaded area in Figures 2–4 (especially in Fig. 2) is clearly related to the width of the error bars.

VI. EXTENSIONS TO AND LIMITATIONS OF THE SII MODEL

The addition of a forward masking function has increased the predictive power of the ESII model, at least for normal-hearing subjects. However, experiments thus far dealt with presentation near 65 dB A only. It is known that with increasing level, the excitation pattern broadens, hence spectral resolution decreases, and temporal resolution increases. Although in principle the extended SII model can account for the increase in temporal resolution (Ludvigsen, 1985), it cannot account for the broadening of the auditory filters, since filter bandwidths are fixed in the model. A future extension to the SII model thus may be to implement a more realistic, level dependent, auditory filterbank.

For listeners with normal hearing or with a mild hearing loss, the SII model in its present form (ANSI S3.5-1997, 1997) is able to predict the speech intelligibility in stationary noise (Pavlovic, 1987; Noordhoek, 2000). However, the model is not meant to predict the speech intelligibility for listeners with moderate to severe hearing loss (Rankovic, 1998; Ching *et al.*, 1998, 2001; Hogan and Turner, 1998; Noordhoek, 2000). With these hearing losses the SII model overestimates performance. Hearing-impaired subjects often require SII values that exceed 0.33, which indicates that correction only for audibility is not sufficient. One reason may be that auditory processing is less than optimal (so-called suprathreshold deficits) (Noordhoek, 2000). Additionally, decreased spectrotemporal resolution may play a role. The latter factor may be accounted for by the extended SII model by parameter adjustment.

As mentioned above, the SRT paradigm is not particularly well suited for sentences in modulated noise where the modulation frequency is low and masking of whole words may occur. It is possible that SRTs are measured that do not reflect the actual masking situation, since the SRT procedure yields a correct score only when the whole sentence is scored correctly. Thus, with these low modulation frequencies, the increase in threshold is actually an experimental artifact. Indeed, when using a different experimental paradigm (Trine, 1995) thresholds do not increase when lowering the modulation frequency. With the present speech materials (Versfeld *et al.*, 2000), the speech rate is about 4–5 syllables per second, hence, a 4-Hz modulated signal may mask half of a word or more. Apparently, this already causes deterioration in intelligibility. Thus, there is a lower limit in the modulation frequency to which the SRT procedure is valid.

VII. SUMMARY

The present paper describes a validation study of the extension to the SII (ANSI S3.5-1997, 1997) proposed by Rhebergen and Versfeld (2005). The extended SII model was validated with SRT experiments with listeners with normal-hearing in nonstationary (or fluctuating) noise conditions that are critical to the extended SII model. From these data, it can be concluded that the extended SII model is able to predict the SRTs for the majority of conditions, but that predictions are better when the extended SII model includes a function to account for forward masking.

ACKNOWLEDGMENTS

Tammo Houtgast, Joost Festen, Gaston Hilkhuysen, and Erwin George are acknowledged for the inspiring discussions on the topic. László Körössy is especially acknowledged for his help with the computer programming and his help with the SRT computer program. The editor Dr. M. Sommers, and two anonymous reviewers are acknowledged for there useful comments.

ANSI (**1996**). "ANSI S3.6-1996, American national standard methods for specification for audiometers" (American National Standards Institute, New York).

ANSI (**1997**). "ANSI S3.5-1997, American national standard methods for calculation of the speech intelligibility index" (American National Standards Institute, New York).

Ching, T. Y. C., Dillon, H., and Byrne, D. (**1998**). "Speech recognition of hearing-impaired listeners: Predictions from audibility and the limited role of high-frequency amplification," J. Acoust. Soc. Am. **103**, 1128–1140.

Ching, T. Y. C., Dillon, H., Katsch, R., and Byrne, D. (**2001**). "Maximising effective audibility in hearing aid fitting," Ear Hear. **22**, 212–224.

de Laat, J. A. P. M., and Plomp, R. (**1983**). "The reception threshold of interrupted speech for hearing-impaired listeners," in *Hearing—Physiological Bases and Psychophysics*, edited by R. Klinke and R. Hartman (Springer-Verlag, Berlin), pp. 359–363.

Dubno, J. R., Horwitz, A. R., and Ahlstrom, J. B. (**2002**). "Benefit of modulated maskers for speech recognition by younger and older adults with normal-hearing," J. Acoust. Soc. Am. **111**, 2897–2907.

Dubno, J. R., Horwitz, A. R., and Ahlstrom, J. B. (**2003**). "Recovery from prior stimulation: Masking of speech by interrupted noise for younger and older adults with normal-hearing," J. Acoust. Soc. Am. **113**, 2084–2094.

Duifhuis, H. (**1973**). "Consequences of peripheral frequency selectivity for nonsimultaneous masking," J. Acoust. Soc. Am. **54**, 1471–1488.

Duquesnoy, A. J. (**1983**). "Effect of a single interfering noise or speech source upon the binaural sentence intelligibility of aged persons," J. Acoust. Soc. Am. **74**, 739–743.

Duquesnoy, A. J., and Plomp, R. (**1983**). "The effect of a hearing aid on the speech-reception threshold of hearing-impaired listeners in quiet and in noise," J. Acoust. Soc. Am. **73**, 2166–2173.

Elliott, L. L. (**1969**). "Masking of tones before, during, and after brief silent periods in noise," J. Acoust. Soc. Am. **45**, 1277–1279.

Festen, J. M. (**1987**). "Speech-perception threshold in a fluctuating background sound and its possible relation to temporal resolution," in *The Psychophysics of Speech Perception*, edited by M. E. H. Schouten (Martinus Nijhoff, Dordrecht), pp. 461–466.

Festen, J. M., and Plomp, R. (**1990**). "Effects of fluctuating noise and interfering speech on the speech-reception threshold for impaired and normal-hearing," J. Acoust. Soc. Am. **88**, 1725–1736.

Fletcher, H., and Galt, R. H. (**1950**). "The perception of speech and its relation to telephony," J. Acoust. Soc. Am. **22**, 89–151.
French, N. R., and Steinberg, J. C. (**1947**). "Factors governing the intelligibility of speech sounds," J. Acoust. Soc. Am. **19**, 90–119.
Gustafsson, H. A., and Arlinger, S. D. (**1994**). "Masking of speech by amplitude-modulated noise," J. Acoust. Soc. Am. **95**, 518–529.
Hogan, C. A., and Turner, C. W. (**1998**). "High-frequency audibility: Benefits for hearing-impaired listeners," J. Acoust. Soc. Am. **104**, 432–441.
Houtgast, T., Steeneken, H. J., and Bronkhorst, A. W. (**1992**). "Speech communication in noise with strong variations in the spectral or the temporal domain," *Proceedings of the 14th International Congress on Acoustics*, Vol. 3, pp. H2–H6.
Jesteadt, W., Bacon, S. P., and Lehman, J. R. (**1982**). "Forward masking as a function of frequency, masking level, and signal delay," J. Acoust. Soc. Am. **71**, 950–962.
Kidd, G., and Feth, L. L. (**1982**). "Effects of masker duration in pure-tone forward masking," J. Acoust. Soc. Am. **75**, 1384–1386.
Koopman, J., Franck, B. A., and Dreschler, W. A. (**2001**). "Toward a representative set of "real-life" noises," Audiology **40**, 78–91.
Kryter, K. D. (**1962a**). "Methods for the calculation and use of the articulation index," J. Acoust. Soc. Am. **34**, 1689–1697.
Kryter, K. D. (**1962b**). "Validation of the articulation index," J. Acoust. Soc. Am. **34**, 1698–1702.
Licklider, J. C. R., and Guttman, N. (**1957**). "Masking of speech by line-spectrum interference," J. Acoust. Soc. Am. **29**, 287–296.
Ludvigsen, C. (**1985**). "Relations among some psychoacoustic parameters in normal and cochlearly impaired listeners," J. Acoust. Soc. Am. **78**, 1271–1280.
Miller, G. A., and Licklider, J. C. R. (**1950**). "The intelligibility of interrupted speech," J. Acoust. Soc. Am. **22**, 167–173.
Moore, B. C. J., and Glasberg, B. R. (**1983**). "Growth of forward masking for sinusoidal and noise maskers as a function of signal delay; implications for suppression in noise," J. Acoust. Soc. Am. **73**, 1249–1259.
Moore, B. C. (**1997**). *An Introduction to the Psychology of Hearing*, 4th ed. (Academic, London).
Mullennix, J. W., Pisoni, D. B., and Martin, C. S. (**1989**). "Some effects of talker variability on spoken word recognition," J. Acoust. Soc. Am. **85**, 365–378.
Nelson, P. B., Jin, S. H., Carney, A. E., and Nelson, D. A. (**2003**). "Understanding speech in modulated interference: Cochlear implant users and normal-hearing listeners," J. Acoust. Soc. Am. **113**, 961–968.
Noordhoek, I. M. (**2000**). "Intelligibility of narrow-band speech and its relation to auditory functions in hearing-impaired listeners," Doctoral thesis, Free University, Amsterdam.
Pavlovic, C. V. (**1987**). "Derivation of primary parameters and procedures for use in speech intelligibility predictions," J. Acoust. Soc. Am. **82**, 413–422.
Plomp, R. (**1964**). "Rate of decay of auditory sensation," J. Acoust. Soc. Am. **36**, 277–282.
Plomp, R., and Mimpen, A. M. (**1979a**). "Improving the reliability of testing the speech reception threshold for sentences," Audiology **18**, 43–52.
Plomp, R., and Mimpen, A. M. (**1979b**). "Speech-reception threshold for sentences as a function of age and noise level," J. Acoust. Soc. Am. **66**, 1333–1342.
Pollack, I. (**1955**). "Masking by a periodically interrupted noise," J. Acoust. Soc. Am. **27**, 353–355.
Rankovic, C. M. (**1998**). "Factors governing speech reception benefits of adaptive linear filtering for listeners with sensorineural hearing loss," J. Acoust. Soc. Am. **103**, 1043–1057.
Rhebergen, K. S., and Versfeld, N. J. (**2005**). "A speech intelligibility index-based approach to predict the speech reception threshold for sentences in fluctuating noise for normal-hearing listeners," J. Acoust. Soc. Am. **117**, 2181–2192.
Rhebergen, K. S., Versfeld, N. J., and Dreschler, W. A. (**2005**). "Release from informational masking by time reversal of native and non-native interfering speech," J. Acoust. Soc. Am. **118**, 1274–1277.
Rosen, S. (**1992**). "Temporal information in speech: Acoustic, auditory and linguistic aspects," Philos. Trans. R. Soc. London, Ser. B **336**, 367–373.
Trine, T. D. (**1995**). "Speech recognition in modulated noise and temporal resolution: Effects of listening bandwidth," Doctoral dissertation, University of Minnesota, Twin Cities (unpublished).
van Wijngaarden, S. J., and Houtgast, T. (**2004**). "Effect of talker and speaking style on the Speech Transmission Index," J. Acoust. Soc. Am. **115**, 38–41.
Versfeld, N. J., Daalder, L., Festen, J. M., and Houtgast, T. (**2000**). "Method for the selection of sentence materials for efficient measurement of the speech reception threshold," J. Acoust. Soc. Am. **107**, 1671–1684.
Versfeld, N. J., and Dreschler, W. A. (**2002**). "The relationship between the intelligibility of time-compressed speech and speech in noise in young and elderly listeners," J. Acoust. Soc. Am. **111**, 401–408.
Widin, G. P., and Viemeister, N. F. (**1979**). "Intensive and temporal effects in pure-tone forward masking," J. Acoust. Soc. Am. **66**, 388–395.

Vowel recognition via cochlear implants and noise vocoders: Effects of formant movement and duration

Paul Iverson[a)]
Department of Phonetics and Linguistics, University College London, 4 Stephenson Way, London NW1 2HE, United Kingdom

Charlotte A. Smith
Department of Human Communication Science, University College London, 4 Stephenson Way, London NW1 2HE, United Kingdom

Bronwen G. Evans
Department of Phonetics and Linguistics, University College London, 4 Stephenson Way, London NW1 2HE, United Kingdom

(Received 21 November 2005; revised 25 September 2006; accepted 26 September 2006)

Previous work has demonstrated that normal-hearing individuals use fine-grained phonetic variation, such as formant movement and duration, when recognizing English vowels. The present study investigated whether these cues are used by adult postlingually deafened cochlear implant users, and normal-hearing individuals listening to noise-vocoder simulations of cochlear implant processing. In Experiment 1, subjects gave forced-choice identification judgments for recordings of vowels that were signal processed to remove formant movement and/or equate vowel duration. In Experiment 2, a goodness-optimization procedure was used to create perceptual vowel space maps (i.e., best exemplars within a vowel quadrilateral) that included F1, F2, formant movement, and duration. The results demonstrated that both cochlear implant users and normal-hearing individuals use formant movement and duration cues when recognizing English vowels. Moreover, both listener groups used these cues to the same extent, suggesting that postlingually deafened cochlear implant users have category representations for vowels that are similar to those of normal-hearing individuals. © *2006 Acoustical Society of America.* [DOI: 10.1121/1.2372453]

PACS number(s): 43.71.Es, 43.71.Ky [AJO] Pages: 3998–4006

I. INTRODUCTION

Monophthongal English vowels have long been thought to be recognized by their F1 and F2 target frequencies, but it has become clear that finer-grained phonetic variation, such as intrinsic formant movement and duration, is also important for recognition by normal-hearing native English speakers. For example, vowel recognition accuracy in quiet declines by about 15–23 percentage points when vowel formant movement is flattened in synthesized or signal-processed speech (e.g., Assmann and Katz, 2005; Hillenbrand and Nearey, 1999), and vowels can be recognized even when the relatively steady-state portions (i.e., where the formant frequencies meet their targets) have been removed (e.g., Strange, 1989). At least in American English, vowel duration likely has a smaller influence on intelligibility (e.g., lengthening or shortening vowels reduces vowel identification accuracy by about 5 percentage points), although speakers systematically vary vowel duration in their productions (e.g., Hillenbrand *et al.*, 2000). This recent emphasis on fine-grained phonetic variation in vowels parallels work on episodic memory and talker differences, which suggests that such phonetic details are an important contributor to speech understanding, rather than a nuisance that must be normalized or removed (e.g., Hawkins and Smith, 2001; Johnson, 2005; Nygaard and Pisoni, 1998).

Current evidence suggests that listeners also use fine-grained acoustic variation to recognize vowels under adverse conditions (e.g., noise, hearing impairments, or cochlear implants). For example, Neel (1998) found that normal-hearing and elderly hearing-impaired individuals were affected similarly by manipulations of signal-processed vowels; recognition accuracy declined for both groups when formant movement was removed and duration was equated. Ferguson and Kewley-Port (2002) found that normal-hearing and hearing-impaired individuals use formant movement and duration when listening to natural speech in multi-talker babble, but the errors for specific vowels differed between the two groups, suggesting that the two groups had somewhat different cue weightings. Kirk *et al.* (1992) found that both normal-hearing listeners and cochlear implant users were able to recognize vowels above chance based only on consonantal formant transitions (i.e., edited CVC syllables in which the quasi-steady-state vowel portion was removed), although removing these consonantal formant transitions from natural CVCs (i.e., allowing listeners to hear the quasi-steady-state vowel without the consonants) had no effect on vowel recognition.

The present study examined whether vowel-intrinsic formant movement (i.e., formant movement within the vowel,

a)Author to whom correspondence should be addressed.

 © 2006 Acoustical Society of America

rather than the consonantal formant transitions examined by Kirk *et al.*, 1992) and duration are used for vowel recognition by postlingually deafened adult cochlear implant users, and normal-hearing individuals listening to cochlear implant simulations. It would be surprising if exactly the same cues were used when recognizing vowels via cochlear implants and normal hearing, because the sensory information provided by acoustic and electric hearing differ substantially. Modern cochlear implants represent the continuous spectrum of speech with a relatively small number of spectral channels, and vowel recognition accuracy seems to be primarily limited by the effective number of spectral channels that are available (e.g., Dorman *et al.*, 1997; Dorman and Loizou, 1998; Fishman *et al.*, 1997; Friesen *et al.*, 2001; Shannon *et al.*, 1995; Xu *et al.*, 2005). Although some modern cochlear implants have as many as 22 electrodes, the neural populations stimulated by different electrodes overlap to a considerable extent, so most implant users effectively have only around 4–7 independent channels (e.g., Friesen *et al.*, 2001). In contrast, normal-hearing individuals are able to utilize about 20 spectral channels. Given that cochlear implant users have poorer resolution for frequency differences, it may be advantageous for them to give more weight to vowel duration than would normal-hearing individuals; temporal resolution via cochlear implants can be as good as with normal hearing (e.g., Busby *et al.*, 1993; Shannon, 1989, 1992; see Shannon, 1993 for a review). However, vowel formant movement may be less informative; in addition to having reduced spectral resolution, some cochlear implant users appear to have difficulty perceiving changes in formant frequencies (e.g., Dorman and Loizou, 1997).

It is particularly plausible that cochlear implant users would learn to rely on different cues than do normal-hearing listeners, because individuals undergo a period of acclimatization after receiving their cochlear implant; vowel recognition accuracy increases by an average of ~35 percentage points over the first 9 months of implant use (e.g., Tyler *et al.*, 1997; Välimaa *et al.*, 2002). The acclimatization process is not well understood, but the improvements in speech perception probably arise from changes in linguistic categorization, not only from changes in lower-level psychophysical processing. For example, Svirsky *et al.* (2004) tracked best exemplar locations in an F1×F2 vowel space for cochlear implant users following implantation; most individuals had vowels at anomalous locations immediately after implantation, and their best exemplar locations tended to move toward those of normal-hearing individuals as they used their cochlear implant over a 2-year period. This suggests that individuals "remap" their vowel space in some way after implantation. However, even after this remapping has likely been completed, the position of individual vowels in the F1×F2 space can differ from those of normal-hearing individuals, and their vowel categories can overlap significantly (e.g., Harnsberger *et al.*, 2001).

The present study investigated how formant movement and duration contribute to vowel identification accuracy (Experiment 1) and to the underlying representations of the vowel categories (Experiment 2). Experiment 1 was similar to previous studies that examined the effects of removing formant movement and duration on vowel identification for normal-hearing listeners (e.g., Assmann and Katz, 2005; Hillenbrand *et al.*, 2000; Hillenbrand and Nearey, 1999); listeners were tested on natural vowels and on signal-processed versions in which the vowel formant movement was removed and duration was equated. Cochlear implant users were tested on these stimuli without additional processing. Normal-hearing listeners were tested on unprocessed versions and on stimuli that had been passed through two, four, and eight-channel noise vocoders simulating a CIS processing strategy (Shannon *et al.*, 1995). Experiment 2 used synthetic stimuli to find locations of best exemplars within a vowel quadrilateral. Previous work has conducted this kind of mapping in a two-dimensional space composed of Fl and F2 target frequencies (e.g., Harnsberger *et al.*, 2001; Johnson *et al.*, 1993). The present study used a multidimensional extension of this method (Iverson and Evans, 2003), to find best exemplars in a five-dimensional space comprising F1 and F2 frequencies at the beginning and end of the vowels, and duration.

II. EXPERIMENT 1: IDENTIFICATION OF SIGNAL-PROCESSED VOWELS

A. Method

1. Subjects

The cochlear implant users were 11 postlingually deafened adults with an age range of 50–75 years. All were native speakers of British English. The subjects were not selected based on their implant or processor strategy; there were eight Nucleus, two Clarion, and 1 Med-El users. They were tested 0.6–7.3 years postimplantation.

The normal-hearing subjects were ten native speakers of Standard Southern British English, with an age range of 24–34 years. All reported having no known hearing or learning disabilities.

2. Stimuli and apparatus

The stimuli were recorded from two speakers, male and female, who were native speakers of southern British English. They were recorded saying the carrier sentence *Say /hVd/ again* with 13 words: *heed* (/iː/), *hid* (/ɪ/), *hayed* (/eɪ/), *head* (/ɛ/), *had* (/æ/), *heard* (/ɜː/), *hud* (/ʌ/), *hod* (/ɒ/), *hard* (/ɑː/), *hoard* (/ɔː/), *hood* (/ʊ/), *hoed* (/əʊ/), and *who'd* (/uː/). They were also recorded reading a short passage (Aesop's *The north wind and the sun*). The stimuli were recorded in an anechoic chamber, and downsampled for playback with 11 025 16 bit samples per second.

Three additional versions of the vowels were created that (1) removed all formant movement, (2) equated duration, and (3) removed formant movement and equated duration. The changes to the stimuli were made using Praat (Boersma and Weenink, 2002). Formant movement was removed using LPC analysis and resynthesis. Specifically, LPC analyzed the signal from the start of voicing after the /h/ to the start of the /d/ closure, the signal was inverse filtered to produce an LPC residual, a time slice of the LPC analysis was identified that represented the vowel's target formant frequencies (defined as the point where F1 reached a peak),

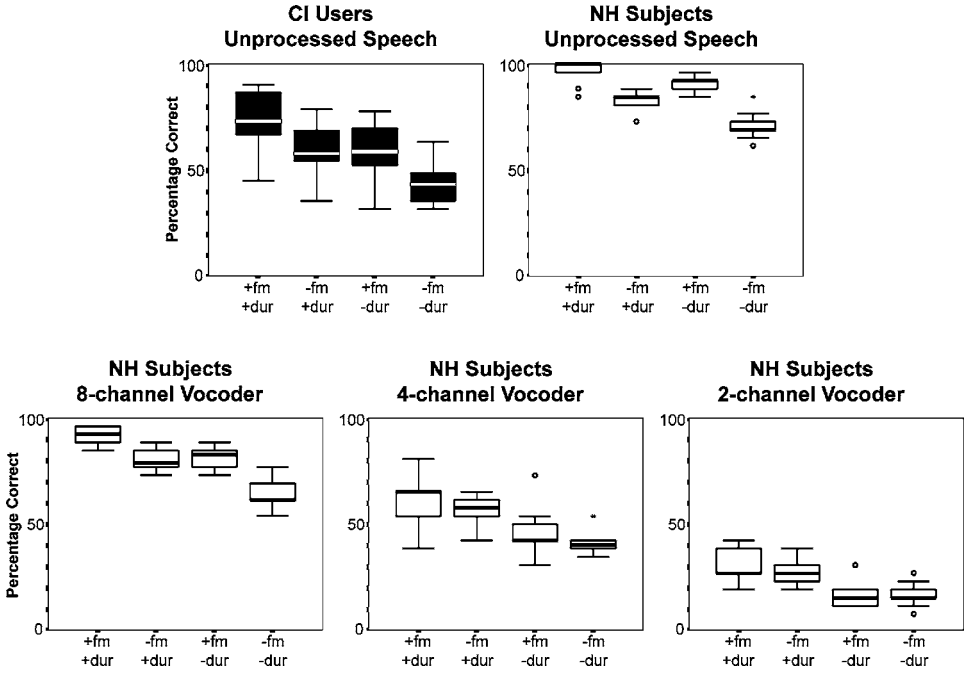

FIG. 1. Boxplots for vowel identification by cochlear implant (CI) users and normal-hearing (NH) subjects, for natural speech (+fm, +dur), vowels with no formant movement but natural duration contrast (−fm, +dur), vowels with natural formant movement and no duration contrast (+fm, −dur), and vowels with no formant movement and no duration contrast (−fm, −dur). The boxes and whiskers display quartile ranges. Circles and asterisks indicate outliers (i.e., more than 1.5 times the inter-quartile range away from the median).

and this single LPC slice was used to filter the entire LPC residual. This process created stimuli that retained the natural F0 of the original stimuli, but had formant frequencies that remained fixed at each vowel's target values. Duration was equated using PSOLA (Pitch Synchronous Overlap and Add), such that the durations of the /h/, the /d/ closure, and the vowel were set to the mean values for each talker. This general approach to signal processing natural speech was similar to that used by Assmann and Katz (2005), although they used STRAIGHT (Kawahara, 1997; Kawahara *et al.*, 1999) rather than the procedures outlined above.

For presentation to normal-hearing subjects, these stimuli were processed by eight, four, and two-channel noise vocoders that were designed to simulate CIS processing (Shannon *et al.*, 1995). Using MATLAB, the stimuli were divided into spectral bands by sixth-order Butterworth filters, amplitude envelopes were calculated by half-wave rectification and low-pass filtering (fourth-order Butterworth, 400 Hz cutoff frequency), a noise carrier was modulated by each envelope, the modulated noise carriers were filtered by the original analysis bands, and the output was summed across bands. Each set of bands spanned a range from 200 to 5000 Hz, and this range was divided into bands based on equal basilar membrane distance (Greenwood, 1990). The filter slopes of the bands crossed at their −3 dB cutoff frequencies.

The stimuli were played to subjects at a comfortable loudness level (adjusted by each listener). Stimuli were delivered over headphones to normal-hearing individuals and in free field (a single speaker placed in a sound-attenuated booth) to cochlear implant patients.

3. Procedure

The speech from each talker was presented in separate blocks. To familiarize the subjects with the talker, subjects heard a short passage read by the talker at the start of the block, and they were simultaneously able to view the text of the passage on a computer screen. In the noise-vocoded conditions, this passage was processed identically to the stimuli that followed. Afterwards, they were presented with *Say hVd again* sentences, and clicked on buttons on a computer screen to indicate which vowel they heard (cochlear implant patients who were unable to use the interface dictated their responses to an assistant). The buttons were labeled both with an hVd word (e.g., *hoed*) and with a familiar word that had the same vowel (e.g., *load*). Subjects did not receive feedback after their response. Before the experiment began, subjects were shown the response interface and completed a few practice trials, until they were satisfied that they understood the task. In each experimental block, subjects heard 52 sentences (13 words × four conditions) presented in an order that was randomized for each subject.

Cochlear implant patients heard unprocessed vowels, and completed four blocks for each talker. Normal hearing subjects were presented with unprocessed versions as well as stimuli processed by eight, four, and two-channel vocoders; they completed two blocks (one for each talker) for each of these four conditions.

B. Results

As displayed in the boxplots of Fig. 1, there were substantial effects of removing formant movement and duration for cochlear implant users. Compared to the natural versions, removing formant movement lowered recognition accuracy by an average of 13.3 percentage points, equating duration lowered accuracy by an average of 14.0 percentage points, and combining the two manipulations lowered accuracy by an average of 29.4 percentage points. These differences were evaluated by transforming the percentages into RAU (Rationalized Arc-sin UnitsStudebaker, 1985) and conducting a MANOVA with two within-subject variables coding the differences between conditions (natural vs flat formant movement; natural vs equated duration). As suggested by the

boxplots, the effects of formant movement, $F(1,10)=64.7, p<0.001$, and duration, $F(1,10)=67.1, p<0.001$, were both significant; there was no significant interaction of formant movement and duration, $p>0.05$.

For normal-hearing subjects, a similar MANOVA was run with the addition of a four-level within-subjects variable for the listening condition (i.e., unprocessed speech; eight, four, and two-band vocoders). There was a significant effect of duration, $F(1,9)=133.0, p<0.001$, but no interaction of duration with the other variables, $p>0.05$; removing duration cues reduced recognition scores by an average of 5.4–15.4 percentage points across the conditions, but there is no clear evidence that subjects put more weight on duration when there was less spectral resolution. There was a significant effect of formant movement, $F(1,9)=87.3, p<0.001$, and a significant interaction between formant movement and noise-vocoder condition, $F(1,9)=33.9, p<0.001$. The interaction occurred because the effect of removing formant movement depended on the amount of spectral resolution available; removing formant movement reduced recognition by an average of 13.5 percentage points for unprocessed speech, and 11.2 percentage points for the eight-channel noise vocoder, but had no significant effects in the four- and two-channel conditions. Finally, the main effect of noise-vocoder condition was also significant, $F(1,9)=421.1, p<0.001$; vowel recognition became less accurate when the number of channels decreased.

Unsurprisingly, removing formant movement had the largest effect on the recognition of diphthongs (i.e., *hayed* and *hoed*). To test whether more subtle patterns of formant movement also had an effect on vowel recognition, the MANOVA analyses were repeated with *hayed* and *hoed* omitted. For cochlear implant patients, removing formant movement had a smaller effect when diphthongs were not included (reducing correct recognition by 4.4 percentage points), but the effect of formant movement remained significant, $F(1,10)=33.5, p<0.001$. For normal-hearing subjects, the effect of formant movement remained significant in the eight-channel condition (reducing correct recognition by 5.2 percentage points), but was eliminated in the unprocessed-speech condition when duration cues were also present. This led to a significant interaction between formant movement, vocoder condition, and duration, $F(3,7)=6.8, p=0.018$.

To further assess the role of formant movement and duration, the percent information transfer (Miller and Nicely, 1955) was calculated for unprocessed vowels, for the features of duration (short vs long) and formant movement (monophthong vs diphthong). For example, the vowels were all classified as long or short, and a 2×2 confusion matrix was constructed to tally how often short vowels were identified as a short vowel (e.g., /ɪ/ identified as /ʌ/), short vowels were identified as a long vowel (e.g., /ɪ/ identified as /i:/), long vowels were identified as a long vowel (e.g., /ɪ/ identified as /eɪ/), and long vowels were identified as a short vowel (e.g., /i:/ identified as /ʌ/). The information transfer statistic ranged from 100% if long vowels were never identified as short vowels (and vice versa) to 0% if the responses for long and short vowels were the same.

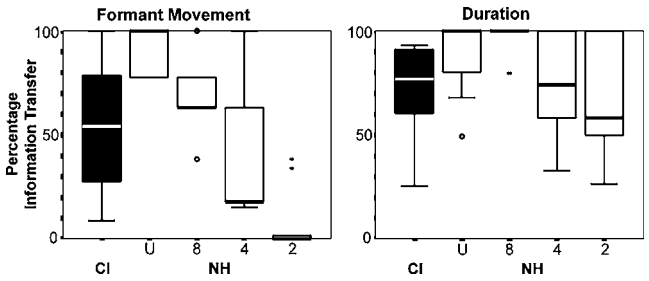

FIG. 2. Boxplots of percent information transfer for formant movement and duration in each of the conditions.

For formant movement, the percentage of information transfer for normal-hearing individuals declined as a function of the number of channels (see Fig. 2); listeners received almost no formant movement information when there were only two channels, but the majority of listeners received 100% of the formant movement information in unprocessed speech. Information transfer for cochlear implant users had a range similar to normal-hearing listeners in the four-channel condition, and a median level of information transfer similar to normal-hearing listeners in the eight-channel condition. This fits with previous findings that cochlear implant users are able to utilize 4–7 channels of spectral information (Friesen *et al.*, 2001). It thus appears that cochlear implant users use formant movement to about the same extent as normal-hearing individuals listening to cochlear implant simulations.

For duration, normal-hearing individuals received less information when the number of channels was low. This likely occurred because the duration feature covaries with spectral differences between vowels in English (e.g., *heed* and *hid* differ both in formant frequencies and duration), and spectral differences would have been clearer in the unprocessed and eight-channel conditions. The range of information transfer scores for cochlear implant users was similar to that of normal-hearing listeners in the four-channel condition, which suggests that both groups of listeners used duration to similar degrees. Given that the perception of duration should not be dependent on spectral resolution, it seems as if all listeners should have been able to achieve 100% information transfer for duration. The upper quartile of normal-hearing subjects achieved 100% information transfer even under the two-channel conditions, but most normal-hearing individuals and all cochlear implant users were below this optimum level. It thus seems as if the vowel recognition accuracy of cochlear implant users could be further improved if they learned to make more effective use of duration.

III. EXPERIMENT 2: VOWEL-SPACE MAPPING WITH FORMANT MOVEMENT AND DURATION

Despite the fact that the cue use of long-term cochlear implant users has the potential to change over time, the results of Experiment 1 suggested that cochlear implant users use formant movement and duration cues to the same extent as do normal-hearing listeners. The present experiment assessed their cue weightings in more detail by examining what combinations of formant frequencies, formant movement, and duration produce best exemplars (i.e., prototypes)

of vowel categories. Although most phonetic categorization research has focused on how different acoustic cues alter the locations of category boundaries (e.g., Hoffman, 1958), examinations of best exemplars can also reveal the structure of phonetic categories and the relative use of different acoustic cues (e.g., Allen and Miller, 2001; Evans and Iverson, 2004; Iverson and Kuhl, 1996). In the present case, mapping boundaries is difficult because they exist as four-dimensional surfaces within the five-dimensional stimulus space; locating best exemplars is easier computationally because they can be represented as a single point within the space.

Previous work (Harnsberger *et al.*, 2001; Svirsky *et al.*, 2004) has mapped best exemplars of vowels using a graphical computer interface in which cochlear implant users interactively clicked on stimuli in a F1 × F2 grid, until they found vowels that they thought matched words printed on the computer screen (e.g., *heed*). Such an approach is not feasible for higher-dimensional stimulus sets, because the additional dimensions increase the number of possible stimuli (e.g., there were 100,700 stimuli in the present experiment). We have developed a goodness optimization method to search spaces like this more efficiently (Evans and Iverson, 2004; Iverson and Evans, 2003). On each trial, subjects see a word printed on the computer screen, hear a synthesized vowel, and rate how closely the word that they hear matches the printed target. After each rating, a computational algorithm analyzes the goodness ratings and changes the acoustic parameters on the next trial to iteratively converge on the best exemplar location. Using this technique, we are able to locate best exemplars within this large stimulus space after 35 trials per vowel.

A. Method

1. Subjects

The subjects were the same as in Experiment 1.

2. Stimuli and apparatus

The stimuli consisted of hVd syllables embedded in recordings of the carrier sentence *Say_again*. The carrier sentence was produced by the male speaker in Experiment 1. Initial and final words, plus the burst of the /d/, were edited from a natural recording. The hVd syllables were created using a cascade-parallel synthesizer (Klatt and Klatt, 1990) to match the vocal timbre, pitch, and higher formant frequencies of the talker. Each syllable had static formant frequencies during the /h/ that matched the onset of the vowel. The F1 and F2 formant frequencies changed linearly from the onset to the offset of the vowel, and F1 fell at the end of the vowel to simulate the /d/ closure. The durations of /h/ and the /d/ closure were fixed, and the duration of the vowel was allowed to vary from 148 to 403 ms. F1 frequency was restricted so that it had a lower limit of 5 ERB_N (Glasberg and Moore, 1990) and an upper limit of 15 ERB_N. F2 frequency was restricted so that it had a lower limit of 10 ERB_N, was always at least 1 ERB_N higher than F1, and had an upper limit defined by the equation $F2 = 26 - (F1 - 5)/2$. The stimuli were synthesized in advance with a 1 ERB_N spacing of the vowel space, and with seven 1evels of log-spaced duration values, for a total of 100 700 individual stimuli. The ERB_N, and log-duration transforms were chosen so that the stimuli would be spaced roughly equally with regard to perception. This spacing allowed us to efficiently distribute the stimuli, although the goodness optimization procedure does not require this equal perceptual spacing.

In addition to these unprocessed stimuli, a second set of stimuli was created by passing them through an eight-channel noise vocoder, following the procedures detailed in Experiment 1.

3. Procedure

On each trial, subjects heard one sentence and rated on a continuous scale whether the hVd was close to being a good exemplar of a word that was displayed on the computer screen. Their ratings were given by mouse clicking on a continuous bar presented on a computer screen. They gave ratings for 12 words: *heed*, *hid*, *hayed*, *head*, *had*, *hard*, *hod*, *hoard*, *heard*, *hoed*, *hood*, and *who'd*. To familiarize subjects with the speaker and task, they first heard the speaker read *The North Wind and The Sun* (as in Experiment 1), and gave a set of practice ratings for the word *hud*.

The goodness optimization procedure involved searching along individual vectors through the stimulus space (i.e., one-dimensional straight-line paths), and finding the best exemplar on each vector. There were a total of seven search vectors and five trials per vector for each vowel. The vectors were chosen so that Vector 1 would allow most subjects to find a close approximation of their best exemplar (the search path passed through formant frequencies measured from natural productions), Vectors 2–6 orthogonally varied the five acoustic dimensions over a wide range, and Vector 7 fine tuned the position of the best exemplar. Specifically, Vector 1 was a straight-line path that passed through two points: (1) the F1 and F2 formant frequencies at the beginning and ending of the natural productions of the target word, and (2) a neutral stimulus in the middle of the vowel space (F1 = 500 Hz and F2 = 1500 Hz, at both the onset and offset); duration was not varied along Vector 1. Vector 2 varied duration, keeping formant frequencies fixed. Vector 3 varied the onset F1 and F2 formant frequencies (i.e., duration and offset formant frequencies were fixed) along the same basic path as the first vector (i.e., through a straight-line path including a neutral vowel and the onset formant frequencies of the natural production). Vector 4 was orthogonal to Vector 3 in the F1/F2 onset space. Vectors 5 and 6 were analogous to Vectors 3 and 4, except that the offset F1 and F2 frequencies were varied. Vector 7 varied all dimensions, passing through the best values found thus far on all dimensions and the neutral vowel.

The end points of all vectors were constrained by the boundaries of the vowel space. For example, Vector 1 for *heed* crossed diagonally across the vowel space, starting from the high-front boundary of the space (i.e., low F1 and high F2), passing through the middle of the space, and ending at the low-back boundary of the space (i.e., high F1 and low F2).

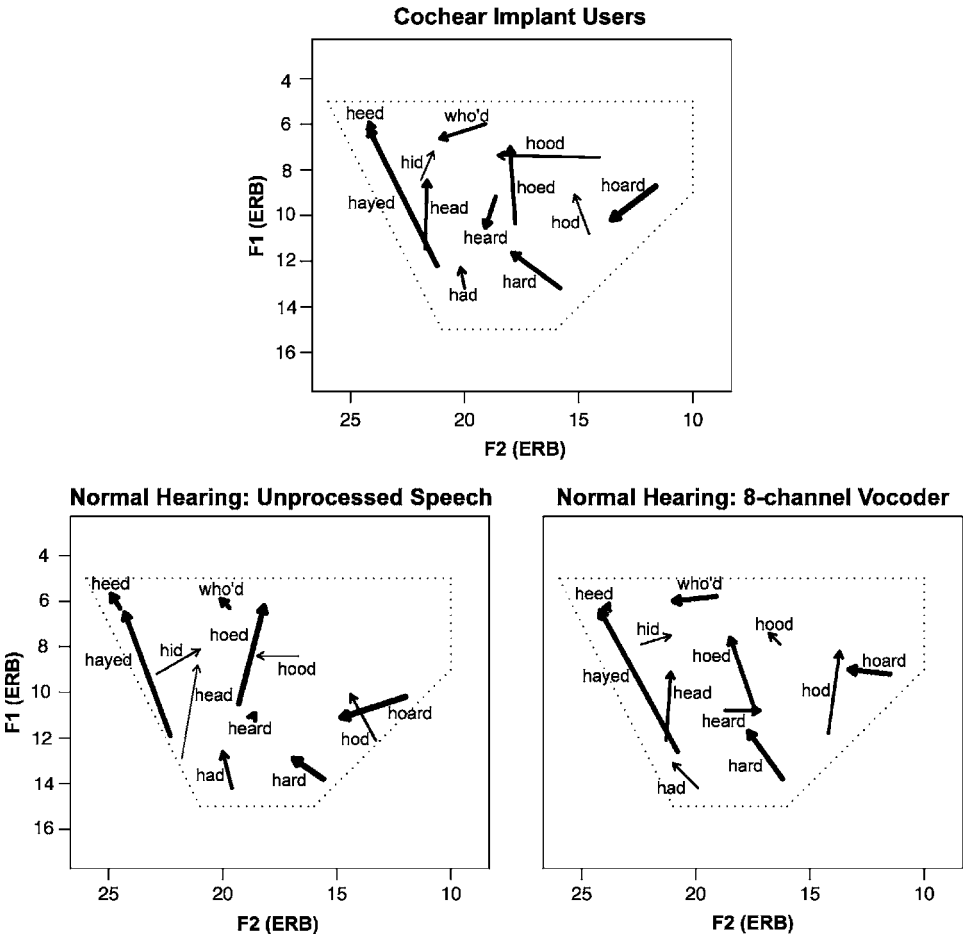

FIG. 3. Best exemplars of vowels with formant movement and duration, for cochlear implant users and normal-hearing individuals. Vowels are plotted as an arrow from the F1 and F2 frequencies at the start of the vowel to the F1 and F2 frequencies at the end. The thickness of the line indicates the preferred duration, with thicker lines for longer vowels.

The best exemplars were found for each vector over five trials. On the first two trials, subjects heard the most extreme stimuli that it was possible to synthesize along the vector (e.g., in the case of *heed*, they heard extreme high-front and low-back vowels, with the order of these two trials randomized). The selection of stimuli on the remaining trials was based on the subjects' judgments, using formulas that were designed to find stimuli along the path that would be perceived as better exemplars. On the third trial, subjects heard a stimulus that was selected by a weighted average of the first two stimuli, according to the equation

$$c = a * \frac{f(b)}{f(a)+f(b)} + b * \frac{f(a)}{f(a)+f(b)}, \quad (1)$$

where a and b are the positions on the search path for the first two trials, $f(a)$ and $f(b)$ are the goodness ratings for the stimuli on those trials (the goodness responses of close to far away were scaled from 0 to 1), and c is the new path position selected for the third trial. On the fourth and fifth trials, the stimuli were selected by finding the minimum of a parabola that was defined by the equation

$$\min = \frac{b-0.5*\{[b-a]^2*[f(b)-f(c)]-[b-c]^2*[f(b)-f(a)]\}}{[b-a]*[f(b)-f(c)]-[b-c]*[f(b)-f(a)]}, \quad (2)$$

where b is the path position of the best stimulus found thus far; a and c are the most recently tested positions on either side of b; and $f(a)$, $f(b)$, and $f(c)$ are the goodness ratings for those stimuli. At the completion of the fifth trial, subjects were allowed to repeat the search if it had produced a poor exemplar. If the best exemplar was correct, the parameters of the best stimulus found thus far were passed onto the next stage of the search algorithm (i.e., to search along the next vector).

B. Results

As displayed in Fig. 3, there were few overall differences between the vowel spaces of cochlear implant users and normal-hearing individuals. On average, both groups of listeners preferred vowels with similar formant frequencies, similar amounts of formant movement, and similar duration contrasts. The results of cochlear implant and normal-hearing individuals (listening to unprocessed speech) were compared using MANOVA analyses with subject type as a between-subject variable and word as a within-subject variable; the analyses were conducted separately for F1 and F2 target frequencies (average of the onset and offset values), F1 and F2 formant movement (offset minus onset), and duration. There was a significant effect of subject type for F1 target frequencies, $F(1,16)=15.1, p=0.001$; the average F1 formant frequencies were slightly lower for cochlear implant users (9.2 ERB_N) than for normal-hearing listeners (9.8 ERB_N). However, there were no other significant effects of subject for any of the other acoustic dimensions, $p>0.05$, demonstrating that there were few overall differences between the best exemplars of normal-hearing and cochlear implant-using individuals. Unsurprisingly, there were significant dif-

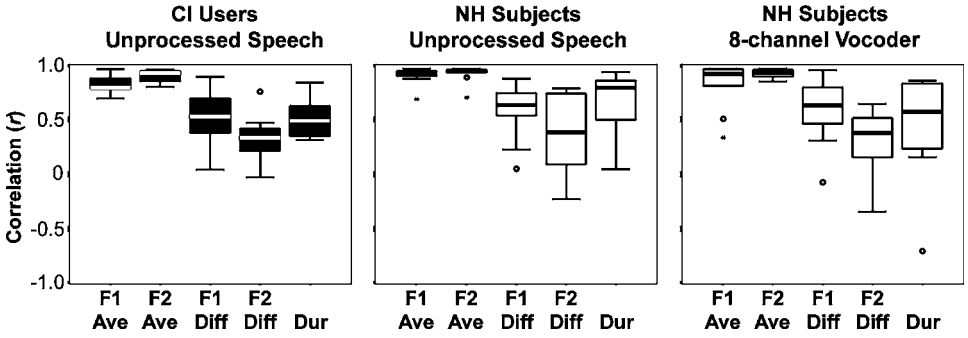

FIG. 4. Boxplots of correlations between the best exemplars of individual subjects and the average best exemplars for normal-hearing individuals listening to unprocessed speech. The pattern of results was similar for cochlear implant (CI) users, normal-hearing (NH) subjects listening to unprocessed speech, and normal-hearing subjects listening to eight-channel vocoders.

ferences between the words in terms of F1 target frequencies, $F(11,6)=269.4, p<0.001$, F2 target frequencies, $F(11,6)=42.6, p<0.001$, F1 formant movement, $F(11,6)=40.5, p<0.001$, F2 formant movement, $F(11,6)=4.7, p=0.034$, and duration, $F(11,6)=10.8, p=0.004$, but there were no interactions between word and subject type, $p>0.05$. The words thus differed significantly for both groups of listeners on all acoustic dimensions.

The best exemplars of normal-hearing individuals for unprocessed and noise-vocoded speech were compared with repeated-measure ANOVAS, with word and condition (unprocessed vs vocoded) coded as within-subject variables. The results were very similar to the comparison between cochlear implant users and normal-hearing individuals above. There was a significant effect of condition for F1 target frequencies, $F(1,9)=12.2, p=0.007$; the average F1 formant frequencies were slightly lower in the noise-vocoder condition (9.5 ERB_N) than for unprocessed speech (9.8 ERB_N). There were no other significant effects of condition for any of the other acoustic measurements, $p>0.05$. There were significant differences between the words in terms of F1 target frequencies, $F(4.4,39.7)=69.4, p<0.001$, F2 target frequencies, $F(4.3,38.7)=111.9, p<0.001$, F1 formant movement, $F(3.0,27.2)=10.2, p<0.001$, F2 formant movement, $F(4.3,38.6)=4.4, p=0.004$, and duration, $F(2.8,24.8)=10.5, p<0.001$, but there were no interactions between word and condition, $p>0.05$.

In order to examine individual differences, the average best exemplar for normal-hearing subjects listening to unprocessed speech was calculated for each vowel, and Pearson correlations were calculated between these averages and the data for individual subjects along each acoustic dimension (i.e., F1 and F2 target frequencies, F1 and F2 formant movement, and duration). This measure thus quantified how closely individual subjects approximated standard British English vowels on each of these dimensions. When this analysis was conducted for normal-hearing individuals listening to unprocessed speech, each individual was compared to an average that did not include themselves.

As displayed in Fig. 4, F1 and F2 target frequencies for individuals consistently approximated the normal averages, but there were poorer correlations and more variability for formant movement and duration. This pattern was generally the same for cochlear implant users and normal-hearing subjects. The individual variability in formant movement and duration likely reflects the fact that these are secondary cues (i.e., not as critical for identification as target F1 and F2 frequencies) rather than being indicative of perceptual difficulties. Independent-samples t tests were used to compare the correlations for normal-hearing individuals and cochlear implant users listening to unprocessed speech. The differences were significant for F1 target frequencies, $t(18.9)=2.49, p=0.022$; the preferred F1 frequencies of normal-hearing individuals (mean $r=0.90$) matched the normal-hearing averages better than did those of cochlear implant users (mean $r=0.82$). There were no significant differences between normal-hearing individuals and cochlear implant users for the other acoustic measures, $p>0.05$. Paired t tests were used to compare the correlations for normal-hearing listeners for unprocessed and noise-vocoded speech; there were no significant differences, $p>0.05$.

Pearson correlations were used to assess the relationship between these correlations and vowel identification accuracy for cochlear implant users in Experiment 1. For F1 target frequencies, there were significant correlations for unprocessed vowels, $r=0.68, p=0.021$, vowels with formant movement removed, $r=0.69, p=0.020$, vowels with duration equated, $r=0.71, p=0.014$, and vowels with both formant movement removed and duration equated, $r=0.72, p=0.012$. This demonstrates that subjects had higher vowel recognition scores when their best exemplars more closely matched the F1 values of normal-hearing individuals. There were no significant correlations for the other acoustic measures, $p>0.05$.

IV. GENERAL DISCUSSION

The results demonstrate that formant movement and duration are important cues for vowel recognition via cochlear implants and noise-vocoder simulations. In Experiment 1, removing both formant movement and duration contrast reduced recognition accuracy for cochlear implant users by an average of 29.4 percentage points. The results were similar for normal-hearing individuals recognizing noise-vocoded vowels, although the effect of formant movement was diminished with reduced numbers of channels. In Experiment 2, both normal-hearing individuals and cochlear implant users preferred vowels with formant movement and duration contrast, although their preferences for these secondary cues were less consistent than their preferences for target F1 and F2 frequencies.

Despite the fact that cochlear implant users undergo a substantial period of relearning following implantation, there was no evidence that they used formant movement and du-

ration any differently than did normal-hearing individuals who were listening to cochlear implant simulations for the first time. The only significant difference was in the use of F1 target frequencies; the F1 frequencies chosen by cochlear implant users in Experiment 2 were less closely correlated with the normal-hearing averages, and individual differences in these correlations were related to vowel recognition accuracy. It is unknown what caused the variability in best F1 frequencies; listeners may have had anomalous F1 frequency targets in their underlying category representations (e.g., Svirsky *et al.*, 2004) or they may have had impaired spectral resolution in this frequency range.

It was particularly surprising that cochlear implant users and normal-hearing individuals had similar best exemplars in Experiment 2, considering that Harnsberger *et al.* (2001) found that cochlear implant users were often more variable in their best exemplar locations than were normal-hearing individuals, and the present cochlear implant users made many errors when recognizing natural vowels in Experiment 1 (averaging 74% correct). In contrast to Harnsberger *et al.*, which used isolated vowels, our method played vowels embedded in natural sentences, and subjects listened to a short story read by the talker before starting the experiment. Subjects were thus able to make their goodness judgments with reference to a particular talker, and this may have made their responses more reliable. Several subjects in our experiment reported that they had difficulty hearing any difference between the vowels in the practice of Experiment 2 (even stimuli at opposite ends of the vowel space), but they were encouraged to repeatedly play the stimuli and make responses based on any small differences that they could hear. The task demands were thus lower than in Experiment 1 (i.e., where individuals heard stimuli only once), which may have improved accuracy and consistency.

Why did normal-hearing individuals and cochlear implant users make such similar use of formant movement and duration? All of the cochlear implant users were postlingually deafened, so presumably they had had phoneme representations, at some point in their history, that matched those of normal-hearing individuals. It is possible that acclimatization to a cochlear implant involves a change in perceptual processing that does not alter these phoneme representations. For example, shallow insertions of an electrode array into the cochlea can cause a mismatch between the electrode sites and the frequency bands analyzed by the cochlear implant processor, such that the stimulation patterns that a cochlear implant user receives are shifted to higher frequencies relative to the stimulation patterns that they experienced when they had normal hearing; learning to adjust to these spectral shifts is thought to be a major component of acclimatizing to a cochlear implant (e.g., Fu *et al.*, 2005; Rosen *et al.*, 1999). It is plausible that such an adjustment involves a change in how the sensory information from the cochlear implant is mapped onto existing phoneme representations, without involving changes to the phoneme representations themselves. Training may be required (e.g., Fu *et al.*, 2005) in order for cochlear implant users to alter their category representations to place more weight on cues such as duration.

A complicating factor is that the same underlying category representations may be involved in production. That is, the best exemplars in Experiment 2 may reflect hyperarticulated target values that speakers aim to achieve when speaking clearly (Johnson *et al.*, 1993). If a cochlear implant user were to modify their use of secondary cues in order to identify vowels more accurately, then this would presumably have consequences for production. For example, an individual who learns to place greater weight on duration when distinguishing /ɪ/ and /i/ may begin to produce these vowels with more duration contrast and less spectral contrast, and thus produce speech that is less intelligible to normal-hearing speakers. Production considerations may thus tend to promote cochlear implant users to rely on the same acoustic cues as normal-hearing individuals.

ACKNOWLEDGMENT

We thank Tim Green for comments on this manuscript.

Allen, J. S., and Miller, J. L. (**2001**). "Contextual influences on the internal structure of phonetic categories: A distinction between lexical status and speaking rate," Percept. Psychophys. **63**, 798–810.

Assmann, P. F., and Katz, W. F. (**2005**). "Synthesis fidelity and time-varying spectral change in vowels," J. Acoust. Soc. Am. **117**, 886–895.

Boersma, P., and Weenink, D. (**2002**). Praat (Computer Software), Amsterdam, The Netherlands.

Busby, P. A., Tong, Y. C., and Clark, G. M. (**1993**). "The perception of temporal modulations by cochlear implant patients," J. Acoust. Soc. Am. **94**, 124–131.

Dorman, M. F., and Loizou, P. C. (**1997**). "Mechanisms of vowel recognition for Ineraid patients fit with continuous interleaved sampling processors," J. Acoust. Soc. Am. **102**, 581–587.

Dorman, M. F., and Loizou, P. C. (**1998**). "The identification of consonants and vowels by cochlear implant patients using a 6-channel continuous interleaved sampling processor and by normal-hearing subjects using simulations of processors with two to nine-channels," Ear Hear. **19**, 162–166.

Dorman, M. F., Loizou, P. C., and Rainey, D. (**1997**). "Speech intelligibility as a function of the number of channels of stimulation for signal processors using sine-wave and noise-band outputs," J. Acoust. Soc. Am. **102**, 2403–2411.

Evans, B. G., and Iverson, P. (**2004**). "Vowel normalization for accent: An investigation of best exemplar locations in northern and southern British English sentences," J. Acoust. Soc. Am. **115**, 352–361.

Ferguson, S. H., and Kewley-Port, D. (**2002**). "Vowel intelligibility in clear and conversational speech for normal-hearing and hearing-impaired listeners," J. Acoust. Soc. Am. **112**, 259–211.

Fishman, K. E., Shannon, R. V., and Slattery, W. H. (**1997**). "Speech recognition as a function of the number of electrodes used in the SPEAK cochlear implant speech processor," J. Speech Lang. Hear. Res. **40**, 1201–1215.

Friesen, L. M., Shannon, R. V., Baskent, D., and Wang, X. (**2001**). "Speech recognition in noise as a function of the number of spectral channels: Comparison of acoustic hearing and cochlear implants," J. Acoust. Soc. Am. **110**, 1150–1163.

Fu, Q. J., Nogaki, G., and Galvin, J. III (**2005**). "Auditory training with spectrally shifted speech: Implications for cochlear implant patient auditory rehabilitation," J. Assoc. Res. Otolaryngol. **6**, 180–189.

Glasberg, B. R., and Moore, B. C. J. (**1990**). "Derivation of auditory filter shapes from notched-noise data," Hear. Res. **47**, 103–138.

Greenwood, D. D. (**1990**). "A cochlear frequency-position function for several species—29 years later," J. Acoust. Soc. Am. **87**, 2592–2605.

Harnsberger, J. D., Svirsky, M. A., Kaiser, A. R., Pisoni, D. B., Wright, R., and Meyer, T. A. (**2001**). "Perceptual "vowel spaces" of cochlear implant users: Implications for the study of auditory adaptation to spectral shift," J. Acoust. Soc. Am. **109**, 2135–2145.

Hawkins, S., and Smith, R. (**2001**). "Polysp: a polysystemic, phonetically-rich approach to speech understanding," J. Italian Linguistics – Rivista di Linguistica **13**, 99–188.

Hillenbrand, J. M., Clark, M. J., and Houde, R. A. (**2000**). "Some effects of duration on vowel recognition," J. Acoust. Soc. Am. **108**, 3013–3022.
Hillenbrand, J. M., and Nearey, T. M. (**1999**). "Identification of resynthesized /hVd/ utterances: Effects of formant contour," J. Acoust. Soc. Am. **105**, 3509–3523.
Hoffman, H. S. (**1958**). "Study of some cues in the perception of the voiced stop consonants," J. Acoust. Soc. Am. **30**, 1035–1041.
Iverson, P., and Evans, B. G. (**2003**). "A goodness optimization procedure for investigating phonetic categorization." *Proceedings of the International Congress of Phonetic Sciences*, Barcelona, August, 2003, pp. 2217-2220.
Iverson, P., and Kuhl, P. K. (**1996**). "Influences of phonetic identification and category goodness on American listeners' perception of /r/ and /l/," J. Acoust. Soc. Am. **99**, 1130–1140.
Johnson, K. (**2005**). "Speaker normalization in speech perception." *The Handbook of Speech Perception* (Blackwell, Oxford, England).
Johnson, K., Flemming, E., and Wright, R. (**1993**). "The hyperspace effect: Phonetic targets are hyperarticulated," Language **69**, 505–528.
Kawahara, H. (**1997**). "Speech representation and transformation using adaptive interpolation of weighted spectrum: Vocoder revisited," *Proceedings of the ICASSP*, Munich, Germany, April, 1997, pp. 1303–1306.
Kawahara, H., Masuda-Katsuse, I., and de Cheveigné, A. (**1999**). "Restructuring speech representations using a pitch-adaptive time-frequency smoothing and an instantaneous-frequency-based F0 extraction," Speech Commun. **27**, 187–207.
Kirk, K. I., Tye-Murray, N., and Hurtig, R. R. (**1992**). "The use of static and dynamic vowel cues by multichannel cochlear implant users," J. Acoust. Soc. Am. **91**, 3487–3498.
Klatt, D. H., and Klatt, L. C. (**1990**). "Analysis, synthesis, and perception of voice quality variations among female and male talkers," J. Acoust. Soc. Am. **87**, 820–857.
Miller, G. A., and Nicely, P. (**1955**). "An analysis of perceptual confusions among some English consonants," J. Acoust. Soc. Am. **27**, 338–352.
Neel, A. (**1998**). "Factors influencing vowel identification in elderly hearing-impaired listeners," Doctoral dissertation, Indiana University, 1989.
Nygaard, L. C., and Pisoni, D. B. (**1998**). "Talker-specific learning in speech perception," Percept. Psychophys. **60**, 355–376.
Rosen, S., Faulkner, A., and Wilkinson, L. (**1999**). "Adaptation by normal listeners to upward spectral shifts of speech: Implications for cochlear implants," J. Acoust. Soc. Am. **106**, 3629–3636.
Shannon, R. V. (**1989**). "Detection of gaps in sinusoids and pulse trains by patients with cochlear implants," J. Acoust. Soc. Am. **85**, 2587–2592.
Shannon, R. V. (**1992**). "Temporal modulation transfer functions in patients with cochlear implants," J. Acoust. Soc. Am. **91**, 2156–2164.
Shannon, R. V. (**1993**). "Psychophysics," in *Cochlear Implants: Audiological Foundations*, edited by R. S. Tyler (Singular, San Diego), pp. 357–388.
Shannon, R. V., Zeng, F. G., Kamath, V., Wygonski, J., and Ekelid, M. (**1995**). "Speech recognition with primarily temporal cues," Science **270**, 303–304.
Strange, W. (**1989**). "Dynamic specification of coarticulated vowels spoken in sentence context," J. Acoust. Soc. Am. **85**, 2135–2153.
Studebaker, G. A. (**1985**). "A 'rationalized' arcsine transform," J. Speech Hear. Res. **28**, 455–462.
Svirsky, M. A., Silveira, A., Neuburger, H., Teoh, S. W., and Suarez, H. (**2004**). "Long-term auditory adaptation to a modified peripheral frequency map," Acta Oto-Laryngol. **124**, 381–386.
Tyler, R. S., Parkinson, A. J., Woodworth, G. G., Lowder, M. W., and Gantz, B. J. (**1997**). "Performance over time of adult patients using the Ineraid or nucleus cochlear implant," J. Acoust. Soc. Am. **102**, 508–522.
Välimaa, T. T., Määttä, T. K., Löppönen, H. J., and Sorri, M. J. (**2002**). "Phoneme recognition and confusions with multichannel cochlear implants: Vowels," J. Speech Lang. Hear. Res. **45**, 1039–1054.
Xu, L., Thompson, C. S., and Pfingst, B. E. (**2005**). "Relative contributions of spectral and temporal cues for phoneme recognition," J. Acoust. Soc. Am. **117**, 3255–3267.

Isolating the energetic component of speech-on-speech masking with ideal time-frequency segregation

Douglas S. Brungart[a)]
Air Force Research Laboratory, Human Effectiveness Directorate, 2610 Seventh Street, Wright-Patterson AFB, Ohio 45433

Peter S. Chang[b)]
Department of Computer Science and Engineering, The Ohio State University, Columbus, Ohio 43210

Brian D. Simpson
Air Force Research Laboratory, Human Effectiveness Directorate, 2610 Seventh Street, Wright-Patterson AFB, Ohio 45433

DeLiang Wang
Department of Computer Science and Engineering and Center for Cognitive Science, The Ohio State University, Columbus, Ohio 43210

(Received 2 January 2005; revised 25 August 2006; accepted 15 September 2006)

When a target speech signal is obscured by an interfering speech wave form, comprehension of the target message depends both on the successful detection of the energy from the target speech wave form and on the successful extraction and recognition of the spectro-temporal energy pattern of the target out of a background of acoustically similar masker sounds. This study attempted to isolate the effects that energetic masking, defined as the loss of detectable target information due to the spectral overlap of the target and masking signals, has on multitalker speech perception. This was achieved through the use of ideal time-frequency binary masks that retained those spectro-temporal regions of the acoustic mixture that were dominated by the target speech but eliminated those regions that were dominated by the interfering speech. The results suggest that energetic masking plays a relatively small role in the overall masking that occurs when speech is masked by interfering speech but a much more significant role when speech is masked by interfering noise. © *2006 Acoustical Society of America.* [DOI: 10.1121/1.2363929]

PACS number(s): 43.71.Gv, 43.66.Pn, 43.66.Rq [GDK] Pages: 4007–4018

I. INTRODUCTION

When a target speech signal is masked by one or more interfering voices, two related but distinct processes are required for the listener to successfully understand the message spoken by the target talker. First, the listener must be able to *detect* the acoustic energy present in the target voice. In general, a listener would only be able to reliably detect those portions of the target voice that occur in time and frequency regions where the target contains at least as much energy as the masker. The acoustic elements of the target that occur in regions that overlap in time and frequency with a more powerful masking sound would be effectively eliminated from the stimulus and thus are unable to contribute to the perception of the target utterance. In this paper, the loss of acoustic information from the target that is caused by this type of masking will be referred to as *energetic masking.*

In situations where no interfering sounds are present in the stimulus, detection alone is generally sufficient to allow the listener to understand a target utterance. If enough acoustic elements of the target talker are detectable in the stimulus, the listener should be able to determine the spectro-temporal energy pattern of the speech and use it to recognize the target utterance. When an interfering sound is present in the stimulus, however, the task becomes more difficult. The listener now detects acoustic elements from both the target and the interferer, and has to find some way to distinguish between the two in order to extract the spectro-temporal energy pattern of the target talker from the combined stimulus.

Of course, this two-stage model of speech perception is in many ways an oversimplification. In particular, it ignores the fact that some spectro-temporal regions of the stimulus will contain enough masker energy to *distort* the target signal, but not enough energy to overwhelm the target signal and render it undetectable. In such cases, it might be perfectly reasonable to expect the distortions caused by the noise to impair the listener's ability to identify those regions as part of the target signal and use them to recognize the target utterance. This raises the specter of whether the loss of performance caused by this kind of distortion should be categorized as *energetic masking*, because it is caused by direct spectral overlap of the target and masker, or whether it should be viewed as nonenergetic masking related to an inability to tease apart the target and masking portions of the stimulus. Either view may be equally valid, but for the purposes of this paper, we will restrict the use of the term "en-

[a)]Author to whom correspondence should be addressed; electronic mail: douglas.brungart@wpafb.af.mil
[b)]Electronic mail: Chang.549@osu.edu

ergetic masking" to the loss of information caused by an overwhelming masker, and exclude confusions caused by signal distortion from that definition. It is worth noting, however, that this distinction is a relatively minor one when the target signal is a spectrally sparse stimulus like speech, because in such cases the acoustic mixture will tend to be dominated either by the target or the masker in almost all the spectro-temporal regions of the stimulus.

Within this conceptual framework, an important question in understanding how listeners process complex auditory stimuli is the extent to which the ability to identify a target speech signal in the presence of a masker is dependent on the elimination of acoustic information about the target signal due to spectral and temporal overlap with the masker (i.e., energetic masking), and the extent to which performance in these situations is limited by the inability to correctly segregate and recognize the spectro-temporal pattern of the detectable acoustic elements of a target signal amid a background of confusingly similar masking sounds. In order to explore this issue, a number of researchers have attempted to develop stimuli that reproduce the potential target-masker confusions that can occur in a speech-on-speech masking task in a stimulus with no spectral overlap between the target and masking speech signals (and thus no significant opportunity for energetic masking to occur). For example, Spieth, Curtis, and Webster (1954) high-pass filtered one talker at 1600 Hz and low-pass filtered the other talker at 1600 Hz, thus creating a stimulus containing two independently intelligible speech signals with no spectral overlap. These stimuli reproduced many of the masking effects associated with normal multitalker stimuli, but presumably generated little or no energetic masking because there was no spectro-temporal overlap in the target and masking signals. This technique was greatly expanded by Arbogast *et al.* (2002), who used cochlear implant simulation software to divide the speech signal into 15 logarithmically spaced envelope-modulated sine waves, and randomly assigned eight of these bands to the target speech and six other bands to the masking speech. Again, this resulted in a stimulus that presumably produced little or no energetic masking but retained the potential target-masker confusions that would normally be present in multitalker speech.

The above studies have attempted to eliminate the energetic masking component that would ordinarily occur in speech-on-speech masking. An alternative approach is to develop a stimulus that approximates the effects of energetic masking but eliminates the potential nonenergetic target-masker confusions that can occur in ordinary multitalker stimuli. In order to be effective, such a stimulus has to account for the amplitude fluctuations that normally occur in a masking speech stimulus, because these fluctuations produce dips in the masking speech that allow listeners to obtain clear "glimpses" of the target speech even when the overall signal-to-noice ratio (SNR) is very unfavorable (Assmann and Summerfield, 2004; Cooke, 2005; Culling and Darwin, 1994; Miller and Licklider, 1950). The simplest approach to this problem is to amplitude modulate a continuous speech-spectrum-shaped noise with the overall envelope of a natural speech masker (Bronkhorst and Plomp, 1992; Brungart *et al.*, 2001; Festen and Plomp, 1990; Hawley *et al.*, 2004). However, this simplistic approach cannot account for the fact that a speech masker can fluctuate differently in different frequency bands, thus allowing the listener the opportunity to hear glimpses of the target in different frequency regions at different times (Buss *et al.*, 2004). Of course, it is possible to amplitude modulate a noise with different envelopes in different frequency bands (Festen and Plomp, 1990). However, signals of this type are known to become recognizable as intelligible speech when they contain more than a few independently modulated frequency bands (Shannon *et al.*, 1995), and, once this happens, there is a real possibility that the masking "noise" could include speech-like spectro-temporal patterns that could be confused with the target speech and thus result in a significant amount of nonenergetic masking.

We propose a new signal processing technique called "ideal time-frequency segregation" (ITFS) that can approximate the energetic masking effects produced by a natural speech masker across both time and frequency in a stimulus with no audible masking signal that could potentially be confused with the target speech. This approach, which is based on the "ideal binary mask" notion that has been used as a performance measure in computational auditory scene analysis (CASA), uses *a priori* information about the time-frequency (T-F) composition of the target and masking signals to eliminate just those spectral and temporal regions of the target signal that would ordinarily be rendered acoustically undetectable by the presence of a more intense masking sound. By eliminating these T-F regions, this procedure is intended to retain the loss of information that would normally occur due to the effects of energetic masking. At the same time, this procedure performs what could be viewed as ideal time-frequency segregation by separating the T-F regions of the stimulus that potentially contain information about the target speech (and thus would be expected to contribute to listener performance in a speech perception task) from those regions that would only contain acoustic information about the masking voice (and thus could potentially reduce performance by distracting the listener's attention away from the T-F regions associated with the target speech). Thus, the net effect of applying this ITFS procedure is to create a stimulus that approximates the effect that energetic masking would have for an "ideal" listener who is able to successfully identify and utilize all of the detectable target information in the stimulus.

The remainder of this paper is organized as follows. Section II describes the technical details of how the ITFS technique was implemented. Section III describes an experiment that applied this technique to multitalker stimuli. Section IV describes an experiment that extended this approach to speech in the presence of a noise masker. Section V describes how the ITFS technique can be used as a conceptual tool in a larger framework for quantifying the roles of energetic and nonenergetic masking in auditory perception. Finally, Sec. VI summarizes the main conclusions from our experiments.

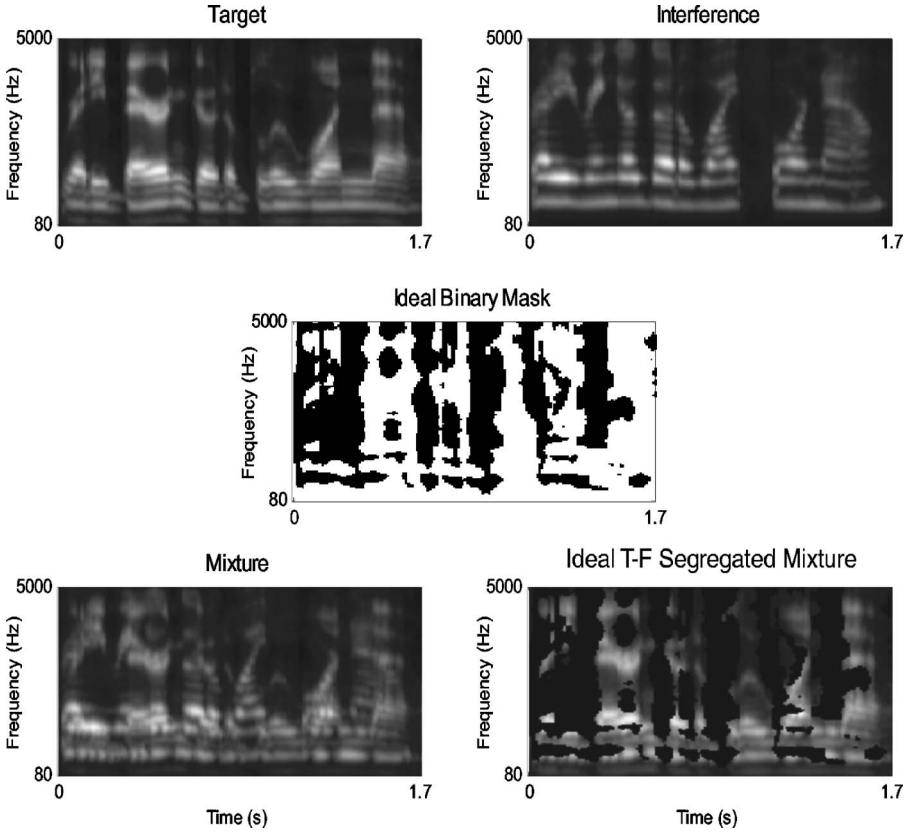

FIG. 1. An illustration of the ideal binary mask for a mixture of two utterances with equal overall rms levels. Top left: Two-dimensional T-F representation of a target male utterance ("Ready Baron go to blue one now"). The figure displays the rectified responses of the gamma-tone filter bank with 128 channels, where the energy value at each T-F unit is scaled to use the gray scale color map from black to white and is raised to the 1/4 power for better display. Top right: Corresponding representation of an interfering female utterance ("Ready Ringo go to white four now"). Middle: Ideal binary mask generated at 0 dB LC, where white pixels indicate 1 and black pixels indicate 0. Bottom left: Corresponding representation of the mixture. Bottom right: Masked mixture using the ideal mask.

II. IDEAL TIME-FREQUENCY SEGREGATION

A. Relationship to "ideal binary masking"

The concept of ITFS is very closely related to the concept of the ideal binary mask in CASA. Ideal binary masking is a signal processing method that simply retains those T-F regions of a mixture where the "target" source is stronger and eliminates the T-F regions where "interfering" sources are stronger. Such processing is called ideal because the mask definition is based on the target and interfering signals before mixing; also the ideal binary mask is the optimal binary mask in terms of SNR gain (Hu and Wang, 2004; Ellis, 2006). In this context, the term "mask" refers not to the addition of an interfering stimulus, as it does in psychoacoustics, but rather to a filter that completely eliminates certain portions of a signal (those assigned to a "zero" value in the mask) while allowing others (those assigned to a "one" value in the mask) to pass through unimpeded. Binary masking is typically based on a two-dimensional T-F representation where the time dimension consists of a sequence of time frames and the frequency dimension consists of a bank of auditory filters (e.g., gammatone filters). Thus the basic element in the ideal binary mask paradigm is a T-F unit corresponding to a specific filter at a particular time frame, and the binary mask itself is a two-dimensional matrix where each element corresponds to a single T-F unit. Those T-F units where the mixture is dominated by the target are assigned a one in the binary mask, and those where the mixture is dominated by an interfering sound are assigned a zero.

The above discussion makes it clear that the ideal binary mask is generated by checking whether the SNR in each T-F unit is greater than 0 dB. We can extend the definition of an ideal binary mask by introducing a predefined local SNR criterion (LC) so that those T-F units where the SNR is greater than a predefined LC value are assigned one in the ideal binary mask, and all the other T-F units are assigned zero. The commonly used ideal binary mask in CASA then corresponds to a LC value of 0 dB.

Figure 1 illustrates the ideal binary mask using a 0 dB LC for a mixture of the male utterance "Ready Baron go to blue one now" and the female utterance "Ready Ringo go to white four now," where the male utterance is regarded as the target. The overall SNR of the mixture (measured from the rms energy in each utterance) is 0 dB. In the figure, the top left panel shows the T-F representation of the target utterance, the top right panel the representation of the interfering utterance, and the bottom left panel the representation of the mixture. The middle panel shows the ideal mask, where white and black indicate 1 and 0, respectively. The bottom right panel shows the masked mixture using the ideal mask. Note that the masked mixture is much more similar to the clean target than the original mixture.

Figure 2 illustrates the effect that varying LC value has on the ideal binary mask for the two-talker speech mixture shown in Fig. 1. The left and right panels show the ideal mask and resulting resynthesized mixture with the LC value set at −12 dB (top row), 0 dB (middle row), and +12 dB (bottom row). As can be seen from the figure, increasing the LC value makes the ideal binary mask more conservative by requiring a higher local SNR in order to retain a particular T-F unit and hence reduces the total number of T-F units retained.

Although very few psychoacoustic experiments have

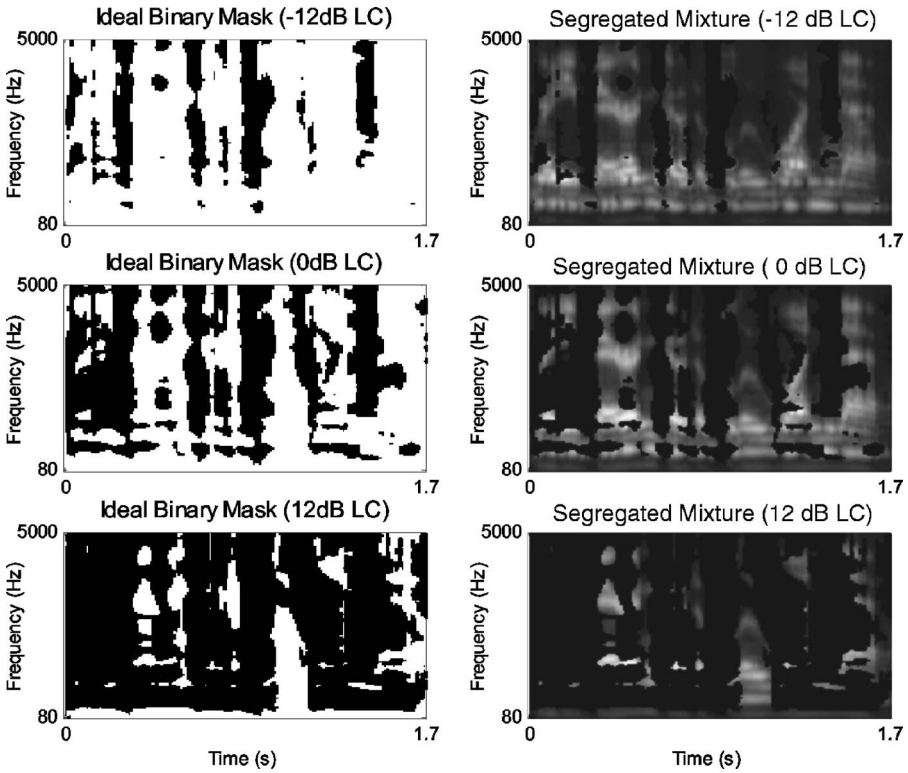

FIG. 2. An illustration of ideal binary masking at different LC values, using the same speech mixture of two utterances from Fig. 1. The three rows show representations for three different LC values (−12 dB, 0 dB, and +12 dB from top to bottom). The left column shows the ideal binary mask in each condition. The right column shows the corresponding masked mixtures using these ideal masks. Note that increasing the LC value makes the binary masking procedure more conservative and thus decreases the number of retained T-F units.

been conducted with ideal binary masks, the binary mask pardigm has been used extensively in CASA. The notion of the ideal binary mask was first proposed by Hu and Wang (2001) as a computational goal of CASA, and was further developed by Roman *et al.* (2003) and Hu and Wang (2004). Binary masks had been used as an output representation in the CASA literature (Brown and Cooke, 1994; Wang and Brown, 1999). Cooke *et al.* (2001) used the *a priori* mask—defined according to whether the mixture energy is within 3 dB of the target energy—in the context of robust speech recognition. Roman *et al.* (2003) conducted speech intelligibility tests and found that estimated masks that are very close to ideal ones yield substantial speech intelligibility improvements compared to unprocessed mixtures. Wang (2005) gave an extensive discussion on the use of the ideal binary mask as the computational goal of CASA.

B. Implementation

In applying the "binary mask" technique to auditory perception, we make the assumption that human listeners also perform a T-F analysis on the stimulus, and that the ideal listener would employ a segregation strategy similar to the one implemented in the ideal binary mask technique. In order to evaluate how real listeners might be able to perform a speech segregation task with such an "ideally segregated" signal, the technique described in the previous section was used to generate ITFS stimuli containing only those T-F regions of the stimulus that were locally dominated by the target speech. The procedures used to generate these stimuli were very similar to those used in previous studies that employed binary masks (e.g., Hu and Wang, 2004). For each stimulus presentation, the ITFS processing was based on a total of three input signals: a *target* signal, an *interfering* signal, and a *mixture* signal of the target and the interference. Each of these was first processed through a bank of 128 fourth-order gammatone filters with overlapping passbands (Patterson *et al.*, 1988) and with center frequencies ranging from 80 to 5000 Hz on an approximately logarithmic scale. The gammatone filter bank effectively decomposed the signals into arrays of 128 narrowband signals, which were further divided into 20 ms time frames with 10 ms overlap in order to produce a matrix of T-F units for each of the input signals. This choice of the filterbank and time windowing is commonly used in speech analysis but it is by no means optimal—other choices are certainly possible. For example, a bank of 64 or even 32 gammatone filters covering the same frequency range has been previously used. Once T-F decomposition is done, within each of the T-F units, a comparison was made between the energy of the target and that of the interference. The resulting local SNR for each T-F unit was then compared to a predefined LC value to determine whether to retain the unit.

Once this binary mask was defined, the output was resynthesized from the mixture using the same method that was described by Weintraub (1985) (see also Brown and Cooke, 1994; Wang and Brown, 1999), which accounts for across-filter phase shifts introduced by the gammatone filter bank. In resynthesis, the binary mask was used to weight the filter outputs in individual frames and the weighted outputs were summed across all frequency channels to yield the resynthesized ITFS wave form.

III. EXPERIMENT 1: EFFECTS OF IDEAL TIME-FREQUENCY SEGREGATION (ITFS) ON SPEECH INTELLIGIBILITY WITH THE CRM TASK

The basic premise of the ITFS technique is that it approximates the signal that would be available to a "perfectly

segregating" listener who could correctly extract all of the T-F units containing useful information about the target speech and completely ignore all of the other extraneous T-F units in the stimulus. Thus, one would expect ITFS processing to produce a large improvement in performance in listening situations where the masker is qualitatively similar to, and thus potentially easily confused with, the target signal. Experiment 1 was designed to examine the effect of ITFS processing on the intelligibility of a stimulus that has been shown to be highly susceptible to these types of target-masker confusions; namely, a target speech signal from the coordinate response measure (CRM) (Brungart *et al.*, 2001) masked by one, two, or three CRM phrases spoken by identical masking talkers and presented at the same level as the target speech. In order to examine the impact of the LC value on performance with ITFS signals, the stimuli were processed with LC values ranging from −60 dB to +30 dB.

A. Methods

1. Listeners

Nine paid listeners participated in the experiment. All had normal hearing and their ages ranged from 18 to 54. Most had participated in previous auditory experiments, and all were familiarized with the CRM task prior to conducting this experiment.

2. Speech stimuli

The speech materials used in the experiment were derived from the publicly available CRM speech corpus for multitalker communications research (Bolia *et al.*, 2000). This corpus, which is based on a speech intelligibility test first developed by Moore (1981), consists of phrases of the form "Ready (call sign) go to (color) (number) now" spoken with all possible combinations of eight call signs ("Arrow," "Baron," "Charlie," "Eagle," "Hopper," "Laker," "Ringo," "Tiger"); four colors ("blue," "green," "red," "white"); and eight numbers (1–8). Thus, a typical utterance in the corpus would be "Ready Baron go to blue five now." Eight talkers—four males and four females—were used to record each of the 256 possible phrases, so a total of 2048 phrases are available in the corpus.

For each trial in the experiment, a total of three audio signals were randomly generated and stored for offline ITFS processing prior to their presentation to the listeners. The first audio signal (the "target" signal) consisted of a CRM phrase randomly selected from all the phrases in the corpus containing the target call sign "Baron." The second audio signal (the "interfering" signal) consisted of one, two, or three different phrases randomly selected from the CRM corpus that were spoken by the same talker used in the target phrase but contained call signs, color coordinates, and number coordinates that were different from the target phrase and different from each other. Each of these interfering phrases was scaled to have the same overall rms power as the target phrase, and then all of the interfering phrases were summed together to generate the overall interfering signal used for the binary mask processing. The third audio signal (the "mixture") was simply the sum of the target and interfering signals for that particular stimulus presentation.

Note that, although all of the individual masking talkers in the mixture were scaled to have the same rms power, the overall SNR was less than 0 dB in the conditions with more than one interfering talker. In previous papers, we have clarified this distinction by referring to the ratio of the target speech to each individual interfering talker as the target-to-masker ratio (TMR), and by referring to the ratio of the target talker to the combined interfering talkers as the overall SNR (Brungart *et al.*, 2001). Under this terminology, the mixture with two equal-level interfering talkers would have a TMR value of 0 dB and an SNR value of approximately −3 dB.

3. Ideal time-frequency segregation

Prior to the start of data collection, each set of three audio signals ("target," "interferer," and "mixture") was used to generate a single ITFS stimulus at a single predetermined LC value. A total of 29 different LC values, ranging from −60 dB to +30 dB in 3 dB increments, were tested in the experiment. In addition, an "unsegregated" condition was included where the stimuli were simply processed using the ITFS technique with a LC value of negative infinity (thus including all T-F units in the resynthesized mixture). This control condition was essentially equivalent to simply presenting the mixture to the listener, but it also captured any distortions that might have occurred during the analysis and resynthesis portions of the ITFS processing.

4. Procedure

The listeners participated in the experiment while seated at a control computer in one of three quiet listening rooms. On each trial, the speech stimulus was generated by a sound card in the control computer (Soundblaster Audigy) and presented to the listener diotically over headphones (Sennheiser HD-520). Then an eight-column, four-row array of colored digits corresponding to the response set of the CRM was displayed on the CRT, and the listener was instructed to use the mouse to select the colored digit corresponding to the color and number used in the target phrase containing the call sign Baron.

The trials were divided into blocks of 50, each taking approximately 5 min to complete. Each subject participated in 90 blocks for a total of 4500 trials per subject. These included 150 trial combinations for each of the 30 LC values (including the unsegregated condition) evenly divided among three talker conditions (two-talker, three-talker, and four-talker, corresponding to one-interferer, two-interferer, and three-interferer, respectively). The trials were also balanced to divide the eight target speakers as evenly as possible across the trials collected in each condition for each subject.

B. Results and discussion

Figure 3 shows the percentage of trials where the listeners correctly identified both the color and the number in the

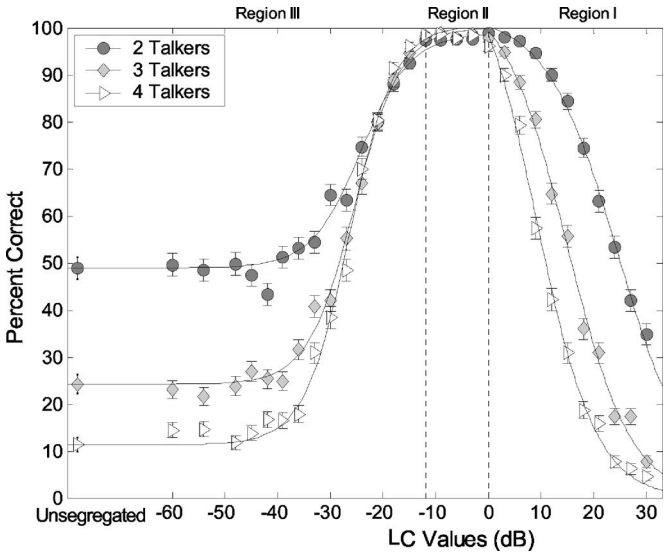

FIG. 3. Percentage of trials in Experiment 1 in which the listeners correctly identified both the color and number coordinates in the target phrase as a function of the LC values. The legend indicates the number of simultaneous talkers tested in the experiment. The error bars represent 95% confidence intervals (±1.96 standard errors) in each condition, calculated from the pooled data collected from all the subjects in the experiment. Because of the discontinuity in the performance curve at 0 dB, two different logistic curves were used to fit the positive and negative LC values in each talker condition (Cavallini, 1993). At negative LC values, this logistic curve was set to asymptote at the performance value achieved in the unsegregated control condition. Note that the target and maskers always were presented at the same overall rms level (i.e., 0 dB TMR) prior to the application of the ITFS procedure.

target phrase as a function of LC for each of two, three, and four simultaneous talker configurations in the experiment. The data were averaged across the listeners used in the experiment, and the error bars in the figure represent the 95% confidence interval of each data point. The points at the far left of the figure (labeled unsegregated) represent the control conditions where all of the T-F units were retained in the resynthesized signal. These points indicate that the listeners were able to correctly identify the color and number coordinates in the stimulus in approximately 50% of the trials with two simultaneous talkers, 25% of the trials with three simultaneous talkers, and 12% of the trials with four simultaneous talkers. These results are consistent with previous experiments that have examined performance in the CRM task with two, three, or four identical talkers (Brungart *et al.*, 2001).

Although the overall number of correct color and number identifications clearly decreased as the number of talkers in the stimulus increased, the general pattern of performance was similar for all three of the talker conditions tested. For purposes of discussion, it is easiest to divide these performance curves into three distinct regions that are clearly defined in all three of these performance curves shown in Fig. 3 and have very different interpretations with respect to the effect of LC. Before discussing each of these regions in detail, we describe the performance for the LC value of 0 dB, which corresponds the standard definition of the ideal binary mask discussed in Sec. II.

1. LC Value of 0 dB: Effects of energetic masking at a TMR value of 0 dB

As discussed earlier, the basic premise of the ITFS technique is that its application with a LC value at or near 0 dB preserves the effects of energetic masking in the stimulus but eliminates errors due to target-masker confusions. Under this premise, the point with 0 dB LC in Fig. 3 can be roughly interpreted as the theoretical maximum level of performance that could be achieved if the listener were able to successfully segregate and identify all of the detectable acoustic elements of the target talker in the stimulus.

An examination of the results in Fig. 3 shows that the listeners in the 0 dB LC condition correctly identified the color and number in the target phrase nearly 100% of the time even in the most difficult four-talker condition. This represents a dramatic improvement in performance over the unsegregated conditions, where performance ranged from 12% correct responses in the four-talker condition to 50% correct responses in the two-talker condition. Since the elimination of the T-F regions with negative local SNR values would not provide additional information about the target, our explanation for the large improvement in performance in the ITFS condition is that performance in the unsegregated condition was primarily dominated by nonenergetic masking effects due to the listener confusing the target and masking voices.

2. Region I: Energetic masking effects at LC values greater than 0 dB

The curves in Region I of Fig. 3 show that performance in the ITFS condition systematically decreased as the LC value increased above 0 dB. The fact that performance was near 100% when LC=0 dB and that it began to decrease almost immediately when LC increased above 0 dB is informative, because it implies that the listeners were able to obtain a significant amount of information from T-F regions of the stimulus that had local SNR values between 0 and +3 dB. This clearly shows that listeners can (and do) extract information from T-F regions of the stimulus with local SNR values as low as 0 dB, thus supporting the somewhat arbitrary choice of 0 dB as the nominal local SNR point differentiating between those T-F units which provide the listener with useful information about the target and those that only provide useful information about the masker.

The drop off in performance when LC$>$0 dB is also informative in another way. By the definition of ITFS, each 1 dB increase in the LC value produces a 1 dB increase in the minimum local SNR value required for a given T-F unit to be retained. This means that each 1 dB increase in LC above 0 dB eliminates exactly the same T-F units from the stimulus that would be eliminated if LC remained unchanged but the level of the masker increased by 1 dB. Thus, to a first approximation, the level of performance achieved for an ITFS stimulus with a LC value of $+L$ dB is approximately equivalent to the level of performance that could be achieved with just the energetic component of speech on speech masking in the corresponding stimulus with the overall SNR reduced by L dB (this assumption will be tested in the next experiment). The Region I performance with positive LC

values could therefore be interpreted as an indicator of the effect of purely energetic masking on multitalker speech perception with the corresponding reduction of overall SNR. These results would then suggest that energetic masking has a remarkably small impact on the performance with the multitalker CRM task. At a TMR of 0 dB, performance was near 100% even for a stimulus containing four simultaneous same-talker speech signals, which corresponds to an overall SNR of approximately −4.8 dB. Even when the effective SNR value was reduced by 30 dB (LC=30 dB), performance was near 35%correct in the two-talker condition and better than chance (3%) even in the four-talker condition.

3. Region II: Plateau in performance at LC values from −12 to 0 dB

In the range of LC values between −12 and 0 dB, the listeners consistently exhibited near-perfect identification performance (100% correct responses) in all three of the talker configurations tested. In this region, the stimulus contained all of the available speech information about the target, but only those T-F regions of the masker that were slightly more intense than the target. These units with stronger masking energy did not significantly interfere with the recognition of the target speech, presumably either because there were not enough of them to be perceived as a competing speech signal or because they only occurred in T-F regions that already contained a significant amount of energy in the target signal.

4. Region III: Target-masker confusion at LC values less than −12 dB

When the LC values used to generate the ITFS stimuli fell below −12 dB, the stimulus started to include progressively more T-F units in places where relatively little or no energy was present in the target. These units produced a rapid decrease in performance, from near 100% at LC value of −12 dB to approximately the same level of performance achieved in the unsegregated condition when LC=−40 dB. Decreasing the LC value below −40 dB caused no further degradation in performance, presumably because all of the relevant phonetic information in the interferer was already present in the stimulus when the LC value was −40 dB.

Decreasing the LC value below 0 dB has essentially no impact on the total amount of phonetic information in the target that is available to the listener. All of the T-F units that include usable information about the target are presumably included in the stimulus at a LC value of 0 dB. What happens when LC is reduced below 0 dB is that some of the T-F regions that primarily include phonetic information about the *interferer* are added back into the stimulus. Thus, the decrease in performance that occurs at negative LC could only be attributed to the listener becoming confused about which acoustic elements belong to the target and which acoustic elements belong to the interferer.

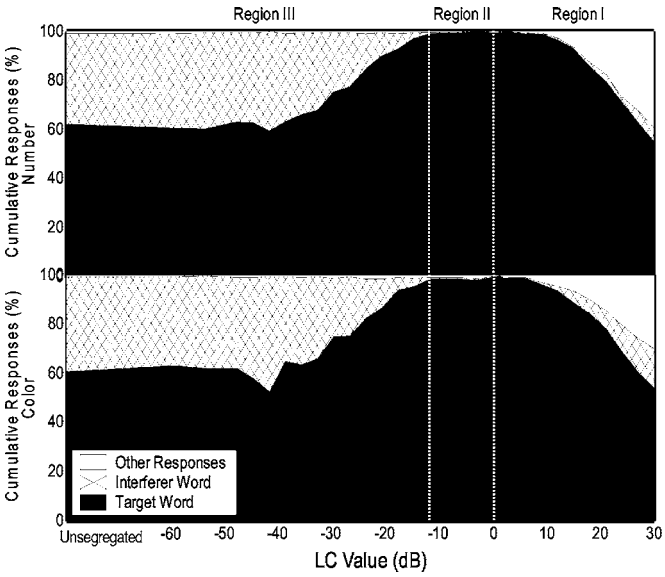

FIG. 4. Distribution of listener color and number responses in the two-talker condition of Experiment 1. The top panel shows the distribution of listener number responses in the experiment: the black area indicates correct responses that matched the number word in the target phrase; the mesh area indicates incorrect responses that matched the number word in the masking phrase; the white area indicates responses that did not match either of the number words contained in the stimulus. The bottom panel shows the same information for the color responses in Experiment 1.

5. Error analysis

Although the error rates shown in Fig. 3 provide an overall picture of the effect that the LC value of the binary mask had on performance in the CRM task, additional insights can be obtained by further analyzing the *types* of errors the listeners made in the experiment. The area graphs in Fig. 4 divide the listeners' color and number responses in the two-talker condition of the experiment into three categories: correct responses that matched the color or number word in the target phrase (black region in the graph), incorrect responses that matched the color or number word in the interfering phrases (meshed region in the graph), and incorrect responses that did not match either of the color or number words present in the stimulus (white region in the graph). Again, the results are somewhat different in the three regions of the figure. In Region II, where the LC value was between −12 and 0 dB, the listeners responded correctly nearly 100% of the time and no meaningful error analysis is possible. In Region I, where the LC value was greater than 0 dB, the incorrect responses were essentially random: the incorrect number responses matched the number in the masking phrase roughly 1/7 of the time, and the incorrect color responses matched the color in the masking phrase roughly 1/3 of the time. Again, this is consistent with the effects of energetic masking: the elimination of phonetic information from the target due to energetic masking has no particular tendency to bias the listener towards any alternative response word, so the incorrect responses are randomly distributed across all the possible alternatives available in the response set.

In Region III, where the LC value was less than −12 dB, the distribution of incorrect responses was much different. In

that region, virtually 100% of the incorrect responses matched the color or number contained in the masking phrase, and almost none contained a color or number word that was not present in the stimulus. This is consistent with the assumption that target-masker confusions are responsible for the decrease in performance in that condition: the addition of the acoustic elements dominated by the masking phrase at negative LC values introduced a second intelligible voice into the stimulus that confused the listener about which voice to respond to.

It is worth noting that there is never any point at any negative LC value where the listeners exhibited a significant number of incorrect responses that did not match the interfering phrase in the stimulus. At modestly negative LC values, one might expect that some point could occur where there would be enough low-level phonetic interferer elements in the stimulus to confuse the listener about the contents of the target phrase, but not enough to allow the listener to understand the contents of the interfering phrase. Such a point would be expected to produce an increase in overall error rate with a random distribution of errors similar to that seen in Region I of the figure. However, no such region exists at negative LC values in Fig. 3. This implies that the acoustic elements of the interferer that are added to the stimulus at negative LC values have no effect on the recognition of the target phrase until they themselves become intelligible and present the listener with an alternative interpretation of key words spoken by the target talker.

IV. EXPERIMENT 2: EFFECTS OF IDEAL TIME-FREQUENCY SEGREGATION ON SPEECH PERCEPTION IN NOISE

The results of Experiment 1 clearly show that application of the ITFS technique produces a dramatic improvement in performance in a multitalker listening task where the confusability of the target and masking signals plays a dominant role in determining overall performance. However, as a comparison it is also helpful to examine what effect the technique might have on the intelligibility of speech in noise, where confusability of the target and masking signals has a much smaller impact on performance than the spectral overlap of the target and masking signals. Also, there was a desire to test the validity of the assumption, outlined in Sec. III B 2, that there was a rough equivalence in terms of energetic masking between the information lost by a 1 dB increase in the LC value of the stimulus at a fixed SNR and a 1 dB decrease in the SNR of the stimulus at a fixed LC value. Thus a second experiment was conducted to examine the effect of ITFS processing on the perception of speech in noise.

A. Methods

1. Listeners

A total of nine paid listeners participated in Experiment 2. All had normal hearing and their ages ranged from 21 to 55. Most had participated in previous auditory experiments, and all were familiarized with the CRM task prior to conducting this experiment.

2. Stimulus generation

The target phrases used in the experiment were derived from the same CRM corpus used in Experiment 1. However, in Experiment 2 these phrases were masked by noise rather than speech. Two different types of Gaussian noise interferers were used to generate the stimuli used in the experiment. The first was a continuous speech-shaped noise masker that was spectrally shaped to match the average long-term spectrum of all of the phrases in the CRM Corpus (Brungart, 2001). The second was a speech-shaped masker that was modulated to match the overall envelope of a speech phrase that was randomly selected from all the nontarget phrases in the CRM corpus. This envelope was extracted by convolving the absolute value of the CRM phrase with a 7.2 ms rectangular window. The resulting envelope was then multiplied with a continuous speech-spectrum-shaped Gaussian noise to generate a modulated noise that simulated the amplitude fluctuations that typically occur in the overall envelope of a natural speech utterance (Brungart, 2001).

3. Ideal time-frequency segregation

Prior to the start of data collection, each of the 256 phrases that contained the call sign Baron was used to construct a total of 60 different stimulus wave forms for eventual presentation in the experiment. These stimulus wave forms consisted of all combinations of two different types of noise (continuous and modulated), ten different effective SNR conditions (ranging from −27 to 0 dB in 3 dB steps), and three different types of ITFS processing. These three types of processing were:

(a) Method 1 ITFS: Fixed mixture SNR, variable LC values. Method 1 used the same procedure for generating the ideal mask that was used in Experiment 1, where the LC value used to calculate the binary mask was varied and the resulting mask was applied to a stimulus with a fixed SNR value of 0 dB. Each Method 1 stimulus was generated by scaling the interfering noise wave form to have the same overall rms power as the target speech (i.e., an SNR of 0 dB), calculating the ideal mask for this mixture with LC set to one of ten values ranging from 0 to 27 dB, and using this ideal mask to resynthesize the speech from the 0 dB SNR mixture.

(b) Method 2 ITFS: Variable mixture SNR values, fixed LC value. Method 2 was designed to test the assumption, outlined in Section III B 2, that each 1 dB increase in LC value was roughly equivalent in terms of the effects of energetic masking to a 1 dB decrease in the overall SNR of the stimulus. Each Method 2 stimulus was generated by scaling the rms power of the interfering noise wave form to one of 10 SNR values relative to the target speech (ranging from 0 to −27 dB in 3 dB steps), calculating the ideal mask for this mixture with LC set to 0 dB, and using this ideal mask to resynthesize the speech from the same SNR mixture used to generate the binary mask. Note that this processing resulted in a stimulus with the same binary mask as the corresponding stimulus generated by Method 1 (i.e., the same set of T-F units retained) but a lower local SNR value within each retained T-F unit.

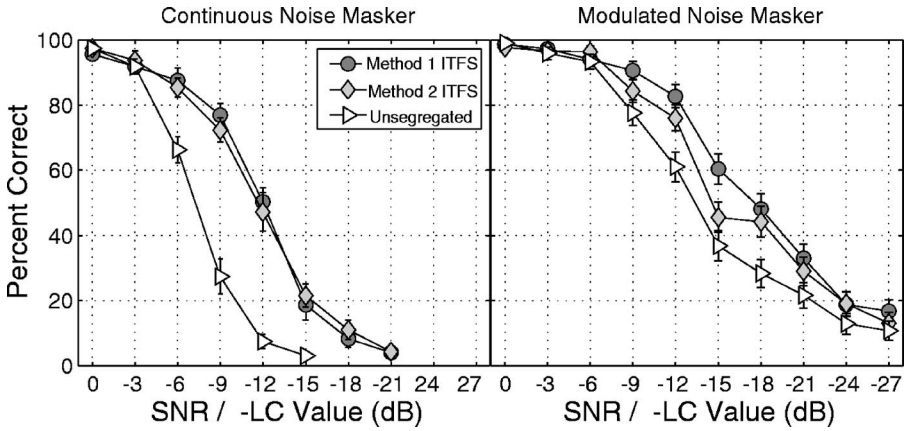

FIG. 5. Percentage of correct identifications of both color and number in each condition of Experiment 2. The left panel shows performance in the continuous noise conditions, and the right panel shows performance in the modulated noise conditions. The circles show performance in the Method 1 ITFS condition as a function of the negative of the LC value used to generate the stimulus. The diamonds in the figure show performance in the Method 2 ITFS condition as a function of the SNR value of the auditory mixture used to generate the stimulus. The open triangles show performance in the unsegregated control condition as a function of the SNR of the target speech. The error bars represent 95% confidence intervals (±1.96 standard errors) in each condition, calculated from the pooled data collected from all the subjects in the experiment.

(c) Unsegregated. Each unsegregated stimulus was generated by scaling the rms power of the interfering speech wave form to the appropriate SNR value relative to the target speech and resynthesizing the resulting mixed speech with a binary mask set to a value of 1 in every T-F unit. This processing was used to ensure that any artifacts introduced by the ideal mask processing software were also included in the unsegregated control condition.

4. Procedure

We used the same procedure as in Experiment 1 except for the following. In stimuli with SNR less than 18 dB, these stimuli were scaled to present the target at the same overall sound level [roughly 60 dB sound pressure level (SPL)]. In those stimuli with a SNR value greater than 18 dB, the stimuli were scaled to ensure that the overall level of the unsegregated stimulus (noise plus speech) would not exceed 80 dB SPL. The trials were divided into blocks of 50–100 trials, with each trial taking approximately 5 min to complete. Preliminary testing revealed that target speech was completely inaudible in the unsegregated continuous noise conditions with SNR lower than −15 dB and in the ITFS continuous noise conditions with SNR values lower than −21 dB (or equivalently those with LC values greater than 15 or 21 dB in Method 1). These eight conditions were eliminated from subsequent data collection. Thus, each listener participated in a total of 48 trials in each of 52 remaining stimulus conditions, for a grand total of 2496 trials for each of the nine listeners in the experiment.

B. Results and discussion

Figure 5 shows the percentage of correct color and number identifications in each condition of Experiment 2. The left panel shows performance in the continuous noise conditions, and the right panel shows performance in the modulated noise conditions. The circles show performance in the Method 1 ITFS condition as a function of the negative of the LC value used to generate the stimulus. The diamonds show performance in the Method 2 ITFS condition as a function of the overall SNR value of the mixture used to generate the stimulus. The open triangles show performance in the unsegregated control condition as a function of SNR.

Overall, the results in the unsegregated control condition were consistent with earlier experiments that have examined CRM performance with similar types of masking noise (Brungart, 2001). In both the continuous and modulated noise conditions, performance was near 100% when the SNR was near 0 dB. At lower SNR values, both conditions exhibited a decrease in performance with the ogive-shaped curve that typically occurs in speech-in-noise intelligibility tests. However, this decrease in performance was much more rapid in the continuous noise condition than in the modulated noise condition. In fact, performance in the unsegregated modulated noise condition was significantly better than chance (3%) even at the lowest SNR value tested. This result clearly illustrates the intelligibility advantages that can be obtained by listening to target speech "in the gaps" of a fluctuating masking sound.

Comparing the results from the unsegregated conditions of the experiment to those from the ITFS conditions, it is apparent that performance curves for the Method 1 and Method 2 stimuli were very similar to one another, and that they were almost identical in shape to those obtained in the unsegregated condition. This suggests that the application of an ideal binary mask with an LC value of 0 dB improved the intelligibility of a speech stimulus masked by noise by roughly 2–5 dB. While not inconsiderable, this improvement appears small relative to the dramatic 50 to 90 percentage point improvements obtained by applying the same binary mask to the 2, 3, and 4-Talker stimuli tested in Experiment 1. Thus it seems that the application of the ideal binary mask had less effect when the target speech signal was masked by noise than when it was masked by speech. These results also have two additional major implications.

The first implication is that there is a very strong (nearly one-to-one) relationship between the amount of masking caused by a 1 dB decrease in the SNR of a noise-masked

speech signal and the loss of acoustic information caused by a 1 dB increase in the LC value used to create an ITFS stimulus.

The second major implication of Experiment 2 is that the pattern of the T-F units preserved by the application of ITFS has a much greater impact on performance than the underlying local SNR values of these T-F units. In this experiment, the Method 1 and Method 2 stimuli were designed to produce exactly the same ideal masks, and thus to retain exactly the same T-F units, at each stimulus SNR. The only difference between the two methods was that the local SNR value within each retained T-F unit of the Method 2 stimulus was substantially lower than in the corresponding T-F unit of the Method 1 condition. Yet, despite these substantially higher local SNR values in the Method 1 condition, the results in Fig. 5 show that performance was nearly identical for the two methods at all SNR values tested. This result suggests that speech perception is much more limited by the listener's ability to determine where the energy in the target speech is located in the T-F domain than by the ability to extract specific target information within individual T-F units.

V. GENERAL DISCUSSION

A. Relationship between ITFS, speech segregation, and informational masking

Speech segregation is an extremely complicated process that depends on many variables. In the introduction, we suggested that a possible way to approximate speech segregation at a basic level is to view it as a relatively simple two-stage analysis of the T-F representation of the auditory mixture. The input to this analysis is provided by the auditory periphery, which can be viewed as a T-F analyzer with resolution that is limited in frequency by the bandwidths (critical bands) of the cochlear filters and in time by the occurrence of forward and backward masking within each critical band. Thus, the output from the auditory periphery could be viewed as an array of individual T-F units, with each unit representing the auditory signal that occurs at a particular time and frequency in the acoustic stimulus, and with the size (i.e., bandwidth and length) of each unit representing the smallest auditory event capable of being individually resolved by the auditory periphery.

Given this array of T-F units, the goal of speech segregation is to find a way to extract target speech from an acoustic mixture containing competing sounds. This can be viewed as consisting of two distinct, but interrelated, stages. The first stage is performed at the level of individual T-F units. Because each T-F unit is, by definition, too small to allow the resolution of individual sounds within the same unit, there are really only a few possible outcomes for a given unit within a complex acoustic mixture. When the unit contains substantially more energy from the target than from the masker, the characteristics of the T-F unit are essentially identical to those of the target alone, and there should be little loss of information due to the presence of the masker. When the unit contains substantially more energy from the masker, information from the target is expected to be lost, and the characteristics of the T-F unit should approximate those of the masker. When the unit contains comparable amounts of energy from the target and masker, the properties of the T-F unit would be corrupted, matching neither the target nor the masker. In the last two cases, where the masker energy in an individual T-F unit is comparable to or greater than the target energy in that unit, the resulting corruption or elimination of the target information would be an example of energetic masking.

In the second stage of the two-stage speech segregation process, the listener examines all of the T-F units in the mixture and uses the acoustic characteristics of each unit determined in the first stage, along with any available *a priori* information about the characteristics of the target, to determine which T-F units should be associated with the target and integrated into the single acoustic image of the target. This is a classic auditory grouping task, and it presumably makes use of a variety of grouping cues such as common onsets or offsets, amplitude or frequency co-modulations, common periodicity across frequency, and *a priori* templates for complex spectro-temporal patterns in speech or nonspeech sounds (Bregman, 1990).

Ideally, the output of the second stage would be a composite signal that includes all of the T-F units containing useful information about the target speech, and excludes all the other units. In reality, however, this segregation process is unlikely to be perfect, as suggested by the performance differences between an unsegregated mixture and the corresponding ITFS processed version shown in Fig. 3. Two kinds of errors could be made in this segregation process. Listeners could inadvertently exclude some T-F units that contain useful information about the target, resulting in a loss of relevant information from the target. They could also inadvertently include some T-F units that only contain acoustic energy from the masker, resulting in a garbled signal that might not be completely intelligible. We contend that these two types of segregation errors represent the very core of the nonenergetic form of masking, often referred to as *informational masking*, that occurs when the listener is unable to segregate the acoustically detectable portions of the target speech from the similar-sounding acoustically detectable portions of the interfering speech (Brungart, 2001; Cahart and Tillman, 1969; Freyman *et al.*, 1999; Kidd *et al.*, 1998; Pollack, 1975).

Because the underlying processes involved in speech segregation are extremely complicated, it is very difficult (or perhaps impossible) to completely isolate the contributions that energetic and informational masking make to overall segregation performance in realistic stimuli. However, if we are willing to make some simplifying assumptions, we could use a tool such as the ITFS technique to get a rough estimate of the effects that energetic and informational masking have on the perception of an arbitrary stimulus. The first approximation is that the application of the ITFS technique with a LC value of 0 dB provides a rough estimate of the effect that purely energetic masking has on the perception of a mixture. The second approximation is that the relative effect of informational masking on an arbitrary acoustic stimulus can be approximated by the smallest positive LC value required to

bring ITFS-processed recognition performance down to the level obtained in the unsegregated condition. This operational metric of informational masking is based on the first approximation plus the assumption that each 1 dB increase in the LC value eliminates the same T-F units (and thus produces approximately the same loss of information) as the energetic masking caused by each 1 dB decrease in the overall SNR value of the stimulus. By this metric, the amount of informational masking produced by the speech maskers in Experiment 1 ranges from 22 to 25 dB, while that produced by the noise maskers in Experiment 2 is from 3 to 5 dB. While this result is clearly consistent with the general notion that speech-on-speech masking produces far more informational masking than speech-in-noise masking, much more data will be needed to determine if this crude metric will prove to be a viable way to compare the effects of informational masking across different types of complex stimuli.

B. Caveats

We believe the ITFS technique can be a valuable tool for assessing the effects of energetic masking in complex speech perception tasks. Because it makes no assumptions about the characteristics of the underlying stimulus, the technique has the potential to be applied to other complex listening tasks that tend to produce informational masking. However, a number of caveats should be kept in mind when applying this technique.

The first is that the technique is much better suited for tasks that require the identification or recognition of acoustic stimuli than for those that require the detection of acoustic stimuli. What we have measured is the intelligibility (or recognition) of target speech in the presence of interfering speech or noise, not the detection of the target signal. In a detection task, there would of course never be any retained T-F unit in the target-absent stimuli, so the use of the ITFS technique would essentially be meaningless (that is to say that the detection level of the stimulus would be determined artificially by the LC value and not by the performance of the subject). Since we have not directly measured target detection, which is closely tied to energetic masking, one should keep in mind that our analysis on energetic masking is based on assumptions and approximations. The ITFS technique is intended to largely remove the effects of informational masking, and our data clearly show that such processing leads to dramatic improvement in target intelligibility despite energy overlap between target and interfering voices. Although we have argued that the technique should introduce minimal impact on energetic masking, future experiments are needed to test whether, or to what extent, our argument holds.

The second important caveat about ITFS technique is that it is intended only as tool to evaluate the relative importance of spectral overlap in the identification or recognition of complex stimuli. It makes assumptions about the segregation of speech stimuli that are clearly not true for human listeners, and it should not be taken as a plausible model of human speech segregation.

The third point of caution about the ITFS technique is that its utility very much depends on how accurately the bandwidths of the auditory filters and the lengths of the temporal windows used to decompose the stimulus into T-F units correspond to the spectral and temporal resolution of the human auditory system. The T-F units used in this experiment are believed to be reasonable estimates of the effective spectral and temporal resolution of human listeners for speech stimuli, but they may not be appropriate for other types of stimuli, particularly those involving transients. Even for speech stimuli, our ITFS processing uses a common but fixed way of decomposing a signal into T-F units and we have not evaluated the effects different T-F resolutions may have on intelligibility performance. In addition, our ITFS processing does not take any nonlinear effects of masking into account, so it will almost certainly provide incorrect results for stimuli involving very high-level masking sounds. Also not incorporated is nonsimultaneous energetic masking which can occur either due to the upward or downward spread of masking in the frequency domain or due to forward or backward temporal masking. In theory, it should be possible to develop a more sophisticated ITFS technique that would take these factors into account and produce a more accurate estimate of the effects of energetic masking in a wider range of listening environments.

Finally, it is important to note that the relatively insignificant role of energetic masking that seemed to occur in this set of experiments was probably related to the relatively small response set used in the CRM corpus. Because they are restricted to four phonetically distinct color alternatives and eight phonetically distinct number alternatives, the key words in the CRM phrases are relatively easy to understand even in extremely noisy environments (Brungart *et al.*, 2001). Presumably, the effects of energetic masking would be substantially greater for other speech perception tests based on speech materials with phonetically similar response alternatives, such as the Modified Rhyme Test (House *et al.*, 1965), or with larger response sets of phonetically balanced words or nonsense syllables. However, a recent study by Roman *et al.* (2003) used unrestricted and semantically predictable sentences from the Bamford-Kowal-Bench corpus (Bench and Bamford, 1979) and found that the binary masks that are very close to ideal binary masks with 0 dB LC are very effective in removing interfering sounds (competing speech or babble noise) and improving speech intelligibility in low SNR conditions. Further research is needed to empirically quantify how much greater the impact of energetic masking is in multitalker listening tasks based on these more difficult speech perception tests.

VI. CONCLUSIONS

This paper has introduced "Ideal Time-Frequency Segregation" as a tool for evaluating the relative contributions that informational and energetic masking make to the overall perception of complex speech stimuli. In general, the results of the experiment are consistent with those of earlier experiments that have examined informational masking in multitalker speech perception. Specifically, they show that informational masking dominates multitalker perception with the Coordinate Response Measure corpus, and that energetic

masking has a relatively much greater impact on speech-in-noise masking than on speech-on-speech masking. Indeed, the effects of energetic masking caused by the speech maskers tested in this experiment were so small relative to those produced by equivalently powerful noise maskers that they suggest that spectral overlap may play only a relatively small role in most speech recognition tasks involving more than one simultaneous talker. Further ITFS tests with different types of speech materials will be needed to determine if this conclusion generalizes beyond the limited CRM corpus tested in this experiment.

Our results also have strong implications for CASA research, where, as discussed in Sec. II, the notion of ideal binary masking was first introduced as a computational goal of CASA. First, the results from our experiments confirm that the ideal binary mask is a very effective technique to improve human speech intelligibility performance in the presence of competing voices. Second, while the commonly used 0 dB LC corresponds to a particularly simple and intuitive comparison, its validity has not been systematically verified in speech intelligibility tests. Our results show that this is indeed a good choice to achieve intelligibility scores near 100%. On the other hand, the 0 dB LC is near the borderline of a performance plateau that centers at −6 dB for the conditions of one, two, and three competing talkers. Since CASA systems must estimate the ideal binary mask, errors in estimation have to be considered. This suggests that the LC value of −6 dB is actually a better criterion to aim for than the 0 dB LC, at least for improving human speech perception in multitalker environments.

ACKNOWLEDGMENTS

This research was supported in part by an AFRL grant via Veridian and an AFOSR grant.

Arbogast, T., Mason, C., and Kidd, G. (**2002**). "The effect of spatial separation on information and energetic masking of speech," J. Acoust. Soc. Am. **112**, 2086–2098.

Assmann, P., and Summerfield, Q. (**2004**). "The perception of speech under adverse conditions," in *Speech Processing in the Auditory System*, edited by S. Greenberg, W. A. Ainsworth, and A. N. Popper (Springer-Verlag, New York).

Bench, J., and Bamford, J. (**1979**). *Speech Hearing Tests and the Spoken Language of Hearing-Impaired Children* (Academic, London).

Bolia, R. W. N., Ericson, M., and Simpson, B. (**2000**). "A speech corpus for multitalker communications research," J. Acoust. Soc. Am. **107**, 1065–1066.

Bregman, A. S. (**1990**). *Auditory Scene Analysis* (MIT Press, Cambridge, MA).

Bronkhorst, A., and Plomp, R. (**1992**). "Effects of multiple speechlike maskers on binaural speech recognitions in normal and impaired listening," J. Acoust. Soc. Am. **92**, 3132–3139.

Brown, G. J., and Cooke, M. (**1994**). "Computational auditory scene analysis," Comput. Speech Lang. **8**, 297–336.

Brungart, D. (**2001**). "Informational and energetic masking effects in the perception of two simultaneous talkers," J. Acoust. Soc. Am. **109**, 1101–1109.

Brungart, D., Simpson, B., Ericson, M., and Scott, K. (**2001**). "Informational and energetic masking effects in the perception of multiple simultaneous talkers," J. Acoust. Soc. Am. **110**, 2527–2538.

Buss, E., Hall, J., and Grose, J. (**2004**). "Spectral integration of synchronous and asynchronous cues to consonant identification," J. Acoust. Soc. Am. **115**, 2278–2285.

Cahart, R., and Tillman, T. (**1969**). "Perceptual masking in multiple sound backgrounds," J. Acoust. Soc. Am. **45**, 694–703.

Cavallini, F. (**1993**). "Fitting a logistic curve to data," Coll. Math. J. **24**, 247–253.

Cooke, M. (**2005**). "Making sense of everyday speech: A glimpsing account," in *Speech Separation by Humans and Machines*, edited by P. Divenyi (Kluwer Academic, Norwell, MA), pp. 305–314.

Cooke, M., Green, P., Josifovski, L., and Vizinho, A. (**2001**). "Robust automatic speech recognition with missing and unreliable acoustic data," Speech Commun. **34**, 267–285.

Culling, J., and Darwin, C. J. (**1994**). "Perception and computational separation of simultaneous vowels: Cues arising from low frequency beating," J. Acoust. Soc. Am. **95**, 1559–1569.

Ellis, D. P. W. (**2006**). "Model-based scene analysis," in *Computational Auditory Scene Analysis: Principles, Algorithms, and Applications*, edited by D. L. Wang and G. J. Brown (IEEE Press/Wiley, New York) (in press).

Festen, J., and Plomp, R. (**1990**). "Effects of fluctuating noise and interfering speech on the speech reception threshold for impaired and normal hearing," J. Acoust. Soc. Am. **88**, 1725–1736.

Freyman, R., Helfer, K., McCall, D., and Clifton, R. (**1999**). "The role of perceived spatial separation in the unmasking of speech," J. Acoust. Soc. Am. **106**, 3578–3587.

Hawley, M., Litovsky, R., and Culling, J. (**2004**). "The benefit of binaural hearing in a cocktail party: Effects of location and type of interferer," J. Acoust. Soc. Am. **115**, 833–843.

House, A., Williams, C., Hecker, M., and Kryter, K. (**1965**). "Articulation testing methods: Consonantal differentiation with a closed response set," J. Acoust. Soc. Am. **37**, 158–166.

Hu, G., and Wang, D. L. (**2001**). "Speech segregation based on pitch tracking and amplitude modulation," in *Proceedings of IEEE Workshop on Applications of Signal Processing to Audio and Acoustics (WASPAA)*, pp. 79–82.

Hu, G., and Wang, D. L. (**2004**). "Monaural speech segregation based on pitch tracking and amplitude modulation," IEEE Trans. Neural Netw. **15**, 1135–1150.

Kidd, G., Mason, C., Rohtla, T., and Deliwala, P. (**1998**). "Release from informational masking due to the spatial separation of sources in the identification of nonspeech auditory patterns," J. Acoust. Soc. Am. **104**, 422–431.

Miller, G., and Licklider, J. (**1950**). "The intelligibility of interrupted speech," J. Acoust. Soc. Am. **20**, Supp. 1.

Moore, T. (**1981**). "Voice Communication Jamming Research," in *AGARD Conference Proceedings 331: Aural Communication in Aviation*, pp. 2:1–2:6. Neuilly-SurSeine, France.

Patterson, R. D., Holdsworth, J., Nimmo-Smith, I., and Rice, P. (**1988**). SVOS final report, part B: Implementing a gammatone filterbank. Rep. 2341, MRC Applied Psychology Unit.

Pollack, I. (**1975**). "Auditory informational masking," J. Acoust. Soc. Am. **82**, Supp. 1.

Roman, N., Wang, D. L., and Brown, G. J. (**2003**). "Speech segregation based on sound localization," J. Acoust. Soc. Am. **114**, 2236–2252.

Shannon, R. V., Zeng, F.-G., Kamath, V., Wygonski, J., and Ekelid, M. (**1995**). "Speech recognition with primarily temporal cues," Science **270**, 303–304.

Spieth, W., Curtis, J. F., and Webster, J. C. (**1954**). "Responding to one of two simultaneous messages," J. Acoust. Soc. Am. **26**, 391–396.

Wang, D. L. (**2005**). "On ideal binary mask as the computational goal of auditory scene analysis," in *Speech Separation by Humans and Machines*, edited by P. Divenyi (Kluwer Academic, Norwell, MA), pp. 181–197.

Wang, D. L., and Brown, G. J. (**1999**). "Separation of speech from interfering sounds based on oscillatory correlation," IEEE Trans. Neural Netw. **10**, 684–697.

Weintraub, M. (**1985**). "A theory and computational model of auditory monaural sound separation," Ph.D. Dissertation, Stanford University.

Perceptual adaptation by normally hearing listeners to a simulated "hole" in hearing

Matthew W. Smith[a] and Andrew Faulkner
Department of Phonetics and Linguistics, UCL, Wolfson House, 4 Stephenson Way, London NW1 2HE, United Kingdom

(Received 28 September 2005; revised 7 September 2006; accepted 7 September 2006)

Simulations of cochlear implants have demonstrated that the deleterious effects of a frequency misalignment between analysis bands and characteristic frequencies at basally shifted simulated electrode locations are significantly reduced with training. However, a distortion of frequency-to-place mapping may also arise due to a region of dysfunctional neurons that creates a "hole" in the tonotopic representation. This study simulated a 10 mm hole in the mid-frequency region. Noise-band processors were created with six output bands (three apical and three basal to the hole). The spectral information that would have been represented in the hole was either dropped or reassigned to bands on either side. Such reassignment preserves information but warps the place code, which may in itself impair performance. Normally hearing subjects received three hours of training in two reassignment conditions. Speech recognition improved considerably with training. Scores were much lower in a baseline (untrained) condition where information from the hole region was dropped. A second group of subjects trained in this dropped condition did show some improvement; however, scores after training were significantly lower than in the reassignment conditions. These results are consistent with the view that speech processors should present the most informative frequency range irrespective of frequency misalignment. © *2006 Acoustical Society of America.* [DOI: 10.1121/1.2359235]

PACS number(s): 43.71.Ky, 43.71.Es, 43.66.Ts [KWG] Pages: 4019–4030

I. INTRODUCTION

Regions of the cochlea where there are no functioning inner hair cells and/or neurons have been referred to as "dead regions" (Moore, 2004; Moore and Glasberg, 1997) and "holes in hearing" (Shannon, Galvin, and Baskent, 2002). The transduction of basilar membrane vibrations into auditory neural impulses is not possible within dead regions. Even so, if a sound contains frequencies corresponding to the characteristic frequencies (CFs) of the dead region, it is still possible for these frequencies to be detected. If the acoustic intensity of this part of the signal is sufficiently great, the vibration pattern of the basilar membrane will spread to locations neighboring the dead region, where the hair cells are still functioning. Consequently, the frequency information is received but activates neurons in the "wrong" tonotopic location. It is questionable whether "off-frequency" listening of this nature is beneficial to speech perception. For example, a number of studies have examined the benefits of amplification for individuals with high frequency hearing loss and suspected associated dead regions. In these studies the gain of the subjects' hearing aids was set to make the high frequencies audible. Amplification, however, often did not improve speech intelligibility and sometimes even resulted in poorer performance (Ching, Dillon, and Byrne, 1998; Hogan and Turner, 1998; Turner and Cummings, 1999). In the studies of Vickers, Moore, and Baer (2001) and Baer, Moore, and Kluk (2002), most listeners benefited from the amplification of frequencies somewhat above (1.7 times) the estimated edge-frequency of the dead region. However, when frequencies higher than this were amplified, performance hardly changed, and even worsened for some individuals. In most cases it was assumed that those individuals who did not benefit from high frequency amplification lacked functional hair cells and/or neurons in the basal part of the cochlea, and that signal detection was being mediated by hair cells at the boundary of, rather than within, the dead region.

Dead regions, or "holes in hearing," may also have a significant impact on speech perception by cochlear implant listeners, for whom the effective performance of their devices relies on there being functioning neurons at electrode locations. Elevated electrical thresholds may be evident for implant electrodes situated within a dead region, and the normal clinical solution in this sort of situation would be to increase the stimulation levels to the relevant electrodes (Shannon *et al.*, 2002). However, this may cause the electrical activation to spread away from the hole region to neighboring areas of surviving neurons, once again resulting in warping of the tonotopic representation of spectral information. Bearing in mind the previously described results from hearing aid users, Shannon *et al.* (2002) hypothesized that spectral warping in cochlear implants may result in poorer levels of speech intelligibility than if the spectral information from the hole was simply lost. The authors assessed the impact of spectral holes of varying size (1.5–6 mm) and location with both implant patients and normally hearing listeners, the latter using noise-vocoder simulations of CI signal processing. Holes were created by turning off certain electrodes, or by eliminating the relevant output noise bands. Also examined was whether the frequency information from the hole regions

[a]Electronic mail: matthew@phon.ucl.ac.uk

could be usefully preserved by remapping the relevant analysis bands to electrodes/output noise bands apical to the hole, basal to the hole, or both sides of the hole; however, these remapping conditions also entailed a warping of the place code of the spectral envelope. The results showed that speech recognition scores were significantly reduced when the holes were at least 4.5 mm wide. Holes in the apical region were the most damaging, while speech information that is highly dependent on spectral cues—vowel identity and consonantal place of articulation—were affected more than information that is predominantly temporally cued—voicing and manner of consonant articulation. Crucially, conditions that attempted to preserve frequency information by remapping it around the hole—and thus warping the place code—appeared to produce results no better than those achieved when the information from the hole region was simply dropped. The authors concluded that these results were not encouraging for the prosthetic restoration of lost information due to a hole in the receptor array, suggesting that the pattern of spectral information becomes unusable when not presented to the correct tonotopic location.

Similar conclusions have been drawn from studies into absolute frequency-place shifting in implants, arising from shallow electrode array insertions. Here, the tonotopic mismatch between the analysis bands in the speech processor and the CFs at implanted electrodes is equivalent to a basalward basilar membrane shift. A number of simulation studies have shown that listeners could tolerate shifts of 3 mm, but that larger shifts produced large decrements in speech recognition performance (Dorman, Loizou, and Rainey, 1997; Shannon, Zeng, and Wygonski, 1998; Fu and Shannon, 1999). However, it is important to note that the subjects in these experiments were given no training and, therefore, had little time to adapt to the effects of tonotopic mismatch. In simulation studies where normally hearing subjects have been given a few hours of training with spectrally shifted speech, the detrimental effects of tonotopic mismatch have been significantly reduced (Rosen, Faulkner, and Wilkinson, 1999; Faulkner, Rosen, and Norman, 2001). Therefore, one might expect that implant users, who are listening with their devices for several hours every day, would also adapt to the frequency mapping provided by their speech processor. This suggestion is supported by the study reported by Harnsberger, Svirsky, Kaiser, Pisoni, Wright, and Meyer (2001). Experienced implant users were asked to provide goodness ratings for synthetic vowel stimuli varying in formant frequencies F1 and F2, in order to construct individual perceptual vowel spaces. If the subjects were failing to adapt to the spectrally shifted information presented by their devices, they would be expected to choose stimuli with lower F1 and F2 formant frequencies than those of natural vowels. However, there was no evidence of any systematic shift in the perceptual vowel spaces.

Shannon *et al.*'s (2002) acute study into "holes in hearing" did not assess the effects of learning. However, listeners might be able to adapt to the distorted representation of information in spectrally warped speech in the same way that they can adapt to spectrally shifted speech. Furthermore, if cochlear implant speech processors were to use analysis filters frequency-aligned to CFs at electrode locations, those patients with large dead regions would be likely to suffer a significant loss of speech information. Kasturi, Loizou, Dorman, and Spahr (2002) examined the effect of the location and size of spectral holes in a cochlear implant simulation, using speech processed through six frequency bands and synthesized as a sum of sine waves. When a 6.25 mm hole was created in the mid-frequency region, between 790 and 2100 Hz, consonant intelligibility fell from more than 90% correct (when all bands were present) to less than 70% correct. Vowel recognition fell to less than 50% accurate in this particular condition. It seems likely then that dropping the information from a hole region is a less than ideal option.

In the present study, an implant simulation with normally hearing listeners was conducted, similar to that of Shannon *et al.* (2002); however, in this study subjects were given training and time to adapt to each condition. Because of the time-consuming nature of the training, a single hole of fixed size (10 mm) and location (mid-frequency region) was examined; acutely, this produced a pronounced detrimental effect on speech intelligibility. The main hypothesis is that, in the context of a hole in hearing, the detrimental effects of a tonotopic mismatch can be significantly reduced with experience. Consequently, it is also hypothesized that, with training, differences might become apparent between conditions which attempt to preserve frequency information by remapping it around a hole, and conditions in which the information from the hole region is lost. In the first experiment subjects were trained in two "preservation" conditions to see if the precise way in which information from the hole region is remapped (warped) around the hole has a significant affect on speech perception. One of these conditions was similar to that examined by Shannon *et al.*, with the warping effect concentrated at the edges of the hole. In the second, however, the warping effect was spread over the entire frequency range. Performance in these conditions was compared to that in a baseline condition in which information from the hole region was simply dropped. In light of the results from this experiment, a second experiment was conducted in which a different group of subjects was trained in the "information dropped" condition.

II. METHOD

A. Test materials

For each processing condition, three tests were used to evaluate performance: Recognition of keywords in sentences, medial vowel identification, and medial consonant identification. No lip-reading cues were provided. Test materials were digitally recorded, at a sampling rate of 48 kHz, by a male and female speaker using standard Southern British English pronunciation. One female speaker recorded the sentence stimuli and another, the vowel and consonant stimuli. The same male speaker was used for all three tests.

The IEEE sentences (IEEE, 1969) were used for the word recognition task. These comprise 72 blocks of ten sentences, with five scored keywords per sentence. The vowel stimuli comprised ten monophthongs (/æ ɑ ɔ i ɛ ɪ ɜ ɒ u ʌ/) and six diphthongs (/eʊ eɪ ɪə aɪ əʊ ɔɪ/) and were presented in

a /b/-vowel-/d/ context: *bad bard bawd bead bed bid bird bod booed bud bared bayed beard bide bode boyd*. These words were presented in the carrier phrase "say /bVd/ again." Test blocks consisted of 48 stimuli from one speaker with three tokens of each word selected at random from a pool containing five tokens of each word.

Each of the nineteen consonant stimuli (/b tʃ d f g k l m n p r s ʃ t θ v w y z/) were recorded in three vCv contexts: /ɑCɑ/, /iCi/, and /uCu/; and were presented in the carrier phrase "say /vCv/ again." Both speakers recorded five tokens of each consonant in each vowel context. Test blocks consisted of 57 stimuli from one speaker with one token of each consonant in each vowel context, selected at random from the full recorded set.

B. Signal processing

Four speech processors were designed, each utilizing noise-band vocoding similar to that described by Shannon, Zeng, Kamath, Wygonski, and Ekelid (1995). The speech signals were band-pass filtered into a number of contiguous frequency bands, from which amplitude envelopes were extracted via half-wave rectification and low-pass filtering. Each envelope was used to modulate a white noise which was subsequently band-pass filtered. All bands were then summed and presented to the listener. Thus, within each band, temporal and amplitude cues were preserved while spectral detail was removed. The center frequencies and −3 dB cut-off frequencies of the analysis and output filters (Table I) were calculated using Greenwood's (1990) equation relating basilar membrane location to characteristic frequency, assuming a basilar membrane length of 35 mm. Signal processing was implemented in two distinct ways: Off-line processing of the recorded test materials, and on-line processing of live speech during training.

Off-line processing was implemented in MATLAB. Analysis and output band-pass filters were sixth-order Butterworth IIR designs, while the low-pass filter used in envelope extraction was a third-order Butterworth filter with a cut-off frequency of 400 Hz. Finally, to limit the signal spectrum, the summed waveform was low-pass filtered at the upper cut-off of the highest frequency band using a sixth-order elliptic filter. Real-time processing was implemented using the Aladdin Interactive DSP Workbench (Hitech AB) and a DSP card (Loughborough Sound Images TMSC31) running at a sampling rate of 11025 Hz. For each processor, the characteristics of the filters were the same as in the off-line processing but in order to reduce the computational load, sixth-order elliptic rather than Butterworth filters were used.

Three of the four processor designs simulated a "hole in hearing" extending from a point on the basilar membrane 25.8 mm from the base (CF 424 Hz) to a point 15.8 mm from the base (CF 2182 Hz). The first of these three processors divided the speech signals into 12 contiguous frequency bands spanning 130–4518 Hz (Table I) and had tonotopically matched analysis and output filters. To create the hole, the middle six output bands were eliminated [Fig. 1(b)]. This processor is subsequently referred to as the "Dropped" condition since spectral information from the hole region was not available to the listener. It should be emphasized that this processor used the same output bands as the two reassignment processors, all having three output bands apical to the hole and three basal to the hole (Table I). However, the three designs differed in the mapping of analysis filters to output filters. In attempting to preserve the spectral information encoded in the frequencies of the hole region, the designs of processors two and three warped the place code of the spectral envelope. Processor two—referred to as "S-warp" (for *Spread warping*)—had six contiguous bands spanning 150–4513 Hz (Table I) and mapped these to the three output bands either side of the hole, entailing a downward spectral shift of the lower three input bands and an upward spectral shift of the three higher input bands [Fig. 1(d)]. Processor three—referred to as "A-warp" (for *Adjacent warping*)—

TABLE I. Filter center and cut-off frequencies, representing: (a) Analysis and output bands for the Matched processor and analysis bands for the S-warp processor; (b) analysis bands for the Dropped and A-warp processors; (c) output bands for the Dropped, A-warp, and S-warp processors.

(a)		(b)		(c)	
Center (Hz)	Cut-off (Hz)	Center (Hz)	Cut-off (Hz)	Center (Hz)	Cut-off (Hz)
	130		130		130
		(1) 166		(1) 166	
(1) 207			207		207
		(2) 252		(2) 252	
	303		303		303
		(3) 360		(3) 360	
(2) 424			424		424
		(4) 496			
	577		577		
		(5) 667			
(3) 769			769		
		(6) 883			
	1011		1011	Hole	
		(7) 1154			
(4) 1316			1316		
		(8) 1496			
	1699		1699		
		(9) 1926			
(5) 2182			2182		2182
		(10) 2468		(4) 2468	
	2789		2789		2789
		(11) 3150		(5) 3150	
(6) 3555			3555		3555
		(12) 4008		(6) 4008	
	4518		4518		4518

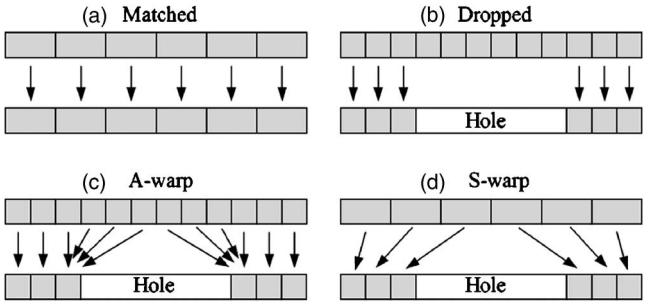

FIG. 1. Mapping of analysis to output bands for the four processors.

analyzed signals into 12 bands; unlike the Dropped processor, however, the middle six bands were not discarded. For both the upper and lower halves of the hole region, envelopes from the three contributing bands were summed and added to the envelope of the band adjacent to the corresponding side of the hole. These two summed envelopes were divided by the number of contributing bands—so that the amplitude was of a similar level to that in neighboring bands (following the method used by Shannon *et al.*, 2002)—and then used to modulate the relevant hole-adjacent output noise-band. All other analysis bands were mapped to tonotopically matched output bands [Fig. 1(c)].

The final processor—referred to as the "Matched" condition—provided an indication of performance level when no hole was present. This was a six-channel, tonotopically matched processor with analysis filters identical to those used in the S-warp condition [Table I and Fig. 1(a)]. As a result of this design the input information to the Matched and S-warp processors was kept the same and enabled a direct test of the effects of warping as implemented in S-warp (an *a priori* assumption was that performance with the S-warp processor would be at least as good as the performance with the A-warp and Dropped processors).

C. Procedure

1. Experiment 1

Experiment 1 investigated the effects of training on the performance with the A-warp and S-warp processors. Eight normally hearing native speakers of English participated in the experiment. Their ages ranged from 18 to 43 and each was paid for taking part. During testing and training, processed speech was presented at a comfortable listening level, via Sennheiser HD25-1 headphones. Presentation was always purely auditory. No feedback was provided in testing and, for the sentence material, subjects never encountered the same sentence twice.

Baseline testing was undertaken in all four processing conditions, the order of presentation being balanced across subjects. First, subjects were familiarized with the sentence task by listening to two lists of BKB sentences (Bench and Bamford, 1979) presented through the Matched processor. The subject attempted to repeat each sentence. A loose scoring method was employed; answers with the same morphological root as that of the target keyword were treated as correct. For familiarization with the vowel task subjects heard an abbreviated test block (16 stimuli) using unprocessed speech. The 16 /b/-vowel-/d/ words were displayed in a grid on a computer screen and subjects attempted to identify each word heard by mouse-clicking on the correct box. A similar familiarization procedure was carried out for the consonant task but with the screen grid displaying orthographic forms of the nineteen consonant stimuli. In the experimental conditions, subjects completed all three tasks before moving on to the next; this meant listening to four lists of IEEE sentences (two each with the male and female speaker), two blocks of vowels (one from each speaker), and two blocks of consonants (one from each speaker) through each processor.

Training commenced once baseline testing was completed. As all subjects trained with both processors, a crossover design was used to control for order effects—four subjects starting with the A-warp processor and four with the S-warp processor. Training consisted of Connected Discourse Tracking (De Filippo and Scott, 1978), an interactive procedure using connected speech in real-time communication. Speaker (author M.S.) and subject sat in separate sound-isolated rooms connected by an audio link, the voice of the speaker being processed in real time. Stories from the Heinemann Guided Readers series were read to the subject who was required to repeat what the speaker had read before he could move on to the next sentence, phrase, or word. If there was an error in the response the speaker re-read the section until the subject could repeat it correctly. A pragmatic approach to correcting errors was taken: The speaker could use intonation and stress to focus the subject's attention on the location of the error, and/or read the next phrase or sentence to provide additional contextual cues. However, three incorrect attempts on the part of the subject were followed by a fourth reading but this time with the audio link switched to unprocessed speech. This way, any potential impasse could be avoided. Subjects were familiarized with the CDT procedure using the Matched processor.

For both the A-warp and S-warp processors, training consisted of five 35 min sessions of CDT, broken down into seven 5 min blocks. After each training session, subjects were tested in the same condition using four lists of sentences (two male and two female), two blocks of vowels (one from each speaker), and two blocks of consonants (one from each speaker). After completing training and testing in the first-trained condition, subjects were tested in the other condition to be trained; this provided a fresh baseline measure for that condition. At the end of the experiment, subjects had five minutes of CDT with the Matched processor; this provided some indication of the optimum tracking rate attainable with a six-channel noise-excited vocoder. Finally, retesting was performed with the Matched and Dropped processors, and with the processor used in earlier training sessions. The order of presentation of the conditions was balanced across subjects. Table II presents the testing and training schedule for a subject trained first with the A-warp processor. Subjects differed in the elapsed time required by the training regime. One week was the maximum time required to complete five sessions for either condition.

2. Experiment 2

Experiment 2 investigated the effects of training on performance with the Dropped processor. A different group of eight normally hearing subjects took part. Again, all were native speakers of English and each was paid for taking part. Their ages ranged from 19 to 43.

Except that subjects were trained in only one condition, and that consonant testing was not conducted (only small training effects being found for these materials in Experiment 1), the procedure was similar to that outlined above. Baseline testing with all four processors was followed by five sessions of training and testing with the Dropped processor. Finally, subjects were re-tested with the Matched, A-warp, and S-warp processors.

TABLE II. Schedule for a subject trained first with the A-warp processor and then with the S-warp processor (m=Matched, d=Dropped).

Session		CDT (35 min)	Number of male and female talker		
			Sentence lists	Vowel blocks	Consonant blocks
Baseline 1	1		m: 2m,2f d: 2m,2f	m: 1m,1f d: 1m,1f	m: 1m,1f d: 1m,1f
	2		a: 2m,2f s: 2m,2f	a: 1m,1f s: 1m,1f	a: 1m,1f s: 1m,1f
A-warp training	3	✓	a: 2m,2f	a: 1m,1f	a: 1m,1f
	4	✓	a: 2m,2f	a: 1m,1f	a: 1m,1f
	5	✓	a: 2m,2f	a: 1m,1f	a: 1m,1f
	6	✓	a: 2m,2f	a: 1m,1f	a: 1m,1f
	7	✓	a: 2m,2f	a: 1m,1f	a: 1m,1f
Baseline 2	8		s: 2m,2f	s: 1m,1f	s: 1m,1f
S-warp training	9	✓	s: 2m,2f	s: 1m,1f	s: 1m,1f
	10	✓	s: 2m,2f	s: 1m,1f	s: 1m,1f
	11	✓	s: 2m,2f	s: 1m,1f	s: 1m,1f
	12	✓	s: 2m,2f	s: 1m,1f	s: 1m,1f
	13	✓	s: 2m,2f	s: 1m,1f	s: 1m,1f
Re-test	14		m: 2m,2f d: 2m,2f a: 2m,2f	m: 1m,1f d: 1m,1f a: 1m,1f	m: 1m,1f d: 1m,1f a: 1m,1f

III. RESULTS

For both experiments data were analyzed by repeated-measures ANOVA ($\alpha=0.05$) using within-subject factors of processor, sessions of training, and speaker gender, and, in Experiment 1, the between-subjects factor of training order. Huynh-Feldt corrections were applied to all F tests, and *post hoc* tests were carried out using Bonferroni-corrected pairwise comparisons. For the linear regression analyses, scores were adjusted in order to remove between-subject variability, while preserving differences across training, by subtracting the difference between the grand mean and the subject's mean score over the five training sessions.

A. Experiment 1

1. Sentences

The results are summarized in Fig. 2. Significant effects of processor were apparent both at baseline [$F(2.61,18.2)=121, p<0.001$] and at the end of the experiment [$F(3,18)=72.8, p<0.001$]—where A-warp and S-warp scores from the final training session were compared with retest scores for the Matched and Dropped processors. At both points in time *a priori* contrasts indicated that scores with the Dropped processor were significantly lower than scores in the other three conditions. In addition, *post hoc* testing showed that scores in the Matched condition were significantly higher than scores in the other conditions at baseline; however, performance in the Matched and S-warp processors was statistically equivalent at the end of the experiment, though this may have been due to a ceiling effect with the Matched processor.

A comparison of sentence scores between the A-warp and S-warp processors, based on scores from the relevant baseline session and all five training sessions, revealed main effects of processor [$F(1,6)=85.5, p<0.001$], speaker [$F(1,6)=115, p<0.001$], and training [$F(5,30)=31.0, p<0.001$]. Performance for S-warp was significantly better than for A-warp, the mean and median scores of the former being higher at every stage, while higher scores were achieved with the female speaker in both conditions. From Fig. 2, it is evident that scores for S-warp and A-warp were much better after the first training session than at baseline. Nevertheless, there were indications that some performance improvements took place between Sessions 1 and 5 of training. *A priori* contrasts showed that scores after Session 5 were greater than scores not only at baseline, but also at Sessions 1 and 2, while linear regression—excluding baseline scores—indicated a significant correlation between performance and training session for S-warp, though not for A-warp (Table III). Even though no training was given with the Dropped processor, scores were significantly better at retest than at baseline [$F(1,7)=9.70, p<0.05$].

The absence of a main effect of training order indicated that there was no difference in the overall performance of subjects who trained first with A-warp and those who trained first with S-warp (Fig. 3). Subjects generally performed better in the condition trained second, suggesting a generalized learning effect for noise-vocoded speech being carried over from the condition trained first. Nevertheless, this advantage was small when the second condition was A-warp and somewhat larger when it was S-warp (5% and 12% differences, respectively). In addition, a condition by training by training order interaction [$F(4.69,28.16)=4.44, p<0.01$] suggested that S-warp scores improved irrespective of training order, while A-warp scores improved only when A-warp was trained first.

2. Vowels

The results are summarized in Fig. 2. Baseline scores represent a significant effect of processor [$F(3,21)=58.0, p<0.001$], as do scores at the end of the experiment [$F(3,18)=61.4, p<0.001$]. Again, *a priori* contrasts indicated significantly poorer performance in the Dropped condition than in the other conditions. At the baseline, *post hoc* contrasts showed that scores with the Matched processor were significantly better than those with the other processors but, as with the sentences, Matched and S-warp processor scores were statistically equivalent at the end of the experiment.

Comparison of A-warp and S-warp scores from the baseline to the end of training, demonstrated significant effects of processor [$F(1,6)=49.0, p<0.001$], speaker [$F(1,6)=17.8, p<0.01$], and training [$F(5,30)=14.4, p<0.001$]. S-warp performance was significantly better than A-warp performance, mean and median scores for S-warp being higher at every stage of training, and scores with the male speaker were significantly higher than with the female speaker. However, there was a significant talker by condition interaction [$F(1,6)=58.5, p<0.001$], a separate analysis for the two speakers indicating that although S-warp scores were significantly better than A-warp scores with the male speaker [$F(1,6)=66.8, p<0.001$], the difference was not significant

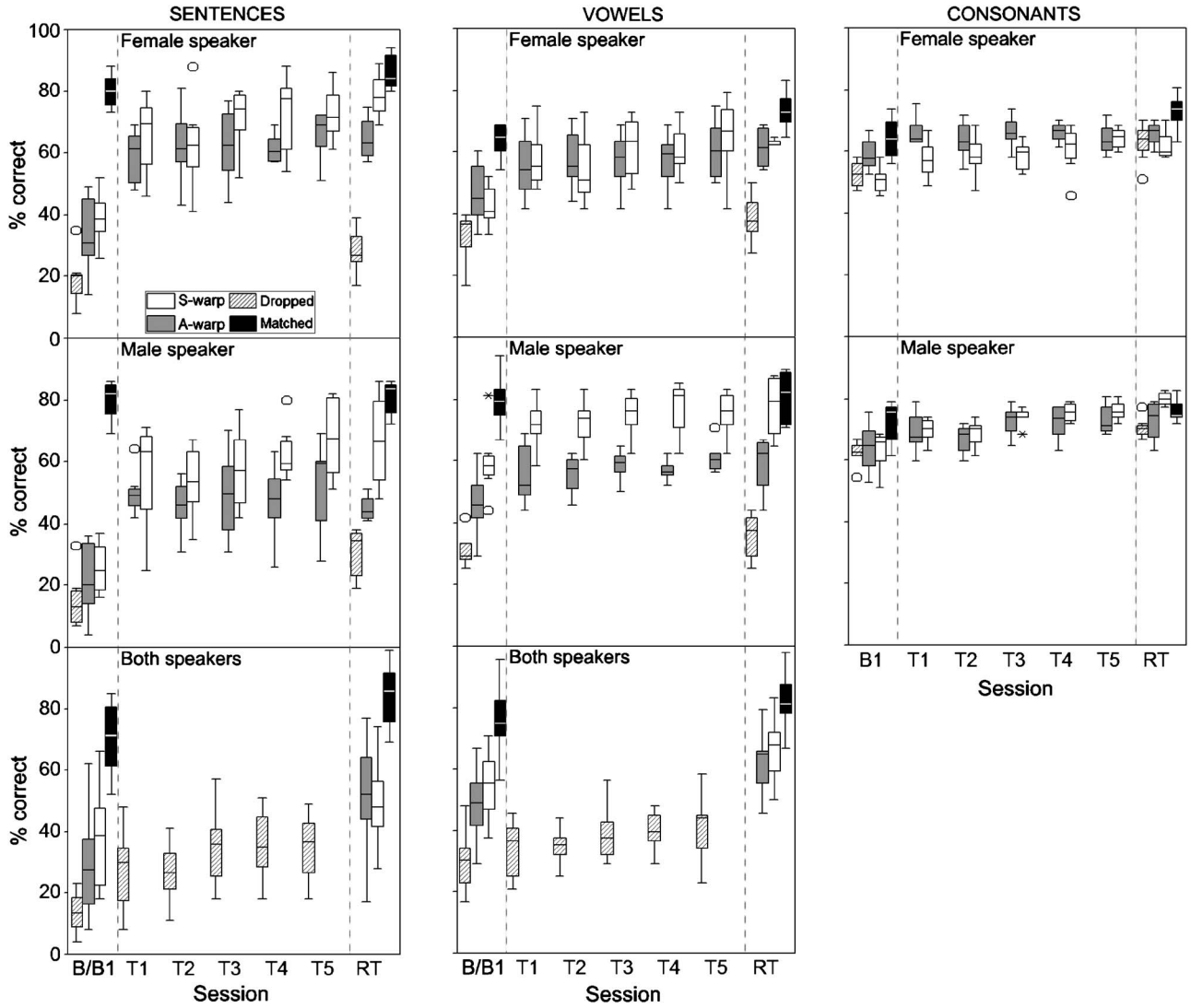

FIG. 2. Performance as a function of session: Baseline B1 (experiment 1) or B (experiment 2), training sessions T1 to T5, retest RT. The upper six panels show data from Experiment 1, and the lower two panels data from Experiment 2 (where consonant testing was not carried out). No effect of speaker was observed in Experiment 2, so data from both speakers is presented in each panel. Baseline and retest data for the "untrained" processors are also shown.

for the female speaker [$F(1,6)=4.31, p=0.083$]. With regard to the training effect, there were indications that, as with the sentences, some improvement in performance occurred after the first training session. *A priori* contrasts showed that scores from the final session were significantly higher than scores from all prior sessions except the fourth, while linear regression across the training sessions demonstrated a significant correlation between training session and scores for both processors (Table III). Comparing the baseline and retest scores of the untrained processors, there was a significant effect of session for the Matched processor [$F(1,7)=5.71, p<0.05$] but not for the Dropped processor.

There was no main effect of training order. However, a significant condition by training order effect was observed [$F(1,6)=37.8, p<0.005$]; subjects who trained second with A-warp achieved almost identical scores for both processors (Fig. 3), while those who trained second with S-warp performed much better in this condition than in the A-warp condition (19% difference in the means).

3. Consonants

Performance was influenced in only minor ways by the different types of spectral manipulation in the four conditions (Fig. 2). Consonant recognition is especially influenced by temporal cues, and these are reasonably well-preserved in noise-band representations of speech, even when only a small number of contiguous bands are available (Shannon *et al.*, 1995). Although main effects of the processor were seen both at the baseline [$F(2.34,16.4)=13.8, p<0.001$] and at the end of training [$F(3,18)=6.52, p<0.005$], the only significant *a priori* contrasts were between the Dropped and Matched conditions. At the end of the training there was no significant difference between Matched, A-warp, and S-warp processors according to *post hoc* testing.

In an ANOVA comparing S-warp and A-warp scores across baseline and training sessions, the effect of the processor narrowly missed significance [$F(1,6)=5.69$, $p=0.054$]. However, male speaker scores were significantly higher than female speaker scores [$F(1,6)=286$, $p<0.001$] and a significant talker by condition interaction was also ob-

TABLE III. Performance as a function of training sessions T1 to T5. Data from linear regression analyses.

	Processor/ Speaker	R	(R^2)	F	p	Regression line (% increase in score/session)
Sentences	S-warp (f)	0.435	0.189	8.86	$p<0.01$	2.35
	S-warp (m)	0.487	0.237	11.8	$p<0.005$	3.28
	A-warp (f)	0.285	0.081	3.36	n.s.	1.31
	A-warp (m)	0.148	0.022	0.85	n.s.	0.68
	Dropped (f)	0.432	0.187	8.71	$p<0.01$	2.31
	Dropped (m)	0.475	0.225	11.1	$p<0.005$	2.15
Vowels	S-warp (f)	0.560	0.313	17.3	$p<0.001$	2.16
	S-warp (m)	0.406	0.165	7.49	$p<0.01$	1.23
	A-warp (f)	0.368	0.135	5.94	$p<0.05$	1.01
	A-warp (m)	0.383	0.147	6.55	$p<0.05$	1.20
	Dropped (f)	0.511	0.261	13.4	$p<0.005$	1.74
	Dropped (m)	0.571	0.326	18.4	$p<0.001$	1.78
Consonants	S-warp (f)	0.483	0.233	11.6	$p<0.005$	1.58
	S-warp (m)	0.643	0.414	26.9	$p<0.001$	1.90
	A-warp (f)	0.082	0.007	0.26	n.s.	–0.20
	A-warp (m)	0.535	0.286	15.2	$p<0.001$	1.34

served [$F(1,6)=83.3$, $p<0.001$], indicating that performance with the A-warp processor was significantly better than performance with the S-warp processor for the female speaker but not for the male speaker. A significant effect of training [$F(5,30)=17.3$, $p<0.001$] and a just significant condition by session interaction [$F(5,30)=2.63$, $p=0.044$] were observed. Consequently, a separate analysis was carried out for the two conditions. S-warp scores at the final training session were significantly higher than at all sessions apart from the fourth, while *post hoc* tests indicated that baseline scores were significantly lower than scores at Sessions 3 and 4. For the A-warp processor, scores at the final training session were significantly higher than those at the baseline and at the second training session. Scores from Session 4 were also higher than at Session 2 according to *post hoc* contrasts. Linear regression analysis (Table III) showed a significant correlation between scores and training session for the S-warp processor. However, for the A-warp processor the correlation was only significant with the male speaker. Again there was evidence of generalized learning for the untrained conditions, with retest scores significantly better than baseline scores for both the Matched [$F(1,7)=11.0$, $p<0.05$] and the Dropped processor [$F(1,7)=75.4$, $p<0.001$].

A significant interaction of condition with training order [$F(1,6)=23.5$, $p<0.005$] showed that scores were higher in the condition trained second. Even so, differences between the two processors were small regardless of training order (Fig. 3).

B. Experiment 2

As the baseline session was essentially identical to that in Experiment 1, it is not surprising that, for both sentence and vowel data, the same pattern of processor effects was seen prior to training (Fig. 2).

1. Sentences

For the Dropped processor there was a main effect of training [$F(5,35)=22.8$, $p<0.001$] but not of the speaker. Again, there were indications that some performance improvements took place between Sessions 1 and 5 of training. *A priori* contrasts showed that Session 5 scores were higher than baseline scores and scores from Sessions 1 and 2. A linear regression analysis of scores from the training sessions—excluding baseline scores—indicated a significant correlation between training session and scores (Table III). Nevertheless, at the end of the experiment (when retest scores for the Matched, S-warp, and A-warp processors were compared with the session five score for the Dropped processor) performance in the Dropped condition was still significantly poorer than performance in the other three conditions. This is at least partly due to the fact that performance also improved in the untrained conditions. There were significant effects of session (baseline versus retest) for the Matched and A-warp processors [$F(1,7)=17.8$, $p<0.005$ and $F(1,7)=27.2$, $p<0.005$, respectively], while the effect of the session narrowly missed significance for S-warp [$F(1,7)=5.38$, $p=0.053$].

2. Vowels

Here, there was a main effect of training [$F(4.93,34.5)=14.1$, $p<0.001$] but not of the speaker. The pattern of contrasts was similar to that seen with sentences. Performance at Session 5 was significantly better than at baseline and at training Sessions 1 and 2, while *post hoc* comparisons showed that baseline scores were significantly lower than scores after the third and fourth training sessions. The results of linear regression analysis (Table III) showed that there was still a significant correlation between the performance and training session, even when baseline scores were excluded. However, as with sentences, a significant effect of processor at the end of the experiment [$F(1.68,11.7)=65.0$, $p<0.001$] indicated that scores in the Dropped condition were still significantly lower than in the other conditions, despite subjects only having had training in the Dropped condition. Once again, S-warp and A-warp scores rose sig-

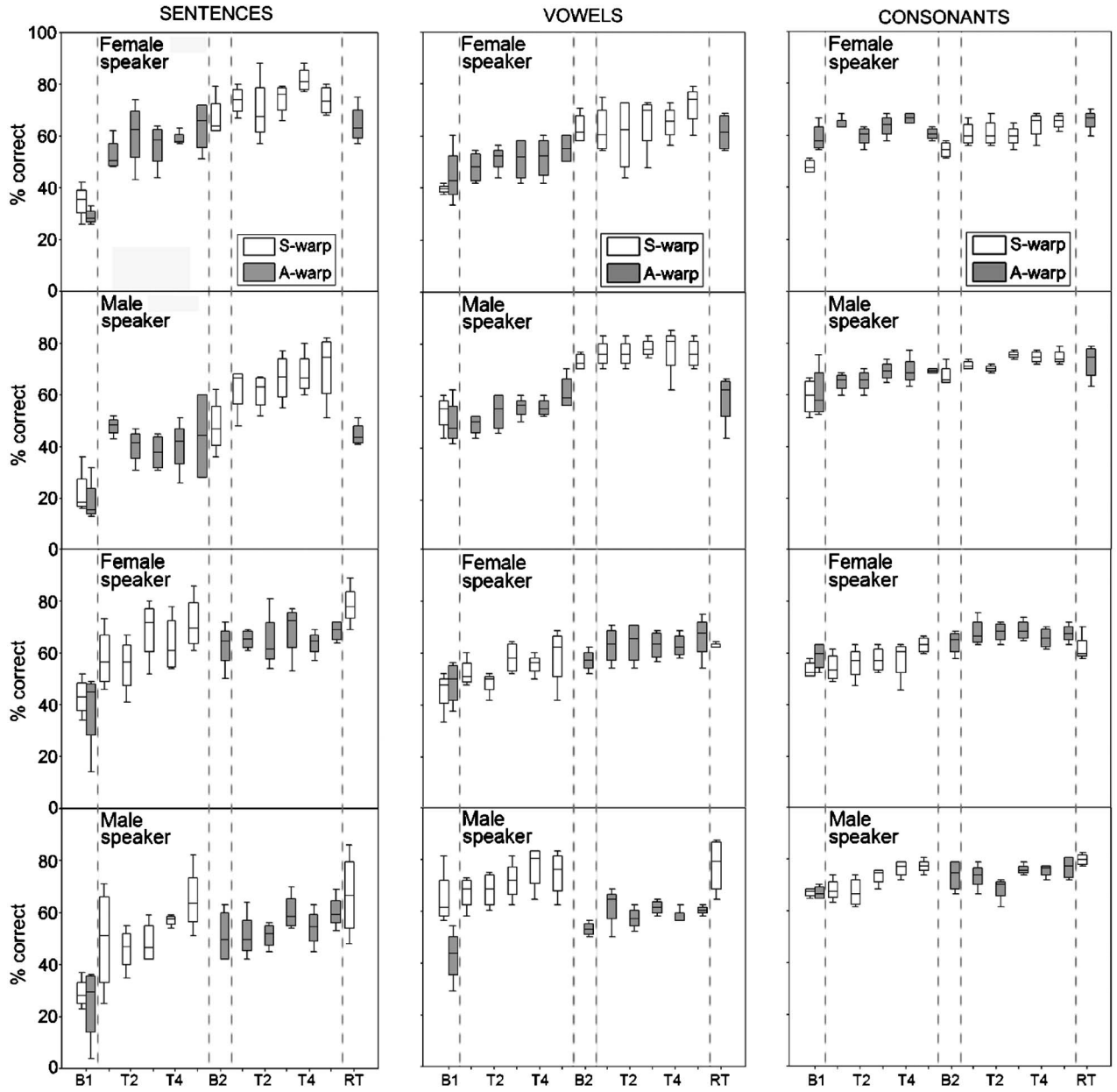

FIG. 3. Experiment 1: The upper six panels represent scores for subjects who trained first with the A-warp processor, and the lower six panels scores for subjects who trained first with the S-warp processor (B2=baseline for the second condition trained). Male and female scores are presented separately.

nificantly between the baseline and retest [$F(1,7)=19.6$, $p<0.005$ and $F(1,7)=41.9$, $p<0.001$, respectively].

C. Between-subjects comparisons: Experiment 1 vs Experiment 2

Subjects in both experiments received the same amount of processor-specific training; however, subjects in Experiment 1 received twice the *overall* amount of training as subjects in Experiment 2. Despite this, the complete data set from Experiment 1 was incorporated into the following analyses in order to increase their power. This is taken into consideration in the discussion of the results.

Between-subjects comparisons across experiments—incorporating data from baseline and all five training sessions—revealed a main effect of processor for sentences [$F(2,21)=30.6$, $p<0.001$] and vowels [$F(2,21)=43.2$, $p<0.001$]. *Post hoc* tests revealed that S-warp and A-warp scores were significantly higher than scores with the Dropped processor for both types of test material.

D. Connected discourse tracking

It should be noted that "corrections"—sections of the training text read with the audio link switched to unprocessed speech—were counted in the final "words per minute" scores. The general pattern of results seen in the analysis of the sentence, vowel and consonant data is also reflected in the CDT rates (Fig. 4). Between-subjects comparisons across experiments showed that overall CDT rates for the Dropped processor were significantly lower than rates for the A-warp and S-warp processors [$F(1,14)=18.0$, $p<0.005$ and $F(1,14)=23.9$, $p<0.001$, respectively], while in Experiment 1, a significant effect of the processing condition indicated that S-warp tracking rates were a little higher than those of

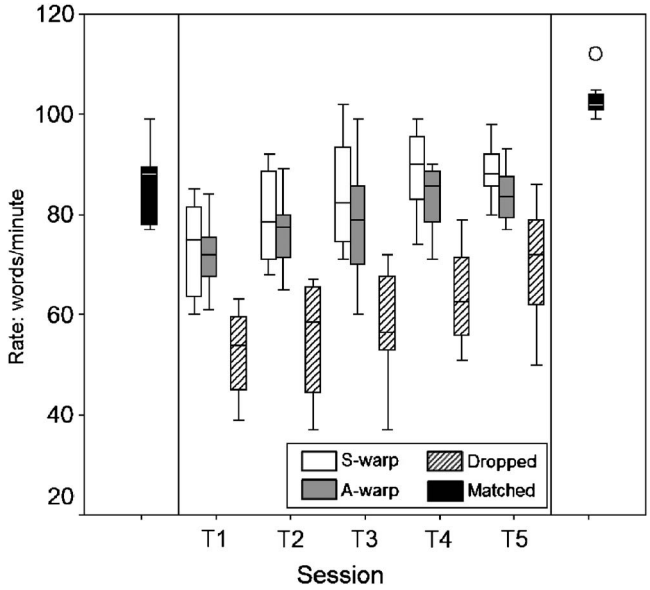

FIG. 4. CDT rates for subjects in experiment 1 (A-warp and S-warp processors) and experiment 2 (Dropped processor). Overall, subjects in experiment 1 had twice as much training as those in experiment 2. Performance with the Matched processor, before and after training, is also shown.

A-warp [$F(1,6)=7.30, p<0.05$]. The rates achieved with the Matched processor at the end of Experiment 1 were the highest of all. When compared with CDT rates from the final training session, a main effect of the condition was seen [$F(2,10)=70.5$, $p<0.001$], *post hoc* tests showing that CDT rates with the Matched processor (103 words per minute) were significantly higher than S-warp rates (90 wpm) and A-warp rates (85 wpm). In addition, a main effect of the training on CDT rates was seen in Experiments 1 and 2 [$F(3.74,22.4)=77.7$, $p<0.001$ and $F(4,28)=21.7$, $p<0.001$, respectively] though some of this improvement may be attributable to increasing experience with the speaker (author M.S.) and the particular training texts used.

IV. DISCUSSION

This simulation of cochlear implant signal processing confirmed that a hole in the spectral representation of speech can have a significant effect on intelligibility. When the information from the hole region was dropped altogether performance was poor, even after three hours of training, with only 34% accuracy achieved in sentence keyword identification, and 41% in vowel identification. The frequency region defined by the hole (424–2182 Hz) included much of the F1 and F2 formant frequency information that is crucial to vowel identification (Peterson and Barney, 1952; Nearey, 1989). However, vowel recognition remains well above chance in noise-vocoder processing, even when there are no spectral cues, because nonspectral cues such as duration and overall amplitude are preserved (Shannon *et al.*, 1995); this supports the conclusion that the Dropped processor transmitted little of the spectral detail required for vowel identification. Consonant scores were less severely affected by the hole, as demonstrated by the fact that scores in the A-warp, S-warp, and Dropped conditions were similar to scores in the Matched, "no hole," condition. This finding is similar to those of Lippmann (1996) and Breeuwer and Plomp (1984,1985,1986) for nonvocoded speech signals, which found that high levels of consonant recognition could be achieved with widely separated bands of high and low frequency information. These results and the findings of the present study show how the preserved temporal and durational cues in speech (including noise-vocoded speech) can provide reasonably good consonant intelligibility. In the present study it can also be inferred that the between-condition differences seen in sentence testing were due primarily to different levels of vowel intelligibility (see Table IV).

TABLE IV. Mean scores at the end of training (Session T5). Matched processor scores and consonant scores for the Dropped processor (in italics) are taken from the Experiment 1 Retest session.

	A-warp	S-warp	Dropped	Matched
Sentences	59%	70%	34%	*83%*
Vowels	61%	70%	41%	*77%*
Consonants	69%	70%	*67%*	*75%*

Subjects in Experiment 1 received twice the overall amount of training received by subjects in Experiment 2. Nevertheless, it seems unlikely that five more training sessions with the Dropped processor would have produced levels of intelligibility equivalent to those observed with the S-warp and A-warp processors: The differences between the mean scores, post-training, were great—S-warp 70%, A-warp 59%, Dropped 34% for sentences; S-warp 70%, A-warp 61%, Dropped 41% for vowels—while the gradients of the regression lines for the Dropped processor were around 2% per session (Table III). Therefore, the critical finding of this study was that speech intelligibility was much higher in the "preservation" conditions than in the condition where information from the hole region was simply dropped, a conclusion supported by the CDT data for the three processors. Indeed, for the sentence and vowel data, scores in the Dropped condition were significantly lower than S-warp and A-warp scores even before training, probably because the size and location of the hole had an especially deleterious effect when listening with the Dropped processor.

Although the S-warp and A-warp processors mapped frequencies to the wrong tonotopic location in the cochlea subjects clearly learned to adapt to the distorted patterns of spectral information; for instance, with the S-warp processor accuracy of keyword identification improved by nearly 40%. Despite it not being possible to conclude that a longer period of training would have led to complete adaptation, it is interesting to note that at the end of Experiment 1, test scores in the S-warp condition were statistically equivalent to scores in the Matched condition; this, however, may be partly due to ceiling effects in the sentence data, and the degree of variability observed among subjects in the S-warp condition. In addition, post-training scores with the Matched processor might have been higher if subjects had been trained in this condition. Scores for the Dropped processor in Experiment 1 were significantly better at retest than at baseline even without training. Thus it was felt necessary to in-

TABLE V. Average frequencies of the first and second formants of the male and female speaker vowels.

		æ bad	ɑ bard	ɔ board	i bead	ɛ bed	ɪ bid	ɜ bird	ɒ bod	u booed	ʌ bud
(M)	F1	683	639	473	294	619	416	500	647	317	613
	F2	1608	1080	810	2337	1871	2080	1601	987	1654	1452
(F)	F1	1140	808	496	303	803	573	678	557	333	763
	F2	1899	1166	912	2708	2196	2340	1811	1125	1956	1532

vestigate whether a greater degree of improvement might be seen if training was provided in this condition; however, the scores achieved after five sessions of training were not dissimilar to those recorded at retest in Experiment 1. Therefore, the improvement in performance with the Dropped processor probably reflected a general learning effect for noise-vocoded speech (performance improvements—with relatively little exposure—with tonotopically matched noise-vocoded speech have been reported elsewhere, e.g., Faulkner, Rosen, and Stanton, 2003; Davis *et al.*, 2005). However, the superior scores achieved with the S-warp and A-warp processors suggest that the pattern of spectral information and the primary speech cues were still usable to some considerable degree in these conditions despite being presented to the wrong tonotopic location.

By the end of training S-warp scores were approximately 10% better than A-warp scores on the sentence and vowel tests, though the conditions were not significantly different at the baseline. In both conditions the frequencies above and below the center of the frequency range (1011 Hz) were compressed, and warped in opposite directions. For S-warp, the warping effect was spread over the entire frequency range; however, the compression factor was nonuniform with frequencies near the center of the hole being shifted by just over an octave while those in the most apical and basal bands were shifted by under one-third of an octave. In contrast, warping in the A-warp condition was localized to the hole-adjacent bands, with tonotopically matched analysis and output bands apical and basal to these. In order to distinguish spectral patterns when speech signals are reduced to a small number of bands, as they are in cochlear implants and implant simulations, listeners must be able to detect differences between the envelope-modulated levels of neighboring output bands. That the ratios between formant frequencies serve as important cues to speech sounds has been demonstrated in many studies; for instance, Peterson and Barney, 1952; Ladefoged and Broadbent, 1957. In the S-warp condition equal acoustic frequency ranges were mapped to output bands representing constant distances along the cochlea. With the A-warp condition much larger frequency ranges were mapped to the hole-adjacent output bands than to other output bands. It appears that this mapping design, and the consequent reduction in the resolution of hole region frequencies, was less effective at preserving (within the apical and basal portions of the output signal) the information carried by the spectral shape of the original signal.

For the preservation conditions performance was better with the male speaker in the vowel and consonant tests but better with the female speaker for words in sentences. The female speaker sentences were delivered at a slightly slower and more deliberate pace than the male speaker sentences. It is possible that the female speaker advantage would have been nullified, or even reversed, if the speaking rate of the two speakers had been the same. It is not entirely clear why scores in the vowel and consonant tests were better with the male speaker. The ratios between the frequencies of formant peaks will have been particularly disrupted if the first formant was warped to the apical side of the hole and the second formant was warped to the basal side. However, an examination of the formant frequencies in Table V (with reference to the processor filter cut-off frequencies in Table I) indicates that the likelihood of "formant splitting" is no greater for the female than the male speaker. Perhaps a more straightforward explanation for the speaker differences is that the CDT was conducted with the same male speaker who recorded the test materials; subjects, therefore, had more experience of listening to this speaker.

Drawing comparisons with the acute investigation into the effect of spectral holes of Shannon *et al.* (2002) is not straightforward because of methodological differences. In that study a larger frequency range was divided into 20 contiguous bands, and the largest hole examined was 6 mm. Their study also examined the effect of holes varying in size and location, and both cochlear implant patients and normally hearing listeners took part. Notwithstanding these differences, it is still interesting to compare the main findings: Shannon *et al.* found no significant differences between conditions that reassigned information from the hole region—including a condition similar to A-warp—and a condition in which the information from the hole region was simply dropped. Their conclusion was that the pattern of spectral information becomes unusable if it is not presented to the correct tonotopic location. However, the results of the present study indicate otherwise, at least for the size and location of hole investigated here. Subjects were clearly able to make use of warped spectral information and performed better in the preservation conditions than in the Dropped condition, even before training. Furthermore, the detrimental effect of distorting the spectral representation of speech was significantly reduced with training, an outcome consistent with results from other implant simulation studies (e.g., Rosen *et al.*, 1999; Faulkner *et al.*, 2001).

A. Implications for Cochlear Implants

Evidence is accumulating to suggest that implant users are able to adapt when their speech processors present infor-

mation to the wrong tonotopic location (Harnsberger *et al.*, 2001; McKay and Henshall, 2002; Fu, Shannon, and Galvin, 2002). If the speech perceptual difficulties resulting from frequency-to-place mismatch can be readily overcome with experience, it would appear preferable that the most informative frequency range is delivered by the speech processor. Evidence from another study simulating holes in hearing suggests that the location and pattern of holes affect mostly vowel recognition (Kasturi *et al.*, 2002). These authors conclude that neuronal "dead" regions ought to account for some of the variability in vowel recognition performance among cochlear implant listeners. They also go on to suggest that speech processor frequency spacing should be customized for each implant user, with frequency-importance functions—a measure of the proportion of speech information in each channel—having smaller weights on less functional electrodes that may be located within dead regions.

However, it is still not clear whether hearing-impaired individuals gain any benefit from acoustic information presented to a dead region. Several studies with hearing aid users have questioned the benefits of providing high-frequency amplification for individuals with steeply sloping losses (e.g., Murray and Byrne, 1986; Ching *et al.*, 1998; Hogan and Turner, 1998; Turner and Cummings, 1999). In these studies some subjects demonstrated no improvement or even reduced speech intelligibility with high-frequency amplification. Vickers *et al.* (2001) found that amplifying frequencies up to one octave above the estimated edge frequency of a dead region provided some benefit to listeners but amplification of frequencies well within the dead region did not benefit listeners and actually led to poorer performance in some cases. For individuals whose high frequency hearing loss may be associated with a neuronal dead region, Turner and colleagues have suggested that such amplification produces a spread of excitation in the cochlea near the amplified region and a consequent distortion of the spectral pattern. Something similar may happen in cochlear implants where there are electrodes located in a dead region. It may be possible to present an audible signal to the patient by increasing the level of electrical stimulation to the electrode(s); however, the result might be a spread of excitation with functional auditory neurons neighboring the dead region being activated. Again, this distortion of the spectral pattern of information might lead to poorer speech recognition performance. Nevertheless, the results of the present study suggest that, because cochlear implant listeners may well be able to adapt to spectrally warped speech (in a controlled reassignment of frequency to cochlear location), effective speech processors could be designed which route spectral information away from electrodes in the hole region.

The findings of the present study are also relevant to the design of speech processing strategies that combine cochlear implant use with a hearing aid in the nonimplanted ear. For instance, it is conceivable that an implant user could have a relatively shallow electrode array insertion in one ear and some residual low frequency hearing, stimulable with a hearing aid, in the opposite ear. If there were no overlap between the stimulable regions of the two cochleae—ignoring the possibility of a precise abutment of these regions—effectively, there would be a "hole" in hearing *across the two ears*. Although benefits, in terms of improved speech recognition, sound localization and sound quality, have been demonstrated for bilateral-bimodal listening (e.g., Ching *et al.*, 2001 and 2004; Hamzavi *et al.* 2004; Dettman *et al.* 2004; Tyler *et al.* 2002; Armstrong *et al.* 1997), there is considerable variability in performance, and many patients revert to using the implant on its own because they receive no benefit, or even experience interference, when using the acoustic device at the same time. Studies, to date, have given little consideration to the likely incongruities in the frequency-to-place code mapping of the two devices and their effect on speech recognition performance. Recently, "soft surgery" techniques have been developed with the aim of preserving residual low frequency hearing by using a relatively shallow insertion electrode array in the same ear (combined electric and acoustic stimulation, EAS). The results of an EAS simulation study (Dorman *et al.*, 2005) demonstrated that speech intelligibility scores were highest in conditions that minimized the frequency gap between low frequency acoustic hearing and simulated electrode locations. The authors also report the findings of a supplementary experiment where the frequency components from the gap (or "hole") region were shifted up instead of being removed. For several simulated electrode insertion depths intelligibility scores were poorer than when "holes" were left in the spectrum; however, subjects received little practice with the up-shifted conditions.

Simulation experiments like the ones described in the present study could also be used to examine questions related to signal processing in bilateral cochlear implants. Differences in insertion depth of bilateral electrode arrays are likely to lead to frequency-place maps that are in conflict between the two ears. Recent studies (e.g., Dorman and Dahlstrom, 2004) suggest that implant users can make use of mismatched information from the two auditory peripheries, such that speech intelligibility scores with both implants are better than when either is used on its own. However, little analytic work appears to have been carried out regarding the effects of parametric manipulations of the two implant speech processor maps.

V. CONCLUSION

In the context of speech recognition with cochlear implants, the present findings suggest that rerouting spectral information around a hole may be better than simply dropping it, even though the pattern of information is warped. Post-training performance levels in two preservation conditions were significantly better than in a condition where information from the hole region was simply dropped. The deleterious effect caused by warping the speech spectrum was significantly reduced with just three hours of training—a period of time that is inconsequential compared to the amount of experience cochlear implant patients have with their devices. Although subjects also adapted somewhat to the Dropped condition, the effect was small by comparison; this is not surprising since much of the formant frequency detail was lost. Of the two preservation conditions, performance was better when the warping was spread over the

entire frequency range; when warping was localized to hole-adjacent bands, sentence and vowel recognition scores were around 10% lower despite the fact that, beyond the hole region, analysis bands were mapped to the correct tonotopic location. This suggests that there may be performance benefits for warping schemes that map equal acoustic frequency ranges to electrodes representing constant distances within the cochlea; however, further experiments, with holes in different locations, would be required to confirm this.

Although the present results cannot predict complete adaptation to spectral warping with further training, they do imply that acute studies probably underestimate the degree to which listeners can adapt to this type of distortion. The findings are also consistent with results from other simulation studies that have suggested that speech processors should present the most informative frequency range irrespective of frequency misalignment.

ACKNOWLEDGMENTS

The authors are grateful to the Royal National Institute for Deaf People for supporting this work through the awarding of a PhD studentship to Matthew Smith.

Armstrong, M., Pegg, P., James, C., and Blamey, P. (**1997**). "Speech perception in noise with implant and hearing aid," Am. J. Otol. **18**, S140–S141.

Baer, T., Moore, B. C. J., and Kluk, K. (**2002**). "Effects of low pass filtering on the intelligibility of speech in noise for people with and without dead regions at high frequencies," J. Acoust. Soc. Am. **112**, 1133–1144.

Bench, R. J., and Bamford, J. M. (Eds.) (**1979**). *Speech-hearing Tests and the Spoken Language of Hearing-impaired Children* (Academic, London).

Breeuwer, M., and Plomp, R. (**1984**). "Speechreading supplemented with frequency-selective sound-pressure information," J. Acoust. Soc. Am. **76**, 686–691.

Breeuwer, M., and Plomp, R. (**1985**). "Speechreading supplemented with formant-frequency information from voiced speech," J. Acoust. Soc. Am. **77**, 314–317.

Breeuwer, M., and Plomp, R. (**1986**). "Speechreading supplemented with auditorily presented speech parameters," J. Acoust. Soc. Am. **79**, 481–499.

Ching, T. Y. C., Dillon, H., and Byrne, D. (**1998**). "Speech recognition of hearing-impaired listeners: Predictions from audibility and the limited role of high-frequency amplification," J. Acoust. Soc. Am. **103**, 1128–1140.

Ching, T. Y. C., Incerti, P., and Hill, M. (**2004**). "Binaural benefits for adults who use hearing aids and cochlear implants in opposite ears," Ear Hear. **25**, 9–21.

Ching, T. Y. C., Psarros, C., Hill, M., Dillon, H., and Incerti, P. (**2001**). "Should children who use cochlear implants wear hearing aids in the opposite ear?" Ear Hear. **22**, 365–380.

Davis, M. H., Johnsrude, I. S., Hervais-Adelman, A., Taylor, K., and McGettigan, C. (**2005**). "Lexical information drives perceptual learning of distorted speech: Evidence from the comprehension of noise-vocoded sentences," J. Exp. Psychol. Gen. **134**, 222–241.

De Filippo, C. L., and Scott, B. L. (**1978**). "A method for training and evaluating the reception of ongoing speech," J. Acoust. Soc. Am. **63**, 1186–1192.

Dettman, S., D'Costa, W. A., Dowell, R. C., Winton, E. J., Hill, K. L., and Williams, S. S. (**2004**). "Cochlear implants for children with significant residual hearing," Arch. Otolaryngol. Head Neck Surg. **130**, 612–618.

Dorman, M. F., and Dahlstrom, L. (**2004**). "Speech understanding by cochlear-implant patients with different left- and right- ear electrode arrays," Ear Hear. **25**, 191–194.

Dorman, M. F., Loizou, P. C., and Rainey, D. (**1997**). "Simulating the effect of cochlear-implant electrode insertion depth on speech understanding," J. Acoust. Soc. Am. **102**, 2993–2996.

Dorman, M. F., Spahr, A. J., Loizou, P. C., Dana, C. J., and Schmidt, J. S. (**2005**). "Acoustic simulations of combined electric and acoustic hearing," Ear Hear. **26**, 1–10.

Faulkner, A., Rosen, S., and Norman, C. (**2001**). "The right information matters more than frequency-place alignment: Simulations of cochlear implant processors with an electrode array insertion depth of 17 mm," Speech, Hearing and Language: Work in Progress **13**, 52–71.

Faulkner, A., Rosen, S., and Stanton, D. (**2003**). "Simulations of tonotopically mapped speech processors for cochlear implant electrodes varying in insertion depth," J. Acoust. Soc. Am. **113**, 1073–1080.

Fu, Q.-J., and Shannon, R. V. (**1999**). "Recognition of spectrally degraded and frequency-shifted vowels in acoustic and electric hearing," J. Acoust. Soc. Am. **105**, 1889–1900.

Fu, Q.-J., Shannon, R. V., and Galvin, J. J. (**2002**). "Perceptual learning following changes in the frequency-to-electrode assignment with the Nucleus-22 cochlear implant," J. Acoust. Soc. Am. **112**, 1664–1674.

Greenwood, D. D. (**1990**). "A cochlear frequency-position function for several species—29 years later," J. Acoust. Soc. Am. **87**, 2592–2605.

Hamzavi, J., Pok, S. M., Gstoettner, W. F., and Baumgartner, W. D. (**2004**). "Speech perception with a cochlear implant used in conjunction with a hearing aid in the opposite ear," Int. J. Audiol. **43**, 61–65.

Harnsberger, J. D., Svirsky, M. A., Kaiser, A. R., Pisoni, D. B., Wright, R., and Meyer, T. A. (**2001**). "Perceptual 'vowel spaces' of cochlear implant users: Implications for the study of auditory adaptation to spectral shift," J. Acoust. Soc. Am. **109**, 2135–2145.

Hogan, C. A., and Turner, C. W. (**1998**). "High-frequency audibility: Benefits for hearing-impaired listeners," J. Acoust. Soc. Am. **104**, 432–441.

IEEE (**1969**). "Recommended practice for speech quality measurements," IEEE Trans. Audio Electroacoust. **17**, 225–246.

Kasturi, K., Loizou, P. C., Dorman, M., and Spahr, T. (**2002**). "The intelligibility of speech with 'holes' in the spectrum," J. Acoust. Soc. Am. **112**, 1102–1111.

Ladefoged, P., and Broadbent, D. E. (**1957**). "Information conveyed by vowels," J. Acoust. Soc. Am. **29**, 98–104.

Lippmann, R. P. (**1996**). "Accurate consonant perception without mid-frequency speech energy," IEEE Trans. Speech Audio Process. **4**, 66–69.

McKay, C. M., and Henshall, K. R. (**2002**). "Frequency-to-electrode allocation and speech perception with cochlear implants," J. Acoust. Soc. Am. **111**, 1036–1044.

Moore, B. C. J. (**2004**). "Dead regions in the cochlea: Conceptual foundations, diagnosis, and clinical applications," Ear Hear. **25**, 98–116.

Moore, B. C. J., and Glasberg, B. R. (**1997**). "A model of loudness perception applied to cochlear hearing loss," Aud. Neurosci. **3**, 289–311.

Murray, N., and Byrne, D. (**1986**). "Performance of hearing-impaired and normal hearing listeners with various high frequency cut-offs in hearing aids," Aust. J. Audiol. **8**, 21–28.

Nearey, T. M. (**1989**). "Static, dynamic, and relational properties in vowel perception," J. Acoust. Soc. Am. **85**, 2088–2113.

Peterson, G. E., and Barney, H. L. (**1952**). "Control methods used in a study of the vowels," J. Acoust. Soc. Am. **24**, 175–184.

Rosen, S., Faulkner, A., and Wilkinson, L. (**1999**). "Adaptation by normal listeners to upward spectral shifts of speech: Implications for cochlear implants," J. Acoust. Soc. Am. **106**, 3629–3636.

Shannon, R. V., Galvin, J. J., and Baskent, D. (**2002**). "Holes in hearing," J. Assoc. Res. Otolaryngol. **3**, 185–199.

Shannon, R. V., Zeng, F.-G., Kamath, V., Wygonski, J., and Ekelid, M. (**1995**). "Speech recognition with primarily temporal cues," Science **270**, 303–304.

Shannon, R. V., Zeng, F.-G., and Wygonski, J. (**1998**). "Speech recognition with altered spectral distribution of envelope cues," J. Acoust. Soc. Am. **104**, 2467–2476.

Turner, C. W., and Cummings, K. J. (**1999**). "Speech audibility for listeners with high-frequency hearing loss," Am. J. Audiol. **8**, 47–56.

Tyler, R. S., Parkinson, A. J., Wilson, B. S., Witt, S., Preece, J. P., and Noble, W. (**2002**). "Patients utilizing a hearing aid and a cochlear implant: Speech perception and localization," Ear Hear. **23**, 98–105.

Vickers, D. A., Moore, B. C. J., and Baer, T. (**2001**). "Effects of low-pass filtering on the intelligibility of speech in quiet for people with and without dead regions at high frequencies," J. Acoust. Soc. Am. **110**, 1164–1175.

Statistical analysis of the autoregressive modeling of reverberant speech

Nikolay D. Gaubitch,[a] Darren B. Ward, and Patrick A. Naylor
Department of Electrical and Electronic Engineering, Imperial College London, Exhibition Road, London SW7 2AZ, United Kingdom

(Received 15 February 2006; revised 27 July 2006; accepted 29 August 2006)

Hands-free speech input is required in many modern telecommunication applications that employ autoregressive (AR) techniques such as linear predictive coding. When the hands-free input is obtained in enclosed reverberant spaces such as typical office rooms, the speech signal is distorted by the room transfer function. This paper utilizes theoretical results from statistical room acoustics to analyze the AR modeling of speech under these reverberant conditions. Three cases are considered: (i) AR coefficients calculated from a single observation; (ii) AR coefficients calculated jointly from an M-channel observation ($M>1$); and (iii) AR coefficients calculated from the output of a delay-and sum beamformer. The statistical analysis, with supporting simulations, shows that the spatial expectation of the AR coefficients for cases (i) and (ii) are approximately equal to those from the original speech, while for case (iii) there is a discrepancy due to spatial correlation between the microphones which can be significant. It is subsequently demonstrated that at each individual source-microphone position (without spatial expectation), the M-channel AR coefficients from case (ii) provide the best approximation to the clean speech coefficients when microphones are closely spaced (<0.3m). © *2006 Acoustical Society of America.* [DOI: 10.1121/1.2356840]

PACS number(s): 43.72.Ar, 43.55.Hy [DOS] Pages: 4031–4039

I. INTRODUCTION

Many hands-free telecommunication applications involving, for example, speech coding and speech enhancement, make use of autoregressive (AR) analysis techniques such as linear predictive coding (LPC). These applications are often employed in systems used inside rooms where the observed speech signal becomes reverberant due to the enclosed space. There is an interest in AR modeling of degraded speech, and the properties of the AR coefficients have been studied in the context of parameter quantization noise and ambient acoustical noise.[1–3] Several dereverberation algorithms have been proposed which operate on the linear prediction (LP) residual under the explicit or implicit assumptions that the AR coefficients are not affected by reverberation.[4–8] These methods utilize known features of the LP residual of speech signals to attenuate components due to reverberation. Yegnanarayana and Satyanarayana[6] provided a comprehensive study on the effects of reverberation on the LP residual. We now present an investigation of the effects of reverberation on the AR coefficients.

We utilize tools from statistical room acoustics (SRA) theory[9–11] for the analysis of the relation between the sets of AR coefficients obtained from clean speech and those obtained from reverberant speech. SRA provides a means for describing the sound field in a room that is mathematically tractable compared to, for example, wave theory.[9] SRA has been shown useful for the analysis of signal-processing techniques in reverberant environments and has recently been applied by several researchers. Radlović *et al.*,[10] Talantzis *et al.*,[12] and Bharitkar *et al.*[13] utilized SRA to investigate the robustness of channel equalization. Further, Talantzis *et al.*[14] investigated the performance of blind source separation, Gustafsson *et al.*[15] analyzed the performance of sound source localization, and Ward[16] used SRA to measure the performance of acoustic crosstalk cancellation in reverberant environments.

In our study, we will consider three cases: (i) AR coefficients calculated from a single observation; (ii) AR coefficients jointly calculated from an M-channel observation ($M>1$); and (iii) AR coefficients obtained from the output of a delay-and-sum beamformer (DSB). Extending the work in Ref. 17, we will show in terms of spatial expectation that the AR coefficients obtained from reverberant speech are approximately equal to those from clean speech for cases (i) and (ii), while the AR coefficients obtained from the output of the delay-and-sum beamformer differ due to spatial correlation between the microphones. Furthermore, it will be demonstrated that the M-channel AR coefficients from (ii) provide the best estimate of the clean speech coefficients compared to the other two cases under consideration. We believe that our results here also relate to and explain the following statement in Ref. 4: "*…it has been recognized that any practical or typical room transfer function has certain properties that make it possible to accurately determine the speaker's vocal tract transfer function from the reverberative speech signal*." and "*…arrays of plural microphones can also be used to advantage…*" which continues "*For this case, each new microphone requires its own correlation computer. The new outputs from this computer* $R'(\tau_1)$, $R'(\tau_2),\ldots,R'(\tau_{14})$ *are added to the other* $R(\tau)$*'s of other microphones thus giving more accurate data for the coefficient computer*."

[a]Electronic mail: ndg@imperial.ac.uk

The remainder of this paper is organized as follows. In Sec. II we review the statistical room acoustic model including the conditions under which the theory is valid. The simulation environment is defined in Sec. III. In Sec. IV an analysis of the effects of reverberation on the AR coefficients and on the residual signal is presented for the single channel case. Section V presents the analysis of the two multichannel AR modeling cases. Simulation results are presented in Sec. VI and finally conclusions regarding AR modeling of reverberant speech are drawn in Sec. VII.

II. STATISTICAL ROOM ACOUSTICS

In this section, the statistical model of room reverberation and the conditions under which this is assumed valid are summarized. Within the framework of SRA, the sound field at a point in a room consists of the superposition of many acoustic plane waves arriving from all possible directions and with randomly distributed amplitudes and phases such that they form a uniform, diffuse sound field.[9,11] Subsequently, the room transfer function (RTF) of the acoustic channel from the source to the mth microphone can be expressed as the sum of a direct component, $H_{d,m}(e^{j\omega})$ and a reverberant component, $H_{r,m}(e^{j\omega})$, such that

$$H_m(e^{j\omega}) = H_{d,m}(e^{j\omega}) + H_{r,m}(e^{j\omega}), \quad m = 1,2,\ldots,M. \tag{1}$$

Under the conditions stated at the end of this section, and due to the different propagation directions and the random relation of the phases of the direct component and all the reflected waves, it can be assumed that the direct and the reverberant components are uncorrelated.[9,11] Hence, the spatial expectation of the cross terms of the squared magnitude of (1) is zero[10] and the spatially expected energy density spectrum of the RTF can be written

$$\mathcal{E}\{|H_m(e^{j\omega})|^2\} = |H_{d,m}(e^{j\omega})|^2 + \mathcal{E}\{|H_r(e^{j\omega})|^2\}, \tag{2}$$

where $\mathcal{E}\{\cdot\}$ is the spatial expectation operator, with the spatial expectation defined over all allowed microphone-source positions in a room.[15,11] Only the reverberant component varies with position, and its spatial expectation is independent of the microphone index m. The computation of $\mathcal{E}\{\cdot\}$ is described in Sec. III. The direct component of the RTF is the free-space Green's function, defined as[11]

$$H_{d,m}(e^{j\omega}) = \frac{e^{jkD_m}}{4\pi D_m}, \tag{3}$$

where D_m is the distance from the source to the mth microphone and $k = 2\pi f/c$ is the wave number, with f denoting frequency and c the speed of sound in air, which we take at room temperature as $c = 344$ m/s. From SRA, the expected density spectrum of the reverberant component is given by[9,10]

$$\mathcal{E}\{|H_r(e^{j\omega})|^2\} = \left(\frac{1-\alpha}{\pi A\alpha}\right), \tag{4}$$

with A being the total surface area of the room and α the average absorption coefficient of the room walls.

The spatial cross correlation of the reverberant paths between the mth and the nth channels has been shown to be[16]

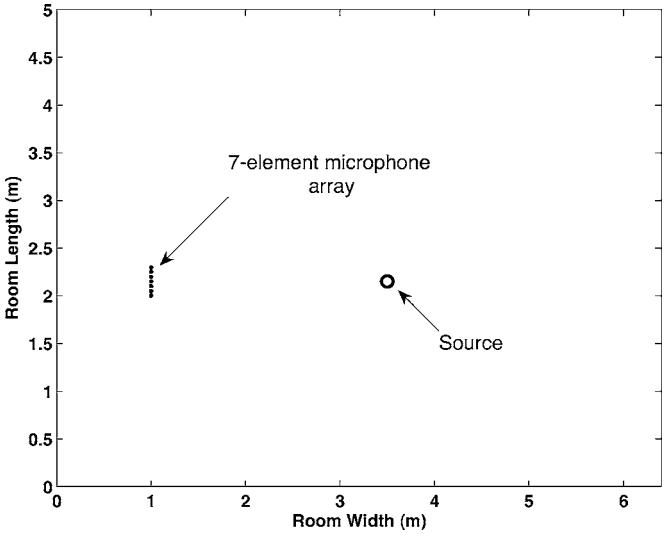

FIG. 1. Plan view of the simulated room environment with the initial position of the microphones (·) and the source (○).

$$\mathcal{E}\{H_{r,m}(e^{j\omega})H_{r,n}^*(e^{j\omega})\} = \left(\frac{1-\alpha}{\pi A\alpha}\right)\frac{\sin k\|\boldsymbol{\ell}_m - \boldsymbol{\ell}_n\|}{k\|\boldsymbol{\ell}_m - \boldsymbol{\ell}_n\|}, \tag{5}$$

where $\|\cdot\|$ denotes the Euclidean norm and $\boldsymbol{\ell}_m$ is the three-dimensional position vector of the mth microphone, with the origin at $(x,y,z) = (0,0,0)$.

These approximations are known to represent closely the acoustic properties of a room provided that the following conditions are satisfied:[9,10]

(1) The dimensions of the room are large relative to the wavelength at all frequencies of interest.
(2) The average spacing between the resonant frequencies of the room is smaller than one-third of their bandwidth. This can be satisfied at all frequencies above the Schroeder frequency defined as

$$f_{\mathrm{Sch}} = 2000\sqrt{\frac{T_{60}}{V}}\ \mathrm{Hz}, \tag{6}$$

where T_{60} is the reverberation time and V is the volume of the room in cubic meters.
(3) Speaker and microphones are situated in the room interior, at least a half-wavelength from the surrounding walls.

These conditions usually hold for most practical situations over the significant speech bandwidth. Also, image method[18] simulations and measured impulse responses of a real room have been demonstrated to coincide closely with SRA theory.[15]

III. EXPERIMENTAL ENVIRONMENT

We consider a room with a single source and an array of microphones as depicted in Fig. 1. All results presented in this paper are based on computer simulations with the simulated environment defined as follows. The dimensions of the room were set to $4 \times 5 \times 6.4$ m. These dimensions were specifically chosen to conform with the ratio (1:1.25:1.6), as in Ref. 10, in order to obtain the best approximation of a diffuse

sound field so as to satisfy the conditions above. Unless stated otherwise, the microphones were positioned in a linear array configuration with the distance between adjacent microphones set to $\|\boldsymbol{\ell}_m - \boldsymbol{\ell}_{m+1}\| = 0.05$ m. The source was at a distance $D = 2.5$ m from the center of the array. The source and the microphones were assumed omnidirectional and were always at least a half-wavelength from the surrounding walls, where the wavelength is taken with respect to the lowest frequency component in the signal. The source-image method for modeling small room acoustics,[18] modified to accommodate fractional sample delays according to Ref. 19, was used to generate finite room impulse responses, $h(n)$. The room transfer function, $H(e^{j\omega})$, was then found by taking the Fourier transform of $h(n)$. Anechoic speech samples were taken from the APLAWD database[20] and all the signals under consideration were bandlimited to 300–7000 Hz with a sampling frequency $f_s = 16$ kHz.

To compute the spatial expectation, $\mathcal{E}\{\cdot\}$, we utilized the method used by Radlovic *et al.*[10] and Gustafsson *et al.*[15] An initial position for the source, $\boldsymbol{y}_0$, and for each of the microphones, $\boldsymbol{\ell}_{m,0}$, was selected. A random translation vector, $\boldsymbol{\theta}$, and a random rotation matrix, $\boldsymbol{\mathcal{R}}$, were generated and applied to the initial coordinates of the source-receiver configuration to obtain the ith realization coordinates $\boldsymbol{y}_i = \boldsymbol{\mathcal{R}}\boldsymbol{y}_0 + \boldsymbol{\theta}$ and $\boldsymbol{\ell}_{m,i} = \boldsymbol{\mathcal{R}}\boldsymbol{\ell}_{m,0} + \boldsymbol{\theta}$. In this way, the distance between the source and the microphones and between successive microphones is kept constant for all $i = 1, 2, \ldots, N$. An estimate of $\mathcal{E}\{\cdot\}$ is obtained by taking the average of the N outcomes.

IV. SINGLE-CHANNEL AR MODELING OF REVERBERANT SPEECH

In this section, we consider AR modeling of speech using linear prediction[21,22] and we present the analysis of the effects of reverberation on the AR coefficients obtained from a single channel. We also discuss the consequences this has on the linear prediction residual.

A. AR modeling of speech

In order to introduce the notation used in the rest of the paper, we provide a brief summary of the AR modeling of speech. A speech signal, $s(n)$, can be expressed as a linear combination of its p past samples using a linear predictor[21]

$$s(n) = -\boldsymbol{a}^T \boldsymbol{s}(n-1) + e(n), \tag{7}$$

where $\boldsymbol{a} = [a_1 \;\; a_2 \;\; \cdots \;\; a_p]^T$ is a $p \times 1$ vector of AR coefficients with $[\cdot]^T$ denoting matrix transpose, $\boldsymbol{s}(n-1) = [s(n-1) s(n-2) \cdots s(n-p)]^T$ is a vector of input samples at time n, $e(n)$ is the LP residual, and p is the prediction order. The prediction error filter and the all-pole predictor are, respectively,

$$A(z) = 1 + \boldsymbol{a}^T \boldsymbol{z} \tag{8}$$

and

$$V(z) = 1/A(z), \tag{9}$$

where $\boldsymbol{z} = [z^{-1} \;\; z^{-2} \;\; \cdots \;\; z^{-p}]$.

The AR coefficients can be obtained by minimizing the sum of the squared prediction error,

$$J = \sum_{n=-\infty}^{\infty} e^2(n) = \sum_{n=-\infty}^{\infty} (s(n) + \boldsymbol{a}^T \boldsymbol{s}(n-1))^2, \tag{10}$$

with respect to each of the coefficients in $\boldsymbol{a}$. Equivalently, by Parseval's theorem, a frequency domain formulation of the error in (10) can be expressed as[21]

$$J = \frac{1}{2\pi}\int_{-\pi}^{\pi} |E(e^{j\omega})|^2 d\omega = \frac{1}{2\pi}\int_{-\pi}^{\pi} |1 + \boldsymbol{a}^T \boldsymbol{d}|^2 |S(e^{j\omega})|^2 d\omega, \tag{11}$$

where $S(e^{j\omega})$ and $E(e^{j\omega})$ are the Fourier transforms of $s(n)$ and $e(n)$ respectively, and $\boldsymbol{d} = [e^{-j\omega} \;\; e^{-j2\omega} \;\; \cdots \;\; e^{-jp\omega}]^T$ is a $p \times 1$ DFT vector. The optimum set of p AR coefficients that minimize the error J is

$$\boldsymbol{a}_{\text{opt}} = \arg\min_{\boldsymbol{a}} J = -\boldsymbol{R}^{-1}\boldsymbol{r}, \tag{12}$$

where

$$\boldsymbol{R} = \frac{1}{2\pi}\int_{-\pi}^{\pi} |S(e^{j\omega})|^2 \boldsymbol{d}\boldsymbol{d}^H d\omega \tag{13}$$

is a $p \times p$ autocorrelation matrix, with $[\cdot]^H$ denoting Hermitian (complex conjugate) matrix transpose and

$$\boldsymbol{r} = \frac{1}{2\pi}\int_{-\pi}^{\pi} |S(e^{j\omega})|^2 \boldsymbol{d} d\omega \tag{14}$$

is a $p \times 1$ vector of autocorrelation coefficients. In practice, the error signal is evaluated over finite windowed frames;[21] however, in this paper the effects of the window will not be considered.

B. Effect of reverberation on the AR coefficients

Consider a speech signal, $s(n)$, produced at a point in a noiseless, reverberant room. The observation by a single microphone positioned at some distance from the speaker is denoted

$$x(n) = \boldsymbol{h}^T \boldsymbol{s}(n), \tag{15}$$

where $\boldsymbol{h} = [h_0 \;\; h_1 \;\; \cdots \;\; h_{L-1}]^T$ is the L-tap impulse response of the acoustic channel from the source to the microphone and $\boldsymbol{s}(n) = [s(n) \;\; s(n-1) \;\; \cdots \;\; s(n-L+1)]^T$ is the input vector at time n. The relation between the AR coefficients obtained by linear prediction from $s(n)$ and those from $x(n)$ is summarized in Theorem 1.

Theorem 1 *Let* $\boldsymbol{a}_{opt} = [a_{opt,1} \;\; a_{opt,2} \;\; \cdots \;\; a_{opt,p}]^T$ *be the optimum set of AR coefficients obtained from the clean speech signal,* $s(n)$, *and* $\boldsymbol{b}_{opt} = [b_{opt,1} \;\; b_{opt,2} \;\; \cdots \;\; b_{opt,p}]^T$ *the optimum set of AR coefficients obtained from the reverberant speech signal,* $x(n)$. *The spatially expected values of the reverberant speech AR coefficients are approximately equal to those of the AR coefficients calculated from clean speech, i.e.,*

$$\mathcal{E}\{\boldsymbol{b}_{\text{opt}}\} \cong \boldsymbol{a}_{\text{opt}}. \tag{16}$$

Proof: We apply LP analysis on the reverberant speech signal, $x(n)$, to obtain the optimum set of AR coefficients

$$\boldsymbol{b}_{\text{opt}} = -\boldsymbol{Q}^{-1}\boldsymbol{q}, \tag{17}$$

with

$$\boldsymbol{Q} = \frac{1}{2\pi}\int_{-\pi}^{\pi} |H(e^{j\omega})|^2 |S(e^{j\omega})|^2 \boldsymbol{d}\boldsymbol{d}^H d\omega \tag{18}$$

and

$$\boldsymbol{q} = \frac{1}{2\pi}\int_{-\pi}^{\pi} |H(e^{j\omega})|^2 |S(e^{j\omega})|^2 \boldsymbol{d} d\omega, \tag{19}$$

where $\boldsymbol{Q}$ is a $p \times p$ autocorrelation matrix and $\boldsymbol{q}$ is a $p \times 1$ vector of autocorrelation coefficients.

In order to study the AR coefficients of reverberant speech, we take the expectation on both sides of (17)

$$\mathcal{E}\{\boldsymbol{b}_{\text{opt}}\} = -\mathcal{E}\{\boldsymbol{Q}^{-1}\boldsymbol{q}\}. \tag{20}$$

However, we would like to consider the expectation of each term of (20). Adopting the approach used in Ref. 10 and Ref. 12, we use the zeroth-order Taylor series expansion to write $\mathcal{E}\{g(x)\} \cong g(\mathcal{E}\{x\})$, as detailed in the Appendix, and therefore (20) can be written as

$$\mathcal{E}\{\boldsymbol{b}_{\text{opt}}\} \cong -\mathcal{E}\{\boldsymbol{Q}\}^{-1}\mathcal{E}\{\boldsymbol{q}\}. \tag{21}$$

This reduces the problem to studying the properties of the AR coefficients in terms of the autocorrelation function.

Now, consider the spatial expectation of the uth element of $\boldsymbol{q}$ in (19)

$$\mathcal{E}\{q_u\} = \frac{1}{2\pi}\int_{-\pi}^{\pi} \mathcal{E}\{|H(e^{j\omega})|^2\} |S(e^{j\omega})|^2 e^{-j\omega u} d\omega, \tag{22}$$

for $u = 1, 2, \ldots, p$. The term $S(e^{j\omega})$ is taken outside the spatial expectation since it is independent of the source-microphone position.

From (2)–(4) the SRA expression for the expected energy density spectrum of the RTF is

$$\mathcal{E}\{|H(e^{j\omega})|^2\} = \frac{1}{(4\pi D)^2} + \left(\frac{1-\alpha}{\pi A \alpha}\right) = \gamma. \tag{23}$$

Since γ is independent of frequency, by substitution of (23) into (22) we arrive at

$$\mathcal{E}\{q_u\} = \frac{\gamma}{2\pi}\int_{-\pi}^{\pi} |S(e^{j\omega})|^2 e^{-j\omega u} d\omega = \gamma r_u, \tag{24}$$

for $u = 1, 2, \ldots, p$, where r_u is the uth element of the clean speech autocorrelation vector $\boldsymbol{r}$, and by similar reasoning the (u,v)th element of $\boldsymbol{Q}$ in (18) becomes

$$\mathcal{E}\{Q_{u,v}\} = \gamma R_{u,v}, \quad u,v = 1,2, \ldots, p, \tag{25}$$

where $R_{u,v}$ is the (u,v)th element of the clean speech autocorrelation matrix $\boldsymbol{R}$. Substituting the results from (24) and (25) into (21) gives (16). □

This result states that if LP analysis is applied to reverberant speech, the coefficients $\boldsymbol{a}_{\text{opt}}$ and $\boldsymbol{b}_{\text{opt}}$ are not necessarily equal at a single observation point in space. However, in terms of spatial expectation, the AR coefficients from reverberant speech are approximately equal to those from clean speech. The accuracy of the approximation depends on the accuracy of estimation of the spatial expectation of the autocorrelation function.

C. Effect of reverberation on the prediction residual

Consider a frequency domain formulation of the source-filter model described in Sec. IV A. The speech signal is expressed as

$$S(e^{j\omega}) = E(e^{j\omega})V(e^{j\omega}), \tag{26}$$

where $E(e^{j\omega})$ is the Fourier transform of the LP residual and $V(e^{j\omega})$ is the transfer function all-pole filter from (9) evaluated for $z = e^{j\omega}$.

Now, consider the speech signal produced in a reverberant room as defined in (15), which in the frequency domain leads to

$$X(e^{j\omega}) = S(e^{j\omega})H(e^{j\omega}) = E(e^{j\omega})V(e^{j\omega})H(e^{j\omega}). \tag{27}$$

Referring to (16), an inverse filter, $B(e^{j\omega}) = 1 + \Sigma_{k=1}^{p} b_k e^{j\omega k}$, can be obtained such that $\mathcal{E}\{B(e^{j\omega})\} \cong A(e^{j\omega})$, where $A(e^{j\omega})$ is given by (8) for $z = e^{j\omega}$. Filtering the reverberant speech signal with this inverse filter, whose coefficients are obtained from the reverberant speech signal, results in

$$\hat{E}(e^{j\omega}) \cong E(e^{j\omega})H(e^{j\omega}), \tag{28}$$

where $\hat{E}(e^{j\omega})$ is the Fourier transform of the LP residual, $\hat{e}(n)$, obtained from the reverberant speech signal. Thus, in the time domain, the LP residual obtained from reverberant speech is approximately equal to the clean speech residual convolved with the room impulse response. The approximation in (28) arises from the AR modeling. Therefore, if the AR coefficients used were identical to those from clean speech, the approximation would be an equivalence.

In summary, we have shown that the AR coefficients obtained from reverberant speech are approximately equal to those from clean speech in terms of spatial expectation. Furthermore, the LP residual obtained from a reverberated speech signal is approximately equal to the clean speech residual convolved with the room impulse response. This approximation depends on the accuracy of the estimation of the AR coefficients. Intuitively, the result in (16) suggests that using a microphone array in a manner so as to approximate the taking of the spatial expectation will give a more accurate estimation of the AR coefficients than use of a single observation alone. This motivates our study of multichannel AR modeling in the following section.

V. MULTICHANNEL AR MODELING OF REVERBERANT SPEECH

Several microphone array techniques have been applied as preprocessing in speech applications, proving advantageous to single-channel algorithms.[23] In this section, we investigate the use of a microphone array to obtain the AR coefficients and how these compare to the AR coefficients from clean speech. Two alternative approaches are considered. In the first alternative, the AR coefficients are obtained by formulating an estimation procedure that jointly minimizes the squared errors over all M channels. In the second

alternative, the AR coefficients are obtained from the output of an M-channel array using delay-and-sum beamforming.

A. *M*-channel AR coefficients

The speech signal observed at the mth microphone in an array of M microphones can be expressed as

$$x_m(n) = \boldsymbol{h}_m^T \boldsymbol{s}(n), \quad m = 1,2,\ldots,M, \tag{29}$$

where $\boldsymbol{h}=[h_{m,0} \;\; h_{m,1} \;\; \cdots \;\; h_{m,L-1}]^T$ is the L-tap room impulse response from the source to the mth microphone.

In linear prediction terms, the observation at the mth sensor from (29) can be written as

$$x_m(n) = -\boldsymbol{b}_m^T \boldsymbol{x}_m(n-1) + e_m(n), \quad m = 1,2,\ldots,M, \tag{30}$$

where $\boldsymbol{b}_m=[b_{m,1} \;\; b_{m,2} \;\; \cdots \;\; b_{m,p}]^T$ are the prediction coefficients, $\boldsymbol{x}_m(n-1)=[x_m(n-1)x_m(n-2)\cdots x_m(n-p)]^T$ is the mth microphone observation vector at time n, and $e_m(n)$ is the prediction residual obtained from the mth microphone signal. From (30), a joint M-channel error function can be formulated as[23]

$$\begin{aligned} J_M &= \frac{1}{M}\sum_{m=1}^{M}\sum_{n=-\infty}^{\infty} e_m^2(n) \\ &= \frac{1}{M}\sum_{m=1}^{M}\sum_{n=-\infty}^{\infty} (x_m(n) + \boldsymbol{b}_m^T \boldsymbol{x}_m(n-1))^2. \end{aligned} \tag{31}$$

The optimum set of coefficients that minimize this error, similarly to (12), is given by

$$\hat{\boldsymbol{b}}_{\text{opt}} = -\hat{\boldsymbol{Q}}^{-1}\hat{\boldsymbol{q}}, \tag{32}$$

with

$$\hat{\boldsymbol{Q}} = \frac{1}{M}\sum_{m=1}^{M} \boldsymbol{Q}_m \tag{33}$$

and

$$\hat{\boldsymbol{q}} = \frac{1}{M}\sum_{m=1}^{M} \boldsymbol{q}_m, \tag{34}$$

where $\hat{\boldsymbol{Q}}$ and $\hat{\boldsymbol{q}}$ are, respectively, the $p\times p$ mean autocorrelation matrix and the $p\times 1$ mean autocorrelation vector across the M microphones. The relation between the clean speech coefficients and the coefficients obtained using (32) is summarized in Corollary 1.

Corollary 1 *Replacing* (18) and (19) *with their averages considered over M microphones* (33) and (34) *and then following the steps of the proof of Theorem 1, it can be shown that the spatial expectation of the AR coefficients obtained from minimization of* (31) *is approximately equal to those from clean speech. That is*,

$$\mathcal{E}\{\hat{\boldsymbol{b}}_{\text{opt}}\} \cong \boldsymbol{a}_{\text{opt}}. \tag{35}$$

This result implies that the optimal AR coefficients obtained using a spatial expectation over M channels are equivalent to the spatial expectation of the AR coefficients in the single-microphone case in (16). However, at each individual position, the M-channel case provides a more accurate estimation of the clean speech AR coefficients than that obtained with a single reverberant channel, as will be shown by simulations in Sec. VI. This is because the averaging of the autocorrelation functions in (33) and (34) is equivalent in effect to the calculation of the spatial expectation operation in the single-channel case (21).

B. AR coefficients from a DSB output

The output of a delay-and-sum beamformer can be written[24] as

$$\bar{x}(n) = \frac{1}{M}\sum_{m=1}^{M} x_m(n-\tau_m), \tag{36}$$

where τ_m is the propagation delay in samples from the source to the mth sensor. Assuming that the time delays of arrival are known for all microphones, linear prediction can be performed on the beamformer output, $\bar{x}(n)$, following the approach in Sec. IV B. This is summarized in Theorem 2.

Theorem 2 *Let* $\boldsymbol{a}_{opt}=[a_{opt,1} \;\; a_{opt,2} \;\; \cdots \;\; a_{opt,p}]^T$ *be the optimum set of AR coefficients obtained from the clean speech signal,* $s(n)$, *and* $\bar{\boldsymbol{b}}=[\bar{b}_{opt,1} \;\; \bar{b}_{opt,2} \;\; \cdots \;\; \bar{b}_{opt,p}]^T$ *be the optimum set of AR coefficients obtained from the DSB output,* $\bar{x}(n)$. *The spatial expectation of the AR coefficients calculated by linear prediction from the output of the DSB is*

$$\mathcal{E}\{\bar{\boldsymbol{b}}_{\text{opt}}\} \cong \boldsymbol{T}\boldsymbol{a}_{\text{opt}} - \boldsymbol{t}, \tag{37}$$

with $\boldsymbol{T}=\boldsymbol{I}-(1/\bar{\gamma})\boldsymbol{R}^{-1}\boldsymbol{\Gamma}(\boldsymbol{\Lambda}^{-1}-\boldsymbol{\Gamma}^H(1/\bar{\gamma})\boldsymbol{R}^{-1}\boldsymbol{\Gamma})^{-1}\boldsymbol{\Gamma}^H$ *and* $\boldsymbol{t}=(\bar{\gamma}\boldsymbol{R}+\boldsymbol{\Xi})^{-1}\boldsymbol{\xi}$, *where these terms are defined in the following proof.*

Proof: Consider a speech signal source, $s(n)$, observed using M microphones and combined using a DSB to give a signal $\bar{x}(n)$. In the frequency domain this can be expressed as

$$\bar{X}(e^{j\omega}) = \left(\frac{1}{M}\sum_{m=1}^{M} H_m(e^{j\omega})e^{-j2\pi f\tau_m}\right)S(e^{j\omega}) = \bar{H}(e^{j\omega})S(e^{j\omega}), \tag{38}$$

where $\bar{X}(e^{j\omega})$ is the Fourier transform of $\bar{x}(n)$, $S(e^{j\omega})$ is the Fourier transform of $s(n)$, $H_m(e^{j\omega})$ is the RTF with respect to the mth microphone, and $\bar{H}(e^{j\omega})$ is the averaged RTF at the DSB output. The AR coefficients, $\bar{\boldsymbol{b}}_{\text{opt}}$, at the beamformer output are calculated as in Sec. IV A,

$$\bar{\boldsymbol{b}}_{\text{opt}} = -\bar{\boldsymbol{Q}}^{-1}\bar{\boldsymbol{q}}, \tag{39}$$

with

$$\bar{\boldsymbol{Q}} = \frac{1}{2\pi}\int_{-\pi}^{\pi} |\bar{H}(e^{j\omega})|^2 |S(e^{j\omega})|^2 \boldsymbol{d}\boldsymbol{d}^H d\omega \tag{40}$$

and

$$\bar{\boldsymbol{q}} = \frac{1}{2\pi}\int_{-\pi}^{\pi} |\bar{H}(e^{j\omega})|^2 |S(e^{j\omega})|^2 \boldsymbol{d} d\omega, \tag{41}$$

where $\bar{\boldsymbol{Q}}$ is a $p\times p$ autocorrelation matrix and $\bar{\boldsymbol{q}}$ is a $p\times 1$ vector.

From this point on, we omit the frequency index for reasons of clarity. The expected energy density spectrum of the averaged RTFs can be written as

$$\mathcal{E}\{|\bar{H}|^2\} = \frac{1}{M^2}\left[\sum_{m=1}^{M}\mathcal{E}\{|H_m|^2\} + \sum_{m=1}^{M}\sum_{\substack{n=1\\ n\neq m}}^{M}\mathcal{E}\{H_m H_n^*\}e^{-j2\pi f(\tau_m-\tau_n)}\right]. \quad (42)$$

From Sec. II, the expected energy density for the mth channel is

$$\mathcal{E}\{|H_m|^2\} = \frac{1}{(4\pi D_m)^2} + \left(\frac{1-\alpha}{\pi A\alpha}\right), \quad (43)$$

and the expected cross correlation between the mth and the nth microphones is

$$\mathcal{E}\{H_m H_n^*\} = \frac{e^{jk(D_m-D_n)}}{16\pi^2 D_m D_n} + \left(\frac{1-\alpha}{\pi A\alpha}\right)\frac{\sin k\|\boldsymbol{\ell}_m-\boldsymbol{\ell}_n\|}{k\|\boldsymbol{\ell}_m-\boldsymbol{\ell}_n\|}. \quad (44)$$

By substituting (43) and (44) into (42) and with $\tau_m = D_m/c$, we obtain the following expression for the mean energy density at the DSB output:

$$\mathcal{E}\{|\bar{H}|^2\} = \bar{\gamma} + \psi(\omega), \quad (45)$$

with

$$\bar{\gamma} = \frac{1}{(4\pi M)^2}\sum_{m=1}^{M}\sum_{n=1}^{M}\frac{1}{D_m D_n} + \left(\frac{1-\alpha}{M\pi A\alpha}\right)$$

and

$$\psi(\omega) = \left(\frac{1-\alpha}{M^2\pi A\alpha}\right)\sum_{m=1}^{M}\sum_{\substack{n=1\\ n\neq m}}^{M}\frac{\sin k\|\boldsymbol{\ell}_m-\boldsymbol{\ell}_n\|}{k\|\boldsymbol{\ell}_m-\boldsymbol{\ell}_n\|} \times\cos(k[D_m-D_n]),$$

where $\bar{\gamma}$ is a frequency-independent component and $\psi(\omega)$ is a component due to spatial correlation.

Now, let

$$\xi_u = \frac{1}{2\pi}\int_{-\pi}^{\pi}\psi(\omega)|S(e^{j\omega})|^2 e^{-j\omega u}d\omega \quad (46)$$

and

$$\Xi_{u,v} = \frac{1}{2\pi}\int_{-\pi}^{\pi}\psi(\omega)|S(e^{j\omega})|^2 e^{-j\omega(u-v)}d\omega \quad (47)$$

be the uth element of a vector $\boldsymbol{\xi}$ and the (u,v)th element of a matrix $\boldsymbol{\Xi}$, respectively. The expected value of the uth element of $\bar{\boldsymbol{q}}$ from (41) then becomes

$$\mathcal{E}\{\bar{q}_u\} = \bar{\gamma}r_u + \xi_u, \quad u = 1,2,\ldots,p, \quad (48)$$

where r_u is the uth element of the vector $\boldsymbol{r}$ in (14). Similarly, the expected value of the (u,v)th element of $\bar{\boldsymbol{Q}}$ from (40) is

$$\mathcal{E}\{\bar{Q}_{u,v}\} = \bar{\gamma}R_{u,v} + \Xi_{u,v}, \quad u,v = 1,2,\ldots,p, \quad (49)$$

where $R_{u,v}$ is the (u,v)th element of the matrix $\boldsymbol{R}$ in (13). The expected set of coefficients for the DSB output is therefore

$$\mathcal{E}\{\bar{\boldsymbol{b}}_{\text{opt}}\} \cong -(\bar{\gamma}\boldsymbol{R} + \boldsymbol{\Xi})^{-1}(\bar{\gamma}\boldsymbol{r} + \boldsymbol{\xi}). \quad (50)$$

Since $\boldsymbol{\Xi}$ is a Hermitian symmetric matrix, it can be factored as

$$\boldsymbol{\Xi} = \boldsymbol{\Gamma}\boldsymbol{\Lambda}\boldsymbol{\Gamma}^H, \quad (51)$$

where $\boldsymbol{\Gamma}$ is a matrix of eigenvectors and $\boldsymbol{\Lambda}$ is a diagonal matrix of eigenvalues. Using the matrix inversion lemma,[25] we can write

$$(\bar{\gamma}\boldsymbol{R} + \boldsymbol{\Xi})^{-1} = \frac{1}{\bar{\gamma}}\boldsymbol{R}^{-1} - \frac{1}{\bar{\gamma}^2}\boldsymbol{R}^{-1}\boldsymbol{\Gamma} \times\left(\boldsymbol{\Lambda}^{-1} - \boldsymbol{\Gamma}^H\frac{1}{\bar{\gamma}}\boldsymbol{R}^{-1}\boldsymbol{\Gamma}\right)^{-1}\boldsymbol{\Gamma}^H\boldsymbol{R}^{-1}. \quad (52)$$

Finally, substituting the result from (52) into (50) we obtain the result in (37). □

Theorem 2 states that, in terms of spatial expectation, the AR coefficients obtained by LP analysis of the DSB output, $\bar{x}(n)$, differ from those obtained from clean speech. This difference depends on the spatial cross correlation between the acoustic channels. It can be seen from (5) that the inter-channel correlation and its significance are governed by the reverberation time, the distance between adjacent microphones, the source-microphone separation, and on the array size if the speaker is in the near field of the microphone array. Of particular interest is the separation of adjacent microphones. From (45) it is evident that the term $\psi(\omega)$ and, consequently, the matrix $\boldsymbol{\Xi}$ and the vector $\boldsymbol{\xi}$, will tend to zero as the source-microphone separation is increased. Therefore, for large intermicrophone separation the matrix $\boldsymbol{T}$ tends to the identity matrix $\boldsymbol{I}$ and the vector $\boldsymbol{t}$ tends to zero and the result in (37) tends to the result in (16). Furthermore, if estimates of $\boldsymbol{T}$ and $\boldsymbol{t}$ were available, since $\boldsymbol{T}$ is a square matrix the effects of the spatial cross correlation could be compensated as $\boldsymbol{a}_{\text{opt}} \cong \boldsymbol{T}^{-1}(\mathcal{E}\{\bar{\boldsymbol{b}}_{\text{opt}}\} + \boldsymbol{t})$. However, estimating these parameters is difficult in practice. Finally, for the special case where the distance between the microphones is exactly a multiple of a half-wavelength at each frequency and the speaker is far from the microphones, then $\psi(\omega) = 0, \forall\,\omega$ and thus $\boldsymbol{\Xi}$ and $\boldsymbol{\xi}$ from (46) and (47) are equal to zero. Therefore, the matrix $\boldsymbol{T}$ becomes exactly the identity matrix $\boldsymbol{I}$ and the vector $\boldsymbol{t}$ is exactly zero, which results in the expression in (37) becoming equivalent to that in (16).

VI. SIMULATIONS AND RESULTS

Having established the theoretical relationship between the AR coefficients obtained from clean speech and those obtained from reverberant speech observations, we now present simulation results to demonstrate and to validate the theoretical analysis. In summary, we demonstrate two specific points: (1) On average over all positions in the room, the AR coefficients obtained from a single microphone as in

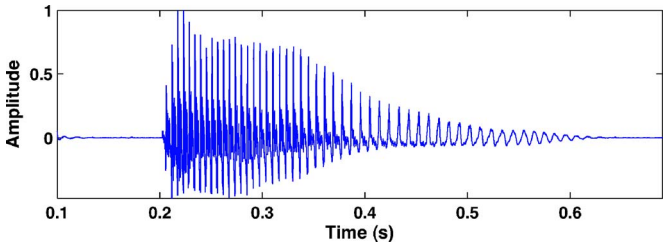

FIG. 2. Speech sample used in the experiments comprising the time-domain waveform of the diphthong /eɪ/ as in the alphabet letter "a" uttered by a male speaker.

case (i) and those calculated from M microphones as in case (ii) are not affected by reverberation while the AR coefficients from the DSB become more dissimilar from the clean speech coefficients with increased reverberation time. (2) The M-channel AR coefficients are the most accurate estimates of the clean speech AR coefficients from the three cases studied.

As an evaluation metric for the similarity between two sets of AR coefficients we use the Itakura distance measure,[22] defined as

$$d_I = \log\left(\frac{\hat{\boldsymbol{a}}^T \boldsymbol{R} \hat{\boldsymbol{a}}}{\boldsymbol{a}^T \boldsymbol{R} \boldsymbol{a}}\right), \tag{53}$$

where $\boldsymbol{a}$ is the set of clean speech coefficients and $\hat{\boldsymbol{a}}$ are the coefficients under test. The Itakura distance can be interpreted as the log ratio of the minimum mean squared errors (MMSE) obtained with the true and the estimated coefficients. The denominator represents the optimal solution for the clean speech and thus $d_I \geqslant 0$. For the experiments, the diphthong /eɪ/ as in the alphabet letter "a" uttered by a male speaker was used as an example and is depicted in Fig. 2. We performed the LP analysis on that sample employing selective linear prediction[26] with a frame length equal to the length of the vowel and a prediction order $p=21$ with sampling frequency $f_s=16$ kHz. The prediction order was chosen using the relation $p=f_s/1000+5$ as recommended in Ref. 22. Thus, this gives a pole pair per kHz of Nyquist sampling frequency and some additional poles to model the glottal pulse. For the selective linear prediction we consider the spectrum in the range 0.3–7 kHz in order to avoid errors due to bandlimiting filters.

A. Experiment 1

The spatial expectation was calculated using $N=200$ realizations of the source-array positions, and thus an average autocorrelation function was calculated for each of the cases under consideration. This was repeated, varying the reverberation time, T_{60}, from 0.1 to 0.9 s in steps of 0.2 s. For each case the Itakura distance measure was applied to the estimation of the spatial expectation of the coefficients. Figure 3 shows the results in which the Itakura distance of the spatially expected coefficients is plotted versus reverberation time for (a) a single channel; (b) $M=7$ channels; and (c) the DSB output simulation and the theoretical expression for the DSB output in (37) (dashed). It can be seen that the experimental outcome closely corresponds to the theoretical results

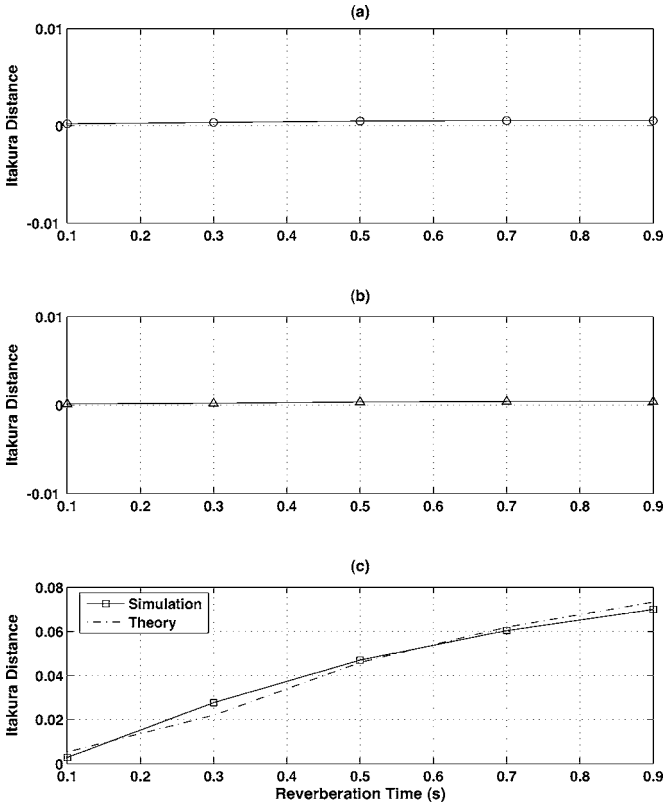

FIG. 3. Itakura distance vs reverberation time for the spatially expected AR coefficients of (a) a single channel; (b) $M=7$ channels; and (c) DSB output simulation and the theoretical expression for the DSB output (37) (dashed).

where the coefficients from the M-channel case and from a single channel are close to the clean speech coefficients with an Itakura distance close to zero. In contrast, the difference between the results from the DSB output and the clean speech increases proportionally to the reverberation time, where the Itakura distance varies from $d_I=0.0028$ for $T_{60}=0.1$ s to $d_I=0.07$ at $T_{60}=0.9$ s.

B. Experiment 2

This experiment illustrates the individual outcomes for the three cases at the $N=200$ different locations. Thus, using the same conditions as in experiment 1, the AR coefficients were computed at each individual source-array position using (17), (32), and (39) and the Itakura distance was calculated. Figure 4 shows the resulting plot in terms of the mean Itakura distance versus increasing reverberation time for (a) a single channel; (b) $M=7$ channels; and (c) a DSB output. The error bars indicate the range between the maximum and the minimum errors while the crosses indicate the mean value for all N locations. It can be seen that the M-channel LPC provides the best approximation of the clean speech AR coefficients. The mean Itakura distance is $d_I=0.01$ on average for all reverberation times, with a maximum distance of $d_I=0.057$ and a minimum distance $d_I=0.0015$ compared to a mean Itakura distance of $d_I=0.027$ for the single-channel case, where the maximum and the minimum distances are, respectively, $d_I=0.079$ and $d_I=0.0067$. It can also be seen that the estimation error for the AR coefficients obtained from the DSB output can become significant with increasing

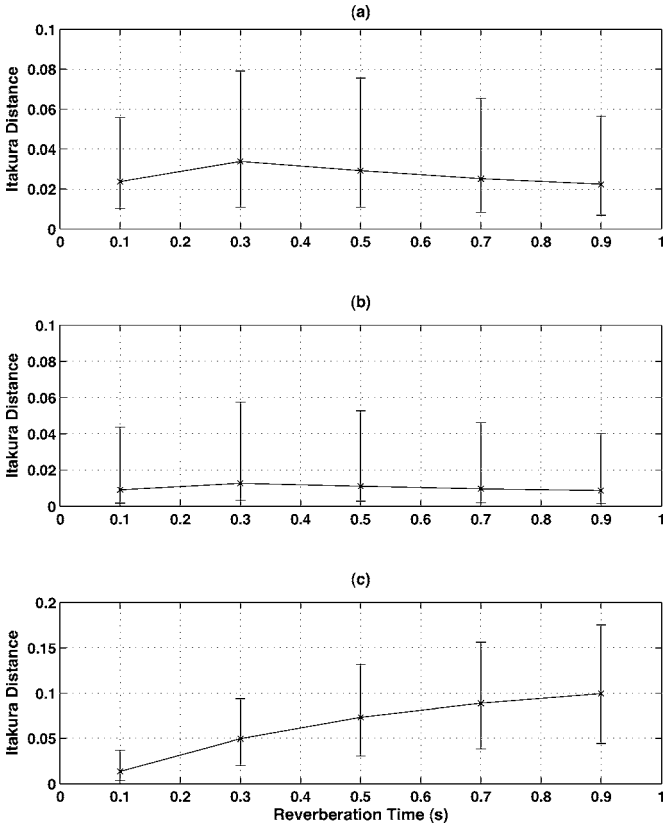

FIG. 4. Itakura distance vs reverberation time in terms of the AR coefficients for each individual outcome for (a) a single channel; (b) $M=7$ channels; and (c) the DSB output. Error bars indicate the maximum and minimum errors while crosses show the mean values.

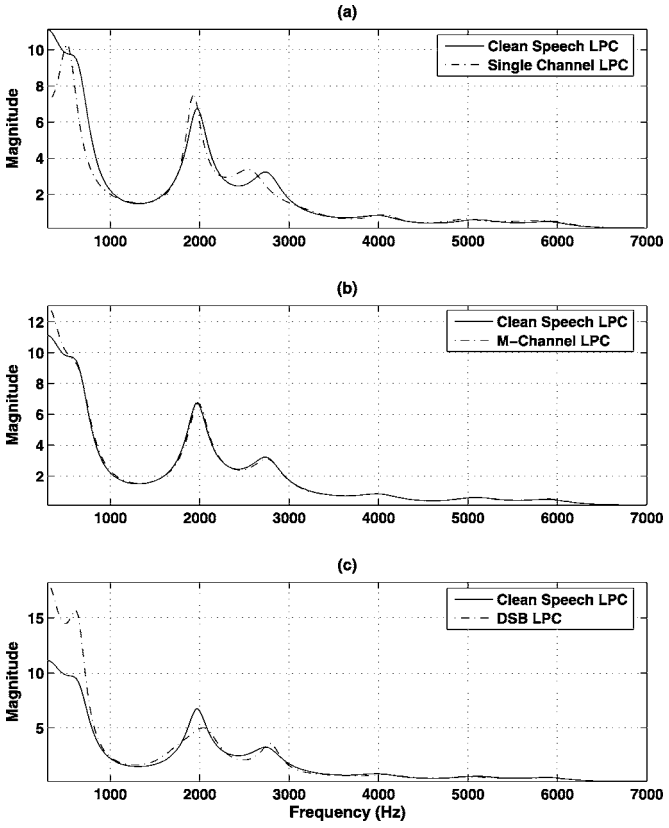

FIG. 5. Spectral envelopes calculated from the AR coefficients of clean speech compared with spectral envelopes obtained from the AR coefficients of (a) a single channel; (b) $M=7$ channels; and (c) the DSB output.

reverberation time, reaching an average of $d_I=0.099$ at $T_{60}=0.9$ with a maximum distance $d_I=0.175$ and minimum $d_I=0.045$ at that reverberation time. This result may appear counterintuitive; however, it conforms with the theoretical expression in (37) and will be clarified further with the following experiment. Figure 5 shows examples of the spectral envelopes from the AR coefficients obtained from reverberant observations using LPC for (a) single channel; (b) $M=7$ channels; and (c) the DSB output. Each case is compared to the resulting spectral envelope from clean speech.

C. Experiment 3

In line with the discussion in Sec. V B, the discrepancy in the estimated AR coefficients at the output of the DSB from those obtained with clean speech is governed mainly by the separation of the microphones. This final experiment demonstrates the effect of the separation between adjacent microphones on the expected AR coefficients obtained at output of a DSB. All the parameters of the room and source-microphone array were kept fixed while the separation, $\|\ell_m - \ell_{m+1}\|$, between adjacent microphones in the linear array was increased from 0.05 to 0.3 m in steps of 0.05 m. The results are shown in Fig. 6, where the Itakura distance is plotted against microphone separation for (a) the theoretical results calculated with (37) (dashed) and the simulated results (crosses) for the spatially expected AR coefficients at the output of the DSB, and (b) the AR coefficients for each individual outcome. Error bars indicate the maximum and the minimum errors while crosses indicate the mean value. It is seen from these results that the estimates at the output of the DSB become more accurate as the distance between the

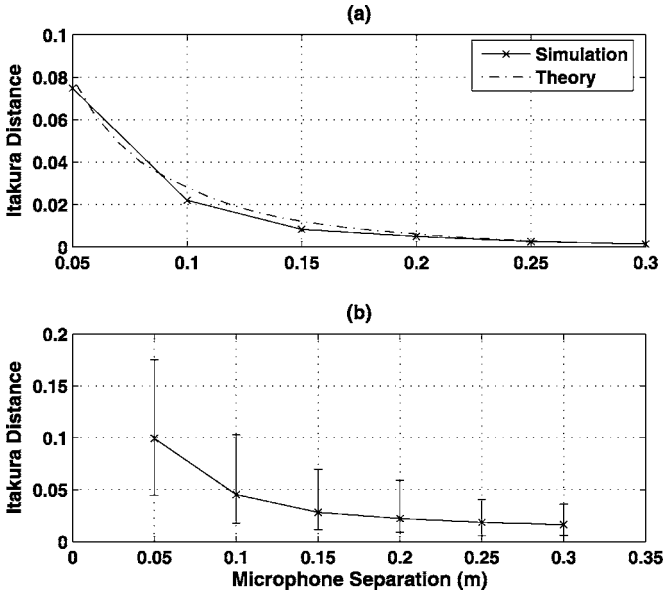

FIG. 6. Itakura distance vs microphone separation for (a) the theoretical results calculated with (37) (dashed) and the simulated results (crosses) for the spatially expected AR coefficients at the output of the DSB and (b) the AR coefficients for each individual outcome. Error bars indicate the maximum and the minimum errors while crosses show the mean value.

microphones is increased. At a microphone separation of $\|\ell_m - \ell_{m+1}\| = 0.3$ m the results are comparable to the M-channel case both in terms of spatial expectation where an Itakura distance of $d_I = 0.0041$ is observed and for the individual outcomes where the mean Itakura distance is $d_I = 0.0164$ with the minimum and maximum distances being $d_I = 0.06$ and $d_I = 0.036$. This is due to the fact that the spatial correlation between microphones becomes negligible with increased microphone separation.

VII. CONCLUSIONS

We have used statistical room acoustic theory for the analysis of the AR modeling of reverberant speech. Investigating three scenarios, we have shown that, in terms of spatial expectation, the AR coefficients calculated from reverberant speech are approximately equivalent to those from clean speech both in the single-channel case and in the case when the coefficients are calculated jointly from an M-channel observation. Furthermore, it was shown that the AR coefficients calculated at the output of a delay-and-sum beamformer differ from the clean speech coefficients due to spatial correlation, which is governed by the room characteristics and the microphone array arrangement. This difference decreases as the distance between adjacent microphones is increased. It was also demonstrated that AR coefficients calculated jointly from the M-channel observation provide the best approximation of the clean speech AR coefficients at individual source-microphone positions and in particular when the microphone separation is small (<0.3 m). Thus, in general, the M-channel joint calculation of the AR coefficients is the preferred option where such an equivalence is important and specifically in the case of closely spaced microphones. Finally, the findings in this paper are of particular interest in speech dereverberation methods using prediction residual processing, where the main and crucial assumption is that reverberation mostly affects the prediction residual. Since most of these methods utilize microphone arrays for the residual processing, M-channel joint calculation of the AR coefficients should be deployed to ensure the validity of this assumption.

APPENDIX

Consider a function, $g(x_1, x_2, \ldots, x_n)$, of random variables[27] with mean values $E\{x_i\} = \mu_i$, which we write $g(x)$ for brevity. Letting $g'(x) = \partial(g(x))/\partial x_i|_{x=\mu}$, the Taylor series expansion of $g(x)$ about the mean, μ, is $g(x) = g(\mu) + \sum_{i=1}^{n} g'(\mu)(x_i - \mu_i) + \breve{g}(x)$, where $\breve{g}(x)$ are the second-order terms and above. All the partial derivatives up to the first order vanish[10] at $(\mu_1, \mu_2, \ldots, \mu_n)$ and, consequently, we can write $\mathcal{E}\{g(x)\} \cong g(\mathcal{E}\{x\})$ up to the zeroth order of approximation. In practice, the accuracy of this approximation will depend on the estimation of the mean value of the random variables.

[1] R. Viswanathan and J. Makhoul, "Quantization properties of transmission parameters in linear predictive systems," IEEE Trans. Acoust., Speech, Signal Process. **23**, 309–321 (1975).
[2] M. R. Sambur and N. S. Jayant, "LPC analysis/synthesis from speech inputs containing quantizing noise or additive white noise," IEEE Trans. Acoust., Speech, Signal Process. **24**, 488–494 (1976).
[3] J. S. Lim and A. V. Oppenheim, "All-pole modeling of degraded speech," IEEE Trans. Acoust., Speech, Signal Process. **26**, 197–210 (1978).
[4] J. B. Allen, "Synthesis of pure speech from a reverberant signal," U.S. Patent No. 311,731 (1974).
[5] S. M. Griebel and M. S. Brandstein, "Microphone array speech dereverberation using coarse channel estimation," in *Proceedings of the IEEE Int. Conf. Acoust., Speech, Signal Processing*, Vol. **1**, pp. 201–204 (2001).
[6] B. Yegnanarayana and P. Satyanarayana, "Enhancement of reverberant speech using LP residual signal," IEEE Trans. Acoust., Speech, Signal Process. **8**, 267–281 (2000).
[7] B. Yegnanarayana, S. R. M. Prasanna, and K. S. Rao, "Speech enhancement using excitation source information," in *Proceedings of the IEEE Int. Conf. Acoust., Speech, Signal Processing*, Vol. **1**, pp. 541–544 (2002).
[8] B. W. Gillespie, H. S. Malvar, and D. A. F. Florêncio, "Speech dereverberation via maximum-kurtosis subband adaptive filtering," in *Proceedings of the IEEE Int. Conf. Acoust., Speech, Signal Processing*, Vol. **6**, pp. 3701–3704 (2001).
[9] H. Kuttruff, *Room Acoustics*, 4th ed. (Taylor & Francis, London, 2000).
[10] B. D. Radlović, R. C. Williamson, and R. A. Kennedy, "Equalization in an acoustic reverberant environment: Robustness results," IEEE Trans. Acoust., Speech, Signal Process. **8**, 311–319 (2000).
[11] P. A. Nelson and S. J. Elliott, *Active Control of Sound* (Academic, London, 1993).
[12] F. Talantzis and D. B. Ward, "Robustness of multichannel equalization in an acoustic reverberant environment," J. Acoust. Soc. Am. **114**, 833–841 (2003).
[13] S. Bharitkar, P. Hilmes, and C. Kyriakakis, "Robustness of spatial average equalization: A statistical reverberation model approach," J. Acoust. Soc. Am. **116**, 3491–3497 (2004).
[14] F. Talantzis, D. B. Ward, and P. A. Naylor, "Expected performance of a family of blind source separation algorithms in a reverberant room," in *Proceedings of the IEEE Int. Conf. Acoust., Speech, Signal Processing*, Vol. **4**, pp. 61–64 (Montreal, Canada) (2004).
[15] T. Gustafsson, B. D. Rao, and M. Trivedi, "Source localization in reverberant environments: Modeling and statistical analysis," IEEE Trans. Speech Audio Process. **11**, 791–803 (2003).
[16] D. B. Ward, "On the performance of acoustic crosstalk cancellation in a reverberant environment," J. Acoust. Soc. Am. **110**, 1195–1198 (2001).
[17] N. D. Gaubitch, P. A. Naylor, and D. B. Ward, "On the use of Linear Prediction for dereverberation of speech," in *Proceedings of the Int. Workshop Acoust. Echo Noise Control*, pp. 99–102 (Kyoto, Japan) (2003).
[18] J. B. Allen and D. A. Berkley, "Image method for efficiently simulating small-room acoustics," J. Acoust. Soc. Am. **65**, 943–950 (1979).
[19] P. M. Peterson, "Simulating the response of multiple microphones to a single acoustic source in a reverberant room," J. Acoust. Soc. Am. **80**, 1527–1529 (1986).
[20] G. Lindsey, A. Breen, and S. Nevard, "SPAR's archivable actual-word databases," Technical Report, University College London(1987).
[21] J. Makhoul, "Linear Prediction: A tutorial review," Proc. IEEE **63**, 561–580 (1975).
[22] J. R. Deller, J. H. L. Hansen, and J. G. Proakis, *Discrete-time Processing of Speech Signals* (Macmillan, New York, 1993).
[23] *Microphone Arrays: Signal Processing Techniques and Applications*, edited by M. S. Brandstein and D. B. Ward (Springer, Berlin, 2001).
[24] B. D. V. Veen and K. M. Buckley, "Beamforming: A versatile approach to spatial filtering," IEEE Signal Process. Mag. **5**, 4–24 (1988).
[25] V. Golub and C. H. Gene, *Matrix Computations*, John Hopkins Series in the Mathematical Sciences, 3rd ed. (John Hopkins University Press, London, 1996).
[26] J. Makhoul, "Spectral linear prediction: Properties and applications," IEEE Trans. Acoust., Speech, Signal Process. **23**, 283–296 (1976).
[27] M. Kendall, A. Stuart, and J. K. Ord, *Kendall's Advanced Theory of Statistics*, 6th ed. (Hodder Arnold, 1994), Vol. **1**.

Binaural segregation in multisource reverberant environments

Nicoleta Roman[a)]
Department of Computer Science and Engineering, The Ohio State University, Columbus, Ohio 43210

Soundararajan Srinivasan[b)]
Department of Biomedical Engineering, The Ohio State University, Columbus, Ohio 43210

DeLiang Wang[c)]
Department of Computer Science and Engineering & Center for Cognitive Science, The Ohio State University, Columbus, Ohio 43210

(Received 27 September 2005; revised 12 June 2006; accepted 24 August 2006)

In a natural environment, speech signals are degraded by both reverberation and concurrent noise sources. While human listening is robust under these conditions using only two ears, current two-microphone algorithms perform poorly. The psychological process of figure-ground segregation suggests that the target signal is perceived as a foreground while the remaining stimuli are perceived as a background. Accordingly, the goal is to estimate an ideal time-frequency (T-F) binary mask, which selects the target if it is stronger than the interference in a local T-F unit. In this paper, a binaural segregation system that extracts the reverberant target signal from multisource reverberant mixtures by utilizing only the location information of target source is proposed. The proposed system combines target cancellation through adaptive filtering and a binary decision rule to estimate the ideal T-F binary mask. The main observation in this work is that the target attenuation in a T-F unit resulting from adaptive filtering is correlated with the relative strength of target to mixture. A comprehensive evaluation shows that the proposed system results in large SNR gains. In addition, comparisons using SNR as well as automatic speech recognition measures show that this system outperforms standard two-microphone beamforming approaches and a recent binaural processor. © *2006 Acoustical Society of America.* [DOI: 10.1121/1.2355480]

PACS number(s): 43.72.Ne [DOS] Pages: 4040–4051

I. INTRODUCTION

A typical auditory environment contains multiple concurrent sources that are reflected by surfaces and change their locations constantly. While human listeners are able to attend to a particular sound signal even under such adverse conditions, simulating this perceptual ability or solving the cocktail party problem (Cherry, 1953) remains a grand challenge. A solution to the problem of sound separation in real environments is essential for many applications including automatic speech recognition (ASR), audio information retrieval and hearing prosthesis. In this paper we study the binaural (two-microphone) separation of speech in multisource reverberant environments.

The sound separation problem has been investigated in the signal processing field for many years for both one-microphone recordings as well as multi-microphone ones (for reviews see Kollmeier, 1996; Brandstein and Ward, 2001; Divenyi, 2005). One-microphone speech enhancement techniques include spectral subtraction (e.g., Martin, 2001), Kalman filtering (Ma *et al.*, 2004), subspace analysis (Ephraim and van Trees, 1995), and autoregressive modeling (e.g., Balan *et al.*, 1999). While having the advantage of requiring only one sensor, these algorithms make strong assumptions about the environment and thus have difficulty in dealing with general acoustic mixtures. Microphone array algorithms are divided in two categories: beamforming and independent component analysis (ICA) (Brandstein and Ward, 2001). While performing essentially the same linear demixing operation, these two algorithms differ in how they compute the demixing coefficients. Specifically, to separate multiple sound sources, beamforming takes advantage of their different directions of arrival while ICA relies on their statistical independence (ICA also requires different arrival directions of sound sources). A fixed beamformer, such as that of the delay-and-sum, constructs a spatial beam to enhance signals arriving from the target direction independent of the interfering sources. The primary limitations of a fixed beamformer are: (1) a poor spatial resolution at lower frequencies, i.e., the spatial response has a wide main lobe when the intermicrophone distance is smaller than the signal wavelength; and (2) spatial aliasing, i.e., multiple beams at higher frequencies when the intermicrophone distance is greater than the signal wavelength. To solve these problems a large number of microphones is required and constraints need to be introduced in order to impose a constant beam shape across the frequencies (Ward *et al.*, 2001). Adaptive beamforming techniques, on the other hand, attempt to null out the interfering sources in the mixture (Griffiths and Jim, 1982; Widrow and Stearns, 1985; Van Compernolle, 1990). While they improve spatial resolution significantly, the main disadvantage of such beamformers is greater computation

[a)]Electronic mail: roman.45@osu.edu
[b)]Electronic mail: srinivasan.36@osu.edu
[c)]Electronic mail: dwang@cse.ohio-state.edu

and adaptation time when the locations of interfering sources change. Note also that while an adaptive beamformer with two microphones is optimal for canceling a single directional interference, additional microphones are required as the number of noise sources increases (Weiss, 1987). A subband adaptive algorithm has been proposed by Liu *et al.* (2001) to address the multisource problem. Their two-microphone system estimates the locations of all the interfering sources and uses them to steer independent nulls that suppress the strongest interference in each T-F unit. The underlying signal model is, however, anechoic and the performance degrades in reverberant conditions. Similarly, the drawbacks of ICA techniques include the requirement in the standard formulation that the number of microphones be greater than or equal to the number of sources and poor performance in reverberant conditions (Hyväarinen *et al.*, 2001). Some recent sparse representations attempt to relax the former assumption (e.g., Zibulevsky *et al.*, 2001), but their application has been limited to anechoic conditions. Other multi-microphone algorithms include nonlinear processing schemes that attempt to remove incoherent components by attenuating T-F units based on the cross-correlation between corresponding microphone signals (Allen *et al.*, 1977; Lindemann, 1995).

Human listeners excel at separating target speech from multiple interferences. Inspired by this robust performance, research has been devoted to build speech separation systems that incorporate the known principles of auditory perception. According to Bregman (1990), the auditory system performs sound separation by employing various grouping cues, including pitch, onset time, spectral continuity, and location in a process known as auditory scene analysis (ASA). This ASA account has inspired a series of computational ASA (CASA) systems that have significantly advanced the state-of-the-art performance in monaural separation as well as in binaural separation. Monaural separation algorithms rely primarily on the pitch cue and therefore operate only on voiced speech. On the other hand, the binaural algorithms use the source location cues—time differences and intensity differences between the ears—which are independent of the signal content, and thus can be used to track both voiced and unvoiced speech. A recent overview of CASA approaches can be found in Brown and Wang (2005).

CASA research, however, has been largely limited to anechoic conditions, and few systems have been designed to operate on reverberant inputs. In reverberant conditions, anechoic modeling of time delayed and attenuated mixtures is inadequate. Reverberation introduces potentially an infinite number of sources due to reflections from hard surfaces. As a result, the estimation of location cues in individual T-F units becomes unreliable with an increase in reverberation and the performance of location-based segregation systems degrades under these conditions. A notable exception is the binaural system proposed by Palomäki *et al.* (2004), which includes an inhibition mechanism that emphasizes the onset portions of the signal and groups them according to a common location. The system shows improved speech recognition results across a range of reverberation times. Evaluations in reverberation have also been reported for two-microphone algorithms that combine pitch information with binaural cues or other signal-processing techniques (Luo and Denbigh, 1994; Wittkop *et al.*, 1997; Shamsoddini and Denbigh, 1999; Barros *et al.*, 2002).

From an information processing perspective, the notion of an *ideal T-F binary mask* has been proposed as the computational goal of CASA (Roman *et al.*, 2003; see also Wang, 2005). Such a mask is constructed from target and interference before mixing; specifically a value of 1 in the mask indicates that the target is stronger than the interference within a particular T-F unit and 0 indicates otherwise. This particular definition results in the optimal SNR gain among all possible binary masks because the local SNR is greater than 0 dB for all the retained T-F units and less than or equal to 0 dB for all the discarded T-F units (see Hu and Wang, 2004). Speech reconstructed from ideal binary masks has been shown to be highly intelligible, even when extracted from multisource mixtures of very low SNRs. In Roman *et al.* (2003), we tested the intelligibility of speech reconstructed from binary masks that are very close to ideal binary masks at three SNR levels of 0, −5, and −10 dB. The tests were done in two and three source configurations. The reconstructed speech improves the intelligibility scores of normal-hearing listeners in all test conditions, and the improvement becomes larger as the SNR decreases. For example, for the two-source condition with the input SNR of −10 dB, binary mask processing improves the intelligibility score from about 20% to 81%. Similar improvements were found in later studies (Chang, 2004; Brungart *et al.*, 2006). In addition, binary mask processing produces substantial improvements in robust speech recognition (Cooke *et al.*, 2001; Roman *et al.*, 2003).

As stated earlier, only one wideband source can be canceled through linear filtering in binaural processing. In this paper we pursue a binaural solution to target segregation under reverberant conditions and in the presence of multiple concurrent sound sources. We propose a two-stage model that combines target cancellation through adaptive filtering and a subsequent stage that estimates the ideal binary mask based on the amount of target cancellation. Specifically, we observe that the amount of target cancellation within individual T-F units is correlated with the relative strength of target to mixture. Consequently, we employ the output-to-input attenuation level within each T-F unit resulting from adaptive filtering to estimate the ideal binary mask. Since the system depends only on the location of the target, it works for a variety of interfering sources including moving intrusions and impulsive ones. Álvarez *et al.* (2002) proposed a related system that combines a first-order differential beamformer to cancel the target and obtain a noise estimate, and spectral subtraction to enhance the target source, but their results are not satisfactory in reverberant conditions.

Although the speech reconstructed directly from the ideal binary mask is highly intelligible, typical ASR systems are sensitive to the small distortions produced during resynthesis and hence do not perform well on the reconstructed signals. Two methods have been proposed to alleviate this problem: (1) the missing-data ASR proposed by Cooke *et al.* (2001) that utilizes only the reliable (target dominant) features in the acoustic mixture; and (2) a target reconstruction

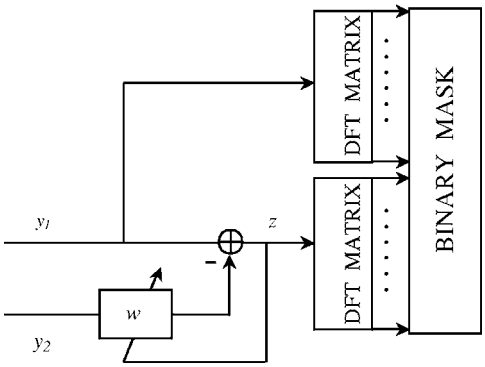

FIG. 1. Schematic diagram of the proposed model. The input signal is a mixture of reverberant target sound and acoustic interference. At the core of the system is an adaptive filter for target cancellation. A T-F decomposition is performed on the output of the adaptive filter and the input signal at microphone 1. The output of the system is an estimate of the ideal binary mask.

method for the unreliable (interference dominant) features proposed by Raj *et al.* (2004) followed by a standard ASR system. The first method requires the use of spectral features, whereas the second method, thanks to reconstruction, can operate on cepstral features. It is well known that cepstral features are more effective for ASR than spectral features. Hence, in our evaluations we use a spectrogram reconstruction technique similar to the one proposed by Raj *et al.* (2004). Our technique leads to substantial speech recognition improvements over baseline and other related two-microphone approaches.

The rest of the paper is organized as follows. In the next section we define the problem and describe the model. In Sec. III we give an extensive evaluation of our system as well as a comparison with related models. In the last section we conclude the paper.

II. MODEL ARCHITECTURE

The proposed model consists of two stages, as shown in Fig. 1. In the first stage, an adaptive filter is applied to the mixture signal, which contains both target and interference, in order to cancel the target signal. In the second stage, the system labels as 1 those T-F units that have been largely attenuated in the first stage since those units are likely to have originated from the target source. This mask is then applied to suppress all the T-F units dominated by noise. The adaptive filter needs to be trained in the absence of noise.

The input signal to our system assumes that a desired speech source s has been produced in a reverberant enclosure and recorded by two microphones to produce the signal pair (x_1, x_2). The transmission path from the target location to microphones is a linear system and is modeled as

$$x_1(t) = h_1(t) * s(t), \tag{1a}$$

$$x_2(t) = h_2(t) * s(t), \tag{1b}$$

where h_i corresponds to the room impulse response for the ith microphone. The challenge of source separation arises when an unwanted interference pair (n_1, n_2) is also present at the input of the microphones resulting in a pair of mixtures (y_1, y_2):

$$y_1(t) = x_1(t) + n_1(t), \tag{2a}$$

$$y_2(t) = x_2(t) + n_2(t). \tag{2b}$$

The interference here is a combination of multiple reverberant sources and additional background noise. In this study, the target is assumed to be fixed but no restrictions are imposed on the number, location, or content of the interfering sources. In realistic conditions, the interference can suddenly change its location and may also contain impulsive sounds. Under these conditions, it is hard to localize each individual source in the scene. The goal is therefore to remove or attenuate the noisy background and recover the reverberant target speech based only on the target source location.

Our objective here is to develop an effective mechanism to estimate an ideal binary mask, which selects the T-F units, where the local SNR exceeds a threshold of 0 dB. The relative strength of target to mixture for a T-F unit is defined as

$$R(\omega,t) = \frac{|X_1(\omega,t)|}{|X_1(\omega,t)| + |N_1(\omega,t)|}, \tag{3}$$

where $X_1(\omega,t)$ and $N_1(\omega,t)$ are the corresponding Fourier transforms of the reverberant target signal and the noise signal at frequency ω and time t corresponding to microphone 1 (primary microphone). Note that the noise signal includes all the interfering sources. As seen in Eq. (3), $R(\omega,t)$ is related to the mixture SNR in a T-F unit. A T-F unit is then set to 1 in the ideal binary mask if $R(\omega,t)$ exceeds 0.5, otherwise it is set to 0. Note that $R(\omega,t)=0.5$ corresponds to the situation where the target and the noise are equally strong.

In the classical adaptive beamforming approach with two microphones (Griffith and Jim, 1982), the filter learns to identify the differential acoustic transfer function of a particular noise source and thus perfectly cancels only one directional noise source. Systems of this type, however, are unable to cope well with multiple noise sources or diffuse background noise. As an alternative, we propose to use the adaptive filter only for target cancellation and then process the noise estimate obtained using a nonlinear scheme described below in order to obtain an estimate of the ideal binary mask (see also Roman and Wang, 2004). This two-stage approach offers a potential solution to the problem of multiple interfering sources in the background.

In the experiments reported here, we assume a fixed target location and the filter w in the target cancellation module (TCM) is trained in the absence of interference (see Fig. 1). A white noise sequence of 10 s duration is used to calibrate the filter. We implement the adaptation using the Fast-Block Least Mean Square algorithm with an impulse response of 375 ms length (6000 samples at a 16 kHz sampling rate) (Haykin, 2002). After the training phase, the filters parameters are fixed and the system is allowed to operate in the presence of interference. Both the TCM output $z(t)$ and the noisy mixture at the primary microphone $y_1(t)$ are analyzed using a short time-frequency analysis. The time-frequency resolution is 20-ms time frames with a 10-ms frame shift and

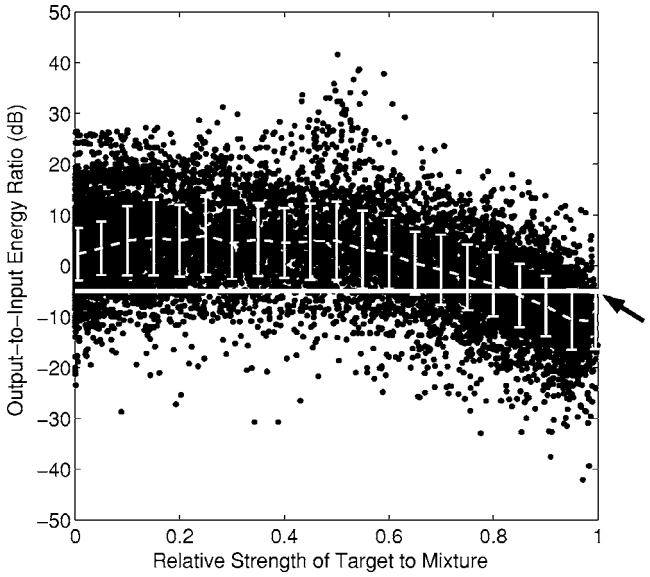

FIG. 2. Scatter plot of the output-to-input ratio with respect to the relative strength of the target to the mixture for a frequency bin centered at 1 kHz. The mean and the standard deviation are shown as the dashed line and vertical bars, respectively. The horizontal line corresponds to the −6 dB decision threshold used in the binary mask estimation.

257 discrete Fourier transform coefficients. Frames are extracted by applying a running Hamming window to the signal.

As a measure of signal suppression at the output of the TCM unit, we define the output-to-input energy ratio as follows:

$$\mathrm{OIR}(\omega,t)=\frac{|Z(\omega,t)|^2}{|Y_1(\omega,t)|^2}. \tag{4}$$

Here $Y_1(\omega,t)$ and $Z(\omega,t)$ are the corresponding Fourier transforms of $y_1(t)$ and $z(t)$, respectively, where $z(t)=y_1(t)-w*y_2(t)$, as shown in Fig. 1.

Consider a T-F unit in which the noise signal is zero. Ideally, the TCM module cancels perfectly the target source resulting in zero output and therefore $\mathrm{OIR}(\omega,t)\rightarrow 0$. On the other hand, T-F units dominated by noise are not suppressed by the TCM and thus $\mathrm{OIR}(\omega,t)\gg 0$. Hence, a simple binary decision can be implemented by imposing a decision threshold on the estimated output-to-input energy ratio. The estimated binary mask is 1 in those T-F units where $\mathrm{OIR}(\omega,t)>\theta(\omega)$, which is a frequency-dependent threshold, and 0 in all the other units. Due to the additional filtering introduced by the target cancellation stage, the noise estimate may have different characteristics compared with the noise in the primary microphone hence degrading the quality of the ideal mask estimation.

Figure 2 shows a scatter plot of R and OIR measured in dB, as well as the mean and the standard deviation, which is obtained for individual T-F units corresponding to a frequency bin at 1 kHz. Similar results are seen across all frequencies. The results are extracted from 100 mixtures of reverberant target speech fixed at 0° azimuth mixed with four interfering speakers at −135°, −45°, 45°, and 135° azimuths. The room reverberation time, T_{60}, is 0.3 s (see Sec. III for simulation details); T_{60} is the time required for the sound level to drop by 60 dB following the sound offset. The input SNR considering reverberant target as signal is 5 dB. Observe that there exists a correlation between the amount of cancellation in the individual T-F units and the relative strength of target to mixture. In order to simplify the estimation of the ideal binary mask we have used in our evaluations a frequency-independent threshold of −6 dB on the output-to-input energy ratio, i.e., $\theta(\omega)$ is set to −6 dB. The −6 dB threshold is obtained when the reverberant target signal and the noise have equal energy in Eq. (3). As seen in the figure, the binary masks estimated using this threshold remove most of the noise at the expense of some target speech energy loss.

III. EVALUATION AND COMPARISON

We have evaluated our system on binaural stimuli, simulated using the room acoustic model described in Palomäki *et al.* (2004). The reflection paths of a particular sound source are obtained using the image reverberation model for a small rectangular room (6 m × 4 m × 3 m) (Allen and Berkley, 1979). The resulting impulse response is convolved with the measured head related impulse responses (HRIR) (Gardner *et al.*, 1994) of a KEMAR dummy head (Burkhard and Sachs, 1975) in order to produce the two binaural inputs to our system. Typically, the room reverberation is influenced by the absorption properties of surface materials, which are frequency dependent, as well as by a low-pass filtering effect due to air absorption. Specific room reverberation times are obtained here by varying the absorption characteristics of room boundaries, as described in Palomäki *et al.* (2004). The position of the listener was fixed asymmetrically at (2.5 m × 2.5 m × 2 m) to avoid obtaining near identical impulse responses at the two microphones when the source is in the median plane. All sound sources are presented at different angles at a distance of 1.5 m from the listener. For all our tests, the target is fixed at 0° azimuth unless otherwise specified. To test the robustness of the system to various noise configurations, we have performed the following tests: (1) an interference of rock music at 45° (scene 1); (2) two concurrent speakers (one female and one male utterance) at azimuth angles of −45° and 45° (scene 2); and (3) four concurrent speakers (two female and two male utterances) at azimuth angles of −135°, −45°, 45°, and 135° (scene 3). The silence before and after each of the interfering utterances is deleted in scene 2 and scene 3 making them more comparable with scene 1. Note that we do not expect the performance to vary significantly with respect to test material because of the spatial filtering principle employed in our model. The signals are upsampled to the HRIR sampling frequency of 44.1 kHz and convolved with the corresponding left and right ear HRIRs to simulate the individual sources for the above three testing conditions (scene 1–scene 3). Finally, the reverberated signals at each simulated ear are summed and then downsampled to 16 kHz. In all our evaluations, the input SNR is calculated at the left ear using reverberant target speech as signal. While in scene 2 and scene 3, the SNR at the two ears is comparable; the left ear is the "better ear"—the ear with a

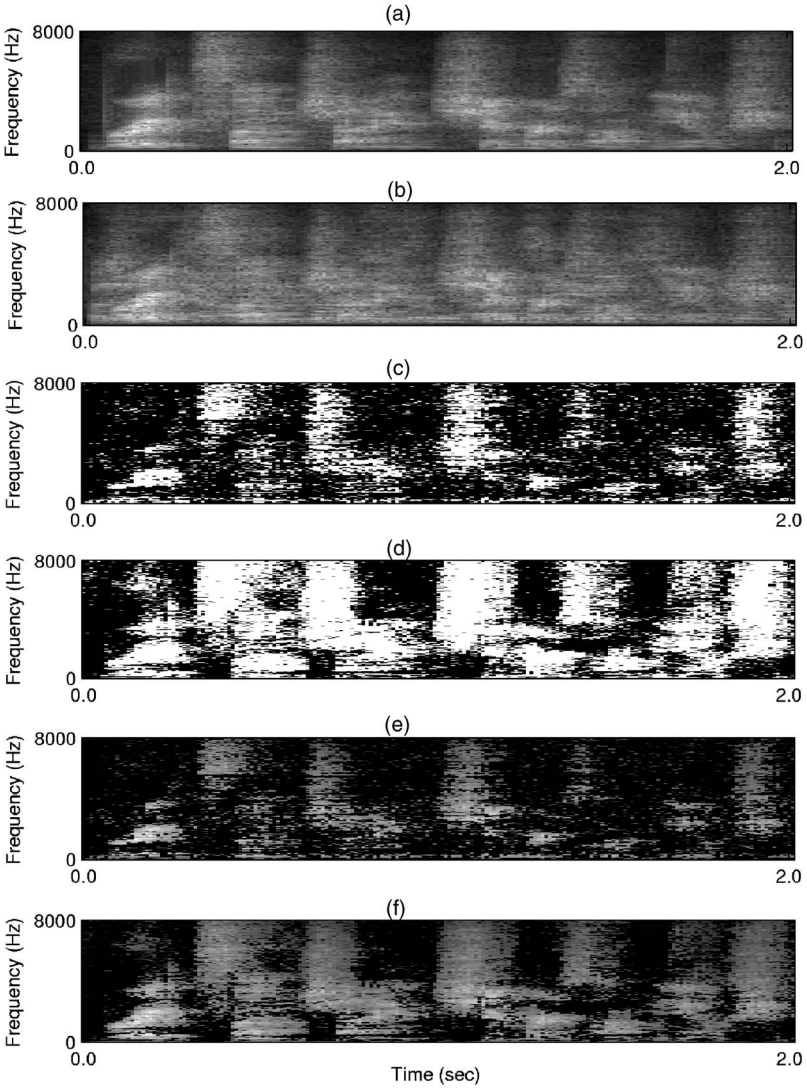

FIG. 3. A comparison between the estimated mask and the ideal binary mask for a five-source configuration. (a) Spectrogram of the reverberant target speech. (b) Spectrogram of the mixture of target speech presented at 0° and four interfering speakers at locations −135°, −45°, 45°, and 135°. The SNR is 5 dB. (c) The estimated T-F binary mask. (d) The ideal binary mask. (e) The mixture spectrogram overlaid by the estimated T-F binary mask. (f) The mixture spectrogram overlaid by the ideal binary mask. The recordings correspond to the left microphone.

higher SNR—in the scene 1 condition. In the case of multiple interferences, the interfering signals are scaled to have equal energy at the left ear.

The binaural input is processed by our system as described in Sec. II in order to estimate the ideal T-F binary mask that is defined as 1 when the reverberant target energy is greater than the interference energy and 0 otherwise. In all our results, the signal simulated at the left ear corresponds to the input signal at the primary microphone. Hence, the binary mask is computed and the signal is resynthesized at the left simulated ear. Figure 3 illustrates the output of our system for scene 3 when the target is the male utterance "Bright sunshine shimmers on the ocean." The room conditions are T_{60}=0.3 s and 5 dB input SNR. Figures 3(a) and 3(b) show the spectrograms of the reverberant target speech and the mixture, respectively. Figures 3(c) and 3(d) show the estimated binary mask and the ideal binary mask, respectively. Figures 3(e) and 3(f) show the output by applying the estimated mask and the ideal mask to the mixture in Fig. 3(b), respectively. Observe that the estimated mask is able to estimate well the ideal binary mask, especially in the high target energy T-F regions.

To systematically evaluate our segregation system, we use the following performance measures: (1) SNR evaluation using the reverberant target speech as signal; and (2) ASR accuracy using our model as a front end. Quantitative comparisons with related approaches are also provided.

A. SNR evaluation

We perform SNR evaluations for the three conditions described above using ten speech signals from the TIMIT database (Garofolo *et al.*, 1993) as target: five female utterances and five male utterances, as used in Roman *et al.* (2003). Results are given in Table I, Table II, and Table III. The room reverberation time is 0.3 s in all conditions and the system is evaluated for the following four input SNR values:

TABLE I. SNR evaluation for a one-source interference (scene 1).

Input SNR	−5 dB	0 dB	5 dB	10 dB
Output SNR (db)	6.36	11.55	15.87	19.69
RSR (%)	59	74	84	91

TABLE II. SNR evaluation for a two-speaker interference (scene 2).

Input SNR	−5 dB	0 dB	5 dB	10 dB
Output SNR (dB)	4.82	10.18	14.68	18.54
RSR (%)	58	73	83	90

−5, 0, 5, and 10 dB. In order to assess the system performance, output SNR and retained speech ratio (RSR) are computed as follows:

$$\text{Output SNR} = 10\log_{10}\left(\sum_t s_E^2(t) \Big/ \sum_t n_E^2(t)\right), \tag{5}$$

$$\text{RSR} = \sum_t s_E^2(t) \Big/ \sum_t s_T^2(t), \tag{6}$$

where $s_T(t)$ is the reverberant target signal resynthesized through an all-one mask, $s_E(t)$ is obtained by applying the estimated binary mask to the reverberant target signal, and $n_E(t)$ is obtained by applying the estimated mask to the noise signal. While the output SNR measures the level of noise that remains in the reconstructed signal, the RSR measures the percentage of target energy loss. The RSR measure is needed because the output SNR measure can be maximized by a strategy that retains very few T-F units containing little noise and hence loses much target energy. The results, averaged across the ten input signals, show SNR improvements in the range of 8–11 dB while preserving much of the target energy (~70%–90%) for input SNR levels greater than or equal to 0 dB. Observe that the system performance degrades at lower SNR values because of an increased overlap between target and interference. The RSR may be improved by imposing a higher threshold on the output-to-input attenuation level at the expense of increasing the residual noise in the output signal. For example, in the scene 3 condition at a 5 dB input SNR, a 0 dB threshold on the output-to-input energy ratio retains 92% of the target signal while improving the SNR only by 4.29 dB. These numbers should be compared with the RSR of 79% and the SNR gain of 8.68 dB reported in Table III using a −6 dB threshold.

Table IV shows the performance of our system for six reverberation times between 0.0 (anechoic) and 0.5 s (e.g., large living rooms and classrooms) that are obtained by simulating room impulse responses with different room absorption characteristics. Results are reported for scene 1 and 0 dB input SNR. For each room configuration, the filter in the TCM module is adapted using 10 s of white noise simulated at the target location, as mentioned earlier. Overall, the system performance degrades by 8 dB output SNR when T_{60} is 0.2 s compared to the anechoic case while preserving the same retained speech ratio. This is partly due to the spectral smearing of individual sources as the reverberation time increases, which results in increased overlap between target and interference. However, note that the RSR is above 70% across all conditions.

TABLE III. SNR evaluation for a four-speaker interference (scene 3).

Input SNR	−5 dB	0 dB	5 dB	10 dB
Output SNR (dB)	3.41	8.94	13.68	17.79
RSR (%)	52	66	79	89

TABLE IV. SNR evaluation at different reverberation levels for a one source interference and 0 dB input SNR.

	Output SNR (dB)	RSR (%)
T_{60}=0.0 s	18.74	70
T_{60}=0.1 s	13.14	73
T_{60}=0.2 s	10.89	74
T_{60}=0.3 s	11.55	74
T_{60}=0.4 s	11.49	75
T_{60}=0.5 s	10.99	74

We compare the performance of our algorithm with the standard delay-and-sum beamformer that is computationally simple and requires no knowledge about the interfering sources. As discussed in the Introduction, while fixed beamformers are computationally simple and require only the target direction, they require a large number of microphones to obtain a good resolution. For our two-microphone configuration, the delay-and-sum beamformer produces only an average of 1.2 dB SNR gain across all three conditions.

To compare our model with adaptive beamforming techniques, we have implemented the two-stage adaptive filtering strategy described in Van Compernolle (1990) that improves the classic Griffith-Jim model under reverberation. The first stage is identical to our target cancellation module and is used to obtain a good noise reference. The second stage uses another adaptive filter to model the difference between the noise reference and the noise portion in the primary microphone. Here, training for the second filter is done independently for each noise condition (scene 1–scene 3) in the absence of a target signal using 10 s white noise sequences presented at each location in the tested configuration. The length of the filter is the same as the one used in the TCM (375 ms). Note that this approach requires adaptation for any change in both the target source location as well as any interfering source location. As expected, the adaptive beamformer is optimal for canceling out one interfering source and hence gives a SNR gain of 13.61 dB in the scene 1 condition. However, the second adaptive filter is not able to adapt to the noise configuration when multiple interferences are active since each source has a different differential path between the microphones. The adaptive beamformer thus produces a SNR gain of 3.63 dB in the scene 2 condition and only 2.74 dB in the scene 3 condition. The advantage for both the fixed beamformer as well as the adaptive one is that target signal distortions are minimal in the output when the filters are calibrated. By comparison, our system introduces some target energy loss. However, note that in the scene 3 condition our system produces a SNR gain of 8 dB while losing less than 30% energy in the target signal for input SNR levels greater than 0 dB.

Given our computational objective of estimating the ideal binary mask, we also employ a SNR evaluation that uses the signal reconstructed from the ideal binary mask as ground truth (see Hu and Wang, 2004):

TABLE V. A comparison with adaptive beamforming in terms of SNR.

	Input SNR	−5 dB	0 dB	5 dB	10 dB
Scene 1	Adaptive beamformer	6.43	8.83	11.34	13.90
	Proposed system	3.72	6.47	8.92	11.70
Scene 2	Adaptive beamformer	−0.40	4.22	8.47	12.38
	Proposed system	2.94	5.85	8.53	11.33
Scene 3	Adaptive beamformer	−1.51	3.18	7.56	11.75
	Proposed system	2.14	4.88	7.58	10.69

$$\mathrm{SNR}_{\mathrm{IBM}} = 10 \log_{10} \frac{\sum_t s_{\mathrm{IBM}}^2(t)}{\sum_t [s_{\mathrm{IBM}}(t) - s_E(t)]^2}, \quad (7)$$

where $s_{\mathrm{IBM}}(t)$ represents the target signal reconstructed using the ideal binary mask and $s_E(t)$ is the estimated target reconstructed from the binary mask produced by our model. The denominator provides a measure of noise—the difference between the reconstructed signals using the ideal mask and the estimated mask. In a way, $\mathrm{SNR}_{\mathrm{IBM}}$ combines the two measures in Eq. (5) and Eq. (6) into a single indicator in dB. Table V provides a comparison between our proposed system and the adaptive beamformer approach described above using this SNR measure. In order to extend the evaluation to the adaptive beamformer, the waveform at the beamformer output needs to be converted into a binary mask representation. Assuming target energy and noise energy are uncorrelated in individual T-F units, we can construct a binary mask as follows. For each T-F unit, if the energy ratio between the beamformer output and the input mixture is greater than 0.5 we label the unit as 1; otherwise we label the unit as 0. The signal resynthesized by applying this mask to the output waveform is used in Eq. (7) as the estimated target. As seen in the table, our system provides some improvements over the adaptive beamformer in low input SNR scenarios with multiple interferences (scene 2 and scene 3).

A combination of target cancellation using a first-order differential beamformer and a spectral subtraction technique has been proposed previously by Álvarez *et al.* (2002). Since the first stage of our system produces a noise estimate, alternatively we can combine our adaptive filtering stage with spectral subtraction to enhance the reverberant target signal. However, as we will show in the following subsection, the computation of the binary mask improves front-end robustness compared to spectral subtraction in ASR applications.

B. ASR evaluation

We also evaluate the performance of our system as a front-end to a robust ASR system. The task domain is speaker independent recognition of connected digits. Here 13 (the numbers 1–9, a silence, very short pause between words, zero and oh) word-level hidden Markov models (HMM) are trained using the HTK toolkit (Young *et al.*, 2000). All except the short pause model have ten states. The short pause model has three states, tied to the middle state of the silence model. The output distribution in each state is modeled as a mixture of ten Gaussians. The HMM architecture is the same as the one used in Cooke *et al.* (2001). The grammar for this task allows for one or more repetitions of digits and all digits are equally probable, and hence the perplexity for this task is 11.0 (Srinivasan *et al.*, 2004). Note that perplexity here refers to the average number of possible words at any point in the sentence (Rabiner and Juang, 1993). Training is performed using the 4235 anechoic signals corresponding to the male speaker dataset from the training portion of the TIDigits database (Leonard, 1984) downsampled to 16 kHz to be consistent with our model. Testing is performed on a subset of the testing set containing 229 utterances from 3 speakers, which is similar to the test set used in Palomäki *et al.* (2004). The test speakers are different from the speakers in the training set. The test signals are convolved with the corresponding left and right ear target impulse responses and noise is added as described above to simulate the three conditions, scene 1–scene 3.

We have trained the above HMMs with clean, anechoic utterances from the training data using feature vectors consisting of the 13 mel-frequency cepstral coefficients (MFCC) together with their first and second order temporal derivatives. MFCCs are used as feature vectors, as they are most commonly used in state-of-the-art recognizers (Rabiner and Juang, 1993). Mean normalization is applied to the cepstral features in order to improve the robustness of the system under reverberant conditions (Shire, 2000). Frames are extracted using 20 ms windows with 10 ms overlap. A first-order preemphasis coefficient of 0.97 is applied to the signal. The recognition accuracy in the absence of noise using anechoic test utterances is 99%. Using the reverberated test utterances, performance degrades to 94% accuracy.

Cepstral mean normalization applied on the MFCC features provides a relatively robust front end for our task domain under the moderate reverberant conditions considered here. Hence, a reasonable approach is to remove the noise component from our acoustic mixture in the front-end processor and to feed an estimate of the reverberant target to the MFCC-based ASR. Although subjective listening tests have shown that the signal reconstructed from the ideal binary mask is highly intelligible (Roman *et al.*, 2003; Chang, 2004; Brungart *et al.*, 2006), the extraction of MFCC features from a signal reconstructed using such a mask is distorted due to the mismatch arising from the T-F units labeled 0, which smears the entire cepstrum via the cepstral transform (Cooke *et al.*, 2001). A similar problem occurs when the second stage of our model is replaced by spectral subtraction since spectral subtraction performs poorly in the T-F regions domi-

nated by interference where oversubtraction or undersubtraction occurs. One way to handle this problem is by estimating the original target spectral values in the T-F units labeled 0 using a prior speech model. This approach has been suggested by Raj *et al.* (2004) in the context of additive noise, and promising results have been reported under this condition. In this approach, a noisy spectral vector Y at a particular frame is partitioned in its reliable Y_r and its unreliable Y_u components. The reliable components are those that approximate well the clean ones X_r while the unreliable components are those dominated by interference. The task in this approach is to reconstruct the underlying true spectral vector X. A Bayesian decision is employed to estimate the unreliable components X_u given the reliable components and a speech prior. Hence, this approach works seamlessly with the T-F binary mask that our speech segregation system produces. Here, the reliable features are the T-F units labeled 1 in the mask while the unreliable features are the ones labeled 0. The prior speech model is trained on the clean training data described previously. Note that, for practical purposes, it is desirable for robust speech recognition to avoid obtaining a prior speech model for each different reverberant condition in which the system might be deployed.

The speech prior is modeled empirically as a mixture of Gaussians and trained with the same clean utterances used in ASR training:

$$p(X) = \sum_{k=1}^{M} p(k)p(X|k), \tag{8}$$

where $M=1024$ is the number of mixtures, k is the mixture index, $p(k)$ is the mixture weight, and $p(X|k) = N(X;\mu_k,\Sigma_k)$.

Previous studies (Cooke *et al.*, 2001; Raj *et al.*, 2004) have shown that a good estimate of X_u is its expected value conditioned on X_r:

$$E_{X_u|X_r,0\leq X_u\leq Y_u}(X_u) = \sum_{k=1}^{M} p(k|X_r, 0 \leq X_u \leq Y_u) \times \int_0^{Y_u} X_u p(X_u|k, 0 \leq X_u \leq Y_u) dX_u, \tag{9}$$

where $p(k|X_r)$ is the *a posteriori* probability of the kth Gaussian given the reliable data and the integral denotes the expectation $\bar{X}_{u,k}$ corresponding to the kth mixture. Note that under the additive noise condition, the unreliable parts may be constrained as $0 \leq X_u \leq Y_u$ (Cooke *et al.*, 2001); this constraint is an approximation that is, for example, not applicable when the target and the noise have antiphase relations. In our implementation, we have assumed that the prior can be modeled using a mixture of Gaussians with diagonal covariance, which can theoretically approximate any probability distribution if an adequate number of mixtures are used (McLachlan and Basford, 1988). Additionally, our empirical evaluations have shown that for the case of $M=1024$ this approximation results in an insignificant degradation in recognition performance in comparison with using the full covariance matrix, while the computational cost is greatly reduced. Hence, the expected value can now be computed as

$$\tilde{X}_u = \begin{cases} \mu_{u,k}, & 0 \leq \mu_{u,k} \leq Y_u, \\ Y_u, & \mu_{u,k} > Y_u, \\ 0, & \mu_{u,k} < 0. \end{cases} \tag{10}$$

The *a posteriori* probability of the kth mixture given the reliable data is estimated using the Bayesian rule from the simplified marginal distribution $p(X_r|k) = N(X_r;\mu_{r,k},\sigma_{r,k})$ obtained from $p(X|k)$ without utilizing any bounds on X_u. While this simplification results in a small decrease in accuracy, it results in a substantially faster computation of the marginal.

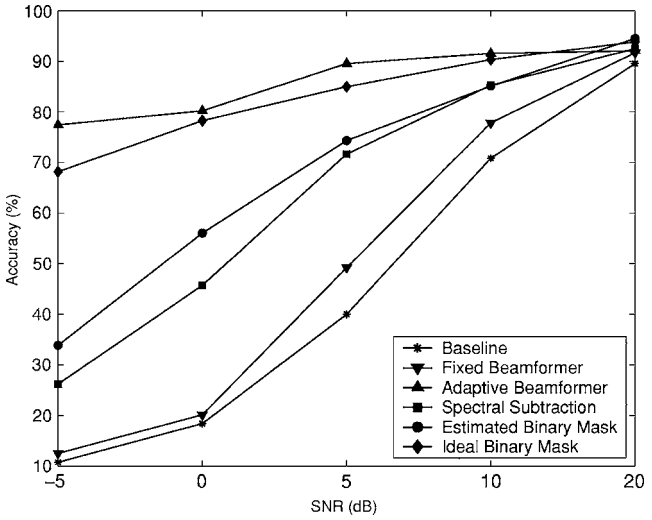

FIG. 4. Digit recognition performance in terms of word-level accuracy for scene 1 at different SNR values for the reverberant mixture (⋆), a fixed beamformer (▼), an adaptive beamformer (▲), a system that combines target cancellation and spectral subtraction (■), our front-end ASR using the estimated binary mask (●), our front-end ASR using the ideal binary mask (♦).

Results

Speech recognition results for the three conditions: scene 1 (one interference of rock music), scene 2 (two concurrent interfering speakers), and scene 3 (four concurrent interfering speakers) are reported separately in Fig. 4, Fig. 5, and Fig. 6 at five SNR levels: −5, 0, 5, 10, and 20 dB. Results are obtained using the same mean normalized MFCC features and the ASR back end described previously for the following approaches: fixed beamforming, adaptive beamforming, target cancellation through adaptive filtering followed by spectral subtraction, our proposed front-end ASR using the estimated mask, and, finally, our proposed front-end ASR using the ideal binary mask. The baseline results correspond to the unprocessed signal at the simulated left ear. Observe that our system achieves improvements over the baseline performance across all conditions. For scene 1, Fig. 4 shows that the word error rate reduction varies from 26% at −5 dB to 58% at 5 dB. For scene 2, Fig. 5 shows that the error rate reduction varies from 50% at −5 dB to 77% at 10 dB. For scene 3, Fig. 6 shows that the error rate reduction

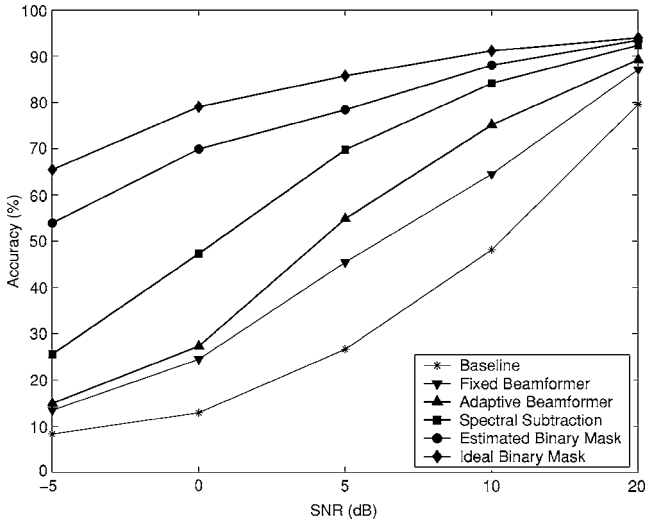

FIG. 5. Digit recognition performance in terms of word-level accuracy for scene 2 at different SNR values for the reverberant mixture (⋆), a fixed beamformer (▼), an adaptive beamformer (▲), a system that combines target cancellation and spectral subtraction (■), our front-end ASR using the estimated binary mask (●), our front-end ASR using the ideal binary mask (◆).

varies from 26% at −5 dB input SNR to 63% at 5 dB input SNR. Additionally, the excellent results reported for the ideal binary mask highlights the potential performance that can be obtained using this approach. Note that the ASR performance depends on the interference type and we obtain the best accuracy score in the two-speaker and four-speaker interference conditions. As seen also in the SNR evaluation, the adaptive beamformer outperforms all the other algorithms in the case of a single interference (scene 1). However, as the number of interferences increases, the performance of the adaptive beamformer degrades rapidly and approaches the performance of the fixed beamformer in the scene 3 condition. As described in the previous subsection, we can combine our adaptive filtering stage with spectral subtraction to cancel the interference. As illustrated by the recognition results in Fig. 5 and Fig. 6, this approach outperforms the adaptive beamformer in the case of multiple concurrent interferences. While spectral subtraction improves the SNR gain in target-dominant T-F units, it does not produce a good target signal estimate in noise-dominant regions. Note that our front-end ASR employs a better estimation of the spectrum in the unreliable T-F units and therefore results in large improvements over the spectral subtraction method.

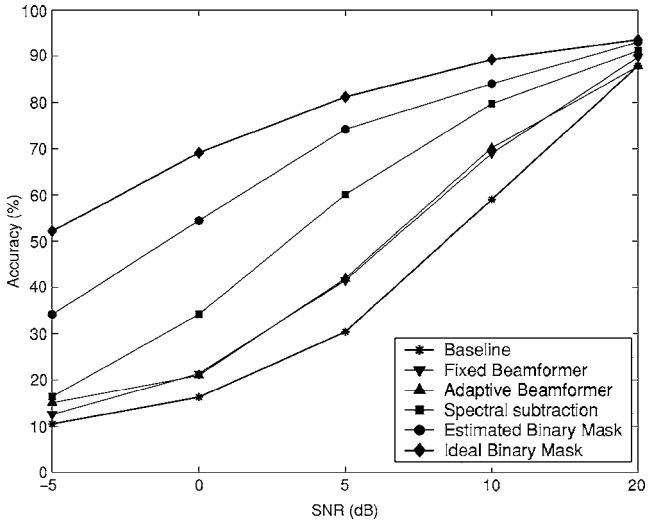

FIG. 6. Digit recognition performance in terms of word-level accuracy for scene 3 at different SNR values for the reverberant mixture (⋆), a fixed beamformer (▼), an adaptive beamformer (▲), a system that combines target cancellation and spectral subtraction (■), our front-end ASR using the estimated binary mask (●), our front-end ASR using the ideal binary mask (◆).

TABLE VI. A comparison with the Palomäki *et al.* system in terms of speech recognition accuracy (%).

Input SNR	0 dB	10 dB	20 dB
Baseline	13.04	43.01	81.85
Palomäki *et al.* system	32.7	78.8	91.9
Proposed system	47.58	81.59	91.80

We compare our system with the binaural system proposed by Palomäki *et al.* (2004), which was shown to produce substantial recognition improvements on the same digit recognition task, as used here. Their system combines binaural localization with precedence effect processing in order to detect reliable spectral regions that are not contaminated by interfering noise or echoes. Recognition is then performed in the log spectral domain by employing the missing data ASR system proposed by Cooke *et al.* (2001). This recognizer takes as input a binary mask that identifies the reliable data in the mixture spectrogram and uses this to compute the state output probabilities for each observed vector based only on its reliable parts. In order to account for the reverberant environment, spectral energy normalization is employed. While our system can handle a variety of interfering sources, the binaural system of Palomäki *et al.* was developed for only one-interference scenarios. Table VI compares the two systems for the case of one interfering source of rock music, which was used in Palomäki *et al.* The recognition results for the Palomäki *et al.* system are the ones reported by the authors while the results for our system have been produced using their configuration setup and our ASR back end described above. The listener is located in the middle of the room while target and interfering sources are located at 20° and −20°, respectively. Here T_{60} is 0.3 s and the input SNR is fixed before the binaural presentation of the signals at three SNR levels: 0, 10, and 20 dB. Note that we obtain a marked improvement over the system of Palomäki *et al.* (2004), in the low SNR conditions. By utilizing interaural time and intensity differences only during acoustic onsets, the mask obtained by their system has a limited number of reliable units. This limits the amount of information available to the missing data recognizer for the decoding (Srinivasan *et al.*, 2004). In our system, on the other hand, a novel encoding of the target source location leads to the recovery of more target dominant regions, and this results in a more robust front end for ASR.

We further compare our system with the negative beamforming approach proposed by Álvarez *et al.* (2002), which is chosen because it also performs target cancellation. The

TABLE VII. A comparison with the Álvarez *et al.* system in terms of speech recognition accuracy (%).

Input SNR	0 dB	10 dB	20 dB
Baseline	11.69	40.99	82.80
Á´lvarez *et al.* system	24.14	51.61	73.39
Proposed system	31.59	75.00	91.94

results are reported in Table VII. In order to compare with this approach, we simulate the input for a two-microphone array with a 5 cm intermicrophone distance using the image reverberation model (Allen and Berkley, 1979). We use the same room configuration, the same interfering signals, and the same spatial configuration as in the scene 3 condition described previously. The system proposed by Álvarez *et al.* uses a first-order differential beamformer to cancel the direct path of the target signal. Since target is fixed at 0°, the adaptation parameter in the differential beamformer is fixed to 0.5 across all frequencies (see Álvarez *et al.*, 2002). The output of the differential beamformer contains both the reverberant part of the target signal as well as an estimate of the additional interfering sources. An additional frequency-equalizing curve is applied on this output since the amount of attenuation performed by this beamformer varies with the frequency of the signal as well as its location. This equalizing-curve is trained using white noise at the corresponding interfering locations. The estimated noise spectrum is finally subtracted from the spectrum of one of the two microphone mixtures (the left one) and the results are fed to the same MFCC-based ASR as used with out system. Our system is trained on the new configuration to obtain the TCM adaptive filter, as described in Sec. II. The T-F mask produced by our system is then used to reconstruct the spectrogram using the prior speech model. As shown in Table VII, our system significantly outperforms the system of Álvarez *et al.* (2002) across a range of SNRs.

IV. DISCUSSION

In natural settings, reverberation alters many of the acoustical properties of a sound source reaching our ears, including smearing of the binaural cues due to the presence of multiple reflections. This is especially detrimental when multiple sound sources are present in the acoustic scene since the acoustic cues are now required to distinguish between the competing sources. Location based algorithms that rely on the anechoic assumption of time delayed and attenuated mixtures are therefore prone to failure in reverberant scenarios. An adaptive filter can be used to better characterize the target location in a reverberant room. We have presented here a novel two-microphone sound segregation system that performs well under such realistic conditions. Our approach is based on target cancellation through adaptive filtering followed by an analysis of the output-to-input attenuation level in individual T-F units. The output of the system is an estimate of an ideal binary mask which labels the T-F components of the acoustic scene dominated by the target sound.

A main novel aspect of the present study lies in the use of a binary mask (Wang, 2005). Techniques that attempt to estimate ratio masks, e.g., the Wiener filter, have been investigated previously in the context of speech enhancement. Although an ideal ratio mask will outperform an ideal binary mask (Srinivasan *et al.*, 2004), the estimation of a ratio mask is more complicated than making binary decisions for estimating a binary mask. Models that estimate ideal binary masks have been recently shown to provide sizable intelligibility as well as ASR gains in anechoic environments (Cooke *et al.*, 2001; Roman *et al.*, 2003). In this study we have further shown that binary mask estimation can result in substantial SNR as well as ASR gains in multisource reverberant situations.

Classic two-microphone noise cancellation strategies process the input using linear adaptive filters and while being optimal in the one-interference condition, they are unable to cope with multiple interferences. By using a binary T-F masking strategy in the second stage, our system is able to cancel an arbitrary number of interferences using only two microphones. As shown in our SNR evaluation, the system is able to outperform existing beamforming techniques across a range of input SNRs. Note that while our processing produces some target signal distortion, we preserve most of the target energy ($>70\%$) at input SNRs greater than 0 dB. The balance between noise cancellation and target distortion can be controlled in our system by varying the output-to-input attenuation threshold. As explained in Sec. III, a more relaxed threshold will ensure less target distortion at the expense of some background noise. Note that target distortion can also be minimized by smoothing the reconstructed signal in a post-processing stage (see, for example, Araki *et al.*, 2005). Our binary mask estimation is currently conducted on the primary microphone, and further improvement may be possible by merging the reconstructed signals at the two microphones.

Since the first stage of our system provides a noise estimate, an alternative nonlinear strategy for the second stage is spectral subtraction. A combination of target cancellation through differential beamforming and spectral subtraction has been proposed previously by Álvarez *et al.* (2002). A SNR evaluation using the reverberant target as signal shows a slight improvement using the spectral subtraction method. However, as seen in the ASR evaluation, the binary masks complement missing data techniques to provide sizable ASR improvements compared to spectral subtraction. Spectral subtraction, however, can also be used in combination with our binary mask estimation. We have observed that additional improvements (an absolute word error rate reduction of 3%–5%) could be obtained when using spectral subtraction to "clean" the reliable regions prior to spectrogram reconstruction.

In terms of application to real-world scenarios, our adaptive filtering strategy has several drawbacks. First, the adaptation of the inverse filter requires data on the order of a few seconds and thus any fast change in target location (e.g., walking) will have an adverse impact on the system. Second, the system needs to identify signal intervals that contain no interference to allow for the filter to adapt to a new target

position. On the other hand, note that our system requires training only with respect to target location and is therefore insensitive to changes in the locations of interfering sources, unlike adaptive beamforming whose training is conditioned on the positions of all sound sources in the environment.

We use the approach proposed by Raj *et al.* (2004) to reconstruct the clean target signal in the unreliable T-F units. This allows for our system to be utilized as a front end to a standard speech recognition system operating using cepstral features. In a systematic comparison, our system shows substantial performance gains over baseline and significant improvements over related approaches. Note that our prior and ASR models are trained on anechoic speech and hence our algorithm is applicable when recognition in changing reverberant environments is desired. However, if samples of reverberant target are available *a priori*, the ASR performance can be further improved through model adaptation (Rabiner and Juang, 1993). We also intend to investigate the possibility of coupling with dereverberation techniques (e.g., Allen *et al.*, 1977) for deriving robust features for recognition.

ACKNOWLEDGMENTS

This research was supported in part by an AFOSR grant (FA9550-04-1-0117), a NSF grant (IIS-0081058) and an AFRL grant via Veridian. We thank B. Raj for helpful discussions. Preliminary versions of this work are included in the Proceedings of 2004 ICASSP and 2006 ICASSP.

Allen, J. B., and Berkley, D. A. (**1979**). "Image method for efficiently simulating small-room acoustics," J. Acoust. Soc. Am. **65**, 943–950.

Allen, J. B., Berkley, D. A., and Blauert, J. (**1977**). "Multimicrophone signal processing techniques to remove room reverberation from speech signal," J. Acoust. Soc. Am. **62**, 912–915.

Álvarez, A., Gómez, P., Nieto, V., Martínez, R., and Rodellar, V. (**2002**). "Speech enhancement and source separation supported by negative beamforming filtering," *Proc. International Conference on Signal Processing*, pp. 342–345.

Araki, S., Makino, S., Sawada, H., and Mukai, R. (**2005**). "Reducing musical noise by a fine-shift overlap-add method applied to source separation using a time-frequency mask," in *Proc. ICASSP*, Vol. **III**, pp. 81–84.

Balan, R., Jourjine, A., and Rosca, J. (**1999**). "AR processes and sources can be reconstructed from degenerate mixtures," *Proc. 1st International Workshop on Independent Component Analysis and Signal Separation*, pp. 467–472.

Barros, A. K., Rutkowski, T., Itakura, F., and Ohnishi, N. (**2002**). "Estimation of speech embedded in a reverberant and noisy environment by independent component analysis and wavelets," IEEE Trans. Neural Netw. **13**, 888–893.

Brandstein, M., and Ward, D. (**2001**). *Microphone Arrays: Signal Processing Techniques and Application* (Springer-Verlag, Berlin).

Bregman, A. S. (**1990**). *Auditory Scene Analysis* (MIT Press, Cambridge, MA).

Brown, G. J., and Wang, D. L. (**2005**). "Separation of speech by computational auditory scene analysis," in *Speech Enhancement*, edited by J. Benesty, S. Makino, and J. Chen, (Springer-Verlag, New York), pp. 371–402.

Brungart, D., Chang, P., Simpson, B., and Wang, D. L. (**2006**). "Isolating the energetic component of speech-on-speech masking with ideal binary time-frequency segregation," J. Acoust. Soc. Am., in press.

Burkhard, M. D., and Sachs, R. M. (**1975**). "Anthropometric manikin for acoustic research," J. Acoust. Soc. Am. **58**, 214–222.

Chang, P. (**2004**). "Exploration of behavioral, physiological, and computational approaches to auditory scene analysis," M.S. thesis, The Ohio State University, available at http://www.cse.ohio-state.edu/pnl/theses/Chang_MSThesis04.pdf. Last accessed 10/30/2006.

Cherry, E. C. (**1953**). "Some experiments on the recognition of speech, with one and with two ears," J. Acoust. Soc. Am. **25**, 975–979.

Cooke, M. P., Green, P., Josifovski, L., and Vizinho, A. (**2001**). "Robust automatic speech recognition with missing and unreliable acoustic data," Speech Commun. **34**, 267–285.

Divenyi, P. (**2005**). *Speech Separation by Humans and Machines* (Kluwer Academic, Norwella, MA).

Ephraim, Y., and van Trees, H. L. (**1995**). "A signal subspace approach for speech enhancement," IEEE Trans. Speech Audio Process. **3**, 251–266.

Gardner, W. G., and Martin, K. D. (**1994**). "HRTF measurements of a KEMAR dummy-head microphone," MIT Media Lab Perceptual Computing Technical Report #280.

Garofolo, J., Lamel, L., Fisher, W., Fiscus, J., Pallett, D., and Dahlgren, N. (**1993**). "DARPA TIMIT acoustic-phonetic continuous speech corpus," Technical Report NISTIR 4930, National Institute of Standards and Technology, Gaithersburg, MD.

Griffiths, L. J., and Jim, C. W. (**1982**). "An alternative approach to linearly constrained adaptive beamforming," IEEE Trans. Antennas Propag. **30**, 27–34.

Haykin, S. (**2002**). *Adaptive Filter Theory*, 4th ed. (Prentice–Hall, Upper Saddle River, NJ).

Hu, G., and Wang, D. L. (**2004**). "Monaural speech segregation based on pitch tracking and amplitude modulation," IEEE Trans. Neural Netw. **15**, 1135–1150.

Hyväarinen, A., Karhunen, J., and Oja, E. (**2001**). *Independent Component Analysis* (Wiley, New York).

Kollmeier, B. (**1996**). *Psychoacoustics, Speech and Hearing Aids* (World Scientific, Singapore).

Leonard, R. G. (**1984**). "A database for speaker-independent digit recognition," *Proc. ICASSP*, pp. 111–114.

Lindemann, E. (**1995**). "Two microphone nonlinear frequency domain beamformer for hearing aid noise reduction," *Proc. IEEE Workshop on Applications of Signal Processing to Audio and Acoustics*, pp. 24–27.

Liu, C., Wheeler, B. C., O'Brien, W. D., Jr., Lansing, C. R., Bilger, R. C., Jones, D. L., and Feng, A. S. (**2001**). "A two microphone dual delay-line approach for extraction of a speech sound in the presence of multiple interferers," J. Acoust. Soc. Am. **110**, 3218–3230.

Luo, H. Y., and Denbigh, P. N. (**1994**). "A speech separation system that is robust to reverberation," *Proc. International Symposium on Speech, Image Processing, and Neural Networks*, pp. 339–342.

Ma, N., Bouchard, M., and Goubran, R. (**2004**). "Perceptual Kalman filtering for speech enhancement in colored noise," *Proc. ICASSP*, Vol. **1**, pp. 717–720.

Martin, R. (**2001**). "Noise power spectral density estimation based on optimal smoothing and minimum statistics," IEEE Trans. Speech Audio Process. **9**, 504–512.

McLachlan, G. J., and Basford, K. E. (**1988**). *Mixture Models: Inference and Applications to Clustering* (Marcel Dekker, New York).

Palomäki, K. J., Brown, G. J., and Wang, D. L. (**2004**). "A binaural processor for missing data speech recognition in the presence of noise and small-room reverberation," Speech Commun. **43**, 361–378.

Rabiner, L. R., and Juang, B. H. (**1993**). *Fundamentals of Speech Recognition*, 2nd ed. (Prentice–Hall, Englewood Cliffs, NJ).

Raj, B., Seltzer, M. L., and Stern, R. M. (**2004**). "Reconstruction of missing features for robust speech recognition," Speech Commun. **43**, 275–296.

Roman, N., and Wang, D. L. (**2004**). "Binaural sound segregation for multisource reverberant environments," *Proc. ICASSP*, **2**, 373–376.

Roman, N., Wang, D. L., and Brown, G. J. (**2003**). "Speech segregation based on sound localization," J. Acoust. Soc. Am. **114**, 2236–2252.

Shamsoddini, A., and Denbigh, P. N. (**2001**). "A sound segregation algorithm for reverberant conditions," Speech Commun. **33**, 179–196.

Shire, M. L. (**2000**). "Discriminant training of front-end and acoustic modeling stages to heterogeneous acoustic environments for multi-stream automatic speech recognition," Ph.D. dissertation, University of California, Berkeley.

Srinivasan, S., Roman, N., and Wang, D. L. (**2004**). "On binary and ratio time-frequency masks for robust speech recognition," *Proc. ICSLP*, pp. 2541–2544.

Van Compernolle, D. (**1990**). "Switching adaptive filters for enhancing noisy and reverberant speech from microphone array recordings," *Proc. ICASSP*, pp. 833–836.

Wang, D. L. (**2005**). "On ideal binary mask as the computational goal of auditory scene analysis," in *Speech Separation by Humans and Machines*, edited by P. Divenyi (Kluwer Academic, Norwell, MA), pp. 181–197.

Ward, D. B., Kennedy, R. A., and Williamson, R. C. (**2001**). "Constant directivity beamforming," in *Microphone Arrays: Signal Processing Techniques and Application*, edited by M. Brandstein and D. Ward (Springer Verlag, Berlin), pp. 3–17.

Weiss, M. (**1987**). "Use of an adaptive noise canceller as an input preprocessor for a hearing aid," J. Rehabil. Res. Dev. **24**, pp. 93–102.

Widrow, B., and Stearns, S. D. (**1985**). *Adaptive Signal Processing* (Prentice-Hall, New Jersey).

Wittkop, T., Albani, S., Hohmann, V., Peissig, J., Woods, W. S., and Kollmeier, B. (**1997**). "Speech processing for hearing aids: Noise reduction motivated by models of binaural interaction," Acust. Acta Acust. 83, 684–699.

Young, S., Kershaw, D., Odell, J., Valtchev, V., and Woodland, P. (**2000**). *The HTK Book (for HTK Version 3.0)*, Microsoft Corporation.

Zibulevsky, M., Pearlmutter, B. A., Bofill, P., and Kisilev, P. (**2001**). "Blind source separation by sparse decomposition," in *Independent Component Analysis: Principles and Practice*, edited by S. J. Roberts, and R. M. Everson (Cambridge University Press, Cambridge).

Model-based sound synthesis of the guqin

Henri Penttinen,[a] Jyri Pakarinen, and Vesa Välimäki
Laboratory of Acoustics and Audio Signal Processing, Helsinki University of Technology, Espoo, Finland

Mikael Laurson
Centre for Music and Technology, Sibelius Academy, Helsinki, Finland

Henbing Li and Marc Leman
Institute for Psychoacoustics and Electronic Music, Department of Musicology, Ghent University, Ghent, Belgium

(Received 5 May 2006; revised 14 September 2006; accepted 14 September 2006)

This paper presents a model-based sound synthesis algorithm for the Chinese plucked string instrument called the guqin. The instrument is fretless, which enables smooth pitch glides from one note to another. A version of the digital waveguide synthesis approach is used, where the string length is time-varying and its energy is scaled properly. A body model filter is placed in cascade with the string model. Flageolet tones are synthesized with the so-called ripple filter structure, which is an FIR comb filter in the delay line of a digital waveguide model. In addition, signal analysis of recorded guqin tones is presented. Friction noise produced by gliding the finger across the soundboard has a harmonic structure and is proportional to the gliding speed. For pressed tones, one end of a vibrating string is terminated either by the nail of the thumb or a fingertip. The tones terminated with a fingertip decay faster than those terminated with a thumb. Guqin tones are slightly inharmonic and they exhibit phantom partials. The synthesis model takes into account these characteristic features of the instrument and is able to reproduce them. The synthesis model will be used for rule based synthesis of guqin music. © *2006 Acoustical Society of America.*
[DOI: 10.1121/1.2360422]

PACS number(s): 43.75.Gh, 43.75.Wx [NHF] Pages: 4052–4063

I. INTRODUCTION

The purpose of this paper is to provide an insight to the acoustical characteristics of the guqin and to propose a model-based synthesis algorithm that is simple enough to run in real time.

The guqin (pronounced ku-ch' in), also called the seven-strings-qin, is the modern name for the fretless plucked string instrument qin, is the oldest Chinese string instrument still used in modern times.[1,2] The current structure of the instrument was formed approximately between the 5th and the 7th centuries, and since then there have been no major changes in the construction. Figure 1 shows the guqin in an *in situ* fashion in the small anechoic chamber at Helsinki University of Technology. This paper proposes a physically inspired sound synthesis technique to generate guqin tones and music using a computer.

The guqin is one of the most important topics in Chinese musicological studies, and due to its long history, rich documentation, and precious old musical notation, there is a good understanding of the role of the guqin in Chinese culture.[3] In contrast, the acoustics of the instrument, as well as the guqin playing techniques, are far less well understood. In addition, transforming of the large body of traditional guqin tabulature into music, i.e., modern music notation and sound, has been a difficult task. The proposed guqin sound synthesizer is the first step in the process of digitizing existing guqin music. With a suitable piece of software, a computer system can be an efficient tool for the guqin tabulature transcription making the work much easier and faster than manual labor. Additionally, a virtual musical instrument system enables composers to create new music for the guqin and extends the possibilities of composing music with new playing styles.

The proposed guqin synthesizer is based on the commuted digital waveguide synthesis technique.[4,5] The digital waveguide technique has been used successfully to synthesize a broad range of traditional and ethnic instruments.[6–8] Since the length of the string is varied in time the instrument model cannot be a purely commuted one. Hence, a body model filter is placed in cascade with the string model. This way the modulation of the body response with the time-varying fundamental frequency is partly avoided. Previously, a neural network based synthesis model for the guqin has been proposed.[9]

The model-based synthesis proposed here takes into account the important characteristics of guqin playing and acoustics, namely, flageolet tones, also called harmonics, gliding of tones, two different ways of terminating the string, and phantom partials.[10] A systematic discussion on the synthesis of flageolet tones has previously been reported.[11] Here, the ripple filter[12] is used for flageolet tone synthesis and a systematic calibration method is introduced. During gliding of tones, the friction noise produced has a harmonic structure and is proportional to the gliding speed. Previously, several computational models for friction sound simulation have been presented.[13–15] See, e.g., Ref. 16 for an overview. For

[a]Electronic mail: Henri.Penttinen@tkk.fi

 © 2006 Acoustical Society of America

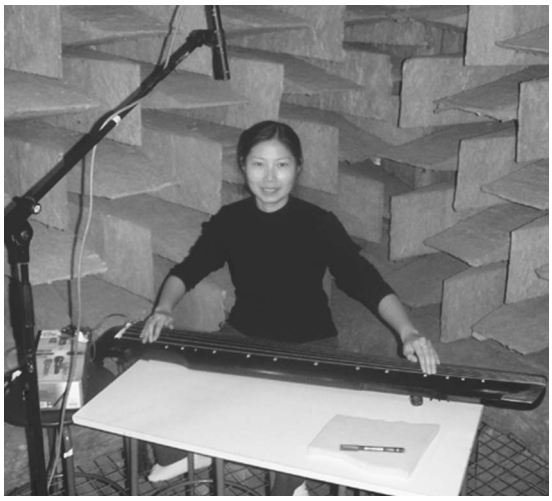

FIG. 1. Ms. Li playing the guqin in the small anechoic chamber at Helsinki University of Technology.

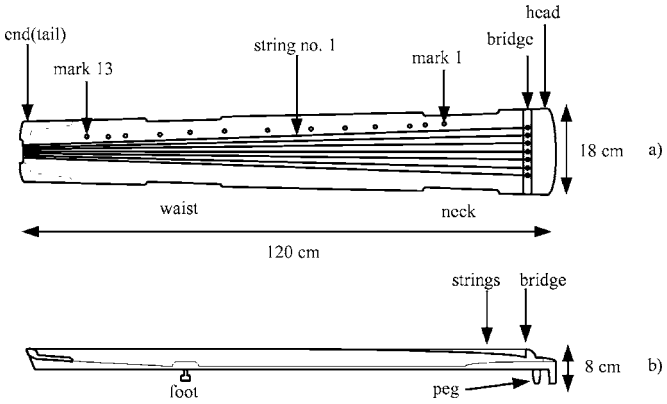

FIG. 2. Construction of the guqin from two angles: (a) top view and (b) side view.

the purposes here a kinetic friction model in the vein of Cook's model-based synthesizers[17] is introduced. Also, due to gliding of tones the string model has to be energetically compensated as described by Pakarinen *et al.*[18] The finger surface, the nail or the fingertip, that terminates the string affects the behavior of the tone and is accounted for in the synthesis model.

Additionally, based on the analysis of the guqin tones it has become evident that the string vibration exhibits phantom partials.[10] The first systematic report on the splitting behavior appeared for the piano by Nakamura and Naganuma[19] and later for the guitar by Woodhouse.[20] Bank and Sujbert explain this to be a result of transverse to longitudinal coupling which is of a nonlinear nature.[21] Many synthesis models for this phenomenon have been proposed recently.[21–23] A computationally efficient solution, that follows the one discussed by Bank and Sujbert,[22] is proposed here.

The remainder of this paper is organized as follows: The structure, tuning, and playing techniques of the instrument are discussed in Sec. II. Section III presents the results of signal analysis of recorded guqin tones to illustrate the characteristics of the timbre of the instrument. The analyzed features include the initial pitch glide of tones, the inharmonicity caused by string stiffness, effects of nail and fingertip terminations of the string, and the friction sounds produced by sliding the finger along the string during gliding tones. In Sec. IV, the waveguide synthesis algorithm, which is loosely based on the physics of the instrument, is introduced. Particular care is paid to the faithful generation of clean gliding tones and realistic friction noise, whose characteristics vary according to the speed of pitch change. Also, the playing of harmonics, which is commonly used in guqin music, can be imitated using the algorithm. Synthetic tones are compared against recordings with the help of signal analysis. Section V addresses the implementation of the synthesizer using a software system developed for physics-based sound synthesis. The software includes a music notation tool called ENP (Expressive Notation Package) that enables the writing and playing of large pieces of computer-generated guqin music. Within ENP, the musical performance parameters, such as timing, dynamics, and playing styles, can be adjusted either manually or by assigning automatic rules.

II. DESCRIPTION OF THE INSTRUMENT

Next, the construction and playing style of the guqin is briefly described.

A. Construction and tuning

The body of the guqin is a long, narrow, hollow box made from two pieces of wooden board, and the top board is carved into an arch while the bottom is flat (see Figs. 1 and 2). For the top board soft wood is usually used (such as tung), while the wood for the bottom board is hard (catalpa or fir). There are two sound holes in the bottom board, and, directly above, on the inner side of the top board there are two protrusions with the same shape as the sound holes.

The surface of the box is covered with a special layer (about 1 mm) of roughcast, which is a mixture of deer horn powder (or bone powder or tile powder) and raw lacquer, and there are several layers of raw lacquer along the top of the roughcast for polishing.

The bridge is made from hard wood, and the strings are attached to it with a twisting-rope system, which allows fine-tuning of the strings in a limited range. The other ends of the strings are bent over the end (tail) and are finally tied up to the feet on the bottom. Traditionally, the strings were made of silk, but after the 1950s they have been replaced mainly by steel-nylon strings. There are 13 marks inlayed on the roughcast at the side of the first string, which indicate the positions of the first to the fifth and the seventh overtone. These marks also function as a reference for stopped strings, i.e., when the string is pressed against the top board. Each part between two contiguous marks is divided into ten parts, for example, mark 2.5 indicates that the tone is played halfway between the second and the third mark.

The seven strings are tuned basically as a pentatonic scale. The basic tuning of the open strings is C_2, D_2, F_2, G_2, A_2, C_3, and D_3 from the lowest string (No. 1) to the highest (No. 7). The pitch range for so called stopped strings is from 65.2 Hz (open string No. 1) to 787.5 Hz (string No. 7, mark 2.6) which roughly correspond to notes C_2 and G_5, respec-

tively. The highest harmonic or flageolet sound is played on string No. 7 on marks No. 1 or No. 13 (f_0=1174.7 Hz, D_6).

The guqin used in this measurement was made by Zhang Jianhua in Beijing in 1999. The boards are made of fir, and the roughcast is deer horn powder and raw lacquer. Shangyin steel-nylon strings are used with the following diameters in mm from string No. 1 to string No. 7: (1) 1.38, (2), 1.20, (3) 1.08, (4) 1.00, (5) 0.90, (6) 0.75, (7) 0.64. The mass density for strings Nos. 5 and 7 were measured to be 1.32 g/m and 0.66 g/m, respectively.

B. Playing techniques

In modern days the guqin is usually played on a table with its two feet standing on the table and the neck laying on the right edge of the table with antislip mats between the contact points of the table and the instrument (see Fig. 1). The right hand plucks the strings between the bridge and the first mark, and the left hand presses the strings against the top plate of the body. The instrument is fretless, which enables smooth sliding tones. Guqin music also incorporates substantial use of harmonics or flageolet tones.

The little fingers of neither hand are used. The other four fingers of the right hand pluck the string from both the fleshy and the nail side. Typically, the nail exceeding the finger is 2–3 mm long for the thumb and 1–2 mm long for the other fingers. The left thumb presses the string on the right side, where the nail and flesh joins, or at the first joint. The other three left fingers press the string with the fleshy top part of the finger or occasionally with the left side of the first ring finger joint.

III. ACOUSTIC MEASUREMENTS AND SIGNAL ANALYSIS

To creat a synthesizer for the instrument, an extensive set of isolated plucks was recorded. The purpose of the isolated plucks is to be able to properly analyze the characteristics of the instrument.

A. Measurement and recording setup

Guqin tones were recorded in the small anechoic chamber of Helsinki University of Technology. The recordings were made with a microphone (AKG C 480 B, cardioid capsule) placed at a distance of about 1 m above the sound board (see Fig. 1). The signals were recorded digitally (44.1 kHz, 16 bits) with a digital mixer (Yamaha 01v) and soundcard (Digigram VX Pocket) onto the hard drive of a PC laptop. To remove infrasonic disturbances the signals were highpass filtered with a fourth-order Butterworth filter with a cutoff frequency of 52 Hz.

As for the tones, four complete sets on a typical scale used in guqin music were recorded. Two different styles for terminating the string with the left-hand finger were used, the nail of the thumb or the fingertip of other fingers. In the following text these styles of string termination will be referred to as nail or fingertip. Furthermore, two different plucking styles were recorded, namely, plucking with the middle finger towards the player or plucking with the index finger away from the player. In addition, a complete set of harmonics or flageolet tones was recorded for all strings and marks. Moreover, three dynamic levels (pp, mf, and ff) were recorded for all open strings and marks seven. Slides, isolated vibratos, scales, and musical pieces were also included in the database. Important for this study are the basic pluck events (281 samples), sliding sounds, and the harmonic sounds (91 samples) that will be analyzed next. All in all, the database contains over 400 samples.

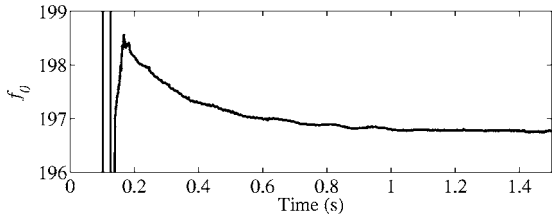

FIG. 3. Initial pitch glide of a forte fortissimo tone played on the guqin (string No. 4, mark 7).

B. Analysis of guqin tones

Next, the essential features in the behavior of guqin tones are illustrated. Their prominent patterns in the time and frequency domain, i.e., the initial pitch glide, decay of sound with different termination, and inharmonicity, are discussed. The discussion of flageolet tones is presented together with its synthesis and results in Secs. IV B and IV C.

1. Initial pitch glide

Initial pitch glide is a phenomenon due to tension modulation and occurs in vibrating strings.[24–26] Even a small transverse displacement of the string causes a second-order change in its length, and therefore in its tension. This causes the pitch to decay after releasing the string from its initial displacement. Hence, some initial pitch gliding occurs in guqin tones. The amount of pitch gliding for tones played as mezzoforte and forte fortissimo notes were measured.

For mezzoforte tones the largest initial pitch glide value obtained was 0.075 ERB (Equivalent Rectangular Bandwidth),[27] while the mean was 0.025 ERB with a standard deviation of 0.021. The number of ERBs is defined as $21.4\log_{10}(4.37F+1)$, where F is frequency in kHz.[27] Similarly, for forte fortissimo tones the mean value for the initial pitch glides was 0.034 ERB with a standard deviation of 0.019. The largest value was 0.096 ERB (for string 5, mark 7). According to Järveläinen,[28] these initial pitch glides would remain inaudible to most listeners, since the limit for the initial pitch glide audibility is about 0.1 ERB. However, the quartile limits are quite large and hence expert listeners, such as instrument players, are able to detect smaller changes than 0.1 ERB.[28]

Figure 3 shows the behavior of the fundamental frequency f_0 in time for a forte fortissimo tone played on string No. 4, mark 7 (about G_3). The x axis displays time and the y axis displays the fundamental frequency. At 0.18 s the fundamental frequency is 198.6 Hz and beyond 1 s it is 197 Hz. This gives a change of 1.6 Hz, which is 0.035 ERB. The fundamental frequency estimations have been calculated

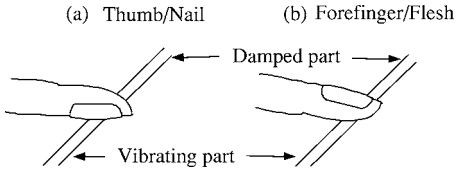

FIG. 4. Sketch of string termination with (a) the nail of the thumb and (b) the fingertip part of the forefinger.

with the autocorrelation-based YIN algorithm.[29] The glitch in Fig. 3 is due to estimation errors during the attack, i.e., when $t<0.18$ s.

The largest measured initial pitch glide can be audible for some listeners, therefore the initial pitch glides are synthesized with the obtained mean value, i.e., 0.025 ERB for *mf* tones and 0.034 ERB for *ff* tones. The initial pitch glides are synthesized by changing the pitch of the string with a break point function in the PWGLSynth system.[30] Alternatively, the synthesis could use the nonlinear approach proposed by Tolonen *et al.*[26]

2. Behavior of tones for nail and fingertip terminations

Two interesting and fundamental phenomena regarding the behavior of the harmonics and their decay were found. First, in guqin playing either the nail of the thumb or the fingertip of another finger terminates stopped strings. This causes a difference in decay times. Secondly, phantom partials were found. The analysis of these phenomena are presented next.

Figure 4 shows a sketch of where the string is terminated with (a) the nail of the thumb and (b) the fingertip of the forefinger. Figure 5(a) presents the time response of a guqin tone played on string 6 mark 5 which is terminated by the nail (f_0=392.25 Hz). The corresponding plot for a tone terminated by the fingertip is depicted in Fig. 5(b) (f_0 =392.44 Hz). Comparing the time responses shows that the string terminated by the nail [Fig. 5(a)] has a steady decay with very slight amplitude modulation. The tone terminated with the fingertip [Fig. 5(b)] exhibits a rapid decay shortly after the attack of the tone and then a steady, slower decay.

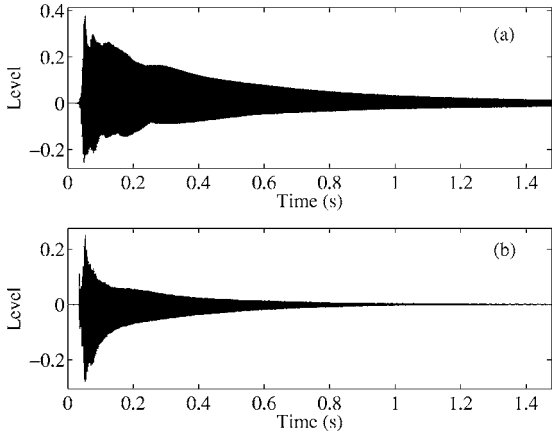

FIG. 5. Time responses of guqin tones played on string 6 mark 5, when (a) the nail of the thumb terminates the string and (b) the fingertip of the forefinger terminates the string.

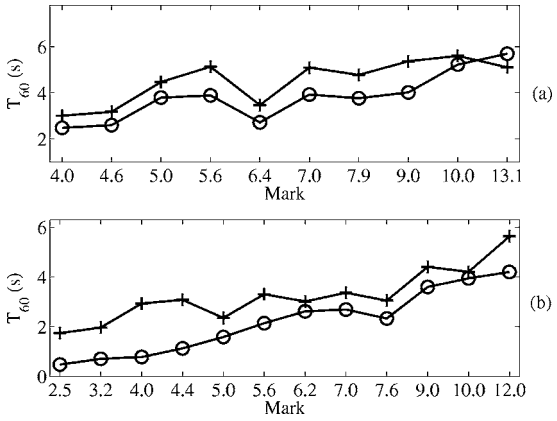

FIG. 6. T_{60} times for all nail (+) and fingertip (○) terminated tones for (a) string 1 and (b) string 7, where the x axis indicates the mark (string length).

The decay times of the tones terminated with nail and fingertip are illustrated in Fig. 6. The figure shows the T_{60} times as a function of the mark, i.e., the y axis indicates the decay times and the x axis where string was pressed from. The results for string 1 are shown in pane (a) and for string 7 in (b). The termination style is indicated as follows, nail with (+) and fingertip with (o). Figure 6 indicates clearly that the decay times of fingertip tones are smaller than those of the nail tones. The reason behind the discovered differences is, naturally, due to a difference in the way the string is terminated with the left hand. When the nail terminates the string, the losses are smaller than when the fingertip terminates the string.

Figure 7 reveals the existence of phantom partials for tones played on string 6 mark 5. Spectral peaks have been manually picked and only spectral peaks that could be reliably identified from the spectrum are shown. Therefore, in Fig. 7(b), peaks above 5 kHz are not shown. The splitting phenomena occur for both nail and fingertip termination. The mode splitting follows the inharmonicity factor B (solid line) and $B/4$ (dashed line) relation, first reported for the piano by

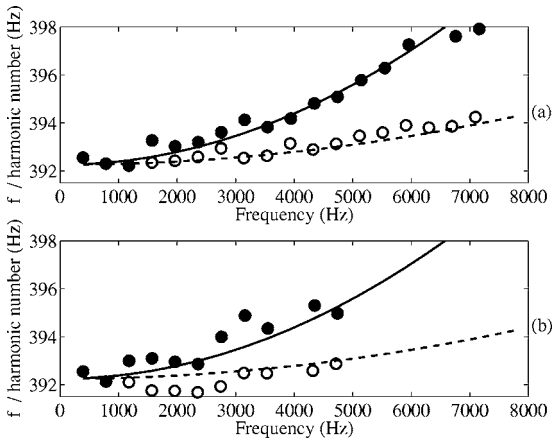

FIG. 7. Splitting of modes for string 6 mark 5, when the (a) nail of the thumb terminates the string and (b) the fingertip of the forefinger terminates the string. Black dots follow the inharmonicity value B=0.00009 (solid line) and the white dots follow the $B/4$ trend (dashed line). Fundamental frequencies obtained with the YIN algorithm for tones in panels (a) and (b) are 392.25 Hz and 392.44 Hz, respectively.

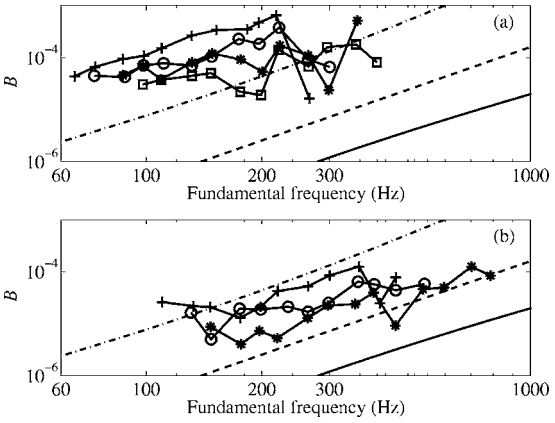

FIG. 8. Estimates of the inharmonicity coefficient B analyzed from recorded guqin tones. Panel (a) shows strings 1–4 and (b) strings 5–7. All seven strings and recorded notes have been covered, hence the overlapping. Strings are presented with the following symbols: in subplot (a) No. 1 with (+), No. 2 with (○), No. 3 with (*), and No. 4 with (□), and in subplot (b) No. 5 with (+), No. 6 with (○), No. 7 with (*). The threshold of audibility is plotted as a dashed line with its 90% confidence intervals as dashed-dotted and solid lines (Ref. 31).

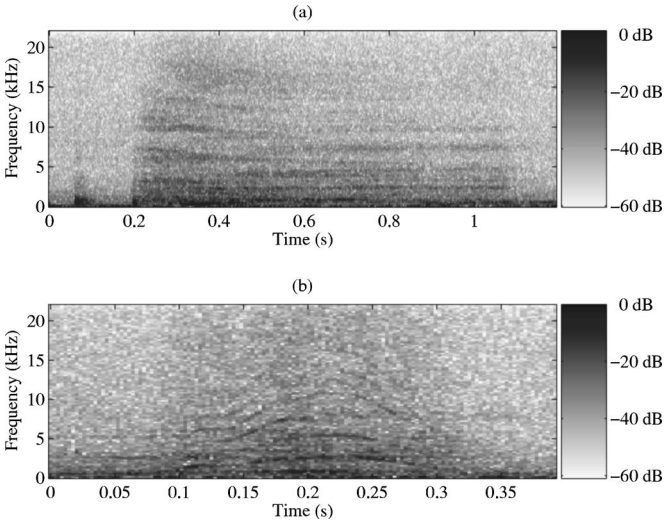

FIG. 9. (a) Spectrogram of the friction noise when sliding slowly from mark 9 to mark 7 on the 1st string (99–131 Hz). (b) Spectrogram of the friction noise when sliding quickly from mark 9 to mark 7 on the 7th string (220–297 Hz).

Nakamura and Naganuma.[19] Hence, the fingertip termination can be considered as increasing losses, but does not prevent the generation of phantom partials.

3. Inharmonicity

The inharmonicity of guqin tones was investigated for all strings and recorded marks. Inharmonicity for the guqin is depicted in Fig. 8 as a function of frequency, on a log-log scale. The threshold of audibility according to Järveläinen *et al.*[31] is also plotted as a dashed line with its 90% confidence intervals as dashed-dotted and solid lines. Results for all seven strings and stopped tones are depicted, and, therefore, overlapping of frequencies occurs.

As for the inharmonicity, two observations can be made. First, the inharmonicity for lower strings (strings 1–4) is larger than for higher strings (strings 5–7), see Figs. 8(a) and 8(b), respectively. This results from a higher Young's modulus value for steel than nylon. The lower strings are made of a combination of steel and nylon, whereas the higher strings are solely of nylon. Secondly, the inharmonicity increases as the length of the string decreases. This can be observed clearly, and especially for strings 1 and 7, as a positive slope of the data points. This is explained by the fact that the length decreases while the diameter stays fixed. This is revealed when inharmonicity is formulated as[32] $B = \pi^3 Q d^4/(64 l^2 T)$, where d is the diameter of the string, l is its length, Q is Young's modulus, and T is tension. In addition, when a string is pressed against the top board or fret board, the tension of the string slightly increases due to elongation.[33] This works against the increasing of inharmonicity as the string becomes shorter, but it does not compensate for the change in length versus the diameter.

According to the threshold of audibility the inharmonicity should be synthesized for at least strings 1–4. However, a recent study shows that the threshold for audibility can be even lower for real plucked string sounds[34] than previously suggested.[31] Additionally, the nature of inharmonicity prevails in the time domain, as the high-frequency waves travel faster than the low-frequency waves as a result of bending stiffness.[20] What is more, a beating effect has been noted to occur with low-inharmonicity conditions.[31,35] In some cases, this beating effect can be a perceptual clue for detecting inharmonicity. More specifically, the beating can be a perceptual clue in relatively long tones, whereas in short tones the beating effect is not perceived, since not enough cycles of the beating occur.[31,35] For these reasons, in high quality sound synthesis of the guqin tones the inharmonicity must be taken into account, while for an average listener it is questionable if it makes any difference. In waveguide models, inharmonicity is typically modeled with allpass filters.[36–39] In this study the inharmonicity is synthesized with a chain of four second-order allpass filters for low tones ($349 < \text{Hz}$) and with a single second-order allpass filter for high tones ($349 > \text{Hz}$).[40]

C. Analysis of friction sounds

The friction noise caused by the sliding finger-string contact was recorded using the setup described in Sec. III A. In order to record only the friction noise, the strings were not plucked. Figure 9(a) shows the spectrogram of the friction noise when the player slides her finger from mark 9 to mark 7 on the lowest string (i.e., from 99 Hz to 131 Hz). In Fig. 9(a), the player was asked to perform the slide slowly. Figure 9(b) shows the friction noise spectrogram with a slide from mark 9 to mark 7 on the highest string (i.e., from 220 Hz to 297 Hz). Here, the player was asked to perform the slide quickly. Note that both sliding styles still fall under the normal playing styles of the guqin, and that they represent the two sliding velocity extremes usually played on the instrument.

The spectrogram plot reveals that the friction signal is similar to lowpass-filtered noise, where the amplitude and cutoff frequency are proportional to the sliding velocity (the amplitude and cutoff frequency are highest in the middle of

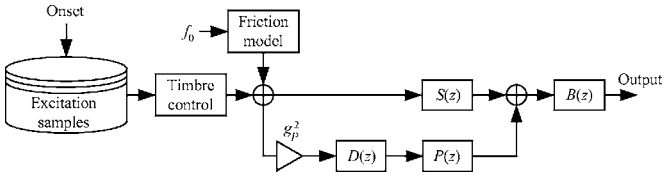

FIG. 10. Block diagram of the guqin synthesizer.

the slide, where also the sliding velocity is highest). In addition to this, there is a clearly observable harmonic structure in the noise [see Fig. 9(b)], consisting of a few modes, each approximately 200–400 Hz wide. The amplitudes and frequencies of these components also seem to be proportional to the slide velocity, the lowest harmonic having its frequency near 2.7 kHz in Fig. 9(b).

The harmonic components in the friction noise imply that the friction signal is somewhat periodic. This periodicity is due to the nylon windings around the string. It is not likely that the harmonicity in the friction is caused by the free vibrations of the string, since the frequencies of the harmonics seem to be controlled by the sliding velocity rather than the string length. Based on Fig. 9(b), we can assume that the slide duration is approximately 150 ms, and the frequency of the lowest harmonic is 2.5 kHz on average during this slide. Since we also know that the distance between the 9th and 7th marks is 183 mm, we can deduce that the width of a single nylon winding should be $183\ \text{mm}/(2.5\ \text{kHz}\times 0.15\ \text{ms}) \approx 0.5$ mm. This is in conjunction with the observations made on the instrument.

IV. SOUND SYNTHESIS OF THE GUQIN

A. General description of synthesis model and time-varying string model

The structure of the synthesis model is illustrated in Fig. 10. The guqin string model essentially constitutes two single-delay loop (SDL) (Ref. 41) digital waveguide (DWG) strings, $S(z)$ and $P(z)$, and a body model filter, $B(z)$. The length of the strings is varied during the synthesis run time.[41] The two SDL string models, $S(z)$ and $P(z)$, synthesize the transversal vibrations and phantom partials of the tone, with the inharmonicity coefficients of B and $B/4$, respectively. The input signal is read from the excitation database. Somewhat similarly as proposed by Bank and Sujbert,[22] the gain g_P for $P(z)$ is squared to model the nonlinear dependence of the amplitude of the phantom partials. Initially, $P(z)$ is a full string model, however, as theory and measurements indicate, the phantom partials do not appear at the same frequency range or frequencies as the transverse vibrations.[10,19–21] Consequently, the unwanted low and high frequencies are filtered out with a bandpass filter $D(z)$.

The string model $S(z)$ is illustrated in Fig. 11. The z^{-L1} block implements the (time varying) integer delay of the SDL. The traditional SDL blocks $H_{\text{LF}}(z)$, $F(z)$, and $A_d(z)$ (Ref. 41) and corresponds to the figure as follows. The $H_{\text{LF}}(z)$ block is the loss filter implementing the frequency dependent decay due to losses in the string and $F(z)$ is a a third-order Lagrange filter applying the fractional part of the loop delay. $A_d(z)$ is the dispersion filter made of a chain of four allpass filters or a single second-order allpass filter. The ripple filter[12] $H_R(z)$ enables efficient modelling of different decay times of partials. In the case of the guqin, the main use of the ripple filter comes in the context of flageolet tones. Coefficient g_{ca} is responsible for gain compensation due to changing length of the string, as will be discussed below. When implementing the string model on a computer, the memory for the maximum length of the string should be allocated beforehand so that the possible elongation can be accounted for. The "Friction" block in Fig. 10, more thoroughly illustrated in Fig. 12, generates the friction noise emanating from the sliding finger-string contact.

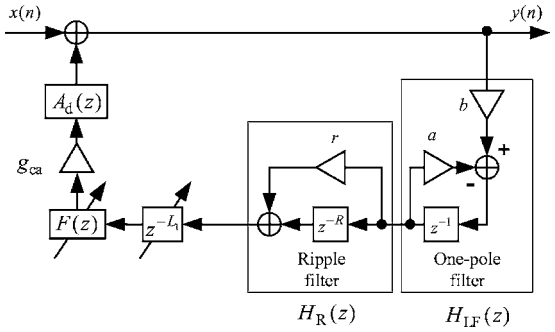

FIG. 11. Signal flow diagram of the guqin string model. The synthesis structure differs from the traditional SDL DWG model in three aspects. First, the length of the delay loop changes during run time. Secondly, the signal values are scaled by g_{ca} in order to avoid the artificial changes in energy due to the pitch change. Thirdly, the ripple filter enables to synthesize flageolet tones.

1. Energy compensation

A problem with conventional time-varying DWGs is the fact that when the pitch of a DWG (i.e., the length of the delay loop) is changed during run time, the energy of the string is artificially altered.[18] In order to fix this problem, the so-called energy compensation method[18] is used, where the samples in the delay loop are scaled to compensate for the artificial energy alteration. This method was chosen over the energy preserving allpass technique discussed by Bilbao,[42] since the energy compensation method is computationally less expensive and seemed to give satisfactory results for the modeling goals.

It must be noted that when simulating small pitch changes, e.g. in the case of a tension modulated string, the artificial attenuation or boosting is very likely to be negli-

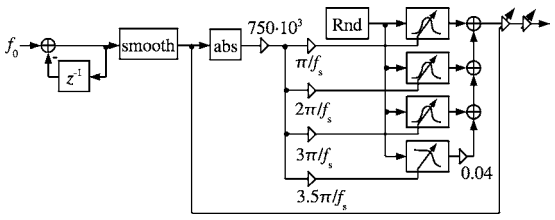

FIG. 12. Signal flow diagram of the friction sound generator. The friction sound generator consists of a noise generator (Rnd), whose output is filtered by a parallel resonator bank and lowpass-filter structure. The sliding velocity controls the central frequencies of the resonators as well as the cutoff frequency of the lowpass filter. Also, the amplitude of the friction is controlled by the slide velocity.

gible. However, when fast and large interval slides are to be simulated, as is the case with the guqin, the artificial damping or boosting can cause audible artifacts in the synthesized sound thus needing to be compensated.

The time-varying scaling coefficient g_{ca} in Fig. 11 takes care of the energy compensation when the pitch of the string is altered. It can be expressed as[18]

$$g_{ca} = \sqrt{1 - \Delta x}, \tag{1}$$

where Δx represents the change in the delay loop length, and is evaluated as

$$\Delta x(n) = x(n) - x(n-1), \tag{2}$$

where x is the delay line length and n is the discrete time index. The delay line length can be easily calculated from the desired fundamental frequency f_0 of the string as

$$x = \frac{f_s}{2f_0} - d_{LF}, \tag{3}$$

where f_s is the sampling frequency (f_s=44 100 Hz was used) and d_{LF} is the group delay imposed by the loss filter $H_{LF}(z)$ at DC.

2. The friction model

As discussed in Sec. III C, the friction noise signal resembles lowpass-filtered noise, whose amplitude and cutoff frequency are proportional to the sliding velocity. More importantly, the friction sound has a few harmonic components, whose amplitudes and frequencies are also proportional to the sliding velocity. For simulating this signal, the friction model as a random noise signal, filtered by a structure of parallel resonators and a lowpass filter, was implemented. The construction of the friction block is illustrated in Fig. 12. This system can be seen as a source-filter structure, where the sound is created in a white noise generator (Rnd block), after which it is inserted into a parallel filter structure consisting of three resonators and a lowpass filter.

The resonator transfer functions are given as

$$R_m(z) = \frac{(1-G)(1-z^{-2})}{1 - 2G\cos(\omega_m)z^{-1} + (2G-1)z^{-2}}, \quad m = 1,2,3, \tag{4}$$

where

$$G = \frac{1}{1+d}, \quad \text{and } d = \tan\left(\frac{B_w}{2}\right). \tag{5}$$

In the equations above, B_w stands for the resonator bandwidth (the distance between the −3 dB locations), normalized between $[0, 2\pi]$, while ω_m is the central frequency of resonator n, also normalized between $[0, 2\pi]$. The transfer function of the lowpass filter is given as

$$H_{LP}(z) = \left(\frac{1-c}{2}\right)\frac{1+z^{-1}}{1-cz^{-1}}, \quad \text{where } c = \frac{1-\sin(\omega_4)}{\cos(\omega_4)}. \tag{6}$$

Here, ω_4 is the cutoff frequency (the −3 dB point) of the filter, normalized to between $[0, 2\pi]$.

The purpose of each resonator is to create a distinguishable noise component in the friction signal. When the resonators' central frequencies are set to harmonic intervals, the resulting noise signal has a harmonic structure. With this in mind, the ω terms can be written as

$$\omega_m = \alpha|\Delta f_0|\frac{n\pi}{f_s}, \quad m = 1,2,3 \tag{7}$$

for the resonators and

$$\omega_4 = \alpha|\Delta f_0|\frac{3.5\pi}{f_s}, \tag{8}$$

for the lowpass filter. In the equations above,

$$\Delta f_0(n) = f_0(n) - f_0(n-1), \tag{9}$$

where $f_0(n)$ is the fundamental frequency of the waveguide at time instant n, and α is a scaling coefficient that defines how much the pitch change signal $\Delta f_0(n)$ will alter the filter frequencies. It must be noted that in practical applications $\Delta f_0(n)$ will be quite small, since the pitch change rate is usually almost negligible when compared to the sampling rate f_s. In experiments performed, it was noted that the value $\alpha = 750 \times 10^3$ worked well.

While testing the system, it was found that since the Δf_0 signal controls the filter frequencies, it should be relatively smooth and not have abrupt changes. If Δf_0 has a significant high-frequency content, the filter structure will produce clearly audible clicks, since the filter characteristics are changed rapidly. For this reason, the Δf_0 single is smoothed before controlling the filters with it. The transfer function of the smoothing operation can be given as

$$T(z) = \left(\frac{1}{M}\right)\frac{1 - z^{-(M+1)}}{1 - z^{-1}}, \tag{10}$$

where M specifies the order of the smoothing operation. In the experiments, the value $M = 1000$ was used.

Finally, as can be seen in Fig. 12, the output of the friction block is scaled by the smoothed Δf_0 signal. This implements the friction amplitude vs sliding velocity dependence phenomenon discussed in Sec. III C. The last scaling coefficient in the signal chain is used for adjusting the overall gain of the friction noise. The user can set its value to between 0 and 100.

3. Body model

The guqin synthesizer cannot purely be a commuted DWG model, since the length of the string is varied as a function of time. Therefore, a body model filter is placed in cascade with the string model. In addition, the excitation signals are filtered with the inverse of the body model filter. This way the effect of the body is roughly simulated in the time varying string.

The average of the excitation signal spectra of open strings was used to create the target body model filter. This target response was then modeled with a cascade of filters. First, the spectral envelope was modeled with a fourth-order linear prediction (LP) model.[43] In this case the low-order LP model is unable to follow the spectral envelope at low fre-

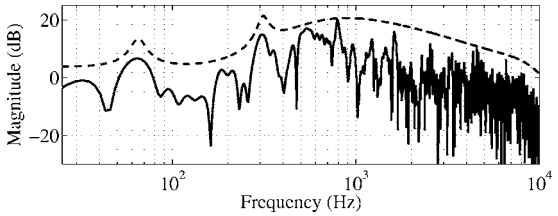

FIG. 13. Magnitude response of the body model filter (dashed line) and the target magnitude response (solid line) with a 6 dB offset.

quencies. Hence, a second-order shelving filter was used to attenuate the low frequencies. As a last step, two prominent low-frequency body modes are modeled with parametric second-order peak filters. The used shelving and peak filters are discussed by Zölzer[44] on pp. 117–125.

Figure 13 shows the magnitude responses of the body model filter and the target response. The excitation signals fed to the instrument model are processed in advance (off-line) with the inverse of the body model filter. This whitens the spectra of the excitations in the same sense as the all-pole model used in linear prediction coding whitens the excitation for the speech coding model.[43] A perfect reconstruction of the effect of the body model filter is achieved with this off-line processing, since when running the instrument model the body filter is in cascade with the string model. The cutoff frequency for the shelving filter is 200 Hz with a 20 dB attenuation. The peak filter parameters are f_c=65 Hz and 310 Hz, and Q_∞=6 and 8, respectively, with a 10 dB amplification for both filters.

This body model filter approximates the spectral envelope and two low-frequency modes of the body. It is a simple and computationally efficient model. A more detailed model would include more body modes, both at low and high frequencies. This kind of resonant structure, especially at high frequencies, could be approximated with a reverb algorithm.[12,45]

B. String model calibration

To produce normal plucked tones the string model parameters must be calibrated as described below. First, the inharmonicity is determined, and then the excitation signals are obtained by canceling the partials of the guqin tone with a sinusoidal model.[46] On the first round, the transversal vibrations are canceled and the parameters for the loss filter $H_{\mathrm{LF}}(z)$ and ripple filter $H_R(z)$ are obtained as described in Refs. 45 and 12, respectively. On the second round, the remaining phantom partials (longitudinal vibrations) similarly are filtered out.

In $H_{\mathrm{LF}}(z)$ the parameter g controls the overall decay, and a controls the frequency dependent decay.[47] The transfer function is $H_{\mathrm{LF}}(z)=b/(1+az^{-1})$, where $b=g(1+a)$. Due to calibration errors and large differences in parameter values, for consecutive tones, the g and a data are smoothed in the same vein as previously proposed.[46] More specifically, the g parameters were treated with a 10th order median filter, and the a parameters were approximated by a linear regression on the logarithmic fundamental frequency scale for each string. Additionally, the excitation signals are normalized. This way a synthesis model was obtained that has natural and subtle changes from a tone to another without drastic unwanted sonic departures. The coefficients for the dispersion filter $A_d(z)$ are obtained as described by Rauhala and Välimäki.[40] As suggested by Bank and Sujbert[21] the decay times of the phantom partials are in the magnitude of the transversal vibrations. Hence, the loss filter parameters for $P(z)$ are copied from $S(z)$. The phantom partials start to become visible in the frequency domain only after the inharmonicity has shifted the transversal partials away from the phantom ones. In addition, high-frequency phantoms seem not to be very prominent. Therefore, $P(z)$ is filtered with a bandpass filter $D(z)$, made of fourth order high-and low-pass Chebyshev type I filters. In this work, $D(z)$ is designed to attenuate partials below the 10th partial and above the 20th.

To produce flageolet tones the parameters for $H_{\mathrm{LF}}(z)$ and $H_R(z)$ are designed with the following heuristic rules. The idea is to use the open string model with properly tuned ripple filter parameters. First, the a parameter for $H_{\mathrm{LF}}(z)$ is calculated for a *flageolet tone* as described in Ref. 46. Then the target decay time T_{60} for the fundamental frequency f_0 of the flageolet tone, obtained from the analysis, is used to determine the loop gain g as

$$g = e^{-(1/f_0 T_{60})}. \tag{11}$$

The ripple rate R is obtained as

$$R = \frac{1}{n}, \tag{12}$$

where n is the harmonic index that functions as f_0 of the flageolet tone, i.e., $f_n=nf_0$. Then the ripple depth r is calculated as

$$r = e^{-(1/f_0 T'_{60})}, \tag{13}$$

where $T'_{60}=T_{60}/200$. This way the ripple filter strangles the decay times of the partials between the ringing ones to be approximately 200 times shorter than for f_0. To obtain the target decay time for the ringing partials g is compensated by $1/(r+1)$. This way the transfer function of the ripply loss filter is

$$H_{\mathrm{LF}}(z)H_R(z) = \frac{g(1+a)}{r+1}\frac{r+z^{-R}}{1+az^{-1}}. \tag{14}$$

Stability is assured when the overall loop gain does not exceed unity. Due to scaling this is assured as long as $g<1$.

There are two advantages for using the ripple filter to produce flageolet tones. First, the open string excitation signal can be used, i.e., no separate excitation signal for flageolet tones is needed. Secondly, the tone of an open string can be changed to a flageolet tone simply by changing the ripple filter coefficients and not by changing f_0 of the string model.

C. Results

Next, synthesis results produced by the model discussed in Sec. IV A are shown, and the measured and synthesized signals and their significant characteristics are compared.

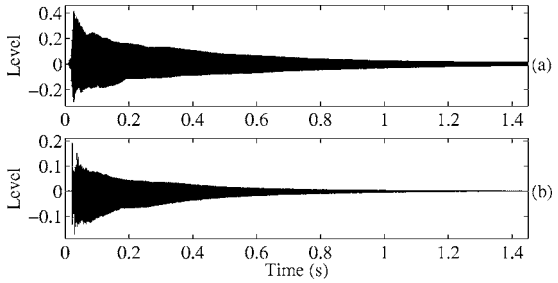

FIG. 14. Time responses of synthesized guqin tones played on string 6 mark 5, when (a) the nail of the thumb terminates the string and (b) the fingertip of the forefinger terminates the string.

1. Normal plucked tones

Figure 14 depicts the time responses of synthesized signals for string 6 mark 5, for (a) nail and (b) fingertip terminations (compare with Fig. 5). The nail tone responses correspond fairly well, as do the fingertip tones, but they have a slight difference during the beginning of the decay. This can be explained by a difference in partial decay times, i.e., the higher frequencies of the real tone decay faster than the synthesized one. This can be improved with a higher loop filter order,[48] but is left for future work. Next, the T_{60} times for recorded and synthesized sounds, shown in Figs. 6 and 15, respectively, are looked at and compared. In both figures the decay times for string 1 is shown in (a) and for string 7 in (b), and the string termination style is indicated for nail (+) and fingertip (○). For all synthesized tones the nail tones decay slower than for the fingertip terminated tones, as they should. The exception for both measured and synthesized is string 1 mark 13.1. The general trend is well preserved in the synthesis. However, synthesis results show a slight departure from the measured tones as a function of the mark, i.e., as the mark increases the difference between the synthesized and measured decay times becomes larger. This can be explained by the parameter smoothing discussed in Sec. IV B.

Figure 16 illustrates the splitting phenomenon produced with the proposed synthesis model (compare with Fig. 7). The splitting phenomenon becomes visible above the eighth partial. As expected, for the synthetic signals the locations of the modes are more systematic than for the measured cases. The inharmonicity of the synthesis follows target behavior

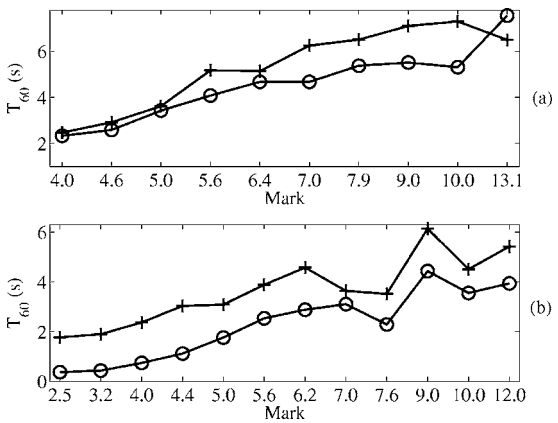

FIG. 15. T_{60} times for all nail (+) and fingertip (○) terminated synthetic tones for (a) string 1 and (b) string 7.

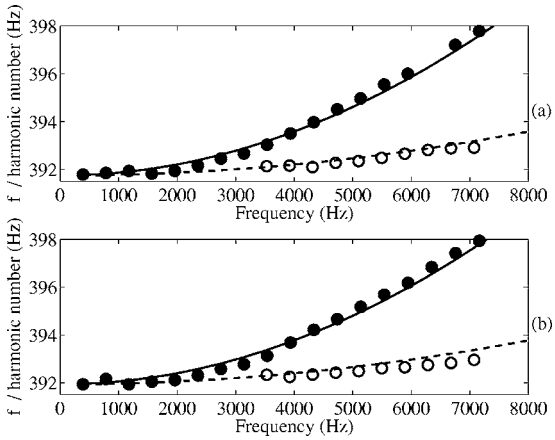

FIG. 16. Splitting of modes when synthesizing string 6 mark 5, for (a) nail and (b) fingertip termination tones. Target inharmonicity coefficient $B=0.00009$ displayed with solid line and the white dots follow the $B/4$ trend (dashed line). Measured f_0 values for tones in panels (a) and (b) are 391.74 Hz and 391.94 Hz, respectively.

(solid and dashed lines) with a 0.5% error marginal up until the 20th partial. The perception of inharmonicity is a complex matter,[34,49] and by interpreting the results obtained by Rocchesso and Scalcon[49] the accuracy achieved with the used method[40] should be adequate. The synthesis of phantom modes is further illustrated in Fig. 17 where magnitude responses of Figs. 17(a) and 17(b) measured and Figs. 17(c) and 17(d) synthesized string 6 mark 5 tones are shown. By comparing Figs. 17(b) and 17(d), one can see that the synthesis of the phantoms is successful. However, tuning of the inharmonicity filters causes some changes in the initial levels of higher harmonics. This is due to the strong variations in the spectrum of the excitation signal, which in proportion causes the changes in the levels of the harmonics. Panel (c) also shows the magnitude response of the bandpass filter $D(z)$ with a dashed line.

2. Flageolet tones

Figure 18 shows decay times regarding flageolet tone synthesis produced with the ripple filter for the fourth string and fifth harmonic. The target decay times are indicated with

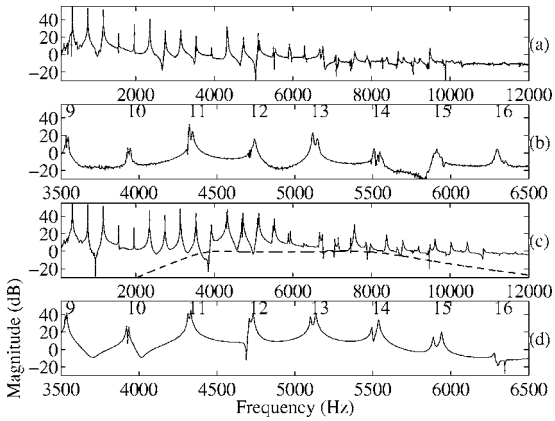

FIG. 17. Magnitude responses of (a–b) measured and (c–d) synthesized string 6 mark 5 tone. Panels (b) and (d) zoom into partials 9–16. The partial number is indicated by the number above. The response of bandpass filter $D(z)$ is also shown in pane (c) with a dashed line.

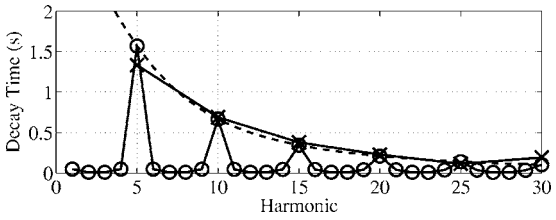

FIG. 18. Flageolet synthesis produced with the ripple filter. Target decay times are shown with (×) and synthesized with (○). The dashed line indicates the decay time response of the loop filter without the ripple filter.

× marks and the synthesized ones with circles, the solid lines interpolate between the points. The dashed line illustrates the response of the loop filter without the ripple filter. The ripple filter is able to reduce the decay times of the partials between the ringing harmonics very well. As a consequence, a flageolet like tone can be produced with an open string synthesis model in the same way as for a real flageolet tone.

3. Friction sounds

The friction sound generator block (Fig. 12) is able to model the real finger-string friction sound relatively well. The spectrogram of a synthesized friction signal is shown in Fig. 19. For the synthesis control signal, a slide similar to that performed in Fig. 9(b) was applied. When comparing Figs. 9(b) and 19, many similarities can be seen. First, the overall shape of the noise is similar, a somewhat lowpass type, and its amplitude is highest when the slide velocity attains its peak. Also, both signals have a harmonic structure, the frequency of which also peaks with the slide velocity. The major difference between Figs. 9(b) and 19 is that the synthesized friction is obviously free of the measurement background noise, which hides some of the features in Fig. 9.

V. SOFTWARE IMPLEMENTATION AND CONTROL OF THE GUQIN SYNTHESIZER

The synthesis and control part of the guqin synthesizer is realized using a visual software synthesis package called PWGLSynth.[30] The PWGLSynth is a part of a larger visual programming environment called PWGL.[30] The control information is generated using the music notation package ENP.[30] As this kind of work is experimental, and the synthesis model must be refined by interactive listening, a system is needed that is capable of making fast and efficient prototypes of the basic components of the system. The system used allows designing instrument models using a copying scheme for patches. Special synth-plug boxes are used in the graphical programming environment to automatically parameterize control entry points. Finally, a musical score is translated into a list of control events. The user can visually associate these events with the instrument definitions by using a mapping scheme. Since the approach used here is to control the synthesis model from the notation software package, a novel representation scheme of the ancient Chinese guqin Jian Zi Pu tabulature has been developed that is suitable for a modern computerized system. A coding system, developed by one of the authors (Henbing Li), based on Western latin characters is used to represent the left-hand and right-hand techniques found in the traditional guqin repertoire. The notation part can be enhanced with editable break-point functions, which allow the realization of the expressive pitch glides and vibrato gestures essential in guqin playing.

VI. CONCLUSIONS

This paper discusses the acoustics and synthesis of the guqin, a traditional Chinese music instrument. The structural features and playing style of the guqin are discussed briefly. The proposed synthesis model is able to reproduce the important characteristics of the instrument, namely flageolet tones, friction sound due to sliding of the finger, different termination behavior, and the phantom partial series. The flageolet tones are produced with a ripply waveguide string model, so that the ripple filter parameters of an open string model are tuned to the desired harmonic. The friction sound is found to be of a harmonic nature and is synthesized with a model-based structure with a noise generator and three filters. The two termination techniques of pressed tones, fingernail and fingertip, cause a difference in decay character, so that tones terminated with the fingernail decay slower than those terminated with a fingertip. Analysis shows the existence of phantom partials. These are modeled with an auxiliary string model placed in parallel with the main string model. Agreement of the output of the synthesis model with measurements is not perfect, but prime features are well captured and synthesized. Moreover, the model is computationally

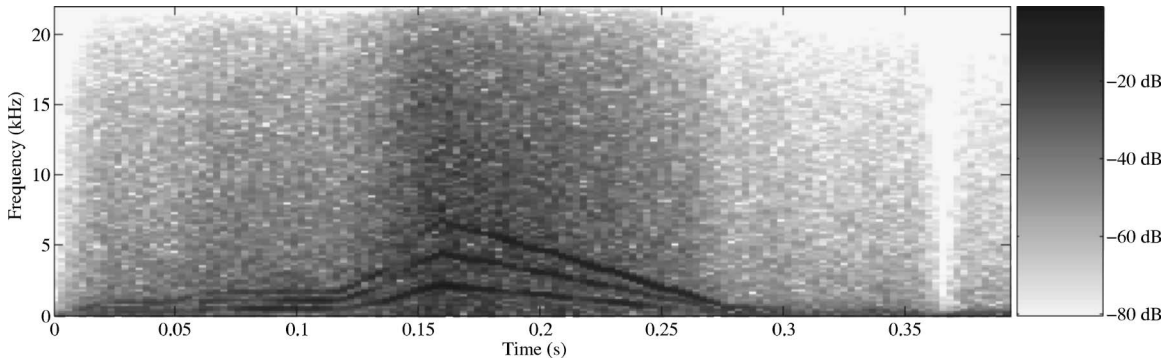

FIG. 19. Spectrogram of the synthesized friction noise when performing a similar slide as in Fig. 9(b). The figure shows that the synthesized friction sound is lowpass filtered noise with harmonic components.

efficient enough to run in real-time. Measured and synthesized guqin tones are available on the Internet at http://www.acoustics.hut.fi/publications/papers/jasa-guqin/. In addition to capturing the prominent properties of the guqin, the model-based synthesis algorithm enables the stretching of reality and the realization of gliding harmonics and sliding of open strings, something that cannot be done in the real world.

A more detailed analysis of the behavior of the phantom partials and their parameterization for the waveguide model could improve the link of the model with the physical world. In addition, future research could include exact modeling of slides and vibrato. In the future, the proposed guqin model will be used for creating rule based guqin music from tablatures, using rule-based control parameters.

ACKNOWLEDGMENTS

The authors are grateful to Jussi Pekonen, Jukka Rauhala, Hanna Järveläinen, Mika Kuuskankare, and Vesa Norilo for their help. Dr. Cumhur Erkut is thanked for his helpful comments. This work has been financially supported by COST287-ConGAS Action (Gesture Controlled Audio Systems), the Academy of Finland (Project No. 104934 and No. 105557), the Pythagoras Graduate School of Music and Sound Research, the Helsinki Graduate School of Electrical and Communications Engineering, and Tekniikan edistämissäätiö.

[1] *The New Grove Dictionary of Music and Musicians*, edited by S. Sadie (Oxford University Press, Oxford, 2001), pp. 630 and 677.
[2] R. V. Gulik, *The Lore of the Chinese Lute* (Charles E. Tuttle, Tokyo, 1969).
[3] M. Gimm, Qin, *Die Musik in Geschichte und Gegenwart*, edited by L. Fincher (Bärenreiter und Metzler, 1997), pp. 1916–1928.
[4] J. O. Smith, "Efficient synthesis of stringed musical instruments," in *Proceedings of the International Computer Music Conference (ICMC'93)* (Tokyo, Japan, 1993), pp. 64–71.
[5] M. Karjalainen, V. Välimäki, and Z. Jánozy, "Towards high-quality sound synthesis of guitar and string instruments," in *Proceedings of the International Computer Music Conference (ICMC'93)* (Tokyo, Japan, 1993), pp. 56–63.
[6] J. O. Smith, "Physical modeling synthesis update," Comput. Music J. **20**, 44–56 (1996), URL: http://www-ccrma.stanford.edu/~jos/pmupd/pmupd.html. Last viewed on 14 September 2006.
[7] C. Erkut, M. Karjalainen, P. Huang, and V. Välimäki, "Acoustical analysis and model-based sound synthesis of the kantele," J. Acoust. Soc. Am. **112**, 1681–1691 (2002).
[8] V. Välimäki, J. Pakarinen, C. Erkut, and M. Karjalainen, "Discrete-time modelling of musical instruments," Rep. Prog. Phys. **69**, 1–78 (2006).
[9] A. W. Y. Su, W. C. Chang, and R. W. Wang, "An IIR synthesis method for plucked-string instruments with embedded portamento," Journal of the Audio Engineering Society **50**, 351–362 (2002).
[10] H. A. Conklin, "Generation of partials due to nonlinear mixing in a stringed instrument," J. Acoust. Soc. Am. **105**, 536–545 (1999).
[11] J. Pakarinen, "Physical modeling of flageolet tones in string instruments," in *Proceedings of the 13th European Signal Processing Conference (EUSIPCO 2005)* (Antalya, Turkey, 2005).
[12] V. Välimäki, H. Penttinen, J. Knif, M. Laurson, and C. Erkut, "Sound synthesis of the harpsichord using a computationally efficient physical model," EURASIP J. Applied Signal Processing **2004**, 934–948 (2004).
[13] C. Canudas de Wit, H. Olsson, K. J. Åström, and P. Lischinsky, "A new model for control of systems with friction," IEEE Trans. Autom. Control **40**, 419–425 (1995).
[14] P. Dupont, V. Hayward, and B. Armstrong, "Single state elasto-plastic models for friction compensation," IEEE Trans. Autom. Control **47**, 787–792 (2002).
[15] F. Avanzini, S. Serafin, and D. Rocchesso, "Interactive simulation of rigid body interaction with friction-induced sound generation," IEEE Trans. Speech Audio Process. **13**, 1073–1081 (2005).
[16] S. Serafin, "The sound of friction: Real-time models, playability and musical applications," Ph.D. thesis, Stanford University (2004), http://www.imi.aau.dk/~sts/serafinthesis.pdf.
[17] P. Cook, "Physically informed sonic modeling (PhISM): Synthesis of percussive sounds," Comput. Music J. **21**, 38–49 (1997).
[18] J. Pakarinen, M. Karjalainen, V. Välimäki, and S. Bilbao, "Energy behavior in time-varying fractional delay filters for physical modeling of musical instruments," in *Proceedings of the IEEE International Conference on Acoustics, Speech, and Signal Processing* (Philadelphia, PA, 2005), pp. 1–4.
[19] I. Nakamura and D. Naganuma, "Characteristics of piano sound spectra," in *Proceedings of the Stockholm Musical Acoustics Conference* (Stockholm, Sweden, 1993), pp. 325–330.
[20] J. Woodhouse, "Plucked guitar transients: Comparison of measurements and synthesis," Acta. Acust. Acust. **90**, 945–965 (2004).
[21] B. Bank and L. Sujbert, "Generation of longitudinal vibrations in piano strings: From physics to sound synthesis," J. Acoust. Soc. Am. **117**, 2268–2278 (2005).
[22] B. Bank and L. Sujbert, "Modeling the longitudinal vibration of piano strings," in *Proceedings of the Stockholm Musical Acoustics Conference* (Stockholm, Sweden, 2003), pp. 143–146.
[23] J. Bensa and L. Daudet, "Efficient modeling of phantom partials in piano tones," in *Proceedings of the International Symposium in Musical Acoustics* (Nara, Japan, 2004), pp. 207–210.
[24] G. Carrier, "On the nonlinear vibration problem of the elastic string," Q. Appl. Math. **3**, 157–165 (1945).
[25] C. Valette, *The Mechanics of Vibrating Strings* (Springer, New York, 1995), pp. 116–183.
[26] T. Tolonen, V. Välimäki, and M. Karjalainen, "Modeling of tension modulation nonlinearity in plucked strings," IEEE Trans. Speech Audio Process. **8**, 300–310 (2000).
[27] B. Glasberg and B. Moore, "Deviation of auditory filter shapes from notched noise data," Hear. Res. **47**, 103–138 (1990).
[28] H. Järveläinen, "Perception of attributes in real and synthetic string instrument sounds," Ph.D. thesis, Helsinki University of Technology, Espoo, Finland (2003), http://lib.tkk.fi/Diss/2003/isbn9512263149/. Last viewed on 14 September 2006.
[29] A. Cheveigné and H. Kawahara, "YIN, a fundamental frequency estimator for speech and music," J. Acoust. Soc. Am. **111**, 1917–1930 (2002).
[30] M. Laurson, V. Norilo, and M. Kuuskankare, "PWGLSynth, a visual synthesis language for virtual instrument design and control," Comput. Music J. **29**, 29–41 (2005).
[31] H. Järveläinen, V. Välimäki, and M. Karjalainen, "Audibility of the timbral effects of inharmonicity in stringed instrument tones," Acoust. Res. Lett. Online (ARLO) **2**, 79–84 (2001).
[32] H. Fletcher, E. D. Blackham, and R. Stratton, "Quality of piano tones," J. Acoust. Soc. Am. **34**, 749–761 (1962).
[33] N. H. Fletcher and T. D. Rossing, *The Physics of Musical Instruments*, 2nd ed. (Springer-Verlag, New York, 1998), p. 620.
[34] M. Karjalainen and H. Järveläinen, "Is inharmonicity perceivable in the acoustic guitar?," in *Proceedings of Forum Acusticum 2005* (Budapest, Hungary, 2005), pp. 435–440.
[35] B. C. J. Moore, R. W. Peters, and B. R. Glasberg, "Thresholds for the detection of inharmonicity in complex tones," J. Acoust. Soc. Am. **77**, 1861–1867 (1985).
[36] D. Jaffe and J. O. Smith, "Extensions of the Karplus-Strong plucked string algorithm," Comput. Music J. **7**, 56–69 (1983), reprinted in *The Music Machine*, edited by C. Roads (MIT Press, Cambridge, 1983), pp. 481–494.
[37] S. A. Van Duyne and J. O. Smith, "A simplified approach to modeling dispersion caused by stiffness in strings and plates," in *Proceedings of the International Computer Music Conference (ICMC'94)* (Aarhus, Denmark, 1994), pp. 407–410.
[38] D. Rocchesso and F. Scalcon, "Accurate dispersion modeling for piano strings," in *Proceedings of the Nordic Acoustical Meeting* (Helsinki, Finland, 1996), pp. 407–414.
[39] B. Bank, F. Avanzini, G. Borin, G. De Poli, F. Fontana, and D. Rocchesso, "Physically informed signal-processing methods for piano sound synthesis: A research overview," EURASIP J. Applied Signal Processing **2003**, 941–952 (2003), special issue on Digital Audio for Multimedia Communications.
[40] J. Rauhala and V. Välimäki, "Tunable dispersion filter design for piano synthesis," IEEE Signal Process. Lett. **13**, 253–256 (2006).

[41]M. Karjalainen, V. Välimäki, and T. Tolonen, "Plucked-string models: From the Karplus-Strong algorithm to digital waveguides and beyond," Comput. Music J. **22**, 17–32 (1998).
[42]S. Bilbao, "Time-varying generalizations of all-pass filters," IEEE Signal Process. Lett. **12**, 376–379 (2005).
[43]J. A. Moorer, "The use of linear prediction of speech in computer music applications," Journal of the Audio Engineering Society **27**, 134–140 (1985).
[44]U. Zölzer, *Digital Audio Signal Processing* (Wiley, Chichester, 1997), p. 279.
[45]D. Rocchesso and J. O. Smith, "Circulant and elliptic feedback delay networks for artificial reverberation," IEEE Trans. Speech Audio Process. **5**, 51–63 (1997).
[46]V. Välimäki and T. Tolonen, "Development and calibration of a guitar synthesizer," J. Audio Eng. Soc. **46**, 766–778 (1998).
[47]V. Välimäki, J. Huopaniemi, M. Karjalainen, and Z. Jánozy, "Physical modeling of plucked string instruments with application to real-time sound synthesis," Journal of the Audio Engineering Society **44**, 331–353 (1996).
[48]H.-M. Lehtonen, J. Rauhala, and V. Välimäki, "Sparse multistage loss filter design for waveguide piano synthesis," in *Proceedings of the IEEE Workshop on Applications of Signal Processing to Audio and Acoustics* (New Paltz, New York, 2005), pp. 331–334.
[49]D. Rocchesso and F. Scalcon, "Bandwidth of perceived inharmonicity for physical modeling of dispersive strings," IEEE Trans. Speech Audio Process. **7**, 597–601 (1999), URL: http://profs.sci.univr.it/~rocchess/. Last viewed on 14 September 2006.

Long-time temperature rise due to absorption of focused Gaussian beams in tissue

Matthew R. Myers
Center for Devices and Radiological Health, HFZ-170, U. S. Food and Drug Administration, Rockville, Maryland 20852

(Received 26 May 2006; revised 7 September 2006; accepted 12 September 2006)

An analytical technique previously developed to study tissue displacement due to acoustic radiation force is extended to analyze temperature rise in tissue for exposure times that are comparable to, or longer than, the tissue perfusion time. A focused transducer with Gaussian amplitude shading is assumed to radiate into a perfused tissue medium with constant thermal and acoustic properties. A simple closed-form expression is derived for the steady-state temperature rise, and a transient correction term is constructed that allows for computation of the equilibrium time of the medium. Comparisons with temperature calculations for non-Gaussian transducers show that the model may be applied to more general intensity profiles. © *2006 Acoustical Society of America.*
[DOI: 10.1121/1.2359695]

PACS number(s): 43.80.Gx, 43.35.Wa [CCC] Pages: 4064–4070

I. INTRODUCTION

Prediction of the temperature rise that is induced by ultrasound absorption over times comparable to the tissue perfusion time is important for therapies such as hyperthermia-enhanced drug delivery (Cho *et al.* 2002), where thermal equilibrium is achieved. Long-term temperature rise is also useful as a conservative safety measure for shorter-duration procedures such as ultrasound ablation or radiation-force imaging, especially when multiple exposures are used or the procedure occurs in a highly perfused medium where the equilibrium time is short. Mathematical models can be employed to predict the long-term temperature rise as a function of important tissue properties such as absorption and perfusion rate, and ultrasound-beam characteristics such as focusing gain.

Nyborg (1988) derived a general solution to the bio-heat transfer equation in terms of a superposition of point heat sources. As an example, he computed the temperature rise due to absorption of an ultrasound beam modeled as a circular cylinder. Bacon and Shaw (1993) used a superposition technique to derive a simple expression for the transient temperature rise due to an absorbed ultrasound beam, also modeled as a circular cylinder. Ellis and O'Brien (1996) used superposition to solve both the lossy Helmholtz equation and the bioheat equation. Their technique was applicable to both cylindrical and rectangular apertures. Wu and Du (1990) considered focused beams with Gaussian amplitude shading and solved for the steady-state temperature rise, in terms of a single convolution integral over the source distribution. Walker (1999) computed the transient temperature rise due to an absorbed beam by modeling the volumetric source as a superposition of heated disks.

More recently, fully numerical techniques have been developed to calculate the thermal effects due to ultrasound absorption. Lizzi *et al.* (2003) used a finite-difference solution to the bioheat transfer equation in cylindrical coordinates to compute the transient temperature during the lesion monitoring associated with a HIFU procedure. Palmeri *et al.* (2004) used the finite-element method to study transient heating during radiation force imaging. A number of numerical investigations into thermal effects of nonlinear propagation have been made [e.g., Curra *et al.* (2000)], though this paper concerns acoustic intensities that are sufficiently low to be adequately described by linear-acoustics theory.

In the present study, an analytic technique previously developed to compute tissue deformation arising from absorption of focused Gaussian ultrasound beams (Myers, 2006) is extended to treat the temperature field. A superposition solution to the bioheat transfer equation in a homogeneous tissue medium is constructed, accounting for perfusion. The convolution integrals are asymptotically evaluated assuming the focal length is long compared to the transducer radius, though computations show that the focal length and transducer radius can be comparable. The analytic expression for the steady-state temperature rise manifests in a simple manner the dependence of the thermal field upon relevant parameters such as the transducer dimension or the perfusion length. A time-varying correction to the equilibrium temperature is also derived, so that the time required to reach steady conditions can be determined.

In the following section, the necessary extensions to the formulation presented in Myers (2006) are presented. Section III contains comparisons with previous studies, for both Gaussian and non-Gaussian beams, as well as with calculations based upon numerical quadrature of the convolution integrals. In Sec. IV the features and limitations of the analytic expressions are examined.

II. METHOD

We first consider the transient temperature induced by a volumetric heat source q in a perfused tissue medium of conductivity K, volume specific heat c_v, and perfusion length L. The medium is assumed infinite and uniform. Nyborg

 © 2006 Acoustical Society of America

(1988) and Nyborg and Wu (1994) have shown that the temperature rise can be computed using the following Green's function solution to the bioheat equation:

$$T(r,z,t) = \int\int F_g(r,z,r',z')q(r',z')r'\,dr'\,dz', \tag{1}$$

where

$$F_g = \frac{1}{4KR}\left\{\exp(-R/L)\left[2-\operatorname{erfc}\left(\sqrt{\frac{t}{\tau}}-\frac{R}{\sqrt{4\kappa t}}\right)\right] + \exp(R/L)\operatorname{erfc}\left(\sqrt{\frac{t}{\tau}}+\frac{R}{\sqrt{4\kappa t}}\right)\right\}, \tag{2}$$

t is time, and $R^2=(r-r')^2+(z-z')^2$, r and z being cylindrical coordinates. It is assumed that the source possesses cylindrical symmetry about the z-axis. Also, κ is the thermal diffusivity, and $\tau=L^2/\kappa$ the perfusion time.

We consider next the case where the heat source is an absorbed ultrasound beam. Within the plane-wave approximation for the beam (Nyborg, 1988)

$$q = 2\alpha I, \tag{3}$$

where I is the local intensity and α is the amplitude absorption coefficient. We suppose that the ultrasound beam is focused and propagating in the $+z$ direction, and that it possesses Gaussian amplitude shading. We also assume that the intensity is low enough that the propagation is governed by the equations of linear acoustics. The intensity profile for the beam is then given by (Wu and Du, 1990)

$$I = I_0 B^{-1} A_1(z)\exp(-2A_1(z)(r/a)^2)\exp(-2\alpha z), \tag{4}$$

where

$$A_1(z) = \frac{B}{\dfrac{B^2 z^2}{r_0^2}+\left(1-\dfrac{z}{z_f}\right)^2}. \tag{5}$$

Here B is the Gaussian coefficient at the transducer, z_f is the geometric focal length of the transducer, and $r_0=\frac{1}{2}ka^2$, k being the acoustic wavenumber and a the transducer radius.

Upon using (3)–(5) in (1), we obtain the following expression for the transient temperature at a point located along the transducer axis:

$$T(r=0,z) = \frac{2\alpha I_0}{B}\int_0^\infty dr'\,r'\int_0^\infty dz'\,A_1(z')e^{-2A_1(z')(r'/a)^2}e^{-2\alpha z'}F_g, \tag{6}$$

where F_g is given by (2) and

$$R = (r'^2+(z-z')^2)^{1/2}. \tag{7}$$

We concentrate now on the steady-state temperature T_0, and consider first the temperature at the focus $z=z_f$. After using

$$F_g \to \frac{\exp(-R/L)}{2KR}, \tag{8}$$

under steady conditions, and making the transformations

$$\rho = \frac{(2A_1)^{1/2}r'}{a}, \quad \zeta = \frac{z'-z_f}{z_f}, \tag{9}$$

we obtain

$$T_0(r=0,z=z_f) = \frac{\alpha I_0 a^2}{2KB}e^{-2\bar{\alpha}}\int_0^\infty d\rho\rho e^{-\rho^2}\int_{-1}^\infty \frac{d\zeta e^{-2\bar{\alpha}\zeta}e^{-(z_f/L)\bar{R}}}{\bar{R}}, \tag{10a}$$

where

$$\bar{R} = [\delta^2\rho^2(\epsilon^2(\zeta+1)^2+\zeta^2)+\zeta^2]^{1/2}, \tag{10b}$$

and

$$\delta = \frac{a}{(2B)^{1/2}z_f} \quad \bar{\alpha} = \alpha z_f \quad \epsilon = \frac{Bz_f}{r_0} = \frac{2Bz_f}{ka^2}. \tag{11}$$

The parameter ϵ is the reciprocal of the transducer gain. The parameter δ, proportional to the reciprocal of the transducer f-number, measures the transducer radius relative to the transducer focal length. We assume $\delta \ll 1$. For δ sufficiently small (the restrictions on δ are discussed further in Sec. IV), $\bar{R}$ appearing in the exponent of (10a) may be approximated by $|\zeta|$, and the steady-state temperature at the focus becomes

$$T_0(r=0,z=z_f) = \frac{\alpha I_0 a^2}{2KB}e^{-2\bar{\alpha}}\int_0^\infty d\rho\rho e^{-\rho^2}\int_{-1}^\infty \frac{d\zeta e^{-2(\alpha\pm 1/2L)z_f\zeta}}{\bar{R}}, \tag{12}$$

where the plus sign applies for $\zeta>0$ and the minus for $\zeta<0$. To make further use of the approximation $\delta \gg 1$, we employ the method of matched asymptotic expansions (Myers, 2006). The integral in (12) is in fact identical to one of the integrals appearing in the displacement calculation of Myers (2006), when the absorption α of the displacement integral is replaced by the "effective" absorption $\alpha\pm 1/2L$. That is, perfusion effectively increases the absorption by an amount $1/2L$ beyond the focal zone, and reduces it by the same amount ahead of the focal zone. Upon repeating steps (13)–(20) of Myers (2006) and using the definitions of δ and ϵ from (11), we obtain

$$T_0(r=0,z=z_f) \approx \frac{\alpha I_0 a^2 e^{-2\alpha z_f}}{2BK}\left\{\log\left(\frac{ka}{\sqrt{B}}\right)-\frac{\log(\alpha_1 z_f)}{2} + \frac{\alpha_2 z_f}{2}+\frac{e^{2\alpha_2 z_f}-1}{4}\right\}. \tag{13}$$

Here

$$\alpha_1 = \alpha + 1/2L, \quad \alpha_2 = \alpha - 1/2L. \tag{14}$$

Equation (13) represents the steady-state temperature at the focus ($z=z_f$). To determine the axial temperature at points on the z axis different from the focus, we return to Eq. (9). We use the coordinate z in the ζ transformation instead of z_f. As shown in Myers (2006), if we define a modified reciprocal

gain based upon the local axial coordinate z via

$$\epsilon' = (\epsilon^2 + (z_f/z - 1)^2)^{1/2}, \tag{15}$$

we may repeat the analysis used to derive (13) using ϵ' in place of ϵ. The resulting expression for the steady-state axial temperature at location z is

$$T_0(r=0,z) \approx \frac{\alpha I_0 a^2 e^{-2\alpha z}}{2BK}\left\{\log\left(\frac{ka\gamma}{\sqrt{B}}\right) - \frac{\log(\alpha_1 z)}{2} + \frac{\alpha_2 z}{2} + \frac{e^{2\alpha_2 z}-1}{4}\right\} \tag{16}$$

where

$$\gamma(z) = \left[1 + \frac{k^2 a^4 (z_f - z)^2}{4B^2 z^2 z_f^2}\right]^{-1/2}. \tag{17}$$

In terms of the gain G, (17) can be expressed as

$$\gamma(z) = \left[1 + G^2\left(1 - \frac{z_f}{z}\right)^2\right]^{-1/2}. \tag{18}$$

Please note that the corresponding expressions defining γ in Myers (2006) contain an error (a factor of z_f^2/z^2). Equations (28) and (29) of Myers (2006) should be replaced with (17) and (18) above.

Equation (16) may be recast in a form that is potentially useful for transducers without Gaussian shading, by introducing the total acoustic power

$$W_0 = \frac{\pi a^2 I_0}{2B}, \tag{19a}$$

and the effective transducer radius

$$a_{\text{eff}} = a/\sqrt{B}. \tag{19b}$$

The steady-state temperature rise may be written

$$T_0(r=0,z) \approx \frac{\alpha W_0 e^{-2\alpha z}}{\pi K}\left\{\log(ka_{\text{eff}}\gamma) - \frac{\log(\alpha_1 z)}{2} + \frac{\alpha_2 z}{2} + \frac{e^{2\alpha_2 z}-1}{4}\right\}. \tag{20}$$

Equation (20) may be applied to any transducer having total power W_0 and radius a_{eff}, with a_{eff} equal to the physical radius in the case of uniform intensity. The accuracy of this approach will be examined in Sec. III.

The behavior of the temperature field for long times may be obtained by analyzing (2) [with R in (2) given by (7)] for large t. We assume that the time is large enough that the following three related conditions apply

$$t \gg \tau, \tag{21a}$$

$$t/\tau \gg R^2/(4\kappa t), \tag{21b}$$

$$r^2/(4\kappa t) \ll 1. \tag{21c}$$

The first condition states that the time of interest is large compared with the perfusion time. The second, which can be rewritten $t \gg \sqrt{\tau(R^2/4\kappa)}$, implies that the time must be large compared with the geometric mean of the perfusion time and the time for diffusion across the distance R (often the focal-zone axial dimension) characterizing the region of interest. In the third condition, r is the radial dimension of the region of interest (often the focal-zone width); we assume heat has diffused a distance large compared to this dimension. It is not assumed that heat has diffused further than the axial dimension of the region of interest.

Conditions (21a) and (21b) ensure that the arguments of the complementary error functions in (2) are large. By employing the asymptotic expansion of the complementary error function

$$\text{erfc}(b) \sim \frac{e^{-b^2}}{\sqrt{\pi} b}(1 - 1/2b^2 + \cdots) \quad (b \gg 1),$$

we obtain a series for which the first term is (8), which leads to the steady-state solution (16). The second term is

$$\frac{-e^{-t/\tau}e^{-R^2/4\kappa t}}{4K\sqrt{\pi\kappa t}\left(\frac{t}{\tau} - \frac{R^2}{4\kappa t}\right)}. \tag{22}$$

Inserting (22) into (6) yields the first-order correction to (16) for long exposure times

$$T_1(r=0,z,t) = \frac{-e^{-t/\tau}}{2K\sqrt{\pi\kappa t}}\frac{\alpha I_0}{B}\int_0^\infty r'dr' \int_0^\infty dz' A_1(z') \times \frac{e^{-2A_1(z')(r'/a)^2}e^{-2\alpha z'}e^{-R^2/4\kappa t}}{\frac{t}{\tau} - \frac{R^2}{4\kappa t}}. \tag{23}$$

We next apply (21c) and (7) to the exponent in the integrand of (23), and use (21b) in the denominator, yielding

$$T_1(r=0,z,t) = \frac{-e^{-t/\tau}}{2K\sqrt{\pi\kappa t}}\frac{\alpha I_0}{B(t/\tau)}\int_0^\infty r'dr' \int_0^\infty dz' A_1(z') \times e^{-2A_1(z')(r'/a)^2}e^{-2\alpha z'}e^{-\frac{(z-z')^2}{4\kappa t}}. \tag{24}$$

After performing the integrals over r' and z', we obtain

$$T_1(r=0,z,t) = \frac{-\alpha I_0 a^2}{8KB}\frac{e^{-t/\tau}}{t/\tau}e^{-2\alpha z'}e^{4\alpha^2\kappa t}\,\text{erfc}(\sqrt{4\alpha^2\kappa t} - z/\sqrt{4\kappa t}). \tag{25}$$

The temperature along the beam axis for long exposure times is given by

$$T(r=0,z,t) = T_0 + T_1, \tag{26}$$

where T_0 is provided in (16) and T_1 in (25).

A measure of the time required to reach thermal equilibrium for a given ultrasound procedure may be determined by using (26) to compute t_{95}, the time at which the temperature reaches 95% of its steady-state value. Evaluating (26) at $t = t_{95}$ and setting the result equal to 0.95 times the equilibrium temperature (16), and canceling common factors, yields

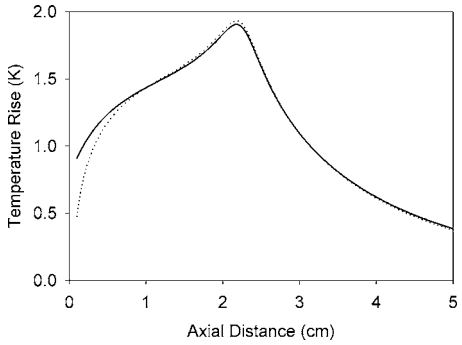

FIG. 1. On-axis steady-state temperature rise as a function of axial distance. Maximum intensity $I_0=0.2$ W/cm^2, transducer radius=0.6 cm, focal length=2.26 cm, frequency=3 MHz. Perfusion length $L=2.0$ cm, absorption $\alpha=0.15$ Np/cm. Solid line—numerical integration of convolution integral. Dotted line—asymptotic model.

$$\frac{e^{-t_{95}/\tau}}{t_{95}/\tau} e^{4\alpha^2\kappa t_{95}} \operatorname{erfc}\left(\sqrt{4\alpha^2\kappa t_{95}} - \frac{z}{\sqrt{4\kappa t_{95}}}\right) = 0.2\left\{\log\left(\frac{ka\gamma}{\sqrt{B}}\right) - \frac{\log(\alpha_1 z)}{2} + \frac{\alpha_2 z}{2} + \frac{e^{2\alpha_2 z}-1}{4}\right\}. \tag{27}$$

The time to reach equilibrium at a location z can be estimated by solving this nonlinear algebraic equation. For highly perfused media, t_{95} is small enough that $4\alpha^2\kappa t_{95} \ll 1$ and $z \gg \sqrt{4\kappa t_{95}}$ for many cases of interest. Under these conditions, the terms on the left side of (27) proportional to α^2 may be neglected, and the erfc function of large negative argument may be set to the asymptotic value of 2. The equilibrium time then satisfies the simpler equation

$$\frac{e^{-t_{95}/\tau}}{t_{95}/\tau} = 0.1\left\{\log\left(\frac{ka\gamma}{\sqrt{B}}\right) - \frac{\log(\alpha_1 z)}{2} + \frac{\alpha_2 z}{2} + \frac{e^{2\alpha_2 z}-1}{4}\right\}. \tag{28}$$

III. RESULTS

The accuracy of the analytical expressions (16) and (25) was examined by comparing with numerical quadrature of the superposition solution (1), and through comparisons with other studies. The double integrals in (1) were computed using a numerical implementation of Simpson's rule on an IBM RS6000/44P workstation. The upper limits of integration on r' and z' [infinite in (1) or (6)] were increased until doubling the values resulted in less than a 0.1% change in the integral. Final values of the upper limits depended upon the exposure time t and perfusion time τ.

In a first set of calculations, the transducer radius (0.6 cm), acoustic frequency (3 MHz), and focal length (2.26 cm), were adopted from the investigation of Wu and Du (1990). The Gaussian parameter B was 1 and the peak intensity I_0 was 0.2 Watts/cm^2. The thermal diffusivity was taken to be 0.15 mm^2/s. Various values of the absorption and perfusion length were considered.

Figure 1 shows the steady-state temperature rise as a function of axial position computed using (16) (dotted line) and numerical quadrature (solid line), for an absorption of $\alpha=0.15$ Np/cm and a perfusion length of $L=2$ cm. The perfusion length corresponds to a moderate amount of perfusion (Nyborg, 1988). The solid line closely resembles that of Wu and Du (1990) for the same parameter values. For this relatively low value of absorption, the temperature profile peaks sharply at the focal region. The analytic and numerical results agree closely beyond an axial distance of about 0.3 cm. A larger absorption of 0.4 Np/cm is featured in Fig. 2. The maximum temperature occurs much closer to the transducer than in Fig. 2. While the accuracy of the analytic result degrades near the transducer, the maximum temperature rise and the location of the maximum is predicted reasonably accurately. In Fig. 3, a value of L (0.4 cm) corresponding to vigorous perfusion is considered. The analytic approach is not as accurate for the high perfusion rate, though the maximum temperature rise (occurring at the focal zone) is predicted to within about 10% error. The time history of the focal zone temperature for the conditions of Fig. 3, determined both by (1) and (26), is shown in Fig. 4. The solid line represents the transient temperature computed via numerical quadrature of (1). The dotted line, based upon the asymptotic model, displays a steeper slope, i.e., larger temperature increase per unit time. The perfusion time $\tau=L^2/\kappa$ for the conditions of Fig. 4 is approximately 107 s. Under the conditions of Fig. 4, the analytic model predicts the transient temperature (relative to steady state) within 20% accuracy at times greater than about half of a perfusion time.

The equilibrium times t_{95} computed using the parameters of Fig. 4, though for different values of the absorption

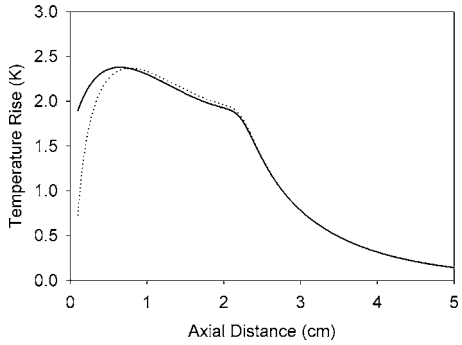

FIG. 2. Same as in Fig. 1, except α is increased to 0.4 Np/cm. Solid line—numerical integration of convolution integral. Dotted line—asymptotic model.

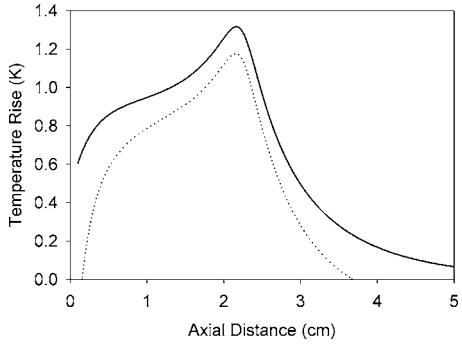

FIG. 3. Same as in Fig. 1, except $\alpha=0.25$ Np/cm and $L=0.4$ cm. Solid line—numerical integration of convolution integral. Dotted line—asymptotic model.

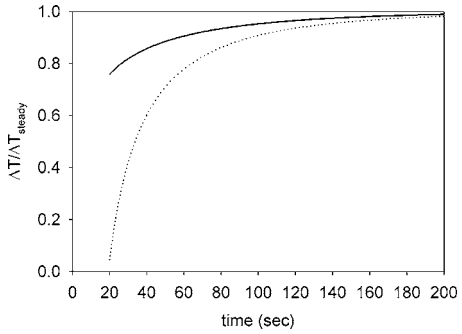

FIG. 4. Time history for the maximum (focal zone) temperatures in Fig. 3. Solid line—numerical integration of convolution integral. Dotted line—asymptotic model.

α, are plotted in Fig. 5. The analytic predictions, based upon (27), overpredict the equilibrium times, with the error decreasing with increasing absorption. Both curves display a region for small α where t_{95} changes little with α, i.e., for small absorption values the time required to reach the steady state is insensitive to the amount of absorption. For larger values of α, a large increase in equilibrium time with increasing α is manifested.

The ability of (20) to predict temperature rise for non-Gaussian amplitude profiles was investigated by comparing with the results of Ellis and O'Brien (1996). A frequency of 3 MHz, focal length of 10 cm, transducer radius of 1 cm, and source power of 0.1 W were used. The perfusion length was 1.18 cm and the absorption 0.15 Np/cm. Figure 6 contains the axial temperature profile derived from (20). The low temperature values very near the transducer, characteristic of the asymptotic model (see Sec. IV), are not present in the corresponding plot of Ellis and O'Brien [Ellis and O'Brien, 1996, Fig. 5(c)]. However, for distances beyond about 1.0 cm, the two curves overlap to within plotting accuracy.

IV. DISCUSSION

The accuracy of the asymptotic method is high in cases of relatively low attenuation and low perfusion length (e.g., Fig. 1). Still, provided the axial location of interest is not very near the transducer, or too far beyond the focal zone, a wide range of perfusion lengths and absorptions of practical interest can be handled by the model with sufficient accuracy. Accuracy criteria for the model may be determined by following the development in Myers (2006), and noting the

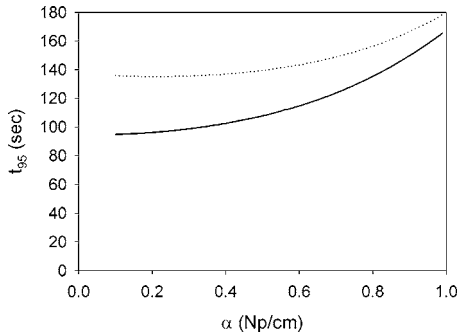

FIG. 5. Equilibrium time t_{95} as a function of absorption, with the other conditions as in Fig. 3.

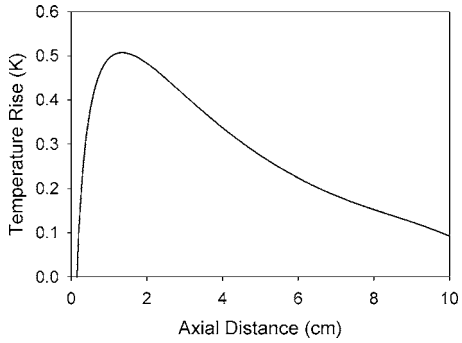

FIG. 6. Steady-state temperature rise computed using the expression for general transducers [Eq. (20)]. Conditions used by Ellis and O'Brien (1996) (frequency=3 MHz, Power=0.2 W, a=1.0 cm, z_f=10 cm, α=0.15 Np/cm, L=1.18 cm) apply.

assumptions required to construct inner and outer asymptotic solutions. Precise limits for the criteria were obtained by numerical experimentation. The criteria are:

(1) $\delta = a/\sqrt{2Bz_f} < 1$;
(2) $\alpha_2 z = (\alpha + 1/2L)z < 4$;
(3) $|(z_f - z)/z|(a/\sqrt{2Bz_f})(\alpha z + z/2L)^{1/2} < 0.5$;
(4) $t > \tau$,
(5) $t > \sqrt{\tau(z_{\text{ref}}^2/(4\kappa))}$.

Physical interpretations of the criteria are given below.

The requirement $\delta \ll 1$, which is stronger than Criterion 1, is the basis for the matched-asymptotic-expansion approach (Myers, 2006). This "large focal length" assumption allows the temperature rise at a given location to be split into contributions due to absorption at that point and distributed heating over the rest of the beam. [See Myers (2006) for further identification of local and global terms.] However, computations revealed that accurate results can be obtained when the radius is comparable to the focal length (Criterion 1). Results from one such set of computations are displayed in Fig. 7, where the temperature rise at the focus computed using both numerical integration (solid line) and the analytic model (dashed line) is plotted as a function of transducer diameter divided by focal length. In each calculation the transducer focal length was 5 cm, the frequency 3 MHz, the absorption 0.15 Np/cm, and the perfusion length 2 cm,

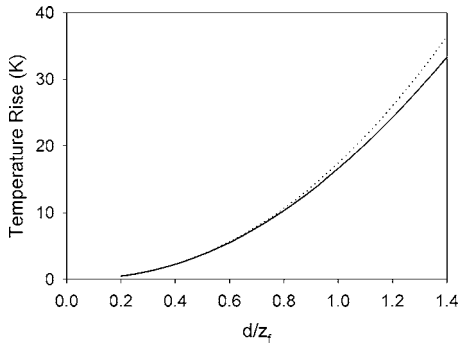

FIG. 7. Steady-state temperature rise at the focus, as a function of transducer diameter. Transducer focal length was maintained at 5 cm while diameter was varied. Frequency is 3 MHz, absorption 0.15 Np/cm, and perfusion length 2 cm. Solid line—numerical integration of convolution integral. Dotted line—asymptotic model.

while the transducer diameter was varied. Acceptable accuracy was achieved even for transducer diameters slightly larger than the focal length.

The second accuracy criterion comes from the local approximation (small ζ) of the absorption and perfusion terms in the integrand of (10). This criterion ensures that there exists a region where gradients in the heat source due to focusing dominate those due to attenuation and perfusion. The third criterion is similar to the first two, but additionally stipulates that for higher attenuations or perfusion rates, or lower f-numbers, attention is restricted to the focal region. It can also be seen from this criterion that the asymptotic predictions will become invalid for large and small values of z.

The fourth criterion is the less precise than the first three, and simply states that the time must be as large as the perfusion time in magnitude in order for (25) to apply. In the case of no perfusion ($\tau=\infty$), e.g., a tissue phantom, the steady-state result (16) is still applicable even though (25) is not. The last criterion requires that the time also be long enough to include sufficient heat conduction. The reference length z_{ref} could be defined by the half-maximum points of the intensity profile in the axial direction for a high-gain transducer. The length z_{ref} is typically a few cm, and the associated diffusion time $z_{\text{ref}}^2/4\kappa$ is on the order of hundreds of seconds. For a moderately perfused tissue, criterion (5) is comparable to criterion (4), but in the case of high perfusion criterion (5) restricts the time to somewhat larger values.

The accuracy of the transient prediction model can be increased by computing more terms in the large-time expansion of (2), though at the price of increased complexity. Equations (27) and (28) are sufficient to provide an estimate of the time to reach steady-state, which is not typically required to high levels of accuracy. Additionally, (27) and (28) display the role played by important parameters. For example, doubling the transducer radius a changes only the right side of (28), by an amount 0.1 log 2. Under the conditions of Fig. 4 (including $z=z_f$), this results in a decrease in t_{95} of about 11%. The actual decrease computed using numerical quadrature of (1) is about 15%. This decrease in equilibrium time with increasing radius is reasonable given that the gain increases with increasing radius, resulting in a smaller focal width. From (4) and (5), it can be seen that the width of the beam at the focus is proportional to $z_f/(ka)$, and hence for fixed wavenumber and focal length the length scale over which radial conduction of heat occurs decreases with increasing radius. The result is a decrease in equilibrium time. The increase in t_{95} with increasing α (Fig. 5) may be understood in a similar manner. A lower value of absorption yields a higher percentage of absorbed energy in the focal region, where the beam radius is small and the characteristic time for radial heat conduction is low.

The insensitivity of the equilibrium time to absorption for small α values (Fig. 5) occurs because perfusion acts immediately to disperse absorbed ultrasound energy, whereas conduction is not significant until the diffusion time $1/(\alpha^2\kappa)$ is reached [see Eq. (27)]. Thus, conduction becomes comparable to perfusion when α is on the order of $1/\sqrt{\kappa\tau}$, which is approximately 0.25 Np/cm for the conditions of Figs. 3–5. In the limit $\alpha\to 0$, Eq. (28) for the equilibrium time becomes

$$\frac{e^{-t_{95}/\tau}}{t_{95}/\tau}=0.1\left\{\log\left(\frac{ka\gamma}{\sqrt{B}}\right)-\frac{1}{2}\log\left(\frac{z}{2L}\right)-\frac{z}{4L}+\frac{e^{-z/L}-1}{4}\right\}. \tag{29}$$

Besides providing t_{95} for small absorption, in light of the above comments this equation also yields the time required to achieve steady-state conditions for a focused beam in a perfused medium where conduction is negligible.

In the manipulations following Eq. (12), it was seen that perfusion can be viewed as decreasing absorption in front of (smaller axial distances) the observation point, and increasing absorption beyond the observation point. This may be understood by noting that absorption serves to shrink the heat source unidirectionally, i.e., the power absorbed at a given axial location decreases monotonically with increasing axial distance. However, due to the nature of the Pennes approximation, perfusion spreads heat in both axial directions from a source located at position z. Thus, in the $+z$ direction perfusion augments absorption, while in the $-z$ direction perfusion opposes absorption. The result is the presence of two effective absorptions, α_1 and α_2, appearing in the solutions such as (20) and (27).

Equation (16) for the steady-state temperature may be combined with the analogous expression for steady-state tissue displacement in Myers, 2006 [Eq. (27) of Myers, 2006] to construct an estimate for the temperature rise expected for a given amount of tissue deformation due to radiation force. After dividing temperature rise by tissue displacement, and ignoring the slight difference in the last additive constant in each expression [$-1/4$ in (16) versus $-3/4$ in Eq. (27) of Myers, 2006], we obtain

$$\frac{T}{w}=\frac{c\mu}{K}. \tag{30}$$

From a safety standpoint, this simple result is conservative, i.e., it overpredicts temperature increase. The overprediction arises from the fact that dynamic equilibrium occurs much faster than thermal equilibrium, and hence for a given exposure time the deformation will reach a higher fraction of its steady-state value. For highly transient processes such as radiation-force imaging with a single beam, the prediction is probably too conservative to be useful. However, Walker (1999) has shown that a conservative estimate of the thermal effects due to radiation force imaging with multiple beam lines may be achieved by assuming the total exposure time to consist of the sum of the times of each of the beams, and assuming each beam to radiate to the same location. The temperature rise per unit of tissue displacement based upon (30) is 2.2 times Walker's value (Walker, 1999) for liver tissue, 2.1 times for breast, and 1.7 times for vitreous. For models such as Walker's, (30) provides a useful order-of-magnitude estimate.

The close agreement of the present model with the results of Ellis and O'Brien (1996) is evidence that the model may be successfully applied to general focused transducers. The long focal length (relative to the transducer radius), moderate perfusion length, and relatively low absorption

considered by Ellis and O'Brien constitute conditions to which the model of this paper is well suited. Equations (27) and (28) may also be applied to determine the thermal equilibrium time of non-Gaussian transducers, provided the quantity $a/\sqrt{B}$ is interpreted as the effective radius a_{eff} of the transducer.

As noted in Myers (2006), use of an infinite-medium Green's function [Eq. (2) for temperature calculations] precludes enforcement of a boundary condition on the transducer face. At low levels of attenuation (Figs. 1 and 4), where the maximum temperature is due primarily to localized heating at the focus, boundary effects can probably be neglected. For higher levels of attenuation, where the maximum temperature is achieved close to the transducer, the error associated with ignoring the boundary condition on $z=0$ is likely to be higher. Assuming an absorption of 0.15 Np/cm, and no perfusion, Wu and Du (1990) found that the temperature rise computed using (8) underestimated the solution imposing a zero-temperature boundary condition on $z=0$. The difference in maximum temperature (occurring at the focus) was less than 10%. The relative error compared to the solution imposing a zero-derivative condition at $z=0$ was about 20%.

V. CONCLUSION

The present model represents a useful method for rapidly calculating the on-axis temperature rise occurring when an ultrasound beam is absorbed in tissue over times that are comparable to, or longer than, the tissue perfusion time. The model is especially accurate in cases of moderate or low perfusion and absorption, and focal lengths that are large compared to transducer radius. However, acceptable accuracy can be achieved even in cases of vigorous perfusion, provided that interest is confined to the region of maximum temperature rise. The capability of the model to simulate temperature rise for long exposure times allows approximate equilibrium times to be computed. Computations involving transducers not possessing Gaussian intensity profiles indicate that the model may be successfully used for more general transducers.

Bacon, D. R., and Shaw, A. (**1993**). "Experimental validation of predicted temperature rises in tissue-mimicking materials," Phys. Med. Biol. **38**, 1647–1659.

Cho, C., Liu, Y., Cobb, W. N., Henthorn, T. K., Lillehei, K., Uwe, C., and Ng, K. (**2002**). "Ultrasound-induced mild hyperthermia as a novel approach to increase drug uptake in brain microvessel endothelial cells," Pharm. Res. **19**, 1123–1129.

Curra, F. P., Mourad, P. D., Khokhlova, V. A., Cleveland, R. O., and Crum, L. A. (**2000**). "Numerical simulations of heating patterns and tissue temperature response due to high-intensity focused ultrasound," IEEE Trans. Ultrason. Ferroelectr. Freq. Control **47**, 1077–1089.

Ellis, D. S., and O'Brien, W. D. (**1996**). "The monopole-source solution for estimating tissue temperature increases for focused ultrasound fields," IEEE Trans. Ultrason. Ferroelectr. Freq. Control **43**, 88–97.

Lizzi, F. L., Muratore, R., Deng, C. X., Ketterling, J. A., Alam, S. K., Mikaelian, S., and Kalisz, A. (**2003**). "Radiation-force technique to monitor lesions during ultrasonic therapy," Ultrasound Med. Biol. **29**, 1593–1605.

Myers, M. R. (**2006**). "Tissue deformation induced by radiation force from Gaussian transducers," J. Acoust. Soc. Am. **119**, 3147–3152.

Nyborg, W. L. (**1988**). "Solutions of the bio-heat transfer equation," Phys. Med. Biol. **33**, 785–792.

Nyborg, W. L., and Wu, J. (**1994**). "Solution of the linear bio-heat transfer equation," Phys. Med. Biol. **39**, 924–925.

Palmeri, M. L., and Nightingale, R. W. (**2004**). "On the thermal effects associated with radiation force imaging of soft tissue," IEEE Trans. Ultrason. Ferroelectr. Freq. Control **51**, 551–565.

Walker, W. F. (**1999**). "Internal deformation of a uniform elastic solid by acoustic radiation force," J. Acoust. Soc. Am. **105**, 2508–2518.

Wu, J., and Du, G. (**1990**). "Temperature elevation generated by a focused Gaussian beam of ultrasound," Ultrasound Med. Biol. **16**, 489–498.

Whistle variability in South Atlantic spinner dolphins from the Fernando de Noronha Archipelago off Brazil

Fernanda S. Camargo
Instituto de Biociências, Universidade de São Paulo, Rua do Matão, travessa 14, no 321, São Paulo, SP, 05508-900, Brazil

Mario M. Rollo, Jr.[a)]
Universidade Estadual Paulista, Campus do Litoral Paulista, Pça. Infante Dom Henrique s/n, São Vicente, SP, 11330-205, Brazil

Viviana Giampaoli
Departamento de Estatística, Instituto de Matemática e Estatística, Universidade de São Paulo, Rua do Matão 1010, São Paulo, SP, 05508-090, Brazil

Claudio Bellini
Projeto TAMAR, R. Dr. Luiz Inacio Pessoa de Melo 81/2051, Recife, PE, 51030-320, Brazil

(Received 9 March 2006; revised 17 July 2006; accepted 13 September 2006)

A series of quali- and quantitative analyses were conducted to evaluate the variability of spinner dolphin whistles from the Fernando de Noronha Archipelago off Brazil. Nine variables were extracted from each whistle contour, and the whistle contours shapes were classified into the seven categories described in Driscoll (1995). The analysis showed mean beginning and ending frequencies values of 10.78 and 12.74 kHz, respectively. On average, whistle duration was relatively short, with mean values around 0.495 s (N=702). Comparative analyses were also conducted to investigate the relationship between the obtained results and those presented in previous studies. When comparing averages, the results of the study of Oswald *et al.*(2003) in the Tropical Eastern Pacific (TEP) presented less significant differences in relation to this study; only whistle duration differed significantly between both works. The results of multivariate classification tests also pointed TEP population as the closest related to the population studied here. The similarities between such disjunct populations might be attributed to a more recent isolation event (the closing of the Panama Isthmus) than the divergence that has driven North and South Atlantic populations apart. © *2006 Acoustical Society of America.* [DOI: 10.1121/1.2359704]

PACS number(s): 43.80.Ka, 43.80.Ev, 43.80.Cs [WWA] Pages: 4071–4079

I. INTRODUCTION

The spinner dolphin, *Stenella longirostris* (Gray, 1828), is a cosmopolitan cetacean found in tropical, subtropical, and less frequently, in warm temperate waters (i.e., Norris *et al.*, 1994). This wide distribution is followed by a notable geographic variation in several morphological characters (i.e., Akin, 1988; Douglas *et al.*, 1992; Perrin and Dolar, 1996; Van Waerebeek *et al.*, 1999) and ecological parameters (Barlow, 1984; Perryman and Westlake, 1998; Perrin *et al.*, 1999). Four subspecies are currently acknowledged (Perrin, 1990; Perrin *et al.*, 1991, 1999): *Stenella longirostris longirostris*, *S. l. orientalis, S. l. centroamericana, and S. l. roseiventris.*

Spinner dolphins, as well as other species of oceanic dolphins, emit clicks and whistles of pure tones, besides a diversified repertoire of pulsed signals (Herman and Tavolga, 1980; Norris *et al.*, 1994; Lammers *et al.*, 2003). Whistles have been characterized in terms of their instantaneous frequency as a function of time (i.e., spectrograms), which is also referred to as a whistle contour. Some authors have studied whistles using subjective classification of their contours, and others have extracted frequency and time parameters from these contours (Bazúa-Durán and Au 2002). The function of whistles in the odontocete communication process has been extensively discussed (Tyack, 1998; McCowan and Reiss, 1995, 2001), and they seem to play an important role in the maintenance of social cohesion and in group organization (Norris *et al.*, 1994; Janik, 2000; Janik and Slater, 1998; Lammers *et al.*, 2003). However, the biological meaning of each frequency and time parameter, as well as of any contour category still needs to be understood (McCowan and Reiss, 1995; Bazúa-Durán and Au, 2002).

Qualitative and quantitative variations in acoustic emissions or phonations, as suggested by Bazúa-Durán and Au, (2002) were recognized and described for *S. longirostris*, but all studies on this variability were developed with populations from the Pacific Ocean (e.g., Norris *et al.*, 1994; Driscoll, 1995; Wang *et al.* 1995a; Bazúa-Durán and Au, 2002). The only work on phonations with a population from the Atlantic Ocean were conducted by Steiner (1981), and aimed to compare different species, excluding any kind of intraspecific analysis. From this scenario, one could note that

[a)]Author to whom correspondence should be addressed. Electronic mail: mario.rollo@csv.unesp.br

it is still necessary to search for any relation between all the information available in the literature, and consequently for a better understanding of the variation within and between populations.

Wang *et al.* (1995a), Driscoll (1995), and Bazúa-Durán and Au (2002) recorded spinner dolphins from Hawaii. However, their results showed significant statistical differences. Some possible reasons for these differences could be differences in the upper frequency limit of the recording systems, different spinner groups being recorded, and observer differences in viewing spectrograms (Bazúa-Durán and Au, 2002). Wang *et al.* (1995a) reported an analysis bandwidth of 0–16 kHz, and Driscoll (1995) and Bazúa-Durán and Au (2002) reported an analysis bandwidth of 0–24 kHz. Since whistles with fundamental frequencies extending into the ultrasonic range have been reported for spinner dolphins (Lammers *et al.*, 2003), the recording and analysis bandwidth upper limit has to be high enough to provide complete representations of the vocal repertoire. It is known that descriptive parameters of the whistles, such maximum and ending frequencies, show significant differences between studies conducted with different upper bandwidth limits (Oswald *et al.*, 2004). Lammers *et al.* (2003) analyzed the acoustic signaling behavior of Hawaiian spinner dolphins in a wider frequency band perspective. The recording system employed allowed them to sample sounds up to 130 kHz and to evaluate the importance of the ultrasonic portion of the sound emissions. Most energy in the fundamental frequency of the whistles was found to be below 24 kHz, as Bazúa-Durán and Au (2002) noted. Based on Lammers *et al.* (2003) conclusions, we can speculate that the major part of the whistles' fundamental frequencies produced by this species is then taken into account here, since the recording limit used in this study is 24 kHz.

It is also known that spinner dolphin whistles can vary geographically (Bazúa-Durán and Au, 2001; Bazúa-Durán *et al.*, 2003; Bazúa-Durán and Au, 2004), as it was already observed for bottlenose dolphins, *Tursiops truncatus* (Wang *et al.*, 1995b; Jones and Sayigh, 2002), and for the estuarine dolphin, *Sotalia guianensis* (Azevedo and Van Sluys, 2005). Nevertheless, the factors influencing this observed geographic variation are still unclear, once the pattern found for spinner dolphins does not follow exactly those observed for the other two species. Studying bottlenose dolphins, Wang *et al.* (1995b) noted that differences in whistle structure were greater between far separated than closer areas. They claimed that, presumably, dolphins in nonadjacent areas have developed unique acoustic characteristics due to geographic isolation. Similarly, Azevedo and Van Sluys (2005), when studying *Sotalia guianensis*, found that the magnitude of the whistles characteristics variation was comparatively smaller between adjacent sites areas than between nonadjacent ones, although in some pairwise comparisons the result was the opposite.

When comparing spinner dolphins whistles from the Hawaiian Islands (Midway Atoll, Kaua'i, O'ahu, Lãna'i, Maui, and Hawai'i) and from Mo'orea, French Polynesia, Bazúa-Durán and Au (2002) found that the macrogeographic variation (between Midway and Mo'orea, and the main Hawaiian Islands) was larger than microgeographic variation (between the main Hawaiian Islands). The authors also found that the variation within each main Hawaiian Island was larger than the variation between them, suggesting the existence of a whistle-specific subgroup (Bazúa-Durán and Au, 2001; Bazúa-Durán and Au, 2004). On the other hand, when the spinner dolphin whistles from the Hawaiian Islands and Mo'orea were compared to the whistles produced by the Tropical Eastern Pacific (TEP) spinner dolphins, greater differences were found between Midway and TEP and Mo'orea groups. O'ahu groups were very similar to TEP and Mo'orea groups, suggesting that there are no differences between oceanic and coastal spinner dolphin whistles. Bazúa-Durán and Au (2002) claimed that the distinctiveness of Midway whistles could be due to the stability of the spinner dolphins in that area, and that the geographic differences found may not occur solely due to geographic isolation, and that other factors, such as fluidity of the spinner dolphin groups may be also affecting this variation (Bazúa-Durán *et al.*, 2003).

In order to evaluate the variability of spinner dolphin whistles from the Fernando de Noronha Archipelago off Brazil (considered as *S. longirostris longirostris*), we conducted a series of quali- and quantitative analyses, which are presented here. No other study on this topic has been done in the Southwestern Atlantic Ocean. Moreover, we used available literature data and some statistical tools to investigate the relationship between our results and those obtained in previous studies, looking for any pattern of geographic variation.

II. METHODOLOGY

Recordings were made in a bay named "Baía dos Golfinhos," located at the Archipelago of Fernando de Noronha (3°51'S and 32°25'W), Brazil (Fig. 1). The "Baía dos Golfinhos" is an intangible inlet inside the National Marine Park of Fernando de Noronha, where regular access of people and boats is prohibited. This bay carries its name because it is visited daily by spinner dolphins, providing an invaluable site for performing acoustic recordings.

The sound samples were collected on free diving sessions in the "Baía dos Golfinhos" from 4 October to 27 December 2002. Underwater behavioral and acoustic data were recorded using a system composed by a SONY® PD150 digital camcorder housed in an AMPHIBICO® VHPD0150 underwater case equipped with dual external hydrophones. All the recordings were made using a sampling rate of 48 kHz, i.e., the frequency upper limit was 24 kHz.

The recordings were imported to an Apple® Macintosh computer using the software IMOVIE 4.0.1. (Apple Computer, Inc.). This application breaks the simultaneous audio and video data into clips accordingly to the data code registered in the digital tape, resulting in a different clip per take. This is very important because each take may correspond to a different context or situation. The audio was then extracted from the video files using the software FINALCUT PRO 3.0 (Apple Computer, Inc.), and stored as AIFF format files. CANARY®V.1.2.4 analysis software (Bioacoustics Research Program, Cornell Lab of Ornithology) was used to generate the spectrograms, with a FFT size of 1024 points, an overlap

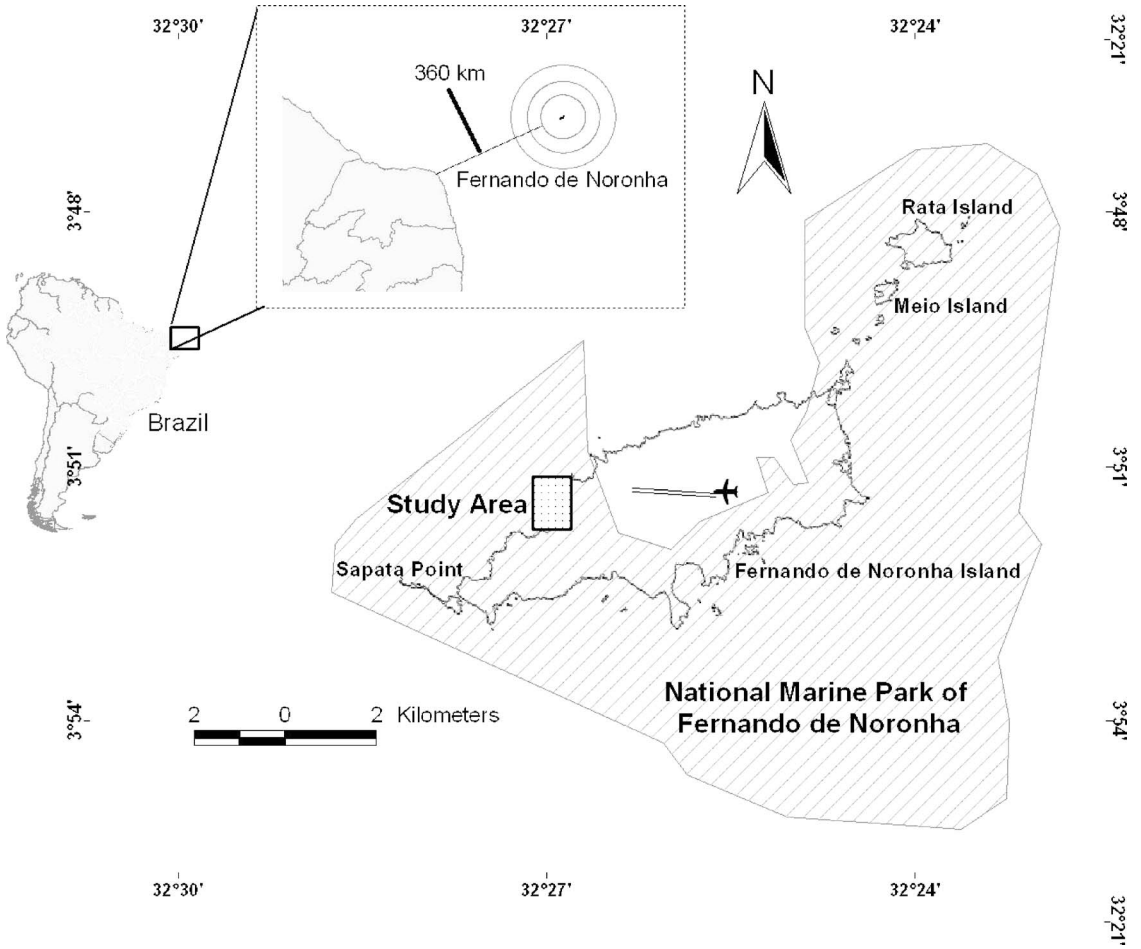

FIG. 1. Map of the study site. The "Baía dos Golfinhos" is situated in the small rectangular inset in the main island of the Fernando de Noronha.

of 50%, a frame length of 512 points, and using a smooth Hamming window. We only used whistles for which all parameters of the spectral contour were distinctly measured and that were not cut off by the upper limit of the recording system (Bazúa-Durán and Au, 2002; Azevedo and Van Sluys, 2005).

From each whistle contour, we extracted nine variables: (1) Beginning frequency (BF), (2) ending frequency (EF), (3) maximum frequency (MAF), (4) minimum frequency (MIF), (5) duration (DUR), (6) number of inflection points (defined as a change from positive to negative or negative to positive slope) (NI), (7) number of breaks (defined as an abrupt variation in frequency in a specific point in time) (NBR), (8) number of loops (a loop was defined as a region where the whistle assumed a parabolic-like shape) (NLO), (9) number of harmonics below the upper frequency limit of the recording system (NHA). These variables were chosen because they can be easily measured from a spectrogram and most of them were chosen to be consistent with the majority of the previous studies with the species, being useful for comparisons.

We also classified the whistle contour into the seven categories described in Driscoll (1995) and Bazúa-Durán and Au (2002), which were used during the comparison process with previous studies: (1) Upsweep, (2) downsweep, (3) concave, (4) convex, (5) constant, (6) sine, and (7) chirps.

In an exploratory phase, a *principal component analysis* (PCA) was used as an effort to find variables unimportant to explain data variability so that they could be excluded from the analyses. Preliminary results showed that the two first components of this analysis explained only 66% of the variability, and only in the sixth component 90% of the variability was achieved and all variables were already included in the previous components. This implies that any of the variables chosen could not be excluded from the analysis.

Following this step, still as an exploratory analysis, a cluster analysis named *CLARA* (Clustering Large Applications) (Kaufman and Rousseeuw, 2005) was performed to determine the existence of any grouping pattern of data according to their similarities. The groups formed were then tested with the *Silhouette width test* (Kaufman and Rousseeuw, 2005), which measures the average dissimilarity between point i and all other points of the cluster, which i belongs to. The *CLARA* analysis revealed that the whole sample of spinner dolphin whistles could be clumped together into four or five groups, and the *Silhouette width test* resulted in a score of 0.23 and 0.22, respectively. None of these results can be considered as a good grouping (Kaufman and Rousseeuw, 2005), and does not seem to have any biological meaning, therefore, not discussed in the present study.

TABLE I. Descriptive analysis of the whistles (mean, standard deviation, minimum, and maximum values, and variation coefficients). Legend: BF—initial frequency; EF—ending frequency; MIF—minimum frequency; MAF—maximum frequency, SP—frequency range; DUR—duration; NI—number of inflection points, NBR—number of breaks, NLO—number of loops, NHA—number of harmonics, nd=not reported.

Study	Statistics	N	BF (kHz)	EF (kHz)	MIF (kHz)	MAF (kHz)	SP (kHz)	DUR (ms)	NI	NBR	NLO	NHA
This Study	Mean	702	10.78	12.74	9.03	14.48	5.44	495	1.16	0.86	0.66	0.63
	Min	702	2.06	2.03	2.03	3.30	0	1.25	0	0	0	0
	Max	702	23.08	22.52	19.36	23.08	16.6	1800	6	12	4	3
	Std Dev.	702	4.08	4.02	2.79	3.87	3.44	394.69	1.15	1.72	0.77	0.67
	C. V.	702	37.88	31.54	30.85	26.73	63.20	79.78	99.17	198.28	116.48	106.97
Wang *et al.* (1995a)	Mean	271	10.61	14.05	9.03	15.20	*nd*	750	1.07	*nd*	*nd*	*nd*
	Min	271	3.91	7.19	3.91	8.75	*nd*	100	0	*nd*	*nd*	*nd*
	Max	271	18.92	22.46	14.38	22.46	*nd*	1820	9	*nd*	*nd*	*nd*
	Std Dev.	271	3.44	2.37	2.24	1.66	*nd*	330	1.19	*nd*	*nd*	*nd*
Bazúa-Durán and Au (2002)	Mean	961	12.02	14.91	10.68	16.50	5.82	449	*nd*	*nd*	0.42	*nd*
	Min	961	2.58	2.29	1.99	2.66	0.39	28	*nd*	*nd*	0	*nd*
	Max	961	22.90	24.00	18.34	24.00	16.93	2256	*nd*	*nd*	12	*nd*
	Std Dev.	961	3.66	3.80	2.68	3.54	3.67	372	*nd*	*nd*	0.75	*nd*
Oswald *et al.* (2003)	Mean	112	10.40	12.40	9.10	13.70	4.6	600	1.9	*nd*	*nd*	*nd*
	Min	112	*nd*	*nd*	*nd*	*nd*	*nd*	*nd*	*nd*	*nd*	*nd*	*nd*
	Max	112	*nd*	*nd*	*nd*	*nd*	*nd*	*nd*	*nd*	*nd*	*nd*	*nd*
	Std Dev.	112	3.40	3.60	2.50	3.50	3.40	400	4.1	*nd*	*nd*	*nd*
Steiner (1981)	Mean	2088	9.76	13.17	8.76	14.32	*nd*	430	0.55	*nd*	*nd*	*nd*
	Min	2088	*nd*	*nd*	*nd*	*nd*	*nd*	*nd*	*nd*	*nd*	*nd*	*nd*
	Max	2088	*nd*	*nd*	*nd*	*nd*	*nd*	*nd*	*nd*	*nd*	*nd*	*nd*
	Std Dev.	2088	3.51	3.10	2.62	2.76	*nd*	330	0.97	*nd*	*nd*	*nd*
Driscoll (1995)	Mean	965	11.80	14.46	10.19	16.80	*nd*	661	*nd*	*nd*	*nd*	*nd*
	Min	965	4.64	4.00	4.00	5.60	*nd*	40	*nd*	*nd*	*nd*	*nd*
	Max	965	21.44	23.04	21.22	23.04	*nd*	1870	*nd*	*nd*	*nd*	*nd*
	Std Dev.	965	3.66	3.91	2.40	3.17	*nd*	334	*nd*	*nd*	*nd*	*nd*
Lammers *et al.* (2003)	Mean	167	*nd*	*nd*	10.10	17.40	7.3	660	*nd*	*nd*	*nd*	1.83
	Min	167	*nd*	*nd*	*nd*	*nd*	*nd*	*nd*	*nd*	*nd*	*nd*	*nd*
	Max	167	*nd*	*nd*	*nd*	*nd*	*nd*	*nd*	*nd*	*nd*	*nd*	*nd*
	Std Dev.	167	*nd*	*nd*	2.50	3.0	3.9	330	*nd*	*nd*	*nd*	0.87

To compare the mean values obtained for the frequency and time parameters with the results presented in previous studies, we applied a series of univariate and multivariate tests, using the Program "R" (R Development Core Team, 2004). First, we used Levene's *F* test to evaluate the homogeneity of variances. Later, we used the *t* test for homogeneous variances and Welch's *t* test for nonhomogeneous variances so as to compare the means (the mean of each variable observed in this study and the correspondent mean found in other studies, as described in the literature).

We also used a classification method through a multivariate statistic test in order to identify which of the results presented in earlier studies would be closer to the results found here. We considered, as a classification criterion, the minimum distance between each value observed in this study and the mean for each of the variables obtained for each other study included in the comparison, weighted for the inverse of the covariance matrix. The distance was defined as

$$D_j = (\mathbf{y} - \overline{\mathbf{y}}_j)^t \mathbf{S}_j^{-1} (\mathbf{y} - \overline{\mathbf{y}}_j)$$

Where the Dj is the minimum distance, y represents each value for the variable j found in this study and $\overline{y}_j$ is the mean value presented in the earlier studies for the variable j. This method is complementary to the *T Test* in comparison between different populations, and allowed us not only to compare means but also to better visualize which population is closest to the Fernando de Noronha population.

Finally, in order to investigate differences in the categorization of whistles between the present study, and in the Driscoll (1995) and Bazúa-Durán and Au (2002) studies, we used the *Pearson's X-squared* statistic.

III. RESULTS AND DISCUSSION

A. Frequency and time parameters

A summary of the descriptive statistics (mean, minimum, maximum, standard deviation, and variation coefficients) of all frequency and time parameters for the 702 whistles included in the analysis is shown in Table I. Our analysis showed that the mean BF was lower than the mean

TABLE II. Correlation matrix of the whistle frequency and time parameters observed in this study, considering. Legend: BF—Initial frequency; EF—Ending frequency; MIF—Minimum frequency; MAF—Maximum frequency; DUR—Duration.

	BF	EF	MIF	MAF	DUR
BF	1.000 000 00	0.245 820 9[a]	0.720 415 6[a]	0.573 526 2[a]	0.048 873 47
EF	0.245 820 94[a]	1.000 000 0	0.505 342 0[a]	0.737 041 1[a]	0.141 473 78[a]
MIF	0.720 415 64[a]	0.505 342 0[a]	1.000 000 0	0.489 662 9[a]	−0.142 518 17[a]
MAF	0.573 526 25[a]	0.737 041 1[a]	0.489 662 9[a]	1.000 000 0[a]	0.417 467 74[a]
DUR	0.048 873 47	0.141 473 8[a]	−0.142 518 2[a]	0.417 467 7[a]	1.000 000 00

[a]Significant correlation at the 0.01 level.

EF, as it had already been observed by Bazúa-Durán and Au (2002). On average, whistle spanning times were relatively short, with mean values around 0.495 s (SD=0.79; N=702). We also conducted an analysis of the degree of association between all variables by using a Correlation Matrix, which is shown in Table II. A significant association was observed between all variables, excluding BF and DUR, which were shown to be independent. The greatest correlation values were observed between BF and MIF (r=0.720, P=0.01), and EF and MAF (r=0.737, P=0.01). Both were positively correlated, indicating that when one of these variables increases its value, the other does the same. We also observed a small negative correlation between MIF and DUR (r=−0,142, P=0.01), indicating that when the minimum frequency increases, the duration of the whistle decreases.

The parameters of whistle frequency and time had the lowest variation coefficient of all analyzed variables (Table I), and they were, therefore, treated separately. Furthermore, these variables are present in all previous studies conducted with spinner dolphin whistles, which allowed us to perform a series of comparisons, as shown below. From the parameters of frequency and time, those associated with frequency had lower variation coefficients when compared to the duration, indicating that the time parameter is more variable, as it has already been observed for *Sotalia guianensis* (Azevedo and Van Sluys, 2005). For *S. longirostris*, Steiner (1981), Wang *et al.* (1995a), and Oswald *et al.* (2003) also found a lower value of variation coefficients for frequency parameters, with the exception to the frequency range, which exceed the duration's one in the third study.

As a first effort of inserting our results in the literature context, we conducted a *t Test*, and the results are shown in Table III. The study of Oswald *et al.* (2003) presented less significant differences in relation to ours; with only whistle duration differing significantly between both works.

Later, in order to find which of the earlier studies on populations of spinner dolphins would have the closest results to those obtained in Fernando de Noronha, we conducted a classification test (according to the criteria of minimum distance described above). It is important to take into account that, as we did not have the variance and covariance matrices observed in the earlier studies, we performed the classification test assuming three possibilities of different matrices: (1) All variables being independent (i.e., the corre-

TABLE III. Comparison of the values obtained in this study with the results presented in the available literature to each of the considered whistle variables.

		Wang *et al.* 1995a	Bazúa-Durán and Au 2002	Oswald *et al.* 2003	Steiner 1981	Driscoll 1995	Lammers *et al.* 2003
BF	*t Test*	0.655	−6.389[a]	1.066	5.927[a]	−5.260[a]	–
	Degrees of Freedom	577.295	1411.277	166.470	1070.988	1410.47	–
	p-value	0.513	<0.001	0.288	<0.001	<0.001	–
EF	*t Test*	−6.263[a]	−11.223[a]	0.843	−2.587[a]	−8.763[a]	–
	Degrees of Freedom	815.406	1661	812	995.950	1665	–
	p-value	<0.001	<0.001	0.400	<0.001	<0.001	–
MIF	*t Test*	0	−12.187[a]	−0.250	2.252[a]	−8.881[a]	−4.540[a]
	Degrees of Freedom	606.459	1661	812	1149.498	1370.121	867
	p-value	1	<0.001	0.803	0.025	<0.001	<0.001
MAF	*t Test*	−4.056[a]	−10.895[a]	2.001	1.012	−13.021[a]	−10.646[a]
	Degrees of Freedom	961.427	1429.777	812	951.895	1323.101	311.871
	p-value	<0.001	<0.001	0.045	0.311	<0.001	<0.001
DUR	*t Test*	−10.207[a]	2.426[a]	−2.601[a]	3.923	−9.031[a]	−5.580[a]
	Degrees of Freedom	582.619	1661	812	1049.19	1353.577	290.452
	p-value	<0.001	0.015	<0.001	<0.001	<0.001	<0.001

[a]The mean difference is statistically different at the 0.05 level.

TABLE IV. Classification of the observations according to the distance (the numbers mean the amount of whistles that had the minimum distance value from each variable observed in this study and the correspondent mean value of each study).

Matrix of Variance-Covariance	Wang *et al.* 1995a	Bazúa-Durán and Au 2002	Oswald *et al.* 2003	Steiner 1981	Driscoll 1995	Total
Independent	26	196	278	84	118	702
With Variance-Covariance Matrix equal to the one observed in this study	103	170	119	223	87	702
With the Variances presented in each study and the same correlations observed in this study	1	0	701	0	0	702

lation is zero), (2) variance and covariance matrices being equal to those observed in this study, (3) combining the variances presented in each study together with our correlation. The result of this classification can be observed in Table IV. As in the univariate analysis, we had a concentration of minor distances in the study of Oswald *et al.* (2003) in two situations: When we considered the variable set independent and when we used the true variances, presented in each study, together with our correlations. However, when we assumed the matrix exactly equal to the one presented in our study, the concentration of minor distances moved to Steiner, 1981 (Table IV).

There are many problems when comparing different efforts. At first, the methods and equipment used to record the sound samples were sometimes distinct. In this study, we recorded the animals during free diving. Although this apparently does not disturb the animals, changing their natural behavior can interfere in their communication process. The earlier studies recorded in the presence of a boat, which can also cause alterations. Moreover, recording equipments were not equal, and varied in the upper frequency limit of the recording system. In the majority of studies, the upper frequency limit of the recording system was greater than 22 kHz (with sample rates of 44.1 or 48 kHz), with the exception to the Wang *et al.* (1995a) study, who used a system with an upper frequency limit of around 16 kHz. Differences in the whistle selection and in the sample size could also conduct to different results.

Additionally, we have to consider that animals engaged in different activities during the recording sessions, as well as being present in different group sizes, can have a significant influence in the sound emission of the group envelope (for example, Norris *et al.*, 1994; Herzing, 2000). Bazúa-Durán and Au (2002), for example, compared their study with Wang *et al.* (1995a) and Driscoll (1995), which were all made in the same place ("Island of Hawaii"), and found significant differences between them when comparing duration and the same frequency variables analyzed in this study. Nevertheless, in their study of geographic variation of spinner dolphin whistles among the Hawai'ian Islands, Bazúa-Durán and Au (2004) did not find any significant differences in whistles emmitted by dolphins with behavioral state and pod size.

In spite of all these difficulties what we intended to do here, in addition to presenting insights to the whistle repertoire of spinner dolphins from the Fernando de Noronha Archipelago (which has never been acoustically studied before), was to test if there was some closeness between this population and other ones studied earlier as an attempt to clarify any geographic variation pattern. We judged the results acquired here as very interesting, pondering that our population would supposedly be closer to the Tropical Eastern Pacific population, studied by Oswald *et al.* (2003). When comparing means, the spinner dolphins from the Fernando de Noronha differ significantly from the TEP only on the duration of the whistles (considering that the variation coefficient of this variable were higher than the frequency ones in both studies). If this is true, the difference in duration could be associated with the recording of different individuals, engaged in different activities, as explained by Bazúa-Durán and Au (2004) for Hawaiian spinner dolphins, and suggested by Whitten and Thomas (2001) for *Lagenorhynchus obliquidens*, and by Janik *et al.* (1994), and Wang *et al.* (1995b) for *Tursiops truncatus*. Otherwise, the similarities between populations so disjunct could possibly be attributed to biogeographic reasons, reflecting that these two populations were more recently isolated than the North and South Atlantic populations, being in contact before the formation to the Panama Isthmus. Other studies have made an approach to this question, although using coastal teleost fishes, such as those of Tringali *et al.* (1999), Craig *et al.* (2004), and Craig *et al.* (2006). In the case of spinner dolphins, such a question is beginning to be addressed (Farro *et al.*, 2005).

Heeding to the results of the classification test, we could consider two different types of results. If we suppose that our population should be more similar to the population from North Atlantic, studied by Steiner (1981), when choosing a variance-covariance matrix exactly equal to that obtained in this study, the results would be associated to some degree of information exchange through intermediate groups, as were already observed by Bazúa-Durán and Au (2002) for Hawaiian spinner dolphins, by Wang *et al.* (1995b) for *Tursiops truncatus*, and by Azevedo and Van Sluys (2005) for *Sotalia guianensis*; and the differences between the Fernando de Noronha population and the Pacific Ocean population could be due to geographic isolation. However, we believe that the third option of variance-covariance matrix is the closest to the real one, where the correlation values that compose the matrix are the ones provided by other studies. Using this matrix, the concentration of minimum distances in the study of Oswald *et al.* (2003) correspond to most of the observations, which confirm the result obtained in the univariate

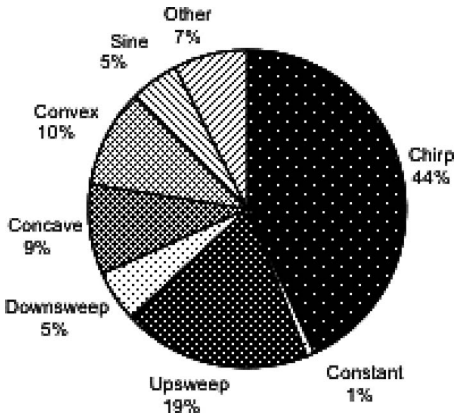

FIG. 2. Distribution of analyzed whistles into categories, being "Other" the category that includes all gradation between other two categories.

analysis and reinforce the idea of proximity between these two populations.

B. Whistle contour

Taking the contour variables of the whistles into consideration, we noticed that all of them (number of breaks, number of inflection points, number of loops, and number of harmonics) have a higher variation coefficient than the frequency and time parameters, as it is shown in Table I. This was already been observed in the studies of Steiner (1981), Wang *et al.* (1995a), and Oswald *et al.* (2003), especially for the number of inflection points and the number of harmonics (when it appears as a whistle parameter). This high intraspecific variability may be a result of individual modulation, transmitting information about identity or context (Bazúa-Durán and Au (2004); Azevedo and Van Sluys, 2005), or the directionality of the emissive animal, in the specific case of number of harmonics (Lammers *et al.* 2003).

Regarding the classification in categories and according to the contour shape of the whistles in the spectrograms, 7% of the whistles could not be ascribed to any of the categories created by Driscoll (1995) and Bazúa-Durán and Au (2002), because they looked like a gradation between two other categories. These whistles were thus set in a category named "Other," as is shown in Fig. 2. This new category is very heterogeneous in the whistle contours that were classified here, and must be reevaluated in the near future. With the aim of comparing the whistles categories distribution found here with the distributions presented by Driscoll (1995) and Bazúa-Durán and Au (2002), we excluded all the assemblage of whistles ascribed to this new category, as it is shown in Fig. 3.

The distribution of the whistles grouped into categories is different between the present study and each of the previous ones (Driscoll, 1995; Bazúa-Durán and Au (2002)), at least in the percentage of two categories, as it is shown by the results of the *Pearson's X-squared* statistic test in Table V. However, the two categories of whistles more frequently recorded, "Chirps" and "Upsweep" were not significantly different between our study and the one of Bazúa-Durán and Au (2002). The "Constant" category, which was very rare, is not significantly different between the three studies. Further, the whistle category "Sine" is very abundant in the studies of Driscoll (1995) and Bazúa-Durán and Au (2002), while it was not in the present study. We believe that this situation occurred because we set a great number of whistles that could have been called by these authors as "Sine," in the "Other" category, due to the great variability of this kind of whistle shape.

Although other authors have shown that whistles have a graded nature and that categorization have not been, therefore, a precise way to represent a repertoire of a given species or population of dolphins, we used it as an additional available resource of comparison between different populations, as it was suggested by Bazúa-Durán and Au (2002). The results are interesting due to the similarity in the general distribution of the whistles in all categories, especially between our study and that of Bazúa-Durán and Au (2002), from which we differed only in two categories, "Sine" and "Concave" (see Fig. 3 and Table V). The comprehension of the significance of these similarities is still difficult due to the lack of biological meaning of this categorization.

We firmly believe that more accurate studies comparing different populations and using more controlled sources of bias should be conducted and are fundamental to achieve this knowledge. Studies focusing in the correlation of sound production and the individual dolphin associated with, should also be conducted, taking into account characteristics such as sex, age class, and behavior.

IV. CONCLUSIONS

Acoustic characteristics of the whistles emitted by dolphins have been described and quantified in a number of studies, and have shown to be useful during comparisons

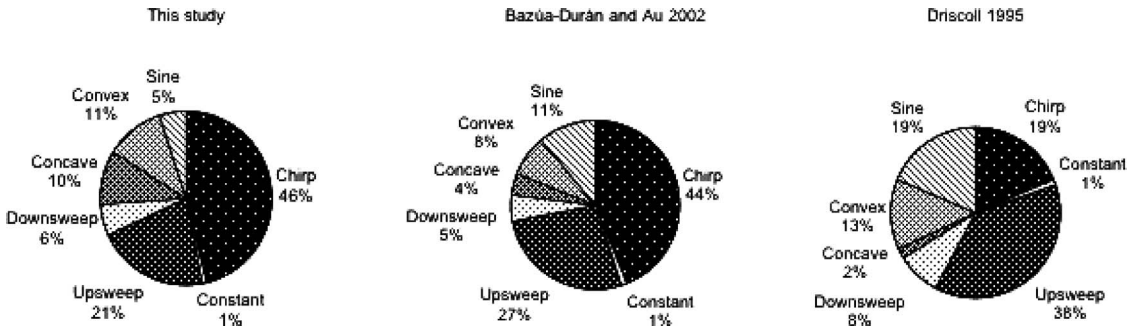

FIG. 3. Comparison of the whistle distribution in the seven categories described by Driscoll (1995) and Bazúa-Durán and Au (2002).

TABLE V. Comparison of the percentage of whistles ascribed to the seven categories with the correspondent results presented by Bazúa-Durán and Au (2002) and Driscoll (1995).

	Bazúa-Durán and Au, 2002		Driscoll, 1995	
Category	*Pearson's X-squared* statistics	*p*-value	*Pearson's X-squared* statistics	*p*-value
Sine	18.077[a]	<0.001	23.535[a]	<0.001
Convex	3.993	0.046	12.277[a]	<0.001
Concave	22.945[a]	<0.001	5.953	0.015
Downsweep	0.608	0.435	6.642[a]	<0.001
Upsweep	7.581	0.006	26.054[a]	<0.001
Constant	0.000	1	0	1
Chirp	0.578	0.447	138.373[a]	<0.001

[a]The mean difference is statistically different at the 0.05 level.

between groups and populations, as during categorization of different species (for instance, see Steiner, 1981; Wang *et al.*, 1995a and 1995b; Bazúa-Durán and Au, 2002, 2004; Oswald *et al.* 2004). In this context, the description presented here, as well as the comparisons conducted with the results available in the literature for other populations, contributes to this huge effort of knowing how populations are organized geographically, and which characteristics of whistles are important to differentiate populations and/or species. Increasing the effort on bioacoustical studies for other known populations of spinner dolphins would allow us to better recognize the existence of any pattern of geographic variation and its correlation to biological features, and these in turn could help to ascribe, in a better resolution, the taxonomic status of each population and subspecies.

ACKNOWLEDGMENTS

We thank Lawrence Wabba, Guillian Buhl, and Alice Grossman for the help and support during different phases of the fieldwork. We also thank Melina Baumgarten and Luis Fábio Silveira for their important comments and for reviewing earlier versions of the manuscript, and the two anonymous reviewers who have made insightful suggestions for improving the manuscript. We also thank CAPES and Projeto TAMAR for the financial and logistical support and IBAMA for giving the necessary permits to data collection inside the National Marine Park of Fernando de Noronha.

Akin, P. A. (**1988**). "Geographic variation in tooth morphology and dentinal patterns in the spinner dolphin, *Stenella longirostris*," Marine Mammal Sci. **4**(2), 132–140.

Azevedo, A. F., and Van Sluys, M. (**2005**). "Whistles of tucuxi dolphins (*Sotalia fluviatilis*) in Brazil: Comparisons among populations," J. Acoust. Soc. Am. **117**(3), 1456–1464.

Barlow, J. (**1984**). "Reproductive seasonality in pelagic dolphins (Stenella spp.): Implications for measuring rates," Rep. Int. Whal. Comm. **6**, 191–198.

Bazúa-Durán, C., and Au, W. L. (**2001**). "Geographic variation in whistles of spinner dolphins (*Stenella longirostris*)," 14th Biennial Conference on Biology of Marine Mammals, Vancouver, Canada, 28 Nov.-3 Dec.

Bazúa-Durán, C., and Au, W. L. (**2002**). "The whistles of Hawaiian spinner dolphins," J. Acoust. Soc. Am. **112**(6), 3064–3072.

Bazúa-Durán, C., and Au, W. L. (**2004**). "Geographic variations in the whistles of spinner dolphins (*Stenella longirostris*) of main Hawaiian Islands," J. Acoust. Soc. Am. **116**(6), 3757–3769.

Bazúa-Durán, C., Au, W. L., and Oswald, J. N. (**2003**). "Possible reasons for the geographic variations in the whistles of spinner dolphins (*Stenella longirostris*) of the Pacific Ocean," 17th *Conference of the European Cetacean Society*, Las Palmas de Gran Canaria 9–13 March.

Craig, M. T., Hastings, P. A., and Pondella, D. J. (**2004**). "Speciation in the Central American seaway: The importance of taxon sampling in the identification of trans-isthmian geminate pairs," J. Biogeogr. **31**, 1085–1091.

Craig, M. T., Hastings, P. A., Pondella, D. J., Ross Robertson, D., and Rosales-Casián, J. A. (**2006**). "Phylogeography of the flag cabrilla *Epinephelus labriformis* (Serranidae): Implications for the biogeography of the Tropical Eastern Pacific and the early stages of speciation in a marine shore fish," J. Biogeogr. **33**, 969–979.

Douglas, M. E., Schnell, G. D., Hough, D. J., and Perrin, W. F. (**1992**). "Geographic variation in cranial morphology of spinner dolphins *Stenella longirostris* in the Eastern Tropical Pacific Ocean," Fish. Bull. **90**, 54–76.

Driscoll, A. D. (1995). The whistles of Hawaiian spinner dolphins, Stenella longirostris. Master's thesis, University of California at Santa Cruz.

Farro, A. P. C., Rollo, M. M. Jr., Silva, J. M. Jr., and Marino, C. L. (**2005**). "Skin sampling for genetic analysis of a South Atlantic spinner dolphin (*Stenella longirostris*) population," in 16th Biennial Conference on Biology of Marine Mammals, 2005, San Diego, CA. (Abstract).

Gray, J. E. (**1828**). *Specilegia Zoologica; or Original Figures and Short Systematic Description of New and Unfigured Animals*, Treuettel, Wurtz and Wood, London.

Herman, L. H., and Tavolga, W. N. (**1980**). "The communication system of cetaceans" in *Cetacean Behavior: Mechanisms and Functions*, edited by L. H. Herman (Wiley, New York), pp. 149–209.

Herzing, D. L. (**2000**). "Acoustics and social behavior of wild dolphins: implications for a sound society" in *Hearing by Whales and Dolphins*, edited by W. W. L. Au, A. N. Popper, and R. F. Fay (Springer Verlag, New York), pp. 225–272.

Janik, V. M. (**2000**). "Source levels and the estimated active space of bottlenose dolphin (*Tursiops truncatus*) whistles in the Moray Firth, Scotland," J. Comp. Physiol. **186**, 673–680.

Janik, V. M., and Slater, P. J. B. (**1998**). "Context-specific use suggests that bottlenose dolphin signature whistle are cohesion calls," Anim. Behav. **56**(4), 829–838.

Janik, V. M., Dehnhardt, G., and Todt, D. (**1994**). "Signature whistle variation in the bottlenosed dolphin, *Tursiops truncatus*," Behav. Ecol. Sociobiol. **35**(4), 243–248.

Jones, G. J., and Sayigh, L. S. (**2002**). "Geographic variation in rates of vocal production of free-ranging bottlenose dolphin," Marine Mammal Sci. **18**(2), 374–393.

Kaufman, L., and Rousseeuw, P. J. (**2005**). *Finding groups in data: An introduction to cluster analysis*, (Wiley, New York), pp. 342.

Lammers, M. O. and Au, W. L. (**2003**). Directionality in the whistles of Hawaiian spinner dolphins (Stenella longirostris): A signal feature to cue direction of movement?, Marine Mammal Science, **19**(2), pp. 249–264.

Lammers, M. O., Au, W. L., and Herzing, D. L. (**2003**). "The broadband social acoustic signaling behavior of spinner and spotted dolphins," J. Acoust. Soc. Am. **114**(3), 1629–1639.

McCowan, B., and Reiss, D. (**1995**). "Maternal Aggressive contact vocalizations in captive bottlenose dolphins (*Tursiops truncatus*): Wide-band, low-frequency signals during mother/aunt-infant interactions," Zoo Biol. **14**, 293–309.

McCowan, B., and Reiss, D. (**2001**). "The fallacy of 'signature whistles' in bottlenose dolphin: A comparative perspective of 'signature information' in animal vocalizations," Anim. Behav. **62**, 1151–1162.

Norris, K. S., Wursig, B., Wells, R. S., and Wursig, M. (**1994**). *The Hawaiian Spinner Dolphin*, (University of California Press, Berkeley), p. 408.

Oswald, J. N., Barlow, J., and Norris, T. F. (**2003**). "Acoustic identification of nine delphinid species in the eastern tropical Pacific Ocean," Marine Mammal Sci. **19**(1), 20–37.

Oswald, J. N., Rankin, S., and Barlow, J. (**2004**). "The effect of recording and analysis bandwidth on acoustic identification of nine delphinidae species," J. Acoust. Soc. Am. **116**(5), 3178–3185.

Perrin, W. F. (**1990**). "Subespecies of *Stenella longirostris* (Mammalia: Cetacea: Delphinidae)," Proc. Biol. Soc. Wash. **103**, 453–463.

Perrin, W. F., Akin, P. A., and Kashiwada, J. V. (**1991**). "Geographic variation in external morphology of the spinner dolphin *Stenella longirostris* in the Eastern Pacific and implications for conservation," Fish. Bull. **89**, 411–428.

Perrin, W. F., and Dolar, L. L. (**1996**). "Preliminary results on spinner dolphins, *Stenella longirostris*, from Philippines," IBI Rep. **6**, 25–33.

Perrin, W. F., Dolar, M. L. L., and Robineau, D. (**1999**). "Spinner dolphins

(*Stenella longirostris*) of the Western Pacific and Southeast Asia: Pelagic and shallow water forms," Marine Mammal Sci. **15**(4), 1029–1053.

Perryman, W. L., and Westlake, D. (**1998**). "A new geographic form of the spinner dolphin, *Stenella longirostris*, detected with aerial photogrammetry," Marine Mammal Sci. **14**(1), 38–50.

R Development Core Team (**2004**). "R: A language and environment for statistical computing," Vienna, Austria, R Foundation for Statistical Computing. http://www.R-project.org. Last accessed 11/10/06.

Steiner, W. W. (**1981**). "Species-specific differences in pure tonal whistle vocalizations of five Western North Atlantic dolphin species," Behav. Ecol. Sociobiol. **9**, 241–246.

Tringali, M. D., Bert, T. M., Seyoum, S., Bermingham, E., and Bartolacci, D. (**1999**). "Molecular Phylogenetics and Ecological Diversification of the Transisthmian Fish Genus *Centropomus* (Perciformes: Centropomidae)," Mol. Ecol., **13**, 193–207.

Tyack, P. L. (**1998**). "Acoustic Communication under sea," in *Animal Acoustics Communication–Sound Analysis and Research Methods*, edited by S. L. Hopp, M. J. Owen, and C. S. Evans (Springer-Verlag, New York), pp. 163–219.

Van Waerebeek, K. V., Gallagher, M., Baldwin, R., Papastravrou, L., and Al-Lawati, S. M. (**1999**). "Morphology and distribution of the spinner dolphin, *Stenella longirostris*, rough-toothed dolphin, *Steno bredanensis* and melon-headed whale, *Peponocephala electra*, from waters off the Sultanate of Oman," J. Cetacean Res. Manage. **1**(2), 167–177.

Wang, D., Wursig, B., and Evans, W. (**1995a**). "Comparison of whistles among seven odontocete species," in *Sensory systems of Aquatic Mammals*, edited by R. A. Kastelein, J. A. Thomas, and P. E. Nachtingall (The Spil Publishers, Woerden, The Netherlands), pp. 299–323.

Wang, D., Wursig, B., and Evans, W. (**1995b**). "Whistles of bottlenose dolphins: Comparison among populations," Aquat. Mamm. **21**(1), 65–77.

Whitten, J. L., and Thomas, J. A. (**2001**). "Whistle repertoire of Pacific white-sided dolphins (*Lagenorhynchus obliquidens*) at the John G. Shedd Aquarium," J. Acoust. Soc. Am. **109**, p. 2391.

Cepstral coefficients and hidden Markov models reveal idiosyncratic voice characteristics in red deer (*Cervus elaphus*) stags

David Reby[a)]
Department of Psychology, University of Sussex, Brighton BN1 9QH, United Kingdom

Régine André-Obrecht, Arnaud Galinier, and Jerome Farinas
Institut de Recherche en Informatique de Toulouse, UPS, 31062 Toulouse, France

Bruno Cargnelutti
UR Comportement et Ecologie de la Faune Sauvage, INRA, 31326 Toulouse, France

(Received 28 December 2005; revised 27 July 2006; accepted 5 September 2006)

Bouts of vocalizations given by seven red deer stags were recorded over the rutting period, and homomorphic analysis and hidden Markov models (two techniques typically used for the automatic recognition of human speech utterances) were used to investigate whether the spectral envelope of the calls was individually distinctive. Bouts of common roars (the most common call type) were highly individually distinctive, with an average recognition percentage of 93.5%. A "temporal" split-sample approach indicated that although in most individuals these identity cues held over the rutting period, the ability of the models trained with the bouts of roars recorded early in the rut to correctly classify later vocalizations decreased as the recording date increased. When Markov models trained using the bouts of common roars were used to classify other call types according to their individual membership, the classification results indicated that the cues to identity contained in the common roars were also present in the other call types. This is the first demonstration in mammals other than primates that individuals have vocal cues to identity that are common to the different call types that compose their vocal repertoire. © *2006 Acoustical Society of America.*
[DOI: 10.1121/1.2358006]

PACS number(s): 43.80.Ka, 43.80.Lb, 43.80.Ev [DOS] Pages: 4080–4089

I. INTRODUCTION

Individual differences in the acoustic structure of vocalizations have been described in several mammal species (e.g., spider monkeys, *Ateles geoffroyi:* Champman and Weary, 1990; mouse lemurs, *Microcebus murinus*: Zimmerman and Lerch, 1993; timber wolves, *Canis lupus*: Tooze *et al.*, 1990; arctic foxes, *Alopex lagopus*: Frommolt *et al.*, 1997; swift foxes, *Vulpes velox*: Darden *et al.*, 2003; spotted hyenas, *Crocuta crocuta*: East and Hofer, 1991; harbour seals, *Phoca vitulina*: Hanggi and Schusterman, 1994; sea otters, *Enhydra lutris*: McShane *et al.*, 1995; elephants, *Loxodonta africana*: McComb *et al.*, 2003; Clemins *et al.*, 2005; bottlenose dolphins, *Tursiops truncatus*: Tyack, 1986; Sayigh *et al.*, 1990; Janik *et al.*, 2006). In deer, studies of individual recognition based on acoustic cues have focused on the vocalizations emitted during early mother/young interactions, and have described how information on individual identity present in vocalizations facilitated either mutual (reindeer, *Rangifer tarandus*: Espmark, 1971, 1975) or partial (red deer: Vankova and Malek, 1997; Vankova *et al.*, 1997) recognition. Individual vocal cues have also been found in the barks given by roe deer (*Capreolus capreolus*) bucks during inter- and intraspecific interactions (Reby *et al.*, 1999) and in the groans of fallow deer (*Dama dama*) bucks during the rutting period (Reby *et al.*, 1998). Although roaring in red deer stags has been extensively studied (Clutton-Brock and Albon, 1979; McComb, 1987, 1988, 1991; Reby *et al.*, 2001; Reby and McComb, 2003a, 2003b; Reby *et al.*, 2005), the potential for red deer rutting calls to convey information on the identity of the caller has not been systematically investigated. Red deer stags give loud and repeated calls during the period of reproduction. Although the roar has received most attention red deer stags actually give four different call types: common roars, harsh roars, chase barks, and barks, each differing in their temporal and spectral acoustic structure, and each being associated with specific postures, social contexts and motivational levels (Reby and McComb, 2003b).

The aim of this study is to evaluate the interindividual variability of the most frequent call type (the *common roar*) and to assess the temporal variation in this identity information over the rutting period. We also assess whether the identity information we detect in the common roars is also present in the other three call types (harsh roars, chase barks, and barks). As three of the studied call types (common roars, harsh roars, and chase barks) are typically composed of more than one vocalization, we use signal detection and classification tools that are compatible with the analysis of series of nonstereotypical signals (rather than focusing our analyses on the first vocalization in the series or treating each vocalization as independent). For this, we use digital signal processing techniques initially developed for the automatic clas-

[a)]Electronic mail: reby@sussex.ac.uk

 © 2006 Acoustical Society of America

sification of human speech utterances, and based on the source-filter theory of voice production.

Despite the fact that the source-filter theory was initially designed for the study of human speech production, several recent studies have shown that it can be successfully generalized to most vocalizations emitted by terrestrial mammalian species (Fitch and Hauser, 1995; Fitch, 1997; Rendall *et al.*, 1998; Fitch and Reby, 2001; Reby and McComb, 2003a, 2003b; McComb *et al.*, 2003; Reby *et al.*, 2005). According to this theory, the spectral structure of mammalian voiced vocalizations results from two successive and independent mechanisms. The glottal wave is generated by the vibration of the vocal folds caused by the passage of air through the closed glottis. It is characterized by its fundamental frequency (F0) and its series of harmonic overtones, which are determined by variation in the subglottal pressure and tension of vocal folds (Titze, 1994) and affect the pitch of the vocalization. The relative amplitude of these frequency components is then modulated due to resonances occurring in the supralaryngeal vocal tract. This supralaryngeal filtering generates broadband frequency components in the sound spectrum, which are called vocal tract resonances or formants. Variation of the relative positions and movement of articulators (the larynx, mandibles, tongue, and lips) throughout the call and among different call types will affect the shape of the vocal tract and therefore the formant characteristics (Liebermann, 1968, 1969; Fitch and Hauser, 1995; McComb, 1988; Owren and Rendall, 1997). Both the individual morphology of the animal's vocal tract and the individual variation in its operation are likely to yield individual differences in the central frequencies and bandwidth of formant frequencies, affecting the "timbre" of the vocal signal.

Analyses of the fundamental frequency in red deer roars have suggested that the fundamental frequency varies with motivational state (although the average F0 in adults is 107 Hz, it can drop as low as 20 Hz in "lazy roars") (Reby and McComb, 2003a, 2003b, and unpublished data). Moreover, three of the four call types studied here are either largely (harsh roars) or totally (chase barks and single barks) aperiodic, and therefore do not contain measurable fundamental frequency and harmonics. On this basis, we decided to focus instead on interindividual variation in the filter-related formant frequencies (as in Rendall *et al.*, 1998). In order to separate the characteristics of the formant frequencies (filter) from the fundamental frequency contour (source), we use "homomorphic analysis," a method based on the source-filter paradigm of voice production (Oppenheim and Schafer, 1968). We then run a series of classification experiments using hidden Markov models, in which the bouts of roars are modeled as a succession of silences and roars, and each roar is modeled as a succession of states of the filter-related frequency components. First, we train a model of each individual's bout of roars using the most commonly uttered vocalization in the repertoire, the bout of common roars. Different identification tests are then performed to evaluate the model's ability to recognize and predict the individual membership of these bouts of vocalizations. Second, we test the stability of the information on individual identity conveyed by the formants throughout the rut. For this, we train a model with the bouts uttered in the first days of vocal activity, and we test the remaining bouts as additional cases. Finally, we test whether this individuality holds across the different vocalizations that compose the vocal repertoire of the stags during the rut, i.e., whether red deer stags have individual voice characteristics. For this, we classify the other call types as additional cases, using a model exclusively trained with bouts of common roars.

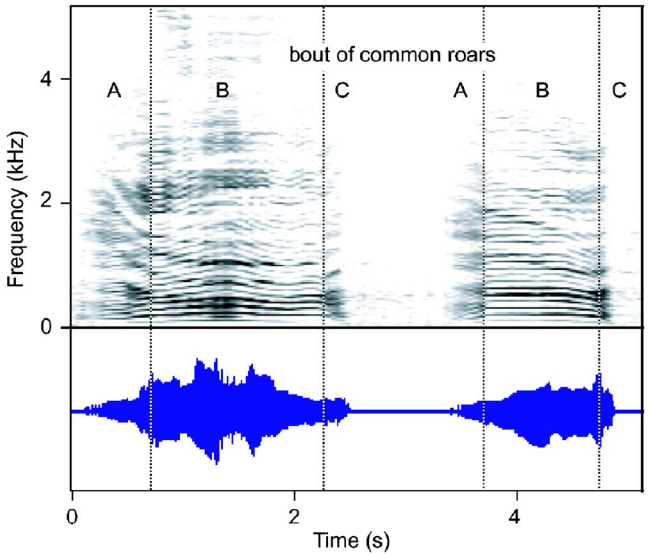

FIG. 1. Narrow band spectrogram of a bout of common roars. The common roar typically includes three phases, A, B, and C. In phase A, the formants fall while the fundamental frequency increases. During phase B the formants are more stationary. Phase C is shorter, with rising formants and a decreasing fundamental frequency.

II. DATA

A. Study animals

We recorded the vocalizations of three adult red deer stags (aged 5, 9, and 12) at the Picarel red deer farm (Southwest France) between September 25 and October 18, 1995, and from four additional adult stags (aged 5, 6, 6, and 8 years, and, respectively, weighing 210, 210, 215, and 230 kg) at the INRA experimental station of Redon (Puy de Dôme) between September 13 and October 4, 1996.

B. Sound recording

Vocalizations were recorded with a Telinga pro-III-S /DAT Mike microphone and a DAT Sony TCD7 recorder, (amplitude resolution: 16 bits, sampling rate: 48 kHz). Digital signals were directly transferred on to a Quadra 950 Macintosh computer using an Audiomedia II sound card and Sound Designer software. Each sound file consisted of a series (bout) of 1–10 consecutive vocalizations (roars) uttered by a stag during a single exhalation. Canary 1.2 (Charif *et al.*, 1995) was used to edit spectrograms of vocalizations. We considered 696 bouts of vocalizations from the seven males. Bouts were classified into four different categories on the basis of their acoustic structure and the postural and social context in which they were given.

We recorded 625 bouts of *common roars* (Fig. 1) from

TABLE I. Distribution of stags' recordings across the period of vocal activity. Each cell represents the number or recorded bouts of common roars. Day 1 is the first day when the stag is heard to vocalize. Bold figures indicate the vocalizations used in the training set of the "temporal" classification test.

	Days of recording																			
Stag	1	2	3	4	5	6	8	10	11	12	13	14	15	16	18	19	22	23	24	25
1	**14**		35					24								3				
2	**20**	6	11	24	22										54		28			
3	**22**	24			7	13	17					7					7			
4	**5**	**10**	11						26							43				
5	**7**								**3**	**8**			4	13	9		16	5	3	
6	**5**	**2**	**2**				31				4									
7	**18**								48	3			9	5	14		1			11

the seven stags, regularly distributed across the periods of vocal activity (Table I). Bouts of common roars contain between 1 and 11 roars, and each roar within the bout is typically composed of three distinct phases that reflect changes in vocal fold vibration and vocal tract shape that occur during the production of the roar [described in detail in Fitch and Reby (2001) and in Reby and McComb (2003a, 2003b)]. In the first phase the stag lowers its larynx and extends its neck to lengthen its vocal tract, inducing the decrease of the formants frequencies and spacing. During the second phase, the vocal tract remains extended and formant spacing remains minimal. Finally, the stag relaxes its vocal tract in the last (and usually shorter) phase, causing formants to rise. We recorded 40 bouts of *harsh roars* from six different individuals (Fig. 2). These bouts are less frequent, and usually characteristic of high motivational states following a contest or a period of intensive herding. Typically the bout starts with a series of short roars (also called grunts) followed by a couple of longer roars with comparable formants. The harsh roar is louder and less periodic than the common roar, and often contains no noticeable harmonics. It is also characterized by little or no formant modulation, reflecting the static body posture adopted by the animal while producing a bout of harsh roars (the larynx is fully lowered and the neck fully extended before the onset of the call and both remain almost static throughout the production of the bout). We also recorded 13 series of *chase barks* (Fig. 3) from three different stags. These calls are short series of short, loud, and explosive barks typically emitted by stags while they chase a hind or a young stag (Clutton-Brock *et al.*, 1982). Finally, we recorded 18 *single barks* (Fig. 4) from five different stags. These louder and longer calls are typically given by stags immediately before a bout of roaring or sometimes singly, and appear to be directed at females (Reby and McComb, 2003b).

III. METHODS

A. Signal processing and analyses

Sound files were low-pass filtered, converted to 8 bits, 8 kHz, SunAU files format, and transferred to a Sun SPARC station. In order to detect the time labels indicating the beginning and ending of each roar in the recorded bouts, we used a preprocessing automated segmentation technique followed by a relative threshold voice detection technique.

The segmentation was performed with the *a priori*

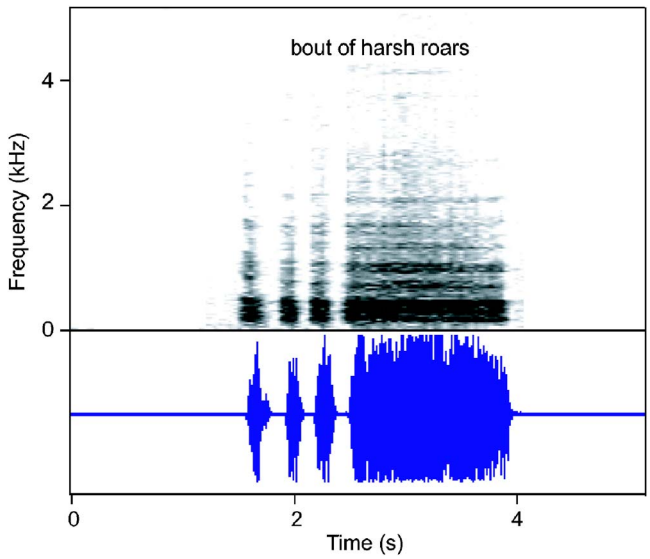

FIG. 2. Narrow band spectrogram of a bout of harsh roars. Compared to common roars, harsh roars are louder, atonal, and characterized by little frequency or energy modulation.

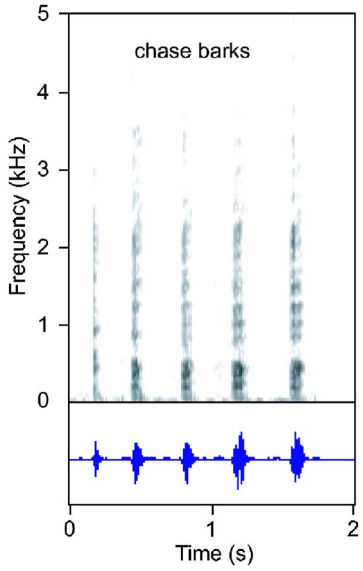

FIG. 3. Narrow band spectrogram of a chase bark series. Chase barks are short vocalizations that are emitted in series.

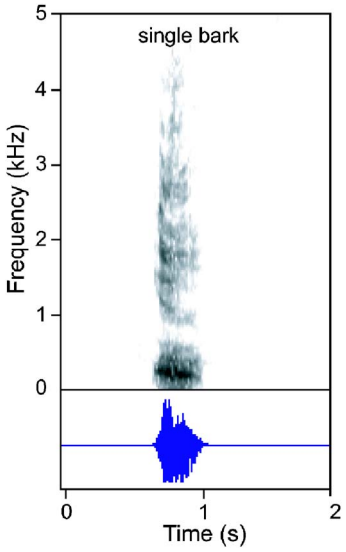

FIG. 4. Narrow band spectrogram of a single bark. Single barks are typically longer than chase barks.

"forward-backward divergence" algorithm (André-Obrecht, 1988). By detecting changes in the parameters of an autoregressive model, this method fragments the signal into stationary segments of variable size, on which statistical parameters can be computed.

Then, in order to define the vocalization boundaries in the sound file by separating intervals of "silence" from intervals of "vocalization," we used the relative energy of each segment. For this, we (1) identified the least energetic segment in the bout, presumably consisting of background noise; (2) calculated the difference between the energy of each segment in the bout, and the energy of the least energetic one; (3) calculated the ratio of each segment's differences to the highest difference. If *Ei* is the energy of a segment *i*, and *n* the number of segments in the bout, the ratio *k* for the considered segment was calculated as follows:

$$k_i = \frac{E_{i-\mathrm{MIN}_{i=1}^{n}}(E_i)}{\mathrm{MAX}\left[E_{i-\mathrm{MIN}_{i=1}^{n}}(E_i)\right]}.$$

Each segment was considered as vocalization if this ratio was greater than 0.75, and silence (or background noise) if it was less than 0.75. This threshold value was determined experimentally with the aim of minimizing the number of misclassified segments. Examination of spectrograms showed that this technique was highly successful at identifying voiced segments; almost all the misclassified segments were very short segments located at the end of the vocalizations. Consecutive segments of silence were then merged into silence phases, and consecutive vocalization segments were merged into vocalization phases. An example of this automated segmentation and energy threshold computation is presented in Fig. 5. The resulting time labels were used to indicate the location of common roars and silences in the bout file for the training phase of the hidden Markov model classifications.

As mentioned previously, we used homomorphic analysis (Oppenheim and Schafer, 1968; Deller, 1999; Quatieri, 2002) to separate the contributions of the excitation source and the vocal tract filter to the sound wave. According to the source-filter theory, the sound wave is produced by filtering the output of the excitation source through the vocal tract filter. In the wave form domain this process can be thought of as the convolution of the excitation wave form with the

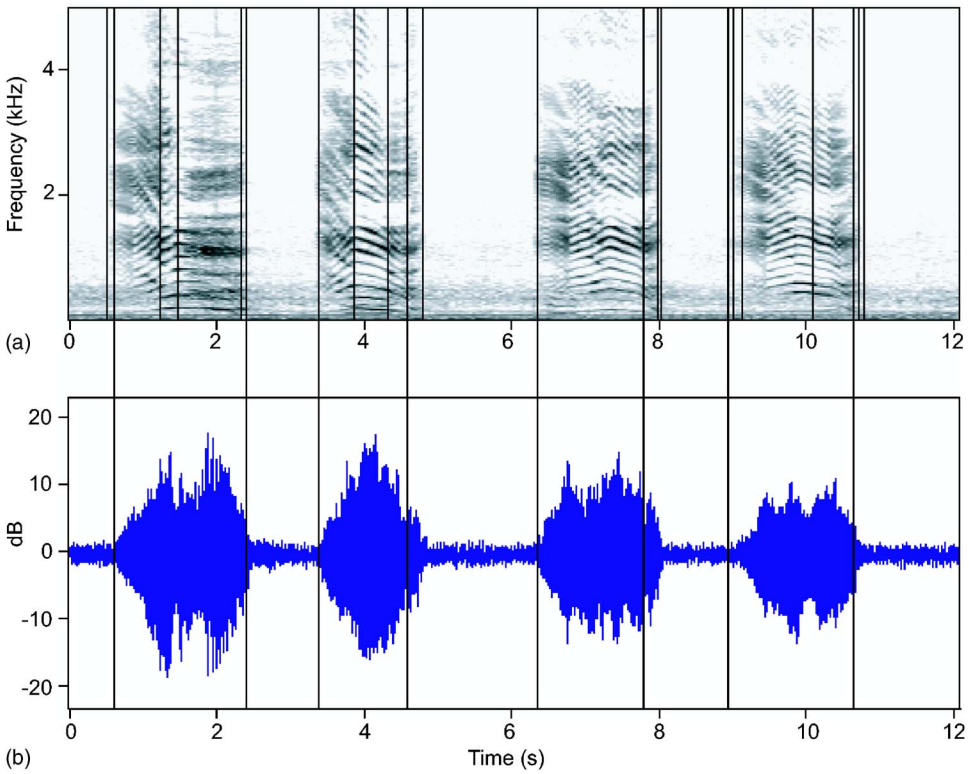

FIG. 5. Automatic detection of vocalization and silence phases in a bout of common roars. (a) Segmentation: the "forward-backward divergence" algorithm fragments the signal into stationary segments of variable size. (b) Energy thresholding: segments are classified as silence or vocalization using the relative energy of each segment. Consecutive silence segments are merged into silence phases and consecutive vocalization segments are merged into vocalization phases.

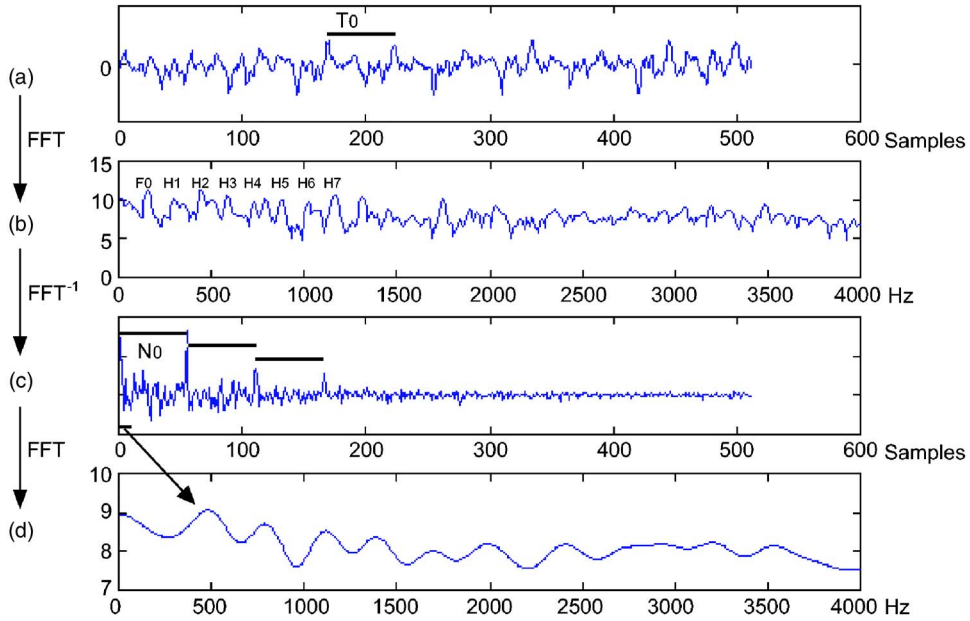

FIG. 6. Homomorphic analysis performed on a 512 samples window of a red deer stag common roar (sampling rate: 8 kHz). Panel A represents the sound wave in the time domain; the signal is periodic with a period T_0. Panel B represents the spectrum (fast Fourier transform) of this sample, with the fundamental frequency (F0) and its harmonic series (the first six harmonics H1–H6 are labeled). Panel C shows the cepstrum Yn. The cepstrum is calculated by taking the inverse Fourier transform of the logarithm of the energy spectrum of the signal. The contribution of the glottal source is represented by impulses spaced by N_0 samples (corresponding to the pitch period), while the contribution of the filter is represented by the lower part of the cepstrum. Finally, panel D shows the frequency spectrum obtained by applying a Fourier transform to the first eight coefficients of the cepstrum, illustrating the smoothing effect of the deconvolution process.

impulse response of the vocal tract. In the spectral domain this same process can be thought of as multiplying the spectrum of the excitation function by the vocal tract's transfer function. Taking the logarithm of the energy spectrum changes this multiplication to an addition, and homomorphic analysis decomposes these additive components of the log spectrum into *cepstral* components, in an exactly analogous way to that in which frequency components are obtained from a complex sound wave. The low "quefrency" cepstral coefficients represent slowly changing aspects of the spectrum—namely the formant frequencies imposed by the vocal tract filter, whereas the high quefrency cepstral coefficients represent rapidly changing aspects of the spectrum—the spectral ripple that is the harmonic structure (the fundamental frequency and its harmonic series). In order to selectively capture the contribution of the vocal tract we used the low quefrency cepstral coefficients. The application of cepstral analysis to a red deer roar is represented in Fig. 6.

When the Mel scale (Stevens *et al.*, 1937), a human logarithmic perceptual scale, is applied to the signal in the frequency domain in order to reduce the dimensionality of the feature vector, these coefficients are called Mel frequency cepstrum coefficients (MFCC). The use of the Mel scale in the classification of red deer vocalizations is supported by the fact that the hearing range of hoofed mammals is comparable to that of humans (Flydal *et al.*, 2001), and that studies of the mammalian auditory system indicate that frequencies are perceived along a roughly logarithmic scale (Fay, 1974; Greenwood, 1990; Clemins, 2005). In our study, we analyzed windows of 25 ms (200 samples at the 8 kHz sampling rate), with a 10 ms overlap. Each window was considered stationary, and the first eight MFCC were retained. For each recorded roar, we obtained a sequence of observation vectors $Y=(Y_1, Y_2, \ldots, Y_T)$ each corresponding to the eight cepstral coefficients of the T subsequent analysis windows.

B. Models

Hidden Markov models are doubly stochastic processes characterized by an underlying stochastic process that is not observable (it is hidden), but can be assessed through another stochastic process that produces the sequence of observed symbols or vectors. Hidden Markov models (HMM) (Rabiner and Juang, 1986) are typically used to model the processes underlying a sequential behavior whose inner workings cannot be directly observed. Here, we make the hypothesis that interindividual differences in the way vocalizations are produced will result in observable interindividual differences in the acoustic structure of the vocalizations. Although we cannot directly observe the individual vocal gestures that are at the origin of the observed individual differences in the acoustic structure of the calls, we can use a HMM to model these underlying mechanisms, and then use these models to predict the individual membership of additional vocalizations. The analyses were run using HTK version 2.2 (Cambridge University Engineering Department). Our Markov model analysis can be formally described as follows: our purpose was to identify one deer among N through the analysis of its bout of vocalization. As a bout consists of a series including up to 11 vocalizations, the bout model M^k_{bou} of the deer D^k is sequence of alternating silence models M_{sil} and vocalization models M^k_{voc}, where the number of vocalizations is variable [Fig. 7(a)]. Each elementary model (M_{sil}, M^k_{voc}, $k=1, \ldots, N$) is a HMM with a Bakis to-

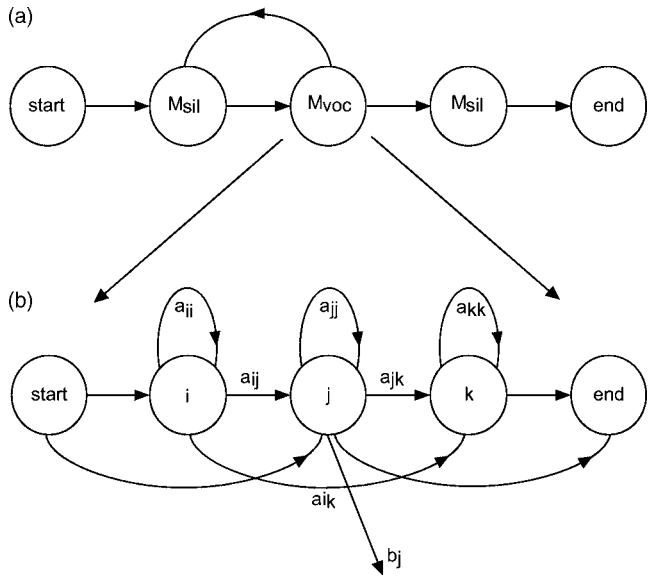

FIG. 7. (a) The model of the roar bout is a succession of silences (M_{sil}) and vocalizations (M_{voc}). The silence model is independent of the considered individuals. (b) In contrast, each individual has its own roar model, a hidden Markov model of three states, where each state emits a vector of eight cepstral coefficients according to a Gaussian mixture probability distribution. Each state is assumed to correspond to one of the three phases that characterize the roar (see Fig. 1).

pology [Fig. 7(b)]. In a Bakis topology, each state can be repeated or omitted. This topology is used in speech recognition in order to take into account the rhythm differences that typically occur in speech sequences. In the case of red deer roaring, this topology enables the HMM automates to model the variability that characterizes deer vocalizations.

The silence model M_{sil} is independent of the considered deer D_k, so that:

$$M^k_{bou} = (M_{sil}, M^k_{voc}).$$

In our study, the hidden process is a finite state, first order Markov chain, meaning that each transition only depends on the very preceding state (and not on the way that state was reached). At each time step, a new state is entered based upon a transition probability distribution ($a_{i,j}$) which depends on the previous state (the Markov property), and an observation output symbol (or vector Y) is produced according to a probability distribution which depends on the current state (b_j). In our case, the distributions b_j are Gaussian mixture models (order 5). During the training phase, we use a subset of records of each deer D_k to adjust the parameters of the corresponding model $M^k_{voc}(a^k_{i,j}, b^k_j)$, using the Baum Welch algorithm (Rabiner and Juang, 1986). The silence model M_{sil} is estimated using all the silence segments available within the training set. During the test phase [performed using the Viterbi algorithm (Forney, 1973)], for each unknown bout characterized by an observation vector sequence $Y=(Y_1, Y_2, \ldots, Y_T)$, and for each individual bout of roar model M^k_{bou}, the likelihood $P(Y|M^k_{bou})$ is calculated. The predicted membership is determined by the best likelihood.

TABLE II. Confusion matrix from the hidden Markov model validation classification computed on the cepstral coefficients from 654 roaring bouts from seven red deer stags. 93.4% of tested bouts are correctly classified.

	Predicted group membership								
Stag	1	2	3	4	5	6	7	% correct	N
1	**73**	1	0	0	1	0	1	96.0	76
2	1	**149**	9	1	1	0	4	90.3	165
3	0	10	**87**	0	0	0	0	89.7	97
4	0	1	0	**94**	0	0	0	98.9	95
5	0	0	0	0	**63**	4	1	92.6	68
6	0	1	0	0	3	**38**	2	86.4	44
7	1	0	0	0	0	1	**107**	98.1	109

C. Classification experiments

Several data sets were constituted in relation to the individual and call type memberships of the vocalization bouts. The first stages (training stage and validation stage) consisted of training the HMM to establish a vocalization model for each individual, with all the 654 bouts of roars. All these bouts were then reclassified using this model in order to test its ability to memorize the dataset (reclassification performance). In the second stage, we tested the model's ability to generalize by performing a random cross-validation test. This evaluated the model's ability to classify additional vocalizations (prediction performance). For this purpose, we trained a HMM with a sample which constituted two thirds of each individual's vocalizations (N=436). This model was then tested with its validation set of remaining vocalizations (N=218). In order to assess the possible degradation of acoustic cues to identity in the course of the rutting period, we conducted a temporal cross validation. To achieve this, we constituted individual training sets including only the vocalizations recorded in the early day(s) of vocal activity (N =165, Table I). We performed a logistic regression on the classification results of the vocalizations recorded later in the rut (N=489) in order to assess the time-related change of the prediction performances of each individual's model. To test if the individuality modeled in common roars holds in the three other vocalization types, we used the subset of common roar bouts as the training set (n=625) and all the other vocalizations (n=71) as test sets. Because stags relatively rarely produce harsh roars, chase barks, and barks, our vocalizations sets are unbalanced among call types, with samples too small to conduct a split-sample approach (Rendall *et al.*, 1998). However, in our case, from the biological point of view, our approach is consistent as recipients are more likely to learn individuality from the most currently uttered call type. Therefore, we do not compare individuality among call types, but we instead test if individuality in the most currently emitted one carries over into the others.

IV. RESULTS

A. Classification of common roars

In the validation stage, 93.4% of the roars were correctly attributed (Table II), with individual scores ranging from

TABLE III. Confusion matrix from the hidden Markov model classification computed on the cepstral coefficients from 654 roaring bouts from seven red deer stags. The model is trained with two-thirds of the available bouts randomly selected within each individual, and the remaining third ($N=218$) are tested as additional cases. 84.9% of tested bouts are correctly classified.

	Predicted group membership								
Stag	1	2	3	4	5	6	7	% correct	N
1	**24**	0	0	1	0	0	0	96.0	25
2	2	**48**	4	1	0	0	0	87.3	55
3	0	5	**27**	0	0	0	0	84.4	32
4	0	1	0	**30**	0	0	1	93.8	32
5	0	1	0	0	**16**	1	5	69.6	23
6	0	0	1	0	4	**9**	1	60.0	15
7	0	0	0	0	4	1	**31**	86.1	36

TABLE IV. Confusion matrix from the hidden Markov model classification computed on the cepstral coefficients from 654 roaring bouts from seven red deer stags. The model is trained with the bouts uttered on the first days of vocal activity ($N=165$), and the bouts uttered during the rest of the period of vocal activity ($N=489$) are tested as additional cases. 58.1% of tested bouts are correctly classified.

	Predicted group membership								
Stag	1	2	3	4	5	6	7	% correct	N
1	**49**	8	3	1	0	0	1	79.0	62
2	0	**95**	35	4	1	0	10	65.5	145
3	1	15	**56**	0	0	0	3	74.7	75
4	6	1	17	**35**	0	0	21	43.8	80
5	0	3	0	0	**12**	4	21	24.0	50
6	0	1	0	0	3	**1**	30	2.9	35
7	2	0	1	0	1	2	**36**	85.7	42

86.4% to 98.9%. In the one-third holdout cross validation, 84.9% of the 218 randomly selected and tested bouts of common roars are correctly classified (Table III). Individual percentages range between 60.0% and 96.0%.

B. Degradation of individuality in common roars with time

In the temporal cross validation, 58.1% of the roars were correctly classified with models constituted with the roars uttered on the first days of vocal activity (Table IV). Percentages were highly variable between individuals, ranging from 2.9% for stag 6 to 85.7% for stag 7. A logistic regression performed on the classification scores of each individual shows that, for three of the seven stags (stag 1: $R=-0.361$, $p<0.005$; stag 2: $R=-0.205$, $p<0.005$, and stag 4: $R=-0.114$, $p=0.06$) the percentage of correctly classified bouts decreases significantly across the period of vocal activity.

C. Across call recognition

In the cross validation performed with the model trained on common roars, 63.4% of the chase barks, harsh roars, and barks are correctly classified (Table V). Last, when chase barks, harsh roars, and barks were included with the common roars in the training set, in the validation phase, the classification score of the common roars was not affected (93.3%) and 91.5% of the calls from the three other types were correctly recognized.

V. CONCLUSIONS

A. Automatic analysis of vocalization sequences

In this paper, we use entirely automated analysis techniques that are particularly appropriate for the processing of large amounts of acoustic data of variable format. The automatic segmentation is particularly well adapted for the detection of calls given in series, and it could be generalized for the automatic detection and identification of animal signals in the context of wildlife population monitoring for conservation or management purposes. The homomorphic analysis is particularly appropriate for disentangling the formants from the fundamental frequency contour in harmonically rich vocalizations, and it has the advantage of characterizing the filter function with a set of largely uncorrelated coefficients suitable for multivariate classifications (Clemins *et al.*, 2005).

In red deer roars, the movement of the larynx causes variation in the filter components. The use of Markov models

TABLE V. Classification of chase barks (cb), barks (ba), and harsh roars (hr) from six stags, using Hidden Markov Models trained with the cepstral coefficients from 625 common roars from seven red deer stags. 63.4% correctly classified. Chase barks: 84.6%, $N=13$; barks: 55.5%, $N=18$; harsh roars: 60%, $N=40$.

	Predicted group membership																						
	1			2			3			4			5			6			7				
Stag	cb	ba	hr	cb	ba	hr	cb	ba	hr	cb	ba	hr	cb	ba	hr	cb	ba	hr	cb	ba	hr	N correct	N total
1	-	-	**1**	-	-	-	-	-	-	-	-	-	-	-	-	-	-	-	-	-	-	1	1
2	-	-	-	**10**	-	**8**	-	-	1	-	-	-	-	1	-	-	-	-	-	-	-	18	20
3	-	-	-	-	-	-	-	-	-	-	-	-	-	-	-	-	-	-	-	-	-	-	-
4	-	-	-	-	1	7	-	-	1	-	-	**6**	-	-	-	-	-	-	-	1	-	6	16
5	-	-	-	-	2	-	-	-	-	-	-	-	**1**	**9**	**4**	-	1	-	-	-	1	14	18
6	-	-	-	-	-	-	-	-	-	-	-	-	2	1	1	-	-	-	-	-	-	0	4
7	-	-	-	-	-	-	-	-	-	-	-	-	-	-	5	-	1	-	-	**1**	**5**	6	12

enables us to take into account these different states as well as the transition probabilities between these states. However, it is important to note that the process being *hidden*, we cannot verify whether the states used in the model actually correspond to those anticipated on the basis of our knowledge of formants production in red deer roaring. It would be interesting in further investigations to assess the effect of varying the number of states and the possible transitions on the predictive performance of the different models. This method has recently been applied successfully to the automatic recognition of call types and individuals from elephant vocalizations (Clemins *et al.*, 2005). The use of Markov models also enables us to include bouts of vocalizations. Such techniques are particularly suited for the study of the acoustic variability of vocalizations emitted in bouts or series, which is the case in many animal acoustic signals.

B. Individual differences in common roars

The results of the validation phase and 1/3 random sample test classifications show that common roar bouts uttered during the rutting period by red deer stags are highly individually structured. Individuality is relatively stable across the period of vocal activity, as a model trained with the vocalizations uttered over a few days at the onset of vocal activity was sufficient to predict the group membership of a majority of the vocalizations uttered later in the rut. In three of the stags studied, we observe a significant decrease in membership prediction, probably resulting from a progressive alteration of the formant characteristics. The very low score obtained for stag 6 may indicate that a drastic change had occurred between the roars given in the first days and those from the rest of the rutting period. It may also be a consequence of the small number of bouts available in the training set ($n=9$) for this individual.

These results suggest that cues to caller's identity exist in the filter-related components of red deer stags' common roars. This variability is likely to result from interindividual differences in the shape of the vocal tract. These differences may have three origins: (1) differences in body size affecting vocal tract length, (Reby and McComb, 2003a), (2) interindividual differences in vocal tract shape independent from body size, and (3) interindividual differences in vocal gesture control of vocal tract length and shape involving larynx, mandible, tongue, and lip positions.

It is notable that classification percentages indicate that cues to individual identity also appear to vary over time. This suggests that the temporal approach described in this paper should be used more often when designing training and testing sets in studies of individual differences based on modeling and classification experiments. Indeed, pooling recordings from different dates, and using classifications percentages from validation phases, *leave-one-out* validations or any cross validations where recordings made on the same date as the tested case(s) are included in the training sample is very likely to result in serious over-estimations of the actual predictive potential of the models.

C. Across calls recognition

When we tested the membership of the three other components of the males' rutting vocal repertoire (harsh roars, chase barks, and barks) using models trained on the cepstral coefficients of the 625 common roars, we obtained percentages of correct classification higher than expected if the membership had been determined randomly. Our sample is too small and our data set is too unbalanced among individuals and call types to allow a comparison of the percentage of recognition between the three types of vocalizations. Nevertheless, our results suggest that although the four vocalizations are produced in different body postures, likely to affect the length and shape of the vocal tract, their formant frequencies share cues to identity. This result indicates that red deer stag have individual voice characteristics, as seen in humans (Doddington, 1985; Furui, 1997) and rhesus monkeys (Rendall *et al.*, 1998). The percentages of correct classification obtained in the validation phase using models trained with tokens from all four vocalization types are higher, showing that the individuality of the voice may consist of individual features shared by all call types as well as individual features specific to each call type (the later being partially lost when a particular call type is not used for the training of the model).

This is the first demonstration of across call individuality in a nonprimate mammal (for primates, see Cheney and Seyfarth, 1988; Rendall *et al.*, 1998). Indeed, to our knowledge, all previous studies on individual cues in acoustic communication in nonprimate mammals have been conducted on the individual differences occurring within each type of call, never across several types of calls (Lambrecht and Dhondt, 1995). Rendall *et al.* (1998) found more mixed evidence for individual voice characteristics across the vocal repertoire of rhesus monkey *Macaca mulatta* (harmonically rich coos were more individually distinctive than either grunts or noisy screams), raising the interesting possibility of interspecific differences in the "individual voice" phenomenon. The ability of red deer receivers to discriminate the identity information discussed above and to transfer it from one call type to another could be assessed by means of playback experiments using the habituation/discrimination paradigm (Rendall *et al.*, 1996; Reby *et al.*, 2001).

D. Potential biological significance of cues to identity in red deer roaring

Studying the acoustic structure of the first roar emitted in a bout, Reby and McComb (2003a) have found that in red deer, formant frequencies and their spacing decreased with increasing age and/or body weight, and that stags attended to these cues during agonistic interactions (Reby *et al.*, 2005). Formant spacing is correlated with the length of the vocal tract and therefore indirectly related to overall body size and body weight. In the present study the recorded males are all adult farmed animals, which are likely to have reached their maximum body weight. The body weight of the four stags for which we had access to biometrical data ranged between 210 and 230 kg, and their roars were characterized by very similar formant frequency spacing corresponding to esti-

mated vocal tract lengths of 81.0, 81.5, 81.5, and 81.8 cm (Reby and McComb, 2003a). Therefore, the individual differences modeled here are more likely to rest in the relative positioning and bandwidth of individual formants rather than in the size-related overall spacing of the formants in the frequency domain. Playback experiments have suggested that females may be preferentially attracted to males with high roaring rates, but indifferent to differences in roar pitch (McComb, 1991). As females often leave or enter male harems, McComb (1991) suggested that females choose which harem to join on the basis of male roaring rate, a potentially reliable cue of the stag's fitness. More recently, Reby *et al.* (2001) have shown that red deer hinds could discriminate between the common roars of their current harem holder and the roars of neighboring males (Reby *et al.*, 2001), and suggested that estrus hinds may choose to mate with stags that they are most familiar with (familiarity being an indicator of the stag's ability to hold mating stands for significant periods), a choice that may partially rely on acoustic individual recognition. The results presented here suggest that hinds may use characteristics of formant frequencies to achieve this individual discrimination, and that these characteristics are available both within and across call types, constituting the equivalent of an individual voice.

ACKNOWLEDGMENTS

The authors thank Marcel Verdier and Alain Brelurut for letting us record the stags at INRA and Catherine Souef at Picarel le Haut, Dominique Pépin, George Gonzales and Mark Hewison for help with the data collection, and Chris Darwin, Karen McComb, Ben Charlton, Loic Hardouin, Drew Rendall and three anonymous referees for their very helpful comments on earlier versions of the manuscript.

Andre-Obrecht, R. (**1988**). "A new statistical approach for the automatic segmentation of continuous speech signals," IEEE Trans. Acoust., Speech, Signal Process. **36**(1), 29–40.

Chapman, C. A., and Weary, D. M. (**1990**). "Variability in spider monkeys' vocalisations may provide basis for individual recognition," Am. J. Primatol **22**, 279–284.

Charif, R. A., Mitchell, S., and Clark, C. W. (**1995**). *Canary 1.2 User's Manual* (Cornell Laboratory of Ornithology, Ithaca, NY).

Cheney, D. L., and Seyfarth, R. M. (**1988**). "Assessment of meaning and the detection of unreliable signals in by vervet monkeys," Anim. Behav. **36**, 477–486.

Clemins, P. J. (**2005**). "Automatic classification of animal vocalizations," Ph.D. thesis, Marquette University.

Clemins, P. J., Johnson, M. T., Leong, K. M., and Savage, A. (**2005**). "Automatic classification and speaker identification of African elephant (*Loxodonta africana*) vocalizations," J. Acoust. Soc. Am. **117**, 956–963.

Clutton-Brock, T. H., and Albon, S. D. (**1979**). "The roaring of red deer and the evolution of honest advertisement," Behaviour **69**, 124–134.

Clutton-Brock, T. H., Guinness, F. E., and Albon, S. D. (**1982**). *Red Deer: Behavior and Ecology of Two Sexes* (The University of Chicago Press, Chicago, IL).

Darden, S. K., Dabelsteen, T., and Pedersen, S. B. (**2003**). "A potential tool for swift fox (Vulpes velox) conservation: Individuality of long-range barking sequences," J. Mammal. **84**, 1417–1427.

Deller, J. R., Hansen, J. H. L., and Proakis, J. G. (**1999**). *Discrete-Time Processing of Speech Signals* (Wiley-IEEE, New York).

Doddington, G. (**1985**). "Speaker Recognition—Identifying people by their voices," Proc. IEEE **73**, 1651–1662.

East, L. E., and Hofer, H. (**1991**). "Loud calling in a female dominated society: I. Structure and composition of whooping bouts of spotted hyenas, *Crocuta crocuta*," Anim. Behav. **42**, 637–649.

Espmark, Y. (**1971**). "Individual recognition by voice in reindeer mother-young relationship," Behaviour **40**, 295–301.

Espmark, Y. (**1975**). "Individual characteristics in the calls of reindeer calves," Behaviour **54**, 50–59.

Fay, R. R. (**1974**). "Auditory frequency discrimination in vertebrates," J. Acoust. Soc. Am. **56**, 206–209.

Fitch, W. T. (**1997**). "Vocal tract length and formant frequency dispersion correlate with body size in rhesus macaques," J. Acoust. Soc. Am. **102**, 1213–1222.

Fitch, W. T., and Hauser, M. D. (**1995**). "Vocal production in nonhuman primates: acoustics, physiology and functional constraints on honest advertising," Am. J. Primatol. **37**, 191–219.

Fitch, W. T., and Reby, D. (**2001**). "The descended larynx is not uniquely human," Proc. R. Soc. London **268**, 1669–1675.

Flydal, K., Hermansen, A., Enger, P. S., and Reimers, E. (**2001**). "Hearing in red deer," J. Comp. Physiol.. **187**, 265–269.

Forney, G. D. (**1973**). "The Viterbi algorithm," Proc. IEEE **61**, 268–278.

Frommolt, K. H., Kruchenkova, E. P., and Russig, H. (**1997**). "Individuality of territorial barking in arctic foxes, *Alopex lagopus*," in *Proceedings of the First International Symposium on Physiology and Ethology of Wild and Zoo Animals*, edited by F. Klima and R. R. Hofman (Gustav Fisher), Jena, pp. 66–70.

Furui, S. (**1997**). "Recent advances in speaker recognition," in *Audio and Video-Based Biometric Person Authentification*, edited by J. Bigun, G. Chollet, and G. Borgefors (Springer-Verlag), Berlin, pp. 237–252.

Greenwood, D. (**1990**). "A cochlear frequency-position function for several species—29 years later," J. Acoust. Soc. Am. **87**, 2592–2650.

Hanggi, E. B., and Schusterman, R. J. (**1994**). "Underwater acoustic displays and individual variation in male harbour seals, *Phoca vitulina*," Anim. Behav. **48**, 1275–1283.

Janik, V. M., Sayigh, L. S., and Wells, R. S. (**2006**). "Signature whistle shape conveys identity information to bottlenose dolphins," Proc. Natl. Acad. Sci. U.S.A. **103**, 8293–8297.

Lambrecht, M. M., and Dhondt, A. A. (**1995**). "Individual voice discrimination in birds," in *Current Ornithology*, edited by D. M. Power (Plenum, New York) Vol. 12, pp. 115–139.

Lieberman, P. (**1968**). "Primate vocalization and human linguistic ability," J. Acoust. Soc. Am. **44**, 1574–1584.

Lieberman, P., Klatt, D. H., and Wilson, W. H. (**1969**). "Vocal tract limitations on the vowel repertoires of rhesus monkeys and other nonhuman primates," Science **164**, 1185–1187.

McComb, K. (**1987**). "Roaring by red deer stags advances the date of oestrus in hinds," Nature (London) **330**, 648–649.

McComb, K. (**1988**). "Roaring and reproduction in red deer, *Cervus elaphus*," Ph.D. thesis, University of Cambridge.

McComb, K. (**1991**). "Female choice for high roaring rate in red deer, *Cervus elaphus*," Anim. Behav. **41**, 79–88.

McComb, K., Reby, D., Baker, L., Moss, C., and Sayialel, S. (**2003**). "Long-distance communication of social identity in African elephants," Anim. Behav. **65**, 317–329.

McShane, L. J., Estes, J. A., Riedman, M. L., and Staedler, M. M. (**1995**). "Repertoire, structure, and individual variation of vocalisations in the sea otter," J. Mammal. **76**, 414–427.

Oppenheim, A. V., and Schafer, R. W. (**1968**). "Homomorphic analysis of speech," IEEE Trans. Audio Electroacoust. **16**(2), 221–226.

Owren, M. J., and Rendall, D. (**1997**). "An affect-conditioning model of nonhuman primate vocal signaling," in *Perspectives in Ethology: Vol. 12. Communication*, edited by D. H. Owings, M. D. Beecher, and N. S. Thompson (Plenum, New York), pp. 299–346.

Quatieri, T. F. (**2002**). *Discrete-Time Speech Signal Processing, Principles and Practice* (Prentice-Hall, Upper Saddle River, NJ).

Rabiner, L. R., and Juang, B. H. (**1986**). "An introduction to hidden Markov models," IEEE ASSP Mag. **3**(1), 4–16.

Reby, D., Joachim, J., Lauga, J., Lek, S., and Aulagnier, S. (**1998**). "Individuality in the groans of fallow deer (*Dama dama*) bucks," J. Zool. **245**, 79–84.

Reby, D., Cargnelutti, B., Joachim, J., and Aulagnier, S. (**1999**). "Spectral acoustic structure of barking in roe deer (*Capreolus capreolus*). Sex-, age- and individual-related variations," C. R. Acad. Sci. III **322**, 271–279.

Reby, D., Izquierdo, M., Hewison, A. J. M., and Pepin, D. (**2001**). "Red deer (*Cervus elaphus*) hinds discriminate between the roars of their current harem holder stag and those of neighbouring stags," Ethology **107**, 951–959.

Reby, D., and McComb, K. (**2003a**). "Anatomical constraints generate hon-

esty: Acoustic cues to age and weight in the roars of red deer stags," Anim. Behav. **65**, 519–530.
Reby, D., and McComb, K. (**2003b**). "Vocal communication and reproduction in deer," Adv. Stud. Behav. **33**, 231–264.
Reby, D., McComb, K., Cargnelutti, B., Darwin, C., Fitch, W. T., and Clutton-Brock, T. H. (**2005**). "Red deer stags use formants as assessment cues during intrasexual agonistic interactions," Proc. R. Soc. London **272**, 941–947.
Rendall, D., Rodman, P. S., and Edmond, R. E. (**1996**). "Vocal recognition of individuals and kin in free-ranging monkeys," Anim. Behav. **51**, 1007–1015.
Rendall, D., Owren, M. J., and Rodman, P. S. (**1998**). "The role of vocal tract filtering in identity cueing in rhesus monkey *(Macaca mulatta)* vocalizations," J. Acoust. Soc. Am. **103**, 602–614.
Sayigh, L. S., Tyack, P. L., Wells, R. S., and Scott, M. D. (**1990**). "Signature whistles of free-ranging bottlenose dolphins (*Tursiops truncatus*): Stability and mother-offspring comparisons," Behav. Ecol. Sociobiol. **26**, 247–260.
Stevens, S. S., Volkmann, J., and Newman, E. B. (**1937**). "A scale for the measurement of the psychological magnitude pitch," J. Acoust. Soc. Am. **8**, 185–190.
Titze, I. R. (**1994**). *Principles of Voice Production* (Prentice-Hall, Englewood Cliffs, NJ).
Tooze, Z. J., Harrington, F. H., and Fentress, J. C. (**1990**). "Individually distinct vocalisations in timber wolves, *Canis lupus*," Anim. Behav. **40**, 723–730.
Tyack, P. L. (**1986**). "Whistle repertoires of two bottlenose dolphins, *Tursiops truncatus*: Mimicry of signature whistles?," Behav. Ecol. Sociobiol. **18**, 251–257.
Vankova, D., and Malek, J. (**1997**). "Characteristics of the vocalisations of red deer (*Cervus elaphus*) hinds and calves," Bioacoustics 7, 281–289.
Vankova, D., Bartos, L., and Malek, J. (**1997**). "The role of vocalizations in the communication between red deer hinds and calves," Ethology **103**, 795–808.
Zimmerman, E., and Lerch, C. (**1993**). "The complex acoustic design of an advertisement call in male Mouse lemurs (*Microcebus murinus*) and sources of its variation," Ethology **93**, 211–224.

Variation in the hearing sensitivity of a dolphin population determined through the use of evoked potential audiometry

Dorian S. Houser[a)]
Biomimetica, 7951 Shantung Drive, Santee, California 92071

James J. Finneran
U.S. Navy Marine Mammal Program, Space and Naval Warfare Systems Center, San Diego, Code 2351, 49620 Beluga Rd., San Diego, California 92152

(Received 26 April 2006; revised 9 August 2006; accepted 2 September 2006)

A portable electrophysiological data collection system was used to assess hearing in a captive population of bottlenose dolphins by recording auditory evoked potentials (AEPs). The AEP system used a transducer embedded in a suction cup to deliver amplitude modulated tones to the dolphin through the lower jaw. Evoked potentials were recorded noninvasively using surface electrodes. Adaptive procedures allowed hearing thresholds to be estimated from 10 to 150 kHz in a single ear in about 45 min. Hearing thresholds were measured in 42 bottlenose dolphins (28 male, 14 female), ranging in age from 4 to 47 years. Variations in hearing sensitivity with age and sex followed patterns seen in humans and terrestrial mammals: generally, within the population there was a progressive loss of high frequency hearing with age and an earlier onset of hearing loss in males than in females. Hearing loss generally occurred between the ages of 20 and 30, and all animals over the age of 27 had some degree of hearing loss. Two dolphins with profound hearing loss were found within the population. Aberrant hearing patterns were observed in related dolphins suggesting genetic links to hearing ability may exist. © *2006 Acoustical Society of America.*
[DOI: 10.1121/1.2357993]

PACS number(s): 43.80.Lb, 43.64.Ri [WWA] Pages: 4090–4099

I. INTRODUCTION

Increased frequency of hearing impairment with age (presbycusis) and sex differences in the onset of hearing impairment have long been known for human populations. The 2003 survey by the National Center for Health Statistics (United States Department of Health and Human Services, 2005) on the health status of individuals within the United States indicated that incidence of profound hearing loss increased from 1% for those under the age of 44, to 15% for those over the age of 74. The incidence of hearing loss among males was nearly twice as high as that of females until the age of 75, supporting the pattern of age-related hearing loss and male bias toward hearing loss at a younger age in human populations. Within the United States, the causes of hearing loss are primarily attributed to noise exposure (33.7%), presbycusis (28%), and ear infections (12.2%) (United States Department of Health and Human Services, 1994).

It seems reasonable to expect that the auditory systems of marine mammals are similarly subject to impairment. Prior work on some odontocete species has demonstrated hearing loss in individuals (Ridgway and Carder, 1993, 1997; Brill *et al.*, 2001; Finneran *et al.*, 2005b; Yuen *et al.*, 2005), although the etiology of the deficit is not certain in most cases. That hearing loss occurs in marine mammals is an important consideration because the ability to produce, receive, and interpret sound permits most marine mammals to thrive in the ocean. Understanding how a marine mammal with hearing loss functions in natural contexts is important to understanding how sensory impairment affects the ability of marine mammals to survive and exploit their environment. Similarly, determining the impact that anthropogenic sound has on marine mammal populations is important to mitigating the environmental consequences of human activity in the world's oceans (National Research Council (NRC), 1994, 2000, 2003). To address either of these issues at the population level, the variation in hearing sensitivity within a population of marine mammals must be determined.

Behavioral audiometry has been the standard approach for assessing hearing sensitivity in marine mammals for many decades (see Nachtigall *et al.*, 2000, for review). Because behavioral approaches to audiometry require subjects to be conditioned to respond to acoustic stimuli, and because such conditioning requires long-term access to the subject, behavioral approaches have been cited as an impediment to large scale testing of hearing in any marine mammal species (NRC, 2000). Electrophysiological approaches to assessing hearing sensitivity increase the rapidity with which tests can be performed. Because they are relatively fast, and the auditory nerve of odontocetes is large (thus providing for a robust neural response to acoustic stimuli), such tests have become increasingly popular in odontocete audiometry (e.g., Popov and Supin, 1990a, 1990b; Szymanski *et al.*, 1999; Andre *et al.*, 2003; Nachtigall *et al.*, 2004; Yuen *et al.*, 2005; Houser and Finneran, 2006).

The presentation of a sinusoidal amplitude modulated (SAM) tone elicits a rhythmic evoked response from the au-

[a)]Electronic mail: biomimetica@cox.net

 © 2006 Acoustical Society of America

ditory system, termed the envelope following response (EFR). Since the fundamental frequency of an EFR to a SAM tone matches the stimulus modulation rate (Campbell *et al.*, 1977; Hall, 1979; Stapells, 1984; Picton *et al.*, 1987), the magnitude of the evoked response can be assessed in the frequency domain. By tracking the magnitude of the evoked response at a range of stimulus levels, sensitivity at the tonal frequency can be obtained (e.g., Campbell *et al.*, 1977). This approach to electrophysiological estimates of hearing sensitivity provides substantial improvement in frequency specificity relative to other approaches (e.g., clicks or tone pips as stimuli). However, direct comparisons between behavioral and EFR thresholds have only recently been described in bottlenose dolphins (*Tursiops truncatus*) (Nachtigall *et al.*, 2004; Finneran and Houser, 2006; Houser and Finneran, 2006) and a false killer whale (*Pseudorca crassidens*) (Yuen *et al.*, 2005). In two of the studies, the transducer used for stimulus presentation was coupled to the lower jaw of a dolphin via a suction cup (Finneran and Houser, 2006; Houser and Finneran, 2006). The EFR thresholds were obtained on dolphins while they were submerged and while they were resting in air. In both instances, EFR thresholds were compared to behavioral thresholds obtained underwater with the dolphin in the direct field. Differences in EFR thresholds obtained on submerged animals and underwater behavioral thresholds (−20–21 dB) (Houser and Finneran, 2006) compared similarly to those observed between in-air EFR thresholds and underwater behavioral thresholds (−26–20 dB) (Finneran and Houser, 2006). Average differences and standard deviations of the differences were also similar (3±13 dB vs −2±13 dB, respectively). Most importantly, EFR and behavioral thresholds were shown to agree closely as to the shape of the audiogram and the upper cutoff frequency of hearing.

This paper presents population level estimates of auditory sensitivity for a cetacean, the bottlenose dolphin. Utilizing the EFR approach, the hearing sensitivity of 42 dolphins maintained by the United States Navy Marine Mammal Program was surveyed. The purpose of the study was to address hearing sensitivity of animals in the population with the expectation that hearing deficits would correlate with reduced echolocation performance. Variation in hearing sensitivity is discussed as a function of subject age and sex, providing the first insight into how hearing losses might develop in a population of marine mammals.

II. METHODS

A. Subjects

All subjects were Atlantic bottlenose dolphins (*Tursiops truncatus truncatus*) maintained by the United States Navy Marine Mammal Program at the Space and Naval Warfare Systems Center, San Diego, California (SSC San Diego). Subjects ranged from 4 to 47 years of age and consisted of 28 males and 14 females. Nine of the 42 animals were captive born. The distribution of subjects by age and sex is provided in Fig. 1. The study followed a protocol approved by the Institutional Animal Care and Use Committee of the Biosciences Division, SSC San Diego, and followed all applicable U.S. Department of Defense guidelines for the care of laboratory animals.

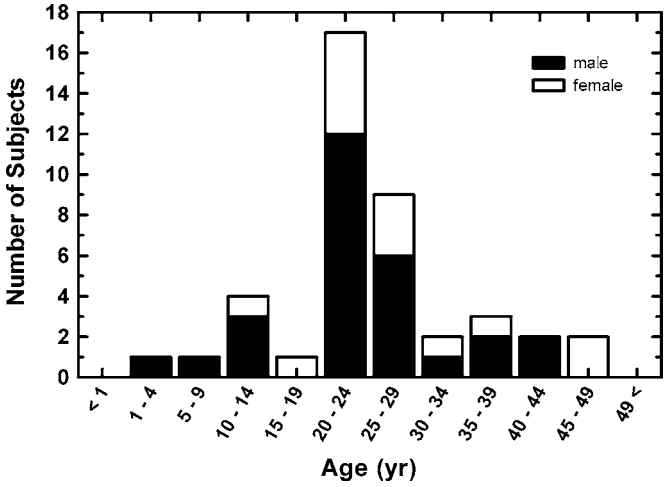

FIG. 1. Age and sex distribution of bottlenose dolphin subjects for which AEP audiograms were collected.

B. EFR Measurements

1. Stimuli, evoked responses, and response detection

The equipment and techniques for stimulus generation and EFR recording have been previously detailed (Finneran and Houser, 2006); only the salient features are described here. SAM tones were used as stimuli to generate the EFR. Eleven carrier frequencies, from 10 to 150 kHz, were tested. All carrier frequencies were 100% amplitude modulated at a rate of 1 kHz, which has been shown to produce a strong EFR in *T. truncatus* (Dolphin *et al.*, 1995; Supin and Popov, 2000). SAM tones were generated with a 1 ms rise/fall time, tone durations of 13–23 ms, and presentation rates of ~40–50/s. In order to improve the signal-to-noise ratio, tone durations were in some instances extended to 62 ms for a dolphin that was tested in the water (see below).

Stimuli were presented to the subjects via a jawphone (a piezoelectric sound projector embedded in a Rhodia V-1065 silicon rubber suction cup) coupled to the dolphin's lower jaw over the pan region (Moore *et al.*, 1995; Brill *et al.*, 2001). The calibration procedures and resulting transmitting voltage responses for the jawphones used in this study (JP1 and JP4), as well as the calibration of EFR-estimated thresholds against behavioral thresholds using these jawphones, are described in Finneran and Houser (2006).

All but one of the subjects was tested while resting out of the water on a padded beaching mat. This subject was tested while stationed on a biteplate and partially submerged (dorsal surface above the waterline) in San Diego Bay (SD Bay). This subject is identified by the superscript "e" in Table I. A different approach was used for this animal because age and poor eyesight prohibited him from voluntarily "beaching" himself out of the water. Since the jawphone permits coupling of the stimulus generator to the lower jaw, similar stimulus conditions can be created for animals that are underwater or in air. Prior comparisons of underwater and in-air estimates of hearing sensitivity derived from EFR measurements with jawphones have been shown to be com-

TABLE I. Subject ID number, age at time of testing, sex and upper cutoff frequency of hearing for each individual in the hearing survey. Unless otherwise noted, frequency-specific thresholds are presented for each individual and each ear. Thresholds are given as dB re: 1 μPa.

					Frequency (kHz)										
ID	Sex	Age	Ear	F_L(kHz)[f]	10	20	30	40	50	60	80	100	115	130	150
1	M	4	L	149	94	86	74	67	64	74	73	92	94	71	127
			R			84	77	71	62	79	75	92	94	74	120
2	M	7	L	147	99	75	83	71	63	77	66	71	73	72	
			R			88	85	76	73	79	78	73	64	73	129
3	M	13	L	73	88	105		71	64	73	154				
			R		75	83	95		66	67	140	163			
4	M	13	L	76	79	78	74	74	70	81	132	151			
			R		75	76	55	54	72	84	126	144			
5	M	13	L	142	80	73	72		70	75	90	79	79	84	145
			R		83	85	78		86		88	65	80	76	147
6[a]	F	12	L	149	88	83	67	74	69	74	77	89	90	78	120
			R		92	86	76	69	65	78	75	95	86	73	127
7[b,e]	M	41	L	53	87	121	115	83	94	155	137	167			
			R		92	137	133	111	116	153	158	173			
8	F	39	L	61	76	69	72	92	112	123	143	152			
			R		78	73	74	85	108	116	137	147			
9	F	28	L	100	75	75	80	79	74	81		116	147		
			R			73	69	72	76	77	75	123	142		
10	M	26	L	49	81	77	71	63	130						
			R		87	67	62	63	124	166					
11	M	23	L	71	66	71	67	64	95	91	146	152			
			R		78	63	60	69	75	83	147	149	147		
12	M	24	L	36	84	79	104	140	147						
			R		84	80	101	127	140						
13[a,d]	F	21	L	126											
			R		74	73	70	69	69		75	93	103	126	132
14	F	26	L	98	78	82	72	81	82	74	75	141	140	106	126
			R		81	82	71	79	99	75	78	116	141		
15	M	24	L	96	101	60	70	75	71	75	76	137			
			R		71	67	73	59	71	76	77	127			
16	F	20	L	142	80		68	63	72	74	74	77	81	100	134
			R				69	69	71						144
17	M	28	L	49	84	69	75	80	122	150					
			R		78	74	87	71	113	151					
18[c,d]	M	25	L												
			R				134		153	148	154	167	164	168	168
19[d]	M	40	L	50											
			R			78		97		146	155	151		139	
20	M	22	L	55	76	76	63	72	105	142	144				
			R		80	70		61	86	155					
21	M	24	L	73		89		86	84	93	142				
			R				91	80	56	83	133	150			
22	M	35	L	93	103	113	119	93	62	75	89	139	146		
			R		87	111	102	117	95	89	91	131			
23	F	27	L	149		89	90	70	64	74	77	88	98	80	121
			R		111	67	73	73	65	76	78	84	93	74	122
24[d]	F	20	L	54	85	74	68	69	115	129	135				
			R												
25	F	30	L	54	80	80	91	103	114	131	134	151			
			R		80	77	84	111	115	136	146	151			
26[c]	F	47	L												
			R												
27	M	25	L	55	69	84	85	62		136	124	153	153		
			R		91	75	79	105	107	133	141	150	159		
28	M	34	L	53	81	68	71	76	109	129	135	153			
			R		102	80	87	67	120	146					
29	M	39	L	125		72	73	67	73	72	72	90	100	131	136

TABLE I. (*Continued.*)

ID	Sex	Age	Ear	F_L(kHz)[f]	Frequency (kHz)										
					10	20	30	40	50	60	80	100	115	130	150
			R				78	71	71	81	86	93	96	128	
30[b]	M	26	L	64	104	109	135	70	71	107	140	148			
			R		100	121	86	84	75	122	153				
31[a]	M	22	L	43		100	82	116	131						
			R			87	86	113	117						
32	M	20	L	80	87	60	73	63	67	80	126	126	111	142	
			R		82	70	65	69	62	76	115	156			
33	M	26	L	39		70	68	131	135	139	164	167			
			R		118	63	61	122	128	113	154	150			
34	M	20	L	44	111	63	68	93	138	143	147	159			
			R		115	69	80	120	123	134	152	151			
35	F	23	L	146	81	75	70	80	65	76	79		88	84	144
			R		83	88		69	72	76	77	93	87	68	123
36	M	24	L	74		90	88	81	66	79	138	148			
			R		86		87	62	58	82	137	152			
37[d]	M	24	L	143											
			R		124	61	74	76	79	80	82	94	95	80	144
38	F	21	L	137	105	64	104	108	61	75	94	97	102		128
			R		105	64	79	108	61	75	85	102	102		128
39	F	46	L	126		66	67	60		77	110	86	81	137	150
			R		74		66	72	83	75	86	84	86	134	130
40	M	13	L	121	92	78	75	84	70	80	82	90	105	137	129
			R		81	79	66	67	54	84	70	98	115	129	
41	M	21	L	147	71	72	70	64	64	75	77	84	83	83	136
			R		77	79	73	80	78	84	71	73	81	78	131
42	F	17	L	108	85	84	72	72	58	81	79	103	136	129	125
			R		83	74	82	61	67	77	78	104	133	123	119

[a]Subjects received an intramuscular injection of midazolam, prior to testing, to reduce anxiety.
[b]Subjects with aberrant audiograms. Subject No. 7 is the father of subject No. 30.
[c]Subjects that are considered to have profound hearing loss based upon high thresholds or lack of evoked responses at the highest levels tested. No F_L was determined for these animals.
[d]Subjects for which thresholds were only obtained in one ear.
[e]This single subject was tested underwater because he could not voluntarily beach himself onto a padded mat.
[f]F_L is calculated from the averaged thresholds of the two ears, when possible.

parable (Houser and Finneran, 2006), so the data from this individual were pooled with the data from the other subjects. For all of the animals tested while resting out of the water on a padded mat, the total time out of the water was typically on the order of 90 min or less. During the testing period animals were periodically sprayed with water to keep the skin moist.

EFRs were measured using electrodes consisting of flexible, conductive, self-adhesive Ag/Ag–Cl pads (Ambu Neuroline 710 series) or 6 and 10 mm diameter gold cup electrodes (e.g., Grass FH-E6G series) embedded in 25 mm diameter silicon suction cups. Attachment sites were dried with gauze pads and alcohol swabs prior to placement of the electrodes. Since the dolphins were periodically sprayed with water during the testing period to keep the skin moist, disposable electrodes were covered with waterproof bandages (Nexcare Absolute Waterproof). Evoked responses were measured between a noninverting (+) electrode placed ~10 cm posterior of the rear edge of the blowhole and offset ~2 cm contralateral of the ear being tested and an inverting (–) electrode placed contralateral of the ear being tested, just posterior to the external auditory meatus. A common reference (ground) electrode was placed on the subject's back near the dorsal fin. Electrode signals were differentially amplified (100 000 gain), filtered (300–3000 Hz), and digitized at 15 or 20 kHz. Signals exceeding 20 μV were rejected from analysis. For each frequency and stimulus pairing, 500 evoked response epochs were recorded.

A small number of the test subjects (N=4) demonstrated an aversion to the attachment of the test equipment (see below). Movement by these individuals created myogenic artifacts sufficient to prevent the recording of evoked potentials. For three of these subjects (see Table I—subjects identified by the superscript "a"), an intramuscular injection of midazolam HCl (Versed; Hoffman-LaRoche, Inc.) at a dose of 0.075–0.1 mg/kg was administered to provide sedation throughout the procedure. Midazolam is a member of the family of sedatives known as the benzodiazepines (e.g., Valium and Xanax), of which at least Valium has been shown to have a mild effect on the latencies of short latency auditory evoked responses, but not the amplitude (Adams *et al.*, 1985). The sedatives are unlikely to have affected threshold estimates in these animals since only the amplitude of the evoked response is used for threshold estimation (see below).

Frequency analysis was performed on 11–21 ms ep-

ochs, excluding the first and last millisecond of the evoked response. Frequency analyses on data collected when tone durations were extended to 62 ms (for the male dolphin tested in water) were performed on 60 ms epochs. Leading and trailing portions of the evoked response were not included so as to avoid transients resulting from signal onset or termination. Durations for frequency analysis were constrained to integral multiples of 1 ms. Magnitude-squared coherence (MSC) was used to determine if the amplitude of the evoked response at the frequency of the modulation rate was significantly greater than measurement noise (Dobie and Wilson, 1989; Dobie, 1993; Dobie and Wilson, 1996). The MSC was calculated by dividing the total number of epochs obtained for each frequency/stimulus pairing into 20 subaverages. Using $\alpha=0.01$, critical values for MSC, MSC_{crit}, were obtained from Amos and Koopmans (1963) and Brillinger (1978). EFRs with $MSC > MSC_{crit}$ were therefore statistically different from noise and were considered to be detected responses.

2. Data collection and threshold estimation

An automated modified staircase technique, similar to that described in Finneran and Houser (2006), was used to adjust stimulus levels and acquire data necessary for threshold estimation. Data collection began with a stimulus SPL of 80–100 dB re 1 μPa. The step size began at either 20 or 30 dB and was reduced after each reversal (i.e., change from a detection to no detection, or vice versa). The staircase procedure ended when the step size was $\leqslant$4 dB. A linear regression utilizing EFR amplitude as the response variable and stimulus SPL as the independent variable was subsequently performed. All detected responses were included in the regression except those exceeding 400 nV. The test was concluded if the regression r^2 value from a minimum of four detected responses reached 0.9; otherwise, additional measurements and regression analyses were performed until the criterion r^2 was met or a maximum of eight detections was made. This procedure for determining the termination of data collection for a specific test frequency ensured that sufficient data existed for the estimation of auditory thresholds at that frequency.

Following data collection, a rules-based modification of a linear regression technique was used to estimate the hearing threshold for each frequency tested (Supin *et al.*, 2001; Yuen *et al.*, 2005; Finneran and Houser, 2006). As previously, the analysis utilized detected responses recorded at each of the frequencies and their associated stimulus levels as the dependent and independent variables, respectively. Details of the rules-based approach are found in Finneran and Houser (2006). Threshold testing was discontinued prior to testing at 150 kHz if a threshold in excess of 140 dB re 1 μPa was obtained for a lower frequency.

3. Analysis

Thresholds were obtained for both ears in all but five individuals; these individuals are indicated by the superscript "d" in Table I. In these individuals, time limitations in the beaching mat resulting from noise issues, equipment malfunctions, or veterinary restrictions prevented testing of both ears. Thresholds were averaged for the left and right ears to produce a mean audiogram for each animal. When only one ear was tested, it was used as the representative audiogram. The upper frequency limit of hearing, F_L, arbitrarily defined as the frequency at which the threshold equaled 120 dB re 1 μPa, was calculated for each audiogram by linear interpolation. Audiograms were considered part of the baseline group if F_L exceeded 140 kHz and there were no notches in the audiogram that exceeded the 120 dB re 1 μPa threshold. Audiograms that qualified as base line were averaged to produce a mean base line audiogram to which all other audiograms could be compared. An analysis of covariance (ANCOVA) was applied to the distribution of F_L within the population using sex as the fixed factor and age as the covariate. Statistical analysis was conducted with STATISTICA© v.7.1 with a significance level of 0.05.

Patterns of variation in hearing sensitivity related to age were investigated by grouping subjects according to age and calculating mean thresholds across the range of hearing for each group. Means were determined by summing the thresholds of individual ears and dividing by the total number of ears tested for a given frequency in an age group. Age groups were divided accordingly: 0–9, 10–19, 20–24, 25–29, 30–39, and 40–47 yr. Since thresholds in excess of 140 dB re 1 μPa became more frequent at higher frequencies, many individuals with compromised hearing were not tested above 100 kHz.

III. RESULTS

Table I provides the age, sex, F_L, and audiometric information for each dolphin tested. The average age of subjects was 23.8 yr for males and 25.4 yr for females. The youngest and oldest males tested were 4 and 41 yr, respectively, and the youngest and oldest females were 12 and 47 yr, respectively. Bilateral testing of the ears was obtained for all but five of the subjects ($N=38$ for the left ear, $N=41$ for the right ear; these subjects are denoted by the subscript "d" in Table I). Comparisons between the records of animals sedated with midazolam HCl and those that were not sedated were similar and no differences in the range and mean amplitudes and latencies were noted.

The base line mean audiogram is shown in Fig. 2(a). Nine of the 42 animals qualified as having base line hearing. These animals ranged in age from 4 to 27 yr. All dolphins over the age of 27 had some degree of hearing loss when compared to the baseline audiogram. Examples of audiograms of the animals that did not qualify as baseline hearing are provided in Figs. 2(b)–2(d). Six of the animals tested had F_L between 100 and 140 kHz and 16 of them had F_L between 50 and 100 kHz [Figs. 2(b) and 2(c), respectively]. Of the remaining animals, seven had F_L below 50 kHz [Fig. 2(d)], two demonstrated aberrant audiograms, and two were considered to have profound hearing loss across the range of frequencies tested. The high frequency roll-off in sensitivity generally occurred across less than one octave.

In general, younger dolphins had a better range of hear-

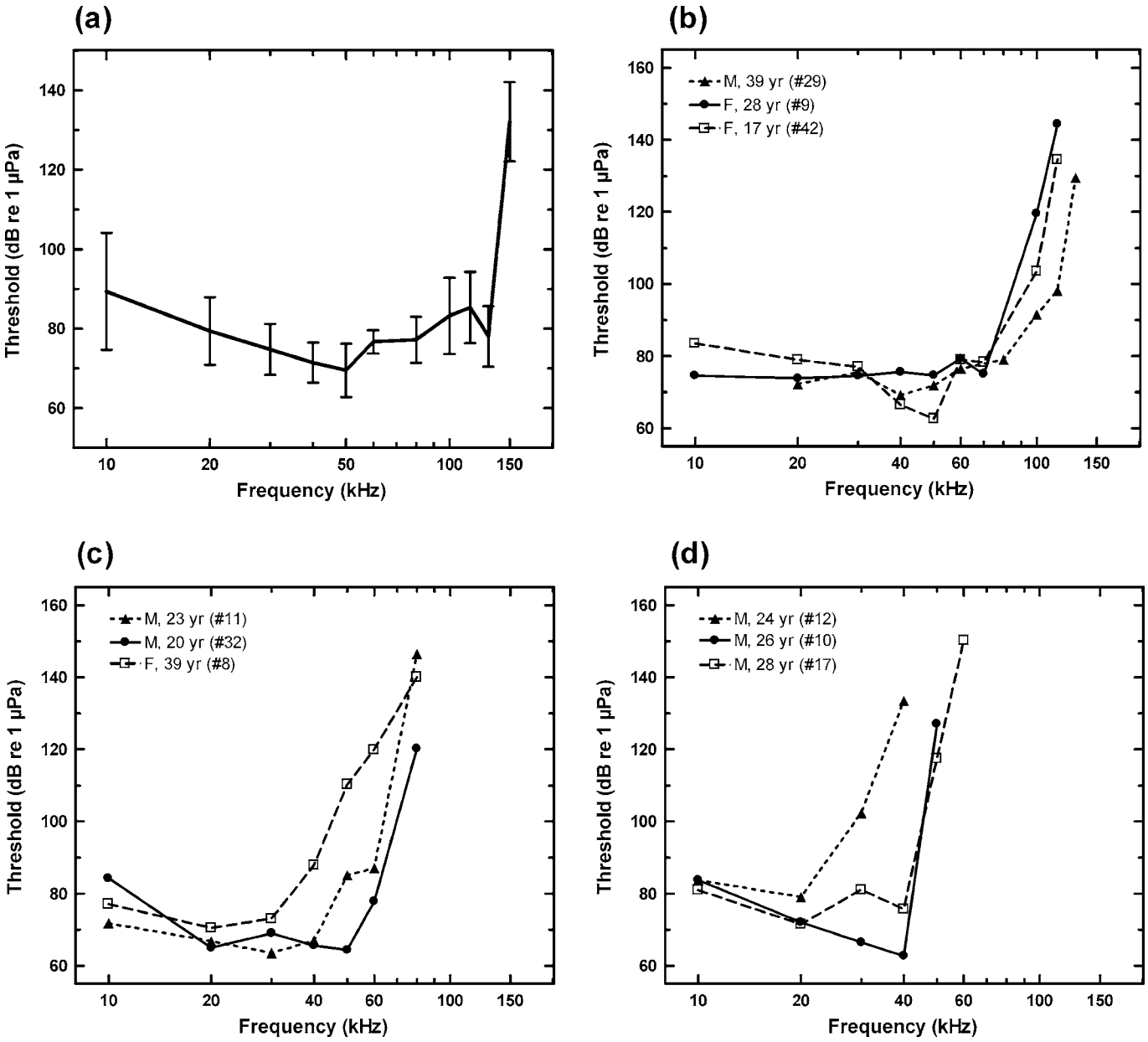

FIG. 2. (a) Mean base line audiogram (n=9). Symbols represent mean thresholds. Error bars indicate ±1 standard deviation. The other panels are representative audiograms for dolphins with upper cutoff frequencies between (b) 100 and 140, (c) 50 and 100, and (d) below 50 kHz. The values presented in the legend correspond to the sex of the animal (M or F), the age of the animal, and the ID number of the animal in Table I (the last value in parentheses).

ing than older dolphins and less variability in mean thresholds than older animals (Fig. 3 and Table II). As animals increased in age there was an overall trend for a reduction in sensitivity at progressively higher frequencies. The F_L generally appear to decline between the ages of 20 and 30 yr, although some animals older than 30 yr had a frequency range of hearing in excess of 120 kHz, and some animals younger than 20 yr showed hearing loss (Fig. 4). ANCOVA utilizing sex as a fixed factor and age as the covariate showed a significant impact of sex on the relationship between age and F_L (Table III). For a covariate mean of 24.3 yr, significant differences existed between the mean F_L of females (113 kHz) and males (81 kHz).

The aberrant audiograms of two male dolphins were characterized by notches below F_L (subjects are identified in Table I with the superscript "b"). The notches are reductions in sensitivity that occur between higher and lower frequencies to which the animal is more sensitive. Figure 5 depicts the aberrant audiogram of a 41 yr male (circles) characterized by a notch in hearing sensitivity at 20 and 30 kHz. The audiogram of this male shows a similar pattern of hearing sensitivity across the range of hearing to that of his male offspring (filled triangles), 15 years younger. The upper cutoff frequencies for the two animals differ by ~10 kHz.

Animals with profound hearing loss produced no detectable EFR across a broad range of frequencies (Fig. 6). For both of these animals, a 41 yr female and a 26 yr male, all detected evoked responses were in excess of 130 dB re 1 μPa. The inability to detect evoked responses always occurred at test frequencies below 50 kHz. These subjects are identified in Table I by the superscript "c".

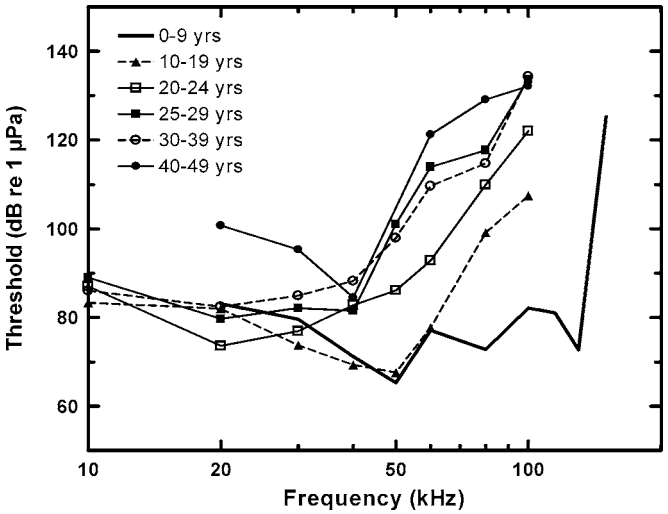

FIG. 3. Mean audiograms for bottlenose dolphins grouped by age. Mean threshold for a given frequency was not plotted if there were fewer than four thresholds obtained at that frequency. Except for the 0–9 yr age group, plots are terminated at 100 kHz; there were a number of individuals for which data above 100 kHz was not obtained because $F_L < 100$ kHz (see Table II). The plot for the 0–9 yr age group is extended so that the reduction in high frequency hearing for animals with a full range of hearing can be viewed for comparison.

IV. DISCUSSION

The variability in hearing sensitivity of a population of bottlenose dolphins observed in the present study follows patterns that are similar to those observed in human populations (Corso, 1959; Northern and Downs, 1971; United States Department of Health and Human Services, 2005) and animal models (Hunter and Willott, 1987; Boettcher, 2002); primarily, both sex and progression in age collectively contribute to reductions in the hearing range of bottlenose dolphins and the loss of hearing generally spreads from the higher frequencies to the lower frequencies. Most of the dolphins in the studied population showed reductions in the range of hearing between the ages of 20 and 30 yr, with the magnitude of the reduction being generally larger in males. Presbycusis in human and animal populations has long been documented (e.g., Corso, 1959), and this process is augmented by the deterioration of the hearing apparatus culminating from noise exposure throughout one's life (Macrae, 1971, 1991a, 1991b; Mills *et al.*, 1997). It seems reasonable that dolphins, having an inherently mammalian inner ear, would suffer from similar phenomena. Additionally, that

TABLE II. Mean threshold, standard deviation, and number of samples (thresholds for individual ears) for bottlenose dolphins grouped by age categories.

		Age (yr)						
Frequency (kHz)		0–9	10–19	20–24	25–29	30–39	40–49	All ages
10	Mean	96.4	83.3	87.0	89.0	86.0	84.3	86.7
	SD	3.6	5.8	15.3	14.9	10.7	9.1	12.6
	n	2	12	23	13	8	3	61
20	Mean	83.1	82.0	73.6	79.7	82.4	100.7	79.7
	SD	5.4	8.3	10.7	15.6	17.1	34.0	15.2
	n	4	12	25	16	9	4	70
30	Mean	79.6	73.7	76.9	82.1	84.9	95.3	79.9
	SD	5.2	10.2	12.5	21.3	15.5	34.1	16.7
	n	4	11	26	17	10	4	72
40	Mean	71.2	69.3	82.8	81.5	88.2	84.5	81.1
	SD	3.8	8.4	22.6	20.4	18.1	20.3	19.7
	n	4	9	29	16	10	5	73
50	Mean	65.3	67.6	86.1	101.1	97.9	97.5	87.3
	SD	5.4	7.7	27.9	28.9	21.4	16.5	26.4
	n	4	12	29	16	10	3	74
60	Mean	77.1	77.7	92.8	113.9	109.6	121.2	98.9
	SD	2.3	5.1	26.5	33.2	27.6	41.1	29.9
	n	4	11	23	16	10	5	69
80	Mean	72.8	99.1	109.9	117.7	114.7	129.1	109.2
	SD	5.0	29.8	31.6	37.5	29.5	30.8	32.5
	n	4	12	23	12	9	5	65
100	Mean	82.1	107.4	122.0	133.7	134.3	132.1	121.7
	SD	11.3	31.3	30.8	28.3	25.3	44.1	32.2
	n	4	11	19	12	9	5	60
115	Mean	81.0	103.0	98.2	137.3	114.1	83.7	107.4
	SD	15.1	23.0	19.0	25.2	27.8	3.5	27.8
	n	4	8	11	9	3	2	37
130	Mean	72.7	103.6	95.1	107.1	129.5	136.8	102.7
	SD	1.3	28.0	26.1	43.0	2.1	2.5	29.8
	n	4	8	8	4	2	3	29
150	Mean	125.3	130.1	134.2	134.1	135.7	140.4	132.6
	SD	4.8	11.4	7.6	22.4	⋯	14.1	11.5
	n	3	7	10	4	1	2	27

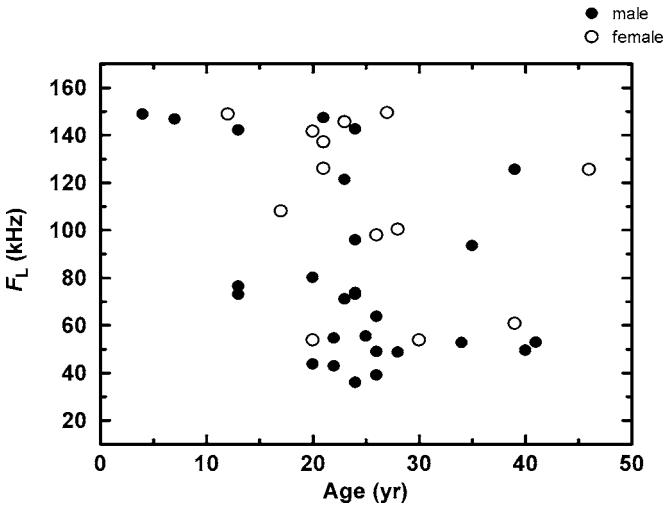

FIG. 4. Upper frequency limit of hearing (F_L), defined as the frequency at which the threshold equaled 120 dB re 1 μPa, as a function of animal age and sex.

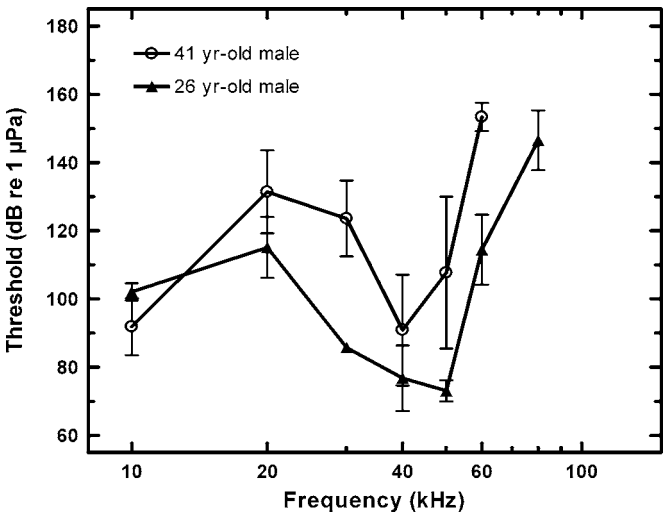

FIG. 5. Audiograms of a 41 yr-old male dolphin (No. 7 in Table I) and his 26 yr-old male offspring (No. 30 in Table I) showing unusual patterns of hearing loss. Threshold values are means of the left and right ears ±1 standard deviation (denoted by the error bars).

males tend to lose their higher frequency hearing at an earlier age than females suggests that similar physiological or behavioral factors contributing to earlier hearing loss in human males may also exist in dolphin populations.

The impact of aging on the ability of dolphins to utilize echolocation remains relatively unexplored. Dolphins have been noted to preferentially emit echolocation clicks in which the spectral content is dominated by frequencies to which they are sensitive (Houser *et al.*, 1999, 2005). This suggests active compensation for hearing deficits and the practice may be common in dolphins with age-related hearing loss. However, the interpretation of echoes received from ensonified targets may additionally be impacted by reductions in temporal sensitivity. Age-related temporal and spectral pattern processing deficits in humans are believed to interact with sensorineural hearing loss in the reduction of speech intelligibility (Fitzgibbons and Gordon-Salant, 2001, 2004; Divenyi *et al.*, 2005). This process is confounded by reverberation (Duquesnoy and Plomp, 1980), a common trait of the environments that bottlenose dolphins typically inhabit. The temporal processing capability of the dolphin has been studied by both psychophysical and physiological means (e.g., Johnson *et al.*, 1988; Dolphin *et al.*, 1995; Supin and Popov, 1995; Popov and Supin, 1997; Helweg *et al.*, 2003). Future studies, similarly designed but utilizing differently aged dolphins could be conducted to determine whether age impacts temporal or spectral pattern processing in the dolphin.

Humans, even under low noise exposure conditions, demonstrate a sex bias in the rate of hearing loss (Pearson *et al.*, 1994). The loss of high frequency hearing in this dolphin population follows a similar trend; however, noise exposure histories do not exist for the animals in this study so differences in noise exposure histories cannot be excluded from contributing to the variability in male-female comparisons. Reasons for the sex bias in human populations remain to be definitively determined, but onset of the phenomenon in males has been identified at ages as young as the late 20s and early 30s (Corso, 1959; Pearson *et al.*, 1994). This age range is similar to that observed for the appearance of reduced F_L in male dolphins and it seems reasonable to conclude that the onset of hearing loss in male dolphins tends to occur after sexually maturity.

Many of the audiograms for the tested animals had best sensitivities that were 10–20 dB less sensitive than those previously recorded by Johnson (1966). Differences in test-

TABLE III. Results of the ANCOVA performed on F_L utilizing sex as a fixed factor and age as a covariate.

	Df	MS	F	p
Intercept	1	82796.29	67.13	<0.001
Age	1	7940.03	6.43	0.016
Sex	1	9629.84	7.51	0.009
Error	37	1233.20		

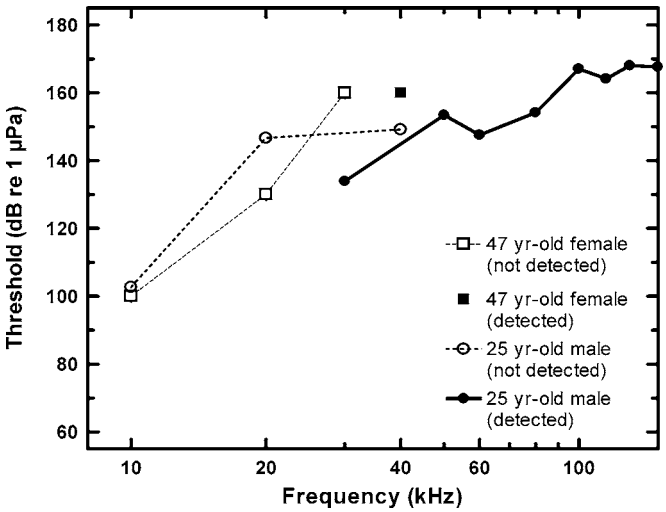

FIG. 6. Thresholds for two dolphins [a 47 yr-old female (No. 26 in Table I) and 26 yr-old male (No. 18 in Table I)] having significant high-frequency hearing loss. Filled symbols represent measured thresholds; open symbols indicate maximum SPLs for which no response was detected (the actual threshold would be higher). Note that thresholds are high for all frequencies at which EFRs were detected.

ing methodologies could explain the differences in threshold, since Johnson used a behavioral paradigm as opposed to the physiological measurements used here. The in-air method of estimating underwater hearing thresholds, using auditory evoked potentials (AEP) recordings obtained when a jawphone is used as the sound source, has been benchmarked against behavioral audiometry conducted within the same subjects, underwater, and in direct sound fields (Finneran and Houser, 2006). Considering behavioral audiometry conducted by Finneran and Houser (2006) on an animal in a pool, which is a closer approximation to the Johnson (1966) setup than the masked behavioral thresholds obtained by Finneran and Houser (2006) from animals housed in SD Bay, AEP threshold estimates are expected to be 0–18 dB higher than behavioral thresholds (with a mean of +8 dB). Thus, differences between the AEP threshold estimates presented here and the behavioral thresholds obtained by Johnson (1966) are near the expected range of differences for the test methodology.

The dolphin population studied here is maintained in netted enclosures within SD Bay. These animals are exposed not only to noise generated by the natural environment (dominated by snapping shrimp and conspecifics), but also to varying amounts of shipping, boating, and construction noise. Mean ambient noise spectral density levels within San Diego Bay range from 67 to 87 dB re: 1 μPa^2/Hz across the range of 0.1–50 kHz (Finneran *et al.*, 2005a). In future measurements of dolphin hearing sensitivity, it would be worthwhile to assess the ambient noise levels of the environment in which the animals lived. By this means, potential relationships between chronic noise exposure and variation in hearing sensitivity might be determined.

Some drug therapies may pose risks of ototoxicity, with the risk being generally related to the total dose administered and the rate of administration. Of particular concern are the aminoglycoside antibiotics which have the potential to produce irreversible hearing loss in mammals. Indeed, the aminoglycoside amikacin has not only been implicated in the loss of hearing in humans, but in odontocetes as well (Finneran *et al.*, 2005b). Some of the dolphins tested in this study, and that had notable hearing loss, had prior amikacin treatments for ailments in which gram-negative bacterial infections were suspected. Gentamicin is also of concern as the 25-yr old male dolphin determined to have profound hearing loss in this study (Fig. 6; No. 18 in Table I) received 1.0 g of gentamicin via combined intravenous and intramuscular injections several years prior to the determination of his hearing loss. Whether gentamicin or amikacin were contributing factors in the loss of hearing for any of these dolphins remains uncertain. The dosages administered were conservative in that exposure to the antibiotics was acute. Prolonged exposures are more likely to result in hair cell damage (Begg and Barclay, 1995; Aran *et al.*, 1999), as was observed in the case of a beluga treated for *Nocardia* spp. infection (Finneran *et al.*, 2005b). However, because of the documented deleterious effects of gentamicin and amikacin on human and lab animal hearing (Kahlmeter and Dahlager, 1984), and because there has never been a controlled study of the effects of any aminoglycoside on sensorineural hearing loss in a cetacean, the possibility that exposure to aminoglycoside antibiotics might contribute to hearing loss in delphinids deserves consideration. Additional data mining of the veterinary records of dolphins for which hearing sensitivity is known (such as might be obtained from marine parks and aquaria or during the rehabilitation of stranded marine mammals) will be useful in determining the impact of aminoglycoside antibiotics on the hearing sensitivity of odontocetes.

The similarity in the audiograms of the father and son pairing, and the atypical shape of the audiograms relative to the rest of the population, is suggestive of a familial link in progressive hearing loss. Genetic predispositions for hearing loss and auditory system abnormalities are documented in humans and laboratory animals (Brown, 1973; Erway *et al.*, 1993) and it seems reasonable that genetic causes of hearing loss would also exist in marine mammals. Whether the animals that were found with profound hearing loss had a genetic predisposition for the condition is unknown.

V. CONCLUSIONS

(1) Evoked potential audiometry was used to assess the hearing sensitivity of a population of bottlenose dolphins.

(2) Bottlenose dolphins experience progressive hearing loss with age (presbycusis), with the higher frequencies being affected first and males losing their hearing before females, as in humans.

(3) There may be genetic factors in an individual dolphin's susceptibility to hearing loss.

(4) The potential for certain antibiotics to contribute to cetacean hearing loss deserves continued investigation.

ACKNOWLEGMENTS

The authors thank R. Dear and C. Schlundt for invaluable help in data collection, M. Patefield for organizing most of the dolphin tests, and the numerous animal training staff of the United States Navy Marine Mammal Program that assisted in the tests. S. Ridgway, D. Carder, and P. Moore provided much helpful advice and technical assistance. Financial support was provided by the Office of Naval Research, Marine Mammal S&T Program and the SSC San Diego In-house Laboratory, Independent Research program.

Adams, D. A., McClelland, R. J., Houston, H. G., and Gamble, W. G. (**1985**). "The effects of diazepam on the auditory brain stem responses," Br. J. Audiol. **19**, 277–280.

Amos, D. E., and Koopmans, L. H. (**1963**). *Tables of the Distribution of the Coefficient of Coherence for Stationary Bivariate Gaussian Processes* (Sandia Corporation, Livermore, CA), p. 328.

Andre, M., Supin, A., Delory, E., Kamminga, C., Degollada, E., and Alonso, J. M. (**2003**). "Evidence of deafness in a striped dolphin, *Stenella coeruleoalba*," Aquat. Mamm. **29**, 3–8.

Aran, J. M., Erre, J. P., Lima da Costa, D., Debbarh, I., and Dulon, D. (**1999**). "Acute and chronic effects of aminoglycosides on cochlear hair cells," Ann. N.Y. Acad. Sci. **884**, 60–68.

Begg, E. J., and Barclay, M. L. (**1995**). "Aminoglycosides—50 years on," Br. J. Clin. Pharmacol. **39**, 597–603.

Boettcher, F. A. (**2002**). "Susceptibility to acoustic trauma in young and aged gerbils," J. Acoust. Soc. Am. **112**, 2948–2955.

Brill, R. L., Moore, P. W. B., and Dankiewicz, L. A. (**2001**). "Assessment of dolphin (*Tursiops truncatus*) auditory sensitivity and hearing loss using jawphones," J. Acoust. Soc. Am. **109**, 1717–1722.

Brillinger, D. R. (**1978**). "A note on the estimation of evoked response," Biol. Cybern. **31**, 141–144.

Brown, K. S. (**1973**). "Genetic features of deafness," J. Acoust. Soc. Am. **54**, 569–575.
Campbell, F. W., Atkinson, J., Francis, M. R., and Green, D. M. (**1977**). "Estimation of auditory thresholds using evoked potentials," in *Auditory Evoked Potentials in Man. Psychopharmacology Correlates of Evoked Potentials*, edited by J. E. Desmedt (Karger, Basel), pp. 68–78.
Corso, J. F. (**1959**). "Age and sex differences in pure-tone thresholds," J. Acoust. Soc. Am. **31**, 498–507.
Divenyi, P. L., Stark, P. B., and Haupt, K. M. (**2005**). "Decline of speech understanding and auditory thresholds in the elderly," J. Acoust. Soc. Am. **118**, 1089–1100.
Dobie, R. A. (**1993**). "Objective response detection," Ear Hear. **14**, 31–35.
Dobie, R. A., and Wilson, M. J. (**1989**). "Analysis of auditory evoked potentials by magnitude-squared coherence," Ear Hear. **10**, 2–13.
Dobie, R. A., and Wilson, M. J. (**1996**). "A comparison of *t* test, *F* test, and coherence methods of detecting steady-state auditory-evoked potentials, distortion-product otoacoustic emissions, or other sinusoids," J. Acoust. Soc. Am. **100**, 2236–2246.
Dolphin, W. F., Au, W. W., Nachtigall, P. E., and Pawloski, J. (**1995**). "Modulation rate transfer functions to low-frequency carriers in three species of cetaceans," J. Comp. Physiol., A **177**, 235–245.
Duquesnoy, A. J., and Plomp, R. (**1980**). "Effect of reverberation and noise on the intelligibility of sentences in cases of presbyacusis," J. Acoust. Soc. Am. **68**, 537–544.
Erway, L. C., Willott, J. F., Arch, J. R., and Harrison, D. E. (**1993**). "Genetics of age-related hearing loss in mice: I. Inbred and F1 hybrid strains," Hear. Res. **65**, 125–132.
Finneran, J. J., Carder, D. A., Schlundt, C. E., and Ridgway, S. H. (**2005a**). "Temporary threshold shift (TTS) in bottlenose dolphins (*Tursiops truncatus*) exposed to midfrequency tones," J. Acoust. Soc. Am. **118**, 2696–2705.
Finneran, J. J., Dear, R., Carder, D. A., Belting, T., McBain, J., Dalton, L., and Ridgway, S. H. (**2005b**). "Pure tone audiograms and possible antibiotic drug-induced hearing loss in the white whale (*Delphinapterus leucas*)," J. Acoust. Soc. Am. **117**, 3936–3943.
Finneran, J. J., and Houser, D. S. (**2006**). "Comparison of in-air evoked potential and underwater behavioral hearing thresholds in four bottlenose dolphins (*Tursiops truncatus*)," J. Acoust. Soc. Am. **119**, 3181–3192.
Fitzgibbons, P. J., and Gordon-Salant, S. (**2001**). "Aging and temporal discrimination in auditory sequences," J. Acoust. Soc. Am. **109**, 2955–2963.
Fitzgibbons, P. J., and Gordon-Salant, S. (**2004**). "Age effects on discrimination of timing in auditory sequences," J. Acoust. Soc. Am. **116**, 1126–1134.
Hall, J. W. (**1979**). "Auditory brainstem frequency following responses to waveform envelope periodicity," Science **205**, 1297–1299.
Helweg, D. A., Moore, P. W., Dankiewicz, L. A., Zafran, J. M., and Brill, R. L. (**2003**). "Discrimination of complex synthetic echoes by an echolocating bottlenose dolphin," J. Acoust. Soc. Am. **113**, 1138–1144.
Houser, D. S., and Finneran, J. J. (**2006**). "A comparison of underwater hearing sensitivity in bottlenose dolphins (*Tursiops truncatus*) determined by electrophysiological and behavioral methods," J. Acoust. Soc. Am. **120**, 1713–1722.
Houser, D. S., Helweg, D. A., and Moore, P. W. B. (**1999**). "Classification of dolphin echolocation clicks by energy and frequency distributions," J. Acoust. Soc. Am. **106**, 1579–1585.
Houser, D. S., Martin, S. W., Bauer, E. J., Phillips, M., Herrin, T., Cross, M., Vidal, A., and Moore, P. W. (**2005**). "Echolocation characteristics of free-swimming bottlenose dolphins during object detection and identification," J. Acoust. Soc. Am. **117**, 2308–2317.
Hunter, K. P., and Willott, J. F. (**1987**). "Aging and the auditory brainstem response in mice with severe or minimal presbycusis," Hear. Res. **30**, 207–218.
Johnson, C. S. (**1966**). "Auditory thresholds of the bottlenosed porpoise (*Tursiops truncatus, Montagu*)," U.S. Naval Ordnance Test Station, NOTS TP 4178, China Lake, p. 28.
Johnson, R. A., Moore, P. W. B., Stoermer, M. W., Pawloski, J. L., and Anderson, L. C. (**1988**). "Temporal order discrimination within the dolphin critical interval," in *Animal Sonar Processes and Performance*, edited by P. E. Nachtigall and P. W. B. Moore (Plenum, New York), pp. 317–321.
Kahlmeter, G., and Dahlager, J. L. (**1984**). "Aminoglycoside toxicity—A review of clinical studies published between 1975 and 1982," J. Antimicrob. Chemother. **13**, 9–22.
Macrae, J. H. (**1971**). "Noise-induced permanent threshold shift and presbyacusis," Audiology **10**, 323–333.
Macrae, J. H. (**1991a**). "Noise-induced permanent threshold shift and presbyacusis," Aust. J. Audiol. **13**, 23–29.
Macrae, J. H. (**1991b**). "Presbycusis and noise-induced permanent threshold shift," J. Acoust. Soc. Am. **90**, 2513–2516.
Mills, J. H., Boettcher, F. A., and Dubno, J. R. (**1997**). "Interaction of noise-induced permanent threshold shift and age-related threshold shift," J. Acoust. Soc. Am. **101**, 1681–1686.
Moore, P. W. B., Pawloski, D. A., and Dankiewicz, L. (**1995**). "Interaural time and intensity difference thresholds in the bottlenose dolphin (*Tursiops truncatus*)," in *Sensory Systems of Aquatic Mammals*, edited by R. A. Kastelein, J. A. Thomas, and P. E. Nachtigall (De Spil, Woerden).
Nachtigall, P. E., Lemonds, D. W., and Roitblat, H. L. (**2000**). "Psychoacoustic studies of dolphin and whale hearing," in *Hearing by Whales and Dolphins*, edited by W. W. L. Au, A. N. Popper, and R. R. Fay (Springer, New York), pp. 330–363.
Nachtigall, P. E., Supin, A. Y., Pawloski, J., and Au, W. W. L. (**2004**). "Temporary threshold shifts after noise exposure in the bottlenose dolphin (*Tursiops truncatus*) measured using evoked auditory potentials," Marine Mammal Sci. **20**, 673–687.
National Research Council (NRC) (**1994**). *Low-Frequency Sound and Marine Mammals: Current Knowledge and Research Needs* (National Academy Press, Washington, DC).
National Research Council (NRC) (**2000**). *Marine Mammals and Low-Frequency Sound: Progress Since 1994* (National Academy Press, Washington, DC).
National Research Council (NRC) (**2003**). *Ocean Noise and Marine Mammals* (National Academies Press, Washington, DC).
Northern, J. L., and Downs, M. P. (**1971**). "Recommended high-frequency audiometric threshold levels (8000–18 000 Hz)," J. Acoust. Soc. Am. **52**, 585–595.
Pearson, J. D., Morrell, C. H., Gordon-Salant, S., Brant, L. J., Metter, E. J., Klein, L. L., and Fozard, J. L. (**1994**). "Gender differences in a longitudinal study of age-associated hearing loss," J. Acoust. Soc. Am. **97**, 1196–1205.
Picton, T. W., Skinner, C. R., Champagne, S. C., Kellett, A. J., and Maiste, A. C. (**1987**). "Potentials evoked by the sinusoidal modulation of the amplitude or frequency of a tone," J. Acoust. Soc. Am. **82**, 165–178.
Popov, V., and Supin, A. (**1990a**). "Electrophysiological studies of hearing in some cetaceans and a manatee," in *Sensory Abilities in Cetaceans*, edited by J. A. Thomas and R. A. Kastelein (Plenum, New York), pp. 405–415.
Popov, V. V., and Supin, A. (**1997**). "Detection of temporal gaps in noise in dolphins: Evoked-potential study," J. Acoust. Soc. Am. **102**, 1169–1176.
Popov, V. V., and Supin, A. Y. (**1990b**). "Auditory brainstem responses in characterization of dolphin hearing," J. Comp. Physiol., A **166**, 385–393.
Ridgway, S. H., and Carder, D. A. (**1993**). "High-frequency hearing loss in old (25+ years old) male dolphins," J. Acoust. Soc. Am. **94**, 1830.
Ridgway, S. H., and Carder, D. A. (**1997**). "Hearing deficits measured in some *Tursiops truncatus*, and discovery of a deaf/mute dolphin," J. Acoust. Soc. Am. **101**, 590–594.
Stapells, D. R., Linden, D., Suffield, J. B., Hamel, G., and Picton, T. W. (**1984**). "Human auditory steady-state potentials," Ear Hear. **5**, 105–113.
Supin, A. Y., and Popov, V. V. (**1995**). "Temporal resolution in the dolphin's auditory system revealed by double-click evoked potential study," J. Acoust. Soc. Am. **97**, 2586–2593.
Supin, A. Y., and Popov, V. V. (**2000**). "Frequency-modulation sensitivity in bottlenose dolphins, *Tursiops truncatus*: Evoked-potential study," Aquat. Mamm. **26**, 83–94.
Supin, A. Y., Popov, V. V., and Mass, A. M. (**2001**). *The Sensory Physiology of Aquatic Mammals* (Kluwer Academic, Boston, MA).
Szymanski, M. D., Bain, D. E., Kiehl, K., Pennington, S., Wong, S., and Henry, K. R. (**1999**). "Killer whale (*Orcinus orca*) hearing: Auditory brainstem response and behavioral audiograms," J. Acoust. Soc. Am. **106**, 1134–1141.
United States Department of Health and Human Services (**1994**). "National Health Interview Survey," *Series 10* (U.S. Dept. of Health and Human Services, National Center for Health Statistics).
United States Department of Health and Human Services (**2005**). "Health, United States, 2005 with chartbook on trends in the health of Americans," (United States Department of Health and Human Services, National Center for Health Statistics, Hyattsville, MD), p. 535.
Yuen, M. M. L., Nachtigall, P. E., Breese, M., and Supin, A. Y. (**2005**). "Behavioral and auditory evoked potential audiograms of a false killer whale (*Pseudorca crassidens*)," J. Acoust. Soc. Am. **118**, 2688–2695.

Modeling acoustic propagation of airgun array pulses recorded on tagged sperm whales (*Physeter macrocephalus*)[a)]

Stacy L. DeRuiter[b)] and Peter L. Tyack
Biology Department, Woods Hole Oceanographic Institution, Woods Hole, Massachusetts 02543

Ying-Tsong Lin, Arthur E. Newhall, and James F. Lynch
Department of Applied Ocean Physics and Engineering, Woods Hole Oceanographic Institution, Woods Hole, Massachusetts 02543

Patrick J. O. Miller
Sea Mammal Research Unit, University of St. Andrews, Fife KY16 8LB, Scotland

(Received 26 January 2006; revised 1 September 2006; accepted 13 September 2006)

In 2002 and 2003, tagged sperm whales (*Physeter macrocephalus*) were experimentally exposed to airgun pulses in the Gulf of Mexico, with the tags providing acoustic recordings at measured ranges and depths. Ray trace and parabolic equation (PE) models provided information about sound propagation paths and accurately predicted time of arrival differences between multipath arrivals. With adequate environmental information, a broadband acoustic PE model predicted the relative levels of multipath arrivals recorded on the tagged whales. However, lack of array source signature data limited modeling of absolute received levels. Airguns produce energy primarily below 250 Hz, with spectrum levels about 20–40 dB lower at 1 kHz. Some arrivals recorded near the surface in 2002 had energy predominantly above 500 Hz; a surface duct in the 2002 sound speed profile helps explain this effect, and the beampattern of the source array also indicates an increased proportion of high-frequency sound at near-horizontal launch angles. These findings indicate that airguns sometimes expose animals to measurable sound energy above 250 Hz, and demonstrate the influences of source and environmental parameters on characteristics of received airgun pulses. The study also illustrates that on-axis source levels and simple geometric spreading inadequately describe airgun pulse propagation and the extent of exposure zones. © *2006 Acoustical Society of America.* [DOI: 10.1121/1.2359705]

PACS number(s): 43.80.Nd, 43.20.Mv, 43.30.Dr [WWA] Pages: 4100–4114

I. INTRODUCTION

Airgun arrays are often used as sources of low-frequency underwater sound for geophysical research and exploration, especially by the oil industry. Airguns generate sound by rapidly releasing compressed air from an airgun cylinder, creating an oscillating air bubble that acts as a source of loud, broadband impulsive sound. The oscillating air bubble also produces a sequence of exponentially decaying bubble pulses following the initial pulse (Parkes and Hatton, 1986). Airguns are generally deployed as horizontal planar towed arrays, minimizing the bubble pulses and directing the main beam of low-frequency sound toward the seafloor (Parkes and Hatton, 1986). Airgun arrays are reported to have theoretical on-axis (directly downward) signatures with peak energy in the 10–200 Hz range, and far-field measurements yield typical peak-to-peak source levels in the range 222–261 dB re 1 μPa when corrected to a source range of 1 m, treating the full array as a point source (Richardson *et al.*, 1995). During seismic surveys, a streamer of hydrophones is also generally towed to record sound reflected from below the seafloor, and characteristics of these reflections are used to invert for bottom properties and map subseafloor features (Barger and Hamblen, 1980; Caldwell and Dragoset, 2000; Dragoset, 2000; Richardson *et al.*, 1995). Although much of the acoustic energy produced by an airgun array is in the frequency range below 250 Hz, both field recordings and models of source spectra illustrate that airguns can produce significant energy at frequencies up to at least 1 kHz [source energy at 1 kHz is about 40 dB re 1 μPa^2/Hz less than at 50 Hz (Blackman *et al.*, 2004; Caldwell and Dragoset, 2000; Goold and Fish, 1998)]. Due to their high source levels and their low frequency content, airgun array transmissions in suitable ocean environments have been detected above background noise at distances of up to 3000 km (Nieukirk *et al.*, 2004).

The source level and frequency range of airgun pulses have generated concern that they may adversely affect fish and marine mammals. Airgun noise could produce adverse effects by direct injury, for example by damaging the animals' ears, or by less direct mechanisms, such as by masking

[a)]Portions of this work were presented in "Preliminary modeling of Dtag acoustic arrivals from the Gulf of Mexico in 2002 and 2003," Proceedings of the Twenty-Third Gulf of Mexico Information Transfer Meeting, U.S. Department of the Interior Minerals Management Service, Gulf of Mexico OCS Region, 2005, and "Quantification and Acoustic Propagation Modeling of Airgun Noise Recorded on Dtag-tagged Sperm Whales in the Gulf of Mexico," Proceedings of the 16th Biennial Conference on the Biology of Marine Mammals, San Diego, CA, December 2005.

[b)]Author to whom correspondence should be addressed. Electronic mail: sderuiter@whoi.edu

 © 2006 Acoustical Society of America

sounds or disrupting behavior. In terms of wildlife conservation, the primary concern regarding these alterations involves questions about whether they could affect populations by reducing survival, reproductive success, or foraging effectiveness. Experiments have documented that exposure to airgun pulses at close range can damage fish ears (McCauley *et al.*, 2003), that fish catches are reduced during airgun surveys in an area (Engås *et al.*, 1996), and that some marine mammals may change their behavior in response to airgun exposure (Engås *et al.*, 1996; McCauley *et al.*, 2003; Richardson *et al.*, 1995).

One method for determining whether, and how, airgun transmissions might affect marine mammals involves controlled exposure experiments (CEEs), in which animals are observed pre-exposure and then exposed to a controlled level of sound. A set of CEEs to measure the response of sperm whales to airgun sounds took place during the Sperm Whale Seismic Study (SWSS) in the Gulf of Mexico during September 2002 and June 2003 (Jochens and Biggs, 2003, 2004). During the experiments, sperm whales were tagged with a Dtag, an archival tag that records acoustic, depth, and orientation information (Johnson and Tyack, 2003). Tagged whales were exposed to airgun array transmissions at ranges from 1 to 13 km. The tags recorded whale movements and vocalizations during the exposure as well as airgun sound arrivals at a variety of source-whale ranges and whale depths. Analysis of the effects of airgun exposure on sperm whale foraging behavior in the Gulf of Mexico and determination of airgun received levels at the whales during these two studies will be presented in two other papers [Miller *et al.* (unpublished) and Madsen *et al.* (2006)]. In this paper, we study the acoustic propagation of airgun signals recorded on Dtags with standard acoustic propagation models. We show that seasonally and spatially variable environmental characteristics play critical roles in determining spectra and levels of airgun arrivals at the whales. Our results also show how source directivity and a surface ducting effect may proportionally increase the high-frequency content of airgun signals arriving at whales near the surface compared to on-axis airgun spectra.

To put the discussion of our modeling techniques and results in context, we have structured this article as follows. Before addressing the CEEs of the Sperm Whale Seismic Study (SWSS) in the Gulf of Mexico, we will begin by discussing the sound sources and receivers employed during the experiments and the acoustic environment in which the CEEs took place. We reiterate that there were two components to the experiment, one that took place in September 2002 and one in June 2003, and we outline differences and similarities between the 2 years. Next, we describe the field experimental techniques and the acoustic models used to analyze the data. We then present the modeling results for each year. Finally, we discuss the implications and significance of our work, emphasizing that near-surface receivers may detect significant sound energy above 250 Hz in certain conditions and that geometric spreading approximations, which have traditionally been used to determine the extent of marine animal exposure zones, are inadequate to describe transmission loss in our study environments.

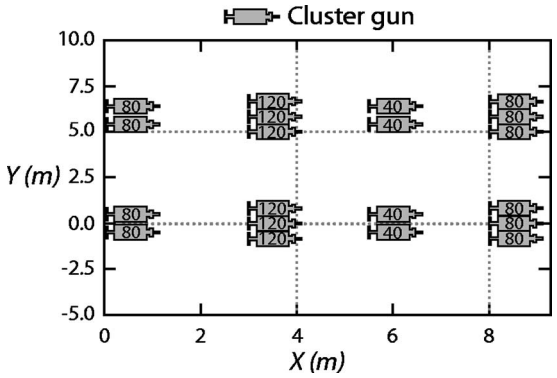

FIG. 1. Configuration of the M/V *Speculator* airgun array, used in the 2002 experiment. Numbers inside individual airguns indicate the displacement (in cubic inches) of each gun.

II. ACOUSTIC SOURCES, RECEIVERS, AND ENVIRONMENT

A. Sound sources: Airgun arrays

In 2002, tagging operations were based on the R/V *Gyre*, and the airgun source vessel was the M/V *Speculator* (the coastal vessel *Speculator* was mounted aboard the deep-water service vessel M/V *Rylan T* to allow work in deep-water research areas). The *Speculator* airgun array was a tuned array 8 m long and 6 m wide, including 20 external sleeve type airguns of various volumes for a total volume of 1680 in^3. Figure 1 shows the configuration of the *Speculator* array. During CEEs, the airgun array was towed at a nominal depth of 6 m and fired every 15 s, with a ramp-up at the start of each firing period during which the number of airguns fired was gradually increased. In this study, we analyzed only recordings of full-array airgun arrivals. The equivalent point-source source level of the array, backcalculated from the on-axis (directly downwards) theoretical far-field signature [shown in Fig. 2(a)], was reported to be 258 dB re 1 μPa @ 1 m (peak-peak) in the 3–800 Hz frequency band (Jochens and Biggs, 2003). Frequency notches in the spectrum of the theoretical far-field signature, which is shown in Fig. 2(b), indicate a Lloyd's mirror effect.

Because sound from an airgun array will reflect at the ocean surface (which is approximately a pressure-release boundary), a Lloyd's mirror effect will occur, and airgun pulse arrivals at distant (far-field) receivers will include, in addition to the direct arrival, a 180-degree-phase-shifted, surface-reflected arrival (Frisk, 1994). This reflected arrival is equivalent to the sound that would be received from a virtual mirror image source located above the sea surface, with approximately the same source amplitude as the airgun array but with opposite polarity [the exact mirror source amplitude depends on sea-surface roughness and source frequency (Jovanovich *et al.*, 1983)]. Interference between the direct pulse and the surface reflection affects the time and frequency structure of pulses recorded at distant receivers, lengthening the pulse and introducing frequency nulls into the source spectrum (Caldwell and Dragoset, 2000; Parkes and Hatton, 1986). The effect varies with airgun array tow depth: as tow depth increases, frequency nulls occur at more

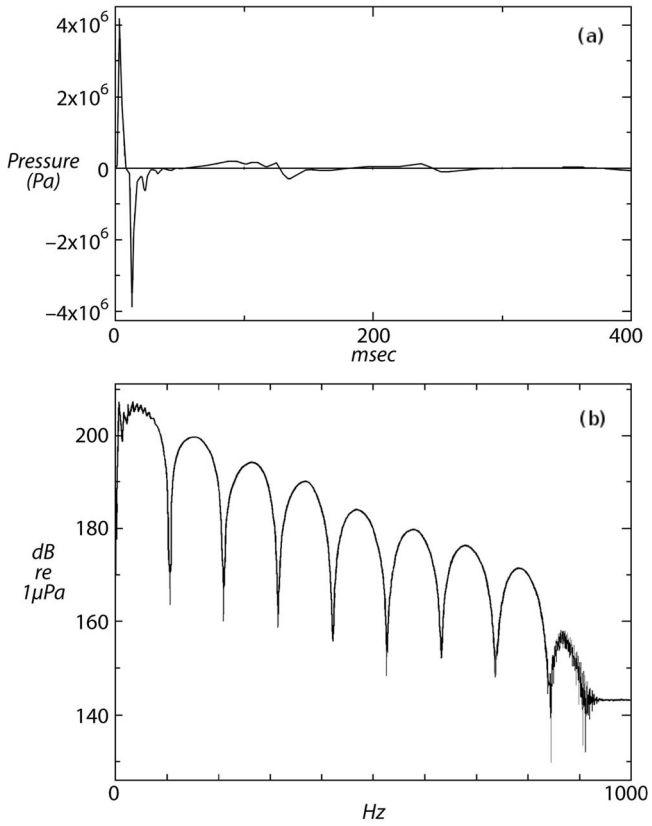

FIG. 2. (a) On-axis theoretical source signature of the M/V *Speculator* airgun array and (b) its amplitude spectrum. Both plots are extracted from Jochens and Biggs (2003).

closely spaced intervals in the source spectrum, and source pressure amplitude increases at frequencies below 100 Hz (Parkes and Hatton, 1986).

The beampattern of a planar array composed of identical point sources has grating lobes when the spacing between array elements, d, is greater than $\lambda/2$ (where λ is source wavelength). The grating lobes are centered at angles θ from the acoustic axis such that $n\lambda = d\sin(\theta)$ (where $n = 1, 2, 3, \ldots$) (Tipler and Llewellyn, 2003). For the *Speculator* array, the spacing between airgun clusters was about 3 m in the x dimension (along the bow-stern axis of the source vessel) and about 6 m in the y dimension (perpendicular to the bow-stern axis of the source vessel). Therefore, the array beampattern should have grating lobes for source frequencies above approximately 250 Hz in the x-z plane and approximately 125 Hz in the y-z plane (assuming a sound speed of 1500 m/s), although array shading will affect the pattern of grating lobes somewhat (Urick, 1975). The presence of grating lobes in the array beampattern at higher frequencies increases the proportion (but not the absolute amount) of higher-frequency energy transmitted by the array at launch angles close to parallel to the sea surface. Detailed modeling of the *Speculator* array beampattern will be presented later in the paper, and will include the Lloyd's mirror effect from sea-surface reflection as well as the effects of array geometry mentioned here.

The Fresnel zone or near field of an acoustic array extends to a range of about D^2/λ, where D is the array dimension (length or width) and λ is sound wavelength (Clay and Medwin, 1977). Assuming a sound speed of 1500 m/s, the far field of the *Speculator* array begins about 2 m from the source at 50 Hz and about 85 m from the source at 2 kHz. All airgun pulses used in this study were recorded in the far field.

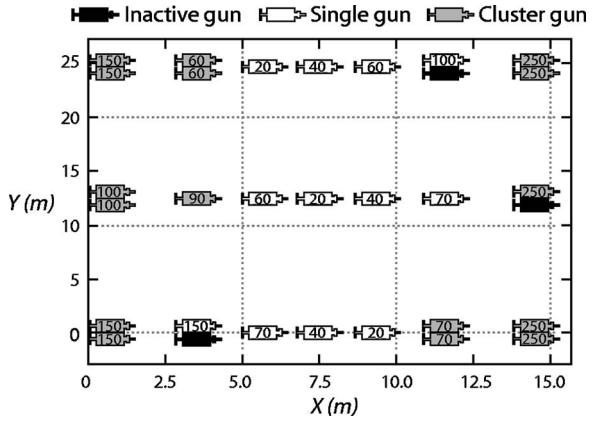

FIG. 3. Configuration of the M/V *Kondor* airgun array, used in 2003 experiment. Numbers inside individual airguns indicate the displacement (in cubic inches) of each gun.

In 2003, tagging operations and visual and acoustic monitoring were based on the R/V *Maurice Ewing*, and the airgun source vessel was the M/V *Kondor Explorer*. The *Kondor* array was a tuned array, 15 m long and 10 m wide, with 31 guns of various sizes for a total volume of 3090 in^3. Only 28 of the guns were active during the experiment, making the total volume of the active guns 2590 in^3. Figure 3 shows the configuration of the array. The private geoservice firm PGS Exploration (Walton-on-Thames, Surrey, UK) provided the on-axis theoretical far-field signature of the array (shown in Fig. 4). Backcalculating from the signature, the equivalent point-source source level was 261 dB re 1 μPa @ 1 m (peak-peak) in the 3–218 Hz frequency band. During CEEs, the airgun array was towed at a nominal depth of 7.5 m and fired every 15 s, with a ramp-up at the start of each firing period during which the number of guns fired was gradually increased to 28. In this study, we analyzed only recordings of full-array airgun arrivals. Like the *Speculator* array, the *Kondor* array source signature is also affected by a Lloyd's mirror effect. The *Kondor* array beampattern should also have grating lobes for source frequencies above approximately 375 Hz in the x-z plane and approximately 75 Hz in the y-z plane (calculated as explained earlier for the *Speculator* array, only using airgun cluster spacings of 2 m in the x dimension and 10 m in the y dimension), again increasing the proportion of higher-frequency energy transmitted by the array at launch angles close to parallel to the sea surface. The Fresnel near field of the Kondor array begins at about 8 m from the array at 50 Hz and 300 m from the array at 2 kHz (calculated as above for the *Speculator* array). Again, all airgun pulses used in this study were recorded in the far field.

B. Receivers: Dtags

Sperm whales (*Physeter macrocephalus*) were tagged with Dtags, digital archival tags that record acoustic, depth,

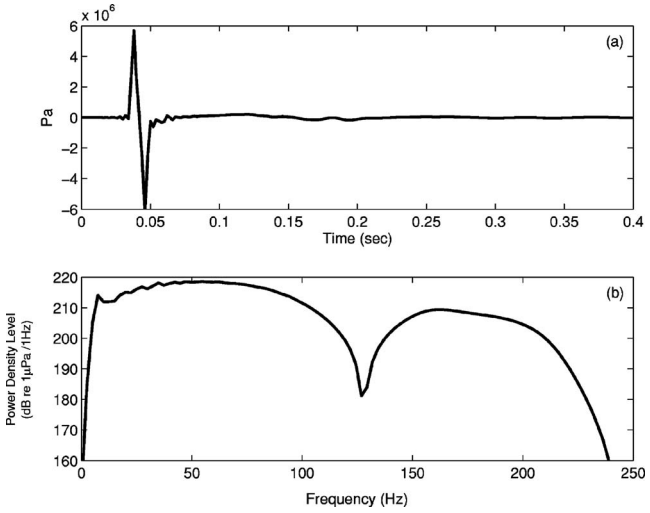

FIG. 4. (a) On-axis theoretical source signature of the M/V *Kondor* airgun array and (b) its amplitude spectrum (0–250 Hz). Both plots were provided by PGS Exploration (Walton-on-Thames, Surrey, UK).

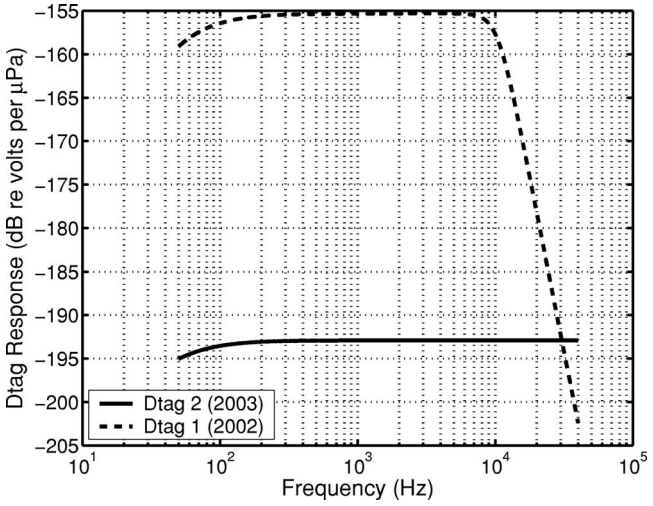

FIG. 5. Frequency response of acoustic sampling of Dtags 1 and 2.

and animal orientation data (Johnson and Tyack, 2003). Orientation data recorded by the tag can be combined with visual tracks to derive an estimate of the position of the tagged whale (Zimmer *et al.* 2005). Two versions of the Dtag were used in the experiments. In 2002, Dtagl tags were used. Dtagl recorded audio at a sampling rate of 32 kHz (12 bit resolution), with flat frequency response (±3 dB) between 400 Hz and 10 kHz and clip level of 155 dB re 1 μPa (0-peak). Filtering was applied to postemphasize the audio recordings at low frequencies. With postemphasis, the frequency response was flat (±1.5 dB) from 60 Hz to 12 kHz. Dtagl also recorded data from three-axis accelerometers and magnetometers, ambient pressure (depth), and temperature at a sampling rate of 48 Hz. In 2003, both Dtagl and Dtag2 tags were used, but only Dtag2 data were analyzed in this study. Dtag2 recorded audio at a sampling rate of 96 kHz (16 bit resolution), with flat (±1.5 dB) frequency response between 400 Hz and 45 kHz and clip level of 193 dB re 1 μPa (0-peak). Filtering was applied to postemphasize the audio recordings at low frequencies. With postemphasis, the frequency response was flat (±1.5 dB) from 50 Hz to 45 kHz. Dtag2 also recorded data from three-axis accelerometers and magnetometers, ambient pressure (depth), and temperature at 50 Hz. Figure 5 shows the sensitivity curves of Dtagl and Dtag2. Both Dtagl and Dtag2 measured temperature near the crystal used to control clock speed of the tag. Their thermistors did not measure ambient water temperature.

C. Ocean and ocean acoustic environment

The CEE components of the SWSS in the Gulf of Mexico were performed in September 2002 and July 2003, and we analyzed data from one exposed whale per year. Figure 6 shows the study areas where the data modeled in this study were collected. On September 11, 2002, the modeled CEE took place on a bathymetric slope of about 1.5° in the west Mississippi Canyon region, in an area where the water depth varies from 400 to 800 m. On June 13, 2003, the modeled CEE took place in the Mississippi Canyon, in an area where the bathymetry is locally flat and the water depth is about 800 m.

During the CEE cruises in both years, CTD (conductivity, temperature, depth) and XBT (expendable bathythermograph) casts were made periodically to estimate the sound speed profile (Jochens and Biggs, 2003, 2004). For acoustic modeling of 2002 airgun pulses, we chose one XBT profile from the 2002 data set, closest to the experiment site and the airgun exposure time. The profile [Fig. 7(a)] indicates a 40 m thick mixed layer below the sea surface, which created a strong surface duct that trapped high-frequency sound and allowed it to propagate with little transmission loss (Urick, 1975). All sound speed profiles taken from the CTD and XBT casts in 2002 showed a similar surface duct. For acoustic modeling of 2003 airgun pulses, we averaged data from two CTD profiles taken near the experiment site to obtain our sound speed profile. Unlike the 2002 sound speed profile, the 2003 profile did not include a strong surface duct [Fig. 7(b)].

No bottom surveys were conducted during the CEE cruises, but marine geology and geoacoustic reports near the experiment areas are available to help establish the geoacoustic bottom model. According to the NGDC Seafloor Surficial Sediment (Deck41) Database (http://www.ngdc.noaa.gov), the dominant lithological component of the surficial seafloor in the CEE areas is clay, and the secondary lithological component is silt. The ratio of bottom sound speed to water sound speed at the seafloor should be about 0.995, a typical value for silty-clay sediments (Hamilton, 1980).

A chirp sonar subbottom survey during the Littoral Acoustic Demonstration Center experiment in August 2001 (Turgut *et al.*, 2002) was conducted in the same area as the 2002 modeled CEE, and sound speed and density profiles from that report are reproduced in Fig. 8(a). Comparing the ocean bottom sound speed to the water sound speed, as shown in Fig. 7(a), confirms that the sound speed ratio at the 2002 study site matches the ratio typical of silty-clay sedi-

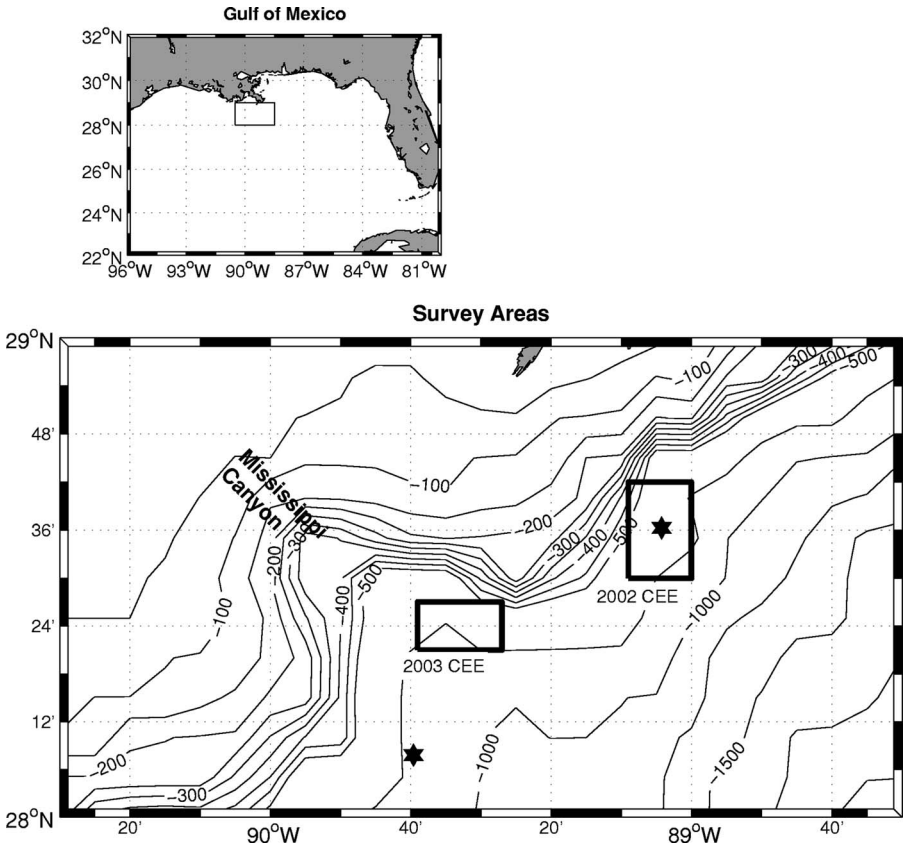

FIG. 6. Sites of airgun operations measured in 2002 and 2003. Upper panel: Location of the study areas. Lower panel: Detail of the 2002 and 2003 study sites (boxes) and locations where data on bottom properties were collected by Turgut *et al.* (2002) and Geresi *et al.* (2005) (stars).

ments. Figure 8(b) shows reflection coefficient versus grazing angle on the seafloor at the site of the 2002 modeled CEE, calculated with the acoustic modeling package OASES (Schmidt, 2004) using data on bottom properties from Turgut *et al.* (2002). For acoustic modeling of the 2002 CEE, we adopted a smoothed version of Turgut's seafloor sound speed and density profiles.

We did not find data on the bottom properties at the site of the 2003 modeled CEE in the literature; the closest detailed studies of the sea floor were conducted in 2003 on Mississippi Canyon Block 798 (about 20 km from the 2003 CEE site, but on the opposite side of the canyon; see Fig. 6)

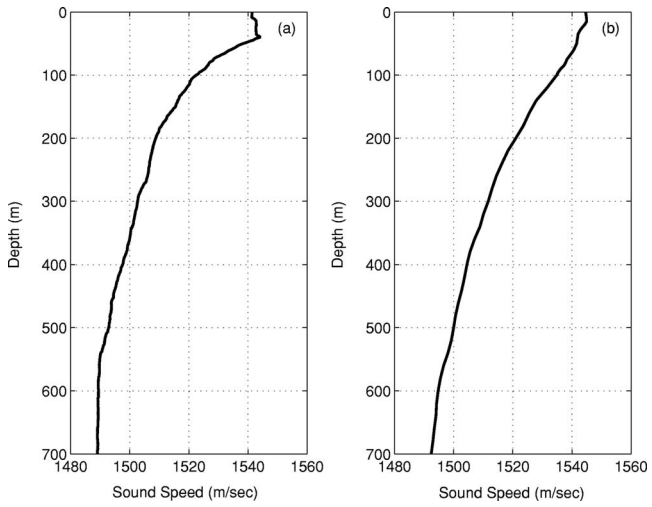

FIG. 7. Sound speed profiles for 2002 (left) and 2003 (right) used for acoustic modeling.

(McGee *et al.*, 2003). Geresi *et al.* (2005) applied a migration velocity analysis to McGee and colleagues' seismic reflection data and obtained the bottom sound speed to 600 m depth, which is reproduced in Fig. 9(a). The sound speed ratio between the top layer of the bottom and deep water [shown in Fig. 7(b)], 0.993, is typical of silty-clay sediments. Figure 9(b) shows the bottom reflection coefficient as a function of frequency and grazing angle on the seafloor at the site of the 2003 modeled CEE, calculated with the acoustic modeling package OASES (Ocean Acoustics and Seismic Exploration Synthesis) (Schmidt, 2004) using bottom properties from Geresi *et al.* (2005). We used Geresi's seafloor sound speed profiles to model the 2003 CEE data.

We applied Hamilton's regression equations to the selected bottom profiles to estimate the bottom density (Hamilton, 1978) at the 2003 study site and the bottom attenuation (Hamilton, 1972) at both sites.

III. METHODS

A. Experiments

Dtags were deployed by approaching sperm whales at the surface in a small inflatable boat, then using a long pole to place the tag atop a whale's back, where it attached with suction cups. The tags were positively buoyant and programmed to release from the whales after a maximum recording time of 12 h (Dtagl) or 16 h (Dtag2), at which point they floated to the surface and were located and recovered with the help of a built-in radio beacon. Since the tags were attached to the whales, it is possible that shadowing by the whales' bodies might have affected recorded airgun pulses.

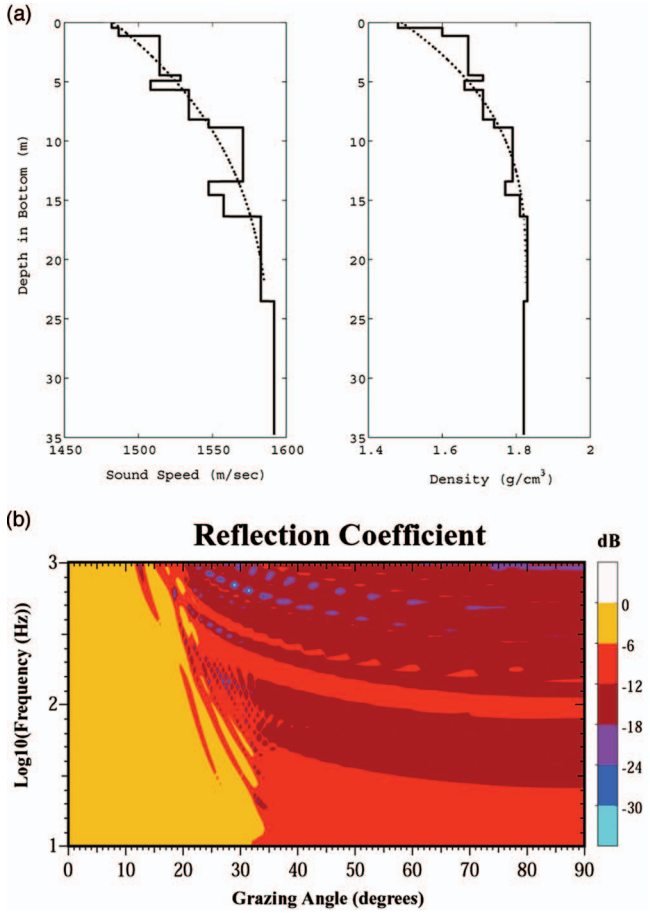

FIG. 8. (a) Bottom sound speed and density profiles for the 2002 study area. The solid lines are the geoacoustic inversion results from wideband (2–12 kHz) chirp sonar data obtained from a Littoral Acoustic Demonstration Center experiment on the east of the Mississippi Canyon in 2001 (Turgut *et al.*, 2003). The dotted lines are fitted curves. (b) Corresponding reflection coefficient contour (grazing angle vs frequency) for the 2002 study area. The corresponding density and attenuation profiles were calculated using Hamilton's regression equations (Hamilton, 1972, 1978).

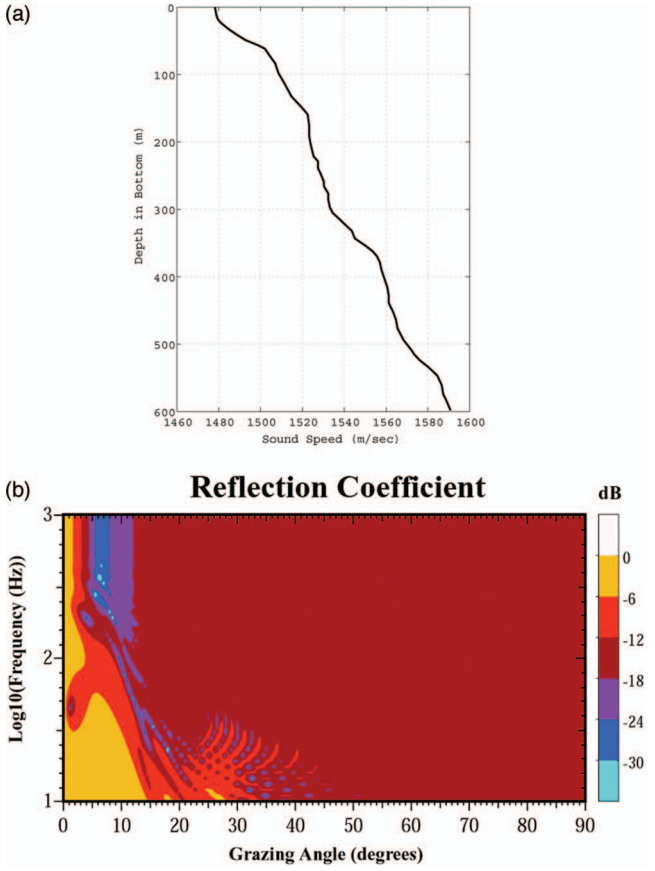

FIG. 9. (a) Bottom sound speed profile for the 2003 study area. The sound speeds were obtained by applying the migration velocity analysis to reflection seismic data on Mississippi Canyon Block 798 (Geresi *et al.*, 2005). (b) Corresponding reflection coefficient contour (grazing angle vs frequency) for the 2003 study area. The corresponding density and attenuation profiles were calculated using Hamilton's regression equations (Hamilton, 1972, 1978).

However, body shadowing should have negligible impact on the timing of pulse arrivals, and only minor influence on relative levels at the frequencies we studied. In fact, body shadowing would have a greater effect in reducing high frequencies than low, which would only reduce the surface ducting effect described in this study. In 2002, one whale underwent a CEE on September 10, and three simultaneously tagged whales underwent a CEE on September 11. In 2003, CEEs were performed on individual tagged whales on June 13 and 22, and two simultaneously tagged whales underwent a CEE on June 14. Each CEE lasted about 1 h, and was preceded and followed by tagged control periods with no airgun exposure. Visual observers on the observation vessel tracked the tagged whales using reticle-binoculars and the radio-beacon in the tag. A derived three-dimensional (3D) track for the entire tag attachment period, estimated to be accurate to ±0.5 km, was calculated using dead-reckoning based on the orientation sensors and the visual locations [Johnson and Tyack, 2003; Madsen *et al.* (2006)]. Horizontal ranges between the airgun arrays and the whales were calculated to the nearest 0.1 km using the derived tracks.

In this study, we modeled airgun arrivals recorded on one tagged whale each year (whale sw02_254b, tagged on September 11, 2002, and whale sw03_164a, tagged on June 13, 2003). Table I presents the exact durations and timing of the tag deployments that included the modeled CEEs. During the 2002 exposure, source-whale range varied from 5.4 to 12.0 km, and water depth varied from 600 to 800 m. During the 2003 exposure, source-whale range varied from 11.0 to 12.0 km, and water depth was about 800 m. Figure 10 shows the locations of the airgun source vessels and tagged whales during the modeled exposures, along with the bathymetry of each study area.

B. Acoustic models

1. Normal mode model for determination of the cutoff frequency

Surface ducts are shallow (generally less than 100 m deep), so only higher-frequency (shorter-wavelength) sound

TABLE I. Duration and timing of modeled tag deployments and CEEs in 2002 and 2003.

Date	Whale ID	Tagged time	Airgun exposure time
9/11/2002	sw02_254b	10:28–22:52	12:16–14:20
6/13/2003	sw03_164a	09:48–23:20	18:26–19:26

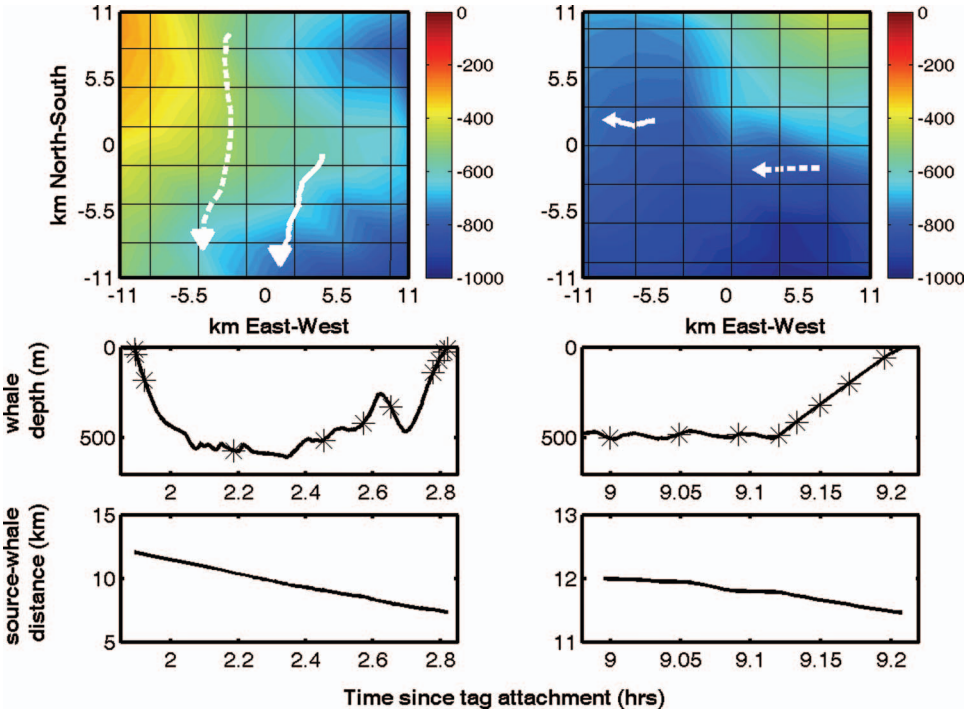

FIG. 10. The left column contains information related to the controlled exposure experiment on September 11, 2002, and the right column contains information on the controlled exposure experiment on June 13, 2003. Top panels: Airgun array source vessel (dotted lines) and tagged sperm whale (solid lines) locations during the two modeled airgun exposures. Arrowheads indicate direction of travel. The x and y axis values indicate distance in km from approximate centers of the study locations: 28.600°N, 89.070°W (2002) and 28.380°N, 89.520°W (2003). Middle panels: Dive profiles of the tagged whales during the modeled exposures. Asterisks indicate the time of firing of modeled airgun pulses. Lower panels: Range from the airgun source vessels to the tagged whales during the modeled exposures.

is trapped and propagates efficiently in surface ducts (Urick, 1975). The cutoff frequency of a surface duct is the approximate frequency below which sound is not trapped in the duct. Cutoff frequency is approximate because sound below the cutoff frequency may be only partially trapped in the duct (a "leaky duct"), and sound may need to be significantly above the cutoff frequency for maximal trapping to occur. To estimate the cutoff frequency of the surface duct in our 2002 study area, we performed a series of KRAKEN normal mode model runs (Porter, 1995) at five frequencies ranging from 50 to 1600 Hz. We used the model output to determine the mode number n and modal eigenvalue k_n for the lowest-numbered mode trapped in the duct at each frequency (a mode was considered trapped if it had high intensity in the duct, and exponentially decaying intensity below the duct). Then, to determine whether mode n would propagate, we calculated its mode-propagation cutoff frequency, ω_n (the frequency above which at least n modes will propagate). Trapped modes with ω_n less than the frequency of the KRAKEN model run that generated them would propagate. We estimated ω_n according to Frisk (1994):

$$\omega_n = k_{zn} c, \tag{1}$$

where

$$k_{zn} = \sqrt{\left(\frac{\omega}{c}\right)^2 - k_n^2}, \tag{2}$$

ω is radian frequency and c is sound speed. We used 1543 m/s for sound speed in the calculations [see Fig. 7(a)]. This procedure determined whether or not the trapped modes would propagate in the duct at each frequency tested, and therefore allowed us to estimate the cutoff frequency of the surface duct as the lowest frequency at which the trapped modes would propagate.

2. Airgun array beampattern model

An airgun array usually contains airgun elements with different volumes, which produce sound pulses with different amplitudes, damping rates and bubble pulse periods (Ziolkowski, 1970). This variability makes airgun array signature modeling complex and difficult. One can estimate the signature from near-field measurements of an airgun array (Ziolkowski *et al.*, 1982, 1997; Laws *et al.*, 1998), but during the CEEs we studied, no near-field measurements of airgun pulses were made. An alternative way to estimate the signature of an airgun array is to treat each element as a monopole source and consider the geometric configuration of the array. The volume of every element in the *Speculator* and *Kondor* arrays was known, and since the amplitude of an airgun element is approximately proportional to the cube-root of its volume, we could estimate the relative amplitude of the elements in each array (Caldwell and Dragoset, 2000). We modeled the array according to the following normalized formulation in a free space bounded by the sea surface

$$S(\vec{x},\omega) = \sum_i \nu_i^{1/3} \frac{e^{-jk_w R_i}}{R_i} + \sum_i (-1)\nu_i^{1/3} \frac{e^{-jk_w R_i'}}{R_i'}, \tag{3}$$

where $\vec{x}$ is the position of the receiver, ω is the acoustic frequency, $k_w = \omega/c$ is the acoustic wave number in water

(where c is the sound speed, 1500 m/s), ν_i is the volume of ith airgun element, and R_i is the distance from the receiver to the ith airgun element. In the second term, the (-1) indicates the contribution from the virtual "mirror image source" due to the Lloyd's mirror effect of the sea surface (modeled as a pressure release boundary), and R_i' is the distance from the receiver to the image source of the ith airgun element. Therefore, our airgun array beampattern model includes both the effects of array geometry and the Lloyd's mirror effect caused by sea-surface reflection. Using this model, we calculated the acoustic pressure at a certain radius from the array and normalized it to obtain an estimate of the source beampattern. The airgun elements in this model were treated as monopole sources with a single impulse, while real airgun pulses include a series of bubble pulses (Ziolkowski, 1970). However, the model could still predict the locations of spatial and frequency notches in the airgun array beampattern, since notch locations are mainly determined by the geometric configuration of the array (Parkes and Hatton 1986, Tipler and Llewellyn 2003).

3. Acoustic ray-tracing model

In this study, we modeled range-dependent acoustic propagation but considered only reflection from the sea-floor and sea-surface boundaries and refraction due to soundspeed variations. We used the ray-tracing program RAY (Bowlin *et al.*, 1992), which can deal with a range-dependent environment, to calculate sound propagation paths and travel times of the airgun pulses recorded during the modeled CEEs. The fundamental theory underlying RAY is well known; the reader interested in more detail is referred to the relevant literature (e.g., Bowlin *et al.*, 1992; Jensen *et al.*, 1994).

4. Broadband acoustic propagation modeling

To model the transient airgun pulse signals recorded on Dtags in the CEEs, we developed a two-dimensional (2D) broadband range-dependent acoustic propagation program based on Fourier synthesis (Jensen *et al.*, 1994). The model, described below, can compute received sound pulses over a specified bandwidth at a single position.

The Fourier pulse synthesis technique is based on the Fourier transform of the continuous wave frequency-domain response multiplied by the spectrum

$$p(r,z,t) = \frac{1}{2\pi}\int_{-\omega_{\max}}^{\omega_{\max}} S(\bar{\omega})H(r,z,\omega)e^{-j\omega t}d\omega, \tag{4}$$

where $p(r,z,t)$ is the pressure signal of a sound source received at the position (r,z) on a vertical plane, which also includes the source; r is horizontal range; and z is depth. $S(\omega)$ is the source spectrum with a finite bandwidth $2\omega_{\max}$, and $H(r,z,\omega)$ is the frequency response of a monopole source at a frequency ω. In our program, $H(r,z,\omega)$ is calculated by the existing time-harmonic acoustic model RAM (range-dependent acoustic model), a parabolic equation (PE) model developed by Michael D. Collins at the Naval Research Laboratory in Washington, DC (Collins, 1993). Discretizing the transform Eq. (4), we obtain

$$\sum_{m=-\infty}^{\infty} p(r,z,k\Delta t + mT) = \frac{\Delta\omega}{2\pi}\sum_{n=-(N/2-1)}^{N/2}[S(\omega)H(r,z,n\Delta\omega) \times e^{-jt_0 n\Delta\omega}]e^{-j(2\pi nk)/N}, \tag{5}$$

where on the right hand side, the frequency within a finite bandwidth is discretized as N samples with values $n\Delta\omega$, with $n=(N/2-1)\sim N/2$. On the left-hand side, the time within a finite window $T(=1/\Delta\omega)$ is sampled at $k\Delta t$, with $k=1,2,3\ldots$N. The sampling rate must obey the Nyquist criterion, or aliasing will occur in the frequency domain. Similarly, discretization in the frequency domain can cause wrap-around in the time domain if $\Delta\omega$ is too large, with m (on the left-hand side of the equation) being the index of the periodicity of the discretized time-domain signal. To minimize the wrap-around effect while keeping $\Delta\omega$ large enough for reasonable computation time, we applied complex frequency integration (Malick and Frazer, 1987; Jensen *et al.*, 1994). If N is an integer power of two, the fast Fourier transform algorithm is efficient for evaluating the summation.

For all model runs, we placed an artificial absorbing layer in the sediments to prevent sound energy from being reflected or refracted back to the water from the deep bottom. The sound source in our model runs was a bell-shaped single pulse, containing most of its energy in the frequency band from 0 Hz to three times its central frequency. Mathematically, this pulse can be represented as

$$s(t) = 0.75 - \cos 2\pi f_c t + 0.25\cos 4\pi f_c t, \quad 0 \leqslant t \leqslant T = 1/f_c, \tag{6}$$

where f_c is the center frequency. We used $f_c=250$ Hz. The model source does not accurately represent the output of an airgun array, but the resulting model output can still predict the arrival time pattern measured at the receiver. Because the low-frequency flow noise is very high in the 2002 Dtag record, and the model source produces 95% of its energy in the 0–600 Hz frequency band, we bandpass filtered the 2002 data and model results from 100 to 600 Hz before comparing them.

IV. RESULTS

A. 2002 experiment and model results

Figure 11 shows the wave form and spectrogram of two airgun pulses from the 2002 experiment, recorded on the same whale near the surface (at 24 m depth) and in deep water (at 420 m depth). There are three clear arrivals in the pulse recorded at 24 m depth. The spectrogram shows that the first arrival contains significant high-frequency energy but almost no energy below 250 Hz. In the pulse recorded at 420 m depth, two strong whale clicks appear at 0.12 and 0.56 s (reduced arrival time), followed by their echoes. Five arrivals from the airgun pulse also can be seen. The first two weak arrivals at 0.25 and 0.32 s contain only high frequency

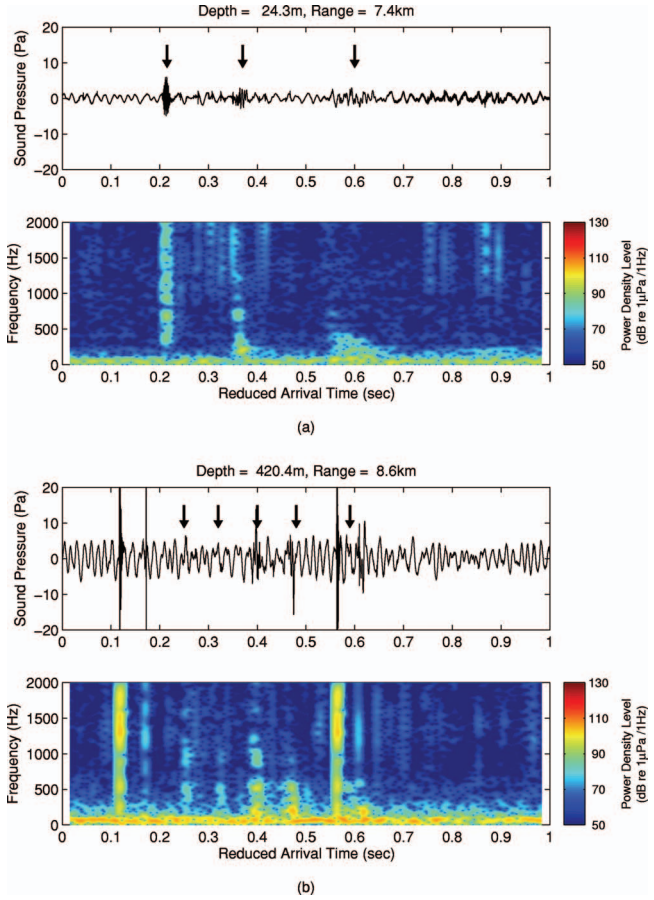

FIG. 11. The wave form and spectrogram of two airgun pulses recorded on the Dtag when the tagged whale was at (a) 24 m depth and (b) 420 m depth during the 2002 experiment. Arrows indicate the airgun arrivals. The intense broadband signals at about 0.12 s and about 0.56 s (both followed by their echoes) are clicks produced by the tagged whale.

energy. The last arrival, at 0.6 s, overlaps with the echo of the second whale click. Spectrograms from both depths also show high level, low frequency flow noise.

The first airgun arrivals recorded when the whale was near the surface lacked low-frequency energy because of the high-pass filtering effect of the surface duct (Fig. 7). Figure 12 shows a plot of RAM parabolic equation model output (transmission loss as a function of range and depth for a 600 Hz source), illustrating the surface ducting effect. Based on our normal mode model runs, we estimated that the cutoff frequency of the surface duct in the 2002 sound speed profile was about 250 Hz, which agrees well with the cutoff frequency shown in the data (Fig. 11). Grating lobes in the airgun array beampattern can also channel energy to near-horizontal launch angles from the array, and thus into the surface duct. Modeling the beampattern of the *Speculator* source array at 7 m depth showed that grating lobes (due to both array geometry and sea-surface reflection) start emerging at 120 Hz, an octave below the duct cutoff frequency. Figure 13 shows examples of the *Speculator* airgun array beampattern at six frequencies from 50 to 650 Hz. Our beampattern model predicts frequency notches occurring in the downward direction at 107 and 214 Hz, in good agreement with the predicted amplitude spectrum of the on-axis airgun array signature [see Fig. 2(b)]. At 650 Hz, the energy

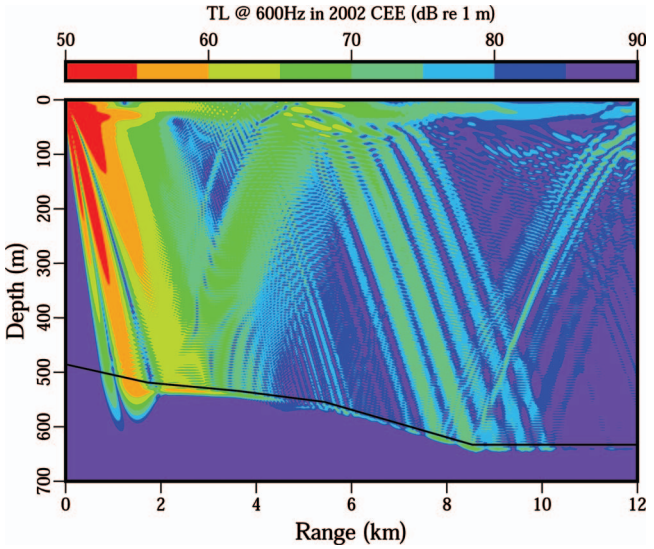

FIG. 12. Transmission loss as a function of range and depth for a 600 Hz omnidirectional point source at 7 m depth in the 2002 study environment. The sea floor is indicated by a solid black line.

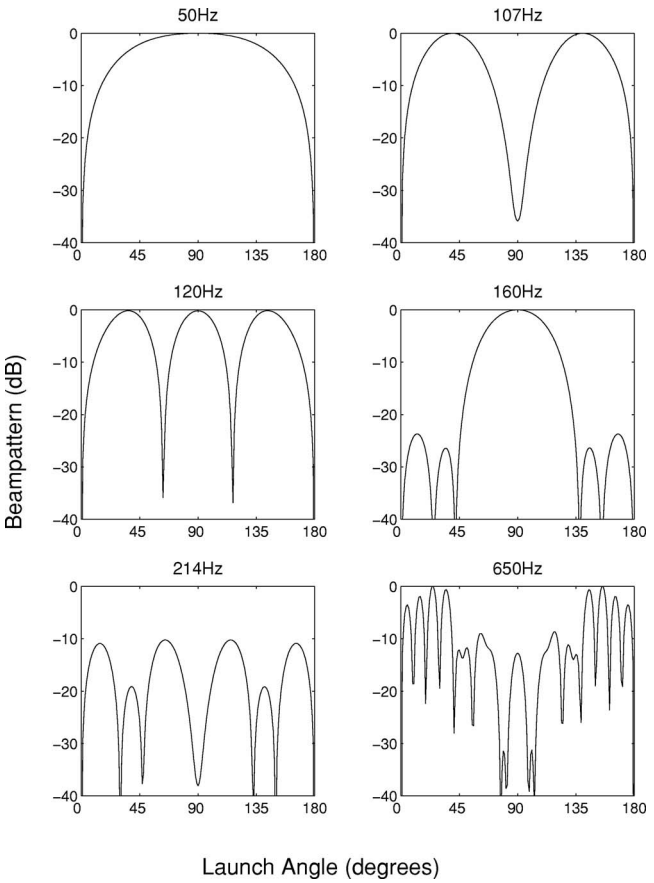

FIG. 13. The modeled beampattern of the M/V *Speculator* airgun array at several frequencies, in a vertical plane along the towing direction. Modeled beampattern includes the effects of sea-surface reflection as well as array geometry, as noted in the text. The airgun array was 7 m below the sea surface for consistency with the modeled source signature (Fig. 2). Launch angles were measured relative to a line extending from bow to stern, and a 3D normalized beampattern was calculated at each frequency. (Because the figure shows 2D beampatterns, the maximum plotted beampattern levels may be less than 0 dB if the maximum-amplitude lobe of the beampattern occurred outside the plane plotted in this figure.)

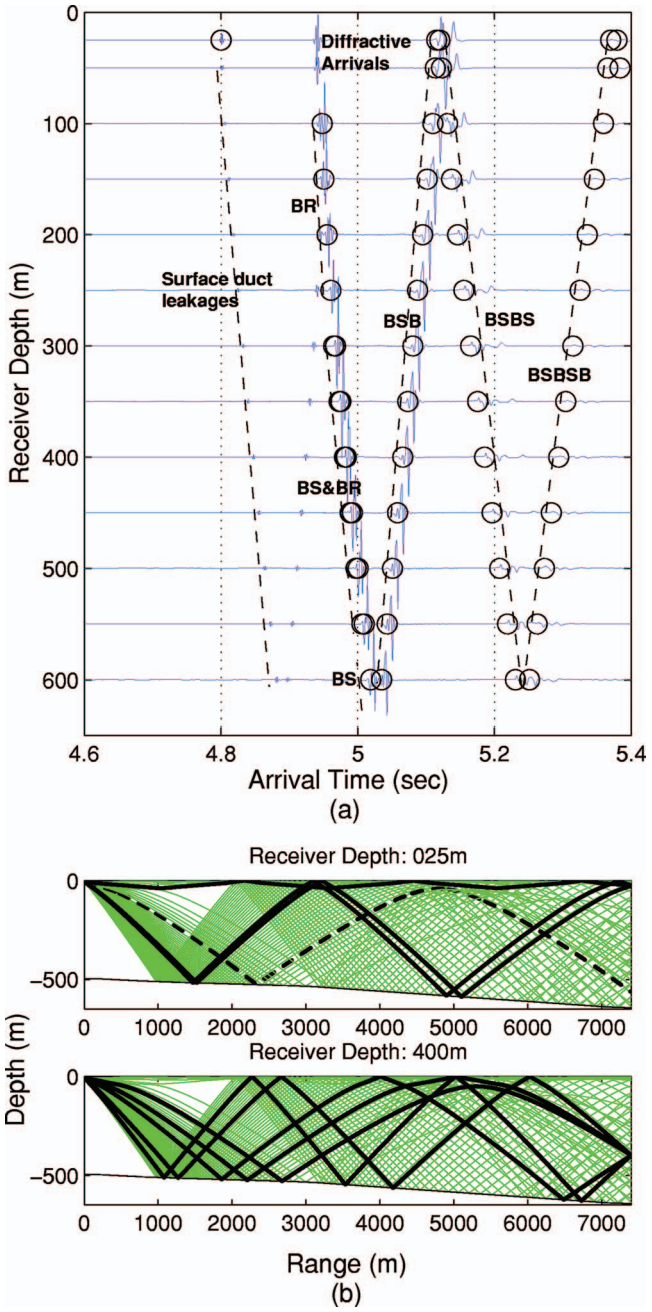

FIG. 14. (a) Modeled wave forms (blue traces) and eigenray arrival times (highlighted by black circles) at 7.4 km range and various depths in 2002. Ray labels are as follows: B indicates a bottom reflection, S indicates a surface reflection, and R indicates refraction in the water column. (b) Modeled eigenray paths (thick black lines) to receivers at 25 m and 400 m depth and sound propagation paths (thin green lines) for the 2002 experiment. The dashed line in the 25 m depth panel is the ultimate BR ray with the shallowest turning point.

emitted by the array at near-horizontal launch angles is even greater than in the downward direction. The model also illustrates that, even at frequencies where the greatest proportion of sound is directed toward the sea floor (e.g., 160 Hz), sound carried by the sidelobes (at launch angles closer to the horizontal) is only 20 dB lower than that in the main, downward-directed lobe [see Fig. 2(b)].

The modeling of the pulse arrivals, including the eigenray arrival time at 7.4 km range and various depths, is shown in Fig. 14(a). The corresponding ray labels are also included; the labels consist of a "B" for every bottom reflection, an "S" for each reflection at the sea surface, and an "R" to indicate refraction in the water column. For example, a BS ray leaves the source, bounces off the bottom, reflects at the surface, and finally arrives at the receiver, and a BSB ray is like a BS ray with one more bottom bounce before arriving at the receiver. The pulse arrivals calculated from the broadband model arrive exactly when the ray-tracing model predicts, except in the case of the diffractive arrivals near the surface and the surface duct leakages, where ray theory fails (Frisk, 1994). The eigenray paths are also calculated and shown in Fig. 14(b) for two selected depths, 25 and 400 m. The first arrival at the 25 m-depth receiver travels in the surface duct, in concordance with our observation that the first arrival has little low-frequency energy. The BSB and BSBS eigenray paths also produce pulses at the 25 m receiver depth; however, they arrive almost at the same time and combine into a single pulse. Figure 14(a) also shows that as the receiver goes deeper, the pulses traveling along BSB and BSBS ray paths separate, and the grazing angles of the bottom bounces of these two rays also change. The reflection coefficient contour for 2002 [Fig. 8(b)] shows that the BSBS ray (grazing angle 24°) has more bottom loss than the BSB ray (grazing angle of 18°), explaining the difference in amplitudes of the BSB and BSBS rays [Figs. 14(a) and 15]. A plot of eigenrays to the 400 m receiver is shown in Fig. 14(b); as shown in Fig. 14(a), the BR ray path arrives at the receiver almost at the same time as the BS ray. Ray trace output also shows that BR rays can arrive at a receiver at 7.4 km range only above 560 m depth. Below that, only BS rays can reach. Conversely, BR and not BS rays arrive at receivers at depths shallower than 330 m.

Figure 14(a) also shows surface duct leakage and the diffractive arrivals. Sound energy leaks from the surface duct due to diffraction and scattering at the boundaries of the duct (Weston *et al.*, 1991). Since the propagation model we used does not account for interface roughness at the boundaries of the duct, the leakage seen in our modeling results is due only to diffraction. Sound energy trapped in a surface duct and subject to leakage has been previously described, from a modal sound propagation perspective, as a virtual mode (Labianca, 1972). When such a virtual mode occurs, some surface ducted energy continuously seeps from the duct, but remains trapped in the waveguide as a whole. The leakages eventually return to the duct after bouncing off the bottom or refracting in the water column (Porter and Jensen, 1993). Figure 14(a) shows two arrivals resulting from surface duct leakages; the second of those arrivals actually leaks from the duct first, but undergoes a bottom bounce before arriving at the whale. The broadband PE model also predicts that a receiver in the surface duct will detect diffractive arrivals [Fig. 14(a); Murphy and Davis, 1974]. Unlike the surface duct leakages, diffractive arrivals in the duct are from an upward-directed ray that is below the duct. As shown in Fig. 14(b), the ray in question is the ultimate BR ray, which has a turning point closer to the base of the surface duct than any other BR ray. The ray turns down at the lower bound of the surface duct (a local maximum in the sound speed profile), and some of its energy enters the duct.

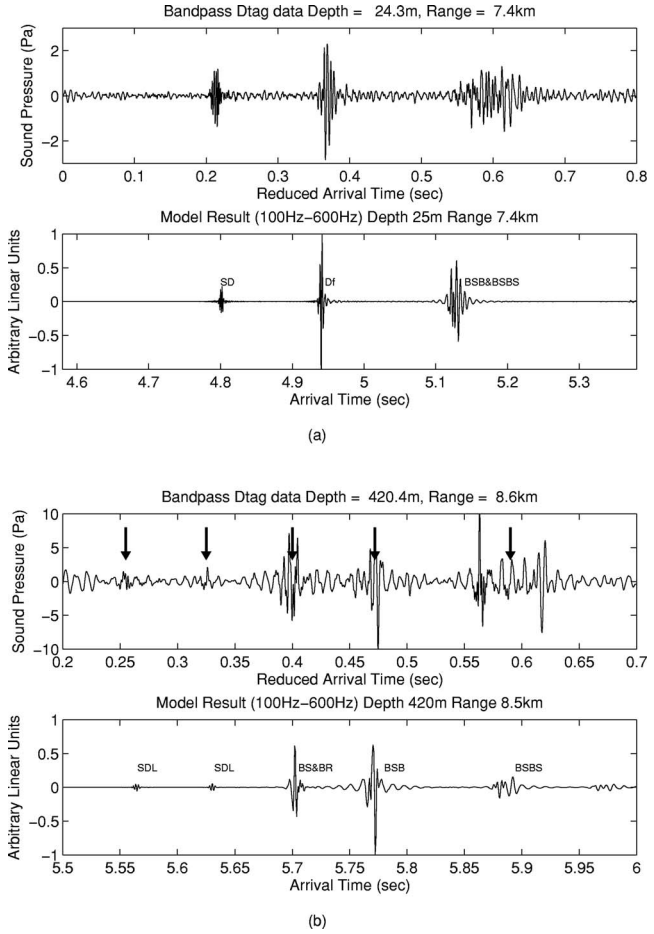

FIG. 15. Wave form comparison between the 2002 Dtag recordings and broadband model results for a receiver at (a) 7.4 km range and 24.3 m depth and (b) 8.5 km range and 420 m depth. All wave forms were bandpass filtered between 100–600 Hz, as described in Sec. III. Ray path labels are as follows: B indicates a bottom reflection, S indicates a surface reflection, SD indicates a surface ducted arrival, SDL indicates a surface duct leakage, and Df indicates diffraction in the water column.

A comparison of wave forms from the Dtag records and the broadband model results is shown in Fig. 15. As shown in Fig. 15(a), the timing and relative amplitudes of modeled arrivals match the data very well for a receiver at 7.4 km range and 24.3 m depth. The broadband model also provides very good results compared with the Dtag data at 8.6 km range and 420 m depth, where the relative differences between the surface duct leakages and the single bottom bounce pulses are especially well described.

B. 2003 experiment and model results

Figure 16 shows the wave form and spectrogram of a typical airgun pulse recorded on a tagged whale 11.2 km from the source at 450 m depth (the intense broadband signals at about 0.4 and 0.9 s are clicks produced by the tagged whale). The spectrogram illustrates that, in contrast to the 2002 data, all arrivals from the airgun pulse contain mainly low-frequency energy (below 500 Hz, and concentrated below 200 Hz). Because the sound speed profile for the modeled 2003 CEE did not include a significant surface duct, high-frequency sound did not undergo ducted propagation to

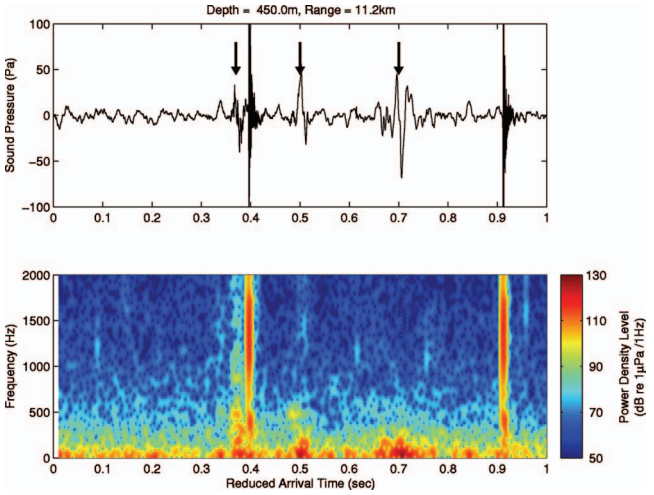

FIG. 16. The wave form and spectrogram of an airgun pulse recorded on the Dtag when the tagged whale was at 450 m depth and 11.2 km range during the 2003 experiment. Arrows indicate airgun arrivals. The intense broadband signals at about 0.4 and 0.9 s are clicks produced by the tagged whale.

the tagged whale near the surface, but rather reached the whale after reflecting from the bottom and the sea surface [see Fig. 17(b)].

The modeled pulse arrivals and eigenray arrival times at 11.2 km range and various depths are shown in Fig. 17(a). The eigenray paths for receivers at 150 and 450 m depth are also shown in Fig. 17(b). As they did in the 2002 model runs, the ray and broadband models predicted nearly identical airgun pulse arrival times. The modeled arrival times match fairly well with the data (Figs. 18 and 19). Figure 17(a) shows that the first airgun arrival at 150 m depth is a BR ray, while that at 450 m depth is a BS ray, because no BR rays arrive at receivers below about 200 m depth at 11.2 km range. Figure 17 also indicates that the third-arriving rays undergo one more surface reflection than the second-arriving rays, which explains why the third arrivals (shown in Fig. 18) are about 180° out of phase with the second arrivals (Frisk, 1994).

Figure 19 shows a wave form comparison between the Dtag records and the broadband PE model results for a receiver at 450 m depth and 11.2 km range. These model results did not match the data as well as the 2002 model results because our information about bottom characteristics was less precise for the 2003 site, as will be clarified further in the discussion section.

V. DISCUSSION AND CONCLUSIONS

Most reviews on the effects of airgun array pulses on marine life have accepted the assumption that airgun noise is limited to low frequencies, and have concentrated on species thought to have good low-frequency hearing (Caldwell, 2002; Popper *et al.*, 2004; Richardson *et al.*, 1995). We found that animals located near the surface when surface-ducting conditions are present may be exposed to measurable levels of airgun sound above 500 Hz. The surface ducting effect described here means that even animals with poor low-frequency hearing (for example, dolphins and other small odontocetes) could potentially detect and be affected by air-

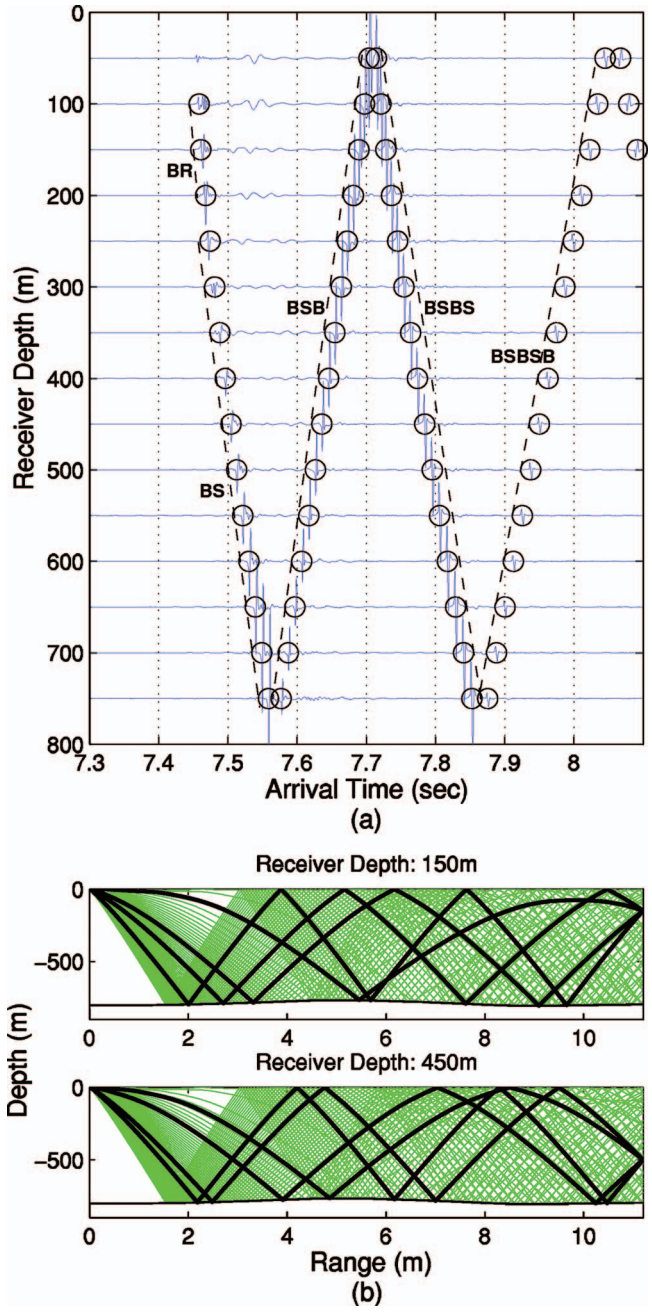

FIG. 17. (a) Modeled wave forms (blue traces) and eigenray arrival times (highlighted by black circles) at 11.2 km range and different depths in 2003. Ray path labels are as follows: B indicates a bottom reflection, S indicates a surface reflection, and R indicates refraction in the water column. (b) Modeled eigenray paths (thick black lines) to receivers at 150 and 450 m depth and sound propagation paths (thin green lines) for the 2003 experiment.

gun noise. However, we did not observe the surface ducting effect in all environmental settings, which underscores the influence of temporally and spatially variable oceanographic conditions on acoustic propagation. The received level of airgun pulses clearly depends not only on source-receiver range and on-axis airgun array source level, but also on array beampattern, sound speed profile, bathymetry, and bottom properties.

Our ability to model the absolute intensity of airgun pulses at the whales was limited by incomplete data in a few key areas. First, we did not have an adequate measurement of the source signatures of the airgun arrays (at all launch

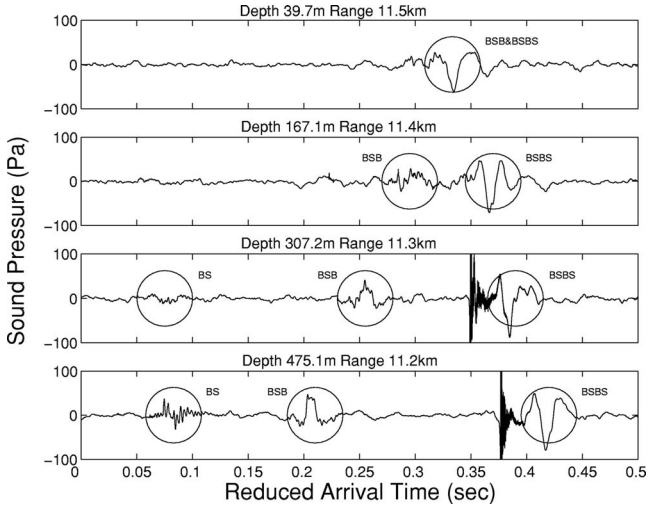

FIG. 18. Wave forms of airgun arrivals recorded on Dtags at different depths and about 11 km range in 2003. Black circles highlight the time of each airgun arrival. Ray path labels are as follows: B indicates a bottom reflection, and S indicates a surface reflection.

angles). Also, the lack of suitably detailed information on environmental properties in the 2003 study area explains the mismatch between 2003 model and data wave forms (Fig. 19). First, the 2003 bottom property data was taken about 20 km from the 2003 CEE site, on the opposite side of the Mississippi Canyon, and errors in bottom parameters result in inaccurate modeling of sound amplitude. Second, in 2003, sound speed data were collected temporally and spatially further from the study area than in 2002. Consequently, inaccuracies in the 2003 sound speed profile resulted in differences between modeled and observed relative arrival times; any errors in bathymetry could also have caused arrival-time discrepancies. Finally, the numerical source used in the models is a point source, which acts like a dipole at low frequencies and emits less energy at launch angles close to the horizontal than does an airgun array. This difference helps explain why airgun arrivals that left the source at near-horizontal launch

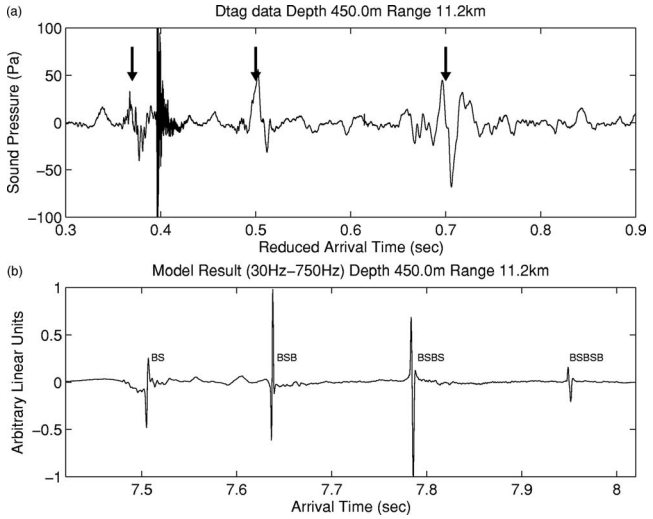

FIG. 19. Wave form comparison between (a) the 2003 Dtag recording and (b) broadband model results for a receiver at 11.2 km range and 450 m depth.

angles have more energy than the model predicts. The observed mismatch between 2003 data and model results emphasizes the fact that accurate modeling of airgun pulse arrivals is impossible without adequate environmental data and source information.

Surface ducted propagation increased the proportion of high-frequency content compared to the seismic (low frequency) content of some airgun arrivals recorded on whales at shallow depths (<50 m) in 2002, but not in 2003, when no surface duct was observed. A reasonable "ducting gain" estimate for the reduction in transmission loss for sound trapped in a surface duct can be obtained by a simple physical argument. The surface duct confines the low-angle trapped energy to its thickness h, as opposed to the full water column depth H, so that there is an H/h geometric ducting gain for the trapped energy. Also, the ducted energy does not interact with the bottom and suffer bottom loss, so the ducted rays will "gain" the amount of energy they would have lost in bottom interaction if the duct did not exist. Thus we can predicate a "surface duct gain" G in dB of

$$G = 10\log(H/h) + \mathrm{TL}(f, r, \theta) \tag{7}$$

for the portion of the rays trapped in the duct, where TL is the transmission loss for a nonducted ray of source angle θ. Of course, exact model calculations are preferable, and we would recommend that any calculations requiring precision be based on such models.

The exact levels notwithstanding, the data from the 2002–2003 Dtag controlled exposure studies do show that airgun arrays produce significant energy at frequencies well above those actually utilized for geophysical surveys (Caldwell and Dragoset, 2000; see Madsen *et al.* (2006) for quantification of received levels). Our model results and source beampattern analysis explain why there was more energy in the 500–2500 Hz frequency band in the airgun signals recorded at a whale near the surface when a surface duct was present.

We recommend that future research should include both modeling and measurement of airgun array source signatures at a full range of angles and at frequencies up to several kilohertz. Collecting (and publishing) accurate and detailed data on airgun array sources would allow for correspondingly accurate and detailed predictions of airgun sound propagation in the ocean. Failure to properly quantify the acoustic source properties of airgun arrays presently limits our ability to predict, test for, and mitigate any potential negative effects they may have. In addition, the ability to predict received levels of airgun pulses as a function of source-receiver range depends on having detailed, current information about the ocean and seabed environment in which the sounds are propagating.

The data we used were collected as part of a controlled exposure experiment designed to study the effect of airgun activity on sperm whale behavior (Miller *et al.*, unpublished). Even assuming behavioral effects can be well-described, there are several major obstacles to the interpretation of such controlled exposure data and their integration into policies designed to mitigate adverse effects of airgun sounds on marine life. First, one must quantify received levels of airgun noise in a manner that accurately relates to the animals' perception of the sound; ideally, this measured level should be directly proportional to the risk of physical damage or adverse behavioral modifications (Madsen, 2005). Second, most management guidelines for mitigating potential airgun effects on marine mammals define maximum allowable exposure levels and then design regulations to protect animals from exposure to unacceptable sound levels. One popular framework for current discussions on potential effects of human-made sounds on marine species, proposed by Richardson *et al.* (1995), suggests that a sound source is surrounded by several zones of potential influence on receiving animals: at very close ranges, animals may be injured by a very loud sound; at greater ranges, their behavior or fitness may be affected by the sound; at even greater ranges, they can detect the sound but are not affected by it; and finally, beyond some range, the animals cannot detect the sound at all. While conceptually useful, the model assumes that sound exposure decreases monotonically with range from the source. Accordingly, an allowable exposure level is generally translated to a range from the airgun array within which potentially impacted marine mammals must not occur during airgun operation (Barlow and Gentry, 2004; Richardson *et al.*, 1995). This range is usually estimated from the maximum allowable exposure level using the backcalculated, broadband, on-axis source level of the airgun array. Most allowable range estimates also assume a geometric spreading transmission loss or a range-independent acoustic model with an omnidirectional sound source (Barlow and Gentry, 2004; Gordon *et al.*, 2004). Since most airgun array source levels are calculated only on-axis and for frequencies below 250 Hz (Gausland, 2000), the range estimation described above does not account for the full frequency range produced by the array or the directionality of the array [although some regulatory approaches include a correction for array beampattern effects (NMFS, 2003)]. Moreover, the detailed aspects of the multipath acoustic propagation, such as the existence of convergence zones and shadow zones, surface ducts, etc., are disregarded.

Our ray trace and PE model results show a convergence zone at 6–8 km range (2003) or 4–6 km range (2002) (shown in Fig. 12), which is further confirmed by data on received levels in the Dtag recordings (for details, see Madsen *et al.*, 2006). These results illustrate that in many cases airgun received levels will not decrease monotonically with increasing range, so that a simple spherical or cylindrical spreading law will not accurately predict the observed pattern of received levels. Regulation based on inappropriate application of a geometric spreading law to calculate the extent of exposure zones could result in exposing animals to higher-than-intended noise levels. For example, using a geometric-spreading based calculation method to estimate the range from an airgun array at which a near-surface sperm whale in the Gulf of Mexico would be exposed to a potentially harmful received level of 180 dB re 1 μPa [root-mean-squared (rms)] results in a range of 295 m (NMFS, 2003). However, received airgun array levels of 180 dB re 1 μPa (rms) at 18 m depth in the Gulf of Mexico have been mea-

sured at ranges up to ~3.5 km from the source—over ten times the range predicted by the geometric spreading calculation (Tolstoy *et al.*, 2004).

Regulations defining allowable ranges between airgun array sound sources and marine species must take into account the potentially complicated relationship between source-receiver range and depth, acoustic frequency, and received sound level. Other mitigation actions, such as ramp-up, assume that potentially affected animals will swim away from a source during ramp-up. Our results show, however, that animals may experience increased exposure levels as they swim away from a source under some conditions, and decreased levels as they approach. In this case, an animal seeking to reduce exposure in the short-term may actually approach the source. Source beampattern may also vary dramatically during ramp-up, resulting in variation in received levels and frequency spectra over time at a given location. There is clearly an urgent need better to define the acoustic signatures of airgun arrays and how sound propagates from them. Any efforts to reduce the risk of airguns to marine mammals must include accurate predictions of exposure.

ACKNOWLEDGMENTS

The authors thank the crews and science parties of the research cruises on which data for this study were collected. Funding for this work was provided by the Office of Naval Research, the U.S. Department of the Interior Minerals Management Service Cooperative Agreements Nos. 1435-01-02-CA-85186 and NA87RJ0445, and the Industry Research Funding Coalition. S.L.D.R. was supported by a National Science Foundation Graduate Research Fellowship. Peter Madsen performed airgun pulse extraction, and Peter Madsen and Mark Johnson provided helpful comments on the manuscript. All approaches to animals for tagging were made following the conditions of NMFS research permits 981-1578 and 981-1707. The Woods Hole Oceanographic Institution Animal Care and Use Committee approved this research.

Barger, J. E., and Hamblen, W. R. (**1980**). "The air gun impulsive underwater transducer," J. Acoust. Soc. Am. **68**, 1038–1045.

Barlow, J., and Gentry, R. (**2004**). "Report of the NOAA Workshop on Anthropogenic Sound and Marine Mammals, 19–20 February 2004," NOAA Technical Memorandum NMFS-SWFSC-361.

Blackman, D. K., de Groot-Hedlin, C., Harben, P., Sauter, A., and Orcutt, J. A. (**2004**). "Testing low/very low frequency acoustic sources for basin-wide propagation in the Indian Ocean," J. Acoust. Soc. Am. **116**, 2057–2066.

Bowlin, J. B., Spiesberger, J. L., Duda, T. F., and Freitag, L. F. (**1992**). *Ocean Acoustic Ray-Tracing Software RAY*, WHOI Technical Report, WHOI-93-10 (Woods Hole Oceanographic Institution, Woods Hole, MA).

Caldwell, J. (**2002**). "Does air-gun noise harm marine mammals?," The Leading Edge **21**, 75–78.

Caldwell, J., and Dragoset, W. (**2000**). "A brief overview of seismic air-gun arrays," The Leading Edge **19**, 898–902.

Clay, C. S., and Medwin, H. (**1977**). *Acoustical Oceanography: Principles and Applications* (Wiley, New York).

Collins, M. D. (**1993**). "A split-step Padé solution for the parabolic equation method," J. Acoust. Soc. Am. **93**, 1736–1742.

Dragoset, W. (**2000**). "Introduction to air guns and air-gun arrays," The Leading Edge **19**, 892–897.

Engås, A., Løkkeborg, S., Ona, E., and Soldal, A. V. (**1996**). "Effects of seismic shooting on local abundance and catch rates of cod (*Gadus morhua*) and haddock (*Melanogrammus aeglefinus*)," Can. J. Fish. Aquat. Sci. **53**, 2238–2249.

Frisk, G. V. (**1994**). *Ocean and Seabed Acoustics* (P.T.R. Prentice-Hall, Upper Saddle River, NJ).

Gausland, I. (**2000**). "Impact of seismic surveys on marine life," The Leading Edge **19**, 903–905.

Geresi, E., Chapman, N. R., McGee, T., and Woolsey, J. R. (**2005**). "Gas hydrate geohazard assessment in the northern Gulf of Mexico using a vertical line array," *Proceedings of the AAPG Annual Convention*, Calgary, Alberta.

Goold, J. C., and Fish, P. J. (**1998**). "Broadband spectra of seismic survey air-gun emissions, with reference to dolphin auditory thresholds," J. Acoust. Soc. Am. **103**, 2177–2184.

Gordon, J., Gillespie, D., Potter, J., Frantzis, A., Simmonds, M. P., Swift, R., and Thompson, D. (**2004**). "A review of the effects of seismic surveys on marine mammals," Mar. Technol. Soc. J. **37**, 16–34.

Hamilton, E. L. (**1972**). "Compressional-wave attenuation in marine sediments," Geophysics **37**, 620–646.

Hamilton, E. L. (**1978**). "Sound velocity-density relations in sea-floor sediments and rocks," J. Acoust. Soc. Am. **63**, 366–377.

Hamilton, E. L. (**1980**). "Geoacoustic modeling of the sea floor," J. Acoust. Soc. Am. **68**, 1313–1340.

Jensen, F. B., Kuperman, W. A., Porter, M. B., and Schmidt, H. (**1994**). *Computational Ocean Acoustics* (AIP, Woodbury, NY).

Jochens, A. E., and Biggs, D. C. (**2003**). *Sperm Whale Seismic Study in the Gulf of Mexico, Annual Report: Year 1* (U.S. Department of the Interior Minerals, Management Service, Gulf of Mexico OCS Region, New Orleans, LA).

Jochens, A. E., and Biggs, D. C. (**2004**). *Sperm Whale Seismic Study in the Gulf of Mexico, Annual Report: Year 2* (U.S. Department of the Interior Minerals, Management Service, Gulf of Mexico OCS Region, New Orleans, LA).

Johnson, M. P., and Tyack, P. L. (**2003**). "A digital acoustic recording tag for measuring the response of wild marine mammals to sound," IEEE J. Ocean. Eng. **28**, 3–12.

Jovanovich, D. B., Sumner, R. D., and Akins-Easterlin, S. L. (**1983**). "Ghosting and marine signature deconvolution: a prerequisite for detailed seismic interpretation," Geophysics **48**, 1468–1485.

Labianca, F. M. (**1972**). "Normal modes, virtual modes, and alternative representations in the theory of surface-duct sound propagation," J. Acoust. Soc. Am. **53**, 1137–1147.

Laws, R., Landrø, M., and Amundsen, L. (**1998**). "An experimental comparison of three direct methods of marine source signature estimation," Geophys. Prospect. **46**, 353–389.

Madsen, P. T. (**2005**). "Marine mammals and noise: Problems with root mean square sound pressure levels for transients," J. Acoust. Soc. Am. **117**, 3952–3957.

Madsen, P. T., Johnson, M., Miller, P. J. O., Aguilar de Soto, N., Lynch, J., and Tyack, P. L. (**2006**). "Quantitative measures of air gun pulses recorded on sperm whales (*Physeter macrocephalus*) using acoustic tags during controlled exposure experiments,"J. Acoust. Soc. Am. **120**, 2366–2379

Mallick, S., and Frazer, L. N. (**1987**). "Practical aspects of reflectivity modeling," Geophysics **52**, 1355–1364.

McCauley, R. D., Fewtrell, J., and Popper, A. N. (**2003**). "High intensity anthropogenic sound damages fish ears," J. Acoust. Soc. Am. **113**, 638–642.

McGee, T., Geresi, E., Lutken, C., Woolsey, B., Higley, P., and Sharpe, S. (**2003**). Operation Report: The 8–14 October, 2003, Cruise of the R/V PELICAN, to deploy the CMRET vertical line array in Mississippi Canyon 798 and Atwater Valley 14, northern Gulf of Mexico, MMRI/CMRET, University of Mississippi.

Miller, P. J. O., Johnson, M. P., Madsen, P. T., Quero, M. E., Biassoni, N., King, R., and Tyack, P. L. (unpublished). "At-sea experiments provide preliminary evidence that airguns affect the foraging behavior of sperm whales in the Gulf of Mexico."

Murphy, E. L., and Davis, J. A. (**1974**). "Modified ray theory for bounded media," J. Acoust. Soc. Am. **56**, 1747–1760.

National Marine Fisheries Service (NMFS) (**2003**). "Taking and importing marine mammals; Taking marine mammals incidental to conducting oil and gas exploration activities in the Gulf of Mexico," Federal Register **68**, 9991–9996.

Nieukirk, S. L., Stafford, K. M., Mellinger, D. K., Dziak, R. P., and Fox, C. G. (**2004**). "Low-frequency whale and seismic airgun sounds recorded in the mid-Atlantic Ocean," J. Acoust. Soc. Am. **115**, 1832–1843.

Parkes, G., and Hatton, L. (**1986**). *The Marine Seismic Source* (D. Reidel, Dordrecht, Holland).
Popper, A. N., Fewtrell, J., Smith, M. E., and McCauley, R. D. (**2004**). "Anthropogenic sound: Effects on the behavior and physiology of fishes," Mar. Technol. Soc. J. **37**, 35–40.
Porter, M. B. (**1995**). *The KRAKEN Normal Mode Program* (SACLANT Undersea Research Center, La Spezia, Italy).
Porter, M. B., and Jensen, F. B. (**1993**). "Anomalous parabolic equation results for propagation in leaky surface ducts," J. Acoust. Soc. Am. **94**, 1510–1516.
Richardson, W. J., Greene, Jr., C. R., Malme, C. I., and Thompson, D. H. (**1995**). *Marine Mammals and Noise* (Academic, San Diego, CA).
Schmidt, H. (**2004**). OASES version 3.1 User Guide and Reference Manual; http://acoustics.mit.edu/faculty/henrik/oases.html. Last accessed 10/30/2006.
Tipler, P. A., and Llewellyn, R. (**2003**). *Modern Physics* (W.H. Freeman and Company, New York).
Tolstoy, M., Diebold, J. B., Webb, S. C., Bohnenstiehl, D. R., Chapp, E., Holmes, R. C., and Rawson, M. (**2004**). "Broadband calibration of R/V *Ewing* seismic sources," Geophys. Res. Lett. **31**, L14310.
Turgut, A., McCord, M., Newcomb, J., and Fisher, R. (**2002**). "Chirp sonar sediment characterization at the northern Gulf of Mexico Littoral Acoustic Demonstration Center experimental site," Oceans '02 MTS/IEEE **4**, 2248–2252.
Urick, R. J. (**1975**). *Principles of Underwater Sound for Engineers* (McGraw-Hill, New York).
Weston, D. E., Esmond, C. G., and Ferris, A. (**1991**). "The duct leakage relation for the surface sound channel," J. Acoust. Soc. Am. **89**, 156–164.
Zimmer, W. M. X., Tyack, P. L., Johnson, M. P., and Madsen, P. T. (**2005**). "Three-dimensional beam pattern of regular sperm whale clicks confirms bent-horn hypothesis," J. Acoust. Soc. Am. **117**, 1473–1485.
Ziolkowski, A. (**1970**). "A method for calculating the output pressure waveform from an air gun," Geophys. J. R. Astron. Soc. **21**, 137–161.
Ziolkowski, A., Parkes, G., Hatton, L., and Haugland, T. (**1982**). "The signature of an airgun array: Computation from near-field measurements including interactions," Geophysics **47**, 1413–1421.
Ziolkowski, A., and Johnston, R. G. K. (**1997**). "Marine seismic sources: QC of wavefield computation from near-field pressure measurements," Geophys. Prospect. **45**, 611–639.